



20th

Iranian Physical chemistry Conference



بیستمین کنفرانس شیمی فیزیک ایران

مکان برگزاری: دانشگاه اراک، پردیس دانشگاه اراک، دانشکده علوم پایه

تاریخ برگزاری کنفرانس: ۳۱-۲۹ مرداد ماه ۱۳۹۶

محور های کنفرانس

ترمودینامیک
مکانیک آماری
طیف سنتی مولکولی
شیمی سطح و حالت جامد

شیمی کو انتومی
الکتروشیمی
شیمی محاسباتی
نانو شیمی فیزیک
مهندسی شیمی

شیمی فیزیک کاربردی
بیوشیمی فیزیک
آموزش شیمی
سینتیک شیمیایی



Email : ipcc20@araku.ac.ir

Website : physchem20.araku.ac.ir



بیستمین کنفرانس شیمی فیزیک ایران

دانشکده علوم پایه - دانشگاه اراک ۲۹-۳۱ مرداد ۱۳۹۶
20th Iranian Physical Chemistry Conference



اعضاء کمیته های علمی و اجرایی

اعضاء کمیته اجرایی	اعضاء کمیته علمی
۱- علیرضا صلابت (دبیر کمیته)	۱- علیرضا صلابت (دبیر کمیته)
۲- محمد سلیمان نژاد	۲- محمد سلیمان نژاد
۳- حسین صادقی	۳- وحید مهدوی
۴- علیرضا بهرامی	۴- سعید امانی
۵- عزیزاله آزاد	۵- جواد ذوالقرنین
۶- رضا پاکبازی	۶- خلیل فقیهی
۷- کاوه خسروی	۷- علیرضا فضلعلی
۸- فرهاد حیدری	۸- ابوالفضل براتی
۹- سعید محمودی	۹- عبدالرضا مقدسی
۱۰- یاسر رنجبر	۱۰- غلامرضا نبیونی
۱۱- علیرضا مجرد	
۱۲- سید فرید میرحسینی	
۱۳- سعیده کمالی نهاد	
۱۴- سید علی منجمی	
۱۵- معصومه اورجلو	
۱۶- زینب فرامرزی	

وب سایت کنفرانس: <http://physchem20.araku.ac.ir>

پست الکترونیک کنفرانس: IPCC20@araku.ac.ir

برنامه زمان بندی بیستمین کنفرانس شیمی فیزیک ایران (مردادماه ۱۳۹۶)

مکان	عنوان جلسه	زمان برگزاری
سالن A (شهید چمران)	مراسم افتتاحیه	۸:۳۰-۱۰
پذیرایی		۱۰-۱۰:۱۵
ارائه پوسترها-بخش اول		۱۰-۱۱:۱۰
سالن A	سخنرانی عمومی (استاد پیشکسوت شیمی فیزیک) جناب آقای دکتر ایلوخانی	۱۱:۱۰-۱۱:۵۰
سالن A	سخنرانی محقق جوان جناب آقای دکتر عزیز حبیبی ینگجه	۱۱:۵۰-۱۲:۳۰
ناهار- نماز و استراحت		۱۲:۳۰-۱۴:۳۰

B: سالن دفاعیه دانشکده علوم

A: سالن شهید چمران

یکشنبه ۲۹ مرداد ۱۳۹۶ (عصر)

ارائه دهنده	کد مقاله	مکان	عنوان مقاله	زمان برگزاری
خانم دکتر معصومه فروتن	PHYSICHEM20	سالن A	Understanding the molecular origin of surface phenomena in water/metal interface based on molecular dynamics approach	۱۴:۳۰ - ۱۵:۱۰
آقای دکتر امیرعباس رفعتی	1040-PHYSICHEM20	سالن A	A novel molecularly imprinted sensor for imidacloprid based on poly (levodopa) /TiO2 nanoparticles composite	۱۵:۱۰ - ۱۵:۳۰
آقای دکتر ستار ارشدی	1058-PHYSICHEM20	سالن A	A theoretical study of gas adsorption on Boron nitride Nanocone induced with Zn-porphyrin	۱۵:۳۰ - ۱۵:۵۰
خانم سعیده کمالی نهاد	1063-PHYSICHEM20	سالن A	physisorption of toxic cyanogen gas onto exterior surface of pristine Al12N12 nanocluster: A theoretical study	۱۵:۵۰ - ۱۶:۱۰
خانم زهرا محمدیان	1071-PHYSICHEM20	سالن B	Selective Hydrogenation of Benzene to Cyclohexane on Various Ni- Supported Catalysts	۱۵:۱۰ - ۱۵:۳۰
آقای دکتر امیری ماجد	PHYSICHEM20	سالن B	Kinetic Studies of DMSO Deuteration Process and Introduction of an Ideal Isotopic Exchange Reactor Type	۱۵:۳۰ - ۱۵:۵۰
خانم الهام پارسی	1328-PHYSICHEM20	سالن B	Improvement of Celecoxib solubility using microemulsion systems	۱۵:۵۰ - ۱۶:۱۰
پذیرایی				۱۶:۱۰ - ۱۶:۳۰
ارائه پوسترها - بخش دوم				۱۶:۱۰ - ۱۷:۲۰
خانم هانیه ندیمی	1250-PHYSICHEM20	سالن A	Molecular Dynamics Studies of Cation Aggregation in two Amino Acid Ionic Liquids	۱۷:۲۰ - ۱۷:۴۰
آقای دکتر سید محمد اعظمی	1114-PHYSICHEM20	سالن A	Theoretical analysis of pi-type hyperconjugative interaction	۱۷:۴۰ - ۱۸
خانم فرشته یعقوبی	1275-PHYSICHEM20	سالن A	The influence of non-covalent interaction of PHCl2 on the activation energy of Aza-Diels-Alder Reaction	۱۸ - ۱۸:۲۰
آقای علی منجمی	1295-PHYSICHEM20	سالن B	Selective Catalytic Oxidation of O-xylene to Phthalic Anhydride over VPO/HZSM-5: An Optimization Study	۱۷:۲۰ - ۱۷:۴۰
خانم دکتر مژگان نجفی	1389-PHYSICHEM20	سالن B	Template assisted synthesis of metallic and conductive polymers nanowire :application in sensors	۱۷:۴۰ - ۱۸
آقای احمد رئیسی	1350-PHYSICHEM20	سالن B	New formulation based on poly(β -cyclodextrin-ester) for preparation of safe PVC	۱۸ - ۱۸:۲۰

دوشنبه ۳۰ مرداد ۱۳۹۶ (صبح)

زمان برگزاری	عنوان جلسه	مکان	کد مقاله	ارائه دهنده
۸:۳۰-۹:۱۰	Docking and Molecular Dynamic Simulation in Virtual Screening for computational Design of Novel $\alpha\beta$ -Tubulin and Survivin Inhibitors	سالن A	PHYSICHEM20	آقای دکتر عبدالخالق بردبار
۹:۱۰-۹:۳۰	Biophysical Studies on the Interaction of Cationic Urethane Gemini Surfactant with Insulin	سالن A	1194-PHYSICHEM20	خانم دکتر پونه سادات پورحسینی
۹:۳۰-۹:۵۰	Soluting-In and Soluting-Out of Water-Soluble Polymers in Aqueous Carbohydrate Solutions Studied by Vapor Pressure Osmometry	سالن A	1226-PHYSICHEM20	خانم دکتر نوسیه ابراهیمی
۹:۵۰-۱۰:۱۰	Binding forces between bovine milk β -lactoglobulin and novel palladium(II) comple	سالن A	1049-PHYSICHEM20	خانم دکتر شهرکی
۹:۱۰-۹:۳۰	Comparison of the Adsorption of Sulfur Mustard on Graphene and Graphene Oxide: A Molecular Dynamics Simulation Study	سالن B	1149-PHYSICHEM20	خانم لیلا ابراهیمی
۹:۳۰-۹:۵۰	Application of decaborane (B ₁₀ H ₁₄) and its fluoro derivatives as an anode in Li- ion battery: A DFT Study	سالن B	1068-PHYSICHEM20	خانم مریم یوسفی زاده
۹:۵۰-۱۰:۱۰	A closed formula for the distribution function in the Renyi statistical mechanic	سالن B	1342-PHYSICHEM20	خانم فهیمه مختاری
پذیرایی				۱۰:۱۰-۱۰:۳۰
ارائه پوستر				۱۰:۱۰-۱۱:۲۰
۱۱:۲۰-۱۱:۵۰	Graphene and graphene doped surface as metal free catalyst for oxygen reduction reaction	سالن A	PHYSICHEM20	آقای دکتر کریم کاکایی
۱۱:۵۰-۱۲:۱۰	The evaluation of electrochemical and physical properties of cationic membranes in the electro-dialysis reversal system of the Imam Khomeini Petrochemical Complex	سالن A	PHYSICHEM20	آقای دکتر علیرضا خدابخشی
۱۲:۱۰-۱۲:۳۰	Preparation of polyethersulfone membrane coated by a nanocomposite structure	سالن A	1384-PHYSICHEM20	آقای دکتر فرهاد حیدری
۱۱:۵۰-۱۲:۱۰	Advance polymeric membrane to CO ₂ separation	سالن B	1053-PHYSICHEM20	خانم سمانه بنده علی
۱۲:۱۰-۱۲:۳۰	Graft (co)polymerization of acrylamide and styrene onto silica nanoparticles by free radical polymerization: Determining molecular weight by measuring intrinsic viscosity	سالن B	1217-PHYSICHEM20	آقای حسین بی آزار
ناهار ، نماز و استراحت				۱۲:۳۰-۱۴:۳۰

دوشنبه ۳۰ مرداد ۱۳۹۶ (عصر)

زمان برگزاری	عنوان جلسه	مکان	کد مقاله
۱۴:۳۰ - ۱۵:۱۰	Photophysics of Organic Compounds: Theoretical Studies	سالن A	PHYSICHEM20 آقای دکتر رضا امیدیان
۱۵:۱۰ - ۱۵:۳۰	Simulation of Clonazepam and Diazepam in DPPC membrane: Investigation of the movemen	سالن A	1288-PHYSICHEM20 آقای دکتر خالد عزیزی
۱۵:۳۰ - ۱۵:۵۰	NO Oxidation Catalysed by Ir3M (M= Ir, Co, Cu) Nanoclusters	سالن A	1164-PHYSICHEM20 خانم نسیم حسنی
۱۵:۵۰ - ۱۶:۱۰	Hydrogen bonding interaction between a new Schiff base ligand and H2PO4 ⁻ : A DFT stud	سالن A	1382-PHYSICHEM20 خانم دکتر معصومه اورجلو
۱۶:۱۰ - ۱۶:۳۰	A Molecular Dynamics Study of SO2 Sorbed in Nonporous Silica Y Zeolite: Temperature and Loading Dependence	سالن A	1134-PHYSICHEM20 خانم یلدا صباحی
۱۵:۱۰ - ۱۵:۳۰	Studying of Electron Transfer Rate Constant of Cytochrome c Immobilized on Nanoparticle Decorated Hybrid System by Cyclic Voltammetry Technique	سالن B	1102-PHYSICHEM20 آقای دکتر ولی علی زاده
۱۵:۳۰ - ۱۵:۵۰	The soluting-out effect in aqueous solutions of 1-butyl-3-methylimidazolium tetrafluoroborate and carbohydrates at various temperatures	سالن B	1333-PHYSICHEM20 آقای بهمن جامه بزرگی
۱۵:۵۰ - ۱۶:۱۰	On the Evaluation of Dieterici Model Via The Study of Bulk Modulus and Tait-Marnagan Regularity of Associating Fluids	سالن B	1379-PHYSICHEM20 آقای دکتر محسن نجفی
۱۶:۳۰ - ۱۶:۴۵	پذیرایی		
۱۶:۳۰ - ۱۷:۴۰	ارائه پوستر		

۱۸:۱۵ حرکت وسایل نقلیه از دانشکده علوم پایه برای ضیافت در مزرعه دانشگاه

۱۸:۳۰ حرکت وسایل نقلیه از دانشگاه مرکزی (میدان شریعتی) برای ضیافت در مزرعه دانشگاه

سه شنبه ۳۱ مرداد ۱۳۹۶ (صبح)

زمان برگزاری	عنوان جلسه	مکان	کد مقاله	
۸:۳۰-۹	Shazand Petrochemical Company Production of polypropylene of bumper grade in shazand petrochemical Co.	سالن A	PHYSICHEM20	آقای دکتر سودیر
۹-۹:۲۰	Using Electrolysis for Accurate Measurement of Oxygen Isotopes Abundance in 18O enriched Water	سالن A	1394-PHYSICHEM20	خانم دکتر بی تا دادپو
۹:۲۰-۹:۴۰	Prediction of Hydrate Dissociation Conditions for system of Tetrahydrofuran + Water	سالن A	1056-PHYSICHEM20	آقای دکتر سیدمحمدجوکار
۹:۴۰-۱۰	Fluorine Lewis Acids	سالن A	1247-PHYSICHEM20	خانم نسیم اورنگی
۹-۹:۲۰	Calculation of a New Correlation Function for Disc Molecules Systems	سالن B	1069-PHYSICHEM20	آقای صمد امینی
۹:۲۰-۹:۴۰	Theoretical Studies on Nonlinear Optical (NLO) Response of Si12C12 Nanocage Decorated with Alkali Metals (M = Li, Na and K)	سالن B	1166-PHYSICHEM20	خانم رضوان رحیمی
۹:۴۰-۱۰	Elucidation of the Spin-Orbit and Relativistic Effects on the Plasmon Excitations of Silver and Gold Nanowire: Time-Dependent Density Functional Theory	سالن B	1326-PHYSICHEM20	خانم نرگس اسدی
۱۰-۱۰:۱۵	پذیرایی			
۱۰-۱۱:۱۰	ارائه پوستر			
۱۱:۱۰-۱۲:۱۵	مراسم اختتامیه	سالن A		
۱۲:۱۵-۱۴	ناهار ، نماز			

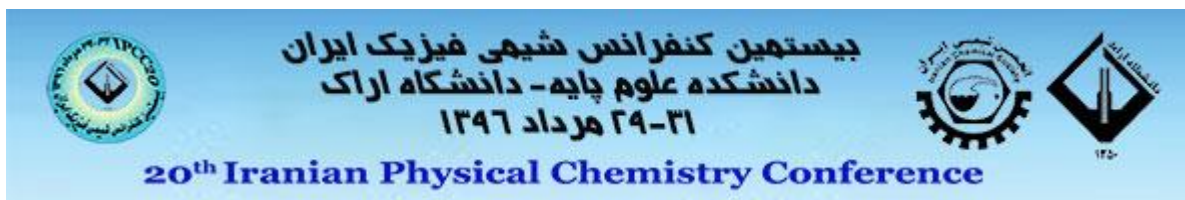


بیستمین کنفرانس شیمی فیزیک ایران
دانشکده علوم پایه - دانشگاه اراک
۳۱-۲۹ مرداد ۱۳۹۶



20th Iranian Physical Chemistry Conference

Invited Speakers



History of Physical Chemistry

H. Iloukhani

Department of Physical Chemistry, Faculty of Chemistry, Bu-Ali Sina University, Hamedan, Iran
khaterehkanlarzadeh@gmail.com

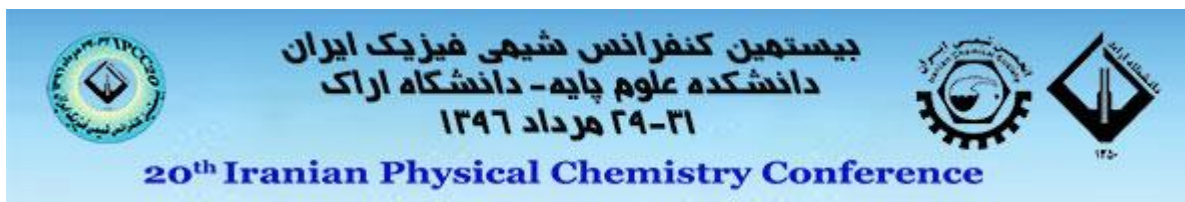
The term "physical chemistry" was coined by Mikhail Lomonosov in 1752, when he presented a lecture course entitled "A Course in True Physical Chemistry". In the preamble to these lectures he gives the definition: "Physical chemistry is the science that must explain under provisions of physical experiments the reason for what is happening in complex bodies through chemical operations". Modern physical chemistry originated in the 1860s to 1880s with work on chemical thermodynamics, electrolytes in solutions, chemical kinetics and other subjects. One milestone was the publication in 1876 by Josiah Willard Gibbs of his paper, On the Equilibrium of Heterogeneous Substances. This paper introduced several of the cornerstones of physical chemistry, such as Gibbs energy, chemical potentials, and Gibbs' phase rule. The first scientific journal specifically in the field of physical chemistry was the German journal, *Zeitschrift für Physikalische Chemie*, founded in 1887 by Wilhelm Ostwald and Jacobus Henricus van't Hoff. All two were awarded the Nobel Prize in Chemistry between 1901–1909. Developments in the following decades include the application of statistical mechanics to chemical systems and work on colloids and surface chemistry, where Irving Langmuir made many contributions. Another important step was the development of quantum mechanics into quantum chemistry from the 1930s, where Linus Pauling was one of the leading names. Theoretical developments have gone hand in hand with developments in experimental methods, where the use of different forms of spectroscopy, such as infrared spectroscopy, microwave spectroscopy, electron paramagnetic resonance and nuclear magnetic resonance spectroscopy, is probably the most important 20th century development.

What is Physical chemistry?

Physical chemistry is the branch of chemistry dealing with the relations between the physical properties of substances and their chemical composition and transformations which study macroscopic, atomic, subatomic, and particulate phenomena in chemical systems in terms of the principles, practices and concepts of physics such as motion, energy, force, time, thermodynamics, quantum chemistry, statistical mechanics, analytical dynamics and chemical equilibrium. Physical chemistry, in contrast to chemical physics, is predominantly (but not always) a macroscopic or supra-molecular science, as the majority of the principles on which it was founded relate to the bulk rather than the molecular/atomic structure alone (for example, chemical equilibrium and colloids). Chemical reactions underpin the production of pretty much everything in our modern world. But, what is the driving force behind reactions? Why do some reactions occur over geological time scales whilst others are so fast that we need femtosecond-pulsed lasers to study them? Ultimately, what is going on at the atomic level? Discover the answers to such fundamental questions and more on this course in introductory physical chemistry.

Some of the relationships that physical chemistry strives to resolve include the effects of:

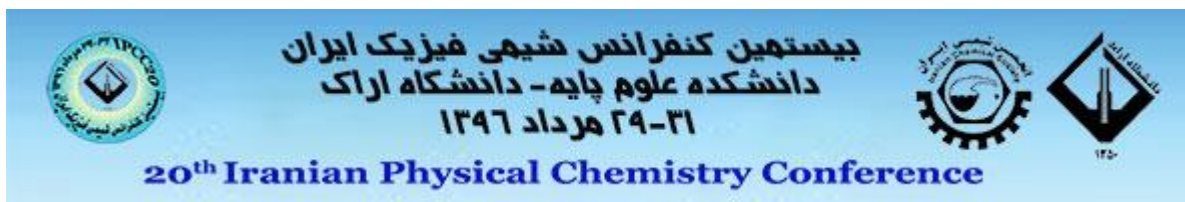
1. Intermolecular forces that act upon the physical properties of materials (plasticity, tensile strength, surface tension in liquids).



2. Reaction kinetics on the rate of a reaction.
3. The identity of ions and the electrical conductivity of materials.
4. Surface science and electrochemistry of cell membranes.
5. Interaction of one body with another in terms of quantities of heat and work called thermodynamics.
6. Transfer of heat between a chemical system and its surroundings during change of phase or chemical reaction taking place called thermochemistry.
7. Study of colligative properties of number of species present in solution.
8. Number of phases, number of components and degree of freedom (or variance) can be correlated with one another with help of phase rule.
9. Reactions of electrochemical cells.

What Do Physical Chemists Do?

Physical chemists are focused on understanding the physical properties of atoms and molecules, the way chemical reactions work, and what these properties reveal. Their work involves analyzing materials, developing methods to test and characterize the properties of materials, developing theories about these properties, and discovering the potential use of the materials. Using sophisticated instrumentation and equipment has always been an important aspect of physical chemistry. Physical chemists' discoveries are based on understanding chemical properties and describing their behavior using theories of physics and mathematical computations. Physical chemists predict properties and reactions of chemicals, then test and refine those predications. They use mathematical analysis and statistics on huge datasets, sometimes with millions of data points, to reveal hidden information about compounds, materials, and processes. They may also conduct simulations, developing mathematical equations that predict how compounds will react over time. Recently, more and more physical chemists have found homes in the emerging fields of materials science and molecular modeling where their skills in analyzing and predicting the behavior of physical properties have exciting new applications. By combining the mathematical rigidity of physical chemistry with the practicality of new materials and new applications, the field of physical chemistry is expanding in new and exciting ways.



Docking and Molecular Dynamic Simulation in Virtual Screening for computational Design of Novel $\alpha\beta$ -Tubulin and Survivin Inhibitors

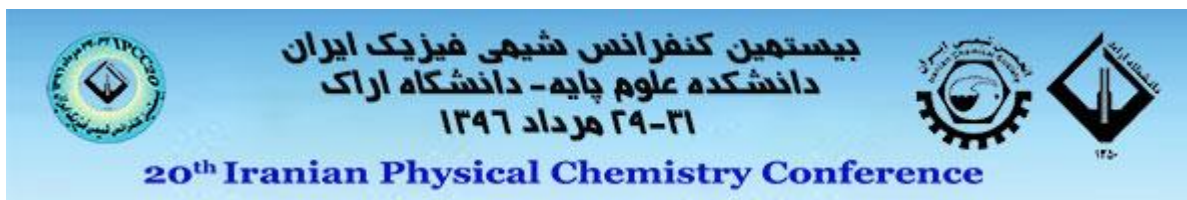
Abdol-Khalegh Bordbar

*Department of Chemistry, University of Isfahan, Isfahan, 8174673441, Iran
bordbar@chem.ui.ac.ir and akbordbar@gmail.com*

In the first part of this study, consensus docking of AutoDock and AutoDock Vina has been used for improving the reliability of docking in a virtual screening of a library of 2497 Piperine derivatives, as novel group of Survivin inhibitors. The initial docking of these compounds into the binding site of Survivin, by using AutoDock Vina program, resulted to the selection of top100 derivatives with highest binding affinities. The subsequent screening was done on these 100 compounds by recalculation of binding energies using Auto Dock program. Considering the obtained binding energies, the top two highest ranked compounds, as well as Piperine, were selected and subjected to three independent 10 ns molecular dynamics (MD) simulations for further validate the proposed binding modes and interactions. Subsequently, the contributions of van der Waals interactions, electrostatic forces, polar and non-polar solvation in the total binding free energies, accompanying entropy component as a further refinement of total free energy, were calculated using the MMPB/GBSA methods and nabnmode module of AMBER, respectively. In addition to MMPB/GBSA methods, by using alanine scanning, the contribution of each active site residue in to the total binding free energy were assessed. The results represent the main role of hydrophobic forces in molecular interactions and elucidate the binding mode of Piperine analogs for further experimental studies.

In this second part of this paper, docking tools were utilized in order to study the binding properties of more than five hundred of proline-based 2, 5-diketopiperazine in the binding site of $\alpha\beta$ -tubulin. Results revealed that 20 compounds among them showed lower binding energies in comparison with tryprostatin-A, a well known tubulin inhibitor and therefore could be potential inhibitors of tubulin.

However, the precise evaluation of binding poses represents the similar binding modes for all of these compounds and tryprostatin-A. Finally, the best docked complex was subjected to a 25 ns molecular dynamics simulation to further validate the proposed binding mode of this compound.



Photophysics of Organic Compounds: Theoretical Studies

Reza Omidyan

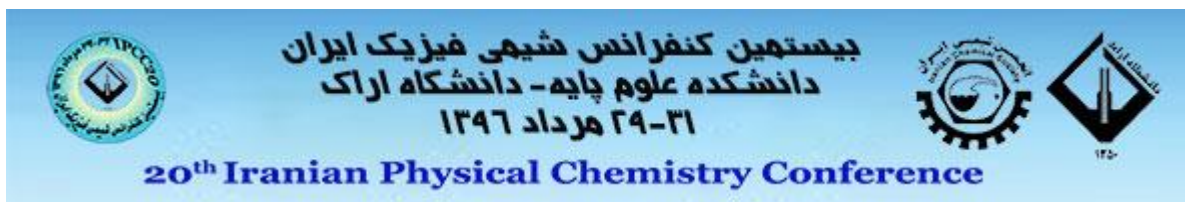
Department of Chemistry, University of Isfahan, 81746-73441 Isfahan, Iran

r.omidyan@sci.ui.ac.ir, reza.omidyan@u-psud.fr

Organic molecules are not stable under persistent irradiation with ultraviolet (UV) light. UV photons can break covalent bonds and thus can induce a great variety of chemical transformations (isomerizations or fragmentations). In this view, it is amazing that life can thrive under full exposition to sunlight. Moreover, biogenesis took place long before the formation of the stratospheric ozone layer (which today filters out the most dangerous UV components of sunlight) and thus under conditions of extremely intense short-wavelength UV radiation. Thus, it must have resulted in an extreme selection pressure for UV protection. These considerations suggest that photostability may have been the decisive selection criterion which has determined the molecular architecture of life at the beginning of the biological evolution.

Fortunately, during last two decades, new advancements in Quantum chemical methods and Laser spectroscopy, provided the opportunity to investigate several challenging subjects such as photostability and photophysics of life and organic systems in molecular scales. The non-Born Oppenheimer potential energy surfaces have been introduced as powerful tools for predicting the so-called Conical Intersections (CIs), being responsible for ultrafast deactivation pathways of excited molecules via internal conversions.

Thus, in this lecture, a brief discussion on recent theoretical results, supporting the hypothesis that the fundamental building blocks as well as the supramolecular structures of life are optimized with respect to photostability, will be presented.



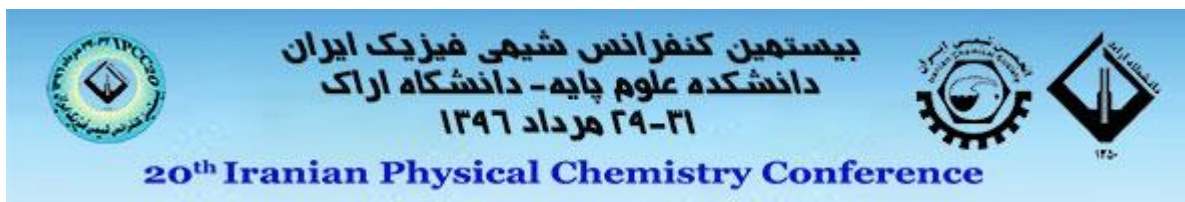
Understanding the molecular origin of surface phenomena in water/metal interface based on molecular dynamics approach

Masumeh Foroutan

Department of Physical Chemistry, School of Chemistry, College of Science, University of Tehran, Tehran, Iran. foroutan@khayam.ut.ac.ir

The interaction of water with solid substrates plays an important role in various natural phenomena such as catalysis, electrochemistry, and motion of water while having important applications in production of hydrogen, fuel cells, and biological sensors, etc. Understanding the interaction of water and solid surfaces can help in comprehension and control of reactivity of water and surfaces. In the last two decades, water adsorption on metallic surfaces has been studied as a result of great progress in laboratory techniques which along with quantum computations and molecular dynamics simulations, can improve our understanding of water/substrate interfaces and reveal valuable information regarding these interfaces. Stability and structure of adsorbed water on the metallic surfaces are affected by two important aspects of water/metal interfaces; (i) water-surface interaction at the interfacial layer of water/metal and, (ii) the nature and strength of hydrogen bonds in the water which can be affected by the substrate. Molecular dynamics simulation is a helpful tool in studying both aspects.

In this study, several systems like water-gold, water-titanium dioxide and water-molybdenum disulfide systems were chosen and, the interactions of water-substrate along with dynamic structure of water were analyzed using molecular dynamics simulations. Furthermore, the relation between structural and dynamical behavior of water and surface properties were studied. The obtained results showed that the positioning, adsorption, and movement of water on a substrates is dependent upon the chemical nature and arrangement of the atoms of the surface. Therefore, the behavior of water molecules on a substrate is a reflection of properties of the surface.



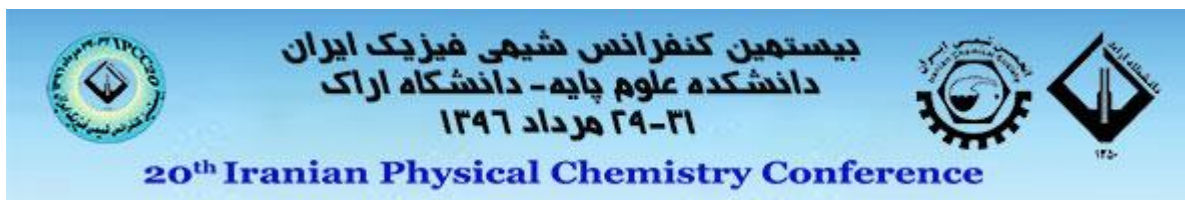
Graphene and graphene doped surface as metal free catalyst for oxygen reduction reaction

Karim Kakaei

Department of Physical Chemistry, Faculty of Science, University Of Maragheh, Maragheh, Iran

The rising global energy demand and environmental impact of traditional energy resources pose serious challenges to human health, energy security, and environmental protection. One promising solution is fuel cell technology, which provides clean and sustainable power. Fuel cell as energy conversion technology currently receives intensive research and development focus because of its high energy conversion efficiency, virtually no pollution, and potential large-scale applications. However, fuel cells require a catalyst for oxygen reduction reaction (ORR) ($\sim 0.4 \text{ mg cm}^{-2}$). Thus, efforts are needed to identify alternative catalysts that are readily available, cost effective, and show comparable or even better catalytic effects than Pt for cathodic oxygen reduction reaction (ORR) in fuel cells. Recent intensive research efforts have led to the development of less expensive and more abundant electro-catalysts for fuel cells. In particular, it was found that vertically aligned carbon allotrope can act as a metal-free electrode to catalyze an ORR process with a 3-times higher electrocatalytic activity and better long-term operational stability than that of commercially available platinum/C electrodes (e.g., C2-20, 20% platinum on Vulcan XC-72R; E-TEK) in alkaline fuel cells. One of the promising alternatives is graphene and graphene based materials for ORR.

This lecture aims to present recent advances for electrocatalysis in oxygen reduction, with a particular focus on graphene as a rising star material including graphene surface, graphene top down synthesis, diagnostic tools characterization, graphene doped with heteroatoms. Finally, we present electrochemical response of oxygen reduction reaction on the graphene and graphene doped heteroatom for ORR. On the other hand we report the F- Cl- and N- doped in RGO by chemical and one pot electrochemical step to obtain graphene-based high performance metal-free ORR electrocatalysts and also better price/performance ratio than any other ORR electrocatalysts.



Heterogeneous Photocatalysts: Promising Materials to Address Energy and Environmental Challenges

A. Habibi-Yangjeh*, M. Mousavi, M. Pirhashemi, M. Shekofteh-Gohari, A. Akhundi

Department of Chemistry, University of Mohaghegh Ardabili, Ardabil, Iran

Email: ahabibi@uma.ac.ir

Nowadays, pollution of the environment with different hazardous compounds is one of the environmental issue that human being is facing. On the other hand, global energy shortage and climate changes have become challenges in the present century. Although various methods such as microbial, adsorption, and ion exchange methods have been used to handle some of environmental pollutants, the application of these methods is restricted due to high cost, poor efficiency, secondary pollution generation, and complicated technology. In recent years, photocatalytic processes have been considered as one of advanced, environmentally friendly, low-cost, and high efficiency strategies to directly harvest, convert and store renewable solar energy for generating sustainable and green energy and addressing a broad range of environmental issues. Potential applications of this green technology include photodegradation of hazardous chemicals, photocatalytic water splitting to produce hydrogen gas, inactivation of microorganisms, photoreduction of carbon dioxide to small molecules of fuels, and synthesis of various organic compounds. Semiconductor materials have vital role in photocatalytic reactions.

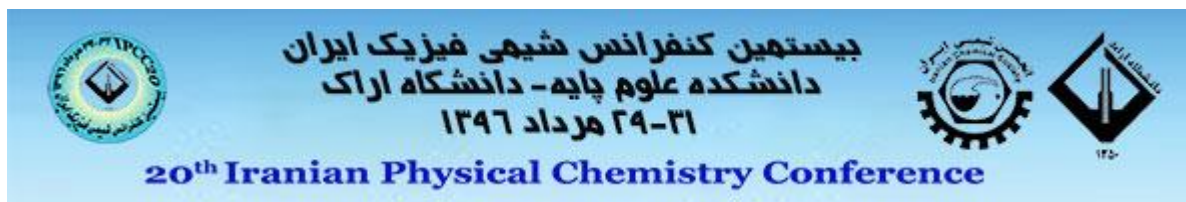
The overall mechanism for heterogeneous photocatalytic processes involves light harvesting, production of electron/hole pairs, charge separation and transfer, and surface oxidation/reduction reactions. It has been confirmed that to achieve the desired efficiency, the fabricated photocatalysts should have good solar-light response, minimal recombination of the charge carriers, and high photostability. Nonetheless, one component photocatalysts such as TiO_2 , ZnO , $\text{g-C}_3\text{N}_4$, SnO_2 , and ZnS do not have remarkable photocatalytic activity under solar irradiation. Hence, in recent years, much more efforts have been paid for designation and fabrication of visible-light-driven photocatalysts with efficient activity. The superior photoactivity of multicomponent photocatalysts are attributed to the high separation and easy transportation of the photogenerated charge carriers at the heterojunction interfaces formed between two or more semiconductors. Based on the abovementioned idea, our research group have focused on designation and fabrication of some novel binary, ternary, and quaternary photocatalysts using usual photocatalysts of TiO_2 , ZnO , and $\text{g-C}_3\text{N}_4$ [1-10]. Properties of the as-prepared nanocomposites such as structure, morphology, composition, optical, and magnetical properties were characterized using some sophisticated instruments. Photocatalytic activity of the nanocomposites was evaluated using different target pollutants. The results showed that multicomponent photocatalysts have highly enhanced activity relative to the counterparts of the nanocomposites.

Acknowledgment

The authors genuinely appreciate University of Mohaghegh Ardabili–IRAN, for financial support of this project.

References

[1] M. Pirhashemi, A. Habibi-Yangjeh, Ultrasonic-assisted preparation of plasmonic $\text{ZnO}/\text{Ag}/\text{Ag}_2\text{WO}_4$ nanocomposites with high visible-light photocatalytic performance for degradation of organic pollutants, *Journal of Colloid and Interface Science*, 491 (2017) 216–229.



- [2] A. Habibi-Yangjeh, M. Shekofteh-Gohari, Novel magnetic $\text{Fe}_3\text{O}_4/\text{ZnO}/\text{NiWO}_4$ nanocomposites: Enhanced visible-light photocatalytic performance through p-n heterojunctions, *Separation and Purification Technology*, 184 (2017) 334–346.
- [3] A. Akhundi, A. Habibi-Yangjeh, Graphitic carbon nitride nanosheets decorated with CuCr_2O_4 nanoparticles: Novel photocatalysts with high performances in visible light degradation of water pollutants, *Journal of Colloid and Interface Science*, 504 (2017) 697–710.
- [4] M. Shekofteh-Gohari, A. Habibi-Yangjeh, $\text{Fe}_3\text{O}_4/\text{ZnO}/\text{CoWO}_4$ nanocomposites: Novel magnetically separable visible-light-driven photocatalysts with enhanced activity in degradation of different dye pollutants, *Ceramics International*, 43 (2017) 3063–3071.
- [5] M. Shekofteh-Gohari, A. Habibi-Yangjeh, Novel magnetically separable $\text{ZnO}/\text{AgBr}/\text{Fe}_3\text{O}_4/\text{Ag}_3\text{VO}_4$ nanocomposites with tandem n-n heterojunctions as highly efficient visible-light-driven photocatalysts, *RSC Adv.* 6 (2016) 2402–2413.
- [6] A. Akhundi, A. Habibi-Yangjeh, Facile preparation of novel quaternary g- $\text{C}_3\text{N}_4/\text{Fe}_3\text{O}_4/\text{AgI}/\text{Bi}_2\text{S}_3$ nanocomposites: magnetically separable visible-light-driven photocatalysts with significantly enhanced activity, *RSC Adv.* 6 (2016) 106572–106583.
- [7] M. Shekofteh-Gohari, A. Habibi-Yangjeh, Fabrication of novel magnetically separable visible-light-driven photocatalysts through photosensitization of $\text{Fe}_3\text{O}_4/\text{ZnO}$ with CuWO_4 , *Journal of Industrial and Engineering Chemistry*, 44 (2016) 174–184.
- [8] M. Mousavi, A. Habibi-Yangjeh, M. Abitorabi, Fabrication of novel magnetically separable nanocomposites using graphitic carbon nitride, silver phosphate and silver chloride and their applications in photocatalytic removal of different pollutants using visible-light irradiation, *Journal of Colloid and Interface Science*, 480 (2016) 218–231.
- [9] A. Habibi-Yangjeh, M. Shekofteh-Gohari, $\text{Fe}_3\text{O}_4/\text{ZnO}/\text{Ag}_3\text{VO}_4/\text{AgI}$ nanocomposites: Quaternary magnetic photocatalysts with excellent activity in degradation of water pollutants under visible light, *Separation and Purification Technology*, 166 (2016) 63–72.
- [10] M. Mousavi, A. Habibi-Yangjeh, Magnetically separable ternary g- $\text{C}_3\text{N}_4/\text{Fe}_3\text{O}_4/\text{BiOI}$ nanocomposites: Novel visible-light-driven photocatalysts based on graphitic carbon Nitride, *Journal of Colloid and Interface Science*, 465 (2016) 83–92.



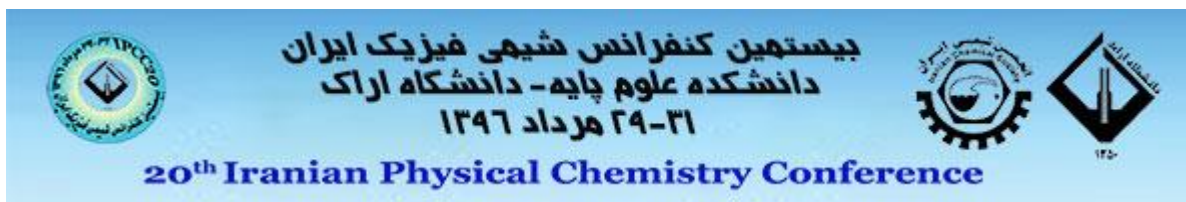
بیستمین کنفرانس شیمی فیزیک ایران
دانشکده علوم پایه - دانشگاه اراک
۲۱-۲۴ مرداد ۱۳۹۶



20th Iranian Physical Chemistry Conference

شیمی فیزیک کاربردی

Applied physical chemistry



Physicochemical properties of PAA-GO-Amylose nanocomposite hydrogel

Mohammad Taghi Taghizadeh, Reza Abdollahi*

^aDepartment of physical chemistry, Faculty of Chemistry, University of Tabriz, Tabriz, Iran)

*r.abdollahi@tabrizu.ac.ir

Abstract: In the present study, a nanocomposite hydrogel was synthesized based on poly (acrylic acid) grafted onto amylose (PAA-g-amylose) which was containing different loadings of graphene oxide (GO) nanosheets. The structural properties of optimized sample were characterized by scanning electron microscopy (SEM), X-ray analysis (XRD) and Fourier transform infrared spectroscopy (FTIR). The thermal behaviors of synthesized hydrogel were investigated by thermal gravimetric analysis (TGA) and differential scanning calorimetry (DSC). XRD and scanning electron microscopy study demonstrates the formation of highly exfoliated GO layers and its homogenous dispersion throughout the polymer matrix with 3 and 5wt% GO. However, the intercalated structure is predominant with 5wt% GO. The homogenous and the strong interaction of the GO layers and the PAA-g-amylose hydrogel matrix induced the significant improvement in thermal properties of the nanocomposite hydrogel. The thermal stability improved by 67°C and T_g shifted to the higher temperature by 53°C at 5wt% GO loading, compared to the pristine hydrogel matrix.

Keywords: PAA-g-amylose, hydrogel, thermal stability, nanocomposite

Introduction

Hydrogels are a class of wet and soft materials, constituted by weakly cross-linked polymers that are composed of a hydrophilic three-dimensional network. Due to their flexible cross-linked chains, hydrogel can absorb a large amount of water [1]. Hydrogels offer high physical and chemical stability in their swollen state [2]. This special soft-wet structure of hydrogels make possible them to be applied as biocompatible materials for a variety of biomedical applications including controlled drug delivery systems, wound dressing, coating for biosensors, membranes for bio separation and tissue scaffold engineering. Therefore, most methods developed to modify hydrogels mechanical properties via chemical engineering methods or change in the steps of synthesis pathway.

Recently, polysaccharide-based polymers such as amylose and amylopectin have been the subject of many studies. Amylose is an anhydro-glucose polysaccharide that is low soluble in water rather than amylopectin. To increase its hydrophobic and hydrophilic properties, amylose backbone can be grafted by several monomers, i.e. acrylic acid. Pal et al. reported a developed pathway for synthesis of grafting binary monomer mixture of acrylamide and acrylic onto amylopectin backbone [3]. Both of poly (acryl amide) and poly (acrylic acid) chains are not biodegradable and amylopectin is biodegradable. Therefore, grafting of PAA and PAM onto the amylopectin backbone reduced the environmental stability of PAA and PAM and on the other hands, flexible nature of PAA and PAM chains help to reduce rigidity of amylopectin chains.

On the basis of this background, in the present study, we attempted to prepare GO/PAA-g-amylose nanocomposite hydrogel with good dispersion of GO

into hydrogel, based on the graft copolymer of poly (acrylic acid) onto amylos (PAA-g-amylose). The structural characterization of GO/PAA-g-amylose hydrogel was investigated by scanning electron microscopy (SEM), X-ray analysis (XRD) and Fourier transform infrared spectroscopy (FTIR) methods. Furthermore, to confirm the thermal and mechanical modifications the techniques of thermogravimetry analysis (TGA) and differential scanning calorimetry (DSC) as well as tensile testing was performed. A well dispersion of GO nanosheets throughout the PAA-g-amylose network matrix result in modified three-dimensional network that represents better thermal stability.

Materials and method

Amylose (C₆H₁₀O₅)_n purified from potato starch, with a purity of 99% was purchased from Gamay Industrial Technology Co. Ltd, Shanghai-China and Graphite was purchased from Aldrich. Acrylic acid, potassium persulfate (KPS) and all organic solvents were obtained from Merck.

GO/PAA-g-amylose nanocomposite hydrogel films were prepared by solution technique followed for PAA-g-amylose hydrogel films. A 1, 3 and 5 wt% of GO nanosheets (with respect to the total weight of PAA-g-amylose hydrogel film) added to graft copolymer network as follows: firstly dried GO was dispersed in 20mL of distilled water and sonicated for 30 min to avoid forming any aggregation and get a homogenous dispersion. Afterwards, the desired PAA-g-amylose hydrogel powder was dissolved in distilled water heated up to 70°C and was then stirred for 12h. Then, the GO dispersion was poured into the PAA-g-amylose solution and the GO/hydrogel mixture solution was stirred for another 5h. Calcium oxide suspension (10mL) was then added and temperature of

all resulting mixture was kept at 85°C for 8h to initiate cross-linking. After the formation process, the mixture was cooled to room temperature and the as-prepared hydrogel was casted on glass plates followed by drying at 65°C. The dried film were peeled off and used for further analysis.

Results and Discussion

FT-IR spectroscopy

FTIR spectroscopy analysis was used to describe the chemical structure of GO/PAA-g-amylose nanocomposite hydrogel and nature of chemical bonds. In the FTIR spectrum of GO (Fig. 1(a)), the broad peaks at 3615 cm⁻¹, 1625 cm⁻¹ and 1725 cm⁻¹ can be attributed to O-H, C=C and C=O band, respectively. According to Hummer's method, through the oxidization process of graphite powder abundant oxygen-containing functional groups are generated on the surface of GO nanosheets. These phenomena can facilitate the physical and chemical interactions with the functionalities of the polymer matrix. The bands at 1248cm⁻¹ are appointed to ring stretching and the band at 640 cm⁻¹ is assigned to symmetric ring deformation of epoxy group that is located on the GO nanosheets. The FTIR spectrum of PAA (fig.2(b)) exhibits a characteristic peak at 1720 cm⁻¹ and between 3420 and 3350 cm⁻¹ are associated with the O-C=O stretching of carboxylic acid groups and O-H vibration. For amylose in Fig. 1(c), the stretching and bending of O-H occurs at 3410 cm⁻¹ and 1646 cm⁻¹, respectively. The band at 1157 cm⁻¹ and 1084 cm⁻¹ are attributed to the stretching of C-O in C-O-H and the bands at the 1018 cm⁻¹ are attributed to the stretching of C-O in C-O-C glycosidic bond which is reported in the literature to be at 1150-1040 cm⁻¹ [4]. The FTIR spectra of PAA-g-amylose (Fig. 1(d)) clearly show characteristics of both amylose and PAA spectrum. In this case, there are few additional bands present in comparison to amylose. The band at 1655 cm⁻¹ is attributed to C=O stretching vibration. One peak at 1450 cm⁻¹ is for C-N stretching vibrations. The presence of these additional peaks confirms successful grafting of PAA chains onto amylose backbone. The FTIR spectrum of GO/PAA-g-amylose hydrogel (Fig. 1(e)) indicates that the decrease of the intensity and little shifting of the C=O peak to 1700 cm⁻¹, clearly indicate that the oxygen in AA groups can interact with the surface of GO nanosheets.

DSC analysis

The glass transition (T_g) behavior of the pure PAA, amylose and grafted PAA-g-amylose as well as GO/PAA-g-amylose containing of 1, 3 and 5wt% of GO nanosheets are investigated by differential scanning calorimetry and the curves are presented in

Fig. 2. In comparison with T_g of pure PAA and amylose (respectively, 110 and 56°C), the T_g of the PAA-g-amylose hydrogel resulted an average amount and is monitored 72°C. The changes in T_g for PAA-g-amylose clearly approve the modified behavior of PAA-g-amylose in contrast with pure PAA and amylose. The advantage of adding GO into PAA-g-amylose hydrogel matrix is the improving of compatibility via an electrostatic interaction between the abundant hydroxyl groups of amylose and oxygen functional groups located on the GO nanosheets. The glass transition temperature of the PAA-g-amylose increase significantly from 72°C to 125°C with 5wt% of GO. It is also observed that the T_g increases by 7 and 19°C as compared to the pristine PAA-g-amylose when the GO content is 1 and 3wt%, respectively. The increase in T_g can be explained by reduced mobility of the polymer chains attached to the surface of the GO sheets by electrostatic interaction such as hydrogen bonds.

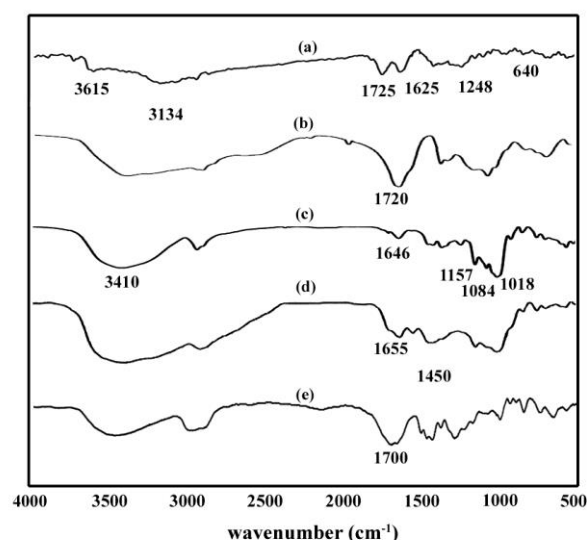


Fig.1. FTIR spectra of (a) GO nanosheets, (b) PAA, (c) amylose, (d) PAA-g-amylose hydrogel and (e) GO/PAA-g-amylose nanocomposite hydrogel.

Thermogravimetry analysis

Fig 3(a) and (b) illustrate the TGA and DTG curves of the PAA-g-amylose and the GO/PAA-g-amylose (containing 1, 3 and 5wt% of GO). A two step process of degradation is detected; a small first loss of mass is observed in the range of 110-200°C temperature and is attributed to the removal of water molecules trapped inside the GO structure. Moreover, the formation of dehydrated acrylic acid was arise upper than 200°C [5]. A second degradation step observed in the 350-516°C temperature range corresponds to pyrolysis of the labile oxygen containing functional groups in the forms of CO, CO₂ and steam. It is observed that GO

and PAA-g-amylose hydrogel matrix has synergistic effect on the thermal stability of PAA-g-amylose hydrogel, whereas the nanocomposite hydrogel containing GO has much improved thermal stability than pristine PAA-g-amylose hydrogel. Furthermore, according to the relative mass loss it seems to have a direct correlation between the amount of GO nanosheets and the extension of the degradation process. The thermal stability of the GO/PAA-g-amylose nanocomposite hydrogel increases gradually with increasing GO content.

Indeed, the Tonset and Tdmax of the GO loaded PAA-g-amylose nanocomposite hydrogels are higher than those of the pristine hydrogel network. As seen from the data which are represented in Table 1, by the increasing of GO content in the matrix of PAA-g-hydrogel the Tdmax was shifted to the higher temperatures. As in the case of 5wt% GO loading, the Tdmax increased to the 486°C. This state is an evidence of the nanocomposite hydrogels improved stability [6].

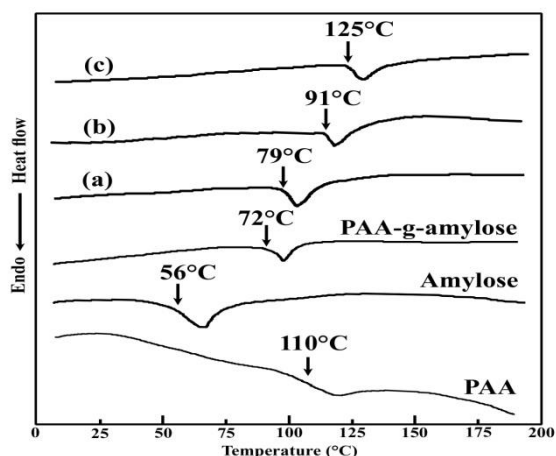


Fig. 2. DSC curves of PAA, amylose, PAA-g-amylose and for GO/PAA-g-amylose containing (a) 1wt%, (b) 3wt% and (c) 5wt% GO nanosheets.

Table 1. Thermogravimetric data of the pristine PAA-g-amylose with different loadings of GO nanosheets.

GO content (wt %)	Td (°C)	Tonset	Td _{max}	Weight loss (%) at temperature (°C)			
				200	300	400	500
0	311	256	402	9	25	73	89
1	332	281	415	7	23	68	88
3	359	309	435	4	20	55	87
5	385	323	486	2	13	48	85

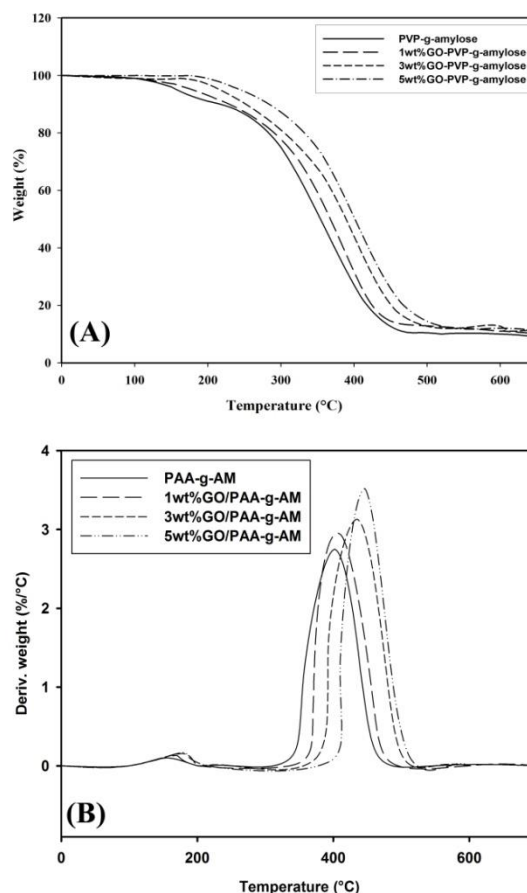


Fig.3. TGA (A) and DTG (B) curves for PAA-g-amylose hydrogel and GO/PAA-g-amylose nanocomposite hydrogels.

References

- [1] M. Sakthivel, D. S. Franklin, S. Guhanathan, pH-sensitive Itaconic acid based polymeric hydrogels for dye removal applications. *Ecotox. Environ. Safe.* 134 (2016) 427-432.
- [2] M. Raphael, *Bio medical Applications of Hydrogels*. Springer Science Business Media, LLC., (2010) Springer-Verlag, New York, Kinam Park Teruo Okano.
- [3] S. Pal, A. Pal, Synthesis and characterizing a novel polymeric flocculant based on amylopectin-graft-polyacrylamide-graft-polyacrylic acid [(AP-g-PAM)-g-PAA], *Polym. Bull.* 69 (2012) 545-560.
- [4] Y. He, X. Wang, D. Wu, Q. Gong, H. Qiu, Y. Liu, T. Wu, J. Ma, J. Gao, Mater. Preparation and structural characterization of turbostratic-carbon/graphene derived from amylose film *Chem. Phys.* 142 (2013) 1-11.
- [5] T. Krivorotova, J. Jonikaite-Svegziene, P. Radzevicius, R. Makuska Constructing nanosized CdTe nanocrystal clusters with thermo-responsive photoluminescence characteristics, *React. Func. Polym.* 76 (2014) 32-40.

Binding forces between bovine milk β -lactoglobulin and novel palladium(II) complex

Somaye Shahraki

Department of Chemistry, University of Zabol, Zabol, Iran

E-mail addresses: s-shahraki@uoz.ac.ir, somaye_shahraki@yahoo.com

Abstract : Ligand binding studies on carrier proteins are crucial in determining the pharmacological properties of drug candidates. Here, a new palladium(II) complex was synthesized and characterized. The *in vitro* binding studies of this complex with β -lactoglobulin (β LG) were investigated by employing biophysical techniques at three temperatures (pH 7.4). The experimental results showed that the Pd(II) complex interacted above carrier proteins with moderate binding affinity ($K_b \sim 0.2 \times 10^3 \text{ M}^{-1}$). Binding of Pd(II) complex to β LG caused strong fluorescence quenching of protein through static quenching mechanism. In studied system hydrogen bonds and van der Waals forces were the major stabilizing forces in the drug-protein complex formation. UV-Visible measurements indicated that the binding of above complex to β LG may induce conformational and micro-environmental changes of proteins. All these experimental results suggest that β LG might act as carrier protein for Pd(II) complex to deliver it to the target molecules.

Keywords: *β -lactoglobulin, Schiff base, Pd(II) complex, Protein interactions*

Introduction

Bovine β -lactoglobulin (β LG) is a soluble globular protein that constitutes 50% of whey proteins. This protein exists in the milk of most mammalian species but is absent from that of human. It has 162 amino acids and molecular mass of 18.3 kDa [1, 2]. The native form of β LG shows a generally β -sheet structure folded into a calyx geometry consist of an α -helix and eight antiparallel β -strands at the outer surface of the β -barrel. For oral delivery applications, because of good biocompatibility and biodegradability of milk proteins, β LG could be considered as natural carrier for lipid-soluble drugs and many biological hydrophobic molecules. Its cost effectiveness, abundant availability, and acceptability make it an attractive alternative protein that can be used as a suitable carrier molecule for a lot of drugs [3]. The ability of β LG to bind various ligands results from its structure. Many studies have confirmed that the main site for specific hydrophobic ligand binding to β LG is located in the internal cavity, calyx, of the β -barrel. Other potential binding sites as second and third sites have been reported though so far lack convincing crystallographic data.

Materials and method

Synthesis and characterization of Pd(II) complex

To a stirred methanol solution (10 ml) of 2,3-butanedione monoxime, (0.202 g, 2 mmol), 2,2-dimethyl-1,3-diaminopropan (0.12 mL, 1 mmol) was added. The bright yellow solution was stirred and heated to reflux for 2 h. In another beaker NaCl (0.117 g, 2 mmol) and PdCl₂ (0.177 g, 1 mmol) in 20 mL of hot double distilled water was stirred for 2 h to a brown solution containing Na₂[PdCl₄]. The solution of prepared Schiff base was added to a stirred solution of

Na₂[PdCl₄]. Then the mixture was stirred and heated to reflux for 2 h. A yellow precipitate separated, which was filtered, washed with methanol and acetone, and finally dried in desiccator. Yield (0.276 g, 62%) with a melting point of 247-249 °C, Anal. Calculated for C₁₃H₂₄N₄O₂Cl₂Pd (445.41): Calc. C, 35.02; H, 5.38; N, 12.57 %. Found. C, 34.83; H, 5.32; N, 12.09 %. FT-IR (KBr, ν / cm^{-1}): 3324 [ν (OH) of oxime], 1610 [ν (C=N) of Schiff-base], 1487 [ν (C=N) of oxime], 1189 [ν (N-O)]. ¹H NMR (500 MHz, DMSO-*d*₆): 0.87–1.25 (12H, 4CH₃ oxime), 1.70–2.24 (6H, 2CH₃ diamine), 2.85–3.17 (4H, 2CH₂ diamine), 7.91 (2H, NOH oxime). The electronic spectra of this complex exhibit three bands. The bands at 211 (log ϵ = 2.13) and 257 nm (log ϵ = 3.12) assigned to intraligand $\pi \rightarrow \pi^*$ and $n \rightarrow \pi^*$ transitions of the azomethine C=N bond and the band at 313 nm (log ϵ = 2.63) assigned to metal to ligand charge transfer transition [4, 5].

Carrier protein interaction studies

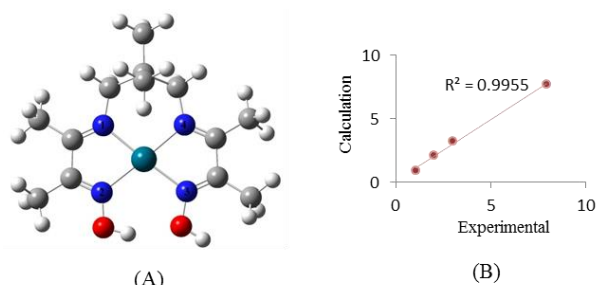
The protein-binding experiments were done in Tris-HCl buffer medium (pH 7.4) at three temperatures; 303, 310 and 317 K. Tris-HCl buffer solution (0.1 mol L⁻¹ Tris, pH 7.4) containing NaCl (0.1 mol L⁻¹) was prepared to keep the pH value and maintain the ionic strength of the solution. The working solution of carrier protein ($1 \times 10^5 \text{ mol L}^{-1}$) was prepared by dissolving them in Tris-HCl buffer solution and stored in a refrigerator at 4 °C prior to use. The concentration of protein was determined by absorbance measurement at 280 nm by the relevant molar absorption coefficient ($\epsilon_{\beta\text{LG}} = 17600 \text{ M}^{-1} \text{ cm}^{-1}$) [6]. The stock solutions of Pd(II) complex ($5 \times 10^{-3} \text{ mol L}^{-1}$) was prepared by dissolving it in Tris-HCl buffer solution.

Results and Discussion



Computational analysis

Generally, when the X-ray crystallography information of compound didn't exist, to obtain appropriate information about structural description we can use of DFT calculations [7]. So, optimized geometry by using the DFT/B3LYP method and 6-311G*+ LANL2DZ mixed basis set and some geometrical parameters (bond lengths and bond angles) of Pd complex is shown in Fig. 1.



Bond lengths (Å)		Bond angles (°)	
Pd-N ₁	2.023	N ₁ -Pd-N ₂	78.473
Pd-N ₂	2.050	N ₁ -Pd-N ₄	99.462
Pd-N ₃	2.045	N ₂ -Pd-N ₃	104.345
Pd-N ₄	2.040	N ₃ -Pd-N ₄	77.719

Fig. 1: The optimized structure of Pd complex, Carbon: Gray, nitrogen: blue, Palladium: light purple (A) Graphic correlation between the experimental and the calculated NMR chemical shifts (B) and selected bond lengths (Å) and bond angles (°) for the Pd complex at B3LYP/6-311G++(d) level (inserted table)

Fluorescence spectral study

As can be seen in Fig. 1, the fluorescence intensity of protein decreases regularly with increasing Pd(II) complex concentrations. This result suggests that Pd(II) complex can bind to βLG, the binding of Pd(II) complex to βLG quenches the intrinsic fluorescence of this protein.

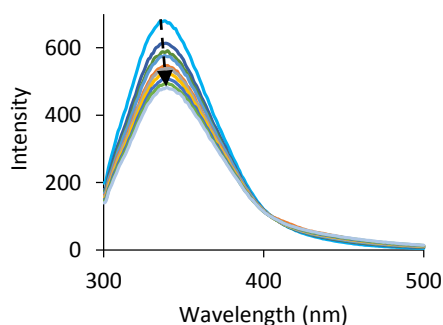


Fig. 2: Fluorescence spectra of βLG with increasing concentration of Pd(II) complex (0–45 μM) at pH 7.4.

Analysis of binding and thermodynamic parameters

By the plot of $\log(F_0-F)/F$ vs. $\log[\text{Complex}]$ the number of binding sites n and binding constant K_b can be obtained (Fig. 3).

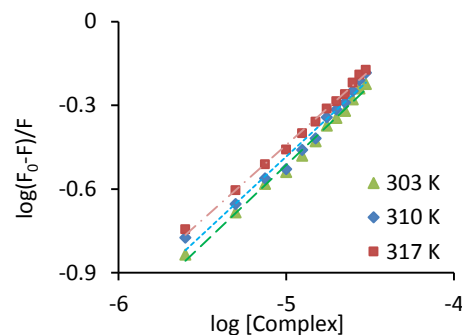


Fig. 3: The plots of $\log(F_0-F)/F$ versus $\log[\text{Complex}]$ for Pd complex-βLG system at three different temperatures.

In Pd(II) complex-βLG system as temperature was increased the values of binding constant decreased that indicate the static quenching was occurred in this system.

Thermodynamics of the carrier protein-Pd(II) complex interaction

The thermodynamic parameters are important for confirming interaction mode [8]. In view of the small positive ΔS values and large negative ΔH values, obtained for Pd(II) complex-βLG system (Fig. 4), hydrogen bonds and van der Waals forces seem to favour the stabilization of drug-protein complex in this system. Of course, due to imine group in structure of complex and obtained small positive ΔS values, the presence of hydrophobic interactions is not unexpected)

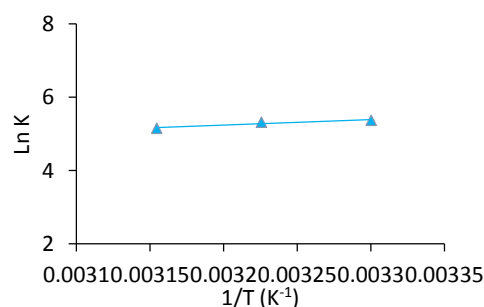


Fig. 4: Arrhenius plots for Pd complex-βLG system at three different temperatures.

Absorption spectral study of the interaction

The double reciprocal plot of $1/\Delta A$ versus $1/[\text{Complex}]$ is linear and the binding constant (K_b) can be calculated from the ratio of the intercept to the slope (Fig. 5). Binding constants of βLG to Pd(II) complex was calculated $3.38 \times 10^4 \text{ M}^{-1}$. These values of association constants for Pd(II) complex/carrier protein

systems confirm the result of fluorescence measurement.

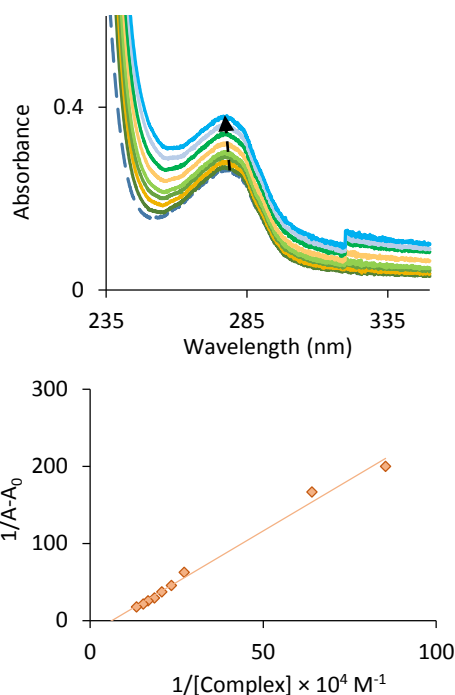


Fig. 5: UV-Vis spectra of Pd(II) complex-protein system in the absence (dash line) and presence of Pd(II) complex (solid lines). (A) Pd complex-HSA system, [HSA] = 5 μ M and [Pd complex] = 0-65 μ M and (B) Pd complex- β LG system, [β LG] = 5 μ M; [Pd complex] = 0-100 μ M at pH 7.4.

Conclusions

Binding of novel Pd(II) complex with β LG was studied by multi-spectroscopic techniques (under simulated physiological conditions). UV-Vis results showed that the binding of Pd(II) complex to protein induced conformational changes on protein. The results of fluorescence suggested that Pd(II) complex can bind to β LG and quench the fluorescence of it with static mechanism. The thermodynamic results showed that hydrogen bonds and van der Waals forces play a major role for β LG-Pd(II) complex associations. Binding parameters between protein and Pd(II) complex such as binding sites number and binding constant were determined.

Acknowledgment

We are grateful to the University of Zabol for financial support.

References

[1] A. Rohit, K. Sathisha, H. Aparna, A variant peptide of buffalo colostrum β -lactoglobulin inhibits angiotensin I-converting enzyme activity, *European journal of medicinal chemistry* 53 (2012) 211-219.

- [2] B. Ghalandari, A. Divsalar, A.A. Saboury, T. Haertlé, K. Parivar, R. Bazl, M. Eslami-Moghadam, M. Amanlou, Spectroscopic and theoretical investigation of oxali-palladium interactions with β -lactoglobulin, *Spectrochimica Acta Part A: Molecular and Biomolecular Spectroscopy* 118 (2014) 1038-1046.
- [3] A.H. Sneharani, J.V. Karakkat, S.A. Singh, A.A. Rao, Interaction of curcumin with β -lactoglobulin stability, spectroscopic analysis, and molecular modeling of the complex, *Journal of agricultural and food chemistry* 58(20) (2010) 11130-11139.
- [4] T.N. Sorrell, C. O'Connor, O.P. Anderson, J.H. Reibenspies, Synthesis and characterization of phenolate-bridge copper dimers with a copper-copper separation of > 3.5 Å. Models for the active site of oxidized hemocyanin derivatives, *Journal of the American Chemical Society* 107(14) (1985) 4199-4206.
- [5] M.F. Iskander, L. El-Sayed, N.M. Salem, R. Werner, W. Haase, Synthesis, characterization and magnetochemical studies of dicopper (II) complexes derived from bis (N-salicylidene) dicarboxylic acid dihydrazides, *Journal of Coordination Chemistry* 58(2) (2005) 125-139.
- [6] J. Essemine, I. Hasni, R. Carpentier, T. Thomas, H. Tajmir-Riahi, Binding of biogenic and synthetic polyamines to β -lactoglobulin, *International journal of biological macromolecules* 49(2) (2011) 201-209.
- [7] S. Jayakumar, D. Mahendiran, V. Viswanathan, D. Velmurugan, A. Kalilur Rahiman, Heteroscorpionate-based heteroleptic copper (II) complexes: Antioxidant, molecular docking and in vitro cytotoxicity studies, *Applied Organometallic Chemistry* (2017).
- [8] Y.-J. Hu, Y. Liu, X.-H. Xiao, Investigation of the interaction between berberine and human serum albumin, *Biomacromolecules* 10(3) (2009) 517-521.

Investigation of Surface and Micellar Properties of Mixed Cationic Surfactant and Ionic Liquid in Aqueous Medium

, Ahmad Bagheri*

Department of Chemistry, Semnan University, Semnan, Iran
 abagheri@semnan.ac.ir

Abstract: Surfactants are a class of organic compounds that can reduce the surface tension of water by configuration in solution surface. The performance of synergism (synergistic) can be far more than their pure state. Recently, ionic liquids with surface-active properties due to the specific characteristics (such as green solvent) have been considered. In this research, the interfacial and micellization behaviors of binary mixtures of an ionic liquid (1-hexyl 3-methylimidazolium chloride or C₆mimCl) and cationic surfactant (CTAB) were studied at various mole fractions. The surface tension and conductivity techniques were used to determine values of surfactants in pure and mixed states. The Experimental results were analyzed according to the regular solution model developed by Client, Rubingh, Rosen and others. Interaction parameters (β^s , β^m), mole fraction (X^s , X^m), activity coefficient (f^s , f^m) were calculated and analyzed at the interface and micellar phases. The thermodynamic parameters such as maximum surface excess (Γ_{max}), surface pressure (Π), excess free Gibbs energy of micellization (ΔG_{ex}^m), minimum area per molecule (A_{min}) calculated and investigated.

Keywords: Surfactants; Ionic liquid; Interaction parameter; Synergism; Excess free Gibbs energy of micellization

Introduction

Surfactant mixture is commonly used in practical application. Molecular interaction between two surfactants in mixed micelle and mixed monolayer is commonly measured by so-called β parameter (β^s and β^m). This parameter is calculated from critical micelle concentration data. According to Rubing's non-ideal solution theory after measuring the critical concentration of the mixed surfactants, CMC_{mix} , and the cmc of individual surfactants the value of the parameter β can be calculated from following equations[1-2]:

$$(X_1)^2 \ln \left(\frac{y_1 CMC_{mix}}{X_1 CMC_1} \right) = (1 - X_1)^2 \ln \left(\frac{(1 - y_1) CMC_{mix}}{(1 - X_1) CMC_2} \right) \quad (1)$$

$$\beta = \frac{1}{(1 - X_1)^2} \ln \frac{y_1 CMC_{mix}}{X_1 CMC_1} \quad (2)$$

Since the value of β is related to the free energy of mixing of the system, a negative value of β means that attractive interaction between two surfactants is stronger than individual surfactants with themselves. The values of molecular interaction parameter (β) and the mole fraction of components (X_i) at the micellar region were calculated on the basis of Rubingh's model

(RST) and Rosen's theory[1-3].

Materials and method

C₆mimCl were obtained from Io-il-tec and CTAB were obtained from Merck Company. The surface tensions of the pure liquids and their mixtures were measured using the platinum-iridium ring method with a KSV (Sigma 70, Finland) tensiometer. The platinum-iridium ring was cleaned with chromosulfuric acid and boiling distilled water. Each measurement was repeated up to ten times to check for reproducibility. The uncertainty of the surface tension measurement is $\pm 0.2 \text{ mNm}^{-1}$ of the final value of surface tension, and the corresponding reproducibility is $\pm 0.01 \text{ mNm}^{-1}$. The temperature was kept constant by a water bath circulator (Pharmacia Biotech) and with the uncertainty $\pm 0.1 \text{ K}$. The binary and ternary mixtures were prepared by mass using an analytical balance (Sartorius, model BP 121S, accurate to $\pm 0.1 \text{ mg}$). The uncertainty of the mole fractions was estimated to be within ± 0.0001 .

Results and Discussion

Fig. 1 shows plots of β^m values versus the mole fraction of mixture (CTAB), typically. β^m are negative values for all mole fractions of all investigated mixture which suggest that interaction in mixed micelles are more attractive than single components systems.



This indicates that the interactions between the two different surfactants after mixing are more attractive or less repulsive than before mixing.

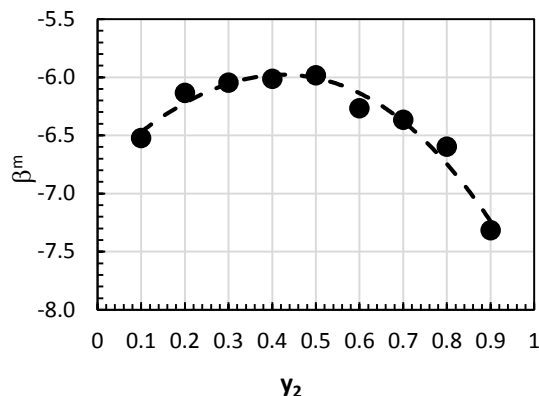


Fig.1. Plots of β^m values versus the mole fraction of CTAB

Fig.2 shows plots of ΔG_m^0 values versus the mole fraction of mixture (CTAB). The negative values of Gibbs energy of micellization indicates the micellization occurs spontaneously, and also, the micellization process of the mixture became more stable with increasing the bulk mole fraction of C_6mimCl .

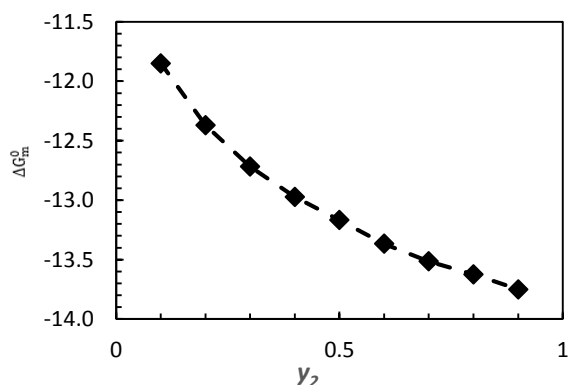


Fig.2. Plots of ΔG_m^0 values versus the mole fraction of CTAB

Conclusions

Binary surfactant systems consisting of C_6mimCl and CTAB exhibit one single break point of micellization. Surface tension measurement shows that this system at 298.15 K exhibit negative synergistic phenomenon. As a result the molecules of C_6mimCl has less interaction with molecules of CTAB, but with increasing of mole fraction of CTAB the number of C_6mimCl monomers decreases since molecules of CTAB are unstable in aqueous solution, the molecules interact with monomers of C_6mimCl and β values get negative.

The results show that the numbers of monomers that participate in formation of mixture micelle are more than first one on the presumption that it is more stable.

This stability is considered to be increasing the counter-ion binding (Cl^-) to micellar surfactant that makes reduction of repulsion between monomers of surfactant and perching together with less gap with more number of monomers.

This synergistic effect observed can be explained by the fact that counter-ion from IL adsorb to the charge head group (N^+) of CTAB molecules and reduce the repulsion between monomer of CTAB surfactant, hence CMC of mixture decreases.

References

- [1] M. J. Rosen, Z. Qiong, "Surfactant-surfactant interactions in mixed monolayer and mixed micelle formation", *Langmuir*, 17 (2011) 3532-3537
- [2] Z. Qiong, M. J. Rosen, "Molecular interactions of surfactants in mixed monolayers at the air/aqueous solution interface", *Langmuir* 19 (2003) 455-462
- [3] A. Bagheri, A. Abolhasani, "Binary mixtures of cationic surfactants with triton X-100 and the studies of physicochemical parameters of the mixed micelles", *Korean J. Chem. Eng.*, 32 (2015) 308-315.

Examination of Optical Spectroscopy of Cadmium Chalcogenide Nanocrystals

Samad Amini^a; Mahmood Moradi LM^a

^a Department of Chemistry, Yasouj University, Yasouj, Iran

e-mail: moradi.mahmood85@yahoo.com

Abstract: High optical quality Cd chalcogenide (Te, Se, and S) quantum dots with average size at the near Bohr radius were synthesized using a colloidal chemical reaction. The Cd chalcogenide (Te, Se, and S) nanocrystals exhibited strong blue shift and discrete energy states which were significantly modified from bulk crystals. The discrete structure of energy states leads to a discrete absorption spectrum of quantum dots, which is in contrast to the continuous absorption spectrum of a bulk semiconductor. Atomic-like discrete energy states of exciton indicate a quantum confinement effect. The energy spacing between the first and second peaks of exciton absorption is less than 50 meV for bigger than ~4 nm quantum dot size, and is more than several hundred meV for ~2 nm size of CdTe quantum dots. The emission of CdSe nanocrystals tuned from near-infrared to dark blue by a reduction in the dot radius from 8 to 0.8 nanometers. The quantum confinement modifies the optical absorption, the photoluminescence, the radiative decay time, and the nonlinear optical properties of nanocrystals. The optical properties of quantum dots are also sensitive to the dielectric effects of surrounding environment, which can be utilized for the detection of nanoscale crack on the spacecraft.

Keywords: Optical Properties, Quantum Confinement, Semiconductor.

1. Introduction

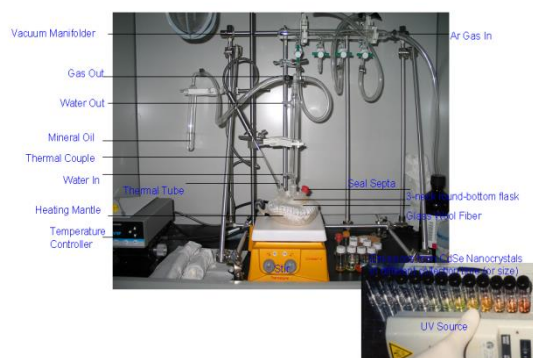
The optical materials with nanoscale sizes are also sensitive to the surrounding environment, which can be utilized for the detection of nanoscale crack on the spacecraft. During the last decade, considerable theoretical and experimental efforts have been made in the fundamental aspects of quantum confinement effects, and optical properties of nanoscale materials. The term nanoscale particle refers to an intermediate in size, between isolated atoms and molecules and bulk materials, where the transitional properties between two limits can be controlled. As it is well known, a decrease of particle size will influence two of the most important contributions to the optical properties of nanoscale materials, which are quantum size effects, surface effects, and surrounding environments[1].

2. Synthesis of semiconductor nanocrystals

High optical quality Cd chalcogenide (Te, Se, and S) nanocrystals with sizes near the Bohr radius ($\alpha_B \sim 7$ nm (CdTe), $\alpha_B \sim 5.6$ nm (CdSe), and $\alpha_B \sim 1.8$ nm (CdS)) were synthesized by the chemical colloidal reaction. Many synthesis techniques were developed for preparing Cd chalcogenide semiconductor nanocrystals, however, the following synthesis methods were mostly applied for our current research samples. For CdS nanocrystals synthesis, a mixture of CdO, oleic acid (OA), and technological-grade 1-octadecene (ODE) is heated to 300 °C. A solution of sulfur in ODE is swiftly injected into the heated solution, and the mixture is allowed to cool to 250 °C for the growth of CdS nanocrystals. The synthesis can be carried out under argon or in open air. Aliquots are taken at different time intervals, and UV-Vis and PL spectra are recorded for each aliquot. For CdSe nanocrystal synthesis, CdO is mixed with Stearic Acid (SA), and heated until CdO is completely dissolved by the SA. The mixture of CdO and SA is optically clear

at around 160 °C, while at room temperature the solution solidified as a waxy or a white substance. Hexadecylamine (HAD) and trioctylphosphine oxide (TOPO) are added in the mixture of CdO and SA, and heated to 320 °C. Then, the solution Se, tributylphosphine (TBP) and dioctylamine (DOA) are injected quickly. The growth temp is 290 °C. The first exciton absorption peaks after 90 seconds of growth are near 600 nm. For CdTe nanocrystal synthesis, CdO is mixed with tetradecyl phosphonic acid (TDPA), and ODE for the slow reaction, and is heated to 300 °C. Also, OA instead of TDPA can be used for the fast reaction. Then the mixture of Te, TBP, toluene and ODE is quickly injected into the solution. The growth temperature is around 245 °C. The first exciton absorption peaks are at ~600-630 nm after ~60 seconds for the slow reaction or after ~10 seconds for the fast reaction. The first absorption peak varies up to ~730 nm continuously adding Te and Cd precursors.

The optical spectroscopy at room temperature is performed using an UV-VIS absorption spectrometer (Agilent Tech, 8453). Size quantization of nanocrystal quantum dots is carried out using an electron transmission microscopy (Hitachi, H-9000NAR).



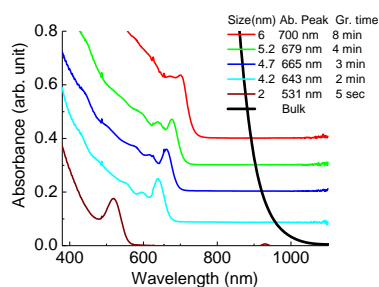
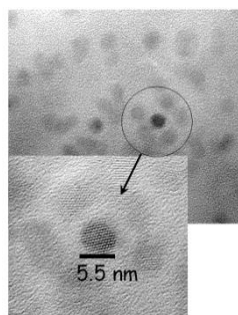


Figure 1. Experimental setup for colloidal-semiconductor nanocrystals, Transmission electron microscopy (Hitachi, H-9000NAR) and absorption spectra of cadmium telluride semiconductor nanocrystals.

3. Optical properties of semiconductor nanocrystals

One of the defining features of a semiconductor is the energy gap between the conduction and valence energy bands. The emission spectrum of semiconductor is determined by the energy bandgap. The energy bandgaps ($E_g \sim 863$ nm), CdSe ($E_g \sim 714$ nm), and CdS ($E_g \sim 513$ nm) of bulk semiconductors are a fixed parameter determined by the material's identity. The situation changes, however, in the case of nanoscale semiconductor particles with sizes near the Bohr radius ($\alpha_B \sim 7$ nm (CdTe), $\alpha_B \sim 5.6$ nm (CdSe), and $\alpha_B \sim 1.8$ nm (CdS)). This size range corresponds to the regime of quantum confinement, for which the spatial extent of the electronic wave function is comparable with the dot size. As a result of these geometrical constraints, electrons feel the presence of the particle boundaries and respond to changes in particle size by adjusting their energy.² This phenomenon is known as the quantum-size effect, and it plays a very important role in quantum dots. For weak confinement ($a \sim \alpha_B$), the energy of exciton in a spherical box potential model is expressed in the form of [3]

$$\Delta E = \frac{\hbar^2 x_{ml}^2}{2MR^2} - \frac{\mu e^4}{2\epsilon^2 \hbar^2} \quad (1)$$

where, \hbar is the Planck's constant $\hbar = h/2\pi$, x_{ml} is the roots of the Bessel function, M is the exciton translation

mass, R is the dot radius, μ is the electron-hole reduced mass, and ϵ is the dielectric constant. For a spherical quantum dots with radius R , the equation (1) indicates that a size dependent contribution to the energy gap is simply proportional to $1/R^2$, implying that the gap increases as the nanocrystal size decreases.

Absorption spectra of CdTe nanocrystals have the strong blue-shift of optical bandage as shown in figure 2. Atomic-like discrete energy states of exciton indicate a quantum confinement effect, which is completely different with the bulk crystals.

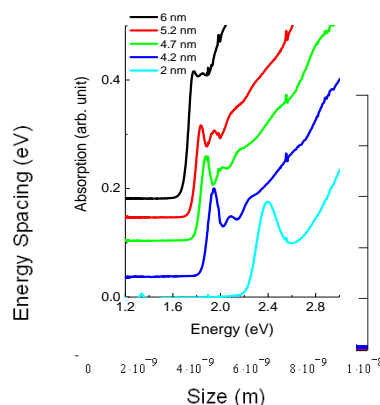


Figure 2. Absorption spectra of CdTe, confinement energy states at the conduction-band and energy transitions.

The discrete structure of energy states leads to a discrete absorption spectrum of quantum dots, which is in contrast to the continuous absorption spectrum of a bulk semiconductor. Because of the quantum-size effect, this ability to tune the nanocrystal size translates into a means of controlling various nanocrystal properties, such as emission and absorption wavelengths. For example, the emission of CdSe nanocrystals can be tuned from near-infrared to dark blue by a reduction in the dot radius from 8 to 0.8 nanometers.

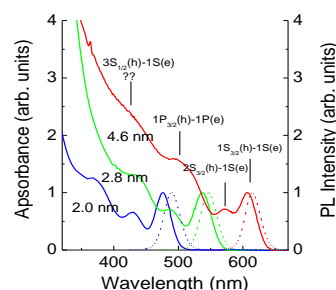


Figure 3. Absorption (solid lines) and photoluminescence (dot lines) spectra of TOPO-passivated CdSe nanocrystals.

Figure 3 shows typical absorption spectra of a series of TOPO-passivated colloidal NC's with mean radii from 2 to 4.6 nm. Because of the narrow NC size distribution, the absorption spectra clearly exhibit discrete features due to transitions coupling electron and hole quantized states. The electron quantized states are labeled using letter (l) to denote the angular momentum of the envelop wave function (S for l=0, P for l=1, D for l=2, etc) and a digit to denote the number of the state of the given symmetry. The three lowest electron states in the order of increasing energy are 1S, 1P, 1D. A similar notation is used for hole states with an addition of a subscript which denotes the total hole angular momentum, which is the sum of the valence-band Bloch-function momentum and the momentum of the hole envelope wave function. For CdSe nanocrystals, the first three hole states in the order of increasing energy are $1S_{3/2}$, $1P_{3/2}$, $2S_{3/2}$.

The photoluminescence (PL) spectra (dot lines) of CdSe nanocrystals are also shown in figure 3. The stark shifts ($\Delta\lambda_S$) of CdSe nanocrystals are $\Delta\lambda_S \sim 7.7$ nm for 4.6-nm size, $\Delta\lambda_S \sim 9.9$ nm for 2.8-nm size, and $\Delta\lambda_S \sim 13.7$ nm for 2.0-nm size. It implies that the nanocrystals have a wider stark shift with the smaller size. The change of stark shift can be expected even crystal structure dependent on ligand or shape of nanocrystals.

4. Conclusion

High optical quality Cd chalcogenide (Te, Se, and S) quantum dots with average size at the near Bohr radius were synthesized using a colloidal chemical reaction. The Cd chalcogenide (Te, Se, and S) nanocrystals exhibited strong blue shift and discrete energy states which were significantly modified from bulk crystals. The discrete structure of energy states leads to a discrete absorption spectrum of quantum dots, which is in contrast to the continuous absorption spectrum of a bulk semiconductor. Atomic-like discrete energy states of exciton indicate a quantum confinement effect. The energy spacing between the first and second peaks of exciton absorption is less than 50 meV for bigger than ~ 4 nm quantum dot size, and is more than several hundred meV for ~ 2 nm size of CdTe quantum dots. The emission of CdSe nanocrystals tuned from near-infrared to dark blue by a reduction in the dot radius from 8 to 0.8 nanometers. The quantum confinement modifies the optical absorption, the photoluminescence, the radiative decay time, and the nonlinear optical properties of nanocrystals. The optical properties of quantum dots are also sensitive to the dielectric effects of surrounding environment, which can be utilized for the detection of nanoscale crack on the spacecraft.

References

¹ X. Wu, R. Wang, B. Zou, P. Wu, L Wang, and J. Xu, "The effects of different interfacial environments on

the optical nonlinearity of nanometer-sized CdO organo," *Appl Phys. Lett.* 71(15), 2097 (1997).

² V. I. Klimov, "Nanocrystal Quantum Dots from fundamental photophysics to multicolor lasing," *Los Alamos Science* 28, 214 (2003).

³ S.V. Gaponenko, *Nanoscale Linear and Nonlinear Optics*, edited by M. Bertolotti, (American Institute of Physics, 2001) pp. 157-177.



DFT study on the structural, properties and electrical conductivity of all Fluorostyrenes

Hossein Shirani Il Beigi* and Reza Fatollahi Geshlag

Department of chemistry, Nazhand Higher Education Institute, Urmia, 5719883896, Iran
shiranihossein@gmail.com

Abstract Electrical and structural properties of all fluorostyrenes (fluorovinylbenzene) have been studied using B3LYP method with 6-311++G** basis set. Effects of the number and position of the substituent fluorine atoms on the properties of the vinyl benzene have been studied using optimized structures obtained for these molecules. Vibrational frequencies, dipole moment, HOMO-LUMO gaps, electronic energy, IR and NMR spectra of these compounds have been calculated and analysed. The analysis of vibrational frequencies showed that we do not have any negative vibrational frequencies for optimized structures and also the positive vibrational frequency suggest that these molecules are on optimized minimum potential energy surface. Data shows 3-(1, 2difluorovinyl)-1, 2, 4, 5-tetrafluoro benzene has the minimal electronic energy and it's more stable among these molecules. Also we found the 1, 4-difluoro-2-vinylbenzene molecule has the lowest, HOMO-LUMO gaps, and electron transfer for this molecule is more favourable in a polymer chain.

Keyword: B3LYP, vibrational frequency, HOMO-LUMO gaps, electron transfer

Introduction

In 1865, the German chemist [Emil Erlenmeyer](#) found that Styrol could form a [dimer](#) [1]. Polystyrene, Polystyrene can be solid or foamed. General-purpose polystyrene is clear, hard, and rather brittle. It is an inexpensive resin per unit weight. It is a rather poor barrier to oxygen and water vapor and has a relatively low melting point. Polystyrene is very slow to [biodegrade](#) and is therefore a focus of controversy among environmentalists. Polystyrene results when styrene monomers interconnect. In the polymerization, the carbon-carbon π bond of the [vinyl group](#) is broken and a new carbon-carbon σ bond is formed, attaching to the carbon of another styrene monomer to the chain [2].some theoretical study on conducting polymers are in literature [3].

Method

B3LYP method with 6-311++G** basis set calculations by Gaussian 09 have been carried out successfully to study the structural and the energetically properties of all fluorostyrenes (fig.1) energy IR frequency, NMR spectra, vibrational frequencies and HLG have been calculated for all designed for molecules Fig.1

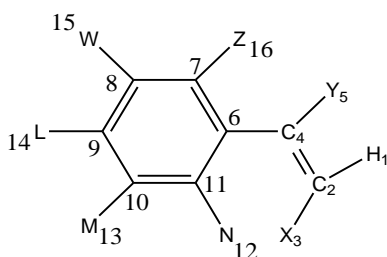


Fig 1: all possible fluorostyrenes(fluoeovinylbenzenes) molecules studied in this work

1;	X=Y=Z=W=L=M=N=H	styrene(vinyl benzene)
2;	X=F, Y=Z=W=L=M=N=H	(Z)-(2-fluorovinyl)benzene
3;	N=F, X=Y=Z=W=L=M=H	1-fluoro-2-vinylbenzene
4;	M=F, X=Y=Z=W=L=N=H	1-fluoro-3-vinylbenzene
5;	W=F, X=Y=Z=L=M=N=H	1-fluoro-3-vinylbenzene
6;	Z=F, X=Y=W=L=M=N=H	1-fluoro-2-vinylbenzene
7;	Y=F, X=Z=W=L=M=N=H	(1-fluorovinyl)benzene
8;	X=N=F, Y=Z=W=L=M=H	(Z)-1-fluoro-2-(2-fluorovinyl)benzene
9;	X=M=F, Y=Z=W=L=N=H	(Z)-1-fluoro-3-(2-fluorovinyl)benzene
10;	X=W=F, Y=Z=L=M=N=H	(Z)-1-fluoro-3-(2-fluorovinyl)benzene
11;	X=Z=F, Y=W=L=M=N=H	(Z)-1-fluoro-2-(2-fluorovinyl)benzene
12;	X=Y=F, Z=W=L=M=N=H	(E)-(1,2-difluorovinyl)benzene
13;	M=N=F, X=Y=Z=W=L=H	1,2-difluoro-3-Vinylbenzene
14;	W=N=F, X=Y=Z=L=M=H	1,4-difluoro-2-vinylbenzene
15;	Z=N=F, X=Y=W=L=M=H	1,3-difluoro-2-vinylbenzene
16;	Y=N=F, Z=W=L=M=X=H	1-fluoro-2-(1-fluorovinyl)benzene
17;	W=M=F, X=Y=Z=L=N=H	1,3-difluoro-5-vinylbenzene
18;	Z=M=F, X=Y=W=L=N=H	1,4-difluoro-2-vinylbenzene
19;	Y=M=F, X=Z=W=L=N=H	1-fluoro-3-(1-fluorovinyl)benzene
20;	Z=W=F, X=Y=L=M=N=H	1,2-difluoro-3-Vinylbenzene
21;	Y=W=F, X=Z=L=M=N=H	1-fluoro-3-(1-fluorovinyl)benzene
22;	X=N=M=F, Y=Z=W=L=H	(Z)-1,2-difluoro-3-(2-fluorovinyl)benzene
23;	X=W=N=F, Y=Z=L=M=H	(Z)-1,4-difluoro-2-(2-fluorovinyl)benzene
24;	X=Z=N=F, Y=W=L=M=H	(Z)-1,3-difluoro-2-(2-fluorovinyl)benzene
25;	X=Y=N=F, Z=W=L=M=H	(E)-1-(1,2-difluorovinyl)-2-fluorobenzene
26;	W=M=N=F, X=Y=Z=L=H	1,2,5-trifluoro-3-vinylbenzene
27;	Z=M=N=F, X=Y=W=L=H	1,2,4-trifluoro-3-vinylbenzene
28;	Y=M=N=F, X=Z=W=L=H	1,2-difluoro-3-(1-fluorovinyl)benzene
29;	Z=W=M=F, X=Y=L=N=H	1,2,5-trifluoro-3-vinylbenzene
30;	Y=W=M=F, X=Z=L=N=H	1,3-difluoro-5-(1-fluorovinyl)benzene
31;	Y=Z=M=F X=W=L=N=H	1,4-difluoro-2-(1-fluorovinyl)benzene
32;	X=Y=W=F, Z=L=M=N=H	(E)-1-(1,2-difluorovinyl)-3-fluorobenzene
33;	X=Y=Z=F, W=L=M=N=H	(E)-1-(1,2-difluorovinyl)-2-fluorobenzene
34;	Y=Z=W=F, X=L=M=N=H	1,2-difluoro-3-(1-fluorovinyl)benzene
35;	Y=Z=N=F, X=W=L=M=H	1,3-difluoro-2-(1-fluorovinyl)benzene
36;	Z=W=N=F, X=Y=L=M=H	1,2,4-trifluoro-3-vinylbenzene
37;	X=Z=W=F, Y=L=M=N=H	(Z)-1,2-difluoro-3-(2-fluorovinyl)benzene
38;	X=W=M=F, Y=Z=L=N=H	(Z)-1,3-difluoro-5-(2-fluorovinyl)benzene
39;	X=Y=M=F, Z=W=L=N=H	(E)-1-(1,2-difluorovinyl)-3-fluorobenzene
40;	X=W=M=N=F, Y=Z=L=H	(Z)-1,2,5-trifluoro-3-(2-fluorovinyl)benzene
41;	X=Z=M=N=F, Y=W=L=H	(Z)-1,2,4-trifluoro-3-(2-fluorovinyl)benzene
42;	X=Y=M=N=F, Z=W=L=H	(E)-1-(1,2-difluorovinyl)-2,3-difluorobenzene
43;	Z=W=M=N=F, X=Y=L=H	1,2,4,5-tetrafluoro-3-vinylbenzene
44;	Y=W=M=N=F, X=Z=L=H	1,2,5-trifluoro-3-(1-fluorovinyl)benzene
45;	Y=Z=W=M=F, X=L=N=H	1,2,5-trifluoro-3-(1-fluorovinyl)benzene
46;	X=Y=Z=M=F, W=L=N=H	(E)-2-(1,2-difluorovinyl)-1,4-difluorobenzene
47;	Y=Z=W=M=F, X=L=M=H	1,2,4-trifluoro-3-(1-fluorovinyl)benzene
48;	X=Y=Z=W=F, L=M=N=H	(E)-1-(1,2-difluorovinyl)-2,3-difluorobenzene
49;	X=Z=W=M=N=F, Y=L=H	(Z)1,2,4,5-tetrafluoro-3-(2-fluorovinyl)benzene



- 50; X=Y=W=M=N=F, Z=L=H (E)-1-(1,2-difluorovinyl)-2,3,5-trifluorobenzene
51; Y=Z=W=M=N=F, X=L=H 1,2,4,5-tetrafluoro-3-(1-fluorovinyl)benzene
52; X=Y=Z=W=M=F, L=N=H (E)-1-(1,2-difluorovinyl)-2,3,5-trifluorobenzene
53; X=Y=Z=W=M=N=F, L=H (E)-3-(1,2-difluorovinyl)-1,2,4,5-tetrafluorobenzene

Table1: B3LYP/6-311++G** optimized values of electronic energies(E_{ele}), Gibbs free energies(G), Zero point energies(G) and enthalpy(H)in Hartree Particle and Entropy (S) in K Cal/Mole

n	ZPE	E_{ele}	G	H	S
1	-194275.9	-194359.2	-194295.6	-194271.0	82.4
2	-256571.9	-256650.8	-256592.3	-256566.7	86.1
3	-256572.3	-256650.8	-256592.4	-256567.1	85.0
4	-256573.4	-256651.4	-256594.2	-256568.0	88.0
5	-256573.2	-256651.3	-256593.8	-256567.8	87.0
6	-256572.8	-256650.9	-256592.3	-256567.9	81.9
7	-256573.9	-256652.3	-256594.5	-256568.7	86.8
8	-318866.2	-318939.8	-318887.3	-318860.4	90.0
9	-318869.3	-318942.9	-318890.6	-318863.6	90.6
10	-318869.2	-318942.9	-318890.4	-318863.4	90.6
11	-318869.0	-318942.8	-318890.3	-318863.3	90.7
12	-318863.9	-318937.7	-318885.2	-318858.1	91.0
13	-318865.0	-318938.3	-318885.9	-318859.1	89.8
14	-318868.4	-318941.6	-318889.3	-318862.6	89.7
15	-318868.3	-318941.6	-318889.3	-318862.5	90.0
16	-318869.9	-318943.3	-318891.0	-318864.2	89.9
17	-318869.8	-318942.8	-318891.1	-318864.0	91.2
18	-318868.9	-318941.9	-318890.4	-31863.08	91.8
19	-318870.9	-318944.1	-318892.3	-318865.1	91.1
20	-318865.3	-318938.4	-318887.9	-318859.4	95.5
21	-318870.9	-318944.1	-318892.6	-318865.1	92.3
22	-381158.8	-381227.3	-381180.7	-318852.6	94.5
23	-381162.1	-381230.6	-381184.0	-380986.4	94.4
24	-381175.1	-381231.1	-381184.4	-381156.3	94.2
25	-381157.7	-381226.3	-381179.6	-381151.4	94.4
26	-381160.4	-381228.5	-381182.2	-381154.0	94.4
27	-381159.9	-381228.1	-381181.6	-381153.5	94.2
28	-381162.1	-381230.4	-381184.3	-381155.9	95.4
29	-381160.9	-381228.8	-381183.4	-381154.4	97.2
30	-381168.0	-381235.0	-381189.4	-381160.7	96.1
31	-381163.3	-381231.4	-381185.2	-381157.0	94.6
32	-381160.8	-381229.4	-381183.1	-381154.5	96.1
33	-381157.5	-381226.0	-381179.5	-381151.2	95.3
34	-381160.0	-381228.1	-381181.8	-381153.7	94.5
35	-381162.3	-381230.4	-381184.2	-381156.0	94.6
36	-381159.9	-381228.1	-381181.6	-381153.5	94.1
37	-381161.5	-381230.3	-381183.5	-381155.2	94.7
38	-381165.6	-381234.1	-381187.7	-381159.4	95.1
39	-381160.7	-381229.4	-381182.9	-381154.5	95.3
40	-443454.1	-443517.5	-443476.7	-443447.3	98.8
41	-443454.1	-443517.6	-443476.7	-443447.3	98.7
42	-443449.8	-443513.4	-443472.5	-443443.0	98.7
43	-443450.8	-443514.0	-443473.3	-443443.9	98.6
44	-443457.3	-443501.5	-443480.1	-443450.5	99.4
45	-443454.9	-443517.9	-443477.6	-443448.1	98.9
46	-443452.9	-443416.2	-443475.8	-443446.1	99.8
47	-443453.5	-443413.0	-443476.2	-443446.7	99.0
48	-443562.5	-443413.0	-443472.4	-443442.7	99.8
49	-505744.9	-505803.3	-505768.3	-505737.6	103.1
50	-505744.7	-505803.0	-505768.1	-505737.4	103.1
51	-505744.2	-505802.0	-505767.6	-505768.1	103.5
52	-505744.3	-505802.6	-505768.0	-505737.0	104.1
53	-568033.6	-568086.8	-568057.9	568025.7	108.3

Results and Discussion

In the study of molecules optimized with 6-311++G** basis set, it is observed that the most negative molecules belonging to 53th molecule ((E)-3-(1, 2-difluorovinyl)-1, 2, 4, 5-tetrafluorobenzene) with -568086.8 energy, indicating that the molecule is stable.

In the analysis of the Gibbs, show that the 53th molecule ((E)-3-(1, 2-difluorovinyl)-1, 2, 4, 5-tetrafluorobenzene) has least Gibbs value. In the analysis of entropy, we can see in table 1, the 53th molecule ((E)-3-(1, 2-difluorovinyl)-1, 2, 4, 5-tetrafluorobenzene) is unstable.

Table 2: B3LYP/6-311++G** optimized values of dipole moment and HOMO-LUMO gaps (HLG) of all fluorostyrene.

molecule	Dipole Moment(D)	H L G(e.V)
1	0.3544	5.0320
2	4.8728	5.1136
3	4.0702	5.1136
4	2.5872	5.0048
5	2.5179	5.0393
6	2.4845	4.9789
7	2.3593	5.0592
8	3.3842	5.3975
9	4.5931	5.0834
10	2.1828	5.1076
11	0.7325	5.0575
12	3.2216	5.0320
13	2.7734	5.1136
14	0.3668	5.0320
15	2.7528	5.0864
16	2.4057	5.0864
17	1.8710	5.0592
18	0.3815	4.8897
19	0.7005	5.0515
20	4.3727	5.0298
21	2.7778	5.0320
22	4.4922	5.4457
23	1.0012	5.2713
24	1.8045	5.4269
25	2.4532	5.2430
26	0.8432	5.0961
27	1.8474	5.0461
28	2.4252	5.1255
29	2.3404	4.9803
30	2.7128	5.0673
31	1.8478	5.3059
32	2.2706	4.9776
33	2.0983	5.3339
34	5.5778	5.4843
35	4.8120	5.4734
36	2.9176	5.0752
37	2.7934	5.0959
38	2.3481	5.1198
39	2.0620	5.0102
40	3.0761	5.3605
41	2.7359	5.372
42	3.1249	5.2612
43	0.6160	5.0592
44	0.6663	5.0646
45	3.9613	5.3613
46	2.0847	5.1796
47	5.5450	5.3885

molecule	Dipole Moment(D)	H L G(e.V)
48	4.5241	5.3132
49	1.9972	5.4117
50	1.5593	5.1807
51	2.8747	5.4076
52	2.6302	5.2094
53	0.8919	5.3875

”, *Canadian Journal of Chemistry*, 90(11) (2012) 902-914.

In the results of optimized molecules with 6-311++G** basis set, see the lowest HLG belonging to the 18th molecules (1, 4-difluoro-2-vinylbenzene) with 4.8897, which shows the highest conductivity (electron transfer) is end also observed that dipole moment molecules (1, 2- difluoro-3- (1-fluorovinyl) benzene) with (5.5778, which represents the solubility of the molecule polar.

Conclusions

B3LYP method with 6-311++G** basis set calculations have been carried out successfully to study the structural parameters. Values of vibrational frequencies, electronic Energy IR, NMR spectra, dipole moment and HLG have been calculated and analysed. According to the results showed no negative vibration frequency showing that the molecules are in the lowest level of optimal energy and also the positive vibrational frequency suggest that these molecules are on optimized minimum potential energy surface. Data shows 3-(1,2difluorovinyl)-1,2,4,5-tetrafluoro benzene has the minimal electronic energy and its more stable among these molecules. Also we found the 1, 4-difluoro-2-vinylbenzene molecule has the lowest, HOMO-LUMO gaps, and electron transfer for this molecule is more favorable in a polymer chain.

References

- [1] Erlenmeyer, Emil “Ueber Distyrol, ein neues Polymere des Styrols”, *Annalen der Chemie*, 135 (1865) 122-123
- [2] Kwon, BG; *et al.* “Regional distribution of styrene analogues generated from polystyrene degradation along the coastlines of the North-East Pacific Ocean and Hawaii”, *Environmental Pollution*, 188 (2014) 45-49
- [3] Hossein Shirani IL Beibi. “Density functional theory study on the structural, reactivity, and electronic properties of all mono-, di-, tri-, tetra-, and penta-fluoroanilines as monomers for conducting polymers

A Density Functional Theory study on the oligomers of the 1-Fluoro-3-(2-Fluorovinyl) benzene as a nanopolymer

Hossein Shirani Il Beigi* and Reza Fatollahi Geshlag

Department of chemistry, Nazhand Higher Education Institute, Urmia, 5719883896, Iran

*Corresponding author. E-mail address: shiranihossein@gmail.com

Abstract: Electrical and structural properties of mono-, di-, tri- and tetra fluorostyrene have been studied using the density functional theory and B3LYP method with 6-311++G** basis set. Vibrational frequencies, IR, NMR spectra, electronic Energy, Dipole moment, energy electron, HOMO-LUMO gaps of these compounds have been calculated. The analysis of these data showed that the polymer molecules become mono-di-tri and tetrafluorostyrene electron energy is increased which demonstrates the greater stability of the molecule. The survey showed that by reducing the HLG gaps electron transfer is made easier. The examination of the results of the polymerization of the molecules was observed that the molecule (Z)-1-fluoro-3-(2-fluorovinyl) benzene is increased dipole moment that reflects its high solubility of polar molecules.

Keywords: B3LYP, Electron energy, Stability, HLG, Dipole moment

Introduction

Polymer properties are broadly divided into several classes based on the scale at which the property is defined as well as upon its physical basis [1]. Polymerization is the process of combining many small molecules known as monomers into a covalently bonded chain or network. During the polymerization process, some chemical groups may be lost from each monomer. The characterization of a polymer requires several parameters which need to be specified. This is because a polymer actually consists of a [statistical](#) distribution of chains of varying lengths, and each chain consists of monomer residues which affect its properties. NMR can be used to determine composition [2].

Method

B3LYP method with 6-311++G** basis set calculations by Gaussian 09 have been carried out successfully to study the structural, energetically properties. Values of dipole moment, energy electron, IR, NMR spectra, vibrational frequencies, HLG and have been calculated and analysed.

Results and Discussion

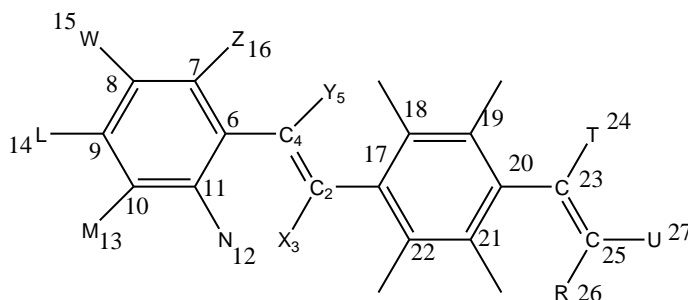


Fig 2: the shape of the molecule (Z)-1-fluoro-3-(2-fluorovinyl) benzene in 6-311++G** basis set calculation

Table 1: B3LYP/6-311++G** optimized values of bond lengths for (Z)-1-fluoro-3-(2-fluorovinyl) benzene.

6C-4C	4C-2C	2C-3X	2C-17C	17C-18C	17C-22C
1.46164	1.34506	1.36652	1.46307	1.40237	1.41019

The least length of the [4C-2C] in B3LYP/6-311++G** optimized structures of for (Z)-1-fluoro-3-(2-fluorovinyl) benzene.

Table 2: B3LYP/6-311++G** optimized values of angle for (Z)-1-fluoro-3-(2-fluorovinyl) benzene.

6C-4C-2C	6C-4C-5Y	4C-2C-3X	4C-2C-17C	3X-2C-17C	2C-17C-18C	2C-17C-22C
129.9	115.1	118.6	129.9	111.5	125.0	119.8

Table 3: B3LYP/6-311++G** optimized values of dihedral for (Z)-1-fluoro-3-(2-fluorovinyl) benzene.

6C-4C-2C-3X	6C-4C-2C-17C	5Y-4C-2C-17C	5Y-4C-2C-3X	4C-2C-17C-18C	4C-2C-17C-22C
0.0	-180.0	0.0	180.0	0.0	180.0

Table 4: B3LYP/6-311++G** optimized values of energies of mono-di-tri and tetrafluorostyrene

Molecule	HLG	E _{ele}	dipo
Monomer	5.107616	-318942.878307	2.1828
Dimer	3.773728	-637135.276304	2.9385
Trimer	3.256112	-955327.93296	4.7529
Tetramer	2.99472	-1273520.66636	6.8520

In the study of molecules optimized with 6-311++G** basis set, it is observed that the lowest HLG was related to the tetrafluorostyrene that has the highest electrical conductivity as well as the stability and solubility of the molecule tetramer shows. In the analysis of the energy electron, we can see in the table 4, the tetramer of molecule has the most of Eel value and it show that tetramer is more stable. Also in the analysis of the dipole moment, we can see the tetramer of molecule is more solubility.

Table 5: B3LYP/6-311++G** optimized values of energies all molecules

MOLECULE	Gibbs	H	S
Monomer	-318890.4	-318863.4	90.6
Dimer	-637029.5	-636988.9	136.2
Trimmer	-55169.4	-955114.7	183.4
Tetramer	-1273309.4	-1273240.6	230.7

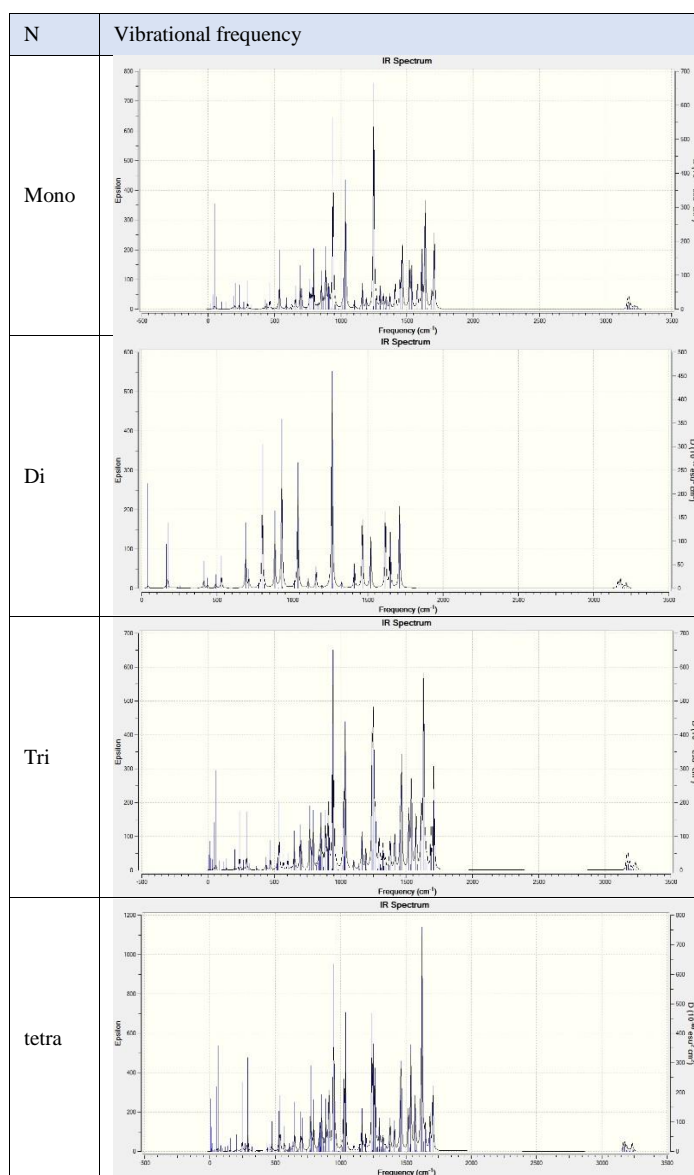
In The optimal molecular analysis of the entropy

(S), we can see the table 5, the monomer molecule has least of entropy, and in the analysis of enthalpy, we can see the, tetramer molecule has least enthalpy show that inner energy of tetramer molecule is low and The possibility of further reaction of molecule. In study of Gibbs free energy, we can see the tetramer molecule has the most Gibbs free energy value.

In the analysis vibrational frequency of the mono-di-tri and tetrafluorostyrene, It is observed that the tetramer in the spectral range of 1600 cm^{-1} have the highest peak

Conclusions

B3LYP method with 6-311++G** basis set calculations have been carried out successfully to study the structural energy, spectroscopic. Values of dipole moment, energy electron, IR frequency, NMR spectrum, vibrational frequencies, HLG. Values of vibrational frequencies, dipole moment and HLG have been calculated and analysed.



References

- [1] S.A. Baeurle "Multiscale modeling of polymer materials using field-theoretic methodologies: a survey about recent developments", *Journal of Mathematical Chemistry*, 46 (2) (2009) 363-426.
- [2] Alb, A. M.; Drenski, M. F.; Reed, W. F "Implications to Industry: Perspective. Automatic continuous online monitoring of polymerization reactions (ACOMP)", *Journal of Mathematical Chemistry*, 57 (3) (2008) 390-396.

Hydrogen solar fuel generation from photocatalytic decomposition of H₂S-containing media via nanostructured solid-solution semiconductor

M. Ghanimati^{a*}, Sh. Afshari^a, M. Lashgari^{a,b}

^aDepartment of Chemistry, Institute for Advanced Studies in Basic Sciences (IASBS), Zanjan, 45137-66731, Iran.

^bHydrogen and Fuel Cell Laboratory, Center for Research in Climate Change and Global Warming (CRCCGW), Zanjan 45137-66731, Iran.

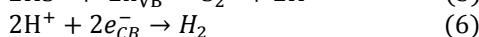
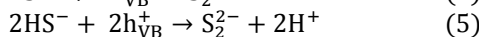
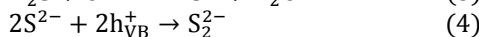
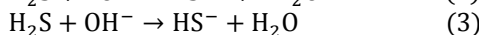
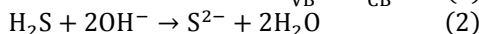
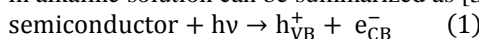
* m.ghanimaty@iasbs.ac.ir

Abstract: Hydrogen sulfide is a flammable, malodorous, highly toxic and corrosive compound which is produced in large quantities as a by-product in many industrial processes. However, it will be economically and environmentally advantageous if it is photodecomposed to generate hydrogen, which is a clean and renewable energy carrier. In this paper, a nanostructured solid-solution semiconductor material from the family of cadmium-zinc-sulfide was synthesized through a facile hydrothermal method and was applied as alloy photocatalyst to generate hydrogen fuel via a H₂S photodecomposition process. Morphological and optical properties of the sample have been characterized by XRD, FE-SEM, EDS and UV-vis DRS techniques. Solid-solution semiconductor exhibited a good photocatalytic performance.

Keywords: solar hydrogen generation; H₂S photodecomposition; solid-solution semiconductor; photocatalyst

Introduction

Hydrogen sulfide is a colourless, corrosive, flammable and greatly perilous gas with a “rotten egg” smell. Every year, millions of tons of H₂S are produced as a by-product in petroleum refineries and natural-gas extraction. Hence, decomposition of H₂S to H₂ over semiconductor photocatalysts has attracted attention because that could satisfy both energy and environment requirements [1-3]. In a photocatalytic H₂S decomposition reaction, photocatalysts play a crucial role. The photocatalytic decomposition of H₂S in alkaline solution can be summarized as [3]:



There, the photo-excited electrons can reduce the protons and the sulfide ion behaves as a hole scavenger.

Among diverse photocatalysts, just the sulfide type semiconductor materials can act stably in the hydrogen sulfide aqueous solution, while metallic or oxide type photocatalysts are sulfurized. Among the various metal sulfides, CdS and ZnS are the two finest semiconductors that have attracted extensive attention for H₂ production from photocatalytic decomposition of hydrogen sulfide [4]. However, their stability and photoactivity was observed to be very poor. To resolve these problems, forming solid solutions out of them is the most promising method [5]. Although the photocatalytic performance of Cd_{1-x}Zn_xS solid solution was higher than those of CdS and ZnS but its band gap was wider than that of CdS. For efficient photocatalytic H₂ generation, we need materials with

narrow band gap for the full utilization of the solar spectrum. Hence, metal ion doping is one of the solutions for reducing the band gap and enhancing the photocatalytic activities of solid solutions under visible light [6]. Several metal ion dopants in CdZnS have been reported to enhance the photocatalytic activity of CdZnS solid solution [7]. In our previous work, a novel photocatalyst Cd_{0.1}Zn_{0.87}Sn_{0.01}Ag_{0.02}S was synthesized and was used as alloy photocatalyst to generate hydrogen from water splitting [8]. Since photocatalytic hydrogen production with simultaneous photodecomposition of H₂S containing media is very more noteworthy, the Cd_{0.1}Zn_{0.87}Sn_{0.01}Ag_{0.02}S solid solution photocatalyst was synthesized according to our previous reports [8] and was used as alloy photocatalyst to generate hydrogen fuel from decomposition of hydrogen sulfide aqueous solution under visible light irradiation.

Materials and method

A solid solution sample was synthesized in a similar way to the previous literature [8]. In a typical synthesis for Cd_{0.1}Zn_{0.87}Sn_{0.01}Ag_{0.02}S, we prepared a 50-mL aqueous solution containing 0.04M Cd(NO₃)₂ (Merck; 98%, Darmstadt, Germany), 0.36M Zn(CH₃COO)₂ (Fluka; 98%, Gillingham, United Kingdom), 0.004M SnCl₄ (Merck; 98%), 0.008M AgNO₃ (Fluka; 98%), and 0.4M CH₃CSNH₂ (Merck; 99%), and agitated for 20 min at room temperature. The solution was heated in an oven at 433 K for 8 h and then cooled to room temperature naturally. The precipitates were washed with distilled water for several times and dried in vacuum at room temperature.

Powder X-ray diffraction pattern of the sample was recorded using a Philips X 'Pert Pro X-ray powder

diffractometer ($\lambda = 1.54\text{\AA}$; Cu K α beam). Field emission scanning electron microscopy (FE-SEM) images were taken by a ZEISS SIGMA VP. UV-vis absorption spectra were recorded on a Varian Cary 5 UV-visible-NIR spectrometer (BaSO₄ was used as a blank).

Photocatalytic hydrogen evolution was performed in home-made photoreactor, consisting of a 500-W power-tunable Xe lamp (Ushio xenon short arc lamp, Tokyo, Japan) and a double-walled cylindrical glassy vessel equipped with a temperature-controlling bath circulator (WCR-P6). In the typical experiment, 50 ml of 0.5 M aqueous NaOH solution in the reactor dispersed with 0.2 g of the photocatalyst powder, stirred and thermostated at 25°C was first purged with nitrogen for 1 h to eliminate the dissolved oxygen and then with bubbling H₂S for about 90 min until saturation of the alkali solution. Then aqueous dispersion in the reactor was irradiated with light from a 500 W xenon lamp. The volume of gas being evolved during the test was measured under atmospheric conditions at 298 K by leading the released gas into an inverted burette (± 0.1 cc) filled with water.

Results and Discussion

The XRD patterns of the solid solution and the standard diffraction patterns of cubic ZnS are depicted in Fig. 1. Sample showed diffraction pattern at 2θ angles of 28.8, 47.9 and 57.4 corresponding to the (111), (220), (311) planes of cubic zinc-blend structure [9]. Compared with the pure ZnS, XRD data shows that the peaks position of alloy photocatalyst shift toward larger values. The successive shift clearly indicates that solid solution was formed. No other peaks were detected, indicating the purity of the solid solution. No CdS, SnS₂ and Ag₂S derived peaks were observed, suggesting that the Cd, Sn and Ag dispersed well in the ZnS crystal [5]. The average crystal size of alloy semiconductor was determined by Scherrer's formula and was calculated as 4 nm [8].

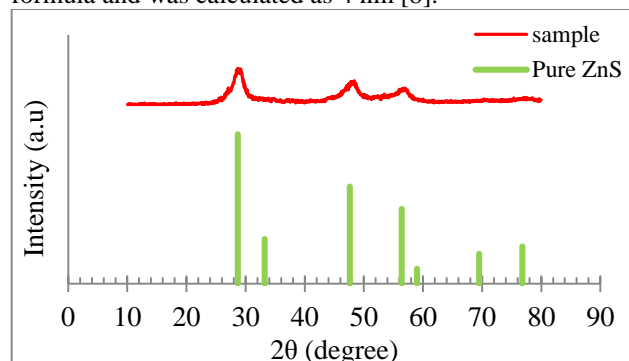


Fig.3: XRD pattern of the alloy photocatalyst synthesized in this work.

Figure 2 shows the optical absorbance spectrum of alloy semiconductor. The spectrum indicated that the

photocatalysts have good absorption in the region 300-700 nm. This means that photocatalysts can absorb visible light. The values of E_g were determined through Kubelka–Munk method [8]. The values of E_g was 2.64 eV for the photocatalyst.

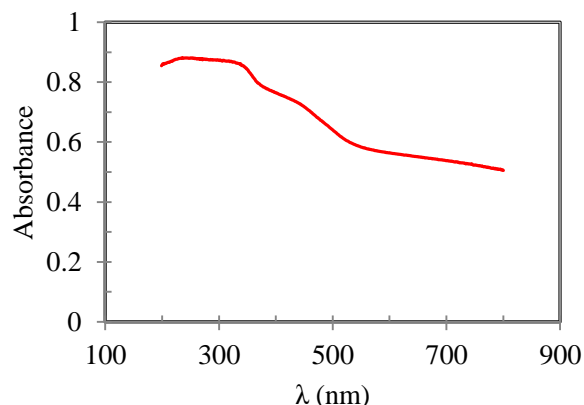


Fig.2: Diffuse reflectance UV-visible spectra of the photocatalyst.

The FESEM images of a solid solution photocatalyst at different magnification are presented in Figure 3. It can be observed that the photocatalyst consists of nanospheres, nanoplatelets, and dense microspheres (nanoparticles aggregated to form microspheres) in the range of 400-500 nm.

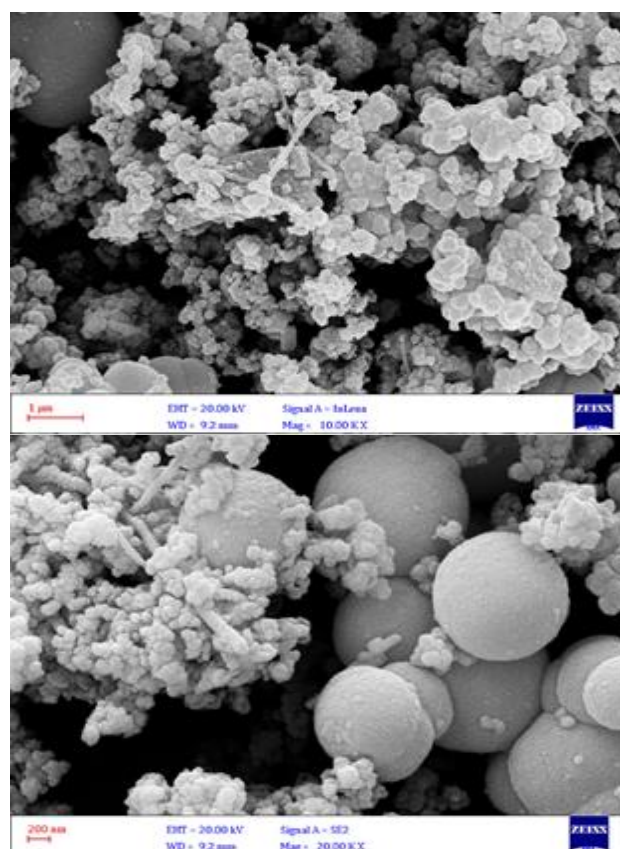


Fig.3: Field emission scanning electron micrograph (FE-SEM) of alloy semiconductor.

The energy dispersive x-ray spectroscopy analysis (Table1) revealed that the obtained solid solution are composed of Ag, Sn, Cd, Zn and S.

Table1: Energy dispersive X-ray spectroscopy (EDS/EDX) data (Wt. %).

Semiconductor	Cd	Zn	Sn	Ag	S
$Cd_{0.1}Zn_{0.87}Sn_{0.01}Ag_{0.02}S$	4.4	70	0.8	0.1	24.7

Hydrogen production rates from the photodecomposition of hydrogen sulfide solution are shown in Fig. 4. The figure indicates that the semiconductor synthesized here have an excellent photocatalytic performance with average hydrogen production rate of 15 ml/h.

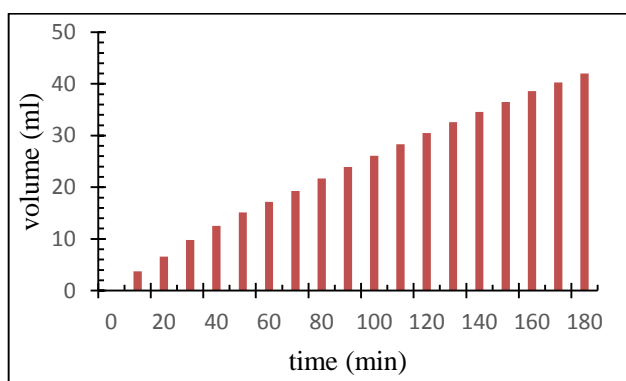


Fig.4: The volume of hydrogen gas being evolved over the semiconductor photocatalyst in alkaline solution.

Conclusions

Using a facile hydrothermal method, an efficient nanostructured semiconductor was synthesized and was applied as alloy photocatalyst to generate hydrogen fuel via a hydrogen sulfide photodecomposition process. The nanostructured solid-solution compound photocatalyst was confirmed by X-ray diffraction (XRD), field emission scanning electron microscopy (FE-SEM) and energy dispersive X-ray spectroscopy (EDX/EDS) analyses. The crystallite sizes of the solid solution samples are in a range of 3–4 nm. Solid-solution semiconductor exhibited a fairly good photocatalytic performance with average hydrogen production rate of 15 ml/h.

References

- [1] E. Subramanian, J. O. Baeg, S. M. Lee, S. J. Moon, K. J. Kong, "Nanospheres and nanorods structured Fe_2O_3 and $Fe_{2-x}Ga_xO_3$ photocatalysts for visible-light mediated ($\lambda \geq 420$ nm) H_2S decomposition and H_2 generation", International Journal of Hydrogen Energy, 34 (2009) 8485-8494.
- [2] V. Preethi, S. Kanmani, "Photocatalytic hydrogen production over $CuGa_{2-x}Fe_xO_4$ spinel", International Journal of Hydrogen Energy, 37 (2012) 18740-18746.
- [3] E. Subramanian, J. O. Baeg, S. M. Lee, S. J. Moon, K. Kong, "Dissociation of H_2S under visible light irradiation ($\lambda \geq 420$ nm) with $FeGaO_3$ photocatalysts for the production of hydrogen", International Journal of Hydrogen Energy, 33 (2008) 6586-6594.
- [4] R. Priya, S. Kanmani, "Solar photocatalytic generation of hydrogen from hydrogen sulphide using CdS-based photocatalyst", Current Science, 94 (2008) 102-104.
- [5] W. Zhang, Z. Zhong, Y. Wang, R. Xu, "Doped solid solution: $(Zn_{0.95}Cu_{0.05})_{1-x}Cd_xS$ nanocrystals with high activity for H_2 evolution from aqueous solutions under visible light", Journal of Physical Chemistry C, 112 (2008) 17635-17642.
- [6] J. N. Hart, M. Cutini, N. L. Allan, "Band gap modification of ZnO and ZnS through solid solution formation for applications in photocatalysis", Energy Procedia, 60 (2014) 32-36.
- [7] M. Kimi, L. Yuliati, M. Shamsuddin, "Photocatalytic hydrogen production under visible light over $Cd_{0.1}Sn_xZn_{0.9-2x}S$ solid solution photocatalysts", International Journal of Hydrogen Energy, 36 (2011) 9453-9461.
- [8] M. Lashgari, M. Ghanimati, "A highly efficient nanostructured quinary photocatalyst for hydrogen production", International Journal of Energy Research, 39 (2015) 516-523.
- [9] L. Wang, W. Wang, M. Shang, W. Yin, S. Sun, L. Zhang, "Enhanced photocatalytic hydrogen evolution under visible light over $Cd_{1-x}Zn_xS$ solid solution with cubic zinc blend phase", International Journal of Hydrogen Energy, 35 (2010) 19-25.

Liquid Phase Equilibria of the System (Water + Phosphoric acid + Amyl acetate) at T = 308.2 K

Behnaz Mohammadi-Khanghah^a, Ali Ghanadzadeh-Gilani^{a,*}, Maryam Nasouri-Gazani^a

^aDepartment of Chemistry, Faculty of science, University of Guilan, Rasht, Iran

*aggilani@gmail.com

Abstract: Experimental solubility and tie-line data for the ternary system of (water + phosphoric acid + amyl acetate) were measured at T = 308.2 K and ambient pressure. Data for the binodal curve were determined by cloud-point titration method. The concentration of each phase was determined by acidimetric titration, the Karl–Fischer technique, and refractive index measurements. A type-1 LLE phase diagram was obtained for this ternary system [1]. The experimental values were regressed and acceptably correlated using the UNIQUAC and NRTL models. The reliability of the experimental data was determined through the Othmer–Tobias plot. Distribution coefficients and separation factors were evaluated over the immiscibility region.

Keywords: “Solubility”, “Tie-line”, “Phosphoric acid”, “Amyl acetate”.

Introduction

Phosphoric acid (PA) is one of the most widely used inorganic acids in the chemical industry. Pure anhydrous PA is a white solid at room temperature and pressure. It has an important role in various industries such as chemical, agriculture, and medical industries. This acid is used as a reagent or chemical intermediate for production of detergents, agricultural feeds, activated carbon, waxes, polishes, soaps, and phosphate fertilizers [2]. This acid has been used as an electrolyte additive for fuel cells and batteries [3]. The pure PA is extensively used in food, beverage, and medicinal industries, where high purity raw materials are required. For example, it is added to cola soft drinks as acidulent, and it is used in dentistry as an etching solution.

In this work, the solubility and tie-line data for the ternary System consisting of water, PA and organic solvent at 308.2 K were determined. The selected organic solvent is amyl acetate.

Materials and method

In this work, analytical grade phosphoric acid containing

85% (by weight) was used. In order to obtain the solubility of the organic-rich side of the curve, anhydrous phosphoric acid (with more than 98% purity) was used.

amyl acetate (stated mass fraction purity > 0.99) was supplied from Merck. Deionized and distilled water was used throughout the experiments. All materials were used as received without any further purification.

Solubility for the system studied was determined by the cloud-point method [4]. The measurements were carried out in an equilibrium glass cell (50 mL) equipped with a magnetic stirrer and isothermal water jacket to hold the temperature of the mixture constant. Addition of the solvent into the cell was carried out using a Brand Transferpette micropipette with an accuracy of ± 0.001 mL. The titration endpoint was

determined visually by observing the transition from a homogeneous to a heterogeneous mixture. The visual measurements were repeated at least three times. The average of these

readings was taken for the component compositions. The equilibrium point was determined by preparing the ternary mixture of known compositions of water, PA, and amyl acetate in an equilibrium cell (250 mL). The mixtures were vigorously agitated by a magnetic stirrer for 5 h, and then left to settle for 6 h for phase separation. Preliminary tests showed that these times are adequate to achieve the phase equilibrium. The samples of acetate-rich were taken by a glass syringe from the upper layer and that of water-rich phase from a sampling tap at the bottom of the cell.

Results and Discussion

Experimental LLE values for the (water + PA + amyl acetate) ternary system were determined at 308.2 K and atmospheric pressure. The experimental values for the ternary system at this temperature are listed in Table 1.

Table 1: Experimental tie-line data in mass fraction for (water + phosphoric acid + amyl acetate) at T = 308.2 K and atmospheric pressure.

W ₁₁	W ₂₁	Organic phase	
		W ₁₃	W ₂₃
0.811	0.182	0.006	0.010
0.711	0.281	0.007	0.016
0.632	0.360	0.007	0.023
0.573	0.418	0.008	0.030
0.528	0.463	0.009	0.037
0.490	0.501	0.009	0.043

The triangular phase diagram for the studied ternary system at 308.2 K is plotted and shown in Fig. 1. As can be seen from the LLE phase diagram, the ternary system exhibit the type-1 behavior of LLE.

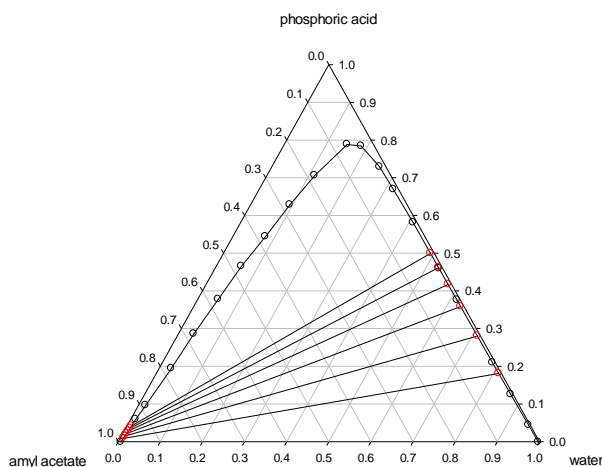


Figure 1: Ternary phase diagram [water (1) + PA (2) + amyl acetate (3)] at $T = 308.2$ K and $p = 101.3$ kPa; (○) experimental cloud points, (◌) experimental tie-lines.

Distribution coefficients (D) and separation factors (S) were determined from the tie-line data to establish the possibility of the use of this solvent for the separation of PA from water. The separation factor is defined as the ratio of distribution coefficients of the acid ($D_2 = w_{23}/w_{21}$) to water ($D_1 = w_{13}/w_{11}$), i.e. $S = D_2/D_1$; w_{13} , and w_{23} represent the mass fraction of water and PA in the organic phase, respectively; w_{11} , and w_{21} represent the mass fraction of water and PA in the aqueous phase, respectively[5]. The experimental distribution coefficients and separation factors for each temperature are given in Table 2.

Table 2: Separation factors (S) and distribution coefficients of PA (D_2) and water (D_1) at $T = 308.2$ K and $P = 101.3$ kPa

D_1	D_2	S
0.008	0.053	6.85
0.010	0.057	5.98
0.012	0.063	5.47
0.014	0.072	5.14
0.016	0.079	4.90
0.018	0.086	4.68

Separation factors, which found to be greater than 1 for this system. It means that extraction of the acid by amyl acetate is possible

The quality of experimentally measured tie lines for the system studied was determined by the Othmer–Tobias

equation [6]. $\{ \ln(1 - w_{33}/w_{33}) = A + B(1 - w_{11}/w_{11}) \}$ correlation equation [6]. A and B are the Othmer–Tobias equation parameters. These parameters are numerical constants which depend on type of system, degree of

immiscibility, and equilibrium compositions. The linearity of the Othmer–Tobias plot (shown Figure 2) indicates a high degree of quality of the measured LLE values.

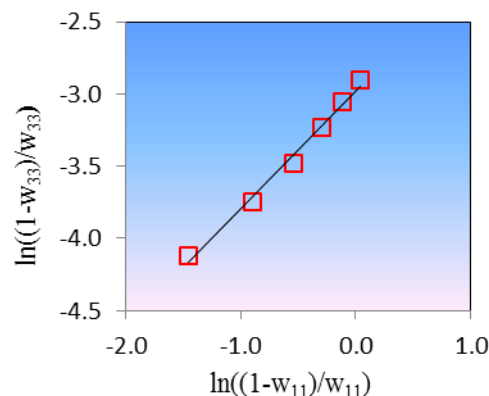


Figure 2: The Othmer–Tobias plot for the ternary system of (water + PA + amyl acetate) at 308.2 K.

Conclusion

Experimental LLE values for the (water + PA + amyl acetate) ternary system were determined at 308.2 K. Experimental results show that amyl acetate serve as appropriate solvent to extract phosphoric acid from the mixture of PA and water. The separation factors and distribution coefficients for the solvent used in this work were calculated. The obtained result confirms the ability of this esteric solvent for extraction of phosphoric acid from aqueous solutions.

References

- [1] H. Ghanadzadeh, A. Ghanadzadeh, Z. Aghajani, S. Abbasnejad, S. Shekarsaraee, (Liquid + liquid) equilibria in ternary aqueous mixtures of phosphoric acid with organic solvents at $T = 298.2$ K, *J. Chem. Thermodyn.* 42 (2010) 695–699.
- [2] H. Ghanadzadeh, A. Ghanadzadeh, Kh. Bahrpaima, Liquid phase equilibria of (water + phosphoric acid + 1-butanol or butyl acetate) ternary systems at $T = 308.2$ K, *J. Chem. Thermodyn.* 40 (2008) 1666–1670.
- [3] A.V. Slack, in: M. Dekker (Ed.), *Phosphoric Acid*, Marcel Dekker Publishers, New York, 1968.
- [4] V. Fischer, W. Borchard, M. Karas, *J. Phys. Chem.* 100 (1996) 15992–15999
- [5] H. Ghanadzadeh Gilani, A. Ghanadzadeh Gilani, S. Shekarsaraee, H. Usluc, *J. Chem. Thermodyn.* 53 (2012) 52–59.
- [6] D.F. Othmer, and P.E. Tobias. “Liquid-Liquid Extraction Data - The Line Correlation”. *Ind. Eng. Chem*, 34, June, (1942). 690–692.

Measurement of phase equilibrium data of ternary aqueous solution of phosphoric acid with ester using thermodynamic models at T=318.2 K

Maryam Nasouri-Gazani^a, Ali Ghanadzadeh-Gilani^{a,*}, Behnaz Mohammadi-Khanghah^a

^aDepartment of Chemistry, Faculty of science, University of Guilan, Rasht, Iran

*aggilani@gmail.com

Abstract: Solubility and liquid-liquid phase equilibrium data for ternary system of [water – phosphoric acid - ester (amyl acetate)] were measured and correlated at T = 318.2 K and atmospheric pressure. The solubility curve data were determined using the cloud-point titration method. A type-1 LLE phase diagram was obtained for this ternary system, where the two liquid pairs (acid + water) and (acid + amyl acetate) are totally miscible and one liquid pair (water + amyl acetate) is partially miscible. Tie lines experimental data with the use of acidimetric titration method, the Karl Fischer technique and measuring the refractive indexes were determined. The experimental distribution coefficients and separation factors were evaluated for this system. The thermodynamic models of UNIQUAC and NRTL were utilized to correlate the experimental tie line data. The reliability of the tie line data was determined by the Othmer-Tobias equation. Maximum and minimum amount of separation factor are 6.21 and 3.89 respectively. The results show separation factors confirm the ability of these solvent for extraction of phosphoric acid from water.

Keywords: Phosphoric acid; Ester; NRTL model; Extraction

Introduction

Phosphoric acid (PA) is an important non-toxic and tri-protic inorganic acid, which has various scientific and industrial applications [1]. PA which has a wide variety of uses could be produced by 3 main commercial processes: wet process, thermal process and dry kiln process. Wet process is nowadays the most common method but the produced acid is diluted with water and various impurities [2].

The necessity of very pure phosphoric acid has increased in recent years because of its increased use in foodstuffs, animal feed additives, and liquid fertilizers [3, 4]. Several solvents have been tested to extract the acid from dilute solutions. In this study, amyl acetate was selected as an organic solvent for the recovery of phosphoric acid from aqueous mixture. Due to the suitable molecular structure, high boiling point and very low solubility in water, amyl acetate has a number of benefits as a high-quality extracting for separating HPO from aqueous solution. This solvent has already been used to extract organic acids from water [5].

The present study obtains a practical LLE data for the extraction of HPO from aqueous solutions, for which no such data have never been published before. The solubility and tie-line data for the ternary systems consisting of water, PA and amyl acetate at 318.2 K were determined and compared. The quality of the experimental tie-line data was determined through the Othmer–Tobias and Hand correlation equations, distribution coefficients (D) and separation factors (S) were determined to establish the possibility of the use of solvent for the separation process. The experimental LLE data were correlated by employing two thermodynamic models, the universal quasi-chemical (UNIQUAC) method of Abrams and Prausnitz [6]

together with the non-random two-liquid (NRTL) model of Renon and Prausnitz [7]

Materials and method

Amyl acetate (stated mass fraction purity > 0.99) was supplied from Merck. The molecular structure of this ester is shown in Figure 1. Deionized water was further distilled before use. Analytical grade PA (H₃PO₄) containing 85% (by weight) was used. In order to obtain the solubility of the organic-rich side of the curves, anhydrous phosphoric acid (with 98% purity) was used. Aqueous solutions of phosphoric acid with a known concentration was prepared as feed.

The solubility data for the ternary mixture were determined by the cloud point method in an equilibrium glass cell. The end-points were determined by observing the transition from an appearance to disappearance mixtures. Type-1 LLE phase diagrams were obtained for all the ternary systems studied. The tie line data were determined using an experimental glass cell. The equilibrium data were determined by preparing the ternary mixtures of known compositions. After separation, samples of both phases were transparent and were carefully analyzed to determine their compositions.

Results and Discussion

The solubility data for the ternary mixture were determined by the cloud point method in an equilibrium glass cell. The end-points were determined by observing the transition from an appearance to disappearance mixtures. Type-1 LLE phase diagrams were obtained for all the ternary systems studied. The tie line data were determined using an experimental glass cell. The equilibrium data were determined by

preparing the ternary mixtures of known compositions. After separation, samples of both phases were transparent and were carefully analyzed to determine their compositions.

Table1: Experimental tie-line data in mass fraction for (water + phosphoric acid + amyl acetate) at T = 318.2 K and atmospheric pressure.

Aqueous phase		Organic phase	
w_{11}	w_{21}	w_{13}	w_{23}
0.809	0.183	0.008	0.011
0.709	0.282	0.009	0.018
0.627	0.364	0.009	0.026
0.571	0.419	0.010	0.033
0.524	0.466	0.011	0.039
0.488	0.502	0.011	0.045

The corresponding phase diagram for this ternary systems at T = 318.2 K are plotted in Figure 1. From the LLE phase diagram, the ternary system exhibits the type-1 behavior of LLE. As, the only one liquid pair (water + solvent) is partially miscible and the (PA + water) and (PA + solvent) are two liquid pairs that are completely miscible.

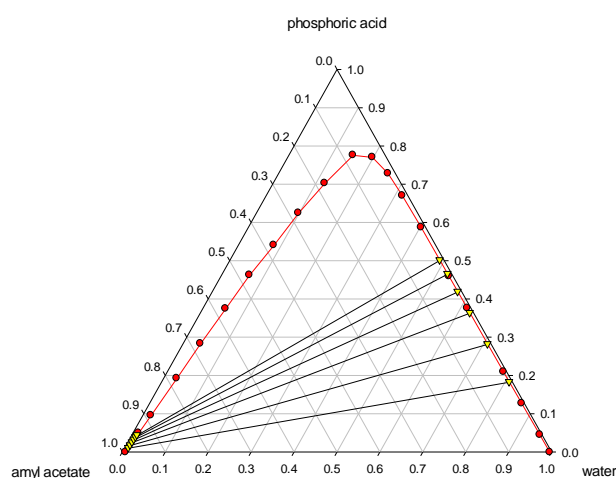


Fig.4: Phase diagram for the ternary system [water (1) + PA (2) + amyl acetate (3)] at T = 318.2 K and $p = 101.3$ KPa; (●) experimental cloud points, (▲) experimental tie-line.

The variation of experimental distribution coefficient separation factor of PA as a function of the mass fraction of the acid in aqueous phase for the ternary system at T = 318.2 K is shown in Figures 2. This factor is found to be greater than 1 ($S > 1$) for the studied system, which means that the acid must have different affinity in the two phases and extraction of PA by this solvent is possible.

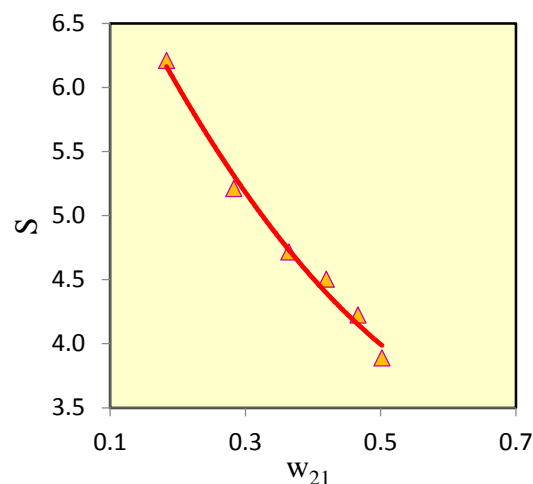


Fig. 2: Plot of the experimental separation factor (S) of phosphoric acid as a function of mass fraction of the acid in the aqueous phase (w_{21}) at T = 318.2K and atmospheric pressure.

Conclusions

Experimental and correlated tie-line data for aqueous mixtures of phosphoric acid with amyl acetate were obtained at T = 318.2 K. The ternary system exhibits type-1 behaviour of the LLE. Distribution coefficients and separation factors were measured to evaluate the extracting capability of the solvent. The separation factors and distribution coefficients for the solvents used in this work were calculated. Maximum and minimum amount of separation factor are 6.21 and 3.89 respectively. The obtained experimental separation factors confirm the ability of amyl acetate for the extraction of phosphoric acid from aqueous solutions and reduce pollution in the environment.

References

- [1] H. Ghanadzadeh Gilani, A. Ghanadzadeh Gilani, and S. Shekarsaraee, "Experimental study of phase equilibria in aqueous mixtures of phosphoric acid with isoamyl acetate and methyl isoamyl ketone at T = (298.2, 308.2, and 318.2) K", *Fluid Phase Equilibria*, 337 (2013) 32–38.
- [2] S. Shekarsaraee, "Phase Equilibria of the Ternary System Water + Phosphoric Acid + 1-Nonanol at Different Temperatures", *PHYSICAL CHEMISTRY RESEARCH*, 4 (2016) 507–518.
- [3] A. Gómez-Siurana, F. Ruiz-Bevia, J. Fernández-Sempere, and E. Torregrosa-Fuerte, "Purification of Phosphoric Acid by Extraction with 2-Ethyl-1-Hexanol: Equilibrium Data and Mass Transfer Coefficients", *Ind. Eng. Chem. Res.*, 40 (2001) 892–897.



- [4] A. Go´mez-Siurana, F. Ruiz-Bevia, J. Ferna´ndez-Sempere, and E. Torregrosa-Fuerte, “Purification of Phosphoric Acid by Extraction with 2-Ethyl-1-Hexanol: Equilibrium Data and Mass Transfer Coefficients”, *Ind. Eng. Chem. Res.*, 40 (2001) 892-897.
- [5] L. Wang, Y. Cheng and X. Li, “Liquid-Liquid Equilibria for the Acetic Acid + Water + Amyl Acetate and Acetic Acid + Water + 2-Methyl Ethyl Acetate Ternary Systems”, *J. Chem. Eng. Data*, 52 (2007) 2171–2173.
- [6] H. Renon, J. M. Prausnitz. “Local compositions in thermodynamic excess functions for liquid mixtures”, *AIChEJ*, 14 (1968) 135-144.
- [7] N. Peschke, S. I. Sandler. “Liquid-liquid equilibria of fuel oxygenate + water + hydrocarbon mixtures”, *J. Chem. Eng. Data*, 40 (1995) 315-320.

Thermodynamic properties and sPC-SAFT modeling of 2-ethoxyethanol, 2-propoxyethanol and 2-butoxyethanol from $T = (293.15-413.15)$ K and pressure up to 30 MPa

Sattar Mahmoudi Asl* Hosseinali Zarei

Department of Physical Chemistry, Faculty of Chemistry, Bu-Ali Sina University, Hamedan, Iran

* sattarmahmoudiasl@gmail.com

Abstract: New experimental $P\rho T$ data of three glycols ethers, namely, 2-ethoxyethanol, 2-propoxyethanol and 2-butoxyethanol were measured in a wide range of temperatures (293.15 to 413.15) K and pressures (0.1 to 30) MPa with a vibrating-tube densimeter. The experimental $P\rho T$ data were correlated with the modified Tait equation. The study is completed with modelling in terms of the simplified perturbed-chain statistical associating fluid theory (sPC-SAFT) equation of state. The pure compound parameters of the sPC-SAFT equation are generally determined by fitting the equation to experimental saturated vapour pressure and liquid density. In this work, new correlation by minimizing the total objective function of temperature, pressure and density simultaneously were developed to estimate the sPC-SAFT equation with two association scheme parameters of three glycols ethers with using $P\rho T$ data. The validity of the parameters and the employed association scheme were tested by prediction of derivative properties. All correlated/predicted results were compared with experimental literature data. The obtained results showed that the sPC-SAFT equation of state along with the proposed correlations, presents good results for modelling of these glycols ethers.

Keyword: 2-Alkoxyethanol; Density; High Pressure; sPC-SAFT;

Introduction:

The study of properties of pure glycol ethers is very important from both theoretical and industrial points of view. 2-alkoxyethanols are used as a solvent for many different purposes such as varnishes, dyes, and resins¹. The simplified PC-SAFT provides a way to predict thermodynamic properties of liquids. In the present investigation, we report new experimental data for the density of pure, 2-ethoxyethanol, 2-propoxyethanol and 2-butoxyethanol at $T = (293.15$ to $413.15)$ K and pressure $P = (0.1$ to $30)$ MPa. Densities of pure component were correlated with the modified Tait and sPC-SAFT equations.

Materials and method:

The following materials with mole fraction purity as stated were used: 2-ethoxyethanol (2EE, Merck, GC > 99 mole fraction), 2-propoxyethanol (2PE, Sigma-Aldrich, GC > 99.4 mole fraction), 2-butoxyethanol (2BE, Merck, GC > 99 mole fraction), Benzene (Merck, GC > 99.4 mole fraction), deionized distilled water. Densities of the pure solvents at atmospheric pressure were measured using an Anton Paar density and sound velocity analyzer (DSA 5000) provided with automatic viscosity correction. The high pressure density measurements were obtained using an Anton Paar (model DMA HP) vibrating densimeter connected to a model DMA 4500 master instrument. The DMA HP was calibrated using deionized distilled water and benzene. The overall uncertainty in the high pressure density measurements was estimated to be within ± 1 kg m⁻³.

Results and Discussion:

The density data used for the calibration were taken from values reported in the manual of DMA HP, literatures,

and NIST website. The reference data were used to correlate the density of solvents at the above-mentioned temperature and pressure ranges using the following equation²:

Table 1. sPC-SAFT parameter for pure components

component	m	$\sigma \times 10^{-10}$	u/k_B	κ^{AB}	ε^{AB}	%AAD ^a
	m	K	K	K	K	
2-EE (inter)	6.027	2.771	229.459	0.020	1200.65	0.17
2-EE (intra)	5.023	2.948	160.076	0.397	1558.27	0.21
2-PE (inter)	5.619	3.002	235.599	0.030	1220.65	0.16
2-PE (intra)	5.060	3.138	190.104	0.291	1256.13	0.24
2-BE (inter)	6.075	3.074	237.637	0.020	1200.65	0.10
2-BE (intra)	5.952	3.111	186.640	0.206	1557.16	0.16

^aAAD% percent average absolute deviation

$$\rho = \sum_{i,j,k} a_{ijk} \tau^i T^j P^k \quad (1)$$

where ρ is the reference density (kg.m⁻³), τ is the oscillation period (μ s), T is the temperature ($^{\circ}$ C), P is the pressure (bar)², and a_{ijk} are the fitting parameters, with $i = 0, 2, j = 0, 1, 2,$ and $k = 0, 1, 2$. In order to correlate correctly experimental values over entire temperature and pressure ranges, and consequently to get a correct evaluation of the derived properties, following modified Tait equation was used:

$$\rho(T, P) = \frac{A_0 + A_1 T + A_2 T^2 + A_3 T^3}{1 - C \ln \left(\frac{B_0 + B_1 T + P}{B_0 + B_1 T + 0.1 \text{ MPa}} \right)} \quad (2)$$

The maximum deviations between the correlated and experimental $P\rho T$ data were obtained 0.016%, 0.023% and 0.019%, for 2-ethoxyethanol, 2-propoxyethanol,

and 2-butoxyethanol, respectively. The plot of this study and literatures are shown in Fig1.

sPC-SAFT Modeling:

The Perturbed-Chain SAFT is one of the successful modifications of SAFT equation for the asymmetric and highly non-ideal systems. The PC-SAFT EoS has been developed by Gross and Sadowski³. Von Solms et al⁴ proposed a simplified version in terms of mixing rules of PC-SAFT equation. They realized that the segment diameters are usually similar for segments belonging to different molecules and subsequently modified certain mixing rules that led to a simpler expression for g_{hs} (radial distribution function) and the expression for a^{hs} (hard-sphere term of Helmholtz energy) reduces to the Carnahan–Starling equation. The equation of state in the expression of the residual molar Helmholtz energy is given as:

$$a = \frac{A}{NkT} = a^{ideal} + a^{hc} + a^{disp} + a^{assoc}, \quad (3)$$

According to the theory for intramolecular association, the contribution to the Helmholtz free energy from the association (inter- as well as intramolecular) in a pure component given :

$$a^{assoc} = \frac{A^{assoc}}{NkT} = \ln X_0 + \frac{1}{2} \sum_A (1 - X_A) - \frac{1}{2} \sum_A \sum_{A \neq B} X_{AB} \Delta_{AB}^{int,ra} \quad (4)$$

The 3 (2:1) scheme (one proton donor site and one proton acceptor site for the hydroxyl group and one proton acceptor site for the ether oxygen) is the simplest reasonable scheme for which intramolecular association is possible, and only this scheme is used in this work.

The sPC-SAFT equation of state contains five pure compound parameters: σ , the segment diameter, u the segment energy, m , the chain-length parameter, ε , the association energy and κ , the association volume. Two parameter sets have been estimated for each of the three glycol ethers: one set for regular sPC-SAFT plus intermolecular association and another for sPC-SAFT plus intramolecular association. The parameters were optimized obtained from experimental based on $P\rho T$ data liquid density of the components and using the following objective function:

$$OF = \sum_i^N \left| \frac{P_i^{exp} - P_i^{calc}}{P_i^{exp}} \right| + \sum_i^N \left| \frac{\rho_i^{exp} - \rho_i^{calc}}{\rho_i^{exp}} \right| + \sum_i^N \left| \frac{T_i^{exp} - T_i^{calc}}{T_i^{exp}} \right|, \quad (5)$$

The parameters for the three glycol ethers are reported in Table 1. In this table, Inter shows parameter sets for sPC-SAFT without intramolecular association (sPC-SAFT-inter), and intra indicates parameter sets for

sPC-SAFT plus intramolecular association (sPC-SAFT-intra). The new correlation were developed by minimizing the total objective function of pressure, density and temperature, pressure and density simultaneously were developed to estimate the sPC-SAFT equation parameters with two association scheme parameters of three glycols ethers including, 2-ethoxyethanol, 2-propoxyethanol and 2-butoxyethanol with using $P\rho T$ data and with a fitting %AAD of 0.17 on average. The sPC-SAFT equation of state was used to predict derivative properties such as the isobaric heat capacities (C_p), isobaric thermal expansion coefficients (α_p), the isothermal compressibility (κ_T) and speed of sound (u). The plot of this study for 2-ethoxyethanol and literatures are shown in Fig 2.

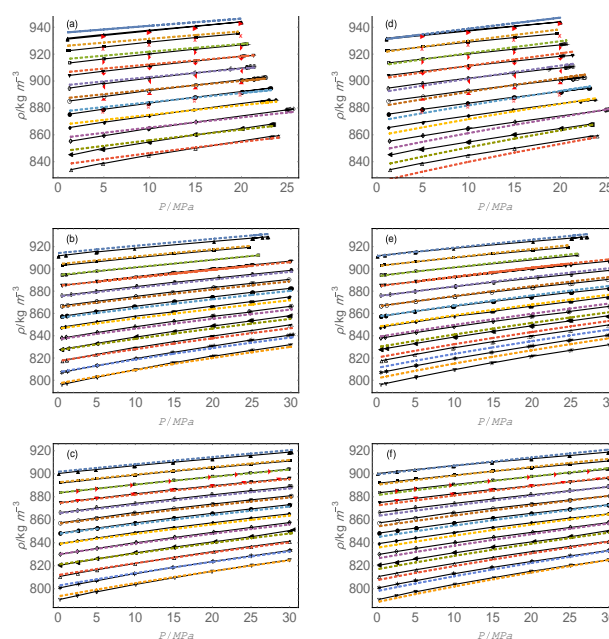


Fig.5: Plots of experimental $P\rho T$ data against pressure of pure solvents with two association scheme, intermolecular association(a,b,c)and intramolecular association(d,e,f),2-ethoxyethanol(a,d),2-propoxyethanol(b,e),2-butoxyethanol (c,f)at temperatures 293.15 K (\blacktriangle), 303.15 K (\blacksquare), 313.15 K(\square), 323.15 K(\blacktriangledown), 333.15 K (\diamond), 343.15 K (\circ), 353.15 K (\bullet), 363.15 K (\blacklozenge), 373.15 K (\diamond), 383.15 K (\blacktriangleleft), 393.15 K (Δ),403.15 K (\star), and 413.15 K (∇),modified Tait correlations were presented with solid lines and sPC-SAFT correlations were presented with dash lines and literature data at temperatures 293.15 K (\blacktriangleright),303.15 K (\times), 313.15 K(\blacktriangleright), 323.15 K(\blacktriangleright), 333.15 K (\blacktriangleright), 343.15 K(\blacktriangleright), and 353.15 K (\blacktriangleright).

Conclusions:

The density of the 2-ethoxyethanol, 2-propoxyethanol and 2-butoxyethanol were measured at $T = (293.15$ to $413.15)$ K and pressure $P = (0.1$ to $30)$ MPa. The densities of pure solvents were correlated using the modified Tait equation. The maximum deviations

between the correlated and experimental $P\rho T$ data were obtained 0.016%, 0.023% and 0.019%, for 2-ethoxyethanol, 2-propoxyethanol, and 2-butoxyethanol, respectively. The simplified perturbed-chain statistical associating fluid theory (sPC-SAFT) with inter and intramolecular association parameters were obtained for 2-ethoxyethanol, 2-propoxyethanol, and 2-butoxyethanol through the experimental $P\rho T$ data. Finally, the EoS was used to predict derivative properties such as isobaric heat capacities, isobaric thermal expansion coefficients, the isothermal compressibility and speed of sound. The obtained results show that the intermolecular association method for 2-ethoxyethanol, 2-propoxyethanol and butoxyethanol better than intramolecular association prediction. The results obtained for the pure solvents were in good agreement with the experimental data. The observed deviation is Probably due to the approximation type used in the site assignment.

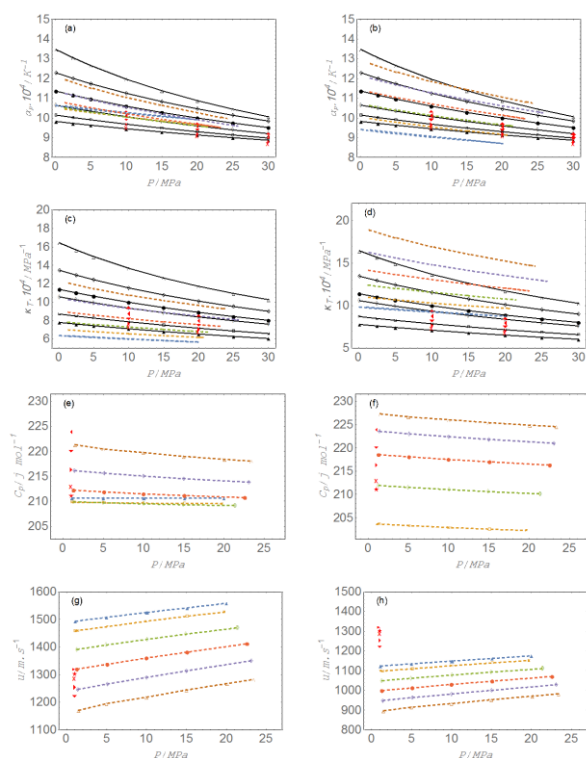


Fig 2. Experimental thermodynamic properties, 2-ethoxyethanol with two association scheme, intermolecular association (a,b,c) and intramolecular association (d,e,f) such as isobaric thermal expansivity (a,b), isothermal compressibility (c,d), isobaric heat capacities (e,f), speed of sound (g,h), at 293.15 K (\blacktriangle), 313.15 K (\square), 333.15 K (\diamond), 353.15 K (\bullet), 373.15 K (\diamond), and 393.15 K (Δ), and literature data at temperatures, 293.15 K (\blacktriangleright), 298.15 K ($*$), 303.15 K (\times), 313.15 K (\blacktriangleright), 323.15 K (\blacktriangledown), 333.15 K (\blacktriangleleft), 343.15 K (\blacktriangle), and 353.15 K (\blacktriangleright).

References

- [1] I. Mozo, I. García de la Fuente, J. González, J. Cobos, N. Riesco, Thermodynamics of mixtures containing alkoxyethanols. Part XXVI. Densities, excess molar volumes, speeds of sound at (293.15, 298.15, and 303.15) K, and isentropic or isothermal compressibilities at 298.15 K for 2-methoxyethanol+ alkoxyethanol or 2-propoxyethanol+ dibutylether systems, *Journal of Chemical & Engineering Data*, 53, (2008), 1404-1410.
- [2] H. Zarei, V. Keley, $P\rho T$ measurement and PC-SAFT modeling of N, N-dimethyl formamide, N-methyl formamide, N, N-dimethyl acetamide, and ethylenediamine from $T=(293.15-423.15)$ K and pressures up to 35 MPa, *Fluid Phase Equilibri*, 427, (2016), 583-593.
- [3] J. Gross, G. Sadowski, Perturbed-chain SAFT: An equation of state based on a perturbation theory for chain molecules, *Industrial & engineering chemistry research*, 40, (2001), 1244-1260.
- [4] N. von Solms, M. Michelsen, G. Kontogeorgis Computational and physical performance of a modified PC-SAFT equation of state for highly asymmetric and associating mixtures, *Industrial & engineering chemistry research*. 42, (2003), 1098-1105.

Production and Identification of V₂O₅ Nanoparticles Using Hydrothermal Synthesis Method

Sara Masoudi Nejad*, Vahid Mahdavi

Department of chemistry, Arak University, Arak, 3815688349, Iran

*masoudi.sara@yahoo.com

Abstract: In this paper, the synthesis of vanadium oxide by hydrothermal method and in the presence of Template molecules, which are different carboxylic acids (malonic acid, succinic acid, adipic acid and glutaric acid) of chain length, have been reported. The effect of the type of carboxylic acid on the structure and morphology of the catalysts were characterized by X-ray diffraction (XRD), scanning electron microscope (SEM) and FT-IR analysis. The results revealed that the morphologies of the vanadium pentoxide Nano crystals could be controlled by template molecules. This facile method to fabricate V₂O₅ Nano particle with well-defined morphologies would be of great significance to design other complicated micro-architectures with advanced functions.

Keywords: Ammonium metavanadate; Hydrothermal; Carboxylic acid

Introduction

Vanadium oxide (V₂O₅) has attracted much interest [1] owing to its excellent properties for various important applications, such as in lithium batteries [2], actuators [3], sensors [4] and catalysis [5]. Compared to bulk V₂O₅, vanadium oxides with Nano and micro-structures have significantly improved the performances in devices for energy storage and sensing [6]. Vanadium oxides were a good example to be studied, because extremely rich chemistry of vanadium oxides and vanadium oxide based catalysts results from a number of different interrelated electronic and structural factors. These compounds have partially filled d-orbitals which are responsible for a wide variety of electronic, magnetic and catalytic properties. The phase diagram shows that vanadium atoms exist in different formal oxidation states, which vary from two to five. The easy conversion between oxides of different stoichiometry and formation of oxygen vacancies enables the oxide to function as catalyst in selective oxidation [7]. From the many different compositions of vanadium oxide, V₂O₅ is the most widely studied vanadium oxide, especially because of its unique layered structure, which also makes it a very good intercalation material [8-10]. It is well known that many nanomaterial properties depend on their size and shape Control of the synthesis is generally a prerequisite for fabricating the desired size and morphology of a nanomaterial. Various chemical methods have been adopted for the preparation of metal oxide nanoparticles including gas-phase methods, sol-gel methods, evaporative decomposition of solutions, and wet chemical synthesis [11]. Herein, we developed a simple way to fabricate V₂O₅ Nano

particle. The synthesis was performed in water solvent using ammonium met vanadate and different carboxylic acid as reactants.

Materials and method

2.1. Preparation of materials

All chemicals are commercially available and were used as received. The synthesis was performed via a hydrothermal method in water solvent. In a typical procedure, 0.02 mol oxalic acid was dissolved in the 30 ml DW water solvent and then 0.015 mol ammonium metavanadate (NH₄VO₃) was added into the solution under stirring for 2 h at room temperature. After that the solution was transferred to a 50 ml Teflonlined stainless autoclave, sealed, kept at 180 °C for 3 days and cooled to room temperature. The black product was filtered, washed with deionized water and absolute ethanol, and dried at 60 °C for 12 h. The dried product was calcined at 500 °C for 2 h and orange Sediment is obtained. By replacing different acids such malonic acid , succinic acid, adipic acid and glutaric acid , which differ over the carbon chain, instead of oxalic acid (table1), the synthesis of vanadium oxide nanoparticles has also been addressed by changing the acid-type parameter.

2.2. Characterizations

The X-ray diffraction device (Diffract meter Philips) of the PW1800 model, with the use of K α Cu and nickel filters, has been used to determine the phases in the catalyst. The SEM machine is the electronic microscope model (Philips XL30) to determine the morphology of the catalyst, to determine the particle shape and particle size of the catalyst. Catalysts from



the Galaxy FT-IR5000 are taken in the form of a KBr infrared spectrum tablet.

Results and Discussion

A sample of vanadium catalyst with oxalic acid prepared in the XRD spectrum lab is compared and compared to Fig.1 with the XRD catalyst spectrum reported in References. As can be seen, these two spectra are in perfect agreement. All catalysts were taken before and after calcination the FT-IR infrared spectrum. The observed peaks at 6110 cm^{-1} and $10893/10\text{ cm}^{-1}$ and $969/40\text{ cm}^{-1}$ and 1309 cm^{-1} and $3196/25\text{ cm}^{-1}$, which belong to the organic groups, were removed after calcination. Fig.2 show the FT-IR spectrum of vanadium Nano oxide catalysts is the IR spectrum of V_2O_5 with different template, exhibiting a series of bands at $1016, 844, 617$ and 523 cm^{-1} . The new band at $835/23\text{ cm}^{-1}$ for oxalic acid, $833/03\text{ cm}^{-1}$ for malonic acid, $806/03\text{ cm}^{-1}$ for succinic acid, $817/87\text{ cm}^{-1}$ for glutaric acid and $814/01\text{ cm}^{-1}$ for adipic acid template assigned to V-O-V deformation modes, which was shifted toward higher wavenumbers than that of the bulk V_2O_5 [12]. To determine the morphology, apparent shape and approximate size of particle size of vanadium nanoparticle catalysts, we used SEM images using electron microscopy. Fig.3 shows the results of this analysis. As evidenced by SEM images, the structure of the morphology of the V_2O_5 has changed completely.

Table1: Type of carboxylic acid.

Common name	IUPAC name	Chemical formula	Structural formula
Oxalic acid	ethanedioic acid	HOOC-COOH	
Malonic acid	propanedioic acid	$\text{HOOC-(CH}_2\text{)-COOH}$	
Succinic acid	butanedioic acid	$\text{HOOC-(CH}_2\text{)}_2\text{-COOH}$	
Glutaric acid	pentanedioic acid	$\text{HOOC-(CH}_2\text{)}_3\text{-COOH}$	
Adipic acid	hexanedioic acid	$\text{HOOC-(CH}_2\text{)}_4\text{-COOH}$	

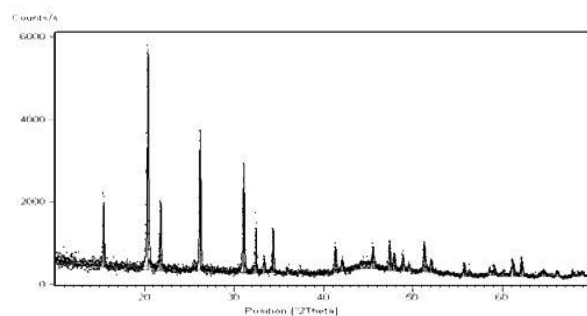


Fig.1: The XRD pattern for V_2O_5 with oxalic acid template.

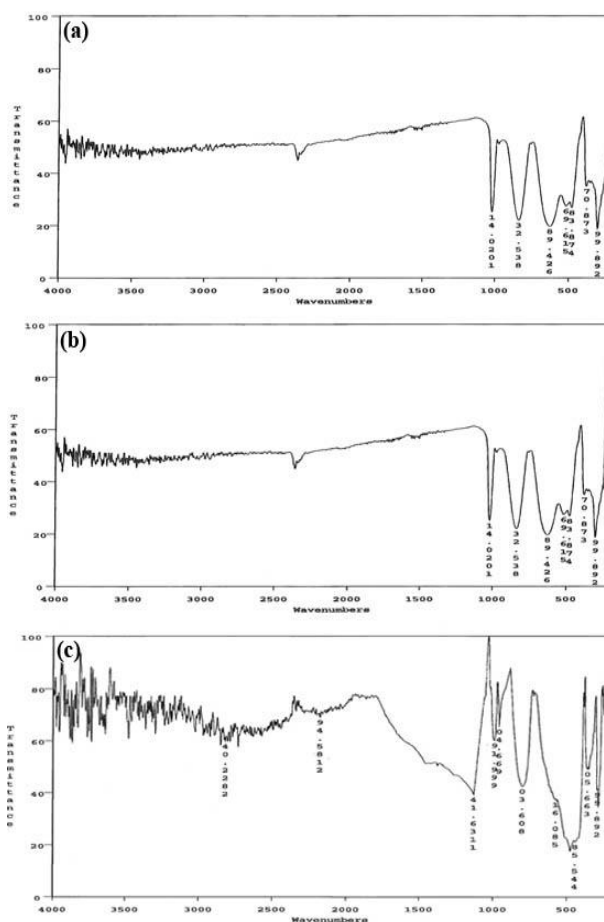


Fig.2: FT-IR spectrum of V_2O_5 with (a) oxalic acid, (b) malonic acid, (c) succinic acid, (d) glutaric acid and (e) adipic acid templates.

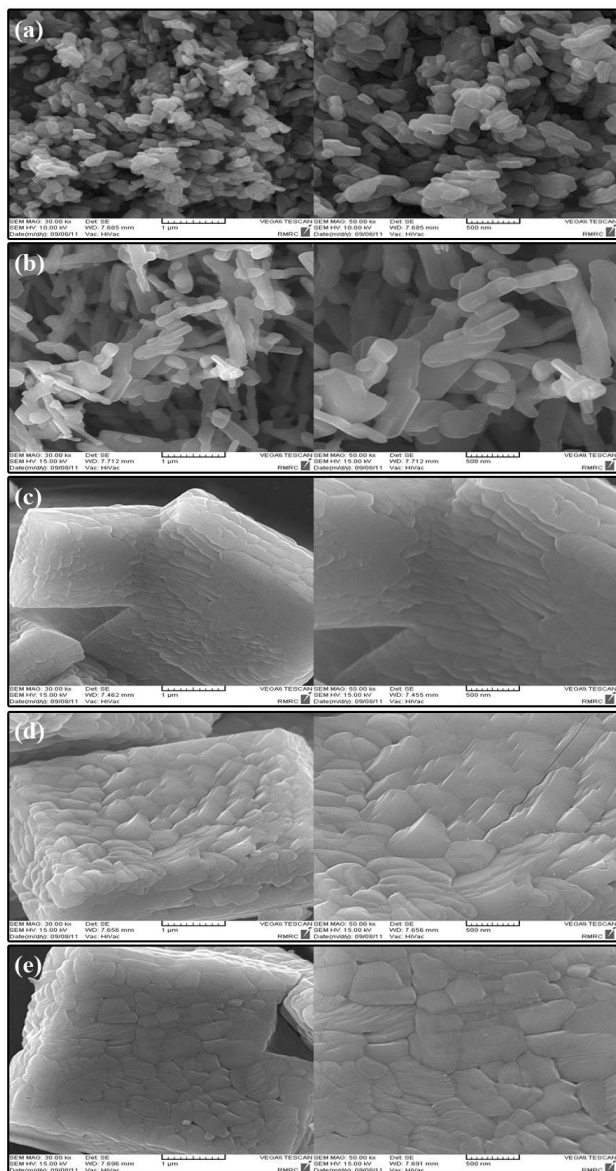


Fig.3: SEM images of V_2O_5 with (a) oxalic acid, (b) malonic acid, (c) succinic acid, (d) glutaric acid and (e) adipic acid templates.

Conclusions

It may be found that the types of carboxylic acid an effect on the morphologies and crystalline structures of the precursors. It could be predicted that precursors with various morphologies would appear by replacing the carboxylic acid mentioned above with other acids. This facile method to fabricate V_2O_5 Nano particle with well-defined morphologies would be of great significance to design other complicated micro-architectures with advanced functions.

References

- [1] T. Chirayil, P.Y. Zavalij, M.S. Whittingham, "Hydrothermal Synthesis of Vanadium Oxides" *Chem. Mater.* 10 (1998) 2629.
- [2] M.S. Whittingham, "Lithium Batteries and Cathode" *Materials Chem. Rev.* 104 (2004) 4271.
- [3] G. Gu, M. Schmid, "V₂O₅ nanofibre sheet actuators" P.W. Chiu, A. Minett, J. Fraysse, G.T. Kim, S. Roth, M. Kozlov, E. Unoz, R.H. Baughman, *Nat. Mater.* 2 (2003) 316.
- [4] J.F. Liu, X. Wang, Q. Peng, Y.D. Li, "Hydrothermal Synthesis and Thermoelectric Transport Properties of Impurity-Free Antimony Telluride Hexagonal Nanoplates" *Adv. Mater.* 17 (2005) 764.
- [5] I.E. Wachs, Y. Chen, J.M. Jehng, L.E. Briand, T. Tanaka, *Catal. Today* 78 (2003) 13.
- [6] Y. Wang, G.Z. Cao, "Synthesis and Enhanced Intercalation Properties of Nanostructured Vanadium Oxides" *Chem. Mater.* 18 (2006) 2787.
- [7] J. Haber, "Fifty years of my romance with vanadium oxide catalysts" *Catalysis Today* 142 (2009) 100–113.
- [8] F. Amano, T. Ito, S. Takenaka, T. Tanaka, "Study of the Reaction Mechanism of Selective Photooxidation of Cyclohexane over V_2O_5/Al_2O_3 " *Phys. Chem. B* 2005, 109, 10973.
- [9] F. Amano, T. Tanaka, T. Funabiki, "Membrane Fusion of Giant Unilamellar Vesicles of Neutral Phospholipid Membranes Induced by La^{3+} " *Langmuir* 2004, 20, 4236.
- [10] B. Li, Y. Xu, G. Rong, M. Jing, Y. Xie, "Vanadium pentoxide nanobelts and nanorolls: from controllable synthesis to investigation of their electrochemical properties and photocatalytic activities" *Nanotechnology* 2006, 17, 2560.
- [11] N. Asim, S. Radiman, M. A. Yarmo, M.S. B. Golriz, "Vanadium pentoxide: Synthesis and characterization of nanorod and nanoparticle V_2O_5 using CTAB micelle solution" *Microporous and Mesoporous Materials* 120 (2009) 397–401.
- [12] H.L. Fei, M. Liu, H.J. Zhou, P.C. Sun, D.T. Ding, T.H. Chen, "Synthesis of V_2O_5 micro-architectures via in situ generation of single-crystalline nanoparticles", *Solid State Sciences* 11 (2009) 102–107.

Alkenes oxidation with hydrogen peroxide by Silica porous and Ultralight with covered metal oxide using Phase-boundary Catalysis method

Shakiba Samady, Hadi Shafiei*, Davood Soudbar

Department of chemistry, Arak Branch, Islamic Azad University, Arak, Iran

*Hshafie2005@yahoo.com

Abstract: The catalytic oxidation of alkenes is an important reactions in the chemical industry and the efficient route for the chemicals and pharmaceuticals synthesis. The process of oxidation is formed in reflux system using H₂O₂ and alkene in the presence of Phase Boundry Catayst (PBC). H₂O₂ and solid catalyst in this process are positive steps towards green chemistry. Herein is reported a highly efficient green process for the oxidation of 1-hexene using H₂O₂ oxidant and modified silver on the SiO₂ support porous catalysts at 65°C. The method enjoys >90% conversion. The catalysts are easily recovered by filtration and are reusable several times and H₂O₂ is cheap, environmentally clean and easy to handle, so these processes have great value nowadays.

Keywords: Oxidation; Alkenes; hydrogen peroxide; Silica porous; Phase-boundary Catalysis

Introduction

Catalysts play a major role in establishing the economic strength of the chemical industry in the first half of the 20th century [1]; Also catalytic oxidation of alkenes is very important in the chemical industry and very important intermediates in the synthesis of many fine chemicals and pharmaceuticals [2]. As we approach the first half the 21st century increasingly demanding environmental legislation, public and corporate pressure and the resulting drive towards clean technology in the industry will provide new opportunities for catalysis and catalytic processes. Some of the major goals of Green Chemistry' are to utilize the environmental friendly substrate, to increase processes selectivity, to maximize the use starting materials, to replace stoichiometric reagents with catalysts and facilitate easy separation of the final reaction mixture [3]. One route to advancing this goal is catalytic system namely phase boundary catalysis (PBC) in order to utilize hydrogen peroxide (H₂O₂) as promising 'Green Chemistry'. Utilization of H₂O₂ as an oxidant for organic substrates; it gives only water as a product in oxidation reactions. Hadi Noor and his colleagues from Ibn Sina Institute of Malaysia university investigated the PBC catalyst [3]. However, H₂O₂ is generally supplied as aqueous solution and, when a substrate to be oxidized is insoluble in water, it is necessary to add co-solvent to obtain reaction mixture [3]. a new integrated chemical PBC system that aqueous H₂O₂ in the oxidation reaction without any co-solvent has been proposed [4]; Furthermore a large number of catalytic oxidation processes are known, but still the chlorohydrin process and catalytic processes based on organic peroxides and organic peracids are used extensively [5]. These processes are unfavourable both from an economic and environmental point of view, being costly and producing large amounts of waste. In contrast to such

processes, catalytic oxidation with hydrogen peroxide (H₂O₂) oxidant is very rewarding because: (i) it generates only water as a by-product, (ii) it has a high content of active oxygen species, and (iii) it is rather compared to organic peroxides and peracids [6]. effective catalysts for the oxidation of alkenes using H₂O₂ at ambient conditions are still being sought.

Tebandeke and co-workers reported that modified silver polyoxometalate catalysts are highly efficient for the oxidation of alkenes using H₂O₂ oxidant. In this work, a catalytic system comprised of silver and polyoxometalates after undergoing heat treatment is employed in the oxidation process [7].

Here in we reported that Alkene oxidation in the presence of H₂O₂ and silver on the SiO₂ support well done and it is very cheap, rewarding and eco-friendly.

Materials and Methods

Alkene were received from Arak Petrochemical company. Solvents and commercially available reagents were used as received from Merck and used. The FTIR spectra catalysts were recorded on a Shimadzu 470 using KBr discs. The elemental composition of the samples was determined using Gas chromatography Shimadzu 14A.

The analytical conditions for GC includes the:

Column temperature: 100°C

Injection temperature: 150°C

Detector temperature: 180°C

0.8 Carrier gas pressure: 0/8 atm

Air-to-hydrogen ratio: 0/5 to 0/55

Injection volume: 0.6 μlit

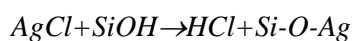
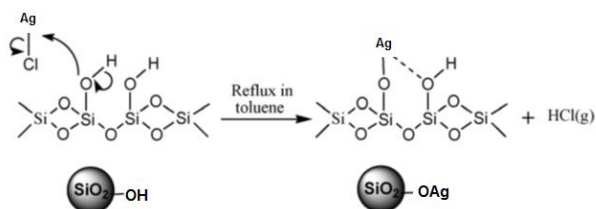
Sensitivity of the detectors: 10⁴



Figure 1: SiO₂ Support ultralight with high porosity

For PBC we prepared solid support (SiOH) with high porosity, ultralight and metal (Ag) that pinned on support. The SiOH was washed with HCl 1M, followed by deionized water, H₂O₂ 30%, and then again deionized water. After being washed, the SiOH was dried overnight at 373 K in vacuum to give preconditioned SiOH.

SiOH (10g) was first refluxed in toluene for 2 h. Then anhydrous AgCl (0.2g) was added to the stirring mixture. This mixture was allowed to react for 1 day under refluxing condition, during which the color of the solution changed into yellow. Then the mixture was filtered in a drybox, washed three times with absolute ethanol and dried at 373 K to give product.



We have investigated the presence of acid with litmus paper.

The catalyst oxidation reaction done under atmospheric pressure involved refluxing a mixture of Si-O-Ag (5g) and 1-hexene at our disposal as organic substance and H₂O₂ 30% as aqueous oxidant and acetonitrile as auxiliary solvent at 65°C during the 24 hours. The used catalyst was recovered by filtration and washing with acetone.

Results and Discussion

The FTIR spectrum of SiO₂ and Si-o-Ag were recorded in the range 400-4000 cm⁻¹, using FTIR spectrometer, is given in figure 2. From the FTIR spectrum, various functional groups and metal-oxide

(MO) bond present in the compound were analyzed. In the FTIR spectrum, a significant band at ~ 1100 cm⁻¹ is assigned to the characteristic stretching mode of Si-o-Ag bond before and after reflux.

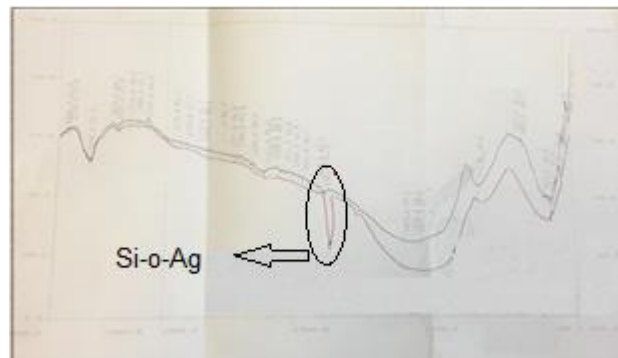
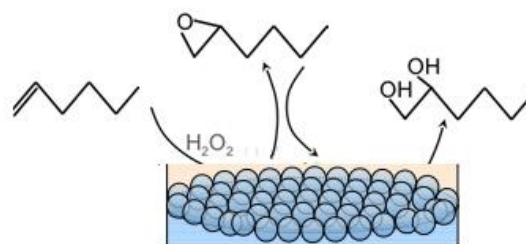


Figure 2. An overlay of the FTIR spectra of SiOH, Si-O-Ag

Initially the oxidation of 1-hexene with 30% aqueous hydrogen peroxide with Si-O-Ag catalyst was investigated. Substrates 1-hexene and H₂O₂ could be oxidized and produce the new production that is alcohol.



primary alkene (before oxidation) have specific spectrums in GC but when reaction finished, we found that GC shows additional spectrum that indicate new product.

Table 1. Conversion and the oxidation of alkene using H₂O₂ 30% with catalyst at 65°C

Primary substance	Time (h)	Conversion	Product
	24	%92	

In this present work, the inclusion of silver onto a SiOH improved the catalytic activity of the system in



terms of conversion . However, the nature of active silver species in the catalyst is not yet clear. The observed catalytic activity could be attributed to silver or a combination of Si-O-Ag. Further studies are ongoing to shed some light on the mechanism and the role of silver in the oxidation process.

Conclusions

We have successfully prepared Si-O-Ag catalysts as Phase Boundry Catalysts. These catalysts are efficient in the oxidation of a alkene with H₂O₂ oxidant producing the corresponding oxides in excellent yields.

The support have three properties simultaneously:

- 1) High ability to functionalized.
- 2) Penetration capability of solvent which causes the availability of catalytic active centers.
- 3) Comfortable and complete separation of products, by simple smoothing or centrifugation.

The catalyst system easily recovered by filtration and are reusable several times and it is cheap and stable.

This protocol has advantages of high yield, mild condition, no environmental pollution, efficient, recyclable and reusable and simple work-up procedure. Also Utilization of H₂O₂ as an oxidant for organic substrate gives only water as a product in oxidation reactions.its mean we design green system for oxidation.

Acknowledgment

The authors gratefully appreciate department of chemistry and especially research department of Islamic Azad University of Arak for their kind supports.

References

- [1] G. Ertl , H. Knözinger, J. Weitkamp , “Handbook of Heterogeneous Catalysis”, 1997, Wiley–VCH, Weinheim.
- [2] M. Hudlucky, “Oxidations in Organic Chemistry”, 1990, Washington DC:Am. Chem Soc, p.1, Washington DC.
- [3] N. Mohd Ran, Sh. Chandren, H Nur “Phase-Boundry Catalyst for oxidation reaction”, 2000, University Technology Malaysia
- [4] H. Nur, S.Ikeda and B. Ohtani, “Phase-boundary catalysis: a new approach in alkene epoxidation with hydrogen peroxide by zeolite loaded with alkylsilane-covered titanium oxide”, *Chemicals Communications*, 22 (2000) 2235-2235.
- [5] K.Jørgensen, “Transition-metal-catalyzed epoxidations”, *Chem.Rev.* 89 (1989) 431-458.

[6] C W.Jones , “Applications of hydrogen peroxide and derivatives”, 1999, Royal Society of Chemistry , p.80,London,United Kingdom

[7] E. Tebandeke, H. Ssekaalo and O. Wendt “Highly efficient epoxidation of olefins with hydrogen peroxide oxidant using modified silver polyoxometalate catalysts” *African Journal of Pure and Applied Chemistry* ,7 (2013) 50-55.



بیستمین کنفرانس شیمی فیزیک ایران
دانشکده علوم پایه - دانشگاه اراک
۳۱-۲۹ مرداد ۱۳۹۶



20th Iranian Physical Chemistry Conference

نانو شیمی فیزیک

Nano physical chemistry

Molecular dynamics study of water oil separation by polymer surface

Masumeh Foroutan, Hojat Zahedi*, Hamideh Babazadeh

^a Department of Physical Chemistry, School of Chemistry, College of Science, University of Tehran,
Tehran, Iran.

*zahedi_hojat@ut.ac.ir

Abstract: The current study investigates the behavior of two immiscible fluids, water and oil on polymeric surfaces using molecular dynamics simulation. The presence of nano roughness and domains with positive and negative charges on polymer surface causes the water molecules to form water clusters of various sizes. Clusters consisting of a small number of water molecules on the nano domains have less mobility, while clusters with more water molecules can slide on the surface which leads to the formation of larger clusters. The formation of large clusters of water molecules results in separation of oil and water molecules. The orientation and the order parameter of water molecules in different layers from polymer surface is investigated as well.

Keyword : Water-Oil Separation, Molecular Dynamic Simulation, Surface, Polymer

Introduction

Oil and gas are the most vital fuels needed in human societies and, water-oil separation process is one of the most important operations in the oil industry. Researchers are continuously optimizing their methods in order to improve this process. There are several ways to separate water from oil. Nanotechnology provides proper tools and novel approaches that can be used in the field of energy [1-5]. The use of polymers, as the separation substrate is more attractive due to low energy consumption, cost and small size of equipment compared to other conventional methods [2, 6]. Recently, PMMA copolymer and poly (4-vinylpyridine) [7] and its copolymer and poly (N, N-diethylamino-2-ethylmethacrylate [8] have been used to separate water and oil. The current study aims to investigate the adsorption behavior of water and oil molecules on a polymer as an oleophilic and hydrophilic surface.

Simulation details

NVT ensemble was used during 5 NS with time step of 1 fs. 300 K temperature by Nose-Hoover thermostat [9] was maintained and damping coefficient was 0.1 ps-1. Non covalent van der Waals interactions were in terms of 12-6 Lennard-Jones potentials [10] with a cutoff distance of 10 Å. In this simulation TIP4P potential model was used for water molecules [11]. The OPLS force field for covalent terms among hexane molecules include of bond, angle, dihedral was used [12]. 1204 water molecules and 358 hexane molecule were put on the substrate.

Results and Discussion

Fig- 1 shows the wettability of water droplet on polymer surface. On the other hand, oil molecules have spread completely on the same surface. Thus, the surface of the polymer is hydrophilic but is super-oleophilic and may be used in the water-oil separation to study their behavior.

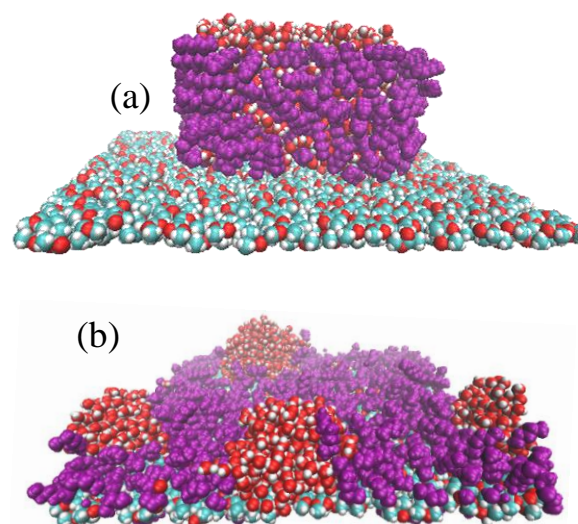


Fig 1: Water- oil and polymer surface configurations in (a) initial and (b) final

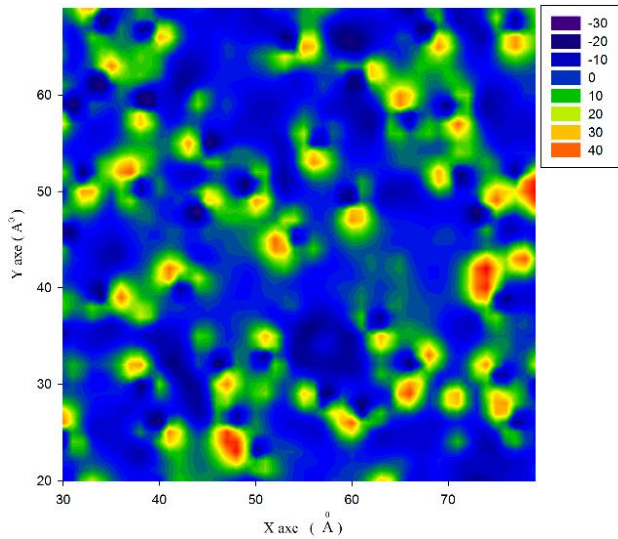


Fig 2: Energy distribution diagrams; electrical energy distribution on the surface of PMMA. Red and black colored parts show the most and the least concentration of positive and negative charges, respectively

Configurations of oil -water-polymer system after 5 nanoseconds of simulation. Fig- 1 shows that oil molecules adsorb to the surface of the polymer center, while water molecules are moving away from it. The hydrogen and carbon atoms of hexane are displayed with the same color for a comprehensible view. Fig-1 shows that water molecules prefer to gather near the sides of the substrate. However, small clusters of water molecules can be seen to reside near the polymer surface. Color illustrations are acceptable, but they should remain clear when printed in monochrome.

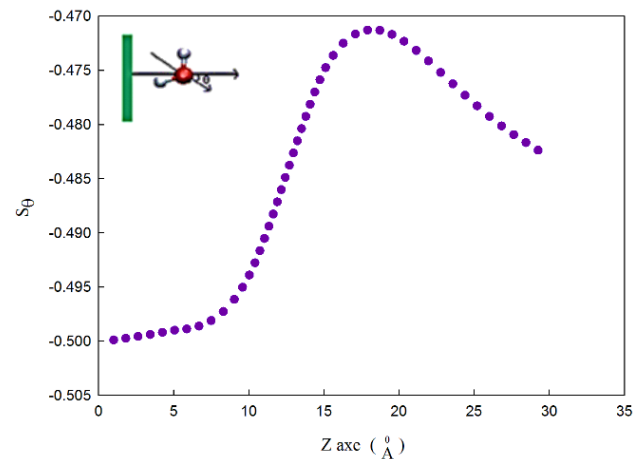
Therefore, electrostatic and van der Waals interaction energy between this point charge and the water molecule with all the atoms in the XY plane of polymer were extracted. Fig- 2 illustrates the acquired data where red and black colors represent the accumulation of positive and negative charges on the polymer. Green and blue colors show areas with almost uniform charge distribution. Based on fig-2, it can be concluded that the polymer surface has domains where the like charges are concentrated. Water molecules tend to gather in domains where positive charges are accumulated to have higher interactions with the surface. Fig-2 shows that these nano domains are scattered on the polymer surface. Water molecules are scattered on the polymer surface, since they prefer to reside close to these domains. The other point in Fig-2 is that the number of negatively charged nano domains is more than the positively charged ones. The higher number of negatively charged nano domains compared to the positively charged ones on a completely neutral polymer can be attributed to the oxygen atom of the carbonyl group. The oxygen atom

of the carbonyl group results in more negatively charged distribution on the surface

The orientation of water molecules at different layers along Z axis, are plotted in fig -3 to present the differences in the behavior of water molecules. On this premise, the order parameter, S_{Θ} , was calculated as follows.

$$S_{\Theta} = \frac{1}{2} \langle (3\cos^2\Theta - 1) \rangle \quad (1)$$

Where, Θ is the angle between normal to the surface and dipole moment vector of water molecules. If the dipole moment vector of all water molecules is parallel to the surface, $S_{\Theta} = -0.5$. In contrast, if the dipole moment vector of all water molecules is perpendicular to the surface, $S_{\Theta} = 1$. The random distribution of water molecules would cause the order parameter to be equal to zero [13].



(b)

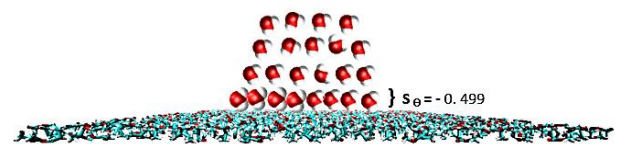


Fig 3 : (a) Order parameter of water molecules to the surface in line with Z parameter;; (b) schematic view of water molecules' orientation to the surface.

Conclusions

This study investigated the behavior of two immiscible fluids, water and oil on the amorphous polymer surface by using molecular dynamics simulation. Water molecules can be separated from water-oil mixture on the polymer surface. The study of the orientation and



ordering parameter of water molecules in different layers from polymer hydrogen atoms are close to the surface.

References

1. Li, J., Yan, L., Hu, W., Li, D., Zha, F., & Lei, Z.. Facile fabrication of underwater superoleophobic TiO₂ coated mesh for highly efficient oil/water separation. *Colloids and Surfaces A: Physicochemical and Engineering Aspects*, 489, (2016), 441-446.
2. Darvishi, M., & Foroutan, M.. Molecular investigation of oil–water separation using PVDF polymer by molecular dynamic simulation. *RSC Advances*, 6(78), (2016), 74124-74134.
3. Buckley, J. S., Bousseau, C., & Liu, Y.. Wetting alteration by brine and crude oil: from contact angles to cores. *SPE Journal*, 1(03), (1996), 341-350.
4. Sheng, J. J.. Investigation of alkaline–crude oil reaction. *Petroleum*, 1(1), (2015), 31-39.
5. Nikkhah, M., Tohidian, T., Rahimpour, M. R., & Jahanmiri, A.. Efficient demulsification of water-in-oil emulsion by a novel nano-titania modified chemical demulsifier. *Chemical Engineering Research and Design*, 94, (2015), 164-172.
6. Ali, U., Karim, K. J. B. A., & Buang, N. A.. A review of the properties and applications of poly (methyl methacrylate)(PMMA). *Polymer Reviews*, 55(4), (2015), 678-705.
7. Li, J. J., Zhou, Y. N., & Luo, Z. H.. Smart fiber membrane for pH-induced oil/water separation. *ACS applied materials & interfaces*, 7(35), (2015), 19643-19650.
8. Che, H., Huo, M., Peng, L., Fang, T., Liu, N., Feng, L., & Yuan, J. CO₂-Responsive Nanofibrous Membranes with Switchable Oil/Water Wettability. *Angewandte Chemie*, 127(31), (2015), 9062-9066.
9. Hoover, W. G.. Canonical dynamics: equilibrium phase-space distributions. *Physical review A*, 31(3), (1985), 1695.
10. Lennard-Jones, J.E.. *Cohesion. Proceedings of the Physical Society*, 43(5), (1931), 461.
11. Jorgensen, W. L., Chandrasekhar, J., Madura, J. D., Impey, R. W., & Klein, M. L. *The Journal of chemical physics*, 79(2), 1983, 926-935.
12. Jorgensen, W. L., Maxwell, D. S., & Tirado-Rives, J. Development and testing of the OPLS all-atom force field on conformational energetics and properties of organic liquids. *Journal of the American Chemical Society*, 118(45), (1996), 11225-11236.
13. Park, J. H., & Aluru, N. R.). Ordering-induced fast diffusion of nanoscale water film on graphene. *The Journal of Physical Chemistry C*, 114(6), (2010), 2595-2599.

Molecular dynamics study of water oil separation by nanoparticles

Masumeh Foroutan, Hojat Zahedi*, Hamideh Babazadeh

Department of Physical Chemistry, School of Chemistry, College of Science, University of Tehran,
Tehran, Iran.

*zahedi_hojat@ut.ac.ir

Abstract: The current study investigates the behaviour of two immiscible fluids, water and oil in the absence and presence of nanoparticles using molecular dynamics simulation. In the presence of nanoparticles, accumulation of water molecules around the particles leads to larger water clusters formation and improves separation water from oil. Nanoparticle acts faster in the adsorption of water molecules and forms larger clusters and is more successful in adsorbing water molecules from the water-oil mixture. The orientation and the order parameter of water molecules in surface and around the nanoparticles are investigated as well and Order parameter and orientation angle increase in regions between 10 and 20 Å for water molecules.

Keywords :Water-Oil Separation, Molecular Dynamic Simulation, Surface, Nanoparticle

Introduction

Oil and gas are the most vital fuels needed in human societies and, water-oil separation process is one of the most important operations in the oil industry. Researchers are continuously optimizing their methods in order to improve this process. There are several ways to separate water from oil. Nanotechnology provides proper tools and novel approaches that can be used in the field of energy [1-5]. Molecular dynamics simulation has shown that hydrophilic nanoparticles enhance separation of water from oil, while it was not possible through empirical methods [6-8]. Recently, nanoparticles were used at the water-oil interface and their effect were studied through a molecular dynamics simulation [9]. The simulation of protein nanoparticles [10], poly aromatic nanoparticles [11], silica nanoparticles [12] and tri-N-butyl phosphate nanoparticles [13] in the presence of two immiscible liquids of water and oil with the aim of exploring the performance of nanoparticles and providing a mechanism to predict and control their behavior for separation of water from oil has been presented as well.

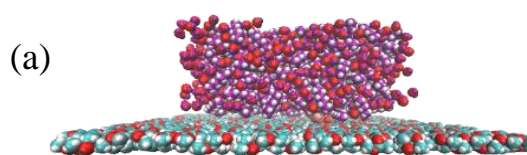
Simulation details

NVT ensemble was used during 5 NS with time step of 1 fs. 300 K temperature by Nose-Hoover thermostat [14] was maintained and damping coefficient was 0.1 ps⁻¹. Non covalent van der Waals interactions were in terms of 12-6 Lennard-Jones potentials [15] with a cutoff distance of 10 Å. In this simulation TIP4P potential model was used for water molecules [16]. The OPLS force field for covalent terms among

hexane molecules include of bond, angle, dihedral was used [17]. 1204 water molecules and 358 hexane molecule were put on the substrate. The nanoparticle atoms and substrate atoms were fixed in their initial position [2].

Results and Discussion

Fig- 1 shows the initial and the final configuration of oil-water system, polymer surface and nanoparticle after 5 ns. Fig- 1 shows that oil molecules occupy polymer surface and water molecules are gathered on the hydrophilic nanoparticle surface in a large cluster. Therefore, an efficient separation of water and oil has occurred where the two phases can be readily distinguished from one another. With the use of nanoparticle in the center of the surface, a large cluster of water molecules was formed in a specific area i.e. around the nanoparticle. This indicates the importance of using super-hydrophilic nanoparticle in the system



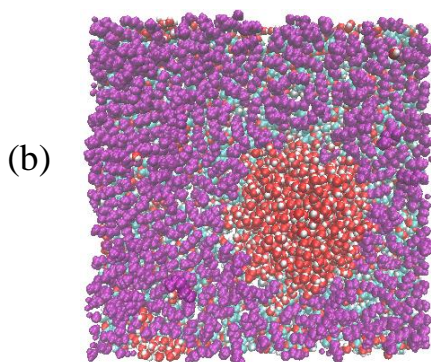


Fig 1: Water- oil and polymer surface configurations in the presence of nanoparticle (a) initial and (b) final of simulation.

The hydrogen and carbon atoms of hexane are displayed with the same color in a comprehensible view. Fig- 1 shows that water molecules prefer to gather near the sides of the substrate. However, small clusters of water molecules can be seen to reside near the polymer surface.

The orientation of water molecules at different layers along the Z axis, are plotted in Fig- 2 to present the differences in the behavior of water molecules. On this premise, the order parameter, S_{θ} , was calculated as follows.

$$S_{\theta} = \frac{1}{2} \langle (3\cos^2\theta - 1) \rangle \quad (1)$$

Where, θ is the angle between normal to the surface and dipole moment vector of water molecules. If the dipole moment vector of all water molecules is parallel to the surface, $S_{\theta} = -0.5$. In contrast, if the dipole moment vector of all water molecules is perpendicular to the surface, $S_{\theta} = 1$. The random distribution of water molecules would cause the order parameter to be equal to zero [18]. There are different order parameters for water molecules in the presence of the nanoparticle. Given the calculated order parameter, S_{θ} , and orientation of water molecules in Fig- 2, three orientations of water molecules around the nanoparticles are suggested in Fig- 2. Given that in the presence nanoparticles the angle, θ is 90 degrees for regions lower than 10 and 7 Å along Z axis, the order parameter is in the range of $-0.5 < S_{\theta} < -0.4$. Fig- 2 (a) is suggested for the aforementioned areas. Order parameter and orientation angle increase in regions between 10 and 20 Å for water molecules.

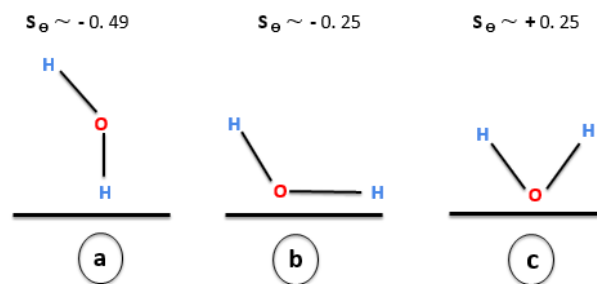


Fig 2: Order parameter of water molecules to the surface in line with Z parameter schematic view of water molecules' orientation to the surface.

Conclusions

This study investigated the behavior of two immiscible fluids, water and oil in the presence of nanoparticles on polymer surface using molecular dynamics simulation. In the presence of nanoparticles, accumulation of water molecules around the particles leads to larger water clusters formation and improves separation water from oil. In addition, the study of the orientation and ordering parameter of water molecules in different layers from polymer and nanoparticle surfaces showed that in lower layers water molecules tend to reside in such a way that their hydrogen atoms are close to the surface and nanoparticle while in the higher layers change their orientation with their oxygen atoms towards the surface.

References

- Li, J., Yan, L., Hu, W., Li, D., Zha, F., & Lei, Z.. Facile fabrication of underwater superoleophobic TiO₂ coated mesh for highly efficient oil/water separation. *Colloids and Surfaces A: Physicochemical and Engineering Aspects*, 489, (2016), 441-446.
- Darvishi, M., & Foroutan, M.. Molecular investigation of oil–water separation using PVDF polymer by molecular dynamic simulation. *RSC Advances*, 6(78), (2016), 74124-74134.
- Buckley, J. S., Bousseau, C., & Liu, Y.. Wetting alteration by brine and crude oil: from contact angles to cores. *SPE Journal*, 1(03), (1996), 341-350.
- Sheng, J. J.. Investigation of alkaline–crude oil reaction. *Petroleum*, 1(1), (2015), 31-39.

5. Nikkhah, M., Tohidian, T., Rahimpour, M. R., & Jahanmiri, A.. Efficient demulsification of water-in-oil emulsion by a novel nano-titania modified chemical demulsifier. *Chemical Engineering Research and Design*, 94, (2015), 164-172.
6. Gao, F., Xu, Z., Liu, G., & Yuan, S.. Molecular dynamics simulation: the behavior of asphaltene in crude oil and at the oil/water interface. *Energy & Fuels*, 28(12), (2014), 7368-7376.
7. Ruiz-Morales, Y., & Mullins, O. C. Coarse-grained molecular simulations to investigate asphaltenes at the oil–water interface. *Energy & Fuels*, 29(3), (2015). 1597-1609.
8. Liu, J., Zhao, Y., & Ren, S. Molecular dynamics simulation of self-aggregation of asphaltenes at an oil/water interface: formation and destruction of the asphaltene protective film. *Energy & Fuels*, 29(2), (2015). 1233-1242.
9. Ranatunga, R. U., Nguyen, C. T., Wilson, B. A., Shinoda, W., & Nielsen, S. O. Molecular dynamics study of nanoparticles and non-ionic surfactant at an oil–water interface. *Soft Matter*, 7(15), (2011). 6942-6952.
10. Cheung, D. L. Molecular simulation of hydrophobin adsorption at an oil–water interface. *Langmuir*, 28(23), (2012). 8730-8736.
11. Teklebrhan, R. B., Ge, L., Bhattacharjee, S., Xu, Z., & Sjöblom, J. Initial partition and aggregation of uncharged polyaromatic molecules at the oil–water interface: a molecular dynamics simulation study. *The Journal of Physical Chemistry B*, 118(4), (2014). 1040-1051.
12. Fan, H., Resasco, D. E., & Striolo, A. Amphiphilic Silica Nanoparticles at the Decane–Water Interface: Insights from Atomistic Simulations. *Langmuir*, 27(9), (2011). 5264-5274.
13. Baaden, M., Burgard, M., & Wipff, G.. TBP at the water-oil interface: The effect of TBP concentration and water acidity investigated by molecular dynamics simulations. *The Journal of Physical Chemistry B*, 105(45), (2001) 11131-11141.
14. Hoover, W. G. Canonical dynamics: equilibrium phase-space distributions. *Physical review A*, 31(3), (1985). 1695.
15. Lennard-Jones, J. E. Cohesion. *Proceedings of the Physical Society*, 43(5), (1931). 461.
16. Jorgensen, W. L., Chandrasekhar, J., Madura, J. D., Impey, R. W., & Klein, M. L. *The Journal of chemical physics*, 79(2), 1983, 926-935.
17. Jorgensen, W. L., Maxwell, D. S., & Tirado-Rives, J. Development and testing of the OPLS all-atom force field on conformational energetics and properties of organic liquids. *Journal of the American Chemical Society*, 118(45), (1996). 11225-11236.
18. Park, J. H., & Aluru, N. R.). Ordering-induced fast diffusion of nanoscale water film on graphene. *The Journal of Physical Chemistry C*, 114(6), (2010), 2595-2599.

A novel molecularly imprinted sensor for imidacloprid based on poly (levodopa) /TiO₂ nanoparticles composite

J. Ghodsi^a and A. A. Rafati^{a*}

^a Department of Physical Chemistry, Faculty of Chemistry, Bu-Ali Sina University, Hamedan, Iran
*aa_rafati@basu.ac.ir

Abstract

This research reports the first applying of poly (levodopa) in development of a molecularly imprinted sensor. A novel electrochemical sensor with the high selectivity and sensitivity was developed for imidacloprid (IMD) based on imprinted poly (levodopa) electropolymerized on glassy carbon electrode (GCE) modified with electrodeposited TiO₂ nanoparticles (TiO₂NPs). High affinity of IMD imprinted Poly (levodopa) to IMD caused the very selective response of electrode to IMD and electrodeposited TiO₂NPs at electrode surface resulted the electrocatalytically reduction of IMD and subsequently high sensitivity of modified electrode. IMD imprinted poly (levodopa) electropolymerized on TiO₂NPs was well characterized by FT-IR, SEM and EDX techniques. Sensor response to IMD was investigated by using square wave voltammetry (SWV), cyclic voltammetry (CV) and differential pulse voltammetry (DPV) techniques. Sensor showed really vast linear range of 2-400 μM, suitably low detection limit (LoD) of 0.3 μM and limit of quantitation (LoQ) of 1 μM. By SWV measurements that are very acceptable in comparison to other reported IMD sensor. Sensor application in real samples for IMD determination was completely successful. Response time is completely short and sensor showed good repeatability and stability in several times of use.

Keywords: *Molecularly imprinted sensor; Pesticide; Imidacloprid; Poly (levodopa); TiO₂ nanoparticles.*

Introduction

Neonicotinoids, a class of new insecticides, have become one of the most widely used and most important synthetic insecticides used in crop protection and animal health care with a global market share of more than 25%. IMD [1-(6-chloro-3-pyridylmethyl)-N-nitroimidazolidin-2-ylidene amine] is the first commercial member of the neonicotinoid family with high systemic properties which is available in the market since 1991. Because of the widespread usage of IMD in agriculture to control insect pests, such as aphids and termites, its residue may occur in various foods like as beans, fruits and vegetables [1]. IMD Previously was thought to have low toxicity to humans and other mammals, but increasingly evidence clearly verified that exposure of IMD may be related with the uncomplimentary results on animals and particularly humans health. Thus IMD spreading through the environment can cause serious concern about environment problems and consequently human and other mammal's health [2].

According to the above mentioned reasons, developing of a fast, sensitive, accurate and easy to apply procedure for IMD determination in environment and agricultural products is very important. So far, various analytical methods such as liquid chromatography tandem mass spectrometry, enzyme-linked immunosorbent assay (ELISA), high-performance liquid chromatography with diode array, micellar electrokinetic chromatography and so on were reported to IMD determination in different real samples [1]. Being sensitive and selective, these methods suffer

from some disadvantages such as high cost, time-consuming sample-preparation and need to expert persons as analyzer [1]. In contrast electro-analytical techniques, as an efficient analytical approach, attract substantial interest for the determination of inorganic and organic compounds, including pesticides because of their several advantages such as high sensitivity, short time analysis, low-cost, compact nature and minimum use of toxic organic solvent [1]. Several modified electrode such as boron-doped diamond (BDD) electrode, poly (carbazole)/chemically reduced graphene oxide modified GCE, grapheme oxide modified GCE and so on were used as electrochemical sensor for the recognition and determination of IMD [3]. Some works applied TiO₂NPs as promising electrocatalyst for reduction of IMD in electrochemical measurement. In this work a molecularly imprinted sensor was developed based on IMD imprinted poly (levodopa) electropolymerized on TiO₂NPs electrodeposited on GCE surface for determination of IMD in highly sensitive and selective manner. Electrochemical sensors based on molecularly imprinted polymers (MIPs) have received more and more attention in recent years. These sensors show high affinity and selectivity toward particular target compounds as template molecules because the recognition sites are formed in MIPs, which have been described as artificial locks for target molecules. A variety of MIP sensors have been reported such as the amperometric and voltammetric sensor.

Poly (levodopa), as a biocompatible polymer which was used in developing of a molecularly imprinted

sensor for first time in this work, electropolymerized on TiO₂NPs electrodeposited on GCE surface and was applied for selective and sensitive determination of IMD.

Materials and method

Titanium sulphate (Ti(SO₄)₂) was purchased from Merck and was used as received. Ethanol and H₂O₂ were from Sigma-Aldrich. L-3,4-dihydroxyphenylalanine (levodopa) with a purity higher than 99% was from Darou Pakhsh Co. (Iran). All other reagents were of analytical grade. Phosphate buffers (PB) (50 mM) were prepared from H₃PO₄, NaH₂PO₄ and Na₂HPO₄ and pH values were adjusted by HCl and NaOH solutions. All phosphate buffers used in the experiments were in pH 7, unless otherwise stated. The solutions were prepared using deionized water and deoxygenated by bubbling high purity (99.99%) nitrogen gas through them for 15 min prior to the experiments. All experiments were carried out at room temperature.

To preparation of Preparation of the GCE/TiO₂NPs/IMD imprinted poly (levodopa), GCE firstly (diameter 3 mm) was polished with alumina slurry and then ultrasonically cleaned with mixture of ethanol and double distilled water and dried with acetone. GCE was immersed into electrolyte consisting of 3 M KCl, 10mM H₂O₂ and 10mM Ti(SO₄)₂ and constant potential of -0.1 V was applied for 30 min. Modified GCE was washed with double distilled water three times and dried at room temperature for next IMD imprinted poly (Levodopa) electropolymerization. TiO₂NPs modified GCE was immersed in phosphate buffer (pH = 5.2) containing 1mM IMD and 5 mM levodopa. Levodopa was electropolymerized and IMD was captured by 10 consecutive cyclic scans in the potential range of -0.2 to +0.8V at a scan rate of 50 mVS⁻¹. Then resulted electrode was dried at room temperature and washed with HCl 0.5 M three times each 20 min to remove the IMD template. Finally electrode was washed with deionized water three times and dried to next IMD rebinding and determination measurements.

Results and Discussion

Figure 1 shows SEM images of electrodeposited TiO₂NPs (a), TiO₂NPs/IMD imprinted poly (levodopa) before (b) and after washing with HCl 0.5 M to remove IMD template (c). As shown in figure 1a, electrodeposited TiO₂NPs on GCE surface are highly uniform in terms of size and shape and average diameter of nanoparticles is about 50 nm. Figure 1b shows the solid layer of IMD imprinted poly (levodopa) which completely covered the TiO₂NPs. As can be seen in figure 1c, due to the HCl washing and removing the IMD template, poly (levodopa) seems porous. This template removed polymer layer supplies

many selective sites to IMD penetration and next its electrocatalytic reduction on TiO₂NPs. (levodopa) and IMD template captured in poly (levodopa).

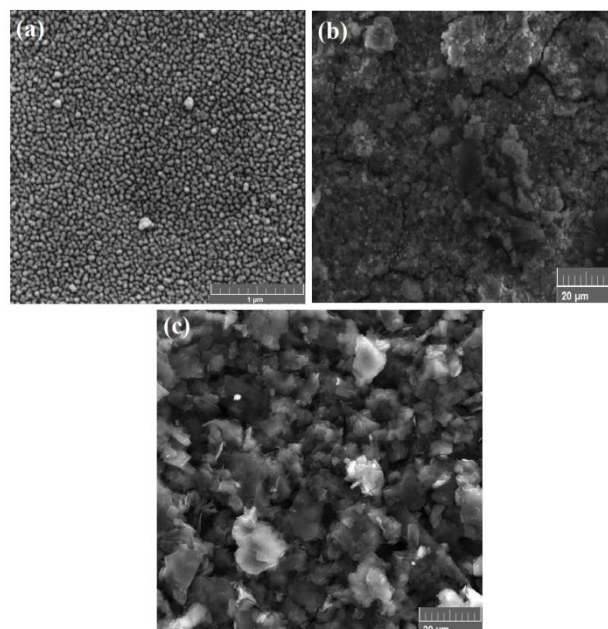


Fig. 1: SEM images of a) TiO₂NPs, b) TiO₂NPs/IMD imprinted poly (levodopa) and c) TiO₂NPs/IMD imprinted poly (levodopa) after washed with HCl 0.5 M (IMD templates were removed).

To confirm the synergic effect of TiO₂NPs and IMD imprinted poly (levodopa) layer in electrocatalytic and sensitive response of modified electrode (IMD molecularly imprinted poly (levodopa)), SWV voltammograms of 60 μM IMD in phosphate buffer obtained by 1) GCE, 2) GCE/IMD imprinted poly (levodopa) and 3) GCE/TiO₂NPs/IMD imprinted poly (levodopa) as working electrode were shown at figure 2. As can be seen at figure 2, CV voltammogram obtained by GCE don't show any significant reduction peak to IMD in comparison to two other electrodes. CV resulted from final modified electrode (3) shows more sensitive reduction peak current to IMD at less negative potential which clearly verifies the more sensitive response of modified electrode with electrocatalytic role of TiO₂NPs in IMD reduction (in comparison with voltammogram 2 which obtained by GCE/IMD imprinted poly (levodopa)).

To correlate the IMD concentration to reduction peak currents in laboratory and real samples, SWV was applied and resulted the vast linear range of 2-400 μM and suitably low LoD of 0.3 μM and LoQ of 1 μM. It should be said LoD and LoQ were calculated by 3s/m and 10s/m respectively. Where s is the standard deviation of obtained calibration curve and m is the slope of calibration curve. SWV voltammograms of IMD in concentration range of 2-400 were measured and its respective calibration plot with linear regression equation is showed at figure 3.

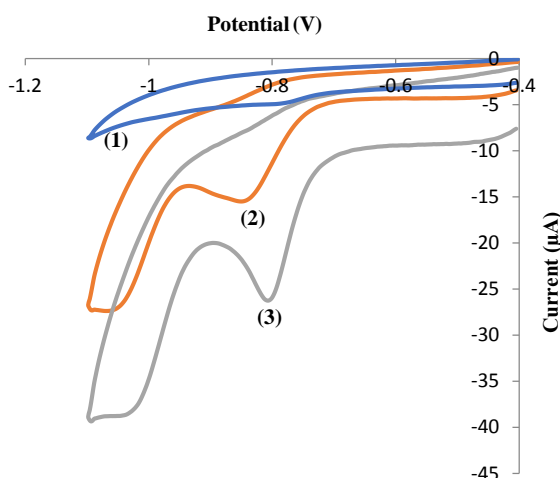


Fig. 2: CV voltammograms of 60 μM IMD in phosphate buffer corresponded to 1) GCE, 2) GCE/IMD imprinted poly (levodopa) and 3) GCE/ TiO_2NPs /IMD imprinted poly (levodopa).

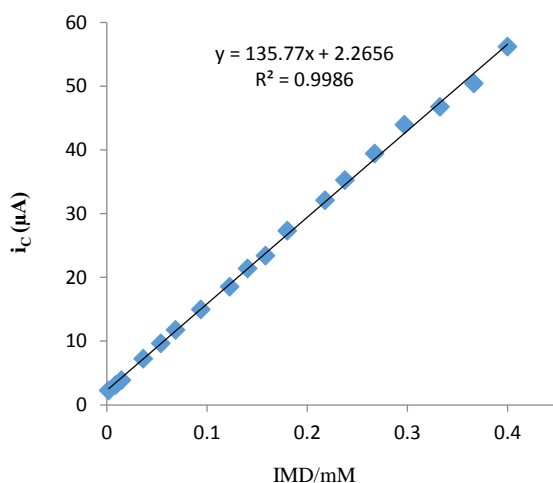


Fig. 3: Linear regression plot obtained by SWV voltammograms of IDM in concentration range of 2-400 μM .

To test the applicability of developed sensor for IMD determination in real samples, two samples including tap water and lake water were investigated by standard addition method. Samples freshly received and were spiked with three amounts of IMD (10, 20 and 30 μM). Results are showed at table 1. Each reported recovery amount is average of three measured concentration. As showed recovery amounts is between 96% and 105.7% which are very reliable and acceptable for IMD determination in real samples. Repeatability of developed sensor was examined by 10 successive determination of a fixed amount of IMD and relative standard deviation (RSD) of determined amounts was calculated as 4.5% which was completely satisfying. Finally developed IMD sensor showed %91 of its initial signal to IMD after 3 weeks in room temperature which verified the good stability of modified electrode.

The sensor achieves to 92% of its maximum response to a fixed amount of IMD in 7 s so that has completely short response time.

Table1: IMD determination in two real samples including tap water and lake water.

Sample	Added (μM)	Expected (μM)	Found (μM)	Recovery (%)
Tap water	10.0	10.0	9.7	97.0
	20.0	20.0	19.2	96.0
	30.0	30.0	31.7	105.7
Lake water	10.0	10.0	9.8	98.0
	20.0	20.0	21.0	105.0
	30.0	30.0	31.2	104

Conclusions

This work applied the poly (levodopa) for developing a molecularly imprinted voltammetric sensor for first time. Developed sensor incorporates the advantages of good selectivity due to high affinity of imprinted poly (levodopa) and high sensitivity due to electrocatalytic properties of TiO_2NPs for determination of IMD in laboratory and real samples. Relatively low price material is required for fabrication of modified electrode and also it has suitable stability and completely short response time. Its vast linear range and low detection limit are other advantage of the developed electrode. According to results applicability of modified electrode in real samples is very acceptable.

Acknowledgment

The authors greatly acknowledge Bu-Ali Sina University for the financial support.

References

- [1] K. Kobashi, T. Harada, Y. Adachi, M. Mori, M. Ihara, D. Hayasaka "Comparative ecotoxicity of imidacloprid and dinotefuran to aquatic insects in rice mesocosms", *Ecotoxicology and Environmental Safety*, 138 (2017) 122-129.
- [2] Y. Jeria, A. Bazaes, M.E. Báez, J. Espinoza, J. Martínez, E. Fuentes "Photochemically induced fluorescence coupled to second-order multivariate calibration as analytical tool for determining imidacloprid in honeybees", *Chemometrics and Intelligent Laboratory Systems*, 160 (2017) 1-7.
- [3] M.B. Brahim, H.B. Ammar, R. Abdelhédi, Y. Samet "Electrochemical behavior and analytical detection of Imidacloprid insecticide on a BDD electrode using square-wave voltammetric method", *Chinese Chemical Letters*, 27 (2016) 666-672.



Biophysical Study of Human Serum Albumin upon Interaction with $\text{La}_2\text{O}_2\text{CO}_3$ Nanoparticles

Somaye Shahraki

Department of Chemistry, University of Zabol, Zabol, Iran

E-mail addresses: s-shahraki@uoz.ac.ir, somaye_shahraki@yahoo.com

Abstract: The production and utilization of nanomaterials unavoidably lead to their accumulation in the environment, thereby posing a threat to human and environment. These compounds go into the human body, soil, or water. The interaction between $\text{La}_2\text{O}_2\text{CO}_3$ nanoparticles and human serum albumin (HSA) was studied by using spectroscopic measurements. The apparent association constant has been deduced ($K_{\text{app}} = 1.1 \times 10^3 \text{ M}^{-1}$) from the absorption spectral changes of HSA- $\text{La}_2\text{O}_2\text{CO}_3$ nanoparticles. Addition of $\text{La}_2\text{O}_2\text{CO}_3$ nanoparticles effectively quenched the intrinsic fluorescence of HSA. The number of binding sites ($n = 1.11$) and apparent binding constant ($K = 3.1 \times 10^4 \text{ M}^{-1}$) were calculated by relevant fluorescence data. The interaction between $\text{La}_2\text{O}_2\text{CO}_3$ nanoparticles and HSA occurs through static quenching mechanism. The effect of $\text{La}_2\text{O}_2\text{CO}_3$ nanoparticles on the conformation of HSA has been studied by means of FT-IR and UV-visible absorption spectra.

Keywords: $\text{La}_2\text{O}_2\text{CO}_3$ nanoparticles, Fluorescence quenching, Human serum albumine

Introduction

The binding properties of HSA and drugs were investigated by many researchers. Nanoparticle probes acting as biosensors in chemical and biochemical field have been researched recently and their applications are becoming more extensive. Three types of nanoparticles in biochemical analysis are used: metal nanoparticles, silica nanoparticles and luminescence quantum dots. Synthesis of nanoparticles with inorganic compounds has been interested [1]. Reduction in size of particles to nanometer scale results in different interesting properties compared with the bulk properties. The metal oxide and hydroxide nanoparticles due to large surface area, show many benefits over conventional materials in various applications. For example, La_2O_3 has various applications such as synthesis of ferroelectric and optical materials [2], catalyst for the oxidative coupling of methane [3, 4] and photo-catalysts for wastewater treatment.

Materials and method

Synthesis of $\text{La}_2\text{O}_2\text{CO}_3$ nanoparticles

$[\text{La}(\text{Trp})_3(\text{OH})_2]$, was used as a new precursor for preparation of the La(III) nanoparticles ($\text{La}_2\text{O}_2\text{CO}_3$). La(III) complex was completely powdered and calcined stepwise at 500°C for 3 h and 700°C for 2 h by a heating rate of $10^\circ\text{C}/\text{min}$ from room temperature (Fig. 1). FT-IR (KBr pellet, cm^{-1}) for $\text{La}_2\text{O}_2\text{CO}_3$ nanoparticles: 1109, 1492 (CO_3^{2-}) [5].

Steady-state measurements

The fluorescence quenching measurements were carried out with JASCO FP-6500 spectrofluorimeter.

The excitation wavelength of HSA was 280 nm and the emission was monitored at 340 nm. The excitation and emission slit widths (each 5 nm) and scan rate ($500 \text{ nm}/\text{min}$) were maintained constant for all the experiments. Samples were carefully purged using pure nitrogen gas for 15 min. Quartz cells with high vacuum Teflon stopcocks were used for purging. Absorption spectral measurements were recorded using Cary 300 UV-visible spectrophotometer.

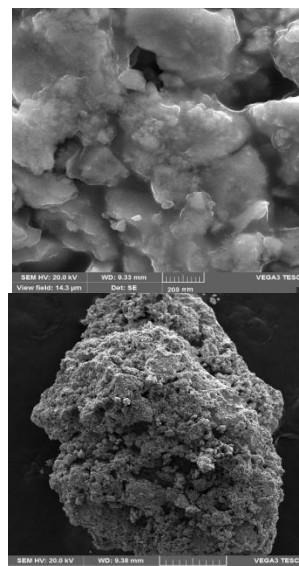


Fig. 1: SEM picture of $\text{La}_2\text{O}_2\text{CO}_3$ nanoparticles

Results and Discussion

Absorption characteristics of HSA- $\text{La}_2\text{O}_2\text{CO}_3$ nanoparticles

Fig. 2 shows the absorption spectrum of HSA in water and in water containing colloidal $\text{La}_2\text{O}_2\text{CO}_3$ nanoparticles at different concentrations. In the presence of $\text{La}_2\text{O}_2\text{CO}_3$ nanoparticles the absorbance of HSA is increased markedly, without change in the location of the peak (280 nm). This inference is due to, while adding $\text{La}_2\text{O}_2\text{CO}_3$ nanoparticles to the solution of HSA some of the HSA molecules gets adsorbed on the surface of $\text{La}_2\text{O}_2\text{CO}_3$ nanoparticles and involved in the formation ground state complex of the type HSA.

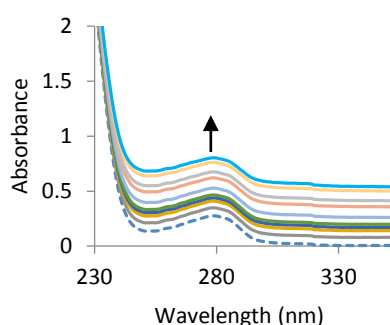


Fig. 1: Absorption spectrum of HSA ($1 \times 10^{-6}\text{M}$) in the presence of $\text{La}_2\text{O}_2\text{CO}_3$ nanoparticles.

Fluorescence quenching of HSA by $\text{La}_2\text{O}_2\text{CO}_3$ nanoparticles

Fig. 3 shows the effect of increasing concentration of $\text{La}_2\text{O}_2\text{CO}_3$ nanoparticles on the fluorescence emission spectrum of HSA. Addition of $\text{La}_2\text{O}_2\text{CO}_3$ nanoparticles to the solution of HSA resulted in the quenching of its fluorescence emission.

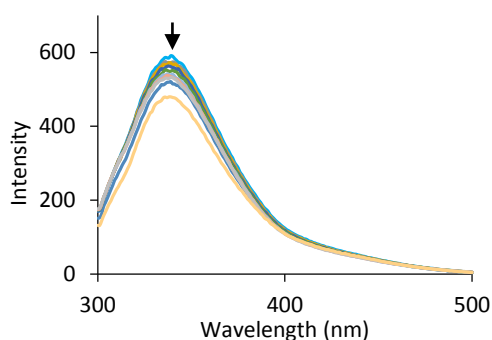


Fig. 3: Fluorescence quenching of HSA in the presence of various concentration of $\text{La}_2\text{O}_2\text{CO}_3$ nanoparticles [$\text{La}_2\text{O}_2\text{CO}_3$] = $0-16 \times 10^{-5}\text{M}$.

Binding constant and number of binding sites

By the plot of $\log (F_0-F)/F$ vs. $\log[\text{La}_2\text{O}_2\text{CO}_3]$ the number of binding sites n and binding constant K_b can be obtained (Fig. 4).

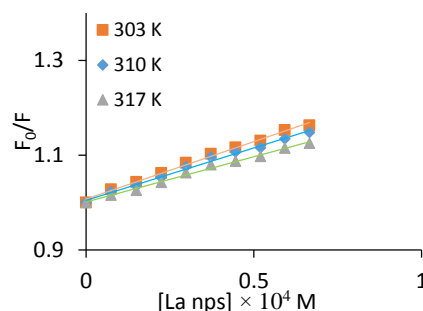


Fig. 4: The plots of $\log (F_0-F)/F$ versus $\log [\text{La}_2\text{O}_2\text{CO}_3]$ for (A) $\text{La}_2\text{O}_2\text{CO}_3$ -HSA system at three different temperatures.

In $\text{La}_2\text{O}_2\text{CO}_3$ -HSA system as temperature was increased the values of binding constant decreased that indicate the static quenching was occurred in this system.

Thermodynamics of the HSA- $\text{La}_2\text{O}_2\text{CO}_3$ nanoparticles interaction

The thermodynamic parameters are important for confirming interaction mode [6]. In view of the small positive ΔS values and large negative ΔH values, obtained for HSA- $\text{La}_2\text{O}_2\text{CO}_3$ nanoparticles system (Fig. 5), hydrogen bonds and van der Waals forces seem to favour the stabilization of drug-protein complex in this system.

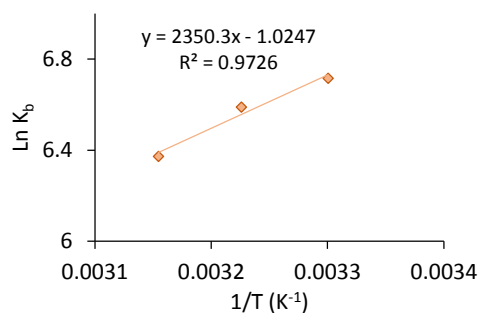


Fig. 5: Arrhenius plots for HSA- $\text{La}_2\text{O}_2\text{CO}_3$ nanoparticles system at three different temperatures.

FT-IR characterization

Fig. 6 shows the FT-IR spectra of HSA, a sharp peak near 1650 cm^{-1} appears while a broad peak appears near 1550 cm^{-1} . In this figure HSA in the absence of $\text{La}_2\text{O}_2\text{CO}_3$ nanoparticles shows the amide I peak at 1654.84 cm^{-1} and in the presence of $\text{La}_2\text{O}_2\text{CO}_3$ nanoparticles the amide I peak was shifted to 1652.91 cm^{-1} .

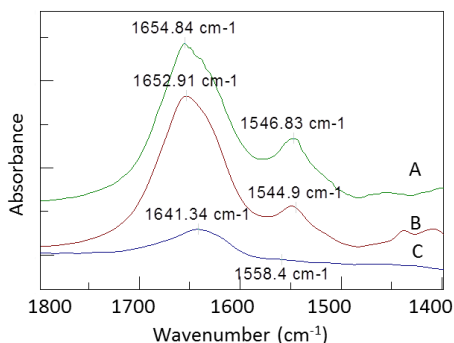


Fig. 6: The FT-IR spectra of HSA in the absence and presence of $\text{La}_2\text{O}_2\text{CO}_3$ nanoparticles.

Conclusions

The interaction between $\text{La}_2\text{O}_2\text{CO}_3$ nanoparticles and HAS has been studied by spectroscopic measurements. The results presented clearly indicated that $\text{La}_2\text{O}_2\text{CO}_3$ nanoparticles quench the fluorescence of HSA through complex formation. The quenching rate constant, binding constant, and number of binding sites were calculated according to the relevant fluorescence data. From FT-IR spectra, it is established that the conformational changes of HSA occurs due to the interaction with $\text{La}_2\text{O}_2\text{CO}_3$ nanoparticles. The binding study of $\text{La}_2\text{O}_2\text{CO}_3$ nanoparticles with HSA is of great importance in pharmacy, pharmacology, and biochemistry.

Acknowledgment

We are grateful to the University of Zabol for financial support.

References

[1] S. Shahraki, F. Shiri, M. Saeidifar, Evaluation of in silico ADMET analysis and human serum albumin

interactions of a new lanthanum (III) complex by spectroscopic and molecular modeling studies, *Inorganica Chimica Acta* 463 (2017) 80-87.

[2] R. Vali, S.M. Hosseini, First-principles study of structural, dynamical, and dielectric properties of A-La 2 O 3, *Computational materials science* 31(1) (2004) 125-130.

[3] A. Vishnyakov, I. Korshunova, V. Kochurikhin, L. Sal'nikova, Catalytic activity of rare earth oxides in flameless methane combustion, *Kinetics and Catalysis* 51(2) (2010) 273-278.

[4] H.L. Wan, X.P. Zhou, W.Z. Weng, R.Q. Long, Z.S. Chao, W. De Zhang, M.S. Chen, J.Z. Luo, S.Q. Zhou, Catalytic performance, structure, surface properties and active oxygen species of the fluoride-containing rare earth (alkaline earth)-based catalysts for the oxidative coupling of methane and oxidative dehydrogenation of light alkanes, *Catalysis today* 51(1) (1999) 161-175.

[5] M. Ghiasi, A. Malekzadeh, Synthesis, characterization and photocatalytic properties of lanthanum oxy-carbonate, lanthanum oxide and lanthanum hydroxide nanoparticles, *Superlattices and Microstructures* 77 (2015) 295-304.

[6] Y.-J. Hu, Y. Liu, X.-H. Xiao, Investigation of the interaction between berberine and human serum albumin, *Biomacromolecules* 10(3) (2009) 517-521.

Effect of ZnS shell on optical properties of Ni-doped ZnSe nanocrystals

Ehsan Soheyli^{a,*}, Gholamreza Nabiyouni^a, Reza Sahraei^b

^a Department of Physics, Faculty of Science, Arak University, Arak, 3815688394, Iran

^b Department of Chemistry, University of Ilam, Ilam, 65315-516, Iran

*ehs.soheyli@gmail.com

Abstract: The present paper aims to suggest a simple/fast route for direct preparation of the Ni-doped ZnSe/ZnS core/shell NCs in aqueous solution. Using XRD measurement, the zinc blend structure and sub-5 nm average size of the NCs was proved. The FT-IR spectrum also showed the passivation of the NCs surface by means of the deprotonated thiol terminals of the NAC molecules. The intensity of the dopant-related emission at about 476 nm in Ni:ZnSe doped NCs was found to experience more than four times enhancement by utilization of the extra ZnS shell. It was also observed that the increasing of the shell overcoating time from 1 to 3 h, has effective role on better passivation of the surface of the NCs and increasing of the emission intensity.

Keywords: Colloidal synthesis; Ni-doped ZnSe NCs; Core/shell structures; Photoluminescence emission.

Introduction

Colloidal nanocrystals (NCs) are nanometer-sized semiconductor particles synthesized and suspended in the both of organic and aqueous solution phases [1]. Evergrowing interest in these materials derives from the convenient fabrication of solids directly from the solution-phase, as well as their rationally-engineered, wide-ranging spectral tunability afforded by the quantum confinement effect [2]. Meanwhile, one of the most important breakthroughs was the development of direct aqueous-based synthesis approaches which fostered their scope in both terms of chemical synthesis and technological point of views [3]. In other hand, introduction of the dopant element opens a new window for making a desired characteristic and optimizing the optical properties in the NCs [4]. Using Ni²⁺ ions and by overcoating the additional shell on core NCs, here, we report a facile way for preparation of Ni-doped ZnSe/ZnS core/shell NCs.

Materials and method

Zn(OAc)₂·2H₂O, Ni(OAc)₂·4H₂O, Se, NaBH₄, N-acetyl-L-cysteine (NAC), NaOH and acetone were purchased from Merck company. The deionized water was also used in all experiments. The Ni-doped ZnSe NCs were prepared as follows; first, the suitable amounts of Zn and Ni precursors were dissolved in aqueous solution of the NAC with molar ratios of Zn:Ni:NAC equal to 1:0.02:3. After titration by 1 M NaOH (pH=9.5) and N₂ bubbling in 3-necked flask, the solution temperature was increased to 100 °C. Next, the freshly prepared NaHSe solution (by reaction of Se and NaBH₄) was swiftly injected and the temperature was cooled down to 80 °C. The flask was refluxed for 1 h yielding to Ni:ZnSe NCs. After that, 3 ml of the NCs solution was exited for optical measurements. Then, the reaction temperature was further decreased to 75 °C and the pre-prepared solution of Zn, NAC (Zn:NAC

molar ratio of 1:2) and 11 ml deionized water was added to stirring solution and the refluxing process was continued for 1, 2 and 3 h for formation of core/shell NCs. After cooling to room temperature, the required amounts of solution was used for PL and PLE spectroscopies. The powder of the NCs were obtained by adding of acetone to as-prepared solution. XRD, FT-IR, PLE and PL analysis were carried out for characterization of the prepared samples.

Results and Discussion

As is observed in Fig. 1, the XRD pattern ($\lambda_{Co}=1.79 \text{ \AA}$) of the NCs powder, show a zinc blend cubic structure of ZnSe with three broad peak at 32, 53.6 and 63.5 degrees which are attributed to (111), (220) and (311), respectively [5]. The obvious broadening of the peaks indicates the small size of the core/shell NCs. Using the well-known Scherrer equation, the size of the NCs were estimated to be near 3.5 nm.

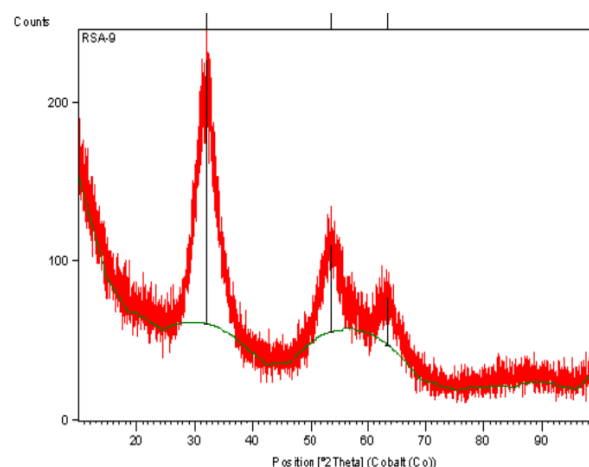


Fig. 1: The XRD pattern of the Ni:ZnSe/ZnS NCs



The FT-IR transmittance spectra show the complete disappearance of the thiol-related peak which is located about 2500 cm^{-1} in pure NAC (Fig. 2). This demonstrates the possible passivation of the NCs with deprotonated thiol group of NAC molecules and their interaction with Zn^{2+} ions in the surface of the NCs. Whereas the carboxylate group were found to be still presented in NAC-capped Ni:ZnSe/ZnS NCs which exhibit their possible interaction with surrounding medium [6].

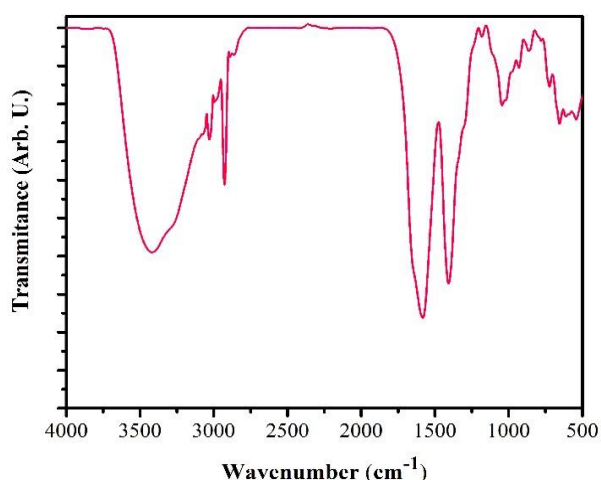


Fig. 2: FT-IR spectrum of the Ni:ZnSe/ZnS NCs.

As an important factor for application of NCs in light emitting systems, the excitation and emission PL spectra of the core and core/shell- doped NCs were recorded and showed in Fig. 3. There are several conclusions, implied from these spectra. The large Stokes shift between absorption and emission peaks (100 nm) indicates that the PL emission can be related to impurity states. Indeed, it can be attributed to recombination of the charge carriers between conduction band and Ni^{2+} energy levels. Interestingly, this dopant-related peak experiences a very substantial enhancement by addition of Zn-NAC solution. It demonstrates the effective surface passivation of the NCs and formation of doped- core/shell structure. When we do use the additional inorganic shell with higher band gap energy, it can prohibit the charge carriers from surface of the NCs where the surface defects can act as trap states for them, leading to non-radiative recombination and decreasing of the emission intensity [7]. However, increasing of the shell growth (by increasing of the shell overcoating time duration) from 1 to 3 h, the emission intensity goes higher. It can be related to increasing of the shell thickness and better surface passivation. In fact, it can truly force on the Ni^{2+} dopant ions to be located at the inside lattice of

the core structure. There are another behavior by injection of shell precursor. As the refluxing time is increased, it is expected to make a red-shift in spectra, but blue-shift in both of the PL and PLE spectra is observed. Such behavior can be related to partial hydrolyzing of the S-H group in NAC molecules and subsequent insertion of the S^{2-} ions to lattice of the ZnSe NCs and formation of the ZnSe(S) alloys.

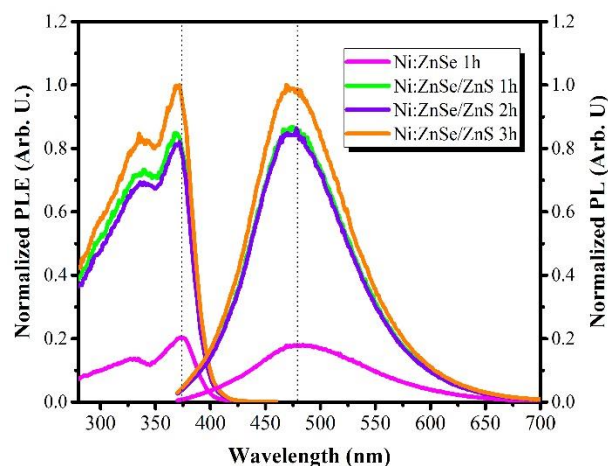


Fig. 3: Effect of shell overcoating on PLE and PL spectra of the as-prepared NCs.

Conclusions

A facile and one-pot method was suggested for preparation of the aqueous-based Ni:ZnSe/ZnS NCs with intense cyan emission and cubic zinc blend crystal structure. The coordinating interaction between cations and deprotonated thiol terminals of the NAC molecules was proved by elimination of the S-H related peak in FT-IR spectra. These phenomena in high temperature may lead to diffusion of the S^{2-} species to lattice structure of the ZnSe NCs and formation of the ZnSe(S) alloys which was indicated by blue-shift of the PLE and PL spectra after growth of the ZnS shell. The obtained optical results have also demonstrated that the Ni^{2+} ions show their own PL emission peak at around 476 nm which was further intensified by using of higher band gap ZnS shell. In addition, increasing of the refluxing time for shell overcoating was accompanied to further enhancement of the emission intensity which is attributed to better surface passivation of the doped NCs.

Acknowledgment

The authors would like to thank Deputy President for Culture and Student Affairs of the Arak University for financial supports.



References

- [1] Y. Yin, A. P. Alivisatos, "Colloidal nanocrystal synthesis and the organic-inorganic interface", *Nature*, 437 (2005) 664-670.
- [2] E. Soheyli, R. Sahraei, G. Nabiyouni, "pH-dependent optical properties of N-acetyl-L-cysteine-capped ZnSe(S) nanocrystals with intense/stable emissions", *J Nanopart Res*, 19 (2017) 92.
- [3] L. Jing *et al.*, "Aqueous Based Semiconductor Nanocrystals", *Chem Rev*, 116 (2016) 10623-10730.
- [4] R. Sahraei, F. Mohammadi, E. Soheyli, M. Roushani, "Synthesis and photoluminescence properties of Ru-doped ZnS quantum dots", *J Lumin*, 187 (2017) 421-427.
- [5] S. Jana, B. B. Srivastava, S. Jana, R. Bose, N. Pradhan, "Multifunctional doped semiconductor nanocrystals", *J Phys Chem Lett*, 3 (2012) 2535-2540.
- [6] C. Shu, B. Huang, X. Chen, Y. Wang, X. Li, L. Ding, W. Zhong, "Facile synthesis and characterization of water soluble ZnSe/ZnS quantum dots for cellular imaging" *Spectrochim. Acta Mol. Biomol. Spectrosc.*, 104 (2013) 143-149.
- [7] K. Saikia, P. Deb, B. Mondal, E. Kalita, "Significant improvement in dopant emission and lifetime in water soluble Cu: ZnSe/ZnS nanocrystals", *Mater. Res Exp*, 1 (2014) 015014.



The electrical and structural study of interaction HCN gas with SiCNTs : A DFT approach

M. Rezaei-Sameti, S. Taghizadeh Najaf Abad, E. Shiravand, K. Abdoli

Department of Physical Chemistry, Faculty of Science, Malayer University, Malayer, 65174, Iran

mrsameti@malayeru.ac.ir

Abstract: In this research, we investigate the interaction of HCN gas with SiCNTs to making new absorber and sensor for HCN gas. All stable adsorption structures are individually optimized by using density function theory at the cam-B3LYP level of theory using the Gaussian 09 set of programs. From optimized structures the DOS plots, MEP plot and quantum molecular descriptors: gap energy, chemical potential (μ), global hardness (η), electrophilicity index (ω), and electronegativity (χ) of the nanotubes are calculated. The results indicate that the adsorption of HCN from N and H head in the vertical direction of surface of SiCNTs is favourable than other those models in thermodynamically approach. The quantum parameters demonstrate that the SiCNTs is a good candidate for detecting HCN gas.

Keywords : SiCNTs, DFT, HCN interaction, quantum parameters

Introduction

Hydrogen cyanide (HCN) is highly lethal to man and animals, so the monitoring and control of its exposure in both industrial and residential environments are of special interest. Therefore, effective methods for monitoring and suppressing the HCN concentration have been highly demanded for atmospheric environmental measurements and controls [1]. Since the discovery of carbon nanotubes (CNTs), extensive studies have focused on the application of CNTs in sensors. Prepared CNT sensors have advantages of low power consumption, fast response and

easy recovery capability over the traditional bulk material sensors. [2-3] Silicon carbide nanotubes (SiCNTs) is one of the important nanotube that it is used to making sensor. The surface-to-volume ratio of the SiCNTs is higher than that of the bulk SiC materials. These results indicate that SiCNTs are good candidates for HCN detecting. The theoretical results show that the BNNTs and AlNNTs is a good candidate to detection HCN molecule[4-6].

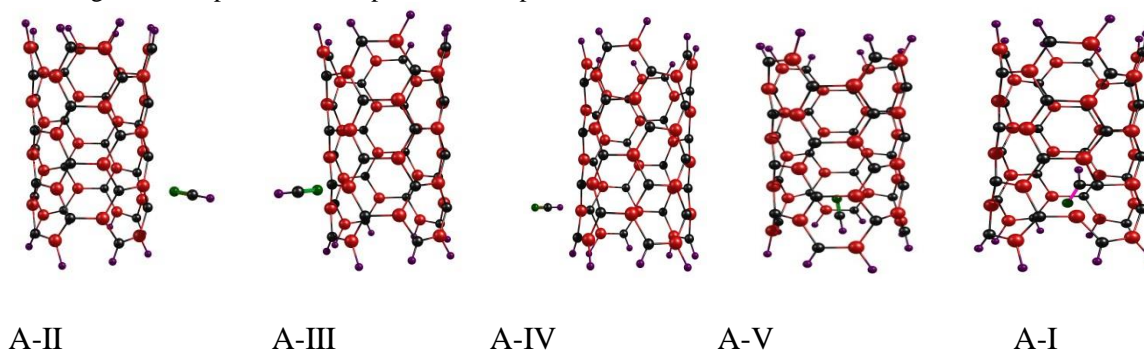


Fig 1. 2D geometrical structures for adsorption HCN molecule on SiCNTs

Results and Discussion

The adsorption energy for HCN adsorption on surface of undoped and B-doped SiCNTs at representative (A-I to B-V) models are tabulated in table 1. Inspections of results show that the adsorption energy of all considered models is in range -3.7 to 23.7 kcal/mol. It is notable that the adsorption energy of B-III models is more negative than other those models and so the adsorption of HCN molecule at this model is favorable than other models. Whereas the adsorption energy of B-II is more positive

than other models and so this model is unspontaneously in view of thermodynamic approach.

Table 1. The adsorption energy for adsorption HCN gas on the surface of SiCNTs

$E_{ads}(Kcal/mol)$	A-I	A-II	A-III	A-IV	A-V
Pristin	-۳/۷	-۳/۷	-۲/۷	۴/۴	۲۳/۷
B-Doped	B-I	B-II	B-III	B-IV	B-V
	-۰/۸	۲۶/۸	-۴/۳	۹/۰	۱۶/۸

The electrophilicity index (ω) determines maximum flow of electron from donor to acceptor species and supplies data connected to structural stability, reactivity and toxicity of chemisorbed on the surface of nanotube, a fairly large charge transfer occurs between two related

species, thus their electronic transport properties could be significantly changed upon physisorption of HCN gas. The results show that the electrophilicity index of B-doped adsorption models increase significantly from original values.

Table 2 The NBO charge around HCN gas after adsorption

<i>Pristine</i>	A-I	A-II	A-III	A-IV	A-V
<i>$\Delta\rho_{NBO}$</i>	0.15	0.15	-0.015	0.022	-0.451
B DOPED	B-I	B-II	B-III	B-IV	B-V
<i>$\Delta\rho_{NBO}$</i>	-0.001	-0.208	-0.014	0.024	-0.05
N DOPED	C-I	C-II	C-III	C-IV	C-V
<i>$\Delta\rho_{NBO}$</i>	0.15	-0.46	-0.023	0.035	-0.36
N B DOPED	D-I	D-II	D-III	D-IV	D-V
<i>$\Delta\rho_{NBO}$</i>	0.01	-0.018	-0.007	0.035	-0.34

The molecular electrostatic potential results reveal that the negative charge densities are localized on the surface of nanotube and positive charge are dispersed around HCN. Thereby in this adsorption process HCN gas has

donor electron effects and so the gap energy, NBO, DOS plot (see Fig. 2) change significantly from original values and the electrical parameters of system is suitable for making sensor for HCN gas.

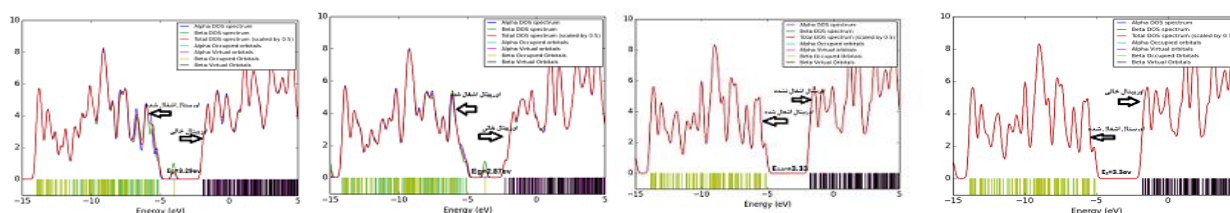


Fig 2. 2D DOS plots for adsorption HCN molecule on SiCNTs

Conclusions

The structural parameters reveal that the bond lengths (Si-C) of neighbourhood of doping and adsorbing sites undergo increase and bond angles (Si-Si) undergo decrease. The band gaps of HCN adsorption on the surface of undoped and B-doped SiCNTs reduced. The adsorption energy of the HCN gas shows that the

adsorption process is weak physisorption in thermodynamic approach. These results demonstrate that SiCNTs is not a good candidate to making HCN absorber. The quantum calculation is shown that the pristine SiCNTs is a good candidate to making HCN sensor

References

- [1] N.G. Wright, A.B. Horsfall. J Phys D: Appl Phys, , 40 (2007) 6345



بیستمین کنفرانس شیمی فیزیک ایران
دانشکده علوم پایه - دانشگاه اراک
۲۱-۲۴ مرداد ۱۳۹۶



20th Iranian Physical Chemistry Conference

- [2] S.K. Padigi, R.K.K. Reddy, S. Prasad, sensor. Biosensors and Bioelec., 22(6) (2007) 829
- [3] M. Menon, E. Richter, M. Andreas, et al. Phys Rev B, 69 (2004) 115322
- [4] A. Gali, Phys Rev B, 73(2006) 245415-8
- [5] M. Rezaei-Sameti, F. Saki, Phys.Chem. Res., 3(4) (2015) 265-277
- [6] Y. Zhang, D. Zhang, C. Liu J Phys Chem B 110(2006) 4671-4674



The electrical and structural study of interaction HCN gas with SiCNTs : A DFT approach

M. Rezaei-Sameti, S. Taghizadeh Najaf Abad, E. Shiravand, K. Abdoli

Department of Physical Chemistry, Faculty of Science, Malayer University, Malayer, 65174, Iran

mrsameti@malayeru.ac.ir

Abstract: In this research, we investigate the interaction of HCN gas with SiCNTs to making new absorber and sensor for HCN gas. All stable adsorption structures are individually optimized by using density function theory at the cam-B3LYP level of theory using the Gaussian 09 set of programs. From optimized structures the DOS plots, MEP plot and quantum molecular descriptors: gap energy, chemical potential (μ), global hardness (η), electrophilicity index (ω), and electronegativity (χ) of the nanotubes are calculated. The results indicate that the adsorption of HCN from N and H head in the vertical direction of surface of SiCNTs is favourable than other those models in thermodynamically approach. The quantum parameters demonstrate that the SiCNTs is a good candidate for detecting HCN gas.

Keywords : SiCNTs, DFT, HCN interaction, quantum parameters

Introduction

Hydrogen cyanide (HCN) is highly lethal to man and animals, so the monitoring and control of its exposure in both industrial and residential environments are of special interest. Therefore, effective methods for monitoring and suppressing the HCN concentration have been highly demanded for atmospheric environmental measurements and controls [1]. Since the discovery of carbon nanotubes (CNTs), extensive studies have focused on the application of CNTs in sensors. Prepared CNT sensors have advantages of low power consumption, fast response and

easy recovery capability over the traditional bulk material sensors. [2-3] Silicon carbide nanotubes (SiCNTs) is one of the important nanotube that it is used to making sensor. The surface-to-volume ratio of the SiCNTs is higher than that of the bulk SiC materials. These results indicate that SiCNTs are good candidates for HCN detecting. The theoretical results show that the BNNTs and AlNNTs is a good candidate to detection HCN molecule[4-6].

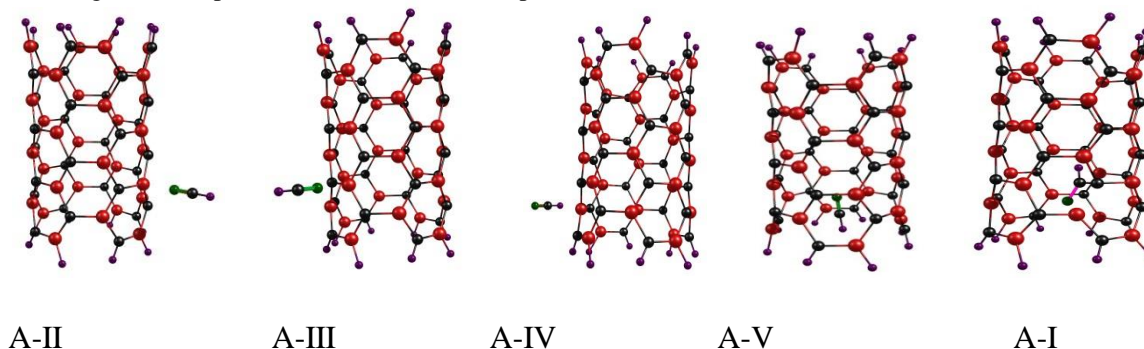


Fig 1. 2D geometrical structures for adsorption HCN molecule on SiCNTs

Results and Discussion

The adsorption energy for HCN adsorption on surface of undoped and B-doped SiCNTs at representative (A-I to B-V) models are tabulated in table 1. Inspections of results show that the adsorption energy of all considered models is in range -3.7 to 23.7 kcal/mol. It is notable that

the adsorption energy of B-III models is more negative than other those models and so the adsorption of HCN molecule at this model is favorable than other models. Whereas the adsorption energy of B-II is more positive than other models and so this model is unspontaneously in view of thermodynamic approach.

Table 1. The adsorption energy for adsorption HCN gas on



the surface of SiCNTs

$E_{ads}(\text{Kcal/mol})$	A-I	A-II	A-III	A-IV	A-V
Pristin	-۳/۷	-۳/۷	-۲/۷	۴/۴	۲۳/۷
B-Doped	B-I	B-II	B-III	B-IV	B-V
	-۰/۸	۲۶/۸	-۴/۳	۹/۰	۱۶/۸

The electrophilicity index (ω) determines maximum flow of electron from donor to acceptor species and supplies data connected to structural stability, reactivity and toxicity of chemisorbed on the surface of nanotube, a fairly large charge transfer occurs between two related

species, thus their electronic transport properties could be significantly changed upon physisorption of HCN gas. The results show that the electrophilicity index of B-doped adsorption models increase significantly from original values.

Table 2 The NBO charge around HCN gas after adsorption

<i>Pristine</i>	A-I	A-II	A-III	A-IV	A-V
$\Delta\rho_{NBO}$	0.15	0.15	-0.015	0.022	-0.451
B DOPED	B-I	B-II	B-III	B-IV	B-V
$\Delta\rho_{NBO}$	-0.001	-0.208	-0.014	0.024	-0.05
N DOPED	C-I	C-II	C-III	C-IV	C-V
$\Delta\rho_{NBO}$	0.15	-0.46	-0.023	0.035	-0.36
N B DOPED	D-I	D-II	D-III	D-IV	D-V
$\Delta\rho_{NBO}$	0.01	-0.018	-0.007	0.035	-0.34

The molecular electrostatic potential results reveal that the negative charge densities are localized on the surface of nanotube and positive charge are dispersed around HCN. Thereby in this adsorption process HCN gas has

donor electron effects and so the gap energy, NBO, DOS plot (see Fig. 2) change significantly from original values and the electrical parameters of system is suitable for making sensor for HCN gas.

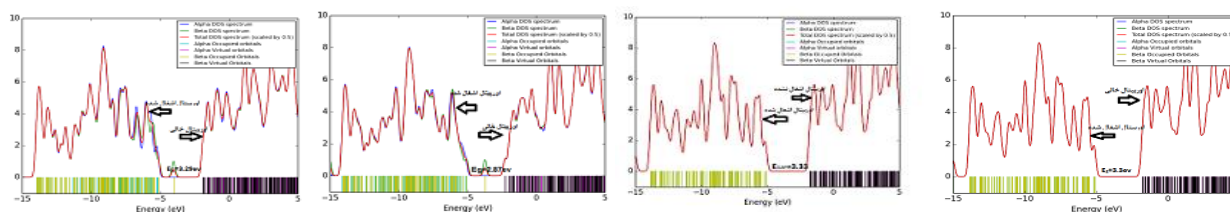


Fig 2. 2D DOS plots for adsorption HCN molecule on SiCNTs

Conclusions

The structural parameters reveal that the bond lengths (Si-C) of neighbourhood of doping and adsorbing sites undergo increase and bond angles (Si-Si) undergo decrease. The band gaps of HCN adsorption on the surface of undoped and B-doped SiCNTs reduced. The adsorption energy of the HCN gas shows that the

adsorption process is weak physisorption in thermodynamic approach. These results demonstrate that SiCNTs is not a good candidate to making HCN absorber. The quantum calculation is shown that the pristine SiCNTs is a good candidate to making HCN sensor

References

- [1] N.G. Wright, A.B. Horsfall. J Phys D: Appl Phys, , 40 (2007) 6345
- [2] S.K. Padigi, R.K.K. Reddy, S. Prasad, sensor. Biosensors and Bioelec., 22(6) (2007) 829
- [3] M. Menon, E. Richter, M. Andreas, et al. Phys Rev B, 69 (2004) 115322



بیستمین کنفرانس شیمی فیزیک ایران
دانشکده علوم پایه - دانشگاه اراک
۲۱-۲۴ مرداد ۱۳۹۶



20th Iranian Physical Chemistry Conference

- [4] A. Gali, Phys Rev B, 73(2006) 245415–8
- [5] M. Rezaei-Sameti, F. Saki, Phys.Chem. Res.,
3(4) (2015) 265–277
- [6] Y. Zhang, D. Zhang, C. Liu J Phys Chem B
110(2006) 4671–4674

DFT study of potassium decorated γ -graphyne: Electronic structure and optical properties

M. Shams-Ghamsary, A. Reisi-Vanani*

Department of Physical Chemistry, Faculty of Chemistry, University of Kashan, Kashan, Iran

E-mail: areisi@kashanu.ac.ir

Abstract: In this work, first-principle calculations of graphyne and K-decorated graphyne were carried out and their optical and structural properties were investigated. This structure of the graphyne family is a direct band gap semiconductor with a band gap of 0.43 eV in absence of potassium, but K-decorated γ -graphyne compounds are metallic, and can then be employed as carbon-based conductors. Through the analysis of the structural properties of pristine and K-decorated γ -graphyne, we find that the most favorable adsorption site of K atom is the hollow site of a 12-C hexagon with adsorption energy equal to -5.86 eV that has chemisorption essence.

Keywords: Graphyne; Carbon nano sheet; Decoration; Adsorption energy; Potassium.

Introduction

In the latest years, the carbon materials family of graphynes, two-dimensional carbon allotropes containing C atoms with sp and sp^2 hybridization states, has become a hub of research. Graphyne, a novel 2D carbon allotrope, was predicted to have a high possibility of synthesis by Baughman et al. in 1987 [1]. Graphyne consists of planar carbon sheets containing sp and sp^2 bonds which can be described as hexagonal rings joined together by the acetylenic linkages ($C - C \equiv C - C$). There are five different types of graphyne, namely α , β , γ , δ and 6,6,12-graphyne which have been identified γ -graphyne is the most stable structure with respect to energy between its family [2, 3]. Graphyne properties can be tuned by decoration with metal atoms. In this work, we investigated the stability of different adsorption sites for K atom including various hollows, top of carbon atoms and bonds on graphyne structure based on their adsorption energy of K to graphyne. The analysis of the band structure and partial density of state (PDOS) showed that the most suitable adsorption site of K atom is H1 position.

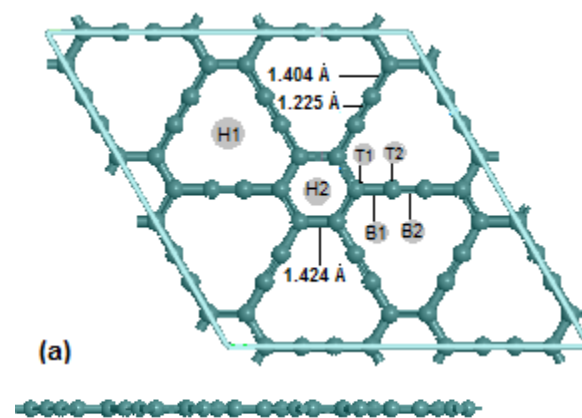
Computational methods

All computations were performed using the spin-polarized first-principle method as implemented in the DMOL³ code. The generalized gradient approximation (GGA) with the Perdew-Burke-Ernzerh of (PBE) exchange-correlation functional was used, in combination with the double numerical plus polarization (DNP). The empirically-corrected density functional theory (DFT+D) method within in Grimme scheme was employed in all the calculation to consider the van der waals forces [4]. To accelerate the convergence of SCF, we apply the direct inversion of iterative subspace (DIIS)

approach. To avoid the inter layer interaction between neighboring layers, a vacuum space of 20 Å is applied along the direction perpendicular to the γ -graphyne sheet. The total density of states (PDOS) in the super cells is calculated with a k-point of (4×4×1).

Results and discussion

We considered the case of a single metal K adsorption on 2×2 γ -graphyne super cell. The optimized structures of pristine and K-decorated graphyne are presented in Fig. 1. There are only two types of C atoms in pristine graphyne, the optimized bonds of $C(sp^2)-C(sp^2)$, $C(sp^2)-C(sp)$ and $C(sp)-C(sp)$ in pristine graphyne are equal to 1.424, 1.404 and 1.225 Å, respectively, which are in good agreement with previous work [5]. Bond lengths of $C(sp^2)-C(sp^2)$, $C(sp^2)-C(sp)$ and $C(sp)-C(sp)$ in K-decorated graphyne are equal to 1.433, 1.403



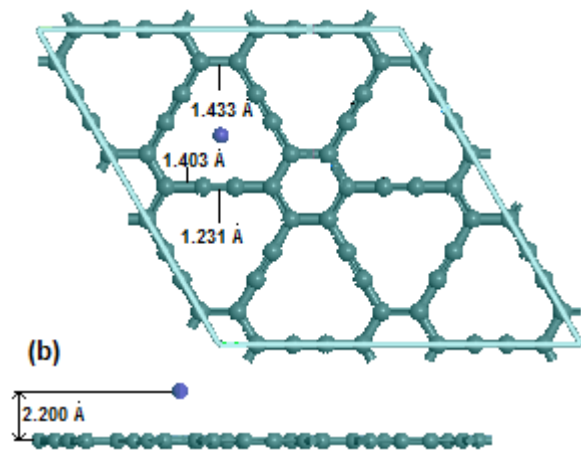


Fig. 1: The optimized structures of pristine and K-decorated graphyne: (a) the top and side view of pristine graphyne; (b) the top and side view of K-decorated graphyne in the best position. The six possible adsorption sites are labeled by H1, H2, T1, T2, B1, B2; (green and purple atoms are C and K, respectively).

and 1.231 Å, respectively. For the adsorption of K atom on graphyne, there are six possible adsorption sites in Fig. 1 (a): the hollow site of a 12-C hexagon (H1), the hollow site of a 6-C hexagon (H2), the bridge sites (namely B1 and B2) and the top of the C atoms (namely T1 and T2).

To determine which site is preferable in energy for the adsorption of K atom, we calculated the adsorption energy for the adsorption of K atom on graphyne by the following equation:

$$E_{\text{ads}} = E_{(\text{graphyne-K})} - E_{(\text{graphyne})} - E_{(\text{K})} \quad (1)$$

where $E_{(\text{graphyne-K})}$ is the total energy of K-decorated graphyne, $E_{(\text{graphyne})}$ is the total energy of pristine graphyne and $E_{(\text{K})}$ is the total energy of free K atom. For the adsorption of K atom on graphyne, a positive value of adsorption energy

demonstrates that the adsorption is endothermic and a negative value of adsorption energy illustrates that the adsorption is exothermic. We presented in Table 1 the calculated adsorption energy of the optimized structure from putting K atom at different adsorption sites. The calculated band structure, density of states (DOS) and partial density of states (PDOS) for pristine graphyne and K-decorated are presented in Fig. 2. Fermi energy is set to zero for all of the plots. In pristine graphyne the high energy level of DOS is mainly comprised of C2p orbitals as shown in Fig. 2 (a). In comparison to pristine graphyne, the DOS of the K-decorated graphyne shift towards the lower energy region. Moreover, it is found that the DOS of K-decorated graphyne approximate to that of pristine graphyne, except for the contribution of K atom. It is well established that the K atom is much easier to done its 4s electron due to its relatively low ionization potential. The valence-band maximum (VBM) and conduction band minimum (CBM) of graphyne (represented in Fig. 2 (a)) are located at the same (Z) point in the hexagonal Brillouin zone, making this a direct band gap semiconductor.

Conclusions

DFT-D calculations are carried out to explore K-decorated graphyne through the analyses of structure and density of states, for pristine and K-decorated graphyne. It is found that K atom adsorbed on the hollow site of a 12-C hexagon is more preferable with adsorption energy equal to -5.86 eV. The γ -graphyne is a direct band gap semiconductor in absence of potassium, with a band gap of 0.43eV but potassium adsorption changes band gap into 0.186eV which makes the structure metallic and improves its conduction.

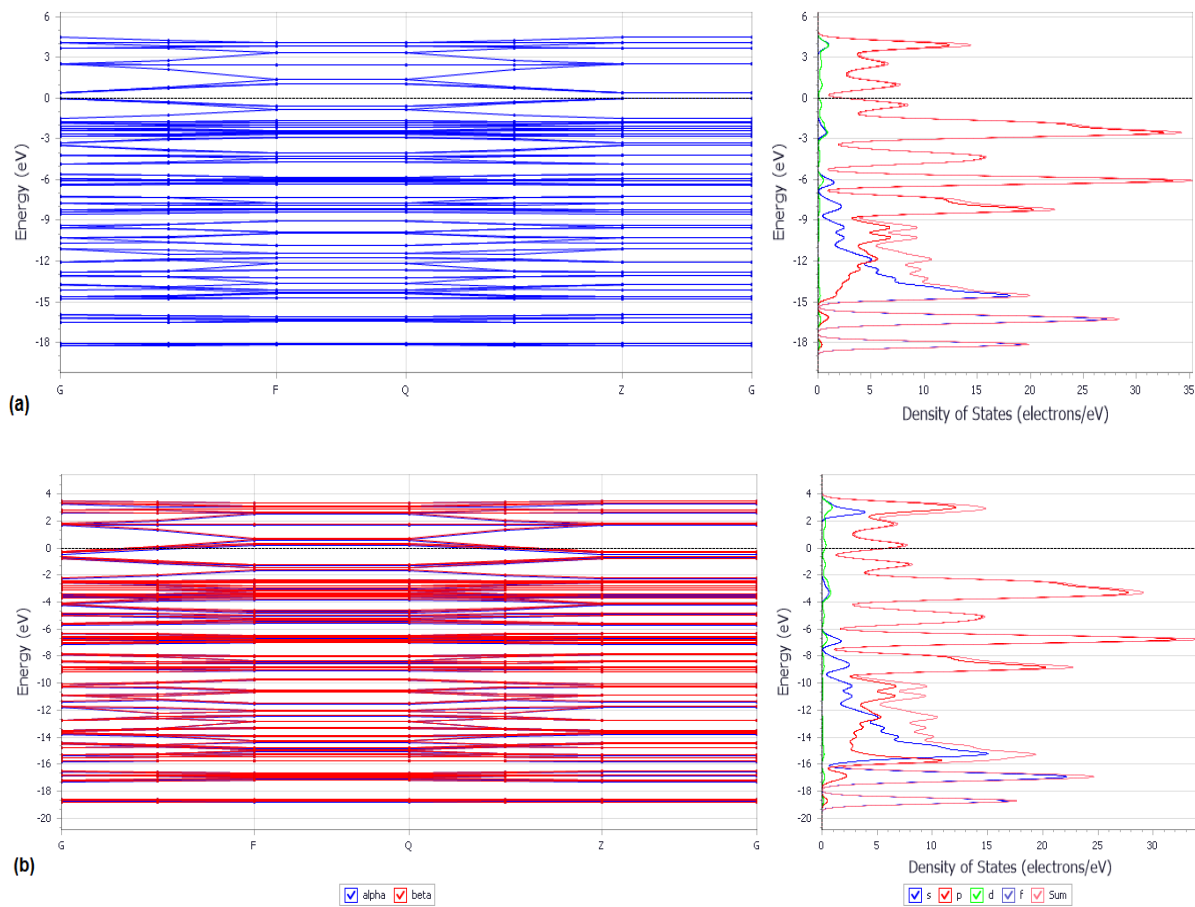


Fig. 2: The band structure and partial density of states (PDOS) for (a) pristine graphyne; (b) K-decorated graphyne.

Adsorption site	Adsorption energy (eV)
H1	-5.86
H2	-5.46
T1	-5.39
T2	-5.44
B1	-5.42
B2	-5.48

Table 1: Adsorption energy of K atom on graphyne in various sites.

References

- [1] R. Baughman, H. Eckhardt, M. Kertesz, Structure-property predictions for new planar forms of carbon: layered phases containing sp^2 and sp atoms, *Journal of Chemical Physics*, 87 (1987) 6687-99.
- [2] M.W. Zhao, W.Z. Dong, A.Z. Wang, Two-dimensional carbon topological insulators superior to graphene, *science reports*, 3 (2013) 3532-37.

- [3] W.Z. Wu, W.L. Guo, X.C. Zeng, Intrinsic electronic and transport properties of graphyne sheets and nanoribbons, *Nanoscale*, 5 (2013) 9264-9276.
- [4] S. Grimme, Semiempirical GGA-type density functional constructed with a long-range dispersion correction, *Journal of Computational Chemistry*, 27 (2006) 1787-1799.
- [5] N. Narita, S. Nagai, S. Suzuki, Potassium intercalated graphyne, *Physical Review B*, 64(24) (2001) 245408-14.

Prediction of elastic properties of TiSe₂ nanosheet under external electric using density functional theory

A. Shahnazari^a, R. Ansari Khalkhali^{a*}, M. Darvizeh^a, S. Rouhi Garkaroudi^b

^aDepartment of Mechanical Engineering, University of Guilan, P.O. Box 3756, Rasht, Iran

^bYoung Researchers and Elite Club, Langarud Branch, Islamic Azad University, Langarud, Guilan, Iran

*r_ansari@guilan.ac.ir

Abstract: In this present investigation, density functional theory is used to study the elastic properties of titanium diselenide (TiSe₂) located in the uniform external electrical field. At the first step, the unit cell of the TiSe₂ is optimized using the SIESTA software to obtain the equilibrated dimensions of the unit cell, bond length and bond angle. Then, using the concept of strain energy against the uniaxial and biaxial strain in the harmonic region, Young's and bulk modulus of the TiSe₂ nanosheet in the external electrical field are computed. For this objective, density functional theory calculations are employed based on the generalized gradient approximation (GGA) with the Perdew–Burke–Ernzerhof (PBE) flavor. It is found that the both Young's modulus and bulk modulus of the TiSe₂ nanosheet increase by increasing the applied external electric field.

Keywords: Density functional theory; Titanium diselenide; Young's modulus; Bulk modulus

structure. The calculations are performed on this optimized structure. In Fig.1, the atoms' positions of planar TiSe₂ structure and the unit cell are shown. Moreover, the values of a, b and c after optimization procedure are given in Table 1 for the TiSe₂ nanosheet located in the electric field of 0 V/Ang.

In this paper, the value of mesh cut off and Kpoint are equal 425 Ry and 10 × 10 × 1, respectively. Besides, the TiSe₂ nanosheet is considered under uniform external electric fields with different values of 0, 1, 2, 3 and 4 V/Ang.

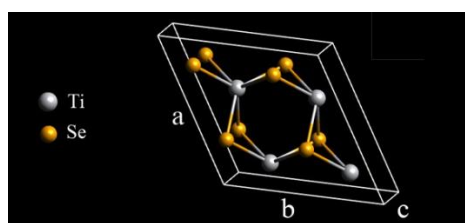


Fig.1: Atoms' positions and unit cell of TiSe₂ nanosheet

Table1: The values of bond length, bond angle and lattice constants of TiSe₂ nanosheet.

Bond length (Å)		Bond angle (Å)	
Ti -Se	2.624	Se-Ti-Se	76.9
Lattice constants (Å)			
a=b	7.119		
c	17		

2.1. Young's modulus

To obtain the Young's modulus of a structure, the second derivative of strain energy with respect to axial strains is employed:

1. Introduction

Because of their layered quasi two-dimensional structure, transition metal dichalcogenides have been attracted much attention in recent years [1, 2]. They have a wide range of applications such as electric power generators, devices and automotive [3, 4]. Titanium diselenide (TiSe₂) is one of the members of layered transitional-metal dichalcogenide consisting of covalently bonded Ti and Se atoms in a two-dimensional hexagonal arrangement [5, 6]. It has been widely utilized as a heavily doped semiconductor or semimetal [7-9].

Recently, several studies have been carried out to investigate various characteristics and applications of TiSe₂. Ataca et al. [10] predicted the stability of 88 different combinations of MX₂ compounds. Chen et al. [11] studied the dimensional effects on the charge density waves in ultrathin films of TiSe₂. Bianco et al. [12] analyzed the electronic and vibrational properties of TiSe₂ in the charge-density-wave phase from first principles. Lioi et al. [13] studied the photon-induced selenium migration in TiSe₂.

In the current study, the effect of external electric field on Young's modulus and Bulk modulus of TiSe₂ nanosheet is investigated. For this purpose, Young's and bulk moduli of the TiSe₂ nanosheet are computed.

2. Mechanical properties

Firstly, 12 atoms of TiSe₂ nanosheet is optimized using SIESTA software [14] in order to obtain the structure with the least energy level which have the most suitable bond lengths and bond angles. The calculations are performed on this optimized

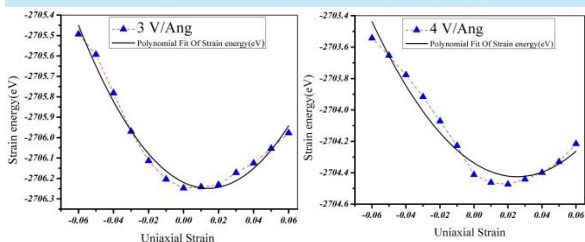


Fig.3: Variations of strain energy are plotted against the applied uniaxial strain in different external electric field

According to Fig.3, the second derivative of strain energy with respect to applied uniaxial strain can be calculated corresponding to different external electric fields. By using the related values in Eq. (1), the value of Young's modulus for TiSe₂ nanosheet subjected to various external electric fields are obtained. Calculated Young's moduli of TiSe₂ nanosheet in different external electric fields are plotted in Fig.4. It is observed that the Young's modulus of TiSe₂ nanosheets varies by changing the value of external electric field. It can be said that, generally, applying the external electrical field leads to increasing Young's modulus.

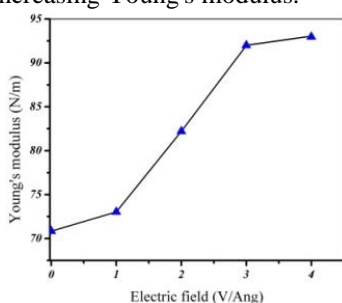
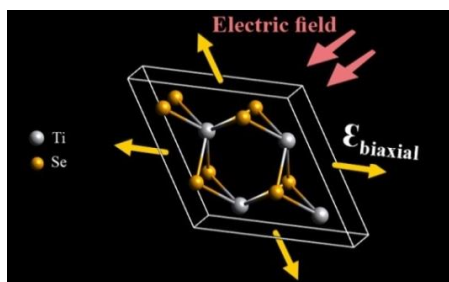


Fig.4: Young's moduli of TiSe₂ nanosheet in different external electric fields

2.2. Bulk modulus

To obtain the bulk modulus, the unit cell is subjected to the biaxial strain (see Fig.5). The bulk modulus is obtained from the second derivative of strain energy with respect to surface area of the unit cell subjected to biaxial strain:

$$B = A_0 \frac{\partial^2 E_s}{\partial A^2} \quad (2)$$



$$Y = \frac{1}{A_0} \frac{\partial^2 E_s}{\partial \varepsilon^2} \quad (1)$$

in which A_0 denotes the equilibrium surface area of the hexagonal unit cell of TiSe₂ nanosheet, E_s is the strain energy of structure and $\varepsilon = \Delta a/a$ represents the applied uniaxial strain. In accordance with the concept of Young's modulus, the unit cell of structure including 12 number of atoms is subjected to uniaxial strains and uniform external field as shown in Fig.2.

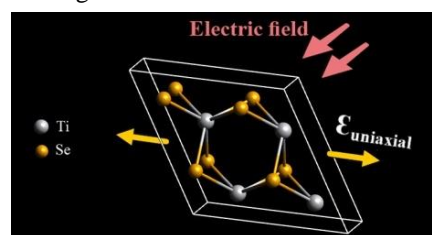
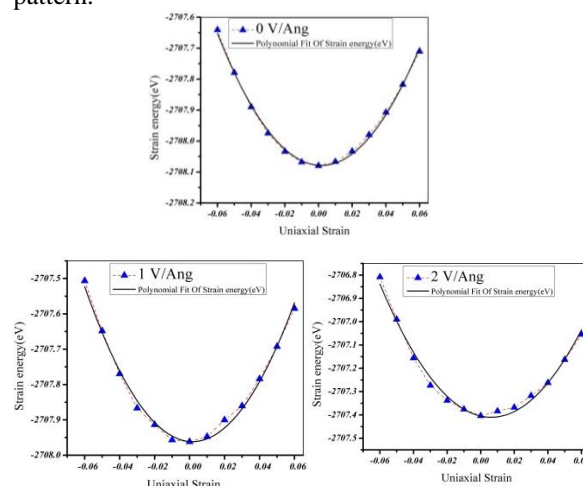


Fig.2: Schematic view of the unit cell subjected to uniaxial strain and external electric field

The unit cell of structure is subjected to tensile and compressive uniaxial strains in the range of -6% and 6% with step of 1%. Then, the strain energies relevant to each value of applied are calculated. In Fig.3, the variations of strain energy are plotted against the applied uniaxial strain in different external electric field. The minimum point with the lowest value of energy represents the optimum point of TiSe₂ nanosheet at the equilibrium state and other points with applied uniaxial strains are located in two sides of this point with a symmetric pattern.



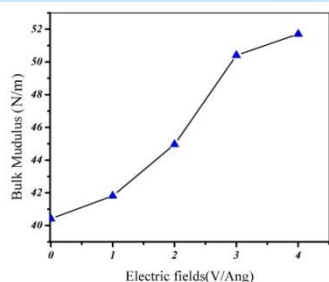


Fig.7: Variation of bulk modulus versus the external electric fields

3. Conclusions

The prime aim of the current study was to predict the elastic properties of TiSe₂ nanosheet subjected to various values of external electric field within the range of 0 V/Ang to 4 V/Ang. In an overall view it was observed that by increasing the value of external electric field, Young's modulus of TiSe₂ nanosheet increases by applying the external electric field which indicates that by applying an external electric field, the stiffness of structure increases. Besides, the external electric field causes to increasing the bulk modulus of TiSe₂ nanosheet.

References

- [1] R. Lv, J.A. Robinson, R.E. Schaak, D. Sun, Transition metal dichalcogenides and beyond: synthesis, properties, and applications of single- and few-layer nanosheets, *Accounts of chemical research* 48 (2014) 56-64.
- [2] A.A. Tedstone, D.J. Lewis, P. O'Brien, Synthesis, Properties, and Applications of Transition Metal-Doped Layered Transition Metal Dichalcogenides, *Chemistry of Materials* 28 (2016) 1965-1974.
- [3] R. Bhatt, S. Bhattacharya, R. Basu, S. Ahmad, Enhanced Thermoelectric Properties of Selenium-Deficient Layered TiSe_{2-x}: A Charge-Density-Wave Material, *ACS applied materials & interfaces* 6 (2014) 18619-18625.
- [4] R. Bhatt, R. Basu, S. Bhattacharya, A. Singh, Surfers, Low temperature thermoelectric properties of Cu intercalated TiSe₂: a charge density wave material, *Applied Physics A* 111 (2013) 465-470.
- [5] A.M. Novello, B. Hildebrand, A. Scarfato, C. Didiot, Scanning tunneling microscopy of the charge density wave in 1T-TiSe₂ in the presence of single atom defects, *Physical Review B* 92 (2015) 081101.
- [6] X.-Y. Fang, H. Hong, P. Chen, T.-C. Chiang, X-ray study of the charge-density-wave transition in single-layer TiSe₂, *Physical Review B* 95 (2017) 201409.
- [7] S. Huang, G. Shu, W.W. Pai, H. Liu, F. Chou, Tunable Se vacancy defects and the unconventional

Fig.5: Schematic view of the unit cell subjected to biaxial strain and external electric field

In other words, the unit cell of TiSe₂ nanosheet is subjected to biaxial strains in the range of -6% and 6% with strain step of 1%. Subsequently, the values of surface area of the unit cell and related strain energy of structure are calculated at each step. Fig.6 illustrates the variation of strain energy of structure against the surface area of the unit cell corresponding to various values of external electric fields. In accordance with Fig.6 and Eq. (2), the values of bulk modulus of TiSe₂ nanosheet subjected to different values of external electric field can be extracted from.

Fig.7 demonstrates the variation of obtained bulk modulus versus the external electric field. It can be seen that by increasing the external electrical field leads to increasing the Bulk modulus.

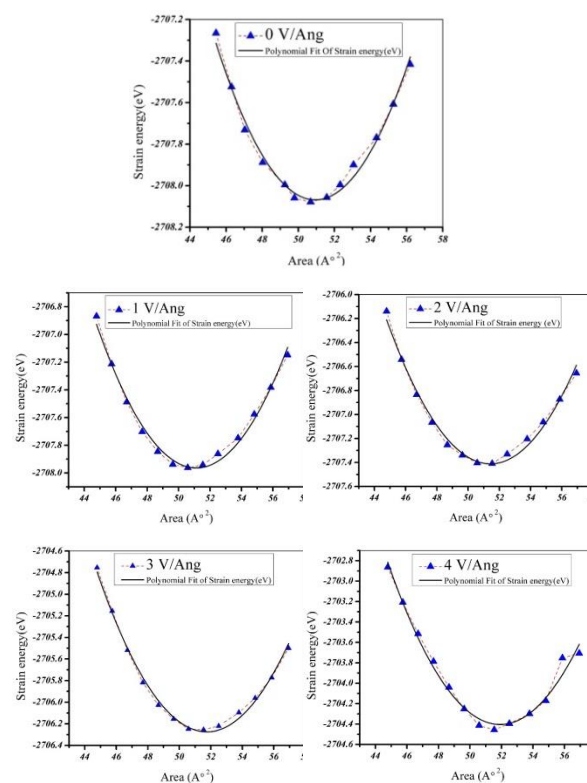


Fig.6: Variation of strain energy against the surface area of the unit cell corresponding to various values of external electric fields



بیستمین کنفرانس شیمی فیزیک ایران
دانشکده علوم پایه - دانشگاه اراک
۳۱-۲۹ مرداد ۱۳۹۶



20th Iranian Physical Chemistry Conference

waves in ultrathin films of TiSe₂, Nano Letters 16 (2016) 6331-6336.

[12] R. Bianco, M. Calandra, F. Mauri, Electronic and vibrational properties of TiSe₂ in the charge-density-wave phase from first principles, Physical Review B 92 (2015) 094107.

[13] D.B. Lioi, D.J. Gosztola, G.P. Wiederrecht, G. Karapetrov, Photon-induced selenium migration in TiSe₂, Applied Physics Letters 110 (2017) 081901.

[14] J.M. Soler, E. Artacho, J.D. Gale, A. García, J. Junquera, P. Ordejón, D. Sánchez-Portal, The SIESTA method for ab initio order-N materials simulation, Journal of Physics: Condensed Matter 14 (2002) 2745.

charge density wave in 1 T- TiSe₂- δ , Physical Review B 95 (2017) 045310.

[8] D.R. Merrill, D.B. Moore, J. Ditto, D.R. Sutherland, The Synthesis, Structure, and Electrical Characterization of (SnSe)_{1.2} TiSe₂, European Journal of Inorganic Chemistry 2015 (2015) 83-91.

[9] D.L. Duong, G. Ryu, A. Hoyer, C. Lin, M. Burghard, K. Kern, Raman Characterization of the Charge Density Wave Phase of 1T-TiSe₂: From Bulk to Atomically Thin Layers, ACS nano (2017).

[10] C. Ataca, H. Sahin, S. Ciraci, Stable, single-layer MX₂ transition-metal oxides and dichalcogenides in a honeycomb-like structure, The Journal of Physical Chemistry C 116 (2012) 8983-8999.

[11] P. Chen, Y.-H. Chan, M.-H. Wong, X.-Y. Fang, Dimensional effects on the charge density



The Role of Functionalization of Carbon Nanotube in Delivery of Gemcitabine

N.Karachi*, N.Abidi

Department of chemistry, Marvdasht Branch, Islamic Azad University, Marvdasht, Iran
nimakarachi@miau.ac.ir

Abstract

In recent years, a lot of attention has been focused on nanoparticles as carriers for drug delivery. Nano-carriers can cause better performance and minimize side effects of drugs. This article explores the potential of carbon nanotubes for delivering anticancer drug, Gemcitabine with and without Folic acid and Chitosan. Using these groups help to decrease the deficiencies of carbon nanotube and increase the stability of the system. Drawing the structures and optimization the systems has been done by using HyperChem, Gauss View, Gaussian and Nanotube Modeler. Energy, dipole moment and NMR parameters (σ_{iso} , σ_{aniso} , $\Delta\sigma$ and δ) of the systems were calculated by HF/STO-3G. Finally, it was observed that systems that were functionalized with Folic acid and Chitosan are proper agents for targeted delivery of Gemcitabine.

Keywords: Carbon nanotubes; Gemcitabine; Folic acid; Chitosan

Introduction

Nano is currently well-recognized in various sophisticated fields especially in medical science [3-5]. Drug Delivery Systems (DDS) are developed in order to improve pharmaceutical and therapeutic properties of drugs and typically hold the drug like a reservoir [1,2]. These systems release the drug in determined location and dosage and hence, are effective on drug pharmacokinetics and distribution inside the body. Nanoparticles are extensively exploited in drug delivery. In recent years, abundant attempts have been concentrated on making nanostructures as drug delivery carriers. That is because such structures, due to their capability in controlling and slow release of drugs, protecting the drug molecule, having particle size smaller than cells, the ability of crossing biological barrier to deliver the drug in targeted place, enhancing the drug durability in blood, targeted drug delivery, and biocompatibility can be considered as a truly effective drug delivery system increasing the therapeutic efficiency of drugs [6,7].

Methods

In our study, drawing molecular structures of Gemcitabine ($\text{C}_9\text{H}_{11}\text{F}_2\text{N}_3\text{O}_4$), Folate ($\text{C}_{19}\text{H}_{19}\text{N}_7\text{O}_6$), chitosan ($\text{C}_8\text{H}_{13}\text{NO}_5$) and SWNT were done by using Nanotube Modeler and HyperChem softwares. After optimizing the single structures, connections between the molecules were done by Gauss View. Gemcitabine molecules bound to carbon nanotube through Amine group that was connected to pyrimidin. The systems were optimized using Gaussian by HF method and STO-3G as the basic set. The frequency test was applied to investigate the presence of negative frequencies. Finally energy and dipole moment and NMR parameters of system were calculated by using HF method.

Discussion and Conclusion

In this article, it was tried to construct the combination of CNT and Gemcitabine because of the side effect of anticancer drug on untargeted tissues, but this system was unstable and can't be exist. So secondary agent was investigated. Considering the fact that folic acid is one of the most important and applicable targeting molecules and can specifically attach to folate receptor, it can

be an appropriate option to stabilize the system and to make it targeted. Thus, folate agent was attached to the system and the optimization of resulting structure was studied.

Since Carbon nanotubes are hydrophobic and have a very low solubility in aqueous solutions that impedes them to be utilized in biological systems, however, functionalization of nanotubes with chitosan agents can enhance their polarity and solubility of the system.

Comparing the energy values of the system (table 1) is observed that trend of stability changes for the above system is as follow:

FUL > JEM > FUL: CHI: CNT: JEM > CNT > CHI

The trend of dipol moment for the system is as follow:

CHI > FUL > JEM > FUL: CHI: CNT: JEM > CNT

Parameter Systems	E (Kcal.mol ⁻¹)	Dipole moment (debye)
JEM	-995.7194	4.7385
FUL	-1540.9835	3.5957
CHI	-1744.4292	0.0027
CNT	-2242.0962	5.4872
FUL:CHI:CNT:JEM	-6818.8566	7.9723

NMR calculations were used to determine the active centers of the system. This method is highly sensitive to the structure and surroundings of atoms and molecules and is a critical method for analyzing molecular structure and finding active sites of them. NMR parameters (σ_{iso} , σ_{aniso} , $\Delta\sigma$ and δ) for the system's atoms were calculated using GIAO. According to NMR calculations, O₂₅ is

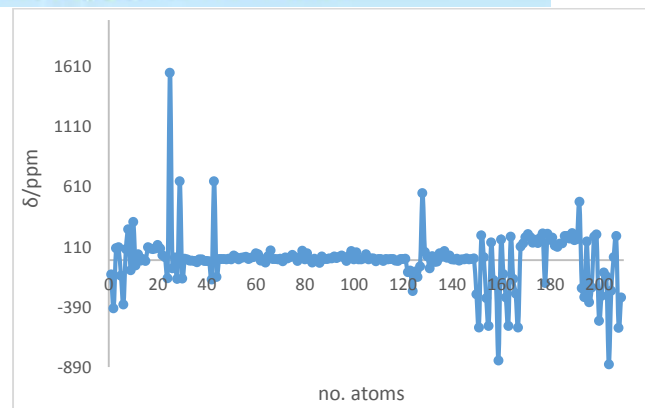
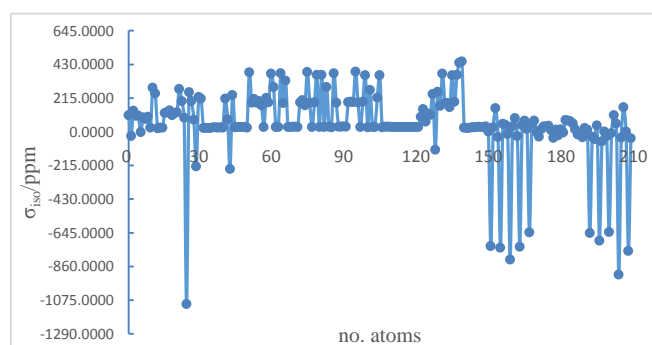


Fig 1. The NMR parameter δ for the system FUL:CHI:CNT:JEM



CHI: CNT: JEM

determined as the active center of the system. (Fig. 1, 2)

Conclusion

This paper investigated the use of carbon nanotubes together with folic acid and chitosan in targeted delivery of Gemcetabine. It was observed that adding folic acid and chitosan to the system containing nanotubes and Gemcetabine can reduce the energy, increase stability, polarity and solubility of the system and therefore, improves drug delivery and performance inside the body. Additionally, O₂₅ was introduced as the active center in NMR calculations.

References:



- [1] M.Yen , J.Yang , J.Mau “Physicochemical characterization of chitin and chitosan from crab shells”, *Carbohydrate Polymers*, 75(2009) 15-21.
- [2] T.Wang, X.K.Zhu, X.T. Xue, D.Y. Wu “Hydrogel sheets of chitosan, honey and gelatin as burn wound dressings”, *Carbohydrate Polymers*, 88(2012) 75-83.
- [3] V.Sgobba, D. M. Guldi “Carbon nanotubes—electronic/electrochemical properties and application for nanoelectronics and photonics”, *Chemical Society Review*, 38(2009) 165–184.
- [4] M.Pumera, A.Ambrosi, A.Bonanni, E. L. K. Chng, H. L. Poh “Graphene for Electrochemical Sensing and Bio Sensing”, *Trends in Analytical Chemistry*, 29(2010)954–965.
- [5] H.Dai “Carbon nanotubes: Synthesis, integration, and properties”, *Accounts of Chemical Research*, 35(2002) 1035-1044.
- [6] V.V.Chaban, T.I.Savchenko, S.M. Kovalenko, O.V.Prezhdo “Heat-driven release of a drug molecule from carbon nanotubes: a molecular dynamics study”, *Journal of Physical Chemistry*, 114(2010)13481-13486.
- [7] S.Dhar, Z. Liu, J. Thomale, H.Dai, S.J. Lippard “Targeted single-wall carbon nanotube mediated Pt (IV) prodrug delivery using folate as a homing device”, *Journal of American. Chemical. Society*, 130(2008) 11467-11476.

Asphaltene Adsorption onto SiO₂ nanoparticles and demulsification behavior

S. Morteza. Sadrpoor^a and Soheila. Javadian^{b*}

Department of physical chemistry, faculty of science, Trabiati Modares University, Tehran-Iran
Department of physical chemistry, faculty of science, Trabiati Modares University, Tehran-Iran

Abstract

Asphaltene Adsorption onto surface nanoparticles is an attractive subject for the oil industry because nanoparticles would remove asphaltenes from the crude oil rapidly and thus make the remaining fraction of crude oil transportable for conventional processing. In this work, the adsorption of asphaltenes from crude oil model solutions onto colloidal nanoparticles of SiO₂ nanoparticles were investigated. Asphaltene Adsorption isotherms were obtained and the resultant shows isotherm is in good Compromise with the Langmuir isotherm model. Bottle test uses for evaluation demulsification of crude oil. Also, the result of demulsification of SiO₂ indicates this nanoparticle better than industrial demulsifier for dehydration of crude oil in all concentration.

Keywords: Crude oil, demulsification, Asphaltene Adsorption

1. Introduction

Emulsification is a critical process as oil field emulsions are, in principal, stable liquid-liquid colloidal suspensions comprising of dispersed/internal phase, continuous/external phase, and emulsifying agents basically (surface active material) present at the oil-water interface. An effectual demulsifying route must thus be capable of annulling/minimizing the stability of targeted emulsion, leading to separation of immiscible phases. Demulsification ways are generally classified into three groups, i.e., chemical, physical, and biological treatments [1].

Asphaltenes are a large molecule with high-molecular-weight, are very complex and can not chemically identifiable compounds easily. Asphaltene defined as the fraction of crude oil that is soluble in light aromatic hydrocarbons, such as toluene and insoluble in low molecular-weight paraffin, such as n-pentane or n-heptane. Their composition, structure, and stability depend on their source oil field, their method of extraction of asphaltene, and the type of solvent (n-heptane or n-pentane) used for extraction. The general structure of asphaltenes is based on polyaromatic nuclei carrying aliphatic chains include heteroatoms, such as nitrogen, oxygen, sulfur, and some metals, especially vanadium, iron, and nickel, asphaltene has an average aromatic sheet comprising 5-10 benzene-condensed rings that forming monomers has an average sheet dimension in the range of 1.2-1.7 nm.

In this work, the use of SiO₂ nanoparticles for adsorption of asphaltenes from oil model solutions is investigated. Silica is commonly used as a catalyst or support for oil upgrading. [1-2].

2. Materials and Methods

Commercially available SiO₂ nanoparticles were purchased from Sigma-Aldrich. The reported particle size is 20-30 nm. Asphaltenes were prepared from a south of Iran oil field. Solvents used in the extraction and precipitation of asphaltenes from south of Iran oil field were n-heptane (99%, HPLC grade, Sigma-Aldrich, and toluene (analytical grade, Merck).

3. Results and discussion

As shown in figure 1 the demulsification ability of SiO₂ compare to industrial demulsifier as different concentrations. According to figure 1 dehydration efficacy of SiO₂ is more than industrial demulsifier as all concentrations.

The Batch adsorption experiments were prepared at a ratio 1:10 (L/g) model oil solution/ mass of the silica nanoparticles. The vials were sealed properly to avoid loss of toluene by evaporation and shaken at 400 rpm in an incubator at a room temperature until equilibrium was established. Then, the asphaltene-containing nanoparticles were separated via centrifugation at 4500 rpm for 20 min. [2-3].

The concentrations of the silica in the supernatant were evaluated using a UV-vis spectrophotometer device (Nicolet Evolution 100). The supernatant solution was analyzed for its asphaltene concentration by usage the UV-vis spectrophotometer device.

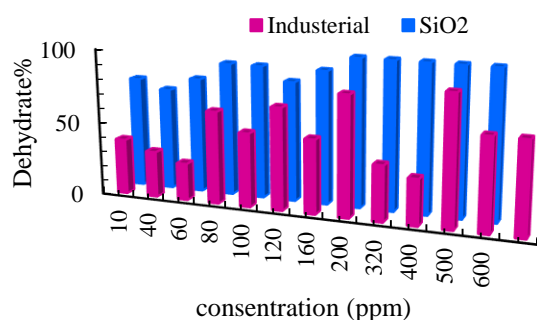


Figure 1: demulsification ability of SiO₂ and industrial demulsifier as a different concentrations

A calibration curve of UV-vis absorbance at ~295 nm versus the asphaltene concentration was created using standard model solutions with known concentrations. To determine the maximum adsorption of asphaltenes and equilibrium isotherm constants, the adsorption isotherms obtained at room temperatures were further investigated (Figure 2). In this case, Langmuir type isotherms were observed, suggesting coverage surface silica by monolayer asphaltene. The Langmuir equilibrium adsorption constant related to the affinity of binding sites (L/mg), and q_m is defined as the monolayer saturation capacity, representing the maximum amount of asphaltenes per unit mass of nanoparticles for complete monolayer coverage (mg/g). The value of q_m was obtained 188.6 for this system.

Reference

[1] R. Zolfaghari et al. "Demulsification techniques of water-in-oil and oil-in-water emulsions in the petroleum industry." *Separation and Purification Technology* 170 (2016): 377-407.

4. Conclusion

Current research trends for oil focus on nanotechnology that maximize recovery of oil while minimizing the environmental effect. This study demonstrated the use of SiO₂ nanoparticles, as typical catalysts/supports commonly present in the oil industry, for asphaltene adsorption and good ability for demulsification of crude oil.

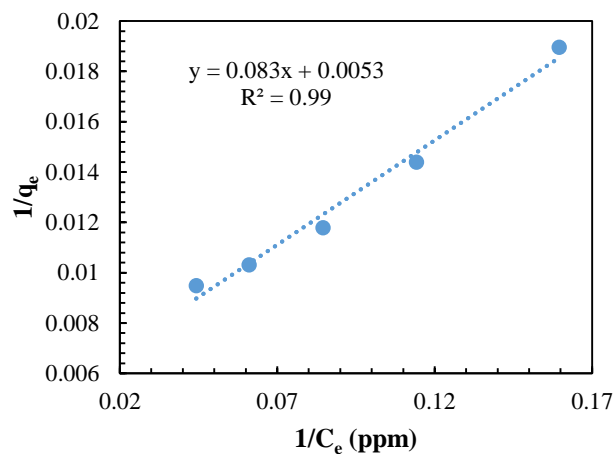


Figure 2: Linearized Langmuir isotherms of asphaltene molecules onto SiO₂ nanoparticles at room temperature. Shaking rate, 400 rpm; contact time, 24 h.

[2] N.Nashaat. "Asphaltene Adsorption onto alumina nanoparticles: kinetics and thermodynamic studies." *Energy & Fuels* 24.8 (2010): 4116-4122.

[3] I. N. Evdokimov, N. Yu Eliseev, and B. R. Akhmetov. "Assembly of asphaltene molecular aggregates as studied by near-UV/visible spectroscopy: II. Concentration dependencies of absorptivities." *Journal of Petroleum Science and Engineering* 37.3 (2003): 145-152.

Synthesis of PEGylated iron oxide nanoparticles as drug delivery carrier

Khadijeh Najafi and Soheila. Javadian*

Department of physical chemistry, faculty of science, Trabiati Modares University, Tehran-Iran

Department of physical chemistry, faculty of science, Trabiati Modares University, Tehran-Iran

Abstract

Targeted and efficient delivery of therapeutics to tumor cells is one of the key issues in cancer therapy. In the present work, we report a core-shell nanoparticles comprising polymer shell coated on magnetic nanoparticles as an anti-cancer drug carrier. Magnetite nanoparticles (MNPs), prepared by simple co-precipitation method, was coated with polyethylene glycol (PEG). X-ray diffraction (XRD) was used for study of the crystalline structure of Fe₃O₄ nanoparticles. Size of Fe₃O₄ and Fe₃O₄@PEG core-shell nanoparticles was investigated by Dynamic light scattering (DLS) that demonstrated diameter of about 38 and 225 nm, respectively. Fourier transform infrared spectra (FTIR) provided the sufficient evidence for the presence of PEG in the Fe₃O₄@PEG core-shell nanoparticles. These nanoparticles was used as a carrier for Doxorubicin (DOX).it could be efficiently loaded in Fe₃O₄@PEG nanoparticles.

Keywords: Magnetic nanoparticles, Drug delivery, Doxorubicin, Polyethylene glycol

1. Introduction

Cancer is one of the most fatal diseases in the world, and the number of new cases increases each year. Despite the fact that chemotherapeutic and radiotherapeutic options are available for cancer, the critical challenge is to deliver them specifically to cancer cells with the additional concern of minimizing toxic effects to normal cells.[1]

Magnetic nanoparticles (MNPs) are a class of NPs that can be manipulated using a magnetic field. These NPs possess unique physical properties and the ability to function at the cellular and molecular levels of biological interactions. Within the last few decades, MNPs have been extensively investigated for biomedical applications, such as magnetic resonance imaging contrast agents for diagnosis and magnetic hyperthermia agents for cancer treatment. Superparamagnetic Iron Oxide NPs(SPIONs) are superior to other metal oxide NPs due to their biocompatibility and stability and are the most commonly employed MNPs for biomedical applications.[2]

Bare SPIONs tend to agglomerate due to van der Waals and magnetic dipole-dipole attractive forces. Surface functionalization of SPIONs with biocompatible molecules is a useful approach to avoid NP agglomeration and permit the conjugation of therapeutic molecules (drugs) to NPs.[3]

In this paper, we have prepared polyethylene glycol modified iron oxide nanoparticle (Fe₃O₄@PEG) as cancer theranostic agent, which shows good loading for the anti-cancer drug.

2. Materials and Methods

Magnetite NP was synthesized chemically by the co-precipitation reaction from an aqueous mixture of Fe³⁺/Fe²⁺ in the molar ratio of 2:1 using concentrated ammonium hydroxide solution in an inert atmosphere of nitrogen. PEGylation of magnetite nanoparticles was carried out by ultrasonic probe at room temperature for 1.5 min.[4]

3. Results and discussion

The size distributions of magnetite were shown in Fig1. The average size of Fe₃O₄ and Fe₃O₄@PEG in was found to be 37.84 nm and 225 nm with a PDI value of 0.3.

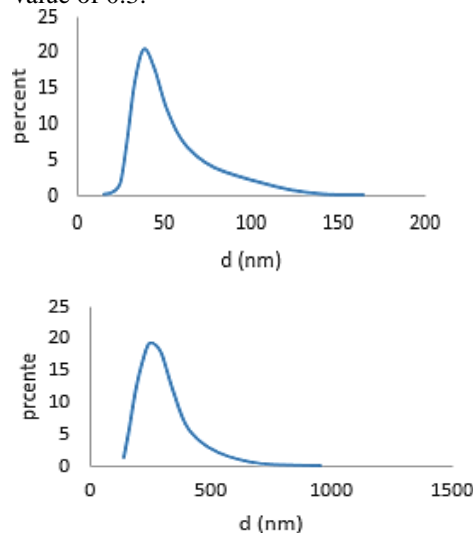


Fig1. The size distribution from DLS result (a) magnetite NP, (b) poly@MNPs

As it can be seen in Fig2. The characteristic diffraction peaks of water-based Fe₃O₄ nanoparticles at 30.2°, 35.7°, 43.3°, 53.6°, 57.2° and 62.6° corresponded to [2

2 0],[3 1 1], [4 0 0], [4 2 2], [5 1 1] and [4 4 0] lattice planes, respectively[35].

To know about the modification of the NPs by the PEG molecules FTIR spectra were displayed in Fig 3. The bare Fe₃O₄ NPs showed characteristic bands related to the Fe–O vibrations near 618 (shoulder) and 569 cm⁻¹. The bare Fe₃O₄ NPs showed characteristic bands related to the Fe–O vibrations near 618 (shoulder) and 569 cm⁻¹.

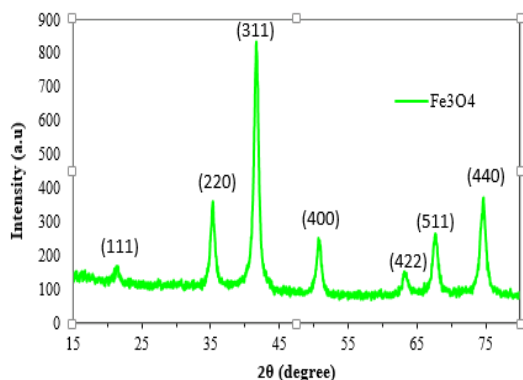


Fig2. XRD patterns of (a) water-based Fe₃O₄nanoparticles. The bare Fe₃O₄ NPs showed characteristic bands related to the Fe–O vibrations near 618 (shoulder) and 569 cm⁻¹. Similar peaks have been observed in the spectra of the PEG@MNPs (at 633 and 569 cm⁻¹), but not Apart from that, a broad –O– H stretch around 3450 cm⁻¹, a sharp –C–H stretch around 2885 cm⁻¹ and a sharp –C–O stretch around 1105 cm⁻¹ are observed in both PEG and the PEG-coated NPs, revealing the presence of PEG residue in the final product. However, these peaks are not observed in the spectrum of bare Fe₃O₄ NPs. These results clearly showed a surface modification of Fe₃O₄ NPs with PEG.

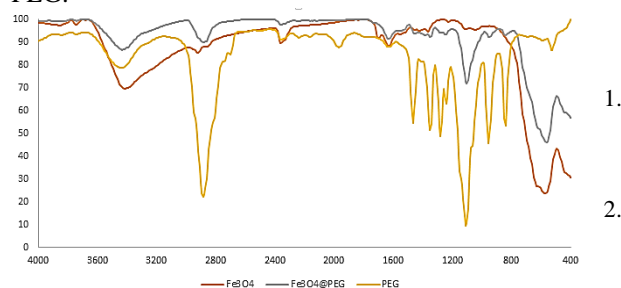


Fig3. FTIR spectrum of Fe₃O₄, PEG-coated Fe₃O₄, PEG

Doxorubicin (DOX) an anti-cancer drug model used for the present study, was loaded into the nanoparticles was studied. DOX drug Entrapment efficiency (Ea) is defined as the following equation

$$E = \frac{C_0 - C_1}{C_0}$$

Where C₀ is the initial concentration of drug molecules, C₁ is the concentration of unbound drug

molecules after adsorption. C₀ and C₁ are based on by measuring DOX concentrations at 480 nm of absorption spectra after calibration.

To find the optimal concentration of drug loading on the nanocarrier, a similar concentration of nanocarrier with different concentrations of the drug was stirred in dark conditions. From the supernatant was taken UV absorption after the completion of the loading process, the results are shown in Fig4.

It is observed that the highest percentage of drug entrapment is related to a ratio of 3:4.

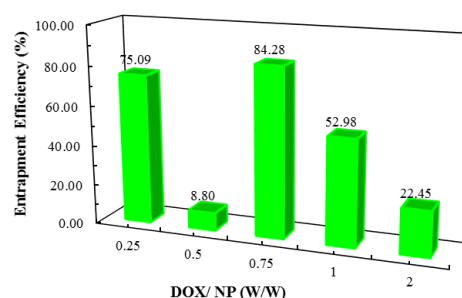


Fig4. Percentage of drug entrapment

4. Conclusion

In summary, magnetic carriers consisting of polyethylene glycol coated superparamagnetic iron oxide (magnetite) nanoparticles were synthesized by co-precipitation of iron ions and subsequently coated with polyethylene glycol. The magnetic carriers were characterized by XRD, FT-IR and DLS techniques.

The drug entrapment has been evaluated using UV-Vis absorption.

This designed system can be used as drug delivery Nanocarriers in biomedical applications.

Reference

- Li, Z., et al., *Synthesis and characterization of monodisperse magnetic Fe₃O₄@ BSA core-shell nanoparticles*. Colloids and Surfaces A: Physicochemical and Engineering Aspects, 2013. **436**: p. 1145-1151.
- Santos, M., et al., *Synthesis, characterization and cytotoxicity of glutathione-and PEG-glutathione-superparamagnetic iron oxide nanoparticles for nitric oxide delivery*. Applied Surface Science, 2016. **367**: p. 26-35.
- Khachatryan, V., et al., *Precise determination of the mass of the Higgs boson and tests of compatibility of its couplings with the standard model predictions using proton collisions at 7 and 8*. The European Physical Journal C, 2015. **75**(5): p. 212.
- Sun, L., et al., *Malachite green adsorption onto Fe₃O₄@ SiO₂-NH₂: isotherms, kinetic and process optimization*. RSC Advances, 2015. **5**(16): p. 11837-11844.

A Novel Sonochemical Method for the Synthesis of Amorphous Iron Oxide Nanoparticles and Its Photocatalytic Application

V. Saheb*, A. Motamednia, S.M.A. Hosseini

Master of Science in Nanochemistry, University of Shahid Bahonar, Kerman, Iran

vskermanu@gmail.com

June 29, 2017

Abstract: Amorphous metal oxides magnetic nanoparticles possess fascinating properties and a wide range of potential applications because of their unique structural and magnetic properties, nontoxicity, and high chemical stability. This work reports the preparation of amorphous Fe₃O₄ nanoparticles by ultrasound irradiation of a mixture of iron filings, Sodium hypochlorite, and PEG surfactant. The PEG surfactant acts as stabilizer and it is nontoxic, non-flammable and easy to handle. The structure and morphology of particles are analyzed by X-Ray Diffraction (XRD), FT-IR and UV-Vis spectra, SEM and TEM microscopy. The Amorphous Fe₃O₄ nanoparticles show good catalytic activity in degradation of methylene blue.

Keywords: Fe₃O₄; amorphous; nanoparticles; sonochemical; photocatalytic

Introduction

Nanometer-scale metal oxide nanoparticles are found to have a great perspective in fundamental sciences and novel technological applications. [1] Amorphous metal oxides magnetic nanoparticles possess fascinating properties and a wide range of potential applications because of their unique structural and magnetic properties, nontoxicity, and high chemical stability. The preparation of iron oxide nanoparticles has been intensively studied due to their potential and practical applications in biotechnology and biomedicine, magnetic separation, drug delivery, magnetic resonant imaging (MRI), catalytic, optical, sorption, and other properties. [2] There are various chemical methods for preparing Fe₃O₄ nanoparticles such as solvothermal, sol-gel, hydrothermal, thermal decomposition, and co-precipitation techniques. [3] In general, these methods do not yield pure amorphous phases, and good control of particle size and achievement of monodispersity are still the challenges in all these techniques. In the present research work, a simple, clean and low-cost method for the synthesis of amorphous Fe₃O₄ nanoparticles is developed. The amorphous nanoparticles were synthesized by sonochemical method in the presence of suitable surfactants. [4] Much effort has been made to modify the surface of amorphous Fe₃O₄ nanoparticles by using molecular, polymeric, and inorganic layers to minimize their agglomeration. Polyethylene glycol (PEG) is one of the polymers with major interest in this area as it is nontoxic, non-flammable and easy to handle. [3]

In this study, PEG-coated Fe₃O₄ nanoparticles were synthesized by sonochemical method and we used the amorphous Fe₃O₄ nanoparticles for the photocatalytic degradation of methylene blue dye.

Materials and method

In a typical procedure, PEG was dissolved into distilled water. Next, iron filings (2g) and NaOCl (25 mL, 6-14 % solution) were added to the PEG solution. This solution was put in a bath type sonicator (160/640W) for 1 hours. A black precipitate was obtained which was centrifuged, washed several times with distilled water and dried. The obtained product was characterized by X-ray diffraction (XRD), SEM microscopy, FT-IR and UV-Vis spectroscopy. In order to evaluate of photocatalytic activity of prepared products for degrading methylene blue dye solution, experiments were performed in a photochemical reactor.

Results and Discussion

The XRD spectrum of synthesized product is shown in Fig. 1. The XRD spectrum shows a noisy pattern and no peaks attributable to an iron product are observed. There are some small peaks which are attributed to NaCl. The XRD pattern shows that an amorphous product is obtained.

FT-IR spectra of Fe₃O₄ nanoparticle is shown in Fig. 2. The peaks appeared at 617.71 and 485.97 cm⁻¹ are assigned to Fe-O bond and the characteristic peak of -OH bond at 3424.66 cm⁻¹ is obviously enhanced.

The morphologies of the Fe₃O₄/PEG were examined by the scanning-electron microscope that is shown in Fig. 3. The bare Fe₃O₄ particles are in the shape of spheres with about 80 nm in diameter.

UV-Vis spectrum of methylene blue is shown in Fig.4. The progress of reduction reaction of MB can be monitored by measuring the decrease in absorption of MB on UV-Vis spectrum at a λ_{max} of 664 nm. The time dependent electronic absorption spectrum of MB during visible light photo irradiation is presented in Fig. 4. After 17 min of irradiation under visible light in



the presence of amorphous Fe_3O_4 nanoparticles, more than 80% of dye got degraded and the solution became colorless. This could be attributed to the fact that when Fe_3O_4 nanoparticle is irradiated with the visible light, electrons get promoted from the valence band to the conduction band of the semiconducting oxide to give electron-hole pairs. Generally, these electron-holes recombine to reduce the photocatalytic activity of semiconductors.

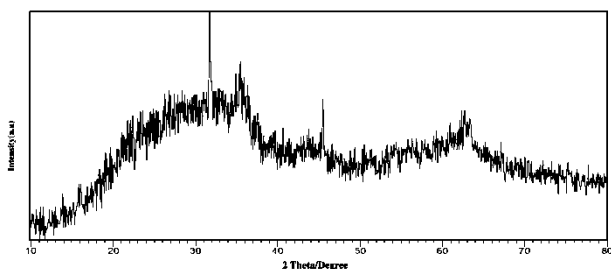
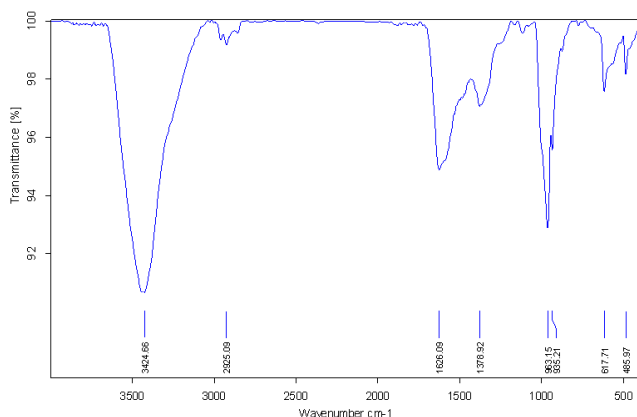


Fig.2: X-ray diffraction patterns of the amorphous Fe_3O_4 nanoparticles.



Conclusions

In summary, in this research work, a facile method for the synthesis of PEG encapsulated Fe_3O_4 nanoparticles is presented. Fe_3O_4 nanoparticles are formed during oxidation of Iron fillings by sodium hypochlorite. PEG 1000 is used as capping agent. The synthesized nanoparticles are characterized by XRD, SEM, and IR spectroscopy. The Fe_3O_4 nanoparticles displayed good catalytic activity compared to the commercial TiO_2 for the methylene blue dye.

References

- [1] L. Beigi, V. Saheb, " A facile one-pot method for the synthesis of CdO_2 and CdO nanoparticles by oxidation of cadmium metal by hydrogen peroxide", *Nano-Structures & Nano-Objects*, 9 (2017) 13–18
- [2] Z. Wang, L. Zhao, P. Yang, Z. Lv, H. Sun, Q. Jiang, " Water-soluble amorphous iron oxide

Fig. 2: FT-IR spectra the amorphous Fe_3O_4 nanoparticles

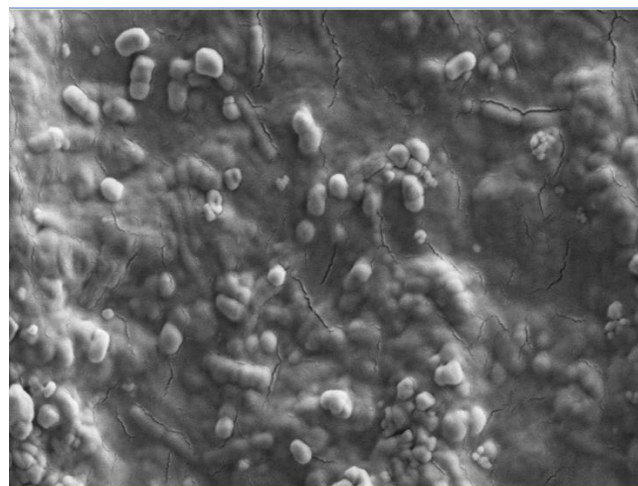


Fig.3: SEM micrographs of $\text{Fe}_3\text{O}_4/\text{PEG}$

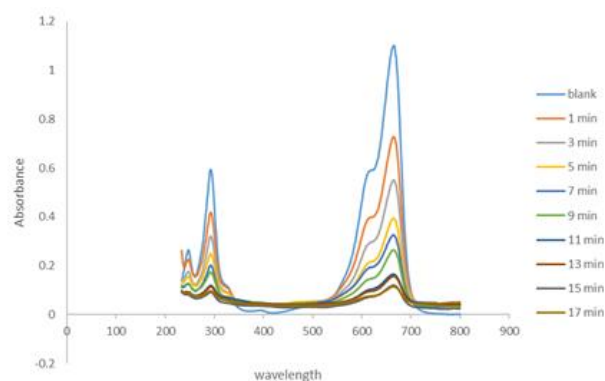


Fig. 4: UV-Visible absorption spectra for the degradation of methylene blue in the presence of amorphous Fe_3O_4 nanoparticles

nanoparticles synthesized by a quickly pestling and nontoxic method at room temperature as MRI contrast agents", *Chemical Engineering Journal*, 235 (2014) 231–235

[3] A. M. Elbarbary, I.A. Ibrahim, H.M. Shafik, S. H. Othman, " Magnetic $^{99\text{m}}\text{Tc}$ - core-shell of polyethylene glycol/polyhydroxyethyl methacrylate based on Fe_3O_4 nanoparticles: Radiation synthesis, characterization and biodistribution study in tumor bearing mice", *Advanced Powder Technology*, 8 (2017) 1898–1910

[4] K. V. P. M. Shafi, A. Ulman, X. Yan, N. Yang, C. Estourne`s, H. White, and M. Rafailovich, "Sonochemical Synthesis of Functionalized Amorphous Iron Oxide Nanoparticles", *Langmuir*, 17 (2001) 5093-5097



Sustainable super-fast adsorptive removal of DBA and BPA from water by a Novel nanocomposite adsorbent

M. H. Ahmadi Azqhandi^a, M. H. Omid^b

^a Applied Chemistry Department, Faculty of Petroleum and Gas (Gachsaran), Yasouj University, Gachsaran, 75813-56001, Iran.

^b Department of Chemistry, Faculty of Science, University of Guilan, P.O. Box 41996-13776, Guilan, Iran.

*mhahmadia58@gmail.com, m.ahmadi@yu.ac.ir

Abstract: The present study focused on the ultrasonic assisted simultaneous removal of dibenzyl amine (DBA) and 2-biphenyl amine (BPA) from aqueous media following using Magnetic Fe₃O₄/bentonite nanocomposite as a new adsorbent. The structure and morphology of nanocomposite was identified by SEM and XRD analysis. The evaluation and estimation of equilibrium data from traditional isotherm models display that the Tempkin model indicated the best fit to the equilibrium data, while the adsorption rate efficiently follows the pseudo-second-order model. The obtained thermodynamic parameters (i.e. namely, ΔG^0 , ΔH^0 and ΔS^0) showed that the adsorption on the nanocomposite was endothermic and spontaneous. Results indicated that the synthesized nanocomposite may be costly adsorbents for organic removal.

Keywords: Nanocomposite; dibenzyl amine (DBA) and 2-biphenyl amine (BPA); Isotherm.

Introduction

Aromatic amines as a branch of organic pollutants can be mutagenic or carcinogenic even at low concentrations [1]. Some main sources of amines in the environment include oil refining, synthetic polymers, dyes, paint, pigments, plastics and rubbers, pesticides, pharmaceuticals, explosives and so on [1,2]. Due to the high production of these kinds of pollutants, an effective and economical method to remove them from the water should be developed.

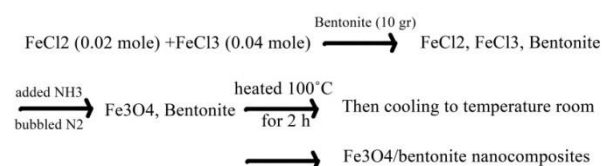
In this study, firstly Fe₃O₄/bentonite nanocomposite was synthesized and characterized by XRD and SEM technique. The prepared Fe₃O₄/bentonite nanocomposite was applied to remove 2-biphenylamine (BPA) and dibenzyl amine (DBA) as a model of aromatic amines from aqueous solution. The kinetics equilibrium and thermodynamic parameters Simultaneously was determined. Furthermore the effect of BPA and DBA concentration, dose of adsorbent, contact time, pH and temperature on the adsorption process was also investigated.

Materials and method

Fe₃O₄/bentonite magnetic composites were prepared using a co-precipitation method [3]. Process Scheme and Reaction Conditions for the Synthesis of nanocomposite was shown in below.

Batch adsorption experiments were carried out in 100 ml glass bottles with Fe₃O₄/bentonite nanocomposite. In all of them, 0.035 g of solid adsorbent was introduced to 50 ml of BPA or DBA solution of increased initial concentrations (C₀) from 5 to 50 mg/l. The pH of the samples was adjusted by dropwise addition of 0.1 N HCl or 0.1 N NaOH to pH 12. At the end of the equilibrium period, the mixture was filtered

and also the remaining DBA and BPA concentration in the filtrate was measured using a spectrophotometer.



Scheme 1: Preparation of Fe₃O₄/bentonite magnetic composites

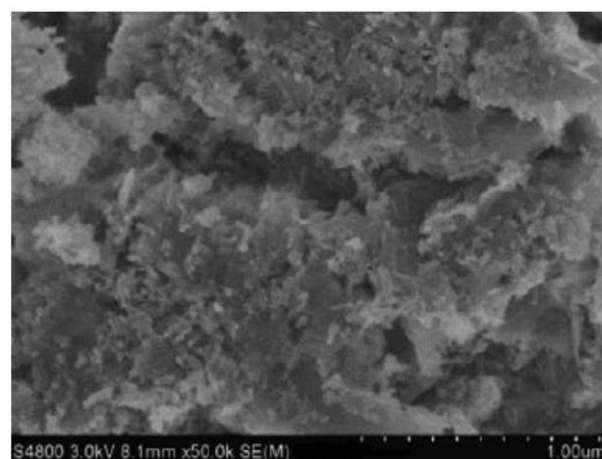


Fig. 1: SEM micrographs of Fe₃O₄/bentonite nanocomposite.

BPA and DBA adsorption

Batch adsorption experiments were carried out in 100 ml glass bottles with nanocomposite. In all of them, 0.035 g of solid adsorbent was introduced to 50 ml of BPA or DBA solution of increased initial concentrations (C₀) from 5 to 50 mg/l. The glass bottles were sealed and then transferred to a shaker and

shaken at 160 rpm and 25°C for specific time to ensure that the adsorption process reached equilibrium. The pH of the samples was adjusted by dropwise addition of 0.1 N HCl or 0.1 N NaOH to pH 12. The pH of solutions was measured with a pH meter (GLP22, Crison, Spanish). At the end of the equilibrium period, the mixture was filtered. The remaining DBA and BPA concentration in the filtrate was measured using a spectrophotometer. The amount of BPA or DPA adsorption at equilibrium q (mg/g) was calculated from the following equation:

$$q = \frac{(C_0 - C)V}{m} \quad (1)$$

Where q is the amount of organic molecules adsorbed (mg/g), C_0 and C are the initial and equilibrium concentration of the adsorbate (mg/ml), respectively; V is the solution volume (ml) and m is the adsorbents dosage (g).

The effect of parameters such as adsorbent dose, contact time, solution pH and temperature for the removal of BPA and DBA were studied.

Results and Discussion

The morphology and the size studding Fe_3O_4 and Fe_3O_4 /bentonite nanocomposite by FE-SEM reveal many microfine particles with diameter of about 0.3-0.8 for Fe_3O_4 /bentonite nanocomposite, which lead to a rough surface and the presence of a porous structure. Also, the aggregation of Fe_3O_4 particles seemed to decrease and their dispersity increase (Fig. 1). The X-ray powder diffraction pattern (Fig. 2) of the nanocomposite indicated the presence of silica and alumina along with iron. These peaks reveal that the nanocomposite were pure Fe_3O_4 with a spinel structure that the bentonite did not result in the phase change of Fe_3O_4 .

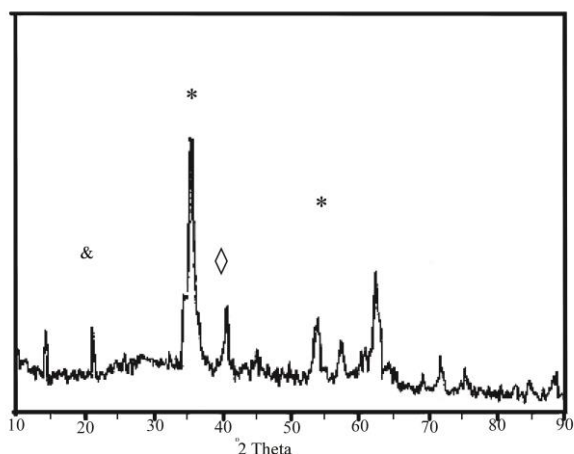


Fig. 2: XRD of Fe_3O_4 /bentonite nanocomposites, * Fe_3O_4 , \diamond Al_2O_3 , & SiO_2 .

Adsorption characteristics:

Adsorbent dosage, Effect of pH and concentration of DBA and DPA was investigated. Optimized values were found at 0.035 g, 2 and 50 ppm for the variables adsorbent mass, pH and initial DBA and DPA concentration respectively and lead to achievement 98.19 and 95.12% removal percentage which strongly confirmed by five replicates at these conditions.

The adsorption isotherms:

The equilibrium adsorption isotherms are fundamental in describing the interactive behaviour between adsorbates and adsorbent and are essential in giving an idea of the adsorption capacity of the adsorbent (Table1 and 2).

Table1: isotherms parameters for BPA

Isotherm	Isotherm coefficient		R ²
Langmuir	$K_L=0.016$ (L/mg)	$q_m=31.25$ (mg/g)	0.964
Freundlich	$K_F=1.605$ ($mg^{1-n}L^n/gr$)	$1/n=0.506$	0.969
Tempkin	$K_T=1.037$ (L/mg)	$b=5862.427$ (j/mol)	0.927
Dubinin-Radushkevich	$K_D=0.272$	$q_m=15/440$	0.924

Table2: isotherms parameters for DBA

Isotherm	Isotherm coefficient		R ²
Langmuir	$K_L=0.070$ (l/mg)	$q_m=13.717$ (mg/g)	0.963
Freundlich	$K_F=1.823$ ($mg^{1-n}L^n/gr$)	$1/n=0.538$	0.984
Tempkin	$K_T=5.340$ (L/mg)	$b=427.167$ (j/mol)	0.967
Dubinin-Radushkevich	$K_D=0.101$	$q_m=360.178$	0.974

Kinetics of adsorption:

The pseudo-second-order model was found to explain the adsorption kinetics most effectively and the theoretical q_e values were closer to the experimental q_e values. As a result, the adsorption fits to the pseudo-second order better than the pseudo-first-order kinetic model.

Effect of adsorbent dosage on removal

The influence of adsorbent dosage on the adsorption of DPA and DBA is shown in Fig. 3. The adsorption of the organic molecules increased with increasing dosage of the nanocomposite, and the adsorption was almost constant at higher dosages than 0.035 g. However, it can be seen from figure 3 that in the same dose of adsorbent, the removal of DPA is more than DBA.

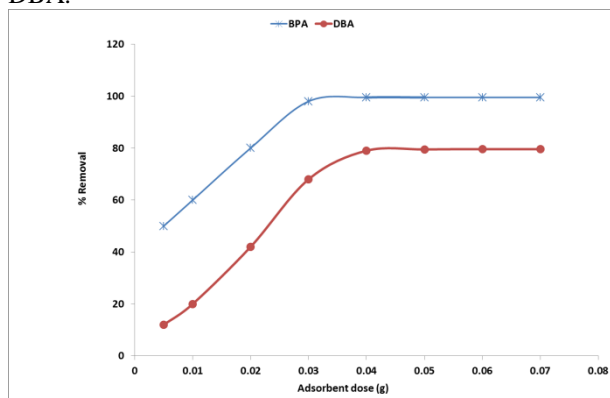


Figure 4: Adsorption of BPA and DBA on nano adsorbent.

Thermodynamic parameters of adsorption

The ΔH^0 and ΔS^0 parameters can be calculated from the slope and intercept of the plot of $\ln K$ vs $1/T$ yields, respectively (Fig. 4 and 5). The positive ΔH^0 (i.e. 35.815 kJ/mol for BPA and 21.756 kJ/mol for DBA) proposed that the adsorption were carried out as an endothermic process at 20–50 °C. Furthermore, the positive ΔS^0 value (i.e. 116.493 kJ/mol.K for BPA and 70.800 kJ/mol.K for DBA) indicates the increased randomness at the solid–solution interface during the fixation of BPA and DBA on the active sites of the adsorbent. Gibbs free energy change (ΔG^0) was also calculated to be -15.820, -17.210, -18.790 and -19.170 kJ/mol for BPA and -19.680, -21.240, -22.380 and -24.020 kJ/mol for DBA in 20, 30, 40, and 50 °C respectively. The negative values of ΔG^0 at different temperatures indicate the feasibility of the process and the spontaneous nature of the adsorption. In addition, the increase in ΔG^0 values with increase in temperature shows that the adsorption was relatively favourable at higher temperatures. Generally, the change in adsorption enthalpy for physisorption is in the range of -20 to 40 kJ.mol⁻¹, but for chemisorption, the range is between -400 and -80 kJ.mol⁻¹. The values of ΔH^0 obtained in this study were within the range of -20 and 40 kJ/mol, indicating that physisorption was the dominant mechanism.

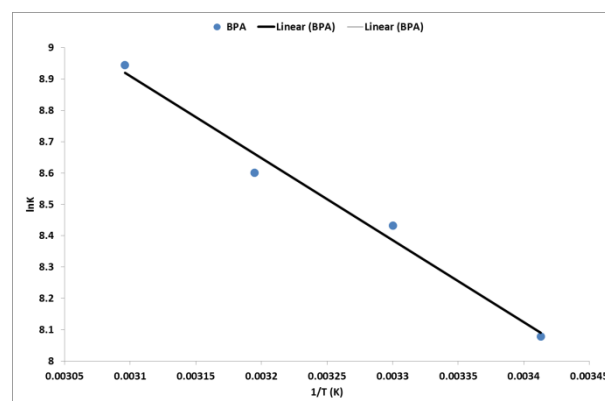


Figure 5: A plot of $\ln K$ versus $1/T$ for BPA.

Conclusion:

Equilibrium, thermodynamics, kinetics and process design are conducted for the adsorption of BPA and DBA from aqueous solutions onto Fe₃O₄/bentonite nanocomposite. The process kinetics can be successfully fitted with pseudo-second-order model. Adsorptions of BPA and DBA on adsorbent follow the Langmuir isotherm. The negative ΔG^0 indicates the overall adsorption processes are spontaneous and also the positive values of ΔH^0 show that both BPA and DBA adsorption processes are endothermic but dominated by physical adsorption, since the enthalpy change is a lower than 40 kJmol⁻¹. The value of ΔS^0 is also positive.

References

1. M. Maclure, R.B. Katz, M. S. Bryant "Elevated blood levels of carcinogens in passive smokers", *American Journal of Public Health*, 79 (1989), 1381–1384.
2. H. Mazaheri, M. Ghaedi, M. H. Ahmadi Azqhandi, A. Asfaram "Application of machine/statistical learning, artificial intelligence and statistical experimental design for the modeling and optimization of methylene blue and Cd (ii) removal from a binary aqueous solution by natural walnut carbon", *Physical Chemistry Chemical Physics*, 19 (2017) 11299-11317.
- [3] A. Asfaram, M. Ghaedi, M. H. Ahmadi Azqhandi "Statistical experimental design, least squares-support vector machine (LS-SVM) and artificial neural network (ANN) methods for modeling the facilitated adsorption of methylene blue dye", *RSC Advances*, 46 (2016) 40502-40516.



ration of spherical super magnetic iron oxide nanoparticles and its application as drug delivery systems

M. H. Ahmadi Azqhandi*

Applied Chemistry Department, Faculty of Petroleum and Gas (Gachsaran), Yasouj University, Gachsaran, 75813-56001, Iran.

[*mhahmadia58@gmail.com](mailto:mhahmadia58@gmail.com) , m.ahmadi@yu.ac.ir

Abstract: In this research, spherical superparamagnetic iron oxide nanoparticles with mean diameter of 6 -10 nm were prepared by a reduction–precipitation method. The surface of spherical superparamagnetic iron oxide nanoparticles SPION were coated with poly (methacrylic acid) (PMAA) and followed by loading with the anticancer drug DOX (doxorubicin). The drug loading efficiency was (14.64 ± 0.29) . In vitro drug release studies were realized for 8 h at two different pH values. The drug release rate at acidic pH was much faster than that at natural pH. These results also indicate that DOX/PMAA nanoparticles have a favourable release property and drug release kinetics followed the Korsmeyer–Peppas model. The samples were characterized by XRD, SEM, TEM, FTIR, and UV-Vis.

Keywords: Release kinetic studies; magnetite drug targeting; functionalization; poly(methacrylic acid); anticancer drug.

Introduction

In the last years, Fe_3O_4 magnetic nanoparticles (MNs) have been widely used in immunoassay, drug delivery and magnetic resonance imaging due to chemical stability, low toxicity and ultra-fine size, etc. [1]. Bare magnetite nanoparticles on account of their large surface area/volume ratio tend to agglomerate. To prevent agglomeration, a variety of polymeric coatings have been applied to nanoparticles [2].

In this research, one kind of novel nano-scale carrier for doxorubicin was prepared using Fe_3O_4 les, the dried nanoparticles (Fe_3O_4) were dispersed in deionised water using ultrasound. A solution of PMAA in deionized water were added into the suspension under stirring, and stirred for 24 h. The Fe_3O_4 :PMAA mass ratio was 1:2. The product was washed with deionized water and freeze-dried under vacuum at -20°C for 24 h.

Preparation of doxorubicin/spherical superparamagnetic iron oxide nanoparticles (DOX–SPION): A solution of DOX– Fe^{2+} complex of 1.5:1

nanoparticles as the core, poly methacrylic acid (PMAA) as a polymeric shell and doxorubicin as a drug to form drug-loaded magnetic nanoparticles.

Materials and method

Fe_3O_4 nanoparticles were prepared by using the reduction–precipitation method that explained elsewhere [3]. For preparation of PMAA-functionalized magnetite nanopartic

drug:iron molar ratio was obtained by adding an aqueous solution of $(\text{NH}_4)_2\text{Fe}(\text{SO}_4)_2 \cdot 6\text{H}_2\text{O}$ to DOX in tris buffer pH 7.6. Then the DOX– Fe^{2+} complex was incubated in the dark with the PMAA-coated SPION (PS), the mass ratio of DOX:PS was 0.31 (w/w). After incubation for 30 min, the drug-loaded PS was separated by centrifugation at 19,000 rpm for 15 min (4°C). Finally, the resulting solid product was washed with ice-cold fresh aqueous buffer pH 7.6 and used immediately afterwards.

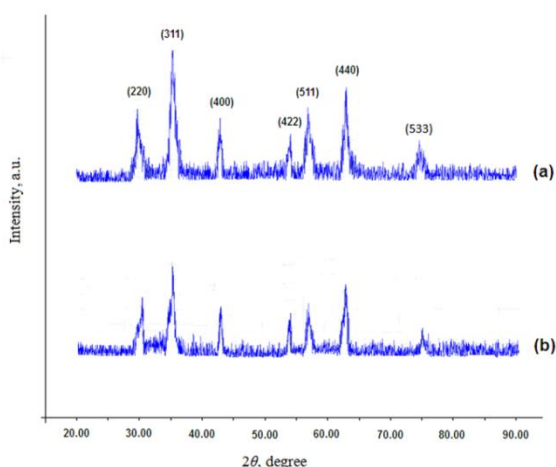


Fig. 1. XRD patterns of (a) uncoated Fe₃O₄ MNs, (b) PMAA-coated Fe₃O₄ MNs.

Results and Discussion

The XRD patterns of the bare Fe₃O₄ and PS shows the nanocrystalline structure and the seven diffraction peaks visible in both patterns, ascertained by comparison with Joint Committee on Powder Diffraction Standards (JCPDS card, File No. 79-0418). These coincidences suggests that the crystalline structure of Fe₃O₄ did not change on modification of the particles with PMAA chains and shows that the PMAA coating occurred only at the surface of Fe₃O₄ MNs and resulted in no detectable chemical/physical change in bulk of the nanoparticles (Fig. 1). The morphologies of magnetic nanoparticles were investigated by FE-SEM and TEM, as shown in Fig. 1a–d. These images showed that the prepared

Drug loading and in vitro release analysis: The drug loading efficiency of DOX was (14.69 ± 0.11) . The low values of the standard deviation indicate uniformity of the drug content in the Nano carriers. The drug-loaded nanoparticles were incubated in acetate buffer and phosphate buffer at different pH values to examine the drug release. The chosen pH levels replicated those found in the acidity environment of cancer cells (pH 4.2), as well as blood (pH 7.4). The drug release at pH 4.2 was much faster than that at pH 7.4. This is likely due to protonation of the phenol group of DOX in the acidic environment, which leads to the faster dissociation of the DOX–iron complex.

Conclusion:

1. M. R. Khanmohammadi, B. Vasheghani F., M. H. Ahmadi Azqhandi, R. Najafipour “Methoxy poly (ethylene glycol)-block-polycaprolactone copolymer:

nanoparticles had regular spherical shape and a core–shell structure. PMAA coating reduced the aggregation and enhanced the particle dispersion. It is an important factor in drug delivery applications that nanoparticles are individually dispersed and are not agglomerated. The FTIR spectra of bare Fe₃O₄ MNs (a) and PS (b) was investigated. The results of FTIR suggested that the Fe₃O₄ MNPs had been successfully coated by PMAA.

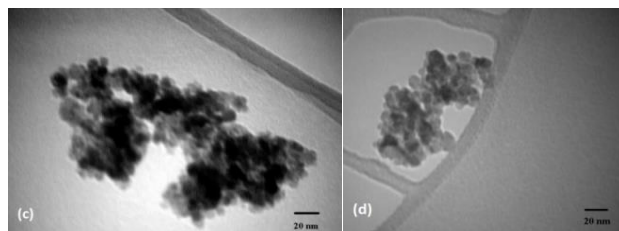
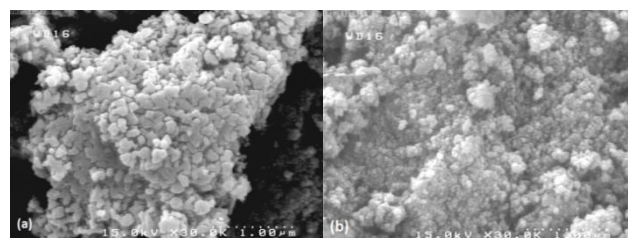


Fig. 2. FE-SEM images of (a) uncoated Fe₃O₄ MNs, (b) PMAA coated Fe₃O₄ MNs and TEM images of (c) uncoated Fe₃O₄ MNs, (d) doxorubicin-loaded PMAA-coated Fe₃O₄ MNs.

Fe₃O₄ nanoparticle, prepared using a reduction–precipitation method, were successfully modified with PMAA and confirmed by FTIR spectroscopy. Based on X-ray diffraction, introduction of the PMAA coating did not affect the crystalline structure of Fe₃O₄, whereas, based on FE-SEM, it enhanced the uniform dispersion of the nanoparticles. Drug loading was confirmed by UV-Vis and in vitro release behavior was investigated. At pH 4.2, Korsmeyer–Peppas kinetics of drug release were observed while at pH 7.4, drug release kinetics followed the zero order model. The values of the release exponent ‘n’ suggested a super case II transport release mechanism in both phosphate and acetate buffer.

References

formulation and optimization by experimental design; determination of diblock molar mass by multivariate



بیستمین کنفرانس شیمی فیزیک ایران
دانشکده علوم پایه - دانشگاه اراک
۱۳۹۶ هرداد ۲۹-۳۱



20th Iranian Physical Chemistry Conference

regression analysis of ¹H NMR spectra”, *Anal. Methods*, 5 (2013) 2840-2846.

2. M. H. Ahmadi Azqhandi, M. R. Khanmohammadi, B. Vasheghani F., R. Najafipour “Biotin-encoded and Fe₃O₄-loaded Polymeric Nano Micelles: Preparation, Optimization and in Vitro characterization”, *Letters in Drug Design & Discovery*, 10 (2013) 105-109.

3. L. Ji, Z. Tan, T. R. Kuykendall, S. Aloni, S. Xun, E. Lin, V. Battaglia “Fe₃O₄ nanoparticle-integrated graphene sheets for high-performance half and full lithium ion cells”, *Physical chemistry chemical physics*, 15 (2011) 7170-7177.

Microemulsion route to fabrication of biocompatible spherical gold nanoparticles

Somayah Tiani moghadam¹, Alireza Salabat^{2,3}, Farid Mirhoseini², Hamid Reza Shamlouei¹

¹ Department of Chemistry, Faculty of Science, Lorestan University, 68137-1-7133, Khorram abad, Iran

² Department of Chemistry, Faculty of Science, Arak University, 38156-8-8349, arak, Iran

³ Institute of Nanosciences & Nanotechnology, Arak University, 38156-8-8349, arak, Iran

s.tiani@yahoo.com

Abstract: Preparation of gold nanoparticles has attracted a great deal of interest due to their interesting optical properties and potential in biomedical applications. For this purpose, one challenge is to find a non-toxic chemical and/or physical method for functionalizing gold nanoparticles with biomolecule compounds. In the current study, a new microemulsion system composed of tetraoctyl ammonium bromide was introduced and studied in details. By using this microemulsion system a novel methodology was applied to prepare biocompatible gold clusters protected by a monolayer of monohydroxy thioalkylated PEG ligand. The morphology, size and size distribution of the prepared functionalized gold nanoparticles were obtained by different methods including dynamic light scattering (DLS), UV-visible spectrophotometry and transmission electron microscopy (TEM).

Keywords: Gold nanoparticles; Microemulsion; Thioalkylated polyethylene glycol; Biocompatible nanoparticles

Introduction

Gold nanoparticles (AuNPs) have been widely employed in biological assemblies and are useful materials for a range of biomedical applications based on their unique properties and multiple surface functionalities [1]. The ease of AuNPs functionalization provides a versatile platform for nanobiothechnology [2]. Brust *et al* prepared biocompatible AuNPs for use in the manufacturing of stable water soluble AuNPs with thioalkylated polyethylene glycol ligand [3].

Biofunctionalized of AuNPs has also become promising candidates in the design of novel biomaterials for the investigation of biological systems [4].

In continuing of our previous research work in the microemulsion systems as soft template to preparation of nanomaterials [5-7], in the current study monohydroxy thioalkylated PEG capped Au (Au MPCs) as biocompatible and water soluble AuNPs has been fabricated based on a new W/O microemulsion system containing of tetraoctyl ammonium bromide (TOAB) as cationic surfactant and toluene as continuous phase. The resulted Au MPCs was characterized with UV-vis spectroscopy, transmittance electron microscopy (TEM) and dynamic light scattering (DLS) analysis.

Experimental section

At the first step of this research the phase diagram of the proposed microemulsion system was constructed and studied in details. At the second step a

microemulsion system was prepared by mixing yellow aqueous solution of hydrogen tetrachloroaurate (HAuCl₄) and a solution of TOAB/toluene. The same microemulsion containing NaBH₄ was also prepared separately. Au nanoparticles were formed by addition of these two systems to each other and reducing the Au(III) ions to obtain a stable light ruby red colour solution, indicating the formation of Au nanoparticles. Then ethanol was added to the above system and centrifuged. Consequently, a colloid system of Au nanoparticles suspended in toluene was obtained.

A solution of 7 mg of monohydroxy PEG ligand dissolved in 2 ml of 2-propanol was added to the prepared colloid system and stirred for 10 min. Finally 10 ml of water was added to this solution and stirred vigorously. The toluene phase became completely colourless while the aqueous phase was changed to red color, indicating that the Au clusters have been transferred to aqueous phase.

A feasible mechanism for the formation of the thiol-stabilized Au nanoparticles by microemulsion system is also shown in Fig. 1.

Results and Discussion

UV-vis spectroscopy

Fig. 2 shows the UV-vis absorption spectra of the MPCs ligand (a) and Au MPCs NPs after 2 h of preparation (b). The results indicate that the Au MPCs NPs in water has a plasmon absorption band at around 522 nm, a feature shift typical for spherical Au MPCs

NPs. Fig 2 (c) present a stable Au MPCs colloidal in water that was diluted for 5 times.

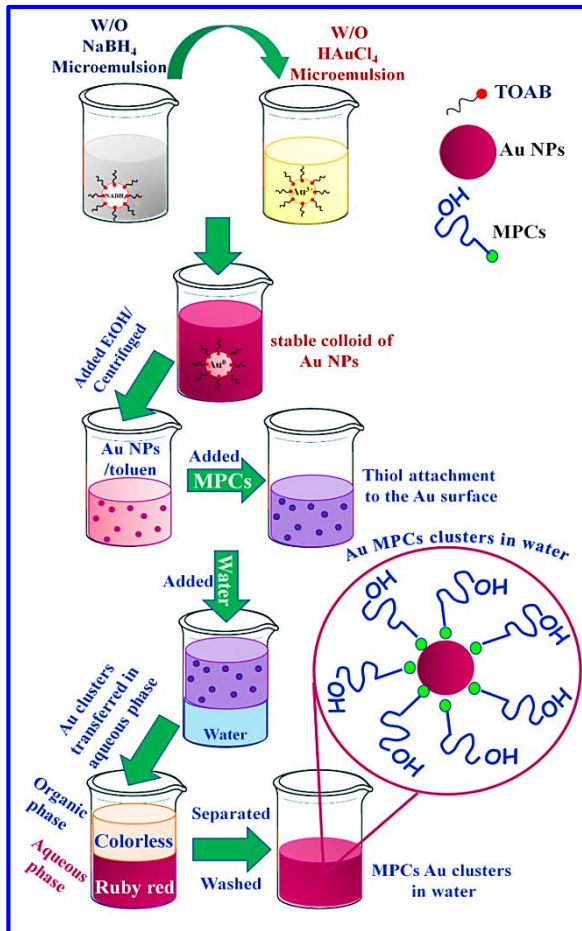


Fig1: Schematic illustration of preparation of biocompatible Au MPCs nanoparticles in microemulsion system

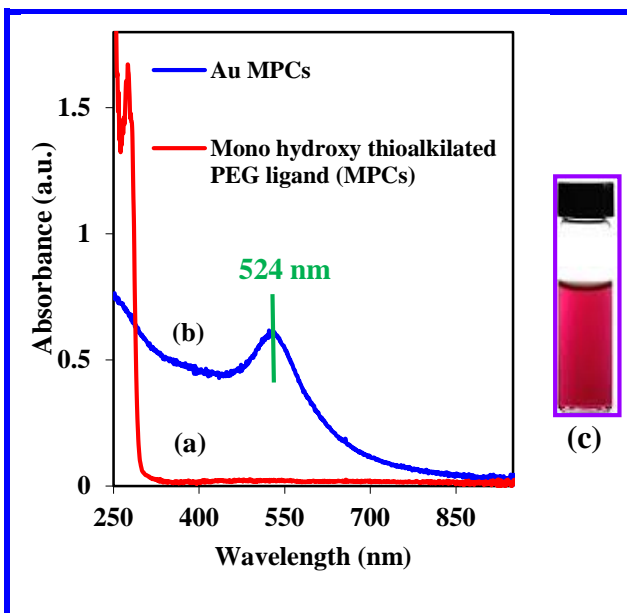


Fig 2: UV-vis spectra of (a) MPCs ligand, (b) Au MPCs in water and (c) image of Au MPCs in water (diluted 5 times)

DLS analysis

In order to clarify the monodispersity, size and stability of Au MPCs nanoparticles in water, the DLS technique was applied. As can be seen from Fig. 3, the average diameter of Au MPCs particles was obtained about 10 nm. The zeta potential of Au MPCs nanoparticles at 25 °C was obtained as +36.5 mV, indicating the high stability of Au MPCs nanoparticles in water.

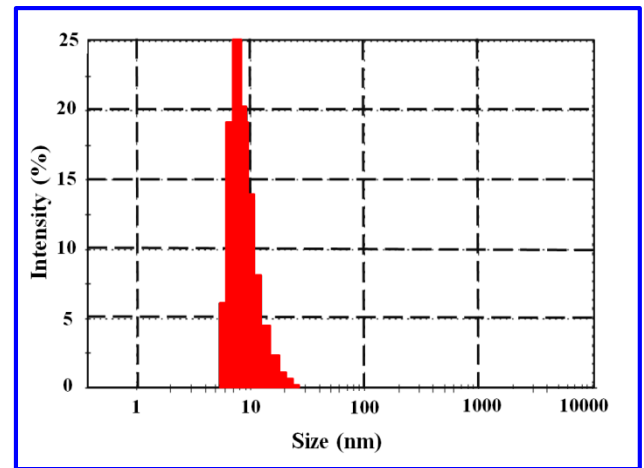


Fig 3: DLS analysis of Au MPCs nanoparticles in water

TEM analysis

Fig. 4 shows the TEM image and distribution histogram of the prepared Au MPCs nanoparticles in water. As can be seen the resulted Au MPCs nanoparticles have mainly spherical structure and are monodisperse with a mean diameter approximately equal to 9 nm. This result also confirms the DLS measurement.

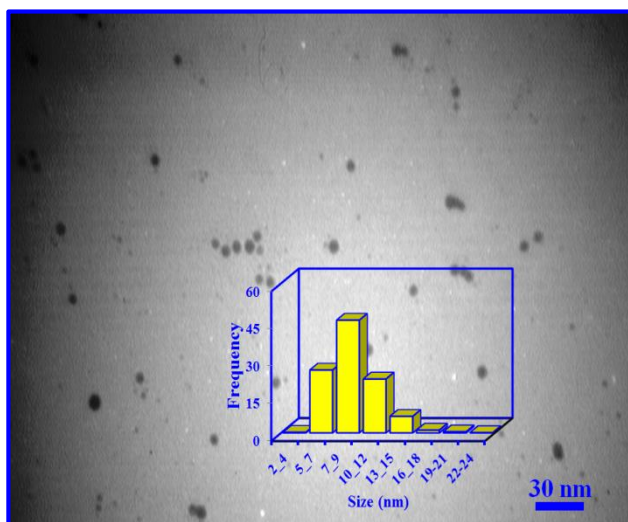


Fig 4: TEM micrograph of Au MPCs nanoparticles in water

Conclusions

In summary, thioalkylated polyethylene glycol (PEG) ligand has been used for the manufacturing of stable water soluble and biocompatible gold MPCs based on microemulsion system. TOAB as a cationic surfactant and toluene as continues phase was used to form microemulsion system. The morphology and size distribution of gold nanoparticles were confirmed by different techniques including dynamic light scattering (DLS), UV-visible spectrophotometry and transmission electron microscopy (TEM). The resulted biocompatible gold nanoparticles exhibit a plasmon absorption band at around 520 nm in the UV-vis and spherical morphology with an average diameter size of 10 nm was confirmed by DLS and TEM analysis.

References

- [1] Y. C. Yeh, B. Creran, V. M. Rotello, Gold nanoparticles: preparation, properties, and applications in Bionanotechnology, *Nanoscale*, 4 (2012) 1871-1880.
- [2] T. Zhang, P. Chen, Y. Sun, Y. Xing, Y. Yang, Y. Dong, L. Xu, Z. Yang and D. Liu, A new strategy improves assembly efficiency of DNA mono-modified gold nanoparticles, *Chemical Communication*, 47 (2011) 5774-5776.
- [3] T. R. Tshikhudo, Z. Wang, M. Brust, Biocompatible gold nanoparticles, *Materials Science and Technology*, 20 (2004) 980-984.

[4] D. F. Moyano and V. M. Rotello, Nano meets biology: structure and function at the nanoparticle interface, *Langmuir*, 27 (2011) 10376-10385.

[5] A. Salabat, G. Nabiyouni, M. Rahmatifar, Effect of platinum precursor on the nanoparticle size synthesized in microemulsion system, *J. Exp. Nanosci.*, 6 (2011) 305-310.

[6] S. Soleimani, A. Salabat, R. F. Tabor, Composite Pt/ α -Al₂O₃ catalysts synthesized by a microemulsion method, *J. Colloid Interface Sci.*, 426 (2014) 287-292.

[7] F. Mirhoseini, A. Salabat, Ionic liquid based microemulsion method for the fabrication of poly(methyl methacrylate)-TiO₂ nanocomposite as a highly efficient visible light photocatalyst, *Rsc Adv.*, 5 (2015) 12536-12545.



Sodium Adsorption on Boron Nitride Armchair Nanoribbon: Insight from DFT

R. Habibpour

Department of Chemical technologies, Iranian Research Organization for Science and Technology, Tehran, 3353-5111, Iran
Habibpour@irost.ir

Abstract: We have studied the adsorption of sodium atoms at the hollow, bridge, and top sites of pristine boron nitride armchair nanoribbon using the density functional theory method. Sodium interacts with armchair nanoribbon through the charge transfer from sodium, with binding energies per adatom of about 3.04eV, 2.97eV, 3.18 and 3.04eV at hollow, bridge, and top sites, respectively. By sodium adsorption, the Fermi level is shifted upwards from -3.53eV in pristine BNNR to ~ -0.594 eV in Na-BNNR due to the extra electrons that are achieved from donor sodium atom. It is found that the total DOS curves of Na adsorbed nanoribbons is symmetric. So, it can be concluded that all the Na adsorbed nanoribbons show non ferromagnetic behavior.

Keywords: Na adsorption, Boron nitride nanoribbon, DFT

Introduction

Among rechargeable batteries, lithium ion batteries (LIBs) have been widely used in different power devices, light vehicles, and portable electronics over the past decade [1]. Although LIBs have demonstrated good performance as rechargeable batteries, sodium ion batteries (SIBs) have been in the spotlight in recent years due to their low cost and the natural abundance of sodium, which makes up approximately 2.6 percent of Earth's crust [2-4]. However, the performance of SIBs needs to be improved in order to reach, or exceed, the power densities and reversible capacities of LIBs. Graphite has already been used as the anode material in LIBs, but it cannot be applied to SIBs [5,6]. Since the radius of the sodium ion is morphologically larger than the interplanar distance between graphite sheets, it is difficult to intercalate sodium into graphite [7]. BN nanostructures have a wide band gap, high oxidation resistance constant, high thermal conductivity, superb mechanical properties, high structural and chemical stability and lower toxicity [8]. It has been indicated that BN can be used as an additive of organic cathode to increase the lifetime (cycle numbers) of the batteries [9]. Here, using density functional theory (DFT) calculations, we study the interaction of atomic Na with the BN nanoribbon to inspect its application as anode in NIB.

Computational details

The steady configuration associated to the Na-adsorbed boron nitride nanoribbon in hollow, bridge, and top sites are shown in Figure 1. The geometric, electronic, and chemical properties of the above-mentioned Na-adsorbed nanoribbons are studied by a quantum espresso-5.0.2 package which performs the first-principles plane-wave calculations within the density functional theory (DFT) framework. The

electron-ionic interaction is represented by the projector augmented wave (PAW) potentials [10].

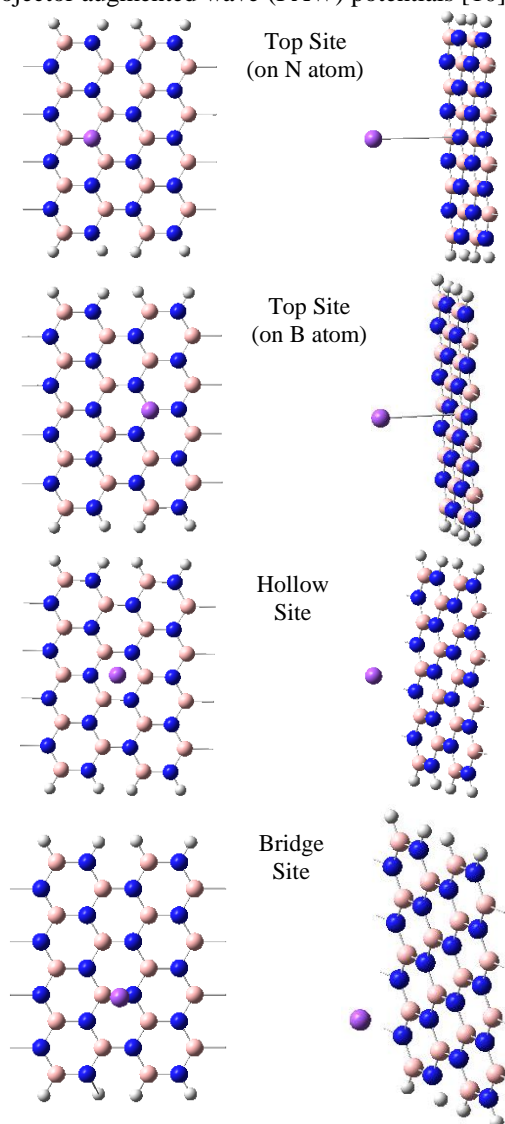


Fig.1: 3×4 Supercells used for modeling the Na-adsorbed



boron nitride nanoribbon in hollow, bridge, and top sites

The exchange and correlation potentials are explained by the generalized gradient approximation of Perdew et al., known as PW91 [11]. In all cases, the plane-wave expansion was limited at a cutoff energy of 25 Ry (340.1 eV), assuring a good convergence in energy. The geometrical structures are fully optimized until the residual force on each atom is smaller than $0.0001\text{eV}/\text{\AA}$. The Brillouin zone integration is done according to the Monkhorst–Pack automatic generation scheme [12] using a 3×4 supercell together with a Gaussian smearing broadening of 0.05 eV. A total of 11 K-points were included in the band structure calculations along $-0.25 (0, 0, -0.25)$ to $0.25 (0, 0, 0.25)$.

Results and Discussion

Fig. 2 presents a comparison of the electronic band structures of the Na-adsorbed boron nitride nanoribbon in hollow, bridge, and top sites. As in the case of graphene, Na adsorption on armchair nanoribbons does not induce spin polarization in these systems. As we know, the pristine a-BNNR is a semiconductor (nonzero band gap) with a direct band gap. The valence band (π band) and the conduction band (π^* band) are separated from each other by a band gap of $\sim 4\text{eV}$. By absorbing sodium, this nanoribbon becomes metallic. The important point is that the Na adsorption on all adsorption sites gives rise to metallic states. The adsorption energy for Na atom on BNNR are calculated by the following equation:

$$E_{\text{ads}} = E_{\text{t}} - E_{\text{Na atom}} - E_{\text{BNNR}} \quad (1)$$

Where E_{t} , $E_{\text{Na atom}}$, and E_{BNNR} are the total energy of the adsorbed Na atoms on the BNNR, the isolated Na atom, and the BNNR, respectively. The negative values of E_{ads} means that the adsorption process is exothermic and that the adsorption of Na atom on the boron nitride nanoribbon is energetically favorable. The calculated adsorption energies of Na atom on different adsorption sites and Na-BNNR surface vertical distances are reported in Table 1. As it is seen, Na atom cannot distinguish different adsorption site on BNNR surface and by high positive adsorption energy indicating a strong endothermic interaction.

Table1: Na adsorption energy and its vertical distance from BNNR surface.

Adsorption site	Adsorption energy (eV)	Na-BNNR surface vertical distances (\AA)
Top (on B)	3.18	4
Top (on N)	3.24	4.5
Bridge	2.97	4.5
Hollow	3.04	4.2

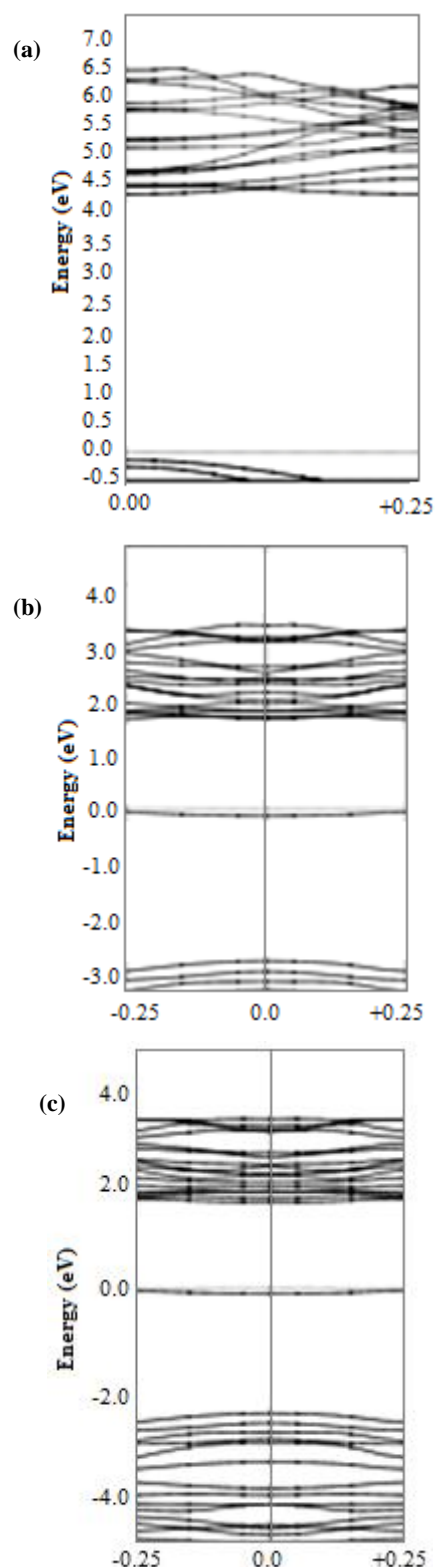


Fig.2: Electronic band structure of pristine a-BNNR (a), Na-BNNR (on B atom) (b), and Na-BNNR (on N atom) (c).

In order to better understand the electronic properties of the adsorption of Li in a-GNR. Their total density of states (DOS) and local density of states (LDOS) are plotted in Fig. 3. It is clear in Fig. 3 that the total DOS curves of Na adsorbed nanoribbons is symmetric. So, it can be concluded that all the Na adsorbed nanoribbons show non ferromagnetic behavior.

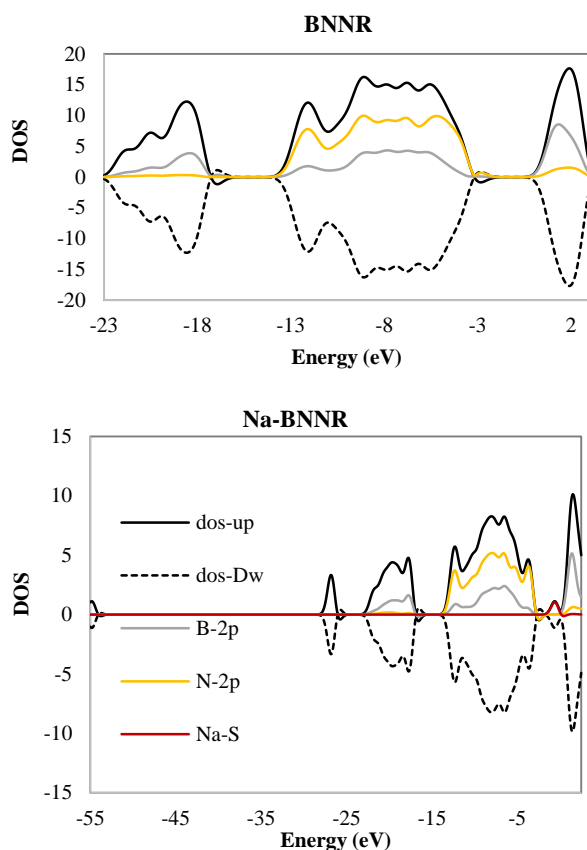


Fig.3: DOS and LDOS of a-BNNR and Na adsorbed a-BNNR.

Conclusions

In summary, we have studied the adsorption of Na atom at the hollow, bridge, and top sites of a-BNNR by means of density functional theory within the local spin density and generalized gradient approximations. Na interacts with armchair nanoribbon through the charge transfer from Na, with binding energies per adatom of about 3.04eV, 2.97eV, 3.18 and 3.24eV at hollow, bridge, and top sites, respectively. The results show that all the Na adsorbed a-BNNR structures are stable at the level of pristine a-BNNR.

References

- [1] J.R. Dahn, T. Zheng, Y. Liu, J. Xue, "Mechanisms for Lithium Insertion in Carbonaceous Materials", *Science*, 270 (1995) 590-593.
- [2] D. Kundu, E. Talaie, V. Daffort, L.F. Nazar, "The emerging chemistry of sodium ion batteries for electrochemical energy storage *Angew*", *Chem. Int. Edit.* 54 (2015) 3431-48.
- [3] A.A. Yaroshevski, "Abundances of chemical elements in the Earth's crust", *Geochem. Int.* 44 (2006) 48-55.
- [4] N. Yabuuchi, M. Yano, H. Yushida, S. Kuze, S. Komaba, "Synthesis and Electrode Performance of O3-Type NaFeO₂-NaNi_{1/2}Mn_{1/2}O₂ Solid Solution for Rechargeable Sodium Batteries", *J. Electrochem. Soc.* 160 (2013) A3131-A7.
- [5] M. Dahbi, N. Yabuuchi, K. Kubota, K. Tokiwa, S. Komaba, "Negative Electrodes for Na-Ion Batteries", *Phys. Chem. Chem. Phys.* 16 (2014) 15007-28.
- [6] S. Komaba, T. Itabashi, M. Watanabe, H. Groult, N. Kumagai, "Electrochemistry of Graphite in Li and Na Salt Codissolving Electrolyte for Rechargeable Batteries", *J. Electrochem. Soc.* 154 (2007) A322-A30.
- [7] Y.J. Kang, S.C. Yung, J.W. Choi, Y.K. Han, "Important Role of Functional Groups for Sodium Ion Intercalation in Expanded Graphite", *Chem. Matter.* 27 (2015) 5402-6.
- [8] D. Golberg, Y. Bando, Y. Huang, T. Terao, M. Mitome, C. Tang, C. Zhi, "Boron Nitride Nanotubes and Nanosheets" *ACS Nano.* 4 (2010) 2979-2993.
- [9] Y.X. Yu, "A dispersion-corrected DFT study on adsorption of battery active materials anthraquinone and its derivatives on monolayer graphene and h-BN", *J. Mater. Chem. A.* 2 (2014) 8910-8917.
- [10] P.E. Blöchl, "Projector augmented-wave method", *Phys. Rev. B.* 50 (1994) 17953-17978.
- [11] J.P. Perdew, Y. Wang, "Accurate and simple analytic representation of the electron-gas correlation energy", *Phys. Rev. B.* 45 (1992) 13244-13249.
- [12] H.J. Monkhorst, J.D. Pack, "Special points for Brillouin-zone integrations", *Phys. Rev. B.* 13 (1976) 5188-5192.

Effect of zinc oxide nanoparticles on azo dye

Elham asgari^a

^aDepartment of Chemistry, Boroujerd Branch, Islamic Azad University, Boroujerd, Iran

*e-mail: e.asgari@iaub.ac.ir

Abstract:

In this research, zinc Oxide nanoparticles were prepared by sol-gel technique. After preparing sol and ensure its sustainability, nanoparticles prepared by annealing from certain temperature. The structure and surface morphology were investigated by X-ray diffraction (XRD) and scanning electron microscopy (SEM). In the following Photocatalytic activities of nanopowders were performed using degradation of azo dyes. The influence of pH, time of irradiation and dye azo concentration on the photocatalytic activity was investigated. The result showed that Zinc Oxide photocatalyst cannot degradation azo dye without irradiation UV-vis and presence of all three factors Azo dye, Zinc Oxide photocatalyst and UV-Vis radiation are necessary for degradation.

Keywords: “Zinc Oxide”, “Dye Azo”, “Photocatalytic Activity”

Introduction

Semiconductors are interesting because of their potential applications in biomedicine, photocatalysis, and nanodevices that are not found in the single individual component. Among the transition metal oxides, zinc oxide and titanium dioxide are interesting because of high refractive index, good optical band gap, low optical loss and high transparency in the visible and Uv-visible region. Zinc oxide is non-toxic, possessing a high luminous transmittance, good electrical properties, and excellent piezoelectric properties [1]. These metal oxides have been prepared by various techniques, that among them, sol-gel technology is perspective and low cost [2].

In this research, zinc oxide nanoparticles prepared by sol gel method. After preparing sol and ensure its sustainability, nanoparticles prepared by annealing from 300 to 600°C temperature. The results indicated that a higher percent of zinc oxide is formed at 600 °C in 60 min. The SEM image showed flat surface without cracks with an average size of less than 100nm.

In continuation of our research, we have examined photocatalic activity of the zinc oxide on azo dye degradation. The result showed that zinc Oxide photocatalyst cannot degradation azo dye without irradiation UV-vis and presence of all three factors Azo dye, Zinc Oxide photocatalyst and UV-vis radiation are necessary for degradation [3, 4].

Materials and method

Zinc acetate (ZA) dihydrate (99.9%) was supplied by Sigma-Aldrich. Isopropanol (IP) and monoethanolamine (MEA) obtained from Merck.

Zinc oxide sol was obtained as follows: One mmol zinc acetate dehydrate was dissolved in 20 mL of IP.

After 10 mm MEA (1 mL) was added very slowly to solution in 5 mn. The solution was thoroughly mixed by a magnetic stirrer at 70 °C for 1 h, until a clear light yellow solution was formed. The sol aged for 72 h and heated at 200°C for 60 min to evaporate the solvent, and then put into the furnace at 300, 400and 600 °C in air for 60 min to crystallize the zinc oxide nanoparticles.

Results and Discussion

Figure 1 shows the XRD pattern of ZnO nanoparticles for different temperature °C. The X-ray diffraction patterns were detected with Miller indices (002), (101), and (100) indexed to the hexagonal wurtzite structure with good crystallinity. The peak intensity increase, with increase the temperature [5].

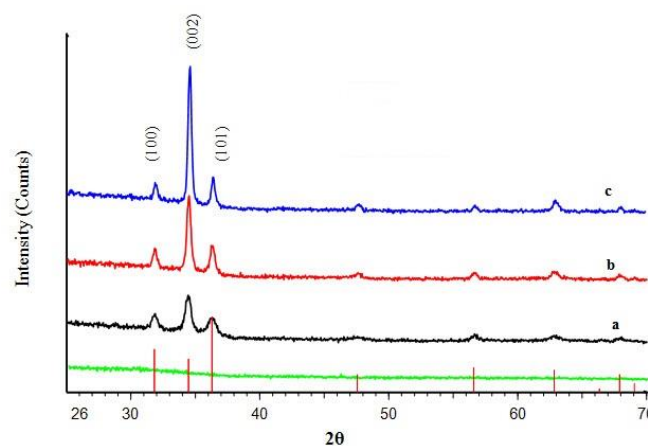


Fig.3: XRD pattern of ZnO nanoparticles annealed at 300(a), 400(b) and 600(c) °C

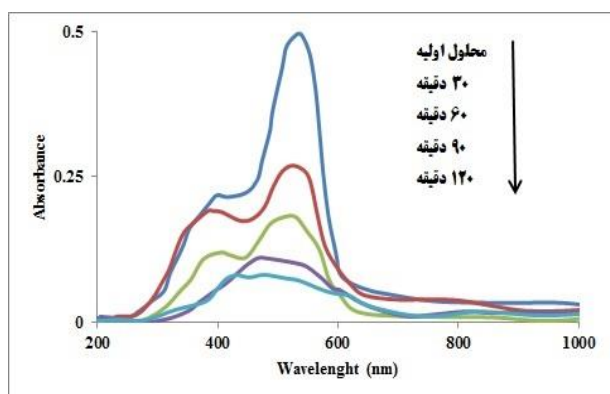


Fig.2: UV-vis spectra of dye azo (15 ppm) after photocatalytic reaction using Zinc oxide nanoparticles

Figure 2 represents the degradation of dye azo with the irradiation time using Zinc oxide nanoparticles. The intensity of absorption peak at 520 nm decreases with increase in the irradiation time. The results showed complete degradation of azo dye solution degraded within 120 min. This suggests that zinc oxide nanoparticle is an efficient catalyst for degradation of azo dye.

The degradation efficiencies of Zinc oxide photocatalysts at different solution pH are shown in Fig. 3. It can be observed from Fig. 3 that in the pH 9, the degradation efficiency reached the maximum value of 84%. Higher the pH value can provide higher concentration of hydroxyl ions to react with holes (h^+) to form hydroxyl radicals (OH^\cdot), subsequently enhancing the photodegradation rate of Azo dye which indicates that, the alkaline pH of reaction mixture has good photocatalytic.

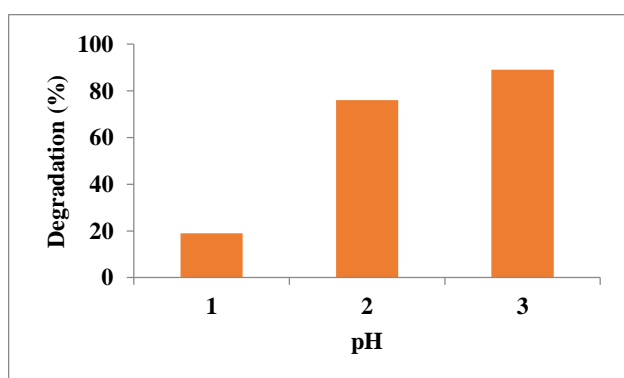


Fig.3: Effect of pH on photodegradation of Azo dye using zinc oxide nanoparticles catalyst.

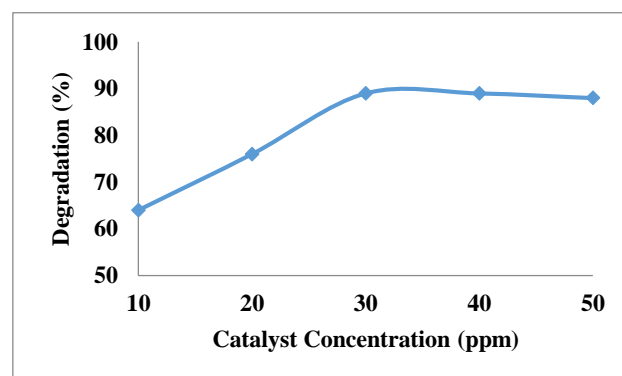


Fig.4: Effect of photocatalyst dosage on photodegradation of Azo dye using zinc oxide catalyst.

The degradation efficiency of Zinc oxide nanoparticle at different amounts of catalyst increased up to 30 mg/L are examined. Enhancement of degradation is due to the increase in the number of dye molecules adsorbed on the Zinc oxide nanoparticles and the increase in the density of Zinc oxide nanoparticles in the area of illumination.

Conclusions

Zinc oxide nanoparticle with average diameter less than 100 nm was successfully prepared by the sol-gel technique in combination with calcination. The Zinc oxide nanoparticles crystallites were produced at calcination temperature at 600 °C. Zinc oxide nanoparticles, is found to be an efficient photocatalyst for degradation of Azo dye.

The optimum pH and catalyst concentration for efficient removal of dye are found to be 9 and 30 mg/L, respectively.

Acknowledgment

The authors wish to thank the Islamic Azad University of Boroujerd for providing partial financial support for this study.

References

- [1] M. Ghaedi, J. Tashkhourian, A. A. Pebdani, B. Sadeghian, F. N. Ana, "Equilibrium, kinetic and thermodynamic study of removal of reactive orange 12 on platinum nanoparticle loaded on activated carbon as novel adsorbent", *Kor J Chem Eng*, 34 (2011) 1-7.
- [2] M. Ghaedi, A. Hassanzadeh, S. N. Kokhdan, B. Sadeghian, F. N. Ana, "Multiwalled carbon nanotubes as adsorbents for the kinetic and equilibrium study of the removal of Alizarin red S and morin", *J Chem Eng Data*, 56 (2011) 2511-2520.
- [3] B. Ramezanzadeh, M. Attar, "Effect of ZnO nanoparticles on the thermal and mechanical properties of epoxy based nanocomposite", *J Therm Anal Calorim*, 103 (2011) 731-739.



بیستمین کنفرانس شیمی فیزیک ایران
دانشکده علوم پایه - دانشگاه اراک
۱۳۹۶ هـ. ش ۲۹-۳۱



20th Iranian Physical Chemistry Conference

[4] M. H. Habibi, R. Sheibani, "Preparation and characterization of nanocomposite ZnO–Ag thin film containing nano-sized Ag particles: influence of preheating, annealing temperature and silver content on characteristics", *J Sol Gel Sci Technol*, 54 (2010) 195-202.

[5] M. H. Habibi, R. Mokhtari, "sulfur-doped niobium pentoxide nanoparticles: fabrication, characterization, visible light sensitization and redox charge transfer study", *J Sol Gel Sci Technol*, 59 (2011) 352-359.

Atomic Scale Investigation of nitrogen doping effects on the structural and electronic properties of Boron Nitride Embedded Armchair Graphene Nanoribbons

R. Habibpour

Department of Chemical technologies, Iranian Research Organization for Science and Technology, Tehran, 3353-5111, Iran
Habibpour@irost.ir

Abstract: We study the electronic and chemical properties of boron nitride embedded armchair graphene nanoribbons under nitrogen doping in comparison with pristine graphene armchair nanoribbon and pristine hybrid graphene and boron nitride armchair nanoribbon using the density functional theory method. Two types of nitrogen species were identified at the atomic level: pyridinic-N (N bonded to two nearest neighbour atoms) and graphitic-N (N bonded to three nearest neighbour atoms). Distinct electronic states of localized π states were found to appear in the occupied and unoccupied regions near the Fermi level at the atoms around pyridinic-N and graphitic-N species, respectively. The results show that all the mentioned nanoribbons are nonmagnetic direct semiconductors.

Keywords: Nitrogen doping, Structural properties, Electronic Properties, a-GBNNR, DFT

Introduction

Graphene nanoribbons (GNRs), because of their semiconducting behavior and their atomic thickness, appear to be very promising candidates for use in potential carbon based opto-electronic devices as well as alternatives to existing silicon based opto-electronics [1]. As a material that is structurally similar to GNRs, the hexagonal boron nitride sheet (h-BN) has attracted much attention in material science research due to their potential applications in optics and opto-electronics [2]. Unlike graphene, h-BN has a large band gap (~ 4.64 eV) and is an insulator [3]. Theoretical studies have found that BNNRs are semiconductors and non-magnetic. Due to their novel electronic properties and potential applications in nanoelectronics, some researchers proposed the hybridization of GNRs and BNNRs. According to experimental and theoretical investigations, the electronic properties of pristine graphene can be considerably altered and improved by substitutional doping with foreign elements [4]. The doping of nitrogen atoms is a good idea because nitrogen atoms have a similar atomic radius as carbon atoms. Using a first-principles method based on the density functional theory (DFT) within the generalized gradient approximation (GGA), we explore the geometric, electronic, and chemical properties of pristine a-GNR (C), hybrid a-GBNNR (C-3BN), and N-doped hybrid a-GBNNR structures including graphitic and pyridinic substitution.

Computational details

The geometric, electronic, and chemical properties of all the nanoribbons are studied by a quantum espresso-5.0.2 package which performs the first-principles

plane-wave calculations within the density functional theory (DFT) framework.

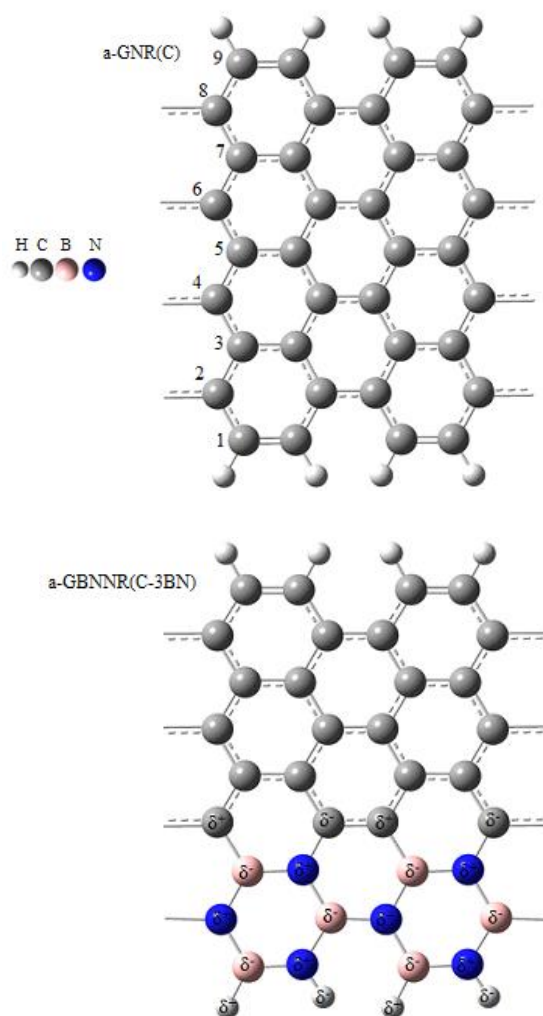


Fig.1: 3×4 Supercells used for modeling pristine a-GNR (C),

hybrid a-GBNRR (C-3BN).

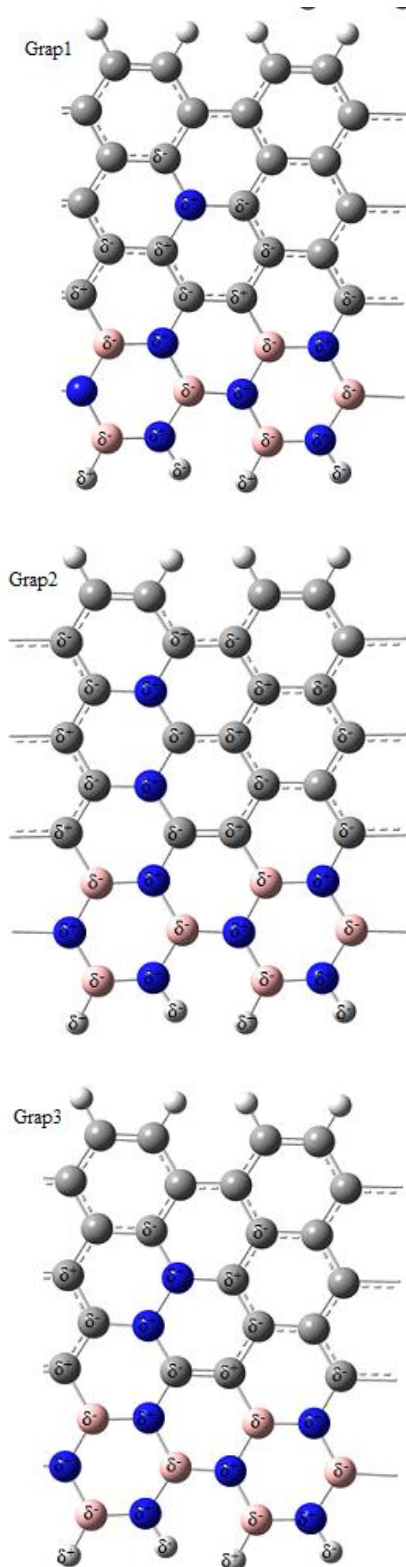


Fig.2: 3×4 Supercells used for modeling graphitic N-doped hybrid a-GBNRRs.

The electron-ionic interaction is represented by the projector augmented wave (PAW) potentials [5]. The exchange and correlation potentials are explained by

the generalized gradient approximation of Perdew et al., known as PW91 [6]. In all cases, the plane-wave expansion was limited at a cutoff energy of 25 Ry (340.1 eV), assuring a good convergence in energy. The geometrical structures are fully optimized until the residual force on each atom is smaller than 0.0001 eV/Å. The pristine a-GNR (C), hybrid a-GBNRR (C-3BN), and N-doped hybrid a-GBNRR structures for our theoretical study are shown in Fig.1, Fig.2, and Fig.3, respectively.

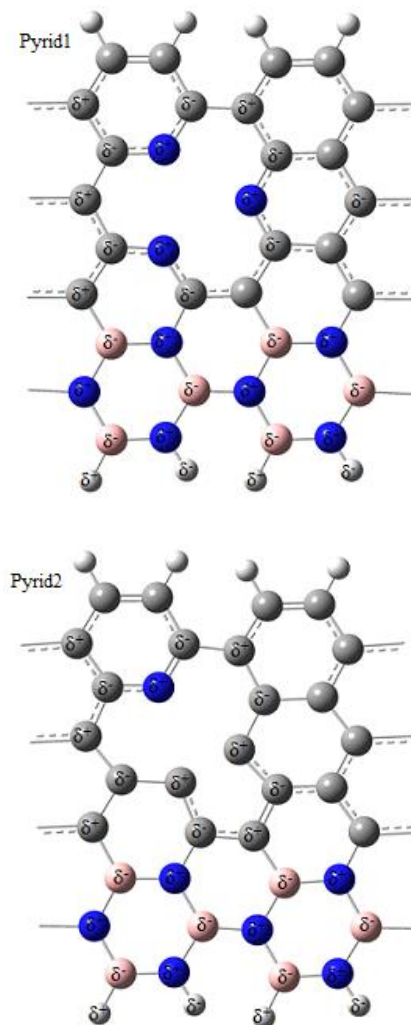


Fig.3: 3×4 Supercells used for modeling pyridinic N-doped hybrid a-GBNRRs.

Results and Discussion

To investigate the thermodynamic stability of the nanoribbons, we calculated the formation energy (E_{form}) using the following formula:



$$E_{\text{form}} = \frac{E_{\text{tot}} - [n_{\text{C}}E_{\text{C}} + n_{\text{B}}E_{\text{B}} + n_{\text{N}}E_{\text{N}} + n_{\text{H}}E_{\text{H}}]}{n_{\text{C}} + n_{\text{B}} + n_{\text{N}} + n_{\text{H}}} \quad (1)$$

where E_{tot} is the total energy of the nanoribbon supercell; E_{C} , E_{B} , E_{N} , and E_{H} are the total energies of the isolated C, B, N, and H atoms, respectively, and n_i is the number of atom i ($i = \text{C, B, N, H}$) in the system. Table 1 presents the formation energy, HOMO-LUMO gap, work function and Lowdin charges of pristine a-GNR (C), hybrid a-GBNNR (C-3BN), and N-doped hybrid a-GBNNRs (Graphitic and Pyridinic).

Table1: formation energy, HOMO-LUMO gap, work function and Lowdin charges of nanoribbons.

nanoribbon	E_{form} (eV)	H-L gap (eV)	work function (eV)	Lowdin charge
a-GNR (C)	-7.48	0.19	4.47	149.4
a-GBNNR (C-3BN)	-7.04	0.43	4.35	150.2
graphitic 1	-7.34	0.82	4.85	151.3
graphitic 2	-7.29	1.15	3.65	152.2
graphitic 3	-7.27	0.76	3.74	152.3
pyridinic 1	-7.21	1.39	4.82	149.2
pyridinic 2	-7.22	1.27	4.69	147.3

The plots of the LDOS show the contribution of different atomic states (2s, 2p) of C, B, and N atoms on the total DOS. In the total DOS, the upper (blue lines) and lower (brown lines) segments represent the up and down spins, respectively. It is clear in Figure 4 that the total DOS curves of all the nanoribbons are symmetric. So, it can be concluded that all the nanoribbons show non ferromagnetic behavior.

Conclusions

The results show that unlike the hybrid C-3BN nanoribbon, all the N-doped hybrid a-GBNNR structures are stable at the level of pristine a-GNR. By using different doping positions and doping patterns, we can tune the electronic and chemical properties of nanoribbons. The shifting of the Fermi energy level into the valence region and conduction region by the doping pattern is observed. We found that the N-doped graphitic2 and N-doped graphitic3 structures are n-type semiconductors with the lowest work function and therefore, they are promising carbon-based materials for building highly efficient field electron emission (FEE) sources. Graphitic N-doped hybrid GBNNRs are n-type semiconductors while pyridinic N-doped hybrid

GBNNRs are p-type semiconductors. Consequently, easily by suitable doping position and doping dose adjustments, can be achieved p-n junctions inside the N-doped hybrid GBNNRs which are the primary construction blocks of most semiconductor electronic devices such as diodes, transistors, solar cells, etc.

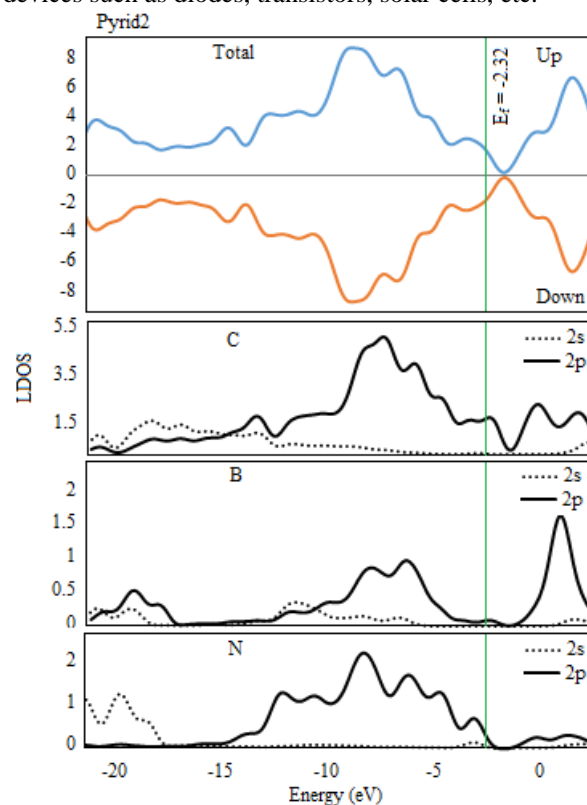


Fig.4: DOS and LDOS of pyridinic 2 N-doped hybrid a-GBNNRs.

References

- [1] F. Bonaccorso, Z. Sun, T. Hasan, A.C. Ferrari, Graphene photonics and optoelectronics, *Nat. Photonics*. 4 (2010) 611-622.
- [2] K. Watanabe, T. Taniguchi, H. Kanda, Direct-bandgap properties and evidence for ultraviolet lasing of hexagonal boron nitride single crystal, *Nat. Mater.* 3 (2004) 404-409.
- [3] M. Topsakal, E. Aktürk, S. Ciraci, First-principles study of two- and one-dimensional honeycomb structures of boron nitride, *Phys. Rev. B*. 79 (2009) 115442/1-11.
- [4] N.P. Bellafont, D.R. Mañeru, F. Illas, Identifying atomic sites in N-doped pristine and defective graphene from ab initio core level binding energies, *Carbon*. 76 (2014) 155-164.
- [5] P.E. Blöchl, Projector augmented-wave method, *Phys. Rev. B*. 50 (1994) 17953-17978.
- [6] J.P. Perdew, Y. Wang, Accurate and simple analytic representation of the electron-gas correlation energy, *Phys. Rev. B*. 45 (1992) 13244-13249.



Optimization of Tensile Strength of NBR/PVC/NiFe₂O₄ Nanocomposites Using Response Surface Methodology

Keivan Torabi¹, Saeed Mirsafai², Mahdi Ashrafi³, Masood Hamadani^{3,*}

Department of Mechanical Engineering, Faculty of Engineering, University of Isfahan, Isfahan, I.R. Iran

Department of Mechanical Engineering, Najafabad Branch, Islamic Azad University, Najafabad, I.R. Iran

Institute of Nanoscience and Nanotechnology, University of Kashan, Kashan, I.R. Iran

hamadani@kashanu.ac.ir

Abstract: NBR/PVC mixtures are physical mixtures with wide commercial importance. The presence of PVC helps to improve the ozone and ageing resistance of NBR, which enables the use of this mixture in the automotive industry. This paper reports the development of acrylonitrile butadiene rubber (NBR) nanocomposite toughened by the combination of polyvinyl chloride (PVC) and NiFe₂O₄NPs. NiFe₂O₄ NPs were synthesized by Sol-Gel Auto-Combustion route for this study. Response surface methodology (RSM) was applied for optimization and modeling of the impact strength of NBR/PVC/NiFe₂O₄ quaternary nanocomposite. NiFe₂O₄ NPs and Optimized NBR/PVC/NiFe₂O₄ nanocomposite were characterized by XRD, SEM, EDX, VSM and the mechanical properties of NBR/PVC/NiFe₂O₄ nanocomposite were investigated.

Keywords: NBR; PVC; NiFe₂O₄; RSM, Nanocomposite

Introduction

NBR/PVC mixtures are physical mixtures with wide commercial importance. The elastomeric component, NBR, can act as a continual plasticizer for PVC applications, as in electrical wires and cables coatings, wrapping films for the food industry, conveyor belts, domestic appliances, etc. The presence of PVC helps to improve the ozone and ageing resistance of NBR, which enables the use of this mixture in the automotive industry as gaskets, wires and cables, and in the manufacture of soles, footwear, artificial leather and others. nanofillers have improved physical and mechanical behaviour and thus offer new technology and business opportunities [1-3].

Response surface methodology (RSM) is a set of mathematical and statistical techniques that are widely used for experimental modeling and analysis of problems in which a response of interest is influenced by several variables and the response surface can be explored to set optimum conditions [4].

In this study, RSM with central composite design (CCD) was used to investigate the effects of processing variables and amount of PVC and NiFe₂O₄nanoparticles (NPs) loading on the tensile strength of OptimizedNBR/PVC/NiFe₂O₄ nanocomposites. Significant parameters that affect the tensile strength of NBR/PVC/NiFe₂O₄ nanocomposite will be determined.

Materials and method

Acrylonitrile butadiene rubber (NBR) and (polyvinyl chloride) PVC resins were supplied by LG Company. Nickel nitrate [Ni(NO₃)₂.6H₂O], ferric nitrate [Fe(NO₃)₃.9H₂O] were supplied by Merck company.

Maltose was supplied by Daejung Chemical & Metals Company.

The NiFe₂O₄ NPs are prepared by the sol-gel auto-combustion method. An appropriate amount of metal nitrates are first dissolved in a low volume of de-ionized water. The molar ratio of nitrates (Ni:Fe) is 1:2. Then a small amount of maltose is added to the solution. The final solution is magnetically stirred for 1 h at room temperature and then extra water is removed in a vacuum rotary evaporator at 120 °C until a gel is achieved. The obtained gel is dried in a hot air oven at 100 °C for about 10 h. Finally dark brown colour nickel ferrite powder is obtained.

The two-roll mill was used to prepare mixtures of NBR/PVC/NiFe₂O₄ with Different percentages of NBR, PVC and NiFe₂O₄NPs obtained from RSM. Mixing was done at room temperature for about 20 min. The samples of almost 2.5mm thicknesses were vulcanized in plate vulcanization machine at 120°C and 20 MPa pressure for 10 min. The vulcanized sheets were laid out aside at room temperature for 24 h, and then they were used to calculate their performances.

Results and Discussion

Characterization of NiFe₂O₄ NPs

XRD study: The XRD pattern of NiFe₂O₄ NPs is shown in Fig.1 and is indexed as a cubic phase (space group: Fd-3m), which are in a good agreement with the standard XRD pattern (JCPDS No. 74-2081). The average particle size was estimated to be ≈35nm by the Scherrer equation.

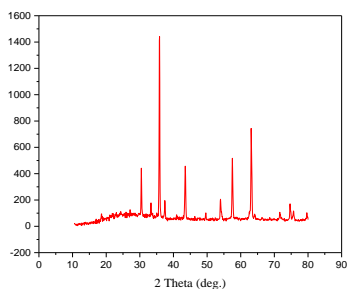


Fig.1: XRD pattern of the nickel ferrite sample.

SEM and EDX study: The SEM images of the NiFe₂O₄NPs are shown in Fig.2(a). SEM images show that nanoparticles exhibits a triangle-like structure with agglomeration in nature. The EDX spectra of pure NiFe₂O₄NPs is shown in Fig.2(b), that shows the peaks of Fe, Ni and O fundamentals and free from other peaks, which established the purity of the sample and no other formation of impurity.

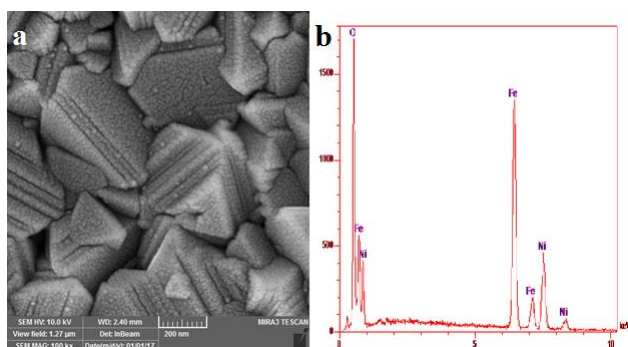


Fig.2: (a) SEM images and (b) EDX spectrum of the nickel ferrite NPs.

Design of experiment: Response surface methodology (RSM) is a set of mathematical and statistical methods that are used for modeling and analysis of problems in which a response or output variable of interest is influenced by several input variables and the aim is to optimize this response. In the present study, the most commonly used technique in RSM design, called central composite design (CCD), was selected for modeling and optimization of impact strength of the quaternary nanocomposite [4]. The multiple regression analysis on the experimental data. The general first degree equation model points out Eq. (1):

$$Y = \beta_0 + \sum_{i=1}^k \beta_i x_i + \sum_{i=1}^k \beta_{ii} x_i^2 + \sum_{i < j} \beta_{ij} x_i x_j + \varepsilon \quad (1)$$

Where Y represents the responses (dependent variables), β_0 is the constant coefficient; β_i , β_{ii} and β_{ij} are coefficients for the linear, quadratic and interaction effects, respectively. x_i and x_j are factors (independent variables), and ε is the standard error.

The experimental data obtained was analysed. First degree model was found to fit adequately the experimental data. The adequacy of the model was established by ANOVA, normal probability plot and Residual Analysis. Through the estimation of all regression coefficients, the experimental response could be modelled as a polynomial equation that shows the effect of experimental factors on the tensile strength. The first degree function in terms of coded factors (parameters) obtained is given in Eq. (2):

$$Y_{\text{tensile strength}} = 16.46 + 1.74 A - 0.53 B \quad (2)$$

Where Y is the impact strength of the quaternary nanocomposite, A and B are PVC and NiFe₂O₄ NPs contents, respectively. The R² value for Eq. (2) was 0.6578. This indicated that 65.78% of the total variation in tensile strength was assigned to the experimental variable studied.

Fig.6 exhibits the comparison between the actual response values as obtained from the experimental runs and predicted response values based on the first degree model equation. It demonstrates that the model is an accurate description of the experimental data, indicating that it was successful in comparing the correlation between the two variables.

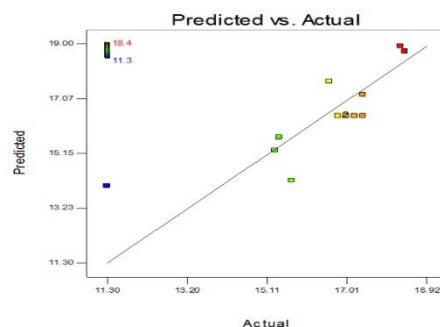


Fig.6: Comparison between the predicted and actual experiment values for the tensile strength.

Fig.7 shows the 3D plot of the interaction of the PVC and NiFe₂O₄NPs loading on tensile strength. The maximum tensile strength of NBR/PVC/NiFe₂O₄ nanocomposites was provided at 0.93 and 41.58 wt% of NiFe₂O₄NPs and PVC loading respectively.

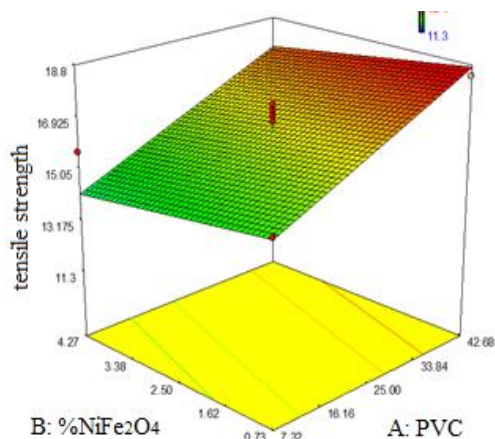


Fig.7: Three-dimensional response surface plots of tensile strength as a function of PVC and NiFe₂O₄NPs loading

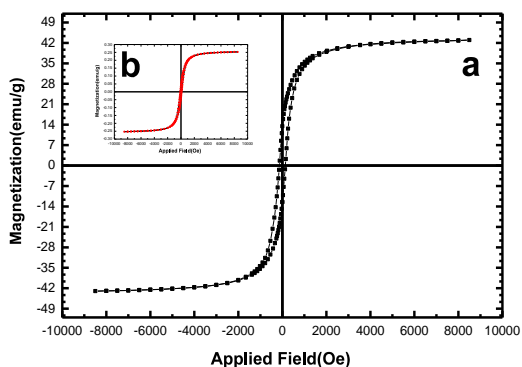
Characterization of Optimized nanocomposite

VSM study: the magnetic hysteresis loop was measured at room temperature for the NiFe₂O₄ NPs is shown in Fig.5(a). NiFe₂O₄ NPs shows ferromagnetic behaviour at room temperature with coercive force (H_c) value of ≈135.93Oe and saturation magnetization (M_s) value of ≈42.94 emu/g.

The magnetic hysteresis loop was measured at room temperature for the NBR/PVC/NiFe₂O₄ is shown in Fig.5(b). NBR/PVC/NiFe₂O₄ shows weak ferromagnetic behaviour at room temperature than NiFe₂O₄ NPs with coercive force (H_c) value of 110Oe and saturation magnetization (M_s) value of ≈0.25 emu/g. Magnetization decreases with increasing polymer content. Since the NBR and PVC powders are not magnetic, the magnetic properties of the Optimized NBR/PVC/NiFe₂O₄ nanocomposite, are attributed to the ferromagnetic properties of the NiFe₂O₄ NPs.

Fig.5: Hysteresis curve of the NiFe₂O₄ NPs (a) and Optimized NBR/PVC/NiFe₂O₄ (b) nanocomposite at room temperature

SEM and EDX study: The SEM images of the Optimize



Synthesis of Cr, Si/TiO₂ nano particles by sol-gel method and modelling of their photocatalytic performance utilizing experimental design with response surface methodology (RSM)

Motahare Mehdipour, Masood Hamadani*

Institute of Nanoscience and Nanotechnology, University of Kashan, Kashan, Iran
hamadani@kashanu.ac.ir

Abstract: Recently, doping with suitable transitional metals has been attempted as a facile method to Performance improvements of TiO₂. Chromium and silicon co-doped TiO₂ photocatalyst was synthesized by modified sol-gel method using titanium (IV) isopropoxide, Cr(NO₃)₃.6H₂O and Tetraethyl orthosilicate (SiC₈H₂₀O₄) as precursors. Using Response Surface methodology (RSM), it was possible to evaluate the role of interaction between Cr and Si in the codoped TiO₂ nanoparticles. The photocatalytic activities of Cr and Si-TiO₂ nanoparticles were evaluated using the photodegradation of methyl orange (MO) as probe reaction under the irradiation of visible light and it was observed that the Cr, Si-TiO₂ photocatalyst shows higher visible photocatalytic activity than the pure TiO₂.

Keywords: sol-gel method; Cr, S-codoped TiO₂; photocatalytic activities; RSM

Introduction

Among all advanced oxidation technologies, photocatalysts has proved to be a promising alternative for their vast applications in environmental protection processes in water, air and waste treatment. A favourable treatment procedure is one which is low in cost, friendly with environment, sustainable and able to remove microorganisms as well as chemical compounds. Compared with other photocatalysts, semiconductors have shown great potential in this regard [1].

TiO₂ semiconductor photocatalyst has attracted much interest due to its chemical and photo stability, low cost and non-toxicity. Although titanium dioxide (TiO₂) is the most popular photocatalytic material, it is active only in the ultraviolet (UV) region because of its wide band gap. Therefore, many researchers have attempted to modify the electronic properties of TiO₂ in order to extend its optical absorption edge into the visible light region and to improve the photocatalytic activity. Recently, doping with suitable transitional metals has been attempted as a facile method to Performance improvements of TiO₂. The dopant transitional metal works by introducing a donor and/or acceptor level in the wide forbidden band of TiO₂, which allows photons with some lower energy can also excite photocatalyst to exhibit a visible light photocatalytic activity [2,3].

In this work, novel chromium and silicon codoped TiO₂ photocatalysts were synthesized by the sol-gel method and optimized by response surface methodology (RSM). RSM is a powerful tool used for reducing the number of experimental runs needed to provide sufficient information for statistically acceptable results. The photocatalytic activity of the samples was investigated by using methyl orange (MO) solutions under visible irradiation.

Materials and method

The chemicals were purchased from Merck and were used as such without any further purification. The typical synthesis procedure for TiO₂ and Cr, Si-codoped TiO₂ nanoparticles was as follows: Titanium(IV) isopropoxide (2 ml) was hydrolysed using 4.60 mL glacial acetic acid at 0 °C. Then, 46.5 mL of deionized water was added drop wise under vigorous stirring for 1 h. Subsequently, the solution ultrasonicated for 15 min in ice bath until a clear solution was formed. The prepared solution was kept in dark for nucleation process for 24 h. The solution was gel in an oven at 70 °C for 12 h. The gel was dried at 120 °C and then prepared powder was crushed well and calcined in the air atmosphere at 550 °C for 2 h.

Results and Discussion

Different percentages of Cr and Si according to [table 1](#) were dissolved in 46.5mL deionized water. Other steps were repeated as in above mentioned process. Degradation of MO in the presence various amounts of Cr, Si-codoped TiO₂ photocatalyst under visible irradiation was investigated by UV-visible spectroscopy and results depicted in [Fig1](#).

Table 1: Experimental factors, experimental and predicted values of MO degradation

Run	Cr/TiO ₂ mol%	S/TiO ₂ mol%	Actual Value	Predicted Value
1		1.50	71.	71.58
2	2.50	3.00	45.	54.91
3	1	3.00	87.50	84.70
4	2.50	3.00	50.00	46.09
5	4.00	1.94	70	63.83
6	1.44	4.06	46	46.17
7	3.56	3.00	78	84.70
8	2.50	4.50	50	55.42
9	2.50	3.00	88	84.70
10	2.50	3.00	83	84.70

11	2.5	3.00	87	84.70
12	1.44	4.06	66	56.40
13	3.56	1.94	58	61.60

Fig.1 shows MO degradation by 3.24% Cr, and 3.14% Si, codoped TiO₂ under visible irradiation is the best catalyst.

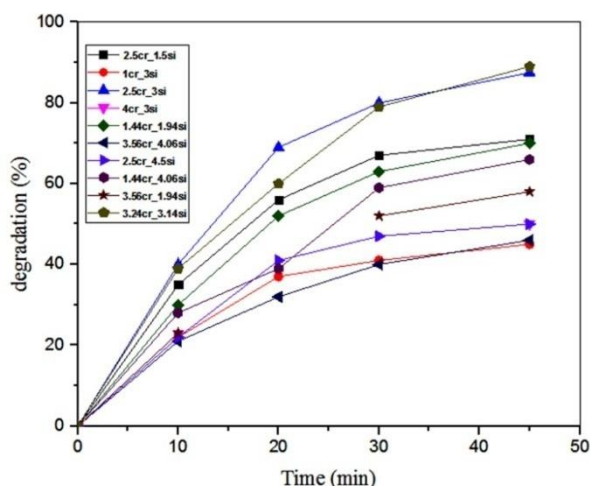


Fig. 4: Degradation of MO in the presence various amounts of Cr,Si-codoped TiO₂.

Fig. 2 shows the predicted versus actual graph for the degradation of MO, indicate good agreement between predicted and experimental results.

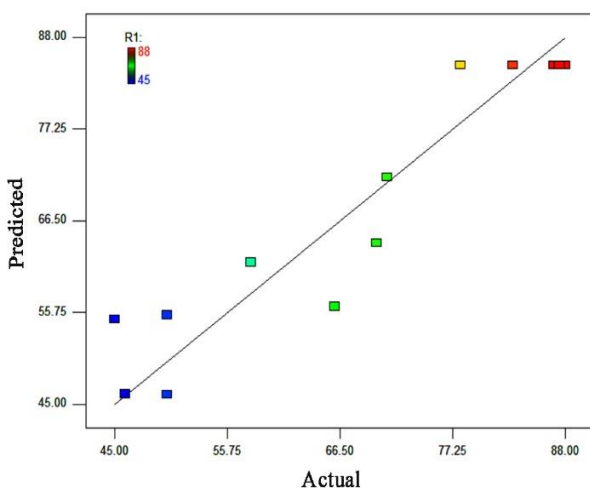


Fig. 2: Plot of actual vs predicted values in photo degradation of MO

The plot of normal probability of the residual for MO is depicted in Fig. 3. The trend shown in this figure reveals reasonably well-behaved residual of MO dye and that the residual is

normally distributed and resembles a straight line. In Fig. 4, the response surface was developed as a function of amount of Cr and Si doping in TiO₂, while the irradiation time was kept constant at 45 min.

Conclusions

The present study investigates the efficient utilization of visible light photocatalyst in decomposition of MO through doping both of chromium and silicon into TiO₂ photocatalyst. The optimal Cr, Si-TiO₂ concentration to obtain the highest photocatalytic activity was 3.24 mol% for Cr and 3.14 mol% for Si. Degradation for best catalyst of Cr_Si_TiO₂ in 45 min under visible irradiation was 87%.

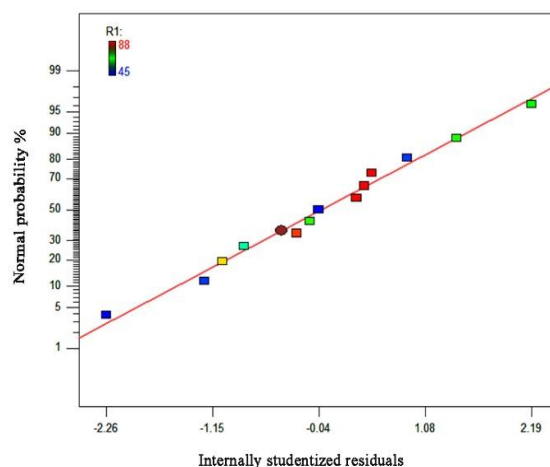


Fig. 3: Normal probability plots for color removal efficiency of MO

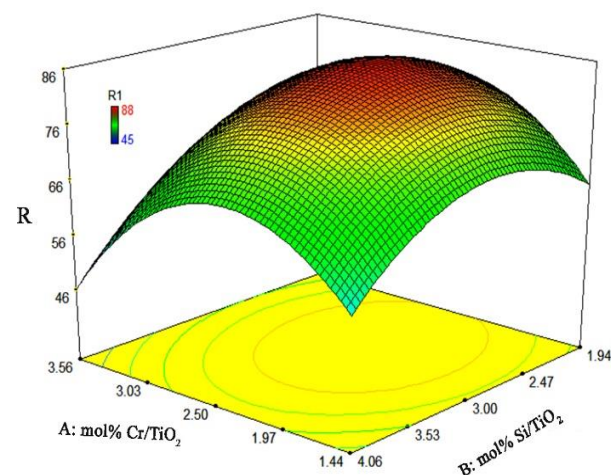


Fig. 4: 3-D response surface plots of MO degradation.

References



بیستمین کنفرانس شیمی فیزیک ایران
دانشکده علوم پایه - دانشگاه اراک
۳۱-۲۹ مرداد ۱۳۹۶



20th Iranian Physical Chemistry Conference

[1] X. Luo, S. Zhang, X. Lin, New insights on degradation of methylene blue using thermocatalytic reactions catalyzed by low-temperature excitation, *Journal of hazardous materials*, 260 (2013) 112-121.

[2] L. Jing, Z. Xu, X. Sun, J. Shang, W. Cai, The surface properties and photocatalytic activities of ZnO ultrafine particles, *Applied Surface Science*, 180 (2001) 308-314.

[3] Z. Xu, J. Yu, Visible-light-induced photoelectrochemical behaviors of Fe-modified TiO₂ nanotube arrays, *Nanoscale*, 3 (2011) 3138-3144.



Response surface methodology (RSM) for optimization of water treatment by $\text{Fe}_3\text{O}_4@\text{SiO}_2@\text{Cr-TiO}_2\text{-S}$ nanocomposite and enhanced performance with deposited Ag on the its surface

Mohammad-Peyman Mazhari, Masood Hamadanian*

Institute of Nanoscience and Nanotechnology, University of Kashan, Kashan, Iran

hamadani@kashanu.ac.ir

Abstract: In this work, first a magnetic chromium and sulfur co-doped TiO_2 photocatalyst was synthesized by modified sol-gel method. Degradation of methyl orange(MO) considered as a model organic pollutant in water. For a high efficiency, we have optimized amount of codoped chromium and sulfur in the $\text{Fe}_3\text{O}_4@\text{SiO}_2@\text{Cr-TiO}_2\text{-S}$ nano particles by using of response surface methodology (RSM). Then different amounts of silver nanoparticle have been deposited on the surface of optimum sample by photodeposition method. The samples were characterized by techniques such as XRD, SEM and EDS. The magnetic nanocomposite samples easy recycling by external magnet. Also, they show a good photocatalyst activity after multiple recycles.

Keywords: *Magnetic nanocomposite; Responsesurface methodology; Cr, S co-doped TiO_2 ; Photodeposition method*

Introduction

Semiconductor titanium dioxide is the most preferred material for decomposition of pollutants wastewater because of its low toxicity, chemical and photo stability, high photocatalytic activity, no-photocorrosion and strong oxidizing power [1-3]. TiO_2 having an energy band gap of about 3.0 eV for rutile and 3.2 eV for anatase, therefore it often absorbs the ultraviolet region of the solar spectrum and only a small amount of visible light. To utilize visible light more effectively in photocatalytic reactions, it is necessary to develop absorption region of TiO_2 by modification of optical properties. Doping TiO_2 with metal or non-metal is one of the most promising strategies for sensitizing TiO_2 to visible light and enhancing photocatalytic activity [4].

In this work, magnetic nanoparticle Fe_3O_4 were synthesized by co-precipitation method were used as themagnetic cores and deposition of a SiO_2 layer by Stöber method. chromium and sulfur ions doped magnetic TiO_2 ($\text{Fe}_3\text{O}_4@\text{SiO}_2@\text{Cr-TiO}_2\text{-S}$) was synthesized with sol-gel method. For investigation and optimization of chromium and sulfur ion amount, we used Response Surface Methodology(RSM). For increasing the photocatalytic activity, we deposit different values of silver nanoparticle on surface of optimize sample by photodeposition method.

Materials and method

All the chemicals were purchased from Merck and were used as such without any further purification. The catalyst support comprised of silica-coated magnetic NPs was synthesized by a simple co-precipitation method. The prepared magnetic nanoparticles were

dispersed in 30 ml of Merck 2-propanol and sonicated for 20 minutes. Then chromic nitrate solution and thiourea (based on mol ratio of Cr and S optimization with RSM) added to the mixed above solution and sonicate for 10 min (table 1).In second beaker, 2.74 ml titanium(IV) isopropoxide was added to 10 ml of Merck 2-propanol with 1 ml acetyl acetone and stirred. Then second beaker was added very slowly to the mixture under stirring. After 30 min added 2ml deionized water to the mixture and refluxing at 80 °C for 12 hours. the particles were driedat 70 °C for 10 h and calcined at 400°C in air atmosphere for 2 hours. Then, deposit different amounts of silver nanoparticle on the surface of optimum sample by photodeposition method.

Results and Discussion

Fig. 1a and 1b show the XRD analysis of the $\text{Fe}_3\text{O}_4@\text{SiO}_2@\text{Cr-TiO}_2\text{-S}$ and $\text{Fe}_3\text{O}_4@\text{SiO}_2@\text{Cr-TiO}_2\text{-S/Ag}$ nanocomposite, respectively. The diffraction peaks in $2\theta= 38.08, 54.06, 63$ and $2\theta= 25.55, 38 .7, 48.20, 53$ corresponding to the Fe_3O_4 and anatase phase of TiO_2 nanoparticle, respectively.

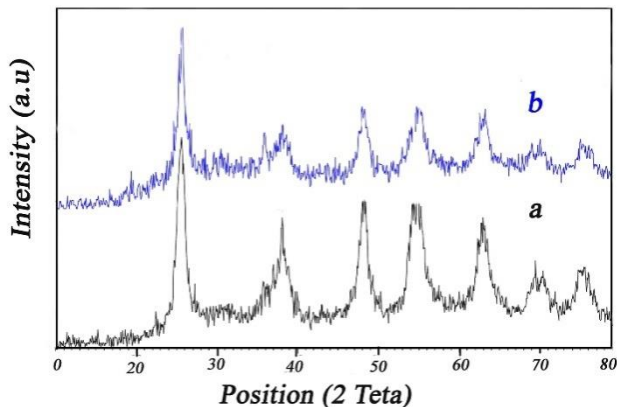


Fig. 1: XRD pattern of samples (a) $\text{Fe}_3\text{O}_4@SiO_2@Cr-TiO_2-S$ (b) $\text{Fe}_3\text{O}_4@SiO_2@Cr-TiO_2-S/Ag$

For confirm the chemical composition were taken energy dispersive X-ray spectroscopy (EDS) analysis of the samples (Fig. 2). The EDS data shows that the samples is composed of O, Fe, Si, Ti, Cr, S and Ag in the nanocomposite structure.

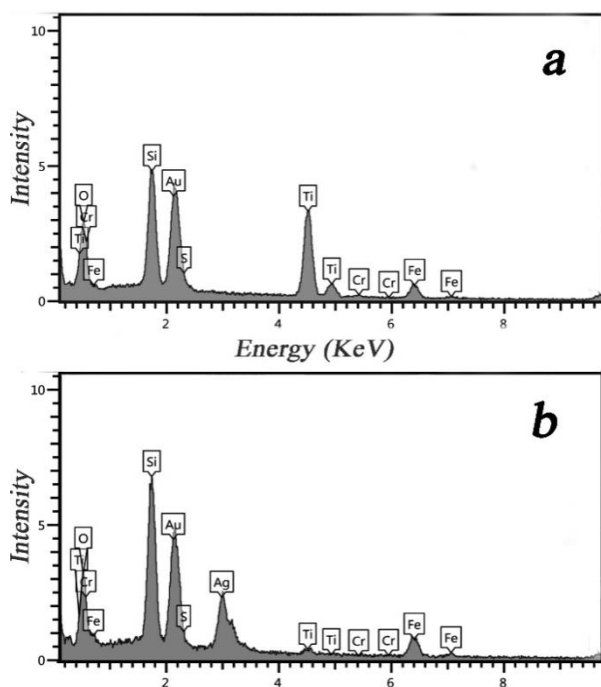


Fig.2: (a) EDS data of $\text{Fe}_3\text{O}_4@SiO_2@Cr-TiO_2-S$ (b) $\text{Fe}_3\text{O}_4@SiO_2@Cr-TiO_2-S/Ag$

The FE-SEM was studied for analyzing the morphology of the samples and image shown in Fig. 3. The FE-SEM $\text{Fe}_3\text{O}_4@SiO_2@Cr-TiO_2-S$ and $\text{Fe}_3\text{O}_4@SiO_2@Cr-TiO_2-S/Ag$ indicate particles are uniform and slightly agglomerated with mediocre size about 26 nm and 33nm, respectively.

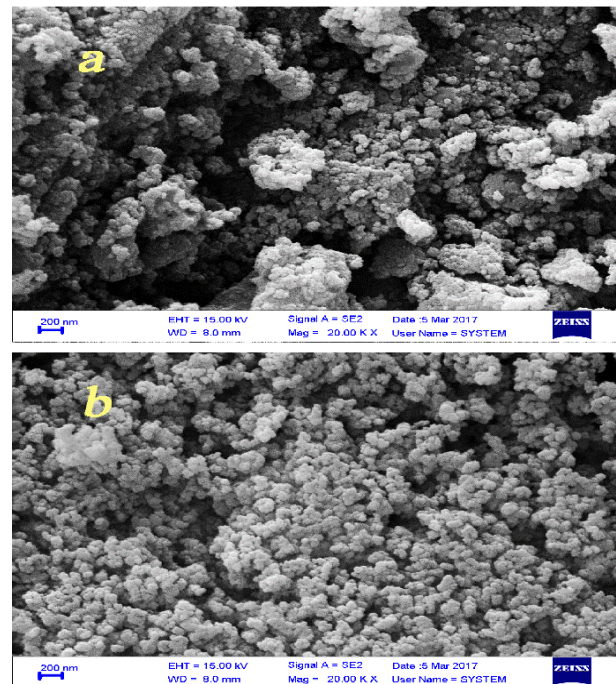


Fig. 3: SEM images of (a) $\text{Fe}_3\text{O}_4@SiO_2@Cr-TiO_2-S$ (b) $\text{Fe}_3\text{O}_4@SiO_2@Cr-TiO_2-S/Ag$

Results of photocatalytic activity of $\text{Fe}_3\text{O}_4@SiO_2@Cr-TiO_2-S$ photocatalyst with various amount of chromium and sulfur under visible irradiation show in Table 1

Table 1: Experimental factors, experimental and predicted values of MO degradation.

Run	A: Cr/TiO ₂ mol%	B: S/TiO ₂ mol%	Actual Value	Predicted Value
1	5	5	84.27	83.80
2	8	8	70.35	70.58
3	8	2	80.49	79.54
4	8	5	73.4	75.06
5	5	5	84.18	83.80
6	5	8	80.36	79.33
7	5	5	83.11	83.80
8	5	2	89.2	88.28
9	5	5	82.85	83.80
10	2	8	88.23	88.07
11	2	5	92.36	92.55
12	5	5	84.52	83.80
13	2	2	96.11	97.02

Fig. 4 show variation of the response as a function of the amount of mol ratio of Cr/TiO₂ and mol ratio of S/TiO₂ at the room temperature. These 3D space diagrams show that MO degradation increases when amount of Cr/TiO₂ and S/TiO₂ little increases (2.03 and 2.24 mol% respectively).

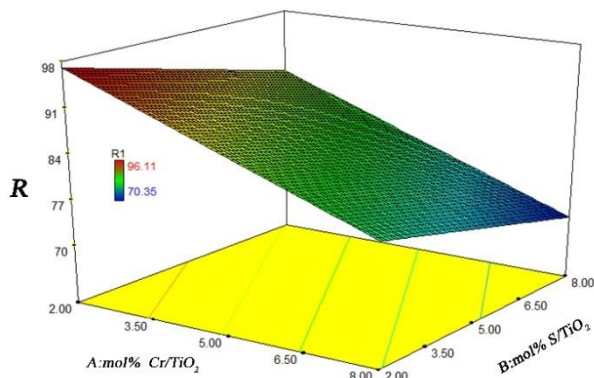


Fig. 4: .3-D response surface plots of MO degradation.

Degradation of MO in the presence of optimize $\text{Fe}_3\text{O}_4@ \text{SiO}_2@ \text{Cr-TiO}_2\text{-S}$ nanocomposite with various amounts of silver nanoparticles on surface visible irradiation was evaluated by UV-visible spectroscopy and results depicted in Figs 5.

The time for almost complete degradation of MO by $\text{Fe}_3\text{O}_4@ \text{SiO}_2@ \text{Cr-TiO}_2\text{-S/Ag}$ (%4) was 120 min under visible irradiation, while the optimize $\text{Fe}_3\text{O}_4@ \text{SiO}_2@ \text{Cr-TiO}_2\text{-S}$ decompose 89% of dye during the same time. In general, when silver (with a low Fermi level) deposit on the surface, Fermi level (E_f) of the composites shift to a negative potential. Also they can help to the charge separation and slow recombination by attracting photoelectrons.

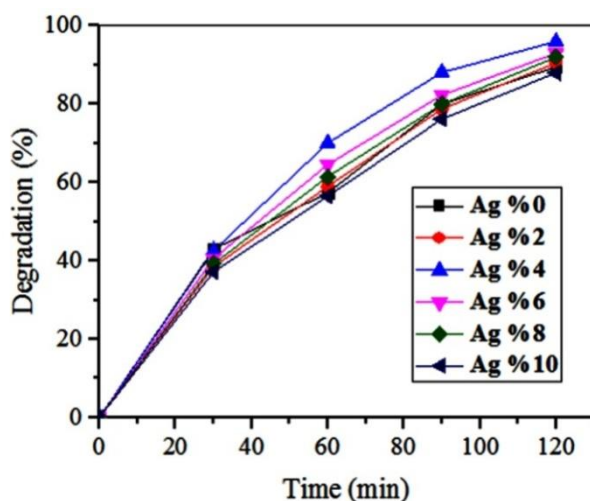


Fig. 5: Photocatalytic degradation of MO by various amount of silver on $\text{Fe}_3\text{O}_4@ \text{SiO}_2@ \text{Cr-TiO}_2\text{-S}$ nanoparticle under visible light.

Conclusions

In this study a photocatalytic process using recoverable magnetic nanocomposite was used to degradation of the MO dye as a model pollutant in wastewater. Optimization of the $\text{Fe}_3\text{O}_4@ \text{SiO}_2@ \text{Cr-TiO}_2\text{-S}$ was performing by Response Surface Methodology with CCD approach and the optimum conditions for MO degradation were found (2.03 and 2.24 mol% for Cr and S, respectively). Deposition of 4% silver nanoparticle on the surface of optimum sample by photodeposition method enhancing of photocatalytic activity.

References

- [1] G. Sivalingam, K. Nagaveni, M. Hegde, G. Madras, Photocatalytic degradation of various dyes by combustion synthesized nano anatase TiO_2 , Applied Catalysis B: Environmental, 45 (2003) 23-38.
- [2] W.-C. Hung, S.-H. Fu, J.-J. Tseng, H. Chu, T.-H. Ko, Study on photocatalytic degradation of gaseous dichloromethane using pure and iron ion-doped TiO_2 prepared by the sol-gel method, Chemosphere, 66 (2007) 2142-2151.
- [3] H. Khojasteh, M. Salavati-Niasari, M.-P. Mazhari, M. Hamadianian, Preparation and characterization of $\text{Fe}_3\text{O}_4@ \text{SiO}_2@ \text{TiO}_2@ \text{Pd}$ and $\text{Fe}_3\text{O}_4@ \text{SiO}_2@ \text{TiO}_2@ \text{Pd-Ag}$ nanocomposites and their utilization in enhanced degradation systems and rapid magnetic separation, RSC Advances, 6 (2016) 78043-78052.
- [4] M.E. Kurtoglu, T. Longenbach, K. Sohlberg, Y. Gogotsi, Strong coupling of Cr and N in Cr-N-doped TiO_2 and its effect on photocatalytic activity, The Journal of Physical Chemistry C, 115 (2011) 17392-17399.
- [5] F. Wang, Z. Ma, P. Ban, X. Xu, C, N and S codoped rutile TiO_2 nanorods for enhanced visible-light photocatalytic activity, Materials Letters, 195 (2017) 143-146.



A DFT study on the phosgene adsorption behavior onto the pristine and substituted sumanenes

Maryam Baji, Zabiollah Mahdavifar*, Ehsan Shakerzadeh

Department of Chemistry, Faculty of Science, Shahid Chamran University of Ahvaz, Ahvaz, Iran

z_mahdavifar@scu.ac.ir

Abstract: Sumanene ($C_{21}H_{12}$, C_{3v}) is a typical representative of the class of compounds known as the molecular bowls, π -bowls, or simply buckybowls. In the present paper we have investigated the adsorption of phosgene molecule on the surface of sumanene and its derivatives. The adsorption processes have been investigated with density functional theory (DFT) approach. The adsorption properties of sumanene molecules toward phosgene are discussed through analysis of the adsorption energy and electronic properties. Results indicate that the physisorption is occurred. Our results indicate that the sumanene can be very useful in the practical application for monitoring phosgene.

Keywords: Sumanene, Phosgene, Adsorption energy, DFT

Introduction

Sumanene ($C_{21}H_{12}$, C_{3v}) is a typical representative of the class of compounds known as the molecular bowls, π -bowls, or simply buckybowls [1]. It can be described as a slice of buckminsterfullerene with twenty one carbon atoms with all vacant valences terminated by hydrogens [2]. The core of the sumanene is a benzene ring and the periphery consists of alternating benzene rings and cyclopentadiene rings. Unlike fullerene, sumanene has benzyl positions which are available for organic reactions. Since the successful synthesis of sumanene by Sakurai et al. in 2003 [1], several experimental and theoretical studies had been performed [3-8]. Sastry and coworkers [9] reported pioneering research on theoretical calculations on heteroatom-substituted sumanenes. The aromaticity and nonlinear optical properties of sumanene modified with boron and nitrogen atoms are investigated through DFT calculations by Armačić et al. [10]. They showed that sumanene substitution with BH and NH groups leads to significant improvement of the first hyperpolarizability. Moreover, theoretical assessment of the small molecules such as CO, CO₂ and NH₃ adsorption properties onto sumanene are also reported [11]. Furthermore, the structure and electronic properties of ozone addition to pristine and functionalized sumanene with NH and BH groups are systematically studied using density functional theory (DFT) calculations by our research group [12].

$C_{59}P$

Computational Method

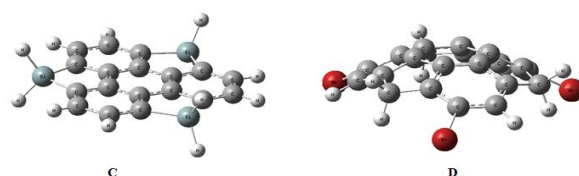
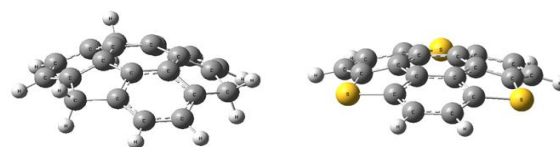
The structures are fully optimized through density functional theory using conventional B3LYP method and 6-31G(d,p) basis set. The nature of the stationary points is checked by frequency analysis at the same computational level and no imaginary frequency is observed for the considered structures. The HOMO-LUMO

gap

($HLG = (\epsilon_L - \epsilon_H)$) which is calculated in terms of the obtained energies of the highest occupied molecular orbital (ϵ_H) and the lowest unoccupied molecular orbital (ϵ_L), is applied to explore electronic properties of the considered systems.

Results and Discussion

First, The pristine and substituted sumanenes are investigated. The optimized structures of the pristine and substituted sumanenes are presented in Figure 1. The core of the sumanene is a benzene ring and the periphery consists of three alternating benzene rings and three cyclopentadiene rings. The CH₂ group of cyclopentadiene rings could be substituted by hetero groups. Thus, the three bridging CH₂ groups of sumanene are replaced by S and Si hetero groups as B and C structures. The benzene rings are also substituted by Br in Panel D of Figure 1. The obtained HOMO (ϵ_H) and LUMO (ϵ_L) energies and HOMO-LUMO gap (HLG) values are listed in Table 1. The results indicate that the HLG are slightly decreased due



Type	HOMO (eV)	LUMO (eV)	Energy Gap (eV)
A	-5.476	-0.716	4.760
B	-5.707	-1.365	4.342
C	-5.981	-1.633	4.348
D	-5.956	-1.369	4.587



In continue, the adsorption of phosgene molecule onto pristine and substituted sumanenes is studied. The obtained stable complexes are presented in Figure 2. The obtained HOMO (ϵ_H) and LUMO (ϵ_L) energies, HOMO-LUMO gap and adsorption energies for the considered complexes are summarized in Table 2.

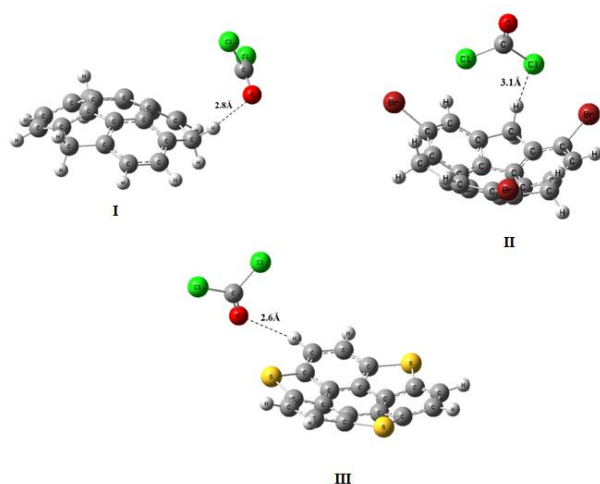


Fig. 1. The sumanene-phosgene complexes

Table 2. The obtained values for sumanene-phosgene complexes

Type	HOMO (eV)	LUMO (eV)	Energy Gap (eV)	E_{ads} (KJ/mol)
I	-5.481	-1.678	3.803	-4.800
II	-6.017	-1.641	4.376	-11.085
III	-5.647	-1.928	3.719	-5.641

According to the results of Table 2, the phosgene molecule adsorbed at the edge of Br-substituted sumanene with adsorption energy of -11.085 kJ/mol. Because of phosgene adsorption the HLG of the considered systems are decreased.

Conclusions

The adsorption of phosgene molecule on the surface of pristine and substituted sumanenes is scrutinized. The adsorption processes have been investigated with DFT approach. The adsorption properties of sumanene molecules toward phosgene are discussed through analysis of the adsorption energy and electronic properties. Results indicate that the physisorption is occurred. The results may provide novel insight for designing suitable materials for removal of phosgene pollutant.

References

- H. Sakurai, T. Daiko, T. Hirao, A synthesis of sumanene, a fullerene fragment, *Science* 301 (2003) 1878-1878.
- T. Amaya, T. Hirao, A molecular bowl sumanene, *Chem. Commun.* 47 (2011) 10524-10535
- T.C. Wu, H.J. Hsin, M.Y. Kuo, C.H. Li, Y.T. Wu, Synthesis and structural analysis of a highly curved Buckybowl containing corannulene and sumanene fragments, *J. Am. Chem. Soc.* 133 (2011) 16319-16321.
- Y.T. Wu, J.S. Siegel, Aromatic molecular-bowl hydrocarbons: synthetic derivatives, their structures, and physical properties, *Chem. Rev.* 106 (2006) 4843-4867.
- A.T. Mori, H.L. Wu, S. Ishida, J.I. Nakamura, K. Murata, T. Hirao, Synthesis and characterization of π -extended bowl-shaped π -conjugated molecules, *Chem. Commun.* 19 (2007) 1902-1904
- T. Amaya, S. Seki, T. Moriuchi, K. Nakamoto, T. Nakata, H. Sakane, A. Saeki, S. Tagawa, T. Hirao, Anisotropic electron transport properties in sumanene crystal, *J. Am. Chem. Soc.* 131 (2008) 408-409
- A.A.S. Karunarathna, S. Saebo, Computational studies of π - π interactions in dimers of heterosubstituted sumanenes, *Struct. Chem.* 26 (2015) 1689-1695.
- S. Armaković, S.J. Armaković, J.P. Šetrajčić, I.J. Šetrajčić, Optical and bowl-to-bowl inversion properties of sumanene substituted on its benzylic positions; a DFT/TD-DFT study, *Chem. Phys. Lett.* 578 (2013) 156-161.
- A.A.S. Karunarathna, S. Saebo, Computational studies of the intermolecular interactions in dimers of the bowl-shaped sumanene molecule, *Struct. Chem.* 25 (2014) 1831-1836.
- U.D. Priyakumar, M. Punnagai, G.P.K. Mohan, G.N. Sastry, A computational study of cation- π interactions in polycyclic systems: exploring the dependence on the curvature and electronic factors, *Tetrahedron* 60 (2004) 3037-3043.
- S. Armaković, S.J. Armaković, J.P. Šetrajčić, V. Holodkov, Aromaticity, response, and nonlinear optical properties of sumanene modified with boron and nitrogen atoms, *J. Mol. Model.* 20 (2014) 2538-2550.
- S. Armaković, S.J. Armaković, J.P. Šetrajčić, S.K. Jaćimovski, V. Holodkov, Sumanene and its adsorption properties towards CO, CO₂ and NH₃ molecules, *J. Mol. Model.* 20 (2014) 2170-2184.
- E. Tahmasebi, Z. Biglari, E. Shakerzadeh, Theoretical insight into the impact of sumanene functionalization with BH and NH groups on its ozone addition features, *Vacuum*, 136 (2017) 82-90.

Preparation and Evaluation of Manganese Catalysts of Alumina and Mesoporous Silica Mesh (HMS) (Mn / Al₂O₃, Mn / HMS) and their Catalytic Activity in Liquid Phase

Mehrnoosh kazemi^{a*}, Vahid mahdavi^b

^aDepartment of chemistry, Arak University, Arak, 3815688349, Iran

^bDepartment of chemistry, Arak University, Arak, 3815688349, Iran

Mehr.k7133@yahoo.com

Abstract: In this paper Mesoporous silica catalyst (HMS) are prepared and (5%-7.5%-10%-15%) weight of different salts of manganese (Nitrate manganese, acetate, sulfate, chloride) by impregnation method. It has been observed that the manganese nitrate salt has the highest percentages. This catalyst is used in the reaction of cyclohexane oxidation to cyclohexanone and cyclohexanol. The results are investigated using FT-IR analysis and X-ray diffraction (XRD) techniques, and the size of particles is determined using the Scherrer equation. Scanning electron microscope (SEM) also confirms the morphology of the mesoporous structure and changes in morphology after the placement of manganese salt on the base.

Keywords: HMS, mesoporous, oxidation

Introduction

HMS can be considered a member of the M41S family, which has many differences with molecular sieves made by electrostatics [1]. Mesoporous M41S class of materials have attracted a lot of interest because of its large surface area, high porosity, controllable and narrowly distributed pore sizes, and high thermal stability, making it self-potentially suitable for a great number of applications, such as catalysis, host-guest chemistry, environmental technology, adsorption, chemical sensors and electrodes in solid state ionic device [2]. The introduction of Ti into the mesoporous structure increases its catalytic characterization [3]. Mesoporous titanium containing M41S and HMS materials have recently been prepared and tested as catalysts. Ti-MCM-41, in which the titanium is incorporated into the framework of siliceous MCM-41, is an effective catalyst for epoxidations of bulky reactants [4,5]. Ti-HMS prepared via templating with a neutral surfactant is also very active towards such reactions [6,7]. Oxidation of cyclohexane to cyclohexanone and cyclohexanol in the presence of oxidizing TBHP and manganese catalyst on the Ti-HMS base in the liquid phase.

Materials and method

2.1. Preparation of materials

The synthesis of mesoporous Si-HMS silicates from a method first described by Pinawia et al. Two solutions A and B were prepared as follows: A solution: 21 g of ethanol + 15 g of tetra-orthosilicate (TEOS) Mix A

1	Ti-HMS (Si/Ti=45)	inoculated	0.45	0
---	-------------------	------------	------	---

solution for 30 minutes at ambient temperature. B solution: 46 g of water + 3.5 g of dodecylamine (DDA) as template agent + 4.1 ml of HCl of 0.1N. Dissolve B solution at ambient temperature for 5 minutes.

Then mix A and B and mix the resulting mixture at room temperature for 24 hours to obtain a gel solution. The gel is then smooth and is dried in an oven for 1-2 nights at 100 °C. At this stage, the precipitate dried in an electric furnace at 500 °C is calcined during a thermal program, and finally the HMS is produced in a perfectly uniform, soft and white powder. After making the base catalyst, we mixed the various manganese salts with different percentages of 2.5, 5, 7, 5, 10 and 15 wt% on the base by inoculum. After preparation of the catalysts, the reflux is carried out at 90 °C in the presence of the measured value of the solvent, cyclohexane as the primary material, TBHP as an oxidizing agent for 8 hours, and then the product is injected into the G.C. device and the conversion percentage of the products is calculated.

2.2. Characterizations

The X-ray diffraction device (Diffract meter Philips) of the PW1800 model, with the use of K α Cu and Ni filters, has been used to determine the phases in the catalyst. The SEM machine is the electronic microscope model (Philips XL30) to determine the morphology of the catalyst.

No	Catalyst	Preparation method	Ti (wt%)	Mn salt used
----	----------	--------------------	----------	--------------

2	Mn(2.5%)/Ti-HMS	inoculated	0.45	0.57
---	-----------------	------------	------	------

3	Mn(5%)/Ti-HMS	inoculated	0.45	0.114
4	Mn(7.5%)/Ti-HMS	inoculated	0.45	0.171
5	Mn(10%)/Ti-HMS	inoculated	0.45	0.228

Table1: Characteristics of the Ti-containing catalysts To prepare 0.5 g of catalyst

Results and Discussion

The properties of the materials prepared for this study are given in table 1.

In this table, the amounts of manganese nitrate salt are used, as well as the amount of titanium.

7	Mn(10%)/Ti-HMS	45.96	NO ₃ ⁻
8	Mn(15%)/Ti-HMS	25.63	NO ₃ ⁻
9	Mn(5%)/Ti-HMS	58.64	Cl ⁻
10	Mn(5%)/Ti-HMS	48.01	CH ₃ COO ⁻
11	Mn(5%)/Ti-HMS	43.51	SO ₄

Table2. conversion percentage of catalysts

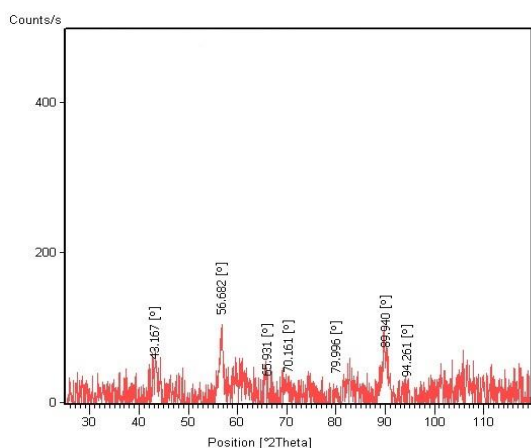


Fig2: The XRD pattern for Mn/Ti-HMS(Si/Ti=45)

To determine the morphology, apparent shape and approximate size of particle size of manganese nanoparticle catalysts, we used SEM images using electron microscopy. Fig.1 shows the results of this analysis. Changing the salt and changing the amount of salt used has changed morphology.

No	Catalyst	conversion percentage	Anion from salt
1	HMS	13.62	-
2	Ti-HMS(Si/Ti=15)	14.74	-
3	Ti-HMS(Si/Ti=25)	45.21	-
4	Ti-HMS(Si/Ti=45)	47.23	NO ₃ ⁻
5	Mn(2.5%)/Ti-HMS	48.48	NO ₃ ⁻
6	Mn(5%)/Ti-HMS	64.47	NO ₃ ⁻

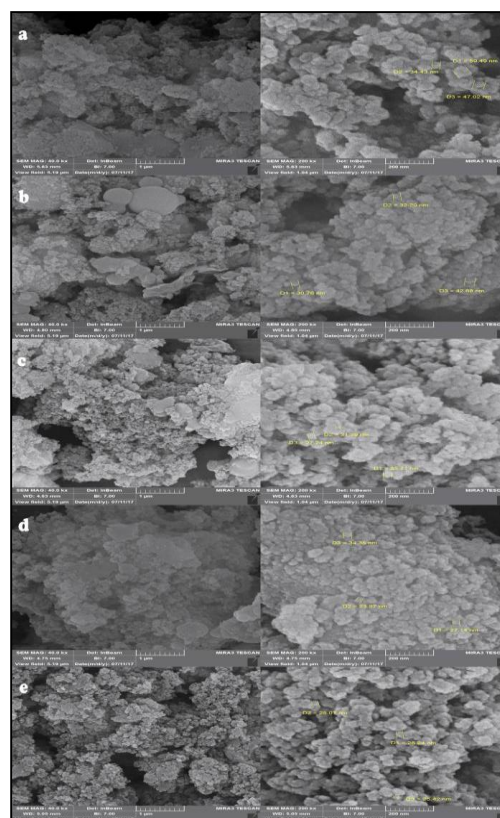


Fig1: FE-SEM images of Ti-HMS with a) 5% Mn(NO₃)₂ b) 10% Mn(NO₃)₂ c) 5% Mn(CH₃COO)₂ d) 5% MnSO₄ e) 5% Mn(NO₃)₂.Al₂O₃ After preparing the catalysts and placing them in reaction with (0.1 g of catalyst, 15 ml cyclohexane was injected as an initial material of 15 ml TBHP and 30 ml of acetonitrile as a solvent) to the G.C machine and the conversion of cyclohexane to cyclohexanone and cyclohexanol was as shown in Table 2 It has been reported. Fig.2 show XRD catalyst spectrum for a sample of Mn/Ti-HMS(Si/Ti=45) Which is similar to the reference spectrum. All catalysts were taken before and after calcination the FT-IR infrared spectrum and show in Fig3. In all three

forms, the Ti-HMS peak appears in the region 1370.82-970.14 cm^{-1} .

Conclusions

In this work, HMS research with specific physical and chemical properties, such as high chemical stability, high thermal stability, has been used as the basis for the production of non-homogeneous solid catalyst.

Therefore, the HMS base appears to increase catalytic activity and non-homogeneity in the reaction system. The activity of these catalysts in the oxidation reaction of cyclohexane with oxidizing TBHP has been investigated. The experimental data showed that the highest activity was for the catalyst Mn5%/Ti-HMS(Si/Ti=45)

The mole ratio of TBHP to cyclohexane was 1: 1, the catalyst was 0.1 g, the reaction time was 8 hours, and the reaction temperature was 90°C.

References

- [1] M.E. Davis, Nature 417 (2002) 813–821.
- [2] M.E. Davis, Nature 417 (2002) 813–821.
- [3] T.A. Zepeda, J.L.G. Fierro, B. Pawelec, R. Nava, T. Klimova, G.A. Fuentes, T. Halachev, Chem. Mater. 17 (2005) 4062–4073
- [4] T. Blasco, A. Corma, M.T. Navarro and J. P. Pariente, J. Catal. 156 (1995) 65.
- [5] A. Sayari, Chem. Mater. 8 (1996) 1840.
- [6] P.T. Tanev, M. Chibwe and T. Pinnavaia, Nature 368 (1994) 321.
- [7] W. Zhang, M. Froba, J. Wang, P.T. Tanev, J. Wong and

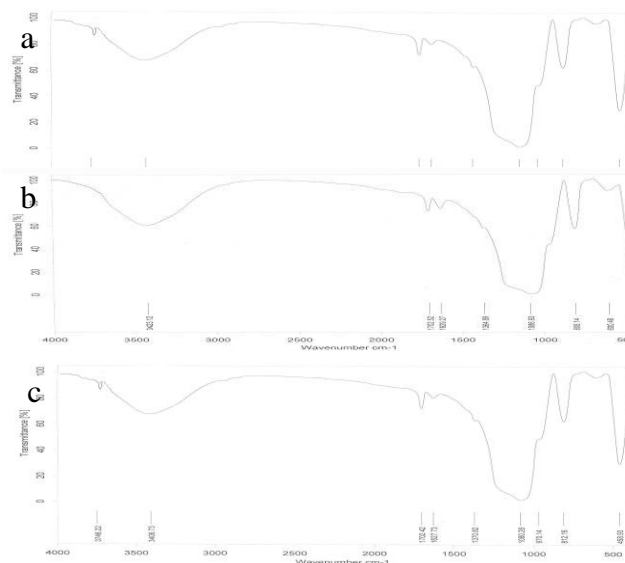


Fig3: FT-IR spectrum of Ti-HMS with a)5% Mn(NO₃)₂
b)5% Mn(CH₃COO)₂ c)5% MnSO₄

Preparation of polymeric nanocomposites with hollow spherical structure composed of magnetic nanoparticles by microemulsion method; Application in deep desulfurization

R. Valirasti¹, A. Salabat^{1,2*}

^{1,2}Department of Chemistry, Faculty of Science, Arak University, 38156-8-8349, Arak, Iran

²Institute of Nanosciences & Nanotechnology, Arak University, 38156-8-8349, Arak, Iran

*Corresponding E-mail address: a-salabat@araku.ac.ir

Abstract: Poly(methyl methacrylate) (PMMA) hollow nanospheres composed of Fe₂O₃ nanoparticles have been synthesized using a new microemulsion method. In this stepwise method a core/shell nanocomposite was prepared in an oil-in-water microemulsion system. The polymerized core of the system removed by a solvent to obtain a hollow sphere particle. The synthesized nanocomposite sample was identified using TEM and FT-IR techniques. The fabricated PMMA/Fe₂O₃ hollow nanosphere sample was used as an excellent magnetic adsorbent for removal of sulphur compounds from gasoline. Removal experiment over PMMA/Fe₂O₃ showed that the desulfurization yield is around 94 % for initial sulfur concentration of 100 ppm for maximum removal time of 60 min.

Keywords: Microemulsion; Hollow Sphere; Nanocomposite; PMMA

Introduction

Polymeric hollow sphere nano-architectures have attracted great interest for their applications [1,2], since surface area and capacity for entrapping of drugs or other substances. Several approaches are reported for hollow sphere structure fabrication such as layer-by-layer adsorption, sole-gel and seed-mediated growth process, which not applied for preparation of polymer nanocomposite materials. Procedure based on microemulsion systems as a nano-reactor for core or shell growth is our interesting field [3].

Sulfur in gasoline reduces the activity of vehicle catalytic converters by poisoning the active sites, thus increasing exhaust gases from motor vehicles that adversely affect human health and the environment. The European Union stipulates that the limitation of sulfur in gasoline should be minimized to 10 ppm since 2009. In recent years, various adsorbents have been investigated in desulfurization process, such as zeolites, metal oxides and carbon based materials. Among these adsorbents, carbon based materials have gained much attention due to their controllable textural and chemical properties. For deep desulfurization of gasoline and diesel fuels as the environment regulations it is necessary to introduce new and effective adsorbents [4-5]. Herein, we report a novel fabrication of polymer hollow nanospheres containing Fe₂O₃ nanoparticles using a stepwise microemulsion method. Besides, as-synthesized PMMA/Fe₂O₃ hollow nanospheres were used as a

magnetic adsorbent for magnetic removal of sulfur compounds from gasoline.

Materials and method

Most reagents, including N-Heptan, Ammonia 25%, methyl methacrylate and pyrrole monomers, methanol, Fe(SO₄).7H₂O, copper chloride (CuCl₂), potassium persulfate (K₂S₂O₈), cetyltrimethylammonium bromide (CTAB), anionic surfactant AOT, benzothiophene (99%) were purchased from Merck.

Fabrication of PMMA/Fe₂O₃ hollow nanosphere

PMMA/ Fe₂O₃ with hollow spherical structure was synthesized in a stepwise manner via microemulsion method. In the first step a microemulsion system containing AOT was prepared by mixing appropriate amounts of AOT, methyl methacrylate monomer (MMA) and aqueous solution of ferric nitrate, so keep the water-to-surfactant molar ratio (W) as 5. This microemulsion (microemulsion containing iron ions) was mixed with another microemulsion having the same composition and containing ammonia. After reduction process a transparent brown stabilized colloid system was obtained.

In the second step cationic surfactant of CTAB was used to form O/W microemulsion systems containing pyrrole monomer as oil phase. The chemical oxidation polymerization of the oil phase was initiated upon addition of CuCl₂ as initiator. After polymerization of the micelles core, the MMA monomer and the prepared Fe₂O₃ colloid were subsequently introduced into the system to obtain swelled micelles with PPy



core and MMA/Fe₂O₃ shell. The core/shell system then polymerized at 70°C by potassium persulfate initiator. At the last step the prepared core/shell nanocomposite was washed with methanol to remove PPy core and excess surfactants. A schematic of the fabrication process is shown in Fig.1. TEM micrograph and FTIR spectrum of the prepared hollow sphere nanocomposite was obtained.

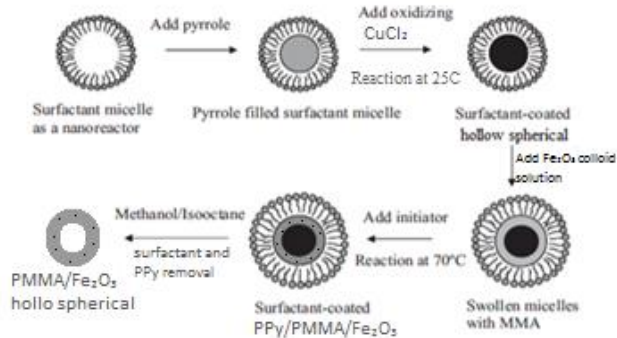


Fig. 1. schematic diagram of the fabrication process of PMMA/Fe₂O₃ hollow spherical structure

Desulfurization Process

The model fuel was prepared by dissolving benzothiophene (BT) in *n*-octane. In a typical experiment, 1mg of the prepared hollow nanosphere as adsorbent was mixed with the model fuel (3 ml) in a sealed glass bottle and stirred for 2 h at 25 C. Then, the adsorbent was separated by a magnet and then centrifuged to ensure complete separation. Fig. 2 shows the dispersed hollow nanospheres in *n*-heptane before and after separation by a magnet. The concentration of the BT in the fuel model was then evaluated using Gas chromatography (GC) method.



Fig.2. Photograph of the dispersed composite in the model Fuel and separation by magnet.

Results and Discussion

Figure 3 shows TEM micrograph of the fabricated PMMA/Fe₂O₃ hollow nanosphere. As can be seen Fe₂O₃ nanoparticles are embedded into the polymer

layer of the spherical (or bowl like) composite particles.

FTIR spectrum of the PMMA and PMMA/Fe₂O₃ hollow nanospheres are shown in Fig. 4. The characteristic band at 687 nm confirms the presence of the Fe₂O₃ nanoparticles and assigned as vibration of Fe-O bonds (Fig. 4 B). Fig. 4 (C) shows the FTIR of the PMMA/Fe₂O₃ sample after adsorption of benzothiophene. The existence of two characteristic bands of 554 and 621 related to vibration of C-S bond of the BT molecule adsorbed on the nanocomposite.

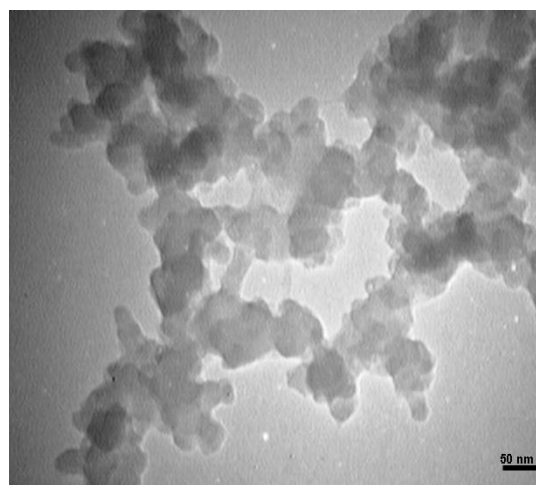


Figure 3. TEM Image of the PPy/PMMA/Fe₂O₃ hollow spherical structure

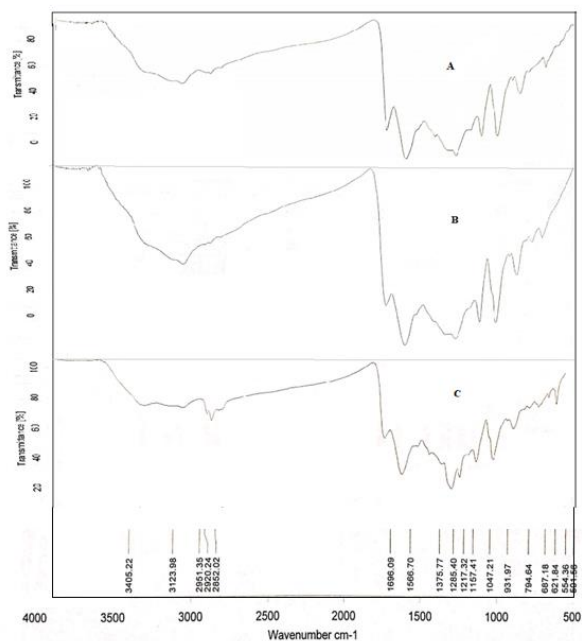


Figure 4. FTIR spectra of the pure PMMA (A), PMMA/Fe₂O₃ hollow sphere (B) and PMMA/Fe₂O₃ after absorption of benzothiophene

The concentration of the BT in the fuel model before and after adsorption process was determined by gas chromatography. The adsorption capacity was calculated by the following equation:

$$\text{Removal}\% = \frac{C_0 - C_e}{C_0} \times 100$$

where C_0 and C_e are the initial and final concentrations of the BT in the model fuel (mg L^{-1}), respectively. BT removal experiment over PMMA/Fe₂O₃ showed that the desulfurization yield is 94 % for initial sulfur concentration of 100 ppm. Time of maximum removal of BT was around 60 min.

References

[1] J. Jang, X. Li Li and J. Hak Oh, Facile fabrication of polymer and carbon nanocapsules using polypyrrole

core/shell nanomaterials, Chem. Commun. 7 (2004) 794-795.

[2] X. Zhang, M. Lin, X. Lin, C. Zhang, H. Wei, H. Zhang, B. Yang, Polypyrrole-Enveloped Pd and Fe₃O₄ Nanoparticle Binary Hollow and Bowl-Like Superstructures as Recyclable Catalysts for Industrial Wastewater Treatment, ACS Appl. Mater. Jilin University, Interfaces, 6 (2014) 450-458.

[3] A. Salabat, F. Mirhoseini, M. Mahdieh, H. Saydi, A novel nanotube-shaped polypyrrole-Pd composite prepared using reverse microemulsion polymerization and its evaluation as an antibacterial agent, New J. Chem. 39 (2015) 4109-4114.

[4] Y.Z. Yang, X.G. Liu, B. Xu, Recent advances in molecular imprinting technology for the deep desulfurization of fuel oils, New Carbon Materials, Taiyuan University 71 (2014) 343.

[5] Li. Ben, Shengnan Yu, Zhongyi Jiang, Wanpeng Liu, Ruijian Cao, Hong Wu. Efficient desulfurization by polymer-inorganic nanocomposite membranes fabricated in reverse microemulsion. Journal of Hazardous Materials 211 (2012) 296– 303.



بیستمین کنفرانس شیمی فیزیک ایران
دانشکده علوم پایه - دانشگاه اراک
۲۱-۲۹ مرداد ۱۳۹۶



20th Iranian Physical Chemistry Conference

مهندسی شیمی

Chemical Engineering

Investigation of acetone as co-solvent on performance PES nanofiltration membrane

Hamideh Aminifard^{*}, Abdolreza Moghadassi, Ehsan Bagheripour

Department of Chemical Engineering, Faculty of Engineering, Arak University, Arak 38156-8-8349, Iran

^{*}Corresponding author (Hamideh Aminifard): h-aminifard@msc.araku.ac.ir

Abstract : Polyethersulfone (PES)-based on mixed matrix nanofiltration membrane was developed by amalgamation with Partially reduced acetone nanocomposite. The effect of acetone fillings on the morphology and performance of the prepared membranes was examined by scanning electron microscopy (SEM) and water contact angle analysis. The blended membranes showed improved water permeability and fouling resistance likened to the simple PES. When the content of acetone was 100 wt.%, the water flux touched a maximum value (10.5 kg/m² h) nearly twice of that of the simple PES membrane (3.5 kg/m² h). Fouling confrontation of the membranes studied by stupid serum albumin solution filtration presented that 10 wt.% acetone membrane had the best antifouling property. Nanofiltration performance of the prepared membranes was assessed by rejection of three organic dyes with different molecular masses.

Keywords: Nanofiltration, acetone, Antifouling, Dye separation, Mixed membrane

Introduction

In the recent periods, nanofiltration (NF) technology has involved growing attention in the fields of water unstiffening and filtration of micro molecules due to its compensations such as low energy consumption, dense design, absence of phase change, and ease of operation [1]. Besides the stated advantages, a main limitation of NF membranes used in the separation procedures is flux weakening due to membrane fouling, which is caused by unwanted adsorption and sedimentation of foul ants onto the membrane surface or into pores [2]. The main swaying factors in the fouling of a membrane are its surface properties like unevenness and hydrophobicity and also, feed solution chemistry and process conditions. It is believed that an increase in the membrane hydrophilicity can recover its fouling resistance because many foul ants are naturally hydrophobic [3]. Several modification methods have been quantified to improve the hydrophilicity of polymeric membranes

Materials and method

Manufacturing grade powder was produced from Qingdao Ruisheng Co., Ltd., China (327/6 mesh, 95/5% purity). Those were full by Merck Co., Germany. Analytical score dimethyl acetamide (DMAC) and Polyethersulfone (PES ultrason E6020P with MW=58,000 g/mol) were bought from BASF Company (Germany). Polyvinyl pyrrolidone (PVP, MW = 29,000 g/mol), were got from Sigma-Aldrich Co., Germany. Three carbon-based dyes, C. I. Reactive Green 19, C. I. Direct Yellow 12 and C. I. Sensitive Blue 21, were bought from Shimi Boyakhsaz Co., Iran[7].

Results and Discussion

The SEM images of acetone, PES and acetone/PES examples are obtainable in Fig. 1. As can be seen in the SEM image of acetone (Fig. 1a), it has a crumpled area and worm-like construction that shows the successful exfoliation of graphite coatings. In the SEM image of hydrothermally manufactured acetone sample (Fig. 1b), the combination of co-solvent and a non-identical particle size distribution are clear. But, as is clear in the SEM image of acetone/PES co-solvent (Fig. 1c), the acetone is consistently dispersed on the crumpled surface of PES sheets with a suitable density.

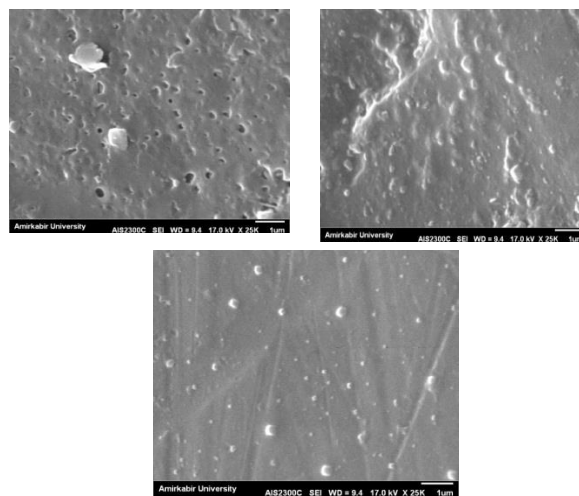


Fig.5: . Surface SEM images of the fabricated membranes.

Table1: Regularity parameters of blended matrix PES membranes resulted from four chosen components.

Acetone (weight %)	DMAC (weight % num.	PVP(weight %)	PES(weight %)	
0	100	1	18	1
10	90	1	18	2
20	80	1	18	3
30	70	1	18	4
40	60	1	18	5

As can be seen from Fig. 2, the rejection value of RB21 is only 70.5% using original PES membrane and 74.4, 80.1 and 85.6% for 10 wt.% acetone/ PES, 10 wt.% acetone/PES and 10 wt.% acetone/PES membranes, respectively. Instead, the rejection performance of the mixed matrix membranes was augmented by increasing the amount of acetone/PES nanocomposite in the membrane matrix up to 20 wt.%.

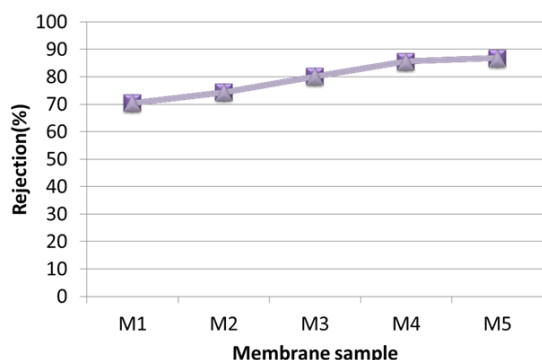


Fig. 2. Dye rejection presentation of the ready nanofiltration membranes (pH= 7.0 ± 0.1)

The filtration recital of the prepared membranes was studied using a dead-end system with an operative membrane area of 19.587 cm². The compaction of the membranes was complete at 0.6 MPa for 29 min before filtration tests to get constant water flux. All of the experiments were did at an operation pressure of 0.5 MPa and ambient temperature[5]. The rejection tests were showed with an aqueous solution of organic tints (100mg/L). The UV-vis spectrophotometric method was used to compute the deduction efficiency of the dyes by a Shimadzu UV-2450, Japan device. The water flux, J_{w,1} (kg/m² h) and rejection, R, were calculated using Eqs. (1) and (2), consistently:

$$J_{w,1} = \frac{M}{At} \quad (1)$$

$$R\% = \left(1 - \frac{C}{C_0}\right) \times 100 \quad (2)$$

where M, A and t represent the weight of the composed permeate (kg), the membrane effective area (m²) and the infusion time (h), respectively. R is the peroxide rejection (%), C₀ and C are the concentration of dye in the feed and permeate solution (mg/L), correspondingly. The antifouling property and flux recovery ratio (FRR) of the acetone/PVP/PES membranes were assessed using the following development: after water flux tests, a solution as a good fouling agent (500 mg/L) was directly substituted in the stirred cell and the flux of solution, J_p (kg/m² h), was chronicled based on the weight of permeated water at 0.5 MPa for 90 min. After percolation of solution, the contaminated membranes were left in purified water for 20 min. Lastly, the pure water flux was restrained again using washed membranes, J_{w,2} (kg/m² h). The FRR, as a parameter for compare the antifouling property of the membranes, was calculated using Eq. (3) based on the gotten results:

$$FRR\% = \left(\frac{J_{w,2}}{J_{w,1}}\right) \times 100 \quad (3)$$

Also, to study the fouling procedure in detail, fouling resistance parameters were measured to investigate the fouling resistant ability of the fortified membrane [4].

Conclusions

Fig. 2 shows the top surface photographs of the ready simple and mixed PES membranes. This picture demonstrates that the top surface of the membranes modified with acetone was darker than the original PES membrane due to the color of this preservative[6]. Also, the nano composite acetone/PVP/PES membranes had a darker surface due to the attendance of acetone with higher molar relation (DMAC/acetone: 70/30) and the gloom of the membranes was increased by increasing the deliberations of acetone/ PES nanocomposite in the molding solutions

Acknowledgment

The authors thank the University of Arak (Iran) for altogether of the provision provided and the financial support of this development.

References

- [1] V. Vatanpour, M. Esmaili, M.H.D.A. Farahani, Fouling discount and retention increase of polyethersulfone nanofiltration membranes entrenched by amine functionalized multi-walled carbon nanotubes, J. Membr. Sci. 466 (2014) 70–81.

[2] C. Liu, 2.5 — advances in membrane technologies for drinking water purification, in: S. Ahuja (Ed.), *Comprehensive Water Excellence and Purification*, Elsevier, Waltham 2014, pp. 75–97.

[3] M. Safarpour, A.R. Khataee, V. Vatanpour, Preparation of a novel polyvinylidene fluoride

(PVDF) ultrafiltration membrane adapted with reduced graphene oxide/titanium dioxide (TiO₂) nanocomposite with improved hydrophilicity and antifouling properties, *Ind. Eng. Chem. Res.* 53 (2014) 13370–13382.

[4] F. Liu, Y.-Y. Xu, B.-K. Zhu, F. Zhang, L.-P. Zhu, Groundwork of hydrophilic and fouling resistant poly(vinylidene fluoride) hollow fiber membranes, *J. Membr. Sci.* 345 (2009) 331–339.

[5] L. Yan, Y.S. Li, C.B. Xiang, S. Xianda, Effect of nano-sized Al₂O₃-particle addition on

PVDF ultrafiltration membrane enactment, *J. Membr. Sci.* 276 (2006) 162–167.

[6] V. Vatanpour, S.S. Madaeni, A.R. Khataee, E. Salehi, S. Zinadini, H.A. Monfared, TiO₂ entrenched mixed matrix PES nanocomposite membranes: influence of different sizes and types of nanoparticles on antifouling and performance, *Desalination* 292 (2012) 19–29.

[7] N.A. Hashim, Y. Liu, K. Li, Preparation of PVDF hollow fiber membranes using SiO₂ particles: the result of acid and alkali treatment on the membrane performances, *Ind. Eng. Chem. Res.* 50 (2011) 3035–3040.

Advance polymeric membrane to CO₂ separation

S.Bandehali¹, A.R. Moghadassi¹

¹ Department of Chemical Engineering, Faculty of Engineering, Arak University,
Arak 38156-8-8349, Iran.

*a-moghadassi@araku.ac.ir

Abstract:

Global CO₂ emissions have increased steadily due to use of fossil fuels and industrial applications. Therefore, it is necessary to decrease of energy consumption and CO₂ concentration by CO₂ separation from natural gas. There are different technologies to CO₂ separation. CO₂ separation membranes prepared by green, simple, and efficient methods have faced great challenges. In recent years, Polymer based membrane materials be applied in vast variety of the membrane materials. Polymeric membrane materials show high permeability to CO₂. But having excellent selectivity should be considering to prepare polymeric membranes. This review summarizes advances in polymeric materials having very high CO₂ permeability and excellent CO₂/N₂ selectivity that enhance the performance of polymeric membranes. Five important classes of polymer membrane materials are highlighted: polyimides, thermally rearranged polymers (TRs), substituted polyacetylenes, polymers with intrinsic microporosity (PIM) and poly (ethylene oxide) (PEO) that are high performance to CO₂ separation.

Keywords: *polymeric membrane; CO₂ separation; gas transport properties; gas separation membrane*

Introduction

The increasing of CO₂ emission in world due to industrial activities is great problem to developed country and developing country. The level of CO₂ emission due to fossil fuel combustion and other industrial activities was 37Gt CO₂ in 2014. According to the National Oceanic and Atmospheric Administration (NOAA), USA, the concentration of CO₂ at atmosphere show the level of CO₂ reach 400ppm in 2015 that the highest level of concentration. It be predicted the level of CO₂ in atmosphere have had increasing trend[1].

There are lots of methods to CO₂ separation. CO₂ separation technologies are Cryogenic distillation, absorption, adsorption and membrane separations. The selection of this methods has related to operation condition such as temperature, pressure, concentration. Also it depends on desirable purity CO₂, cost, reliability. etc. despite of high efficiency Cryogenic distillation method in CO₂ separation, the operating of temperature is very low [2]. Also, Physical and chemical absorption are favourable

Method to CO₂ separation but applying these methods need to recovery absorbent after separation operation. Therefore, absorption technology need to high cost and high energy. And the other hand, about all technologies should be considered the problems of environmental impacts. Recently, Membrane

technology has attracted to CO₂ separation from gas mixture. membrane technology is favorable method reasons of intrinsic advantages such as high energy, high efficiency, operation simplicity and reliability, module compactness and modularity. Membrane technology do not occur changing in phase and need to low maintenance. Also, membrane technology has high flexibility in scale up and can be run in areas that have some benefits[1].

The importance of problems about membrane technology is the selection of material. In fact, the type of material is the core of membrane preparing. Generally, membranes classified three type base on material that be used in membrane preparing: polymeric, inorganic and polymer-inorganic hybrid. Polymeric membrane has high efficiency, excellent mechanical properties, high processability for gas separations.

polymeric membranes be used to CO₂ gas separation During the past decades[3].

In general, to high performance of separation operating is required high permeability and high selectivity for a specific species in a mixture. glassy or rubbery polymers show an empirical relationship between permeability (P) and selectivity (α) in gas mixtures. Membranes that have high permeability show low selectivity. upper bound Robeson show relationship between permeability and selectivity in 1991. Also with new polymeric material be modified in 2008.

There are lots of material that have been investigated for gas separation membranes but a few polymeric membranes have processability in industrial application[4].

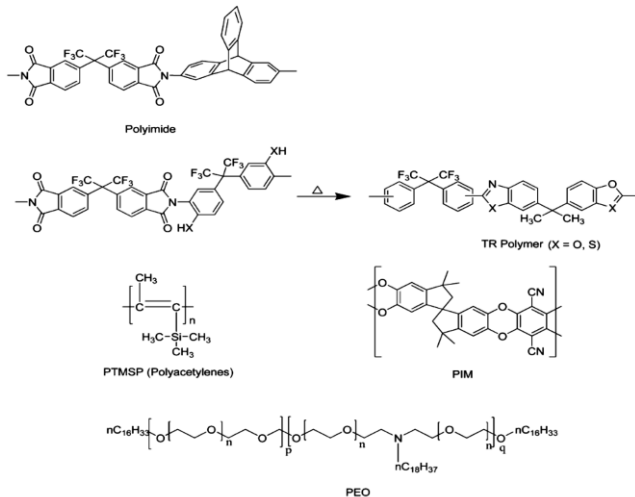


Fig 6 Representative chemical structure of polymer with high CO₂ permeability [3].

General principles of membrane gas separation

The gas transport membrane be explained with permeability and selectivity and the separation performance investigated with two parameter addition to solubility. Permeability be defined as the flux that across from, diffusivity is as known mobility of the molecules within the membrane and solubility is the solubility of gas molecules into membrane. membrane The relationship for permeability, selectivity and solubility be followed by equation[3]:

$$P = DS \quad (1)$$

that P is the permeability coefficient (cm³ (STP) cm⁻² s⁻¹ cmHg⁻¹), D is diffusivity coefficient (cm² s⁻¹) and S is the solubility coefficient (cm³ (STP) cmHg⁻¹). The common measurement of P is the barrer (10⁻¹⁰ cm³ (STP) cm⁻² s⁻¹ cmHg⁻¹).

P permeability is an index to determine separation performance. Addition of barrer the unit of GPU can be used to gas transport membrane. The unit of GPU is 10⁻⁶ cm³ (STP) cm⁻² s⁻¹ cmHg⁻¹.

Permeability be determined by experimental relationship as follow[4]:

$$\frac{P}{L} = \frac{Q}{A\Delta p} \quad (2)$$

L is the effective thickness of the membrane, Q the flux that cross from membrane, A is the surface area of membrane and Δp is the gradient of pressure across membrane.

Ideal selectivity is the ratio of A gas permeability to B gas permeability (α) be explained by equation[3]:

$$\alpha = \frac{P_A}{P_B} = \frac{D_A}{D_B} \times \frac{S_A}{S_B} \quad (3)$$

There are experimental relationships to determined solubility but commonly it be determined experimental dates. The solubility coefficient depends on the type of material that be applied within membrane.

Generally, membranes base on polymer be derived To rubbery and glassy polymers that depends on glass transition temperature. There is low gas-polymer interaction for permeable gases, especially glassy polymer and the gases with little diameter have more diffusion via membrane.

Therefore, improvement of gas separation membrane should be considering by two type of polymer and the choice of the type of polymer is important [2, 3].

In this review be tried to describe polymeric membrane that have high efficiency to CO₂ separation and be highlighted high efficiency polymers that be use to gas separation membrane such as: polyimides, thermally rearranged polymers (TR polymers), substituted polyacetylenes, polymers of intrinsic microporosity (PIM), (ethylene oxide) (PEO)-based polymers (Fig 6).

Polyimides

Polyamides (PAs) are amorphous polymers that have special chemical resistance, high mechanical strength, good thermal stability [5, 6]. These polymers are as primary material to produce polyimides. Among glassy polymers, aromatic polyimides (PIs) are appealing materials for gas separation owing to their excellent gas permeability and selectivity and also good physico-chemical properties [3, 7, 8] other applications of aromatic polyimides (specially polyamide and polyimides contain of oxiazole are good selection to electronic application [9]) are microelectronics and photoelectronics industries as alignment films in displays, circuit boards, photoresists and dielectric films [8]. polyimides are produced by condensation reaction of an aromatic amine and an aromatic anhydride group (Poly ethylene oxide (PEO))

Ordinary, poly ethylene oxide (PEO) base membranes apply to separation of CO₂ because of high affinity for acidic gases and organic vapors. PEOs have high performance and easy fabrication due to drastic interaction polar ether oxygen atoms and CO₂. Permeability of H₂, N₂, and O₂ gases don't change by increasing of end of polar ether oxygen. But oxygen atoms case be crystallite and high chain packing that



lead to decrease gas permeability. Pure PEOs usually don't use for gas separation. Some strategy proposes to reduce of crystallization. In fact, molecular weight and content of ethylene oxide or regulation of micron-domain morphology able for reduction of crystallization in PEO. For example, preparing of purely PEO polymers with highly amorphous can be help it. Some purely PEO structure is block copolymer with short ethylene oxide segment that case be reduction of crystallization in temperature room, and enhancing of branch with bulky group, cross-links are most attractive such as using of DME end group of PEG decrease PEO crystallization and increase separation by micro-phase separation [3, 18-20]. This polymer has properties like reverse-selective membrane [18]. Copolymers have structure of micro phase-separate including of soft PEO segments and hard segments such as polyamides (Pebax, polyether block amide for different application such as wire coating and textile fibers), polysulfons and nanocomposite, Hard segment lead to increase of mechanical stability and obstruct crystallization in PEO that case be application it in the actual practical [3, 20, 21]. Also, Multi block copolymer contain of PEO be used to separation CO₂. Such as Poly (ethylene oxide-b-amide), Pebax (producing from various poly(ether-amide) s. Studying of these copolymers is limit because of some problem in solubility. Therefore, new multi block copolymers be investigated such as poly (ethylene oxide)- (butylene terephthalate)

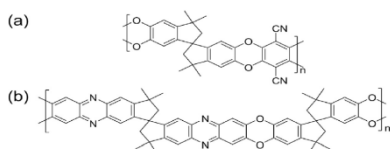


Figure 3. Complete mechanism for thermal rearrangement of hydroxyl-polyimide to polybenzoxazole [17].

with Commercial name Polyactive. Howbeit, there are solubility problems. Crystallization of the structure polymer in the hard phase increase separation performance due to inducing of flexible segments inter-dispersed). One of the main characteristics of PIs as compared to PAs is their higher thermal stability [5]. Also low solubility aramids is result of their rigid backbones and strong interchain interactions therefore polyamides have problems in processing [10]. Polyimide membranes are suitable to separate aromatics from aromatic and aliphatic mixtures because of high affinity polar imide functional groups with electrons of aromatic rings. Another special trait of polyimides is the intra and interchain charge transfer complex (CTC).

Aromatic polyimides have low

solubility, however, there are some method to increase solubility such as incorporating of ester, amide or other flexible and pendant group. These methods induce CTC, chain packing and electronic polarization interaction [11].

A few commercial polyimides are soluble such as Ultem, P84 and Matrimid These polyimides have high selectivity and low permeability [12]. Intrinsically, polyimides and polyamides have high potential to create interchain hydrogen bonding because of high resistance toward aggressive feeds containing condensable components [13].

Thermally rearrangement polymer (TR)

As be known, high performance of membrane is in means of high permeability and selectivity. Heat treatment is another method to increase performance of membrane. The size of voids in polymeric membranes create porosity. Thermal post-membrane conversion can be used to lead to uniform size of voids that is known to rearranged (TR) process. Park et al. synthesized TR polymers that be used to CO₂/CH₄ separation.[14]high free volume in TR membrane related to micropore that case be increase permeability while selectivity is stable due to rigid-rod benzoxazole structure [15]

Hence, connecting of voids morphology is good in tailored free volume. TR membrane have high permeability and selectivity for gas molecules and ions[3]. Depend on ortho position can be forms of polybenzimidazoles, polybenzothiazoles, and polybenzoxazoles[16]. The random chain conformation is one of the reasons tuning size cavity. Dense polybenzoxazole (PBO) and polybenzothiazole (PBT) membranes be produced from thermally rearrangement polyimides cantaning of -SH, -OH ortho functional groups[3]. Ordinary, Polybenzoxazoles be applied to prepare TR membranes due to insolubility in organic solvents and high resistance to chemical environment [16]. TR mebranes show high selectivity for CO₂/CH₄ separation. [3]. PBO be produced from thermally rearrangement aromatic polyimides and ortho-hydroxyl group and N-C bound. Ordinary, thermally rearrangement be done under 300-500°C. Complete mechanism be shown in **Error! Reference source not found.**[17].

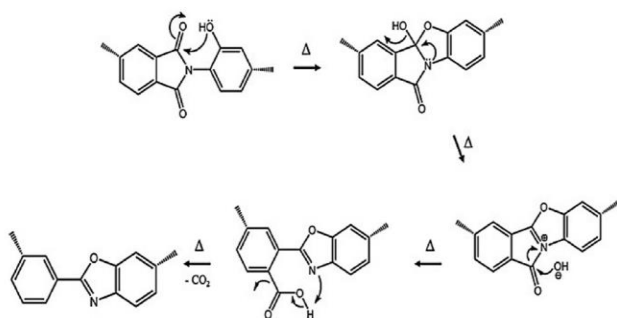


Figure 2. reaction of amine with anhydride to form an imide [5].

Poly ethylene oxide (PEO)

Ordinary, poly ethylene oxide (PEO) base membranes apply to separation of CO₂ because of high affinity for acidic gases and organic vapors. PEOs have high performance and easy fabrication due to drastic interaction polar ether oxygen atoms and CO₂. Permeability of H₂, N₂, and O₂ gases don't change by increasing of end of polar ether oxygen. But oxygen atoms case be crystallite and high chain packing that lead to decrease gas permeability. Pure PEOs usually don't use for gas separation. Some strategy proposes to reduce of crystallization. In fact, molecular weight and content of ethylene oxide or regulation of micron-domain morphology able for reduction of crystallization in PEO. For example, preparing of purely PEO polymers with highly amorphous can be help it. Some purely PEO structure is block copolymer with short ethylene oxide segment that case be reduction of crystallization in temperature room, and enhancing of branch with bulky group, cross-links are most attractive such as using of DME end group of PEG decrease PEO crystallization and increase separation by micro-phase separation [3, 18-20]. This polymer has properties like reverse-selective membrane [18]. Copolymers have structure of micro phase-separate including of soft PEO segments and hard segments such as polyamides (Pebax, polyether block amide for different application such as wire coating and textile fibers), polysulfons and nanocomposite, Hard segment lead to increase of mechanical stability and obstruct crystallization in PEO that case be application it in the actual practical [3, 20, 21]. Also, Multi block copolymer contain of PEO be used to separation CO₂. Such as Poly (ethylene oxide-b-amide), Pebax (producing from various poly(ether-amide) s. Studying of these copolymers is limit because of some problem in solubility.

Therefore, new multi block copolymers be investigated such as poly (ethylene oxide)- (butylene terephthalate)

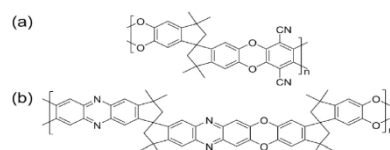


Figure 3. Complete mechanism for thermal rearrangement of hydroxyl-polyimide to polybenzoxazole [17].

with Commercial name Polyactive. Howbeit, there are solubility problems. Crystallization of the structurepolymer in the hard phase increase separation performance due to inducing of flexible segments inter-dispersed between the rigid segments, PEO, PDMS and a rigid segment in the tri-block copolymers increase solubility, permeability, the mechanical and thermal stability, similar to di-block copolymer including of PEO and PDMS [19]. PEO phase in these copolymers increase diffusivity due to continuous pathway. Morphology by domain shape and spatial arrangement due to the hard segment composition and the lengths of the PEO and hard segment blocks effect on gas permeability (figure 4) [3, 20] Copolyimides containing of ethylene oxide comparing to pure polyimides have higher diffusivity for CO₂, N₂ gases. The mobility of chain decrease due to glassy polyimides. Also polyimides enhance mechanical properties of copolyimides. So Mico-phase in PEO contribute in gas diffusion and micro-domain in polyimide improve mechanical strength. As shown in figure 15 with increasing of PEO molecular weight induce diffusivity and permeability. PEO-polyurethane be used for biomedical and gas separation applications due to high mechanical properties and structural interchangeability. Other rubbery material with PEO can be used in copolymers such as poly(propylene oxide) , PDMS, siloxanes, and dendrimers [20].

Substituted polyacetylenes

these polymers be produced from bulky pendant groups and be prepared from polymerization acetylenic monomers. The pendant groups obstruct of rotation membrane backbone. These polymers have large free volume fraction. Hence, they show high permeability. cis-rich poly(1-trimethylsilyl-1-propyne) (PTMSP) and polymers in this class often have high permeability for any gases. In spite of high permeability show low selectivity according to Robeson upper bound limit. And the other hand, if polyacetylene-based membranes will be applied to CO₂ separation, they will be show strong physical aging. Nevertheless, some methods be applied to modification of structure polymer such as cross-linking and grafting [3].

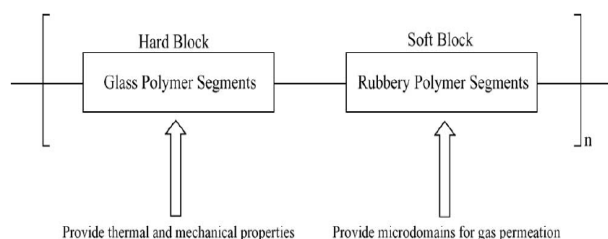


Figure 4. Synthetic strategy for polymer structure used as CO₂ separation membrane [1].

Polymers intrinsic microporosity (PIM)

PIMs are new class of polymer that show high permeability, selectivity and firstly be introduced by Budd and McKeown research groups. PIMs have high solubility in common solvents. Most PIMs that be used to preparing embrane are PIM-1 and PIM-2 (figure 5) Usually, poly(trimethyl-silyl-propyne) (PTMSP) be compared with PIM-1 [18]. Generally, PIMs be produced from polycondensation reaction of tetrahydroxy-monomers containing spiro- or contorted centres with tetrafluoromonomers. PIMs are including of pores with the diameter of less 2 nm[3].

Conclusions

Membrane technology has important role to CO₂ separation and improvement performance of polymeric membrane can be helped it. thus, the choice of suitable material to gas separation membrane is key parameter to enhance of gas transport properties that have high permeability and excellent selectivity. Polyimides, TR polymers, poly(ethylene oxide)s, substituted polyacetylenes and PIMs have high potential to improve polymeric membrane.

References

1. S. Wang, X.L., H. Wu, Z. Tian, Q. Xin, G. He, D Peng, S. Chen, Yan Yin, Z. Jiang, M. D. Guiver, *Advances in high permeability polymer-based membrane materials for CO₂ separations*. Energy Environ. Sci., 2016. **9**(6): p. 1863-1890
2. Seader, J.D., *SEPARATION PROCESS PRINCIPLES*. second ed. 2006, Utah: Department of Chemical Engineering University
3. N. Du, H.B.P., M. M. Dal-Cin, M. D. Guiver, *Advances in high permeability polymeric membrane materials for CO₂ separations*. Energy Enviromental Science, 2012. **5**: p. 7306-7322.
4. C. E. Powell, G.G.Q., *Polymeric CO₂/N₂ gas separation membranes for the capture of carbon*

dioxide from power plant flue gases. Journal of Membrane Science 2006. **279**: p. 1-49.

5. McKeen, L.W., *FATIGUE AND TRIBOLOGICAL PROPERTIES OF PLASTICS AND ELASTOMERS*. Third ed. 2015: M. Deans.
6. M. I. Loría-Bastarrachea, M.A.-V., *Membranes from rigid block hexafluorocopolyaramides: Effect of block length on gas permeation and ideal separation factor*. Membrane Science, 2013. **443**: p. 36-44.
7. S. T. Muntha, A.K.M.S., *Progress on Polymer-Based Membranes in Gas Separation Technology*. Polymer-Plastics Technology and Engineering, 2016. **10.1080/03602559.2016.1163592**: p. 1-68.
8. C-D. Varganici, D.R., C. Barbu-Mic, Liliana Rosua, Dumitru Popovici, Camelia Hulubei, B. C. Simionescu, *On the thermal stability of some aromatic-aliphatic polyimides*. Analytical and Applied Pyrolysis, 2015. **113**: p. 390-401.
9. M. Grucela-Zajac, M.F., L. Skorka, K. Bijak, K. Smolarek, S. Mackowski, E. Schab-Balcerzak, *Photophysical, electrochemical and thermal properties of new (co)polyimides incorporating oxadiazole moieties*. Synthetic Metals, 2014. **188**: p. 161- 174.
10. S-H Hsiao, K.-H.L., *A comparative study on the properties of aromatic polyamides with methyl- or trifluoromethyl-substituted triphenylamine groups*. Fluorine Chemistry, 2016: p. 1-35.
11. D. Serbezeanu, I.-D.C., M. Bruma, I. A. Ronova, *Correlation between physical properties and conformational rigidity of some aromatic polyimides having pendant phenolic groups*. Structural Chemistry, 2016. **27**(3): p. 973-981.
12. Y. J. Cho, H.B.P., *High Performance Polyimide with High Internal Free Volume Elements*. Macromolecular 2011. **32**: p. 579-586.
13. J. Vaughn, W.J.K., *Effect of the Amide Bond Diamine Structure on the CO₂, H₂S, and CH₄ Transport Properties of a Series of Novel 6FDA-Based Polyamide-Imides for Natural Gas Purification*. Macromolecules, 2012. **45**: p. 7036-7049.
14. Q. Liu, H.B., D. R. Paul, J.S. Riffle, J. E. McGrath, B. D. Freeman, *Gas permeation properties of thermally rearranged (TR) isomers and their aromatic polyimide precursors*. Membrane Science, 2016. **518**: p. 88-99.
15. Y. M. Xu, N.L., J. Zuo, T-S. Chung, *Aromatic polyimide and crosslinked thermally rearranged poly (benzoxazole-co-imide) membranes for isopropanol dehydration via pervaporation*. Membrane Science, 2016. **499**: p. 317-325.

Modeling of Systems Containing Glycols with CPA EoS and Performance Investigation of the Two Different Association Schemes

Z. Pourdehzaad^a, K. Peyvandy^{b*}

^aDepartment of Chemical Engineering, Semnan University, Tehran, 14896-54913, Iran

^bDepartment of Chemical Engineering, Semnan University, Semnan, 35196-45399, Iran

*k_peyvandy@semnan.ac.ir

Abstract

Since mixtures containing glycols are very important in oil-gas and chemical industries, modeling of such systems is one of the topics to be considered. The cubic-plus-association(CPA) equation of state(EoS) is employed using two different association schemes for glycols to model liquid density and vapor pressure of pure glycols and vapor-liquid equilibria(VLE) of several binary systems. The performance of two various association schemes compared with each other and our predictions were generally in agreement with the experimental data available in the literature. A discussion about the most appropriate association scheme for glycols is presented and according to the results that obtained, one of the association schemes introduced as a better association scheme.

Keywords: CPA; Association scheme; Liquid density; Vapor pressure; VLE

Introduction

Mixtures of association compound especially mixtures of water and glycols are important in the oil-gas industries. For example Monoethylene glycol(MEG) is the common thermodynamic inhibitor used to prevent gas hydrate formation. Thus, investigation of such systems is more important in contrast to other glycols. Generally, glycols applied for natural gas transport and petrochemical processes and Triethylene glycol(TEG) has the most contributions(95%) in dehydration units.

Therefore, it is essential to predict the vapor pressure and the liquid density of pure glycols and phase equilibria of their mixtures. From a thermodynamic viewpoint, accurate prediction of these properties of before-mentioned systems is an important and challengeable subject. Furthermore, common existing models are unable to accurately predict the themophysical properties. Recently CPA equation of state was successfully applied to model complex systems containing glycol[1,2,3].

In previous works, Drawai et al., Folas et al. have modeled phase equilibria of different glycol systems[1,2,3]. However, they are considered just one association scheme for glycols and generally, in the literature the performance of the 4C scheme is evaluated.

In this work, the capability of the CPA EoS is investigated to calculate the vapor pressure, liquid density and phase equilibria of systems containing glycols. Moreover, the performance of two different association schemes is investigated for glycols. Finally, we have illustrated and compared the applicability of 2B and 4C schemes in several cases.

Thermodynamic modeling

The CPA EoS proposed by Kontogeorgis et al. in 2010[4]. The definition of this equation in terms of pressure(P) is as follows:

$$P = \frac{RT}{V_m - b} - \frac{\alpha(T)}{V_m(V_m + b)} - \frac{1}{2} \frac{RT}{V_m} \left(1 + \frac{1}{V_m} \frac{\partial \ln g}{\partial \left(\frac{1}{V_m} \right)} \right) \sum_i x_i \sum_{A_i} (1 - X_{A_i}) \quad (1)$$

Where b, V_m and g denote the co-volume parameter, molar volume and radial distribution function respectively and $\alpha(T)$ refers to energy parameter which is determined from the following equation:

$$\alpha(T) = a0[1 + c_1(1 - \sqrt{T_r})]^2 \quad (2)$$

Where T_r is reduced temperature.

X_{A_i} depicts the fraction of A-sites that do not make bonds with other existing sites on the molecule i and depends on association strength($\Delta^{A_i B_j}$) and x_i is the mole fraction of component i. X_{A_i} parameter can be obtained from the following relation:

$$X_{A_i} = \frac{1}{1 + \frac{1}{V_m} \sum_j x_j \sum_{B_j} X_{B_j} \Delta^{A_i B_j}} \quad (3)$$

Where

$$\Delta^{A_i B_j} = g(V_m) \left[\exp\left(\frac{\varepsilon^{A_i B_j}}{RT}\right) - 1 \right] b_{ij} \beta^{A_i B_j} \quad (4)$$

Where $\varepsilon^{A_i B_j}$ and $\beta^{A_i B_j}$ are the parameters of CPA and show the association energy and the association volume respectively. Kontogeorgis et al.[5] proposed following equation for radial distribution function(g):

$$g(\rho) = \frac{1}{1 - 1.9\eta} \quad \text{where} \quad \eta = \frac{1}{4V_m} b \quad (5)$$



In order to use the CPA EoS for mixtures, the mixing rules should be applied for a and b parameters. In current work, we employed the following mixing rule[6]:

$$a = \sum_i \sum_j x_i x_j a_{ij} \quad (6)$$

Where

$$a_{ij} = a_i^{\frac{1}{2}} a_j^{\frac{1}{2}} (1 - kij) \quad (7)$$

And

$$b = \sum_i \sum_j x_i x_j b_{ij} \quad (8)$$

Where

$$b_{ij} = \frac{b_i + b_j}{2} (1 - lij) \quad (9)$$

Where kij and lij are the adjustable parameters and adjusted with experimental solubility data.

Especially we need a combining rule because it takes into account the effects of self and cross-associating. Hence, we used from CR-1 relationships:

$$\varepsilon^{A_i B_j} = \frac{\varepsilon^{A_i B_i} + \varepsilon^{A_j B_j}}{2} \quad (10)$$

And

$$\beta^{A_i B_j} = \sqrt{\beta^{A_i B_i} \beta^{A_j B_j}} \quad (11)$$

In order to predict the liquid density, vapor pressure and phase equilibria of glycol systems using CPA EoS, we applied the MATLAB software because it is a powerful software in the evaluation of these properties and presents accurate results.

Results and Discussion

The purpose of this article is to predict liquid density, vapor pressure and phase equilibria of systems containing glycols with CPA EoS using two association schemes for glycols. Studying the literatures showed that there is no evidence for comparing different schemes. Thus, we can say that the comparison of the performance of two schemes is the main objective of this work.

Eq. (3) depends on choosing the appropriate schemes for the components. Hence, we consider the 4C scheme for water, 2B scheme for ethanol and the 4C and 2B schemes for glycols (MEG and TEG). The CPA EoS has five parameters for the association compounds and these parameters are usually obtained by simultaneous fitting experimental vapor pressure and saturated liquid density data. Therefore we considered the following relationship as the objective function:

$$OF = \frac{1}{N_p} \left(\sum_{i=1}^N \left| \frac{p_i^{exp} - p_i^{calc}}{p_i^{exp}} \right| + \sum_{i=1}^N \left| \frac{\rho_i^{L.exp} - \rho_i^{L.calc}}{\rho_i^{L.exp}} \right| \right) \quad (12)$$

Where N_p depicts the number of experimental data. The information related to the experimental data are shown in Table1. The values of CPA parameters presented in Table2 and the average absolute deviations(AADs) are inferior to 2.5%.

Table1. The information related to experimental data of compounds

Fluid	N_p	$T_c(K)$	T-range(K)	Ref. of exp. Data
H ₂ O	120	647.13	274-631	[7]
Ethanol	72	514.00	293-506	[8]
MEG	86	719.90	275-685	[9]
TEG	88	769.5	285-720	[9]

The CPA parameters dimensions consist of:

$a_0(J m^3 mol^{-2})$, $b(m^3 mol^{-1})$, $\varepsilon(J mol^{-1})$ and c_1 and β are dimensionless.

According to the results of pure glycols, the performance of the 2B scheme is very satisfactory. The investigation results of vapor pressure and liquid density of MEG presented in fig.1 and 2.

Table2. The CPA parameters of pure components

Fluid	Scheme	a_0	$B \times 10^{-5}$	c_1	ε	β	AAD% ρ^{sat}/ρ^{liq}
H ₂ O	4C	0.12	1.45	0.67	16655	0.069	2.2/1.3
Ethanol	2B	0.77	4.87	1.03	17703	0.033	1.2/0.2
MEG	4C	0.99	5.18	0.834	18999	0.019	0.4/1.2
	2B	1.39	5.15	0.806	24403	0.010	0.2/0.7
TEG	4C	4.69	13.12	1.126	18517	7E-4	1.4/1.2
	2B	4.73	13.09	1.143	25156	3.3E-4	1.2/1.1

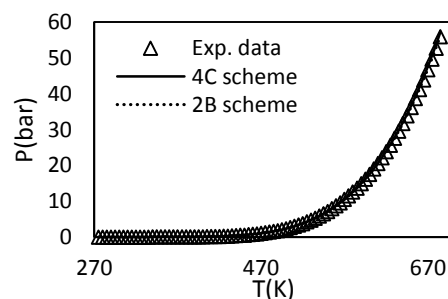


Fig.1: The vapor pressure of MEG

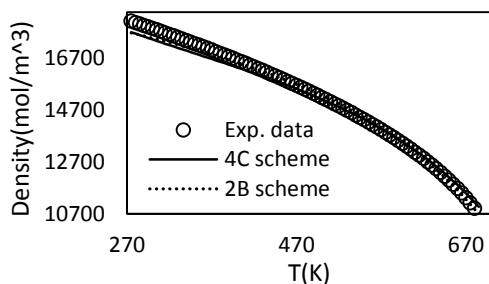


Fig.2: The liquid density of MEG

On the other hand, we investigated the phase equilibria of some binary systems containing glycols. There are two adjustable parameters and these parameters were optimized with following objective function:

$$OF = \frac{1}{N_p} \sum_{i=1}^N \left| \frac{S_i^{L,exp} - S_i^{L,calc}}{S_i^{L,exp}} \right| \quad (13)$$

Where S is solubility of component i. The adjusting the binary interaction parameters done with following correlations[10]:

$$k_{ij} = A + \frac{B}{T} \quad (14)$$

And

$$l_{ij} = C + \frac{D}{T} \quad (15)$$

The temperature ranges of mixtures are shown in Table3 and the results of optimization of k_{ij} and l_{ij} presented in Table4. As can be seen from Table4, the results of model accurately predict the experimental data

Table3. Temperature ranges of experimental data of mixtures

Mixture	T_{min}	T_{max}	N_p	Ref. of exp. data
H ₂ O-MEG	376.05	462.57	19	[11]
H ₂ O-TEG	371.55	421.25	18	[12]
Ethanol-MEG	354	389.79	15	[11]

Table4. The binary interaction parameters of mixtures

Mixture	Scheme s	k _{ij}		l _{ij}		AAD (%)
		A	B	C	D	
H ₂ O-MEG	4C-4C	-	1107.8	3.15	-1095	1.69
	4C-2B	1.110	343.24	1.15	-302	2.68
H ₂ O-TEG	4C-4C	0.570	-	3.46	-1400	0.85
	4C-2B	-	838.6	4.6	-1747	0.33

Mixture	Scheme s	k _{ij}		l _{ij}		AAD (%)
		A	B	C	D	
		2.510		7		
Ethanol-MEG	2B-4C	-	4.4	0.02	0.891	0.35
	2B-2B	0.004	23.4	0.03	19	0.30

The results of one of the mixtures that studied in this work presented in Fig. 3. Generally, the 2B scheme is better than the 4C scheme, except for the water-MEG mixture.

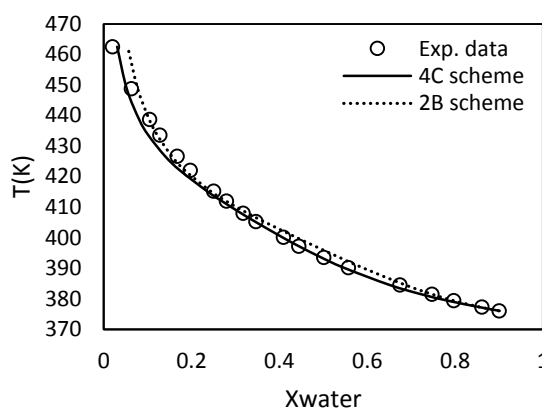


Fig.3: The mutual solubility of MEG-water

Conclusions

In the current work, the CPA EoS was used to predict the vapor pressure, liquid density and phase equilibria of systems containing glycols. The performance of two schemes (2B and 4C) for glycols was evaluated. The results of the investigation were accurate and very satisfactory.

References

- [1] SO. Derawi, GM. Kontogeorgis, ML. Michelsen, EH. Stenby "Extension of the Cubic-Plus-Association Equation of State to Glycol-Water Cross-Associating Systems", *Ind. Eng. Chem. Res.*, 42 (2003) 1470-1477.
- [2] GK. Folas, OJ. Berg, E. Solbraa, AO. Fredheim, GM. Kontogeorgis, ML. Michelsen, EH. Stenby "High-pressure vapor-liquid equilibria of systems containing ethylene glycol, water and methane Experimental measurements and modeling", *Fluid Phase Equilibria*, 251 (2007) 52-58.
- [3] GK. Folas, GM. Kontogeorgis, ML. Michelsen, EH. Stenby "Vapor-liquid, liquid-liquid and vapor-liquid-liquid equilibrium of binary and multicomponent systems with MEG Modeling with the



CPA EoS and an EoS/GE model", *Fluid Phase Equilibria*, 249 (2006) 67-74.

[4] GM. Kontogeorgis, GK. Folas "Thermodynamic Models for Industrial Applications", *Wiley*, 262 (2010).

[5] GM. Kontogeorgis, IV Yakoumis, H Meijer, EM. Hendriks, T Moorwood "Multicomponent phase equilibrium calculations for water – methanol – alkane mixtures", *Fluid Phase Equilibria*, 201 (1999) 158-160.

[6] SH. Mushrif (2004). Determining equation of state binary interaction parameters using K- and L points (Master's thesis, University of Saskatchewan, Saskatoon, Canada). Retrieved from <http://www.collectionscanada.gc.ca>.

[7] NIST Chemistry WebBook, <http://www.webbook.nist.gov/chemistry/fluid/>.

[8] DIPPR 801 Thermophysical Property Database and DIADEM Predictive Professional, 2011 version 5.0.1.

[9] SO. Derawi, ML. Michelsen, GM. Kontogeorgis, EH. Stenby "Application of the CPA equation of state to glycol/hydrocarbons liquid-liquid equilibria", *Fluid Phase Equilibria*, 209 (2003) 163-184.

[10] H. Haghghi, (2009). Phase Equilibria Modelling of Petroleum Reservoir Fluids Containing Water, Hydrate Inhibitors and Electrolyte Solutions(Ph.D. thesis, University of Heriot-Watt, Institute of Petroleum Engineering). Retrieved from <http://www.ros.hw.ac.uk>.

[11] N. Kamihama, H. Matsuda , K. Kurihara, K. Tochigi, S. Oba "Isobaric Vapor-Liquid Equilibria for Ethanol + Water + Ethylene Glycol and Its Constituent Three Binary Systems", *J. Chem. Eng.*, 57 (2012) 339-344.

[12] AK. Mostafazadeh, MR. Rahimpour, A. Shariati "Vapor-Liquid Equilibria of Water+Triethylene Glycol(TEG) and Water + TEG + Toluene at 85 kPa", *J. Chem. Eng.*, 54 (2009) 876-881.



Correlation between Fractional Free Volume and Diffusivity of CO₂ Gas Molecules Through Neat and Blended Pebax Based Membranes

Hossein Biazar¹, Mahdi Abdollahi^{*1}, Morteza Khoshbin¹

1. Polymer Reaction Engineering Department, Faculty of Chemical Engineering, Tarbiat Modares University, Tehran, Iran

*Corresponding author: abdollahim@modares.ac.ir

Abstract : Gas transport properties of poly(ether-b-amide6) (under Pebax trademark) and poly(vinyl-ran-dibutyl maleate) (PVAc-co-DBM) blends were measured. It was shown the CO₂/CH₄ selectivity (α) parameter enhanced twice of its primary amount with addition in P(VAc-co-DBM) wt%, however the permeability (P) of CO₂ had a reduction trend. Calculation of CO₂ diffusivity (D) and solubility (S) indicated the reduction in permeability was because of diffusivity parameter reduction. To study this matter more precisely fractional free volume (FFV) of membranes were calculated with two different methods. It was shown with P(VAc-co-DBM) increment, FFV of membranes have been reduced. Correlation between FFV and diffusivity of membranes confirmed gas transport data of prepared membranes fitted properly in equations.

Keywords: Poly(ether-b-amide), Vinyl acetate- based copolymer, Blend membrane, Fractional free volume (FFV), Carbon dioxide, Methane

Introduction

Gas permeability and selectivity are the most important characteristics of membranes. Gas permeability is composed of gas solubility and diffusivity parameters. Gas diffusivity is rather influenced by free volume of polymer matrix and gas solubility is more concerned by physical and chemical interactions between polymer and gas.

Because of the importance of CO₂ separation from CH₄ in industrial processes, increase in CO₂-philicity of Pebax based membranes which blended with P(VAc-co-DBM), have been researched [1]. However in this study, CO₂/CH₄ selectivity increased incredibly because of new interactions between CO₂ and acetate groups and increase in CO₂ solubility, but CO₂ permeability decreased because of gas diffusivity reduction. Studying this matter better, needs more information about amount of free volume in polymer matrix and establishment a correlation between free volume of matrix and gas diffusivity.

Lee established a method to relate gas diffusivity with free volume of system [2]. He defined $(V-V_0)/V$ as dimensionless fractional free volume (FFV). V is the specific volume of polymer and V₀ is the specific volume of polymer chains which is obtained by Bondi's group contribution method. Park & Paul inserted a correction factor for each chemical group in chain structure and depended to the type of gas in Lee's equations [3].

The aims of present study are calculation of FFV by two different methods and establishment a correlation between FFV and gas diffusivity.

Theoretical

As noted before membrane matrix free volume is the most important factor which determines diffusivity. Lots of investigations have been done in this area shows relationship between diffusivity and FFV of matrix is as follows:

$$D = A \exp(-B / ffv) \quad (1)$$

$$ffv = (V - V_0) / V \quad (2)$$

in above equations A and B are the constants. V is reached easily by dividing the molar mass to the density of blend ($V=M/\rho_b$). The most usual method to achieve V₀ is Bondi's group contribution method.

$$V_0 = 1.3 \sum_{k=1}^n (V_w)_k \quad (3)$$

Which here, (V_w)_k is the vanderwaals volume of each constituent groups of chain structure and n is the number of this groups.

In order to consider the effect of preamble gas, eq (3), modified as follows:

$$(V_0)_n = \sum_{k=1}^m \gamma_{nk} (V_w)_k \quad (4)$$

Here γ_{nk} is the correction factor which for each group is determined to type of permeation gas.

Results and Discussion

Gas transport properties of Pebax/ P(VAc-co-DBM) blends has been shown in table 1. As it's seen, in spite of α increment because of solubility increase, permeability has been reduced because of diffusivity reduction. In order to understand relationship between CO₂ gas diffusivity and existing free volume in membrane, FFV of membranes have been calculated



with and without gas type consideration by Lee and Park & Paul methods, respectively, and correlation established between diffusivity and FFV. From obtained R^2 values, it would be found out whether relationship between gas diffusivity and FFV, is according to equation (1) or not.

Table. 1. Gas transport properties of neat and blended membranes

blends	S_{CO_2}	D_{CO_2}	P_{CO_2}	P_{CH_4}	Selectivity
Pebax	0.127	9.87	167.13	9.51	17.57
10% ¹	0.179	6.48	154.69	7.93	22.59
20%	0.187	5.42	135.52	5.36	25.11
30%	0.193	4.01	103.35	2.76	37.47
40%	0.214	3.03	86.59	2.57	31.39
50%	0.392	1.55	81.02	5.63	14.4

1.Wt% of P(VAc-co-DBM)

Table. 2. Calculated FFVs of membranes

blends	ρ_b	FFV ¹	FFV ²
Pebax	1.14	0.1764	0.6394
10%	1.1419	0.1760	0.5861
20%	1.1439	0.1756	0.5326
30%	1.1459	0.1752	0.4789
40%	1.1479	0.1749	0.4251
50%	1.1499	0.1745	0.3710

1. without and 2.with gas type consideration

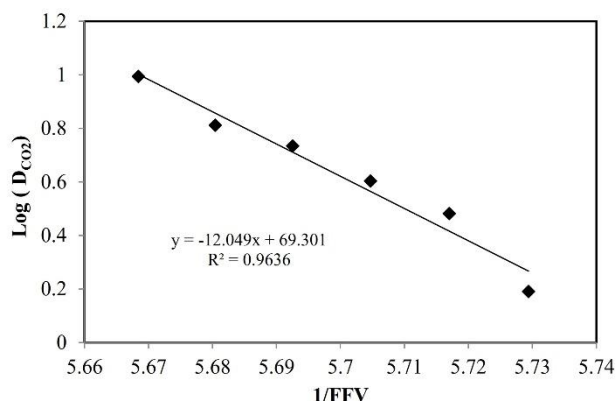


Fig. 1. Correlation between D_{CO_2} and FFV plot without gas type consideration

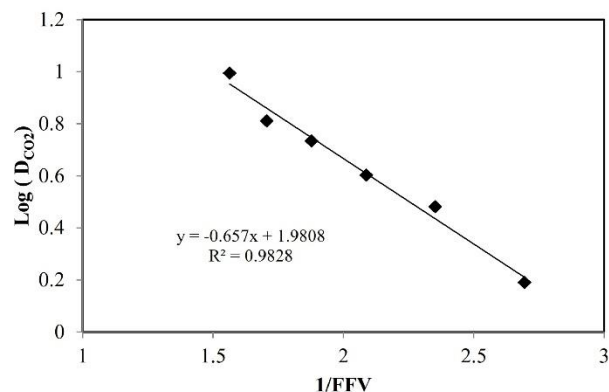


Fig. 2. Correlation between D_{CO_2} and FFV plot with gas type consideration

Conclusion

According to data for FFV in two condition (without/with permeate gas consideration, respectively) calculated in table 2, $\text{Log}(D_{CO_2})$ versus $1/\text{FFV}$ was drawn up in fig 1 and fig 2. R^2 values shown in fig 1 and fig 2 ($R^2 > 0.9$) have been proved that relationship between gas diffusivity parameter and FFV value of membranes, has been established correctly without and with permeate gas consideration. Although results showed that with permeate gas effect considering in calculations by Park and Paul method, $\text{Log}(D_{CO_2})$ versus $1/\text{FFV}$ relationship has been established by more accuracy (bigger R^2).

References

- [1] Abdollahi M., Khoshbin M., Biazar H., Khanbabaei G., preparation, morphology and gas permeation properties of carbon dioxide-selective vinyl acetate-based polymer/ poly(ethylene oxide-b-amide 6) blend membranes, *Polymer*, 121, 274-285, 2017.
- [2] Lee W., selection of barrier materials from molecular structure, *Polym. Eng. Sci.*, 20, 65-69, 1980.
- [3] Park J., Paul D., correlation and prediction of gas permeability in glassy polymer membrane material via a modified free volume based group contribution method, *J. Membr. Sci.* 125, 23-39, 1997



Graft (co)polymerization of acrylamide and styrene onto silica nanoparticles by free radical polymerization: Determining molecular weight by measuring intrinsic viscosity

Hossein Biazar¹, Mahdi Abdollahi*¹

1. Polymer Reaction Engineering Department, Faculty of Chemical Engineering, Tarbiat Modares University, Tehran, Iran

* Corresponding author: abdollahim@modares.ac.ir

Abstract: Free radical (co)polymerization of acrylamide (AAM) and styrene (St) in the presence of vinyl functionalized silica nanoparticles (VSN) was performed and chains' molecular weight were determined by measuring intrinsic viscosity. To synthesize VSN, first silica nanoparticles (SN) were modified by amine groups (Aminated SN, ASN) and in the next step, ASN was the vinyl (VSN) functionalized by treatment of nanoparticles with acryloyl chloride. Acrylamide homopolymerization and acrylamide/styrene copolymerization were done by free radical graft polymerization using ammonium persulfate (APS) as the initiator and sodium dodecyl sulfate (SDS) as the surfactant in the presence of VSN nanoparticles. Acrylamide nature of VSNs' double bonds causes participation of them in the polymerization reaction. Non-attached chains were separated by centrifugation and were dissolved in water. Intrinsic viscosities of dilute polymer solutions were measured by Ubbelohde viscometer. With intrinsic viscosity data in hand, viscosity- average molecular weight of the synthesized chains was calculated by existing experimental relationships.

Keywords: free radical graft polymerization, acrylamide, vinyl- functionalized silica nanoparticle

Introduction

Modification of inorganic nanoparticles with a polymer shell is interesting due to application of modified particles in various fields. The polymer shell can change the interfacial properties of these modified particles. Silica nanoparticles (SNs) have received more attention due to their facile synthesis, high specific surface area, hydrophilic surface and easy modification because of their surface chemistry. Free radical polymerization is a powerful strategy for modifying surface properties of nanoparticles. Thermal initiators like persulfates have been used extensively in the aqueous polymerizations as well as in the graft polymerizations.

In the present study, first SNs were aminated by introduction of amino-silane agent to their surface, then aminated SNs (ASNs) were vinyl functionalized by acryloyl chloride to yield VSN. Synthesized VSNs were participated in the polymerization reaction and polymer chains were grafted onto nanoparticles. To measure molecular weight of the polymer chains, first non-attached free chains were separated by centrifugation, then they were dissolved in water. Intrinsic viscosity was measured by Ubbelohde viscometer. Viscosity- average molecular weight also was calculated from intrinsic viscosity data.

Experimental

Materials

Acrylamide (AAM), styrene (St), SN (7 nm, Sigma-Aldrich), SDS, acetone, APTES, APS and acryloyl chloride were used.

Synthesis of polymer-grafted SN

To synthesize vinyl- functionalized SNs (VSNs), SNs were first aminated via reacting with APTES, then the product was reacted with acryloyl chloride with a procedure reported in the literature [1].

1.2 g monomer(s) (according to Table 1) and SDS (0.89 g) were dissolved in the suspension of 0.2% VSN in 40 ml water prepared by 30 min magnet stirring and then 15 min ultrasonication. The reaction mixture was purged with nitrogen for 45 min, then APS (20 mg) was quickly added. The polymerization was continued for 8 h at 60°C (Fig. 1).

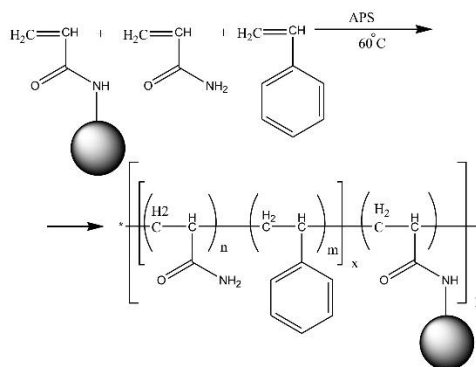


Fig. 1. Schematic representation of the reaction
After polymerization, the polymer- grafted nanoparticles were separated from a portion of suspension via centrifugation. Non-attached free

polymer chains in the solution were then precipitated by adding excess amount of the acetone as a nonsolvent. The obtained polymer was dissolved in water and precipitated with acetone again. This procedure was repeated three times and then the white solid powder was dried in a vacuum oven at 70°C for 24 h. Remaining suspension was precipitated by acetone and then dispersed in water. This procedure was repeated three times and product was dried under vacuum at 70 °C for 24 h. Two synthesized samples were named as P1 and P2 (AAM homopolymer and AAm/St copolymer, respectively). FTIR test was done to prove occurrence of graft polymerization reaction. TGA tests also were done to measure ratio of polymer weight to silica weight (G) and conversion of monomers (P). All of the calculations were done according to equations given in our previous work [2]. Also molecular weight of the free chains were calculated by intrinsic viscosity data obtained from viscometry of dilute polymer solutions in Ubbelohde viscometer.

Theoretical

Ubbelohde viscometer was used to measure viscosity of the dilute polymer solutions. Reduced (η_{red}) and intrinsic ($[\eta]$) viscosities were obtained using viscometry data by equation (1) and (2), respectively.

$$\eta_{red} = \frac{\left(\frac{\eta}{\eta_s} - 1\right)}{c} = \frac{\eta_{sp}}{c} \quad (1)$$

$$[\eta] = \lim_{c \rightarrow 0} \eta_{red} = \lim_{c \rightarrow 0} \frac{\eta_{sp}}{c} = \lim_{c \rightarrow 0} \eta_{inh} = \lim_{c \rightarrow 0} \frac{\ln \frac{\eta}{\eta_0}}{c} \quad (2)$$

With extrapolating η_{red} versus concentration (c) plots, $[\eta]$ would be obtained in zero concentration. Obtained $[\eta]$ value can then be used to calculate viscosity-average molecular weight using equation (3) [2].

$$[\eta] = 9.33 \times 10^{-3} M_w^{0.75} \quad (3)$$

Results and Discussion

Graft (co)polymerization initiated by APS has been performed according to Table 1. Because of almost same FTIR spectrums between synthesized homo- and co-polymer, just one of them has been given in Fig 1. A strong absorption band in 1094 cm^{-1} was assigned to the Si-O-Si in the SN. Amine adsorption band appeared at around 3180 and 3350 and carbonyl band located at 1680, showing that polyacrylamide has been formed on surface of the SNs. Because of little amount

of styrene in copolymer sample, there was no detectable peak concerning to styrene.

Thermogravimetric analysis (TGA) also was performed for all ASNs and polymer-grafted SNs (PSNs) samples and grafting percentage, conversion, chain density and degree of polymerization of chains were calculated (Table 1).

Table 1. Grafting percentage, conversion, chain density and chains' degree of polymerization of samples

samples	AAM(wt%)	St(wt%)	G (%)	P (%)
P1	100	0	593.7	39.6
P2	98.29	1.71	508.3	33.9

By drawing η_{red} versus c (Fig 2) and extrapolating graph to zero concentration, intrinsic viscosities were obtained, and by putting them in equation (3), viscosity- average molecular weights were calculated (Table 2). Results showed that in the presence of styrene as a comonomer in the reaction, molecular weight reduces intensely. This reduction can be attributed to increase in entropy of system with increase in number of participant monomers and formation of styrene micelles with existing SDS.

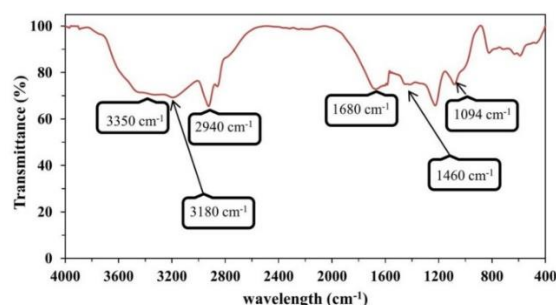


Fig 1. FTIR spectrum of P2

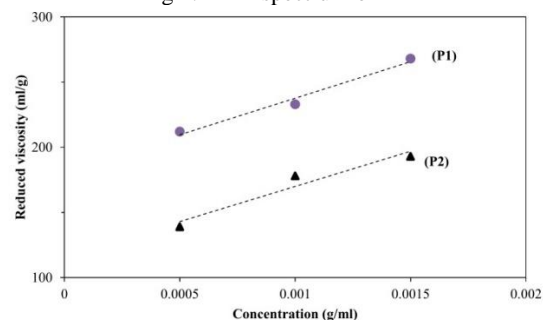


Fig 2. Reduced viscosity versus concentration plots

Table 2. Intrinsic viscosity, viscosity molecular weight and correlation coefficient of plots in Fig. 2

samples	$[\eta]$ (ml/g)	M_v (g/mole)	R^2
P1	181.34	522575.8	0.979
P2	115.98	287962.1	0.942

Conclusion

Free radical graft polymerization of AAm and St onto VSN were successfully performed. FTIR and TGA

results proved formation of polymer chains and their linkage to VSN. To determine molecular weight of formed chains, intrinsic viscosity method was used. Results showed that by copolymerizing AAm with St, M_v of chains reduced intensely. It was attributed to increase in entropy of the system by addition of styrene.

References

- [1] Macquarrie D., Fairfield S., The Heck reaction at a silica surface: functionalization of simple organo-modified silicas, *J. Mater. Chem.* 7(11), 2201-2204, 1997.
- [2] Khakpour H., Abdollahi M., Nasiri A., Synthesis, microstructural characterization and hydrophobic intermolecular nano-aggregation behavior of acrylamide/2-acrylamido-2-methy-1-propane sulfonic acid/butyl acrylate co-and terpolymers, *J. Polym. Res.*, 22(10) 189-201, 2015.

Size –Controlled Synthesis of Ni-MgO nanoparticles in CO₂- steam reforming of methane

M. Mousavi^{a*}, A. Nakhaeipour^a

^aDepartment of Chemistry, Faculty of Sciences, Ferdowsi University of Mashhad, Mashhad, Iran

*Mary_Mousavi44@yahoo.com

Abstract: The influence of Ni –MgO particle size on catalyst performance, product selectivity and coke formation in simultaneous steam and CO₂ reforming of methane to syngas has been investigated. The Ni-MgO nanoparticles were prepared by the incipient wetness impregnation method. In this work, the Ni-MgO particle sizes in the range of 7/13 to 29/7 nm have been studied using well-defined Catalysts based on α -Al₂O₃ support. Experimental results indicated that both products selectivity's and H₂/CO ratio to be independent of Ni-MgO particle size. Nevertheless, formation rates on the surface of catalyst are increased by increasing Ni-MgO particle size. In addition, the carbon atoms deposited on one site of catalyst is shown an opposite trend.

Keywords: CO₂- steam reforming, Ni- catalyst, Methane, syngas, size dependent

Introduction

A number of studies have been dedicated to the development of active and coke- resistant catalyst for in this process [1]. Among these catalysts, Ni-base catalysts are the usual choice of Catalytic material for commercialized steam reforming reactions at an industrial scale [2,3,4]. The Influence of various parameters on particle size such as :active metal content, support type and promoter will be discussed regarding carbon deposition and catalytic activity in this section. But Particle size played a key role in the suppression of carbon deposition, higher catalytic activity and stability [5].

In present work, the effect of particle size on catalyst activity, product selectivity's and coke formation are evaluated.

Materials and method

The supported Ni catalysts were prepared via incipient wetness impregnation on the MgO pre-coated α -Al₂O₃ support using Ni (NO₃)₂·6H₂O (Merk) as the Ni precursor compound. The XRD spectrum of the catalysts were collected using an X-ray diffract meter, Philips PW1840 X-ray diffract meter, using monochromatized Cu/K α radiation (40 kV, 40 mA) with scan rate of 0.02° (2 θ) per second from 10-80°. Catalytic reaction runs were conducted in a fixed-bed quartz reactor with inner-diameter of 1.2 cm at atmospheric pressure.

Results and Discussion

BET surface area: Table 1 gives the BET surface of the catalysts after calcination. AS it is revealed, both specific surface and total pore volume of the catalyst were decreased by increasing the Ni- loading.

Ni- MgO nanoparticle sizes: Table 1 shows that the Ni- MgO nanoparticle sizes were calculated from the Ni- and Mg loading. As shown in table 1, by increasing the Ni-loading, Ni-MgO Particle size is increased.

Catalyst activity: Table 2 listed the results for CH₄, H₂O and CO₂ Conversion and syngas (H₂+CO) selectivity. As shown in table 2, by increasing of loading Ni-particles, Conversations of CH₄, H₂O and CO₂ were increased [6-7].

coke study: Fig 1 gives that the coke deposition amount on the catalyst. Was increased by increasing Ni- Loading [7-9]. As reported in prior studies, by increasing Ni-MgO particle size, the amount of coke deposition is increased.

Table 1: BET surface are, Total pore volume, Ni and Mg loadings, surface Ni and Mg densities dispersions and particle sizes as determined by H₂ chemisorption of the various catalysts.

Mg loading (wt.%)	Ni loading (wt.%)	BET surface area (m ² /g)	Total pore volume (cm ³ /g)	Ni-Mg dispersion ^b (%)	d _{Ni-Mg} ^b (nm)
0	0 ^a	11.2	0.161	0	0
1.0	1.0	10.9	0.158	7.5	13.7
1.0	1.8	10.6	0.155	6.1	16.9
1.0	2.6	10.3	0.153	5.1	20.1
1.0	3.4	10.1	0.150	4.4	23.3
1.0	4.2	9.8	0.147	3.9	26.5
1.0	5.0	9.5	0.145	3.5	29.7

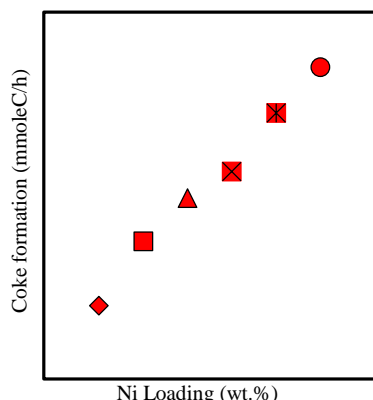


Figure 1. The amount of deposited carbon (C) over spent catalysts by the TPO measurements against Ni loading wt.%.
Conclusions

The influence of size-particle on catalyst activity, Product selectivity and coke deposition over Ni/ MgO/ α - Al₂O₃ catalyst in CO₂-steam reforming of methane was studied. Results indicated that products selectivity's and H₂/Co ration to be independent of nickel particle size. But coke formation rate is increased by increasing nickel particle size.

References

- [1] N. A. Pechimuthu, K. K. Pant, S. C. Dhingra, R. Bhalla, *Industrial and Engineering chemistry*. 45(2006) 7435–7443.
- [2] P. Ferreira-Aparicio, I. Rodr_guez-Ramos, J. A. Anderson, A. Guerrero-Ruiz, *Applied catalysis A: General*.202(2000) 183–196.
- [3] A. D. Ballarini, S. R. de Miguel, E. L. Jablonski, O. A. Scelza, A. A. Castro, *Catalysis Today*.107(2005) 481–486.
- [4] Y. Zhao, Y. X. Pan, Y. B. Xie, C. J. Liu, *Catalysis Communications*.9(2008) 1558–1562.
- [5] V. Kroll, H. Swaan, C. Mirodatos. Methanereformingreactionwithcarbondioxide OverNi/SiO₂ catalyst:I.Deactivationstudies. *Journal Catalyst* 161 1996:409–22.
- [6] DAJM. Ligthart, RA. van Santen, EJM. Hensen. “Influence of particle size on the activity and stability in steam methane reforming of supported Rh nanoparticles”. *Journal of Catalysis*280(2011) 206-20.
- [7] DAJM. Ligthart, JAZ. Pieterse, EJM. Hensen. “The role of promoters for Ni catalysts in low temperature (membrane) steam methane reforming”. *Applied Catalysis A: General*. 405(2011) 108-19.
- [8] D. Baudouin, U. Rodemerck, F. AD. Krumeich, Mallmann, KC. Szeto, H. Ménard, et al. “Particle size effect in the low temperature reforming of methane by

carbon dioxide on silica-supported Ni nanoparticles”. *Journal of Catalysis*. 297(2013) 27-34.

[9] J. Juan-Juan, MC. Román-Martínez, MJ. Illán-Gómez. “Nickel catalyst activation in the carbon dioxide reforming of methane: Effect of pretreatments”. *Applied Catalysis A: General*. 355(2009) 27-32.

The effect of magnetic field on particle Size of NiO nanoparticles

M. Mousavi^{a*}, A. Nakhaeipour^a, M. Gholizadeh^a

^aDepartment of Chemistry, Faculty of Sciences, Ferdowsi University of Mashhad, Mashhad, Iran

*Mary_Mousavi44@yahoo.com

Abstract: In this paper, the effect of magnetic field over NiO nanoparticles has been investigated. Also experimental results on the effects of a magnetic field on water are reported. Purified water was circulated at a constant flow rate in a magnetic field. After this treatment, the physicochemical properties of water were changed, shown as the decrease of surface tension in addition, by decreasing of the surface tension of the solvent in the precipitation step, average particle size of NiO nano particles decreased. Also the structure and morphology of NiO-nanoparticles were characterized by x-ray diffraction (XRD), Bruner Emmet-Teller (BET) and Transmission electron microscopy (TEM).

Key words: NiO nanoparticles, solvent, surface tension, precipitation.

Introduction

The magnetic treatment has remained a controversial process for industrial and domestic water treatment for over 50 years [1]. This type of physical treatment helps to prevent the use of chemicals such as polyphosphates or corrosive substances that are expensive and can be harmful to human life or disruptive to the environment. Independent review of the performance of the magnetic treatment has been highly controversial, while the increase in the number of commercial magnetic treatment devices might seem to be an indicator of the effectiveness of magnetic fields in the water processing. Many claims have been made that magnetic fields (MFs) change the physicochemical properties of water, or prepared laboratory solutions [2,3], by influencing pH value, nucleation and growth, surface tension and chemical equilibria. Tombacz et al. have tested both flowing and static systems, and concluded that only in a flowing system is the magnetic effect observed [4]. The magnetic flux density ranges from 0.1 to 0.8 T among those magnetic treatment experiments. Kobe et al. took 0.5 T as the magnetic flux density in their experiments to obtain successful treatment results [5]. Chang and Weng investigated the effects of the MF on the hydrogen-bonded structure of water and found that the number of hydrogen bonds increased by approximately 0.34% when the MF strength increased from 1 to 10 T [6].

The aim of this paper is to measure surface tension of the magnetized solvent on the characteristics of the NiO nanoparticles.

Materials and method

The NiO nanoparticles were synthesized of Ni (NO₃)₂·6H₂O (Merck) by homogeneous precipitation in presence and absence of magnetic field. The deionized water was magnetized by passing into the static

magnetic field (AQUA CORRECT device with a coaxial static magnetic system of 6500G field strength). (BET) method, pore volume, average pore diameter, and pore size distribution of the iron nanoparticles were determined by N₂ physisorption using a Micrometrics ASAP 2010 automated system. The XRD spectrum of the samples were collected using an X-ray diffractometer, Philips PW1840 x-ray diffractometer, using Cu/K_α radiation (40 kV, 40 mA) and a step scan mode at a scan rate of 0.02° (2θ) per second from 20-90°. The morphology of prepared iron nanoparticles after calcinations was observed with a transmission electron microscope (TEM, LEO 912 AB, Germany).

Results and Discussion

Effects of magnetic field on the surface tension of solvent: The influence of magnetic field and number of passes through the magnetic field on the surface tension of the distilled water is presented in Fig 1. As shown in Fig 1, the magnetic field caused a significant decrease in the surface tension of solvent. Also, by increasing the number of passes through the magnetic field, the surface tension of solvent decreased. [7-8]

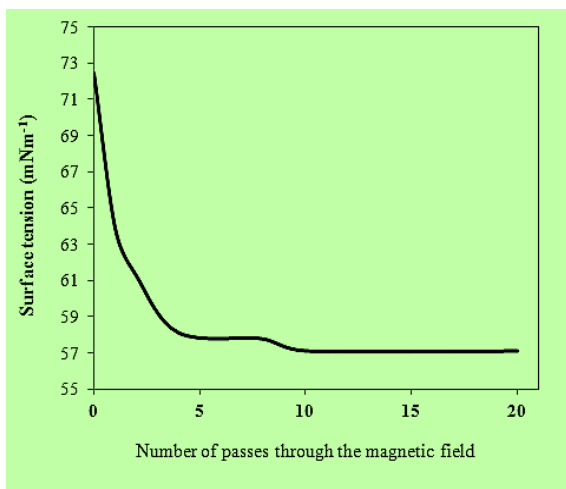


Figure 1. The influence of the magnetic field and number of passes through the magnetic field on the surface tension of the distilled water.

Catalyst characterization

X-ray diffraction: The crystal phases of the prepared samples were analysed by powder x-ray diffraction (XRD). As shown in Fig 2, only the diffraction peaks are attributed to NiO nanoparticles with cubic structure. Also, based on the diffraction data, the crystalline phase of two samples showed the hexagonal structures of NiO crystal, which is independent of the water pre-treatment in precipitation of NiO nanoparticles (magnetization process). [9]

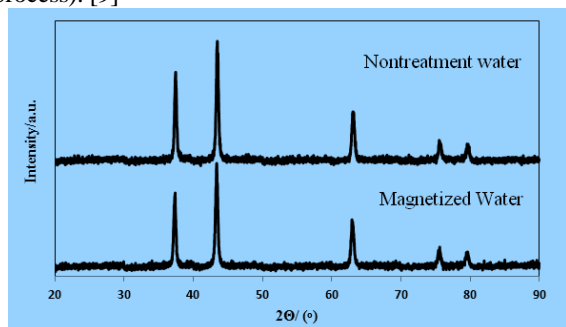


Figure 2. Powder XRD patterns of prepared samples

BET surface area: Table 1 shows that surface area and calculated particle size from BET results.

As shown in Table 1 particle size of NiO nanoparticles increased by increasing the surface tension of the solvent in the precipitation step. [10]

Table 1. Surface tension of water, average particle size and textural properties of the prepared samples.

Method	Surface tension of water (mNm ⁻¹)	Average particle size (nm)			BET surface area (m ² /g)	Average pore size (nm) ^a
		BET	XRD	TEM		
Non-treatment	72.5	179	28.3	30.2	5.03	40.5
Magnetized	51.1	124	42.1	39.7	7.3	43.9

TEM microscopy: The TEM images and histograms of particle size distribution for synthesized nanoparticles in magnetized and no treatment water are shown in Fig 3.

It can be seen the magnetized water do not change the shape of nanoparticles. But, the particle size distribution and the average particle size of NiO nanoparticles prepared in magnetized water is lower than that of no treatment sample.

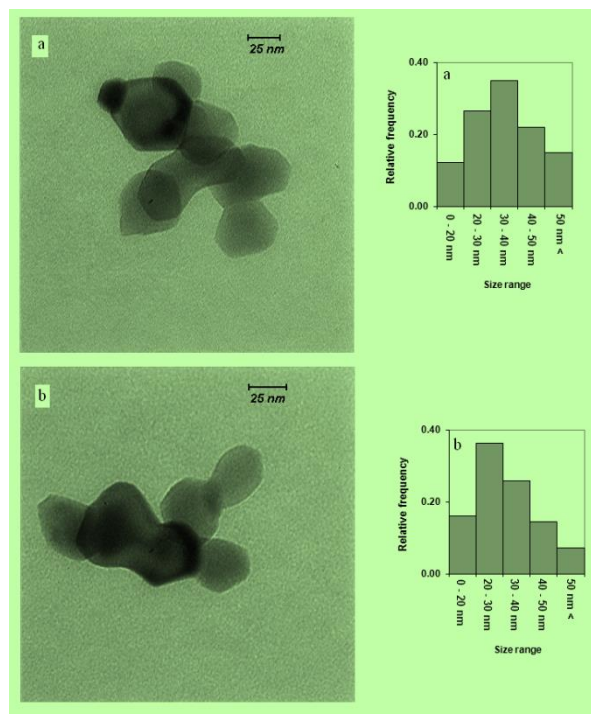


Figure 3. TEM micrographs of the NiO nanoparticles synthesized in precipitating method. a: No treatment water, b: Magnetized water

Conclusions

Many claims have been made that magnetic fields change the physicochemical properties of water. Our experimental results verified again that magnetic treatments have changed some properties of water. The surface tension was decreased. In this study NiO nanoparticles are prepared by homogenous precipitation in presence and absence of magnetic field. The particle shape, particle size and Particle size distribution of the prepared samples was determined by BET, XRD, TEM Techniques.

Also the results shown that the surface tension of distilled water decrease under the effect of magnetic field.

References

- [1] J.S. Baker, S.J. Judd, *Water Res.* 30 (1996) 247.
- [2] M. Morimitsu, K. Shiomi, M. Matsunaga, *Journal Colloid Interface Science.* 229 (2000) 641.



- [3] L. Holysz, M. Chibowski, E. Chibowski, *Colloid Surface A* 208 (2002) 231.
- [4] E. Tombacz, C. Ma, K.W. Busch, M.A. Busch, *Colloid Polymer Science*. 269 (1991) 278.
- [5] S. Kobe, G. Draz̃ić, P.J. McGuinness, J. Straz̃išar, *journal of magnetism and magnetic materials*.. 236 (2001).
- [6] K.T. Chang, C.I. Weng, *journal of Applied physics*. 100 (2006) 043917.
- [7] R.V. Martín Algarra, L. Lahuerta Zamora, G.M. Antón Fos, P.A. Alemán López, "Magnetized Water: Science or Fraud?", *Journal of Chemical Education*. 85 (2008) 1416.
- [8] M.C. Amiri, A.A. Dadkhah, "On reduction in the surface tension of water due to magnetic treatment, Colloids and Surfaces"A: *Physicochemical and Engineering Aspects*, 278 (2006) 252-255.
- [9] D. Adityawarman, A. Voigt, P. Veit, K. Sundmacher, "Precipitation of nanoparticles in a non-ionic microemulsion: Identification of suitable control parameters", *Chemical Engineering Science*. 60 (2005) 3373-3381.
- [10] K.S.W. Sing, "Reporting physisorption data for gas/solid systems with special reference to the determination of surface area and porosity", *Pure and Applied Chemistry*. 54 (1982) 17.

Preparation and characterization of cation-exchange membranes based on polycarbonate (PC) & acrylonitrile butadiene styrene (ABS) modified by NiFe₂O₄ nanoparticles

S. Asgari^{a*}, A. R. Khodabakhshi ^a

^a Department of Chemistry, Faculty of Science, Arak University, Arak 38156-8-8349, Iran

*asgary_saeed@yahoo.com

Abstract: In this research, polycarbonate (PC) and acrylonitrile butadiene styrene (ABS) based heterogeneous cation exchange membranes modified by NiFe₂O₄ (Nickel Ferrite) nanoparticles were prepared by casting-solution techniques, and their morphological and electrochemical properties were studied. Ion exchange capacity, transport number, permselectivity and ionic flux were investigated. The results show that in membranes prepared with different percentages of nanoparticles, the ion exchange capacity and ionic flux increased toward the membranes without nanoparticles. By adding nanoparticles of nickel ferrite, due to the magnetic properties and absorption of these nanoparticles, and their accumulation around the resin, access to the functional group is reduced and the ion exchange capacity decreases and with the improvement of the path of the transfer channels increased of the flux.

Keyword: Nickel Ferrite; nanoparticles; polycarbonate; acrylonitrile butadiene styrene; heterogeneous

Introduction

Ion-exchange membranes (IEMs) are involved in several separative and production processes, including dialysis, Donnan dialysis, and electro dialysis [1]. Ion-exchange membranes due to high selectivity, were used in desalination, water treatment and industrial wastewater treatment and recovery of metals [2]. nowadays, using modify methods, such as mixing polymers, using nanoparticles and etc., can be improved structural and electrochemical properties. ABS is a commercial material with relatively low cost and good mechanical properties. Due to the nature of hydrophobicity and hydrophobicity, may be changed the properties of the membrane. PC is also a polymer with appropriate thermal resistance outstanding impact strength and suitable electrical properties. Moreover PC has a good adsorption property due to its structure which provides high electrostatic interaction [4, 5]. In this research cation exchange membranes were prepared using polymeric mixture of ABS and PC by casting-solution techniques. The effect of nickel ferrite nanoparticles on physical properties of membranes was investigated.

Materials and methods

Polycarbonate (PC) supplied by DSM (Xantar®) and Acrylonitrile-butadiene-styrene (ABS), supplied by T.P.C, Iran were used as binders. Tetrahydrofuran (THF) as solvent and cation exchange resin by Merck Inc., were used to prepare the membranes.

Magnetic nanoparticles of nickel ferrite (NiFe₂O₄) have been synthesized by co-precipitation route using stable ferric and nickel salts with sodium hydroxide as the precipitating agent and Polyethylene glycol as the surfactant [3].

The cell used to study membrane electrochemical properties in shown is Fig.1.

Membranes with various compounds using THF as solvents of specific proportions were made in a glass reactor equipped with a mechanical stirrer at room

temperature and then placed in the NaCl for further testing. Solution compounds are shown in Table 1[4, 5,6].

Characterization of Prepared Membranes

After the membranes were prepared, their ion exchange capacity was investigated. To measure the ion exchange capacity, the membrane sample was placed in 1M HCl solution for 24 hours. then the sample was washed with distilled water and placed in the 1M NaCl solution, and finally, the solution is titrated with 0.01M NaOH solution and can be calculated by the following equation [1, 4, 7]:

$$IEC = \frac{a}{W_{dry}} \quad (1)$$

Where *a* is the milli-equivalent of ion exchange group in membrane and *W_{dry}* is the weight of dry membrane (gr).

Table1: compositions of casting solution

When the membrane surfaces in contact with two solutions with different concentrations of 0.1 and 0.01 M NaCl, a potential is created. A two-compartment cell and two calomel electrodes are used for testing. After measuring the potential, the transport number is calculated using the Nernst relationship [5, 6]:

$$E_m = (2t_i^m - 1) \left(\frac{RT}{nF} \right) \ln \left(\frac{a_1}{a_2} \right) \quad (2)$$

Where t_i^m transport number, T is the temperature, R is gas constant, n is electrovalence of counter-ion and a_1 , a_2 are electrolyte activities in the solution. The ionic permselectivity of membranes is obtained from the following equation [8] :

$$P_s = \frac{(t_i^m - t_0)}{(1 - t_0)} \quad (3)$$

Where, t_0 is transport number of counter-ion in solution phase.

To calculate the ion flux on both sides the cell of the solution, 0.1 and 0.01M NaCl are used. By applying a constant voltage, the sodium ion permeated of the anodic section to the cathode part, and pH increased in the cathode section of the ion production OH^- . By changing pH, the amount of passing moles can be calculated [8, 9].

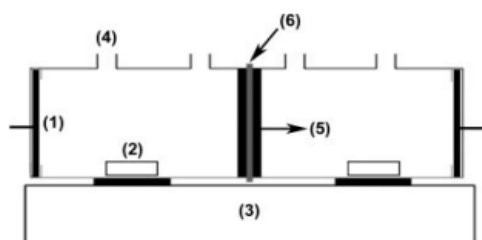


Fig.1: Schematic of test cell : (1) platinum electrode; (2) magnetic bar; (3) stirrer; (4) orifice; (5) rubber ring; (6) membrane

Results and Discussion

Figure. 2 shows the ion exchange capacity of the prepared membranes. With the increasing in the percentage of nanoparticles, the initially increased ion exchange capacity, but with the filling of the surface and the accumulation of nanoparticles. Led to decreased in IEC [5, 6].

The permselectivity and transport number of membrane are showed in figure 3.

The transport number and permselectivity of membranes is improved by increasing the percentage of nanoparticles

This may be due to the electrical properties and absorption of nickel ferrite nanoparticles and increased the conductivity in the ionic transfer channels [5, 7, , 8].

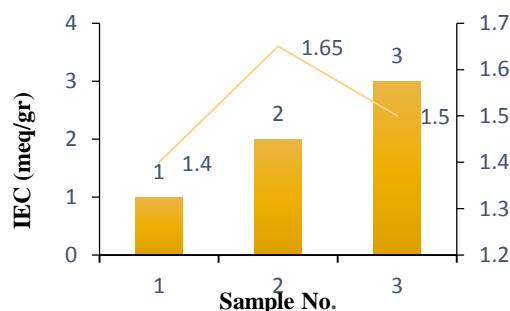
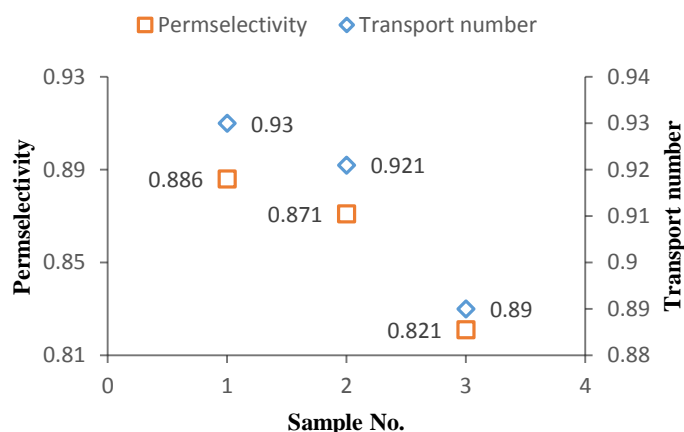


Fig.2: ion exchange capacity of the prepared membranes

The figure. 4 showed the ionic flux. The flux increased with increasing nanoparticles. This is due to increased porosity and water channels in the membrane network [10].



Membrane code	Polymer binder (PC:ABS) (w/w)	Nanoparticle :binder (w/w)	Solvent (THF:bi nder) (v/w)	Resin:binder (w/w)
M1	50:50	0	20:1	50:50
M2	50:50	2	20:1	50:50
M3	50:50	6	20:1	50:50

Fig. 3: The permselectivity and transport number of prepared membranes

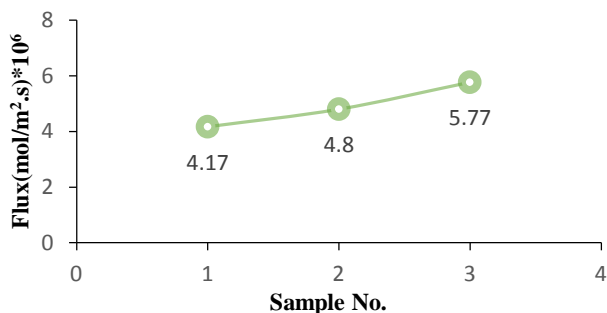


Fig.4: The ionic flux of prepared cation exchange membrane

Conclusions

Nickel ferrite nanoparticles have a significant effect on the electrochemical and physicochemical properties of membranes. The addition of nanoparticles in the membrane network, initially increased properties including, ion exchange capacity, transport number, and permselectivity. The ionic flux increased significantly as a result of the improvement transfer channels in the membrane network and increased porosity.

References

- [1] J. Schauer, V. Ku dela, K. Richau, R. Mohr, Heterogeneous ion-exchange membranes based on sulfonated poly(1,4-phenylene sulfide), *Desalination* 198 (2006) 256–264.
- [2] Nagarale, R. K., Kittur, A. A. & Kulkarni, S. S. Ion-exchange membranes " preparative methods for electro dialysis and fuel cell applications. 197, 225–246 (2006).
- [3] K. Maaz, S. Karim, A. Mumtaz, S.K. Hasanain, J. Liu, J.L. Duan, Synthesis and magnetic characterization of nickel ferrite nanoparticles prepared by co-precipitation route, *Journal of Magnetism and Magnetic Materials*, 321(2009) 1838-1842.
- [4] C. Klaysom, S. H. Moon, B. P. Ladewig, G. Q. M. Lu, L. Wang (2011) *J. Colloid Interface Sci.* 363, 431.
- [5] A. R. Khodabakhshi, S. S. Madaeni, and S. M. Hosseini, "Effect of Polymers Blend Ratio Binder on Electrochemical and Morphological Properties of PC / S-PVC-Based Heterogeneous Cation-Exchange Membranes," 2010.
- [6] H. Farrokhzad *et al.*, "Novel composite cation exchange films based on sulfonated PVDF for electromembrane separations," *J. Memb. Sci.*, vol. 474, pp. 167–174, 2015.
- [7] S. M. Hosseini, A. Gholami, S. S. Madaeni, A. R. Moghadassi, and A. R. Hamidi, "Fabrication of (polyvinyl chloride / cellulose acetate) electro dialysis heterogeneous cation exchange membrane : Characterization and performance in desalination process," vol. 306, pp. 51–59, 2012.
- [8] S. M. Hosseini, F. Jeddi, M. Nemati, S. S. Madaeni, and A. R. Moghadassi, "Electrodialysis heterogeneous anion exchange membrane modi fi ed by PANI / MWCNT composite nanoparticles : Preparation , characterization and ionic transport property in desalination," *DES*, vol. 341, pp. 107–114, 2014.
- [9] T. Xu, "Ion exchange membranes : State of their development and perspective," vol. 263, no. 2, pp. 1–29, 2005.
- [10] A. R. Khodabakhshi, S. S. Madaeni, and S. M. Hosseini, "Investigation of electrochemical and morphological properties of S-PVC based heterogeneous cation-exchange membranes modified by sodium dodecyl sulphate," *Sep. Purif. Technol.*, vol. 77, no. 2, pp. 220–229, 2011.

Studying the effects of Gas&Liquid velocities in modeling of the simultaneous removal of CO₂ and H₂S using MEA in a hollow fiber membrane contactor

E. Amirahmadi^a, M. Talaghat^{*a}Chemical Petroleum & Gas Eng, Shiraz university of technology, Shiraz, 9871, Iran

*talaghat@sutech.ac.ir

Abstract: A two-dimensional mathematical model was studied for the transport of CO₂ and H₂S through hollow fiber membrane (HFM) contactors while using MEA (monoethanolamine) as the chemical absorber. The model considered non-wetted where the gas and the solvent liquid fill the membrane pores for counter current gas-liquid flow direction. There is an axial and radial diffusion in the tube, through the membrane and the shell. The model validation was on the physical and chemical absorption of CO₂ using water and MEA, respectively. The percentage of removal of CO₂ increased while increasing the absorbent velocity. As for H₂S, low flow rate of amine was efficient in complete removal. The percentage removal of CO₂ decreased while increasing gas velocity because of lower hold up time, whereas H₂S removal did not change with increasing gas velocity at low gas velocities. However the effect is more obvious at high gas velocities.

Keywords: CO₂; Natural gas; H₂S; MEA

Introduction

CO₂ is considered as a major greenhouse gas that causes global warming and lowers the efficiency of several industrial processes. On the otherhand, H₂S is a poisonous gas and highly toxic and flammable that causes major health concerns upon contact. Several technologies for natural gas treatment in the petrochemical industry include absorption towers and packed and plate columns. Although these conventional processes are being used up to date, these methods possess many disadvantages such as flooding foaming and demand high capital and operating costs [1, 2]. In a typical hollow fiber membrane contactor device, a considerable number of hollow fibers membranes are assembled together in a large tube where two phases come into a direct contact with each other for the purpose of mass transfer without the dispersion of one phase into another due to the presence of a very fine barrier (membrane). Membrane contactors offer several practical advantages including high surface area per unit contactor volume, independent control of gas and liquid flow rates, no flooding or foaming formation occurring, and low operation and capital costs[3]. The objective of this paper is to develop and solve a comprehensive 2D mathematical model for simultaneous removal of CO₂ and H₂S using MEA in hollow fiber membrane contactors.

Materials and method

We have studied a 2D mathematical modelling for the removal of both CO₂ and H₂S through membrane contactor using MEA as the chemical solvent. There is an axial and radial diffusion in the tube, shell, and the membrane as well. The model is useable for none, partial, and complete wetted. A material balance has been used on a shell-and-tube membrane contactor system to develop the main equations for the

mathematical model. The system is made of three sections: tube, membrane, and shell side. The gas stream (CH₄, H₂S, and CO₂) flows through the shell side, while the liquid flows through the tube in a counter-current direction. The gas stream is entered to the shell side (at $z = L$), while the solvent is entered through the tube side (at $z = 0$). CO₂ and H₂S are removed from the gas stream by diffusing through the membrane and then absorbing with the amine. We can see the model development for a segment of a hollow fiber in **Figure1**, which the solvent flows with a fully-developed laminar parabolic velocity profile.

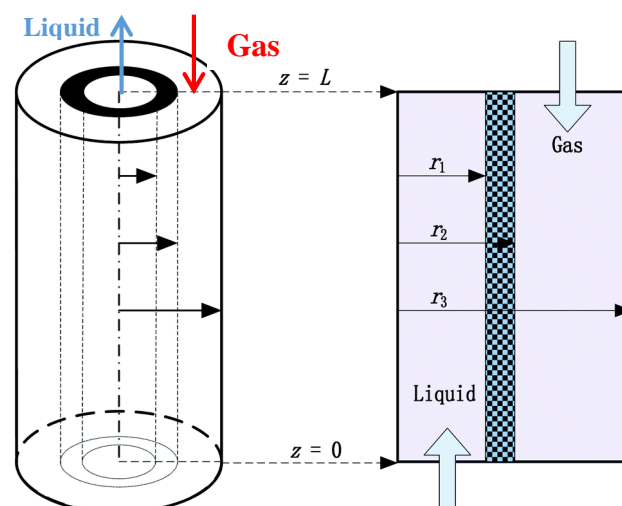


Fig. 4: A schematic diagram for the membrane contactor used for modeling

Results and Discussion

1 molar MEA was used as a solvent in the tube side while the gas mixture (10% CO₂, 10% H₂S, and 80% CH₄) was sent through the shell side in a counter-



current direction. The model equations with the boundary conditions were solved for different gas, liquid flow rates, and MEA concentrations. The temperature was set at 298 K, and 1 atm pressure. The objective is to study the effect of different gas, and liquid velocities on the removal of CO₂ & H₂S. The concentration gradient and the total flux vectors of CO₂ in the tube, membrane and shell sides of the contactor are shown in **Figure 2**. The gas mixture streams in the shell side at ($z = L$) where the concentration of CO₂ is the highest $C_{CO_2} = 4 \text{ mol m}^{-3}$, while MEA flows in the tube side at ($z = 0$) where CO₂ has a concentration amount of zero. The gas in the shell side moves to the membrane due to the concentration difference, and then is absorbed by the MEA in the tube. The steady state material balance for the transport CO₂ and H₂S in the shell side, may be written as

$$D_{i-shell} \left[\frac{\partial^2 C_{i-shell}}{\partial r^2} + \frac{1}{r} \frac{\partial C_{i-shell}}{\partial r} + \frac{\partial^2 C_{i-shell}}{\partial z^2} \right] = V_{z-shell} \frac{\partial C_{i-shell}}{\partial z} \quad (1)$$

Assuming Happel's free surface model [4], the velocity profile in the shell is given by

$$V_{z-shell} = 2(V) \left[1 - \left(\frac{R_2}{R_3} \right)^2 \right] \times \left[(r/R_3)^2 - (R_2/R_3)^2 + 2 \ln(R_2/r)/R_3 \right] \quad (2)$$

$$\text{At } z = L, C_{i-shell} = C_0 \quad (i = CO_2 \& H_2S) \quad (3)$$

$$\text{At } r = R_2, C_{i-shell} = C_{i-mem} \quad (4)$$

$$\text{At } r = R_3, \frac{\partial C_{i-shell}}{\partial r} = 0 \quad (\text{symmetry}) \quad (5)$$

The steady state material balance for the transport of CO₂ and H₂S inside the membrane can be considered to be due to diffusion only and may be written as

$$D_{i-mem} \left[\frac{\partial^2 C_{i-mem}}{\partial r^2} + \frac{1}{r} \frac{\partial C_{i-mem}}{\partial r} + \frac{\partial^2 C_{i-mem}}{\partial z^2} \right] = 0 \quad (6)$$

Boundary conditions are given as

$$\text{At } r = R_1, C_{i-mem} = \frac{C_{i-tube}}{m_i} \quad (i = CO_2 \& H_2S) \quad (7)$$

$$\text{At } r = R_2, C_{i-mem} = C_{i-shell} \quad (8)$$

Where m_i is solubility of CO₂ and H₂S in MEA.

Steady state material balance for the transport of CO₂ and H₂S while reacting with MEA inside the tube side may be written as

$$D_{i-tube} \left[\frac{\partial^2 C_{i-tube}}{\partial r^2} + \frac{1}{r} \frac{\partial C_{i-tube}}{\partial r} + \frac{\partial^2 C_{i-tube}}{\partial z^2} \right] + R_i =$$

$$V_{z-tube} \frac{\partial C_{i-tube}}{\partial z} \quad (9)$$

Boundary conditions are given as:

$$\text{at } z = 0, C_{i-tube} = 0, C_{MEA-tube} = C_0 \quad (10)$$

$$\text{at } r = 0, \frac{\partial C_{i-tube}}{\partial r} = 0 \quad (\text{symmetry}) \quad (11)$$

$$\text{at } r = R_1, C_{i-tube} = C_{i-membrane} \times m_i \quad (12)$$

$$\frac{\partial C_{i-tube}}{\partial r} = 0 \quad (13)$$

(s = other species than H₂S&CO₂)

Table 1: Membrane module dimensions, properties, and model parameters for CO₂-H₂S-MEA system.

Parameter	Value	Reference
Inner tube diameter (mm)	0.22	-
Outer tube diameter (mm)	0.3	-
Inner shell diameter (mm)	0.529	-
Module length L (cm)	22	-
Number of fibers	3600	-
$D_{CO_2-shell}$ (m ² s ⁻¹)	1.8×10^{-5}	Cussler [36]
D_{CO_2-tube} (m ² s ⁻¹)	1.51×10^{-9}	Paul et al. [37]
$D_{CO_2-membrane}$ (m ² s ⁻¹)	$D_{CO_2-shell}(\epsilon/\tau)$	Calculated
$D_{H_2S-shell}$ (m ² s ⁻¹)	2.01×10^{-5}	Cussler [36]
$D_{H_2S-tube}$ (m ² s ⁻¹)	1.52×10^{-9}	Estimated
$D_{H_2S-membrane}$ (m ² s ⁻¹)	$D_{H_2S-shell}(\epsilon/\tau)$	Calculated
$D_{MEA-tube}$ (m ² s ⁻¹)	9.32×10^{-10}	Paul et al. [37]
$D_{MEA+ -tube}$ (m ² s ⁻¹)	$D_{MEA-tube}$	Assumed
$D_{MEACO_2 -tube}$ (m ² s ⁻¹)	$D_{MEA-tube}$	Assumed
$D_{H_2S -tube}$ (m ² s ⁻¹)	$D_{H_2S-tube}$	Assumed
m_{CO_2} (mol mol ⁻¹)	0.8	Paul et al. [37]
m_{H_2S} (mol mol ⁻¹)	2.3	Estimated
ϵ (porosity)	0.4	-
τ (tortuosity)	2	-

Fig. 3 shows the concentration gradient of H₂S in the tube, membrane and shell sides of the system. H₂S is consumed very quickly in the first 20% of the module length. This is because of the higher solubility of H₂S in MEA ($m_{H_2S} = 2.3$) and the instant reaction with MEA. The flux vectors in the shell side also disappear after 20% of the module length.

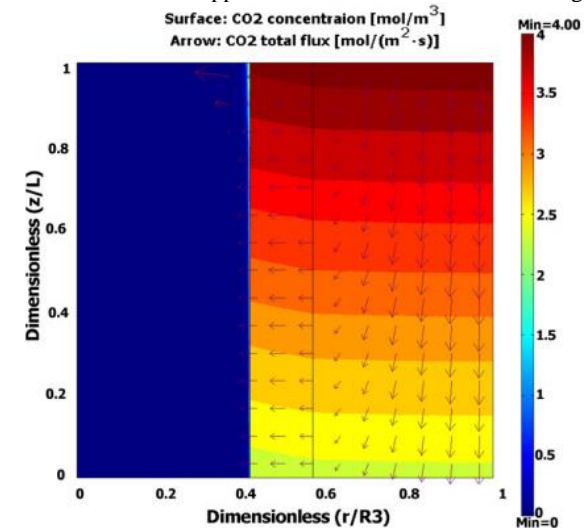


Figure 2: Model solution for CO₂. $r_1 = 0.11 \text{ mm}$, $r_2 = 0.15 \text{ mm}$, $r_3 = 0.265 \text{ mm}$, $L = 22 \text{ cm}$, $CCO_2 = 4 \text{ mol}$



m^{-3} , $C_{\text{MEA0}} = 1000 \text{ mol m}^{-3}$, $V_{\text{Gas}} = 3.33 \text{ m s}^{-1}$, $V_{\text{Liq}} =$

0.67 m s^{-1} .

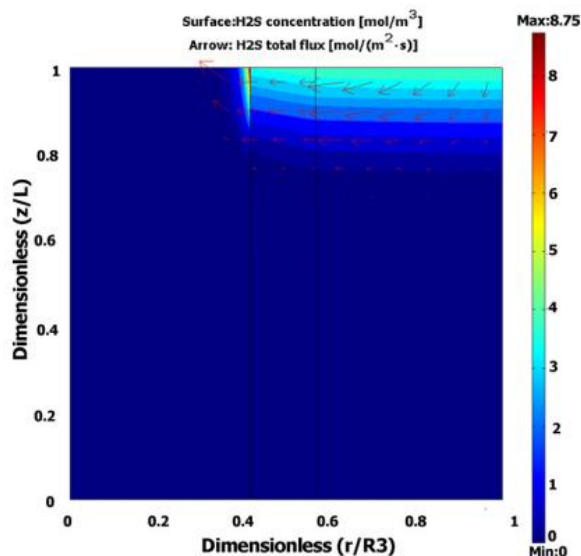


Figure 3: Model solution for H₂S. $r_1 = 0.11 \text{ mm}$, $r_2 = 0.15 \text{ mm}$, $r_3 = 0.265 \text{ mm}$, $L = 22 \text{ cm}$, $C_{\text{H}_2\text{S}0} = 4 \text{ mol m}^{-3}$, $C_{\text{MEA0}} = 1000 \text{ mol m}^{-3}$, $V_{\text{Gas}} = 3.33 \text{ m s}^{-1}$, $V_{\text{Liq}} = 0.67 \text{ m s}^{-1}$.

We can see the deduction in absorption of CO₂ by increasing the velocity of gas through the shell side in **Figure 4**, but it is evident that the increase of gas velocity almost doesn't influence the removal of H₂S and all of the H₂S is being absorbed through the shell side at considered situations.

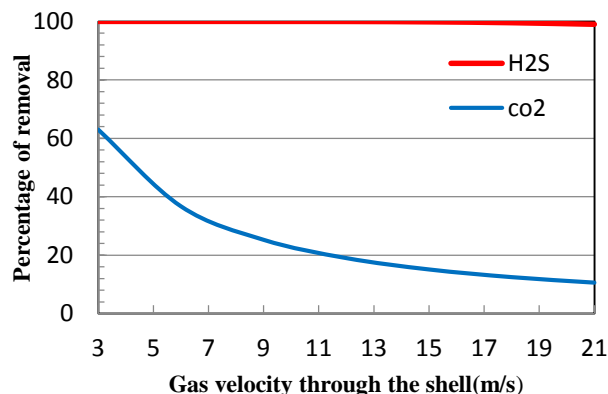


Figure 4: Removal of CO₂ and H₂S in different gas velocities. $r_1 = 0.11 \text{ mm}$, $r_2 = 0.15 \text{ mm}$, $r_3 = 0.265 \text{ mm}$, $L = 22 \text{ cm}$, $C_{\text{CO}_20} = 4 \text{ mol m}^{-3}$, $C_{\text{H}_2\text{S}0} = 4 \text{ mol m}^{-3}$, $C_{\text{MEA0}} = 1000 \text{ mol m}^{-3}$, $V_{\text{Liq}} = 0.67 \text{ m s}^{-1}$.

It is obvious that we have a rise of removal efficiency for H₂S by increasing the speed of liquid in **Figure 5**, but it is not important to rise the absorption of H₂S because it is fully absorbed even in lower liquid velocities.

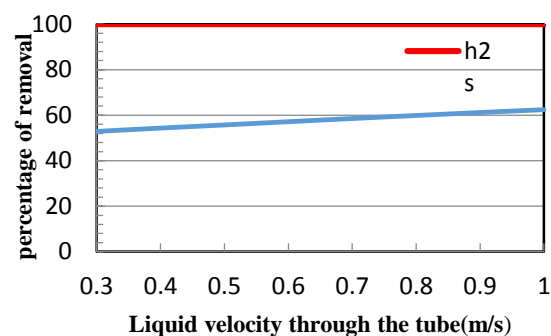


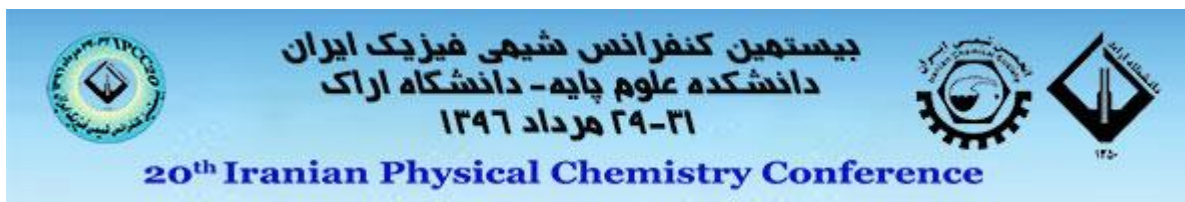
Figure 5: Removal of CO₂ and H₂S in different liquid velocities. $r_1 = 0.11 \text{ mm}$, $r_2 = 0.15 \text{ mm}$, $r_3 = 0.265 \text{ mm}$, $L = 22 \text{ cm}$, $C_{\text{CO}_20} = 4 \text{ mol m}^{-3}$, $C_{\text{H}_2\text{S}0} = 4 \text{ mol m}^{-3}$, $C_{\text{MEA0}} = 1000 \text{ mol m}^{-3}$, $V_{\text{Gas}} = 3.33 \text{ m s}^{-1}$

Conclusions

A 2D mathematical model was developed for the simultaneous transport of CO₂ and H₂S in HFM contactors using MEA as chemical absorber. The model assumed to be non-wetted for countercurrent gas-liquid flow direction. Axial and radial diffusion were considered in the fiber, membrane and the shell. We had no experimental data for validation, so the model was validated for physical and chemical absorption of CO using water and MEA, respectively. The model results has an excellent agreement for physical and chemical absorption while considering non-wetted and partial-wetted conditions, respectively. After the model was validated, the effect of gas and liquid flow rates were studied on the efficiency of simultaneous removal of CO₂ and H₂S. The % removal of CO₂ increased while increasing the MEA flow rate. But for H₂S, low flow rate of MEA was more efficient in complete removal. The percentage of removal of CO₂ decreased while increasing gas velocity, whereas, H₂S % removal did not change with increasing gas velocity when operating at low gas velocity. However, the effect is more pronounced while operating at high gas velocities.

References

- [1] A. Gabelman, S. Hwang, Hollow fiber membrane contactors, *J. Membr. Sci.* 159 (1999) 61–106.
- [2] D. deMontigny, P. Tontiwachwuthikul, A. Chakma, Comparing the absorption performance of packed columns and membrane contactor, *Ind. Eng. Chem. Res.* 44 (2005) 5726–5732
- [3] J-L. Li, B-H. Cheng, Review of CO₂ absorption using chemical solvents in hollow fiber membrane contactors, *Sep. Purif. Technol.* 41 (2005) 109–122.
- [4] J. Happel, Viscous flow relative to arrays of cylinders, *AIChE J.* 5 (1959) 174–177.



Simulation of the absorption tower of the gas dehydration unit and estimation of the BTEX solubility in TEG

Maryam Ansari and Farzad Alavi*

Department of Chemical, Petroleum, and Gas engineering, Shiraz University of Technology, Shiraz, 71557-13876, Iran
*alavi@sutech.ac.ir

Abstract: One of the most important steps of gas processing is the gas dehydration. In this unit, water vapor from the natural gas stream is removed by absorption into a solvent such as tri-ethylene glycol (TEG). From the environmental point of view, a problem of this unit is the solubility of the aromatic compounds, mainly benzene, toluene, ethylbenzene, xylenes (BTEX) in TEG and then release of these compounds into the atmosphere. Accurate simulation of this units can be a great help to optimize the operating parameters and reduce the emission rate of this materials. In this work, the Peng-Robinson (PR) Equation of State (EOS) is used for estimating the BTEX solubility in TEG in the absorber. Since the final emission rate is determined by the solubility in absorber, this work focuses on the simulation of absorber. The absorber is simulated using a customized code and no simulation software is used. At steady conditions, the amount of absorption of BTEX into TEG determines the amount of BTEX emissions into atmosphere.

Keywords: Natural Gas; Dehydration; PR EOS; TEG; BTEX

Introduction

Natural gas is the cleanest, least expensive and most used form of energy in the world. Gas is an environmentally friendly energy source compared to oil and coal. At present, about 20% of the world's energy is supplied by natural gas. Before the gas transfer to the pipelines, processes are carried out on it. One of the important processes is dehydration (removal of water from the gas). The presence of water in the gas causes corrosion and hydrate formation in transportation pipelines, and diminution of the thermal energy of the gas. Glycols are one of the most important materials for gas dehydration. TEG is used in about 95% of glycol dehydration units due to high boiling point, low vapor pressure and selective solubility [1]. TEG form hydrogen bonds with water and BTEX and similar compounds. BTEX are the aromatic hydrocarbons and they are known as environmental pollutants. Inhalation of large amounts of these substances can lead to drowsiness, headaches, visual impairment, respiratory problems and leukemia [2]. After absorption, these materials enter the atmosphere at the time of the regeneration of TEG and cause environmental problems. The Clean Air Act Amendments of 1990 have increased the regulatory pressure on emissions of BTEX and other volatile organic compounds (VOC) from glycol units. According to the contract, the maximum emission of aromatic compounds can be 25 tons per year (tpy) [3]. Therefore, the thermodynamic study of mixtures containing natural gas, water, TEG and BTEX is essential for modeling and simulation of unit and then estimating of BTEX emission. So much research has been done in this regard. Gupta et al.[4] achieved experimental isobaric vapor-liquid equilibria data for the systems TEG+benzene, TEG+toluene and

benzene+N-methylpyrrolidone. Ng et al.[5] determined vapor liquid equilibria for the system contain of CH₄, benzene, toluene, ethylbenzene, o-xylene in the presence of pure TEG and mixture of TEG and water. Equilibrium data achieved in the range of operating conditions of equipment including contactor, flash-tank, regenerator. They also used an extended functional form of Peng-Robinson for system modeling and they observed good matching between model and experimental data. Yu et al.[6] presented liquid-liquid equilibria for two-component systems containing alkanol-alkane, water-alkane, aceticacid-alkane, water-ester, aniline-alkane and three-component systems containing alkane-methanol-benzene, methanol-toluene-alkane. They also used the PR and SAFT EOS, and the UNIFAC model to predict the behavior of the systems and by drawing the binodal curves they concluded that the SAFT EOS was more adapted to empirical results due to considering the chemical effects of the bonds. Tsuji et al.[7] realized that they were able to remove the azeotrope point from the mixture of water+2-propanol PEG can be used with a specific concentration because PEG reduces the volatility of water and azeotrope disappears. They, for more experiments on this phenomena, examined vapor-liquid equilibria of systems TEG-H₂O, TEG-ethanol, and TEG-2-propanol. Finally, they used a modified version of the PR EOS to correlate the data and found a good fit. Khosravanipour et al. [8] obtained the VLE data for the systems of water+TEG, water+toluene+TEG by the modified Othmer. The Van Laar, NRTL, and Uniquac models were used to correlate the data. The Root Mean Square Deviation (RMSD) for first and second systems was respectively Van Laar and NRTL. Aniya et al. [9] reported experimental isobaric vapor-liquid equilibria data for



the systems TEG+water at several sub-atmospheric pressure and local atmospheric pressure. The experimental data was correlated using NRTL and Wilson activity models and found that Wilson's model correlates data well.

Thermodynamic Model

Gas dehydration by TEG is often conducted in a tray tower, so that the TEG is introduced from above and wet gas from the bottom of the tower. In this work, we used Tomich's technique [10] to simulate the tower. In this method, flash calculations are performed on all trays. To perform equilibrium calculations, the $\Phi - \Phi$ approach used and we obtained the fugacity coefficient Φ , from PR-EOS. The calculations to be continued until the conditions of material and energy balances are satisfied on each tray. More details can be found elsewhere [10]. The fugacity coefficient from the PR EOS can be written as follows:

$$\ln \Phi_i = \frac{b_i}{b} (Z-1) - \ln(Z-B) - \frac{A}{2\sqrt{2}B} \left(\frac{2 \sum_{k=1}^n x_i a_{ik}}{a} - \frac{b_i}{b} \right) \quad (1)$$

$$\times \ln \frac{Z + 2.41B}{Z - 0.414B}$$

Where

$$A = \frac{aP}{R^2 T^2} \quad (2)$$

$$B = \frac{bP}{RT} \quad (3)$$

$$a = \sum_{i=1}^n \sum_{j=1}^n x_i x_j \sqrt{a_i a_j} (1 - k_{ij}) \quad (4)$$

$$b = \sum_{i=1}^n x_i b_i \quad (5)$$

And

$$a_i = ac_i \times \alpha_i \quad (6)$$

$$ac_i = 0.45724 \frac{R^2 T_{ci}^2}{P_{ci}} \quad (7)$$

$$\alpha_i = (1 + m_i (1 - \sqrt{T_{ri}}))^2 \quad (8)$$

$$m_i = 0.37464 + 1.54226 w_i - 0.26992 w_i^2 \quad (9)$$

$$b_i = 0.0778 \frac{RT_{ci}}{P_{ci}} \quad (10)$$

Results and Discussion

The results of simulation with MATLAB are presented in Tables 1 and 2. To validate this results, the results are compared with ProMax® results which were adopted from [11]. In this reference in order to increase the purity of glycol, two methods including the application of a stripping gas and Drizo® cycle have been compared. Schematic views of these processes are shown in Figures 1 and 2. The results are also given in Tables and 2. As may be appreciated, the results from ProMax and Drizo cycle are in a good agreement with the results of MATLAB.

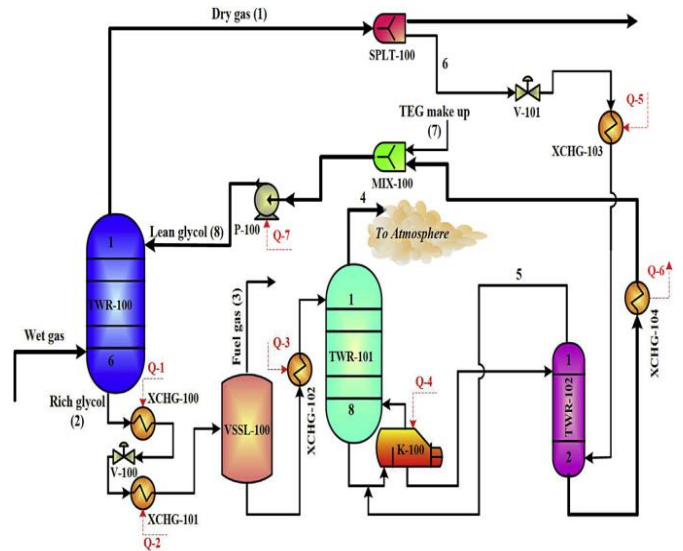


Fig. 1. Schematic diagram of the natural gas dehydration unit using stripping gas injection.

Table1: Weight% of TEG output from absorber:

components	$W_i^{ProMax,stripping_gas}$ [11]	W_i^{MATLAB}
CO2	0.12	0.1214
N2	0.03	0.3702
H2O	5.82	3.0737
Alkanes (C1-C7)	0.83	0.5863
BTEX compounds	3.80	4.2805
TEG	89.40	91.5679

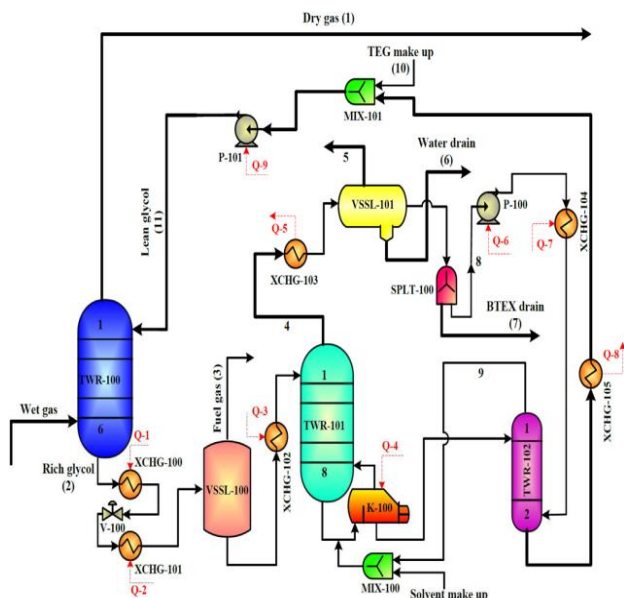


Fig. 2. Schematic diagram of the natural gas dehydration unit using Drizo process.

Table2: Weight% of TEG output from absorber:

components	$W_i^{ProMax, Drizo_cycle}$ [11]	W_i^{MATLAB}
CO ₂	0.11	0.1215
N ₂	0.28	0.3703
H ₂ O	3.01	3.1011
Alcanes (C ₁ -C ₇)	0.59	0.5860
BTEX compounds	4.90	4.2605
TEG	91.11	91.5601

Conclusions

One of the most important problems of natural gas dehydration units is the BTEX releases. Knowledge of equilibrium behavior of components and then simulation of this unit is very important for estimation of the BTEX emissions. In this work, a special method plus PR EOS was used for simulation of the absorption tower of the dehydration unit and then the results were compared with the results of reference 11 and good agreement was seen between the MATLAB results and the ProMax results plus Drizo cycle. This suggests further thermodynamic studies in this field.

References

- [1] C.U. Ikoku "Natural Gas Engineering: A systems approach", Petroleum publishing company: Houston, (1980).
- [2] C.S. Chen, Y.C. Hseu, S.H. Liang, J.Y. Kuo, S.C. Chein "Assessment of genotoxicity of methyl-tert-butyl ether, benzen, toluene, ethylbenzene, and xylene to human lymphocytes using comet assay", *Hazardous Materials*, (2008), 351-356.
- [3] J. Collie, M. Hlavinka "An analysis of BTEX emissions from amine sweetening and glycol dehydration facilities", Laurance Reid Gas Conditioning Conference, Norman, Oklahoma, (1998).
- [4] S.K. Gupta, B.S. Rawat, A.N. Goswami, S.M. Nanoti, R. Krishna "Isobaric vapor liquid equilibria of the systems: benzene-triethylene glycol, toluene-triethylene glycol and benzene-n-methylpyrrolidone", *Fluid phase equilibria*, 16 (1989), 95-102.
- [5] H.J. Ng, C.J. Chen, M. Razzaghi "vapor liquid equilibria of selected aromatic hydrocarbons in TEG", *Fluid phase equilibria*, (1993), 207-214.
- [6] M.L. Yu, Y.P. Chen, "correlation of liquid-liquid phase equilibria using the SAFT equation of state", *Fluid phase equilibria*, (1994), 149-165.
- [7] T. Tsuji, T. Haiki, M. Hongo "vapor liquid equilibria of the Three Binary Systems: Water+Tetraethylene Glycol (TEG), Ethanol+TEG and 2-propanol+TEG", *Ind. Eng. Chem. Res.*, 37, (1998), 1685-1691.
- [8] A. Khosravanipour mostafazadeh, M.R. Rahimpour, A. Shariati "vapor liquid equilibria water+Triethylene Glycol (TEG) and water+TEG+Toluene at 85kPa", *J. Chem. Eng. Data*, 54, (2009), 876-881.
- [9] V. Aniya, A. Singh, D. De, R. Rebby, B. Satyavathi "Experimental isobaric vapor-liquid equilibria at sub-atmospheric and local atmospheric pressure, volumetric properties and molar refractivity from 293.15 to 313.15K of water+triethylene glycol", *Fluid phase equilibria*, 405 (2015), 132-140.
- [10] J.F. Tomich, "A new simulation method for equilibrium stage processes", *AIChE*, 16 (1970), 229-332.
- [11] M. Saidi, M. Parhoudeh, M.R. Rahimpour "mitigation of BTEX emission from gas dehydration unit by application of Drizo process: A case study in Farashband gas processing plant; Iran", *Natural Gas Science and Engineering*, 19 (2014), 32-45.



Prediction of water content of carbon dioxide using the PC-SAFT equation of state

Mina Keshavarz, Farzad Alavi*, Jafar Javanmardi

Department of Chemical Engineering, Shiraz University of Technology, Shiraz, Iran

*alavi@sutech.ac.ir

Abstract : Information about water content in carbon dioxide is of particular importance to the transfer and processing of natural gas. Experimental results for the water content are collected in literatures for the carbon dioxide-rich phase at temperatures ranging from 298.15(K) to 373.15(K) and pressure of 0.69 (MPa) to 7.17(MPa). The goal of this work is to check the ability of the PC-SAFT equation to predict the solubility of water (H₂O) in CO₂. The computer algorithm used for isothermal multiphase flash calculations is based on the minimization of the Gibbs energy along with stability analysis to find the most stable state of the system.

Keywords: water content, PC-SAFT, carbon dioxide.

Introduction

The aim of this work is to test the capabilities of the PR and PC-SAFT EoS for predicting the water content of CO₂. The main reason to select the PR and the PC-SAFT EoS in an attempt to compare their performance in this work is that these equations are very widely used for phase equilibrium calculations of fluid mixtures, including those mixtures encountered in the natural-gas and petroleum industries [1]. Using Gibbs free energy analysis, phase stability analysis can be formulated by calculating the distance between Gibbs free energy surface and the tangent plane, called the tangent plane distance (TPD). Stability analysis is to locate the minimum of the TPD at all compositions. It is further suggested that checking the positivity at stationary points is sufficient. Here, equations for calculation the water content of carbon dioxide were developed using the tangent plane criterion for stability. At a given pressure P and temperature T, a mixture of composition Z is stable if and only if the tangent plane to the Gibbs free energy surface at Z always lies below the Gibbs free energy surface. This can be mathematically [2].

PC-SAFT equation

The perturbed-chain EoS was developed in 2001 by Gross and Sadowski [3] by extending the perturbation theory of Barker and Henderson [4] to a hard-chain reference. The PC-SAFT equation is usually written in terms of the residual Helmholtz free energy. Each term in the equation represents a different microscopic contribution to the total free energy of the fluid. The equation is given by statistical associating fluid theory (PC-SAFT).

$$\tilde{a}^{res} = \tilde{a}^{hc} + \tilde{a}^{disp} + \tilde{a}^{assoc} \quad (1)$$

Where \tilde{a}^{res} is the residual Helmholtz free energy of the system. The superscripts hc, disp, and assoc refer to

a reference hard-chain contribution, a dispersion contribution, and an associating contribution, respectively, where

$$\tilde{a}^{\sim} = \frac{a}{RT} \quad (2)$$

The hard-sphere chain contribution was provided and defined by Gross and Sadowski as

$$\tilde{a}^{hc} = \bar{m}\tilde{a}^{hs} - \sum_{i=1}^{nc} x_i (m_i - 1) \ln g_{ij}^{hs} \quad (3)$$

It depends on the radial pair distribution function for segments in the hard-sphere system (g_{ij}^{hs}), the hard-sphere contribution (\tilde{a}^{hs}), and the mean segment number (\bar{m}), which is a function of m, the number of segment per chain.

The dispersion contribution to the Helmholtz free energy, accounts for van der Waals forces. In this work, we use the dispersion expression defined by Gross and Sadowski

$$\tilde{a}^{disp} = -2\pi\bar{\rho}I_1\bar{m}^2\varepsilon\sigma^3 - \pi\bar{\rho}I_2C_1\bar{m}^2\varepsilon^2\sigma^3 \quad (4)$$

Where the coefficient C_1 depends on the mean segment number (\bar{m}).

For evaluating the VLE of normal fluids, inclusion of \tilde{a}^{hc} and \tilde{a}^{disp} in the PC-SAFT approach is sufficient. Three parameters, the segment number (m), the segment energy parameter (ε/k), and the segment diameter (σ) are required to characterize each compound.

The Helmholtz free energy due to association \tilde{a}^{assoc} is defined as

$$\tilde{a}^{assoc} = \sum_{i=1}^{nc} x_i \left[\sum_{A_i} \left(\ln X^{A_i} - \frac{X^{A_i}}{2} \right) + \frac{1}{2} M_i \right] \quad (5)$$

Where X^{A_i} is the mole fraction of molecules i not bonded at site A , M_i is the number of association sites on each molecule, and \sum_{A_i} represents a sum over all associating sites on each molecule.

The water content experimental and predicted data are reported in Table (2) and plotted in figures (1).

Pure component parameters for PC-SAFT equation of state can be found in Table 1.

The AAD are defined by equation [6]

$$AAD = \sum_{i=1}^n \left| \frac{y_{exp,i} - y_{cal,i}}{y_{exp,i}} \right| \quad (6)$$

Where $y_{cal,i}$ is the calculated water content and $y_{exp,i}$ is the experimental water content in literature.

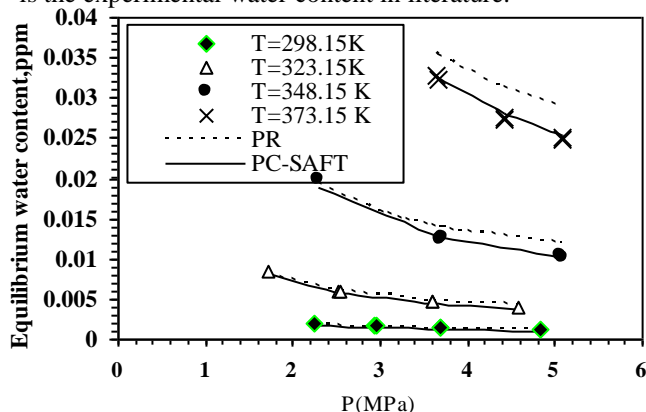


Fig.7: Predicted water content of carbon dioxide using PC-SAFT. Experimental data are from references[6,7]. Kij=0

Table1: Pure component Physical Properties and Characteristic parameters for the PR and PC-SAFT Eos^{3,5}

Compound	Carbon dioxide	Water
Symbol	CO2	H2O
MW(g/mol)	44.010	18.015
T_c (K)	304.2	647.3
P_c (MPa)	73.765	220.483
ω	0.225	0.344
$\frac{\epsilon}{k}$ (K)	169.21	366.51
m	2.0729	1.0656
σ (Å)	2.7852	3.0007

Compound	Carbon dioxide	Water
k^{AB}	----	0.034868
$\frac{\epsilon^{AB}}{k}$	----	2500.7

The set of PC-SAFT parameters for carbon dioxide was taken from the literature and is presented in Table 1

Table2: The average absolute deviation (AAD) obtained in this work

EoS	AAD
PR	133.25
PC-SAFT	39.2137

Results and Discussion

The PC-SAFT and PR equations of state are applied for predicting the water content of CO₂ over an extensive range of temperature and pressure. The resulting pressure water content diagram are shown in Figure 1 for the carbon dioxide. We showed that PC-SAFT EoS is able to reproduce the solubility of water in CO₂ in a wide range of temperatures and pressures. The AAD% among all the experimental and predicted data are 0.133% for PR EoS and 0.039% for PC-SAFT EoS. The agreements between the experimental and predicted data of PC-SAFT equation are satisfactory.

References

- [1] W.A.Fouad, M Yarrison, K.Y.Song, K.R.Cox, W.G.Chapman. "High pressure measurements and molecular modeling of the water content of acid gas containing mixtures", *AIChE*.61(2015) 3038-3052
- [2] Z.Li, A.Firoozabadi. "General strategy for stability testing and phase-split calculation in two and three phases", *SPE*.17 (2012) 1096-1107
- [3] J. Gross, G. Sadowski, "Perturbed-chain SAFT: An equation of state based on a perturbation theory for chain molecules", *Ind. Eng. Chem. Res.* 40 (2001) 1244- 1260
- [4] J.A. Barker, D. Henderson. "Perturbation Theory and Equation of State for Fluids: The Square-Well Potential", *J. Chem. Phys.*47 (1967) 2856-2861.
- [5] J.G.Gross,G. Sadowski, "Application of the perturbed-chain SAFT equation of state to associating systems", *Ind. Eng. Chem. Res.*41(2002)5510-5515

Fabrication of polyethersulfone based nanofiltration membrane modified by TiO_2 nanoparticles

A. Rasouli^a, A. R. Khodabakhshi^{b*}

^aDepartment of Chemistry, Arak University, Arak 38156-8-8349, Iran

^{*}A-khodabakhshi@Arak.ac.ir

stract: In the recent research, $PEs - TiO_2$ are made by the phase-inversion method by the method of casting the solution. In this method, polyvinylpyrrolidone (PVP) was used as a cavity and N-N dimethyl acetamide (DMAC) as a solvent, and from the nanoparticle TiO_2 as an (additive) membrane construct. Water permeability and salt Rejection flow tests, and water content and water contact angles were used to describe the membrane. Water flux showed the tendency to maintain a good stability. By using the atomized nanoparticle TiO_2 to the solution, the salt rejection increased sharply and improved with the use of nanoparticles TiO_2 . the water content increased by applying more than 0.05 wt% of the nanoparticles TiO_2 and then decreasing. The water contact angle also decreased.

Keyword: nanofiltration; Titanium dioxide (TiO_2); phase inversion/casting solution; Water permeability; salt rejection

Introduction

NF is a membrane method that is widely and worldly used in the processes of water treatment, desalination, purification and content ration, pharmaceutical, and so on. [10]

Polymers are materials used to make NFs. Organic polymers due to their affordability, low prices and vast resources have many benefits various polymers such as polysulfone (PS) and polyethersulfone (PES), polyimide (PI) and polyvinylpyrrolidone fluoride (PVDF), polyamide (PA), etc. are used as basic polymers in membrane manufacturing. PES is one of the most important poly-series materials and widely used in the field of separation. [2, 6]

PES membranes have good chemical and thermal resistance and always have an asymmetric structure and are ready for the phase inversion process. But this PES also has some disadvantages. PES is a hydrophobic polymer and is easily susceptible to clogging. [1]

Modification of the PES membrane due to the increased hydrophobicity can be implemented in a number of ways, such as chemical-surface grafting and incremental mixing. [9]

Recently, PES has been modified with some inorganic nanoparticles, such as graphene oxide nanoparticles, silver nanoparticles, and here the nanoparticles TiO_2 are modified, and these reforms increase the hydrophilicity-salt rejection - and improve the anti-fouling properties. Among tiny nanoparticles, Titanium dioxide TiO_2 has the most beneficial properties due to its excellent stability and crystalline structure, and more is used for the preparation of adsorbents, catalysts, sensors and photovoltaic devices. High-fluency, antibacterial properties, availability, low sodium and low prices lead to using of this nanoparticle. [3]

TiO_2 Minimizes system decomposition (fracture and cracking) when combined with a polymer. In this section, the Latin photo is taken exactly. In this research, water contact angle, water content, water

permeability and salt rejection were investigated. Particularly the reaction between TiO_2 and PES was considered.

Materials

N,N-Dimethyl acetamide (DMAC, Mw= 87.12 g/mol, density= g/cm³) polyvinylpyrrolidone (PVP, Mw= 25,000 g/mol) from Merck, Germany, was used as solvent and pore former agent, respectively. Polyethersulfone (PES) provided by BASF (Ultrason E6020P, MW= 58,000 g/mol) was used as basic polymer. Titanium dioxide (TiO_2) nanoparticle (nano powder, <500 nm particle size, Iran) was employed as inorganic filler additives. All other chemicals were supplied by Merck.

Preparation of TiO_2 /PES Nanofiltration membrane

The PES membrane combined with TiO_2 by 0.05 wt% to 1 wt% of nanoparticles TiO_2 , proportional to PES weight, prepared by phase inversion method using DMAC as solvent and deionized water as non-solvent. To make the membrane, a reliable amount of (18 wt%) PES and (1 wt%) PVP was solved in the DMAC solvent by a mechanical stirrer for 2 hours, initially. Then a nanoparticle TiO_2 was dispersed at a concentration of (0, 0.05, 0.1, 0.5, 1) and stirred in a polymer solution for 14 hours. The prepared solution was then kept in steady-state air without stirrer for 24 hours, until the bubbles were completely removed, then pulled onto a glass plate with a clean film, with a 200pm blade. Finally, the glass plate was immersed horizontally immediately in a distilled water container for approximately 24 hours to completely remove it. Then place the prepared membrane between 2 strips of paper for 24 hours to dry. The composition of different polymeric solutions is shown in Table 1.

Table 1: Composition of casting solutions



Sample no.	PES (wt%)	PVP (wt%)	TiO ₂ (wt%)	DMAC (wt%)
1	18	1	0	81
2	18	1	0.05	81
3	18	1	0.1	81
4	18	1	0.5	81
5	18	1	1	81

Result and Discussion

Water Flux and Salt Rejection:

The performance of the prepared membranes was analyzed through a dead-end stirred cell setup (Fig. 1) with effective area of membrane about 17.36 cm². The experiment was performed at fixed pressure (5bar). Permeation flux was calculated by the following equation. [8]

$$J_v = Q/A \cdot t \quad (1)$$

Where J_v (L/m²h), Q (L), A (m²), t (h) are expressed as permeation flux, content of permeated water, membrane area and permeation time, respectively. CaCl₂ aqueous solution (0.835 gr/cm³), was used as feed solution for the determining of rejection. [4]

$$\text{Rejection \%} = 1 - \left(\frac{C_p}{C_f}\right) \times 100 \quad (2)$$

Where C_p and C_f are ionic solution concentration in permeate and feed, respectively.

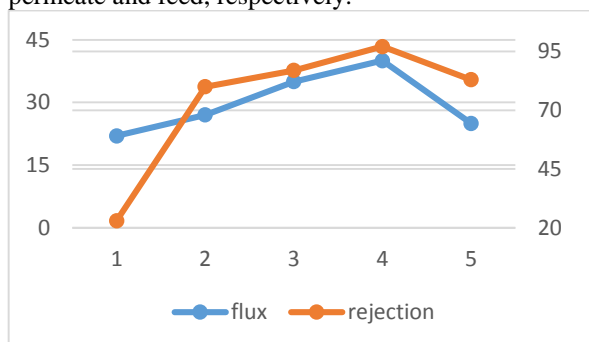


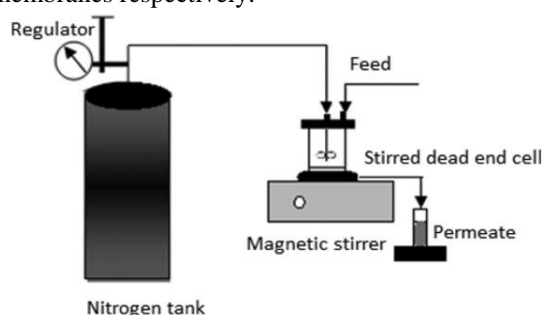
Fig. 1 Effect of TiO₂ nanoparticle concentration on flux and rejection

Water Content:

The water content was measured as the weight difference between the dried membranes and wet ones. The wet membranes were weighed initially and then they were dried in an oven at a fixed temperature (50°C) for 24hr until constant weight was achieved as dry-membrane. The following equation was used for water content calculation. [5]

$$\% \text{ water content} = \left(\frac{W_w - W_d}{W_w}\right) \times 100 \quad (3)$$

Where W_w and W_d are the weight of wet and dried membranes respectively.



Water Contact Angle:

For observing membrane surface hydrophobicity, the water contact angle was measured by using a contact angle measuring instrument. De-ionized water was the probe liquid in this test. To minimize the experimental errors, the contact angle was measured in three different locations of membranes and the average was reported. All experiments were at ambient temperature. [7]

Table1: Water content and water contact angle of fabricated membranes

Sample no.	Water content%	Water Contact Angle%
1	78.3	66
2	80.4	54
3	83.1	61
4	83.4	53
5	83.7	60

Conclusion

The phase inversion method was used to modify the membrane of the PES modification effect were obtained by nanoparticles TiO₂. Membrane properties the most important results are:

1. All modified membranes have less water contact angle than compared to unfilled PES.
2. Add the Nano particle TiO₂ improved salt retention for membranes prepared from 70% for base membranes up to 97.8 for sample no.4
3. Water content: All the modified membranes had higher water content compared to unfilled PES. Water content of bare PES was 78.3, while this amount was 83.4 for membrane with 0.5 wt% of TiO₂. This means modification increased the membranes' hydrophobicity.
4. As mentioned, properties such as hydrophobicity, water contact angle, water content and salt rejection all improved. It can be said that 0.5 wt% of TiO₂ was the optimum concentration of TiO₂ and showed that TiO₂ was a suitable modifier for membrane modification.

Acknowledgement

The authors gratefully acknowledge Arak University for the financial support during this research.

Reference

- [1] C. Barth, M.C. Goncalves, A. T. N. Pires, J. Roeder, B.A. Wolf, "Asymmetric polysulfone and polyethersulfone membranes: effects of thermodynamic conditions during formation on their performance" J. Membr. Sci., 169 (2000), 287–299.
- [2] C. Zhao, J. Xue, F. Ran and S. Sun, "Modification of polyethersulfone membranes – A review of methods", Progress in Materials Science, 58 (2013), 76-150.



- [3] J. F. Li, Z. L. Xu, H. Yang, L. Y. Yu, M. Liu, "Effect of TiO₂ nanoparticles on the surfacemorphology and performance of microporous PES membrane", *Appl. Surf. Sci.*, 255(2009), 4725–4732.
- [4] H. S. Lee, S. J. Im, J. H. Kim, H. J. Kim, J. P. Kim, B. R. Min, "Polyamide thin-film nanofiltration membranes containing TiO₂ nanoparticles" *Desalination*, 219 (2008), 48-56.
- [5] M. Sivakumar, A. K. Mohanasundaram, D. Mohan, K. Balu, R. Rangarajan, "Modification of Cellulose Acetate: Its Characterization and Application as an Ultrafiltration Membrane", *J. Appl. Polym. Sci.*, 67 (1998), 1939-1946.
- [6] N. Ghaemi, S. S. Madaeni, A. Alizadeh, P. Daraei, M. M. S. Badieh, M. Falsafi, V. Vatanpour, "Fabrication and modification of polysulfone nanofiltration membrane using organic acids: Morphology, characterization and performance in removal of xenobiotics", *Sep. Purif. Technol.*, 96 (2012), 214-228.
- [7] N. Giovambattista P. G. Debenedetti, P. J. Rossky, "Effect of Surface Polarity on Water Contact Angle and Interfacial Hydration Structure", *American Chemical Society*, 111 (2007), 9581–9587.
- [8] R. Han, S. Zhang, C. Liu, Y. Wang, X. Jian, "Effect of NaA zeolite particle addition on poly(phthalazinone ether sulfone ketone) composite ultrafiltration (UF) membrane performance", *J. Membr. Sci.*, 345 (2009), 5-12.
- [9] S. Zinadini, A. Zinatizadeh, M. Rahimi, V. Vatanpour, H. Zangeneh, "Preparation of a novel antifouling mixed matrix PES membrane by embedding graphene oxide nanoplates", *J. Membr. Sci.*, 453 (2014), 292–301.
- [10] V. V. Goncharuk, A. A. Kavitskayam M. D. skaya, "Nanofiltration in drinking water supply" *J. Water Chem. Technol.*, 33 (2011), 37-54.

Effect of β -cyclodextrin based polyester on the reduction of DEHP migration in plasticized PVC

Ahmad Raeisi*, Khalil Faghieh

Organic Polymer Chemistry Research Laboratory, Department of Chemistry, Faculty of Science, Arak University, ahmad.raeisi66@gmail.com

Abstract: Efficient reduction of migration of di(2-ethylhexyl) phthalate (DEHP) is challenging because migration of DEHP poses a serious threat to human health and the ecosystems. In the present study, water-insoluble β -cyclodextrin based polyester (β -CDPE) was synthesized by reaction of β -cyclodextrin with sebacoyl chloride (SCI) as a cross-linker using micro-emulsion method. The β -CDPE was incorporated to PVC/DEHP systems (PVC/DCPEs) as a reactive inhibitor to reduce DEHP migration. DEHP migration tests were carried out for the flexible PVC according to the ISO3826:1993(E) test method and the quantity of migrated DEHP were then determined with UV-vis spectroscopy. It was found that the addition of β -CDPE decreases the levels of DEHP migration from the PVC/DCPEs samples by almost 58.61%. Mechanical properties of PVC/DCPEs films including the tensile strength (TS), Young's modulus (YM) and elongation at break (E_B) were investigated. All the mechanical data in PVC/DCPEs samples were slightly improved in the presence of β -CDPE as compare to PVC/DEHP system

Keywords: β -cyclodextrin based polyester, DEHP migration, plasticized PVC

Introduction

Poly(vinyl chloride) (PVC) is one of the effective and most promising polymers which have many good properties such as low heat release profile, low flammability, low combustibility, good chemical resistance, good electrical insulation properties and low cost. Therefore, they can be used widely in electronic devices, medical devices, infant care products, food packaging, toys and construction materials [1].

Usually, PVC materials are mixed with phthalates plasticizers to obtain desired properties such as flexibility, transparency, and durability. Phthalates account for 80% of all plasticizer production while DEHP is responsible for over 50% of worldwide phthalate production. To date DEHP is regarded as the best additive for the plasticization and processability of PVC [2]. Because phthalates are additives and not covalently bound to the plastic matrix of PVC, they are able to migrate from PVC and enter into the environment. The migration of phthalates from PVC not only leads to a progressive loss of its initial properties but, more importantly, also implies potential serious health hazards [3, 4]. The leached phthalates may contaminate their contacted environment and get into the human body directly. So migration of DEHP has aroused wide concern and is exigent to be solved. To address this problem three main strategies have been pursued by researchers, namely the development of safe plasticizers alternative to DEHP, reduction of the leaching aptitude of plasticizers and the substitution of P-PVC with alternative safe polymers [5, 6]. Among the strategies reduction of the leaching aptitude of plasticizers would be easier and more applicable as compare to the other methods. It can be explain that the factory use PVC and DEHP and

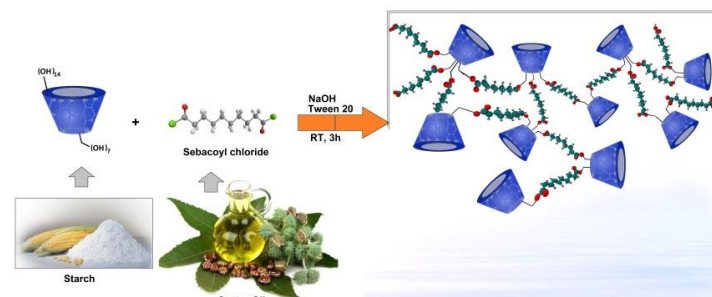
change them is not easy way. If small amount of additive could reduce the migration of DEHP it would be a promising way.

The main purpose of this work was to study the effects of water-insoluble β -cyclodextrin based polyester (β -CDPE) on reduction of DEHP migration in P-PVC and theoretical study to find its mechanism and interaction.

Materials and method

Sebacoyl chloride (SCI), β -cyclodextrin (β -CD) and polyoxyethylene sorbitan monolaurate (Tween 20) were obtained by Sigma-Aldrich Chemical Company. Emulsion grade poly(vinyl chloride), (LG PB1752) and Di-(2-ethylhexyl) phthalate (DEHP) were obtained by LG Chemical Company. Also cyclohexane, chloroform and tetrahydrofuran (THF) were purchased from Fluka Chemical Company.

Water-insoluble β -cyclodextrin based polyester (β -CDPE) was prepared according to the pervious reported articles [7].



Scheme 1. Synthesis route of poly(β -cyclodextrin-ester)

Preparation of plasticized PVC films

Depending on the percentage of the additives (DEHP and β -CDPE) in PVC matrix, appropriate amounts of



PVC were dissolved in 50 ml THF at 40°C for 30 min under mechanical stirring. Then, the solutions were kept under stirring to reach room temperature. In order to prepare formulations with different compositions, the obtained PVC solutions were mixed with various amounts of the additives according to table 1 and stirred for 24h at room temperature. To ensure the successful dispersion of additives in PVC matrix, an ultrasonic treatment for 1h was applied. The resulting mixtures were casted in clean petri dishes and dried at room temperature under ambient pressure for 5 days. At last, these obtained solid films were removed out of the petri dishes and dried in vacuum oven for 3 days. In each film, the total weight of PVC-plasticizer mixtures should be 2g. The compositions of the films are presented in Table 1.

Table 1. The composition of resulting plasticized PVC films

Formulation	PVC (%)	DEHP (%)	β -CDE (%)
PVC/DEHP	70	30	0
PVC/DEHP-CDE ₁	68	30	2
PVC/DEHP-CDE ₂	66	30	4
PVC/DEHP-CDE ₃	64	30	6

Migration Tests

The plasticized PVC films (i.e., PVC/DEHP, PVC/DCPE₁, PVC/DCPE₂, and PVC/DCPE₃) were prepared with dimensions of 20 × 40 × 0.2 (L × H × D mm³).

Migration tests of DEHP were carried out on the prepared plasticized PVC films based on the International Organization for Standardization (ISO) analyse method 3826:1993(E). In all of the migration tests, a mixture of ethanol/water in equal proportions (123.77/50 v/v) was used as extraction solution. The PVC films were washed with distilled water to remove dust and impurities from the surface, and then immersed into 200 mL flasks including 100 mL of the extraction solution. Migration tests were conducted at 37 °C in an oven for 24 h, 48 h, 72h, 96h, 120h and 144h. At the end of the contact time, the flasks were removed from the oven, turned 10 times, and the contents were transferred to a sample cell. In order to evaluate the quantity of DEHP which had migrated from the plasticized PVC films into the extraction solution, the contents of sample cells were analyzed using UV-vis spectroscopy at 275 nm.

Results and Discussion

The mechanical properties of the samples including the tensile strength (Ts), Young's modulus (Ym), and elongation at break (EB) were evaluated from the stress-strain curve (Figure 1) and the data are listed in Table 2. The tensile strength increased from 14.75MPa for PVC/DEHP to 16.7 MPa for

PVC/DCPE₂. The tensile strength (Ts) values of PVC/DCPE₁ and PVC/DCPE₂ and PVC/DCPE₃ were about 15.99, 16.7 and 16.69MPa, respectively which were slightly higher as compared to the PVC/DEHP.

Another important parameter in mechanical properties is Young's modulus. Young's modulus (Ym) values (Table 2), determined for PVC/DCPE₁, PVC/DCPE₂ and PVC/DCPE₃ were about 13.15, 12.91 and 12.54MPa, respectively which were higher as compared to the PVC/DEHP. PVC/DCPE₁ showed the highest Young's modulus reached 13.15 GPa, which is 5.2% higher than PVC/DEHP sample.

Table 2 indicated elongation at break values (E_B) of all the samples that showed increases with increasing β -CDPE loading from 214.96 for the PVC/DEHP to 230.29 for PVC/DCPE₃. The E_B values of PVC/DCPE₁ and PVC/DCPE₂ and PVC/DCPE₃ were about 228.84, 230.29 and 246.00 MPa, respectively which were about 6.4%, 7.13% and 14.43% higher as compared to the PVC/DEHP. This suggested that, the prepared β -CDPE networks had a positive effect as a modifier for increasing of E_B values. These may be due to good dispersion of β -CDPE in the PVC/DEHP matrix allowing the higher elongation at break which increased the polymers chains mobility.

Table 2. Mechanical properties of PVC/DEHP and PVC/DCPEs

Data	PVC/DEHP	PVC/DCPE ₁	PVC/DCPE ₂	PVC/DCPE ₃
T _S (MPa) ^a	14.75	16.09	16.7	16.69
Y _M (GPa) ^b	12.50	13.15	12.91	12.54
E _B (%) ^c	214.9	228.84	230.29	246.27

^aTensile strength, ^bYoung's modulu, ^cElongation at break

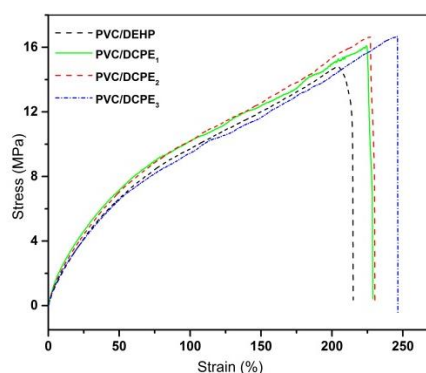


Figure 1. Tensile stress-strain curves for the PVC/DEHP and PVC/DCPEs samples.

Migration tests:

The value of migrated DEHP in the extraction solutions were quantitatively calculated by using a UV-Visible spectroscopy.

Resulting data from migration test show that DEHP migration from P-PVC into extraction solution mostly occurs in the initial times (~96h) and after about 96h of

contact migration rate of DEHP was significantly decreased. This event arises because when DEHP migration of DEHP happens from P-PVC in large amounts, the resulted empty locations in the P-PVC matrix are slowly filled by the extraction solution caused saturated PVC matrix. Further, due to saturating phenomenon, PVC can shrink and become hard and stiff, thus migration rate of DEHP are deeply decreased by progress of time as a result in all the P-PVC samples. After 144 h of contact time, the concentration of migrated DEHP from PVC/DCPEs sheets was lower than that of the PVC/DEHP sheet, as listed in Table 3. Results shows that the loading of β -CDPE into P-PVC matrix resulted to a highly decrease of DEHP migration associated to inclusion complexes and polar interactions between β -CDPE and DEHP molecules. The polar interactions occurred between ester groups of DEHP with hydroxyl and ester functions in β -CDPE were resulted. Also inclusion complexes between the cavities of TCCT dispersed in the P-PVC matrix and the DEHP molecules were formed (Scheme 2). The reduction efficiency of the DEHP migration for PVC/DCPEs can be calculated according to following equation:

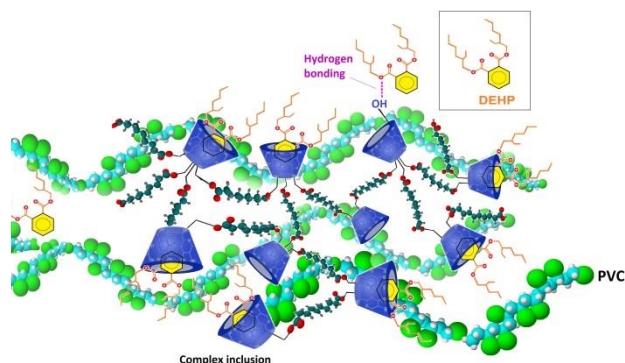
$$\text{Anti - migration efficiency (\%)} = \left(1 - \frac{C_{\text{PVC/DCPEs}}}{C_{\text{PVC/DEHP}}} \right) \times 100$$

$C_{\text{PVC/DCPEs}}$ and $C_{\text{PVC/DEHP}}$ are the concentration of the DEHP migrated to the extraction solution at 144h in the PVC/DCPEs and PVC/DEHP sheets respectively.

The anti-migration efficiency of PVC/DCPE₁, PVC/DCPE₂ and PVC/DCPE₃ were 42.9%, 48.18% and 58.61% respectively. As a result, it was found that the addition of β -CDPE significantly reduces migration of DEHP from flexible PVC.

Table1. The concentration of DEHP into extracted solutions

Sample	Concentration of DEHP (ppm)					
	24 h	48 h	72 h	96 h	120 h	144 h
PVC/DCPE ₃	20.2	39.9	54.02	64.32	66.38	66.67
PVC/DCPE ₂	22.2	42.2	65.79	71.97	81.38	83.47
PVC/DCPE ₁	34.3	55.5	67.85	87.85	91.67	91.97
PVC/DEHP	51.0	91.0	121.0	134.6	154.9	161.0



Scheme 2. Schematic illustration of anti-migration mechanism of DEHP into PVC/DCPEs films

Conclusions

In this work, a new selective and powerful inhibitor to reduce DEHP migration from P-PVC was easily synthesized by crosslinking the renewable cyclic oligosaccharide β -cyclodextrin with Sebacoyl chloride.

The synthesized β -cyclodextrin based polyester has been used in PVC/DEHP system as a reactive nano-inhibitor to reduce DEHP migration. To compare the properties of PVC/DEHP and PVC/DCPEs, mechanical and migration properties were. Mechanical properties studies showed that loading of β -CDPE inhibitor into PVC matrix had a role as a plasticizing agent to improve tensile properties of PVC/DEHP. According to the migration results into PVC/DCPEs samples, it can be concluded that β -CDPE inhibitors are good enough to effectively reduce the DEHP migration into P-PVC samples. As a result, the presence of β -CDPE inhibitor into the PVC/DEHP samples played a key role to improve stability of DEHP in the plasticized PVC matrix and it could provide a new way to prepare safe PVC.

References

- [1] W. Choi, J.W. Chung, S.-Y. Kwak, Unentangled Star-Shape Poly (ϵ -caprolactone) s as Phthalate-Free PVC Plasticizers Designed for Non-Toxicity and Improved Migration Resistance, ACS applied materials & interfaces 6(14) (2014) 11118-11128.
- [2] G. Wypych, Handbook of plasticizers, ChemTec Publishing 2004.
- [3] F. Chiellini, M. Ferri, A. Morelli, L. Dipaola, G. Latini, Perspectives on alternatives to phthalate plasticized poly (vinyl chloride) in medical devices applications, Progress in Polymer Science 38(7) (2013) 1067-1088.
- [4] L. Bernard, B. Décaudin, M. Lecoœur, D. Richard, D. Bourdeaux, R. Cuffe, V. Sautou, A.S. Group, Analytical methods for the determination of DEHP



بیستمین کنفرانس شیمی فیزیک ایران
دانشکده علوم پایه - دانشگاه اراک
۲۱-۲۴ مرداد ۱۳۹۶



20th Iranian Physical Chemistry Conference

plasticizer alternatives present in medical devices: a review, *Talanta* 129 (2014) 39-54.

[5] G. Latini, C. De Felice, A. Del Vecchio, A. Barducci, M. Ferri, F. Chiellini, Di-(2-ethylhexyl) phthalate leakage and color changes in endotracheal tubes after application in high-risk newborns, *Neonatology* 95(4) (2008) 317-323.

[6] W. Kim, I. Choi, Y. Jung, J. Lee, S. Min, C. Yoon, Phthalate levels in nursery schools and related factors, *Environmental science & technology* 47(21) (2013) 12459-12468.

[7] L.D. Wilson, R. Guo, Preparation and sorption studies of polyester microsphere copolymers containing β -Cyclodextrin, *Journal of colloid and*

interface science 387(1) (2012) 250-261.

Mathematic modeling of purification of biodiesel with PES polymeric membrane

S.Koudzari Farahani^{a*}, E.Gandomkar Ghalhari^a, A.R. Moghadassi^a, S.M. Hosseini^a, E.Joudaki^a

^aDepartment of Chemical Engineering, Faculty of Engineering, Arak University, Arak, 38156-8-8349, Iran

*e-mail: s-godzarifarahani@phd.araku.ac.ir

Abstract: One of the new separation methods for purifying biodiesel used in recent years, is the membrane separation process. In the current research, purification of produced biodiesel was carried out using Polymeric Poly Ether Sulfone (PES) based membrane. The prepared PVP membranes was containing 1, 1.5, 2 and 3 wt.% of PVP concentration with 16 wt.% PES. as additive. Reported experimental determining the membrane flux and separation efficiency (glycerol rejection) membrane was modeled by Maxwell Model. The result, including penetration rate, theory graph and experimental data comparison for biodiesel and glycerin, and error graphs have been explained. Results showed that the experimental data's have Compatibility with the model and, membrane with 2 percent PVP has provided more acceptable results.

Keywords: Mathematic model; Maxwell Model; Biodiesel; PES; PVP.

Introduction

Biodiesel is produced from renewable sources such as vegetable oils or animal fats [1-6]. Biodiesel is produced through different techniques such as microemulsion, pyrolysis and transesterification [3,5]. However, the most notable way to produce biodiesel fuel is through transesterification reaction. Transesterification is the reaction of triglycerides and low molecular weight alcohols such as methanol and ethanol in the presence of catalyst. Non-purified biodiesel will contain impurities such as glycerol, unreacted methanol, residual catalyst, bound glycerol (i.e., unreacted triglyceride (TG), diglyceride (DG) and monoglyceride (MG), and perhaps small amounts of soap and water. it is necessary to remove these impurities, because they will strongly affect engine performance [1].

The reported works showed that, the membrane separation process is a suitable alternative for biodiesel purification. In the present article, polymeric membranes were prepared for the separation of free glycerol dispersed in crude biodiesel. The polymeric membranes developed via phase inversion by immersion precipitation technique. In order to improve the properties and performance of the asymmetric poly ether sulfone (PES) membrane as the vital factors to purify the raw FAME by membrane processes [7], different contents of pvp polymer were added to the casting solution. It was attempted to understand the effects of different concentrations of pvp polymer on the structure and morphology of the pes membrane with the aim of glycerol removal from biodiesel. In this study we modeled experimental data from published experimental last works [12] by Maxwell model and comparing ability of permeation matrix membrane.

schematic diagram of an ideal MMM showed in Fig1.

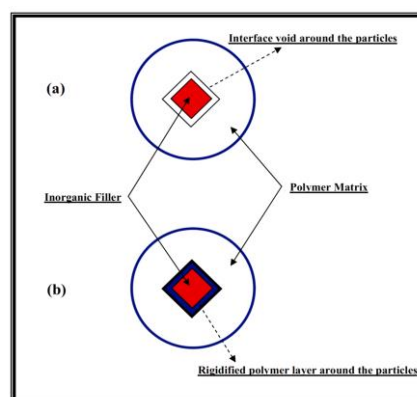


Fig 1. schematic diagram of an ideal MMM [8]

Materials and Method

Poly ether sulfone (PES Ultrason E6020P with MW=58,000 g/mol) and dimethyl acetamide (DMAC) as the solvent, polyvinyl pyrrolidone (PVP) with 25,000 g/mol as the pore former. waste cooking oils, methanol (99.9% purity) and sodium hydroxide (NaOH) for biodiesel production.

Preparation of membranes:

blend PES membrane with PVP polymer were prepared as method reported in last work [12] by using phase inversion induced by immersion precipitation technique. Casting solutions consisting of PES (16wt.%), DMAC and different concentration of PVP polymer (1, 1.5, 2 and 3 wt.%) as an additive and pore former were prepared by mechanical stirrer at 200-400 rpm and room temperature (25°C). After formation of homogeneous solution, the films were

cast by a casting knife with 250 μm thickness. The prepared films were immersed in non-solvent bath for precipitation. The immersion process was carried out at room temperature. The non-solvent was only water. The prepared membranes were washed and stored in water for at least 1 day to completely leach out the residual solvents and additives. As the final stage, the membranes were dried by placing between two sheets of filter paper for 24 h at room temperature.

Maxwell's Model Method:

Maxwell's model is the most famous equation to predict the permeability and electrical conductivity in composite materials [10]. Maxwell presented this equation in 1873 heterogeneous media [8]. Development of proper model(s) for prediction of MMMs different properties, especially those of separation performance, is essential for approaching this goal. On the other hand, having of this model(s) potentially can reduce necessity of the experimental measurements' time and money for preparation and evaluation of different MMMs. Many theoretical and empirical predictive models have been adapted or developed for prediction of MMMs separation performance. the penetrates permeation through MMMs as follows:

$$P_r = P_c \left[\frac{P_d + 2P_c - 2\phi_d(P_c - P_d)}{P_d + 2P_c + \phi_d(P_c - P_d)} \right] \quad (3)$$

$$\phi = \frac{V_{fil}}{V_{fil} + V_{pol}} \quad (4)$$

Where P_r is the ratio of MMM permeability (P_{MMM}) to that of continuous polymer phase (P_c) as (P_{MMM}/P_c), P_d is the incorporated dispersed filler particles, and ϕ_d is the volumetric filler particles loading. Even though many other models have been proposed for predicting the permeability of mixed matrix membranes but Maxwell model has been accepted most widely in the literature [10,11]. In the case of MMMs containing impermeable filler particles ($P_d = 0$), this model is reduced to the following equation [10]:

$$P_r = P_c \left[\frac{1 - \phi_d}{1 + 0.5\phi_d} \right] \quad (5)$$

In the present study, 4 PES membranes separation ability were comparison. In addition, in order to enhance the separation performance of the prepared membranes, different amounts of PVP polymer effect on this separation, were incorporated into the membrane matrices. It is reasonably a novel work to examine the separation properties of PES membranes

for the biodiesel purification. Then we predicted performance of membrane with Maxwell model and calculated AARE%.

Table 1. Experimental data and Theoretical data of the Maxwell model

AARE (%) The Maxwell model		Theoretical P_r		Experimental P_r		sample
P_{gly}	P_{bio}	P_{gly}	P_{bio}	P_{gly}	P_{bio}	
66.66	44.23	0.09	0.58	0.27	1.04	18%PES+1%PVP
52.17	44.03	0.11	0.61	0.23	1.09	18%PES+1.5%PVP
29.41	39.63	0.12	0.67	0.17	1.11	18%PES+2%PVP
58.33	40.74	0.1	0.64	0.24	1.08	18%PES+3%PVP

Results and Discussion

The results of permeability for the biodiesel and glycerol in PES/PVP blend membranes are given in Table 1 at 25 °C and 1 bar. As it is observed that PES/PVP introduced the high permeability.

However, several researchers were reported some increment in permeabilities of MMMs with incorporated impermeable filler particles. They concluded that increasing in the resultant MMMs' permeabilities may be due to disrupting the polymer chain packing density by adding filler and increment of the matrix polymer's free volume, especially in the vicinity of the filler particles. but According to the Maxwell model for impermeable filler particles, MMMs' permeabilities are decreased as filler particles loadings increases (Fig. 3). It seems there is a better explanation for the case and that is the surface flux on the external surface of the incorporated filler particles [8]. The optimization criteria of prediction accuracy of the current developed model is absolute average relative error percentage (AARE %) of predicted MMMs' permeabilities by the following equation [8]:

$$AARE\% = \frac{100}{N} \sum_{i=0}^N \left| \frac{P_i^{cal} - P_i^{exp}}{P_i^{exp}} \right| \quad (6)$$

Fig 2 and 3 shows the comparison between P_r experimental data and P_r computational data of the glycerine and biodiesel component. However it is commonly that there is a difference between theoretical and experimental data. In this clearly, If the difference between theoretical and experimental data is less, it's better. So sample No.3 represents the smallest difference among all samples, it is the best sample.

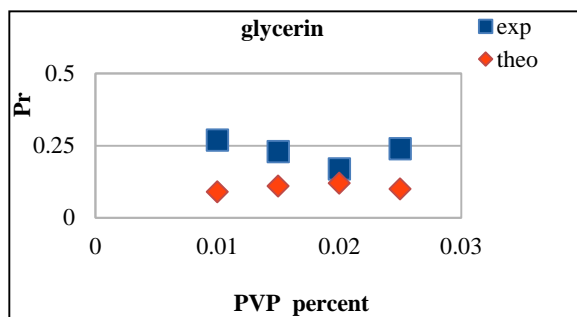


Fig. 2. Comparison of theoretical and experimental data for glycerin

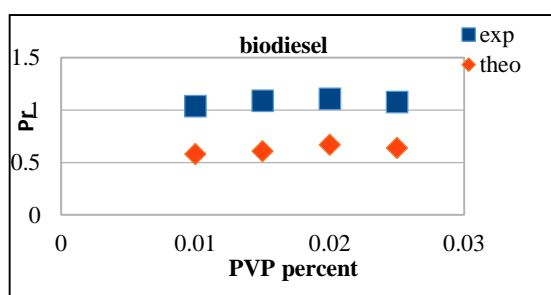


Fig. 3. Comparison of theoretical and experimental data for Biodiesel

The computational error rate between observed data and computational Maxwell model data is shown in Fig 4. The lower the error rate explained the less the difference between the empirical data and the theory, and the predicted model could well cover the experimental data. As it is seen, the membrane No.3 has the most matching.

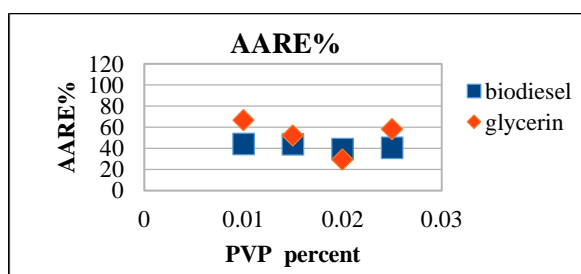


Fig. 4. error rate between theoretical and experimental data

Conclusions:

PES/PVP blend membranes were successfully prepared with different PVP contents to investigate their behaviour in biodiesel/glycerol separation. The results demonstrated that Due to the data obtained in the laboratory and the modelling performed by the software and as it is shown in

diagrams, the model and experimental data has excellent accordance together. As the purpose of this study was to isolate glycerin from biodiesel, the amount of glycerin penetration in the outflow of membranes was minimal. In the case of experimental data and Pr theory, in both cases glycerine and biodiesel of the 2% PVP membrane showed more suitable values. The error rate of this sample was lowest.

References:

- [1] I. M. Atadashi, A. R. Abdul-Aziz, N. M. N. Sulaiman, The effects of water on biodiesel production and refining technologies: A review. *Renewable and Sustainable Energy Reviews*, 16,(2012), 3456- 3470.
- [2] I. M. Atadashi, M. K. Aroua, A. R. Abdul Aziz, N.M.N Sulaiman, High quality biodiesel obtained through membrane technology. *Journal of Membrane Science*, 421-422,(2012), 154-164.
- [3] I. M. Atadashi, M. K. Aroua, A. R. Abdul Aziz, N. M. N. Sulaiman, Membrane biodiesel production and refining technology: A critical review. *Renewable and Sustainable Energy Reviews*, 15,(2011), 5051– 5062.
- [4] M. José Alves, S. M. Nascimento, I. G. Pereira, M. I. Martins, M. R. V. L. Cardoso, M. Reis, Biodiesel purification using micro and ultrafiltration membranes. *Renewable Energy*, 58,(2013), 15-20.
- [5] Yong Wang, X. Wang, Y. Liu, S. Ou, Y. Tan, S. Tang, Refining of biodiesel by ceramic membrane separation. *Fuel Processing Technology*, 90,(2009), 422-427.
- [6] J. Saleh, M. A. Dube, A.Y. Tremblay, Separation of glycerol from FAME using ceramic membranes. *Fuel Processing Technology*, 92,(2011), 1305–1310.
- [7] Roy S, Ntim SA, Mitra S, Sirkar KK. Facile fabrication of superior nanofiltration membranes from interfacially polymerized CNT-polymer composites. *J Membr Sci*;375,(2011), 81-87.
- [8] Aroon .M.A., Ismail .A.F., Matsuura.T, Rahmati.M.M.M., "Performance studies of mixed matrix membranes for gas separation", *Sep&pur. Tech.* 75, (2010), 229–242.
- [9] F. T. Minhas, S. Memon, M. I. Bhangar, N. Iqbal, M. Mujahid, Solvent resistant thin film composite nanofiltration membrane: Characterization and permeation study. *Applied Surface Science*, 282 (2013), 887– 897.
- [10] Z. Rajabi, A.R. Moghadassi, S.M. Hosseini, M. Mohammadi, "Preparation and characterization of PVC based MMM filled with MWCNT for CO₂ separation", *J. of Ind. and Eng. Che.* 19 (2013) 347-352.
- [11] M. Hussain.M.S, "Mixed Matrix Membranes For Gas Separation", 2013.



Evaluation of CO₂/CH₄ Gas Separation in PVA and PVC Mixed Matrix Membrane Permeation Models

E.Gandomkar Ghalhari^{a*}, S.Koudzari Farahani^a, A.R.Moghdassi^a, E.Joudaki^a, S.M. hosseini^a

^aDepartment of Chemical Engineering, Faculty of Engineering, Arak University, Arak, 38156-8-8349, Iran

*e-mail: e-gandomkar@phd.araku.ac.ir

Abstract: The purpose of this paper is to examine, predict and compare gas transport behavior of mixed matrix membranes (MMMs) combined with porous particles with different polymeric matrix. In this regard, composite flat sheet membranes are prepared from different amounts of poly(Polyvinyl alcohol) (PVA) and poly vinyl chloride(PVC) Gas permeability were studied for the prepared membranes. Then these membranes modelled was performed by Maxwell, and the results of Maxwell model with the experimental data were compared and the percentage of error was shown. Studied results showed that despite higher permeability emissions of carbon dioxide with PVC membrane grid with carbon nanotubes in the membrane of PVA but Maxwell model for PVA membranes without any additive as a polymeric membrane has provided more acceptable results.

Keywords: Mathematic modeling; Maxwell Model; mixed matrix membrane; PVA; CO₂/CH₄ separation; PVC.

Introduction

Gas separation is an important unit operation employed widely throughout the chemical industries[1-4]. Typical applications are O₂/N₂ separation, H₂ recovery from process gas streams, natural gas sweetening and drying and hydrocarbon recovery from off-gas[5]. These processes have traditionally been carried out using absorption, adsorption, cryogenic and other techniques. [1,4,6,7] Membranes are barriers that permit the preferential transport of certain penetrants, thereby enabling the separation of mixtures of such components. Recently, gas separation membrane technology has proved as a major gas separation technique over the traditional gas separation procedures like cryogenic distillation and pressure swing adsorption. Therefore researches on this membrane have attracted much interest and some kinds of material have been utilized for these membranes in the last two decades [8–12]. Among them, polymeric membranes have received much attention and have been used in a wide range of industrial applications [13] such as CO₂/N₂ and CO₂/CH₄ gas separation processes. These membranes offer many advantages such as low energy costs, environmental endurance, simplicity of operations and good thermal and mechanical properties [14,15]. Also efforts on the novel membranes preparation with better gas separation performance (combining high permeability with high selectivity) is continuing [10,16]. Despite of polymeric membranes advantages, there is significant limitation in the development of newer gas separation membranes which is the important Robeson trade-off between perm-selectivity and permeability [16]. One of the best methods to overcome this restriction is utilizing mixed matrix membranes which combine the polymers process ability with greater gas separation

properties of inorganic materials [17]. Several factors can affect the structure and consequently gas permeation properties through the polymer/inorganic MMMs including: (1) polymer and inorganic intrinsic properties, (2) morphology of MMMs, e.g. shape and size dispersion of the filler particles through polymer matrix, (3) interfacial defects such as void formation and the polymer matrix's chains rigidification around the filler particles (if any), and (4) MMMs preparation procedure. Knowing the transport properties of MMMs constituents is basic important data for their proper selection and true structure design to improve their separation performance and consequently increment of the MMMs competition for current and potential membrane gas separation. In this study we modeled experimental data from published experimental works by Maxwell model and comparing ability of permeation matrix membrane [18,19]. schematic diagram of an ideal MMM showed in Fig1.

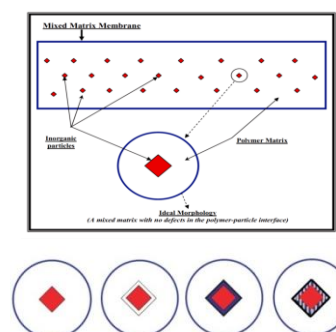


Fig 1. schematic diagram of an ideal MMM [20].

Materials and method

Maxwell's model is the most famous equation to predict the permeability and electrical conductivity in composite materials [19]. Maxwell presented this



equation in 1873 heterogeneous media [20]. Development of proper model(s) for prediction of MMMs different properties, especially those of separation performance, is essential for approaching this goal. On the other hand, having of this model(s) potentially can reduce necessity of the experimental measurements' time and money for preparation and evaluation of different MMMs. Many theoretical and empirical predictive models have been adapted or developed for prediction of MMMs separation performance. the penetrates permeation through MMMs as follows:

$$P_r = P_c \left[\frac{P_d + 2P_c - 2\phi_d(P_c - P_d)}{P_d + 2P_c + \phi_d(P_c - P_d)} \right] \quad (1)$$

$$\phi = \frac{V_{fill}}{V_{fill} + V_{pol}} \quad (2)$$

Where P_r is the ratio of MMM permeability (P_{MMM}) to that of continuous polymer phase (P_c) as (P_{MMM}/P_c), P_d is the incorporated dispersed filler particles, and ϕ_d is the volumetric filler particles loading. Even though many other models have been proposed for predicting the permeability of mixed matrix membranes but Maxwell model has been accepted most widely in the literature [19,21]. In the case of MMMs containing impermeable filler particles ($P_d = 0$), this model is reduced to the following equation [19]:

$$P_r = P_c \left[\frac{1 - \phi_d}{1 + 0.5\phi_d} \right] \quad (3)$$

In the present study, two mixed matrix nanocomposite membranes were comparison ability PVA/ GA /DEA , PVC/ MWCNTs for CO_2/CH_4 separation. In addition, in order to enhance the separation performance of the prepared membranes, different amounts of nano particle and different matrix to compare effect of matrix on this separation, were incorporated into the membrane matrices. It is reasonably a novel work to examine the gas separation properties of mixed matrix membranes for the CO_2 separation from natural gas (CH_4). Then we predicted performance of membrane with Maxwell model and calculated AARE%

Results and Discussion

As it shown Fig.2, Presented Mixed matrix membranes were successfully prepared with different PVA and PVC contents to investigate their behavior in CO_2/CH_4 separation. The results demonstrated that PVA matrix in the membranes caused a significant increase in the overall gas permeability due to chemical structure. According to the Maxwell model for impermeable filler particles, MMMs' permeabilities are decreased as filler particles loadings increases (Fig. 3). However, several researchers were reported some increment in permeabilities of MMMs with incorporated impermeable filler particles . They concluded that increasing in the resultant MMMs'

permeabilities may be due to disrupting the polymer chain packing density by adding filler and increment of the matrix polymer's free volume, especially in the vicinity of the filler particles. It seems there is a better explanation for the case and that is the surface flux on the external surface of the incorporated filler particles [20]. The optimization criteria of prediction accuracy of the current developed model is absolute average relative error percentage (AARE %) of predicted MMMs' permeabilities by the following equation [18]:

$$AARE\% = \frac{100}{N} \sum_{i=0}^N \left| \frac{P_i^{cal} - P_i^{exp}}{P_i^{exp}} \right| \quad (4)$$

Table 1 showed the Summary of the estimated filler particles' permeabilities and AAREs of MMMs' permeabilities prediction using different predictive models.

AARE (%) The Maxwell model		Theoretical Pr		Experimental Pr		Membrane
PCO ₂	PCH ₄	PCO ₂	PCH ₄	PCO ₂	PCH ₄	
55.10	55.10	0.72	0.01	1.62	0.04	PVA MMM
72.05	72.91	0.98	0.02	3.52	0.08	PVA MMM1
76.81	73.19	1.05	0.02	4.54	0.09	PVA MMM2
71.05	68.00	1.09	0.02	3.77	0.08	PVA MMM3
56.05	64.74	1.13	0.02	2.58	0.08	PVA MMM4
44.29	52.25	1.16	0.02	2.09	0.06	PVA MMM5
55.10	55.10	0.72	0.01	1.62	0.04	PVC MMM9

Table1: Permeability values for a)PVA and b)PVC MMMs.

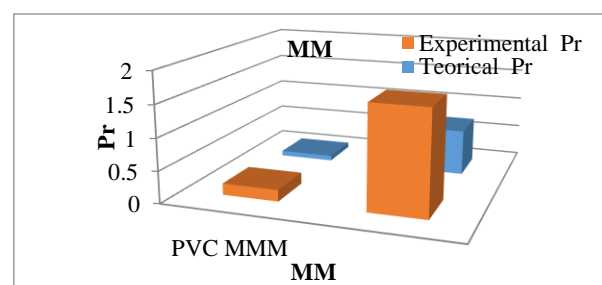


Fig.2: the polymeric matrix membranes' CO_2 permeabilities prediction using the Maxwell model.

Conclusions

Presented Mixed matrix membranes were successfully prepared with different PVA and PVC contents to investigate their behavior in CO_2/CH_4 separation. The results demonstrated that PVA matrix in the membranes caused a significant increase in the overall gas Permeability due to chemical structure. also it is seen a significant increase in the new creation of voids

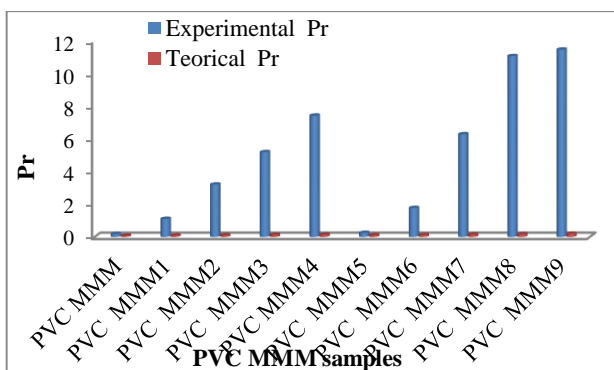
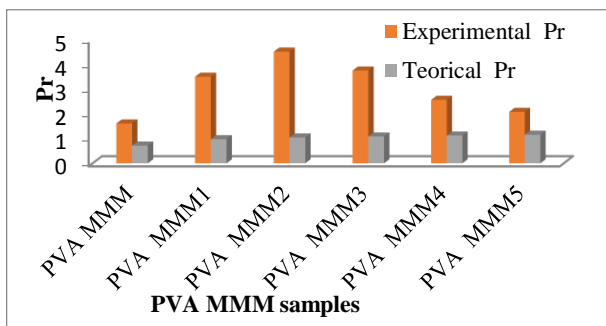


Fig.3 Effect of volumetric impermeable (e.g. Pd= 0) filler particles loadings on the MMMs' permeabilities prediction using the Maxwell model.

especially adjacent to the polymer-particle interface [18] but nano additive had a sharp improvement of adsorption ability and capacity the calculated AAREs for MMMs' permeability's were reduced considerably. The results support the aim of the current study that the incorporated nonporous filler particles are not really impermeable. Absolutely more accurate approach should be developed to provide better estimation of the

AARE (%) The Maxwell model		Theoretical Pr		Experimental Pr		Membrane
PCO ₂	PCH ₄	PCO ₂	PCH ₄	PCO ₂	PCH ₄	
55.10	55.10	0.08	۰.۰۸	0.18	0.00	PVC MMM
92.06	93.01	0.09	۰.۰۹	1.11	0.03	PVC MMM1
96.63	97.35	0.11	۰.۱۱	3.22	0.09	PVC MMM2
97.60	98.15	0.13	۰.۱۳	5.21	0.15	PVC MMM3
98.10	98.35	0.14	۰.۱۴	7.45	0.19	PVC MMM4
55.10	55.10	0.11	۰.۱۱	0.25	0.01	PVC MMM5
93.12	88.48	0.12	۰.۱۲	1.78	0.03	PVC MMM6
97.61	95.98	0.15	۰.۱۵	6.31	0.12	PVC MMM7
98.43	97.35	0.17	۰.۱۷	11.08	0.21	PVC MMM8
98.29	97.14	0.20	۰.۲۰	11.48	0.22	PVC MMM9

so-called impermeable filler particle.

References

- [1] N. A. Downie, "Industrial Gases London", Blackie Academic & Professional 1997.
- [2] Y. Y. B. Freeman, "Membrane Gas Separation", W. S. John Wiley & Sons Ltd, 2010.
- [3] S. Kulprathipanja, "Zeolites in Industrial Separation and Catalysis", WILEY-VCH Verlag GmbH & Co., 2010.
- [4] M. Mulder, "Basic Principles of Membrane Technology", Kluwer Academic Pub., 1996.
- [5] P. Bernardo, et al., "Membrane Gas Separation: A Review/State of the Art. In" *Industrial & Engineering Chemistry Research*, 48 (2009), No. 10, pp. 4638-4663.
- [6] F. I. Khan and A. Kr. Ghoshal, "Removal of Volatile Organic Compounds from polluted air. In" *J. of Loss Preven. in the Pro. Ind.*, 13 (2000), No. 6, pp. 527-545.
- [7] K. K. S. W.S.W Ho, "Membrane Handbook", New York: Van Nostrand Reinhold, 1992.
- [8] A.F. Ismail, W. Lorna, "Suppression of plasticization in polysulfone membranes for gas separations by heat-treatment technique" *Sep. Puri. Tech.* 30 (2003) 37-46.
- [9] M. Anson, J. Marchese, et al., "ABS copolymer-activated carbon mixed matrix membranes for CO₂/CH₄ separation", *J. of Mem.Sci* 243 (2004) 19-28.
- [10] S.H. Huang, C.C. Hu, K.R. Lee, et al., "Gas separation properties of aromatic poly(amide-imide) membranes", *European Polymer Journal* 42 (2006) 140-148.
- [11] R. Xing, W.S.W. Ho, "Synthesis and characterization of crosslinked Polyvinylalcohol/ polyethyleneglycol blend membranes for CO₂/CH₄ separation" *J. of the Taiwan Institute of Che. Engineers* 40 (2009) 654-662.
- [12] S.K. Sen, S. Banerjee, "Gas transport properties of fluorinated PEI films containing phthalimidine moiety in the main chain" *J. of Mem.Sci* 350 (2010) 53-61.
- [13] W. Albrecht, K. Kneifel, T. Weigel, et al., "Preparation of highly asymmetric hollow fiber membranes from PEI by a modified dry-wet phase inversion technique using a triple spinneret" *J. of Mem.Sci.* 262 (2005) 69-80.

Preparation of polyethersulfone membrane coated by a nanocomposite structure

F. Heidary*

Department of Chemistry, Faculty of Science, Arak University, Arak 38156-8-8349, Iran

*F-heidary@araku.ac.ir

Abstract: Nanocomposite membranes were prepared by coating a porous Polyethersulfone (PES) support containing 8-hydroxyquinoline (as complexing agent) with poly (vinyl alcohol) (PVA)/Fe₃O₄ nanocomposite solution. The prepared membranes were applied for removal of Zn(II) ions from water. The effect of membrane modification on the membranes performance for removal of metal ions was investigated. The results indicated that presence of ligand and Fe₃O₄ nanoparticles in the membrane structure enhanced the ions rejection. The prepared samples were characterized by scanning electron microscopy. SEM images indicated appropriate distribution of nanoparticles in the polymeric matrix.

Keywords: Nanocomposites; Magnetite nanoparticles; Polyethersulfone

Introduction

Various techniques such as ion-exchange, evaporation, chemical precipitation, chemical oxidation or reduction, flocculation, electrochemical treatment, membrane filtration and reverse osmosis have been used to remove heavy metal ions from industrial wastewater and urban water supplies [1-3].

Membrane adsorption is an applicable technique for removal of metal ions from aqueous solutions. Compared to the conventional methods for separation of metal ions e.g. ion exchange, chemical precipitation and adsorption columns, adsorptive membranes present several advantages such as higher flow rate, excellent removal efficiency, lower pressure drop, reusability, faster kinetic and facility of scale up [4-6]. A suitable adsorbent should offer a stable structure with abundant binding sites which is appropriate for adsorption of metal ions. The use of nanomaterials in the wastewater treatment has attracted significant attention due to their numerous active groups and large specific surface area. However, the instability in separation of nanomaterials from water and their regeneration limited their applications. Nanomaterials can be loaded on porous materials as supports to resolve mentioned problems. Also, these supports themselves might be employed as the additional adsorbents in enhancing the adsorption. Use of the nanostructure in membrane (as a porous medium) is alternative techniques to improve the removal efficiency of metal ions via polymeric membranes. However, metal oxides are classified as one of the desired agents for metal ions removal from aqueous systems due to their large surface area, suitable adsorption capacity and high activity.

Magnetite is a type of the most durable iron oxide under ambient conditions and can be prepared by a facile

procedure and easy to be incorporated with other components because of its surface hydroxyl groups [7]. Moreover, magnetite has attracted great interest due to its unique adsorption, excellent reactivity, ion exchange capacity, environmental safety and low cost. However, recycling of magnetite nanoparticles is difficult after using. Therefore, improvement of recycle abilities and prevention from agglomeration are important for the use of magnetite nanoparticles. In order to overcome the problem and to modify adsorption properties of the nanoparticles, they are typically dispersed on a high surface area carrier. In addition, introducing of additives such as ligands is an efficient method to provide high performance membranes. Polyethersulfone (PES) is a high-Tg polymer, which has suitable thermal, mechanical and chemical resistances. This is widely used in preparing asymmetric membranes with various pore sizes in the active layer.

In current work, PES/PVA/Fe₃O₄ nanocomposite membrane containing a chelating agent was prepared using magnetite nanoparticles to obtain a new mixed matrix membrane with the suitable affinity for Zn(II) ions. During this experiment, metal ions solutions were employed for membranes investigation.

Materials and method

Polyethersulfone (PES, Ultrason E 6020P, Mw= 58,000 g/mol and glass transition temperature $T_g = 225$ °C) and dimethylacetamide (DMAC) were obtained from BASF, Germany. The solvent (DMAC) was used without any purification.

Polyvinylidene fluoride and polyvinylpyrrolidone (PVP) with 25,000 g/mol molecular weight as pore former were purchased from Alfa-Aesar and Merck, respectively. Poly (vinylalcohol) (PVA, Mw = 72000 g/mol), FeCl₂·4H₂O and NaOH were obtained from Merck Company. Distilled water was used



throughout this study. $\text{Zn}(\text{NO}_3)_2 \cdot 6\text{H}_2\text{O}$ and 8-hydroxyquinoline were obtained from Sigma–Aldrich. PES flat membranes were prepared by phase inversion via immersion precipitation. Dope solution was prepared by dissolving PES polymer in DMAC and adding PVP as pore former at around 25 °C with mechanical stirring at 200 rpm for 4 h. The homogeneous polymer solution was kept to remove bubbles. The concentration of membrane matrix (PES) and pore former (PVP) were selected as 16 and 2wt. %, respectively. Then, a certain amount of the complexing agent (8-HQ) was added to the solution. The solution was cast using a home-made casting knife with 150 μm thickness on glass plate substrate. This was immediately immersed in the non-solvent bath at room temperature without any evaporation. The fabricated membrane was then further treated with prepared nanocomposite solution of PVA/ Fe_3O_4 nanoparticles.

Results and Discussion

The performances of virgin and modified membranes were examined using a dead-end filtration cell under 3 bars at room temperature. Experimental setup composed of nitrogen gas cylinder, pressure regulator, membrane stirred cell and permeate tube. The detail of the experimental setup is shown in Fig. 1. Each membrane sample with an area of 12.56 cm^2 was located into the cell, and connected to a nitrogen tank via pressure tubing. The feed solution was stirred at 400 rpm using a magnetic stirrer to minimize concentration polarization. The permeated product was collected in a beaker and weighed using a balance. The rejections of the ions were evaluated by measuring the ions concentration in the feed and permeate using atomic absorption. Fig. 2 illustrates the SEM cross-sections of PES membranes after addition of PVP. As can be seen, after addition of PVP the formation of pores in the membrane's structure is clearly obvious. All the membranes showed a characteristic morphology of asymmetric membrane, consisting of a dense skin-layer and a porous sub-layer with finger-like structure.

Fig. 3 shows the influence of the ligand addition and membrane coating with nanocomposite solutions on removal of Zn(II) ions from aqueous single metal solutions.

Unmodified PES/PVDF membrane offered negligible capacity for rejection of the ions. The ion rejection was enhanced by addition of 8-HQ to the casting solution. This is due to the improvement in the quantity of reactive sites for adsorption of metal ions.

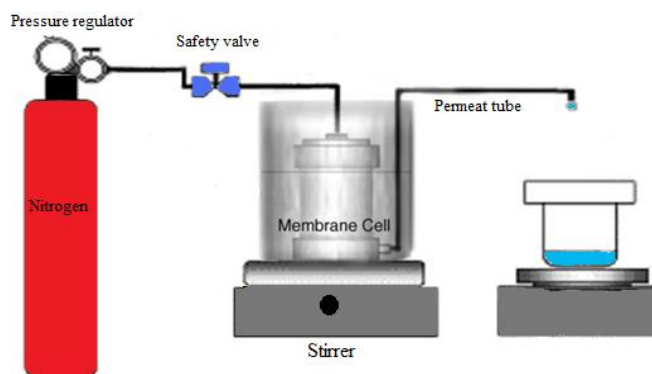


Fig.8: Dead-end filtration system



Fig.2: SEM cross-sections of PES/PVDF membranes

Results also show that coating of membranes with PVA containing Fe_3O_4 nanoparticles can affect the membrane performance. Whereas the membranes act as an adsorptive barrier, the increase of available active sites and higher surface area enhances the ions removal efficiency. In prepared nanocomposite membranes, higher amount of magnetite nanoparticles resulted in enhancement of ions rejection which supports this fact that unmodified membranes have weaker adsorption ability. Introduction of more reactive sites on the membrane surface (magnetite nanoparticles) increases the interactions between the ions and reactive sites leading to enhancement of adsorption and ions rejection.

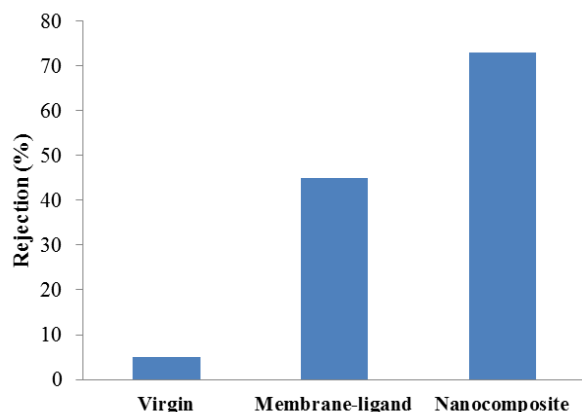


Fig.2: The metal ions rejection of prepared membranes

Isotherms, thermodynamics and kinetics, *Sep. Purif. Technol.*, 94 (2012) 1–8.

[7] F. Wang, D. Liu, P. Zheng, X. Ma Synthesis of rectorite/Fe₃O₄-CTAB composite for the removal of nitrate and phosphate from water, *J. Ind. Eng. Chem.*, 41 (2016) 165–174.

Conclusions

Novel PES nanocomposite membranes with suitable metal ions separation properties were developed using coating procedure. Compared to virgin membrane, the coating of membranes with PVA/Fe₃O₄ nanocomposite solution led to significantly improvement in membrane performance for removal of metal ions. Also, the results demonstrated that surface modification has enhanced the surface hydrophilicity of membranes.

References

- [1] I.H. Alsohaimi, S.M. Wabaidur, M. Kumar, M.A. Khan, Z.A. Allothman, M.A. Abdalla Synthesis, characterization of PMDA/TMSPEDA hybrid nanocomposite and its applications as an adsorbent for the removal of bivalent heavy metals ions, *Chem. Eng. J.*, 270 (2015) 9–21.
- [2] S.S. Madaeni, F. Heidary “Improving separation capability of regenerated cellulose ultrafiltration membrane by surface modification”, *Appl. Surf. Sci.*, 257 (2011) 4870–4876.
- [3] Y. Yurekli Removal of Heavy Metals in Wastewater by Using Zeolite Nano-Particles Impregnated Polysulfone Membranes, *J. Hazard. Mater.*, 309 (2016) 53–64.
- [4] A. Ghaee, M. Shariaty-Niassar Effects of chitosan membrane morphology on copper ion adsorption, *Chem. Eng. J.*, 165 (2010) 46–55.
- [5] R. S. Vieira, E. Guibal, E. A. Silva, M. M. Beppu Adsorption and desorption of binary mixtures of copper and mercury ions on natural and crosslinked chitosan membranes *Adsorption*, 13 (2007) 603–611.
- [6] E. Salehi, S.S. Madaeni, F. Heidary Dynamic adsorption of Ni(II) and Cd(II) ions from water using 8-hydroxyquinoline ligand immobilized PVDF membrane:



بیستمین کنفرانس شیمی فیزیک ایران
دانشکده علوم پایه - دانشگاه اراک
۳۱-۲۹ مرداد ۱۳۹۶



20th Iranian Physical Chemistry Conference

شیمی محاسباتی

Computational chemistry

A DFT study of cooperativity effect on stability and NLO response of bifurcated lithium bonds

F. Rezaie, M. Solimannejad*

Department of Chemistry, Faculty of Science, Arak University, Arak, 38156-8-8349, Iran
m-solimannejad@araku.ac.ir

Abstract Density functional calculations at the CAM-B3LYP/6-311++G(d,p) level are performed to analyze intermolecular interactions and nonlinear optical properties in complexes connected via bifurcated lithium bonds. Linear clusters of $(\text{LiN}(\text{CHO})_2)_{1-5}$ with bifurcated lithium bonds (BLB) are selected as a model system in present work. Stabilization energies of these clusters are in the range of -1.95 to -9.682 eV. Cooperativity effects based on energy are computed for these selected complexes. Also, in these clusters, first hyperpolarizability increased by cluster size and its values were obtained in ranges of 606.1-1327.443 a.u. To determine the cooperativity effect on electric properties, effect of monomer addition to clusters was computed.

Keywords: *Bifurcated lithium bond; Cooperativity; DFT; NLO*

Introduction

Noncovalent interactions play a vital role in various fields of chemistry and biochemistry. They are responsible for stabilizing many important molecules, for example, DNA and proteins [1]. One groups of noncovalent interactions including lithium bonds are interesting intermolecular interactions which has investigated lately [2,3]. Optical properties of molecular aggregations have been the focus of recent experimental as well as theoretical investigations, due to their importance for many technological applications. Beginning of the field of nonlinear optics (NLO) is often taken to be the detection of second-harmonic generation by Franken et al. in 1961 [4]. Recently, researches have shown that having an additional electron in atoms can create NLO properties [5,6].

Cooperativity effects of diformamide, fluoroacetylene, urea and $\text{HCHO}\cdots(\text{HF})_{1-9}$ clusters on the NLO properties were studied previously [7,8]. Also, effect of cluster size on NLO properties was studied in two types of lithium bonded chains of $(\text{NCLi})_{1-8}$ and $(\text{NC}_3\text{Li})_{1-8}$ [9]. In this present work, we have chosen $(\text{LiN}(\text{CHO})_2)_{1-5}$ linear clusters and an attempt has been made to evaluate effect of cooperativity on their stability and NLO response. The present results might be of interest when investigating the transition between monomers and solid state properties.

Materials and method

All calculations were carried out by Gaussian 09 package [10]. All molecular clusters were fully optimized at the CAM-B3LYP/6-311++G(d,p) level [11]. Stabilization energy was computed for all clusters from this equation:

$$\Delta E_N = E_{\text{cluster}} - N E_{\text{monomer}} \quad (1)$$

where E_{cluster} and E_{monomer} represent energies of complex and isolated monomer from optimized structures and N is number of monomers that connected together to form cluster.

The counterpoise computations were implemented for correction of stabilization energy [12]. The cooperative effect (CE_n) was obtained for energies of the clusters using the following equations [13]:

$$\text{CE}_n = \frac{\Delta E_{\text{cluster}} - (n-1) \Delta E_{\text{dimer}}}{n-2} \quad (2)$$

where $\Delta E_{\text{cluster}}$ is defined as the stabilization energy of clusters, while ΔE_{dimer} is the stabilization energy of the dimer (taken as a reference) and n is the number of monomers in the cluster. The above equation is divided by $n-2$, to take into account additional fragments because the dimer taken as reference.

In the presence of electric field [14], by the finite-field (FF) approach [15,16] under an electric field magnitude of 0.0001 a.u. the z-component of μ , α and β were computed. Also, effect of adding one monomer to studied linear clusters was determined from equation that given below:

$$P_{1-2\dots N}^{\text{coop}} = \Delta P_{1-2\dots N} - \Delta P_{1-2} \quad (3)$$

when $P_{1-2\dots N}^{\text{coop}}$ is cooperative effects of lithium bond between molecule 1 and 2 for electric property, $\Delta P_{1-2\dots N}$ is namely as interaction-induced property of 1-2...N complex and ΔP_{12} is interaction-induced property of dimer 12.

$\Delta P_{1-2\dots N}$ calculated from property of cluster ($P_{1-2\dots N}$) minus properties of monomer frozen in related cluster (monomer 1) and subsystem 2...N:

$$\Delta P_{1-2\dots N} = P_{1-2\dots N} - P_1 - P_{2\dots N} \quad (4)$$

Results and Discussion

The optimized structure and BLBs distances of the $(\text{LiN}(\text{CHO})_2)_5$ cluster, at the CAM-B3LYP/6-311++G(d,p) level of theory, are presented in Fig. 1 and interaction distances of other clusters are classified in Table 1. All of the $(\text{LiN}(\text{CHO})_2)_n$ clusters corresponds to

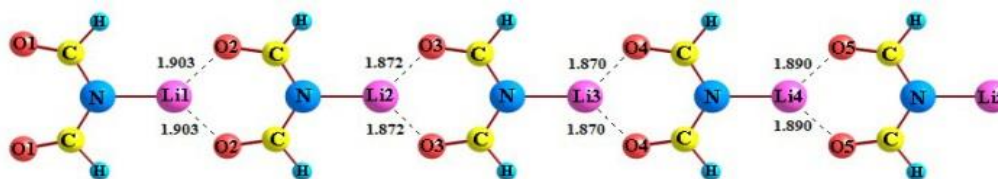


Fig. 1: Optimized $(\text{LiN}(\text{CHO})_2)_5$ cluster at the CAM-B3LYP/6-311++G(d,P) level of theory (all intermolecular distances are in Å).

Table 1: Binding distances (r , Å) in the $(\text{LiN}(\text{CHO})_2)_n$ clusters.

N	R_{12}	R_{23}	R_{34}	R_{45}	R_{avr}
2	1.933				1.933
3	1.912	1.902			1.907
4	1.906	1.879	1.894		1.893
5	1.903	1.872	1.870	1.890	1.883

a minimum on the potential surface with C_{2v} symmetry.

One important initial finding is the slight contraction of 11 mÅ in $r_{\text{Li}\cdots\text{O}}$ binding distances from the dimer to trimer. Non-additive effects also lead to small Li \cdots O contraction for the different clusters. This situation has been reported in linear lithium-bonded clusters of LiCN and LiNC, previously [2]. The observed contraction with the cluster size in the $r_{\text{Li}\cdots\text{O}}$ binding distances of studied clusters can be interpreted as signature of cooperative effects in these systems.

The interaction energy provides a measure of the strength of the BLBs between $\text{LiN}(\text{CHO})_2$ monomers in the $(\text{LiN}(\text{CHO})_2)_{2-5}$ clusters. Table 2 shows the interaction energies of the studied clusters.

Table 2: Calculated stabilization energies (corrected with BSSE), cooperative effect (CE_n) on eV units.

N	ΔE_N	BSSE	$\Delta E_N + \text{BSSE}$	CE_n
2	-1.993	0.044	-1.950	-
3	-4.478	0.088	-4.391	-0.491
4	-7.132	0.132	-7.000	-0.576
5	-9.858	0.176	-9.682	-0.628

The magnitudes of the interaction energies increase with increasing cluster size. Considering the results, it can be seen that $(\text{LiN}(\text{CHO})_2)_3$ is bound about 2.485 eV more strongly than $(\text{LiN}(\text{CHO})_2)_2$. The CE_n values of studied complexes are enhanced with complex size, too. Based on the magnitude of this contribution, cooperative phenomena play a significant role in the behavior of larger clusters.

The responses of studied clusters to nonlinear optics (NLO) were evaluated and results of this analysis are listed in Table 3.

Table 3: Calculated NLO properties of bifurcated lithium bonds. Dipole moment (μ_z), linear polarizability (α_{zz}) and first hyperpolarizability (β_{zzz}) are in a.u. and energy gap (E_g) is in eV.

N	μ_z	α_{zz}	β_{zzz}	E_g
1	4.671	56.747	606.114	6.158
2	11.071	114.083	791.189	3.828
3	17.857	172.865	973.192	2.871
4	24.777	232.219	1151.704	2.391
5	31.758	291.876	1327.443	2.114

Table 3 shows that the energy gap (E_g) of studied clusters are downturn along with increasing size of clusters. Generally, results from Table 3 points out that due to reduction of energy gap from monomer to pentamer, electron transfer has been made easier and this process can lead to increase β_{zzz} . Linear chains of $(\text{NCLi})_{1-8}$ and $(\text{NC3Li})_{1-8}$ have been show that in convenience lithium bonds in energies of HOMO-LUMO gap has dropped with growth of chain [9] and these findings confirm the correctness of our calculations. Also, our results show that aggregation of monomers lead to increase α_{zz} and β_{zzz} in all complexes, which are in agreement with previous studies [7,8]. According to these results, it should be noted that the main reason for enhancing the polarizability and hyperpolarizability is the increase in the values of dipole moment. Fortunately, our results showed that dipole moment values increase with cluster size and this observed trend is in agreement with increasing trend of polarizability and hyperpolarizability. Fig. 2 display correlation between α_{zz}/N and β_{zzz}/N versus number of monomers with good correlation coefficients 0.99. Fig. 2 confirms the cooperativity effect in polarizability of lithium bonds clusters but first hyperpolarizability of BLB clusters is obtained anticlimactic trend. For this reason, we calculated cooperativity effects for electric properties of bifurcated lithium bonds and results from these calculations are



gathered in Table 4. These findings confirm that adding one monomer to cluster lead to increasing dipole moment, polarizability and first hyperpolarizability with increasing cluster size and this trend confirm the cooperativity effect on electric properties of all BLB and BSB clusters.

Table 4: Computed cooperativity effects for electric properties of bifurcated metal bonds formed by linear clusters of $(MN(CHO)_2)_{3-5}$, $M=Li$ and Na .

N	μ_z^{coop}	α_{zz}^{coop}	β_{zzz}^{coop}
3	0.254	1.977	38.075
4	0.339	2.693	47.800
5	0.376	3.008	51.401

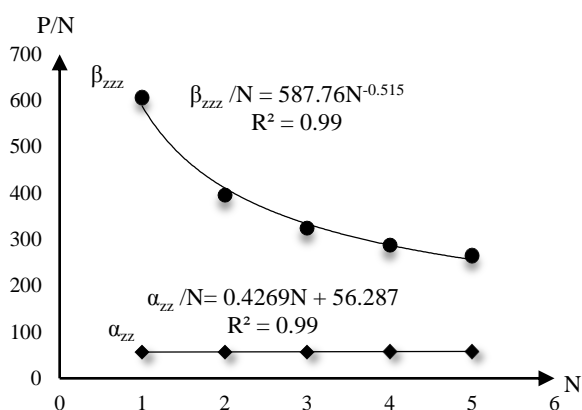


Fig. 2: Correlation between P/N and number of monomers in bifurcated lithium bond clusters. (P is polarizability or hyperpolarizability).

Conclusions

Study of cooperativity effect on stability and nonlinear optic properties of clusters including bifurcated lithium bonds at CAM-B3LYP/6-311++G(d,p) level were carried out. Our results from optimization were indicated that cluster size leads to more stability in considering complexes. Furthermore, calculation of cooperativity effect on electric properties was shown that dipole moment, polarizability and first hyperpolarizability were increased with growth of cluster. Briefly, effects of cooperativity lead to reduction the stabilization energy and increase the NLO response with cluster size.

References

[1] S. Scheiner, "Hydrogen bonding. A theoretical perspective", 1997, Oxford University Press, Oxford.
[2] M. Solimannejad, S. Ghafari, "Theoretical insight into cooperativity in lithium-bonded complexes: linear

clusters of $LiCN$ and $LiNC$ ", *Chemical Physics Letters*, 577 (2013) 6-10.

[3] M. Solimannejad, F. Rezaie, "Cooperativity in bifurcated lithium-bonded complexes: A DFT study" *Chemical Physics Letters*, 657 (2016) 195-8.

[4] R. W. Boyd, "Nonlinear optics", 2003, Academic press.

[5] R. -L. Zhong, H. -L. Xu, "Role of excess electrons in nonlinear optical response", *Journal of Physical Chemistry Letters*, 6 (2015) 612-619.

[6] G. Yu, X. Houang, "Theoretical insights and design of intriguing nonlinear optical species involving the excess electron", *International Journal of Quantum Chemistry*, 115 (2015) 671-679.

[7] B. Skwara, W. Bartkowiak, "On the cooperativity of the interaction-induced (hyper) polarizabilities of the selected hydrogen-bonded trimer", *Chemical Physics Letters*, 436 (2007) 116-123.

[8] A. Baranowska, A. Zawada, "Interaction-induced electric properties and cooperative effects in model systems", *Physical Chemistry Chemical Physics*, 12 (2010) 852-862.

[9] F. Ma, D. Bai, "A theoretical investigation of one-dimensional lithium-bonded chain: enhanced first hyperpolarizability and little red-shift", *Journal of Molecular Modeling*, 20 (2014) 1-9.

[10] M. Frisch, G. Trucks, Gaussian 09, revision A02, (2009), Gaussian Inc, Wallingford.

[11] T. Yanai, R. Harrison, "Multiresolution quantum chemistry in multiwavelet bases: time-dependent density functional theory with asymptotically corrected potentials in local density and generalized gradient approximations", *Molecular Physics*, 103 (2005) 413-424.

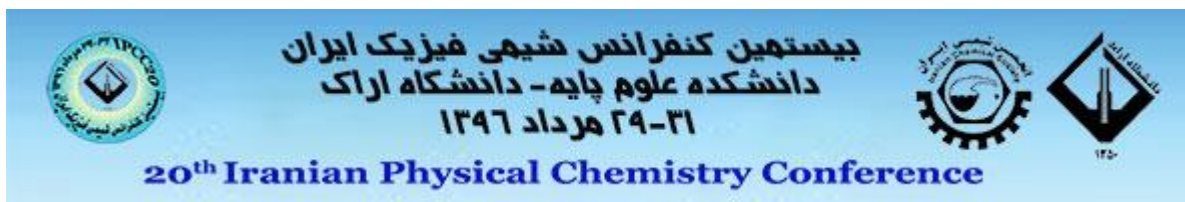
[12] S. F. Boyd, F. D. Bernardi, "The calculation of small molecular interactions by the differences of separate total energies. Some procedures with reduced errors", *Molecular Physics*, 19 (1970) 553-566.

[13] R.D. Parra, S. Bulusu, "Cooperative effects in one-dimensional chains of three-center hydrogen bonding interactions", *The Journal of Chemical Physics*, 118 (2003) 3499-3509.

[14] K. D. Bonin, V. V. Kresin, "Electric-dipole polarizabilities of atoms, molecules, and clusters" (1997) World Scientific.

[15] A. McLean, M. Yoshimine, "Theory of molecular polarizabilities", *Journal of Chemical Physics*, 47 (1967) 1927-1935.

[16] H. A. Kurtz, J. J. Stewart, "Calculation of the nonlinear optical properties of molecules", *Journal of Computational Chemistry*, 11 (1990) 82-87.



Mechanism Interpretation of Thermal Decomposition Reactions of Vinyl Ethers in Gas Phase Using DFT Method

B. Behnaz Shahrokh

ACECR -University of Applied Science and Technology, Ahvaz, Iran

*r10719853@yahoo.com

Abstract: The mechanism thermal decompositions of propyl vinyl ether (PVE), isopropyl vinyl ether (IPVE) and butyl vinyl ether (BVE) compounds were investigated in the gas phase using density functional theory (DFT). The DFT calculations for the decomposition of considered ethers were performed at B3LYP/6-31G level of theory. Changes in thermodynamic functions including ΔH^\ddagger , ΔS^\ddagger and ΔG^\ddagger were also determined and interpreted. The calculation results revealed that thermal decompositions of PVE, BVE and IPVE species occur via a proton transfer mechanism, where formation of a hydrogen bridge between a hydrogen atom of the alkyl group and the extreme carbon atom of the vinyl group is responsible for the decomposition reaction. The theoretical results compare rather well with the experimental findings available in the literature.

Keywords: DFT, vinyl ethers, proton transfer mechanism, decomposition, rate constant

Introduction

During thermal activation and the following decomposition of polyatomic molecules, such as organic compounds, atoms and radicals can be formed. Because of the variety of intramolecular rearrangements, the decomposition products can take the form of various products. Blades and Murphy [1] studied the thermal unimolecular decomposition of isopropyl vinyl ether (IPVE) using toluene as the carrier gas. The rate measurements were also conducted using a Beckman Spectrophotometer at 302, 305, and 310 μ absorbance bands where the acetaldehyde was strongly absorbing but the ether remained transparent. It was also found that the rate of decomposition of the parent IPVE obeys the first-order rate law, and the experimental data conform to the Arrhenius equation, Eq. 1

$$k = 3.8 \times 10^{12} \exp(-43560/RT) \quad (1)$$

In few reported investigations, there were some interesting findings about the mechanism of thermal decay of the ethers while the quantitative values of kinetic parameters were determined in order to describe the decomposition process [2-4].

Computational Details

In the field of computational chemistry, the calculation of molecular properties that depend on the electronic distribution through the molecule are reliable due to the explicit representation of electrons in this methodology. The density functional theory (DFT) method was chosen to perform the calculations so all the molecular properties of the considered ethers are calculated based on their electronic density

distributions [5, 6]. The geometries of reactants, products and transition state structures were fully optimized at B3LYP/6-31G level of theory and the geometries of various stationary points and the harmonic vibrational frequencies were also calculated at the same level of theory. All calculations were performed using Gaussian 03 program package [7].

where there is a formula allowing one to define the rate constant of decay for a given energy equal to or above the threshold energy required for dissociation, as shown in eq. 2

$$k_n = \frac{1}{h} \int_{E^\ddagger}^{\infty} \rho(E) \exp(-E/kT) dE \quad (2)$$

Where k_n is the rate constant of the reaction threshold energies, $\rho(E)$ defines the line width of quantum state (eV) and h is the Planck constant (eV. s).

Frequently, the precise calculation of the activation energy value (to determine the rate constant) is not possible. Instead, for excluding the activation energy from calculations, it is convenient to determine the dependency of the rate constant to the pressure by considering the k/k_∞ ratio, and to use a formula called the Slater equation as shown in Eq. 3 [8].

$$k/k_\infty = 1/(1 + \nu/\omega) \quad (3)$$

Where the k_∞ parameter is the rate constant of a thermal decomposition reaction at high pressure limit (when the k_∞ value is not dependent on the pressure), ν is the frequency factor (s⁻¹) and ω defines the collision frequency of the molecule at a given pressure (s⁻¹).

While using Eq. 3 to calculate the pressure

dependency of the rate constant of a thermal decomposition reaction, the frequency factor (ω) is the only unknown parameter which can be derived from a calculation in ChemBio3D Ultra 11.0 program package [9].

Results and Discussion

The optimized geometries of reactants, transition states (TS) and products for decomposition of PVE, IPVE and BVE at the B3LYP/6-31G level of theory are shown in Figs. 1, 3 and 4, respectively.

Thermal Decomposition of PVE: The proposed mechanism of decomposition of PVE molecule is shown in Fig. 1.

Fig.1: Optimized geometries of the species involved in the thermal decomposition of PVE calculated at B3LYP/6-31G level of theory: parent PVE (a), transformed structure for activating the parent PVE via formation of a α H---C hydrogen bridge (b), optimized transition state (c), products (d).

The rate constant for a molecule decomposition can be calculated using the formula presented by Slater (Eq. 4) [8]:

$$k = \omega \cdot \exp(-E_a/RT) \quad (4)$$

Where ω , the frequency resulting in the decay of a molecule (s^{-1}), E_a the activation energy (kcal mol^{-1}) and T the temperature (K). Using Eq. 4, it is possible to calculate the rate constant for PVE molecule decomposition. For this purpose, the least negative frequency of the TS structure was selected as it corresponds to the formation of TS, and has a calculated value of $1.5 \times 10^{11} \text{ s}^{-1}$. Further, the value of activation energy for decay of PVE was determined theoretically in ref. [10] to be $E_a = 43.6 \text{ kcal mol}^{-1}$. Therefore, the rate constant for decomposition of PVE at 700K is calculated to be 0.156 s^{-1} . Literature survey reveals that there is no available experimental data to make a comparison with the calculated rate constant.

The dependence of k/k_∞ is obtained in the pressure limit for PVE decay. The value of collision frequency at the atmospheric pressure is $\omega_0 = 6 \times 10^{10} \text{ s}^{-1}$, and the actual collision frequency can be obtained from Eq. 5

$$\omega = \omega_0 \left(\frac{P}{760} \right) \quad (5)$$

Where P is the pressure (Torr). The calculated ΔH^\ddagger is $56.84 \text{ kcal mol}^{-1}$, ΔS^\ddagger is $-4.154 \text{ cal mol}^{-1}\text{K}^{-1}$ and ΔG^\ddagger is $56.199 \text{ kcal mol}^{-1}$ at 298K, which are reported for the first time.

It is easy to calculate the dependence of k/k_∞ from the pressure of the reaction mixture. The pressure dependency for the rate constants of PVE (and also for BVE and IPVE) decay was calculated using the software MATHKAD 2001i and is presented in Fig. 2.

Fig 2: Dependence of $-\ln(k/k_\infty)$ on the pressure (kPa) for thermal unimolecular decomposition of BVE (—1), PVE (---2) and IPVE (....3)

Thermal Decomposition of IPVE: The proposed mechanism of decomposition of PVE molecule is shown in Fig. 3.

Fig 3. Optimized geometries of the species involved in the thermal decomposition of IPVE calculated at B3LYP/6-31G level of theory: parent IPVE (a), transformed structure for activating the parent IPVE via formation of a β H---C hydrogen bridge (b), optimized transition state (c), products (d)

In order to calculate the rate constant for IPVE decomposition, Eq. 4 is used. For this purpose, the smallest negative frequency of the TS structure was calculated to be $2.23 \times 10^{12} \text{ s}^{-1}$. Additionally, the value of activation energy for decomposition of IPVE was determined experimentally in ref. [10] to be $E_a = 42.32 \text{ kcal mol}^{-1}$. Therefore, the rate constant for decomposition of PVE at 700K is determined to be $k = 0.211 \text{ s}^{-1}$. It should be mentioned that in Ref. [10] the rate constant at 721.3K was determined to be $k = 0.172 \text{ s}^{-1}$ [11,12]. The calculated pressure dependency of the rate constant of IPVE decay is presented in Fig.2. At 700K and a 1 atm, the value of molecular collision frequency for IPVE is $\omega_0 = 8 \times 10^{10} \text{ s}^{-1}$. Additionally, the thermodynamic functions at 298K are calculated to be $\Delta H^\ddagger = 50.34 \text{ kcal mol}^{-1}$, $\Delta S^\ddagger = -4.7 \text{ cal mol}^{-1}\text{K}^{-1}$ and $\Delta G^\ddagger = 64.30 \text{ kcal mol}^{-1}$, and the results obtained are in good agreement with the available literature data [11].

Thermal Decomposition of BVE: The proposed mechanism of decomposition of BVE molecule is shown in Fig. 4.

Fig 4. Optimized geometries of the species involved in the thermal decomposition of BVE calculated at B3LYP/6-31G level of theory: parent BVE (a), transformed structure for activating the parent BVE via formation of a α H---C hydrogen bridge (b), optimized transition state (c), products (d)

Once again, Eq. 4 is used to calculate the rate constant



of BVE decomposition reaction. For this purpose, the smallest negative frequency of the TS structure was calculated to be $4.50 \times 10^{-1} \text{ s}^{-1}$. The value of activation energy for decay of BVE was determined both experimentally and theoretically in refs. [10-12] to be: $E_a = 44.6 \text{ kcal mol}^{-1}$, and using the same approach as PVE and IPVE, the rate constant for the decomposition of BVE at 700K is calculated to be $k = 0.219 \text{ s}^{-1}$. For the comparison purposes, the value of rate constant at 721K was determined to be $k = 0.129 \text{ s}^{-1}$ in refs. [11, 12].

The calculated pressure dependency of the rate constant of BVE decay is illustrated in Fig.2. At 700K and a 1 atm, the molecular collision frequency for BVE is $\omega_0 = 8 \times 10^9 \text{ s}^{-1}$. Further, the value of thermodynamic functions at 298K are determined to be $\Delta H^\ddagger = 63.87 \text{ kcal mol}^{-1}$, $\Delta S^\ddagger = -12.83 \text{ cal mol}^{-1} \text{ K}^{-1}$ and $\Delta G^\ddagger = 65.25 \text{ kcal mol}^{-1}$, and such thermodynamic data are reported for the first time which are in good agreement with the available literature data [12].

Conclusions

The results of the theoretical investigations in the present work revealed that the thermal decomposition of vinyl ethers can proceed via a proton transfer mechanism, where a hydrogen bridge is formed between a hydrogen atom of the alkyl group and the extreme carbon atom of the vinyl group. For PVE and BVE species, the only pathway towards the reaction products is to incorporate the α -hydrogen of the alkyl group whereas for IPVE species, it is the participation of a β -hydrogen on the alkyl group that leads to the decomposition reaction.

The calculated values of thermodynamic parameters including ΔH^\ddagger , ΔS^\ddagger and ΔG^\ddagger for the studied vinyl ether decomposition reactions corresponded to non-spontaneous decay processes. From these results, it can be concluded that the use of computational chemistry methods, and specifically the DFT approach, to predict the mechanism, kinetics and thermodynamics of thermal decomposition reactions, can be very promising and acts as a suitable alternative

when there are no available experimental observations.

References

- [1] A. T. Blades, G. W. Murphy "kinetics of the thermal decomposition of vinyl ethyl ether" J. Am. Chem. Soc, 74(1952) 1039-1041.
- [2] T. O. Bamkole "calculation of the Arrhenius parameters for the pyrolysis of some alkyl vinyl ether using Mopac" J. Appl Sci, 6(2006) 41-63.
- [3] T. S. Pokidova, A. F. Shestakov the breakdown of vinyl ethers as a two-center Synchronous reaction" Russian J. Phys. Chem. A: Focus on Chemistry 83(2009) 1860-1870.
- [4] K. Shimofuji, K. Saito, A. Imamura "unimolecular thermal decomposition of ethyl vinyl ether and the consecutive thermal reaction of the intermediate product acetaldehyde" J. Chem. Phys, 95(1991) 155-165.
- [5] A. D. Becke "Densityfunctional thermochemistry. III. the role of exact exchange" J. Chem. Phys, 98(1993) 5648-5656
- [6] C. Lee, W. Yang, R. G. Parr "development of Colle-Salvetti correlation-energy formula into a functional of electron density" J. Phys. Rev. B, 37(1988) 785-789
- [7] M. J. Frisch, et al Gaussian 03 (Revision C.02) 2004 Gaussian Inc Wallingford CT.
- [8] N. B. Slater, 1959 Theory of Unimolecular Reactions, Cornell University, New York.
- [9] ChemBio3D Ultra 11.0, CambridgeSoft, (2007).
- [10] G. N. Sargsyan, B. Shakhrokh, A. B. Harutyunyan "semi-empirical method for calculating the activation energies of the unimolecular thermal decomposition of vinyl ethers" J. Phys. Chem A, 89(2015) 252-257
- [11] A. T. Blades "The kinetics of the decomposition of vinyl isopropyl ether" Can. J. Chem, 31(1953) 418-421.
- [12] T. O. Bamkole, E. U. Emovon "the thermal decomposition of alkyl vinyl ethers" J. Chem. Soc. B, (1968) 332-329.

A theoretical study on the role of ortho, meta and para situation of different electron donating functional groups on the electronic structure and aromaticity of phenol molecule

M. Souri*, Z. Doroumali

Department of Chemistry, Payame Noor University, Kangan, IRAN

*e-mail: msouri@pnu.ac.ir

Abstract: Aromaticity is of fundamental importance to chemistry. In this paper, the role of ortho, meta and para situation of different electron donating functional groups on the electronic structure and aromaticity of phenol molecule have been investigated. The stability energy of each molecule have been considered. Results show that, the stability energy of three isomers of each phenol derivative have not considerable differences. In NH₂ and OCH₃ functionalized phenol the O-H bond length in ortho isomers are higher than in the other isomers. Simultaneously, in each case, the O-C bond is shorter. About CH₃ functionalized phenol there is not a meaningful difference between O-H and O-C bond length in different isomers. In all considered derivatives the electronic charge on H atom in ortho isomer is more than two other isomers. Variation of NICS (1) and NICS (1)_{zz}, calculated for ortho, meta and para isomers follow a similar trend. In the case of NH₂ and CH₃ substitution, the maximum aromaticity has been obtained when the ortho situation occupied with functional group. On the other hand, para substitution of OCH₃ functional group cause to maximize the aromaticity of phenol.

Keywords: substitution effect, electron donating functional groups, NICS

Introduction

Aromaticity is of fundamental importance to chemistry. Even after two centuries, the concept that electron delocalization in closed circuits endows molecules with special properties continues to increase in its scope of applicability and in its importance. Since aromaticity is not a directly measurable quantity, its magnitude is now generally evaluated in terms of structural, energetic, and magnetic criteria. However, magnetic properties are the most closely related to aromaticity, as they depend directly on the induced ring currents associated with cyclic electron delocalization [1-2].

The NICS index is another simple, easy and reference independent method to evaluate the aromaticity of molecules. When cyclic compounds with delocalized p-electrons are subjected to the external magnetic field perpendicular to the ring, the p-electrons in the closed circuit provide a ring current. This circular ring current produces an induced magnetic field, opposite the external one. Shielding of the external magnetic field will be intensified by the nuclear magnetic resonance chemical shift. Schleyer et al. [3] efforts lead to a method to calculate the chemical shift not only at every nucleus but also at any point in the space in the vicinity of molecules. NICS is the negative of the isotropic component of the chemical shielding tensor. It is very often to calculate NICS at the geometric center of the ring. To avoid the shielding effects of the framework of electrons, calculations were carried out at points 1 Å above the center of pentagonal and hexagonal rings of 7AI (NICS(1)). Additionally, since ring current is induced by the external magnetic field applied perpendicular to the ring, the out of plane (zz) component of the magnetic

shielding tensor (NICS(1)_{zz}) is considered as a better descriptor of aromaticity. Negative values of NICS show aromaticity and positive values denote anti aromaticity behaviour; moreover the magnitude of NICS index indicates the degree of aromaticity or anti aromaticity. Using the standard basis sets for calculation of magnetic properties yields the results depended to gauge origin. Elimination of this gauge dependence is possible using gauge invariant atomic orbitals (GIAOs) as basic functions. Therefore, in this study, the NICS indices have been calculated using GIAO method [4].

Dipole moment (μ) is a quantity describing the polarity of a system. The total molecular dipole moment is approximated as the vector sum of the dipole moments related to the individual bonds. The dipole moment is an important property to describe the chemical reactivity of a system. The higher the dipole moment, the stronger will be the intermolecular interactions,

The aim of the recent study is to investigate the role of ortho, meta and para situation of different electron donating functional groups on the electronic structure and aromaticity of phenol molecule.

Theoretical method

Electron donating NH₂, CH₃ and OCH₃ functional groups have been chosen to investigate the role of ortho, meta and para substitution effect on the stability and geometrical properties of functionalized phenol molecule.

Geometry optimization of all considered molecules were carried out at B3LYP/6-311++G** level of theory using Gaussian 09 suite program [5]. Vibrational frequency calculation has been performed on each molecule: and it



has been demonstrated that all optimized structures are in ground states.

Gauge invariant atomic orbitals (GIAO) method was applied to estimate the magnetic tensor shielding within the same level of theory.

Results and Discussion

To investigate the substitution effect, different electron donating functional groups, including: NH_2 , CH_3 and OCH_3 , have been substituted on the ortho, meta and para situation in phenol molecule.

The schematic structures of the considered molecules have been indicated in Figure 1.

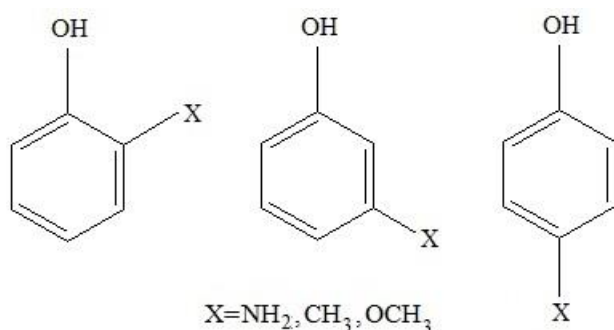


Figure 1: Schematic structures of studied derivatives of phenol.

Geometry of considered phenol derivatives have been optimized in B3LYP/6-311++G** level of theory. The stability energy of each molecule have been indicated in Table 1.

Table 1: Stability energy and geometrical properties of studied molecule.

functional group	situation	stability energy in Hartree)	$d_{\text{O-H}}$ (in Å)	$d_{\text{O-C}}$ (in Å)	charge of O	charge of H
NH_2	Ortho	-362.9348	0.975	1.356	-0.275	0.310
	Meta	-362.9352	0.963	1.371	-0.229	0.254
	Para	-362.9317	0.962	1.377	-0.252	0.256
OCH_3	Ortho	422.1170	0.967	1.363	-0.254	0.291
	Meta	422.1057	0.963	1.366	-0.226	0.262
	Para	-422.1024	0.962	1.371	-0.370	0.244
CH_3	Ortho	-346.8860	0.962	1.372	-0.238	0.279
	Meta	-346.8865	0.963	1.371	-0.227	0.256
	Para	-346.8855	0.963	1.372	-0.241	0.262

In addition, to investigate the substitution effect on geometrical properties, the O-H and C-O bond lengths (in phenol parent molecule), and the natural charges on the involving O and H atoms have been summarized in this table.

With a glance to Table 1, the stability energy of three isomers of each phenol derivative have not considerable differences. In the case of NH_2 and CH_3 substitution, the meta isomer and in OCH_3 substitution the ortho isomer are a little more stable than the others. In NH_2 and OCH_3 functionalized phenol the O-H bond length in ortho isomers are higher than in the other isomers. Simultaneously, in each case, the O-C bond is shorter. About CH_3 functionalized phenol there is not a meaningful difference between O-H and O-C bond length in different isomers.

In all considered derivatives the electronic charge on H atom in ortho isomer is more than two other isomers.

In order to investigate the role of substitution of functional groups on the electron distribution and aromaticity of benzene ring, the NMR calculations have been performed for each molecule, and NICS (1) and NICS (1)_{zz} indices have been summarized in Table 2.

Table 2: dipole moment and aromaticity indices NICS (1) and NICS (1)_{zz}, calculated for different molecules in B3LYP/6-311++G** level of theory.

Functional group	situation	μ (in Debye)	Nics (1)	Nics (1) _{zz}
NH_2	Ortho	2.609	-9.369	-25.103
	Meta	2.743	-8.276	-21.656
	Para	2.127	-9.053	-23.620
OCH_3	Ortho	2.863	-8.886	-24.932
	Meta	1.786	-9.306	-24.018
	Para	0.494	-10.613	-25.5096
CH_3	Ortho	1.786	-9.593	-26.152
	Meta	1.075	-9.443	-25.139
	Para	1.426	-9.577	-25.781

Results in Table 2 indicate that variation of NICS (1) and NICS (1)_{zz}, calculated for ortho, meta and para isomers follow a similar trend. In the case of NH_2 and CH_3 substitution, the maximum aromaticity has been obtained when the ortho situation occupied with functional group. On the other hand, para substitution of OCH_3 functional group cause to maximize the aromaticity of phenol.

As mentioned above, the NICS (1)_{zz} is more reliable and we have considered it as the proper criteria of aromaticity. Based on it, the substitution of methyl group in ortho situation causes the most aromaticity of benzene ring among all considered molecules.

The other geometrical property, summarized in Table 2, is the dipole moment (μ) of each considered molecule.

OCH₃ group on the ortho situation results the most value, 2.863 Debye, of dipole moment among all considered phenol derivative.

Conclusions

Geometry of some phenol derivatives, and the O-H and C-O bond lengths (in phenol parent molecule), and the natural charges on the involving O and H atoms have been optimized in B3LYP/6-311++G** level of theory. The stability energy of each molecule have been considered. Results show that, the stability energy of three isomers of each phenol derivative have not considerable differences. In NH₂ and OCH₃ functionalized phenol the O-H bond length in ortho isomers are higher than in the other isomers. Simultaneously, in each case, the O-C bond is shorter. About CH₃ functionalized phenol there is not a meaningful difference between O-H and O-C bond length in different isomers. In all considered derivatives the electronic charge on H atom in ortho isomer is more than two other isomers.

Variation of NICS (1) and NICS (1)_{zz} calculated for ortho, meta and para isomers follow a similar trend. In the case of NH₂ and CH₃ substitution, the maximum aromaticity has been obtained when the ortho situation occupied with functional group. On the other hand, para substitution of OCH₃ functional group cause to maximize the aromaticity of phenol.

OCH₃ group on the ortho situation results the most value, 2.863 Debye, of dipole moment among all considered phenol derivative.

References

- [1] Special issue on Aromaticity, Phys. Chem. Chem. Phys. 2004, 2.
- [2] P. v. R. Schleyer, , Guest Editor. Thematic issue on Delocalization-Pi and Sigma, Chem. Rev. 2005, 105.
- [3] P. v. R. Schleyer, C. Maerker, A. Dransfeld, H. Jiao, N.J. Rv, E. Hommes, Nucleus-independent chemical shifts: a simple and efficient aromaticity probe, J. Am. Chem. Soc. 118 (1996) 6317–6318.
- [4] F. Jensen, Introduction to Computational Chemistry, John Wiley & Sons Ltd., Chichester, England, 2007.
- [5] M.J. Frisch, G.W. Trucks, H.B. Schlegel, G.E. Scuseria, M.A. Robb, J.R. Cheeseman, G. Scalmani, V.

Barone, B. Mennucci, et al. (2009) Gaussian 09, revision A.02. Gaussian Inc, Pittsburgh, PA

Investigation of the role of ortho, meta and para situation of halide functional groups on the electronic structure and aromaticity of phenol molecule

M. Souri*, S. Sirab

Department of Chemistry, Payame Noor University, Kangan, IRAN

*e-mail: msouri@pnu.ac.ir

Abstract: In this study the role of ortho, meta and para situation of different halide functional groups on the electronic structure and aromaticity of phenol molecule has been investigated. Results indicate that the stability energy of three isomers of bromophenol are so closed together. About the chlorophenol, the para isomer have lower stability energy, comparing with two other isomers. On the other hand, the stability energy of ortho and para isomers are so closed together. In the case of fluorophenol, the para isomer is meaningfully less stable than two other isomers. In all studied derivatives the O-H bond length in ortho isomers have the most value between three isomers. Simultaneously, the O-C bond lengths are the shortest. All considered functionalized phenol compounds have the most value of dipole moment in para state. The most value of the dipole moment among all considered molecules is belong to para boromo phenol. Substitution of Br and F in ortho situation causes to maximize the aromaticity of benzene ring. On the other hand, substitution of Cl group in para situation causes to maximize the aromaticity of chlorophenol. The most value of the NICS (1)ZZ among all considered molecules is belong to ortho fluoro phenol.

Keywords: aromaticity, NICS, substitution effect

Introduction

The terms aromaticity and aromatic are firmly entrenched in the scientific literature and indeed are among those most often used in organic chemistry. Aromaticity to a greater or lesser extent is expected in the following classes of organic compounds: (a) monocyclic annulenes (n is the number of π -electrons) including benzenoid hydrocarbons and their substituted derivatives and fully conjugated carbocyclic (mono and poly) anions and cations containing peripheral π -electrons; (b) condensed conjugated carbocycles including benzenoid systems such as naphthalene and other such as azulene; (c) fully conjugated heterocycles (heteroaromatics) of which a vast variety exist as was pointed out early on by Balaban; and (d) ferrocenes and related sandwich systems [1,2].

The Nucleus Independent Chemical Shift (NICS) is the magnetic probe for the evaluation of aromaticity; it is computationally inexpensive and easy to compute, moreover, this simple and efficient probe is reference independent and can be used for comparing aromaticity of molecules from different families. The aromaticity has been very often assessed by calculating the NICS at the geometric center of the rings and also, to specifically avoid the shielding effects of the framework of r electrons, at some point somewhat (generally 1.0 Å) above the geometric center of the ring [3]. Additionally, it has also been recognized that, since ring currents resulting from cyclic π -electron delocalization are induced primarily by the external magnetic field applied perpendicularly to the ring (conventionally the ZZ direction), the out of plane (ZZ) component of the magnetic shielding tensor

should contain the most relevant information for the aromaticity evaluation, as was first envisioned by Pople [4].

Dipole moment (μ) is a quantity describing the polarity of a system. The total molecular dipole moment is approximated as the vector sum of the dipole moments related to the individual bonds. The dipole moment is an important property to describe the chemical reactivity of a system. The higher the dipole moment, the stronger will be the intermolecular interactions,

The aim of the recent study is to investigate the role of ortho, meta and para situation of different halide functional groups on the electronic structure and aromaticity of phenol molecule.

Theoretical method

The electron donating functional groups, including: F, Cl and Br, have been chosen to investigate the role of ortho, meta and para substitution effect on the electronic structure and geometrical properties of phenol molecule.

Geometry optimization of all considered molecules were carried out at B3LYP/6-311++G** level of theory using Gaussian 09 suite program [5]. Vibrational frequency calculation has been performed on each molecule: and it has been demonstrated that all optimized structures are in ground states.

Gauge invariant atomic orbitals (GIAO) method was applied to estimate the magnetic tensor shielding within the same level of theory.



Results and Discussion

To investigate the substitution effect, different functional groups including: F, Cl and Br have been substituted on the ortho, meta and para situation in phenol molecule. The schematic structures of the considered molecules have been indicated in Figure 1.

Figure 1: Schematic structures of studied derivatives of phenol.

Geometry of considered phenol derivatives have been optimized in B3LYP/6-311++G** level of theory. The stability energy of each molecule have been indicated in Table 1. In addition, to investigate the substitution effect on geometrical properties, the O-H and C-O bond lengths (in phenol parent molecule), and the natural charges on the involving O and H atoms have been summarized in this table.

Table 1: Stability energy and geometrical properties of studied molecule.

Functional group situation Stability energy
(in Hartree)

Results in Table 1 indicate that the stability energy of three isomers of bromophenol are so closed together. About the chlorophenol, the para isomer have lower stability en

Functional group	situation	stability energy (in Hartree)	r_{OH} (in Å)	r_{OC} (in Å)	charge of O	charge of H
Br	Ortho	-2881.1031	0.968	1.356	-0.168	0.255
	Meta	-2881.1011	0.963	1.366	-0.221	0.260
	Para	-2881.1005	0.963	1.368	-0.231	0.262
Cl	Ortho	-767.1828	0.967	1.357	-0.173	0.252
	Meta	-767.1813	0.963	1.367	-0.215	0.259
	Para	-767.1731	0.963	1.368	-0.228	0.258
F	Ortho	-406.8265	0.965	1.362	-0.234	0.276
	Meta	-406.8273	0.963	1.366	-0.223	0.260
	Para	-406.425	0.963	1.371	-0.236	0.255

ergy, comparing with two other isomers. On the other hand, the stability energy of ortho and para isomers are so closed together. In the case of fluorophenol, the para

isomer is meaningfully less stable than two other isomers. The meta fluorophenol is the most stable isomer of fluorophenol compounds.

A considerable point is that, in all studied derivatives the O-H bond length in ortho isomers have the most value between three isomers. Simultaneously, the O-C bond lengths are the shortest. On the other hand, charge distribution on different isomers show no clear pattern.

Dipole moment (μ) of considered molecules have been summarized in Table 2. With a glance to this table, all considered functionalized phenol compounds have the most value of dipole moment in para state. The most value of the dipole moment among all considered molecules is belong to para bromo phenol. The para fluoro phenol and para chloro phenol are in the next orders, respectively.

Table 2: dipole moment and aromaticity indices NICS (1) and NICS (1)ZZ, calculated for different molecules in B3LYP/6-311++G** level of theory.

Functional group	situation	μ (in Debye)	Nics (1)	Nics (1) _{zz}
Br	Ortho	1.074	-9.499	-24.865
	Meta	0.868	-9.468	-24.506
	Para	2.299	-9.450	-24.440
Cl	Ortho	1.043	-9.815	-25.227
	Meta	0.8762	-9.344	-24.559
	Para	1.798	-9.783	-25.788
F	Ortho	0.997	-10.284	-26.263
	Meta	0.830	-9.754	-25.176
	Para	2.147	-9.957	-25.647

In order to investigate the role of substitution of functional groups on the electron distribution and aromaticity of benzene ring, the NMR calculations have been performed for each molecule, and NICS (1) and NICS (1)ZZ indices have been summarized in Table 2.

Results in Table 2 indicate that variation of NICS (1) and NICS (1)ZZ, calculated for ortho, meta and para isomers are not the same for all derivatives. As mentioned above, the NICS (1)ZZ is more reliable and we have considered it as the proper criteria of aromaticity.

Results show that, substitution of Br and F in ortho situation causes to maximize the aromaticity of benzene ring. On the other hand, substitution of Cl group in para situation causes to maximize the



aromaticity of chlorophenol. The most value of the NICS (1)ZZ among all considered molecules is belong to ortho fluoro phenol.

Conclusions

Geometry of considered phenol derivatives have been optimized in B3LYP/6-311++G** level of theory. In addition, to investigate the substitution effect on geometrical properties, the O-H and C-O bond lengths (in phenol parent molecule), and the natural charges on the involving O and H atoms have been summarized in this table.

Results indicate that the stability energy of three isomers of bromophenol are so closed together. About the chlorophenol, the para isomer have lower stability energy, comparing with two other isomers. On the other hand, the stability energy of ortho and para isomers are so closed together. In the case of fluorophenol, the para isomer is meaningfully less stable than two other isomers. In all studied derivatives the O-H bond length in ortho isomers have the most value between three isomers. Simultaneously, the O-C bond lengths are the shortest. On the other hand, charge distribution on different isomers show no clear pattern.

All considered functionalized phenol compounds have the most value of dipole moment in para state. The most value of the dipole moment among all considered molecules is belong to para boromo phenol. The para fluoro phenol and para chloro phenol are in the next orders, respectively.

Substitution of Br and F in ortho situation causes to maximize the aromaticity of benzene ring. On the other hand, substitution of Cl group in para situation causes to maximize the aromaticity of chlorophenol. The most value of the NICS (1)ZZ among all considered molecules is belong to ortho fluoro phenol.

References

- [1] A. Heilbronner E. Azulenes. "In Nonbenzenoid Aromatic Compounds" Ginsburg, D., Ed.; Interscience: New York, 1959; p 171
- [2] A. Balaban, T. Studii Cercerati Chim. Acad. Romania 7 (1958) 257
- [3] P.v.R. Schleyer, M. Manoharan, Z.X. Wan, B. Kiran, H. Jiao, R. Puchta, N.J.R.v.E. Hommes, Org. Lett. 3 (2001) 2465.
- [4] J.A. Pople, J. Chem. Phys. 24 (1956) 1111.
- [5] M.J. Frisch, G.W. Trucks, H.B. Schlegel, G.E. Scuseria, M.A. Robb, J.R. Cheeseman, G. Scalmani, V. Barone, B. Mennucci, et al. (2009) Gaussian 09, revision A.02. Gaussian Inc, Pittsburgh, PA

Theoretical study of the ortho, meta and para substitution of different electron withdrawing functional groups in phenol derivatives

M. Souri*, L. Nikoopour

Department of Chemistry, Payame Noor University, Kangan, IRAN

*e-mail: msouri@pnu.ac.ir

Abstract: Even though aromaticity cannot be directly probed, it has, nevertheless, traditionally been associated with at least three types of measurable molecular effects: structural, energetic and magnetic. In this study the role of ortho, meta and para situation of different electron withdrawing functional groups on the electronic structure and aromaticity of phenol molecule has been investigated. Geometry of considered phenol derivatives have been optimized in B3LYP/6-311++G** level of theory. Results show that, the stability of ortho isomers of various substituted phenols are more than meta and para isomers. In addition, ortho isomers have more acidic characteristic, comparing with meta and para substituted derivatives of phenol. The natural charges confirm this statement. On the other hand, when functional groups sit on meta position, NICS (1)_{zz} values are close together, no matter what is the functional group. But different functional groups cause to different NICS (1)_{zz} for benzene ring, when they sit on the ortho position. In ortho position, COCH₃ substituted phenol have the most aromaticity. CN and CHO functionalized phenol are in the next orders.

Keywords: substitution effect, electron withdrawing groups, phenol, NICS

Introduction

Around 50% of all known organic compounds may be classified as containing aromatic ring systems. The many aromatic compounds of great biological importance include the porphyrins and the nucleic acids. In addition to these typically organic cyclic π -electron systems, the term aromatic is also used for many systems on the border of organic and inorganic chemistry (e.g. borazine), or which are typically inorganic (e.g. boroxine, aluminobenzene, etc)[1-3].

Even though aromaticity cannot be directly probed, it has, nevertheless, traditionally been associated with at least three types of measurable molecular effects: structural, energetic and magnetic. In this work we choose to assess the aromatic behaviour of the systems on the basis of the analysis of their magnetic properties. The importance of the these properties in studying the aromaticity of molecular systems arises because when they are subjected to external magnetic fields perpendicular to the (putative) aromatic ring, a ring current arises, which is closely dependent on the existence of a system of delocalized p-electrons in closed circuits with-in the ring. This circular ring current produces an induced magnetic field opposing the external one, and the final result is a shielding of the external magnetic field manifested by the nuclear magnetic resonance chemical shifts, which can be experimentally measured at each nucleus. In order to generalize this concept and make it useful in aromaticity studies Schleyer et al. [4] have developed a methodology involving the calculation of the chemical shifts not just at every nucleus but at any point in the space in the vicinity of molecules, leading to what is now described as Nucleus Independent Chemical Shifts (NICS); these are just the negative of the isotropic component (the trace) of

the chemical shielding tensor evaluated at the specific points.

It is very often to calculate NICS at the geometric center of the ring. To avoid the shielding effects of the framework of electrons, calculations were carried out at points 1 Å above the center of pentagonal and hexagonal rings of 7AI (NICS(1)). Additionally, since ring current is induced by the external magnetic field applied perpendicular to the ring, the out of plane (zz) component of the magnetic shielding tensor (NICS(1)_{zz}) is considered as a better descriptor of aromaticity. Negative values of NICS show aromaticity and positive values denote anti aromaticity behaviour; moreover the magnitude of NICS index indicates the degree of aromaticity or anti aromaticity.

Dipole moment (μ) is a quantity describing the polarity of a system. The total molecular dipole moment is approximated as the vector sum of the dipole moments related to the individual bonds. The dipole moment is an important property to describe the chemical reactivity of a system. The higher the dipole moment, the stronger will be the intermolecular interactions,

The aim of the recent study is to investigate the role of ortho, meta and para situation of different electron withdrawing functional groups on the electronic structure and aromaticity of phenol molecule.

Theoretical method

The electron withdrawing functional groups, including: CN, COCH₃ and COH, have been chosen to investigate the role of ortho, meta and para substitution effect on the geometry, dipole moment (μ) and aromaticity of functionalized phenol molecule.



Geometry optimization of all considered molecules were carried out at B3LYP/6-311++G** level of theory using Gaussian 09 suite program [5].

Vibrational frequency calculation has been performed on each molecule: and it has been demonstrated that all optimized structures are in ground states.

Gauge invariant atomic orbitals (GIAO) method was applied to estimate the magnetic tensor shielding within the same level of theory.

Results and Discussion

To investigate the substitution effect, different electron withdrawing functional groups, including: CN, COCH₃ and COH, have been substituted on the ortho, meta and para situation in phenol molecule. The schematic structures of the considered molecules have been indicated in Figure 1.

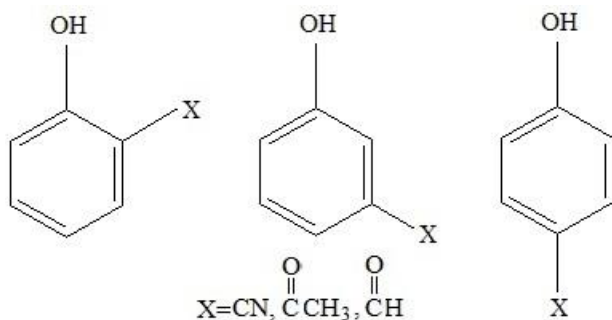


Figure 1: Schematic structures of studied derivatives of phenol.

Geometry of considered phenol derivatives have been optimized in B3LYP/6-311++G** level of theory. The stability energy of each molecule have been indicated in Table 1. In addition, to investigate the substitution effect on geometrical properties, the O-H and C-O bond lengths (in phenol parent molecule), and the natural charges on the involving O and H atoms have been summarized in this table.

As has been indicated in Table 1, the stability of ortho isomers of various substituted phenols are more than meta and para isomers. On the other hand, the O-H bond length in ortho isomers is higher, and the O-C bond is shorter, than relative values in two other isomers. All of this indicate that more stable ortho isomers have more acidic characteristic, comparing with meta and para substituted derivatives of phenol. The natural charges confirm this statement. With a glance to Table 1, the H atom in ortho isomer have more positive charge than in para and meta isomers. This higher positive charge on H atom is accompanied with higher negative charge on O atom, in CHO and COCH₃ substituted phenol molecules.

Table 1: Stability energy and geometrical properties of studied molecule.

Functional group	situation	stability energy (in Hartree)	r _{O-H} (Å)	r _{O-C} (Å)	charge of O	charge of H
CHO	Ortho	420.9283	0.984	1.341	.245	0.319
	Meta	420.9173	0.963	1.366	.223	0.269
	Para	420.9190	0.963	1.361	.213	0.266
COCH ₃	Ortho	460.2616	0.988	1.339	.267	0.342
	Meta	460.2501	0.963	1.367	.232	0.273
	Para	460.2512	0.963	1.362	.223	0.270
CN	Ortho	399.8277	0.967	1.354	.194	0.297
	Meta	399.8249	0.963	1.364	.222	0.270
	Para	399.8266	0.963	1.361	.214	0.265

In order to investigate the role of substitution of functional groups on the electron distribution and aromaticity of benzene ring, the NMR calculations have been performed for each molecule, and NICS (1) and NICS (1)_{zz} indices have been summarized in Table 2.

Table 2: dipole moment and aromaticity indices NICS (1) and NICS (1)_{zz}, calculated for different molecules in B3LYP/6-311++G** level of theory.

Functional group	situation	μ (in Debye)	Nics (1)	Nics (1) _{zz}
CHO	Ortho	3.335	-9.023	-22.939
	Meta	2.208	-9.863	-25.107
	Para	3.454	-9.501	-24.103
COCH ₃	Ortho	3.490	-10.138	-26.158
	Meta	2.059	-9.761	-25.031
	Para	2.654	-9.393	-24.065
CN	Ortho	3.608	-9.552	-24.409
	Meta	3.590	-9.480	-25.296
	Para	5.199	-9.729	-24.795

Results in Table 2 indicate that variation of NICS (1) and NICS (1)_{zz}, calculated for ortho, meta and para isomers are not the same for all derivatives. As mentioned above, the NICS (1)_{zz} is more reliable and we have considered it as the proper criteria of aromaticity.

A considerable point is that, when functional groups sit



on meta position, NICS (1)_{zz} values are close together, no matter what is the functional group. But different functional groups cause to different NICS (1)_{zz} for benzene ring, when they sit on the ortho position. In ortho position, COCH₃ substituted phenol have the most aromaticity. CN and CHO functionalized phenol are in the next orders.

The other geometrical property, summarized in Table 2, is the dipole moment (μ) of each considered molecule. Dipole moment of considered molecules have been summarized in Table 2. CN functional group shifts the dipole moment to greater values (comparing with two other functional groups). Specially, CN on the para situation terminates to considerable value, 5.199 Debye, of dipole moment in the resulting phenol derivative.

Conclusions

Geometry of considered phenol derivatives have been optimized in B3LYP/6-311++G** level of theory. To investigate the substitution effect on geometrical properties, the stability energy of each molecule and the O-H and C-O bond lengths (in phenol parent molecule), and the natural charges on the involving O and H atoms have been considered.

Results show that, the stability of ortho isomers of various substituted phenols are more than meta and para isomers. In addition, ortho isomers have more acidic characteristic, comparing with meta and para substituted derivatives of phenol. The natural charges confirm this statement.

In order to investigate the role of substitution of functional groups on the electron distribution and aromaticity of benzene ring, the NICS (1) and NICS (1)_{zz}

indices have been calculated. A considerable point is that, when functional groups sit on meta position, NICS (1)_{zz} values are close together, no matter what is the functional group. But different functional groups cause to different NICS (1)_{zz} for benzene ring, when they sit on the ortho position. In ortho position, COCH₃ substituted phenol have the most aromaticity. CN and CHO functionalized phenol are in the next orders.

CN on the para situation terminates to considerable value, 5.199 Debye, of dipole moment in the resulting phenol derivative.

References

- [1] E. D. Jemmis, B.Kiran, Inorg. Chem. 34 (1998) 2110.
- [2] P. V. R. Schleyer, H. Jiao, N. J. R. v. E. Hommes, V. G. Malkin, O. Malkina, J. Am. Chem. Soc. 119 (1997) 669.
- [3] I. Madura, T. M. Krygowski, M. K. Cyran^{ski}, Tetrahedron 54 (1998) 14913.
- [4] P.v.R. Schleyer, C. Maerker, A. Dransfeld, H. Jiao, N.J.R.v.E. Hommes, J. Am. Chem. Soc. 118 (1996) 6317.
- [5] M.J. Frisch, G.W. Trucks, H.B. Schlegel, G.E. Scuseria, M.A. Robb, J.R. Cheeseman, G. Scalmani, V. Barone, B. Mennucci, et al. (2009) Gaussian 09, revision A.02. Gaussian

DFT Study and Molecular Docking Simulation of Some Lung Cancer Drugs with Epidermal Growth Factor Receptor Tyrosine Kinase

M. H. Ghatee*, M. Behrouz

Department of Chemistry, Shiraz University, Shiraz, 71946-84795, Iran

*ghatee@susc.ac.ir

Abstract: Inspired by the significance of gefitinib, afatinib and erlotinib as extensively used drugs for treatment of lung cancer, the quantum chemical and molecular docking studies of these drugs was performed to obtain details of structural properties of lung anticancer drugs for drug discovery purposes. Computational study showed that the afatinib is a more active and softer drug than gefitinib and erlotinib. In this research, we selected three epidermal growth factor receptor tyrosine kinase (EGFR) to simulate interactions between drugs and receptors. A clear picture of interactions, relative orientations and hydrogen bonds in the case of each complex system is described.

Keywords: DFT calculations; Drug discovery; Lung cancer; Molecular docking.

Introduction

Lung cancer continues to be a major global health problem with more than 1.6 million new patients diagnosed each year with this disease [1]. There are three main types of lung cancer including (a) non-small cell lung cancer (NSCLC), (b) small cell lung cancer (SCLC), and (c) the lung carcinoid tumour (LCT) [2]. The NSCLC is the most popular type (85%) of lung cancer.

In advanced NSCLC, chemotherapy improves survival and is used as first-line treatment [3]. Several drugs that target molecular pathways in lung cancer are available, especially for the treatment of advanced disease. Commonly used drugs are paclitaxel, gemcitabine, pemetrexed, methotrexate, gefitinib, afatinib and erlotinib. The gefitinib, afatinib and erlotinib, typically inhibit tyrosine kinase at the EGFR. Tyrosine kinases are a subgroup of the larger class of protein kinases that attach phosphate groups to other amino acids (serine and threonine). Phosphorylation of proteins by kinases is an important mechanism in communicating signals within a cell (signal transduction) and regulating cellular activity, such as cell division. A tyrosine kinase can become an unregulated receptor within an organism due to influences discussed, such as mutations and more [4,5]. In this research, we have chosen these drugs to investigate for a clear understanding of their interaction with EGFR tyrosine kinase by quantum chemical calculations. See Fig. 1 for the structure of the drugs.

Computational Methods

Geometry of all drugs has been optimized with Density functional theory (DFT) at the B3LYP/6-31+G** level of theory, by Gaussian09 program package [6]. The docking simulation was undertaken using the Molegro Virtual Docker (MVD) software [7] and the geometry of resulting complexes was studied using the MVD

Pose Viewer utility. Ligand-bound crystallographic structures of EGFR tyrosine kinases obtain from Protein Data Bank (PDB) was applied.

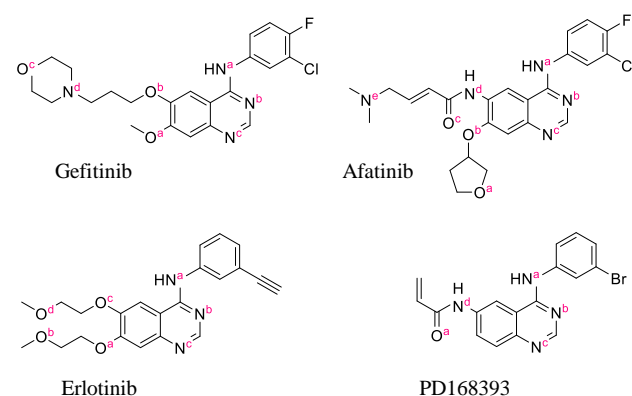


Fig. 1: Structure of gefitinib, afatinib, erlotinib and PD168393.

Results and Discussion

To generate the optimized geometry conformation for all drugs, we set the required jobs with DFT method using hybrid gradient corrected exchange functional by Becke [8] by the gradient corrected correlation functional of Lee, Yang and Parr [9]. The Pople type split valence basis sets [10] are extensively used in *ab initio* quantum chemistry calculations.

In this study, we chose 6-31+G**, a double- ζ Pople type basis set in Gaussian 09 package (B3LYP method and 6-31+G** basis set). Also, frequency calculations were performed to confirm attaining the state of energy minima. Calculated enthalpy, Gibbs free energy, entropy, hardness and softness of each drugs are shown in Table 1.

Table 1. Enthalpy, Gibbs free energy, entropy, hardness and softness calculated at B3LYP/6-31+G** level.

Drug	H ^a	G ^a	S ^b	η ^a	σ ^a
Gefitini	-	-	196.40	0.078	12.79
b	1857.09174 5	1857.18506 4	6	1	8
Afatini	-	-	212.41	0.071	14.00
b	1988.65614 1	1988.75706 5	2	4	5
Erlotini	-	-	193.59	0.078	12.77
b	1316.87235 5	1316.96433 9	5	3	8

^a in Hartree, ^b in cal mol⁻¹ K⁻¹

The comparison of hardness and softness factors between gefitinib, afatinib and erlotinib reveals that the afatinib is softer than gefitinib and erlotinib. The IR spectrum for gefitinib is shown in Fig. 2. The principal peaks were observed at 1028, 1013, 1110, 1248, 1500, 1578, 1625, 2956, 3400 cm⁻¹ [11]. Assignments for the major infrared absorption band are provided in Table 2.

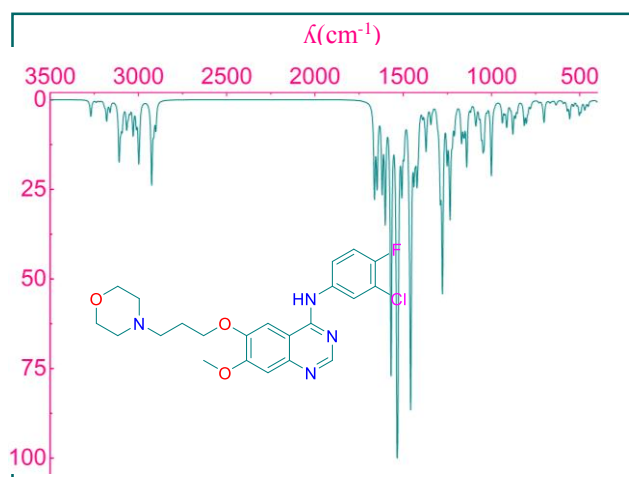


Fig. 2: IR spectra of gefitinib at B3LYP/6-31+G** level.

Table 2. Infrared spectroscopic data for gefitinib in B3LYP/6-31+G**, absorption peaks (at λ_{max}) in cm⁻¹.

C-F	C-Cl	C-O	C-N	HC=C H ^a	C=N	C=C	CH ₂ C H ^b	N-H
1001	1140	1278	1334	1458	1534	1569	2925	3269

^a in aryl, ^b in alkyl

The more activity of afatinib with respect to other selected drugs in EGFR tyrosine kinase receptor is expected due to its softer nature. For better illustration of this concept and drug-receptor interactions, EGFR tyrosine kinase crystal structure 1XKK, 1M14, 4LQM was selected for docking study with MVD docking package, where the receptors errors were also corrected by the structure preparation process. The first step in the generation of suitable receptor structure is the assignment of hydrogen positions on the basis of default rules. Water molecules contained in the PDB

file have been removed. Finally, partial charges (the Gasteiger methodology) were calculated, and the active site of the ensemble was defined as the collection of residues within 7 Å of the bound inhibitor and comprised the union of all ligands of the ensemble. The cavities that are identified by the cavity detection algorithm are used by the guided differential evolution search algorithm to focus the search, to that specific area during the docking simulations. In the case of the crystal structures for 1XKK, 1M14 and 4LQM the program by default, identified five different binding sites. From these predicted binding sites, the one with the highest volume is 229.376 Å³. Highest volume cavity for 1M14 and 4LQM are 198.144 Å³ and 562.688 Å³ respectively. Next, the correct atom types (including hybridization states) and correct bond types were defined, and missing H atom were compensated. We have used the optimized structure of selected drugs as ligands for docking study (details given in computational methods section). Five top ranking pose from forty runs for each ligands were returned in the simulations, out of which one best pose for each ligand was selected on the basis of their rerank score.

Initially, PD168393 was redocked at the active site of EGFR tyrosine kinase receptor (4LQM crystal structure) to validate our docking protocol. In Fig. 3, we have shown the docking image of PD168393 in active site and superposed the docking image of the best pose obtained using MVD. It is observed that both of them are placed at the same binding site and show strong interaction with EGFR tyrosine kinase receptor. Also, we have superposed the docking image for the best obtained pose of gefitinib, afatinib and erlotinib with this receptor (Fig. 3). The RMSD value between the docked and co-crystallized PD168393 was found to be 1.56 Å, which is lower than the limit, i.e., 2 Å [12].

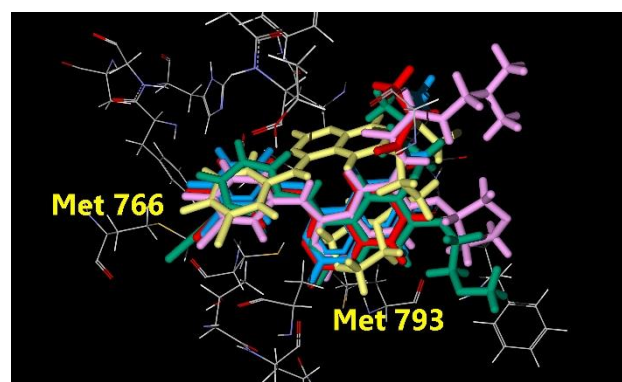


Fig. 3: Superposition of the PD168393 (blue) in active site of 4LQM crystal structure, docked image of PD168393 (red), gefitinib (pale-yellow), afatinib (pink) and erlotinib (cyan) in active site of 4LQM.



Table 3 presents the interaction energy between the ligand and protein, Lennard-Jones 12-6 potential energy, protein-ligand interactions, Gibbs free energy, hydrogen bond energy and rerank scores for the selected alignment and conformation of each complex of ligand with receptors. According to Table 3, afatinib has better interaction with three EGFR tyrosine kinase receptors which confirm the validity of our obtained DFT results. Table 3 indicates that afatinib has more interaction energy and hydrogen bonding energy between drug and receptor complexes.

Table 3. Thermodynamic and docking parameters of selected drugs in active site of EGFR tyrosine kinase receptors.

Parameter	Receptor	Gefitinib	Afatinib	Erlotinib
E^a	1XKK	-172.123	-177.258	-161.120
	1M14	-137.761	-146.224	-132.629
	4LQM	-142.001	-152.043	-144.316
LJ-12-6 ^a	1XKK	-56.070	-48.899	-52.825
	1M14	-37.881	-41.370	-33.490
	4LQM	-32.262	-46.650	-45.677
ΔG^a	1XKK	-167.802	-166.261	-151.688
	1M14	-135.833	-137.129	-133.126
	4LQM	-139.130	-147.622	-128.375
HB ^a	1XKK	-4.681	-11.045	-8.049
	1M14	-1.242	-4.997	-4.613
	4LQM	-3.817	-2.500	-4.983
Re-rank score	1XKK	-129.203	-132.150	-119.141
	1M14	-97.030	-108.300	-93.922
	4LQM	-93.120	-114.441	-104.543

^a in kcal mol⁻¹

Conclusions

In this study, the gefitinib, afatinib and erlotinib drugs were evaluated for their anti-cancer activity with respect to 1XKK, 1M14, 4LQM EGFR tyrosine kinase receptor. The most strong hydrogen bonding interactions are between drugs and Met793 in the case of 1XKK receptor, Met769 in 1M14, and Met793 in 4LQM receptors. DFT study and docking simulations indicated that the afatinib has better inhibition with all three EGFR tyrosine kinase receptors.

References

- [1] A. J. Alberg, M. V. Brock, J. M. Samet, "Murray and Nadel's Textbook of Respiratory Medicine", 2016, Saunders Elsevier, 6th Ed., 927-939.e5.
- [2] M. J. Thun, B. D. Carter, D. Feskanich "50-Year Trends in Smoking-Related Mortality in the United States", N. Engl. J. Med., 368 (2013) 351-364.
- [3] NSCLC Meta-Analyses Collaborative Group "Chemotherapy in Addition to Supportive Care Improves Survival in Advanced Non-Small-Cell Lung Cancer: A Systematic Review and Meta-Analysis of Individual Patient Data from 16 Randomized Controlled Trials", J. Clin. Oncol., 26 (2008) 4617-25.
- [4] J. Ansari, D. H. Palmer, D. W. Rea, S. A. Hussain "Role of Tyrosine Kinase Inhibitors in Lung Cancer", Anticancer Agents Med. Chem., 9 (2009) 569-575.
- [5] W. C. Dempke, T. Suto, M. Reck "Targeted Therapies for Non-Small Cell Lung Cancer", Lung Cancer, 67 (2010) 257-274.
- [6] Gaussian 09, Revision A.01, M. J. Frisch, G. W. Trucks, H. B. Schlegel, G. E. Scuseria, M. A. Robb, J. R. Cheeseman, G. Scalmani, V. Barone, B. Mennucci, G. A. Petersson, H. Nakatsuji, M. Caricato, X. Li, H. P. Hratchian, A. F. Izmaylov, J. Bloino, G. Zheng, J. L. Sonnenberg, M. Hada, M. Ehara, K. Toyota, R. Fukuda, J. Hasegawa, M. Ishida, T. Nakajima, Y. Honda, O. Kitao, H. Nakai, T. Vreven, J. A. Montgomery, Jr., J. E. Peralta, F. Ogliaro, M. Bearpark, J. J. Heyd, E. Brothers, K. N. Kudin, V. N. Staroverov, R. Kobayashi, J. Normand, K. Raghavachari, A. Rendell, J. C. Burant, S. S. Iyengar, J. Tomasi, M. Cossi, N. Rega, J. M. Millam, M. Klene, J. E. Knox, J. B. Cross, V. Bakken, C. Adamo, J. Jaramillo, R. Gomperts, R. E. Stratmann, O. Yazyev, A. J. Austin, R. Cammi, C. Pomelli, J. W. Ochterski, R. L. Martin, K. Morokuma, V. G. Zakrzewski, G. A. Voth, P. Salvador, J. J. Dannenberg, S. Dapprich, A. D. Daniels, O. Farkas, J. B. Foresman, J. V. Ortiz, J. Cioslowski, D. J. Fox, 2009, Gaussian, Inc., Wallingford CT.
- [7] R. Thomsen, M. H. Christensen "MolDock: a New Technique for High-Accuracy Molecular Docking", J. Med. Chem., 49 (2006) 3315-3321.
- [8] A. D. Becke "Density-Functional Thermochemistry. III. The Role of Exact Exchange", J. Chem. Phys., 98 (1993) 5648-5652.
- [9] C. Lee, W. Yang, R. G. Parr "Development of the Colle-Salvetti Correlationenergy Formula into a Functional of the Electron Density", Phys. Rev. B, 37 (1988) 785-789.
- [10] R. Ditchfield, W. J. Hehre, J. A. Pople "Self-Consistent Molecular-Orbital Methods. IX. An Extended Gaussian-Type Basis for Molecular-Orbital Studies of Organic Molecules", J. Chem. Phys., 54 (1971) 724-728.

DFT Study of a Novel Cucurbit[n]uril-type Molecular Container

M. H. Ghatee*, M. Behrouz

Department of Chemistry, Shiraz University, Shiraz, 71946-84795, Iran

*ghatee@susc.ac.ir

Abstract: For carriers in drug delivery, it is important to have high aqueous solubility which is equally or even more important than the good solubility of container-drug complex. Cucurbit[n]uril-type (CB[n]) molecular container has excellent aqueous solubility and ability to solubilize a wide range of insoluble pharmaceuticals. Density functional theory (DFT) calculations have been carried out for 1CB with Gaussian 09 using B3LYP density functional method, 6-31G** and 6-31+G** basis sets with and without explicit water molecules solvent. In this research, we investigate the structural and thermodynamical properties of this drug carrier in detail. The frequency analysis on 1CB is consistent with that of obtained by experimental IR data.

Keywords: Cucurbit[n]uril; Drug container; DFT calculations; Drug delivery.

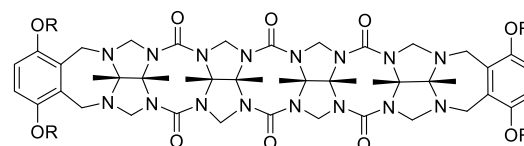
Introduction

A major thrust in the area of supramolecular chemistry is the development of macrocyclic compounds that act as molecular containers [1]. Accordingly, basic molecular recognition properties of numerous classes of macrocycles including cyclodextrins, calixarenes, cyclophanes, crown ethers and most recently pillararenes have been extensively studied [2,3]. In the wide area of supramolecular chemistry, cucurbit[n]urils, CB[n], present as a new family of macrocyclic host molecules that are cyclic oligomers of n (n=5, 6, 7, 8, 10, 14) glycoluril units bridged by 2n methylene groups. CB[n] are able to form stable complexes with various guests, including drug molecules, amino acids and peptides, saccharides, hydrocarbons, perfluorinated hydrocarbons, and even high molecular weight guests such as proteins (e.g., human insulin).

A major problem facing the pharmaceutical industry over the past 20 years has been the increase in the percentage of new chemical entities with excellent biological activity but such poor solubility characteristics that they cannot be formulated on their own [4]. The great interest in CB[n] compounds arises from the availability of a homologous series of hosts that display both high binding affinity and high selectivity toward their insoluble drugs, as guests, in water [5]. Jeon *et al.* [6] examined CB[7] as a potential drug carrier for oxaliplatin (anticancer). They found that CB[7] forms a stable 1:1 inclusion complex with oxaliplatin in aqueous solution and showed that the encapsulation of drug, not only increases the stability of the drug but also may reduce unwanted side effects caused by protein binding of the drug in aqueous solution.

Inspired by the significance of CB[n]-type, 1CB, as an extensively drug container in order to increase drug solubility, we investigated 1CB molecular container by DFT, to obtain details of structural and thermodynamic properties of this drug container with and without

explicit water molecules solvent. The molecular structure of 1CB container is shown in Fig. 1.



R = (CH₂)₃SO₃Na

Fig. 1: Structure of 1CB.

Computational Methods

1CB was constructed and initially optimized by molecular dynamics (MD) simulation using the HyperChem 7.0 [7]. The simulation was performed at low temperature with Amber force field. Then, the full optimization of 1CB was performed by *ab initio* HF/6-31G**, and subsequently by DFT on the B3LYP/6-31G** and B3LYP/6-31+G** level of theory (at 1 atm and 300 K in the gas phase and solution phase with implicit water molecules as solvent, PCM model). We confirmed the absence of imaginary frequency for attaining energy minima on the potential energy surface. All these calculations were performed by Gaussian09 software [9].

Results and Discussion

In DFT study of 1CB, no significant effect has been observed on the 1CB ground state energy by using different basis set. The total energy of 1CB in different optimization methods is shown in Table 1.

For the gas phase we observed that the stability of 6-31+G** basis set vs. 6-31G** was just 91.847 kcal mol⁻¹, and the energy of 6-31+G** basis set in the solution phase optimization was 108.415 kcal mol⁻¹ less than 6-31G** basis set. Table 1 shows that the stability of 1CB in ground state energy in solution phase is about 163 kcal mol⁻¹ more than that of gas phase. The comparison

between *ab initio* and DFT study of gas phase in 6-31G** basis set has shown that only 0.46% difference in total energy.

Table 1: Optimized energy (E , kcal mol⁻¹) at B3LYP level with two basis sets. The difference in energy (ΔE) between gas and solution phase.

Basis set	E	ΔE
6-31+G** ^a	-4405209.3071939	163.419
6-31+G** ^b	-4405372.7266707	
6-31G** ^a	-4405117.4595798	146.851
6-31G** ^b	-4405264.3115341	
6-31G** ^{ac}	-4384902.3716832	

^a in gas phase, ^b in solution phase, ^c in HF method.

The vibrational spectral assignments were carried out to validate the accuracy of data and the optimized structure of 1CB with the same level of theory as was employed for the geometry optimization of the molecule. The IR spectrum of 1CB is shown in Fig. 2 and the selected vibrational wave number are shown and compared with experiment in Table 2. It can be seen a good agreement between calculated and experimental frequencies. The maximum deviation rise to 61 cm⁻¹ at 1286.

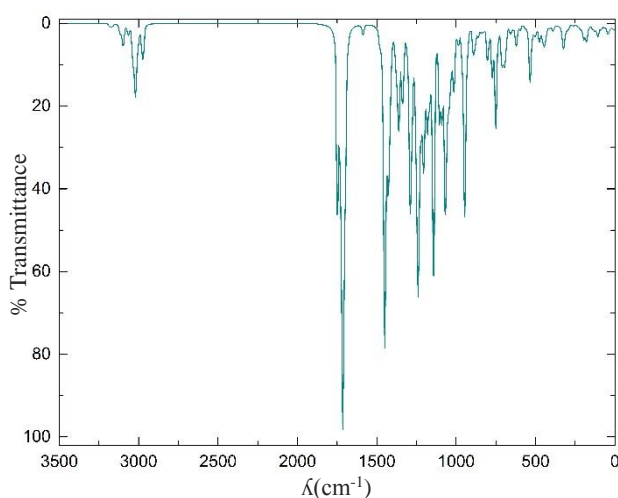


Fig. 2: IR spectrum of 1CB on B3LYP/6-31G** in gas phase.

Frontier molecular orbitals play an important role in the electric and optical properties. Both the highest occupied molecular orbital, HOMO, and the lowest unoccupied molecular orbital, LUMO, are the main orbitals taking part in chemical reaction. The HOMO energy characterizes the ability of electron giving and the LUMO characterizes the ability of electron accepting, while their gap characterizes the molecular chemical stability. In the B3LYP/6-31G** gas phase study of 1CB, we observed -5.35 eV, -1.64 eV and 3.70 eV for HOMO, LUMO and the energy gap, respectively.

The electrophilicity index, ω , is a measure of the energy stabilization of a molecule when it acquires an electron. Table 2: Comparison between observed and calculated IR vibrational wave number (cm⁻¹) for 1CB obtained at B3LYP/6-31G** level of theory.

Calc.	675	751	801	823	945	997	1123
Exp.	665	756	797	822	920	972	1076
Calc.	1190	1286	1339	1500	1766	3022	
Exp.	1178	1225	1313	1456	1711	3000	

additional amount of electron density, from the environment. The ω has become a powerful tool to study the reactivity of organic molecules. 1CB has $\omega=42.043$ kcal mol⁻¹ with a moderate electrophilic character. Hardness, η , and softness, σ , of 1CB are 58.985 kcal mol⁻¹ and 3344.591 kcal mol⁻¹, respectively. These results are shown that 1CB is a soft drug carrier that could have good reactivity in the presence of inclusion drugs in the 1CB cavity.

The total thermal energy, vibrational energy, zero point energy, ZPE, enthalpy, Gibbs free energy, entropy and heat capacity for 1CB were computed from DFT studies. Furthermore, we have investigated the effect of solvent on these thermodynamic functions of 1CB. We have calculated these functions in the presence of implicit water solvent by the PCM model. The computed thermodynamic functions are listed in Table 3. The results indicate that the ZPE for 1CB in the solution phase has 0.315 kcal mol⁻¹ (0.04%) energy less than gas phase. According to Table 1, 1CB in solution phase was 146.851 kcal mol⁻¹ (0.003%) more stable from the isolated molecule.

Table 3: Thermodynamic functions for 1CB in the gas and solution phases and 300 K calculated at B3LYP/6-31G**

Thermodynamic functions	Gas phase	Solution phase
ZPE, Zero point energy ^a	793.498878	793.183872
H, Enthalpy ^a	-4404264.320180	-4404411.089367
G, Gibbs free energy ^a	-4404412.159259	-4404559.080929
E _t , Total thermal energy ^a	852.552	852.635
E _v , Vibrational energy ^a	850.763	850.847
S, Entropy ^b	492.802	493.310
C _v , Heat capacity ^b	358.271	359.348

^a in kcal mol⁻¹, ^b in cal mol⁻¹ K⁻¹

Conclusions

The molecular properties for the novel 1CB drug container using the full geometry optimization, thermodynamical functions and IR spectra have been determined by *ab initio* and DFT studies. The 1CB in implicit water was more stable (by 163 kcal mol⁻¹) than isolated 1CB. The theoretical values for IR are in good



agreement with the observed values even in the low frequency region. The calculated HOMO and LUMO energies show the high chemical reactivity of the 1CB. According to the results, 1CB is a soft drug container with moderate electrophilicity which is a demanding property for drug container.

References

- [1] C. J. Pedersen "The Discovery of Crown Ethers", *Angew. Chem. Int. Ed. Engl.*, 27 (1988) 1021-1027.
- [2] M. Xue, Y. Yang, X. Chi, Z. Zhang, F. Huang "Pillararenes, a New Class of Macrocycles for Supramolecular Chemistry", *Acc. Chem. Res.* 45 (2012) 1294-1308.
- [3] T. Ogoshi, S. Kanai, S. Fujinami, T-A. Yamagishi, Y. Nakamoto "Para-Bridged Symmetrical Pillar[5] Arenes: Their Lewis Acid Catalyzed Synthesis and Host-Guest Property", *J. Am. Chem. Soc.* 130 (2008) 5022-5023.
- [4] C. A. Lipinski "Drug-Like Properties and the Causes of Poor Solubility and Poor Permeability", *J. Pharmacol. Toxicol. Methods*, 44 (2000) 235-249.
- [5] L. Isaacs "Stimuli Responsive Systems Constructed Using Cucurbit[n]uril-type Molecular Containers", *Acc. Chem. Res.*, 47 (2014) 2052-2062.
- [6] Y. J. Jeon, S-Y. Kim, Y. H. Ko, S. Sakamoto, K. Yamaguchi, K. Kim "Novel Molecular Drug Carrier: Encapsulation of Oxaliplatin in Cucurbit[7]uril and its Effects on Stability and Reactivity of the Drug", *Org. Biomol. Chem.*, 3 (2005) 2122-2125.
- [7] HyperChem(TM) Professional 7.0, 2002, Hypercube,



Inc., 1115 NW 4th Street, Gainesville, Florida 32601, USA.

[8] S. Profeta, N. L. Allinger “Molecular Mechanics Calculations on Aliphatic Amines”, *J. Am. Chem. Soc.* 107 (1985) 1907-1918.

[9] Gaussian 09, Revision A.01, M. J. Frisch, G. W. Trucks, H. B. Schlegel, G. E. Scuseria, M. A. Robb, J. R. Cheeseman, G. Scalmani, V. Barone, B. Mennucci, G. A. Petersson, H. Nakatsuji, M. Caricato, X. Li, H. P. Hratchian, A. F. Izmaylov, J. Bloino, G. Zheng, J. L. Sonnenberg, M. Hada, M. Ehara, K. Toyota, R. Fukuda, J. Hasegawa, M. Ishida, T. Nakajima, Y. Honda, O. Kitao, H. Nakai, T. Vreven, J. A. Montgomery, Jr., J. E. Peralta, F. Ogliaro, M. Bearpark, J. J. Heyd, E. Brothers, K. N. Kudin, V. N. Staroverov, R.

Kobayashi, J. Normand, K. Raghavachari, A. Rendell, J. C. Burant, S. S. Iyengar, J. Tomasi, M. Cossi, N. Rega, J. M. Millam, M. Klene, J. E. Knox, J. B. Cross, V. Bakken, C. Adamo, J. Jaramillo, R. Gomperts, R. E. Stratmann, O. Yazyev, A. J. Austin, R. Cammi, C. Pomelli, J. W. Ochterski, R. L. Martin, K. Morokuma, V. G. Zakrzewski, G. A. Voth, P. Salvador, J. J. Dannenberg, S. Dapprich, A. D. Daniels, O. Farkas, J. B. Foresman, J. V. Ortiz, J. Cioslowski, D. J. Fox, 2009, Gaussian, Inc., Wallingford CT.

[10] J. Aihara “Reduced HOMO-LUMO Gap as an Index of Kinetic Stability for Polycyclic Aromatic Hydrocarbons”, *J. Phys. Chem. A*, 103 (1999) 7487-7495.

A theoretical study on the structure, strength and bonding properties of bifurcated chalcogen bonds:

Fariba sadat Mohammadian-Sabet^a, Mehdi D. Esrafil^{a*}

^aLaboratory of Theoretical Chemistry, Department of Chemistry, University of Maragheh, Maragheh, Iran

*E-mail: esrafil@maragheh.ac.ir

Abstract: We present a detailed DFT study on structure, interaction energy and nature of bifurcated chalcogen bonds formed between XCY molecule (X = O, S; Y = S, Se and Te) and 1,2-dihydroxybenzene or 1,2-dimethoxybenzene. The interaction energies for these complexes are in the range of -1.96 to -6.91 kcal/mol. To better understand the nature of bifurcated chalcogen bonds, molecular electrostatic potential and quantum theory of atoms in molecules analyses are performed.

Keywords: Bifurcated Chalcogen bond; σ -hole; Electrostatic potential; DFT; AIM.

Introduction

Noncovalent interactions play a vital role in various fields of chemistry and biochemistry. They are responsible for the stability and structure of biomacromolecules, such as DNA and proteins. Numerous experimental and theoretical studies indicate that atoms of Group-VI, due to the localization of a positive electrostatic potential region (σ -hole), can form attractive noncovalent interactions with potential electron-rich sites [1-3]. This interaction is named as “chalcogen bond”, in which the chalcogen containing molecule plays the role of Lewis acid.

The importance of chalcogen bonds is evident from their critical roles in controlling molecular recognition processes and host-guest interactions in biological systems [4,5]. For example, the S \cdots O chalcogen bonds seem to play an important role in the stability of protein β -sheets [6]. The electron donor in chalcogen bond interactions is usually an atom with a negative site (e.g. lone pair of electrons). Only a few studies have been devoted to chalcogen bond interactions with two electron-rich species (three-center or bifurcated chalcogen bond) [7]. The aim of this study is to investigate the bonding properties in bifurcated chalcogen-bonded complexes formed between XCY (X = O, S; Y = S, Se and Te) and 1,2-dihydroxybenzene (DHB) or 1,2-dimethoxybenzene (DMB) molecules (Fig. 1).

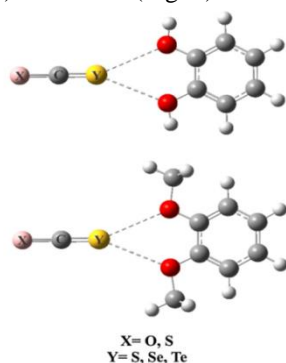


Fig. 1: Schematic representation of bifurcated chalcogen bonds

Materials and method

All DFT calculations were performed using Gaussian 09 suite of programs [8]. The structures of the isolated monomers and the complexes were fully optimized using M06-2X method. A large def2-TZVPPD triple- ζ [9] basis set equipped with two sets of polarization and diffusion functions was used for the description of all atoms. The corresponding harmonic frequency calculations were also performed at the same level.

Results and Discussion

The chalcogen-bonding is defined as a directional interaction where the positive region representing the σ -hole of the chalcogen atom points toward the most negative region of the chalcogen bond acceptor. The molecular electrostatic potential (MEP) analysis shows that there is a region of negative potential located approximately between the two oxygen atoms of the chalcogen bond acceptors (DHB and DMB). The computed MEPs are -39.5 and -42.3 kcal/mol for DHB and DMB, respectively.

Table 1 shows that the chalcogen bond distances are in the range of 3.200–3.296 Å and 3.067–3.159 Å in the XCY \cdots DHB and XCY \cdots DMB complexes, respectively. All of them are shorter than the sum of the van der Waals radii of the respective atoms (1.56 Å for O, 1.80 Å for S, 1.90 Å for Se and 2.06 Å for Te) [10].

As can be seen from Table 1, the interaction energies for these complexes vary in a relatively narrow range, between -1.96 and -6.91 kcal/mol. The chalcogen bond becomes stronger in the order of OCS < OCSe < OCTe and SCS < SCSe < SCTe for the same chalcogen bond acceptor. The weakest chalcogen bond interactions in the SCS complexes are attributed to the smaller polarizability of S atom with respect to the Se and Te as well as its smaller electronegativity compared to O atom. Fig.2 shows the correlation between the interaction energies and positive σ -hole potentials on the chalcogen atoms Y. Almost a linear relationship is found between them with a correlation coefficient R^2 value of 0.983 and 0.980 in the XCY \cdots DHB and XCY \cdots DMB complexes, respectively.



According to quantum theory of atoms in molecules (QTAIM) analysis, electron densities at the Y...O bond critical points (BCPs) are in the range of 0.007–0.013 au, which are consistent with the criteria proposed for the existence of noncovalent bonds [11]. Moreover, the values of the Laplacian at the BCPs are all positive, which correspond to a local depletion of the electron density from the bonding region. The electron energy density values are all positive, which supports the electrostatic nature of these bifurcated chalcogen bonds.

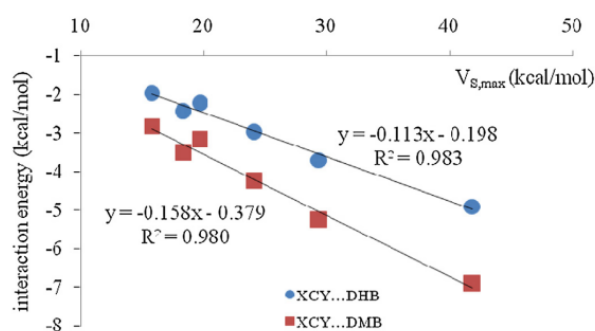


Fig.2: Maximum electrostatic potentials ($V_{s,max}$) of Y atom of XCY molecule versus interaction energies of XCY...DHB and XCY...DMB complexes.

Table1: Binding distances (r_{int}), C–Y...O angles, interaction energy (E_{int}), NBO atomic charge (Q) of Y atom and second-order charge-transfer energy ($E^{(2)}$) in XCY...DHB and XCY...DMB complexes.

Molecule	r_{int} (Å)	Angle(°)	E_{int} (kcal/mol)	Q(e)	$E^{(2)}$ (kcal/mol)
OCS...DHB	3.204	156	-2.22	0.048	0.70
OCSe...DHB	3.218	156	-2.98	0.068	1.19
OCTe...DHB	3.200	152	-4.90	0.085	1.77
SCS...DHB	3.233	156	-1.96	0.251	0
SCSe...DHB	3.256	156	-2.44	0.303	0
SCTe...DHB	3.296	157	-3.70	0.364	1
OCS...DMB	3.093	156	-3.17	0.043	0
OCSe...DMB	3.088	156	-4.24	0.061	1.83
OCTe...DMB	3.067	155	-6.91	0.074	3.27
SCS...DMB	3.121	156	-2.82	0.265	0.70
SCSe...DMB	3.159	156	-3.52	0.294	1.11
SCTe...DMB	3.153	156	-5.26	0.353	2.02

Conclusions

In summary, we have investigated the structure, interaction energy and bonding properties of bifurcated chalcogen bonds in the XCY...DHB and XCY...DMB complexes using M06-2X/def2-TZVPPD calculations (X = O, S; Y = S, Se, Te; DHB = 1,2- dihydroxybenzene and DMB = 1,2 dimethoxybenzene). The optimized chalcogen bond distances are in the range of 3.200–3.296 Å and 3.167–3.159 Å in the XCY...DHB and XCY...DMB complexes, respectively. The chalcogen bond becomes stronger in the order of OCS < OCSe < OCTe and SCS < SCSe < SCTe for the same chalcogen bond acceptor.

Acknowledgment

This work has been supported by University of Maragheh through a research fund.

References

- [1] U. Adhikari, S. Scheiner, Comparison of P...D (D = P,N) with other noncovalent bonds in molecular aggregates, *Chem. Phys. Lett.*, 514 (2011) 36-39.
- [2] S. Scheiner, Detailed comparison of the pnictogen bond with chalcogen, halogen, and hydrogen bonds, *Int. J. Quantum Chem.*, 113 (2013) 1609-1620.
- [3] U. Adhikari, S. Scheiner, Effects of Charge and Substituent on the S...N Chalcogen Bond, *J. Phys. Chem. A*, 118 (2014) 3183-3192.
- [4] M.E. Brezgunova, J. Lie-rig, E. Aubert, S. Dahaoui, P. Fertey, S. Lebegue, J.G. Angyan, M. Fourmigue, E. Espinosa, Chalcogen Bonding: Experimental and Theoretical Determinations from Electron Density Analysis. Geometrical Preferences Driven by Electrophilic–Nucleophilic Interactions, *Cryst. Growth Des.*, 13 (2013) 3283-3289.
- [5] Bauza, D. Quiñonero, P.M. Deya, A. Frontera, Halogen bonding versus chalcogen and pnictogen bonding: a combined Cambridge structural database and theoretical study, *Cryst. Eng. Comm.*, 15 (2013) 3137-3144.
- [6] M. Iwaoka, S. Takemoto, S. Tomoda, Statistical and Theoretical Investigations on the Directionality of Nonbonded S...O Interactions. Implications for Molecular Design and Protein Engineering, *J. Am. Chem. Soc.*, 124 (2002) 10613-10620.
- [7] V.P. Nziko, S. Scheiner, Intramolecular S...O Chalcogen Bond as Stabilizing Factor in Geometry of Substituted Phenyl-SF₃ Molecules, *Org. Chem.*, 80 (2015) 2356-2363.
- [8] M.J. Frisch, G.W. Trucks, H.B. Schlegel, et al., Gaussian 09, Revision A.02, Gaussian, Inc., Wallingford, CT, 2009.
- [9] D. Rappoport, F. Furche, Property-optimized gaussian basis sets for molecular response calculations, *J. Chem. Phys.*, 133 (2010) 134105.
- [10] Bondi, van der Waals Volumes and Radii, *J. Phys. Chem.*, 68 (1964) 441-451.
- [11] U. Koch, P.L.A. Popelier, Characterization of C-H...O Hydrogen Bonds on the Basis of the Charge Density, *J. Phys. Chem.*, 99 (1995) 9747-9754.

DFT calculations and thermodynamic stability of sulfa drugs

Hossein Nikoofard* and Mohsen Sargolzaei

Faculty of Chemistry, Shahrood University of Technology, Shahrood 63199-95161, Iran

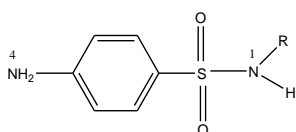
*nikomahdieh@yahoo.com

Abstract: A computational study at the density functional theory (DFT) was carried out on the structural and physico-chemical properties of a series of sulfonamide derivatives (SAs) as WHO essential medications in the treatment of basic health system. The B3LYP/6-311++G(d,p) level of theory carried out on sulfadiazine (SDZ), sulfathiazole (STZ), sulfaquinolaxine (SQX), sulfacetamide (SAA), and the reference unsubstituted sulfonamide (SA) was discussed and rationalized in term of the N¹-sulfonamide substituent. The geometric structures and the electronic properties related to the bacteriostatic reactivity were revealed to be affected by the steric and "push-pull" characteristics of the substituents. From the molecules studied it is evident that SDZ act as the most electro-active agent, possessing the highest biological activity. DFT computations carried out using the standard molar enthalpies of formation in the gas phase predicted improvements in the thermodynamic stabilization of the SDZ, SQX, and SAA molecules and an unstabilization of STZ with respect to the parent molecule SA.

Keywords: Standard enthalpy of formation; Sulfonamide; Density functional theory; Bacteriostatic.

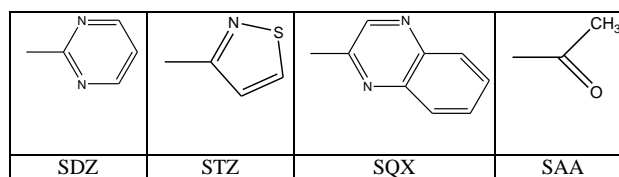
Introduction

The relationship between the chemical structure and pharmaceutical activity of sulfa drugs (sulfonamide derivatives, SAs) has prompted the current experimental and theoretical investigations for new sulfa compounds that would possess a greater pharmacological activity [1-3]. The sulfonamide mechanism has been recognized at the enzyme level. In bacteria, anti-bacterial sulfonamides act as the competitive inhibitors of dihydropteroate synthetase. Hence, sulfonamide interferes with the enzyme folic acid synthetase, which is involved in changing PABA to folic acid, which results in the deficiency of folic acid, causing injury to the bacterial cell. Most bacteriostatic SAs have been derivatized basically by variation in the R-substitution linked to the N¹ atom of the sulfonamido group (Scheme 1). In this way, sulfadiazine is one of the substantial sulfonamide antibiotics that are listed as WHO crucial medications in the cure of basic health system. In comparison to the SA derivatives, it has been found that the original SA is at the lowest end of the activity spectrum. Although these drugs are clinically effective in the treatment of various medical disorders, they cause some negative side-effects, which may lead to hepatitis and arthritis. Through relocation, these drugs reach the environment and cause acute toxicity and serious public health hazards [4].



Scheme 1: Molecular structure of SA with N atom numbering.

In the current work, we wish to report a theoretical investigation carried out on the SA derivatives including SAA, SDZ, SQX, STZ, and the original sulfonamide SA as the reference molecule, which can be used to evaluate the relevance of the physico-chemical and structural properties toward the steric and electronic influences of the N1-substituents. The R groups were chosen by taking into account the structures of some sulfonamide-based drugs. The sketch map of the substituent structures for all the studied SAs is depicted in Scheme 2. Investigations have been carried out to identify the geometric structure, energy disparity between the lowest unoccupied molecular orbital and the highest occupied molecular orbital, atomic and group Mulliken charge distribution, and some appropriate quantum descriptors.



Scheme 2: Sketch map of R group structure for all studied SAs.

Computation method

The ground-state geometry of each sulfonamide was fully optimized using the gradient procedure at the restricted DFT technique, as implemented in the Gaussian 09 program package. The fully-optimized structures by the DFT-B3LYP level were confirmed to be the real minima through the zero imaginary frequencies. For all cases, both the radical cation and



radical anion were treated as open-shell systems by UB3LYP/6-311++G(d,p). The standard molar enthalpies of formation in the gas phase at 298.15 K for all the studied species were estimated by the atomization energy route. The detailed description of this calculation procedure has been reported in the literature.

Results and Discussion

According to Scheme 1, for the dihedral angle D_{N^4-ph} , defining the torsion between the amino group (NH_2) and phenyl ring (ph), a value of 178° is an evidence of complete planarity, and our calculated results indicated that all SAs presented values for D_{N^4-ph} close to 180° . It is interesting that introduction of the selected R groups did not affect the planarity of the amino group and phenyl ring present in the parent molecule (SA). It has been found that this planarity in the SA drugs is a necessary condition for a pharmaceutical activity. The dihedral angle between the SO_2 group and the phenyl ring, D_{ph-SO_2} , was also close to 180° in all SAs. However, for the SAA, SDZ, and SQX species, the C-S- N^1 bond angle (\angle_{CSN^1}) displayed a value of nearby 105° , although it was found to be 100° for the STZ molecule. This may be attributed to the different steric effects resulting from the proximity of the substituent R to the sulfonamido group. Our calculated results for all SAs revealed that the bond angle for O-S-O was near 120° , indicating that introduction of the R group did not affect it considerably.

Table 1: Bond length values (Å) for SA species in the both radical cation (+) and radical anion (-) states at B3LYP/6-311++G(d,p) level of theory.

Ions	N ⁴ -ph	S-ph	S-N ¹	N ¹ -R
SA(+)	1.3342	1.8149	1.6642	--
SAA(+)	1.3341	1.8112	1.6818	1.4463
SDZ(+)	1.3380	1.7975	1.6946	1.3997
SQX(+)	1.3478	1.7738	1.7479	1.3699
STZ(+)	1.3456	1.7670	1.7420	1.3690
SA(-)	1.4050	1.7315	1.7715	--
SAA(-)	1.42305	1.7696	1.8332	1.3588
SDZ(-)	1.3916	1.7861	1.6828	1.4168
SQX(-)	1.4039	1.7998	1.7059	1.4369
STZ(-)	1.4120	1.7670	1.7240	1.3691

In the case of the radical anion and radical cation species, some selected bond lengths of the studied molecules are given in Table 1. As we can see in this table, for all SAs, the bond length for N⁴-ph is 1.38 Å, which is in the order of the C-C bond length in the resonance structure of phenyl ring (on average, 1.39 Å). This means that the amino group is well-conjugated with the phenyl ring, and is not affected by the substituent type. In this way, the N⁴-ph bond distances varied in the following order: anionic (1.40 Å) > neutral (1.38 Å) > cationic (1.34 Å). It is interesting that the S-ph and S-N¹ bond lengths were not varied considerably by the R groups, where the distance between the S atom and R group changed due to the substituent steric hindrance. It was established [5] that the sulfonamide activity is accompanied by a small distance between the N¹ atom and R group corresponding to the large bond order for N¹-R. It was concluded that the electronic and structural properties of the substituent could contribute to the bacteriostatic activity of a sulfa drug.

It is expected that the presence of a desired R substituent on the sulfonamido group could improve the electron delocalization along the molecular structure. For the case of the SA derivatives, delocalization of the π -electrons onto the molecular backbone led to satisfactory conjugation systems and improved stabilizations. The extended aromatic structure can correspond to the narrow HOMO-LUMO (H-L) gap energy, which provides a reasonable qualitative indication of the excitation properties and of the ability of electron or hole transport. Table 2 displays the H-L gaps for all the SA molecules. According to this data, reduction in the H-L gap values for both the radical anion and radical cation species becomes more considerable with respect to the ones in the neutral state. Thus we may predict that the SA derivatives have the most reactivity in their ionic forms. It is interesting that the H-L gaps for the R substituted species are lower with respect to the reference SA molecule, which is in good agreement with the less bacteriostatic reactivity of the original SA [5]. Among the compounds studied, SDZ and SQX have the lower H-L gaps, indicating that they can be show the higher reactivity. The results obtained revealed that the HOMO-LUMO electronic transitions could be attributed to the tendency of the considered R groups to contribute the π -electrons with the molecular system.

Table 2: HOMO-LUMO gaps (eV) for SA species in neutral and ionic states.

SAs	Neutral	Cationic	Anionic
-----	---------	----------	---------

SA	0.197	0.074	0.034
SAA	0.192	0.052	0.034
SDZ	0.174	0.050	0.025
SQX	0.166	0.049	0.034
STZ	0.193	0.054	0.034

Some thermochemical quantities of the sulfonamide derivatives including the total energy (E), zero-point energy (ZPE), enthalpy (H), and Gibbs free energy (G) were calculated at 298.15 K for their optimized structures by means of the B3LYP/6-311++G(d,p) level of theory. The gas-phase standard molar enthalpies of formation at 298 K, $\Delta H_{f,298}^{\circ}(g)$, for SAs were calculated through the atomization energy route, and the results obtained were displayed in Table 3. As it can be seen in this figure, in a comparative study in the gas phase, the improvement in stability (corresponding to $\Delta H_{f,298}^{\circ}(g) < 0$) was obtained for the SAA, SDZ, and SQX species with respect to the reference molecule SA. Indeed, attachment of an electron-attracting substituent to the sulfonamido group leads to an evident decrease in the standard molar enthalpies of formation and followed by an increase in the thermodynamic stabilization. In agreement with the electronic results, we observed that the thermodynamic stability of the STZ molecule decreased with respect to the unsubstituted parent SA. Since the thermal stability of compounds is an important factor to be considered for the standardization of drugs and pharmaceuticals, it may be concluded that the considered processor helps us to predict the relative thermodynamic stability of new SA derivatives for which the respective experimental determination has not been reported.

SA species	$\Delta H_{f,298}^{\circ}(g)$
Sulfanamide	212.64
Sulfacetamide	-39.64
Sulfadiazine	-22.37
Sulfaquinoxaline	-54.27
Sulfathiazole	243.78

Conclusions

In this study, the B3LYP/6-311++G(d,p) level of theory was employed to investigate the influence of the N1-sulfonamide substituent on the geometrical structure and electronic properties of the SAA, SDZ, SQX, and STZ molecules. Substituting the hydrogen atom of the sulfanamido group by four different substituents played a fine-tune effect on the physico-

chemical properties and thermodynamic stabilities of the SA derivatives. In the case of the R substituted species, improvements were obtained in the HOMO-LUMO gap, charge density, and some electronic descriptors with respect to the ones in the reference SA molecule, which were in good agreement with the higher bacteriostatic reactivity of these molecules. The calculations carried out on the neutral and ionic SAs showed that the SDZ molecule had a more satisfactory structural and electronic characteristic for the bacteriostatic reactivity. Besides, the calculated results for the standard molar enthalpies of formation in the gas phase revealed an improvement in the thermodynamic stabilization of the SDZ, SQX, and SAA molecules with respect to the unsubstituted parent molecule. Generally, the theoretical data obtained for the efficient injection and transport of the carrier charges involving holes and electrons can be applied for the rational design of a sulfa drug of desired properties.

Acknowledgment

The authors wish to thank the Shahrood University of Technology for the financial support of this research work.

References

- [1] S. Alyar, Ü. Özdemir Özmen, N. Karacan, O.Ş. Şentürk, K.A. Udachin, Tautomeric properties, conformations and structure of 2-hydroxyacetophenone methanesulfonylhydrazone, *J. Mol. Struct.* 889 (2008) 144-149.
- [2] A. Chandran et al., Vibrational spectroscopic and quantum chemical calculations of (E)-N-Carbamimidoyl-4-((naphthalen-1-yl-methylene) amino) benzene sulfonamide, *Spectrochim. Acta A* 87 (2012) 29-39.
- [3] H.A. Dabbagh, A. Teimouri, R. Shiasi, A. Najafi Chermahini, DFT, Ab initio and FT-IR studies of the structure of sulfonamide triazenes, *J. Iran. Chem. Soc.* 5 (2008) 74-82.
- [4] K.H. Lu, C.Y. Chen, M.R. Lee, Trace determination of sulfonamides residues in meat with a combination of solid-phase microextraction and liquid chromatography-mass spectrometry, *Talanta* 72 (2007) 1082-1087.
- [5] C. Soriano-Correa, R.O. Esquivel, R.P. Sagar, Physicochemical and structural properties of bacteriostatic sulfonamides: Theoretical study, *Int. J. Quant. Chem.* 94 (2003) 165-172.

Ab initio calculations of the molecular structure and vibrational frequencies of fluorine-substituted pyrroles

Hossein Nikoofard

Faculty of Chemistry, Shahrood University of Technology, Shahrood, 36199-95161, Iran
nikomahdieh@yahoo.com

Abstract: In this work, the structural, electronic and energetic properties of neutral and singly ionized fluouromethyl-pyrroles (FMPs) were carried out by means of Hartree-Fock (HF) and B3LYP-DFT methods. The characterization of the titled molecules was discussed and rationalized in term of the number and position of the fluorine atoms. The calculations were performed on the *mono*-, *di*-, and *tri*-fluorosubstitued methyl-pyrroles by employing the B3LYP/6-31G(d,p) level of theory. The results obtained reveal that the fluorine-substituted methyl groups play a fine-tune effect on the properties of the FMT monomers. It is found that the electronic properties can be successfully correlated with the electronic character of the substitution via a linear dependence behavior on the Hammet function. Moreover, the frontier molecular study reveals that the p- and n-doped states had more suitable properties respect to un-substituted pyrrole, reflecting the hole and electron transport characteristics of the FMT derivatives. It was found that characteristics of the fluorinated substitutions in these molecules have important role in the polymerization process and their polymer products. We hope that the results obtained can be helpful in designing a series of modified materials with the facility of hole and electron injections and the efficient charge transport.

Keywords: Density functional theory; Conducting polymer; Pyrrole; Fluorine-substituted.

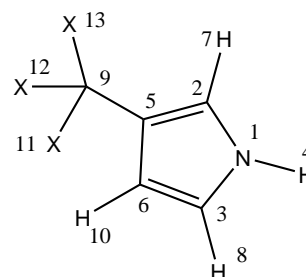
Introduction

Conducting polymers are attractive for use in energy storage devices and organic light-emitting diodes (OLEDs) because they can exist in both oxidized and reduced states [1-3]. The electrical and optical properties of conducting polymers can be fine-tuned by derivatization of the monomer back bone with suitable substituents.

Substitution of pyrrole monomer with appropriate 3-substituents (β -position) induces a push-pull effect on the π -electrons and alters the electrical conductivity of the corresponding polymers compared with that of polypyrroles. Fluoropolymer are characterized by their excellence in resisting chemical attack, their very good thermal stability, chemical inertness, outstanding electrical properties and excellent weathering [4]. These properties differentiate fluoropolymers from their hydrocarbon analogues, and make them preferable materials for high energy radiation environments in the chemical, microelectronic and nuclear industries as well as in medicine and aerospace. The fluorine-substituents have significant effects on the structure, charge distribution and electro-polymerization of the pyrrole ring [5].

In this work, we report a theoretical investigation carried out on a series of fluoromethyl-pyrroles (FMTs), which can be used desirable for designing novel functional materials for conducting polymers. In these molecules, the hydrogen atoms on the b-position of the pyrrole ring substituted by the fluorine-substituted methyl groups, which leads to the different structures

displayed in Scheme 1. We show that these new derivatives can be modified some physical and electronic characteristics of the pyrrole monomer.



Scheme1: Molecular structure of FMPs with atom numbering (X=H or F).

Computational details

The optimized structural parameters were used in the vibrational frequency calculations at the DFT level. We employed a 6-31G(d,p) basis set as implemented in Gaussian 09 program. All the parameters were allowed to relax and all the calculations converged to an optimized geometry. The preliminary study showed that HF is not capable of effectively describing vibrational frequencies of these compounds and the B3LYP-DFT method rendered better results compared with HF method.

Results and Discussion

In Table 1, are tabulated some selected bond lengths, planer and the dihedral angles defining the torsion between the methyl group and thiophene ring (D_{9527}) of

the FMT derivatives. According to this table (column 5), our calculations indicate that all monomers have planar structures $D_{9527} \approx 0$, in which the fluoro-substituted methyl groups are slightly away from the thiophene ring due to their steric hindrances (C_9-C_5 bond length). It is interesting that introduce of fluorine atoms on the methyl group does not effect on the planarity structure of the parent molecule (pyrrole). Planarity of the pyrrole derivatives is an important parameter in their electrical conductivity. According to Table 1, the C-H bond length of all monomers in α positions (R_{83} and R_{72} bonds, respectively) is affected slightly by substituent group.

Table 1: Some selected geometrical parameters for FMP molecular structures at B3LYP/6-31G** level of theory.

Monomer	R_{83}	R_{72}	A_{213}	D_{9527}
Pyrrole	1.0797	1.0797	109.78	0
PyCH ₃	1.0799	1.0799	109.54	0
PyCH ₂ F	1.0796	1.0803	109.73	1.41
PyCHF ₂	1.0795	1.0785	109.95	-1.80
PyCF ₃	1.0793	1.0784	110.03	0.01

In the case of the FMP derivatives, delocalization of the π -electrons onto the molecular structure leads to satisfactory resonance systems and improved stabilization. It has been clear that extended aromatic structure may correspond to the narrow gap for the highest occupied molecular orbital (HOMO) and lowest unoccupied molecular orbital (LUMO), which provides a reasonable qualitative indication of the excitation properties and of the ability of electron or hole transport. Table 2 (column 3) displays the HOMO-LUMO gaps (HLGs) for all molecules under study. As it can be seen in this table, the HLG values for all substituted monomer show a reduction respect to un-substituted monomer (except for PyCF₃). Results obtained was also shown that the HLG values for the p-doped species are less than those of the n-doped species, providing that conductivity of p-doped polymer can be facilities respect to n-doped ones. In the case of p-doped conducting polymers, the ionization potential of monomer (IP) is important parameter for estimating the energy barrier for the injection of holes into the polymer backbone. According to table 2 (column 4), these quantities were shifted to more positive values as the number fluorine atoms on the methyl group increased. This trend is reasonable because higher the electron withdrawing character of the substituent destabilized the product of

oxidized reaction. This deviation can be explained via the proximity of the fluorine atom to the branching center on the pyrrole ring (α -carbon). Consequently, it caused strain effect and interaction with reaction zone of monomer ring.

Table 2: Calculated values of HLG (eV) and IP (kcal/mol) for studied species in neutral state.

Monomer	HLG	IP
Pyrrole	0.2517	180.18
PyCH ₃	0.2507	173.82
PyCH ₂ F	0.2497	180.20
PyCHF ₂	0.2512	187.00
PyCF ₃	0.2521	192.46

Analysis of the spectra information such as wave numbers of normal vibrational modes, intensities and force constances for mono-, di-, and tri-FMPs confirm the structural and electronic results. Vibrational analysis of FMPs is very complex due to their low. For brevity, the number (n) of low frequencies ($< 1000 \text{ cm}^{-1}$) and corresponding the Zero Point Energy (ZPE) for all FMPs are listed in Table 3. According to Table 3, among the studied molecules, Py-CF₃ monomer have higher number of low frequencies and so we may predict that Py-CF₃ may have higher thermodynamic stability compared to other FMPs. The ZPE values predict some comparative stability.

Table 3: The number (n) and percent ($n\%$) of IR transitions with frequencies lower than 1000 cm^{-1} for FMPs and their ZPE values obtained at B3LYP/6-31G** level of theory.

Monomers	n ($\nu < 1000 \text{ cm}^{-1}$)	$n\%$ ($\nu < 1000 \text{ cm}^{-1}$)	ZPE (kcal/mol)
PyCH ₃	12	36.36	69.09
PyCH ₂ F	13	39.39	64.92
PyCHF ₂	15	45.45	60.35
PyCF ₃	17	51.52	55.07

The gas-phase standard molar enthalpies of formation at 298 K, $\Delta H_{f,298}^{\circ}(g)$, for the titled molecules were calculated through the atomization energy route. The calculated values of $\Delta H_{f,298}^{\circ}(g)$ for mono-, di- and tri-fluoro-substituted pyrroles with their corresponding $\Delta G_{f,298}^{\circ}(g)$ are presented in Table 4. The results obtained show that attachment of a fluorine atom to

pyrrole ring leads to an evident reduction in the standard molar enthalpies of formation respect to un-substituted parent molecule. In general, it may be concluded that the relationships obtained between the standard molar enthalpies of formation and the number and position of fluorine atom helps us to predict the relative thermodynamic stability of poly(FMPs) for which the respective experimental determination was not reported.

Table 4: Gas-phase standard molar enthalpy of formation for FMPs at 298 K at B3LYP/6-31G(d,p) level of theory.

Monomer	ΔH_f^0	ΔG_f^0
Pyrrrole	-1340.47	-1243.31
PyCH ₃	-657.40	-531.69
PyCH ₂ F	-461.67	-335.52
PyCHF ₂	-279.37	-150.44
PyCF ₃	-101.87	28.0017

Conclusions

In the current work, the B3LYP/6-31G(d,p) level of theory has been employed to investigate the influence of fluoro-substituted methyl groups on the structural, electronic, and vibrational spectra properties of FMPs. Replacing the hydrogen atoms of methyl ring by *momo*-, *di*-, and *tri*-fluoro atoms plays a fine-tune effect on the electronic properties and thermodynamic stabilities of the FPT monomers. FMPs are proposed in this series of research as candidate monomers for conducting polymers with modified characteristics compared to polypyrrole. The calculations carried out on the neutral and both ionic monomers show that the doped states have more satisfactory structural and electronic characteristics for conductivity. The results obtained for the standard molar enthalpies of formation reveals an improvement in the thermodynamic stabilization of the FPTs respect to the un-substituted

parent molecule.

Acknowledgment

The financial support of Shahrood University of Technology gratefully acknowledged.

References

- [1] A.C. Grimsdale, K.L. Chan, R.E. Martin, P.G. Jokisz, A.B. Holmes, Synthesis of Light-Emitting Conjugated Polymers for Applications in Electroluminescent Devices, *Chem. Rev.*, 109 (2009) 897-1091.
- [2] S. Günes, H. Neugebauer, N.S. Sariciftci, Conjugated Polymer-Based Organic Solar Cells, *Chem. Rev.*, 107 (2007) 1324-1338.
- [3] P. Heremans, D. Cheyns, B.P. Rand, Strategies for Increasing the Efficiency of Heterojunction Organic Solar Cells: Material Selection and Device Architecture, *Acc. Chem. Res.*, 42 (2009) 1740-7.
- [4] H. Sabzyan, A. Omrani, Ab Initio and DFT Study of All Mono-, Di-, Tri-, and Tetrafluoropyrroles and Their Cations: Predicting Structural, Spectroscopic, Electropolymerization, and Electrochemical Properties, *J. Phys. Chem. A* 107 (2003) 6476-6482.
- [5] Y. Huang, Y. Wang, G.Y. Sang, E.J. Zhou, L.J. Huo, Y.Q. Liu, Y.F. Li, Polythiophene Derivative with the Simplest Conjugated-Side-Chain of Alkenyl: Synthesis and Applications in Polymer Solar Cells and Field-Effect Transistors, *J. Phys. Chem. B* 112 (2008) 13476-13482.

Computational study of solvent effect on ruthenium catalyzed click synthesis of 1,2,3-triazoles

S.Mahdavian*, T. Hosseinejad, M. M. Heravi

Department of Chemistry, Alzahra University, Vanak, Tehran, Iran

*S_mahdavian_66@yahoo.com

Abstract: In this study, ruthenium catalyzed azide-alkyne cycloaddition reaction mechanism has been modeled by quantum mechanical methods. In this respect, we have investigated regioselectivity in azide-alkyne reaction on the presence of ruthenium catalysts in solution phases. Density functional theory and polarized continuum model were utilized to demonstrate that 1,5-disubstituted triazole is the main product. We demonstrated that the presence of $Cp^*RuCl(PH_3)_2$ catalyst has an important role on the energy barriers of transition states and so the regioselective behavior of synthesis. The thermodynamic stability of Ru-azide-alkyne complexes in transition state structures was comparatively evaluated in the presence of solvent. It was shown that the production of 1,5-disubstituted triazoles in 1,2-dichloroethane solution is more favorable thermodynamically than dimethylformamide.

Keywords: Ruthenium catalyst; Disubstituted 1,2,3-triazoles; Click reaction; DFT computations; Polarized continuum model.

Introduction

Recently, the experimental and computational chemists have been attracted widely to the click synthesis of 1,2,3 triazoles and their derivatives. Huisgen's dipolar cycloaddition of organic azides and alkynes is the most direct route to 1,2,3-triazoles [1]. In 2001, Kolb, Finn and Sharpless published a review describing a new strategy for organic chemistry [2]. They have termed the foundation of the approach "click chemistry", and defined a set of stringent criteria that a process must meet to be useful in this context. A major advance in the chemistry was achieved recently, with the discovery that Cu(I) complexes can mediate the cycloaddition reactions of terminal alkynes with azides to give selectively 1,4-disubstituted 1,2,3-triazoles under mild conditions [3,4]. In 2005, ruthenium catalysis was found as a complementary reaction to CuAAC which shown an inverse regioselectivity with reasonable yield and rate increase [5,6]. The very success of the CuAAC highlights the need for selective access to the complementary regioisomers, the 1,5-disubstituted triazoles. In this content, a large number of ruthenium mediated reactions of azide-alkynes have been developed from the experimental and computational viewpoints [3,7]. In this research, we have focused on investigation of the regioselective nature of click synthesis of 1,2,3-triazoles using $Cp^*RuCl(PH_3)_2$ as catalyst in the solution phase. In this respect, computational chemistry methods were employed to interpret the solvent effect (including: dimethylformamide (DMF), 1,2 dichloroethane (1,2DCE)) on the energetic and electronic stability in the production of 1,5-disubstituted triazole.

Computational details

The optimized geometry of all compound was calculated at M06/6-31G* level of theory. It is worthwhile to note that M06 functional has been introduced as a top performer within modern functionals with a high performance and accuracy and has been parameterized including both transition metals and non-metals [8]. All stationary points and transition states were confirmed after frequencies analysis. The effect of solvation was taken into account using the polarized continuum model (PCM) calculations [9]. The GAMESS suite of programs [10] has been used in DFT calculations.

Results and Discussion

In the first step, we have determined the optimized structures corresponding to the ground states and transition states in the presence of $Cp^*RuCl(PH_3)_2$ at M06/6-311G** level of theory in the solution phase.

The main goal of this research is the assessment of solvent effect to present the theoretical basis for the catalytic role of $Cp^*RuCl(PH_3)_2$ in regioselective click synthesis of 1,5-disubstituted 1,2,3-triazole derivatives from benzyl azide and phenyl acetylene. The M06/6-311G** calculated reaction electronic energies in the gas and solution phases have been reported in Table 1. As it was clear from the calculated reaction electronic energies, in the absence of catalyst, there is no energetic preference in the production of disubstituted triazoles in the gas and solution phases that is in agreement with the experimental observations. Moreover, PCM computations confirm the near calculated reaction electronic energies for the synthesis of disubstituted triazoles in 1,2-DCE and DMF solutions.

Table 1. Reaction electronic energies of click synthesis of disubstituted 1,2,3-triazoles calculated at M06/6-311G** level of theory in the gas and two solution phases.

	1,5 disubstituted triazoles	1,4 disubstituted triazoles
Gas phases	ΔE_r -44.5531	ΔE_r -45.9964
Solution phases		
1,2-DCE	-43.1726	-48.6946
DMF	-43.0471	-49.0712

In the next step, the we determined M06/6-31G* optimized geometries of transition states in the presence of Cp*RuCl(PH₃)₂ catalyst (Figs. 1 and 2). We demonstrated that the presence of Cp*RuCl(PH₃)₂ catalyst has a considerable effect on the energy barriers of transition states and so the regioselective behavior of synthesis. In this context, we assessed the solvent effect on the energy barriers of transition states regioisomers in the presence of Cp*RuCl(PH₃)₂ catalyst. The comparative analysis of the calculated electronic energies of transition states regioisomers is in confirmation with regioselective production of 1,5-disubstituted triazole (Table2).

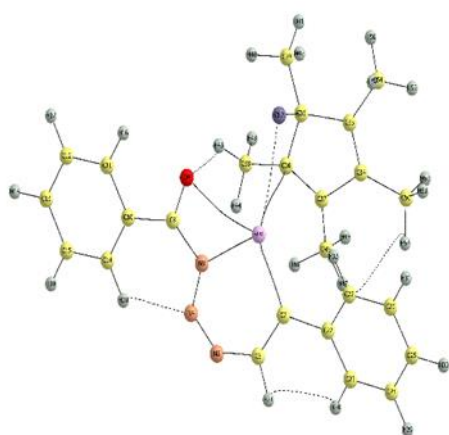


Fig1: optimized structures of TS-Cat1,5 calculated at M06/6-311G** level of theory.

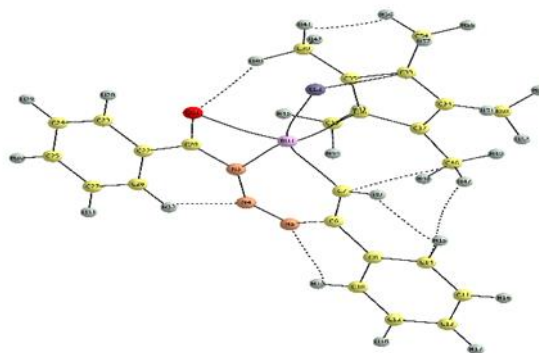


Fig2: optimized structures of TS-Cat1,4 calculated at M06/6-311G** level of theory.

Moreover, the reported results of Table2 shows that the production of 1,5-disubstituted via Ru catalyzed reaction in the presence of DMF as solvent should be more favorable than 1,2-DCE, from the kinetical viewpoint.

Table 2. Thermochemistry of click synthesis of disubstituted 1,2,3-triazoles in presence of Cp*RuCl(PH₃)₂ catalyst calculated at M06/6-311G** level of theory in the gas and three solution phases.

	TS-Ru1,5	TS-Ru1,4
Gas phases	Energy(Hartree) -6090/3165	Energy(Hartree) -6090/2968
Solution phases		
1,2DCE	-6090/3356	-6090/3211
DMF	-6090/3374	-6090.3233

Conclusions

Our calculated reaction energies in the gas and solution phases indicate that there is no considerable distinction in the production of disubstituted triazoles in the gas and solution phases that is in agreement with the experimental observations. Furthermore, there is a small distinction between the calculated stability of regioisomers in solution phases. In the next step, we investigated comparatively the role of solvents on energy barriers of transition states considering the Ru catalyst. The obtained results show that DMF is more suitable solvent rather than 1,2 DCE. More importantly, our calculated reaction energy barriers in the gas and



solution phases indicate that the production of 1,5 disubstituted triazoles is more favorable than its 1,4 disubstituted regioisomer that is in agreement with the experimental observations.

Acknowledgments

The authors are thankful from Alzahra Research Council for the partial financial support.

References

- [1] M. M. Heravi, M. Tamimi, H. Yahyavi, T. Hosseinejad, "Huisgen's Cycloaddition Reactions: A Full Perspective", *Curr. Org. Chem*, 20(2016) 1591-1647.
- [2] H. C. Kolb, M. G. Finn, K. B. Sharpless, "Click Chemistry: Diverse Chemical Function from a Few Good Reactions", *Angew. Chem. Int. Ed.* 40 (2001) 2004.
- [3] T. Hosseinejad, B. Fattahi, M. M. Heravi, "Computational studies on the regioselectivity of metal-catalyzed synthesis of 1,2,3 triazoles via click reaction: A review", *J.Mol.Modeling*, 21 (2015) 264-301.
- [4] T. Hosseinejad, M. Dinyari, "Computational study on stereoselective synthesis of substituted 1H tetrazoles via a click reaction: DFT and QTAIM approaches", *Comput. Theor. Chem*, 1071 (2015) 53-60.
- [5] BC. Boren, S. Narayan, L.K. Rasmussen, L. Zhang, H. Zhao, Z. Lin, G.Jia, V. Fokin, "Ruthenium-Catalyzed Azide-Alkyne Cycloaddition: Scope and Mechanism", *J. Am. Chem. Soc*, 130(2008) 8923-8930.
- [6] E. Boz, N.S. Tüzün, "Reaction mechanism of ruthenium-catalyzed azidealkyne cycloaddition reaction: A DFT study", *J.Organometal.Chem*, 724, (2013) 167-176.
- [7] a) B. M. Trost, "On Inventing Reactions for Atom Economy", *Acc. Chem. Res.* 35(2002) 695.
- b) B. M. Trost, M.U. Frederiksen, M. T. Rudd, "Ruthenium-catalyzed reactions--a treasure trove of atom-economic transformations", *Angew. Chem. Int. Ed.* 44 (2005) 6630.
- [8] Y.Zhao, D. G.Truhlar, "The M06 suite of density functionals for main group thermochemistry, thermochemical kinetics, noncovalent interactions, excited states, and transition elements: two new functionals and systematic testing of four M06-class functionals and 12 other functional", *Theor. Chem. Acc*, 120(2006) 215-223.
- [9] V. Barone, M. Cossi, "Quantum Calculation of Molecular Energies and Energy Gradients in Solution by a Conductor Solvent Model", *J. Phys. Chem.A.* 102 (1998) 1995.
- [10] M.W.Schmidt, K.K.Baldrige, J.A. Boatz, S.T.Elbert, M.S. Gordon, J.H. Jensen, S.Koseki, N.Matsunaga, K.A.Nguyen, S.J.Su, T.L.Windus, M.Dupuis, J.A.Montgomery, "General Atomic and Molecular Electronic Structure System", *J.Comput. Chem*, 14(1993) 1347-1363.

ONIOM Study of Binding Affinity of Breast Cancer Imine Drugs to Estrogen Receptor- α

Mohsen Sargolzaei*, Mohammad Soltanali

Faculty of Chemistry, Shahrood University of Technology, Shahrood 63199-95161, Iran

*mohsen.sargolzaei@gmail.com

Abstract: We used computational method of ONIOM to obtain drug binding energy. Three-layer ONIOM (M06-2x/6-31+G*:PM6: AMBER) method was used for studying of drug binding. Initial models were constructed using binding sites derived from Hotspot Wizard Server and capping of their amino acids. Binding energy values demonstrated that strongest binding belong to drug of 4,4'-((o-tolylimino)methylene)diphenol and weakest binding happen with drug of 4,4'-(((2-chlorophenyl)imino)methylene)diphenol. Also, we have found that binding energy depend on substitute group on studied drugs. Interaction energy data showed that drug binding strength depend on hydrogen bonding with residues of Glu353, Arg394 and Thr347 and also hydrophobic interaction with other residues.

Keywords: Cancer; Binding energy; DFT.

Introduction

Breast cancer is important diseases among females which affect one out of ten women. Excessive exposure to estrogens is an important factor for breast cancer risk. Estrogen receptor in breast cells is a protein that transduces signals of their binding ligands. This protein has four important regions including N-terminal regulatory domain (A-B), DNA-binding domain (C), Hing region (D) and Ligand binding domain (E). Binding of drug to ligand domain causes a conformational deformation in receptor protein. This deformation leads to several events that result to gene expression [1-6].

In this study, three-layer ONIOM method was used to obtain binding affinity for six breast cancer drugs. Then, optimized structures were applied to achieve interaction energy between drug and binding pocket using a high level of theory.

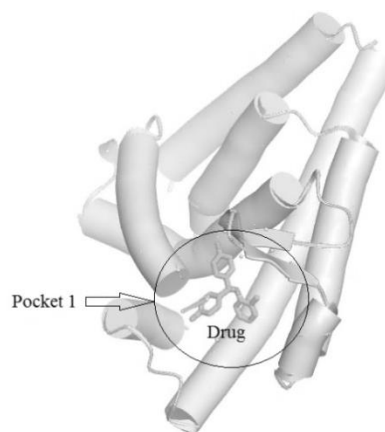


Fig. 2. Crystal structure of Ligand Binding Domain of estrogen receptor along with catalytic or main pocket.

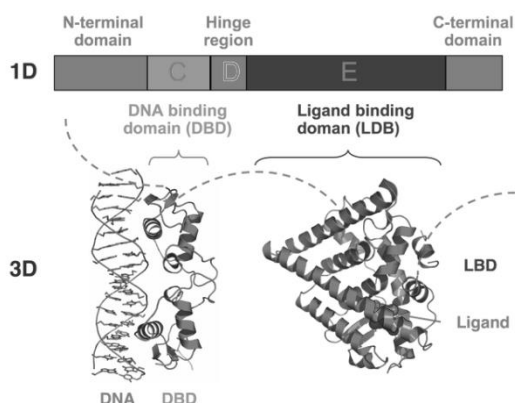


Fig. 1. The structure of estrogen receptor.

Materials and method

The catalytic pocket along with drug was extracted from X-ray structure. Then cutting residues were capped by acetyl and methyl amino groups. Models generated were optimized by three-layer ONIOM (M06-2x/6-31+G*:PM6: AMBER) method with Gaussian 09 software.

We used following equations to derive binding energy for optimized structures.

$$BE = INT + DEF^{pocket} + DEF^{drug} \quad (1)$$

$$BE = E_{opt}^{model} - E_{opt}^{pocket} - E_{opt}^{drug} \quad (2)$$

$$INT = E_{opt}^{model} - E[pocket]_{sp}^{model} - E[drug]_{sp}^{model} \quad (3)$$

$$DEF^{drug} = E[drug]_{sp}^{model} - E_{opt}^{drug} \quad (4)$$

$$DEF^{pocket} = E[pocket]_{sp}^{model} - E_{opt}^{pocket} \quad (5)$$

where BE, INT, DEF^{pocket} and DEF^{drug} are binding, interaction and pocket deformation and drug deformation energy, respectively. E_{opt}^{model} , E_{opt}^{pocket} and E_{opt}^{drug} are optimized energy of model, optimized pocket and optimized ligand, respectively. $E[drug]_{sp}^{model}$ and $E[pocket]_{sp}^{model}$ are single point energy of pocket and ligand derived from optimized structure of models, respectively.

Model	INT	DEF^{drug}	DEF^{pocket}	BE
1	-17.961	0.007	17.467	-0.487
2	-0.089	0.006	0.001	-0.082
3	-0.042	0.111	-0.004	0.065
4	-0.019	0.018	-0.007	-0.008
5	-3.363	0.011	3.275	-0.077
6	-0.088	0.014	0.003	-0.071

Results and Discussion

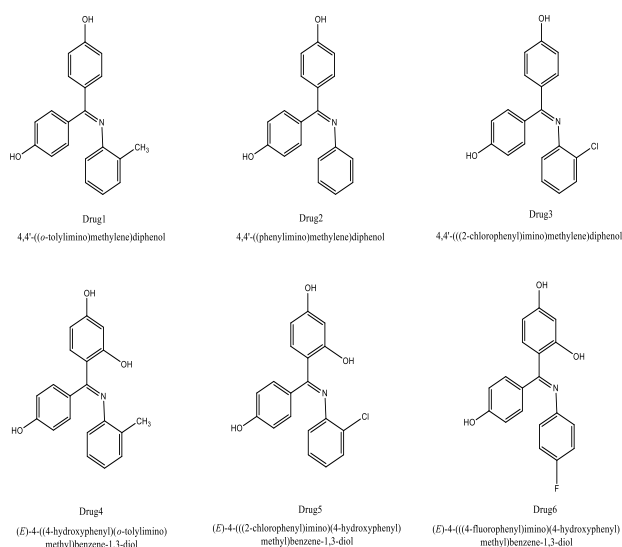


Fig. 3. The structure of imine drugs used for deriving of binding energy.

Table 1 shows decomposition of binding energy to INT and DEF for all drugs mentioned in Fig.3. The decomposition of energy components are achieved from equation 1-5 in computational details section. As seen, the major contribution in binding energy belongs to INT energy term. Moreover, the INT term is favorable for binding process for all models. Tighter binding is seen for model 1 than that of other models. DEF^{drug} and DEF^{pocket} energy terms represent conformational change of drug and pocket, respectively. Comparison of DEF^{drug} for all models shows that drugs of 1 to 6 require energy for conformation adaption upon binding to its pockets. On the other hand, DEF^{pocket} values show that conformational change is unfavorable except for pocket 3 and 4. Comparison of BE demonstrates following order for models 1 to 6 as follows:

$$1 > 2 > 5 > 6 > 4 > 3$$

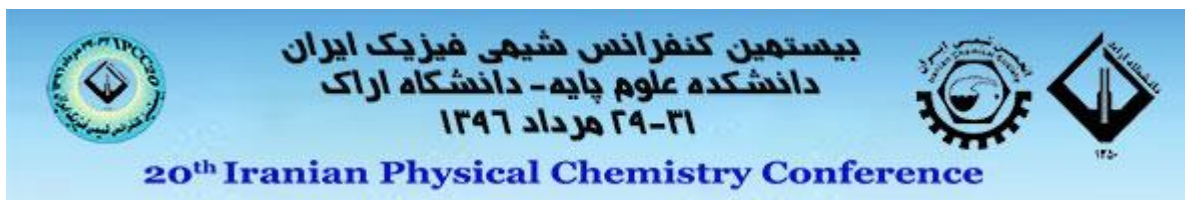
By looking at the structure of drug 1 to 6, we can discuss derived order. If we look at structure of drug 3, we can see an electron withdrawing group ($-Cl$ group). This group lead to withdrawing of electron and decreasing of hydrogen bond strength between drug and its pocket. Therefore, its conformational change or its DEF^{drug} reduces significantly. So, drug cannot bind to pocket strongly.

Two electron donor (i.e. $-CH_3$ and $-OH$) on drug 4 lead to increasing of electrons on different parts of molecule. Increasing of electron increases resonance and also bond order of drugs. So, rotation of benzene rings containing $-OH$ group for creation of hydrogen bond with its pocket cannot be done.

For drug 5 and 6, the existence of one electron donor and one electron acceptor in drug result to moderate condition for rotation of drugs. Drug 2 without any electron donor and acceptor has more flexible structure for formation of hydrogen bond. Finally, electron donor group of $-CH_3$ in drug 1 lead to strong binding of this drug to its pocket because this group increases electron in drug without changing of its bond order.

Conclusions

In this study, we used ONIOM method to calculate binding energy for some imine drugs. Models used in our study were constructed using available x-ray for imine drugs. Binding energy was derived after optimization of constructed models. It was found that major interaction in binding energy belongs to interaction energy term. On the other hand, the effect



of substitute group of drug is important factor to BE values.

References

- [1] E.N. Imyanitov, K.P. Hanson, Mechanisms of breast cancer, *Drug Discovery Today: Disease Mechanisms*, 1 (2004) 235-245.
- [2] M. Clemons, P. Goss Estrogen and the Risk of Breast Cancer, *New England Journal of Medicine*, 344 (2001) 276-285.
- [3] K. McPherson, C.M. Steel, J.M. Dixon, Breast cancer—epidemiology, risk factors, and genetics, *BMJ* 321 (2000) 624-628.
- [4] S.E. Singletary, Rating the Risk Factors for Breast Cancer, *Annals of Surgery*, 237 (2003) 474-482.
- [5] M. Dieterich, J. Stubert, T. Reimer, N. Erickson, A. Berling, Influence of Lifestyle Factors on Breast Cancer Risk, *Breast Care*, 9 (2014) 407-414.
- [6] E.G. Hohenstein, S.T. Chill, C.D. Sherrill, Assessment of the Performance of the M05-2X and M06-2X Exchange-Correlation Functionals for Noncovalent Interactions in Biomolecules, *Journal of Chemical Theory and Computation*, 4 (2008) 1996-2000.

Substitution effect on singlet-triplet energy gap and electrophilicity of silylenes at Density Functional Theory

Shiri, Azam

Department of chemistry, Faculty of Science, Malayer University, Malayer, Iran: amshiri@gmail.com

Abstract: The effect of different substituents on stability of several *N*-heterocyclic silylenes study with the aid of ΔE_{S-T} parameter at DFT using B3LYP/6-311++G** basis set. The field of stable silylene research has grown dramatically since the first isolation of a stable silylene in 1994. Prior to 1994, silylenes existed only as reactive intermediates, isolable only in low temperature matrixes. Since then, several stable silylenes have been synthesized, some in fact showing remarkable thermal stability. Here, silylenes with electron donating groups have stability higher than electron withdrawing ones. This stability may be attributed to the effective electron donating character of the nitrogen atoms that enhances with former groups.

Keywords: *Density Functional Theory, Silylene, Stability, Singlet-triplet energy gap*

Introduction

Quantum chemistry is capable of calculating a wide range of electronic and thermodynamic properties of interest to a chemist or physicist. Calculations can be used both to predict the results of future experiments and to aid in the interpretation of existing results. Quantum chemistry can also be applied to biological processes such as toxicity and carcinogenicity.

Silylenes, $RR'Si$, are divalent silicon species analogous to carbenes. Most of them are only known as reactive intermediates in thermal and photochemical reactions. Their existence has been proved by forming adducts with trapping agents while in recent years several stable species have been isolated [1–3]. The first stable silylene was synthesized and isolated as a diamino silylene, *N,N'*-di-*tert*-butyl-1,3-diaza-2-silacyclopent-4-en-2-ylidene, in 1994 by M. Denk et al. [1].

In general, silylenes prefer a singlet configuration in their ground state. Several factors associated to the stabilization of singlet ground state silylenes are well-known, the *p*-electron donating ability from the substituent to the formally empty 3*pz* orbital of silicon being the most important one. Other factors are the aromaticity, and ring stress in the case of cyclic compounds [4–7]. Steric effects due to dialkyl substitutions has been studied and reported [8]. Many workers have addressed interesting questions concerning the generation, reactivity, substituent effects, singlet-triplet energy gaps, relative stabilities and usages of silylenes [9–15].

Two different concepts of stability can be considered in chemistry. In a chemist's mind stability indicates the preservability of a compound. In quantum chemistry, stability means the depth of the minima on the potential energy surface. The first is a kinetic factor, which can be studied and quantified by the reactivity of the compound. The latter is a thermodynamic factor which can be calculated by quantum chemical methods. Two useful

ways have been introduced to estimate the thermodynamic stability of silylenes. On the one hand the singlet-triplet energy separation of silylenes turned out to be a reliable measure: increasing stability of the molecules increases the singlet-triplet energy separation. On the other hand isodesmic reaction energies were used to set up a scale for the relative stability of substituted silylenes [16].

DFT is a computational quantum mechanical modelling method used in physics, chemistry and materials science to investigate the electronic structure (principally the ground state) of many-body systems, in particular atoms, molecules, and the condensed phases.

Density Functional Theory (DFT) based reactivity descriptors were used in conjunction with the molecular electrostatic potential as measures of chemical reactivity, whereas the reaction enthalpy for isodesmic reaction and the singlet-triplet energy difference were used as measures of stability.

Here we will present examples of how quantum chemistry can be used to examine the influence of ΔE_{S-T} on stability of several silylenes.

Computational details

Geometries of all molecules considered in this study were fully optimized using gradient corrected DFT with Becke's three-parameter hybrid exchange functional, the Lee-Yang-Parr correlation functional (B3LYP) and with the 6-311++G** basis set using Spartan' 10 program [17]. ΔE_{S-T} was obtained as $E_{(triplet)} - E_{(singlet)}$, where the geometries of both electronic states were separately optimized.

Results and Discussion

As the nature of substituents has a remarkable effect on stability, we decided to evaluate such an effect with ΔE_{S-T} and ω for a series of *N,N'*-disubstituted silylenes **1**

Table 1. ΔE_{s-T} , chemical potential(μ), global hardness(η) and

Entry	X	HOMO O (eV)	LUMO MO (eV)	ΔE_{s-T} (Kcal/mo l)	μ (eV)	η (eV)	ω (e V)
1	NH ₂	-5.45	- 1.23	50.9 0	-3.34	4.2 2	1.3 2
2	OH	-5.74	- 1.30	49.9 5	-3.52	4.4 4	1.3 9
3	OC H ₃	-5.60	- 1.13	49.6 6	-3.36	4.4 7	1.2 7
4	CH ₃	-5.32	- 0.85	54.6 3	-3.08	4.4 7	1.0 6
5	H	-5.54	- 0.83	60.6 2	-3.18	4.7 1	1.0 8
6	F	-6.25	- 1.65	29.1 7	-3.95	4.6	1.6 9
7	Cl	-6.10	- 2.01	24.8 5	-4.05	4.0 9	2.0 1
8	Br	-6.01	- 2.62	20.4	-4.31	3.3 9	2.7 5
9	I	-5.89	- 3.04	18.2 0	-4.46	2.8 5	3.5 0
10	CH O	-6.84	- 2.68	66.1 0	-4.76	4.1 6	2.7 2
11	CN	-7.31	2.91	55.1 7	-5.11	4.4	2.9 7
12	NO ₂	-7.39	- 3.64	50.1 8	-5.51	3.7 5	4.0 5

using DFT method at the B3LYP/6-311++G** level of theory that are summarized in table 1. We have already reported the halogens, electron donating and electron withdrawing substituents effects on the stability and the singlet-triplet splitting.

The electron donating substituents and the electron withdrawing groups lead to high singlet-triplet energy gap and so have high stability.

Chemical potential μ and η were obtained using:

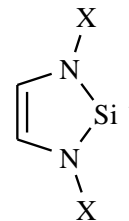
$$\mu = \frac{E_{HOMO} + E_{LUMO}}{2} \quad (1)$$

$$\eta = E_{LUMO} - E_{HOMO} \quad (2)$$

$$\omega = \mu^2 / 2\eta \quad (3)$$

Notably, the order of ω for electron donating groups is as follows $CH_3 < OCH_3 < NH_2 \cong H < OH$ indicating that inductive effect is more significant than resonance effects. The NO_2 substituent leads to high ω value because of its σ and π -withdrawing character. Species with high ω values have high μ .

electrophilicity (ω) of **1-12** computed at the B3LYP/6-31+G level of theory



1

Scheme 1. N-Heterocyclic silylenes

Conclusions

In this paper, DFT calculation has determined that substitutions have dramatic effect on stability and reactivity of silylenes.

Acknowledgment

The authors gratefully acknowledge the financial support for this work from the Malayer University, Malayer, Iran.

References

- [1] M. Denk, J.C. Green, N. Metzler, M. Wagner, *J. Chem. Soc. Dalton Trans.* (1994) 2405.
- [2] J. Heinicke, A. Oprea, M.K. Kindermann, T. Kárpáti, L. Nyulászi, T. Veszprémi, *Chem. Eur. J.* 4 (1998) 541.
- [3] M. Kira, S. Ishida, T. Iwamoto, C. Kabuto, *J. Am. Chem. Soc.* 121 (1999) 9722.
- [4] B.T. Luke, J.A. Pople, M.B. Krogh-Jespersen, Y. Apeloig, M. Karni, J. Chandrasekar, P.V.R. Schleyer, *J. Am. Chem. Soc.* 108 (1986) 270.
- [5] L. Nyulászi, A. Belghazi, S. Kis-Szetsi, T. Veszprémi, J. Heinicke, *J. Mol. Struct. (Theochem)* 313 (1994) 73.
- [6] C. Heinemann, T. Müller, Y. Apeloig, H. Schwarz, *J. Am. Chem. Soc.* 118 (1996) 2023.
- [7] T. Veszprémi, L. Nyulászi, T. Kárpáti, *J. Phys. Chem.* 100 (1996) 6262.
- [8] M. Z. Kassaei, B. N. Haerizade and Z. Hossaini, *J. Mol. Struct. (Theochem)* 681(2004) 129.
- [9] P.P. Gaspar, M. Xiao, D. Ho Pae, D.J. Berger, T. Haile, T. Chen, D. Lei, W.R. Winchester and P. Jiang, *J. Organometallic Chem.* 646 (2002) 68.
- [10] M. Weidenbruch, *J. Organometallic Chem.* 646 (2002) 39.
- [11] M. Haaf, T.A. Schmedke and R. West, *Acc. Chem. Res.* 33 (2000) 704-714.

A computational study on Gauche Effect of C₈H₁₅O-X (X: OH, NH₂, CH₃) Conformers

G. Kouchakzadeh

Department of chemistry, Khorramabad Branch, Islamic Azad University, Khorramabad, Iran

gh_kouchakzadeh@yahoo.com

Abstract: Theoretical calculations of chemical hardness and stability energy on C₈H₁₅O-X (X: OH, NH₂, CH₃) carried out by NBO at the B3LYP/6-311+G** level. C₈H₁₅O-X have been two distinguishable conformations: one CO-anti position, and the other CO-gauche position. This calculations confirm importance of LP₂O₁₆ → σ*_{C12-Y} (Y=O, N, C) hyperconjugation interactions that can stable the CO-gauche conformers. Chemical hardness of CO-gauche conformers is in good agreement with the energy results. This results show that molecular interaction in the gauche geometries increases from compound with X=OH to X=CH₃. Actually, the gauche effect with hyperconjugation factor play important role in the stability of the gauche geometries.

Keywords: “Gauche Effect, Chemical Hardness, C₈H₁₅O-X (X: OH, NH₂, CH₃)”

Introduction

The gauche effect is a tendency to conform to a structure that has the maximum number of gauche interactions between adjacent electron pairs or polar bands[1]. This effect characterizes any gauche-conformer which is more stable than the anti-conformer[2]. There are two main explanations for the gauche effect: hyperconjugation and bent bonds.

In this work, We used C₈H₁₅O-X compounds with X= OH, NH₂, CH₃ and expected that C₈H₁₅O-X have been two distinguishable conformations: one CO-anti position, and the other CO-gauche position(Fig.1). The gauche-conformations were found to be more stable by hyperconjugation factor of the gauche effect.

Also, in this study, Natural Bond Orbital (NBO) analysis provides an efficient method for studying intra and intermolecular bonding and interaction among bonds[3].

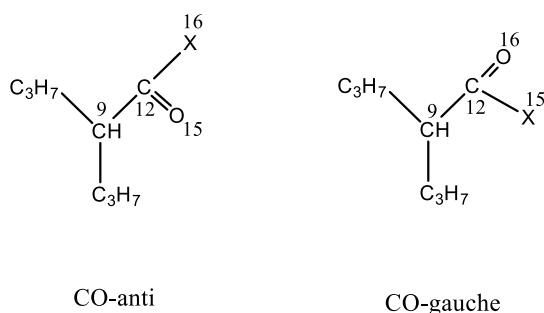


Fig.2: The structures of C₈H₁₅O-X (X=OH, NH₂, CH₃) in conformation CO-gauche and CO-anti

Computational method

This study was carried out by the Gaussian 09 program. Geometry optimizations of compounds

[CO- gauche and CO-anti conformers] was performed at the B3LYP/6-311+G** level. Natural Bond Orbital analysis was also performed at the B3LYP/6-311+G** level of theory.

NBO analysis was carried out by considering all possible interactions between filled donor and empty acceptor NBOs and estimating their energy importance by second-order perturbation theory [4].

Chemical hardness is an important reactivity property of matter that is defined as the resistance towards electron cloud polarization or deformation of chemical species is a measure of stabilities and reactivates of molecules [5]. Global chemical hardness (η) was calculated as follows:

$$\eta = 0.5(\epsilon_{LUMO} - \epsilon_{HOMO}) \quad (1)$$

Results and Discussion

Table 1 shows the values of the chemical hardness of the CO-gauche and CO-anti conformers. In C₈H₁₅O-X geometries, hyperconjugation factor of the gauche effect increases the stability to gauche conformers.

Also, there is a stereoelectronic preference for conformations in which the best donor lone pair is antiperiplanar to the best acceptor bond.

Chemical hardness of gauche conformers decreases from compound with X=OH to X=CH₃ and the E₂ too. This results show that molecular interaction in the gauche geometries increases from compound with X=OH to X=CH₃.

Table1: Chemical hardness for different compounds of C₈H₁₅O-X (X: OH, NH₂, CH₃)

compound	$\epsilon_{\text{LUMO}} - \epsilon_{\text{HOMO}}$	η
C ₈ H ₁₅ O-OH,anti	۰,۲۷۲۲۳	0.136115
C ₈ H ₁₅ O-OH, gauche	۰,۲۷۳۸۸	0.136940
C ₈ H ₁₅ O-NH ₂ ,anti	0.24693	0.123465
C ₈ H ₁₅ O-NH ₂ ,gauche	0.24515	0.122575
C ₈ H ₁₅ O-CH ₃ ,anti	0.22304	0.11152
C ₈ H ₁₅ O-CH ₃ , gauche	0.22474	0.11237

Table 2 shows the stability energies of the CO-gauche and CO-anti conformers.

Table2: Molecular interaction and calculated energies (in Hartree) of the HOMO and the LUMO for different compounds of C₈H₁₅O-X (X: OH, NH₂, CH₃)

compound	donor-accepter	E ₂ (stability energy)
C ₈ H ₁₅ O-OH,anti	LP ₂ O ₁₆ →σ*C ₁₂ -O ₁₅	34.05
C ₈ H ₁₅ O-OH, gauche	LP ₂ O ₁₆ →σ*C ₁₂ -O ₁₅	34.15
C ₈ H ₁₅ O-NH ₂ ,anti	LP ₂ O ₁₅ →σ*C ₁₂ -N ₁₆	24.88
C ₈ H ₁₅ O-NH ₂ ,gauche	LP ₂ O ₁₆ →σ*C ₁₂ -N ₁₅	25.61
C ₈ H ₁₅ O-CH ₃ ,anti	LP ₂ O ₁₅ →σ*C ₁₂ -C ₁₆	20.25
C ₈ H ₁₅ O-CH ₃ , gauche	LP ₂ O ₁₆ →σ*C ₁₂ -C ₁₅	20.58

Conclusions

The origin of the gauche effect in C₈H₁₅O-X is hyperconjugation. The gauche effect plays important role in the stability of gauche geometries. LP₂O₁₆→σ*C₁₂-Y(Y=O, N, C) interaction is responsible for gauche preference in C₈H₁₅O-X. The results show that chemical hardness of gauche geometries decrease from compound with X=OH to X=CH₃, the stability energy (E₂) is also same trend.

References

- [1] M. B. Smith, J. March, "March's Advanced Organic Chemistry", 2007, A John Wiley & Sons Publication, 6th Ed, 200.
- [2] N. C. Craig, A. Chen, K. Hwan Suh, S. Klee, G. C. Mellau, B. P. Winnewisser, and M. Winnewisser, "Contribution to the Study of the Gauche Effect. The Complete Structure of the *Anti* Rotamer of 1,2-Difluoroethane", J. Am. Chem. Soc., 119(20) (1997) 4789-4790.
- [3] P.Rubarani ,S.Gangadharan, Sampath Krishnan, " Natural Bond Orbital (NBO) Population Analysis of 1-Azanaphthalene-8-ol", J. ACTA PHYSICA POLONICA A, 125(2014) 18-22.
- [4] G. Kouchakzadeh, D. Nori-Shargh, " Symmetry breaking in the planar configurations of disilicon tetrahalides: Pseudo Jahn-Teller effect parameters, hardness and electronegativity", J. Phys. Chem. Chem. Phys., 17(43) (2015) 29252-61.
- [5] N.R.Sheela, S. Muthu, S. Sampathkrishnan, " Molecular orbital studies (hardness, chemical potential and electrophilicity), vibrational investigation and theoretical NBO analysis of 4-4'-(1H-1, 2, 4-triazol-1-yl methylene) dibenzonitrile based on abinitio and DFT ", J. Molecular and Biomolecular Spectroscopy, 120(2014) 237-251.



Theoretical Study on the Reaction Mechanism Of NH And HO₃

S. khoie^{a*}, H.douroudgary^a, M. Vahedpour^a

^aDepartment of chemistry, University Zanjan, P.O. Box 45371-38791, Zanjan, Iran

^aDepartment of chemistry, University Zanjan, P.O. Box 45371-38791, Zanjan, Iran

*samira.khoie68@gmail.com

Abstract : The gas phase reaction of imidogen, NH, and HO₃ have been studied computationally on the doublet potential energy surface (PES). The mechanism of two main products are discussed in this work. In kinetic point of view, suitable barrier energies and the number of transition state can caused the suggested pathways are possible and favour. In thermodynamic aspect, two obtained products with large value in standard Gibbs free energies of reactions are most stable in comparison with the reactants.

Keywords: "Imidogen;doublet state;mechanism;potential energy surface"

Introduction

The imidogen radical is found in a wide variety of environments and has been observed in various of astrophysical sources. It is the key for understanding the fate of nitrogen in combustion systems regardless of whether the nitrogen originates from nitrogen-containing fuel or from the air. NH was first observed in a nonlaboratory source in the spectrum of the sun. Since then NH was detected again in the spectrum of the sun and in comets. NH is important in understanding the photochemistry of ammoniacal planetary atmospheres and interstellar chemistry. It is also observable in the Earth's atmosphere. The imidogen radical was one of the first radicals which was detected in stellar atmospheres. NH is one of the few species with a triplet electronic ground state ($^3\Sigma^-$), isoelectronic with O(3P) and CH₂ ($\bar{X}^3 B_1$). NH can be produced in the gas phase as well as in a Liquid or in the solid state (matrices). In a collision-free situation, the excited electronic state has a maximum lifetime, since collisions depopulate the excited states [1]. Trioxy radicals O₃R are assumed to play key roles in hydrocarbon oxidation, combustion, atmospheric chemistry, as well as chemical and biochemical oxidations. Specifically, the HO₃ radical has been postulated repeatedly in the past as an important intermediate in atmospheric processes, although it had never been detected experimentally. In particular, it was not clear whether the combination of atomic hydrogen with ozone might lead to a long-lived HO₃ radical or if immediate dissociation into O₂ and OH takes place. In 1996, ion cyclotron resonance mass spectrometry was used by Speranza to estimate the enthalpy of formation of HO₃ to -4.2 ± 21 kJ mol⁻¹. This estimate implies that the reaction enthalpy of O₂ + OH → HO₃ is -41.8 ± 21 kJ mol⁻¹ [2].

The goal of the present work is the computational study of the mechanisms of NH+ HO₃ reaction to identify some final products and their production pathway. Also, special notice has been given to the thermodynamics aspect of the reaction by MP2

calculation. We also carry out a complete analysis of the triplet potential energy surface of the reaction.

Materials and method

All the calculations have been carried out using Gaussian 09 software package program [3]. All geometry optimizations were carried out using second order Møller–Plesset perturbation theory MP2 approach in connection with the 6-311++g(d, p) basis set.

Results and Discussion

According to the reaction mechanism, two products in possible pathways are yielded, As shown in the figure1. geometries of all species represented in figure 2. Thermodynamic parameters of obtained product tabulated in table 1. We found one pre-reaction complex between NH and HO₃ denoted as C1. C1 is converted into IN1 via TS1 with the energy barrier of 46.55 kcal/mol. Then IN1 is transformed into CP2 and CP3 via two transition state which are TS2 and TS3 with the energy barriers of 3.27 and 14.83 kcal/mol, respective. CP2 can directly transform into P2(HO₂+NOH) and CP3 can directly transform into P3(O₂+H₂NO).

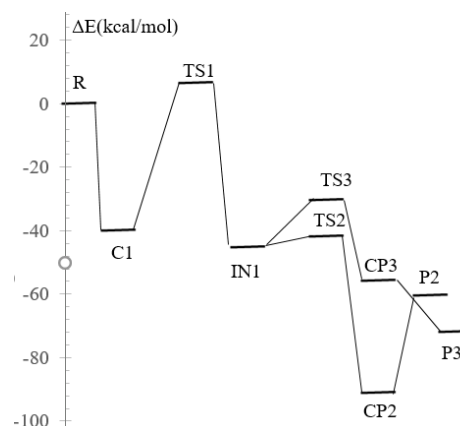




Fig 1: Schematic representation of the doublet potential energy surface of [NH+HO₃] system computed at the MP2/6-311++g (d,p) level.

Table 1. The standard internal energies, enthalpies, Gibbs free energies in kcal mol⁻¹, and entropies of reaction in cal mol⁻¹K⁻¹ at the MP26-311++g (d,p) level.

MP2	ΔE°	ΔH°	ΔG°	ΔS°
P2	-71.68	-71.98	-72.76	57.63
P3	-62.38	-60.24	-60.41	54.56

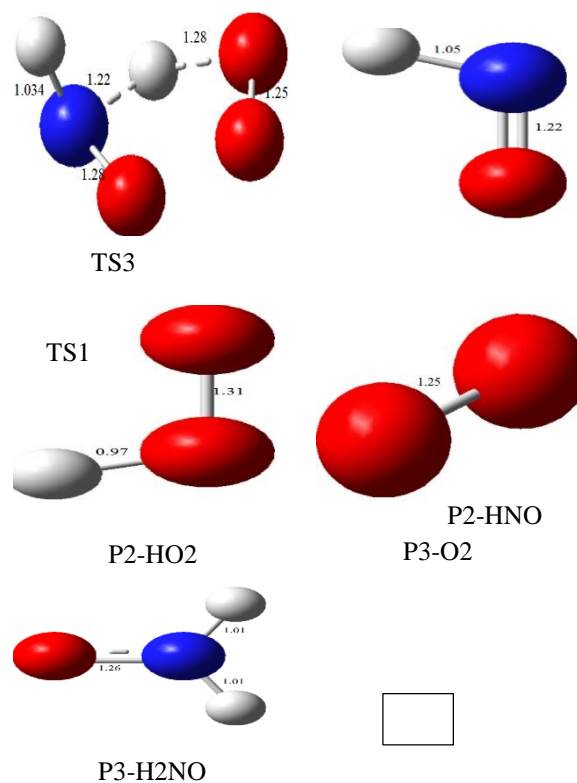
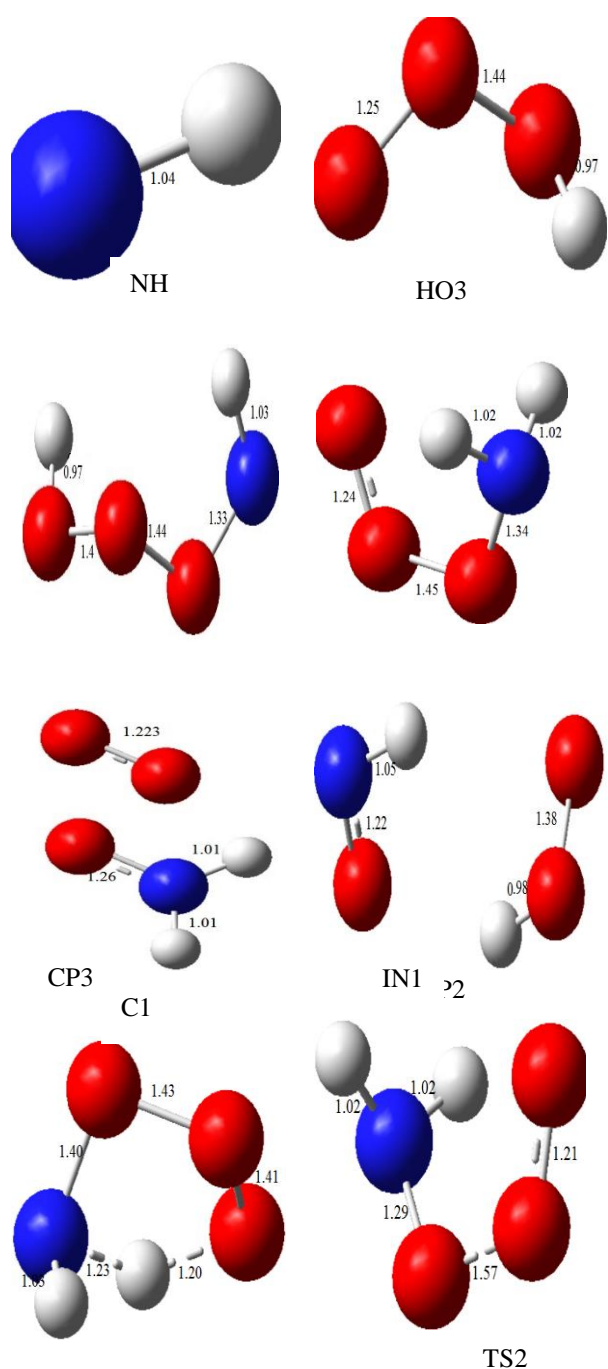


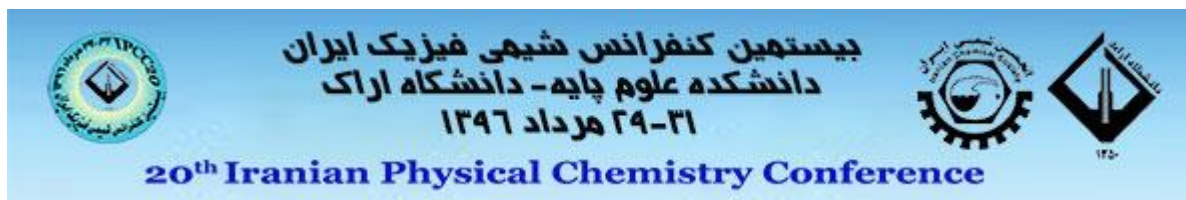
Fig 2. geometries of optimized structures at MP2/6-311++g(d,p) level.

Conclusions

In the present work, we have characterized the details of the gas-phase reaction between NH and HO₃ on the doublet PES with MP2 level of theory in connection with the 6-311++G(d,p) basis set. Based on our suggested mechanism, for the most important products, two reaction pathways with suitable energy of transition state are obtained. The reaction is initiated via association of two reactant(C1) and in the entrance channels ended to final products complexes then these complexes release to corresponding final stable adducts.

References

- [1] W. Hack, R. Haubold, C. H-Sterzel, H. Keller-Rudek, U. Ohms-Bredemann, D. Schioberg, C. Strametz, "Gmrelin Handbook of Inorganic and Organometallic Chemistry", Springer-Verlag Berlin Heidelberg, 1993, 8rd Ed., 14-17.
- [2] W. M. F. Fabian, J. Kalcher, R. Janoschek, "Stationary points on the energy hypersurface of the reaction O₃ + H → [HO₃]* ↔ O₂ + OH and thermodynamic functions of HO₃ at G3MP2B3, CCSD(T)-CBS (W1U) and MR-ACPF-CBS levels of theory", *Theoretical Chemistry Accounts*, 114 (2005) 182–188.



Predicting the entropy of benzene derivatives Using Topological Indices and Quantitative Structure Property Relationship

B. Bijani^a, F. Shafiei^{*}

^{a,b}Department of Chemistry, Science Faculty, Arak Branch, Islamic Azad University,

P.O. Box 38135-567, Arak 38361-1-9131, Iran

*e-mailcorresponding author: *f-shafiei@iau-arak.ac.ir*

Abstract: Topological indices are digital values that are assigned based on chemical composition. These values are purported to correlate chemical structures with various chemical and physical properties. They have been successfully used to construct effective and useful mathematical methods to establish clear relationships between structural data and the physicochemical properties of these materials.

In this study, a QSPR study relating topological indices to the entropy of 113 benzene derivatives is reported. The entropy values were calculated at HF level of theory (6-31 G basis sets) by Gaussian 98. Multiple linear regression (MLR) provided good models with three to seven independent variables. The best model obtained is based on three descriptors: Randić, Wiener and Szeged topological indices, with values of the correlation coefficient ($r=0.927$), the standard error ($s=16.430\text{J/mol}$) and the adjusted correlation coefficient was calculated as 0.859.

Keywords: Topological indices; benzene derivatives; QSPR; MLR method.

Introduction

One of the most important purposes in application of mathematical and statistical methods is to find a relationship between molecular structure and values of physical properties, chemical reactivity or biological activity. As a result, quantitative structure-property relationship (QSPR) and quantitative structure-activity (QSAR) studies have been promoted.

QSAR or QSPR modeling methods have been used for more than 50 years but there is still, surprisingly, considerable confusion on the best way to characterize the quality of models.

Topological indices (TIs), as molecular descriptors, are important tools in QSPR/QSAR studies [1-5]. A topological index is a graph invariant number calculated from a graph representing a molecule.

The physicochemical properties of compounds are important in many fields, including pharmaceuticals, chemistry, biochemistry and environmental sciences. Property estimations can help to minimize time and cost in producing new chemical materials with desired properties.

Predictive methods for estimating thermodynamic properties, such as enthalpies of formation, Gibbs free energy and entropies of acyclic and aromatic compounds, on the basis of fundamental concepts on molecular structure have been reported [6].

Artificial Neural Networks were also used in developing QSPR models for prediction of physicochemical properties [7,8].

Prediction of entropies and enthalpies of organic compounds by using group contribution methods was also published [9]. Prediction of standard absolute

entropy ($S_{298\text{K}}$) of gaseous organic and inorganic compounds was reported in [10,11].

The main aim of this study is to illustrate the usefulness of topological indices in QSPR study of entropy (S) of benzene derivatives. As far as we are aware, this is the first QSPR study for prediction of benzene derivatives entropies using topological indices.

Materials and method

The entropy (S) of 113 benzene derivatives (benzene included) was computed at the Hartree-Fock (HF) level of theory, using the ab initio 6-31G basis sets. The benzene derivatives in this set have seven different substituents, each substituent being present in at least six compounds. These substituents are amino, bromo, chloro, hydroxyl, methyl, methoxyl and nitro groups. To obtain an appropriate QSPR model we used multiple linear regression (MLR) procedure, by SPSS software, version 16, and backward stepwise regression was used to construct the QSPR models.

The best predictive QSPR model is developed on a reduced training set of 69 chemicals, having an acceptable predictive capability on 44 test set compounds.

For drawing the graphs of our results, we used the Microsoft Office Excel – 2003 program.

Seven topological indices tested in the present study are Randić (1χ), Balaban (J), Harary (H), Szeged (Sz), Hyper Wiener (WW), Wiener Polarity (Wp) and Wiener (W) indices.

All the used topological indices were calculated in

hydrogen suppressed graphs. The descriptors were calculated with Chemicalize program [12].

Statistical Analysis

Structure-Property models (MLR models) are generated using the multi linear regression procedure of SPSS, version 16. The entropy (S, J/mol K) is used as the dependent variable and 1χ , J, H, Sz, WW, Wp and W indices are used as the independent variables. The models are assessed with r value (correlation coefficient), the r^2 (coefficient of determination), the r^2 - adjusted, the s value (root of the mean square of errors), the F value (Fischer statistic), the D value (Durbin-Watson) and the Sig (significant).

Results and Discussion

Several linear QSPR models involving three to seven descriptors were established and the strongest multivariable correlations were identified by the backward method, with significant at the 0.05 level and regression analysis of the SPSS program.

For obtaining appropriate QSPR models we used maximum R2 method and followed backward regression analysis. The predictive ability of the model is discussed on the basis of predictive correlation coefficient.

The best linear model contains three topological descriptors, namely, Randić (1χ), Wiener (W) and Szeged (Sz) indices with an acceptable predictive power on the test set. The regression parameters of the best three descriptor correlation model is gathered in equation 1.

$$S = 70.258 + 59.9661\chi + 2.748Sz - 4.163W \quad (1)$$

$$N_{\text{train}}=69; r_{\text{train}}=0.927; r^2_{\text{train}}=0.859; S_{\text{train}}=16.43; D_{\text{train}}=2.033; F_{\text{train}}=132.299$$

$$N_{\text{test}}=44; r_{\text{test}}=0.984; r^2_{\text{test}}=0.968; S_{\text{test}}=10.06; D_{\text{test}}=1.790; F_{\text{test}}=406.452$$

This model produced a standard error of 16.430 J mol⁻¹ K⁻¹, a correlation coefficient of 0.927, and the adjusted correlation coefficient (adjusted r-squared) was calculated as 0.859.

The result is therefore very satisfactory. Fig 1 shows the linear correlation between the observed and the predicted entropy values obtained using equation (1).

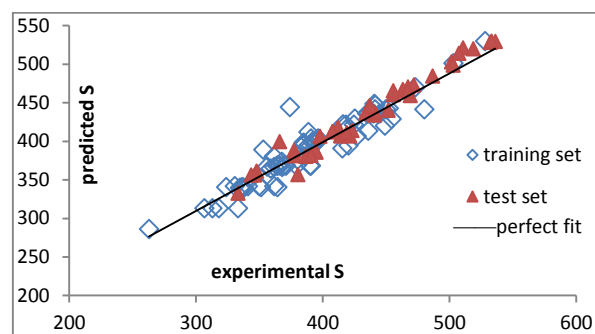


Fig. 1: Comparison between the predicted and observed entropy by MLR method (cf. eq. 1)

Residual Values

The residual values of entropy calculated by equation (1) show a fairly random pattern (see Figure 2). This random pattern indicates that a linear model provides a decent fit to the data.

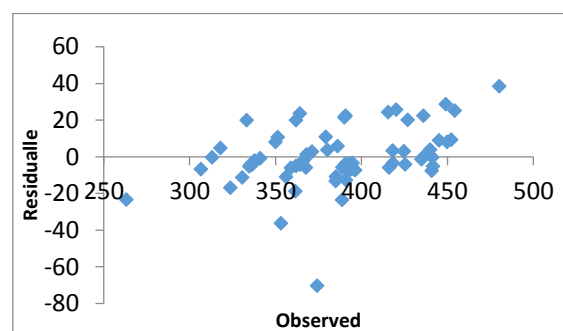


Figure 5. Plot of residuals against observed values of benzene derivatives entropy (S).

Conclusions

In this work, QSPR models for the prediction of entropy for a training set of benzene derivatives using MLR based on topological descriptors calculated from molecular structure have been developed. MLR model is proved to be a useful tool in the prediction of entropy.

The QSPR models found on a training set composed of 69 compounds have an acceptable predictive performance on a test set including 44 compounds.

The aforementioned results and discussion lead us to conclude that combining the three descriptors (Sz, W, 1χ) could be used successfully for modeling and predicting entropy (S) of compounds. This model contains fewer topological descriptors, maximum of Fischer statistic value (F) and minimum root of the mean square of errors (s).

References



- [1] A.A. Taherpour, F. Shafiei, The structural Relationship Between Randic Indices, Adjacency Matrix, Distance Matrixes and Maximum wavelength of linear simple Conjugated Polyene Compounds, *J. Molec. Struct. THEOCHEM*, 726(2005) 183-188.
- [2] F. Ashrafi, A.A. Rostami, and N. Mahdavi pour, Study on QSPR Method for Theoretical Calculation of Boiling Point of Some Organic Compounds, *Asian J. Chem.* 21(3) (2009) 1667-1671.
- [3] D. Janežič, B. Lučić, S. Nikolić, A. Miličević, and N. Trinajstić, Boiling Points of Alcohols – A Comparative QSPR Study, *Internet Electron. J. Mol. Des.* 5 (2006) 192–200.
- [4] M. Kompany-Zareh, A QSPR study of boiling point of saturated alcohols using genetic algorithm, *Acta Chim. Slov.* 50(2003)259-273.
- [5] F. Shafiei , H. Hosseini , Quantitative Structure Property Relationship Models for the Prediction of Gas Heat Capacity of Benzene Derivatives Using Topological Indices, *MATCH Commun. Math. Comput. Chem.* 75, (2016) 583-588.
- [6] P. R. Duchowicz, E. A. Castro, F. M. Fernández, M. P. González, A new search algorithm for QSPR/QSAR theories: Normal boiling points of some organic molecules, *Chem. Phys. Lett.* 412 (2005) 376–380.
- [7] Li. Qianfeng, Chen. Xingguo, Hu. Zhide, Quantitative structure-property relationship studies for estimating boiling points of alcohols using calculated molecular descriptors with radial basis function neural network, *Chemometrics and Intelligent Laboratory Systems*, 72 (1) (2004) 93-100.
- [8] J. Taskinen, J. Yliruusi, Prediction of Physicochemical Properties, *Advan. Drug Delivery Rev.* 55 (2003) 1163-1183.
- [9] J. S. Chickos, C. M. Braton, D. G. Hesse and J. F. Liebman, Estimating Entropies and Enthalpies of Fusion of Organic Compounds, *J. Org. Chem.* 56 (1991) 927-938.
- [10] Mu. Lailong, Feng. Changjun, Topological Research on Molar Diamagnetic Susceptibilities for Inorganic Compounds, *MATCH Commun. Math. Comput. Chem.* 58(2007) 591-607.
- [11] Mu. Lailong, He. Hongmei, Estimation of Ideal Gas Entropy of Organic Compounds, *Ind. Eng. Chem. Res.* 50 (2011) 8764-8772.
- [12] Web search engine developed by ChemAxon; software available at <http://WWW.Chemicalize.Org>.



Ion-Pairs Formed in $[\text{MiM}^+]_2[\text{C}(\text{CN})_3^-]_2$ Ionic Liquid: A Theoretical Study

B. Makiabadi^a, M. Zakarianezhad^{*b}

^a Department of Chemical Engineering, Sirjan University of Technology, P.O. Box: 7813733385, Sirjan, Iran

^b Department of Chemistry, Payame Noor University, Tehran, Iran

*bmakiabadi@Yahoo.com

Abstract: Intermolecular interactions between cations and anions in $[\text{MiM}^+]_2[\text{C}(\text{CN})_3^-]_2$ ionic liquid have been studied using B3LYP, M052X and M056X methods in conjunction with the 6-311++G(2d,2p) basis set. Structures, interaction energies, charge transfer and hydrogen bonding of the ionic complexes have been investigated. The effect of different solvents on the stability of complexes and monomers was examined. The obtained natural bond orbital parameters show that in all ion pairs the charge transfer takes place from anions to cations. The $\text{LP}(\text{N}) \rightarrow \sigma^*(\text{N}-\text{H})$ and $\text{LP}(\text{N}) \rightarrow \sigma^*(\text{C}-\text{H})$ donor-acceptor interactions are the most important interactions in these complexes. It is predicted that $\text{N} \cdots \text{H}-\text{N}$ interaction is stronger than $\text{N} \cdots \text{H}-\text{C}$ one.

Keywords: Aggregation, Ionic liquids, Interaction energy, Charge transfer

Introduction

Ionic liquids are the most important new family of green solvents which can be used to substitute traditional organic solvents [1]. They are usually organic salts that melt below 100°C, generally composed of organic cations and inorganic or organic anions [2]. In the last two decades, ILs have received a wide attention due to their attractive properties, such as low flammability, extremely low vapor pressure, high thermal and chemical stability, as well as large liquid state temperature range and wide electrochemical window [3,4]. Some of scientists have shown that ionic liquids can be aggregated in aqueous and non-aqueous solutions. The aggregation behaviors of such surface-active ILs have attracted the most attention in the colloid and interface fields; numerous aggregates formed by the surface-active ILs have been investigated over the past years [5,6]. Many electrochemical applications of ionic liquids depend on ionic conductivities [7,8] which can be changed by their aggregation. The main aim of this work is to find the clusters formed from interaction between 2MIM⁺ and 2C(CN)₃⁻ ions, calculation of binding energy, geometrical parameters and characterization of the nature of intermolecular interactions in $[\text{MiM}^+]_2[\text{C}(\text{CN})_3^-]_2$ complexes.

Materials and method

All structures studied in this work were optimized by B3LYP, M052X and M062X methods using 6-311++G(2d,2p) basis set. Geometries, energies, and topologic properties were determined by using the Gaussian 03 program. The solvent effect on complexes stability was examined using B3LYP/6-311++G(2d,2p) method by applying the polarizable continuum model (PCM). NBO analysis were carried out at the B3LYP/6-311++G(2d,2p) level of theory.

Results and Discussion

In this work, complexes formed by interaction two cations with two anions of $[\text{MIM}^+][\text{C}(\text{CN})_3^-]$ ionic liquid were modeled. The optimized structures of aggregates were illustrated in Figure 1. Totally, four stable complexes were found on the potential energy surface. In all aggregates, N-H and C-H bonds of cation rings are involved in hydrogen bonds having different strength, which leads to slightly different intermolecular distances. It seems that the number and type of hydrogen bonds present in the complex play an important role in the stability of the complexes.

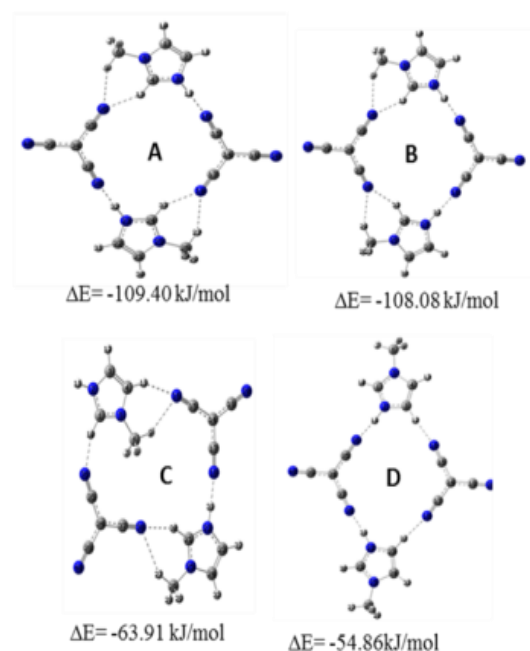


Fig.1: Optimized structures for complexes A–D at the B3LYP/6-311++G(2d,2p) level of theory.



Based on the Table 1, the relative stability of complexes decreases in the order $A > B > C > D$. The results show that, the interaction energies using B3LYP method is greater than that of M052X and M062X ones.

Table 1: Interaction energy for A-D complexes in different levels of theory.			
complex	method		ΔE_{elec}
A	B3lyp/ 6-311++G(2d,2p)		-109.40
B			-108.08
C			-69.91
D			-54.86
A	M052X /6-311++G(2d,2p)		-103.40
B			-102.51
C			-68.82
D			-41.21
A	M062X/ 6-311++G(2d,2p)		-104.30
B			-103.10
C			-63.53
D			-41.32

The results show that the tendency for aggregation decreases as the temperature increases. Also, the binding energy decreases on going from gas phase to solution phase. The association of ions to form the aggregates decreases with increase in polarity of solvent. The investigation of data shows that in all four complexes A–D the charge transfer takes place from anions to cations. The amount of the charge transfer in the most stable complexes (A and B) is greater than in the other two.

Conclusions

The aggregated ion pairs of $[MIM^+]_2[C(CN)_3^-]_2$ ionic liquid have been studied using B3LYP, M052X and M056X methods in conjunction with the 6-311++G(2d,2p) basis set. The results show that, the tendency for aggregation decreases as the temperature and polarity of solvent increases. NBO results show that the charge transfer taking place from anions $C(CN)_3$ to cations MIM upon complex formation.

Acknowledgment

The authors sincerely thank the Sirjan University of Technology and the Payame Noor University for providing financial support of this work.

References

- [1] R. D. Rogers, K. R. Seddon” Chemistry. Ionic liquids--solvents of the future?” *Science*, 302 (2003) 792-802.
- [2] J. Palomar, V. R. Ferro, J. S. Torrecilla, F. Rodríguez” Density and Molar Volume Predictions Using COSMO- RS for Ionic Liquids. An Approach to Solvent Design” *Ind. Eng. Chem. Res.*, 46 (2007) 6041-6049.
- [3] W. Liu, L. Cheng, Y. Zhang, H. H. Wang, M. Yu” The physical properties of aqueous solution of room-temperature ionic liquids based on imidazolium: Database and evaluation” *J. Mol. Liq.*, 140(2008) 140, 68-73.
- [4] J. Dupont “On the solid, liquid and solution structural organization of imidazolium ionic liquids”*J. Braz Chem. Soc.*, 15 (2004) 15, 341–350.
- [5] M. Armand, F. Endres, D. R MacFarlane, H. Ohno, B. Scrosati” Ionic-liquid materials for the electrochemical challenges of the future” *Nat. Mater.* 2009, 8, 621–629.
- [6] A. Farnicola, B. Scrosati,; H Ohno” Potentialities of ionic liquids as new electrolyte media in advanced electrochemical devices” *Ionics*, 2006, 12, 95–102.
- [7] M. Armand, F. Endres, D. R. MacFarlane, H. Ohno, B. Scrosati” Ionic-liquid materials for the electrochemical challenges of the future” *Nat. Mater.*, 8 (2009) 621–629.
- [8] A. Farnicola, B. Scrosati, H. Ohno” Potentialities of ionic liquids as new electrolyte media in advanced electrochemical devices” *Ionics*, 12 (2006) 95– 102.

Theoretical Study on Cooperative Effects between the Hydrogen Bonding and Anion- Π Interactions in Ternary Complexes of C₆H₆-M-YBBY (M= F⁻, Cl⁻ and Y= CN, CO, F)

B. Makiabadi^a, M. Zakarianezhad^{*b}

^a Department of Chemical Engineering, Sirjan University of Technology, P.O. Box: 7813733385, Sirjan, Iran

^b Department of Chemistry, Payame Noor University, Tehran, Iran

*bmakiabadi@Yahoo.com

Abstract: A DFT calculation was carried out on the ternary complex formed C₆H₆-M-YBBY (M= F⁻, Cl⁻ and Y= CN, CO, F). The cooperative effect between the hydrogen-bonding and anion... Π interactions were investigated. The result shows that the H...M and anion ... Π interactions are strengthened in the ternary complex in comparison with those in the corresponding binary system. The cooperativity is negative for all the ternary complexes. This means that both of the interactions, hydrogen bond and anion... Π , are reinforced and the cooperativity effects occur. The cooperativity effect of anion... Π interaction on the hydrogen bond is more pronounced than that of the hydrogen bond interaction on the anion... Π interaction for the ternary system. The obtained natural bond orbital (NBO) parameters show that in all systems the charge transfer takes place from anion to ring.

Keywords: Cooperative, Interaction energy, Ternary system, NBO

Introduction

Noncovalent interactions between molecules play a very important role in supramolecular chemistry, molecular biology, and materials science [1-3]. Although research has traditionally focused on the more common hydrogen-bonded (HB) interactions, more recently, interest has grown in other types of intermolecular interactions, namely, halogen bonding, σ -whole bonding, dihydrogen bonding, and hydride bonding, among others. Also, substituent effects on anion- interactions have received much attention in experimental and theoretical investigations as a result of their extremely important role in determining the structures and activities of organic, organometallic and biological molecules, including enzyme-substrate recognition, catalyst development, new drug and nanomaterial design, etc [4-8]. More recently, interest has been growing in another non-covalent interaction between anions, namely, the anion- Π interaction. We performed a theoretical study on C₆H₆-M-YBBY trimers (M= F⁻, Cl⁻ and Y=F, CN, CO, CH₃) triads with the aim of investigating of hydrogen bonding and Π -interactions and the cooperativity between them.

Materials and method

The B3LYP calculations with cc-pVTZ basis set were used to analyse intermolecular interactions in C₆H₆-M-YBBY trimer (M= F⁻, Cl⁻ and Y=F, CN, CO, CH₃). To better understanding the properties of these systems, the corresponding dimers are also studied. Molecular geometries, binding energies, vibrational frequency of monomers, dimers, and trimers are investigated at the B3LYP/cc-pVTZ computational level

Results and Discussion

The interaction energy in the dyads can be regarded as the energy difference between the complex and the monomers: $E_i(A-B) = E_{AB} - (E_A + E_B)$ and the corresponding value in the triads ($E_i(A-B-C)$) is calculated in the similar way. $E_i(AB, T)$ and $E_i(BC, T)$ are the interaction energies of AB and BC dyads while they are in the geometry of triads. Table 1 gives the most important interactions of studied triads. Also, the systems studied form stable triads are shown in Figure 1.

Trimer	$E_i(ABC)$	$E_i(AB)$	$E_i(BC)$
C ₆ H ₆ -Cl-B ₂ F ₂	-217.67	-36.49	-50.34
C ₆ H ₆ -Cl-B ₂ CO ₂	-133.57	-36.49	-44.12
C ₆ H ₆ -Cl-B ₂ CN ₂	-90.25	-31.01	-36.49
C ₆ H ₆ -F-B ₂ F ₂	-314.13	-28.33	-68.30
C ₆ H ₆ -F-B ₂ CO ₂	-152.58	-68.30	-69.17
C ₆ H ₆ -F-B ₂ CN ₂	-123.12	-48.47	-68.30
Trimer	$E_i(AB,T)$	$E_i(BC,T)$	$E(\text{coop})$
C ₆ H ₆ -Cl-B ₂ F ₂	-88.42	-181.17	-130.83
C ₆ H ₆ -Cl-B ₂ CO ₂	-29.45	-37.08	-52.96
C ₆ H ₆ -Cl-B ₂ CN ₂	-7.76	-13.24	-22.75
C ₆ H ₆ -F-B ₂ F ₂	-26.80	-245.84	-217.51
C ₆ H ₆ -F-B ₂ CO ₂	16.58	-84.29	-15.12
C ₆ H ₆ -F-B ₂ CN ₂	-111.58	-384.82	-6.36

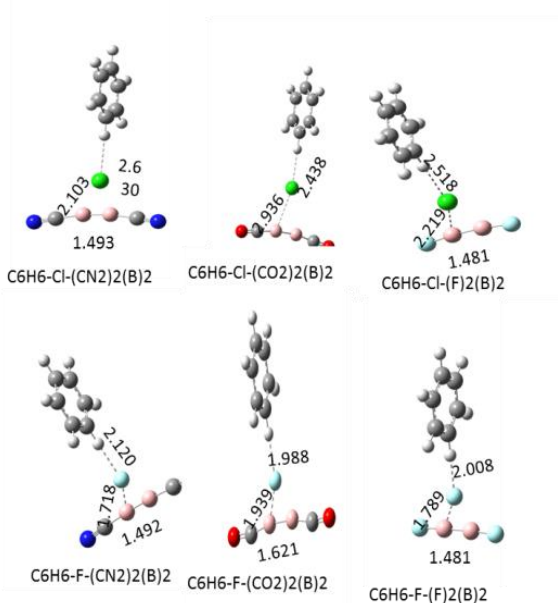


Fig.1: Optimized structures for ternary complexes at the B3LYP/cc-pVTZ level of theory.

Particular attention is paid to cooperative energies. The cooperativity between hydrogen bond and anion- π interactions in C6H6-M-YBBY complexes is studied by DFT calculations. The estimated values of cooperative energy (E_{coop}) are all negative. The results show that, the cooperativity effect of the anion- π interaction on M...YBBY interaction is more pronounced than that of hydrogen bond on the H...M interaction for the ternary system. Also, the H...M and H...M π interactions are strengthened in the ternary complex in comparison with those in the corresponding binary system. The electronic properties of the complexes are analyzed using parameters derived from the atoms in molecules (AIM) and natural bond orbital (NBO) methodology. Atom in molecule analysis confirms that all hydrogen and anion- π interactions have electrostatic nature. The NBO analysis shows that in all complexes the electronic charge is transferred from anion to YBBY and C6H6 molecules.

Conclusions

The cooperativity effect between the hydrogen-bonding and anion(M)... π (M = F, Cl⁻) interactions is investigated in the ternary complex C6H6-M-YBBY (M= F⁻, Cl⁻ and Y= CN, CO, F) by the B3LYP method. The results show that the cooperativity effect

of anion... π interaction on the hydrogen bond is more pronounced than that of the hydrogen bond interaction on the anion... π interaction for the ternary systems. The findings are helpful for understanding the cooperative and competitive role of hydrogen and anion(M)... π interactions in molecular recognition and biological systems.

Acknowledgment

The authors sincerely thank the Sirjan University of Technology and the Payame Noor University for providing financial support of this work.

References

- [1] K. Muller-Dethlefs, P. Hobza "Noncovalent interactions: a challenge for experiment and theory" *Chem. Rev.* 100 (2000) 143-168.
- [2] P. Metrangolo, H. Neukirch, T. Pilati, G. Resnati "Halogen Bonding Based Recognition Processes: A World Parallel to Hydrogen Bonding" *Acc. Chem. Res.*, 38 (2005) 386-395.
- [3] M. Fourmigue "Halogen bonding: Recent advances" *Curr. Opin. Solid State Mater. Sci.*, 13 (2009) 36-45.
- [4] P. Lipkowski, S. J. Grabowski, J. Leszczynski "Properties of the halogen-hydride interaction: an ab initio and "atoms in molecules" analysis" *J. Phys. Chem. A*, 110 (2006) 10296-10302.
- [5] A. Frontera, F. Saczewski, M. Gdaniec, E. Dziemidowicz-Borys, A. Kurland, P. M. Deya, D. Quiçõnero, C. Garau "Anion- π Interactions in Cyanuric Acids: A Combined Crystallographic and Computational Study" *Chem. Eur. J.*, 11 (2005) 6560-6567.
- [6] Y. S. Rosokha, S. V. Lindeman, S. V. Rosokha, J. K. Kochi "Halide Recognition through Diagnostic „Anion- π “ Interactions: Molecular Complexes of Cl, Br, and I with Olefinic and Aromatic π Receptors" *Angew. Chem.*, 116 (2004) 4750-4752.
- [7] A. Garcia-Raso, F. M. Alberii, J. J. Fiol, A. Tasada, M. Barcel-Oliver, E. Molins, C. Estarellas, A. Frontera, D. Quiçõnero, P. M. Deya "2-Aminopyrimidine Derivatives Exhibiting Anion- π Interactions: A Combined Crystallographic and Theoretical Study" *Cryst. Growth Des.*, 9 (2009) 2363-2376.
- [8] S. Demeshko, S. Dechert, F. Meyer "Anion- π Interactions in a Carousel Copper(II)-Triazine Complex" *J. Am. Chem. Soc.*, 126 (2004) 4508-4509.

Quantitative Structure Property Relationship Models for the Prediction of Heat Capacity of Amino Acid Derivatives Using Topological Indices

T. Momeni Isfahani*, F. Shafiei

Department of Chemistry, Arak Branch, Islamic Azad University, Arak, Iran
P.O. Box 38135-567, Arak 38135-567, Iran

* Corresponding E-mail address: t-momeni@iau-arak.ac.ir

Abstract: The present work represents a quantitative structure–property relationship (QSPR) study for predicting of heat capacity (C_v) of 35 amino acids derivatives based on the Randic (1X), Balaban (J), Szeged (Sz), Harary (H), Wiener (W), Hyper Wiener (W_w) and Wiener Polarity (W_p) topological indices. The calculation was performed by the ab-initio method at HF/6-31G (d) level of theory. The correlation coefficients (R) between experimental and predicted heat capacity (C_v) for the prediction set by multiple linear regressions (MLR) and partial least square (PLS) methods are 0.9263 and 0.998, respectively. The results demonstrated that the calculated C_v values by PLS were in good agreement with the experimental ones, and the performance of the PLS model was superior to MLR approach.

Keywords: "quantitative structure–property relationship", "Amino Acid Derivatives", "PLS".

Introduction

The analyses of amino acids are very important in biochemical[1], pharmaceutical[2] and clinical studies[3]. Quantitative structure activity relationship (QSAR) studies, which is useful in molecular design and medicinal chemistry [4]. Topological indices (Tis) play an important role for the analysis of molecular diversity and lead to optimization through well-established structure-property/activity relationships. Tis are numerical quantities derived from a graph-theoretical representation of the molecular structure through mathematical in- variants[5]. The main aim of this work is to illustrate the usefulness of topological descriptors in QSPR study of amino acids derivatives.

Materials and method

The heat capacity (C_v) of 35 amino acids derivatives [6] is taken from the quantum mechanics methodology with Hartree-Fock (HF) level using the ab initio 6-31G basis sets and the standard procedure in GUSSIAN 03. The topological indices (TIs) used for the QSPR analysis were Wiener (W), Szeged (Sz), first order molecular connectivity(1X), Balaban(J), Hyper-Wiener(W_w), Wiener Polarity(W_p) and Harary(H) indices. The total data set was randomly divided into two groups. A training set of 30 compounds and a prediction set of 5 compounds. The training set was used to adjust the parameters of the models and the prediction set was used to evaluate the prediction aptitude of the constructed models. The leave-one-out (LOO) cross-validation analyses were performed to assess the modeling ability of the method. In the present work, regression analyses were performed using multiple linear regression (MLR) and partial least square regression (PLS).

Results and Discussion

Principal components analysis (PCA) was performed on the calculated structural descriptors to the whole data set, for investigation the distribution in the chemical space, which shows the spatial location of samples to assist the separation of the data into training and prediction sets. The PCA results show that two PCs (PC_1 and PC_2) describe 95.69% of the overall variances (Fig. 1).

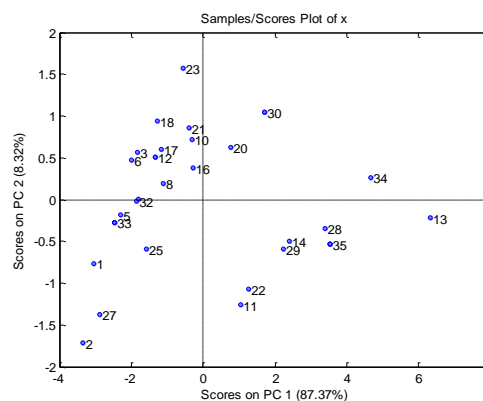


Fig.1: Principal components analysis, PC_1 versus PC_2 of the descriptors for the data set.

The two PCs, their score plot is a reliable presentation of the spatial distribution of the points for the data set. As can be seen in Fig. 1, there is not a clear clustering between compounds. For regression analysis, data set was randomly separated into two groups, a training set (30 data) and a prediction set (5 data). For the selection of the most relevant descriptors, stepwise variable selection method was applied. Finally, stepwise MLR

(SW-MLR) model based on training set and using the chosen descriptors was created for predicting of heat capacity (C_v). To ensure of independent characteristic of the used variables, the correlation matrix was calculated for both approaches and the results are listed in Table 1. As is obvious in Table 1 Correlation values for the two descriptors J and W_p are 0.57 which means, that the descriptors are independent of each other.

Table 1: Correlation matrix for the selected descriptors in the proposed models

	1χ	J	H	w	ww	W_p	Sz
1χ	1						
J	-0.67	1					
H	0.98	-0.64	1				
w	0.96	-0.62	0.98	1			
ww	0.94	-0.61	0.96	0.99	1		
W_p	0.95	-0.57	0.97	0.94	0.91	1	
Sz	0.84	-0.68	0.88	0.88	0.87	0.87	1

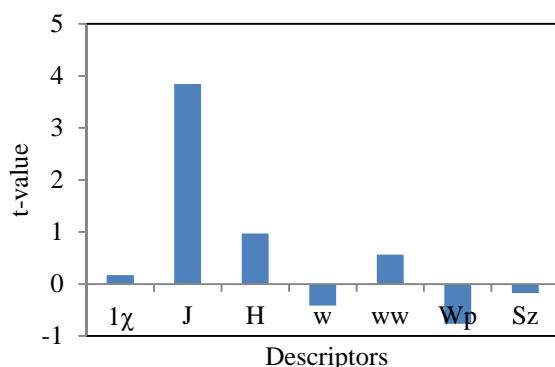


Fig. 2: Plot of descriptor's versus t-value.

Fig.2 show the value and sign of t-value, they are likely to have significant effects in the model. The t-value close to zero is non-significant.

The best equation obtained by SW-MLR for the heat capacity (C_v) of amino acid derivatives was:

$$Y(C_v) = 14.37 + 1.72(J) - 2.98(W_p)$$

As seen, the resulting model has two significant descriptors.

The data set and corresponding observed PLS predicted values of heat capacity (C_v) for all molecules studied in this investigation.

Fig.3 shows the specifications of the best models for PLS and MLR.

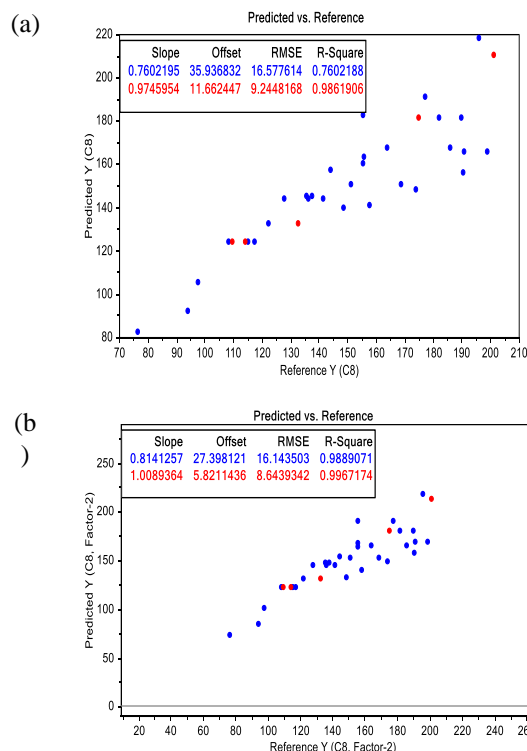


Fig.3: Plot of MLR(3a) and PLS (3b) calculated versus experimental heat capacity (C_v)

Table 2: Statistical parameters obtained using the MLR and PLS models.

Model	R^2	R_p^2	RMSE _t	RMSE _p	Q^2
MLR	0.760	0.926	6.576	5.244	0.760
PLS	0.988	0.996	6.143	4.643	0.929

Note: a_t , training set; a_p , prediction set

Table 2 shows RMSE and R^2 for prediction C_v . As can be seen, the good results were achieved in PLS model.

Conclusions

QSPR models for the prediction of heat capacity for a training set of amino acids derivatives. Using MLR and PLS based on topological descriptors calculated from molecular structure alone have been developed. PLS model is proved to be a useful tool in the prediction of heat capacity. This model contains fewer parameters having to be optimized the Balaban(J) and Wiener Polarity(W_p) indices.

Acknowledgment

The authors gratefully acknowledge the support to this work from, Islamic Azad University, Arak Branch, and research council.



References

- [1] R.M. Hazen, T.R. Filley, G.A. Goodfriend, Selective adsorption of L-and D-amino acids on calcite: Implications for biochemical homochirality, *Proceedings of the National Academy of Sciences*, 98 (2001) 5487-5490.
- [2] R. Yoshioka, Racemization, optical resolution and crystallization-induced asymmetric transformation of amino acids and pharmaceutical intermediates, *Novel Optical Resolution Technologies*, (2007) 83-132.
- [3] Y. Matsumura, Poly (amino acid) micelle nanocarriers in preclinical and clinical studies, *Advanced drug delivery reviews*, 60 (2008) 899-914.
- [4] S. Wold, J. Trygg, A. Berglund, H. Antti, Some recent developments in PLS modeling, *Chemometrics and intelligent laboratory systems*, 58 (2001) 131-150.
- [5] E. Estrada, Generalization of topological indices, *Chemical Physics Letters*, 336 (2001) 248-252.
- [6] F. Tian, P. Zhou, Z. Li, T-scale as a novel vector of topological descriptors for amino acids and its application in QSARs of peptides, *Journal of molecular structure*, 830 (2007) 106-115.

Physisorption of toxic cyanogen gas onto exterior surface of pristine Al₁₂N₁₂ nanocluster: A theoretical study

M. Solimannejad^{a*}, S. Kamalinahad^a, E. Shakerzadeh^b

^aDepartment of Chemistry, Faculty of Science, Arak University, 38156-8-8349, Arak, Iran

^bChemistry Department, Faculty of Science, Shahid Chamran University of Ahvaz, Ahvaz, Iran

*m-solimannejad@araku.ac.ir

Abstract In this research, the interaction of cyanogen molecule with pristine Al₁₂N₁₂ nanocluster is studied to understand the electronic properties of the designated adsorption complexes. To this end, the cyanogen adsorption over Al₁₂N₁₂ in the gas phase is investigated using density functional theory (DFT) at the CAM-B3LYP/6-31+G(d) level of theory. Geometry and electronic structures of the fragments and their interacting systems are studied, and then natural bond orbitals (NBO) analysis is applied to interpret the perturbation caused by molecular adsorption. Our results confirm a physical adsorption between cyanogen molecule and exterior surface of pristine Al₁₂N₁₂ with adsorption energy (E_{ads}) equal to -55.36 kJ/mol. It is expected that Al₁₂N₁₂ will be used in designing novel materials for potential applications to detect toxic cyanogen molecule.

Keywords: Sensing of cyanogen; pristine Al₁₂N₁₂; Density of state; DFT.

Introduction

Aluminum nitride (AlN) ceramics have unique properties such as large band gap (about 6.3 eV), a high thermal conductivity (up to 320 W/mK), a small thermal-expansion coefficient, low electron affinity and chemical inertness [1,2]. These properties make this material an interesting candidate for applications as semiconductor processing and microelectronics. In previous studies it was shown that (AlN)_n fullerene-like cage structures form highly symmetric structures with closed electronic shell and spherical shapes [3]. Most interesting and stable is the case of n=12 for extraordinary and high sphericity [4].

Cyanogen (NCCN), a colorless and toxic flammable gas with a pungent almonds-like odor, was first prepared by Gay-Lussac in 1815 by the thermal decomposition of silver cyanide [5]. It is used as a rocket propellant, an insecticide, and a chemical weapon. Cyanogen gas is very toxic and an irritant to the eyes and respiratory system. The maximum permissible vapor concentration is 10 parts per million [6]. Thus, the design of cyanogen sensors is very important for monitoring cyanogen concentration in the environment. Therefore, in this study we have investigated the potential possibility of pristine Al₁₂N₁₂ nanocage as a new promising sensor for detection of toxic cyanogen molecule.

Computational methods

Structure optimizations and all energy calculations were calculated using spin-restricted CAM-B3LYP/6-31+ G(d) level of theory [7]. Harmonic vibrational frequency calculations approved the stationary points

as a minima structure on the potential energy surfaces. The charge polarization between the nanocage and the adsorbed molecules was calculated by using natural bond orbitals (NBO) analysis [8]. All calculation was performed using Gaussian09 package [9]. Energy gap (E_g) and Fermi level energy (E_F), have been calculated. The energy gap has the following operational equation:

$$E_g = (\text{HOMO} - \text{LUMO}) \quad (1)$$

Where HOMO and LUMO are the highest occupied molecular orbital and the lowest unoccupied molecular orbital energies, respectively.

Density of states (DOS) and partial density of states (PDOS) analyses were performed on the pristine and NCCN-Al₁₂N₁₂ complex at the same level of theory using the GaussSum program [10].

The adsorption energy (E_{ads}) of cyanogen on the surface of pristine Al₁₂N₁₂ was defined as:

$$E_{\text{ads}} = E_{\text{complex}} - E_{\text{NCCN}} - E_{\text{AlN nanocage}} + E_{\text{BSSE}} \quad (2)$$

Where E_{complex}, E_{NCCN} and E_{AlN nanocage} are total energies of pristine Al₁₂N₁₂ with adsorbed molecules, isolated NCCN and the pristine Al₁₂N₁₂, respectively. The basis set superposition error (BSSE) [11] was also evaluated using counterpoise method to remove basis functions overlap effects. Based on the Eq. (2), negative adsorption energy indicates that the formed complex is stable.

Results and Discussion

Structure optimization and geometry of pristine Al₁₂N₁₂

The optimized geometry structure of pristine Al₁₂N₁₂ with T_h symmetry have been achieved at the CAM-

B3LYP level with 6-31+G(d) basis set. $Al_{12}N_{12}$ including six tetragonal and eight hexagonal AlN rings with two nonequivalent Al-N bonds: one is shared between a tetragonal and a hexagonal ring and the other between two hexagonal rings. (see Fig. 1a). The electronic properties of this nanocage are also studied. The results of frontier molecular orbital energies (HOMO and LUMO) and the computed energy gap (E_g) values for the considered nanocage are shown in Table 1. The outcome energy gap for the $Al_{12}N_{12}$ is about 6.49 eV (Table 1). The density of state (DOS) and graphic presentation of the HOMO and LUMO distribution of pristine $Al_{12}N_{12}$ is present in Fig. 1c. According to this figure, the HOMO is concentrated over the N atoms of the nanocage and the LUMO is spread more on Al atoms. Also, the optimized structure of cyanogen molecule is investigated. According to Fig. 1b, the NCCN molecule is linear; the calculated bond length of $N\equiv C$ and $C - C$ is about 1.386 and 1.156 Å, respectively.

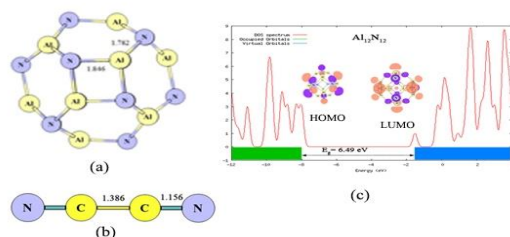


Fig.3: Optimized structure of (a) $Al_{12}N_{12}$, (b) NCCN and (c) total density of states (TDOS) of $Al_{12}N_{12}$ (Bonds in Å).

Table 1. Highest occupied molecular orbital (HOMO), lowest unoccupied orbital (LUMO), energy gap (E_g), the change of energy gap of nanocage after adsorption (ΔE_g %) and Fermi level energies (E_F) calculated for pristine $Al_{12}N_{12}$ and A configuration.

Cyanogen adsorption on the pristine $Al_{12}N_{12}$

In this section, we have searched for a suitable position

Configuration	HOMO (eV)	LUMO (eV)	E_g (eV)	ΔE_g (%)	E_F (eV)
$Al_{12}N_{12}$	-8.01	-1.52	6.49	-	-4.76
$Al_{12}N_{12}/NCCN$	-7.69	-2.68	5.00	22.92	-5.18

on the exterior surface of pristine $Al_{12}N_{12}$ for cyanogen detection. After full geometry optimization of difference initial structure only one stable adsorption configuration is obtained (see Fig. 2). In $Al_{12}N_{12}/NCCN$ configuration, the nitrogen atom in the NCCN molecule is close to a Al atom of the external surface of the $Al_{12}N_{12}$ cage with interaction distance of 2.057 Å. In this configuration, the cyanogen adsorption leads to a local structural deformation on both the

cyanogen and the $Al_{12}N_{12}$ nanocage. The $N\equiv C$ and $C - C$ bonds of cyanogen are decreased (Fig. 2). Moreover, the Al-N bonds of the $Al_{12}N_{12}$ are increased from 1.782 and 1.846 Å in the pristine form to 1.802 and 1.867 Å in the $Al_{12}N_{12}/NCCN$ configuration.

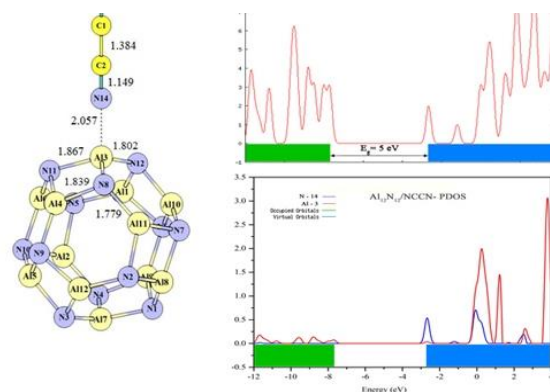


Fig.4: Optimized structures, total density of states (TDOS) and partial density of states (PDOS) of $Al_{12}N_{12}/NCCN$ configuration. (Bonds are in Å).

The calculated E_{ads} and BSSE values for this configuration using Eq. (2) are reported in Table 2. According to the results of this table, E_{ads} values for $Al_{12}N_{12}/NCCN$ configuration is -55.36 kJ/mol with ΔH_{ads} and ΔG_{ads} values -57.16 and -25.54 kJ/mol respectively. Negative values of adsorption energy indicate that the structures are stable but the interaction between cyanogen molecule and $Al_{12}N_{12}$ is physisorption. The calculated NBO charge indicates that charge polarization of 119 |mili-esu| occurs from $Al_{12}N_{12}$ nanocage to cyanogen molecule, confirming physisorption adsorption.

Table 2. Charge polarization from cage to molecule (Q_T), adsorption energy (E_{ads}) and BSSE of NCCN adsorbed on pristine $Al_{12}N_{12}$.

Configuration	Q_T (mili-esu)	E_{ads} (kJ/mol)	BSSE (kJ/mol)
$Al_{12}N_{12}/NCCN$	119	-55.36	6.39

The electronic properties of nanocage/cyanogen system such as HOMO-LUMO energy gap and Fermi level energy (E_F) are shown in Tables 1. The results implying E_g in the $Al_{12}N_{12}/NCCN$ configuration is 5 eV. The shift of E_g (ΔE_g) within the adsorption process is connected to the adsorption onto external surface of pristine $Al_{12}N_{12}$. To better understand the nature of cyanogen molecule adsorption over the electronic properties of nanocage, we have performed



the electronic density of states (DOS) and partial density of state (PDOS) analysis (Fig. 2). According to the DOS spectrum of $Al_{12}N_{12}/NCCN$ configuration the valance and conduction levels have closed in comparison with that $Al_{12}N_{12}$ nanocage. Also, it is obvious from PDOS analysis that there is interaction between Al3 with N14 in $Al_{12}N_{12}/NCCN$ configuration and new band (-2.68 eV) is appeared in the vicinity of Fermi level because of the interaction between cyanogen molecule and the nanocage. For this reason the band gap of the $Al_{12}N_{12}/NCCN$ decreases by 22.92% which correspond to more reactivity.

Conclusions

We have performed DFT calculations to study the adsorption of cyanogen molecule on the surface of $Al_{12}N_{12}$ nanocage. Structural and electrical calculations confirmed that cyanogen molecule can be absorbed on the surface of the nanocage. NBO analysis display charge polarization from cage to cyanogen molecule and interaction between gas/nanocage is physisorption with changes in its electrical conductance.

References

- [1] E. Ruiz, S. Alvarez, P. Alemany, "Electronic structure and properties of AlN", *Physical Review B*, 49 (1994) 7115-7123.
- [2] E. Rille, R. Zarwasch, H. Pulker, "Properties of reactively d.c.-magnetron-sputtered AlN thin films", *Thin Solid Films*, 228 (1993) 215-217.
- [3] C. Chang, A. Patzer, E. Sedlmayr, T. Steinke, D. Sülzle, "Computational evidence for stable inorganic fullerene-like structures of ceramic and semiconductor materials", *Chemical Physics Letters*, 350 (2001) 399-404.
- [4] C. Chang, A. Patzer, E. Sedlmayr, T. Steinke, D. Sülzle, "A density functional study of small $(AlN)_x$ clusters: structures, energies, and frequencies", *Chemical Physics*, 271 (2001) 283-292.
- [5] J.L. Gay-Lussac, "Recherches sur l'acide prussique", 1815, Imprimerie de Mme. Ve. Perronneau, 1-103.
- [6] H.B. Elkins, "The Chemistry of Industrial Toxicology", 1959, New York: John Wiley & Sons, Inc. 2nd Ed., 1-452, London: Chapman & Hall.
- [7] T. Yanai, D.P. Tew, N.C. Handy, "A new hybrid exchange–correlation functional using the Coulomb-

attenuating method (CAM-B3LYP) ", *Chemical Physics Letters*, 393 (2004) 51-57.

[8] A.E. Reed, R.B. Weinstock, F. Weinhold, "Natural population analysis", *The Journal of Chemical Physics*, 83 (1985) 735-746.

[9] M. Frisch, G. Trucks, H. Schlegel, G. Scuseria, M. Robb, J. Cheeseman, J. Montgomery Jr, T. Vreven, K. Kudin, J. Burant, Gaussian Inc, Wallingford.

[10] N.M. O'boyle, A.L. Tenderholt, K.M. Langner, "cclib: A library for package-independent computational chemistry algorithms", *Journal of Computational Chemistry*, 29 (2008) 839-845.

[11] L. Turi, J. Dannenberg, "Correcting for basis set superposition error in aggregates containing more than two molecules: ambiguities in the calculation of the counterpoise correction", *The Journal of Physical Chemistry*, 97 (1993) 2488-2490.

Boron nitride nanotubes (BNNTs) as a potential sensor for detection of hydroperoxyl radical (HO₂): A DFT study

M. Noormohammadbeigi^a, M. Solimannejad^{b*}

^aDepartment of Chemistry, Lorestan University, Khorram Abad, 44316-6-8151, Iran

^bDepartment of Chemistry, Faculty of Science, Arak University, Arak, 38156-8-8349, Iran

*m-solimannejad@araku.ac.ir

Abstract: In this present study, the adsorption behavior of HO₂ radical on the exterior surface of (5, 0) zigzag boron nitride nanotube (BNNT) using density functional theory (DFT) has been investigated. The electronic structures and geometries of studied complexes were calculated at B3LYP-D3/6-31++G (d, p) computational level. After full optimization without symmetry constrain, three desirable configurations (**A**, **B**, **C**) were obtained. The value of adsorption energy for the most stable configuration (**A**) is computed -0.68 eV, indicating physisorption process. Meaningful change of HOMO-LUMO gap after adsorption process confirming BNNT can be introduced as a promising sensor for sensing of HO₂ radical.

Keywords: BNNT; HO₂; DFT; DOS.

Introduction

In the last years, enhancement of pollution in the air lead

to decrease width of ozone layer. The HO₂(hydroperoxyl)

radical, an oxygenated radical, was known as an ozone layer destructor [1–3]. It was observed by Foner and Hudson for the first time [4]. They generated the radical by the termolecular reaction between hydrogen atom, oxygen molecule, and a third body.

Nanostructures have significant capacity in diverse fields

such as gas sensor, hydrogen storage, electronic devices

and drug delivery [5]. Because of the extraordinary physical and chemical properties of boron nitride nanotubes (BNNTs) [6], these compounds have received considerable research interests. They are semiconductors, with a constant band gap of ~3.5–5.5 eV, almost being independent from tubular diameter and helicity and wall [7–10]. BNNTs were firstly theoretically predicted in 1994 [11] and then experimentally synthesized by arc discharge in 1995 [12].

The interaction of free radicals and nanoadsorbents was

investigated previously. Baei et al. have indicated sensitivity of single-walled carbon nanotubes to the OCN radical [13]. In addition, adsorption of NO on Pt-decorated graphene [14] and NO₂, N₂O on Aldoped graphene nanostructure [15] was considered recently.

In the present work, an attempt has been made to scrutinize the adsorption of HO₂ radical onto external surface of BNNT. This interaction will be studied based on analyses of structures, energies and electronic properties. The main aim of this investigation was answering to this question: Is BNNT a proper candidate for detecting of HO₂ radical or not? It should be

noted that despite importance of HO₂ radical as an ozone layer destructor, no theoretical study has been done to sense of it.

Materials and method

All calculations such as equilibrium geometries, adsorption energies, energy gaps, density of state and thermodynamic properties for complexes pairing BNNT and HO₂ were performed at spin-unrestricted B3LYP-D3 functional [16] and 6-31++G(d,p) basis set in the Gaussian 09 [17]. All optimized structures, completely set on a local minimum and we obtained real frequencies.

To evaluate adsorption energy (E_{ad}) of HO₂ on BNNT we have used the following equation:

$$E_{ad} = E_{complex} - (E_{HO_2} + E_{BNNT}) + BSSE \quad (1)$$

Where $E_{complex}$, E_{HO_2} and E_{BNNT} are total energies of BNNT with adsorbed HO₂, free HO₂ and pristine BNNT. Also we calculated basis set superposition error (BSSE), using the counterpoise method [18] to eliminate basis functions overlap effects. Negative amount of adsorption energy indicates that whole complexes are stable. GaussSum program has been used to exhibit density of state (DOS) plots, on the pristine BNNT and different complexes [19]. In order to calculate the charge transfer between boron nitride nanotube and HO₂ radical, we have performed natural bond orbitals (NBO) analysis [20].

Results and Discussion

The pristine (5,0) zigzag single-walled boron nitrogen nanotube consisting of 20 boron and 20 nitrogen atoms was considered, which its end atoms were saturated by hydrogen atoms to reduce the boundary effects. In Fig. 1, the optimized structure and geometry of pristine zigzag (5, 0) single-walled BNNT and HO₂ radical are shown. As mentioned, all calculations carried out at



B3LYP-D3 /6-31++G (d, p) computational level. Fig. 1 reveals that two individual bonds in BNNT structure recognizable. One of them is in parallel with tube axis that has bond length 1.45Å and another one is diagonal to the tube axis that has bond length 1.47Å. To investigate the accuracy of structural data, our results were compared with previous work and they were in a fair agreement with it [21]. In addition, geometry of

	E_{ad}	HOMO	E_H	LUMO	E_g	$Q_i e $
Pristine	-	-6.78	-4.80	-2.81	3.97	0
A	-0.48	-6.88	-5.90	-4.93	1.95	0.167
B	-0.36	-6.78	-5.88	-4.98	1.80	0.170
C	-0.32	-6.67	-5.73	-4.79	1.88	0.147

HO₂ radical is in conformity with similar study [22]. The difference between electronegativity of boron and nitrogen atoms can be formed an ionic B-N bond that proved by NBO analysis.

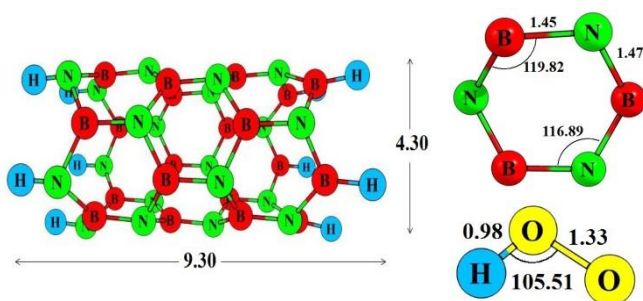


Fig. 1. Optimized structures of BNNT and HO₂ (bonds in Å and angles in degree).

In order to detect the most favourable adsorption configuration, HO₂ radical was located around the exterior surface of BNNT with different orientations. Molecule was approached to the tube from O or H sites or both of them. After full optimization without symmetry constrain, three desirable configurations (A, B, C) were obtained observing in Fig. 2. In all configurations oxygen and hydrogen atoms of HO₂ are bonded to boron and nitrogen of tube respectively but in different positions. The value of calculated adsorption energy for the most stable configuration (A), was -0.48 eV (Table 1). In this complex, equilibrium distance of B-O and N-H are computed 1.64Å, 1.53Å respectively confirming almost strong interactions. In addition, bond length of O-H and angle of H-O-O in HO₂ after adsorption process were increased while bond length of O-O approximately unchanged. In contrast of most stable mode, Adsorption energy for B and C complexes were determined -0.36 eV and -0.32 eV. According to Fig. 2, binding distance of B-O and N-H respect to A configuration was enhanced while a value of H-O-O angle has deducted significantly in the other complexes. It is obvious that interaction of HO₂ molecule with BNNT in B and C structures are more fragile than A.

To comprehend electronic properties of complexes, NBO analysis was performed. Obtained results reveal that in the most stable configuration (A), 0.167 e charge is transferred from HO₂ to the tube (Table 1). In fact neutral BNNT molecule will gain charge from HO₂ due to adsorption and this charge lead to modification in electronic properties of the tube. B and C configurations have received more and less charge respect to A.

Table 1. Adsorption energy (E_{ad}), HOMO, fermi energies (E_H), LUMO, energy gap (E_g) (all in eV) and charge transfer from HO₂ to BNNT (Q_i) computed for pristine and HO₂/BNNT complexes (A,B,C)

In order to gain a deep understanding of the electronic properties, the plots of density of state depicted as can be seen in Fig.3. A value of energy gap (E_g) in pristine BNNT is 3.98 eV confirming semiconductor nature of tube which in a good agreement with previous report [11]. With the approach of molecule to the surface and formation of complexes, E_g has been deducted to 1.95 eV in A configuration. Because of appearing new peaks around conduction level resulting newly formed LUMO has been closed to Fermi level of pristine BNNT. This phenomenon leading to decrease of energy gap. For this reason, conductivity of the system significantly changed and therefore this tube is sensitive enough for sensing HO₂ radical.

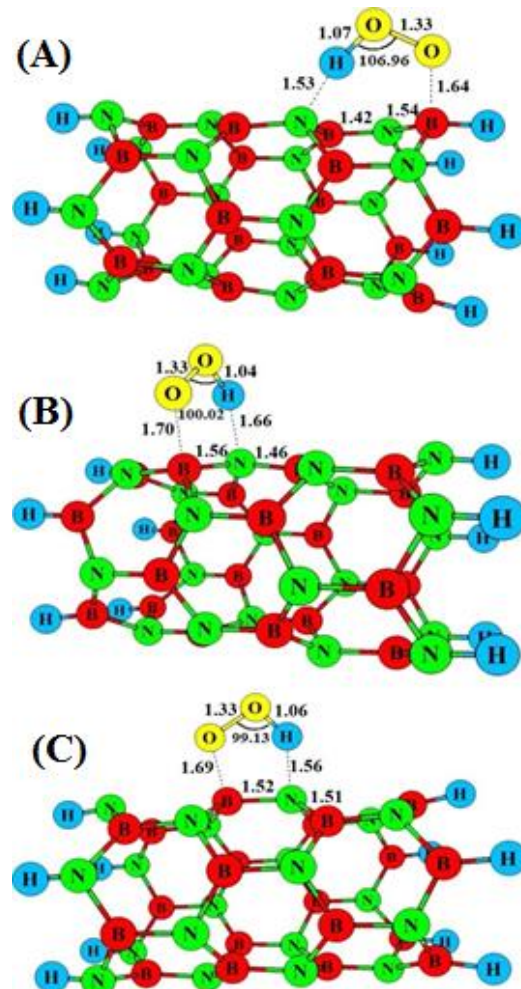
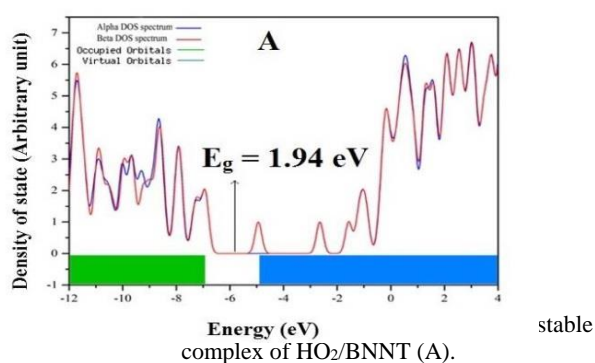
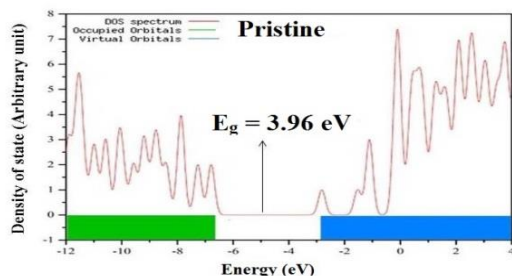


Fig. 2. Models for three stable complexes of HO₂/BNNT (A, B, C).



Conclusions

The tendency of HO₂ radical toward adsorption on exterior surface of BNNT was considered. Obtained results from this process indicated that significant changes in structural and electrical properties are occurred. Based on NBO analysis charge transfer occurs from HO₂ molecule to pristine BNNT that leads to change conductance in tube. It is expected that BNNT can be act as a promising device to detect of HO₂.

References

- [1] P.S. Monks, "Gas-phase radical chemistry in the troposphere", *Chemical Society Reviews*, 34 (2005) 376-395.
- [2] D. Jacob, "Introduction to Atmospheric Chemistry", 1999, Princeton University Press, 280, Princeton, USA.
- [3] R. Wayne, "Chemistry of Atmospheres", 2000, Oxford University Press, New York, UK.
- [4] S. Foner, R. Hudson, "Detection of the HO₂ radical by mass spectrometry", *The Journal of Chemical Physics*, 21 (1953) 1608-1609.
- [5] J. Wang, C.H. Lee, Y. Bando, D. Golberg, Y.K. Yap, "B-C-N Nanotubes and Related Nanostructures", 2009, Springer, New York, UK.
- [6] A. Loiseau, F. Willaime, N. Demoncy, N. Schramchenko, G. Hug, C. Colliex, H. Pascard, "Boron nitride nanotubes", *Carbon*, 36 (1998) 743-752.
- [7] H. Xiang, J. Yang, J. Hou, Q. Zhu, "First-principles study of small-radius single-walled BN nanotubes", *Physical Review B*, 68 (2003) 035427.
- [8] A. Soltani, N. Ahmadian, A. Amirazami, A. Masoodi, E.T. Lemeski, A.V. Moradi, "Theoretical investigation of OCN adsorption onto boron nitride nanotubes", *Applied Surface Science*, 261 (2012) 262-267.
- [9] A. Soltani, N. Ahmadian, Y. Kanani, A. Dehnohalaji, H. Mighani, "Ab initio investigation of the SCN chemisorption of single-walled boron nitride nanotubes", *Applied Surface Science*, 258.24 (2012) 9536-9543.
- [10] J. Beheshtian, A.A. Peyghan, Z. Bagheri, "Detection of phosgene by Sc-doped BN nanotubes", *Sensors and Actuators B: Chemical* 171 (2012) 846-852.
- [11] A. Rubio, J.L. Corkill, M.L. Cohen, "Theory of graphitic boron nitride nanotubes", *Physical Review B*, 49.7 (1994) 5081.
- [12] N.G. Chopra, R. Luyken, K. Cherrey, V.H. Crespi, M.L. Cohen, S.G. Louie, A. Zettl, "boron nitride nanotubes", *Science*, 269.5226 (1995) 966.
- [13] M.T. Baei, S.Z. Sayyed-Alangi, A. Soltani, M. Bahari, A. Masoodi, "Adsorption properties of OCN radical on (6, 0), (8, 0), and (10, 0) zigzag single-walled carbon nanotubes: a density functional study", *Monatshefte für Chemie-Chemical Monthly*, 142.1 (2011) 1-4.
- [14] A.S. Rad, E. Abedini, Appl. "Chemisorption of NO on Pt-decorated graphene as modified nanostructure media: a first principles study" *Applied Surface Science*, 360 (2016) 1041-1046.
- [15] A.S. Rad, "First principles study of Al-doped graphene as nanostructure adsorbent for NO₂ and N₂O: DFT calculations", *Applied Surface Science*, 357 (2015) 1217-1224.
- [16] S. Grimme, J. Antony, S. Ehrlich, H. Krieg, "A consistent and accurate ab initio parametrization of density functional dispersion correction (DFT-D) for the 94 elements H-Pu", *The Journal of chemical physics*, 132.15 (2010) 154104.
- [17] M. J. Frisch, et al, "Gaussian 09, Revision A. 02. Gaussian Inc., Wallingford, CT" (2009).
- [18] L. Turi, J. Dannenberg, "Correcting for basis set superposition error in aggregates containing more than two molecules: ambiguities in the calculation of the counterpoise correction", *The Journal of Physical Chemistry*, 97.11 (1993) 2488-2490.
- [19] N.M. O'boyle, A.L. Tenderholt, K.M. Langner, "Cclib: a library for package-independent computational chemistry algorithms", *Journal of computational chemistry*, 29.5 (2008): 839-845.
- [20] A.E. Reed, R.B. Weinstock, F. Weinhold, "Natural population analysis", *The Journal of Chemical Physics*, 83(2), 735-746.
- [21] R. Wang, R. Zhu, D. Zhang, "Adsorption of formaldehyde molecule on the pristine and silicon-doped boron nitride nanotubes" *Chemical Physics Letters*, 467.1 (2008) 131-135.
- [22] D.H. Liskow, H.F. Schaefer III, C.F. Bender, "Geometry and electronic structure of the hydroperoxyl radical", *Journal of the American Chemical Society*, 93.25 (1971) 6734-6737.



Application of decaborane (B₁₀H₁₄) and its fluoro derivatives as an anode in Li-ion battery: A DFT Study

M. Yousefizadeh, E. Shakerzadeh*, M. Bamdad

Chemistry Department, Faculty of Science, Shahid Chamran University of Ahvaz, Ahvaz, Iran

e.shakerzadeh@scu.ac.ir

Abstract: Application of decaborane (B₁₀H₁₄) and its fluoro derivatives in Li-ion batteries has been investigated through density functional theory (DFT) computations. The results indicate that decaborane (B₁₀H₁₄) has a negative value of cell voltage which is meaningless. A strategy is introduced to improve the performance of B₁₀H₁₄. The hydrogen atoms in different positions are substituted by fluorine atoms. The cell voltage of decaborane fluoro derivatives remarkably increase up to 1.10 V. This investigation may evoke one's attention to the design of novel anode in Li-ion batteries based on boron nanomaterials.

Keywords: Li-ion battery; Cell voltage; Decaborane, Fluorination; DFT calculations; Nanostructure.

(H is a bridging atom). The bridging hydrogen participates most often in a multicenter two-electron bond both within the cluster and in the interaction with metals. These hydrogens are distinctly protonic, and their relative acidity depends on the cage size as well as other parameters. Decaborane (B₁₀H₁₄) is the most stable nido-boranes [6, 7]. The B₁₀H₁₄ possess four equivalent electron-deficient terminal hydrogen atoms and exhibits a wide range of properties. Sneddon and co-workers have devised several ingenious strategies for synthesis of the substituted decaboranes [8]. Decaborane with double the number of boron atoms in the shape of a basket, a very useful starting material for a lot of borane chemistry.

Li-ion battery is a common electric energy storage device, and it can be applied as the main power for many electronic devices [9]. A Li-ion battery is composed of two electrodes (a cathode and an anode) separated by an electrolyte. The applications of nanomaterial in Li-ion batteries have been attracted great interest [10]. Hence there is an increasing demand for finding efficient nanomaterial as anode of Li-ion batteries, and this has stimulated research activities in this field. The main contribution of the present study is to investigate the performance of decaborane and its fluoro derivatives in anode of Li-ion battery.

Materials and method: All of the optimized geometries for the Li@B₁₀H₁₄ and Li⁺@B₁₀H₁₄ as well as their fluoro derivatives are obtained using TPSSH/6-311+G(d) level of theory. All calculations are performed using Gaussian 09 software.

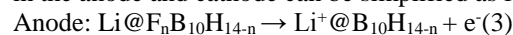
Results and discussion:

The optimized geometries of the Li@B₁₀H₁₄ and its fluoro derivatives are shown in Figure 1. The adsorptions of Li and Li⁺ are considered on the surface of these structures. The structure of lithium decaborane

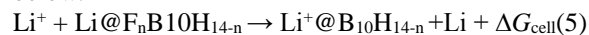
which adsorbed the Li atom, E(F_nB₁₀H_{14-n}) corresponds to the energy of an isolated F_nB₁₀H_{14-n}, E(Li) is the energy of an atomic Li. Indeed,

$$E_{ad} = E(\text{Li}^+ @ \text{F}_n \text{B}_{10} \text{H}_{14-n}) - E(\text{F}_n \text{B}_{10} \text{H}_{14-n}) - E(\text{Li}^+) \quad (2)$$

where E(Li⁺@F_nB₁₀H_{14-n}) is the energy of and F_nB₁₀H_{14-n} which adsorbed the Li⁺ cation and E(Li⁺) is the energy of a Li⁺ cation. All of these energies are obtained using the optimized structures. A Li-ion battery (LIB) is composed of two electrodes (a cathode and an anode) separated by an electrolyte. The reaction in the anode and cathode can be simplified as follows:



Thus overall reaction for the LIB can be written as below.



For calculating the voltage for this cell the Nernst equation can be applied as:

$$V_{\text{cell}} = \frac{-\Delta G_{\text{cell}}}{zF} \quad (6)$$

of the total reaction of cell at 298 K and 1 atm. It can be assessed as the internal energy ($\Delta G = \Delta E + P\Delta V - T\Delta S$). Since the entropy contributions and volume effects are very small (<0.01 V) to the cell. So the V_{cell} can be obtained by predicting internal energy change as follows:

$$\Delta E = E(\text{Li}) + E(\text{Li}^+ @ \text{F}_n \text{B}_{10} \text{H}_{14-n}) - E(\text{Li}^+) - E(\text{Li} @ \text{F}_n \text{B}_{10} \text{H}_{14-n}) \quad (7)$$

the ΔG_{cell} (Gibbs free energy change) could be calculated for the reaction (5) by performing frequency analysis for the most stable Li@F_nB₁₀H_{14-n} and Li⁺@B₁₀H_{14-n} complexes too. The calculated value for ΔG_{cell} is approximately equal to the difference between the E_{ads} values of the most stable Li@B₁₀H_{14-n} and Li⁺@B₁₀H_{14-n} complexes, Eq. (7). The Eq. (7) reveals that the Li⁺@F_nB₁₀H_{14-n} system interaction is favorable for the ΔE, and the stronger interaction will cause a



more negative ΔE . In addition, the $\text{Li}@F_n\text{B}_{10}\text{H}_{14-n}$ interaction is not favorable for the ΔE and V_{cell} .

The obtained V_{cell} from Eq. 7 are presented in Figure 1 for the studied structure. It is found that the the pristine $\text{B}_{10}\text{H}_{14}$ has the $V_{\text{cell}} = -0.66$ V which is meaningless. Thus the pristine decaborane is not suitable for anode in LIB. In continue the fluoro derivatives of decaborane are taken into account. The results indicate that the fluorination significantly enhance the cell voltage ranging from 0.73 to 1.10 V. The 1,3,6,9- $\text{F}_4\text{B}_{10}\text{H}_{10}$ compound has the maximum V_{cell} of 1.10 V. Therefore, the fluorination is an appropriate strategy to enhance the efficiency of decaborane as an anode of LIB.

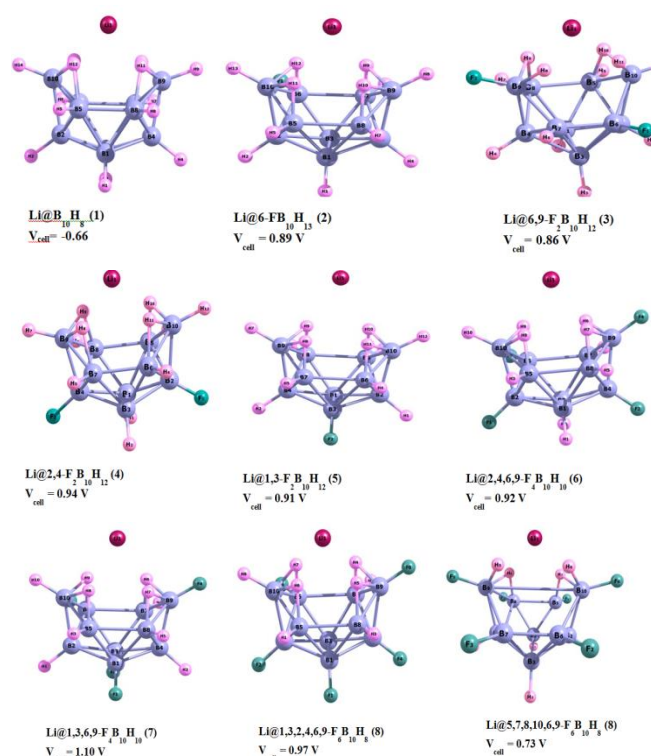


Fig. 1. Optimized structures of $\text{Li}@B_{10}H_{14}$ and its fluoro derivatives and calculated V_{cell} values.

It is shown that the interaction of Li^+ with $F_n\text{B}_{10}\text{H}_{14-n}$ is much more favorable than the Li interaction which makes the application of these systems proper in anode of LIB.

Conclusions

By means of DFT calculations we have investigated the performance of pristine $\text{B}_{10}\text{H}_{14}$ and fluoro derivatives of $\text{B}_{10}\text{H}_{14}$ structures as anode compounds

for LIBs. It is found that although the pristine $\text{B}_{10}\text{H}_{14}$ suffers from low V_{cell} , its fluoro derivatives improve the performance of the LIB by increasing the V_{cell} .

References

- [1] M. F. Hawthorne "The role of chemistry in the development of boron neutron capture therapy of cancer", *Angew chem, Int. Ed. Engl.* 32 (1993) 950–984.
- [2] D. Hnyk, J. Holub, S. A. Hayes, M. F. Robinson, D. A. Wann, H. E. Robertson, D. W. H. Rankin "Molecular structures of arachno-heteroboranes with decaborane frameworks: Two C_s-symmetrical azacarbaboranes and carbathiaboranes", *Inorg. Chem.* 45 (2006) 8442–8446.
- [3] H. M. Colquhoun, D. F. Lewis, P. L. Herbertson, K. Wade "Polyetherketones based on para-carborane: synthesis, sulfonation, and membrane-forming characteristics", *Polymer*, 38 (1997) 4539–4546. (b) E. Hong, Y. Kim, Y. Do "A neutral group 4 poly (methyl methacrylate) catalyst derived from o-carborane", *Organometallics*, 17 (1998) 2933–2935.
- [4] K. A. Nguyen, K. Lammertsma "Structure, Bonding, and Stability of Small Boron–Lithium Clusters", *J. Phys. Chem. A* 102 (1998) 1608–1614.
- [5] G. N. Srinivas, T. P. Hamilton, J. A. Boatz, K. Lammertsma "Theoretical Studies of B_2Li_n ($n = 1-4$)", *J. Phys. Chem. A* 103 (1999) 9931–9937.
- [6] I. Sioutis, R. M. Pitzer "Theoretical Investigation of the Binding Energies of the Iodide Ion and Xenon Atom with Decaborane", *J. Phys. Chem. A* 110 (2006) 12528–12534.
- [7] D. F. Gaines, H. Beal "Hydrogen–deuterium exchange in decaborane (14): Mechanistic studies", *Inorg. Chem.* 39 (2000) 1812–1813.
- [8] S. Muhammad, H. Xu, Z. su, "Capturing a synergistic effect of a conical push and an inward pull in fluoro Derivatives of $\text{Li}@B_{10}H_{14}$ basket: toward a higher vertical ionization potential and nonlinear optical response", *J. Phys. Chem.* 115 (2011) 923–931.
- [9] N. Nitta, F. Wu, J. T. Lee, G. Yushin "Li-ion battery materials: present and future", *Materials Today*, 18 (2015) 252–264.
- [10] X. Fan, W. T. Zheng, J-L. Kuo, D. Singh "Adsorption of single Li and the formation of small Li clusters on graphene for the anode of Lithium-ion batteries", *Applied Materials*, 5 (2013) 7793–7797

Estimating the Boiling Point of Amino Acids by using QSPR and MLR methods

A. Safaria, F. Shafiei *

Department of Chemistry, Faculty of Science, Arak Branch, Islamic Azad University,

P.O. Box 38135-567, Arak 38361-1-9131, Iran

f-shafiei@iau-arak.ac.ir

Abstract

Chemical Graph theory is used to mathematically model the molecules in regularity to gain insight into their physical and chemical properties. Graph-theoretical topological indices are high potential descriptors for modeling and predicting physicochemical properties of chemical compounds. A QSPR study was performed for prediction of boiling point (Bp°C) of 60 type different Amino acid derivatives by using topological indices such as Wiener (W), Szeged (Sz), first order molecular connectivity (¹X), Balaban (J), hyper-Wiener(WW), Wiener polarity (WP) and Harary (H). The goal of quantitative structure -Property relationship studies find a relationship between the physicochemical actions a molecule with structural parameters.

The calculation was performed by the ab-initio method at HF/6-31G level of theory. The relationship analysis between boiling point and topological indices was done by using multiple linear regression (MLR) method, with boiling point as dependent variable and seven independent variables to generate the equation that relates the structural features to the boiling point (Bp°C). The results have shown that combining the three descriptors ((J, H, Sz) could be efficiently used for boiling points compounds.

Keywords : Topological indices; Amino acids; QSPR ; multiple linear regression;

Introduction

Quantitative structure-activity relationship (QSAR) and quantitative structure property relationship (QSPR) is the process by which chemical structure is quantitatively correlated with a well defined process, such as biological activity or chemical reactivity [1].

Numerous studies have been made relating to the various fields by using what are called topological indices (TI) [2]. Topological indices are the numerical value associated with chemical constitution purporting for correlation of physical properties, chemical activity or biological activity. T-scale as a novel vector of topological descriptor for amino acids based on 67 kinds of structural topological variables of 135 amino acids established [3]. New chemical descriptors used for the design of biologically active of 87 amino acids [4]. Pioneering work in applying QSPR to boiling points was done by Wiener who introduced the path number defined as the sum of the distances between any two carbon atoms in the molecule [5].

Materials and Methods

The boiling point of a compound is predetermined by the intermolecular interactions in the liquid and by the difference in the molecular internal partition function in the gas phase and in the liquid at the boiling temperature. The physicochemical properties are taken from the chemspider program [6].

In this paper, such topological indices as Wiener, W [7], Hyper-Wiener, WW[8], Wiener polarity, WP [9], Randić, ¹X[10], Balaban, J [11], Harary number, H [12] and Szeged, Sz [13] have been used for evaluating this relation. The descriptors were calculated with chemicalize program [14].

Regression Analysis

Structure- Property models (MLR models) are generated using the multi linear regression procedure of SPSS version 20 (Inc., Chicago, IL, USA) and backward stepwise regression was used to construct the QSPR models. For drawing the graphs of our results, we used the Microsoft Office Excel – 2010 program. The boiling point (Bp°C) are used as the dependent variable and ¹X, J, H, W, WP, WW and Sz indices as the independent variables. Criteria for selection of the best multiple linear regression model were the statistics: squared multiple correlation coefficient (R²), adjusted correlation coefficient (R²_{adj}), Fisher-ratio(F), root of the mean square of errors(RMSE), Durbin-Watson value (D) and significance (Sig).

Results and Discussion

Several linear QSPR models involving three-seven descriptors are established and strongest multivariable correlations are identified by the Back ward step wise regression routine implemented in SPSS is used to develop the linear model for the prediction of the properties. We studied the relationship between

topological indices to the boiling point of 60 amino acids.

QSPR models for the Boiling points (Bp⁰C)

Initial regression analysis indicated that topological indices play a dominating role in modeling the Boiling point. In Table 1 are given the regression parameters and quality of correlation of the proposed models for Boiling point of 60 amino acids.

Table 1. Regression parameters and quality of correlation of the proposed models for the Boiling point.

Model	Independent variables	R	R ²	R ² _{adj}	F	RMSE
1	J,H,WW	0.915	0.838	0.829	96.274	277.0647

The best linear model for Bp contains three topological descriptors, namely, Balaban (J), Harary number (J) and Hyper-Wiener(WW) indices. Fig 1 shows the linear correlation between the observed and the predicted the boiling point values obtained using Eq. (1).

Model 1

$$Bp = 113.497 + 26.067(J) + 6.286(H) - 0.028(WW) \quad (1)$$

N=60, R=0.915, R²=0.838, R²_{adj}=0.829, RMSE=277.0647 F=96.274, Sig=0.000, DW=1.973

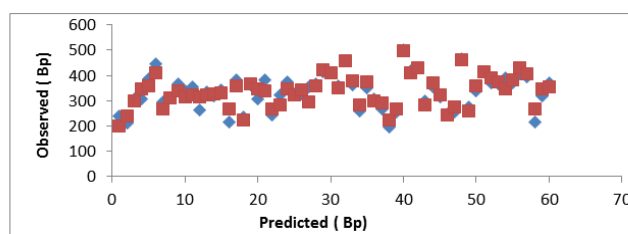


Figure 1. Comparison between the predicted and observed values of boiling point by MLR.

In this study, to find the best model for predict the properties mentioned, we will use the following sections:

The Durbin-Watson statistics

The Durbin-Watson statistic ranges in value from 0 to 4. A value near 2 indicates non-autocorrelation; a value toward 0 indicates positive autocorrelation; a value toward 4 indicates negative autocorrelation. Therefore the value of Durbin-Watson statistic is close to 2 if the errors are uncorrelated. In our all models, the value of Durbin-Watson statistic is close to 2(See eq.1) and hence the errors are uncorrelated.

The residuals values

The residuals values of boiling point expressed by equation .The residual values show a fairly random pattern (see Figure 2). This random pattern indicates that a linear model provides a decent fit to the data.

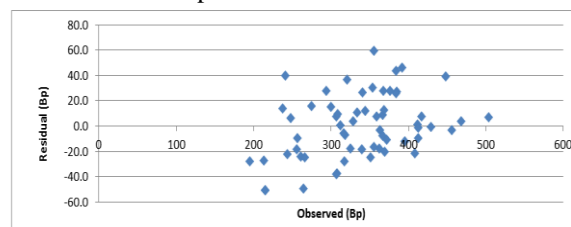


Figure 2. Comparison between the residual and observed values of boiling point by MLR.

Conclusion

QSPR models for the prediction of the boiling point 60 amino acids derivatives using MLR method based on topological descriptors calculated from molecular structure alone have been developed. Multiple linear regression model benefiting from various descriptors, factors and efficient coefficients can suggest the best algorithm for determining this physical property of chemical molecules. However, MLR model is proved to be a useful tool in the prediction of Boiling point. We can use only three topological index (J),(H) and (ww) for predicting Boiling point.

References

- [1] R.W. Taft, "Separation of polar, steric and resonance effects in reactivity", In: Newman MS(ed.): Steric effects in organic chemistry New York: Wiley, (1956) 556-675.
- [2] A. A. Taherpour, F. Shafiei, "The structural relationship between Randić indices, adjacency matrices, distance matrices and maximum wave length of linear simple conjugated polyene compounds", J. Mol. Struct. theochem, 726 (2005) 183-188.
- [3] F. Tian, P. Zhou, Z. Li, "T-scale as a novel vector of topological descriptors for amino acids and its application in QSARs of peptides", J. Mol. Struct, 830(2007)106-115.
- [4] M. Sandberg, L. Eriksson, J. Jonsson, M. Sjöström, S. Wold, "New chemical descriptors relevant for the design of biologically active peptides. A multivariate characterization of 87 amino acids", J. Med. Chem, 41(1998)2481-2491.
- [5] H. Wiener, "Structural Determination of Paraffin Boiling Points", J. Am. Chem. Soc, 69 (1947) 17-20.
- [6] Web search engine developed by Chemspider; software available at <http://WWW.Chemspider.Com>
- [7] P. V. Khadikar, N. V. Deshpande, P. P. Kale, A. Dobrynin, I. Gutman, G. Dömötör, "The Szeged index and an analogy with the Wiener index", J. Chem. Inf. Compt. Sci, 35(1995) 547-550.

Applications of Graph Theory to modeling and predicting some physico-chemical properties and QSPR study

A. Safari, F. Shafiei*

Department of Chemistry, Science Faculty, Arak Branch, Islamic Azad University,

P.O. Box 38135-567, Arak 38361-1-9131, Iran
f-shafiei@iau-arak.ac.ir

Abstract: Graph theory is a branch of mathematics which about graph are discussed and commonly called topological indices, which are important descriptors of molecular structure. In this study the relationship between the Randić' (${}^1\chi$), Balaban (J), Szeged (Sz), Harary (H), Wiener (W), Hyper-Wiener (WW), and Wiener Polarity (WP) to the thermal energy (E_{th}), and heat capacity (C_v) of 80 Amino acids is represented. Physicochemical properties are taken from the quantum mechanics methodology with HF level using the ab initio 6-31G basis sets. The multiple linear regressions (MLR) and Back ward methods (with significant at the 0.05 level) were employed to give the QSPR models. The satisfactory obtained results show that combining the two descriptors (J, 1X) are excellent descriptors for predicted (C_v), and (E_{th}) of the amino acids derivatives.

Keywords: *Amino acids; QSPR; MLR method; Topological indices*

Introduction

Aminoacids are organic compounds containing amine ($-NH_2$) and carboxyl ($-COOH$) functional groups, along with a side chain (R group) specific to each amino acid.

Quantitative structure- property relationship (QSPR) and Quantitative structure- activity relationship (QSAR) are mathematical models designed for predictions the properties of a wide range of chemical compounds based on the correlation between these properties and molecular descriptors as topological indices[1]. Topological indices (TI) are the digital values associated with chemical constitution for correlation of chemical structure with various physical properties, chemical reactivity or biological activity and useful mathematical methods for finding good relationship between several data of the properties in these materials [2-5].

Relationship between topological indices and thermodynamic properties such as heat capacity, standard Gibbs energy of formation, thermal energy and entropy of the monocarboxylic acids, alkanes [6,7], alcohols [8,9], aldehydes and ketones [10] has been searched.

Materials and methods

The chemical structure of the 80 amino acids derivatives was drawn by Gauss View Software and then was transferred into Gaussian 03 program to optimize the physicochemical properties of the molecules at the RHF/6-31 G level of theory.

Topological indices

Mathematical descriptors have been widely used in structure-property/ activity studies [11]. The topological indices (Tis) used for the QSPR analysis were Wiener (W),

Szeged (Sz), first order molecular connectivity (${}^1\chi$), Balaban(J), Hyper-Wiener(WW), Wiener (W), Wiener Polarity(WP) and Harary(H) indices.

The aim of this study is to provide reliable QSPR models for predicting physicochemical properties of amino acids derivatives. The descriptors were calculated with chemicalize program [12].

Statistical analysis

In the present study, structure- property models (MLR models) are generated using the multilinear regression procedure of SPSS version 20 and backward stepwise regression was used to construct the QSPR models.

Regression Analyses

The thermal energy (E_{th} kJ/mol) and heat capacity (C_v J/molK) are used as the dependent variable and topological indices as the independent variables. The models are assessed with R value (correlation coefficient), the R^2 (squared multiple correlation coefficient), the R^2_{adj} (adjusted correlation coefficient), the RMSE value (root of the mean square of errors), the F value (Fischer statistic), the D value (Durbin-Watson) and the Sig (significant).

QSPR models for the gas heat capacity (C_v) and thermal energy (E_{th})

The best linear model for C_v and E_{th} contains five topological descriptors, namely, Randić' (1X), Balaban (J), Hyper-Wiener (WW), Wiener polarity (Wp),

Wiener (W) and Szeged (Sz) indices. The regression parameters of the best five descriptors correlation model are gathered in equation (1, 2).

Model 1

$$C_v = 28.472 + 11.471(X) + 8.946(J) + 0.234(W) + 3.439(W_p) - 0.144(Sz) \quad (1)$$

N=80, R=0.973, R²=0.946, R²_{adj}=0.943, RMSE=154.642 F=261.317, Sig=0.000, DW=1.783

Model 2

$$E_{th} = -246.159 + 150.104(X) + 66.416(J) - 1.834(W) + 0.355(WW) \quad (2)$$

N=80, R=0.934, R²=0.873, R²_{adj}=0.867, DW=1.872 RMSE=590.322, F=129.218, Sig=0.000

Test for autocorrelation by using the Durbin-Watson statistic

We will focus on the Durbin-Watson statistic and unstandardized predicted and residual values. The Durbin-Watson statistic ranges in value from 0 to 4. A value near 2 indicates non-autocorrelation; a value toward 0 indicates positive autocorrelation; a value toward 4 indicates negative autocorrelation. Therefore the value of Durbin-Watson statistic is close to 2 if the errors are uncorrelated. In our all models, the value of Durbin-Watson statistic is close to 2 (See eqs.1-2) and hence the errors are uncorrelated.

Multicollinearity

Good regression model should not exist correlation between the independent variables or not happen multicollinearity. Test multicollinearity as a basis the variance inflation factor (VIF) value of multicollinearity test results using SPSS. If the VIF value lies between 1-10, then there is no multicollinearity, and if the VIF < 1 or > 10, then there is multicollinearity.

In all our final models, the Multicollinearity has existed, because the values of correlations between independent variables are near to one and VIFs value lies are not use of between 1-10.

Results and discussion

Multiple linear regression method predictive power for a QSAR/QSPR analyses. It can be conveniently estimated by statistical parameters. A good QSPR model should have both suitable relativity and good predictability. In the constructed model internal validation is usually done by leave-one-out (LOO). The new QSPR models are expected to have low R²_{cal} and LOO-cross-validation (Q²_{loo}) values [13,14]. We studied the validation of linearity between the molecular descriptors in the models 1 and 2. We

obtained by SPSS the Pearson coefficient correlation and collinearity statistics as follows Tables (3, 4).

For model 1 the Pearson correlation (Sz,W),(W_p,X) and (X,W) are near one, and VIF (W_p),(W), (Sz) and (1X) > 10. After removed (W) from this model, we corrected model 1 as follow:

$$C_v = -22.418 + 26.498(X) + 17.460(J) \quad (3)$$

N=80, R=0.964, R²=0.930, R²_{adj}=0.928, RMSE=242.414 F=513.412, Sig=0.000, DW=1.795, Q²_{LOO}=0.824

Table 3: Correlation between the molecular descriptors (model 1)

Collinearity						Corrected model		VIF
Sz	J	W _p	X	w	Tolerance	VIF		
Sz	1	0.622	-0.678	0.617	-0.945	0.024	42.376	-
J	0.622	1	-0.568	0.639	-0.605	0.287	3.489	1.992
W _p	0.678	-0.568	1	-0.846	-0.643	0.010	97.175	-
X	0.617	0.639	-0.846	1	-0.743	0.041	24.607	1.992
W	-0.945	-0.605	0.643	-0.743	1	0.011	89.146	-

For model 2 the Pearson correlation (WW, W),(W,X) and (X,WW) are near one, and VIF (1X),(W) and (WW) > 10. After removed (W) from this model, we corrected model 2 as follow:

$$E_{th} = -93.740 + 87.647(X) + 65.787(J) \quad (4)$$

N=80, R=0.921, R²=0.848, R²_{adj}=0.845, DW=1.967 RMSE=822.886, F=215.544, Sig=0.000, Q²_{LOO}=0.746

Table 4: Correlation between the molecular descriptors (model 2)

Collinearity					Corrected model		VIF
W _w	J	X	w	Tolerance	VIF		
W _w	1	0.017	-0.836	-0.983	0.027	148.05	-
J	0.17	1	-0.209	-0.032	0.531	1.883	1.869
X	0.836	-0.209	1	-0.914	0.003	37.321	1.869
W	-0.983	-0.032	-0.914	1	0.007	293.564	-

we have computed Q² (Eq.5) by 50% of data, randomly, that are positive and less than one.

$$Q^2 = 1 - \frac{\sum(Y_i - \hat{Y}_{i|i})^2}{\sum(Y_i - \bar{Y})^2} \leq 1 \quad (5)$$

Where the notation i|i indicates that the response is predicted by a model estimated when the i-th sample was left out from the training set.

Comparison between predicted and observed values of C_v and E_{th} of respect amino acids derivatives show the linear correlation between them. Figure 1, 2 shows the observed and the predicted heat capacity and thermal energy values obtained using equation (3,4) respectively.

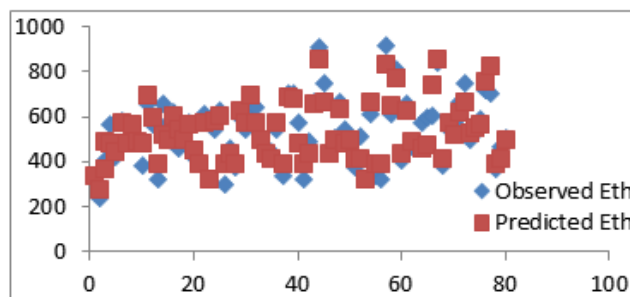


Figure 1. Comparison between the predicted and observed thermal energy by MLR method.

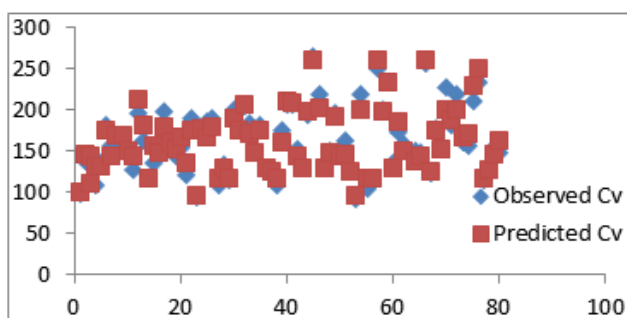


Figure 2. Comparison between the predicted and observed heat capacity by MLR method.

Conclusion

At present study, QSPR mathematical models for the prediction of the heat capacity (C_v) and thermal energy (E_{th}) of 80 amino acids derivatives by using MLR method based on topological descriptors calculated from molecular structure alone have been developed. MLR model is proved to be a useful tool in the prediction of C_v and E_{th} . Cross-validation as the evaluation technique has been designed to evaluate the quality and predictive ability of the MLR model. The obtained results showed that the only Randic and balaban indices are good topological indices for modeling heat capacity and thermal energy.

References

- [1] M. Randic', S. C. Basak, "Multiple regression analysis with optimal molecular descriptors", SAR QSAR Environ. Res, 11 (2000) 1–23.
- [2] Y. P. Du, Y. Z. Liang, B.Y. Li, C. J. Xu, "Orthogonalization of block variables by subspace-projection for quantitative structure property relationship (QSPR) data", J.

Chem. Inf. Comput. Sc, 42 (2002) 1128–1138.

[3] M. Randić, "Characterization of molecular branching", *J. Am. Chem.*, 97(1975)6609–6615.

[4] Z. Slanina, F. Uhlik, S. L. Lee, E. Osawa, "Geometrical and thermodynamic approaches to the relative stabilities of Fullerene isomers", *MATCH Commun. Math. Comput. Chem.*, 44 (2001) 335–348.

[5] B. Lučić, N. Trinajstić, "New developments in QSPR/QSAR modeling based on topological index", *SAR QSAR Environ. Res.*, 7 (1997) 45–62.

[6] O. Ivanciuc, T. Ivanciuc, D. Cabrol-Bass, A. T. Balaban, "Evaluation in quantitative structure–property relationship models of structural descriptors derived from information-theory operators", *J. Chem. Inf. Comput. Sci.*, 40 (2000) 631–643.

[7] D. Bonchev, "Over all connectivities / topological complexities: A new powerful tool for QSPR/QSAR", *J. Chem. Inf. Comput. Sci.*, 40 (2000) 934–941.

[8] S. Liu, H. Liu, Z. Xia, C. Cao, Z. Li, "Molecular distance edge vector (m): An extension from alkanes to alcohols", *J. Chem. Inf. Comput. Sci.*, 39 (1999) 951–957.

[9] V. Sharma, R. Goswami, A. K. Madan, "A novel highly discriminating topological descriptor for structure–property and structure–activity studies", *J. Chem. Inf. Comput. Sci.*, 37 (1997) 273–282.

[10] Z. Lin, J. Xu, X. Zheng, Z. Li, "Study on quantitative structure- property relationship of chain hydrocarbons, aldehydes and alkanones by molecular distance-edge vector",

Acta Phys. Chem. Sin., 16 (2000) 153–161.

[11] M. Randic, "Topological Indices. Encyclopedia of Computational Chemistry (P. von Rague Schleyer, Editor-in-Chief", London: Wiley, (1998)3018-3032.

[12] Web search engine developed by ChemAxon; software available at [http:// WWW.Chemicalize. Org](http://WWW.Chemicalize.Org).

[13] K. Baumann, N. Stiefl, "Validation tools for variable subset regression, *J. Comput. Aided. Mol. Des.*, 18(2004) 549-562.

[14] N. Chirico, P. Gramatica, "Real External Predictivity of QSAR models: How to evaluate it Comparison of Different Validation Criteria and Proposal of Using the Concordance Correlation Coefficient", *J. Chem. Inf. Model.*, 51 (2011)2320-2335.



Quantum hard spheres in a slit pore

A. Helmi

Department of Chemistry, Isfahan University of Technology, Isfahan, 8415683111, Iran

A.helmi@ch.iut.ac.ir

Abstract: In this paper, the density functional theory is employed to investigate the effects of quantum correction on the structure and such thermodynamic properties of quantum-mechanical hard sphere fluids confined in nano-slit pore as excess adsorption and wall pressure. It is found that the repulsion between hard sphere molecules because of quantum effect play an important role in determining the structure and thermodynamic properties of the confined fluid. Another finding of the present study involves the key role of the excluded volume in determining the structure and thermodynamic properties of quantum mechanical hard sphere fluids. By increasing of the quantum effect, λ^* , the periodic oscillation in the density profile becomes more obvious and the order of layers in the pore increases. Increasing the values of λ^* is found to lead not only to drastic changes in the structure of the fluid molecules but also, to increased excess adsorption and wall pressure of the fluid confined in slit pores.

Keywords: DFT; Semi-classical quantum fluid; Slit pore; Excess adsorption.

Introduction

The thermodynamic properties of confined quantum fluids are a major area of basic and applied research in nanotechnology [1]. In classical systems, quantum effects for heavy molecules at high temperature are so small that quantum corrections are often neglected. But it should be noted that the thermodynamic properties of such quantum fluids as hydrogen, deuterium, and neon whose de Broglie's wavelengths are of the same magnitude as the mean distance between particles greatly depend on quantum corrections[1].

It is clear that in most theoretical studies, the hard sphere fluid is the one most commonly employed as a reference system to study such realistic fluids as the Lennard Jones fluid and electrolyte solutions. Hence, hard sphere fluids have attracted a lot of attention by researchers due to their importance in modeling real systems, especially confined quantum fluids.

The present work aims to investigate the effects of quantum correction on the structure and such thermodynamic properties as excess adsorption of quantum-mechanical hard sphere fluids confined in nano-scale slit pore. In this work among the different theoretical methods for studying the thermodynamic properties of fluids confined in nano-scale pores, the successful versions of the DFT, modified fundamental measure theory (MFMT), that gives improved contact density for hard sphere fluids has been used.

Materials and method

In the density functional theory, the grand canonical potential of an inhomogeneous system is defined as [2]:

$$\Omega[\rho(\mathbf{r})] = \beta F[\rho(\mathbf{r})] + \int d\mathbf{r} \rho(\mathbf{r}) [V^{ext}(\mathbf{r}) - \mu] \quad (1)$$

where, μ is the chemical potential and V^{ext} is the external potential for this component. Generally, the

equilibrium density profile of an inhomogeneous fluid can be obtained by minimizing the grand canonical potential as follows:

$$\rho(\mathbf{r}') = \rho_b \exp \left[-\beta V^{ext}(\mathbf{r}') + \beta \mu^{ext} - \int \sum_{\alpha} d\mathbf{r}'' \frac{\partial \Phi}{\partial n_{\alpha}} w_i^{(\alpha)}(\mathbf{r} - \mathbf{r}') \right] \quad (2)$$

where, μ^{ext} and ρ_b are the bulk excess chemical potential and bulk fluid density, respectively. In this work, used has been made of the effective diameter method, in which the quantum-mechanical hard sphere has an effective diameter larger than that of the classical hard sphere [3].

$$\sigma_{eff} = \sigma \left(1 + \sum_l a_l \lambda^{*l} + \sum_m \sum_n c_{mn} \rho^{*n} \lambda^{*m} \right)^{1/3} \quad (3)$$

where, $\lambda^* = \lambda/\sigma$ and $\rho^* = \rho\sigma^3$. The term $\sum_l a_l \lambda^{*l}$ is a series in the thermal wavelength, and the double summation, $\sum_m \sum_n c_{mn} \rho^{*n} \lambda^{*m}$, expresses the dependence of the ratio on both density and thermal wavelength. In this work, the coefficients in Table 1 were used to calculate the properties of the fluid confined in a spherical pore and in equilibrium with the bulk fluid.

Table1: Optimal coefficients

a_1	a_2	a_3	C_{21}	C_{22}
1.08016	0.752081	-0.489996	-0.471077	-1.29761

Results and Discussion

In this section, we study the effects of quantum correction on the structure, adsorption and contact density of a hard sphere fluid confined in a nano-slit pore.

Effects of quantum correction on the structure

It is known that the structure of a quantum mechanical fluid in nano-pore systems depends on such parameters as pore size, intermolecular interactions, wall–fluid interactions, and the quantum effect, λ^* . Since the simultaneous study of these effects is complex, we consider a quantum mechanical hard sphere particles confined in a hard and structureless slit pore. Fig. 1 depict the density profiles of the hard sphere fluid with bulk density equal to 0.5 confined in a nano-slit pore with distance between the walls, $H=5\sigma$, for different values of the λ^* including 0, 0.2, 0.4 and 0.6. It is also clear that the density profile of the fluid exhibits an oscillatory behavior for different values of λ^* and that the number of peaks corresponds to the number of molecular layers in the nano-spherical pore. It is clear that in the absence of wall-molecule and molecule-molecule interactions, the structure of the fluid is determined by entropy effects because of the excluded volume near the walls. This excluded volume, increases with the effective diameter of the particles confined in the slit pore. The excluded volume has direct effects on the density distribution of molecules in the pore. Moreover the quantum effect causes the hard spheres to repel each other before they come into contact, while the classical ones repel each other only upon contact. This effect causes to more molecules accumulate at the wall due to the tendency of the molecules to escape from this repulsion. Also the repulsion among the molecules enhances the orderliness of the layers in the pore; which is reflected in the growing heights of the peaks and depths of the valleys in the density profiles.

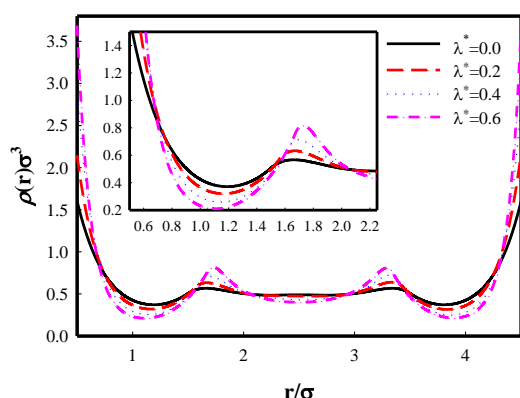


Fig.5: Density profiles of a quantum hard sphere fluid with bulk density equal to 0.5 confined in a slit pore with distance between the walls equal to 5σ , in a nano-slit pore versus r/σ for different values of the λ^* including 0, 0.2, 0.4 and 0.6.

Effects of quantum correction on the excess adsorption

As we know, the excess adsorption of fluids Γ , in a nano-slit pore is defined by:

$$\Gamma = \frac{1}{H} \int d\mathbf{r} [\rho(\mathbf{r}) - \rho_b] \quad (4)$$

where ρ_b refers to bulk density. Fig. 2 plots the adsorption isotherm of a hard sphere fluid for different values of λ^* including 0, 0.2, 0.4, and 0.6 for a bulk density equal 0.6 versus H/σ . Based on this figure, adsorption of the fluid has an oscillatory behavior with maximum and minimum values for integral and half integral values of H respectively. It is clear that the adsorption is negative for all values of λ^* and H . For a fixed value of λ^* , adsorption increases with H and also for a fixed value of H , it increases with λ^* . It is also clear from these Figures that the height and depth of the oscillations increase with increasing λ^* .

It is known that the excluded volume plays the key role in determining the structure and thermodynamic properties of classical and quantum mechanical hard sphere fluids. In fact, the excluded volume increases with increasing quantum effect, λ^* . This will lead to increases in the periodic oscillations of excess adsorption in nano slit pore. In fact, when λ^* increases, the quantum hard sphere fluid exhibits a rising tendency for being adsorbed onto the nano-pore as a result of both the entropy effect and the breaking up of the repulsion between the molecules at the pore walls. From the figure, it is easy to realize that excess adsorption is become nearly uniform by increasing of the distance between the walls, H .

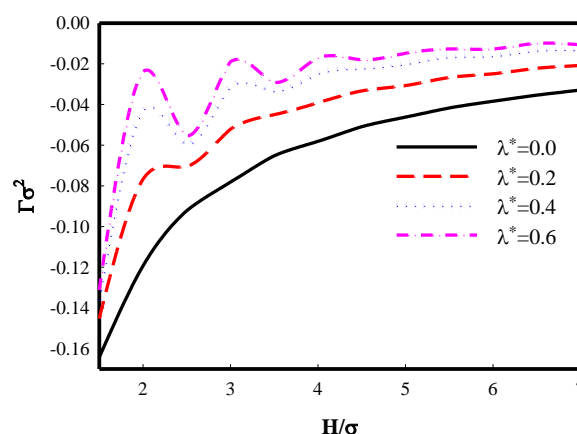


Fig.2: Adsorption isotherm of a hard sphere fluid for different values of λ^* including 0, 0.2, 0.4, and 0.6 for a bulk density equal 0.6.

Effects of quantum correction on the wall pressure

To investigate the effect of the distance between the walls, H , on the contact density of the fluid at the walls, we used the contact theorem directly set the contact density of the fluids at the walls equal to wall pressure, $P_w = \rho(0)$, and plotted it versus H , for different values of λ^* , as shown in Figure 3. In this figure, the wall pressure, of a hard sphere fluid with a bulk density of 0.6 confined in a pore between two flat walls for different values of λ^* including 0, 0.2, 0.4, and 0.6 has been plotted versus the H .

The wall pressure of the fluid at the pore walls versus H/σ clearly exhibits an oscillatory behavior. This oscillatory behavior increases with λ^* . In fact the height and depth of the wall pressure oscillations increase with increasing λ^* .

According to this figure for a fixed value of H , wall pressure increases with λ^* .

As mentioned the excluded volume plays the key role in determining the structure and thermodynamic properties of quantum mechanical hard sphere fluids. In fact, the excluded volume increases with increasing λ^* . This will lead to increases in the periodic oscillations of wall pressure.

In the classical hard-sphere system, pressure arises due to the direct contact collisions but that quantum mechanical pressure arises from the collisions without any direct contact, that is, from inter-particle repulsions due to quantum effects. This is because the periodic oscillation in the wall pressure becomes more obvious and wall pressure grows larger with increasing values of λ^* . Once the repulsion between fluid molecules is increased, the wall pressure increases as result of the enhanced quantum effect, λ^* . The increased quantum effect, λ^* , then causes the hard spheres to repel each other before they come into contact; the repulsion is then broken at the wall and the molecules escaping the repulsion have a greater tendency to accumulate at the pore wall.

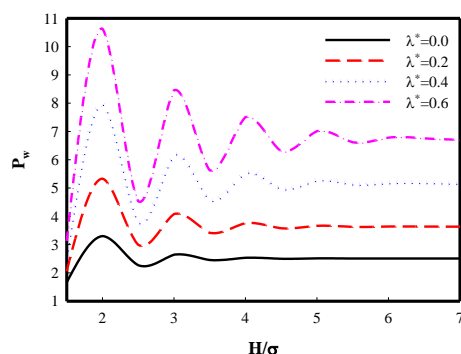


Fig.3: The wall pressure of the hard sphere fluid with a bulk density of 0.6 confined in a pore between two flat walls versus the H for different values of λ^* including 0, 0.2, 0.4, and 0.6.

Conclusions

The effective diameter method was used, in which the quantum-mechanical hard sphere has an effective diameter larger than that of the classical hard sphere. Results showed that the excluded volume increases by quantum effect in slit pore. This excluded volume causes the hard spheres to repel each other before they come into contact, while the classical ones repel each other only upon contact. This effect causes to more molecules accumulate of the molecules at the wall due to the tendency of the molecules to escape from this repulsion.

Our results also showed that, due to the effective diameter of hard molecules, Synergy's entropy effect and the broken repulsion between molecules at the pore wall causes the quantum-mechanical hard sphere fluid exhibits an increasing tendency to be adsorbed onto the nano-slit pore with increasing values of λ^* .

Acknowledgment

The authors would like to acknowledge the Isfahan University of Technology Research Council for their financial support.

References

- [1] V.M. Trejos, A.G. Villegas, A. Martinez "Computer simulation of liquid-vapor coexistence of confined quantum fluids", *J. Chem. Phys.* 139 (2013) 184505.
- [2] E. Keshavarzi, A. Helmi "The Effects of Inserting a Tiny Sphere in the Center of a Nanospherical Pore on the Structure, Adsorption, and Capillary Condensation of a Confined Fluid (A DFT Study)", *J. Phys. Chem. B.* 119 (2015) 3517–3526.
- [3] A. Helmi, M. D. Esrafilii "A hard sphere fluid with quantum correction in nanospherical pores: A DFT study", *J. Mol. Liq.* 238 (2017) 160–169.

The influence of the Li₂ interaction with pristine and halogenated B₁₀H₁₄ on their electronic and nonlinear optical properties

M. Rasteh^a, E. Shakerzadeh^{*.b} and S. Fakhraie^a

^aDepartment of chemistry, College of sciences, Payame Noor University, Tehran, Iran

^bChemistry Department, Faculty of Science, Shahid Chamran University of Ahvaz, Ahvaz, Iran

*e.shakerzadeh@scu.ac.ir

Abstract: In this study the influence of Li₂ interaction with pristine and halogenated decaborane (B₁₀H₁₄) derivatives on their electronic and optical properties are investigated through DFT calculations. For this purpose, all structures are fully optimized at B3LYP/6-311++G** level of theory and different properties such as energy gap, polarizability and hyperpolarizability are calculated for the relaxed geometries. It is found that the electro-optical features of pristine and halogenated B₁₀H₁₄ could be efficiently tuned by interaction with Li₂ molecule. The results could be valuable for designing novel boron-based electro-optical devices. The present results will be beneficial for further theoretical and experimental studies on the NLO properties of boron-based compounds.

Keywords: Decaborane, energy gap, Polarizability, Hyperpolarizability, halogenated, halogen.

Introduction

The last few decades the design and synthesis of nonlinear optical (NLO) materials have been attracted great interest¹. Research on designing new high-performance nonlinear optical (NLO) materials is being an intriguing issue for scientist². Among many strategies for enhancing the NLO response of materials, introducing the diffuse excess electron, such as alkali metals, proposed an efficient approach to improve the NLO properties of different systems. In the present study the influence of Li₂ interactions with pristine and halogenated decaborane (B₁₀H₁₄) on their electro-optical features are investigated through DFT calculations.

Results and Discussion

In order to investigate the Li₂ interaction with decaborane, the Li₂ molecule is located at different positions of pristine and halogenated B₁₀H₁₄ and the geometry optimizations are carried out at B3LYP/6-311++G** level of theory. The optimized structures are depicted in Fig.1. Notice that fluorine (F) and chlorine (Cl) atoms replace by different hydrogen

atom in the considered Li₂@1-F-B₁₀H₁₃, Li₂@2-F-B₁₀H₁₃, Li₂@5-F-F-B₁₀H₁₃, Li₂@in9-F-F-B₁₀H₁₃, Li₂@out9-F-F-B₁₀H₁₃, Li₂@1-Cl-B₁₀H₁₃, Li₂@2-Cl-F-B₁₀H₁₃, Li₂@5-Cl-F-B₁₀H₁₃, Li₂@in9-Cl-F-B₁₀H₁₃ and Li₂@out9-F-B₁₀H₁₃ complexes which are presented in Fig. 1. The obtained highest occupied molecular orbital (HOMO) and the lowest unoccupied molecular orbital (LUMO) energies together with energy gap (E_g) values as well as polarizability and the first static hyperpolarizability of the considered structures are listed in Table 1. It is found the Li₂ interactions with pristine and halogenated B₁₀H₁₄ narrow their energy gaps. Such a reduction of HLG is mainly due to the formation of a high energy level as the new HOMO levels locating between the original HOMO and LUMO of pristine B₁₀H₁₄. Thus the electronic properties of these considered systems are strongly sensitive to interaction with the Li₂. As can be seen in Table 1, the first static hyperpolarizability (β_0) is induced in both pristine and halogenated B₁₀H₁₄, especially in the case of Li₂@B₁₀H₁₄ complex with remarkable value of 34891.8 a.u.

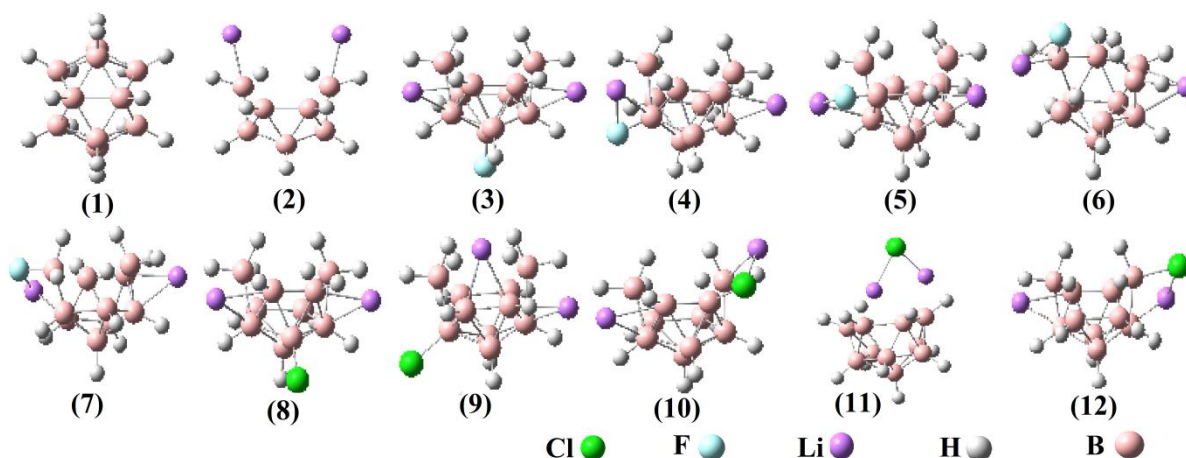


Fig. 1. The optimized structures of the considered complexes

Table 1. The obtained electro-optical parameters of the considered compounds

systems	μ (au)	α (au)	β_0 (au)	HOMO (eV)	LUMO (eV)	E_g (eV)	B-X(X=F, Cl)
1	1.29	124.70	69.7	-8.319	-2.854	5.465	-
2	6.13	236.80	34891.8	-4.259	-2.708	1.551	-
3	2.55	147.93	466.0	-5.203	-1.475	3.728	1.375
4	2.23	147.10	420.8	-5.311	-1.406	3.905	1.456
5	1.73	146.33	140.2	-5.203	-1.366	3.837	1.459
6	1.78	145.54	222.7	-5.606	-1.371	4.235	1.513
7	2.18	146.24	451.9	-5.323	-1.416	3.918	1.478
8	1.95	160.15	334.9	-5.235	-1.476	3.759	1.843
9	4.93	159.97	893.5	-6.247	-1.882	4.365	1.830
10	2.73	162.00	531.5	-5.312	-1.428	3.884	1.923
11	1.07	154.56	90.5	-7.282	-2.437	4.846	3.620
12	2.41	160.86	455.9	-5.421	-1.491	3.930	1.950

Conclusions

To sum up, it is concluded the electro-optical features of pristine and halogenated B₁₀H₁₄ could be efficiently tuned by interaction with Li₂ molecule.

References

- G. de la Torre, P. Vázquez, F. A. López and T. Torres, *Chem. Rev.* 2004, **104**, 3723
- R.L. Zhong, H.L. Xu, Z.R. Li and Z.M. Su *J. Phys. Chem. Lett.* 2015, **6**, 612
- S. Muhammad, H.L. Xu, Y. Liao, Y.H. Kan and Z.M. Su *J. Am. Chem. Soc.* 2009, **131**, 11833

A Computational study of pristine and Al-doped boron nitride nanosheet as CNCl sensor

R. Moladoust^a, S.M. Mousavi-Khoshdel^{b*}, E. Vessally^c

^aDepartment of Chemistry, University of Mohaghegh Ardabili, Ardabil, 5619911367, Iran

^bDepartment of Chemistry, Iran University of Science and Technology, Tehran, 1684613114, Iran

^cDepartment of Chemistry, Payame Noor University, Zanjan, Iran

* mmousavi@iust.ac.ir

Abstract:

In order to explore a novel sensor to detect the cyanogen chloride (CNCl) molecule, we study the adsorption and electronic properties of the interaction CNCl with the pristine and Al-doped boron nitride nanosheet using density function theory. The most stable adsorption geometries, adsorption energies, charge transfers, and density of states of these systems are thoroughly discussed. Comparing the results of the pristine BN nanosheet with CNCl, we found that Al-doped BN nanosheet is more sensitive to the CNCl molecule, which is indicated by the calculated optimized geometry and electronic properties of these systems. Al-doped BN nanosheet is expected to be a potential candidate for detecting of toxic CNCl molecule.

Keywords: Gas Sensor; Cyanogen Chloride; BN nanosheet; DFT

Introduction

Cyanogen chloride (CNCl) is a highly volatile and toxic. It has strong irritant and choking effects. Exposure to cyanogen chloride can be rapidly fatal. Its vapors are extremely irritating and corrosive [1]. Boron nitride nanostructures, because of their unique properties including high thermal conductivity and chemical stability, strong resistance to oxidation have been applied in the nanodevices such as transistors and chemical sensors [2-4]. BN sheet possesses polar B-N bond and a wide band gap that is independent of its helicity. Because of the polar nature of B-N bonds, BN nanostructures are expected to have higher reactivity than their carbon analogs. It indicates that BN nanostructures could be good candidates for gas sensors.

In this research, we study the adsorption of CNCl molecule on pristine and Al-doped BN sheets using density functional theory (DFT), to verify whether or not the sheets can be used as gas sensors.

Computational methods

The full geometry optimizations and electronic properties calculations on the pristine and Al-doped sheet to the CNCl molecule were performed using hybrid meta generalized gradient approximation with the M06-2X functional and the 6-31+G(d) basis set, as implemented in the GAMESS suite of program. Adsorption energy calculations and density of states (DOS) analysis were performed at the same level of theory. GaussSum program was used to obtain DOS results. We have defined the adsorption energy (E_{ad}) as follows:

$$E_{ad} = E_{(CNCl/sheet)} - (E_{(sheet)} + E_{(CNCl)}) + E_{(BSSE)}$$

HOMO-LUMO energy gap is defined as:

$$E_g = E_{LUMO} - E_{HOMO}$$

Results and Discussion

In order to find the most stable configuration, full geometrical optimization was performed with different orientations of the CNCl molecule with surface sheet. After relaxation, in the most stable structure, CNCl molecule attaches to a B atom of the sheet from its nitride (-N-) head (Fig. 1), and its corresponding calculated E_{ad} value is about -4.77 kcal/mol, indicating a weak adsorption.

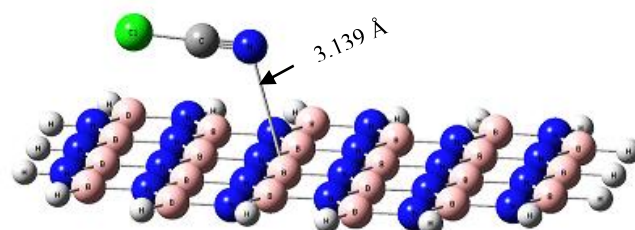


Figure 6 : The most stable configuration after optimization.

The calculated energy gaps of the pristine and CNCl adsorbed sheet are about 7.86 and 7.15 eV, respectively. The HOMO and LUMO are mainly localized on the CNCl molecule and BN sheet (Fig. 2) at -7.97 and -0.82 eV, respectively.

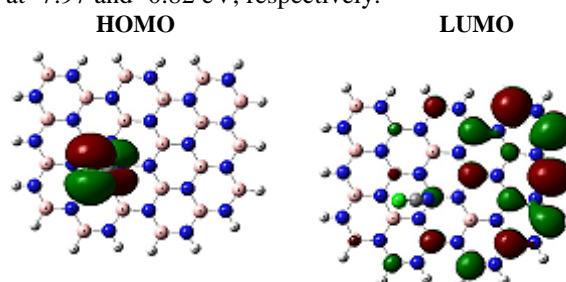


Figure 2: The HOMO and LUMO profile of the CNCl/BN sheet complex.

Our calculated indicated that small amount of charge transfer between CNCl and BN sheet, So a net charge of 0.17 $|e^-|$ is transferred from the molecule to the sheet (Table 1). For the bare BN sheet (Fig. 3), after adsorption process of CNCl molecule, E_g value decreased to -7.15 eV for BN sheet/CNCl complex due to charge transfer to the molecule. As the energy gap of the pristine sheet is only slightly changed during the adsorption process, the pristine nanosheet will not be sensitive to CNCl molecule. So, we investigated the influence of Al-doping on adsorption and electronic characteristics of the sheet on CNCl.

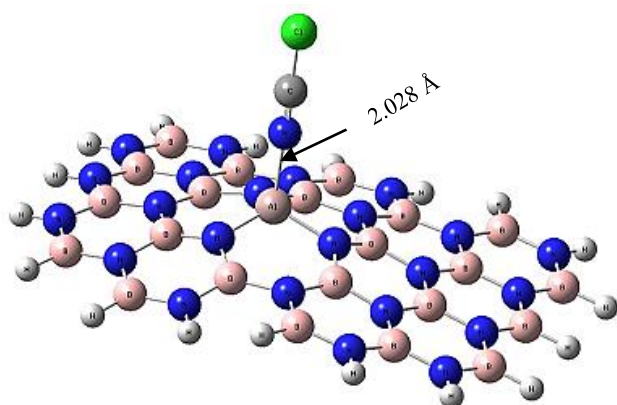


Figure 3: The optimized structure of Al-doped BN sheet with CNCl molecule.

When one boron atom is substituted by Al atom in the BN Sheet, it is found that the geometric structure of the Al-BN Sheet, changes dramatically. Due to the large size of Al atom, it protrudes out of plane in order to relieve the stress. After the adsorption of CNCl molecule, the length of Al-N bond is increased from 1.737 to 1.773 Å, indicating that the Al site is transformed from sp^2 hybridization to more sp^3 like hybridization. Moreover, the adsorption energy of CNCl on the Al-BN sheet is - 22.71 kcal/mol, which is larger than that of CNCl on the pristine BN Sheet. The interaction distance in the CNCl molecule interacted with the Al atom of BN sheet is about 2.028 Å that is reduced than distance with the B atom of BN sheet. Mulliken population analysis indicated that the charge about 0.66 $|e^-|$ is transferred from the CNCl molecule to the Al-BN sheet. These adsorption energy values, interaction distances and charge transfer exhibit that the CNCl molecule is favourably adsorbed in the Al-BN sheet owing to the strong covalent interaction between CNCl molecule and Al-BN sheet.

To further understand the electronic properties of BN sheet, the density of states (DOS) plots for sheet to the CNCl molecule, were calculated.

DOS plot of the CNCl/Al-BN Sheet complexe shows a considerable change (Fig. 4). New states have appeared in the DOS of complexe in comparison to the bare BN sheet. This indicates that the electronic

properties of the Al-BN sheet are sensitive to the CNCl adsorption.

The energy gap value of the Al-BN sheet decreased from 7.62 to 5.77 eV in the CNCl/Al-BN sheet complexes.

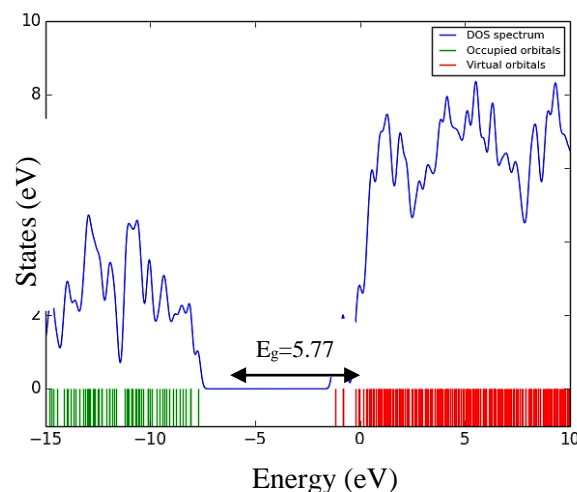


Figure 4: The DOS profile of the Al-BN/CNCl complex.

These changes would result in an electrical conductivity change of the sheet according to Eq. (1). The electrical conductance is exponentially related to E_g value according to the following equation:

$$\sigma \propto \exp\left(-\frac{E_g}{2kT}\right)$$

(1)

According to the equation, smaller E_g values lead to higher conductance at a given temperature. Compared with the pristine BN sheet, the Al-BN sheet would have excellent CNCl detection ability.

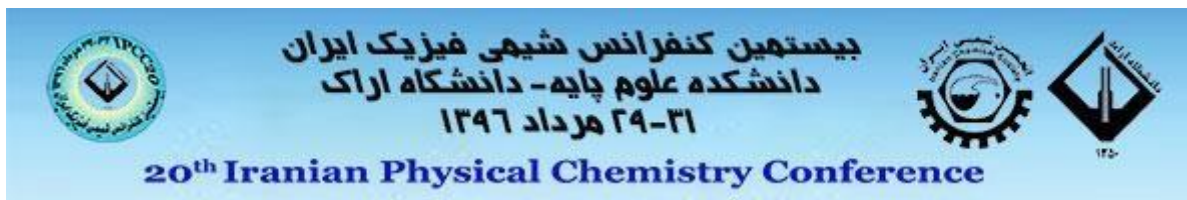
So, we believe that Al doping process may be a good strategy for improving the sensitivity of the sheet to CNCl, which cannot be detected by the pristine BN Sheet (Table 1).

Table 1: Adsorption energies, the electronic properties and charge transfer of the BN complexes.

Compound	E_{ad} (kcal/mol)	E_{HOMO} (eV)	E_{LUMO} (eV)	E_g (eV)	q_{CT} (e)
BN-CNCl	-4.77	-7.97	-0.82	7.15	0.17
Al-BN-CNCl	-22.71	-7.74	-1.97	5.77	0.66

Conclusion

In this research, we have performed upon the reliable chemical gas sensors for the detection of toxic gas molecule. The electronic sensitivity of pristine and Al-doped BN sheet to the CNCl molecule were investigated using density functional theory. The



results indicate that Al-doped BN sheet is more sensitive and reactive to the CNCl molecule.

References

- [1] GC. Deng, ZH. Zhang, B. Li, XD. Gao, SL. Zang, "Determination of cyanogen chloride in the air pollution by spectrophotometry", Chin J Anal Chem, 29 (2001) 565-568.
- [2] A.B. Preobrajenski, M.A. Nesterov, M.L. Ng, A.S. Vinogradov, N. Mårtensson, Chem. Phys Lett, 446 (2007) 119.
- [3] J.Y. Dai, P. Giannozzi, J.M. Yuan, Surf. Sci. 603 (2009) 2328–3234.
- [4] X. Jiang, Q. Weng, X. Wang, X. Li, J. Zhang, "Recent progress on fabrications and applications of boron nitride nanomaterials: a review", Journal of Materials Science & Technology, 31(2015) 589–598.

Quantum Chemical Evaluation of Optoelectronic Properties of Oligoselenophene:Fullerene BJJ Solar Cells

ZabiollahMahdavifar*, Samira Tajdinan, Ehsan Shakerzadeh

Department of Chemistry, Faculty of Science, Shahid Chamran University of Ahvaz, Ahvaz, Iran

*z_mahdavifar@scu.ac.ir

Abstract: In this work, in order to model the active layer in the bulk hetero-junction solar cells, the fullerene structures such as C₆₀, C₇₀, PC₆₀BM, PCBDAN as acceptor and oligoselenophenes ((OS)_n=14) as donor were considered. The (OS)_n=14/C₆₀, (OS)_n=14/C₇₀, (OS)_n=14/PC₆₀BM and (OS)_n=14/PCBDAN blends (complexes) as a model of the active layer in the BJJ solar cell were chosen and the opto-electronic properties were studied. Results show the width of the absorption spectrum of all investigated blends in the range of 400-700 nm and maximum wavelength in the range of 516.65 - 536.03 nm. Base on obtained data the calculated efficiency of these blends based on Scharber diagram was obtained namely 8% and 8.2% respectively.

Keywords: Oligoselenophenes, fullerene, bulk hetero-junction solar cells optoelectronic properties, DFT

Introduction

Nowadays because of the fossil fuels declining and the environmental damage, clean and renewable solar energy as an inexhaustible resource has attracted increasing attention over the past decades due to nontoxic and nonpolluting operation [1]. The annual solar radiation coming to earth (including 5% UV, 43% visible and 52% IR) is several times the world's annual energy consumption [2]. In this context, organic photovoltaic (OPV) device have attracted much attention in recent years [3, 4, 5, 6,7]. There are many reasons for the interest in OPVs comparing with silicon-based photovoltaics (PV). The OPVs offer low cost, solution-based processing, low thermal budget and the capability to fabricate flexible layer-area devices [3, 8]. Organic photovoltaics are devices, which convert solar energy or light directly into electrical power by photovoltaic effect [9]. The photovoltaic effect describes the fundamental interaction of light with matter to produce electricity.

C₅₉P

Computational Method

Quantum-chemical calculations using density functional theory (DFT) with the aim of Gaussian 09 were performed to investigate the electronic structure of these (OS)_n/fullerene blends by employing the B3LYP hybrid density functional. The basis sets used for the calculations are the split valence 6-311G(d) basis set. Time-dependent DFT (TD-DFT) calculations were performed to assess the excited-state vertical transition energies and oscillator strengths based on the optimized molecular geometries at the same level of theory.

Results and Discussion

On the basis of the optimized ground-state geometries of (OS)₁₂/C₆₀, (OS)₁₄/C₇₀ and (OS)₁₄/C₆₀ complex (Fig. 1), the deformation energy (E_{def}), interaction energy (E_{int}), binding energy (E_b) were calculated and are presented in Table 1. A negative value of binding energy indicates more stability of considered system. Compare the values of binding energy of (OS)₁₂/C₆₀ and (OS)₁₄/C₆₀ show that the structure with with karger number on *n* is more stable and generally, the (OS)₁₄/C₆₀ blends is more stable than others. According to the values specified in the Table 1, the interaction energy contribution in the complex formation process are obtained large and negative values, which indicate that the deformation in the direction sustainability is take place. Among all cases, (OS)₁₄/C₆₀ blend has the largest deformation and interaction energy.

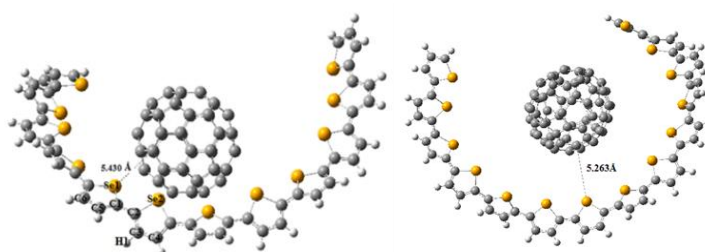


Fig. 1: Optimized structures of (OS)₁₂/C₆₀ and (OS)₁₄/C₆₀

Table 1: deformation energy (E_{def}), interaction energy (E_{int}), binding energy (E_b) of (OS)_n/fullerene with the B3LYP/6-311G(d) method.

In organic solar cells, frontier molecular orbital energy levels have a close relation with V_{oc} and energy driving force ($\Delta E1$) for exciton dissociation. Namely, the V_{oc} is determined by the difference between the HOMO of the donor and the LUMO of the acceptor, according empirical equation summarized by Scharber and co-workers, which can be expressed as

$$V_{oc} = \left(\frac{1}{e}\right) (|E_{HOMO}^{Donor}| - |E_{LUMO}^{Acceptor}|) - 0.3V$$

here, e is the elementary charge, and the value of 0.3 is an empirical factor. The energy difference $\Delta E1$ between the LUMOs of the donor and the acceptor should be larger than 0.3 eV, which guarantees efficient exciton split and charge dissociation at the D/A interface. To explore these relationships, the frontier molecular orbital (FMO) energies of all the acceptors with regard to the electron donors (OS) $n=10-15$ were depicted in Fig. 2. The values of $\Delta E1$ and V_{oc} parameters are reported in Table 2.

Table 2: ΔE_{LL} & V_{oc} of (OS) $_n$ /fullerene with the B3LYP/6-311G(d) method.

	ΔE_1 (LUMO $_{OS_n}$ - LUMO $_{C_n}$) (eV)	V_{oc} (V)
(OS) $_{n=12}$ /C $_{60}$	0.854	1.055
(OS) $_{n=14}$ /C $_{60}$	0.825	1.029
(OS) $_{n=14}$ /C $_{70}$	0.820	1.034

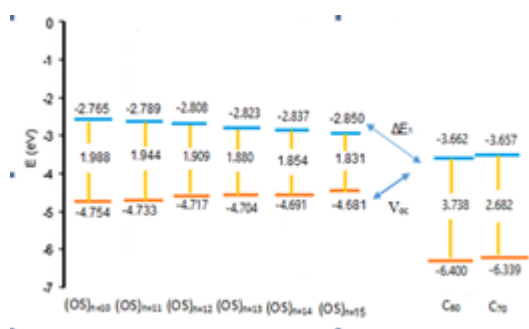


Fig. 2: Frontier molecular orbital energy levels of (OS) $n=10-15$ and C $_{60}$ and C $_{70}$.

The results show that the most favorable amount of $\Delta E1$ is owned by (OS) $_{14}$ /C $_{70}$ blend, because of the LUMO level are located relative to each other therefore this complex has the lowest $\Delta E1$ and highest

	E_{def} (kJ.mol $^{-1}$)	E_{int} (kJ.mol $^{-1}$)	E_b (kJ.mol $^{-1}$)
(OS) $_{n=12}$ /C $_{60}$	-28.701	-0.798	-29.499
(OS) $_{n=14}$ /C $_{60}$	-33.020	-1.974	-34.994
(OS) $_{n=14}$ /C $_{70}$	-31.766	-1.040	-32.806

V_{OC} compared to other complexes under study. As we know, with increasing the V_{OC} , the power conversion efficiency (PCE) of blend will be increased (see Table 3).

Table 3: PCE values of (OS) $_n$ /fullerene with the B3LYP/6-311G(d) method

	Power conversion efficiency (PCE)
C $_{60}$ /(OS) $_{n=12}$	7.7%
C $_{60}$ /(OS) $_{n=14}$	8.0%
C $_{70}$ /(OS) $_{n=14}$	8.2%

The vertical singlet-singlet electronic transition energies and optical absorption spectra of all (OS) n /fullerene blends were calculated by the TD-DFT/6-311G(d) level of theory. Fig. 3 shows the simulated absorption spectra (considering the first 40 excited states), along with the absorption wavelength. The absorption spectrum of all blends shows only an extreme peak. The main transitions of all blends occurred in the visible range. The difference in chain length oligomers in the (OS) $_{14}$ /C $_{60}$ and (OS) $_{12}$ /C $_{60}$ blends has led to the hyperchromic effect was occurred. This effect defined as increase in absorptivity at a particular wavelength of light by a solution or substance due to structural changes in a molecule.

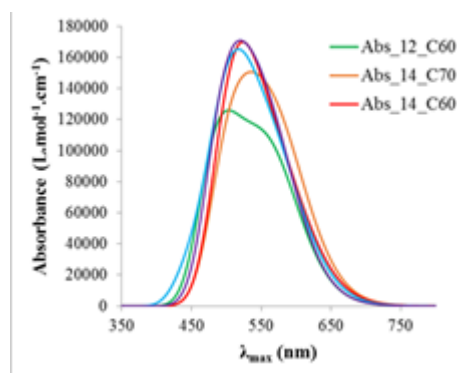


Fig. 3: Simulated absorption spectra of (OS) $_{12}$ /C $_{60}$, (OS) $_{14}$ /C $_{70}$, and (OS) $_{14}$ /C $_{60}$ blends.



Conclusions

The method of B3LYP/6-311G(d) has been used to investigate the electronic and the optical features of (OS)_n/fullerene blends. Results show the width of the absorption spectrum of all investigated blends in the range of 400-700 nm and maximum wavelength in the range of 516.65 - 536.03 nm. The highest open circuit voltage (V_{OC}) is belonging to the (OS)₁₄/C₇₀ blend. Based on obtained results, the (OS)₁₄/C₇₀ is a favorable candidate as model for BHJ solar cell than that of the other blends. In order to investigate the effect of chain length of oligomers on the solar cell properties, the optoelectronic properties of (OS)₁₂/C₆₀ blend was also studied. In comparison, the electronic and optical properties and the obtained efficiency values for (OS)₁₂/C₆₀ and (OS)₁₄/C₆₀ (7.7% and 8% respectively) indicated that (OS)₁₄/C₆₀ complex is more suitable candidate than the (OS)_{n=12}/C₆₀ for modeling the active layer in the BHJ solar cells.

Acknowledgment

The authors should thank Shahid Chamran University for their supports in this scientific research.

References

- [1] Y. Wang, W. Wei, X. Liu, Y. Gu, *Sol. Energy Mater. Sol. Cells*, 98 (2012) 129–145.
- [2] Y. Li, T. Pullerits, M. Zhao, M. Sun, *J. Phys. Chem. C* 115 (2011) 21865–21873.
- [3] E. Bundgaard, F.C. Krebs, *Sol. Energy Mater. Sol. Cells* 91 (2007) 954–985.
- [4] S. Xiao, A.C. Stuart, S. Liu, W. You, *Appl. Mater. Interfaces* 1 (2009) 1613–1621.
- [5] S. Gunes, D. Baran, G. Gunbas, A. Durmus, A. Fuchsbaauer, N.S. Sariciftci, L. Toppare, *Polym. Chem.* 1 (2010) 1245–1251.
- [6] T.A. Skotheim, R.L. Elsenbaumer, J.R. Reynolds, *Handbook of Conducting Polymers*, ed., Marcel Dekker, Inc, New York, 1998.
- [7] C.N. Hoth, P. Schilinsky, S.A. Choulis, C.J. Brabec, *Nano Lett.* 8 (2008) 2806–2813.
- [8] S. Tang, J. Zhang, *J. Phys. Chem. A* 115 (2011) 5184–5191.
- [9] C.J. Brabec, V. Dyakonov, J. Parisi, N.S. Sariciftci, *Organic Photovoltaics: Concepts and Realizations*, Springer-Verlag Berlin Heidelberg, New York (2003).

Tuning the Electronic Properties of C₅₉M Hetro-Fullerenes; Computational Approach

ZabiollahMahdavifar*, Zahra Nomresaz, Ehsan Shakerzadeh

Department of Chemistry, Faculty of Science, Shahid Chamran University of Ahvaz, Ahvaz, Iran

*z_mahdavifar@scu.ac.ir

Abstract: In this study the structural and electronic properties of C₅₉M [M = B, Al, Ga, Si, Ge, N, P, As] heterofullerenes and C₆₀ fullerene using density functional theory calculations (MPW1PW91/6-31g (d)) were investigated. The results of the geometrical structures, relative stabilities, and electronic properties hetro-fullerenes were discussed to achieve a further understanding of structure- property relationship of the hetro-cages. Based on our calculations, the heterofullerenes with smaller heteroatom have more thermodynamic stability and on the other hand, the heterofullerenes with heavier heteroatoms have less reactivity. The most stable structures based on calculated binding energy are related to the C₅₉N and C₅₉B structures. Furthermore, the C₅₉Ga fullerenes have the most reactivity based on the calculated HOMO–LUMO energy gap.

Keywords: Hetro-fullerene, Electronic properties, DFT

Introduction

Existence of heterofullerenes that make from substitution of one or more of carbon atoms with other elements was reported first time in 1991 by Smalley group [1]. Since then researchers have done much effort to production and separation of heterofullerenes. In 1995, Hirsch et al achieved to method for synthesis [2] and Hamelin achieved to a method for purification Azafullerene C₅₉N [3]. In the same year Mohr was succeed to synthesize C₅₉B and C₆₉B [4,5]. Also C₅₉P and C₆₉P, heterofullerenes of transition metals C₅₉X [X = Pt, Fe, Co, Ni, Rh, Ir, ...] and clusters of silicon identified and synthesized by researchers in 1998.

In this paper, the impact of the heteroatom substitutionary of (B, Al, Ga, Si, Ge, N, P, As) instead one carbon atoms in fullerene cage is investigated. Electronic and structural properties of all hetro-fullerenes with C₁ symmetry are namely thermodynamic and kinetic stability, natural bond orbitals (NBO) analysis using MPW1PW9/6-31g (d) level of theory are considered.

Computational Method

DFT hybrid functional with MPW1PW91/6-31G(d) level of theory was used to consider geometry optimization and the electronic properties of C₅₉M hetro-fullerenes with the aim of Gaussian09 program. According to the dipole moment (~ 0.0) and no contradistinction between carbons atom of C₆₀ fullerene, therefore a carbon atom was chosen for substitution. The neighboring carbon atoms in the periodic table such as B, Al, Ga from group III and N, P, As from the group V and Si, Ge periodic table were chosen as heteroatoms to succeed instead of carbon atom in fullerene cage.

Results and Discussion

Fully geometry optimized of C₆₀ and C₅₉M fullerenes were carried using MPW1PW91/6-31G(d) level of theory (as shown in Fig. 1).

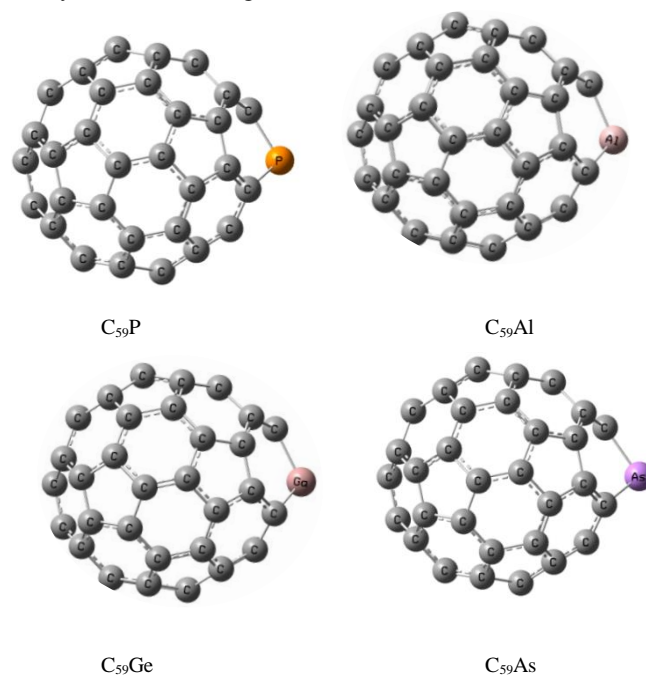


Fig. 1: Optimized structures of C₅₉M [M= P, Al, Ga, As]

The stability of new formed fullerenes is fundamentally determined by the binding energy per atom (E_b), so the binding energy per atom for these clusters is calculated as below:

$$E_b = \frac{1}{60} [E_{C_{59}M} - (59E_C + E_M)]$$

It is known that both the thermodynamic stability and kinetic stability have crucial influence on the relative abundances of different fullerene structures. It has been pointed out that higher kinetic stability is usually related with a larger HOMO-LUMO energy gap

because exciting electrons from low HOMO to a high LUMO is energetically unfavorable, which would be necessary to activate or action.

Obtained data show that the stability of studied hetero-fullerenes was decreased in compared with pristine C₆₀ fullerene (Fig. 2). Based on this Figure, C₅₉N with -9.236 eV/atom and C₅₉Ga with -9.116 eV/atom have the highest and the lowest thermodynamic stability between the studied heterofullerenes.

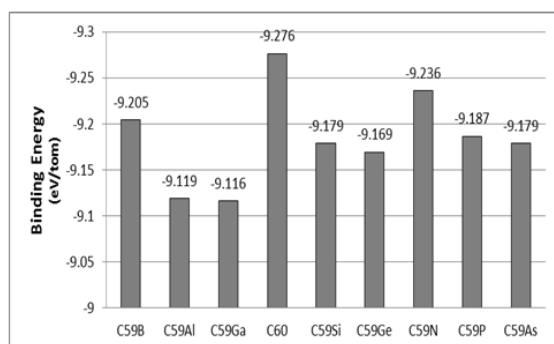


Fig. 2: Calculated binding energy of C₅₉M fullerenes.

The calculated HOMO–LUMO energy gap of all hetero-fullerenes are plotted in Fig. 3.

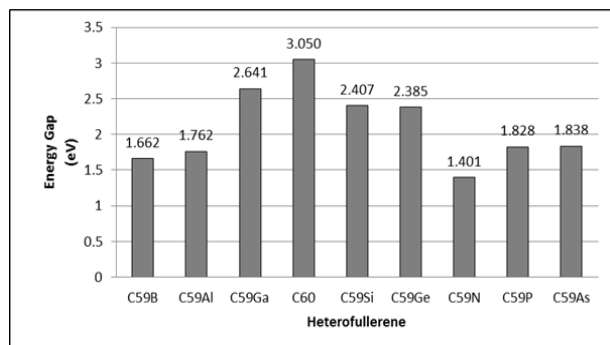


Fig. 3: Calculated HOMO-LUMO energy gap of C₅₉M fullerenes.

As can be seen in Fig.3, the HOMO-LUMO energy gap of C₅₉M fullerenes are in the range of 1.401–2.641 eV. The largest HOMO–LUMO energy gap is related to the C₅₉Ga hetero-fullerene 2.641 eV while the lowest energy gap is belonging to C₅₉N hetero-fullerene. This means that C₅₉N has the lowest kinetic stability among the studied structures. In conclusion, from kinetic and thermodynamic points of view, C₅₉N, it was theoretically determined that this cluster must be extremely chemical reactivity. In continue atomic charge using natural bond orbital analysis and Hirshfeld method for entitled structures were

calculated. Results show the positive charge on hetero-atom and also the charge transfer take place from hetero-atoms to carbon atoms (Fig. 4). It should be noted that the C₅₉N fullerene because of the high electronegativity of nitrogen atom than carbon atom, the partial charge on N is negative which means the charge transfer from carbon atoms to the nitrogen is occurred.

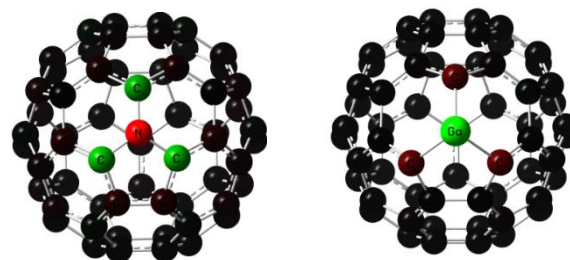


Fig. 4: Calculated partial charge distribution of (a) C₅₉Ga and (b) C₅₉N

Conclusions

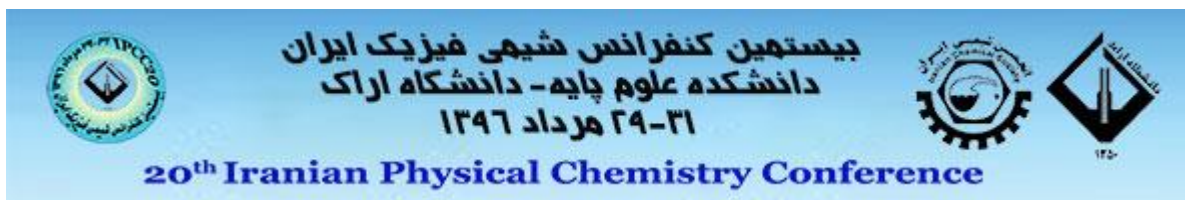
Theoretical studies of the C₅₉X (X= B, N, Al, Si, P, Ga, Ge, and As) have been performed systemically based on the DFT calculations. The results of the geometrical structures, relative stabilities, and electronic properties hetero-fullerenes were discussed to achieve a further understanding of structure- property relationship of the hetero-cages. It is found that the hybrid cages undergo some distortions due to the substitution of the heteroatoms. According to the calculated binding energies, the C₅₉M cage with smaller heteroatom is more stable. HOMOs of the hetero-fullerenes are all increased, but the HOMO-LUMO gaps are decreased compared with those of the C₆₀. As for binding energy, the cages doped with III Group elements are obviously larger than other cages.

Acknowledgment

The authors should thank Shahid Chamran University for their supports in this scientific research.

References

- [1] T. Cuo, C. Jin, and R. E. Smalley, Doping Bucky: Formation and Properties of Boron-Doped Buckminsterfullerene, *J. Phys. Chem*, 95 (1991) 4948-4950.
- [2] C. Lee, S. S. Park, W. R. Lee, K. H. Lee, Structure and Energetics of (C₆₀)₂₂⁺, Conformers: Quantum Chemical Studies, *Bull. Korean Chem. Soc.* 31 (2010) 457-.
- [3] U. Reuther, A. Hirsch, Synthesis, properties and chemistry of aza [60] fullerene *Carbon*, 38 (2000)1539–1549.



Molecular Dynamic Simulation of 5-Fluorouracil Drug Adsorption in Zeolite Imidazolate Framework ZIF-8

Maryam Gomar*, Saeid Yeganegi

Department of Physical Chemistry, Faculty of Chemistry, University of Mazandaran, Babolsar, Iran

*maryam_gomar63@yahoo.com

Abstract : Zeolitic imidazolate frameworks (ZIFs) are a class of metal-organic frameworks. Research on biomedical applications of ZIFs has recently started, and ZIFs have been identified as promising materials for drug storage. In this study, Molecular dynamic simulations were performed to study the adsorption of anti-cancer drug namely 5-Fluorouracil (5-FU). Our results showed that the studied ZIF have high capacities (0.65-0.68 g/g) for the adsorption of 5-FU drug. The analysis of radial distribution function (RDF) showed that hydrogen bonding played an important role for adsorption of drug. results showed that studied ZIFs compared to conventional metal organic frameworks(MOFs), had higher capacity for the adsorption of studied drug, showing they can be used as more efficient carriers.

Keywords: *Molecular dynamic Simulation, Zeolite Imidazolate Framework, RDF*

Introduction

Metal organic frameworks (MOFs) as drug-delivery nanocarriers are highly desirable due to their large loading of drugs, biodegradability and versatile functionality [1]. Mesoporous MOFs with well-defined pores provide a wealth of opportunities for drug delivery. Currently, the microscopic understanding of drug-MOF interaction remains elusive and molecular-level study is crucial for the development of MOFs as novel drug devices with ideal loading and specific delivery. Horcajada et al. performed QM calculation to examine the interaction of ibuprofen (IBU) with MIL-53(Fe) [2]. A strong binding energy of 57 kJ mol⁻¹ was found, which is in the same magnitude for IBU interacting with zeolites. They observed the formation of a strong hydrogen bond between the carboxylic oxygen of IBU and the hydroxyl group of MIL-53(Fe). Babarao and Jiang reported a computational study on the energetics and dynamics of IBU in two host carriers, MIL-101 and UCMC-1.68 [3]. The predicted maximum loading of IBU in MIL-101 is 1.11 g IBU g⁻¹ MIL-101, which agrees fairly well with experimentally determined loading of 1.37 g/g.

Liédana et al. studied adsorption of caffeine in ZIF-8 and reported a lower uptake capacity (28 wt%) compared to Cunha et al. [23] for MIL-100(Fe) (49.5 wt%). However, caffeine uptake reported for ZIF-8 was still higher than that of mesoporous silica, SBA-15 (23 wt%) and non-ordered silicas (20.4 wt%) [4].

Here, we studied adsorption, molecular interactions, diffusion behavior of anti-cancer drug in ZIF namely ZIF-8 using molecular dynamics (MD) simulation at

298 K. Molecular dynamics simulations can be used as a valuable tool to understand the adsorption and release of drugs inside the porous structure at the molecular level.

We used MD simulations to study the interactions between guest molecules and ZIF. For this purpose, radial distribution functions (RDFs) were analyzed to examine the most favorable interaction sites between drug and ZIF.

Computational Details

MD simulations were performed using NVT ensemble with a time step of 1 fs up to a total of 4 ns simulation time at 298 K. We considered 1×10⁶ and 3×10⁶ steps for equilibrium and production phases, respectively. The temperature was held constant with a Nose-Hoover chain (NHC) thermostat. Van der Waals interactions were treated using the Lennard-Jones (LJ) potential function where atomic parameters for ZIF were taken from the Universal force field. The Lennard-Jones interactions were cut at the 12.5 Å. The electrostatic interactions were calculated using the Ewald summation method. Periodic boundary conditions were applied in all three dimensions. Crystal structures of ZIFs were taken from Crystallography Open Database. The ZIF structure were assumed to be rigid which has a negligible effect on the adsorption of molecule.

Results and Discussion

3.1. Validation of the Force Field

To validate the employed force field simulated adsorption capacity of 5-FU in ZIF-8 at 298 K was compared to the experimental values reported in the literature. Figure 1 shows the relative concentration of drug as simulation box length before and after simulation. Area under the curve can show the number of adsorbed drug molecules. The adsorption value for 5-FU in ZIF-8 was calculated to be 674.58 mg/g which agrees well with the experimental value (0.66 g/g or 66 wt%) reported by Sun et al [5]. Therefore, this force field based on the LJ potential model will be utilized for further study in this work.

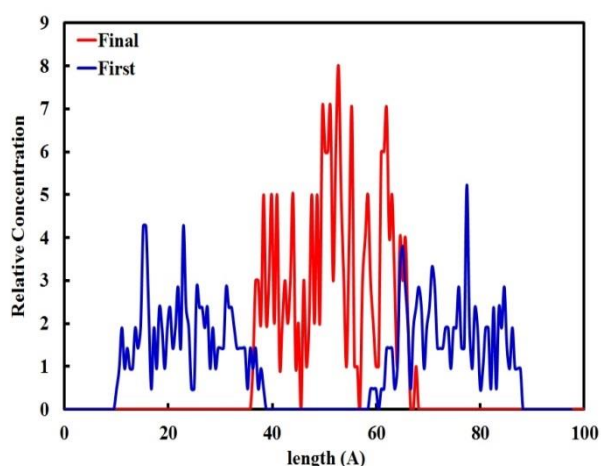


Fig.1: The relative concentration of drug as simulation box length before and after simulation.

3.2. Adsorption of drugs

Table 1 shows the adsorption capacity of drug in ZIF. It is evident that the adsorption capacity of ZIF-8 was more than that of other MOFs.

ZIF structure	adsorption capacity(mg drug/g ZIF)
ZIF-8	5-FU 674.58

Table.1: Adsorption capacity of drug in ZIF.

We also calculated radial distribution functions (RDF) that show the probability of finding an atom at a spherical shell of certain thickness at a distance (r) from the reference atom which is generally located at the origin [6]. In order to examine the distribution of drug molecule inside the ZIF framework in detail, radial distribution functions (RDFs) were calculated by:

$$g_{\alpha\beta}(r) = \frac{N}{\rho N_{\alpha} N_{\beta}} \sum_{i=1}^{N_{\alpha}} \sum_{k=1}^{N_{\beta}} \langle \delta(r - |r_k - r_i|) \rangle \quad (1)$$

Where N is the total number of atoms, ρ is density, r is distance, N_{α} and N_{β} are the number of α and β atoms, respectively.

Fig.2 shows the calculated RDF for the studied drug in ZIF-8. The sharpness Zn-Od and Zn-Nd peaks were noticeably indicating metal sites in ZIF-8 are generally the primary adsorption sites for guest drug.

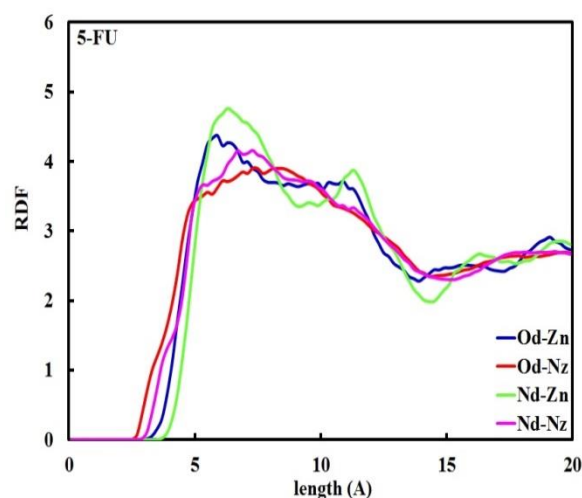


Fig.2: The RDF diagram for the studied drug in ZIF-8.

Conclusion

The analysis of RDF showed that metal sites in ZIF are the primary adsorption sites for drug. The results showed the adsorption of MP drug was the maximum. The result showed ZIF-8 were good system for adsorption and of 5-FU drug.

Acknowledgments

Financial support from the University of Mazandaran is highly appreciated.

References

- [1] An, J., S.J. Geib, and N.L. Rosi, "Cation-triggered drug release from a porous zinc-adeninate metal-organic framework. *Journal of the American Chemical Society*", 131 (2009) 8376-8377.
- [2] Horcajada, P., et al., "Flexible Porous Metal-Organic Frameworks for a Controlled Drug Delivery. *Journal of the American Chemical Society*", 130 (2008) 6774-6780.
- [3] Babarao, R. and J. Jiang, "Unraveling the energetics and dynamics of ibuprofen in mesoporous metal-organic frameworks". *The Journal of Physical Chemistry C*, 2009. 113 (2009) 18287-18291.
- [4] Liédana, N., et al., "One-step encapsulation of caffeine in SBA-15 type and non-ordered silicas". *Chemical engineering journal*, 223 (2013) 714-721



Application of decaborane (B₁₀H₁₄) and its fluoro derivatives as an anode in Li- ion battery: A DFT Study

M. Yousefizadeh, E. Shakerzadeh*, M. Bamdad

Chemistry Department, Faculty of Science, Shahid Chamran University of Ahvaz, Ahvaz, Iran

e.shakerzadeh@scu.ac.ir

Abstract: Application of decaborane (B₁₀H₁₄) and its fluoro derivatives in Li-ion batteries has been investigated through density functional theory (DFT) computations. The results indicate that decaborane (B₁₀H₁₄) has a negative value of cell voltage which is meaningless. A strategy is introduced to improve the performance of B₁₀H₁₄. The hydrogen atoms in different positions are substituted by fluorine atoms. The cell voltage of decaborane fluoro derivatives remarkably increase up to 1.10 V. This investigation may evoke one's attention to the design of novel anode in Li-ion batteries based on boron nanomaterials.

Keywords: Li- ion battery; Cell voltage; Decaborane, Fluorination; DFT calculations; Nanostructure.

Introduction:

Boranes and borides compounds have spanned a large area of chemistry due to their aesthetically appealing structures and unique bonding features and the formation of cages and clusters [1-5]. Among the borides, lithium borides have been extensively studied and showed that the lithium atom preferably forms a bridge around the central B-B bond. Boranes can also form metal-hydrogen-boron (MHB) bonds with metals (H is a bridging atom). The bridging hydrogen participates most often in a multicenter two-electron bond both within the cluster and in the interaction with metals. These hydrogens are distinctly protonic, and their relative acidity depends on the cage size as well as other parameters. Decaborane (B₁₀H₁₄) is the most stable nido-boranes [6, 7]. The B₁₀H₁₄ possess four equivalent electron-deficient terminal hydrogen atoms and exhibits a wide range of properties. Sneddon and co-workers have devised several ingenious strategies for synthesis of the substituted decaboranes [8]. Decaborane with double the number of boron atoms in the shape of a basket, a very useful starting material for a lot of borane chemistry.

Li-ion battery is a common electric energy storage device, and it can be applied as the main power for many electronic devices [9]. A Li-ion battery is composed of two electrodes (a cathode and an anode) separated by an electrolyte. The applications of nanomaterial in Li-ion batteries have been attracted great interest [10]. Hence there is an increasing demand for finding efficient nanomaterial as anode of Li-ion batteries, and this has stimulated research activities in this field. The main contribution

decaborane and its fluoro derivatives in anode of Li-ion battery.

Materials and method: All of the optimized geometries for the Li@B₁₀H₁₄ and Li⁺@B₁₀H₁₄ as well as their fluoro derivatives are obtained using TPSSH/6-311+G(d) level of theory. All calculations are performed using Gaussian 09 software.

Results and discussion:

The optimized geometries of the Li@B₁₀H₁₄ and its fluoro derivatives are shown in Figure 1. The adsorptions of Li and Li⁺ are considered on the surface of these structures. The structure of lithium decaborane (Li@B₁₀H₁₄) resembles a basket, and the Li atom merely forms the handle of this basket. In this basketlike molecule, the Li atom is located along the principal C₂ axis in a bridging fashion. The adsorption energy for Li and Li⁺ is predicted by the following equations:

$$E_{ad} = E(\text{Li}@F_n\text{B}_{10}\text{H}_{14-n}) - E(F_n\text{B}_{10}\text{H}_{14-n}) - E(\text{Li}) \quad (1)$$

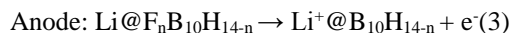
where $E(\text{Li}@F_n\text{B}_{10}\text{H}_{14-n})$ is the energy of an $F_n\text{B}_{10}\text{H}_{14-n}$ which adsorbed the Li atom, $E(F_n\text{B}_{10}\text{H}_{14-n})$ corresponds to the energy of an isolated $F_n\text{B}_{10}\text{H}_{14-n}$, $E(\text{Li})$ is the energy of an atomic Li. Indeed,

$$E_{ad} = E(\text{Li}^+@F_n\text{B}_{10}\text{H}_{14-n}) - E(F_n\text{B}_{10}\text{H}_{14-n}) - E(\text{Li}^+) \quad (2)$$

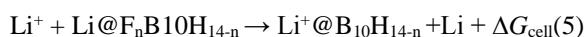
where $E(\text{Li}^+@F_n\text{B}_{10}\text{H}_{14-n})$ is the energy of $F_n\text{B}_{10}\text{H}_{14-n}$ which adsorbed the Li⁺ cation and $E(\text{Li}^+)$ is the energy of an Li⁺ cation. All of these energies are obtained using the optimized structures. A Li-ion



battery (LIB) is composed of two electrodes (a cathode and an anode) separated by an electrolyte. The reaction in the anode and cathode can be simplified as follows:



Thus overall reaction for the LIB can be written as below.



For calculating the voltage for this cell the Nernst equation can be applied as:

$$V_{\text{cell}} = \frac{-\Delta G_{\text{cell}}}{zF} \quad (6)$$

where F is the Faraday constant (96500 C/mol) and z is the charge of Li^+ . The ΔG_{cell} is the Gibbs free energy of the total reaction of cell at 298 K and 1 atm. It can be assessed as the internal energy ($\Delta G = \Delta E + P\Delta V - T\Delta S$). Since the entropy contributions and volume effects are very small (<0.01 V) to the cell. So the V_{cell} can be obtained by predicting internal energy change as follows:

$$\Delta E = E(\text{Li}) + E(\text{Li}^+\text{@F}_n\text{B}_{10}\text{H}_{14-n}) - E(\text{Li}^+) - E(\text{Li@F}_n\text{B}_{10}\text{H}_{14-n}) \quad (7)$$

the ΔG_{cell} (Gibbs free energy change) could be calculated for the reaction (5) by performing frequency analysis for the most stable $\text{Li@F}_n\text{B}_{10}\text{H}_{14-n}$ and $\text{Li}^+\text{@B}_{10}\text{H}_{14-n}$ complexes too. The calculated value for ΔG_{cell} is approximately equal to the difference between the E_{ads} values of the most stable $\text{Li@B}_{10}\text{H}_{14-n}$ and $\text{Li}^+\text{@B}_{10}\text{H}_{14-n}$ complexes, Eq. (7). The Eq. (7) reveals that the $\text{Li}^+\text{@F}_n\text{B}_{10}\text{H}_{14-n}$ system interaction is favorable for the ΔE , and the stronger interaction will cause a more negative ΔE . In addition, the $\text{Li@F}_n\text{B}_{10}\text{H}_{14-n}$ interaction is not favorable for the ΔE and V_{cell} .

The obtained V_{cell} from Eq. 7 are presented in Figure 1 for the studied structure. It is found that the the pristine $\text{B}_{10}\text{H}_{14}$ has the $V_{\text{cell}} = -0.66$ V which is meaningless. Thus the pristine decaborane is not suitable for anode in LIB. In continue the fluoro derivatives of decaborane are taken into account. The results indicate that the fluorination significantly enhance the cell voltage ranging from 0.73 to 1.10 V. The 1,3,6,9- $\text{F}_4\text{B}_{10}\text{H}_{10}$ compound has the maximum V_{cell} of 1.10 V. Therefore, the fluorination is an

appropriate strategy to enhance the efficiency of decaborane as an anode of LIB.

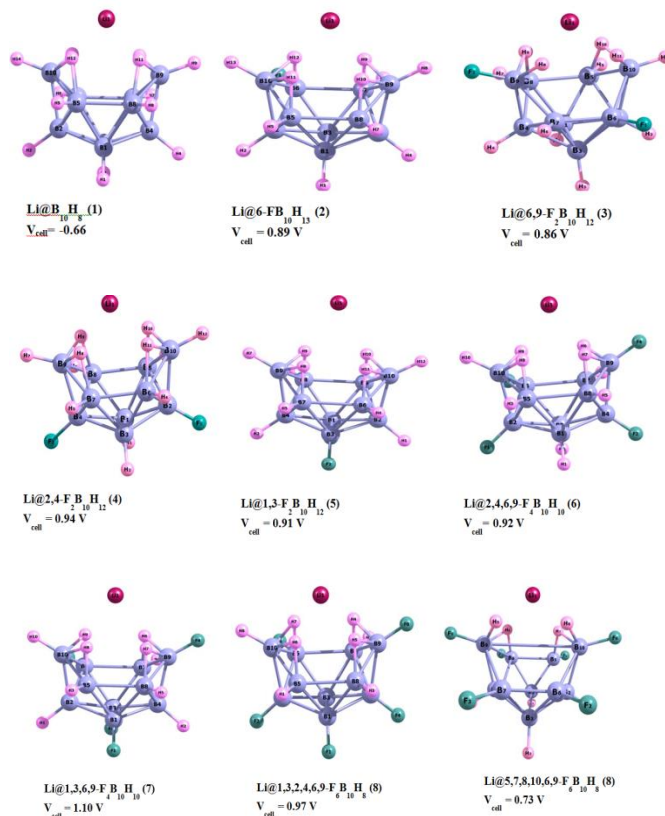


Fig. 1. Optimized structures of $\text{Li@B}_{10}\text{H}_{14}$ and its fluoro derivatives and calculated V_{cell} values.

It is shown that the interaction of Li^+ with $\text{F}_n\text{B}_{10}\text{H}_{14-n}$ is much more favorable than the Li interaction which makes the application of these systems proper in anode of LIB.

Conclusions

By means of DFT calculations we have investigated the performance of pristine $\text{B}_{10}\text{H}_{14}$ and fluoro derivatives of $\text{B}_{10}\text{H}_{14}$ structures as anode compounds for LIBs. It is found that although the pristine $\text{B}_{10}\text{H}_{14}$ suffers from low V_{cell} , its fluoro derivatives improve the performance of the LIB by increasing the V_{cell} .

References

- [1] M. F. Hawthorne "The role of chemistry in the development of boron neutron capture therapy of cancer", *Angew chem, Int. Ed. Engl.* 32 (1993) 950–984.
- [2] D. Hnyk, J. Holub, S. A. Hayes, M. F. Robinson, D. A. Wann, H. E. Robertson, D. W. H. Rankin



“Molecular structures of arachno-heteroboranes with decaborane frameworks: Two C_s-symmetrical azacarba- and carbathiaboranes”, *Inorg. Chem.* 45 (2006)8442–8446.

[3] H. M. Colquhoun, D. F. Lewis, P. L. Herbertson, K. Wade “Polyetherketones based on para-carborane: synthesis, sulfonation, and membrane-forming characteristics”, *Polymer*, 38 (1997) 4539–4546. (b) E. Hong, Y. Kim, Y. Do “A neutral group 4 poly (methyl methacrylate) catalyst derived from o-carborane”, *Organometallics*, 17 (1998) 2933–2935.

[4] K. A. Nguyen, K. Lammertsma “Structure, Bonding, and Stability of Small Boron– Lithium Clusters”, *J. Phys. Chem. A* 102 (1998) 1608–1614.

[5] G. N. Srinivas, T. P. Hamilton, J. A. Boatz, K. Lammertsma “Theoretical Studies of B₂Li_n (n = 1–4)”, *J. Phys. Chem. A* 103 (1999)9931–9937.

[6] I. Sioutis, R. M. Pitzer “Theoretical Investigation of the Binding Energies of the Iodide Ion and Xenon Atom with Decaborane”, *J. Phys. Chem. A* 110 (2006) 12528–12534.

[7] D. F. Gaines, H. Beal “Hydrogen– deuterium exchange in decaborane (14): Mechanistic studies”, *Inorg. Chem.* 39 (2000) 1812–1813.

[8] S. Muhammad, H. Xu, Z. su, “Capturing a synergistic effect of a conical push and an inward pull in fluoro Derivatives of Li@B₁₀H₁₄ basket: toward a higher vertical ionization potential and nonlinear optical response”, *J. Phys. Chem.* 115 (2011) 923-931.

[9] N. Nitta, F. Wu, J. T. Lee, G. Yushin “Li- ion battery materials: present and future”, *Materials Today*, 18 (2015) 252-264.

[10] X. Fan, W. T. Zheng, J-L.Kuo, D. Singh “Adsorption of single Li and the formation of small Li clusters on graphene for the anode of Lithium-ion batteries”, *Applied Materials*, 5 (2013) 7793-7797



Estimating the Boiling Point of Amino Acids by using QSPR and MLR methods

A. Safaria, F. Shafiei *

Department of Chemistry, Faculty of Science, Arak Branch, Islamic Azad University,

P.O. Box 38135-567, Arak 38361-1-9131, Iran

f-shafiei@iaau-arak.ac.ir

Abstract

Chemical Graph theory is used to mathematically model the molecules in regularity to gain insight into their physical and chemical properties. Graph-theoretical topological indices are high potential descriptors for modeling and predicting physicochemical properties of chemical compounds. A QSPR study was performed for prediction of boiling point (Bp°C) of 60 type different Amino acid derivatives by using topological indices such as Wiener (W), Szeged (Sz), first order molecular connectivity (¹X), Balaban (J), hyper-Wiener(WW), Wiener polarity (WP) and Harary (H). The goal of quantitative structure -Property relationship studies find a relationship between the physicochemical actions a molecule with structural parameters.

The calculation was performed by the ab-initio method at HF/6-31G level of theory. The relationship analysis between boiling point and topological indices was done by using multiple linear regression (MLR) method, with boiling point as dependent variable and seven independent variables to generate the equation that relates the structural features to the boiling point (Bp°C). The results have shown that combining the three descriptors ((J, H, Sz) could be efficiently used for boiling points compounds.

Keywords : Topological indices; Amino acids; QSPR ; multiple linear regression;

Introduction

Quantitative structure-activity relationship (QSAR) and quantitative structure property relationship (QSPR) is the process by which chemical structure is quantitatively correlated with a well defined process, such as biological activity or chemical reactivity [1]. Numerous studies have been made relating to the various fields by using what are called topological indices (TI) [2]. Topological indices are the numerical value associated with chemical constitution purporting for correlation of physical properties, chemical activity or biological activity. T-scale as a novel vector of topological descriptor for amino acids based on 67 kinds of structural topological variables of 135 amino acids established [3]. New chemical descriptors used for the design of biologically active of 87 amino acids [4]. Pioneering work in applying QSPR to boiling points was done by Wiener who introduced the path number defined as the sum of the distances between any two carbon atoms in the molecule [5].

Materials and Methods

The boiling point of a compound is predetermined by the intermolecular interactions in the liquid and by the difference in the molecular internal partition function in the gas phase and in the liquid at the

boiling temperature. The physicochemical properties are taken from the chemspider program [6].

In this paper, such topological indices as Wiener, W [7], Hyper-Wiener, WW[8], Wiener polarity, WP [9], Randić, ¹X[10], Balaban, J [11], Harary number, H [12] and Szeged, Sz [13] have been used for evaluating this relation. The descriptors were calculated with chemicalize program [14].

Regression Analysis

Structure- Property models (MLR models) are generated using the multi linear regression procedure of SPSS version 20 (Inc., Chicago, IL, USA) and backward stepwise regression was used to construct the QSPR models. For drawing the graphs of our results, we used the Microsoft Office Excel – 2010 program. The boiling point (Bp°C) are used as the dependent variable and ¹X, J, H, W, WP, WW and Sz indices as the independent variables. Criteria for selection of the best multiple linear regression model were the statistics: squared multiple correlation coefficient (R²), adjusted correlation coefficient (R²_{adj}), Fisher-ratio(F), root of the mean square of errors(RMSE), Durbin-Watson value (D) and significance (Sig).

Results and Discussion

Several linear QSPR models involving three-seven descriptors are established and strongest multivariable correlations are identified by the Backward step wise regression routine implemented in SPSS is used to develop the linear model for the prediction of the properties. We studied the relationship between topological indices to the boiling point of 60 amino acids.

QSPR models for the Boiling points (Bp⁰C)

Initial regression analysis indicated that topological indices play a dominating role in modeling the Boiling point. In Table 1 are given the regression parameters and quality of correlation of the proposed models for Boiling point of 60 amino acids.

Table 1. Regression parameters and quality of correlation of the proposed models for the Boiling point.

Model	Independent variables	R	R ²	R ² _{adj}	F	RMS
1	J,H,WW	0.915	0.838	0.829	96.274	277.06

The best linear model for Bp contains three topological descriptors, namely, Balaban (J), Harary number (J) and Hyper-Wiener(WW) indices. Fig 1 shows the linear correlation between the observed and the predicted the boiling point values obtained using Eq. (1).

Model 1

$$\text{Bp} = 113.497 + 26.067(\text{J}) + 6.286(\text{H}) - 0.028(\text{WW}) \quad (1)$$

N=60, R=0.915, R²=0.838, R²_{adj}=0.829, RMSE=277.0647 F=96.274, Sig=0.000, DW=1.973

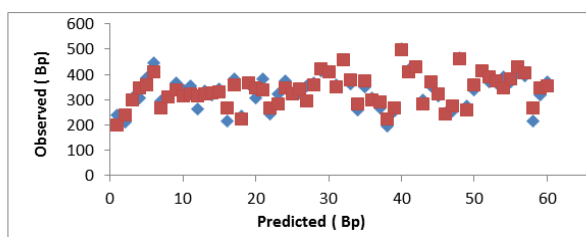


Figure 1. Comparison between the predicted and observed values of boiling point by MLR.

In this study, to find the best model for predict the properties mentioned, we will use the following sections:

The Durbin-Watson statistics

The Durbin-Watson statistic ranges in value from 0 to 4. A value near 2 indicates non-autocorrelation; a

value toward 0 indicates positive autocorrelation; a value toward 4 indicates negative autocorrelation. Therefore the value of Durbin-Watson statistic is close to 2 if the errors are uncorrelated. In our all models, the value of Durbin-Watson statistic is close to 2(See eq.1) and hence the errors are uncorrelated.

The residuals values

The residuals values of boiling point expressed by equation .The residual values show a fairly random pattern (see Figure 2). This random pattern indicates that a linear model provides a decent fit to the data.

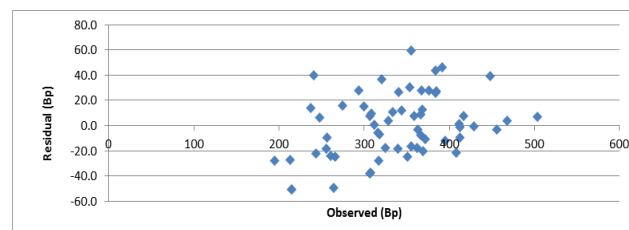


Figure 2. Comparison between the residual and observed values of boiling point by MLR.

Conclusion

QSPR models for the prediction of the boiling point 60 amino acids derivatives using MLR method based on topological descriptors calculated from molecular structure alone have been developed. Multiple linear regression model benefiting from various descriptors, factors and efficient coefficients can suggest the best algorithm for determining this physical property of chemical molecules. However, MLR model is proved to be a useful tool in the prediction of Boiling point. We can use only three topological index (J),(H) and (ww) for predicting Boiling point.

References

- [1] RW. Taft, "Separation of polar, steric and resonance effects in reactivity", In: Newman MS(ed.): Steric effects in organic chemistry New York: Wiley, (1956) 556-675.
- [2] A. A. Taherpour, F. Shafiei, "The structural relationship between Randić indices, adjacency matrices, distance matrices and maximum wave length of linear simple conjugated polyene compounds", J. Mol. Struct. theochem,726 (2005) 183-188.
- [3] F. Tian, P. Zhou, Z.Li, "T-scale as a novel vector of topological descriptors for amino acids and its application in QSARs of peptides", J. Mol. Struct,830(2007)106-115.
- [4] M. Sandberg, L. Eriksson, J. Jonsson, M. Sjöström, S. Wold, "New chemical descriptors



relevant for the design of biologically active peptides.

A multivariate characterization of 87 amino acids", J. Med. Chem, 41(1998)2481-2491.

[5] H. Wiener, "Structural Determination of Paraffin Boiling Points", J. Am. Chem. Soc, 69 (1947) 17-20.

[6] Web search engine developed by Chemspider; software available at [http:// WWW. Chemspider. Com](http://WWW.Chemspider.Com)

[7] P. V. Khadikar, N. V. Deshpande, P. P. Kale, A. Dobrynin, I. Gutman, G. Dömötör, "The Szeged index and an analogy with the Wiener index", J. Chem. Inf. Comput. Sci, 35(1995) 547-550.

[8] D. J. Klein, I. Lukovits, I. Gutman, "On the definition of the hyper-Wiener index for cycle-containing structures", J. Chem. Inf. Comput. Sci, 35 (1995) 50-52.

[9] M. Liu, B. Liu, "On the Wiener polarity index", MATCH Commun. Math. Comput. Chem, 66 (2011) 293-304.

[10] M. Randić, "Generalized molecular descriptors", J. Math. Chem, 7 (1991) 155-168.

[11] A. T. Balaban, "Highly Discriminating Distance Based Topological Indices", Chem. Phys. Lett, 89 (1982) 399-404.

[12] C. K. Das, B. Zhou, N. Trinajstić, "Bounds on Harary index", J. Math. Chem, (2009) 1369-1376.

[13] I. Gutman, S. Klavžar, "An algorithm for the calculation of the Szeged index of benzenoid hydrocarbons", J. Chem. Inf. Comput. Sci, 35 (1995) 1011-1014

[14] Web search engine developed by ChemAxon; software available at [http:// WWW. Chemicalize. Org](http://WWW.Chemicalize.Org).



Applications of Graph Theory to modeling and predicting some physico-chemical properties and QSPR study

A. Safari, F. Shafiei*

Department of Chemistry, Science Faculty, Arak Branch, Islamic Azad University,

P.O. Box 38135-567, Arak 38361-1-9131, Iran

*f-shafiei@iau-arak.ac.ir

Abstract: Graph theory is a branch of mathematics which about graph are discussed and commonly called topological indices, which are important descriptors of molecular structure. In this study the relationship between the Randic' ($^1\chi$), Balaban (J), Szeged (Sz), Harary (H), Wiener (W), Hyper-Wiener (WW), and Wiener Polarity (WP) to the thermal energy (E_{th}), and heat capacity (C_v) of 80 Amino acids is represented. Physicochemical properties are taken from the quantum mechanics methodology with HF level using the ab initio 6-31G basis sets. The multiple linear regressions (MLR) and Back ward methods (with significant at the 0.05 level) were employed to give the QSPR models. The satisfactory obtained results show that combining the two descriptors (J, 1X) are excellent descriptors for predicted (C_v), and (E_{th}) of the amino acids derivatives.

Keywords: Amino acids; QSPR; MLR method; Topological indices

Introduction

Amino acids are organic compounds containing amine ($-NH_2$) and carboxyl ($-COOH$) functional groups, along with a side chain (R group) specific to each amino acid.

Quantitative structure- property relationship (QSPR) and Quantitative structure- activity relationship (QSAR) are mathematical models designed for predictions the properties of a wide range of chemical compounds based on the correlation between these properties and molecular descriptors as topological indices[1]. Topological indices (TI) are the digital values associated with chemical constitution for correlation of chemical structure with various physical properties, chemical reactivity or biological activity and useful mathematical methods for finding good relationship between several data of the properties in these materials [2-5].

Relationship between topological indices and thermodynamic properties such as heat capacity, standard Gibbs energy of formation, thermal energy and entropy of the monocarboxylic acids, alkanes [6,7], alcohols [8,9], aldehydes and ketones [10] has been searched.

Materials and methods

The chemical structure of the 80 amino acids derivatives was drawn by Gauss View Software and then was transferred into Gaussian 03 program to

optimize the physicochemical properties of the molecules at the RHF/6-31 G level of theory.

Topological indices

Mathematical descriptors have been widely used in structure-property/ activity studies [11]. The topological indices(Tis) used for the QSPR analysis were Wiener (W), Szeged (Sz), first order molecular connectivity ($^1\chi$), Balaban(J), Hyper-Wiener(WW), Wiener (W), Wiener Polarity(WP) and Harary(H) indices. The aim of this study is to provide reliable QSPR models for predicting physicochemical properties of amino acids derivatives. The descriptors were calculated with chemicalize program [12].

Statistical analysis

In the present study, structure- property models (MLR models) are generated using the multilinear regression procedure of SPSS version 20 and backward stepwise regression was used to construct the QSPR models.

Regression Analyses

The thermal energy (E_{th} kJ/mol) and heat capacity (C_v J/molK) are used as the dependent variable and topological indices as the independent variables. The models are assessed with R value (correlation coefficient), the R^2 (squared multiple correlation coefficient), the R^2_{adj} (adjusted correlation coefficient), the RMSE value (root of the mean



square of errors), the F value (Fischer statistic), the D value (Durbin-Watson) and the Sig (significant).

QSPR models for the gas heat capacity (C_v) and thermal energy (E_{th})

The best linear model for C_v and E_{th} contains five topological descriptors, namely, Randić (¹X), Balaban (J), Hyper-Wiener (WW), Wiener polarity (Wp), Wiener (W) and Szeged (Sz) indices. The regression parameters of the best five descriptors correlation model are gathered in equation (1, 2).

Model 1

$$C_v = 28.472 + 11.471(X) + 8.946(J) + 0.234(W) + 3.439(Wp) - 0.144(Sz) \quad (1)$$

$$N=80, R=0.973, R^2=0.946, R^2_{adj}=0.943, RMSE=154.642, F=261.317, Sig=0.000, DW=1.783$$

Model 2

$$E_{th} = -246.159 + 150.104(X) + 66.416(J) - 1.834(W) + 0.355(WW) \quad (2)$$

$$N=80, R=0.934, R^2=0.873, R^2_{adj}=0.867, DW=1.872, RMSE=590.322, F=129.218, Sig=0.000$$

Test for autocorrelation by using the Durbin-Watson statistic

We will focus on the Durbin-Watson statistic and unstandardized predicted and residual values. The Durbin-Watson statistic ranges in value from 0 to 4. A value near 2 indicates non-autocorrelation; a value toward 0 indicates positive autocorrelation; a value toward 4 indicates negative autocorrelation. Therefore the value of Durbin-Watson statistic is close to 2 if the errors are uncorrelated. In our all models, the value of Durbin-Watson statistic is close to 2 (See eqs.1-2) and hence the errors are uncorrelated.

Multicollinearity

Good regression model should not exist correlation between the independent variables or not happen multicollinearity. Test multicollinearity as a basis the variance inflation factor (VIF) value of multicollinearity test results using SPSS. If the VIF value lies between 1-10, then there is no multicollinearity, and if the VIF < 1 or > 10, then there is multicollinearity.

In all our final models, the Multicollinearity has existed, because the values of correlations between

independent variables are near to one and VIFs value lies are not use of between 1-10.

Results and discussion

Multiple linear regression method predictive power for a QSAR/QSPR analyses. It can be conveniently estimated by statistical parameters. A good QSPR model should have both suitable relativity and good predictability. In the constructed model internal validation is usually done by leave-one-out (LOO). The new QSPR models are expected to have low R²_{cal} and LOO-cross-validation (Q²_{loo}) values [13,14]. We studied the validation of linearity between the molecular descriptors in the models 1 and 2. We obtained by SPSS the Pearson coefficient correlation and collinearity statistics as follows Tables (3, 4).

For model 1 the Pearson correlation (Sz,W),(Wp,X) and (X,W) are near one, and VIF (Wp),(W), (Sz) and (1X) > 10. After removed (W) from this model, we corrected model 1 as follow:

$$C_v = -22.418 + 26.498(X) + 17.460(J) \quad (3)$$

$$N=80, R=0.964, R^2=0.930, R^2_{adj}=0.928, RMSE=242.414, F=513.412, Sig=0.000, DW=1.795, Q^2_{LOO}=0.824$$

Table 3: Correlation between the molecular descriptors (model 1)

	Collinearity					Corrected model		VIF
	Sz	J	W _p	X	w	Tolerance	VIF	
Sz	1	0.622	-0.678	0.617	-0.945	0.024	42.376	-
J	0.622	1	-0.568	0.639	-0.605	0.287	3.489	1.992
W _p	0.678	-0.568	1	-0.846	-0.643	0.010	97.175	-
X	0.617	0.639	-0.846	1	-0.743	0.041	24.607	1.992
W	-0.945	-0.605	0.643	-0.743	1	0.011	89.146	-

For model 2 the Pearson correlation (WW, W),(W,X) and (X,WW) are near one, and VIF (¹X),(W) and (WW) > 10. After removed (W) from this model, we corrected model 2 as follow:

$$E_{th} = -93.740 + 87.647(X) + 65.787(J) \quad (4)$$

$$N=80, R=0.921, R^2=0.848, R^2_{adj}=0.845, DW=1.967, RMSE=822.886, F=215.544, Sig=0.000, Q^2_{LOO}=0.746$$

Table 4: Correlation between the molecular descriptors (model 2)



Collinearity				Corrected	model	v
W _w	J	X	w	Tolerance	VIF	
W _w	1	0.017	-0.836	-0.983	0.027	148.05
J	0.17	1	-0.209	-0.032	0.531	1.883
X	0.836	-0.209	1	-0.914	0.003	37.321
W	-0.983	-0.032	-0.914	1	0.007	293.564

we have computed Q^2 ($E_{q,5}$) by 50% of data, randomly, that are positive and less than one.

$$Q^2 = 1 - \frac{\sum(Y_i - \hat{Y}_{i|i})^2}{\sum(Y_i - \bar{Y})^2} \leq 1 \quad (5)$$

Where the notation $i|i$ indicates that the response is predicted by a model estimated when the i -th sample was left out from the training set.

Comparison between predicted and observed values of C_v and E_{th} of respect amino acids derivatives show the linear correlation between them. Figure 1, 2 shows the observed and the predicted heat capacity and thermal energy values obtained using equation (3,4) respectively.

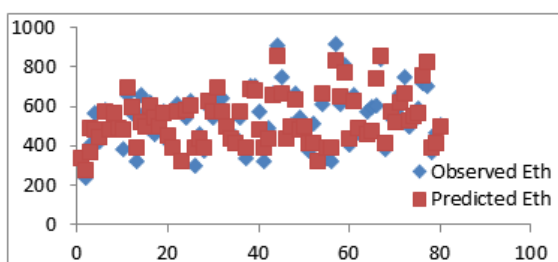


Figure 1. Comparison between the predicted and observed thermal energy by MLR method.

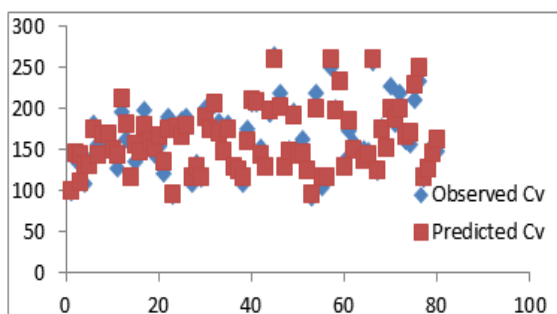


Figure 2. Comparison between the predicted and observed heat capacity by MLR method.

Conclusion

At present study, QSPR mathematical models for the prediction of the heat capacity (C_v) and thermal energy (E_{th}) of 80 amino acids derivatives by using MLR method based on topological descriptors calculated from molecular structure alone have been developed. MLR model is proved to be a useful tool in the prediction of C_v and E_{th} . Cross-validation as the evaluation technique has been designed to evaluate the quality and predictive ability of the MLR model. The obtained results showed that the only Randic and balaban indices are good topological indices for modeling heat capacity and thermal energy.

References

- [1] M. Randić, S. C. Basak, "Multiple regression analysis with optimal molecular descriptors", SAR QSAR Environ. Res, 11 (2000) 1–23.
- [2] Y. P. Du, Y. Z. Liang, B.Y. Li, C. J. Xu, "Orthogonalization of block variables by subspace-projection for quantitative structure property relationship (QSPR) data", J. Chem. Inf. Comput. Sci, 42 (2002) 1128–1138.
- [3] M. Randić, "Characterization of molecular branching", J. Am. Chem, 97(1975)6609–6615.
- [4] Z. Slanina, F. Uhlik, S. L. Lee, E. Osawa, "Geometrical and thermodynamic approaches to the relative stabilities of Fullerene isomers", MATCH Commun. Math. Comput. Chem, 44 (2001) 335–348.
- [5] B. Lučić, N. Trinajstić, "New developments in QSPR/QSAR modeling based on topological index", SAR QSAR Environ. Res, 7 (1997) 45–62.
- [6] O. Ivanciuc, T. Ivanciuc, D. Cabrol-Bass, A. T. Balaban, "Evaluation in quantitative structure-property relationship models of structural descriptors derived from information-theory operators", J. Chem. Inf. Comput. Sci, 40 (2000) 631–643.
- [7] D. Bonchev, "Over all connectivities / topological complexities: A new powerful tool for QSPR/QSAR", J. Chem. Inf. Comput. Sci, 40 (2000) 934–941.
- [8] S. Liu, H. Liu, Z. Xia, C. Cao, Z. Li, "Molecular distance edge vector (m): An extension from alkanes to alcohols", J. Chem. Inf. Comput. Sci, 39 (1999) 951–957.
- [9] V. Sharma, R. Goswami, A. K. Madan, "A novel highly discriminating topological descriptor for structure-property and structure-activity studies", J. Chem. Inf. Comput. Sci, 37 (1997) 273–282.



[10] Z. Lin, J. Xu, X. Zheng, Z. Li, "Study on quantitative structure- property relationship of chain hydrocarbons, aldehydes and alkanones by molecular distance-edge vector",

Acta Phys. Chem. Sin, 16 (2000) 153–161.

[11] M. Randic, " Topological Indices. Encyclopedia of Computational Chemistry (P. von Rague Schleyer, Editor-in-Chief", London: Wiley, (1998)3018-3032.

[12] Web search engine developed by ChemAxon; software available at [http:// WWW.Chemicalize. Org](http://WWW.Chemicalize.Org).

[13] K. Baumann, N. Stiefl, "Validation tools for variable subset regression, J. Comput. Aided. Mol. Des, 18(2004) 549-562.

[14] N. Chirico, P. Gramatica, "Real External Predictivity of QSAR models: How to evaluate it Comparison of Different Validation Criteria and Proposal of Using the Concordance

Correlation Coefficient", J. Chem. Inf. Model,51 (2011)2320-2335.



Quantum hard spheres in a slit pore

A. Helmi*

Department of Chemistry, Isfahan University of Technology, Isfahan, 8415683111, Iran

*A.helmi@ch.iut.ac.ir

Abstract: In this paper, the density functional theory is employed to investigate the effects of quantum correction on the structure and such thermodynamic properties of quantum-mechanical hard sphere fluids confined in nano-slit pore as excess adsorption and wall pressure. It is found that the repulsion between hard sphere molecules because of quantum effect play an important role in determining the structure and thermodynamic properties of the confined fluid. Another finding of the present study involves the key role of the excluded volume in determining the structure and thermodynamic properties of quantum mechanical hard sphere fluids. By increasing of the quantum effect, λ^* , the periodic oscillation in the density profile becomes more obvious and the order of layers in the pore increases. Increasing the values of λ^* is found to lead not only to drastic changes in the structure of the fluid molecules but also, to increased excess adsorption and wall pressure of the fluid confined in slit pores.

Keywords: DFT; Semi-classical quantum fluid; Slit pore; Excess adsorption.

Introduction

The thermodynamic properties of confined quantum fluids are a major area of basic and applied research in nanotechnology [1]. In classical systems, quantum effects for heavy molecules at high temperature are so small that quantum corrections are often neglected. But it should be noted that the thermodynamic properties of such quantum fluids as hydrogen, deuterium, and neon whose de Broglie's wavelengths are of the same magnitude as the mean distance between particles greatly depend on quantum corrections[1].

It is clear that in most theoretical studies, the hard sphere fluid is the one most commonly employed as a reference system to study such realistic fluids as the Lennard Jones fluid and electrolyte solutions. Hence, hard sphere fluids have attracted a lot of attention by researchers due to their importance in modeling real systems, especially confined quantum fluids.

The present work aims to investigate the effects of quantum correction on the structure and such thermodynamic properties as excess adsorption of quantum-mechanical hard sphere fluids confined in nano-scale slit pore. In this work among the different theoretical methods for studying the thermodynamic properties of fluids confined in nano-scale pores, the successful versions of the DFT, modified fundamental measure theory (MFMT), that gives improved contact density for hard sphere fluids has been used.

Materials and method

In the density functional theory, the grand canonical potential of an inhomogeneous system is defined as [2]:

$$\Omega[\rho(\mathbf{r})] = \beta F[\rho(\mathbf{r})] + \int d\mathbf{r} \rho(\mathbf{r}) [V^{ext}(\mathbf{r}) - \mu] \quad (1)$$

where, μ is the chemical potential and V^{ext} is the external potential for this component. Generally, the equilibrium density profile of an inhomogeneous fluid can be obtained by minimizing the grand canonical potential as follows:

$$\rho(\mathbf{r}') = \rho_b \exp \left[-\beta V^{ext}(\mathbf{r}') + \beta \mu^{ext} - \int \sum_{\alpha} d\mathbf{r}'' \frac{\partial \Phi}{\partial n_{\alpha}} w_i^{(\alpha)}(\mathbf{r}'' - \mathbf{r}') \right] \quad (2)$$

where, μ^{ext} and ρ_b are the bulk excess chemical potential and bulk fluid density, respectively. In this work, used has been made of the effective diameter method, in which the quantum-mechanical hard sphere has an effective diameter larger than that of the classical hard sphere [3].

$$\sigma_{eff} = \sigma \left(1 + \sum_l a_l \lambda^{*l} + \sum_m \sum_n c_{mn} \rho^{*n} \lambda^{*m} \right)^{1/3} \quad (3)$$

where, $\lambda^* = \lambda/\sigma$ and $\rho^* = \rho\sigma^3$. The term $\sum_l a_l \lambda^{*l}$ is a series in the thermal wavelength, and the double summation, $\sum_m \sum_n c_{mn} \rho^{*n} \lambda^{*m}$, expresses the dependence of the ratio on both density and thermal wavelength. In this work, the coefficients in Table 1 were used to calculate the properties of the fluid

confined in a spherical pore and in equilibrium with the bulk fluid.

Table1: Optimal coefficients

a_1	a_2	a_3	C_{21}	C_{22}
1.08016	0.752081	-0.489996	-0.471077	-1.29761

Results and Discussion

In this section, we study the effects of quantum correction on the structure, adsorption and contact density of a hard sphere fluid confined in a nano-slit pore.

Effects of quantum correction on the structure

It is known that the structure of a quantum mechanical fluid in nano-pore systems depends on such parameters as pore size, intermolecular interactions, wall–fluid interactions, and the quantum effect, λ^* . Since the simultaneous study of these effects is complex, we consider a quantum mechanical hard sphere particles confined in a hard and structureless slit pore. Fig. 1 depict the density profiles of the hard sphere fluid with bulk density equal to 0.5 confined in a nano-slit pore with distance between the walls, $H=5\sigma$, for different values of the λ^* including 0, 0.2, 0.4 and 0.6. It is also clear that the density profile of the fluid exhibits an oscillatory behavior for different values of λ^* and that the number of peaks corresponds to the number of molecular layers in the nano-spherical pore. It is clear that in the absence of wall-molecule and molecule-molecule interactions, the structure of the fluid is determined by entropy effects because of the excluded volume near the walls. This excluded volume, increases with the effective diameter of the particles confined in the slit pore. The excluded volume has direct effects on the density distribution of molecules in the pore. Moreover the quantum effect causes the hard spheres to repel each other before they come into contact, while the classical ones repel each other only upon contact. This effect causes to more molecules accumulate at the wall due to the tendency of the molecules to escape from this repulsion. Also the repulsion among the molecules enhances the orderliness of the layers in the pore; which is reflected in the growing heights of the peaks and depths of the valleys in the density profiles.

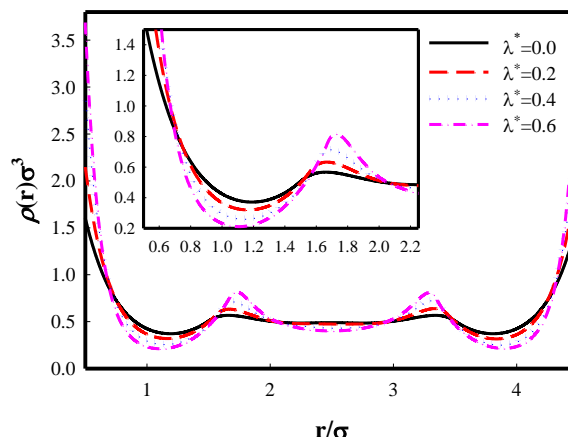


Fig.1: Density profiles of a quantum hard sphere fluid with bulk density equal to 0.5 confined in a slit pore with distance between the walls equal to 5σ , in a nano-slit pore versus r/σ for different values of the λ^* including 0, 0.2, 0.4 and 0.6.

Effects of quantum correction on the excess adsorption

As we know, the excess adsorption of fluids Γ , in a nano-slit pore is defined by:

$$\Gamma = \frac{1}{H} \int d\mathbf{r} [\rho(\mathbf{r}) - \rho_b] \quad (4)$$

where ρ_b refers to bulk density. Fig. 2 plots the adsorption isotherm of a hard sphere fluid for different values of λ^* including 0, 0.2, 0.4, and 0.6 for a bulk density equal 0.6 versus H/σ . Based on this figure, adsorption of the fluid has an oscillatory behavior with maximum and minimum values for integral and half integral values of H respectively. It is clear that the adsorption is negative for all values of λ^* and H . For a fixed value of λ^* , adsorption increases with H and also for a fixed value of H , it increases with λ^* . It is also clear from these Figures that the height and depth of the oscillations increase with increasing λ^* .

It is known that the excluded volume plays the key role in determining the structure and thermodynamic properties of classical and quantum mechanical hard sphere fluids. In fact, the excluded volume increases with increasing quantum effect, λ^* . This will lead to increases in the periodic oscillations of excess adsorption in nano slit pore. In fact, when λ^* increases, the quantum hard sphere fluid exhibits a rising tendency for being adsorbed onto the nano-pore as a result of both the entropy effect and the breaking up of the repulsion between the molecules at the pore walls. From the figure, it is easy to realize that excess adsorption is become nearly uniform by increasing of the distance between the walls, H .

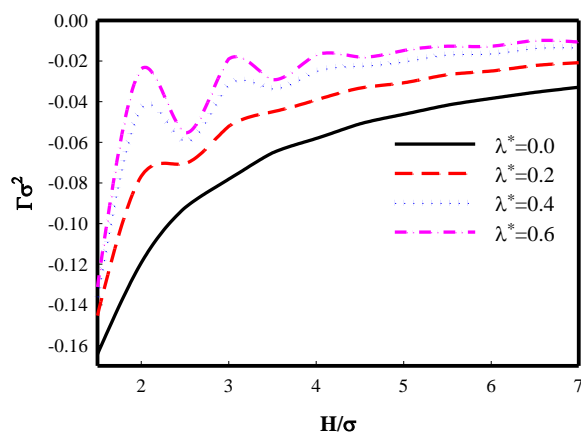


Fig.2: Adsorption isotherm of a hard sphere fluid for different values of λ^* including 0, 0.2, 0.4, and 0.6 for a bulk density equal 0.6.

Effects of quantum correction on the wall pressure

To investigate the effect of the distance between the walls, H , on the contact density of the fluid at the walls, we used the contact theorem directly set the contact density of the fluids at the walls equal to wall pressure, $P_w = \rho(0)$, and plotted it versus H , for different values of λ^* , as shown in Figure 3. In this figure, the wall pressure, of a hard sphere fluid with a bulk density of 0.6 confined in a pore between two flat walls for different values of λ^* including 0, 0.2, 0.4, and 0.6 has been plotted versus the H .

The wall pressure of the fluid at the pore walls versus H/σ clearly exhibits an oscillatory behavior. This oscillatory behavior increases with λ^* . In fact the height and depth of the wall pressure oscillations increase with increasing λ^* .

According to this figure for a fixed value of H , wall pressure increases with λ^* .

As mentioned the excluded volume plays the key role in determining the structure and thermodynamic properties of quantum mechanical hard sphere fluids. In fact, the excluded volume increases with increasing λ^* . This will lead to increases in the periodic oscillations of wall pressure.

In the classical hard-sphere system, pressure arises due to the direct contact collisions but that quantum mechanical pressure arises from the collisions without any direct contact, that is, from inter-particle repulsions due to quantum effects. This is because the periodic oscillation in the wall pressure becomes more obvious and wall pressure grows larger with increasing values of λ^* . Once the repulsion between fluid molecules is increased, the wall pressure increases as result of the enhanced quantum effect, λ^* . The increased quantum effect, λ^* , then causes the hard spheres to repel each other before they come into contact; the repulsion is then broken at the wall

and the molecules escaping the repulsion have a greater tendency to accumulate at the pore wall.

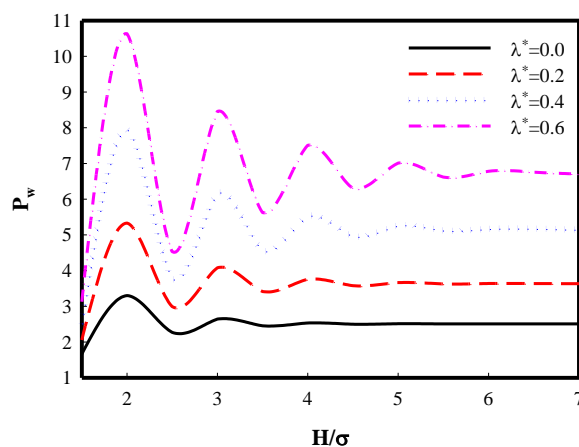


Fig.3: The wall pressure of the hard sphere fluid with a bulk density of 0.6 confined in a pore between two flat walls versus the H for different values of λ^* including 0, 0.2, 0.4, and 0.6.

Conclusions

The effective diameter method was used, in which the quantum-mechanical hard sphere has an effective diameter larger than that of the classical hard sphere. Results showed that the excluded volume increases by quantum effect in slit pore. This excluded volume causes the hard spheres to repel each other before they come into contact, while the classical ones repel each other only upon contact. This effect causes to more molecules accumulate of the molecules at the wall due to the tendency of the molecules to escape from this repulsion.

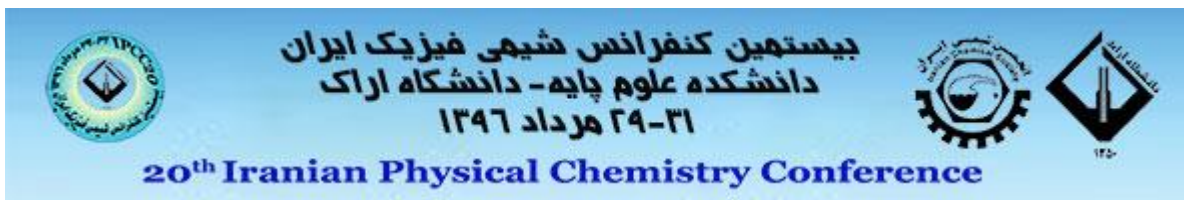
Our results also showed that, due to the effective diameter of hard molecules, Synergy's entropy effect and the broken repulsion between molecules at the pore wall causes the quantum-mechanical hard sphere fluid exhibits an increasing tendency to be adsorbed onto the nano-slit pore with increasing values of λ^* .

Acknowledgment

The authors would like to acknowledge the Isfahan University of Technology Research Council for their financial support.

References

- [1] V.M. Trejos, A.G. Villegas, A. Martinez "Computer simulation of liquid-vapor coexistence of confined quantum fluids", *J. Chem. Phys.* 139 (2013) 184505.



[2] E. Keshavarzi, A. Helmi “The Effects of Inserting a Tiny Sphere in the Center of a Nanospherical Pore on the Structure, Adsorption, and Capillary Condensation of a Confined Fluid (A DFT Study)”, *J. Phys. Chem. B.* 119 (2015) 3517–3526.

[3] A. Helmi, M. D. Eshrafi “A hard sphere fluid with quantum correction in nanospherical pores: A DFT study”, *J. Mol. Liq.* 238 (2017) 160–169.



Theoretical study on the atmospheric reaction of Hydroxycyclohexadienyl with acetylene using DFT calculations

P.alikhani*, H.douroudgary, M. Vahedpour

Department of chemistry, University Zanjan, P.O. Box 45371- 38791, Zanjan, Iran

*parvin.alikhani94@gmail.com

Abstract: The gas phase reaction of Hydroxycyclohexadienyl and acetylene have been studied computationally on the doublet potential energy surface. The potential energy surface for one product, P1, is obtained. Enthalpy and Gibbs free energy of reaction are -7.159 and -7.195 kcal/mol.

Keywords: hydroxycyclohexadienyl; analysis of the kinetics; quantum mechanics;

(ZPE) corrections and characterization of the stationary points as minima or saddle points. All structures including transition states and stationary points are confirm with vibrational frequency analysis. Connection among transition states and corresponding stationary points are confirmed by intrinsic reaction coordinate calculation.

Introduction

Over the past years, a growing concern about the quality of air in the industrial and urban zones has been controls, specifically targeting HC (hydrocarbon) air toxics, which constitute a class of the most widespread atmospheric pollutants. Polycyclic aromatic hydrocarbons (PAHs) account for the largest and very dangerous portion of the HC emissions because many of them are potent mutagens and carcinogens And since they escape the combustion sources in a form of easily inhaled ultrafine particles ($d < 0.1 \mu\text{m}$), their presence in the atmosphere can cause acute and long-term respiratory effects [1]. In addition, air deposition of PAH on soil and directly on plants is likely to be responsible for contamination of such food products as cereal and vegetables, which then become the main PAH sources in a human diet. A better understanding of the mechanisms of PAH and soot formation during HC combustion is essential for the development of more efficient combustion devices with minimal environmental impact [2]. The purpose of the present research is the study of potential energy surface of Hydroxycyclohexadienyl (HCHD) and acetylene reaction in the selected path. We also compute thermodynamic parameters of obtained products on doublet potential energy surface.

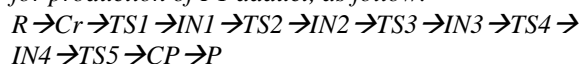
Materials and method

The purposes of this work by means of computational methods based on density functional theories carried out. A details of the doublet potential energy surfaces (PES) for the reaction of hydroxycyclohexadienyl (HCHD) and acetylenewith the aim of clarifying the reaction mechanism. High-level methods consist of M06-2X [3] and B3LYP [4] in connection with 6-311++g(d,p) and 6-311++g(3df,2p) basis sets applied for geometry optimization of all species. Harmonic vibrational frequencies calculated at the same level of theory were used for zero-point energy

Result and Discussion

Potential energy profile and geometrical parameters of all spices are depicted in figure 1 and 2, respectively.

According to the doublet PES, there is one pathway for production of P1 adduct, as follow:



We found one pre reactive complex between HCHD and C_2H_2 which name of this complex is Cr. The pre-reactive complex Cr1 is transform into Cp via five transition states, TS1, TS2, TS3, TS4 and TS5, the barrier energies of theses transition states are 21.38 kcal/mol, 47.78 kcal/mol, 46.66 kcal/mol, 36.89 kcal/mol and 55.66 kcal/mol at M06-2X/6-311++g(d, p) method. Then, Cp1 transforms into the P1 ($C_8H_7+H_2O$) with barrier less process. Enthalpy computed for this products is $\Delta H^0 = -7.159 \text{ kcal/mol}$ which is negative that shows this reaction is exothermic process. Also, this process has negative Gibbs free energy $\Delta G^0 = -7.195 \text{ kcal/mol}$ that indicates production of P1 is spontaneous in gas phase and at atmospheric pressure and 298.15 K. The small positive ΔS value of P1 shows that the entropy change of the product is negligible that is related to the difference of internal degree of freedoms. The calculated internal energies, enthalpies, Gibbs free energies and entropies of this reaction in gas phase at atmospheric pressure and temperature (298.15 K) at M06-2X/6-311++g(d,p) level, have been summarized in Table 1.

Table1. Calculated thermodynamic parameters of P (Spiro [2,5] octatrienyl and water) adducts. Values are in kcal/mol

method	ΔE^0	ΔH^0	ΔG^0	$T\Delta S^0$
--------	--------------	--------------	--------------	---------------



M06-2X/6-311++g(d,p)	-7.158	-7.159	-7.195	0.036
----------------------	--------	--------	--------	-------

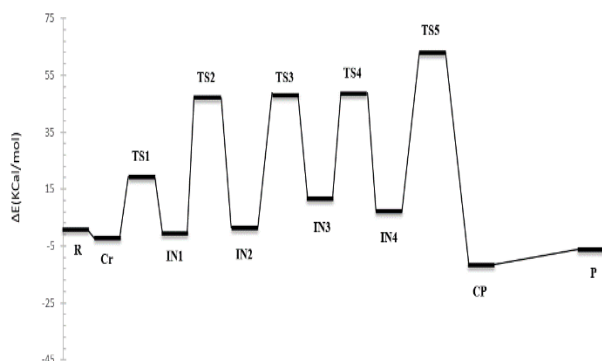


Fig. 1. singlet potential energy profile of HCHD + C₂H₂ reaction at M06-2X/6-311++g(d,p) level.

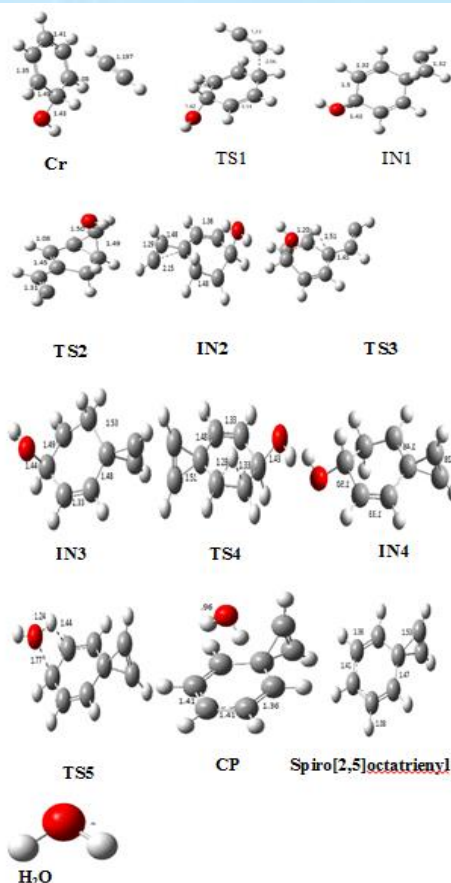


Table2. total energies taking into zero point energy (in Hartree) and relative energies (in kcal/mol) in parentheses.

Species	M06-2X (d,p) ¹	B3LYP (3df,2p) ²	Species	M06-2X (dp) ¹	B3LYP(3df,2p)
R	-385.126 (0.00)	-385.338 (0.00)	CP	-385.146 (-12.51)	-385.346 (-5.06)
Cr	-385.131 (-3.11)	-385.328 (-0.385)	TS1	-385.097 (18.27)	-385.303 (21.84)
IN1	-385.129 (-1.53)	-385.328 (6.695)	TS2	-385.052 (46.24)	-385.258 (50.63)
IN2	-385.125 (0.41)	-385.318 (12.938)	TS3	-385.051 (47.07)	-385.261 (48.54)
IN3	-385.109 (10.75)	-385.302 (22.88)	TS4	-385.050 (47.65)	-385.245 (58.36)
IN4	-385.116 (6.25)	-385.309 (18.138)	TS5	-385.027 (61.91)	-385.233 (66.09)
P(H ₂ O+A ³)	-385.138 (-7.20)	-385.344 (-12.48)			

- M06-2X(d,p) stands for at M06-2X/6-311++g(d,p) and
- B3LYP(3df,2p) stands for B3LYP/6-311++g(3df,2p).
- A=Spiro [2,5] octatrienyl.

1. Geometries of all species computed at M06-2X/6-311++g(d,p) level.

Conclusions

The reaction of HCHD with acetylene can be considered as an elementary reaction. The formation of intermediates and transition states confirm by DFT calculations.

Thermodynamic variables obtained by implemented methods.

References

- [1] Durant, J. L.; Busby, W. F.; Lafleur, A. L.; Penman, B. W.; Crespi, C. L. *Mutat. Res.* 1996, 371, 123-157.
- [2] Samanta, S. K.; Singh, O. V.; Jain, R. K. *Trends Biotechnol.* 2002, 20, 243-248.
- [3] Zhao and D. G. Truhlar, *Theoretical Chemistry Accounts*, 2008, 120, 215-241.
- [4] E. G. Hohenstein, S. T. Chill and C. D. Sherrill, *Journal of chemical theory and computation*, 2008, 4, 1996-2000



QSPR Study on the Estimation Melting Point of Barbiturates by Using Topological Indices and MLR Method

E.Esmaili^a F. Shafiei^{b*}

^{a,b}Department of Chemistry, Arak Branch, Islamic Azad University, Arak, Iran
P.O. Box 38135-567, Arak 38361-1-9131, Iran

* Corresponding E-mail address: f-shafiei@iau-arak.ac.ir

Abstract: In this study the relationship between the Randic' (¹X), Balaban (J), Szeged (Sz), Harary (H), Wiener (W), HyperWiener (WW) and Wiener Polarity (WP) to the Melting Point (M.P) of 17 barbiturate Compounds is represented. The Melting Point (M.P) of 17 barbiturate Compounds were calculated with Chem Draw software. The multiple linear regressions (MLR) and Back ward methods were employed to give the QSPR models. After MLR analysis, we studied the validation of linearity between the molecular descriptors in the best models for used properties. The predictive powers of the models were discussed by using the method of cross-validation. The results have shown that descriptor (WP), could be efficiently used for estimating, modeling and predicting the Melting Point (M.P) for of respect compounds.

Keywords: Topological indices; Barbiturates; MLR method; QSPR

Introduction

QSAR models were studied to predict heat capacities of organic combinations in 25 c temperature, [1, 2].

By using physical and chemical describer of octanol-water partition coefficient (log P), Hansch indicated quantitative relationship between structure- activity of barbiturates and investigated penetration coefficient to biological membrane of these materials [3].

The importance of barbiturates and thiobarbiturates is well established in pharmaceutical chemistry and drug design. This class of drugs exhibit hypnotic, anticonvulsant and anaesthetic activity. [4,5]

Materials and Method

The descriptors were calculated with chemicalize program [8]. In the present work, linear regression analyses were performed using SPSS-16 (SPSS Inc., Chicago, IL, USA).

Melting Point (M.P) are used as the dependent variable and ¹X, J, H, W, W_p, WW and Sz indices as the independent variables. Criteria for selection of the best multiple linear regression model were the statistics: squared multiple correlation coefficient (R^2), adjusted correlation coefficient (R^2_{adj}), Fisher ratio (F), root mean square error (RMSE), Durbin-Watson value (DW) and significant (Sig).

Barbiturates are drugs that act as central nervous system depressants. By virtue of this, they produce a wide spectrum of effects, from mild sedation to total anesthesia. Barbiturates are also effective as anxiolytics, hypnotics, and anticonvulsants [6].

Quantitative Structure- Property Relationship (QSPR) and Quantitative Structure- Activity Relationship (QSAR) methods are based on the hypothesis that change in chemical structure of a compound is reflected in change to its physico-chemical properties [7].

In this section for verification and validity of the regression models, we will focus on the Durbin-Watson statistic and unstandardized predicted and residual values. The Durbin-Watson statistic ranges in value from 0 to 4 (See eq.1). If the VIF value lies between 1-10, then there is no multicollinearity, and if the VIF < 1 or > 10, then there is multicollinearity.

Results and Discussion

The best linear model for Melting Point contains four topological descriptors, namely, Hyper Wiener (WW), Wiener polarity (W_p), Randic' (X), Harary (H)

and Wiener (W) indices. The model is found as $M.P = 387.914 - 72.665(X) + 31.330(H) - 2.451(W) + 0.437(WW) - 9.515(WP)$ (1)

$N=17$ $R=0.991$ $R^2=0.983$ $R^2_{adj} = 0.975$ $RMSE=80.862$ $F=123.869$ $Sig=0.000$ $DW=2.748$

For model.1. the Pearson correlation (WW,WP),(H,W),(H,WW) is near one, and $VIF(WW), VIF(H)$ and $VIF(W) > 10$, therefore there is a linearity between (WW, WP),(H,W) and (H,WW). After removed W from this model four indices H, WW,WP and X remains the Pearson correlation (H, WP) is near one, and $VIF(H), VIF(WP) > 10$, therefore there is a linearity between H and WP. After removed H from this model, we corrected model (2) as follow:

$$M.P = 415.067 + 5.141(WP) \quad (2)$$

$N=17$ $R=0.928$ $R^2=0.861$ $R^2_{adj} = 0.852$ $RMSE=169.266$ $F=92.96$ $Sig=0.000$ $DW=1.268$ $Q^2=0.9$

The residual is the difference between the observed and predicted values.

Figures (1) show the linear correlation between the observed and the predicted Melting Point(M.P) of

Conclusions

QSPR models for the prediction of the Melting Point(M.P) for a training set of barbiturates using MLR based on topological descriptors calculated from molecular structure alone have been developed. MLR model is proved to be a useful tool in the prediction of Melting Point(M.P). Cross-

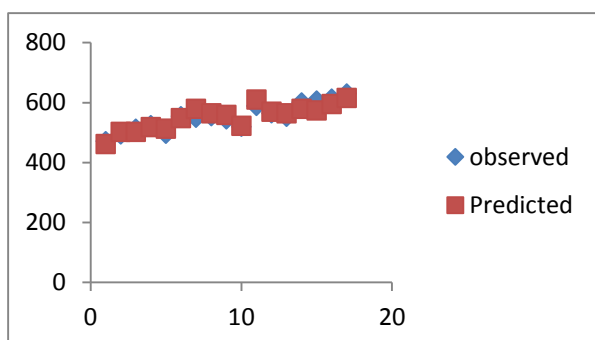


Figure 1. Comparison between the predicted and observed of models calculated validation of M.P by MLR method.

below:

Table 1: Correlation between the molecular descriptors (model .1)

	Collinearity statistical				Corrected model		VIF
	WW	X	WP	HW	VIF		
ww	1.000	.009	-.990	.669	.085	1.814E3	-
X		1.000	.007	-.551	.489	144.17	-
wp			1.000	-0.603	0.013	69.88	1
H				1.000	0.737	925.48	-
W					1.000	4.091E3	-

barbiturates value obtained using equation model (2).

validation as the evaluation technique has been designed to evaluate the quality and predictive ability of the MLR model. The obtained results showed that (WP) for predicting M.R is good topological index for modeling M.P.



References

- [1] X .Yao, B. Fan, J. P. Doucet, A. Panaye, "Quantitative structure- property relationship models for the prediction of liquid heat capacity", *QSAR Comb.Sci.* 22 (2003) 29- 48.
- [2] A. Ivanova, V. A. Palyulin, A. N. Zefirov and N. S. Zefirov. "Fragment Descriptors in QSPR: Application to heat Capacity Calculation", *Russ. J. Org. Chem.* 40 (2004) 644-649.
- [3] C. Hansch, A. R. Steward, S.M. Anderson, D. Bentley, " Quantitative Aspects of Chemical Pharmacology: Chemical Ideas in Drug Action ", *J. Med. Chem.* 11 (1967)1-11.
- [4] K.S. Jain, T.S. Chitre, P.B. Miniyar, M.R. Kathiravan, V.S. Bendre, V.S. Veer, S.R. Shahane and C.J. Shishoo, " Biological and medicinal significance of pyrimidines", *Curr. Sci.* .90(2006) 793-803.
- [5] U.Rudolph and B. Antkowiak," Molecular and neuronal substrates for general anaesthetics", *Nat. Rev.*, 5(2004) 709-720.
- [6]http://www.dignitas.ch/index.php?option=com_content&view=article&id=22&Itemid=62&lang=de. Retrieved 2011-06-14.
- [7] Tu. Le, V. Chandana Epa, F. R. Burden, D. A. Winkler, "Quantitative Structure–Property Relationship Modeling of Diverse Materials Properties", *Chem. Rev.* 112 (2012) 2889
- [8] Web search engine developed by ChemAxon; software available at <http://WWW.Chemicalize.org>

The influence of the Li₂ interaction with pristine and halogenated B₁₀H₁₄ on their electronic and nonlinear optical properties

M. Rasteh^a, E. Shakerzadeh^{*.b} and S. Fakhraie^a

^aDepartment of chemistry, College of sciences, Payame Noor University, Tehran, Iran

^bChemistry Department, Faculty of Science, Shahid Chamran University of Ahvaz, Ahvaz, Iran

*e.shakerzadeh@scu.ac.ir

Abstract: In this study the influence of Li₂ interaction with pristine and halogenated decaborane (B₁₀H₁₄) derivatives on their electronic and optical properties are investigated through DFT calculations. For this purpose, all structures are fully optimized at B3LYP/6-311++G** level of theory and different properties such as energy gap, polarizability and hyperpolarizability are calculated for the relaxed geometries. It is found that the electro-optical features of pristine and halogenated B₁₀H₁₄ could be efficiently tuned by interaction with Li₂ molecule. The results could be valuable for designing novel boron-based electro-optical devices. The present results will be beneficial for further theoretical and experimental studies on the NLO properties of boron-based compounds.

Keywords: Decaborane, energy gap, Polarizability, Hyperpolarizability, halogenated, halogen.

Introduction

The last few decades the design and synthesis of nonlinear optical (NLO) materials have been attracted great interest¹. Research on designing new high-performance nonlinear optical (NLO) materials is being an intriguing issue for scientist². Among many strategies for enhancing the NLO response of materials, introducing the diffuse excess electron, such as alkali metals, proposed an efficient approach to improve the NLO properties of different systems. In the present study the influence of Li₂ interactions with pristine and halogenated decaborane (B₁₀H₁₄) on their electro-optical features are investigated through DFT calculations.

Results and Discussion

In order to investigate the Li₂ interaction with decaborane, the Li₂ molecule is located at different positions of pristine and halogenated B₁₀H₁₄ and the geometry optimizations are carried out at B3LYP/6-311++G** level of theory. The optimized structures are depicted in Fig.1. Notice that fluorine (F) and chlorine (Cl) atoms replace by different hydrogen

atom in the considered Li₂@1-F-B₁₀H₁₃, Li₂@2-F-F-B₁₀H₁₃, Li₂@5-F-F-B₁₀H₁₃, Li₂@in9-F-F-B₁₀H₁₃, Li₂@out9-F-F-B₁₀H₁₃, Li₂@1-Cl-B₁₀H₁₃, Li₂@2-Cl-F-B₁₀H₁₃, Li₂@5-Cl-F-B₁₀H₁₃, Li₂@in9-Cl-F-B₁₀H₁₃ and Li₂@out9-F-B₁₀H₁₃ complexes which are presented in Fig. 1. The obtained highest occupied molecular orbital (HOMO) and the lowest unoccupied molecular orbital (LUMO) energies together with energy gap (E_g) values as well as polarizability and the first static hyperpolarizability of the considered structures are listed in Table 1. It is found the Li₂ interactions with pristine and halogenated B₁₀H₁₄ narrow their energy gaps. Such a reduction of HLG is mainly due to the formation of a high energy level as the new HOMO levels locating between the original HOMO and LUMO of pristine B₁₀H₁₄. Thus the electronic properties of these considered systems are strongly sensitive to interaction with the Li₂. As can be seen in Table 1, the first static hyperpolarizability (β_0) is induced in both pristine and halogenated B₁₀H₁₄, especially in the case of Li₂@B₁₀H₁₄ complex with remarkable value of 34891.8 a.u.

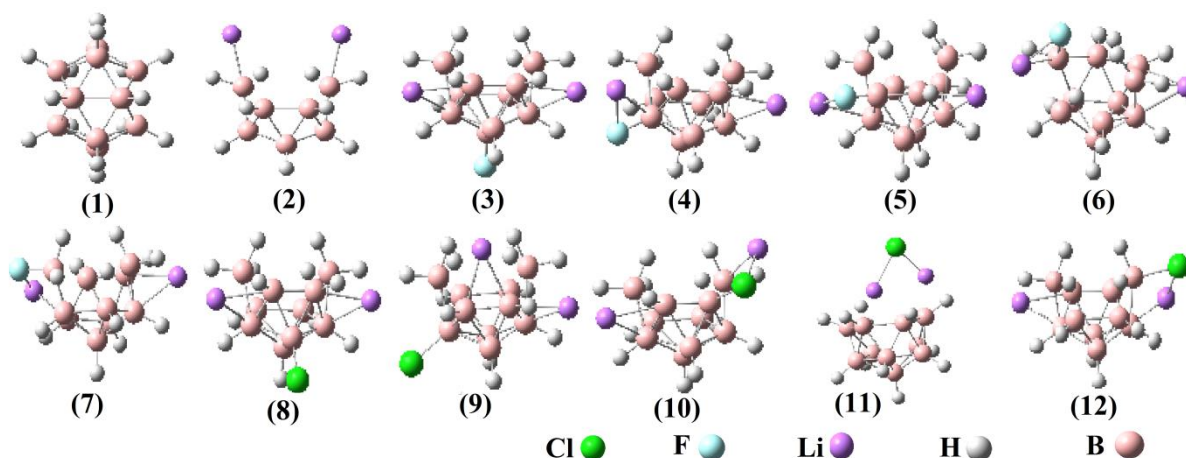


Fig. 1. The optimized structures of the considered complexes

Table 1. The obtained electro-optical parameters of the considered compounds

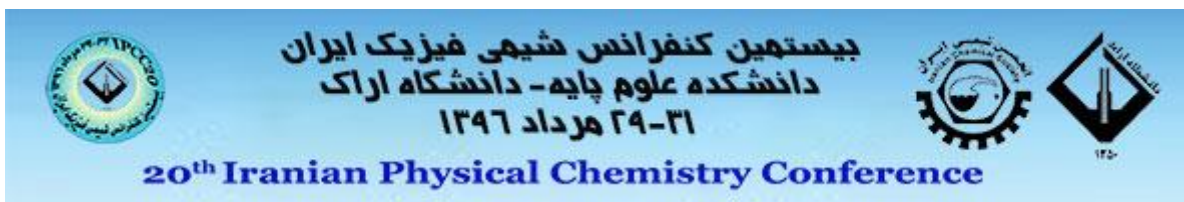
systems	μ (au)	α (au)	β_0 (au)	HOMO (eV)	LUMO (eV)	E _g (eV)	B-X(X=F, Cl)
1	1.29	124.70	69.7	-8.319	-2.854	5.465	-
2	6.13	236.80	34891.8	-4.259	-2.708	1.551	-
3	2.55	147.93	466.0	-5.203	-1.475	3.728	1.375
4	2.23	147.10	420.8	-5.311	-1.406	3.905	1.456
5	1.73	146.33	140.2	-5.203	-1.366	3.837	1.459
6	1.78	145.54	222.7	-5.606	-1.371	4.235	1.513
7	2.18	146.24	451.9	-5.323	-1.416	3.918	1.478
8	1.95	160.15	334.9	-5.235	-1.476	3.759	1.843
9	4.93	159.97	893.5	-6.247	-1.882	4.365	1.830
10	2.73	162.00	531.5	-5.312	-1.428	3.884	1.923
11	1.07	154.56	90.5	-7.282	-2.437	4.846	3.620
12	2.41	160.86	455.9	-5.421	-1.491	3.930	1.950

Conclusions

To sum up, it is concluded the electro-optical features of pristine and halogenated B₁₀H₁₄ could be efficiently tuned by interaction with Li₂ molecule.

References

- G. de la Torre, P. Vázquez, F. A. López and T. Torres, *Chem. Rev.* 2004, **104**, 3723
- R.L. Zhong, H.L. Xu, Z.R. Li and Z.M. Su *J. Phys. Chem. Lett.* 2015, **6**, 612
- S. Muhammad, H.L. Xu, Y. Liao, Y.H. Kan and Z.M. Su *J. Am. Chem. Soc.* 2009, **131**, 11833



QSPR Study on the Estimation Solubility of Barbiturates by Using Topological Indices

E. Esmaceli, F. Shafiei*

Department of Chemistry, Arak Branch, Islamic Azad University, Arak, Iran
P.O. Box 38135-567, Arak 38361-1-9131, Iran

* f-shafiei@iau-arak.ac.ir

Abstract: Graph theory is a delightful playground for the exploration of proof techniques in discrete mathematics and its results have application in many areas of sciences. In this study the relationship between the Randić' (1X), Balaban (J), Szeged (Sz), Harary (H), Wiener (W), HyperWiener (WW) and Wiener Polarity (WP) to the Solubility (Log S) of 17 barbiturate Compounds is represented. The Solubility (Log S) of 17 barbiturate Compounds were calculated with chemicalize program. The multiple linear regressions (MLR) and Back ward methods were employed to give the QSPR models. After MLR analysis, we studied the validation of linearity between the molecular descriptors in the best models for used properties. The predictive powers of the models were discussed by using the method of cross-validation. The results have shown that descriptor Hyper-wiener(WW), could use for estimating, modeling and predicting the Solubility (Log S) for of respect compounds.

Keywords: Topological indices; Barbiturates; MLR; QSPR; Validation

Introduction

In 2009, Vulpes studied quantitative relationship between structure- activity and anesthesia power of number of Barbiturates and thiobarbiturates and modeling it by multiple linear regressions [1].

Variety of methods for predicting aqueous solubility have been reported in the literature, including Yalkowsky's semiempirical equation[2] the group contribution methods[3,4] and the in

silico quantitative structure–property relationships (QSPR) [5–8]. By physical and chemical describer of octanol-water partition coefficient (log P), Hansch indicated quantitative relationship between structure- activity of barbiturates and investigated penetration coefficient to biological membrane of these materials [9].

Materials and Method

The Solubility (Log S) of 17 barbiturate Compounds were calculated with chemicalize program[10].

Structure- Property models (MLR models) are generated using the multi linear regression procedure of SPSS version 16.0 and backward stepwise regression was used to construct the QSPR models. For drawing the graphs of our

results, we used the Microsoft Office Excel – 2010 program.

All the used topological indices were calculated using all hydrogen suppressed graph by deleting all the carbon hydrogen as well as heteroatomic hydrogen bonds from the structure of the barbiturate.

Criteria for selection of the best multiple linear regression model were the statistics: correlation coefficient (R), squared multiple correlation coefficient (R^2), adjusted correlation coefficient (R^2_{adj}), Fisher ratio (F), root mean square error (RMSE), Durbin-Watson value (DW) and significant (Sig). In this section for verification and

validity of the regression models, we will focus on the Durbin-Watson statistic and unstandardized predicted and residual values. The Durbin-Watson statistic ranges in value from 0 to 4(See eq.1). If the VIF value lies between 1-10, then there is no multicollinearity, and if the $VIF < 1$ or > 10 , then there is multicollinearity.

Results and Discussion

The best linear model for Solubility (Log S mol/L) contains topological descriptor, HyperWiener (WW) indices.

The statistical items of the best three descriptors correlation model were as follows:

$$\text{Model (1)} \\ \text{Log S} = 3.979 - 1.135(^1X) - 0.003(WW) + 0.008(Sz) \\ N=17 \quad R=0.983 \quad R^2=0.967 \quad R_{adj}^2 = 0.959 \quad RMSE=0.23450 \\ F=125.748 \quad Sig=0.000 \quad DW=2.412$$

We studied the relationship between topological indices to the Solubility (Log S mol/L) of 17 barbiturate compounds.

In this study, to find the best model for predict the properties mentioned, we will use the following sections.

In our model, the value of Durbin-Watson statistic is close to 2 (See eq.1) and hence the errors are uncorrelated.

We studied the validation of linearity between the molecular descriptors in the model.1. We obtained $Q^2_{LOO} = 0.857$

The residual is the difference between the observed and predicted values. Comparison

Figure (1) show the linear correlation between the observed and the predicted Solubility (Log S mol/L) value obtained using equation (2) .

Conclusions

In this study, QSPR mathematical models for the prediction of the Solubility (Log S mol/L) of barbiturates by using MLR method based on topological descriptors calculated from molecular structure alone have been developed. MLR model

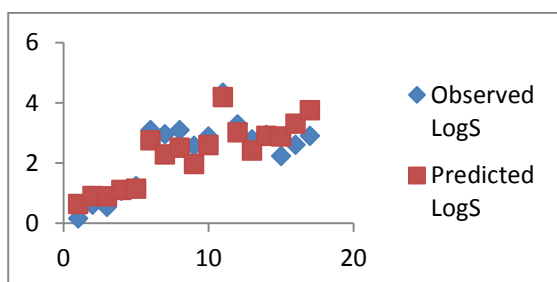


Figure 1. Comparison between the predicted and observed

by SPSS the Pearson coefficient correlation and collinearity statistics as follows Table 1.

For model.1 the Pearson correlation ($Sz, ^1X$) is near one, and $VIF(Sz), (^1X)$ and $VIF(Sz) > 10$, therefore there is a linearity between Sz and 1X . After removed Sz from model, we corrected models as follow :

$$\text{Model (2)} \\ \text{Log S} = -0.284 - 0.002(WW) \\ N=17 \quad R=0.911 \quad R^2=0.830 \quad R_{adj}^2 = 0.818 \quad RMSE=0.49340 \\ F=64.120 \quad Sig=0.000 \quad DW=0.294$$

In equation(2) Q^2_{LOO} is the squared cross-validation coefficients for leave one.

We have computed Q^2_{LOO} (Eq.3) by 50% of data, randomly, that are positive and less than one.

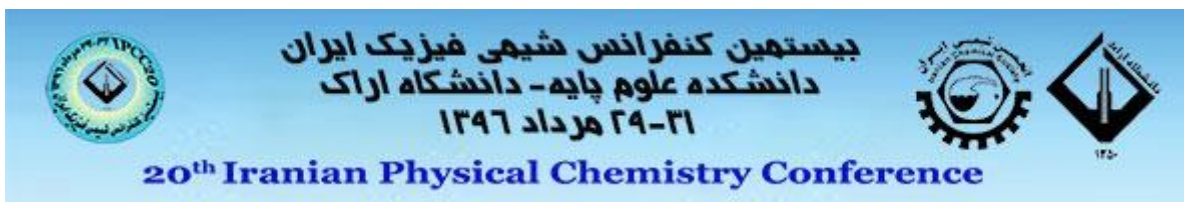
$$Q^2 = 1 - \frac{\sum(Y_i - \hat{Y}_{i|i})^2}{\sum(Y_i - \bar{Y})^2} \quad Q^2 \leq 1 \quad (3)$$

In the equation (3), the notation $i|i$ indicates is predicted by a model estimated when the i -th sample was left out from the training set.

Table 1. Correlation between the molecular descriptors (model.1)

Collinearity statistical			Corrected model		
Sz	WW	¹ X	Tolerance	VIF	VIF
Sz	1	-0.363	0.045	22.137	-
WW	-0.363	1	0.044	22.810	1
¹ X	-0.545	-0.563	0.036	28.149	-

is proved to be a useful tool in the prediction of Solubility (Log S mol/L). The obtained results showed that HyperWiener(WW) index is good topological index for for predicting Solubility (Log S mol/L).



of Log S by MLR method

References

- [1] D.Vulpes, M.V.Putz, A.Chiriac" QSAR study on the anaesthetic activity of some barbiturates and thiobarbiturates", *Revue Roumaine de Chimie*, , 54(9) (2009) 723-732
- [2] S.H .Yalkowsky, S.C .Valvani "Solubility and partitioning I: Solubility of nonelectrolytes in water", *J Pharm Sci* 69(1980)912-922.
- [3] G. Klopman, S .Wang, D.M .Balthasar "Estimation of aqueous solubility of organic molecules by the group contribution approach Application to the study of biodegradation", *J Chem Inf Comput Sci* 32 (1992)474-482.
- [4] P.B. Myrdal, A.M .Manka, S.H. Yalkowsky. AQUAFAC 3: "Aqueous functional group activity coefficients; application to the estimation of
- [5] P.D .Huibers, A.R. Katritzky" Correlation of the aqueous solubility of hydrocarbons and halogenated hydrocarbons with molecular structure", *J Chem Inf Comput Sci* 38 (1998)283-292.
- [6] T.M Nelson, P.C Jurs" Prediction of aqueous solubility of organic compounds", *J ChemInf Comput Sci* 34 (1994)601-609.
- [7] J .Huuskonen, M .Salo, J .Taskinen" Aqueous solubility prediction of drugs based on molecular topology and neural network modeling", *J Chem Inf Comput Sci* 38 (1998)450-456.
- [8] J. Huuskonen" Estimation of aqueous solubility for a diverse set of organic compounds based on molecular topology", *J Chem Inf Comput Sci* 40 (2000)773-777.
- [9]C. Hansch, A. R. Steward, S.M. Anderson,D. Bentley " Quantitative Aspects of Chemical Pharmacology: Chemical Ideas in Drug Action ", *J. Med. Chem.*, 11 (1967)1-11.
- [10] Web search engine developed by ChemAxon; software available at <http://WWW.Chemicalize.org>



A Computational study of pristine and Al-doped boron nitride nanosheet as CNCl sensor

R. Moladoust^a, S.M. Mousavi-Khoshdel^{b*}, E. Vessally^c

^aDepartment of Chemistry, University of Mohaghegh Ardabili, Ardabil, 5619911367, Iran

^bDepartment of Chemistry, Iran University of Science and Technology, Tehran, 1684613114, Iran

^cDepartment of Chemistry, Payame Noor University, Zanjan, Iran

* mmousavi@iust.ac.ir

Abstract:

In order to explore a novel sensor to detect the cyanogen chloride (CNCl) molecule, we study the adsorption and electronic properties of the interaction CNCl with the pristine and Al-doped boron nitride nanosheet using density function theory. The most stable adsorption geometries, adsorption energies, charge transfers, and density of states of these systems are thoroughly discussed. Comparing the results of the pristine BN nanosheet with CNCl, we found that Al-doped BN nanosheet is more sensitive to the CNCl molecule, which is indicated by the calculated optimized geometry and electronic properties of these systems. Al-doped BN nanosheet is expected to be a potential candidate for detecting of toxic CNCl molecule.

Keywords: Gas Sensor; Cyanogen Chloride; BN nanosheet; DFT

Introduction

Cyanogen chloride (CNCl) is a highly volatile and toxic. It has strong irritant and choking effects. Exposure to cyanogen chloride can be rapidly fatal. Its vapors are extremely irritating and corrosive [1]. Boron nitride nanostructures, because of their unique properties including high thermal conductivity and chemical stability, strong resistance to oxidation have been applied in the nanodevices such as transistors and chemical sensors [2-4]. BN sheet possesses polar B-N bond and a wide band gap that is independent of its helicity. Because of the polar nature of B-N bonds, BN nanostructures are expected to have higher reactivity than their carbon analogs. It indicates that BN nanostructures could be good candidates for gas sensors.

In this research, we study the adsorption of CNCl molecule on pristine and Al-doped BN sheets using density functional theory (DFT), to verify whether or not the sheets can be used as gas sensors.

Computational methods

The full geometry optimizations and electronic properties calculations on the pristine and Al-doped sheet to the CNCl molecule were performed using hybrid meta generalized gradient approximation with the M06-2X functional and the 6-31+G(d) basis set, as implemented in the GAMESS suite of program. Adsorption energy calculations and density of states (DOS) analysis were performed at the same level of theory. GaussSum program was used to obtain DOS results. We have defined the adsorption energy (E_{ad}) as follows:

$$E_{ad} = E_{(CNCl/sheet)} - (E_{(sheet)} + E_{(CNCl)}) + E_{(BSSE)}$$

HOMO-LUMO energy gap is defined as:

$$E_g = E_{LUMO} - E_{HOMO}$$

Results and Discussion

In order to find the most stable configuration, full geometrical optimization was performed with different orientations of the CNCl molecule with surface sheet. After relaxation, in the most stable structure, CNCl molecule attaches to a B atom of the sheet from its nitride (-N-) head (Fig. 1), and its corresponding calculated E_{ad} value is about -4.77 kcal/mol, indicating a weak adsorption.

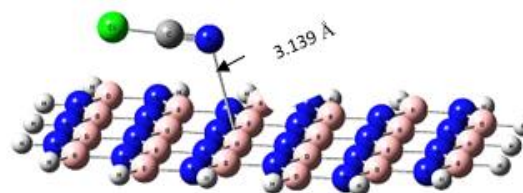


Figure 2 : The most stable configuration after optimization.

The calculated energy gaps of the pristine and CNCl adsorbed sheet are about 7.86 and 7.15 eV, respectively. The HOMO and LUMO are mainly localized on the CNCl molecule and BN sheet (Fig. 2) at -7.97 and -0.82 eV, respectively.

HOMO

LUMO

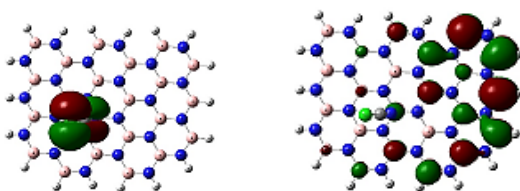


Figure 2: The HOMO and LUMO profile of the CNCl/BN sheet complex.

Our calculated indicated that small amount of charge transfer between CNCl and BN sheet, So a net charge of 0.17 $|e^-|$ is transferred from the molecule to the sheet (Table 1). For the bare BN sheet (Fig. 3), after adsorption process of CNCl molecule, E_g value decreased to -7.15 eV for BN sheet/CNCl complex due to charge transfer to the molecule. As the energy gap of the pristine sheet is only slightly changed during the adsorption process, the pristine nanosheet will not be sensitive to CNCl molecule. So, we investigated the influence of Al-doping on adsorption and electronic characteristics of the sheet on CNCl.

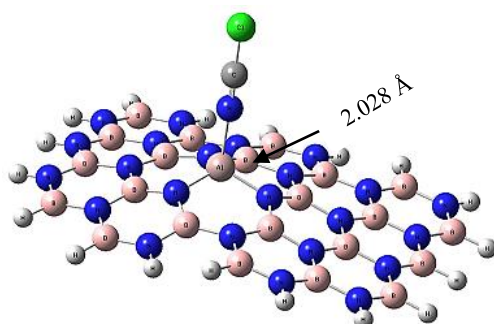


Figure 3: The optimized structure of Al-doped BN sheet with CNCl molecule.

When one boron atom is substituted by Al atom in the BN Sheet, it is found that the geometric structure of the Al-BN Sheet, changes dramatically. Due to the large size of Al atom, it protrudes out of plane in order to relieve the stress. After the adsorption of CNCl molecule, the length of Al-N bond is increased from 1.737 to 1.773 Å, indicating that the Al site is transformed from sp^2 hybridization to more sp^3 like hybridization. Moreover, the adsorption energy of CNCl on the Al-BN sheet is - 22.71 kcal/mol, which is larger than that of CNCl on the pristine BN Sheet. The interaction distance in the CNCl molecule interacted with the Al atom of BN sheet is about 2.028 Å that is reduced than distance with the B atom of BN sheet. Mulliken population analysis indicated that the charge about 0.66 $|e^-|$ is transferred from the CNCl molecule to the Al-BN sheet. These adsorption energy values, interaction distances and charge transfer exhibit that the CNCl molecule is favourably adsorbed in the Al-BN

sheet owing to the strong covalent interaction between CNCl molecule and Al-BN sheet.

To further understand the electronic properties of BN sheet, the density of states (DOS) plots for sheet to the CNCl molecule, were calculated.

DOS plot of the CNCl/Al-BN Sheet complex shows a considerable change (Fig. 4). New states have appeared in the DOS of complex in comparison to the bare BN sheet. This indicates that the electronic properties of the Al-BN sheet are sensitive to the CNCl adsorption.

The energy gap value of the Al-BN sheet decreased from 7.62 to 5.77 eV in the CNCl/Al-BN sheet complexes.

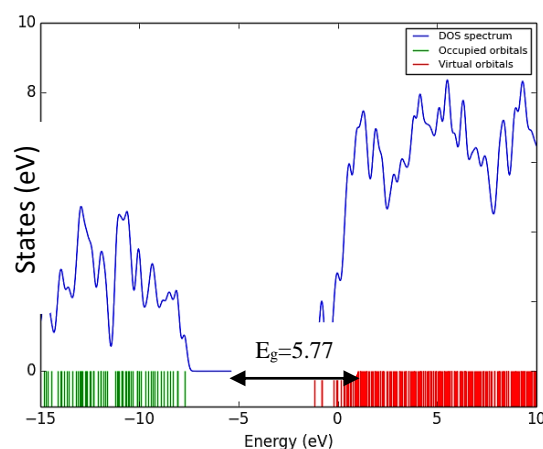


Figure 4: The DOS profile of the Al-BN/CNCl complex.

These changes would result in an electrical conductivity change of the sheet according to Eq. (1). The electrical conductance is exponentially related to E_g value according to the following equation:

$$\sigma \propto \exp\left(-\frac{E_g}{2kT}\right) \quad (1)$$

According to the equation, smaller E_g values lead to higher conductance at a given temperature. Compared with the pristine BN sheet, the Al-BN sheet would have excellent CNCl detection ability. So, we believe that Al doping process may be a good strategy for improving the sensitivity of the sheet to CNCl, which cannot be detected by the pristine BN Sheet (Table 1).

Table 1: Adsorption energies, the electronic properties and charge transfer of the BN complexes.

Compound	E_{ad} (kcal/mol)	E_{HOMO} (eV)	E_{LUMO} (eV)	E_g (eV)	q_{CT} (e)
BN-CNCl	-4.77	-7.97	-0.82	7.15	0.17
Al-BN-CNCl	-22.71	-7.74	-1.97	5.77	0.66



Conclusion

In this research, we have performed upon the reliable chemical gas sensors for the detection of toxic gas molecule. The electronic sensitivity of pristine and Al-doped BN sheet to the CNCl molecule were investigated using density functional theory. The results indicate that Al-doped BN sheet is more sensitive and reactive to the CNCl molecule.

References

- [1] GC. Deng, ZH. Zhang, B. Li, XD. Gao, SL. Zang, "Determination of cyanogen chloride in the air pollution by spectrophotometry", Chin J Anal Chem, 29 (2001) 565-568.
- [2] A.B. Preobrajenski, M.A. Nesterov, M.L. Ng, A.S. Vinogradov, N. Mårtensson, Chem. Phys Lett, 446 (2007) 119.
- [3] J.Y. Dai, P. Giannozzi, J.M. Yuan, Surf. Sci. 603 (2009) 2328–3234.
- [4] X. Jiang, Q. Weng, X. Wang, X. Li, J. Zhang, "Recent progress on fabrications and applications of boron nitride nanomaterials: a review", Journal of Materials Science & Technology, 31(2015) 589–598.

Quantum Chemical Evaluation of Optoelectronic Properties of Oligoselenophene:Fullerene BJJ Solar Cells

ZabiollahMahdaviFar*, Samira Tajdinin, Ehsan Shakerzadeh

Department of Chemistry, Faculty of Science, Shahid Chamran University of Ahvaz, Ahvaz, Iran

*z_mahdaviFar@scu.ac.ir

Abstract: In this work, in order to model the active layer in the bulk hetero-junction solar cells, the fullerene structures such as C₆₀, C₇₀, PC₆₀BM, PCBDAN as acceptor and oligoselenophenes ((OS)_n=14) as donor were considered. The (OS)_n=14/C₆₀, (OS)_n=14/C₇₀, (OS)_n=14/PC₆₀BM and (OS)_n=14/PCBDAN blends (complexes) as a model of the active layer in the BJJ solar cell were chosen and the opto-electronic properties were studied. Results show the width of the absorption spectrum of all investigated blends in the range of 400-700 nm and maximum wavelength in the range of 516.65 - 536.03 nm. Base on obtained data the calculated efficiency of these blends based on Scharber diagram was obtained namely 8% and 8.2% respectively.

Keywords: Oligoselenophenes, fullerene, bulk hetero-junction solar cells optoelectronic properties, DFT

Introduction

Nowadays because of the fossil fuels declining and the environmental damage, clean and renewable solar energy as an inexhaustible resource has attracted increasing attention over the past decades due to nontoxic and nonpolluting operation [1]. The annual solar radiation coming to earth (including 5% UV, 43% visible and 52% IR) is several times the world's annual energy consumption [2]. In this context, organic photovoltaic (OPV) device have attracted much attention in recent years [3, 4, 5, 6,7]. There are many reasons for the interest in OPVs comparing with silicon-based photovoltaics (PV). The OPVs offer low cost, solution-based processing, low thermal budget and the capability to fabricate flexible layer-area devices [3, 8]. Organic photovoltaics are devices, which convert solar energy or light directly into electrical power by photovoltaic effect [9]. The photovoltaic effect describes the fundamental interaction of light with matter to produce electricity.

C₅₉P

Computational Method

Quantum-chemical calculations using density functional theory (DFT) with the aim of Gaussian 09 were performed to investigate the electronic structure of these (OS)_n/fullerene blends by employing the B3LYP hybrid density functional. The basis sets used for the calculations are the split valence 6-311G(d) basis set. Time-dependent DFT (TD-DFT) calculations were performed to assess the excited-state vertical transition energies and oscillator strengths based on the optimized molecular geometries at the same level of theory.

Results and Discussion

On the basis of the optimized ground-state geometries of (OS)₁₂/C₆₀, (OS)₁₄/C₇₀ and (OS)₁₄/C₆₀ complex (Fig. 1), the deformation energy (E_{def}), interaction energy (E_{int}), binding energy (E_b) were calculated and are presented in Table 1. A negative value of binding energy indicates more stability of considered system. Compare the values of binding energy of (OS)₁₂/C₆₀ and (OS)₁₄/C₆₀ show that the structure with with karger number on n is more stable and generally, the (OS)₁₄/C₆₀ blends is more stable than others. According to the values specified in the Table 1, the interaction energy contribution in the complex formation process are obtained large and negative values, which indicate that the deformation in the direction sustainability is take place. Among all cases, (OS)₁₄/C₆₀ blend has the largest deformation and interaction energy.

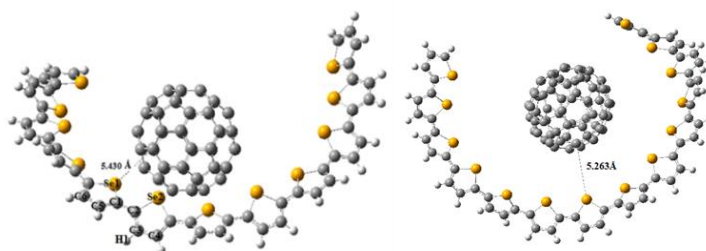


Fig. 1: Optimized structures of (OS)₁₂/C₆₀ and (OS)₁₄/C₆₀

Table 1: deformation energy (E_{def}), interaction energy (E_{int}), binding energy (E_b) of (OS)_n/fullerene with the B3LYP/6-311G(d) method.

	ΔE_i (LUMO _{OS} - LUMO _{OS}) (eV)	V_{oc} (V)
(OS) _{n=12} /C ₆₀	0.854	1.055
(OS) _{n=14} /C ₆₀	0.825	1.029
(OS) _{n=14} /C ₇₀	0.820	1.034

In organic solar cells, frontier molecular orbital energy levels have a close relation with V_{oc} and energy driving force ($\Delta E1$) for exciton dissociation. Namely, the V_{oc} is determined by the difference between the HOMO of the donor and the LUMO of the acceptor, according empirical equation summarized by Scharber and co-workers, which can be expressed as

$$V_{oc} = \left(\frac{1}{e}\right) (|E_{HOMO}^{Donor}| - |E_{LUMO}^{Acceptor}|) - 0.3V$$

here, e is the elementary charge, and the value of 0.3 is an empirical factor. The energy difference $\Delta E1$ between the LUMOs of the donor and the acceptor should be larger than 0.3 eV, which guarantees efficient exciton split and charge dissociation at the D/A interface. To explore these relationships, the frontier molecular orbital (FMO) energies of all the acceptors with regard to the electron donors (OS)_n=10-15 were depicted in Fig. 2. The values of $\Delta E1$ and V_{oc} parameters are reported in Table 2.

Table 2: ΔE_{LL} & V_{oc} of (OS)_n/fullerene with the B3LYP/6-311G(d) method.

	E_{def} (kJ.mol ⁻¹)	E_{int} (kJ.mol ⁻¹)	E_b (kJ.mol ⁻¹)
(OS) _{n=12} /C ₆₀	-28.701	-0.798	-29.499
(OS) _{n=14} /C ₆₀	-33.020	-1.974	-34.994
(OS) _{n=14} /C ₇₀	-31.766	-1.040	-32.806

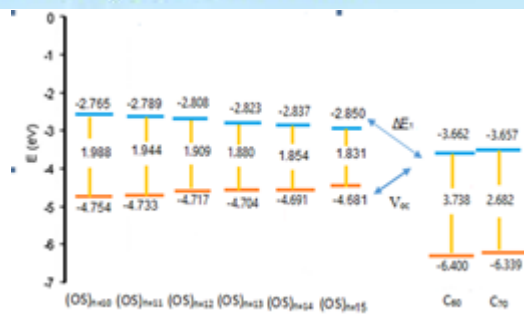


Fig. 2: Frontier molecular orbital energy levels of (OS)_n=10-15 and C₆₀ and C₇₀.

The results show that the most favorable amount of $\Delta E1$ is owned by (OS)₁₄/C₇₀ blend, because of the LUMO level are located relative to each other therefore this complex has the lowest $\Delta E1$ and highest V_{oc} compared to other complexes under study. As we know, with increasing the V_{oc} , the power conversion efficiency (PCE) of blend will be increased (see Table 3).

Table 3: PCE values of (OS)_n/fullerene with the B3LYP/6-311G(d) method

	Power conversion efficiency (PCE)
C ₆₀ /(OS) _{n=12}	7.7%
C ₆₀ /(OS) _{n=14}	8.0%
C ₇₀ /(OS) _{n=14}	8.2%

The vertical singlet-singlet electronic transition energies and optical absorption spectra of all (OS)_n/fullerene blends were calculated by the TD-DFT/6-311G(d) level of theory. Fig. 3 shows the simulated absorption spectra (considering the first 40 excited states), along with the absorption wavelength. The absorption spectrum of all blends shows only an extreme peak. The main transitions of all blends occurred in the visible range. The difference in chain length oligomers in the (OS)₁₄/C₆₀ and (OS)₁₂/C₆₀ blends has led to the hyperchromic effect was occurred. This effect defined as increase in absorptivity at a particular wavelength of light by a solution or substance due to structural changes in a molecule.

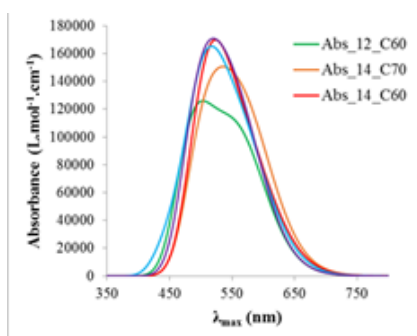


Fig. 3: Simulated absorption spectra of (OS)₁₂/C₆₀, (OS)₁₄/C₇₀, and (OS)₁₄/C₆₀ blends.

Conclusions

The method of B3LYP/6-311G(d) has been used to investigate the electronic and the optical features of (OS)_n/fullerene blends. Results show the width of the absorption spectrum of all investigated blends in the range of 400-700 nm and maximum wavelength in the range of 516.65 - 536.03 nm. The highest open circuit voltage (V_{OC}) is belonging to the (OS)₁₄/C₇₀ blend. Based on obtained results, the (OS)₁₄/C₇₀ is a favorable candidate as model for BHJ solar cell than that of the other blends. In order to investigate the effect of chain length of oligomers on the solar cell properties, the optoelectronic properties of (OS)₁₂/C₆₀ blend was also studied. In comparison, the electronic and optical properties and the obtained efficiency values for (OS)₁₂/C₆₀ and (OS)₁₄/C₆₀ (7.7% and 8% respectively) indicated that (OS)₁₄/C₆₀ complex is more suitable candidate than the (OS)_{n=12}/C₆₀ for modeling the active layer in the BHJ solar cells.

Acknowledgment

The authors should thank Shahid Chamran University for their supports in this scientific research.

References

- [1] Y. Wang, W. Wei, X. Liu, Y. Gu, *Sol. Energy Mater. Sol. Cells*, 98 (2012) 129–145.
- [2] Y. Li, T. Pullerits, M. Zhao, M. Sun, *J. Phys. Chem. C* 115 (2011) 21865–21873.
- [3] E. Bundgaard, F.C. Krebs, *Sol. Energy Mater. Sol. Cells* 91 (2007) 954–985.
- [4] S. Xiao, A.C. Stuart, S. Liu, W. You, *Appl. Mater. Interfaces* 1 (2009) 1613–1621.

[5] S. Gunes, D. Baran, G. Gunbas, A. Durmus, A. Fuchsbaue, N.S. Sariciftci, L. Toppare, *Polym. Chem.* 1 (2010) 1245–1251.

[6] T.A. Skotheim, R.L. Elsenbaumer, J.R. Reynolds, *Handbook of Conducting Polymers*, ed., Marcel Dekker, Inc, New York, 1998.

[7] C.N. Hoth, P. Schilinsky, S.A. Choulis, C.J. Brabec, *Nano Lett.* 8 (2008) 2806–2813.

[8] S. Tang, J. Zhang, *J. Phys. Chem. A* 115 (2011) 5184–5191.

[9] C.J. Brabec, V. Dyakonov, J. Parisi, N.S. Sariciftci, *Organic Photovoltaics: Concepts and Realizations*, Springer-Verlag Berlin Heidelberg, New York (2003).

Tuning the Electronic Properties of C₅₉M Hetro-Fullerenes; Computational Approach

ZabiollahMahdavifar*, Zahra Nomresaz, Ehsan Shakerzadeh

Department of Chemistry, Faculty of Science, Shahid Chamran University of Ahvaz, Ahvaz, Iran

*z_mahdavifar@scu.ac.ir

Abstract: In this study the structural and electronic properties of C₅₉M [M = B, Al, Ga, Si, Ge, N, P, As] heterofullerenes and C₆₀ fullerene using density functional theory calculations (MPW1PW91/6-31g (d)) were investigated. The results of the geometrical structures, relative stabilities, and electronic properties hetro-fullerenes were discussed to achieve a further understanding of structure- property relationship of the hetro-cages. Based on our calculations, the heterofullerenes with smaller heteroatom have more thermodynamic stability and on the other hand, the heterofullerenes with heavier heteroatoms have less reactivity. The most stable structures based on calculated binding energy are related to the C₅₉N and C₅₉B structures. Furthermore, the C₅₉Ga fullerenes have the most reactivity based on the calculated HOMO–LUMO energy gap.

Keywords: Hetro-fullerene, Electronic properties, DFT

Introduction

Existence of heterofullerenes that make from substitution of one or more of carbon atoms with other elements was reported first time in 1991 by Smalley group [1]. Since then researchers have done much effort to production and separation of heterofullerenes. In 1995, Hirsch et al achieved to method for synthesis [2] and Hamelin achieved to a method for purification Azafullerene C₅₉N [3]. In the same year Mohr was succeed to synthesize C₅₉B and C₆₉B [4,5]. Also C₅₉P and C₆₉P, heterofullerenes of transition metals C₅₉X [X = Pt, Fe, Co, Ni, Rh, Ir, ...] and clusters of silicon identified and synthesized by researchers in 1998.

In this paper, the impact of the heteroatom substitutionary of (B, Al, Ga, Si, Ge, N, P, As) instead one carbon atoms in fullerene cage is investigated. Electronic and structural properties of all hetro-fullerenes with C₁ symmetry are namely thermodynamic and kinetic stability, natural bond orbitals (NBO) analysis using MPW1PW91/6-31g (d) level of theory are considered.

Computational Method

DFT hybrid functional with MPW1PW91/6-31G(d) level of theory was used to consider geometry optimization and the electronic properties of C₅₉M hetro-fullerenes with the aim of Gaussian09 program. According to the dipole moment (~ 0.0) and no contradistinction between carbons atom of C₆₀ fullerene, therefore a carbon atom was chosen for substitution. The neighboring carbon atoms in the periodic table such as B, Al, Ga from group III and N, P, As from the group V and Si, Ge periodic table were chosen as heteroatoms to succeed instead of carbon atom in fullerene cage.

Results and Discussion

Fully geometry optimized of C₆₀ and C₅₉M fullerenes were carried using MPW1PW91/6-31G(d) level of theory (as shown in Fig. 1).

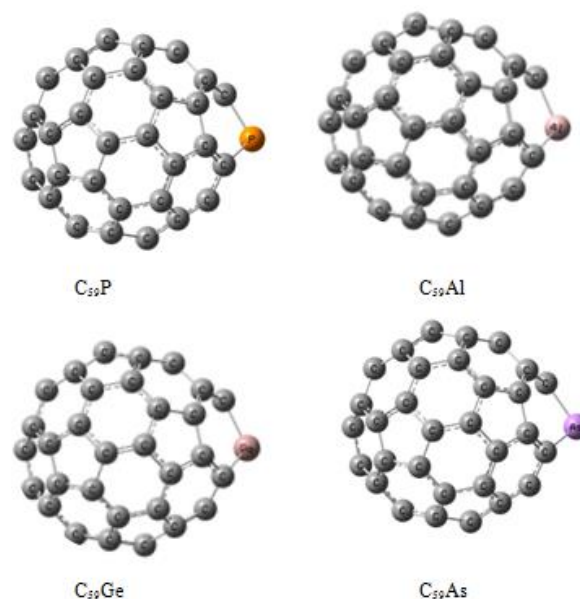


Fig. 1: Optimized structures of C₅₉M [M= P, Al, Ga, As]

The stability of new formed fullerenes is fundamentally determined by the binding energy per atom (E_b), so the binding energy per atom for these clusters is calculated as below:

$$E_b = \frac{1}{60} [E_{C_{59}M} - (59E_C + E_M)]$$

It is known that both the thermodynamic stability and kinetic stability have crucial influence on the relative abundances of different fullerene structures. It has been pointed out that higher kinetic stability is usually related with a larger HOMO-LUMO energy gap

because exciting electrons from low HOMO to a high LUMO is energetically unfavorable, which would be necessary to activate or action.

Obtained data show that the stability of studied hetero-fullerenes was decreased in compared with pristine C₆₀ fullerene (Fig. 2). Based on this Figure, C₅₉N with -9.236 eV/atom and C₅₉Ga with -9.116 eV/atom have the highest and the lowest thermodynamic stability between the studied heterofullerenes.

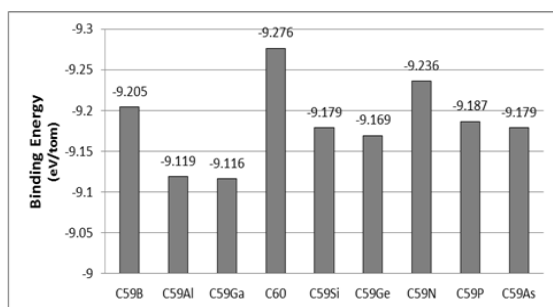


Fig. 2: Calculated binding energy of C₅₉M fullerenes.

The calculated HOMO–LUMO energy gap of all hetero-fullerenes are plotted in Fig. 3.

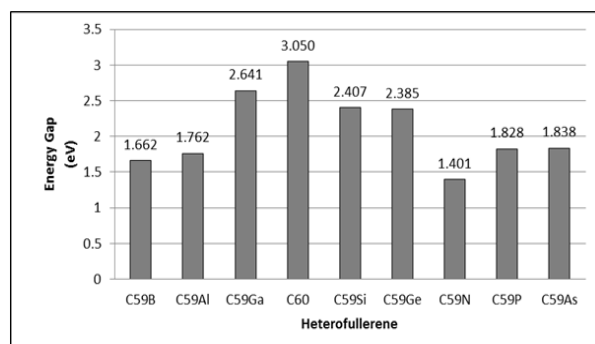


Fig. 3: Calculated HOMO-LUMO energy gap of C₅₉M fullerenes.

As can be seen in Fig.3, the HOMO-LUMO energy gap of C₅₉M fullerenes are in the range of 1.401–2.641 eV. The largest HOMO–LUMO energy gap is related to the C₅₉Ga hetero-fullerene 2.641 eV while the lowest energy gap is belonging to C₅₉N hetero-fullerene. This means that C₅₉N has the lowest kinetic stability among the studied structures. In conclusion, from kinetic and thermodynamic points of view, C₅₉N, it was theoretically determined that this cluster must be extremely chemical reactivity. In continue atomic charge using natural bond orbital analysis and Hirshfeld method for entitled structures were calculated. Results show the positive charge on hetero-atom and also the charge transfer take place

from hetero-atoms to carbon atoms (Fig. 4). It should be noted that the C₅₉N fullerene because of the high electronegativity of nitrogen atom than carbon atom, the partial charge on N is negative which means the charge transfer from carbon atoms to the nitrogen is occurred.

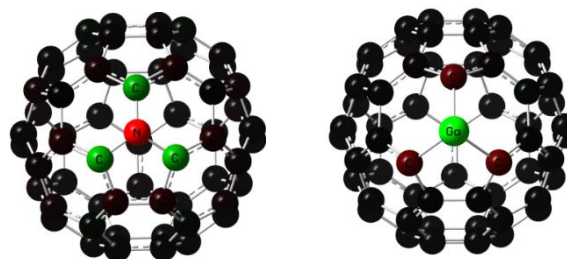


Fig. 4: Calculated partial charge distribution of (a) C₅₉Ga and (b) C₅₉N

Conclusions

Theoretical studies of the C₅₉X (X= B, N, Al, Si, P, Ga, Ge, and As) have been performed systemically based on the DFT calculations. The results of the geometrical structures, relative stabilities, and electronic properties hetero-fullerenes were discussed to achieve a further understanding of structure-property relationship of the hetero-cages. It is found that the hybrid cages undergo some distortions due to the substitution of the heteroatoms. According to the calculated binding energies, the C₅₉M cage with smaller heteroatom is more stable. HOMOs of the hetero-fullerenes are all increased, but the HOMO-LUMO gaps are decreased compared with those of the C₆₀. As for binding energy, the cages doped with III Group elements are obviously larger than other cages.

Acknowledgment

The authors should thank Shahid Chamran University for their supports in this scientific research.

References

- [1] T. Cuo, C. Jin, and R. E. Smalley, Doping Bucky: Formation and Properties of Boron-Doped Buckminsterfullerene, *J. Phys. Chem.*, 95 (1991) 4948-4950.
- [2] C. Lee, S. S. Park, W. R. Lee, K. H. Lee, Structure and Energetics of (C₆₀)₂₂⁺, Conformers: Quantum Chemical Studies, *Bull. Korean Chem. Soc.* 31 (2010) 457-.
- [3] U. Reuther, A. Hirsch, Synthesis, properties and chemistry of aza [60] fullerene *Carbon*, 38 (2000)1539–1549.

Theoretical Study of the effects of some electron donating groups on intramolecular hydrogen bonding in a phosphorus ylide of pyrrole

A. Azadi*, M. Shahraki, S.M. Habibi-Khorassani

Department of Chemistry, University of Sistan and Baluchestan, Zahedan, Iran

*ghj.afsaneh@yahoo.com

Abstract: In this paper, intramolecular hydrogen bond strength (IHB) in a phosphorus ylide of the pyrrole, in the presence of electron-donating substituents of the pyrrole ring, is examined theoretically. Analysis of the data obtained in this paper show that with increasing electron donating obvious strength of substitution, intramolecular hydrogen bond strength (N-H ...O) is reduced.

Keywords: Ylide, Intramolecular hydrogen bonding; AIM; NBO; Electron-donating group

Introduction

Phosphorus ylides are active systems that as reactant can be used in the synthesis of organic compounds in multiple reactions. Triphenyl phosphine with active acetylenic esters in the presence of pyrrole in a solution of water and acetone produces stable ylides. Product of this reaction constitute of a single isomer, due to intramolecular hydrogen bond is forming [1]. In this paper, the effects of electron-donating groups are examined on the intramolecular hydrogen bond strength (substituted in α and β positions of the pyrrole ring). The list groups, electron-donating substituents as either below:

O⁻- NR₂- NH₂- OH- OR- NHCOR- OCOR- R- Ph- CHCR₂

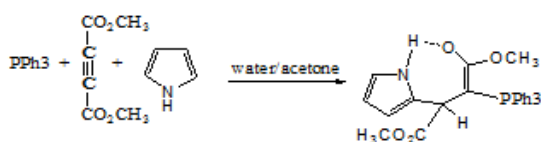


Fig. 1 The reaction between triphenylphosphine, dimethyl acetylenedicarboxylate, and pyrrole for generation of stable phosphorus ylide in a solution of water and acetone

Computational Methods

The geometry of the molecules has been fully optimized with the DFT method and B3LYP level of theory [2, 3], and the 6-31++G (d, p) basis set [4], using the ultrafine grid option and the Berny algorithm with the default parameters of the Gaussian-03, package [5]. The atomic charges schemes were

employed and compared in this study include the AIM, NBO, Mulliken, and CHELPG methods [6,7]. The atoms in molecules (AIM) theory of Bader was also applied here to study the properties of the bond critical point and to analyses dependencies between topological, energetic and geometrical parameters of the IHB [8,9].

Results and Discussion

Bond length (N-H) and angle (N-H ... O) and the distances (N-O) and (O ... H) including parameters are that used for comparing the strength of hydrogen bonds. Whatever the combined strength of hydrogen bond increases, intervals (N ... O) and (O ... H) shorter but the length of bond (N-H) and angle (N-H ... O) will be more reduced. By analyzing and comparing, these parameters in the Figs 2 and 3 can be concluded that decreased the intramolecular hydrogen bond strength is decreased.

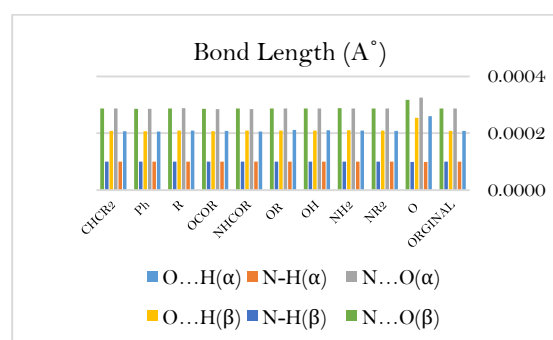


Fig 2. Bond lengths calculated at the B3LYP/6-31++g (d, p) level of theory

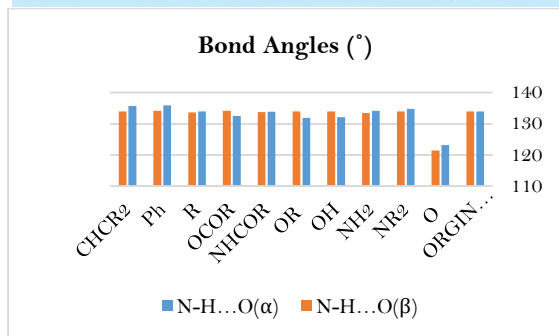


Fig 3. Bond angles calculated at the B3LYP/6-31 + g (d, p) level of theory

Comparison of charge distribution in hydrogen atoms

Partial atomic charges serve a different, but even more important, purpose in the qualitative rationalization of organic and inorganic reactivity [6]. In part following analysis of charge atoms H, O and N are engaged in intramolecular hydrogen distributions. Of the AIM, NBO, CHELPG, Milliken; for at bonds compared. The results of the analysis of NBO and AIM in the Table 1.

Table 1. Partial charges (q in units of e) of the hydrogen atom

H ₆	qAIM(α)	qNBO(α)	qAIM(β)	qNBO(β)
ORIGINAL	0.4817	0.4588	0.4817	0.4588
O ⁻	0.4288	0.4311	0.4168	0.4256
NR ₂	0.4817	0.4575	0.4869	0.4592
NH ₂	0.4829	0.4581	0.4821	0.4573
OH	0.4922	0.4637	0.4852	0.4590
OR	0.4926	0.4630	0.4875	0.4592
NHCOR	0.4931	0.4640	0.4862	0.4607
OCOR	0.4964	0.4650	0.4889	0.4519
R	0.4779	0.4555	0.4821	0.4576
Ph	0.4832	0.4586	0.4865	0.4607
CHCR ₂	0.4834	0.4584	0.4834	0.4592

calculated in level of B3LYP/6-31 + g (d, p) level of theory

AIM analysis

Charge density and Laplacian values at the critical point provides valuable information on the hydrogen bond strength. If the charge density is in the range of between 0.002 to 0.035 e/au³ and Laplacian of the charge density in the range 0.024 to 0.139 e/au³, represents hydrogen bonds [10]. Data contained in the Table 2, the charge density and Laplacian intramolecular hydrogen bond shows that the existence of substitution on the ring pyrrole desired compound, in many cases caused a

decrease is the charge density and density Laplacian critical point that of the it can be concluded, intramolecular hydrogen bond strength is decreased.

Table 2. Geometrical (in °A) and electron density (ρ (BCP), e/au³), Laplacian ($\nabla^2\rho$ (BCP), e/au⁵), and energy density (H_{BCP} , hartrees/au³) calculated at the bond critical points of the

	$\rho(\alpha)$	$\nabla^2\rho(\alpha)$	$H(\alpha)$	$\rho(\beta)$	$\nabla^2\rho(\beta)$	$H(\beta)$
ORIGINAL	0.02025	0.06364	-0.00002	0.02025	0.06364	-0.00002
O ⁻	0.00726	0.02788	0.00100	0.00836	0.03192	0.00100
NR ₂	0.02033	0.06344	-0.00007	0.02013	0.06328	-0.00001
NH ₂	0.02002	0.06276	-0.00003	0.01963	0.06192	0.00000
OH	0.01955	0.06216	0.00008	0.02013	0.06320	-0.00003
OR	0.01924	0.06136	0.00011	0.02018	0.06332	-0.00003
NHCOR	0.02130	0.06664	-0.00006	0.01990	0.06264	0.00000
OCOR	0.02039	0.06436	0.00002	0.02097	0.06568	-0.00006
R	0.02000	0.06284	-0.00001	0.01986	0.06260	0.00001
Ph	0.02136	0.06604	-0.00015	0.02075	0.06496	-0.00005
CHCR ₂	0.02081	0.06476	-0.00010	0.02035	0.06388	-0.00003

Z-isomer at the B3LYP/6-31 + g (d, p) level of theory

NBO analysis

Natural bond orbital (NBO) theory is useful method for study intramolecular hydrogen bond (IHB). The results of NBO analyzing, can be achieved information about charge transfer between different orbitals, occupation numbers, and the charge on the atoms in the molecular structure. From the two criteria charge, transfer and occupation numbers is used direction of check the strength of intramolecular hydrogen bonds in here. In Tables 3 and 4 values of the occupation numbers for anti-bonding orbitals, as well as unshared pair of electrons of oxygen) numbers (51) (substituted in the position α) numbers 50 (substituted in position β) and orbital energy related to its, are reported.

Table 3. Occupation numbers (electrons) and corresponding orbital energies (e in unit au) bonds of the acceptor and the lone pairs of the donor atom (NO), and their second order perturbation stabilization energies $E_T^{(2)}$ (kcal/mol)



Table 4

	$O.N_T(LP$ $O_{51})(\beta)$	$E_T^{(2)}$ (β)	$\epsilon(\sigma^* N5-$ $H6)(\beta)$	$O.N_T(\sigma^*$ $N5-H6)(\beta)$
ORIGINAL	3.8131	4.36	0.5212	0.0269
O ⁻	5.3771	0.56	0.6475	0.0252
NR ₂	3.8129	4.31	0.5217	0.0267
NH ₂	3.8128	4.03	0.5259	0.0261
OH	3.8129	4.29	0.5182	0.0269
OR	3.8129	4.31	0.5204	0.0270
NHCOR	3.8126	4.12	0.5187	0.0263
OCOR	3.8130	4.84	0.5162	0.0276
R	3.8129	4.16	0.5243	0.0264
Ph	3.8132	4.61	0.5153	0.0275
CHCR ₂	3.8131	4.38	0.5209	0.0271

Conclusion

Theoretical calculations in this paper was performed on the stable phosphorus ylide of the pyrrole and some electron-donating groups as the substituent is on the pyrrole ring. A succession of different substitution on the ring, have the different effects on the resonance and intramolecular hydrogen bond strength, that all these factors can be reduced or increased hydrogen bond strength. According to the results, and in some cases a few factors contradicted in a substituent specific sum of all these data, we can conclude that the existence of substituted electron donor on the ring pyrrole compound decreases the intramolecular hydrogen bond strength (N₅-H₆...O₅₁).

References

- [1]. Hazeri N, Habibi-Khorassani SM, Maghsoodlou MT, Marandi G, Nassiri M, Shahzadeh AG (2006) J Chem Res 4:215
- [2]. Becke AD (1993) J Chem Phys 98:5648
- [3]. Lee CT, Yang WT, Parr RG (1988) Phys Rev B 37:785
- [4]. Hari Haran PC, Pople JA (1973) Theor Chim Acta 28:213
- [5]. Frisch MJ, Trucks GW, Schlegel HB, Scuseria GE, Robb MA, Cheese man JR, Montgomery JJA, Vreven T, Kudin KN, Burant

	$O.N_T(LP$ $O_{51})(\alpha)$	$E_T^{(2)}$ (α)	$\epsilon(\sigma^* N5-$ $H6)(\alpha)$	$O.N_T(\sigma^*$ $N5-H6)(\alpha)$
ORIGINAL	3.8131	4.36	0.5212	0.0269
O ⁻	3.8054	-	0.6568	0.0196
NR ₂	3.8126	4.52	0.5141	0.0292
NH ₂	3.8128	4.28	0.5153	0.0282
OH	3.8123	4.17	0.5113	0.0268
OR	3.8125	4.02	0.5114	0.0269
NHCOR	3.8130	5.02	0.4984	0.0295
OCOR	3.8131	4.64	0.5017	0.0281
R	3.8128	4.41	0.5167	0.0280
Ph	3.8124	5.15	0.5124	0.0308
CHCR ₂	3.8122	5.09	0.5217	0.0301

JC, Millam JM, Iyengar SS, Tomasi J, Barone V, Mennucci B, Cossi M, Scalmani G, Rega N, Petersson GA, Nakatsuji H, Hada M, Ehara M, Toyota K, Fukuda R, Hasegawa J, Ishida M, Nakajima T, Honda Y, Kitao O, Nakai H, Klene M, Li X, Knox JE, Hratchian HP, Cross JB, Bakken V, Adamo C, Jaramillo J, Gomperts R, Stratmann RE, Yazyev O, Austin AJ, Cammi R, Pomelli C, Ochterski JW, Ayala PY, Morokuma K, Voth GA, Salvador P, Dannenberg JJ, Zakrzewski VG, Dapprich S, Daniels AD, Strain MC, Farkas O, Malick DK, Rabuck AD, Raghavachari K, Foresman JB, Ortiz JV, Cui Q, Baboul AG, Clifford S, Cioslowski J, Stefanov BB, Liu G, Liashenko A, Piskorz P, Komaromi I, Martin RL, Fox DJ, Keith T, Al-Laham MA, Peng CY, Nanayakkara A, Challacombe M, Gill PMW, Johnson B, Chen W, Wong MW, Gonzalez C, Pople JA (2003) Gaussian-03. Gaussian, Inc., Wallingford CT

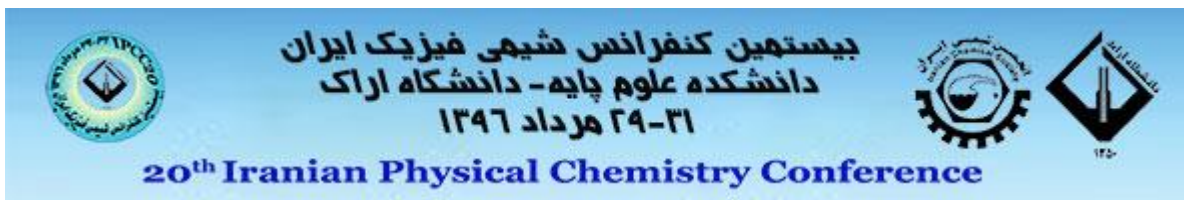
[6]. Cramer CJ (2002) Essentials of computational chemistry. Wiley, New York

[7]. Martin F, Zipse H (2005) J Comput Chem 26:97-105

[8]. Dakkouri M, Typke V (2007) Struct Chem 18:357-372

[9]. Szatyłowicz H, Krygowski TM, Jezierska-Mazzarello A (2011) J Mol Model 17:125-131.

[10]. Grabowski, S.J. J. Mol. Struct. (2001) 562, 137-143.



Molecular Dynamic Simulation of 5-Fluorouracil Drug Adsorption in Zeolite Imidazolate Framework ZIF-8

Maryam Gomar*, Saeid Yeganegi

Department of Physical Chemistry, Faculty of Chemistry, University of Mazandaran, Babolsar, Iran

*maryam_gomar63@yahoo.com

Abstract : Zeolitic imidazolate frameworks (ZIFs) are a class of metal-organic frameworks. Research on biomedical applications of ZIFs has recently started, and ZIFs have been identified as promising materials for drug storage. In this study, Molecular dynamic simulations were performed to study the adsorption of anti-cancer drug namely 5-Fluorouracil (5-FU). Our results showed that the studied ZIF have high capacities (0.65-0.68 g/g) for the adsorption of 5-FU drug. The analysis of radial distribution function (RDF) showed that hydrogen bonding played an important role for adsorption of drug. results showed that studied ZIFs compared to conventional metal organic frameworks(MOFs), had higher capacity for the adsorption of studied drug, showing they can be used as more efficient carriers.

Keywords: Molecular dynamic Simulation, Zeolite Imidazolate Framework, RDF

Introduction

Metal organic frameworks (MOFs) as drug-delivery nanocarriers are highly desirable due to their large loading of drugs, biodegradability and versatile functionality [1]. Mesoporous MOFs with well-defined pores provide a wealth of opportunities for drug delivery. Currently, the microscopic understanding of drug-MOF interaction remains elusive and molecular-level study is crucial for the development of MOFs as novel drug devices with ideal loading and specific delivery. Horcajada et al. performed QM calculation to examine the interaction of ibuprofen (IBU) with MIL-53(Fe) [2]. A strong binding energy of 57 kJ mol⁻¹ was found, which is in the same magnitude for IBU interacting with zeolites. They observed the formation of a strong hydrogen bond between the carboxylic oxygen of IBU and the hydroxyl group of MIL-53(Fe). Babarao and Jiang reported a computational study on the energetics and dynamics of IBU in two host carriers, MIL-101 and UMCM-1.68 [3]. The predicted maximum loading of IBU in MIL-101 is 1.11 g IBU g⁻¹ MIL-101, which agrees fairly well with experimentally determined loading of 1.37 g/g.

Liédana et al. studied adsorption of caffeine in ZIF-8 and reported a lower uptake capacity (28 wt%) compared to Cunha et al. [23] for MIL-100(Fe) (49.5 wt%). However, caffeine uptake reported for ZIF-8 was still higher than that of mesoporous silica, SBA-15 (23 wt%) and non-ordered silicas (20.4 wt%) [4]. Here, we studied adsorption, molecular interactions, diffusion behavior of anti-cancer drug in ZIF namely ZIF-8 using molecular dynamics (MD) simulation at

298 K. Molecular dynamics simulations can be used as a valuable tool to understand the adsorption and release of drugs inside the porous structure at the molecular level.

We used MD simulations to study the interactions between guest molecules and ZIF. For this purpose, radial distribution functions (RDFs) were analyzed to examine the most favorable interaction sites between drug and ZIF.

Computational Details

MD simulations were performed using NVT ensemble with a time step of 1 fs up to a total of 4 ns simulation time at 298 K. We considered 1×10⁶ and 3×10⁶ steps for equilibrium and production phases, respectively. The temperature was held constant with a Nose-Hoover chain (NHC) thermostat. Van der Waals interactions were treated using the Lennard-Jones (LJ) potential function where atomic parameters for ZIF were taken from the Universal force field. The Lennard-Jones interactions were cut at the 12.5 Å. The electrostatic interactions were calculated using the Ewald summation method. Periodic boundary conditions were applied in all three dimensions. Crystal structures of ZIFs were taken from Crystallography Open Database. The ZIF structure were assumed to be rigid which has a negligible effect on the adsorption of molecule.

Results and Discussion

3.1. Validation of the Force Field

To validate the employed force field simulated adsorption capacity of 5-FU in ZIF-8 at 298 K was compared to the experimental values reported in the

literature. Figure 1 shows the relative concentration of drug as simulation box length before and after simulation. Area under the curve can show the number of adsorbed drug molecules. The adsorption value for 5-FU in ZIF-8 was calculated to be 674.58 mg/g which agrees well with the experimental value (0.66 g/g or 66 wt%) reported by Sun et al [5]. Therefore, this force field based on the LJ potential model will be utilized for further study in this work.

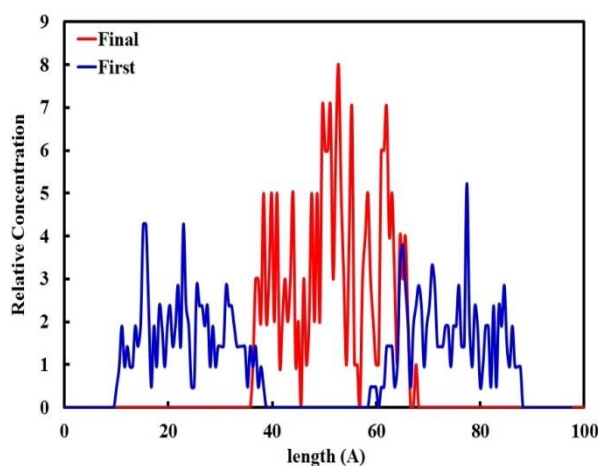


Fig.1: The relative concentration of drug as simulation box length before and after simulation.

3.2. Adsorption of drugs

Table 1 shows the adsorption capacity of drug in ZIF. It is evident that the adsorption capacity of ZIF-8 was more than that of other MOFs.

ZIF structure	adsorption capacity(mg drug/g ZIF)
ZIF-8	5-FU 674.58

Table.1: Adsorption capacity of drug in ZIF.

We also calculated radial distribution functions (RDF) that show the probability of finding an atom at a spherical shell of certain thickness at a distance (r) from the reference atom which is generally located at the origin [6]. In order to examine the distribution of drug molecule inside the ZIF framework in detail, radial distribution functions (RDFs) were calculated by:

$$g_{\alpha\beta}(r) = \frac{N}{\rho N_{\alpha} N_{\beta}} \sum_{i=1}^{N_{\alpha}} \sum_{k=1}^{N_{\beta}} \langle \delta(r - |r_k - r_i|) \rangle \quad (1)$$

Where N is the total number of atoms, ρ is density, r is distance, N_{α} and N_{β} are the number of α and β atoms, respectively.

Fig.2 shows the calculated RDF for the studied drug in ZIF-8. The sharpness of Zn-Od and Zn-Nd peaks were noticeably indicating metal sites in ZIF-8 are generally the primary adsorption sites for guest drug.

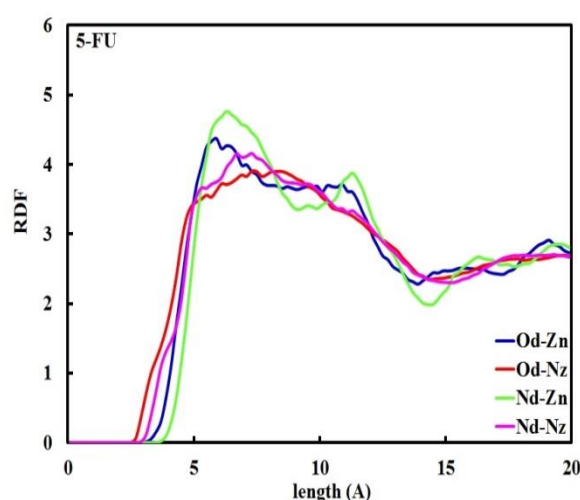


Fig.2: The RDF diagram for the studied drug in ZIF-8.

Conclusion

The analysis of RDF showed that metal sites in ZIF are the primary adsorption sites for drug. The results showed the adsorption of MP drug was the maximum. The result showed ZIF-8 were good system for adsorption and of 5-FU drug.

Acknowledgments

Financial support from the University of Mazandaran is highly appreciated.

References

- [1] An, J., S.J. Geib, and N.L. Rosi, "Cation-triggered drug release from a porous zinc-adeninate metal-organic framework. *Journal of the American Chemical Society*", 131 (2009) 8376-8377.
- [2] Horcajada, P., et al., "Flexible Porous Metal-Organic Frameworks for a Controlled Drug Delivery. *Journal of the American Chemical Society*", 130 (2008) 6774-6780.
- [3] Babarao, R. and J. Jiang, "Unraveling the energetics and dynamics of ibuprofen in mesoporous metal-organic frameworks". *The Journal of Physical Chemistry C*, 2009. 113 (2009) 18287-18291.

Release of Mercaptopurine Drug in Zeolite Imidazolate Framework ZIF-8 by Molecular Dynamic Simulations

Maryam Gomar*, Saeid Yeganegi

Department of Physical Chemistry, Faculty of Chemistry, University of Mazandaran, Babolsar, Iran

*maryam_gomar63@yahoo.com

Abstract : Research on biomedical applications of zeolite imidazolate frameworks (ZIFs) has recently started, and several ZIFs have been identified as promising materials for drug storage. In this study, we used molecular simulations to investigate release of an anti-cancer drug, Mercaptopurine (MP) in biocompatible ZIF. results showed that the rate of drug release for MP was the lowest rate in ZIF-8. The analysis of radial distribution function (RDF) showed that hydrogen bonding played an important role for release of drug. . Our results showed that the computational approach is a powerful strategy for the efficient identification of bioactive compounds in novel porous materials.

Keywords: Drug Delivery, Molecular dynamic Simulation, RDF, Zeolite Imidazolate Framework

Introduction

Metal organic frameworks (MOFs) are a new group of nanoporous materials with exceptional physical properties, such as large surface areas, high pore volumes, low densities and well-defined pores [1]. MOFs are obtained by the self-assembly of metal clusters and organic linkers, resulting in tailored nanoporous host materials with pore sizes up to 6 nm. One of the most important advantages of MOFs over traditional nonporous materials is the tenability of chemical and structural properties during synthesis. Thousands of MOFs have been reported to date,³ and theoretically unlimited number of materials can be generated. The tailorability of pore sizes and chemical functionalities makes MOFs promising candidates in various applications such as gas storage and separation,⁶ catalysis⁷ and chemical sensing. MOFs are also promising carriers for biomedical applications such as drug storage, drug delivery and imaging. Lipids, polymeric nanoparticles, metal clusters and carbon structures have been tested as drug storage materials. However, these materials have several limitations such as low drug loading capacities (<5 wt%), rapid drug release and toxicity. MOFs have been recently studied as alternative drug storage materials due to the possibility of tuning the host-guest interaction, not only by varying their pore size but also by functionalizing the building blocks with chemical groups, providing the possibility of controlling the kinetic release of a therapeutic agent. MOFs offer extremely high drug capacity (for example, up to 1.4 g of ibuprofen per gram of porous solid: four times higher than the adsorption achieved with mesoporous silica materials) and very long release times (e.g. up to 21 days) of several therapeutic agents.

Zeolite imidazolate frameworks (ZIFs), being considered as a new subclass of MOFs, are constructed with tetrahedral units formed by one bivalent metal M^{2+} cations (usually Zn^{2+}) and four

imidazolate anions (Im^-), analogous to SiO_2 tetrahedra in zeolites [2], have characteristics of both conventional MOFs (e.g. easily tuneable pores and cavities) and zeolites (e.g. high aqueous stability) which provide them excellent platforms for drug delivery[3].

Here, we studied release of anti-cancer drug in ZIF-8 using molecular dynamics (MD) simulation at 298 K. Molecular dynamics simulations can be used as a valuable tool to understand the release of drugs inside the porous structure at the molecular level. .

To the best of our knowledge, no simulation study has been reported in the literature for drug diffusion in ZIFs. We used MD simulations to study the interactions between guest molecules and ZIF. For this purpose, radial distribution functions (RDF) were analyzed to examine the most favorable interaction sites between drug and ZIF.

Computational Details

MD simulations were performed using NVT ensemble with a time step of 1 fs up to a total of 4 ns simulation time at 298 K. We considered 1×10^6 and 3×10^6 steps for equilibrium and production phases, respectively. The temperature was held constant with a Nose-Hoover chain (NHC) thermostat. Van der Waals interactions were treated using the Lennard-Jones (LJ) potential function where atomic parameters for ZIFs were taken from the Universal force field. The Lennard-Jones interactions were cut at the 12.5 Å. The electrostatic interactions were calculated using the Ewald summation method. Periodic boundary conditions were applied in all three dimensions. Crystal structures of ZIF were taken from Crystallography Open Database. The ZIFs structures were assumed to be rigid which has a negligible effect on the adsorption of molecules. The release of drug also studied using MD simulations with NVT ensemble and a time step of 1 fs up to a total of 2 ns at 298 K.



Results and Discussion

3.1. Radial Distribution Functions (RDF) of drug

We calculated radial distribution functions (RDF) that show the probability of finding an atom at a spherical shell of certain thickness at a distance (r) from the reference atom which is generally located at the origin. In order to examine the distribution of drug molecules inside the ZIF framework in detail, radial distribution functions (RDF) were calculated by [4]:

$$g_{\alpha\beta}(r) = \frac{N}{\rho N_{\alpha} N_{\beta}} \sum_{i=1}^{N_{\alpha}} \sum_{k=1}^{N_{\beta}} \langle \delta(r - |r_k - r_i|) \rangle$$

(1)

Where N is the total number of atoms, ρ is density, r is distance, N_{α} and N_{β} are the number of α and β atoms, respectively.

Fig.3 shows the calculated RDF for the studied drug in ZIF-8. The RDF diagram for MP showed that Sd-Zn peak is the most pronounced one, indicating more tendency of Sd atom of MP for interacting with Zn in ZIF-8.

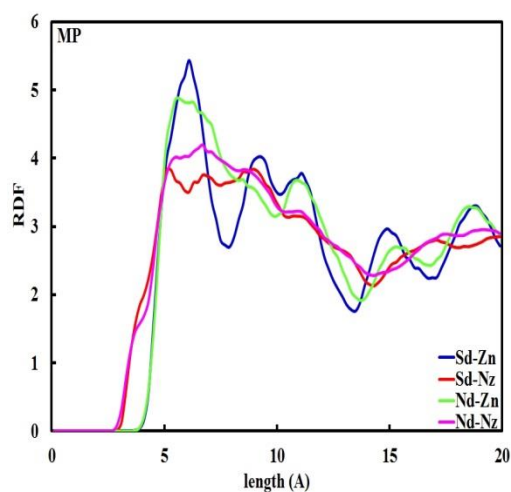
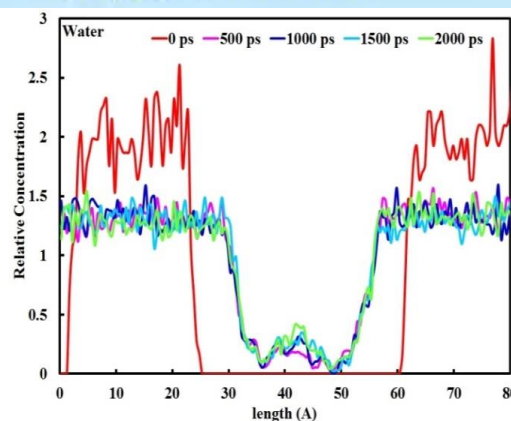


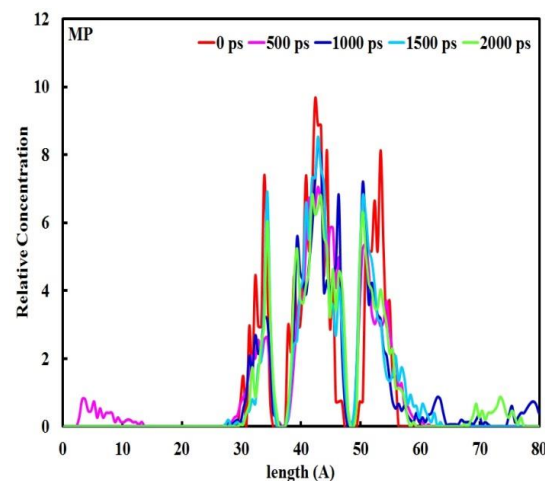
Fig.1: The RDF diagram for the studied drug in ZIF-8.

3.2. Release of drug

The release of drug from ZIF are also studied in aqueous medium. The relative concentration of water and MP molecules in ZIF-8 at different times of simulation is also shown in Fig 2. As can be seen, diffusing of water molecules toward the ZIF-8. The sharpness of peaks at the center of box for MP molecules didn't change a lot showing MP molecules diffused to aquatic medium very slowly.



(a)



(b)

Fig.2: Relative concentration of (a) water and (b) MP molecules as function of box length for ZIF-8 at different times of simulation.

Conclusion

The results showed the release of MP drug was the least. The results showed ZIF-8 were good system for and release of MP drug.

Acknowledgments

Financial support from the University of Mazandaran is highly appreciated.

References

- [1] M. Eddaoudi, H. Li, and O. Yaghi, "Highly porous and stable metal-organic frameworks: structure design and sorption properties", *Journal of the American Chemical Society*, 122 (2000), 1391-1397.
- [2] Tian, Y.Q., et al., "The Silica-Like Extended Polymorphism of Cobalt (II) Imidazolate Three-Dimensional Frameworks: X-ray Single-Crystal Structures and Magnetic Properties". *Chemistry-A European Journal*, 9 (2003) 5673-5685.

A theoretical study on the [Al(DFX)₂]³⁻, [Fe(DFX)₂]³⁻ and [Ga(DFX)₂]³⁻ complexes

S. Kaviani, M. Izadyar*

Department of Chemistry, Faculty of Sciences, Ferdowsi University of Mashhad, Mashhad, Iran

[*izadyar@um.ac.ir](mailto:izadyar@um.ac.ir)

Abstract

In this work, density functional theory (DFT) study on the electronic structures and binding energies of deferasirox coordinated to Al³⁺, Fe³⁺ and Ga³⁺ metal ions was carried out, using the CAM-B3LYP/6-31G(d) level of the theory in the water. The results indicate that deferasirox has the most stable complex with Fe³⁺ metal ion, because of maximum interaction of Fe³⁺ metal ion with oxygen and nitrogen atoms of the deferasirox. Because of the importance of the charge transfer in the complex formation, donor-acceptor interaction energies were evaluated. Finally, the probable correlation between the binding energy values and electronic chemical hardness was analyzed.

Keywords: Binding energy, Deferasirox, NBO, Electronic chemical hardness

Introduction

Because humans are enabled to remove iron from the body, a clinically relevant state can occur if toxic levels of iron accumulate. Excess iron deposited in the liver, spleen and myocardium, which this iron accumulation leads to progressive organ dysfunction and finally death [1]. Iron-chelating agents slowly mobilize iron by binding of iron present in a transit pool, which is in equilibrium with the insoluble iron deposits. Then iron chelate is excreted in the urine.

4-[3,5-Bis(2-hydroxyphenyl)-1,2,4-triazol-1-yl] benzoic acid, known as deferasirox (DFX) is a promising drug approved for the oral treatment of iron overload in patients suffering from chronic anemia such as β -thalassemia [2]. DFX is highly selective for Fe³⁺ metal ion, which forms a stable complex in a 2:1 molar ratio at physiological pH [3]. Furthermore, DFX increases aluminium and other toxic metal absorption such as gallium [4]. Despite the fact that theoretical investigations have been performed for metal ion uptake by biomolecules, but a few theoretical studies have been performed on the metal-DFX complexes [5].

Computational methods

The geometry of the complexes have been optimized at the CAM-B3LYP level [6] using the 6-31G(d) basis set. Solvent effects were taken into account by the conductor like polarizable continuum model (CPCM) [7]. In order to estimation of the main

donor-acceptor interactions, natural bond orbital (NBO) analysis was performed on the optimized structures. Finally, molecular orbital analysis was also done to evaluate the difference between the HOMO and LUMO energies and electronic chemical hardness, at the same level of theory.

Results and Discussion

After optimizing the complex and ligand, separately (Figure 1), metal-ligand binding energy (E_b) have been computed according to Eq. 1.

$$E_b = \frac{-(E_{\text{complex}} - E_{\text{metal}} - 2E_{\text{ligand}})}{2} \quad (1)$$

Where E_{complex} , E_{metal} and E_{ligand} are the energies of the complex, corresponding metal ion and ligand components, respectively. Theoretical metal-ligand binding energies have been calculated and the metal-ligand binding energy trend is accordance to: Fe³⁺>Al³⁺>Ga³⁺.

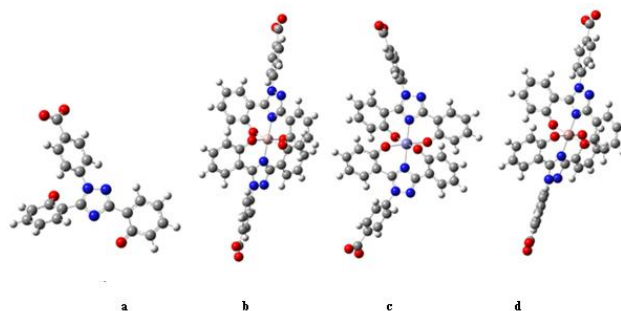


Fig. 1: Optimized structures of a) DFX, b) [Al(DFX)₂]³⁻, c) [Fe(DFX)₂]³⁻ and d) [Ga(DFX)₂]³⁻.



Natural bond orbital (NBO) analysis indicates the charge transfer from the oxygen and nitrogen atoms of the DFX to the metal ions. The important donor-acceptor interaction energies of the complexes are related to the interaction of the lone pair (LP) electrons of the oxygen and nitrogen atoms of the DFX and nonbonding orbital of the metal ion (LP^*_M). According to data, it is confirmed that $[Fe(DFX)_2]^{3-}$ complex is more stable than $[Al(DFX)_2]^{3-}$ and $[Ga(DFX)_2]^{3-}$ complexes.

According to the frontier molecular orbital (FMO) theory, electronic chemical hardness (η) can be defined on the basis of the energy gap between the highest energy occupied molecular orbital (HOMO) and lowest energy unoccupied molecular orbital (LUMO), according to Eq. 2.

$$\eta = \frac{E_{LUMO} - E_{HOMO}}{2} \quad (2)$$

HOMO-LUMO energies and electronic chemical hardness of the metal-DFX complexes in the aqueous solution have been calculated. Based on the data, $[Fe(DFX)_2]^{3-}$ has the maximum chemical hardness among the studied metal-ligand complexes. Moreover, there is a linear correlation between the binding energy and the electronic chemical hardness.

Conclusion

DFT calculations have been employed to investigate the complexation of Al^{3+} , Fe^{3+} and Ga^{3+} metal ions and DFX. From the energy view point, DFX is the best receptor for Fe^{3+} metal ion. NBO analysis indicated charge transfer from oxygen and nitrogen atoms of the DFX to the metal ions. Finally, according to calculations of HOMO-LUMO energy gap, a linear correlation between the binding energy and the electronic chemical hardness was obtained.

References

- [1] Y. Kohgo, K. Ikuta, T. Ohtake, Y. Torimoto, J. Kato, Body iron metabolism and pathophysiology of iron overload, *International journal of hematology*, 88 (2008) 7-15.
- [2] E. Nisbet-Brown, F.N Olivieri, P.J. Giardina, R.W. Grady, E.J. Neufeld, R. Sechaud, A.J. Krebs-Brown, J.R Anderson, D. Alberti, K.C Sizer, *The Lancet*, 361 (2003) 1597-1602.
- [3] H. Nick, P. Acklin, R. Lattmann, P. Buehlmayer, S. Hauffe, J. Schupp, D. Alberti, Development of tridentate iron chelators: from desferrithiocin to ICL670, *Current medicinal chemistry*, 10 (2003) 1065-1076.
- [4] G.J. Kontoghiorghes, *Hemoglobin*, 32 (2008) 608-615.

[5] S. Salehi, A.S. Saljooghi, M. Izadyar, *Computational Biology and Chemistry*, 64 (2016) 99-106.

[6] T. Yanai, D.P. Tew, N.C.A. Handy, *Chemical Physics Letter*, 393 (2004) 51-57.

[7] V. Barone, M. Cossi, *The Journal of Physical Chemistry A*,

Theatrical study of the effects of some electron withdrawing groups on intramolecular hydrogen bonding in a phosphorus ylide of pyrrole

A. Diali*, M. Shahraki, S. M. Habibi-Khorassani

Department of chemistry, University of Sistan and Baluchestan, Zahedan, Iran

*admch65@gmail.com

Abstract The ylide compounds are often hard to assign by experimental techniques, particularly with intramolecular hydrogen bonding (IHB) system. In the present study, theoretical calculations were carried out for the z-isomer (2-substituted pyrrole stable Phosphorus ylide) and similar molecules with ten electron withdrawing groups (EWGs) from weak to strong for positions of the α and β pyrrole rings. Topological parameters at the bond critical point (BCP) of IHB from Bader's atoms in molecules (AIM) theory and Winhold's natural bond orbital (NBO) calculations were analyzed at the B3LYP/6-311++g** level in details. The loss of charge of the hydrogen atom and gain of charge of oxygen and nitrogen atoms in IHB (N-H...O) was concluded by details of AIM and NBO analysis.

Keywords: Electron Withdrawing groups, Phosphorus ylide, Intramolecular Hydrogen bonding, AIM, NBO

Introduction

In the present study IHB in Z-isomer was analysed. The synthesis reaction of triphenylphosphine, dimethyl acetylenedicarboxylate in the presence of pyrrole in a mixture of water-acetone has been previously reported. Experimental data were shown that the main product is in a Z-isomer from [1] (Fig. 1).

The main objective of this study was to investigate whether theoretical results would provide clear evidence for the existence of intramolecular hydrogen bonding to confirm the experimental data and evaluate strength of the IHB (N-H...O) to fix Z-isomer and also evaluation of electron withdrawing groups from weak to strong for position of the α and β pyrrole ring. The list of electron withdrawing groups were as below:

F, COR, CO₂R, CO₂H, CF₃, CN, SO₃H, NO₂, NR₃⁺, NH₃⁺.

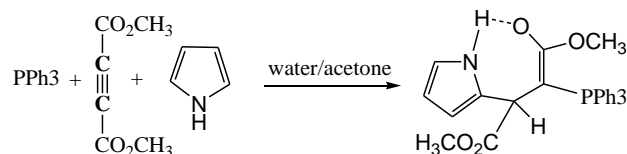


Fig.1 The reaction between triphenylphosphine, dimethyl acetylenedicarboxylate, and pyrrole for generation of stable phosphorus ylide in a mixture of water-acetone

Computational method

The Geometrical of the molecules has been fully optimized with the DFT method and B3LYP/6-31++g** level of theory [2,3], and the 6-31++G (d,p) basis set [4] using the ultrafine grid option and the Berny algorithm with the default parameters of the Gaussian-03, package [7]. The atomic charges

schemes were employed and compared in this study include the AIM, NBO, Mulliken and CHELPG methods [5,6]. That atoms in molecules (AIM) theory of Bader was also applied here to study the properties of the bond critical point and to analyses dependencies between topological, energetic and geometrical parameters of the IHB [8,9]. The AIM calculations were carried out using the AIM2000 package [10]. The natural bonding orbital (NBO) calculations were analyzed at the B3LYP/6-31++g** level in details.

Results and Discussion

Geometrical parameters analysis

Geometrical parameters such as bonding length O...H, N-H, N...O and angle N-H...O were used to compare the strength of hydrogen bonding. The strength of IHB will be increased with the shorter distances of O...H and N...O and greater the angle N-H...O and length N...H. By analysis these parameters can be concluded that the IHB strength are in the below order:

$$\text{NO}_2 < \text{N}^+\text{R}_3 < \text{N}^+\text{H}_3$$

The data is reported in Table .1

AIM analysis

The object of AIM theory was to find the topological and geometrical parameters in the critical points and to analyze them in terms of electronic densities ρ (BCP), their Laplacian $\nabla^2\rho$ (BCP), kinetic energy density (G), potential energy density (V), Hamiltonian of electronic energy density. By increasing the effects of electron Withdrawing, Electron density and Laplacian increase that leads to increase the strength of IHB. The -G/V parameter correlate with properties covalence the more -G/V

parameter, the less properties covalence and the more properties electrostatic of IHB. Therefore, the strong EWGs have the strongest IHB. (Table .1)

NR ₃ ⁺	3.80757	18.14	0.37232	0.05695
NH ₃ ⁺	5.42844	22.37	0.35599	0.05699

Table 1 Geometrical (in° A) and electron density ($\rho(\text{BCP})$, e/au³), Laplacian ($\nabla^2\rho(\text{BCP})$, e/au⁵), calculated at the bond critical points of the Z-isomer at the B3LYP/6-31++g** level

(α)	R(O...H)	r(N-H)	$\rho(\text{N-H}\dots\text{O})$	$\nabla^2\rho$
Original	2.0859	0.9964	0.02025	0.06360
F	2.0641	0.9981	0.02109	0.06640
COR	2.0348	0.9976	0.02250	0.06944
CO ₂ R	2.0899	0.9979	0.02001	0.06336
CO ₂ H	2.0798	0.9985	0.02040	0.06440
CF ₃	2.0416	0.9991	0.02207	0.06856
CN	2.0316	0.9993	0.02274	0.07048
SO ₃ H	2.0348	1.0007	0.02227	0.06908
NO ₂	2.0526	1.0004	0.02151	0.06792
NR ₃ ⁺	1.7965	1.0062	0.03763	0.11428
NH ₃ ⁺	1.7823	1.0107	0.03869	0.11720

NBO analysis

The analysis NBO was used to study hydrogen bonding, spin rotation dam and effect anomery. The Occupation numbers for the $\sigma^*(\text{N-H6})$ antibonds, occupation numbers for the LPT(O), delocalization interactions, $E^{(2)}$, by second order perturbation theory were reported in the table. 2.

The results of NBO analysis show that in N-H6...O, lone pairs of oxygen atom participate as donor and the $\sigma^*(\text{N-H6})$ antibond as acceptor.

In summary, putting electron withdrawing groups in position α and β pyrrole ring increase IHB.

Table 2 Occupation numbers (electrons) and corresponding orbital energies (e in unit au) of the N-H bonds of the acceptor and the lone pairs of the donor atom (nO), and their second order perturbation stabilization energies $E^{(2)}$ (kcal/mol)

(α)	O.N(LP _T -O51)	$E^{(2)}$	$\varepsilon(\sigma^* \text{N5-H6})$	O.N($\sigma^* \text{N5-H6}$)
original	3.81304	4.36	0.52121	0.02695
F	3.81301	4.94	0.50066	0.02822
COR	3.81252	6.05	0.50064	0.03183
CO ₂ R	3.81221	4.47	0.50668	0.02904
CO ₂ H	3.81208	4.67	0.50326	0.02876
CF ₃	3.81236	5.41	0.50078	0.03000
CN	3.81254	5.66	0.48993	0.03015
SO ₃ H	3.81197	5.25	0.48691	0.03136
NO ₂	3.81174	5.21	0.48269	0.03201

Comparison of charge distribution in hydrogen atom Calculations are important for determining the electrostatic interactions of molecules. There are four different ways to assign charge of hydrogen atom engaged in IHB including of AIM, NBO, Mulliken and CHELPG methods (Fig.2).

Reduced charge density around the hydrogen atom shows that is increases the strength of IHB with the EWGs on structure (Table.3)

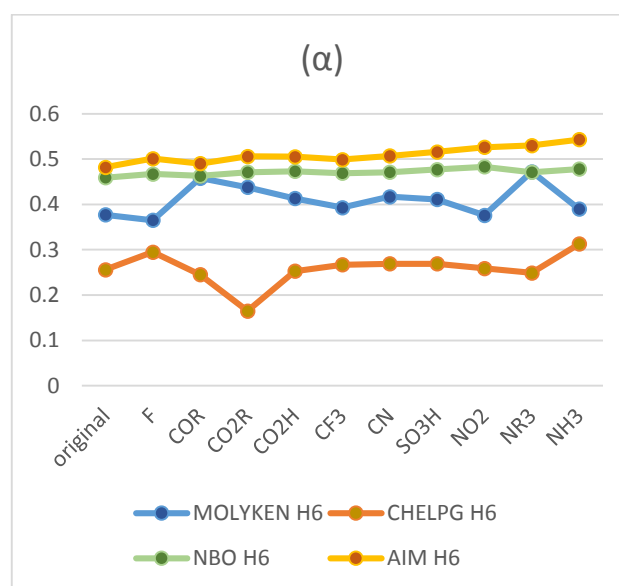


Fig.2 charge distribution (q in units of e) of the hydrogen atom

Table.3 charge distribution (q in units of e) of the hydrogen atoms

H6	qNBO (α)	qAIM (α)	qNBO (β)	qAIM (β)
Original	0.459	0.482	0.459	0.482
F	0.467	0.501	0.461	0.489
COR	0.463	0.490	0.464	0.347
CO ₂ R	0.471	0.506	0.464	0.492
CO ₂ H	0.473	0.505	0.465	0.494
CF ₃	0.469	0.499	0.465	0.497
CN	0.471	0.507	0.468	0.499
SO ₃ H	0.477	0.516	0.469	0.503
NO ₂	0.483	0.526	0.469	0.504
NR ₃ ⁺	0.471	0.530	0.482	0.530
NH ₃ ⁺	0.478	0.543	0.485	0.535



Conclusions

In the present study strength of IHB were investigated in Z-isomer of a special phosphorus ylide and similar molecules with ten EWGs from weak to strong for positions of α and β pyrrole rings. Comparison all data between different structures show interesting results about the effect of electron withdrawing groups on structure and strength of IHB. The overall result is that the both α and β pyrrole rings, electron withdrawing groups position compounds are evaluated for increased strength of IHB the EWGs that are stronger more effect on the strength of this bond. The overall result is that the electron withdrawing groups on the both positions of α and β pyrrole rings for increased IHB strength.

References

- [1] M. Shahraki, S. M. Habibi-Khorassani, A. Ebrahimi • M.T Maghsoodlou • Y. Ghalandarzahi, *Struct Chem* (2013) 24:623–635
- [2] Becke AD (1993) *J Chem Phys* 98:5648
- [3] Lee CT, Yang WT, Parr RG (1988) *Phys Rev B* 37:785
- [4] Hari Haran PC, Pople JA (1973) *Theor Chim Acta* 28:213
- [5] Cramer CJ (2002) *Essentials of computational chemistry*. Wiley, New York
- [6] Martin F, Zipse H (2005) *J Comput Chem* 26:97–105
- [7] Frisch MJ, Trucks GW, Schlegel HB, Scuseria GE, Robb MA, Cheeseman JR, Montgomery JA, Vreven T, Kudin KN, Burant JC, Millam JM, Iyengar SS, Tomasi J, Barone V, Mennucci B, Cossi M, Scalmani G, Rega N, Petersson GA, Nakatsuji H, Hada M, Ehara M, Toyota K, Fukuda R, Hasegawa J, Ishida M, Nakajima T, Honda Y, Kitao O, Nakai H, Klene M, Li X, Knox JE, Hratchian HP, Cross JB, Adamo C, Jaramillo J, Gomperts R, Stratmann RE, Yazyev O, Austin AJ, Cammi R, Pomelli C, Ochterski JW, Ayala PY, Morokuma K, Voth GA, Salvador P, Dannenberg JJ, Zakrzewski VG, Dapprich S, Daniels AD, Strain MC, Farkas O, Malick DK, Rabuck AD, Raghavachari K, Foresman JB, Ortiz JV, Cui Q, Baboul AG, Clifford S, Cioslowski J, Stefanov BB, Liu G, Liashenko A, Piskorz P, Komaromi I, Martin RL, Fox DJ, Keith T, Al-Laham MA, Peng CY, Nanayakkara A, Challacombe M, Gill PMW, Johnson B, Chen W, Wong MW, Gonzalez C, Pople JA (2003) *Gaussian 03, Revision A.1*. Gaussian Inc., Pittsburgh
- [8] Dakkouri M, Typke V (2007) *Struct Chem* 18:357–372
- [9] Szatyłowicz H, Krygowski TM, Jezierska-Mazzarello A (2011) *J Mol Model* 17:125–131
- [10] Bader RFW (1990) *Atoms in molecules. A quantum theory*. Clarendon, Oxford



Photoswitching in 11H- indeno[1,2-b]quinolin-4-ol (HIQO): A TD-DFT approach

H. Mahboub, H. Roohi*

Department of Chemistry, University of Guilan, Rasht, 419383369, Iran

*hroohi@guilan.ac.ir

Abstract: Photoswitching in 11H- indeno[1,2-b]quinolin-4-ol (HIQO) and its derivatives was investigated theoretically at TD-DFT 6-311++G(2d,2p) level of theory in the first excited state (S_1). molecule is able to render both normal and tautomer emissions and exhibit the large Stokes-shifted fluorescence in gas phase. The potential energy surfaces at ground and excited states, structural parameters, absorption and emission bands, vertical excitation and emission energies and dipole moment were calculated. The results were shown that enol form in ground state is more stable than the Keto one. The potential of these molecules as emissive materials in designing and generation of new displays and light sources were predicted based on their high Stokes shifts.

Keywords: ESIPT; Photoswitches; HIQO; TD-DFT

Introduction

Molecular switches can toggle between two (or more) stable states that have different physical feature. They play an important role in biology and information technology and have become important components of advanced material. Many types of molecular switches found in nature and many of synthetic switches developed by Chemists [1].

Photo switches, are a class of chemical compounds that undergo reversible photochemistry so that many rounds of active/inactive states can be formed. A range of molecules undergo photoswitchable behavior such as ring-opening/closing and isomerization [2]. ESIPT reactions involve proton (or hydrogen atom) transfer from adonor hydrogen bond to a proton acceptor upon excitation in the excited state [3]. Due to this structural change, the excited tautomer possesses photophysical properties, different from those of the ground state species. Large stokes shift is a typical indication for ESIPT occurrence [4]. ESIPT molecules are used in luminescent materials, chemo-sensors, proton transfer laser, photo-stabilizers and organic light emitting devices (OLEDs) [5].

Computational details

The stationary points on the S_0 and S_1 potential energy surfaces of HIQO was optimized using DFT methods (PBE0 for S_0) and (PBE0-TD for S_1) [6] in conjunction with the 6-311++G(2d,2p) basis set. Vibration frequency calculations were performed at the same level to validate that the optimized structures as the energy-minima or transition states. The calculations were carried out using GAUSSIAN 09 program package [7]. The Bader theory was also applied to find and to characterize the critical points. Topological properties of bond critical points (BCPs) were calculated at the PBE0/6-311++G(2d,2p) level

of theory by using the AIM2000 program package [8].

Results and Discussion

The molecular structures of the HIQO are explored at S_0 and S_1 states using PBE0 approaches. The optimized isomeric structures of HIQO are shown in Fig. 1.

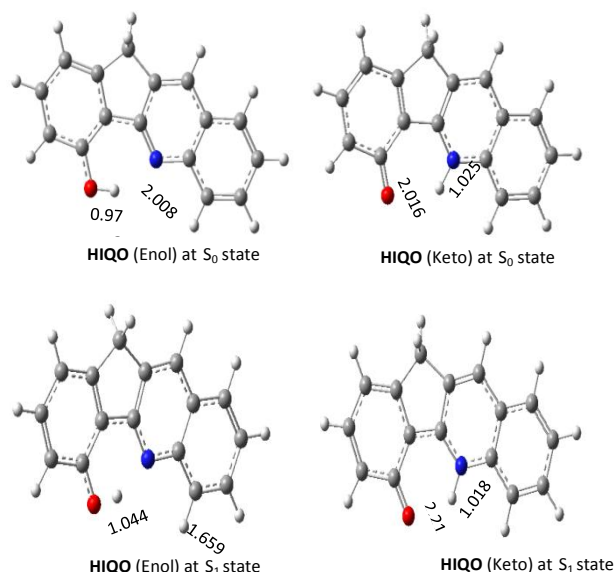


Fig.1: PBE0 optimized minima structures of HIQO (distance:Å) at S_0 and S_1 states.

The calculated relative energies of HIQO are given in Table 1. According to the results shown in Table 1; Enol form in ground state is more stable than the Keto one. The energy difference between S_1 -Enol and S_1 -Keto forms of HIQO, indicating that the photo-transformation at the S_1 state is energetically a favored process.

Table1: Relative energies (kcal/mol), dipole moments (Debye), absorption and emission wavelengths (nm) of HIQO molecule at S_0 and S_1 states.

State	λ (nm)	ΔE (kcal/mol)	μ/D
S_0 -E	-	0.0	3.3
S_0 -K	-	11.4	6.1
S_1 (FC)	330.3	86.6	3.3
S_1 -E	389.6	77.4	3.8
S_1 -K	641.8	64.5	7.7

As can be seen in Table 1, the first calculated vertical excitation energy (VEE) is 3.753 eV for HIQO. The normal emission of HIQO is observed in 389.6 nm ev that is red-shifted by 59.3nm compared to the excitation wave length. The calculated S_1 -Keto \rightarrow S_0 -Keto fluorescence emission wavelength of HIQO is 641.86 nm at the PBE0/6-31++G(2d,2p) level of theory.

Fig. 2 illustrates the FC and relaxed potential energy curves along the proton transfer (PT) pathway in the ground and excited states as a function of the reaction coordinate (RC = d_{OH}) for HIQO calculated by using PBE0 functional. Inspection of the Figs. shows that the enol (S_0 -E) form is the most stable tautomer.

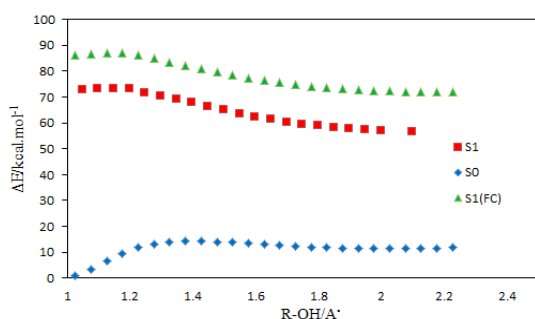


Fig.2: potential energy curves along the proton transfer (PT) pathway in the ground (S_0) and excited (S_1) states as a function of the reaction coordinate RC (O-H) for HIQO.

As mentioned above, HIQO has two minima (S_1 -E and S_1 -K) on the PES at S_1 state.

The quantum theory of atoms in molecules (QTAIM) is a useful gadget to determine hydrogen bonding. AIM theory can take information on changes in the electron distribution as a result of either bond formation or complex formation [9]. Topological properties of bond critical points (BCPs) were calculated at the PBE0/6-311++G(2d,2p) level of theory. Fig. 3 shows the change in the $\rho(r)$ and $\nabla^2\rho(r)$ at the $OH\cdots N$ and $O\cdots HN$ bond critical points (BCPs) versus RC at S_0 state. As can be seen, an

increase in value ($\rho(r)$ and $\nabla^2\rho(r)$) in $OH\cdots N$ bond is accompanied by a decrease in those $O\cdots HN$ bond.

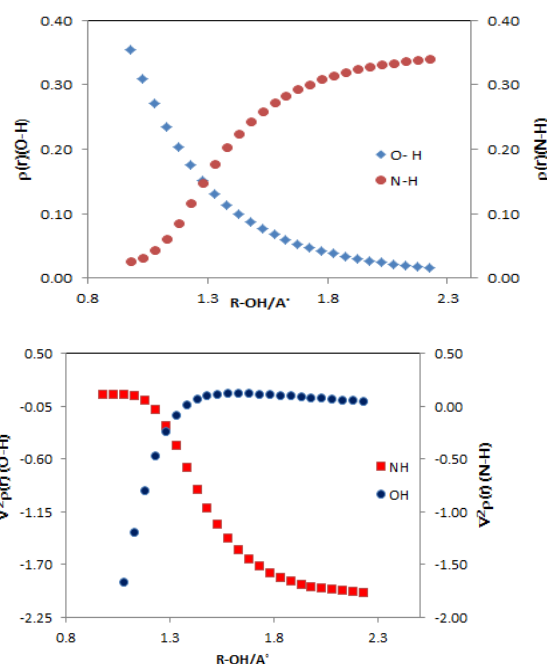


Fig.3: Variation of electron density and Laplacian of electron density at the $N(O)$ -H BCP in terms of RC along the PT pathway of the HIQO at the S_0 .

Conclusions

In the present paper, the ES IPT reaction and the photophysical properties were studied by DFT method. Ground state calculations show that Enol form is more stable than the corresponding Keto form. However the excited state keto form is found to be more stable than the respective enol form. From the results, it can be estimated that proton transfer in the ground state is impossible, while upon photoexcitation this process becomes possible.

References

- [1] T. Dirk "Molecular switches and cages", *Beilstein J. Org. Chem*, 8 (2012) 870-871.
- [2] AA. Beharry, GA. Woolley "Azobenzene photoswitches for biomolecules", *Chemical Society Reviews*, 40.8 (2011) 4422-4437.
- [3] Z. Zhiyun, et al. "Control of the Reversibility of Excited-State Intramolecular Proton Transfer (ESIPT) Reaction: Host-Polarity Tuning White Organic Light Emitting Diode on a New Thiazolo [5, 4-d] thiazole ESIPT System", *Chemistry of Materials*, 28.23 (2016) 8815-8824.



- [4] S. Hristova, et al. "10-Hydroxybenzo [h] quinoline: switching between single-and double-well proton transfer through structural modifications", *Rsc Advances*, 5.124 (2015) 102495-102507.
- [5] V. Padalkar, P. Ramasami, N. Sekar "TD-DFT Study of excited-state intramolecular proton transfer (ESIPT) of 2-(1,3-benzothiazol-2-yl)-5-(N,N-diethylamino)phenol with benzoxazole and benzimidazole analogues", *Procedia Computer Science*, 18 (2013) 797-805.
- [6] R. Abbel, AP.H.J. Schenning, E.W. Meijer "Fluorene-based materials and their supramolecular properties", *Journal of Polymer Science Part A: Polymer Chemistry*, 47.17 (2009) 4215-4233.
- [7] M. J. Frisch, et al. "Gaussian 09, Revision A, Gaussian", *Inc., Wallingford CT*(2009).
- [8] A. Otero-de-la-Roza, E. R. Johnson, V. Luaña "Critic2: A program for real-space analysis of quantum chemical interactions in solids", *Computer Physics Communications*, 185.3 (2014) 1007-1018.
- [9] U. Koch, P. L. A. Popelier "Characterization of CHO hydrogen bonds on the basis of the charge density", *The Journal of Physical Chemistry* 99.24 (1995) 9747-9754.

A DFT study on all Chloro-2,3-dihydrothieno[3,4-b] [1,4] dioxines

Hossein Shirani Il Beigi*, Ahmadreza Shakibi

Department of chemistry, Nazhand Higher Education Institute, Urmia, 5719883896, Iran
*shiranihossein@gmail.com

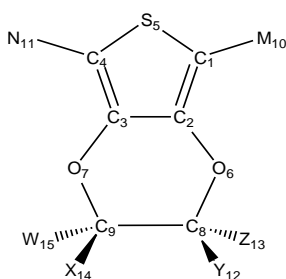
Abstract: The structural and electrical properties of mono, di, tri, tetra and perchlorothieno-2,3-dihydrothieno[3,4-b] [1,4] dioxine have been developed and studied using B3LYP method with 6-311++G** basis set. highest occupied molecular orbital (HOMO) and lowest unoccupied molecular orbital (LUMO) energies, HLG (the gap between HOMO and LUMO orbitals) and size of dipole moment vector, total electrical energies, Gibbs energies, Enthalpies, Entropies, IR spectrums of the molecules, NMR spectrums and Zero-Point vibrational energies have been calculated and studied as well. The conductivity of each molecule, which can be known from the HLG values and dipole moment vectors are explained and studied in this paper.

Keywords: Theoretical calculations; DFT-B3LYP; Electric dipole moment; 2,3-dihydrothieno[3,4-b] [1,4] dioxine.

Introduction

Given compounds have specific electrochemical properties, which make them unique. They have been employed as a standard counter electrode in dye-sensitized solar cell (DSSC). The use of computational techniques in catalysis has become widespread and extensive, mainly because of the sophistication of several densities functional theory (DFT) software codes. However, the reliability of such DFT calculations depends on the particular approximation of the exchange–correlation functional. Nowadays, DFT studies usually go beyond the so-called local density approximation (LDA) and are based on the generalized gradient approximation (GGA) or on hybrid functional (e.g.: B3LYP) [4].

The main models of each molecule are showed in Fig.1.



Where:

- 1- M, N, W, X, Y, Z=H
2,3-dihydrothieno[3,4-b] [1,4] dioxine
- 2- Z=Cl / M, N, X, Y, W=H
2-chloro-2,3-dihydrothieno[3,4-b] [1,4] dioxine
- 3- Z, Y=Cl / M, N, W, X=H
2,2-dichloro-2,3-dihydrothieno[3,4-b] [1,4] dioxine
- 4- X, Y=Cl / M, N, W, Z=H
(2R,3S)-2,3-dichloro-2,3-dihydrothieno[3,4-b] [1,4] dioxine
- 5- W, Y=Cl / M, N, X, Z=H
(2S,3S)-2,3-dichloro-2,3-dihydrothieno[3,4-b] [1,4] dioxine
- 6- Y, Z, X=Cl / M, N, W=H

- 7- X, Y, Z, W=Cl / M, N=H
2,2,3,3-tetrachloro-2,3-dihydrothieno[3,4-b] [1,4] dioxine
- 8- M, N=Cl / X, Y, Z, W=H
5,7-dichloro-2,3-dihydrothieno[3,4-b] [1,4] dioxine
- 9- M=Cl / N, X, Y, Z, W=H
5-chloro-2,3-dihydrothieno[3,4-b] [1,4] dioxine
- 10- M, W=Cl / X, Y, Z, N=H
2,5-dichloro-2,3-dihydrothieno[3,4-b] [1,4] dioxine
- 11- M, X=Cl / W, Y, Z, N=H
2,5-dichloro-2,3-dihydrothieno[3,4-b] [1,4] dioxine
- 12- M, Y=Cl / W, X, Z, N=H
2,7-dichloro-2,3-dihydrothieno[3,4-b] [1,4] dioxine
- 13- M, Z=Cl / W, X, Y, N=H
2,7-dichloro-2,3-dihydrothieno[3,4-b] [1,4] dioxine
- 14- M, N, X=Cl / W, Y, Z=H
2,5,7-trichloro-2,3-dihydrothieno[3,4-b] [1,4] dioxine
- 15- M, N, W=Cl / X, Y, Z=H
2,5,7-trichloro-2,3-dihydrothieno[3,4-b] [1,4] dioxine
- 16- M, N, Y=Cl / W, X, Z=H
2,5,7-trichloro-2,3-dihydrothieno[3,4-b] [1,4] dioxine
- 17- M, N, Z=Cl / W, X, Y=H
2,5,7-trichloro-2,3-dihydrothieno[3,4-b] [1,4] dioxine
- 18- M, N, Z, W=Cl / X, Y=H
2,3,5,7-tetrachloro-2,3-dihydrothieno[3,4-b] [1,4] dioxine
- 19- M, N, X, Y=Cl / W, Z=H
2,3,5,7-tetrachloro-2,3-dihydrothieno[3,4-b] [1,4] dioxine
- 20- M, N, W, Y=Cl / X, Z=H
2,3,5,7-tetrachloro-2,3-dihydrothieno[3,4-b] [1,4] dioxine
- 21- M, N, X, Y, Z, W=Cl
perchlorothieno[3,4-b] [1,4] dioxine

Fig.3: All possible mono, di, tri, tetra and perchlorothieno-2,3-dihydrothieno[3,4-b] [1,4] dioxine studied in this work.

Computational method

These molecular calculations were performed with the Gaussian-09 suite of programs for geometry optimization and for calculation of vibrational frequencies using B3LYP/6-311++G** method. In this paper, all of the calculations were carried out using program gauss view.

Results and Discussion

In this section, optimized configurations (B3LYP/6-311++G**level of theory) of mono, di, tri, tetra and perchlorothieno-2,3 dihydrothieno[3,4-b] [1,4] dioxine and their radical cations have been studied have been studied. The NMR spectrums are absent in this paper.

Table1: Electric dipole moments, HOMO, LUMO, HLG (Homo-Lumo gaps) calculated at B3LYP/6-311++G** level of theory for the optimized structures of molecules. In this table HOMO, LUMO, HLG are studied in (eV) and Electric dipole moments in (D).

Molecule	HOMO	LUMO	HLG	Dipole
1	-0.21243	-0.01488	0.19755	1.7756
2	-0.22275	-0.02216	0.20059	2.1096
3	-0.23169	-0.03576	0.19593	1.8068
4	-0.23189	-0.03162	0.20027	2.2064
5	-0.22871	-0.03174	0.19697	0.5784
6	-0.23972	-0.04328	0.19644	2.3337
7	-0.24276	-0.05073	0.19203	2.0243
8	-0.21714	-0.04263	0.17451	2.4757
9	-0.21716	-0.02578	0.19138	2.5016
10	-0.22361	-0.03271	0.1909	2.6036
11	-0.22705	-0.03633	0.19072	0.4109
12	-0.22772	-0.03612	0.1916	2.1219
13	-0.22607	-0.03264	0.19343	2.5548
14	-0.22611	-0.05091	0.1752	1.1323
15	-0.22314	-0.04776	0.17538	2.4748
16	-0.22668	-0.05069	0.17599	0.9931
17	-0.22461	-0.04753	0.17708	2.4860
18	-0.22973	-0.05210	0.17763	1.2409
19	-0.23440	-0.05776	0.17664	0.9892
20	-0.23165	-0.05509	0.17656	1.7898
21	-0.33627	-0.06319	0.27308	1.2033

It is observable in the Tabel the HLG values of 5,7-dichloro-2,3-dihydrothieno[3,4-b] [1,4] dioxine (8) and 2,5,7-trichloro-2,3-dihydrothieno[3,4-b] [1,4] dioxine (14) are extremely smaller than the other compounds. It is noteworthy to mention that when HLG values of a compound is low, it indicates that the molecule would be able to transfer electrons and of course electricity through itself. That is also mean the gap between HOMO and

LUMO are very small and the electrons can easily move from HOMO to LUMO. We also can see in this table that values of dipole moment vectors in 2,5-dichloro-2,3-dihydrothieno[3,4-b] [1,4] dioxine (10) and 2,7-dichloro-2,3-dihydrothieno[3,4-b] [1,4] dioxine (13) are higher among other compounds. By studying these values of dipole moments, we would be able to predict their electro polymerization properties. From the calculation presented in Table 2, we can see that in the first compound (2,3-dihydrothieno[3,4-b] [1,4] dioxine (1)) which is without chlorine group the total electrical energy is very low which make this compound more stable than the others. Furthermore, the total electrical energy in perchlorothieno[3,4-b] [1,4] dioxine (21) is higher among the others. The calculated Zero-Point Vibrational Energy (ZPE) values for all of the compounds are listed in Table 2. Having in mind the contents of the table it can be said that ZPE for perchlorothieno[3,4-b] [1,4] dioxine is greater than other compounds, as a result the relative thermal stability of perchlorothieno[3,4-b] [1,4] dioxine is higher than other compounds. The values of the total enthalpy (H), entropy (S), Gibbs energy (G) calculated for each molecule in Table 2. All of the molecules showed positive frequency. Having a positive frequency indicates that the molecule reached the minimum values of the potential optimized state. Further, it should be noticed that Gibbs energies and Enthalpies of the 2,3-dihydrothieno[3,4-b] [1,4] dioxine (1) compound is higher than the other compounds. Indeed, the entropy of the last molecule(perchlorothieno[3,4-b] [1,4] dioxine (21)) is higher than the other molecules, because the stability of the perchlorothieno[3,4-b] [1,4] dioxine (21) molecule is lower than the other molecules. The most important IR spectrums are assembled below.

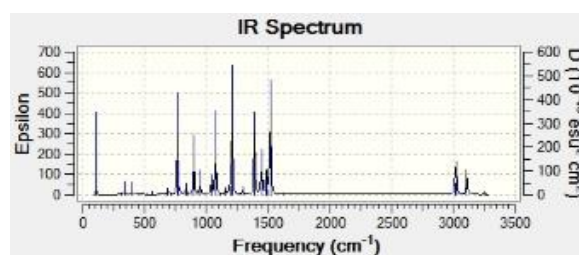


Fig.2: IR spectrum of the 2,3-dihydrothieno[3,4-b] [1,4] dioxine (1). The numbers are in (nm).

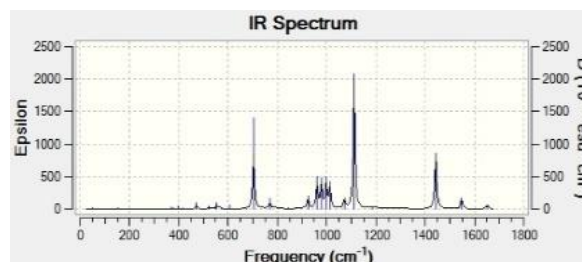


Fig.3: IR spectrum of the perchlorothieno[3,4-b] [1,4] dioxine (21). The numbers are in (nm).

Table2: B3LYP/6-311++G** optimized values of Total electrical energies, Gibbs energies, Enthalpies, Entropies and Zero-Point vibrational energies calculated at B3LYP/6-311++G** level of theory for the optimized structures of molecules. In this table Total electrical energies, Gibbs energies, Enthalpies, Entropies and Zero-Point vibrational energies are studied in (Kcal/mol).

Molecule	Eele	G	H	S	ZPE
1	-490066.48	-490016.28	-489991.18	52698.29	-489997.46
2	-778488.91	-778444.98	-778419.88	57009.28	-778426.16
3	-1066898.78	-1066867.40	-1066836.03	60962.60	-1066842.30
4	-1066898.78	-1066867.40	-1066836.03	61125.75	-1066842.30
5	-1066905.05	-1066873.68	-1066842.30	61169.67	-1066848.58
6	-1355314.92	-1355283.55	-1355252.17	65022.59	-1355258.45
7	-1643724.79	-1643705.97	-1643668.32	68097.38	-1643680.87
8	-1066892.50	-1066861.13	-1066829.75	62299.19	-1066836.03
9	-778482.63	-778438.70	-778413.60	57467.37	-778419.88
10	-1066898.78	-1066867.40	-1066836.03	61734.43	-1066842.30
11	-1066898.78	-1066861.13	-1066836.03	62343.12	-1066842.30
12	-1066898.78	-1066861.13	-1066836.03	62324.29	-1066842.30
13	-1066898.78	-1066867.40	-1066836.03	61753.26	-1066842.30
14	-1355308.65	-1355283.55	-1355252.17	67105.92	-1355258.45
15	-1355314.92	-1355283.55	-1355252.17	66509.78	-1355258.45
16	-1355308.65	-1355283.55	-1355252.17	67105.92	-1355258.45
17	-1355314.92	-1355283.55	-1355252.17	66509.78	-1355258.45
18	-1643731.07	-1643712.24	-1643674.59	70638.80	-1643680.87
19	-1643724.79	-1643705.97	-1643668.32	71787.14	-1643674.59
20	-1643724.79	-1643705.97	-1643668.32	70651.35	-1643680.87
21	-2220544.54	-2220538.26	-2220506.89	77553.96	-2220513.16

Conclusions

In the nutshell, using Gaussian-09 with B3LYP method and 6-311++G** basis set has been performed aiming at the understanding of the influence of the chlorine group in the conductivity of the molecules. The results and calculations have been carried out using the program gauss view. When the number of the chlorine group rises, the total electrical energy is higher, that means the stability decreases.

References

- [1] S. Jameh-Bozorgi, H. S. IL Beigi “Theoretical study on the electronic, structural, properties and reactivity of a series of mono-, di-, tri- and tetrafluorothiophenes as monomers for new conducting polymers”, *Journal of Fluorine Chemistry*, 132 (2011) 190-195.
- [2] Vera L.S. Freitas, Maria D.M.C. Ribeiro da Silva, José R.B. Gomes “A computational study on the thermochemistry of methylbenzo- and methyl dibenzothiophenes”, *Journal of Molecular Structure: THEOCHEM*, 946 (2010) 20-25.
- [3] Fangyuan Tian, Hongji Li, Mingji Li, Cuiping Li, Yingjie Lei, Baohe Yang “Synthesis of one-dimensional poly(3,4-ethylenedioxythiophene)-graphene composites for the simultaneous detection of hydroquinone, catechol, resorcinol, and nitrite”, *Journal of Synthetic Metals*, 226 (2017) 148-156.
- [4] Ana M. Pessoa, José L.C. Fajn, José R.B. Gomes, M. Natlia D.S. Cordeiro “Cluster and periodic DFT calculations of adsorption of hydroxyl on the Au (h k l) surfaces”, *Journal of Molecular Structure: THEOCHEM*, 946 (2010) 43-50.

Computational study on oligomers of 2,3,5,7-tetrachloro-2,3-dihydrothieno[3,4-b] [1,4] dioxine as intelligent nano-conducting polymers

Hossein Shirani Il Beigi*, [Ahmadreza Shakibi](#)

Department of chemistry, Nazhand Higher Education Institute, Urmia, 5719883896, Iran

[*shiranihossein@gmail.com](mailto:shiranihossein@gmail.com)

Abstract: A series of conductive polymers have been calculated and developed using B3LYP method with 6-311++G** basis set. Energy band gap (HOMO (the highest occupied molecular orbital)–LUMO (the lowest unoccupied molecular orbital)), HLG (the gap between HOMO and LUMO orbitals) and size of dipole moment vector, total electrical energies, Gibbs energies, Enthalpies, Entropies and Zero-Point vibrational energies have been calculated and studied. The IR spectrums of the molecules and NMR spectrums are calculated and studied as well. The conductivity of each polymer, which can be known from the HLG values and dipole moment vectors are explained and studied in this paper.

Keywords: DFT-B3LYP; Electrochemistry; Electric dipole moment.

Introduction

Conductive polymers composites have recently attracted tremendous attention because they possess the excellent properties of conductive polymers, e.g., high electrical conductivity, long-term environmental stability, good electrochemical activity, and biocompatibility, as well as the unique electrical and chemical properties of them. In this paper we used B3LYP method with 6-311++G** basis set in order to optimize each polymer. The properties of 2,3,5,7-tetrachloro-2,3-dihydrothieno[3,4-b] [1,4] dioxine have been studied as well. we built the Dimer and Trimer molecule of the 2,3,5,7-tetrachloro-2,3-dihydrothieno[3,4-b] [1,4] dioxine, shown in the figure 1 and figure 2.

Computational procedures

All calculations were performed within the framework of DFT, using B3LYP method with 6-311++G** basis set. In this paper the calculations were carried out using program gauss view.

Results and Discussion

According to the Table 1 which has shown in the next page, the total electrical energy of the Trimer molecule is smaller than the Dimer molecule, which make the Trimer molecule more stable than the Dimer molecule. The values of bond lengths between C₁ and C₁₀ in both Dimer and Trimer molecules assembled in Table 2, shows that the electron density is higher in both polymers. It should be noted that the Gibbs energies and Enthalpies of the Dimer molecule is higher than the Trimer molecule. Indeed, the entropy of the Trimer molecule is higher than the Dimer molecule, because the stability of the Trimer molecule is lower than the Dimer molecule. We also can see in Table 1 that values of dipole moment vectors in

Trimer molecule is higher than the other molecule. By studying these values of dipole moments, we would be able to predict their electro polymerization properties.

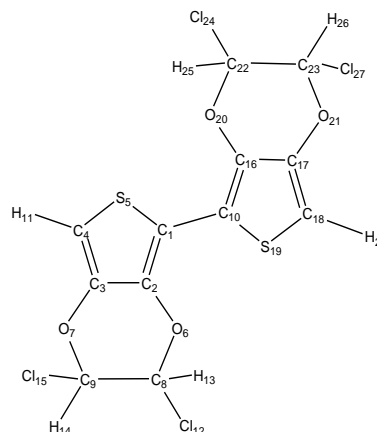


Fig.4: Dimer of the 2,3,5,7-tetrachloro-2,3-dihydrothieno[3,4-b] [1,4] dioxine.

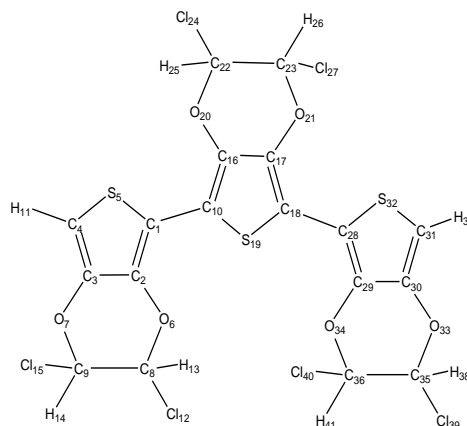


Fig.2: Trimer of the 2,3,5,7-tetrachloro-2,3-dihydrothieno[3,4-b] [1,4] dioxine.

Table1: B3LYP/6-311++G** optimized values of Total electrical energies, Gibbs energies, Enthalpies, Entropies and Zero-Point vibrational energies calculated at B3LYP/6-311++G** level of theory for the optimized structures of polymers. In this table Total electrical energies, Gibbs energies, Enthalpies, Entropies and Zero-Point vibrational energies are studied in (Kcal/mol) and Electric dipole moments in (D).

Polymer	Eele	HLG	G	H	S	ZPE	Dipole
1	-2133048.94	0.14754	-2132978.65	-2132932.85	97080.82	-2132946.02	0.0941
2	-3199198.47	0.13298	-3199093.04	-3199030.92	131436.36	-3199050.37	1.8422

Table2: B3LYP/6-311++G** optimized values of bond lengths studied in angstrom (Å)

Polymer	1C-2C	1C-10C	1C-5S	2C-3C	2C-6O	3C-7O	4C-11H	4C-5S	6O-8C	7O-9C	8C-13H	8C-12Cl	9C-15Cl	9C-14H
1	1.38	1.44	1.76	1.42	1.37	1.37	1.08	1.73	1.42	1.41	1.09	1.79	1.79	1.09
2	1.38	1.44	1.76	1.42	1.37	1.37	1.08	1.73	1.42	1.41	1.09	1.78	1.79	1.09

Table3: Dihedral angles studied in (°) and calculated at B3LYP/6-311++G** level of theory for the optimized structures of the polymers.

Polymer	4C-5S-1C-10C	4C-5S-1C-2C	5S-1C-2C-6O	2C-6O-8C-13H	2C-6O-8C-12Cl	9C-8C-6O-2C	14H-9C-8C-6O	15Cl-9C-8C-6O	7O-9C-8C-6O	3C-7O-9C-8C	11H-4C-3C-7O
1	-179.85282	-0.05315	178.62251	-78.14347	165.34840	44.45538	63.33318	-177.58261	-59.90220	45.36955	-1.39173
2	-179.62999	-0.00942	178.48564	-78.51588	164.93007	44.06570	63.39839	-177.49994	-59.79268	45.65098	-1.45175

Table4: Angles studied in (°) and calculated at B3LYP/6-311++G** level of theory for the optimized structures of the polymers.

Polymer	8C-9C-14H	9C-8C-13H	8C-9C-15Cl	9C-8C-12Cl	4C-3C-7O	7O-9C-8C	2C-6O-8C	3C-7O-9C	1C-2C-6O	4C-3C-2C	5S-1C-2C	5S-4C-3C	5S-4C-11H	4C-5S-1C
1	110.24	110.34	111.17	111.39	125.05	110.66	114.28	114.13	123.79	113.35	108.79	110.86	120.95	92.57
2	110.21	110.37	111.17	111.38	125.02	110.68	114.41	114.06	123.74	113.39	108.72	110.87	120.95	92.57

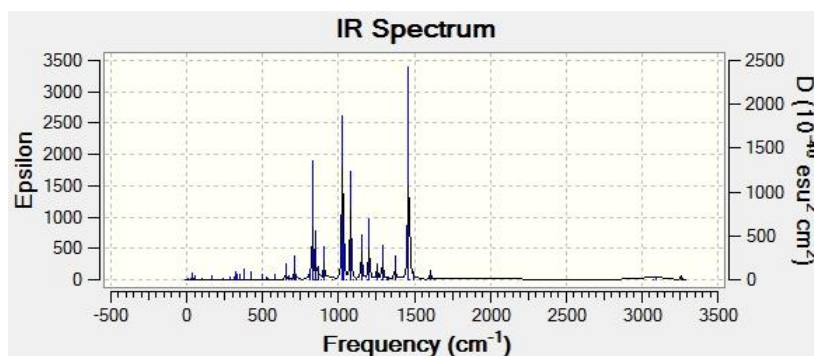


Fig.3: IR spectrum of the Dimer molecule. The numbers are in (nm).

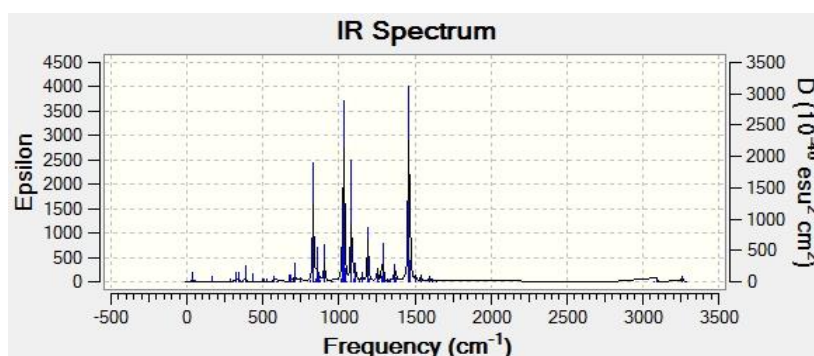


Fig.4: IR spectrum of the Trimer molecule. The numbers are in (nm).

The IR spectrums of Dimer and Trimer molecules are shown in Fig 3 and Fig 4. These figures are prepared by extracting the frequency of each single polymer. The NMR spectrums are absent in this paper.

Conclusions

In this paper, Energy band gap (HOMO–LUMO), HLG (the gap between HOMO and LUMO orbitals) and size of dipole moment vector, total electrical energies, Gibbs energies, Enthalpies, Entropies and Zero-Point vibrational energies have been calculated. we have studied the characteristics of Dimer and Trimer Molecules The most important results are summarized below:

1-The B3LYP/6-311++G** optimized values of bond lengths between C_1 and C_{10} of the both polymers assembled in Table 2, shows that the electron density is higher in these bonds and the electron transfer is very easy through themselves.

2-The values of Total electrical energies which have been shown in Table one shows that the stability of the polymers decreases when chlorine group increases.

References

- [1] S. Jameh-Bozorgi, H. S. IL Beigi “Theoretical study on the electronic, structural, properties and reactivity of a series of mono-, di-, tri- and tetrafluorothiophenes as monomers for new conducting polymers”, *Journal of Fluorine Chemistry*, 132 (2011) 190-195.
- [2] Vera L.S. Freitas, Maria D.M.C. Ribeiro da Silva, José R.B. Gomes “A computational study on the thermochemistry of methylbenzo- and methylthiophenes”, *Journal of Molecular Structure: THEOCHEM*, 946 (2010) 20-25.
- [3] Fangyuan Tian, Hongji Li, Mingji Li, Cuiping Li, Yingjie Lei, Baohe Yang “Synthesis of one-dimensional poly(3,4-ethylenedioxythiophene)-graphene composites for the simultaneous detection of hydroquinone, catechol, resorcinol, and nitrite”, *Journal of Synthetic Metals*, 226 (2017) 148-156.

Density prediction of aliphatic hydrocarbons using nonlinear group contribution method

M. motevalli*, Z. Kalantar

School of Chemistry, Shahrood University of Technology, Shahrood, Iran

*motevalli.m71@yahoo.com

Abstract: In this work, we propose a quantitative structure property relationship (QSPR) approach in order to model the density of saturated and unsaturated aliphatic hydrocarbons including linear and branched alkanes, substituted and unsubstituted cycloalkanes and cycloalkenes and linear and branched alkenes up to the high temperature, high pressure conditions. The group contribution method was used to select the most important descriptors of compounds structure. Levenberg -Marquardt artificial neural network (ANN) was used to link molecular structures and density data. The data set was randomly divided into three data set: training set (4358 point), validation set (643 point) and test set (643 point). After training and optimization of the ANN parameters, the performance of the model was investigated by the test set. The result indicates that this model can simulate the relationship between the experimental descriptors and the density of the desired molecules accurately.

Keywords: QSPR, Group Contribution Method, Artificial Neural Network, density, hydrocarbons.

Introduction

The liquid density is a very important for both heat and mass transfer calculation in the design of chemical processes. Although experimental data can be very accurate however, it is not always possible to find reliable experimental values of density for every compound over a wide range of temperature and pressure in the literature, nor is it practical to measure such property as the need arises [1]. Therefore, this characteristic can be obtained using different estimation methods such as equation of state (EOS), group contribution method or quantitative structure – property relationship (QSPR) studies.

One of the most widely used methods to estimate various physical and chemical properties is QSPR methodology. In QSPR methodology, the property under consideration is correlated using some chemical structure-based parameters. These parameters are calculated by known mathematical algorithms only from the chemical structure of compounds. There are many types of chemical structure-based parameters. Functional groups which are selected based on group contribution method (GCM), are one of the simplest classes of these parameters [2]. Also, many different techniques have been used for constructing QSPR models; however, artificial neural networks (ANNs) have become popular for constructing these models in the past decade [3]. The popularity of this technique is due to its success in data analysis; it indeed has a self-learning mechanism that does not require the traditional skills of a programmer.

The literature surveys by the authors of this manuscript showed that there are some limited attempts to develop QSPR models to predict the density of hydrocarbons [4-6]. Among others, Moosavi et al. developed an ANN model for

prediction of density for saturated hydrocarbons (linear and branched alkanes and cycloalkanes) and aromatic hydrocarbons over a wide range of temperature and pressure [6].

The main subject of this study is to present an accurate method for estimation of density of a wide variety of hydrocarbons over a wide range of temperatures and pressures. To do so, a combination of GCM with ANN was employed to density prediction of these compounds. The combined proposed method (GCM+ANN) follows the classical scheme of dividing the molecule in defined groups but instead of determining the value of the group contributions, an artificial neural network is trained to learn the relation between the density and the molecular structure.

2. Methodology

2.1. Data set

A population of 4346 experimental value of density for 48 aliphatic hydrocarbons over a wide range of temperatures and pressures was collected from the literature and was used as the main data set. These compounds contain linear and branched alkanes, substituted and unsubstituted cycloalkanes and cycloalkenes and linear and branched alkenes with the number of carbon atoms varying from 2 to 40. The pVT data set was randomly divided into 3 groups: training set, validation set and test set consisting of 3070, 638 and 638 data point, respectively.

2.2. Generation and selection of descriptors

The selection of relevant descriptors, which relate the density to the molecular structure, is an important

step to construct a predictive model. The first selected descriptors were temperature and pressure because the density is related to both them. The molecular mass (M) is another training descriptor. The other descriptors are selected based on group contribution method. In this step, the chemical structures of all 48 hydrocarbons were analyzed, and to represent the structure of the molecules to predict density, 10 functional groups were found useful.

These group are $-\text{CH}_3$, >CH_2 , $-\overset{|}{\underset{|}{\text{C}}}\text{H}$, $-\overset{|}{\underset{|}{\text{C}}}-$,

>CH_2^\oplus , $-\overset{|}{\underset{|}{\text{C}}}\text{H}^\oplus$, $=\text{CH}_2$, $=\text{CHR}$, $=\text{CR}_2$ and

$=\text{CHR}^\oplus$. Therefore, the number of these functional groups in each compound was selected as the other descriptors. If each of these functional groups not exists in these compounds, the related descriptor will be considered as zero.

2.3. QSPR modelling

A three-layer feed-forward neural network with the tangent-sigmoid (tansig) transfer function was designed to model the density of the studied hydrocarbons. This artificial neural network consists of an input layer, an output layer and one hidden layer (figure 1). Each layer contains a few neurons and each neuron in any layer was fully connected to the neurons of a succeeding layer. Also a bias term was added to the neurons in the hidden layers. The number of neurons presented in the input and output layer depends on the number of variables (in this work descriptors and density, respectively). The number of neurons used for the hidden layer and the ANN parameters (weights and biases) is optimized using Levenberg-Marquardt back-propagation algorithm (TRAINLM). The ANN algorithm was written in MATLAB R2008a. [7] using the MATLAB Neural Networks Toolbox and the programs were executed on a Pentium PC with 4 G RAM and CPU speed of 2.5 GHz.

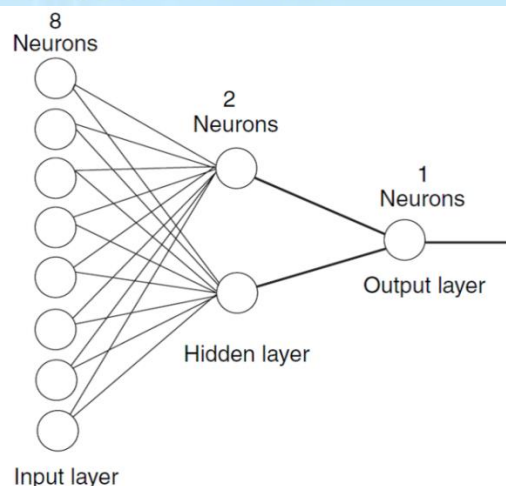


Fig. 1: Used three layer ANN.

3. Results and Discussion

The ANN architecture was constructed with 13 neuron in input layer include T , p , M and 6 functional groups and 1 neuron in output layer that predicts density by network. The number of neuron in the hidden layer is unknown and need to be optimized. Also, the tangent-sigmoid function (tansig) for computation of hidden layer node activities and the linear transfer function (PURELIN) for computation of output activities were employed.

In order to find the optimized architecture of ANN, networks with different number of hidden nodes from 6 to 12 with a step of 1 and learning epochs of 60 to 500 with a step of 10 were trained simultaneously. The obtained results showed that ANN with 12 neurons in the hidden layer and 360 number of epoch had the lowest MSE error for validation set. The capability of the optimized ANN model has been evaluated by predicting values of density using that for the validation and test sets. The statistical parameters for these two sets are reported in Table 1. Also, the performance of this model was evaluated by plotting the estimated values versus the experimental values of density for the validation and test sets, see figure 2.

Table 1. Statistical parameters for the calculated densities of hydrocarbons in validation and test sets using optimized ANN model

set	R ²	AAD	MSE
validation	0.9989	0.37406	30.625
test	0.9990	0.38242	80.089

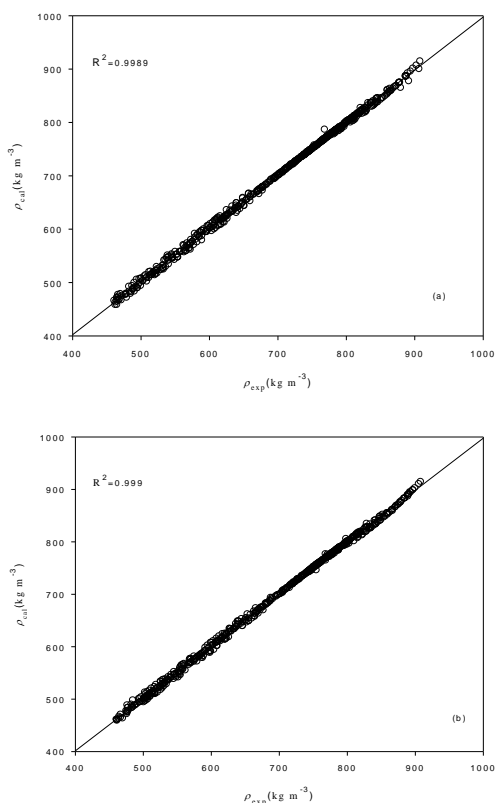


Fig.2: Plot of predicted density versus experimental density for (a) validation and (b) test sets.

The excellent results in Table 1 and Figure 2 show that the GCM+ANN model can be accurately predict the density of hydrocarbons over a wide range of temperature and pressure conditions.

4. Conclusion

The ANN model was developed for predicting the density aliphatic hydrocarbons over a wide range of temperature and pressure. Network modelling and analysis was performed using the MATLAB software with particular use of Neural Network Toolbox. Training was performed using Levenberg–Marquardt algorithm. The most accurately ANN model has a 13-12-1 architecture. The accuracy of the optimized ANN model was checked by comparing predicted and experimental values of density of hydrocarbons not used during training. The results indicate that the proposed model has good prediction ability.

References

- [1] L. Constantinou, R. Gani, “New group contribution method for estimating properties of pure compounds”; *AIChE J*, 40 (1994) 1697-1710.
- [2] F. Gharagheizi, “New neural network group contribution model for estimation of lower

flammability limit temperature of pure compounds” *Ind. Eng. Chem. Res.*, 48 (2009) 7406–7416

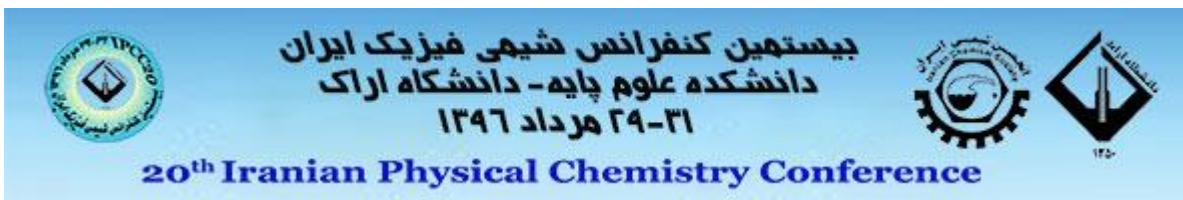
[3] P. C. Jurs, “Assessing the reliability of a QSAR models predictions” *J. Mol Graph Model*, 23 (2005) 503-523.

[4] R. Haghbakhsh, H. Adib, P. Keshavarz, M. Koolivand, S. Keshtkari, “Development of an artificial neural network model for the prediction of hydrocarbon density at high-pressure, hightemperature conditions”, *Thermochim. Acta*, 551 (2013) 124–130.

[5] J. Homer, S.C. Generalis, J.H. Robson, “Artificial neural networks for the prediction of liquid viscosity, density, heat of vaporization, boiling point and Pitzer's acentric factor. Part I. Hydrocarbons”, *Phys. Chem. Chem. Phys.* 1 (1999) 4075-4081.

[6] M. Moosavi, N. Soltani, “Prediction of hydrocarbon densities using an artificial neural network -group contribution method up to high temperatures and pressures”, *Thermochimica Acta*, 556 (2013) 89– 96

[7] MATLAB R2008a, The Math Works, Inc., Natick, MA, USA.



GA-ANN modeling for density prediction of hydrocarbons over a wide range of temperature and pressure

M. Motevalli*, Z. Kalantar, Mohsen Sarglozaie

School of Chemistry, Shahrood University of Technology, Shahrood, Iran

*motevalli.m71@yahoo.com

Abstract: Genetic algorithm (GA) and artificial neural network model (ANN) were successfully developed for density prediction of hydrocarbons. A large number of molecular descriptors were calculated with Dragon software and a subset of calculated descriptors was selected with a genetic algorithm as a feature selection technique. Only 11 descriptors were obtained by GA as the most feasible descriptors, and then they were used as inputs for neural network. These descriptors are: pressure, temperature, molar mass, MATs1e, GATs2v, MLOGP, R3u, R4e, E2p, BEN, HATsm. A total of 4464 data points of density at several temperatures and pressures have been used to train, validate and test the model. These data points were randomly divided into three data sets: training (2480), validation (992) and test set (992). The predictive model was built using the Levenberg-Marquardt artificial neural network (LM-ANN) and its architecture and parameters were optimized using training set. The prediction ability of the model was evaluated using the validation and test sets. The mean square error (MSE) and R^2 were 20.1084, 0.9989 for the validation set and 12.6649, 0.9990 for the test set, respectively. The obtained results showed the excellent prediction ability of the proposed model in the prediction of density for different hydrocarbons.

Keywords: artificial neural network (ANN), genetic algorithm (GA), hydrocarbons.

Introduction

The thermodynamic studies are important for efficient design of chemical processes, and to develop correlation and prediction methods applicable over wide temperature and pressure ranges. Among others, volumetric properties such as density and its derivatives are of great interest not only for industrial applications but also for fundamental aspects [1]. Although experimental data can be very accurate, it is difficult to provide all the data needed for every compound from literatures. Thus, new predictive technique for liquid density is not only welcomed but a necessity for the chemical industries.

In recent years, quantitative structure property relationships (QSPR) method which relates chemical structure-based parameters to the properties of chemical compounds has been reported quite extensively in the literature for the prediction of chemical or physicochemical properties of materials. In the QSPR methodology, many molecular-based parameters which are called "molecular descriptors" are used. Molecular descriptors are numeric characteristics of a pure component directly calculated from its molecular structures with special algorithms. Several molecular descriptors are then selected by heuristic method or genetic algorithm (GA) to correlate the desired property of material. The QSPR approach use linear and nonlinear regression techniques to represent the relations among the variables of a given system. The relationship between molecular descriptors and thermodynamic or transport properties is highly

nonlinear, and consequently, an artificial neural network (ANN) can be a suitable alternative to model those properties.

In the present work, a QSPR study was performed to predict the density of a wide variety of hydrocarbons containing linear and branched alkanes, cycloalkanes, linear and branched alkenes and cycloalkenes over a wide range of temperatures and pressures using GA-ANN model.

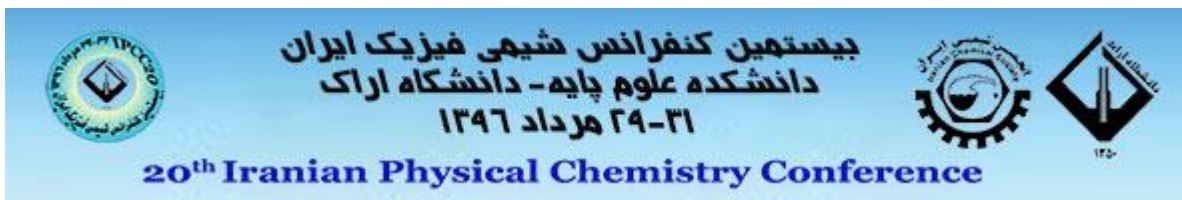
Materials and method

The data set used in this study is the density of different aliphatic hydrocarbons over a wide range of temperature and pressures. Type of hydrocarbons with the number of compounds and data point for each of them was reported in Table 1.

Table 1. The number of compounds and data point for all types of hydrocarbons used in this study

Type of hydrocarbon	No. of compounds	No. of data point
Linear alkanes	17	1589
Branched alkanes	7	752
Linear alkenes	14	1298
Branched alkenes	1	279
Cycloalkanes (substituted or unsubstituted)	10	546

These data was randomly divided into 3 groups: training set, validation set and test set consisting of 2480, 992, 992 data point, respectively. In order to



calculate the theoretical descriptors, the molecular structures were constructed with aid of hyperchem 7.1 [2] and optimized by the AM1 semi-empirical method of the software until the root-mean square gradient was 0.001. 21 electronic descriptors were calculated by the HyperChem software. The molecular geometries of compounds were further optimized by dragon package 2.1 [3]. A total of 1481 theoretical descriptor were calculated for each compound in the data set using Dragon software. These descriptors are calculated using 2D representation of the molecules. As a result, the total theoretical descriptors were being found for each compound in the data set is 1502.

The selection of significant descriptors, which relate the property data to the molecular structure, is an important step in QSPR modelling. Selection of the significant structural descriptors among the 1502 ones was performed as follows: all descriptors with same values for all molecules were omitted, and one of the two descriptors having a pairwise correlation coefficient above 0.9 ($R > 0.9$) was removed. Finally, 233 molecular descriptors remained. To account the effects of experimental temperature and pressure on the density data of the studied compounds, two other columns were added to the descriptor data matrix. Also, the molecular mass (M) of each compound is another training descriptor which added to the descriptor data matrix.

The most relevant descriptors are needed to be selected from the remained descriptors. This is the prominent problem in QSPR studies to choose the minimum number of descriptors with high prediction ability of the model. Conventional variable selection methods like stepwise regression are based upon a single solution or a few solutions. To overcome this problem, a genetic algorithm (GA) designed for the selection of variables was used. GA is a stochastic method used to solve optimization problems defined by fitness criteria, applying the evolution hypothesis of Darwin and different genetic functions, i.e. crossover and mutation. In this work, the genetic algorithm analysis with partial least squares (PLS) regression method was used for selection of important descriptors from the remaining descriptors. In this work, the GA parameters were cross-validation random subset: number of subsets, 5; iteration, 100; population size, 64; initial terms (%) 30; maximum generations, 100; convergence (%) 50; mutation rate, 0.01; and cross-over, double. Eight calculated descriptors namely; MATs1e, GATs2v, MLOGP, R3u, R4e, E2p, BEN, HATsm and three experimental descriptors, pressure, temperature and molecular mass were selected as the most feasible descriptors by genetic algorithm.

In this work a three layer feed-forward ANN with Levenberg-Marquardt back-propagation learning algorithm was operated. The artificial neural network

model was constructed using 11 neurons in input layer and 1 neuron in output layer. The number of neurons in the hidden layer is unknown and need to be optimized. Furthermore, the ANN parameters including the number of nodes in input layer, the transfer function, the number of epoch, the momentum value, and also weights and biases of network must be optimized using Levenberg-Marquardt algorithm. To do so, the training and validation data sets were used to optimize the network parameters. To ensure that the over-fitting and under fitting of the ANN model did not occur, for each configuration, the root mean square errors of training and validation (RMSET and RMSEV, respectively) was used to evaluate the performance of each network. The training of each network was stopped after no improvement was observed for RMSET and RMSEV. The result showed that a 10-10-1 architecture with sigmoid transfer function and Levenberg-Marquardt algorithm for back-propagation of error at 290 iterations has the best performance for the prediction of hydrocarbons density. The architecture and specification of the optimized ANN are shown in Table 2.

Table 2. Architecture and specification of the optimized artificial neural network

Parameter	Value
No. of nodes in the input layer	10
No. of nodes in the hidden layer	10
No. of nodes in the output layer	1
Transfer function of hidden layer	Tan-Sig
Transfer function of output layer	Linear
Epoch	290
Learning Algorithm	LM

The capability of the model has been evaluated by predicting values of density by the optimized ANN model for the validation and test sets. The excellent prediction results, reveals the capability of this model. The correlation coefficient (R^2) and mean squared error (MSE) for test set with optimized model were 0.9990 and 12.6649, respectively. Also, the performance of the model was evaluated by plotting the estimated values versus the experimental values of density for the validation and test sets, see figure 1. From this figures, it is clear that there is not systematic differences between the two sets of results.

Conclusions

We have successfully developed a GA-ANN model to predict the density of different aliphatic hydrocarbons over a wide range of temperature and pressure. The most feasible descriptors were selected by employing genetic algorithm analysis with partial least square (GA-PLS) method from a pool of

theoretically derived descriptors. The most accurately ANN model which relates selected descriptors with density has a 10-10-1 architecture that was trained with the Levenberg-Marquardt algorithm. Our results showed that the predicted density with optimized model is in a good agreement with experimental data. As a result, it was found that properly selected and train ANN could fairly represent dependents of the density for hydrocarbons to the molecular descriptors.

References

- [1] Z. Kalantar, H. Nikoofard, F. Javadi, "Extension of LIR equation of State to Alkylamines Using Group Contribution Method"; *ISRN Physical Chemistry*, 1 (2013) 1-8.
- [2] HyperChem (2002) 7.1. Toronto, Canada, HyperCube Inc.
- [3] Todeschini R., Milano Chemometrics and QSPR Group. [http:// www.disat.unimib.it/vhml](http://www.disat.unimib.it/vhml).

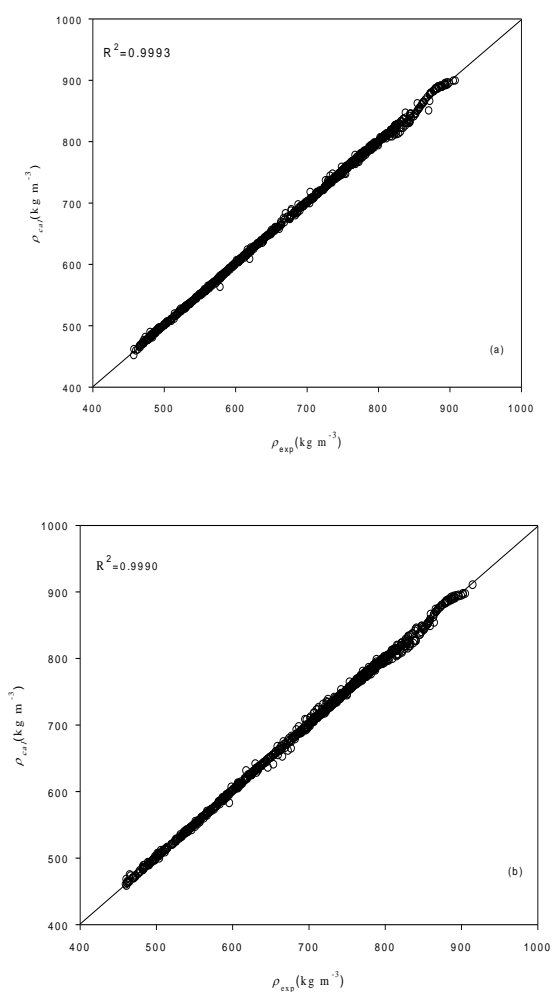


Fig.5: Plot of predicted density versus experimental density for (a) validation and (b) test sets.



A theoretical assignment of the stability of the isomerism in coumarin

F. Bayestizehi*, M. Shahraki, F. Ghodsi

Department of Chemistry, University of Sistan and Baluchestan, Zahedan, Iran

*farkhondehbayestizehi@gmail.com

Abstract: The reaction between dialkyl acetylenedicarboxylates (DAADs) and trialkyl phosphites in the presence of 4-hydroxycoumarin lead to product 3-[2-(dialkoxyphosphoryl)-1, 2-dialkoxycarbonyl-ethyl]-4-hydroxycoumarins. Quantum mechanical calculations were undertaken for ascertain of stability of two isomers possible product 4. Herein, theoretical calculations have been employed for the assignment of the most stable isomers anti and gauche product 4 at both the HF/6-31G (d, p) level and the B3LYP method with 6-311++G (d, p) basis set. The results showed that product 4 with anti HCCH arrangements are more stable than 4 with gauche HCCH arrangements. The results (theoretical calculations) were consistent with the experimental data obtained from NMR spectroscopy.

Keywords: Stereoselectivity, 4-Hydroxycoumarin, Phosphonates, Isomerism, Computational methods

Introduction

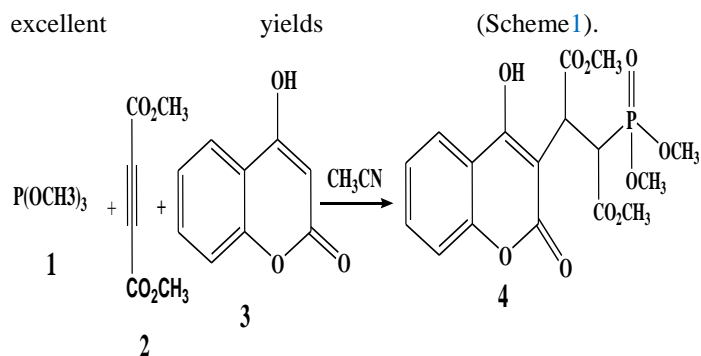
Coumarin (2H-1-benzopyran-2-ones) are important oxygen containing fused heterocycles used in drugs and dyes [1]. Coumarins continue to receive attention for their diverse bioactivities. Some natural coumarins have been used as human therapeutics, while 4-hydroxycoumarins are prominent examples of microbial modification which gave rise to the first generation molecules developed along with aspirin and heparin as anticoagulants [2]. The synthesis of the reaction between dialkyl acetylenedicarboxylate (DMAD), trialkyl phosphite and 4-hydroxycoumarin (Scheme 1) for the preparation of product 4 has been earlier published [3]. In this study, an assignment of the stability of gauche and anti-forms of the synthesis compound is investigated by the some computational methods.

Materials and method

For assignment of the two isomers compound 4, first their structures were optimized at the HF/6-31G (d, p) level of theory by the GAMESS program. The relative stabilization energies for both isomers have been calculated at the HF/6-31G (d, p) and B3LYP/6-311++ G (d, p) levels. Further investigation was undertaken to determine more effective factors in the stability of the two isomers on the basis of AIM calculation at the HF/6-31G(d,p) level of theory by the AIM2000 program package. The number of critical points and intramolecular hydrogen bonds have been recognized for the two isomers.

Results and Discussion

The reaction between trialkyl phosphites 1 and dialkyl acetylenedicarboxylate 2 in the presence 4-hydroxycoumarins 3 proceeds in the appropriate solvent at room temperature to lead product 4 in



Scheme 1: Synthesis compound 4

Table 1. The relative energy (kcal /mol) between the two possible product 4 obtained at the HF/6-31G (d, p) and B3LYP/6-311++G (d, p) levels

conformer	HF	B3LYP
anti	0.01	0.008
gauche	0.0	0.0

Table 2. The values of ρ , $\nabla^2 \rho$ and Hamiltonian -H(r) for the configuration of 4 calculated at the BCP

anti	$\rho(r) \times$	$\nabla^2 \rho(r) \times$	-H(r)
O(36),O(27)-1	4.4	21.2	7.4
C(5),O(26)-2	10.7	8.8	4.5
O(38),H(17)-3	9.1	37.6	13.3
O(21),H(43)-4	5.3	23.2	10.09
O(25),H(41)-5	5.7	22.4	9.3
O(24),H(34)-6	6.9	27.2	9.7

Table 3. The values of ρ , $\nabla^2 \rho$ and Hamiltonian $-H(r)$ for the configuration of 4 calculated at the BCP

gauche	$\rho(r) \times 10^3$	$\nabla^2 \rho(r) \times 10^3$	$-H(r)$
O(36),O(24)-1	6.2	26.8	7.8
H(37),O(21)-2	30.1	27.2	10.1
O(38),H(31)-3	5.8	23.2	8.7

Table 4. Most important geometrical parameters involving the value of $-H_{tot}$ (in au), dipole moment (ind), and the number of hydrogen bonds and relative energy (kcal/mol) for the two isomers of 4

	Dipole moment	NO.OF.HB S	$-H_{tot}$ (au)	Relative energy (kcal/mol)
anti	9.46	6	54.29	0.008
gauche	4.85	3	26.6	0.0

^a At B3LYP/6-311 ++G (d, p)

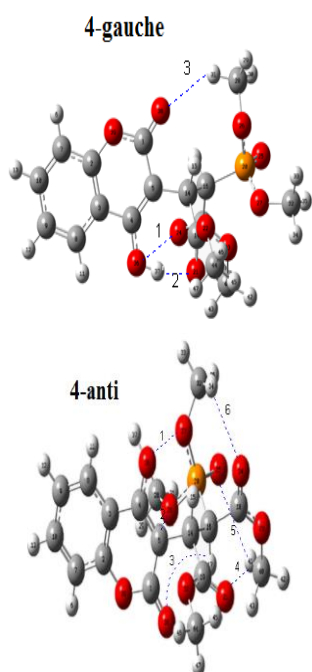


Figure 1. Intramolecular hydrogen bonds (dotted line) in two isomers compound 4

In recent years, AIM theory has often been applied in the analysis of H bonds. In this theory, the topological properties of the electron density distribution are derived from the gradient vector field of the electron density $\nabla \rho(r)$ and on the Laplacian of the electron density, $\nabla^2 \rho(r)$, identifies regions of space where the electronic charge is locally depleted [$\nabla^2 \rho(r) > 0$] [4]. Two interacting atoms in a molecule form a critical point in the electron density, where $\nabla \rho(r) = 0$, called the bond critical point (BCP). The

values of the charge density and its Laplacian at these critical points give useful information regarding the strength of the H bonds [5]. The ranges of $\nabla \rho(r)$ and $\nabla^2 \rho(r)$ are 0.002–0.035 e/a_0^3 and 0.024–0.139 e/a_0^3 , respectively, if H bonds exist [6].

The numbers of hydrogen bonds in both isomers anti and gauche 4 are 6 and 3, and the values of ρ and $\nabla^2 \rho(r) \times 10^3$ for them are in the ranges 0.004–0.01 and 8.8–37.6 e/a_0^3 , and 0.005–0.030 and 23.2–26.8 e/a_0^3 respectively (see Tables 2,3). In addition, the Hamiltonians [$-H(r) \times 10^4$] are in the ranges 4.5–13.3 and 7.8–10.1 au, respectively (see Tables 2, 3). These HBs show $\nabla^2 \rho(r) > 0$ and $H(r) < 0$, which according to the classification of Rozas et al [V] are medium-strength hydrogen bonds. although in according data from Table 1 dipole moment in 4-gauche (4.85D) is less than 4-anti (9.46D) and appears to be an effective factor for the instability 4-anti, the value of $-H_{tot}$ in 4-anti (58.29 au) is more than in 4-gauche (26.6 au), and is taken as a factor in the stability of 4-anti (Table 4). It seems that the instability in the 4-anti ratio 4-gauche stems from the two opposite factors (dipole moment and total Hamiltonian) in which the influence of total Hamiltonian is superior to that of dipole moment. this behavior is in good agreement with the experimental results based upon the 1H , ^{13}C , and ^{31}P NMR data. also Intramolecular H-BCP along with partial molecular graphs for 4 are shown in Figure 1 (dotted lines). The electron densities (ρ) $\times 10^3$, Laplacian of electron density $\nabla^2 \rho(r) \times 10^3$, and energetic density $-H(r) \times 10^4$ are also reported in Tables 2 and 3.

Conclusions

The Quantum mechanical calculation at HF and B3LYP levels of theory exhibiting that compound 4 with anti HCCH arrangements are more stable than gauche HCCH arrangements these results were in agreement with the NMR experimental data.

References

1. S. Rajasekaran, G. K. Rao, S. P. N. Pai, A. Ranjan, *International journal of chem tech research*, 3 (2011) 555-559
2. RL. Mueller First-generation agents: aspirin, heparin and coumarins. *Best Pract Res Clin Haematol* 17(2004) 23–53
3. M. Anary-Abbasinejad, Kh. Charkhati, A. Hassanabadi, *J. Chem. Res*, (2009)319-321
4. R.F.W. Bader, *Atoms in Molecules a Quantum Theory Oxford University Press, New York*, (1990)



A Molecular Dynamics Study of SO₂ Sorbed in Nonporous Silica Y Zeolite: Temperature and Loading Dependence

Y. Sabahi, F. Moosavi*

Department of Chemistry, Ferdowsi University of Mashhad, Mashhad, 91775-1436, Iran

*moosavibaigi@um.ac.ir

Abstract: The dynamical and structural properties of sulfur dioxide (SO₂) guest gas inside nonporous silica Y zeolite were studied by molecular dynamics (MD) simulation for different loadings (8, 12, 16, 20 and 24) of SO₂ per unit cell at temperatures of 300, 400, 500 and 600 K. The order of calculated self-diffusion coefficient of SO₂ guest molecules at different temperatures, is in the range of 10⁻⁹ up to 10⁻⁸ m²s⁻¹. Overall rate for cage-to-cage diffusion shows an Arrhenius temperature dependence with $E_{act} \sim 3.5$ to 5.5 kJ. mol⁻¹. Generally, the SO₂ self-diffusion coefficients increase with temperature.

Keywords: Molecular dynamic simulation; Y zeolite; Diffusion coefficient

Introduction

The emissions of SO₂ are known to cause clear impacts on human health and the environment. Therefore, the removal of SO₂ mainly from the burning of fossil fuels in power plants is a goal of many air pollution researchers [1]. Acidic gases such as SO₂ are one of the main causes for the greenhouse effect, photochemical smog, acid rain, ground layer ozone formation and great hazards to human health [2]. But besides these risks, SO₂ is fundamental for chemical industry, for instance, in producing sulfuric acid [3].

Zeolites are crystalline inorganic microporous materials with well-defined pore structure and cages of varying dimensions. The basic building blocks of zeolites are mainly composed of corner-sharing SiO₄ tetrahedra, and by repeating their periodic tetrahedral network [4]. Because of their regular structure, high internal surface, and high hydrothermal stability, faujasite (FAU) zeolites have been broadly employed in practical applications such as adsorption, separation, and catalysis, especially as desulfurization adsorbents in the process of producing clean fuels [5]. Y zeolite has a network of almost spherical supercages which are interconnected with each other in a tetrahedral manner by 12 membered oxygen rings forming windows. The diameter of these windows is about 7.8 Å while the supercages have a diameter of 11.8 Å [6].

In this work, molecular dynamic (MD) simulation technique, has been employed to investigate static or dynamic behavior at the molecular level.

Computational method

All simulations have been done using DL_POLY_2.17 [7] program on a Linux workstation. One unit cell of FAU was used as the simulation box. Moreover, periodic boundary conditions were applied. The behavior of SO₂ was investigated for loadings of 8, 12, 16, 20 and 24 mol/u.c.(molecule per unit cell). Simulations are carried out in 300 ,

400, 500 and 600 K. The initial structure was equilibrated for 2000 ps. The length of MD runs for data production is 1000 ps. Time step in all simulations was 1 fs and cut-off radius was considered 12 Å.

The self-diffusion coefficient can be obtained from the long time limit of mean square displacement (MSD) using well-known Einstein relation,

$$D_i = \frac{1}{6} \lim_{t \rightarrow \infty} \frac{d}{dt} \langle [r_i^c(t) - r_i^c(0)]^2 \rangle \quad (1)$$

where $r_i^c(t)$ is the location of the center of mass of particle if at time t .

To calculate the diffusion activation energy, Arrhenius equation is used,

$$D = D_0 e^{-\frac{E_{act}}{RT}} \quad (2)$$

where E_{act} , R , and T are the diffusion activation energy, gas constant and temperature, respectively [4].

Results and Discussion

MD simulations at different temperatures and loadings are carried out for SO₂ guest molecules in the fixed silica Y zeolite framework.

The center of mass MSD, self-diffusion, activation energy for SO₂ diffusion process, and main radial distribution functions (RDFs) are computed and discussed.

For instance, Fig. 1 shows the time variation of center of mass MSD of SO₂ diffusion within the pores of silica Y zeolite for loading 8 SO₂ molecules per unit cell at different temperatures.

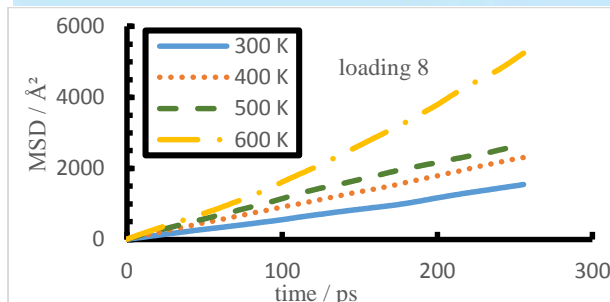


Fig. 1: The effect of temperature on the computed center of mass MSD of SO_2 within pores of silica Y zeolite from simulation at loadings 8.

These results show that within the range of simulation conditions, the motion is in the diffusion regime and there is a linear relationship for MSD over time. As expected generally, the slope of MSD curves increases with increasing temperature due to an increase in the kinetic energy of the guest molecules which allows them to move more easily within the pores of zeolite.

Fig. 2 indicates the time variation of center of mass MSD of SO_2 calculated from simulations at different loadings of guest molecules at 500 K, as a typical sample. It can be expected that at higher loadings collisions between guest molecules may prevent the diffusion of guest molecules which causes a reduction in MSD of guest molecules at high loading.

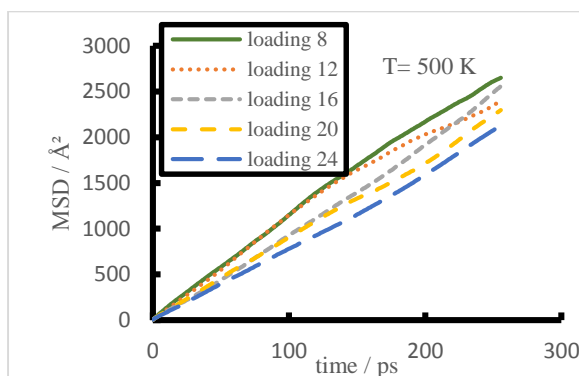


Fig. 2: The effect of loading (molecules per unit cell) change on the computed center of mass MSD of SO_2 within pores of silica Y zeolite from simulation at 500 K.

The calculated self-diffusion coefficients and activation energy values for SO_2 in the silica Y zeolite at different temperatures and loadings have been presented in Table 1.

T (K)	8 mol/u.c.	12 mol/u.c.	16 mol/u.c.	20 mol/u.c.	24 mol/u.c.
300	1	0.95	0.79	0.56	0.69
400	1.49	1.39	1.39	0.88	0.94
500	1.74	1.58	1.64	1.45	1.36
600	3.41	2.24	1.65	1.28	1.36
E_{act}	5.44	3.93	3.84	4.22	3.66

After our initial studies of the dynamics and self-diffusion coefficient of SO_2 molecules in the silica Y zeolite, we particularly focus on RDF between the center of mass of SO_2 and Si atom of zeolite framework. For instance, the RDF curves between center of mass of SO_2 and Si atom of the zeolite framework is given in Fig. 3 for loading 8 at different temperatures.

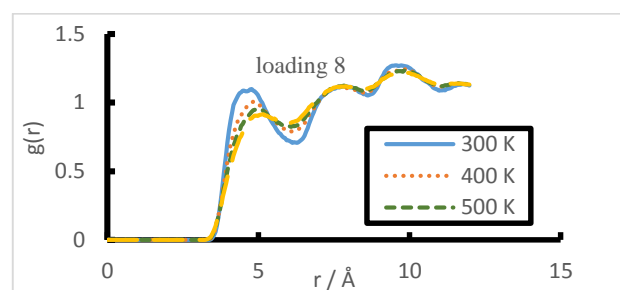


Fig. 3: The RDFs between the center of mass of SO_2 and Si atom of the zeolite from simulation at different temperatures and loadings 8.

As seen in Fig. 3, increasing the temperature decreases the intensity of the RDF peak. Furthermore, with decreasing the temperature the first RDF peak of SO_2 with Si atom appears in shorter distances.

Fig. 4 displays RDFs of COM SO_2 - Si (COM refers to the mass of the center of a sulfur dioxide molecule) in silica Y zeolite at 500 K, with the loading of SO_2 varying from 8 to 24 molecules/u.c. The position of the main peaks over the whole loading range remained at 4.975 Å, which represents that the locations of SO_2 molecules adsorbed before kept their original positions when new molecules came into the zeolite. That means the molecules that adsorbed later had no effect on the relative location of molecules that existed before. This can also be confirmed by RDFs between sulfur atoms (Fig. 5), where the main peak always remained at 4.675 Å.

Table 1: The computed self-diffusion coefficients, D in $10^{-8} \text{ m}^2 \text{ s}^{-1}$ and activation barriers E_{act} ($\text{kJ} \cdot \text{mol}^{-1}$) of SO_2 in silica Y zeolite at different temperatures and loadings.

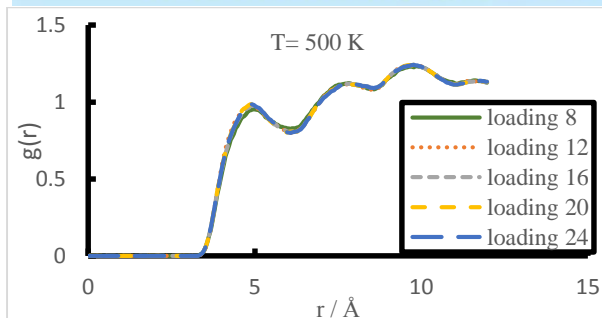


Fig. 4: The RDFs between the center of mass of SO₂ and Si atom of the zeolite from simulation at 500 K and different loadings.

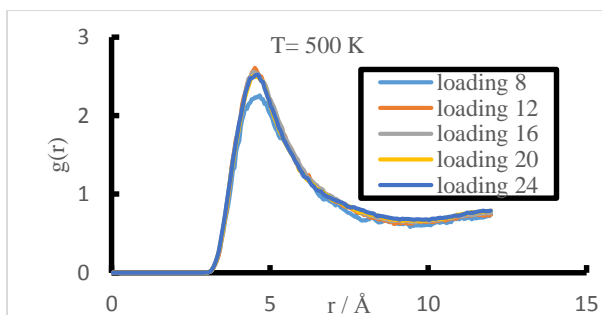


Fig. 5: The RDFs between the sulfur atoms guest molecules from simulation at 500 K and different loadings.

Conclusions

In this study, the dynamics, self-diffusion coefficient, and structural properties of SO₂ guest molecules within the pores of silica Y zeolite were investigated using MD simulations. It was observed that the computed center of mass MSD of SO₂ molecules in silica Y zeolite increases with increasing temperature. Moreover, at each temperature, the MSD of SO₂ decreases when the guest loading is increased in the range of 8-24 SO₂ molecules per unit cell of silica Y zeolite. Temperature dependence of the self-diffusion coefficient of SO₂ for this process is followed.

Structural study shows that height of first peak RDF of COM SO₂- Si decreases with increasing temperature. The simulation results can also help to better understand the roles of the temperature and loading parameters in the behavior of the guest gases through the crystalline compounds at molecular level.

References

- [1] J. Yang, G. Hu, H. Gao "Influence of operating parameters on performance of SO₂ absorption in fulvic acid solution", *Chem. Eng. J.*, 288 (2016) 724–738.
- [2] S. Yun, H. Lee, W. E. Lee, H. S. Park "Multiscale textured, ultralight graphene monoliths for enhanced CO₂

and SO₂ adsorption capacity", *Fuel*, 174 (2016) 36–42.

[3] M. C. C. Ribeiro "Molecular Dynamics Simulation of Liquid Sulfur Dioxide", *J. Phys. Chem. B*, 110 (2006) 8789-8797.

[4] M. H. Kowsari, S. Naderlou "Understanding the dynamics, self-diffusion, and microscopic structure of hydrogen inside the nonporous Li-LSX zeolite", *Microporous Mesoporous Mater.*, 240 (2017) 39-49.

[5] S. Dang, L. Zhao, J. Gao, C. Xu "Loading Dependence of the Adsorption Mechanism of Thiophene in FAU Zeolite", *Ind. Eng. Chem. Res.*, 55 (2016) 11801–11808.

[6] S. Mitra, V. K. Sharma, S. L. Chaplot, R. Mukhopadhyay "Diffusion of hydrocarbon in zeolite and effect due to pore topology: Neutron scattering and MD simulation studies", *Chem. Phys.*, 430 (2014) 69–77.

[7] W. Smith, T. R. Forester, I. T. Todorov, THE DL POLY 2 USER MANUAL", 2007, STFC Daresbury Laboratory, Version 2.17, Cheshire, UK.

Predicting the entropy of benzene derivatives Using Topological Indices and Quantitative Structure Property Relationship

B. Bijani^a, F. Shafiei^{*}

^{a,b}Department of Chemistry, Science Faculty, Arak Branch, Islamic Azad University,

P.O. Box 38135-567, Arak 38361-1-9131, Iran

^{*}e-mailcorresponding author: *f-shafiei@iau-arak.ac.ir*

Abstract: Topological indices are digital values that are assigned based on chemical composition. These values are purported to correlate chemical structures with various chemical and physical properties. They have been successfully used to construct effective and useful mathematical methods to establish clear relationships between structural data and the physicochemical properties of these materials.

In this study, a QSPR study relating topological indices to the entropy of 113 benzene derivatives is reported. The entropy values were calculated at HF level of theory (6-31 G basis sets) by Gaussian 98. Multiple linear regression (MLR) provided good models with three to seven independent variables. The best model obtained is based on three descriptors: Randić, Wiener and Szeged topological indices, with values of the correlation coefficient ($r=0.927$), the standard error ($s= 16.430\text{J/mol}$) and the adjusted correlation coefficient was calculated as 0.859.

Keywords: *Topological indices; benzene derivatives; QSPR; MLR method.*

Introduction

One of the most important purposes in application of mathematical and statistical methods is to find a relationship between molecular structure and values of physical properties, chemical reactivity or biological activity. As a result, quantitative structure-property relationship (QSPR) and quantitative structure-activity (QSAR) studies have been promoted.

QSAR or QSPR modeling methods have been used for more than 50 years but there is still, surprisingly, considerable confusion on the best way to characterize the quality of models.

Topological indices (TIs), as molecular descriptors, are important tools in QSPR/QSAR studies [1-5]. A topological index is a graph invariant number calculated from a graph representing a molecule.

The physicochemical properties of compounds are important in many fields, including pharmaceuticals, chemistry, biochemistry and environmental sciences. Property estimations can help to minimize time and cost in producing new chemical materials with desired properties.

Predictive methods for estimating thermodynamic properties, such as enthalpies of formation, Gibbs free energy and entropies of acyclic and aromatic compounds, on the basis of fundamental concepts on molecular structure have been reported [6].

Artificial Neural Networks were also used in developing QSPR models for prediction of physicochemical properties [7,8].

Prediction of entropies and enthalpies of organic compounds by using group contribution methods was also published [9]. Prediction of standard absolute

entropy ($S_{298\text{K}}$) of gaseous organic and inorganic compounds was reported in [10,11].

The main aim of this study is to illustrate the usefulness of topological indices in QSPR study of entropy (S) of benzene derivatives. As far as we are aware, this is the first QSPR study for prediction of benzene derivatives entropies using topological indices.

Materials and method

The entropy (S) of 113 benzene derivatives (benzene included) was computed at the Hartree-Fock (HF) level of theory, using the ab initio 6-31G basis sets. The benzene derivatives in this set have seven different substituents, each substituent being present in at least six compounds. These substituents are amino, bromo, chloro, hydroxyl, methyl, methoxyl and nitro groups. To obtain an appropriate QSPR model we used multiple linear regression (MLR) procedure, by SPSS software, version 16, and backward stepwise regression was used to construct the QSPR models.

The best predictive QSPR model is developed on a reduced training set of 69 chemicals, having an acceptable predictive capability on 44 test set compounds.

For drawing the graphs of our results, we used the Microsoft Office Excel – 2003 program.

Seven topological indices tested in the present study are Randić (1χ), Balaban (J), Harary (H), Szeged (Sz), Hyper Wiener (WW), Wiener Polarity (Wp) and Wiener (W) indices.

All the used topological indices were calculated in hydrogen suppressed graphs. The descriptors were calculated with Chemicalize program [12].

Statistical Analysis

Structure-Property models (MLR models) are generated using the multi linear regression procedure of SPSS, version 16. The entropy (S , J/mol K) is used as the dependent variable and 1χ , J , H , Sz , WW , Wp and W indices are used as the independent variables. The models are assessed with r value (correlation coefficient), the r^2 (coefficient of determination), the r^2 - adjusted, the s value (root of the mean square of errors), the F value (Fischer statistic), the D value (Durbin-Watson) and the Sig (significant).

Results and Discussion

Several linear QSPR models involving three to seven descriptors were established and the strongest multivariable correlations were identified by the backward method, with significant at the 0.05 level and regression analysis of the SPSS program.

For obtaining appropriate QSPR models we used maximum R^2 method and followed backward regression analysis. The predictive ability of the model is discussed on the basis of predictive correlation coefficient.

The best linear model contains three topological descriptors, namely, Randić (1χ), Wiener (W) and Szeged (Sz) indices with an acceptable predictive power on the test set. The regression parameters of the best three descriptor correlation model is gathered in equation 1.

$$S = 70.258 + 59.966^1\chi + 2.748Sz - 4.163W \quad (1)$$

$$N_{\text{train}}=69; r_{\text{train}}=0.927; r^2_{\text{train}}=0.859; s_{\text{train}}=16.43; D_{\text{train}}=2.033; F_{\text{train}}=132.299$$

$$N_{\text{test}}=44; r_{\text{test}}=0.984; r^2_{\text{test}}=0.968; s_{\text{test}}=10.06; D_{\text{test}}=1.790; F_{\text{test}}=406.452$$

This model produced a standard error of 16.430 J mol⁻¹ K⁻¹, a correlation coefficient of 0.927, and the adjusted correlation coefficient (adjusted r -squared) was calculated as 0.859.

The result is therefore very satisfactory. Fig 1 shows the linear correlation between the observed and the predicted entropy values obtained using equation (1).

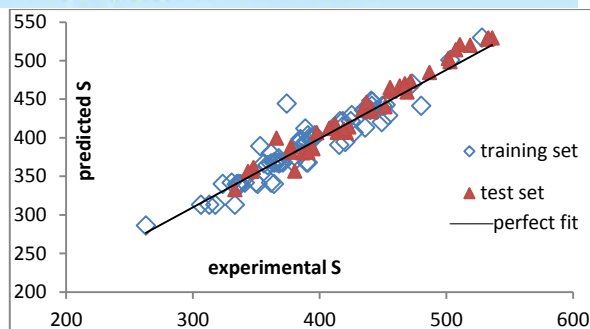


Fig. 1: Comparison between the predicted and observed entropy by MLR method (cf. eq. 1)

Residual Values

The residual values of entropy calculated by equation (1) show a fairly random pattern (see Figure 2). This random pattern indicates that a linear model provides a decent fit to the data.

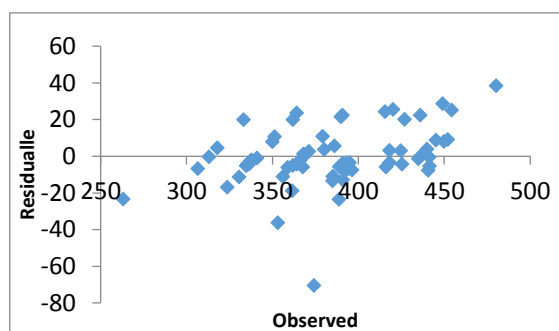


Figure 5. Plot of residuals against observed values of benzene derivatives entropy (S).

Conclusions

In this work, QSPR models for the prediction of entropy for a training set of benzene derivatives using MLR based on topological descriptors calculated from molecular structure have been developed. MLR model is proved to be a useful tool in the prediction of entropy.

The QSPR models found on a training set composed of 69 compounds have an acceptable predictive performance on a test set including 44 compounds.

The aforementioned results and discussion lead us to conclude that combining the three descriptors (Sz , W , 1χ) could be used successfully for modeling and predicting entropy (S) of compounds. This model contains fewer topological descriptors, maximum of Fischer statistic value (F) and minimum root of the mean square of errors (s).



References

- [1] A.A. Taherpour, F. Shafiei, The structural Relationship Between Randic Indices, Adjacency Matrix, Distance Matrixes and Maximum wavelength of linear simple Conjugated Polyene Compounds, *J. Molec. Struct. THEOCHEM*, 726(2005) 183-188.
- [1] [2] F. Ashrafi, A.A. Rostami, and N. Mahdavi pour, Study on QSPR Method for Theoretical Calculation of Boiling Point of Some Organic Compounds, *Asian J. Chem.* 21(3) (2009) 1667-1671.
- [3] D. Janežič, B. Lučić, S. Nikolić, A. Miličević, and N. Trinajstić, Boiling Points of Alcohols – A Comparative QSPR Study, *Internet Electron. J. Mol. Des.* 5 (2006) 192–200.
- [4] M. Kompany-Zareh, A QSPR study of boiling point of saturated alcohols using genetic algorithm, *Acta Chim.Slov.* 50(2003)259-273.
- [5] F. Shafiei , H. Hosseini , Quantitative Structure Property Relationship Models for the Prediction of Gas Heat Capacity of Benzene Derivatives Using Topological Indices, *MATCH Commun. Math. Comput. Chem.* 75, (2016) 583-588.
- [6] P. R. Duchowicz, E. A. Castro, F. M. Fernández, M. P. González, A new search algorithm for QSPR/QSAR theories: Normal boiling points of some organic molecules, *Chem. Phys. Lett.* 412 (2005) 376–380.
- [7] Li. Qianfeng, Chen. Xingguo, Hu. Zhide, Quantitative structure-property relationship studies for estimating boiling points of alcohols using calculated molecular descriptors with radial basis function neural network, *Chemometrics and Intelligent Laboratory Systems*, 72 (1) (2004) 93-100.
- [8] J. Taskinen, J. Yliruusi, Prediction of Physicochemical Properties, *Advan. Drug Delivery Rev.* 55 (2003) 1163-1183.
- [9] J. S. Chickos, C. M. Braton, D. G. Hesse and J. F. Liebman, Estimating Entropies and Enthalpies of Fusion of Organic Compounds, *J. Org. Chem.* 56 (1991) 927-938.
- [10] Mu. Lailong, Feng. Changjun, Topological Research on Molar Diamagnetic Susceptibilities for Inorganic Compounds, *MATCH Commun. Math. Comput. Chem.* 58(2007) 591-607.
- [11] Mu. Lailong, He. Hongmei, Estimation of Ideal Gas Entropy of Organic Compounds, *Ind. Eng. Chem. Res.* 50 (2011) 8764-8772.
- [12] Web search engine developed by ChemAxon; software available at <http://WWW.Chemicalize.Org>.

Interaction between nanostructured tetrazolium based ionic liquids and aromatic sulfur compounds: A M062X functional approach

N. Pourghasemi, H. Roohi*

Department of Chemistry, Faculty of Science, University of Guilan, Rasht, Iran

*hroohi@guilan.ac.ir

Abstract: Density functional theory has been used to investigate the interactions between aromatic sulfur compounds (dibenzothiophene, diphenylsulfide and thiophene) and nanostructured ionic liquid 1-ethyl-3-methyltetrazolium tetrafluoroborate ([EMTT][BF₄]). The M062X functional and 6-311++G(d,p) basis set were employed for optimization of structures in the gas phase. The natural bond orbital analysis (NBO) and the quantum theory of atoms in molecules (AIM) have been employed to elucidate the interaction characteristics between the 1-ethyl-3-methyltetrazolium tetrafluoroborate ionic liquid and aromatic sulfur compounds. Results have demonstrated that both cation and anion in ionic liquid play the important roles in extraction and separation of aromatic sulfur compounds. The interaction energy between ionic liquid and sulfur compounds decreases in the following order: diphenylsulfide < thiophene < dibenzothiophene. The charge analysis reveals that there is a charge transfer during the process. The AIM results confirm the existence of hydrogen bonding between the aromatic sulfur compounds and the ionic liquid.

Keywords: Density functional theory; Hydrogen bonding; Ionic liquid; NBO

Introduction

Desulfurization methods of liquid fuel such as hydrodesulfurization, oxidative desulfurization, bio-desulfurization, reactive adsorption, non-destructive adsorption, N-adsorption, and extractive desulfurization [1-9] has attracted the attention of scientists and engineers due to the stringent regulations imposed on the presence of sulfur in fuel. However, each of these strategies faces its own challenges. In particular, most current methods are used of large quantities of volatile organic solvents in the extraction process, which can be a serious concern to the health and environment [10-11]. Recently, the application of ionic liquids (ILs) in the fields of extraction have gained increasing interest. ILs are entirely composed of organic cations and various inorganic and organic anions that exist in the liquid state around room temperature. Due to the specific characteristics such as wide electrochemical windows, negligible vapor pressure, high ionic conductivity and good solubility, ILs can be widely used as green solvents in the extractive desulfurization of liquid fuels [12]. Computational chemistry techniques such as density functional theory (DFT) can contribute to a more focused development of ILs for extractive applications. DFT can be useful by studying the interactions between aromatic sulfur compounds and ionic liquid [13]. In this work has been investigated the interactions between aromatic sulfur compounds (dibenzothiophene, diphenylsulfide and thiophene) and nanostructured ionic liquid 1-ethyl-3-methyltetrazolium tetrafluoroborate ([EMTT][BF₄]). The main goal of this work is to find the most stable complexes and to characterize the nature of intermolecular interactions in [EMTT][BF₄] IL and aromatic sulfur compounds.

Materials and method

Density functional theory at the M06-2X/6-311++G(d,p) level of theory was employed to study the structural parameters, electronic properties and the interaction energies of the IL...aromatic sulfur compounds complexes. All of the initial structures were fully optimized with above methods in gas phases. The NBO analysis was carried out on the MP2/6-311++G(d,p) wave functions using version 3.1 of NBO package. Topological properties of electron charge density [electron density, $\rho(r)$, Laplacian of electron density, $\nabla^2\rho(r)$, and electronic energy density, $H(r)$] were calculated using Bader's theory at MP2/6-311++G(d,p) level of theory by the AIM2000 program package.

Results and Discussion

In this work, complexes formed from interaction between 1-ethyl-3-methyltetrazolium tetrafluoroborate [EMTTZ][BF₄] IL and aromatic sulfur compounds, thiophene (TS), dibenzothiophene (DBT) diphenylsulfide (DFS) has been studied by means of density functional theory. Optimized structures of the IL, TS, DBT, DFS is shown in Figure 1. The optimized structures of the most stable complexes from interaction between [EMTTZ][BF₄] IL and various aromatic sulfur compounds (TS, DBT, DFS) (named as A, B and C, respectively) are given in Figure 2.

The extractive performance can be correlated with the structure, composition and intermolecular forces solvent- solute. Hence, it is important to investigate the interaction energy between [EMTT][BF₄] IL and aromatic sulfur compounds. The interaction energy (ΔE) between the [EMTT][BF₄] IL and aromatic

sulfur compounds was calculated according to the equations given below:

$$\Delta E = E_{\text{complex}} - (E_{\text{IL}} + E_{\text{S}}) \quad (1)$$

where E_{S} and E_{IL} are the individual energy of the aromatic sulfur compounds (TS, DBT, DFS) and [EMTT][BF₄] IL, respectively, E_{complex} is the energy of the complexes (A, B and C).

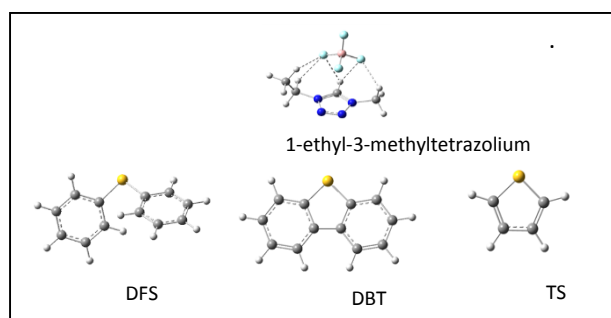


Fig. 1: Optimized structures of [EMTT][BF₄] ionic liquid, TS, DBT, DFS at the M06-2X/6-311++G(d,p) level of theory

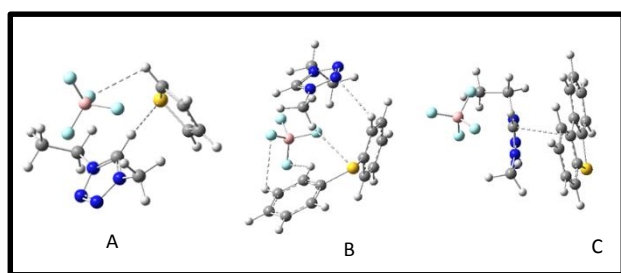


Fig. 2: Optimized structures of A, B and C complexes at the M06-2X/6-311++G(d,p) level of theory.

The calculated electronic interaction energies of the A, B and C complexes at M06-2X / 6-311++G (d, p) level of theory are listed in Table 1. For the calculation of interaction energies, basis set superposition errors (BSSE) and zero-point vibrational energies (ZPVE) were considered. According to the results given in this table, the interaction energies for A, B and C complexes are -5.85, -8.36, -5.29, kcal mol⁻¹, respectively. Based on the BSSE and ZPVE corrected ΔE s, the strength of the inter-molecular interactions in the complexes decreases in the following order: **B > A > C**.

As can be seen in figure 2, Ts and DFS can interact with both the cation and anion of the ionic liquid. Therefore, it is predicted that the hydrogen bonds to be formed between F atom of the anion and CH of the Ts as well as the CH tetrazolium ring of cation and S atom of the Ts in A complex. The H-bonding distances in A complex are 2.722 and 2.613 Å, respectively. B complex can be had four hydrogen bonds formed from the interaction of N atom of tetrazolium ring of the cation with CH phenyl ring of

DFS as well as the CH bonds of phenyl ring and S atom of the DFS are generally involved in interaction with F atoms of the anion. The CH...N, CH...F and S...F hydrogen bonding distances in B complex is 2.751, 2.634, 2.751 and 2.974 Å, respectively. The results of geometrical parameters indicate that the π - π interaction is the major interaction between IL and DBT in C complex. The equilibrium distance between the closest atoms of tetrazolium ring of the cation (C atom) and thiophene ring of DBT (C atom) is about 3.351 Å for C complex.

Table 1: Interaction energies (kcal mol⁻¹) calculated for most stable forms A, B and C complexes with the BSSE and ZPVE correction in M06-2X / 6-311 ++ G (d, p) level of theory

Complex	ΔE (kcal/ mol)	ΔE_0^{BSSE} (kcal/mol)
A	-10.24	-5.85
B	-14.23	-8.36
C	-9.71	-5.29

Natural bond orbital (NBO) analysis:

A better understanding of charge transfer processes in the complexes is provided by NBO calculation. The results of NBO analysis including sum natural charge (Σq_s) in the aromatic sulfur compounds of complexes at MP2/6-311++G(d,p) level of theory are given in Table 2. Comparison of Σq_s shows that the interaction between aromatic sulfur compounds and nanostructured ionic liquid of [EMTT][BF₄] involves some charge transfer between the interacting components. The Σq_s values obtained for A, B and C complexes are 0.032, -0.271 and -0.007 au, respectively.

NBO results allow us to investigate the amount of the charge transfer (CT) due to the electron delocalization between interacting subunits. The charge transfer of A complex occurs from thiophene to [EMTT][BF₄] IL, while in B and C complexes it is transferred from [EMTT][BF₄] IL to the aromatic sulfur compounds. The amount of |CT| is in good agreement with the greater interaction energy obtained (ΔE) for the complexes.

AIM analysis

The quantum theory of AIM is useful quantities to characterize the bonds. Topological criteria are also useful in detecting the existence of H-bond and van der Waals interactions. For all complexes, the calculated values of the sum electronic density, $\Sigma \rho(r)$, at the bond critical points (BCPs), ring critical points (RCPs) and cage critical points (CCPs) of inter-molecular regions at MP2/6-311++G(d,p) level of theory are listed in Tables 2.

The sum of electron densities, $\Sigma\rho(r)$, at all bond, ring and cage critical points in the inter-ionic regions of A, B and C complexes is 0.070, 0.045 and 0.151 au, respectively. Comparison of $\Sigma\rho(r)$ values reveals that the electron densities of the complexes in the inter-ionic regions decreases in the order of $C > A > B$. The results show that the sum electron density of C complex is greater than other ones. Also, there is a reverse situation between ΔE and $\Sigma\rho(r)$ in the complexes.

Table 2: NBO and AIM data calculated at MP2/6-311++G(d, p) level of theory for most stable complexes.

Complex	$\Sigma q_{s\text{-compound/au}}$	$\Sigma\rho(r)/\text{au}$
A	0.032	0.070
B	-0.271	0.045
C	-0.007	0.151

Conclusions

In this work, a computational approach based on quantum chemical methods at M06-2X/6-311++G(d,p) level of theory are described to predict the interactions between aromatic sulfur compounds (dibenzothiophene, diphenylsulfide and thiophene) and nanostructured ionic liquid 1-ethyl-3-methyltetrazolium tetrafluoroborate ([EMTT][BF₄]) in the gas phase.

The interaction strength due to variation of the aromatic sulfur compounds was well displayed by change in interaction energy, structural parameter, electron density properties, natural charge and charge transfer in the complexes. Our results predicted that the hydrogen bonds (in A and B complexes) and the π - π interaction (in C complex) is formed between [EMTT][BF₄] IL and the aromatic sulfur groups of thiophene, diphenylsulfide and dibenzothiophene. The results show that C complex has lower interaction strength compared to the other complexes. It is predicted that nanostructured ionic liquid [EMTT][BF₄] is more suitable for extractive desulfurization of thiophene than other aromatic sulfur compounds.

References

[1] Y. Nie, Y. Dong, L. Bai, H. Dong, X. Zhang "Fast oxidative desulfurization of fuel oil using dialkylpyridinium tetrachloroferrates ionic liquids", *Fuel*, 103 (2013) 997-1002.

[2] W. Jiang, W. Zhu, H. Li, Y. Chao, S. Xun, Y. Chang, Z. Zhao "Mechanism and optimization for oxidative desulfurization of fuels catalyzed by Fenton-like catalysts in hydrophobic ionic liquid",

Journal of Molecular Catalysis A: Chemical, 382 (2014) 8-14.

[3] X. Chen, D. Song, C. Asumana, G. Yu "Deep oxidative desulfurization of diesel fuels by Lewis acidic ionic liquids based on 1-n-butyl-3-methylimidazolium metal chloride", *Journal of Molecular Catalysis A: Chemical*, 359 (2012) 8-13.

[4] H. Song, X. Wan, M. Dai, J. Zhang, F. Li, H. Song, "Deep desulfurization of model gasoline by selective adsorption over Cu-Ce bimetal ion-exchanged Y zeolite", *Fuel processing technology*, 116 (2013) 52-62.

[5] C. Sentorun-Shalaby, S. Saha, X. Ma, C. Song "Mesoporous-molecular-sieve-supported nickel sorbents for adsorptive desulfurization of commercial ultra-low-sulfur diesel fuel", *Applied Catalysis B: Environmental*, 101 (2011) 718-726.

[6] J. E. Ber, P. Wasserscheid, A. Jess "Deep desulfurization of oil refinery streams by extraction with ionic liquids" *Green chemistry*, 6 (2004) 316-322.

[7] A. Bosmann, L. Datsevich, A. Jess, C. Schmitz, P. Wasserscheid "Deepdesulfurization of diesel fuel by extraction with ionic liquids", *Chem Commun*, (2001) 2494-5.

[8] S. Zhang, Z. Zhang "Novel properties of ionic liquids in selective sulfur removal from fuels at room temperature", *Green Chemistry*, 4 (2002), 376-379.

[9] Y. Nie, C. Li, H. Meng, Z. Wang "N, N-dialkyl imidazoliumdialkylphosphate ionic liquids: their extractive performance for thiophene series compounds from fuel oils versus the length of alkyl group", *Fuel processing technology*, 89(2008), 978-983.

[10] P. Kulkarni, C. Afonso "Deep desulfurization of diesel fuel using ionic liquids: current status and future challenges", *Green Chemistry*, 12 (2010), 1139-1149.

[11] J. CamposMartin, M. CapelSanchez, P. Perez-Press, "Oxidative processes of desulfurization of liquid fuel", *Journal of Chemical Technology and Biotechnology*, 85 (2010) 879-890.

[12] H. Zhao, G. A. Baker, D. V. Wagle, S. Ravula, Q. Zhang "Tuning Task-Specific Ionic Liquids for the Extractive Desulfurization of Liquid Fuel", *ACS Sustainable Chem. Eng.*, 4 (9) (2016) 4771-4780.

[13] H. Zhu, W. Guo, M. Li, L. Zhao, S. Li, Y. Li, X. Lu, H. Shan "Density Functional Theory Study of the Adsorption and Desulfurization of Thiophene and Its Hydrogenated Derivatives on Pt(111): Implication for the Mechanism of Hydrodesulfurization over Noble Metal Catalysts", *ACS Catal.* 1 (2011) 1498-1510.

Comparison of the Adsorption of Sulfur Mustard on Graphene and Graphene Oxide: A Molecular Dynamics Simulation Study

L. Ebrahimi^{a,b,*}, A. Khanlarkhani^a, M. R. Vaezi^a and M. Babri^b

^aDepartment of Nanomaterial, Materials and Energy Research Center, Karaj, P.O. Box: 31787-316, Iran

^bDefense Chemical Research Lab (DCRL), Karaj, P.O. Box: 31585-1461, Iran

*chemistry8084@gmail.com

Abstract: In this work, the adsorption behaviour of sulfur mustard on graphene and graphene oxide was studied by molecular dynamics simulation. For this purpose, pair interaction energy and orientational distribution function analyses have been done to determine the adsorption properties. Results showed that there is a specific interaction between sulfur mustard and graphene oxide (-17.175 kcal/mol) which is stronger than graphene and correspond to parallel orientation of sulphur mustard near the surface of the adsorbent while there are two distinct peaks in distribution of interaction energy between sulphur mustard and graphene (centered at -11.875 and -6.125 kcal/mol) and related to the parallel and tilted orientations of sulfur mustard on graphene. These findings indicates that graphene oxide may retain much more sulfur mustard than graphene, and can be used as a superior adsorbent against these type of chemical warfare agents.

Keywords: sulfur mustard; graphene; graphene oxide; molecular dynamics simulation

Introduction

Sulfur mustard (HD), a blistering agent (Fig. 1), is one of the most toxic chemical warfare agents used in battlefields. Skin, eyes and respiratory system are the main target organs, and DNA, RNA and proteins are the most important cellular target of HD toxicity [1, 2]. Introducing an appropriate adsorbent for personal protection against this hazardous compound is much required.

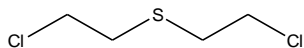


Fig. 1: The structure of sulfur mustard.

In this study, graphene (GRA) and graphene oxide (GO) are considered as the adsorbents. Graphene is a two dimensional material consisting of a hexagonal (honeycomb) lattice of covalently bound sp^2 carbon atoms; and graphene oxide is an oxygen-rich carbonaceous layered material by distributing carboxylic groups at its edges, and hydroxyl and epoxy groups on its basal plane [3]. Because of their high surface area, there are lots of reports which indicates that these materials are used to adsorb different kinds of organic and inorganic compounds [4-7]. The aim of this article is to present results of the investigation of adsorption pair interaction energy (PIE) of HD molecules on these adsorbents as well as structural studies using molecular dynamics (MD) simulation. To achieve these goals, energy distributions and orientational distribution function must be calculated. Pair interaction energy distribution consists of energy distributions of individual molecule–molecule interactions. Orientational analysis provides information about the relative positional structure of HD molecules on the adsorbents [8]. To date, no research has been found that surveyed the atomic-level insight of adsorption of HD on GRA and GO.

Materials and method

In this work, all-atom OPLS model [9] was used for liquid HD [10, 11] and solid graphene and graphene oxide [3]. Both GRA and GO with dimensions of $50 \times 40 \text{ \AA}^2$ were considered in the middle of two cubic boxes with their basal planes parallel to xy -plane. The z position of carbon atoms of both adsorbents were taken as a reference z position ($z = 0 \text{ \AA}$). GO was constructed based on a molecular formula of $C_{10}O_1(OH)_1$ (i.e., one epoxy group and one hydroxyl group per 10 carbon atoms were attached randomly to the both graphene basal planes) [12]. Then 646 HD molecules were equally distributed on both sides of the simulation boxes with periodic boundary conditions applied in all directions. The typical size of the simulation boxes were $52.1 \times 43.0 \times 62.7 \text{ \AA}^3$ for GRA and $52.1 \times 43.0 \times 63.9 \text{ \AA}^3$ for GO. The simulations were performed under canonical (NVT) ensemble at 298 K using a Langevin dynamics method. The particle-mesh Ewald method [13-14] was applied to calculate electrostatic interactions, whereas non-bonded van der Waals interactions were modeled by a Lennard–Jones potential with a cut-off distance 15 \AA . The systems were initially equilibrated for 5 ns with 1000 step energy minimization at first, followed by a 5 ns production run. A time step of 1 fs was used to integrate the equation of motion. All MD simulations were carried out using NAMD package [15].

Results and Discussion

In this study, distributions of the intermolecular interaction energies between HD molecules and both adsorbents were investigated. Fig. 2 compares pair interaction energy distribution of HDs and GRA and or GO near the surface of these adsorbents. As can be seen, there are different interaction mechanisms

between HD and GRA. The position of a maximum (-11.875 kcal/mol) with good probability corresponds to a strong interaction and the position of other peak (-6.125 kcal/mol) with lower probability indicates another weaker interaction. There is also a small peak which located at -1 kcal/mol.

The shape of the distribution for graphene oxide is different from graphene. This observation reveals different interaction nature near two surfaces. The maximum (-17.175 kcal/mol) with medium probability shows that there is one kind of specific interaction between HDs and GO near the surface. Another important point is that the interaction between HDs and GO (-17.175 kcal/mol) is more favorable than HDs and GRA (-11.875 kcal/mol). It means that functional groups on graphene oxide can cause stronger interaction with sulfur mustard and adsorb it better.

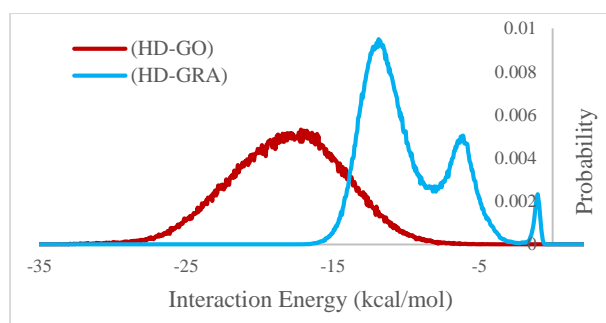


Fig. 2: Distribution of individual interaction energies between HDs and GRA and GO near the surface of the adsorbents.

To deeper insight into the interaction between HD and the adsorbents and how they can accommodate HD molecules on their surfaces, orientational distribution function analysis has been done. For this purpose, the axis between two terminal carbons of HD was considered as the main axis of the molecule. Then the angle between this axis and reference z position of GRA or GO was regarded as the structural factor and the distribution of this factor (angel) was calculated. In order to obtain these data, each peak in the plot of interaction energy distribution of each adsorbents (Fig. 2) was considered separately. The obtained results (Fig. 3) showed that HD molecules placed on GRA in the configurations of parallel (one sharp peak at around 90°) and tilted (two wide peaks at around 30° and 150°) related to the first and second peaks of PIE respectively. Also, the number of parallel configurations is more and according to PIE, this orientation is energetically more favorable.

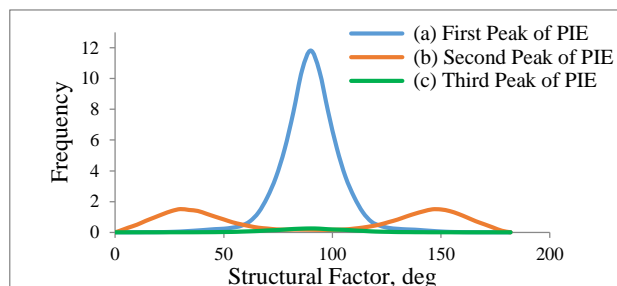


Fig. 3. Distribution of the average angle between axis of the HD molecule and reference z position of GRA.

The results of the orientational distribution function of GO indicates that HD molecules are located in parallel configuration near the surface of GO (a sharp peak at around 90°). This result is shown in Fig. 4.

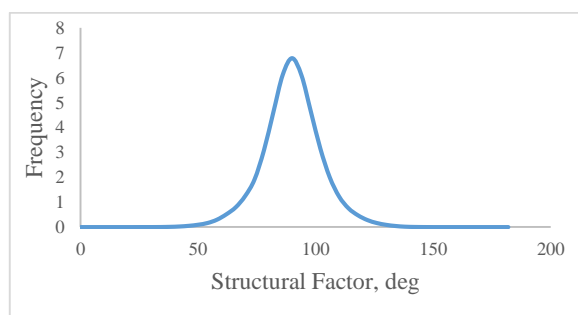


Fig. 4. Distribution of the average angle between axis of the HD molecule and reference z position of GO.

In addition, the interaction energies between HD molecules near both surfaces and also into the bulk was studied. Fig. 5 represents these distributions near the surface of the GRA and into the bulk. The comparison between Fig. 2 and Fig. 5 indicates that interactions nature between HDs are different from the interactions between HDs and GRA. As can be seen in Fig. 5, on the negative energy side the distributions show a slightly more pronounced shoulder structure for HDs. There are also large spikes located near 0.0 kcal/mol due to the many relatively weak interactions related to the HD molecules in far distances. Also, the interaction of HDs near the surface is stronger than into the bulk. This result may be explained by specific orientations of HDs with respect to the GRA which may cause to strengthen the intermolecular interaction between HDs.

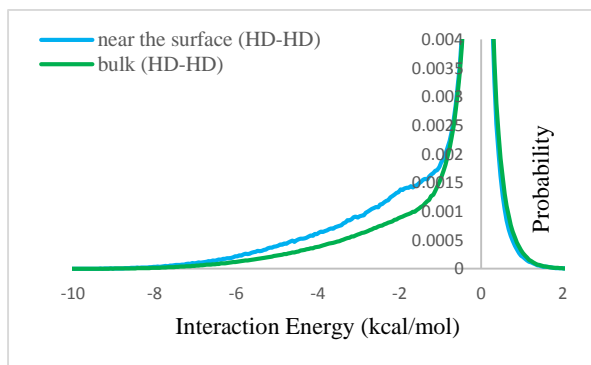


Fig. 5: Distribution of individual interaction energies between HD molecules near the surface of GRA and into the bulk.

The results of this analysis for GO is shown in Fig. 6. It is clear that the obtained results are similar to the results of HD-HD interaction near the surface of GRA and also into the bulk. The main difference is that in some parts, the pair interaction energy between HDs near the surface of GO is weaker than into the bulk. This observation can be attributed to the fact that the stronger interaction between HDs and GO may weaken the interaction between HDs near the surface of GO.

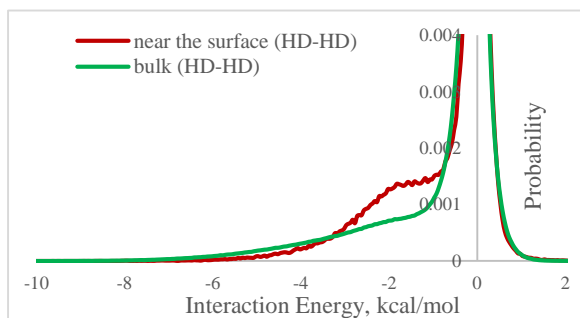


Fig. 6: Distribution of individual interaction energies between HD molecules near the surface of GO and into the bulk.

Conclusions

The purpose of this study was to investigate the interaction energy and structural properties for the adsorption of sulfur mustard on graphene and graphene oxide using molecular dynamics simulation. To achieve this goal, pair interaction energy analysis and orientational distribution function were carried out near the surface of adsorbents and into the bulk. The obtained data showed that HD preferred to place on both adsorbents in parallel configuration. The results indicate that the presence of functional groups on graphene oxide causes stronger interaction with HDs relative to graphene. Therefore graphene oxide may be used as more suitable adsorbent in protective equipment.

References

- [1] R. C. Malhotra, K. Ganesan, K. Sugendran, R. V. Swamy "Chemistry and Toxicology of Sulphur Mustard-A Review", *Defence Science Journal*, 149 (1999) 97-116.
- [2] M. P. Shakarjian, D. E. Heck, J. P. Gray, P. J. Sinko, M. K. Gordon, R. P. Casillas, N. D. Heindel, D. R. Gerecke, D. L. Laskin, J. D. Laskin "Mechanisms Mediating the Vesicant Actions of Sulfur Mustard after Cutaneous Exposure", *Toxicological Sciences*, 114 (2010) 5-19.
- [3] J. Chen, X. Wang, C. Dai, S. Chen, Y. Tu "Adsorption of GA molecule onto graphene and graphene oxide: a molecular dynamics simulation study" *Physica E*, 62 (2014) 59-63.
- [4] J. -G. Yu, L. -Y. Yu, H. Yang, Q. Liu, X. -H. Chen, X. -Y. Jiang, X. -Q. Chen, F. -P. Jiao "Graphene Nanosheets as Novel Adsorbents in Adsorption, Preconcentration and Removal of Gases, Organic Compounds and Metal Ions", *Sci. Total Environ*, 502 (2015) 70-79.
- [5] S. Chowdhury, R. Balasubramanian "Recent Advances in the Use of Graphene-Family Nano-adsorbents for Removal of Toxic Pollutants from Wastewater", *Adv. Colloid Interface Sci*, 204 (2014) 35-56.
- [6] G. Z. Kyzas, E. A. Deliyanni, K. A. Matis "Graphene oxide and its application as an adsorbent for wastewater treatment", *J. Chem. Technol. Biotechnol*, 89 (2014) 196-205.
- [7] G. K. Ramesha, A. V. Kumara, H. B. Muralidhara, S. Sampath "Graphene and graphene oxide as effective adsorbents toward anionic and cationic dyes" *J. Colloid Interface Sci*, 361 (2011) 270-277.
- [8] M. Tafazzoli, A. Khanlarkhani "Investigation of the Enhanced Solubility of Fluorinated Methanes in CO₂ by Monte Carlo Simulation: Absolute Free Energy of Solvation and Structural Properties of Solution", *J. Supercrit. Fluids*, 40 (2007) 40-49.
- [9] W. L. Jorgensen, J. Tirado-Rives "The Opls [Optimized Potentials for Liquid Simulations] Potential Functions for Proteins, Energy Minimizations for Crystals of Cyclic Peptides and Crambin", *J. Am. Chem. Soc.*, 110 (1988) 1657-1666.
- [10] W. L. Jorgensen, D. S. Maxwell, J. Tirado-Rives "Development and Testing of the Opls All-Atom Force Field on Conformational Energetics and Properties of Organic Liquids" *J. Am. Chem. Soc.*, 118 (1996) 11225-11236.
- [11] W. L. Jorgensen, P. Schyman "Treatment of Halogen Bonding in the Opls-Aa Force Field: Application to Potent Anti-Hiv Agents" *J. Chem. Theory Comput*, 8 (2012) 3895-3901.

[12] C.-J. Shih, S. Lin, R. Sharma, M.S. Strano, D. Blankschtein "Understanding the pH-dependent behavior of graphene oxide aqueous solutions: a comparative experimental and molecular dynamics simulation study" *Langmuir*, 28 (2011) 235-241.

[13] T. Darden, D. York, L. Pedersen "Particle Mesh Ewald: An $N \cdot \log(N)$ Method for Ewald Sums in Large Systems", *J. Chem. Phys*, 98 (1993) 10089-10092.

[14] U. Essmann, L. Perera, M. L. Berkowitz, T. Darden, H. Lee, L. G. Pedersen, "A Smooth Particle Mesh Ewald Method" *J. Chem. Phys*, 103 (1995) 8577-8593.

[15] J. C. Phillips, R. Braun, W. Wang, J. Gumbart, E. Tajkhorshid, E. Villa, C. Chipot, R.D. Skeel, L. Kale, K. Schulten "Scalable molecular dynamics with NAMD", *J. Comput. Chem*, 26 (2005) 1781-1802.



Adsorption of Baclofen drug on Silicon Carbide nanotube as a new drug delivery system: A theoretical study

Davood Farmanzadeh^{a*}, Haniye Badeli^a, Leila Tabari^a

^aDepartment of Physical Chemistry, Faculty of Chemistry, University of Mazandaran, Babolsar, 47416-95447, Iran

*Corresponding author: d.farmanzad@umz.ac.ir

Fax: +98-1135302350

Abstract: In the paper interaction of Baclofen drug molecule with armchair silicon carbide nanotubes (6,6) has been theoretically investigated using density functional theory (DFT). The generalized gradient approximation (GGA) with the Perdew, Burke, and Ernzerhof (PBE) functional was employed to describe the exchange and correlation terms. It has been found that the molecule is chemically adsorbed on top of C site of nanotube with adsorption energy -178.32 (kJ/mol) and a c-o binding distance is 2.066Å. The adsorption result indicated that charge transfers from the SiCNT toward Baclofen drug (.099e). These results were extremely relevant in order to identify the potential applications of SiC nanotube as drug delivery systems.

Keywords: Baclofen, DFT study, Drug delivery, SiC nanotube.

Introduction

The development of new and effective drug delivery systems with the ability to improve the therapeutic profile and efficacy of therapeutic agents is one of the key issues faced by modern medicine. In the past decade, the rapid development of nanotechnology has brought many fascinating ideas and opportunities to disease diagnosis and treatment. The carbon nanomaterials have projected tremendous research interest for biomedical applications since their discovery [1]. The recently synthesized silicon carbide nanotube has been found to be a semiconducting material and is of great technological interest for devices designed to operate at high temperatures, high power, and in harsh environments. And the stability of SiC nanotube is diameter dependent. More importantly, SiC nanotube is a semiconductor, weakly dependent on the helicity. An attractive point is that SiC nanotube has higher reactivity than carbon nanotube due to its great polarity. Obviously, these unique properties of SiC nanotube are the key advantages for its applications to the building blocks in the fabrication of electronic/optics nanodevices [2].

Spasticity is a potentially disabling symptom in patients with multiple sclerosis. Although limb spasticity is a well known complication arising from MS, the prevalence, associated disability and treatment patterns are not adequately defined. The resulting disability may take the form of gait disorders, fatigue, 'spasms' and pain. Current medical treatments are partially effective and have side effects including sedation, weakness and cognitive difficulties. Oral baclofen, commonly prescribed for spasticity, is often sub optimally managed. It is most often under dosed for fear of ensuing weakness and fatigue [3, 4]. baclofen rather selectively activates GABAB receptors, which are mainly found

presynaptically. Baclofen has also been found to depress the transmitter release from Ia afferents in the cat without any postsynaptic effects on the motoneurons [5, 6]. The focus of this study was on quality of life issues as they pertain to the experience of spasticity and the relative effectiveness of current treatment, including baclofen, in patients with MS.

In this work, we study the adsorption behaviors of the baclofen drug on the armchair SiC nanotube using density functional theory (DFT). The main objective of this DFT calculations is analyze the effects of the interactions on the geometrical parameters and the interaction energies of the considered complexes.

Materials and method

All calculations were carried out by using the DMol3 program based on the density functional theory. The generalized gradient approximation (GGA) with the Perdew, Burke, and Ernzerhof (PBE) functional was employed to describe the exchange and correlation terms. All electron calculations are employed with the double numerical plus d-function (DNP). Structural optimizations were obtained without any symmetry constraints by using a convergence tolerance of energy of 2.0×10^{-5} Ha. The Adsorption energy was calculated by the following formula:

$$E_{ads} = E(\text{Bac-SiCNT}) - E(\text{SiCNT}) - E(\text{Bac})$$

where $E(\text{Bac-SiCNT})$ is the total energy of Baclofen-SiCNT complex and $E(\text{SiCNT})$ and $E(\text{Bac})$ are the total energy of optimized pristine SiCNTs and the total energy of isolated Baclofen, respectively.

Results and Discussion

At the first, we calculated the stable configuration and electronic structures of Baclofen drug and

pristine SiC nanotube. Figure 1 show the optimized most stable structures of Baclofen and SiC nanotube.

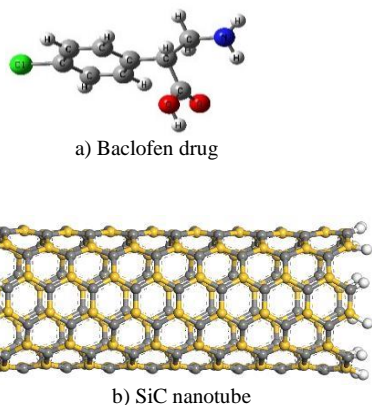


Fig.1: The optimized structure of a) Baclofen drug and b) SiC nanotube.

Further, we studied the interaction of SiCNT with a Baclofen, To find stable Baclofen adsorbed configurations, several distinct starting structures have been used for optimization, including a Cl, N, O head or OH located on top of the Si or C atom (Fig 2).

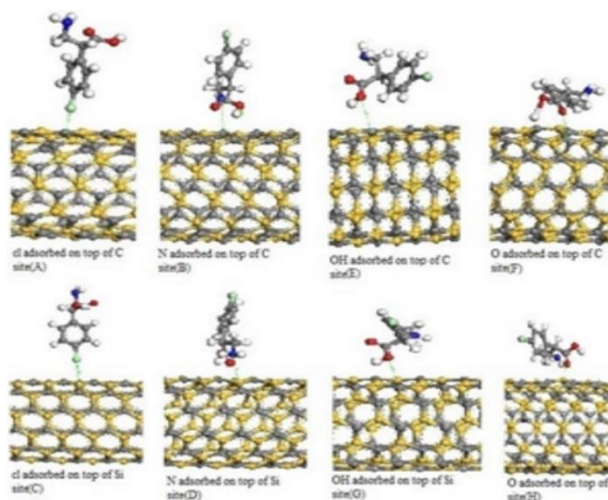


Fig.2: The optimized structures of Baclofen-SiCNT complexes.

Relevant data for Eads, equilibrium distance are given in Table 1. Interestingly, after full relaxation with no constraints, all of the initial configurations have turned into one stable configuration (F) with a high exothermic adsorption energy of -178.32 kJ/mol, in which the oxygen atom of Baclofen is closeto the C atom of the tube by a distance of 2.06 Å.

Table1: Adsorption energy and distance of systems .

configurations	E _{ads} (kJ/mol)	Distanse(Å)
A	-39.83	2.435
B	-65.44	3.449
C	-37.95	3.103

D	-137.81	3.139
E	-53.10	3.143
F	-178.32	2.066
G	-41.55	3.298
H	-87.13	2.877

In the F configuration, a local structural deformation at the adsorption site has been predicted after the Baclofen adsorption, where the adsorbing Carbon atom is slightly pulled out of the surface and the corresponding Si-C bond is thus elongated from 1.792 Å in the pristine tube to 1.798 Å in the adsorbed form. The calculated Absorption energy and average C-O equilibrium distance, after optimization for configuration R, are about -178.32eV and 2.06Å, respectively. The small distance of adsorbed O atom from the plane and the negative adsorption energy indicate strong interaction (chemisorption) of Baclofen with the SiCNT. we employed methods Mulliken for calculating the charge transfer. Mulliken charge analysis shows a charge transfer (~.099e) from SiC nanotube to baclofen drug.

Conclusions

Our results suggest that SiC nanotube for drug delivery system is favorable and energetically the SiCNT-Baclofen system is stable. the best adsorption sites for Baclofen are the C atom of the SiCNTs when the O atom pointing. SiCNT can be considered as a promising drug delivery system for Baclofen to transport it to target cells.

Acknowledgments

Financial support from the University of Mazandaran is highly appreciated.

References

- [1] F. Safdari, "DFT calculations and molecular dynamics simulation study on the adsorption of 5-fluorouracil anticancer drug on graphene oxide nanosheet as a drug delivery vehicle". *Journal of Inorganic and Organometallic Polymers and Materials*, 27 (2017) 805-817.
- [2] B. Xiao. "Theoretical studies of chemisorption of NO₂ molecules on SiC nanotube". *Surface Science*, 604 (2010) 1882-1888.
- [3] M. Barnes. "Spasticity in multiple sclerosis". *Neurorehabilitation and neural repair*, 17 (2003) 66-70.
- [4] J. Kesselring, A. Thompson. "Spasticity, ataxia and fatigue in multiple sclerosis". *Bailliere's clinical neurology*, 6 (1997) 429-445.
- [5] N. J. Tillakaratne, L. Medina-Kauwe, K. M. Gibson. "Gamma-aminobutyric acid (GABA) metabolism in mammalian neural and nonneural tissues. *Comparative Biochemistry and Physiology Part A: Physiology*, 112 (1995) 247-263.
- [6] I. Jimenez, P. Rudomin, M. Enriquez. "Differential effects of (-)-baclofen on Ia and descending monosynaptic EPSPs". *Experimental brain research*, 85 (1991) 103-113.

Theoretical study of oxidation of acetonitrile with nitrogen trioxide and formation of secondary organic aerosol

Morteza Alihosseini*, Morteza vahedpour, Mahsa Yousefian

Department of Chemistry, University of Zanjan, Zanjan, P.O. Box 38791-45371, Iran

*alihosseyni_2008@yahoo.com

Abstract : This theoretical study investigated the oxidation reaction mechanism of acetonitrile as a volatile organic compound by nitrogen trioxide in formation of secondary organic aerosol. The B3LYP level with 6-311++G(3df,3pd) basis set was used to optimize geometries of reactants, products, and transition states. One product was obtained and the reaction pathway of the product was discussed and potential energy surface was plotted. The rate constant calculated at atmospheric pressure over the temperature range 300-2500 K. Finally formation of secondary organic aerosol has been discussed.

Keywords: VOC; SOA; acetonitrile; nitrogen trioxide; potential energy surface.

Introduction

Secondary organic aerosol, (SOA), is tiny particulate matter that is created from chemical transformation of atmospheric organic compounds[1]. Experiments indicate that large amount of total organic particulate mass is because of SOA. As a result, understanding SOA formation mechanisms is important in atmospheric chemistry [2]. Studies have proven that oxidation of volatile organic compounds (VOCs), is the major mechanism of formation of SOA. Volatile organic compounds are chemical compounds that can evaporate in temperature and pressure of atmospheric conditions [3,12] and have two major sources: natural(primary) and chemical reactions(secondary) in the atmosphere[4]. They can impact on air quality by producing atmospheric pollutants, ozone, and organic aerosol.

Acetonitrile(CH₃CN, methyl cyanide), is one of the volatile organic compounds which has gained much attention in recent years because of its importance in atmospheric chemistry[5]. There are various sources of acetonitrile to the atmosphere that the major source is biomass burning [6].

To our knowledge no study has been done over reaction of acetonitrile with nitrogen trioxide. On the other hand no research has been done over the role of acetonitrile in the formation of SOA. Therefore In this paper we first aim to study reaction pathways of acetonitrile with NO₃. Then, we focus on the potential of adducts of this reaction in producing secondary organic aerosol.

Materials and method

All of the calculations were carried out with the GAUSSIAN 03 program. Therefore geometries of reactants, products (denoted as P), and transition states (denoted as TS) were optimized using B3LYP[7] with 6-311++G(3df,3pd) basis set.

Connections between transition states, and products are confirmed by the intrinsic reaction coordinate (IRC)[8] analysis at the B3LYP level of theory. All these calculations are done at a temperature of 298.15K and under atmospheric pressure. Finally rate constant have been calculated by transition state theory (TST)[9] with GPOP program.

Results and Discussion

The optimized geometries of the reactants, transition states, and products at the B3LYP level and 6-311++G(3df,3pd) are shown in Fig. 1. The relative energies and zero point energy corrections have been listed in Table 1. for the B3LYP level. To simplify our discussion, the energy of reactant (CH₃CN+NO₃) is set to be zero as reference. The thermodynamic functions values at room temperature and atmospheric pressure are tabulated in Table 2.

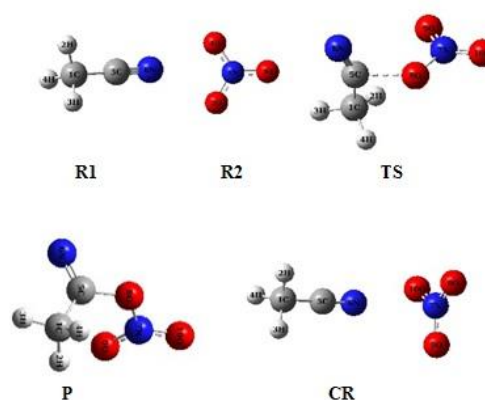


Fig.6: Geometries of reactants, transition states, and products optimized at B3LYP level.

Then, by means of the transition states and their connected products, the PES profile has been plotted at the B3LYP level in Fig. 2. Finally the rate constant

k for the reaction pathway of P is plotted in Fig. 3 and rate constant values over the range 200-2500 K and atmospheric pressure are listed in Table 3.

Reaction pathway

The pathway initiated from one pre-reactive complex, CR, that has been found between reactants CH₃CN and NO₃ on PES.

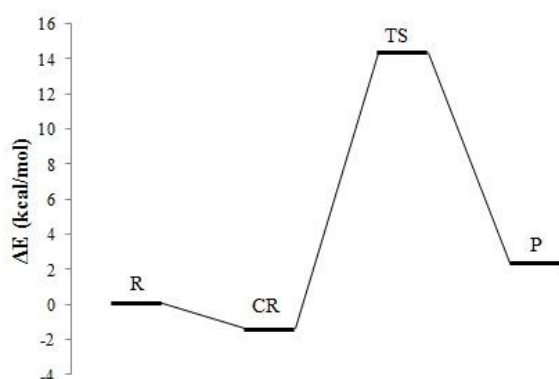


Fig. 2 The potential energy profile of the CH₃CN+NO₃ reaction at the b3lyp/6-311++G (3df,3pd) level.

The complex lies -1.545 kcal/mol below the original reactant (CH₃CN+ NO₃) at the B3LYP level. In this path CR converts to P via TS with energy barrier of 15.803 kcal/mol and one imaginary frequency at -499i cm⁻¹ at the B3LYP level.

Table1: The relative energies of the reactants and product in the CH₃CN + NO₃ reaction.

Species	B3LYP
CH ₃ CN+NO ₃	0.00
CR	-1.5456
TS	14.2575
P	2.2453

Thermodynamic data shows that the overall process is endothermic with the reaction enthalpy of 1.34 kcal/mol and nonspontaneous in gas phase with 13.67 kcal/mol Gibbs free energy.

Table2: The reaction energies, enthalpies, and Gibbs free energies, and entropies (kcal/mol)

Reaction	ΔE°	ΔH°	ΔG°	TΔS°
CH ₃ CN + NO ₃ →CH ₃ C(N)ONO ₂	1.93	1.34	13.67	-12.33

Calculation of rate constant

The rate constant has been calculated for this

pathway by the transition state theory (TST) implemented in the GPOP program. As shown in Fig.2 the pathway P includes only one transition state, TS. The overall rate constant values of the CH₃CN+ NO₃ reaction through path P have been listed in table 3 at the temperature range of 300-2500K.

Table1: rate constants k (cm⁻¹ molecule⁻¹ s⁻¹) at the temperature range of 300-2500 K

T	K	T	K	T	K
300	6.33E-26	1100	1.46E-17	1900	7.76E-16
400	3.22E-23	1200	3.01E-17	2000	1.06E-15
500	1.52E-21	1300	5.66E-17	2100	1.42E-15
600	2.14E-20	1400	9.89E-17	2200	1.86E-15
700	1.51E-19	1500	1.63E-16	2300	2.40E-15
800	6.83E-19	1600	2.54E-16	2400	3.04E-15
900	2.30E-18	1700	3.81E-16	2500	3.80E-15
1000	6.25E-18	1800	5.52E-16		

Figure 3, also shows the Arrhenius plot for the k rate constant. Arrhenius parameters for the k rate constant are as follows:

$$k = 5.69 \times 10^{-14} \exp(-71.30 \text{ kJ mol}^{-1}/RT)$$

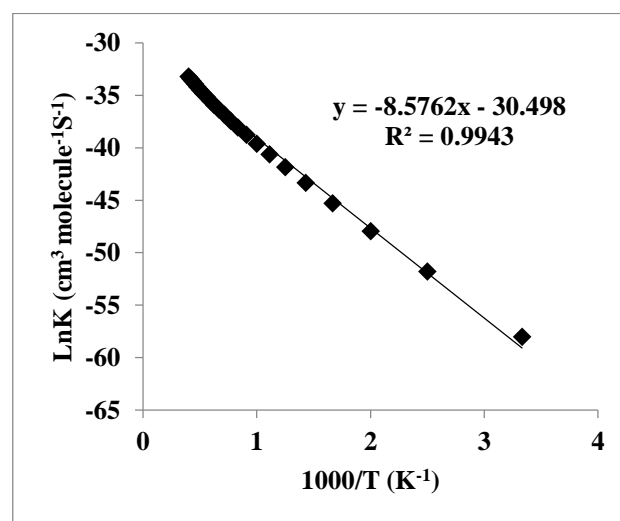


Fig. 3 Arrhenius plot for the k rate constant

SOA Formation

One of the important factors that controls secondary organic aerosol formation of organic compounds in the atmosphere is volatility. Organic species in oxidation reactions can lower volatility by adding functional groups or increase volatility by breaking C-C bonds. On the other hand, formation of species with high molecular weight can also affect volatility. Therefore oxidation reactions of volatile organic compounds (VOCs), are determinant in

formation of SOA[1]. In term of volatility, polarity and size are two key functions that determining the vapor pressure of a molecule. The more polarity is, the less volatility will become. As a result, oxidation reactions which increase polarity or size of a molecule can play important role in formation of SOA[10]. nitrogen trioxide is one of the main oxidants in the atmosphere that as a polar functional group can be added to carbon skeleton and facilitate formation of SOA[11]. This product will have decrease in volatility because of the addition of polar nitrogen trioxide. Moreover they can react with oxygen molecules and new formed products can lead to much decrease in volatility. Therefore, they have potential to produce SOA. An alternative mechanism that is likely is non-oxidative reaction in the condensed phase. Because there is a reverse relation between vapor pressure and every two carbon added by order of magnitude, these reactions can form low volatile products and hence help yielding the SOA[12].

Conclusions

In this work, the mechanism for the reaction of $\text{CH}_3\text{CN} + \text{NO}_3$ was studied at B3LYP level with 6-311++G(3df,3pd) basis set. The potential energy profile was drawn and thermodynamic data was calculated. Then the rate constant values for the P production pathway has been calculated using TST theory at atmospheric pressure and temperature range of 300-2500 K. Finally, formation of secondary organic aerosol from given adducts was studied. This research reveals that oxidation of acetonitrile by NO_3 can result in formation of secondary organic aerosol.

References

- [1] J.H. Kroll, J.H. Seinfeld, Chemistry of secondary organic aerosol: Formation and evolution of low-volatility organics in the atmosphere, *Atmos. Environ.*, 42 (2008) 3593-3624.
- [2] H.-J. Lim, B.J. Turpin, Origins of Primary and Secondary Organic Aerosol in Atlanta: Results of Time-Resolved Measurements during the Atlanta Supersite Experiment, *Environ. Sci. Technol.*, 36 (2002) 4489-4496.
- [3] T. Salthammer, Very volatile organic compounds: an understudied class of indoor air pollutants, *Indoor Air*, 26 (2016) 25-38.
- [4] J. Murphy, D. Oram, C. Reeves, Measurements of volatile organic compounds over West Africa, *Atmos. Chem. Phys.*, 10 (2010) 5281-5294.
- [5] B.S. Jursic, Density functional theory and ab initio study of CH_3NC and HNC isomerization, *Chem. Phys. Lett.*, 256 (1996) 213-219.

- [6] J. De Gouw, C. Warneke, D. Parrish, J. Holloway, M. Trainer, F. Fehsenfeld, Emission sources and ocean uptake of acetonitrile (CH_3CN) in the atmosphere, *J Geophys Res Atmos*, 108 (2003).
- [7] A.D. Becke, A new mixing of Hartree-Fock and local density-functional theories, *J. Chem. Phys.*, 98 (1993) 1372-1377.
- [8] J. Cizek, J. Paldus, Coupled Cluster Approach, *Phys. Scripta*, 21 (1980) 251.
- [9] A.G. Baboul, L.A. Curtiss, P.C. Redfern, K. Raghavachari, Gaussian-3 theory using density functional geometries and zero-point energies, *J. Chem. Phys.*, 110 (1999) 7650-7657.
- [10] J.F. Pankow, W.E. Asher, SIMPOL.1: a simple group contribution method for predicting vapor pressures and enthalpies of vaporization of multifunctional organic compounds, *Atmos. Chem. Phys.*, 8 (2008) 2773-2796.
- [11] R.J. Griffin, D.R. Cocker, R.C. Flagan, J.H. Seinfeld, Organic aerosol formation from the oxidation of biogenic hydrocarbons, *J Geophys Res Atmos*, 104 (1999) 3555-3567.
- [12] M. Alihosseini, M. Vahedpour, M. Yousefian, New trace of secondary organic aerosol from oxidation of acetonitrile with radical hydroxyl, *Computational and Theoretical Chemistry*, 1113 (2017) 72-81.

QM study on the mechanism of Carbonic anhydrase II inhibition with non-zinc mediated inhibitor

Mina Ghiasi^{*a}, Masumeh Zolfi^a and Mansour Zahedi^b

^aDepartment of Chemistry, Faculty of Physics & Chemistry, Alzahra University, 19835-389, Vanak, Tehran, Iran.

ghiasi@alzahra.ac.ir

^bDepartment of Chemistry, Faculty of Science, Shahid Beheshti University, G. C., Evin, 19839-63113, Tehran, Iran.

Abstract: In the present study, experimentally observed inhibition mechanism of zinc enzyme carbonic anhydrase II (CAII) by new class of suicide inhibitors, has been modeled using of density functional theory (DFT) to investigate the geometrical parameters and thermochemical aspects of this mechanism. It should be mentioned that this distinctive feature of the CA active site architecture and details of CA-inhibitor complex structure is little understood at present. Many of the CA isozymes involved in these processes are important therapeutic targets with the potential to be inhibited to treat a range of disorders. The results of our calculations indicate that studied inhibitor do not directly interact with the metal ion from the CA active center.

Keywords: Carbonic anhydrase; Nano scale inhibitor; Inhibition mechanism; QM calculation.

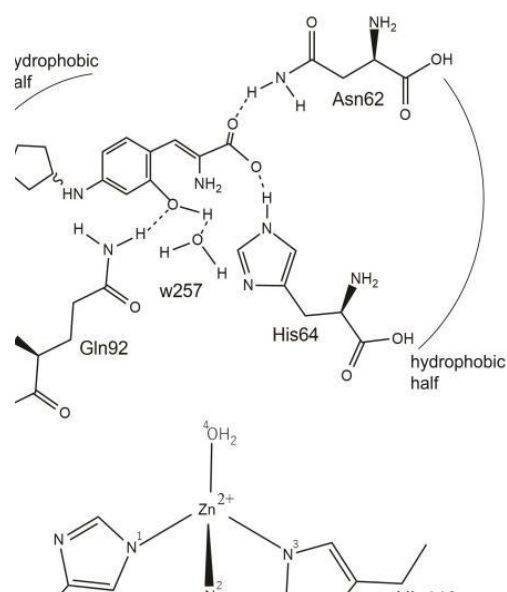
Introduction

Carbonic anhydrases (CAs, EC 4.2.1.1) belong to biological metalloenzymes that facilitate the proton transport and present in all three domains of life, Eucarya, Bacteria and Archaea [1, 2]. These superfamily of metalloenzymes efficiently catalyze very simple physiological reaction, the conversion of carbon dioxide to bicarbonate ion, and then bicarbonate replaced by a water molecule to generate catalytically inactive form of this enzyme.

Carbonic anhydrase is inhibited by an extended numbers of different deterrents and often using their anion, for instance: metal complexing anion, sulfonamides, phenols and polyamines that bind to the metal ion through the enzyme active site or are anchored to the water molecule coordinated to the metal ion [3, 4]. In recent years a novel group of inhibitors of CA that belong to the new chemotype molecules including coumarins and their derivatives have been reported [5-7] that inhibit CA isoforms IX, XII, and XIII, Figure 1. This new class of carbonic anhydrase inhibitors binds to the entrance of active form of the CA active center (hydrolyzed form) and does not directly interact with the metal ion such as

presently available inhibitors of the sulfonamide and sulfamate type [4]. Scheme 1 presents the proposed inhibition mechanism of CAs by this new class of inhibitors, leading to cis- or trans-2-hydroxy-cinnamic acid. So in the present research we use the quantum mechanical calculations to investigate on the inhibition mechanism of new class of inhibitor, as potent inhibitor of CA II.

Fig.7: Proposed inhibition mechanism of CA by nano scale inhibitor that leading to cis/trans-2-hydroxycinnamic acid



Materials and method

Ab initio calculations were carried out with the Gaussian program series 2003. The structure of carbonic anhydrase active center in active (zinc-bound hydroxide) and inactive (zinc-bound water) forms, nano scale inhibitor the complex between inhibitor and CA were fully optimized employing a hybrid Hartree-Fock- density functional scheme, the adiabatic connection method –Becke three-parameter with Lee-Yang-Parr (B3LYP) functional of density functional theory (DFT) with the standard 6-31+G* basis set. Full optimizations were performed without any symmetry constrains. The harmonic vibrational frequencies were computed to confirm that an optimized geometry correctly corresponds to a local minimum that has only real frequencies. Also the thermodynamic properties of all compounds were obtained from frequency calculations at 298.15 K and 1.0 atmosphere pressure.

Results and Discussion

Structure of carbonic anhydrase active center in active and inactive form were fully optimized at B3LYP method using 6-31+G* basis set with no initial symmetry restrictions and assuming C_1 point group. Figure 2 and Table 1 shows the optimized structure and some structural details of carbonic anhydrase active center in both form. As the results indicate the average N(His)-Zn-O(OH₂) and N(His)-Zn-N(His) bond angles is equal to 92.3° and 119.7° respectively in active and inactive form respectively, so both active and inactive forms of β -CA have tetrahedral geometry.

Calculation of vibrational frequencies has confirmed stationary point with no negative eigenvalue observed in the force constant matrix.

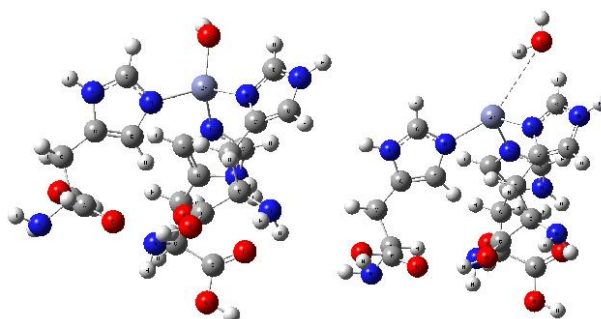


Fig.2: The optimized geometry of carbonic anhydrase active site in active (left) and inactive (right) form.

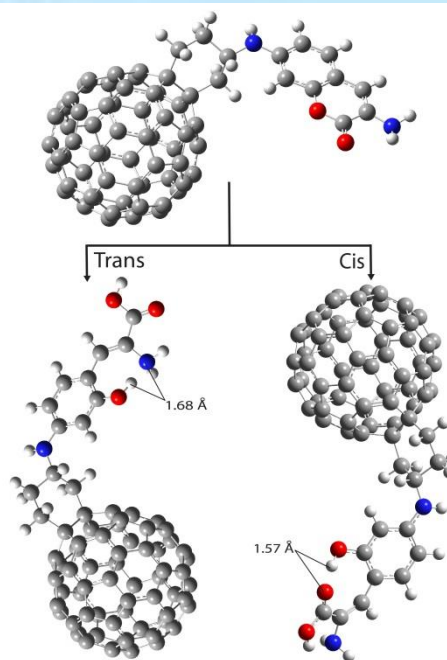


Fig.3: The optimized geometry of nano scale inhibitor in cis and trans isomer.

The minimization procedure for the studied inhibitor has been performed at the B3LYP/6-31+G* method yields a non-planar conformation as the more stable one, Figure 3.

According to previous study on human carbonic anhydrase II one molecule of the coumarin hydrolysis product (cis-2-hydroxycinnamic acid) as a new inhibitor bound within the hCA II active site [8]. So according to proposed mechanism in Figure 1 the most stable conformer of inhibitor undergo hydrolysis by the zinc bound hydroxide ion which acts as a potent nucleophile. In addition at the presence of water molecule cis-2-hydroxy-cinnamic acid intermediate is formed and the active form of the enzyme is converted to inactive form, water bonded to the zinc ion. According to the results of our calculation cis-2-hydroxy-cinnamic acid cannot bind in the restricted space near the zinc ion thus reoriented toward the exit of the active center cavity. In continue a rearrangement of the inhibitor/enzyme adduct occur which leading to provide the trans-2-hydroxy-cinnamic acid isomer.

Table1: Some structural details of active and inactive form of CA.



Connected Atoms	CA (active)	CA (inactive)
Bond Distance(Å)		
Zn-N1	2.09	2.17
Zn-N2	2.08	2.15
Zn-N3	2.06	2.12
Zn-O4	1.87	3.49
Bond Angle(°)		
N1 Zn N2	112.88	111.12
N1 Zn O4	111.52	151.25

Conclusions

In the present research, the inhibition mechanism of CA II by new inhibitor using DFT method has been investigated. In the next step the inhibition mechanism of natural carbonic anhydrase II by nano scale inhibitor has been investigated. According to our calculated results the hydroxycinnamic acids formed by the active center mediated hydrolysis of the coumarin derivatives in active site region which is different in all CA isoforms and the enzyme active form convert to inactive form. The formed hydroxycinnamic acid after hydrolysis may adopt cis/trans conformations which can interact with around amino acids residues at the entrance of the enzyme active center without binding to the zinc ion. We are hopeful that our results be helpful to design new inhibitors with interesting pharmacological applications to synthesize new drugs to manage the brain disease.

Acknowledgment

Technical support of the Chemistry Computation Center at Shahid Beheshti University is greatly acknowledged.

References

- [1] S. Elleuche, S. Pöggeler, Carbonic anhydrases in fungi, *Microbiology* 156 (2010) 23-29.
- [2] M. Hilvo, M. Tolvanen, A. Clark, B. Shen, G.N. Shah, A. Waheed, P. Halmi, M. Hänninen, J.M. Hämäläinen, M. Vihinen, W.S. Sly, S. Parkkila, Characterization of CA XV, a new GPI-anchored form of carbonic anhydrase, *Biochem. J.* 392 (2005) 83-92.
- [3] A. Maresca, C. Temperini, L. Pochet, B. Masereel, A. Scozzafava, C.T. Supuran, Deciphering the mechanism of carbonic anhydrase inhibition with coumarins and thiocoumarins, *J. Med.* 53 (2009) 335-344.

[4] J.Y. Winum, A. Scozzafava, J. L. Montero, C.T. Supuran, New Zinc Binding Motifs in the Design of selective Carbonic Anhydrase Inhibitors, *Mini-Rev. Med. Chem.* 6 (2006) 921-936.

[5] A. Maresca, C. Temperini, H. Vu, N.B. Pham, A. Scozzafava, R.J. Quinn, C.T. Supuran, Non-Zinc Mediated Inhibition of Carbonic Anhydrases : Coumarins Are a New Class of Suicide Inhibitors Non-Zinc Mediated Inhibition of Carbonic Anhydrases : Coumarins Are a New Class of Suicide Inhibitors #, *Society.* 131 (2009) 3057-3062.

[6] A. Maresca, C. Temperini, L. Pochet, B. Masereel, A. Scozzafava, C.T. Supuran, Deciphering the mechanism of carbonic anhydrase inhibition with coumarins and thiocoumarins, *J. Med.* 53 (2009) 335-344.

[7] (a) A. Maresca, C.T. Supuran, Coumarins incorporating hydroxy-and chloro-moieties selectively inhibit the transmembrane, tumor-associated carbonic anhydrase isoforms IX and XII over the cytosolic ones I and II , *Bioorg. Med. Chem. Lett.* 20 (2010) 4511-4514. (b) A. Maresca, A. Scozzafava, C.T. Supuran, 7, 8-Disubstituted-but not 6, 7-disubstituted coumarins selectively inhibit the transmembrane, tumor-associated carbonic anhydrase isoforms IX and XII over the low nanomolar/subnanomolar range, *Bioorg. Med. Chem.* 20 (2010) 7255-7258.

[8] A. Maresca, C. Temperini, H. Vu, N.B. Pham, A. Scozzafava, R.J. Quinn, C.T. Supuran, Non-Zinc Mediated Inhibition of Carbonic Anhydrases : Coumarins Are a New Class of Suicide Inhibitors Non-Zinc Mediated Inhibition of Carbonic Anhydrases : Coumarins Are a New Class of Suicide Inhibitors #, *Society.* 131 (2009) 3057-3062.

NO Oxidation Catalysed by Ir₃M (M= Ir, Co, Cu) Nanoclusters

A. Mohajeri*, N. Hassani

Department of Chemistry, Shiraz University, Shiraz, 71454, Iran

*amohajeri@shirazu.ac.ir

Abstract: Density functional theory (DFT) has been used to demonstrate the crucial influence of the alloying on the energy barriers for the NO oxidation reaction over Ir-based bimetallic nanoclusters. The Langmuir–Hinshelwood (LH) mechanism is explored to gain insights into the fundamental mechanism for the reaction between NO and O₂. The adsorption energies, reaction pathways, and reaction barriers are calculated systematically for square planar geometry of Ir₃M (M= Ir, Co, Cu) clusters. Comparing the calculated barriers of monometallic Ir₄ cluster with those of bimetallic clusters (Ir₃Co and Ir₃Cu) indicates that the catalytic activity of Ir centres seems not to be dependent on its surroundings.

Keywords: Nitrogen oxides; catalytic oxidation; Ir₄ cluster; alloying

Introduction

Nano sized clusters perusal has been one of the attractive topics of research in some science for example physics, biology and chemistry [1]. Clusters can be applied to catalysis, data storage, medical diagnosis, bio sensing and etc. [2]. However, properties of metal clusters are different from those of bulk metals, due to their size. During the last decade, iridium-based catalysts have attracted much attention, because of their ready availability and high reactivity. Accordingly, a number of theoretical and experimental studies have been devoted to investigating the adsorption of NO and O₂ molecules as well as and their reaction on the iridium surface. For example, Gardner et al. [3] studied the dissociative process of NO adsorption on the (1×1)–Ir (100) surface at 300 K using vibrational spectroscopy and low-energy electron diffraction (LEED). A combined experimental and theoretical study of NO adsorption on Ir(100) surface has been carried out to evaluate a function of NO coverage versus temperature.²³ King et al. [4] explained that both molecular and dissociative chemisorption and reactions of NO can happen on Ir surfaces. Endou et al. [5] carried out a comparative investigation on the adsorption properties of several metal clusters such as Rh, Pd, Ag, Ir, Pt, and Au toward NO. Furthermore, it has been reported that Ir can be highly active and selective to be catalyst, when it is present in the form of nanoparticles. By now it is well known that the different types of factors which influence the electronic and catalytic behavior of Iridium clusters include the size and morphology of the cluster, the charge on the cluster, the supporting material, ligand adsorption, doping and so on.

The present study is devoted to investigating the detailed reaction process of NO oxidation on the Ir₄ cluster by performing density functional theory (DFT) calculations. On the other side, it is known that bimetallic catalysts often exhibit advantageous properties compared to those of their pure constituent

metals, because alloying offers opportunities for the synergistic inter-metallic interactions that may improve the catalytic performance [6-8]. In this context, developing bimetallic nanoclusters with improved catalytic activity is also of great interest. Accordingly, we also study the effect of alloying on the reactivity and catalytic behaviour of the Ir₄ cluster by introducing Cu and Co atoms.

Method

In order to find the correct atomic arrangement for Ir₃M (M= Co, Cu) clusters, we performed geometrical optimization on square planar configuration with all possible spin multiplicities. All calculations were carried out within the framework of the DFT methods embedded in the Gaussian 09 suites of program [9]. Becke's hybrid three-parameter exchange functional (B) and the correlation approach of Perdew-Wang's referred as BPW91 is used to describe the reaction system. The minimum energy configurations of Ir₃M (M= Co, Cu) are predicted to be a square planar structure with nonet, septet and septet spin states for Ir₄, Ir₃Cu and Ir₃Co respectively. After the establishment of lowest energy states for square planar configurations of Ir₃M (M= Co, Cu) clusters, their catalytic behaviours for the NO oxidation are examined. The standard 6-31G (d) basis set is used for N and O atoms and the LANL2DZ pseudo potential is employed for transition metals.

We calculated the zero-point energy (ZPE) corrected adsorption energy (E_{ads}) of adsorbate A with an Ir₃M cluster as

$$E_{ads} = (E_{Ir_3M-A} - E_{Ir_3M} - E_A) + (E_{Ir_3M-A}^{ZPE} - E_{Ir_3M}^{ZPE} - E_A^{ZPE}) \quad (1)$$

In this equation, E_{Ir₃M-A}, E_{Ir₃M} and E_A correspond to the energies of the complex between the adsorbed species (A) and the cluster, the bare Ir₃M clusters, and a gas phase adsorbate, respectively. A more negative E_{ads} corresponds to stronger adsorption,

which means that the corresponding adsorption is thermodynamically more favourable.

Results and Discussion

3.1. Adsorption of O₂ and NO on Ir₃M (M= Ir, Co, Cu) clusters

In the first step, we examined the adsorption of O₂ and NO molecules over the Ir₃M (M= Ir, Co, Cu) clusters. Various orientations have been taken into account to design the initial configurations. After full geometry optimization, both O₂ and NO adsorbed through binding with one of the Ir atoms. The calculated adsorption energies for all possible spin multiplicities of Ir₃M-O₂, Ir₃M-NO, and Ir₃M-ON complexes are showed that the adsorption of NO via its nitrogen results in more stable complexes. The lowest energy structure of Ir₃M-O₂ (M= Ir, Co, Cu) with square planar geometry are in quintet state with the adsorption energy of -1.43, 1.53 and 1.50 eV for Ir₄, Ir₃Cu and Ir₃Co respectively.

The optimized geometries together with structural parameters for the adsorption of NO and O₂ Ir₃M (M= Ir, Co, Cu) clusters are displayed in Fig.1 It can be seen that, after adsorption, the O-O bond distance increased as compared to the bond length of free standing O₂ (1.229Å). The bond elongation is accompanied by notable red shifts in the O-O stretching frequency that are 223~294 cm⁻¹ upon the adsorption of O₂ on Ir₃M (M= Ir, Co, Cu). The decrease in stretching frequency is due to the back-donation from Ir₃M to π* orbital of O₂ leading to bond weakening and highlighting the activation of O₂ molecule on the surface of Ir₃M (M= Ir, Co, Cu) clusters. Unlike O₂, the NO bond is less affected by the adsorption over Ir₃M (M= Ir, Co, Cu) clusters. The N-O bond is red shifted by 82~96 cm⁻¹ upon the adsorption on Ir₃M (M= Ir, Co, Cu).

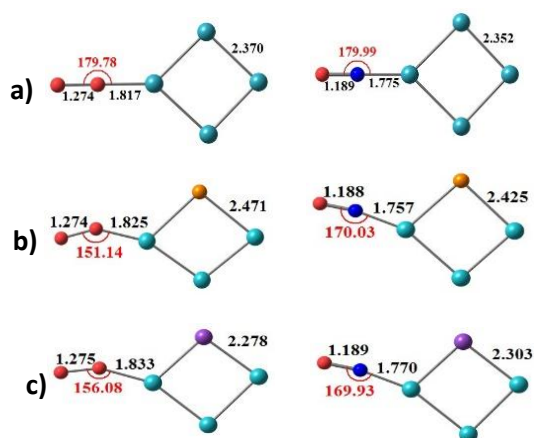


Fig.8: The lowest energy structures of Ir₃M -O₂ and Ir₃M -ON in square planar configuration. Bond length and bond angles are given in angstrom and degree. Ir (●), Cu (●), Co (●), N (●), O (●).

3.2. NO oxidation catalyzed by Ir₃M (M= Ir, Co, Cu) clusters

For NO oxidation, we considered the LH mechanism which is proposed to be the most probable mechanism for this reaction [10, 11]. To search for the minimum-energy pathway we calculated ground PES for the reaction promoted by Ir₃M (M= Ir, Co, Cu) the reaction starts from Ir₃M -O₂ in the quintet state and NO in its doublet ground states. Thus the reaction proceeds either on sextet or on quartet spin multiplicity states. The detailed results for the ground state surfaces which is sextet surface for NO oxidation on Ir₃M (M= Ir, Co, Cu) are presented here. As shown in Figure 2, NO and O₂ are initially co-adsorbed on the single Ir atom to form a chemically energized intermediate **IM1** which lies below the entrance channel by -1.76, -1.95, -2.22 eV for Ir₄, Ir₃Co and Ir₃Cu respectively. Comparing these values with the co-adsorption of NO and O₂ on pristine Ir₄ with an adsorption energy of -1.76 eV indicates a stronger adsorption on Ir₃Cu and Ir₃Co clusters. After co-adsorption, the dissociation of adsorbed O₂ has taken place and one of the oxygen atoms approaches to NO to form ONO (**IM2**) + O by surmounting transition state **TS1**. The barrier heights of the transition states are 0.81, 0.96 and 0.99 for Ir₄, Ir₃Co and Ir₃Cu respectively. Comparing the first energy barriers of the doped cluster with the corresponding values in the case of pristine Ir₄ reveals a decrease in catalytic efficiency for doped clusters. In saddle point **TS1**, which an O-O bond is breaking, one of the oxygen atoms approaches to the NO to form ONO. The formed ONO locates in such a way that one of its oxygen is adsorbed on the neighbouring Ir atom with the corresponding co-adsorption energy of -3.41, -3.70, -3.41 eV for Ir₄, Ir₃Co and Ir₃Cu respectively. The **IM2** further evolves into more stable intermediate **IM3** through adsorption of ONO on the neighbouring Ir atom adjacent to Ir-O bond via **TS2**. The intermediate **IM3** is an energized ONO-Ir₄-O complex which lies 3.85, 3.47, 3.03 eV for Ir₄, Ir₃Co and Ir₃Cu, respectively below the entrance channel and serves as the precursor of forming NO₂. The produced ONO is adsorbed on the doped atom in Ir₃Co and Ir₃Cu or on neighbour Ir in Ir₄ via one of its oxygen atoms. On the final state, the NO₂ molecule desorbs from the cluster surfaces while leaving an adsorbed oxygen atom on the surface of the clusters. On the final state, the NO₂ molecule desorbs from the cluster surfaces while leaving an adsorbed oxygen atom on the surface of the clusters. As shows in Fig.2 that NO oxidation over the surfaces of Ir₃Cu and

Ir_3Co clusters features second energy barriers (0.47 and 0.58 eV) that are lower than that of the Ir_4 cluster in square planar geometries (0.68 eV).

The results show that the geometrical parameters for the stationary points located along the reaction coordinates and the mechanistic details regarding the NO oxidation on bimetallic clusters are very similar to those discussed above for pristine Ir_4 . In summary, the potential energy surface profiles along the pristine Ir_4 and its doped analogues have common features: the overall reaction is highly exothermic and the initial activation of O_2 is the rate-determining step (TS1). Although the second transition state energy barrier turns out to be significantly lower for the Ir_3M -mediated reactions, the activation energies for NO oxidation promoted by Ir_3M are higher than those obtained for pristine Ir_4 . This seems to imply that the general bifunctional properties proposed in the literature for a bimetallic catalyst does not apply to the present systems and for NO oxidation the reaction prefers to be catalysed by monometallic Ir cluster.

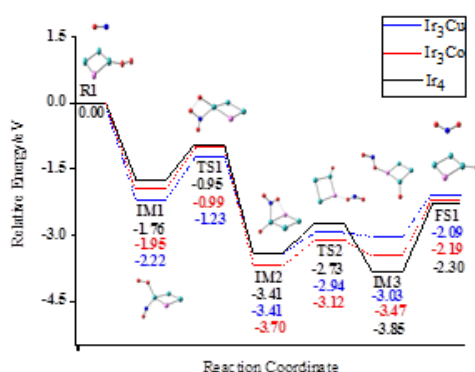


Fig.9: Potential energy surfaces for NO oxidation promoted by square planar Ir_3M ($\text{M} = \text{Ir}, \text{Co}$ and Cu) with multiplicity sextet. The sum of energies of free Ir_3M , O_2 , and NO is taken as the zero energy.

Conclusions

In summary, the catalytic properties of monometallic Ir_4 and bimetallic Ir_3M clusters ($\text{M} = \text{Cu}, \text{Co}$) toward NO oxidation are studied by DFT calculations. The PESs for sextet spin states of square planar configuration were obtained and the effect of alloying has been scrutinized along the reaction paths. In all cases, the reaction proceeds according to the single-centre mechanism. The Ir site is the active centre and the oxidation proceeds through the adsorption of O_2 and NO on the Ir atom. The results show that O_2 can be effectively activated upon adsorption on Ir atom which is crucial to determine the rate of NO oxidation. The doped clusters adsorb NO and O_2

more strongly than the pristine Ir_4 . Nonetheless, the activation barriers for NO oxidation reaction are almost in the same order of magnitude for Ir_4 and its doped counterparts. This implies that the catalytic activity of Ir centre in the bimetallic clusters is independent of its surroundings and the NO oxidation reaction prefers to be catalysed by monometallic Ir cluster.

Acknowledgment

The authors would like to acknowledge support of the Shiraz University Research Council.

References

- [1] A. M. Argo, J. F. Odzak, B. C. Gates "Role of Cluster Size in Catalysis: Spectroscopic Investigation of $\gamma\text{-Al}_2\text{O}_3$ -Supported Ir_4 and Ir_6 during Ethene Hydrogenation", *J. Am. Chem. Soc.*, 125 (2003), 7107-7115.
- [2] R. Ferrando, J. Jellinek, R. L. Johnston "Nanoalloys: From Theory to Applications of Alloy Clusters and Nanoparticles Johnston", *Chem. Rev.* 108 (2008), 845-910.
- [3] P. Gardner, R. Martin, R. Nalezinski, C.L.A. Lamont, M.J. Weaver, A.M. Bradshaw "Adsorption of Nitric Oxide on Ir(100): Influence of Substrate Reconstruction", *J. Chem. Soc., Faraday Trans.* 91 (1995) 3575-3584.
- [4] Z. P. Liu, S.J. Jenkins, D.A. King "Car Exhaust Catalysis from First Principles: Selective NO Reduction under Excess O_2 Conditions on Ir", *J. Am. Chem. Soc.*, 126 (2004) 10746-10756.
- [5] A. Endou, N. Ohashi, K. Yoshizawa, S. Takami, M. Kubo, A. Miyamoto "Comparative Investigation on the Adsorption Properties of Precious Metal Clusters toward NO: A Density Functional Study", *Jpn. J. Appl. Phys.*, 104 (2000) 5110-5117.
- [6] D. Palagin, J. P. K. Doye "CO Oxidation Catalysed by Pd-based Bimetallic Nanoalloys", *Phys. Chem. Chem. Phys.*, 17 (2015) 28010-28021.
- [7] W. Chen, S. Chen "Iridium-Platinum Alloy Nanoparticles: Composition-dependent Electrocatalytic Activity for Formic Acid Oxidation", *J. Mater. Chem.*, 21 (2011) 9169-9178.
- [8] H. I. Karan, K. Sasaki, K. Kuttiyiel, C. A. Farberow, M. Mavrikakis, R. R. Adzic "Catalytic Activity of Platinum Monolayer on Iridium and Rhenium Alloy Nanoparticles for the Oxygen Reduction Reaction", *ACS Catal.*, 2 (2012) 817-824.
- [9] M. J. Frisch, G. W. Trucks, H. B. Schlegel, G. E. Scuseria, M. A. Robb, J. R. Cheeseman, G. Scalmani, V. Barone, B. G. A. Mennucci, Petersson, et al. Gaussian 09, revision A.02, Gaussian, Inc.: Wallingford, CT, 2009.
- [10] D. Torres, S. Gonzalez, K. M. Neyman, F. Illas "Adsorption and Oxidation of NO on Au (111) Surface: Density functional studies", *Chem. Phys. Lett.*, 422 (2006) 412-416.

A DFT study on sensing performance of Cu-decorated Si₁₂C₁₂ (Cu@Si₁₂C₁₂) nanocage for detecting toxic cyanogen gas

Mohammad Solimannejad*, [Azin Karimi Anjiraki](#), Saeedeh Kamalinahad

Department of Chemistry, Faculty of Science, Arak University, 38156-8-8349, Arak, Iran

*m-solimannejad@araku.ac.ir

Abstract: The adsorption of NCCN molecule onto the outer surfaces of pristine and Cu-decorated Si₁₂C₁₂ (Cu@Si₁₂C₁₂) nanocage is investigated using density functional theory (DFT) calculations. According to the results of the calculations, the NCCN molecule could not strongly adsorb on the exterior surfaces of Si₁₂C₁₂ nanocage. Therefore, in order to increase the efficiency of Si₁₂C₁₂ nanocage for NCCN adsorption, Cu decorating process was investigated. The results show that interaction between the NCCN molecule and Cu@Si₁₂C₁₂ is chemisorptions with appreciable adsorption energy. Therefore Cu@Si₁₂C₁₂ is a suitable adsorbent and it is expected that can potentially to be used as nanosensors for detecting the presence of toxic NCCN molecule.

Keywords: Sensing of cyanogen, Si₁₂C₁₂ nanocage, DFT, Cu-decorated, Sensor.

Introduction

Cyanogen is a very toxic gas, highly flammable, colorless with the smell of bitter almonds that it was the first time synthesized by Gay-Lussac in 1815 via pyrolysis of silver cyanide (AgCN) [1]. Therefore, the design of cyanogen nanosensors is very important to monitor and control of cyanogen gas. Nanoscale silicon carbide materials are one of the most functional materials for technological applications because they can be used in high power, high temperature and high-frequency devices and semiconductors due to their superior properties [2,3]. A substantial category of fullerene-like structures such as nanocages may display novel chemical and physical properties of themselves. Also, nanocages can be used effectively as nanocontainers for the storage of gases [4-7]. Wang et al [8] designed and evaluated a family of Si_nC_n (n=6-36) nanocages and their energy stability using density functional theory calculations. The results of Wang et al calculations demonstrate that the (SiC)₁₂ nanocage was the highest stability in the energy value cluster among other cage-like structures. Our purpose of this study is to investigate the possibility of pristine and Cu-decorated Si₁₂C₁₂ nanocage as a new nanosensor for detecting and sensing of the toxic cyanogen gas.

Materials and method

The electronic structures, geometry optimizations and density of states (DOS) analyses were carried on the Si₁₂C₁₂ nanocage, Cu-decorated Si₁₂C₁₂ nanocage and different NCC/Si₁₂C₁₂ and NCCN/Cu@Si₁₂C₁₂ complexes using WB97XD functional [9] with 6-31+G(d) basis set. All calculations were performed utilizing the Gaussian 09 quantum chemistry code [10].

Results and Discussion

Si₁₂C₁₂ includes eight hexagonal and six tetragonal SiC rings with T_h symmetry. In pristine Si₁₂C₁₂ two types of Si-C bonds are recognizable: the one with a bond length of 1.823 Å is common between a hexagonal and a tetragonal ring (bond 6-4), and another with a bond length of 1.767 Å corresponds to common bond between two hexagonal rings (bond 6-6). The C-C and N≡C bond length of linear cyanogen molecule is about 1.386 and 1.159 Å, respectively. These outcomes are consistent with the results of previous studies [11,12]. NBO analysis demonstrates that natural charge of C and Si atoms in Si₁₂C₁₂ is about -1.822 and 1.822 esu respectively, because of the difference in electronegativity between two atoms. Also, we calculated frontier molecular orbital energies (HOMO/LUMO) and the energy difference between HOMO and LUMO (E_g) for intended nanocage by using the Eq. (1) that the outcome E_g for the Si₁₂C₁₂ is about 7.00 eV (see table 1).

$$E_g = (\text{LUMO} - \text{HOMO}) \quad (1)$$

We investigated different probable adsorption structures in order to obtain the most stable configurations of the adsorbed cyanogen molecule on the outer surface of the Si₁₂C₁₂ nanocage. The results of reviews indicate that there are two sustainable adsorption configurations for cyanogen adsorption on the pristine Si₁₂C₁₂ (Fig. 1). In one of them, the nitrogen atom of the cyanogen molecule is bonded with Si atom of the outer surface of the Si₁₂C₁₂ (A) and in another, C-C bond of the NCCN is located in parallel on C atom of the nanocage (B). Using Eq. (2), E_{ads} and E_{BSSE} values were calculated for two configurations (table 2).

$$E_{\text{ads}} = E_{\text{complex}} - (E_{\text{NCCN}} + E_{\text{Nanocage}}) + E_{\text{BSSE}} \quad (2)$$

According to the results of this table, value obtained for the E_{ads} of A and B configurations is about -45.55 and -18.52 kJ.mol⁻¹, respectively.

Negative values of E_{ads} show that the structures are sustainable even if the interaction of NCCN molecule with $Si_{12}C_{12}$ is very weak.

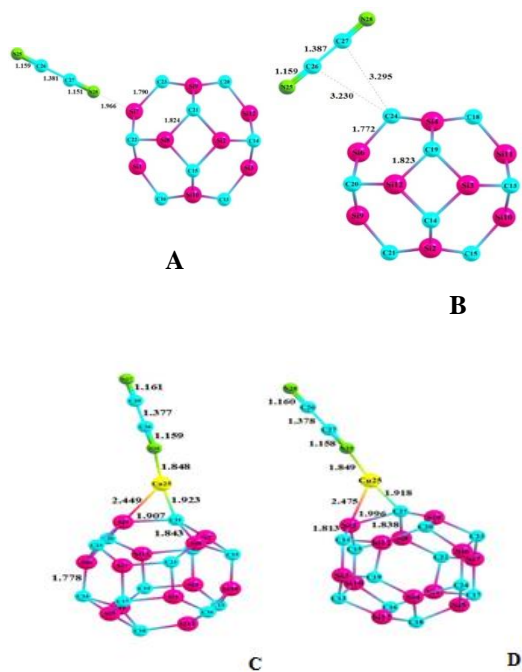


Fig. 1. The presentation optimized structure of A and B configurations (Bonds in Å).

The results showed that the pristine $Si_{12}C_{12}$ is not sensitive enough for sensing NCCN molecule. Therefore, to solve this problem and improve the performance of the cyanogen nanosensor, we used the Cu-decorated $Si_{12}C_{12}$ nanocage for the adsorption of cyanogen. Because, in addition to the doping process [11,13,14], the metal decoration is another way to intensify the adsorption property of nanostructures [15,16] and the sensitivity of the nanocage can be increased by metal-decorated technology.

There are two separate locations in $Si_{12}C_{12}$ nanocage for the process of decorating. One common bond between a hexagonal and a quadrilateral ring (bond 6-4), and another common bond between two hexagonal rings (bond 6-6). Highest occupied molecular orbital (HOMO), lowest unoccupied molecular orbital (LUMO), energy gap (E_g) for $Cu@Si_{12}C_{12}$ are calculated and gathered in Table 1. These obtained results of this table indicate that in the decoration process of $Si_{12}C_{12}$ nanocage with Cu, reduced energy gap (E_g) in comparison with pristine nanocage, because this process leading to increasing the HOMO energy level and decrease the LUMO energy level, thus the energy gap between HOMO and LUMO are reduced.

After the optimization of Cu-decorated $Si_{12}C_{12}$ structures, the NCCN adsorption was examined on the Cu-decorated $Si_{12}C_{12}$ in several positions. The result was that only two stable structures were obtained: C and D configurations. As is depicted in Fig. 2, the N atom in the NCCN molecule is bonded to Cu atom of the outer surface of the $Cu@Si_{12}C_{12}$ and in these (C and D) configurations, the Cu-N distance is 1.848 and 1.849 Å, respectively. Also for two configurations, E_{ads} and E_{BSSE} values were calculated by using Eq. (2) (see table 2). E_{ads} values for C and D configurations are -101.91 and -102.84 $kJ.mol^{-1}$, respectively. More negative values of the adsorption energy (E_{ads}) demonstrate that the structure is more stable. Therefore, D configuration is stronger and more stable than of the C configuration.

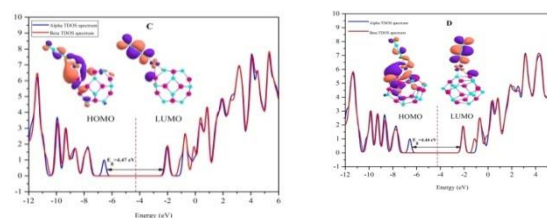


Fig. 2. The show Optimized structures and total density of states (TDOS) for C and D configurations (bond lengths are in Å). The dashed line in TDOS plots indicates Fermi energy.

Conclusions

Using density functional theory, the adsorption of cyanogen molecule on the pristine and Cu-decorated $Si_{12}C_{12}$ is investigated. Based on the results obtained from the calculations, the NCCN molecule could not strongly adsorb on the exterior surfaces of $Si_{12}C_{12}$ nanocage thus the adsorption of the NCCN molecule is a weak physisorption. As a result, in this process, the electronic and structural properties of $Si_{12}C_{12}$ nanocage do not change dramatically. In order to increase the efficiency of $Si_{12}C_{12}$ nanocage for NCCN adsorption, the Cu-decorated $Si_{12}C_{12}$ nanocage under investigation is located. The results show that interaction between the NCCN molecule and $Cu@Si_{12}C_{12}$ is chemisorptions with appreciable adsorption energy. Also TDOS diagram and NBO analysis, in order to justify and understand better of these interactions were calculated that confirm sizeable charge transfers in the adsorption of NCCN on the Cu-decorated $Si_{12}C_{12}$. Due to, the high sensitivity of Cu-decorated $Si_{12}C_{12}$ nanocage and other features, so it seems that this nanocage is a good candidate as the sensor for detecting and sensing NCCN molecule.

References

- [1] J.L. Gay-Lussac, Recherches sur l'acide prussique, Imprimerie de Mme. Ve. Perronneau 1815.
- [2] M. Bhatnagar, B.J. Baliga, Comparison of 6H-SiC, 3C-SiC, and Si for power devices, IEEE Transactions on Electron Devices 40 (1993) 645-655.
- [3] W.-j. Cho, R. Kosugi, J. Senzaki, K. Fukuda, K. Arai, S. Suzuki, Study on electron trapping and interface states of various gate dielectric materials in 4H-SiC metal-oxide-semiconductor capacitors, Applied Physics Letters 77 (2000) 2054-2056.
- [4] M. Dresselhaus, K. Williams, P. Eklund, Hydrogen adsorption in carbon materials, Mrs Bulletin 24 (1999) 45-50.
- [5] S. Trasobares, O. Stephan, C. Colliex, G. Hug, W. Hsu, H. Kroto, D. Walton, Electron beam puncturing of carbon nanotube containers for release of stored N₂ gas, The European Physical Journal B-Condensed Matter and Complex Systems 22 (2001) 117-122.
- [6] M. Terrones, R. Kamalakaran, T. Seeger, M. Rühle, Novel nanoscale gas containers: encapsulation of N₂ in CN_x nanotubes, Chemical Communications (2000) 2335-2336.
- [7] M.B. Javan, M. Ganji, M. Sabet, N. Danesh, Incorporation of Hydrogen Molecules into Carbon Nitride Heterofullerenes: An Ab Initio Study, Journal of Computational and Theoretical Nanoscience 8 (2011) 803-807.
- [8] R. Wang, D. Zhang, C. Liu, Theoretical prediction of a novel inorganic fullerene-like family of silicon-carbon materials, Chemical physics letters 411 (2005) 333-338.
- [9] J.-D. Chai, M. Head-Gordon, Long-range corrected hybrid density functionals with damped atom-atom dispersion corrections, Physical Chemistry Chemical Physics 10 (2008) 6615-6620.
- [10] M. Frisch, G. Trucks, H. Schlegel, G. Scuseria, M. Robb, J. Cheeseman, J. Montgomery Jr, T. Vreven, K. Kudin, J. Burant, Pittsburgh PA, Pople JA (2009) Gaussian 09, revision A02, Gaussian Inc, Wallingford.
- [11] M. Solimannejad, S. Kamalinahad, E. Shakerzadeh, Sensing Performance of Sc-doped B₁₂N₁₂ Nanocage for Detecting Toxic Cyanogen Gas: A Computational Study, Physical Chemistry Research 4 (2016) 315-332.
- [12] M.B. Javan, Adsorption of CO and NO molecules on SiC nanotubes and nanocages: DFT study, Surface Science 635 (2015) 128-142.

Theoretical Studies on Nonlinear Optical (NLO) Response of Si₁₂C₁₂ Nanocage Decorated with Alkali Metals (M = Li, Na and K)

Mohammad Solimannejad*, Rezvan Rahimi, Saeedeh Kamalinahad

Department of Chemistry, Faculty of Science, Arak University, 38156-8-8349 Arak, Iran
 Institute of Nanosciences and Nanotechnology, Arak University, 38156-8-8349 Arak, Iran

*m-solimannejad@araku.ac.ir

Abstract: Electronic structure and nonlinear optical (NLO) response of Si₁₂C₁₂ nanocage decorated with alkali metals (M = Li, Na and K) are investigated by ab initio quantum chemistry method. The results of present study indicate that interaction of alkali metals with Si₁₂C₁₂ nanocage narrow the energy gap of nanocage remarkably. It is shown that, decoration of Si₁₂C₁₂ with alkali metals play significant role in enhancement of first hyperpolarizability (β_0) and consequence NLO response of Si₁₂C₁₂ nanocage.

Keywords: Si₁₂C₁₂ nanocage; Alkali metals; Hyperpolarizability

Introduction

Design and fabrication of the nonlinear optical (NLO) materials is an important task in current researches due to their wide applications in optical communication, optical computing, photonic and electro-optical devices and laser [1, 2]. Many guidelines have been introduced for the design of new NLO materials [2–8]. Interaction of alkali metals with nanomaterial's, through excess electrons redounds to enhancement in first hyperpolarizability and large NLO response in electronic devices [9–11].

In addition, doping of alkali metal atoms is an effective strategy for significant change in the electronic and nonlinear optical properties of nanomaterial's [1, 5, 8, and 12]. Excellent physicochemical properties of silicon carbide nanomaterial such as high-power, high frequency, high temperature semiconductors, wide band gap and high thermal conductivity [13–15], lead to abundant study of these materials in contemporary investigations. Theoretical results have shown that Si₁₂C₁₂ nanocage appears to be more stable than the other silicon carbide derivatives [13]. This nanocage has many applications in laser devices, optical communication, optical computing, and optical data storage [16, 17]. The motivation of the present study is investigation influence of interaction between alkali metals (M = Li, Na and K) with Si₁₂C₁₂ nanocage in enhancement of first hyperpolarizability (β_0) and NLO response of Si₁₂C₁₂ nanocage for the first time. The prospect of this research is providing more useful information for the development of new devices based on nanoscale silicon carbon materials with large NLO response.

Materials and method

The geometry optimization, electronic structure, and NLO properties of interacted Si₁₂C₁₂ nanocage with alkali metals (M = Li, Na and K) described by the spin-

unrestricted approach and are investigated by means of density functional theory (DFT) and second order Møller–Plesset (MP2) calculations with 6-31+G(d) basis set. All calculations were performed using Gaussian 09 program package [28].

Results and Discussion

This nanocage is consisted with six tetragonal and eight hexagonal rings. Two individual Si–C bonds are distinguishable in the Si₁₂C₁₂ nanocage, one is shared between two hexagons (b66) with length about 1.767 Å and the other is shared between a tetragon and a hexagon (b64) with length of 1.823 Å (see Fig. 1). It seems that the participation of p orbital is increased for (b64) bonds in comparison to (b66). Therefore, the bond lengths of (b64) are larger than (b66). In the present study interaction between Si₁₂C₁₂ nanocage and alkali metals (M = Li, Na and K) and consequence effect of it on the electronic and nonlinear optical properties of nanocage is investigated. For this purpose, different initial positions for alkali atom over the nanocage including: the on top of a C or Si atom, over hexagonal and square rings, and on the top of a b66 or a b64 bond, are considered. After full optimization of considered systems, two stable structures with no imaginary vibrational frequencies were identified for each Si₁₂C₁₂–M (M = Li, Na and K) complexes. These stable structures are obtained from interaction of alkali atoms on the C atom (S1) and over hexagonal ring (S2) of Si₁₂C₁₂ nanocage (Fig. 1).

The vertical distances between the alkali atom and the C (S1 configurations) adherence to the following trend: 2.003 (S1–Li) < 2.353 (S1–Na) < 2.793 (S1–K). Hence, it is obvious that interaction of Li atom with C atom of Si₁₂C₁₂ nanocage is more prominent than other alkali metals.



The electronic properties of the interacted nanocage are also investigated; the obtained frontier molecular orbital energies ε_H , ε_L and HOMO–LUMO gap (HLG) values for this mentioned nanocage are listed in Table 1. The obtained energies of HOMO, LUMO and HOMO–LUMO gap of $\text{Si}_{12}\text{C}_{12}$ nanocage are -8.10 , -1.09 and 7.01 (eV) respectively. The obtained results indicate that interaction of alkali metals with $\text{Si}_{12}\text{C}_{12}$ nanocage significantly narrows the HOMO–LUMO gaps, and leads to decrease of HLG from 7.01 eV for pristine $\text{Si}_{12}\text{C}_{12}$ to range of 5.31 – 5.53 eV for six studied complexes. In order to more accurate display HLG, the total density of states (TDOS) of the pristine nanocage, is depicted in Fig. 2. It was found that the interaction of the alkali atoms with these nanocage leads to the formation of a high energy level as the new HOMO level locating between the original HOMO and LUMO of pristine nanocage.

The HOMO–LUMO gap (HLG) of the intended systems defined as:

$$\text{HLG} = (\varepsilon_L - \varepsilon_H) \quad (1)$$

The calculated polarizability (α) and the first hyperpolarizability (β_0) of $\text{Si}_{12}\text{C}_{12}$ –M (M = Li, Na, K) complexes at MP2/6 – 31 + G (d) level are summarized in Table 2. The value of α and hyperpolarizability (β_0) for pristine $\text{Si}_{12}\text{C}_{12}$ is 370.87 a.u. and 0.00 a.u. respectively so this considered nanocage has no NLO response. After interaction of alkali metals with $\text{Si}_{12}\text{C}_{12}$, the $\text{Si}_{12}\text{C}_{12}$ –M (M = Li, Na, and K) complexes exhibit large α values ranging from 393.49 to 414.97 a.u. According to Table 2, our results reveal that first hyperpolarizability (β_0) is observed in $\text{Si}_{12}\text{C}_{12}$ –M due to the interaction of alkali atoms with nanocage. The obtained β_0 values are 4277.06 (Li), 5771.99 (Na) and 4015.57 (K) a.u. for S1 configurations and 851.37 (Li), 1889.38 (Na), and 1252.11 (K) a.u. for S2 configuration, respectively. The first hyperpolarizability (β_0) values for S2 configuration are less than corresponding values in S1 configuration.

The polarizability (α) and first hyperpolarizability (β_0) is assessed according to the following equations:

$$\alpha = 1/3 (\alpha_{xx} + \alpha_{yy} + \alpha_{zz}) \quad (2)$$

$$\beta_0 = (\beta_x^2 + \beta_y^2 + \beta_z^2) \quad (3)$$

According to NBO analysis performed on the $\text{Si}_{12}\text{C}_{12}$ –M complexes, indicating that charge transfer is occurred from alkali metal atom to the $\text{Si}_{12}\text{C}_{12}$ nanocage. The results have been collected in Table 1.

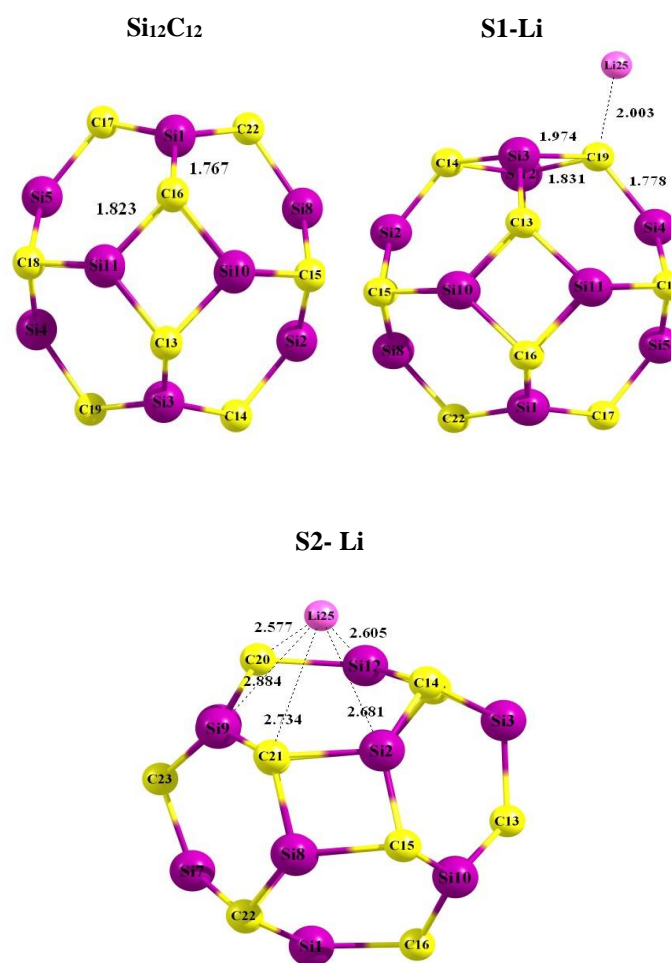


Fig. 1 the optimized structures of pristine $\text{Si}_{12}\text{C}_{12}$ and $\text{Si}_{12}\text{C}_{12}$ –M (M = Li, Na, K) complexes.

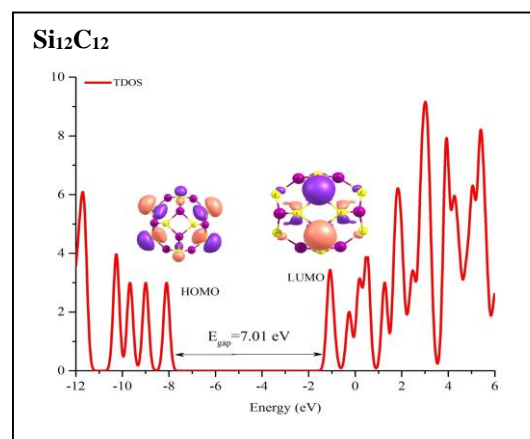


Fig. 2. TDOS of pristine $\text{Si}_{12}\text{C}_{12}$



Conclusions

In this study, we have inspected structure, electronic properties and nonlinear optical specifications of pristine $\text{Si}_{12}\text{C}_{12}$ nanocage and $\text{Si}_{12}\text{C}_{12}\text{-M}$ ($\text{M} = \text{Li}, \text{Na}, \text{K}$) via theoretical calculations. The density of states, and NBO analysis showed that interaction of the alkali metals with $\text{Si}_{12}\text{C}_{12}$ nanocage narrows the HOMO-LUMO gap. It is shown that electro-optical property of considered nanocage is sensitive to the interaction with the alkali metals remarkably. Interaction of the Na atom over C atom gives largest NLO response among studied complexes. Finally it is our expectation that interaction of the alkali metals with considered nanocage provide promising strategy for developing of high performance NLO materials.

References

- [1] N. Hou, Y.Y. Wu, J.Y. Liu, Theoretical studies on structures and nonlinear optical properties of alkali doped electrides $\text{B}_{12}\text{N}_{12}\text{-M}$ ($\text{M} = \text{Li}, \text{Na}, \text{K}$). *Int. J. Quantum. Chem.*, 116(17) (2016)1296-1302.
- [2] E. Shakerzadeh, Z. Biglari, E. Tahmasebi, M@B_{40} ($\text{M} = \text{Li}, \text{Na}, \text{K}$) serving as a potential promising novel NLO nanomaterial. *Chem. Phys. Lett.*, 654(2016)76-80.
- [3] M. Solimannejad, A theoretical study of nonlinear optical features of alumina nanostructures with the groups III and VI dopants. *Phys. Chem. Res.*, 4(4) (2016)627-641.
- [4] S. Kamalinahad, M. Solimannejad, E. Shakerzadeh, Nonlinear optical (NLO) response of pristine and functionalized dodecahydrotribenzo [18] annulene ([18] DBA): a theoretical study. *Bull. Chem. Soc. Jpn.*, 89(6) (2016)692-699.
- [5] H.-L. Xu, Z.-R. Li, D. Wu, B.-Q. Wang, Y. Li, F.L. Gu, Y. Aoki, Structures and large NLO responses of new electrides: Li-doped fluorocarbon chain. *J. Am. Chem. Soc.*, 129(10) (2007)2967-2970.
- [6] E. Shakerzadeh, N. Barazesh, S.Z. Talebi, A comparative theoretical study on the structural, electronic and nonlinear optical features of $\text{B}_{12}\text{N}_{12}$ and $\text{Al}_{12}\text{N}_{12}$ nanoclusters with the groups III, IV and V dopants. *Superlattices Microstruct.*, 76 (2014)264-276.
- [7] E. Shakerzadeh, E. Tahmasebi, H.R. Shamlouei, The influence of alkali metals (Li, Na and K) interaction with $\text{Be}_{12}\text{O}_{12}$ and $\text{Mg}_{12}\text{O}_{12}$ nanoclusters on their structural, electronic and nonlinear optical properties: a theoretical study. *Synth. Met.*, 204 (2015)17-24.
- [8] M. Niu, G. Yu, G. Yang, W. Chen, X. Zhao, X. Huang, Doping the alkali atom: an effective strategy to improve the electronic and nonlinear optical properties of the inorganic $\text{Al}_{12}\text{N}_{12}$ nanocage. *Inorg.Chem.* 53(1) (2013)349-358.
- [9] P. Karamanis, R. Marchal, P. Carbonnière, C. Pouchan, Doping-enhanced hyperpolarizabilities of silicon clusters: a global ab initio and density functional theory study of $\text{Si}_{10}(\text{Li}, \text{Na}, \text{K})_n$ ($n = 1, 2$) clusters. *J. Chem. Phys.*, 135(4) (2011)044511.
- [10] P. Karamanis, C. Pouchan, Fullerene-C60 in contact with alkali metal clusters: Prototype nano-objects of enhanced first hyperpolarizabilities. *J. Phys. Chem. C*, 116(21) (2012)11808-11819.
- [11] Glendening ED, Feller D (1995) Cation-Water Interactions: The $\text{M}^+(\text{H}_2\text{O})_n$ Clusters for Alkali Metals, $\text{M} = \text{Li}, \text{Na}, \text{K}, \text{Rb},$ and Cs . *J Phys Chem* 99 (10):3060-3067.
- [12] Xu H-L, Li Z-R, Wu D, Ma F, Li Z-J, Gu FL (2009) Lithiation and Li-doped effects of [5] cyclacene on the static first hyperpolarizability. *J Phys Chem C* 113 (12):4984-4986.
- [13] Duan XF, Burggraf LW (2015) Theoretical investigation of stabilities and optical properties of $\text{Si}_{12}\text{C}_{12}$ clusters. *J Chem Phys* 142 (3):034303.
- [14] Mo Y, Shajahan M, Lee Y, Hahn Y, Nahm K (2004) Structural transformation of carbon nanotubes to silicon carbide nanorods or microcrystals by the reaction with different silicon sources in rf induced CVD reactor. *Synth Met* 140 (2):309-315.
- [15] Pan Z, Lai H-L, Au FC, Duan X, Zhou W, Shi W, Wang N, Lee C-S, Wong N-B, Lee S-T (2000) Oriented silicon carbide nanowires: synthesis and field emission properties. *Adv Mater* 12 (16):1186-1190.

Theoretical investigation on gas-phase reaction of C₂H₆ with HO₂

Sh. Shirmohammadi*, H. douroudgari, M. Vahedpour

Department of chemistry, University of Zanjan, P.O. Box 45371-38791, Zanjan, Iran

*shohreh.shm1992@gmail.com

Abstract: The gas phase reaction of ethane with hydroperoxyl radical has been studied computationally on the doublet potential energy surface (PES). In the first step, association of reactants (C₂H₆ and HO₂) yield one pre reaction complex (CR) and in the last step, before releasing of adducts reaction ended to post-reactive complex. Thermodynamic parameters of product, CH₄+CH₂O + HO₂ are obtained. Standard Gibbs free energy ($\Delta G^0 = -28.23$ kcal/mol) and standard enthalpy ($\Delta H^0 = -18.19$ kcal/mol) of reaction show the production of mentioned adducts are spontaneous and exothermic process in atmospheric condition. Also, the number of transition states and barrier heights of them show that the reaction pathway for CH₄+CH₂O+OH adducts is kinetically favour.

Keywords: “Ethane; doublet state; mechanism; potential energy surface”

Introduction

The transient species HO₂ has long been postulated to play an important role in atmospheric chemistry [1].

Ethane is of the most important tropospheric organic trace gases. Ethane is the second most abundant hydrocarbon in the atmosphere and has a lifetime of approximately two months [2]. Ethane which is primarily emitted from fossil fuel sources as tracer species. Also, it is a useful tracer for fossil fuel-derived CH₄ because it is not emitted by methane’s microbial sources. Major global sources of C₂H₆ are the oil and gas sector, biofuel production and use and biomass burning.

Ethane is a ubiquitous constituent of the Earth’s atmosphere, with surface concentrations typically ranging from 500 to 2200 ppt over the northern hemisphere [3]. The main C₂H₆ sources are of anthropogenic origin (62% from leakage during production and transport of natural gas (NG), 20% from biofuel combustion and 18% from biomass burning; e. g) [4]. Ethane can be used as a refrigerant in cryogenic refrigeration systems [5]. The purpose of this work is carry out details of the doublet PES for the reaction of C₂H₆ with HO₂ of by means of computational methods based on DFT theories with the aim of clarifying the reaction mechanism.

Electronic calculations

All calculations have been carried out using Gaussian 09 package program [6]. The geometries of reactants, products, intermediate and transition states (TSs) involved in reaction are optimized using the B3LYP [7] level in connection with 6-311++G(d,p) basis set [8]. Connections between intermediates, transition states, and products are confirmed by intrinsic reaction coordinate (IRC) [9] at B3LYP level. Also, At this level of theory we calculated the harmonic vibrational frequencies to verifying the nature of stationary points (minima or transition state), zero point vibrational energy (ZPE) and the thermodynamic contributions to the enthalpy and free

energy. Transition states were characterized by one imaginary vibrational frequency and in minimum points all frequencies are real.

Results and Discussion

In figure 1 PES at doublet state and in figure 2 geometrical parameters of all species are shown. Total and relative energies are tabulated in table 1.

There is one favor pathway on doublet PES for obtained product as follow:



In the first step, association of reactants (C₂H₆ and HO₂) yield one pre reaction complex (CR). CR transform into CP via two transition states, TS1 and TS2. The energy barrier of these transition states are 56.54 kcal/mol and 10.39 kcal/mol at B3LYP/6-311++ g (d,p) level. In the first step, CR through TS1 converts to IN and in the second step IN via TS2 transforms to CP. IRC calculation confirms the connection between computed transition states and their corresponding stationary points. Form geometrical point of view TS1 (with C_s symmetry) involves migration of methyl group from 4C atom toward 9O atom with -1039i cm⁻¹ imaginary frequency and TS2 with C_s symmetry involves hydrogen shift (H-shift) from 4C toward 1C with -1622i cm⁻¹ imaginary frequency at B3LYP/6-311++g(d,p) level. Then, CP release into corresponding adducts without any energy barrier. CH₄+CH₂O+OH are stable products. Calculated thermodynamic parameters indicate that production of these adducts are exothermic ($\Delta H^0 = -18.19$ kcal/mol) and spontaneous ($\Delta G^0 = -28.23$ kcal/mol).

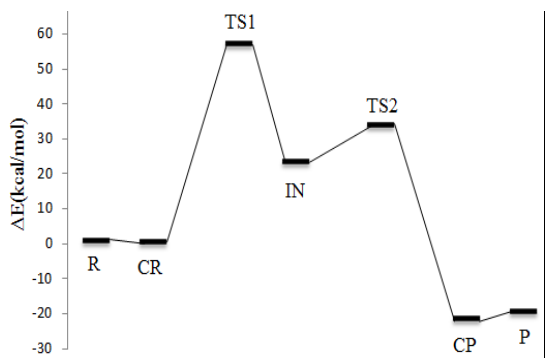


Fig.1. Doublet potential energy profile of $C_2H_6+HO_2$ reaction at B3LYP/6-311++g(d,p) level

Table 1. The total energies (in Hartree) and relative energies (in kcal/mol) calculated for this reaction.

Species	B3LYP/6-311G++g(d,p)	
	Total energy	relative energy
R	-230.726	0.0
CR	-230.726	-0.401
TS1	-230.690	22.573
IN	-230.762	-22.503
TS2	-230.636	56.143
CP	-230.673	32.925
P	-230.758	-20.375

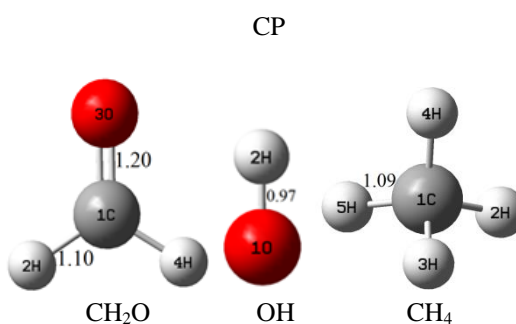
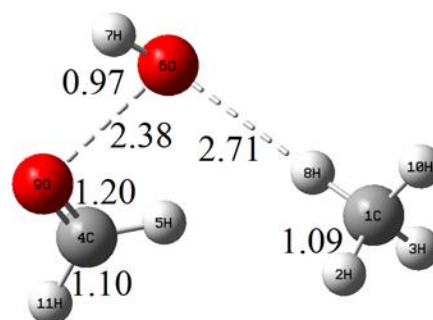
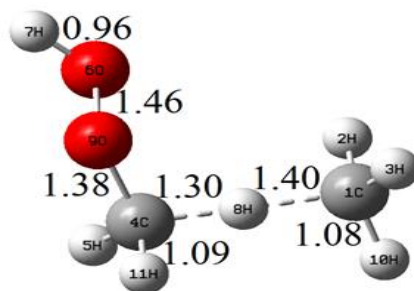
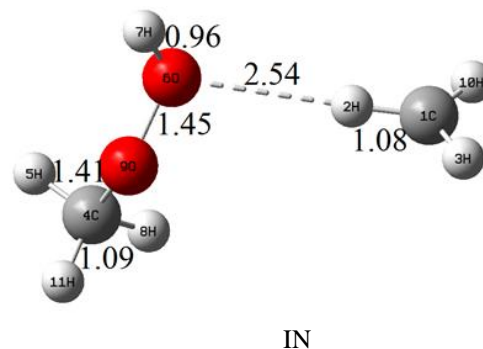
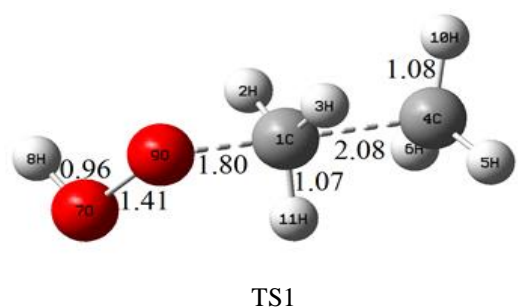
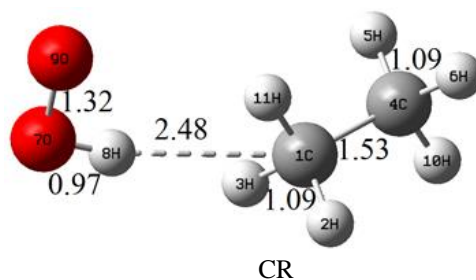
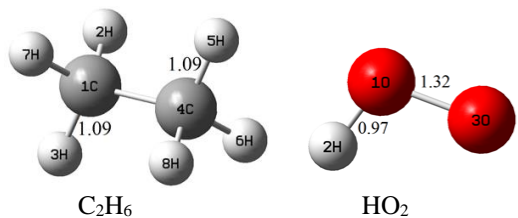


Fig. 2. Geometries of all species for $C_2H_6+HO_2$ reaction at B3LYP/6-311++g(d,p) level.

Conclusions

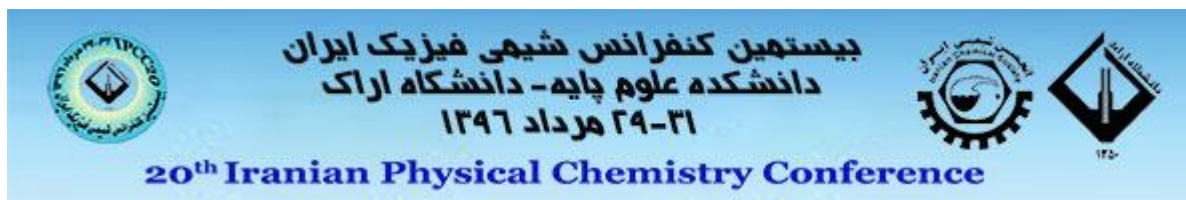
In the present work, we have characterized the details of the gas-phase reaction of ethane and HO_2 on Doublet PES with B3LYP level of theory in connection 6-311G++g(d,p) basis set. Based on our suggested mechanism,



for the product P, one reaction pathway with suitable heights is obtain. The reaction begins via formation of the reactant complex and ended to the post reactive complex before releasing to product.

References

- [1] B. G. Hunt “Photochemistry of Ozone in a Moist Atmosphere”, *Geophysical Fluid Dynamics Laboratory Environmental Science Services Administration Washington D, .C.*, 71 (1966) 1385-98.
- [2] J. Rudolph, “The tropospheric distribution and budget of ethane”, *Journal Of Geophysical Research*, 100 (1995) 11369-11381.
- [3] I. J. Simpson, M. P. S. Andersen, S. Meinardi, L. Bruhwiler, N. J. Blake, D. Helmig, F. S. Rowland & D. R. Blake “Long-term decline of global atmospheric ethane concentrations and implications for methane”, *Nature*, 488 (2012) 490–494.
- [4] Y. Xiao, J. A. Logan, D. J. Jacob, R. C. Hudman, R. Yantosca, and D. R. Blake “Global budget of ethane and regional constraints on U.S. sources”, *Journal Of Geophysical Research*, 113 (2008)1-13.
- [5] D. A. Vallero, “Environmental Biotechnology: A Biosystems Approach”, 2010, Duke University, 1st Ed., 641, Durham North Carolina, Usa.
- [6] P. Bhasi, Z. P. Nhlabatsi, S. Sitha “Possible interstellar formation of phosphorus analogue of hydrazoic acid: A computational study on the reaction between HN and PN”, *Computational And Theoretical Chemistry*, 1078 (2016) 129-137.
- [7] C. Lee, W. Yang, and R. G. Parr “Development of the Colic-Salvetti correlation-energy formula into a functional of the electron density”, *Physical Review B*, 37 (1988) 785-789.
- [8] K. Raghavachari, G. W. Trucks “A fifth-order perturbation comparison of electron correlation theories”, *Chemical Physics Letters*, 157 (1989) 479-483.
- [9] Carlos Gonzalez and H. B. Schlegel “Reaction Path Following in Mass-Weighted Internal Coordinates”, *Journal of Chemical Physics*, 94 (1990) 5523-5527.



Study of functional groups effect on the stability of single-walled carbon nanotubes with different diameters

Mehdi kheirmand, Neda Tamimi*

Department of chemistry, School of Basic sciences, Yasouj University, Yasouj 75914, Iran

*Email:neda.tamimi67@gmail.com

Abstract: The structures of ideal zigzag single-wall carbon nanotubes (SWCNTs) with coordinates (3,0), (4,0), (5,0), (6,0), (7,0) (In order to measure the effect of changing the diameter of single-wall carbon nanotubes on its stability) and two different lengths included 6 and 8 Å (In order to measure the effect of changing the length of single-wall carbon nanotubes on its stability) with a hydroxyl group was fully optimized at the B3LYP/6-311++G** level using the gaussian03w software, and the Gibbs free energy(ΔG) and total molecular energy (HF) parameters associated with the attachment of the OH substituent was determined. The results of the studies show that there is a direct correlation between the size(diameter and length) of the hydroxylized of single walled carbon nanotubes and their stability.

Keywords: hydroxyl group; zigzag single walled carbon nanotubes (SWCNTs); Density functional theory (DFT)

Introduction

Since their discovery in 1991 [1], single-walled carbon nanotubes (SWCNTs) have attracted extensive interest all over the world due to their unique structural, mechanical, and electrical properties [2] and a variety of potential applications, such as hydrogen storage [3], chemical sensors [4], and nanobioelectronics [5], etc. Three different structural types of single-wall carbon nanotubes exist: armchair, zigzag and chiral. Here we will focus on zigzag carbon nanotubes with “saw-tooth” like shaped ends and metallic or semiconductor electronic properties. The structures of carbon nanotubes could be described as a perfect graphene sheet wrapped up into a cylinder [6]. During cleaning raw carbon nanotubes various functionalized structures are formed as result of oxidation. Functionalized carbon nanotubes are promising candidates for basic studies in material sciences and numerous technical applications (e.g. in polymer chemistry, composites engineering, catalysis, nanomedicine)[7,8]. Density functional theory (DFT) and, in particular, the B3LYP hybrid density functional is widely used in molecular modeling studies to predict structure, spectroscopic parameters and energy changes of small, middle and large size molecules in chemistry, physics, material engineering, pharmacy and medicine. End substituted SWCNTs during mild oxidation are formed [9]. Pristine CNTs are insoluble in water, greatly limiting its bio- compatibility. Chemical functionalized of CNTs by introducing molecules and groups is a conventional way to improve this issue [10,11]. The structure, energy and energy gaps of CNTs with hydroxyl group at the end of CNTs with different length and diameters were evaluated by theoretical calculations [12,13]. The recent theoretical and experimental studies demonstrated that the presence of the functional groups significantly modifies the electron structure and bioactivity of CNTs [14,15].

Materials and method

The geometries and electronic wave functions of the species are obtained at B3LYP/6-311++G** level of theory[16] were performed using Gaussian 03 program. In our short study the structures of ideal SWCNTs, and with one hydroxyl groups at the end of the nanotubes, were fully optimized and the energy of the -OH substituent attachment was determined.

Results and Discussion

In order to evaluate the hydroxyl group effect on the stability of carbon nanotubes with different diameters and length, five different coordinate hydroxylized SWCNTs (3,0), (4,0), (5,0), (6,0), (7,0) and two lengths of them (6 and 8 Å) using the gaussian 03 software at the computational level B3LYP/6-311++G** were fully optimized then Gibbs free energy(ΔG) and total molecular energy (HF) parameters were calculated for them. The process of changing the values of ΔG and HF show that by increasing the diameter and length of hydroxylized single-walled carbon nanotubes, the amount of energy released also increased.

Conclusions

In summary, the structural of hydroxylized zigzag SWCNTs have been studied theoretically. The present density functional theory studies using B3LYP/6-311++g(d,p) calculations indicate that it is possible to hydroxylized one end of an zigzag SWCNT. The results of computations performed on functionalized single walled carbon nanotubes show a measure of the length and diameter of hydroxylized carbon nanotubes with the



stability it has a direct relationship. So in the hydroxylized single-walled carbon nanotubes which have the highest length and diameter the minimum activity is observed.

References

- [1] S. Iijima, *Nature* **354** (1991) 56.
- [2] M.S. Dresselhaus, G. Dresselhaus, A. Jorio, *Annu. Rev. Mater. Res.* **34** (2004) 247.
- [3] C. Liu, Y.Y. Fan, M. Liu, H.T. Cong, H.M. Cheng, M.S. Dresselhaus, *Science* **286** (1999) 1127.
- [4] J. Kong, N.R. Franklin, C.W. Zhou, M.G. Chapline, S. Peng, K.J. Cho, H.J. Dai, *Science* **287** (2000) 622.
- [5] E. Katz, I. Willner, *ChemPhysChem* **5**(2004) 1085.
- [6] D.Wang, C. Zhao, G. Xin, D. Hou, *J.Mol. Struct-THEOCHEM* **962** (2010) 62–67
- [7] E.G. Rakov, Y. Gogotsi (Ed.), *Nanotubes and Nanofibers*, Taylor & Francis, Boca Raton, London, New York (2006) 37–108.
- [8] T. Kar, B. Akdim, X. Duan, R. Patcher, *Chem. Phys. Lett.* **423** (2006) 126–130.
- [9] E. Chelmeckaa, K. Pasternyb, T. Kupkac, L. Stobińskid,, *J. Mol. Structure-THEOCHEM* **948** (2010)93–98
- [10] T. G. Abi, S. Taraphder, *Comput. Theor. Chem.*,**1027**(2014)19.
- [11] T. G. Abi, T. Karmakar, S. Taraphder, *Comput. Theor. Chem.* **1010**(2013)53.
- [12] M. Francisco-Marquez, A. Galano, A. Martínez, On the free radical scavenging capability of carboxylated single-walled carbon nanotubes, *J. Phys. Chem. C.*, **114** (2010) 6363.
- [13] J. Chen, A.M. Rao, S. Lyuksyutov, M.E. Itkis, M.A. Hamon, H. Hu, R.W. Cohn, P.C. Eklund, D.T. Colbert, R.E. Smalley, R.C. Haddon, Dissolution of full-length single-walled carbon nanotubes, *J. Phys. Chem. B* **105** (2001) 2525.
- [14] L.R. Arias, L. Yang, *Inactivation of bacterial pathogens by carbon nanotubes in suspensions*, *Langmuir*, **25** (2009) 3003–3012.
- [15] Y.X. Wang, Y.X. Bu, *J. Phys. Chem. B*, **111** (2007)6520–6526.
- [16] C. Lee, W. Yang, and R. G. Parr, *Phys. Rev. B.*,**37**(1988) 785.



QSPR modeling of thermal energy and entropy of amines using molecular descriptors

M. Talaei, E. Mohammadinasab*

Department of Chemistry, Arak Branch, Islamic Azad university, Arak, Iran

*e-mohammadinasab@iau-arak.ac.ir

Abstract : In this study, multiple linear regression method that is based on property-structure model has been used to predict of the thermal energy and entropy of the 31 different types of amines. This model is based on topological and geometrical and quantum descriptors and the important rule of these molecular descriptors are specified for predicting the studied thermodynamic functions in this class of organic molecules. It is indicated that among studied molecular descriptors to predict the thermal energy, minimum Z Length, minimum projection area, lumo descriptors have more importance than the other descriptors. Also, it is observed that such descriptors as minimum Z Length, Balaban, Hyper-Wiener and volume are the best descriptors for predicting the values of entropy of this class of amines.

Keywords: "Amines", "Thermodynamic Function", "Molecular Descriptors".

Introduction

The structure-property relationship among numerous computational methods plays the most important role in predicting chemicals' properties. Chemical structure changes reflect changes in the physicochemical properties. One of the applications of this relationship is to predict various thermodynamics functions of amines and their derivatives [1-6].

Materials and method

Amines are considered as one of the most abundant nitrogen-containing organic compounds which are present in definite plants and a restricted chemical intermediary, histamine that arises in most animal tissues. They are used for different applications from industrial manufacturing to medicine (see Table 1).

In present research, the thermal energy and entropy of the 31 different types of amines are considered as dependent and topological and geometrical and quantum descriptors and independent variables in the regression model, respectively. Recent studies have showed that molecular indices of molecules determine the thermodynamics functions of them, so it's especially important to know that how change in the molecular structures changes the thermodynamics properties.

The thermal energy and entropy of 31 different types of the amines is performed by the DFT method based on B3LYP method and 3-21G standard basis sets. The quantum descriptors are calculated using mechanic quantum computation and also topological and geometrical descriptors are computed using the literatures, we investigated the relationship between

values of the thermal energy and entropy and the above descriptors using Excel software.

The multiple linear regression method was used to explore the relationship between the thermal energy and entropy in contrast to molecular descriptors using SPSS software version 16 with multiple linear regression method and backward procedure with an estimated error of 0.05.

Results and Discussion

Whether or not the regression model explains a statistically significant percentage of data was found through the *ANOVA Table* of output based on the MLR model in terms of the relationship between properties and structural indices.

The comparison of models and the values of statistical coefficients showed that the best models for predicting thermal energy and entropy of amines using the MLR method are as follows:

$$E_{th} = -118.375 + 43.015 \text{ Lumo} + 12.571 \text{ Min Z L} + 3.688 \text{ Min P A}$$

$$R=0.991, \quad R^2=0.981, \quad R^2_{\text{Adjust}}=0.979, \quad \text{std}=5.3527, \\ \text{DW}=1.957, \text{F}=474.963$$

$$\text{VIF Values: Lumo: 1.063, Min Z L: 1.054, Min P A: 1.091}$$

$$S = 0.019 + 0.017 \text{ J} - 5.616\text{E-}5 \text{ WW} + 0.000 \text{ V} + 0.0003 \text{ Min Z L}$$

$$R=0.976, \quad R^2=0.953, \quad R^2_{\text{Adjust}}=0.946, \quad \text{std}=0.00317, \\ \text{DW}= 1.913, \text{F}=131.301$$

$$\text{VIF Values: J: 1.244, WW: 1.098, V: 2.265, Min Z L: 2.105}$$

From a statistical regression analysis lens of view, Durbin-Watson (DW) statistic is a number to



examine autocorrelation in the residuals. The DW values 1.957, 1.913 in final models are considered acceptable indicating that there is poor correlation between the errors and the independence of residuals. These numerical values indicate that our final models are perfect. In Table 2 the values of observed, predicting, residual thermal energy and entropy is showed, respectively.

Table 1: The used amines

Number	Name	Number	Name
1	aminoethan	17	diallylamine
2	3-amino-1-propen	18	allylpropylamine
3	1-aminopropan	19	1-aminohexane
4	2-aminopropane	20	di-n-propylamine
5	methylethyl amine	21	butyldimethylamine
6	trimethyl amine	22	triethylamine
7	1-aminobutane	23	1-aminoheptane
8	1-amino-2-methylpropane	24	propyl-n-butylamine
9	2-aminobutane	25	propylisobutylamine
10	2-methyl-2-aminopropane	26	propyl-sec-butylamine
11	diethylamine	27	1-amino-2-ethylhexane
12	ethyldimethyl amine	28	di-n-butylamine
13	allylethyl amine	29	ethyldi-n-propylamine
14	1-aminopentane	30	triallylamine
15	methylbutyl amine	31	tri-n-propylamine
16	ethylisopropyl amine	32	

84.64	81.62	3.01	.072	.069	-.002
84.33	79.83	4.50	.071	.073	.004
104.70	110.70	-5.99	.079	.076	-.001
104.44	105.39	-.95	.077	.078	-.001
104.30	102.20	2.10	.078	.078	-.007
103.68	95.80	7.88	.076	.083	.004
104.58	113.22	-8.64	.079	.076	.000
104.33	97.77	6.56	.078	.078	-.001
108.51	112.26	-3.75	.085	.087	-.001
124.67	128.87	-4.20	.087	.088	-.001
124.60	130.20	-5.60	.087	.088	-.002
123.94	124.86	-.92	.086	.088	.003
112.44	110.93	1.51	.091	.088	-.004
128.50	130.87	-2.38	.093	.096	-.003
144.65	148.04	-3.39	.094	.097	-.001
144.54	152.88	-8.34	.094	.095	-.004
144.21	140.22	3.99	.093	.097	-.001
144.27	145.22	-.95	.091	.092	-.001
164.63	151.35	13.28	.101	.102	-.001
164.52	157.48	7.04	.101	.102	.002
164.26	162.58	1.68	.100	.098	-.001
164.24	160.77	3.47	.101	.102	.002
184.54	177.68	6.86	.106	.104	.002
184.46	189.06	-4.60	.109	.107	-.002
184.07	185.27	-1.21	.108	.110	.005
156.21	158.69	-2.48	.105	.100	.007
204.01	205.59	-1.58	.115	.108	.001

In Figures 1 and 2, the values of $R^2 = 0.981$ for E_{th} , $R^2=0.953$ show the linear correlation between observed and predicting values resulted from the model that is related to the dependent variable. The larger values of R^2 indicate a stronger correlation.

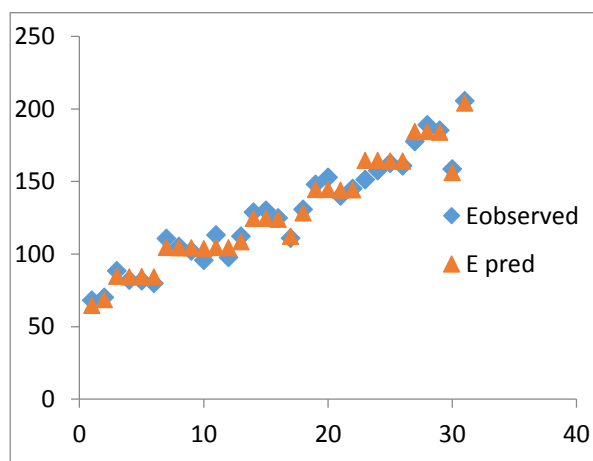


Fig.2: Comparison of the experimental and predicted E_{th}

Table 2: The values of observed, predicting, residual related to thermal energy (E_{th})/kcalmol⁻¹ and entropy (S)/kcalmol⁻¹.

$E_{th(obs)}/$ Kcal mol ⁻¹	$E_{th(pred)}/$ Kcal mol ⁻¹	Res(E)/ Kcal mol ⁻¹	$S_{(obs)}/$ Kcal mol ⁻¹	$S_{(pred)}/$ Kcal mol ⁻¹	Res(S)/ Kcal mol ⁻¹
64.76	68.21	-3.45	.065	.063	.001
68.65	70.28	-1.63	.071	.070	.001
84.72	88.64	-3.92	.072	.071	-.003
84.28	82.18	2.10	.071	.073	.003

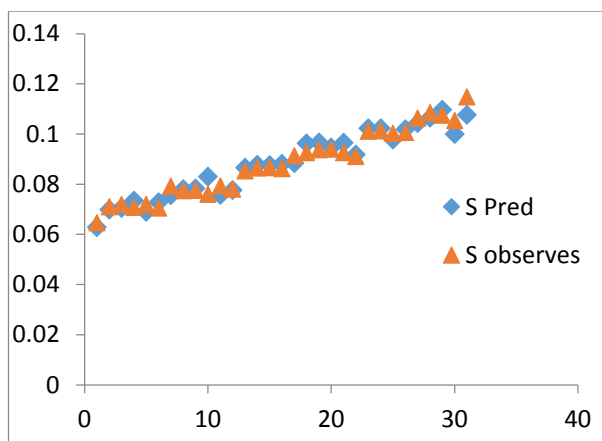


Fig.2: Comparison of the experimental and predicted S

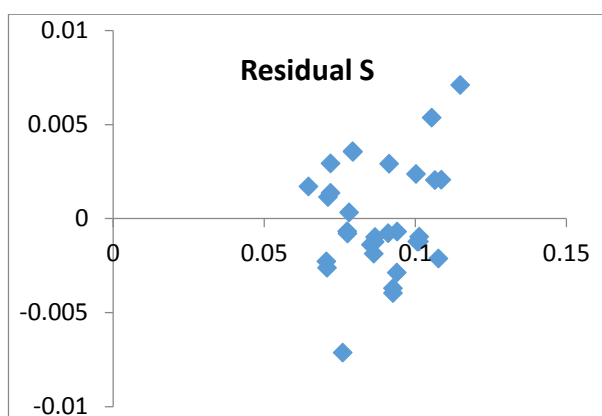


Fig.3: The scatter curve of the residual against observed S

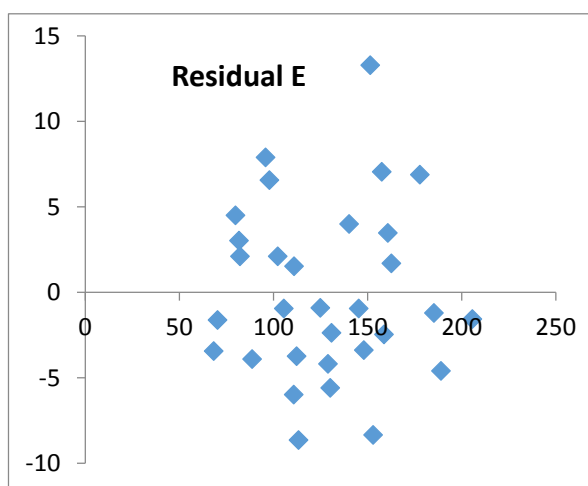


Fig.4: The scatter curves of the residuals against observed E

Conclusion

In this study, a model was presented for predicting the thermal energy and entropy of amines. Considering the research studies in which several two-dimensional indices were used, the current paper makes an attempt to

investigate several three-dimensional indices as molecular descriptors and their application for prediction of thermodynamic function of amines. It was also witnessed that among the proposed models to predict the thermodynamic function, the model including a combination of descriptors minimum Z Length, minimum projection area, lumo is the most appropriate one. And the last but not least, this was the first time that the relationship between thermodynamic properties with molecular descriptors of amines and their derivatives was investigated through the use of SPSS software and MLR method.

References

- [1] Web search engine developed by ChemAxon; software available at [http:// WWW. Chemicalize. Org.](http://WWW.Chemicalize.Org)
- [2] A. T. Balaban, T. S. Balaban, "New Vertex Invariant and Topological Indices of Chemical Graphs Based on Information on Distance", *Math. Chem.* 8 (1991) 383-397.
- [3] G. Cash, S. Klavzar, M. Petkovsek, "Three Methods for Calculation of the Hyper-Wiener Index of Molecular Graphs", *J. Chem. Inf. Comput. Sci.* 42 (2002) 571-576.
- [4] J. Devillers, A. T. Balaban, "Topological indices and related descriptors in QSAR and QSPR", 1999, Gordon and Breach Science, Netherlands.
- [5] R. T. Morison and R. Neilson Boyd, "Organic Chemistry", 2003, Allyn & Bacon.
- [6] M. Goodarzi and E. Mohammadinasab, "Theoretical investigation of relationship between quantum chemical descriptors, topological indices, energy and electric moments of zig-zag polyhex carbon nanotubes TUHC₆[2p,q] with various circumference [2p] and fixed lengths", *Fullerenes, Nanotubes and Carbon Nanostructures.* 21 (2013) 102-112.

Theoretical Study on Interaction of Boron-nitride Nanotube Ammonia as a Biomarker Gases

Sadegh Afsharia*, Ameneh Izadi, S. Ahmad Nabavi Amri

School of Chemistry, Damghan University, Damghan, Iran
s.afshari@du.ac.ir

Abstract: The interaction of pristine and Al-doped and Ga-doped boron-nitride nanotube ammonia have been studied by the density functional theory's method at the B3YP/6-31+(d) level of theory. The interaction of the ammonia from two sides (Hydrogen and Nitrogen atom) with the mentioned systems. There is no interaction from Hydrogen sides of ammonia with the mentioned structures, but there are interaction between the Nitrogen atom of ammonia. The esp's of structures have been calculated, too. The esp of the structures had the same trend with the interactions. Also, the density of states has been studied for the interactions. The interaction cause to increase the E_g for all of the three system. In addition, the interaction energy and difference Gibbs free energy have been calculated. The calculated interaction energy's show that the interaction for Al doped BN nanotube/ NH_3 was the strongest and the interaction for pristine BN nanotube/ NH_3 was the weakest. The calculated difference Gibbs free energies show the same result. This means that ammonia adsorption on the Al doped BN nanotube is easiest and on the pristine BN nanotube is hardest for these three systems in the room temperature.

Keywords: "Biomarker gases; Ammonia; Boron Nitride nanotubes; Density Functional Theory; Dopping"

Introduction

Analysis of human exhaled a noninvasive method to diagnose some diseases. It is one of the oldest forms of diagnosis through the smell of human breath [1]. About 3000 different volatile organic compounds and aerosol particles in human breath has been identified by researchers [2,3]. The presence of some gases in human breath may indicate certain diseases. So, these gases are used to detect disease through human breath tests, Hence, they are known as a biomarker. In this work ammonia is selected for examination and identification. Ammonia is a colorless and pungent gas composed of nitrogen and hydrogen. The existence of this gas in exhaled, indicates the kidney disease and bacterial infection [4,5]. The biomarkers are generally measurable indicators of certain biological conditions. They often use for search about natural biological processes, pathogenic processes or pharmacological responses to a particular treatment [6]. The advantages of studying biomarkers are being high sensitivity, simplicity, and time [7]. The interaction of gases with the nanotubes is a method that is commonly used to study the gases. Therefore, in this paper the interaction of ammonia with pristine, aluminum and gallium doped boron nitride nanotubes has been studied [8].

Materials and method

All calculations were performed using DFT at the B3LYP/ 6-31+G(d) level of theory as implemented in the GAUSSIAN 09 program suite. The nanotubes used as an adsorbent is the zigzag (6,0) form of boron nitride

nanotube. The density of states (DOS) for the structures has been obtained by the GaussSum program. In graphs of the DOS (figure 1), E_g generally refers to the energy difference between the valence (HOMO) and the conduction (LUMO) levels in semiconductors. For the sake of clarity, the Fermi level has been set to zero. In order to verify the structures, the corresponding frequency calculations were carried out at the same level. The interaction energy ($E_{\text{interaction}}$) of a molecule interacted with a nanotube is obtained using the following equation:

$$E_{\text{Interaction}} = E_{(\text{nanotube-NH}_3)} - E_{(\text{nanotube})} - E_{(\text{NH}_3)}$$

where $E_{(\text{nanotube+NH}_3)}$ is the total energy of a NH_3 molecule adsorbed on the nanotube, E_{NH_3} is the energy of the isolated NH_3 molecule, and E_{nanotube} is the energy of the isolated nanotube. Here the pristine, Al and Ga-doped BN nanotube were used as the nanotube.

Results and Discussion

In this work the interaction of molecule ammonia with pure, aluminum and gallium-doped boron nitride nanotubes has been investigated. For this purpose, the interaction of ammonia molecule from possible sides (Nitrogen and Hydrogen atoms) and the boron atom of the boron nitride nanotubes, the aluminum atom of the Al-doped boron nitride nanotube and the gallium atom of the gallium-doped boron nitride nanotube have been investigated. The results have show that ammonia can have interaction with mentioned nanotube from the Nitrogen side and have no interaction from Hydrogen atom sides. The amount of some correspond bond length before and after interaction have been shown in Table 1.

Table 1. Bond Lengths for some bonds of BN nanotube, Al-doped BN nanotube and Ga-doped BN nanotube before and after interaction with ammonia

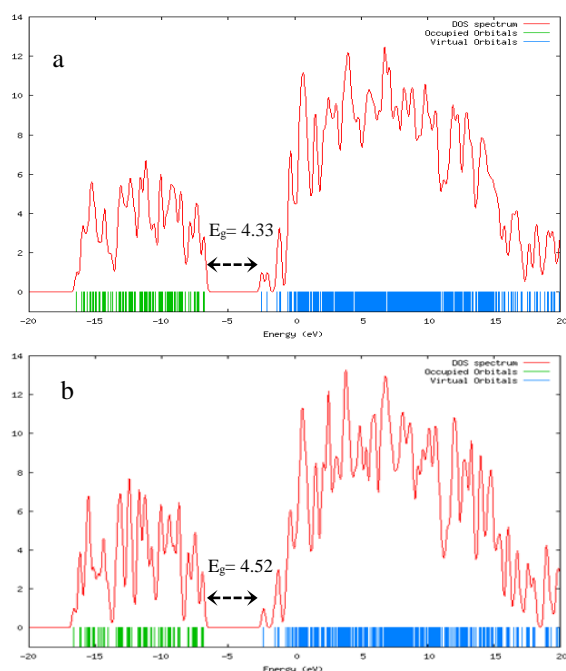
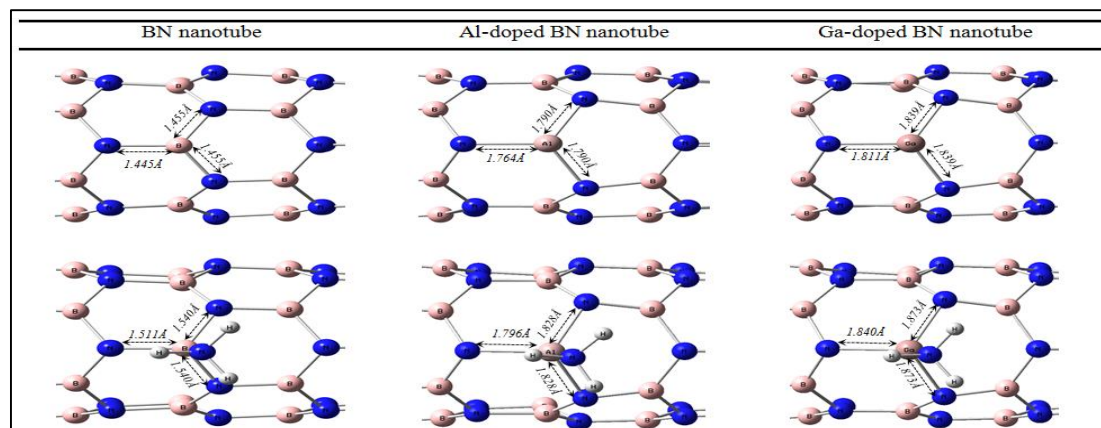


Figure 1. The density of states for a) BN-Ga-doped, b) BN-Ga-doped/ NH_3 .

As can be seen, the interaction cause to be increasing the near bonds of correspond atom in interaction. For example, the B-N bond length has been changed from 1.445 to 1.511 Å, the Al-N bond length has been changed from 1.764 to 1.796 Å and the Ga-N bond length has been changed from 1.811 to 1.840 Å.

The density of states (DOS) diagrams has been calculated for the interactions. Figure 1, shows the DOS diagrams before and after the interaction BN-Ga-doped and ammonia. The gap energy, E_g , (the difference between

LUMO energy and HOMO energy states) increases with interaction. This means that the E_g value have been changed 4.33 to 4.52 eV. It is a large-gap semiconductor range. In brief the other E_g , HOMO and LUMO values

Table 2. Calculated interaction energy, HOMO energy (E_{HOMO}), LUMO energy (E_{LUMO}) and HOMO-LUMO energy gap (E_g) by (eV)

	$E_{\text{Interaction}}$	ΔG	E_{LUMO}	E_{HOMO}	E_g
BN nanotube/ NH_3	-3078.82	-3076.838	-2.04	-6.70	4.66
Al _B -doped BN nanotube/ NH_3	-3079.78	-3077.363	-1.96	-6.48	4.51
Ga _B -doped BN nanotube/ NH_3	-3079.74	-3077.292	-1.96	-6.47	4.52
BN nanotube	-	-	-2.34	-6.90	4.56
NH_3	-	-	0.46	-7.29	7.79
Al _B -doped BN nanotube	-	-	-2.29	-6.78	6.49
Ga _B -doped BN nanotube	-	-	-2.46	-6.79	4.33

have been mentioned in table 1. Also, the interaction energy and the difference Gibbs free energy of interactions have been shown in table 2. As can be seen for this table, the results show interaction energy for the BN-Al-doped/ NH_3 system has the highest value (-3079.78 eV) and the BN/ NH_3 system has the lowest value (-3078.82 eV). This trend is like for difference Gibbs free energy. The difference Gibbs free energy for the BN-Al-doped/ NH_3 system has the highest value (-3077.363 eV) and the BN/ NH_3 system has the lowest value (-3076.838 eV). This shows that the interaction between BN-Al-doped and ammonia is stronger than the BN/ NH_3 and BN-Ga-doped/ NH_3 .

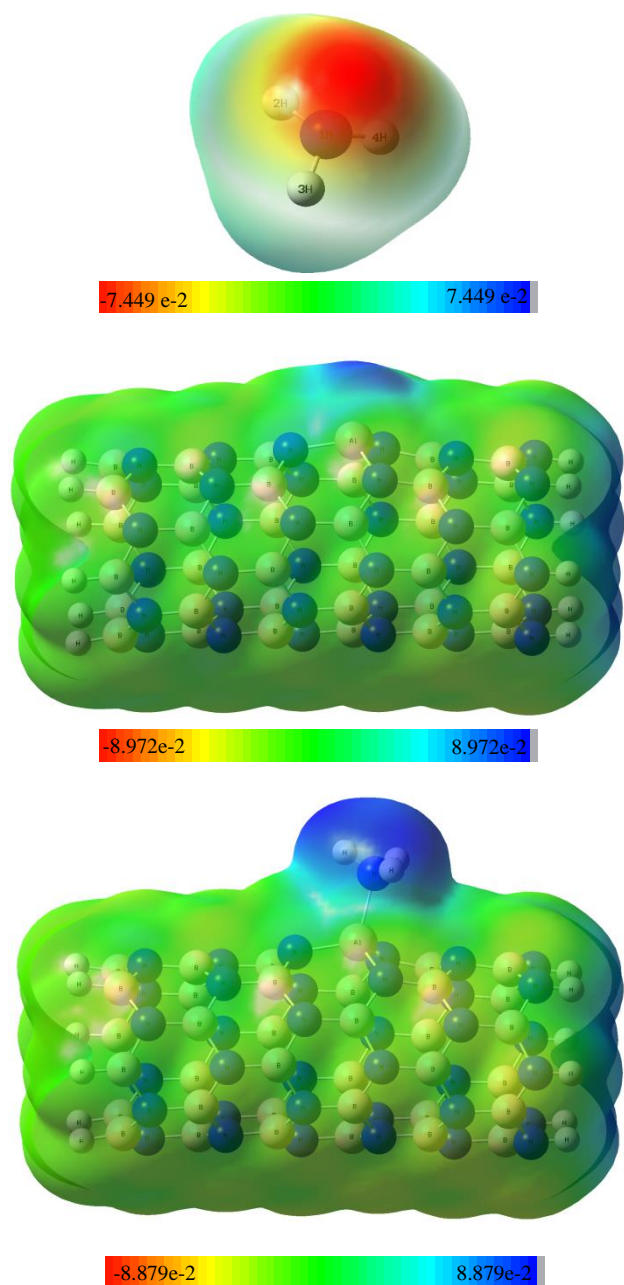


Figure 2. The electrostatic potential of NH_3 , Al doped BN nanotube and Al doped BN nanotube/ NH_3 .

Having knowledge about the active sites of the studied structures is necessary. So, the electrostatic potential (esp) of the studied structures has been computed. esp shows that where the molecule side has less or more electron density. It shows that the active and inactive sides in per molecule. Figure 2 shows the esp for NH_3 , Al doped BN nanotube and Al doped BN nanotube/ NH_3 . As can be seen the Nitrogen atom in ammonia have the active side of this molecule and the Aluminum atoms is the active side of the Al doped BN nanotube. So, as the results show Al doped BN nanotube and ammonia can

interact from mentioned sides and we can see adsorption. The other electrostatic potentials had good agreement results with studied interactions and did not show in this paper for shorten.

Conclusions

The interaction of pristine and Al-doped and Ga-doped boron-nitride nanotube ammonia have been studied theoretically. There is no interaction from Hydrogen sides of ammonia with of mentioned structures, but there are interaction between the Nitrogen atom of ammonia. The prediction of this can be possible by the study of the esp of structures. This interaction cause to increase the E_g for all of the three system. The calculated interaction energy's show that the interaction for Al doped BN nanotube/ NH_3 was the strongest and the interaction for pristine BN nanotube/ NH_3 was the weakest. The calculated difference Gibbs free energies show the same result. This means that ammonia adsorption on the Al doped BN nanotube is the easiest and on the pristine BN nanotube is the hardest for these three systems in the room temperature.

References

- [1] T. Wasilewski and G. Jacek "Bioelectronic nose: Current status and perspectives." *Biosensors and Bioelectronics* 87 (2017): 480-494.
- [2] M. Phillips, K. Gleeson and J. M. B. Hughes Greenberg "Volatile organic compounds in breath as markers of lung cancer: a cross-sectional study". *Lancet*, 353 (1999)1930-1933.
- [3] I. Horvath, J. Hunt and P. J. Barnes "Exhaled breath condensate: methodological recommendations and unresolved questions", *J. European Respiratory* 26 (2005) 523-548.
- [4] J. Pereira and P. Porto-Figueira "Breath analysis as a potential and non-invasive frontier in disease diagnosis: an overview", *J. Metabolites*, 5 (2015) 3-55.
- [5] C. Wang and P. Sahay "Breath analysis using laser spectroscopic techniques: breath biomarkers, spectral fingerprints, and detection limits", *J. Sensors*, 9 (2009) 8230-8262.
- [6] P. K. Lam, "Use of biomarkers in environmental monitoring" *J. Ocean & Coastal Management*, 52 (2009) 348-354.
- [7] P.G. Wells, K. Lee, and C. Blaise, "*Microscale testing in aquatic toxicology*" , 1997 *advances, techniques, and practice*. CRC Press.
- [8] D. Golberg, Y. Bando, Y. Huang, T. Terao, M. Mitom , C. Tang & C. Zhi "Boron nitride nanotubes and nanosheets", *J. ACS nano*, 4 (2010) 2979-2993.

Theoretical Study on adsorption Hydrogen cyanide of Pristine and Doped Boron-nitride Nanotube

Sadegh Afsharia*, Ameneh Izadi, S. Ahmad Nabavi Amri

School of Chemistry, Damghan University, Damghan, Iran

*s.afshari@du.ac.ir

Abstract: The adsorption of hydrogen cyanide on pristine and Al-doped and Ga-doped boron-nitride nanotube have been studied by the density functional theory's method at the B3YP/6-31+(d) level of theory. For this aim, the adsorption of the HCN from two sides (Hydrogen and Nitrogen atom) with the mentioned systems has been investigated. HCN has no adsorption on the pristine BN nanotube, and also, there is no adsorption from Hydrogen sides of HCN on the mentioned structures, but the adsorption is by the Nitrogen side of HCN. The esp's of structures have been calculated, too. The esp of the structures had the same trend with the adsorption. Also, the density of states has been studied for the interactions. The interaction cause to decrease the E_g for all of the two system. In addition, the interaction energy and difference Gibbs free energy have been calculated. The calculated interaction energy's show that the interaction for Al doped BN nanotube/HCN was the strongest. The calculated difference Gibbs free energies show the same result. This means that HCN adsorption on the Al doped BN nanotube is easiest at the room temperature.

Keywords: "Hydrogen cyanide; Boron Nitride nanotubes; Density Functional Theory; Dopping"

Introduction

Volatile organic compounds (VOCs) in human breath were identified as early as 1970 [1] as a non-invasive indicator of health. Composition and the amount of some of the VOCs in human breath have been related to different diseases [2]. Despite the obvious advantages, only a little breath tests is used in the routine application. More sensitive and non-invasive methods are being investigated utilizing the fact that hydrogen cyanide (HCN) is a biomarker for *P. aeruginosa* and the cystic fibrosis [3-5]. In nature, *P. aeruginosa* emits the poisonous gas HCN in order to kill competitive microorganisms. In this work HCN is selected for examination and identification. The biomarkers are generally measurable indicators of certain biological conditions. They often use for search about natural biological processes, pathogenic processes or pharmacological responses to a particular treatment [6]. The advantages of studying biomarkers are being high sensitivity, simplicity, and time [7]. The interaction of gases with the nanotubes is a method that is commonly used to study the gases. Therefore, in this paper the interaction of HCN with pristine, aluminum and gallium doped boron nitride nanotubes has been studied.

Materials and method

All calculations were performed using DFT at the B3LYP/ 6-31+G(d) level of theory as implemented in the GAUSSIAN 09 program suite. The nanotubes used as an adsorbent is the zigzag (6,0) form of boron nitride nanotube. The adsorption energy (E_{ad}) of a molecule interacted with a nanotube is obtained using the following equation:

$$E_{ad} = E_{(nanotube-NH_3)} - E_{(nanotube)} - E_{(HCN)}$$

where $E_{(nanotube+HCN)}$ is the total energy of a HCN molecule adsorbed on the nanotube, E_{HCN} is the energy of the isolated HCN molecule, and $E_{nanotube}$ is the energy of the isolated nanotube. Here the pristine, Al and Ga-doped BN nanotube were used as the nanotube.

The density of states (DOS) for the structures has been obtained by the GaussSum program. In graphs of the DOS (figure 1), E_g generally refers to the energy difference between the valence (HOMO) and the conduction (LUMO) levels in semiconductors. For the sake of clarity, the Fermi level has been set to zero. In order to verify the structures, the corresponding frequency calculations were carried out at the same level.

Results and Discussion

In this work the adsorption of the Hydrogen cyanide molecule on pure, aluminum and gallium-doped boron nitride nanotubes has been investigated. For this purpose, the interaction of the HCN molecule from possible sides (Nitrogen and Hydrogen atoms) and the boron atom of the boron nitride nanotubes, the aluminum atom of the Al-doped boron nitride nanotube and the gallium atom of the gallium-doped boron nitride nanotube have been investigated. The results have shown that the HCN can adsorb on Al-doped and Ga-doped BN nanotube and no adsorb on pristine BN nanotube from the Nitrogen side and also, have no interaction from Hydrogen atom sides.

The amount of correspond bond length and bond angle before and after adsorption have been shown in Table 1.

As can be seen, the adsorption cause to be increasing the bond length and decreasing the bond angle of correspond atoms. The Al-N bond length has been changed from 1.763 to 1.789Å and the Ga-N bond length has been changed from 1.811 to 1.833Å and also, the N-Al-N bond

Table 1. Bond Lengths and angels for bonds of BN nanotube, Al-doped BN nanotube and Ga-doped BN nanotube before and after interaction with ammonia

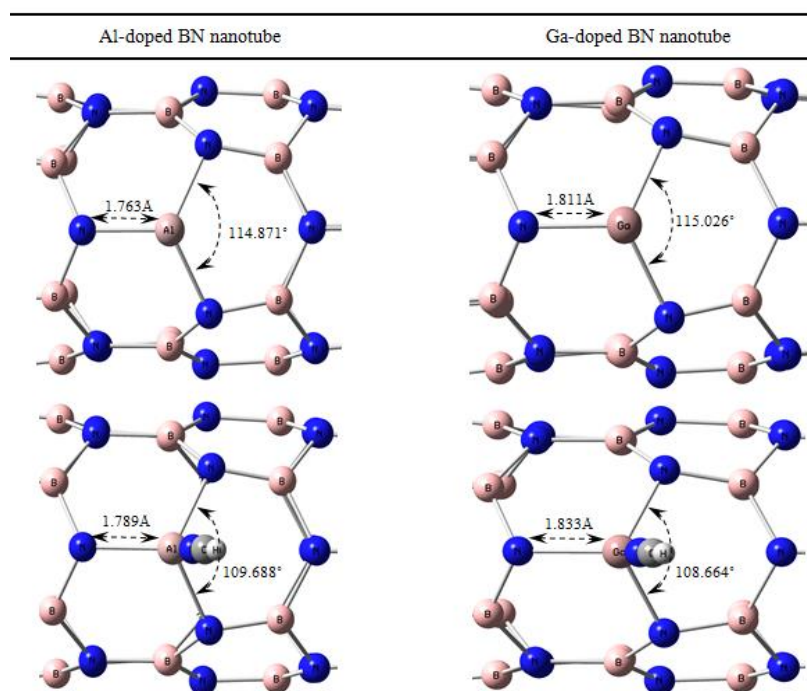


Table 2. Calculated interaction energy, HOMO energy (E_{HOMO}), LUMO energy (E_{LUMO}) and HOMO-LUMO energy gap (E_g) by (eV)

	E_{ad}	ΔG	E_{LUMO}	E_{HOMO}	E_g
Al_B -doped BN nanotube/HCN	-2543.411	-5083.962	-2.47	-6.33	3.86
Ga_B -doped BN nanotube/HCN	-2543.398	-5083.900	-2.27	-6.33	4.06
HCN	-	-	-2.34	-6.90	4.56
Al_B -doped BN nanotube	-	-	-2.29	-6.78	6.49
Ga_B -doped BN nanotube	-	-	-2.46	-6.79	4.33

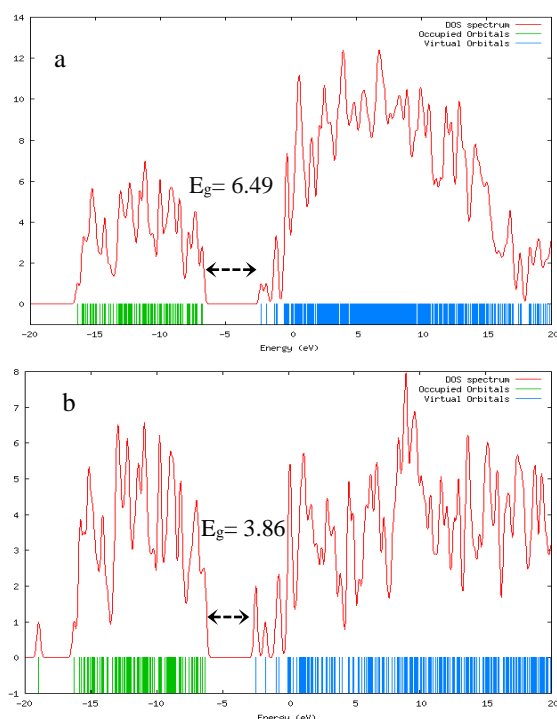


Figure 1. The density of states for a) BN-Al-doped, b) BN-Ga-doped/HCN.

angle has been changed from 114.871 to 109.688° and the N-Ga-N bond angle has been changed from 115.026 to 108.664°.

The electrostatic potential (esp) of the studied structures has been computed to recognize the active sites of studied structures. The esp can show the active sites by showing that where the molecule side has less or more electron density. It shows that the active and inactive sides in per molecule. Figure 2 shows the esp for HCN, Ga doped BN nanotube and Ga-doped BN nanotube/HCN. As can be seen the Nitrogen atom in HCN have the active side of this molecule and the Ga atoms is the active side of the Ga-doped BN nanotube. So, as the results show the HCN can adsorb on Ga-doped BN nanotube from mentioned sides and we can see adsorption. The other electrostatic potentials did not show in this paper for shorten. The density of states (DOS) diagrams has been calculated for the interactions.

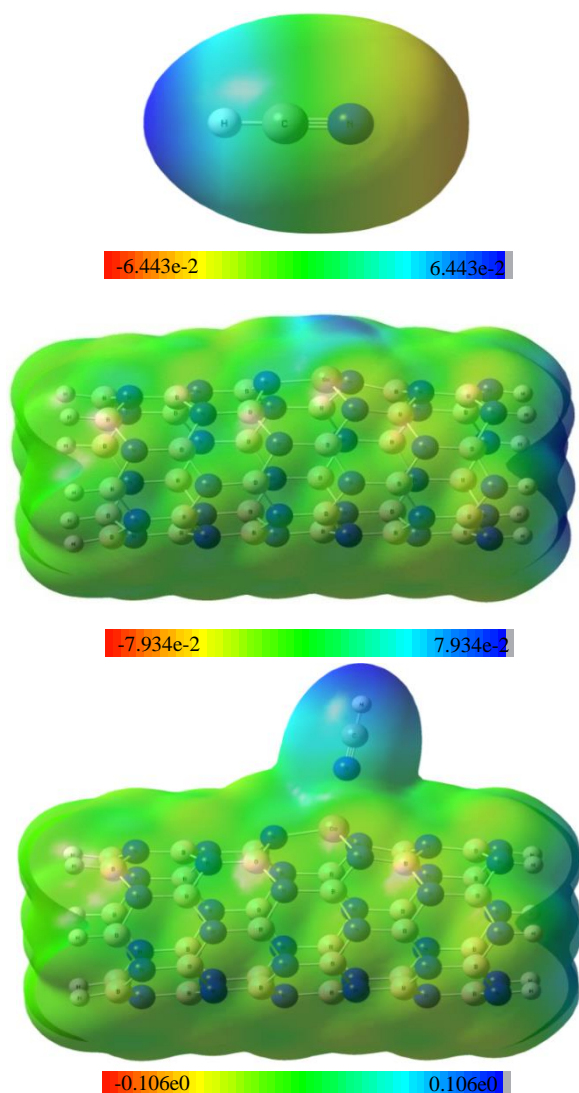


Figure2. The electrostatic potential of HCN, Ga doped BN nanotube and Ga doped BN nanotube/HCN.

Figure 1, shows the DOS diagrams before and after the adsorption HCN on BN-Al-doped. The gap energy, E_g , (the difference between LUMO energy and HOMO energy states) decreases by adsorption. This means that the E_g value have been changed 6.49 to 3.86 eV. It is a large-gap semiconductor range. In brief the other E_g , HOMO and LUMO values have been mentioned in table 1. Also, the adsorption energy and the difference Gibbs free energy of interactions have been shown in table 2. As can be seen this table, the results show interaction energy for the BN-Al-doped/HCN system (-2543.411 eV) is higher than the BN-Ga-doped/HCN system (-2543.398 eV). This trend is like for difference Gibbs free energy.

The difference Gibbs free energy for the BN-Al-doped/HCN system (-5083.962 eV) is lower than and the BN-Ga-doped/HCN system (-5083.900 eV). This shows that the HCN adsorption on BN-Al-doped is stronger than and BN-Ga-doped/HCN.

Conclusion

The adsorption of the HCN on pristine and Al-doped and Ga-doped boron-nitride nanotube have been studied theoretically. There is no interaction from Hydrogen sides of HCN with of the mentioned structures and also, there is no interaction from Nitrogen sides of HCN with pristine BN nanotube, but there are interaction between the Nitrogen atom of HCN with two other studied structures. The prediction of this can be possible by the study of the esp's of structures. This interaction cause to decrease the E_g for all of the three system. The calculated adsorption energies show that the interaction for Al doped BN nanotube/HCN was stronger than the Ga doped BN nanotube/HCN. The calculated difference Gibbs free energies show the same result. This means that HCN adsorption on the Al doped BN nanotube is easier than Ga doped BN nanotube at the room temperature.



References

- [1] S. Chen, L. Zieve, V. Mahaderan, J. Lab. Clin. Med. 75 (1970) 628.
- [2] A. Amann, D. Smith, Breath Analysis for Clinical Diagnosis and Therapeutic Monitoring, Word Scientific, Singapore, 2005.
- [3] Enderby, B., Smith, D., Carroll, W. & Lenney, W. Hydrogen cyanide as a biomarker for Pseudomonas aeruginosa in the breath of children with cystic fibrosis. *Pediatr. Pulm.* 44, 142–147 (2009).
- [4] Ryall, B., Davies, J., Wilson, R., Shoemark, A. & Williams, H. Pseudomonas aeruginosa, cyanide accumulation and lung function in CF and non-CF bronchiectasis patients. *Eur. Resp. J* 32(3), 740–747 (2008).
- [5] Sanderson, K., Wescombe, L., Kirov, S., Champion, A. & Reid, D. Bacterial cyanogenesis occurs in the cystic fibrosis lung. *Eur. Resp. J* 32, 329–333 (2008).
- [6] P. K. Lam, "Use of biomarkers in environmental monitoring" *J. Ocean & Coastal Management*, 52 (2009) 348-354.
- [7] P.G. Wells, K. Lee, and C. Blaise, "*Microscale testing in aquatic toxicology*", 1997 *advances, techniques, and practice*. CRC Press.
- [8] D. Golberg, Y. Bando, Y. Huang, T. Terao, M. Mitom, C. Tang & C. Zhi "Boron nitride nanotubes and nanosheets", *J. ACS nano*, 4 (2010) 2979-2993.

Experimental and Theoretical Studies on Acid Dissociation Constants of 4-Hydroxycoumarin

M. Ashtari-Delivand^a, B. Ghalami-Choobar^{a,*}, A. Ghiami-Shomami^{a,b}

^aDepartment of Chemistry, University of Guilan, Rasht, 19141, Iran;

^bYoung Researchers and Elite Club, Rasht Branch, Islamic Azad University, Rasht, Iran;

*B-Ghalami@guilan.ac.ir

Abstract: In this work, we investigated the pK_a values of the 4-Hydroxycoumarin using the experimental and computational methods. Experimentally, we used pH metric method to measure the pK_a values of 4-Hydroxycoumarin. deprotonation constant in NaNO_3 aqueous solutions with different ionic strength ($0 \leq I \text{ (mol.kg}^{-1}) \leq 2.18$) at $T=308.2$ K. Computationally, we report on the performance of several protocols for predicting the pK_a values of aqueous solution. Calculations were carried out at the B3LYP/6-31+G(d) and MP2/6-311++G(2d,2p) levels of theory combined with CPCM model with a mean absolute deviation less than 0.7 pK_a units. By comparing the calculated pK_a 's for 4-hydroxycoumarin drug from various methods to their experimental values, it was found an optimal combination of methods for gas and solution phase energies.

Keywords: 4-Hydroxycoumarin "pK_a" CPCM model" Gas-Phase" Solution-Phase" pH metric

Introduction

Most drugs have acidic or basic functionalities. Acid dissociation constants are important physicochemical parameters, which can provide critical information about properties such as solubility, lipophilicity, acidity, transport behavior, bonding to receptors, and permeability. Formulation procedures for optimizing drug delivery also benefit from the determination of the pK_a . Because acid-base properties of a drug are dependent on experimental conditions (e.g., temperature, ionic strength, ionic media), it is necessary to provide reliable model for the description of its acid-base behavior as a function of these different conditions [1, 2].

Coumarins (chromone-2-ones, benzopyran-2-ones) are naturally occurring classes of compound, which having variety of pharmacological activity dependent on the substitution patterns. Coumarins core structure represents a highly privileged and biologically relevant molecular scaffold which occurs in many natural products [3].

4-Hydroxycoumarin, have also been important starting materials for the preparation of several simple coumarins derivatives, which are known to possess important biological and pharmacological properties [4]. In the present work, calculations and measurements of pK_a values have been performed on the 4-Hydroxycoumarin in water and water-ethanol solvents.

Materials and method

a. Experimental section

All the potentiometric measurements were made using a digital multimeter (Martini instruments Mi180). The output of the multimeter was connected to a personal computer for data acquisition. The Mi5200 software together with Microsoft Excel (Office 2007) software

were used for data acquisition and calculations. A Model GFL circulation water bath was used to control the temperature of the test solution at $T=308.2$ K. The pH combination electrode was calibrated with pH 4 and 7 buffer solutions. All titrations were carried out under magnetic stirring and bubbling N_2 through the solution in order to exclude O_2 and CO_2 inside.

b. Computational section

The gas phase Gibbs free energies for Neutral (AH) and anion (A^-) species were calculated for 4-hydroxycoumarin at the B3LYP/6-31+G(d) and MP2/6-311++G(2d,2p) levels of theory. Also, the solvation free energies values of AH and A^- species for 4-hydroxycoumarin in water solvent were calculated using CPCM with UAHF, UAKS, UA0, UFF, Bondi, Pauling and Klamt atomic radii at the HF/6-31+G(d) level of theory. All calculations were performed using Gaussian 09 and Gaussian 03 program packages [5]. For computational efficiency, ΔG_{soln}^* were determined through the thermodynamic cycles defined in Figs. 1-3 based on Eq. (1).

$$\Delta G_{\text{soln}}^* = \Delta G_{\text{gas}}^* + \sum_{i=1}^{N_{\text{products}}} n_i \Delta G_{\text{soln},i}^* - \sum_{j=1}^{N_{\text{reactants}}} n_j \Delta G_{\text{soln},j}^* \quad (1)$$

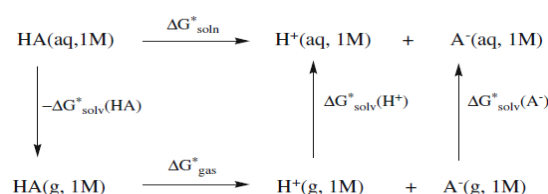


Fig. 1: Thermodynamic cycle A used in pK_a calculations with direct method. Ref. [6]

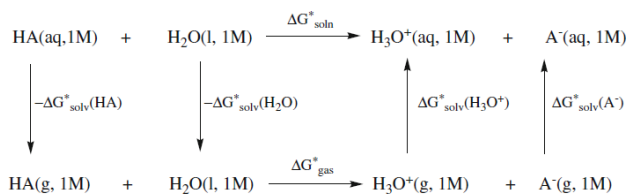


Fig. 2: Thermodynamic cycle B used in pK_a calculations with direct method. Ref. [6]

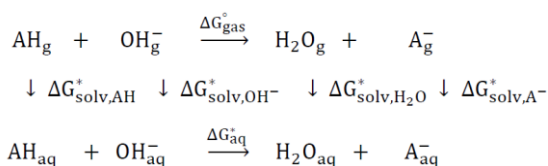


Fig. 3: Thermodynamic cycle C used in pK_a calculations with direct method. Ref. [7]

Results and Discussion

a. Experimental section

The change in pH due to titrant (NaOH) volume addition was recorded at different ionic strengths of $\text{NaNO}_3(\text{aq})$ solutions. The equivalence point pH was determined by using titration curve and plotting first and second derivative curves. The experimental deprotonation constants of 4-hydroxycoumarin obtained from titration curves at different ionic strengths are reported in table 1.

Table1: Experimental deprotonation constants of 4-hydroxycoumarin in $\text{NaNO}_3(\text{aq})$ at different ionic strength and at $T=308.2\text{ K}$

I(mol kg ⁻¹)	pK_a
0	4.86
0.52	4.87
1.03	4.84
1.60	4.77
2.18	4.69

b. Computational section

The Gibbs free energies of gas and solution phase were used to calculate the pK_a values. Firstly, the Gibbs free energies were calculated at the B3LYP/6-31+G(d), MP2/6-311++G(2d,2P) and HF/6-31+G(d) levels of theory. Then, the ΔG_g° and $\Delta \Delta G_{\text{solv}}^*$ were calculated through the thermodynamic cycles. Finally, ΔG_{soln}^* were calculated using the CPCM with UAHF, UAKS, UA0, UFF, Bondi, Pauling and Klamt atomic radii. It can be noted, the choice of cavities in CPCM is important because the computed energies and properties depend on the cavity size and shape. In this study, the different cavities were used to evaluate the solvation effects. Also, the calculated and experimental pK_a values of 4-hydroxycoumarin drug in water solvent were reported in

Table 2. Comparison of results in Table 2 shows a good agreement between the experimental and the calculated pK_a values of investigated compounds in water solvent. The pK_a value was obtained using thermodynamic cycles A, B and C in according to Eqs. 2-4 respectively. It can be noted; Gas phase and solvation free energies of H^+ , H_2O and H_3O^+ were taken from literatures [6].

$$pK_a = \frac{\Delta G_{\text{soln}}^*}{RT \ln(10)} \quad (2)$$

$$pK_a = \frac{\Delta G_{\text{soln}}^*}{RT \ln(10)} - \log[\text{H}_2\text{O}] \quad (3)$$

$$pK_a = \frac{\Delta G_{\text{aq}}^*}{2.303} - RT + \ln \Delta V \quad (4)$$

Table2: Experimental and computational pK_a values through the thermodynamic cycles A, B and C, respectively.

Method	Cycles	$pK_a(\text{Calc.})$						
		UAHF	UAKS	UA0	UFF	Bondi	Pauling	Klamt
B3LYP	A	2.52	2.25	5.69	2.10	2.43	3.07	2.63
	B	2.96	2.70	6.14	2.54	2.87	3.51	3.07
	C	4.45	4.18	7.62	4.03	4.36	5.00	4.56
MP2	A	5.24	4.97	8.41	4.82	5.15	5.79	5.35
	B	4.44	4.18	7.61	4.02	4.35	4.99	4.55
	C	4.31	4.04	7.48	3.89	4.22	4.86	4.42

¹ Experimental pK_a value of 4-Hydroxycoumarin is 4.16 and was taken from ref. [8]

Conclusions

Calculation of pK_a values for 4-Hydroxycoumarin drug in water solvent were successfully performed using CPCM/UAHF, UAKS, UA0, UFF, Bondi, Pauling, Klamt/HF/6-31+G(d) level of theory in solution-phase and B3LYP/6-31+G(d) and MP2/6-311++G(2d,2P) levels of theory in gas-phase. Comparison of results shows a good agreement between the experimental and the calculated pK_a values of investigated drugs. It can be concluded that the mentioned method can be applied in the prediction of pK_a values of the compounds with similar structure. Also Results obtained show that deprotonation constant of 4-Hydroxycoumarin decreases with increasing the ionic strength.

Acknowledgment

We gratefully acknowledge the graduate office of University of Guilan for supporting this work.

References

[1] M. Meloun, S. Bordovska, A. Vrana "The thermodynamic dissociation constants of the anticancer Drugs camptothecine, 7-ethyl-10-hydroxycamptothecine,



10-hydroxycamptothecin and 7-ethylcamptothecin by the least-squares nonlinear regression of multiwavelength Spectrophotometric pH-titration data”, *Anal. Chim. Acta*, 584 (2007) 419–432.

[2] M. Sanchool “Evaluation of Acidity Constants and Evolution of Electronic Features of Phenol Derivatives in Different Compositions of Methanol/Water Mixture”, *Journal of Chemistry*, 2012 (2013) 1.

[3] Pramod K. Sahu, Praveen K. Sahub, Dau D. Agarwal “Role of basicity, calcinations, catalytic activity and recyclability of hydrotalcite in eco-friendly synthesis of coumarin derivatives”, *J. Mol. Catal. A: Chem.*, 395 (2014) 251–260.

[۴] F. Borges, F. Roleira, N. Milhazes, L. Santana, E. Uriarte “Simple Coumarins and Analogues in Medicinal Chemistry: Occurrence, Synthesis and Biological Activity”, *Curr. Med. Chem.*, 12 (2005) 887–916.

[5] M.J. Frisch, G.W. Trucks, H.B. Schlegel, G.E. Scuseria, M.A. Robb, (2004) J.R. Cheeseman, Gaussian 03, Revision E.01, Gaussian, Inc., Wallingford (CT).

[6] J. Ho, M.L. Coote “A universal approach for continuum solvent pKa calculations: are we there yet? ”, *Theor. Chem. Acc.*, 125 (2010) 3–21.

[7] N. Sadlej-Sosnowska “Calculation of acidic dissociation constants in water: solvation free energy terms. Their accuracy and impact”, *Theor. Chem. Acc.*, 118 (2007) 281–293.

[8] P. Nowak, P. Olechowska, M. Mitoraj, M. Wozniakiewicz, P. Koscielniak “Determination of acid dissociation constants of warfarin and hydroxywarfarins by capillary electrophoresis”, *J. Pharm. Biomed. Anal.* 112 (2015) 89–97.

Theoretical investigation of 4-(2,3-dihydro[3,4-6][1,4][dioxin-5-yl) aniline copolymer

F. Kalantari Fotooh*, M. R. Nateghi, M. Mohammadi

Department of chemistry, Yazd branch, Islamic Azad University, Yazd, Iran

*f-kalantari-f@iauyazd.ac.ir

Abstract: Poly 4-(2,3-dihydro[3,4-6][1,4][dioxin-5-yl) aniline (EDOT-Ani) is an interesting novel monomer which can be used as an electrode in fabrication of dye synthesized solar cells. In this paper a DFT method with B3LYP/6-31G* level of theory was used for investigating the structural, electronic and optical properties of different configurations of 4-EDOT-Ani. The structural parameters were calculated and indicated that the EDOT-Aniline has a benzoid structure. Gibbs free energy calculations show that gauche-anti configuration is the most energetically stable structure. The HOMO-LUMO gaps were calculated their counterparts were interpreted. The IR spectrum was simulated and show good correlation with experimental values. Finally, TDDFT calculations were used for obtaining the UV spectra of all configurations.

Keywords: Copolymer, EDOT, DFT, Optical properties.

Introduction

Electronically conducting polymers have received considerable attention because of their wide range of technological applications in optical and electronic devices [1], energy storage systems [2], plastic solar cells [3], biosensors [4] and electromagnetic shielding [5]. These applications can be attributed to their band structures. There have been a number of attempts over the past decades to the preparation of novel organic conjugated polymers with low band gaps [6]. Among the conjugated polymers, poly (3,4-ethylenedioxythiophene) (PEDOT) is a promising organic electrode material for its low band gap, low oxidation potential and remarkable environmental stability [7-9]. This polymer has chains which block the 3,4 positions of thiophene ring, exerting an electron donating effect which reduce the band gap of polythiophene about 1.2-1.7 eV and causes a high degree of visible light transmission [10]. Several studies have been carried out for random copolymerization of aniline-EDOT monomers in order to comprise the conductivity and electro catalytic effect of both Aniline and EDOT [11, 12]. In this work we exploit DFT calculations to investigate the conformational, electronic and optical properties of 3,4 -Ethylenedioxythiophene -Aniline copolymer (n-EDOT-Ani).

Computational details

All calculations were carried out using Gaussian 09 [13] and density functional theory at B3LYP level in combination with 6-31G(d) basis set. Different configurations were considered for 2-4 oligomers and let them to fully optimized. Higher Occupied Molecular Orbital (HOMO) and Lower Unoccupied Molecular Orbitals (LUMO) energies were calculated and their isosurfaces plots are depicted using Gauss view program with isodensity value =0.02au. The HOMO-LUMO energy gap was evaluated as the difference between the HOMO and LUMO energy levels. Then the frequency calculations were applied for all species and the most

energetically stable configurations were selected. IR spectra were simulated and scaled with a common scaling factor of 0.9613 [13, 14]. TD-DFT/B3LYP/6-31G* calculations were also performed for simulating UV-visible spectra in DMSO medium on polarized continuum model (PCM).

Results and Discussion

Fig 1 shows the all studied configuration of 4-EDOT-Ani, after full optimization. Gibbs free energy results show that gauche-anti conformation (Tet3) is the most stable structure among all studied conformations. The inter ring distance in all conformation is about 1.39- 1.40 Å for N-C bond lengths and about 1.46Å for C-C bond lengths which show the benzoid structure of this copolymer [15]. Table 1 reports the HOMO-LUMO energy levels for the most stable conformations of 1-4 EDOT-Ani. The results show that the band gap of EDOT-Aniline is about 4.32eV and reduces to 3.39 eV by increasing the number of monomers in 4-EDOT-Ani which is due to the higher conjugation between monomers. This band gap is lower than the band gap obtained for PEDOT [16]. Among all conformations of 4-EDOT-Ani, Tet 3 show the most narrowing band gap which is due to its higher structural planarity and therefore higher conjugation and electron conductivity.

Contours of HOMO and LUMO are depicted in Fig 2 for Tet 3 configuration. In all oligomers the HOMOs are mostly located on the rings and the LUMOs are concentrated on the inter ring bonds which confirm the benzoid structure of EDOT-Ani polymer.

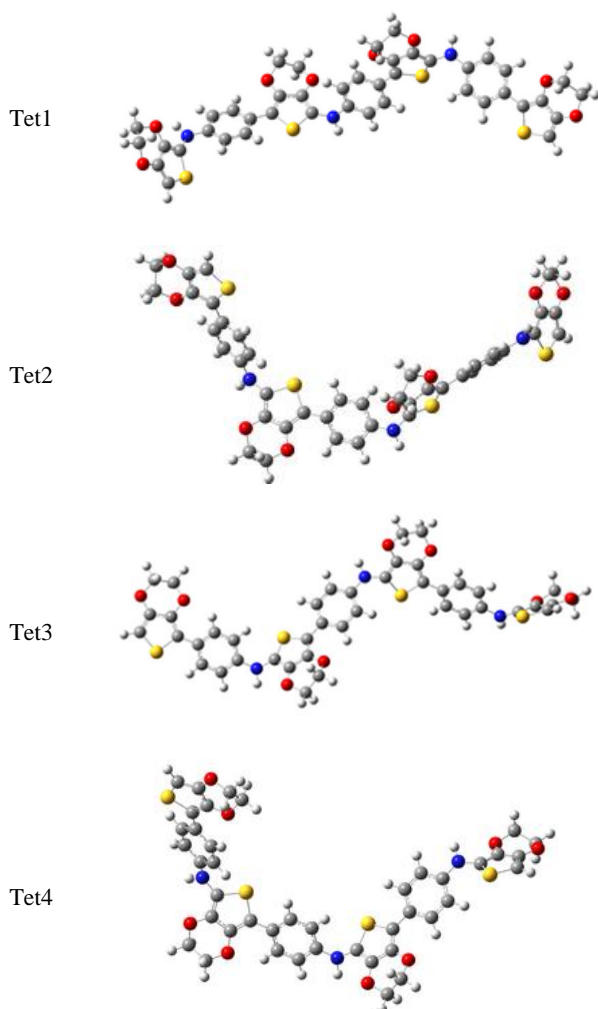


Fig 1: Optimized structure of all configuration of 4-EDOT-Ani, red, yellow and blue balls are used for C, O, S and N atoms respectively.

By increasing the number of monomers to 4- EDOT-Ani the HOMO is more prominent over the N-C inter ring bonds which is due to its higher conjugation.

Table 1: Gibbs free energies(kJ/mol) of different isomers of monomer to pantamer structures of EDOT-Aniline

	HOMO/eV	LUMO/eV	Gap/eV
M	-4.82621	-0.50259	4.32
D	-4.41831	-0.72056	3.70
T	-4.45287	-0.76845	3.68
Tet1	-4.33559	-0.79457	3.54
Tet2	-4.35464	-0.77689	3.58
Tet3	-4.22947	-0.84355	3.39
Tet4	-4.24198	-0.8294	3.41

The delocalization of HOMO and LUMO orbitals are higher in Tet3 and Tet 4 conformations with higher planarity than Tet1 and 2.

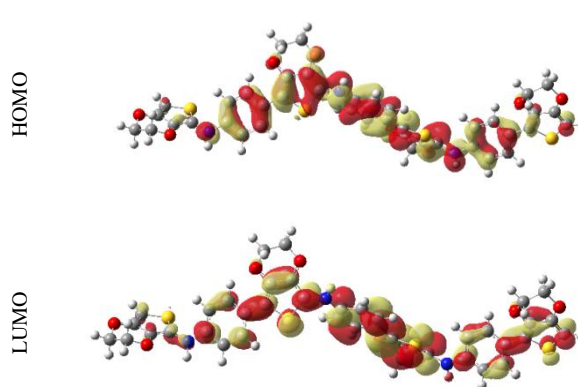


Fig 2: The isosurface plot of HOMO-LUMO states from B3LYP/6-31G*for 4-EDOT-Ani the electron accumulation is indicated with dark gray (Red) and the charge depletion with light gray (yellow) colors.

The theoretically simulated IR spectra of 4- EDOT- Ani copolymer is presented in Fig 3.

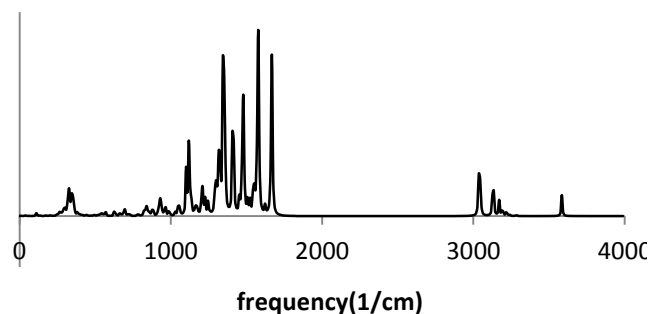


Fig 3: IR spectrum of 4-EDOT-Ani calculated by B3LYP/6-31G*

A peak at 3584- 3589 is assigned to N-H stretching which is different from experimental data [12]. The difference in simulated and observed N-H stretching can be attributed to the fact that theoretical data is for an isolated oligomer in vacuum state while the experimental is that of condensed phase. The bands at 3035- 3133 are assignable to asymmetric C-H stretching of dioxan ring. The band around 1646- 1670 are corresponding to C-C and C=C stretching of thiophen ring in close agreement with experimental data [12]. The vibrations at 1178, 1103- 1120 are assigned for C-O-C bond stretching in the ethylenedioxy group [17]. C-S stretching band is observed at about 845 cm⁻¹ and 960 cm⁻¹.

The theoretically simulated UV-vis spectra of 4-EDOT-Anilin at TD/DFT/6-31G* level of theory are given in Fig 4 for all conformations, respectively. The peaks at 300- 366 nm corresponds to $\pi - \pi^*$ excitation of the para substituted benzene segment in Aniline.

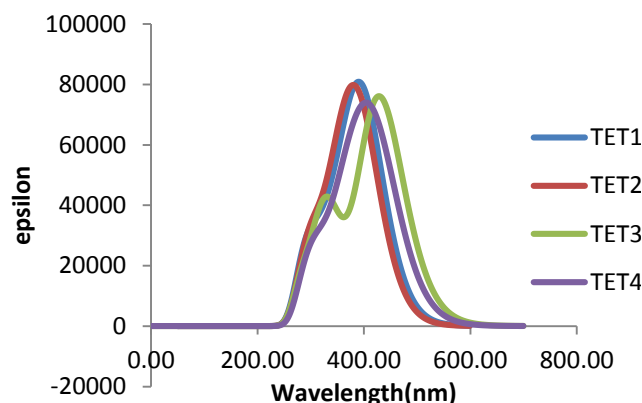


Fig 4: UV-visible spectra of 4-EDOT-Aniline using TD/DFT/6-31G*

The broad peak at 420-426 nm can be attributed to $\pi-\pi^*$ electronic transition of EDOT ring. The highest intensity can be attributed to Tet3 conformation with low band gap and highest conjugation. Two peaks at 430 and 330 nm in Tet 3 are in close agreement with experimental results [12] at 330 and 410nm.

Conclusions

In this paper structural, electronic and optical properties of Poly 4-(2,3-dihydro[3,4-6][1,4][dioxin-5-yl] aniline) was investigated using B3LYP/6-31G* level of theory. Gibbs free energy results show that gauche- anti conformation (Tet3) is the most stable structure among all studied conformations. Structural results show the benzoid structure for this copolymer which are confirmed by HOMO- LUMO counters. The H-L gap of EDOT-Aniline monomer is about 4.32eV and reduces to 3.39 eV by increasing the number of monomers in 4-EDOT-Ani. Theoretically IR and UV-vis spectra were calculated and show close agreement with experimental data.

References

- [1] H. He, J. Zhu, N.J. Tao, et al., "A Conducting Polymer Nanojunction Switch", *Journal of the American Chemical Society*, 123 (2001) 7730-7731.
- [2] F. Cheng, W. Tang, C. Li, et al., "Conducting Poly(aniline) Nanotubes and Nanofibers: Controlled Synthesis and Application in Lithium/Poly(aniline) Rechargeable Batteries", *Chemistry - A European Journal*, 12 (2006) 3082-3088.
- [3] P. Vanlaeke, G. Vanhoyland, T. Aernouts, et al., "Polythiophene based bulk heterojunction solar cells: Morphology and its implications", *Thin Solid Films*, 511-512 (2006) 358-361.
- [4] G. Inzelt, M. Pineri, J.W. Schultze, et al., "Electron and proton conducting polymers: recent developments and prospects", *Electrochimica Acta*, 45 (2000) 2403-2421.
- [5] J.-M. Yeh, C.-L. Chen, Y.-C. Chen, et al., "Enhancement of corrosion protection effect of poly(o-ethoxyaniline) via the formation of poly(o-ethoxyaniline)-clay nanocomposite materials", *Polymer*, 43 (2002) 2729-2736.
- [6] R.L.E. T. A. Skotheim, In *Handbook of Conducting Polymers*, Marcel Dekker, New York, 1998.
- [7] J. Yu, S. Holdcroft, "Synthesis, Solid-Phase Reaction, and Patterning of Acid-Labile 3,4-Ethylenedioxythiophene-Based Conjugated Polymers", *Chemistry of Materials*, 14 (2002) 3705-3714.
- [8] M.A. Najeeb, S.M. Abdullah, F. Aziz, et al., "Structural, morphological and optical properties of PEDOT:PSS/QDs nano-composite films prepared by spin-casting", *Physica E: Low-dimensional Systems and Nanostructures*, 83 (2016) 64-68.
- [9] T. Rebiš, G. Milczarek, "A comparative study on the preparation of redox active bioorganic thin films based on lignosulfonate and conducting polymers", *Electrochimica Acta*, 204 (2016) 108-117.
- [10] H. Huang, P.G. Pickup, "A Donor-Acceptor Conducting Copolymer with a Very Low Band Gap and High Intrinsic Conductivity", *Chemistry of Materials*, 10 (1998) 2212-2216.
- [11] G.M. El-Enany, M.A. Ghanem, M.A.A. El-Ghaffar, "Electrochemical Deposition and Characterization of Poly(3,4-ethylene dioxythiophene), Poly(aniline) and their Copolymer onto Glassy Carbon Electrodes for Potential Use in Ascorbic Acid Oxidation", *Portugaliae Electrochimica Acta*, 28 (2010) 336-348.
- [12] L. Shahhosseini, M.R. Nateghi, M. Kazemipour, et al., "Electrochemical synthesis of novel polymer based on (4-(2,3-dihydrothieno[3,4-6][1,4][dioxin-5-yl] aniline) in aqueous solution: Characterization and application", *Materials Chemistry and Physics*, 177 (2016) 554-563.
- [13] M.J. Frisch, G.W. Trucks, H.B. Schlegel, et al., *Gaussian 09*, Gaussian, Inc., Wallingford, CT, USA, 2009.
- [14] P. Rosmus, H. Bock, B. Solouki, et al., "Silathene: Highly Correlated Wave Functions and Photoelectron Spectroscopic Evidence", *Angewandte Chemie International Edition in English*, 20 (1981) 598-599.
- [15] M. Garcia, L. Fomina, S. Fomine, "Electronic structure evolution of neutral and dicationic states of conjugated polymers with their band gap", *Synthetic Metals*, 160 (2010) 2515-2519.
- [16] C. Alemán, E. Armelin, J.I. Iribarren, et al., "Structural and electronic properties of 3,4-ethylenedioxythiophene, 3,4-ethylenedisulfanylthiophene and thiophene oligomers: A theoretical investigation", *Synthetic Metals*, 149 (2005) 151-156.
- [17] L. Zhang, H. Peng, P.A. Kilmartin, et al., "Poly(3,4-ethylenedioxythiophene) and Polyaniline Bilayer Nanostructures with High Conductivity and Electrocatalytic Activity", *Macromolecules*, 41 (2008) 7671-7678.



DFT calculations on 2-N-ethylidynesaminiumoxane, 2-N-ethylidynesaminiumthiane, 2-N-ethylidynesaminiumselenane

Hossein Shirani Il Beigi^{a,*}, Peyvand Ghanbarpour^a, Farhad Gholampour^b

^aYoung Researchers and Elites Club, Urmia Branch, Islamic Azad University, Urmia, Iran

^bDepartment of Chemistry, Payame Noor University, P.O.Box 19395-3697, Tehran, Iran

*shiranihossein@gmail.com

Abstract

The structural parameters of 2-N-ethylidynesaminiumoxane (1), 2-N-ethylidynesaminiumthiane (2), 2-N-ethylidynesaminiumselenane (3) were calculated by means of the hybrid density functional (B3LYP and M06-2X) theory based methods with the 6-311+G** basis set on all atoms, natural bond orbital (NBO) interpretation and atoms in molecules theory (AIM). Levels of theory used in this work showed that the axial conformations of compounds 1–3 are more stable than their corresponding equatorial forms. The hyper-conjugative anomeric effect (HCAE) is in favor of the axial conformations of compounds 1–3. The axial conformations of compounds 1–3 are harder than their corresponding equatorial conformations but their conformational behaviors could not be interpreted with the Maximum Hardness Principle.

Keywords: DFT-B3LYP, Natural Bond Orbital, 2-N-ethylidynesaminiumoxane

Introduction

The anomeric effect is a stereoelectronic effect that was discovered by Edward in 1955 while studying carbohydrates; the term was later coined by Lemieux and Chu in 1958 [1]. Due to steric hindrance in the axial conformations of the six membered rings, substituent groups prefer to be equatorial and the chair conformer predominates in equilibrium, but the anomeric effect is in favor of the axial conformation of a six membered saturated ring in opposition to the steric effect [2-4]. Obviously, there is no general consensus about the actual origin of the anomeric effect [3]. Accordingly, the origin of the anomeric effect has remained an open question. To gain further insight on the origin of the anomeric relationships in compounds of 2-N-ethylidynesaminiumoxane (1), 2-N-ethylidynesaminium thiane (2), 2-N-ethylidynesaminium selenane (3), we have investigated the correlations between the differences in the total energies, electrostatic model associated with the dipole–dipole interactions, hyperconjugative anomeric effect (HCAE) and structural parameters among the axial and equatorial conformations of compounds 1–3 (Fig. 1)

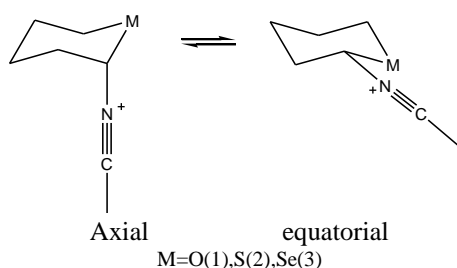


Fig. 1. Schematic representation of the axial and equatorial conformations of compounds 1–3.

Computational method

All the structural parameters optimizations and the electronic energies and the thermodynamic functions calculation in this work were performed at the B3LYP/6-311+G** and M06-2X/6-311+G** with the GAMESS US package of programs [5-8]. The hyper-conjugative anomeric effects (HCAEs), bonding and antibonding orbital occupancies and energies, attractive electrostatic interactions between two adjacent atoms (AEI), dipole–dipole interactions and their influences on the structural and conformational properties of compounds 1–3 were quantitatively investigated by means of the natural bond orbital (NBO) interpretations.

Representative structural parameters [bond lengths (r), bond angles (θ), torsion angles (ϕ) and their differences: Δr , $\Delta\theta$ and $\Delta\phi$ parameters] for the axial and equatorial conformations of compounds 1–3 as calculated at the B3LYP/6-311+G** level of theory, are summarized in Tables 1 and 2. The σ_{M1-C2} bond lengths in the axial conformations of compounds of 1–3 are smaller than those in their corresponding equatorial conformations. The hyper-conjugative interactions between the non-bonded lone pairs of the six-membered rings [LPM, M = O(1), S (2), Se (3)] and the $\sigma^*_{C-Nethyl}$ tend to decrease the σ_{M1-C2} bond lengths by increasing their double bond characters but the $\sigma_{M1-C2} \rightarrow \pi^*_{Nethyl}$ and $\sigma_{M1-C2} \rightarrow \sigma^*_{Nethyl}$ electron delocalizations have opposite impacts. Note that the impacts of the $\sigma_{M1-C2} \rightarrow \pi^*_{Nethyl}$, $\sigma_{M1-C2} \rightarrow \sigma^*_{Nethyl}$ and $\pi_{Nethyl} \rightarrow \sigma^*_{M1-C2}$ electron delocalizations on the decrease of the $\sigma_{C2-Nethyl}$ bond lengths and also on the increase of the σ_{M1-C2} bond lengths in the axial and equatorial conformations of compounds 1–3 are relatively the same. The calculated Gibbs free energy,

Table 1. B3LYP/6-311+G**and M06-2X calculated thermodynamic functions and parameters [ΔH , ΔG (in kcal mol⁻¹), S and ΔS (in cal mol⁻¹K⁻¹)] at 25°C and 1 atm pressure for the axial and equatorial conformations of compounds 1-3.

Compounds	H	S	G	ZPE	E ₀	ΔH	ΔS	ΔG	ΔZPE	ΔE_0
1-ax	-403.924530	96.291	-403.634756	0.183173	-403.597639	0.00	0.000	0.00	0.00	0.00
	<i>-403.740312</i>	<i>92.427</i>	<i>-403.445123</i>	<i>0.185773</i>	<i>-403.407988</i>	<i>0.00</i>	<i>0.000</i>	<i>0.00</i>	<i>0.00</i>	<i>0.00</i>
1-eq	-403.583768	97.808	-403.630240	0.183225	-403.594222	7.16	1.517	2.83	0.03	2.1
	<i>-403.397836</i>	<i>93.574</i>	<i>-403.442296</i>	<i>0.185843</i>	<i>-403.405938</i>	<i>7.80</i>	<i>1.147</i>	<i>1.77</i>	<i>0.04</i>	<i>1.28</i>
2-ax	-726.568414	101.165	-726.617062	0.179790	-726.579460	0.00	0.000	0.00	0.00	0.00
	<i>-726.377847</i>	<i>98.471</i>	<i>-726.424634</i>	<i>0.181618</i>	<i>-726.388663</i>	<i>0.00</i>	<i>0.000</i>	<i>0.00</i>	<i>0.00</i>	<i>0.00</i>
2-eq	-726.565839	102.389	-726.613906	0.179938	-726.576872	1.61	1.224	1.98	0.09	1.62
	<i>-726.374659</i>	<i>99.284</i>	<i>-726.421832</i>	<i>0.181735</i>	<i>-726.385550</i>	<i>2.00</i>	<i>0.813</i>	<i>1.76</i>	<i>0.07</i>	<i>1.95</i>
3-ax	-2729.902542	102.943	-2729.951454	0.178657	-2729.913892	0.00	0.000	0.00	0.00	0.00
	<i>-2729.744461</i>	<i>100.986</i>	<i>-2729.792443</i>	<i>0.180654</i>	<i>-2729.755542</i>	<i>0.00</i>	<i>0.000</i>	<i>0.00</i>	<i>0.00</i>	<i>0.00</i>
3-eq	-2729.900466	104.230	-2729.949989	0.178684	-2729.911878	1.30	1.287	0.92	0.02	1.26
	<i>-2729.741892</i>	<i>102.329</i>	<i>-2729.790512</i>	<i>0.180956</i>	<i>-2729.753118</i>	<i>1.61</i>	<i>1.343</i>	<i>1.21</i>	<i>0.19</i>	<i>1.52</i>

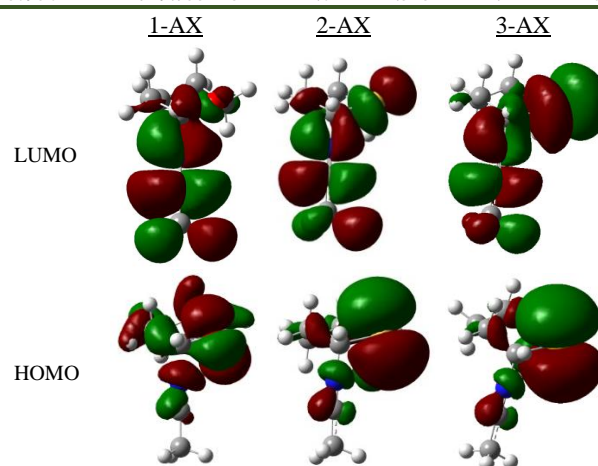


Fig. 2. Schematic representation of the HOMO and LUMO in the axial conformations of compounds 1-3 [M = O(1), S (2), Se (3)]

enthalpy, entropy, corrected electronic energy differences (i.e. ΔG , ΔH , ΔS and ΔE_0) for the axial and equatorial conformations of compounds 1-3 as calculated at the B3LYP/6-311+G** and M06-2X/6-311+G** are given in Table 1. The results showed that the axial conformations of compounds 1-3 are more stable than their corresponding equatorial conformations. The strong $LP_{ax}M_1 \rightarrow \sigma_{C_2-N_7}^*$ Nethyl electron delocalizations in the axial conformations of compounds 1-3 cause the greater HCAEs values compared to their corresponding equatorial forms. The second-order perturbation theory has been employed to evaluate the magnitude of the plausible donor-acceptor hyperconjugative interactions. The NBO-B3LYP/6-311+G** analysis showed that the $LP_{ax}M_1 \rightarrow \sigma_{C_2-N_7}^*$ [M=O (1),S(2),Se(3)] electron delocalizations have the most impacts on the magnitudes of the total hyperconjugative anomeric effect (HCAE) of compounds 1-3. In fact, the calculated HC-endo-AE values in the axial conformations of compounds 1-3 are controlled by the $LP_{ax}M_1 \rightarrow \sigma_{C_2-N_7}^*$ electron delocalizations, respectively. By means NBO DEL calculations we found the variations of the $\sigma_{C_2-N_7}$ bond lengths in the axial and equatorial conformations of compounds 1-3, respectively, results from the confrontations between the impacts of the $LP_{ax}M_1 \rightarrow \sigma_{C_2-N_7}^*$ Nethyl and $\sigma_{M_1-C_2} \rightarrow \pi_{N_7}^*$ Nethyl electron delocalizations in compounds 1-3 (Table 4). Our results showed that the $LP_{ax}M_1 \rightarrow \pi_{N_7-C_8}^*$ [LPM1, M=O(1),S(2), Se(3)] electron delocalizations have much weaker impacts on the axial conformation preferences in compounds 1-3 than the $LP_{ax}M_1 \rightarrow \sigma_{C_2-N_7}^*$ hyperconjugative interactions.

Table 2. B3LYP/6-311+G** calculated energies (in hartree) of HOMO (ϵ_{HOMO}), LUMO (ϵ_{LUMO}), see Fig. 2, $\epsilon_{\text{LUMO}} - \epsilon_{\text{HOMO}}$ and global hardness (η) for the axial and equatorial conformations of compounds 1-3.

	ϵ_{HOMO}	ϵ_{LUMO}	$\epsilon_{\text{LUMO}} - \epsilon_{\text{HOMO}}$	I	A	η	$\Delta\eta$
1-ax	-0.58200	-0.02157	0.56043	0.58200	0.02157	0.280215	0.01306(8.20)
1-eq	-0.56335	-0.02905	0.5343	0.56335	0.02905	0.26715	0.00000
2-ax	-0.38698	-0.21115	0.17583	0.38698	0.21115	0.08791	0.00788(4.95)a
2-eq	-0.37543	-0.21537	0.16006	0.37543	0.21537	0.08003	0.00000
3-ax	-0.37056	-0.21235	0.15821	0.37056	0.21235	0.07910	0.00601(3.77)a
3-eq	-0.36177	-0.21559	0.14618	0.36177	0.21559	0.07309	0.00000

Conclusions

We investigate electronic energies, structural parameters, bonding and stereoelectronic points for compounds 1–3 by means of the DFT, NBO and AIM analyses. The calculations showed that the axial conformations of compounds 1–3 are more stable than their corresponding equatorial conformations and the dipole moments (μ) of the axial conformations of compounds 1–3 are smaller than those of their equatorial forms. The results of NBO Deletion have been proved that $LP_{ax}M \rightarrow \sigma_{C2-N7}^*$ hyperconjugative interactions are responsible for the axial conformation preferences in compounds 1-3. The axial conformations of compounds 1–3 are harder than their corresponding equatorial conformations. The calculated values of $\rho(r)$, between the axial and equatorial conformations of compounds 1–3 are in good agreement with the amounts of the anomeric effect in axial and equatorial conformations.

References

- [1] Edward, J. T. Stability of glycosides to acid hydrolysis. *Chem. Ind. (Lond.)* 1102–1104 (1955).
- [2] Lemieux, R. U. & Chu, P. in 133rd National Meeting of the American Chemical Society 31N (American Chemical Society, 1958).
- [3] E. Juaristi and G. Cuevas, *The Anomeric Effect*, CRC Press Inc, Boca Raton, FL, 1995.
- [4] P. Deslongchamps, *Stereoelectronic Effects in Organic Chemistry*, Wiley, New York, 1983.
- [5] H. Shirani Il Beigi, P. Ghanbarpour, *Journal of Structural Chemistry*, 2014, 55: 2, 217-222.
- [6] C. J. Cramer, *J. Org. Chem.*, 1992, 57, 7034. 5 C. J. Cramer, D. G. Truhlar and A. D. French, *Carbohydr. Res.*, 1997, 298, 1.
- [7] H. Shirani Il Beigi, *J. Phys. Chem., A*, 2013, 87:9, 1537-1541.
- [8] C. L. Perrin, K. B. Armstrong and M. A. Fabian, *J. Am. Chem. Soc.*, 1994, 116, 715.



Doping the Buckminsterfullerene by Nitrogen Substitution ($C_{54}N_6$); a Density Functional Theory Study

Hossein Shirani Il Beigi^{a,*}, Peyvand Ghanbarpour^a, Farhad Gholampour^b

^aYoung Researchers and Elites Club, Urmia Branch, Islamic Azad University, Urmia, Iran

^bDepartment of Chemistry, Payame Noor University, P.O.Box 19395-3697, Tehran, Iran

*Corresponding author. E-mail address: shiranihossein@gmail.com

Abstract

C_{60} and $C_{54}N_6$ fullerene was studied by Density Functional Theory DFT at the B3LYP/6-31G* level of theory. The structure parameters, vibrational frequencies, dipole moment, polarizability, highest occupied molecular orbital (HOMO) and lowest unoccupied molecular orbital (LUMO), used to understand the properties of the doped $C_{54}X_6$ ($X = N$) and fullerene C_{60} . The obtained result indicates that the C-C bond length increases as a result of doping. The calculations show that the doped fullerene $C_{54}N_6$ is more thermal stability than other C_{60} fullerene. Also, the $C_{54}N_6$ fullerene has the lowest electronic energy. The minimal and the maximal values of bond lengths is correspond to C_{60} and $C_{54}N_6$ fullerenes, respectively. The highest HOMO-LUMO gap associated by C_{60} and the lowest HOMO-LUMO gap belongs to $C_{54}B_6$ fullerene. The higher total dipole moment value associated by fullerene doped nitrogen $C_{54}X_6$ ($X = N$).

Keywords: B3LYP/6-311+G; Fullerene; HOMO-LUMO gap; Stabilization Energy

Introduction

Nowadays, the interest in nanoscale materials has rapidly increased due to their positive use in various technical and scientific researches relating on the energy, environment, and biomedical fields. Carbon is one of the most amazing elements with a vast range of exotic properties. These properties have shed the light on carbon-based nanostructures, such as fullerenes [1], carbon nanotubes [2], and graphene [3]. The fullerene molecules C_{60} discovered in 1985 [4]. Since this finding, a whole range of studies have been conducted on these particles. Fullerenes are accepted as the fourth form of solid carbon after amorphous, graphite and diamond forms [5]. Fullerenes and their derivatives are attractive compounds, especially for carbon nanotechnology. Variation of the number, type and positional relationship of chemical moieties attached to the fullerene core allows the formation of fullerene-containing systems with adjustable properties (e.g., solubility, biological activity, photochemical and conductive properties) [6].

stable compounds here. We have investigated the theoretical methods to elucidate the doped fullerenes using molecular and structural properties. This was done by discussing quantum chemical parameter.

Result and Discussion

The geometry of fullerene cages has been optimized by means B3LYP/6-31G*. These substituents have selected in order to show the effect of doping on the structural and electronic properties of the fullerene molecule. The optimized geometries of the C_{60} cages and hetero atoms $C_{54}X$ ($X = N$) are presented in Figure 1. The structures of fullerenes are described in terms of two bond lengths close to the doping element. The optimized bond lengths (r), bond angles (θ) and torsion angles (ϕ) for C_{60} and $C_{54}N_6$ are listed in Tables 1-3, which obtained from DFT level calculations at B3LYP/6-31G*.

Computational method

All the structural parameters optimizations and the electronic energies and the thermodynamic functions calculation in this work were carried out using the B3LYP/6-31G* level with the GAMESS US package of programs. It has been found that $C_{54}N_6$ are the most



Table 1. Bond Lengths (in Å) in C₆₀ and C₅₄X₆ (X = N), structures calculated at the B3LYP/6-31G* level

Compound	r _{1,2}	r _{2,3}	r _{3,4}	r _{4,5}	r _{5,6}	r _{6,1}	r _{1,7}	r _{2,8}	r _{3,9}	r _{4,10}	r _{5,11}	r _{6,12}
C ₆₀	1.4532	1.3955	1.4534	1.3956	1.4534	1.3956	1.4533	1.4535	1.4534	1.4533	1.4536	1.4533
C ₅₄ N ₆	1.5320	1.5478	1.5312	1.5476	1.5317	1.5475	1.4204	1.4205	1.4198	1.4207	1.4200	1.4203

Table 2. Bond angle (θ) in C₆₀ and C₅₄X₆ (X = N), structures calculated at the B3LYP/6-31G* level

Compound	$\theta_{1,2,3}$	$\theta_{2,3,4}$	$\theta_{3,4,5}$	$\theta_{4,5,6}$	$\theta_{5,6,1}$	$\theta_{6,1,2}$	$\theta_{7,1,2}$	$\theta_{8,2,3}$	$\theta_{9,3,4}$	$\theta_{10,4,5}$	$\theta_{11,5,6}$	$\theta_{12,6,1}$
C ₆₀	120.0	120.0	120.0	120.0	120.0	120.0	108.0	120.0	108.0	120.0	108.0	120.0
C ₅₄ N ₆	120.0	120.0	120.0	120.0	120.0	120.0	105.2	114.2	105.2	114.2	105.2	114.2

Table 3. Torsion angles (ϕ) in C₆₀ and C₅₄X₆ (X = N), structures calculated at the B3LYP/6-31G* level

Compound	$\phi_{1,2,3,4}$	$\phi_{2,3,4,5}$	$\phi_{3,4,5,6}$	$\phi_{4,5,6,1}$	$\phi_{5,6,1,2}$	$\phi_{6,1,2,3}$	$\phi_{7,1,2,3}$	$\phi_{8,2,3,4}$	$\phi_{9,3,4,5}$	$\phi_{10,4,5,6}$	$\phi_{11,5,6,1}$	$\phi_{12,6,1,2}$
C ₆₀	0.0	0.0	0.0	-0.1	0.0	0.0	-142.6	-138.2	-142.6	-138.2	-142.6	-138.2
C ₅₄ N ₆	-0.1	0.1	0.0	0.0	0.0	0.0	-130.3	-126.3	-130.4	-126.3	-130.4	-126.3

Table 4. B3LYP/6-31G* calculated zero-point energies (ZPE), electronic energies (E_{ele}), thermodynamic functions (H, G in kcal/mol, S in cal/mol K) and parameters (ΔH , ΔG , ΔZPE , ΔE_{ele} (in kcal/mol) and ΔS (in cal/mol.k) at 298 K and 1 atm for C₆₀, C₅₄N₆ compounds.

Compound	H	S	G	ZPE	E _{ele}	ΔH	ΔS	ΔG	ΔZPE	ΔE_{ele}
C ₆₀	-1434348.3	136.3	-1434388.9	235.3	-1434597.2	62476.2	0.0	62479.3	10	62470.5
C ₅₄ N ₆	-1496824.5	146.6	-1496868.2	227.9	-1497067.7	0.0	10.3	0.0	2.6	0.0

Table 5. B3LYP/6-31G* calculated energies (in e.V) of HOMO (ϵ HOMO), LUMO (ϵ LUMO), ϵ LUMO - ϵ HOMO and I (ionization potential) and A (electron affinity) for the compounds 1-4

Compound	HOMO ⁻¹	HOMO	LUMO	LUMO ⁺¹	HLG	I	A
C ₆₀	-6.0	-6.0	-3.2	-3.2	2.8	6.0	3.2
C ₅₄ N ₆	-5.9	-5.3	-3.5	-3.0	1.8	5.3	3.5

According to Table 1, the C-C bond distance is around 1.453Å. As a consequence of the doping the computed bond distance increases to around 1.729Å. Thereby, an average increase of 0.276Å in C₆₀ bond lengths was attributed to the doping. When the carbon cage is doped by B, the C-X bonds increased but when the carbon cage is doped by N, the C-X bonds decreased. The minimal and The calculated Gibbs free energy, enthalpy, entropy, electronic energy, zero point energy and their differences (i.e. ΔG , ΔH , ΔS , ΔE_{ele} and ΔZPE) for the all fullerenes (C₆₀, C₅₄N₆) are presented in Tables 4.

This calculation performed at B3LYP/6-31G* level. Our results show that the doped fullerene C₅₄N₆ is more thermal stability than C₆₀. The electronic structure of the fullerene doped metal compared to pure fullerene C₆₀ has been calculated with density functional theory using the B3LYP/6-31G basis set. The HOMO represents the ability to donate an electron, LUMO as an electron acceptor represents the ability to obtain an electron. Highest occupied molecular orbital (HOMO) and Lowest unoccupied molecular orbital (LUMO) are the basic electronic parameters associated with the orbital in a molecule and the difference between them, resulting in energy gap. This HOMO and LUMO helps to describe the

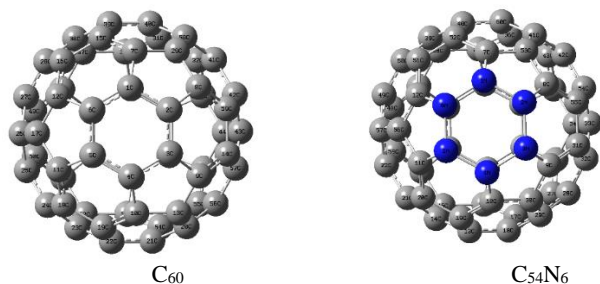


Fig. 1. The optimized geometries of the C_{60} cages and hetero atoms $C_{54}N_6$

chemical reactivity and kinetic stability of the molecule. These HOMO and LUMO orbitals find out the way to the molecule interacts with other species (Fig. 2). Therefore, while the energy of the HOMO is directly related to the ionization potential, LUMO energy is directly related to the electron affinity. According to the frontier molecular orbital theory, the relative chemical reactivity of a molecular system can be estimated using HOMO and LUMO energies, atomic orbital coefficients, net atomic charges and by the overlaps of molecular orbital.

The HOMO-LUMO gap of doped fullerenes varies depending on the type of hetero atoms. The increase of gap leading to the enhanced stability against electronic excitations. The energies of the HOMO and LUMO of fullerenes are in the Table 5. The HOMO-LUMO gap of doped fullerenes decrease from C_{60} to $C_{54}N_6$.

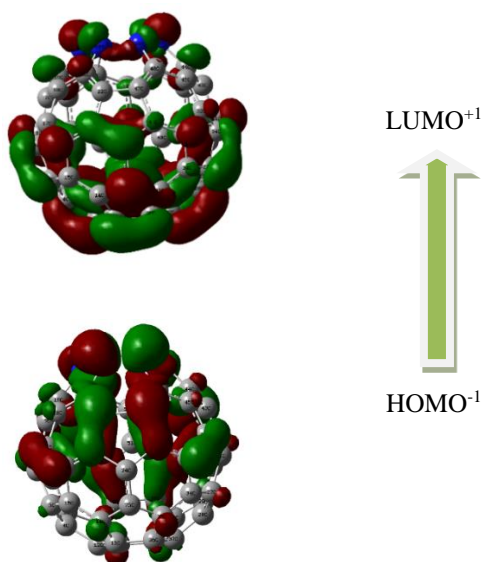


Fig. 2. The HOMOs and LUMOs calculated with density functional theory using the B3LYP/6-31G basis set associated by $C_{54}N_6$.

We have also calculated the vertical ionization potentials and electron affinities for all the isomers and reported the results in Table 5.

Conclusion

Theoretical studies of the C_{60} and $C_{54}N_6$ fullerene have been performed systematically based on the DFT calculations. The results of the geometrical structures, vibrational frequencies, the HOMO-LUMO gap, dipole moment and polarizability of the doped cages were discussed to achieve a further understanding of structure property relationship of the doped cages. According to the results, the doped fullerene $C_{54}N_6$ is more thermal stability than C_{60} fullerenes. HOMO values are increased in doped fullerene cage but the HOMO – LUMO gaps are decreased compared with those of fullerene C_{60} .

References

- [1] H.W. Kroto, J. R. Heath, S. C. O'Brien, R. F. Curl and R. E Smalley, C_{60} : Buck-minsterfullerene, *Nature*, vol.318,no.6042,pp.162-163,1985.
- [2] S. Iijima, "Helical microtubules of graphitic carbon," *Nature*, vol. 354, no. 6348, pp. 56–58, 1991.
- [3] K. S. Novoselov, A. K. Geim, S. V. Morozov et al., "Electric field in atomically thin carbon films," *Science*, vol. 306, no. 5696, pp.666–669, 2004.on solid sup
- [4] W. A. Kratschmer, L. D. Lamb, K. Fostiropoulos, and D. R. Huffman, Solid C_{60} : a new form of carbon, *Nature (London)*, vol. 347, pp.354-358, 1990.
- [5] H.W. Kroto, A.W. Allaf and S.P.Balm, *Chem. Rev.* 91, 1213 (1991)
- [6] W. Weltner and R.J. VanZee, *Chem. Rev.* 89, 1713 (1989)

Determining the octanol-water partition coefficient of amines using MLR method

M. Talaei, E. Mohammadinasab*

Department of Chemistry, Arak Branch, Islamic Azad university, Arak, Iran

*e-mohammadinasab@iau-arak.ac.ir

Abstract : In this study, the MLR method based on QSPR method was applied to predict the LogP of 31 different type amines. The results of experimental for used molecules were compared with the results of MLR calculations and was represented that minimum Z Length, minimum projection area, Maximum Z Length indices are the best descriptors for predicting the values of LogP of used amines. The best model in this study indicated that those structural descriptors, play an important role in effect on LogP of amines. For the first time, the relationship between LogP of amines and some molecular indices using SPSS and multiple linear regression model is investigated. The obtained results demonstrated that there are good relationships between some geometrical indices of this class amines.

Keywords: "Amines", "Octanol-Water Partition Coefficient", "Molecular Descriptors".

Introduction

The octanol—water partition coefficient $P_{o/w}$ is defined as the ratio of the equilibrium concentration of a solute in octanol to that in water. $\log P_{o/w}$ has for a long time been known to be one of the quantitative physical properties that correlates with biological activity.

$\log P_{o/w}$ is considered as an essential property in new or problematic chemicals studies. It is mainly expressed as the n-octanol/water partition coefficient $\log P_{o/w}$ regarding the hydrophobicity of the compound. Chemical graph theory is a branch of mathematics which combines graph theory and chemistry and has been extensively applied to predicting the physic-chemical and biological properties of organic compounds through the quantitative structure-activity/property relationship.

In present work, multiple linear regression modeling was used to construct a relation between coefficient partition of amines and their molecular descriptors.

Materials and method

Multiple regression is a statistical tool that examine how multiple independent variables are related to a dependent variable. When identified how these multiple variables relate to your dependent variable, we can take information about all of the independent variables and use it to make much more powerful and accurate predictions about why things are the way they are.

In this study, the experimental LogP values for 31 amines were extracted from the literature. (see Table.1) and then the relationship between the experimental LogP and topological, geometrical and quantum descriptors of 31 different types of amines was investigated.

The quantum descriptors of 31 different types of the amines is computed by the DFT method based on B3LYP method and 3-21G standard basis set and also topological and geometrical descriptors are computed using the literatures[1-4]. we investigated the relationship between values of the LogP and the above descriptors using Excel software.

Results and Discussion

In table 1 is showed the values of observed, predicting, residual LogP of used amines.

Table 1: The values of the observed, predicting, residual LogP

Name	LogP _{ex}	LogP _{Pred}	Residual
aminoethan	-.130	-.11338	-.01662
3-amino-1-propen	.030	-.04996	.07996
1-aminopropan	.480	.33971	.14029
2-aminopropane	.260	.21096	.04904
methylethyl amine	.150	.35720	-.20720
trimethyl amine	.160	-.01287	.17287
1-aminobutane	.970	.80467	.16533
1-amino-2-methylpropane	.730	.79158	-.06158
2-aminobutane	.740	.71355	.02645
2-methyl-2-aminopropane	.400	.68320	-.28320
diethylamine	.580	.77676	-.19676
ethylmethyl amine	.700	.71375	-.01375
allylethyl amine	.810	.87399	-.06399
1-aminopentane	1.490	1.29291	.19709
methylbutyl amine	1.330	1.20443	.12557
ethylisopropyl amine	.930	1.18582	-.25582
diallylamine	1.110	1.16283	-.05283
allylpropylamine	1.330	1.43501	-.10501
1-aminohexane	2.060	1.59041	.46959
di-n-propylamine	1.670	1.80588	-.13588
butyldimethylamine	1.700	1.63007	.06993
triethylamine	1.450	1.67273	-.22273
1-aminoheptane	2.570	2.40023	.16977
propyl-n-butylamine	2.120	2.47446	-.35446
propylisobutyl amine	2.070	2.00386	.06614
propyl-sec-butylamine	1.910	2.18747	-.27747
1-amino-2-ethylhexane	2.820	2.58396	.23604
di-n-butylamine	2.830	2.78950	.04050
ethyl-di-n-propyl amine	2.680	2.69708	-.01708
triallylamine	2.590	2.19787	.39213
tri-n-propylamine	2.790	2.92629	-.13629

Whether or not the regression model explains a statistically significant percentage of data was found through the Table 2. of output based on the MLR model in terms of the relationship between LogP and molecular indices.



Table 2: Efficient output Parameters of MLR Method in 7 models

Model	R	R ²	R ² _{Adj}	STD	Mean square	F
1	0.98	0.96	0.95	0.206	2.732	64.481
2	0.98	0.96	0.95	0.201	3.073	75.962
3	0.98	0.96	0.95	0.202	3.505	85.571
4	0.98	0.96	0.95	0.199	4.088	103.719
5	0.98	0.96	0.95	0.196	4.902	126.975
6	0.98	0.96	0.95	0.201	6.105	150.841
7	0.98	0.95	0.95	0.207	8.106	189.233

The comparison of 7 models and the values of statistical coefficients showed that the best models for predicting the octanol-water partition coefficient for amines using the MLR method are as follows:

$$\text{LogP} = -4.739 + 0.265 \text{MaxZL} + 0.070 \text{MinPA} + 0.313 \text{MinZL} \quad ; \text{DW}=2.6$$

Final Descriptors	MaxZL	MinPA	MinZL	VIF
MaxZL	1			1.325
MinPA	0.397	1		1.190
MinZL	0.364	0.183	1	1.155

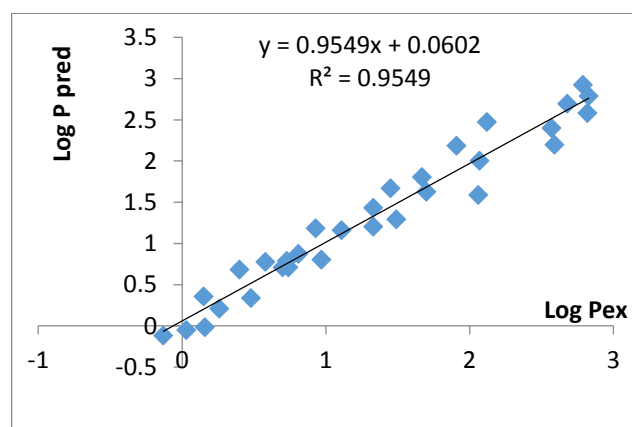


Fig.1: The curve of the LogP_{pred} versus the LogP_{ex}

In Figures 1, the values of $R^2 = 0.9549$ show the linear correlation between experimental and predicting values resulted from the model that is related to the LogP_{ex}. The larger values of R^2 indicate a stronger correlation.

It is worth mentioning that there are many partial differences between the experimental and predicted LogP of the model.

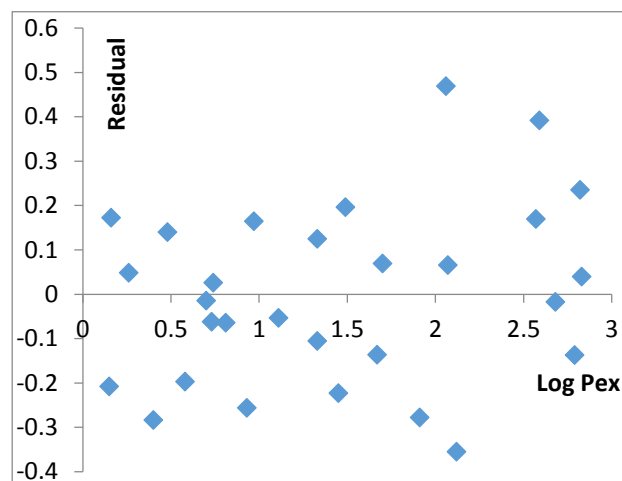


Fig.2: The scatter curves of the residuals against experimental LogP

Conclusion

The results of experimental for used molecules were compared with the results of multiple nonlinear regression calculations and was represented that minimum Z Length, minimum projection area, Maximum Z Length indices are the best descriptors for predicting the values of LogP of amines. According to the literature search, to the best of our knowledge this is the first report on amines which their LogP in contrast to mentioned descriptors is predicted by SPSS software and linear multiple regression model.

References

- [1] Web search engine developed by ChemAxon; software available at [http:// WWW. Chemicalize. Org](http://WWW.Chemicalize.Org).
- [2] A. T. Balaban, T. S. Balaban, "New Vertex Invariant and Topological Indices of Chemical Graphs Based on Information on Distance", *Math. Chem.* 8 (1991) 383-397.
- [3] G. Cash, S. Klavzar, M. Petkovsek, "Three Methods for Calculation of the Hyper-Wiener Index of Molecular Graphs", *J. Chem. Inf. Comput. Sci.* 42 (2002) 571-576.
- [4] J. Devillers, A. T. Balaban, "Topological indices and related descriptors in QSAR and QSPR", 1999, Gordon and Breach Science, Netherlands.

A DFT study on the molecular hydrogen (H₂) storage on Sc-decorated B₃₆ nanosheet

E. Tahmasebi^{a,*}, Z. Biglari^a, E. Shakerzadeh^b

^a Chemistry Department, Faculty of Science, Lorestan University, Khorram Abad, Lorestan, Iran Email: Email

^b Chemistry Department, Faculty of Science, Shahid Chamran University of Ahvaz, Ahvaz, Iran

Email: tahmasebi621@gmail.com

Abstract: The hydrogen storage capacity of transition metal Sc atoms decorated porous boron nanosheet B₃₆ is investigated by the density functional method. It is shown that the ScB₃₆ could adsorb up to four H₂ molecules. The obtained adsorption energies per H₂ molecule are found to be in the range of 0.35-0.55 eV, imply to physisorption adsorption process. Therefore, the results suggest a quasi-molecular adsorption for nH₂@ScB₃₆ complexes which introduce this nanostructure as a good candidate material for hydrogen storage media. This investigation may evoke one's attention to the design of novel hydrogen storage media based on boron nanomaterials such as B₃₆.

Keywords: H₂ molecule; Storage; Adsorption; DFT calculations; Boron nanostructure.

Introduction:

Hydrogen energy has been attracting much interest as an ideal kind of energy because of its abundant, renewable, cheap, and environmentally friendly in nature. Hydrogen energy can reduce the dependence of the world on fossil fuels and help to resolve the global warming issue [1]. However, the greatest challenge in the realization of H₂ economy is to find a feasible storage media. For most hydrogen storage materials, there are many problems such as low storage capacity, high desorb temperature, absence or low reversibility, slow kinetics will preclude their practical applications. Generally, the adaptable average adsorption energy per H₂ of the hydrogen storage materials should be intermediate between physisorbed and chemisorbed states (0.2-0.6 eV).

It is well known that carbon-based nanostructures, such as nanotubes, fullerenes, graphene have been widely researched in recent years. Boron is the fifth element in the periodic table and posses a richness of chemistry second to carbon. It is lighter than carbon, so the boron nanostructures are attracting more attentions now. Recently, the B₃₆ nanosheet has been synthesized by Piazza et al. [2]. It is a quasiplanar all-boron sheet with a central hexagonal hole. It was reported that the B₃₆ nanosheet with C_{6v} symmetry is highly stable. The B₃₆ nanosheet is a hot spot for scientists due to its unique features. [3-7]. For the pure nanomaterials, due to the simple Van der Walls interaction dominates the adsorption of hydrogen molecules, the surface cannot store hydrogen efficiently. This inertness becomes a main hindrance in the actualization of its possible applications. The main contribution of the present

study is to investigate the possibility of hydrogen storage on to Sc-decorated B₃₆ nanosheet through density functional theory.

Materials and method

All of the optimized geometries are obtained using M06L/6-311+G(d) level of theory. All calculations are performed using Gaussian 09 software.

Results and discussion:

The adsorption energy per H₂ molecule is predicted by the following equations:

$$E_{ad} = [E(nH_2@ScB_{36}) - E(ScB_{36}) - nE(H_2)]/n \quad (1)$$

where $E(nH_2@ScB_{36})$, $E(ScB_{36})$ and $E(H_2)$ are referred to the total energy of complex in which nH₂ molecules are adsorbed on nanosheet, the energy of isolated Sc-decorated B₃₆ nanosheet and the energy of a free H₂ molecule, respectively. Also n denote number of adsorbed H₂ molecule.

At first the Sc-decorated B₃₆ nanosheet is investigated. the B₃₆ structure has bowl shape with a central hexagonal hole. This structure has C_{6v} symmetry with different kinds of B-B bonds. The Sc atom decorates on the top of hexagonal hole. The obtained binding energy is found to be 4.55 eV. Thus, Sc atom binds tightly to the surface of B₃₆ nanoheet. The optimized Sc-decorated B₃₆ nanosheets are depicted in Figure 1. Therefore, Sc atom is most stably located outside the hollow site of B₃₆ cavity with the appreciable adsorption energy, which is much larger than the experimental cohesive energy of bulk Sc (3.90 eV/atom). Hence, it could be possible promising media for hydrogen storage. In continue. The adsorption of H₂

molecules onto Sc-decorated B₃₆ nanosheet is considered through M06L/6-311+G(d) level of theory.

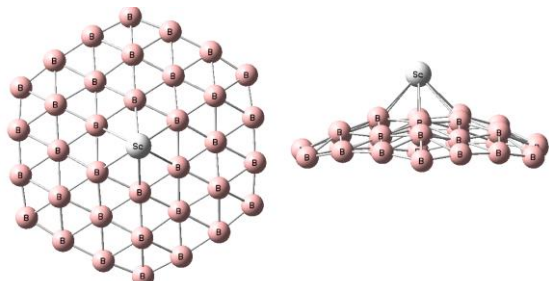


Figure 1. The Sc-decorated B₃₆ nanosheet from top and side views.

The adsorption one to six hydrogen molecules (H₂) are investigated on the Sc-decorated B₃₆ nanosheet. After full optimization, it is found that only four H₂ molecules could be adsorbed over Sc atom. The obtained optimized structures are presented in Figure 2. The obtained adsorption energies per H₂ molecule are in the range of 0.35-0.55 eV. This implies that the hydrogen likely bonds with the considered nanosheet through physisorption. This adsorption is not dissociative and during the formation of complex no clustering for H₂ molecules is observed. This kind of adsorption is known as quasi-molecular adsorption which is reported as a favorable adsorption for hydrogen-storage materials.

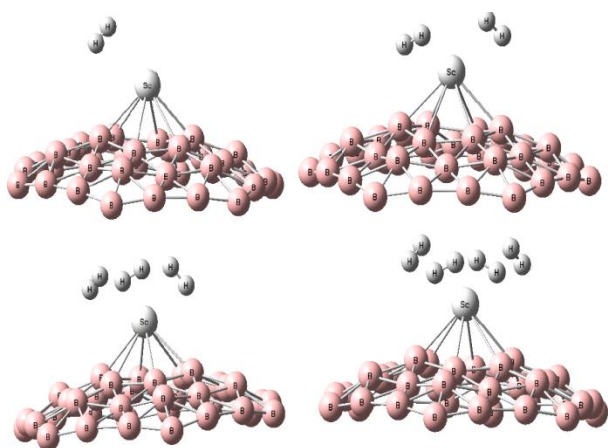


Figure 2. The optimized structures of nH₂@ScB₃₆

Conclusions

By means of DFT calculations we have investigated the performance of Sc-decorated B₃₆ nanosheet as hydrogen storage media. It is found that ScB₃₆ nanosheet could be

applied as promising candidate for hydrogen storage materials under near ambient conditions. Consequently, the results demonstrate a quasi-molecular adsorption for H₂ over ScB₃₆ nanosheet, which introduce this nanostructure as a good candidate material for hydrogen storage. This investigation may develop the design of novel hydrogen storage media based on boron nanomaterials.

References

- [1] R. Cortright, R. Davda, J.A. Dumesic, Hydrogen from catalytic reforming of biomass-derived hydrocarbons in liquid water., *Nature* 418 (2002) 964-967
- [2] Z.A. Piazza, H.-S. Hu, W.-L. Li, Y.-F. Zhao, J. Li, L.-S. Wang, Planar hexagonal B₃₆ as a potential basis for extended single-atom layer boron sheets, *Nat. Commun.* 5 (2014) 3113–3117.
- [3] Q. Chen, G.F. Wei, W.J. Tian, H. Bai, Z.P. Liu, H.J. Zhai, S.D. Li, Quasi-planar aromatic B₃₆ and B₃₆-clusters: all-boron analogues of coronene, *Phys. Chem. Chem. Phys.* 16 (2014) 18282–18287.
- [4] C.S. Liu, X. Wang, X.J. Ye, X. Yan, Z. Zeng, Curvature and ionization-induced reversible hydrogen storage in metalized hexagonal B₃₆, *J. Chem. Phys.* 141 (2014) art. No.194306.
- [5] Y. Valadbeigi, H. Farrokhpour, M. Tabrizchi, Adsorption of small gas molecules on B₃₆ nanocluster, *J. Chem. Sci.* 127 (2015) 2029–2038.
- [6] Z. Rostami, H. Soleymanabadi, N–H bond cleavage of ammonia on graphene-like B₃₆ borophene: DFT studies, *J. Mol. Model.* 22 (2016) 70-76
- [7] A.S. Kootenaiea, G. Ansari, B₃₆ borophene as an electronic sensor for formaldehyde: Quantum chemical analysis, *Phys. Lett. A*, 380 (2016) 2664–2668.
- [8] A. Rastgou, H. Soleymanabadi, A. Bodaghi, DNA sequencing by borophene nanosheet via an electronic response: A theoretical study, *Microelectronic Engineering* 169 (2017) 9–15

Computation of Heats of Formation for Imidazolium-Based Ionic Liquids Using G3(MP2) Compound Model Chemistry

M. Zare*, Z. Asakereh and E. Shakerzadeh

Department of Chemistry, Faculty of Science, Shahid Chamran University of Ahvaz, Ahvaz, Iran

*email: m.zare@scu.ac.ir

Abstract: Theoretical studies of the thermodynamic properties of the ionic liquids (ILs) have attracted extensive attention in recent times as a result of the possibility of prediction. In the present work, atomization approach is used to calculate the heat of formation ($\Delta_f H^\circ$) of 1-alkyl-3-methylimidazolium dicyanamide [$C_n\text{mim}$][dca] ($n=2, 4, \text{ and } 6$) with G3(MP2) compound model chemistry. A good agreement with the experimental result has been observed. The predicted heat of formation was found to decrease in magnitude with increasing alkyl side chain length. Linear correlation was found to exist in calculated heat of formation with alkyl side chain of the imidazolium ring.

Keywords: Ionic Liquids; Imidazolium; Heat of Formation; thermochemistry; G3(MP2).

Introduction

Ionic liquids (ILs) are a class of compounds composed of bulky cations and anions and thereby melt below 100 °C [1]. They have been found applications as solvent in organic synthesis and extraction processes, in electrochemical devices and lubrication, due to their negligible vapour pressure, low melting point, high ionic conductivity, and high thermal stability [2, 3].

At present there has been considerable growth in the number of theoretical investigations pertaining to ionic liquids, whereby scientists are attempting to predict many of the physical properties that characterize ionic liquids. In this work, quantum mechanical calculations are used to predict $\Delta_f H^\circ$ of imidazolium-based ionic liquids by Gaussian-3 theory using reduced Møller-Plesset order (G3(MP2)).

Methods

The atomization approach uses known $\Delta_f H^\circ$ of isolated atoms and calculated atomization energies (D_0) to predict $\Delta_f H^\circ$ of molecules [4]:

$$\Delta_f H^\circ(A_x B_y, 0K) = x\Delta_f H^\circ(A, 0K) + y\Delta_f H^\circ(B, 0K) - \sum D_0 \quad (1)$$

Then, $\Delta_f H^\circ(A_x B_y, 298K)$ can be obtained as follows:

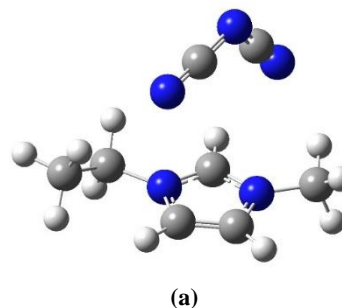
$$\begin{aligned} \Delta_f H^\circ(A_x B_y, 298K) &= \Delta_f H^\circ(A_x B_y, 0K) + \\ &[H^\circ(A_x B_y, 298K) - H^\circ(A_x B_y, 0K)] - \\ &x[H^\circ(A, 298K) - H^\circ(A, 0K)] - y[H^\circ(B, 298K) - \\ &H^\circ(B, 0K)] \end{aligned} \quad (2)$$

This method is used to calculate the values of $\Delta_f H^\circ$ for 1-alkyl-3-methylimidazolium dicyanamide [$C_n\text{mim}$][dca] ($n=2, 4, \text{ and } 6$) using G3(MP2) theory, a composite one for calculation of total energies of molecules with an impressive accuracy. This theory uses geometries from second-order perturbation theory and scaled zero-point

energies from Hartree-Fock theory followed by a series of single-point energy calculations at the MP2(Full)/6-31G(d), QCISD(T)/6-31G(d), and MP2/GTMP2Large levels of theory [5,6]. Gaussian 03 is used for all of the G3(MP2) calculations [7].

Results and Discussion

Figures 1 shows the optimized structures of the [$C_2\text{mim}$][dca], [$C_4\text{mim}$][dca] and [$C_6\text{mim}$][dca]. The values of calculated atomization energy (D_0), Heats of formation at 0K and 298K are listed in Table 1. This table also contains comparisons of predicted values for heats of formation which obtained in this work and the literature values. A very good agreement between the calculated value with only experimental value is evident. The $\Delta_f H^\circ$ of ionic liquids is dependent on their molecular structure. It can be seen that the heat of formation decreases with the alkyl chain lengthening. Figure 2 shows the heat of formation values versus number of carbon in alkyl side chain of the imidazolium ring. There is a linear correlation with $R^2=1.0000$.



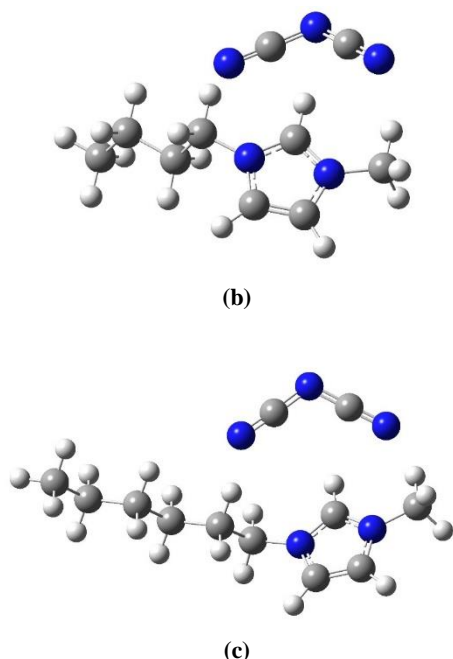


Fig.1. Optimized structures of (a) [C₂mim][dca], (b) [C₄mim][dca] and (c) [C₆mim][dca].

Table 1. Calculated atomization energy (D_0), Heats of formation at 0K ($\Delta_f H^0(0K)$) and 298K ($\Delta_f H^0(298K)$) in kcal.mol⁻¹.

Ionic liquids	D_0	$\Delta_f H^0(0K)$	$\Delta_f H^0(298K)$	$\Delta_f H^0(298K)^a$
[C ₂ mim][dca]	2385.90	104.51	95.96	---
[C ₄ mim][dca]	2940.10	96.83	85.50	86.85
[C ₆ mim][dca]	3494.23	89.15	75.04	---

^aExperimental value. Ref [8].

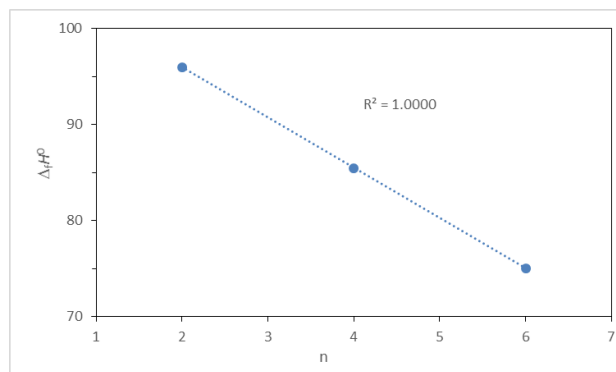


Fig. 2. Correlation of calculated heat of formation and number of carbon in alkyl side chain (n).

Conclusions

The values of heat of formation of 1-alkyl-3-methylimidazolium dicyanamide [C_nmim][dca] (n=2, 4, and 6) were predicted using G3(MP2), a computationally expensive method with high degree of accuracy. We found good agreement between G3(MP2) calculated results and only experimental value in the literature. The

calculated heat of formation was found to decrease in magnitude with increasing alkyl chain length. It seems atomization approach is a tractable and reasonable method in predicting heat of formation of ionic liquids

References

- [1] K. Marsh, J. Boxal, R. Lichtenthaler, "Room temperature ionic liquids and their mixtures—a review", *Fluid Phase Equilib.* 219 (2004) 93-98.
- [2] D. Kuang, P. Wang, S. Ito, S. Zakeeruddin, M. Gratzel, "Mesoscopic dye-sensitized solar cells based on tetracyanoborate ionic liquid electrolyte", *J. Am. Chem. Soc.*, 128 (2006) 7732-7733.
- [3] R. deSouza, J. Padilha, R. Gonclaves, J. Dupont, "Chemical modelling: applications and theory", *J. Electrochem. Commun.*, 5 (2003) 728-731.
- [4] L. Curtiss, K. Raghavachari, P. Redfern, J. Pople, "Assessment of Gaussian-2 and density functional theories for the computation of enthalpies of formation", *J. Chem. Phys.* 106 (1997) 1063-1079.
- [5] L. Curtiss, P. Redfern, K. Raghavachari, V. Rassolov, J. Pople, "Gaussian-3 theory using reduced Moller-Plesset order", *J. Chem. Phys.*, 110 (1999) 4703-4709.
- [6] L. Curtiss, P. Redfern, K. Raghavachari, V. Rassolov, J. Pople, "Gaussian-3 (G3) theory for molecules containing first and second-row atoms", *J. Chem. Phys.*, 109 (1998) 7764-7776.
- [7] M. Frisch, et al., Gaussian, Inc., Wallingford, CT, 2004.
- [8] V. Emel'yanenko, S. Verevkin, A. Heintz, "The gaseous enthalpy of formation of the ionic liquid 1-butyl-3-methylimidazolium dicyanamide from combustion calorimetry, vapor pressure measurements, and ab Initio calculations", *J. Am. Chem. Soc.* 129 (2007) 3930-3937.

A DFT Study of Adsorption of Anti cancer drug Phenoxodiol onto the surface of BNNT and BNNT-Ge Nanotubes

R. Kouchyandard, M. Kia*

Young Researcher and Elite Club, Rasht Branch, Islamic Azad University, Rasht, Iran

Department of Chemistry, Rasht Branch, Islamic Azad University, Rasht, Iran

*Kia@iaurasht.ac.ir

Abstract : In this work, the adsorption properties of phenoxodiol upon surface of BN nanotubes were theoretically investigated in the gas phase using density functional theory (DFT) calculations. Herein, boron nitride and drug molecule phenoxodiol were drawn through "Nanotube modeler" Software and were optimized by the method of DFT/B3LYP, Basis function 6-31G (d) and using Gaussian software 09. finally, some studies were conducted dipole moment, gap between HOMO and LUMO, ionization potential, hardness, softness, electron affinity and chemical potential of drug molecules before and after placing on to the nanotubes. It was found that the adsorption behavior of phenoxodiol molecule on the pristine (5,5) and Ge-doped BNNTs are electrostatic in nature and optima structures using this method have shown good conductivity and chemical absorption than using free State of the drugs.

Keywords: phenoxodiol; Adsorption; Density functional theory; Boron nitride nanotubes

Introduction

Phenoxodiol (2H-1-benzopyran-7-0, 1, 3-[4-hydroxyphenyl], PXD) is a synthetic analogue of the naturally-occurring plant isoflavone and anticancer agent, genistein. PXD is currently undergoing clinical trials, as a chemotherapeutic in ovarian and prostate cancers [1]. Phenoxodiol being assessed in several clinical studies against a range of cancer types and showed to have a good efficacy and safety profile. Prostate cancer the most common cancer in men, with an estimated incidence of >230,000 new cases, and the second with ~30,000 new deaths. Advanced disease has a 5-year survival of only 30 % [2]. BN is a binary compound made of Group III and Group V elements in the periodic table. The band gap of BNNTs has been reported to be between 5.0 and 6.0 eV independent to tube chirality. This provides good electrical. Boron nitride nanotubes (BNNTs) have been increasingly investigated for use in a wide range of applications due to their unique physicochemical properties including high hydrophobicity, heat and electrical insulation, resistance to oxidation, and hydrogen storage capacity[3]. While CNTs can be a metal or a narrow band-gap semiconductor BNNTs are a structural analogy to CNTs that instead alternate boron and nitride atoms to replace the carbon atoms in the hexagonal structure. Although CNTs and BNNTs have similar structures, their properties are quite different The aim of this study is to investigate adsorption of anti-cancer Phenoxodiol on Boron nanotubes using Density Functional Theory (DFT).

Materials and method

BNNT (5,5), BNNT-Ga nanotubes and Phenoxodiol molecule has optimized. The quantum chemical computations were carried out using the hybrid-DFT (Beck 3 parameters plus LYP functional, B3LYP)

coupled with the 6-31G* basis set, implemented in the GAMESS program package[4]. The quantum molecular descriptors for nanotubes were determined as follows:

$$E_{ad} = E_{BN(5,5)/Phenoxodiol} - (E_{BN(5,5)} + E_{Phenoxodiol}) \quad (1)$$

$$E_{ad} = E_{BNNT-Ge/Phenoxodiol} - (E_{BNNT-Ge} + E_{Phenoxodiol}) \quad (2)$$

$$\mu = - (I + A) / 2 \quad (3)$$

$$\eta = (I - A) / 2 \quad (4)$$

$$S = 1 / \eta \quad (5)$$

$$\omega = (\mu^2 / 2\eta) \quad (6)$$

$$\Delta N_{max} = - \mu / \eta \quad (7)$$

Where I ($-E_{HOMO}$) is the energy of the Fermi level and A ($-E_{LUMO}$) is the first given value of the conduction band. Hardness (η) can be approximated using the Koopmans' theorem. I ($-E_{HOMO}$) is the ionization potential and A ($-E_{LUMO}$) is the electron affinity of the molecule. The maximum amount of electronic charge, ΔN_{max} , that the electrophone system may accept is given by Eq.

Results and Discussion

We investigate the quantum molecular descriptors for Phenoxodiol molecule in the interactions with



BNNT(5,5) and BNNT-Ge showed in Table 1.

Table1: Quantum parameter of interaction between Phenoxodiol, BNNT(5,5) and BNNT-Ge

Property	pheno xodiol	BN(5,5)	BNNT-Ge	PXD/BNNT(5,5)	PXD/BNNT-Ge
E_{HOMO} (eV)	-5.01	-7.28	-6.53	-5.19	-5.45
E_{LUMO} (eV)	-1.03	7.16	-3.6	-1.48	-1.6
E_g (eV)	-3.98	-14.44	-2.93	-3.71	-3.85
D_M	1.75	0.00	11.63	1.19	15.60
E_{ad} (eV)	-	-	-	945.21	76.19
I (eV)	+5.01	+7.28	+6.53	+5.19	+5.45
A (eV)	+1.03	-7.16	+3.6	+1.48	+1.6
η	1.99	7.22	1.46	1.85	1.92
μ	-3.02	-0.06	-5.06	-3.33	-3.52
S	0.50	0.13	0.68	0.53	0.51
ω	2.29	2.49	8.75	2.99	3.22
ΔN_{max}	1.51	8.31	3.45+	1.79	1.83

Phenoxodiol

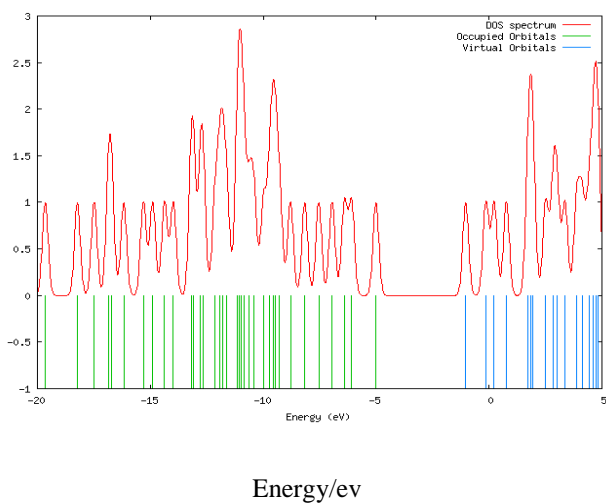
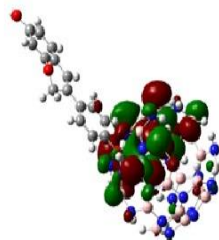
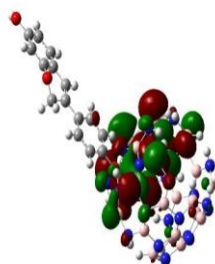


Fig.1: Optimized structure phenoxodiol and their density of state plot.

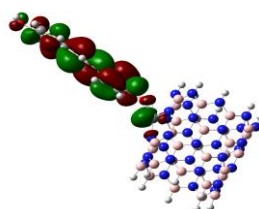


HOMO BNNT (5,5), Phenoxodiol



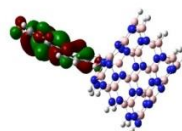
LUMO BNNT (5,5), Phenoxodiol

Fig.2: HOMO and LUMO orbitals of Phenoxodiol adsorbed on



the surface of BNNT (5,5).

HOMO BNNT-Ge, Phenoxodiol



LUMO BNNT-Ge, Phenoxodiol

Fig.3: HOMO and LUMO orbitals of Phenoxodiol adsorbed on the surface of BNNT-Ge.

E_{HOMO} is the energy of the highest occupied molecular orbital and E_{LUMO} is the energy of the lowest unoccupied molecular orbital of the considered structure. In addition, whatever the difference between HOMO and LUMO energy level is higher, the molecular stability better, reactivity and conductivity will be less. In addition, the following result was obtained:

1. The dipole moment of Phenoxodiol decreased after connecting with BN55 nanotubes.
2. The dipole moment of Phenoxodiol increased after connecting with BNNT-Ga nanotubes.
3. Whatever I (ionization potential) increases, the conductivity of the system is lower and become more stable.
4. Absorption of molecules on the nanotubes was better when μ (chemical potential) is negative

Conclusions

We investigated the adsorption phenomena of phenoxodiol on the BNNT (5,5) and BNNT-Ge surfaces using density functional with B3LYP/6-31G* level. Our results show that the chemical adsorption of phenoxodiol on the BNNT-Ge system is larger than that on the pristine BNNT (5,5). Our calculation indicates that bond gap phenoxodiol on the BNNT (5,5) is larger than that on the BNNT-Ge and it is more stable.

References

- [1] J. R. Gamble, P. Xia, C. N. Hahn, J. J. Drew, C. J. Drugemuller, D. Brown, M. A. Vadas, Phenoxodiol an experimental anticancer drug, shows potent antiangiogenic properties in addition to its antitumour effects, *International journal of cancer*, 118(10) (2006) 2412-2420.
- [2] H. Y. Zhang, J. Cui, Y. Zhang, Z. L. Wang, T. Chong, Z. M. Wang, Isoflavones and Prostate Cancer, *Chinese medical journal*, 129(3) (2016) 341-347.
- [3] M. J. Meziani, W. L. Song, P. Wang, F. Lu, Z. Hou, A. Anderson, Y. P. Sun, Boron nitride nanomaterials for thermal management applications, *Chemical physics and physical Chemistry*, 16(7) (2015) 1339-1346.
- [4] M. Gallo, A. Favila, D. Glossman-Mitnik, DFT studies of functionalized carbon nanotubes and fullerenes as nanovectors for drug delivery of antitubercular compounds, *Chemical Physics Letters*, 447(1) (2007) 105-109.



Conformational analysis of 2-(((1-phenylethyl)imino)methyl)phenol and its halogen substitutions, as a Schiff base with chiral carbon, A DFT study

M. Afkanpoor^{a*}, M. Vakili^a, G. Grivani^b, S. F. Tayyari^a

^aDepartment of Chemistry, Ferdowsi University of Mashhad, Mashhad 91775-1436, Iran

^bSchool of Chemistry, Damghan University, P.O. Box 36715-364, Damghan, Iran

* monirafkanpoor@chmail.ir

Abstract:

The molecular structure and conformational analysis of 2-(((1-phenylethyl)imino)methyl)phenol, as a Schiff base with a chiral atom, has been done by calculation methods. According to our calculations at B3LYP and MP2 levels of theory, three stable conformers (C1-C3) can be drawn for target molecule. The C1 conformer is the most stable, and relative stability of C2 and C3 are in the range of 1.20-2.67 kcal/mol, in the gas phase and solutions. Also we considered the halogen substitution effects, X=F, Cl, and Br, on the conformation stability at both gas phase and solution. According to our results, the para halogen substitutions have no significant effect on the relative stability of three stable conformers.

Keywords: DFT; Chiral carbon; substitution effect; Conformers stability, Schiff base.

Introduction

Schiff bases have a wide variety of applications in various field such as biology, pharmacy, industry, and etc. [1-4].

2-(((1-phenylethyl)imino)methyl)phenol (PIMP), as a Schiff base, with one chiral carbon are particularly eye-catching. This molecule shows a fairly strong intramolecular H-bonding (IHB) between the H-atom of the hydroxyl group and the N-atom of the imine moiety. The IHB is caused to an intramolecular proton transfer, associated with a change in π -electron configuration, from the hydroxyl's O atom to the imine's N atom. The mentioned transfer occur under the influence of light, for photochromic, and temperature for thermochromic, Schiff bases, [5].

The aim of present work is to investigate the structure and conformational stability of target molecule and its para halogen substitutions, in gas phase and solution with different solvents by theoretical methods.

Materials and method

All quantum calculations have been done by the Gaussian 09 [6]. The conformation and structure of target molecules have been optimized at the B3LYP, and MP2 levels with using the 6-311++G**, 6-311G**, and 6-31G** basis sets. The SCRF-PCM method were selected for conformation study in acetonitrile and carbon tetrachloride solutions, as a nonpolar and polar solvents, at selected levels and basis sets.

Dipole moments of mentioned structures in both phase calculated at B3LYP/6-311++G** level of theory.

Results and Discussion

Three stable conformers of our molecules, PIMP and X-PIMP, with X=F, Cl, and Br are shown in Fig. 1.

Their relative stabilities of three forms of X-PIMP with respect to the most stable form, calculated at different

level and basis set, in the gas phase and solution are tabulated in Table1. According to this table, the C1 conformer is the stable form in all target molecules in gas phase and solution.

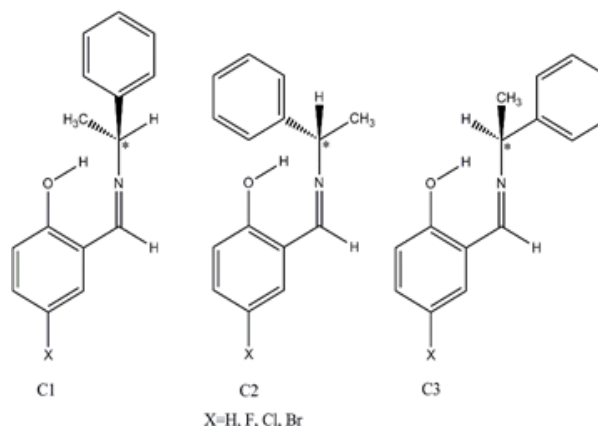


Fig.1: Three stable conformers of PIMP and its halogen substitutions. * is shown chiral atom.



Table 1: The relative energies and dipole moments of three conformers in gas phase and solution at different levels of theory.

	Gas			CCl ₄			CH ₃ CN		
	C1	C2	C3	C1	C2	C3	C1	C2	C3
B3LYP/6-311++G**									
PIMP	0.0	2.34	1.34	0.0	2.39	1.41	0.0	2.05	1.79
Cl-PIMP	0.0	2.25	1.22	0.0	2.14	1.31	0.0	1.98	1.73
F-PIMP	0.0	2.30	1.24	0.0	2.19	1.32	0.0	1.99	1.73
Br-PIMP	0.0	2.23	1.20	0.0	2.13	1.31	0.0	2.00	1.73
B3LYP/6-311G**									
PIMP	0.0	2.47	1.69	0.0	2.29	1.64	0.0	2.16	1.97
Cl-PIMP	0.0	2.37	1.49	0.0	2.22	1.50	0.0	2.08	1.85
F-PIMP	0.0	2.41	1.57	0.0	2.24	1.54	0.0	2.11	1.90
Br-PIMP	0.0	2.34	1.51	0.0	2.20	1.56	0.0	2.05	1.90
MP2/6-31G**									
PIMP	0.0	2.67	1.44	0.0	2.60	1.47	0.0	2.45	1.69
Cl-PIMP	0.0	2.58	1.27	0.0	2.52	1.34	0.0	2.37	1.58
F-PIMP	0.0	2.41	1.57	0.0	2.55	1.38	0.0	2.40	1.62
Br-PIMP	0.0	2.56	1.42	0.0	2.43	1.28	0.0	2.27	1.55
Dipole moment(Debye)									
PIMP	3.06	2.69	2.88	3.21	2.81	3.28	3.62	3.62	3.81
Cl-PIMP	2.55	2.93	3.14	2.91	3.31	3.48	3.44	3.88	3.83
F-PIMP	2.42	2.79	3.02	2.77	3.19	3.36	3.32	3.77	3.71
Br-PIMP	2.58	2.94	3.17	2.93	3.32	3.50	3.46	3.88	3.85

According to This Table, in different computational levels and basis sets the following trend is obtained for the stable forms of PIMP and X-PIMP in both gas phase and solution:

C2 < C3 < C1.

The energy differences between three stable enol conformers of the p-substituted PIMP in the gas phase and solutions are negligible, in the range of 1.20-2.67, 1.28-2.60, and 1.55-2.45 kcal/mol in the gas phase, CCl₄, and CH₃CN solvents.

Conclusion

From the theoretical point of view, three stable conformers can be considered for PIMP, a molecule with a chiral carbon, and its para halogen substitutions. Our calculations, for target molecules, at different level of theory are shown, that the energy differences between three stable forms are in the range of 1.20-2.67 kcal/mol, in the gas phase and solutions. By the way, the Cl, F, and Br substitutions in the para position decreases the absolute energies and increase the stability, but do not significantly effect on the relative energies.

Acknowledgment

This work was financially supported by the Ferdowsi University of Mashhad, Iran.

References

- [1] A. McAuliffe, R.V. Parish, S.M. Abu-El-Wafa, R.M. Issa, "High-valent manganese complexes of tetradentate schiff base ligands. ESR-active and ESR-silent dimeric species", *Inorg. Chim. Acta*, 115 (1986) 91-94.
- [2] V. Ambike, S. Adsule, F. Ahmed, Z. Wang, Z. Afrasiabi, E. Sinn, F. Sarkar, S. Padhye, "Copper conjugates of nimesulide Schiffbases targeting VEGF, COX and Bcl-2 in pancreatic cancer cells", *J. Inorg. Biochem.*, 101 (2007) 1517-1524.
- [3] R. Jones, D. Summerville, F. Basolo, "Synthetic oxygen carriers related to biological systems", *Chem. Rev.*, 79 (1979) 139-179.
- [4] T.Ma. Ismail, "Mononuclear and binuclear Co(II), Ni(II), Cu(II), Zn(II) and Cd(II) complexes of schiff-base ligands derived from 7-formyl-8-hydroxyquinoline and diazaminophthalenes", *J Coord Chem*, 58 (2005) 141-151.
- [5] A. Koll, J. Janski, A. Karpfen, P. Wolschann, "Bifunctional influence of 3-chloro substitution on structural and energetic characteristics of N-methyl-salicylidene imine s", *J. Mol. Struct.*, 976 (2010) 19-29.
- [6] Gaussian 09, Revision B.05, M. J. Frisch, G. W. Trucks, H. B. Schlegel, G. E. Scuseria, M. A. Robb, J. R. Cheeseman, J. A. Montgomery, Jr., T. Vreven, K. N. Kudin, J. C. Burant, J. M. Millam, S. S. Iyengar, J. Tomasi, V. Barone, B. Mennucci, M. Cossi, G. Scalmani, N. Rega, G. A. Petersson, H. Nakatsuji, M. Hada, M. Ehara, K. Toyota, R. Fukuda, J. Hasegawa, M. Ishida, T. Nakajima, Y. Honda, O. Kitao, H. Nakai, M. Klene, X. Li, J. E. Knox, H. P. Hratchian, J. B. Cross, C. Adamo, J. Jaramillo, R. Gomperts, R. E. Stratmann, O. Yazyev, A. "Gaussian 09", Revision B.05. CT, (2009).

Fluorine Lewis Acids

N. Orangi* and K. Eskandari

Department of Chemistry, Isfahan University of technology, Isfahan, 84156-83111, Iran

*n.orangi@ch.iut.ac.ir

Abstract: When R is sufficiently electron withdrawing, the fluorine in the R-F molecules could interact with electron donors (e.g. ammonia) and form a non-covalent bond (F \cdots N). Inasmuch as there are fundamental differences between these interactions and halogen bonds of iodine, bromine and chlorine, the term “fluorine bond” is preferred for describing these type of interactions. Natural energy decomposition analysis (NEDA) and interacting quantum atoms (IQA) methods reveal that fluorine and halogen bonds are different in their geometrical preference. In contrast to the halogen bonds (R – X \cdots Y) that are highly directional and the R – X – Y angle tends to be linear, fluorine bonds are not directional.

Keywords: Fluorine bond; Halogen bond; Directionality; IQA; NEDA

Introduction

Fluorine bond is a non-covalent interaction in which a fluorine atom (F) connecting to a very strong electron-withdrawing group acts as a Lewis acid and interacts with the electron donor species. The “fluorine bonds” are fundamentally different with the halogen bonds of iodine, bromine and chlorine. In contrast to the halogen bonds, both ESP and $\nabla^2\rho$ analyses indicate that the electron density around a fluorine atom is spherical, so it is usually said that the fluorine could not participate in halogen bonds. [1-2] Nevertheless, recent theoretical studies show that when R in the R-F is adequately electron withdrawing, the fluorine atom can interact with a Lewis base and form a weak noncovalent bond. [3] F₂, NCF, NC-CC-F, CF₃-CC-F and FCCF molecules are some examples in which the fluorine atoms are able to interact with a nucleophile (e.g. ammonia) and create a non-covalent (F \cdots N) bond. Although, these interactions were categorized as “halogen bonds”, in a recent work, we found several vital differences between these non-covalent interactions and halogen bonds. [4] Newly, Noorizadeh et al. used steric charges to study the halogen bonds. They also showed that the fluorine bonds could not be halogen bond. [5] Directionality and tendency toward linearity is one of the most important features of halogen bonds. In fact, the halogen bonds are extremely directional and the R-X-Y angle, θ , tends toward 180°. [6] In the present work, to reach a deeper understanding of the nature and directionality of these two interactions, we used NEDA, IQA and IQF (interacting quantum atoms and interacting quantum fragments) methods. To compare the orientation favourite and directional features of these bonds, we have investigated a series of complexes formed between ammonia and some fluorine-containing molecules, including F₂, NCF, FCCF and their chlorine/bromine-containing analogous.

Materials and method

In this work, the geometries of all of the molecules were optimized at MP2/aug-cc-pvDZ level of theory using Gaussian 09 package. The wavefunctions were obtained by B3LYP single point calculations on the above-mentioned MP2 optimized geometries for NEDA and IQA/IQF calculations. IQA/IQF terms were calculated by AIMAll program package. The NBO 5.0 program implemented in the GAMESS (US) was used to calculate the NEDA energy components.

Results and Discussion

NEDA calculations

Halogen bonds are typically classified as electrostatic interactions, mostly due to the presence of an area of positive electrostatic potential (the so-called σ -hole) on the extension of R-X bonds. Furthermore, because of the relatively narrow and focused form of the σ -holes, it has been said that the electrostatic interactions are the main reason for the linearity of R-X-Y angles. [7] However, decomposition analyses of interaction energies do not confirm the predictions based on the σ -hole notion. The variations of NEDA energy components with θ angle have been represented in the Fig. 1. The linear structures are the energetically most favorable position of these halogen bonds. In the linear complexes, the sum of attractive terms (i.e. EL+CT) overwhelms the CORE repulsion between the monomers. Figure 1 displays that the CT component of interaction energy is largely responsible for the bond directionality.

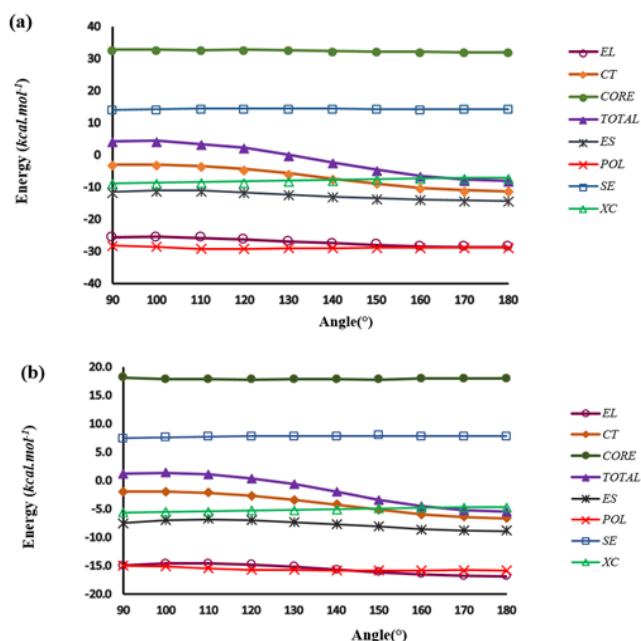


Fig.3: The angular distortion of NEDA energy components in a) NCBBr...NH₃, b) NCCl...NH₃ complexes.

Fig. 2 shows the changes in the NEDA interaction energy and its components for the NCF...NH₃ complex. Interestingly, the perpendicular position of complex is the most stable structure. In contrast to the halogen bonds, the charge transfer and electrical components favor the perpendicular structure. Fig. 2 indicates that in the fluorine bonded NCF...NH₃ complex, the electrical component displays a high angular distortion and is basically responsible for the orientation preference. The classical electrostatic term shows major sensitivity to the angular dependency among the different components of electrical term (ES, POL and SE).

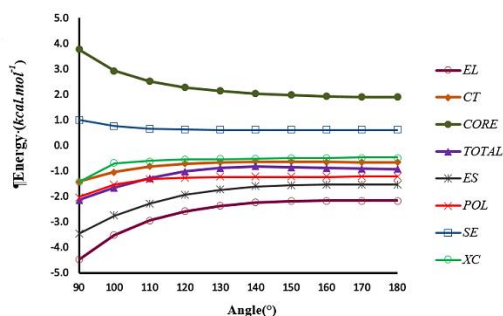


Fig.2: The angular distortion of NEDA energy components in NCF...NH₃ complex.

IQF and IQA analyses

IQA/IQF analyses have been studied on the NCX...NH₃ complexes for investigation the directional features of X...N interactions. In the linear structure of complexes, there is an attractive interaction between the NCX and

NH₃ fragments based on IQF calculations. In all arrangements, the quantum-mechanical term, V_{XC} (NCX,NH₃), is the dominate stabilizing component in the total inter-fragment interaction energy, though the classical interactions, V_{cl} (NCX,NH₃) are not insignificant. The variations of the total inter-fragment interaction energy between NCX and NH₃, E_{int}^{IQF} (NCX.NH₃), with θ angle for the NCBBr...NH₃ and NCCl...NH₃ complexes have been presented in the fig 3. As exposed, the linear arrangements of NCBBr...NH₃ and NCCl...NH₃ complexes are more favorable. Also, the classical component of inter-fragment interaction energy is more sensitive to the angular distortion than the exchange-correlation term.

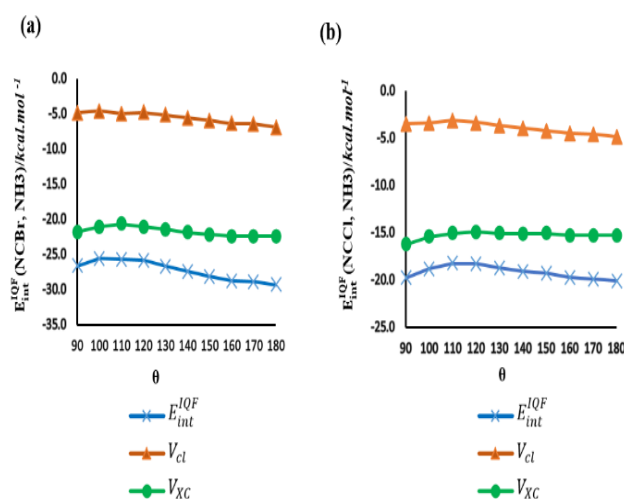


Fig.3: The angular distortion of IQF energy and its classical and exchange-correlation terms for the NCBBr...NH₃ (a) and NCCl...NH₃ (b) complexes

Fig 4 displays the variations of the IQF energy terms with the θ angle in the NCF...NH₃ system. Unlike to the halogen bonded complexes, the interaction energy between NCF and NH₃ fragments and also its quantum and classical terms favor the perpendicular arrangement. In this case, the exchange-correlation term indicates more angular dependencies and is largely responsible for the orientation favorite of E_{int}^{IQF} (NCF,NH₃).

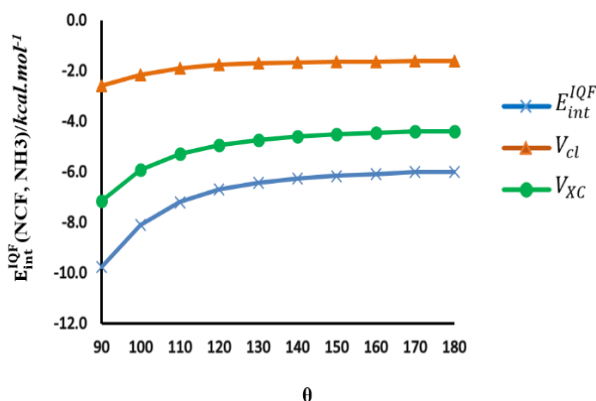


Fig.4: The angular distortion of IQF energy and its classical and exchange-correlation terms for the NCF...NH₃ complex.

The intra-atomic and interatomic terms in halogen bonded complexes have been studied using the IQA analyses. In all orientations in the NCB_r...NH₃ and NCCl...NH₃ complexes, the interaction between the halogen and nitrogen shows a stabilizing role and always is negative. Although the classical term of $E_{int}^{IQA}(N,X)$ is more sensitive to the angular changes, both classical and quantum components are responsible for bond directionalities. The interaction between carbon (of NCF) and nitrogen (of ammonia), $E_{int}^{IQA}(N,C)$ is another interatomic interaction that is effective to the bond directionalities. This component is negative for all the C-X-N angles and its nature is principally classical (around 99% of $E_{int}^{IQA}(N,C)$ arises from the classical components). In contrast to the halogen-nitrogen interaction, $E_{int}^{IQA}(N,C)$ favors the perpendicular orientation. In the IQA viewpoint, in all orientations, the interaction between fluorine and nitrogen atoms is repulsive and $E_{int}^{IQA}(N,F)$ has a weakening role in the formation of NCF...NH₃, so it is said that there is a clear difference between fluorine and other halogens.

Conclusions

There are several facts that show the fluorine bonds are not similar to halogen bonding interactions. In contrast to the chlorine/bromine-containing complexes that are more favorable in the linear structure, the perpendicular orientation of the fluorine containing complexes is the most stable arrangement. According to the NEDA analyses, the CT component is extremely sensitive to the angular changes in the halogen bonds, and is mostly responsible for the bond directionality. In contrast to the halogen bonds, the electrical component plays an essential role and is more favorable in the perpendicular orientation of the fluorine bonded complexes. Based on IQA analyses, the interatomic interaction between nitrogen (of ammonia) and carbon (of NCF) is mostly

responsible for the creation and orientation favorite of NCF...NH₃ complex.

Acknowledgment

The author gratefully acknowledges the Sheikh Bahaei National High-Performance Computing Center (SBNHPCC) for providing free access to its computational facilities. SBNHPCC is supported by scientific and technological department of presidential office and Isfahan University of Technology (IUT).

References

- [1] T. Clark, M. Hennemann, J. S. Murray, P. Politzer "Halogen bonding: the σ -hole", *J. Mol. Model*, 13 (2) (2007) 291-296.
- [2] K. Eskandari, H. Zariny "Halogen bonding: A lump-hole interaction Chem", *Phys. Lett*, 492 (1) (2010) 9-13.
- [3] J. S. Murray, P. Lane, P. Politzer "Expansion of the σ -hole concept" *J. Mol. Model*, 15 (6) (2009) 723-729.
- [4] K. Eskandari, M. Lesani "Does Fluorine participate in the halogen bonding?", *Chem. Eur. J*, 21 (12) (2015) 4739-4746.
- [5] A. M. Koohi, Z. Mahdaviifar, S. Noorizadeh "Can Fluorine form Halogen Bond? Investigation of Halogen Bonds through Steric Charge", *ChemistrySelect*, 2 (9) (2017) 2716-2720.
- [6] P. Politzer, J. S. Murray, T. Clark "Halogen bonding: an electrostatically-driven highly directional noncovalent interaction" *Phys. Chem. Chem. Phys.*, 12 (28) (2010) 7748-7757.
- [7] Z. P. Shields, J. S. Murray, P. Politzer "Directional tendencies of halogen and hydrogen bonds", *Int. J. Quant. Chem*, 110 (15) (2010) 2823-2832.

Quantum mechanical comparison between two isomers of C₂₄ fullerene nanocage

Saeed Ekrami, Hamid Reza Shamlouei*

Lorestan University, Chemistry Department, Khorram Abad

*shamlouei.ha@lu.ac.ir

Abstract: The C₂₄ is one of the small fullerenes which has many structures. Between these structures two isomers are more common. One of the isomers has six 4-member rings and eight 6-member rings (6-4) and another has two 6-member rings and twelve 5-member rings (6-5). In this article the structure and stability of these isomers were studied using Gaussian 09 package. The result of energy calculates shown that C₂₄ (6-5) isomer has lower energy that means more stability. Also calculation of Free energy and Enthalpy proved same results. In the calculation of electrical properties, the 6-5 isomer has lower E_g that cause more conductivity.

Keywords: Fullerene, stability, C₂₄

Introduction

Fullerene family, a spherical shape of carbon atoms following discovery of buckminsterfullerene C₆₀ and others nanotubes; open a new interesting window of chemistry world. In past decade fullerene and its derivatives attract scientific opinion to its wonderful and unique properties in biotechnology, molecules electronic Devices, biomedical engineering [1,2], nanomaterials [3] and biomedical science [4]. These special properties are related to fullerene structure and special geometry. Among the kind of fullerenes, in recent years the attention of researchers has been attracted to small ones (where C < 60). In small fullerene, C₂₄ is most favorite because of its application in molecule electronic devices, nanotechnology, and biomedical engineering. Also the orientation effect of C₂₄ fullerene reported by Wen-Kai Zhao et al [5] pointed to the application of C₂₄ in nanometer electronics field. First time Fullerenes theoretically was predicted to exist but its existence was proved by spectral analysis of red carbon in the atmosphere [6].

After discovery of C₆₀ Bucky-ball, on the other hand, several experimental and theoretical studies be accomplished for finding stable form of different fullerenes especially for the smaller ones.

Here we explain a computational method for examining the structure and stability of C₂₄ fullerene isomers.

Computational Details

The results reported here were carried out using density functional theory by Gaussian 09 package.

All calculation was performed at B3LYP/6-311+G(d), WB97XD/6-311+G(d), M06/6-311+G(d), PBE/6-311+G(d) computational level of theory. All Optimization and frequencies calculation where achieved in mentioned method. The result of frequencies has

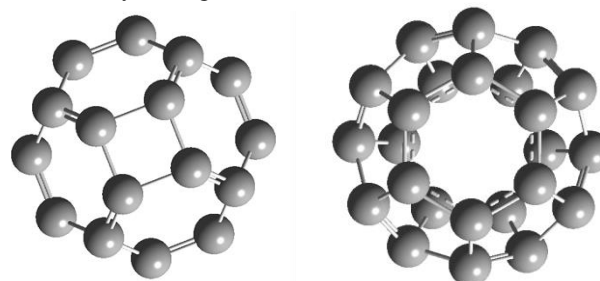
showed no negative values means that our structures are in global minima.

The frequency calculations were used to calculate the Enthalpy, Free-Energy and Energy of these two isomers.

Results and Discussion

Structural investigation

The optimized structures of two 6-4 and 6-5 isomers of C₂₄ were calculated at B3LYP and M062X/6-31+G (d) level of theory. In Fig.1, their structure was illustrated.



4-6 isomer of C₂₄

6-5 isomer of C₂₄

Fig.1: the optimized structures of two 6-4 and 6-5 isomers of C₂₄

As illustrated in Fig1, the 6-4 isomer consists of six 4-member and eight 6-member rings. The 6-5 isomer construct from 2 six-member and 12 five-member rings. In continue, the energetic parameters of these two structural isomers were studied.

Energetic considerations

Relative energies of these two structures were calculated and reported in Table 1. Additionally the enthalpy and free energy difference

Table 1: the energies of two isomers and energy difference between them

Method	$E_{6-4}(H)$	$E_{6-5}(H)$	ΔE (kCal.mol ⁻¹)
b3lyp/6-311+g(d)	-913.9829583	-914.0265144	27.33145
WB97XD/6-311+G(d)	-913.6731339	-913.7121171	24.46196
PBE/6-311+G(d)	-912.9750828	-913.0222348	29.58788
M06/6-311+g(d)	-913.3527272	-913.4015543	30.63901

As shown in Table 1, the 6-5 isomer has higher stability in comparison to 6-4 isomer of C₂₄ nanocage. It is considerable that all considerable method used for calculations has same results. Additionally the CBS method which is the very accurate methods was used to estimate the enthalpy and free energy difference between two isomers and the results were gathered in Table 2.

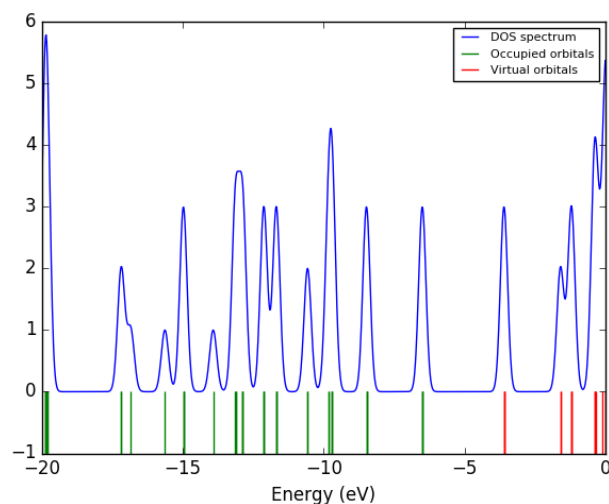
Table 2: The enthalpy and Free Energy of two structural isomers of C₂₄, ΔH and ΔG

Isomer	6-4	6-5	$\Delta H=$	$\Delta G=$
Enthalpy(H)	-902.724348	-902.774841	31.68 (Kcal.mol ⁻¹)	
Free Energy (H)	-902.766901	-902.816629	31.20 (Kcal.mol ⁻¹)	

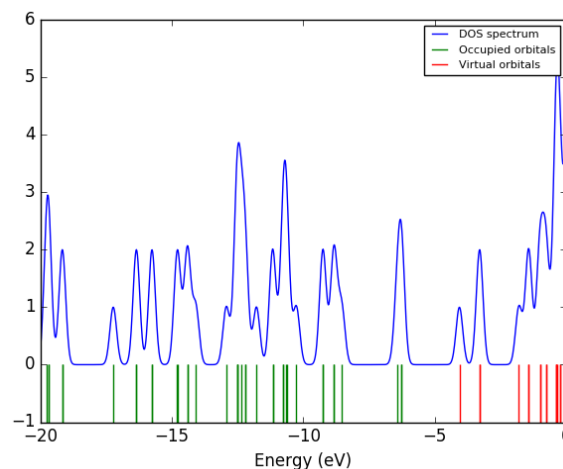
The results in Table 2 show that in accordance with previous section the 6-5 isomer has higher stability.

Electronic consideration

The DOS spectrums of two isomers of C₂₄ were illustrated in Fig2.



a



b

Fig2: the DOS spectrums of 6-4 (a) and 6-5 (b) isomers of C₂₄

The energies of HOMO and LUMO orbitals were calculated and gathered in Table 3. The E_g for these nanocages were estimated using the HOMO and LUMO energies (Table3).

Table 3: the energies of HOMO and LUMO of two isomers of C₂₄ nanocage

Isomer	E_{HOMO}		E_{LUMO}		E_g	
	b3lyp/6-311+g(d)	M06/6-311+g(d)	b3lyp/6-311+g(d)	M06/6-311+g(d)	b3lyp/6-311+g(d)	M06/6-311+g(d)
6-4	-6.35	-6.5	-3.85	-3.6	2.5	2.9
6-5	-6.12	-6.26	-4.31	-4.06	1.81	2.2

The E_g results show that the 6-4 isomer has more E_g than the 5-6 isomer, which demonstrate the higher electrical conductivity of 6-5 isomers.

Conclusions

There are many isomers for C₂₄ fullerene and we choose two isomers that earlier analysis shown their relative stability among all others. We used some reliable method for calculating the energy difference between two isomers. The result of energy calculates shown that C₂₄(6-5) isomer has lower energy that means more stability. Also calculation of Free energy and Enthalpy proved same results. In the calculation of electrical properties, the 6-5 isomer has lower E_g that cause more conductivity.

Acknowledgment

The authors gratefully acknowledge the Sheikh Bahaei National High Performance Computing Center (SBNHPCC) for providing computing facilities and time. SBNHPCC is supported by scientific and technological department of presidential office and Isfahan University of Technology (IUT).



References

- [1] S.Nagase, T. Kobayashi, T. Akasaka, and T. Wakahara, "Fullerenes: chemistry, physics and technology, In:Endo-hedral Metallofullerenes: Theory, Electrochemistry, and Chemical Reactions" , (2000) Wiley, 395-429, New York, Chapter 9.2.
- [2] D. Baowan, B. J. Cox, and J. M. Hill, *J. Mol. Model.*, 18 (2012) 549-557
- [3] T. Akasaka, and S. Nagase, "New, Family of Carbon Clusters" (2002) Kluwer Academic Publisher: Dordrecht, The Netherlands.
- [4] K. Uthukumar, and J. A. Larsson, *J. Mater. Chem.*, 18 (2009) 3347.
- [5] Z.Wen-Kai, Y. Chuan-Lu, Z. Jing-Fen, W. Mei-Shan, and M. Xiao-Guang, *Physica B* , 407 (2012) 2247 – 2253.
- [6] E.D. Isergin G.I. Mironove, *Low Temperature Physics*, 33 (2007) 1038-1042

Intramolecular hydrogen bond strength in three stable conformers of 2-(((1-phenylethyl)imino) methyl)phenol and its halogen substitutions, as a Schiff base with chiral carbon; A theoretical study

M. Afkanpoor^{a*}, V.R. Darugar^a, G. Grivani^b, M. Vakili^a

^aDepartment of Chemistry, Ferdowsi University of Mashhad, Mashhad 91775-1436, Iran

^bSchool of Chemistry, Damghan University, P.O. Box 36715-364, Damghan, Iran

* monirafkanpoor@chmail.ir

Abstract:

The molecular structure and intramolecular hydrogen bond strength of 2-(((1-phenylethyl)imino)methyl)phenol, as a Schiff base with a chiral atom, has been studied by calculation methods, at B3LYP/6-311++G** level of theory. According to our results, three stable conformers (C1-C3) can be drawn for target molecule. In addition, we considered the para halogen substitution effects, X=F, Cl, and Br, on the molecular structure and intramolecular hydrogen (IHB) strength of title molecule at gas phase. According to our results, the para halogen substitutions have no significant effect on the molecular geometry and topological parameters related to IHB strength of three stable conformers of target molecules.

Keywords: DFT; Chiral carbon; substitution effect; IHBs, Schiff base.

Introduction

Schiff bases, with C=N groups (imine) and benzene rings in their main chain, are interested for a wide spectrum of applications, such as metal ion complex agents [1], catalyst carriers [2], antitumor properties [3]. These compounds show thermochromism and photochromism properties in the solid state, which can cover reversibility of the intramolecular proton transfer.

2-(((1-phenylethyl)imino)methyl)phenol (PIMP), as a Schiff base, with one chiral carbon are particularly eye-catching. This molecule shows a fairly medium intramolecular H-bonding (IHB) between the H-atom of the hydroxyl group and the N-atom of the imine moiety. The mentioned transfer occur under the influence of light, for photochromic, and temperature for thermochromic, Schiff bases, [4].

In this study, optimized geometry and topological parameters related to IHB strength of title compound have been investigated by DFT method. Also the para halogen substitution effect on the structure and IHBs of target molecule have been studied.

Materials and method

The entire calculations for the PIMP and X-PIMP were done by a hybrid functional B3LYP at 6-311++G(d,p) basis set. All the calculations were performed using the Gaussian 09W program package [5].

AIM 2000 software was applied to obtain electron density and the Laplacian of electron density at the hydrogen bond critical points (BCPs) according to Bader's atoms in molecules (AIM) theory [6].

Results and Discussion

Three stable conformers of our molecules, PIMP and X-PIMP, with X=F, Cl, and Br, are shown in Fig. 1.

According to our calculations at B3LYP/6-311++G**, the C1 form is the most stable conformers.

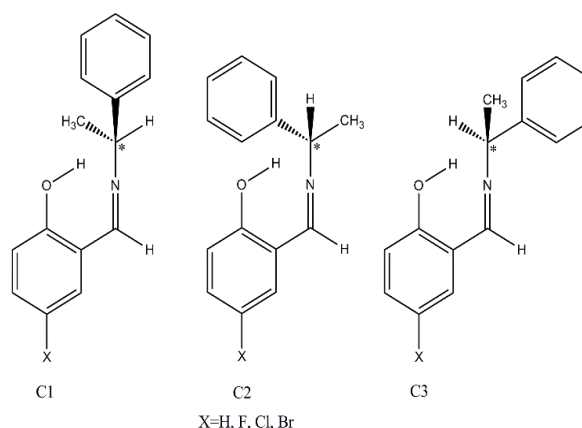


Fig.1: Three stable conformers of PIMP and its halogen substitutions. * is shown chiral atom.

The theoretical geometry and topological parameters related to IHB strength for X-PIMP molecules are listed in Table 1.

According to this Table, the C2 and C3 conformers in X-PIMP molecules have the most IHB strength. The shorter N...O bond distance are in agreement with increasing of topological parameters related to IHBs in these conformers.

E_{IHB} is the IHB energy in kcal/mol, calculated according to Espinosa *et al.* suggestion [7]. The E_{IHB} is one of important factors for description of intramolecular hydrogen bond strength. According to our theoretical calc



ulations, the following trend in IHB strength for three conformers is obtained for the three stable conformers of X-PIMP: 3 ~ 2 > 1

Also the hydrogen bond strength of X-PIMP when X=F, Cl, Br, do not significantly changed in comparison with that in parent molecule (PIMP). So, the values of IHBs in the mentioned substitutions are near together.

Table 1: The geometrical and topological parameters related to IHB strength of target molecules in gas phase at B3LYP/6-311++G** level.

	PIMP			Cl-PIMP			F-PIMP			Br-PIMP		
	C1	C2	C3	C1	C2	C3	C1	C2	C3	C1	C2	C3
d(O...H)	0.984	0.996	0.996	0.994	0.997	0.996	0.993	0.995	0.995	0.994	0.997	0.997
d(N...H)	1.779	1.730	1.728	1.739	1.750	1.727	1.743	1.736	1.730	1.737	1.730	1.726
d(O...N)	2.628	2.628	2.627	2.634	2.625	2.625	2.637	2.629	2.627	2.633	2.625	2.624
<OHN	147.9	147.6	148.1	147.7	147.4	147.9	147.7	147.3	147.8	147.8	147.4	147.9
ρ_{BCP}	0.049	0.051	0.051	0.050	0.051	0.051	0.049	0.050	0.051	0.050	0.051	0.052
V_{BCP}^2	-0.1113	-0.1111	-0.1111	-0.1111	-0.1111	-0.1111	-0.1114	-0.1111	-0.1114	-0.1112	-0.1110	-0.1111
E_{HB}	14.2	14.8	14.9	14.3	14.9	15.0	14.2	14.6	14.8	14.4	14.9	15.1

Conclusion

From the theoretical point of view, three stable conformers can be considered for PIMP, a molecule with a chiral carbon, and its para halogen substitutions. Our calculations, for target molecules, at B3LYP/6-311++G** level of theory are shown that the halogens do not significant effect on the H bond strength and molecular geometry of title molecules.

Acknowledgment

This work was financially supported by the Ferdowsi University of Mashhad, Iran.

References

- [1] S.A. Zarei, D. Khaledian, K. Akhtari, K. Hassanzadeh, "Copper(II) and nickel(II) complexes of tetradentate Schiff base ligand: UV-Vis and FT-IR spectra and DFT calculation of electronic, vibrational and nonlinear optical properties", *Mol. Phys.*, 113 (2015) 3296-3302.
- [2] J.L. Sessler, P.J. Melfi, G. Dan Pantos, "Uranium complexes of multidentate N-donor ligands" *Coord. Chem. Rev.*, 250 (2006) 816-843.
- [3] M. Kabak, A. Elimali, Y. Elerman, T.N. Durlu, "Conformational study and structure of bis-N,N'-p-bromo-salicylideneamine-1,2-diaminobenzene", *J. Mol. Struct.*, 553 (2000) 187-192.
- [4] T.Ma. Ismail, "Mononuclear and binuclear Co(II), Ni(II), Cu(II), Zn(II) and Cd(II) complexes of schiff-base ligands derived from 7-formyl-8-hydroxyquinoline and dia-

minonaphthalenes", *J. Coord. Chem.*, 58 (2005) 141-151.

[5] M. J. Frisch, G. W. Trucks, H. B. Schlegel, G. E. Scuseria, M. A. Robb, J. R. Cheeseman, J. A. Montgomery, Jr., T. Vreven, K. N. Kudin, J. C. Burant, J. M. Millam, S. S. Iyengar, J. Tomasi, V. Barone, B. Mennucci, M. Cossi, G. Scalmani, N. Rega, G. A. Petersson, H. Nakatsuji, M. Hada, M. Ehara, K. Toyota, R. Fukuda, J. Hasegawa, M. Ishida, T. Nakajima, Y. Honda, O. Kitao, H. Nakai, M. Klene, X. Li, J. E. Knox, H. P. Hratchian, J. B. Cross, C. Adamo, J. Jaramillo, R. Gomperts, R. E. Stratmann, O. Yazyev, "Gaussian 09", Revision B.05. CT, (2009).

[6] R.F.W. Bader, *Atoms in Molecules*, Wiley OnlineLibrary, (1990).

[7] E. Espinosa, E. Molins, C. Lecomte, "Hydrogen bond strengths revealed by topological analyses of experimentally observed electron densities" *Chem. Phys. Lett.*, 285 (1998) 170-173.

Molecular Dynamics Studies of Cation Aggregation in two Amino Acid Ionic Liquids

H. nadimi, F. Moosavi*, M. Housaindokht

Department of chemistry, ferdowsi, mashhad, 9177948974, iran

* moosavibaigi@um.ac.ir

Abstract: The structure of two aqueous dodecyl betaine chloride and dodecyl betaine N-acetyl glycinate solutions were studied using molecular dynamic (MD) simulations. The distance between the same atoms of cations from each other follows the following procedure: C17-C17 > C12-C12 > C6-C6 > C5-C5 > N1-N1, that confirm spontaneous self-assembly of cations into small micellar aggregates. Results were presented for the organization of solvent around the carboxylate of both cations with a hydrogen bonding between hydrogen of water and oxygen of cation. The number of more hydrogen bonds between water-cation, water-anion, anion-cation and anion-anion were observed in dodecyl betaine N-acetyl glycinate than dodecyl betaine chloride that were led to a decrease of gradient of cation, anion and water in MSDs and thereby less diffusion of the cation and anion.

Keywords: Aggregation; Amino Acid Ionic Liquid; Surfactant; Simulasion

Introduction

Ionic liquids (ILs) have attracted great attention in researches due to their specific physicochemical properties, such as nonvolatility, nonflammability, high stability, high ionic conductivity, and easy recyclability during the past years. Aqueous solutions of long alkyl chain substituted IL compounds were found to aggregate, forming micelles. The self-assemblies of amphiphilic molecules have many potential applications such as nanomaterial, organic or bioorganic synthesis ,drug delivery, separation process, and other dispersant technologies. In this sense, the clarification of self-assembling phenomena of ILs must be a significant research subject [1].

A easy way to prepare functional IL systems is to mix functional molecules with ILs in order to **preparing** of them for certain applications. therefore amino acids are candidates to act as a platform for functional ILs because of their low cost, availability, biodegradability and biological activity [2].

In recent years, the properties of ionic liquid solutions have been studied extensively by molecular dynamics (MD) simulations. MD simulations provide a unique resolution of structural details down to the Angstrom scale [3].

In this regard, we have carried out atomistic level MD simulations of two amino acid based ionic liquid surfactants in bulk aqueous solution.

Method

All the simulations reported in here were performed with the GROMACS 4.5.4 [4] simulation program. The AMBER force field [5] was used to determine the intra- and intermolecular force constants for both anion and cation. Nose'-Hoover thermostat and Parrinello-Rahman barostat were used to control the temperature at 300K and pressure at 1 bar. Water was described by the rigid

SPC/E model and a time step of 1 fs was used. Further details were reported in Table 1.

Table 1: details of simulation

	Surfactant type	Ion pair number	Numbe r of water molecu les	Lenght of cubic box (nm)	Cut off (nm)
System1	[C ₁₇ H ₃₆ NO ₂] ⁺ [Cl] ⁻	30	1987	4.26	2.0
System2	[C ₁₇ H ₃₆ NO ₂] ⁺ [C ₄ H ₅ NO ₃] ⁻	30	1987	4.4	2.0

A schematic drawing of two ionic liquid were provided as Figure 1 to aid the discussion.

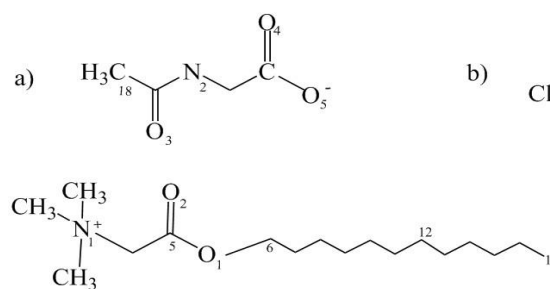


Figure.1: schematic drawing of cation and anion a) N-acetyl glycinate , b) chloride

Results and Discussion

The radial distribution function (RDF) between the cation of dodecyl betaine N-acetyl glycinate and hydrogen of water was shown in Figure 2. The RDF plot displayed a peak at 0.18 nm, indicating the presence of strong hydrogen bonds between water and the carboxylate group of cation. The same result were obtained for system 1, which we did not show here.

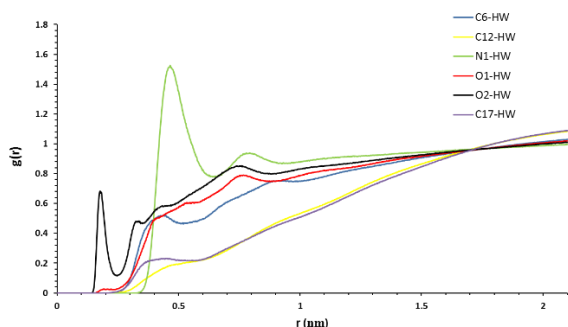


Figure.2: Radial distribution functions, $g(r)$ for hydrogen of water and atoms of cation in dodecyl betaine N-acetyl glycinate.

The aggregation of cation due to their amphiphilic nature is obvious from Figure 3, which shows the RDFs for several sites on the cation with the same sites of other cations. It can be seen that the C12 atom on the dodecyl chain is ordered to a great extent with a narrow peak at 0.42 nm. RDFs corresponding to C6, C5 and N1 do not show any peak suggesting strong ordering around each other. The spherical nature of the cation aggregates is also evident from the RDFs in according to Bhargava et al [6], which show the distance between the same atoms from each other that follows the following procedure:

$$C17-C17 > C12-C12 > C6-C6 > C5-C5 > N1-N1$$

The same results were obtained for dodecyl betaine N-acetyl glycinate, which we did not show here.

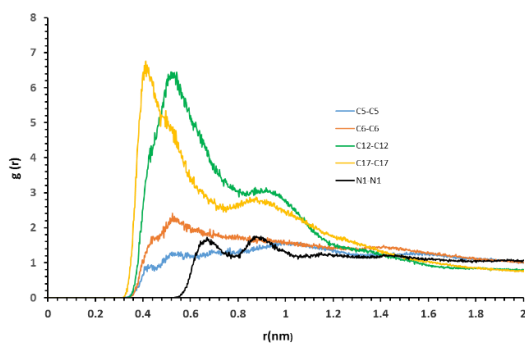


Figure.3: Radial distribution functions, $g(r)$ for cation-cation atoms in dodecyl betaine chloride.

Comparison of the diffusion and movement of particles in the system shows the molecular mobility and the presence of interaction in the studied systems. For this reason, the Mean Square Displacement (MSD) of two surfactants were compared in Figure 4. As can be seen from the figure, replacement of Chloride anion with N-acetyl glycinate led to a decrease in gradient of cation, anion and water MSDs, that is indicative of stronger interactions between anion-water, cation-water, cation-anion and anion-anion in accordance with table 2, thereby providing a less space for the diffusion of the cation and

anion.

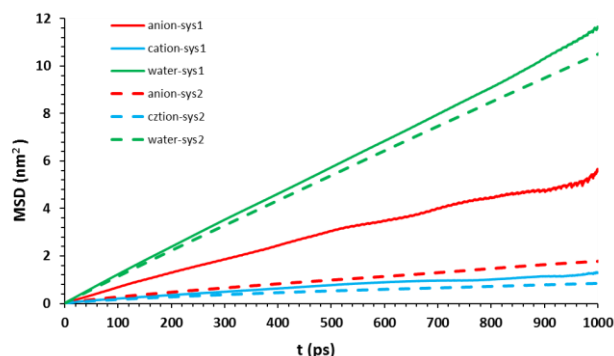


Figure.4: Mean Square Displacement (MSD) in both of systems.

In addition, the large difference in the anion gradient is also due to the small size of the anion.

Table 2: number of hydrogen bond

	Anion-water	Cation-water	Cation-anion	Cation-cation	Anion-anion	Water-water
Sys 1	0	22.9	0	0	0	3396.5
Sys 2	201	29.5	2	0	1	3388.5

Conclusions

Aqueous solutions of two amino acid based ionic liquid surfactants have been studied using MD simulations. The strong hydrogen bond have been between water and the carboxylate group of cation. The structure of the aggregate has been found to be spherical. Anion of N-acetyl glycinate has more stronger interactions than Chloride anion thereby providing a less diffusion of the cation, anion and water. Clearly, long trajectory simulations on large systems have been provided additional insight into the nature of the aggregates.

Acknowledgment

This research was supported by Department of Chemistry, Ferdowsi University of Mashhad.

References

- [1] Y. Gu, L. Shi, X. Cheng, F. Lu, L. Zheng, "Aggregation Behavior of Dodecyl-3-methylimidazolium Bromide in Aqueous Solution: Effect of Ionic Liquids with Aromatic Anions", *Langmuir*, 29 (2013) 6213-6220.
- [2] H. Ohno, K. Fukumoto, "Amino Acid Ionic Liquids", *Acc. Chem. Res*, 40 (2007) 1122-1129.
- [3] T. Mendez-Morales, J. Carrete, O. Cabeza, L. Gallego, L. Varela, "Molecular Dynamics Simulation of the Structure and Dynamics of Water_1-Alkyl-3-methylimidazolium Ionic Liquid Mixtures", *Phys. Chem. B*, 115 (2011) 6995-7008.

Electric Field Gradient for Prediction of Effect of Cation Na⁺ on Nucleic Acid Bases: Aromaticity by Cyclic References

N. Bagheri*, P. Abbasi, F. Tavakkol

Department of Chemistry, Islamic Azad University, Firoozabad Branch, Firoozabad, Iran

*nrgs.bagheri@gmail.com

Abstract

In this research, it has been studied the effects of Na⁺ ion on Nitrogenous Organic Bases (NOB) in the nucleic acids by using of a new index. This index is according to Electric Field Gradient (EFG) in the middle of bond and evaluated as a reference by corresponding cyclic same compounds. The studied molecules were Adenine, Guanine, Cytosine, Thymine and Uracil that has been investigated. The trend of changes of aromaticity by putting Na⁺ in the middle of cycle and change of distance according to degree of Angstrom (Å). It has been used Density Functional Theory (DFT) as a method for geometrical optimization Beck 3 Lee Yang Parr (B3LYP) in 6-311++G** and 6-31G standard basis set. These calculations have been done in two steps. In the first step, it has been calculated electric field gradient in the middle of bond in absence of Na⁺ (EFG⁰) and in the second step in presence of Na⁺, it has been calculated in 1 Å distance of middle of bond without Na⁺ (EFG^{0.5}) and with Na⁺ that compared amount of aromaticity between EFG⁰ and EFG^{0.5} in 6 distance (d = 0.5, 1, 1.5, 2, 2.5 and 3 Å).

Keywords: Nucleic Acid, Na⁺, Aromaticity, Electric field gradient (EFG)

Introduction

In molecular biology, two nucleotides on opposite complementary deoxyribonucleic acid (DNA) or ribonucleic acid (RNA), strands that are connected via hydrogen bonds are called a base. DNA and RNA were first isolated by the Swiss physician Friedrich Miescher who, in 1869, discovered a microscopic substance in the pus of discarded surgical bandages. As it resided in the nuclei of cells, he called it "nuclein". In the canonical Watson-Crick DNA base pairing, adenine (A) forms a base pair with thymine (T) and guanine (G) with cytosine (C). In RNA, thymine is replaced by uracil (U) [1]. Uracil (C₄H₄N₂O₂) is a common and naturally occurring pyrimidine derivative. Uracil [Pyrimidine-2,4(1H,3H)-dione] undergoes amide-imidic acid tautomeric shifts because any nuclear instability the molecule may have from the lack of formal aromaticity is compensated by the cyclic-amidic stability. The amide tautomer is referred to as the lactam structure, while the imidic acid tautomer is referred to as the lactim structure [2].

Aromaticity is a chemical property in which a conjugated ring of unsaturated bonds, lone pairs, or empty orbitals exhibit a stabilization stronger than would be expected by the stabilization of conjugation alone. This property led to the term "aromatic" for this class of compounds, and hence the term "aromaticity" for the eventually-discovered electronic property. The circulating π electrons in an aromatic molecule produce ring currents that oppose the applied magnetic field in NMR. The NMR signals of protons in the plane of an aromatic ring are shifted substantially further down-field than those on non-aromatic sp² carbons. This is an important way of detecting aromaticity [3]. Aromatic molecules are able to interact with each other in so-called π - π stacking: the π systems form two parallel rings overlap in a "face-to-face" orientation and interact with each other in an "edge-to-face" orientation: the slight positive charge of the substituents on the ring atoms of one molecule are attracted to the slight negative charge of the aromatic system on another molecule. An atom in an aromatic system can have other electrons that are not part of the system, and are therefore ignored for the 4n + 2 rule. uracil that make up the sequence of the genetic code in RNA is aromatic pyrimidine.

Considering that aromaticity is a multidimensional phenomenon, the investigation of new aromaticity indices is very important. In this sense, it has been introduced the corrected total electron density (CTED) as



an index of aromaticity based on ellipticity (ϵ) and bond length variations from those for a system assumed as full aromatic. The validity of this index was checked for a series of rings in monocyclic and polycyclic structures. Also, the aromaticity of polycyclic benzene rings was evaluated from the calculation of the average g -factor for a hydrogen placed perpendicularly at geometrical center of related ring plane at a distance of 1.2°A . The results have been compared with the other commonly used aromatic indices, such as HOMA, NICSs, PDI, FLU, MCI and CTED [4].

Computational Details

All the compounds have been fully optimized energies at equilibrium geometries by using DFT at B3LYP level with 6-311++G** [5] basis set. Frequency test has been done to ensure that all the optimized geometries are in ground state. The optimized geometries show that all rings are planar (in xy plane). The EFG calculations at the sites of atoms and in the middle and above the bonds have been made according to the procedure (see Results and discussion below) for optimized structures. The calculations have been done by Gaussian09 [6] package.

Results and Discussion

In atomic, molecular, and solid-state physics, EFG measures the rate of change of the electric field at an atomic nucleus generated by the electronic charge distribution and the other nuclei. The electric field gradient tensor, V_{ij} , which is defined by the second derivatives of the potential generated by electron density with respect to desired position of molecule, is a useful tool to obtain some molecular information. The electric field gradient tensor is a symmetric second rank tensor with zero off diagonal elements which can be expressed in an axis system. This component has been assigned to "EFG" in this manuscript. The unit of computed EFG value is Volt per square meter (Vm^{-2} or $\text{NC}^{-1} \text{m}^{-1}$) [7].

In this research, to finding compounds in their cyclic form have four kinds of bonds such as: C=C, C-C, C-N, C=N. So, it has been selected two cyclic references that have localized electrons in bonds named cyclohexene and 1, 2, 5, 6-tetra hydro pyrimidine [8].

By using of a new index of corresponding amount of aromaticity (electric field gradient) in two steps amount of aromaticity in NOB in DNA and RNA has been calculated.

We have calculated amount of aromaticity in NOB being in the Nucleic acids without Na^+ ion by using EFG. That style of putting Bq in the cycle has been observed in fig

1 and amount of aromaticity of seven styles has been shown in Table 1. Na^+ ion has been located in 0.5, 1, 1.5, 2, 2.5 and 3 A° distances of middle of cycle and according to this, aromaticity of NOB has been calculated. Style of putting Na^+ ion has been shown in Fig 1. The amount of aromaticity of seven cycles has been listed in table 1 and 2.

The EFG is non-zero only if the charges surrounding the nucleus violate cubic symmetry and therefore generate an inhomogeneous electric field at the position of the nucleus. EFGs are highly sensitive to the electronic density in the immediate vicinity of a nucleus. This is because the EFG operator scales as r^{-3} , where r is the distance from a nucleus. This sensitivity has been used to study effects on charge distribution resulting from substitution, weak interactions, and charge transfer. $A = \sum_{\text{localized}} \text{EFG}$ is sum of references EFG, $B = \sum_{\text{delocalized}} \text{EFG}$ is sum of Eigen values in v_{zz} and $\Delta = B - A$ is aromaticity amount of uracil as an example of these molecules.

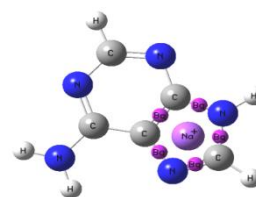


Fig 1: Uracil molecule with cation

By putting Na^+ ion in the middle of cycle according to different distances of studied 7 cycles. Whenever Na^+ ion localized in 3A distance is stable structure than other and whenever Na^+ ion localized in 0.5 A distance is unstable structure than other.

Table 1: The amount of aromaticity without Na^+

Molecule	$A = \sum_{\text{localize}} \text{EFG}$	$B = \sum_{\text{delocalize}} \text{EFG}$	$\Delta \text{EFG}^{0.5}$
Uracil	5.3373	7.1189	1.7816
Thymine	5.3373	7.0975	1.7602
Cytosine	5.3373	7.4928	2.1555
Adenine(5)	4.6196	6.2015	1.5819
Adenine(6)	5.3373	7.7832	2.4459
Guanine(5)	4.6196	6.2437	1.6241
Guanine(6)	5.3373	7.2948	1.9575

Table 2. The amount of aromaticity with Na^+

Molecule	$A=\Sigma_{\text{localize}} \text{EFG}$	$B=\Sigma_{\text{delocalize}} \text{EFG}$	$\Delta \text{EFG}^{0.5}$
Uracil	5.3373	6.1478	0.8105
Thymine	5.3373	6.1278	0.7914
Cytosine	5.3373	6.4894	1.1521
Adenine(5)	4.6196	5.9173	1.2977
Adenine(6)	5.3373	6.7426	1.4053
Guanine(5)	4.6196	5.8944	1.2748
Guanine(6)	5.3373	6.3215	0.9842

Amount of aromaticity in this 7 cycle calculated by EFG in the middle of bond (ΔEFG^0) and in 0.5 and 1 \AA have the same trends.

So, standard test of EFG has been determined for cycles in 0.5 \AA distance of bond. Results show by entrance of Na^+ ion, amount of aromaticity of compounds has been reduced as seen in Table 2. Whatever distance of it get away from cycle, amount of aromaticity of compounds has been increased.

So, the trend of changes of stability from these compounds is such as below:

Without $\text{Na}^+ > 3 > 2.5 > 2 > 1.5 > 1 > 0.5$

The amounts of aromaticity in these compounds have been calculated in some different distances of cations. The results have shown the same trends such as in 1 \AA by $\text{EFG}^{0.5}$ at different distances 0.5, 1, 1.5, 2, 2.5, 3 \AA (Fig 2).

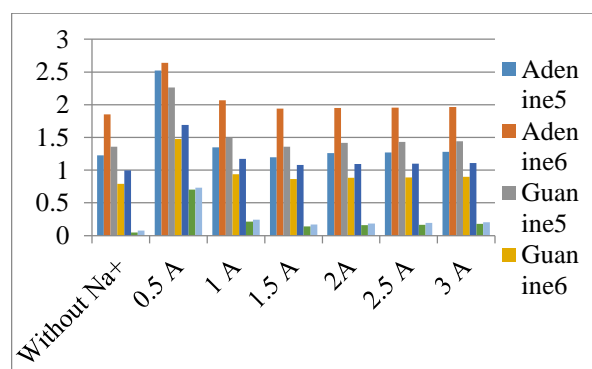


Fig 2: The comparison of aromaticity of different distances of Na^+ in EFG^0

Also, hexa-membered cycles show that in both standard in EFG^0 and $\text{EFG}^{0.5}$ and EFG^1 and have similar trend. Adenine, cytosine, thymine, and uracil have more aromaticity. The trend of changes of aromaticity in 5 cycles investigated and all of them have same trend that in contrast this trend with other standard of aromaticity like NICS and HOMA has been showed good adaptation.

So, we have found from trends of changes of aromaticity, when EFG on bond in 0.5 \AA distance changes, amount of aromaticity in more distances increases.

Conclusion

Several nitrogenous Organic Bases have been optimized at B3LYP/6-311++G** level of theory with no imaginary frequencies. All the rings which have been optimized are planar. Electric field gradient EFG calculations have been performed for these species and presented a new criterion for aromaticity, which are indicated by ΔEFG . Positive ΔEFG values indicate the presence of aromaticity, whereas negative values denote antiaromaticity.

Our method is computationally much easier and inexpensive to compute. Since EFG calculations are used the most in some other quantum mechanical programs, this type of aromaticity evaluations will be readily available.

References

- [1] D.J. Brown, Heterocyclic Compounds: Thy Pyrimidines, 1994, Vol 52. New York: Interscience, 1994.
- [2] N.K. Kochetkov, E.I. Budovskii Organic, Chemistry of Nucleic Acids Part B, 1972, New York: Plenum Press, 1972.
- [3] A.H. Pakiari, M. Farrokhnia, S.M. Azami, "Multicenter bond index analysis of influence of metal cations on the aromaticity of aromatic amino acids: Phenylalanine and tyrosine" Chem. Phys. Lett., 457 (2008) 211-215.
- [4] F. Uzun, A. Tokatli, "The new aromaticity index based on g-factor calculation applied for polycyclic benzene rings", Chem. Phys. Lett. 621 (2015) 5-11.
- [5] C. Lee, W. Yang, R.G. Parr, (1988) Phys Rev B, 37(1988)785-789.
- [6] M.J. Frisch et al., GAUSSIAN 09, Revision E.01, Gaussian, Inc., Wallingford, CT, 2004.
- [7] A.H. Pakiari, N. Bagheri, "A new approach for aromaticity criterion based on electrostatic field gradient", J. Mol. Model. 17 (2011) 2017-2027.
- [8] N. Bagheri, K. Ghaed, Thesis of M.S, Islamic azad university of firoozabad (2014).

Molecular Dynamics Simulations of the effect of Trifluoroethanol on the Conformation of α -synuclein peptide

S.Jalili^a, A.pakzadiyan^{b*}

^aDepartment of Chemistry, Faculty of chemistry, K.N. Toosi University of Technology, Tehran, Iran

^bDepartment of Chemistry, Faculty of chemistry, K.N. Toosi University of Technology, Tehran, Iran

*a.pakzadiyan@email.kntu.ac.ir

Abstract

The accumulation of alpha-synuclein (α -syn) fibrils in neuronal inclusions is the defining pathological process in Parkinson disease (PD). Solvation structure and association alpha-synuclein (α -syn) in aqueous TFE solutions are investigated. Using molecular dynamics simulation and the AMBER03 force field. This conformational transition with concomitant peptide aggregation is a possible mechanism of plaque formation. Here, in order to gain more insight into the mechanism of α -helix formation of α -syn peptide by TFE, which particularly stabilizes α -helical conformation, we studied the secondary-structural elements of α -syn peptide by molecular dynamics simulations. Secondary structural elements determined from NMR spectroscopy in aqueous TFE solution are preserved during the MD simulation. TFE/water mixed solvent has reduced capacity for forming hydrogen bond to the peptide compared to pure water solvent. TFE allows α -syn to form bifurcated hydrogen bonds to TFE as well as to residues in peptide itself. MD simulation in this study supports the notion that TFE can act as a α -helical structure forming solvent.

Keywords: Alpha-synuclein (α -syn); Parkinson disease (PD); Hydrogen bond; TFE; MD simulation

Introduction

Investigating the onset and development of high-impact human pathologies like Alzheimer's and Parkinson's diseases cannot be separated from an accurate description of inter- and intramolecular interactions involved in the formation and stability of amyloid aggregates. Depending on the environment on several species can be formed during amyloid aggregate growth: oligomeric partially ordered structures may occur as on- or off-pathway intermediates of the process [1] and are often recognized as the toxic species, rather than the mature fibrils [2,3].

In this paper, because of the wide usage of 2,2,2-trifluoroethanol (TFE) as a solvent in experimental and theoretical studies of biosystems [4], TFE/water mixtures have been considered as solvent. Molecular dynamics simulation, as one of the major computational methods developed for biosystems, is used to study the solvation effects. Surprisingly, it adopts α -helical conformation without aggregation in the presence of trifluoroethanol (TFE). TFE is known as a secondary-structure-inducing agent. Since influence of TFE on the conformation of peptides is not well understood, characterization of the effects of TFE is important to understand protein folding. Here, in order to gain more insight into the mechanism of α -helix formation of α -syn peptide in

TFE, which particularly stabilizes α -helical conformation, we studied the secondary-structural elements of the α -syn peptide in TFE aqueous solution by molecular dynamics simulations.

Materials and method

MD simulations on a molecule of α -syn in pure water, pure TFE, and eleven different TFE–water mixtures were performed using Gromacs simulation package [5] with the Amber03 force field [6]. Table 1 shows the composition of the simulated systems. The TFE molecules were modeled using a flexible nine-site model [7] involving all possible angles and dihedrals in the molecule and water molecules were represented by the TIP3P model [8]. Inter-atomic interactions were described by a sum of pair-wise Coulomb and Lennard–Jones potential terms. Each system was energy-minimized during 50,000 steps of steepest descent method and then was equilibrated at 300 K with an NVT-MD simulation for 500 ps followed by a simulation in NPT ensemble (at 300 K and 1 bar) for 500 ps. Production simulations were initiated from the last snapshot of the corresponding equilibration runs. All runs were performed at constant pressure and temperature for 1 ns and configurations of the system were saved every 2 ps. The pressure was maintained by using a Parrinello–



Rahman barostat [9] with a coupling time of $\tau_p = 1$ ps, whereas the temperature was controlled by a Berendsen thermostat [10] with a coupling time of $\tau_t = 1$ ps. The equations of motion were integrated using the leap-frog algorithm [11] and the integration time step was 2 fs. The bond lengths were kept constant by applying the LINCS algorithm [12] and periodic boundary conditions were applied to the systems in all directions. Long-range electrostatic interactions were calculated by the particle-mesh Ewald method [13].

Results and Discussion

RMSD (*Root Mean Square Deviation*), as a function of time in MD simulations shows the RMS deviations from the starting structure during 10 ns MD simulations. The RMSD values of the protein backbone atoms between the structures resulting from the simulations and the starting structure are compared in Figure 1. In the simulations a rapid initial increase of the RMSD was observed during the first 100 ps. RMSD values in a TFE/water mixed solvent tended to be relatively constant after 100ps including heating and equilibrium periods.

Figure 1 presents the calculated residual secondary structure α -syn and TFE molecules during MD simulation in TFE/H₂O. Plots of secondary structure changes obtained from MD simulations are shown in (Fig. 2).

The diagram of the secondary structure is based on the reduction of the concentration of trifluoroethanol, which as you can see in Figure, reduces the alpha-helix Conformation by decreasing its concentration.

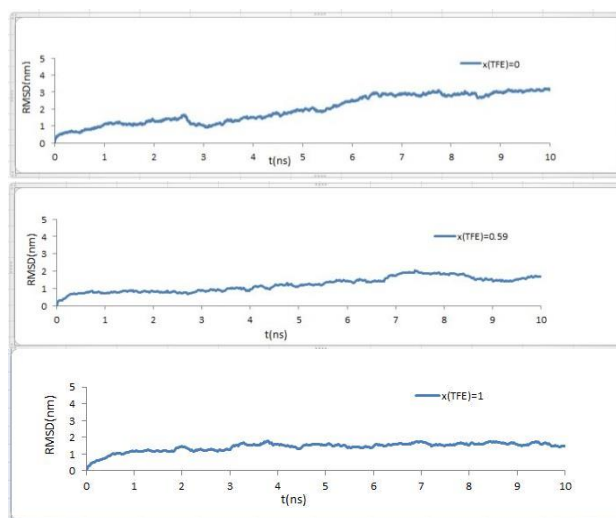
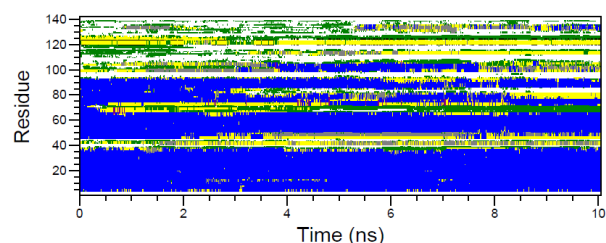


Fig. 1: RMSD of atomic positions from the minimized and equilibrated structure averaged over 10 ns MD simulations.

Table1: Composition of the systems in the first set of simulations.

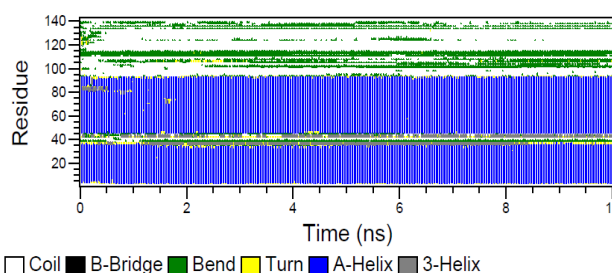
n (H ₂ O)	n (TFE)	x (TFE)	n (α -syn)
9573	0	0	1
1098	1613	0.59	1
0	1856	1	1

Secondary structure



(a)

Secondary structure



(b)

Fig. 2: Secondary structures of a α -syn peptide at the water/TFE. (a) $x(\text{TFE})=0$, (b) $x(\text{TFE})=1$



Conclusions

The solvation structure and thermodynamics of α -syn in aqueous and TFE solutions have been investigated at various concentrations. Water molecule destabilizes the α -helix in the peptide due to the strong interactions between the charged atoms in peptide and water.

Dielectric constant of TFE is about one-third that of water, resulting in a strengthening of interactions between charged groups in the peptides. TFE is much weaker base than water resulting in a weaker capacity for accepting protons in hydrogen bonds. TFE has only one O-H group and has a much larger size than water. TFE/water mixed solvent has reduced capacity for forming hydrogen bond to the peptide compared to pure water solvent. Therefore, TFE forms hydrogen bonds to α -syn and allows α -syn to maintain the intramolecular hydrogen bond. In conclusion, α -helical secondary structure elements in α -syn determined from NMR spectroscopy in TFE/water mixed solvent are preserved during the MD simulation. TFE allows the peptide to form bifurcated hydrogen bonds to TFE as well as to peptide itself. Since it is important to develop a tool to control the amyloid deposition observed in Alzheimer's disease patients.

References

- [1] F. Chiti, C.M. Dobson, Protein misfolding, functional amyloid, and human disease, *Annu. Rev. Biochem.* 75 (2006) 333–366.
- [2] M. Stefani, Structural features and cytotoxicity of amyloid oligomers: implications in Alzheimer's disease and other diseases with amyloid deposits, *Prog. Neurobiol.* 99 (2012) 226–245.
- [3] R.M. Koffie, M. Meyer-Luehmann, T. Hashimoto, K.W. Adams, M.L. Mielke, M. Garcia-Alloza, et al., Oligomeric amyloid β associates with postsynaptic densities and correlates with excitatory synapse loss near senile plaques, *Proc. Natl. Acad. Sci.* 106 (2009) 4012–4017.
- [4] A.R. van Buuren, H.J.C. Berendsen, *Biopolymers* 33 (1993) 1159–1166.
- [5] A.P. Eichenberger, W.F. van Gunsteren, L.J. Smith, *J. Biomol. NMR* 55 (2013) 339–353.
- [6] D. Van Der Spoel, E. Lindahl, B. Hess, A.R. Van Buuren, E. Apol, P.J. Meulenhoff, et al., *Gromacs user manual version 4.5*, Available at: www.gromacs.org 2005.
- [7] Y. Duan, C. Wu, S. Chowdhury, M.C. Lee, G. Xiong, W. Zhang, et al., *J. Comput. Chem.* 24 (2003) 1999–2012.
- [8] R. Chitra, P.E. Smith, *J. Chem. Phys.* 115 (2001) 5521–5530.
- [9] W.L. Jorgensen, J. Chandrasekhar, J. Madura, M.L. Klein, *J. Comput. Chem.* 79 (1983) 926–935.
- [10] A. Aspect, J. Dalibard, G. Roger, *Phys. Rev. Lett.* 49 (1982) 1804–1807.
- [11] H.J.C. Berendsen, J.P.M. Postma, W.F. Van Gunsteren, A. Di Nola, J.R. Haak, *J. Chem. Phys.* 81 (1984) 3684–3690.
- [12] M.P. Allen, D.J. Tildesley, *Computer Simulation of Liquids*, Oxford University Press, Oxford, 1989.
- [13] B. Hess, H. Bekker, H.J.C. Berendsen, J.G.E.M. Fraaije, *J. Comput. Chem.* 18 (1997) 1463–1472.

Al-doped Boron Nitride Nanosheets as CO₂ Gas Sensor: A DFT Study

K. Azizi*, R. Omidirad

^aDepartment of Science, University of Kurdistan, Sanandaj, Iran
reyhan.omidirad@gmail.com

Abstract: The adsorption of CO₂ on both cases of the Al-doped boron nitride nanosheets, B atom replaced by Al (Al_B) and N atom replaced by Al (Al_N), was studied at the DFT-M062-X/6-311g (d,p) level. The results indicate that CO₂ prefers to adsorb via O head on both Al_B-BNNS and Al_N-BNNS systems through physisorption process. Moreover, for both Al_B and Al_N cases the direction of charge transfer is from CO₂ to the Al-doped nanosheets and upon the CO₂ adsorption the energy gap of adsorbents decreases remarkably.

Keywords: Al-doped BNNS; adsorption; CO₂; DFT;

Introduction

CO₂ is a colourless, odourless and it exists in the Earth's atmosphere as a trace gas. Also CO₂ is the major contributor for global warming. Climate change due to greenhouse emissions has become a significant global challenge and methods to efficiently and effectively separate, capture, store and convert greenhouse gases, especially CO₂ have attracted increasing attention. [1]

Therefore, designing promising sorbents for removal or detection of low concentration levels of this gas is of great importance. Among category of materials that presents a great potential for gas adsorption are the nanostructured systems. Because of great features such as excellent sensing capabilities, high specific surface area, fast response, high mechanical strength, uniform porosity, and low operating temperature have attracted certain attention. In recent years, boron nitride nanostructures, such as boron nitride nanosheets, have attracted increasing attention due to their unique properties. [2-6]

Despite satisfying some of the most desirable properties, these nanostructures are not good at absorbing in a pure state than some gases. A variety of approaches have been selected to improve the gas absorption of nanomaterials, including the application of electric field, wall defects, chemical functionalization, or doping with particular atoms. [7]

Doping the heteroatom on the structural and electron properties of boron nitride nanostructures has a significant effect on the storage potential of gases in them. In this regard, extensive empirical and theoretical studies have been carried out. For example Ping Shao and colleagues [8] showed with DFT that BNNT is not a good adsorbent for the CO₂ molecule, and the doping of metal

elements such as Al can affect the electronic and structural properties of BNNT and can significantly improve CO₂ absorption.

In this paper, the structural properties, electron properties and the applicability of Al-BNNS for absorption of CO₂ molecule were studied by DFT method.

COMPUTATIONAL METHODS

For all studied systems, geometry optimizations were done at the M062-X functional and 6-311Gdp basis set using the Gaussian 03 software. Also, GaussSum 2.2 program was used to obtain the molecular orbital energies (HOMO and LUMO) and evaluating the density of states (DOS) results. After full optimization of the considered structures, we evaluated the adsorption energy of adsorbate molecule according to the following equation:

$$E_{ads} = E(\text{CO}_2\text{-Al}_x\text{-BNNS}) - (E(\text{Al}_x\text{-BNNS}) + E(\text{CO}_2))$$

(x=B or N)

Where $E(\text{CO}_2\text{-Al}_x\text{-BNNS})$ is the total energy of the complex that is formed when one molecule of CO₂ is adsorbed on the surface of considered Al_x-BNNS and also $E(\text{Al}_x\text{-BNNS})$ and $E(\text{CO}_2)$ are the total energies of Al_x-BNNS and CO₂ molecules, respectively.

RESULTS AND DISCUSSION

Initially, the geometric structure of the nano adsorbent boron nitride (consists of 39 B atoms and 39 N atoms) doped with Al atom without the presence of a gas molecule and then in the presence of the CO₂ gas molecule was optimized, the results are shown in Fig1.

As shown in the picture, due to the larger Al radius than N and the weaker Al-B bonds than Al-N, the amount of expulsion of doped atoms in Al_N form is larger than Al_B. In fact, in the form of the Al_B N atoms, transmit a significant electron density from the Al atom to their side and distributes the electron cloud throughout the nanostructure, which reduces the angular pressure in the nanostructure and reduces the amount of protrusion of the doped atom.

Al_B form has a HOMO negative surface and LUMO is more positive than Al_N, and the energy gap of the Al_N form is approximately half that of Al_B. From the results of table (1) it can be seen that the doping of the Al atom, instead of N, can turn the BNNS from the non-conductive state into a semiconductor due to a reduction in the energy gap which the DOS graphs confirm this. (Fig 2)

If, by the DOS charts, we compare the energy gap between the capacity layer and the conductivity layer in the doped system to pure state, the energy gap in the Al_N-BNNS system is reduced to that of the pure state, And as a result, electrical conduction raised, this could be due to an increase in the electron distribution in the nanostructure capacity band and to reduce its distance from the conduction band. But in the Al_B-BNNS system, the gap is approximately equal to the initial energy gap. According to the reported data, the greatest changes in the energy gap for the Al_N form of the nanosheet is ۰.۵۷eV, because a significant change in the energy gap this from of nanostructure can be as an appropriate sensor for the CO₂ molecule.

E_{ads} values indicate that the absorption of CO₂ molecule on the surface of the Al doped boron nitride nanosheets is physical type.

Comparison of E_{ads} values for the absorption of CO₂ molecules in both Al_B and Al_N forms shows that E_{ads} for the Al_N state is more negative than Al_B, indicating that electrostatic forces are not the main factor in the interaction of CO₂ with nanoparticles.

The results show that in all cases the transfer of charge from the CO₂ molecule to the boron nitride nanostructure is carried out.

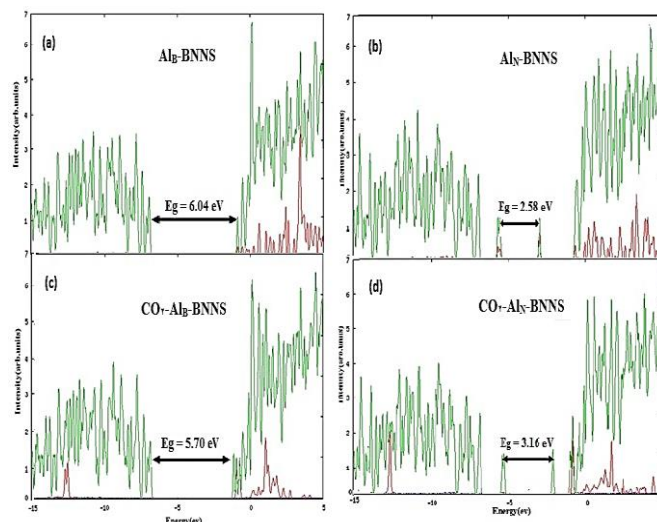
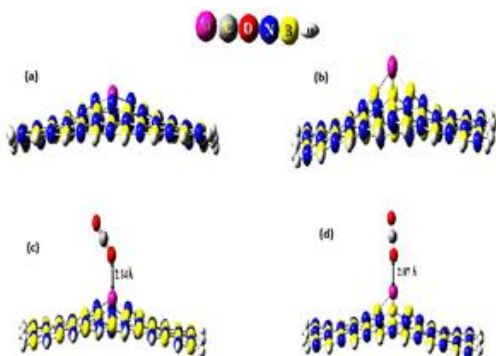


Fig. 1: Optimized structure of (a) Al_B-BNNS, (b) Al_N-BNNS, (c) CO₂-Al_B-BNNS, (d) CO₂-Al_N-BNNS.

Fig. 2: Density of state plot of (a) Al_B-BNNS, (b) Al_N-BNNS, (c) CO₂-Al_B-BNNS, (d) CO₂-Al_N-BNNS.

Table 1: Calculated parameters for adsorption of CO₂ on the Al_x-BNNS.

system	R _{min} (Å)	E _{ads} (kcal/mol)	E _{gap} (eV)	ΔE _{gap} (eV)	CT (e)
CO ₂ -Al _B -BNNS	۲/۱۴	-۱۹/۳۲	۵/۷۰	-۰/۳۳	۰/۱۰
CO ₂ -Al _N -BNNS	۲/۰۷	-۲۱/۴۷	۳/۱۶	۰/۵۸	۰/۱۲

Conclusions

In summary, by means of spin-polarized DFT computations, we exploited the potential of utilizing Al-doped BNNS as the CO₂ gas sensor. Our computations showed that CO₂ adsorption on the Al-doped BN sheet is dependent on the doping site: the Al_N sheet adsorbs the CO₂ molecule more strongly to prepare its application as gas sensor, while the Al_B sheet adsorbs the CO₂ molecule moderately.

References

- [1] L. Li, Y. Liu, X. Yang, X. Yu, Y. Fang, Q. Li, P. Jin, and C. Tang, "Ambient Carbon Dioxide Capture Using Boron-Rich Porous Boron Nitride: A Theoretical Study", *Applied Materials & Interfaces*, 9 (2017) 15399–15407.
- [2] J. Zhao and Z. Chen "Carbon-Doped Boron Nitride Nanosheet: An Efficient Metal-Free Electrocatalyst for the Oxygen Reduction Reaction", *Physical Chemistry C*, 119 (2015) 26348–26354.
- [3] L.H. Li, E. J. G. Santos, T. Xing, E. Cappelluti, R. Roldan, Y. Chen, K. Watanabe, and T. Taniguchi,

“Dielectric Screening in Atomically Thin Boron Nitride Nanosheets”, *Nano Letters*, 15 (2015) 218–223.

[4] Y. Wang, L. Wang, and C. Yan, “Field Emission Properties of Carbon Nanotubes with Boron Doping and H₂O Adsorption”, *Nanomaterials*, (2013) 1-6.

[5] J. Beheshtian, A. Ahmadi Peyghan, Z. Bagheri, “Ab initio study of NH₃ and H₂O adsorption on pristine and Na-doped MgO nanotubes”, *Structural Chemistry*, 24 (2013) 165–170.

[6] M.Y. DUAN, G. S. SHI, C. L. WANG, L. P. ZHOU, X. R. CHEN, and H.P. FANG, “A Theoretical Study of a Single-Walled ZnO Nanotube as a Sensor for H₂O Molecules”, *Communications in Theoretical Physics*, 58 (2012) 275–279.

[7] C. Zhi, Y. Bando, C. Tang, D. Golberg, “Boron nitride nanotubes”, *Materials Science and Engineering*, 70 (2010) 92-111.

[8] P. Shao, X.Y. Kuang, L.P. Ding, J. Yang, and M.M. Zhong, “Can CO₂ molecule adsorb effectively on Al-doped boron nitride singlewalled nanotube? ”, *Applied Surface Science*, 285 (2013) 350-356.

The influence of non-covalent interaction of PHCl_2 on the activation energy of Aza-Diels-Alder Reaction

Fereshteh Yaghoobi*

Faculty of Science, University of Nahavand, Nahavand, Iran

*yaghoobifereshteh@gmail.com

Abstract: Using DFT calculations, the combination of $\text{X}_2\text{C}=\text{NNH}_2$ ($\text{X} = \text{F}, \text{Cl}, \text{Br}$) and 1,3-butadiene to form a six-membered was investigated. At first, the effect of various substituents of $\text{X}_2\text{C}=\text{NNH}_2$ ($\text{X} = \text{F}, \text{Cl}, \text{Br}$) and then the effect of non-covalent interaction of PHCl_2 with $\text{X}_2\text{C}=\text{NNH}_2$ on the activation barriers of these reactions were studied. It was shown that $\text{X}=\text{F}$ decreases the activation barriers of these reactions more than other substituents ($\text{X} = \text{Cl}$ or Br). Also, the energy barriers for these reactions are substantially lowered by non-covalent interaction PHCl_2 with $\text{X}_2\text{C}=\text{NNH}_2$. The PHCl_2 retards the formation of the incipient N-C bond from imine to diene while simultaneously accelerating the C-C bond formation.

Keywords: “Aza-Diels-Alder” “density functional theory (DFT)” “activation energy” “non-covalent interaction”

Introduction

The Diels–Alder reaction (DA), including a large variety of dienes and dienophiles, is one of the most useful reactions in modern organic chemistry that widely used to form six-membered rings structures since it was discovered in 1928[1]. Since the remarkable acceleration of DA reaction catalyzed by AlCl_3 was first reported by Yates and Eaton [2], LA catalysis in DA reactions has achieved much attention due to its striking rate acceleration and high regio- and stereospecificities in comparison with the uncatalyzed process [3].

The Aza-Diels–Alder reactions make a powerful route for constructing nitrogen including six-membered heterocycles from readily available imines, coupled with diene components [4]. Just as in the standard Diels-Alder reactions, chiral Lewis acids play an important catalytic role in the Aza-Diels–Alder reactions [5]. Although Lewis acids have played the most important roles in these reactions, it is believed that most Lewis acids would be trapped by basic nitrogen atoms of the starting materials and/or final heterocyclic products in these reactions [6].

Also, organic molecules that have the potential to form non-covalent interaction with and substrate as Lewis acids play an important catalytic role in Aza-Diels-Alder reactions. Those Organic molecules that interact with substrate through a hydrogen bond (HB) or halogen bonds (XB) have been especially widely developed and used [7].

Herein we attempt to demonstrate detailed information about the effect of various substituents of $\text{X}_2\text{C}=\text{NNH}_2$ ($\text{X} = \text{F}, \text{Cl}, \text{Br}$) and also the effects of non-covalent interaction of PHCl_2 on Aza-Diels-Alder reaction studied here that is involving $\text{X}_2\text{C}=\text{NNH}_2$ ($\text{X} = \text{F}, \text{Cl}, \text{Br}$) and 1,3-butadiene. Therefore, effect of the absence and presence of the PHCl_2 in the reaction was studied.

The computational chemistry is applied in order to take advantage of their ability to elucidate fine details of the structure and energy of transient species such as the transition state in these reactions. In recent years, the

M06-2X method becomes more and more widely accepted for the cycloaddition [8]. The M06-2X method was employed at the TZVPP basis set level in the current work.

Computational method

Density functional theory (DFT) calculation were carried out with the Gaussian 09 suite of programs [9]. The structure of the reactants, transition states and the products were optimized using M06-2X/TZVPP level of theory. The nature of the minimums and transition states was confirmed by the absence and presence of the imaginary frequency, respectively. Intrinsic reaction coordinate (IRC) calculations were done to confirm the identity of the transition state structures.

Results and Discussion

The structures that were considered as the reactant and product are presented in Fig. 1. To investigate the influence of the PHCl_2 on the activation energies of DA reactions of $\text{X}_2\text{C}=\text{NNH}_2$ ($\text{X} = \text{F}, \text{Cl}, \text{Br}$) and 1,3-butadiene, these reactions was investigated (1) in the absence of PHCl_2 and (2) in the presence of PHCl_2 .

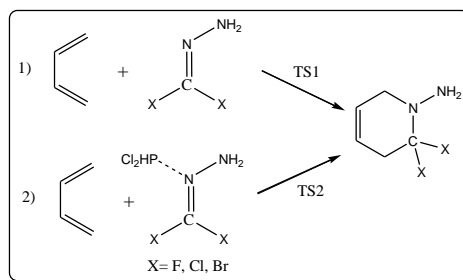


Fig.4: Investigated structures as reactant and product (1) in the absence of PHCl_2 and (2) in the presence of PHCl_2 .

At first, the DA reaction in the absence of PHCl_2 was investigated. The M06-2x/TZVPP geometries for all

transition states are given in Fig. 2.

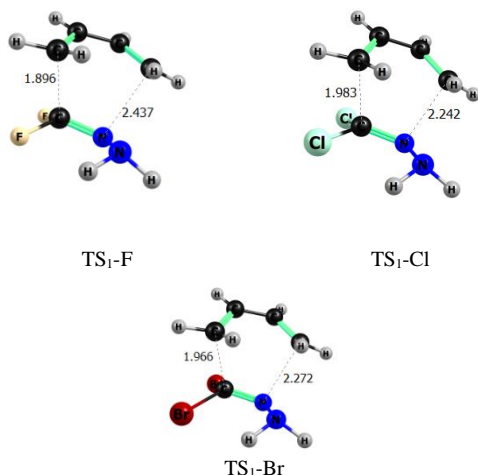


Fig.2: Optimized geometries of the transition states at M06-2x/TZVPP in the absence of PHCl_2 .

The values of the energies related to these structures are shown in Table 1.

Table. 1: ZPE energies (kcal/mol) of Aza-Diels-Alder reaction for various substitutions in the absence of PHCl_2

After binding of the PHCl_2 with $\text{X}_2\text{C}=\text{NNH}_2$, these pair

Substituent type	Reactants	TS	Product
F	-316457.57	-316432.31	-316498.60
Cl	-768702.06	-768670.70	-768734.53
Br	-3421805.15	-3421773.70	-3421838.11

then interact with the diene substrate. Therefore, the DA reaction in the presence of PHCl_2 was investigated. The M06-2x/TZVPP geometries of all transition state are given in Fig. 3.

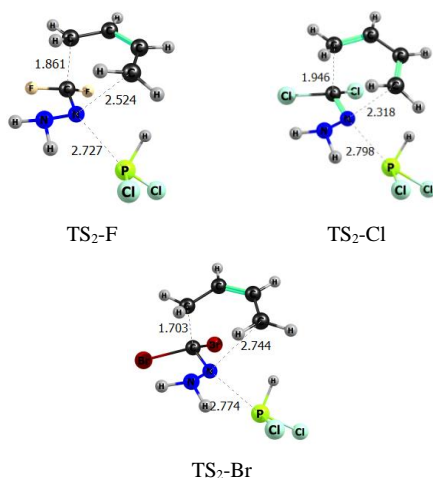


Fig.3: optimized geometries of the transition states at M06-2x/TZVPP in the presence of PHCl_2 .

The values of the energies related to the DA reaction in

the presence of PHCl_2 are shown in Table 2.

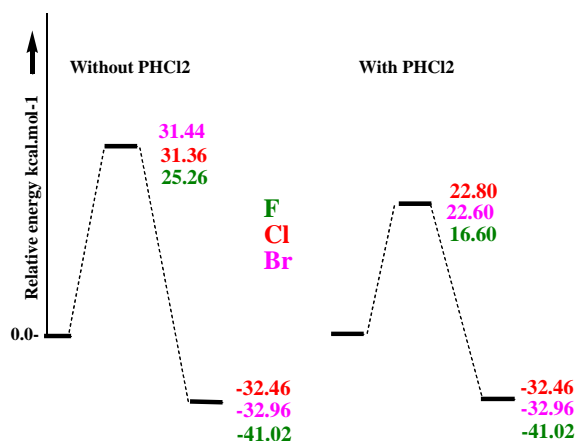
The comparison of the transition state structures in Figs. 1 and 2 shows that binding of the PHCl_2 to $\text{X}_2\text{C}=\text{NNH}_2$, leads to decrease of the newly forming C...C bond lengths

Substituent type	Reactants	TS	Product
F	-1108606.15	-1108589.55	-1108647.17
Cl	-1560850.64	-1560827.83	-1560883.11
Br	-4213953.72	-4213931.13	-4213986.68

in transition structures and to increase of the newly forming C...N bond lengths in transition structures.

The energy profiles related to the investigated reactions in the absence of PHCl_2 and in the presence of PHCl_2 are presented in Fig.4. according to the diagrams, the activation barrier with F, Cl and Br substituents in the absence of PHCl_2 are 25.26, 31.36 and 31.44 kcal/mol⁻¹ endothermic, respectively. It is clear that the Fluorine more than other substituent decreases activation barrier.

Fig.4: Energy diagram for the investigated reactions.



As it is shown in Fig. 4, the presence of PHCl_2 decreases the activation energy by 8.66, 8.84 and 8.56 kcal/mol for F, Br and Cl substituents, respectively. On the other hand, according to data in Figs. 3, and 4, increasing of non-covalent interaction between PHCl_2 with $\text{X}_2\text{C}=\text{NNH}_2$, will decrease the activation barriers of Aza-Diels-Alder reaction studied here.

Conclusions

Theoretical investigation on Aza-Diels-Alder reaction of $\text{X}_2\text{C}=\text{NNH}_2$ ($\text{X} = \text{F}, \text{Cl}, \text{Br}$) and 1,3-butadiene in the absence of PHCl_2 and in the presence of PHCl_2 revealed that the reaction with the fluorine substituent has the lowest activation barrier. The non-covalent interaction of PHCl_2 with $\text{X}_2\text{C}=\text{NNH}_2$ influences activation barriers of the Aza-Diels-Alder reaction studied here. In all cases, presence of PHCl_2 leads to decreasing the activation



energy.

References

- [1] O. Diels, K. Alder "Synthesen in der hydroaromatischen Reihe", *Justus Liebigs Ann. Chem.*, 460 (1928) 98–122.
- [2] P. Yates, P. Eaton "Acceleration of the Diels-Alder reaction by aluminium chloride" *Chem. Rev.*, 82 (1960) 4436- 4437
- [3] U. Pindur, G. Lutz, C. Otto "Acceleration and selectivity enhancement of Diels-Alder reactions by special and catalytic methods", *Chem. Rev.*, 93 (1993), 741- 761
- [4] P. Buonora, J. C. Olsen, T. Oh "Recent developments in imino Diels–Alder reactions", *Tetrahedron*, 57 (2001) 6099–6138.
- [5] X. Jiang, R. Wang "Recent Developments in Catalytic Asymmetric Inverse-Electron-Demand Diels–Alder Reaction" *Chem. Rev.*, 113 (2013) 5515- 5546.
- [6] S. Kobayashi, K. A. Jorgensen "Cycloaddition Reactions in Organic Synthesis", 2002, Wiley-VCH:Weinheim.
- [7] V de. P. Nziko. S. Scheiner "Catalysis of the Aza-Diels-Alder Reaction by Hydrogen and Halogen Bonds", *J. Org. Chem.*, 81(2016) 2589-2597.
- [8] B. J. Levandowski, K. N. Houk, A. G. Ross, S. J. Danishefsky, K. Houk, *Angew* "Theoretical analysis of reactivity Patterns in Diels–Alder Reaction of cyclopentadiene, cyclohexadiene, and cycloheptadiene with symmetrical and unsymmetrical dienophiles", *J. Org. Chem.*, 80 (2015) 3530-3537.
- [9] M. J. Frisch, G. W. Trucks, H. B. Schlegel, G. E. Scuseria, M. A. Robb, J.R. Cheeseman, G. Scalmani, V. Barone, B. Mennucci, G. A. Petersson, H. Nakatsuji, M. Caricato, X. Li, H. P. Hratchian, A. F. Izmaylov, J. Bloino, G. Zheng, J. L. Sonnenberg, M. Hada, M. Ehara, K. Toyota, R. Fukuda, J. Hasegawa, M. Ishida, T. Nakajima, Y. Honda, O. Kitao, H. Nakai, T. Vreven, J. J. A. Montgomery, J. E. Peralta, F. Ogliaro, M. Bearpark, J. J. Heyd, E. Brothers, K. N. Kudin, V. N. Staroverov, R. Kobayashi, J. Normand, K. Raghavachari, A. Rendell, J. C. Burant, S.S. Iyengar, J. Tomasi, M. Cossi, N. Rega, J. M. Millam, M. Klene, J. E. Knox, J. B. Cross, V. Bakken, C. Adamo, J. Jaramillo, R. Gomperts, R.E. Stratmann, O. Yazyev, A. J. Austin, R. Cammi, C. Pomelli, J. W. Ochterski, R. L. Martin, K. Morokuma, V. G. Zakrzewski, G. A. Voth, P. Salvador, J. J. Dannenberg, S. Dapprich, A. D. Daniels, O. Farkas, J. B. Foresman, J. V. Ortiz, J. Cioslowski, D. J. Fox, Revision A, 02 ed., Gaussian, Inc., Wallingford CT, (2009).

Computational investigation on the ground and low-lying electronic states of PH

R. Ahmadpour and Z. Biglari*

Chemistry Department, Faculty of Science, Lorestan University, Khorram Abad, Lorestan, Iran

*biglari.z@lu.ac.ir

Abstract: Ab initio potential energy curves and transition dipole moments have been calculated for the 16 low-lying electronic states including eight triplet states: $X^3\Sigma^-$, $2^3\Sigma^-$, $1^3\Pi$, $1^3\Delta$, $1^3\Sigma^+$, $2^3\Pi$, $3^3\Sigma^-$ and $3^3\Pi$; three quintet states: $1^5\Sigma^-$, $1^5\Pi$ and $2^5\Sigma^-$ and five singlet states: $1^1\Sigma^-$, $1^1\Pi$, $1^1\Delta$, $1^1\Sigma^+$ and $2^1\Pi$ of Phosphorus Hydride, PH, using the multi-reference configuration interaction method with large active space and basis sets. Potential energy and transition dipole moments have been computed from $1.0 a_0$ to $30.0 a_0$, and were used to calculate average lifetimes of excited state vibrational levels. The spectroscopic parameters of the bound states were determined.

Keywords: PH; ab initio; potential energy curves; MRCI; dipole moment.

Introduction

The low lying electronic states of simple hydride radicals often need to be considered in many different areas from astrophysics to plasma chemistry. Group V hydrides have an open shell configuration $\dots\sigma^2\pi^2$ that gives rise to a $X^3\Sigma^-$ ground state [1]. The $A^3\Pi-X^3\Sigma^-$ electronic spectrum of PH was first observed and assigned by Pearse [2] in 1930 from a continuous discharge through a mixture of hydrogen and phosphorus vapor. Since then the $A^3\Pi-X^3\Sigma^-$ transition of PH and PD has been analysed many times, most by Rostas et al. [3]. The PH molecule can be made by photochemical decomposition of PH_3 . Theoretical calculations are available for PH [4,5]. Finally, PH may occur in the sun and cool stellar atmospheres [6,7]. In this paper we present details of an extensive *ab initio* investigation in which all the adiabatic potential energies correlating to the first four dissociation asymptotes study to obtain transition dipole moment and radiation lifetimes. These potential energy curves have been calculated at both the CASSCF and the configuration interaction (MRCI) level with a large basis sets.

Materials and method

All calculations were carried out using the ORCA 2.9.0 quantum chemistry program. In this research was used the augmented correlation-consistent polarized valence quadruple zeta (aug-cc-pVQZ) basis sets of Woon and Dunning for P ($42s19p3d2f1g \rightarrow 6s5p3d2f1g$) and H ($7s4p3d2f \rightarrow 5s4p3d2f$) atoms. These calculations were performed at 80 different P–H distances. Ab initio points of the potential curves were imported in program LEVEL to calculate vibrational energy levels and equilibrium internuclear distances (r_e). Computed vibrational energies of the $v = 0$ to 3 levels were then fitted to Dunham energy expression, and the vibrational constants ω_e and $\omega_e x_e$ were obtained.

Results and Discussion

The calculated energy at $r = 30.0 a_0$ is taken as the separated-atom limit energy. For Phosphorus atom, the ground state is $^4S^o$ and the excited states are $^2D^o$, $^2P^o$ and 4P which lie 11361, 18723 and 55939 cm^{-1} higher than ground state, respectively. We considered the first four dissociation asymptotes and wavefunctions for the two electronic states arising from the interaction of P ($^4S^o$) + H (2S), i.e., $^3,5\Sigma^-$; and six electronic states arising from the interaction of P ($^2D^o$) + H (2S), i.e. $^1,3\Sigma^-$, $^1,3\Pi$ and $^1,3\Delta$; and four states arising from the interaction of P ($^2P^o$) + H (2S), i.e. $^1,3\Sigma^+$, $^1,3\Pi$ and four states arising from the interaction of P (4P) + H (2S), i.e. $^3,5\Sigma^-$, $^3,5\Pi$ were computed using state-averaged CASSCF (SA-CASSCF) and MRCISD methods. The *ab initio* potential energies at the MRCISD level for all states of PH were calculated and for triplet states are plotted in Fig.1. The $2^3\Sigma^-$, $1^3\Delta$, $1^3\Sigma^+$ and $3^3\Sigma^-$ states of PH are repulsive.

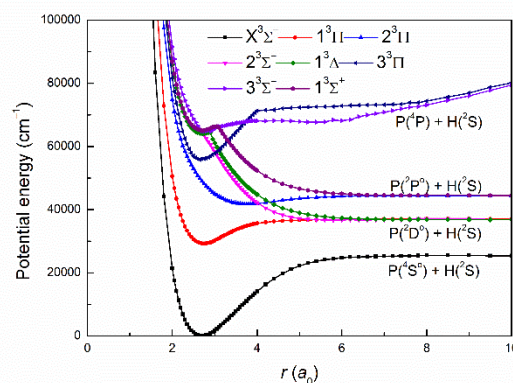


Fig.5: MRCI potential energy curves of ground and excited triplet states of PH.

The calculated dipole moments for all triplet states are plotted in Fig. 2 for $r = 1.0 a_0$ to $10.0 a_0$. Ab initio points of potential energy curves and dipole moments were imported in program LEVEL, in order to calculate

vibrational energy levels and equilibrium internuclear distances (r_e). The energies of all bound vibrational levels are computed for the low-lying electronic states of PH using the LEVEL program is presented in Table 1. The obtained calculations suggest that the $v = 16$ level is the highest bound vibrational level of the $X^3\Sigma^-$ state for PH and the $v = 6$ is the highest bound vibrational for $1^3\Pi$ and $2^3\Pi$.

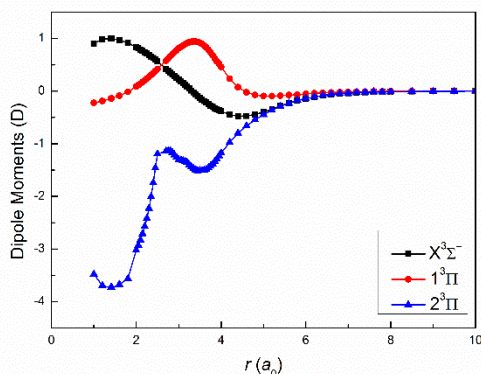


Fig.2: Dipole moment for the triplet states of PH.

Table 1: Vibrational energy levels in the triplet states of PH.

v	$X^3\Sigma^-$	$1^3\Pi$	$2^3\Pi$
0	1205.4	30302.8	42192.3
1	3508.7	32246.3	43018.1
2	5714.7	33905.1	43670.7
3	7811.9	35273.4	44136.4
4	9830.0	36243.1	44403.2
5	11745.7	36761.2	44484.0
6	13576.8	36993.8	44536.9
7	15313.0		
8	16947.0		
9	18478.3		
10	19899.9		
11	21199.8		
12	22368.4		
13	23387.8		
14	24231.1		
15	24864.1		
16	25264.1		

The computed vibrational energies of the $v = 0 - 3$ levels were fitted to Dunham energy expression, and the harmonic vibrational frequencies ω_e and anharmonicity constants $\omega_e x_e$ were calculated. The equilibrium rotational constants (B_e) were calculated from r_e values, and the vibration-rotation interaction constants (α_e) were obtained from LEVEL outputs and were presented in Table 2.

Table 2: Spectroscopic constants (in cm^{-1}) triplet states of PH.

Constant	$X^3\Sigma^-$	$1^3\Pi$	$2^3\Pi$
T_e	0.0	29241	41735
D_e	25524	7826	2729
r_e (\AA)	1.432	1.444	1.992
B_e	8.422	8.283	4.352
α_e	0.195	0.403	0.312

ω_e	2408.3	2223.1	1008.1
$\omega_e x_e$	51.53	143.88	90.03

Matrix elements of the dipole moment operator between all triplet states were computed at the MRCISD level using the ORCA program. The Einstein A coefficients for all vibronic transitions were calculated using the following equation;

$$A_{v' \rightarrow v''} = \frac{16\pi^3 \nu^3}{3h\epsilon_0 c^3} |\langle \psi_{v'} | R_e(r) | \psi_{v''} \rangle|^2 \quad (1)$$

where $R_e(r)$ is the electronic transition dipole moment and ν is the transition frequency. To obtain an average lifetime for a vibrational level of an excited electronic state should calculate the sum of Einstein A coefficients for transitions to all lower state vibrational levels:

$$\tau_{v'} = \left(\sum_{v''} A_{v' \rightarrow v''} \right)^{-1} \quad (2)$$

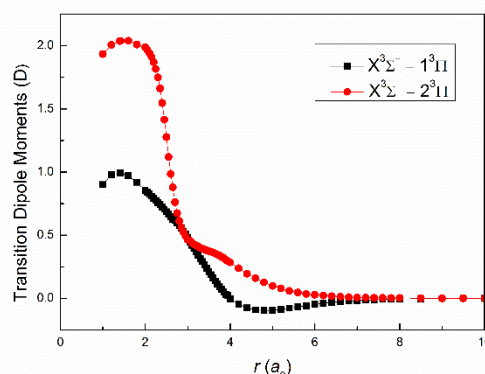


Fig.3: Transition dipole moment for triplet states of PH.

The Einstein A coefficients and lifetimes are calculated for the vibrational levels of the $1^3\Pi$, and $2^3\Pi$ states for PH. We computed a lifetime of 398 ns for the $v' = 0$ level of the $1^3\Pi$ state and for the $v' = 0$ level of the $2^3\Pi$, radiation lifetime was determined 1054 ns.

Conclusions

Ab initio potential energy curves and transition dipole moments have been calculated for the $X^3\Sigma^-$, $1^5\Sigma^-$, $1^1\Sigma^-$, $1^1\Pi$, $1^1\Delta$, $1^3\Pi$, $2^3\Sigma^-$, $1^3\Delta$, $2^3\Pi$, $1^3\Sigma^+$, $2^1\Pi$, $1^1\Sigma^+$, $3^3\Sigma^-$, $2^5\Sigma^-$, $3^3\Pi$ and $1^5\Pi$ states of PH at the MRCI level of theory with large active space and basis sets using the ORCA program. The computed transition dipole moments were used to calculate average lifetimes of excited state vibrational levels for PH. These highly accurate transition dipole moments can be used to calculate the Einstein A coefficients for all rovibronic transitions of PH.

References

[1] R.N. Dixon and H.M. Lambertson, The $A^3\Pi-X^3\Sigma^-$ band systems of AsH and AsD, J. Mol. Spectrosc., 25 (1968) 12-33.

- [2] R.W.B. Pearse, The ultra-violet spectrum of Magnesium Hydride. 1. The band at λ 2430, Proc. R. Soc. London Ser. A, 129 (1930) 328-354.
- [3] J. Rostas, D. Cossart, and J. R. Bastien, Rotational Analysis of the PH and PD $A^3\Pi_i-X^3\Sigma^-$ Band Systems, Canad. J. Phys. 52 (1974) 1274-1287.
- [4] R. S. Ram and P. F. Bernath, Infrared Fourier Transform Spectroscopy of PH, J. Mol. Spectrosc., 122 (1987) 275-281.
- [5] J. A. J. Fitzpatrick, Oleg V. Chekhlov, D. R. Morgan, R.W. Burrows and C.M. Western, Predissociation dynamics in the $A^3\Pi$ state of PH: An experimental and ab initio investigation, Phys. Chem. Chem. Phys., 4 (2002), 1114-1122.
- [6] E.M. De Gouveia and P.D. Singh, The 3410 Å band of the PH molecule in the solar photospheric spectrum, Sol. Phys., 90 (1984) 259-268.
- [7] H.R. Johnson and A.J. Sauval, Molecules in red-giant stars. I - Column densities in models for K and M stars, Astron. Astrophys. Suppl. Ser., s49 (1982) 77-87.

Van der Waals interaction of nitrobenzene with Pd (111)

Zahra Tavangar, Zahra haji Ahmadi*

Faculty of chemistry Kashan University, Kashan, Iran

*zhahmadi@gradkashanu.ac.ir

Abstract: Understanding the interaction of organic molecule on metal surfaces is important for a wide range of technological applications. In this study, the adsorption of nitrobenzene (NB) on Pd (111) surface in different positions is investigated. The most favorable adsorption site energetically was calculated with different corrected vdw-DF functional. To further explain this adsorption, the partial density of states (PDOS) and lowdin charges before and after adsorption are compared.

Keywords: adsorption, surface, nitrobenzene, van der Waals interaction

Introduction

The interaction of organic molecules on metal surfaces has been a topic of interest to study both experimentally [1] and theoretically [2]. This wide study is due to the variety of applications of organic/metal interaction, such as in modern electronic and optical devices [3] (like organic gas sensors, organic light emitting diodes, organic field effect transistors, solar cells, ultrafast optical switches), nanolithography devices, and also organic molecule containing hetero atoms utilized as corrosion inhibitors [4]. Another vital application is in heterogeneous catalytic reactions. Catalytic reaction of aromatic compounds is a key reaction in many petrochemical processes [5]. We chose to study the adsorption of nitrobenzene as aromatic molecule on metal because of its industrial applications. Aniline is one of the most important chemical materials applied in rubber, dyes and pigments, agrochemicals and pharmaceutical industry that is produce by hydrogenation of nitrobenzene (NB) in heterogeneous catalytic reactions. Several support materials have been used for hydrogenation of NB to aniline. Group 10 and face centered cubic crystal structure metals have great results in hydrogenation aromatic rings [6]. So palladium (Pd) which has experimental usage was chosen for this reaction [7]. To calculate adsorption energy in different reactions, the DFT level of theory was widely applied within Generalized Gradient Approximation (GGA) functional in the form of Perdew-Burker-Ernzerhof (PBE) [8], but usually doesn't gain great results in energy and position of

adsorption [9]. Since there are weak overlaps between organic molecule and metal orbitals, this interaction is physisorption with just van der Waals (vdw) forces. So in the last decade vdw forces in DFT method were considered. Different dispersion corrected DFT like vdw-DF (2004), vdw-DF2 [10], C09 (2010), vdw-DFcx (2014) and more consistent functionals (vdW-DF-obk8, vdW-DF-ob86, vdw-DF2-c09, vdw-DF2-b86r) are published till now. Based on the importance of producing aniline this article is devoted to study the interaction of NB with Pd (111) that can help with preliminary studies of catalytic hydrogenation of NB in industry. Also, studying electronic calculation, charge density and densities of states can help simulate this complex as an organic/metal electronic device.

Computational details

The quantum espresso package (version 6.0) [11] was used to perform plane wave DFT calculations. The ultrasoft pseudopotentials were utilized to describe the core electron interactions. The plane wave basis set with an energy cutoff of about 400 eV. The lattice constant of palladium fcc bulk was obtained to be 3.908 Å with 15×15×15 kpoint mesh. The metal slab was modeled with 3×3 unit cell with four atomic layers and 3×3×1 Monkhorst-Pack k-point sampling for brillouin zone. In all calculations the two bottom layers were frozen in bulk positions. The vacuum space between the slabs was set to at least 15 Å to

ensure the slab interaction was omitted. For accurate total energies, we used the Methfessel-Paxton method with smearing parameter of 0.02. Six different configurations for adsorption of NB on Pd (111) were performed using the PBE. The position with the lowest adsorption energy was considered in nonlocal interactions through the self-consistent (SCF) van der Waals density functional theory. Eventually the most appropriate configuration in view of adsorption energy was analyzed in electronic structure at the metal/molecule interface by evaluating the density of states and charge density difference.

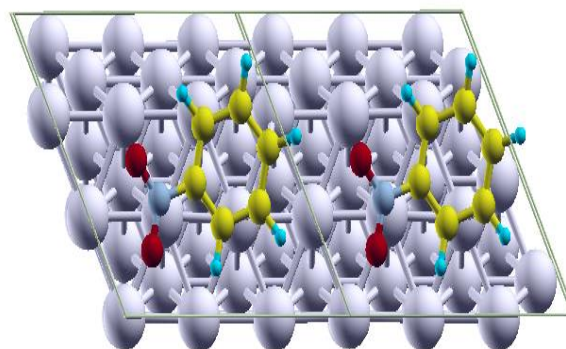


Fig 1 Pd(111)/NB (Pd-top-N)

Results and discussion

At first we optimized Pd (111) surface and NB separately with PBE functional. Two possible adsorption models of NB parallel and vertical were considered. Adsorption energies for different configurations are shown in table 1. In vertical configuration 3 initial sites were investigated. The NB is located perpendicular to the surface, Pd-top-N, Pd-top-O, and Pd-bridge-C. After optimization of vertical sites, the distance between the two top layers and between the two Pd atoms in surface increased about 0.03 Å and 0.01 Å, respectively. The angle between NB molecule and Pd surface changed about 7 degree. In parallel position hydrogens and NO₂ exited from the plane that benzene ring is located. In this case the distance of two top layers of Pd decreased. We try to investigate more different initial positions with SCF calculation to find the most stable adsorption. The results confirm that the parallel Pd-top-N (Fig1) is the most stable adsorption. For this configuration we calculated adsorption energy by different corrected vdw-DF functionals as shown in table 1. We found vdw-DF2-C09 functional to have the most negative adsorption energy (-3.0615 ev). Considering the vdw interaction modification indicated an interaction which was thought to be a weak physisorption bonding is in fact a strong chemisorption.

Table 1 adsorption energies of different positions and functionals

	initial adsorption position	E _{ads} (eV) PBE	parallel Pd- top- N	
			functional	E _{ads} (eV)
vertical			vdw-DF	-0.6661
	Pd-top-O	-0.2358	vdw-DF-C09	-2.4603
	Pd-top-N	-0.1562	vdw-DF-ob86	-1.9676
	Pd-top-C	-0.1016	vdw-DF-obk8	-1.4892
parallel	Pd-top-N	-0.6369	vdw-DF-cx	-2.1611
	Pd-bridge-C	-0.0457	vdw-DF2	-0.0044
	Pd-fcc-C	-0.0037	vdw-DF2-C09	-3.0615
			vdw-DF2-b86r	-1.7163

In order to identify the adsorption of NB molecule on Pd (111) surface, the partial density of states (PDOS)

for (p) orbital (Fig2) of nitrogen and (d) orbitals of the Pd atom that are located under nitrogen are compared before and after adsorption. They are close to each other in HOMO place. Decrease in the peaks of LUMO indicates that there is an interaction between p orbitals of NB and d orbitals of surface. Lowdin charges of each atom displayed that after adsorption the charge of all atoms except nitrogen decreased.

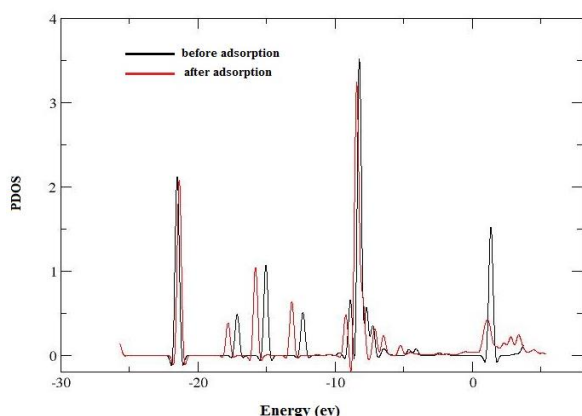


Fig 2 PDOS for p orbitals of nitrogen before and after adsorption

Conclusion

We have studied the adsorption and electronic properties of NB on Pd (111) surface by employing PBE and vdW-DF approaches. The strongest adsorption belongs to parallel Pd-top-N site. VdW-DF2-C09 functional considerably changes results significantly compared to different vdW-DFs functionals that was investigated here. The PDOS plot and lowdin charges before and after adsorption, confirm this rather strong interaction.

References

- [1] M. Pope and C. E. Swenberg, *Electronic Processes in Organic Crystals and Polymers* (Oxford University Press, New York, USA, 1999)
- [2] Priya Sony, Peter Puschnig, Dmitrii Nabok, and Claudia Ambrosch-Draxl. Importance of Van DerWaals Interaction for Organic Molecule-Metal Junctions: Adsorption of Thiophene on Cu(110) as a Prototype. *PRL* 99, 176401 (2007)
- [3] L.S. Hunga, C.H. ChenRecent. progress of molecular organic electroluminescent materials and devices. *Materials Science and Engineering R* 39 (2002) 143–222

[4] Mehdi Mousavi, Hossein Safarizadeh, Azita Khosravan. A new cluster model based descriptor for structure-inhibition relationships: A study of the effects of benzimidazole, aniline and their derivatives on iron corrosion. *Corrosion Science* 65 (2012) 249–258

[5] Somorjai GA chemistry in two dimensions: surfaces. Cornell university press, Ithaca, NY (1981)

[6] Mark Saeys, Marie-Françoise Reyniers, and Guy B. Marin. Density Functional Study of Benzene Adsorption on Pt(111). *J. Phys. Chem. B* 2002, 106, 7489-7498

[7] Jae Seung Oh, Sang Moo Lee, Jong Kee Yeo, Chul Woo Lee, Jae Sung Lee. Palladium-catalyzed synthesis of N,N'-diphenylurea from nitrobenzene, aniline, and carbon monoxide. *Ind. Eng. Chem. Res.*, 1991, 30 (7), pp 1456–1461

[8] Perdew, J. P.; Burke, K.; Ernzerhof, M. *Phys. Rev. Lett.* 1996, 77, 3865–3868.

9- Erik R. McNellis, Jörg Meyer, and Karsten Reuter . Azobenzene at coinage metal surfaces: Role of dispersive van der Waals interactions. *PHYSICAL REVIEW B* 80, 205414 (2009)

10- K. Lee, E.D. Murray, L. Kong, B.I. Lundqvist, D.C. Langreth, *Phys. Rev. B* 82 (2010)081101

[11] P. Giannozzi, et al *J.Phys.:Condens.Matter*, 21, 395502(2009)

DFT study of Molecular structure, and optical properties of charge transfer complexes derived from Tetrathiafulvalene and Tetracyanoquinodimethane derivatives

Vahideh Hadigheh-Rezvan*

Chemistry Department, Islamic Azad University, Ardabil Branch, Ardabil, Iran

*v_h_rezvan@yahoo.com

Abstract:

During the past decades organic nonlinear optical (NLO) materials have been attracted much attention because NLO materials have potential applications in the field of optoelectronic [1]. Experimental measurements and theoretical calculations on molecular hyperpolarizability become one of the key factors in the NLO materials design. Theoretical determination of hyperpolarizability is quite useful both in understanding the relationship between the molecular structure and nonlinear optical properties. Several organic derivatives are designed with large first hyperpolarizability (β). Among the interesting type of organic materials, charge transfer complexes (CTC) have recently been identified as promising NLO materials. The present study is dedicated to perform a theoretical investigation using B3LYP/6-311G++ (d, p) level of theory, about the linear and nonlinear optical properties, represented as dipole moment (μ), α , and β of CTCs of, tetracyanoquinodimethane derivatives (TCNQ, **1**) and tetrathiafulvalene (TTF, **2**). Our aim is designing new NLO materials that can be synthesized in future.

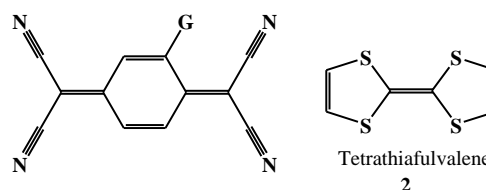
Keywords: tetrathiafulvalene (TTF), tetracyanoquinodimethane (TCNQ), polarizability, hyperpolarizability, charge transfer complex, and DFT

Introduction

In recent years, great efforts had been made to develop new organic, inorganic, and semiorganic nonlinear optical materials due to their widespread applications in technologies like lasers, optoelectronics, frequency conversion, high-speed information processing, optical advantage of both inorganic (high thermal and mechanical stability) and organic (broad optical frequency range and second harmonic conversion efficiency) materials. The development of materials with non-linear optical properties is an active topic of research with industrial applications for optical devices [1–4].

So far several kinds of organic compounds have designed with large first hyperpolarizability. Among these compounds, charge transfer complexes have recently been identified as promising NLO materials due to long range conjugation and mesomeric effect in the molecules. The term of charge transfer complex was introduced firstly by Mulliken [5-6], and discussed widely by Foster [7].

In this work our designed CTCs were obtained from imaginary following reaction (Scheme 1). Then molecular geometry, and optical property of these CTCs theoretically were studied.



1a	G=H	1f	G=Et
1b	G=F	1g	G= <i>iso</i> -Pr
1c	G=Cl	1h	G=OHCH ₂ CH ₂ O
1d	G=Br	1i	G=NO ₂
1e	G=CH ₃	1j	G=CN

Quantum chemical calculations were performed on ten molecules at DFT/ B3LYP level of theory, employing the split valence basis set 6-311G (d, p). Calculated optimized molecular structure, dipole moment, polarizability, and first hyperpolarizability for all of molecules were dedicated.

Computational details

At first all the molecules were obtained by Gussview05 program. Then the dipole moment (μ value), polarizability (α value), and the first static hyperpolarizability (β value) of all aimed molecules, were calculated by Gaussian09 program based on the finite field approach. All the ground state geometries of the molecules are optimized without imposing any symmetry constraint. The stationary points of all structures were found and potential energy hyper surfaces were characterized using freq keyword and standard analytical harmonic vibrational analysis. The absence of the imaginary (negative) frequencies, as well as of negative eigenvalues of the second-derivative matrix, confirms that

all molecules correspond to local true minima of the potential energy.

Density functional theory has been employed using Becker's three parameter hybrid exchange functional with Lee-Yang-Parr correlation functional and 6-311G++ (d, p) basis sets to optimization and calculating the optical properties of all molecules by polar keyword after optimization, in alternative step as separately.

Results

1-Polarizability

The polarizability and hyperpolarizability are the tendency for a molecule to form an induced dipole in an applied electric field. This parameter evaluates the linear optical property of a system. They determine not only the strength molecular interactions (long-range intermolecular induction, dispersion forces, etc.) as well as the cross sections of different scattering and collision processes, but also the nonlinear optical properties of the system.

Polarizability was calculated at B3LYP/ 6-311++G (d, p) level of theory using the standard Gaussian09w keyword 'Polar'. This keyword means that the polarizabilities were obtained analytically rather than by numerical differentiation. The polarizability is presented in the output from Gaussian09w in the standard orientation in lower triangular order: α_{xx} , α_{xy} , α_{yy} , α_{xz} , α_{yz} , α_{zz} . The average polarizability (α_{ave}), using xx, yy, and zz components are defined as the equation given below:

$$\alpha_{ave} = (\alpha_{xx} + \alpha_{yy} + \alpha_{zz}) / 3 \quad (1)$$

Since the values of polarizability tensors on the output file of Gaussian09w are reported in atomic units (a.u.), the calculated values (α_{ave}) were converted into electrostatic units. (1 a.u. equals with 0.1482×10^{-24} esu). The results for studied molecules are mentioned in the Table.

Polarizability values show linear optical property for these CTSs are more because of long conjugated system in these compounds.

2. Hyperpolarizability

To investigate the nonlinear optical properties of the molecules is very important because of the key functions of frequency shifting, optical modulation, optical switching, optical logic and optical memory for the emerging technologies in areas such as in telecommunications, signal processing and optical interconnections.

The first hyperpolarizability is a third-rank tensor that can be described by a $3 \times 3 \times 3$ matrix. The 27 components of the 3D matrix can be reduced to 10 components due to the Kleinman symmetry. It can be given in the lower tetrahedral format. The complete equation for calculating the magnitude of the total first static hyperpolarizability is given by the following equation:

$$\beta_{total} = [(\beta_{xxx} + (\beta_{zzz} + \beta_{zyy} + \beta_{zxx})^2 (\beta_{yyy} + \beta_{yzz} + \beta_{xzz})^2)]^{1/2} \beta_{xyy} \beta_{yxx}^2$$

As hyperpolarizability is difficult to measure directly, computational calculation is an alternate choice. The first-order hyperpolarizability of these novel molecular systems were calculated using B3LYP level of theory with the standard 6-311++G (d, p) basis set, based on the finite field approach. Since calculated values of β are in atomic units (a.u), these values have been converted into electrostatic units (esu) ($1 \text{ a.u.} = 8.6393 \times 10^{-33} \text{ esu}$). The results of hyperpolarizability for molecules are mentioned in the below Table. β_{tot} values of all these molecules are at least 7 times more than that of urea (0.77×10^{-30}) at the same level of theory B3LYP/6-311++G(d, p) (Urea is one of the prototypical molecules used for the NLO properties of the molecular systems for comparative purposes).

1. Discussions and Conclusions

The molecular structures of 10 CTCs were studied using DFT/ B3LYP level of theory and 6-311++ G (d, p) basis sets. Linear and Non-linear optical properties were studied by calculating the dipole moment, the mean polarizability and the first hyperpolarizability using the same method. This research showed that the investigated compounds are good candidates as a nonlinear optical material. Especially have larger the first hyperpolarizability β values, which makes these compounds attractive objects for future studies of nonlinear optics.

Table Calculated polarizability, first hyperpolarizability (β) and using B3LYP level of theory and 6-311G++(d,p) basis sets for some

Complex	$\alpha_{ave} \times 10^{-24}$ (in esu)	β_{total} (in a.u.)
2+1a	58.72	11494.9
2+1b	58.93	9317.64
2+1c	59.87	7578.39
2+1d	60.67	7659.43
2+1e	59.33	12201.62
2+1f	60.54	6091.18
2+1g	63.34	14463.04
2+1h	35.55	335428.62
2+1i	60.54	4952.48
2+1j	60.99	5403.95

References:

- [1] J. Stamatoff, R. DeMartino, D. Haas, G. Khanarian, H.T. Man, R. Norwood, H.N. Yoon, *Angew. Makromol. Chem.* 183 (1990) 151.
- [2] T. Kaino, S. Tomaru, *Adv. Mater.* 5 (1993) 172.
- [3] T.J. Marks, M.A. Ratner, *Angew. Chem.* 107 (1995) 167.
- [4] C. Bosshard, *Adv. Mater.* 8 (1996) 385.
- [5] R.S. Mulliken, *J. Am. Chem. Soc.* 72 (1950) 4493.
- [6] R.S. Mulliken, W.B. Pearson, *Molecular Complexes*, Wiley Publishers, New York, 1969.

Simulation of Clonazepam and Diazepam in DPPC membrane: Investigation of the movement

Khaled Azizi ^{a,b,*} and Mokhtar Ganjali Koli ^{a,b}

^aDepartment of Chemistry, University of Kurdistan, Sanandaj, Iran

^bResearch center of Nanotechnology, University of Kurdistan, 66177-15175, Sanandaj, Iran

* k.azizi@uok.ac.ir

* azizkhalid822@yahoo.com

Abstract: Mobility of DPPC molecules in the presence of two kinds of benzodiazepines (BZDs) (Diazepam; Clonazepam) within model membranes was investigated by molecular dynamics simulation. Observations can be explained by more free space in the Clonazepam containing system that leads to more movement of DPPC molecules in this system. Mobility of Diazepam in DPPC membrane is more than Clonazepam. It seems the presences of bulky atoms like Oxygen and Nitrogen in the structure of Clonazepam caused less movement of this molecule. More ability of Clonazepam molecules in establishing the hydrogen bond is another reason for slower movement of this molecule in DPPC membrane.

Keywords: Benzodiazepines, Molecular dynamics simulation, Mean Square Displacement, Membrane

Introduction

Benzodiazepines (BZDs) are one of the most widely prescribed pharmacologic agents in the United States (more than 112 million prescriptions in 2007) [1]. BZDs are used for numerous indications, including anxiety, insomnia, muscle relaxation, relief from spasticity caused by central nervous system pathology, and epilepsy. BZDs are also used intraoperatively because of their amnesic and anxiolytic properties. However, these properties become undesired side effects in nearly all other clinical instances. The severity of BZD-induced adverse effects forces physicians to exercise caution and pay attention to side effects when prescribing this class of agents. Tolerance, dependence, age-related physiological changes, and drug-drug interactions are all important considerations. This review explains the mechanisms of action of BZDs, compares and contrasts popular BZDs on the market today, and describes specific BZD-mediated effects and side effects [2]. Molecular dynamics simulations enable us to get a very detailed picture of the molecular events and are powerful and precise tools that may provide valuable complementary to experiment information about details of interactions between the drug molecules and biomembranes. Despite the enormous development of computer simulations of lipid bilayers and utilizing GROMACS package for MD simulations, investigations on computer modeling of BZDs in the lipid bilayer are rather scarce. Hence, in this work, effects of Diazepam and Clonazepam on dipalmitoylphosphatidylcholine (DPPC) lipid bilayer (Fig 1) were considered.

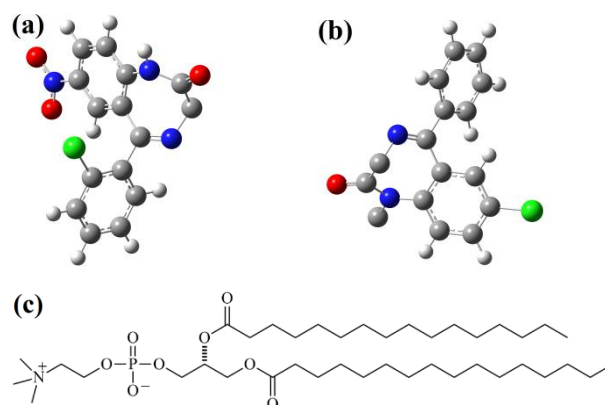


Fig.1: Molecular structures of Clonazepam (a), Diazepam (b) and DPPC (c)

Materials and method

In this study, three different systems were chosen to carry out the simulation study. The first system which comprises only lipid and water molecules was utilized as a reference. The second one includes 128 DPPC lipids (64 per leaflet) with one Diazepam molecule in each leaflet, within the bilayer. Another system contains one Clonazepam molecule in each leaflet, which were hydrated by 4000 water molecules. The simulations were executed in the NPT ensemble using GROMACS 4.5.5 package [3]. All simulations were carried out under pressure (1 bar) and temperature (323 K), and with periodic boundary conditions. Temperature was controlled by the Nose-Hoover thermostat with a coupling time of 0.5 ps [4]. Constraining the bond lengths was done by using the LINCS algorithm [5]. Coulomb and Van der Waals interactions were cut-off at 1.2 nm,

whereas for long-range electrostatics the particle mesh Ewald treatment was applied [6]. Starting structure for DPPC lipid bilayer was taken from the Berger lipid [7] modified by Tieleman [8]. At first, positions of drugs were restrained and equilibration conducted in the NVT ensemble for 2 ns and then followed by equilibration in NPT ensemble for 8 ns. After equilibration steps, all simulations were run for 100 ns from their starting conditions and coordinates of the atoms. For water molecules, the simple point charge model (SPC) was used [9]. The topology and coordinates files of drugs based on the GROMOS 53A6 force field was received from ATB server [10,11].

Results and Discussion

It is confirmed that many cell signalling processes of the membrane, are controlled by lipid molecules diffusion, an indicator of lipid viscosity [12]. Therefore, calculations of the lateral diffusion coefficients for all ILs as well as lipids in all simulated systems were done. The lateral diffusion constant can be obtained from the Einstein relation [13]:

$$D = \lim_{t \rightarrow \infty} \frac{1}{4} \frac{d}{dt} \langle |\Delta r(t)|^2 \rangle \quad (1)$$

where $\langle |\Delta r(t)|^2 \rangle$ is the mean square displacement (MSD) in XY plane during the time t , starting from the initial time t_0 and D stand for the lateral diffusion coefficient. Averaging is taken over all molecules and over all initial time t_0 . Figure 2 shows the kinetic behaviour of drug molecules.

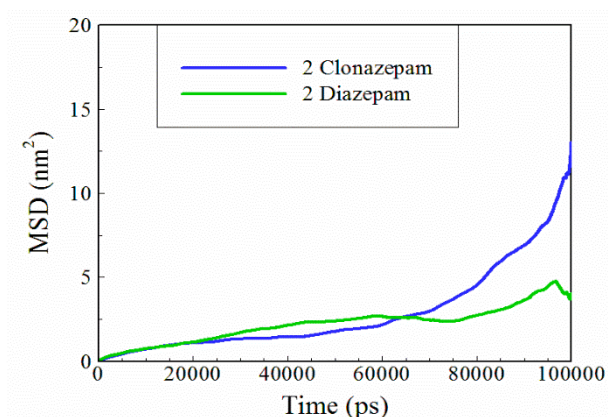


Fig.2: The mean square displacement of the drugs in the simulated systems.

The linear range of this figure is 0-65ns and movement of Diazepam in this range is more than Clonazepam. It seems that less mobility of Clonazepam in this range is due to the presence of additional Oxygen and Nitrogen molecules in the structure of Clonazepam as one can be seen in Fig 1. These bulky atoms caused slower movement of the Clonazepam molecules in DPPC

membrane. Another reason can be explained by more ability of Clonazepam molecules in establishing the hydrogen bond that caused slower movement. Figure 3 shows the behavior of DPPC molecules in the presence of these drugs. As seen in this figure, movement of DPPC molecules in all drugs containing systems is less than reference system. This reduction of mobility for DPPC molecules, in the linear range of MSD, is less in the Diazepam containing system than that one. As mentioned in the description of Fig 2, because of more mobility of Diazepam, there is less free space for movement of DPPC molecules in this system and the same discussion applies to Clonazepam. Due to less mobility of Clonazepam than

Diazepam, free space in the Clonazepam containing system is more than the Diazepam containing system, hence, movement of DPPC molecules in this system are more than the Diazepam containing system.

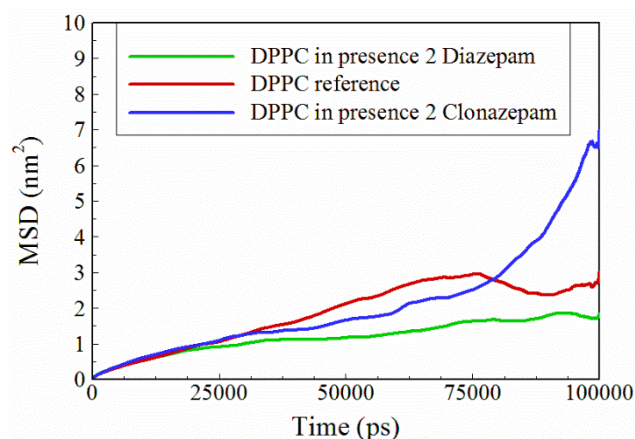


Fig.3: The mean square displacement of the DPPC molecules in the simulated systems.

Conclusions

Mobility of Clonazepam and Diazepam in DPPC membrane is affected from their structure and mobility of DPC molecules depended on these structures.

References

- [1] E. Cascade, A.H. Kalali, Use of benzodiazepines in the treatment of anxiety, *Psychiatry* (Edgmt). 5 (2008) 21.
- [2] C. Fox, H. Liu, A.D. Kaye, L. Manchikanti, A.M. Trescot, P.J. Christo, *Clinical Aspects of Pain Medicine and Interventional Pain Management: A Comprehensive Review*, Paducah, KY ASIP Publ. *Antianxiety Agents*. (2011) 543–552.
- [3] B. Hess, C. Kutzner, D. Van Der Spoel, E. Lindahl, *GROMACS 4: algorithms for highly efficient, load-balanced, and scalable molecular simulation*, *J. Chem. Theory Comput.* 4 (2008) 435–447.



- [4] M.B. Boggara, R. Krishnamoorti, Partitioning of nonsteroidal antiinflammatory drugs in lipid membranes: a molecular dynamics simulation study, *Biophys. J.* 98 (2010) 586–595.
- [5] B. Hess, H. Bekker, H.J.C. Berendsen, J.G.E.M. Fraaije, LINCS: a linear constraint solver for molecular simulations, *J. Comput. Chem.* 18 (1997) 1463–1472.
- [6] U. Essmann, L. Perera, M.L. Berkowitz, T. Darden, H. Lee, L.G. Pedersen, A smooth particle mesh Ewald method, *J. Chem. Phys.* 103 (1995) 8577–8593.
- [7] O. Berger, O. Edholm, F. Jähnig, Molecular dynamics simulations of a fluid bilayer of dipalmitoylphosphatidylcholine at full hydration, constant pressure, and constant temperature., *Biophys. J.* 72 (1997) 2002.
- [8] D.P. Tieleman, J.L. MacCallum, W.L. Ash, C. Kandt, Z. Xu, L. Monticelli, Membrane protein simulations with a united-atom lipid and all-atom protein model: lipid–protein interactions, side chain transfer free energies and model proteins, *J. Phys. Condens. Matter.* 18 (2006) S1221.
- [9] H.J.C. Berendsen, J.P.M. Postma, W.F. van Gunsteren, J. Hermans, Interaction models for water in relation to protein hydration, in: *Intermol. Forces*, Springer, 1981: pp. 331–342.
- [10] S. Canzar, M. El-Kebir, R. Pool, K. Elbassioni, A.K. Malde, A.E. Mark, D.P. Geerke, L. Stougie, G.W. Klau, Charge group partitioning in biomolecular simulation, *J. Comput. Biol.* 20 (2013) 188–198.
- [11] K.B. Koziara, M. Stroet, A.K. Malde, A.E. Mark, Testing and validation of the Automated Topology Builder (ATB) version 2.0: prediction of hydration free enthalpies, *J. Comput. Aided. Mol. Des.* 28 (2014) 221–233.
- [12] R.R. Gullapalli, M.C. Demirel, P.J. Butler, Molecular dynamics simulations of DiI-C 18 (3) in a DPPC lipid bilayer, *Phys. Chem. Chem. Phys.* 10 (2008) 3548–3560.
- [13] H. Mosaddeghi, S. Alavi, M.H. Kowsari, B. Najafi, Simulations of structural and dynamic anisotropy in nano-confined water between parallel graphite plates, *J. Chem. Phys.* 137 (2012) 184703.

The study of photo-tautomerization in Coumarin-benzothiazole as a drugnanocarrier

T. Pouryahya, H. Roohi*

Department of Chemistry, Faculty of Science, University of Guilan, Rasht, Iran

* hroohi@guilan.ac.ir

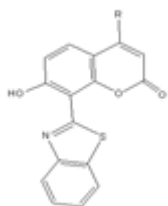
Abstract:

Based on DFT and TD DFT methods, the excited state intramolecular proton transfer (ESIPT) reaction of Coumarin-2-(2'-hydroxyphenyl)-benzothiazole (Cou-HBT) as a fluorophore in the gas phase has been explored. The geometric structures in the ground (S_0) and first excited states (S_1) were analyzed to make clear the mechanism of proton transfer. The potential energy curves in the ground and excited states also demonstrate the tautomerism mechanism between enol and keto. The Cou-HBT-enol can be converted in to Cou-HBT-keto via ESIPT. The photophysical behaviour of substituted Cou-HBT has been studied. The electron- withdrawing and electron-donating groups in to the coumarin caused red and blue shifts of the ESIPT fluorescence emission band, respectively.

Keywords: TD DFT methods; ESIPT; fluorophore; coumarin-benzothiazole.

Introduction

Dye chemistry covers a large numbers of researches in many fields [1]. In particular, excited-state intramolecular proton transfer (ESIPT) dyes have found many applications, e.g., they can be used to probe some analytes in many different biological environments [2] or in laser dyes [3] and luminescent metaterials [4]. Most of the ESIPT reactions include enol-keto photo-tautomerization. In ESIPT dyes, the absorption occurs from the S_0 -enol form while the emission takes place from the S_1 -keto isomer. Chemists are interested in exploring more over excited state interamolecular proton transfer reaction because of its desirable characteristics, such as, emission and more specially environmentally sensitive fluorescence properties [5] Today, theoretical methods such as density-functional theory (DFT) and time dependent density-functional theory (TD-DFT) are useful tools to consider the hydrogen bonding which occurs in excited state intramolecular proton transfer dyes [6]. In this work, proton transfer in excited state in coumarin-benzothiazol (Cou-HBT) and the photophysical properties of substituted coumarin-benzothiazole that having NH_2 , OH , H and NO_2 substituents (C_{1-4} = R_{1-4} Cou-HBT, $\text{R}_1=\text{NH}_2$, $\text{R}_2=\text{OH}$, $\text{R}_3=\text{H}$ and $\text{R}_4=\text{NO}_2$) (Scheme 1) have been studied theoretically. Coumarin derivaties are well-known dyes due to their strong fluorescence nature and their wide application in drug delivery systems as phototriggers [7]. Among the different ESIPT molecules, 2-(2'-hydroxyphenyl) benzothiazole (HBT) exhibits remarkable properties such as a large Stokes shift and dual emission [8].



Scheme. 1 Substituted Cou-HBT. $\text{C}_{1-4} = \text{R}_{1-4}$ Cou-HBT ($\text{R}_1=\text{NH}_2$, $\text{R}_2=\text{OH}$, $\text{R}_3=\text{H}$ and $\text{R}_4=\text{NO}_2$)

Computational details

The ground-state and excited-state geometric optimizations were followed out with DFT and TD-DFT level using PBE1PBE method and 6-311++G(d,p) basis set. DFT methods are employed as a valid standard tool for the theoretical treatment of electronic structures.

Results and Discussion

The optimized Cou-HBT-enol and Cou-HBT-keto in the ground-state (S_0) and excited-state (S_1) have been shown in Fig. 1.

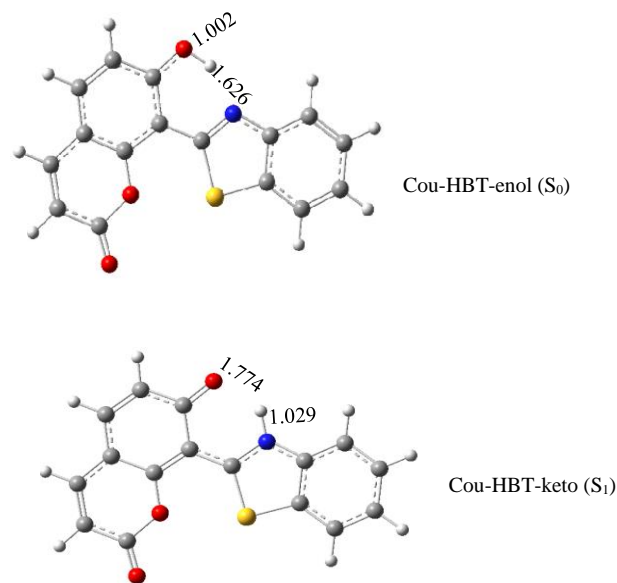


Fig.1 Optimized structures for Cou-HBT (distance: \AA) based on PBE1PBE/6-311++g (d,p) theoretical level at ground (S_0) and excited (S_1) states.

The energy diagram of photo-tautomerization in Cou-HBT has been shown in Fig. 2. At first, the molecule is in ground state S_0 -E. Upon photoexcitation, the molecule is vertically excited to the Franck-Condon excited state S_1 -

E(FC). The molecule, from S_1 -E(FC) state, directly undergoes a tautomerization via ESIPT to the excited state S_1 -K.

shift. The Stokes shift observed for other molecules is nearly 150 nm.

Table 1. Absorption and emission wavelengths (λ) and oscillator strengths (f) for C1 to C4 molecules in the gas phase.

	C1		C2	
	S_0 -E	S_1 -K	S_0 -E	S_1 -K
λ /nm	332.3	481.53	328.03	479.55
f	0.1	0.14	0.41	0.13
	C3		C4	
λ /nm	327.63	482.48	449.8	660.02
f	0.14	0.14	0.03	0.07

The calculated relative energies and dipole moment values are given in Table 2. Based on PBE1PBE method in the gas phase, energy of S_1 -E(FC) form of the Cou-HBT at S_1 state is greater than that of its keto form at S_1 by 15.66 kcal/mol, showing that the conversion of S_1 -E(FC) to keto form is not an energetic process. An increase in the dipole moment value is observed on going from S_0 -E to S_1 -K.

Table. 2 Calculated relative energies (kcal/mol) and dipole moment values (μ /D) for C1 to C4 molecules in the gas phase.

Molecule		ΔE (kcal/mol)	μ /D
C1	S_0 -E	0.0	2.1
	S_1 -E(FC)	86.08	2.1
	S_1 -K	71.74	3.6
C2	S_0 -E	0.0	2.7
	S_1 -E(FC)	87.16	2.7
	S_1 -K	71.83	4.1
C3	S_0 -E	0.0	4.5
	S_1 -E(FC)	87.26	4.5
	S_1 -K	71.60	7.2
C4	S_0 -E	0.0	3.5
	S_1 -E(FC)	63.56	3.5
	S_1 -K	56.40	4.9

Conclusion

In the present exploration, we have found that the keto form of all molecules studied here are not stable in ground state, while keto form in excited state is most stable tautomer. The S_1 -E(FC) state of Cou-HBT is converted to its phototautomer keto. The large Stokes shift is found for chromophores, so

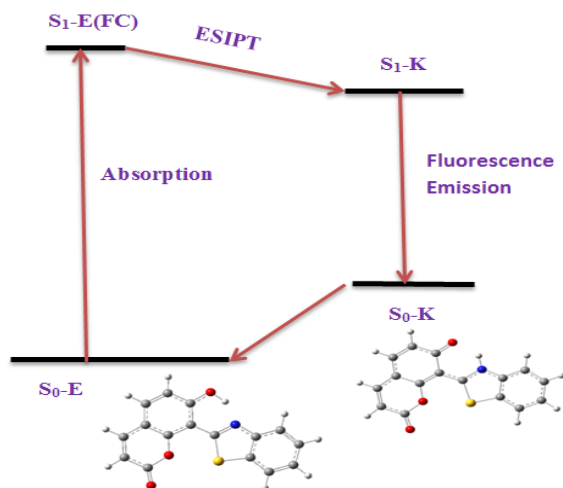


Fig.2 Energy diagram of phototautomerization for Cou-HBT.

Fig.3 illustrates the potential energy curves (PECs) along the proton transfer (PT) at the ground and excited states, to understand the enol-keto photo-tautomerization mechanism clearly. It can be seen that in the S_1 state, the Cou-HBT-enol can be easily isomerized to the Cou-HBT-keto. Therefore, the proton transfer process is likely to proceed in the excited state. However, in the S_0 state, the Cou-HBT-enol is barely converted to Cou-HBT-keto because of the high energy barrier.

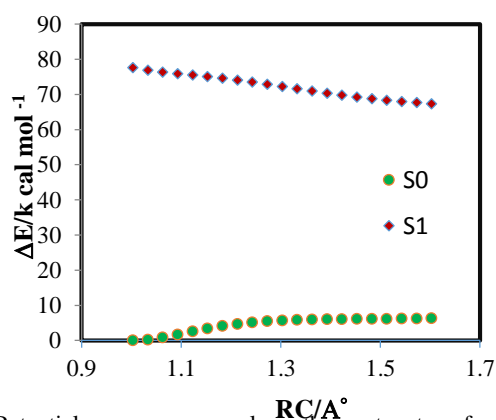


Fig.3 Potential energy curves along the proton transfer (PT) pathway in the ground (S_0) and excited (S_1) states as a function of the reaction coordinate (RC) for Cou-HBT.

In this study, TD DFT calculations have been utilized to observe the photophysical properties of C1 to C4 in the gas phase (see Table 1). The calculated excitation wavelength for the S_0 to S_1 transition for C4 chromophore is 449.8 nm, while the emission band for its keto tautomer is observed at 660.02 nm, indicating that a large Stokes

that the greatest value of shift in wavelength is observed for C4 molecule.

References

- [1] C. Azarias, AD. Laurent “Tuning ESIPT fluorophores into dual emitters”, *Chemical Science*, 7 (2016) 3763-3774.
- [2] Y. Pan, J.Huang “A new ESIPT-based fluorescent probe for highly selective and sensitive detection of HClO in aqueous solution”, *Tetrahedron Letter*, 58.13 (2017) 1301-1304.
- [3] Zhang. Wei, Yan.Yongli “Low-Threshold Wavelength-Switchable Organic Nanowire Lasers Based on Excited-State Intramolecular Proton Transfe ”, *Angewandte Chemie International Edition*, 54.24 (2015) 7125-7129.
- [4] Lu. Fengxian, Hu.Rui “Luminescent properties of benzothiazole derivatives and their application in white light emission ”, *RSC Advances* 7.7 (2017) 4196-4202.
- [5] Z. Jianzhang, Ji. Shamin “Excited state intramolecular proton transfer (ESIPT): from principal photophysics to the development of new chromophores and applications in fluorescent molecular probes and luminescent materials”, *Physical Chemistry Chemical Physics*, 14.25 (2012) 8803-8817.
- [6] A. Carlo, Vi. Barone “Toward reliable density functional methods without adjustable parameters: The PBE0 model”, *The Journal of chemical physics*, 110.13 (1999) 6158-6170.
- [7] B. Shrabani, B.Sandipan “Coumarin–benzothiazole–chlorambucil (Cou–Benz–Cbl) conjugate: an ESIPT based pH sensitive photoresponsive drug delivery system”, *Journal of Materials Chemistry B*, 3.17 (2015) 3490-3497.
- [8] P.Majumdar, Ji. Zhao “2-(2-hydroxyphenyl)-benzothiazole (HBT)-rhodamine dyad: acid-switchable absorption and fluorescence of excited-state intramolecular proton transfer (ESIPT)”, *The Journal of Physical Chemistry B*, 119.6 (2014) 2384-2394.

A computational and conceptual DFT study on the mechanism of producing 3,8-dimethyl-3H-imidazo[4,5-a]acridine-11-carbonitrile DFT study

F. Zonozi^{a*}, M. Halleh^b

^aDepartment of Chemistry, Mashhad Branch, Islamic Azad University, Mashhad, Iran

^bDepartment of Biology, Parand Branch, Islamic Azad University, Tehran, Iran

*Fzonozi@gmail.com

Abstract

In this paper, proper mechanism based on valuable thermodynamics information of producing 3,8-dimethyl-3H-imidazo[4,5-a]acridine-11-carbonitrile as a new fluorescent compound has been theoretically investigated in detail, employing DFT(density functional theory) and the polarizable continuum model (PCM).

In addition gas phase calculations, the mechanism was fully investigated in methanol. Methanol for analysis of solvent effect, as a polar solvent, results decreasing activation energy for the tautomerization and final step, while for the cyclization step activation energy increased. Based on our theoretical calculation, final step, losing H₂O for formation of product is the **rate determining step**. By considering NBO information, could be understood that cyclization step has **Electrophilic** mechanism. Solvent effect, activation energy and free Gibbs energy for all steps were calculated.

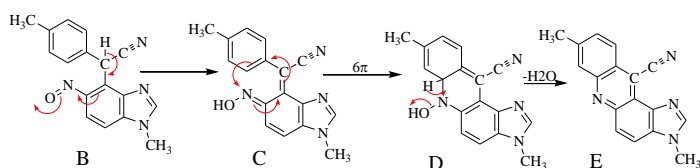
Keywords: “DFT study” “Electrophilic Mechanism” “NBO calculation” “Imidazo[4,5-a]Acridine”

1. Introduction

Nowadays, it is demonstrated that Imidazo Acridine derivatives considerably noted for the synthesis of drugs for treatment many disease [1] and other aspects of industrial organic material's usage, in a large number of cases. [2-4]

Today, many kinds of important acridine derivatives have been used for producing such compounds of dyes and some valuable drugs .[5]

Although imidazo acridine derivatives are used widely as an antimicrobial and other aspect of industrial compounds, mechanisms of their synthesis are not clear exactly. Thus understanding of the mechanism of formation the products are so important. In spite of increasing attention to the synthesis of these compounds, we have no evidence for theoretical study to their mechanism, especially in one-pot synthesis. Because of all, we decided to investigate theoretical study on the mechanism of formation of 3, 8-dimethyl-3H-imidazo [4,5-a] acridine-11-carbonitrile as an imidazo-acridine derivative that is synthesized as a new fluorescent compound by Dr.Pordel [6]. The product was obtained at room temperature and 1 atm. Pressure with good yields of Product, they presented the following mechanism (Scheme1).



Scheme 1

In basicity media experimentally, they [13] reported valuable data for producing 3,8-dimethyl-3H-imidazo[4,5-a]acridine-11-carbonitrile were synthesized from 1-methyl-5-nitrobenzimidazole as a one-pot synthesis, through the mechanism has shown in the scheme1[6].

In this paper, here we have theoretically investigated the mechanism of reactions. More specifically, for the cyclization and rate determining step, losing H₂O, which are not very clear experimentally, a mechanism was proposed, which is compatible with experimental data.

2. Computational methods

All of calculations have been performed with the B3LYP [7-9] hybrid density functional level using the Gaussian 09 package [10]suite of programs.

The 6-311++ g(d, p) basis sets were employed [11].

First, all degrees of freedom for all geometries were optimized.

The transition states obtained were confirmed to have only one imaginary frequency of the Hessian.

Then, the gas-phase-optimized geometries were used to perform frequency calculations in gas phase and methanol (PCM model).

In both of the gas phase and PCM model, the zero-point-energy (ZPE) corrections were made to obtain energies.

Herein, the used methods are widely applicable in theoretical investigation of the mechanism of chemical reactions [12-18].

The related thermodynamic quantities were obtained at room temperature and 1 atm. for giving exact conditional on the experimental results [6].

In the gas phase and PCM model, sum of electronic and zero point energies and sum of electronic and thermal Free Energies

derived from the frequency calculations were included to obtain relative activation energies and Free Gibbs energies. The zero-point corrections were also considered to obtain activation energies.

The Chem. craft program was used for drawing illustrations.

3. Results and discussion

Regarding the formation of 3,8-dimethyl-3H-imidazo[4,5-a]acridine-11-carbonitrile that has been an one-pot synthesis[6] we decided to investigate theoretically by using G09 and got a confirmation or refusal for proposed mechanism. Our investigation has been involved an analysis of DFT calculation for all species which carried out by G09, then based on this calculation we obtained all possibility reaction's activation energies and geometries then from results of NBO analysis of the stationary points, we will discuss in order to establish the electronic nature and reality of the mechanism of the cyclization (step2) from Path II. Moreover, we calculated relative energies and free Gibbs Energies for all species, and all possibility reactions. All thermodynamics data collected in Table 1. Additionally, energy profile which is reported by drawing plot for illustrating the proper path way that is based on relative energies, will be coming in Fig.7.

Table 1: Relative energies (kJ/mol) for all species which involved in our proposed mechanism, E and G are electronic considered zero point energy and Gibbs free energy, respectively

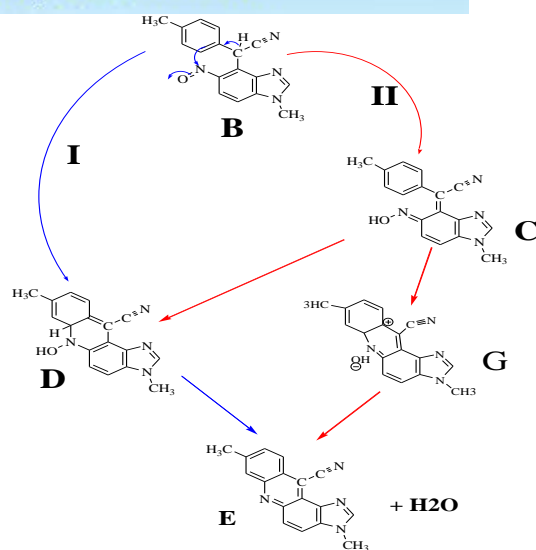
Species	E(g)	G(g)	E(pcm)	G(pcm)
E+H ₂ O	0.00	0.00	0.00	0.00
B	286.24	285.03	292.31	298.16
C11	341.65	341.59	332.01	333.73
C12	344.84	347.82	334.47	341.32
C13	340.98	340.83	344.68	347.84
C14	334.67	335.49	335.48	340.79
D	322.60	331.66	327.01	339.24
G	322.79	331.51	324.08	336.08

First of all, we carried out our calculation on the mechanism of the reactions that is shown in Scheme 2.

As we can see on Scheme 2, for producing E from B, we have two paths, that, path II has three steps, 1) tautomerization 2) cyclization, 3) losing H₂O for formation of product E, while path I just has two steps because tautomerization and cyclization occurred simultaneously while calculation of activation energies for 1st steps of path I and II, shows that path II is suitable for mechanism of reaction.

In this paper, a new mechanism was proposed for the path I that we supposed, may be tautomerization lead to cyclization simultaneously as well, but as we can see in Fig.1, it has higher activation energy than all reactions related to Path II, therefore, we couldn't suppose this path, thus path I is rejected.

Related activation energies were calculated for path I that is higher than all reactions which are existed in the Path II, therefore there isn't any confirmation for the Path I.



3 : (2R)-(1-methyl-5-nitroso-1H-benzimidazol-4-yl)(4-methylphenyl)ethanenitrile
E : 3,8-dimethyl-3H-imidazo[4,5a]acridine-11-carbonitrile

Scheme 2

3.1. Path I

We will have this conclusion by considering all results as shown in the Energy profile for these paths (Fig.1).

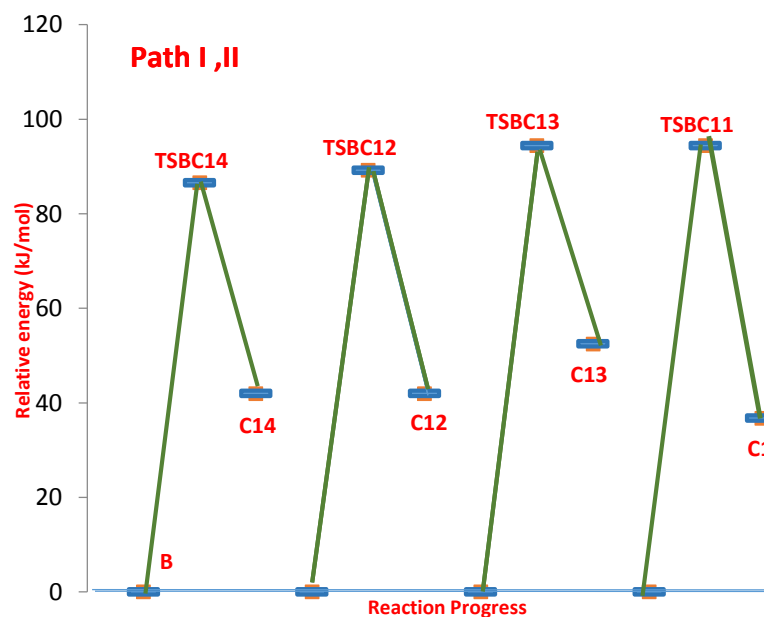


Fig. 1: Energy profile for Pathway I, II

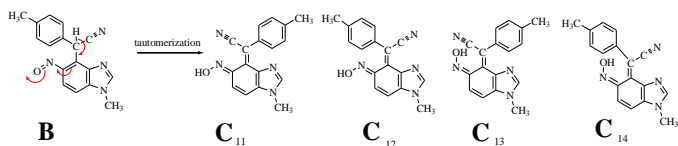
All results about activation energies for two paths will be coming in Table 3. Optimized TS structure in solution is shown in Fig.2.

Solvent effect decreases E_{act} by 9.08 for TSBD by kJ/mol.

3.2 PathII

3.2.1 Tautomerization

In the first step of Path II, we have a tautomerization which is shown in Scheme 3.



C11:(2Z)-[(5E)-5-(hydroxyimino)-1-methyl-1,5-dihydro-4H-benzimidazol-4-ylidene](4-methylphenyl)acetonitrile
 C12:(2E)-[(5E)-5-(hydroxyimino)-1-methyl-1,5-dihydro-4H-benzimidazol-4-ylidene](4-methylphenyl)acetonitrile
 C13:(2Z)-[(5Z)-5-(hydroxyimino)-1-methyl-1,5-dihydro-4H-benzimidazol-4-ylidene](4-methylphenyl)acetonitrile
 C14:(2E)-[(5Z)-5-(hydroxyimino)-1-methyl-1,5-dihydro-4H-benzimidazol-4-ylidene](4-methylphenyl)acetonitrile

Scheme 3

As we can see, there is four possibility of configuration for C species.

The keto form **B** could be converted to each of **C** forms by tautomerization (or vice versa) via an intermolecular proton transfer (IPT) reaction.

Obviously, the plot of Fig.1 shows that for the Path II reaction, B-C14 or B-C12 is possible than others because of low activation energies.

The obtained structure for the TS isn't planar, breaking of the C7-H11 bond at the same time, formation O1-H11 bond, which is occurring in the optimized structure of TSs.

Some of the most important structural parameters of the keto form change via the keto \rightarrow enol IPT tautomerization, gathered in Table 2.

As we can see the angle of C₄-C₇-C₈ for all enol forms increased via tautomerization as well as bond length of N₄-O₁, but the length of C₈-C₇ and C₇-C₄ for the enol forms decreased.

Table 2 : Some of the most important structural parameters of the keto-enols form in Å

Bond length (Å)	B	C11	C12	C13	C14	D
C ₇ -H ₁₁	1.092	4.624	4.687	2.336	2.263	4.655
O ₁ - H ₁₁	3.447	0.972	0.973	0.976	0.975	0.966
N ₄ - O ₁	1.227	1.374	1.377	1.368	1.365	1.426
C ₈ - C ₇	1.530	1.377	1.372	1.384	1.382	1.460
C ₇ - C ₄	1.535	1.488	1.495	1.486	1.489	1.372
Angle (°)						
C ₄ -C ₇ -C ₈	112.693	125.690	126.240	126.500	125.550	120.27

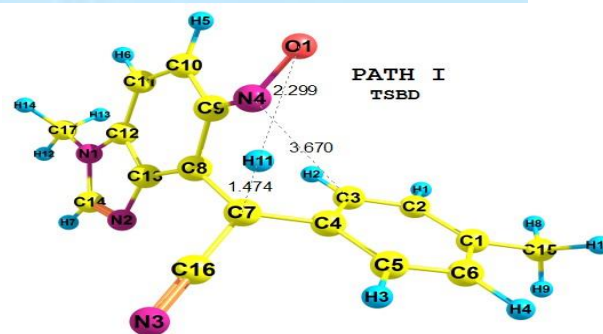


Fig.2: Optimized structure of TSBD in solvent phase

3.2.1.1 Solvent effects on the tautomerization step

The tautomerization mechanism has been theoretically fully investigated and optimized for reactant (keto form), products (enol forms) and their transition states, in the gas phase and methanol, which structures of TSs in solvent are shown in Fig.3.

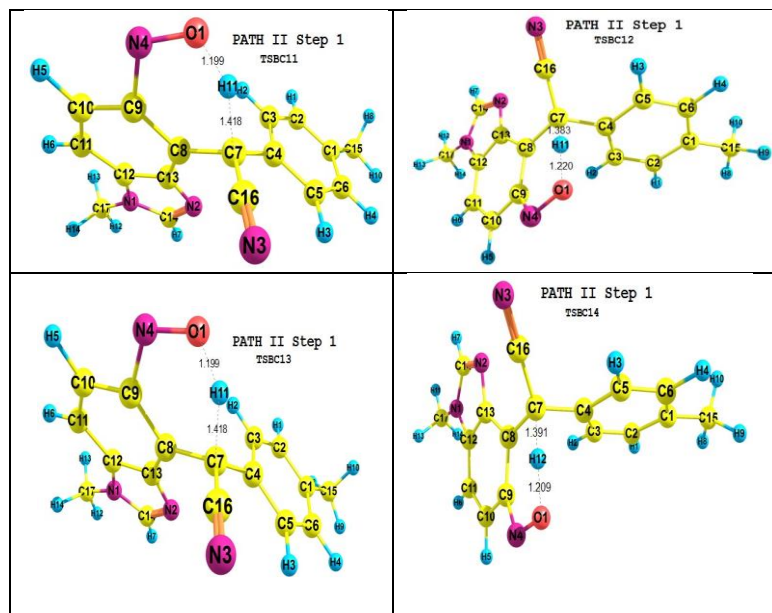


Fig.3: The optimized structure of the transition state (TS) of the enol-keto tautomerization in methanol phase

We know that, polar solvent stabilizes all the species and their dipole moments are increased during tautomerization. Therefore, larger dipole moment leads to finer stabilization in polar solvents.

In additional, the solvent with higher dielectric constant results greater stabilization for the polar species.

Usually, transition state has the lower dipole moments than both of tautomer which results less barrier energy in the polar solvents than the gas phase.

All related activation energies for tautomer's of TSs were computed in the gas phase and solvent (methanol) which are reported for this step in Table 3.

Table 3: Related Eact for all tautomerization reactions by kJ/mol

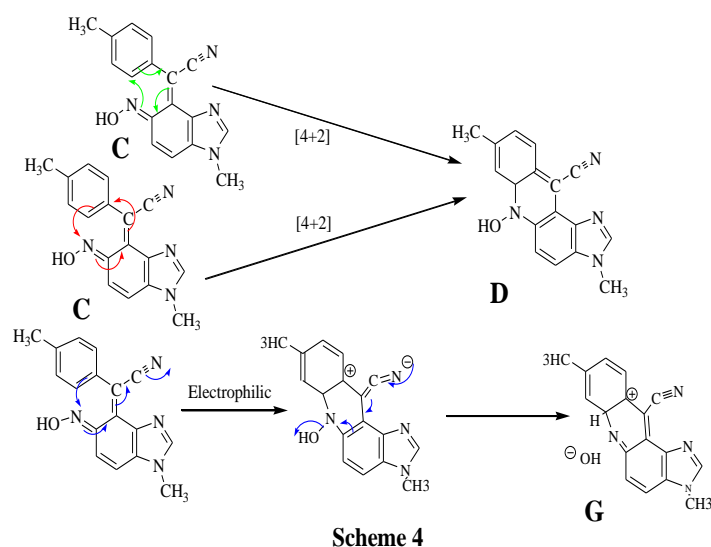
Spices	Gas phse	Methanol phase
B-C11	102.44	96.06

B-C12	98.22	89.26
B-C13	102.44	95.93
B-C14	98.22	87.43
B-D	116.77	107.69

However, considering the solvent effects prefers methanol phase by 6.38, 8.96, 6.51, 10.79, 9.08 kJ/mol for B-C₁₁, B-C₁₂, B-C₁₃, B-C₁₄ and B-D respectively. In the solution, C₁₄ is more stable than others, while keto form B is the most stable, in both phases. By comparing the activation energies for all possibility tautomerization reactions that are reported in the Table 3, we concluded that there is a possibility for B - C₁₂ or B - C₁₄ reactions by just 2 kJ/mol differences in methanol phase.

3.2.2 Cyclization

We supposed four mechanisms, may be happened in the cyclization step, that one of them B-D was rejected in the previous section (Scheme2), now we would discuss about others, which are shown in Scheme 4.



Optimized structures in solution are shown in Fig.4.

Activation energies was calculated with using of $E_a = E_{TS} - E_R$, which E_{TS} and E_R , are energies related to transition state and reactant respectively. We reported activation energies for all possibility reactions for proving and decided which reaction really was happened, all the E_a quantities for this step are reported in Table 4 by kJ/mol.

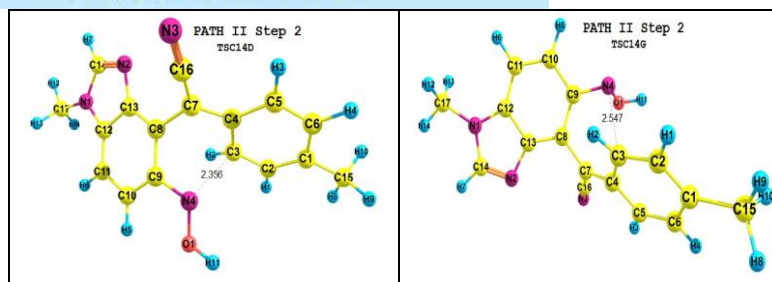
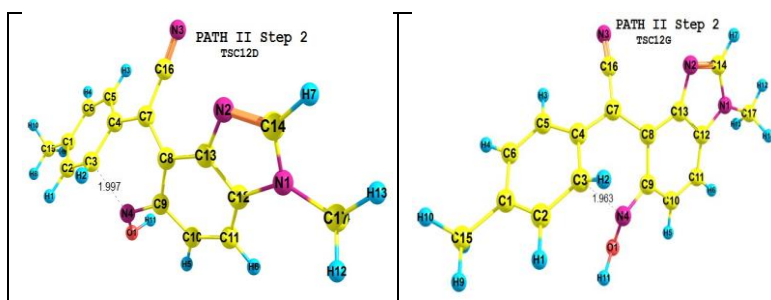


Fig. 4 : The optimized structure of the transition state (TS) for the cyclization step in methanol phase

Table4: Related E_{act} for all species of cyclization step (Path II) by kJ/mol

Species	Gas phse	Methanol phase
C ₁₂ -D	55.81	69.47
C ₁₄ -D	127.88	127.22
C ₁₂ -G	43.37	57.54
C ₁₄ -G	132.72	132.25

Obviously, in the methanol solution, the energy barrier has increased by 13.66, 0.66, 14.17, 0.47 kJ/mol for C₁₂D, C₁₄D, C₁₂G and C₁₄G respectively because of the polarity of solvent (methanol) that could stable reactants more than the transition state, thus related activation energies have been increased. On the other hand, in solution phase, partial charges are more stable than transition states by affecting of polarity of solvent. Therefore, cyclization, which is based on partial charges, is more difficult and related activation energies are increased. Moreover, these results have been illustrated with drawing a plot as shown in Fig.5.

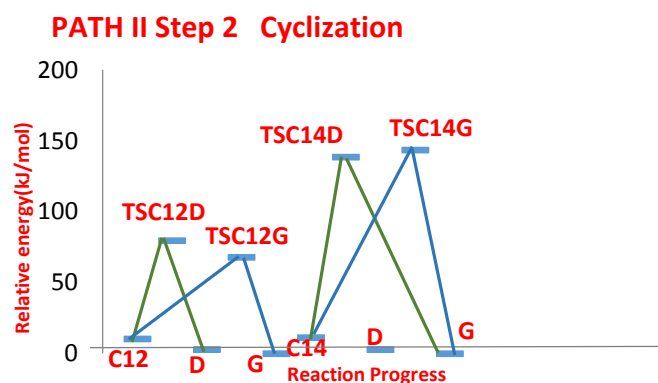


Fig.5: Energy profile for Path II Step 2 Cyclization
 According to results, could be understood that possibility of reaction C₁₂- G is more than others. Of course, it is expected due to related activation energy of C₁₂ - G is less than C₁₄ - G because in the structure of C₁₄, there is a OH group that disturbed cyclization step. Some important results can be deduced from this energy database. Actually, it can clearly demonstrate that the C₁₂-G reaction was happened. It means, the **mechanism of cyclization is Electrophilic** that C₃ attacked to N₄ because of analyzing the results of charge distributions based on NBO calculation for each mechanism that will be discussed about them.

From analysis of useful information of NBO's method, which is suitable for studying intra and inter molecular bonding interactions and investigation of charge transfer in chemical compounds [19-20] it can be understood that during the cyclization, there is interest that C₃ (NO C₅) starts to attack (attaching) to N₄ because of partial negative charge, which existed on C₃ atom on the reactant (C) while this charge is decreased on TS CD or TSCG. It means; the mechanism of Cyclization is Electrophilic, while if we supposed that the mechanism of this step was Nucleophilic, N₄ atom must have more negative partial charge than C₃ for starting cyclization. We gathered all NBO data on the Table 5.

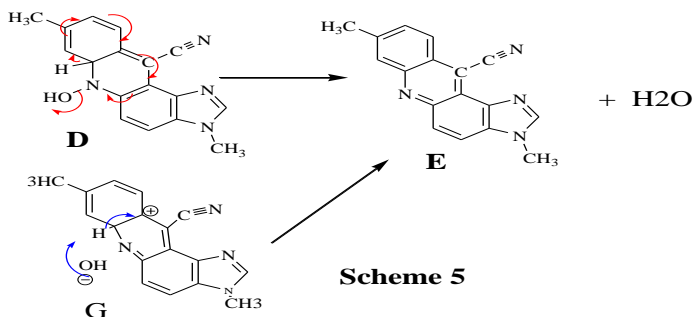
Table 5: Related NBO Atomic charges for species (pcm) that involved on cyclization step

Atoms/species	C	D	TSCD	TSCG
C3	-0.619	-0.061	-0.069	-0.183
N4	-0.204	-0.209	-0.148	-0.115
C5	-0.489	-0.141	-0.171	-0.179

The transition states were verified by rationalizations of the Hessian matrix, and by analysis of the internal reaction coordinates (IRC) for both reactions.

3.2.3 Losing H₂O for formation product

Proposed mechanism for producing E has three main steps. The final step, the formation of the product E, is the **rate-determining step** of the Path II, because of higher activation energy, which are shown in the Scheme 5.



According to the energy quantities, E_a of this step in the methanol is less than gas phase by 10.24 and 7.12kJ/mol for producing the final product from D or G respectively. Thus, the solvent effects decreased the energy barrier.

Table 6: Related activation energies for final step reactions calculated theoretically by kJ/mol

	Gas phase	Methanol phase
D – E	102.95	92.71
G – E	102.76	95.63

As we could see both reactions are the same in the gas phase but have a little differences in solvent. The latest reaction for producing 3,8-dimethyl-3H-imidazo[4,5-a]acridine-11-carbonitrile as the final step, simply losing H₂O, fully optimized and investigated theoretically by DFT calculation that related transition states in solvent are shown in Fig. 6.

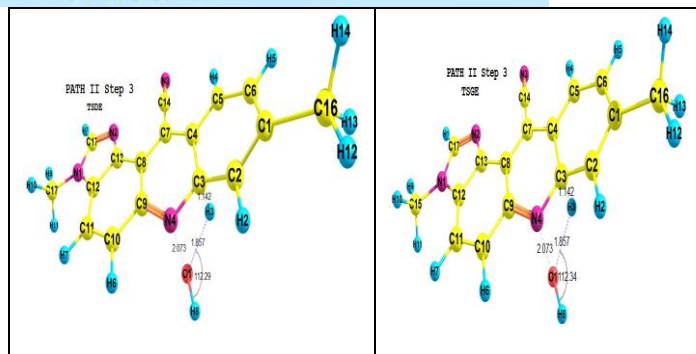


Fig.6: The optimized structures of the transition state (TS) for the final step, formation product in methanol phase

In Fig. 7 all energy profiles that we have reported by drawing plots for illustrating all steps in this paper are based on relative Energies, which are reported in Table 1.

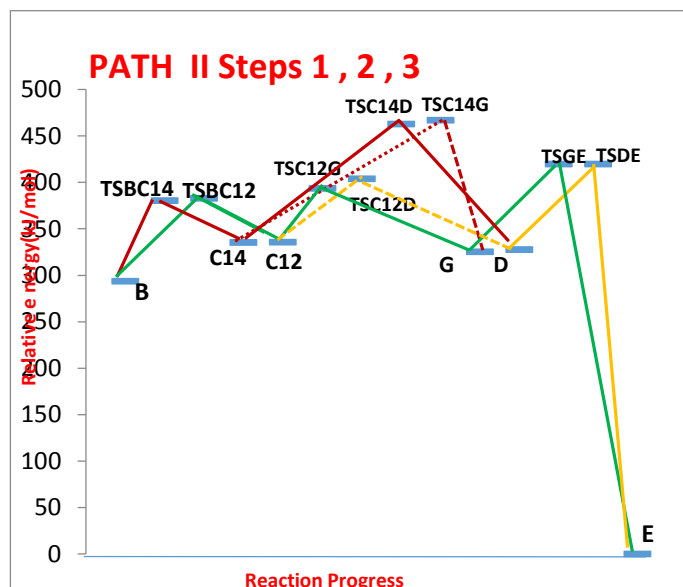


Fig. 7 : Relative energies for all steps of Path II by kJ/mol

4. CONCLUSION

The computed activation energies, reveal that the major path and mechanism for producing E, through a small barrier are the Pathway II which is shown in the Fig.7, obviously we could find that the most proper path is: **B-C₁₂-G-E**. Additionally, we can prove Electrophilic mechanism for cyclization step as well. This finding is inconsistent with previous experimental studies [6]. Moreover, by considering activation energies for all steps, it could be clearly understood that losing H₂O for Producing E, is the **rate-determining** step.

References

- [1] M. Wainwright “ Review of Acridine a neglected antibacterial chromophore” Journal of antimicrobial chemotherapy 47 (2001)1-13.

- [2] F. Bellina¹, S. Cauteruccio², R. Rossi³ "Synthesis and biological activity of vicinal diaryl-substituted 1H-imidazoles" *Tetrahedron* 63(22) (2007) 4571-4624.
- [3] Z.J. Hu, J.X. Yang, Y.P. Tian, H.P. Zhou, X.T. Tao, G.B. Xu "Synthesis and optical properties of two 2,2': 6',2"-Terpyridyl-based two-photon initiators" *J. Mol. Struct.*, 839 (2007) 50-57.
- [4] M.H. Tsai¹, Y.H. Hong², C.H. Chang³, H.C. Su⁴, C.C. Wu⁵, A. Matoliukstyte⁶ "3-(9-Carbazolyl)carbazoles and 3,6-Di(9-carbazolyl)carbazoles as Effective Host Materials for Efficient Blue Organic Electrophosphorescence" *Adv. Mater.* 19 (2007) 862-866.
- [5] R. Sahraei, M. Pordel, H. Behmadi, B. Razavi "Synthesis of a new class of strongly fluorescent heterocyclic compounds: 3H-imidazo[4,5-a]acridine-11-carbonitriles" *J. Luminescence* 136 (2013) 334-338.
- [6] M. Pordel "Synthesis of new fluorescent compounds from benzimidazole" *J. Chem. RESEARCH*, (2012) 595-597.
- [7] A.D. Becke "Density-functional thermochemistry. III. The role of exact exchange" *J. Chem. Phys.* 98 (1993) 5648-5652.
- [8] A.D. Becke "Density-functional exchange-energy approximation with correct asymptotic behavior" *Phys. Rev. A*. 38 (1988) 3098-3100.
- [9] C. Lee¹, W. Yang², R.G. Parr³ "Development of the Colle-Salvetti correlation energy formula into a functional of the electron density" *Phys. Rev. B*. 37 (1988) 785-789.
- [10] M. J. Frisch, G. W. Trucks, H. B. Schlegel, G. E. Scuseria, M. A. Robb, J. R. Cheeseman, J. A. Montgomery, Jr., T. Vreven, K. N. Kudin, J. C. Burant, J. M. Millam, S. S. Iyengar, J. Tomasi, V. Barone, B. Mennucci, M. Cossi, G. Scalmani, N. Rega, G. A. Petersson, H. Nakatsuji, M. Hada, M. Ehara, K. Toyota, R. Fukuda, J. Hasegawa, M. Ishida, T. Nakajima, Y. Honda, O. Kitao, H. Nakai, M. Klene, X. Li, J. E. Knox, H. P. Hratchian, J. B. Cross, C. Adamo, J. Jaramillo, R. Gomperts, R. E. Stratmann, O. Yazyev, A. J. Austin, R. Cammi, C. Pomelli, J. W. Ochterski, P. Y. Ayala, K. Morokuma, G. A. Voth, P. Salvador, J. J. Dannenberg, V. G. Zakrzewski, A. D. Daniels, O. Farkas, A. D. Rabuck, K. Raghavachari, J. V. Ortiz, Gaussian 03, Gaussian Inc., Pittsburgh, PA, 2003.
- [11] P.J. Hay¹, W.R. Wadt² "Ab initio effective core potentials for molecular calculations. Potentials for K to Au including the outermost core orbitals" *J. Chem. Phys.* 82 (1985) 299-310.
- [12] P. Pe´rez¹, D. Yepes², P. Jaque³, E. Chamorro⁴, L. R. Domingo⁵, R. S. Rojas⁶, A. Toro-Labbe⁷ "A computational and conceptual DFT study on the mechanism of hydrogen activation by novel frustrated Lewis pairs" *Phys. Chem. Chem. Phys.*, 17(2015) 10715 - 10726.
- [13] C. N. Alves¹, A. S. Carneiro², J. Andre´³, L. R. Domingo⁴ "A DFT study of the Diels-Alder reaction between methyl acrole in derivatives and cyclopentadiene. Understanding the effects of Lewis acids catalysts based on sulfur containing boron Heterocycles" *Tetrahedron* 62(2006) 5502-5509.
- [14] M. Jose´ Aurell¹, Luis R. Domingo², Patricia Pe´rez³, Renato Contreras⁴ "A theoretical study on the regioselectivity of 1,3-dipolar cycloadditions using DFT-based reactivity indexes" *Tetrahedron* 60 (2004) 11503-11509.
- [15] L. R. Domingo¹, J. A. Sa´ez², P. Pe´rez³ "A comparative analysis of the electrophilicity of organic molecules between the computed IPs and EAs and the HOMO and LUMO energies" *Chemical Physics Letters* 438 (2007) 341-345.
- [16] P. Pe´rez¹, L. R. Domingo², M. J. Aurell³, R. Contreras⁴ "Quantitative characterization of the global electrophilicity pattern of some reagents involved in 1,3-dipolar cycloaddition reactions" *Tetrahedron* 59 (2003) 3117-3125.
- [17] Ali Beyramabadi¹, Ali Morsali² "Tautomerization of 4-(2-thiazolylazo) resorcinol: A DFT study" *OCAIJ*, 8(2), (2012) 46-51.
- [18] S. Banjo¹, A. Olatunbosun² "Quantum Chemical Calculations on molecular structures and solvents effect on 4-nitropicolinic and 4-methoxy picolinic acid" *International Journal of Physical Sciences* 8(26), (2013) 1382-1392.
- [19] M. Snehathal¹, C. Ravikumar², I. Hubert Joe³, N. Sekar⁴, V. S. Jayakumar⁵ "Spectrochim. Acta A" 72 (2009) 654-662.
- [20] C. James¹, A. Amal Raj², R. Reghunathan³, I. Hubert Joe⁴, V.S. Jayakumar⁵ "Vibrational Spectral Analysis of TCHS used in Self Assembled Monolayer and Formation Dynamics" *J. Raman Spectrosc.* 37 (2006) 1381-1389.



Fluorine substitution: a theoretical study

Hossein shirani Beigi*, Sepideh Bibak

Department of chemistry /nazhand high education institute, Urmia 5779883896 iran

*shiranihoseini@gmail.com

Abstract:

Replacing the fluoride c5 and c6 instead of hydrogen using the theoretical level of Hf and B3LYP with the base level 6-311++G** it has been investigated and parameters such as dipole moment, vibrating frequencies, highest homo molecular orbital and Lomo largest molecular orbital occupied. Fluorine as a substitute for hydrogen causes a change in the length of the transplants.

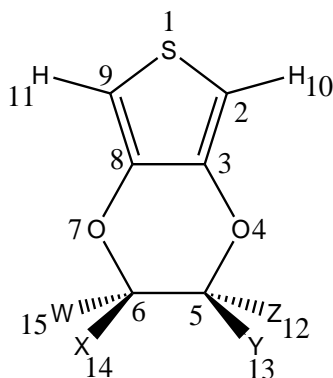
Keywords: B3LYP/6_311++G**, full energy homo Lomo oxygen, dipole moment

Introduction:

Given the properties of fluorine atoms and put it down

To c5 and c6 provides different structures and properties to the molecule this is a great way to study the particular parameters mentioned. The report states that the molecule is optimized by the four substrates in terms of persistence and variance, and these differences are significant in the

molecule there are identical residues that are chemically identical and only the variable fluorine atom by changing or displacing each one produces separate fluorine- derived results and the shape of the molecule changes. We reported the fluorine variable in each of the contributors. $1; z=F; 2; Y=F; 3; X=F; 4; W=F; 5; Z=Y=F; 6; Y=X=F; 7; Z=X=F; 8; Z=Y=X=F; 8; Z=Y=X=W=F$



And we combined our findings separately in the tables what is important is a careful comparison of the stability and structure of the waves of these.

Chemical sites with other molecular carbons as well as between c5 and c6 substituents and which is expressed in every paragraph and in the table.

Computational method:

Optimization of electron structure and energy parameters with thermodynamic calculations using their base usage of B3LYP and the most abundant mode of molecule were identified and these results were carried out by discussing the quantum chemical parameter.

Result and discussion:

Fluorine that is optimized in each of the chemical locations provided by B3LYP/6-311++G** and the result of optimizing and replacing the divergent bond between the different bipolar and homo and lomo which are compared in the tables.

In table(1) the length of the bonds in the molecule has been shown to be reduced by the presence of the dispersing atom of each of the four substitutions (x,z,y,w) in c5 and c6. The bond length is reduced to that of the fluorine free substrate this is due to the electronegative properties of fluorine relative to carbon, which causes a difference in the length of the bond in the molecule.



1C-9C	2C-3C	8C-3C	3C-4C	4C-5C	5C-6C	6C-7C	7C-8C	8C-9C	2C-10H	9C-11H	5C-12F.H	5C-13F.H	6C-14F.H	6C-15F.H
1.8126	1.35294	1.4349	1.40355	1.4235	1.5265	1.4683	1.4000	1.3539	1.07340	1.0735	1.0842	1.4573	1.0910	1.0840
1.8093	1.3529	1.4376	1.4095	1.4181	1.5172	1.3641	1.3558	1.3558	1.0733	1.0733	1.0844	1.4559	1.0845	1.0932
1.8107	1.3539	1.4349	1.400	1.4683	1.5265	1.4235	1.4335	1.3529	1.0735	1.0734	1.0840	1.09110	1.4571	1.0842
1.8069	1.3559	1.4376	1.3967	1.4630	1.5173	1.4181	1.4094	1.3529	1.0733	1.0733	1.0845	1.0932	1.0844	1.4559
1.8080	1.3519	1.4359	1.4150	1.3954	1.5189	1.4598	1.3989	1.3553	1.0733	1.0734	1.4224	1.4041	1.4117	1.0884
1.7344	1.3599	1.4266	1.3823	1.3918	1.5382	1.4029	1.3736	1.3618	1.0776	1.0776	1.0897	1.3821	1.3641	1.0970
1.7339	1.3620	1.4271	1.3742	1.4055	1.5376	1.4055	1.3742	1.3620	1.0776	1.0776	1.3654	1.0956	1.3654	1.0956
1.8079	1.3510	1.4319	1.4164	1.3539	1.3981	1.5361	1.4296	1.4036	1.0732	1.0732	1.3916	1.4102	1.4117	1.0884
1.8055	1.3512	1.4311	1.4150	1.3899	1.5479	1.4149	1.4149	1.3511	1.0732	1.0732	1.4157	1.3810	1.4157	1.3811

Table 2 shows that angles with method by B3LYP/6-311++G**

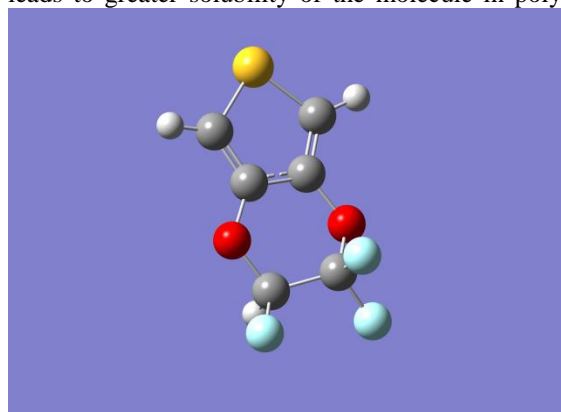
1C-2C-10H	1C-9C-11H	2C-3C-10H	9C-8C-11H	2C-3C-4C	9C-8C-7C	1C-9C-8C	1C-2C-3C	3C-4C-5C	8C-7C-6C	4C-5C-13F.H	4C-5C-12F.H	7
120.5776	120.5231	22.1662	28.4098	124.7716	126.6760	110.0493	109.9552	118.1824	110.4278	107.8464	107.5383	10
120.7565	120.5437	22.3437	22.3452	123.6818	124.4965	110.5004	110.2162	115.5540	113.9345	109.1578	106.4144	10
120.5213	120.5799	22.1617	22.1676	126.6778	124.7708	109.9563	110.0478	110.4245	118.1792	109.6152	106.0820	10
120.5633	120.7363	22.3553	22.3316	124.5053	123.6756	110.2085	110.5045	113.9099	115.5612	109.6416	105.5067	10
120.8783	120.5833	22.2992	22.3457	123.4742	124.9641	110.4491	109.9708	115.7802	113.3504	106.5662	109.4477	11
121.4213	121.3807	22.7071	22.7255	124.8568	124.9912	110.5650	110.4369	113.5877	113.3390	110.2393	107.2912	11
121.4356	121.4143	22.7317	22.7200	124.9800	124.9915	110.5233	110.5295	113.9439	113.9220	111.363	105.9763	11
120.9689	120.6853	129.2527	22.2826	124.630	124.3204	110.1757	109.7781	114.0311		106.5105	110.2895	11
120.8965	120.9190	22.2643	22.2785	124.3451	124.3386	109.8583	109.8694	115.2902	115.3060	107.6129	110.3620	10

Dipolar moments have increased effects on molecule properties .

For example the magnitude of bipolar moments leads to greater solubility of the molecule in poly

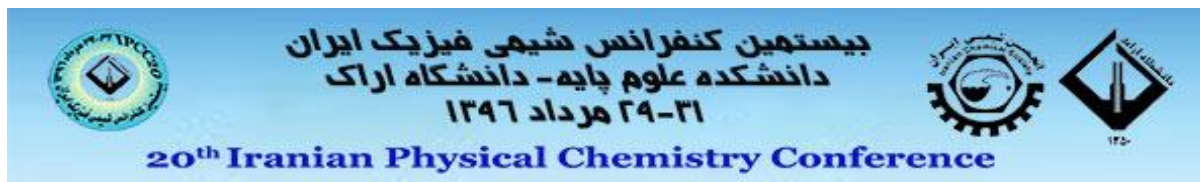
solvents and its interaction in the polar and intermediate environments increases.

The dipolar moments also depends on the length of



Calculate the dipolar moment by B3LYP/6-311++G** in table 6

T ممان دوقطبی	B3LYP/6-311++G**	M062X/6-311++G**	LCWpb/6-311++G**
1	1.1373	1.0158	1.8324
2	2.4826	2.2828	2.3677
3	1.6354	1.5408	1.4938
4	2.4325	2.2388	2.3249
5	2.0945	1.9091	0.9474
6	2.9834	2.7373	2.7086
7	2.8415	2.6029	2.4693
8	3.7464	3.4352	-1.6476
9	3.5309	3.2252	3.0775



After the electron placement at the electronic equations the largest and smallest molecules of orbital HOMO and LUMO can be calculated for the molecule. Any one of the HOMO and LUMO is less able to say for each structure that the process

of electron. Transfer from the bonding band to the conduction band is easier.

Usually HOMO is more stable than LUMO which is calculated HOMO and LUMO

structure and is more convenient is soluble polar for the molecule

Fig 8 (o4) HOMO has more and more light but however the large dimensional dipole moment of figure 8 to 317464 is more than the other

Conclusion

We examined the structure of the proposed variable 4, as shown. For example by placing the fluorine atom instead of bond 2 which is the same in terms of chemical location the difference in the parameters.

The length of the graft bond and HOMO and LUMO the dipole moments and electrons that cause changes in the structure of the molecule which is why we designed nine structures for the molecule with distinct properties and consistency.



Doping fullerene by Boron Substitution; a Theoretical Study

Hossein Shirani Il Beigi^{a,*}, Peyvand Ghanbarpour^b, Sepideh Bibak^a

^aDepartment of Chemistry, Nazhand Higher Education Institute, Urmia, 5719883896, Iran

^bYoung Researchers and Elites Club, Urmia Branch, Islamic Azad University, Urmia, Iran

* shiranihossein@gmail.com

Abstract

C_{60} , and $C_{54}B_6$ fullerene was studied by Density Functional Theory DFT at the B3LYP/6-31G* level of theory. The structure parameters, vibrational frequencies, dipole moment, polarizability, highest occupied molecular orbital (HOMO) and lowest unoccupied molecular orbital (LUMO), used to understand the properties of the doped $C_{54}X_6$ ($X = B$) and fullerene C_{60} . The obtained result indicates that the C-C bond length increases as a result of doping. The calculations show that the doped fullerene $C_{54}B_6$ is more thermal stability than C_{60} fullerene. The minimal and the maximal values of bond lengths is correspond to C_{60} and $C_{54}B_6$ fullerenes, respectively. The highest HOMO-LUMO gap associated by C_{60} and the lowest HOMO-LUMO gap belongs to $C_{54}B_6$ fullerene

Keywords: B3LYP/6-311+G; Fullerene; HOMO-LUMO gap

Introduction

The unique structural and electronic properties of fullerenes led to another type of doping, named substitutional doping where one or more carbon atoms of fullerene are substituted by other atoms, as well as the endohedral doping and exohedral doping [1]. Doped fullerenes have attracted a great deal of interest due to their remarkable structural, electronic, optical, and magnetic properties [2]. Molecular nanoscale electronic devices have attracted a great deal of attention in recent years. Carbon fullerene is one of the most stable and a well-known nanoscale molecular structure; C_{60} often acts as a semiconductor [3]. Introduction of heteroatoms into C fullerene leads to distinguished physical and chemical properties which make them promising materials for some unique applications [4]. In particular, BN substituted C cages have been studied several times [5]. On a parallel track, there have also been several theoretical investigations dealing with the structural and stability aspects as well as electronic properties of heterofullerene $C_{60-n}X_n$ ($X = N$ and B, $n = 1-2$) [6]. We report the structure parameters, vibrational spectra, HOMO-LUMO gap, dipole moment and polarizability used to understand the properties of the doped $C_{54}X_6$ ($X = B$) and fullerene C_{60} .

Computational method

All the structural parameters optimizations and the electronic energies and the thermodynamic functions

calculation in this work were carried out using the B3LYP/6-31G* level with the GAMESS US package of programs. It has been found that $C_{54}B_6$ are the most stable compounds here. We have investigated the theoretical methods to elucidate the doped fullerenes using molecular and structural properties. This was done by discussing quantum chemical parameter.

Result and Discussion

The geometry of fullerene cages has been optimized by means B3LYP/6-31G*. These substituents have selected in order to show the effect of doping on the structural and electronic properties of the fullerene molecule. The optimized geometries of the C_{60} cages and hetero atoms $C_{54}X$ ($X = B$) are presented in Figure 1. The structures of fullerenes are described in terms of two bond lengths close to the doping element. The optimized bond lengths (r), bond angles (θ) and torsion angles (ϕ) for C_{60} and $C_{54}B_6$ are listed in Tables 1-3, which obtained from DFT level calculations at B3LYP/6-31G*.

Table 1. Bond Lengths (in Å) in C₆₀ and C₅₄X₆ (X = B), structures calculated at the B3LYP/6-31G* level

Compound	r _{1,2}	r _{2,3}	r _{3,4}	r _{4,5}	r _{5,6}	r _{6,1}	r _{1,7}	r _{2,8}	r _{3,9}	r _{4,10}	r _{5,11}	r _{6,12}
C ₆₀	1.4532	1.3955	1.4534	1.3956	1.4534	1.3956	1.4533	1.4535	1.4534	1.4533	1.4536	1.4533
C ₅₄ B ₆	1.7292	1.7251	1.7296	1.7252	1.7294	1.7251	1.5604	1.5604	1.5605	1.5605	1.5605	1.5603

Table 2. Bond angle (θ) in C₆₀ and C₅₄X₆ (X = B), structures calculated at the B3LYP/6-31G* level

Compound	$\theta_{1,2,3}$	$\theta_{2,3,4}$	$\theta_{3,4,5}$	$\theta_{4,5,6}$	$\theta_{5,6,1}$	$\theta_{6,1,2}$	$\theta_{7,1,2}$	$\theta_{8,2,3}$	$\theta_{9,3,4}$	$\theta_{10,4,5}$	$\theta_{11,5,6}$	$\theta_{12,6,1}$
C ₆₀	120.0	120.0	120.0	120.0	120.0	120.0	108.0	120.0	108.0	120.0	108.0	120.0
C ₅₄ B ₆	120.0	120.0	120.0	120.0	120.0	120.0	103.0	115.4	103.0	115.4	103.0	115.4

Table 3. Torsion angles (ϕ) in C₆₀ and C₅₄X₆ (X = B), structures calculated at the B3LYP/6-31G* level

Compound	$\phi_{1,2,3,4}$	$\phi_{2,3,4,5}$	$\phi_{3,4,5,6}$	$\phi_{4,5,6,1}$	$\phi_{5,6,1,2}$	$\phi_{6,1,2,3}$	$\phi_{7,1,2,3}$	$\phi_{8,2,3,4}$	$\phi_{9,3,4,5}$	$\phi_{10,4,5,6}$	$\phi_{11,5,6,1}$	$\phi_{12,6,1,2}$
C ₆₀	0.0	0.0	0.0	-0.1	0.0	0.0	-142.6	-138.2	-142.6	-138.2	-142.6	-138.2
C ₅₄ B ₆	0.0	0.0	0.0	0.0	0.0	0.0	-130.0	-124.2	-129.9	-124.2	-129.9	-124.2

Table 4. B3LYP/6-31G* calculated zero-point energies (ZPE), electronic energies (E_{ele}), thermodynamic functions (H, G in kcal/mol, S in cal/mol K) and parameters (ΔH , ΔG , ΔZPE , ΔE_{ele} (in kcal/mol) and ΔS (in cal/mol.k) at 298 K and 1 atm for C₆₀, C₅₄B₆ compounds.

Compound	H	S	G	ZPE	E _{ele}	ΔH	ΔS	ΔG	ΔZPE	ΔE_{ele}
C ₆₀	-1434348.3	136.3	-1434388.9	235.3	-1434597.2	62476.2	0.0	62479.3	10	62470.5
C ₅₄ B ₆	-1384346.2	145.6	-1384389.6	225.3	-1384586.7	112478.3	9.3	112478.6	0.0	112481

Table 5. B3LYP/6-31G* calculated energies (in e.V) of HOMO (ϵ HOMO), LUMO (ϵ LUMO), ϵ LUMO - ϵ HOMO and I (ionization potential) and A (electron affinity) for the compounds 1-4

Compound	HOMO ⁻¹	HOMO	LUMO	LUMO ⁺¹	HLG	I	A
C ₆₀	-6.0	-6.0	-3.2	-3.2	2.8	6.0	3.2
C ₅₄ B ₆	-5.8	-5.6	-4.5	-3.2	1.1	5.6	4.5

According to Table 1, the C-C bond distance is around 1.453 Å. As a consequence of the doping the computed bond distance increases to around 1.729 Å. Thereby, an average increase of 0.276 Å in C₆₀ bond lengths was attributed to the doping. When the carbon cage is doped by B, the C-X bonds increased but when the carbon cage is doped by B, the C-X bonds decreased. The minimal and The calculated Gibbs free energy, enthalpy, entropy, electronic energy, zero point energy and their differences (i.e. ΔG , ΔH , ΔS , ΔE_{ele} and ΔZPE) for the all fullerenes (C₆₀, C₅₄B₆) are presented in Tables 4.

This calculation performed at B3LYP/6-31G* level. Our results show that the doped fullerene C₅₄B₆ is more thermal stability than C₆₀. The electronic structure of the fullerene doped metal compared to pure fullerene C₆₀ has been calculated with density functional theory using the B3LYP/6-31G basis set. The HOMO represents the ability to donate an electron, LUMO as an electron acceptor represents the ability to obtain an electron. Highest occupied molecular orbital (HOMO) and Lowest



unoccupied molecular orbital (LUMO) are the basic electronic parameters associated with the orbital in a molecule and the difference between them, resulting in energy gap. This HOMO and LUMO helps to describe the chemical reactivity and kinetic stability of the molecule. These HOMO and LUMO orbital find out the way to the molecule interacts with other species (Fig. 2). Therefore, while the energy of the HOMO is directly related to the ionization potential, LUMO energy is directly related to the electron affinity. According to the frontier molecular orbital theory, the relative chemical reactivity of a molecular system can be estimated using HOMO and LUMO energies, atomic orbital coefficients, net atomic charges and by the overlaps of molecular orbital.

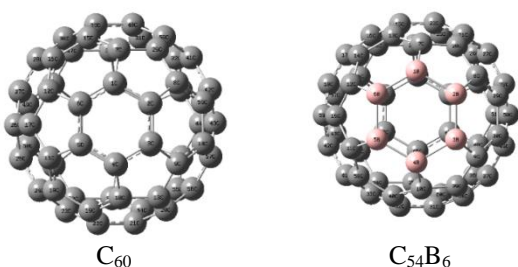


Fig. 1. The optimized geometries of the C_{60} cages and hetero atoms $C_{54}B_6$

The HOMO-LUMO gap of doped fullerenes varies depending on the type of hetero atoms. The increase of gap leading to the enhanced stability against electronic excitations. The energies of the HOMO and LUMO of fullerenes are in the Table 5. The HOMO-LUMO gap of doped fullerenes decrease from C_{60} to $C_{54}B_6$.

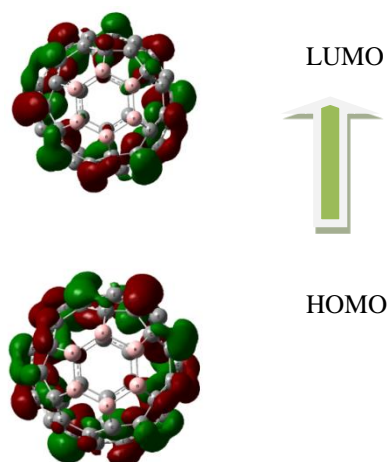


Fig. 2. The HOMOs and LUMOs calculated with density functional theory using the B3LYP/6-31G basis set associated by $C_{54}B_6$.

We have also calculated the vertical ionization potentials and electron affinities for all the isomers and reported the results in Table 5.

Conclusion

Theoretical studies of the C_{60} and $C_{54}B_6$ fullerene have been performed systemically based on the DFT calculations. The results of the geometrical structures, vibrational frequencies, the HOMO-LUMO gap, dipole moment and polarizability of the doped cages were discussed to achieve a further understanding of structure property relationship of the doped cages. According to the results, the doped fullerene $C_{54}B_6$ is more thermal stability than C_{60} fullerenes. HOMO values are increased in doped fullerene cage but the HOMO – LUMO gaps are decreased compared with those of fullerene C_{60} .

References

- [1] A. Nitzan and M. A. Ratner, Electron transport in molecular wire junctions, *Science*, vol. 300, pp.1384, 2003.
- [2] M. S. Dresselhaus, G. Dresselhaus, and P. C. Eklund, *Science of Fullerenes and Carbon Nanotubes*, Academic Press, New York, NY, San Diego, CA, 1996.
- [3] R. H. Xie, J. Zhao, and Q. Rao, Doped carbon nanotubes, in *Encyclopedia of Nanoscience and Nanotechnology*, I edited by H. S. Nalwa, American Scientific Publisher, California, 2003.
- [4] A. Nitzan and M. A. Ratner, Electron transport in molecular wire junctions, *Science*, vol. 300, pp.1384, 2003.
- [5] Guo, T., Jin, C., Smalley, R.E.: Doping bucky: formation and properties of boron-doped buckminsterfullerene. *J. Phys. Chem.* 95, 4948–4950 (1991)
- [6] Pradeep, T., Vijayakrishnan, V., Santra, A.K., Rao, C.N.R. Interaction of nitrogen with fullerenes: nitrogen derivatives of C_{60} and C_{70} . *J. Phys. Chem.* 95, 10564–10565 (1991)

Theoretical study on the mechanism of the NH₃ plus NO reaction on the doublet potential energy surfaces

R. hosengolilo, L. sagatforosh*, S.asgharzade

Department of Chemistry, Payame Noor University, Tehran, I.R. IRAN

*saghatforoush@gmail.com

Abstract

Kinetic and mechanism of atmospheric reaction of ammonia (NH₃) and nitric oxide (NO) on the doublet potential energy surfaces have been investigated in details using ab initio and DFT methods. All stationary points involved in the title reaction were optimized at the B3LYP and MP2 methods of computation in connection with the 6-311++G (d, p) and 6-311++G (3df, 3pd) basis set. For calculation of accurate energies, the CCSD(T) method is applied. Also, thermodynamic parameters and rate constant are calculated at B3LYP method with the mentioned basis set. The results show that direct hydrogen abstraction mechanism is the most important pathways of reaction. Two pre-reactive complex, C1, was formed between ammonia and nitric oxide. Three different products are suggested which all of them have enough thermodynamic stability. The production of NH₂ + HON is the main reaction channel in thermodynamic viewpoint with standard Gibbs free energy of $\Delta G^0 = -10.56$ kcal/mol at B3LYP level. The rate constant is calculated at the 300-2500 K temperature range for the reliable pathway of the mentioned at MP2/6-311++(d, p) method.

Keyword: kinetic; mechanism; ammonia; rate constant; thermodynamic

Introduction

Ammonia, NH₃, and nitric oxide, NO, are important atmospheric species that participate in atmospheric reactions. Most of the NH₃ reactions are pertinent to hydrogen abstraction to produce NH₂ radical [1-3]. Ammonia, the most important alkaline compound found in the atmosphere, has a key role in aerosol chemistry. Gaseous ammonia is released at the Earth's surface primarily through the decomposition of organic material and, due to extremely large solubility in water and reactivity with acid aerosol components, is efficiently removed by interaction with aqueous and acid aerosols. Ammonia is the most third abundant nitrogen species in the terrestrial atmosphere and it plays a critical role in both homogeneous and heterogeneous atmospheric reaction. Being the dominant basic gas in the atmosphere, ammonia partially neutralizes atmospheric acids in precipitation [4].

Ammonia has been at the forefront of advances in refrigeration technology, making it essential to the food processing, storage and delivery infrastructure of our economy. The advantages of ammonia in refrigeration are well known. Ammonia does not destroy atmospheric ozone and does not contribute to the greenhouse effect linked to global warming. In fact, ammonia, one of the most common compounds found in nature, is essential to the earth's nitrogen cycle and its release in the atmosphere is immediately recycled. The use of ammonia as a refrigerant is consistent with international

agreements on reducing global warming and ozone depletion. The most important advantage of ammonia for using in refrigeration industry is an environmentally compatible refrigerant because it has an ozone depletion potential (ODP) of zero and a global warming potential (GWP) of zero.

Ammonia can act as a nucleophile in substitution reactions and is an important source of nitrogen for living systems. Many physical and chemical mechanisms are responsible for the removal of NH₃ from the atmosphere. The main pathways for NH₃ removal from the atmosphere involve atmospheric moisture (e.g., clouds, rain, and fog) and surface water (e.g., seas, rivers, lakes) and deposition on vegetation and soil. So, in this work we perform a detailed theoretical study on the different paths for NH₃ and nitric oxide radical.

Theoretical methods

All the calculations were performed with the GAUSSSIAN 03 program [5]. All geometry optimizations were carried out using Møller–Plesset perturbation theory MP2 and B3LYP level approach in connection with the 6-311++g (d, p) and 6-311++G (3df, 3pd) basis set. Single point calculations were performed for all species at the CCSD (T)//B3LYP level. The Gpopt [6] program as standard software is used for calculation of rate parameters of reaction.

Result and discussion

Figure 1 show the relative energy profile of ammonia and nitric oxide reaction. Total and relative energies for all species of reaction are tabulated in table 1 at MP2 and B3LYP level of computations. We found two pre-reactive complex formed between NH₃ and nitric oxide denoted as C1 and C2. The pre-reactive complex C1 is transformed to CP1 occurring via transition state TS1 with the energy barrier of 60.642 kcal/mol. CP1 can be followed two different pathways. In first pathway, CP1 directly and without passing any transition state converts into the final adduct (HNO+NH₂), which is energetically 14.361 kcal mol⁻¹ above the original reactants. In second pathway, CP1 can be converted into the product complex CP2 via transition state TS2 with the energy barrier of 46.824 kcal mol⁻¹. Then CP2 can directly convert to P2 (OH+H₂N₂) without any transition state. In path P3, the pre-reactive complex C2 is transformed to CP3 after passing from transition state TS3. The energy barrier for this conversation is 50.374 kcal/mol. Product complex CP3 can be converted to product P3 without any transition state. P3 is the most stable product in comparison with the others. So, it is the main product in thermodynamic approach. Structures of transition state (TS1 and TS3) are found H-abstraction from ammonia molecule to nitric oxide.

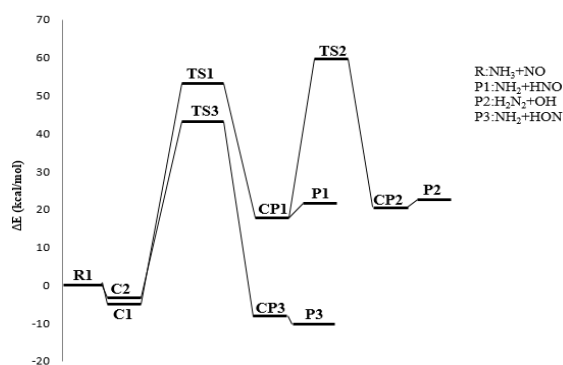


Fig.6: Doublet potential energy profiles of the NH₃+NO reaction at B3LYP level

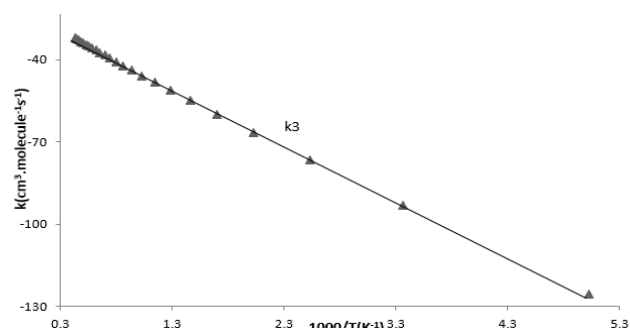


Fig2: Arrhenius curves for the reaction rate constant k_3 for path P3 in the NH₃+NO reaction at MP2 method

Table 1: The relative energies (taking into account ZPE for all methods and the BSSE corrections just for RMP2) (in kcal/mol)

at various methods and basis sets for all species of NH₃+NO reaction

species	B3LYP	MP2	CCSD(T)//B3LYP
R(NH ₃ +NO)	0.000	0.000	0.000
C1	-1.366	-1.457	-2.546
C2	-1.009	-1.021	-0.717
CP1	16.402	18.919	23.833
CP2	16.553	12.109	13.877
CP3	-9.238	-11.898	-10.357
P1	14.361	7.818	12.366
P2	15.786	14.403	14.617
P3	-10.875	-8.170	-7.082
TS1	59.275	60.122	58.801
TS2	63.224	68.398	62.786
TS3	49.374	48.553	49.965

Conclusion

The theoretical study carried out in this work lead to the following conclusions:

1. The present work, The reaction of NH₃ with the NO carried out using the MP2 and B3LYP theoretical approaches in connection with the 6-311++G(d, p) and 6-311++G (3df, 3pd) basis set.
2. Reaction of NH₃ with the NO is produced three kinds of products after passing three transition states. P3 is the most stable product.

References

1. L.V. Moskaleva, M.C. Lin, Theoretical Study of the NH₂ + C₂H₂ Reaction, J. Phys. Chem. A 102(1998) 4686-4693.
2. A. Ianniello & F. Spataro, Occurrence of gas phase ammonia in the area of Beijing (China), (2010) Atmos Chem Phys 10:9487-9503.
3. D. Papousek Geometry changes in molecular photoionization: The NH₃⁺ (\tilde{X}^2A_2'') ← NH₃ (X^1A_1) transition (1983) J Molecular Struct 100: 179.
4. Rennard JJ, Calidonna SE, Henley MV Fate of ammonia in the atmosphere--a review for applicability to hazardous releases ,2004 J Hazard Mat 108:29-60.
5. Frisch etal; "GAUSSIAN 03, Revision B.03, Gaussian"; Inc., Pittsburgh, PA; 2003.
6. Miyoshi A (2010) Gaussian Post Processor (GPOP) University of Tokyo.



A First-principles study of Li adsorption and diffusion on graphene nanoflakes under the effect of external electric field as an anode material for Li-ion battery

Seyyed Mahdi Atashzar*, Soheila Javadian

Department of Chemistry, Faculty of Science, Tarbiat Modares University, P.O. Box 14115-175, Tehran, Iran

*mahdi.atashzar@gmail.com

Abstract: In this work the interaction between Li ion and graphene surface with the absence and the presence of external electric field (EEF) applied perpendicular to the surface was investigated. M06-2X/6-31G(d) DFT calculations were performed to describe the adsorption and diffusion properties. Meaning of the binding energy and scanning the potential energy surface (PES) of the charged molecular systems in the presence of EEF is different from that in the absence of electric field as the binding energy is an anisotropic characteristic which depends on the orientation of molecules with respect to the EEF. With the electric field increased from 0.0 a.u to 0.02 a.u, the diffusion barriers were decreased from 24 to 20 KJ/mol, for the Li ion in the graphene nanoflakes. We concluded that the external electric field can increase the charging speed of rechargeable ion batteries based on the graphene anode materials.

Keyword: external electric field; grapheme; rechargeable ion batteries

Introduction

Layered structural materials are convenient for intercalation/deintercalation of metal ions, thus can be used as the appropriate materials for rechargeable ion batteries [1-2]. Lithium ion batteries have been the subject of intense investigations due to their good cycling performance, high storage capacity and high energy density. Despite all the studies, finding excellent anodes with good electrical conductivity and high reversible lithium storage are still under development. Among them, graphite is the key anode material for the commercial lithium ion batteries with an energy capacity of 372 mAhg⁻¹. Some experimental results have shown that graphene, a single atomic-layer thickness of graphite, can adsorb higher amounts of Li (e.g. specific capacity of ~540 mAhg⁻¹) than graphite.

In this work, we investigated the effects of an external electric field on adsorption and diffusion of Li ion in the graphene monolayer based on DFT analysis. We have reported that adsorption and mobility of the transporting ion can be significantly enhanced in the graphene monolayer with an external electric field.

Materials and method

First, the model cluster with a molecular formula of C₈₈H₂₆ was constructed and fully optimized using the M06-2X meta-hybrid GGA functional merged with the 6-31G(d,p) basis set as implemented in the GAMESS program [3]. Then the Li ion was positioned above the surface. Three different orientations of the ion with respect to the graphene surface, namely, top, hollow and bridge, were considered as starting structures (Fig. 1). In the top site geometry the Li ion located directly above the C-atom, in the hollow site conformation the ion is above the centre of a hexagon in the graphene layer and in the bridge site structure the ion positioned above the centre of a C-C bond. During the calculation in the absence and presence of different homogeneous external electric fields

in which the electric field was directed perpendicularly from the Li ion to the graphene flake, the rigid model was used: the geometry of the cluster was frozen as it obtained in the first step and the optimized ion position was determined by varying the distance between the ion and the graphene plane until the most stable position is found. The site with the largest adsorption energy was ascribed as the most stable site of adsorption.

The binding energies for our systems in the presence of EEF were calculated from Equation

$$E_{binding} \perp = E_{complex}^{field} - (E_{Li}^{field} + E_G^{field}) + FQ(R_1 - R_0)$$

In this equation, complex, Li, and G subscripts denote the complex, Li ion, and graphene surface, respectively. The term $FQ(R_1 - R_0)$ corrects the energy of the reference Li ions for their distance to the coordinate origin in the complexes. In other words, this term measures the electric work which is required to move free ions from the origin to their coordinates in the complexes.

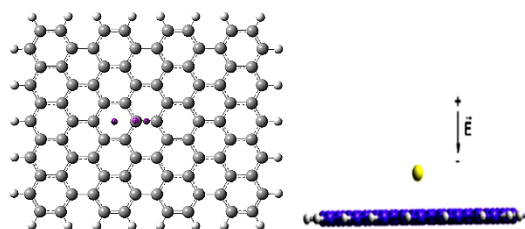


Fig.7: The different orientations of the ion with respect to the graphene surface: (T) top, (H) hollow and (B) bridge (down).

Results and Discussion

In this work, the effect of a uniform and directed external electric field on Li ion adsorption and diffusion on a graphene flake was investigated. The perpendicularly

applied external electric field was directed from the Li ion to the graphene surface. The results of calculated



equilibrium distances between the Li ion and the graphene flake surface (R_{Gr-Li}), the residuary atomic charges on the Li ion ($Z_{Li\ ion}$), the adsorption energies of the Li ion-graphene molecular complexes (E_{ads}) and the dipole moments of Li-graphene complexes are displayed in Table 1.

When the external electric field is increased from 0.0 to 0.02 a.u., the adsorption energies increase from -231.18 to -439.32 kJ/mol, for the Li ion adsorbed at H sites.

In this study the diffusion barriers were calculated using a constrained method in the present work, in which the ions were constrained in the direction along the diffusion path, whereas it is allowed to relax in the direction perpendicular to the diffusion path.

Because of the high symmetry of the cluster we have studied two different diffusion paths: both cases the starting position of the ion is the hollow position in the middle of the cluster (H) and the ion migrate through the middle of the bond (B) or on the top of the C atom (T), denoted as path A or B, respectively. To eliminate the electric field induced bending of the graphene plane the rigid model was used to determine the energies for different adsorption positions.

Energy barriers of the diffusion of Li ion on Path A and B in the absence and presence of applied electric field on the graphene monolayer is shown in Fig. 2

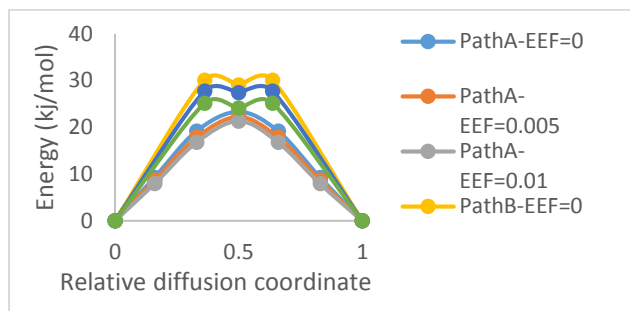


Fig.2: The energy barrier as a function of the relative distance along the tow paths. The relative distance is defined by the ratio of the horizontal distance from the starting site to the position of the Li ion along a given pathway and that from the starting site to the ending site.

Table1: The adsorption energies (E_{ads}), Mulliken atomic charge (electron charge), the natural bond orbitals (NBO) analysis charge (electron charge), the Li ion-graphene equilibrium distances and the dipole moments of the graphene-Li ion complexes represented when the Li ion, is adsorbed on the $C_{88}H_{26}$ graphene cluster

Ion-graphen complex	Electric field strength (a.u.)	E_{ads} (kJ mol ⁻¹)	R _{Ion-Gr} (Å)	Mulliken chargea (e)	NBO chargea (e)	Dipole moment (Debye)
$C_{88}H_{26}$	0	-231.18	1.80	0.516	0.941	5.183
	0.005	-337.45	1.74	0.448	0.92	1.877
	0.01	-359.48	1.70	0.390	0.898	3.109
	0.02	-439.32	1.85	-0.079	-0.079	15.180

Conclusions

In conclusion, the adsorption and diffusion behaviors of the Li ion on graphene monolayer with an external electric field were investigated using the DFT method. The diffusion barriers were decreased after applying the electric field. The results suggest that the electric field can be used to realize a fast charging process of rechargeable ion batteries

References

[1] X. Bian, Q. Fu, C. Qiu, X. Bie, F. Du, Y. Wang, Y. Zhang, H. Qiu, G. Chen, Y. Wei "Carbon black and vapor

grown carbon fibers binary conductive additive for the $Li_{1.18}Co_{0.15}Ni_{0.15}Mn_{0.52}O_2$ electrodes for Li-ion batteries", *Mater. Chem. Phys.*, 156 (2015) 69e75.

[2] W. He, X. Li, J. Chen, F. Peng, R. Zhang, Y. Liu, Z. Xiao "Effects of ionothermal and hydrothermal methods on structure and electrochemical performance of $LiNi_{1/3}Co_{1/3}Mn_{1/3}O_2$ cathode materials", *Mater. Chem. Phys.*, 155 (2015) 9e16.

[3] M.W. Schmidt, K.K. Baldrige, J.A. Boatz, S.T. Elbert, M.S. Gordon, J.H. Jensen, S. Koseki, N. Matsunaga, K.A. Nguyen, S. Su "General atomic and molecular electronic structure system", *J. Comput. Chem.*, 14 (1993) 1347-1363.



Decomposition of activation barrier of the Aza-Diels-Alder in the presence of PHX₂ (X=F, Cl, Br)

Fereshteh Yaghoobi*

Faculty of Science, University of Nahavand, Nahavand, Iran

*yaghoobifereshteh@gmail.com

Abstract: The effect of PHX₂ (X=F, Cl, Br) on the activation barriers of H₂C=NNH₂ (dienophile) and 1,3-butadiene (diene) cycloaddition has been explored by means of density functional theory (DFT) and energy decomposition analysis (EDA). For these cycloadditions, the activation barriers were investigated using activation strain model and decomposition of the activation barrier (ΔE^\ddagger) into orbital interaction (ΔE_{orb}), electrostatic interaction (ΔE_{elstat}), pauli repulsion (ΔE_{pauli}) and distortion energy (ΔE_{dist}) was reported. Also, the relationship between interaction energies and distortion energies of transition states these cycloadditions were investigated. The results show that in the presence of PHX₂ (X= F, Cl, Br), distortion energy of diene and dienophile decreased and also the interaction energies between reactants increased. Therefore, in presence of PHX₂ (X= F, Cl, Br), activation barrier for this cycloaddition decreased.

Keywords: “Aza-Diels-Alder” “density functional theory” “energy decomposition analysis” “activation strain model”

Introduction

The Diels–Alder cycloaddition reactions (DA) are a useful tool for accessing unsaturated six-membered rings in the modern organic chemistry [1]. The DA reaction usually requires electron-withdrawing groups in the dienophile and electron-rich dienes. In the past few decades, investigation of novel Lewis acid catalysis is still a major research area in organic chemistry. The Lewis acids (LA) can act as catalyst in the DA reactions and can promote these reactions. These catalysts can enhance the reaction DA rates [2].

The Aza-Diels–Alder reactions provide an alternative route for synthesis of nitrogen-containing heterocyclic rings from imine and diene components [3]. Just like DA reaction, Lewis acids play an important catalytic role in the Aza-Diels-Alder reaction [4].

The reactions between H₂C=NNH₂ and 1,3-butadiene in the absence and presence of PHX₂ (X=F, Cl, Br), in order to understand the effects of PHX₂ on these reactions were investigated. According to activation strain model [5], the activation energy (ΔE^\ddagger) is decomposed into the distortion energy (ΔE_d^\ddagger) and interaction energy (ΔE_i^\ddagger). Activation energy, distortion energy and interaction energy of all transition states studied here, were calculated.

EDA is a valuable analytical tool that partition the interaction energy (ΔE_i^\ddagger) into electrostatic interaction (ΔE_{elstat}), orbital interaction (ΔE_{orb}), pauli repulsion (ΔE_{pauli}). These values allowed us to conclude that the main factor responsible for the existence of positive values of ΔE^\ddagger for all reaction studied here and also allow extraction of information on the role of PHX₂ (X=F, Cl, Br) in determination of ΔE^\ddagger .

Computational method

All of structure under investigation optimized using the Gaussian 09 suite of programs [6] at M06-2X/TZVPP level of theory. The EDA analysis with the program

package ADF13.01, were carried out at M06/TZVP (ZORA)// M06-2X/TZVPP with C₁ symmetry. The nature of the minimums and transition states was confirmed by the absence and presence of the imaginary frequency, respectively. Intrinsic reaction coordinate (IRC) calculations were done to confirm the identity of the transition state structures.

Results and Discussion

The transition structures of the cycloadditions involving H₂C=NNH₂ and 1,3-butadiene in the absence of PHX₂ (X= F, Cl, Br) and in the presence of PHX₂ (X= F, Cl, Br) are presented in Fig. 1.

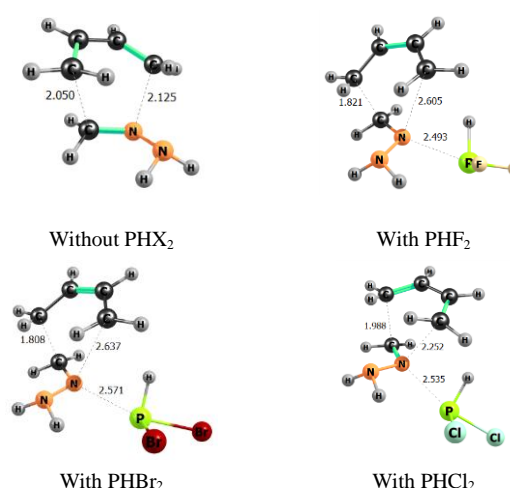


Fig.8: Optimized geometries of the transition states at M06-2x/TZVPP in the absence of PHX₂ (X= F, Cl, Br) and in the presence of PHX₂

The activation strain model was applied in order to determine reactivity of the compound studied here. The values of activation energy (ΔE^\ddagger), interaction energy (ΔE_i^\ddagger) and distortion energy (ΔE_d^\ddagger), which was

decomposed as the sum of the diene distortion energy ($\Delta E_{d-dien}^\ddagger$) and dienophile distortion energy ($\Delta E_{d-CH_2=N-NH_2}^\ddagger$) for all reactions at M06/TZP (ZORA)//M06-2X/TZVPP were calculated (Fig. 2).

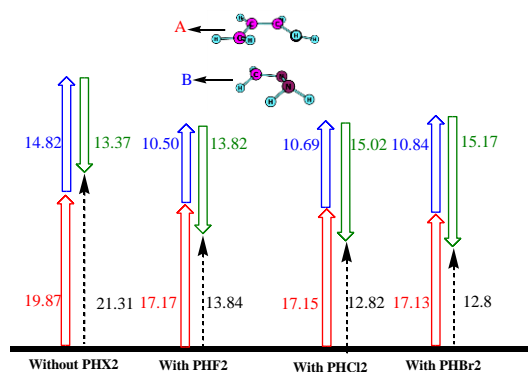


Fig.2: values of ΔE^\ddagger (dash line), ΔE_i^\ddagger (in green), $\Delta E_{d-dien}^\ddagger$ (in red) and $\Delta E_{dienophile}^\ddagger$ (in blue) for reactions under study.

The difference in the reactivity between the reactants under study is related to both the distortion energy and interaction energy. As can be seen in Fig. 2, the distortion energies of diene and dienophile after binding PHX_2 (X= F, Cl, Br) to reactants are decreased and also after binding PHX_2 to reactants, the dienophile distortion energy more than diene distortion energy are increase in all substituents of PHX_2 .

As shown in Fig.2, the interaction energies display a range between 13.37 and 15.17. The interaction between energy between $H_2C=NNH_2$ and 1,3-butadiene in the presence of PHX_2 for X= Cl and Br show the maximum values.

The activation strain analyses show that after binding PHX_2 to dienophile reactant, the interaction energy between reactants have the most effect on activation energy of reactions.

The interaction energy between strained reactants decomposed into three terms as shown in eq. 1.

$$\Delta E_i^\ddagger = \Delta E_{elstat} + \Delta E_{orb} + \Delta E_{pauli} \quad (1)$$

Table. 1: Interaction energies decomposition (in kcal/mol) for transition states of $H_2C=NNH_2$ and 1,3-butadiene cycloaddition.

Butadiene+CH ₂ NNH ₂ cycloaddition	ΔE_{pauli}	ΔE_{orb}	ΔE_{elstat}
Without PHX ₂	162.64	-99.32	-76.69
With PHF ₂	151.14	-93.26	-71.70
With PHCl ₂	155.25	-96.38	-73.90
With PHBr ₂	156.22	-96.81	-74.58

The values of ΔE_{elstat} , ΔE_{orb} and ΔE_{pauli} in the transition state are listed in Table 1.

The results of Table 1 show that the main portion of ΔE_i in the transition states study here is attributed to ΔE_{orb} .

The greatest amounts of ΔE_{orb} corresponding to transition states of $H_2C=NNH_2$ and 1,3-butadiene cycloaddition in absence of PHX_2 and also this structure has the greatest amounts of ΔE_{pauli} . Also this cycloaddition in presence of PHF_2 have lowest amounts of ΔE_{orb} and ΔE_{pauli} . The value of ΔE_{orb} for transition states of $H_2C=NNH_2$ and 1,3-butadiene cycloaddition in presence of $PHCl_2$ is -96.38 and in presence of $PHBr_2$ is -96.81 kcal/mol.

Conclusions

The activation barriers of $H_2C=NNH_2$ and 1,3-butadiene cycloaddition in the absence and in the presence of PHX_2 (X= F, Cl, Br) using density functional theory (DFT) and energy decomposition analysis (EDA) has been explored. For these cycloaddition, the activation barriers were investigated using activation strain model. The decomposition of the activation barrier into ΔE_{orb} , ΔE_{elstat} , ΔE_{pauli} and ΔE_{dist} studied here. The results show that with binding PHX_2 (X= F, Cl, Br) to $H_2C=NNH_2$, distortion energy of diene and dienophile decreased and also the interaction energies between reactants increased. Therefore, in presence of PHX_2 (X= F, Cl, Br), activation barrier for this cycloaddition decreased. The ΔE_{orb} has the maximum effect on stabilization of these cycloadditions.

References

- [1] O. Diels, K. Alder "Synthesen in der hydroaromatischen Reihe", *Justus Liebigs Ann. Chem*, 460 (1928) 98–122.
- [2] U. Pindur, G. Lutz, C. Otto "Acceleration and selectivity enhancement of Diels-Alder reactions by special and catalytic methods", *Chem. Rev*, 93 (1993), 741-761.
- [3] P. Buonora, J. C. Olsen, T. Oh "Recent developments in imino Diels–Alder reactions", *Tetrahedron*, 57 (2001) 6099–6138.
- [4] X. Jiang, R. Wang "Recent Developments in Catalytic Asymmetric Inverse-Electron-Demand Diels–Alder Reaction" *Chem. Rev*, 113 (2013) 5515- 5546.
- [5] W-J. V. Zeist, F. M. Bickelhaupt "The activation strain model of chemical reactivity", *Org. Biomol. Chem*, 8 (2010) 3118-3127.
- [6] M. J. Frisch, G. W. Trucks, H. B. Schlegel, G. E. Scuseria, M. A. Robb, J.R. Cheeseman, G. Scalmani, V. Barone, B. Mennucci, G. A. Petersson, H. Nakatsuji, M. Caricato, X. Li, H. P. Hratchian, A. F. Izmaylov, J. Bloino, G. Zheng, J. L. Sonnenberg, M. Hada, M. Ehara, K. Toyota, R. Fukuda, J. Hasegawa, M. Ishida, T. Nakajima, Y. Honda, O. Kitao, H. Nakai, T. Vreven, J. J. A. Montgomery, J. E. Peralta, F. Ogliaro, M. Bearpark, J. J. Heyd, E. Brothers, K. N. Kudin, V. N. Staroverov



Interplay between hydrogen bond and single-electron tetrel bond: $\text{H}_3\text{C}\cdots\text{COX}_2\cdots\text{HY}$ and $\text{H}_3\text{C}\cdots\text{CSX}_2\cdots\text{HY}$ ($\text{X} = \text{F}, \text{Cl}$; $\text{Y} = \text{CN}, \text{NC}$) complexes as a working model

Z. Rezaei^{*a}, M. Solimannejad^a, M. D. Esrafil^b

^aQuantum Chemistry Group, Department of Chemistry, Faculty of Sciences, Arak University, Arak, Iran;

^bLaboratory of Theoretical Chemistry, Department of Chemistry, University of Maragheh, Maragheh, Iran

*z.rezaei.chem@gmail.com

Abstract : UMP2 calculations with aug-cc-pVDZ basis set were performed to analyze intermolecular interactions in a series of ring-shaped molecular complexes formed by CH_3 , $\text{CO}(\text{S})\text{X}_2$ ($\text{X} = \text{F}, \text{Cl}$) and $\text{HCN}(\text{NC})$ which are connected via two hydrogen bonds and a single-electron tetrel bond interactions. Molecular geometries and interaction energies of dyads and triads are investigated at the UMP2/aug-cc-pVDZ computational level. Particular attention is paid to many-body interaction energies. The impacts of the hydrogen bonds on the single-electron tetrel bond in each complex are systematically investigated. The electronic properties of the complexes are analyzed using parameters derived from the atoms in molecules (AIM) methodology.

Keywords : cooperativity; hydrogen bonding; Tetrel bonding; MP2

Introduction

Theoretical investigation on noncovalent single-electron interactions helps us to gain a deeper insight in chemistry of reactions involving radicals.

The tetrel bond (TB) is a Lewis acid–Lewis base attractive interaction in which covalently-bonded Group-IV atoms (C, Si, Ge or Sn) act as the Lewis acid [1]. Politzer and Murray [2, 3] associated its origin with the presence of an σ -hole region along the extension of the covalent bond to these atoms. Furthermore, there can also exist a “ π -hole”, a positive region of the molecular electrostatic potential that is perpendicular to an adjacent portion of the molecular framework. The tendency of Group IV atoms to interact with a given Lewis base increases in going from the lighter to the heavier atoms ($\text{C} < \text{Si} < \text{Ge} < \text{Sn} < \text{Pb}$), and as the electron-withdrawing ability of the remainder of the molecule increases.

This work is designed to address the issue of cooperativity effects between hydrogen bond and single electron tetrel bond interactions in a systematic and thorough manner. We present an ab initio study on concerted interactions in eight ring shaped complexes $\text{H}_3\text{C}\cdots\text{COX}_2\cdots\text{HY}$ and $\text{H}_3\text{C}\cdots\text{CSX}_2\cdots\text{HY}$, where $\text{X} = \text{F}, \text{Cl}$ and $\text{Y} = \text{CN}, \text{NC}$ (Fig. 1).

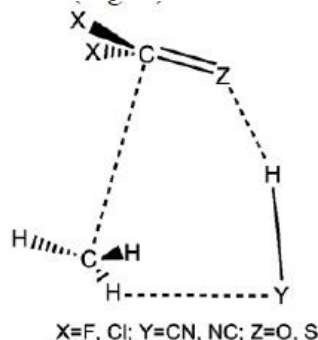


Fig.1: Disposition of the monomers within the complexes.

Method

Structures have been optimized and characterized by frequency computations at the UMP2/aug-cc-pVDZ computational level. The stabilization energy was calculated by supramolecular approach and the full counterpoise (CP) method was used to correct them. To characterize the topological properties of the dyads and ringshaped triads, atoms in molecules (AIM) analysis was performed with the help of AIMAll program using the wave functions generated at the UMP2/aug-cc-pVDZ level by Gaussian 03 computational package. All geometry optimizations, interaction energies and energy components were calculated using the GAMESS package [4].

Results and Discussion

To further understand the cooperativity effects, an analysis of many-body decomposition of the stabilization energy was performed. The total stabilization energy of triad equals the sum of relaxation energy and many-body terms: $E_i(\text{ABC}) = E_R + E_{\text{A-B}} + E_{\text{A-C}} + E_{\text{B-C}} + E_{\text{A-B-C}}$

The strain energy (E_R) is defined as the energy sum of the monomers frozen in the geometry of the triads minus the energy sum of the optimized monomers. The $E_{\text{A-B}}$, $E_{\text{B-C}}$ and $E_{\text{A-C}}$ are two-body terms. Results presented in Table 1 shows that two-body interaction energy provides the largest contribution of the total interaction energy.

Table 1. Decomposition of stabilization energy [kJ mol^{-1}] of the studied triads using the geometry within the triads.



Cooperativity has been calculated using equation: $E_{\text{Coop}} = E_i(\text{ABC}) - E_i(\text{AB}) - E_i(\text{BC}) - E_i(\text{AC})$. Here $E_i(\text{ABC})$ is the stabilization energy of the trimer, $E_i(\text{AB})$ and $E_i(\text{BC})$ are the stabilization energy of the isolated dimers within their corresponding minima configuration and $E_i(\text{AC})$ is the interaction energy of the molecules A and C in the geometry they have in the trimer. In all of the cases, a favorable cooperativity is observed for triads (Table 2).

Electron density analysis

The shift of electron density which is the difference in density between the complex and the sum of isolated monomers, in the same positions as those in the complex, provides useful information about the formation of a complex. Fig. 2 shows the electron density difference maps of $\text{CH}_3 \cdots \text{CSX}_2 \cdots \text{HNC}$ and $\text{CH}_3 \cdots \text{COX}_2 \cdots \text{HNC}$ (X = F, Cl) complexes.

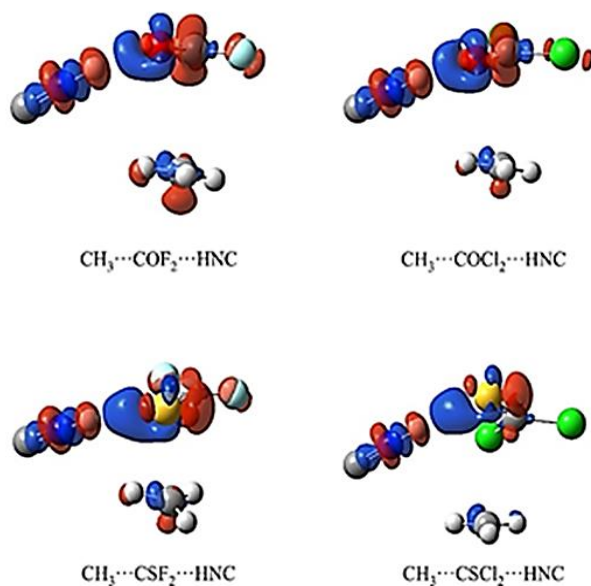


Fig. 2: Electron density difference maps of $\text{CH}_3 \cdots \text{CSX}_2 \cdots \text{HNC}$ and $\text{CH}_3 \cdots \text{COX}_2 \cdots \text{HNC}$ (X=F, Cl) complexes. The selected isosurface is 0.001 au. Charge depletion and accumulation sites are shown in red and blue, respectively.

An increase in the electron density is indicated by blue area, whereas the red regions represent the density loss.

A red density loss is found in the p-hole of the carbon atom of COX_2 and CSX_2 (X = F, Cl) in all structure, caused by CH_3 single electron revealing the electrostatic nature of this kind of interaction. Red region around CH_3 carbon atom indicating electronic density depletion is larger in complexes including more positive p-hole such

Triads(A...B...C)	$\Delta E_{\text{A-B}}$	$\Delta E_{\text{B-C}}$	$\Delta E_{\text{A-C}}$	$\Delta E_{\text{A-B-C}}$	E_s
$\text{CH}_3 \cdots \text{COCl}_2 \cdots \text{HCN}$	-4.32	-9.75	-3.22	-0.26	0.45
$\text{CH}_3 \cdots \text{COCl}_2 \cdots \text{HNC}$	-4.22	-17.63	-3.21	-0.37	1.00
$\text{CH}_3 \cdots \text{CSCl}_2 \cdots \text{HCN}$	-4.21	-7.75	-3.48	0.03	0.22
$\text{CH}_3 \cdots \text{CSCl}_2 \cdots \text{HNC}$	-3.74	-14.48	-3.64	0.20	0.52
$\text{CH}_3 \cdots \text{COF}_2 \cdots \text{HCN}$	-4.45	-8.08	-3.19	-0.70	0.67
$\text{CH}_3 \cdots \text{COF}_2 \cdots \text{HNC}$	-4.28	-15.22	-3.40	-1.00	1.14
$\text{CH}_3 \cdots \text{CSF}_2 \cdots \text{HCN}$	-2.51	-5.84	-3.11	-1.59	0.42
$\text{CH}_3 \cdots \text{CSF}_2 \cdots \text{HNC}$	-1.64	-11.17	-2.83	-2.66	0.71

as COF_2 and CSF_2 but it vanishes in $\text{CH}_3 \cdots \text{CSCl}_2 \cdots \text{HNC}$ complex as CSCl_2 monomer has the weakest p-hole comparing others. The similar features were also reported in hydrogen bonds. The blue area of the lone pair on the O and S atom is larger at the side close to the H atom of HNC than that at the other side, and simultaneously the H atom of the HNC near the lone pair on the O and S atom is surrounded by a larger red region.

Conclusions

Ab initio calculations at UMP2/aug-cc-pVTZ level were used to characterize intermolecular interactions in $\text{H}_3\text{C} \cdots \text{COX}_2 \cdots \text{HY}$ and $\text{H}_3\text{C} \cdots \text{CSX}_2 \cdots \text{HY}$ (X = F, Cl; Y = CN, NC) triads. The equilibrium structures and interaction energies of the complexes were analyzed. All binding distances are approximately shorter than the sum of van der Waals radii of those related interacting atoms, which indicates there is an attractive interaction between the monomers in the ternary complexes. The impacts of the hydrogen bonds on the single-electron tetrel bonding each complex were systematically investigated by calculating the three-body $E_{\text{A-B-C}}$ values. In all ternary complexes studied, the two-body energy term is the source of the interaction energy. The nature of the X and Y substituent strongly determine the contribution of the three-body energy terms which is largest and smallest for the $\text{CH}_3 \cdots \text{CSF}_2 \cdots \text{HNC}$ and $\text{CH}_3 \cdots \text{CSCl}_2 \cdots \text{HNC}$, respectively. A linear relationship was obtained between the interaction energies and electron density values at RCPs with an R^2 value of 0.943. The results of this study are useful for the applications in molecular recognition and supermolecular chemistry involving single electron tetrel bonds.

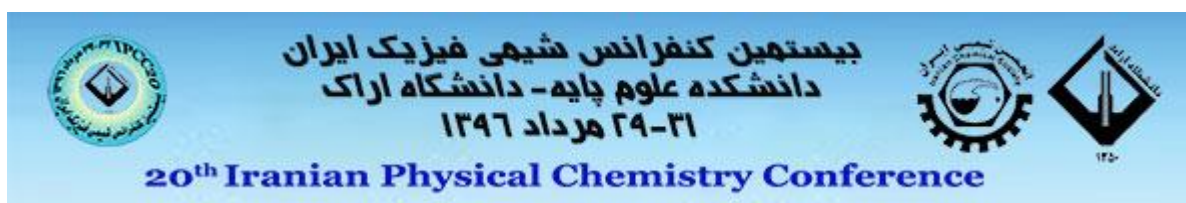


Table 2. Interaction energies E_i [kJ mol^{-1}] of hydrogen and lithium bonding in the studied dyads (D) and triads (T).

Triads(A...B...C)	$E_i(ABC)$	$E_i(AB)$	$E_i(BC)$	$E_i(AB, T)$	$E_i(BC, T)$	E_{coop}
$\text{CH}_3 \cdots \text{COCl}_2 \cdots \text{HCN}$	-17.09	-4.49	-10.44	-3.90	-9.44	-0.71
$\text{CH}_3 \cdots \text{COCl}_2 \cdots \text{HNC}$	-24.42	-4.49	-17.85	-3.32	-16.78	-1.37
$\text{CH}_3 \cdots \text{CSCl}_2 \cdots \text{HCN}$	-15.19	-4.08	-9.08	-4.02	-7.61	-0.19
$\text{CH}_3 \cdots \text{CSCl}_2 \cdots \text{HNC}$	-21.13	-4.08	-15.15	-3.33	-14.05	-0.32
$\text{CH}_3 \cdots \text{COF}_2 \cdots \text{HCN}$	-15.74	-4.42	-9.66	-3.82	-7.70	-1.37
$\text{CH}_3 \cdots \text{COF}_2 \cdots \text{HNC}$	-22.76	-4.42	-16.05	-3.19	-14.40	-2.14
$\text{CH}_3 \cdots \text{CSF}_2 \cdots \text{HCN}$	-12.62	-3.24	-6.83	-2.13	-5.53	-2.01
$\text{CH}_3 \cdots \text{CSF}_2 \cdots \text{HNC}$	-17.59	-3.24	-12.06	-0.99	-10.60	-3.37

References

- [1] I. Alkorta, I. Rozas, J. Elguero "Molecular complexes between silicon derivatives and electron-rich groups", *J. Phys. Chem. A*, 105 (2001) 743–749.
- [2] J.S. Murray, P. Lane, P. Politzer "Expansion of the r-hole concept", *J. Mol. Model*, 15 (2009) 723–729.
- [3] A. Bundhun, P. Ramasami, J.S. Murray, P. Politzer "Trends in r-hole strengths and interactions of F_3MX molecules (M = C, Si, Ge and X = F, Cl, Br, I)", *J. Mol. Model*, 19 (2013) 2739–2746.
- [4] M.W. Schmidt, K.K. Baldrige, J.A. Boatz, S.T. Elbert, M.S. Gordon, J.H. Jensen, S. Koseki, N. Matsunaga, K.A. Nguyen, S. Su "General atomic and molecular electronic structure system", *J. Comput. Chem*, 14 (1993) 1347–1363.

Theoretical study of substituent effects on the barrier energy of $\text{CH}_2\text{NH} + \text{NO}$ reaction in gas phase

S. Asgharzadeh*, M. Vahedpour and H. Sagafi

Department of Chemistry, Faculty of Science, University of Zanjan, Iran

*somaieasgarzade@znu.ac.ir

Abstract

The reaction of methanimine with NO on the doublet potential energy surface was carried out using the UMP2, UB3LYP and CCSD(T)//B3LYP theoretical approaches in connection with the 6-311++G (d, p) and some other basis sets. Two pre-reactive complex, C1 and C2 was formed between CH_2NH and nitric oxide. From a variety of this complex, two types of products are obtained that one of them are found to be thermodynamically stable. In thermodynamic viewpoint, $\text{CH}_3+\text{N}_2\text{O}$ adduct is spontaneous and exothermic with -14.30 and -13.63 kcal/mol in Gibbs free energy and enthalpy of reaction at the UB3LYP level, respectively. In kinetic point of view, the mentioned products after passing one transition state is the most favor pathway of reaction. In this reaction, for $\text{HCN}+\text{HNOH}$ adduct is the main kinetically product. So, we have studied the substituent effects on the barrier energy in this path. The obtained substituent effects analysis showed that the barrier energy is reduced when one of the hydrogen atom in $-\text{CH}_2$ is substituent via activating group such as $-\text{NH}_2$.

Keywords: Mechanism; methanimine; Potential energy surface; substituent; activating group

Introduction

Amines are organic compounds and functional groups which contain a basic nitrogen atom and emitted into the atmosphere from a variety of oceanic, biogenic and anthropogenic sources. Also, amines released into the atmosphere from carbon capture and storage technologies. Amines are participate in conversion reaction in atmosphere and convert to secondary organic aerosol (SOA) and brown carbon in aqueous phase. Schade and crutzen studied the atmospheric chemistry of amines and show that amines are not very harmful at ambient atmosphere concentrations. But when they are participate in reactions produce suspected carcinogens such as nitrosamines. The photo oxidation of methylamine (CH_3NH_2) and the decomposition of methyl azides are produced methanimine in the atmosphere [1].

Methanimine is the simplest molecule containing a carbon-nitrogen double bond that is also called methylenimine or formaldimine (H_2CNH). Gas phase methylenimine was first produced by Johnson and Lovas through hydrogen atom abstraction and pyrolysis of methylamine. Methanimine is a reactive species and unstable in the terrestrial environment, and it is an important molecule in prebiotic chemistry, because it is a possible precursor of glycine (via its reactions with HCN and H_2O). Also, H_2CNH was observed in dark interstellar dust clouds, and in the upper atmosphere of Titan. In the atmosphere of Titan, methanimine produced via the reaction of $\text{N} (^2\text{D})$ with both methane and Ethan [2].

Methylene imine (methanimine, formaldimine, $\text{CH}_2=\text{NH}$) is a pyrolysis product of amines as well as a photolysis product of methylamine [3] and diazomethane [4]. It has obvious chemical importance as the simplest imine, and with its carbon-nitrogen double bond, methylenimine is a bonding paradigm for numerous nitrogen-containing heterocyclic. The molecule is also of astrophysical interest, having been detected in dark interstellar dust clouds.

Theoretical methods

All the electronic structure calculations were performed using the GAUSSIAN03 program package [5]. All geometry optimizations were carried out using Møller-Plesset perturbation theory MP2 and B3LYP level approach in connection with the 6-311++g (d, p) basis set. Single point calculations were performed for all species at the CCSD (T)//B3LYP level.

Result and discussion

In spite of numerous attempts, two complexes are formed between the reactants CH_2NH and NO that have been noted as C1 and C2. Pre-reactive complex C1 is 2.234kcal/mol more stable than original reactant. In path P1, pre-reactive complex C1 is converted to final products $\text{HCN}+\text{HNOH}$ via transition state TS1 with the energy barrier of 35.124 kcal/mol. In this path we are substituent the hydrogen of $-\text{CH}_2$ group with two different group: activating group $-\text{NH}_2$ and deactivating group $-\text{F}$. the obtained substituent effects analysis showed that the deactivating group is increasing the barrier energy of reaction by 24.543 kcal/mol. Whereas

the activating group is reduce the barrier energy by 7.247kcal/mol. the obtained results are depicted graphically in figure 2.

In path P2, pre-reactive complex ¹C2 is evolves to the intermediate IN1 through the transition state TS2 with the high energy barrier (37.78 kcal mol⁻¹). The high value of the dipole moment ($\mu=8.35$ Debye) suggestive to the zwitterionic character of intermediate IN1 and it points to that the solvent effects can play a conclusive role when the reaction befalls in a polar protic solvent. From an energetic points of view, IN1 is 23.86 kcal mol⁻¹ unstable than the reactants. From IN1, the hydrogen of -NH group migrate to -CH2 group through TS3 with an energy barrier of about 41.67 kcal mol⁻¹. Finally intermediate IN2 decomposes into the products CH₃+N₂O over the transition state TS4 with the barrier energy of 39.56 kcal mol⁻¹. Product P2 is 8.89 kcal mol⁻¹ more stable than the original reactants. Thermodynamic data shows that P2 formation process is exothermic by -9.72 kcal mol⁻¹ and spontaneous in gas phase with -11.90 kcal mol⁻¹ standard Gibbs free energy.

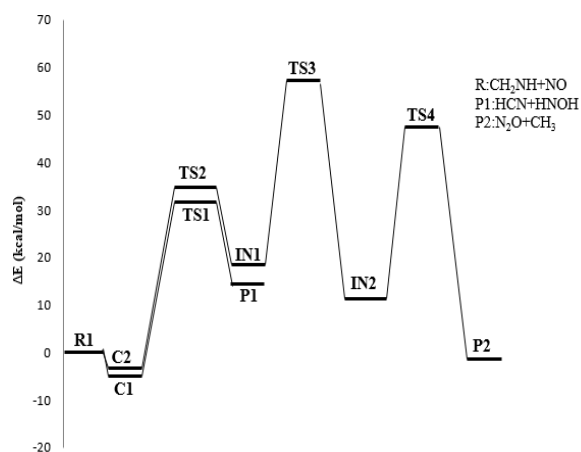


Fig.9: Doublet potential energy profiles of the CH₂NH+NO reaction at B3LYP level

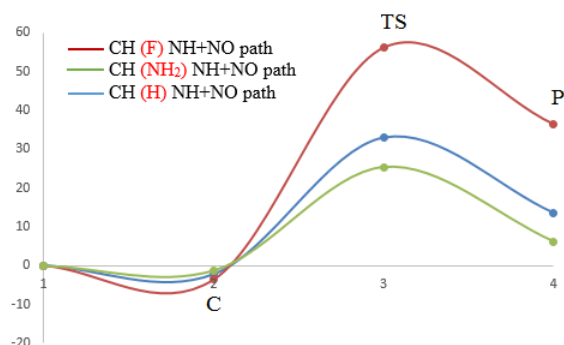


Fig.2: The substituent effect on the P1 path

Table1. The reaction energies, enthalpies, free energies and entropies are (kcal/mol) in 298K at the B3LYP level

Reaction	ΔE°	ΔH°	ΔG°	$T\Delta S^\circ$
CH ₂ NH+NO→HCN+HNOH	12.36	11.25	13.17	-1.92
CH ₂ NH+NO→CH ₃ +N ₂ O	-11.32	-13.63	-14.30	0.67

Conclusion

The theoretical study carried out in this work lead to the following conclusions:

1. In this study, the reaction of CH₂NH with the NO carried out using the MP2 and B3LYP theoretical approaches in connection with the 6-311++G (d, p) basis set.
2. The obtained substituent effects analysis reveals that the barrier energy is reduced when the activating group is substituent instead of hydrogen in -CH₂ group.

References

1. C. Lindley; J. Calvert.; J. Shaw, Rate Studies of the Reactions of the (CH₃)₂N Radical with O₂, NO, and NO₂. Chem. Phys. Lett. 1979, 67, 57–62.
2. C.Nielsen, ; B. D'Anna,; .Karl.; M. Aursnes, ; A. Boreave; R. Bossi.; A. Bunkan; M. Glasius; A. Hansen; M. Hallquist, et al. Summary Report: Photo-Oxidation of Methylamine, Dimethylamine and Trimethylamine; Climit Project No. 201604; NILU OR 2/ 2011, ISBN 978-82-425-2357-0; NILU: 2011.
3. Y Lazarou;P. Papagiannakopoulos, Kinetic Studies of the Reactions of Atomic Chlorine with N-Methylmethylenimine and 1,3,5- Trimethylhexahydro-1,3,5-Triazine. J. Phys. Chem. 1993, 97, 4468– 4472.
4. E. Tuazon; R. Atkinson; S. Aschmann; J. Arey, Kinetics and Products of the Gas-Phase Reactions of O₃ with Amines and Related Compounds. Res. Chem. Intermediat. 1994, 20, 303–320.
5. Frisch etal; "GAUSSIAN 03, Revision B.03, Gaussian"; Inc., Pittsburgh, PA; 2003.



DFT Investigation $C_{16}Be_8O_8$ nano-cage as selective nano-sensor for CO and NO gases

Zahra Rostami, Leyla Namdari*

Department of Chemistry, Payame Noor University (PNU), P.O. Box 19395-3697, Tehran, Iran

*leylanamdari@gmail.com

Abstract: The molecular structure and properties of the $C_{16}Be_8O_8$ nano-cage were analyzed, using DFT performed at B3LYP level of theory and 6-31G (d) as a basis set. More changes in the electrical conductivity of the cluster occurred, in effect of CO adsorption. $C_{16}Be_8O_8$ nano-cluster could be potentially used as a selective nano-sensor for CO and NO molecules. The electrical conductivity of the cluster, arising from HOMO/LUMO energy gap, was more sensitive to CO gaseous molecule rather than NO one, indicating that the heterogeneous $C_{16}Be_8O_8$ nano-cage may be potential nano-sensor for CO and NO molecule. These findings were specified by analyzing the characteristics in the electron density of states.

Keywords: DFT; selective ; sensitive; nano-sensor

Introduction

Nanostructured materials may be defined as ultrafine materials with the structures, elements, clusters, crystallites or molecules in dimensions range of 1 to 100 nm. These novel materials have widely varied potential applications ranging from the fields of nano-electronics to nano-scale biotechnology. Extensively and multidisciplinary, the field includes multilayer films, atomic clusters, nano-crystalline materials, and nano-composites having remarkable variations in substantial electrical, optic, and magnetic properties [1-3]. During the last decade, modeling, manufacturing, and efficiency of new nanostructured materials especially, fullerene-related materials have attracted considerable attention due to their novel physical and chemical properties. Since the discovery of C_{60} , the number of carbon allotropes greatly expanded, which were limited to graphite, diamond, and amorphous carbon such as soot and charcoal. Fullerenes have been extensively used in the form of nano-cage structures, nanotubes, nano-capsules, and nano-polyhedral in electronics, nanotechnology, biotechnology, and for several biomedical applications [4-5]. Utilization as nano-sensor in all mentioned applications is one of the most significant function of fullerenes. The modern lives rely on sensors, with several functional areas, to allow society to run smoothly. The performance of nano-sensors is similar to sensors but they can detect either minute particles or miniscule quantities of something. Nano-sensors can be chemically or mechanically utilized to detect the presence of gases in an area for applications such as identifying potentially hazardous gas leaks, used on oil rigs, monitoring manufacture processes, firefighting, and industrial plants. In recent years, numerous efforts have been dedicated to the study of possible [XY] n fullerene-like structures in which X and Y are constructed of other elements, rather than carbon, for their specific physical and chemical properties. So far, a large volume of researches are devoted to the fullerene-

related materials (C_n) and the (X, Y)_n nano-cluster individually, but very little effort has thus far been put towards carbon heterogeneous $C_nX_nY_n$. Here, we report the first theoretical study on the adsorption of NO and CO molecules on a new heterogeneous $C_{16}Be_8O_8$ nano-cluster composed of carbon, Beryllium, and oxygen atoms. In this work, computations based on DFT calculations were performed to elucidate the electronic and geometrical structures of the cluster and also the relationship between the electronic structures of $C_{16}Be_8O_8$ and the characteristics of adsorbed molecules.

Computational method

A $C_{16}Be_8O_8$ nano-cage consisted of six squares, six hexagons and two octagons was chosen as models for density functional studies. Geometry optimizations were performed at B3LYP level of theory and 6-31G (d) as a basis set without any symmetry constrain.

We define the E_{ad} of a gas molecule as follows:

$$E_{ads} = E_{(adsorbate/cluster)} - E_{(adsorbate)} - E_{(cluster)}$$

Where $E_{(adsorbate/cluster)}$ is the total energy of CO and NO molecules adsorbed on the surface of $C_{16}Be_8O_8$ nano-cage, $E_{(cluster)}$ and $E_{(adsorbate)}$ are the total energies of the pristine cluster and an adsorbate cluster, respectively. According to the definition, a negative value of E_{ads} corresponds to exothermic adsorption.

energy gap (E_g) is defined as

$$E_g = E_{LUMO} - E_{HOMO}$$

where E_{LUMO} and E_{HOMO} are energy of HOMO and LUMO.

Results and Discussion

The optimized structure of pure $C_{16}Be_8O_8$ nanocluster shown in Fig. 1, was obtained with the above-mentioned DFT functional. In the next step the adsorption of CO and NO molecules was analysed on the $C_{16}Be_8O_8$ surface of nanocluster. In order to obtain the most favorable complexes, various configurations were used for optimization including the gas molecules located on top of the surface Be, O, and C atoms in different positions above the cluster surface with different orientations. However, upon optimization only two local minima were obtained for CO and NO adsorbed on the cluster. The optimized structures for both adsorbed systems were reported in Fig. 2. More detailed information from the simulation of the CO/NO on the $C_{16}Be_8O_8$ system, including values electronic properties for this configuration is listed in Table 1. Based on the density of state analysis (DOS), it was found that CO and NO adsorption appreciably decreased the electrical conductivity of $C_{16}Be_8O_8$ nano-cluster, impacting HOMO/LUMO energy gap variations, therefore, the $C_{16}Be_8O_8$ nano-cluster could be potentially used as selectively nano-sensor devices towards CO and NO molecules.

Fig.10: structure of optimized $C_{16}Be_8O_8$ nanocluster

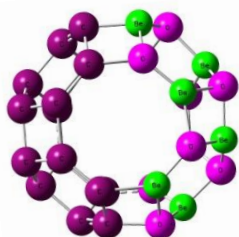


Fig.2: The optimized structures for both adsorbed systems

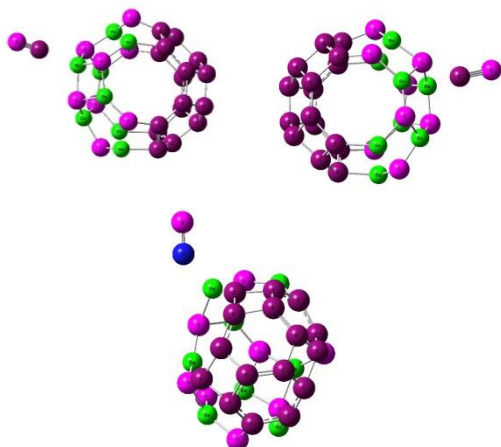


Table1: Calculated HOMO, and LUMO energies, and HOMO-LUMO energy gap (E_g) of the systems

SYSTEM	E_{HOMO}	E_{LUMO}	E_g
$C_{16}Be_8O_8$	-4.47	-2.44	2.02
$C_{16}Be_8O_8/CO$	-4.29	-2.73	1.55
$C_{16}Be_8O_8/NO$	-4.90	-3.02	1.81

Conclusions

DFT calculations were performed to study the adsorption of a series of gaseous molecules (CO and NO) on the heterogeneous $C_{16}Be_8O_8$ fullerene-like nano-cluster. The electrical conductivity of the cluster, arising from HOMO/LUMO energy gap, was more sensitive to CO gaseous molecule rather than NO one, indicating that the heterogeneous $C_{16}Be_8O_8$ nano-cage may be potential nano-sensor for CO and NO molecule. These findings were specified by analyzing the characteristics in the electron density of states.

References

- [1] A Salvatore Aricò, P Bruce, B Scrosati, J Tarascon, and W van Schalkwijk, Nanostructured materials for advanced energy conversion and storage devices, *Nature Materials* 4, 366 - 377 (2005).
- [2] G Konstantatos and E H. Sargent, Nanostructured materials for photon detection, *Nature Nanotechnology* 5, 391-400 (2010).
- [3] S. Zhuiykov, W. Wlodarski, Y. Li, Nanocrystalline $V_2O_5-TiO_2$ thin-films for oxygen sensing prepared by sol-gel method, *Sensors and Actuators B: Chemical* 77 (2001) 484.
- [4] H. Chang, J. D. Lee, S. M. Lee, Y. H. Lee, Adsorption of NH_3 and NO_2 molecules on carbon nanotubes, *Applied Physics Letters* 79 (23) (2001) 3863.
- [5] J. Lu, S. Nagase, Y. Maeda, T. Wakahara, T. Nakahodo, T. Akasaka, D. Yu, Z. Gao, R. Han, H. Ye, Adsorption configuration of NH_3 on single-wall carbon nanotubes, *Chemical Physics Letters* 405 (1-3) (2005) 90.

Theoretical study on the mechanism of the glyoxal plus O atom reaction on the singlet potential energy surfaces

H. Sagafi*, M. Vahedpour and S. Asgharzadeh

¹Department of Chemistry, Faculty of Science, University of Zanjan, Iran

*h_saghafi@znu.ac.ir

Abstract

Kinetic and mechanism of atmospheric reaction of glyoxal and atomic oxygen (O) on the singlet potential energy surfaces have been investigated in details using ab initio and DFT methods. All stationary points involved in the title reaction were optimized at the B3LYP, MP2 and G3B3 methods of computation in connection with the 6-311++G (3df, 3pd) basis set. For calculation of accurate energies, the CCSD(T) method is applied. Also, thermodynamic parameters and rate constant are calculated at B3LYP method with the mentioned basis set. The results show that direct hydrogen abstraction mechanism is the most important pathways of reaction. One pre-reactive complexes, C1, on the singlet and triplet potential energy surfaces were formed between glyoxal and oxygen. Two different products are suggested which both of them have enough thermodynamic stability. The production of OCHCO + OH is the main reaction channel in thermodynamic viewpoint with standard Gibbs free energy of $\Delta G^0 = -61.9$ kcal/mol at B3LYP level. The rate constant for OCHCO+OH and OCC+2OH production pathways calculated at the 300-2500 K temperature range.

Keyword: mechanism; glyoxal; rate constant; ab initio

Introduction

Glyoxal is an organic compound with the chemical formula OCHCHO. It is a yellow-colored liquid that evaporates to give a green-colored gas. Glyoxal is the smallest dialdehyde (two aldehyde groups). Its structure is more complicated than typically represented because the molecule hydrates and oligomerizes. It is produced industrially as a precursor to many products. Glyoxal was first prepared and named by the German-British chemist Heinrich Debus (1824–1915) by reacting ethanol with nitric acid [1]. The bifunctionality of glyoxal is used to cross-link functionalized macromolecules such as cellulose, polyacrylamides, polyvinyl alcohol, keratin and other polycondensates. For example, glyoxal is used as a cross-linking agent for imparting wet strength to coated paper. With cellulose, unstable hemiacetals are obtained in the cold, which irreversibly form acetals when heated in the presence of acid catalysts. Glyoxal is also the starting point for the production of a number of other compounds. The dual functionality and the ability of glyoxal to form heterocyclic compounds are used in the production of resins for imparting crease resistance to textiles, ion exchange resins, and cross-linking agents. Glyoxal bisulfide is used as a resist agent in printing with reactive dyes and as a levelling agent in dyeing polyamide with acid dyes. The reducing properties of glyoxal are used in the photographic industry and in glassmaking for the production of silvered glass mirrors. Glyoxal has bactericidal properties comparable with those of glutaraldehyde and is used as a bactericide in preparation with other components (formaldehyde,

glutaraldehyde, quaternary ammonium). The role of hydrogen bonded molecular complexes on the kinetics and dynamics of gas-phase free radical reactions has been the focus of interest of both experimental and theoretical investigations [2-3]. The atmospheric reactions of glyoxal with radicals and atmospheric oxidant have been investigated. Also, the dimerization of glyoxal have been studied. Glyoxal is not volatile and is not expected to accumulate in biota or soil/sediment. It is clearly readily biodegradable. Glyoxal have an important role in atmospheric reaction and can be react with many radicals of atmosphere and removed radicals from atmosphere. So, we have studied the atmospheric reaction of glyoxal with the atomic oxygen.

Theoretical methods

All the calculations were performed with the GAUSSIAN 03 program [4]. All geometry optimizations were carried out using Møller–Plesset perturbation theory MP2 and B3LYP level approach in connection with the 6-311++g (d, p) and 6-311++G (3df, 3pd) basis set. Single point calculations were performed for all species at the CCSD (T)//B3LYP level. The Gpop [5] program as standard software is used for calculation of rate parameters of reaction.

Result and discussion

Figure 1 show the relative energy profile of glyoxal and atomic oxygen reaction. As seen, We found one pre-reactive complex formed between glyoxal and O denoted

as C1. The structure of C1 was confirmed by an atom in molecule, AIM, topological analysis of the wave function. This investigation reveals the presence of bond critical points (bcp), located between the oxygen atom of molecular oxygen and the hydrogen of hydrazine [$\rho(r_{bcp}) = 0.0551 \text{ e bohr}^{-3}$ and $\nabla^2\rho(r_{bcp}) = 0.1335 \text{ e bohr}^{-5}$]. The pre-reactive complex C1 is transformed to CP1 occurring via transition state TS1 with the energy barrier of 24.763 kcal/mol. CP1 can be followed two different pathways. In first pathway, CP1 directly and without passing any transition state transform into the final adduct (OCHCO + OH), which is energetically 64.162 kcal mol⁻¹ more stable than the original reactants. In second pathway, CP1 can be converted into the product P2 via transition state TS2 with the energy barrier of 46.710 kcal mol⁻¹. Product P2 (CCO + 2OH) is 14.250 kcal/mol more stable than reactants. In both of path the hydrogen abstraction of glyoxal occurred. The thermodynamic data shows that the production of P1 and P2 are exothermic and spontaneous according to the enthalpy and Gibbs free energy data.

The theoretical study carried out in this work lead to the following conclusions:

1. The present work, The reaction of glyoxal with the O carried out using the MP2 and B3LYP theoretical approaches in connection with the 6-311++G(d, p) and 6-311++G(3df, 3pd) basis set.
2. Reaction of OCHCHO + O is produced two kinds of products after passing two transition states. P1 is the most stable product in title reaction. The rate constants are calculated for both products.

References

1. S. Aloisio, J. Francisco, ACC, chem, Res, 33(2000)825.
2. L.W Smith, A. Ravishankara, J, phys, chem. A 106(2002)4798.
3. J. Hansen, J. Francisca, chem,phys, chem, 3 (2002)833.
4. Frisch et al; "GAUSSIAN 03, Revision B.03, Gaussian"; Inc., Pittsburgh, PA; 2003.
5. Miyoshi A (2010) Gaussian Post Processor (GPOP).

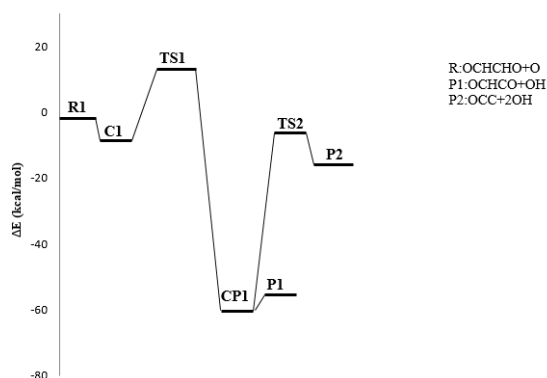


Fig.11: singlet potential energy profiles of the OCHCHO + O reaction at B3LYP level

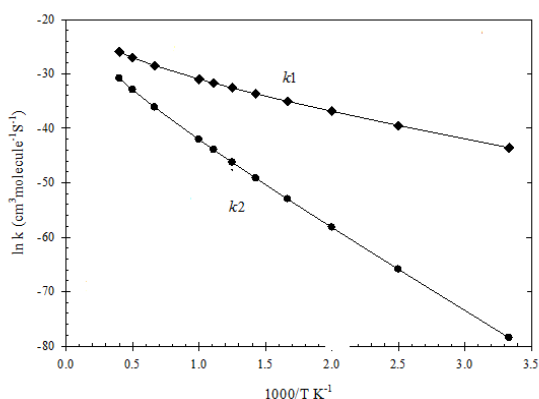


Fig2: Arrhenius curves for the reaction rate constant k_1 for path P1 and k_2 for path P2 in the OCHCHO + O reaction at MP2 method

Conclusion

DFT Investigation of Adsorption of F₂ Molecule on Pristine and defected Graphene

Zahra Rostami^{*a}, Tahmine Rastkhiz^a, Hamed Soleymanabadi^b

^a Department of Chemistry, Payame Noor University (PNU), P.O. Box 19395-3697, Tehran, Iran

^b Department of Chemistry, College of Science, Central Tehran Branch, Islamic Azad University, Tehran, Iran

^{*}rostami@pnu.ac.ir

Abstract: We investigated fluorine adsorption on the pristine, double vacancy defected graphenes by using density functional at B3LYP level of theory and 6-31G (d) as a basis set calculations in terms of geometric, energetic and electronic properties. These processes also significantly change the electronic properties of complex by decreasing its HOMO/LUMO energy gap and increasing the work function. The results were determined by comparing the defect graphene with pure graphene showed that the graphene with defect is suitable than pure graphene for adsorption of selected halogen. We believe that the obtained results may be helpful in several fields of study such as sensors, catalysts, and field emission investigations.

Keywords: fluorine; double vacancy; halogen

Introduction

Graphene, first isolated by Novoselov and Geim in 2004 is two-dimensional crystal composed of atomic layers of carbon arranged in a lattice of hexagon rings. Its interesting electric and transport properties have spawned a considerable interest since its discovery in 2004. Structural defects which are commonly present in atomic structure of graphene and carbon nanotubes during its growth play a key role in the chemistry and physics of graphene and deteriorate the performance of devices based on graphene and carbon nanotubes [1-4]. In addition, introduction of defects in the carbon network can be useful in some applications. It is an interesting way to tailor intrinsic properties of graphene and create new functionalization. The Stone-Wales (SW) defect, single and double vacancies are the most common defects formed in graphene and carbon nanotubes and alter the properties of these nanomaterials. It is well-known that defects associated with dangling bonds increase the reactivity of graphene and allow adsorption of other atoms on it. It is also shown that reconstructed defects without dangling bonds such as SW defects or reconstructed vacancies locally changed the density of π -electrons and enhance the local reactivity. Structural defects have impact on the bond lengths and curvature around defects which leads to a local rehybridization of s and π orbitals. All defects cause scattering of the electron waves and change the electron trajectory. Therefore, defects strongly affect the electronic properties. As the presence of defects alters the chemical reactivity and the electronic properties of graphene, fully exploit of graphene sensors is dependent on considering the effect of defects on the electronic properties of graphene. Fluorine, as a strong electron acceptor, can act as a bonding modifier by either making the adsorbate-substrate bond stronger or weaker.

Computational method

A graphene sheet consisted of 130 carbon atoms was considered, which its end atoms were saturated with hydrogen atoms to reduce boundary effects. Geometry optimizations, energy calculations, and density of states (DOS) analysis were performed on pristine and defected graphene employing B3LYP functional with 6-31G(d) basis set as implemented in GAUSSIAN program. The B3LYP has been demonstrated to be a reliable and commonly used level of theory in the study of different nanostructures. We define the E_{ad} of a F₂ atom as follows:

$$E_{ad} = E(\text{F}_2\text{-nanosheet}) - E(\text{F}_2) - E(\text{nanosheet})$$

where $E(\text{F}_2\text{-nanosheet})$ is the total energy of the F₂-nanosheet complex, and $E(\text{nanosheet})$ and $E(\text{F}_2)$ are related to the energy of an isolated nanosheet and F₂ atom, respectively. Energy gap (E_g) is defined as

$$E_g = E_{LUMO} - E_{HOMO}$$

where E_{LUMO} and E_{HOMO} are energy of LUMO and HOMO.

Results and Discussion

At first, we have focused on the adsorption of F₂ on the graphene and defected graphene surface. In order to find minimum adsorption configurations (local minima), the F₂ was initially placed at different positions above the nano sheets, four different sites for outside adsorption (as shown in fig. 1) are selected to examine the interaction between the nano sheets and F₂ molecule. F₂ prefers to be weakly adsorbed on the top of a carbon atom of the surface graphene with E_{ad} is about -0.08 and -0.12 eV. The adsorption of the F₂ on the C site in graphene can be rationalized by the fact that the LUMO is mainly located on the C atoms. F₂ molecule was located vertically and horizontally on the graphene. More detailed information from the simulation of the F₂/graphene and defected graphene system, including values of E_{ad} , electronic properties for this configuration is listed in Table 1. Also in fig. 2 we have shown structure of the optimized

F_2 /graphen and defected graphen system, the E_{ad} values of adsorption F_2 on the defected graphene calculated to be about -0.87 and -1.13. It was found that the adsorption of fluorine on the defected graphene facilitate the field electron emission from its surface by shifting the Fermi level to higher energies and decreasing the work function, significantly.

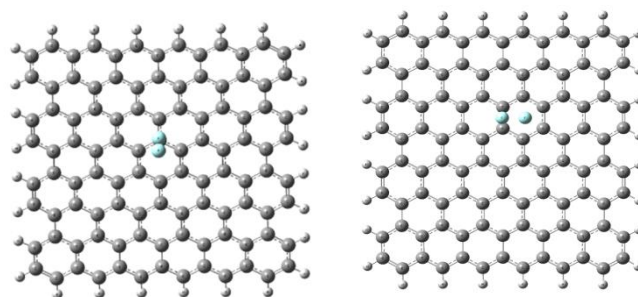


Fig.2: structure of optimized F_2 /graphen and defected graphen system.

Conclusions

We have studied fluorine (F_2) adsorption on pristine graphene and defected graphene by using DFT (B3LYP)/6-31G* method and basis set, The results were determined by comparing the defect graphene with pure graphene showed that the graphene with defect is suitable than pure graphene for adsorption of selected halogen. We believe that the obtained results may be helpful in several fields of study such as sensors, catalysts, and field emission investigations.

References

- [1] A. Y. Zou, C.-Z. Wang, Z.-B. Fu, Y.-J. Tang, H. Zhang, Effects of various defects on the electronic properties of single-walled carbon nanotubes: a first principle study, *Front. Phys.* 9 (2014) 200–209.
- [2] J. Kang, J. Bang, B. Ryu, K.J. Chang, Effect of atomic-scale defects on the lowenergy electronic structure of graphene: perturbation theory and local-density-functional calculations, *Phys. Rev. B* 77 (2008) 11545.
- [3] B. Akdim, T. Kar, X. Duan, R. Pachter, Density functional theory calculations of ozone adsorption on sidewall single-wall carbon nanotubes with Stone–Wales defects, *Chem. Phys. Lett.* 445 (2007) 281–287.
- [4] S. Roh, J. Oh, Y. Choi, D. Shon, W. Kim, Ch Cho, Wh. Yi, J. Yoo, Ch Lee, J. Kim, Adsorption of alkanethiol molecules onto carbon nanotube surface, *J. Vac. Sci. Technol. B* 22 (2004) 1411–1415.

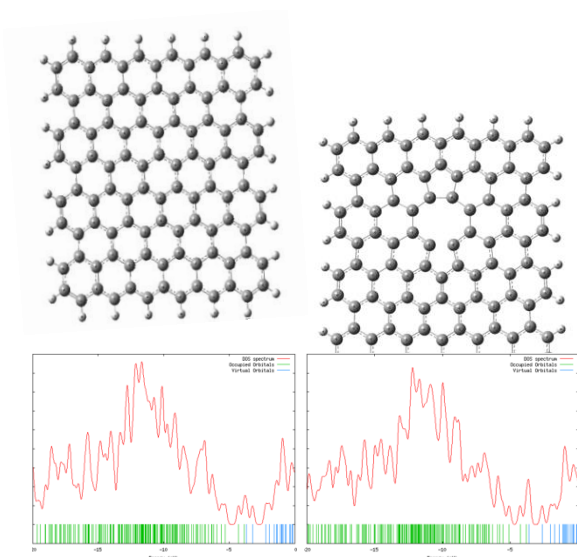
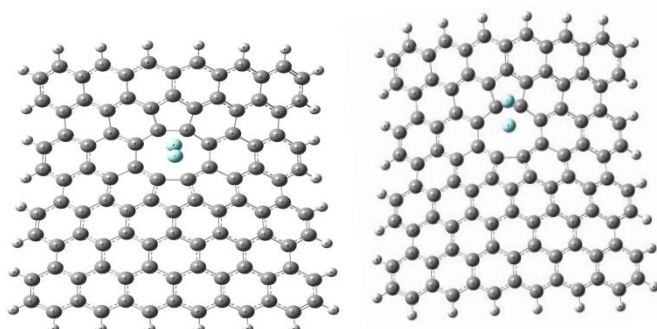


Fig.12: structure of optimized graphen and defected graphen and its density of state (DOS) plot

Table1: Calculated adsorption energies (E_{ad} , eV), HOMO, and LUMO energies, and HOMO-LUMO energy gap (E_g) of the systems

graphen	E_{ad}	E_{HOMO}	E_{LUMO}	E_g
horizontal	-0.087	-3.88	-3.70	0.18
vertical	-0.120	-3.89	-3.71	0.18
defected	-----	-----	-----	-----
horizontal	-0.87	-3.81	-3.65	0.16
vertical	-1.13	-3.85	-3.65	0.19



Structure determination of noble metal clusters using resonance Raman scattering: determination of the efficiency and sensitivity of the messenger technique

Z. Jamshidi^{a*}, S. Ashtari Jafari^b,

^aChemistry and Chemical Engineering Research Center of Iran, P.O. Box 14335-186, Tehran, Iran

^bChemistry and Chemical Engineering Research Center of Iran, Postal, Tehran, Iran

*na.jamshidi@gmail.com

Abstract: The increasing importance of noble metal clusters has made their structure determination one of the hot topics of the day. Vibrational spectroscopy is one of the classically efficient ways for this goal. In this work we have used a particular kind of photon-dissociation spectroscopy called “the messenger technique” alongside resonance Raman scattering to increase the efficiency and sensitivity of the structure determination process. We have used three closed-shell silver clusters Ag_{4, 6, 8} interacted with ligand N₂ for our research. The results show great improvements compared to other spectroscopic methods indicating that this method could be a great replacement in cases that IR spectroscopy fails to give accurate results.

Keywords: “Raman”, “resonance Raman”, “metal clusters”, “messenger technique”

Introduction

In recent years, increasing application of noble metal clusters has led to numerous studies trying to determine their structure and properties. Nowadays, noble metal clusters are widely used in electronic industries, medical sciences, etc. Spectroscopy methods are one of the best ways of structure determination and amongst them, vibrational spectroscopy has played an important role in studying noble metal clusters. (Multiple) photon dissociation is a kind of vibrational spectroscopy in which the vibrational spectra is produced as a result of the dissociation of the system after interacting with photons. The problem with this method is for strongly bound clusters, it is almost impossible to do so within the mid to far-IR light region where the vibrational peaks of noble metal clusters occur.

As a solution “the messenger technique” [1] is introduced which is a kind of action spectroscopy. In this method the cluster is interacted with a weakly-bound small ligand called the messenger. The interaction of the photons with this complex breaks the weak bond between the cluster and the ligand and produces the vibrational spectrum. What we should pay attention to is the fact that determination of the structure of the cluster using this spectrum is only possible if it is compared with a calculated vibrational spectrum which shows the importance of computational chemistry in structure determination of clusters [2]. The interaction between the cluster and the ligand must be weak enough to not to affect the intercluster vibrational modes. Noble gas atoms and small inert molecules such as N₂ are usually used as messenger ligands [3]. In this method the vibrational normal modes between the cluster and the ligand are carefully studied. The modes are one out of plane bending (rocking), an in the plane bending (wagging) and stretching.

The messenger technique has been usually applied in IR vibrational spectroscopy so in our previous work we decided to extend this method to Raman and resonance Raman spectroscopy for the cases that no intense and efficient IR spectra exists. At first, we tried to find a proper messenger ligand that would enhance the Raman absolute intensities and at the same time have all the significant characteristics of a good messenger. We chose several small ligands and interacted them with quartet silver clusters. The results showed that amongst our set of ligands, N₂ enhances the Raman absolute intensities very well while forming a very weakly-bound complex with the cluster. In the present work, we studied the efficiency of our method with the increasing cluster size choosing Ag_{4, 6, 8} as our system. We also investigated the sensitivity of this method by comparing the results for pure and complex isomers of Ag₈ which are very similar in energy level and hard to separate from each other. This is an example of the cases where IR spectroscopy can't provide the desired information.

Materials and method

All ground state geometry optimizations, vibrational frequencies and polarizabilities were calculated using Amsterdam Density Functional (ADF) software [4] with the long-range corrected functional CAM-B3LYP [5] and a TZ2P basis set. Based on the Placzek's classical theory of polarizability and by including the finite lifetime of the electronic state, we calculate the on- and off-resonance Raman spectra from the derivatives of the frequency-dependent polarizability with respect to normal coordinate by including the finite lifetime $\Gamma=0.004$ a.u. Absolute Raman intensities are presented as the differential Raman scattering cross-section (DRSC) in terms of the derivative of the polarizability.



Results and Discussion

For our purposes, we chose Ag_6 cluster with D_{3h} symmetry and also two more stable Ag_8 cluster isomers with symmetries T_d and D_{2d} . Since the interaction of N_2 with silver clusters gets weaker with the increasing size, larger clusters will reproduce the same trend as our selected clusters. After interacting the clusters with N_2 ligand and performing energy optimization, numerical frequency and td calculations we obtained the IR and UV spectra for $Ag_{4, 6, 8-N_2}$ complexes. The IR spectra proves to be a not efficient tool because of the low IR intensities that are a result of small dipole moments especially for the very symmetric Ag_8-T_d cluster. Obtaining the UV spectrum allows us to choose the highly allowed electronic transition for each complex which indicates the energy of the incident light used to obtain resonance Raman spectra. For the normal Raman spectra we choose an incident light that is far enough from the highly allowed electronic transition to make sure the resonance will not happen. By obtaining the resonance Raman spectra of the four complexes (figure 1) we see that the interaction with N_2 has produced large Raman intensities with big enhancement factors (the proportion of resonance Raman intensity to normal Raman intensity for each vibrational normal mode) for both the inter cluster and cluster-ligand interaction regions.

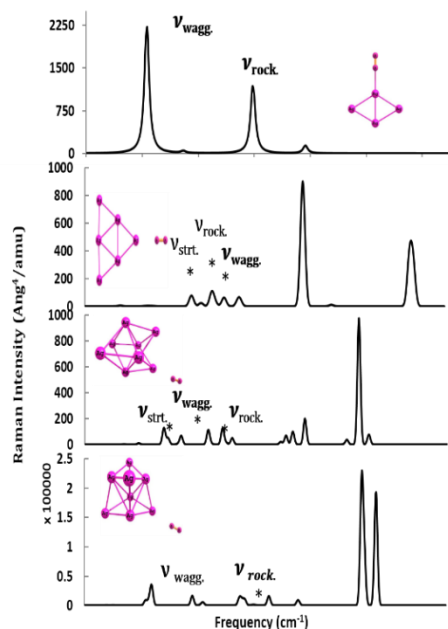


Figure 13. The resonance Raman spectra of $Ag_{4, 6, 8-N_2}$.

In one case $Ag_8-T_d-N_2$ complex shows an up to 3×10^3 enhancement factor. The proper resonance Raman intensities makes it the best way out IR, normal Raman and UV spectroscopy for structure determination of strongly bound clusters. Also the intercluster bonds show little displacement compared to pure cluster bonds which

indicates that the weak interaction of N_2 makes it a good messenger. Among the cluster-ligand vibrations, stretching and wagging move to the red with the increasing cluster size while rocking vibration shows no special trend.

In order to test the sensitivity of our method we managed to compare the pure Ag_8 isomers with their complexes with N_2 ligand. This choice lies in several reasons: the octet silver clusters have important roles in many research fields but their similar energy levels make them very difficult to identify and separate from each other. In fact our calculations showed that the T_d isomer is more stable but the D_{2d} isomer has a stronger interaction with N_2 ligand. Also their high symmetries causes in not so crowded, almost similar IR spectra with low intensities. Former studies have shown that the UV spectra for these two clusters is also very similar [6] which makes Raman and especially resonance Raman spectroscopy the best way to study these systems. As it is shown in figure 2, the complexes rR spectra in comparison to ones obtained from pure isomers show much higher absolute Raman intensities and the difference between the two isomers enhancement factors can lead to identifying them in the mixture.

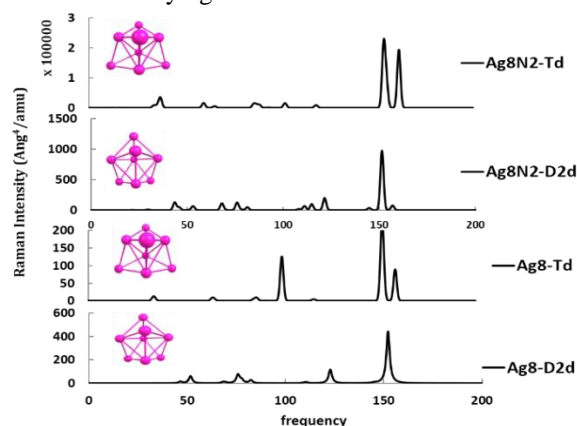


Figure 14. The resonance Raman spectra of pure and complex Ag_8-T_d and D_{2d} clusters.

Conclusions

We decided to investigate the efficiency of the messenger technique coupled with resonance Raman spectroscopy for structure determination of the silver clusters and the effects of increasing size. In order to do so, we studied the vibrational and UV spectra of $Ag_{4, 6, 8-N_2}$ complexes and the displacements of the cluster-ligand peaks. The results showed that N_2 -ligand proves to be a good messenger ligand as the bond gets weaker with the increasing size. The rR spectra are shown to be the best way for studying these system compared to IR and UV spectra. This method also shows great sensitivity being able to produce intense, not similar spectra for the two Ag_8 isomers.



References

- [1] Klaus D. Sattler "Handbook of Nanophysics: Clusters and Fullerenes", 2010, CRC Press
- [2] Gruene, Philipp, David M. Rayner, Britta Redlich, Alexander FG van der Meer, Jonathan T. Lyon, Gerard Meijer, and André Fielicke. "Structures of neutral Au₇, Au₁₉, and Au₂₀ clusters in the gas phase." *Science* 321, no. 5889 (2008): 674-676.
- [3] Fielicke, André, Irene Rabin, and Gerard Meijer. "Far-infrared spectroscopy of small neutral silver clusters." *The Journal of Physical Chemistry A* 110.26 (2006): 8060-8063.
- [4] Baerends, E. J., et al. "Amsterdam density functional." *Theoretical Chemistry, Vrije Universiteit, Amsterdam*, URL <http://www.scm.com> 42 (2013).
- [5] Yanai, Takeshi, David P. Tew, and Nicholas C. Handy. "A new hybrid exchange–correlation functional using the Coulomb-attenuating method (CAM-B3LYP)." *Chemical Physics Letters* 393.1 (2004): 51-57.
- [6] Harb, M., Rabilloud, F., Simon, D., Rydlo, A., Lecoultre, S., Conus, F., & Félix, C. (2008). Optical absorption of small silver clusters: Ag_n, (n= 4–22). *The Journal of chemical physics*, 129(19), 194108.

Cooperative and diminutive interplay between the sodium bonding with hydrogen and dihydrogenbondings in ternary complexes of NaC₃N with HMgH and HCN (HNC)

Mohaddeseh Rabbani, Amineh Ahmadi, Mohammad Solimannejad*

Quantum Chemistry Group, Department of Chemistry, Faculty of Sciences, Arak University, Arak, Iran;

*m-solimannejad@araku.ac.ir

Abstract: Ternary complexes of NaC₃N with HMgH and HCN (HNC) are connected by sodium, hydrogen and dihydrogen bonds. Molecular geometries and interaction energies of dyads and triads are investigated at the MøllerPlesset perturbation theory of the second order/aug-cc-pVDZ computational level. Particular attention is paid to parameters, such as cooperative energies and many-body interaction energies. Triads with the HMgH molecule located at the end of the chain show an energetic cooperativity ranging between -2.13 and -10.53 kJ.mol⁻¹. When the HMgH molecule is located in the middle, the obtained cluster is diminutive with an energetic effect with values 4.39 and 6.77 kJ mol⁻¹. The electronic properties of the complexes are analysed using parameters derived from the atoms in molecules methodology.

Keywords: hydrogen bonding; sodium bonding; dihydrogen bonding; cooperativity

Introduction

Noncovalent interactions between molecules play an important role in supramolecular chemistry, molecular biology and materials science [1]. Although research has traditionally focused on the most common hydrogen bond (HB) interactions, more recently, interest has grown for other types of intermolecular interactions, such as sodium bonds and dihydrogen bonds.

As a member of the unusual HB family, the concept of dihydrogen bond (DHB) is interesting and unique, which is an attractive intermolecular or intramolecular H...H interaction, arising from the close approach of a protonic H atom and a hydridic H atom [2–4]. In the DHB, a metal hydride often plays the role of electron donor. Up to now, DHBs have been the topic of numerous experimental and theoretical studies [5–12].

It is known that the positively charged sodium atom with relatively small atomic radius can also form weak sodium bond interaction with other molecules, which was experimentally verified by Ault as early as in the 1970s [13]. However, the investigation on unusual sodium bond is limited to the work of the Li's group who reported singleelectron sodium bond [14–16] and π -sodium bond [17]. Other than those endeavours, little information is available on the sodium bonding systems with other electron donors.

If several weak bonds are present in one complex, there are mutual influences between them, irrespective of whether they are of the same type [18,19] or different [20–23]. Recently, an article concerning cooperativity in multiple unusual weak bonds with HBs, hydric bonds, DHBs, halogen bonds and ion- π interactions has been published [24]. It has been shown that the cooperative and anticooperative or diminutive effects are highly dependent on the geometrical disposition of the interacting molecules [20–26].

Careful studies of simple models are of interest in order to extend their conclusions to larger ones. Herein, we design some simple structures, including sodium, hydrogen and dihydrogenbondings. We perform a

theoretical study on the six triads with the aim of investigating the effect of sodium bonding on an HB and a DHB and the cooperativity between them. To the best of our knowledge, the study of cooperativity in triads with sodium, hydrogen and dihydrogenbondings is reported here for the first time.

Materials and method

Structures of the monomers and the complexes were optimised and characterised by frequency computations at the MP2/aug-cc-pVDZ computational level [27]. The interaction energies were calculated as the difference of the total energy of the complexes and the sum of the isolated monomers in their minima configuration. The full counterpoise (CP) method [28] was used to correct the interaction energies from the inherent basis set superposition error (BSSE) All ab initio calculations were performed using the Gaussian 03 program package [29]. The atoms in molecules (AIM) methodology [30] was used to analyse the electron density of the systems considered at the MP2/aug-cc-pVDZ level. The topological analysis was carried out with the AIM2000 program [31]

Results and Discussion

Geometries: The systems studied form stable triads with C_{∞v} symmetry (Scheme1). The intermolecular distances found for these systems are in the range of 2.19–2.55 Å° for Na...H(N,C) sodium bonds and 1.50–2.05 Å° for HBs and DHBs(Table1).

For systems with HMgH...NaC₃N...HCN(HNC) and NC₃Na...NCH(CNH)...HMgH arrangements, the Na...H(N,C), N...H and H...H distances in the triads are smaller than the corresponding values in the dyads. The differences in distances between triads and dyads are in the range 0.004–0.036 Å° for sodium bonds and 0.011–0.142 Å° for HBs and DHBs (Table 1). This trend can be interpreted as a cooperative effect of sodium bond with hydrogen, and DHBs.



For systems with $\text{NC}_3\text{Na}\cdots\text{HMgH}\cdots\text{HCN}(\text{HNC})$ arrangement, the $\text{Na}\cdots\text{H}$ and $\text{H}\cdots\text{H}$ distances in the triads Scheme 1. Disposition of the monomers within the complexes, are larger than the corresponding values in the dyads, with differences in values 0.021 , 0.034 Å and 0.082 , 0.090 Å, respectively (Table 1). This trend can be interpreted as a diminutive effect of sodium bond and DHB, which is reported here for the first time.

Interaction energies: The interaction energies in the dyads can be regarded as the energy difference between the complex and the monomers: $E_{\text{int}(\text{AB})} = E_{\text{AB}} - (E_{\text{A}} + E_{\text{B}})$ and the corresponding value in the triads ($E_{\text{int}(\text{ABC})}$) is calculated in a similar way. $E_{\text{int}(\text{AB,T})}$ and $E_{\text{int}(\text{BC,T})}$ are the interaction energies of AB and BC dyads while they are in the geometry of triads. In Table 2, the interaction energies of the six studied triads and respective dyads are listed. All results were corrected for BSSE using the CP method. As shown in Table 2, the interaction energy of the title complexes ranges from -54.88 to -98.99 kJ mol⁻¹. An energetic cooperativity parameter was calculated using Equation (1) [32,33]:

$$E_{\text{coop}} = E_{\text{int}(\text{ABC})} - E_{\text{int}(\text{AB})} - E_{\text{int}(\text{BC})} - E_{\text{int}(\text{AC, T})} \quad (1)$$

where $E_{\text{int}(\text{ABC})}$ is the interaction energy of the triad, $E_{\text{int}(\text{AB})}$ and $E_{\text{int}(\text{BC})}$ are the interaction energies of the isolated dyads within their corresponding minima configurations. $E_{\text{int}(\text{AC,T})}$ is the interaction energy of the molecules A and C in the trimer geometry. In $\text{HMgH}\cdots\text{NaC}_3\text{N}\cdots\text{HCN}(\text{HNC})$ and $\text{NC}_3\text{Na}\cdots\text{NCH}(\text{HNC})\cdots\text{HMgH}$ studied complexes, a favourable cooperativity is observed with values that range between -2.13 and -10.53 kJ mol⁻¹. In the same way, diminutive effects are observed for two complexes with $\text{NaC}_3\text{Na}\cdots\text{HMgH}\cdots\text{HCN}(\text{HNC})$ arrangement with values 4.39 and 6.77 kJ mol⁻¹.

Many-body interaction analysis The two- and three-body contributions to total interaction energy are obtained by many-body analysis [34,35]. The two-body terms ($E_{\text{A-B}}$, $E_{\text{A-C}}$, and $E_{\text{B-C}}$) can be calculated as the total energy of each molecular pair in the geometry of triad minus the energy sum of the monomers, all of them frozen in the geometry of the triad. The threebody term $E_{\text{A-B-C}}$ is calculated as the total interaction energy of the triad minus the interaction energy of each pair of monomers, all of them frozen in the geometry of the triad using Equation (2) [35]:

$$E_{\text{A-B-C}} = E_{\text{int}(\text{ABC})} - E_{\text{A-B}} - E_{\text{A-C}} - E_{\text{B-C}} \quad (2)$$

$E_{\text{int}(\text{ABC})}$ is obtained by subtracting the total energy of the optimised triads from the energy sum of the monomers frozen in the geometry of the triads. The relaxation energy (E_{relax}) is defined as the energy sum of the monomers frozen in the geometry of the triads minus the energy sum of the optimised monomers. Thus, the total interaction energy of the triad is obtained using Equation (3) [35]:

$$E_{\text{int}(\text{ABC})} = E_{\text{A-B}} + E_{\text{A-C}} + E_{\text{B-C}} + E_{\text{A-B-C}} + E_{\text{relax}} \quad (3)$$

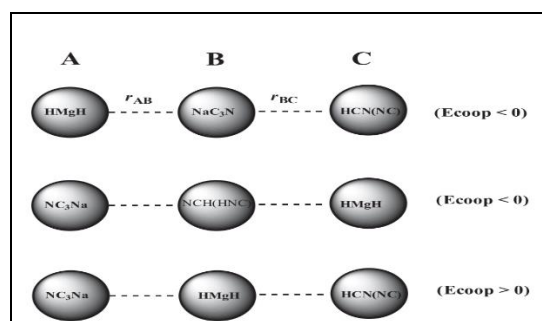
The results are presented in Table 4, in which all energies are corrected for BSSE. As seen in Table 4, two-body interaction energy in some cases provides the largest contribution to the total interaction energy up to 99%. For all the triads, the two-body interaction energies $E_{\text{A-B}}$

and $E_{\text{B-C}}$ are attractive, that is, they make a positive contribution to the total interaction energy. $E_{\text{A-C}}$ is attractive for triads with cooperativity and repulsive for triads with diminutive effect. For all triads $E_{\text{A-C}}$ is the smallest two-body interaction term, consistent with the largest distance between them.

In $\text{HMgH}\cdots\text{NaC}_3\text{N}\cdots\text{HCN}$, $\text{NC}_3\text{Na}\cdots\text{NCH}\cdots\text{HMgH}$ and $\text{NC}_3\text{Na}\cdots\text{HMgH}\cdots\text{HCN}$ studied complexes, $E_{\text{A-B}}$ is larger than $E_{\text{B-C}}$. This means that the sodium bonding contributes more to the bonding interaction between two molecules in a triad than the HB and DHB. In other three complexes, $E_{\text{B-C}}$ is larger than $E_{\text{A-B}}$ which means more contribution of hydrogen and dihydrogenbondings to the bonding interaction between two molecules in a triad than the sodium bond.

The three-body interaction energy $E_{\text{A-B-C}}$ is attractive in triads with cooperativity and repulsive for triads with diminutive effect. This situation is similar to twobody interaction energies $E_{\text{A-C}}$. The contribution of the three-body interaction energy is much smaller than that of twobody interaction energy. The relaxation energy can be taken as a measure of the degree of strain that drives the distortion of the ternary system. As seen in Table 4, the relaxation energies are positive, so they make a destabilising contribution to the total interaction energies of the triads. The relaxation energy is largest for $\text{NC}_3\text{Na}\cdots\text{CNH}\cdots\text{HMgH}$ and smallest in $\text{NC}_3\text{Na}\cdots\text{HMgH}\cdots\text{HCN}$ which is in line with order of stabilities in these triads.

Electron density analysis: The values of the electron density in the intermolecular bond critical points (BCPs) show a clear dependency on the interatomic distance. It has been manifested in numerous studies that the charge density at BCPs, ρ_{BCP} , gives valuable information about the strength and origin of the intermolecular interactions [36]. Therefore, the variation in the ρ_{BCP} value at the BCP in the triad with respect to the corresponding dyad can be used to analyse the mutual influence of the two interactions. Table 5 lists the variations in electron density and the Laplacian of electron density at two BCPs located between molecules A, B and C. An enhancement in electron density and Laplacian of electron density is observed for triads with cooperativity, whereas in the triads with diminutive effect a reduction of electron density and Laplacian of electron density upon triad formation is observed.



Scheme 1. Disposition of the monomers within the complexes.



Table 1. Intermolecular distances R (Å) in the investigated triads (T) and dyads. R indicates the changes relative to the respective dyads.

Triads(A...B...C)	E _{A-B}	E _{B-C}	E _{A-C}	E _{A-B-C}	E _{relax}
HMgH-NaC ₃ N-HCN	-48.56	-32.36	-0.25	-1.45	0.98
HMgH-NaC ₃ N-HNC	-48.64	-50.42	-0.31	-2.07	2.47
NC ₃ Na-NCH-HMgH	-55.63	-15.12	-4.03	-7.62	0.89
NC ₃ Na-CN ₃ H-HMgH	-27.53	-57.38	-4.43	-11.36	3.12
NC ₃ Na-HMgH-HCN	-48.20	-15.59	4.23	4.38	0.28
NC ₃ Na-HMgH-HNC	-26.62	-48.13	5.28	6.83	0.50

Table 2. Interaction energy (kJ mol⁻¹) of sodium, hydrogen and dihydrogenbondings in the studied dyads and triads at MP2/aug-cc-pVDZ level

Triads(A...B...C)	E _{int(ABC)}	E _{int(AB)}	E _{int(BC)}	E _{int(AB,T)}	E _{int(BC,T)}	E _{COOP}
HMgH-NaC ₃ N-HCN	-81.65	-47.97	-31.91	-47.88	-31.68	-2.13
HMgH-NaC ₃ N-HNC	-98.99	-47.97	-48.54	-47.75	-48.28	-4.06
NC ₃ Na-NCH-HMgH	-81.51	-55.30	-15.67	-54.85	-14.47	-6.86
NC ₃ Na-CN ₃ H-HMgH	-97.59	-56.56	-26.55	-54.43	-24.73	-10.53
NC ₃ Na-HMgH-HCN	-54.88	-47.97	-15.67	-47.94	-15.40	4.39
NC ₃ Na-HMgH-HNC	-62.12	-47.97	-26.55	-47.88	-26.19	6.77

Table 3. Decomposition of interaction energy (kJ mol⁻¹) of the studied triads using the geometry within the triads.

Triads(A..B..C)	Δρ _{AB}	ΔV ² _{AB}	Δρ _{BC}	ΔV ² _{BC}
HMgH-NaC ₃ N-HCN	0.0001	0.0007	0.0005	0.0020
HMgH-NaC ₃ N-HNC	0.0002	0.0012	0.0009	0.0023
NC ₃ Na-NCH-HMgH	0.0012	0.0085	0.0252	0.0076
NC ₃ Na-CN ₃ H-HMgH	0.0014	0.0090	0.0080	0.0078
NC ₃ Na-HMgH-HCN	-0.0007	-0.0037	-0.0025	-0.0043
NC ₃ Na-HMgH-HNC	-0.0010	-0.0055	-0.0042	-0.0065

Table 4. Changes in AIM parameters of the triads relative to the respective dyads

Triads(A..B..C)	R _{AB,T}	R _{AB}	ΔR _{AB}	R _{BC,T}	R _{BC}	ΔR _{BC}
HMgH-NaC ₃ N-HCN	2.193	2.197	-0.004	2.050	2.061	-0.011
HMgH-NaC ₃ N-HNC	2.190	2.197	-0.007	1.801	1.813	-0.012
NC ₃ Na-NCH-HMgH	2.427	2.453	-0.026	1.783	1.925	-0.142
NC ₃ Na-CN ₃ H-HMgH	2.552	2.588	-0.036	1.506	1.633	-0.127
NC ₃ Na-HMgH-HCN	2.218	2.197	0.021	2.015	1.925	0.090
NC ₃ Na-HMgH-HNC	2.231	2.197	0.034	1.715	1.633	0.082

Conclusions

Ternary complexes of NaC₃N with HMgH and HCN (HNC) were investigated with quantum chemical calculations at the MP2/aug-cc-pVDZ level. The equilibrium structures, energetics and cooperative effects on the properties of the complexes were analysed. The triads with the HMgH molecule located at the end of the chain showed an energetic cooperativity. When the HMgH molecule was located in the middle, the obtained cluster was diminutive. Similar conclusion was obtained from the analysis of the intermolecular distances. These findings are helpful for understanding the cooperative and competitive roles of sodium, hydrogen and dihydrogenbondings in molecular recognition, crystal engineering and biological systems.

References

- [1] K. Muller-Dethlefs, P. Hobza, *Chem. Rev.*,(2000) 100-143.
- [2] I. Alkorta, J. Elguero, *Chem. Soc. Rev.*, 27 (1998) 163.
- [3] R. Custelcean, J.E. Jackson, *Chem. Rev.*, 101 (2001) 1963.
- [4] B.G. de Oliveira, *Phys. Chem. Chem. Phys.* 15 (2013) 37.
- [5] I. Alkorta, K. Zborowski, J. Elguero, M. Solimannejad, *J. Phys. Chem. A*, 110 (2006) 10279.
- [6] P.L.A. Popelier, *J. Phys. Chem. A* 102(1998) 1873.
- [7] T. Kar, S. Scheiner, *J. Chem. Phys.* 119(2003) 1473.
- [8] S.J. Grabowski, *J. Phys. Chem. A* 104 (2000) 5551.
- [9] I. Alkorta, J. Elguero, C. Foces-Foces, *Chem. Commun.* 1996, 1633.
- [10] G.N. Patwari, T. Ebata, and N. Mikami, *J. Chem. Phys.* 114 (2001) 8877.



20th Iranian Physical Chemistry Conference

- [11] W.T. Klooster, T.F. Koetzle, P.E.M. Siegbahn, T.B. Richardson, and R.H. Crabtree, *J. Am. Chem. Soc.* 121, (1999)6337.
- [12] R. Custelcean, J.E. Jackson, *J. Am. Chem. Soc.* 120, (1998) 12935.
- [13] B.S. Ault, *J. Am. Chem. Soc.* 100(1978) 2426.
- [14] Z.F. Li, Y.C. Zhu H.X. Li, *Phys. Chem. Chem. Phys.* 11(2009)11113.
- [15] Z.F. Li, H.X. Li, Y.C. Zhu, and G.F. Zuo, *Chem. Phys. Lett.* 482(2009)160.
- [16] Z.F. Li, Y.C. Zhu, G.F. Zuo, H.A. Tang, H.Y. Li, *Int. J. Quantum Chem.* 111 (2011) 570.
- [17] Z. Li, X. Zhang, H. Li, Y. Zhu, and X. Yang, *Chem. Phys. Lett.* 510(2011)273.
- [18] M.D. Esrafil, N.L. Hadipour, *Mol. Phys.* 109(2011) 2451.
- [19] M.D. Esrafil, H. Behzadi, N.L. Hadipour, *Theor. Chem. Acc.* 121 (2008) 135.
- [20] M. Solimannejad, *ChemPhysChem* 13(2012)3158. [21] M. Solimannejad, M. Malekani, *Comput. Theor. Chem.* 998(2012) 34.
- [22] M. Solimannejad, M. Malekani I. Alkorta, *Mol. Phys.* 109(2011) 1641.
- [23] M. Solimannejad, M. Malekani, I. Alkorta, *J. Phys. Chem. A* 114(2010)12106.
- [24] I. Alkorta, F. Blanco, P.M. Deya, J. Elguero, C. Estarellas, A. Frontera, D. Quinonero, *Theor. Chem. Acc.* 126(2010)1.
- [25] O. Mo, M. Yáñez, J.E. Del Bene, I. Alkorta, J. Elguero, *ChemPhysChem* 6 (2005)1411.
- [26] S.A.C. McDowell and A.D. Buckingham, *J. Chem. Phys.* 132(2010)064303.
- [27] C. Møller and M.S. Plesset, *Phys. Rev.* 46 (1934) 618.
- [28] S.F. Boys and F. Bernardi, *Mol. Phys.* 19 (1970)553.
- [29] M.J. Frisch, G.W. Trucks, H.B. Schlegel, G.E. Scuseria, M.A. Robb, J.R. Cheeseman, V.G. Zakrzewski, J.A.M. Zakrzewski, Jr., R.E. Stratmann, J.C. Burant, S. Dapprich, J.M. Millam, A.D. Daniels, K.N. Kudin, M.C. Strain, O. Farkas, J. Tomasi, V. Barone, M. Cossi, R. Cammi, B. Mennucci, C. Pomelli, C. Adamo, S. Clifford, J. Ochterski, G.A. Petersson, P.Y. Ayala, Q. Cui, K. Morokuma, D.K. Malick, A.D. Rabuck, K. Raghavachari, J.B. Foresman, J. Cioslowski, J.V. Ortiz, A.G. Baboul, B.B. Stefanov, G. Liu, A. Liashenko, P. Piskorz, I. Komaromi, R. Gomperts, R.L. Martin, D.J. Fox, T. Keith, M.A. Al-Laham, C.Y. Peng, A. Nanayakkara, C. Gonzalez, M. Challacombe, P.M.W. Gill, B. Johnson, W. Chen, M.W. Wong, J.L. Andres, C. Gonzalez, M.H. Gordon, E.S. Replogle, and J.A. Pople, Gaussian03; Revision C. 02 ed. (Gaussian, Inc., Pittsburgh, PA, 2004). [30] R.F.W. Bader, *Atoms in Molecules: A Quantum Theory* (Oxford University Press, Oxford, UK, 1990). [31] F. Biegler-König and J. Schönbohm, AIM 2000 Program Package, Ver.2.0 (University of Applied Sciences, Bielefeld, Germany, 2002). [32] X. Lucas, C. Estarellas, D. Escudero, A. Frontera, D. Quinonero, and P.M. Dey a, *ChemPhysChem* 10, 2256 (2009).
- [33] B. Gong, B. Jing, Q. Li, Z. Liu, W. Li, J. Cheng, Q. Zheng, J. Sun, *Theor. Chem. Acc.* 127(2010)303.
- [34] P. Valiron and I. Mayer, *Chem. Phys. Lett.* 275(1997) 46.
- [35] D. Hankins, J.W. Moskowitz F.H. Stillinger, *J. Chem. Phys.* 53 (1970)4544.

The response of rational barrier of spindle ring of single-molecule electric revolving door

Alireza Gholipour* Razieh Sadat Neyband

Department of Chemistry, Faculty of Sciences, Lorestan University, Khoramabad, Iran

Phone: +98 6633120619 Fax: +98 6633120612

*Alir.gholipour@gmail.com,

Abstract: We studied the response of rotation of spindle ring on energies, aromaticity and quadrupole moment in single-molecule revolving door (S-MERD) by using M05-2X/6-311++G** level of theory. Rotational barrier of energies, aromaticity and quadrupole moment for all substituents produces a $\cos^2 \theta$ function. All substituents have the maximum energy when the spindle and stator are coplanar ($E@0$ and $E@180$). The energies decrease as the spindle ring gradually rotates out of planarity and passes from a minimum ($E@40$) then the energies reach the transition state in the perpendicular conformation ($E@90$). The strong strict repulsion between the hydrogen atoms of the stator and substituents of the spindle ring significantly raises the energy of the flat configuration. The rational barrier of the energies for all substituent are higher than those for $X = H$. On the base of calculated energies, the rational barrier of the energies of S-MERD is in order $OH > F > CH_3 > Cl > H$. The rotation of spindle ring is accompanied by an increase in the aromaticity of spindle ring from $N@0$ to $N@90$ then decrease from $N@90$ to $N@180$ of this ring.

Keywords spindle ring; aromaticity and quadrupole moment.

Introduction

Molecular machines have been particularly interesting because of their increasing importance in nanoscience chemistry. In the last two decades, a wide variety of artificial molecular machines have been reported including so-called molecular gyroscope, elevator, nanocars [1] and molecular turnstiles. Among them, the molecular turnstiles have received considerable attention due to their resemblance to ordinary revolving doors. Molecular turnstiles include different kinds of motion, and fuel by different driving forces such as light, heat, or chemical reactions. Molecular machines have been particularly interesting because of their increasing importance in nanoscience chemistry. In the last two decades, a wide variety of artificial molecular machines have been reported including so-called molecular gyroscope elevator nanocars [2-5] and molecular turnstiles. Among them, the molecular turnstiles have received considerable attention due to their resemblance to ordinary revolving doors. Molecular turnstiles include different kinds of motion, and fuel by different driving forces such as light, heat, or chemical reactions [6].

Computational method

We explored the response of rotation of spindle rings on the energies, aromaticity and quadrupole moment of S-MERD. The rotational barrier was considered about the spindle ring from 0° to 180° by 10° intervals. The S-MERDs were optimized for each 10° intervals. Calculations have been performed by using the M05-2X density functional theory (DFT) paired with the 6-311++G** basis sets.

This methodology constitutes an economical approach to the calculation electric properties. So that we focus carefully on the suitable theoretical method for computational data. M05-2X is the best performers, in fact, by some criteria they are the very best available functional at this time. We encourage readers to use these functional for their applications; they have already been quite successful and shown good robustness.

Nucleus-independent chemical shifts (NICS) have been used extensively for the identification of aromaticity properties of molecules since the NICS index is one of the most widely employed indicators of aromaticity. It is defined as the negative value of the absolute shielding computed at a ring center or at some other interesting point of a system. Though NICS (1) (1 \AA above/below the plane of the ring) was recommended as being a better aromaticity diagnostic than NICS (0). NICS (1) reflects π -effects because at this point the effects of the local σ -bonding contributions are diminished.



NMR calculations have been performed at M05-2X/6-311++G** level of theory using GIAO method. All optimizations have been carried out using the GAMESS program.

Results and Discussion

The energies were computed as the difference between the energy of the S-MERD and the minimum energy ($E-E_{min}$). Rotational barrier of energies for all substituents produces a $\cos^2 \theta$ function with two energy minima at the 40° and 130° of comparable stabilities conformation and peak energy at the nearly perpendicular conformation (See Figure 1).

Energy predicts that the most stable conformer for all substituents is a tilted conformation with angle of about 40° between the spindle ring and the stator. For all substituents, $E@0$ and $E@180$ are maximum value (See Figure 1). The energies decrease as the spindle ring gradually rotates out of planarity and passes from a minimum ($E@40$) then the energies reach the transition state in the perpendicular conformation ($E@90$).

As shown in the Figure 2, Energy changes during the rotation. The presence of substituent at the spindle ring results in change on the energy profile and increases the rotational barriers curves. As can be seen in Figure 2, the shapes of the profile have been obtained by plotting the respective NICS values as functions of angle θ which shows the NICS values of spindle ring as $\cos^2 \theta$ function.

The values of NICS have been evaluated for all substituents the change of values of NICS at the center of spindle ring are negative before rotation. $N@0$ is equal to -9.56, -9.47, -9.56, -9.20 and -8.86 ppm at the center of spindle ring for H, F, CH_3 , Cl and OH, respectively (Figure 2). The NICS of spindle ring increase as spindle ring gradually rotates out of planarity and reach the highest NICS in the perpendicular conformation ($N@90$). Spindle ring is aromatic and becomes more aromatic with rotation; $N@90$ is minimum because the overlap of current ring of spindle with the current ring stator in perpendicular conformation leads to the highest NICS ($N@90$), where the molecule is fully π -conjugated. The values of $N@90$ are equal to -9.89, -9.83, -9.70, -9.42 and -9.21 ppm for H, F, CH_3 , Cl and OH, respectively (Figure 2).

The S-MERD is equipped with a quadrupole moment, which is distributed along the z-axis in (Scheme 1). The nature of the electrostatic of the S-MERD correlates with the magnitude of the Q_{zz} .

We calculated quadrupole moment tensor components for the entire system at the M05-2X/6-311++G** level of theory.

The values of Q_{zz} evaluated for all substituents are negative. The $Q_{zz}@0$ are equal to -65.24, -63.98, -60.48, -64.94 and -54.77 B (Buckingham, $1\text{B}=3.336\times 10^{-40}\text{ cm}^2$), for X = H, F, CH_3 , Cl and OH, respectively (Figure 5). For all substituents, the values of Q_{zz} of spindle ring decrease with rotation. As can be seen in Figure 5, the value of Q_{zz} of spindle ring decreases from $Q_{zz}@0$ to $Q_{zz}@90$ then increase from $Q_{zz}@90$ to $Q_{zz}@180$. The Q_{zz} value passes from a maximum in $Q_{zz}@90$. The Q_{zz} decreases as spindle ring gradually rotates out of planarity and reaches the lowest in the perpendicular conformation ($Q_{zz}@90$). The values of $Q_{zz}@90$ are equal to -52.62, -50.42, -52.23, -59.86 and -51.94 B for H, F, CH_3 , Cl and OH, respectively.

After the maximum at 90° , the values of Q_{zz} increase by rotation and $Q_{zz}@180$ are equal to -64.22, -62.02, -60.00, -65.10 and -55.60 B for H, F, CH_3 , Cl and OH, respectively. As can be seen in Figure 1, the values of Q_{zz} for all substituents are the highest when the spindle and stator are coplanar ($N@0, 180$).

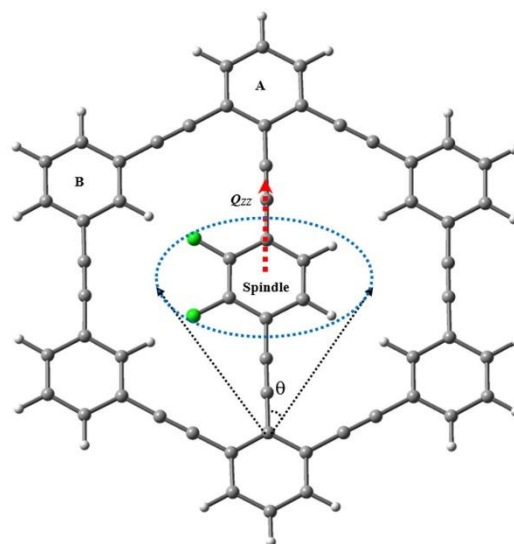


Fig 1. Model employed to describe the motion of the spindle ring between two sites related by 180° . The spindle ring is equipped with a quadrupole moment which is perpendicular to the spindle ring and distributed along the z-axis in S-MERD. Green spherical X = F, Cl, H, CH_3 , and OH substituents

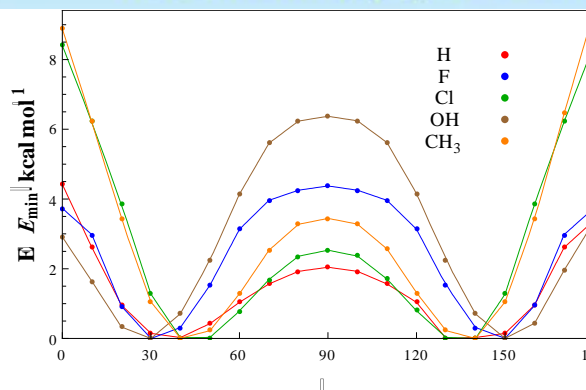


Fig. 2 The Rotational barrier energy (in kcal mol⁻¹) of the conformation obtained for S-MERD calculated M05-2X/6-311++G** at level of theory as a function of the rotation angle θ .

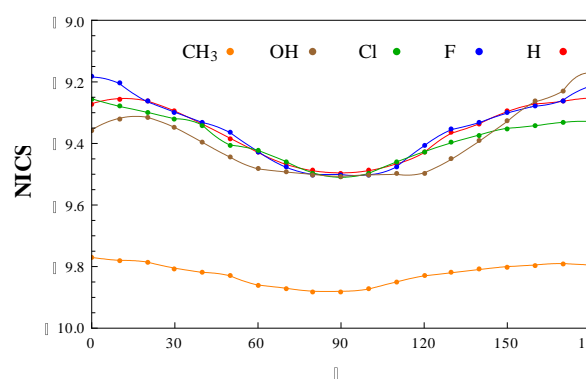


Fig.3: The profile of NICS values (in ppm) calculated at the center of B rings obtained from M05-2X/6-311++G** level of theory as a function of the rotation angle.

Conclusions

The rotation of spindle ring is accompanied by an increase in the aromaticity of spindle ring from N@0 to N@90 then decrease from N@90 to N@180 of this ring.

For all substituents, the value of Q_{zz} of spindle ring decreases from $Q_{zz}@0$ to $Q_{zz}@90$ then increase from $Q_{zz}@90$ to $Q_{zz}@180$. The Q_{zz} value passes from a maximum in $Q_{zz}@90$. All substituents have the maximum energy when the spindle and stator are coplanar ($E@0$ and $E@180$). The energies decrease as the spindle ring gradually rotates out of planarity and passes from a minimum ($E@40$) then the energies reach the transition state in the

perpendicular conformation ($E@90$). The strong strict repulsion between the hydrogen atoms of the stator and substituents of the spindle ring significantly raises the energy of the flat configuration. The rotational barrier of the energies for all substituent are higher than those for $X = H$. On the base of calculated energies, the rotational barrier of the energies of S-MERD is in order $OH > F > CH_3 > Cl > H$.

References

- [1] I.E. Wachs, Catalysis science of supported vanadium oxide catalysts, *Dalton Transactions*, 42 (2013) 11762-11769.
- [2] A.S. Kootenaei, J. Towfighi, A. Khodadadi, Y. Mortazavi, Stability and catalytic performance of vanadia supported on nanostructured titania catalyst in oxidative dehydrogenation of propane, *Applied Surface Science*, 298 (2014) 26-35.
- [3] S. Bagheri, N. Muhd Julkapli, S. Bee Abd Hamid, Titanium dioxide as a catalyst support in heterogeneous catalysis, *The Scientific World Journal*, 14 (2014) 21-51.
- [4] T. Mongkhonsi, L. Kershenbaum, The effect of deactivation of a V_2O_5/TiO_2 (anatase) industrial catalyst on reactor behavior during the partial oxidation of o-xylene to phthalic anhydride, *Applied Catalysis A: General*, 170 (1998) 33-48.
- [5] T. Zhang, J. Liu, D. Wang, Z. Zhao, Y. Wei, K. Cheng, G. Jiang, A. Duan, Selective catalytic reduction of NO with NH_3 over HZSM-5-supported Fe-Cu nanocomposite catalysts: The Fe-Cu bimetallic effect, *Appl. Catal. B* 148-149 (2014) 520-531.
- [6] J. Hu, Z. Lu, H. Yin, W. Xue, A. Wang, L. Shen, S. Liu, Aldol condensation of acetic acid with formaldehyde to acrylic acid over SiO_2 -, SBA-15-, and HZSM-5-supported V-P-O catalysts, *J. Ind. Eng. Chem.* 40 (2016) 145-151.

DFT study of structural and electronic properties of N-Doped Graphenylene

Fatemeh Fotovi, Mohsen Vafae* and Mohammad Reza Hosseini

Department of physical chemistry, faculty of science, Trabiati Modares University, Tehran-Iran

*m.vafae@modares.ac.ir

Abstract

In this work we have performed density functional theory with the plane-wave basis set to study structural and electronic properties of N-doped Graphenylene. Our results show like other nanosheets such as graphene nitrogen, it can affect the intrinsic properties of Graphenylene. The most important effect on electronic properties is the change of direct and narrow band gap. On the other hand, structural properties, like cell parameters modify after nitrogen doping. The results of this research can be considered as promising use of graphenylene in electronic device industry. This two dimensional structure and N-doped one show promising features for the future researches.

Keywords: density functional theory, Graphenylene, plane-wave, Quantum ESPRESSO

Introduction

Graphene has been a topic of intensive investigation since the pioneering work on synthesis of this unique two-dimensional material by Geim, Novoselov and co-workers. It has attracted enormous attention due to its fascinating physical properties, such as abnormal quantum Hall effects and massless Dirac fermions, which are attributed to the special linear behavior of electronic bands near the Fermi level in the K (or K0) point of the Brillouin zone. However, the linear gapless spectrum of graphene is bound to conflict with the basic requirement for its application in traditional electronic devices. [1]

Recently, a hypothetical two-dimensional sp^2 -carbon structure dubbed graphenylene, which was first described by Balaban *et al.*, has acquired great interest due to its thermodynamic stability and well-defined pore structure. It is a possible isomerization product of graphyne and its structural properties have been well documented. It is composed of cyclohexatriene units with two quite distinct C-C bonds in the hexagonal ring and has periodic pores with a diameter of 3.2 Å.

In this paper, we study the electronic and electromagnetic properties of nitrogen doped graphenylene based on the theory of density functional theory by Quantum ESPRESSO software.[2]

1. Computational details

Quantum ESPRESSO is a software suite for ab initio quantum chemistry methods of electronic-structure calculation and materials modeling, distributed for free under the GNU General Public License. It is based on Density Functional Theory, plane wave basis sets, and pseudopotentials (both norm-conserving and ultrasoft). ESPRESSO is an acronym for opEn-Source Package for Research in Electronic Structure, Simulation, and Optimization. The core plane wave DFT functions of QE are provided by the PWscf component, PWscf previously existed as an independent project. PWscf (Plane-Wave Self-Consistent Field) is a set of programs for electronic structure calculations within density functional theory and density functional perturbation theory, using plane wave basis sets and pseudopotentials. [3]

Density functional theory (DFT) is a computational quantum mechanical modelling method used in physics, chemistry and materials science to investigate the electronic structure (principally the ground state) of many-body systems, in particular atoms, molecules, and the condensed phases. Using this theory, the properties of a many-electron system can be determined by using functionals, i.e. functions of another function, which in this case is the spatially dependent electron density. Hence the name density functional theory comes from the use of functionals of the electron density. DFT is

among the most popular and versatile methods available in condensed-matter physics, computational physics, and computational chemistry.[4]

3. Results and discussion

In the present study, we explore the hypothetical two dimensional sp²-carbon structure dubbed graphenylene, through the use of computational methods based on density functional theory (DFT). Graphenylene is a two dimensional sp²-carbon network formed by the fusion of hexatomic rings and tetraatomic rings. Graphenylene can be obtained by substituting each benzenoid C-C bond and connected two carbon atoms with a biphenylene unit, forming a two dimensional carbon honeycomb network that possesses the same point group, D_{6h}

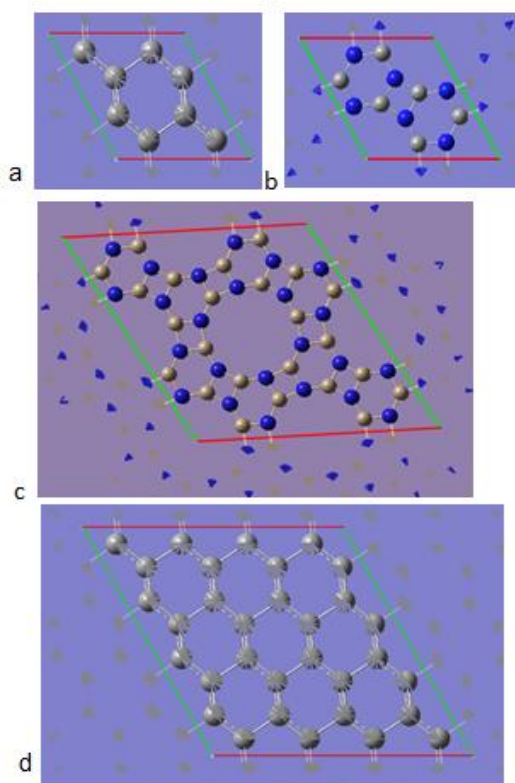


Fig1. The two-dimensional structures of (a) graphenylene and (b) graphene are shown. They are both honeycomb structures composed of sp²-carbon networks with the D_{6h} point group. The 2 × 2 supercells of (c) graphenylene and (d) graphene.

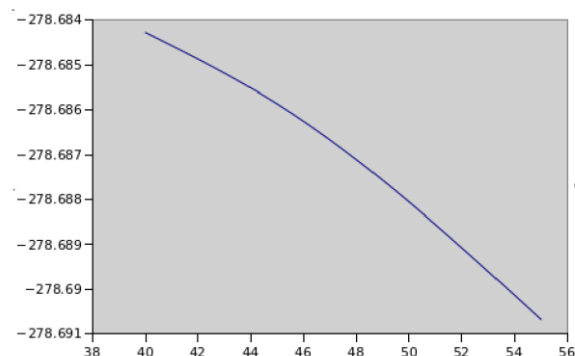


Fig2. Cut-off energy optimization

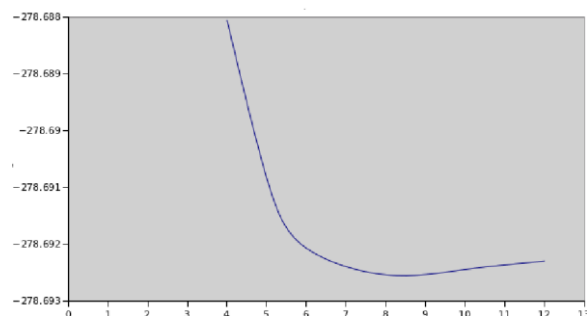


Fig3. K-point sampling optimization

4. Conclusion

In this project, we calculated the electromagnetic properties and learned the significant effect of Nitrogen on properties of Graphenylene.

Reference

- Hirunsit, Pussana, Monrudeem Liangruksa, and Paisan Khanchaitit. "Electronic structures and quantum capacitance of monolayer and multilayer graphenes influenced by Al, B, N and P doping, and monovacancy: Theoretical study." *Carbon* 108 (2016): 7-20.
- Song, Qi, et al. "Graphenylene, a unique two-dimensional carbon network with nondelocalized cyclohexatriene units." *Journal of Materials Chemistry C* 1.1 (2013): 38-41.
- Muhammad, Rafique, Yong Shuai, and He-Ping Tan. "First-principles study on hydrogen adsorption on nitrogen doped graphene." *Physica E: Low-dimensional Systems and Nanostructures* 88 (2017): 115-124.

Nature of Metal-ligand Bond in some derivatives of [(NHC(R))₄Re(N)(Y)] complexes:

(Y = F, Cl, Br; R = H, CH₃, F, Cl, Br): A Theoretical Study

S. Aghigh Hamrahian, Mehdi Bayat*, Sadegh Salehzadeh
 Faculty of Chemistry, Bu-Ali Sina University, Hamedan, Iran
 *Mehdi806@gmail.com(mbayat@basu.ac.ir)

Abstract: Theoretical studies on structure and nature of C→Re bonds in some derivatives of [(NHC(R))₄Re(N)(Y)] (Y = F, Cl, Br R = H, CH₃, F, Cl, Br) complexes have been reported at PBE1PBE/def2-SVP level of theory and We investigated the trend in interaction energy in [NHC(R)₂Re(N)Y] complexes with same substitutions by changing the R atoms from F to Br.

Key words: Theoretical study; Nature of Metal-ligand Bond; NHC Ligand.

Introduction

N-heterocyclic carbenes are most accessible organic ligands in both organometallic and coordination chemistry, which is reflected by thousands of applications involving NHC-bearing metal complexes in areas ranging from homogeneous catalysis to material science [1]. The chemistry of N-heterocyclic carbenes (NHCs) and their metal complexes has advanced significantly over the last two decades in the field of organometallic catalysis and medicinal chemistry [2]. Herein we want to report a theoretical study on structure and nature of C→Re bonds in some derivatives of [(NHC(R))₄Re(N)(Y)] (Y = F, Cl, Br R = H, CH₃, F, Cl, Br) complexes at PBE1PBE/def2-SVP level of theory.

Computational methods

The geometries of all complexes were fully optimized at PBE1PBE/def2—SVP level of theory by using GAUSSIAN-D program. The interaction energy for the complexes was calculated at mentioned level using def2—TZVP basis set. In all cases, the vibrational frequency analysis, calculated at the same level of theory, indicated that the optimized structures are at the stationary points corresponding to local minima without any imaginary frequency. The nature of C→Re bonds in the complexes are also analysed via NBO and EDA analysis.

Result and discussion

The interaction energy between [NHC(R)]₄ and Re(N)Y in optimized structures of [(NHC(R))₄Re(N)(Y)] (Y = F, Cl, Br R = H, CH₃, F,

Cl, Br) complexes have been studied at PBE1PBE/def2-TZVP // PBE1PBE/def2-SVP level of theory complexes are calculated. The data showed that the C→Re bonds in the complexes especially with electron donating substituents are stronger than other complexes. Also the results on changing R substituents from F to Br atoms show that there is increasing trend in the interaction energy in the complexes.

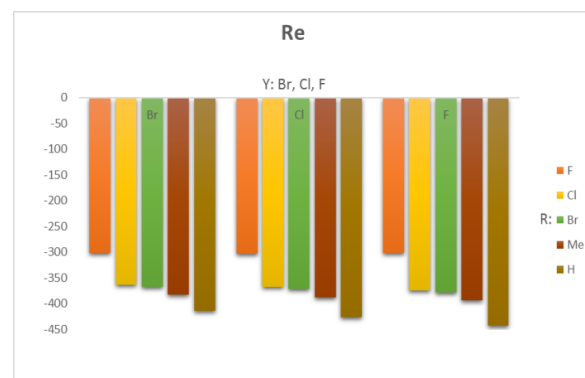


Fig 1. Trend of the variation of interaction energy in [(NHC(R))₄Re(N)(Y)] (Y = F, Cl, Br R = H, CH₃, F, Cl, Br) complexes.

Conclusions

The data show that there is a increasing trend in interaction energy in [NHC(R)₂M(N)Y] complexes with same substitutions by changing the R atoms from F to Br.

References

- Nolan, S. P., W.-V. Weinheim, "N-Heterocyclic Carbenes in Synthesis", 2006, university of new orleans.
- Tran, Hai Ngan. "Novel Metal Complexes of Imidazolyl-Substituted N-Heterocyclic Carbenes and Catalytic Applications", 2011, University of San Diego State.
- E. Ochlik, S. Kong, P. Arciszewski, S. Wiebalek, U. Abram, "Aryl and NHC Compounds of Technetium and Rhenium", Journal of the American chemical society, 134 (2012) 9118–9121.
- S. J. Hoek, L.-A. Schaper, W. A. Herrmann, F. E. Kuu'hn. "Group 7 transition metal complexes with N-heterocyclic carbenes", Royal Society of Chemistry, 42 (2013) 5073-5089.

Hydrogen bonding interaction between a new Schiff base ligand and H_2PO_4^- : A DFT study

Masoumeh Orojloo* and Saeid Amani

Department of Chemistry, Faculty of Sciences, Arak University, Dr. Beheshti Ave.
Arak 38156-88349, Iran

* m-orojloo@phd.araku.ac.ir

Abstract: Quantum chemical calculation and molecular studies were used to estimate the electronic structure, Physical properties, energy of optimized structures and the probable mode of binding of the Ligand (2-((3-hydroxy propyl imino) methyl)-4-(thiazol-2 yldiazanyl) phenol) (L) with the guest H_2PO_4^- anion. Molecular geometries of the complexes are investigated using the Density Functional Theory (DFT) method employing 6-311++G(d,p) basis set. Our results reveal that each H_2PO_4^- anion remained with the ligand (L) through two hydrogen bonding interactions. Theoretical calculations also revealed the lowest orbital energy gap of [L- H_2PO_4^-] complex is lower than that of free receptor (L) due to hydrogen bonding interactions.

Keywords: DFT Calculations; Schiff base; Hydrogen bonding.

Introduction:

Anions play vital role in the areas of biology, environmental hazard, medicine, catalysis among others, hence its recognition and sensing has gained considerable interest. The design of molecular probes, which is capable of recognizing anions, is a welcoming development in the biological industry and environmental processes due its significant potential applications [1]. Based on our previous works, colorimetric receptor possessing two phenolic and alcoholic OH binds to cyanide ions by involving azomethine cyanide reaction sites and phenolic OH via hydrogen bonding interaction [2]. To gain a deeper insight into the mechanism and structure for binding of Ligand (L) with the guest ion H_2PO_4^- , in addition to the spectral aspects of the complex, quantum chemical calculations were performed using Density Functional Theory (DFT) to supplement the experimental results.

Materials and method:

Quantum chemical calculations were carried out using Gaussian03 program package [3]. Molecular geometry optimizations of the receptor (L) and [L- H_2PO_4^-] complex were obtained by density functional theory (DFT) employing the 6-311++G(d,p) basis set.

Results and Discussion:

The optimized complex structure of (L) plus H_2PO_4^- showed that one H_2PO_4^- anion was attached with two OH parts of L to form a stable 1:1 complex (Fig. 1). At this point, each H_2PO_4^- anion remained

with L through two hydrogen bonding interactions, where both phenolic and alcoholic hydroxyl groups interacted with two different 'O' atoms of H_2PO_4^- . The intermolecular distances found for the [L- H_2PO_4^-] complex are 1.447 Å and 1.830 Å, since hydrogen bonds of phenolic and alcoholic O-H of L interacted with two oxygen atoms of H_2PO_4^- fragment, respectively.

To have a better understanding of the response mechanism of Ligand (L), the representative transition energy diagram for the Highest Occupied Molecular Orbital (HOMO) and the Lowest Unoccupied Molecular Orbital (LUMO) of the Ligand (L) and [L- H_2PO_4^-] complex were obtained, which is shown in Fig. 2. The complexation of (L) with H_2PO_4^- distorted the electron density distribution of the receptor due to the formation of hydrogen bonds. HOMO's for L were localized mainly on the O-H of phenolic moiety and nitrogen of imine group whereas; LUMO was distributed only on the phenolic moiety of the receptor (L). As a result, hydrogen bond is formed between phenolic O-H and imine group. Conversely, the electron density distribution changed for both receptor moieties and H_2PO_4^- of the complex. One of the hydrogen bond was formed between phenolic O-H and oxygen atom of H_2PO_4^- group. The second hydrogen bond was formed between alcoholic O-H and oxygen atom of H_2PO_4^- anion. The total energy of the optimized complex (-1915.4588 a.u.) in the gas phase was lower compared to the energy of the receptor (-1271.6654 a.u.) thereby protecting the greater stability of the

complex (Table 1). Theoretical calculations also revealed the lowest orbital energy gap of [L-H₂PO₄⁻] complex ($\Delta E = 2.9453$ eV) which is lower than that of free receptor L ($\Delta E = 3.3137$ eV). Calculation of optimized energy of the free L and [L-H₂PO₄⁻] complex in DMSO solvent was also carried out. The results of the calculation in gas phase and solution phase are in agreement with each other and can be seen in Table 1.

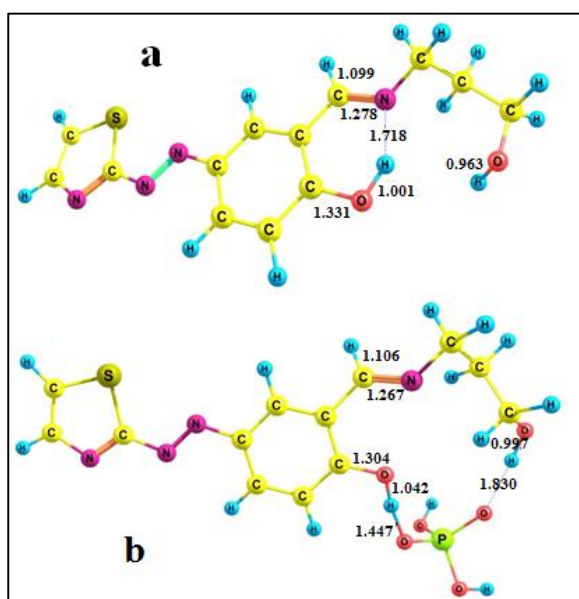


Fig. 1 (a) optimized structure of L, (b) optimized structure of L: H₂PO₄⁻ complex, by B3LYP/6-311++G(d,p).

Table 1. Computational optimized Energy (a. u.) of free receptor L and [L-H₂PO₄⁻] complex in gas phase and in DMSO solvent

phase	receptor (L)	[L-H ₂ PO ₄ ⁻] complex
gas phase	-1271.6654	-1915.4588
solvent (DMSO)	-1271.6936	-1915.5410

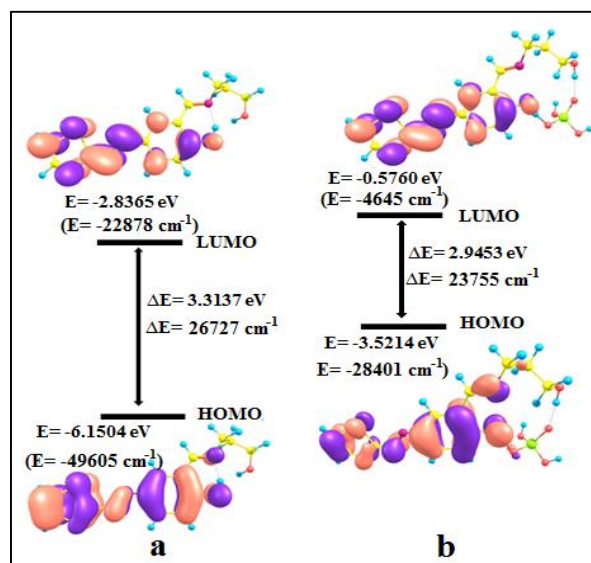


Fig.2 Energy level diagrams of the HOMO and LUMO orbital of (a) (L) and (b) L-H₂PO₄⁻ complex (using the DFT/B3LYP/6-311++G(d,p) method).

Conclusions:

Compared with our previous work [2], azoazomethine receptor (L) binds to H₂PO₄⁻ ions by involving phenolic and alcoholic OH via hydrogen bonding interaction.

Acknowledgment:

The authors would like to thank the Research Council of Arak University for financial support of this research.

References:

- [1] P.D. Beer, P.A. Gale, Anion recognition and sensing: the state of the art and future perspectives. *Angewandte Chemie International Edition* 40 (2001) 486-516.
- [2] M. Orojloo, S. Amani, Naked-eye detection of cyanide ions in aqueous media based on an azoazomethine chemosensor, *Comptes Rendus Chimie*, 20 (2016) 415-423.
- [3] M. Frisch, G. Trucks, H. Schlegel, G. Scuseria, M. Robb, J. Cheeseman, J. Montgomery Jr, T. Vreven, K. Kudin, J. Burant, Gaussian 03, revision D. 01. Gaussian Inc., Wallingford, CT 2004, 26.



Simulation of Hydrated Nafion as Fuel Cell Membrane by Dissipative Particle Dynamics

Majid Sedighi*, Abbas Ali Rostami, Saeid Yeganegi

Department of Chemistry, Mazandaran University, Babolsar, Iran.

*Sedighi49@gmail.com

Abstract: The microphase separation of hydrated perfluorinated sulfonic acid membrane Nafion was investigated using Dissipative Particle Dynamics (DPD). The Nafion as a polymer was modelled by connecting coarse grained beads which corresponds to the hydrophobic backbone of polytetrafluoroethylene and perfluorinated side chains terminated by hydrophilic end particles of sulfonic acid groups. The morphology of hydrated Nafion is studied for polymer molecular weight of 5720, 11440 and 17160 in water content of 10%, 20% and 30%. The results show water particles and hydrophilic particles of Nafion side chains spontaneously form aggregates and are embedded in the hydrophobic phase of Nafion backbone. The averaged water pore diameter and the averaged water clusters distance were found to rises with water volume fraction.

Keywords: Fuel cell, Membrane, Nafion, Mesosacle, DPD.

Introduction

During the last two decades, world-wide efforts have been mounted into the research, design and development of polymer electrolyte membrane (PEM) fuel cells, for stationary and portable applications [1]. Perfluorinated sulfonic acid membrane Nafion is the most common membrane materials used in polymeric electrolyte fuel cell. It is due to their exceptional chemical, mechanical and thermal stability as well as their advantage to conducting proton [2]. Although Nafion has received the extensive studies among the various membranes types, there is still some serious limitations such as of high manufacturing technology and cost, restrictive range stability and a significant degree of hydration is required in order to obtain sufficient proton conductivity [3]. Chemical formula of Nafion is show in Fig. 1.

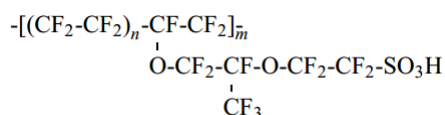


Fig. 1. Chemical formula of Nafion

The Nafion equivalent weight (EW) is determined by the average distance between the side chains along the backbone. Expressing the water content by the average number of water molecules per SO₃ group, then for a membrane with an EW of 1100 (g/eq.) at room temperature the water uptake ranges from $\lambda \sim 1$ at 0% relative humidity to $\lambda = 14$ at 100% relative humidity [4, 5]. Dissipative particle dynamics (DPD) simulations has been employed to study the modeling morphology evolution of a wide range of copolymer systems in order to investigate microphase separation

in copolymers and block copolymers [3, 4]. Dissipative particle dynamics was used for first time by Yamamoto and Hyodo [5] to investigate the micro phase separation in Nafion morphology at varying degrees of hydration. The aim of present study is to investigate the hydrated PSFA membrane morphology at different hydrated level via Dissipative Particle Dynamics method. The morphology is obtained via the membrane network contours, water cluster sizes and structure characteristics. A Nafion polymer is modelled via connecting soft core potential bead which corresponds to a group of several atoms by a bond potential.

Theory and mathematical formulation

Dynamics of soft DPD particles are governed by Newton's second law of motion in Lagrangian reference coordinates System as follow:

$$\begin{aligned} d\mathbf{r}_i &= \mathbf{v}_i dt, \quad d\mathbf{v}_i = \frac{\mathbf{F}_i}{m_i} dt = \frac{1}{m_i} \sum_{j \neq i} \mathbf{F}_{ij} \\ \mathbf{F}_{ij} &= \mathbf{F}_{ij}^C + \mathbf{F}_{ij}^D + \mathbf{F}_{ij}^R + \mathbf{F}_{ij}^S \end{aligned} \quad (1)$$

where \mathbf{r}_i and \mathbf{v}_i are the position and velocity vectors of the indexed bead i in Cartesian coordinate respectively, dt is the simulation time step, m_i is the bead mass and \mathbf{F}_i is the overall force vector applied on the bead i . \mathbf{F}_{ij} is the vector sum of the three pairwise-additive conservative (\mathbf{F}_{ij}^C), dissipative (\mathbf{F}_{ij}^D) and random (\mathbf{F}_{ij}^R) and a harmonic spring force (\mathbf{F}_{ij}^S) as follows:

$$\mathbf{F}_{ij}^C = A_{ij} \omega^C(r_{ij}) \frac{\mathbf{r}_{ij}}{r_{ij}} = A_{ij} \left(1 - \frac{r_{ij}}{R_C} \right) \frac{\mathbf{r}_{ij}}{r_{ij}} \quad (2)$$

Where A_{ij} is maximum repulsion force adjusting the repulsive strength between beads i, j , R_C is the cut-off radius (or particle effective diameter) and DPD



length scale beyond which the interparticle repulsive interactions are ignored, and $\omega^c(r_{ij})$ is the conservative weight function. The repulsive parameter A_{ij} is set at $25K_B T$ for density $\rho = 3$ to match the compressibility of water at room temperature if each bead represents a water molecule [6]. In the present study as will be discussed later each bead stands for four water molecule, so the repulsive parameter is set at $100K_B T$ for water beads. The repulsion parameter between other same type beads is chosen to have the same value of water beads. The repulsion parameters of different type beads corresponds to the mutual solubility, expressed as Flory-Huggins χ - parameter. The relation is as follow when the reduced density has the value of $\rho = 3$.

$$A_{ij} = A_{ii} + 3.27\chi_{ij} \quad (3)$$

The values of the repulsion parameters A_{ij} and Flory-Huggins χ - parameter were determined previously in ref [5] and are listed in Table 1 and Table 2 respectively.

Table 1. DPD beads definitions and repulsion parameters [5].

	A	B	C	W
$CF_2CF_2CF_2CF_2$	104	-	-	-
$OCF_2CF(CF_3)O$	104.1	104	-	-
$CF_2 - CF_2 - SO_3H$	114.2	108.5	104	-
$(H_2O)_4$	122.9	120	94.9	104

Table 2. Flory Huggins parameters for each bead pair [5].

Pair	χ
A-B	0.022
A-C	3.11
A-W	5.79
B-C	1.37
B-W	4.90
C-W	-2.79

The pairwise random force is present as follows to induce movement by stochastic agitation and to compensate for the lost degrees of freedom due to coarse-graining:

$$\mathbf{F}_{ij}^R = \sigma \omega^R(r_{ij}) \xi_{ij} dt^{-\frac{1}{2}} \frac{r_{ij}}{r_{ij}}, \langle \xi_{ij}(t) \rangle = 0$$

$$\xi_{ij}(t) \xi_{kl}(t') = (\delta_{ik} \delta_{jl} + \delta_{il} \delta_{jk}) \delta(t - t') \quad (4)$$

Where $\omega^R(r_{ij})$ is the random force weight function, σ is the noise amplitude for randomly generated numbers (ξ_{ij}) with Gaussian white-noise statistics, zero mean and unit variance. They are uncorrelated for different pairs of particles while meeting the condition $(\xi_{ij} = \xi_{ji})$ to maintain centrality of the pairwise force.

The present study concerns with the Nafion polymer with equivalent weight of 1144. The Nafion morphology is then investigated in three water volume fraction of 0.1, 0.2 and 0.3 which correspond

to hydration level of $\lambda = 2.7, 6$ and 10.3. A cubic with a unit cell length of 40 is considered in the present study which is scaled by the unit of length R_c and corresponds to a dimension of 28.4 nm in each direction. Periodic boundaries were assumed in all boundaries. Each simulation run involved the dynamics of 192,000 beads and contained several thousand of polymer chains. The number of A, B, C and W beads in various water content and corresponding hydration level are presented in Table 3. The modeled membrane polymers are shown in Fig. 2. The present Nafion modelling corresponds to the Nafion with equivalent weight of 1200 which can stand for Nafion EW1200 a commercial one.

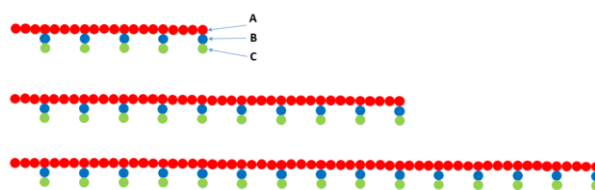


Fig. 2. Bead representation of the membrane polymers structure.

Table 3. Number of polymer molecule in the system for various molecular weights at different percentage of water content.

Water content%	MW=5720	MW=11440	MW=17160	Hydration level
10	5760	2880	1920	2.67
20	5120	2560	1706	6
30	4480	2240	1493	10.28

The time evolution of DPD beads is calculated up to the equilibrium structure of hydrated Nafion polymer. The maximum equilibration is observed about $t = 50000$, which corresponds to 1000000 time step according to the time step size of 0.05 in DPD reduced unit. In addition the size of time step was examined to test if the energy levels changes near its correct value $K_B T = 1$. The numerical simulation is accomplished by DL_Meso_DPD open source package [13].

Results and Discussion

The size of the water aggregates or clusters and the average distance between them are demonstrated via the Radial Distribution Function (RDF) or pair correlation function $g(r)$ of the water beads. Interpretation of RDF plots is straightforward. The time progressing morphology of Nafion1200 with three molecular weight of at different hydration level is shown in figure 4. At initial times a small domain of water aggregation forms very small water clusters. As time progressing, the formed aggregated water which is surrounded by hydrophilic beads of polymer (sulfonic group in Nafion molecule) which were the end bead of Nafion chains (beads C in figure 2). The water and hydrophilic beads of Nafion are embedded in the hydrophobic Nafion beads. The structure

equilibrium is obtained at different time for various hydration levels as indicated in caption of Fig. 5. It also shows that the water cluster becomes larger by increasing the hydration level. This phenomenon is observed for Nafion morphology with other molecular weight. Water cluster size augmentation are shown in figure 5 in which the water beads with sulfonic group are shown in by iso-surfaces at density $\rho = 1.5$ for Nafion with MW = 11440 and three hydration level.

The Nafion morphology quantitative parameter should be extracted via the RDF graph. The RDF of water beads are shown in Fig. 6 at different hydration level. The RDF curves experience two peaks in their raising which corresponds to first and second nearest water accumulation in the water clusters. The curve in its decreasing manner cut the RDF=1 value in first peak which shows the averaged water cluster size in the system. Then the RDF reach to second peak at a position which stands for the second water cluster and its position in distance axis shows the distances of water clusters.

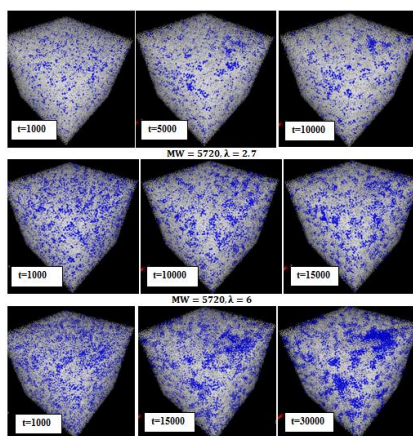


Fig. 4. Morphologies of the Nafion with as time progressing for different hydration level. (Nafion polymers are shown with silver and water beads are shown with blue beads.)

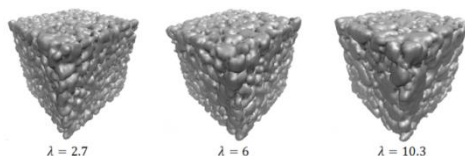


Fig. 5. Iso-surface Representation of water beads region including sulfonic acid group at density $\rho = 1.5$ for hydrated Nafion with MW = 11440 and three different hydration levels.

The values at which RDF drops below the value 1 increase with water content. Also the 2nd maximum shifts towards larger distance with increase of water content. This indicates that for these membranes, the water cluster size R_{pore} and the distance between clusters D_{cl} increase with hydration level. These

trends are observed for Nafion with MW = 5720, 17160 (figure 7).

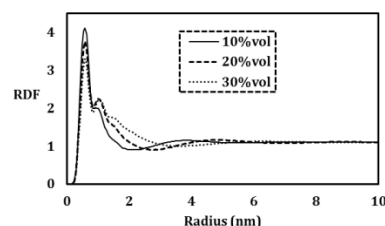


Figure 6. Radial distribution function(RDF) for water beads at three water content of 10%, 20% and 30% for Nafion 1144 with molecular weight of MW = 11440

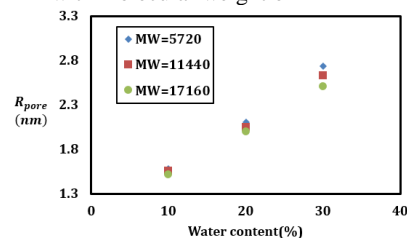


Figure 7. Average pore radius R_{pore} versus water content at different molecular weight.

Finally it is observed that the Nafion polymer structure experiences more changes by water content with respect to molecular weight. The meso scale simulation of hydrated Nafion by DPD is confirmed to be one of the reputable structures for actual materials. The results of mesoscopic study can be used to extract the atomistic level properties such as proton conductivity [8].

Conclusions

Dissipative particle dynamics as a mesoscopic method is implemented to study the structure of hydrated Nafion membrane. Nafion structure is made via connecting three different beads with spring force. Each four water molecules is coarse grained in a bead to reach the same size with respect to other beads. The system starts from a random distribution of beads and equilibrated. The calculated pore radius in structure shows agreement with the results of experiments in range of 4 to 5 nm. The pore radius and water cluster distances shows increment with water content. Pore radius becomes smaller by increasing the molecular weight in the studied range. Finally the water cluster distances become larger at higher molecular weight.

References

- [1] K. A. Mauritz , R. B. Moore, "State of understanding of Nafion". Chemical reviews, 104(2004) 4535-4586.
- [2] B. Smitha, S. Sridhar,A. Khan, "Solid polymer electrolyte membranes for fuel cell applications—a review". Journal of membrane science, 259(2005) 10-26.



- [3] M. A. Horsch, Z. Zhang, C. R. Iacovella, S. C. Glotzer, "Hydrodynamics and microphase ordering in block copolymers: Are hydrodynamics required for ordered phases with periodicity in more than one dimension?". The Journal of chemical physics, 121(2004) 11455-11462.
- [4] X. Cao, G. Xu, Y. Li, Z. Zhang, "Aggregation of poly (ethylene oxide)-poly (propylene oxide) block copolymers in aqueous solution: DPD simulation study". The Journal of Physical Chemistry A, 109(2005) 10418-10423.
- [5] S. Yamamoto, S.-a. Hyodo, "A computer simulation study of the mesoscopic structure of the polyelectrolyte membrane Nafion". Polymer journal, 35(2003) 519-527.
- [6] R. D. Groot, K. Rabone, "Mesoscopic simulation of cell membrane damage, morphology change and rupture by nonionic surfactants". Biophysical journal, 81(2001) 725-736.
- [7] M. A. Seaton, R. L. Anderson, S. Metz, W. Smith, "DL_MESO: highly scalable mesoscale simulations". Molecular Simulation, 39(2013) 796-821.
- [8] M. Eikerling, A. Kornyshev, U. Stimming, "Electrophysical properties of polymer electrolyte membranes: a random network model". The Journal of Physical Chemistry B, 101(1997) 10807-10820.

Computational examination of functionalization of the armchair boron-nitride nanotubes by borazine

E. Ahmadi, M. Anafcheh*

Department of Chemistry, Faculty of Physics & Chemistry, Alzahra University, P. O. Box 1993893973, Tehran, Iran
*m_anafcheh@alzahra.ac.ir

Abstract: In this work, we analyze by means of density functional theory calculations the reaction of [2+2] cycloadditions of borazine $B_3N_3H_6$ to armchair single-walled boron nitride nanotube (3,3) BNNTs. For all the armchair boron nitride nanotubes, diagonal BN bonds, either at the edge or at the middle of the tube, prefer [2+2] cycloaddition, but BN bonds perpendicular to the tube axis undergo bond-cleavage and ring-expansion. Our DFT calculations reveal that bonding of borazine with perpendicular BN bonds are more favorable, with negative interaction energies, but interaction energies for BN bonds are obtained to be positive which are not favorable for the formation of these complexes. Such expanded structures are stabilizing by 20–35 kcal/mol depending on the reactive site of the tube. These findings suggest that BN nanotubes can be used as a carrier of different derivatives of borazine and that a wide range of new materials can be developed.

Keywords: armchair BNNTs, cycloaddition; borazine; DFT

Introduction

Since the first experimental realization [1] many chemists have focused the chemical modifications of BNNTs. BNNTs take the advantage of more chemically and thermally stable than their carbon analogues. In view of that, it is not difficult to imagine the synthesis of interesting materials developed from BNNTs, which not only allow tuning their several properties but also make new functionalized materials [2]. Such modifications include substitutional doping and covalent and noncovalent functionalization by a wide range of chemicals at the surface [3]. To this aim, in the present investigation, we explore the reaction between the surface of BN nanotubes and borazine ($B_3N_3H_6$). Borazine has been called the inorganic benzene, due to the remarkable similarity in its physical properties with benzene.

Computational Aspects

All quantum chemical calculations were performed at the level of density functional theory (DFT) by GAUSSIAN 09 package. The zigzag BNNTs, (5,0), (6,0), (7,0) and (8,0) consisting of six zigzag rings stacked along the tube axis, were considered to interact with borazine. Hydrogen atoms were added at open ends to avoid dangling bonds. Geometries of all the systems were allowed to be fully relaxed during the B3LYP/6-31G* optimization, followed by vibrational analyses that ensure the identification of true minima.

Results and Discussion

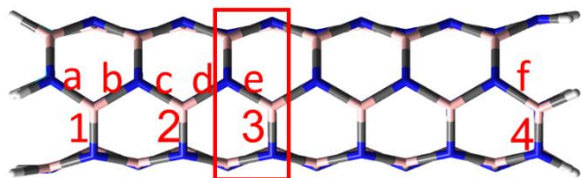
Several sites at the surface of BNNT are available to interact with $B_3N_3H_6$, shown in Scheme 1. First, with

respect to (3,3)-BNNT, the sites a, b, c, d, e and f are diagonal BN bonds while the sites 1–4 refer to BN bonds that lie perpendicular to the tube axis. Borazine was initially positioned directly above these sites (B/N of borazine $B_3N_3H_6$ over N/B of the tube) with the distance of 2 Å, and then geometries were fully optimized. All diagonal BN bonds, either at the edge or at the middle of the tube undergo [2+2] cycloaddition, making an additional square rings with the BN bond of tubes. But BN bonds perpendicular to the tube axis undergo bond-cleavage and ring-expansion, i.e., the borazine molecule pulls apart the BN bond of the tube at these sites and becomes an integral part of the tube by expanding the original hexagonal BN ring at the tube surface by forming an 8-membered BN ring. The geometries of these two types of BNNT- $B_3N_3H_6$ complexes are depicted in Fig.

1, and the interaction energies of all (3,3) BNNT- $B_3N_3H_6$ complexes are summarized in Table 1. Our density functional results show negative interaction energies for all the perpendicular BN sites, bond cleavage reaction and ring expansion, while positive interaction energies for diagonal ones, cycloaddition reaction. This shows that the [2+2] borazine cycloaddition does not favor reaction pathway. Instead borazine prefers to interact with perpendicular BN sites of (3,3) BNNT forming more stable complexes with borazine. In the most stable complex, (3,3)-BNNT- $B_3N_3H_6$ -1, the borazine molecule pulls apart the BN bond of the tube at site 1 and becomes an integral part of the tube by expanding the original hexagonal BN ring at the tube surface by forming an 8-membered BN ring, shown by the dotted bonds in Fig. 1. This BN bond cleavage and expansion of the surface stabilizes the complex by more than 34 kcal/mol. The two newly formed BN bonds with borazine $B_3N_3H_6$ in (3,3)-BNNT- $B_3N_3H_6$ -1 are only slightly longer than the

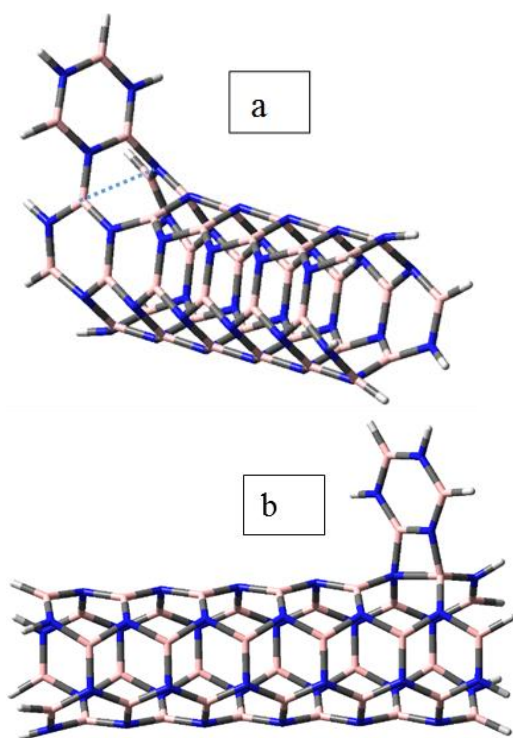
standard BN double bond (1.45 Å) of borazine (B₃N₃H₆).

Scheme 1. Active Sites of (3,3) BNNT. Blue, pink, and gray spheres represent N, B, and H atoms, respectively.



In this complex, the BN bond distance of 1.44 Å, at the attached sites in nanotube, stretches to 2.831 Å in complex which shows no bond between these atoms. The change in internal geometry of nanotube at the attached sites, B and N, are in accord with the change from sp² hybridization to sp³ in the complex.

Fig.15: B3LYP/6-31+G* optimized structures of (3,3)-BNNT-B₃N₃H₆ complexes: an example of a) diagonal BN site and b) BN site perpendicular to the axis of tube. Blue, pink, and gray spheres represent N, B, and H atoms, respectively.



In fact, all other five BN bonds of the octagon are in the range of 1.43–1.48 Å, indicating delocalization of π-electrons, as in the case of borazine. The next most stable structures (3,3)-BNNT-B₃N₃H₆-2 and (3,3)-BNNT-B₃N₃H₆-3 also exhibit similar structural features, i.e., cleavage of the BN bond at site 2 and 3, respectively,

which lie near the middle and at the middle of the BN tube. In the complexes of (3,3)-BNNT-B₃N₃H₆-2 and (3,3)-BNNT-B₃N₃H₆-3 borazine binds to the tube by about 20 kcal/mol. A slightly lower interaction energy of 0.691 is found in B₃N₃H₆-2

Table 1: HOMO-LUMO gaps (v.s. eV) and interaction energy (v.s. kcal/mol) in the complexes of (3,3) BNNT-borazine.

Complex-sites	Gap	E _{int}
(3,3)BNNT-B ₃ N ₃ H ₆ -1	6.212	-34.675
(3,3)BNNT-B ₃ N ₃ H ₆ -2	6.126	-20.136
(3,3)BNNT-B ₃ N ₃ H ₆ -3	6.145	-20.827
(3,3)BNNT-B ₃ N ₃ H ₆ -a	5.348	18.517
(3,3)BNNT-B ₃ N ₃ H ₆ -b	5.582	12.682
(3,3)BNNT-B ₃ N ₃ H ₆ -c	6.133	15.192
(3,3)BNNT-B ₃ N ₃ H ₆ -d	5.535	14.815
(3,3)BNNT-B ₃ N ₃ H ₆ -f	6.024	16.949

Conclusions

Interactions between borazine B₃N₃H₆ with BN nanotube have been studied using DFT theory. In addition to the expected [2+2]-cycloaddition products, making an additional square rings with the BN bond at the surface of BN nanotubes, an unusual feature has been revealed. Borazine B₃N₃H₆ is able to break a BN bond at the surface of the tube, not only at the edge or near the edge of the tube, but also at the middle, and become an integral part of the tube by expanding the original hexagonal BN ring at the tube surface by forming an 8-membered BN ring. Interestingly such breaking and expansion of a ring at the surface depends on the site of the tube. All BN bonds perpendicular to the tube axis are broken, but not the diagonal bonds. Bond cleavage and expansion processes are energetically more favorable than the [2+2]-cycloaddition process. Such expansion processes stabilize the complexes by about 20–35 kcal/mol. Both ring-expansion and cycloaddition products may have a wide range of applications in BN nanotube chemistry and warrant further investigation.

Acknowledgment

Supporting of this investigation by Alzahra University is gratefully acknowledged.

References

- [1] N. G. Chopra, R. J. Luyken, K. Cherrey, V. H. Crespi, M. L. Cohen, S. G. Louie, A. Zettl, Boron Nitride Nanotubes. *Science* 269 (1995) 966–967.
- [2] D. Golberg, Y. Bando, Y. Huang, T. Terao, M. Mitome, C. Tang, C. Zhi, Boron Nitride Nanotubes and Nanosheets. *ACS Nano* 4 (2010) 2979–2993.



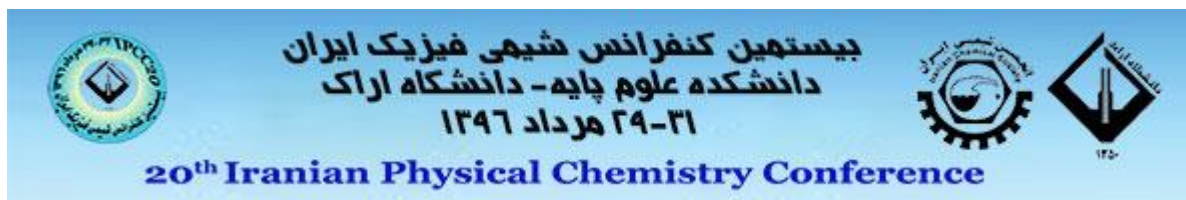
بیستمین کنفرانس شیمی فیزیک ایران
دانشکده علوم پایه - دانشگاه اراک
۳۱-۲۹ مرداد ۱۳۹۶



20th Iranian Physical Chemistry Conference

شیمی کوانتوم

Quantum Chemistry



Semi-empirical Quantum Mechanical Methods for Tetracycline Interactions on Graphene

R. Rostamian*, H. Behnejad

Department of Physical Chemistry, School of Chemistry, University College of Science, University of Tehran, Tehran, Iran.

*r.rostamian@gmail.com, r.rostamian@ut.ac.ir

Abstract: Graphene nanosheet (GNS) has been paid attention to as the thinnest molecule in the world. GNS has presented excellent benefits and utilizations which extremely depend on a large-scale preparation of high quality GNS. In this study the interaction between tetracycline (TC) molecule and GNS will be investigated using semi-empirical quantum mechanics calculations. The VdW energy interaction, Mulliken charges, and dipole moment calculated by computational approaches. These kind of interactions are important to better understand in drug delivery process, catalytic applications and it is also approved that the graphene new generation carbon family are promising materials for extracting TTC from water.

Keywords: *Graphene nanosheet, Semi-empirical method, Tetracycline, Interaction.*

Introduction

The name semiempirical molecular orbital theory indicates that the methods used have been parameterized to reproduce experimental results. Semiempirical techniques use the same Linear Combination of Atomic Orbitals-Self Consistent Field (LCAO-SCF) theory as ab initio programs. However, many of the more complex integrals are removed or replaced using simple approximations. Empirical parameters and functions are used to compensate for the errors introduced by removing integrals. These empirical parameters are fitted to reproduce experimental data. The basic approximations for neglecting less important integrals were developed by Pople's group in the 1950s and 1960s. The method that arose from this method and used in this research is NDDO approximations. These methods are still in use, although usually in modifications intended for interpreting molecular spectra. NDDO is a basic approximation for neglecting less important integrals. It is available in a variety of modifications, each adapted to accurately compute certain properties or for calculations on particular types of compounds.

Tetracycline (TCs) is a class of antibiotics that have widely administered to human and veterinary treatments to maintain health and prevent diseases. In 2005, it was estimated approximately 3.8 million kilograms of TC were utilized to animal treatments and livestock production in USA; the amount increased about 30% compared to that used in 2004. TC released from human treatments could survive residential wastewater treatment phenomena, and disseminate in the environment. Sorption and fate of TC in the environment is a pivotal factor in assessing their exposure and risks in the ecosystems.

The thorough understanding of the TC-GNS interaction is essential for the understanding and successful prediction of the intermolecular interaction of antibiotic-adsorbent system. Our results provide

fundamental information about the systems and demonstrate that using semi empirical method for this aim can be a useful means of identifying the phenomena that control surface chemistry [1, 2].

Materials and method

The electronic properties and structural of GNS interacting with one molecule of TC, in different arrangements and structural conformations were obtained via ab initio computations based on semi-empirical method. The semi-empirical computations were performed using the Material Studio package (available from Accelrys, San Diego, CA). All geometry optimizations and quantum chemical computations were fulfilled using VAMP module which is a semi empirical molecular orbital program that has been optimized to be highly numerically stable and fast. VAMP includes routines implementing the natural atomic orbital/point charge (NAO-PC) model. It lets us have comprehensive information about dipole, quadrupole and high quality molecular electrostatic potentials (MEPs).

VAMP is generally faster than comparable methods and this property makes it attractive. The computation was done with SCF (self-consistent field) quality which controls specify the accuracy when the SCF is converged. Molecular properties have evaluated using the highest occupied molecular orbital (HOMO) energies, lowest unoccupied molecular orbital (LUMO) energies and the other properties which derived from these two main HOMO and LUMO energies. The NDDO and AM1 hamiltonians were applied to optimize geometrical parameters of GNS as well as TC to obtain the most stable complexes

Mulliken Population Distribution

Mulliken population distribution is generally utilized in quantum calculations to evaluate the active centers of organic molecule responsible for interaction with molecules. It has been frequently reported that the

more negative the atomic charges, the more easily electron donating to the unoccupied molecular orbital.

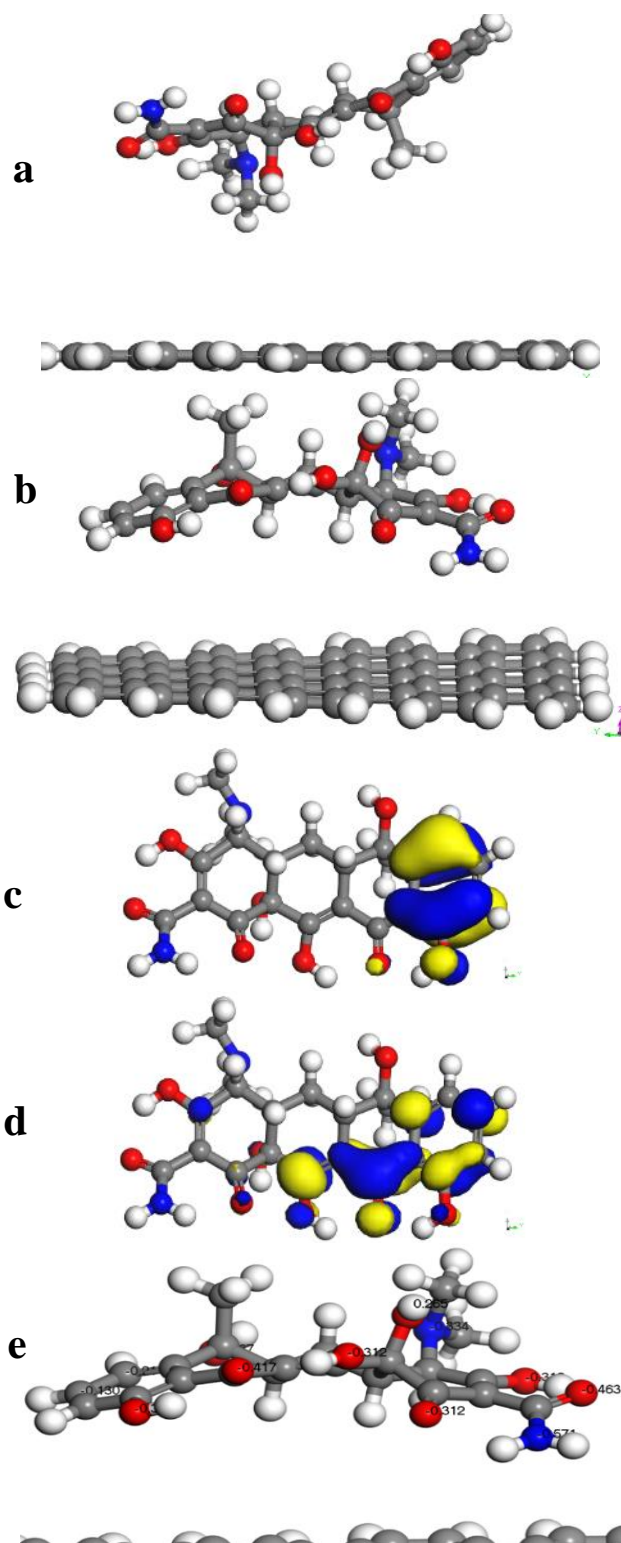


Fig. 1. The final optimized structures of TC onto GNS (a & b), the pictures of HOMO (c) and LUMO (d) orbitals of TC, Mulliken charges of TC (e) in the most stable configuration after optimization.

Results and Discussion

Two different configurations of TC on GNS were obtained in which configuration 2 was the most stable structure (Fig. 1b).

As displayed in Table 1, HOMO-LUMO gaps for configuration 1 is more than configuration 2 and that is a reason that configuration 2 was selected as the most stable structure. The dipole moment (μ) of two configurations of TC onto GNS were listed in Table 1 as well. The dipole moment for configuration 2 as the most stable configuration is the maximum. This data has verified that both π - π interaction (via terminal phenyl group) and electrostatic interactions (between heteroatoms of TC and GNS surface) are in the optimized TC-GNS system.

Table 1. The HOMO-LUMO energies, E_g and dipole moment (μ) of two configurations of TC onto GNS.

VAMP Module	System	E_{HOMO} (ev)	E_{LUMO} (ev)	E_g (ev)	μ
Config. 2	2	-5.089	-4.109	0.98	-4.599
	GNS	-5.067	-4.104	0.963	
	TTC	-9.207	-0.81	8.397	
Config. 1	1	-5.443	-3.217	2.226	-4.330
	GNS	-5.067	-4.105	-0.962	
	TTC	-9.205	-0.808	-8.397	

Fig. 1.e displays the Mulliken charge distributions of TC. As shown in this Figure, Mulliken atomic charge of N (of NH_2) is -0.571 , which is bigger than that of N (of $+\text{NHCH}_2\text{O}$) (-0.334). That is to say, the electronegativity of N (of $+\text{NHCH}_2\text{O}$) is larger.

As the larger the electronegativity is, the stronger the interactions will be, thus the distance between N (of NH_2) and GNS is shorter than that between N (of $+\text{NHCH}_2\text{O}$) and GNS. It can be concluded that because the space steric hindrance of N (of $+\text{NHCH}_2\text{O}$) is much larger than that of N (of NH_2).

Another main point which results from semi empirical calculation is a little torsion and twist in the GNS surface after semi empirical optimization which is clearly displayed in Fig 2. It totally agrees with experimental SEM image of GNS.

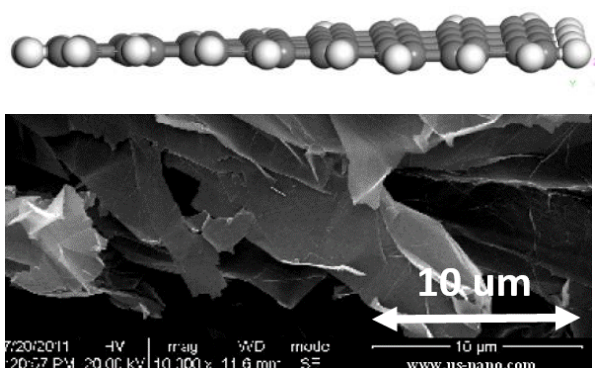


Fig 2. GNS structure after optimization and SEM image of GNS

Conclusions

In this research, the interactions of TC drug onto GNS were studied using first principles of calculations based on quantum mechanics. The VdW energy interaction, Mulliken charges, and dipole moment calculated by computational approaches. These results inform us that the GNS is promising materials for removing TC from wastewater samples and it is also approved that the graphene new generation carbon family are promising materials for extracting TTC from water.

References

- [1] R. Rostamian, H. Behnejad, "A unified platform for experimental and quantum mechanical study of antibiotic removal from water", *Journal of Water Process Engineering*, 17 (2017) 207-215.
- [2] R. Rostamian, H. Behnejad, "A comparative adsorption study of sulfamethoxazole onto graphene and graphene oxide nanosheets through equilibrium, kinetic and thermodynamic modeling", *Process Safety and Environmental Protection*, 102 (2016) 20-29.

Quantum chemistry study on the regioselective behavior of 1,3-dipolar cycloaddition reaction of azides with various substituted cyclooctynes

M.Omrani*, T.Hosseinnejad

Department of Chemistry, Alzahra University, Vanak, Tehran, Iran

*marzieh.omrani@yahoo.com

Abstract: The 1,3-Dipolar cycloaddition reactions are the classic reaction in modern synthetic organic chemistry. The Huisgen cycloaddition is the reaction of a dipolarophile with a 1,3-dipolar compound that leads to 5-membered heterocycles. With the goal of identifying alkyne-like reagents for use in azide-alkyne Huisgen cycloaddition reactions, we used density functional theory (DFT) and polarized continuum model (PCM) computations. In this respect, we investigated the structure and energy of transition states in the reaction path and assessed the trends in the calculated activation barriers for the 1,3-dipolar cycloaddition of azides with various substituted cyclooctynes in the gas and solution phases to interpret theoretically the origin of regioselectivity in the synthesis of disubstituted 1,2,3-triazole derivatives.

Keywords: 1,3-Dipolar cycloaddition, 1,2,3-triazole, regioselectivity, density functional theory, polarized continuum model.

Introduction

The azide-alkyne Huisgen cycloaddition is a 1,3-dipolar cycloaddition reaction between an azide and a terminal or internal alkyne to give a 1,2,3-triazole compound.

Rolf Huisgen[1] was the first to understand the scope of this organic reaction (Fig. 1).

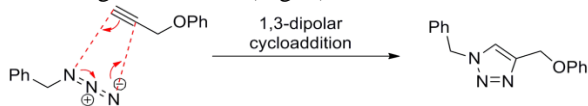


Fig1: 1,3-dipolar cycloaddition reactions.

In 2001, Sharpless and Meldal independently proposed processes in which azide and alkyne produce 1,2,3 triazoles in the presence of copper catalyst at room temperature, entitled as click reaction [2].

1,2,3-Triazole derivatives are pharmacologically important class of compounds. They are chemically stable, inert to severe hydrolytic, oxidizing and reducing conditions even at high temperatures. Their derivatives show anti-HIV [3], anti-bacterial [4], anti-histamine [5] and anti-tumor [6] activity. Besides their pharmacological features, they are used in agro chemistry, dye industry and anti-corrosion agent [7].

Recently, the Bertozzi group [8] demonstrated a new strain-release cyclooctyne labelling reagent (fig.2) that proceeds azide-alkyne cycloaddition reaction in the absence of a Cu catalyst at physiological temperatures. Thus, these labeling reagents that avoid using copper are highly desirable.

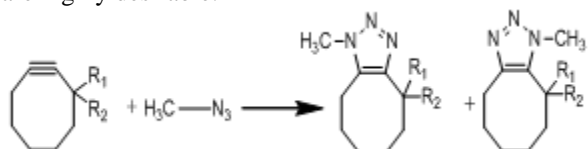


Fig2: azide-alkyne cycloaddition reactions.

In this research, we have focused on the regioselective behaviour of the aforementioned azide-alkyne cycloaddition reaction in the presence of various substituted cyclooctynes (with hydrogen and fluorine) using density functional theory (DFT) [9] and polarized continuum model (PCM) [10] approaches.

Quantum calculation of molecular energies and energy gradients in solution by a conductor solvent model.

Computational details

All calculations were performed using the M08-HX/6-311+G** level of theory with no symmetry constraints in geometry optimization procedure. It is important to mention that M08-HX functional has been introduced as a modern hybrid meta-GGA (generalized gradient approximation) exchange-correlation functional combined with Hartree-Fock exchange contribution [11].

We also utilized harmonic frequency analysis to confirm that the found optimized geometries correspond to the true minima or saddle points. In order to assess the solvent effects, PCM calculations have been performed based on a continuum representation of the solvent surrounding the substances. The GAMESS suite of programs [12] has been employed in DFT calculations.

Results and Discussion

We first concentrated on non-substituted cyclooctyne and two fluorinated cyclooctyne models. To determine how various substituents affect the reactivity of



cyclooctyne with methyl azide, we calculated the activation energies and the reaction energies in gas phase at M08-HX/6-311+G** level of theory (that were reported in Table1) for the formation of 1,2,3-triazole regioisomers (as illustrated in Fig. 3).

Table1: Activation energy for transition states TS1 and TS2 and reaction energy for the production of Isomer1 and Isomer2 (in kcal/mol), calculated at M08-HX/6-311+G** level of theory.

Reactant	R ₁	R ₂	Activation energy		Reaction energy	
			TS1	TS2	Isomer1	Isomer2
1a	H	H	10.805	-	-82.887	-
1b	H	F	9.532	6.327	-78.825	-78.930
1c	F	F	7.507	4.219	-80.905	-86.118

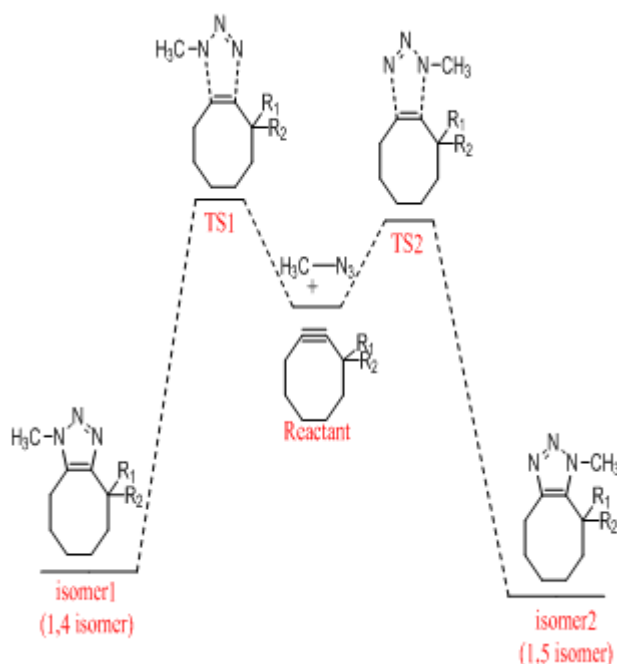


Fig3: azide-cyclooctyne cycloaddition reaction pathways.

In Fig.4, we have presented the obtained structure of TS1 and TS2 calculated at M08-HX/6-311+G** level of theory.

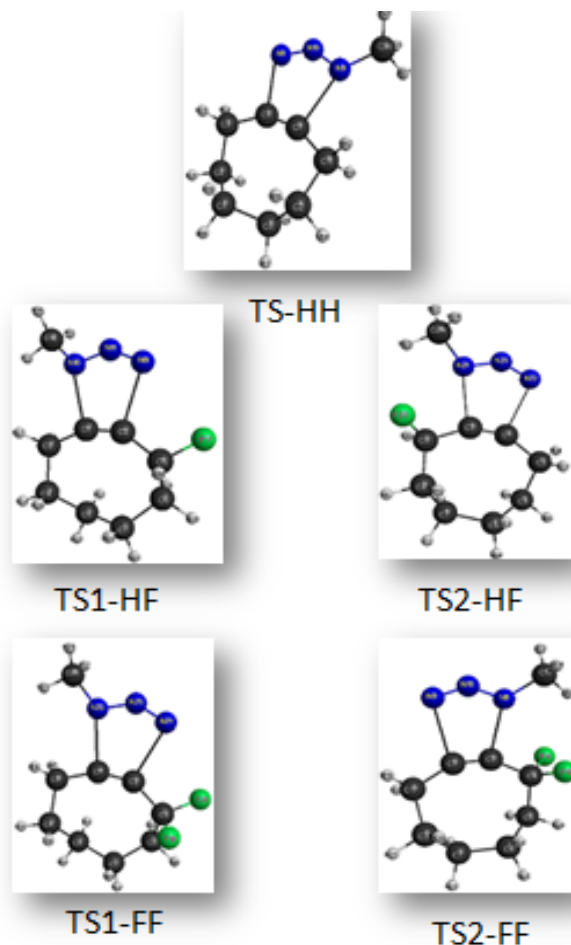


Fig.4. The obtained structures of TS1 and TS2 calculated at M08-HX/6-311+G** level of theory.

Then, we calculated reaction energies in solution phase at M08-HX/6-311+G** level of theory in two solvents, dimethyl formamide (DMF) and ethanol. (Table2).

Table2: Reaction energy, ΔE_r , (in kcal/mol) for the production of Isomer1 and Isomer2 in two solution phases at calculated M08-HX/6-311+G** level of theory

R ₁	R ₂	Solution phases	
		ΔE_r	
		DMF	ethanol
H	H	Product=-85.774	Product=-85.714
H	F	Isomer1=-86.872 Isomer2=-85.689	Isomer1=-86.870 Isomer2=-85.667
F	F	Isomer1=-84.480 Isomer2=-85.893	Isomer1=-84.405 Isomer2=-85.890

Conclusions

The comparison of calculated reaction energies in the gas and solution phases reveals that there is no considerable preference between the productions of two region-isomers. While our calculated reaction activation energies indicate that the production of Isomer2 is more favorable from the kinetic viewpoint. Moreover, cycloaddition of methyl azide and FF substituted cyclooctyne corresponds with the lower activation energy and is more convenient kinetically. Comparative analysis of PCM computations show that applying DMF as solvent decrease the reaction energies and so can be considered as more appropriate solvent.

Acknowledgment

The authors gratefully acknowledge the financial support received from the research council of Alzahra University.

References

- [1] Huisgen, Rolf. 1,3-Dipolar Cycloaddition. 75(1963)604-637.
- [2] V.V. Rostovtsev, L.G. Green, V.V. Fokin, K.B. Sharpless, A stepwise Huisgen cycloaddition process: copper(I)-catalyzed regioselective ligation of azides and terminal alkynes, *Angew. Chem. Int. Ed.* 41 (2002) 2596–2599.
- [3] S. Velaquez, R. Alvarez, C. Perez, F. Gago, C. De, J. Balzarini, M.J. Camarasa, Regiospecific synthesis and anti-human immunodeficiency virus activity of novel 5-substituted N-alkylcarbamoyl and N,N-dialkyl carbamoyl 1,2,3-triazole-TSAO analogues, *Antivir. Chem. Chemother.* 9 (1998) 481–489.
- [4] M.J. Genin, D.A. Allwine, D.J. Anderson, M.R. Barbachyn, D.E. Emmert, S.A. Garmon, D.R. Graber, K.C. Grega, J.B. Hester, D.K. Hutchinson, J. Morris, R.J. Reischer, C.W. Ford, G.E. Zurenko, J.C. Hamel, R.D. Schaadt, D.B. Stapert, H.J. Yagi, Substituent effects on the antibacterial activity of nitrogen-carbon-linked (azolylphenyl)oxazolidinones with expanded activity against the fastidious gram-negative organisms *haemophilus influenzae* and *moraxella catarrhalis*, *Med. Chem.* 43 (2000) 953–970.
- [5] D.R. Buckle, C.J.M. Rockell, H. Smith, B.A. Spicer, Studies on 1,2,3-triazoles. 13. (Piperazinylalkoxy) [1]benzopyrano[2,3-d]-1,2,3-triazol-9(1H)-ones with combined H1-antihistamine and mast cell stabilizing properties, *J. Med. Chem.* 29 (1986) 2262–2267.
- [6] P. Norris, D. Horton, B.R. Levine, Cycloaddition of acetylenes with 5-azido-5-deoxy-d-aldopentose derivatives: synthesis of triazole reversed nucleoside analogs, *Heterocycles.* 43 (1996) 2643–2665.
- [7] H.A. Orgueira, D. Fokas, Y. Isome, P.C.M. Chan, C.M. Baldino, Regioselective synthesis of [1,2,3]-triazoles catalyzed by Cu(I) generated in situ from Cu(0) nanosize activated powder and amine hydrochloride salts, *Tetrahedron Lett.* 46 (2005) 2911–2914.
- [8] N. J. Agard, J. A. Prescher and C. R. Bertozzi, J. Am. A Comparative Study of Bioorthogonal Reactions with Azides. *Chem. Soc.* 126 (2004) 15046.
- [9] A.D. Becke J. Densityfunctional thermochemistry .*Chem. Phys.* 2 (1993)98.
- [10] V. Barone, M. Cossi, "Quantum calculation of molecular energies and energy gradients in solution by a conductor solvent model" *J. Phys. Chem.* 102(1998)1995-2001.
- [11] Y. Zhao, D.G. Truhlar, *J. Chem. Theory Computational.* 4 (2008)11.
- [12] M.W. Schmidt, K.K. Baldrige, J.A. Boatz, S.T. Elbert, M.S. Gordon, J.H. Jensen, S.Koseki, N.Matsunaga, K.A. Nguyen, S.J. Su, T.L. Windus, M. Dupuis, J.A. Montgomery, *J. Comput. Chem.* 14 (1993) 1347-1363.

Quantum chemistry study on modification of poly (styrene-co-maleic anhydride) with 5-amino-4-imidazole carboxamide

T.Hosseinnejad^a, S. Keshavarzi^{b*}, M.M. Heravi^a

^aDepartment of Chemistry, Alzahra University, Vanak, Tehran, Iran.

^bDepartment of Chemistry, Science and Research Branch, Islamic Azad University, Tehran, Iran.

*shabnaz67@yahoo.com

Abstract: The imidization reaction of modified Poly (styrene-co-maleic anhydride) (SMA) with 5-amino-4-imidazole carboxamide can be occurred via two different amino nucleophilic sites to afford the poly (styrene-co-maleimide) (SMI). These two reaction modes were assessed comparatively from the structural and electronic viewpoints, using the quantum chemistry computations. For this purpose, the mathematical properties of electron density functions were calculated and analyzed topologically using density functional theory (DFT) and quantum theory of atoms in molecules (QTAIM) indicators. In overall, all of our calculated quantum chemical results approve the more electronic propensity to generate SMI-N-Amine maleimide compound. This theoretical feature as a firm basis usable for the high experimental affordance in producing SMI-N-Amine maleimide compound as poly (styrene-co-maleimide) (SMI).

Keywords: 5-Amino-4-imidazole carboxamide; SMI; DFT; QTAIM approach

Introduction

The study of polymer for the construction of supported catalysts has been largely overlooked. In continuation of our interest in the synthesis of heterocyclic systems under heterogeneous catalysis and computational design of new heterogeneous catalysts [1-3], we have recently concentrated on several coordinating modes of copper metal ions on modified SMA ligand models [4-6], via density functional theory (DFT) [7] and quantum theory of atoms in molecules (QTAIM) approaches [8].

In the present study, we have investigated the reaction of Poly (styrene-co-maleic anhydride) (SMA) with 5-amino-4-imidazole carboxamide examining the corresponding SMI as ligand for coordination with Cu(I) nano particles.

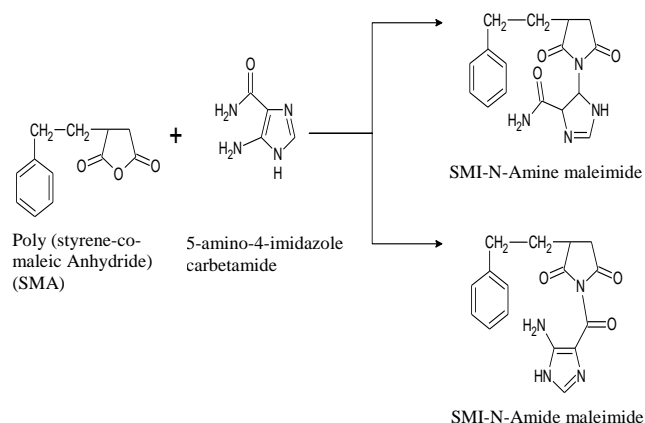
This novel modified support using a different base was examined as a recoverable and reusable heterogeneous catalyst in the synthesis of 1,2,3-triazoles via click reaction. This imidization reaction can be occurred through two different amino nucleophilic sites.

In this respect, the imidization reactions were assessed based on the analysis of mathematical properties of electron density functions using DFT and QTAIM computations and compared with experimental observations.

Computational details

The geometries of all compounds have been optimized using M06 functional [9] as a hybrid meta-GGA (generalized gradient approximation) exchange-correlation functional in connection with 6-31G* orbital basis set. All stationary points were determined as minima after verifying the presence of all real frequencies. The GAMESS suite of programs [10] has

been employed in DFT calculations. Topological analysis of electron density at DFT optimized structure of SMI-N-Amine and SMI-N-Amide maleimides was performed via QTAIM computations using AIMALL program package[11].



Scheme 1. The reaction of SMA with 5-amino-4-imidazole carboxamide via two different amino nucleophilic sites.

Results and Discussion

In the present section, we have investigated the reaction of SMA polymeric support with 5-amino-4-imidazole carboxamide via DFT and QTAIM calculations. SMA with reactive anhydride groups can be modified and reacted with 5-amino-4-imidazole carboxamide via two different amino nucleophilic sites to obtain the SMI. These two reaction modes lead to two different SMI denoted as SMI-N-Amine and SMI-N-Amide maleimides which have been modeled and displayed in Scheme 1. On the basis of obtained experimental data, it was fully characterized that the

reaction of maleic anhydride moiety in SMA with 5-amino-4-imidazole carboxamide produces SMI-N-Amine maleimide with high affordance, while SMI-N-Amide maleimide can be also produced from the mechanistical viewpoint.

In the first step, we calculated the optimized structure of SMI-N-Amine and SMI-N-Amide maleimides at M06/6-31G* level of theory (which have been illustrated in Fig. 1).

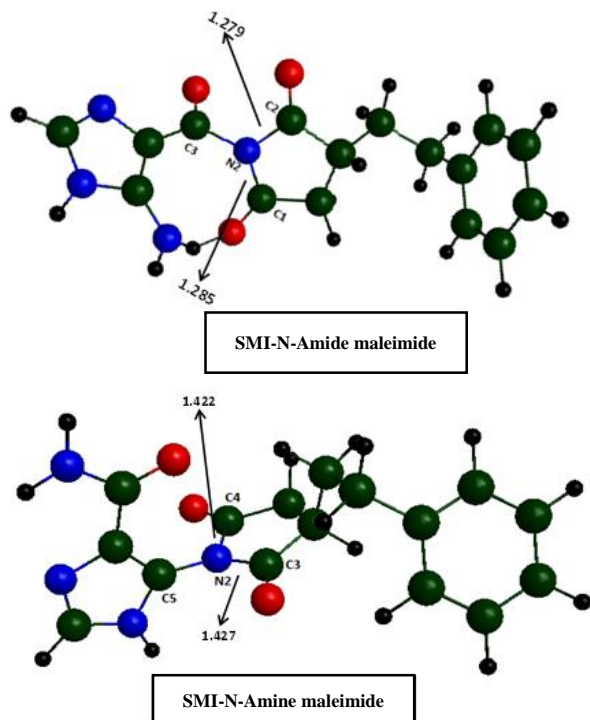


Fig. 1: The optimized structure of SMI-N-Amine and SMI-N-Amide maleimides calculated at M06/6-31G* level of theory. Note that M06/6-311+G** calculated bond order values of some key bonds have been also reported.

Moreover, we have

also reported M06/6-311+G** calculated bond order values of new formed imide bonds in Fig. 1. As it has been illustrated in Fig. 1, the calculated bond order of C-N imides in SMI-N-Amine maleimide is higher and consequently richer electronically than that of SMI-N-Amide maleimide (with 1.427 and 1.422 bond order calculated values for N2-C3 and N2-C4 and 1.285 and 1.279 bond order calculated values for N2-C1 and N2-C2 in SMI-N-Amine and SMI-N-Amide maleimides, respectively) that confirms the higher experimental affordance of producing SMI-N-Amine maleimide.

In order to present more sound theoretical interpretation for the preference in producing of SMI-N-Amine maleimide with high affordance in comparison with SMA-N-Amide maleimide, we topologically analyzed the electron density functions using QTAIM indicators. In this respect, we applied the M06/6-31G* and M06/6-311+G** wave function

files corresponding to the optimized structures of SMI-N-Amine and SMI-N-Amide maleimides were used as inputs to AIM2000 program package[11]. Then, we calculated some key bond and ring critical points (BCPs and RCPs, respectively) and their associated bond paths and assessed comparatively the bond strength of newly formed bonds. QTAIM molecular graphs of SMI-N-Amine and SMI-N-Amide maleimides containing (including) all bond and ring critical points and their associated bond paths were also presented in Fig. 2.

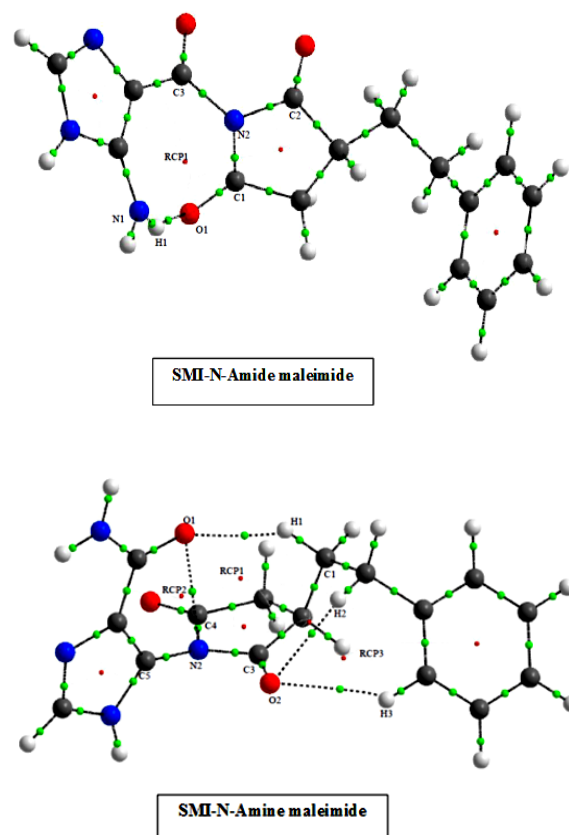


Fig. 2: Complete molecular graphs (MGs) of SMI-N-Amine and SMI-N-Amide maleimides calculated by QTAIM analysis of M06/6-311G** electron density functions. Bond Critical Points: green circles; Ring Critical Points: red circles; Bond Paths: gray lines.

The following facts can be extracted from the comparative assessment of the calculated QTAIM results:

I) the large positive values of electron density with the negative values of $\nabla^2 \rho_b$ and H_b and also $|V_b|/G_b > 2$ values on C-N imide bonds confirm the covalent character of these new formed bonds, II) The calculated values of electron density properties and indicators on C-N imide BCP in SMI-N-Amine maleimide is larger and electron-richer than that of SMI-N-Amide maleimide (with 0.291 and 0.288

electron density values for N2-C3 and N2-C4 BCPs and 0.265 and 0.259 electron density values for N2-C1 and N2-C2 BCPs in SMI-N-Amine and SMI-N-Amide maleimides, respectively). On the other hand, the comparative analysis of QTAIM molecular graphs of SMI-N-Amine maleimide and SMI-N-Amide maleimide shows that O1-H1 and O1-N2 intramolecular interactions in SMI-N-Amine maleimide lead to the formation of two RCPs (RCP1 and RCP2 with M06/6-311G** calculated 0.005 and 0.019 electron density values, respectively) and consequently stabilize the molecule while in SMI-N-Amide maleimide there exist only one RCP from the intramolecular interaction of O1-H1.

Conclusions

In summary, we have investigated comparatively two reaction modes for the reaction of SMA with 5-amino-4-imidazole carboxamide via DFT and QTAIM calculations. All of our calculated quantum chemical results approve the more electronic propensity to generate SMI-N-Amine maleimide compound. We can evaluate this theoretical feature as a firm basis for the high experimental affordance in producing SMI-N-Amine maleimide compound as poly (styrene-co-maleimide) (SMI).

Acknowledgment

The authors are thankful for partial financial supports from Alzahra University Research Council.

References

- [1] E. Hashemi, Y.S. Beheshtiha, S. Ahmadi, M.M. Heravi "In situ prepared CuI nanoparticles on modified poly (styrene-co-maleic anhydride): an efficient and recyclable catalyst for the azide-alkyne click reaction in water", *Transition Metal Chemistry*, 39 (2014) 593-601.
- [2] M.M. Heravi, E. Hashemi, Y.S. Beheshtiha, S. Ahmadi, T. Hosseinejad "PdCl₂ on modified poly (styrene-co-maleic anhydride): A highly active and recyclable catalyst for the Suzuki-Miyaura and Sonogashira reactions", *Journal of Molecular Catalysis A: Chemical*, 394 (2014) 74-82.
- [3] M.M. Heravi, S. Sadjadi, N.M. Haj, H.A. Oskooie, F.F. Bamoharram "Role of various heteropolyacids in the reaction of 4-hydroxycoumarin, aldehydes and ethylcyanoacetate", *Catalysis Communications*, 10 (2009) 1643-1646.
- [4] T. Hossiennejad, M. Daraie, M.M. Heravi, N.N. Tajoddin "Computational and Experimental Investigation of Immobilization of CuI Nanoparticles on 3-Aminopyridine Modified Poly(styrene-co-maleic anhydride) and Its Catalytic Application in Regioselective Synthesis of 1,2,3-Triazoles", *Journal of Inorganic and Organometallic Polymers and Materials*, (2017) 1-10.
- [5] M.M. Heravi, T. Hosseinejad, N. Nazari "Computational investigations on structural and electronic properties of CuI nanoparticles immobilized on modified poly(styrene-co-maleic anhydride), leading to unexpected but an efficient catalyzed synthesis of 1,4-dihydropyridine via Hantzsch pyridine synthesis", *Canadian Journal of Chemistry*, 95 (2017) 530-536.
- [6] T. Baie Lashaki, H.A. Oskooie, T. Hosseinejad, M.M. Heravi "CuI nanoparticles on modified poly (styrene-co-maleic anhydride) as an effective catalyst in regioselective synthesis of 1,2,3-triazoles via click reaction: A joint experimental and computational study", *Journal of Coordination Chemistry*, (2017) 1-38.
- [7] C. Lee, W. Yang, R.G. Parr "Development of the Colle-Salvetti correlation-energy formula into a functional of the electron density", *Physical Review B*, 37 (1988) 785-789.
- [8] R.F.W. Bader "Atoms in Molecules: a Quantum Theory", 1990, Oxford University Press, Oxford, UK.
- [9] D.G. Truhlar, Y. Zhao "The M06 suite of density functionals for main group thermochemistry, thermochemical kinetics, noncovalent interactions, excited states, and transition elements: two new functionals and systematic testing of four M06-class functionals and 12 other functionals", *Theoretical Chemistry Accounts*, 120 (2008) 215-241.
- [10] M.W. Schmidt, K.K. Baldrige, J.A. Boatz, S.T. Elbert, M.S. Gordon, J.H. Jensen, S. Koseki, N. Matsunaga, K.A. Nguyen, S.J. Su, T.L. Windus, M. Dupuis, J.A. Montgomery "General atomic and molecular electronic structure system", *Journal of Computational Chemistry*, 14 (1993) 1347-1363.
- [11] T.A. Keith, AIMAll (Version 16.05.18), TK Gristmill Software, (2010), Overland Park KS, USA.

Theoretical study on the gas phase reaction mechanism of methanethiol and nitroxyl

M. HaghdoostManjily^{a*}, H.douroudgari^a, M. Vahedpour^a

^aDepartment of chemistry, University of Zanjan, P.O. Box 45371-38791, Zanjan, Iran

[*marjanhaghdoost@yahoo.com](mailto:marjanhaghdoost@yahoo.com)

Abstract: The reaction of methanethiol and nitroxyl at atmospheric conditions have been studied computationally on the singlet potential energy surface (PES). Thermodynamic parameters for adducts, H₂CO and H₂NSH, are obtained. Gibbs free energy and enthalpy of reaction indicate that the production of mentioned adducts are spontaneous and exothermic. Also, from thermodynamic and kinetic viewpoints, we can conclude that the reaction pathway for H₂CO + H₂NSH products is favour. In kinetic point of view, suitable barrier energies and the number of transition state can cause the suggested pathways are possible. In thermodynamic aspect, two obtained products with large value in standard Gibbs free energies of reactions are most stable in comparison with the reactants.

Keywords: “singlet state; atmospheric condition; reaction mechanism; potential energy surface”

Introduction

The chemistry of sulfur compounds has an important effect on our environment via acid rain, visibility reduction and climate modification. Generation of sulfur compounds are from two important sources: The largest origin of sulfur in the atmosphere (>60% of the total emission) is the SO₂ released by fossil fuel combustion and industrial processes. The second largest source is the oceanic emission of sulfides, mainly dimethyl sulfide (DMS), by marine phytoplankton [1].

Reduced forms of sulfur compounds, such as RSH, RSR', and RSSR', are released into the atmosphere mainly due to biogenic activity. These sulfur species play an important role in the atmospheric sulfur cycle and it is quite important to understand their fate in the troposphere [2].

Methanethiol (CH₃SH) is one of the most important products of degradation of organic matter, it is released from decaying organic matter in marshes and it is present in coal tar and some crude oils [3]. In addition, colonic bacteria produce large quantities of the highly methanethiol [4].

The rates of elementary chemical reactions involving NO and HNO are important to understanding complex processes such as pollution formation, energy release in advanced propellants, and fuel combustion [5].

A series of studies indicate that HNO is a unique and near-perfect treatment for heart failure. HNO also has the potential to be used to prevent ischemia reperfusion injury and has been used in the past to treat alcoholism.

Others have found that HNO has the properties of an endothelium-derived hyperpolarizing factor and/or endothelium-derived relaxing factor. Thus, it is becoming increasingly evident that HNO can be developed as a therapeutic agent of significant importance (or is an endogenously generated signaling species). Driven by these recently reported biological effects, as well as others, efforts to elucidate the

possible physiological targets and signaling mechanisms of HNO have been substantial. To date, two particular biological moieties have been reported to be primary targets for HNO, thiols, and metals (i.e., thiol- and metallo-proteins) [6].

The purposes of this work by means of computational methods based on quantum theories to carry out a detail of the singlet potential energy surfaces (PES) for the reaction of CH₃SH and HNO with the aim of clarifying the reaction mechanism.

Materials and method

All calculations were performed with the GAUSSIAN 09 program [7]. All geometry optimizations were carried out using B3LYP [8] and M06-2X [9] approach in connection with the 6-311++g(3df,3pd) [10] basis set. At these level of theories vibrational frequency calculations are performed for verifying the nature of the corresponding stationary point (true minima or true transition state). Reactants, prereactive complex, intermediate and postreactive complex have all real vibrational frequency and transition states have one imaginary frequency. Also, via frequency calculation we obtain zero point of stationary points and thermodynamic parameters.

Results and Discussion

In Figure 1 PES at singlet state and in figure 2 geometrical parameters of all species are depicted. Total and relative energies are tabulated in table 1.

There is one possible pathway on singlet PES for P1 product as follows:



In the first step association of reactants (CH₃SH and HNO) yields one product complex Cr1. The pre-reactive complex Cr1 is transformed into Cp1 via three transition states TS1, TS2 and TS3. The barrier energies of these transition states are 65.761 kcal/mol, 39.274 kcal/mol and 58.885 kcal/mol (at B3LYP/6-311++g(3df,3pd) level), respectively. In



first step Cr1 through TS1 converts to IN1 and in second step IN1 via TS2 transforms to IN2 in third step IN2 through TS3 convert to Cp1. IRC calculation confirm the connection between computed transition states and their stationarypoints.

Form geometrical point of view TS1(with Cs symmetry) involves hydrogen shift (H-shift) from 6C atom toward 3S atom with imaginary frequency of 886i cm⁻¹, TS2(with Cs symmetry) involves H-shift from 3S toward 6C with imaginary frequency of 1098i cm⁻¹ and TS3(with Cs symmetry) involves H-shift from 1O toward 2N with imaginary frequency of 704i cm⁻¹ (at B3LYP/6-311++g(3df,3pd) level).Then CP1 release into the P1 (H₃CS+H₂NO) without any energy barrier. P1 is a stable product.

Calculated thermodynamic parameters indicate that production of this adduct is exothermic ($\Delta H^0 = -36.997$ kcal/mol) and spontaneous ($\Delta G^0 = -36.802$ kcal/mol).

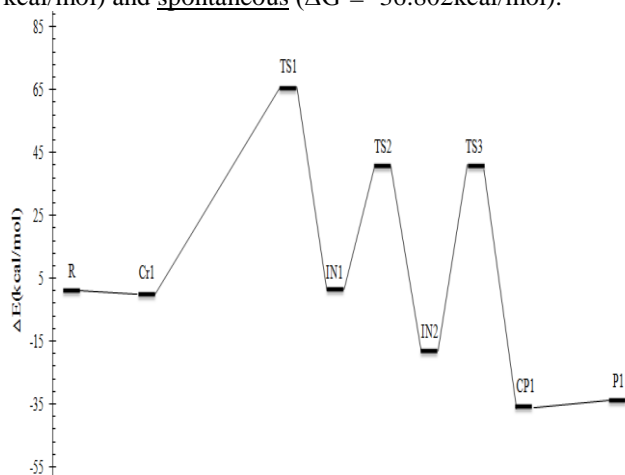
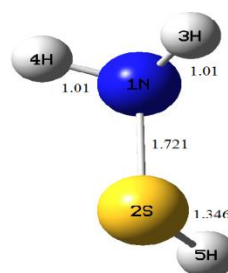
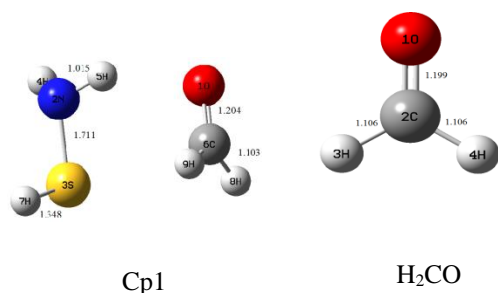
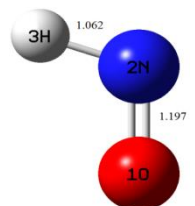


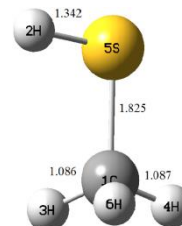
Fig.1: Singlet potential energy profile of [H₃CSH + HNO] reaction at B3LYP/6-311++g(3df,3pd) level



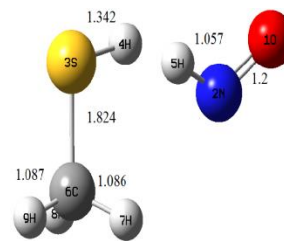
H2NSH



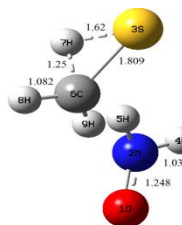
HN



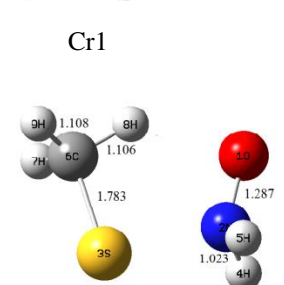
CH₃SH



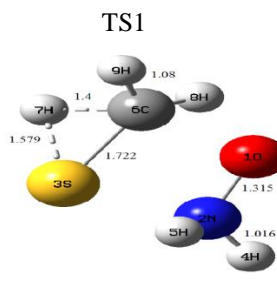
Cr1



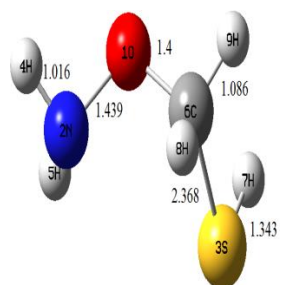
TS1



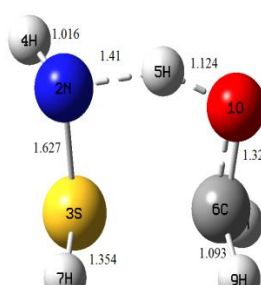
IN1



TS2



IN2



TS3

Fig.1: Geometries of all species for H₃CSH+HNO reaction at B3LYP/6-311++g(3df,3pd) level.



Table1: The total energies (in hartree) and relative energies (in kcal/mol) calculated for this reaction.

Species	B3LYP/6-311G ++g(3df,3pd)		M06-2X/6-311G ++g(3df,3pd)	
	Total energy	relative energy	Total energy	relative energy
R	-569.199	0.0	-569.095	0.0
Cr1	-569.201	- 1.190	-569.098	-1.845
IN1	-569.198	0.551	-569.093	1.571
IN2	-569.230	-19.216	-569.134	-24.390
Cp1	-569.258	-36.808	-569.160	-40.517
TS1	-569.096	64.571	-568.994	63.384
TS2	-569.136	39.825	-569.030	41.134
TS3	-569.136	39.669	-569.126	-19.136
P1	-569.255	-34.958	-569.154	-36.754

Conclusions

In the present work, we have characterized the details of the gas-phase reaction of methanethiol and nitroxyl on the singlet PES with the B3LYP and M06-2X level of theory in connection with the 6-311G++g(3df,3pd) basis set. Based on our suggested mechanism, for the product P1, one reaction pathway with suitable barrier energies of transition states is obtained. The reaction is initiated via the formation of the reactant complex and ended to postreactive complex before releasing to product.

References

- [1] Zh. Qingzhu, T. Sun, X. Zhou, and W. Wang "Rate parameters and branching ratios for the multiple-channel reaction of dimethyl sulfide DMS with atomic H", *Chemical physics letters*, 414 (2005)316-321.
- [2] U. Tadafumi, S. Tsuzuki, M. Sugie, K. Tokuhashi, and A. Sekiya "A theoretical study on the strength of two-center three-electron bonds in the NO₃ radical adducts of reduced sulfur molecules, H₂S, CH₃SH, CH₃SCH₃, and CH₃SSCH₃", *Chemical physics*, 324 (2006) 465-473.
- [3] S. Nourbakhsh, K. Norwood, H-M. Yin, C-L. Liao, and C. Y. Ng "Vacuum ultraviolet photodissociation and photoionization studies of CH₃SH and SH", *The Journal of chemical physics*, 95(1991) 946-954.
- [4] F. Julie, J. Springfield, T. Koenig, E. DeMaster, and M. D. Levitt "Oxidation of hydrogen sulfide and methanethiol to thiosulfate by rat tissues: a specialized function of the colonic mucosa", *Biochemical pharmacology*, 62(2001) 255-259.
- [5] K. Yuzuru, and T. Takayanagi "Ab initio molecular orbital study of potential energy surface for the H₂NO (2 B 1) → NO (2 Π) + H₂ reaction", *Journal of Molecular Structure: THEOCHEM*, 507(2000) 119-126.
- [6] F. Jon M, and S. J. Carrington "HNO signaling mechanisms", *Antioxidants & redox signalling*, 14 (2011) 1649-1657.
- [7] M. J. Frisch, G. W. Trucks, H. B. Schlegel, G. E. Scuseria, M. A. Robb, J. R. Cheeseman, G. Scalmani et al. "09, Revision D. 01, Gaussian." *Inc., Wallingford, CT* (2009).
- [8] H. Edward G, S.T. Chill and C. D. Sherrill. "Assessment of the performance of the M05- 2X and M06- 2X exchange-correlation functionals for noncovalent interactions in biomolecules." *Journal of Chemical Theory and Computation*, 4 (2008) 1996-2000.
- [9] Zh. Yan and D. G. Truhlar. "The M06 suite of density functionals for main group thermochemistry, thermochemical kinetics, noncovalent interactions, excited states, and transition elements: two new functionals and systematic testing of four M06-class functionals and 12 other functionals." *Theoretical Chemistry Accounts: Theory, Computation, and Modeling (Theoretica Chimica Acta)*, 120 (2008) 215-241.
- [10] M. J. Frisch, J. A. Pople and J. S. Binkley. "Self-consistent molecular orbital methods 25. Supplementary functions for Gaussian basis sets." *The Journal of chemical physics*, 80 (1984) 3265-3269.

Theoretical analysis of pi-type hyperconjugative interaction

S.M. Azami

Department of Chemistry, Yasouj University, Yasouj 7591874934, Iran.
azami@yu.ac.ir

Abstract: The critical point (CP) responsible for hyperconjugative interaction is identified, which cannot be detected by means of conventional electron density based calculations. This CP is detected via π electron density topology, by excluding σ electron density from the total one. To achieve this, the density matrix is projected onto perpendicular p orbitals of the molecular plane. Since the presence of hyperconjugation phenomenon in carbocation systems is well understood, several carbocations are benchmarked and the results show the positive carbon atom establishes hyperconjugative CP with the adjacent methyl group(s). Also, π localization and delocalization indices are employed to support the conclusions made by the CP properties.

Keywords: QTAIM; Hyperconjugation; Critical Point.

Introduction

The conjugation phenomenon can be easily pictured by delocalized molecular orbitals (MOs) as π -type MOs which are distributed over the entire molecule. QTAIM is also able to identify the conjugation phenomenon via delocalization indices as the number of delocalized electrons over atomic basins. According to quantum mechanics, the two π and two π^* orbitals located on adjacent double bonds can be considered as four unperturbed states, which are then mixed to form perturbed (delocalized) and more stable states with lower energies. In this mixing, only π -type orbitals are included and σ -type orbitals do not contribute to the conjugation phenomenon. In planar molecules, σ and π -type orbitals are strictly unmixed. However these two types of orbitals might be mixed to result more stable orbitals in non-planar molecules. The mixture between π -type and σ -type orbitals is called hyperconjugation which has been pointed out by Mulliken [1]. For example, propene (Fig. 1) is a non-planar system whose double bond is mixed by certain C-H bonds. This mixing is occurred so that the resultant π -type orbital possess the same nodal plane as the hypothetical (unperturbed) π bond does. Consequently, one may consider this π -type MO in order to characterize the hyperconjugative interaction in propene.

One way to analyze the molecular electronic structure is to take advantage of electron density topology in the context of QTAIM. In QTAIM, a chemical bond is accompanied by the corresponding bond critical point (BCP) whose properties are used for characterization of the bond. One disadvantage of QTAIM is that BCP cannot be detected for π bonds; instead, they can be extracted from several other parameters such as delocalization indices. Since hyperconjugation phenomenon is closely related to π electron density, the hyperconjugative CP cannot be also detected via conventional QTAIM. However, in a

recent work by the present author, QTAIM is generalized to π -type electron density topology [2]; which enables one to detect hyperconjugative BCP. This method is also used for characterization of several concepts and interactions including aromaticity, antiaromaticity, heteroaromaticity, metal- π interaction, and van der Waals complexes [3-8].

In the present work, we wish to detect the hyperconjugative CP, explore its properties, and examine if the presented work agrees with chemical interpretation of hyperconjugation in several neutral molecules and carbocations in which the presence of hyperconjugative interaction is well understood.

Computational details

The molecular geometries and their electronic wave functions are optimized at B3LYP/6-311++G** levels of theory utilizing Gaussian 03 suite of programs [9]. Frequency test for neutral molecules detected no imaginary frequency which reveals that the molecular geometries are energetically located in a local minimum. In contrast, all studied carbocations possessed imaginary frequency which was unavoidable; because the molecule must have the symmetry plane coincident with the nodal plane of π -type MOs. Otherwise, the procedure in Ref. [9] cannot be employed to detect the hyperconjugative BCP. The π component of delocalization and localization indices, were also calculated from atomic overlap matrices (AOM) [10].

Results and Discussion

The simplest carbocation, methyl cation, possess no π system and consequently no hyperconjugation is expected. Ethyl cation (pictured inside Table 1), has appropriate molecular symmetry plane; however, the molecule is identified as transition structure (TS) with one imaginary frequency. Although the presence of a CP in a TS does not necessarily imply a stabilizing



interaction, the CP properties are still helpful to get insight into the interaction [10-14] Several TS systems have also been previously evaluated by the present author via π CPs in antiaromatic rings [2].

Table 1 includes chemical structure of carbocations with their CP properties, π delocalization indices and their labels used in the text. According to the formal picture of carbocations, secondary carbocations are able to establish two hyperconjugative interactions with either methyl group in **aII**; and similarly three ones in **aIII**. Therefore, stronger hyperconjugative interaction is expected in **aI**, as the positive charge is imposed to one methyl group. This phenomenon can also be seen as descending trend of $\nabla^2\rho_{\pi}^{CP}$ and δ_{π} values from **aI** to **aIII**. In contrast to the polyenes, all $\nabla^2\rho_{\pi}^{CP}$ values are negative for carbocations which reveals the presence of sharing interaction between the formally positive carbon and adjacent atoms. Another result which can be concluded from the electron density at the attractors located on the carbon atoms nuclei (ρ_{π}^{att}) and their π localization index (λ_{π}) is the ascending trend of these two quantities from **aI** to **aIII**. These trends explicitly show that methyl groups are able to populate the formally empty p orbital on the formally positive carbon atom; which gives rise to the carbocation's stability.

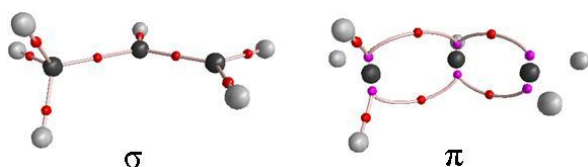


Fig. 2: Critical points of σ and π electron densities.

Table1: CP, localization and delocalization indices analysis of carbocations.

		ρ_{π}^{CP}	$\nabla^2\rho_{\pi}^{CP}$	ρ_{π}^{att}	λ_{π}	δ_{π}
aI		0.02 6	-0.075	0.04 7	0.04 9	0.30 0
aII		0.02 3	-0.040	0.06 1	0.08 0	0.20 6
aIII		0.02 0	-0.023	0.06 4	0.08 9	0.15 3

Conclusions

The π -type bonding critical point responsible for hyperconjugative interaction can be detected via

electron density topology analysis of π molecular orbitals. Carbocations, in which hyperconjugation phenomenon is known as a stabilizing factor, are analyzed and the results showed apparent hyperconjugative CPs between the formally positive carbon atom and adjacent methyl groups. Also, the π -graphs of carbocations suggest that the adjacent carbon atoms play primary role in the hyperconjugative interaction.

References

- [1] R.S. Mulliken, *J. Chem. Phys.*, 7 (1939) 339.
- [2] S.M. Azami, *J. Phys. Chem. A*, 114 (2010) 11794.
- [3] R. Firouzi, S. Sharifi Ardani, *Phys. Chem. Chem. Phys.*, 16 (2014)11538.
- [4] R. Firouzi, *Chem. Phys. Lett.*, 48 (2014) 595.
- [5] Y. Zeng, J. Hao, S. Zheng, L. Meng, *J. Phys. Chem. A*, 115 (2011) 11057.
- [6] W. Wu, X. Li, *J. Phys. Chem. A*, 119 (2015) 2091.
- [7] Y. Zeng, W. Wu, *ChemPhysChem*, 14 (2013)1591.
- [8] Y. Zeng, M. Zhu, *ChemPhysChem*, 12 (2011) 3584.
- [9] M.J. Frisch, et al., Gaussian 09, Gaussian, Pittsburgh, PA, 2009.
- [10] C.F. Matta, J. Hernandez-Trujillo, *J. Phys. Chem. A.*, 107 (2003) 7496.
- [11] R.F.W. Bader, *J. Phys. Chem. A*, 102 (1998) 7314.
- [12] R.F.W. Bader, *Chem. Eur. J.*, 12 (2006) 2896.
- [13] J. Poater, M. Solà, F.M. Bickelhaupt, *Chem. Eur. J.*, 12 (2006) 2902.
- [14] R.F.W. Bader, *J. Phys. Chem. A*, 113 (2009) 10391.



A computational study of 1:1 and 1:2 clusters of NAP and DME

Zeinab Korkani, Mohammad Solimannejad*

Quantum Chemistry Group, Department of Chemistry, Faculty of Sciences,
Arak University, Arak, Iran

* Corresponding author: m-solimannejad@araku.ac.ir

Abstract: DFT calculations at M05-2X computational level using aug-cc-pVDZ basis set were used to analyze the interactions in 1:1 and 1:2 complexes of naphthalene (NAP) with dimethyl ether (DME). The structures obtained have been analyzed with the Atoms in Molecules (AIM), and many-body interaction energies methodologies. Two minima were located on the potential energy surface of the 1:1 complexes. Four different structures have been obtained for the 1:2 complexes. Two types of interactions are observed, CH...O and CH... π hydrogen bonds. Stabilization energies of the 1:1 and 1:2 clusters including BSSE and ZPE are in the range 9–12 kJ mol⁻¹ and 20–27 kJ mol⁻¹ respectively at M05-2x/aug-cc-pVDZ computational level.

Keywords: Hydrogen bonding ; AIM.

Introduction

Noncovalent interactions between molecules play an important role in supramolecular chemistry, molecular biology, and materials science [1]. There are being shortages of studies using large aromatic systems, though works in larger polycyclic have been performed as a way to explain graphite interactions [6-13]. Naphthalene is one of the simplest polycyclic aromatic hydrocarbons, thus it is one of the first choices to generalize the studies of interaction with aromatic rings to polycyclic.

DME has properties that make it of specific interest. In the first place, its central O atom is an ideal acceptor of a proton from naphthalene. Moreover, the position of a pair of methyl group's neighbor to this electronegative oxygen makes DME a strong candidate for the formation of CH...O H-bonding interactions. In addition DME has two internal rotors and has thus received considerable attention as a prototypical double internal rotor system [14]. On a different note, to date several weakly bound complexes of DME have been studied [15-21].

In the present work the interaction in systems inclusive a NAP molecule and one or two DME molecules were computationally studied. This type of study permits locating the following prospects: (1) The geometries of clusters vocalized between NAP and DME have not been located to date. (2) The value of the interaction energy of these clusters is also unknown. (3) In larger clusters the poise between C₁₀H₈...C₂H₆O and C₂H₆O...C₂H₆O interactions could play a proper role. The systems studied permit surmising the comparative importance of these proportions.

Materials and method

In the present study, the geometries of the isolated NAP, and DME molecules and their clusters were fully optimized at the M05-2X/aug-cc-pVDZ computational level [22]. The atoms in molecules (AIM) methodology [23] has been used to analyze the electron density of the systems considered at the MP2/aug-cc-pVDZ computational level.. The topological analysis has been carried out with the AIM2000 program [24]. All geometry optimizations, interaction energies and energy components were calculated using GAMESS suite of programs [25].

Results and Discussion

The electronic properties of the isolated NAP and DME monomers have been used to generate a set of initial structures that have been considered for the exploration of the potential energy surface resulting in the location of two 1:1 minima. The binding energies of these complexes are reported in Table 2 and their structures are depicted in Fig1. Binding energies of the NAP...DME dimers in the range of 9–12 kJmol⁻¹ at M05-2X/aug-cc-pVDZ computational level. The most important intermolecular interactions within the most stable minimum 11-t corresponds to a structure with a pair of CH... π hydrogen bonds. The electron density analysis of the 11-t dimer (Fig. 1 and Table S1) presents two bcp between the CH group of DME and the π electrons of two aromatic rings of NAP.

A total of four minima structures have been found for the trimers (Fig 2). All complexes are formed through all the possible combination of CH... π , and CH...O HBs interactions. The interaction energies of the four minima structures located in the potential energy surface of the trimer are reported in Table 1. Binding energies of the 1:2 complexes of NAP and DME including zero-point vibrational corrections and



BSSE lie in the range of 20–27 kJ mol⁻¹ at M05-2X/aug-cc-pVDZ computational level. Molecular graphs of trimers from the AIM analysis are shown in Fig. 2. All the CH...O, CH... π and C...O hydrogen interactions in studied trimer structures are confirmed with the presence of BCPs between atoms of DME and NAP molecules. As in the case of the dimers, the electronic characteristic of the intermolecular bond critical points indicate that they correspond to weak interactions. The two- and three- and four-body contributions to the total interaction energy in the trimers and tetramers have been obtained by many-body analysis [26-27]. In this work, many-body analysis has been performed for four studied trimers clusters. As seen in Table 2, two-body interaction energy in all cases provides the largest contribution of the total interaction energy. However, the three-body terms have been contributed lower than two-body terms in the total interaction energy. The total relaxation energy (E_R) is described as the energy sum of the monomers with all of them frozen in the geometry of the trimers minus the energy sum of the optimized monomers. The relaxation energy can be taken as a measure of the degree of strain that drives the distortion of the ternary and tetramer systems.

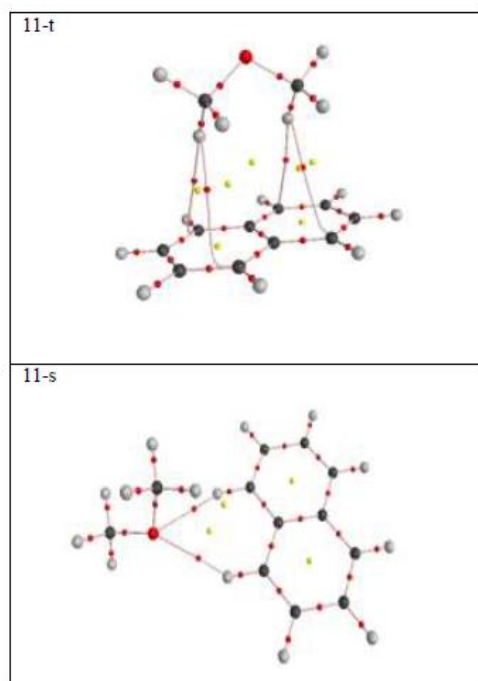


Fig.1: The molecular graphs of C₁₀H₈...C₂H₆O binary clusters, where the BCP and RCP are denoted as small red and yellow dots, respectively

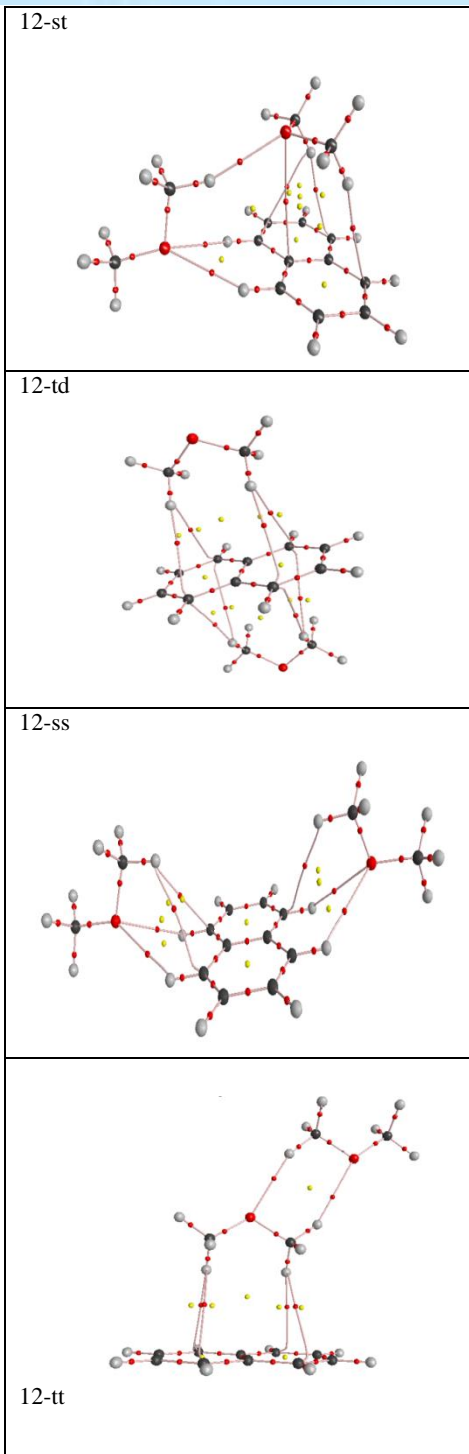


Fig.2 : The molecular graphs of C₁₀H₈... (C₂H₆O)₂ ternary clusters, where the BCP and RCP are denoted as small red and yellow dots, respectively

Table 1: Relative energy ($\text{kJ}\cdot\text{mol}^{-1}$), stabilization energy ($\text{kJ}\cdot\text{mol}^{-1}$) corrected with BSSE and ZPE calculated at M05-2X/aug-cc- pVDZ computational level.

J. C. Rayez, M. T. Rayez, *J. Mol. Struct (THEOCHEM)*, 772 (2006) 1.

Complex	2-body	3-body	E_R	E_{total}
12-st	-40.23	-2.17	0.55	-41.86
12-td	-36.36	-0.18	0.17	-36.37
12-ss	-32.36	1.38	0.35	-30.63
12-tt	-29.98	-0.21	0.27	-29.92

Table 2: Decomposition binding energies ($\text{kJ}\cdot\text{mol}^{-1}$) of the studeid trimers.

Conclusions

This work reports a study of the structural and electronic properties of complexes between one naphthalene and two dimethyl ether molecules. The investigated complexes show that the molecules involved approach to each other through a number of possible interactions, namely CH...C and CH...O hydrogen bonds along with C...O weak interactions. All the formed clusters are characterized by the multiple intermolecular H-bonds, where most of H-bonds are closed-shell interactions.

References

- [1] K. Müller-Dethlefs, P. Hobza, *Chem. Rev*, 100 (1999) 143-168.
- [2] R. C. Santos, F. Agapito, E. M. Gonçalves, J. A. Martinho Simões, R. M. Borges dos Santos, *J. Chem. Thermodynamics*, 61(2013) 83-89.
- [3] I. Alkorta, J. Elguero, *J. Phys. Chem. A*, 108 (2004) 9400-9405.
- [4] V. Kalamse, N. Wadnerkar, A. Chaudhari, *Energy*, 49 (2013) 469-474.
- [5] Enrique M. Cabaleiro-Lago, Jesus Rodriguez-Otero, and Angeles Pena-Gallego, *J. Phys. Chem. A*, 112 (2008) 6344-6350.
- [6] S. Tsuzuki, K. Honda, T. Uchimaru, M. Mikami, *J. Chem. Phys.*, 120 (2004) 647.
- [7] D. Feller, K. D. Jordan, *J. Phys. Chem. A*, 104 (2000) 9971.
- [8] J. M. Hermida-Ramon, A. M. Grana, *J. Comput. Chem.*, 28 (2007) 504.
- [9] C. D. P. Zeinalipour-Yazdi, D. P. Ullman, *J. Phys. Chem. B*, 110 (2006) 24260.
- [10] A. Reyes, M. A. Tlenkopatchev, L. Fomina, P. Guadarrama, S. Fomine, *J. Phys. Chem. A*, 107 (2003) 7027.
- [11] T. Sato, T. Tsuneda, K. Hirao, *J. Chem. Phys.*, 123 (2005) 104307/1.
- [12] T. R. Walsh, *Chem Phys Lett*, 363 (2002) 45.
- [13] B. Collignon, P. N. M. Hoang, S. Picaud, D. Liotard,

[14] Y. niide, M. Hayashi, *J. Mol. Spectrosc.*, 223(2004) 152.

[15] Y. Tatamitani et al, *J. Am. Chem. Soc.*, 124 (2002) 2739.

[16] S. Vijayakumar, P. Kolandaivel, *J. Mol. Struct.*,

Complex	SE	SE+BSSE	SE+BSSE+ZPE	E_{rel}
11-t	-18.19	-13.01	-11.96	0.00
11-s	-14.73	-11.31	-9.40	3.46
12-st	-41.86	-32.14	-26.53	0.00
12-td	-36.37	-25.59	-20.40	5.49
12-ss	-30.63	-27.08	-23.74	11.23
12-tt	-29.92	-24.38	-20.64	11.94

734 (2005) 157.

[17] A. Engdahl, B. Nelander, *J. Chem. Soc. Faraday. Trans.*, 88 (1992) 1177.

[18] S. W. Han, K. Kim, *J. Mol. Struct.*, 475 (1999) 43.

[19] P. Ottaviani, W. Caminati, B. velino, S. Blanco, A. Lessari, J. C. Lopez, J. L. Alonso, *Chemphyschem*, 5(2004) 336.

[20] E. Sanchez-Garcia, M. Studentkowski, L. A. Montero, W. Sander, *Chemphyschem*, 6 (2005) 618.

[21] M. Solimannejad, Scheiner, *J. Chemical. Physics. Letters*, 429 (2006) 38.

[22] Y. Zhao, D. G. Truhlar, *J. Chem. Theory. Comput.*, 2 (2006) 1009.

[23] F. Biegler-Konig, *J. Schonbohm, AIM 2000 Program Package, Ver.2.0, University of Applied Sciences, Bielefeld, Germany*, (2002).

[24] M. W. Schmidt, K. K. Baldrige, J. A. Boatz, S. T. Elbert, M. S. Gordon, J. H. Jensen, S. Koseki, N. Matsunaga, K. A. Nguyen, S. J. Su, T. L. Windus, M. Dupuis, J. A. Montgomery "General atomic and molecular electronic structure system", *J. Comput. Chem.*, 14 (1993) 1347.

[25] S. S. Xantheas, *J. Chem. Phys.*, 100 (1994) 7523.

[26] L. Rincón, R. Almeida, D. G. Aldea, *Int J Quantum Chem.*, 102 (2005) 443.

[27] A. Zawada, W. Bartkowiak, *Comput. Theo.r Chem.*, 967 (2011) 120.

DFT study of interaction of Agon and Eozin dyeon functionalized single-walled Carbon Carbon Nanotubes

M. Moghadari*, F. Yousefi
 Chemistry Department, Yasouj University, Yasouj 75918-74831, Iran
 *Corresponding author: **M. Moghadari**
 Tel/fax: + 98 741 222 1711.
 E-mail: fyousefi@mail.yu.ac.ir

ABSTRACT

In this investigation the Density Functional Theory (DFT) of electron method is utilized to study the adsorption of, Ag molecule on the surface of (5, 5), (5, 0) and (6,6), (6,0) carbon nanotubes also software has been used to carry out quantum chemistry calculations., the structural and electronic properties of Eozin molecule on functionalized (5,0) zigzag and (5,5) armchair single-walled carbon nanotube was studied in gas phase on the basis of density functional theory (DFT). The computational results, which includes, indicate that rich adsorption patterns may result from the interaction of metal with the carbon nanotubes. Furthermore, covalent interaction of Eozin with single-walled carbon nanotube was investigated and its quantum molecular descriptors and binding energies were calculated. The DFT B3LYP/6-31G** calculations revealed that the binding energies of multi walled carbon nanotube with Eozin have negative.

Keyword ; density functional theory, zigzag, armchair

1. Introduction

Soon after the discovery of carbon nanotubes (CNTs) considerable efforts have been dedicated on the investigations of non-carbon nano tubes among which the counter parts of third and fifth groups of elements are proposed as proper alternative materials [1]. Carbon nanotubes belong to the family of fullerenes, the third allotropic of carbon after graphite and diamond [۲-۳]. They are very stable molecules and this stability has caused some drawbacks in integrating the nanotubes with the current technology. To this time, numerous experimental and computational studies have been devoted to characterize the properties of boron nitride nanotubes (BNNTs) and aluminum nitride nanotubes (AlNNTs) [۴].

Computational methods

Being different in chirality there are two kinds of nanotubes: zigzag (N,0) and armchair (N,N), where N presents the size of tube diameter. In this paper N = 5 and 6 were taken respectively for both zigzag and armchair of CNT. The B3LYP method of Density Functional Theory (DFT) was employed for calculations. Because of more correlation energy being included, were carried out at the 6-31G** basis set level, which is reasonable and available for such a big system.

Results and discussion

Observed variations for bond length after Ag molecule adsorption on exterior surface of nanotube have shown in Table (1). We can interpret that C-C bond length increasing after Ag molecule adsorption over nanotube, is due to

the fact that metal is more electropositive than carbon. This property, during formation of C-M bond, cause partial positive charge on both carbon atoms and hence create electrostatic repulsion between this two carbon atoms which results in increasing C-C bond length. As inter-particular viewpoint of interactions, metal molecule binding to nano-tube results in transmission of non bonded pair electrons of metal to two Π^* , molecular orbital of C-C bond. This issue causes an increase in electronic population of this anti binding orbital and decrease electronic population of σ binding orbital which result in weakness of C-C bond and increase in its length (Table 1). As shown in Table 1, the changes in length of bonds are much small. This fact show that physical adsorption of metal molecule over nanotube's surface is very difficult. It may be interpreted that sometimes there is not any adsorption which can leads to apparent changes of length and diameter of nanotube. Metal binding to nano-tube results in transmission of electrons of the atomic lattice to Π^* molecular orbital of C-C bond. This issue causes an increase in electronic population of this anti binding orbital and decrease electronic population of Π^* binding orbital which result in weakness of C-C bond and increase in its length (Table 1). It is well known that graphite Π -orbitals of carbon atoms combine to form bonding and antibonding molecular Π -orbitals, which construct conduction bands and valence bands, and the interaction between bands leads to band overlap. Therefore graphite is metallic conductive. The energy band structures can be given from calculated

orbital energies. The calculated the band gaps of CNTs are given in Table 2. It can be seen that CNT(6,0) and CNT(6,6)'s all have wide band gaps (0.2 eV). This result is consistent with that of calculations. The width of band gap calculated for CNT(5,0) and CNT(5,5) ranges from 0.29 eV. A comparison indicates that conductivity of CNT(5,0) and CNT(5,5) is much more than that of CNT (6,0) and (6,6). CNTs displays a wide-gap semiconductor or metallic conductor. The calculated results also indicate that the conductivity of CNTs is with obvious relation to its chirality and diameter. The Ag atom can be adsorbed to the CNT (see fig1). Therefore, upon the metal adsorptions, E_g of the tube dramatically decreases in the all adsorption cases which would result in an electrical conductivity change of the nanotube according to the equation $\sigma = \exp\left(\frac{-E_g}{2kT}\right)$ where σ is the electric conductivity, and k is the Boltzmann's constant (eV). According to the equation, smaller values of E_g at a given temperature ($298K$) lead to larger electric conductivity. The smaller the band gap, the greater the conductivity and the metallic property. We observed the increase in functionalization leads to the decrease the energy gap in compare with SWCNT and Eozin. The energy gap characterizes the molecular chemical stability and it is important parameter in determining molecular electrical properties. It is well known that molecules with high energy gap are kinetically stable. The calculation results of quantum molecular descriptors for functionalized single-walled carbon nanotube and Eozin molecule. (See Table.3)

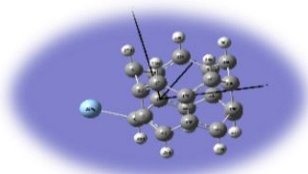


Fig.1.structures of zigzag (5, 0)

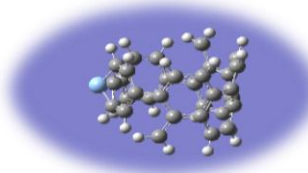


Fig.2.structures of Armchair (5, 5)

Table1.calculated complexation the natural charges on the atoms based on Milliken analysis C-M and C-C bonding with Method B3LYP/6-31G**for CNT

Model	C-Cn,A	C-C,A	C-M
CNT(5,0)			
CNT-Ag	1.53	1.45	2.17
CNT(5,5)			
CNT-Ag	1.47	1.45	1.41
CNT(6,0)			

CNT-Ag	1.50	1.49	2.23
CNT(6,6)			
CNT-Ag	1.41	1.40	3.58

Table.2.Influence of metal adsorptions on the electronic properties of the tubes CNT

Model	E_g (eV)	A(electric conductivity)	Dipole
CNT(5,0)			
Ag	0.29902	0.0029	2.37
CNT(5,5)			
Ag	0.29902	0.0029	5.91
CNT(6,0)			
Ag	0.20941	0.0170	3.21
CNT(6,6)			
Ag	0.20941	0.0170	6.2

Table 3. Quantum molecular descriptors for functionalized (5,0) SWCNT,

	Eozin	CNTAg(5,0)	CNTAg Eozin
E_{gap}	0.268	0.29902	0.22069
μ	0.12593	0.11435	0.092695
I	0.2599	0.26386	0.20304

Fig. 2 shows the optimized structures of (5,0) zigzag carbon nanotube (Ag), Eozin molecule, and Eozin loaded onto (5,0) SWCNT functionalized. For better understanding the nature of the interaction of (5,0)-SWCNT (for example Ag) and Eozin, we examined the electronic structures of the functionalized (5,0) zigzag CNT-Ag with Eozin.

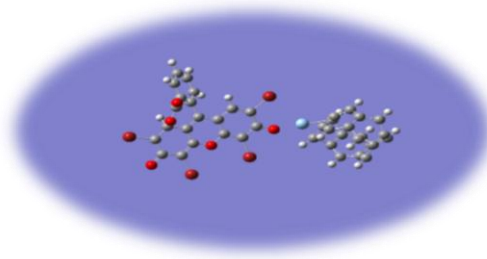


Fig.1.structures of zigzag (5, 0)-CNT-Ag with Eozin

We observed the increase in functionalization leads to the decrease the energy gap in compare with SWCNT and Eozin dye (see Table.3). The energy gap characterizes the molecular chemical stability and it is important parameter in determining molecular electrical properties. It is well known that molecules with high energy gap are kinetically stable. The calculation results of quantum molecular descriptors for functionalized single-walled carbon nanotube, Eozin dye molecule and SWCNT loaded with one Eozin dye are shown in Table 3. In order to investigate the interaction of Eozin dye with SWCNT the resulting Enthalpy energies and Gibbs free energies given by Table.4.

Table4-Calculated complexation enthalpies, Gibbs free energies for CNT with Eozin molecule by method B3LYP/6-31G**



Model	ΔE_f kcal/mol	ΔG_f kcal/mol	ΔS_f cal/mol	ΔG_f kcal/mol
CNT(5,0)				
CNT-Ag	-32143	-32417	-0.0466	-32431
CNT(5,5)				
CNT-Ag	-36093	-36500	-0.0398	-36512

It is observed that the Gibbs free energy is negative and the reactions are spontaneous. A negative enthalpy indicates that the reaction is intense and according to experimental results.

Conclusion

In this work we showed, a theoretical study on adsorption of Eozin dye on sidewall of functionalized (5,0)-SWCNT. Our results showed that thermodynamically covalent functionalization of SWCNT is favorable and energetically the SWCNT-Eozin system is stable. Also B3LYP calculation with 6-31G** basis set performed to obtained binding energies, dipole moment, molecular electrostatic potential, gap energies. The results clearly indicated that electronic properties can be used for prediction of strength interaction between dye molecules and single-walled carbon nanotube.

References

- [1] X. Chen, J. Ma, Z. Hu, Q. Wu, Y. Chen, J. Am. Chem. Soc. 127 (2005) 17144
[۲]. S. Iijima, Nature 354 (1991) 56.
[۳]. D. Tasis, A. Bianco, M. Prato, Chem.Rev. 106 (2006) 1105
.[۴] Q. Dong, X.M. Li, W.Q. Tian, X.R. Huang, C.C. Sun, J. Mol. Struct. (Theochem.) 948 (2010) 83.

Chemical functionalization of single-walled boron nitride nanotube with 1,2,4 triazolium based ionic liquids

H. Roohi^a, R. Salehi^{a*}

^aDepartment of Chemistry, University of Guilan, Rasht, P.O. Box 419383-3697, Iran

*R.Salehi88@ymail.com

Abstract: The study of the structural and electronic properties of ionic liquid functionalized boron nitride nanotube can lead to the development of the applications of BNNTs, such as chemical and biological sensors. In the present work, functionalization of (8,0) zigzag single-walled boron nitride nanotube (BNNT) with [MTZ][X₁₋₄] (X₁₋₄ = BF₄⁻, PF₆⁻, TFO⁻, NTf₂⁻) ionic liquids is explored at the M06-2X/6-31+G(d,p) level of theory. Four types functionalized BNNTs (A–D) were found on the potential energy surface of the interaction between [MTZ]⁺ and BNNT. The HOMO–LUMO gap, electronic chemical potential μ , hardness η and softness S for BNNT and different configurations of functionalized BNNT were calculated. These results show that the functionalization of (8,0) zigzag BNNT results in significant changes in the electronic properties of BNNT.

Keywords: methyl 1,2,4 triazolium; single-walled boron nitride nanotube; Ionic liquid

Introduction

Boron nitride nanotubes (BNNTs)[1,2] are a class of nanomaterials with extraordinary properties such as chemical stability, distinct thermal conductivity and thermal stability that could be potential candidates for a wide range of applications such as the protective shields, sensors, biology or medicine. Thus, it is especially important to find a way to tune BNNT electronic properties in order to widen the application field. The tubular surface could interact with metal nanoparticles [3], organic molecules [4], biomolecules [5], drugs [6], ionic liquids (ILs) [7,8] and other functional groups [9] which could be done in two forms: non-covalent and covalent interaction. Functionalization surface not only modifies the electronic, chemical and optical properties of BNNTs but also improves their dispersion and solubility in various solvents [10].

Due to these excellences, studies of functionalized BNNTs have been the subject of varied research in recent years. Although, experimental methods provide a lot of information about the chemical and physical functionalization of NTs by ILs, but it is still a great challenge to understand the behaviors of these functionalizations at molecular levels using theoretical predictions. The main aims of this work are to find the electronic properties of (8,0) zigzag single-walled boron nitride nanotube functionalized with [MTZ][X₁₋₄] (X₁₋₄ = BF₄⁻, PF₆⁻, TFO⁻, NTf₂⁻) ionic liquids including, energies and energy gaps ($E_{LUMO-HOMO}$), by using DFT method. Furthermore, we investigate the quantum molecular descriptors including electronic chemical potential (μ), global hardness (η), energy gap, global softness (S) and solubility of functionalized BNNTs.

Materials and method

In the present work, calculation of electronic properties of [MTZ][X₁₋₄]-functionalized (8,0) BNNT were carried out using M06-2X method. All specified structures in Fig. 1 was calculated at the ONIOM (M06-2X/6-31+G(d,p): PM6) level of theory in gas phase. All calculations were performed with the Gaussian 09 program package.

Results and Discussion

It is predicted that [MTZ][X₁₋₄] (X₁₋₄ = BF₄⁻, PF₆⁻, TFO⁻, NTf₂⁻) ILs can be connected to exterior sidewall of (8,0) zigzag single-walled BNNT through N atom of MTZ ring. The most stable structures are shown in Fig. 1. As can be seen in Fig. 1, the MTZ ring can be located perpendicular to the tube axis. In order to evaluate the stability of F-BNNTs, the binding energies ($BEs = -\Delta E_{ele}$) of the complexes calculated at M06-2X/6-31+G(d,p) level of theory are summarized in Table 1. According to the data given in this table, the binding energies for (A–D) complexes in gas phase are -61.5, -67.5, -84.2, -84.8 kcal/mol, respectively. Comparison of BEs values reveals that the stability of the complexes decreases in the order of is D > C > B > A.

The energy gap between HOMO and LUMO usually defines the lowest electronic energy absorption band. A high HOMO–LUMO energy gap indicates greater stability and low reactivity of the chemical system. Hard molecules have a large energy gap, and soft molecules have a small energy gap. A soft molecule with a small gap will be more polarizable than hard molecules.



As can be observed from Table 1, the energy gap ($E_{LUMO}-E_{HOMO}$) of F-BNNT complexes decreases compared with the pristine BNNT in gas phase. The decrease in HOMO–LUMO energy gap leads to a decrease in global hardness ($\eta = (I - A)/2$) and an increase in global softness ($S = 1/2\eta$). Therefore, global softness of the (A–D) complexes increases with a decrease in energy gap. The negative values of chemical potential ($\mu = -\chi = -(I + A)/2$) for F-BNNT are greater than that of BNNT ($\mu = -4.56$ eV). Therefore, all the chemical potentials decrease (become more negative) upon functionalization with ILs.

(μ) (eV), hardness (η) (eV) and softness (S) (eV) for pure (8,0) BNNT and F-BNNTs in gas phase at M062X/6–31+G(d,p) level of theory.

Structure	$\Delta E/\text{kcal mol}^{-1}$	$\Delta E_{\text{GAP}}/\text{eV}$	η/eV	S/eV	μ/eV
BNNT		7.30	3.65	0.27	-4.56
A	-61.5	7.08	3.54	0.28	-4.84
B	-67.5	7.12	3.56	0.28	-4.60
C	-84.2	7.02	3.51	0.28	-4.78
D	-84.8	7.02	3.51	0.28	-4.82

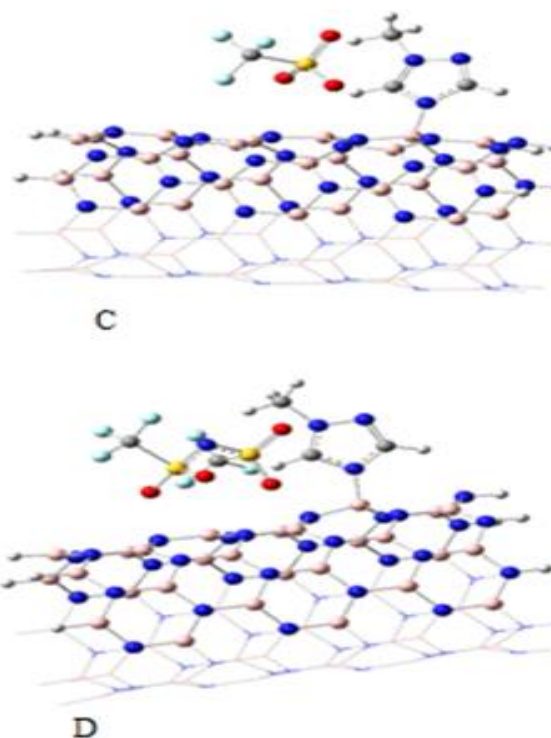
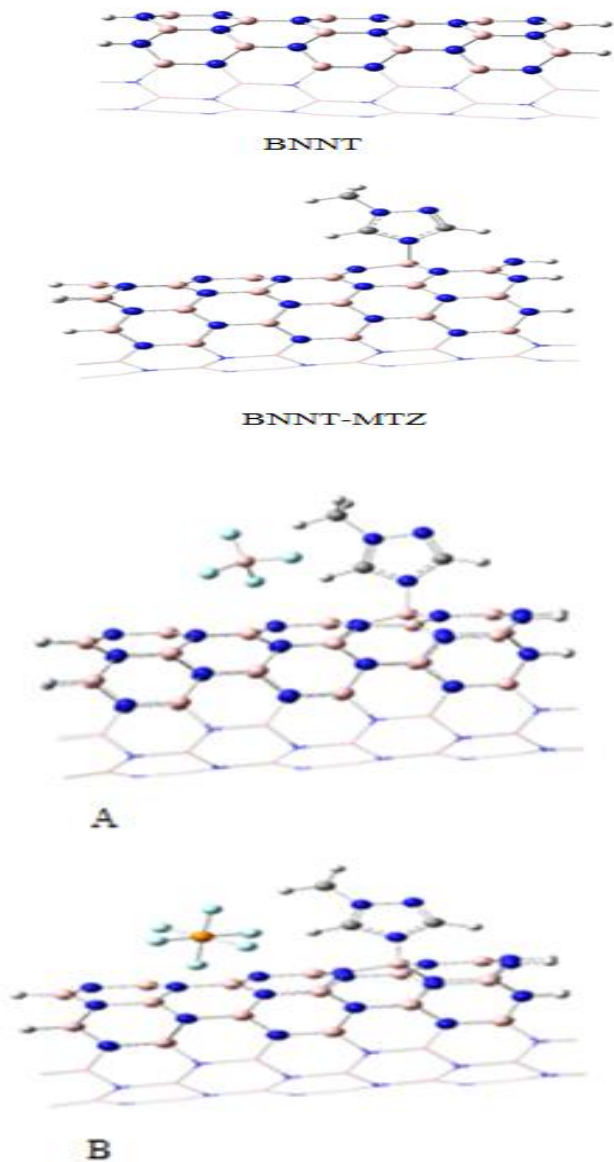


Fig 1. Optimized structures for (A–D) complexes at ONIOM (M06-2X/6-31+G(d,p); PM6) level of theory.

Conclusions

In the present work, calculation of electronic properties of [MTZ][X₁₋₄]-functionalized (8,0) BNNT were investigated using M06-2X functional theory in gas phase. The consequence of binding energies calculated by using M06-2X functional is $D > C > B > A$. The calculated Global reactivity descriptors show that the attachment of ILs to BNNT decreases the band gap between HOMO and LUMO in (A–D) complexes.

References

- [1] X. Blase, A. Rubio, S. G. Louie, A. Cohen, Stability and Band Gap Constancy of Boron Nitride Nanotubes, *Europhys. Lett*, 28(1994) 335-340.

Table 1. Binding energies ($\Delta E_{\text{ele}} = E_{(\text{BNNT}[\text{MTZ}][\text{X}_{1-4}])} - (E_{(\text{X}_{1-4})} + E_{(\text{BNNT}[\text{MTZ}])})$) (kcal.mol^{-1}), energy gap ($E_{\text{L-H}}$), quantum molecular descriptors electronic chemical potential



- [2] Y. Chen, J. Zou, S. J. Campbell, G. Le Caer, Boron nitride nanotubes: Pronounced resistance to oxidation, *Appl. Phys. Lett.*, 84(2004), 2430-2432.
- [3] W.Q. Han, A. Zettl, Functionalized Boron Nitride Nanotubes with a Stannic Oxide Coating: A Novel Chemical Route to Full Coverage, *J. AM. CHEM. SOC.*, 125 (2003) 2062-2063.
- [4] C. Zhi, Y. Bando, C. Tang, S. Honda, K. Sato, H. Kuwahara, D. Golberg, Covalent Functionalization: Towards Soluble Multiwalled Boron Nitride Nanotubes, *Angew. Chem. Int. Ed.*, 44(2005) 7932-7935.
- [5] C. Zhi, Y. Bando, W. Wang, C. Tang, H. Kuwahara, D. Golberg, DNA-Mediated Assembly of Boron Nitride Nanotubes, *Chem. Asian J.* 2(2007) 1581-1585.
- [6] N. Saikia, S. K. Pati, R. C. Deka, First principles calculation on the structure and electronic properties of BNNTs functionalized with isoniazid drug molecule, *Appl Nanosci.*, 2(2012) 389-400.
- [7] C. Zhi, Y. Bando, W. Wang, C. Tang, H. Kuwahara, D. Golberg, Molecule Ordering Triggered by Boron Nitride Nanotubes and “Green” Chemical Functionalization of Boron Nitride Nanotubes, *J. Phys. Chem. C* 111(2007) 18545-18549.
- [8] C. Zhi, Y. Bando, C. Tang, R. Xie, T. Sekiguchi, D. Golberg, Perfectly Dissolved Boron Nitride Nanotubes Due to Polymer Wrapping, *J. AM. CHEM. SOC.*, 127(2005)15996-15997.
- [9] C. Zhi, Y. Bando, C. Tang, D. Golberg, Engineering of electronic structure of boron-nitride nanotubes by covalent functionalization, *physical review B*, 74(2006) 153413-153417.
- [10] C. Zhi, Y. Bando, C. Tang, D. Golberg, Boron nitride nanotubes *Materials Science and Engineering R*, 70 (2010) 92-111.

Study on the Interaction Energy of Imidazolium and Pyrrolidinium-Based Dicyanamide Ionic Liquids: The Effect of Alkyl Chain Length

M. Zare*, Z. Asakereh and E. Shakerzadeh

Department of Chemistry, Faculty of Science, Shahid Chamran University of Ahvaz, Ahvaz, Iran

*Email: m.zare@scu.ac.ir

Abstract: Understanding the relationship between the structures of ionic liquids and their properties is very important. In the present study, on the basis of quantum chemical calculations, the effect of the alkyl side chain length upon the cation-anion interaction energies of 1-alkyl-3-methylimidazolium dicyanoamide [C_nmim][dca] (n=2, 4, 6 and 8) and 1-alkyl-1-methylpyrrolidinium dicyanoamide [C_nmpyrr][dca] (n=2, 4, 6 and 8) ionic liquids were studied using the Gaussian-3 theory using reduced Møller-Plesset order (G3(MP2)). The calculated interaction energy was found to increase in magnitude with decreasing alkyl side chain length. Regardless of the cation type, second degree polynomial correlations have been found.

Keywords: Ionic Liquids; imidazolium; pyrrolidinium; Interaction Energy; G3(MP2).

Introduction

Ionic liquids (ILs) are a class of compounds composed of organic cations and organic or inorganic anions with melting points below 100 °C [1]. The negligible vapour pressure, low melting point, high thermal stability and high ionic conductivity are among remarkable properties that make them suitable as green solvent, electrolyte and lubricant [2].

By altering the cations and anions that form the ion pair, numerous ionic liquids can exist with different physicochemical properties. Thus, understanding the relationship between the structures of cation and anion and their properties is important. Cation-anion interaction is one of the most important factors influencing the properties of ILs which must be known. Quantum mechanical calculation is a powerful tool for studying this interaction.

In this work, we focus on the cation-anion interaction of 1-alkyl-3-methylimidazolium [C_nmim]⁺ and 1-alkyl-1-methylpyrrolidinium cations [C_nmpyrr]⁺ (n refers to the alkyl chain length, n=2, 4, 6 and 8) paired with dicyanoamide anion [dca]⁻. The effect of side-chain length on the extent of interaction has been investigated.

Methods

Optimized structures and energies of the [C_nmim]⁺ and [C_nmpyrr]⁺ cations, anion [dca]⁻, [C_nmim][dca] and [C_nmpyrr][dca] (n=2, 4, 6 and 8) ionic liquid ion pairs were obtained with the Gaussian-3 theory using reduced Møller-Plesset order (G3(MP2)). G3(MP2) theory uses geometries from second-order perturbation theory and scaled zero-point energies from Hartree-Fock theory followed by a series of single-point energy calculations at the MP2(Full)/6-31G(d), QCISD(T)/6-31G(d), and MP2/GTMP2Large levels of theory [3,4].

All calculations were performed using the Gaussian 03 program package [5].

Results and Discussion

Figures 1 and 2 show the optimized structures of the [C_nmim][dca] and [C_nmpyrr][dca] ion pairs, respectively.

The interaction energy (E_{int}) is calculated as the difference between the ion pair energy ($E_{ion-pair}$) and the anion (E_{anion}) and the cations (E_{cation}) energies:

$$E_{int} = E_{ion-pair} - E_{cation} - E_{anion} \quad (1)$$

The magnitude of the interaction energy follows the trends [C₂mim][dca] > [C₄mim][dca] > [C₆mim][dca] > [C₈mim][dca] and [C₂mpyrr][dca] > [C₄mpyrr][dca] > [C₆mpyrr][dca] > [C₈mpyrr][dca]. The interaction energy decreases with the alkyl chain lengthening. However, the changes are not noticeable. It seems Coulombic interaction of oppositely charged ions is more important than the van der Waals interaction of the alkyl chains on the imidazolium and pyrrolidinium cations. Figure 3 shows the interaction energy and the number of carbon atoms in the alkyl chain length correlate in a second-degree polynomial fashion with $R^2 = 0.9741$ and 0.9990 for [C_nmim][dca] and [C_nmpyrr][dca], respectively.

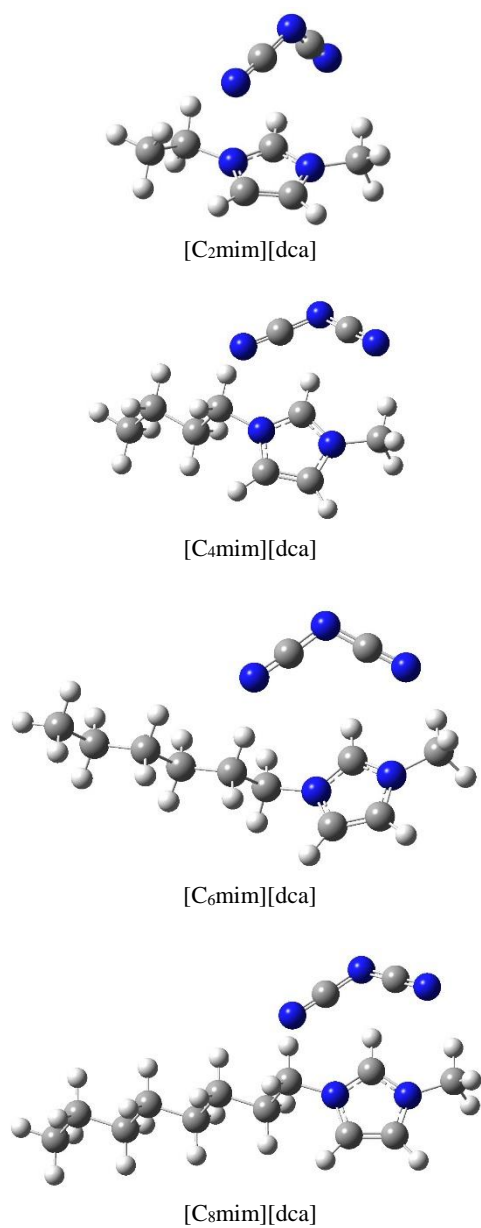


Fig.1. Optimized structures of 1-alkyl-3-methylimidazolium dicyanamide.

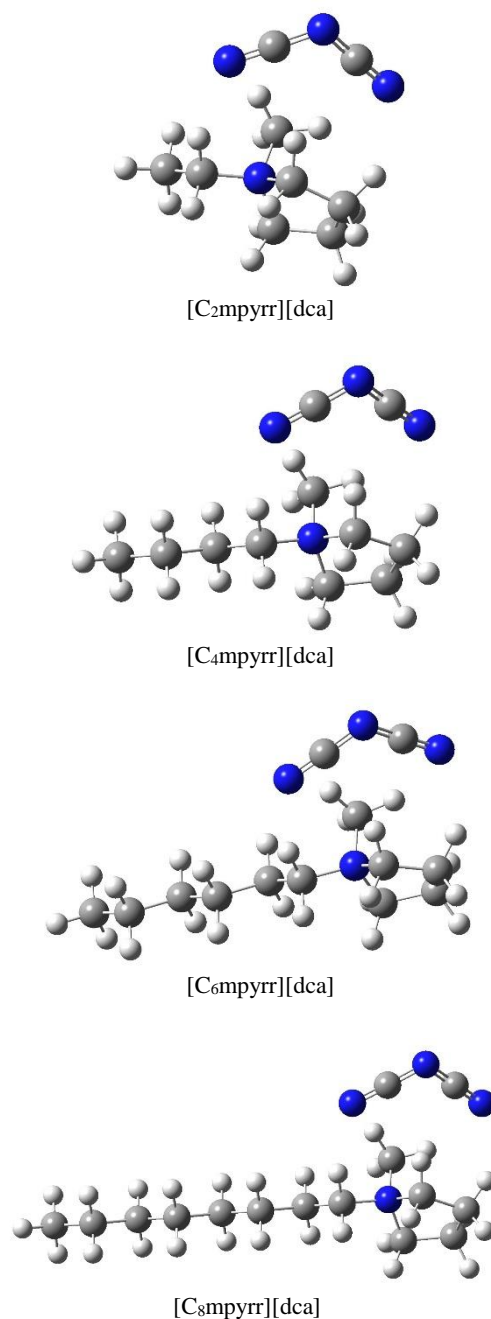


Fig.2. Optimized structures of 1-alkyl-1-methylpyrrolidinium dicyanamide.

Table 1 G3(MP2) electronic energy (E_0 , in a.u.) of the cations, anions, and ion-pairs and cation-anion interaction energies (E_{int} , kcal.mol⁻¹) of ionic liquids.

ILs	$E_{0,cation}$	$E_{0,anion}$	$E_{0,ion-pair}$	E_{int}
[C ₂ mim][dca]	-343.938832	-	-	-
		240.189034	584.263085	84.85
[C ₄ mim][dca]	-422.409500	-	-	-
		240.189034	662.732239	83.90
[C ₆ mim][dca]	-500.878921	-	-	-
		240.189034	741.201376	83.70



[C ₈ mim][dca]	-579.347918	-	-	-
		240.189034	819.670195	83.61
[C ₂ mpyrr][dca]	-330.261183	-	-	-
		240.189034	570.583101	83.40
[C ₄ mpyrr][dca]	-408.731964	-	-	-
		240.189034	649.052893	82.76
[C ₆ mpyrr][dca]	-487.201534	-	-	-
		240.189034	727.521959	82.45
[C ₈ mpyrr][dca]	-565.670589	-	-	-
		240.189034	805.990808	82.32

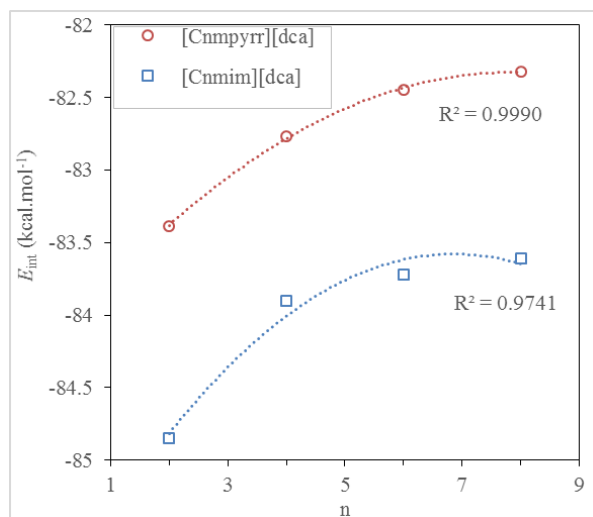


Fig.3. Calculated cation-anion interaction energies of (□) [C_nmim][dca] and (○) [C_nmpyrr][dca] versus the number of carbon atoms in alkyl side chain.

Conclusions

We have calculated the cation-anion interaction energies of ion pairs of 1-alkyl-3-methylimidazolium and 1-alkyl-1-methylpyrrolidinium ionic liquids by the accurate G3(MP2) method. The calculated interaction energy was found to decrease with longer alkyl chain length. Correlation between interaction energy and the alkyl chain length was investigated. Second-degree polynomial correlations were found to exist in both [C_nmim][dca] and [C_nmpyrr][dca]. Some properties of ionic liquids like density, melting point, surface tension and electric conductivity may be governed by the cation-anion interaction.

References

- [1] J. Huddleston, A. Visser, W. Reichert, H. Willauer, G. Broker, R. Rogers, "Characterization and

comparison of hydrophilic and hydrophobic room temperature ionic liquids incorporating the imidazolium cation", *Green Chem.* 3 (2001) 156-164.

- [2] P. Wasserscheid, W. Keim, "Ionic liquids—new solutions" for transition metal catalysis", *Angew. Chem., Int. Ed.* 39 (2000) 3772-3789.

- [3] L. Curtiss, P. Redfern, K. Raghavachari, V. Rassolov, J. Pople, "Gaussian-3 theory using reduced Moller-Plesset order". *J. Chem. Phys.* 110 (1999) 4703-4709.

- [4] L. Curtiss, P. Redfern, K. Raghavachari, V. Rassolov, J. Pople, "Gaussian-3 (G3) theory for molecules containing first and second-row atoms", *J. Chem. Phys.* 109(1998) 7764-7776.

- [5] M. Frisch, et al., Gaussian, Inc., Wallingford, CT, 2004.

A computational investigation on the excited-state intramolecular proton transfer (ESIPT) process in o-Hydroxy analogues of green fluorescent protein chromophore

H. Roohi^a, R. Nokhostin^a *

^aDepartment of Chemistry, University of Guilan, Rasht, 41938-33697, Iran

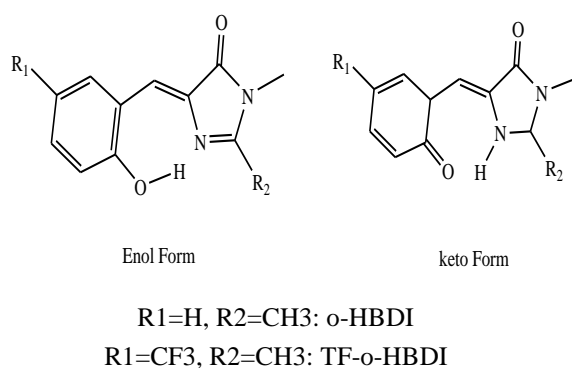
* nokhostin@gmail.com

Abstract: The intramolecular photo-induced proton transfers in o-Hydroxy analogues of the green fluorescent protein (GFP) chromophore were investigated using TD-DFT method at PBE0/6-311++G(d,p) and M06-2X/6-311++G(d,p) levels of theory in both gas and solution phases. The potential energy surfaces (PESs), at ground (S_0) and excited states (S_1) along the reaction coordinate (RC = dOH) were assessed. Changes of Structural parameters, absorption and emission bands, vertical excitation and emission energies, oscillator strength, dipole moment and electron density at critical points in ESIPT process were scrutinized. The results show the photo-physical properties of o-Hydroxy analogues, of the green fluorescent protein chromophore are dependent on substitution patterns and solvents.

Keywords: GFP; TD-DFT; Excitation energy; ESIPT.

Introduction

Green Fluorescent Protein is a significant model system for biologically relevant proton transfer reactions that has been examined widely by many spectroscopical methods [1]. GFP can be used to direct observation at intracellular processes, growth and spreading of cell clones, such as pathogenic bacteria and cancers, and mapping gene expressions, etc. [2]. 4-(2-hydroxybenzylidene)-1, 2-dimethyl-1H-imidazol-5(4H)-one (o-HBDI) is an analogue of the native GFP core that in recent years has been particularly investigated. The main reason for this attention is the exclusive photochemical properties of the o-HBDI [3-4]. In this work, the photophysics and photochemistry of o-Hydroxy analogues of the green fluorescent protein chromophore (o-HBDI and TF-o-HBDI Scheme 1) on the nature and mechanism of the ESIPT reaction in both gas and solution phases were investigated. Finally, the H-bonding interactions along the proton transfer through Atoms-In-Molecules theory (AIM) [5] were probed.



Scheme.1: Chemical Structures of o-HBDI and TF-o-HBDI.

Computational details

The ground state (S_0) and the lowest singlet excited-state (S_1) geometry of the o-HBDI and TF-o-HBDI were optimized using DFT methods (PBE0 and M06-2X for S_0) and (PBE0-TD and M06-2X-TD for S_1) [6] in conjunction with a 6-311++ G (d,p) basis set. The stationary points on the S_0 and (S_1) potential energy surfaces (PESs) of o-HBDI and TF-o-HBDI, were represented at the M06-2X (M06-2X-TD)/6-311++G (d,p). Topological properties of the electron density, were analyzed at the M06-2X/6-311++G (d, p) level of theory by using the AIM2000 program package [7]. The calculations were carried out using GAUSSIAN 09 program package.

Results and Discussion

The M06-2X/6-311++G(d,p) optimized equilibrium structures of the o-HBDI and TF-o-HBDI at S_0 and S_1 states are shown in Fig. 1.

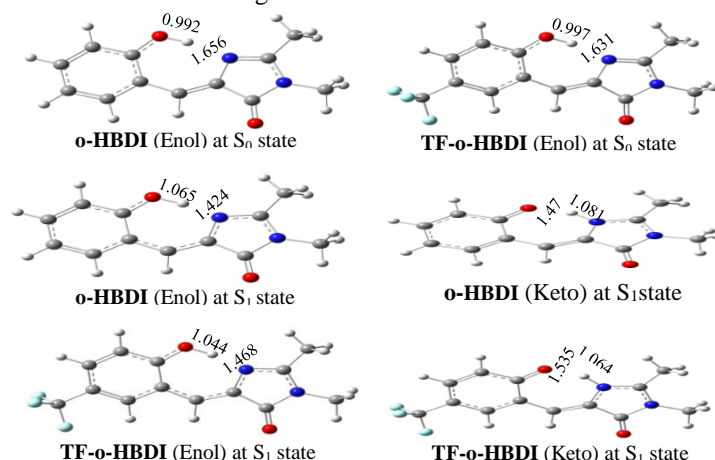


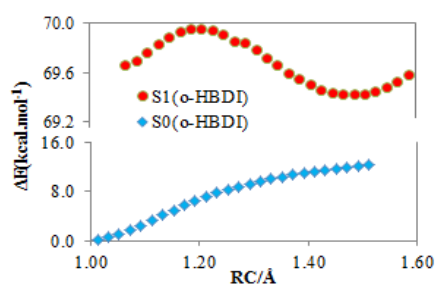
Fig.1: M062X optimized minima structures of o-HBDI and TF-o-HBDI (distances in terms of Å) at S_0 and S_1 states.

The value of H-Bond angle in S_0 -E form of o-HBDI

and TF-o-HBDI is 168.4° and 168.1° respectively. The O–H bond length in o-HBDI and TF-o-HBDI is 0.992 and 0.997 Å, respectively. Thus, it is predicted that the strength of H-bonding interaction increases on going from TF-o-HBDI to o-HBDI.

Fig. 2 represents the relaxed potential energy curves during the minimum-energy proton transfer (PT) path at the S_0 and S_1 states as a function of the RC (d_{OH}) for o-HBDI and TF-o-HBDI. According to Fig. 2, the potential energy diagram of the S_0 state for o-HBDI and TF-o-HBDI clearly shows global minima corresponding to enol forms. Inspection of the Figs. reveals that the enol forms (S_0 -E) with O–H...N H-bonding are more stable than the keto forms (S_0 -K) in the gas phase at S_0 state. Hence, O...H–N tautomers of two compounds at the S_0 state are not stable and transform to O–H...N tautomers.

a) o-HBDI



b) TF-o-HBDI

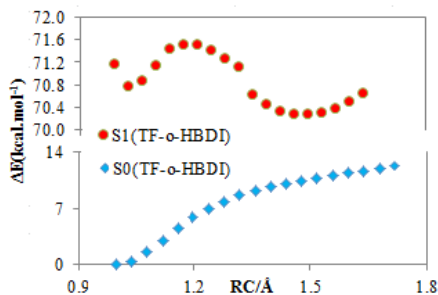


Fig.2: Potential energy curves along the proton transfer pathway in the ground (S_0) and excited (S_1) states as a function of the reaction coordinate (RC) for, (a) o-HBDI and (b) TF-o-HBDI.

In contrast to S_0 state, from PECs given in Fig. 2, it is observed that barrier height for enol to keto tautomerization in o-HBDI and TF-o-HBDI at S_1 state is very low, suggesting that proton transfer is kinetically possible.

The vertical excitation and emission energies on the ESIPT process at the behavior of the first singlet excited state of o-HBDI and TF-o-HBDI are argued by time-dependent density functional theory (TD-DFT).

The computed photo-physical characteristic at PBE0/6-311++G (d,p) is exhibited in Table 1. By probing in the variation of λ_1 values, a red shift in the absorption band is expected. Calculated λ_1 values in the absorption band for o-HBDI and TF-o-HBDI are 380.3 nm and 370.6 nm, respectively. Therefore, the maximum red shift occurs in o-HBDI.

Table1: Absorption and emission wavelengths, oscillator strength (f) and dipole moment, at PBE0/6-311++G(d, p) level, of theory.

	o-HBDI			TF-o-HBDI		
	S_0 -E	S_1 -E	S_1 -K	S_0 -E	S_1 -E	S_1 -K
λ_1 /nm	380.8	431.8	550.2	370.6	419.0	546.1
λ_2 /nm	321.16	344.0	380.6	313.8	335.9	392.3
λ_3 /nm	307.32	317.4	348.5	310.8	324.5	344.7
f_1	0.329	0.324	0.144	0.407	0.451	0.154
f_2	0.296	0.270	0.000	0.178	0.118	0.000
f_3	0.000	0.000	0.485	0.000	0.000	0.493
μ/D	3.6057	3.9	6.3	7.5	7.4	10.9

The oscillator strengths (f), for $S_0 \rightarrow S_1$ absorption bands is 0.329 for o-HBDI and, 0.407 for TF-o-HBDI. If we compare the position and oscillator strength of the $S_0 \rightarrow S_1$ band of molecules, we can observe that the intensity of the $S_0 \rightarrow S_1$ absorption band decreases on going from TF-o-HBDI to o-HBDI.

The normal emissions of o-HBDI and TF-o-HBDI are remarked in 431.8 nm ($f = 0.324$) and 419 nm ($f = 0.451$) that are red-shifted by 51 nm and 48.4 nm compared to the vertical excitation wavelengths, respectively. From Table 1, it can be found that S_1 -K to S_0 -K fluorescence emission wavelength of o-HBDI and TF-o-HBDI is 550.2 nm ($f = 0.144$) and 546.1 nm ($f = 0.154$), respectively. As can be seen, fluorescence emission wavelength decreases on going from o-HBDI to TF-o-HBDI.

Photo-physical features of chromophores strongly depend on the polarity of the solvent. The properties of interested chromophores are explored by TD-DFT/PBE0 method in the solvents by different polarities (acetonitrile and cyclohexane). Tables 2 declare the related results of photo-physical features in two solvents.

Table2: Solvatochromic data for o-HBDI and TF-o-HBDI molecules at PCM-PBE0/6-311++G(d, p) level of theory.



As can be understood by Table 2, dipole moment in S_1 -K

form is more than enol form at both states. In addition, increasing dipole moment changes in order acetonitrile > cyclohexane. The absorption wavelengths of molecules increase on going from cyclohexane to acetonitrile. The S_1 -K forms of o-HBDI and TF-o-HBDI are stable in polar and non-polar solvents and represent a fluorescence emission. The calculated S_1 -K \rightarrow S_0 -K fluorescence emission wavelengths of o-HBDI (TF-o-HBDI) in acetonitrile and cyclohexane are 502 (473.3 nm) and 534 (517.8 nm) and Stock shifts are 96.3 (108.5 nm) and 147.6 (147.1 nm), respectively. This indicates that the Stock shift decreases as the polarity of solvent increases.

AIM method can lead us to better comprehend chemical bond characteristics during PT processes. Topological properties of bond critical points (BCPs) were calculated at the M06-2X/6-311++G(d, p) level of theory. Fig. 3 demonstrates the variation in the $\rho(r)$ at the OH \cdots N and O-HN bond critical points (BCPs), in terms of RC at S_0 and S_1 states for o-HBDI. According to Fig. 3 along the PT reaction, the $\rho(r)$ of OH \cdots N bond increase and those of the O-HN one decrease.

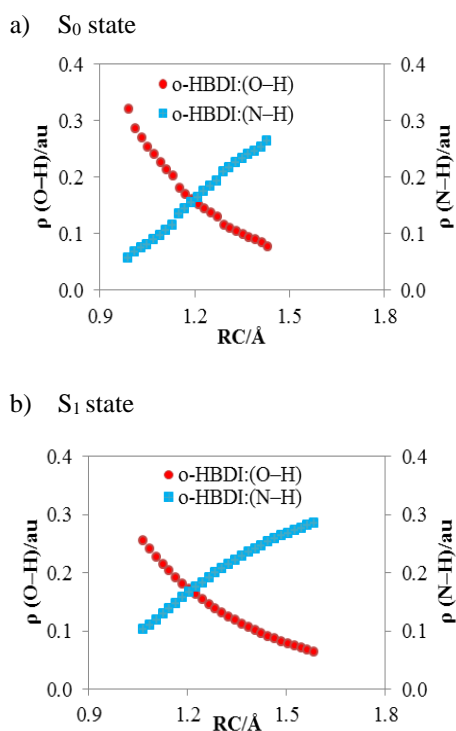


Fig.3: Variation of electron density at the N(O)-H BCP in term of RC along the PT pathway of the o-HBDI S_0 (a) and S_1 (b) states.

Environment	o-HBDI			TF-o-HBDI		
Acetonitrile	S_0 -E	S_1 -E	S_1 -K	S_0 -E	S_1 -E	S_1 -K
λ_l /nm	405.7	440.8	502.0	364.8	432.4	473.3
f_l	0.462	0.658	0.453	0.525	0.716	0.492
μ /D	4.9	5.0	9.5	9.5	9.3	14.4
Cyclohexane						
λ_l /nm	386.4	–	534.0	370.7	422	517.8
f_l	0.470	–	0.238	0.540	0.542	0.253
μ /D	4.1	–	7.8	8.3	8.3	12.5

Conclusions

The intramolecular photo-induced proton transfer in o-Hydroxy analogues of the green fluorescent protein chromophore in both gas and solution phases were investigated using TD-DFT method at PBE0/6-311++G(d,p) and M06-2X/6-311++G(d,p) levels of theory. Both structures show a seven-membered ring intramolecular hydrogen bonding structure. The photo-physical properties of o-Hydroxy analogues, of the green fluorescent protein chromophore depend on substitution patterns and solvents.

References

- [1] B. van Oort, MJT. ter Veer, ML. Groot, IHM. van Stokkum "Excited state proton transfer in strongly enhanced GFP (sGFP2)", *Phys. Chem. Chem. Phys.*, 14 (2012) 8852–8858.
- [2] RR. Alieva, FN. Tomilin, AA. Kuzubov, SG. Ovchinnikov, NS. Kudryasheva "Ultraviolet fluorescence of coelenteramide and coelenteramide-containing fluorescent proteins. Experimental and theoretical study", *J. Photochem. Photobiol.*, 162 (2016) 318–323.
- [3] CC. Hsieh, PT. Chou, CW. Shih, WT. Chuang, MW. Chung, J. Lee, T. Joo "Comprehensive Studies on an Overall Proton Transfer Cycle of the ortho-Green Fluorescent Protein Chromophore", *J. Am. Chem. Soc.*, 133 (2011) 2932–2943.
- [4] YH. Hsu, YA. Chen, HW. Tseng, Z. Zhang, JY. Shen, W. Chuang, TC. Lin, CS. Lee, WY. Hung, BC. Hong, SH. Liu, PT. Chou "Locked ortho- and para-Core Chromophores of Green Fluorescent Protein; Dramatic Emission Enhancement via Structural Constraint", *J. Am. Chem. Soc.*, 136 (2014) 11805–11812.
- [5] RFW. Bader, H. Essén "The characterization of atomic interactions", *J. Chem. Phys.*, 80 (1984) 1943–1960.

Allicin on single-walled carbon nanotubes zigzag physical adsorption using density functional theory

Mehdi Ghaffari Moghaddam

Department of Chemistry, Faculty of Science, University of Abhar, Zanjan, Iran

Email: Mehdi.Moghaddam2014@gmail.com

Abstract: Since the discovery of carbon nanotubes, extensive researches have been done to find the ability of these nanostructures in multiple sciences. One of these areas, is the physical adsorption of important molecules, especially as Allicin, including molecules that have medical applications. One of the ways how Allicin as molecules can be separated and recognized probably is the study of its interactions by carbon nanotubes. The present study tries to investigate the interaction of Allicin with carbon nanotube as zigzag using density functional theory calculations. For this purpose, the method of density functional theory is applied and (6,0) SWCNT, included 72 atoms were used. Allicin in different directions interacted with nanotube while the energy and minimum distances of adsorption were calculated. The results have shown that the (6,0) SWCNT, adsorbed Allicin from a part of sulfur, and of course with the nearest distance. However, further studies should be done in this case.

Keywords: 1- Allicin 2- CNT ۳- DFT ۴- VdW

Introduction

1. Introduction

1-1 Carbon nanotubes

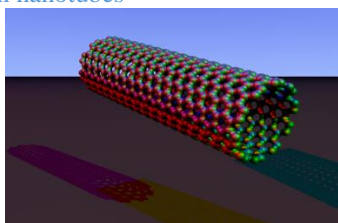


Fig 1-1: three-dimensional view of carbon nanotubes

The nature of the element carbon naturally in the solid state in the form of diamond and graphite. The third type is currently produced in the laboratory of nanotechnology are carbon nanotubes.

The difference properties of carbon nanotubes to replace species that has caused a lot of material in the industry and cause massive upheaval in the material world.

2-1: The discovery of carbon nanotubes. In the mid-1980s, Kroto, Smalley and his colleagues were able to use laser vaporization of graphite in a joint investigation. A large family of 60 carbon atoms for sustainable intensive clusters using mass spectrometry sample vaporized carbon discovered. The molecules of similar geometric surfaces were designed and manufactured by Buckminsterfullerene and called fullerenes were read.

The most famous and enduring yet structure which is produced fullerene is C₆₀. (C represents carbon and carbon-60 atoms in a fullerene molecule are introduced a number), which is also known as a buckyball is made (Figure 2-1).

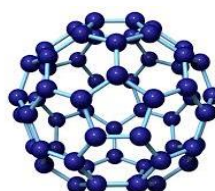


Fig 2-1: fullerenes (C₆₀)

In 1991, Iijima and his colleagues have been studying the carbon residue of an arc between graphite electrodes were Discharge Using transmission electron microscopy (TEM) with high resolution (HRTEM), carbon disciplines and winding observe screw (Figure 3-1).

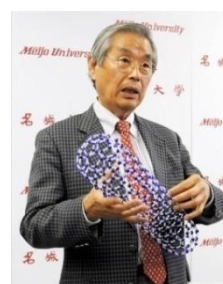
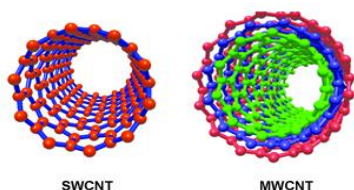


Figure 3-1: Ayljyma (1939 Japan)

Carbon nanotubes are a new breed of nano-structures composed of carbon atoms have been significantly [1]. Carbon nanotubes as a type of nanomaterial attracted a lot of attention limitations [2]. Because of the unique properties of mechanical, chemical and electrical carbon nanotubes [3] Its distinctive properties such as: the ability to accumulate analyte, to minimize the level of fouling and electro-catalytic activity for electrochemical measurement are awesome [4].



SWCNT

MWCNT

Figure 4-1: single-walled and multi-walled nanotubes view. Single-walled carbon nanotubes includes two types of nanotubes (SWCNT) and multi-walled nano-tubes (MWCNT) (Figure 4-1), In 1991 and 1993, respectively, which were discovered by Iijima [6-5]. Single-walled nanotubes are the most simple geometry and a diameter of about 0.8 and 2 nm.

1-3-1- Single-walled carbon nanotubes (SWNT)

Single-walled carbon nanotubes of carbon just one Sakhtarsadh (sheet of regular hexagons) were formed. Some projections indicate that single-walled conductor or semiconductor can be. The high electrical conductivity depends on the exact geometry of the carbon atoms. Since the beginning of their work on single-walled as a one-dimensional phenomenon were called to the stage to stage this theory has evolved.

Due to the angle of torsion pages graphene, single-walled nanotubes are divided into two general categories chiral and zigzag. CNT carbon nanotube is Ghyrkayral mirror image of the original structure is the same. Single-walled carbon nanotubes-sheets of graphite which are wrapped to form a layer with nano dimensions [7].

Single-walled carbon nanotubes according to the arrangement of carbon atoms pipe section into three major categories armrest and metallic properties that are chiral and zigzag is divided semiconductor properties [8].

2-3-1- multi-walled carbon nanotubes (MWCNT) Single-walled carbon nanotubes with additional graphene tubes surrounding a central material called multi-walled nanotubes [9]. Multi-walled carbon nanotubes are always electrically conductive [10].

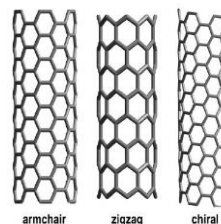
Multiwalled carbon nanotubes (substitute carbon black) in color powders. One of the disadvantages of the single-walled multiwalled nanotubes is that less is strengthening because they are weak internal page links.

4.1.:Armatureandzigzag

CNTs

Due to the angle of torsion pages graphene, single-walled nanotubes are divided into two general categories chiral and zigzag. Ghyrkayral carbon nanotubes that are identical mirror image of the original structure (Figure 5-1).

There are two kinds of chiral nanotubes: Zigzag and the armature. The name comes from the shape of the cross-section of them. So there are three types of single-walled carbon nanotubes. To roll the sheets of graphene and nanotubes diameter of two integers n and m can be achieved.



armchair

zigzag

chiral

Fig 5-1: Types of single-walled nanotubes

5-1: Zigzag Carbon Nanotubes

The chiral vector is equal to zero, one of its components, such as vector $(6, 0)$ of the recurring units such as (Figure 6-1) are formed. The zigzag vectors are vectors in the class. It is named because of the appearance of this unit. The English name of the vectors, the zigzag.



Fig 6-1: repeat unit for chiral vector $(6, 0)$ (zigzag)

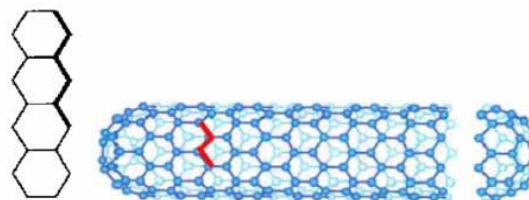


Figure 7-1: atoms joined together to create the kind of zigzag shape.

Sharp zigzag nanotubes are paramagnetic and gradually lose its magnetic properties. Highly dependent on the length - radius - temperature and strong magnetic flux.

2 - Methods of Computational Chemistry

1-2: density functional theory (DFT)

DFT theory within the framework of quantum mechanics to study the electronic structure of many-particle system. In this theory, the introduction of universal energy functional variation of the electron characteristics of the material (in this case the electron density) is obtained.

Density functional theory, in fact, a useful tool for calculating the ground state energy [11] And density distributions [12] Molecular atoms and solids, particularly for systems involving a large number of atoms or molecules is With this theory can be accurate density and energy of the ground state electron systems under the influence of an external potential are calculated. Moreover, by using density functional theory can be non-Hamgin systems with different interactions can be studied. Simple-most used approximation is the local density approximation LDA



[13]. With this theory can be single-atom Schrödinger equation with single-atom potential correlation with the potential LDA exchange earned and calculated the density [14].

The wave function for cease-electron interaction

$$\psi(r_1, r_2, \dots, r_N)$$

Where i've been r_i spatial coordinates and spin of electrons. Schrödinger equation is answered below.

$$\text{Relevance 1-2; } (\hat{T}_e + \hat{H}_{ee} + \hat{H}_{ne})\psi(r_1, r_2, \dots, r_N) = E \psi(r_1, r_2, \dots, r_N)$$

Density functional theory based on the principle that every property of a few interacting particles can be A function of the density of the ground state (r) n_0 considered and its density is a function of the location swing. Prove the existence of such a function in the work Hohenberg Kahn and Mermin [15].

The basic rules of order by density functional theory (Hohenberg and Kohn) and (Cohen and dinner) in the years 1964 and 1965 were presented. Cases Hohenberg - Kohn show That all the properties of the ground state of a cease-electron interaction can be obtained from the density of the ground state, As a result, many devices electron ground state energy function of the density of variational principle comply. Cohen case - you represent the ground state electron density is exclusively determined by the total energy of a system. Mathematically, the electron density ρ at a point in real Fzary by Coordinates x, y, z . Defined by function $\rho = \rho(x, y, z)$

Displays the total energy of the system, E can be defined as a function of electron density.

$$\text{Relevance 2-2; } E = E(\rho(x, y, z))$$

To determine the energy can be divided into three categories as follows:

$$\text{Relevance 3-2; } E[\rho] = T[\rho] + U[\rho] + \text{Exc}[\rho]$$

The (T) kinetic energy of electrons . Coulomb energy U , Exc energy exchange between the electron - electron. Coulomb energy is expressed by the following equation:

$$\text{Relevance 4-2; } U = U_{ne} + U_{nn} + U_{ee}$$

The U_{ne} , U_{ee} , U_{nn} , and U_{nn} represent the attraction between electrons and nuclei, electrons and electron repulsion -The core are repulsive.

2.2- interactions between particles based on molecular mechanics

Intermolecular interactions (non-hybrid) models that form the potential use of this potential is as follows (a combination of potential and electrostatic potential Lnard- Jones):

$$\text{Relevance 5-2; } u(r_{ij}) = 4\epsilon_{ij} \left[\left(\frac{\sigma_{ij}}{r_{ij}} \right)^{12} - \left(\frac{\sigma_{ij}}{r_{ij}} \right)^6 \right] + \frac{q_i q_j}{4\pi\epsilon_0 r_{ij}}$$

To calculate intermolecular interactions, the combination of potential and electrostatic potential is used Lnard- Jones. Lnardjvnz parameters (ϵ and

σ) and atomic charges adsorb gases from the force fields to be earned.

1-2-2- The van der Waals (short-range)

As mentioned earlier, Benard Jones parameters (ϵ and σ) to adsorb and absorbent fields are proudly. To calculate the molecular interactions between absorbent and adsorbent in the simulation All parameters Benard - Jones by mixing the Lorentz - Berthelot determined. The equations of the form are as follows:

$$\text{Relevance 6-2; } \sigma_{ij} = \frac{1}{2}(\sigma_{ii} + \sigma_{jj}), \epsilon = \sqrt{\epsilon_{ij}\epsilon_{ij}}$$

2-2-2; The electrostatic (range - Long)

The second term potential equation (2-11), Coulomb equation for calculating the electrostatic forces are:

$$\text{Relevance 7-2; } E_{\text{coul}} = \frac{1}{2} \sum_{i=1}^N \sum_{j \neq i=1}^{\infty} \frac{q_i q_j}{r_{ij}}$$

Korea radius R_c of the equation when system loads to be cut and in case if $N \rightarrow \infty$ for a position defined and conditionally convergent.

3.2 periodic boundary conditions

The simulation system with more than a few tens of thousands of computers are typically very time consuming and not spend for larger systems. To solve the problem of periodic boundary conditions are used. In this situation, a system containing N atoms in a cube can be considered. These systems are surface atoms to cause the situation that certain behavior show and the main difference is small systems to large systems. Several cubes are placed around the basic cube which is actually a virtual copy of the preliminary system, so that the effect is removed. If an atom of a cube out of funds, with the same speed from the other side of the cube. By this method, boundary conditions simulation system will be large system will have the same treatment. In (Figure 2-1) this behavior is observed.

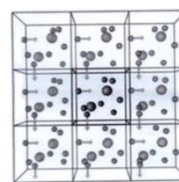


Fig 1-2: periodic boundary conditions

3. Results

LatticeConstant 1.00 Ang

%block LatticeVectors

```
20.00000000 0.00000000 0.00000000
0.00000000 25.00000000 0.00000000
0.00000000 0.00000000 20.00000000
```

%endblock LatticeVectors

MeshCutoff 125 Ry

%block kgrid_Monkhorst_Pack

```
1 0 0 0.0
0 1 0 0.0
0 0 1 0.0
```

%endblock kgrid_Monkhorst_Pack


```

xc.functional GGA # Default value
xc.authors revPBE # Default value
#*****
*****
PAO.EnergyShift 110 meV
PAO.SplitNorm 0.30
PAO.SplitNormH 0.50
PAO.SoftDefault true
PAO.SoftPotential 50.0 Ry
PAO.SoftInnerRadius 0.80
PAO.BasisSize DZP
    
```

Table 3-1: Introduction position and functional groups of

Number	1	2	3	4	5
position	CH2	MID- CH2-2	S	SO-1	SO- 2

allicin

1.3 Interaction Results CNT (6,0) & ALLICIN

In Figure 1-3, three-dimensional images of allicin can be viewed.

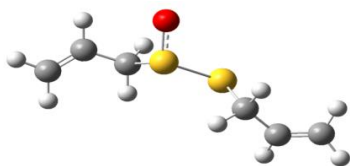


Fig 1-3: three-dimensional images of allicin

Single-walled carbon nanotube three-dimensional schematic in Figure 2-3 (6, 0) can be seen. The ends of the nanotubes by hydrogen atoms have been linked to the cause of this could be due to repeated intermittent nanotubes. The hydrogen atom cut nanotubes and the nanotube block to prevent the recurrence of intermittent endless.

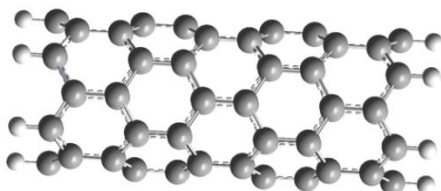


Fig 2-3: three-dimensional image of carbon nanotubes (6,0)

2.3 of allicin molecule functional groups

At the end of a three functional group single-walled carbon nanotubes for molecular absorption by allicin is used in different situations. In order to separate each in various positions (Figure 3-3).

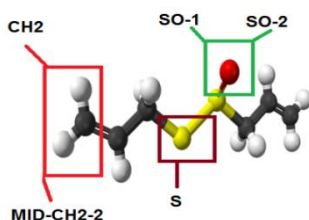


Fig 3-3: Overview of functional groups allicin

Allicin molecules and single-walled carbon nanotubes from 5 to (6,0) are close.

In position 1 hydrogen from the middle of the ring hexagonal carbon nanotubes is close to the outer surface (Figure 4-3). In position 2 hydrogen from the carbon nanotube approaches (Figure 5-3). Allicin, a sulfur atom at position 3 from the outer surface of the nanotube approaches (Figure 6-3). In position four oxygen atoms of allicin from the outer surface of the carbon nanotubes is close to the hexagonal ring (Figure 7-3). As oxygen atom at position 5 to the outer surface of the ring hexagonal nanotubes and carbon nanotube approaches (Figure 8-3).

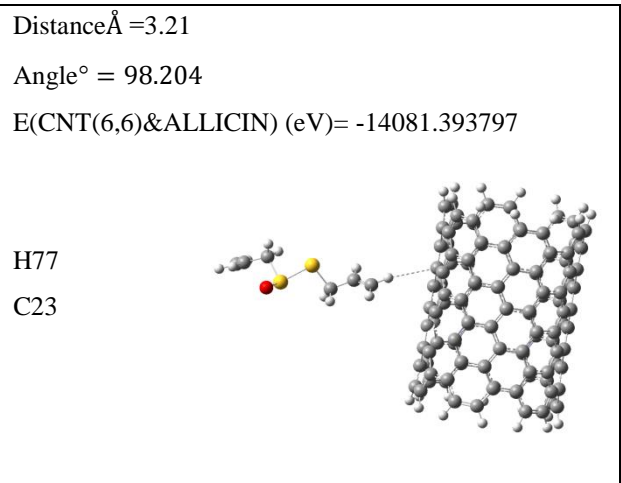


Figure 4-3: Position 1 allicin interaction of the hydrogen with carbon atoms of carbon nanotubes

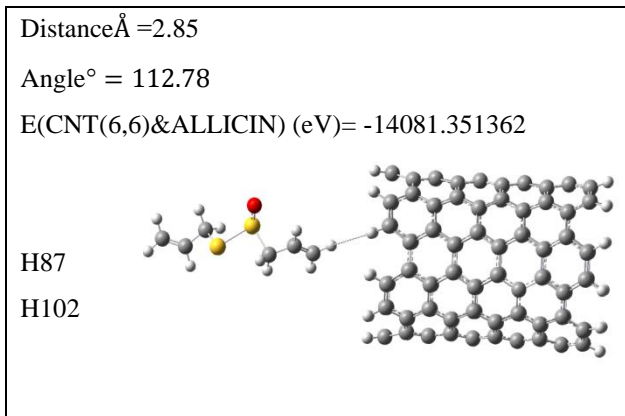


Fig 5-3: Position 2 allicin interaction of the hydrogen with hydrogen from carbon nanotubes

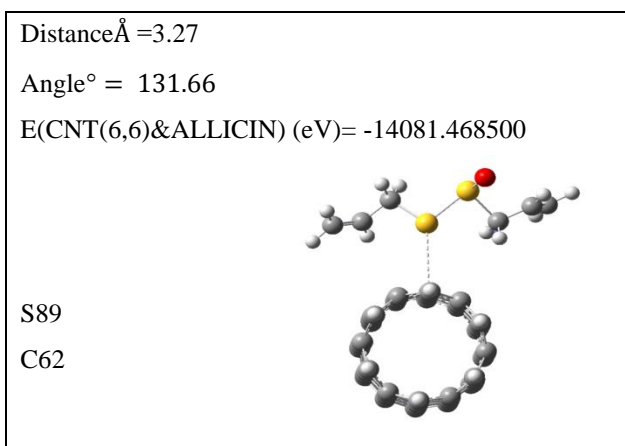


Fig 6-3: Position 3 allicin from garlic, sulfur, carbon

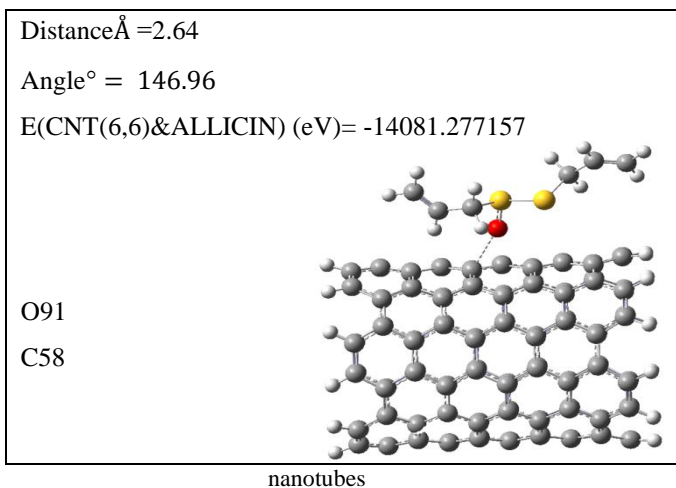


Fig 7-3: position 4 of the carbon atoms of oxygen with carbon nanotubes allicin (the 6-sided carbon rings)

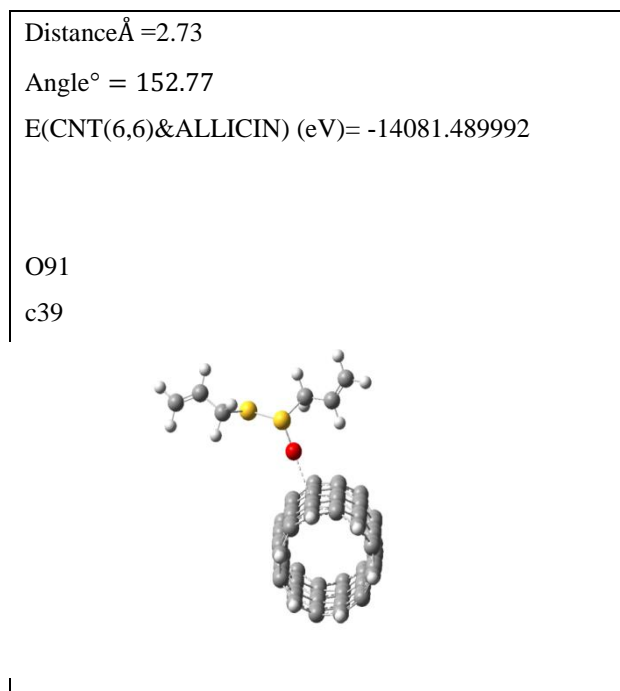


Fig 8-3: Location 5 of garlic, allicin oxygen atom with carbon nanotubes (inside the 6-sided ring)

Table 2-3: allicin and closest link between carbon nanotube uptake in 5 positions

5	4	3	2	1	Number
SO-2	SO-1	S	MID-CH2-2	CH2	position
C ₃₉	C ₅₈	C ₆₂	H ₁₀₂	C ₂₃	CNT _{6,0}
O ₉₁	O ₉₁	S ₈₉	H ₈₇	H ₇₇	Allicin
2.73	2.64	3.27	2.85	3.21	Distance (\AA)

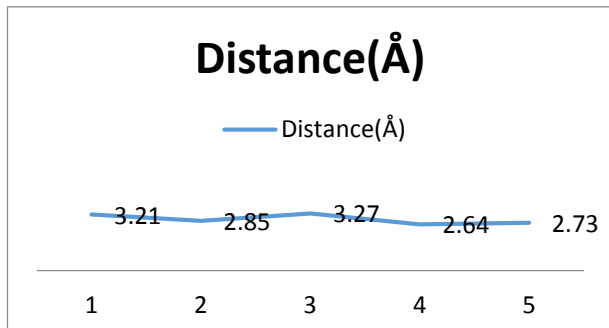
2.3 functional groups at positions absorb bond length

Table 3.3: Minimum distance of each link

Number	1	2	3	4	5
Distance (\AA)	3.21	2.85	3.27	2.64	2.73



Chart 1-3: the shortest distance between the link and allicin interaction of carbon nanotubes (0,6)



The shortest distance between functional groups absorb in position 4 (Å 81/2) and position 2 and 5 (273 Å) also seen close.

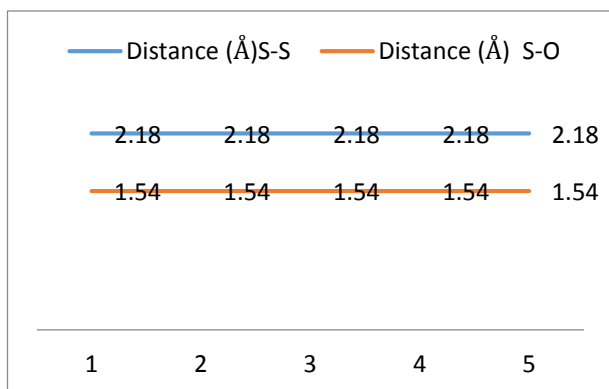
3.3 allicin molecules bond length between atoms in different positions absorption

In connection with this bond length sulfur - sulfur, oxygen and sulfur allicin molecule absorption was measured at different positions (Table4-3) remains permalink distance and direction of impact absorption during the transplant sulfur - sulfur and oxygen - no sulfur (chart 3-3)

Table 4-3: The bond oxygen atoms with oxygen and oxygenSulfur

Number	1	2	3	4	5
Distance(Å)S – S	2.18	2.18	2.18	2.18	2.18
Distance(Å)S – O	1.54	1.54	1.54	1.54	1.54

chart 3-3: oxygen atoms with oxygen and oxygen-sulfur bond length



3.4. Allicin and single-walled nanotube atoms bond angle (6,0)

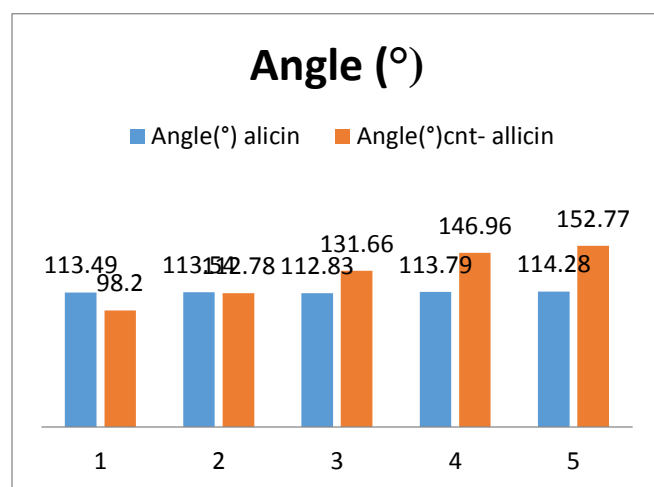
This is the angle between the atoms (oxygen - sulfur - sulfur) and angle of allicin molecules absorb allicin bond between the carbon nanotubes (6,0) measured in different situations (see Table 5-3)

Table 5-3: angle between the link and allicin atoms of carbon nanotubes (6,0)

Number	1	2	3	4	5
Angle(°) Allicin					
S189 – S190 – O191	113.490	113.54	112.83	113.77	114.28
Angle(°) CNT- Allicin	C23- H76- C75	H102- H87- C85	C62- S89- S90	C58- O91- S90	C39- O91- S90
	98.204	112.78	131.66	146.96	146.42

The angle between the atoms in position 5, the angle between the atoms allicin allicin and allicin angle between the interacting atoms and carbon nanotubes (0,6) has its maximum value.

Figure 3-3: the angle between the link and allicin atoms of carbon nanotubes (6,0)



5.3 energy

Vandvalsy allicin absorbed energy equation and density functional theory (DFT) bond length and bond angle with respect to allicin with carbon nanotubes



(6.0) is calculated. Calculated according to the following equation.

Relevance 1-3;

$$E_{ads}(eV) = E(\text{CNT}_{6,0} - \text{Allicin}) - E_{\text{CNT}_{6,0}} - E_{\text{Allicin}}$$

Allicin

$$E_{\text{CNT}_{6,0}} = -11864.644138 \text{ (eV)}$$

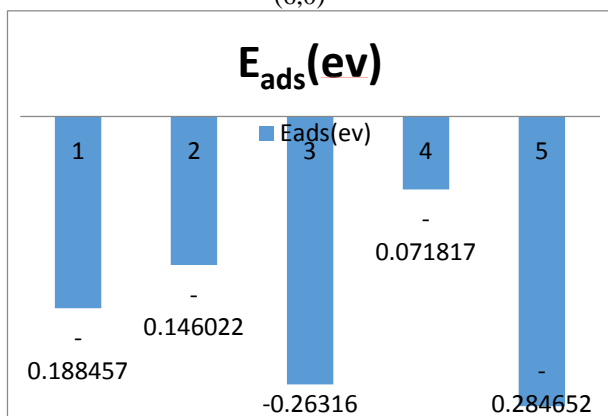
$$E_{\text{Allicin}} = -2216.561203 \text{ (eV)}$$

Table 6-3: allicin and energy between the atoms of carbon nanotubes in different situations

Number	1	2	3	4	5
Position	CH2	MID-CH2-2	S	SO-1	SO-2
$E(\text{CNT}_{6,0} - \text{Allicin}) \text{ (eV)}$	14081.393797 -	14081.351362 -	14081.4 -68500	14081.2771 -57	14081.489 -992
$E_{ads} \text{ (eV)}$	0.1884 -57	0.1460 -22	0.26316 -	0.071 -817	0.284 -652

After calculating the total energy of the interaction between single-walled carbon nanotubes allicin and (0.6) absorbed at different positions (Table 8-6) is considered the lowest and most stable interaction energy is absorbed in the position 3 and position 5 position 4 is also noteworthy unstable position (chart 4-3).

Chart 4-3: allicin energy and nanotube carbon atoms (6,0)



6.3 Calculations density of states (DOS) for the absorption of allicin by CNT (6,0)

To understand the behavior of the electronic orbitals of single-walled carbon nanotubes and find out the nature of the allicin and (6.0) that the binding density of states (DOS) for blending system SWCNT / ALLCIIN with DOS compare the individual parts.

To calculate the density of single-walled nanotubes interact with allicin (6.0) that the 5 one orientation

orientation is acceptable that the review mode DOS (Figure 8-3) Position 5 found that allicin molecules absorb DOS near the Fermi level at the level of single-walled carbon nanotubes (6.0) does not affect the sub-zero energy-Dhd.tnha very small changes can be seen that the results show that allicin molecules absorb carbon single-walled nanotubes (6.0) no effect on the distribution of electronic charge is not carbon nanotube atoms.

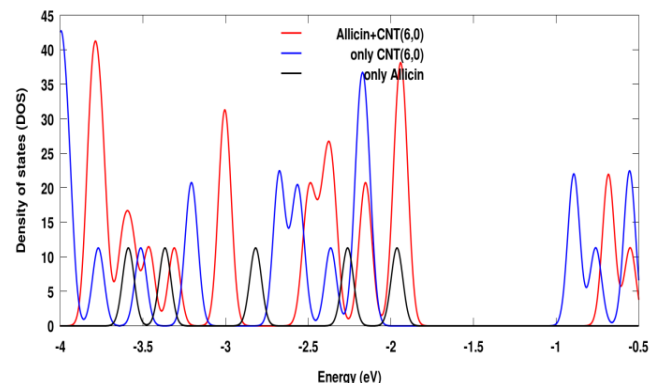


Fig9-3: Calculate the density of states (DOS) for the absorption of allicin in nanotubes (Position 5)

4. Conclusion

Viewed as allicin star turn is closer to Krbnnytk walled nanotubes (6.0) from position 5 (Figure1-4) both in terms of link length, the shortest distance and the nearest size ($2/73 \text{ \AA}$) images. Most angle than the atoms of allicin ($114/280 \text{ degrees}$) Vbrhmknsh allicin nanotubes ($152/77^\circ$) is noteworthy that position 4 is also inclined but inclined position 4 may be caused by the interaction of very high and significant energy is extremely unstable position 4 position 4 Lzamy be ignored. In terms of energy and a more sustainable energy positions 3 and 5 position 3 of the criterion (distance and angle) is unacceptable and energy can be the result of interactions is high.

The closest and most stable energy angle and position 5 (Figure1-4) is more favorable, then it is better interaction between allicin Vnanvlvlh single-walled carbon (6.0) in the fifth position and calculated approach DOS indicated that position 5 allicin has little effect on the optical properties of single-walled carbon nanotubes (6.0) does not.

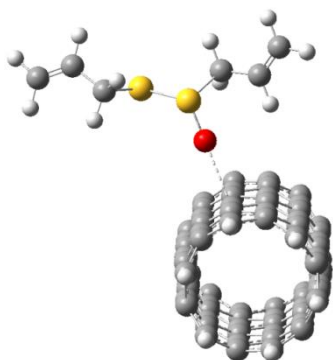


Fig1-4: allicin approach to carbon nanotubes (6,0) (Position 5)

References

- [1] S. Carnpidelli, B. Ballesteros, A. Filoramo, G. Torres, M. A. Rahman, F. Werner, V. Sgobba, C. Cioffi, Chem. Soc., (2008) 11503-11509 .
- [2] K. L. Strong, D. P. Anderson, D. P. Lafdi & Kuhn, sciencedirect, (2003) 1477-488
- [3] A. Morkoci, M. Purnera, X. Liopis, B. Perez, M. delvels, S. Alegret. Anal.Chem,(2005) 826-38
- [4] S. Chapline, M. G. Franklin, N. R. Tomblor, T. W. Cassell, H. Dati, Science, (1999) 512-13.
- [5] R. Yan, D. T. Liang, J. Tay Environ. Pollut, (2003) 399-407.
- [6] R. Hirlekar, Asian J Pharm Clin Res. Review, (2009) 17-27.
- [7] M. S. Dresselhaus, G. Dresselhaus, P. Avouris, Pure Appl. Chem, (2001).
- [8] O. Kumar, Y. K. Singh, V. Rao, R. Vijayaraghavan, Defence Science Journal, (2008) 617-625.
- [9] F. Patolsky, Y. Weizmann, I. Willner, Chem. Int. Ed., (2004) 2113.
- [10] B. Rrthos, D. Mehn, A. Demortier, N. Pierard, Y. Morciaux, G. Demortier, A. Fonseca, Sciencedirect, (2005) 321-11. Y. Anderson, D. C. Langreth, B. T. Lundqvist, Phys. Rev. Lett, (1996) 102.
- [11] L. J. Sham, M. Schlauter, Phys. Rev. B, (1985) 3553.
- [12] N. Metropolis, A. W. Rosenbluth. M. N. Rosenbluth, A. H. Teller, J. Chem. Phys., (1953) 1087-1092.
- [13] P. Hohnenberg, W. Kohn, Phys. Rev. B, (1964) 864.
- [14] G. Vignale, Phys. Rev. Lett., (1987) 2360-2363.

Elucidation of the Spin-Orbit and Relativistic Effects on the Plasmon Excitations of Silver and Gold Nanowire: Time-Dependent Density Functional Theory

N. Asadi Aghbolaghi, M. H. Khodabandeh and Z. Jamshidi*

Chemistry and Chemical Engineering Research Center of Iran, P.O. Box 14335-186, Tehran, Iran

* Corresponding author: na.jamshidi@gmail.com

Abstract: The excitation spectra of linear atomic silver and gold with various sizes have been calculated using time-dependent density functional theory. Our results show strong resonances for the pure Ag nanoparticles and strongly broadened spectra with many transitions for the pure gold structures. Moreover, the resonance energies are strongly dependent on the size of the nano wire. Gold and silver show a continuously decreasing resonance energy with increasing length. Spin orbit interaction does not have a considerable effect on orbital energy and hybridization of orbitals in Ag chain, but for gold chain, it is of particular importance. Without considering the relativity, the electronic spectra of Ag₈ and Au₈ have the same scheme.

Keywords: plasmon, noble metals, optical properties, nanowire, spin-orbit

Introduction

A large number of applications make use of the outstanding optical properties of noble-metal clusters (e.g. Ag and Au) which are due to the localized surface-plasmon resonances (SPR) that dominate the clusters' optical response in the visible and the ultraviolet spectral regions. Applications include surface-enhanced Raman spectroscopy (SERS), biomolecule sensing, labelling of biomolecules, cancer therapy, the plasmonic absorption enhancement in solar cells, and nanophotonics. The SPR depends on the size, shape, composition, and the environment of the nanoparticles [1, 2].

Gold and silver have practically the same lattice constant and are chemically similar. Ag shows a strong SPR down to very small sizes, whereas in Au the resonance gets more broadened and damped with decreasing size. The reason for the different optical of the two materials is the different position of the d states that influence the optical properties. In Ag the collective oscillation is only weakly coupled to the interband transitions from the d band, whereas in Au the coupling is strong [3].

The spin-orbit coupling also has a strong impact in the absorption spectra resonances and oscillator strengths. This is especially true for nanowires, where the effect of spin orbit is large and not substantially reduced with the chain length, in contrast to more compact gold clusters where this spin-orbit effect tends to be quenched [4].

In this work, we apply the time-evolution formalism of TDDFT. Our interest is to understand how the relativistic effects, especially the spin-orbit part, affect

the longitudinal collective plasmonic resonances in the linear silver and gold chains.

Computational methods

The calculations of ground state electronic properties were performed within the framework of density functional theory (DFT) using the statistical averaging of model orbital potential (SAOP) exchange-correlation functional in combination with an all electron triple-zeta basis set with two polarization slater type functions (TZ2P). We performed the scalar-relativistic (SR) and fully relativistic case (including the spin-orbit) using zeroth-order regular approximation (ZORA) formalism.

Results and Discussion

The excitation spectra of silver and gold nanowires are analysed in this section. Silver and gold chains show longitudinal and transverse peaks. The longitudinal peak, corresponding to the $\Sigma_m \rightarrow \Sigma_m'$ transition (along the main axis of the chain), shifts linearly to the red as the length of the system increases. The transverse peak remains at approximately constant energy for all systems studied and corresponds to $\Sigma_m \rightarrow \Pi_m$ transitions with the xy plane perpendicular to the chain.

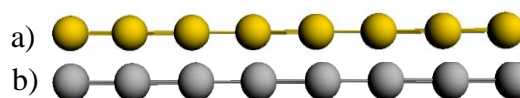


Fig1. a) Au₈ and b) Ag₈ wire

The absorption spectra of silver and gold nanowires Ag_n and Au_n (n = 8- 24) is presented in Fig.2. As the chain grows, transitions arising from d orbitals contribute to the transverse peak, which affects its

oscillator strength. It is explicit that the energy gap of a chain reduces with increasing its length.

The plasmon peak in Ag clusters spectra is more intense than Au. Relativistic effects (scalar and spin orbit parts) are the most important factor in causing above discrepancies. Contrary to silver, gold chains display a strong d- band that converges to a distinct pattern at a chain length of about twelve atoms. The relativity introduces changes in the d-s band separation. The relativistic stabilization of s orbital and relativistic destabilization of d orbitals are seen in both Ag and Au atoms.

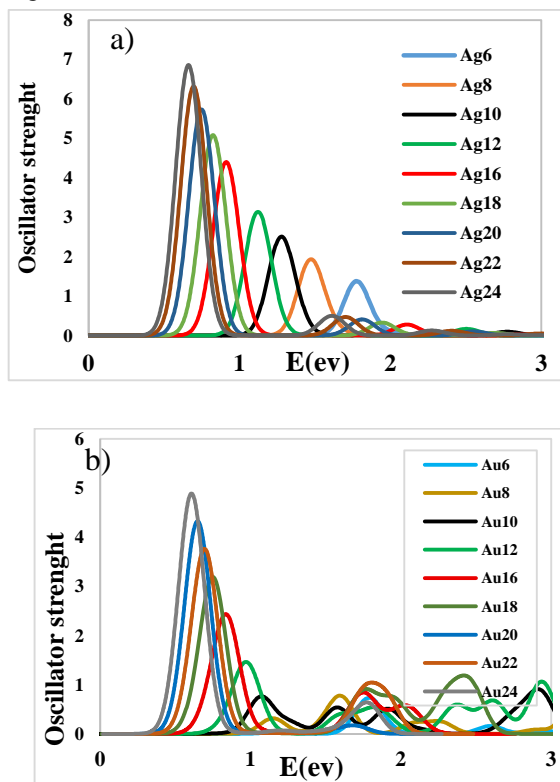


Fig.2. The absorption spectra of silver and gold nanowires a) Ag_n and b) Au_n ($n = 8-24$)

Total and partial density of state for Ag_8 and Au_8 nanowire show in the Fig.3.

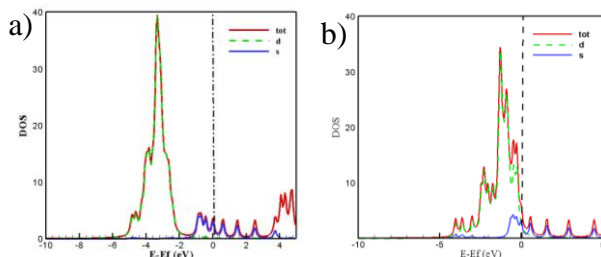


Fig. 3. The total and partial DOS of a) Ag_8 and b) Au_8 chains.

The computed absorption spectra of neutral Ag_8 and Au_8 linear chains using different formalisms are plotted in Fig. 4. These spectra is obtained by

computation of excitation energies at the non-relativistic, scalar relativistic and two-component zeroth-order regular approximation (ZORA) TD-ALDA formalism levels of theory.

In Fig4, we focused on longitudinal excitations which make the plasmonic-like behavior. The longitudinal plasmon peak in Au_8 system has lower intensity and appears at lower in energy than the Ag_8 chain. Fig. 4b clearly shows that the Au_8 spectrum has severely affected by relativistic effects and coupling matrix.

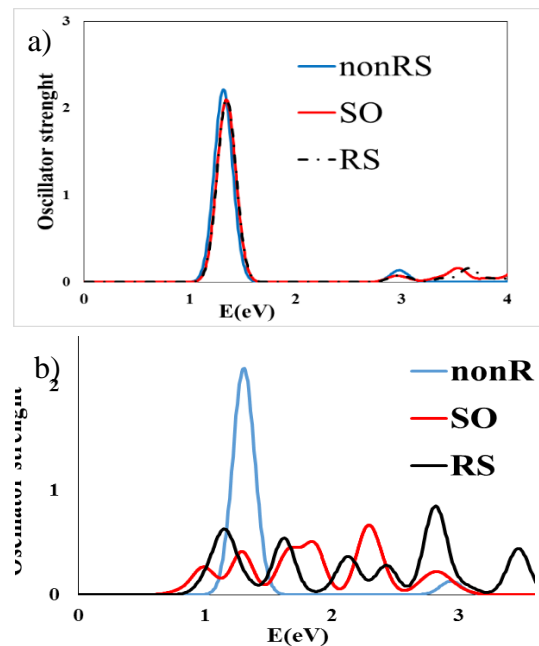


Fig.4. The computed spectra for a) Ag_8 and b) Au_8 at four levels of calculation; SR (scalar-relativistic), nonRS and full relativistic (scalar-relativistic +spin-orbit) level

The evaluation of the d contribution in excitation can help us to describe quantitatively the effect of relativity on the noble metal clusters.

Conclusions

The excitation spectra of linear chains of silver and gold have been studied for systems with different lengths. The longitudinal peak of these structures corresponds to the $\Sigma_m \rightarrow \Sigma_m'$ excitation along the chain. This peak shifts to the red as the chain length increases. It is anticipated that, without considering the relativity, the electronic spectra of Ag_8 and Au_8 have the same scheme. The results can be different after considering the relativistic terms.

References

- [1] E. B. Guidez and Ch. M. Aikens "Theoretical analysis of the optical excitation spectra of silver and gold nanowires" *Nanoscale*, 4 (2012) 4190–4198.
- [2] X. L-Lozano, H. Barron, Ch. Mottet and H. Weissker "Aspect-ratio- and size-dependent emergence of the surface-

plasmon resonance in gold nanorods – an ab initio TDDFT study” *Phys Chem Chem Phys*, 16 (2014) 1820-1823.

[3] X. L-Lozano, C. Mottet, and H. Weissker “Effect of Alloying on the Optical Properties of Ag–Au Nanoparticles” *J Phys Chem. C*, 117. (2013) 3062 – 3068.

Ab initio study on the structures and stability of Si_mC_n ($m + n \leq 4$) cationic nanoclusters

F. Mirshamsy^a, M. R. Noorbala ^{*a}, M. Namazian^a

^a Department of Chemistry, Yazd University, Yazd, Iran

*e-mail: noorbala@yazd.ac.ir

Abstract: An ab initio study of cationic nanoclusters SiC^+ , SiC_2^+ , Si_2C^+ , SiC_3^+ , Si_2C_2^+ and Si_3C^+ has been done. B3LYP method and 6-311++G** basis set have been used to optimize fully the geometries of the nanoclusters. Highest occupied molecular orbital (HOMO)–lowest unoccupied molecular orbital (LUMO) gaps and polarizability calculated using the B3LYP, G4MP2 and G4 methods. Among these methods, G4 has less systematic error, but since its calculation cpu time is higher than G4MP2, G4MP2 method has been used in this study. The most stable structures of these nanoclusters have been determined. In the more stable structures, the carbon atoms are in the majority whereas in the less stable structure the reverse is true.

Keywords: SiC cationic nanoclusters; ab initio method; Nanostructures

Introduction

In recent years, there has been a great deal of interest in theoretical and experimental study of atomic and molecular clusters. Because clusters have unusual properties, studying the geometric structure and their base electronic state are necessary. One of the properties of the clusters is the ratio of large the surface to volume and the quantum effects due to the small dimensions of the clusters. [1].

Among various types of clusters, simple metal and semiconductor clusters continue to be the most important and widely studied clusters, both experimentally and theoretically. In the area of semiconductor clusters, carbon and silicon, though belonging to the same column of the periodic table, vary significantly in their basic chemical and physical properties, so it is a technology point of view [1].

Silicon carbide has been widely studied in recent years, with several reasons. One of the reasons for this studying is the use of silicon carbide in industrial applications, for example, in electronic devices, data storage and the development of chemical reactions due to its prominent properties such as strength, high chemical resistance, high energy gap, high electrical mobility and thermal stability. The other reason is that interstellar space has been discovered [2].

Computational and method

Structural Properties of Small Cationic nanoconductors Si_mC_n with $m + n \leq 4$ including polarizability and energy levels of HOMO-LUMO were studied using B3LYP, G4MP2 and G4 methods. Among the methods, G4 has less systematic error [3], but since its calculation cpu time is higher than G4MP2, G4MP2 method has been used in this study.

Results and Discussion

In this study, all different structures including chain, linear, loop, flat and three dimensional structures are investigated and the most stable structure is specified.

The total hardness using HOMO and LUMO energy is obtained as follows:

$$\eta = \frac{1}{2} (E_{\text{HOMO}} - E_{\text{LUMO}})$$

The mean polarizability is also obtained using the following equation:

$$\alpha = \frac{1}{3} (\alpha_{xx} + \alpha_{yy} + \alpha_{zz})$$

The total hardness, polarizability, and stability are determined for each category of cationic nanoclusters:

SiC^+

Total hardness and polarizability are calculated using the G4MP2 method and the results are presented in



Table 1.

Fig. 1. SiC cationic cluster.

Table 1. Polarizability and total hardness for cationic nanoclusters SiC

Structure	η	α
SiC	0.729	41.84

SiC_2^+

Total hardness and polarizability are calculated using the G4MP2 method and the results are presented in Table 2.

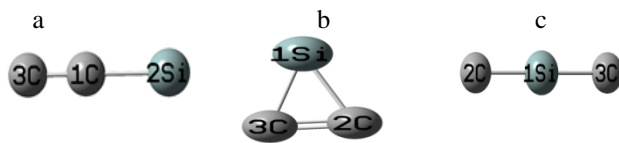


Fig. 2. SiC₂ cationic clusters.

Table 2 Polarizability and total hardness for cationic nanoclusters SiC₂

Structure	η	α
a	0.935	39.83
b	2.356	37.88
c	2.618	41.55

Among the cationic isomers of SiC₂, the most stable isomer is 2-c structure in figure 2.

SiC₃⁺

Total hardness and polarizability are calculated using the G4MP2 method and the results are presented in Table 3.

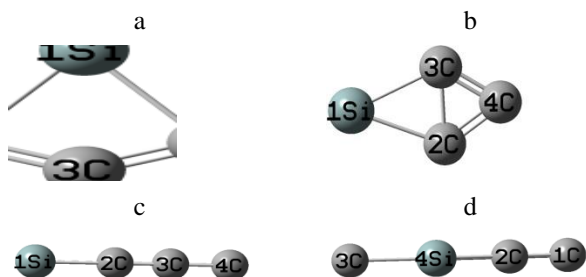


Fig. 3. SiC₃ cationic clusters.

Table 3 Polarizability and total hardness for cationic nanoclusters SiC₃

Structure	η	α
a	1.894	37.69
b	1.638	41.52
c	0.734	59.78
d	0.939	63.28

Among the cationic isomers of SiC₃, the most stable isomer is 3-d structure in figure 3.

Si₂C⁺

Total hardness and polarization are calculated using the G4MP2 method and the results are presented in Table 4.



Fig. 4. Si₂C cationic clusters.

Table 4 Polarizability and total hardness for cationic nanoclusters Si₂C

Structure	η	α
a	2.177	72.78
b	1.942	67.37

Among the cationic isomers of Si₂C, the most stable isomer is 4-a structure in figure 4.

Si₂C₂⁺

Total hardness and polarizability are calculated using the G4MP2 method and the results are presented in Table 5.

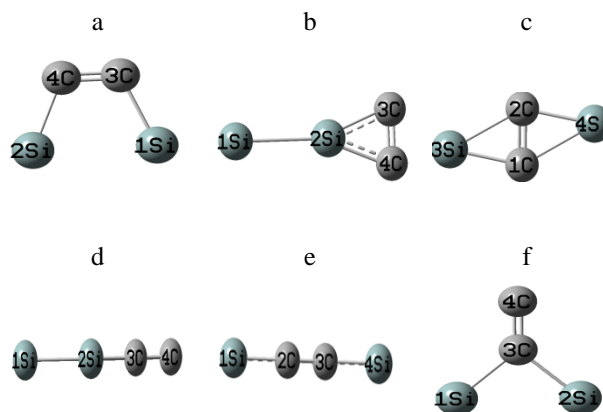


Fig. 5. Si₂C₂ cationic clusters.

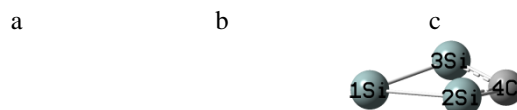
Table 5 Polarizability and total hardness for cationic nanoclusters Si₂C₂

Structure	η	α
a	1.256	67.38
b	0.859	69.79
c	1.847	63.8
d	0.784	81.98
e	0.676	95.61
f	1.3326	63.9

Among the cationic isomers of Si₂C₂, the most stable isomer is 5-d structure in figure 5.

Si₃C⁺

Total hardness and polarizability are calculated using the G4MP2 method and the results are presented in Table 6.



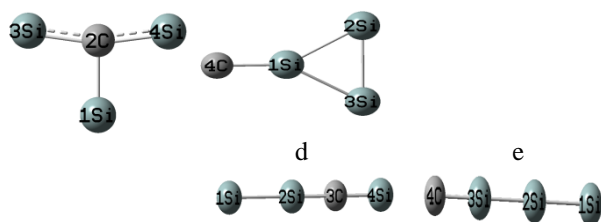


Fig. 6. Si_3C cationic clusters.

Table 6 Polarizability and total hardness for cationic nanoclusters Si_3C

Structure	η	α
a	1.487	90.1
b	1.488	174.5
c	1.053	1.053
d	0.741	113.85
e	0.679	124.85

Among the cationic isomers of Si_3C , the most stable isomer is 6-e structure in figure 6.

Conclusions

In this study, the polarizability and total hardness were calculated using the G4MP2 method on cationic nanocluster Si_mC_n with $(m+n \leq 4)$. The most stable nanocomposites are specified among the isomers.

References

- [1] P. Pradhan and A. K. Ray; "An ab initio study of the electronic and geometric structures of Si_mC_n cationic nanoclusters"; *European. Physics Journal D* **37**, (2006) 393-407.
- [2] P. S. Yadav, R. K. Yadav, S. A. Agrawal and B. K. Agrawal; "Ab initio study of the physical properties of binary Si_mC_n ($m+n \leq 4$) nanoclusters"; *Journal of Physics Condensed Matter* **18** (2006) 7085-7102.
- [3] L. A. Curtiss, P. C. Redfern and K. Raghavachari; "Gaussian-4 theory using reduced order perturbation theory"; *The Journal of Chemical Physics* **127** (2007) 124105-124114.



A theoretical study to evaluation of inhibitory activity of methyl 2-(phenethyl amino)acetate(C₆₀-I_h)[5,6]fullerene

S. Fakhraee*

Department of chemistry, Payame Noor University, Tehran, 19395-3697, Iran

*e-mail: Fakhraee@pnu.ac.ir

Abstract: The design and development of the HIV-inhibitors are one of the most remarkable achievements of molecular medicine. In the present study, a new fullerene based anti-HIV drugs substituted by a pyrrolidine type functional group with chemical name methyl 2-(phenethyl amino)acetate(C₆₀-I_h)[5,6]fullerene has been introduced to inhibit HIV enzymes. Quantum theory of atoms in molecules theory (QTAIM) has been applied to determine the electronic structure and bond natures of the designed anti-HIV drug. The electronic population analyses including the AIM atomic charges, 3D visualization of electrostatic potential energy map (ESP) and Laplacian of electron density have been applied to investigate variation of electronic charge distribution to assess the inhibition activity of designed anti-HIV drug. The results show that the functionalizing C₆₀ fullerene with methyl 2-(phenethyl amino) acetate deforms the uniform distribution of electron density on C₆₀ and increases the polarity of molecules. The more deformation of electron density causes the more capability of drug binding to the HIV enzymes. Therefore, this novel molecule is introduced as a potential of anti-HIV drugs.

Keywords: HIV-inhibitors; inhibitory activity; atoms in molecules; electronic charge distribution.

Introduction

Special characteristics of fullerenes and their derivatives make them very applicable in medical chemistry. Inhibitory activity of fullerenes derivatives against enzymes, such as glutathione transferase, glutathione reductase, and nitric oxide synthase, has been widely reported [1-4]. Nevertheless, the applications of fullerenes in biological environments are limited because of their very low solubility in polar solvents and their toxicity [5,6]. Thirty double bonds in C₆₀ structure make it possible to add particular designed functional groups to C₆₀. These compounds work better than pure fullerenes, due to their polar interactions with harmful or helpful enzymes in the body. The substituted fullerenes are soluble in water and non-toxic to inhibit viruses affecting DNA and RNA [1,7].

The C₆₀ derivatives are suggested as greatest medical potential for human immunodeficiency virus (HIV) inhibitors [8,9]. HIV-protease (HIV-PR) and HIV-reverse transcriptase (HIV-RT) enzymes are two targets for anti-HIV fullerene derivatives. The most offered mechanism for this inhibiting process is occupation of HIV enzyme cavity by C₆₀ core [10-13]. The binding of C₆₀ derivatives to enzymes changes the protein structure of the substrate binding site and results in the inhibition of the reverse transcription reaction [14-16]. Molecular modeling studies have demonstrated that C₆₀ could properly fit within the

active sites of the HIV-PR and HIV-RT core to prevent the vital activity of this enzyme [9-11]. In 2005, Mashino et al. [16] synthesized some amino acid-type C₆₀ derivatives and investigated the inhibitory activity of these compounds on HIV-RT. This was the first report concerning the effect of C₆₀ derivatives on HIV-RT. The investigation of biological properties of HIV-RT inhibitors is a broad but immature area of research yet. On the other hand, the physical and chemical properties of C₆₀ derivatives responsible for inhibiting HIV-RT has such a great biological importance that motivate us to study the electronic structure characterization of C₆₀ derivatives in inhibiting HIVenzyme. According to our previous study [17] the pyrrolidine derivatives of fullerene show the most charge displacement and inhibitory activity on enzyme respect to the malonic acid type derivatives. In the present study, we have designed a new fullerene based anti-HIV drugs substituted by pyrrolidine type functional group with chemical name methyl 2-(phenethyl amino) acetate (C₆₀-I_h)[5,6]fullerene.

The electronic structure of this anti-HIV drug has been investigated to assess its inhibitory activity, using atoms in molecules theory (AIM) [18].

Materials and method

In this study the methyl 2-(phenethyl amino) acetate functional group has been replaced on positions 5 and

BCP	$\rho(r)$	$\nabla^2\rho(r)$	$G(r)$	$V(r)$	$H(r)$
1	0.0051	0.0139	0.0027	-0.0020	0.0007
2	0.0108	0.0353	0.0072	-0.0057	0.0015
3	0.0068	0.0245	0.0050	-0.0040	0.0010
4	0.2055	-0.3629	0.0481	-0.1869	-0.1388
5	0.2425	-0.5288	0.0602	-0.2526	-0.1924
6	0.2409	-0.5195	0.0599	-0.2496	-0.1897

6 of C_{60} fullerene, between two six member rings of C_{60} as shown in Fig. 1.

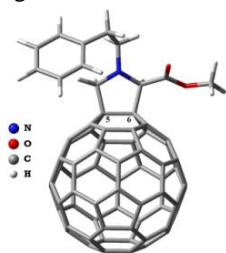


Fig 1: Chemical structures of fullerene derivatives interacting with enzymes of the HIV.

All calculations including geometry optimization, frequency and population analyses have been performed at B97D/6-311++g**[19] extensive density functional level of theory using Gaussian09 [20] package. The atoms in molecules (AIM) analysis has been applied at the same level of theory to analyze the wave function of the molecule and determine the nature of the bonds using AIM2000 [21] program. The optimized structure and AIM molecular graph of anti-HIV drug, including bond paths (BP) and bond critical points (BCPs) have been represented in Fig. 2

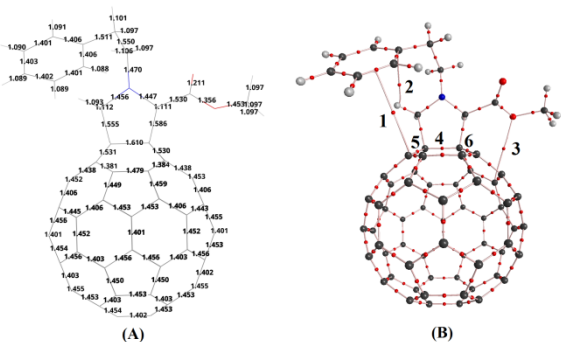


Fig. 2: (A) Optimized structure including bond lengths (B) AIM molecular graph including BPs and BCPs for anti-HIV drug.

Results and Discussion

Table 1 represents the AIM descriptors of BCPs numbered as 1-6 in Fig. 2, including the electron density, $\rho(r)$, Laplacian of electron density, $\nabla^2\rho(r)$, electronic potential energy, $V(r)$, electronic kinetic energy, $G(r)$, the total electronic energy, $H(r)$.

Table 1: AIM descriptors for the BCPs 1-6 represented in Fig. 2 for the anti-HIV drug.

As the results in table 1 show, BCPs 1-3 are associated with three $\pi\dots\pi$, $CH\dots\pi$ and $CO\dots\pi$ closed-shell interactions in drug, respectively. These interactions help to electron delocalization between C_{60} and substitution, leading to increase the polarity of the molecule. The population analysis shows dipole moment 3.698 Debye for drug molecule, while it is zero for C_{60} .

In order to compare the electronic structure of drug with non-substituted C_{60} , the AIM descriptors of common BCPs between two molecules (4-6) were compared. The AIM descriptors for C_{60} fullerene have been computed and reported in table 2.

Table 2: AIM descriptors for BCPs 4-6 in C_{60} , corresponding to the BCPs 4-6 in Fig. 2B.

BCP	$\rho(r)$	$\nabla^2\rho(r)$	$G(r)$	$V(r)$	$H(r)$
4	0.2751	-0.6273	0.0820	-0.3331	-0.2510
5	0.3002	-0.7961	0.1020	-0.3014	-0.4036
6	0.2754	-0.6720	0.0821	-0.3338	-0.2519

Comparing the Table 1 and 2 for covalent interactions corresponding to BCPs 4-6 demonstrates a decrease in $\rho(r)$, $|\nabla^2\rho(r)|$ and $|H(r)|$ values in anti-HIV drug respect to the C_{60} , due to the addition of the substitution. This changes the uniform electronic charge distribution to increase the polarity of anti-HIV drug respect to C_{60} . In order to investigate the electronic charge distribution on anti-HIV drug, the AIM atomic charges have been calculated and represented in Fig 3A by colors. The red and green colors show atoms with negative and positive electric charge, respectively. The dipole vector has been shown in Fig. 3A. As it is clear in this figure, due to the interactions corresponding to BCP 1 and 2, the terminal carbon atoms of the corresponding bond paths on C_{60} and phenyl group become extremely positive.

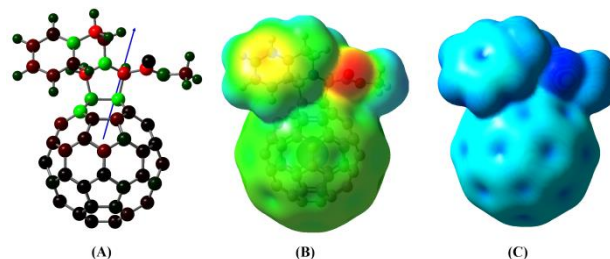


Fig 3: (A) The AIM atomic charges, (B) electrostatic potential energy map, and (C) Laplacian of electron density surface for anti-HIV-drug.

Another method to investigate the variation of the electronic charge distribution is electrostatic potential energy map (ESP) (Fig. 3B). In ESP map, the blue



surfaces, indicating the highest electrostatic potential energy, emerge from the back edges of the above electrostatic potential map on hydrogen atoms. The red surface, indicating lowest electrostatic potential energy, covers the oxygen atoms of methyl acetate. The electric charge difference between atoms of substitution leads to regions with different colors. The greater regions of molecule (C_{60} part) appear in green color demonstrates the smaller electric charge difference. On the other hand, due to the relationship between electrostatic potential and electric charge distribution, the red areas with lowest potential are characterized by a abundance of electrons and the blue areas of high potential are characterized by a relative absence of electrons.

The final method to evaluation of charge distribution is 3D visualization of Laplacian of electron density (Fig. 3C). In this figure blue surfaces have $\nabla^2\rho(r) > 0$ where the kinetic energy density dominates and a depletion of negative charge occurs. As it is observed in Fig. 3C the dark blue areas, located at oxygen atoms of substitution, have more electron density depletion respect to other regions. The regions with $\nabla^2\rho(r) < 0$, indicating the concentration of negative charge with red color are not available on the Laplacian surface for anti-HIV drug. The ESP and Laplacian of electron density surfaces correlate. Finally, the different analyses confirms a non-uniform charge distribution on the anti-HIV-drug. Addition of substitution on C_{60} deforms the balanced distribution of electron density on fullerene. The more deformation of electron density causes the more capability of drug binding to the HIV enzymes.

Conclusion

Addition of methyl 2-(phenethyl amino)acetate on fullerene C_{60} forms an effective HIV enzyme inhibitor. The AIM analysis, ESP map, Laplacian map and dipole moment of the mentioned molecule show that the substitution alters the electron density distribution respect to non-polar C_{60} and increases the ability of this drug to connect to the active sites of enzymes.

References

[1] E. Nakamura, S. Tokuyama, S. Yamago, T. Shiraki, Y. Sugiura "Biological activity of water-soluble fullerenes. structural dependence of DNA cleavage, cytotoxicity, and enzyme inhibitory activities including HIV-protease inhibition", *Bull Chem Soc Jpn.*, 69(1996), 2143-2151.
[2] N. Iwata, T. Mukai, Y. N. Yamakoshi, S. Hara, T. Yanase, M. Shoji, T. Endo, N. Miyata, "Effects of C_{60} , a fullerene, on the activities of glutathione s-transferase and glutathione-related enzymes in rodent and human livers" *Fullerene Science and Technology*, 6(1998), 213-226.

[3] T. Mashino, K. Okuda, T. Hirota, M. Hirobe, T. Nagano, M. Mochizuki, "Inhibitory effect of fullerene derivatives on glutathione reductase", *Fullerene Science and Technology*, 9(2001),191-196.
[4] D.J. Wolff, K. Mialkowski, C. F. Richardson, S. R. Wilson, " C_{60} -fullerene monomalonate adducts selectively inactivate neuronal nitric oxide synthase by uncoupling the formation of reactive oxygen intermediate from nitric oxide production", *Biochemistry*, 40(2001), 37-45.
[5] R. S. Ruoff, D. S. Tse, R. Malhotra, D. C. Lorents, "Solubility of fullerene in a variety of solvents" *J Phys Chem*, 97(1993), 3379-3383.
[6] M. Brettreich, A. Hirsch. "A highly water-soluble dendro[60]fullerene" *Tetrahedron Lett*, 39(1998), 2731-2734.
[7] S. Durdagi, C.T. Supuran, T.A. Strom, N. Doostdar, et al, "In silico drug screening approach for the design of magic bullets; a successful example with anti-HIV fullerene derivatived amino acids". *J Chem Inf Model*, 49(2009), 1139-1143.
[8] R. Sijbesma G. Srdanov, F. Wudl, J.A. Castoro, C. Wilkins, S.H. Friedman, "Synthesis of a fullerene derivative for the inhibition of HIV enzymes", *J Am Chem Soc*, 115(1993), 6510-6512.
[9] S.H. Friedman, D.L. DeCamp, R. Sijbesma, G. Srdanov, F. Wudl, G.L. Kenyon, 'Inhibition of the HIV-1 protease by fullerene derivatives: model building studies and experimental verification' *J Am Chem Soc* 115(1993), 6506-6509.
[10] F. Calvaresi, M. Zerbetto, "Baiting proteins with C_{60} ", *ACS Nano*, 4(2010), 2283-2299.
[11] S.H. Friedman, P.S. Ganapathi, Y. Rubin, G.L. Kenyon, "Optimizing the binding of fullerene inhibitors of the HIV-1 protease through predicted increases in hydrophobic desolvation", *J Med Chem*, 41(1998), 2424-2429.
[12] S. Bosi, T. D. Ros, G. Spalluto, G. alluto, J. Balzarini, M. Prato. "Synthesis and anti-HIV properties of new water-soluble bis-functionalized [60] fullerene derivatives", *Bioorg Med Chem Lett*, 13 (2003), 4437-4440.
[13] S. Bosi, T. D. Ros, G. Spalluto, M. Prato, "Fullerene derivatives: an attractive tool for biological applications", *Eur J Med Chem*, 38 (2003), 913-923
[14] K. A. Cohen, J. Hopkins, R.H. Ingraham, et al., "Characterization of the binding site for nevirapine (BI-RG-587), a nonnucleoside inhibitor of human immunodeficiency virus type-1 reverse transcriptase", *J Biol Chem*, 266 (1991), 14670-14674.
[15] S. J. Smerdon, J. Jäger, J. Wang, et al. "Structure of the binding site for nonnucleoside inhibitors of the reverse transcriptase of human immunodeficiency virus type 1" *Proc Natl Acad Sci USA*, 91(1995), 3911-3915.

Allicin on single-walled carbon nanotubes zigzag physical adsorption using density functional theory.

Mehdi Ghaffari Moghaddam

Department of Chemistry, Faculty of Science, University of Abhar, Zanjan, Iran

Email: Mehdi.Moghaddam2014@gmail.com

Abstract: Since the discovery of carbon nanotubes, extensive researches have been done to find the ability of these nanostructures in multiple sciences. One of these areas, is the physical adsorption of important molecules, especially as Allicin, including molecules that have medical applications. One of the ways how Allicin as molecules can be separated and recognized probably is the study of its interactions by carbon nanotubes. The present study tries to investigate the interaction of Allicin with carbon nanotube as zigzag using quantum chemistry calculations. For this purpose, the method of density functional theory is applied and (6,0), included 72 atoms were used. Allicin in different directions interacted with nanotube while the energy and minimum distances of adsorption were calculated. The results have shown that the (6,0) SWCNT, adsorbed Allicin from a part of sulfur, and of course with the nearest distance. However, further studies should be done in this case.

Keywords: 1- Allicin 2- CNT

Introduction

2. Introduction

1-1 Carbon nanotubes

The nature of the element carbon naturally in the solid state in the form of diamond and graphite. The third type is currently produced in the laboratory of nanotechnology are carbon nanotubes.

The different properties of carbon nanotubes to replace species that has caused a lot of material in the industry and cause massive upheaval in the material world.

2-1- Single-walled carbon nanotubes (SWNT)

Single-walled carbon nanotubes of carbon just one sheet of regular hexagons were formed. Some projections indicate that single-walled conductor or semiconductor can be. The high electrical conductivity depends on the exact geometry of the carbon atoms. Since the beginning of their work on single-walled as a one-dimensional phenomenon were called to the stage to stage this theory has evolved.

Due to the angle of torsion pages graphene, single-walled nanotubes are divided into two general categories chiral and achiral. CNT carbon nanotube is the mirror image of the original structure is the same. Single-walled carbon nanotubes-sheets of graphite which are wrapped to form a layer with nano dimensions [1].

Single-walled carbon nanotubes according to the arrangement of carbon atoms pipe section into three major categories armchair and metallic properties that are chiral and zigzag is divided semiconductor properties [2].

2-3-1- multi-walled carbon nanotubes (MWCNT)

Single-walled carbon nanotubes with additional graphene tubes surrounding a central material called multi-walled nanotubes [3]. Multi-walled carbon nanotubes are always electrically conductive [4].

Multiwalled carbon nanotubes (substitute carbon black) in color powders. One of the disadvantages of the single-walled multiwalled nanotubes is that less is strengthening because they are weak internal page links.

3-1: Zigzag Carbon Nanotubes
The chiral vector is equal to zero, one of its components, such as vector (6, 0) of the recurring units such as (Figure 1-1) are formed. The zigzag vectors are vectors in the class. It is named because of the appearance of this unit. The English name of the vectors, the zigzag.

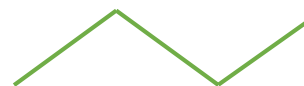


Fig 1-1: repeat unit for chiral vector (6, 0) (zigzag)

Sharp zigzag nanotubes are paramagnetic and gradually lose its magnetic properties. Highly dependent on the length - radius - temperature and strong magnetic flux.

2 - Methods of Computational Chemistry

1-2: density functional theory (DFT)

DFT theory within the framework of quantum mechanics to study the electronic structure of many-particle system. In this theory, the introduction of universal energy functional variation of the electron characteristics of the material (in this case the electron density) is obtained.

Density functional theory, in fact, a useful tool for calculating the ground state energy [5] And density distributions [6] Molecular atoms and solids, particularly for systems involving a large number of atoms or molecules is. With this theory can be accurate density and energy of the ground state electron systems under the influence of an external potential are



calculated. Moreover, by using density functional theory can be non-Hamgin systems with different interactions can be studied. Simple-most used approximation is the local density approximation LDA [7]. With this theory can be single-atom Schrödinger equation with single-atom potential correlation with the potential LDA exchange earned and calculated the density [8].

Relevance 1-2; $E = E < \rho(X, Y, Z) >$
 Relevance 2-2; $E[\rho] = T[\rho] + U[\rho] + Exc[\rho]$
 Relevance 3-2; $U = U_{ne} + U_{nn} + U_{ee}$
 Relevance 4-2; $u(r_{ij}) = 4\epsilon_{ij} \left[\left(\frac{\sigma_{ij}}{r_{ij}} \right)^{12} - \left(\frac{\sigma_{ij}}{r_{ij}} \right)^6 \right] + \frac{q_i q_j}{4\pi\epsilon_0 r_{ij}}$
 Relevance 5-2; $\sigma_{ij} = \frac{1}{2}(\sigma_{ii} + \sigma_{jj}), \epsilon = \sqrt{\epsilon_{ij}\epsilon_{ij}}$

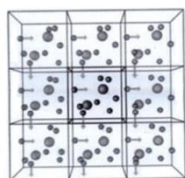


Fig 1-2: periodic boundary conditions

3. Results

```
LatticeConstant 1.00 Ang
%block LatticeVectors
20.00000000 0.00000000 0.00000000
0.00000000 25.00000000 0.00000000
0.00000000 0.00000000 20.00000000
%endblock LatticeVectors
MeshCutoff 125 Ry
%block kgrid_Monkhorst_Pack
1 0 0 0.0
0 1 0 0.0
0 0 1 0.0
%endblock kgrid_Monkhorst_Pack
xc.functional GGA # Default value
xc.authors revPBE # Default value
```

CNT (6,0) & ALLICIN

In Figure1-3, three-dimensional images of allcin can be viewed.



Fig 1-3: three-dimensional images of allcin

Single-walled carbon nanotube three-dimensional schematic in Figure 2-3 (6, 0) can be seen The ends of the nanotubes by hydrogen atoms have been linked to the cause of this could be due to repeated intermittent nanotubes The hydrogen atom cut nanotubes and the

nanotube block to prevent the recurrence of intermittent endless.

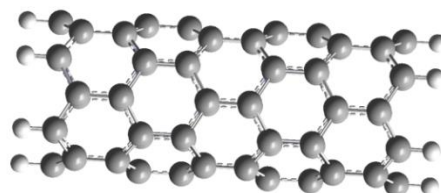
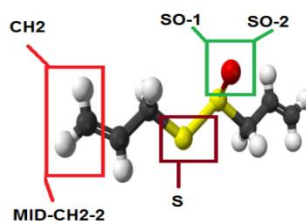


Fig 2-3: three-dimensional image of carbon nanotubes (6,0)

2.3 of allcin molecule functional groups

At the end of a three functional group single-walled carbon nanotubes for molecular absorption by allcin is used in different situations In order to separate each in various positions (Figure 3-3).



Number	1	2	3	4	5
position	CH2	MID-CH2-2	S	SO-1	SO-2

Fig 3-3: Overview of functional groups allcin

Table 3-1: Introduction position and functional groups of allcin

Allcin molecules and single-walled carbon nanotubes from 5 to (6,0) are close.

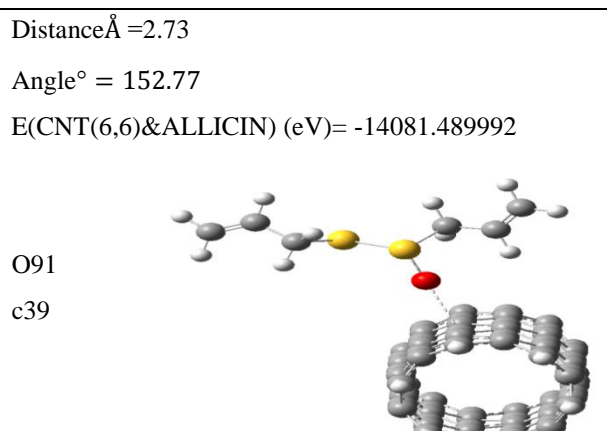
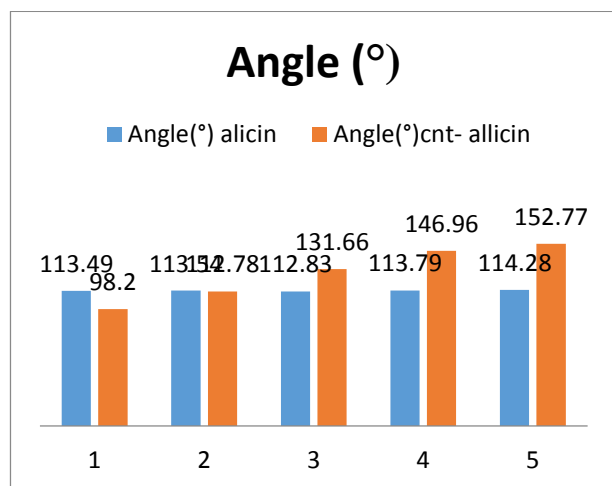


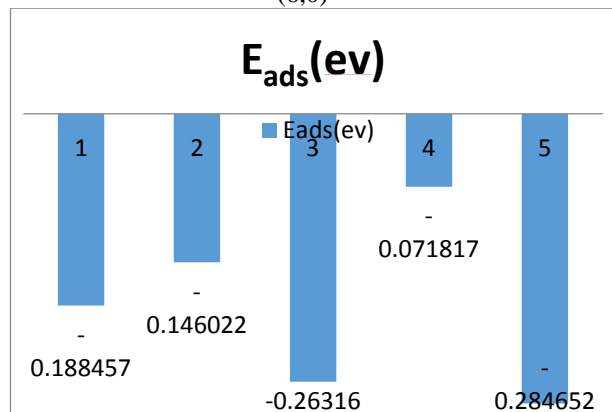
Fig4-3: Location 5 of garlic, allcin oxygen atom with carbon nanotubes (inside the 6-sided ring)

Chart 1-3: the angle between the link and allucin atoms of carbon nanotubes (6,0)



Relevance 1-3;
 $E_{ads}(eV) = E(CNT_{6,0} - Allicin) - E_{CNT_{6,0}} - E_{Allicin}$
 $E_{CNT_{6,0}} = -11864.644138 (eV)$
 $E_{Allicin} = -2216.561203 (eV)$

Chart 2-3: allucin energy and nanotube carbon atoms (6,0)



6.3 Calculations density of states (DOS) for the absorption of allucin by CNT (6,0)

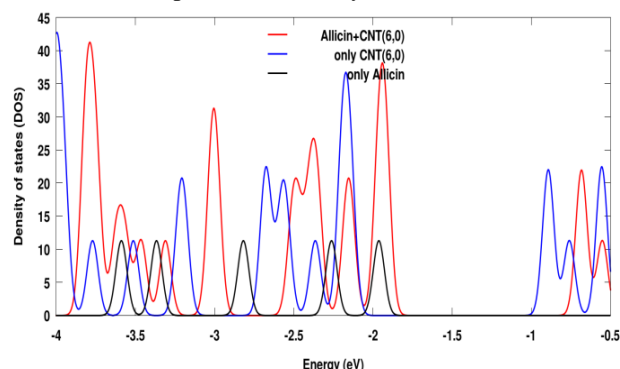


Fig4-3: Calculate the density of states (DOS) for the absorption of allucin in nanotubes (Position 5)

4 . Conclusion

Viewed as allucin star turn is closer to Krbnytk walled nanotubes (6.0) from position 5 (Figure1-4) both in terms of link length, the shortest distance and the nearest size ($2/73 \text{ \AA}$) images. Most angle than the atoms of allucin ($114/280$ degrees) Vbrhmknsh allucin nanotubes ($152/77^\circ$) is noteworthy that position 4 is also inclined but inclined position 4 may be caused by the interaction of very high and significant energy is extremely unstable position 4 position 4 Lzamy be ignored. In terms of energy and a more sustainable energy positions 3 and 5 position 3 of the criterion (distance and angle) is unacceptable and energy can be the result of interactions is high.

The closest and most stable energy angle and position 5 (Figure1-4) is more favorable, then it is better interaction between allucin Vnanvlvlh single-walled carbon (6.0) in the fifth position and calculated approach DOS indicated that position 5 allucin has little effect on the optical properties of single-walled carbon nanotubes (6.0) does not.

References list:

- [1] M. S. Dresselhaus, G. Dresselhaus, P. Avouris, Pure Appl. Chem, (2001).
- [2] O. Kumar, Y. K. Singh, V. Rao, R. Vijayaraghavan, Defence Science Journal, (2008) 617-625.
- [3] F. Patolsky, Y. Weizmann, I. Willner, Chem. Int. Ed., (2004) 2113.
- [4] B. Rrthos, D. Mehn, A. Demortier, N. Pierard, Y. Morciaux, G. Demortier, A. Fonseca, Sciencedirect, (2005) 321-331. Y.
- [5] Anderson, D. C. Langreth, B. T. Lundqvist, Phys. Rev. Lett, (1996) 102.
- [5] L. J. Sham, M. Schlauter, Phys. Rev. B, (1985) 3553.



بیستمین کنفرانس شیمی فیزیک ایران
دانشکده علوم پایه - دانشگاه اراک
۲۱-۲۴ مرداد ۱۳۹۶



20th Iranian Physical Chemistry Conference

مکانیک آماری

Statistical Mechanics

Jahn-Teller effect study of structural deformation of neutral ,anionic and cationic SO₂ molecule structural

A.Esmaeili^a

^aDepartment of Chemistry, Education, Mahallat, Iran

Esmaeili.ali42031@gmail.com

Abstract: The structural properties of SO₂ (SO₂, SO₂⁺, SO₂²⁺, SO₂⁻, SO₂²⁻) have been examined by means of B3LYP/Def2-TZVPP level of theory interpretations. The results obtained showed the expected ground state structure for compounds is linear (D_{∞h} symmetry). The distortion of the high-symmetry configuration of compounds is due to the pseudo Jahn-Teller effect (PJTE), which is the only source of instability of high-symmetry configuration in nondegenerate states. The negative curvatures of the ground state electronic configurations and the positive curvatures of the excited states of the adiabatic potential energy surfaces (APES) which resulted from the mixing of the ground Σ_g⁺ and excited Π_u states are due to the PJTE (i.e. PJTE((Σ_g⁺ + Π_u) ⊗ Π_u problem). [1]. Contrary to the usual expectation, with the decrease of the energy gaps between reference states (Δ), the PJTE stabilization energy decreases from compound 1 to compound 5.

Keywords: TD-DFT, pseudo Jahn-Teller effect, imaginary frequencies,

Introduction

The structural properties of SO₂ (SO₂, SO₂⁺, SO₂²⁺, SO₂⁻, SO₂²⁻) have been examined by means of B3LYP/Def2-TZVPP level of theory interpretations. The results obtained showed the expected ground state structure for compounds is linear (D_{∞h} symmetry). The distortion of the high-symmetry configuration of compounds is due to the pseudo Jahn-Teller effect (PJTE), which is the only source of instability of high-symmetry configuration in nondegenerate states. The distortion is due to the mixing of the ground Σ_g⁺ and excited Π_u states. [1]

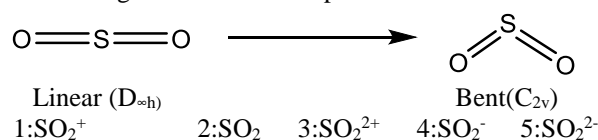
Computational Method:

The linear (D_{∞h} symmetry) and bent (C_{2v} symmetry) geometries of compounds were optimized by B3LYP with Def2-TZVPP basis set on all atoms with the Gaussian 09 package of program. The nature of the stationary points for compounds has been determined by means of the number of imaginary frequencies. Time-dependent density functional theory (TD-DFT) which is one of the most popular tools in the study of excited states of molecular systems, which is used to study the electronic configuration of the linear and bent structure of compounds.

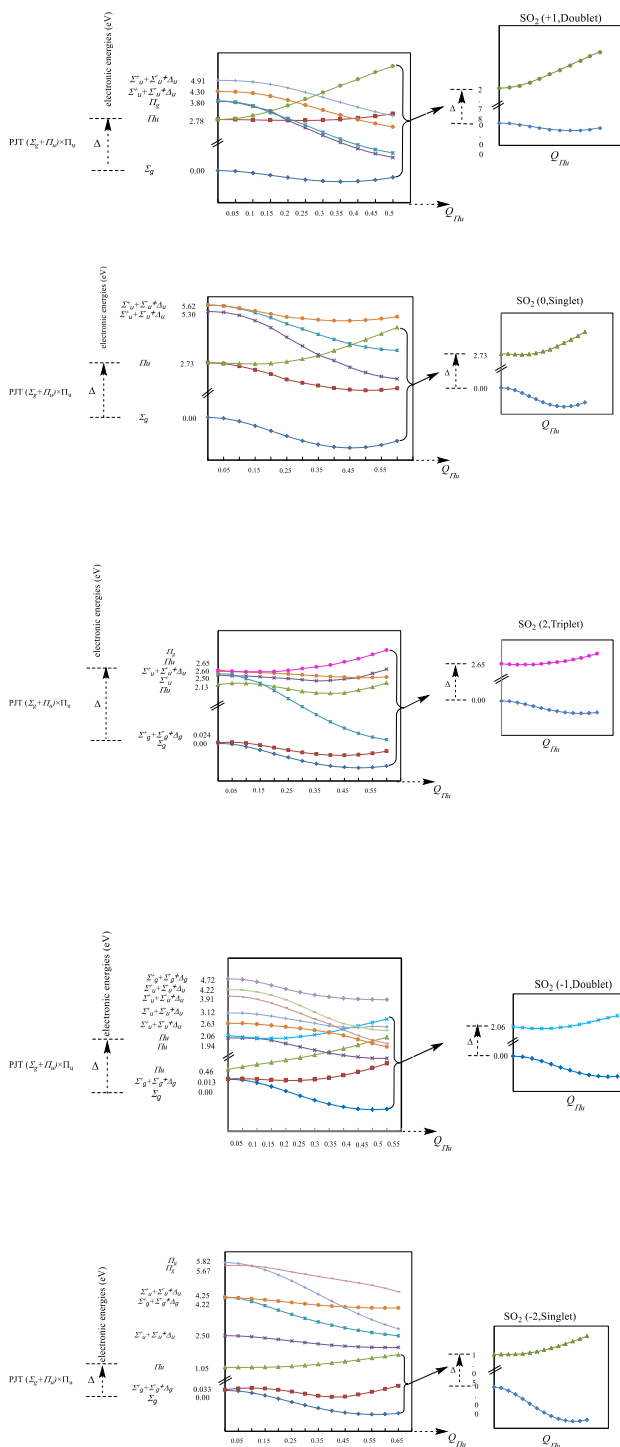
Results and Discussion

It is well-known that the only source of structural distortions of high-symmetry configurations of any molecular system is the Jahn-Teller (JT) effect (JTE), including the proper JTE for systems in electronically degenerate states, the Renner-Teller effect (RTE) for linear molecules, and pseudo JTE (PJTE) for any system [2]. Since the ground state of the molecule of

interest is Σ_g⁺ in the linear configuration, the distortion along the Π_u vibrational bending mode, according to the PJTE, may occur only as a result of the vibronic mixing with one (or more) relatively low-lying Π_u states, which provides for the stabilization of the ground state in the bent configuration. In this work, we have used TD-DFT (B3LYP/Def2-TZVPP) calculations to obtain the energy curves of the ground and excited Σ_g⁺ (with Π_u, Σ_u⁺ + Σ_u⁻ + Δ_u) states in the bending directions of compounds.



In principle, the ground state can interact with the upper Π_u state, but Figures show that it does not since the energy of this excited state decreases with increase of the flap angle rather than increasing as it would if it participated in the PJTE effect. While other interactions may play a very small role, it is clear that the interaction of the ground state and the lowest Π_u excited state in the high-symmetry configuration is the main cause for the bending observed for these compounds. [3]



The distortions in the linear ($D_{\infty h}$) configurations of compounds 1-5 are due to the PJTE, resulting from mixing of the ground Σ_g^+ and excited Π_u states [PJTE ($\Sigma_g^+ + \Pi_u$) \otimes Π_u]. The PJTE ($\Sigma_g^+ + \Pi_u$) \otimes Π_u problems are associated with the mixing of $\Psi_{\text{HOMO}}(\Sigma_g^+)$ and $\Psi_{\text{LUMO}}(\Pi_u)$ molecular orbitals. [4]

References

- [1] I. B. Bersuker, The Jahn-Teller Effect; Cambridge University Press: New York, 2006.
- [2] D. Nori-Shargh, S. N. Mousavi and J. E. Boggs, J. Phys. Chem. A, 2013, 117, 1621.
- [3] G. Kouchakzadeh, D. Nori-Shargh, J. phys. chem. chem. phys., 2015
- [4] Hakan Kayi, I. B. Bersuker and J. E. Boggs, J. Mol. Struct., 1023 (2012) 108-114.

Conclusions

The results obtained showed that the linear ($D_{\infty h}$) structures of compounds 1-5 are more stable than their corresponding bent (C_{2v}) configurations and the energy differences between the $D_{\infty h}$ and C_{2v} configurations decrease from compound 1 to compound 5.



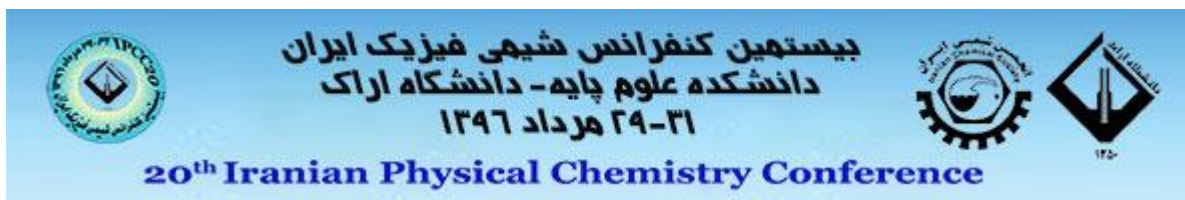
بیستمین کنفرانس شیمی فیزیک ایران
دانشکده علوم پایه - دانشگاه اراک
۳۱-۲۹ مرداد ۱۳۹۶



20th Iranian Physical Chemistry Conference

آموزش شیمی

Chemistry Education



A Closer Look to Le Châtelier's Principle Based on Microscopic Approach

Ebrahim Zarei*, Salma Ehsani

Department of Basic Science, Farhangian University, Tehran, Iran

*e.zarei@cfu.ac.ir

Abstract: In this work, in order to correct understanding of Le Châtelier's principle, it was presented a simple method for teaching of this principle as an important principle in chemistry. Le Châtelier's principle is not related to the notion that "nature favors equilibrium", but rather to the fact that "nature favors probable", that is, the dominating statistical distribution. The applied approach uses microscopic descriptors of matter (energy levels and populations) and does not require any assumptions about the nature of A or B (as two parts of internal equilibrium of a system) or the types of processes that interconvert A and B.

Keywords: *Le Châtelier's Principle; Microscopic Approach; Energy Levels; populations; Distribution*

Introduction

Le Châtelier's principle (LCP) is a ubiquitous "rule-of-thumb" in chemistry and is regularly included in chemistry courses. The principle states that: "A system at equilibrium, when subjected to a disturbance, responds in a way that tends to minimize the effect of the disturbance" [1]. LCP represents a qualitative summary of a wide range of observations, but does not have well-defined terms of reference. This allows LCP to be applied to a variety of fields beyond chemistry itself: biology, physics, geology, and even economics [2]. In economics for example, LCP has been related to the law of supply and demand. In a simplified picture, when supply of a certain commodity equals demand, the price of that commodity is stable. When the supply decreases, the economic system (market) tries to counter the effect of reduced supply by increasing the price of commodity and thus reducing the demand. This phenomenon is well known from everyday experience and may contribute to students' misconception that systems encountered in the world abide by the "principle of stability" [2].

The notion that equilibrium states or situations are favored is not true as Planck has illustrated in a philosophical statement [3, 4]: "The idea that nature has a certain interest to preserve an equilibrium state at all cost is wrong. Nature is essentially indifferent; in certain cases it reacts in one sense, but in other cases in the opposite sense." The connection between the LCP, "principle of stability" and chemical equilibrium is interesting and may stimulate class discussion. Most standard teaching materials only describe the applications of LCP, but not its physical rationale. There have been previous reports relating LCP to Gibbs free energy.

However, such descriptions either use calculus and are hence technically more difficult [5] or involve the reaction coordinate [6], which enhances another misconception that LCP is relevant only to chemical reactions. We aim to present a more general approach

that is applicable to processes involving both physical and chemical transformations. Also, our approach does not

require the constraining assumption about the fixed amount of substance being present in the system, nor the use of reaction coordinate concept.

Discussion

LCP predicts how the system will respond to external perturbation. This response is spontaneous so we shall first comment on "spontaneity" by using microscopic descriptors of matter [7]. The microscopic descriptors have been used previously for describing entropy [8], which plays a very important part in understanding of LCP. The processes of chemical interest often take place at constant temperature, T , and pressure, p , or at constant T and volume, V . The direction of such processes is governed by changes in thermodynamic potentials: Gibbs free energy, G (for processes at constant p and T), and Helmholtz free energy, A (for processes at constant V and T). These potentials must be negative in order for the respective processes to be spontaneous [9]. The maximum quantities of energy that can be exchanged as work between system and surroundings during isobaric and isochoric processes are $\Delta G - p\Delta V$ and ΔA , respectively [9]. We shall first visualize ΔG and ΔA changes using microscopic descriptors and subsequently show how LCP arises out of these conditions.

Let us consider a homogenous, single-component system

that, in its initial state is not in equilibrium. The system will evolve towards equilibrium or final state (Fig. 1) and during this evolution its internal energy changes. The internal energy (U) change is equivalent on the microscopic level to changes in both energy levels (ϵ_i) and their populations (n_i) because $U = E = \sum_i n_i \epsilon_i$ [7]. Although in reality the changes in populations and



levels take place simultaneously, we can visualize them as a two-step process: first the change in energy levels, followed by redistribution of particles among the new set of levels (so as to maximize the entropy of the final state). The change in energy levels represents the energy exchanged as work and corresponds to $\Delta G - p\Delta V$ or ΔA , depending on whether the process is isobaric or isochoric. The change in level populations corresponds to energy exchanged as heat, which is described by $T\Delta S$ term (Fig. 1).

It has been explained the microscopic nature of thermodynamic potentials μ (G and A) and this brings us to the rationalization of LCP itself. Consider the system in internal equilibrium that has two parts A and B and is described by equation $A \rightleftharpoons B$. The parts may comprise different chemical species, different aggregation phases, and so forth. For each part, we can define its thermodynamic potential as μ_A and μ_B . At equilibrium $\mu_A = \mu_B$ so that $\mu = \mu_B - \mu_A = 0$. When the system is perturbed or shifted from its equilibrium state by external influences, for example, changes in temperature, pressure, volume, amount of substance, and so forth the energy levels or populations in both A and B will change (Fig.s 2 and 3). This leads inevitably to changes in the corresponding μ_A and μ_B . However, as we have stated above, A and B have different energy levels, internal structures, and initial level populations, so the changes in chemical potentials will not be equal, that is, $\Delta\mu_A \neq \Delta\mu_B$. Parts A and B must have different levels and populations, because they correspond to different structures, for example, reactants–products, liquid–gas phases, and so forth. How does this observation lead to LCP? As the result of a perturbation we get $\mu_A > \mu_B$ or $\mu_A < \mu_B$. In other words we have increased the free energy of one side of the equilibrium relative to the other. The change in μ for the forward process $A \rightarrow B$ is $\Delta\mu = \Delta\mu_B - \Delta\mu_A$ and for the reverse process $A \leftarrow B$ is $\Delta\mu = \Delta\mu_A - \Delta\mu_B$. If the perturbation makes $\mu_A > \mu_B$ then the forward reaction would proceed spontaneously because only then will $\Delta\mu < 0$. The overall rate of the forward process will increase thus moving the equilibrium to the right. Conversely, the increase in μ_B will favor the reverse process $A \leftarrow B$ and move equilibrium to the left. The relative increase in μ at one side of the equilibrium shifts the equilibrium position to the opposite side. This conclusion is equivalent to LCP statement and is due to the requirement $\Delta\mu < 0$. The $\Delta\mu < 0$ requirement itself is due to the probabilistic character of natural processes, that is, to the tendency of systems to increase total entropy (system and surroundings) as discussed in detail in ref 1.

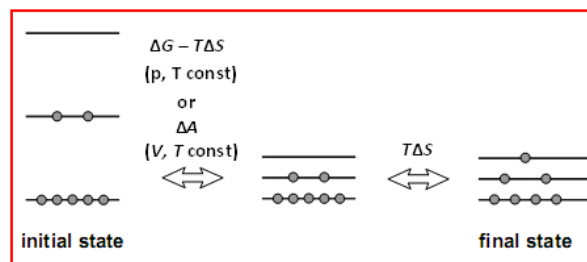


Fig. 1: Microscopic visualization of free energies. The energy level diagram shows what happens in the system when its initial state is perturbed by outside influence. The internal energy of the system changes as it evolves from initial towards final state via an intermediate state. The states involved in each step are linked by double tipped arrows while corresponding changes in thermodynamic functions are listed above.

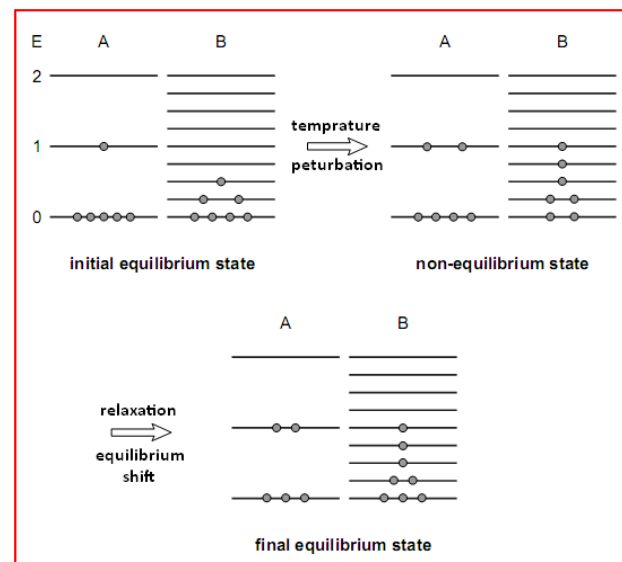


Fig. 2: Change in the equilibrium system ($A \rightleftharpoons B$) containing 6A and 7B species (e.g., ions, atoms) upon perturbation in the form of temperature increase. Increase in temperature leads to population of higher levels in non-equilibrium state. The evolution of the system in time, from initial equilibrium state (before the perturbation) towards the final equilibrium state is shown. After the temperature perturbation, the equilibrium shifts to the right since one A is converted into B.

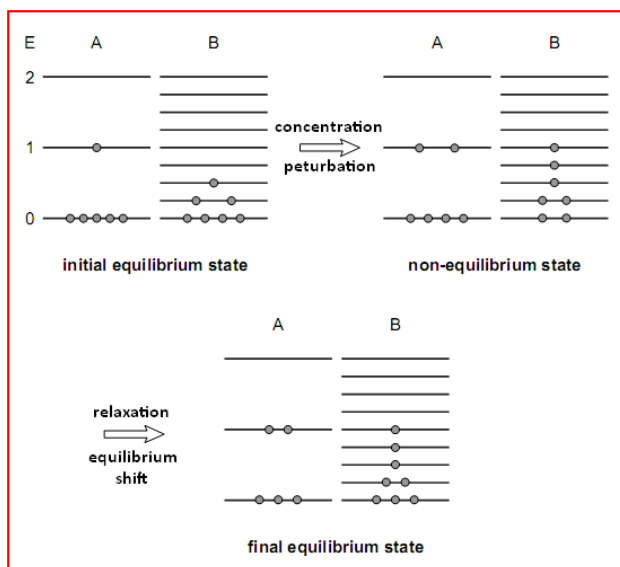


Fig. 3: Change in the equilibrium system ($A \rightleftharpoons B$) containing 6A and 6B species initially, which is perturbed by adding 2A species. As more A is added there are more species to populate energy levels. The evolution of the system from initial towards final equilibrium state is described through energy levels and populations. After the addition of A, the equilibrium state is reestablished by rearranging the system to counter the perturbation (i.e., one A is converted into B, in accordance with LCP).

Conclusions

It has been presented a simple approach that “demystifies” LCP and stimulates students to think about fundamental physical background behind the well-known principles. LCP is not related to the notion that “nature favors equilibrium”, but rather to the fact that “nature favors probable”, that is, the dominating statistical distribution. Our approach uses microscopic descriptors of matter (energy levels and populations) and does not require any assumptions about the nature of A or B or the types of processes that interconvert A and B.

References

- [1] P.W. Atkins, J. de Paula, Atkins' Physical Chemistry, 2010, 9th Ed., Oxford University Press: Oxford, 221-223.
- [2] V.B.E. Thomsen, Le Châtelier's Principle in the Sciences, *J. Chem. Educ.* 77 (2000) 173-176.

[3] J.de Heer, Le Châtelier, Scientific Principle, or "Sacred Cow"?, *J. Chem. Educ.* 35 (1958) 133-136.

[4] M. Planck, Das Prinzip von Le Chatelier und Braun, *Ann. Physik* 19 (1934) 759-768.

[5] M. Deumie, B. Bouilil, O. Henri-Rousseau, On the minimum of the Gibbs Free Energy Involved in Chemical Equilibrium, *J. Chem. Educ.* 64 (1987) 201-204.

[6] K.A. Dill, S. Bromberg, Molecular Driving Forces, 2003, Garland Science: New York, 243.

[7] I. Novak, The Microscopic Statement of the Second Law of Thermodynamics, *J. Chem. Educ.* 80 (2003) 1428-1431.

[8] F.L. Lambert, Entropy is Simple, Qualitatively, *J. Chem. Educ.* 79 (2002) 1241-1246.

[9] A.H. Carter, Classical and Statistical Thermodynamics, 2001, Prentice-Hall: Upper Saddle River, NJ, 134.



A Simple Method for Education of Void Space in Solids

Ebrahim Zarei*, Salma Ehsani

Department of Basic Science, Farhangian University, Tehran, Iran

*e.zarei@cfu.ac.ir

Abstract: The atomic-level structure of crystalline solids can be difficult to comprehend. In this field, one of the subjects that students have basic misconception is void space in solids. In this work, a brief history of void space of solids has been studied. Also, a low cost strategy has been presented for reducing the misconceptions related to void space in solids using simple materials such as small glass beads and water. The idea of bridging analogies has been applied in the physics education community to help students for easy understanding of some concepts. For this purpose, in this study, this approach has been used for better comprehension of students of the void space concept in solids.

Keywords: *Crystalline Solids; Void Space; Misconception; Education*

Introduction

Pick up any freshman chemistry text, turn to the section on the solid state, and there you will find a description of the various ways that atoms, modelled as solid spheres, can pack together. (You will probably also find a picture of stacked oranges). Read further and you will discover that the most efficient way to pack atoms is in the face-centered cubic (FCC) arrangement, which yields a 74% packing efficiency (or, conversely, 26% void space). What you will not find, and may not know, is that mathematicians have only recently been able to prove that the FCC is indeed the densest possible arrangement of spherical objects. The so-called Kepler conjecture, first put forth by Johannes Kepler in the 1600s, troubled mathematicians for several hundred years until a satisfactory proof was offered in 1998 [1]. Until its solution the Kepler conjecture was considered one of the last great unsolved problems in mathematics, comparable in significance to, for example, Fermat's last theorem. It was so significant that an entire book has been devoted to the problem and its solution [2].

Though all of this may be of greater interest to mathematicians than to chemists, it does show that problems of packing efficiency are not as simple as they might at first appear. The reader may wonder why the results of the demonstration presented here do not come closer to the 26% void space predicted for cubic closest packing. While some of the discrepancy may be attributed to experimental error and edge effects, it is also likely that the beads do not pack in a perfectly ordered arrangement. Physicists, as it turns out, have a name for this disordered packing, which they call random close packing or RCP [3]. It has a 64% packing efficiency (36% void space), which agrees well with values obtained in this experiment. This depends of course on how the beads are added to the container. As physicist David Weitz [4] notes, a jar of packed marbles may be transitioned from RCP to FCC by shaking the jar so that the marbles "jump up slightly and rearrange themselves". Instructors who are interested in a

materials science application for this demonstration may find it interesting to explore with their students how the quantity of void space changes when the container is shaken to order the beads. Researchers who are interested in packing problems do not limit their attention to spherical objects. One recent study [5], widely reported in the popular science media [6], concerned the packing of ellipsoids, in particular M&M candies. It turns out that ellipsoids have a much higher RCP efficiency than spheres (about 72%), which may be useful information if you are ever trying to win a contest by guessing the number of M&Ms in a candy jar. All jokes aside, the point is that questions about how solid particles pack together is actually an active and complex area of research with applications in a variety of disciplines.

Materials

Any small spherical objects can be used, although the diameter should not exceed 6 mm or the results become less reliable. If larger spheres are desired, the container volume should be scaled up accordingly, remembering that sphere volume increases as the radius cubed. Good results are obtained with small borosilicate glass beads (0.2–6 mm) of the type used for packing chromatography columns [2]. Less expensive options include metal bbs, shotgun shot, or beads from craft stores. (Note however that bbs tend to rust.) As previously noted, sand can also be used and gives reasonably good results, though of course the particles are neither perfectly spherical nor uniform. If you are going to purchase sand rather than just visiting the local playground, 20–40 mesh sea sand seems to work best.

Results and Discussion

The Demonstration Method

This simple demonstration is used to illustrate the substantial quantity of empty space that remains when solid spheres of any size are packed together. The demonstration is straightforward. A beaker or large



(250-mL) graduated cylinder is filled to an arbitrary mark (100-mL mark is simplest) with small glass beads or metal shot of uniform diameter (2–5 mm). A second container is filled with beads of much smaller diameter, perhaps 500 μm or less. Sand can also be used. For the greatest effect, it is best if the particles in the second beaker are so small as to make the sample appear nearly uniform. Students are then queried as to which sample contains the greatest percentage of empty space. In a class of beginning students nearly all will choose the sample with the larger particles.

There are of course many possible variations to the demonstration presented here. It can be structured as an inquiry activity for students. More than two samples can be used, providing additional experimental data and a greater sense of the continuum from macroscopic to microscopic. For greater precision, the quantity of water added can be determined from its mass and density. However, there are many sources of error, including bubbles of air that adhere to the solids and the “edge effect” that becomes more pronounced when larger particles are used. Thus, time spent improving measurement precision does not necessarily lead to more accurate results and may in fact distract from the “big idea”; namely, void space is independent of particle size.

The Conceptual Challenge for Students

For students, the very concept of void space in a solid can be difficult to grasp. Most students, when asked, would never guess that there can be as much as 48% empty space between the atoms in a crystalline solid. And who can blame them? Nothing about the visual appearance of a solid gives any clues to its atomic-level structure. There are a number of well-documented misconceptions in this area. Johnson [7] found that “The idea of ‘nothing’ between the particles ... appears to cause considerable difficulties for students. Many seem to prefer to think of ‘something’, usually referred to as ‘air’, as being between the particles.” Nussbaum [8], in a review of existing literature on student conceptions of the gaseous state, found that even students who recognized that gases were particulate in nature still resisted the notion that there was empty space between the particles. Most research, however, has centered on student conceptions of the liquid or gaseous state, with little or no attention given to the solid state. Perhaps this is because there are numerous demonstrations and activities to challenge misconceptions about gases and liquids. The compressibility of gases provides some indirect evidence for the existence of empty space between the molecules or atoms. The fact that salt dissolves in water without noticeably increasing its volume suggests that there is empty space between individual water molecules. There are, unfortunately, no compelling demonstrations or activities that provide convincing evidence for the void space in a solid.

Since this void space cannot be observed directly or indirectly, instructional approaches usually rely on molecular models or graphics in which atoms are analogized with macroscopic spherical objects. Unfortunately, existing research has shown that students do not always make the desired connection between the target concept and the analog [9, 10]. Students may believe that a model of a unit cell constructed from model kits or oranges contains 30% void space, but will not necessarily extend this result to the atomic scale.

Bridging Analogies

The idea of bridging analogies has been used in the physics education community to help students make connections between an easily observed “anchoring” phenomenon and an abstract “target” phenomenon or concept. This has proved to be an especially useful approach in situations, such as the one discussed here, in which the similarities between the target concept and the analog are not immediately apparent to the novice learner. In one example from a widely cited article by Clement [11], it is reported that students will accept the idea that a spring pushes up on a book resting on top of it, but do not agree that a book resting on a table experiences the same upward force. The target concept, in this case, is Newton’s third law, or the principle of equal and opposite forces. To help students more clearly make the connection between the target concept and the analog, Clement proposes the use of *bridging analogies*, a series of analogies that successively approximate the target concept. In Clement’s example one intermediate analogy is of a bent, “springy” board. The springy board shares properties of both the bouncy spring and the rigid table, helping students to ultimately see the similarity between the table and the spring. Research conducted with beginning students found that the experimental group (students exposed to the bridging analogies) had larger post test gains than the control group. In the example presented here, the beaker filled with the small glass beads or sand is the bridge that can help students grasp the idea that even substances that appear uniformly solid can still contain large quantities of void space.

Instructional Applications

There are many places in the introductory curriculum where this demonstration might be used. In introductory or high school classes it provides a way to address deep-seated misconceptions about the structure of matter at the atomic scale. In a majors-level course it can be used in conjunction with a unit on the properties of solids. Students in these classes often calculate packing efficiency using the atomic radius, crystal structure, and dimensions of a unit cell; this demonstration provides a visual way to comprehend what they otherwise simply calculate. The demonstration can also be applied to discussions about density. When students in



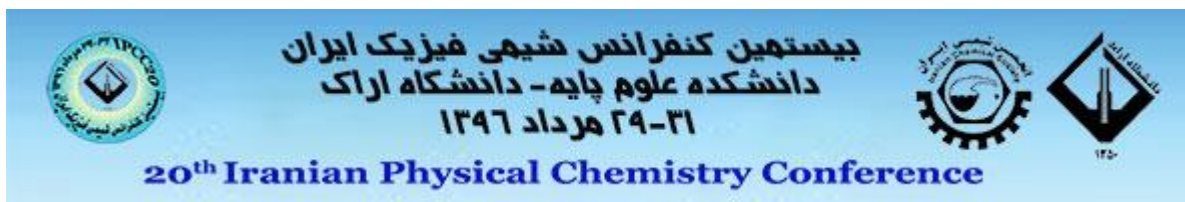
introductory classes are asked to devise a method for determining the density of a crystalline solid (e.g. NaCl) many choose to pour the solid into a graduated cylinder and incorrectly assume that they are measuring the volume of their sample. Even when they do recognize that some volume is unaccounted for, they usually assume that the error is a small one. The above demonstration is an excellent way to dispel that notion. In an interdisciplinary science class with a geology or earth science focus, the demonstration might be relevant to a discussion about soil percolation and drainage. Lastly, there is growing interest in the inclusion of materials science concepts in the general chemistry curriculum. The ACS [12] has published a companion text on materials science that can be used as part of a general chemistry curriculum and numerous articles in this Journal [13] have offered additional resources for instructors who wish to incorporate materials science concepts into their curricula. This demonstration would fit well within any of these instructional programs.

Conclusions

In this study, a brief history of void space of crystalline solids has been presented and students's misconceptions about this subject have been mentioned. In order to reducing these misconceptions, based on the idea of bridging analogies, a simple demonstration has been applied using simple and available substances such as small glass beads and water.

References

- [1] N.J.A. Sloane, *Nature*, 395 (1998) 436-436.
- [2] G. Szpiro, *Kepler's Conjecture: How Some of the Greatest Minds in History Helped Solve One of the Oldest Math Problems in the World*, 2003, John Wiley: Hoboken, NY.
- [3] S. Torquato, T.M. Truskett, P.G. DeBenedetti, *Phys. Rev. Lett.* 84 (2000) 2064-2067.
- [4] D. Weitz, *Science*, 303 (2004) 968-969.
- [5] A. Donev, I. Cisse, D. Sachs, E.A. Variano, F.H. Stillinger, R. Connelly, S. Torquato,; P.M. Chaiken, *Science*, 303 (2004) 990-993.
- [6] P. Weiss, *Sci. News*, 165 (2004) 102-102.
- [7] P. Johnson, *Int. J. Sci. Ed.* 20 (1998) 393-412.
- [8] J. Nussbaum, *The Particulate Nature of Matter in the Gaseous Phase*. In *Children's Ideas in Science*, 1985, R. Driver, E. Guesne, A. Tiberghien, Eds., Open University Press: Philadelphia, 124-144.
- [9] K.S. Taber, *Phys. Ed.* 36 (2001) 222-226.
- [10] A.G. Harrison, D.F. Treagust, *Sci. Ed.* 80 (1996) 509-534.
- [11] J. Clement, *J. Res. Sci. Teach.* 30 (1993) 1241-1257.
- [12] A.B. Ellis, M.J. Geselbracht, B.J. Johnson, G.C. Lisensky, W.R. Robinson, *Teaching General Chemistry: A Materials Science Companion*, 1993, American Chemical Society Books: Washington, DC.
- [13] C.G. Widstrand, K.J. Nordell, A.B. Ellis, *J. Chem. Educ.* 78 (2001) 1044-1046.



Modeling Trial for chemistry tenth of high school base on green chemistry from the experts and related teachers

Tahereh Haghi

Department of Sherafat University Farhangian Tehran Iran

tara_haghi@yahoo.com

Abstract: This study aimed to provide a good model for the design and production experiment of basic chemistry based on the principles of green chemistry. This research is about the relationship between highschool chemistry and green chemistry. The titles of 10th book chemistry, in collaboration with chemistry teachers who taught chemistry last year. Then, based on the results of the surveys and the titles listed for the chemistry book, experiments were designed based on the principles of green chemistry. The method of research was to determine the relationship between the three chapters of the chemistry curriculum of the tenth grade chemistry school with green chemistry. And through an interview with chemistry professors, the appropriate method for preparing and setting up the Green Lab Chemistry Lab was reviewed.

Keywords: *Green Chemistry, Green Solvents, Sustainable Development, Reusability, Green Catalysts, Twelve Principles*

Introduction

Green Chemistry is a set of principles and methods aimed at reducing the use and production of hazardous substances in chemical processes consistent with the three objectives of the sustainable environment, sustainable economy and sustainable society.

Sustainable development means meeting the needs of the present generation without compromising the ability of future generations to meet their needs. Green chemistry is one of the most basic and powerful tools used in sustainability. Green chemistry training can provide the knowledge and knowledge necessary to develop the technology needed to achieve sustainable globalization.

Green chemistry is a complementary and modifying chemistry course that can cover all the basic concepts of chemistry including stoichiometry, acids and bases, enthalpy, reaction speed, etc. In the 1990s, new science was introduced in chemistry, persistent chemistry and green chemistry in chemistry, all of which have a meaning, and it is green chemistry.

Materials and method

Collection of basic information related to the subject of research from the documents, books, magazines and articles of specialized sites and scan Preparation of a questionnaire on the conformity of the chemistry book with the twelve principles of green chemistry

Interviews and interviews with relevant professors and teachers

Examination of experiments and information in science

textbooks, basic chemistry and basic sciences laboratory and the design of experiments based on green chemistry in line with the information in the books. Summarize the collected materials, conclusions and suggestions.

The research method will be combined with a library-documentary and laboratory methodology. The method of data collection is the use of books, journals, articles and specialized websites, interviews with professors and chemistry teachers and the preparation of questionnaires.

A tool for collecting information from study fingers and for academic teachers to consider the appropriate design patterns for testing Conclusion and gathering of information obtained.

Ultimately, the ultimate goal of green chemistry is to make the quality of life on a planet cleaner and safer. In this research, the study of green chemistry, its goals and principles, its future prospects, and the modeling of Green Luminosity experiments for the tenth grade elementary school chemistry book have been studied.

Green chemistry is an effective means of fostering students' interest in chemistry and materials. For an ideal society, and in keeping with the science of the day, we need new ideas in education, such as green chemistry. Green chemistry training can provide a new attitude to life easier and safer, by which one can enhance the skills of thinking and problem solving and exploration in learners.

Principles of Green Chemistry

Green chemistry is usually presented as a set of twelve principles proposed by Anastass and Warner. These principles include guidelines for professional chemists when working with new chemical compounds, synthesis of materials and new technological processes. These principles include:

Preventing the production of vain products

It is better to prevent the production of waste and toxic waste, before it is produced to harm harmful wastes or to clean the environment.

Atomic economy, increasing atomic efficiency

The atomic economy means that the design of chemical reactions is in such a way that a greater percentage of the atoms in the reactants enter the structure of the final products. This also helps to increase the chemical reaction efficiency.

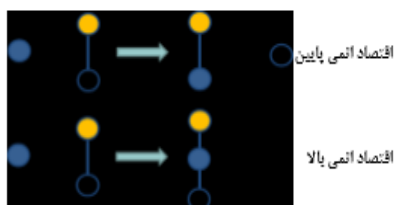


Fig.1 : Atomic economy

Design of lesser chemical processes

Chemists should, as far as possible, design a method or use or produce substances that have less harmful effects for human beings or the environment. There is often a variety of raw materials for a chemical reaction that can be chosen most appropriately.

Designing healthier materials and chemicals

Chemical products should be designed to work well despite the risk of toxicity. New products can be designed to be healthier and, at the same time, work well for them to do.

Minimizing the use of solvents and auxiliaries and more healthy conditions

Many chemical reactions are performed in the presence of a solvent, and most of the time, organic solvents are used that will have many dangers and are highly toxic. Solvents have a widespread use in synthetic reactions. Often, solvents such as alcohols, benzene, carbon tetrachloride, chloroform and dichloromethane are toxic and volatile. Large amounts of solvent in the purification of materials are used, for example, in chromatography, which adds to contamination and

can be very dangerous for humans. Green chemistry development has a new definition for halal role. The ideal green solvent must be natural, non-toxic, inexpensive and easily accessible. Clearly water is the cheapest and most compatible solvent with the environment. Occasionally, solvents may be substituted for less hazardous materials such as water or carbon dioxide.

Increase energy efficiency

In chemical processes, the construction and isolation methods are designed to the extent that they are designed to reduce the need for energy and achieve more energy at the end of the reaction.

Utilization of renewable raw materials

Chemical reactions should be designed in such a way that they can be used for recovery materials.

Avoiding Chemical Derivatives

Derivation (such as the use of limiting groups or transient physical and chemical changes) should be reduced, because the existence of these stages will mean the use of additional reactants that can produce false products.

Utilizing catalysts

Catalytic converters increase the selectivity of a reaction; reduce the required temperature; minimize side reactions; increase the rate of reaction of the reactants to the final products.

Design of easily damaged products

Chemical products must be designed in such a way that at the end of the products they are in the nature of being degradable and remain in the environment and break down as quickly as possible.

Real-time estimation of a reaction to prevent contamination

It is very important that the progress of a reaction is always followed up until the completion of the reaction. Because after the chemical reaction is completed, side effects are generated unwanted products.

Secure intrinsically safe chemicals to prevent accidents

One way to reduce the potential for unwanted chemical events is to use reactants and solvents that reduce the risk of explosions, fires and unwanted chemicals. The damage associated with this data can be reduced by changing the state (solid, liquid, gas) or the composition of the reactants.

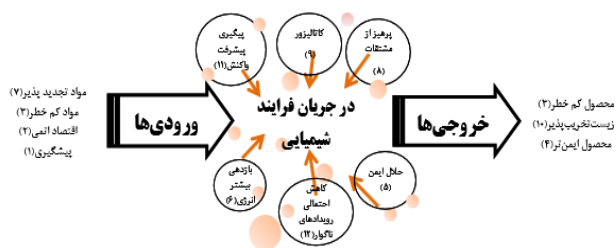


Fig.2: principles 12 of green chemistry at a glance

Results and Discussion

What is the significance of studying these concepts for students? Today's students, and ultimately the global community tomorrow, will dramatically benefit from the introduction of the principles of green chemistry into the curriculum. Green chemistry training can provide the knowledge and knowledge needed to develop the technology needed to achieve the ultimate goal of the sustainable world.

Green chemistry is taught at universities all over the world, but has not formally entered most of the chemistry curriculum. In fact, students do not have enough knowledge about how chemicals affect human health and the environment. Most universities do not have the toxicity of chemicals or environmental concerns in their curriculum. The training of green chemistry programs can inform future students and engineers about these issues. And to play an important role in developing and institutionalizing the ideas of green chemistry among students. In green chemistry experiments, they use and produce less toxic chemicals than traditional ones. At the same time, healthier, more secure and cheaper ones are coming to an end. The following features highlight the need for the educational system to focus on green chemistry.

- Provide a civilian version of traditional chemistry in curriculum
- Designing safer experiments for students
- Teaching Critical Thinking Skills Using Green Chemistry Concepts
- Reduce the cost of preparing and using solvents
- Reduce the cost of removing toxic waste
- Integrating scientific concepts with sustained and responsible monitoring
- Creating opportunities for students and students to participate in meaningful research
- Synchronizing the role of green chemistry in solving the challenges of global sustainability and environmental justice
- Reduce the need for specialized equipment such as hood and gas conditioning and ...

There are many common goals between green chemistry and sustainable development. Because sustainable development means a balance between the economic, social and environmental benefits that education places in the relationship between them. Therefore, green chemistry and industry and sustainable development complement each other. In the following, the relationship between green chemistry, industry and sustainable development has been identified.

Conclusions

According to a survey conducted by asking colleagues, the principles of green chemistry require the study of various chemical reactions and how they affect the green chemistry that we do not have such a specific explanation in the first chapter, and in the second chapter, The topic of chemistry is green, and the third chapter of this book has also been dedicated to life, and the main factor in green chemistry is elaborated, but it is just the same.

References

- [1] Jahanshahi Beyhaghbaghi, Abbasi Mustafa, Shahi Beygh Baghi Manouchehr. Assessing how chemicals are synthesized to meet the goals of green chemistry for better and more sustainable environmental management. *New Quarterly Journal of Management and Accounting*. Number 5, Summer (1395), Pages 209-193.
- [2] Examined by Maryam, Shahin Heydari. A quantitative measure of the amount of absorption of pollutants from vehicles by green walls. *Science and Technology of the Environment* (1393).
- [3] Refresh, d. Q M Green chemistry educational and research views. (1393)
- [4] Arthur Ragauskas, Yunqiao pu " Ionic Liquid as a Green Solvent for Lignin" Article in *Journal of Wood Chemistry and Technology*. April 2007.
- [5] Chao-Jun Li and Barry M. Trost " Green Chemistry for Chemical Synthesis " University of Chicago, Chicago, IL, and approved July 3, 2008 (received for review May 5, 2008).
- [6] Christian Capello, Ulrich Fischer and Konrad Hungerbuhler " What is a green solvent? A comprehensive framework for the environmental assessment of solvents " 9th March 2007.
- [7] Kirchoff, M. M. *Green Chemistry : Principles and Practice What Is Green Chemistry? Green Chem.* (2010).
- [8] Li, C.-J. & Trost, B. M. Green chemistry for chemical synthesis. *Proc. Natl. Acad. Sci. U. S. A.* **105**, 13197–13202 (2008).
- [9] Nameroff, T. J., Garant, R. J. & Albert, M. B. Adoption of green chemistry: An analysis based on US patents. *Res. Policy* **33**, 959–974 (2004).
- [10] Poliakoff, M., Fitzpatrick, J. M., Farren, T. R. &



Anastas, P. T. Green Chemistry : Science and Politics of Change Author (s): Martyn Poliakoff , J . Michael Fitzpatrick , Trevor R . Farren and Paul T . Anastas Published by: American Association for the Advancement of Science Stable URL : **297**, 807–810 (2016).

[11] Rebecca L.Lankey , and Paul T.Anastas " Life-Cycle Approaches for Assessing Green Chemistry Technologies" Ind. Eng. Chem. Res. 2002, 41, 4498-4502.

[12] Sameer P. Nalawade, Francesco picchioni , L.P.B.M.Janssen " Supercritical carbon dioxide as a green solvent for processing polymer melts: processing aspects and applications " Department of chemical Engineering , university of Groningen , The Netherlands (2005).

[13] Singh, A., Jain, D., Upadhyay, M. K. & Khandelwal, N. Green synthesis of silver nanoparticles using Argemone mexicana leaf extracts and evaluation of their antimicrobial activities. *Dig. J. Nanomater. Biostructures* **5**, 483–489 (2010).

[14] Adi Wolfson . Christina Dlugy . Yoram Shotland " Glycerol as a green solvent for high product yields and

selectivities " 15 August 2006.

[15] F-Kheirdoosh , Sh-Sobhani Laboratory Of Green Chemistry - Razi University Press

[16] Zolfaghari, M. Done M Green Chemistry; Prospects and Applications. Eighth Seminar on Chemistry of Iran 95, 43-50 (2009).

[17] Rezaei Meysam, Nouri Ramin, Karami Hussein, Pourian Mohammad Ali, Aryan Reza. Green chemistry and its solutions for environmental protection. Second National Conference on Environmental Health, Health and Sustainable Environment in Khordad (1394).

[18] Shah Mohammadi Ardebili Masoumeh, the mountain of fame. The Role of Green Chemistry in Sustainable Development and the Textbook Approach to It. Eighth Symposium on Chemistry in Iran September 6th and 7th (1392).

[19] Fallahzadeh Reza Ali. Thermodynamic methods for generating energy from waste. Second National Conference on Environmental Health, Health and Sustainable Environment (1394).

Modeling of experiment base on green chemistry for tenth chemistry of high school from the view point experts and related teachers

Tahereh Haghi^a – Dr Seyed Mohsen Mousavi^b – Dr Razieh Nejat^c

^aDepartment of Sherafat University Farhangian Tehran Iran

^bDepartment of Sherafat University Farhangian Tehran Iran

^cDepartment of Sherafat University Farhangian Tehran Iran

* [tara_haghi@yahoo.com](mailto: tara_haghi@yahoo.com)

Abstract: This study aimed to provide a good model for the design and production experiment for chemistry basis on the principles of green chemistry. This research is about the relationship between highschool chemistry and green chemistry. The titles of book chemistry, Was investigated by collaboration of chemistry teachers who taught chemistry last year. Then, based on the results of the surveys and the titles listed for the chemistry book, experiments were designed based on the principles of green chemistry. The method of research was to determine the relationship between the three chapters of the chemistry curriculum of the tenth grade chemistry book of high school with green chemistry. And through an interview with chemistry professors, the appropriate method for preparing and setting up the Green Lab Chemistry Lab was reviewed.

Keywords: *Green Chemistry, Green Solvents, Sustainable Development, Reusability, Green Catalysts, Twelve Principles*

Introduction

Green Chemistry is a set of principles and methods aimed at reducing the use and production of hazardous substances in chemical processes consistent with the three objectives of the sustainable environment, sustainable economy and sustainable society.

Sustainable development means meeting the needs of the present generation without compromising the ability of future generations to meet their needs. Green chemistry is one of the most basic and powerful tools used in sustainability. Green chemistry training can provide the knowledge and knowledge necessary to develop the technology needed to achieve sustainable globalization.

Green chemistry is a complementary and modifying chemistry course that can cover all the basic concepts of chemistry including stoichiometry, acids and bases, enthalpy, reaction speed, etc. In the 1990s, new science was introduced in chemistry, persistent chemistry and green chemistry in chemistry, all of which have a meaning, and it is green chemistry.

Materials and method

Collection of basic information related to the subject of research from the documents, books, magazines and articles of specialized sites and scan Preparation of a questionnaire on the conformity of the chemistry book with the twelve principles of green chemistry

Interviews and interviews with relevant professors and teachers

Examination of experiments and information in science textbooks, basic chemistry and basic sciences laboratory and the design of experiments based on green chemistry in line with the information in the books. Summarize the collected materials, conclusions and suggestions.

The research method will be combined with a library-documentary and laboratory methodology. The method of data collection is the use of books, journals, articles and specialized websites, interviews with professors and chemistry teachers and the preparation of questionnaires.

A tool for collecting information from study fingers and for academic teachers to consider the appropriate design patterns for testing Conclusion and gathering of information obtained.

Ultimately, the ultimate goal of green chemistry is to make the quality of life on a planet cleaner and safer. In this research, the study of green chemistry, its goals and principles, its future prospects, and the modeling of Green Luminosity experiments for the tenth grade elementary school chemistry book have been studied.

Green chemistry is an effective means of fostering students' interest in chemistry and materials. For an ideal society, and in keeping with the science of the day, we need new ideas in education, such as green chemistry. Green chemistry training can provide a new attitude to life easier and safer, by which one can

enhance the skills of thinking and problem solving and exploration in learners.

Principles of Green Chemistry

Green chemistry is usually presented as a set of twelve principles proposed by Anastass and Warner. These principles include guidelines for professional chemists when working with new chemical compounds, synthesis of materials and new technological processes. These principles include:

Preventing the production of vain products

It is better to prevent the production of waste and toxic waste, before it is produced to harm harmful wastes or to clean the environment.

Atomic economy, increasing atomic efficiency

The atomic economy means that the design of chemical reactions is in such a way that a greater percentage of the atoms in the reactants enter the structure of the final products. This also helps to increase the chemical reaction efficiency.

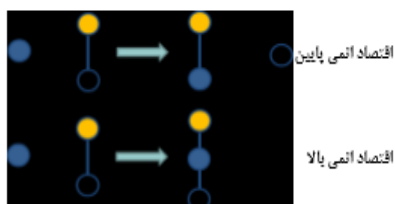


Fig.1 : Atomic economy

Design of lesser chemical processes

Chemists should, as far as possible, design a method or use or produce substances that have less harmful effects for human beings or the environment. There is often a variety of raw materials for a chemical reaction that can be chosen most appropriately.

Designing healthier materials and chemicals

Chemical products should be designed to work well despite the risk of toxicity. New products can be designed to be healthier and, at the same time, work well for them to do.

Minimizing the use of solvents and auxiliaries and more healthy conditions

Many chemical reactions are performed in the presence of a solvent, and most of the time, organic solvents are used that will have many dangers and are highly toxic. Solvents have a widespread use in synthetic reactions. Often, solvents such as alcohols, benzene, carbon tetrachloride,

chloroform and dichloromethane are toxic and volatile. Large amounts of solvent in the purification of materials are used, for example, in chromatography, which adds to contamination and can be very dangerous for humans. Green chemistry development has a new definition for halal role. The ideal green solvent must be natural, non-toxic, inexpensive and easily accessible. Clearly water is the cheapest and most compatible solvent with the environment. Occasionally, solvents may be substituted for less hazardous materials such as water or carbon dioxide.

Increase energy efficiency

In chemical processes, the construction and isolation methods are designed to the extent that they are designed to reduce the need for energy and achieve more energy at the end of the reaction.

Utilization of renewable raw materials

Chemical reactions should be designed in such a way that they can be used for recovery materials.

Avoiding Chemical Derivatives

Derivation (such as the use of limiting groups or transient physical and chemical changes) should be reduced, because the existence of these stages will mean the use of additional reactants that can produce false products.

Utilizing catalysts

Catalytic converters increase the selectivity of a reaction; reduce the required temperature; minimize side reactions; increase the rate of reaction of the reactants to the final products.

Design of easily damaged products

Chemical products must be designed in such a way that at the end of the products they are in the nature of being degradable and remain in the environment and break down as quickly as possible.

Real-time estimation of a reaction to prevent contamination

It is very important that the progress of a reaction is always followed up until the completion of the reaction. Because after the chemical reaction is completed, side effects are generated unwanted products.

Secure intrinsically safe chemicals to prevent accidents

One way to reduce the potential for unwanted chemical events is to use reactants and solvents that reduce the risk of explosions, fires and unwanted chemicals. The damage associated with this data can be reduced by changing the state (solid, liquid, gas) or the composition of the reactants.

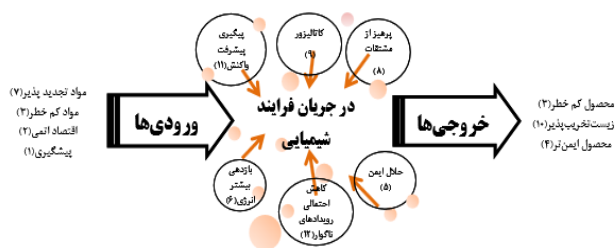


Fig.2: principles 12 of green chemistry at a glance

Results and Discussion

What is the significance of studying these concepts for students? Today's students, and ultimately the global community tomorrow, will dramatically benefit from the introduction of the principles of green chemistry into the curriculum. Green chemistry training can provide the knowledge and knowledge needed to develop the technology needed to achieve the ultimate goal of the sustainable world.

Green chemistry is taught at universities all over the world, but has not formally entered most of the chemistry curriculum. In fact, students do not have enough knowledge about how chemicals affect human health and the environment. Most universities do not have the toxicity of chemicals or environmental concerns in their curriculum. The training of green chemistry programs can inform future students and engineers about these issues. And to play an important role in developing and institutionalizing the ideas of green chemistry among students. In green chemistry experiments, they use and produce less toxic chemicals than traditional ones. At the same time, healthier, more secure and cheaper ones are coming to an end. The following features highlight the need for the educational system to focus on green chemistry.

- Provide a civilian version of traditional chemistry in curriculum
- Designing safer experiments for students
- Teaching Critical Thinking Skills Using Green Chemistry Concepts
- Reduce the cost of preparing and using solvents
- Reduce the cost of removing toxic waste
- Integrating scientific concepts with sustained and responsible monitoring
- Creating opportunities for students and students to participate in meaningful research
- Synchronizing the role of green chemistry in solving the challenges of global sustainability and environmental justice
- Reduce the need for specialized equipment such as hood and gas conditioning and ...

There are many common goals between green chemistry and sustainable development. Because sustainable development means a balance between the economic, social and environmental benefits that education places in the relationship between them. Therefore, green chemistry and industry and sustainable development complement each other. In the following, the relationship between green chemistry, industry and sustainable development has been identified.

Conclusions

According to a survey conducted by asking colleagues, the principles of green chemistry require the study of various chemical reactions and how they affect the green chemistry that we do not have such a specific explanation in the first chapter, and in the second chapter, The topic of chemistry is green, and the third chapter of this book has also been dedicated to life, and the main factor in green chemistry is elaborated, but it is just the same.

References

- [1] Jahanshahi Beyhaghbaghi, Abbasi Mustafa, Shahi Beygh Baghi Manouchehr. Assessing how chemicals are synthesized to meet the goals of green chemistry for better and more sustainable environmental management. *New Quarterly Journal of Management and Accounting*. Number 5, Summer (1395), Pages 209-193.
- [2] Examined by Maryam, Shahin Heydari. A quantitative measure of the amount of absorption of pollutants from vehicles by green walls. *Science and Technology of the Environment* (1393).
- [3] Refresh, d. Q M Green chemistry educational and research views. (1393)
- [4] Arthur Ragauskas, Yunqiao pu " Ionic Liquid as a Green Solvent for Lignin" Article in *Journal of Wood Chemistry and Technology*. April 2007.
- [5] Chao-Jun Li and Barry M. Trost " Green Chemistry for Chemical Synthesis " University of Chicago, Chicago, IL, and approved July 3, 2008 (received for review May 5, 2008).
- [6] Christian Capello, Ulrich Fischer and Konrad Hungerbuhler " What is a green solvent? A comprehensive framework for the environmental assessment of solvents " 9th March 2007.
- [7] Kirchoff, M. M. *Green Chemistry : Principles and Practice What Is Green Chemistry? Green Chem.* (2010).
- [8] Li, C.-J. & Trost, B. M. Green chemistry for chemical synthesis. *Proc. Natl. Acad. Sci. U. S. A.* **105**, 13197–13202 (2008).
- [9] Nameroff, T. J., Garant, R. J. & Albert, M. B. Adoption of green chemistry: An analysis based on US patents. *Res. Policy* **33**, 959–974 (2004).
- [10] Poliakoff, M., Fitzpatrick, J. M., Farren, T. R. &



Anastas, P. T. Green Chemistry : Science and Politics of Change Author (s): Martyn Poliakoff , J . Michael Fitzpatrick , Trevor R . Farren and Paul T . Anastas Published by: American Association for the Advancement of Science Stable URL : 297, 807–810 (2016).

[11] Rebecca L.Lankey , and Paul T.Anastas " Life-Cycle Approaches for Assessing Green Chemistry Technologies" Ind. Eng. Chem. Res. 2002, 41, 4498-4502.

[12] Sameer P. Nalawade, Francesco picchioni , L.P.B.M.Janssen " Supercritical carbon dioxide as a green solvent for processing polymer melts: processing aspects and applications " Department of chemical Engineering , university of Groningen , The Netherlands (2005).

[13] Singh, A., Jain, D., Upadhyay, M. K. & Khandelwal, N. Green synthesis of silver nanoparticles using Argemone mexicana leaf extracts and evaluation of their antimicrobial activities. *Dig. J. Nanomater. Biostructures* 5, 483–489 (2010).

[14] Adi Wolfson . Christina Dlugy . Yoram Shotland " Glycerol as a green solvent for high product yields and selectivities " 15 August 2006.

[15] F-Kheirdoosh , Sh-Sobhani Laboratory Of Green Chemistry - Razi University Press

[16] Zolfaghari, M. Done M Green Chemistry; Prospects and Applications. Eighth Seminar on Chemistry of Iran 95, 43-50 (2009).

[17] Rezaei Meysam, Nouri Ramin, Karami Hussein, Pourian Mohammad Ali, Aryan Reza. Green chemistry and its solutions for environmental protection. Second National Conference on Environmental Health, Health and Sustainable Environment in Khordad (1394).

[18] Shah Mohammadi Ardebili Masoumeh, the mountain of fame. The Role of Green Chemistry in Sustainable Development and the Textbook Approach to It. Eighth Symposium on Chemistry in Iran September 6th and 7th (1392).

[19] Fallahzadeh Reza Ali. Thermodynamic methods for generating energy from waste. Second National Conference on Environmental Health, Health and Sustainable Environment (1394).



بیستمین کنفرانس شیمی فیزیک ایران
دانشکده علوم پایه - دانشگاه اراک
۳۱-۲۹ مرداد ۱۳۹۶



20th Iranian Physical Chemistry Conference

طیف سنجی مولکولی

Molecular spectroscopy

Alkali halides as positive and negative ion source for ion mobility and mass spectrometry

Hassan Shahraki^{a*}, Mahmoud Tabrizchi^a, Hossein Farrokhpour

^aDepartment of Chemistry, Isfahan University of Technology, Isfahan, 84156-83111, Iran

*shahraki.h@gmail.com

Abstract: Filament ion sources have been used in the production of high current of ions for a wide variety of applications. In this work, a new long-life alkali ion source, based on alkali halide salts doped in nano- γ -alumina (Al_2O_3) is proposed. Depending the polarity, the ion source produces both alkali and halide ions. Alkali and halide ion peaks were observed by ion mobility spectrometry (IMS) in positive and negative modes, respectively. The lifetime of the ion source for different alkali halides was measured to be in the range of 216-960 h. The total ion current emitted from the source was about $2\mu A$, while at the collector plate of the IMS it was 12 nA. Finally, the application of the new source in ion mobility spectrometry was demonstrated by observing ion mobility spectra of some compounds ionized via cation attachment reaction.

Keywords: nano- γ -alumina (Al_2O_3); ion source; ion mobility spectrometry; alkali ions; halide ions.

Introduction

Ion source is an essential part of all instruments dealing with ions in gas phase. Alkali ion sources have been used in particle accelerators, mass spectrometers and ion mobility spectrometers. Alkali ions are easily produced by thermal ionization of alkali salts. Thermionic emission of alkali ions with alumino-silicates substrate as ion source were developed for accelerators [1]. The lifetime of these sources are reported to be less than 25 hours.

Alkali ions are also widely used in the ion attachment mass spectrometry (IAMS). This technique provides a sensitive method for detection of volatile compounds in the gas phase. In IAMS the sample is ionized via attachment to a primary ion such as Li^+ or Na^+ [2].

Alkali and halide ion attachment were also used in ion mobility spectrometry (IMS) which is a sensitive, fast and low-cost analytical technique for the detection of volatile compounds [3]. The usage of the IMS instrument for detect of organic compounds strongly depends on ionization source type. This kind of ion source, along with other ionization sources such as corona discharge, and surface ionization were proposed to replace the commonly used ^{63}Ni radioactive source in IMS. Despite the small size, low weight and no need to external power for the ^{63}Ni , its application is discouraged because of safety regulations. Hence, the use of a substitute nonradioactive ionization source for IMS is encouraged.

Few reports are available for alkali ion attachment ion mobility spectrometry. Positive and negative thermal ionization of alkali salts were introduced to be used in IMS [4]. Tabrizchi et al developed an alkali ionization source for IMS, based on graphite intercalation compounds (GICs) [5]. The GICs were synthesised by fusing alkali metal halides with normal graphite. The thermionic emission of the main ion of the

corresponding salt lasted for several days. No negative ions were observed upon reversing the drift field. In order to achieve a good stability, it is necessary to alkali salts coated into the nano porous substrate having high surface area. In fact, the variation of the amount of absorbed alkali metal may affect the lifetime and current intensity ion source. As our interest, we here present the development of a new long-life alkali and halide ion source with high stability, using alkali halides doped in nano-particles of γ - Al_2O_3 . The new ion source was characterized using an ion mobility spectrometer. The important features of the proposed ion source are long lifetime, simplicity, high stability, and high positive and negative ionization efficiency.

Materials and method

γ -alumina nano-particles were obtained from US Research Nanomaterials. Alkali metal halides were obtained from Merck. Alkali halides doped nano- γ -alumina ($MX/nano-\gamma-Al_2O_3$, where $M = K, Na, Li, Cs$ and $X = Cl, I, F$) particles were prepared by the incipient-wetness impregnation (IWI) method. Nano- γ -alumina powder added into a saturated solution of alkali metal halides. The mixture was stirred for 12 h at room temperature. It was then washed twice with distilled water, and dried at $120\text{ }^\circ C$ for 12 h in an oven. The powder was finally calcined at $500-700\text{ }^\circ C$ in a furnace for 3 h. fine Nichrome filament with a diameter of $150\mu m$, was used as the heater for thermal ionization source. The filament was connected to an isolated variable-power supply (1-12 V, 2A) for heating. The prepared nano-particles were coated on the filament by the immersion of the filament into the slurry of the prepared nano-particles. To characterize the prepared alkali halides doped nano- γ -alumina powders as ion source, an ion mobility spectrometer (IMS) was used. The instrument was a desktop research grade IMS manufactured in Isfahan University of Technology. A schematic diagram of an ion source is shown in Fig. 1.

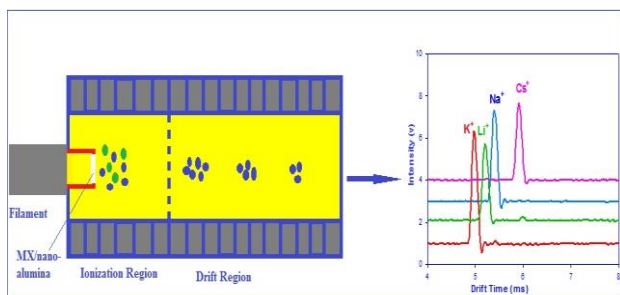


Fig. 1: Schematic setup of the ion mobility spectrometer with alkali ion source.

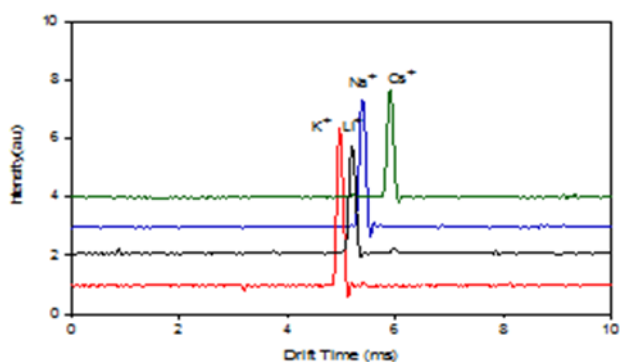


Fig.2: The positive reactant ion mobility spectra of MX/nano- γ - Al_2O_3 ion sources.

Results and discussion

Positive IMS spectra

The recorded ion mobility spectra of alkali ions coming from MX/nano- γ - Al_2O_3 are shown in Fig.2. The peaks appeared at 5.22, 5.38, 4.92 and 5.69 ms, correspond to Li^+ , Na^+ , K^+ and Cs^+ , respectively. The reason for the smaller drift time for K^+ compared to Li^+ and Na^+ can be attributed to the more hydration of Li^+ and Na^+ compared to K^+ in the drift tube. The charge density on Li^+ and Na^+ is larger than K^+ because of their smaller size. The cesium ion is heavy and its peak appears after those of all alkali ions.

Ion Current intensity

The intensity of the ion emission depends strongly on the filament current and its mass and surface size. The typical total ion current that flows between the filament and the first ring of the IMS was measured to be about $2\mu\text{A}$. The measurement was done a filament loaded with 11 mg sodium doped nano-particles at a given filament current of 1.2 A. The filament emission current is in the range of the corona discharge ion current. The ion

current at the IMS collector (~ 16 cm away from the ion source) was also measured for the same amount of different doped nano-particles in the range of 0.9 to 1.2 A filament current, while the shutter grid was left totally open. Fig. 3 shows the effect of current on the ion beam intensity at the IMS collector plate for different ions. It is seen that the intensity generally increases with the filament current up to a certain level. Further increase of the filament current was not possible due to the filament burning. Nevertheless, the ion intensity observed at the collector plate is a small portion of the original ion current emitted by the filament. This is due to the fact that at atmospheric pressure most ions are annihilated during their drifting towards the collector. Despite the loose of ions, the ion intensity is excellent for application in IMS, since it is comparable to the corona discharge ion source and it is much higher than that produced by the conventional radioactive ^{63}Ni ion source.

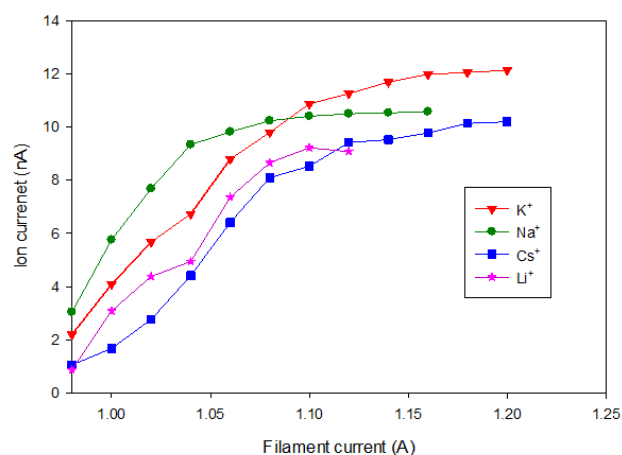


Fig.3: The effect of filament current on the ion beam intensity at the IMS collector.

Life time

Fig. 4 shows the variation of the intensity of the Li^+ , Na^+ , K^+ and Cs^+ peaks versus days of continuous operation. Assuming an exponential decay, the lifetime of the sources were obtained from the fitting of the data to a function of $A \cdot \exp(-t/\tau)$, where τ is the lifetime. The average lifetime is longer than 500 h. This is longer than our previously reported lifetime of graphite intercalated compounds [5]. It should be mentioned that, an ion source fabricated with micro scale alumina, lasted only about 5h in positive and 20 min in negative mode. Hence, the nano-scale alumina has a profound effect on the life time of the source. The specific surface area for nano- γ - Al_2O_3 ($300 \text{ m}^2 \text{ g}^{-1}$) is much higher than that of the micro scale one ($120 \text{ m}^2 \text{ g}^{-1}$). The lifetime of the negative ion sources fabricated in this work was

obtained to be about 43 h. This is shorter than the typical observed lifetimes in positive mode. Nevertheless, this is considered a long life in compare with that observed (only few minutes) for pure alkali halides salts loaded on a bare filament.

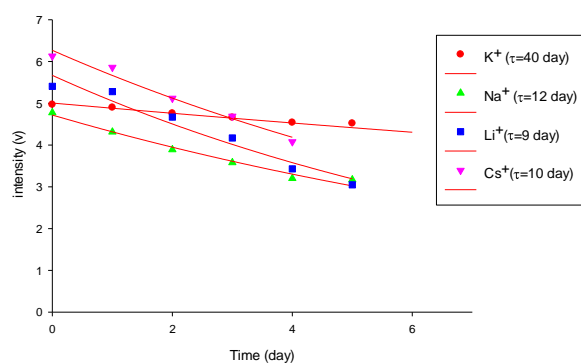


Fig.4: Variation of the Li^+ , Na^+ , K^+ and Cs^+ peaks versus time and the fitting curves (solid lines) assuming an exponential function.

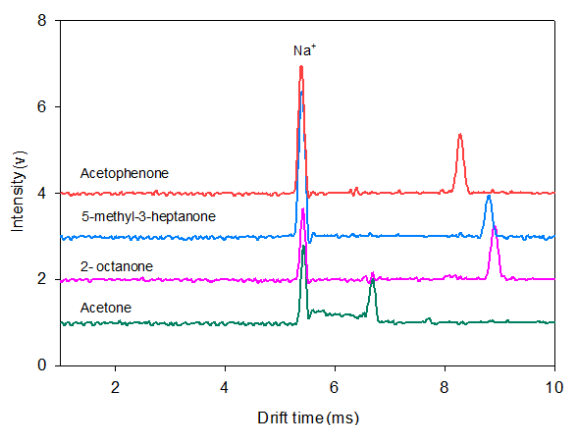


Fig.5: Ion attachment IMS spectra of samples detected by IMS with Na^+ ion source.

Ion attachment ion mobility spectrometry

Similar to the ion attachment mass spectrometry technique, the fabricated source was used in IMS to perform ion attachment ion mobility spectrometry (IAIMS). The possibility of IAIMS was examined for some test compounds, acetone, 2-octanone, acetophenone and 5-methyl-3-heptanone in positive mode. The results are presented in Fig. 5. For each sample, a new peak appeared, in addition to the original cation peak, which is due to the ion attachment to the sample molecule. Alkali ion sources compared to other sources of ions produced as reactive ions do not react with ammonia. It is important to identify organic compounds in the presence of ammonia. The concentration of acetone in human breath is very low, in

the range of several ppb (parts per billion). This concentration makes it difficult to detect acetone in the breath matrix consisting of nitrogen, oxygen, carbon dioxide, water, inert gases, ammonia and other volatile organic compounds (VOCs). Lithium (Li) ion mobility spectrometry is a highly sensitive method for detecting volatile organic compounds (VOCs) without fragmentation in real-time. Acetone/ cation interaction was examined in the gas phase using ion mobility spectrometry. IMS-mass spectrometric studies determined that the reactant ion in a lithium ion emitters is as $\text{Li}^+(\text{H}_2\text{O})_n(\text{N}_2)_m$ and the product ion is formed due to cation attachment to the analyte, $\text{Acetone.Li}^+(\text{H}_2\text{O})_n(\text{N}_2)_m$. Also, lithium ion source does not respond to most small molecules, such as nitrogen, oxygen, carbon dioxide and water which may exist in air and no general background ions are created by this method.

Conclusions

A new surface ionization source was constructed by the impregnation of nano- γ -alumina with the alkali halides and used in ion mobility spectrometry. In addition to positive ions, unlike the intercalated graphite compounds, the new source generated negative halide ions. The lifetime of the new alkali and halide ion source is in the range of several weeks, higher than that previously reported for graphite intercalated potassium and it is comparable to the ultraviolet ionization source. It is simple, low cost, and easy to use. Various types of alkali or halide ion beams can be produced if an appropriate salt is chosen. The capability of using this ion source in qualitative analysis of organic compounds was evaluated. Results indicates that the source fabricated in this work is a very promising non-radioactive dual ion source that can be used in IMS as well as other devices such as accelerators and mass spectrometers.

References

- [1] Roy, P.K., Greenway, W.G., Grote, D.P., Kwan, J.W., Lidia, S.M., Seidl, P.A., Waldron W.L.: Lithium ion sources. *Nucl. Instrum. Meth. Phys. Res., Sect. A* 733(2014) 112–118.
- [2] Fujii, T.: Alkali-metal ion/molecule association reactions and their applications to mass spectrometry. *Mass Spectrom. Rev.*19 (2000) 111 – 138
- [3] Kanu, A.B., Haigh, P.E., Hill, H.H.: Surface detection of chemical warfare agent simulants and degradation products. *Anal. Chim. Acta.*553(2005) 148-159.
- [4] Tabrizchi, M.: Thermal ionization ion mobility spectrometry of alkali salts. *Anal. Chem.*75(2003)3101-3106.
- [5] Tabrizchi, M, Hosseini, Z. S.: An alkali ion source based on graphite intercalation compounds for ion mobility spectrometry. *Meas. Sci. Technol.*19(2008) 075603.

Excited State Proton Transfer Process In The 2-hydroxy –N-Salicylidene Schiff Base

Vali Alizadeh, Ahmad Jamali moghadam*

University of Garmsar P.O.Box 3581755796, Garmsar, Iran

*f.j.moghadam@gmail.com

Abstract: The Excited state reaction coordinates and the consequent energy profiles of a new Schiff Base N-Salicylidene-2-Bromoethylamine (NSBA) have been investigated at the CC2 level of theory. The electron-driven proton transfer and torsional deformation have been identified as the most important photochemical reaction coordinates. The potential energy profiles of the ground and the lowest excited singlet state are calculated. In contrast to the ground state, the excited state potential energy profile shows a barrier-less dissociation pattern along the O–H stretching coordinate which verifies the proton transfer reaction at the S1 ($\pi\pi^*$) state. The calculations indicate S1/S0 conical intersections (CIs) which provide non-adiabatic gates for radiation-less decay to the ground state. At the CI, barrier-free reaction coordinates direct the excited system to the ground state of enol-type minimum. According to calculation results, a trans-keto type structure obtained from photoexcitation of the enol, can be responsible for the photochromic effect of title compound. Furthermore, our results confirm the suggestion that aromatic Schiff Bases are potential candidates for optically driven molecular switches.

Keywords: Schiff Base, Intramolecular Proton Transfer, Photochromism

Introduction

From the beginning of the 21th century, the research for molecular switches based on light-induced conformational changes has been a hot topic. Schiff Base molecules represent a class of advanced materials widely employed in photonic and optoelectronic applications [1–5]. Many of these belong to the family of photo- (PC) or thermo- chromic (TC) materials—that is, systems that change their color after photo- or thermo-irradiation, respectively. It is also well established that the optical properties of Schiff base molecules are related directly to their photochromic nature, which is a reversible reaction between enol and keto forms, giving rise to the reversible photocolouration of a single chemical species between two states. Recently, the photochromic effect of salicylaldehyde Schiff bases have been the subject of several papers, where it was demonstrated that the excited state intramolecular proton transfer (ESIPT) process after photo excitation is the most crucial step in excited state reaction dynamics of these molecules. Beyond this process, producing a keto structure as a new tautomeric form is responsible for photochromic effect with bathochromically shifted spectra. So far, the ESIPT has attracted massive research interest, both in theory and experiment [6–10].

Usually, ortho-hydroxy Schiff bases display two possible tautomeric forms, the enol-imine and the ketoamine forms. Depending on the tautomers, two types of intramolecular hydrogen bonds can exist in Schiff

bases: O—H...N in enol-imine and N—H...O in ketoamine tautomers [11, 12].

Computational Details

The ab initio calculations have been performed with the TURBOMOLE program package [13, 14]. The Resolution of identity Møller–Plesset perturbation theory to second-order (RI-MP2) [15, 16] calculations were performed to obtain the equilibrium geometry of the titled compound at the ground electronic state. Excitation energies and equilibrium geometry of the lowest excited singlet states have been determined at the resolution-of-identity second-order approximate coupled-cluster (RI-CC2) [17, 18] method. The calculations were performed with the correlation-consistent polarized valence double- ζ (cc-pVDZ) basis set [19].

Results and Discussion

The first step of this work is looking for the most stable structure of title compound. The most stable structure in ground state (S0) at the MP2/cc-pVDZ level of theory is enol form (E). While the excited state proton transfer (ESPT) is mainly achieved after the S1 geometry optimization of the E form at the CC2 level as keto form (K), (see Fig. 1).

The potential energy profiles calculated along the minimum energy paths (MEP) for hydrogen (or proton) transfer of the enol form of NSBA together with torsion of the ethylamine group (C1–C2–C7–N1 dihedral



angle) in the keto structure of NSBA in the S_0 and S_1 states are shown in Figure 2a, b. As shown, in the ground state, the local minimum is in the enol side, whereas in the S_1 , the minimum is in the keto side. The minimum energetic level of the S_1 state along the PT coordinate lies in the short distance to the long distance of OH, which corresponds to the new bond formation of H-N. In the ground state, the enol-keto transformation is not favored by considering the energy changes, but in the S_1 state, the PES does not show a barrier, and this transformation will be favored by decreasing the internal energy of the system along the enol-keto transformation. Transfer of a proton between the oxygen and nitrogen atoms in the initial S_1 state of enol leads to create the keto in its $\pi\pi^*$ state. At this minimum, the S_0/S_1 potential energy profiles touch each other and obtain new way to return enol form. Namely reversible structural change along with spectral shift. This result indicates that the photochromism of certain ESIPT systems. The characteristic features of such systems are strong and broad absorption in the UV/vis range, and very fast radiation-less return to the ground state.

The S_0 curve in Figure 2a exhibits a barrier for proton transfer in the S_0 state of NSBA ($E = 0.45$ eV), while the energy profile of the S_1 state calculated along the S_1 reaction path in Figure 2a indicates a barrierless path for proton transfer from oxygen toward the nitrogen atom. It verifies that spontaneous hydrogen transfer takes place, resulting in the formation of keto tautomer on the excited state potential energy surface. The keto-type S_1 structure is estimated to lie 2.84 eV (CC2 result) above the global minimum of the ground state (see Fig. 2a).

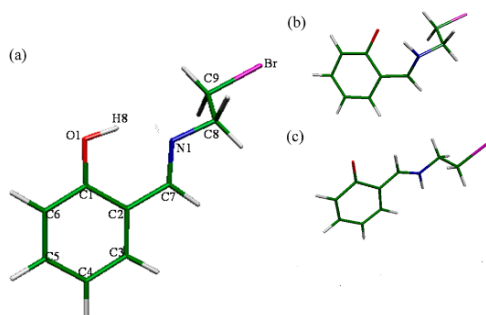


Figure 1: Optimized geometries and numbering pattern: (a) the most stable configuration of the enol form of NSBA (calculated at the MP2/cc-pVDZ level of theory); (b) the S_1 optimized structure of cis-keto form of NSBA (determined at the CC2/cc-pVDZ geometry optimization of the E form); (c) the optimized geometry structure of trans-keto form of NSBA obtained at the MP2/cc-pVDZ level of theory.

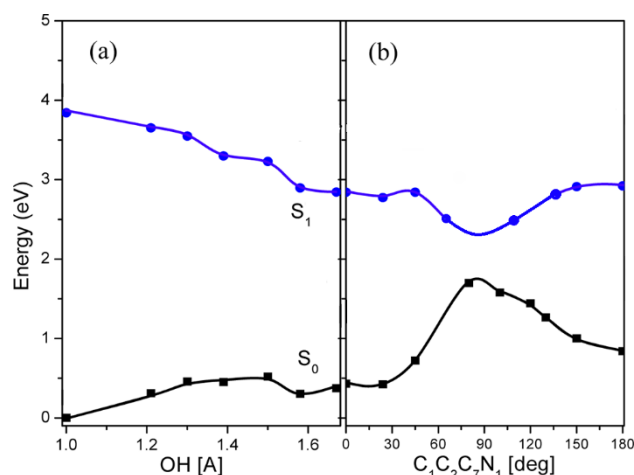


Fig. 2: Potential energy curves of the S_0 state (squares) and the $S_1(\pi\pi^*)$ state (circles), as the functions of hydrogen transfer reaction path in the enol form of NSBA (a) and torsional reaction path in the keto form of NSBA (b). The energy origin is the energy of minimum enol in the ground state.

Electronic Properties:

The vertical electronic transition energies of the most stable enol and keto forms of NSBA are presented in Table 1. The vertical excitation energy at the CC2/cc-pVDZ level on the S_0 geometry of the E identifies two strong electronic transitions: The S_1-S_0 transition at 4.03 eV (307.7 nm) can be described as the $\pi\pi^*$ (H-L) excitation, (H and L indicate to HOMO and LUMO, respectively). The oscillator strength of this transition is 0.125. The S_3-S_0 lies at 5.09 eV (243 nm) with the oscillator strength of 0.255, and can be described as the $\pi\pi^*$ state.

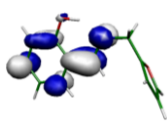
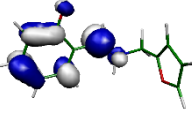
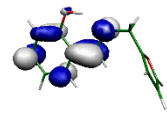
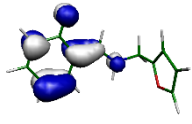
The vertical excitation energies at the same level of theory on the MP2 ground state optimized geometry of trans-keto tautomer indicate two strong electronic transitions; the S_2-S_0 transition at the 3.07 eV (404.56 nm) can be described as the $\pi\pi^*$ (H-L) excitation (see Table 1). The oscillator strength of this transition is 0.320. The S_4-S_0 transition also lies at 4.62 eV (268.8 nm) with the oscillator strength of 0.17 and can be described as the $\pi\sigma^*$ since there is one electron excitation of H-(L+1).

Table 1. Vertical Energy Gap (eV) and Oscillator Strength (f) of the E and trans-Keto Rotamers					
Enol			Trans-Keto		
Transition	eV	f	Transition	eV	f
$S_1 (\pi\pi^*)$	4.03	0.125	$S_1 (\pi\pi^*)$	2.9	0.002
$S_2 (n\pi^*)$	4.95	0.001	$S_2 (\pi\pi^*)$	3.07	0.32
$S_3 (\pi\pi^*)$	5.09	0.255	$S_3 (\pi\pi^*)$	4.37	0.006
$S_4 (\pi\pi^*)$	5.51	0.004	$S_4 (\pi\pi^*)$	4.62	0.172



The vertical electronic transition energies and molecular orbitals of the most stable enol and keto forms of NSBA are presented in Table 2. Calculations shows about 120 nm shift along the intramolecular proton transfer.

Table 2. Molecular Orbital and transition wavelength (S_1-S_0)

form	Enol	Trans- Keto
LUMO	 307 nm	 427 nm
HOMO		

Conclusions

The computational results of the present work suggest the following features of the photophysics of NSBA. This molecule is transparent to visible radiation but strongly absorbent for UV radiation. The primary UV-induced reaction is proton transfer from the hydroxyl group to the imine group. This reaction is predicted to be essentially barrier-less and thus extremely fast. The system switches from the S_1 surface to the S_0 surface via a nonadiabatic transition. It is thus possible that the global minimum structure of NSBA is restored with a probability very close to unity, which is a requirement for the function of SBEA as an effective photostabilizer.

Acknowledgment

The research council of University of Garmsar is gratefully acknowledged. The calculations have been performed via the Computational Center of the Chemistry Department of University of Isfahan.

References

- [1] A. El'tsov, "Organic Photochromes"; 1990, Plenum Press, 1st Ed., 102-200, New York.
- [2] V. Ramamurthy, "Photochemistry in Organized and Constrained Media"; 1991, Wiley-VCH: 2nd Ed, 1-150, New York.

- [3] J.C. Crano, R.J. Guglielmetti, "Organic Photochromic and Thermochromic Compounds"; Topics in Applied Chemistry; 1999, Plenum Press, 1st Ed, 345-357, New York.

- [4] H. Durr, H. Bouas-Laurent, "Photochromism: Molecules and Systems", 2003, 2nd Ed.; Elsevier: Amsterdam.

- [5] M. Irie "Diarylethenes for Memories and Switches" *Chem. Rev*, 100 (2000) 1685-1716.

- [6] A. L. Sobolewski and W. Domcke "Computational Studies of the Photophysics of Hydrogen-Bonded Molecular Systems", *J. Phys. Chem. A*, 111 (2007) 11725-11735.

- [8] A. L. Sobolewski, W. Domcke and C. Ha'ttig "Photophysics of Organic Photostabilizers. Ab Initio Study of the Excited-State Deactivation Mechanisms of 2-(2'-Hydroxyphenyl)benzotriazole", *J. Phys. Chem. A*, 110 (2006) 6301-6306.

- [9] J. M. Ortiz-Sa'nchez, R. Gelabert, M. Moreno, J. M. Lluch "Theoretical Study on the Excited-State Intramolecular Proton Transfer in the Aromatic Schiff Base Salicylidene Methylamine: an Electronic Structure and Quantum Dynamical Approach", *J. Phys. Chem. A*, 110 (2006) 4649-4656.

- [10] M. Z. Zgierski "Theoretical study of photochromism of N-salicylidene- α -methylbenzylamine", *J. Chem. Phys*, 115 (2001) 8351-8358.

- [11] M. Z. Zgierski and A. Grabowska "Theoretical approach to photochromism of aromatic Schiff bases: A minimal chromophore salicylidene methylamine" *J. Chem. Phys*, 112 (2000) 6329-6337.

- [12] M. Juan, S. Ortiz, G. R. Gelabert, M. Moreno "Electronic-structure and quantum dynamical study of the photochromism of the aromatic Schiff base salicylideneaniline", *J. Chem. Phys*, 129 (2008) 7845-7852.

- [13] Ahlrichs, R.; Bär, M.; Häser, M.; Horn, H.; Kölmel, C "Electronic Structure Calculations on Workstation Computers: theProgram System Turbomole", *Chem. Phys. Lett*, 162 (1989) 165-169.

- [14] Turbomole V6.3; Turbomole GmbH: Karlsruhe, Germany, 2007; available from <http://www.turbomole.com>.

- [15] Møller, C.; Plesset, M. S "Note on an Approximation Treatment for Many-Electron Systems", *Phys. Rev*, 46 (1934) 618-622.

- [16] Weigend, F.; Häser, M "RI-MP2: First Derivatives and Global Consistency", *Theor. Chem. Acc*, 97 (1997) 331-340.

- [17] Weigend, F.; Häser, M.; Patzelt, H.; Ahlrichs "R. RI-MP2: Optimized Auxiliary Basis Sets and Demonstration of Efficiency", *Chem. Phys. Lett*, 294 (1998) 143-152.

MRCI calculations for the low-lying electronic states of ScH and ScD

Z. Biglari

Chemistry Department, Faculty of science, Lorestan University, Khorram Abad, Lorestan, Iran
biglari.z@lu.ac.ir

Abstract: Ab initio potential energy curves and transition dipole moments have been calculated for the $X^1\Sigma^+$, $A^1\Delta$, $B^1\Pi$, $a^3\Delta$, $b^3\Pi$, $c^3\Sigma^+$, $1^3\Phi$, $2^3\Pi$, $1^3\Sigma^-$, $2^3\Delta$, $1^5\Pi$, $1^5\Phi$, $1^5\Sigma^-$ and $1^5\Delta$ states of scandium hydride, ScH, using the multi-reference configuration interaction method with large active space and basis sets. Potential energy and transition dipole moments have been computed from 0.5 Å to 20.0 Å, and were used to calculate average lifetimes of excited state vibrational levels. The Deuterium isotope effect of this molecule is also investigated in the LEVEL program using different mass of Hydrogen and Deuterium. The spectroscopic parameters of the bound states were determined for ScH and ScD, which agree well with available experimental results.

Keyword: MRCI; potential energy curves; transition dipole moment; excited electronic states; ScH; ScD

Introduction

The studies of the electronic spectra of diatomic transition-metal hydrides provide some important information, required for understanding the role of d electrons in chemical bond formation, metal-hydrogen bonding in inorganic chemistry, surface science, the chemisorption of the hydrogen atom on catalytic metal surfaces. Thus, several researches have been published in the transition-metal hydrides domain. Indeed, the transition metal-containing molecules are important astrophysical compounds. For instance, TiH and FeH have been observed in the spectra of M-type stars as well as NiH and CrH have been identified in the spectra of sunspots. It is noticeable that scandium hydride (ScH) as the simplest transition metal-containing molecule have been attracted a great number of experimental and theoretical researches.

Several studies using different methods incorrectly predicted the ground state of ScH is a $^3\Delta$ state [1]. Bauschlicher and coworkers theoretically studied the first-row transition metal hydrides and showed that the correct description of the ground state of ScH is a $^1\Sigma^+$ state to be lower than a $^3\Delta$ state by 2420 cm^{-1} [2].

In this paper, the potential energy curves and transition dipole moments for several singlet, triplet and quintet states of ScH are calculated using the multi-reference configuration interaction (MRCI) method with large active space and basis sets. Ab initio calculations were carried out and the transition dipole moment functions were used to calculate the Einstein A coefficients for vibronic transitions and lifetimes of several excited electronic states.

Computational details

All calculations were performed using the ORCA 2.9.0 program. The augmented correlation-consistent polarized valence quadruple zeta (aug-cc-pVQZ) basis sets of Woon and Dunning are applied for both scandium and hydrogen atoms, and were fully decontracted to give

$23s19p12d4f3g2h$ for Sc and $7s4p3d2f$ for H. The C_{2v} point group was used for the linear ScH molecule. The calculations were performed in the following steps; the first step was a restricted Hartree-Fock (RHF) calculation was performed at 65 internuclear distances from 0.5 Å to 20.0 Å, producing 265 molecular orbitals.

The second step, these molecular orbitals were used as initial guess for the state-averaged complete active space self-consistent field (SA-CASSCF) calculations with 4 active electrons in 10 orbitals CAS(4,10), i.e., five molecular orbitals of a_1 , two b_1 , two b_2 and one a_2 symmetry (correlating to 1s of H and 4s, 4p and 3d of Sc). Nine core orbitals correlating to $1s2s2p3s3p$ of Sc were kept doubly occupied in all configuration state functions (CSFs). At the equilibrium geometry of ScH, i.e., 1.800 Å, several low-lying states with spin multiplicity of one, three, and five ($S = 0, 1, 2$) were computed, which belong to $X^1\Sigma^+$, $A^1\Delta$, $B^1\Pi$; $a^3\Delta$, $b^3\Pi$, $c^3\Sigma^+$, $1^3\Phi$, $2^3\Pi$, $1^3\Sigma^-$, $2^3\Delta$ and $1^5\Pi$, $1^5\Phi$, $1^5\Sigma^-$, $1^5\Delta$ states. The CASSCF total energy was $-760.245078 E_h$ and for the $X^1\Sigma^+$ state of ScH $-760.319106 E_h$ at 1.800 Å.

The final step was a multi-reference configuration interaction with single and double excitations (MRCISD), for which the MOs of SA-CASSCF was used. The last 66 external frozen orbitals, i.e., those with energies higher than 10.0 E_h were kept out from the CI space. Finally, potential energy values and transition dipole moments of the ground and excited states were used in program LEVEL, in order to compute Einstein A coefficients and spectroscopic constants.

Results and Discussion

The *ab initio* energies computed at the MRCISD level for all electronic states are plotted together in Figure 1. The calculated energy at $r = 20.0\text{ Å}$ is taken as the separated-atom limit energy. For Scandium atom, the 4F states lie 11520 cm^{-1} higher than 2D states. We considered two first asymptotes and wavefunctions for the six electronic states

arising from the interaction of Sc (2D) + H (2S), i.e., $1,3\Sigma^+$, $1,3\Pi$, $1,3\Delta$; and eight electronic states arising from the interaction of Sc (4F) + H (2S), i.e. $3,5\Sigma^-$, $3,5\Pi$, $3,5\Delta$ and $3,5\Phi$ were computed using state-averaged CASSCF (SA-CASSCF) and MRCISD methods. The second asymptote lies at about 11520 cm^{-1} above the ground state asymptote which is located about 14335 cm^{-1} and 2815 cm^{-1} above the ground state asymptote and experimental asymptote, respectively.

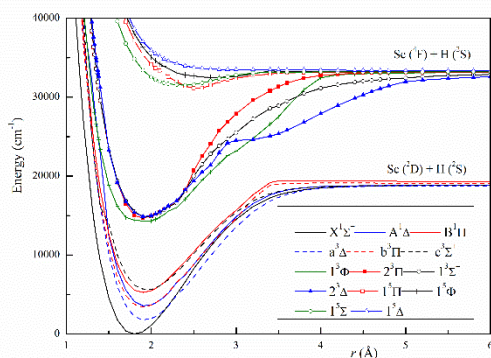


Fig.1: MRCI potential energy curves of all electronic states of ScH.

The calculated dipole moments for all singlet states are plotted in Fig. 2 for $r = 0.5\text{ \AA}$ to 6.0 \AA .

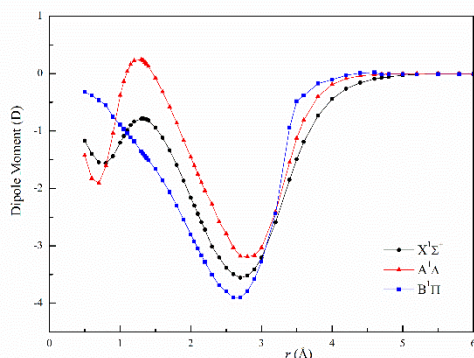


Fig.2: Dipole moments for the singlet states of ScH.

Ab initio points of potential energy curves and dipole moments were imported in program LEVEL, in order to calculate vibrational energy levels and equilibrium internuclear distances (r_e). The Deuterium isotope effect of this molecule is also investigated in the LEVEL program using different mass of Hydrogen and Deuterium. The reduced mass for ScH and ScD is 0.98572693 u and 1.92773591 u , respectively. The energies of all bound vibrational levels are computed for the low-lying

electronic states of ScH and ScD using the LEVEL program and parts of them are presented in Tables 1-2.

Table 1: Vibrational energy levels in the low-lying electronic states of ScH.

ν	$X^1\Sigma^+$	$A^1\Delta$	$B^1\Pi$	$a^3\Delta$	$b^3\Pi$	$c^3\Sigma^+$
0	759.5	4255.9	5927.6	2471.0	4090.6	6234.6
1	2266.2	5644.5	7253.6	3863.6	5451.3	7514.7
2	3733.6	7010.7	8549.9	5240.1	6791.1	8751.9
3	5150.3	8294.7	9794.2	6547.2	8071.1	9971.6
4	6519.5	9493.3	10983.5	7750.1	9259.5	11158.3
5	7860.5	10708.3	12134.7	8979.4	10449.2	12281.8
6	9165.4	11850.9	13231.9	10145.9	11586.3	13352.6
7	10401.0	12978.9	14272.6	11277.8	12674.4	14354.3
8	11576.5	14057.6	15254.0	12366.4	13715.5	15265.6
9	12712.1	15090.5	16184.1	13410.5	14716.2	16113.6
10	13778.4	16056.3	17084.3	14399.5	15685.6	16889.9
11	14779.3	16942.6	17972.7	15337.3	16654.2	17601.9
12	15709.6	17718.7	18818.1	16209.9	17614.4	18202.5
13	16558.9	18338.9	18886.0	17004.1	18518.5	18623.8
14	17311.8	18729.0		17690.8		18816.4
15	17944.9			18246.2		

Table 2: Vibrational energy levels in the low-lying electronic states of ScD.

ν	$X^1\Sigma^+$	$A^1\Delta$	$B^1\Pi$	$a^3\Delta$	$b^3\Pi$	$c^3\Sigma^+$
0	541.7	4055.4	5735.2	2270.2	3893.4	6049.5
1	1625.3	5052.5	6688.4	3269.1	4871.6	6972.8
2	2694.4	6042.3	7633.0	4261.4	5839.3	7870.6
3	3738.3	7024.1	8555.0	5252.8	6800.5	8755.0
4	4755.7	7941.4	9447.9	6191.2	7721.8	9629.5
5	5745.8	8801.2	10312.6	7054.3	8579.0	10494.5
6	6717.8	9682.5	11158.6	7942.9	9441.2	11332.4
7	7680.2	10530.9	11981.1	8816.3	10292.6	12138.5
8	8624.2	11356.4	12776.2	9655.4	11111.2	12923.7
9	9535.3	12175.2	13543.4	10482.7	11910.4	13671.6
10	10407.1	12978.2	14280.6	11287.0	12682.4	14362.5
11	11256.1	13762.2	14987.6	12070.9	13432.1	15007.6
12	12086.0	14519.6	15664.6	12830.4	14157.2	15614.2
13	12880.3	15247.6	16319.0	13564.7	14861.3	16196.6
14	13642.0	15942.0	16965.4	14273.6	15555.3	16764.3
15	14371.6	16594.5	17608.1	14954.6	16251.3	17304.5



The obtained calculations suggest that the $v = 13$ level is the highest bound vibrational level of the $B^1\Pi$ state for ScH and the $v = 18$ is the highest bound vibrational of this state for ScD. The computed vibrational energies of the $v = 0 - 3$ levels were fitted to Dunham energy expression, and the harmonic vibrational frequencies ω_e and anharmonicity constants $\omega_e x_e$ were calculated. The equilibrium rotational constants (B_e) were calculated from r_e values, and the vibration-rotation interaction constants (α_e) were obtained from LEVEL outputs. The molecular constants computed for ScH and ScD are compared with those of the previous *ab initio* studies [4-6] and with the experimental values [3] in Tables 3-4.

Table 3: Computed spectroscopic constants (in cm^{-1}) for the $X^1\Sigma^+$ and excited states of ScH.

state	T_e	D_e	ω_e	$\omega_e x_e$	B_e	α_e	r_e (Å)
$X^1\Sigma^+$	0.0	18857	1554	22.7	5.24	0.107	1.80
	0.0^a	-	1597	-	5.43	0.125	1.78
	0.0 ^b	18868	1587	-	-	-	1.77
	0.0 ^c	17180	1540	-	5.3	-	1.80
$A^1\Delta$	3548.6	15316	1451	26.2	4.6	0.085	1.93
	3914 ^b	-	1428	-	-	-	1.90
	3516 ^c	13712	1390	-	4.5	-	1.95
$B^1\Pi$	5261.2	13602	1371	20.4	4.7	0.121	1.90
	^a	-	1410	23.5	4.99	0.146	1.85
	5856 ^b	-	1380	-	-	-	1.88
$a^3\Delta$	1764.5	17101	1444	21.4	4.6	0.078	1.92
	1868 ^b	-	1432	-	-	-	1.88
	1726 ^c	15487	1395	-	4.6	-	1.94
$b^3\Pi$	3395.3	15469	1408	20.2	4.7	0.110	1.90
	3544 ^b	-	1406	-	-	-	1.88
	6200 ^d	-	1438	-	-	-	1.93
$c^3\Sigma^+$	5579.5	13285	1306	15.1	4.5	0.090	1.95
	6122 ^b	-	1325	-	-	-	1.92
$2^3\Pi$	14691	18465	1195	18.0	4.808	0.247	1.89
$2^3\Delta$	14851	18254	1272	9.6	4.615	0.163	1.93
$1^3\Sigma^-$	14813	18402	1205	10.0	4.582	0.171	1.93
$1^3\Phi$	14268	18925	992	13.0	4.497	0.032	1.95
$1^5\Pi$	31099	2088	1095	145	2.642	0.178	2.54
$1^5\Sigma^-$	31499	1694	-	-	2.969	0.089	2.4

^aExperimental values Ref. [3]; ^bRef. [4]; ^cRef. [5]; ^dRef. [6].

Table 4: Computed spectroscopic constants (in cm^{-1}) for the $X^1\Sigma^+$ and excited states of ScD.

state	T_e	D_e	ω_e	$\omega_e x_e$	B_e	α_e
$X^1\Sigma^+$	0.0	18857.4	1105.196	9.224	2.690	0.037
	0.0^a	-	1141.265	12.380	2.787	0.045
$A^1\Delta$	3548.6	15315.8	1004.757	3.798	2.353	0.035
$B^1\Pi$	5261.2	13602.4	971.219	7.823	2.430	0.046

	^a	-	986.302	-	2.540	0.041
$a^3\Delta$	1764.5	-	1001.693	1.878	2.375	0.032
$1^3\Pi$	3395.3	15469.1	986.062	4.259	2.427	0.045
$2^3\Pi$	14691.0	18465.3	929.878	11.670	2.458	0.107
$1^3\Sigma^+$	5579.5	13284.8	940.742	9.722	2.290	0.027
$2^3\Delta$	14851.4	18254.0	947.670	15.548	2.360	0.062
$1^3\Sigma^-$	14812.6	18401.5	944.142	18.267	2.343	0.068
$1^3\Phi$	14267.7	18924.7	709.012	5.933	2.300	0.028
$1^5\Pi$	31099.5	2087.9	808.706	82.212	1.351	0.029
$1^5\Sigma^-$	31499.5	1694.3	490.221	20.544	1.518	0.008

Matrix elements of the dipole moment operator between all singlet and triplet states were computed at the MRCISD level using the ORCA program. The Einstein A coefficients for all vibronic transitions were calculated using the following equation;

$$A_{v' \rightarrow v''} = \frac{16\pi^3 \nu^3}{3h\epsilon_0 c^3} \left| \langle \psi_{v'} | R_e(r) | \psi_{v''} \rangle \right|^2 \quad (1)$$

where $R_e(r)$ is the electronic transition dipole moment and ν is the transition frequency. To obtain an average lifetime for a vibrational level of an excited electronic state should calculate the sum of Einstein A coefficients for transitions to all lower state vibrational levels:

$$\tau_{v'} = \left(\sum_{v''} A_{v' \rightarrow v''} \right)^{-1} \quad (2)$$

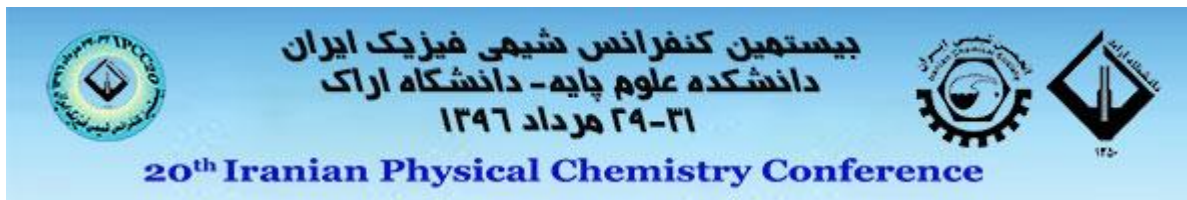
The Einstein A coefficients and lifetimes are calculated for the vibrational levels of the $B^1\Pi$, $b^3\Pi$, and $2^3\Pi$ states for ScH. We computed a lifetime of 74 μs for the $v' = 0$ level of the $B^1\Pi$ state. For the $v' = 0$ level of the two triplet states $b^3\Pi$ and $2^3\Pi$, radiative lifetimes were determined 17 ms and 149 ns, respectively. These values for ScD have been calculated.

Conclusions

Ab initio potential energy curves and transition dipole moments have been calculated for the $X^1\Sigma^+$, $A^1\Delta$, $B^1\Pi$, $a^3\Delta$, $b^3\Pi$, $c^3\Sigma^+$, $1^3\Phi$, $2^3\Pi$, $1^3\Sigma^-$, $2^3\Delta$, $1^5\Pi$, $1^5\Phi$, $1^5\Sigma^-$ and $1^5\Delta$ states of ScH at the MRCI level of theory with large active space and basis sets using the ORCA program. The computed transition dipole moments were used to calculate average lifetimes of excited state vibrational levels for ScH and ScD. These highly accurate transition dipole moments can be used to calculate the Einstein A coefficients for all rovibronic transitions of ScH and ScD.

References

- [1] P.R. Scott and W.G. Richards, On the low-lying electronic states of ScH, J. Phys. B: atomic and Molecular Physics, 7 (1974) 1679-1682.
- [2] C.W. Bauschlicher Jr. and S.P. Walch, On the d bond in ScH, J. Chem. Phys. 76 (1982) 4560-4568.



[3] R.S. Ram and P.F. Bernath, Fourier transform emission spectroscopy of the $B^1\Pi-X^1\Sigma^+$, $C^1\Sigma^+-X^1\Sigma^+$, and $G^1\Pi-X^1\Sigma^+$ systems of ScH and ScD, J. Chem. Phys. 105 (1996) 2668-2674.

[4] L. Lodi, S.N. Yurchenko and J. Tennyson, The calculated rovibronic spectrum of scandium hydride, ScH; Mol. Phys., 113 (2015) 1998-2011.

[5] S. Koseki, Y. Ishihara, D.G. Fedorov, H. Umeda, M.W. Schmidt, and M.S. Gordon, Dissociation Potential Curves of Low-Lying States in Transition Metal Hydrides. 2. Hydrides of Groups 3 and 5, J. Phys. Chem. A, 108 (2004) 4707-4719.

[6] J. Anglada, P.J. Bruna, and S.D. Peyerimhoff, The electronic spectrum of ScH, Mol. Phys., 66 (1989) 541-563.



بیستمین کنفرانس شیمی فیزیک ایران
دانشکده علوم پایه - دانشگاه اراک
۲۱-۲۴ مرداد ۱۳۹۶



20th Iranian Physical Chemistry Conference

ترمودینامیک

Thermodynamics

Lattice energy of Alkyl Boron and Alkyl Carboranes

EnsiehGhasemian

^aDepartment of chemistry, faculty of science, Ilam university, P.O. Box 69315516, Ilam, Iran

*e.ghasemian@gmail.com

Abstract: The lattice energy and enthalpy of 12 new salts of triazolium and imidazolium cations were calculated using Madelung equation. The Madelung equation is based on correlation methods that rely on volume to predict thermodynamic quantities. Density and melting point are only reported physical properties of these compounds in literatures. So predicting lattice energy and enthalpy are important parameters to understand other behaviors of compounds.

Keywords: carboran, borane, lattice energy, density, enthalpy

Introduction

Ionic liquids (“melts”) are receiving renewed attention for their promise as alternative reaction media, catalysis and stabilizer due to the useful properties are negligible vapor pressure, high electrical conductivity, wide electrochemical window, tolerance to strong acids, and excellent thermal and chemical stability [1]. In the present work it has begun an investigation into the properties of a new class of imidazolium salts with two goals in mind. One is to shed light on the factors that contribute to the low melting points of *N,N'*-dialkylimidazolium salts. The other is to incorporate carborane anions into the ionic liquid repertoire. Carborane anions are among the most inert anions in modern chemistry. Their extraordinarily weak nucleophilicity and redox inertness has allowed the exploration of new extremes of cation reactivity and the isolation of new superacids [2,3]. Their incorporation into ionic liquids should expand this utility, opening up new frontiers in reactive cation chemistry.

Theoretical method

Lattice energies are of central importance in the estimation of enthalpies of formation via thermochemical cycles. For ionic materials, at which point the Coulombic forces among the ions overwhelm all other forces of attraction. In this situation, the equation takes the following simple form

$$U_{POT} = AI \left(\frac{2I}{V_m} \right)^{1/3} \quad \text{eq (1)}$$

where $A = 121.39 \text{ kJ.mol}^{-1}.\text{nm}^{-3}$ is the standard electrostatic Madelung constant of the Kapustinskii equation [4].

Results and Discussion

All necessary experimental data have been given from literatures [5,6]. Table 1 shows values of calculated lattice energy and lattice enthalpy.

Table 1: Applied ionic liquids and predicted values

compound	V_m/nm^3	$U/\text{kJ.mol}^{-1}$	$\Delta H/\text{kJ.mol}^{-1}$
[EMIM][CB ₁₁ H ₁₂]	4E-09	71988.27683	86853.7088
[EMIM][CB ₁₁ H ₆ Cl ₆]	5.3E-09	65140.59445	80006.0264
[EMIM][CB ₁₁ H ₆ Br ₆]	5.6E-09	64172.51912	79037.9511
[EMIM][1-CH ₃ -CB ₁₁ H ₁₁]	4.3E-09	70039.16887	84904.6009
[EMIM][1-C ₂ H ₅ -CB ₁₁ H ₁₁]	4.5E-09	69176.99552	84042.4275
[OMIM][CB ₁₁ H ₆ Cl ₆]	6.4E-09	61391.01638	76256.4484
[EDMIM][CB ₁₁ H ₁₂]	4.2E-09	70746.07912	85611.5111
[EDMIM][CB ₁₁ H ₆ Cl ₆]	5.5E-09	64574.30655	79439.7386
[BDMIM][CB ₁₁ H ₆ Cl ₆]	6.1E-09	62302.88671	77168.3187
(C ₃ N ₄ H ₈) ₂ B ₁₂ H ₁₂	4.5E-09	68860.93734	83726.3693
(C ₂ N ₄ H ₆)CB ₁₂ H ₁₂	3.2E-09	77092.13352	91957.5655
(C ₃ N ₄ H ₈)CB ₁₂ H ₁₂	3.6E-09	74105.94646	88971.3785

A further enhancement of the calculation of lattice energy is the conversion of energy to enthalpy, as is generally required in thermochemical applications where $\Delta_L H$ is the lattice enthalpy,

$$\Delta_L H = U_{POT} + \sum_{i=1}^n s_i \left(\frac{c_i}{2} - 2 \right) RT \quad \text{eq(2)}$$

s_i is the number of ions of type i , n is the number of ion types in the formula unit, and c_i is defined

according to whether ion i is monatomic ($c_i = 3$), linear polyatomic ($c_i = 5$), or nonlinear polyatomic ($c_i = 6$) [4,5].

The lattice enthalpy of alkyl carboranes in this research is about 7000-9000 kJ/mol. The well-established, empirical method of structural similarity suggests the lattice enthalpy of halogenated carboranes is lower than alkyl carboranes. Results in Table 1 show increase in number of imidazolium ring decrease lattice enthalpy of carboranes. Unfortunately lattice energy and lattice enthalpy of applied alkyl borane and carboranes don't have reported in literature so far. so the results are approximate.

Conclusions

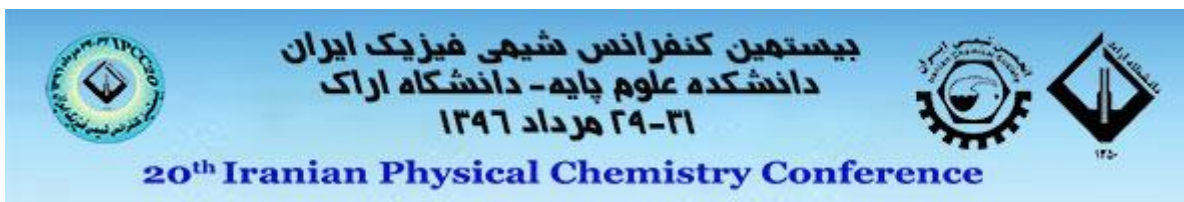
The importance of the present work is reporting lattice energy and lattice enthalpy for the first time. In this paper it has been shown application of depended thermodynamic variables to volumes of molecules is applicable method to predict thermodynamic parameters of new compounds.

Acknowledgment

The authors are grateful for the financial support from the Research Councils of Ilam University.

References

- [1] J. D. Holbrey, R. D. Rogers, *Ionic Liquids in Synthesis*, 2002. VCH Wiley: Weinheim,
- [2] M. J.; Earle, J. M. S. S. Esperanca, M. A. Gilea, J. N. Canongia Lopes, L. P. N. Rebelo, J. W. Magee, K. R. Seddon, J. A. Widegren, The distillation and volatility of ionic liquids. *Nature* 439(2006)831-834.
- [3] J. D. Holbrey, W. M. Reichert, R. P. Swatloski, G. A. Broker, W. R. Pitner, K. R. Seddon, R. Rogers, Efficient, halide free synthesis of new, low cost ionic liquids: 1,3-dialkylimidazolium salts containing methyl- and ethyl-sulfate anions. *Green Chem.* 4 (2002) 407-413.
- [4] H. D. B. Jenkins and L. Glasser, Difference rule - A new thermodynamic principle: Prediction of standard thermo-dynamic data for inorganic solvates, *J. Am. Chem. Soc.* 126 (2004) 15809-15817.
- [5] H. D. B. Jenkins, Thermodynamics of the Relationship between Lattice Energy and Lattice Enthalpy, *J. Chem. Educ.* 82(2005) 950-952.



Coarse-Grained Simulations of Freezing Behavior of Water-NaCl Mixtures

S. Mahmood Fatemi* and Masumeh Foroutan

Department of Physical Chemistry, School of Chemistry, College of Science, University of Tehran, Tehran 14155-6455, Iran

m.fatemi@khayam.ut.ac.ir

Abstract: We performed molecular dynamics simulations using the coarse-grained model to study the freezing behavior of water-salt mixture in a wide range of temperatures for a very long time around 50 nanoseconds. For the salty water, an interface in nanoscale was used. For this system, the freezing behavior of water molecules was studied using some qualities such as density, total energy, and radial distribution function. For the water-salt mixture, the equilibrium freezing temperature depression observed in the simulations was well consistent with the experimental data. The plots of the total energy versus time shows the freezing point of water-salt mixture was 265 K that is 9 K less than the freezing point of pure water. The reduction of freezing point is in very good agreement with the experimental freezing point.

Keywords: Coarse-grained model; Nanoscale; Freezing point; Water-salt mixture.

Introduction

Water is the most utilized solvent in experimental and computational studies [1, 2] particularly for biological systems. The presence of salts significantly modifies the properties of pure water, and also affects the properties of biological molecules in water. Experimental studies of both thermodynamic and kinetic aspects of the equilibrium between salts and their saturated solutions are also crucial in geological studies [3]. Sodium chloride is one of the most abundant salts available on earth, and for this reason many experimental studies have been devoted to determining the properties of NaCl solutions, and the effect of NaCl on biological molecules. It is clear that computer simulations can complement these studies by supplying a molecular perspective of the behavior of the system. For this reason, some simulation studies have been devoted to NaCl solutions [4] and primitive models of ionic systems. The chemical potential of ions in solution has been calculated in many simulation studies. However, it is somewhat surprising to realize that the number of studies devoted to determine from molecular simulations the solubility of salts in water is quite small. In the present work, we have using a developed coarse-grained model of water for studying the freezing behavior of water molecules water-salt mixture.

In this work, the coarse-grained models of water and NaCl in water were used for MD simulation, where a monoatomic model of water (mW) has been used as a computational basis. In an attempt to avoid challenging electrostatics in term of computational methods, ions were modeled without charge. The full details of the coarse-grained models of water and NaCl in water were given in the mentioned Ref. [4].

Simulation Details

The LAMMPS [5] MD package was used to equilibrate the molecules and run the simulations under NPT conditions at different temperatures and 1 atm. The pressure and temperature were controlled using a Nose-Hoover barostat and thermostat with damping parameters 500×10^{-6} nanosecond and 100×10^{-6} nanosecond, respectively. All simulations were performed with periodic boundary (PPP) conditions. The equations of motion were integrated using the velocity Verlet algorithm with a time step of 10×10^{-6} nanosecond. Simulation boxes with dimensions of about $2.0 \times 2.2 \times 5.4$ nanomete³ and $10.4 \times 2.1 \times 2.1$ nanomete³ used for pure water and water-salt mixture, respectively. All simulations were performed for 50 nanoseconds. Long production runs were used to determine with high accuracy the different quantities of NaCl solution. The initial configurations for the pure water simulations had 1584 water molecules in the liquid phase. An interface in nano scale was used for the simulation of salt-water mixture. As the study results in the next section show, the temperature of 274 K has been identified as the freezing temperature of pure water. To study the freezing behavior of pure water, we chose a wide range of temperatures. The initial configuration of the salt water mixture had 1584 water molecules in the liquid phase. The Na and Cl were initially placed by removing 144 water molecules in the middle and nanoscale distance of the cell (see Fig. 1), resulting in a solution concentration of %14. It has been shown that a system with 1584 total molecules is satisfactory for the study of ice growth.

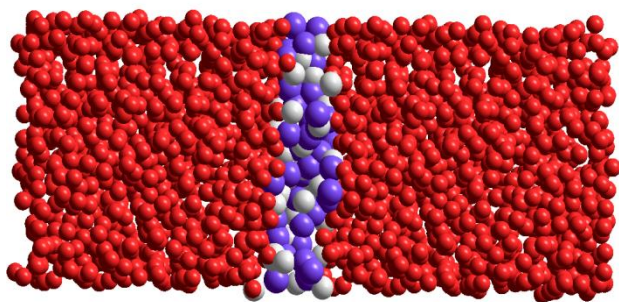


Fig. 1: The Snapshot of initial configuration of 14% water-salt mixture, The Na and Cl were initially placed in the middle and nano scale of the cell (Colors assigned to each molecule: red, water; white, Cl & purple, Na).

Results and Discussion

According to the recent paper of Vega [6] in order to determine the freezing point of pure water, the total energy vs. time was calculated and shown in figure 2.

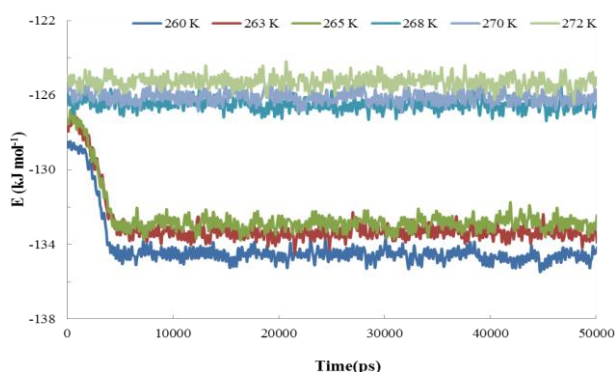


Fig. 2: Total energies of water-salt mixture at several temperatures.

Figure 2 shows the total energy changes of water-salt mixture at 260, 263, 265, 268, 270, and 272 K. As can be observed in figure 2, at 260, 263 and 265 K, the amount of energy was reduced over time before reaching equilibrium. So at these temperatures, system is lower than the freezing point. The constant energy of the system at 268, 270 and 272 K showed that the primary system maintained its liquid state. Therefore, 265 K (maximum temperature at which some part of the liquid is converted into ice) can be introduced as the freezing point of water- NaCl mixture, Figure 3 shows the RDFs for water-water at several temperatures. As the figure shows there are sharp peaks around 2.64×10^{-1} nanometer for all temperatures. Height of the peaks was increased by decreasing the temperature.

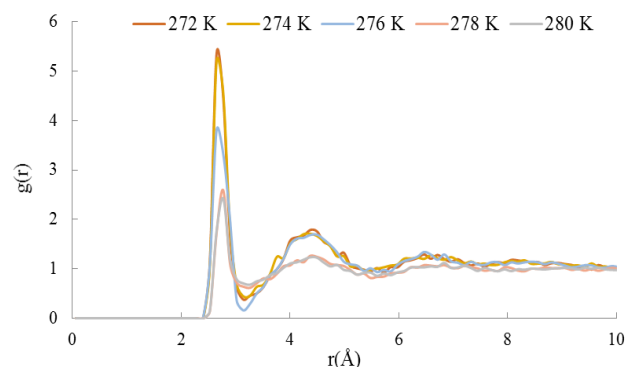


Fig.3- RDFs for water-water

Conclusions

In this study, 50 nanosecond simulations for the freezing of water molecules in water-salt mixture was performed using the coarse-grain model. For constructing the input of the simulation of salty water, an interface in nanoscale distance was used. The comparison of the obtained results for pure water and water-salt mixture shows how salt, as an anti-freezing agent, can make important changes in freezing behavior of water. Using plots of the total energy versus time, 265 K was determined as the freezing point of water-salt mixture which is 9 K below the freezing point of pure water. In the less temperature than obtained freezing point the sodium and chloride ions tendency to network formation and rejection of solution lead to reduction of water molecules accumulation.

References

- [1] S. M. Fatemi, M. Foroutan, Study on formation of unstable clathrate-like water molecules at freezing/melting temperatures of water and salty water, *Fluid Phase Equilib.* 384 (2014) 73-81.
- [2] M. Foroutan, S.M. Fatemi, F. Esmaeilian, A review of the structure and dynamics of nanoconfined water and ionic liquids via molecular dynamics simulation, *Eur. Phys. J. E*, 40 (2017) 19.
- [3] F.Zhang, G. Wang, T. Kamai, W. Chen, D.Zhang, J. Yang, Undrained shear behavior of loess saturated with different concentrations of sodium chloride solution, *Eng. Geol.*, 155 (2013)69-79.
- [4] S. M. Fatemi, M. Foroutan, Molecular Dynamics Simulations of Freezing Behavior of Pure Water and 14% Water-NaCl Mixture Using the Coarse-Grained Model,
- [5] S. Plimpton, Fast parallel algorithms for short-range molecular dynamics. *J. Comput. Phys.* 117 (1995) 1-19.
- [6] R.G. Fernández, J.L.F. Abascal, F.C. Vega, The melting point of ice Ih for common water models calculated from direct coexistence of the solid-liquid interface, *J. Chem. Phys.* 124 (2006) 144506-11.

Melting/Freezing Behavior of Water Confined Between Two-layer Graphene Nanosheets

S. Mahmood Fatemi* and Masumeh Foroutan

Department of Physical Chemistry, School of Chemistry, College of Science, University of Tehran, Tehran 14155-6455, Iran

*m.fatemi@khayam.ut.ac.ir

Abstract: In this work, the melting/freezing point of confined water between two graphene nanosheets was calculated from direct coexistence of the solid-liquid interface. Also, molecular dynamics simulation of confined liquid water-ice between two graphene nanosheets was applied. Phase transition temperature of the confined ice-water mixture was calculated as 240 K that was 29 K less than the non-confined ice-water system. The obtained simulation results showed that water molecules located in the region near each graphene sheet with the thickness of 2 nm had a different behavior from other water molecules located in other regions. Also, coordination number remarkably changed at phase transition temperature. Coordination numbers of water in the bulk system and confined system were 4.9 and 6.2, respectively.

Keywords: Melting/freezing point; Confined ice-water mixture; Graphene sheets; TIP4P/Ice water Model.

Introduction

Confinement of molecules at nanometric scale provides the possibility of exploring the behavior of fluids under special conditions that are not encountered in bulk systems [1, 2]. Studying the unusual properties of confined water is important for designing novel nanofluidic applications. Water confined in different structures like graphite channels, carbon nanotubes, silica pores, mica surfaces, metal oxide-based nanocapsules and reverse micelles has motivated intense investigations both theoretically and experimentally [3]. Recent studies have demonstrated that the confinement of matters at nanometric scale induces phase transition or a supercooling [4]. It has been shown that confinement in cylindrical nanopores decreases the equilibrium melting temperature of water. Pores with the radius of larger than 50 nm have essentially the same melting temperature as water in bulk, while pores with the radius of 1 nm or less do not exhibit first order melting transition. A similar relationship is held for the boiling-point elevation in pores. Recently, rate of capillary evaporation of water confined between two hydrophobic surfaces separated by nanoscopic gaps, as a function of gap, surface size, and temperature has been computed [5].

In this work, phase equilibrium of water and ice mixtures confined between two graphene sheets was examined using MD simulations.

Simulation Details

The simulations were performed using LAMMPS [6] and TIP4P/Ice model as a new water model specifically designed to cope with solid-phase properties. Predictions of this model for both densities and coexistence curves of ice have been demonstrated to be better than those for other water models.

All the interatomic interactions were modeled by the well-known Lennard-Jones potential. The Ewald method was implemented to compute electrostatic interactions. Velocity form of the Verlet algorithm method and the Nosé-Hoover barostat and thermostat were also applied with damping coefficients 1 and 0.1 ps⁻¹, respectively and time step of 3 fs was employed. Moreover, the cutoff distance of 10 Å was utilized for the van der Waals potentials. Computer simulations were carried out using a (30×20×68) Å³ computational cell with the periodic boundary conditions applied in all three principal directions. For the confined system, two open-ended finite-length graphene sheets with the length of 63.9 Å were considered. The distance between these two graphene sheets was 20 Å and the number of their carbon atoms was 1584. Figure 1 shows the initial configuration of the simulation system. All MD simulations were performed in the NVT ensemble. Atoms of the graphene sheets were fixed at their initial positions and 1000 water molecules in liquid and ice Ih halves were placed between two graphene sheets.

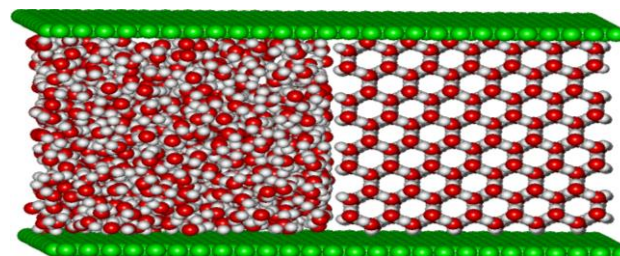


Fig.1: Initial configuration of simulation for confined water between two graphene sheets, green, white and red colors are carbon, hydrogen and oxygen respectively.

Results and Discussion

Figure 2 represents energy changes of the confined ice-water mixture between two graphene nanosheets for several temperatures close to phase transition temperature. As can be observed, energy of the system was reduced over time at 235 K and 237 K, which represented freezing of the water existing in the liquid system at these temperatures. Moreover, increased energy at 242 K and 245 K indicated melting of the ice in the system at these temperatures. At 240 K, energy changes of the system were constant over time. Thus, this point was considered as the solid-liquid phase transition temperature of water confined between graphene sheets.

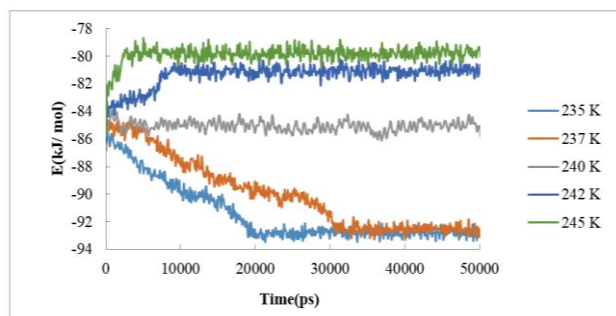


Fig. 2: Total energy changes versus time for confined bulk ice-water mixture between two graphene sheets.

Figure 3 represents the RDF for oxygen-oxygen atoms of water molecules confined between two graphene nanosheets at the temperatures close to the phase transition temperature. This curve showed a sharp peak and a relatively weak peak at distances 2.64 Å and 4.61 Å, respectively. As can be observed in this curve, height of the peaks was different at more and less temperatures than the phase transition temperature. Height of the peaks was reduced with an increase in water temperature; however, this reduction was more evident as a result of changing water phase from solid to liquid states. Higher intensity of peaks at 235 K and 237 K compared to 242 K and 245 K showed higher correlation of water molecules in crystal than liquid states.

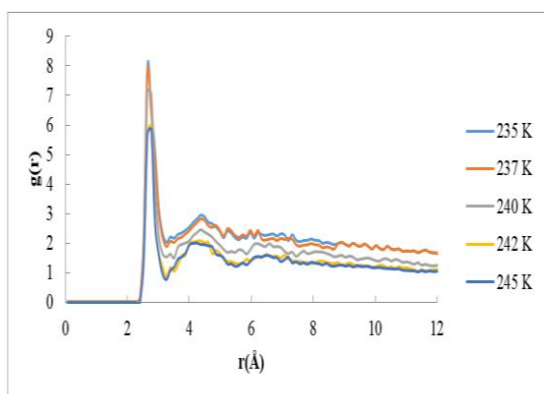


Fig.3- RDF for oxygen-oxygen atom of water molecules confined between two graphene sheets at the temperatures close to the phase transition temperature.

Conclusions

Graphene effects on the phase transition temperature of water and ice confined between two nanosheets of graphene were investigated using plots of total energy versus time, temperature versus density, radial distribution functions, and coordination numbers. Using plots of total energy versus time, phase transition temperature of the confined ice-water mixture was obtained as 240 K that was 29 K less than the non-confined ice-water system. RDF for hydrogen atoms of water in the vicinity of the carbon atom of graphene sheets appeared at less distances than the oxygen atom of water. In other words, at 245 K, orientation of water molecules was such that these molecules got closer to the graphene sheet from the side of their own hydrogen atom.

Also, coordination number remarkably changed at phase transition temperature. Coordination numbers of water in the bulk system and confined system were 4.9 and 6.2, respectively.

References

- [1] M. Foroutan, S.M. Fatemi, F. Esmailian, A review of the structure and dynamics of nanoconfined water and ionic liquids via molecular dynamics simulation, *Eur. Phys. J. E*, 40 (2017) 19.
- [2] M. Foroutan, S.M. Fatemi, F. Shokouh, Graphene confinement effects on melting/freezing point and structure and dynamics behavior of water, *J. Mol. Graphics Modell.* 66 (2016) 85-90.
- [3] M. Foroutan, S.M. Fatemi, *Encyclopedia of Nanoscience and Nanotechnology* edited by H.S.Nalwa, American Scientific Publishers, Valencia, CA, (2017).
- [4] M. Schoeffel, N. Brodie-Linder, F. Audonnet, C. Alba-Simionesco, Wall Thickness Determination of Hydrophobically Functionalized MCM-41 Materials. *J. Mater. Chem.* 22 (2012) 557-567.
- [5] S. Sharma., Pablo G. Debenedetti. Evaporation rate of Water in Hydrophobic Confinement. *Proc. Natl. Acad. Sci. U. S. A.* 119 (2012) 4365-4370
- [6] S. Plimpton, Fast parallel algorithms for short-range molecular dynamics. *J. Comput. Phys.* 117 (1995) 1-19.

Molecular Dynamics Study of Dynamic Criteria of a Nanoalloy in a Melting Process

F. Arianfar*, H. Behnejad

Department of Physical Chemistry, School of Chemistry, University College of Science, University of Tehran, Tehran, Iran.

*f_arianfar@yahoo.com

Abstract: The operations of melting of Au₁₅Ag₄₀ nanoalloy have been studied using the molecular dynamic simulations using the Gupta multiparticle potential and the nonergodicity of simulations is removed by the multiple histogram method. The melting characteristics are determined by the analysis of variations in the potential energy. The dynamic criteria (VACF and power spectrum curves) show that the similarity in the behavior of the atoms increases as the temperature increases.

Keywords: Molecular dynamic simulation, Au₁₅Ag₄₀ nanoalloy, Gupta multiparticle potential, Dynamic criteria.

Introduction

Generally, a bulk material should have constant physical properties regardless of its size, but at the nanoscale size-dependent properties are often observed. bimetallic nanoalloys have received significant observation because their characteristics changed by varying their size and also their composition can be adjusted to get wanted properties. Studying the structures, thermal stability and melting process of different nanoalloys helps us to find and design many applications such as catalysis, optics, magnetism and etc. Molecular dynamics simulation provides the methodology for detailed microscopic modelling on the molecular scale. After all, the nature of matter is to be found in the structure and motion of its constituent building blocks, and the dynamics is contained in the solution to the N-body problem. Molecular dynamics (MD) is a computer simulation of physical movements of atoms and molecules in the context of N-body simulation. The atoms and molecules are allowed to interact for a period of time, giving a view of the motion of the atoms. In the most common version, the trajectories of atoms and molecules are determined by numerically solving the Newton's equations of motion for a system of interacting particles, where forces between the particles and potential energy are defined by interatomic potentials or molecular mechanics force fields.

In current study dynamic criteria of melting mechanism of Au₁₅Ag₄₀ nanoalloy has been defined by molecular dynamic simulation.

Computational part:

In this work, we used second-moment-approximation (SMA) tight-binding analytic potential,

which has been used extensively in structural and thermal studies of metal clusters. In this model, total energy of a system is given by:

$$E = \sum_j E_j^b + E_j^r, \quad (1)$$

where, E_b and E_r are the bonding and the repulsive Born–Mayer term respectively. For binary system consisting α and β type atoms.

Global minimum structures of Au₁₅Ag₄₀ were used as an initial configuration to perform MD simulations at different temperatures using DL-POLY 2.20 simulation package. Potential parameters determined by Gupta. These have been used to mimic the interaction between the atoms. The equation of motions is integrated in the constant temperature ensemble (NVT) using the velocity version of the Verlet algorithm and employing Evans thermostat.

Dynamic Criteria

In a crystalline solid, all atoms located at similar positions and have similar environments and feel equal mean forces. The velocity autocorrelation function (VACF) shows how the present velocity of a particle is related to its previous value and how it affects its subsequent velocities. For liquid systems, VACF decays to zero after a few collisions and for solid systems it decays after a few oscillations. As the temperature of the solid cluster increases its energy also increases and the correlation between atoms reduces. Finally, in the liquid-like region the oscillations in the VACF disappear, which is the signature of an uncorrelated motion of the atoms in the cluster.

Other useful quantity to study the environment similarity between the individual atoms

of the cluster and also diffusive motions within it is the power spectrum which is defined as the fourier transform of VACF:

$$\Omega^{(i)}(\omega) = 2 \int_0^{\infty} C^{(i)}(t) \cos(\omega t) dt, \quad (2)$$

Where $C^{(i)}(t)$ is the velocity autocorrelation of atom i :

$$C^{(i)}(t) = \frac{\langle v_i(t_0) \cdot v_i(t_0+t) \rangle}{\langle v_i(t_0) \cdot v_i(t_0) \rangle}, \quad (3)$$

where v_i is the velocity of atom i , and the angular brackets express time averaging over the product of velocity at the same or different times in MD trajectory. During the simulations, the particles' centers of mass were fixed and the rotational degrees of freedom were restricted, so the velocities in Eq. (3) are only related to the internal degrees of freedom.

Results and Discussion

Figs. 1 and 2 show the dynamical behavior of $Au_{15}Ag_{40}$ as the temperature increases using VACF and power spectrum of the constituent atoms of the $Au_{15}Ag_{40}$ respectively.

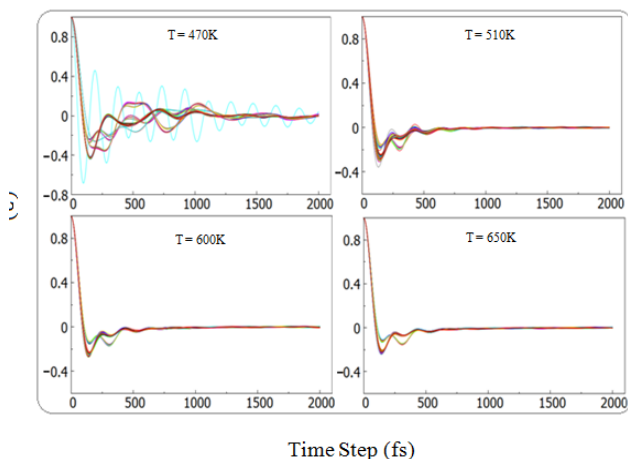


Fig. 1. Velocity auto correlation functions vs temperature for all constituents of the $Au_{15}Ag_{40}$ nanoalloy.

For $Au_{15}Ag_{40}$ the similarity of the behavior increases as the temperature goes up until at melting temperature where the curves for the shell atoms and core atoms as well, merge into two single curves.

Power spectrum is also as an indicator for the beginning of diffusive motions with taking nonzero

values at zero frequency and increase in this value as the melting behavior intensifies.

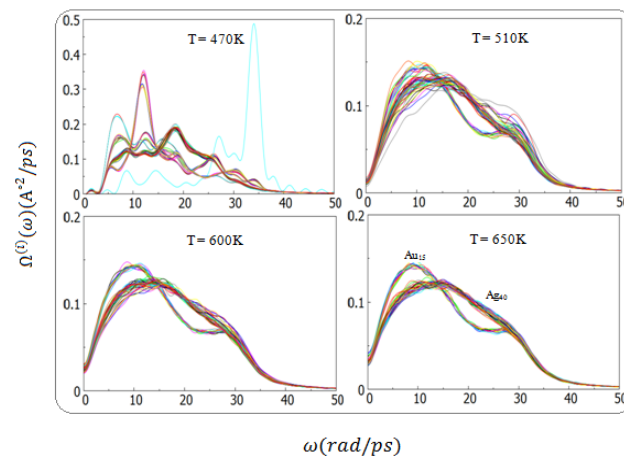


Fig. 2. Power spectra vs frequency at different temperatures.

One can see that, as the temperature goes up, the value of the power spectrum at zero frequency increases, indicating diffusive motions occurring in the system. It is useful to point out that at low temperature the more oscillating atom in the VACF curve has the highest frequency.

Conclusions

In this study several complementary methods were used to investigate the melting mechanisms of $Au_{15}Ag_{40}$ nanoalloy and the MD simulation at constant temperature, starting from global minimum energy structure of $Au_{15}Ag_{40}$ used to study its melting behavior exploiting using dynamical criteria. The VACF and power spectrum curves show that the similarity in the behavior of the atoms increases as the temperature increases. Atoms subjected to stronger forces exhibit more oscillating behavior in their VACF curves and correspondingly higher frequency in the power spectrum curve. Moreover, the power spectrum values at zero frequency can be used to show the intensity of diffusive motions at the given temperature.

Reference

- [1] Arianfar, Fatemeh, Raheleh Rostamian, and Hassan Behnejad. "Molecular Dynamics Simulation of the Melting Process in $Au_{15}Ag_{40}$ Nanoalloys." *Physical Chemistry Research* 5.2 (2017): 359-366.

Study of structure of liquid water on TiO₂(110) using molecular dynamic simulation

Hamideh Babazadeh K.* and Masumeh Foroutan

Department of Physical Chemistry, School of Chemistry, College of Science, University of Tehran, Tehran 14155-6455, Iran

*babazadeh.hh@ut.ac.ir

Abstract: The study of water on titanium dioxide substrate is one the vastly studied systems concerning water-metallic oxide interface. Many quantum and molecular dynamics simulations have been performed to improve the scientific knowledge regarding the interactions between water/titanium dioxide. On this premise, we performed molecular dynamics simulations to study the structure of liquid water on the nanocrystalline titanium dioxide surface. In the current work, we analyzed formation and distribution of water molecules in the first and second layers from a molecular dynamics perspective. For this system, the results are extracted from density profiles and mean squared displacement and are in line with the reported quantum calculations and experimental data.

Keywords: Nanocrystalline titanium dioxide; Water distribution; Nano droplet; Molecular dynamics simulation.

Introduction

Solid-liquid interface is the main contributor in various processes such as electrochemical reactions, catalysis and energy storage and saving which has become a challenge for the field of surface science in recent years [1, 2]. The interactions of water and metallic oxides play an important role in fuel cells and energy generation, additionally; a thin water film can be formed on metallic substrates as a result of the environmental humidity [3, 4]. Titanium dioxide (TiO₂) and its interface with water is one of the most important surfaces. Titanium itself is resistant to corrosion by forming a thin oxide layer which acts as a barrier against additional oxygen diffusion [5]. TiO₂ is widely used as a photocatalyst especially in aquatic environments [6]. Lee and coworkers have studied the formation of water chains on TiO₂ surfaces by quantum and experimental approaches. They reported that at 50 K water molecules adsorb on the titanium dioxide surface. Additionally, as the water spreads on the surface, one dimensional chain of water molecules is observed, which is stable up to 190 K and dissociates at higher temperatures [7]. Tilocca et al. studied the dissociation of water over TiO₂ surface at 160 K by using ab initio molecular dynamics (AIMD) computations. The 160 K was chosen since the two-layer adsorption of water is experimentally stable in vacuum [8]. Their result indicates that dissociation of water is a function of the number of water layers on the surface. Liu and coworkers used a four layer of TiO₂ and observed that the film of water molecules does not dissociate and remains intact. Furthermore, at even number of layers even when water molecules are separately introduced to the system, they become connected through the simulation [9]. Conversely, 3 layers of TiO₂ along with a monolayer of water

molecules results in separation of water molecules. Nevertheless, DFT results indicate that adsorption and dissociation of water molecules on the mentioned titanium dioxide are dependent upon the amount of water covering the surface [10].

In this work, we analyzed formation and distribution of water molecules in the first and second layer from a molecular dynamics perspective.

Simulation Details

All MD simulations were performed using the LAMMPS package [11] and structures were visualized using the VMD package [12] force field and TIP3P [13] model were used for modeling of water molecules. In the current study, 6 systems were simulated in which a box of water comprising 100, 500, 1000, 2000, 4000 and 8000 water molecules were used. The box dimensions were chosen in such a way that the density value was equal to 1 g.cm⁻³. Three layers of neutrally charged TiO₂ were used as the substrate. The substrate dimensions were also changed based on the number of water molecules so that the system could easily achieve equilibrium. The simulation was performed in the NVT ensemble for 2×10⁶ time steps where each time step was set to 1 fs. Nosé-Hoover thermostat [14] was applied to maintain temperature at 300 K, with damping coefficients 0.1 ps⁻¹. Both van der Waals and electrostatic interactions were considered between water molecules and the TiO₂ substrate. Non-bonded van der Waals interactions modeled in terms of 12-6 Lennard-Jones famous potentials [15]. We applied particle-particle particle-mesh (PPPM) method to minimize error in long-range terms in both Coulombic and Lennard-Jones

potentials. Lennard-Jones and Columbic cutoff radiuses were 10 Å and 12 Å, respectively. SHAKE algorithm was used to keep O-H distance fixed at 0.9572 Å and H-O-H angle at 104.52°. The equations of motions were integrated using the Verlet algorithm and periodic boundary conditions were applied along the X and Y axes to eliminate the edge effects. shown that a system with 1584 total molecules is satisfactory for the study of ice growth.

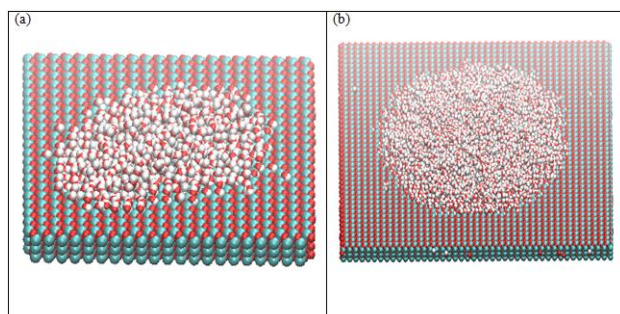


Fig.1: The final snapshot configuration of the systems, (a) 500 and (b) 8000 water molecules. Color code for elements: O, red; Ti, blue; H, white.

Results and Discussion

Density profiles of water molecules on TiO₂ nanocrystal were calculated along Z directions to study the water-TiO₂ interface and determine the behavior of water molecules.

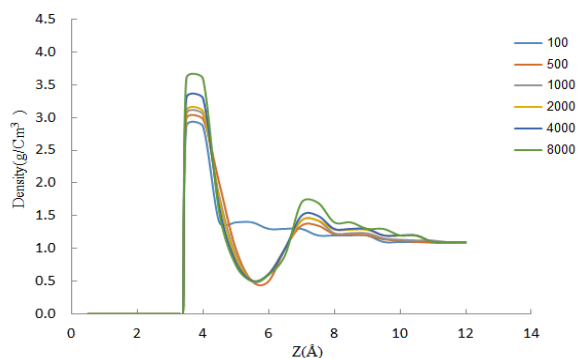


Fig. 2: Density profiles of the Nano droplet with different number of water molecules along z axis.

Fig. 2 shows the density profiles of the nanodroplet with different number of water molecules along z axis. It is apparent in Fig. 2 that for 100 water molecules only one peak exists at 3.6 Å which supports the formation of one layer of water. As the number of water molecules is increased from 500 to 8000 two peaks at 3.6 and 7.4 Å is observed. This is a direct result of the formation of two layers of water which is in line with quantum calculations [16]. It would now be possible to describe the first and second layer based on the density profiles along z axis. On this premise,

the water molecules residing at less than 3.6 Å from the surface form the first layer. Additionally, the water molecules from this point up to 7.4 Å form the second layer while a decrease in density profiles can be observed at 5.78 Å which illustrates the space between the two layers. These results are in agreement with the acquired quantum data [10]. Mean squared displacement (MSD) of water molecules was calculated to study the movement of water molecules in the formed layers. Fig. 3 illustrates the MSD diagram of water molecules in the first and second layers for different sizes of the nanodroplet. The obtained results from Fig. 3 indicate that the MSD of the molecules that reside in the layers increase with the size of the droplet.

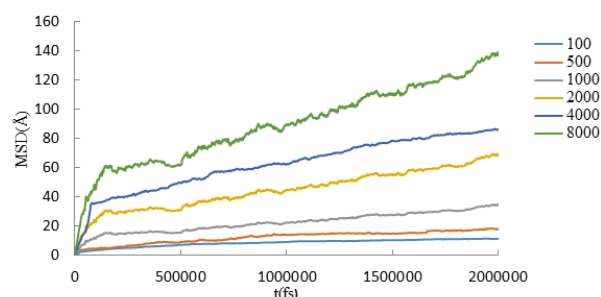


Fig.3 The MSD diagram of water molecules for different sizes of the Nano droplet On TiO₂ surface.

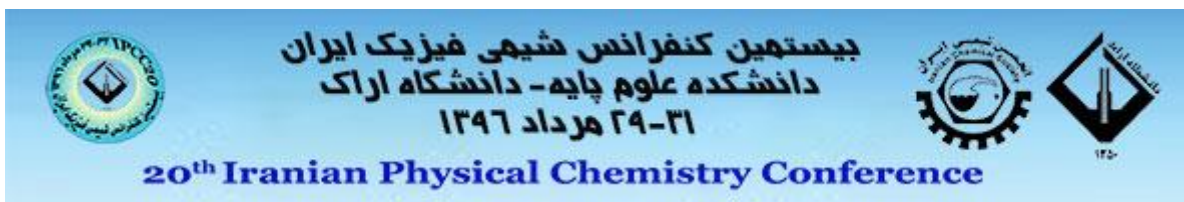
Conclusions

In this study, the behavior of water molecules on the surface of nanocrystalline TiO₂ was studied. As a result of the symmetry of the (110) plane of the retail phase the nanodroplet shows anisotropic wetting behavior. A single layer of water forms on the surface for 100 water molecules. As the number of water molecules increase a second layer of water forms on the surface. The obtained results were in agreement with acquired data from density profile diagrams. The MSD diagram of water molecules show the movement of the molecules that reside in the layers increase with the size of the droplet.

References

- [1] F. Zaera, Probing liquid/solid interfaces at the molecular level. *Chem. Rev.* 112,(2012) 2920-2986.
- [2] F. Zaera, Surface chemistry at the liquid/solid interface. *Surf. Sci.* 605, (2011) 1141-1145.
- [3] M. F. Hochella, M, & A.F.White, A. (1990). Mineral-water interface geochemistry; an overvie. *Rev. Mineral. Geochem.* 23, (1990) 1-16.

- [4] O. Björneholm, M. H. Hansen, A. Hodgson, L. M. Liu, D. T. Limmer, A. Michaelides, & E. Tyrode, Water at interfaces. *Chem. Rev.* 116, (2016) 7698-7726.
- [5] Y. J. Lim, & Y. Oshida, Initial contact angle measurements on variously treated dental/medical titanium materials. *Biomed. Mater.* 11, (2001) 325-341.
- [6] M. Batzill, E. L. Hebenstreit, W. Hebenstreit, & U. Diebold, Influence of subsurface, charged impurities on the adsorption of chlorine at TiO₂ (110). *Chem. Phys. Lett.* 367, (2003) 319-323.
- [7] J. Lee, D. C. Sorescu, X. Deng, & K. D. Jordan, Water chain formation on TiO₂ (110). *Chem. Phys. Lett.* 4, (2012) 53-57.
- [8] A. Tilocca, & A. Selloni, Structure and reactivity of water layers on defect-free and defective anatase TiO₂ (101) surfaces. *J. Phys. Chem. B.* 108, (2004) 4743-4751.
- [9] L. M. Liu, C. Zhang, G. Thornton, & A. Michaelides, Structure and dynamics of liquid water on rutile TiO₂(110). *Phys. Rev. B.* 82, (2010) 161415.
- [10] J. Carrasco, A. Michaelides, M. Forster, S. Haq, R. Raval, & A. Hodgson, A one-dimensional ice structure built from pentagons. *Nat. Mater.* 8, (2009) 427-431.
- [11] S. Plimpton, Fast parallel algorithms for short-range molecular dynamics. *J. Comput. Phys.* 117 (1995) 1-19.
- [12] W. Humphrey, A. Dalke, & K. Schulten, VMD: visual molecular dynamics. *J. Mol. Graph.* 14, (1996) 33-38.
- [13] W. L. Jorgensen, J. Chandrasekhar, J. D. Madura, R. W. Impe, & M. L. Klein, Comparison of simple potential functions for simulating liquid water. *J. Chem. Phys.* (1983) 926-935.
- [14] W. G. Hoover, Canonical dynamics: equilibrium phase-space distributions. *Phys. Rev. A.* 31, (1985) 1695.
- [15] J. E. Lennard-Jones, Cohesion. *Proc. R. Soc. London, Ser. A.* 43, (1931) 461.
- [16] G. Mattioli, F. Filippone, R. Caminiti, & A. A. Bonapasta, Short hydrogen bonds at the water/TiO₂ (anatase) interface. *J. Phys. Chem. C*, 112, (2008) 13579-13586.



Hydrogen bonding of water molecules on TiO₂(110): Amolecular dynamic simulation approach

Hamideh Babazadeh K.* and Masumeh Foroutan

Department of Physical Chemistry, School of Chemistry, College of Science, University of Tehran, Tehran 14155-6455, Iran

*babazadeh.hh@ut.ac.ir

Abstract: The interaction of water with solid substrates plays an important role in various natural phenomena. Understanding the interaction of water and solid surfaces can help in comprehension and control of reactivity of water and surfaces. On this premise, we performed molecular dynamics simulations to study the hydrogen bonds of water molecules on the nanocrystalline titanium dioxide (110) surface. Water on titanium dioxide (110) is the most widely studied water-oxide interface, yet questions about hydrogen bonding are controversial. In this work, the formation of hydrogen bonds between water molecules and titanium dioxide is investigated. Our result show in the first layer fewer numbers of hydrogen bonds exist among water molecules since they tend to form hydrogen bonds with the titanium dioxide substrate.

Keywords: Nanocrystal Titanium Dioxide; Hydrogen bonding; Molecular dynamics simulation.

Introduction

Water molecules in contact with a catalyst surface can play a significant role in heterogeneous catalytic and photocatalytic processes [1]. In particular, this applies to the surfaces of metaloxides, which represent a relevant class of heterogeneous catalysts,[2] and to the surfaces of TiO₂ rutile and anatase polymorphs, likely the most used photocatalysts[3]. Campbell et al. studied the interlayer hydrogen bonding in a number of metallic oxides and their results is in agreement with experimental data [4]. In empirical researches no interlayer hydrogen bonding was detected for water on TiO₂ surface, whereas quantum methods indicate that such bonding should be observed [5]. Mattioli and coworkers studied the formation of hydrogen bonds on anatase surface. They considered two layers of water and observed that short hydrogen bonds occur on anatase substrate. In their work, the first layer of water formed a stronger network than other reported researches. They have also studied the effect of temperature on the first adsorbed layer of water. The short hydrogen bonds result in charge transport from Ti atoms to oxygen atoms of the surface. However, the network of hydrogen bonds disintegrates at higher temperatures [6]. It has also been observed that the hydrogen bond lifetime among interfacial water molecules on TiO₂ surface is longer than in the bulk of water which can be related to stronger interactions between water and titanium dioxide substrate [7].

In this work, to calculate the number of hydrogen bonds between water-water and water-surface Based on the size of the drops.

Simulation Details

All MD simulations were performed using the LAMMPS package [8] and structures were visualized using the VMD package [9] force field and TIP3P [10] model were used for modeling of water molecules. Three layers of neutrally charged TiO₂ were used as the substrate. The substrate dimensions were also changed based on the number of water molecules so that the system could easily achieve equilibrium. The simulation was performed in the NVT ensemble for 2×10^6 time steps where each time step was set to 1 fs. Nosé-Hoover thermostat [11] was applied to maintain temperature at 300 K, with damping coefficients 0.1 ps⁻¹. Both van der Waals and electrostatic interactions were considered between water molecules and the TiO₂ substrate. Non-bonded van der Waals interactions modeled in terms of 12-6 Lennard-Jones famous potentials [12]. We applied particle-particle particle-mesh (PPPM) method to minimize error in long-range terms in both Columbic and Lennard-Jones potentials. Lennard-Jones and Columbic cutoff radiuses were 10 Å and 12 Å, respectively. SHAKE algorithm was used to keep O-H distance fixed at 0.9572 Å and H-O-H angle at 104.52°. The equations of motions were integrated using the Verlet algorithm and periodic boundary conditions were applied along the X and Y axes to eliminate the edge effects.

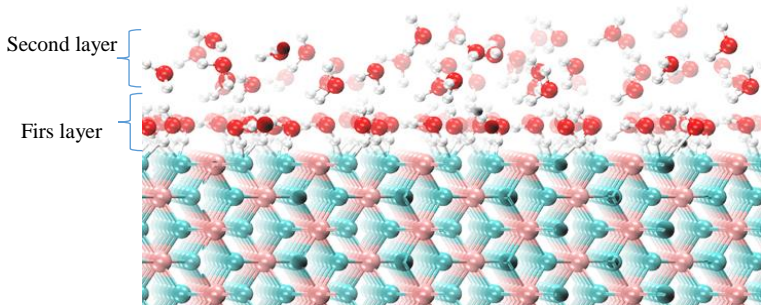
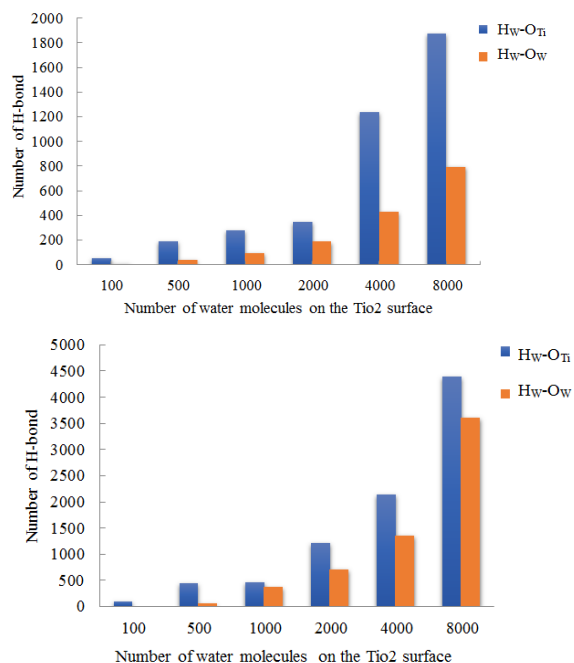


Fig.1: Snapshot of the formation of water-substrate and water-water hydrogen bonds. Colour code for elements: O, red; Ti, blue; H, white.

Results and Discussion

Water molecules reside on the TiO_2 surface with their hydrogens oriented towards the surface. Fig. 1 illustrates the formation of water-substrate and water-water hydrogen bonds. In the first layer fewer numbers of hydrogen bonds exist among water molecules since they tend to form hydrogen bonds with the titanium dioxide substrate. Additionally, increasing the number of water molecules up to 2000 and more results in molecular exchange between the first and second layers which in turn makes way for hydrogen bonding among water molecules.



Compare the number of hydrogen bonds that are formed between (a) water-surface, water-water in first layer, and (b) water-water in first and second layer.

Fig. 2 illustrates the number of possible hydrogen bonds that are formed between either water-water or water-surface. The number of possible hydrogen

bonds in the first and second layer are also presented in the same figure. It can be seen in Fig. 2 (a) that in the first layer water molecules tend to form hydrogen bonds with the surface. In this region the number of possible water-surface hydrogen bonds is more than water-water. This is a direct result of strong interaction between water and TiO_2 surface. It is also observable in Fig. 2(b) that the number of interlayer hydrogen bonds increases especially in the first layer. As the number of water molecules increase, they reside near the oxygen atom of the substrate. After the filling of the first layer completes, second layer forms. Therefore, as a result of more water molecules residing in the second layer, a higher number of possible hydrogen bonds are expected in this layer. However, this is not the case since molecular exchange occurs between the two layers, following which the water molecules reside near the Ti atoms of the surface. Thus, the number of water molecules and consequently the number of possible hydrogen bonds in the first layer increase. Therefore, it is the number of hydrogen bonds in the first layer that increases.

Conclusions

In this study, we performed molecular dynamics simulation to study the hydrogen bonds of water molecules on the nanocrystalline titanium dioxide surface. Our results show in the first layer fewer numbers of hydrogen bonds exist among water molecules since they tend to form hydrogen bonds with the titanium dioxide substrate. By increasing the number of water molecules they reside near the oxygen atom of the substrate. After the filling of the first layer completes, second layer forms. Therefore, as a result of more water molecules residing in the second layer, a higher number of possible hydrogen bonds are expected in this layer. Due to the exchange of water molecules between the layers, the number of possible hydrogen bonds in the first layer increase.

References

- [1] M. A. Henderson, C. L. Perkins, M. H. Engelhard, S. Thevuthasan, & C. H. Peden, Redox properties of water on the oxidized and reduced surfaces of CeO_2 (111). *Surf. Sci.* 526, (2003) 1-18.
- [2] A. L. Linsebigler, G. Lu, & J. T. Yates Jr, Photocatalysis on TiO_2 surfaces: principles, mechanisms, and selected results. *Chem. Rev.* 95, (1995) 735-758.
- [3] O. Carp, C. L. Huisman, & A. Reller, Photoinduced reactivity of titanium dioxide. *Prog. Solid State Chem.* 32, (2004) 33-177.
- [4] M. B. Huggenschmidt, L. Gamble, & C. T. Campbell, The interaction of H_2O with a TiO_2 (110) surface. *Surf. Sci.* 302, (1994) 329-340.



[5] M. A. Henderson, An HREELS and TPD study of water on TiO₂ (110): the extent of molecular versus dissociative adsorption. *Surf. Sci.* 355, (1996) 151-166.

[6] G. Mattioli, F. Filippone, F., R. Caminiti, & A. A. Bonapasta, Short hydrogen bonds at the water/TiO₂ (anatase) interface. *J. Phys. Chem. C* 112, (2008) 13579-13586.

[7] T. Ohto, A. Mishra, S. Yoshimune, H. Nakamura, M. Bonn, & Y. Nagata, Influence of surface polarity on water dynamics at the water/rutile TiO₂ (110) interface. *J. Phys. Condens. Matter* 26, (2014). 244102.

[8] S. Plimpton, Fast parallel algorithms for short-range molecular dynamics. *J. Comput. Phys.* 117, (1995) 1-19.

[12] W. Humphrey, A. Dalke, & K. Schulten, VMD: visual molecular dynamics. *J. Mol. Graph.* 14, (1996) 33-38.

[13] W. L. Jorgensen, J. Chandrasekhar, J. D. Madura, R. W. Impe, & M. L. Klein, Comparison of simple potential functions for simulating liquid water. *J. Chem. Phys.* (1983) 926-935.

[14] W. G. Hoover, Canonical dynamics: equilibrium phase-space distributions. *Phys. Rev. A* 31, (1985) 1695.

[15] J. E. Lennard-Jones, Cohesion. *Proc. R. Soc. London, Ser. A* 43, (1931) 461

Photoswitching of Salicylidene-methyl-furylamine: A Theoretical Photodynamics Study

Vali Alizadeh, Ahmad Jamali Moghadam*
 University of Garmsar P.O. Box 3581755796, Garmsar, Iran
 *f.j.moghadam@gmail.com

Abstract: Potential energy surfaces (PES) for the ground and excited state intramolecular proton transfer (ESIPT) processes in N-salicylidene-methyl-furylamine (SMFA) have been studied using CC2 level of theory. Our calculations suggest the non-viability of ground state intramolecular proton transfer. Excited state PES calculations support the existence of ESIPT process in SMFA. The calculated results show that the intramolecular hydrogen bond were formed in the S₀ state, and upon excitation, the intramolecular hydrogen bonds between -OH group and nitrogen atom would be strengthened in the S₁ state, which can facilitate the proton transfer process effectively. The calculations indicate two S₁/S₀ conical intersections (CIs) which provide radiation-less decay to the ground state. At the CIs, two barrier-free reaction coordinates direct the excited system to the ground state of enol-type minimum. The keto-type S₁ state attained by barrierless proton transfer is found to be unstable via a torsional motion, which provides fast access to a S₁-S₀ conical intersections. From the conical intersection, a barrierless reaction path directs the system back to the enol-type minimum of the S₀ potential energy surface, thus closing the photocycle.

Keywords: Schiff Base, Intramolecular Proton Transfer, Photochromism

Introduction

Excited-state reactions play important roles in the electronic properties of materials and biological systems, including their photoinduced functions. Aromatic Schiff bases and their metal complexes have recently attracted considerable attention because of their interesting and important properties such as biological activities, chemodosimeter, molecular tweezers, photochemical behavior, ionophores, catalytic activities, and pH-responsive [1-6]. Aromatic Schiff bases belong to a broad family of molecular systems whose photophysics is determined by the excited state intramolecular proton-transfer (ESIPT) reaction. Photochromic Schiff bases represent a special group of ESIPT systems, whose depopulation routes of the excited molecule are particularly complex. Besides the PT reaction cycle, returning the system to its original state through the back-PT, a large portion of molecules may be trapped in the ground state as metastable photochromic species. The photochromism and tautomerism features make extensive applications for Schiff bases in the laser dyes, molecular switches, nonlinear optical properties, and molecular electronic devices. The search for molecular switches based on light-induced conformational changes prompted by the ESIPT reaction is drawing special attention [10-12] since the theoretical proposition of a long-distance intramolecular hydrogen-atom transfer due to this phenomenon. According to the significance of proton transfer and tautomerism processes in Schiff

bases, so far, they have been the subject of numerous studies [11-15].

Computational Details

The ab initio calculations have been performed with the TURBOMOLE program package [16, 17]. The Resolution of identity Møller-Plesset perturbation theory to second-order (RI-MP2) [18, 19] calculations were performed to obtain the equilibrium geometry of the titled compound at the ground electronic state. Excitation energies and equilibrium geometry of the lowest excited singlet states have been determined at the resolution-of-identity second-order approximate coupled-cluster (RI-CC2) [20, 21] method. The calculations were performed with the correlation-consistent polarized valence double- ζ (cc-pVDZ) basis set [17].

Results and Discussion

The first step of this work is looking for the most stable structure of title compound. The most stable structure in ground state (S₀) at the MP2/cc-pVDZ level of theory is enol form (E). While the excited state proton transfer (ESPT) is mainly achieved after the S₁ geometry optimization of the E form at the CC2 level as keto form (K), (see Fig. 1). The minimum potential energy (MPE) profiles of E in the S₀ state and in the lowest excited $\pi\pi^*$ state, determined along the PT (OH distance) and along the torsion of the ethyl-furyl group (dihedral angle of θ (C2-C7-N1-C8)) and of the methylamine group (dihedral angle of θ (C1-C2-C7-N1)) are shown in Fig. 3.

The middle panel of Fig. 3, illustrates that the enol form is a typical excited-state intramolecular proton transfer (ESIPT) system. The minimum energy profiles were obtained by optimization of molecular geometry for fixed values of the reaction coordinate for ground and excited states, performed respectively at the MP2/cc-pVDZ or CC2/cc-pVDZ level of theory. The results showed that after optical excitation of E to the first excited singlet state ($\pi\pi^*$), a spontaneous (barrier-free) PT reaction occurs. Although the C2–C7 bond is a single bond in the enol form after the proton transfer, it changes into a double bond of cis-enol form. Considering the MPE curve of the ground state in Fig. 3(b), the enol–keto transformation is not favored any more in the ground state, while in the S1 ($\pi\pi^*$) state, the PES does not show a barrier, and this transformation will be favored by decreasing the internal energy of the system along the enol–keto transformation. It verifies that spontaneous hydrogen transfer takes place on the S1 ($\pi\pi^*$) state, resulting in the formation of the keto tautomer on the excited state potential energy surface. The keto-type S1 structure is estimated to lie 2.80 eV (CC2 result) above the global minimum of the ground state (see Fig. 3(b)). Calculations for PT systems show that the torsion of the proton-accepting group relative to the proton donating group plays an essential role for the effective quenching of the electronic excitation in these systems. Although we didn't find a ground state minimum for the case of cis-keto structure of SMFA. A barrier-less PE profile of the S1 ($\pi\pi^*$) state in the direction of the PT reaction and the small mass of the proton leads to the conclusion that the photophysics of SMFA is dominated by the ESIPT reaction which eventually may result in the formation of the photochromic trans-keto form. However, the reaction pathway leading to the CI-2, is also barrier-less and it plays an essential role in the photochemical behavior of SMFA after excitation. Internal conversion through these CIs, from both sides of Fig. 3, populate the ground state of SMFA at the conformations near to CI1 and CI2. However, the reaction pathway leading to the CI2, is also barrier-less and it plays an essential role in the photochemical behavior of SMFA after excitation. Since a large steric hindrance exists when $\theta > 95$, we didn't find a local minimum for the ground state along with this reaction coordinate. Therefore, this reaction coordinate should only act as a radiation-less deactivation pathway of the S1 ($\pi\pi^*$) state to the ground state via the CI2.

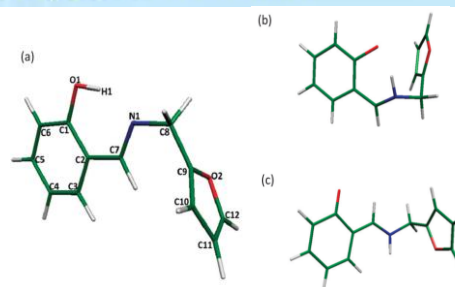


Figure 1: Optimized geometries and numbering pattern: (a) the most stable configuration of the enol form of SMFA (calculated at the MP2/cc-pVDZ level of theory); (b) the S1 optimized structure of cis-keto form of SMFA (determined at the CC2/cc-pVDZ geometry optimization of the E form); (c) the optimized geometry structure of trans-keto form of SMFA obtained at the MP2/cc-pVDZ level of theory.

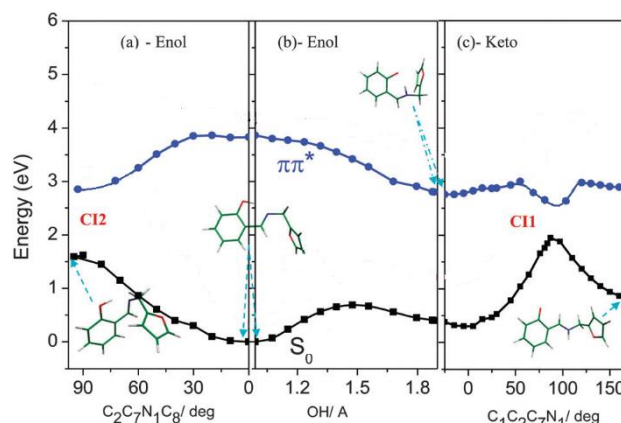


Figure 2: Potential energy curves of the S0 state (squares) and the S1($\pi\pi^*$) state (circles), as the functions of the torsional reaction path (a and c) and the hydrogen transfer reaction path (b). The energy origin is the energy of minimum enol in the ground state.

Electronic Properties:

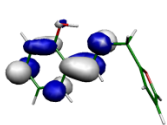
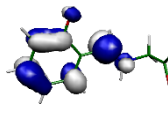
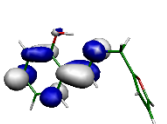
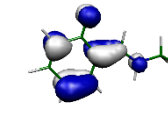
The vertical excitation energy at the CC2 level using cc-pVDZ basis sets on the S0 geometry of most stable enol form (E) and also trans-keto tautomer (K) are presented in Table 1. The vertical excitation energy at the CC2/cc-pVDZ level on the S0 geometry of the E identifies two strong electronic transitions: The S₁–S₀ transition at 4.19 eV (295.7 nm) can be described as the $\pi\pi^*$ (H–L) excitation, (H and L indicate to HOMO and LUMO, respectively). The oscillator strength of this transition is 0.118. The S₃–S₀ lies at 5.39 eV (230 nm) with the oscillator strength of 0.181, and can be described as the $\pi\pi^*$ state. The vertical excitation energies at the same level of theory on the MP2 ground state optimized geometry of trans-keto tautomer indicate two strong electronic transitions; the S₂–S₀ transition at



the 3.28eV (378 nm) can be described as the $\pi\pi^*$ (H-L) excitation (see Table 1). The oscillator strength of this transition is 0.3. The S_4-S_0 transition also lies at 5.6eV (221 nm) with the oscillator strength of 0.155 with electron excitation of H-(L+1).

The vertical electronic transition energies and molecular orbitals of the most stable enol and keto forms of SMFA are presented in Table 2. Calculations shows about 80 nm shift along the intramolecular proton transfer and Trans-keto formation.

Transition	Enol		Trans-Keto	
	eV	f	Transition	eV
$S_1 (\pi\pi^*)$	4.19	0.1180	$S_1 (n\pi^*)$	3.03
$S_2 (n\pi^*)$	5.09	0.0010	$S_2 (\pi\pi^*)$	3.28
$S_3 (\pi\pi^*)$	5.39	0.1810	$S_3 (\pi\pi^*)$	4.88
$S_4 (\pi\pi^*)$	6.07	0.0040	$S_4 (\pi\pi^*)$	5.6

	Enol	Trans-Keto
LUMO	 29 5 n	 37 6 n
HOMO		

Conclusions

The proton transfer is the main character of SMFA at the excited state. In contrast to the ground state, the PT process is significantly exoergic in the excited state. From the barrierless potential energy curve of the enol form at the excited state, one can conclude the fast dynamics for such ESIPT. The calculations indicate that the trans-keto form produced by UV excitation of Enol form is a strong UV/vis absorber and should be highly photostable. Upon strong UV irradiation, a significant concentration of the trans-keto form of SMFA can be produced. This form absorbs strongly in the visible range of the spectrum. The ground state of the trans-keto form is metastable (0.84eV). The thermal back reaction from trans-keto to the more stable E has to overcome a barrier of about

1.1 eV and is therefore expected to be rather slow. Thus, UV irradiation of SMFA may result in a mixture of enol and its photoproduct.

Acknowledgment

The research council of University of Garmsar is gratefully acknowledged. The calculations have been performed via the Computational Center of the Chemistry Department of University of Isfahan.

References

- [1] A. Hameed, M. al-Rashida, M. Uroos, K. Mohammed Khan "Review Schiff bases in medicinal chemistry: a patent review", *Expert Opin. Ther. Pat.*, 27 (2017) 63-79.
- [2] Bhandari, S. V.; Bothara, K. G.; Raut, M. K.; Patil, A. A.; Sarkate, A. P.; Mokale, V. J. Design, Synthesis and Evaluation of Antiinflammatory, "Analgesic and Ulcerogenicity Studies of Novel s-Substituted Phenacyl-1,3,4-oxadiazole-2-thiol and Schiff Bases of Diclofenac Acid as Nonulcerogenic Derivatives", *Biorg. Med. Chem.*, 16 (2008) 1822-1831
- [3] Saghatforoush, L. A.; Chalabian, F.; Aminkhani, A.; Karimzad, G., "Synthesis, Spectroscopic Characterization and Antibacterial Activity of New Cobalt(II) Complexes of Unsymmetrical Tetradentate (OSN2) Schiff Base Ligands" *Eur. J. Med. Chem.*, 44(2009) 4490-4495.
- [4] Lin, W.; Yuan, L.; Feng, J.; Cao, X. A Fluorescence-Enhanced Chemodosimeter for Fe^{3+} Based on hydrolysis of Bis(coumarinyl) Schiff Base" *Eur. J. Org. Chem.*, (2008) 2689-2692.
- [5] Park, M.; Chung, C.; Kim, Y., "Molecular Recognition: Schiff Base as Molecular Tweezers", *Mol. Cryst. Liq. Cryst. Sci. Technol., Sect. A*, 337(1999) 485-488.
- [6] Saha, U. C.; Dhara, K.; Chattopadhyay, B.; Mandal, S. K.; Mondal, S.; Sen, S.; Mukherjee, M.; Van Smaalen, S.; Chattopadhyay, P., "A New Half-Condensed Schiff Base Compound: Highly Selective and Sensitive pH-Responsive Fluorescent Sensor" *Org. Lett.*, 13(2011) 4510-4513.
- [7] J.C. Crano, R.J. Guglielmetti, "Organic Photochromic and Thermochromic Compounds"; Topics in Applied Chemistry; 1999, Plenum Press, 1st Ed, 345-357, New York.
- [8] H. Durr, H. Bouas-Laurent, "Photochromism: Molecules and Systems", 2003, 2nd Ed.; Elsevier: Amsterdam.
- [9] M. Irie "Diarylethenes for Memories and Switches" *Chem. Rev.*, 100 (2000) 1685-1716.
- [10] A. L. Sobolewski and W. Domcke "Computational Studies of the Photophysics of Hydrogen-Bonded Molecular Systems", *J. Phys. Chem. A*, 111 (2007) 11725-11735.
- [11] A. L. Sobolewski, W. Domcke and C. Ha'ttig "Photophysics of Organic Photostabilizers. Ab Initio Study of the Excited-State Deactivation Mechanisms of 2-(2'-Hydroxyphenyl)benzotriazole", *J. Phys. Chem. A*, 110 (2006) 6301-6306.



- [12] J. M. Ortiz-Sánchez, R. Gelabert, M. Moreno, J. M. Lluch "Theoretical Study on the Excited-State Intramolecular Proton Transfer in the Aromatic Schiff Base Salicylidene Methylamine: an Electronic Structure and Quantum Dynamical Approach", *J. Phys. Chem. A*, 110 (2006) 4649–4656.
- [13] M. Z. Zgierski "Theoretical study of photochromism of N-salicylidene- α -methylbenzylamine", *J. Chem. Phys.*, 115 (2001) 8351–8358.
- [14] M. Z. Zgierski and A. Grabowska "Theoretical approach to photochromism of aromatic Schiff bases: A minimal chromophoresalicylidene methylamine" *J. Chem. Phys.*, 112 (2000) 6329–6337.
- [15] M. Juan, S. Ortiz, G. R. Gelabert, M. Moreno "Electronic-structure and quantum dynamical study of the photochromism of the aromatic Schiff base salicylideneaniline", *J. Chem. Phys.*, 129 (2008) 7845–7852.
- [16] Ahlrichs, R.; Bär, M.; Häser, M.; Horn, H.; Kölmel, C "Electronic Structure Calculations on Workstation Computers: theProgram System Turbomole", *Chem. Phys. Lett*, 162 (1989) 165–169.
- [17] Turbomole V6.3; Turbomole GmbH: Karlsruhe, Germany, 2007; available from <http://www.turbomole.com>.
- [18] Møller, C.; Plesset, M. S "Note on an Approximation Treatmentfor Many-Electron Systems", *Phys. Rev*, 46 (1934) 618–622.
- [19] Weigend, F.; Häser, M "RI-MP2: First Derivatives and GlobalConsistency", *Theor. Chem. Acc*, 97 (1997) 331–340.
- [20] Weigend, F.; Häser, M.; Patzelt, H.; Ahlrichs "R. RI-MP2: Optimized Auxiliary Basis Sets and Demonstration of Efficiency", *Chem. Phys. Lett*, 294 (1998) 143–152.
- [21] Christiansen, O.; Koch, H.; Jørgensen "P. The Second-Order Approximate Coupled Cluster Singles and Doubles Model CC2", *Chem. Phys. Lett*, 243 (1995) 409–418.



Investigation of mechanical properties of polypropylene grade 550 J reinforced by Inorganic Nucleation Agent

Fatemeh Norouzi^{a*}, Davood Soudbar^b, Ali Mechershavi^b

^aDepartment of Chemical Engineer, Graduate From Islamic Azad university Farahan, Arak 3819717971, Iran.

^bDepartment of Research and Development, Shazand Petrochemical Company, 575, Iran..

*fatemeh.norouzi1992@gmail.com

Abstract: In This research Talc As a nucleating agent, at mass (2000ppm, 4000ppm, 6000ppm, 8000ppm, 10000ppm) was added into isotactic polypropylene (IPP) matrix by solution/precipitation method and compression-molded method. The crystallization morphology was studied by scanning electron microscope (SEM), Talc particles are also well dispersed in the polypropylene matrix. The result showed that talc can induce α crystal and increase the degree of crystallization of IPP. matrix. The melting peak of IPP analyzed by differential scanning calorimetry (DSC) was raised. It explains that crystalline perfect degree of PP were increased. The mechanical and Physical properties of polypropylene, which was measured using the izod impact test, tensile properties, flexural modulus, was improved by increasing the amount of talc. And the optimal amount of nucleating agent was 10000ppm.

Keywords: isotactic polypropylene, nucleating agent, crystallization properties, mechanical properties

Introduction

Isotactic polypropylene (IPP) is one of the most important commercial thermoplastics because of its relatively low cost, versatility, recyclability and good mechanical performance in engineering applications [1]. However, IPP also has its own disadvantages such as low impact strength, especially at a low temperature, toughness and notch-sensitive, which limit its application range. This paper finds out an efficient way to overcome the disadvantages of IPP. That is to add the nucleating agent to semicrystalline polymers, so that the nucleating agent will control crystallization process of IPP [2]. The subject of polymer crystallization has attracted great scientific and industrial attention for several decades and substantial effort continues to be devoted to this area of research. accelerate formation of crystalline, decrease spherulites dimensions and increase crystallinity, thus improve the thermal and mechanical properties [3]. Polypropylene (PP) is widely used in structural applications, mixed with organic reinforcements such as natural fibers [4] or inorganic reinforcements such as calcium carbonate [5] clay and talc [6]. As efficient nucleating agents, talc have abilities to make the crystal form of IPP. This point is well known and has been thoroughly investigated [7]. Among these reinforcing agents, talc is one of the most used

mineral filler and enables to improve both the thermal and mechanical properties of PP. This

filler also facilitates the shaping of PP by reducing and homogenizing the moldings shrinkage.

The main objective of this study is to investigate the influence of nucleating agent talc on crystallization, thermal and mechanical properties of PP.

Materials and method

The isotactic polypropylene (HP550J, MFR:

3.2g/10 min according to ISO 1133) without any nucleating agents is supplied by Arak PETROCHEMICAL COMPANY.

Talc or talcum is a clay mineral composed of hydrated magnesium silicate with the chemical formula $H_2Mg_3(SiO_3)_4$ or $Mg_3Si_4O_{10}(OH)_2$. (Luzenac) was used in this study.

Sample preparation

IPP was mixed with various concentrations of talc (2000ppm, 4000ppm, 6000ppm, 8000ppm, 10000ppm) was initially prepared, then extruded with (bautek) co-rotating twin-screw extruder. The screw rotation speed was 75 r/min. Temperatures of 7 control zones of the extruder were maintained at 170°C, 175°C, 180°C, 185°C, 190°C, 190°C, 190°C and 180°C from hopper to die.

Scanning electron microscope (SEM)

Surfaces of the samples were characterized by (Cambridge-s360) scanning electron

microscope. Samples were dried for 24h and fixed on a sample platform.

Differential scanning calorimeter (DSC)

DSC scanning of the samples was performed on a Mettler Toledo DSC/SDTA DSC822 differential scanning calorimeter in a nitrogen atmosphere. The sample weight was about 3-4mg. The temperature range of the test was set as 30~230°C. To determine the melting behavior of these samples, the scanning speed was

set as 10°C/min from 30 to 230°C. After the first heating run the sample was kept at 230°C for 5 minutes to erase the thermal history of processing. Melting temperatures were measured and DSC thermograms were recorded.

Mechanical properties

Three different dimensions of specimens, 10×10 mm, dumbbell-shaped 4.1×2 mm and 60×12×4 mm, were prepared by an injection molding machine, and were used for the izod impact, tensile properties and flexural Modulus tests respectively. Following the, the impact strength was tested by the notched Izod impact (ZwickRoell HIT 5.5P) method, at the impact speed of 3.5 m/s, toss energy corrected in all cases and drop height fixed at 61.0 cm. tensile properties following the ASTM D638 and flexural modulus following ASTM D790 were measured By (CHEST). The samples for tensile tests were stretched at room temperature, at the initial gauge length of 25 mm, at a constant elongation speed of 50 mm/min. The tensile stress was determined by dividing the tensile load by the initial cross-section. The tensile strain was calculated by the ratio of the increment of the length between clamps to the initial gauge length.

Results and Discussion

Crystallization morphology

Fig.1 shows the appearances of IPP and nucleated IPP (10000ppm talc), respectively. It is obvious to see that spherulites of IPP with talc have uniform dimensions and neat arrangement. Spherulites dimensions are about 12µm. However, the largest and smallest spherulites can be observed for pure IPP.

Spherulites stop growing when they collide with each other. Homogeneous nucleation, which is

mainly crystallization behavior of pure IPP, supplies small amounts of nuclei. So pure IPP gets lower probability of collision, and its spherulites dimensions are larger than modified IPP.

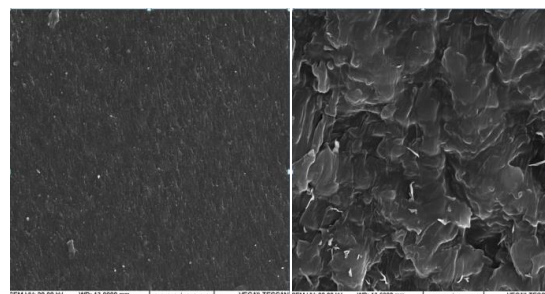


Fig.1 SEM of pure IPP(a) and IPP with 10000 ppm Talc(b)

In Fig.2 DSC melting behaviors of IPP and IPP with the 10000ppm nucleating agent talc are shown. From the diagram, it can be observed that melting peak of IPP with 10000 ppm nucleating agent talc increases by about 2°C, the melting peak is sharper, Thus addition of 10000 ppm can improve crystallinity and crystallization perfect degree of IPP. And the degree of crystallite was increased from 34.78% to 41.46%. Consequently, it has improved the thermal stability of IPP. DSC have revealed that the thermal stability of IPP is significantly affected by addition of 10000 ppm talc.

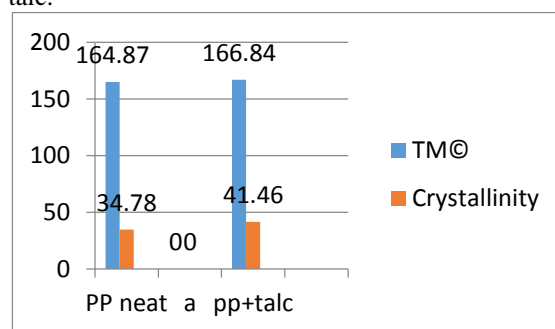


Fig.2 DSC of pure IPP and IPP with 10000ppm talc

Mechanical properties

The mechanical properties of compression molded IPP samples comprising talc were investigated for blends comprising from 0 to 10000 ppm of the additive. When talc was added into IPP matrix, an increase in the notched Izod impact strength, tensile strength, flexural modulus of IPP was detected. Fig 3, When 10000 ppm talc was added into IPP, the notched Izod impact strength, tensile strength, and flexural modulus of IPP were increased by 27.27%, 6.7%, 89.6 respectively.



These results of the mechanical properties are in general accord with the crystallization properties presented above. Generally, mechanical properties of crystalline PP depend on the degree of crystallinity, the dimensions and distribution uniformity of spherulites. The fineness of the crystal grain must be beneficial to impact strength. Furthermore, the nucleating agent impels the degree of orientation of the polymer and improves the crystallization rate, retards the relaxation of the cooling process of the polymer melt. The boundary strength between spherulites increases, thus it will be beneficial to the improvement of the impact strength of the materials. Adding the nucleating agent makes the number of nuclei increasing, crystallization rate accelerating, spherulite dimensions decreasing, particle dimensions distribution of crystallization uniformed, which eliminate the phenomenon of stress concentration under loading. It has demonstrated that crystallization properties of the IPP are directly related to mechanical properties of IPP.

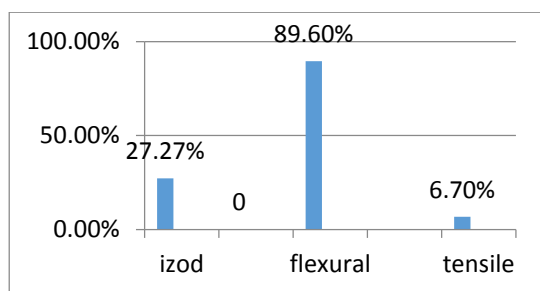


Fig.2 Mechanical properties of polypropylene reinforced

Conclusions

In this study, properties of IPP with nucleating agent talc are investigated. The result has showed that talc is an effective nucleating agent. It can greatly improve crystallization properties, such as uniform spherulites dimensions, neat arrangement and high crystallinity. 10000 ppm talc improves crystallinity and crystallization perfect degree of IPP, so increase melting peak and decomposition temperature and improve the thermal stability of IPP. Mechanical properties of IPP are related to crystallization properties. Thenotched Izod impact strength, tensile strength, and flexural strength of IPP are increased by 27.27%, 6.7%, 89.6 respectively. And the optimal amount of nucleating agent was 10000 ppm.

References

- [1] M. Kersch, H.-W. Schmidt, V. Altst€adt "Influence of different beta-nucleating agents on the morphology of isotactic polypropylene and their toughening effectiveness", *Polymer* 98 (2016) 320-326.
- [2] N. Fanegas, M.A. Go´mez, C. Marco, I. Jimenez, G. Ellis "Influence of a nucleating agent on the crystallization behavior of isotactic polypropylene and elastomer blends", *Polymer* 48 (2007) 5324-5331.
- [3] Ayret Mollova, Rene Androsch, Daniela Mileva, Markus Gahleitner, Sergio S. Funari "Crystallization of isotactic polypropylene containing beta-phase nucleating agent at rapid cooling", *European Polymer Journal* 49 (2013) 1057-1065.
- [4] Shaohong Shi, Xiang Zhang, Yuansen Liu, Min Nie, Qi Wang "Crystalline modification and morphology of polypropylene developed under the combined effects of montmorillonite and self-assembly β nucleating agent", *Composites Science and Technology* 135 (2016) 76-82.
- [5] Arjaree Pradittham, Natthaporn Charitngam, Suttasinee Puttajan, Duangduen Atong, Chiravoot Pechyen "Surface modified CaCO₃ by palmitic acid as nucleating agents for polypropylene film: mechanical, thermal and physical properties", *Energy Procedia* 56 (2014) 264 - 273.
- [6] K. Wang, N. Bahlouli, F. Addiego, S. Ahzi, Y. Remond, D. Ruch, R. Muller "Effect of talc content on the degradation of re-extruded polypropylene/talc composites", *Polymer Degradation and Stability* 98 (2013) 1275-1286.
- [7] Karolth R. Espinosa, Luciana A. Castillo, Silvia E. Barbosa "Blown nanocomposite films from polypropylene and talc. Influence of talc nanoparticles on biaxial properties", *Materials and Design* 111 (2016) 25-35.

Prediction of Hydrate Dissociation Conditions for system of Tetrahydrofuran + Water

M.Raeisi^a, J.Javanmardi^{a*}, F.Alavi^a, S. M.Jokar^a

^aDepartment of Chemical, Petroleum and Gas Engineering, Shiraz University of Technology, Shiraz, Iran

^{*}Javanmardi@sutech.ac.ir

Abstract: Utilization of Tetrahydrofuran (THF) is a common way to moderate the hydrate formation conditions. In this work, attempts have been made to predict the dissociation conditions for system of THF + water using van der Waals-Platteeuw (vdW-P) solid solution theory. Only 50% of THF + water system with THF concentration in the mole fraction range lower than 6% are utilized to optimize the interaction parameters of Kihara potential for the guest THF molecules.

The phase boundaries for system of THF + water and then carbon dioxide + THF + water, methane + THF + water and nitrogen + THF + water in all available concentration ranges are predicted and compared with available literature experimental data. The results showed acceptable agreement between predicted and experimental data for the systems examined in this study. The Peng-Robinson equation of state was used for determining component fugacities in gas phase and UNIQUAC activity model for calculating activity in liquid phase.

Keywords: Hydrate; THF; van der Waals-Platteeuw model; Kihara potential parameters

Introduction

Gas hydrates, or clathrate hydrates, are ice-like compounds composed of water and one or more other hydrate forming compound(s). These nonstoichiometric crystalline compounds are formed by physically stable interactions between water (host) and small molecules (guest) under low temperatures and relatively high pressures. Low molecular-weight gas molecules, like methane, nitrogen, and carbon dioxide and some volatile liquids, like THF are captured into cavities formed by hydrogen bonded water [1]. These organic volatile compounds are water-soluble or water-insoluble hydrate formation promoters [2,3–6].

The promotion effect of THF in the hydrate system has been extensively investigated. Addition of aqueous solutions of THF in concentrations below 6 mole% to the system, normally leads to reduction of gas hydrate formation pressure [7]. THF can form structure II hydrate, independent of the presence of another hydrate former [1]. There are some researches in the literature which report the phase equilibrium measurements of methane + THF + water [4,5,7,8], carbon dioxide + THF + water [7,9–11], and nitrogen + THF + water [4,10] systems. However, few researches addressed thermodynamic models for the prediction of dissociation conditions of pure or mixed-gas hydrates containing THF.

In this work, only 50% of the reported experimental data for system of THF + water with THF concentration less than 6mol% are utilized to estimate the Kihara parameters of THF. In order to validate the estimated parameters, dissociation conditions of hydrates for systems THF+ water (with THF mole fraction lower than 20%), carbon dioxide + THF+ water, methane + THF + water and nitrogen + THF+ water are predicted and compared with the experimental data reported in

the literature. In this regard, the thermodynamic model of van der Waals–Platteeuw with Peng-Robinson equation of state has been coupled with the UNIQUAC activity model.

Thermodynamic Model

The model described in this paper is based on the vdW-P solid solution theory [12]. For a system in which gas, hydrate, and aqueous (consisting of water and soluble organic hydrate formers) phases coexist in equilibrium, the equality of chemical potentials of water in the hydrate and aqueous phases can be written as:

$$\mu_w^H = \mu_w^L \quad (1)$$

where, μ indicates chemical potential, the subscript w refers to water, and the superscripts H and L refer to the hydrate and aqueous phases, respectively. The equality of these chemical potentials can be written as the equality of chemical potential difference of water between the phases and hypothetical empty hydrate phase:

$$\Delta \mu_w^{\beta-H} = \mu_w^\beta - \mu_w^H = \Delta \mu_w^{\beta-L} = \mu_w^\beta - \mu_w^L \quad (2)$$

The difference between chemical potential of water in H and phases, is defined by [12,13]:

$$\Delta \mu_w^{\beta-H} = RT \sum_m \nu_m \ln \left(1 + \sum_j C_{mj} f_j \right) + RT \ln \gamma_w^H \quad (3)$$

where, ν_m is the number of cavities of type m per water molecule in the unit hydrate cell, j runs over all guest components, C_{mj} is the Langmuir constant, which accounts for hydrate former–water interaction in the cavity, f_j is the fugacity of component j including THF and γ_w^H is the activity coefficient of water in hydrate phase [13]. The fugacity of component in gas phase is obtained from Peng-Robinson equation of state [14].

The fugacity of THF in the aqueous liquid phase can be calculated using equations given by refs. [2,5] and the activity coefficient of water in hydrate phase can be estimated by the equations given by ref. [13]:

Results and Discussion

Only half of available hydrate experimental data [9,15,16–20] of system THF + water are used for optimization of Kihara parameters. The optimized THF Kihara parameters and other ones are presented in Table 1.

Table 1: The Kihara interaction parameters.

Comp.	a (Å)	δ (Å)	ϵ/k (K)	Ref.
CH ₄	0.3834	3.14393	155.593	[1]
N ₂	0.3526	3.13512	127.426	[1]
CO ₂	0.6805	2.97638	175.405	[1]
THF	0.9013	3.56214	291.568	This work

Figure 1 shows the comparison between modeling results and the experimental data for system of THF + water.

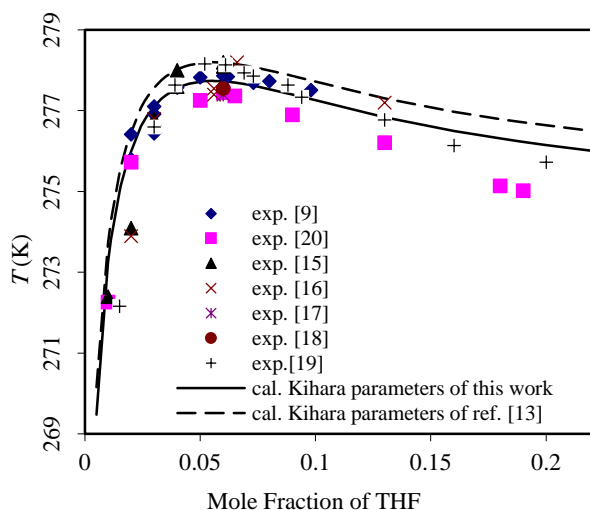


Fig. 1: Experimental and predicted hydrate dissociation conditions of system THF + water at 100 kPa.

The corresponding average absolute errors (AAE) for system THF + water are reported in Table 2. The corresponding AAE for hydrate systems of methane + THF + water, nitrogen + THF + water and carbon dioxide + THF + water are given in Tables 3-5. As it can be observed, the agreement between the predictions and the experimental data for these systems are also found to be acceptable.

Table 2. The average absolute error, AAE*, of hydrate dissociation temperatures for system of THF + water.

Mole fraction of THF	Data points	AAE, (K)	Ref.
0.01-0.2	34	0.42	[9,15,16–20]
0.01-0.06	21	0.43	[9,15,16–20]

$$* AAE = \frac{1}{NP} \sum_{i=1}^{NP} |T_{cal} - T_{exp}|$$

Table 3: The AAE of hydrate dissociation temperatures for system of THF + water + methane.

Mole fraction of THF	Data points	Pres. range, (MPa)	AAE, (K)	Ref.
0.0048	8	0.68-4.66	0.16	[8]
0.0105	9	0.90-5.68	0.08	[8]
0.0107	9	2.051-14.047	0.12	[5]
0.03	4	2.02-8.91	0.18	[4]
0.05	9	2.051-14.047	0.43	[5]
0.0556	12	0.68-12.5	0.22	[7]
overall	51		0.20	

Table 4: The AAE of hydrate dissociation temperatures for system of THF + water + nitrogen.

Mole fraction of THF	Data points	Pres. range, (MPa)	AAE, (K)	Ref.
0.01	5	3.12-9.77	0.30	[4]
0.011	5	3.31-10.09	0.22	[10]
0.03	7	2.975-10.87	0.11	[4]
0.05	5	2.20-10.00	0.22	[4]
overall	22		0.22	

Table 5: The AAE of hydrate dissociation temperatures for system of THF + water + carbon dioxide.

Mole fraction of THF	Data points	Pres. range, (MPa)	AAE, (K)	Ref.
0.011	5	1.3-3.35	0.17	[10]
0.012	11	1.5-4.3	0.06	[11]
0.0156	6	0.5-3.52	0.32	[9]
0.0275	6	0.19-2.5	0.72	[9]
0.0299	4	0.26-3.02	0.49	[9]
0.03	9	0.27-3.2	0.30	[11]
0.05	6	1.08-2.24	0.2	[11]
0.0556	15	0.18-3.17	0.33	[7]
overall	62		0.29	

Overall temperature average absolute error for 169 available experimental data points was about 0.29 (K), show the accuracy of the model.

Conclusions

In this work, the van der Waals–Platteeuw solid solution theory applied to predict dissociation conditions of pure THF hydrate (system of THF + water) and hydrates of methane, nitrogen, and carbon dioxide in the presence of THF as a water-soluble hydrate promoter. Also, the Kihara interaction parameters of THF were optimized using the hydrate dissociation points for the system of THF + water. Although, only few experimental

data of pure THF hydrate formation condition were used in optimization, the achieved results show high accuracy. Furthermore, it was seen that the UNIQUAC activity model is able to predict phase boundaries of hydrate for considering systems.

Acknowledgment

The authors are grateful to the Shiraz University of Technology for supporting this work.

References

- [1] E. D. Sloan, Jr., C. Koh, "Clathrate Hydrates of Natural Gases", 2008, 3rd ed., Marcel Dekker Inc., New York, NY, USA.
- [2] M. D. Jager, R. M. De Deugd, C. J. Peters, J. de SwaanArons, E. D. Sloan, "Experimental determination and modeling of structure II hydrates in mixtures of methane+ water+ 1, 4-dioxane", *Fluid Phase Equilib.*, 165 (1999) 209–223.
- [3] S. Mainusch, C. J. Peters, J. de SwaanArons, J. Javanmardi, M. Moshfeghian, "Experimental determination and modeling of methane hydrates in mixtures of acetone and water", *J. Chem. Eng. Data.* 42 (1997) 948–950.
- [4] Y. T. Seo, S. P. Kang, H. Lee, "Experimental determination and thermodynamic modeling of methane and nitrogen hydrates in the presence of THF, propylene oxide, 1, 4-dioxane and acetone", *Fluid Phase Equilib.*, 189 (2001) 99–110.
- [5] R. M. De Deugd, M. D. Jager, J. De SwaanArons, "Mixed Hydrates of Methane and Water-Soluble Hydrocarbons Modeling of Empirical Results", *AIChE J.*, 47 (2001) 693–704.
- [6] Y. Saito, T. Kawasaki, T. Okui, T. Kondo, R. Hiraoka, "Methane storage in hydrate phase with water soluble guests", Proc. of the 2nd Int. Conf. Gas Hydrate, Toulouse, France, 1996, 459–465.
- [7] Y. J. Lee, T. Kawamura, Y. Yamamoto, J. H. Yoon, "Phase Equilibrium Studies of Tetrahydrofuran (THF)+ CH₄, THF+ CO₂, CH₄+ CO₂, and THF+ CO₂+ CH₄ Hydrates", *J. Chem. Eng. Data.*, 57 (2012) 3543–3548.
- [8] A. H. Mohammadi, D. Richon, "Phase Equilibria of Clathrate Hydrates of Tetrahydrofuran+Hydrogen Sulfide and Tetrahydrofuran+Methane", *J. Chem. Eng. Data.*, 55 (2009) 982–984.
- [9] A. Delahaye, L. Fournaison, S. Marinhas, I. Chatti, J. P. Petitet, D. Dalmazzone, "Effect of THF on equilibrium pressure and dissociation enthalpy of CO₂ hydrates applied to secondary refrigeration", *Ind. Eng. Chem. Res.*, 45 (2006) 391–397.
- [10] A. H. Mohammadi, J. F. Martinez-Lopez, D. Richon, "Determining phase diagrams of tetrahydrofuran+methane, carbon dioxide or nitrogen clathrate hydrates using an artificial neural network algorithm", *Chem. Eng. Sci.*, 65 (2010) 6059–6063.
- [11] K. M. Sabil, C. J. Peters, "Phase equilibrium data of mixed carbon dioxide and tetrahydrofuran clathrate hydrate in aqueous electrolyte solutions", Proc. of the 11th Int. Conf. Properties and Phase Equilibria (PPEPPD), Crete, Greece, 2007.
- [12] J. van der Waals, J. Platteeuw, "Clathrate solutions", *Adv. Chem. Phys.*, 2 (1959) 1–57.
- [13] T. A. Strobel, C. A. Koh, E. D. Sloan, "Thermodynamic predictions of various tetrahydrofuran and hydrogen clathrate hydrates", *Fluid Phase Equilib.*, 280 (2009) 61–67.
- [14] D. Peng, D. B. Robinson, "A New Two-Constant Equation of State", *Ind. Eng. Chem.*, 15 (1976) 59–64.
- [15] R. Anderson, A. Chapoy, B. Tohidi, "Phase relations and binary clathrate hydrate formation in the system H₂-THF-H₂O", *Langmuir.*, 23 (2007) 3440–3444.
- [16] H. J. M. Hanley, G. J. Meyers, J. W. White, E. D. Sloan, "The melting curve of tetrahydrofuran hydrate in D₂O", *Int. J. Thermophys.*, 10 (1989) 903–909.
- [17] D. G. Leaist, J. J. Murray, M. L. Post, D. W. Davidson, "Enthalpies of Decomposition and Heat Capacities of Ethylene Oxide and Tetrahydrofuran Hydrates", *J. Phys. Chem.*, 26 (1982) 4175–4178.
- [18] S. R. Gough, D. W. Davidson, "Composition of Tetrahydrofuran Hydrate and the Effect of Pressure on the Decomposition", *Can. J. Chem. Eng.*, 49 (1971) 2691–2699.
- [19] V. Y. Dyadin, Y. A. Larionov, E. G. Manakov, A. Y. Zhurko, F. V. Aladko, E. Y. Mikina, T. V. Komarov, "Clathrate hydrates of hydrogen and neon", *Mendeleev Commun.*, 9 (1999) 209–210.
- [20] T. Makino, T. Sugahara, K. Ohgaki, "Stability boundaries of tetrahydrofuran + water system", *J. Chem. Eng. Data.*, 50 (2005) 2058–2060.

Calculation of Density of Ionic Liquids From Development Redlich-Kwong Equation of State

A.Moradzadeh^{a*}, S.A. Razavizadeh^b

^aDepartment of Chemistry, Payme Noor University, Urmia, Iran

^bDepartment of Chemistry, Payme Noor University, Shiraz, Iran

*ahlam.moradzadeh@gmail.com

Abstracts

In this study Redlich–Kwong equation of state is developed for calculation PpT properties of some ionic liquids. This equation of state is based on the generic Redlich–Kwong equation of state in which the parameters of this equation of state are dependent of density and temperature. In order to improve the predictive power of the mentioned equation of state for calculation of the density of ionic liquids, modifications on the parameters of this equation of state have been considered. The ionic liquids under consideration in this work include: imidazolium cations: Tetrafluoroborate, Thiocyanate, Trifluoromethanesulfonate, Ethylsulfate, bis (Trifluoromethylsulfonyl)-imide and Hexafluorophosphate. We will see that the comparison of predicted densities from the modified equation of state and experimental data shows high ability of this equation in predicting PpT properties of ionic liquids. The overall average deviation percent of the calculated density of ionic liquids obtained by this equation of state is 0.08 %.

Keywords: Equation of State; Ionic Liquids; Density

Introduction

Ionic liquids (ILs) have attracted many researchers in the areas including physics and chemistry because of their characteristics that are different from conventional molecular liquids and, today, ILs have been one of the interesting subjects of scientific study. ILs are consisted of ions and liquids at or near room temperature, and show negligible vapor pressure, thermal and chemical properties, and so on [1-3]. Also, ILs have been widely used as solvents for organic reactions with the expectation of high yields [1]. Most interesting features of ILs can be attributed to remarkable interionic interactions, and these can be an important key factor to study the characteristics of ILs at the molecular level. From the results of both experimental and theoretical investigations, it has been recognized that the interionic interaction of ILs could determine physical and chemical properties. Equations of state provide a way to predict thermophysical properties of fluids. They are considered as important tools in chemical engineering designs and have a major role in the phase equilibria study of fluids and fluid mixtures. In general, the equations in common use can be classified as belonging to the cubic equations, the extended family of virial equations, or equations based more closely on the results from statistical mechanics and computer simulations. Recently, several models have been proposed for predicting densities of ILs. In this investigation, the modifications are performed to the attractive parameter of the Redlich–Kwong EoS [4-6].

Method

The Redlich-Kwong (1949) equation of state is [7]:

$$p = \frac{RT}{V-b} - \frac{a}{V(V+b)}$$

where

$$a = \frac{a_{RK}}{T^{0.5}} \quad a_{RK} = 0.4278 \frac{R^2 T_c^2}{p_c} \quad b = 0.0867 \frac{RT_c}{p_c} \quad \text{where } R$$

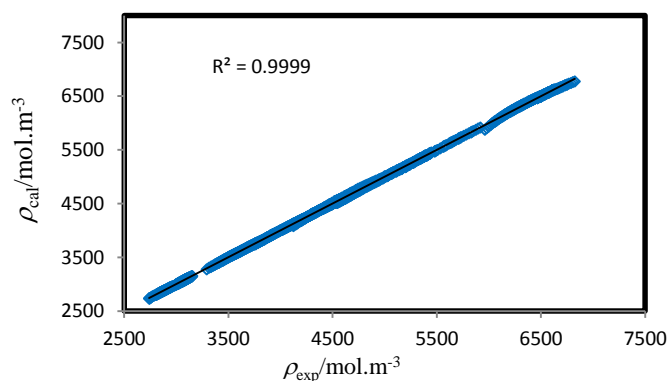
is the universal gas constant, p , V and T are the pressure, volume and temperature respectively. Parameter a is a temperature dependent parameter and, a_{RK} and b are component dependent

constants. This simple equation gives the thermodynamic properties of gases over a wide interval of densities, particularly for temperatures above the critical temperature with reasonable accuracy. In the present research the attractive parameter of the EoS, a , was considered temperature and density dependent and a new correlation was obtained to calculate this parameter. The density of ILs was calculated in a wide range of temperature and pressure from modified equation of state.

Result and Discussion

The density values of all ILs were calculated from the modified RK EoS. The obtained densities compared comprehensively with a large number of experimental liquid densities [8] at pressures from 1 bar up to 2000 bar and temperatures from 293 K to 472 K. The excellent agreement between the calculated and experimental densities [8] of studied ILs reveals that the modifications made on the attractive term of RK make this EoS a promising tool for the density prediction of ILs.

A modification was proposed to improve Redlich–Kwong equation of state and its parameters for ionic liquids. The improved equation of state was used for prediction of PpT properties of ionic liquids. The density has been calculated for 14 ionic liquids in a broad range of temperatures and pressures. This modified equation of state predicted the densities of ionic liquids with an overall average deviation percent of about 0.08%. The advantages of this equation with respect to temperature and density dependence of the coefficient, are high precision and good ability to predict the thermodynamic properties of ionic liquids.



compared with the experimental values.

Fig. 1. The predicted densities for ILs by the modified equation of state

Table 1. Experimental and calculated data for studied ionic liquids.

Ionic Liquid	Number of points	T- range(K)	p- rang(bar)	ρ -rang(mol/m ³)	
				Experimental	Calculated
1 [Emim] [BF ₄]	182	313-472	1-2000	5873-6601	6608-6963
2 [Emim] [EtSO ₄]	29	293-391	1-400	5007-5397	4997-5389
3 [Emim] [NTf ₂]	37	322-414	1-300	5473-5918	5480-5918
4 [Emim] [SCN]	66	298-398	1-100	6466-6627	6465-6628
5 [Bmim] [BF ₄]	47	293-393	1-100	5026-5359	5028-5361
6 [Bmim] [C (CN) ₃]	97	293-393	1-300	4303-4641	4295-4637
7 [Bmim] [PF ₆]	190	312-472	1-2000	4334-5059	4335-5070
8 [Bmim] [SCN]	66	298-338	1-100	5314-5450	5313-5450
9 [Hmim] [BF ₄]	182	313-472	1-2000	4082- 4771	4125-4783
10 [Hmim][NTf ₂]	165	298-333	1-595	2991-3101	2994-3100
11 [Hmim][PF ₆]	182	312-472	1-2000	3744-4385	3761- 4389
12 [Hpmim][NTf ₂]	97	293-393	1-300	2807-2977	2806-2981
13 [Omim][BF ₄]	78	293-393	1-100	3689-3945	3684-3946
14 [Omim][PF ₆]	182	312-472	1-2000	3279-3664	3293-3667

To check the predictive power of the proposed equation of state, the experimental density versus the calculated density from the new equation of state was plotted, as shown in figure 1 for all studied compounds. This figure displays the overall performance of the new equation of state in predicting the density of ionic liquids over wide density range. As figure 1 shows, the calculated densities are well distributed along the diagonal. Figure 1 reconfirms the reliability of the proposed equation state to predict the $P\rho T$ properties of fluids. As this figure shows, the diagram has an excellent fit to the data and the correlation coefficients, R^2 , of the diagram is very good over a wide pressure and density ranges.

Conclusions

The main purpose of this work was to develop an equation of state from van der Waals family. This equation of state has been obtained with the modification of the attractive parameter of Redlich-Kwong equation of state. The density of pure ionic liquids has been calculated at different temperatures and pressures. The obtained results were compared with experimental data. The results showed excellent agreement between experimental and calculated density. The present equation of state was evaluated by examination of 1600 experimental density data for 14 ionic liquids. This

new equation of state predicted the densities of fluids with an overall average deviation percent of the density about 0.08%. Comparison of the obtained results with experimental data indicates the high capability of the proposed equation of state for prediction of the $p\rho T$ properties of pure ionic liquids in a broad range of temperature and pressure.

References

- [1] Wasserscheid, P., & Welton, T. (2008). Ionic Liquids in Synthesis, Weinheim, Wiley-VCH.
- [2] Wasserscheid, P., & Keim, W. (2000). Ionic liquids- New "solutions" for transitionmetal catalysis. *Angew. Chem., Int. Ed.*, 39, 3773-3789.
- [3] Castner, E. W. Jr, Wishart, J. F., & Shirota, H. (2007). Intermolecular Dynamics, Interactions, and Solvation in Ionic Liquids. *Acc. Chem. Res.*, 40, 1217-1227
- [4] Weingaertner, H. (2007). Understanding ionic liquids at the molecular level: facts, problems, and controversies. *Angew. Chem., Int. Ed.*, 47, 654-670.
- [5] Ohno, H. (2005). *Electrochemical Aspects of Ionic Liquids*, Hoboken, Wiley-Interscience.
- [6] Rogers, R. D., & Voth, G. A. (2007). Special Issue on Ionic Liquids. *Special Issue on Ionic Liquids. Acc. Chem. Res.*, 40(11).



Liquid-liquid equilibria of aqueous two phase system containing of PEGDME 2000 and $(\text{NH}_4)_2\text{SO}_4$ at different temperatures and its application in partitioning of lactic acid

Mohammed Taghi Zafarani^a – Moattar^a, Hemayat Shekaari^a, Tohid Hashemzadeh^{a*}

^a Physical Chemistry Department, Faculty of Chemistry, University of Tabriz, Tabriz, 5166616471, Iran

* Engineer_tohid@yahoo.com

Abstract: In this work, the liquid-liquid equilibria (LLE) of (PEGDME₂₀₀₀ + ammonium sulphate + water) was studied at $T = (298.15, 308.15 \text{ and } 318.15) \text{ K}$. Furthermore for this system the free energies, enthalpies and entropies of cloud points were calculated at the mentioned temperatures in order to investigate the driving force for the mentioned two-phase system. For representing the experimental binodal data the Merchuk equation in the original form and with the temperature dependency and an empirical equation were used. Othmer-Tobias and Bancraft, a temperature dependent Setschenow and osmotic virial equations were used to fit the tie-line data. Moreover, the effect of temperature on the binodal curves and the tie-lines for the investigated aqueous two-phase system have been studied. In addition the partitioning behaviour of the lactic acid molecule on the investigated aqueous two-phase system was studied.

Keywords: (Liquid-liquid) equilibrium; Polyethylene glycol di-methyl ether; Ammonium sulphate, Setschenow equation, Lactic acid.

Introduction

ATPSs have been recognized as an economical and efficient downstream processing method, and widely used for recovery and purification of various biomolecules [1]. In this work liquid-liquid equilibrium (LLE) of aqueous two-phase systems containing PEGDME₂₀₀₀ and ammonium sulphate has been studied.

Lactic acid is one of important carboxylic acids in chemical industries. Partitioning of lactic acid in the above two phase system has also been studied.

Materials and method

Poly ethylene glycol di-methyl ether (PEGDME), of molar mass 2000, with CAS number 9003-39-8, was obtained from Merck. Ammonium sulphate with CAS Registry No. 7783-20-2 and minimum mass fraction purity 0.99 was obtained from Merck. The polymer and salt were used without further purification, and double distilled deionized water was used. Concentrated lactic acid solution (mass fraction 98% in water) with CAS number 79-33-4, was obtained from Sigma aldrich.

A glass vessel with an external jacket used around which water at constant temperature was circulated using a thermostat with an uncertainty $\pm 0.05 \text{ K}$. The binodal curves were determined by clouding point titration method. In this method, the composition of the mixture for each point on the binodal curve was determined from the amount of titrate added until turbidity was observed using an analytical balance (Shimatzu, 321-34553,

Shimatzu Co., Japan) with a precision of $\pm 1.10^{-7} \text{ kg}$. The maximum uncertainty was found to be ± 0.002 in determining the mass fraction of both polymer and salt by using of this method.

For determination of the tie-lines, feed samples (about $2 \times 10^{-5} \text{ m}^3$) were prepared by mixing appropriate amounts of polymer, salt and water in the vessel. The thermostat was set at the desired temperature, and the samples were stirred for 1 h. Then, the samples were placed in the thermostat (JULABO model MB, Germany) with temperature control ability of $\pm 0.02 \text{ K}$ and allowed to settle for at least 48 h so that they could be separated into two clear phases. After the separation of the two phases, the concentrations of ammonium sulphate in the top and bottom phases were determined by the formaldehyde method. The chemical reaction is as follows:



The sulfuric acid formed was titrated against sodium hydroxide solution. The analysis of samples with given composition of PEGDME and $(\text{NH}_4)_2\text{SO}_4$ showed that the presence of PEGDME did not interfere with the determination. The uncertainty in the measurement of the mass fraction of the salt is 0.002. The concentration of PEGDME in both phases was determined by refractive index measurements performed at $T = 298.15 \text{ K}$ using a refract meter (ATAGO DR-A1, Japan). The uncertainty in refractive index measurement is 0.0002.

Since concentrated lactic acid solution contains high levels of dimmers, it was first diluted 10-fold and then boiled for (8 to 10) h under reflux to hydrolyze the

dimers. The resulting solution after reflux, titrated by 0.1N potassium hydroxide.

Results and Discussion

The obtained binodal data were fitted to the following empirical relationship developed by Merchuk: [2]

$$w_1 = a \exp(bw_2^{0.5} - cw_2^3) \quad (1)$$

where w_1 and w_2 are the concentrations of polymer and salt, respectively. The results are reported in Table 1.

Table1: Values of parameters (a, b, c) and standard deviation (sd) of Eq. (1), for {PEGDME₂₀₀₀ (1) + ammonium sulphate (2) + water (3)} systems at different temperatures.

T/K	a	b	c.10 ⁴	sd
298.15	110.0920	-0.5682	3.6035	0.35
308.15	97.4627	-0.5314	4.5387	0.20
318.15	105.0797	-0.5228	5.6350	0.22

On the basis of obtained standard deviations, we conclude that the Eq. (1) can be satisfactorily used to correlate the binodal data of the investigated system.

The correlation equations given by Othmer- Tobias (eq2a) and Bancroft (eq 2b) [3] have been used to correlate the tie-line compositions.

$$\left(\frac{1-w_1^t}{w_1^t}\right) = k \left(\frac{1-w_2^b}{w_2^b}\right)^n \quad (2a)$$

$$\left(\frac{w_3^b}{w_2^b}\right) = k_1 \left(\frac{w_3^t}{w_1^t}\right)^r \quad (2b)$$

where, k, n, k_1 , and r represented fit parameters, “top” and “bot” represent top and bottom phases, respectively. These equations have also been used to assess the reliability of LLE data. The corresponding correlation coefficient values, R are given in Table 2. On the basis of the obtained deviations ($Dev.$), we conclude that Eqs. (2a) and (2b) can be satisfactorily used to correlate the tie-line data of the investigated system. From the correlation coefficient values, reported in Table 2, we conclude that the reported tie-line data have acceptable consistency. [8].

Setchenow type equation:

The following Seteschenow type equation proposed by Hey et al. [5] was also used for the correlation of tie-line data:

$$\ln\left(\frac{C_p^{top}}{C_p^{bot}}\right) = k_p + k_s (C_s^{bot} - C_s^{top}) \quad (3)$$

in which the k_s is the salting-out coefficient, k_p is a constant, and C_p and C_s are the molality of polymer and salt respectively. Recently [4] we successfully used the Eq. (3) for the correlation of tie-line data. In this work, for the temperature dependency of fitting parameters of Eq. (3), we adopted a simple form for each parameter as follows [20]:

$$\ln\left(\frac{C_p^{top}}{C_p^{bot}}\right) = \left[\frac{k_p}{T} + \frac{k_s}{T} (C_s^{bot} - C_s^{top})\right] \quad (4)$$

The parameters of the Eq. (4) were obtained from the correlation of the experimental LLE data.

Table 2: Values of parameters of Othmer-Tobias and Bancroft, (k, n, K, r), for {PEGDME₂₀₀₀ (1) + ammonium sulphate (2) + water (3)} at different temperatures.

T/K	k	n	R ²	K	r	R ²	Dev
298.15	0.1902	1.6423	0.994	2.7652	0.6290	0.994	0.37
308.15	0.1051	1.7177	0.999	3.7313	0.5670	0.999	0.08
318.15	0.1690	1.5326	0.997	3.2655	0.6375	0.997	0.09

The locus for the experimental binodals shown in Fig. 1 demonstrated that the two-phase area is expanded with an increase in temperature.

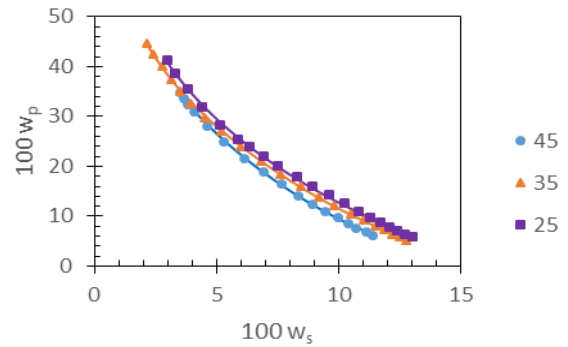


Fig 1. Experimental binodal results for the {PEGDME₂₀₀₀ (p) + di-sodium hydrogen citrate (s) + water (w)} system at different temperatures: (●) T = 298.15;

(▲) T = 308.15 and (■) T = 318.15 K, and (solid line) the calculated from equation (1).

Partition behaviour of lactic acid in different temperatures:

The partition coefficients ($K_{\text{lactic acid}}$) and extraction efficiency (E) of lactic acid in aqueous two phase system were calculated respectively by Eq. (5) and Eq. (6) and presented in figure 2.

$$K_{\text{lactic acid}} = \frac{w_{\text{lactic acid}}^{\text{top}}}{w_{\text{lactic acid}}^{\text{bot}}} \quad (5)$$

$$E = \frac{K_{\text{lactic acid}}}{K_{\text{lactic acid}} + 1} \times 100 \quad (6)$$

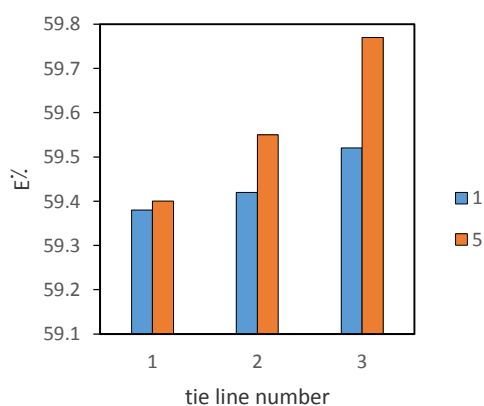


Fig 2. Effect of temperature and TLL on the iodine partitioning for {PEGDME2000 (p) + (NH₄)₂SO₄ (s) + H₂O (w)} system: (1) $T = 298.15$ K; (2) $T = 308.15$ K and (3) $T = 318.15$ K.

This figure shows that the partition coefficient increases with increasing temperature

Conclusions

Liquid-liquid equilibrium data for the {PEGDME₂₀₀₀ + ammonium sulphate + water} system was studied at $T = 298.15$, 308.15 and 318.15 K and the experimental binodal and tie-line data at the mentioned temperatures were reported. Comparison between the experimental data shows that the phase-separation ability of the studied system increased with increasing the temperature. The experimental binodal data were satisfactorily correlated using an empirical equation and the Merchuck equation as a function of temperature with a linear temperature dependency in the form of $(T - T_0)$ K as a variable.

Acceptable consistencies of the experimental tie-lines are obtained using the Othmer-Tobias and Bancroft equations. Additionally, Seteschenow type equation and osmotic virial model were used for the correlation of the (liquid - liquid) phase behaviour of the system studied.

On the base of the obtained results, it can be concluded that, the performances of all the considered models in the

correlation are good. The Setschenow type equation with only two-parameters however, shows the best results in the correlation and prediction of the tie-line compositions of the studied system.

Applicability of this polymer based ATPS has been studied for extraction of lactic acid. We found that this ATPS which is environmentally benign can be used as a simple technique for extraction of lactic acid; so that it can efficiently extract lactic acid in polymer phase. The partition coefficients and extraction percent of lactic acid in this ATPS were obtained; and it was found that these quantities increase as the differences in PEGDME concentrations between the phases increases. From the experimentally determined values for the lactic acid molecule partitioning we concluded that partition coefficients is increased with increasing temperature.

References

- [1] S.P.M. Ventura, C.M.S.S. Neves, M.G. Freire, I.M. Marrucho, J. Oliveira, J.A.P. Coutinho, Evaluation of Anion Influence on the Formation and Extraction Capacity of Ionic-Liquid-Based Aqueous Biphasic Systems, *J. Phys. Chem. B* 113 (2009) 9304–9310.
- [2] Merchuk, J. C. Andrews, B. A. Asenjo, J.A. Aqueous two-phase systems for protein separation Studies on phase inversion *J. chromatogr. B.* 711(1998) 285-293.
- [3] D. F. Othmer, P. E. Tobias. Liquid -Liquid Extraction Data -Toluene and Acetaldehyde Systems, *Ind. Eng. Chem.* 34 (1942) 690-692.
- [4] M. T. Zafarani-Moattar, H. Shekaari, M. Hosseinzadeh, P. Jafari, Aqueous two-phase system of poly ethylene glycol dimethyl ether 2000 and sodium hydroxide at different temperatures: Experiment and correlation, *Fluid Phase Equilib.* 376 (2014) 225-233.
- [5] M. J. Hey, D. P. Jackson, H. Yan, The salting-out effect and phase separation in aqueous solutions of electrolytes and poly (ethylene glycol), *Polymer* 46 (2005) 2567-2572.

The effect of polymer molar mass on the aqueous two-phase system containing Poly ethylene glycol dimethyl ether and ammonium sulphate at 298.15 K and its application of this system in partitioning of iodine

Mohammed Taghi Zafarani –Moattar^a, Hemayat Shekaari^a, Tohid Hashemzadeh^{a*}

^aPhysical Chemistry Department, Faculty of Chemistry, University of Tabriz, Tabriz, 5166616471, Iran

* Engineer_tohid@yahoo.com

Abstract: The partitioning of iodide was studied in an aqueous two phase system (ATPS) comprised of ammonium sulphate, poly ethylene glycol dimethyl ether (PEGDME), and water at 298.15 K. To investigate the effect of molar mass of the polymer on the tie-line, similar measurements were also made at $T=298.15$ K on this two phase system consisting of the PEGDME with molar masses of 250, 500 and 2000 $\text{g}\cdot\text{mol}^{-1}$. Finally the effect of molar mass of polymer on the binodal of {PEGDME + ammonium sulphate +water} was studied by measuring liquid-liquid equilibrium at $T= 298.15$ K for three different molar masses. The experimental binodal data were described using two empirical nonlinear three parameter expressions developed by Merchuk and Zafarani Moattar et al. The increase in the polymer molar mass provides ATPS with larger biphasic region. The tie-line compositions were estimated and correlated using the Othmer–Tobias and Bancroft and Setschenow type equations. In addition the partitioning behaviour of the iodine molecule on the investigated aqueous two-phase system was studied.

Keywords: Liquid-liquid equilibrium; Ammonium sulphate; Setschenow type equation; Poly ethylene glycol dimethyl ether; Iodine Partitioning.

Introduction

Aqueous two phase systems (ATPSs) are increasingly being used in biotechnology for the separation of a wide variety of products. Separation of biological molecules and particles using ATPS was initiated more than half a century by P.-Å. Albertsson [1].

In this work, the binodal and tie-line data are reported for {PEGDME +ammonium sulphate +water} at different molar masses of PEGDME and at 298.15. We also reported iodine partitioning using {PEGDME+(NH₄)₂SO₄ + H₂O} system and reported iodine partition coefficient in this aqueous two-phase system at $T= 298.15\text{K}$.

Materials and method

The chemicals poly ethylene glycol di-methyl ether (PEGDME) with molar mass 2000 $\text{g}\cdot\text{mol}^{-1}$, 500 $\text{g}\cdot\text{mol}^{-1}$, and 250 $\text{g}\cdot\text{mol}^{-1}$ with CAS number 9003-39-8, ammonium sulphate with CAS Registry No. 7783-20-2 purity of 99%, iodine (I₂), of molar mass 253.809 $\text{g}\cdot\text{mol}^{-1}$, with CAS number 9003-39-8 and purity of 99%, were all obtained from Merck.

A glass vessel with an external jacket used around which water at constant temperature was circulated using a thermostat with an uncertainty ± 0.05 K. The binodal curves were determined by clouding point titration method. In this method, the composition of the mixture for each point on the binodal curve was determined from the amount of titrate added until turbidity was observed using an analytical balance (Shimatzu, 321-34553, Shimatzu Co., Japan) with a precision of $\pm 1.10^{-7}$ kg. The maximum uncertainty was found to be ± 0.002 in

determining the mass fraction of both polymer and salt by using of this method.

For determination of the tie-lines, feed samples (about $2 \times 10^{-5} \text{ m}^3$) were prepared by mixing appropriate amounts of polymer, salt and water in the vessel. The thermostat was set at the desired temperature, and the samples were stirred for 1 h. Then, the samples were placed in the thermostat (JULABO model MB, Germany) with temperature control ability of ± 0.02 K and allowed to settle for at least 48 h so that they could be separated into two clear phases. After the separation of the two phases, the concentrations of ammonium sulphate in the top and bottom phases were determined by the formaldehyde method. The chemical reaction is as follows:



The sulfuric acid formed was titrated against sodium hydroxide solution. The analysis of samples with given composition of PEGDME and (NH₄)₂SO₄ showed that the presence of PEGDME did not interfere with the determination. The uncertainty in the measurement of the mass fraction of the salt is 0.002. The concentration of PEGDME in both phases was determined by refractive index measurements performed at $T = 298.15$ K using a refract meter (ATAGO DR-A1, Japan). The uncertainty in refractive index measurement is 0.0002.

The mixture with the same amount of polymer, salt and water used for tie-lines determination were prepared again and the partitioning 0.0014 g of iodine was investigated. The quantity of the iodine is determined by titration with sodium thiosulfate.

Results and Discussion

For the aqueous (PEGDME + ammonium sulphate) system, the binodal data and tie-line compositions determined experimentally at different polymer molar masses and at 298.15 K temperature.

The locus for the experimental binodals is shown in Fig. 1. In fact by increasing molar mass of PEGDME, the polymer becomes less hydrophilic and its solubility in water decreases; therefore, the salting out strength of PEGDME is increased by increasing molar mass of polymer. Also, in Fig.2 the tie-line data are shown at molar masses $M = (2000, \text{ and } 250) \text{ g.mol}^{-1}$ for the temperature 298.15 K. From Fig.2, it can be seen that the slope and length of tie-lines increased with an increase of polymer molar mass.

In this work for the correlation of binodal data, we examined the performances of the Merchuck equation [2] and the empirical equation that we proposed recently [3]:

$$w_p = a \cdot \exp [b \cdot (w_s)^5 - c \cdot (w_s)^3] \quad (1)$$

$$w_p = a + \beta \cdot \ln(w_s) + \gamma \cdot w_s \quad (2)$$

where w_p and w_s are the mass percent of the polymer and salt respectively. Also a, b, c are fitting parameters of Eq. (1) and α, β and γ are the fitting parameters of Eq. (2).

The fitting parameters for these equations along with the corresponding standard deviation for each polymer at 298.15 K are given in Tables 1 and 2. The obtained standard deviations (*sd*) show that both of equations (1) and (2) can be used to reproduce the binodal values; however, on the basis of the obtained standard deviations, we conclude that the performance of equation (2) is better than equation (1).

Table1: Values of parameters (a, b, c) and standard deviation (*sd*) of Eq. (1), for {PEGDME₂₀₀₀ (1) + ammonium sulphate (2) + water (3)} systems with difference in molar mass at $T=298.15$ K.

polymer	a	b	$10^4 \cdot c$	<i>sd</i>
2000	110.0920	-5.682	3.6035	0.35
500	82.6271	-3.635	9.2403	0.11

Table2: Values of parameters (α, β, γ), and standard deviation (*sd*) of Eq. (2), for {PEGDME₂₀₀₀ (1) + ammonium sulphate (2) + water (3)} systems with difference in molar mass at $T=298.15$ K.

polymer	α	β	γ	<i>sd</i>
2000	64.5855	-20.2629	-.5027	0.24

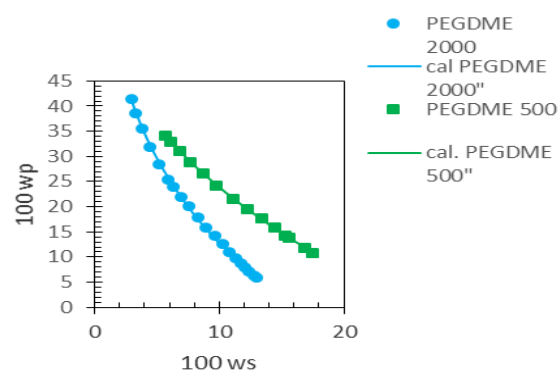


Fig 1. Plot of mass percent polymer against mass percent salt to show binodal curves for the {PEGDME (p) + ammonium sulphate (s) + water (w)} two-phase system at different polymer molar masses: (●) PEGDME2000; (■) PEGDME500; and $T = 298.15$ K; and (solid line) the calculated from equation (1).

For the correlation of LLE data of polymer + salt + water system, several models have been developed. However, in this work we decided to use a Setschenow type equation [4].

A Setschenow type equation is a relatively simple two parameter equation:

$$\ln \left(\frac{C_p^{top}}{C_p^{bot}} \right) = k_p + k_s (C_s^{bot} - C_s^{top}) \quad (3)$$

in which k_s is the salting-out coefficient, k_p is a constant and m_p and m_s are the molality of polymer and salt, respectively. Superscripts “top” and “bot” stand for polymer rich phase and salt rich phase, respectively.

The fitting parameters obtained from the correlation of the experimental LLE data at $T = 298.15$ K are given in Table 3 along with the corresponding standard deviations. On the basis of deviations reported in Table 3, it is interesting to note that equation (3) with only two parameters represents the experimental LLE values with excellent accuracy.

Table 3: Values of parameters of Setschenow type equation, (k_p, k_s) ($\text{kg} \cdot \text{K} \cdot \text{mol}^{-1}$), for {PEGME (p) + ammonium sulphate (s) + water (w)} at different molar masses and temperatures 298.15 K.

polymer	k_p	k_s	<i>sd</i>
2000	1.8025	0.8564	0.07
500	1.0469	0.3930	0.02
250	0.8197	0.4532	0.001

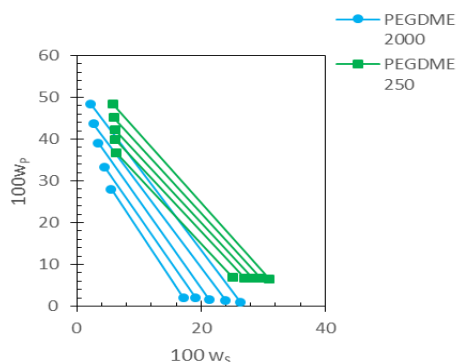


Fig.2: Effect of type of polymer via plot of mass percent polymer against mass percent salt to illustrate the effect of polymer molar mass on the slope and length of tie- lines of the {PEGDME n (p) + ammonium sulphate (s) + H₂O (w)} system: (●) PEGDME2000; (■) PEGDME250; (—), tie-lines were obtained by connecting the experimental equilibrium phase composition values.

Influence of polymer molar mass on partition behaviour of I₂:

The partition coefficients (K_{iodine}) and extraction efficiency (E) of I₂ in aqueous two phase system were calculated respectively by Eq. (4) and Eq. (5) and the results are presented in figure 3.

$$K_{iodine} = \frac{w_{iodine}^{top}}{w_{iodine}^{bot}} \quad (4)$$

$$E = \frac{K_{iodine}}{K_{iodine}+1} \times 100 \quad (5)$$

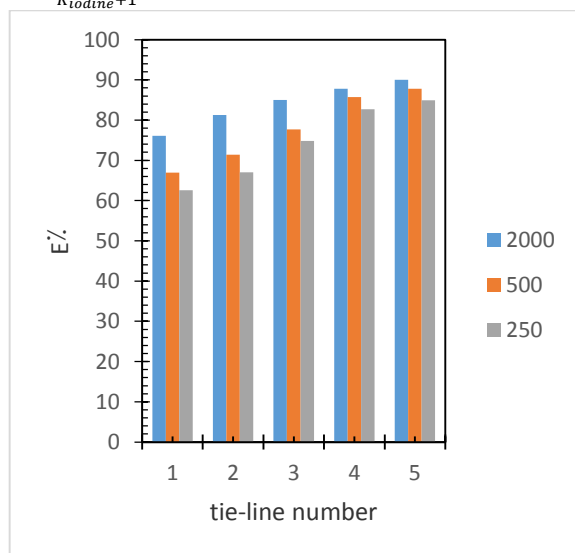


Fig.3: Effect of temperature and TLL on the iodine partitioning for {PEGDME2000 (p) + (NH₄)₂SO₄ (s) + H₂O (w)} system: (blue column) PEGDME₂₀₀₀; (orange column) PEGDME₅₀₀ and (gray column) PEGDME₂₅₀.

This figure shows that the partition coefficient increases with increasing molar mass of polymer.

Conclusions

Phase equilibrium results were obtained for aqueous two-phase system (PEGDME+ (NH₄)₂SO₄ +H₂O) at $T = 298.15$ K and PEGDME molar masses of 2000, 500, 250 g.mol⁻¹. The experimental binodal data were satisfactorily correlated with Merchuck and a new empirical equation.

Acceptable consistencies of the experimental tie-lines are obtained using the Othmer-Tobias and Bancroft equations. Additionally, Seteschenow type equation was used for the correlation of the (liquid - liquid) phase behaviour of the system studied with excellent accuracy.

Applicability of this polymer based ATPS has been studied for extraction of iodine. The partition coefficients and extraction percent of iodine in this ATPS were obtained; and it was found that by increasing molar mass of polymer the K_{iodine} and E are increased.

References

- [1] P.A. Albertsson, Partition of Cell Particles and Macromolecular, Wiley, New York, 1986.
- [2] Merchuk, J. C. Andrews, B. A. Asenjo, J.A. Aqueous two-phase systems for protein separation Studies on phase inversion J. chromatogr. B.711 (1998) 285-293.
- [3] M.T. Zafarani-Moattar, E. Nemati-Kande, Study of liquid-liquid and liquid-solid equilibria of the ternary aqueous system containing poly ethylene glycol dimethyl ether 2000 and tri-potassium phosphate at different temperatures: Experiment and correlation CALPHAD 34 (2010) 478-486.
- [4] M.J. Hey, D.P. Jackson, Hong Yan, The salting-out effect and phase separation in aqueous solutions of electrolytes and poly(ethylene glycol), Polymer 46 (2005) 2567-2572.

Prediction of Liquid Phase Equilibria for Water + Valeric Acid or Levulinic Acid + Dimethyl Phtalate

Forough Mohamadi-Zad*, Sina Shekarsaraee
 Department of Chemistry, Faculty of science, University of Guilan, Rasht, Iran
 shekarsaraee@guilan.ac.ir (S. Shekarsaraee)
 Tel/Fax: +98133333262

Abstract: (Liquid-liquid) equilibrium (LLE) data were investigated for mixtures of (water + propionic acid + trans-decalin or cis-decalin) and (water + propionic acid + trans-decalin + naphthalene) at $T = 298.15$ K and $P = 1019.0$ hPa. The tie-line data were predicted by the UNIFAC method. The distribution coefficients and the separation factors for the immiscibility region are calculated to evaluate the effect of solvent type. Naphthalene was used as a solid additive to investigate the effect of non-polar additive on separation of the acid from aqueous solution. It is concluded that trans-decalin is slightly better than cis-decalin but it is a cheaper and more stable solvent and may serve as an adequate solvent to extract propionic acid from its dilute aqueous solutions. Concentration effect of naphthalene also investigated and result showed that it could be very effective in separation of propionic acid from aqueous solution.

Keywords: LLE Data, UNIFAC Method, Decalin, Naphthalene

Introduction

The separation of carboxylic acids from aqueous fermentation media by solvent extraction has been an actual research area. A large amount of investigation has been carried out in recent years on the (liquid-liquid) equilibrium (LLE) measurements of ternary systems, in order to understand and provide further information about the phase behavior of such systems [1-3]. Propionic acid (PA) is a widely used carboxylic acid in pharmaceutical industry as a cellulosic solvent and can be used to provide propionates as fungicides. It is also used in the electroplating industry, and to prepare perfume esters [4]. Since, the liquid extraction of propionic acid from aqueous solution is industrially and scientifically important, various organic solvents have been investigated and reported for propionic acid extraction [5-7]. Trans-decalin and cis-decalin used in this study may be considered also as suitable solvents for extraction of propionic acid from water, having low vapor pressure, capability to form two phases at reasonable temperatures and rapid phase separation (low density and high viscosity). Naphthalene used as a solid additive to increase the capability of solvent for separation process. The tie-lines were predicted using the UNIFAC method (a group contribution method) developed by Fredenslund et al. [8].

Materials and method

The equilibrium data of the ternary and quaternary mixtures were predicted by UNIFAC method using the interaction parameters between CH₂, CH₃, CH=CH, OH, COOH and H₂O [9]. Eight ternary and five quaternary mixtures were chosen to investigate the effect of solvent structure, acid concentration and additive presence on separation of propionic acid from aqueous solutions. Feed compositions are listed in table 1.

Table 1. Feed compositions of investigated mixtures

solvent	m _{water} (g)	m _{PA} (g)	m _{solvent} (g)	m _{naphthalene} (g)
cis-decalin	20	5	20	-
	20	30	20	-
trans-decalin	20	5	20	-
	20	10	20	-
	20	15	20	-
	20	20	20	-
	20	25	20	-
	20	30	20	-
	20	5	20	2
	20	30	20	2
	20	5	20	4
	20	5	20	10
20	5	20	20	

Results and Discussion

Equilibrium tie-line data for the (water + PA + cis-decalin), (water + PA + trans-decalin) and (water + PA + trans-decalin + naphthalene) ternary and quaternary systems were measured at $T = 298.2$ K and atmospheric pressure. Tie-line data for the ternary and quaternary systems are given in Tables 2. In this study, distribution coefficients of the acid (D₂) and separation factors (S) were calculated from the predicted data to evaluate the effectiveness of the acid extraction by the organic solvents (cis-decalin and trans-decalin) and additive (naphthalene). The experimental separation factor, which is a measure of the ability of a solvent to separate the acid from water, is defined as the ratio of distribution coefficients of the acid (D₂) to water (D₁), i.e.



$$S = \frac{D_2}{D_1} \quad (1)$$

$$D_2 = \frac{w_{23}}{w_{21}} \quad (2)$$

$$D_1 = \frac{w_{13}}{w_{11}} \quad (3)$$

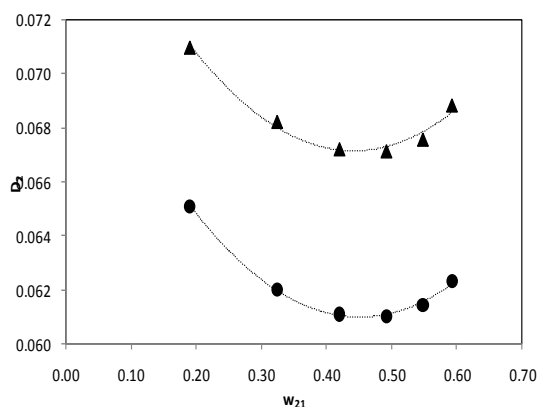


Fig. 1. Plot of the distribution coefficient (D_2) of PA as a function of mass fraction of the acid in the aqueous phase; (●) water + PA + trans-decalin, (▲) water + PA + trans-decalin + naphthalene

Conclusions

In this study, a comparison of the extracting capabilities of the solvents and additive was made with respect to separation factor values. This factor is found to be greater than 1 ($S > 1$) for the systems investigated, which means that the acid must have different affinity in the two phases and extraction of PA by these solvents is possible. As seen from Table 2, a slight solvent effect on the separation factor can be observed between two isomers

but additive (naphthalene) has a noticeable effect on both separation factor and distribution coefficient.

References

- [1] Letcher, T.M., Redhi, G.G., "Phase equilibria for liquid mixtures of (butanenitrile + a carboxylic acid + water) at 298.15 K", *Fluid Phase Equilibria*, 193, 2002.
- [2] Arce, A., Blanco, A., Souza, P., Vidal, I.J., "Liquid-Liquid Equilibria of the Ternary Mixtures Water + Propanoic Acid + Methyl Ethyl Ketone and Water + Propanoic Acid + Methyl Propyl Ketone", *J. Chem. Eng. Data*, Vol. 40, 1995.
- [3] Branios, J.A., Mullins, J.C., Thies, M.C., "Liquid-liquid equilibria for the oleic acid-beta.-sitosterol-water system at elevated temperatures and pressures", *Ind. Eng. Chem. Res.*, Vol. 33, 1994.
- [4] Kirk, R.E., Othmer, D.F., *Encyclopedia of Chemical Technology*, Interscience Encyclopedia Inc., New York, 1947.
- [5] Ehreli, S.C., Bilgin, M., "Quaternary Liquid-Liquid Equilibrium of Water + Acetic Acid + Propionic Acid + Solvent (Amyl Alcohol, Cyclohexyl Acetate, or Toluene) Systems", *J. Chem. Eng. Data*, Vol. 49, 2004.
- [6] Taghikhani, V., Vakili-Nezhaad, G.R., Khoshkbarchi, M.K., Shariaty-Niassar, M., "Liquid-Liquid Equilibria of Water + Propionic Acid + Methyl Butyl Ketone and of Water + Propionic Acid + Methyl Isopropyl Ketone", *J. Chem. Eng. Data*, Vol.46, 2001.
- [7] Ehreli, S.C., Tath, B., Bagman, P., "(Liquid + liquid) equilibria of (water + Propionic acid + cyclohexanone) at several temperatures", *J. Chem. Thermodyn.*, Vol. 37, 2005.
- [8] Fredenslund, A., Jones, R.L., Prausnitz, J.M., "Group-contribution estimation of activity coefficients in nonideal liquid mixtures", *AIChE J.*, Vol. 21, 1975.
- [9] Reid, R.C., Prausnitz, J.M., Poling, B.E., *The Properties of Gases and Liquids*, 4th ed., McGraw-Hill Inc., New York, 1987.

Molecular Interactions Study of Diisobutyl Ketone and 2-Alkanol by Density Measurements

Mohammad Almasi, Behrooz Davodi*

Department of Chemistry, Ahwaz Branch, Islamic Azad University, Ahwaz, Iran

*behroozdavodi@gmail.com

Abstract: In present paper, density values for binary systems of diisobutyl ketone + 2-propanol or 2-butanol or 2-pentanol have been measured over the entire range of composition and within the temperature range of 293.15 to 323.15 K. From these data, excess molar volumes were calculated and interpreted in terms of intermolecular interactions and structural effects. Obtained values of excess molar volumes were correlated for all binary liquid mixtures with Redlich-Kister equation. These values are positive for diisobutyl ketone + 2-alkanol mixtures and increase with rising temperature.

Keywords: Diisobutyl Ketone; 2-Alkanol; Density; Excess molar volume

Introduction

Diisobutyl ketone (DIBK) is a low cast polar compound ($n_D^{20} = 2.70$ D and $d_4^{20} = 9.9$ at 20 °C) that often is used as solvent for various coating systems especially as a solvent for rubbers, paint removers, resins, polystyrene, polyurethane, acrylic coatings, and cleaning solutions. DIBK is also used in the production of synthetic leathers, transparent paper, and aluminum foil and as extraction solvent. It is a colorless, stable liquid with the high boiling point and slow evaporating property that has limited water solubility but miscible with alcohols. Excellent viscosity and surface tension reduction in high solid's coatings and a non-HAP (Hazardous Air Pollutant) solvent are of the other advantages of this chemical [1]. Our studies are directed to investigate non-aqueous binary mixtures by physico-chemical properties [2] to provide useful informations about the molecular interactions.

Materials and method

Diisobutyl ketone, 2-propanol, 2-butanol, 2-pentanol, were purchased from Merck with purity higher than 99% and used without further purifications. Density of the pure compounds and mixtures were measured by SVM 3000 stabinger viscometer, provided with automatic viscosity correction. The mixtures were prepared by weighing known masses of pure liquids in airtight, narrow-mouth ground stoppered bottles taking due precautions to minimize evaporation losses

Results and Discussion

The excess molar volumes V_m^E for the three binary systems were evaluated using the equation

$$V_m^E = \sum_{i=1}^N x_i M_i (\rho^{-1} - \rho_i^{-1}) \quad (1)$$

Where ρ is the density of the mixture, ρ_i is the density of pure component i , x_i is the mole fraction, M_i is the molar mass of component i , and N stands for the number of

components in the mixture. V_m^E for the binary systems were fitted by the least-squares method to the Redlich-Kister [3] equation

$$V_{ij}^E = x_i x_j \sum_{k=0}^n A_k (x_i - x_j)^k \quad (2)$$

Experimental data and fitted equations for the three binary systems are presented in Fig. 1.

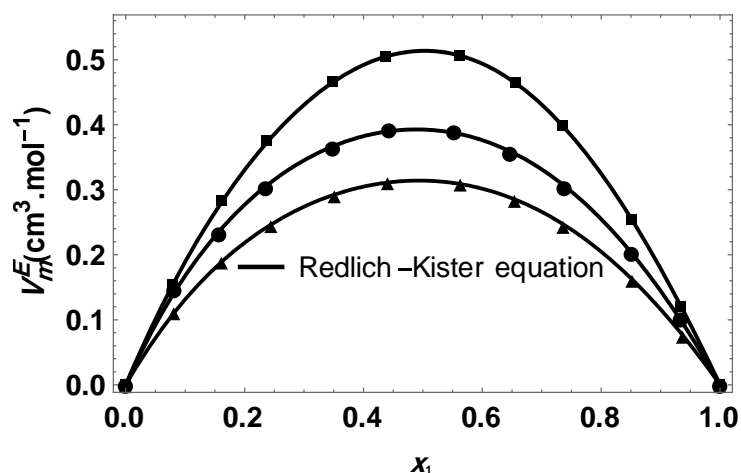


Fig.2: Excess molar volumes at 298.15 K for the binary systems: (▲) diisobutyl ketone+ 2-propanol, (●) diisobutyl ketone+ 2-butanol, (■) diisobutyl ketone+ 2-pentanol.

Generally V_m^E can be considered as arising from three types of interactions between component molecules. Physical interactions mainly consisting of dispersion forces or weak dipole-dipole interaction and making a positive contribution. Chemical or specific interactions which include charge transfer, formation of hydrogen bonds and other complex forming interactions resulting in negative contribution. The structural contributions arising from geometrical fitting of one component into another due to difference in molar volumes resulting in negative V_m^E [4]. Intermolecular

interactions take place during the mixing process can be classified as follows: i) favourable interactions between polar groups (C=O and –OH) responsible for a negative contribution to V_m^E . ii) Unfavourable interactions involving polar substituent and apolar groups. The positive deviation of V_m^E for DIBK (1) + 2-alkanol (2) solvent system is governed by steric hindrances of molecule components which overcome the other effect due to specific interactions between different species. In all the systems, the excess molar volumes are obviously increased with rise of temperature and with increasing the chain length of 2-alkanol. When the number of carbon atoms in the hydrocarbon part of 2-alkanol increases, the polar characteristics starts reducing which resists the formation of intermolecular interactions between DIBK and 2-alkanol and hence the tendency to form associated complex decreases with the lengthening of carbon chain

Conclusions

Values of densities for binary mixtures consisting DIBK + 2-alkanol at various temperatures were measured and the corresponding excess molar volumes have been calculated and fitted by Redlich-Kister polynomial to evaluate the standard errors. Excess molar values are positive for all studied mixtures. The structure of DIBK

/alcohol mixtures is governed by hindrances effects in the carbon chain of alcohols.

Acknowledgment

The Authors thanks the Islamic Azad University, Ahwaz Branch for financial support of this work.

References

- [1] Papa, A. J. Ullmann's Encyclopedia of Industrial Chemistry, Wiley-VCH: Weinheim, England.
- [2] H. Iloukhani, M. Almasi, Densities and Excess Molar Volumes of Binary and Ternary Mixtures Containing Acetonitrile + Acetophenone + 1,2-Pentanediol: Experimental Data, Correlation and Prediction by PFP Theory and ERAS Model. *J. Solution. Chem.* 40 (2011) 284–298.
- [3] O. Redlich, A. T. Kister, Algebraic representation of thermodynamic properties and the classification of solutions. *Ind. Eng. Chem.* 40 (1948) 345-348.
- [4] B. S. Lomte, J. M. Bawa, K. M. Lande, R. B. Arbad, Densities and Viscosities of Binary Liquid Mixtures of 2-Butanone with Branched Alcohols at (293.15 to 313.15) K, *J. Chem. Eng. Data* 54(2009)127–130.

Study of Density and Excess Molar Volume of Ortho Xylene and 2-Alkanol

Mohammad Almasi, FaridehZargar*

Department of Chemistry, Ahwaz Branch, Islamic Azad University, Ahwaz, Iran

*Farideh zargar44@gmail.com

Abstract: Measured densities of Para xylene, 2-propanol, 2-butanol, 2-pentanol and their binary mixtures with Para xylene in the liquid state were reported over the whole composition range at the temperatures 293.15 to 323.15 K and atmospheric pressure. From the experimental data, excess molar volumes were calculated, correlated with Redlich-Kister equation and interpreted in terms of intermolecular interactions and structural effects. These Values are positive for Para xylene + 2- Alkanol mixture and increase with rising temperature.

Keywords: Para xylene; 2-Alkanol; Density; Excess molar volume

Introduction

Oxygenates are compounds that contain oxygen such as ethers, glycol ethers, alcohol, methyl and carbonates or biomass products such as esters of vegetable oils and used as fuel additives. Increasing demand environmental concern, and occasional oil crises turn the researchers to study the use of fuel additive oxygenates. These compounds improve air quality and increase the fuel efficiency by allowing more complete combustion in internal combustion engines as oxygen in oxygenates readily oxidized fuel. The presence of oxygenates in fuel not only reduces the carbon monoxide emission and other toxic emissions but also increases the octane/cetane rating of fuel. Excess properties of mixtures provide information about the molecular interactions between the various components and can be used for the development of molecular models describing the thermodynamic behavior of mixtures. The thermodynamic properties of mixtures are of great industrial interest. The property studied has proved to be meaningful from a thermodynamic point of view, as it provides direct information about the energetic effects arising between the molecules present in the mixture, so it can help to explain the rearranging of the bonding that occurs during the mixing process, which is essential when studying new theoretical approaches to the liquid state, either pure or mixture.[1– 2].

Materials and method

Para xylene, 2-propanol, 2-butanol, 2-pentanol, were purchased from Merck with purity higher than 99% and used without further purifications. Density of the pure compounds and mixtures were measured by SVM 3000 stabinger viscometer, provided with automatic viscosity correction. The mixtures were prepared by weighing known masses of pure liquids in airtight, narrow-mouth ground stoppered bottles taking due precautions to minimize evaporation losses

Results and Discussion

The excess molar volumes V_m^E for the three binary systems were evaluated using the equation

$$V_m^E = \sum_{i=1}^N x_i M_i (\rho^{-1} - \rho_i^{-1}) \quad (1)$$

Where ρ is the density of the mixture, ρ_i is the density of pure component i , x_i is the mole fraction, M_i is the molar mass of component i , and N stands for the number of components in the mixture. V_m^E for the binary systems were fitted by the least-squares method to the Redlich–Kister [3] equation

$$V_{ij}^E = x_i x_j \sum_{k=0}^n A_k (x_i - x_j)^k \quad (2)$$

Experimental data and fitted equations for the three binary systems are depicted in Fig. 1.

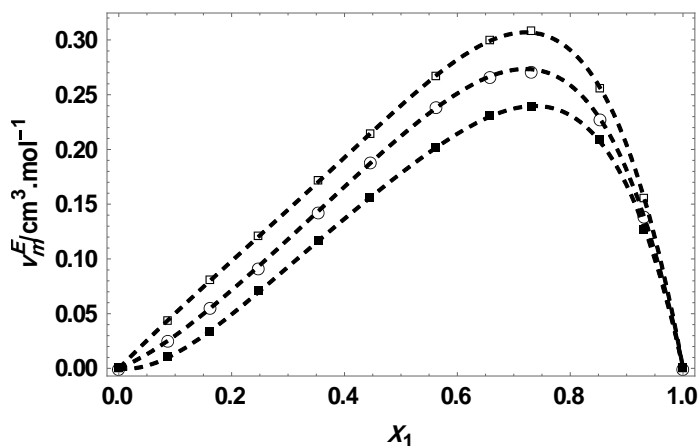


Fig.3: Excess molar volumes at 298.15 K for the binary systems: (■) Para xylene + 2-propanol, (○) Para xylene + 2-butanol, (□) Para xylene + 2-pentanol. Dashed lines calculated with Redlich–Kister equation

At the simplest qualitative level, V_m^E values may be attributed to the resultant of two opposing effects. The positive contribution to V_m^E values arises from the breaking of self-associated 2-propanol and dipole-dipole interactions between monomers and dimers of 2-alkanol



and from the disruption in the favorable orientation order of the aromatic hydrocarbons. The negative contribution is due to the electron-donor-acceptor interactions between 2-alkanol and aromatic hydrocarbons and change in free volume in real mixtures. High positive V_m^E values show that factors of positive contribution dominate over the negative contribution. Excess molar volumes of Para xylene + 2-Alkanol are positive over the whole range of mole fractions. Positive values would indicate that molecular interactions between different molecules are weaker than interactions between molecules in the same pure liquid. In these mixtures, attractive interactions between unlike species decrease and repulsive interactions predominate, leading to positive excess molar volumes.

This may be due to the steric hindrance offered by two bulky methyl groups which restrict the proper orientation of these molecules and obstruct the 2-alkanol toward the ring thus making electron-donor-acceptor interaction weaker. In spite of this qualitative description of the present data, the degree of association of 2-alkanol and the influence of aromatic hydrocarbon on it remain to be investigated.

Conclusions

Densities and excess molar volumes V_m^E for binary mixtures Para xylene + 2-alkanol were measured at various temperatures and fitted by Redlich-Kister polynomial to evaluate the standard errors. Positive excess molar volumes for all binary systems indicate that the governed forces in the mixtures are scattering type.

Acknowledgment

The Authors thanks the Islamic Azad University, Ahwaz Branch for financial support of this work.

References

- [1] H. Iloukhani, M. Almasi, Thermophysical and transport properties of binary mixtures containing triethylene glycol and alcohols at different temperatures, *ThermochimActa* 495 (2009) 139-143.
- [2] H. Iloukhani, M. Almasi, Densities and Excess Molar Volumes of Binary and Ternary Mixtures Containing Acetonitrile + Acetophenone + 1,2-Pentanediol: Experimental Data, Correlation and Prediction by PFP Theory and ERAS Model. *J. Solution. Chem.* 40 (2011) 284-298
- [3] O. Redlich, A. T. Kister, Algebraic representation of thermodynamic properties and the classification of solutions. *Ind. Eng. Chem.* 40 (1948) 345-348.

Measurement density of nanofluids containing MWCNT- OH decorated with soft metal (Au) in ethylene glycol

M. Moghadari*, F. Yousefi

Chemistry Department, Yasouj University, Yasouj 75918-74831, Iran

*Corresponding author: FakhriYousefi

Tel/fax: + 98 741 222 1711.

*fyousefi@mail.yu.ac.ir

Abstract: In the present study, the density of MWCNT-OH-Au in ethylene glycol are presented. Density measurements also showed that the density decreases with increasing temperature and increases with an increasing in the solid weight fraction. Using experimental data indicated that the maximum of density of the nanofluid MWCNT-OH-Au/EG was 1.11737, This occurred at solid weight fraction of 0.2% and temperature of 20°C.

Keyword: Density, Nanofluid

Introduction

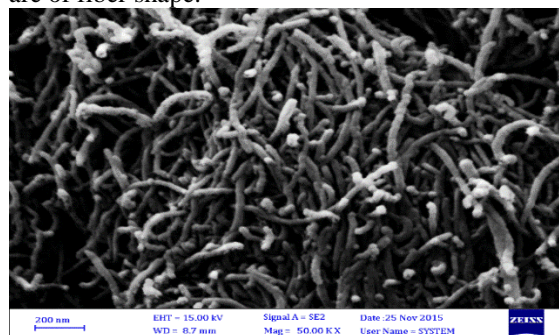
The mixture of nanoparticles with a base fluid (water, ethylene glycol, oil, etc.) is called nanofluid. Nanofluids are new type of fluids which have various applications in industrial and engineering apparatus. [1]. In the recent decade researchers have been found that adding nanoparticles to a working fluid introduces a very significant alteration in its thermophysical properties [2]. Some remarkable increase in the thermal properties of nanofluid such as thermal conductivity and convective heat transfer capability is due to the positively altered thermal properties of nanoparticles in comparison to the conventional fluid. Nanoparticles can be either metal oxide such as Al₂O₃, CuO, ZnO and TiO₂ or carbon based particles like carbon nanotube (CNT), graphene oxide (GO) and graphene nanoplatelets (GNP) [3]. Thermophysical properties are very impressive in efficiency of heating systems. In other words, the main aim of adding nanoparticles to the fluids that are used in heat exchanging systems is improving the thermophysical properties. Also, the amount of these properties will change by adding them to the base fluid [4]. Among these properties the density, viscosity, thermal conductivity and specific heat capacity are citing factors. Researchers have different statements about the effect of adding nanoparticles to the water.

Experimental

1.1. Preparation and synthesis of CNT-OH-Au

0.01 g of H₂AuCl₄ salt was dissolved in 100 mL double distilled water under stirring for 1 h at 70 °C. Then, 0.20 g of NaNO₃ that dissolved in 5 mL distilled water was added to the solution. In the next step, 0.50 g of CNT-OH was dissolved in 100 mL double distilled water under ultrasound bath. After 1 h solution was added to the CNT-OH solution and subsequently keeping in the stirring for 24 h. The solid material was filtered and dried at 60 °C. Synthesized nanoparticles were characterized by

SEM. Fig.1 shows the SEM image of pristine MWCNT-OH which were decorated with Au nanoparticles and it indicates that the nanoparticles are of fiber shape.



1. SEM image of pristine MWCNT-OH which was decorated with Au

1.2 Nanofluid Preparation

The nanoparticles used in the study is MWCNT-OH-Au ethylene glycol (Merck product, Germany) were used as the base fluid. The nanofluids were subjected to a mixing process using the mechanical stirrer for 30 minutes and underwent ultrasonic processor (Hielscher Company, Germany) for 4 h for each concentration to enhance the stability of the nanofluid. This solution remains stable for two week. In the study, Nano fluid sample were prepared by taking 50ml of base fluid in a beaker and then, MWCNT-OH-Au/EG Nano fluids. Stability the applications of nanofluids depend on their properties and stability which can be determined by the quality of the dispersion and suspension of nanoparticles in the base fluid. Stability MWCNTs of the prepared nano fluid was studied by using a pH meter to measure the pH values

2.3 Measurement of density

The density of MWCNT-OH-Au was dispersed into EG base fluid. Composites with solid weight fractions of 0.0125%, 0.025%, 0.05%, 0.1 and 0.2% MWCNTs/EG Nano fluids were measured in a temperature range from 20 °C to 55 °C. A density meter (DMA 4500M) was used to measure the densities of above mentioned nanofluids.

3. Results and discussion

The density of nanofluids has increases with the increase of nanoparticle concentrations, and decreases when the temperature increases. Volumetric behavior of MWCNT-OH-Au nanofluids has investigated from experimental measurements. Fig. (2),(3) shows the density of nanofluid samples as a function of weight fraction and temperature. The data with weight fraction percentages of 0.0125%, 0.025%, 0.05%, 0.1% and 0.2% were measured at 20 to 55 °C and at 5 °C steps. This test is also done for MWCNT-OH /W, MWCNT-OH /EG, and MWCNT-OH /EG-W(60-40), MWCNT-OH -Au/W, MWCNT-OH -Au/EG-W(60-40), MWCNT-OH -Ag/W, MWCNT-OH -Ag/EG, MWCNT-OH -Ag/EG-W(60-40), MWCNT-OH -Pd/W, MWCNT-OH -Pd/EG and MWCNT-OH -Pd/EG-W(60-40) in various temperature (20-55 °C) and solid weight

References

- [1] S. Lee, S.U.S. Choi, S. Li, J.A. Eastman, Measuring thermal conductivity of fluids containing oxide nanoparticles, ASME J. Heat Transf. 121 (1999) 280–288.
- [2] S.P. Jang, S.U. Choi, Effects of various parameters on nanofluid thermal conductivity, J. Heat Transf. 129 (2007) 5 617–623.
- [3] G.-J. Lee, C.K. Rhee, Enhanced thermal conductivity of nanofluids containing graphene nanoplatelets prepared by ultrasound irradiation, J. Mater. Sci. 49 (2014) 4 1506–1511.
- [4] M. Tamizi, M. Kamalvand, M. Namazian, Dependency of the thermophysical properties of nanofluids on the excess adsorption, Int. J. Heat Mass Transf. (2016) 99 630–637.

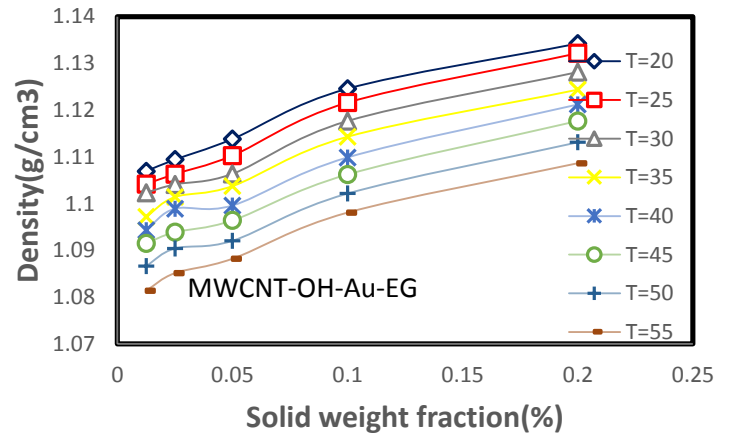


Fig.2. Variations of density of MWCNT-OH and its composites in Ethylene glycol vs solid weight fraction at different temperature (MWCNT-OH-Au/EG).

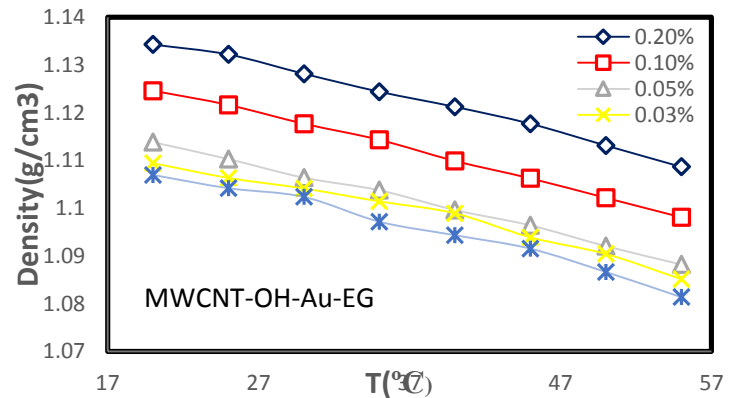
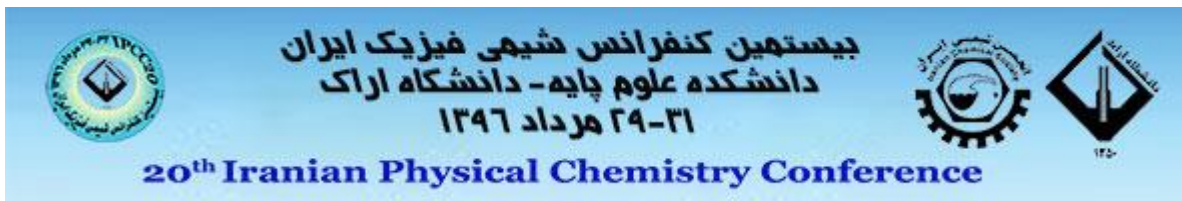


Fig.3. Variations of density with temperature at different solid weight fraction base fluid Ethylene glycol (MWCNT-OH-Au/EG)



Photocatalytic degradation of Auramine O using BiOI/BiOCl/BiOPO₄ nanoparticles under blue light irradiation and modeling by artificial neural networks

M. Mohseniyan, F. Yousefi*

Chemistry Department, Yasouj University, Yasouj 75918-74831, Iran

*Corresponding author: Fakhri Yousefi

Tel/fax: + 98 741 222 1711.

*fyousefi@mail.yu.ac.ir

Abstract: Dyes with complicated structure and their degradation products are highly toxic and carcinogenic. Auramine O was photodegraded under blue light irradiation catalyzed by BiOI/BiOCl/BiOPO₄. Neural network method is employed to estimate photocatalytic degradation. To study this photo degradation, central composite design (CCD) under response surface methodology (RSM) was applied to design a systematic set of experiments. The CCD was used to investigate the significance of the effects of parameters including irradiation time, amount of photo catalyst and initial dye concentration that designed by using the DESIGN EXPORT 7. Variables such as initial dye concentration, photo catalyst dosage and irradiation time were involved in the experiments while the dye photo degradation percentage was considered as response. The effects of variables on the response were studied and optimized.

Keyword: Photocatalytic degradation, artificial neural networks

1. Introduction

The removal of pollutant compounds from aqueous media can be done using various techniques including biological treatments such as bio filtration; physical adsorption, thermal oxidation, water hydrolysis by aqueous alkalis and oxidative chlorination are some of good candidates for reducing pollutants content (1-2). The ANN technique has applied successfully in various fields of modeling and prediction in many engineering systems, mathematics, medicine, economics, metrology and many others. It has become increasingly popular during the last decade. The advantages of ANN compared to conceptual models are its high speed, simplicity and large capacity which reduce engineering attempt. Some recent applications are made in thermos physical properties [3]. Backpropagation neural network (BPNN) is widely used because it can effectively solve non-linear problem. However, there are some deficiencies for BP neural network, such as getting into local extreme and slow convergence. The Artificial neural networks (ANNs) supplies a nonlinear function mapping of a set of input variables into the corresponding network output variables, without the requirement of having to identify the actual mathematics form of the relation between the input and output variables. One kind of feed forward neural network that has been used commonly for the approximate functions is multilayer perceptron (MLP) [4]. The ANNs are discussed in details in the literature, and consequently only a few famous features of it are given as follow to explain the general nature of the network. The MLP neural networks consist of multiple layers of simple activation units named neurons that are arranged in such a way that each neuron in one layer is

joined with each neuron in the next by weighted connections. Neurons are arranged in layers that make up the global architecture. MLP neural networks are contained of one input layer, at least one hidden layer and an output layer. The number of neurons in the input layer is defined by the problem to be solved.

1. Experimental

2.1 Instruments and reagents

The pH measurements were carried out using pH/Ion meter model-686 (Metrohm, Switzerland, Swiss) and the DSB concentrations were determined using Jusco UV-Vis spectrophotometer model V-530 (Jasco, Japan). Nano-BiOI/BiOCl/BiOPO₄ (Synthesized in the laboratory University of Yasouj) was used as photo catalyst. The stock solution (200 mgL⁻¹) was prepared by dissolving 20mg of Auramine O in 100 mL double distilled water and the working solutions prepared following its suitable dilution. All chemicals including, Auramine O, NaOH and HCl with the highest purity available were purchased from Merck (Darmstadt, Germany).

2.2 Central composite design

The CCD was used to investigate the significance of the effects of parameters including irradiation time, amount of photo catalyst and initial dye concentration that designed by using the DESIGN EXPORT 7. A five-level CCD was performed to evaluate the influence of the quantities of degradation yield (Table 1) that leading to 20 runs for the optimization process consists of 2ⁿ factorial points with 2n axial points and Nc central points to estimate the experimental error (reproducibility of the data). The axial points are located at distance of

from center and make the design rotatable. The mathematical relationship between the three independent variables can be approximated by the second order polynomial model:

$$Y = \beta_0 + \sum_{i=1}^3 \beta_i \beta_j + \sum_{i=1}^3 \sum_{j=1}^3 \beta_{ij} X_i X_j + \sum_{i=1}^3 \beta_{ij} X_i^2$$

Where y is the predicted response (photo degradation percentage); X_i 's are the independent variables (irradiation time, amount of photo catalyst and initial dye concentration) that are known for each experimental run. The parameter b_0 is the model constant; b_i is the linear coefficient; b_{ij} are the quadratic coefficients and b_{ij} are the cross-product coefficients. In this study, after the destruction of the data we have used modeling to match.

3. Artificial neural network modeling

ANN modeling was carried out by employing the custom neural network toolbox developed in MATLAB (R2014a). The input and output layer nodes had a linear transfer function (purline) while only the hidden layer nodes had sigmoid transfer function for the ANN model. ANNs were trained according to the Levenberg-Marquardt algorithm available in the neural network toolbox of MATLAB. This network is one of the most common neural network models which is used in engineering applications. In this study, to predict photocatalytic degradation of mentioned nanofluids, the time (t), PH, PPM dye and the amount of adsorbent of the system and one neuron is in the output layer corresponding.

4. Results and discussion

All experimental data point of Photocatalytic degradation that used in this study is 107. The MLP is trained, validated, and tested with random 70% (75 data points), 15% (16 data points), and 15% (16 data points) of all experimental data point, respectively. For this study, the mean square error (MSE) was chosen as a measure of the performance of the net. The net with one hidden layer (20 neurons) with a mean square error of the performance of the net. The net with one hidden layer (20 neurons) with a mean square error of 2.07×10^{-5} leads to the best prediction in Fig. 1. The progress of training, validation, and test errors as a function of the number of training epochs is shown in Figure 2. Based on training and testing data, the best neural network model is utilized to predict the thermal conductivity of nanofluids. Figure 3 shows the comparison of the predictive and experimental values of training and testing data. These figures demonstrate that there are good harmony between the predictive and the experimental values of training and testing data of nanofluids. Besides,

Figure 4 presents the error analysis of train, test and validation data over temperature variation

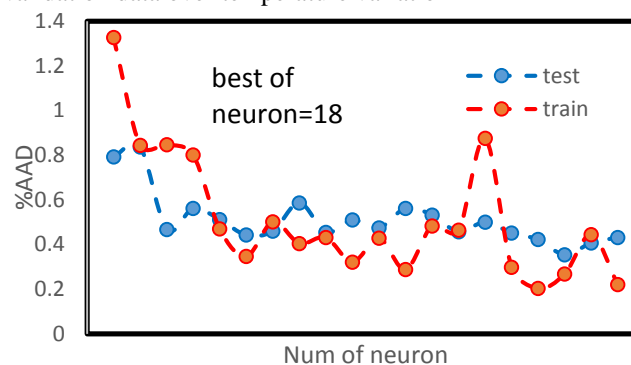


Fig.1. Effect of the number of hidden layer neurons on AAD%

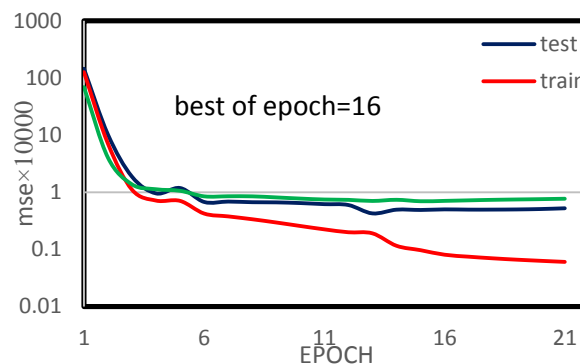


Fig. 2. Evolution of training, validation, and test errors as a function of the number of training epochs during ANN training

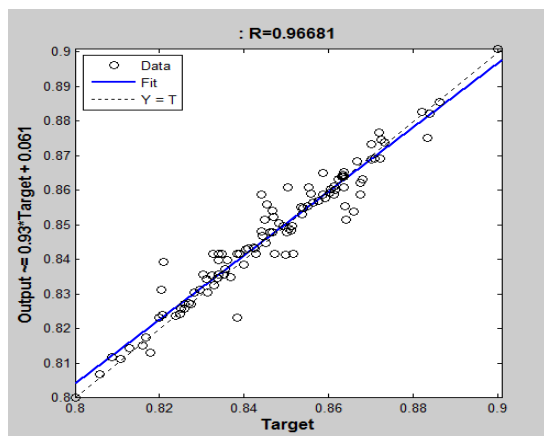


Fig. 3. Modeling ability of the optimized ANN to predicate of effective Photocatalytic degradation: ($R^2 = 0.96681$, AAD = 0.3891%)

Table 1. Experimental factors and levels in the central composite design

absorbent	time	PPM dye	PH	Photodegradation%
0.02	100	2	6	83.63
0.02	100	4	4	79.93
0.02	100	6	2	76.23
0.02	100	6	4	80.58
0.02	100	6	6	84.93
0.0175	95	5	5	81.9
0.015	90	4	4	78.87
0.0175	95	5	5	80.59
0.02	100	6	6	82.31
0.015	100	6	6	74.915
0.01	100	6	6	67.52
0.015	110	6	6	74.72
0.02	120	6	6	81.92
0.0175	105	7	5	76.845
0.015	90	8	4	71.77
0.015	100	6	6	54.15
0.015	110	4	8	36.53
0.0225	105	5	7	65.09
0.03	100	6	6	93.65
0.025	90	6	6	77.67
0.02	80	6	6	61.69

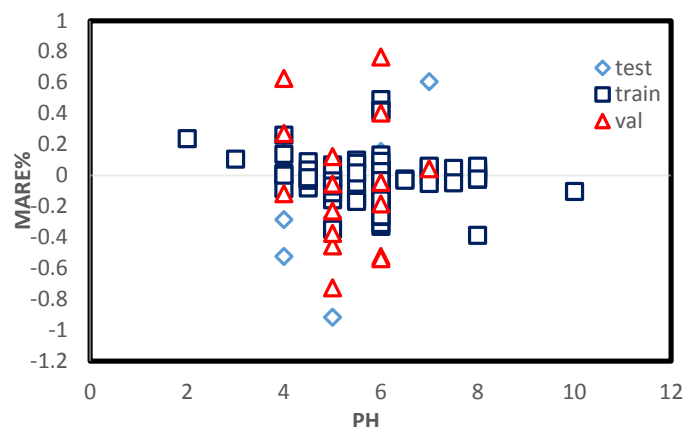


Fig.4 Percentage absolute relative error for Photocatalytic degradation with the experimental data

5. Conclusion

In this study, photocatalytic degradation of Auramine O has been investigated. The MLP is trained, validated, and tested with random 70% (75 data points), 15% (16 data points), and 15% (16 data points) of all experimental data point, respectively. The AADs% of a collection of 107 data points for all nanofluids using the ANN at various temperatures and solid weight fraction is 0.3891% ($R^2=0.96681$).

References

- [1] S. S. Patil, V. M. Shinde, *Environ. Sci. Technol.*, 1988, **22**, 1160-1165.
- [2] B. Mills, *Filtr. Sep.*, 1995, **32**, 147-152.
- [3] H. Karimi, F. Yousefi, *Chinese Journal of Chemical Engineering* 15 (2007) 765-771.
- [4] P.P. Van der Smagt (1994) Minimization methods for training feed forward neural network. *Neural Netw* 7:1994.

Effect of choline chloride / malonic acid deep eutectic solvent on the acetaminophen Solubility at $T = (288.15 \text{ to } 318.15) \text{ K}$

M.Mokhtarpour*, H. Shekaari, M. T. Zafarani-Moattar,

Department of Physical Chemistry, University of Tabriz, Tabriz, Iran

*Masomeh64_m@yahoo.com

Abstract: Deep eutectic solvents (DESs) as a new class of green solvents have been used to overcome the poor solubility of drugs during the recent years. In this work, the effect of DES containing choline chloride as hydrogen bond acceptor and malonic acid as hydrogen bond donor has been studied on acetaminophen (ACP) solubility at temperature ranges (298.15 to 313.15) K. The results indicate that the solubility of ACP increases with increasing concentration of DES and at higher temperatures. The solubility data were correlated by the modified Apelblat, λh (Buchowski) and Yalkowsky models which the Apelblat model is more consistent with experimental data.

Keywords: Deep eutectic solvent; Solubility; Acetaminophen; Modified Apelblat

Introduction

Acetaminophen (ACP) is an analgesic and antipyretic drug widely used in modern therapeutics. This drug is specially indicated in the treatment of several minor diseases presented by pediatric patients [1]. However, it has a low solubility in water ($14 \text{ g}\cdot\text{L}^{-1}$ at 298.15 K [2]). Different methods were used to increase the solubility of drugs such as additions of surface-active agents, cyclodextrins, cosolvents, and pH adjustment. Among them, co-solvency is a simple, effective, most frequent and feasible solubilization method used in the pharmaceutical industry [3]. The use of this method can also improve some other physicochemical properties including solubility, permeability and dissolution rate of drugs [4].

Deep eutectic solvents based on choline chloride (ChCl) first introduced by Abbott [5]. These solvents can overcome the limitations of ILs and they have advantages such as a lower cost and desirable environmental impact [6]. In addition, they can be also prepared from biodegradable and natural components, and it was found that their toxicity is much lower than ILs [7]. These types of solvents are liquid at room temperatures typically formed by mixing two solid compounds, such as a quaternary ammonium salt as hydrogen bond acceptor (HBA) (e.g. ChCl) and a hydrogen bond donor (HBD) (e.g. urea or a carboxylic acid) at their eutectic composition with melting point much lower than that of the individual components [8].

The purpose of this work is providing the aqueous solubility of ACP in the presence of DES based on ChCl as HBA and malonic acid as HBD at $T = (298.15 \text{ to } 308.15) \text{ K}$ and atmospheric pressure. To correlate and predict of the aqueous solubility of drugs, different empirical models are suggested in literature. Among them, Apelblat, Yalkowsky and λh models were applied [9] which used to correlate experimental solubility data of ACP in the aqueous DES solutions at various experimental temperatures.

Materials and method

The binary solvent mixtures (DES + water) were prepared by mixing the appropriate amounts (in grams) of solvents. The shake flask method has been employed in this work. Briefly, the sealed vials containing an excess amount of ACP powder in the solvent mixtures were mixed using a shaker and placed in water bath thermostat for 3 days to reach an equilibrium. When a saturated solution was attained, the solid phase was removed by centrifugation followed by filtration. The clear solutions were diluted with water and assayed by a double beam spectrophotometer at 248 nm. The concentrations of the diluted solutions were determined from the calibration curve with the correlation coefficient of 0.9999. Each experimental data point represented the average of at least three repetitive experiments.

Results and Discussion

Solubility results The aqueous solubility of acetaminophen (ACP) in terms of mole fraction, x_1 , in (ACP (1) + water (2) + DESs (3)) systems is calculated by using of Eq. (1):

$$x_1 = \frac{\frac{w_1}{M_1}}{\frac{w_1}{M_1} + \frac{w_2}{M_2} + \frac{w_3}{M_3}} \quad (1)$$

where M_i and w_i are the molecular weight and mass fractions of i component in the saturated solution, respectively [10]. The relationship between solubility of ACP, mole fraction x_1 , versus temperature in aqueous DES solutions with different weight fractions has been shown in Figs. 1. It can be seen from those figure, the solubility of ACP was increased with increasing the mass fraction of DES (w_{DES}) and at higher temperatures. It seems that these types of green solvents are proper

solvents rather than ILs and organic solvents in pharmaceutical fields.

Solid-liquid phase equilibrium modeling

In this study, some regular empirical solubility equations are used to correlate the solubility data. They are modified Apelblat[11], λh [12] and Yalkowsky[2] equations.

Modified Apelblat equation

The modified Apelblat equation is the most commonly applied mathematical model for both polar as well as for nonpolar systems, hence it was applied in the present study in order to correlate the experimental solubility with the calculated one. According to the modified Apelblat model, the temperature dependent solubility of ACP can be represented by Eq. (2) at the equilibrium[11]:

$$\ln x_1 = A + \frac{B}{T} + C \ln T \quad (2)$$

where A , B , and C are empirical constants.

λh (Buchowski) equation

Buchowski et al. described the behavior of solid solubility in liquid as the Buchowski equation [12]. This equation gave a good description for many solid – liquid systems using two adjustable parameters λ and h , as reported by previous researchers [13]. The Buchowski equation can be written as:

$$\ln\left(1 + \lambda \frac{1 - x_1}{x_1}\right) = \lambda h \left(\frac{1}{T} - \frac{1}{T_{m1}}\right) \quad (3)$$

where λ and h are two parameters and T_{m1} is the melting temperature of ACP. The value of λ is identified as the approximate mean association number of solute molecules, which reflects the non-ideality of the solution system, and h estimates the excess mixing enthalpy of solution [12].

Yalkowsky equation

The log-linear equation describes an exponential increase in a drugs solubility with a linear increasing in co-solvent concentration. This relationship is described algebraically by:

$$\ln x_{1-mix} = \ln x_{1-water} + \sigma w_3 \quad (4)$$

where x_{1-mix} and $x_{1-water}$ are the total solute solubilities in the co-solvent / water mixture and in water, respectively, σ is the co-solvent solubilization power for the particular co-solvent – solute system, and w_3 is the weight fraction of the co-solvent in the aqueous mixture.

Results show that all equations are in good agreement with the experimental data, but Apelblat model showed

better agreement with the experimental data of ACP solubility in DES aqueous solutions that are shown in the Figs. 1.

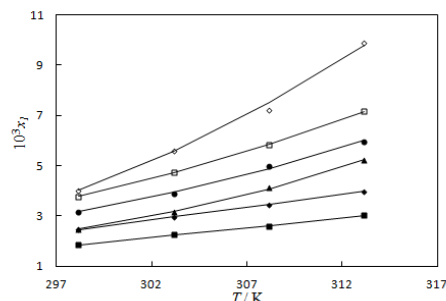


Fig.4: The relationship between solubility of ACP, mole fraction x_1 , versus temperature in aqueous ChCl / malonic acid solutions with w_{DES} : 0.00(■), 0.02 (◆), 0.05 (▲), 0.07 (●), 0.10 (□), 0.15 (◇) and solid lines obtained from Eq. (2).

Conclusions

The aqueous solubility of acetaminophen in the presence of deep eutectic solvent (ChCl / malonic acid), as co-solvents was determined experimentally within the temperature ranges from (298.15 to 318.15) K. The solubility mole fraction of acetaminophen in the studied solvents increased with increasing deep eutectic solvents concentration and temperature.

Acknowledgment

The authors wish to thank financial support from the graduate council of the University of Tabriz.

References

- [1] J.G. Hardman, L.E. Limbird, Chapter 27 (2001) 712.
- [2] S.H. Yalkowsky, Y. He, P. Jain, Handbook of aqueous solubility data, CRC press, 2016.
- [3] S. Vahdati, A. Shayanfar, J. Hanaee, F. Martínez, W.E. Acree Jr, A. Jouyban, Industrial & Engineering Chemistry Research 52 (2013) 16630-16636.
- [4] A.P. Abbott, G. Capper, D.L. Davies, H.L. Munro, R.K. Rasheed, V. Tambyrajah, Chemical Communications (2001) 2010-2011.
- [5] A.P. Abbott, G. Capper, D.L. Davies, R.K. Rasheed, V. Tambyrajah, Chemical Communications (2003) 70-71.
- [6] R.G. Strickley, Pharmaceutical research 21 (2004) 201-230.



- [7] M. Hayyan, M.A. Hashim, A. Hayyan, M.A. Al-Saadi, I.M. AlNashef, M.E. Mirghani, O.K. Saheed, *Chemosphere* 90 (2013) 2193-2195.
- [8] Q. Zhang, K.D.O. Vigier, S. Royer, F. Jérôme, *Chemical Society Reviews* 41 (2012) 7108-7146.
- [9] R. Heryanto, M. Hasan, E.C. Abdullah, A.C. Kumoro, *ScienceAsia* 33 (2007) 469-472.
- [10] A. Forte, C.I. Melo, R. Bogel-Łukasik, E. Bogel-Łukasik, *Fluid Phase Equilibria* 318 (2012) 89-95.
- [11] A. Apelblat, E. Manzurola, *The Journal of Chemical Thermodynamics* 31 (1999) 85-91.
- [12] H. Buchowski, A. Ksiazczak, S. Pietrzyk, *The Journal of Physical Chemistry* 84 (1980) 975-979.
- [13] J. Qing-Zhu, M. Pei-Sheng, Z. Huan, X. Shu-Qian, W. Qiang, Q. Yan, *Fluid phase equilibria* 250 (2006) 165-172.

Volumetric studies of acetaminophen in aqueous solution of ChCl / malonic acid deep eutectic solvent at $T = (293.15 \text{ to } 318.15) \text{ K}$

M. Mokhtarpour*, H. Shekaari, M. T. Zafarani-Moattar,

Department of Physical Chemistry, University of Tabriz, Tabriz, Iran

*Masomeh64_m@yahoo.com

Abstract: One way to check the interactions between drug and solvent to find the best solvent in pharmaceutical fields is volumetric studies. The thermodynamic properties including volumetric properties have been investigated using density measurements at $T = (288.15 \text{ to } 318.15 \text{ K})$ to understand the interactions between the components. The calculated thermodynamic parameters values confirm the strong solute – solvent interactions between acetaminophen and deep eutectic solvent containing choline chloride as hydrogen bond acceptor and malonic acid as hydrogen bond donor. It seems that these types of green solvents are proper solvents rather than ionic liquids and organic solvents in pharmaceutical fields.

Keywords: Deep eutectic solvent; Volumetric; Acetaminophen; density

Introduction

Due to some favorable properties, deep eutectic solvents (DESs) have recently been proposed as solvents for a variety of pharmaceutical applications [1]. These solvents can overcome the limitations of ionic liquids and they have advantages such as a lower cost and desirable environmental impact [2]. They can be used as co-solvent in pharmaceutical fields [3]. To achieve a better understanding and deep insight of the drug-solvent interactions and development of DESs in this field, it is essential to have knowledge of certain physicochemical and thermodynamic properties of such systems including density and speed of sound. In this work the densities of the ternary solutions containing ACP in the aqueous DES solutions were measured at different temperatures and used to calculate the apparent molar volume, V_ϕ , standard partial molar volume, V_ϕ^0 , transfer volume, $\Delta_{tr}V_\phi^0$ values. The calculated parameters were utilized to survey influence of the DES on the solute-solvent interactions in aqueous solution of ACP.

Materials and method

In the present study, the deep eutectic solvent of ChCl / malonic acid was prepared at molar ratios of 1:1 [4].

The binary solvent mixtures (DES + water) were prepared by mixing the appropriate amounts (in grams) of solvents.

Density measurement

The solutions were provided in glass vials and in molal base concentration by weighting using an analytical balance with an uncertainty $\pm 1 \times 10^{-4} \text{ g}$ and closed firmly with parafilm. The density, d , of solutions was measured

with a vibrating tube densimeter (Anton Para, DSA 5000 densimeter). The instrument was calibrated with doubly distilled deionized and degassed water [5].

Results and Discussion

The densities, d , for ACP in water and in the aqueous DES solutions (0.05, 0.1 and 0.15 w/w) are measured. These data in water and in aqueous DES solutions increase with ACP concentrations as well as with DES concentrations but decrease with rise in temperature. These data were used to compute apparent molar volume, V_ϕ :

$$V_\phi = \frac{M}{d} - \left[\frac{(d - d_0)}{m d d_0} \right] \quad (1)$$

where m is the molality of the ACP in water and in binary solvents (DES + water), M is the molar mass of the ACP and d_0 , d are the densities of the solvent and solutions. The apparent molar volumes of ACP in aqueous ChCl / malonic acid solution (0.15 w/w) at experimental temperatures $T = (288.15, 298.15, 308.15, 318.15) \text{ K}$ are plotted in Fig. 1. The positive V_ϕ values demonstrate intense solute-solvent interactions and it is observed that, the apparent molar volumes decrease with increasing of the ACP concentration. In addition, by increasing the temperature thermal kinetic energy of water molecules is increased and then their interactions with ACP molecules are weakened. This phenomenon leads to release some of the water molecules around the drug molecules which reduces the pressure on these molecules and increasing the volume of the ACP [6].

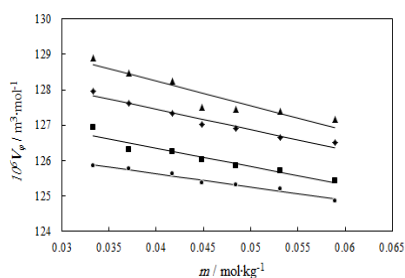


Fig. 1. Apparent molar volumes, V_{ϕ} , of ACP in the aqueous ChCl / malonic acid (0.15 w/w) solutions at $T = 298.15$ K (●), 303.15 K (■), 308.15 K (◆) and 313.15 K (▲).

The standard partial molar volume V_{ϕ}^0 is obtained by least squares fitting of apparent molar volume V_{ϕ} by using Eq. (2):

$$V_{\phi} = V_{\phi}^0 + S_v m \quad (2)$$

where S_v is the experimental slope illustrating solute-solute interactions and m is the molality of the ACP in water and in the aqueous solutions of DES. The values of V_{ϕ}^0 provide a study of (solute + solvent) interactions and the slope, S_v provides information regarding (solute + solute) interactions. The values of V_{ϕ}^0 for aqueous DES solutions at different concentrations is plotted in Fig. 2. It is expected that due to enhanced solute-solvent interactions, the positive V_{ϕ}^0 values increase with increasing in the DES concentration and temperature. This trend, indicates the presence of strong (solute + solvent) interactions and such interactions further strengthen with higher concentrations of DES in the ternary solutions and at elevated temperatures. The values of S_v are negative for all the investigated solutions and all experimental temperatures and become more negative with increase in concentration of the DES. The negative values of S_v indicates weak solute-solute interactions between ACP molecules in the presence of DES solutions. The less values of S_v with compared to V_{ϕ}^0 values suggest the weak solute-solute interactions and stronger solute-solvent interactions.

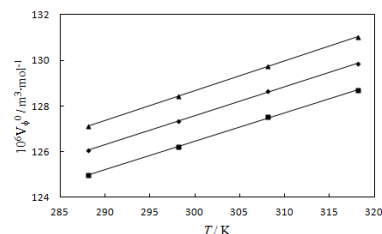


Fig.2: The comparison of the standard partial molar volumes, V_{ϕ}^0 , of ACP in aqueous ChCl / malonic acid solutions at different temperatures: in 0.05 w/w (■), 0.10 w/w (◆), 0.5 w/w (▲).

Conclusions

volumetric parameters of acetaminophen in aqueous ChCl / malonic acid solutions have been used to study the interactions between acetaminophen and the deep eutectic solvents in aqueous medium. The standard partial molar volumes, V_{ϕ}^0 , show that their values have increased by increasing the deep eutectic solvent concentration. This observation indicates that the interactions of the deep eutectic solvent with acetaminophen become stronger with increasing the co-solvent concentration. This results indicate that deep eutectic solvents containing malonic acid is proper solvent for enhancing acetaminophen solubility.

Acknowledgment

The authors wish to thank financial support from the graduate council of the University of Tabriz.

References

- [1] A.P. Abbott, G. Capper, D.L. Davies, R.K. Rasheed, V. Tambyrajah, *Chemical Communications* (2003) 70-71.
- [2] R.G. Strickley, *Pharmaceutical research* 21 (2004) 201-230.
- [3] M. Hayyan, M.A. Hashim, A. Hayyan, M.A. Al-Saadi, I.M. AlNashef, M.E. Mirghani, O.K. Saheed, *Chemosphere* 90 (2013) 2193-2195.
- [4] Q. Zhang, K.D.O. Vigier, S. Royer, F. Jérôme, *Chemical Society Reviews* 41 (2012) 7108-7146.
- [5] T.J. Fortin, A. Laesecke, M. Freund, S. Outcalt, *The Journal of Chemical Thermodynamics* 57 (2013) 276-285.
- [6] M.D. Tehrani, R. Sadeghi, *Journal of Chemical & Engineering Data* 61 (2016) 3144-3156.

Thermodynamic study of salt effect on the Glutamine solubility in aqueous solution at T=(298.2 and 308.2)K

Hatame Fathipour-Pishkhani, Bahram Ghalami-Choobar*

Department of chemistry, University of Guilan, Rasht, 19141, Iran

*B-Ghalami@guilan.ac.ir

Abstract: In the present study, the experimental solubility of Glutamine were determined in aqueous potassium nitrate (KNO₃) and potassium chloride (KCl) solutions at T= (298.2 and 308.2) K by using a 'gravimetric' method. The experimental data on the solubility were measured at different temperatures of Glutamine in aqueous electrolyte solutions with a different concentration of KCl and KNO₃ at T= (298.2 and 308.2) K. Gibbs free energies have been evaluated at both temperatures. It was found the solubility of Glutamine rises with an increase in the KCl and KNO₃ concentration. These results can contribute to a better understanding of the thermodynamic behaviour of Glutamine in aqueous solution.

Keywords: solubility; Glutamine; Gravimetric; Amino acids; electrolyte

Introduction

The knowledge of properties such as activity coefficients, water activity, and solubility are very useful as a support for the design and simulation of separation processes such as extraction or drying [1]. The experimental measurements revealed of importance due to their applications in chemical, pharmaceutical and food industries [2]. The detailed studies on nature and extent of solubility are not only important in protein chemistry, but also important in chemical, pharmaceutical, food, cosmetics and biodegradable plastic industries [3,4]. Also, the solubility of amino acids in different electrolyte solvents are important in many biochemical processes and this plays a crucial role in the determination of proper solvents and the development and operation of crystallization processes [5].

Glutamine is a non-essential amino acid that plays important roles both as building blocks of proteins and as intermediates in metabolism. The experimental measurement shows the electrolyte can increase and decrease the solubility of amino acids. These phenomena are known as the salting-in and salting-out effect, respectively. The difference in the solubility trends is probably due to a kind of complex formation in aqueous phase by the amino acid with different electrolyte [6].

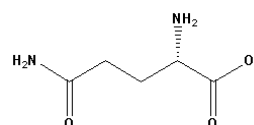
In the present study, the solubility of Glutamine (Scheme 1) in aqueous potassium chloride (KCl) and potassium nitrate (KNO₃) solution were measured by using a 'gravimetric' method.

Materials and method

Firstly, KCl and KNO₃ were dried in an oven for 2 hours and then cooled in a desiccator about 1 hour to use. After drying, the aqueous solution of salts in concentration of 0.0, 0.5, 1, 1.5, 2 and 2.5 molality (mol.kg⁻¹) were made

and 4 ml of the aqueous solvent mixtures of KCl and KNO₃ were mixed with certain amount of Glutamine (0.2g). Then these solutions were poured into a covered glass tubes and maintained at the constant temperature by continuous forced water circulation from a thermostat bath at T= (298.2 and 308.2) K. The solutions were stirred constantly for 4 hours to reach equilibrium conditions. Before sampling, the solutions were allowed to settle about 90 min.

Then, the solubility of Glutamine was determined by gravimetric method. So 1 ml of the sample were placed into weighed glass tubes and immediately weighed. All the solvent was evaporated, and the crystals dried completely in a drying stove. Finally, the glass vessels were cooled and weighed. The solubility of glutamine was calculated from the knowledge of the initial concentration of electrolyte present in solution.



Scheme 1: Structures of Glutamine

Results and Discussion

Figure 1 shows solubility of Glutamine in aqueous solution of KCl in various electrolyte concentrations at T=(298.2 and 308.2) K. It can be seen that the solubility of Glutamine rises with increasing temperature. The solubility were also measured in presence and absence of the electrolyte at T= 298.2 K (See Table 1).

The solubility data of table 1 shows that the solubility of Glutamine in presence of KNO₃ is higher than KCl.

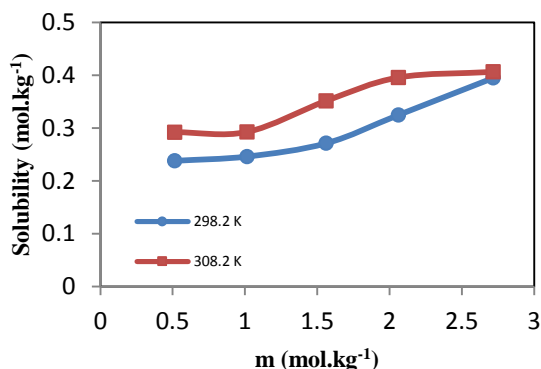


Fig.1: plot of the values of glutamine solubility versus concentration of KCl at T= (298.2 and 308.2) K.

On the other hand, a salting-in effect was observed with nitrate (NO_3^-) and chloride (Cl^-) ions. But at the same temperature, solubility of Glutamine in the presence of KNO_3 is higher than KCl. The difference in the solubility trends is probably due to a kind of complex formation in aqueous phase by the amino acid with different anions.

Table 1: The solubility of Glutamine in aqueous potassium chloride (KCl) and potassium nitrate (KNO_3) at T= 298.2 K in (mol/g) scale.

Molality (m)	Solubility (mol/kg)	$\Delta G/RT$
<u>KCl</u>		
0.5155	0.2673	-0.1330
1.0152	0.2702	-0.1351
1.5625	0.2836	-0.3181
2.0619	0.2975	-0.4365
2.7174	0.3092	-0.4629
<u>KNO_3</u>		
0.5155	0.2922	-0.2596
1.0582	0.2928	-0.2672
1.6304	0.3516	-0.3628
2.1978	0.3958	-0.4157
2.5182	0.3496	-0.4510

The solubility data of Table 1 were used to calculate the free energy of amino acid for each of the electrolyte in according to following equation:

$$\Delta G_{sol} = RT \ln(S_0/S) \quad (1)$$

Where, S_0 and S are the solubilities of Glutamine in pure water and aqueous-electrolytes solution, respectively. For each additive electrolyte, ΔG_{sol} values decrease when the concentration of aqueous electrolyte increases. Moreover, the values of Gibbs free energy for system including KCl component are higher than those system

are consisting of KNO_3 .

Conclusions

The experimental solubility of Glutamine were determined in aqueous potassium nitrate (KNO_3) and potassium chloride (KCl) solutions at T= (298.2 and 308.2) K. The experimental solubility data show a salting-in effect in the present of KCl and KNO_3 . Furthermore, the solubility of the present amino acid follows the order: $\text{KNO}_3 > \text{KCl}$. Although both the experimental anions show salting-in effect, but the effect of NO_3^- is more in comparison to that of Cl^- with common cation. Furthermore ΔG_{sol} for Glutamine with KNO_3 are higher than amino acids with KCl. So, it can be concluded that the complex will be more stable in KNO_3 than KCl.

Acknowledgment

We gratefully acknowledge the graduate office of University of Guilan for supporting this work.

References

- [1] Luísa A. Ferreira, Eugénia A. Macedo, Simão P. Pinho, "The effect of ammonium sulfate on the solubility of amino acids in water at (298.15 and 323.15) K", J. Chem. Thermodyn., 41 (2009) 193-196.
- [2] Mohammad K. Khoshkbarchi and Juan H. Vera, "Effect of NaCl and KCl on the Solubility of Amino Acids in Aqueous Solutions at 298.2 K: Measurements and Modeling", Ind. Eng. Chem. Res., 36 (1997) 2445-2451.
- [3] Amitava Bhattacharyya, Swapan Kumar Bhattacharya, "Chemical Transfer Energies of Some Homologous Amino Acids and the $-\text{CH}_2-$ Group in Aqueous DMF: Solvent Effect on Hydrophobic Hydration and Three Dimensional Solvent Structure", J. Solution Chem., 42 (2013) 2149-2167.
- [4] Luisa A. Ferreira, Eugénia A. Macedo, and Simão P. Pinho, "Effect of KCl and Na_2SO_4 on the Solubility of Glycine and DL-Alanine in Water at 298.15 K", Ind. Eng. Chem. Res., 44(23) (2005) 8892-8898.
- [5] Luísa A. Ferreira, S. P. Pinho, E. A. Macedo, "Solubility of l-serine, l-threonine and l-isoleucine in aqueous aliphatic alcohol solutions", Fluid Phase Equilib., 270 (2008) 1.
- [6] Sanjay Roy a, Partha Sarathi Guina, Kalachand Mahalib, Bijoy Krishna Dolui, "Role of Electrolytes in the Solubility of L-proline and Its Transfer Free Energetics", J. Mol. Liq., 223 (2016) 927-933.

Density and speed of sound of poly(ethylene glycol) dimethyl ether 250 and 500 in 1-propanol mixtures at different temperatures

S. Faraji^a, H. Shekaari^{b*}, M. T. Zafarani-Moattar

Department of Physical Chemistry, University of Tabriz, Tabriz, Iran

*s.faraji1989@yahoo.com

Abstract: In the present study, volumetric and compressibility properties of binary mixtures, 1-propanol + poly(ethylene glycol) dimethyl ether (PEGDME) were determined. Density and speed of sound data were measured to obtain excess molar volumes, isentropic compressibility deviation, and excess speed of sound for the investigated systems at $T = (298.15 \text{ to } 318.15) \text{ K}$. The calculated values for these deviations became more negative with increasing of temperature. Redlich – Kister and Ott *et al.* equations were used to correlate the above mentioned experimental data. The results are interpreted in terms of present solute-solvent interactions in the studied mixtures.

Keywords: Poly(ethylene glycol) dimethyl ether; Density; Speed of Sound; Redlich-Kister Model

Introduction

To study of solute-solvent interactions between the components of binary mixtures, the excess thermodynamic properties such as volumetric and compressibility are useful [1]. In this respect, density and speed of sound were measured for investigated systems in this work to obtain excess molar volumes, isentropic compressibility deviation, and excess speed of sound for the investigated systems at $T = (298.15 \text{ to } 318.15) \text{ K}$. Polyethylene glycol 250 dimethyl ether has proved to be successful for scrubbing waste air and gas streams containing different organic substances, acid gases, and even inorganic compounds. Polyethylene glycol dimethyl ether is an aprotic and powerful diluent that is also used as a solubilizing agent for plastic, textile, paper, and paint stripping applications.

Singh and *et al.* measured the densities, speeds of sound, and refractive indices of PEGDME250 with 1-propanol and 1-butanol. The densities, viscosities, and enthalpies of binary mixtures of PEGDME250 + methanol have been reported at 303.15 K. To the best of our knowledge, the previous studies indicate that there is no report in the literature on the PEGDME500 in 1-propanol binary mixtures.

Therefore, in this work, we measured the density and speed of sound of the investigated systems containing PEGDME250 and PEGDME500 with 1-propanol and calculated excess molar volume, isentropic compression deviation and the deviation in speed of sound and the experimental data have been correlated with use of Redlich – Kister and Ott *et al.* equations [2,3].

Materials and method

All the chemicals were obtained from Merck Co. 1-Propanol with the purity of minimum mass fraction 0.998, poly(ethylene glycol) dimethyl ether 250 and 500 without more purifications were employed.

The density and speed of sound of the solutions at different temperatures were measured with the digital vibrating-tube analyzer (Anton Paar DSA 5000, Austria) that proportional temperature of a apparatus kept the samples temperatures with an uncertainty of 0.001 K using peltier device built in the densimeter. The degassed double distilled water and dry air to calibrate the apparatus at 298.15 K. The density of a known molality of aqueous NaCl was used to test the apparatus given by Pitzer *et al.* [4]. Uncertainty of the measurement is $\pm 0.003 \text{ kg}\cdot\text{m}^{-3}$ for density and $0.1 \text{ m}\cdot\text{s}^{-1}$ for speed of sound.

Results and Discussion

Laplace equation by use of equ (1) is derived from measurement data of density and speed of sound of 1-propanol (1) + PEGDME (2) mixtures together with the isentropic compressibility at 298.15, 308.15, and 318.15 K. Also, experimental data are used to the excess molar volume (V^E), deviation in isentropic compressibility (ΔK_s), and speed of sound (Δu) to following relations as given in table 1 [5].

$$k_s = 1/\rho u^2 \quad (1)$$

$$V^E = \sum_{i=1}^2 x_i M_i \left(\frac{1}{\rho} - \frac{1}{\rho_i} \right) \quad (2)$$

$$\Delta K_s = K_s - \sum_{i=1}^2 (x_i K_{si}) \quad (3)$$

$$\Delta u = u - \sum_{i=1}^2 (x_i u_i) \quad (4)$$

where ρ , and u denote the density, and speed of sound of the mixtures. Also M_1 , M_2 , ρ_1 , ρ_2 , u_1 , u_2 , x_1 , and x_2 indicate molar mass, density, speed of sound, mole fraction, in which that subscripts 1 and 2 are representative of 1-propanol and polymer, respectively.

Derived values for V^E and ΔK_s indicate negative values in the range of mole fraction of polymer and working temperatures, also it indicates that when the temperature increases, obtaining amount decrease. Based

on the figure 3, the process of depression of V^E values is regular with the increasing of temperature. The negative V^E values is related to the positive contributions resulting from breaking of like interactions of the pure liquids and also negative contributions are due to the formation unlike (polymer-solvent) interactions and packing effects. The negative values of V^E pile result from close packing effects and intermolecular interactions. These interactions are between hydrogen atom from hydroxyl group of alcohol and the oxygen atoms from polymer. Therefore, packing effect for negative values of obtained V^E is creditable for alcohol + polymer systems. For the excess molar volume in the 1-propanol + ethylene glycol, + ethylene glycol monomethyl, + ethylene glycol dimethyl, + diethylene glycol dimethyl, + triethylene glycol dimethyl, + diethylene glycol diethyl, and + diethylene glycol dibutyl ethers systems the negative values reported at 298.15 K. This behavior of discrepancy of V^E values with temperature is similar to the studied systems in this study. Difficulty in compressing alcohol + polymer solution in polymer various mass fractions and the working temperature started to be larger with the increasing of temperature. The calculated values for the (Δu) with increasing temperatures much more that this increase was not significant. According to obtained values peak at around mole fraction 0.3 for PEGDME500 and at around mole fraction 0.4 for PEGDME250 can be seen.

Table1: Experimental density (ρ), and speed of sound (u), excess molar volume (V^E), and isentropic compressibility deviations (ΔK_s) for the binary 1-propanol (1) + PEGDME500 (2) mixtures.

X_2	$\rho / \text{g}\cdot\text{cm}^{-3}$	$u / \text{m}\cdot\text{s}^{-1}$	$V^E / \text{cm}^3\cdot\text{mol}^{-1}$	$10^{14}\Delta K_s / \text{T}\cdot\text{Pa}^{-1}$
$T = 298.15 \text{ K}$				
0.0000	0.799597	1205.33	0.000	0.00
0.0030	0.804865	1210.71	-0.029	-0.12
0.0040	0.806505	1211.99	-0.031	-0.15
0.0119	0.819575	1224.00	-0.087	-0.41
0.0222	0.834661	1237.94	-0.171	-0.69
0.0354	0.851885	1253.88	-0.234	-0.99
0.0529	0.871822	1272.92	-0.222	-1.30
0.0729	0.891734	1292.68	-0.317	-1.58
0.1042	0.916985	1318.37	-0.423	-1.88
0.1903	0.964367	1368.89	-0.514	-2.24
0.2755	0.993983	1401.40	-0.542	-2.27
0.3411	1.009973	1419.75	-0.555	-2.20
0.4181	1.024418	1435.65	-0.551	-2.03
0.5488	1.042001	1455.10	-0.522	-1.66
0.6916	1.055044	1469.37	-0.428	-1.17
0.8797	1.066785	1482.69	-0.266	-0.47
1.0000	1.071966	1488.71	0.000	0.00

All of the calculated deviations for V^E , ΔK_s , and Δu are correlated to the Redlich – Kister equation [24];

$$Q = x_2(1-x_2) \sum_{p=0}^N A_p(2x_2 - 1)^p \quad (5)$$

where Q , is stand for all of the deviations; A_p , fitting coefficients; and N , is the degree of the polynomial expansion. With the use of equ (5), N equals to 4 for V^E , ΔK_s , and Δu . The Redlich – Kister five parametric equation have had good relation with calculated values for the above quantities. Because, acceptable standard deviation have for the mentioned quantities. The standard deviation $sdev$, between the calculated values Q_{cal} and experimental data Q_{exp} is estimated with the use of following relation,

$$sdev = \left(\frac{\sum_{i=1}^{n_{Dat}} (Q_{exp} - Q_{cal})^2}{n_{Dat}} \right)^{1/2} \quad (6)$$

where n_{Dat} is the number of experimental points. These quantities are fitted with the use of Ott et al. equation, which are dependents based on exponential;

$$Q = x_1(1-x_1) \left(\exp(-\alpha x_1) \sum_{i=0}^1 B_i(1-2x_1)^i + (1-\exp(-\alpha x_1)) \sum_{i=0}^2 C_i(1-2x_1)^i \right) \quad (7)$$

where, α , B_i and C_i are indicative of fitting coefficients. The best model for the relation between experimental data is predicted with the use of obtained standard deviation for the three recent equations.

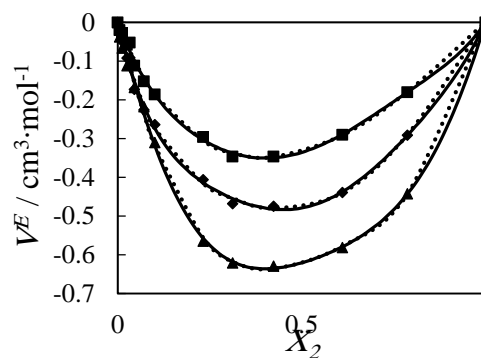


Fig.5: The excess molar volumes (V^E) for the 1-propanol (1) + PEGDME250 (2) system as a function of polymer mole fraction (X_2) at various temperatures (\blacksquare , $T = 298.15 \text{ K}$; \blacklozenge , $T = 308.15 \text{ K}$; \blacktriangle , $T = 318.15 \text{ K}$; — Redlich – Kister model and ... Ott model).

In relation to volumetric properties of polymeric solutions, the apparent specific volumes of investigated systems in this study related to dilute area it was calculated by the use of following equation[5]:

$$V_\phi = (1 + W_p) / W_p \rho - 1 / W_p \rho_0 \quad (8)$$

where ρ , and ρ_0 are the densities of the solution and pure alcohol, respectively, and W_p , weight fraction of polymer (kg polymer per kg of solvent). According to findings, V_ϕ obtained values for PEGDME 500 is less than PEGDME 250.



The limiting apparent specific volume, V_ϕ^0 , of the polymer in investigated solutions was obtained by use of equ (9). The knowledge of thermodynamic behaviour of polymer solutions is extended by the V_ϕ^0 data [5].

$$V_\phi = V_\phi^0 + B_v W_p + C_v W_p^2 \quad (9)$$

In this equation, B_v and C_v which depend on solute-solvent interactions and temperature are considered as empirical parameters.

Another specific volumetric property is excess specific volume (v^E) which can be calculated for the studied solutions by the use of following relation [5]:

$$v^E = \left(\frac{1}{\rho}\right) - \frac{1}{1 + W_p} \cdot \left(\frac{W_p}{\rho_p} + \frac{1}{\rho_0}\right) \quad (10)$$

where ρ_p , is pure polymer density, ρ , solution density, ρ_0 , density of alcohol, and W_p , weight fraction of polymer. The negative values is obtained for excess specific volume for the studied systems in this work, which these values became more negative with the increasing of temperature and the obtained data are more negative for PEGDME250 in comparison to PEGDME500. Experimental density and speed of sound data were measured for the in 1-propanol + PEGDME250, PEGDME500 solutions at $T = (298.15$ to $318.15)$ K. By the use of these data, the excess molar volume (V^E) the isentropic compressibility, (ΔK_s), deviation in speed of sound, (Δu) and excess specific volume were calculated. The calculated values for these deviations became more negative with increasing of temperature. And these values for PEGDME500 have less negative values compared to PEGDME250. By the use of Redlich – Kister and Ottet *al.* equations, the correlation between experimental data and calculated data indicated

the experimental data have good agreement with the Ottet *al.* equation.

Acknowledgment We are grateful to University of Tabriz Research Council for the financial support of this research.

References

- [1] K. Narendra, C. Srinivasu, S. Fakruddin, P. Narayanamurthy, Excess parameters of binary mixtures of anisaldehyde with o-cresol, m-cresol and p-cresol at T=(303.15, 308.15, 313.15, and 318.15) K, *J. Chem. Thermodyn* 43 (2011) 1604-1611.
- [2] O. Redlich, A. Kister, Algebraic representation of thermodynamic properties and the classification of solutions, *Ind. Eng. Chem* 40 (1948) 345-348.
- [3] J. Ott, C. Stouffer, G. Cornett, B. Woodfield, R. Wirthlin, J. Christensen, U. Deiters, Excess enthalpies for (ethanol+ water) at 298.15 K and pressures of 0.4, 5, 10, and 15 MPa, *J. Chem. Thermodyn* 18 (1986) 1-12.
- [4] K.S. Pitzer, J.C. Peiper, R. Busey, Thermodynamic properties of aqueous sodium chloride solutions, *J. Phys. Chem. Ref. Data* 13 (1984) 1-102.
- [5] M.T. Zafarani-Moattar, F. Samadi, R. Sadeghi, Volumetric and ultrasonic studies of the system (water+ polypropylene glycol 400) at temperatures from (283.15 to 313.15) K, *J. Chem. Thermodyn* 36 (2004) 871-875.
- [6] S. Ebrahimi, R. Sadeghi, Density, speed of sound, and viscosity of some binary and ternary aqueous polymer solutions at different temperatures, *J. Chem. Eng. Data* 60 (2015) 3132-3147.

Soluting-In and Soluting-Out of Water-Soluble Polymers in Aqueous Carbohydrate Solutions Studied by Vapor Pressure Osmometry

Nosaibah Ebrahimi, Rahmat Sadeghi*

Department of Chemistry, University of Kurdistan, Sanandaj, Iran

*rsadeghi@uok.ac.ir

Abstract: Precise vapor pressure osmometry (VPO) measurements at 308.15 K have been performed for ternary systems of carbohydrate in aqueous 0.2 w/w polymer solutions. The polymers are polyethylene glycol 400 (PEG400), polyethylene glycol 10000 (PEG10000) and polypropylene glycol 400 (PPG400), and the carbohydrates are xylose, xylitol, glucose, fructose, sucrose and raffinose. In order to study the soluting-out and soluting-in effects occurring in the polymer-carbohydrate aqueous systems, deviations of vapor-liquid equilibria behavior of these systems from the semi-ideal state have been evaluated. The VPO data obtained for PEG-carbohydrate aqueous systems, which are completely miscible, generally show positive deviations (soluting-in effect) from the semi-ideal behaviour that become more positive by increasing hydrophobic nature of PEG and carbohydrates. However, in the case of PPG + carbohydrates aqueous systems that can undergo phase separation, the VPO data in the monophasic and biphasic regions, respectively show negative (soluting-out effect) and positive deviations from the semi-ideal behaviour. In these systems, because of unfavorable PPG-carbohydrate interactions, the solutes exclude themselves from the vicinity of each other and therefore aqueous biphasic systems are entropically formed above a critical concentration.

Keywords: Vapor pressure osmometry, Water-soluble polymer, Carbohydrate, Semi-ideal behavior, Soluting effects

Introduction

Carbohydrates may exert significant influence on the stability and behavior of aqueous polymeric systems in foods and in other fields of application [1]. Moreover, the addition of sufficient amounts of sugars to aqueous solutions of polypropylene glycols leads to the formation of aqueous biphasic systems (ABSs) [2]. ABSs, originally proposed by Albertsson [3], are formed upon mixing two water-soluble but structurally different components in aqueous media under certain concentrations and conditions. The use of ABSs for separation of cells, membranes, viruses, proteins, nucleic acids, enzymes and other biomolecules leads to gentle, safe, low cost and high yield extraction processes [4]. It is interesting to note that polymer-carbohydrate ABS offer greener extraction procedures than polymer-ionic liquid and traditional polymer-salt ABS. The substitution of high charge density salts by carbohydrates for implementation of polymer based ABS can lead to improved biotechnological routes, because high ionic strength or alkaline media created by salts may be deleterious to a number of biomolecules. Also, carbohydrates are more eco-friendly and less expensive than imidazolium or pyridinium based ionic liquids which have been widely used for ABS formation. This fact merits thermodynamic investigations of different ternary polymer-carbohydrate aqueous solutions.

In this work, a precise vapor pressure osmometry method is used to determine water activities of different ternary aqueous solutions containing both polymer and sugar at 308.15 K. Deviations of vapor-liquid equilibria behavior of the studied systems from the semi-ideal state, are scrutinized and related to soluting effects.

Materials and method

D (+) – xylose (≥ 0.99), D (+) – glucose (≥ 0.995), D (-) – fructose (≥ 0.99), sucrose (≥ 0.98), raffinose pentahydrate (≥ 0.97), PEG400 and PEG10000 were purchased from Merck. Xylitol (≥ 0.99) was obtained from Alfa Aesar. PPG400 was obtained from Fluka. Double distilled and deionized water was used. Solutions were prepared by mass with the use of a Sartorius CP124S balance precisely within $\pm 1.10^{-7}$ kg. The vapor pressure osmometry (VPO) measurements were carried out with a Knauer vapor pressure osmometer (model K-7000).

Results and Discussion

Fig. 1 depicts the concentration dependence of the water activity for systems of carbohydrate in aqueous 0.2 w/w polymer solutions. Fig. 1a shows that water activity in carbohydrate-PEG10000 aqueous solutions in the whole concentrations range increases in the order: raffinose < sucrose < glucose < fructose \cong xylitol < xylose. Also, the measured water activities for systems of carbohydrate in aqueous 0.2 w/w PEG400 solutions obey the same order. The values of water activity in the binary carbohydrate + water solutions [5] follow the order: raffinose < sucrose < glucose < xylitol < fructose < xylose, which is similar to that in carbohydrate-PEG aqueous solutions, with the exception of xylitol and fructose. From Fig. 1b, it is possible to observe two different and quit reverse orders for water activities in the one-phase and two-phase regions of carbohydrates in aqueous 0.2 w/w PPG400 solutions: raffinose < sucrose < glucose < fructose <

xylitol < xylose, in the one-phase region, and sucrose > glucose > fructose > xylitol > xylose, in the two-phase region. As can be seen, for each of the carbohydrate + PPG400 aqueous systems, the slope of the plot of water activity against carbohydrate molality (a_w vs. m_c) in the two-phase region is less than that in the one-phase region. This is because of partial dehydration of solutes occurring by ABS formation [2,6]. In addition, the interesting order observed for water activities in the two-phase region indicates that in the case of more hydrophilic carbohydrates, more partial dehydration occurs by phase separation. The concentration point at which the slope of a_w vs. m_c changes and phase separation achieves is 1.17, 1.35, 1.48, 1.62 and 2.04 mol.kg⁻¹ for sucrose, glucose, fructose, xylitol and xylose, respectively. These values increase in the same order of water activity in the one-phase region. Furthermore, these observations are in good agreement with liquid-liquid equilibria phase diagrams (binodal curves) for these systems [2]. The more hydrated the carbohydrate (the lower a_w), the higher soluting-out strength of the carbohydrate and then the lower required carbohydrate concentration for phase separation.

In order to investigate the soluting effect occurring in a ternary A + B + water solution, here, we scrutinize deviations from the following equations:

$$(a_w + 1) - (a_{wA}^\circ + a_{wB}^\circ) = 0 \quad (1)$$

$$\Delta p - (\Delta p_A^\circ + \Delta p_B^\circ) = 0 \quad (2)$$

where a_{wA}° and a_{wB}° are, respectively, the water activities in binary A + water and B + water solutions with solute molalities m_A and m_B , and a_w is the water activity in ternary A + B + water solution with the same solute molalities as the constituent binary aqueous solutions. Also, $\Delta p = p - p^*$ and $\Delta p_i^\circ = p_i^\circ - p^*$ are, respectively, the vapor pressure depressions for ternary A + B + water and binary i + water solutions with the same solute molalities. These equations are established for the semi-ideal solutions in which the A-B interactions are negligible and the A-water and B-water interactions in the ternary solutions are the same as those in the corresponding binary solutions. Therefore, departures from Eqs. 1 and 2 may be taken as an evidence for specific A-B interactions. If in a ternary A + B aqueous system, the A-B interactions are more favorable than the A-water and B-water interactions, the water molecules are allowed to relax to the bulk state and therefore $a_w + 1 > a_{wA}^\circ + a_{wB}^\circ$ and Δp is less negative than $\Delta p_A^\circ + \Delta p_B^\circ$ (positive deviation from the semi-ideal behavior). This is an example of soluting-in phenomenon in which the mutual solubilities of A/water and B/water increase. In other words, each solute acts as cosolvent for another solute. However, if in a ternary A + B aqueous system, the A-B interactions are unfavorable, the interactions of

each solute with water (A-water and B-water interactions) are strengthened in the presence of the other solute. In these systems, unfavorable interactions between two solutes decrease the amount of free water molecules with respect to the semi-ideal state, thus $a_w + 1 < a_{wA}^\circ + a_{wB}^\circ$ and Δp is more negative than $\Delta p_A^\circ + \Delta p_B^\circ$ (negative deviation from the semi-ideal behavior). This is an example of soluting-out phenomenon in which solutes A and B exclude themselves from the vicinity of each other and compete for water molecules. In this case, the quality of solvent for each solute is lowered by the addition of another solute to solution and ultimately above the critical concentration because of entropic reasons ABS formation is favorable [2,6]. As example, plots of $(a_w + 1) - (a_{w,p}^\circ + a_{w,c}^\circ)$ against carbohydrate molality for the ternary systems of xylose in aqueous 0.2 w/w PEG400, PEG10000 and PPG400 solutions are depicted in Fig. 2. The other investigated systems show the similar behavior. According to this figure, in the case of carbohydrate + PPG400 + water system which can produce ABS (soluting-out effect), the negative and positive departures from Eq. 1, that become more negative and more positive with increasing carbohydrate concentration, are seen in the one-phase and two-phase regions, respectively. However, in the carbohydrate + PEG + water solutions which soluting-in phenomenon occurs, positive deviation from Eq. 1, that becomes more positive with increasing carbohydrate concentration is observed. Carbohydrate + PEG400 aqueous systems show smaller deviations from the semi-ideal behavior as compared to Carbohydrate + PEG10000 aqueous systems. This indicates that favorable sugar-PEG interactions are increased by increasing the PEG molar mass. The comparison of departures from the semi-ideal state for different carbohydrate + PEG10000 or PEG400 + water systems shows that positive deviation from Eqs. 1 and 2 increases by decreasing the hydrophilic nature of the sugar, and follows the order: raffinose < sucrose < glucose < fructose < xylitol < xylose. This order is similar to the trend observed in Fig. 1a for the water activity of these solutions. This means that the carbohydrate-PEG interactions increase with increasing hydrophobic nature of carbohydrates. On the other hand, the magnitude of negative deviations from Eqs. 1 and 2 in the one-phase region of carbohydrate + PPG + water systems increases by increasing the hydrophilic nature of the carbohydrates and obey the order: raffinose > sucrose > glucose > fructose > xylitol > xylose. The liquid-liquid equilibria behavior (binodal curves) of carbohydrate-PPG400 aqueous systems [2] ascertains that the soluting-out strength of carbohydrates decreases in the order: raffinose > sucrose > glucose > fructose > xylitol > xylose, which is quite in agreement with the extent of negative deviations from Eq. 1 and 2. In fact, the mutual

exclusion of PPG and carbohydrate from the vicinity of each other is intensified by increasing the carbohydrate hydrophilicity. This is the main reason for more negative deviations from the semi-ideal behavior for the more hydrophilic sugars. Furthermore, the positive deviations from Eqs. 1 and 2 in the two phase region of carbohydrate + PPG + water systems increase in the same order of the water activities in this region.

Conclusions

The VPO data for Carbohydrate + PEG + water solutions show positive deviations from the semi-ideal state. These systems are completely miscible and there are preferential interactions between PEG and Carbohydrate. By increasing the PEG molar mass and decreasing hydrophilicity of the carbohydrate, the PEG-carbohydrate interactions become more favorable, and then the positive deviations from the semi-ideal behavior increase. However for carbohydrate + PPG + water systems, which have limited miscibility, the VPO data in the one-phase region show negative deviations from the semi-ideal state. In fact, because of unfavorable carbohydrate-PPG interactions, aqueous carbohydrate solutions are worse solvents for PPG compared to pure water. In other words, carbohydrates exert soluting-out effect on the aqueous PPG solutions and above critical concentrations induce phase separation which leads to the formation of ABS composed of PPG-rich and carbohydrate-rich phases. Since by ABS formation partial dehydration of solutes occurs, in the biphasic region of PPG-carbohydrate aqueous systems, positive departure from the semi-ideality was observed.

References

- [1] Y.D. Livney, I. Portnaya, B. Faupin, L. Fahoum, O. Ramon, Y. Cohen, S. Mizrahi, U. Cogan, Interactions of glucose and polyacrylamide in solutions and gels, *J. Polym. Sci. Part B Polym. Phys.* 41 (2003) 3053–3063.
- [2] R. Sadeghi, N. Ebrahimi, M.D. Tehrani, Investigation of carbohydrates as non-charged, non-toxic and renewable soluting-out agent for polymer based aqueous biphasic systems implementation, *Polymer (Guildf)*. 98 (2016) 365–377.
- [3] P.-Å. Albertsson, *Partition of cell particles and macromolecules: separation and purification of biomolecules, cell organelles, membranes, and cells in aqueous polymer two-phase systems and their use in biochemical analysis and biotechnology*, Wiley New York etc., 1986.
- [4] A.F.M. Cláudio, M.G. Freire, C.S.R. Freire, A.J.D. Silvestre, J.A.P. Coutinho, Extraction of vanillin using ionic-liquid-based aqueous two-phase systems, *Sep. Purif. Technol.* 75 (2010) 39–47.
- [5] N. Ebrahimi, R. Sadeghi, Osmotic properties of

carbohydrate aqueous solutions, *Fluid Phase Equilib.* 417 (2016) 171–180.

- [6] R. Sadeghi, B. Hamidi, N. Ebrahimi, Investigation of Amino Acid–Polymer Aqueous Biphasic Systems, *J. Phys. Chem. B.* 118 (2014) 10285–10296.

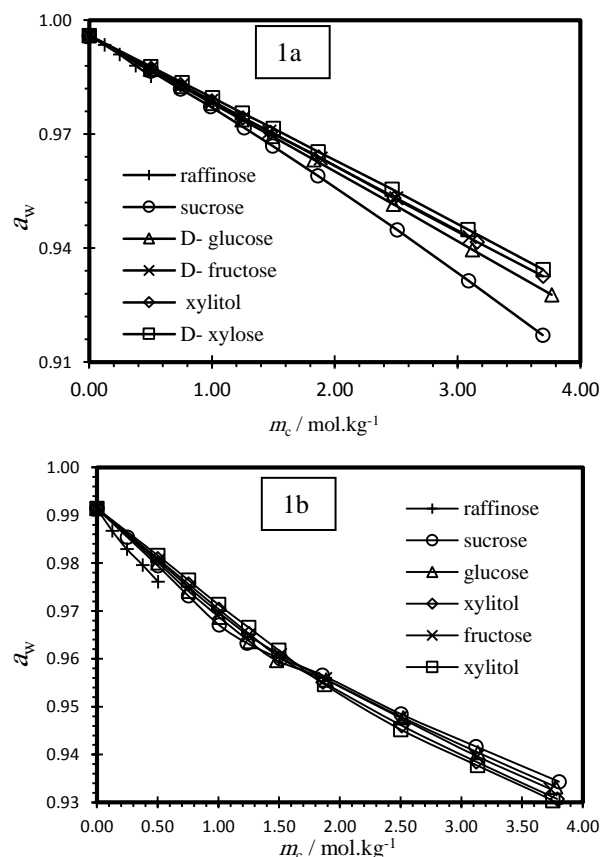


Fig. 1: Plot of water activity, a_w , against carbohydrate molality, m_c , for carbohydrate in aqueous 0.2 w/w of PEG10000 (1a) and PEG400 (1b).

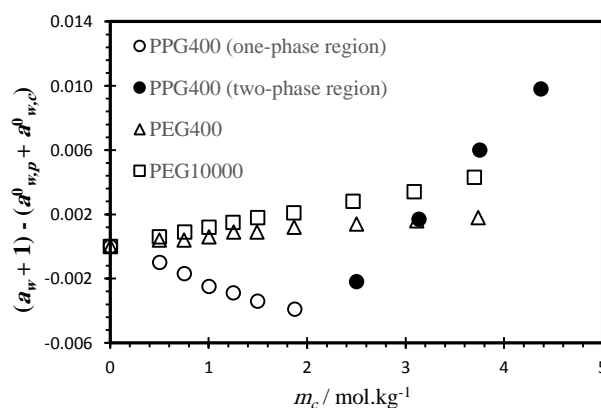


Fig. 2: Plot of $a_w + 1 - (a_{w,p}^0 + a_{w,c}^0)$ against carbohydrate molality for xylose in aqueous 0.2 w/w polymer solutions.

Soluting-In and Soluting-Out of Water-Soluble Polymers in Aqueous Carbohydrate Solutions Studied by Vapor Pressure Osmometry

Nosaibah Ebrahimi, Rahmat Sadeghi*

Department of Chemistry, University of Kurdistan, Sanandaj, Iran

*rsadeghi@uok.ac.ir

Abstract: Precise vapor pressure osmometry (VPO) measurements at 308.15 K have been performed for ternary systems of carbohydrate in aqueous 0.2 w/w polymer solutions. The polymers are polyethylene glycol 400 (PEG400), polyethylene glycol 10000 (PEG10000) and polypropylene glycol 400 (PPG400), and the carbohydrates are xylose, xylitol, glucose, fructose, sucrose and raffinose. In order to study the soluting-out and soluting-in effects occurring in the polymer-carbohydrate aqueous systems, deviations of vapor-liquid equilibria behavior of these systems from the semi-ideal state have been evaluated. The VPO data obtained for PEG-carbohydrate aqueous systems, which are completely miscible, generally show positive deviations (soluting-in effect) from the semi-ideal behaviour that become more positive by increasing hydrophobic nature of PEG and carbohydrates. However, in the case of PPG + carbohydrates aqueous systems that can undergo phase separation, the VPO data in the monophasic and biphasic regions, respectively show negative (soluting-out effect) and positive deviations from the semi-ideal behaviour. In these systems, because of unfavorable PPG-carbohydrate interactions, the solutes exclude themselves from the vicinity of each other and therefore aqueous biphasic systems are entropically formed above a critical concentration.

Keywords: Vapor pressure osmometry, Water-soluble polymer, Carbohydrate, Semi-ideal behavior, Soluting effects

Introduction

Carbohydrates may exert significant influence on the stability and behavior of aqueous polymeric systems in foods and in other fields of application [1]. Moreover, the addition of sufficient amounts of sugars to aqueous solutions of polypropylene glycols leads to the formation of aqueous biphasic systems (ABSs) [2]. ABSs, originally proposed by Albertsson [3], are formed upon mixing two water-soluble but structurally different components in aqueous media under certain concentrations and conditions. The use of ABSs for separation of cells, membranes, viruses, proteins, nucleic acids, enzymes and other biomolecules leads to gentle, safe, low cost and high yield extraction processes [4]. It is interesting to note that polymer-carbohydrate ABS offer greener extraction procedures than polymer-ionic liquid and traditional polymer-salt ABS. The substitution of high charge density salts by carbohydrates for implementation of polymer based ABS can lead to improved biotechnological routes, because high ionic strength or alkaline media created by salts may be deleterious to a number of biomolecules. Also, carbohydrates are more eco-friendly and less expensive than imidazolium or pyridinium based ionic liquids which have been widely used for ABS formation. This fact merits thermodynamic investigations of different ternary polymer-carbohydrate aqueous solutions.

In this work, a precise vapor pressure osmometry method is used to determine water activities of different ternary aqueous solutions containing both polymer and sugar at 308.15 K. Deviations of vapor-liquid equilibria behavior of the studied systems from the semi-ideal state, are scrutinized and related to soluting effects.

Materials and method

D (+) – xylose (≥ 0.99), D (+) – glucose (≥ 0.995), D (-) – fructose (≥ 0.99), sucrose (≥ 0.98), raffinose pentahydrate (≥ 0.97), PEG400 and PEG10000 were purchased from Merck. Xylitol (≥ 0.99) was obtained from Alfa Aesar. PPG400 was obtained from Fluka. Double distilled and deionized water was used. Solutions were prepared by mass with the use of a Sartorius CP124S balance precisely within $\pm 1.10^{-7}$ kg. The vapor pressure osmometry (VPO) measurements were carried out with a Knauer vapor pressure osmometer (model K-7000).

Results and Discussion

Fig. 1 depicts the concentration dependence of the water activity for systems of carbohydrate in aqueous 0.2 w/w polymer solutions. Fig. 1a shows that water activity in carbohydrate-PEG10000 aqueous solutions in the whole concentrations range increases in the order: raffinose < sucrose < glucose < fructose \cong xylitol < xylose. Also, the measured water activities for systems of carbohydrate in aqueous 0.2 w/w PEG400 solutions obey the same order. The values of water activity in the binary carbohydrate + water solutions [5] follow the order: raffinose < sucrose < glucose < xylitol < fructose < xylose, which is similar to that in carbohydrate-PEG aqueous solutions, with the exception of xylitol and fructose. From Fig. 1b, it is possible to observe two different and quit reverse orders for water activities in the one-phase and two-phase regions of carbohydrates in aqueous 0.2 w/w PPG400 solutions: raffinose < sucrose < glucose < fructose <

xylitol < xylose, in the one-phase region, and sucrose > glucose > fructose > xylitol > xylose, in the two-phase region. As can be seen, for each of the carbohydrate + PPG400 aqueous systems, the slope of the plot of water activity against carbohydrate molality (a_w vs. m_c) in the two-phase region is less than that in the one-phase region. This is because of partial dehydration of solutes occurring by ABS formation [2,6]. In addition, the interesting order observed for water activities in the two-phase region indicates that in the case of more hydrophilic carbohydrates, more partial dehydration occurs by phase separation. The concentration point at which the slope of a_w vs. m_c changes and phase separation achieves is 1.17, 1.35, 1.48, 1.62 and 2.04 mol.kg⁻¹ for sucrose, glucose, fructose, xylitol and xylose, respectively. These values increase in the same order of water activity in the one-phase region. Furthermore, these observations are in good agreement with liquid-liquid equilibria phase diagrams (binodal curves) for these systems [2]. The more hydrated the carbohydrate (the lower a_w), the higher soluting-out strength of the carbohydrate and then the lower required carbohydrate concentration for phase separation.

In order to investigate the soluting effect occurring in a ternary A + B + water solution, here, we scrutinize deviations from the following equations:

$$(a_w + 1) - (a_{wA}^\circ + a_{wB}^\circ) = 0 \quad (1)$$

$$\Delta p - (\Delta p_A^\circ + \Delta p_B^\circ) = 0 \quad (2)$$

where a_{wA}° and a_{wB}° are, respectively, the water activities in binary A + water and B + water solutions with solute molalities m_A and m_B , and a_w is the water activity in ternary A + B + water solution with the same solute molalities as the constituent binary aqueous solutions. Also, $\Delta p = p - p^*$ and $\Delta p_i^\circ = p_i^\circ - p^*$ are, respectively, the vapor pressure depressions for ternary A + B + water and binary i + water solutions with the same solute molalities. These equations are established for the semi-ideal solutions in which the A-B interactions are negligible and the A-water and B-water interactions in the ternary solutions are the same as those in the corresponding binary solutions. Therefore, departures from Eqs. 1 and 2 may be taken as an evidence for specific A-B interactions. If in a ternary A + B aqueous system, the A-B interactions are more favorable than the A-water and B-water interactions, the water molecules are allowed to relax to the bulk state and therefore $a_w + 1 > a_{wA}^\circ + a_{wB}^\circ$ and Δp is less negative than $\Delta p_A^\circ + \Delta p_B^\circ$ (positive deviation from the semi-ideal behavior). This is an example of soluting-in phenomenon in which the mutual solubilities of A/water and B/water increase. In other words, each solute acts as cosolvent for another solute. However, if in a ternary A + B aqueous system, the A-B interactions are unfavorable, the interactions of

each solute with water (A-water and B-water interactions) are strengthened in the presence of the other solute. In these systems, unfavorable interactions between two solutes decrease the amount of free water molecules with respect to the semi-ideal state, thus $a_w + 1 < a_{wA}^\circ + a_{wB}^\circ$ and Δp is more negative than $\Delta p_A^\circ + \Delta p_B^\circ$ (negative deviation from the semi-ideal behavior). This is an example of soluting-out phenomenon in which solutes A and B exclude themselves from the vicinity of each other and compete for water molecules. In this case, the quality of solvent for each solute is lowered by the addition of another solute to solution and ultimately above the critical concentration because of entropic reasons ABS formation is favorable [2,6]. As example, plots of $(a_w + 1) - (a_{w,p}^\circ + a_{w,c}^\circ)$ against carbohydrate molality for the ternary systems of xylose in aqueous 0.2 w/w PEG400, PEG10000 and PPG400 solutions are depicted in Fig. 2. The other investigated systems show the similar behavior. According to this figure, in the case of carbohydrate + PPG400 + water system which can produce ABS (soluting-out effect), the negative and positive departures from Eq. 1, that become more negative and more positive with increasing carbohydrate concentration, are seen in the one-phase and two-phase regions, respectively. However, in the carbohydrate + PEG + water solutions which soluting-in phenomenon occurs, positive deviation from Eq. 1, that becomes more positive with increasing carbohydrate concentration is observed. Carbohydrate + PEG400 aqueous systems show smaller deviations from the semi-ideal behavior as compared to Carbohydrate + PEG10000 aqueous systems. This indicates that favorable sugar-PEG interactions are increased by increasing the PEG molar mass. The comparison of departures from the semi-ideal state for different carbohydrate + PEG10000 or PEG400 + water systems shows that positive deviation from Eqs. 1 and 2 increases by decreasing the hydrophilic nature of the sugar, and follows the order: raffinose < sucrose < glucose < fructose < xylitol < xylose. This order is similar to the trend observed in Fig. 1a for the water activity of these solutions. This means that the carbohydrate-PEG interactions increase with increasing hydrophobic nature of carbohydrates. On the other hand, the magnitude of negative deviations from Eqs. 1 and 2 in the one-phase region of carbohydrate + PPG + water systems increases by increasing the hydrophilic nature of the carbohydrates and obey the order: raffinose > sucrose > glucose > fructose > xylitol > xylose. The liquid-liquid equilibria behavior (binodal curves) of carbohydrate-PPG400 aqueous systems [2] ascertains that the soluting-out strength of carbohydrates decreases in the order: raffinose > sucrose > glucose > fructose > xylitol > xylose, which is quite in agreement with the extent of negative deviations from Eq. 1 and 2. In fact, the mutual

exclusion of PPG and carbohydrate from the vicinity of each other is intensified by increasing the carbohydrate hydrophilicity. This is the main reason for more negative deviations from the semi-ideal behavior for the more hydrophilic sugars. Furthermore, the positive deviations from Eqs. 1 and 2 in the two phase region of carbohydrate + PPG + water systems increase in the same order of the water activities in this region.

Conclusions

The VPO data for Carbohydrate + PEG + water solutions show positive deviations from the semi-ideal state. These systems are completely miscible and there are preferential interactions between PEG and Carbohydrate. By increasing the PEG molar mass and decreasing hydrophilicity of the carbohydrate, the PEG-carbohydrate interactions become more favorable, and then the positive deviations from the semi-ideal behavior increase. However for carbohydrate + PPG + water systems, which have limited miscibility, the VPO data in the one-phase region show negative deviations from the semi-ideal state. In fact, because of unfavorable carbohydrate-PPG interactions, aqueous carbohydrate solutions are worse solvents for PPG compared to pure water. In other words, carbohydrates exert soluting-out effect on the aqueous PPG solutions and above critical concentrations induce phase separation which leads to the formation of ABS composed of PPG-rich and carbohydrate-rich phases. Since by ABS formation partial dehydration of solutes occurs, in the biphasic region of PPG-carbohydrate aqueous systems, positive departure from the semi-ideality was observed.

References

- [1] Y.D. Livney, I. Portnaya, B. Faupin, L. Fahoum, O. Ramon, Y. Cohen, S. Mizrahi, U. Cogan, Interactions of glucose and polyacrylamide in solutions and gels, *J. Polym. Sci. Part B Polym. Phys.* 41 (2003) 3053–3063.
- [2] R. Sadeghi, N. Ebrahimi, M.D. Tehrani, Investigation of carbohydrates as non-charged, non-toxic and renewable soluting-out agent for polymer based aqueous biphasic systems implementation, *Polymer (Guildf)*. 98 (2016) 365–377.
- [3] P.-Å. Albertsson, *Partition of cell particles and macromolecules: separation and purification of biomolecules, cell organelles, membranes, and cells in aqueous polymer two-phase systems and their use in biochemical analysis and biotechnology*, Wiley New York etc., 1986.
- [4] A.F.M. Cláudio, M.G. Freire, C.S.R. Freire, A.J.D. Silvestre, J.A.P. Coutinho, Extraction of vanillin using ionic-liquid-based aqueous two-phase systems, *Sep. Purif. Technol.* 75 (2010) 39–47.
- [5] N. Ebrahimi, R. Sadeghi, Osmotic properties of

carbohydrate aqueous solutions, *Fluid Phase Equilib.* 417 (2016) 171–180.

- [6] R. Sadeghi, B. Hamidi, N. Ebrahimi, Investigation of Amino Acid–Polymer Aqueous Biphasic Systems, *J. Phys. Chem. B.* 118 (2014) 10285–10296.

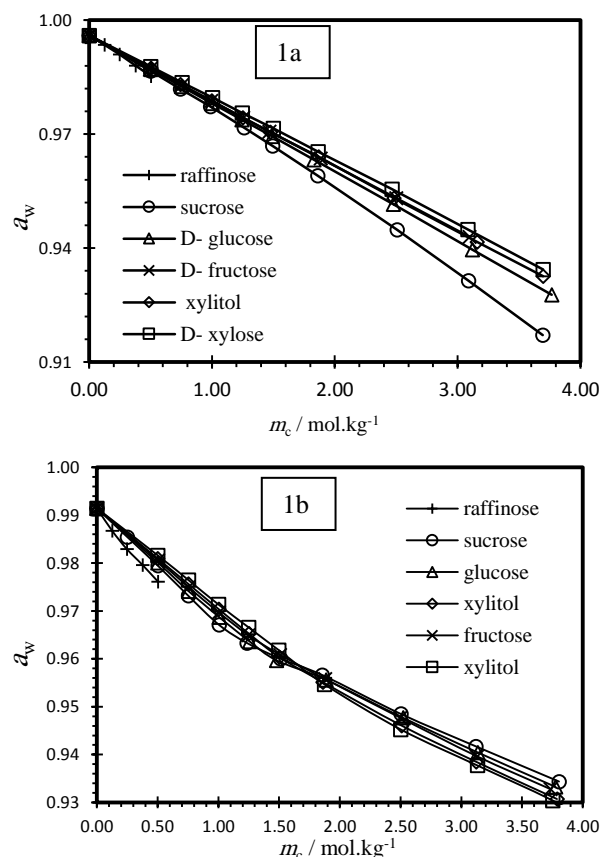


Fig. 1: Plot of water activity, a_w , against carbohydrate molality, m_c , for carbohydrate in aqueous 0.2 w/w of PEG10000 (1a) and PEG400 (1b).

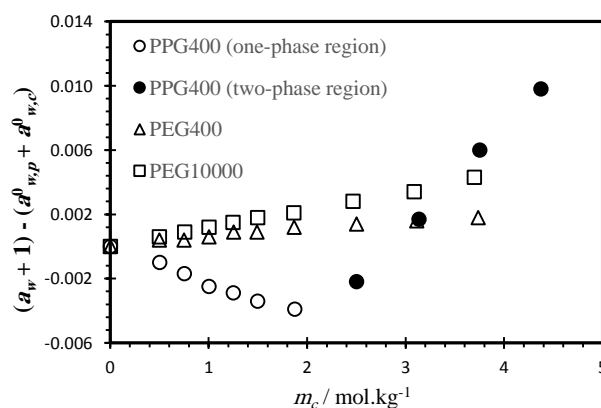


Fig. 2: Plot of $a_w + 1 - (a_{w,p}^0 + a_{w,c}^0)$ against carbohydrate molality for xylose in aqueous 0.2 w/w polymer solutions.

The role of the ionic liquid [C₄C₁im]Br as additive in the formation of the PEG-based ABS at $T = 298.15$ K: Effects of the PEG molecularweight and the salt

S. Hamzehzadeh^{a*}, M. Fardshirayeh^a

^aChemistry and Chemical Engineering Research Center of Iran (CCERCI), Tehran, P.O.Box: 14335-186, Iran

*melissa505@ymail.com

Abstract: Polyethylene glycols (PEGs) are the most common polymers used in the polymer-salt aqueous biphasic systems. However, the hydrophilic nature of PEGs and the lowpolarity of the PEG-rich phase limit the applicability of this technique. To overcome this limitation, in recent years, a new approach has been proposed based on the use of ionic liquids (ILs) as adjuvants in PEG-based ABS. Nevertheless, to develop a full picture of how ILs affect the ABS features, more information is needed. In this regard, this work is devoted to study the influence of the IL 1-butyl-3-methylimidazolium bromide ([C₄C₁im]Br) as additive on the formation of {PEG 4000 + tri-sodium citrate (Na₃C₆H₅O₇)}, {PEG 4000 + di-sodium tartrate (Na₂C₄H₄O₆)}, {PEG 4000 + di-sodium succinate (Na₂C₄H₄O₄)} and {PEG 400 + Na₃C₆H₅O₇} ABS. For this purpose, phase diagrams of the aforementioned ABS were determined with the addition of small quantities (5 wt%) of [C₄C₁im]Br at $T = 298.15$ K. The results obtained indicate that the biphasic region of ABS with [C₄C₁im]Br is larger than that of ternary system for PEG 400; while, it is not remarkably changed for PEG 4000. Furthermore, the salts present the same trend to form the two-phase system in the presence of 5 wt% [C₄C₁im]Br.

Keywords: Aqueous biphasic system; Polyethylene glycol; Ionic liquid; Salt; PEG Molecular weight.

Introduction

Liquid-liquid extraction has often been a favored choice of the process engineer for the development of separation processes. Meanwhile, liquid-liquid extraction utilizing aqueous biphasic systems (ABS) that are usually formed by combining either two incompatible polymers or a polymer and a salt in water above a certain critical concentration is considered to be environmentally friendly because traditional volatile organic compounds (VOCs) are not used in the whole process; therefore, it has already been used to separate and purify various biological products, metal ions, dyes, drug molecules, and small organic species from the complex mixtures in which they are produced. For large-scale enzyme extraction, the aqueous polymer-salt systems are more attractive than the aqueous polymer-polymer systems because of their greater selectivity, lower viscosity, lower cost, rapid phase disengagement, and the availability of commercial separators, which allow a faster and continuous protein separation [1]. Despite the well-known advantages provided by these types of ABS, however, they suffer from the limited range of polarities at their coexisting phases that often originated from the phase-forming polymers. To overcome this limitation, in recent years, ionic liquids (ILs) have been used as adjuvants by some researchers [2, 3] to control the physicochemical properties of ABS. Recently, the influence of the IL 1-butyl-3-methylimidazolium bromide, [C₄C₁im]Br, as additive on the formation of the {PEG 400 + potassium citrate (K₃C₆H₅O₇)} [4], {PEG 600 + K₃C₆H₅O₇} [5], and {PEG (400, 600, 4000, and 6000) + K₃PO₄} [6] at $T = 298.15$ K has been studied by our research group. These studies reveal that the impact of the IL on the promotion

of ABS is decreased with increasing the PEG molecular weight (MW), so that eventually at a certain MW of PEG this effect is reversed, making the ABS formation more difficult [6]. In continuation of our previous works, here, we decided to study the role of the IL [C₄C₁im]Br as additive in the formation of the several PEG-based ABS at $T = 298.15$ K. The effects of the PEG MW and the salt type were examined. For this purpose, the phase diagrams of the {PEG 4000 + tri-sodium citrate (Na₃C₆H₅O₇)}, {PEG 4000 + di-sodium tartrate (Na₂C₄H₄O₆)}, {PEG 4000 + di-sodium succinate (Na₂C₄H₄O₄)} and {PEG 400 + Na₃C₆H₅O₇} ABS were determined with the addition of small quantities (5 wt%) of [C₄C₁im]Br at $T = 298.15$ K.

Materials and method

PEGs with MW of 400 and 4000 g·mol⁻¹, and [C₄C₁im]Br were supplied by Merck and used without further purification. The water content in the [C₄C₁im]Br was determined by the use of the Karl Fischer method to be $w = 0.0098$ in mass fraction, which was in good agreement with the value quoted by the suppliers, approximately less than $w = 0.01$. This water content in the IL was taken into account during the preparation of the aqueous solutions for the treatment of the experimental data. Tri-sodium citrate (Na₃C₆H₅O₇), di-sodium tartrate (Na₂C₄H₄O₆), and di-sodium succinate (Na₂C₄H₄O₄) with purity of minimum $w = 0.99$ were supplied by Sigma Aldrich. Double distilled water was used for preparation of solutions.

The determination of the binodal curves was carried out by a turbidimetric titration method. The polymer stock solution of known concentration was titrated with the salt stock solution or vice versa, until the solution turned



turbid, which indicated the formation of two liquid phases. In accordance with the amount of titrant added until turbidity was observed, the composition of the mixture for each point on the binodal curve was calculated by mass using the analytical balance[6].

Results and Discussion

In this study, the role of the IL $[C_4C_1im]Br$ as additive in the formation of several PEG-based ABS with varying the PEG MW and the type of the phase-forming salt was investigated at $T = 298.15 K$.

Effect of the PEG MW –The binodal curves for the {PEG 400 + $Na_3C_6H_5O_7$ + 5 wt% $[C_4C_1im]Br$ } and {PEG 4000 + salt ($Na_3C_6H_5O_7$, $Na_2C_4H_4O_6$, or $Na_2C_4H_4O_4$) + 5 wt% $[C_4C_1im]Br$ } ABS at $T = 298.15 K$ are depicted in Figs. 1 and 2a-c, respectively. It should be noted that the $[C_4C_1im]Br$ concentration was kept constant (*i.e.*, 5 wt%) in all binodal curves. Fig. 1, shows that for the studied ABS composed of PEG 400, the biphasic region of the system with $[C_4C_1im]Br$ is larger than that of without IL, indicating that lesser quantities of salt needed to form ABS, meaning the ABS formation is promoted by using IL. However, as can be seen in Fig. 2a-c for ABS composed of PEG 4000, the biphasic region of the systems with $[C_4C_1im]Br$ is negligibly smaller than that of the corresponding ternary systems. In our previous work, a similar observation was made with the {PEG (400 or 4000) + K_3PO_4 + 5 wt% $[C_4C_1im]Br$ } ABS at $T = 298.15 K$ [6]. It seems that for the PEGs with higher MW the ABS promoting impact of the hydrogen bonding interactions between Br^- anion of the IL and the terminal $-OH$ groups of the PEG is offset, to a large extent, by the salting-in effects of the PEG-IL cation interactions[6].

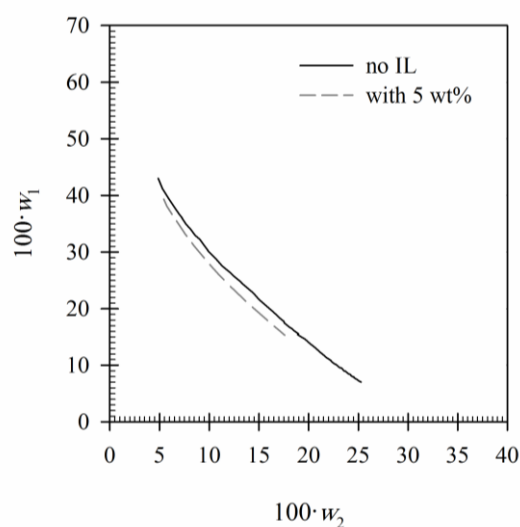


Fig. 1 : Effect of $[C_4C_1im]Br$ on the binodal curve of {PEG 400 (1) + $Na_3C_6H_5O_7$ (2)} ABS at $T = 298.15 K$.

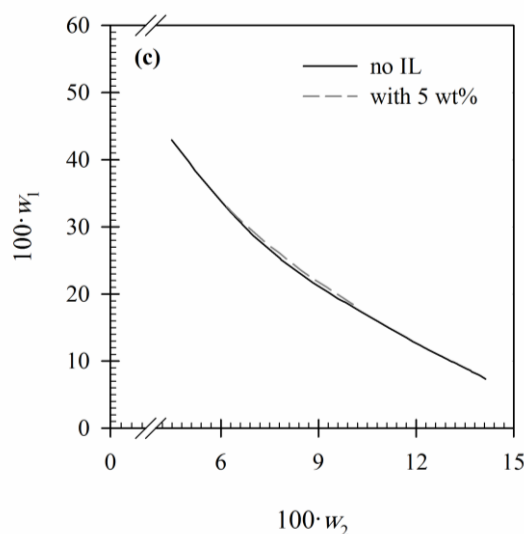
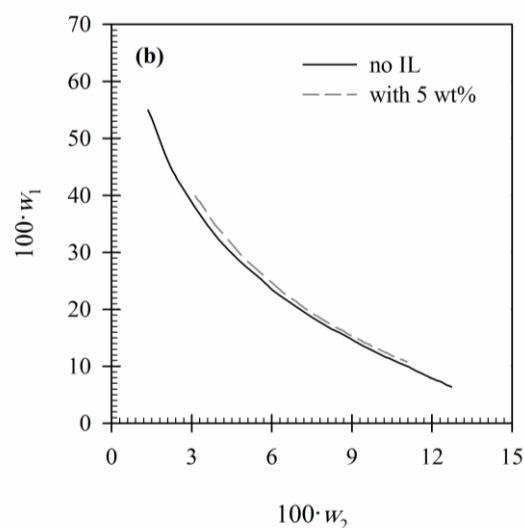
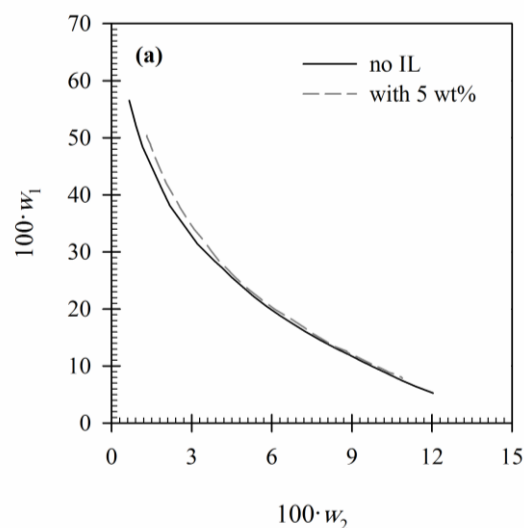


Fig. 2 : Effect of $[C_4C_1im]Br$ on the binodal curves of {PEG 4000 (1) + salt (2)} ABS at $T = 298.15 K$: (a) $Na_3C_6H_5O_7$, (b) $Na_2C_4H_4O_6$, (c) $Na_2C_4H_4O_4$.

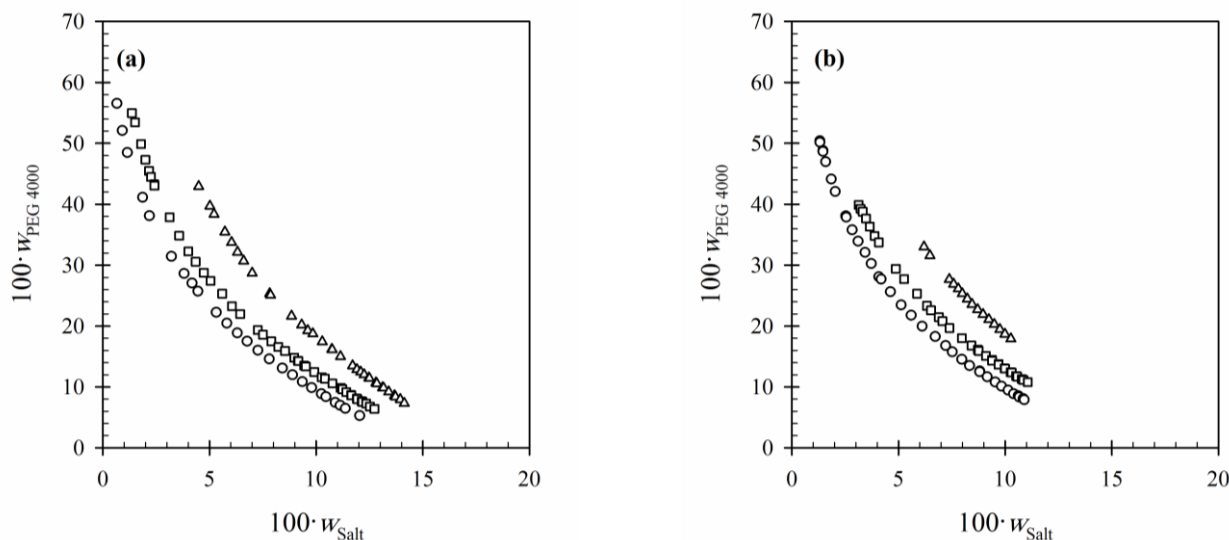


Fig.3: The binodal curves for ABS composed of PEG 4000 and salt at $T = 298.15$ K: (a) without IL; and (b) with 5 wt% $[C_4C_{1im}]Br$.

Effect of the salt – The relative ability of different salts including $Na_3C_6H_5O_7$, $Na_2C_4H_4O_6$, and $Na_2C_4H_4O_4$ to salt-out PEG 4000, and as a result to form ABS in the presence of $[C_4C_{1im}]Br$ as additive was examined. Initially, the ternary PEG-salt ABS were studied. The Phase diagrams for the ternary PEG-salt ABS at $T = 298.15$ K are shown in Fig. 3a. As can be seen, the ability of different salts to form ABS or salting-out the PEG demonstrates the following trend:



Additionally, for the quaternary systems, from Fig. 2a-c the presence of 5 wt% of $[C_4C_{1im}]Br$ has a small impact on the ABS formation, and thus, as we can see in Fig. 3b, the salts present the same trend to form the two-phase system.

Conclusions

In this study, the role of the IL $[C_4C_{1im}]Br$ as additive in the formation of several PEG-based ABS with varying the PEG MW and the phase-forming salt was investigated at $T = 298.15$ K. The binodal curves for the $\{PEG\ 400 + Na_3C_6H_5O_7\}$, $\{PEG\ 4000 + Na_3C_6H_5O_7\}$, $\{PEG\ 4000 + Na_2C_4H_4O_6\}$, and $\{PEG\ 4000 + Na_2C_4H_4O_4\}$ ABS were determined with the addition of small quantities (5 wt%) of $[C_4C_{1im}]Br$ at $T = 298.15$ K. It was found that the biphasic region of ABS with IL is larger than that of ternary system for PEG 400; while, it is not remarkably changed for PEG 4000. Furthermore, the salts present the same trend to form the two-phase system in the presence of 5 wt% IL.

References

- [1] M. T. Zafarani-Moattar and S. Hamzehzadeh, "Phase diagrams for the aqueous two-phase ternary system containing the ionic liquid 1-butyl-3-methylimidazolium bromide and tri-potassium citrate at $T = (278.15, 298.15, \text{ and } 318.15)$ K," *Journal of Chemical & Engineering Data*, 54 (2008) 833-841.
- [2] J. F. B. Pereira, Á. S. Lima, M. G. Freire, and J. A. P. Coutinho, "Ionic liquids as adjuvants for the tailored extraction of biomolecules in aqueous biphasic systems," *Green Chemistry*, 12 (2010) 1661-1669.
- [3] R. L. de Souza, V. C. Campos, S. P. M. Ventura, C. M. F. Soares, J. A. P. Coutinho, and Á. S. Lima, "Effect of ionic liquids as adjuvants on PEG-based ABS formation and the extraction of two probe dyes," *Fluid Phase Equilibria*, 375 (2014) 30-36.
- [4] S. Hamzehzadeh and M. Vasires, "Ionic liquid 1-butyl-3-methylimidazolium bromide as a promoter for the formation and extraction capability of poly (ethylene glycol)-potassium citrate aqueous biphasic system at $T = 298.15$ K," *Fluid Phase Equilibria*, 382 (2014) 80-88.
- [5] S. Hamzehzadeh and M. Abbasi, "The influence of 1-butyl-3-methyl-imidazolium bromide on the partitioning of l-tyrosine within the $\{\text{polyethylene glycol } 600 + \text{ potassium citrate}\}$ aqueous biphasic system at $T = 298.15$ K," *The Journal of Chemical Thermodynamics*, 80 (2015) 102-111.

Modelling photocatalytic degradation of Azur (II) using BiOI/BiOBr/BiPO₄ nanoparticles under blue light irradiation using diffusional neural networks

M. Mohammadi, F. Yousefi*

Chemistry Department, Yasouj University, Yasouj 75918-74831, Iran

*Corresponding author: Fakhri Yousefi

Tel/fax: + 98 741 222 1711.

*fyousefi@mail.yu.ac.ir

Abstract: To study this photodegradation, central composite design (CCD) under response surface methodology (RSM) was applied to design a systematic set of experiments. The CCD was used to investigate the significance of the effects of parameters including irradiation time, amount of photocatalyst and initial dye concentration that designed by using the DESIGN EXPORT 7.) that leading to 20 runs for the optimization process consists of 2ⁿ factorial points with 2n axial points and N_c central points to estimate the experimental error (reproducibility of the data). The axial points are located at distance of from centre and make the design rotatable. Artificial Neural network method is employed to estimate photocatalytic degradation blue light irradiation catalyzed by BiOI/BiOBr/BiPO₄.

Keywords: Artificial Neural network, photocatalytic degradation, BiOI/BiOBr/BiPO₄

Introduction

Dyes with complicated structure and their degradation products are highly toxic and carcinogenic [1]. These processes in despite of their unique advantages have drawbacks such as production and/or consumption of large volumes of toxic solutions or toxic derivatives that generally need next treatments. The combination of ozone with a proper radiation source and immobilized TiO₂ photo catalyst enhances its decomposition into hydroxyl radicals. Hydroxyl radicals are strong oxidizing agents which can react with organic compounds and transform them to CO₂ and H₂O [2]. In recent years, the artificial neural networks (ANN) grabbed the attention of many researchers in various industrial and engineering fields. High speed processing, extensive capacity, and simplicity are the primary benefits of using the ANN compared with the classical methods. Due to these advantages of ANN, many researchers have used this method for predicting the thermos physical features of nanofluids and other engineering applications [3].

Artificial neural network (ANN)

Artificial neural networks (ANNs) are robust statistical approaches that try to be like the human nervous system by establishing a logical model consisting of inter-connective neurons in a computing network. Neural networks are used to solve complex modeling challenges such as estimation, classification, and pattern recognition. Making an artificial neural network for modeling is of three steps. There are two main categories of ANNs which can be applied whether in regression or classification: the supervised and the unsupervised. In

supervised, the network is trained by regulating the values of the weights between neurons which make it possible to assume output value(s) after taking delivery of a number of instructing data from previous experimental. In unsupervised, there is no desired target value while introducing inputs to the structure. Multi-layer perceptron (MLP) feedforward neural network, one of the most popular training algorithms, usually has one or more hidden layers, in which selection of suitable numbers significantly depends upon the analyzer's experience and problem's nature. In the feedforward backpropagation algorithm, inputs pass through the network and at the end, outputs are compared with desired values and error is calculated [4].

Results and Discussion

With increasing the number of neuron, the performance of network in training should increase at meanwhile as the performance of network in testing data lead to optimized value at best or most favorable number of hidden neurons (see Fig. 1). In this path, the trained network is generalized and has largest prognostication on testing data. In this paper, MSE is mean square error that was chosen as a measure of the performance of the net. The net with one hidden layer with a MSE of 6.62×10^{-5} leads to the best prognostication in Fig. 1. Figure 2 shows the assessment of training, validation, and test errors as a subordinate of the number of training epochs. According to testing data, the optimized neural network model was used to forespeak the effective Photocatalytic degradation Azur(II) the analogy between

predictive data and experimental data is carried out and shown in Fig. 3. The results of Fig 3 evaluates good compromise between the predicted data and the experimental data of effective Photocatalytic degradation with absolute average error, AAD = 0.530 % and high correlation coefficients, $R^2 = 0.93219$. Besides, Figure 4 presents the error analysis of train, test and validation data over temperature variation.

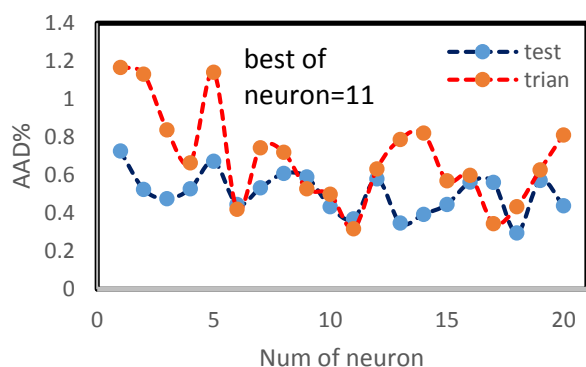


Fig.1. Shows of the number of hidden layer neurons

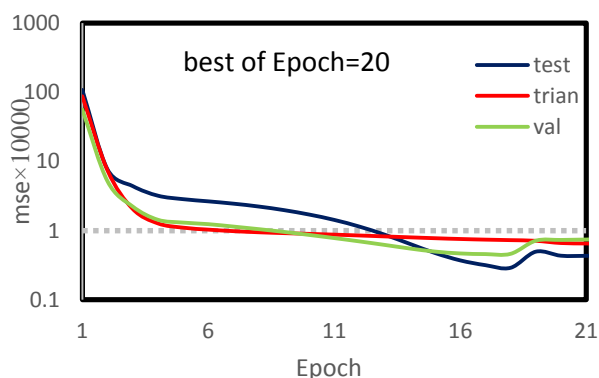


Fig. 2. Evolution of training, validation, and test errors as a function of the number of training Epochs during ANN training

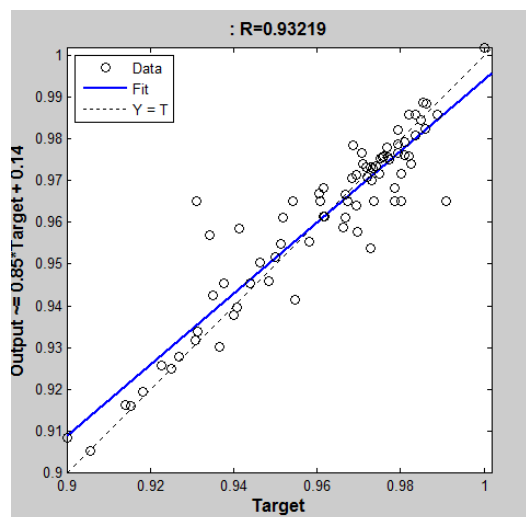


Fig. 3. Modeling ability of the optimized ANN to predicate of effective Photocatalytic degradation: ($R^2 = 0.93219$, AAD =0.530%)

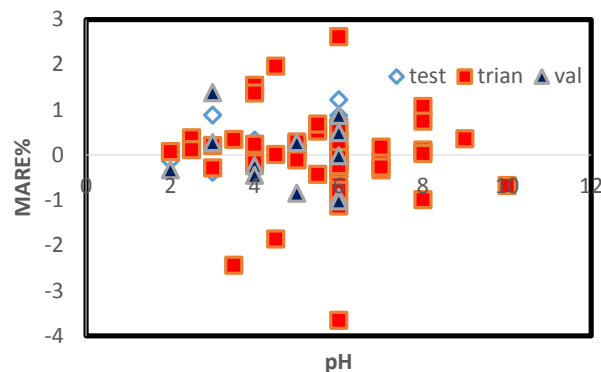


Fig.4 Percentage absolute relative error for Photocatalytic degradation with the experimental data

Conclusion

In this study, photocatalytic degradation of Azur(II) has been investigated using artificial neural network. The MLP is trained, validated, and tested with random 70% (70 data points), 15% (15 data points), and 15% (15 data points) of all experimental data point, respectively. The AADs% of a collection of 100 data points for all experimental data using the ANN at various conditions is 0.530 % ($R^2=0.93219$).

References

- [1] A. Houas, I. Bakir, M. Ksibi, E. Elaloui, *J. Chem. Phys.*, **96** (1999) 479-486.
- [2] M. Mehrjouei, S. Muller, D. Moller, *J. Chem. Eng.*, **248** (2014) 184-190.
- [3] M. Mohanraj, S. Jayaraj, C. Muraleedharan, "Applications of artificial neural networks for refrigeration, air-conditioning and heat pump systems—a review", *Renew. Sustain. Energy Rev.*, **16** (2012) 1340–1358.
- [4] M. Durairaj, C. Science, "Applications of artificial Neural network for IVF data analysis and prediction", *J. Eng. Comput.*, **2** (2013) 11–15.

Pressure Dependence of the Viscosity of Three Polyalkylene Glycol Ether Lubricants

M. Zare* and S. Golabvand

Department of Chemistry, Faculty of Science, Shahid Chamran University of Ahvaz, Ahvaz, Iran

*m.zare@scu.ac.ir

Abstract: Pressure dependence of viscosity of the lubricants is essential for most industrial applications. In the present work, experimental viscosities of three polyalkylene glycol ether lubricants including PAG1 (23 ethylene oxide units), PAG2 (29 ethylene oxide units) and PAG3 (21 ethylene oxide units) were correlated using a linear relation with high accuracy. This simple and accurate linear equation provides reliable extrapolation of viscosity data for this class of lubricant. In addition, we have analysed the pressure–viscosity coefficient (α) for these fluids. This property decreases when the pressure increases for three lubricants. The following sequence have been found for this coefficient $\text{PAG3} > \text{PAG2} > \text{PAG1}$.

Keywords: Correlation; Viscosity; Lubricants; Pressure dependence.

Introduction

At present lubricants are extensively used to facilitate relative motion of solid bodies and minimizing friction and wear between them by adding a thin layer of fluid between the areas in contact. Moreover, lubricating oils are required to carry out a range of other functions, including heat removal, corrosion prevention, transfer of power, and suspension and removal of wear particles [1].

An extensive class of synthetic lubricants is polyalkylene glycol ethers (PAGs). They can be manufactured by the reaction of epoxides, usually ethylene and propylene oxide (EO and PO), with compounds that contain active hydrogen in the presence of a basic catalyst [2].

Dynamic viscosity is an important physical property of lubricants, which affect heat and mass transfer. The variation of the viscosity of lubricants with the pressure is crucial in determining its ability to form a layer of oil between rolling surfaces to reduce friction and wear [2]. Study of the viscosity and its dependence with the pressure are necessary. In this work, our proposed equation is used to describe the viscosity of three poly(propylene oxide) dimethyl ethers as a function of pressure. We also determine the pressure–viscosity coefficient using the literature viscosity data over broad pressure range for three PAGs.

Methods

Ghatee *et al.* [3] have proposed a three-parameter equation for temperature dependent viscosity, which successfully applies for a variety of ionic liquids:

$$\left(\frac{1}{\eta}\right)^\varphi = a + bT \quad (1)$$

where a and b are specific adjustable parameters and φ is a characteristic exponent. This also can be successfully applied as a two-parameter equation with a universal value ($\varphi=0.3$). Viscosity is a non-linear function of

pressure and increases smoothly with pressure. Recently, we modified the Eq. (1) for pressure dependent viscosity as:

$$\eta^\varphi = A + BP \quad (2)$$

where A , B , and φ are fitting parameters. This equation was used to correlate viscosity of a various types of ionic liquids with pressure. In this investigation, we examined the applicability of this equation for three poly(propylene oxide) dimethyl ethers. Viscosity behaviour of PAG1 (23 EO units), PAG2 (29 EO units) and PAG3 (21 EO units) was investigated.

Results and Discussion

Viscosity of a liquid is a non-linear function of pressure. It increases smoothly with the pressure. The values of the viscosity of PAG1, PAG2, and PAG3 are fitted using the Eq. (2) in two-parameter form with $\varphi=0.3$ at constant temperature. The temperature, range of pressure, fitting parameters (A and B), correlation coefficient squared (R^2), and absolute average deviation percent (%AAD) are displayed in Table 1. The values of R^2 and %AAD indicate Eq. (2) can describe the pressure dependent viscosity of polyalkylene glycol ethers quite accurately.



Table 1. Temperature (T), range of pressure (ΔP), fitting parameters of Eq. (2) with $\varphi=0.3$, R^2 , and %AAD of studied lubricants. Viscosity data are taken from Refs [2 and 4].

Lubricant	T/K	$\Delta P/MPa$	A	B	R^2	%AAD ^a
PAG1	303.15	0.1-60	3.48367	0.02165	0.99925	0.89
	313.15	0.1-60	3.09644	0.01747	0.99924	0.81
	333.15	0.1-60	2.53128	0.01247	0.99982	0.36
	353.15	0.1-60	2.17135	0.00952	0.99995	0.17
	373.15	0.1-60	1.94127	0.00807	0.99979	0.33
PAG2	303.15	0.1-60	3.82878	0.02453	0.99898	1.00
	313.15	0.1-60	3.39997	0.01980	0.99951	0.72
	333.15	0.1-60	2.78372	0.01410	0.99975	0.42
	353.15	0.1-60	2.38120	0.01083	0.99999	0.07
PAG3	303.15	0.1-60	2.10518	0.00881	0.99993	0.19
	303.15	0.1-60	3.80777	0.02511	0.99871	1.21
	313.15	0.1-60	3.35141	0.02014	0.99933	0.82
	333.15	0.1-60	2.71511	0.01403	0.99975	0.44
	353.15	0.1-60	2.29683	0.01055	0.99995	0.18
	373.15	0.1-60	2.01780	0.00853	0.99999	0.06

$$^a \%AAD = \frac{1}{m} \sum_m |\eta_{\text{expt.}} - \eta_{\text{calc.}} / \eta_{\text{expt.}}| \times 100$$

In order to characterize the suitability of a lubricant, pressure–viscosity coefficient, $\alpha(p)$, is used [5]:

$$\alpha(p) = \frac{1}{\eta} \left(\frac{\partial \eta}{\partial p} \right)_T \quad (3)$$

The $\alpha(p)$ values are obtained using this equation together with the parameters of Eq. (2) and plotted versus pressure at different temperature for three lubricants in Fig. 1. This property decreases when the pressure increases and decreases strongly with the temperature from 303.15 to 373.15 K. The magnitude of α follows the trends PAG3> PAG2> PAG1.

Conclusions

The variation of viscosity with pressure was studied for three PAGs using Eq. (2). This simple and accurate linear equation provides reliable extrapolation and interpretation of viscosity data for this class of lubricant. The pressure–viscosity coefficients were obtained using the parameters of Eq. (2). The following trend for the α values have been found: PAG3 > PAG2 > PAG1.

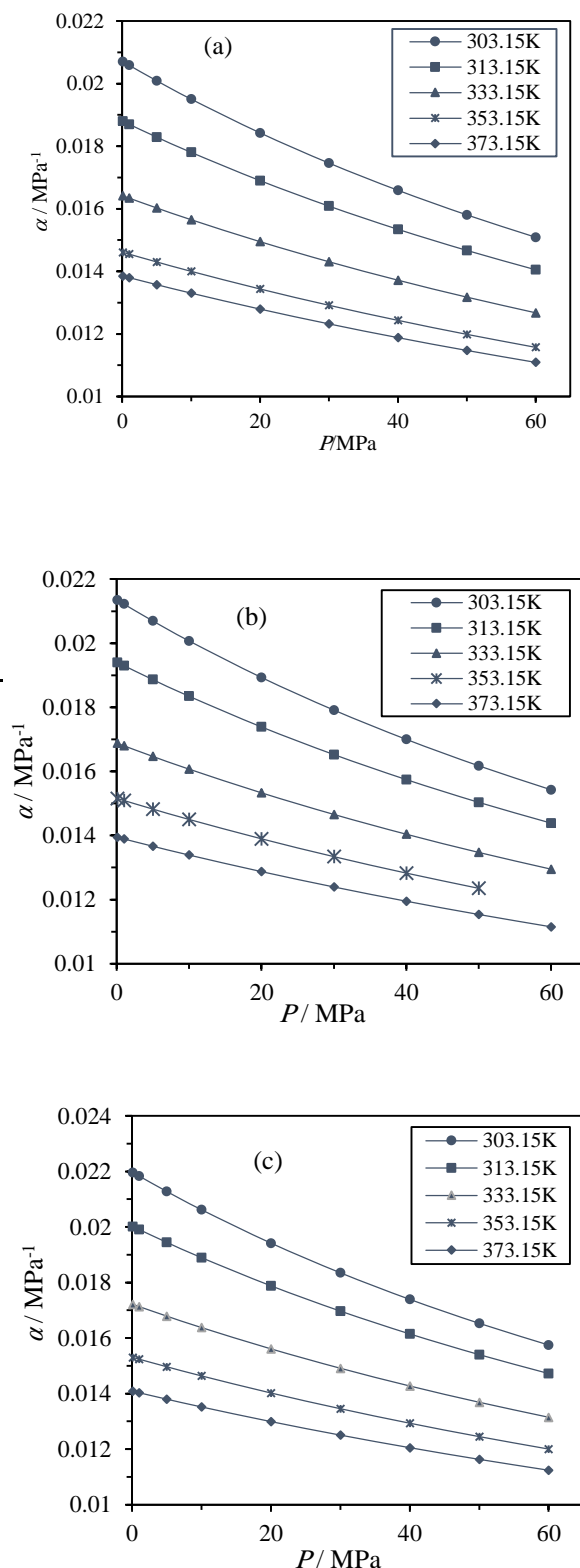


Fig. 1. Pressure–viscosity coefficient as a function of pressure for (a) PAG1, (b) PAG2, and (c) PAG3 at different temperatures.



References

- [1] X. Paredes, A. S. Pensado, M. J. P. Comunas, and J. Fernandez, "Experimental Dynamic Viscosities of Dipentaerythritol Ester Lubricants at High Pressure", *J. Chem. Eng. Data*, 55(2010) 3216–3223.
- [2] X. Paredes, A. S. Pensado, M. J. P. Comunas, and J. Fernandez, "How Pressure Affects the Dynamic Viscosities of Two Poly(propylene glycol) Dimethyl Ether Lubricants", *J. Chem. Eng. Data.*, 55 (2010) 4088–4094.
- [3] M.H. Ghatee, M. Zare, A.R. Zolghadr, F. Moosavi, *Fluid Phase Equilib*, 291 (2010) 188–194.
- [4] X. Paredes, O. Fandino, A. S. Pensado, M. J. P. Comunas, J. Fernandez, *TribolLett* 45 (2012) 89–100.
- [5] F.M. Gacino, X. Paredes, M.J.P. Comunas, J. Fernandez, *J. Chem. Thermodyn*, 54 (2012) 302–309.

Effect of the Temperature on the Viscosities of Three Polyalkylene Glycol Ether Lubricants

M. Zare* and S. Golabvand

Department of Chemistry, Faculty of Science, Shahid Chamran University of Ahvaz, Ahvaz, Iran

*m.zare@ scu.ac.ir

Abstract: Temperature dependence of dynamic viscosity of the lubricants is essential for most industrial applications. In the present work, experimental viscosities of three polyalkylene glycol ether lubricants including PAG1 (23 ethylene oxide units), PAG2 (29 ethylene oxide units) and PAG3 (21 ethylene oxide units) were correlated using a linear relation with the high accuracy. In addition, we have analysed the temperature–viscosity coefficient (β) for these fluids. This property decreases when the temperature increases and increases with the pressure from 0.1 to 60 MPa for three lubricants. The following sequence have been found for this coefficient PAG3 > PAG2 > PAG1.

Keywords: Correlation; Viscosity; Lubricants; Temperature dependence

Introduction

Lubricants are extensively employed to facilitate relative motion of solid bodies and minimizing friction and wear between them by adding a thin layer of fluid between the areas in contact. Moreover, lubricating oils are required to carry out a range of other functions, including heat removal, corrosion prevention, transfer of power, and suspension and removal of wear particles [1]. The polyalkylene glycol ethers (PAGs) are synthetic lubricants, which prepared by the reaction of epoxides, usually ethylene and propylene oxide (EO and PO), with compounds that contain active hydrogen in the presence of a basic catalyst [2].

The analysis of the viscosity of lubricants is essential for their use as lubricants. The variation of the viscosity of PAGs with the temperature and pressure is crucial in determining its ability to form a layer of oil between rolling surfaces to reduce friction and wear [2]. In the present work, viscosity of three poly(propylene oxide) dimethyl ethers as a function of temperature is studied. We also determine the temperature–viscosity coefficient using the literature viscosity data over broad temperature range for three PAGs.

Methods

Ghatee *et al.* [3] have proposed an equation for temperature dependent viscosity of ionic liquids as:

$$\left(\frac{1}{\eta}\right)^\varphi = a + bT, \quad (1)$$

where a and b are specific adjustable parameters and φ is a characteristic exponent. This also can be successfully applied as a two-parameter equation with a universal value ($\varphi=0.3$). In this investigation, we examined the applicability of this equation for three poly(propylene oxide) dimethyl ethers. Viscosity behaviour of PAG1 (23 EO units), PAG2 (29 EO units) and PAG3 (21 EO units) was investigated

Results and Discussion

Viscosity of a liquid is a non-linear decreasing function of temperature. The values of the viscosity of PAG1, PAG2, and PAG3 are fitted using the Eq. (1) in two-parameter form with $\varphi=0.3$ at constant pressure. The pressure, range of temperature, fitting parameters (a and b), correlation coefficient squared (R^2), and absolute average deviation percent (%AAD) are displayed in Table 1.

Table 1. Pressure (p), range of temperature (ΔT), fitting parameters of Eq. (1) with $\varphi=0.3$, R^2 , and %AAD of studied lubricants. Viscosity data are taken from Refs [2 and 4].

Lubricant	p /MPa	ΔT /K	a	b	R^2	%AAD ^a
PAG1	0.1	303-373	-0.71329	0.00331	0.99704	3.63
	1	303-373	-0.71267	0.00330	0.99727	3.31
	5	303-373	-0.70963	0.00327	0.99681	3.59
	10	303-373	-0.70175	0.00322	0.99664	3.75
	20	303-373	-0.69848	0.00316	0.99684	3.63
	30	303-373	-0.69004	0.00309	0.99636	4.05
	40	303-373	-0.68668	0.00304	0.99655	4.20
	50	303-373	-0.68566	0.00300	0.99690	4.30
	60	303-373	-0.68409	0.00295	0.99690	4.01
	PAG2	0.1	303-373	-0.67084	0.00308	0.99872
1		303-373	-0.67250	0.00308	0.99878	2.28
5		303-373	-0.66934	0.00305	0.99873	2.33
10		303-373	-0.66684	0.00302	0.99873	2.50
20		303-373	-0.65991	0.00295	0.99893	2.25
30		303-373	-0.65282	0.00289	0.99880	2.63
40		303-373	-0.64975	0.00284	0.99886	2.55
50		303-373	-0.64897	0.00280	0.99899	2.38
60		303-373	-0.64506	0.00275	0.99903	2.67
PAG3		0.1	303-373	-0.75525	0.00336	0.99900
	1	303-373	-0.75443	0.00335	0.99901	2.36
	5	303-373	-0.75033	0.00332	0.99899	2.17
	10	303-373	-0.74580	0.00328	0.99900	2.26
	20	303-373	-0.73828	0.00321	0.99904	2.24
	30	303-373	-0.73162	0.00315	0.99907	2.45
	40	303-373	-0.72625	0.00309	0.99913	2.21
	50	303-373	-0.72203	0.00304	0.99920	2.28
	60	303-373	-0.71852	0.00299	0.99927	2.23

$$^a \%AAD = \frac{1}{m} \sum_m |\eta_{\text{expt.}} - \eta_{\text{calc.}} / \eta_{\text{expt.}}| \times 100$$

The values of R^2 and %AAD indicate Eq. (1) can describe the temperature dependent viscosity of polyalkylene glycol ethers quite accurately.

In order to characterize the suitability of a lubricant, the temperature-viscosity coefficient, β is used. This coefficient is defined by the following expression:

$$\beta = \frac{1}{\eta} \left(\frac{\partial \eta}{\partial T} \right)_p \quad (2)$$

The β values are obtained using this equation together with the parameters of the Eq. (1) and plotted versus temperature at different pressure for three lubricants in Fig. 1. This property decreases when the temperature increases and increases with the pressure from 0.1 to 60 MPa. The magnitude of β follows the trends $\text{PAG3} > \text{PAG2} > \text{PAG1}$.

Conclusions

The variation of viscosity with temperature was studied for three PAGs using Eq. (1). This simple and accurate linear equation provides reliable extrapolation and interpretation of viscosity data for this class of lubricant. The temperature-viscosity coefficients were obtained using the parameters of Eq. (1). The following trend for the β values have been found: $\text{PAG3} > \text{PAG2} > \text{PAG1}$. More studies on the various types of lubricants at high pressure are required to guarantee the generality of the proposed equation. This work is under proceed in our group.

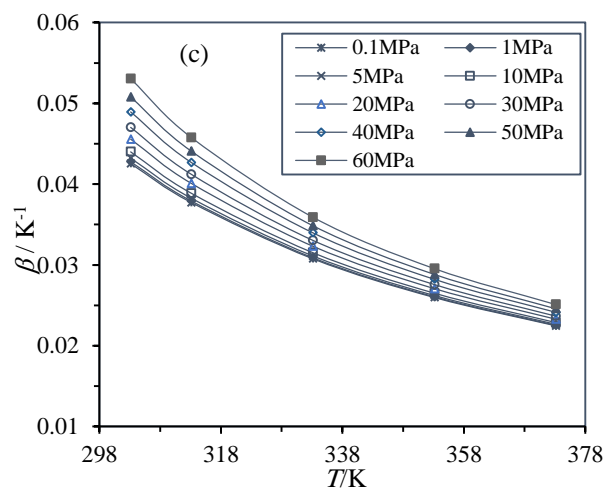
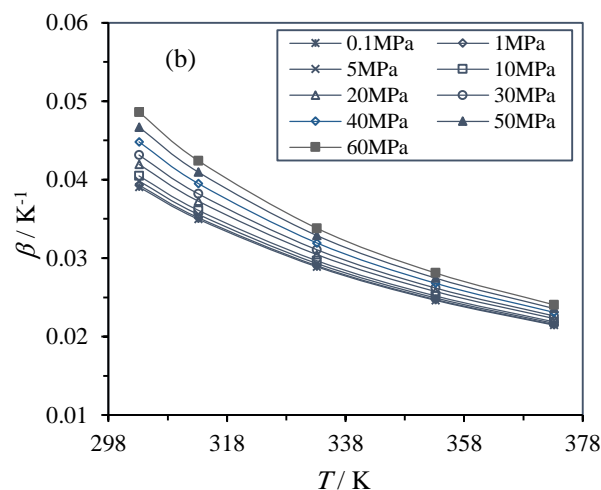
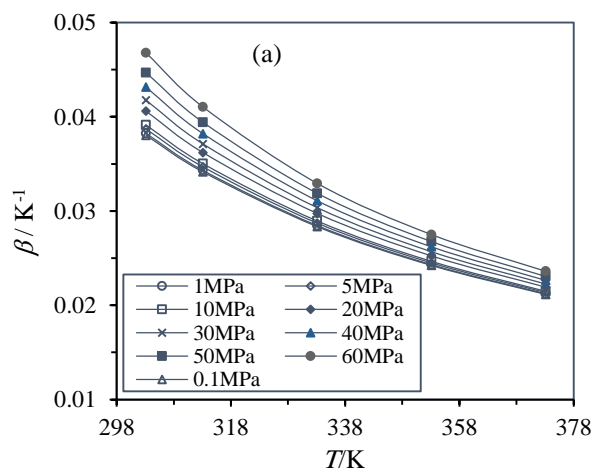
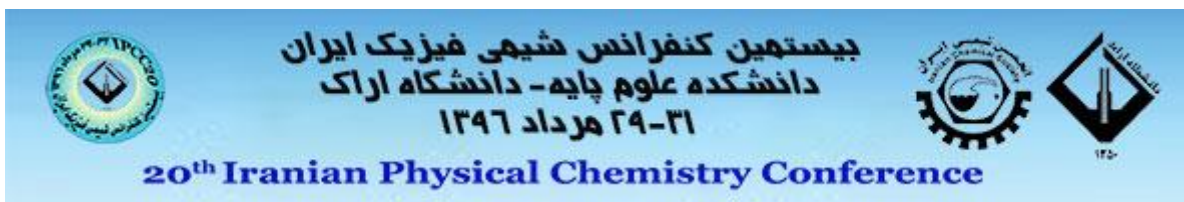


Fig. 1. Temperature-viscosity coefficient as a function of temperature for (a) PAG1, (b) PAG2, and (c) PAG3 at different pressure.

References

- [1] X. Paredes, A. S. Pensado, M. J. P. Comunas, and J. Fernandez, "Experimental Dynamic Viscosities of Dipentaerythritol Ester Lubricants at High Pressure", *J. Chem. Eng. Data*, 55 (2010) 3216–3223.
- [2] X. Paredes, A. S. Pensado, M. J. P. Comunas, and J. Fernandez, "How Pressure Affects the Dynamic Viscosities of Two Poly(propylene glycol) Dimethyl Ether Lubricants", *J. Chem. Eng. Data*, 55 (2010) 4088–4094.
- [3] M.H. Ghatee, M. Zare, A.R. Zolghadr, F. Moosavi, *Fluid Phase Equilib.* 291 (2010) 188–194.
- [4] X. Paredes, O. Fandino, A. S. Pensado, M. J. P. Comunas, J. Fernandez, *TribolLett* 45 (2012) 89–100.



Effect of water soluble polymers on the thermodynamic properties of quaternary ammonium salt aqueous solutions

Masoomeh Baghlani¹, Rahmat Sadeghi²

¹Department of Chemistry, University of Kurdistan, Sanandaj, Iran,

²Department of Chemistry, University of Kurdistan, Sanandaj, Iran,

*rsadeghi@uok.ac.ir

*baghalanim@yahoo.com

Abstract: To investigate the new kinds of aqueous biphasic systems (ABS) produced by the addition of thermosensitive polymer to aqueous solution of ammonium salts, vapor – liquid equilibria (VLE) and liquid – liquid equilibria (LLE) behavior of aqueous ammonium salt (AS) – polymer solutions, were carried out for ternary systems including tetra methyl ammonium bromide (TMAB) + poly (propylene glycol) with an average molecular weight of 400 g.mol⁻¹ (PPG400) + water, tetra ethyl ammonium bromide (TEAB) + PPG400 + water, TMAB + poly (ethylene glycol) with an average molecular weight of 400 g.mol⁻¹ (PEG400) + water and TEAB + PEG400 + water. Our results show that, TMAB and TEAB in aqueous solution of PPG form ABS. The phase forming ability of the investigated AS increase with increasing the hydrophilicity of AS and follows the order TMAB > TEAB. In the VLE section, the water activity and constant water activity lines were obtained for aqueous solutions of TMAB and TEAB in the absence and presence of the polymer at $T = 298.15$ K.

Keywords: Aqueous biphasic systems; vapor – liquid equilibria; liquid – liquid equilibria; ammonium salt; polymer

Introduction

Aqueous biphasic systems (ABS) were introduced in 1956 by Albertsson[1]. These systems are commonly defined as water-rich systems which formed by addition of two water-soluble compounds above a critical concentration. These compounds which have a different chemical structures, polarities and hydration capabilities provide conditions for the partition and separation of valuable and chemically diverse molecules such as cells, organelles, enzymes, protein, metal ions, dyes drug molecules, small organic species and nano and micro solid particles from the complex mixtures in which they are produced in aqueous media [2].

The purpose of this report is to investigate the solubility-effect of polymers PPG400 and PEG400 on aqueous solutions of tetra methyl ammonium bromide and tetra ethyl ammonium bromide. To achieve this purpose, isopiestic equilibrium molalities (vapor–liquid Equilibria (VLE) properties) and binodal curves (liquid–liquid equilibria (LLE) properties) were measured for aqueous solutions of TMAB and TEAB + PPG400 and PEG400. Study on VLE of these ternary aqueous solutions provides useful information on the molecular mechanism of phase separation.

Materials and method

Materials.

Tetra methyl ammonium bromide (> 99% w/w) and tetra ethyl ammonium bromide (> 99% w/w) were obtained from Merck. PPG400 and PEG400 were obtained from Aldrich and Merck, respectively. Polymers were used without further purification, TMAB and TEAB were dried in an electrical oven at about 383.15 K for 24h prior to use. Double-distilled and deionized water was used.

Method.

All the solutions were prepared by mass on a Sartorius CP124S balance precise to within $\pm 1 \times 10^{-4}$ g.

The experimental measurements of water activity of ternary aqueous AS + polymer systems were carried out by the improved isopiestic method, as previously described[3]. The experimental apparatus employed for determination of liquid–liquid equilibrium data is essentially similar to the one used previously[4]. The glass vessel was provided with an external jacket in which water at constant temperature was circulated using a Julabo water thermostat. The temperature was controlled to within ± 0.05 K. The binodal curves were determined by a titration method. An AS solution of known concentration was titrated with the polymer solution or vice versa, until the solution turned turbid. Then water was added to get a clear one-phase system again, and the above procedure was repeated.

Results and Discussion

In the present work, the isopiestic measurements were carried out for binary and ternary aqueous solution of



TMAB + polymer and TEAB + polymer at $T = 298.15$ K. The experimental isopiestic molalities for aqueous AS-polymer systems were tested with ZSR rule which is written as follows:

$$\frac{m_i}{m_i^0} + \frac{w_p}{w_p^0} = 1 \quad a_w = \text{constant} \quad 0 \leq \frac{m_i}{m_i^0} \leq 1 \quad \text{and} \quad 0 \leq \frac{w_p}{w_p^0} \leq 1 \quad (1)$$

where m_i is the molality of AS and w_p is the weight fraction of polymer in the ternary solution and m_i^0 and w_p^0 are the molality of AS and weight fraction of polymer in the binary solution, respectively. Stokes and Robinson theoretically derived this equation for isopiestic mixed nonelectrolyte aqueous solutions from the semi-ideal hydration model.

Both ternary aqueous solutions of TMAB + PEG and TEAB + PEG systems, which cannot form ABS (solting-in effect), show slightly positive deviation from the ZSR equation, that means there is no significant preferential interaction between components in ternary solution of TMAB or TEAB + PEG + H₂O.

However, the constant water activity curves for aqueous solutions of TMAB or TEAB + PPG systems, which are capable of inducing phase separation (solting-out effect), show the negative and positive deviations from the ZSR respectively in the one-phase and two-phase areas.

Conclusions

Novel sustainable, cheap and biodegradable ABS were developed in this work by study of VLE and

LLE properties of ternary TMAB or TEAB + PPG400 or PEG400 + water systems. It was found that the aqueous ternary systems including TMAB + PPG400 and TEAB + PPG400 have solting-out effect but TMAB + PEG400 + H₂O and TEAB + PEG400 + H₂O system have a solting-in effect.

References

- [1] P.-Å. Albertsson, "Partition of cell particles and macromolecules: separation and purification of biomolecules, cell organelles, membranes, and cells in aqueous polymer two-phase systems and their use in biochemical analysis and biotechnology", 1986, vol. 346. Wiley New York etc.
- [2] R. Sadeghi and F. Jahani "Salting-in and salting-out of water-soluble polymers in aqueous salt solutions", *J. Phys. Chem. B*, 116 (2012) 5234–5241.
- [3] L. R. Ochs, M. Kabiri-badr, and H. Cabezas "An improved isopiestic method to determine activities in multicomponent mixtures", *AIChE J*, 36 (1990) 1908–1912.
- [4] R. Sadeghi, B. Hamidi, and N. Ebrahimi "Investigation of Amino Acid-Polymer Aqueous Biphasic Systems," *J. Phys. Chem. B*, 118 (2014) 10285–10296.

Volumetric properties of acetaminophen in aqueous ionic liquid, 1-butyle-3-methylimidazolium bromide, solutions at different temperatures

FaribaGhaffari^{a*}, HemayatShekaari^a, Mohammed TaghiZafaraniMoattar^a

Department of Physical Chemistry, Faculty of Chemistry, University of Tabriz, Tabriz, Iran
*fariba_s2129@yahoo.com

Abstract: Densities of acetaminophen in 0.1, 0.2, 0.3 and 0.4 mol.kg⁻¹ aqueous solution of ionic liquid, 1-butyle-3-methylimidazolium bromide ([BMIm]Br), against the molality of acetaminophen have been measured at T = (293.15 to 308.15) K. Using the density data, standard partial molar volume (V_{ϕ}^0) have been calculated. These parameters have been used to calculation transfer volume for acetaminophen from water to aqueous ionic liquid solution. The transfer quantities are positive and increase with increasing molality of the ionic liquid and decrease with temperature which indicate the dominance of ion or hydrophilic-hydrophilic interactions between [BMIm]Br and acetaminophen and dehydration effect of ionic liquid on the acetaminophen solutions.

Keywords: Acetaminophen; Ionic liquid; Apparent molar volume

Introduction

Acetaminophen, N-acetyl-p-amino phenol (NAPAP) more commonly known as paracetamol is a popular analgesic drug used widely in current therapeutics for the treatment of pain and reducing fever. One of problems for this drug is poorly solubility in water [1]. Ionic liquids (ILs) are usually defined as organic salts with melting points lower than 100 °C. In recent years, ionic liquids (ILs) have been suggested as replacements for volatile organic solvents [2]. In the past few years, ILs have also gained interest for use in several pharmaceutical applications such as solubilization of poorly soluble drugs, synthesize active pharmaceutical ingredients (APIs) with modified solubility, increased their thermal stability, as solvent in the synthesis of APIs or drug intermediates, crystallization, separations, extraction of APIs from natural products, drug delivery, in drug detection as a binder to prepare the modified electrode, as support in liquid membrane, and in fluid chromatography [3-8]. In such studies, drug interactions with ionic liquids at molecular level can be understood through the thermodynamic properties. Therefore, the aim of this work is to calculate some thermodynamic properties of ternary {acetaminophen + 1-butyle-3-methylimidazolium bromide ([BMIm]Br) + H₂O} solutions, as a model to study the solvation (hydration) behavior of acetaminophen in the presence of an ionic liquid.

Materials and method

[BMIM]Br were prepared and purified by using the procedure previously described in the literature [9]. The ionic liquid was analyzed by ¹H NMR (Bruker Av-300) and FTIR (PerkinElmer, Spectrum RXI) to confirm the absence of any major impurities and they were found to be in good agreement with those reported in literature.

Density measurement

The solutions were prepared in mass basis by an analytical balance (Shimadzu, 321-34553, Shimadzu Co.,

Japan) having a standard uncertainty 1×10^{-4} g. The density, d , of solutions was measured with a vibrating tube densimeter (Anton Para, DSA 5000 densimeter). The density is extremely sensitive to temperature, so it was kept constant within $\pm 1.0 \times 10^{-3}$ K by an internal temperature controller built in peltier device. The standard uncertainty of density measurements were found to be within 5.0×10^{-6} g.cm⁻³. Before each series of measurements, the densimeter was calibrated in the experimental temperature.

Results and Discussion

Volumetric results

The experimental density (d) values of acetaminophen in aqueous solutions of [BMIm]Br as a function of acetaminophen molality (m) were measured at temperatures T = (293.15 to 308.15) K. The apparent molar volumes (V_{ϕ}) of acetaminophen in the investigated solutions were determined from the experimentally measured densities using the relation:

$$V_{\phi} = \frac{M}{d} - \frac{(d - d_0)}{m d d_0} \quad (1)$$

where M is the molar mass of acetaminophen, m is the molality of acetaminophen in aqueous [BMIm]Br solutions, d and d_0 are the densities of the solutions containing (acetaminophen + [BMIm]Br + H₂O) and ([BMIm]Br + H₂O) solutions, respectively. The Figure 1 is a representative of the apparent molar volume (V_{ϕ}) values of acetaminophen versus acetaminophen molality in ionic liquid. The V_{ϕ} values increase with increase in concentration of [BMIm]Br at all experimental temperatures. There is a good linear correlation between V_{ϕ} values and acetaminophen molality (m).

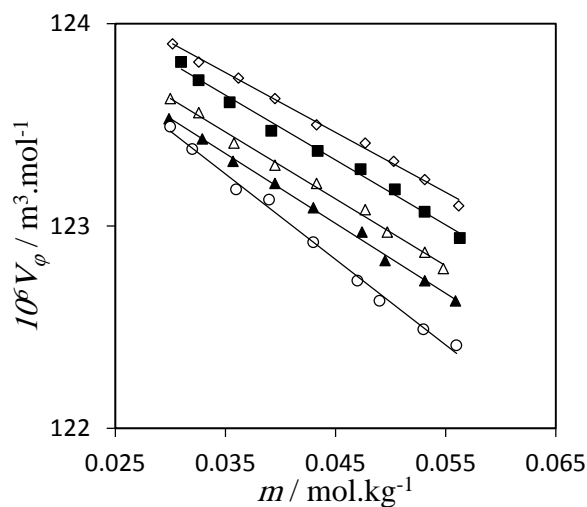


Fig.6: Apparent molar volumes ($V_{\phi} / \text{m}^3 \cdot \text{mol}^{-1}$) of acetaminophen versus its molality ($m / \text{mol} \cdot \text{kg}^{-1}$) in aqueous [BMIm]Br solutions with different molalities of [BMIm]Br: \circ , 0.000; \blacktriangle , 0.1004; \triangle , 0.1995; \blacksquare , 0.2995; \diamond , 0.4009 at $T=293.15$ K.

Therefore, the values of apparent molar volumes at infinite dilution (standard partial molar volume) (V_{ϕ}^0) are estimated by least-squares fitting to Masson's equation [10]:

$$V_{\phi} = V_{\phi}^0 + S_v m \quad (2)$$

Where S_v is the experimental slope indicating solute-solute interactions occurring between acetaminophen molecules. The V_{ϕ}^0 values are independent of solute-solute interactions at infinite dilution and only reflect the presence of solute-solvent interactions between acetaminophen and ionic liquid, [BMIm] Br. The negative values of S_v indicates weak solute-solute interactions between acetaminophen molecules in the presence of ionic liquid solutions. The less values of S_v in compared to V_{ϕ}^0 suggest the weak solute-solute interactions in compared to stronger solute-solvent interactions. The transfer volumes ($\Delta_{tr} V_{\phi}^0$) of acetaminophen at infinite dilution from water to aqueous [BMIm]Br solutions have been calculated as :

$$\Delta_{tr} V_{\phi}^0 = V_{\phi}^0(\text{in [BMIm] + H}_2\text{O}) - V_{\phi}^0(\text{H}_2\text{O}) \quad (3)$$

The $\Delta_{tr} V_{\phi}^0$ values are positive and increase with increase of the ionic liquid molality, which these results indicate the hydrophilic-ionic group interactions,

hydrophilic – hydrophilic group interactions between acetaminophen and ionic liquid.

Conclusions

In the present work, measurements have been used to study of the interactions between a drug, acetaminophen, and the ionic liquid in aqueous medium. The apparent molar volume, V_{ϕ} , of acetaminophen in the aqueous ionic liquid, 1-butyle-3-methyl-imidazolium bromide ([BMIm]Br), solutions calculated from density measurements are used to obtain the standard partial molar properties and transfer partial molar properties. This observation indicates that the interactions of the ionic liquid with acetaminophen were strengthening with the increase of the ionic liquid concentration.

Acknowledgment

The authors wish to thank financial support from the graduate council of the University of Tabriz.

References

- [1] M. J. Earle, K. R. Seddon, Ionic liquids: Green solvents for the future. *J. Pure Appl. Chem*, 72 (2000) 1391-1398.
- [2] T. Welton, Room-Temperature Ionic Liquids. Solvents for Synthesis and Catalysis. *Chem. Rev.* 99 (1999) 2071-2084.
- [3] T.M. Letcher, N. Deenadayalu, Ternary liquid-liquid equilibria for mixtures of 1-methyl-3-octyl-imidazolium chloride + benzene + an alkane at $T=298.2$ K and 1 atm. *J. Chem. Thermodyn.* 35 (2003) 67-76.
- [4] S. Tajik, M.A. Taher, H.c. Beitollahi, Application of a new ferrocene-derivative modified-graphene paste electrode for simultaneous determination of isoproterenol, acetaminophen and theophylline. *Sensors Actuators B Chem.* 197 (2014) 228-236.
- [5] N. Kouki, R. Tayeb, M. Dhahbi, Recovery of acetaminophen from aqueous solutions using a supported liquid membrane based on a quaternary ammonium salt as ionophore. *Chem. Pap.* 68 (2014) 457-464.
- [6] S. Kianipour, A. Asghari, Room temperature ionic liquid/multiwalled carbon nanotube/chitosan modified glassy carbon electrode as a sensor for simultaneous determination of ascorbic acid, uric acid, acetaminophen, and mefenamic acid. *IEEE Sensors J.* 13 (2013) 2690-2698.
- [7] O.A. Cojocaru, K. Bic, G. Gurau, A. Narita, P.D. McCrary, J.L. Shamshina, P.S. Barber, R.D. Rogers, *MedChemComm* 4 (2013) 559-563.

Volumetric studies of cefazolin sodium in aqueous ionic liquid, 1-octyl-3-methylimidazolium bromide at $T = 298.15$ K

Fariba Ghaffari^{a*}, Hemayat Shekaari^a, Mohammed Taghi Zafarani Moattar^a

Department of Physical Chemistry, Faculty of Chemistry, University of Tabriz, Tabriz, Iran

*fariba_s2129@yahoo.com

Abstract: The study of thermodynamic properties of drugs is one method to study the interactions between drug and solvent to find the best solvent in pharmaceutical fields. In this work the thermodynamic properties including volumetric properties have been measured at $T = (288.15 \text{ to } 318.15 \text{ K})$. The measured data have been applied to calculate, standard partial molar volume (V_{ϕ}^0) and transfer volume ($\Delta_{tr}V_{\phi}^0$) and used to discuss various solute-solvent interactions. The transfer quantities are positive and increase with increasing molality of the ionic liquid. The calculated thermodynamic parameters values confirm the strong solute – solvent interactions between Ionic Liquid and cefazolin sodium.

Keywords: Ionic liquid; volumetric; cefazolin sodium; Apparent molar volume

Introduction

Pharmaceutical compounds are chemical substances characterized by the specific properties towards a human body [1]. The pharmaceutical industries are undoubtedly experiencing a series of problems. One of these problems is low solubility [2]. Solubility is the phenomenon of dissolution of solid in liquid phase to give a homogenous system. Solubility is one of the important parameters to achieve desired concentration of drug in systemic circulation for pharmacological response to be shown. Poorly water soluble drugs often require high doses in order to reach therapeutic plasma concentrations after oral administration [3]. Poor water solubility of drug candidates is a major problem in the pharmaceutical industry and it has been estimated that 40% of all newly developed drugs are poorly soluble or insoluble in water [4]. Recently to overcome this problem, ionic liquids (ILs) have been recommended as alternative organic solvents in the pharmaceutical industry [5]. They have been used in pharmaceutical industry as solvent [6]. The study of thermodynamic properties of drugs in ionic liquid mixtures is crucial from a technological point of view but it also provides a better understanding of the mechanisms involved when using these new media. For example, volumetric and acoustic properties are powerful tools to study drug behavior in ionic liquid solutions and were used to provide information on solute–solute and solute–solvent interactions in the mixtures [7].

Materials and method

The ionic liquid [OMIm]Br was synthesized and purified by using the procedure described in literature [8,9]. The ionic liquid was analyzed by ¹H NMR (Bruker Av-300) and FTIR (PerkinElmer, Spectrum RXI) to confirm the absence of any major impurities and they were found to be in good agreement with those reported in literature.

Density measurement

The solutions were prepared in mass basis by an analytical balance (Shimadzu, 321-34553, Shimadzu Co., Japan) having a standard uncertainty 1×10^{-4} g. The density, d , of solutions was measured with a vibrating tube densimeter (Anton Para, DSA 5000 densimeter). The density is extremely sensitive to temperature, so it was kept constant within $\pm 1.0 \times 10^{-3}$ K by an internal temperature controller built in peltier device. The standard uncertainty of density measurements were found to be within 5.0×10^{-6} g.cm⁻³. Before each series of measurements, the densimeter was calibrated in the experimental temperature.

Results and Discussion

Volumetric results

The experimental density (d) values of cefazolin sodium in aqueous solutions of [OMIm]Br as a function of cefazolin sodium molality (m) were measured at temperatures $T = (293.15 \text{ to } 308.15) \text{ K}$. The apparent molar volumes (V_{ϕ}) of cefazolin sodium in the investigated solutions were determined from the experimentally measured densities using the relation:

$$V_{\phi} = \frac{M}{d} - \frac{(d - d_0)}{md_0} \quad (1)$$

where M is the molar mass of cefazolin sodium, m is the molality of cefazolin sodium in aqueous [OMIm]Br solutions, d and d_0 are the densities of the solutions containing (cefazolin sodium + [OMIm]Br + H₂O) and ([OMIm]Br + H₂O) solutions, respectively. Figure 1 is a representative of the apparent molar volume (V_{ϕ}) values of cefazolin sodium versus cefazolin sodium molality in ionic liquid. The V_{ϕ} values increase with increase in concentration of [OMIm]Br at all experimental temperatures. There is a good linear

correlation between V_ϕ values and cefazolin sodium molality (m).

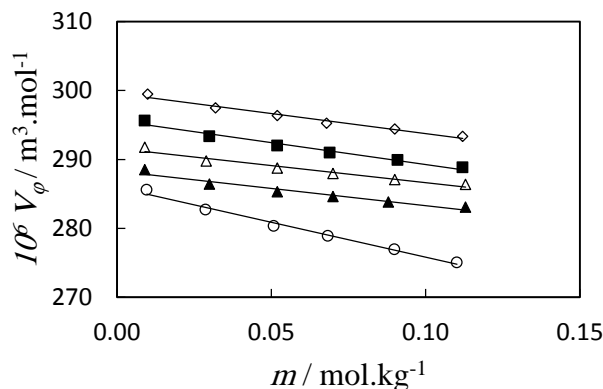


Figure 1: Apparent molar volumes ($V_\phi / \text{m}^3 \cdot \text{mol}^{-1}$) of cefazolin sodium versus its molality ($m / \text{mol} \cdot \text{kg}^{-1}$) in aqueous [OMIm]Br solutions with different molalities of [OMIm]Br: \circ , 0.000; \blacktriangle , 0.1009; \triangle , 0.2001; \blacksquare , 0.2991; \diamond , 0.4005 at $T=298.15 \text{ K}$.

Therefore, the values of apparent molar volumes at infinite dilution (standard partial molar volume) (V_ϕ^0) are estimated by Redlich–Mayer equation [10]:

$$V_\phi = V_\phi^0 + S_v m^{1/2} + B_v m \quad (2)$$

Where S_v and B_v are empirical parameters. The V_ϕ^0 values are independent of solute–solute interactions at infinite dilution and only reflect the presence of solute–solvent interactions between drugs and ionic liquid, [OMIm]Br. The V_ϕ^0 values are positive and increase as the ionic liquid concentration increases. The positive values of V_ϕ^0 show the strong solute–solvent interactions. The transfer volumes ($\Delta_{tr} V_\phi^0$) of drugs at infinite dilution from water to aqueous [OMIm]Br solutions have been calculated as :

$$\Delta_{tr} V_\phi^0 = V_\phi^0 (\text{in [OMIm]} + \text{H}_2\text{O}) - V_\phi^0 (\text{H}_2\text{O}) \quad (3)$$

It is clear that the $\Delta_{tr} V_\phi^0$ values are positive and increase with increase of the ionic liquid molality, which these results indicate the hydrophilic-ionic group interactions, hydrophilic – hydrophilic group interactions between cefazolin sodium and ionic liquid.

Conclusions

In this work, measurements have been used to study of the interactions between a drug, cefazolin sodium, and the ionic liquid in aqueous medium. The apparent molar volume, V_ϕ , of cefazolin sodium in the aqueous ionic liquid, 1-octyle-3-methyl-imidazolium bromide ([OMIm]Br), solutions calculated from density measurements are used to obtain the standard partial molar properties and transfer partial molar properties. This observation indicates that the interactions of the ionic liquid with cefazolin sodium were strengthening with the increase of the ionic liquid concentration.

Acknowledgment

The authors wish to thank financial support from the graduate council of the University of Tabriz.

References

- [1] A.D.D. Santos, A.R.C. Morais, C. Melo, R. Bagol-Lukasik, E. Bagol-Lukasik, Solubility of pharmaceutical compounds in ionic liquids, *Fluid Phase Equilib.* 356 (2013) 18–29.
- [2] M. Moniruzzama, M. Goto, Application of ionic liquids: future solvents and reagents for pharmaceuticals, *J. Chem. Eng. Jpn.* 44 (2013) 370–381.
- [3] Varun Raj Vemula, Venkateshwarlu Lagishetty, Srikanth Lingala, SOLUBILITY ENHANCEMENT TECHNIQUES.
- [4] H. Mizuuchi, V. Jaitely, S. Murdan, A.T. Florence, Room temperature ionic liquids and their mixtures: potential pharmaceutical solvents. *Euro. J. Pharmaceutic. Sci.* 33 (2008) 326–331.
- [5] R.D. Rogers, K.R. Seddon, Ionic liquids — solvents of the future? *Science* 302 (2003) 792–793.
- [6] H. Wang, X. Zhou, G. Gurau, R.D. Rogers, First Edition. Edited by Wei Zhang and Berkeley W. Cue Jr. 2012 John Wiley & Sons, Ltd. Published 2012 by John Wiley & Sons, Ltd.
- [7] R. Elhami-Kalvagh, H. Shekaari, A. Bezaatpour, Application of scaled particle theory to the partial molar volumes of some tetradentate N2O2 type Schiff bases in ionic liquid + DMF solutions, *Fluid Phase Equilib.* 354 (2013) 1–5.
- [8] J.Z. Yang, J. Tong, J.B. Li, Study of the Volumetric Properties of the Aqueous Ionic

Thermodynamic study of electrolyte effect on the micellization of hexadecyltrimethyl ammonium bromide in aqueous solution at T=(298.2 and 308.2)K

Sara Kalavari, Bahram Ghalami-Choobar*

Department of chemistry, University of Guilan, Rasht, 19141, Iran

*B-Ghalami@guilan.ac.ir

Abstract: In this study, electrolyte and temperature effects on the critical micelle concentration (CMC) of hexadecyltrimethyl ammonium bromide (HTAB) were studied by using the conductometric technique. The CMC of HTAB was determined in pure water at T= (298 and 308) K. The obtained results shown that the CMC also increases with increasing temperature. Moreover, CMC of HTAB was measured in the presence of NaCl and KCl electrolytes with 0.003, 0.005 and 0.008 mol. kg⁻¹ at T= (298 and 308) K. The obtained results shown that the CMC decrease with increasing electrolyte concentration. The Gibbs free energy of micellization were also determined by conductometric measurements.

Keywords: conductometry; critical micelle concentration; HTAB; electrolyte

Introduction

Surfactants are the materials which contain a hydrophobic tail group and a hydrophilic head-group together at the same molecule [1,2]. Surfactants in water show different behavior, the polar part is scrambling to communicate with water, while the non-polar part is away from of the water. An amphiphilic molecule can be such a way placed in the water level that polar section being in contact with water molecule and nonpolar part of it is at the top level, in air or non-polar liquid [3]. The presence of these molecules on the surface is to cause reduce to the adhesion energy, and thereby reduce the surface tension, that's why these molecules, called surfactants or surface-active. Another way of placing amphiphilic molecules in such a way which allows each component communicates with its favorable environment, in this case, molecules can form lumps that the part of hydrophobic is orientated to inside of the system and the hydrophilic section dispersed in solution, these masses or lumps are called micelles. The ratio of molecules in solution surface or molecules that act as micelles in the liquid depends on the concentration of amphiphilic [4,5]. At low concentrations, surfactants tend to exposure levels. Once a horde of surfactant was on the surface, the molecules are as well as micelles, this happens occurs for various surfactant in certain concentrations. This specific concentration is called the critical micelle concentration or CMC. The factors that can be changing the critical micelle concentration: temperature, chemical structure of the surfactant (interms of branches or chains of hydrocarbon or number of hydrocarbons, etc.), Pressure, pH, ionic strength in the presence of electrolytes, solvent, [6]. The critical micelle concentration of a surfactant can be examined by changes in the physicochemical properties of surfactant solutions. Some physical properties for this purpose, including cleanliness, viscosity, density, electrical conductivity, surface tension, the osmotic pressure, tension at the interface, light-scattering and refractive index [7]. In the present work, we have studied the effect of two different electrolytes such

as, NaCl, and KCl with 0.003, 0.005 and 0.008 mol. kg⁻¹, on the CMC of hexadecyltrimethyl ammonium bromide (HTAB) by conductometric method. Also, the Gibbs free energy of micellization was determined.

Materials and method

In this work, to find the critical micellar concentration of HTAB surfactant, the conductometry method has been used. The demineralized distilled water with a conductivity of (<2 μs) was purchased and was used for all the experiments. All of the materials, HTAB and electrolytes were prepared from Merck Company. Conductivity measurements were carried out with digital Conductivity Meter Martini Mi 180.

Results and Discussion

3.1. Effect of temperature on the CMC of HTAB

The specific conductivity, k, values of HTAB in aqueous solutions with and without salts at T= (298 and 308) K were measured. Figure 1 shows the behavior of specific conductivity as a function of HTAB concentration in 0.003 mol. kg⁻¹ KCl solution at (298.2 and 308.2) K. Slope of this graph's before the CMC is different from the past of CMC point. Therefore, the CMC has been determined from the intersection of the two straight lines of this conductivity concentration. The results show that the CMC also increases with increasing temperature.

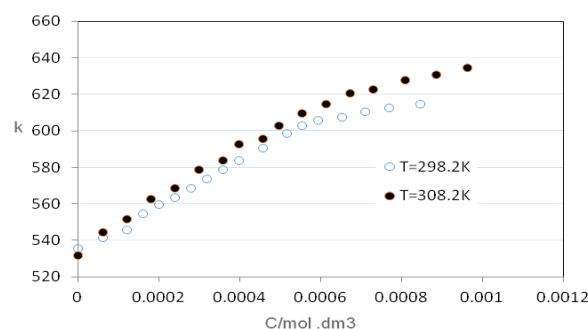


Fig. 1: Plot of the specific conductivity (μS) versus concentration of HTAB in $0.003 \text{ mol.kg}^{-1}$ KCl solution at $T=(298.2 \text{ and } 308.2)$ K.

0.003	0.3010	4.8071×10^{-4}	-47442.32
0.005	0.3829	3.9708×10^{-4}	-47467.86
NaCl			
0.003	0.5293	4.2085×10^{-4}	-42957.46
0.005	0.3780	4.638×10^{-4}	-46987.85

3.2. Effect of electrolytes on the CMC of HTAB

The CMC values of HTAB in NaCl and KCl aqueous solutions were studied at $T=(298 \text{ and } 308)$ K. Figure 2 shows the plot of the specific conductivity (μS) versus concentration of HTAB in $0.003 \text{ mol.kg}^{-1}$ NaCl and KCl solutions at $T=298.2$ K. The critical micelle concentration (CMC) has been determined from the intersection of the two straight lines of these conductivity-concentration plots above and below the abrupt change in the slope.

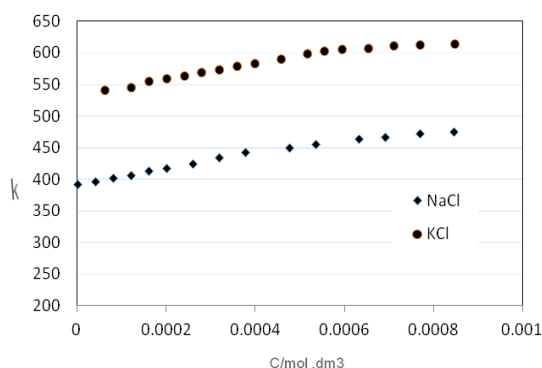


Fig. 2: Plot of the specific conductivity (μS) versus concentration of HTAB in $0.003 \text{ mol.kg}^{-1}$ NaCl and KCl solutions at $T=298.2$ K.

3.3. Thermodynamic properties determination of HTAB micellization

The thermodynamic properties such as standard Gibbs free energy of micellization for HTAB system in pure water and the presence of NaCl and KCl electrolytes have been calculated by using the following equation

$$\Delta G^\circ = (2 - \beta) RT \ln X_{cmc}(1)$$

In table 1 has been illustrated the Gibbs free energy of micellization for HTAB in 0.003 and $0.005 \text{ mol.dm}^{-3}$ NaCl and KCl solutions at $T=298.2$ K.

Table 1. Molality, degree of dissociation (β), CMC and ΔG for NaCl and KCl solutions at $T=298.2$ K

Molality (m)	β	CMC	ΔG
KCl			

Conclusions

The CMC values of HTAB have been calculated in NaCl and KCl aqueous solutions at $T=(298 \text{ and } 308)$ K. From obtained results, it can be concluded that the CMC values of HTAB decrease on the addition of electrolytes. The obtained results show that the CMC also increases with increasing temperature.

Acknowledgment

We gratefully acknowledge the graduate office of University of Guilan for supporting this work.

References

- [1] B. Hwan Lee "Effects of Various Alcohols and Salts on the Mixed Micellization of Cationic Surfactant (CPC) with Nonionic Surfactant (TX-100)", *J. Colloid Interface Sci.*, 19 (2017) 1-4.
- [2] J. M. Ruso, D. A. T. Wool, P. Taboada, V. Mosquera "Self-association of n-hexyltrimethylammonium bromide in aqueous electrolyte solution", *Colloid Polym. Sci.*, 280(2002) 336-341.
- [3] G. Perez, L. Delcastillo, R. Rodriguez "Micellar properties of tetradecyltrimethylammonium nitrate in aqueous solutions at various temperatures and in water-benzyl alcohol mixtures at 25°C ", *Colloid Polym. Sci.*, 282 (2004) 1359-1364.
- [4] E. Fuguet, C. Rafols, M. Roses, E. Bosch "Critical micelle concentration of surfactants in aqueous buffered and unbuffered systems", *Anal. Chim. Acta*, 548 (2005) 95-100.
- [5] C. Erhlin, T. Zenwang, T. Chiachiu, C. Chuanhsuen "Determination of the Critical Micelle Concentration of Cationic Surfactants by Capillary Electrophoresis", *J. High Resol. Chromatogr.* 425 (1999) 265-270
- [6] J. R. Moulins, A. Harris, R. Dean, S. Moore, R. Paleau "Micellar, interfacial and fluorescence investigation on binary mixtures of dodecyl cationic surfactants in aqueous media", *Colloids Surf., A* 302 (2007) 608-615.
- [7] J. Day, K. Ismail "Aggregation of sodium dodecyl sulfate in aqueous nitric acid medium", *J. Colloid Interface Sci.*, 378(2012) 144-151.

Partitioning of L-tryptophan in aqueous biphasic systems composed of PEG 4000 and some biodegradable salts at $T = 298.15$ K

S. Hamzehzadeh^{a*}, M. Fardshirayeh^a

^aChemistry and Chemical Engineering Research Center of Iran (CCERCI), Tehran, P.O.Box: 14335-186, Iran

*melissa505@ymail.com

Abstract: Partitioning in aqueous biphasic systems (ABS) is widely recognized today as a rapid, gentle, and highly efficient technique for the separation of soluble as well as particulate biomaterials. This technique has gained increasing attention as the separation method of choice in biotechnology. Here, the partitioning behaviour of the amino acid L-tryptophan between the two phases of different PEG-based ABS composed of PEG 4000 and various biodegradable salts such as tri-sodium citrate ($\text{Na}_3\text{C}_6\text{H}_5\text{O}_7$), di-sodium tartrate ($\text{Na}_2\text{C}_4\text{H}_4\text{O}_6$), or di-sodium succinate ($\text{Na}_2\text{C}_4\text{H}_4\text{O}_4$) was examined. The partition coefficients of L-tryptophan (K_{Trp}) were determined in the studied systems at $T = 298.15$ K. It seems that in addition to phase hydrophobicity effect, the salt ability to salting-out amino acid can be one of the major factors for transferring amino acid to PEG-rich phase.

Keywords: Aqueous biphasic system; Polyethylene glycol; partitioning; L-tryptophan

Introduction

Partitioning in aqueous biphasic systems (ABS) is widely recognized today as a highly efficient technique for the separation of soluble as well as particulate biomaterials. This technique has gained increasing attention as the separation method of choice in biotechnology. The potential of ABS for the separation of biological materials was first realized over more than half a century ago by Albertsson. Today, ABS that provide a rapid, low-cost, gentle and highly efficient means for the recovery and purification of the bio-based materials from bio-reaction media is known as a promising technique to success of biotechnology for bulk product manufacturing. ABS is considered to be environmentally safe and benign because its application may represent an opportunity to completely eliminate the need for the volatile organic compounds (VOCs) in the whole separation process. Traditional ABS generally forms when an aqueous solution of two water-soluble, but mutually incompatible polymers (e.g., polyethylene glycol (PEG) and dextran), or a water-miscible polymer and a salt (e.g., PEG and K_3PO_4) exceeds specific threshold concentrations and separates into two aqueous phases. PEGs are widely used polymers in aqueous biphasic partitioning studies both in basic and applied research, due in part to their biodegradability, low toxicity, low-cost, relatively low melting points, and very low volatility. The applications of the polymer-based ABS have been well documented [1]. Liquid-liquid extraction processes play a decisive role within the field of chemistry and biotechnology. Especially the recovery and purification of biomolecules from bioreaction media is gaining increasing importance due to a growing demand for biotechnologically manufactured fine chemicals and biomolecules [2].

Here, we decided to study the partitioning behavior of the amino acid L-tryptophan (Trp) within the different

polymer-based ABS formed by PEG 4000 and various biodegradable salts such as tri-sodium citrate ($\text{Na}_3\text{C}_6\text{H}_5\text{O}_7$), di-sodium tartrate ($\text{Na}_2\text{C}_4\text{H}_4\text{O}_6$), and di-sodium succinate ($\text{Na}_2\text{C}_4\text{H}_4\text{O}_4$). The partition coefficients of L-tryptophan (K_{Trp}) were determined in the studied systems at $T = 298.15$ K.

Materials and method

Material

Polyethylene glycol 4000 (PEG 4000), with a quoted molar mass $4000 \text{ g}\cdot\text{mol}^{-1}$, and L-tryptophan ($\text{C}_{11}\text{H}_{12}\text{N}_2\text{O}_2$) were supplied by Merck and used without further purification. Tri-sodium citrate ($\text{Na}_3\text{C}_6\text{H}_5\text{O}_7$), di-sodium tartrate ($\text{Na}_2\text{C}_4\text{H}_4\text{O}_6$), and di-sodium succinate ($\text{Na}_2\text{C}_4\text{H}_4\text{O}_4$) with purity of minimum $w = 0.99$ were purchased from Sigma Aldrich. Double distilled water was used for preparation of solutions.

Determination of the partition coefficients of L-tryptophan

The ABS with different compositions were prepared in the vessels and used to evaluate the L-tryptophan (Trp) partitioning at $T = 298.15$ K. The concentration of Trp in each vessel was about w (mass fraction) = 0.001. Then, the prepared samples were shaken vigorously for 5 min. The samples were placed in a water bath at the working temperature and were left to equilibrate for 36 h to achieve a complete amino acid partitioning between the two phases. After the samples reached equilibrium, a sample of each phase was withdrawn and analyzed for the amino acid contents. The L-tryptophan concentrations, in the top and bottom phases, were determined by UV spectroscopy using a spectrophotometer at a wavelength of 279 nm. For amino acid quantification, to avoid interference from the phase components, the samples were diluted and analyzed against the blanks containing

the same phase components but without amino acid. The partition coefficients for L-tryptophan, K_{Trp} , were determined as the ratio of the concentration of Trp in the aqueous top polymer- and that in the bottom salt-rich phases as describe by equation (1):

$$K_{Trp} = \frac{[Trp]_{PEG}}{[Trp]_{salt}} \quad (1)$$

where $[Trp]_{PEG}$ and $[Trp]_{salt}$ represent the equilibrium compositions (in mass fraction) of L-tryptophan in the polymer-rich phase and salt-rich phase, respectively.

Results and Discussion

The partitioning behavior of Trp in the studied ABS composed of PEG 4000 and various biodegradable salts, $Na_3C_6H_5O_7$, $Na_2C_4H_4O_6$, or $Na_2C_4H_4O_4$ at $T = 298.15$ K is depicted in Fig.1. As shown in Fig.1, for the common initial mixture compositions of the studied PEG-based ABS the partitioning of Trp into the PEG-rich phase decreases in the following order of the used salt:



It seems that the affinity of L-tryptophan to the PEG-rich phase is in accordance with the water-structuring nature of the salt used as the "salting-out" agent to form ABS[3]. It is known that an increase of the salt water-structuring nature causes the water to stay preferably in the salt-rich phase, leading to an increase in the concentration of PEG at the PEG-rich phase, and consequently, to an enhanced phase separation in PEG-based ABS. Thus, the PEG-rich phase becomes more hydrophobic, making the extraction capacity of ABS increase for the hydrophobic L-tryptophan. Therefore, it seems that in addition to the phase hydrophobicity effect, the salt ability to salting-out can be one of the major factors for transferring amino acid to PEG-rich phase.

Furthermore, Trp displays $K_{Trp} > 1.0$ for all ABS and the compositions studied. In other words, L-tryptophan intends to PEG-rich phase. It is also observed that by increasing the composition of ABS, L-tryptophan has more tendency to upper phase i.e. PEG-rich phase that this phenomenon is itself caused by increasing effects of salting-out caused by increasing concentration of salt.

Conclusions

In this study, partitioning of L-tryptophan in {PEG 4000 + $Na_3C_6H_5O_7$ }, {PEG 4000 + $Na_2C_4H_4O_6$ }, and {PEG 4000 + $Na_2C_4H_4O_4$ } ABS was investigated at $T = 298.15$ K. The results obtained indicate that in addition to phase hydrophobicity effect, the salt ability to salting-out amino

acid can be one of the major factors for transferring amino acid to PEG-rich phase.

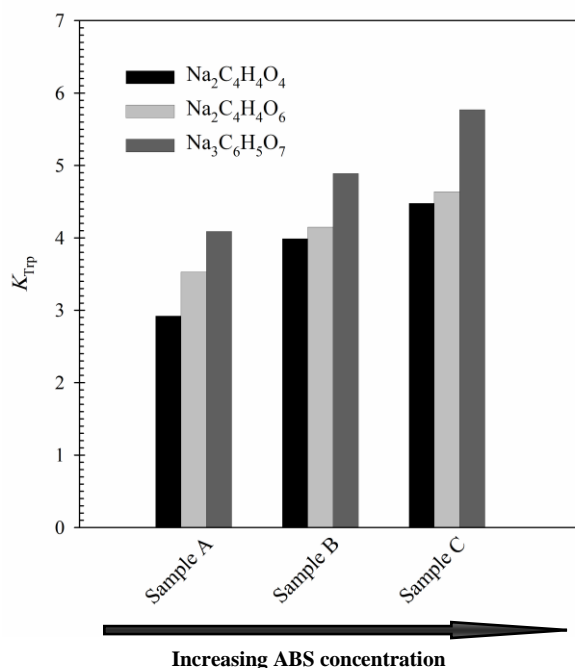


Fig.7: The partitioning of Trp within {PEG 4000 + salt} ABS at $T = 298.15$ K.

References

- [1] B. Y. Zaslavsky, Aqueous two-phase partitioning: physical chemistry and bioanalytical applications: CRC Press, 1994.
- [2] R. Hatti-Kaul, Aqueous two-phase systems: methods and protocols vol. 11: Springer, 2000.
- [3] B. Afzal Shoushtari, J. Rahbar Shahrouzi, and G. Pazuki, "Effect of nanoparticle additives on partitioning of cephalexin in aqueous two-phase systems containing poly (ethylene glycol) and organic salts," Journal of Chemical & Engineering Data, 61 (2016) 2605-2613.

Improvement of Celecoxib solubility using microemulsion systems

E. Parsi^a, A. Salabat^a

^aDepartment of Chemistry, Faculty of Science, Arak University, Arak, 38156-8649, Iran

*a-salabat@araku.ac.ir

Parsielham@ymail.com

Abstract: The aim of this study is to increase the solubility of an analgesic, antipyretic and anti-inflammatory drug named “Celecoxib” using two types of O/W and IL (ionic liquid)/W microemulsion systems. The pseudo-ternary phase diagram was constructed and four microemulsion formulations were selected (denoted as A, B, C, D) for drug loading. The physicochemical properties such as density, refractive index and electrical conductivity of the four different microemulsion formulations were measured. The solubility of the Celecoxib in the constructed formulations of two different types of O/W and IL/W microemulsions were determined and compared. The results showed considerable increase in solubility of the drug in the microemulsion systems specially when containing ionic liquid.

Keywords: Microemulsion systems, Ionic liquid, Drug delivery system

Introduction

Delivery of some poorly soluble drugs in target cell or tissue is difficult due to their insolubility or sparingly solubility in water and most pharmaceutical grade organic liquids. For this reason, such drugs are discarded in the first steps of production. Many researchers have been performed in order to improve drug solubility for example using dimethyl sulfoxide, ethanol and liposomes [1-4]. However such methods are not effective for delivery of drugs with poor solubility. An effective method introduced and developed to increase solubility and improve successful delivery of such drugs is microemulsions. The Microemulsions are isotropic mixtures of oil, water and surfactant (frequently a cosurfactant). They are clear and stable compounds with droplet size between 1-100 nm [5-7]. Microemulsions have some ability in drug delivery such as control their release, increase drugs solubility and bioavailability and reduce patient variability [8]. Microemulsions have some applications such as synthesis of nanocomposite and pharmacy [9,10]. Therefore the aim of this study is to increase the solubility of a drug named “Celecoxib” using microemulsion system. The Celecoxib is an analgesic, antipyretic and anti-inflammatory drug. It is an inhibitor of cyclooxygenase-2 (COX-2). Solubility of Celecoxib is classified in “low” category (0.0033 mg/ml at 25°C in water) [11-13].

Materials and method

Materials

Celecoxib (C₁₇H₁₄F₃N₃O₂S), Polyoxyethylene (20) sorbitan monooleate (Tween 80), diethylene glycol monoethyl ether (Transcutol® P), Isopropyl myristate (IPM), 1-Methyl-3-Octyl- imidazolium hexafluoro phosphate (C₁₂H₂₃F₆N₂P), Distilled and deionized water.

Methods

Construction of pseudo-ternary phase diagrams

In order to determine microemulsion region, a pseudo-ternary phase diagram was constructed by the water titration method. This phase is clear and single phase area. The weight ratio of surfactant (tween 80) to co-surfactant (Transcutol® P) (Smix) was selected 2.96:1 to form a phase diagram. To construct a phase diagram, a mixture of Smix and oil was titrated with water dropwise. The resultant solution was put under magnetic stirring at room temperature. Titration was continued until the solution became cloudy or turbid. The amount of water required for making the solution cloudy was recorded and the concentration of each component was calculated in percent. Finally, pseudo-ternary phase diagram was plotted by using of Tri-plot software version 4.1.2.

Drug incorporation in microemulsions

Four different w/o microemulsion formulations were selected from pseudo-ternary phase diagram. To obtain these formulations, sufficient amount of oil, surfactant, co-surfactant and water were mixed together until 100% weight of the solution and under magnetic stirring was made. In order to prepare Celecoxib-loaded microemulsions, 0.5% (w/w) of the drug was incorporated into each formulation and mixed using magnetic stirring until total of drug dissolved in the microemulsion formulations and homogeneous and clear solutions were obtained.

Equilibrium solubility test

In order to determine the solubility of Celecoxib in microemulsion formulations the following steps were performed: (1) The excess amount of Celecoxib was increased into 1ml of formulations and allowed to reach

equilibrium by stirring for 24h at room temperature. (2) The formulations containing excess amounts of Celecoxib were centrifuged at 20000 rpm for 5 min. (3) The upper solution obtained from centrifuge in step 2 was separated and diluted with methanol. (4) The concentration of Celecoxib was determined by UV-Visible spectrophotometer. Formulations without drug were used as blank which diluted with the same amount of methanol.

Characterization of microemulsion formulations

Density

The densities of the microemulsions formulations were measured by densimeter (model Mettler Toledo (DE51, USA) with precision $\pm 1 \times 10^{-5}$ g/cm³). The temperature was controlled to within ± 0.01 K. Before the measurement of formulations density, the densimeter was calibrated using density of air and distilled and deionized water.

Refractive index

Refractive indices of the microemulsion formulations were measured by refractometer (model Mettler Toledo (RE50, USA) with precision of $\pm 10^{-5}$). The temperature was controlled to within ± 0.01 K. Before the measurement of the refractive index of formulations, the refractometer was calibrated using refractive index of distilled and deionized water.

Electrical conductivity

Electrical conductivity of the microemulsion formulations were measured by a conductivity meter (model Metrohm 712 (Switzerland) with precision of $\pm 10^{-2}$ μ S/cm). The temperature was controlled to within ± 0.01 K. Before the measurement of electrical conductivity of formulations, the conductivity meter was calibrated using a standard KCl solution.

Results and discussion

In this study, Tween 80 was selected as the surfactant which reduces interfacial tension between oil-water interfaces. For increasing the flexibility of interfacial layer to form microemulsion, it is necessary to have a co-surfactant, here we selected transcutool® P as a co-surfactant. Isopropyl myristate is compatible with skin, and it has solubilization capacity for Celecoxib drug due to alkyl chain. Fig.1 shows the pseudo-ternary phase diagram of the microemulsion system (tween 80, transcutool® P, isopropyl myristate, water) at 25°C from which four microemulsion formulations were selected (denoted as A, B, C, D in Fig. 1). Table 1 summarized the physicochemical properties (density, refractive index and electrical conductivity) of the four different microemulsion formulations. As expected, density and refractive index were increased and conductivity was reduced with reducing water content.

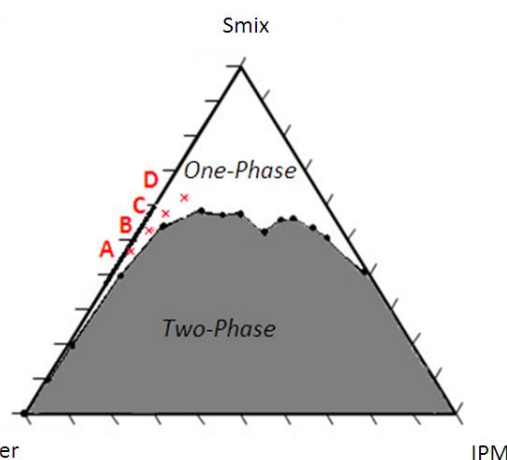


Fig.1. Pseudo-ternary phase diagram of the microemulsion system containing tween 80, transcutool® P, isopropyl myristate and water

Fig.2 shows a comparison of the solubility among our developed formulations (i.e. A, B, C and D), IPM and water and also a formulation labeled "E". The formulation named "E" is actually the formulation "A" in which 1-Methyl-3-Octyl-imidazolium hexafluorophosphate has been used instead of the IPM. From Fig. 2 some conclusion can be made:

- Solubility of Celecoxib in water is extremely low (3.3×10^{-6} mg/L) and its solubility is increased respectively in IPM, A, B, C and D. These results show that the solubility of Celecoxib in O/W microemulsions is increased with increasing the Smix content and with reducing water content.
- The O/W microemulsion named "A" was selected as optimal formulation due to its safety nature. In this formulation ionic liquid (1-methyl-3-octyl imidazolium hexafluoro phosphate) was used instead of IPM. The resultant formulation as stated previously was named "E". The constructed IL/W microemulsion "E" consists of 53% (w/w) water, 46% (w/w) Smix and 3% (w/w) ionic liquid. As expected, Celecoxib has the most solubility in IL/W microemulsion (i.e. E).
- The ionic liquids have the intrinsic ability to dissolve hydrophobic drugs due to having the alkyl chains. When such high soluble ionic liquids are entered into the microemulsions, a significant increase in the solubility of the drugs can be observed.

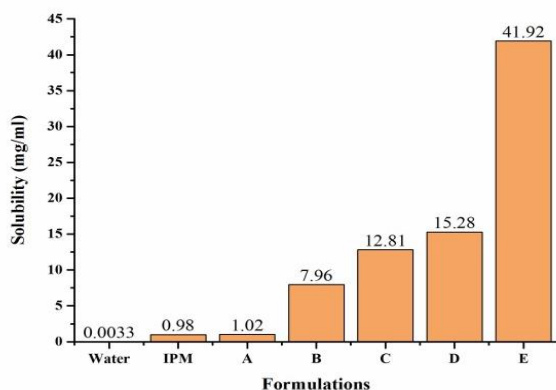


Fig.2. Solubility of Celecoxib in O/W microemulsion systems (A, B, C, D), IL/W microemulsion system (E), water and Isopropyl myristat (IPM)

Table.1. Physicochemical properties of microemulsion systems consist ofween 80, transcutool® P, isopropyl myristate and water

No	Water (w/w%)	IPM (w/w%)	Smix (w/w%)	Density (g/cm ³)	Refractive index	Conductivity (μS/cm)
A	53	3	44	1.01863	1.39801	13.06
B	45	5	50	1.03707	1.41017	9.35
C	40	5	55	1.04071	1.41321	8.04
D	35	5	60	1.04378	1.42320	5.64

Conclusions

In this paper solubility of the Celecoxib in four different O/W microemulsion systems was studied. It was shown that microemulsion systems specially an optimum IL/W microemulsion formulation have the considerable solubility of the Celecoxib. Such systems can be used as a strong method to improve the delivery of poorly soluble drugs.

Acknowledgment

Research was carried out under the current budget of the Arak University, Arak, Iran.

References

[1] B. W. Müller, & E. Albers, "Complexation of dihydropyridine derivatives with cyclodextrins and 2-

hydroxypropyl-β-cyclodextrin in solution", International journal of pharmaceutics, 79 (1992) 273-288.

[2] Y. Barenholz, "Liposome application: problems and prospects", Current opinion in colloid & interface science, 6(1) (2001) 66-77.

[3] M. J. Lawrence, & G. D. Rees, "Microemulsion-based media as novel drug delivery systems", Advanced drug delivery reviews, 45(1) (2000) 89-121.

[4] A. S. Balte, P. K. Goyal, & S. p. Gejji, "Theoretical studies on the encapsulation of paracetamol in the α, β and γ-cyclodextrins", J Chem Pharm Res, 4(5) (2012) 2391-2399.

[5] S. P. Moulik, & B. K. Paul, "Structure, dynamics and transport properties of microemulsions" Advances in Colloid and Interface science, 78(2) (1998) 99-195.

[6] M. Kreilgaard, "Influence of microemulsions on cutaneous drug delivery", Advanced Drug Delivery Reviews, 54 (2002) S77-S98.

[7] S. Tenjarla, "Microemulsions: an overview and pharmaceutical applications" Critical Reviews™ in Therapeutic Drug Carrier Systems, 16(5) (1999) 461.

[8] N. A. T. E. S. A. N. Subramanian, S. K. Ghosal, & S. P. Moulik, "Topical delivery of celecoxib using microemulsion", Acta Pol Pharm, 61(5) (2004) 335-341.

[9] A. Salabat, J. Eastoe, K. J. Mutch, & R. F. Tabor, "Tuning aggregation of microemulsion droplets and silica nanoparticles using solvent mixtures", Journal of colloid and interface science, 318(2) (2008) 244-251.

[10] F. Mirhoseini, & A. Salabat, "Ionic liquid based microemulsion method for the fabrication of poly (methyl methacrylate)-TiO₂ nanocomposite as a highly efficient visible light photocatalyst", RSC Adv.5(17) (2015) 12536-12545.

[11] K. W. Marshall, "Practical implications of cyclooxygenase-2-specific inhibitors in orthopedics", American journal of orthopedics (Belle Mead, NJ), 28(3 Suppl) (1999) 19-21.

[12] J. H. Lee, M. J. Kim, H. Yoon, C. R. Shim, H. A. Ko, S. A. Cho, & G. Khang, "Enhanced dissolution rate of celecoxib using PVP and/or HPMC-based solid dispersions prepared by spray drying method", Journal of Pharmaceutical Investigation, 43(3) (2013) 205-213.

[13] A. M. Samy, M. M. Ghorab, S. G. Shadeed, & Y. I. Mortagi Y, "Effect of different additives on celecoxib release", International Journal of Pharmacy and Pharmaceutical Sciences, 5(2013) 667-671.

The soluting-out effect in aqueous solutions of 1-butyl-3-methylimidazolium tetrafluoroborate and carbohydrates at various temperatures

Rahmat Sadeghi^{a*}, Bahman Jamehbozorg^b

Department of Chemistry, University of Kurdistan, Sanandaj, Iran

Department of Chemistry, University of Kurdistan, Sanandaj, Iran

[*bahmanjamebozorg@gmail.ir](mailto:bahmanjamebozorg@gmail.ir)

[*rsadeghi@uok.ac.ir](mailto:rsadeghi@uok.ac.ir)

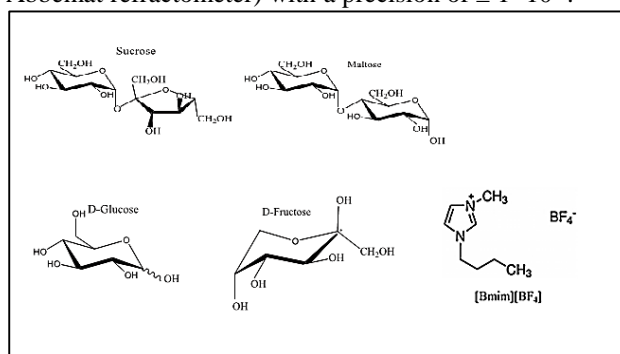
Abstract: Phase diagrams and liquid–liquid equilibrium (LLE) data of the aqueous 1-butyl-3-methylimidazolium tetrafluoroborate+ carbohydrate two-phase systems were determined experimentally at 298.15, 303.15, 308.15, 313.15 and 318.15 K. The soluting-out effect of four carbohydrates including sucrose, maltose monohydrate, D-(+)-glucose, and D-(-)-fructose on the aqueous ionic liquid solutions were investigated. It was found that a decreasing in temperature and increasing the number of hydroxyl groups from monosaccharides (glucose and fructose) to disaccharides (sucrose and maltose monohydrate) caused the expansion of two-phase region. Although glucose and fructose are structural isomers and the numbers of their hydroxyl groups are equal, the soluting-out capability of glucose is more than that of fructose. The soluting-out powers of disaccharides obey the order: maltose > sucrose. It was also found that the concentration of carbohydrate, which is in equilibrium with a certain concentration of ionic liquid, increases by increasing temperature. Based on the cloud point values, the ΔG_C values for all systems are negative and becomes more negative by decreasing the temperature and increasing the hydrophilicity of the carbohydrates.

Keywords: Soluting-out effect; Aqueous biphasic system; Ionic liquid; Cloud point

Introduction

Ionic liquids are organic molten salts with melting points below 100 °C that have interesting properties such as negligible vapor pressures, non-flammability, good thermal and electrochemical stability. One of the most important applications of ILs in biotechnology is their ability to form aqueous biphasic systems (ABS) with wide range of solutes in aqueous solutions. Since the bulk of both phases are composed of water, ABS form a gentle medium for bioproducts and therefore can be used in various extraction processes. For the first time, Zhang et al. reported the formation of IL + carbohydrate aqueous biphasic systems [1]. Carbohydrates are nontoxic, renewable feedstock and biodegradable organic molecules. Studying the thermodynamic properties of aqueous solutions containing ionic liquids and carbohydrates for understanding of molecular mechanism of phase separation is very important. In this work, for better understanding of soluting effect phenomenon in aqueous IL/carbohydrate systems, liquid - liquid equilibria experiments were conducted at various temperatures. In order to study the effects of some parameters such as number of hydroxyl groups and stereochemical properties of sugar molecules on the phase separation capability, four carbohydrates including sucrose, maltose monohydrate, D-(+)-glucose, and D-(-)-fructose were selected.

[Bmim][BF₄] were synthesized and purified according to the procedures described in the literature [2]. All the carbohydrates were obtained from Merck. The binodal curves were determined by a titration method. A carbohydrate solution of known concentration was titrated with the IL solution or vice versa, until the solution turned turbid. To determine the compositions of coexisting phases, feed samples were prepared by mixing appropriate amounts of IL, carbohydrate and water in the vessel and the sample was stirred for 1 h. After separation of the two transparent phases, the concentrations of the carbohydrates in the top and bottom phases were determined by the Anton Paar Gyromat Digital Automatic Polarimeter. The concentration of IL in both phases was determined by using the refractometry analysis at 298.15 K using a refractometer (Anton Paar Abbemat refractometer) with a precision of $\pm 1 \times 10^{-6}$.



Scheme 1. Chemical structures of the carbohydrates and ionic liquid studied.

Materials and method

Results and Discussion

For all the [Bmim][BF₄] + carbohydrate + water systems, by decreasing temperature phase boundary is shifted to the lower concentrations (the biphasic region is expanded) and aqueous two-phase system to be formed easier. At higher temperatures the [Bmim][BF₄]-water interactions become stronger and soluting-out of the IL by the sugars becomes more difficult. According to our results, at a same overall composition, the slope of the all tie-lines decreases by increasing temperature. As mentioned above, the IL-water interactions strengthen with increasing temperature. For this reason, by increasing temperature the water molecules spontaneously migrate from the carbohydrate-rich phase to the IL-rich phase to reach a new equilibrium state. Therefore, with an increase in temperature, the IL- and sugar-rich phases become more dilute and concentrated, respectively. Due to the change of the water content of the coexisting phases, the volumes of IL-rich and sugar-rich phases increased and decreased respectively, by increasing temperature. By decreasing temperature, for the tie-lines near the binodal curve, phase inversion occurs so that the IL-rich phase which is top phase at higher temperatures becomes the bottom phase at lower temperatures.

The soluting-out strength of the investigated sugars on the aqueous IL solutions decreases in the order: maltose > sucrose > D-(+)-glucose > D-(-)-fructose. The formation of ABS is a reflectance of the competition between the solutes (carbohydrate molecules and IL ions) in the creation of hydration complexes. The amounts of hydration for various sugars depend on two factors which include: the number of -OH groups on the sugars molecules and structural and stereochemical natures of carbohydrates. This trend indicates that the disaccharides (maltose and sucrose) are stronger soluting-out agents than monosaccharides (D-(+)-glucose and D-(-)-fructose). Although glucose and fructose are structural isomers and the number of hydroxyl groups is equal, the soluting-out

capability of glucose is more than that of fructose. This is because the pyranose structure (6-sided ring) has more desirable conformation than furanose structure (5-sided ring) for hydrogen bonding with water molecules. The results indicate that the biphasic region is expanded from sucrose (glucose-fructose) to maltose (glucose-glucose). The following equation was used for the calculation of free energy of phase separation or clouding (ΔG_C):

$$\Delta G_C = RT_C \ln X_C \quad (1)$$

where X_C is the mole fraction of sugars at cloud point. The ΔG_C values for all systems are negative and become more negative by decreasing temperature and increasing the hydrophilicity of the carbohydrates.

Conclusions

Phase diagrams and LLE data of the aqueous [Bmim][BF₄] + carbohydrate two-phase systems were determined experimentally at $T = (298.15, 303.15, 308.15, 313.15 \text{ and } 318.15) \text{ K}$. These systems with high differences in hydrophilicity power of constituents and unfavorable solute-solute interactions have strong soluting-out effect. For these systems, the phase separation capability increase by decreasing temperature and increasing the number of hydrogen bonding sites on the carbohydrate molecules (from monosaccharides to disaccharides).

References

- [1] Y. Zhang, S. Zhang, Y. Chen, J. Zhang, "Aqueous Biphasic Systems Composed of Ionic Liquid and Fructose", *Fluid Phase Equilib.* 257 (2007) 173–176.
- [2] G.-H Min, T. Yim, H.-Y Lee, D.-H Huh, E. Lee, J. Mun, S. M Oh, Y.-G Kim, "Synthesis and Properties of Ionic Liquids: Imidazolium Tetrafluoroborates with Unsaturated Side Chains", *Bull. Korean Chem. Soc.* 27 (2006) 847–852.

Speed of sound estimation for some ionic liquids from density and surface tension data

M. Behroozi^{a*}

^aDepartment of chemistry, University of Zanjan, Zanjan, 45371-38791, Iran

*behroozi.m@znu.ac.ir

Abstract: From density and surface tension data, speed of sound estimation was performed for some ionic liquids. Because the experimental data of speed of sound for ionic liquids is very scarce the predictive methods can be useful. The selected ionic liquids were: 1-Ethyl-3-methylimidazolium tetrafluoroborate, 1-propyl-3-methylimidazolium tetrafluoroborate, 1-butyl-3-methylimidazolium tetrafluoroborate, 1-pentyl-3-methylimidazolium tetrafluoroborate, 1-hexyl-3-methylimidazolium tetrafluoroborate and 1-butyl-3-methylpyridinium tetrafluoroborate. Speed of sound data along with density data can be used for calculation of some thermodynamic properties such as isentropic compressibility κ_s , isothermal compressibility κ_T , and isobaric thermal expansivities α_p . The calculated values were compared with the experimental data. Good agreement was observed between the experimental and predicted data.

Keywords: Speed of sound; Density; Surface tension; Ionic liquids.

Introduction

Ionic liquids (ILs) hold many considerable attentions due to their special characteristics such as low vapor pressure, chemical stability, good thermal stability, non-flammability and so on [1-2]. ILs are green solvents. Knowledge of the physical and thermodynamic properties of ionic liquids can be useful for better understanding of the nature of ILs. One important property of ILs is speed of sound. Speed of sound data along with density data can be used for calculation of isentropic compressibility κ_s , isothermal compressibility κ_T , and isobaric thermal expansivities α_p . Although experimental measurements are available for common fluids, experimental data for many new fluids of industrial interest are not are non-existent [3] so estimation of physical properties is very important. In this work, speed of sound of 1-Ethyl-3-methylimidazolium tetrafluoroborate ([emim][BF₄]), 1-propyl-3-methylimidazolium tetrafluoroborate ([prmim][BF₄]), 1-butyl-3-methylimidazolium tetrafluoroborate [bmim][BF₄], 1-pentyl-3-methylimidazolium tetrafluoroborate [pmim][BF₄], 1-hexyl-3-methylimidazolium tetrafluoroborate ([hmim][BF₄]) and 1-butyl-3-methylpyridinium tetrafluoroborate ([bmpyr][BF₄]) were estimated from density and surface tension data.

Materials and method

The speed of sound (u) in ms^{-1} units can be estimated using the theoretical Auerbach's relation [4]

$$u = \left(\frac{\sigma}{6.33 \times 10^{-10} \cdot \rho} \right)^a \quad (1)$$

where $a = 2/3$, σ and ρ are the surface tension in Nm^{-1} units and density in kgm^{-3} units, respectively.

Results and Discussion

The speed of sound of ionic liquids was calculated by theoretical Auerbach's relation from density and surface tension data. The results are shown in Table 1. The agreement between the theoretical and experimental data was good.

Table 1: density ρ , surface tension σ , and speed of sound u of ionic liquids.

Ionic liquid	$\rho / (\text{g} \cdot \text{cm}^{-3})$	$\sigma / \text{mN} \cdot \text{m}^{-1}$	$u \text{ (m s}^{-1}\text{)}$	
			cal	exp
[emim][BF ₄]	1.27760	55.73	1680.84	1622.9 ^a
[bmim][BF ₄]	1.20862	46.39	1543.43	1594.9 ^b
[pmim][BF ₄]	1.18247	40.86	1439.03	-
[hmim][BF ₄]	1.1453	39.47	1436.47	1523.7 ^b
[bmpyr][BF ₄]	1.185655	45.21	1536.67	1598.5 ^b

^aRef. [5]

^bRef. [6]

From the equation 1 can be seen the linear behavior of plot of $\log u$ against $\log(\sigma/\rho)$.

Conclusions

It is shown that the Auerbach's relation was successfully described the speeds of sound of ILs.

Acknowledgment

The authors would like to thank University of Zanjan for providing the necessary facilities to carry out the research.



References

- [1] M. A. Iglesias-Otero, J. Troncoso, E. Carballo, L. Romani, *J. Chem. Thermodynamics* 40 (2008) 949–956.
- [2] M. García-Mardones, A. Barrós, I. Bandrés, H. Artigas, C. Lafuente, *J. Chem. Thermodynamics* 51 (2012) 17–24.
- [3] R. L. Gardas, J. A.P. Coutinho, *Fluid Phase Equilib.* 263 (2008) 26–32
- [4] R. L. Gardas, J. A.P. Coutinho, *Fluid Phase Equilib.* 267 (2008), 188–192.
- [5] M. Srinivasa Reddy, Sk. MdNayeem, C. Soumini, K. Thomas, S.S. Raju, B. Hari Babu, *Thermochim. Acta* 630 (2016) 37-49.
- [6] G. García-Miaja, J. Troncoso, L. Romani, *J. Chem. Thermodynamics* 41 (2009) 334–341.

Evaluating Second Order Thermodynamic Derivative Properties of Hydrocarbon Chain Series by Perturbed Chain-SAFT Equations of State

A. Jamali^{a*}, H. Behnejad^a

^aDepartment of Physical Chemistry, School of Chemistry, University College of Science, University of Tehran, Tehran 14155, Iran

*a_jamali87@ut.ac.ir

Abstract: In order to provide a comprehensive understanding of limitations of the perturbed Chain Statistical associating fluid theory Equations of State (PC-SAFT EoS), this study offers insight into its application for the prediction of derivative properties over extensive ranges of pressure and temperature. Therefore, this paper focused on the second derivative properties of pure components related to Alkanes by PC-SAFT EoS. The pure component parameters used for these calculations were fitted to vapour-liquid equilibrium data. The PC-SAFT EoS is found to be able to acceptably describe the derivative properties including speed of sound and heat capacities as well as Pressure-Vapour-Temperature properties of Alkanes series studied in this work.

Keywords: PC-SAFT, Equation of State, Heat Capacity, Speed of Sound

Introduction

The thermodynamic properties of alkanes is a great challenge for all kinds of equation of state (EoS) and only a few are based on a fundamental theory [1]. It is believed that SAFT-family EoS may have better performance in this type of calculations, because they include all the important molecular contributions. SAFT is an EoS on the basis of statistical mechanics and more specifically to Wertheim's first-order thermodynamic perturbation theory (TPT1) for associating fluids [2]. The perturbed chain SAFT (PC-SAFT) model is among the most recent modifications of the SAFT approach. PC-SAFT has been applied with great success for very different types of fluids. This model considers molecules to be the chains composed of spherical segments with square-well pair potentials for the segments and it may be considered as an extension of the Barker and Henderson perturbation theory to a hard chain reference. Also, it should be considered that successful representation of phase equilibrium depends not only on good models but also on parameter values, i.e., on the parameter fitting strategy.

The objective of this work is evaluating the ability of PC-SAFT EoS in predicting the derivative properties of alkane series and the pure component parameters used for these calculations were fitted to vapour-liquid equilibrium data.

Method

PC-SAFT EoS is written as summation of residual Helmholtz free energy term. The residual Helmholtz free energy is equal to the Helmholtz free energy minus the Helmholtz free energy of the ideal gas

at the same temperature T and density ρ that it can be expressed as [3]:

$$\frac{A^{res}(T, \rho)}{NRT} = a(T, \rho) - a^{ideal}(T, \rho)$$

$$= a^{hs}(T, \rho) + a^{chain}(T, \rho) + a^{disp}(T, \rho) + a^{assoc} \quad (1)$$

The second order properties considered are given by the following equations:

$$C_v(T, \rho) = C_v^{ideal}(T) + C_v^{res}(T, \rho)$$

$$= C_v^{ideal}(T) - T \left(\frac{\partial^2 a^{res}}{\partial T^2} \right)_\rho \quad (2)$$

$$C_p(T, \rho) = C_p^{ideal}(T) + C_p^{res}(T, \rho) = C_v + \frac{T}{\rho^2} \frac{(\partial P / \partial T)_\rho^2}{(\partial P / \partial \rho)_T} \quad (3)$$

$$\mu_{JT} = -\frac{1}{C_p} \left(V + T \frac{(\partial P / \partial T)_V}{(\partial P / \partial V)_T} \right) \quad (4)$$

$$u = \sqrt{-V^2 \left(\frac{C_p}{C_v} \right) \left(\frac{(\partial P / \partial V)_T}{MW} \right)} \quad (5)$$

$$\mu_{JT} = T \left(\frac{\partial P}{\partial T} \right)_\rho - \rho \left(\frac{\partial P}{\partial \rho} \right)_T \quad (6)$$

The ideal contributions of the isochoric and isobaric heat capacities were obtained from a complete data library [4].

Most EoS are able to provide good evaluations of first-order derivatives of Helmholtz free energy, but have difficulty in accurately predicting the above mentioned function derivatives in Eqs. (2)-(6).

Results and Discussion

Pure component parameters were fitted to experimental vapor pressure and saturated liquid density data taken from NIST Chemistry WebBook[4]. In Table 1, a summary of the average absolute deviation (AAD %) between experimental data and EoS predictions for C_v , C_p and speed of sound of all the components examined. Calculation of this thermodynamic properties was performed for all components in the pressure range up to 50 MPa and specified temperature range and compared with experimental data. For the calculation of heat capacities, the ideal gas contribution of the fluid is obtained from the NIST database [4] and the residual contribution from the EoS. It should be considered that in liquid phase and near-critical region, the residual contribution is important, but at high temperatures it becomes less significant.

As it can be observed, very good correlation of the isochoric and isobaric heat capacity is obtained in all cases.

On average, it can be claimed that PC-SAFT performs thoroughly better than cubic EoS and original SAFT EoS for all the properties.

The speed of sound of compounds also are predicted above the critical temperature, utilizing the PC-SAFT EoS. The predicted values for one of them is shown in Figure 1.

Conclusions

The predictive ability of the model on the estimation of the thermodynamic derivative properties for chain fluids has been checked. In fact, the speed of sound is generally represented as a severe consistency test for PC-SAFT EoS, since it involves the temperature and density partial derivatives of pressure and to achieve this the EoS must describe with great accuracy the isothermal properties of pressure, isochoric and isobaric heat capacity.

Table 1. Summary of AAD % for All the Properties Calculated from the PC-SAFT EoS.

component	AAD%			T range (K)
	C_v	C_p	u	
n-Methane	1.80	14.50	4.83	220-310
n-Ethene	4.63	11.74	4.93	275-350
n-Propane	1.654	6.62	4.07	360-500
n-Butane	2.18	5.67	4.80	350-560
n-Pentane	1.42	4.40	4.75	420-570
n-Hexane	1.51	4.24	5.91	400-550
n-Heptane	1.29	4.08	5.86	460-600
n-Octane	1.85	2.45	6.22	400-600
n-Nonane	1.53	2.61	9.26	400-570
n-Decane	0.83	1.81	8.02	425-665
n-Undecane	0.50	0.72	9.85	450-690
n-Dodecane	0.59	1.01	6.88	450-690
Iso-Butane	1.58	5.11	5.29	360-570

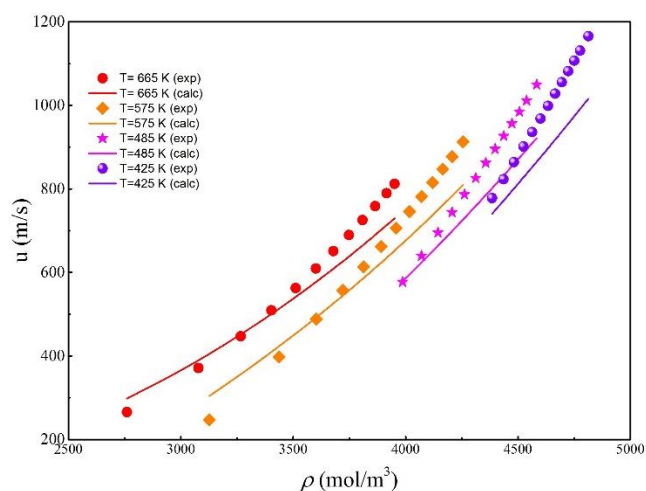


Fig 1. Predicted (symbols) and experimental (solid lines) speed of sound of n-Decane

References

- [1] A. Maghari, M. Hamzehloo, Fluid Phase Equilibria 302 (2011) 195.
- [2] S. Perturbed-Chain, Industrial & Engineering Chemistry Research 40 (2001) 1244.
- [3] A. De Villiers, C. Schwarz, A. Burger, G. Kontogeorgis, Fluid Phase Equilibria 338 (2013) 1.
- [4] Lemmon, E. W.; Linden, M. O.; Friend, D. G., Thermophysical Properties of Fluid Systems. In NIST Chemistry WebBook, NIST Standard Reference Database Number 69; Linstrom, P. J., Mallard, W. G., Eds.; National Institute of Standards and Technology: Gaithersburg, MD, 20899.

Functionalization of halloysite sorbent via carboxylic acid linkage for removal methylene blue: Thermodynamics study

Mohammad Hassan Kanani¹, Somaye Akbari*, Mohammad Haghhighatkish, Elmira Pajootan
 Textile Engineering Department, Amirkabir University of Technology, Tehran, Iran

* akbari_s@aut.ac.ir

Abstract: There are lots of research to improve surface functionalization on the halloysite nanotube (HNT). The aim of this work is enhancement of functional group of HNT by dicarboxylic acid groups. HNT first was reacted through silanization reaction via 3-triethoxysilylpropylamine (APTES) to produce HNT-NH₂. In the next step, HNT-NH₂ was reacted with succinic anhydride in order to create carboxylic acid groups onto the structure. The synthesis process was investigated by FTIR spectra which indicated the addition of carboxylic acid groups to the structure of HNT to increase the adsorption capacity to methylene blue. HNT-HCl (washed HNT using HCl), HNT-NH₂ and HNT-COOH adsorbents were compared together. Effect of pH and temperature on removal of methylene blue was investigated. Thermodynamic study indicate adsorption of methylene blue on HNT-COOH was an endothermic and irreversible. The maximum dye removal rate was about 96% at pH 9 at temperature 318 K.

Keywords: halloysite, synthesis, adsorbent, thermodynamic, functional end-group

Introduction

Dyes are widely used in many industries such as paper, plastic, cosmetics and food industries. Therefore, wastewater containing dye, in these industries must be carefully purification before being discharged in nature, it may cause serious danger environmental problems such as disorder in photosynthesis, catastrophic effect in human being, there are toxic to micro organism and in general leads to damage to the environment [1].

Halloysite nanotubes (HNT_s) are natural-mineral clay adsorbent with hollow nanotube structure. HNT_s are one of the cheapest existing adsorbent. The molecular formula for HNT_s is Al₂Si₂O₅(OH)₄n H₂O and it is composed of multiple-layered structure [2]. There is large number hydroxyl group on its surface of HNT_s and the gap space between layers lead to adsorb many pollutant. On the other hand, HNT_s deposit of hollow channel and surface hydroxyl groups, the functional groups are not available. As a result, lots of surface functionalization on the HNT_s have been done.

HNT_s can be functionalized with carboxylic acid groups to improve removal capacity toward cationic dye. Therefore, in this work, the adsorption of methylene blue as a cationic model dye was investigated by functionalization of washed HNT into HNT-NH₂ and HNT-COOH, respectively. Also, key parameters such as pH, different concentrations and temperature were investigated. The thermodynamic parameters are calculated and reported.

Materials and methods

The HNT, (diameter: 80 nm) was purchased from Delta-Dolsk Co., Poland. All chemicals were analytical grade. First, HNT were purified with HCl for 24h under constant stirring. Then, 5g of dried HNT-HCl was added to toluene (100 mL) containing 10 mL of APTES. The suspension was refluxed at 80°C for 12h under constant stirring.

In the next step, the solid phase was separated and washed 3 times with ethanol and methanol using Buchner funnel. 1g of dried HNT-NH₂ was mixed with 50 mL of DMF and sonicated for 5 minutes. Then 1.2 g of succinic anhydride was added to the solution which was then refluxed and stirred at 90°C for 24h. The solid phase was separated and washed 3 times with DMF using Buchner funnel. Finally, the prepared adsorbent was dried at 60°C for 8h [3]. The route of synthesis is show in Fig.1.

A mass of dried HNT-COOH was added to the 250-mL methylene blue solution (20 mg/L). The pH of dye solution was adjusted to 3,5,7,9 and 11 by NaOH and HCl. Solutions with different concentration of dye (10, 20, 50, 75 and 100 mg/g) were examined. Also, the removal rate at 298, 308 and 318 K was investigated. The samples were taken from solution at different time intervals and examined with spectrophotometer (UNICO 2100) for the absorbance measurement at 665 nm, the maximum absorption wavelength of methylene blue.

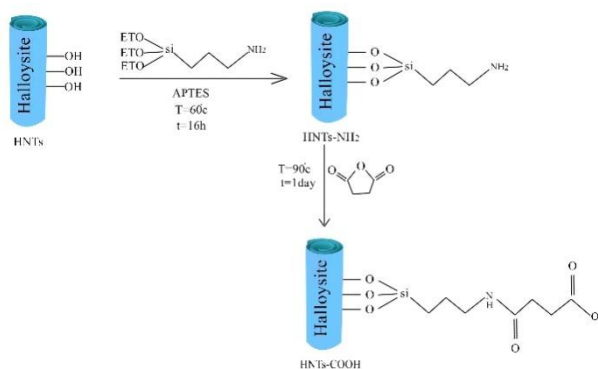


Fig.1: Schematic route of syntheses HNT-COOH

Results and Discussion

FTIR

FTIR spectra of HNT-HCl, HNT-NH₂ and HNT-COOH are shown in Fig.2. Peak assignment was made according to the literature[3]. Spectra of raw halloysite reveals peaks at 475 and 541 cm⁻¹ showing Si-O-Si and Al-O-Si connections bending. The peak at 3620-3690 cm⁻¹ is related to the stretching vibration of the inner surface Al-OH. The peaks at 2929 and 2852 cm⁻¹ are assigned to symmetric and asymmetric stretch CH₂. The peak at 914 cm⁻¹ is attributed to the bending vibration of inner surface hydroxyl groups. In addition, peaks at 1030 and 1630 cm⁻¹ are related to the stretching Si-O and bending vibration absorbing water. After functionalization, carboxylic acid peak at 1699 cm⁻¹ can be observed. Also, the peaks at 1645 and 1555 cm⁻¹ are related to the bending primary and secondary amine groups. The peak at 1410 cm⁻¹ can be also related to the stretching C-O.

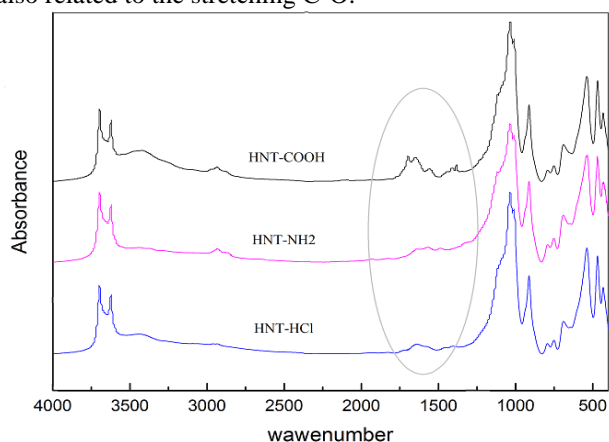


Fig.2: FTIR Spectra of HNT-HCl, HNT-NH₂ and HNT-COOH.

TEM

Transmission electron microscope (TEM) was used to observe morphological structure of original and modified HNTs. Fig.3. TEM image shows a cylinder with a diameter of 100 to 140 nm and a length of 2 to 3 micrometers. Also, the interior lumen with a diameter of 30 to 40 nm clearly seen in the picture. Modified on halloysite adsorbent lead to increase the size with no change in morphology.

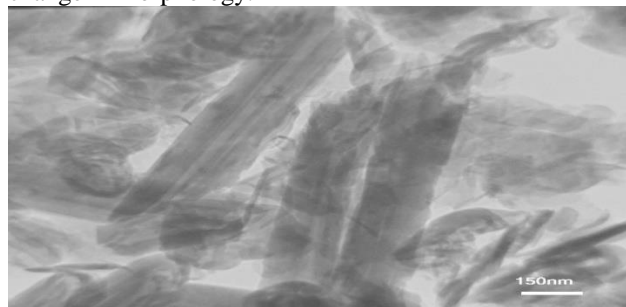


Fig.3: TEM of modified halloysite

Removal of methylene blue

Comparing between removal between three different HNTs are shown in Fig.4. The carboxylic acid functionalization ones leads to improve removal about 96%.

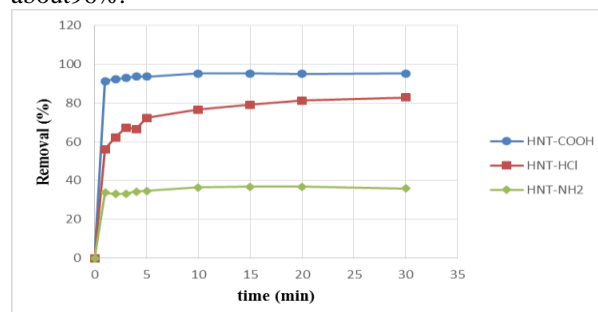


Fig.4: Removal of methylene blue by HNT-HCl, HNT-NH₂ and HNT-COOH (Adsorbent dosage: 0.1 g/L).

One of the most important parameters affecting the adsorption capacity is the pH. The effect of pH on the adsorption of methylene blue shown in Fig 5. By increasing pH, the removal rate of dyes increases. This may be due to the fact that, at higher pH, the HNT_s surface is negatively charged and, by increasing the positive charge of the methylene through electrostatic forces of attraction [4].

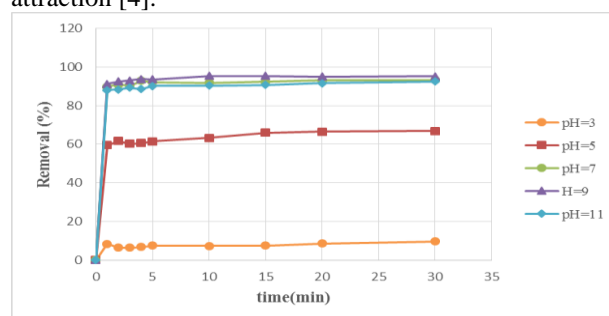


Fig.5: Effect of pH on dye removal ([C₀]: 20 mg/L, adsorbent dosage: 0.3 g/L).

Effect of temperature on the removal capacity was measured at 298, 308 and 318 K. According to Fig. 6 removal of methylene blue increased from 93% to 96% by increasing temperature of solution from 298 to 398 K.



Fig.6: Effect of temperature on dye removal ([C₀]: 20 mg/L, adsorbent dosage: 0.3 g/L).

Increase dye removal may be due to an increase in the

number of active sites for adsorption due to increased mobility of color molecules with increasing temperature [4]. This effect shows the adsorption mechanism of methylene blue on HNT-COOH involves physical adsorption.

Thermodynamic study

Thermodynamic studies were performed based on equilibrium data which was investigated. Thermodynamic parameters include change of Gibbs free energy (ΔG°), enthalpy (ΔH°) and entropy (ΔS°) are calculated through the equations (1) and (2).

$$\log \left(\frac{q_e}{C_e} \right) = \frac{\Delta S^\circ}{2.303R} + \frac{-\Delta H^\circ}{2.303RT} \quad (1)$$

$$\Delta G^\circ = \Delta H^\circ - T\Delta S^\circ \quad (2)$$

Where q_e is the solid-phase concentration at equilibrium, C_e is equilibrium concentration in solution (mg/L), T is temperature in K, and R is gas constant (8.314 J/mol.K). Change in enthalpy (ΔH°) and entropy (ΔS°) are calculated as the slope and intercept of the linear Van't Hoff plot $\log(q_e/C_e)$ vs. $1/T$ intercept, respectively. In the following, the change of Gibbs free energy can be calculated from equation 2 [5].

The Van't Hoff plot related to the adsorption of methylene blue on HNT-COOH is shown in Fig. 7. Furthermore, various thermodynamic parameters are reported in Table 1.

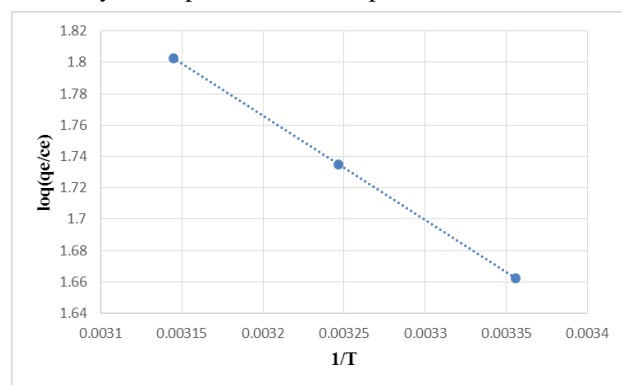


Fig.7: Van't Hoff plot of methylene blue adsorption onto HNT-COOH

Considering that the change of Gibbs free energy is negative at all temperatures while the change in enthalpy has positive values, this shows the nature of adsorption to be endothermic and irreversible.

Table 1: Thermodynamic parameters for adsorption of methylene blue dye on HNT-COOH at different temperatures

T(K)	ΔG° (kJ/mole)	ΔH° (kJ/mole)	ΔS° (kJ/mole)
298	-9.4461		
308	-10.2234	0.0745	12.7349
318	-10.9561		

Conclusions

This study demonstrated that the addition of carboxylic acid groups via succinic anhydride increases the adsorption efficiency of the methylene blue removal in wastewater, which can be explained by the interaction of the negatively charged sorbent and positive methylene blue dye molecules. Also, increasing temperature leads to increased removal of methylene blue on HNT-COOH.

Thermodynamic study indicates that the adsorption of methylene blue on HNT-COOH was an endothermic and irreversible process.

References

- [1] Yu, Liang, et al. "Recent advances in halloysite nanotube derived composites for water treatment." *Environmental Science: Nano* 3.1 (2016): 28-44.
- [2] Li, Ruijun, et al. "Highly selective solid-phase extraction of trace Pd (II) by murexide functionalized halloysite nanotubes." *Analytica Chimica Acta* 713 (2012): 136-144.
- [3] Joo, Yongho, et al. "Aggregation and stabilization of carboxylic acid functionalized halloysite nanotubes (HNT-COOH)." *The Journal of Physical Chemistry C* 116.34 (2012): 18230-18235.
- [4] Shahamati Fard, Farnaz, et al. "Enhanced acidic dye adsorption onto the dendrimer-based modified halloysite nanotubes." *Desalination and Water Treatment* 57.54 (2016): 26222-26239.
- [5] Afroze, Sharmeen, et al. "Adsorption of methylene blue dye from aqueous solution by novel biomass Eucalyptus sheathiana bark: equilibrium, kinetics, thermodynamics and mechanism." *Desalination and Water Treatment* 57.13 (2016): 5858-5878.

Densities and Viscosities for Binary and Ternary Mixtures of Benzene + Cyclohexane and + N,N-Dimethyl acetamide at Temperature of 298.15 K

M.Doost Mohammadi^a and M.Hamzehloo^{b*}

^{a,b}University of Tehran, college of science, school of chemistry, Department of physical chemistry, Tehran, Iran
Email: mhamzehloo@khayam.ut.ac.ir

Abstract: Densities, viscosities and derived properties for binary and ternary mixtures consist of Benzene, Cyclohexane and N,N-Dimethyl acetamide were measured at temperatures of 298.15 K in the whole range of mole fractions. The measured data and calculated values of all systems are in good agreement with literature and Redlich-Kister and the Cibulka equations.

Keywords: Density, Viscosity, Excess molar volume, N,N-Dimethyl acetamide

Introduction

Thermodynamic and transport properties are essential in process design and operation. Density and viscosity of the multicomponent mixtures are required in many chemical engineering calculations involving fluid flow, heat, and mass transfer. [1] The experimental data of excess thermodynamic properties of the liquid mixtures provide useful information about molecular interactions. Excess molar volumes (V^E), deviations in the viscosity ($\Delta\eta$) for the mixtures were derived from the experimental data. The experimental results are considered to talk about the strength of intermolecular interactions between the components of the systems.

Experimental

Chemicals are supplied by Merck with purity higher than 99%. The mixtures were prepared by weighing pure liquids into stoppered bottles to prevent evaporation and reducing possible errors in mole fraction calculation. The densities were measured with digital densitometer and viscosities were measured with an Ubbelohde viscometer. The apparatus was frequently calibrated by known pure liquid viscosity and density. The uncertainty in the mole fraction is estimated to be lower than $\pm 10^{-4}$.

Results and discussions

Dynamic viscosities and viscosity deviations were calculated from the following equation:

$$\eta = \eta_{\text{water}} \frac{\rho \times t}{\rho_{\text{water}} \times t_{\text{water}}} \quad \Delta\eta = \eta - \sum_{i=1}^N x_i \eta_i$$

Where η_{water} , ρ_{water} and t_{water} refers to viscosity, density and efflux time of pure water respectively.

The excess molar volumes (V^E) were calculated from density data by:

$$V^E = \sum_{i=1}^N x_i M_i \left(\frac{1}{\rho} - \frac{1}{\rho_i} \right)$$

The mixing functions V^E , $\Delta\eta$ were represented mathematically by the Redlich-Kister [2] equation for correlating the experimental data:

$$\Delta Q_{ij} = x_i x_j \sum_{k=1}^N A_k (x_j - x_i)^k$$

Derived data (V^E , $\Delta\eta$) for the ternary system were correlated, respectively, using the equation:

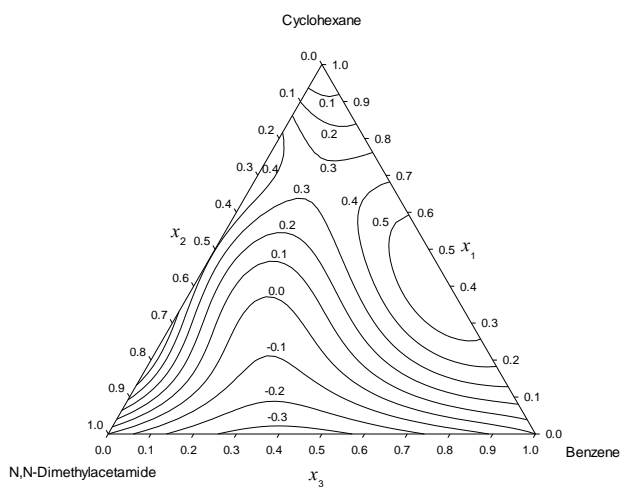
$$\Delta Q_{123} = \Delta Q_{\text{bin}} + x_1 x_2 x_3 \Delta_{123}$$

$$\Delta Q_{\text{bin}} = \sum_{i=1}^3 \sum_{j>i}^3 \Delta Q_{ij}$$

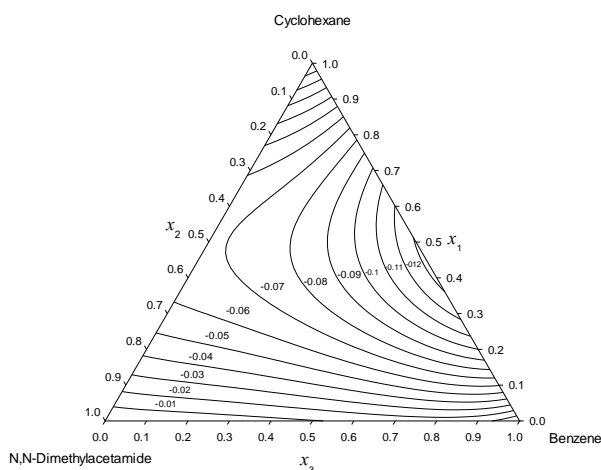
Where ΔQ_{123} refers to V^E , $\Delta\eta$ for the ternary mixtures. The ternary contribution term Δ_{123} was correlated using the expression suggested by Cibulka [3]:

$$\Delta_{123} = B_0 + B_1 x_1 + B_2 x_2$$

Where the ternary parameters B_0 , B_1 , and B_2 were determined with an optimization algorithm similar to that for the binary parameters.



Curves of $V^E/\text{cm}^3.\text{mol}^{-1}$ for the ternary system
Benzene(1) + Cyclohexane (2) + N,N-Dimethylacetamide (3) at 298.18 K



Curves of $\Delta\eta$ for the ternary system
Benzene(1) + Cyclohexane (2) + N,N-Dimethylacetamide (3) at 298.18 K

Figur1: ternary plot for excess molar volume and the deviation of viscosity of ternary system of Benzene, Cyclohexane and N,N-Dimethyl acetamide.

Conclusion

Densities, viscosities and derived properties for binary and ternary mixtures consist of Benzene, Cyclohexane and N,N-Dimethyl acetamide were measured at temperatures of 298.15 K in the whole range of mole fractions. The measured data and calculated values of all systems are in good agreement with literature and Redlich-Kister and the Cibulka equations.

References

- [1] Alvarez, E.; Sanjurjo, B.; Cancela, A.; Navaza, J. M. Mass Transfer and Influence of Physical Properties of Solutions in a Bubble Column. *Chem. Eng. Res. Des.* 2000, 78, 889–893
- [2] Redlich; O. J. Kister. A. T. Algebraic representation of thermodynamic properties and the classification of solutions. *Ind. Eng. Chem.* 1948, 40, 345-348.
- [3] Cibulka, I. Estimation of excess volume and density of ternary liquid mixtures of nonelectrolytes from binary data. *Collect. Czech, Chem. Commun.* 1982, 47, 1414-1419.

On the Calculation of Fugacity Coefficient of Thorium Using van der Waals Model

Mohsen Najafi^{1*} and Masoud Khajehvand²

1-Nuclear Science and Technology Research Institute, AEOI, Tehran, Iran

2-Department of Chemistry, Payam Noor University, Iran

*mnajafi@aeoi.org.ir

*msnnajafi@gmail.com

Abstract: The accurate description of thermodynamic properties and regularities of fluids and solids have been a subject to active research, which has developed continuously during the several decades and will continue to do so. Equation of State (EOS) represents the cornerstone of thermodynamic models. In van der Waals model, compressibility factor (Z) includes the sum of attractive and repulsive terms ($Z=Z_{rep}+Z_{att}$) and this model was the first equation to predict vapor-liquid coexistence. In this paper, we calculate fugacity coefficient for Thorium using some Equations of State (EOS). The EOSs are van der Waals type consist of van der Waals(vdW), Redlich-Kwong(RK) and Berthelot(B). All EOSs predict well the behaviour of fugacity coefficient of thorium qualitatively.

Keywords: Fugacity Coefficient, Thorium, Equation of State, van der Waals model

Introduction

Thorium is a naturally occurring [radioactive chemical element](#). It was discovered in 1828 by the Norwegian mineralogist [Morten Thrane Esmark](#) and identified by the Swedish chemist [Jöns Jakob Berzelius](#) and named after [Thor](#), the [Norse god](#) of thunder. Thorium produces a radioactive gas, [radon-220](#), as one of its [decay products](#). Secondary decay products of thorium include [radium](#) and [actinium](#). In nature, virtually all thorium is found as [thorium-232](#), which undergoes [alpha decay](#) with a [half-life](#) of about 14.05 [billion](#) years. Other [isotopes of thorium](#) are short-lived intermediates in the decay chains of higher elements, and only found in trace amounts. Thorium is estimated to be about three to four times more abundant than [uranium](#) in the Earth's crust, and is chiefly refined from [monazite](#) sands as a by-product of extracting [rare earth metals](#). Thorium was once commonly used as the light source in [gas mantles](#) and as an alloying material, but these applications have declined due to concerns about its radioactivity. Thorium is also used as an alloying element in nonconsumable [TIG](#) welding electrodes. When compared to uranium, there is a growing interest in developing a thorium fuel cycle due to its greater safety benefits, absence of non-[fertile](#) isotopes and its higher occurrence and availability. In this research, fugacity coefficient for Thorium will be calculated using some Equations of State (EOS) based on the equation (1)

$$\ln \phi = \int_0^p \left(\frac{Z-1}{p} \right) dp \quad (1)$$

Equations of State

The accurate description of thermodynamic properties and regularities of fluids and solids have been a subject to

active research, which has developed continuously during the several decades and will continue to do so. Equation of State (EOS) represents the cornerstone of thermodynamic models. They can be used to calculate vapor-liquid and liquid-liquid phase equilibria of fluids and fluid mixtures typically over wide ranges of temperature and pressure. EOSs are being formulated increasingly with the benefit of greater theoretical insights. The van der Waals EOS was the first equation to predict vapor-liquid coexistence in which compressibility factor (Z) includes the sum of attractive and repulsive terms ($Z=Z_{att}+Z_{rep}$). The doctoral thesis of van der Waals and several his works on the behaviour of gases and liquids have influenced and contributed to the development of several areas of physics and thermodynamics of fluids. In this paper, we used some EOSs for calculating fugacity coefficient of Thorium. The EOSs consist of

(I) van der Waals EOS (vdW)

This EOS, proposed in 1873, was the first equation capable of representing vapor-liquid coexistence

$$p = \frac{RT}{V_m - b} - \frac{a}{V_m^2} \quad (2)$$

(II) Redlich-Kwong EOS (RK)

The EOS, proposed in 1949, is one of the most important model for the modification of attractive term of vdW

$$p = \frac{RT}{V_m - b} - \frac{a}{T^{1/2}V_m(V_m + b)} \quad (3)$$

$$p = \frac{RT}{V_m - b} - \frac{a}{TV_m^2} \quad (4)$$

(III) Berthelot EOS (B)

This EOS, proposed in 1907 and like RK EOS, is the model for the modification of attractive term of vdW

$$\ln \phi_{vdW} = \ln(V) - \ln(V - b) - \frac{a}{RTV} - \ln(Z) + (Z - 1)$$

$$\ln \phi_{RK} = \ln(V) - \ln(V - b) - \frac{a}{bT^{1.5}} \ln \frac{V}{V + b} - \ln(Z) + (Z - 1)$$

$$\ln \phi_B = \ln(V) - \ln(V - b) - \frac{a}{RT^2V} - \ln(Z) + (Z - 1) \quad (5)$$

Figures 1 and 2 are the results of the calculations. It is clear that all EOSs predict well the behaviour of fugacity coefficient of thorium qualitatively.

References

Results

In this paper, we calculate fugacity coefficient for Thorium using some Equations of State (EOS). The EOSs are van der Waals type consist of van der Waals(vdW), Redlich-Kwong(RK) and Berthelot(B). The equations (5) show the fugacity coefficients based on these EOSs.

[1] Thorium: *Physico-Chemical Properties of Thorium and Its Compounds and Alloys*, IAEA, 1975

[2] R. Sadus, *Equation of State for The Calculation of Fluid-Phase Equilibrium*, J. AICHE, **46**(2000)169

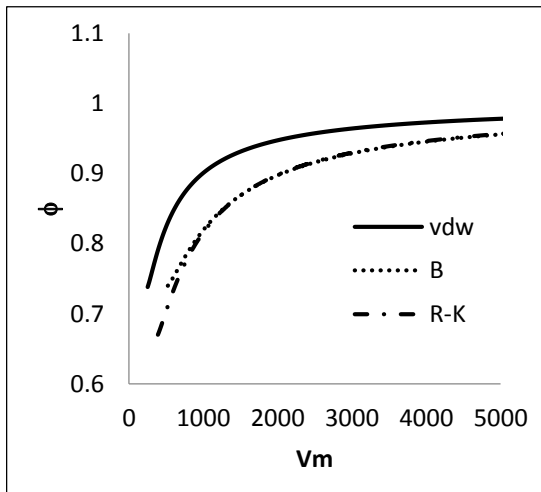


Figure1: Fugacity coefficient of thorium vs volume

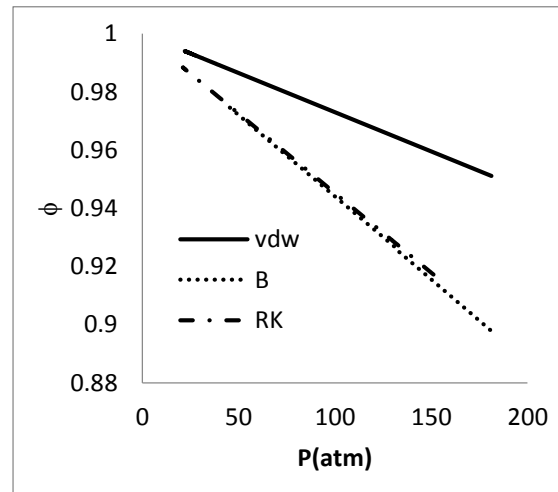


Figure2: Fugacity coefficient of thorium vs pressure

On the Evaluation of Dieterici Model Via The Study of Bulk Modulus and Tait-Marnagan Regularity of Associating Fluids

Mohsen Najafi^{1*} and Mahdi Darvishi²

1-Nuclear Science and Technology Research Institute, AEOI, Tehran, Iran

2-Department of Chemistry, Payam Noor University, Iran

*mnajafi@aeoi.org.ir

*msnnajafi@gmail.com

Abstract: Equations of State (EOS) are major tools for correlation and prediction of thermodynamic properties of fluids, therefore a large number of publications deal with their development or improvement. In 1899, Dieterici proposed an alternative theoretically based EOS involving an exponential term $Z = Z_{rep} e^{Z_{at}}$. There are some advantages in this model, such as a more realistic critical compressibility factor (Z^c). In this paper, we calculate bulk modulus and study Tait-Marnagan regularity of associating fluids in order to evaluate the performance of equations of state (EOS) based on Dieterici model. The investigated EOSs are Dieterici (D), Dieterici-Carnahan-Starling (DCS) and Dieterici-Guggenheim (DG). Our studies show that the bulk modulus and the regularity are predicted well by EOSs for all substances.

Keywords: Bulk Modulus, Tait-Marnagan Regularity and Associating Fluids, Dieterici Model

Introduction

The accurate description of thermodynamic properties of fluids has been a subject to active research, which has developed continuously during the several decades and will continue to do so. Equations of State (EOS) are major tools for correlation and prediction of thermodynamic properties of fluids, therefore a large number of publications deal with their development or improvement. An EOS which is valid over large intervals of temperatures and pressures is a powerful tool in thermodynamic predictions. Generally, three categories of EOS can be established according to their fundamentals: empirical, theoretical and semi-empirical. An empirical EOS is usually needed to several experimental data or many adjustable parameters and therefore their applications are usually restricted to a very limited number of substances. A theoretical EOS is also needed to the same number of molecular parameters, particularly to the intermolecular pair potential function. Semi-empirical EOSs are probably the most extensively used for prediction of thermodynamic properties of fluids. In this paper, we used three semi-empirical EOSs based on Dieterici model for calculating and predicting bulk modulus and Tait-Marnagan Regularity of some associating fluids in order to evaluate them.

Dieterici model

In 1899, Dieterici proposed an alternative theoretically based EOS involving an exponential term $p = \frac{RT}{V_m - b} e^{-a/RTV_m}$. There are some advantages in this model, such as a more realistic critical compressibility factor ($Z^c = 0.2706$). However the Dieterici equation

has not contributed significantly to the development of modern equations of state. This model can be generalized as $Z = Z_{rep} e^{Z_{at}}$. The attractive or repulsive term of Dieterici EOS can be replaced with the other terms. In this respect, we replaced the repulsive term of this model with the Carnahan-Starling and Guggenheim expressions as the following:

(I) Dieterici EOS (D)

$$p_D = \frac{RT}{V_m - b} e^{-a/RTV_m} \quad (1)$$

(II) Dieterici-Carnahan-Starling EOS (DCS)

$$p_{DCS} = \frac{RT(1 + \eta + \eta^2 - \eta^3)}{V_m(1 - \eta)^3} e^{-a/RTV_m} \quad (2)$$

(III) Dieterici-Guggenheim EOS (DG)

$$p_{DG} = \frac{RT}{V_m(1 - \eta)^4} e^{-a/RTV_m} \quad (3)$$

Bulk Modulus and Tait-Murnaghan Regularity

Bulk modulus is a thermodynamic properties of fluids

$$B_T = \rho \left(\frac{\partial p}{\partial \rho} \right)_T \quad (4)$$

Although fluids have different intermolecular interactions and molecular structures, nevertheless, there are some

regularities that nearly all fluids obey them. Several regularities have been reported for supercritical and subcritical fluids. Based on Tait-Murnaghan Regularity, the bulk modulus of fluid is nearly linear in pressure for each isotherm

$$B_T = B_{0,T} + B'_{0,T} P \quad (5)$$

Where $B_{0,T}$ is B_T in zero pressure and $B'_{0,T}$ is slope of bulk modulus in zero pressure. This regularity was first noticed by P. G. Tait over 100 years ago and is now called the Tait-Murnaghan regularity.

Results

In this research, we used three semi-empirical EOSs based on Dieterici model for calculating and predicting bulk modulus and Tait-Murnaghan Regularity of some associating fluids. We chose water, ammonia, methanol and hydrogen sulphide as associating fluids in our study. The obtained results are shown in Figures 1 to 4. It is clear that all EOSs predict well the behaviour of thermodynamic properties of fluids.

References

1. Y. S. Wei and Richard J. Sadus, *AIChE Journal*, **46**, 169(2000)
2. J. O. Valderrama, *Ind. Eng. Chem. Res.*, **42**, 1603(2003)
3. Sadus, R.J., *J. Chem. Phys.*, **115**, 1460 (2001)
4. Sadus, R.J., *Fluid Phase Equilibria*, **210**, 31 (2003)
5. Ali Maghari and Leila Hosseinzadeh-Shahri, *Fluid Phase Equilibria*, **206**, 287 (2003)
6. NIST, Chem Web Book, www.nist.gov

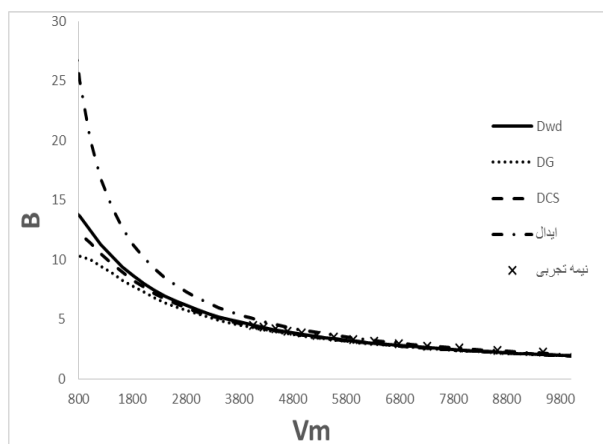


Figure1: Bulk modulus vs volume in 250 K for H₂S

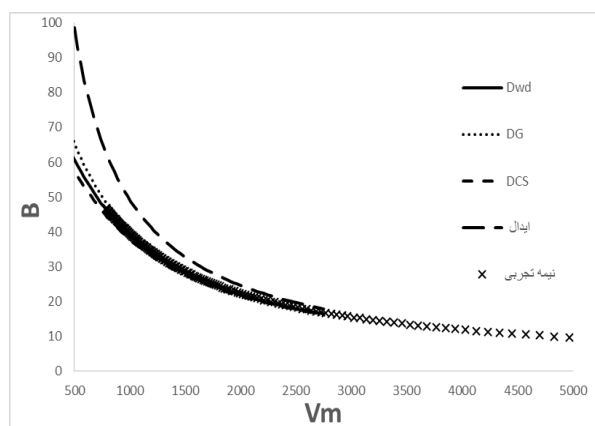


Figure2: Bulk modulus vs volume in 600 K for H₂O

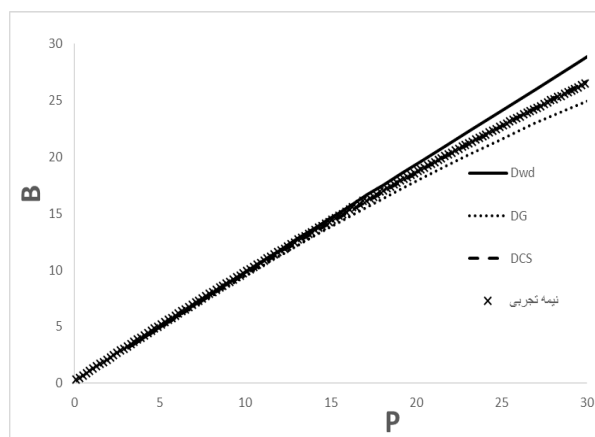


Figure3: Tait-Murnaghan Regularity for NH₃

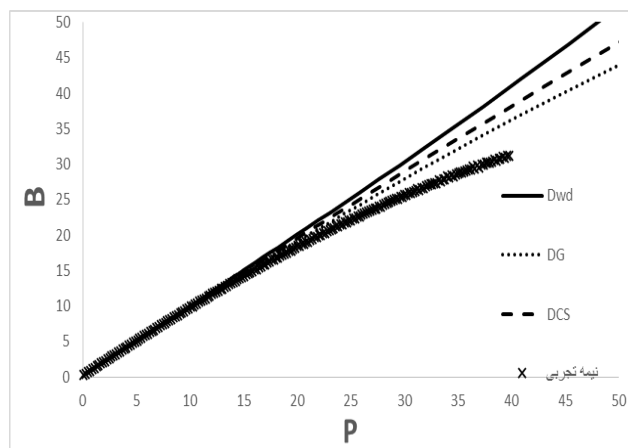


Figure4: Tait-Murnaghan Regularity for CH₃OH

Study of molecular interactions in binary mixtures containing 2-propanol, 1, 3-diaminopropane, and 2, 5-dimethoxytetrahydrofuran using macroscopic properties of solutions at 81.5 kPa and different temperatures

H. Iloukhani^{a,*}, K. Khanlarzadeh^{*a}, F. Panahi

^aDepartment of Physical Chemistry, Faculty of Chemistry, Bu-Ali Sina University, Hamedan, Iran
Khaterehkanlarzadeh@gmail.com

Abstract: Densities, ρ and refractive indices, n_D of binary mixtures consisting of 2-propanol, 1, 3-diaminopropane, and 2, 5-dimethoxytetrahydrofuran have been measured for the whole range of composition at temperatures of (298.15, 308.15, 318.15, and 328.15) K in ambient pressure (81.5 kPa). Excess molar volumes V_m^E , Partial excess molar volumes $\bar{V}_{m,i}^E$, refractive index deviations Δn_D , excess thermal expansion coefficient α^E and isothermal coefficient of pressure excess molar enthalpy $(\partial H_m^E / \partial P)_{T,x}$ for mixtures were derived. V_m^E and Δn_D for binary mixtures were correlated with the Redlich–Kister polynomial equation. The effect of temperature on the excess molar volumes and refractive index deviations are discussed in terms of molecular interaction between unlike molecules. Positive deviation from ideal state were recorded for excess volume in mixture of 1, 3-Diaminopropane + 2, 5-Dimethoxytetrahydrofuran and 2-Propanol + 2, 5-Dimethoxytetrahydrofuran solution. However in mixture of 2-Propanol and 1, 3-Diaminopropane negative deviation in the high composition of 1, 3-Diaminopropane varies to positive in the dominated mole fraction of alcohol which was analyzed to interpret the molecular interactions.

Keywords: Binary mixtures, Density, Excess molar volumes, Refractive index, Molecular interactions

Introduction

Thermodynamic properties of binary mixtures of amines, methoxy and hydroxyl groups are seemed to be interesting and would give great outcomes of molecular interactions in solutions. Meanwhile the studies of volumetric and electromagnetic properties of liquid mixtures provide valuable information on the structure and molecular interactions in solutions. In this sense, changes in structure consequence of molecular interaction can be provided by investigation of deviation of refractive index and the volumetric properties from ideal state due to composition and temperature. Deviation in solution properties from ideal state are resultant of broken bonds of primary pure components and formation of new bonds between molecules of different kinds. In fact, this deviation is affected by three factors: physical, chemical, and molecular structure that includes break the dipole-dipole, ionic, and hydrogen bonds and cause to positive deviation; On the other hand forming solvent-soluble bonds, which can be even hydrogen and dipolar type with proper orientation in some of the molecules, factors that are lead to negative deviations in solutions. In addition to these factors, the steric effect result of some large groups, as well as diversity in size and shape of components in mixtures are effected deviations substantially [1, 2].

The aim of our research group is developing the thermodynamic data for analysis and identification of molecular interactions in non-electrolyte solutions at different temperatures [3-5]. In this regard, present paper reports the density, ρ , and excess molar volume,

V_m^E , and Partial excess molar volumes, $\bar{V}_{m,i}^E$ of 2, 5-Dimethoxytetrahydrofuran (1) + 2-Propanol (2), 2, 5-Dimethoxytetrahydrofuran (1) + 1, 3-Diaminopropane (2), and 1, 3-Diaminopropane (1) + 2-Propanol (2) at temperatures of (298.15, 308.15, 318.15, and 308.15) K and at ambient pressure. Also, refractive index deviations Δn_D , excess thermal expansion coefficient α^E and isothermal coefficient of pressure excess molar enthalpy $(\partial H_m^E / \partial P)_{T,x}$ were reported. Deviation in excess molar volumes and refractive indices were calculated for the studied mixtures and data for the binary systems were fitted to Redlich–Kister equation and their parameters have also been calculated.

Materials and method

The 2-Propanol (CAS No. 67-63-0), 1, 3-Diaminopropane (CAS No. 109-76-2), and 2, 5-Dimethoxytetrahydrofuran (CAS No. 696-59-3) were purchased from Merck, and used without any further purification. The pure components were stored in the dark glasses at constant humidity and temperature.

Binary mixtures were prepared by mass, using electronic balance (Sartorius AG.GK 1203, Germany) with precision of ± 0.0001 g. Density of pure components and mixtures were measured using digital vibrating-tube densimeter (Anton Paar DMA 4500), with an accuracy of ± 0.01 K in temperature. The measurement of refractive indices of pure components and mixtures were obtained by digital automatic refractometer (Anton Paar Abbemat 500) with the accuracy of ± 0.01 K in temperature. The details regarding density and refractive index measurement using Anton Paar DMA4500 and Anton Paar Abbemat



500 are described in our previous literature [3]. The estimated uncertainty for density and refractive index measurement, and mole fraction, are $\pm 1 \times 10^{-5} \text{ g} \cdot \text{cm}^{-3}$, $\pm 5 \times 10^{-5}$, and $\pm 4 \times 10^{-4}$.

Results and Discussion

Excess molar volume for all mixtures was calculated from density results at different temperatures and at ambient pressure using the following equation:

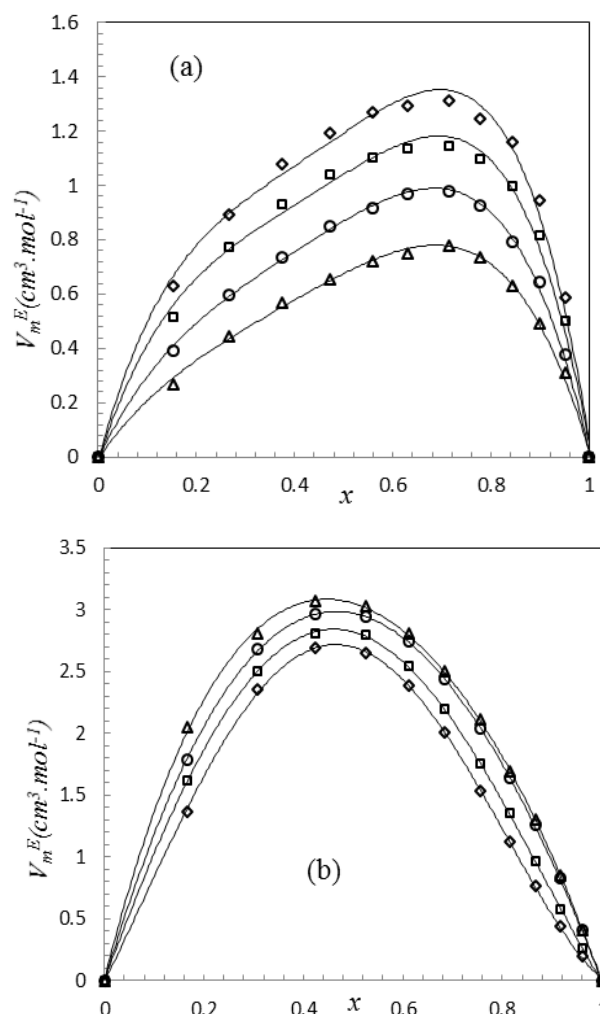
$$V_m^E = \sum_{i=1}^N x_i M_i (\rho^{-1} - \rho_i^{-1}) \quad (1)$$

Where ρ , is the density of the mixture, ρ_i , is the density of pure component, x_i , is the mole fraction, M_i , is the molar mass of component i , and N stands for the number of components in the mixtures. The excess molar volumes are estimated to $\pm 1 \times 10^{-3} \text{ cm}^3 \cdot \text{mol}^{-1}$. 2, 5-Dimethoxytetrahydrofuran (1) + 2-Propanol (2), 2, 5-Dimethoxytetrahydrofuran (1) + 1, 3-Diaminopropane (2), and 1, 3-Diaminopropane (1) + 2-Propanol (2) at temperatures of (298.15, 308.15, 318.15, and 308.15) K and at ambient pressure. The partial molar volumes, $V_{m,i}$, in these mixtures were calculated over the whole composition range using equation (2).

$V_{m,i} = V_m^E + V_{m,i}^* + (1 - x_i) (\partial V_m^E / \partial x_i)_{T,P}$ (2) V_m^E is the results contribution from several opposing effects. These effects may be divided arbitrarily into three types, namely, the physical, chemical, and structural. Physical contributions, that is, nonspecific interactions between the real species present in the mixture, contributes a positive term to V_m^E . The chemical or specific intermolecular interactions results in a volume decrease and these include charge-transfer type forces and other complex-forming interactions. This effect contributes with negative values to V_m^E . The structural contributions are mostly negative and arise from several effects, especially from interstitial accommodation and changes of free volume. The Prigogine-Flory-Patterson (PFP) theory has been commonly employed to analyze thermodynamic function for binary systems. This theory has been used to interpreting the results of measurements of the excess properties of a number of binary systems formed by molecular species which differ in size and shape. According to the PFP theory, excess molar volume calculations include three contributions: (i) interactional, which is proportional to the (χ_{12}) parameters; (ii) the free volume contribution which arises from the dependence of the reduced volume upon the reduced temperature as a result of the difference between the degree of expansion of the two components and (iii) the (P^*) contribution, which

depends both on the differences of internal pressures and differences of reduced volumes of the components. Excess molar volumes for these ternary systems were also predicted using for geometrical solution models. These models use binary contributions evaluated by Redlich-Kisterequation.

As can be seen in figures 1, V_m^E values for binary systems of 2, 5-Dimethoxytetrahydrofuran (1) + 1, 3-Diaminopropane (2), and 2, 5-Dimethoxytetrahydrofuran (1) + 2-Propanol (2) are positive over the whole composition range which indicates the expansion of mixing. As quantified by the Hammett equation, methoxy is an electron-donating group [6]. On the other hand, like ammonia, amines are bases [7]. There is not unexpected that broken bonds of primary pure components and formation of new bonds between molecules of different kinds lead to expansion in volume of mixtures and therefore positive deviations are obtained as can be seen in Figs 1 (a) – 1(b), which clearly indicate that there is a kind of repulsive interactions in these binary mixtures.



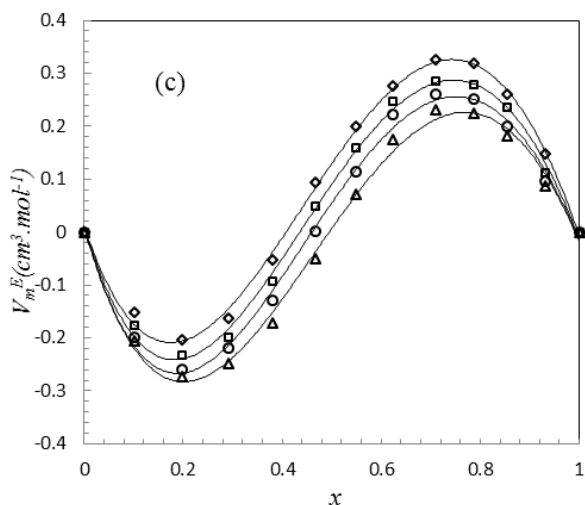


Fig. 1. Plot of experimental excess molar volume V_m^E vs. mole fraction for the binary systems at the temperatures 298.15 K (\diamond), 308.15 K (\square), 318.15 K (\circ), and 328.15 K (Δ). (a) 1,3-Diaminopropane+2,5-methoxytetrahydrofuran, (b) 2-Propanol + 2, 5-Dimethoxytetrahydrofuran, (c) 2-Propanol + 1, 3-Diaminopropane. The solid curves represent the corresponding correlations by the Redlich-Kister equation.

Conclusions

Understanding of molecular interactions is essential in chemical processes and thermodynamic properties are one of the best means to interpret and justify these interactions. In this paper we obtain densities and refractive indices of binary mixtures including of 2, 5-Dimethoxytetrahydrofuran, 1, 3-Diaminopropane, and 2-Propanol. Excess molar volume, V_m^E , Partial excess molar volumes, $\bar{V}_{m,i}^E$, refractive index deviations Δn_D , excess thermal expansion coefficient α^E and isothermal coefficient of pressure excess molar enthalpy $(\partial H_m^E / \partial P)_{T,x}$ were calculated. By using excess molar volume and refractive index deviations from ideal state, molecular interactions are estimated. In general it can be concluded that chemical interactions consequences to negative deviations and the positive quantities are indicated the physical interactions in binary systems.

Acknowledgment

The authors would like to thank the Bu-Ali Sina University for providing the necessary facilities to carry out the research

References

[1] G. Duve, O. Fuchs, H. Overbeck, Hoechst Solvents: Manual for Laboratory and Industry, 5th ed., Hoechst Aktiengesellschaft, 1974.

- [2] B.E. Poling, J.M. Prausnitz, J.P. Ó Connel, J.P., The Properties of Gas and Liquid, 5th ed., McGraw-Hill, New York, 2000.
- [3] H. Iloukhani, M. Jafarnejad, J. Chem. Thermodyn. 96 (2016) 210–221.
- [4] K. Khanlarzadeh, H. Iloukhani, M. Soleimani - J. Mol. Struct. 1139(2017) 78-86.
- [5] M. Jafarnejad, H. Iloukhani, Thermochim. Acta. 639 (2016) 160–172.
- [6] L.P. Hammett, *J. Am. Chem. Soc.* 59 (1937): 96 -103.
- [7] J.W. Smith, S. Parai, Basicity and complex formation, John Wiley & Sons Ltd. 1968.

Volumetric and Compressibility behavior of aqueous carbohydrate – polymer solutions at different temperature

Mehdi Dadkhah Tehrani^a, Rahmat Sadeghi^{b*}

^aDepartment of Chemistry, University of Kurdistan, Sanandaj, 6617715175, Iran

^bDepartment of Chemistry, University of Kurdistan, Sanandaj, 6617715175, Iran

*rahsadeghi@yahoo.com

Abstract: Density and sound velocity of carbohydrates such as glucose, fructose and sucrose in water and in aqueous solutions 10% w/w of polymer of PPG400, PEG400 at $T = (288.15, 293.15, 298.15, 303.15 \text{ and } 308.15) \text{ K}$ have been measured. From the experimental density and sound velocity data, isentropic compressibility values of solvent and aqueous solution of polymer-carbohydrate have been obtained and by using them, hydration number of carbohydrates were calculated. Apparent molar properties such as apparent molar volume, and apparent molar isentropic compressibility of carbohydrates were calculated and discussed about sweet property of carbohydrates. All results are discussed based on locations and type of interaction of OH groups in carbohydrate molecules.

Keywords : *Isentropic compressibility ; Apparent molar properties*

Introduction

Carbohydrates are the most abundant biomolecules on the surface of the earth, which plays a key role in plant and animal life [1]. Carbohydrates, because they can easily be solved in water, generally are placed in the field of green chemistry. Carbohydrate - polymer aqueous systems have the biphasic capability which one of the phases is carbohydrate – rich and other phase polymer – rich. Aqueous biphasic systems (ABS) when formed aqueous solution of two solutes with the power of different hydrophilic above a critical concentration mixed together. ABS formed under the influence of factors such as temperature, pH [2], presence of excess salt, average molar mass polymers [3] and etc. ABS have many advantages including major volume of each of the phases is containing water (> 80%) which creating a gentle environment for the biomolecules and prevents from destruction of macromolecules such as polymers; also tension interface between phases in this systems, is very low which it preserves the biological activity of the biomolecules. All of these advantages has led the aqueous biphasic systems as a powerful method for the extraction and purification of the proteins, cells, nanoparticles, amino acids, microorganisms, enzymes, nucleic acids, fungi, viruses, chloroplasts, mitochondria, membrane vesicles [4], etc.

Materials and method

Table1: Provenance and mass fraction of the chemical studied

Chemical name	Source	mass fraction purity
D (+) - Glucose	Merck	≥ 0.995
D (-) - Fructose	Merck	≥ 0.99
Sucrose	Merck	≥ 0.98
PEG400	Merck	-
PEG4000	Merck	-
PPG400	Aldrich	-

In order to prepare solutions of glucose, fructose and sucrose with different concentrations in water and in aqueous solution of 10% w/w different polymers, Sartorius CP124S balance served precisely within $\pm 1 \cdot 10^{-7} \text{ Kg}$. Density and velocity sound of solutions measured by using a vibrating-tube analyzer (Anton Paar DSA 5000, Austria) with precision $\pm 1 \cdot 10^{-3} \text{ Kg} \cdot \text{m}^{-3}$ and $\pm 1 \cdot 10^{-2} \text{ m} \cdot \text{s}^{-1}$, respectively, at (288.15, 293.15, 298.15, 303.15 and 308.15) K. The around temperature of this cell is controlled by a Peltier device within a precision of $\pm 1 \cdot 10^{-3} \text{ K}$. Before starting work, the device must be calibrated by double distilled water and dry air temperature of 293.15 K.

Results and Discussion

In order to determine how effect of polymers in carbohydrate aqueous solutions and look at changes that may occur in the volumetric and compressibility properties of carbohydrates, these systems were chooses. In this research, density and sound velocity of carbohydrates such as glucose, fructose and sucrose in water and in aqueous solutions 10% w/w of polymers such as PPG400, PEG400, PEG4000 and PEG10000 have been measured.

Isentropic compressibility values of solution, β_s , is expressed with equation $\beta_s = -\frac{1}{v} \left(\frac{\partial v}{\partial p} \right)_s$. This parameter can be calculated from empirical data of density and sound velocity and Laplace-Newton's equation:

$$\beta_s = \frac{1}{d u^2}$$

where d and u , are the density and sound velocity respectively.

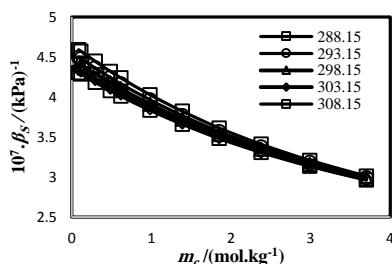


Fig. 1: Plot of isentropic compressibility of solution (β_s) against molality of carbohydrate (m_c). (A): glucose in water at different temperature

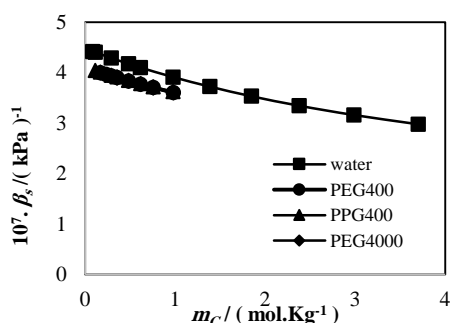


Fig. 2: Glucose in water and aqueous solutions of polymers at $T = 298.15 \text{ K}$.

In fact, before the junction of isotherms, water is a major portion in the solution compressibility; So in the area and similar to β_w of water is decreasing with temperature rising (Fig.1). As can be seen from Fig. 2, Isentropic compressibility of carbohydrates in water greater value than when in the presence of different polymers in constant temperature. In aqueous solution of polymer, more molecules of water interact with carbohydrates so number of water molecules of bulk are reduced and β_s is decreased too.

There are several ways to calculate the **hydration number**, n_h , such as ion mobility, entropy values, infinite dilution apparent molar volume, etc. in this study, this equation has been used [5]:

$$n_h = \frac{n_w}{n_s} \left(1 - \frac{\beta_s}{\beta_w} \right)$$

where n_w and n_s are the number of moles of water and solute respectively. This equation can be used under conditions where it is assumed n_h are number of molecules of water in the first layer of hydration and by a specified manner with solute molecules have interaction which it can be considered incompressible. In order to discussion on the hydration nature three types of carbohydrates in water and in aqueous solutions of polymers, various factors affect such as position of substituent over anomeric carbon, proportion of OH (axial) to OH (equatorial), hydrophobicity and hydrophobicity index [6,7], etc.

Apparent molar volume apparent molar volume of carbohydrates, V_ϕ , density values of these systems were used in the following equation [8]:

$$V_\phi = \frac{M_s}{d} + \frac{1000(d_0 - d)}{m_s d d_0}$$

where M_s and m_s is molecular mass and molality of carbohydrate, d_0 and d represent the density of the solvent and solution, respectively. Fig. 3 shows in a specified concentration with increasing temperature, V_ϕ is increasing a trend. When the temperature rises, thermal kinetic energy of molecules of water is increased and their interaction it with glucose molecules weakened. The trends for all carbohydrates are the same in water and in aqueous solutions of polymers. By comparing the apparent molar volume three carbohydrates in all solutions was observed trend of sucrose > glucose > fructose. Because of the larger structure, existence two rings in structure and presence more the number of OH groups in various situations, apparent molar volume is larger for sucrose.

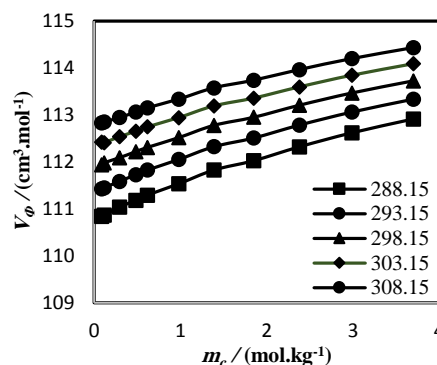


Fig. 3: Plot of apparent molar volume (V_ϕ) against glucose molality (m_c) in water at different temperatures

Apparent molar isentropic compressibility of the solutes, K_ϕ , which defined as $K_\phi = - \left(\frac{\partial V_\phi}{\partial P} \right)_S$ calculated from density and sound velocity experimental data of glucose, fructose and sucrose in different solutions, according to the following equation [8]:

$$K_\phi = \frac{1000(\beta_s d_0 - \beta_{s,0} d)}{m_s d d_0} + \frac{M_s \beta_s}{d}$$

Apparent molar isentropic compressibility of the solutes for these systems, all the values are negative because water molecules in the hydration layer of solute are more compact than water molecules of the bulk. With the increase of fructose molality and solute-solute interactions, gone out part of the water molecules of



fructose hydration layer and Joined to bulk. This causes decreasing electrostriction of fructose molecules and is rising K_ϕ . This behaviour seen for aqueous and polymer aqueous solutions of glucose and sucrose. Fig. 4 shows in a defined concentration, with increasing temperature compressibility rises for three carbohydrates in water and in polymers aqueous solutions. This phenomenon can be attributed to the weakening of the interaction between the molecular by increasing temperature. Amount of compressibility in a special solution this trend follows the: sucrose > glucose > fructose. Whatever molar isentropic compressibility more negative, indicative of the fact that compact water in hydration layer of solute is more difficult from water in bulk. From Fig. 5 it can be seen that By comparing the K_ϕ in solutions mentioned, lowest amount dedicated to aqueous solution of fructose in constant temperature. With the addition of the polymers to water-carbohydrate solution, reduced hydrogen interactions between water and carbohydrate that causes the release of water molecules of hydration layer which this change, increase the compressibility of carbohydrates in solutions than the be two-component solution of water-carbohydrate.

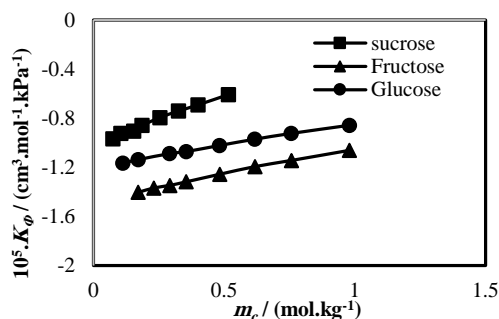


Fig. 4: Glucose fructose and in aqueous solution 10% w/w of PPG400 at $T = 298.15$ K.

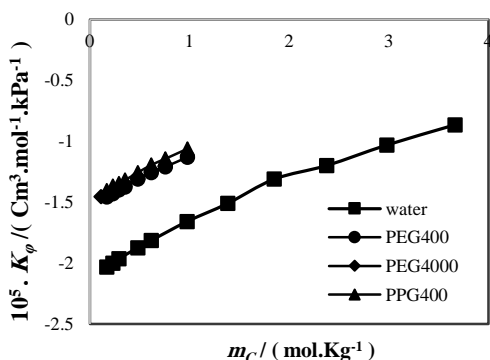


Fig. 5: Fructose in water and in aqueous solutions 10% w/w of polymers PEG400, PEG4000 and PPG400 at $T = 298.15$ K

Conclusions

Density and sound velocity of glucose, fructose and sucrose in aqueous solutions in presence and absence of polymers (PPG400, PEG400 and PEG4000) at different temperature have been reported. By comparing the hydration number and apparent molar volume of three carbohydrates at a specified temperature and concentration, observed the disaccharide of sucrose is higher values than the monosaccharide of glucose and fructose. Also fructose compared to glucose are more hydration as well as confirmed his apparent molar volume smaller than glucose. Also negative values of $\left(\frac{\partial^2 V_\phi^0}{\partial T^2}\right)_P$ for these carbohydrates represents their structure-breaking that this trend obey: sucrose > glucose > fructose.

Acknowledgment

The authors thank the Dr. N Ebrahimi and B Jamehbozorg for this experimental research.

References

- [1] A. Lehninger, D. L. Nelson "Lehninger Principles of Biochemistry", 2008, 5th Ed, 239-240, Madison, USA.
- [2] M. A. Eiteman, J. L. Gainer "The Effect of The pH Difference Between Phases on Partitioning in Poly (Ethylene Glycol)-Phosphate Aqueous Two-Phase Systems", *Chemical Engineering Communications*, 105 (1991), 171-183.
- [3] R. Sadeghi, F. jahani "Salting-in and Salting-out of Water-soluble Polymers in Aqueous Salt Solutins", *J. Phys. Chem. B*, 116 (2012), 5234-5241.
- [4] P. A. Albertsson "Partition of Cell Particles and Macromolecules: Separation and Purification of Biomolecules", 1986, wiley, New York, USA.
- [5] E. Junquera, D. Olmos, E. Aicart "Carbohydrate-Water Interactions of P-nitrophenylglycosides in Aqueous Solution. Ultrasonic and Densitometric Studies", *Physical Chemistry Chemical Physics*, 4 (2002), 352-357.
- [6] H. Uedaira, H. Uedaira "The Relation Between Partial Molar Heat Capacities And the Number of Equatorial Hydroxyl Groups of Saccharides in Aqueous Solution", *The Journal of Chemical Thermodynamics*, 17 (1985), 901-902.
- [7] K. Miyajima, K. Machida, M. Nakagaki "Hydrophobic Indexes for Various Monosaccharides ", *Bulletin of The Chemical Society of Japan*, 58 (1985), 2595-2599.
- [8] R. Sadeghi, R. Golabiazar, H. Shekaari "The Salting-out effect and Phase Separation in Aqueous Solutions of Tri-Sodium Citrate and 1-Butyl-3-Methyl Imidazolium Bromide", *The Journal of Chemical Thermodynamics*, 42 (2010), 441-443.



The solvent activity of binary mixtures 1-propanol + poly (ethylene glycol) dimethyl ether 250 and 500 at T = 298.15 K

S. Faraji^a, H. Shekaari^{b*}, M. T. Zafarani-Moattar

Department of Physical Chemistry, University of Tabriz, Tabriz, Iran

* hemayatt@yahoo.com

Abstract: Thermodynamic properties of binary mixtures, 1-propanol + poly(ethylene glycol) dimethyl ether(PEGDME)250/ poly(ethylene glycol) dimethyl ether(PEGDME)500 were determined. The activity of 1-propanol was measured in the poly (ethylene glycol) dimethyl ether 250 and 500 (PEGDME 250 and PEGDME 500) systems by use of isopiestic method at 298.15 K. The effect of the polymer molar mass on the solvent activity and also vapor pressure were studied. To calculate the activity of the solvent, CaCl₂ was used as isopiestic standard. The results show that the activity of 1-propanol in PEGDME500 is much more than PEGDME250. The obtained solvent activity data were correlated with the modified Flory-Huggins and Flory-Huggins activity equations.

Keywords: "Poly(ethylene glycol) dimethyl ether; Isopiestic method, 1-Propanol activity, vapor pressure"

Introduction

To study the nature and type of intermolecular interactions between the components of the mixtures, thermodynamic properties such as vapor-liquid equilibrium (VLE) are necessary. Vapor-liquid equilibrium data and correlation of solvent activity data using the activity equations as an important thermodynamic property in polymer + solvent systems have been of great importance for a range of different actions such as surface acoustic-wave vapor sensors, recovery of organic vapors from waste-air streams using a polymeric membrane, pervaporation

Different techniques were used to measure the activity of the solvent in the solutions. Among them, the isopiestic method is the easiest technique which is based on variety of solutions including nonvolatile solutes by transferring solvent mass by vaporation, when connected through the vapor space to approach equilibrium.

The chemical potentials of the solvent in each of the solutions in the closed equilibrium systems are equal. Since the solvent activity is known for one or more standard solutions, it will be known for each solution within the isopiestic system.[1] Recent studies are employed isopiestic apparatus for the measurement of the activity of 1-propanol in 1-propanol + poly(ethylene glycol) dimethyl ether 250 and 500 systems with different molar masses of the polymer. Therefore, in this work, the activity of 1-propanol in the binary mixtures (1-propanol (1) + PEGDME250 (2)) and (1-propanol (1) + PEGDME500 (2)) were measured for obtaining vapor pressure depression. The results were correlated with the modified Flory-Huggins and Flory-Huggins equations.[2,3]

Materials and method

All the chemical were obtained from Merck Co. The calcium chloride (G R, minimum 0.995 in mass fraction) were dried in an electrical oven at about 110°C for 24h

prior to use. 1-Propanol with the purity of minimum mass fraction 0.998, poly(ethylene glycol) dimethyl ether 250 and 500 without more purifications were employed.

The isopiestic method was used to measure of solvent activity in the studied solutions. The apparatus was held in constant temperature batch for at least 120 h for equilibration at 298.15 K using a Heto temperature controller (Heto therm PF, Heto Lab Equipment, Denmark) within ± 0.01 K. To determine isopiestic equilibrium molalities, the masses of isopiestic flasks in equilibrium were prepared by an analytical balance (Shimadzu, 321-34553, Shimadzu Co., Japan) with a precision of $\pm 1 \times 10^{-8}$ kg as described previously. [4]

Results and Discussion

At isopiestic equilibrium, the activity of solvent in the reference and PEGDME solutions must be the equal. Thus, the solvent activity (a_s) in the solutions of alcohol + polymer from that of reference solutions is calculated with the isopiestic equilibrium mass fractions with reference standard solutions. Alcohol activity is one of the important thermodynamic properties which gives a deep insight of to solute-solute and solute-solvent interactions. In the current study, the improved isopiestic method was used to study the vapor-liquid equilibria behavior of binary 1-propanol (1) + PEGDME250 (2) and 1-propanol (1) + PEGDME500 (2) mixtures at 298.15 K. The activity of the 1-propanol at isopiestic equilibrium in the reference and sample solutions must be equal. It was understood that the activity data with respect to molality of CaCl₂, m_r , is fitted directly with the a fourth-order polynomial that coefficient of equation for reference and 1-propanol [5] is as following: $b_0 = -0.012 \pm 0.001$, $b_1 = -0.1 \pm 0.01$, $b_2 = 0.06 \pm 0.01$, $b_3 = -0.012 \pm 0.003$;

$$a_s = 1 + b_0(m_r) + b_1(m_r)^2 + b_2(m_r)^3 + b_3(m_r)^4 \quad (1)$$



For the VLE description of polymer solutions, the activity data of solvent are fitted with using Flory Huggins equation indicating the relation between experimental data with the use of the following model

$$\ln a_1 = \ln(\varphi_1) + (1-1/r_2)(1-\varphi_1) + \chi_{12}(1-\varphi_1)^2 \quad (2)$$

where, φ_1 , indicates volume fraction of solvent, χ_{12} , the interaction parameter of Flory Huggins for the system, r_2 is the segments of polymer is expressed as molar volume from polymer to molar volume from solvent correlated with the equation of $r_2 = (M_p/\rho_p)/(M_s/\rho_s)$, where ρ_p and ρ_s are density of polymer and solvent respectively. Derived the interaction parameter for the studied systems which is χ_{12} .

Vapor pressure depression values (Δp) is another important thermodynamic property which is directly attributed to the solute – solvent interactions and can be computed using the vapor pressures of the solutions, with use of the equ (6).

$$\Delta p = p_s^0 - p_{exp} \quad (3)$$

where, p_{exp} experimental vapor pressure and p_s^0 vapor pressure for the pure solvent. The obtained values for the Δp are given in table 1.

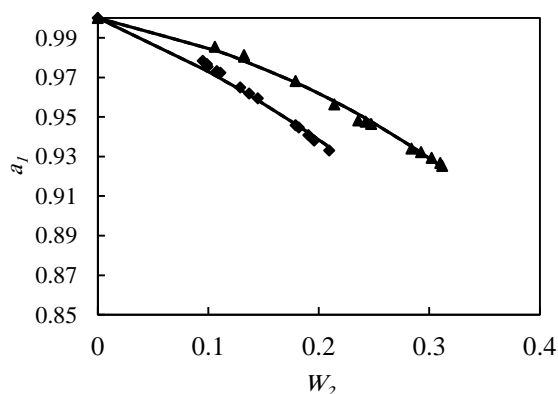


Fig.8: The comparison of activity of 1-propanol in binary mixtures of 1-propanol + PEGDME250 and 1-propanol + PEGDME500 at T = 298.15 K.

Table1: Experimental isopiestic data for the 1-propanol (1) + PEGDME500 (2) at T = 298.15 K.

W_{CaCl2}	W_2	a_1	$p / (\text{kPa})$	$\Delta p / (\text{kPa})$
	1-propanol (1) + PEGDME500 (2)			
0.0000	0.0000	1.000	2.780	0.000
0.0381	0.1062	0.985	2.740	0.040
0.0448	0.1324	0.981	2.728	0.052
0.0458	0.1326	0.980	2.726	0.054

0.0625	0.1792	0.968	2.691	0.089
0.0766	0.2142	0.956	2.658	0.122
0.0860	0.2359	0.948	2.636	0.144
0.0868	0.2425	0.948	2.634	0.146
0.0882	0.2475	0.946	2.631	0.149
0.1022	0.2840	0.934	2.596	0.184
0.1041	0.2927	0.932	2.591	0.189
0.1074	0.3022	0.929	2.583	0.197
0.1103	0.3101	0.927	2.576	0.204
0.1120	0.3119	0.925	2.572	0.208

Standard uncertainties (σ) for each variables are $\sigma(X_2) = 0.0001$; $\sigma(a_1) = 0.001$; $\sigma(T) = 0.01\text{K}$; $\sigma(p) = 0.01 \text{ kPa}$

Conclusions

The modified isopiestic method was successfully used to measure the solvent activity in 1-propanol + PEGDME250 and + PEGDME500 solutions at 298.15 K. The findings have been correlated to the modified Flory-Huggins and Flory-Huggins equations. It was found that the vapor pressure depression in PEGDME500 was less than PEGDME250 solutions. Also, by the use of obtained standard deviations for the solvent activity and vapor pressure, it was understood that the modified Flory-Huggins equation has successfully correlated with experimental data.

Acknowledgment We are grateful to University of Tabriz Research Council for the financial support of this research.

References

- [1] L.R. Ochs, M. Kabiri-badr, H. Cabezas, An improved isopiestic method to determine activities in multicomponent mixtures *AIChE J* 36 (1990) 1908-1912.
- [2] Y. Bae, J. Shim, D. Soane, J. Prausnitz, Representation of vapor-liquid and liquid-liquid equilibria for binary systems containing polymers: applicability of an extended Flory-Huggins equation, *J. Appl. Poly. Sci* 47 (1993) 1193-1206.
- [3] P.J. Flory, Principles of polymer chemistry, Cornell University Press, 1953
- [4] M.T. Zafarani-Moattar, H. Shekaari, E.M.H. Agha, Vapor – Liquid equilibria study of the ternary systems containing sucrose in aqueous solutions of ionic liquids, 1-butyl-3-methyl imidazolium bromide and 1-hexyl-3-methyl imidazolium bromide at 298.15 K and atmospheric pressure, *Fluid Phase Equilib* 429 (2016) 45-54.
- [5] M.T. Zafarani-Moattar, N. Tohidifar, Vapor-Liquid Equilibria, Density, Speed of Sound, and Viscosity for the Poly (ethylene glycol) 400+ 1-Propanol and 1-Butanol Systems, *J. Chem. Eng. Data* 59 (2014) 4070-4080.



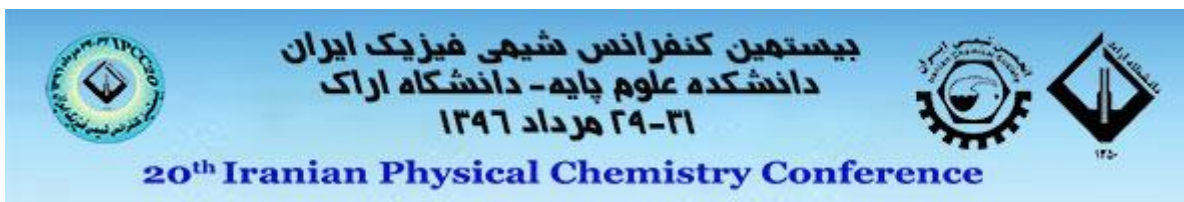
بیستمین کنفرانس شیمی فیزیک ایران
دانشکده علوم پایه - دانشگاه اراک
۳۱-۲۹ مرداد ۱۳۹۶



20th Iranian Physical Chemistry Conference

سینتیک شیمیایی

Chemical Kinetics



Isotherm and Kinetic Modeling of Adsorption of Acridine Orange Using Eucalyptus-Wood Based Activated Carbon Modified with Maghemite Nanoparticles

T. Momeni Isfahani*

Department of Chemistry, Arak Branch, Islamic Azad University, Arak, Iran

P.O. Box 38135-567, Arak 38135-567, Iran

*t-momeni@iau-arak.ac.ir

Abstract: In this study, activated carbon (AC) was prepared from low cost and locally available source such as eucalyptus wood, the activated carbon modified with γ -Fe₂O₃. The activated carbon was produced by the acid treatment of the carbon obtained from eucalyptus wood. The prepared nanomaterial was characterized by field emission scanning electron microscopy (FE-SEM), X-ray diffraction (XRD) and vibrating sample magnetometer (VSM) to examine their size and magnetic moment. The γ -Fe₂O₃ nanoparticle loaded activated carbon (γ -Fe₂O₃-NPs-AC) was used as novel adsorbent for the removal of acridine orange. The Freundlich and Langmuir isotherms were studied. The Langmuir was found to be most applicable isotherm which predicted maximum monolayer adsorption capacities of 154.74 mgg⁻¹ for the adsorption of dye. The pseudo-second order model was found to be applicable for the adsorption kinetics.

Keywords: Maghemite nanoparticles, Acridine Orange, activated carbon

Introduction

Dyes widely applied in textiles, food and beverage industries and printing processes [1]. These materials are important pollutants that lead to producing serious hazards to the human and other animals and organisms. Dyes present in wastewater generate high toxicity following possible accumulation in the various ecosystems and the environment. Therefore, their removals from industrial effluents before discharge into the environment require extreme and great attention [2]. Among versatile protocol for wastewater treatment versatile, the adsorption methods are widely used to remove classes of chemical pollutants from wastewater. Activated carbon is one of the most preferred adsorbent over other adsorbents due to its high surface area and easy availability. However, the high operating cost and difficulties in the regeneration of activated carbon leads to many researchers to search for more economic adsorbents. Use of biomass consisting mainly of agricultural and forestry waste, can be regarded as a renewable energy source with great potential to supply the global material demands [3].

The nano-adsorbents are of high specific surface area and accessible surface adsorption sites which make them well applicable for the adsorption of pollutants. Many authors have documented the technology of magnetic adsorbents by incorporation of magnetic nanoparticles of iron oxide on adsorbent substrates [4]. Magnetite (Fe₃O₄) and maghemite (γ -Fe₂O₃) are the most commonly employed.

In this work, the maghemite (γ -Fe₂O₃) nanoparticles loaded on the activated carbon was synthesized. The prerequisite for magnetic separation is the synthesizing or combining them with nanoparticles

(metal oxides). These nanoparticles that are mainly in the form of γ -Fe₂O₃, were separated or removed accompany with the target pollutants from the aquatic environment by a magnet. The presence of γ -Fe₂O₃ in the adsorbent's structure leads to chemical stability, decreased toxicity, and excellent recyclability of the adsorbent. The main goal of this work was to investigate the adsorption capacity of the γ -Fe₂O₃-NPs-AC as an adsorbent for removal of the Acridine Orange dye from aqueous solution.

Materials and method

After crushing the pruned branches of a number of eucalyptus trees into small pieces, they were washed with distilled water and then dried overnight. The dried small pieces of eucalyptus wood were placed in a furnace and heated. After further grinding in a mortar, they were sieved into a uniform size (50-80 mesh). Then, they were impregnated with a concentrated solution of the HCl and HNO₃. The reaction solution for loading γ -Fe₂O₃ nanoparticles on activated carbon (AC) was prepared as follows: iron (ii) sulfate solution and NH₄Fe (SO₄)₂ were dissolved in deionized water followed by complete mixing with AC. Then sodium hydroxide was added to the prepared mixed solution drop-by drop along with strong stirring at room temperature. The produced γ -Fe₂O₃-NPs-AC was filtered, washed several times with distilled water and dried.

Results and Discussion

In this study, the structure of the produced γ -Fe₂O₃-NPs-AC was characterized by VSM, XRD and FE-SEM techniques. The FE-SEM is useful for

determination of the particle size, shape and porosities, result is shown in Fig.1. An XRD analysis as powerful tools was used to study the crystal structures of the γ -Fe₂O₃ nanoparticles and result is shown in Fig. 2. The magnetization curve in Fig. 3 gives a saturation magnetization value of 30.21 emu/g.

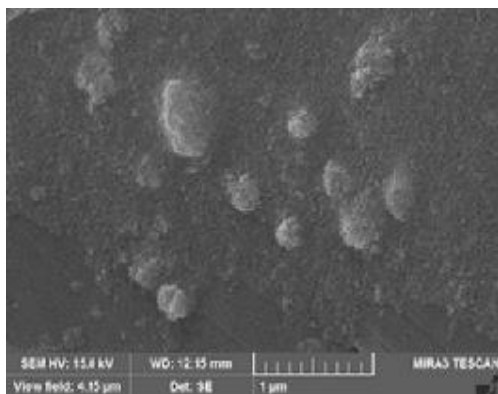


Fig. 1: FESEM image of the γ -Fe₂O₃-NPs,

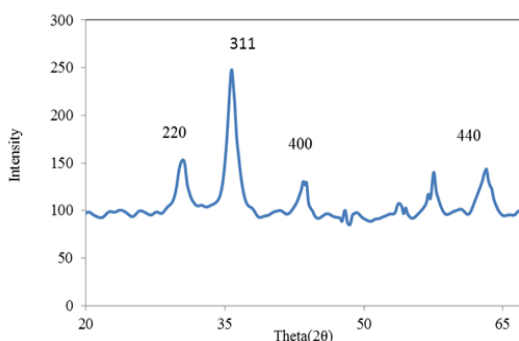


Fig. 2: XRD pattern of γ -Fe₂O₃-NPs.

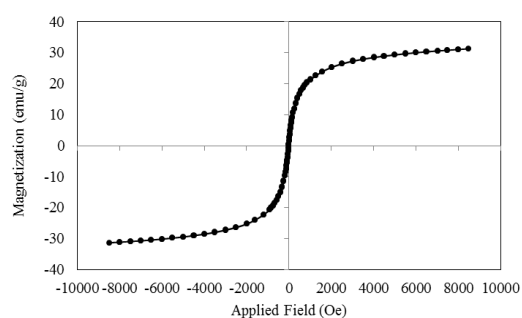


Fig. 3: Magnetization curve of γ -Fe₂O₃.

Kinetic models

The appropriate kinetic models such as pseudo-first order and pseudo-second order kinetics were investigated to study the rate and mechanism of adsorption process. The pseudo-first-order equation is expressed as follows:

$$\log(q_e - q_t) = \log(q_e) - \frac{k_1 t}{2.303}$$

Where K_1 is the Lagergren rate constant of adsorption (min^{-1}). The plot of $\log(q_e - q_t)$ against t gives a linear relationship from which K_1 and q_e are determined from the slope and intercept of the plot, respectively [5]. The relatively low correlation coefficient of this model and higher value of difference between experimental and calculated value of adsorption capacity (Table 1) show its inappropriateness for analyzing kinetic data corresponding to the entire adsorption process.

Table 1: Parameters obtained from the kinetics models

Model	Parameters	Value
Pseudo -first-order	$k_1(\text{min}^{-1})$	0.0140
	$q_e(\text{calc})(\text{mg g}^{-1})$	3.2690
	R^2	0.9405
Pseudo- second-order	$k_2(\text{g mg}^{-1} \text{min}^{-1})$	0.0025
	$q_e(\text{calc})(\text{mg g}^{-1})$	23.1204
	R^2	0.9904
Exp. data	$q_e(\text{exp})(\text{mg g}^{-1})$	24.0134

Therefore, the experimental data was fitted to the second-order rate constant. The pseudo-second-order equation is expressed as follows:

$$\frac{t}{q_t} = \frac{1}{k_2 q_e^2} + \left(\frac{1}{q_e}\right)t$$

Where k_2 is the pseudo-second-order rate constant of adsorption ($\text{g mg}^{-1} \text{min}^{-1}$). The values of q_e and k_2 are determined from the slope and intercept of the t/q_t against t [5]. The high correlation coefficients of this model over the whole adsorption stage in addition to the closeness of theoretical and experimental q_e values show the applicability of this model for analyzing experimental data (Table 1).

Adsorption isotherms

Studies of the adsorption isotherms are necessary to attain useful information about the nature of dye interaction with adsorbents and to evaluate their applicability and efficiency for this purpose. The experimental equilibrium data was fitted to two well-known isotherm models like Langmuir and Freundlich. In the Langmuir isotherm [6] monolayer accumulation of target compound on the surface of the adsorbent is represented in linear form as follows:

$$\frac{C_e}{q_e} = \frac{1}{K_L q_m} + \frac{C_e}{q_m}$$

Where K_L is Langmuir constant or adsorption equilibrium constant ($L mg^{-1}$). Following plotting the C_e/q_e versus C_e , based on the slope and intercept value of achieved line, the value of $1/K_L q_m$ and $1/q_m$ was calculated and their value was presented in Table 2.

The Freundlich isotherm can be expressed in the linear form as follows:

$$\ln q_e = \ln K_f + \frac{1}{n} \ln C_e$$

Where $K_f (mg g^{-1})(L mg^{-1})^{1/n}$ and $1/n$ are isotherm constants that indicate the capacity and intensity of the adsorption, respectively.

Table 2: Isotherm constant parameters and correlation coefficients calculated.

Model	Parameters	Value
Langmuir	$q_m (mg g^{-1})$	154.74
	$K_L (L mg^{-1})$	0.6020
	R^2	0.9594
Freundlich	$1/n$	0.4886
	$K_f (mg g^{-1})(L mg^{-1})^{1/n}$	6.5080
	R^2	0.8954

The fitting results show that the correlation coefficient of Langmuir isotherm was higher than of Freundlich isotherm, indicating that the adsorption of Acridine Orange on γ -Fe₂O₃-NPs-AC can be better fitted using Langmuir model and the adsorption is a monolayer adsorption.

Conclusions

A simple and fast procedure was developed using economic, effective, and eco-friendly adsorbent, the activated carbon modified with γ -Fe₂O₃ for removal of Acridine Orange. Kinetic regression results showed that the adsorption process is more accurately represented by a pseudo-second-order model. Langmuir isotherm model was found to be superior to another model. The results indicated that the removal method has a remarkable ability to improve the efficiency of dyes removal.

Acknowledgment

The authors gratefully acknowledge the support to this work from, Islamic Azad University, Arak Branch, and research council.

References

- [1] A. Mittal, J. Mittal, A. Malviya, V. Gupta, Adsorptive removal of hazardous anionic dye "Congo red" from wastewater using waste materials and recovery by desorption, *Journal of Colloid and Interface Science*, 340 (2009) 16-26.
- [2] M. Ghaedi, A. Ghaedi, M. Hossainpour, A. Ansari, M. Habibi, A. Asghari, Least square-support vector (LS-SVM) method for modeling of methylene blue dye adsorption using copper oxide loaded on activated carbon: Kinetic and isotherm study, *Journal of Industrial and Engineering Chemistry*, 20 (2014) 1641-1649.
- [3] N. Saeidi, M. Parvini, Z. Niavarani, High surface area and mesoporous graphene/activated carbon composite for adsorption of Pb (II) from wastewater, *Journal of Environmental Chemical Engineering*, 3 (2015) 2697-2706.
- [4] M. Yamaura, D.A. Fungaro, Synthesis and characterization of magnetic adsorbent prepared by magnetite nanoparticles and zeolite from coal fly ash, *Journal of Materials Science*, 48 (2013) 5093-5101.
- [5] M. Ravanan, M. Ghaedi, A. Ansari, F. Taghizadeh, D. Elhamifar, Comparison of the efficiency of Cu and silver nanoparticle loaded on supports for the removal of Eosin Y from aqueous solution: Kinetic and isotherm study, *Spectrochimica Acta Part A: Molecular and Biomolecular Spectroscopy*, 123 (2014) 467-472.
- [6] C. Namasivayam, D. Kavitha, Removal of Congo Red from water by adsorption onto activated carbon prepared from coir pith, an agricultural solid waste, *Dyes and pigments*, 54 (2002) 47-58.

Elimination of methylene blue dye by nano clinoptilolite zeolite from aqueous solutions, kinetic and thermodynamic studies

M. Banimahd Keivani^{a,*}

^aDepartment of Chemistry, Payame Noor University, 19395-4697, Tehran, Iran

*mbk_ir@yahoo.com

Abstract: In this paper we study kinetic and thermodynamic parameters for elimination of methylene blue (MB) dye from aqueous solution by application nano clinoptilolite zeolite (NCZ). The effects of some important parameters such as kinetic and thermodynamic parameters were studied. It was found that second-order kinetics model ($r^2 = 0.9994$) is more better than first-order kinetics model ($r^2 = 0.1688$). The change in Gibb's free energy (ΔG°), the change in entropy (ΔS°) and the change in enthalpy (ΔH°) were also investigated and calculated for this removal. this process had negative changes in Gibb's free energy and positive in enthalpy and entropy. This adsorption was an endothermic and spontaneous process.

Keywords: Nano clinoptilolite; Zeolite; Kinetic; Thermodynamic; Methylene blue

Introduction

Some of the physicochemical methods that have been employed to remove dye from wastewater include chemical precipitation, coagulation, membrane filtration, electrolysis and oxidation [1]. Nano clinoptilolite zeolite is a mineral material that obtained from mine in khorasan province.

Study of removal kinetic is important to evaluate an adsorption dynamics. In order to determining mechanism of adsorption processes such as chemical reaction and removal, the pseudo-first-order adsorption and the pseudo-second-order were used to examine the experimental data [2]. To study the effect of thermodynamic parameters, such as, the change in Gibb's free energy (ΔG°), the change in entropy (ΔS°) and the change in enthalpy (ΔH°) were also investigated and calculated for adsorbent using following relations [3].

Materials and method

All chemicals used were analytical reagents grade and prepared in distilled water. Nano clinoptilolite zeolite is a mineral material that obtained from mine in khorasan province. For obtain of nano size of zeolite, use ball mill. Absorbance measurements were carried out on a single beam Perkin-Elmer UV-Vis spectrophotometer with a 1 cm cell was used for measuring all of absorption data.

Results and Discussion

For the further investigation of kinetics data, the pseudo-second-order model was used. The linear forms of the both kinetic models are shown below:

$$\ln(q_e - q_t) = \ln q_e - k_1 t \text{ Pseudo-first order} \quad (1)$$

$$\frac{t}{q_t} = \frac{1}{k_2 q_e^2} + \frac{t}{q_e} \text{ Pseudo-second order} \quad (2)$$

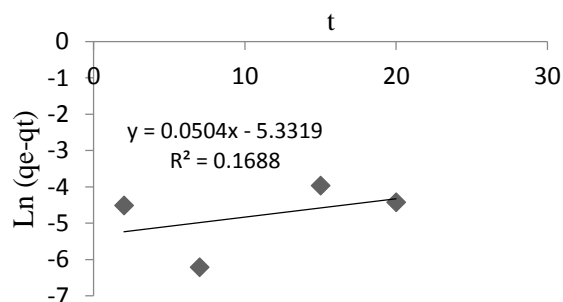


Fig1 : Pseudo-first order model for removal of MB by NCZ

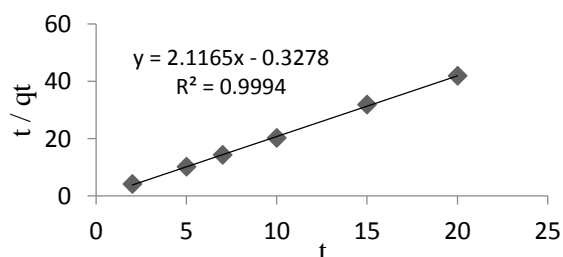


Fig2 : Pseudo-second order model for removal of MB by NCZ

Table1: Adsorption kinetic parameters of MB onto NCZ,
T=298K

Pseudo-first order			
q_e^a	K_1	q_e^b	r_1^2
0.0048	-0.0504	0.478	0.1688
Pseudo-second order			
q_e^a	K_2	q_e^b	r_2^2
0.472	-13.69	0.478	0.9994

^a Calculated ^b Experimental

The change in Gibb's free energy (ΔG°), the change in entropy (ΔS°) and the change in enthalpy (ΔH°) were also investigated and calculated for adsorbent using following relations.

$$\Delta G^\circ = -RT \ln K_c \quad (3) \quad K_c = \frac{C_{Ad}}{C_e} \quad (4)$$

$$\ln K_c = \frac{\Delta S^\circ}{R} - \frac{\Delta H^\circ}{R} \left(\frac{1}{T}\right) \quad (5)$$

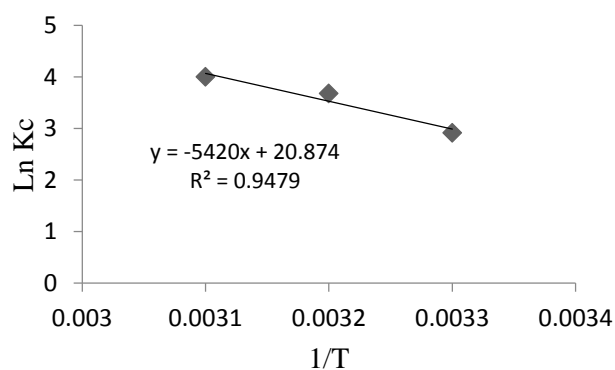


Fig3 : Vantt hoff equation for removal of Mb by NCZ

Table 2: Thermodynamic parameters for adsorption of MB onto NCZ

T (K)	ΔG° (KJ)	ΔH° (KJ)	ΔS° (J)
298	-6.627	45.061	173.54
308	-8.361		
318	-10.096		

Conclusions

Different between experimental and calculated q_e shows no applicability of the pseudo-first order model in predicting the kinetics of the MB adsorption onto the NCZ. For this removal the pseudo-second order model is

better than the pseudo-first order model. Thermodynamic calculation carried out the sorption of MB by NCZ was an endothermic process and this process had negative changes in Gibb's free energy and spontaneously.

References

- [1] V. K. Garg, R. Gupta, A. Yadav, R. Kumar "Dye removal from aqueous solution by adsorption on treated sawdust", *Bioresource Technology*, 89(2), (2003), 121-124.
- [2] M. Zhao, Z. Tang, P. Liu, "Removal of methylene blue from aqueous solution with silica nano-sheets derived from vermiculite", *J. Hazard. Mat.*, 158(1), (2008), 43-51.
- [3] V. Vadivelan, K.V. Kumar, "Equilibrium, kinetics, mechanism, and process design for the sorption of methylene blue onto rice husk", *J. Colloid Interface Sci.*, 286(1), (2005), 90-100.

Bovine Serum Albumin interactions with new derivatives Schiff base study by spectroscopic techniques

H. Dezhampannah and R. Binazir*

Department of Chemistry, Faculty of Science, University of Guilan, Rasht, Iran

h.dpanah@guilan.ac.ir

Abstract The interaction of ternary Cu(II) complexes of Schiff base tyrosine amino acid derivatives and bipyridine heterocycle (S) with bovine serum albumin (BSA) was investigated using fluorescence quenching and Fourier transform infrared (FTIR). Fluorescence quenching data showed that the quenching mechanism of BSA treated by the complex was static quenching, which was highly accord with the non-radioactive energy transfer theory. The quenching data were used for calculation parameters such as binding sites, binding distance. Intermolecular forces between the complex and BSA were also obtained by analyzing the fluorescence spectral data. Fourier transform infrared spectroscopic data demonstrated that BSA interacts with Schiff base molecule mainly via both the hydrophobic and hydrophilic interactions with a minor change in the secondary structure of BSA.

Keywords Schiff base; BSA; Fluorescence; FTIR; interaction

Introduction

Schiff bases, named after Hugo Schiff are formed when any primary amine reacts with an aldehyde or a ketone under specific conditions. Structurally, a Schiff base (also known as imine or azomethine) is a nitrogen analogue of an aldehyde or ketone in which the carbonyl group ($C=O$) has been replaced by an imine or azomethine group. Schiff bases are some of the most widely used organic compounds. They are used as pigments and dyes, catalysts, intermediates in organic synthesis, and as polymer stabilisers. Schiff bases have also been shown to exhibit a broad range of biological activities, including antifungal, antibacterial, antimalarial, antiproliferative, anti-inflammatory, antiviral, and antipyretic properties [1]. BSA has two tryptophans (Trp-134 and Trp-214). Trp-134 of BSA is located on the surface of the molecule while the other Trp is in the hydrophobic pocket (like Trp-214 in HSA) [2]. Bovine serum albumin (BSA) is a globular protein (~66,000 Da) that is used in numerous biochemical applications due to its stability and lack of interference within biological reactions. Bovine BSA is well characterized, abundant and cost effective serum albumin and is homologous to Human Serum Albumin (HSA). The abovementioned properties made BSA a potent tool for protein-drug interaction studies and their specific and firm binding with small molecules. Rugs and dyes can be used for drug delivery. BSA is also found to be a carrier as well as a distributor for several endogenous and exogenous ligands. Therefore these types of interactions have been widely studied [3].

Materials and method

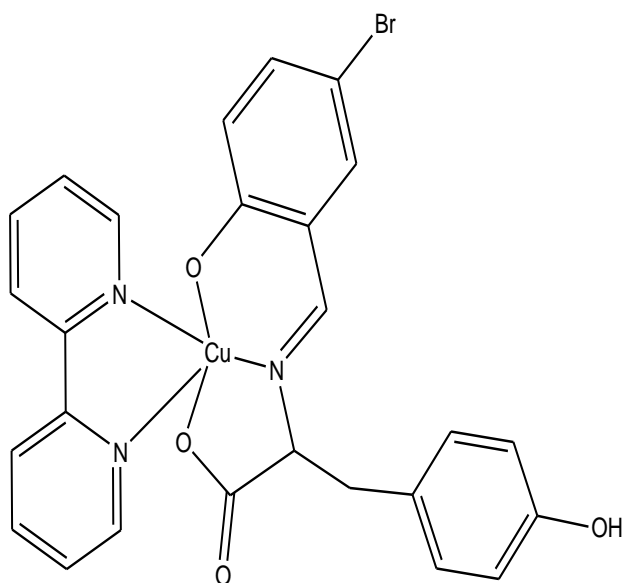
Stock solutions of BSA were made by dissolving BSA in water. The exact concentration of BSA was determined

spectrophotometrically using molecular absorption at 278 nm. Solutions of Schiff base S (scheme 1) complex were first prepared in methanol. Solutions of Schiff base complexes were kept in the dark and all solutions were used freshly.

Fluorescence spectroscopy

Emission spectra were recorded by a Cary eclipse spectrofluorimeter. Schiff base S was dissolved in methanol for fluorescence. The fluorescence emission spectra were recorded in the range of 300–450 nm at the excitation wavelength of 295 nm. The observed fluorescence intensities were corrected for dilution. The quenching of fluorescence for BSA is described by the Stern–Volmer equation. Titration experiments; BSA solution is placed in a quartz cuvette and titrated with various amounts of solution of the Schiff base complex.

FTIR
In order to conduct FTIR measurements, a solution of Schiff base T was added stepwise to the protein solution (0.06 mM) with constant stirring to ensure homogeneity of solution and to reach the target BIM concentrations of 0.03, 0.06, and 0.09 mM. The solutions were then freeze-dried in a Christ Alpha 1-2 LD freeze dryer at -40°C and 0.15 atm pressure for 4 h, the vacuum was broken at the end of the freeze-drying cycle. The pellets were prepared by mixing the freeze-dried sample with KBr and compacted under vacuum for 3 min. FTIR measurements were carried out at room temperature by an ALPHA FTIR spectrometer (Bruker optics) using KBr pellet in the range of $4000\text{--}400\text{ cm}^{-1}$.



Scheme 1. Chemical structure of Schiff base S

Results and Discussion

Fluorescence quenching is a process which decreases the fluorescence intensity of a given substance. The mechanisms of quenching are usually classified as dynamic or static quenching. Dynamic quenching is collisional and encounters between quencher and the fluorophore, but static quenching, is due to complex formation. The fluorescence spectra of BSA in the presence of different concentrations of Schiff base are shown in Fig. 1. It can be observed that increasing the concentration of Schiff base decreased the fluorescence intensity of BSA with 10 nm, blue shift in the maximum wavelengths, respectively. The variation of F_0/F versus total concentration of Schiff base T (Fig. 2). The plot of $F_0/(F_0 - F)$ vs $1/[Q]$ (Fig. 3) in equation 2, yields f^{-1} as the intercept on the y axis and $(fK_b)^{-1}$ as the slope. Thus, the ratio of the ordinate and the slope gives K_b . The number of Schiff base T molecules bound per protein (n) is calculated from equation 3 (Fig. 4, Table 1).

$$\frac{F_0}{F} = 1 + K_{SV}[Q] \quad (1)$$

$$\frac{F_0}{(F_0 - F)} = \frac{1}{fK_b[Q]} + \frac{1}{f} \quad (2)$$

$$\log \frac{(F_0 - F)}{F} = n \log[Q] + \log K_S \quad (3)$$

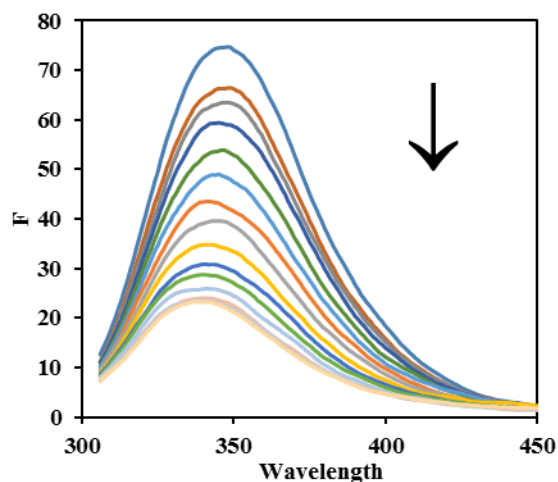


Fig. 1. Fluorescence quenching

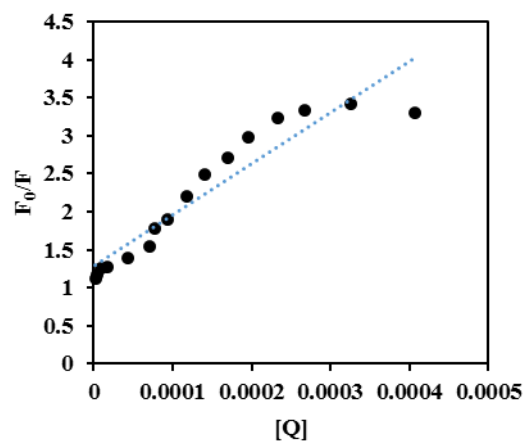


Fig. 2. The variation of F_0/F versus total concentration of Schiff base complex

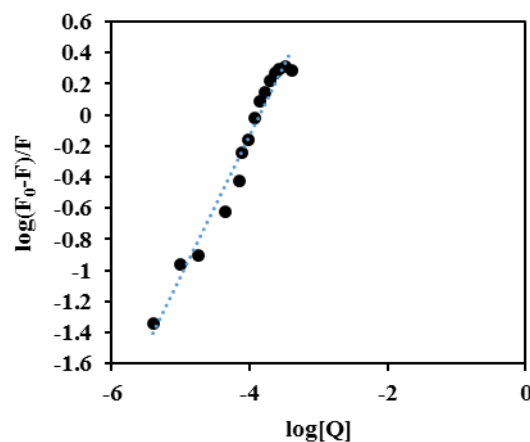


Fig. 3. The plots of $\log(F_0 - F)/F$ as a function of $\log[Q]$.

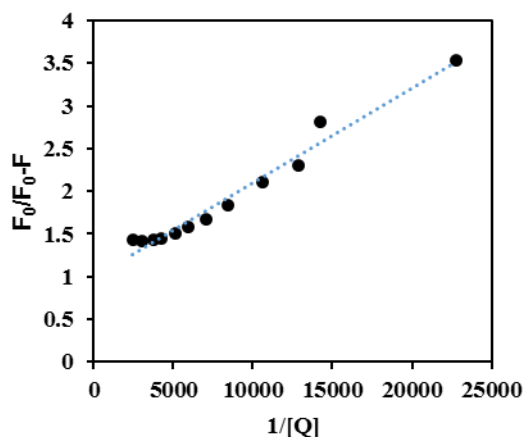


Fig. 4. The plot of F_0/F_0-F as function of $1/[Q]$.

Table 1. Stern–Volmer constant, Binding constants and binding sites

protein	K_{sv} ($L mol^{-1}$)	K_b ($L mol^{-1}$)	n	K_q
BSA	$6.7 \cdot 10^3$	$9.9 \cdot 10^3$	1	$6.73 \cdot 10^{11}$

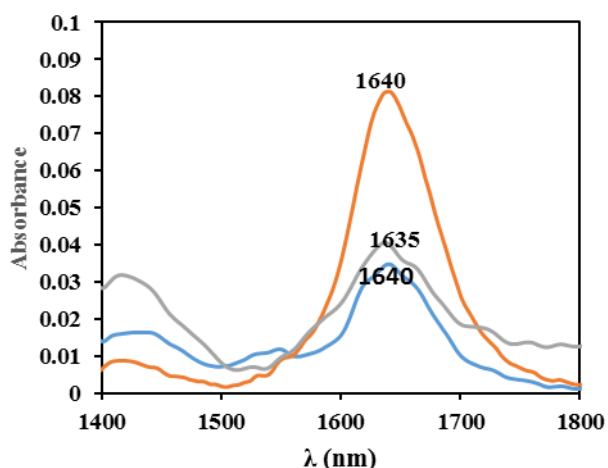


Fig. 5. FTIR spectra in the region of $1400-1800\text{ cm}^{-1}$

Conclusions

In this work, the interaction between a Schiff base complex and BSA has been investigated using fluorescence spectroscopy and FTIR. It was shown that the fluorescence of BSA has been quenched due to reacting with Schiff base complex. So on the basis of spectroscopic studies this Schiff base complex binds strongly to BSA. This work can provide important insight into the binding mechanism of this Schiff base complex with BSA. Based on the results of the present study, FTIR spectra shift in wavelength and change in intensity of absorbance indicate that Schiff base S interacts with BSA molecule mainly via hydrophobic and hydrophilic interactions. This is also accompanied by an increase in the solubility, bioavailability, and antitumor activity of Schiff base.

References

- [1] C. Silva¹, D. Silva², L. Modolo³, R. Alves⁴, M. Resende⁵, Martins⁶, A. Fatima⁷ "Schiff bases: A short review of their antimicrobial activities", *Journal of Advanced Research* (2011) 2, 1–8.
- [2] H. Dezhampanah¹, R. Firouzi² "An Investigation on intermolecular interaction between Bis(indolyl)methane and HSA and BSA using multi technique methods", *Journal of Biomolecular Structure and Dynamics*, 2016
- [3] K. Ghosh¹, S. Rathi², D. Arora. "Fluorescence spectral studies on interaction of fluorescent probes with Bovine Serum Albumin (BSA)", *Journal of Luminescence*.

Study of interaction between ternary Cu(II) complex of Schiff base and bovine serum albumin by spectroscopic methods

H. Dezhampanah* and R. Binazir

Department of Chemistry, Faculty of Science, University of Guilan, Rasht,

Iran h.dpanah@guilan.ac.ir

Abstract The molecular mechanism of a ternary Cu(II) complexes of schiff-base tryptophan amino acid derivatives and bipyridine hetrocycle(T) binding to bovine serum albumin (BSA) under physiological conditions in vitro under optimal physiological condition (pH=7.4) was investigated by fluorescence quenching and Fourier transform infrared .the fluorescence emission of BSA was quenched by this Schiff base complex that has been analyzed for estimation of binding parameters. Fluorescence quenching data showed that the quenching mechanism of BSA treated by the complex was static quenching, which was highly accord with the non-radioactive energy transfer theory Fourier transform infrared spectroscopic data demonstrated that BSA interacts with Schiff base molecule mainly via both the hydrophobic and hydrophilic interactions with a minor change in the secondary structure of BSA.

Keywords Schiff base; BSA; Flourescence; FTIR; interaction;

Introduction

Schiff bases are compounds with a functional group that contains C=N, which are usually synthesized from the condensation of primary amines and active carbonyl groups. Schiff bases and their metal complexes are important class of compounds in medicinal and pharmaceutical field.[1]

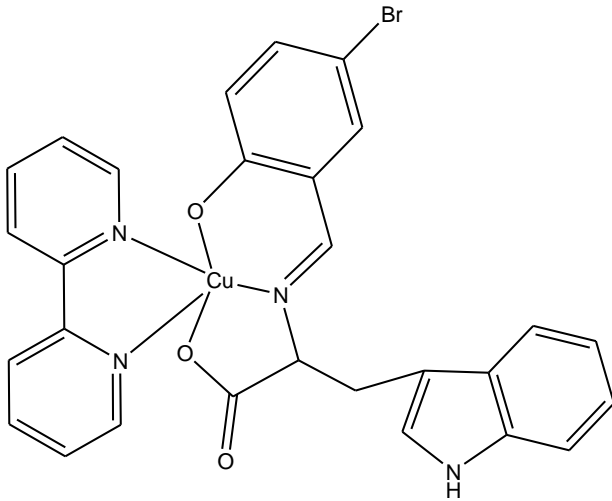
Proteins play a vital role in the life course and are closely related to the origin, evolution and metabolism of life. A great variety of medicinal drugs are bound and [2]

transported in the body usually through plasma proteins, reaching the receptor lesion site and thus pharmacological effects occur. Serum albumin is the most abundant protein in the plasma as it can bind with most of endogenous and exogenous compounds to form stable complexes

Materials and method

Stock solutions of BSA were made by dissolving BSA in water The exact concentration of BSA was determined spectrophotometrically using molecular absorption coefficient of $35,700 \text{ M}^{-1}\text{Cm}^{-1}$ at 278 nm. Solutions of Schiff base complex were first prepared in methanol Solutions of Schiff base complexes were

kept in the dark and all solutions were used freshly Fluorescence spectroscopy Emission spectra were recorded by a Cary eclipse spectrofluorimeter Schiff base S was dissolved in methanol For fluorescenc The fluorescence emission spectra were recorded in the range of 300– 450 nm at the excitation wavelength (kex) of 295 nm. The observed fluorescence intensities were corrected for dilution. The quenching of fluorescence for HSA is described by the Stern–Volmer equation titration experiments, BSA solution is placed in a quartz cuvette and titrated with various amounts of solution of the Schiff base complex FT IR. In order to conduct FTIR measurements, a solution of Schiff base S was added stepwise to the proteinsolution (0.06 mM) with constant stirring to ensure homogeneity of solution and to reach the target BIM concentrations of 0.03, 0.06, and 0.09 mM. The solutions were then freeze-dried in a ChristAlpha 1-2 LD freeze dryer at -40°C and 0.15 atm pressure for 4 h, the vacuum was broken at the end of the freeze-drying cycle. The pellets were prepared by mixing the freeze-dried sample with KBrand compacted under vacuum for 3 min. FTIR measurements were carried out at room temperature by an ALPHA FTIR spectrometer (Bruker optics) using KBr pellet in the range of $4000\text{--}400 \text{ cm}^{-1}$.



Scheme. 1.Chemical structure of Schiff base T

Results and Discussion

Fluorescence quenching is a process which decreases the fluorescence intensity of a given substance. The mechanisms of quenching are usually classified as dynamic or static quenching. Dynamic quenching is collisional and encounters between quencher and the fluorophore, but static quenching, is due to complex formation. The fluorescence spectra of BSA in the presence of different concentrations of Schiff base are shown in Fig.1. It can be observed that increasing the concentration of Schiff base decreased the fluorescence intensity of BSA with 11nm, blue shift in the maximum wavelengths, respectively. The variation of F_0/F versus total concentration of Schiff base T (Fig. 2). The plot of $F_0/(F_0 - F)$ vs $1/[Q]$ (Fig.3) in equation 2, yields f^{-1} as the intercept on the y axis and $(fK_b)^{-1}$ as the slope. Thus, the ratio of the ordinate and the slope gives K_b . The number of Schiff base T molecules bound per protein (n) is calculated from equation 3 (Fig. 4, Table 1).

$$\frac{F_0}{F} = 1 + K_{SV}[Q] \quad (1)$$

$$\frac{F_0}{(F_0 - F)} = \frac{1}{fK_b[Q]} + \frac{1}{f} \quad (2)$$

$$\log \frac{(F_0 - F)}{F} = n \log[Q] + \log K_s \quad (3)$$

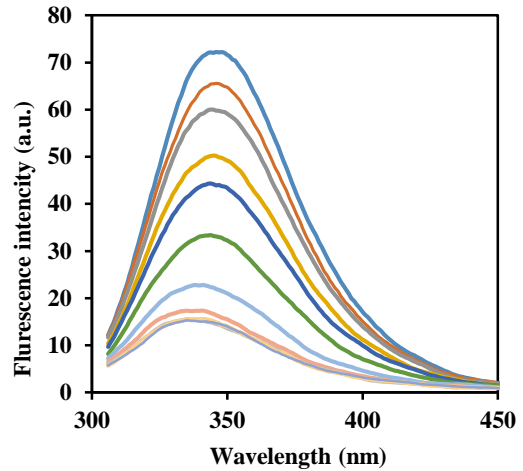


Fig. 1. Fluorescence quenching of BSA-Schiff base solution.

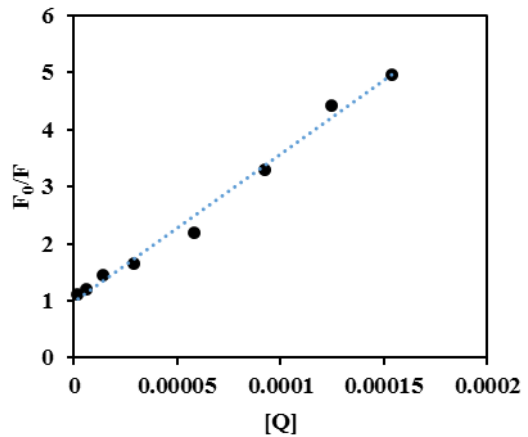


Fig. 2. The variation of F_0/F versus total concentration of Schiff base complex

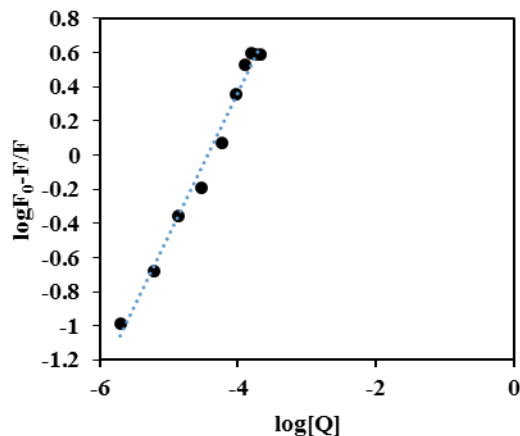


Fig. 3. The plots of $\log (F_0 - F)/F$ as a function of $\log[Q]$.

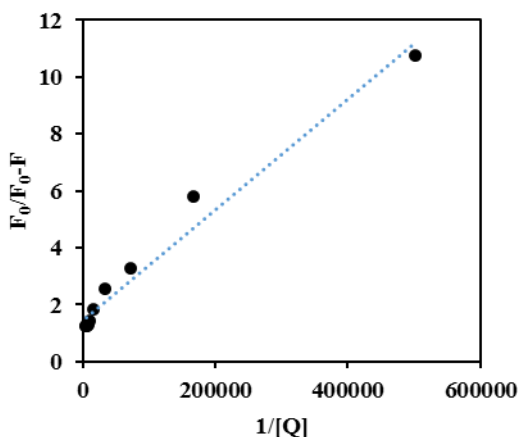


Fig. 4. The plot of F_0/F_0-F as function of $1/[Q]$.

Table 1. Stern–Volmer constant, Binding constants and binding sites

protein	K_{sv} ($L mol^{-1}$)	K_b ($L mol^{-1}$)	n	K_d
BSA	$2.6 \cdot 10^4$	$7.3 \cdot 10^4$	1	$2.6 \cdot 10^{12}$

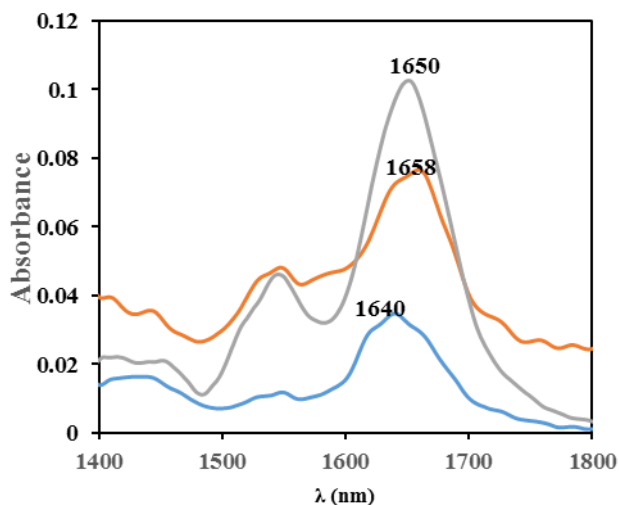


Fig. 5. FTIR spectra in the region of $1400-1800\text{ cm}^{-1}$

Conclusions

In this work, the interaction between a Schiff base complex and BSA has been investigated using fluorescence and FTIR. It was shown that the fluorescence of BSA has been quenched due to reacting with Schiff base complex So, on the basis of spectroscopic studies this Schiff base complex bind strongly to BSA. Based on the results of the present study, FTIR spectra shift in wavelength and change in intensity of absorbance indicate that Schiff base T interacts with BSA molecule mainly via hydrophobic and hydrophilic interactions. This is also accompanied by an increase in the solubility, bioavailability, and antitumor activity of Schiff base T

References

- [1] N. Fani¹, A. Bordbar², Y. Ghayeb³ "A combined spectroscopic, docking and molecular dynamics simulation approach to probing binding of a Schiff base complex to human serum albumin", *Spectrochimica Acta Part A: Molecular and Biomolecular Spectroscopy* 103 (2013) 11–17.
- [2] H. Dezhampanah¹, M. Esmaili², A. Khorshidi³ "Milk β -casein as a vehicle for delivery of bis(indolyl)methane: Spectroscopy and molecular docking studies", *Journal of Molecular Structure* 1136 (2017) 50e58

Effect of ionic strength on the formation of diethyl(1*S*, 2*S*)-3,3 dibenzoylcyclopropane-1,2 dicarboxylate: A kinetics and mechanism study

F. Mahmoudi*, S.M. HabibiKhorassani, M. Shahraki

Department of Chemistry, University of Sistan and Baluchestan, Zahedan, Iran

*mahmoodi.bahar@yahoo.com

Abstract: In this study, the kinetics and mechanism of the reaction between diethyl acetylenedicarboxylate and dibenzoylmethane has been studied in the presence of triphenylarsine as a catalyst with respect to the concentration, solvent, temperature, ionic strength, surfactant and structure. To detect the effect of ionic strength on the reaction rate some salts was used. The best performance was in the presence of potassium iodide salt that rate of the reaction was 6.8-fold faster. Moreover, the effect of cationic, nonionic and anionic surfactants on the reaction rate was investigated that anionic surfactant (sodium dodecylsulfate) has the significant decrease on the rate of the reaction. The kinetic data were provided the reaction order, kinetics values (k_{ovr} and E_a), activation parameters (ΔH^\ddagger , ΔS^\ddagger and ΔG^\ddagger), the rate-determining step (RDS) and the proposed mechanism.

Keywords: Kinetics, Mechanism, Ionic Strength, Surfactant

Introduction

Cyclopropanes have been used as building blocks for the synthesis of organic reactions. Also, they are present in a number of pharmacologically important natural products some of which belong to the group of alkylating anticancer agents. Cyclopropanes have to the significant reactivity due to their high π character, inherent angle strain, and intrinsic torsional strain. M. T. Maghsoodlou and coworkers reported a stereoselective synthesis of trans-cyclopropanes via the reaction between acetylenic esters and C-H acids in the presence of triphenyl arsine [1]. Actually, the stability of triphenyl arsine in air may facilitate the experimental operations. The present method benefits from the catalytic role of triphenylarsine, and also allows access to cyclopropane derivatives stereoselectively [1,2]. In this article, the kinetics and mechanism of the reaction between diethyl acetylenedicarboxylate and dibenzoylmethane has been studied in the presence of triphenylarsine as a catalyst by using the UV-vis spectrophotometry technique.

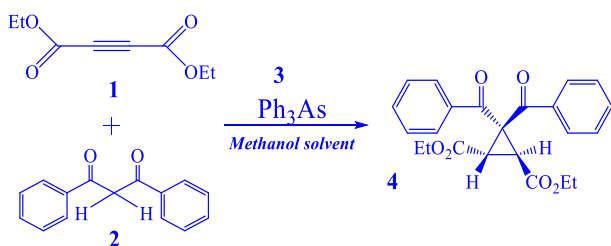


Fig. 1. The reaction between diethyl acetylenedicarboxylate 1 and dibenzoylmethane 2 in the presence of triphenylarsine 3 as a catalyst for generation of diethyl (1*S*, 2*S*)-3,3-dibenzoylcyclopropane-1,2-dicarboxylate 4.

Materials and Instruments

The chemicals used were obtained from Fluka (Buchs, Switzerland). The solvents were purchased from Merck (Darmstadt, Germany). The spectra were recorded by UV-vis spectrophotometer (model Cary Bio-300, CA, USA) with a 10-mm light-path cell.

Results and discussion

The experimental absorbance curve was recorded versus time at the wavelength of 460 nm and 27°C (Fig. 2). This curve (dotted line) is fitted to second-order curve (solid line). Moreover by investigation the effect of concentration, the partial orders of the reaction were obtained one and one, respectively with respect to compounds 1 ($\alpha=1$) and 2 ($\beta=1$) under the pseudo-order condition at the wavelength of 460 nm and at 27°C. The rate law for this reaction is as follows:

$$\text{Rate} = k_{obs}[1]^\alpha[2]^\beta \quad (1)$$

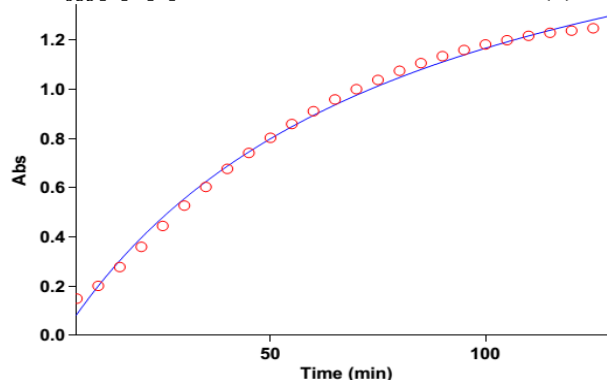


Fig. 2. The second-order fit curve (solid line) accompanied by the experimental curve (dotted line) for the reaction

between **1** (10^{-2} M) and **2** (10^{-2} M) and **3** (5×10^{-3} M) in methanol at 460 nm and 27°C.

Effect of solvents and temperature

The influence of variation of the dielectric constant and polarity was carried out by the addition of ethanol, keeping other parameters unchanged. The rate of the reaction was found to be inhibited by the addition of ethanol. The effect of temperature on the rate was studied by performing the kinetic experiments at various temperatures while keeping other experimental conditions constant. It was observed that the reaction is faster when the temperature is increased. These data are summarized in Table 1.

Table 1. The values of overall second order rate constant (k_{ovr}) for the reaction between **1** (10^{-2} M), **2** (10^{-2} M) and **3** (5×10^{-3} M) at 460 nm.

Solvent ϵ (D)	T (°C) ± 0.1			
	17	22	27	32
Methanol	32.780.25141.24	259.10425.36		
Ethanol	24.54.12 9.5823.2041.54			

By investigation the Arrhenius and Eyring plots, the values of activation parameters for the overall reaction were computed. The results are summarized in Table 2.

Table 2. The values of activation parameters (ΔH^\ddagger , ΔS^\ddagger , ΔG^\ddagger , E_a and $\ln A$) for the reaction between **1** (10^{-2} M), **2** (10^{-2} M) and **3** (5×10^{-3} M) at 460 nm.

Solvent	ΔH^\ddagger	ΔS^\ddagger	ΔG^\ddagger	E_a	$\ln A$
	(kJ.mol ⁻¹)	(J.mol ⁻¹ .K ⁻¹)	(kJ.mol ⁻¹)	(kJ.mol ⁻¹)	
Methanol	80.14	67.98	60.41	82.61	38.63
Ethanol	112.72	155.85	67.50	115.19	49.20

Effect of ionic strength

The influence of ionic strength on the rate of formation of product was evaluated by using the *NaCl*, *NaBr*, *NaI*, *KI* and *NH₄Cl* salts, keeping other experimental conditions constant. In the presence, *NH₄Cl* salt of the reaction was stopped and no progress. But with the addition of other salts have the significant increase the rate, our results show that higher concentration of salts promotes the rate of the reaction. The best performance was in the presence of *KI* salt that of the reaction was 6.8-fold faster. These data are summarized in Table 3.

Table 3. The effect of ionic strength on the overall second order rate constant (k_{ovr}) for the reaction between **1** (10^{-2} M), **2** (10^{-2} M) and **3** (5×10^{-3} M) in methanol at 460 nm and 27°C.

Without salt	<i>NaBr</i>	<i>NaCl</i>	<i>NaI</i>	<i>KI</i>
259.10735.58	1031.08	1511.76	1777.92	

Effect of surfactants

The effect of surfactant on the reaction rate was evaluated by using cationic (*N-dodecyl pyridinium chloride*), nonionic (*Triton X-100*) and anionic (*SDS*) surfactants while keeping other parameters unchanged. The addition of *N-dodecyl pyridinium chloride* and *Triton X-100* surfactants to the reactants have not effect on the rate of reaction. In the presence, of *SDS* surfactant second-order rate constant was found to 6.7-fold slower.

Effect of structure of dialkylacetylenedicarboxylates

For further investigation, the effect of structure of dialkyl acetylenedicarboxylates on the reaction rate, experiments were performed in the presence dimethyl acetylenedicarboxylate **1b** under the same conditions used in the previous experiments. The values of the second order rate constant (k_{ovr}) for the reactions between (**1a**, **2** and **3**) and (**1b**, **2** and **3**) are reported in Table 4. In addition, the effects of temperature, potassium iodide salt, and *SDS* surfactant also on the reaction rate between **1b**, **2** and **3** was evaluated that the same previous results were obtained.

Table 4. The values of overall second order rate constant (k_{ovr}) for the reactions between (**1a**, **2** and **3**) and (**1b**, **2** and **3**) in methanol and at 460 nm.

Reaction	T (°C) ± 0.1			
	17	22	27	32
(1a , 2 and 3)	80.25	141.24	259.10	425.36
(1b , 2 and 3)	86.59	164.14	312.80	590.68

1a: diethyl acetylenedicarboxylate **1b**: dimethyl acetylenedicarboxylate

Mechanism investigation

According to the results of the above experiments, the simplified derive as a possible comment is shown in Fig. 3.

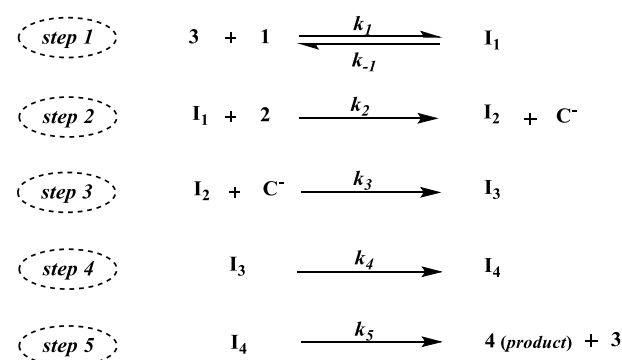


Fig. 3. A simplified Scheme for the proposed reaction mechanism.

Based on the experimental data, the fourth step of proposed mechanism was identified as an *RDS* (k_4) with more likely and this was confirmed by the steady-state assumption.

Conclusions

Kinetics and mechanism of the reaction between diethyl acetylenedicarboxylate **1** and dibenzoyl methane **2** in the presence of triphenylarsine **3a** as a **catalyst** and in methanol solvent were investigated by UV-vis spectrophotometry. The results can be summarized as follows: The proposed mechanism involved five steps. The overall order of reaction followed second-order kinetics and the partial order of the reaction with respect to each reactant is one. The rate of reaction was increased in the presence of the solvent with higher dielectric constant and at the higher temperature. The effect of ionic strength on the reaction rate was evaluated, in the presence of potassium iodide salt of the reaction was 6.8-fold faster. Moreover, the effect of surfactant on the reaction rate was evaluated, in the presence of anionic surfactant (*SDS*) have the significant decrease in the rate the formation of product. For further investigation, the effect of structure of dimethyl acetylenedicarboxylate **1b** on the reaction rate was performed. The fourth step of proposed mechanism was identified as an *RDS* (k_4).

References

- [1] M.T Maghsoodlou, S. M Habibi Khorassani "Highly stereoselective construction of functionalized cyclopropanes from the reaction between acetylenic esters and C-H acids in the presence of triphenylarsine", J Elsevier Ltd, 2009.
- [2] Marchello A. Cavitt, Lien H "Intramolecular donor- acceptor cyclopropane ring-opening cyclizations", J Royal Society of Chemistry, 2014.
- [3] S. M Habibi Khorassani, M.T Maghsoodlou "AIM analysis, synthetic, kinetic and mechanistic investigations of the reaction between triphenylphosphine and dialkyl acetylenedicarboxylate in the presence of 3-methoxythiophenol", J Indian Academy of Sciences, 2013.

Determination of solvatochromic parameter in binary mixtures of deep eutectic solvent with molecular solvents

Zahra Bozorgmehr, Alireza Harifi-Mood*

Department of Chemistry, Kharazmi University, Tehran, Iran

[*harifi@khu.ac.ir](mailto:harifi@khu.ac.ir)

[*alireza.harifi@gmail.com](mailto:alireza.harifi@gmail.com)

Abstract: Binary mixtures of solvents are widely used in chemical processes in order to tune the polarity properties of the media and to facilitate chemical and physical processes. In this study, ethaline as a deep eutectic solvent was considered as new green media for chemical processes. The physicochemical properties of the solvent mixtures, consisting of solvatochromic parameters, were obtained using solvatochromic probes. Solvatochromic parameters of binary mixture of Ethaline with ethanol, butanol, propanol, water, acetonitrile and DMSO, were measured under atmosphere pressure, at the room temperature. Results showed that the polarity and hydrogen bond donor ability of the ethaline decreases with increasing mole fraction of molecular solvents, while hydrogen bond acceptor ability of the media shows a different pattern. Deviation from ideal behavior, observed for solvatochromic parameters, confirmed preferential solvation of the solutes in these media.

Keywords: Deep eutectic solvents; Solvatochromic parameters; physicochemical properties

Introduction

Deep eutectic solvents (DESs) are relatively new class of ionic liquids (ILs) that can be simply prepared via mixing of a quaternary ammonium salt with salts or a hydrogen bond donor compound (HBD). They are considered nowadays as green ionic liquid analogues [1-2]. DESs are systems forming from Lewis or Brønsted acids and bases. They contain large, asymmetric ions with low lattice energy and hence, low melting points. Studies have shown various advantages and special properties for deep eutectic solvents, such as nontoxicity, low cost, and ease of preparation. When a DES is added to another solvent, it improves the chemical and physical properties of that solvent. Understanding solute-solvent interactions in binary mixed solvent systems is more complicated than in pure solvents [3]. The electronic transition energy of solvatochromic indicators of solvent polarity depends on the solvation sphere's composition and properties, and therefore, the use of such indicators is a suitable method for studying solute-solvent interactions.

In this study, we obtained solvatochromic parameters (normalized polarity (E_T^N), polarity/polarizability (π^*), hydrogen-bond donor (α), and hydrogen-bond acceptor (β) abilities) in a binary solvent mixture of ethaline as a DES and ethanol, propanol, butanol, water, DMSO, and acetonitrile. The solvatochromic indicators used in this study were Reichardt's betaine dye, 4-nitroanisole and 4-nitroaniline.

Materials and method

Ethaline was obtained by mixing choline chloride and ethylene glycol at the molar ratio of 1:2 and subsequent stirring under heating up to ~ 353.15 K until a homogeneous and colorless liquid was formed. Binary mixtures of ethaline and ethanol, butanol, propanol, water, acetonitrile and DMSO were gravimetrically prepared over the entire range of ethaline mole fractions.

The appropriate solutions of the solvatochromic probe were prepared and their UV-vis absorption spectra of prepared solutions were recorded. The maximum absorptions were determined for each probe. The E_T^N , π^* , α , and β parameters were calculated from the wavelength of maximum absorption according to the procedure reported in our previous researches [3-4].

Results and Discussion

Figures 1-4 show the variation of solvatochromic parameters of DES versus the mole fractions of molecular solvents as a co-solvent in binary mixtures. It is clear that all solvatochromic parameters show negative or positive deviations from ideality in solvent mixtures. Ethaline/water mixtures show a different trend for E_T^N , π^* , and α parameters. In other mixtures, when small quantities of ethaline are added to molecular solvents, E_T^N , π^* , and α parameters increase sharply and then change smoothly to the value of pure ethaline. There is a different trend in β parameter which decreases sharply at first except for DMSO mixtures which shows a smooth decreasing and water/ethaline and acetonitrile/ethaline mixtures that they demonstrate a completely different behavior. On

the other hand, π^* parameter shows a synergistic behavior in water/ethaline mixtures. It reveals that the aqueous solutions of ethaline are more polar and polarizable than pure components. It can be concluded that the probe is not equally solvated by the two components of the binary solvent mixture, and therefore a “preferential solvation” of the probe is confirmed. Preferential solvation arises whenever the bulk mole fraction solvent composition differs from the solvation microsphere.

Conclusion

By comparing the solvatochromic parameters determined in binary mixtures of ethaline with ethanol, propanol, buthanol, water, DMSO, and acetonitrile, we could conclude that the most explored systems show basically similar polarity and hydrogen bonding ability response patterns. Positive or negative deviation from ideal behavior confirms that the solvatochromic probes are preferentially solvated by one component of the mixture.

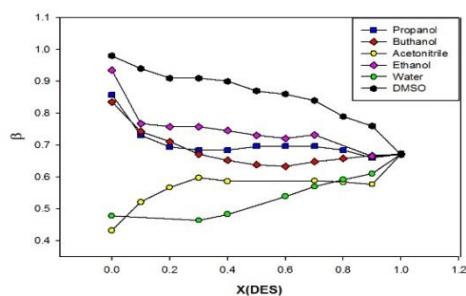


Figure 1. The variation of β parameters for binary mixtures of ethaline with some molecular solvents.

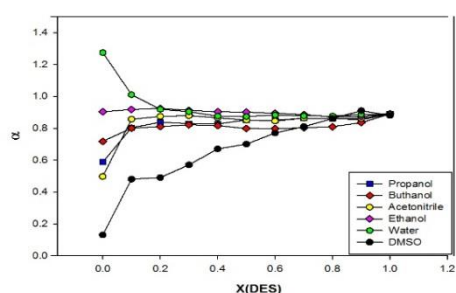


Figure 2. The variation of α parameters for binary mixtures of ethaline with some molecular solvents.

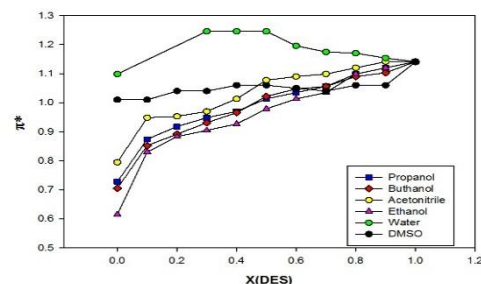


Figure 3. The variation of π^* parameters for binary mixtures of DES with some molecular solvents.

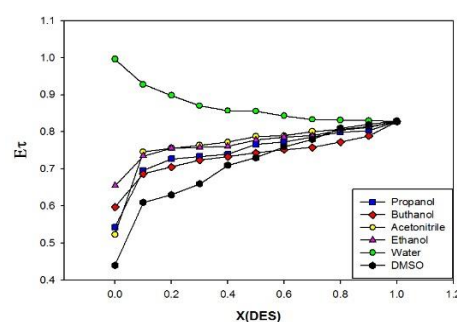


Figure 4. E_T^N parameters for binary mixtures of DES with some molecular solvents.

References

- [1] E.L. Smith, A.P. Abbott, and K.S. Ryder, Deep eutectic solvents (DESs) and their applications. *Chem. rev.*, 114 (2014) 11060-11082.
- [2] A.P. Abbott, D. Boothby, G. Capper, D.L. Davies, R.K. Rasheed, V. Tambyrajah, Novel solvent properties of choline chloride/urea mixtures, *Chem. Commun.* (2003) 70–74.
- [3] A.R. Harifi-Mood, A. Habibi-Yangjeh, M.R. Gholami, Solvatochromic parameters for binary mixtures of 1-(1-butyl)-3-methylimidazolium tetrafluoroborate with some protic molecular solvents, *J. Phys. Chem. B* 110 (2006) 7073–7078.
- [4] A.R. Harifi-Mood, R. Ghobadi, S. Matic, B. Minofar, D. Řeha, Solvation analysis of some solvatochromic probes in binary mixtures of reline, ethaline, and glyceline with DMSO, *J. Mol. Liq.* 222 (2016) 845–853.

Calculation of Pseudo First-order rate constants, k_{obs} , and Activation Parameters Containing ΔS^\ddagger , ΔH^\ddagger and E_a

Bitra Shafaatian*, Mohaddeseh Taherian

School of Chemistry, Damghan University, Damghan 3671641167, Iran

*shafaatian@du.ac.ir

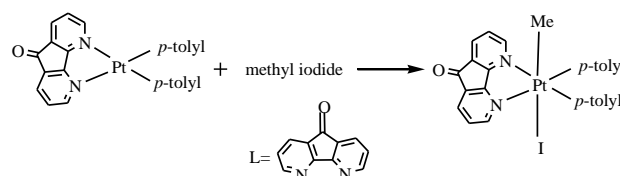
Abstract: Two New organoplatinum(II) and organoplatinum(IV) complexes containing chelated ligand with nitrogen donor atoms, (L), were synthesized and characterized by different methods such as: FT-IR, ^1H NMR, UV/Vis, elemental analysis and conductometry. Kinetic studies of the oxidative addition reaction of MeI with organoplatinum(II) complex were investigated and the temperature dependence of the rate constant was reported. From the temperature dependence of rate constants, the activation parameters were calculated. The activation parameters containing E_a , ΔH^\ddagger and ΔS^\ddagger of the reaction were calculated according to Arrhenius and Eyring equations, respectively. The large negative of ΔS^\ddagger showed that the reaction occurred by the S_N2 mechanism.

Keywords: Activation Parameters; Rate Constants; Organoplatinum

Introduction

The oxidative addition reaction represents one of the most fundamental processes in transition metal chemistry [1]. For example, oxidative addition of the substrate X-Y to a metal center (M) leads to an increase in the coordination number of the complex due to the formation of two new bonds, M-X and M-Y, upon complete dissociation of the X-Y bond. Oxidative addition reactions in platinum complexes were investigated by the addition of a molecule X-Y to a square planar d^8 platinum(II) complex to give an octahedral d^6 platinum(IV) complex represented one of the classic example of such reactions. Oxidative addition and reductive elimination reactions of transition metal complexes form the basis of many catalytic systems [2]. Alkyl, aryl, and alkynyl complexes of transition metals undergo various unique reactions such as reductive elimination, β -hydrogen elimination and insertion of small molecules into the metal-carbon bond. These reactions play important roles in many synthetic organic reactions catalyzed by transition metal complexes such as homo- and cross-coupling reactions, polymerization, hydrogenation and carbonylation of the organic substrates [1].

organoplatinum(II) complex make it possible to monitor the oxidative addition reaction of the platinum(II) complex by UV/Vis spectroscopy (Scheme 1). In acetone the complex reacted with excess of MeI and a yellow solution of organoplatinum(IV) complex was obtained. In this case, excess of MeI was used as a reagent and the disappearance of the MLCT band for the platinum(II) complex ($\lambda_{\max}=441$) nm in acetone was used to monitor the reaction. The intense red color of the platinum(II) complex changed to yellow color upon oxidation to platinum(IV) complex (Fig. 1).



Scheme 1: The reaction of kinetic studies

Materials and method

All chemicals were reagent grade quality purchased from commercial sources and used as received. UV-Vis spectra were recorded on an Analytik Jena Specord 205 spectrophotometer.

Results and Discussion

One of the most important reactions is oxidative addition of alkyl halides with square-planar complexes of platinum [3]. Red to orange color of

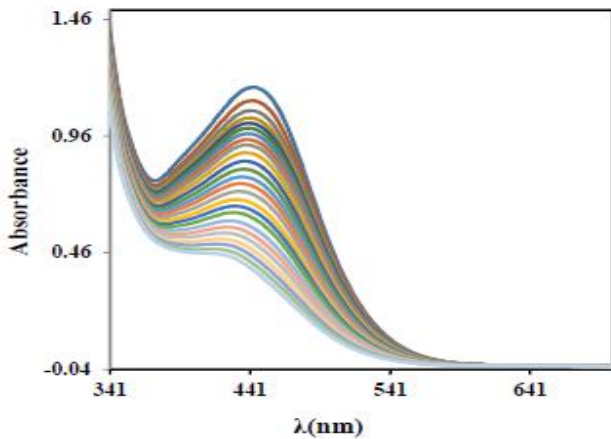


Fig. 1: Decay plot for oxidation of platinum(II) to platinum(IV).

The excess of methyl iodide made the reaction followed good pseudo-first-order kinetics. The pseudo-first-order rate constants (k_{obs}) can be calculated with curve fitting by using Microsoft Excell solver [4]. Two typical of curve fitting plots in dichloromethane was shown in Figs. 2 and 3. Graphs of these first-order rate constants against the concentrations of MeI gave good straight line plots passing through the origin, showing a first-order dependence of the rate on the concentration of the MeI (Fig. 2). The overall second-order rate constants (k_2) can be obtained from the slopes of these figures. The activation parameters were determined from the measurements of k_2 at different temperatures.

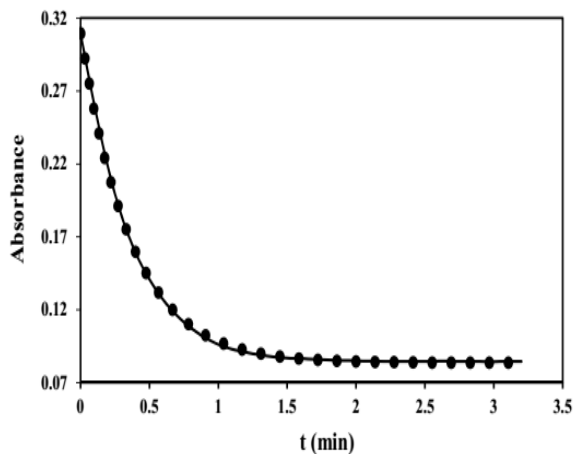


Fig. 2: Curve fitting for the oxidative addition reaction at 35 °C (50 μL of MeI).

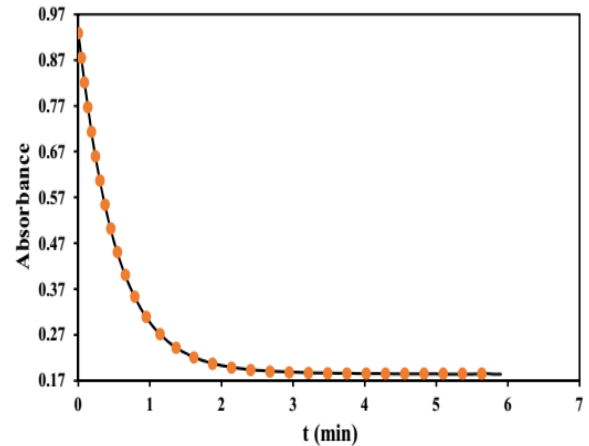


Fig. 3: Curve fitting for the oxidative addition reaction at 30 °C (50 μL of MeI).

The values of k_2 and k_{obs} were given in Table 1. As seen from Table 3, the rates of the reaction with MeI increased with increasing of temperatures.

Table1: The data of k_2 .

T(K)	288.15	293.15	298.15	303.15	308.15
k_2	2.7201	3.7984	4.4313	5.8650	8.1457

The activation energy, E_a , was obtained from the Arrhenius equation as following:

$$\ln k_2 = \ln A - E_a/RT$$

The Arrhenius plot in was shown in Fig. 5.

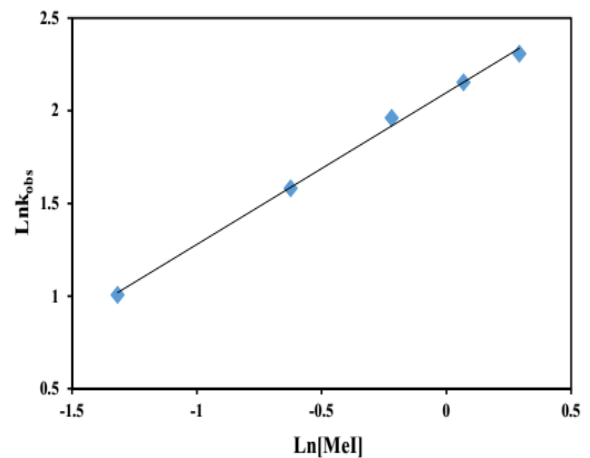


Fig. 4: Plot of first-order rate constants (k_{obs}) for the reaction of $[Pt(p\text{-tolyl})_2(L)]$ with MeI in acetone at different temperatures vs $[MeI]$ at $T=35^\circ C$.

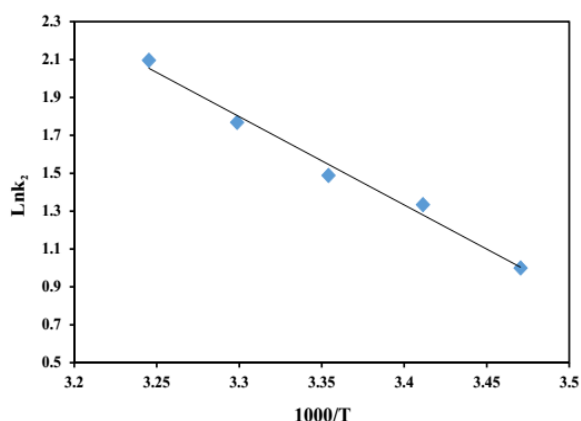


Fig. 5: Arrhenius plot for the reaction of [Pt(*p*-tolyl)₂(L)] with MeI in acetone.

Furthermore, ΔH^\ddagger and ΔS^\ddagger were obtained from the Eyring equation:

$$\ln(k_2/T) = \ln(k'/h) + \Delta S^\ddagger/R - \Delta H^\ddagger/RT$$

The Eyring plots were shown in Fig. 6 and the activation parameters were given in Table 2.

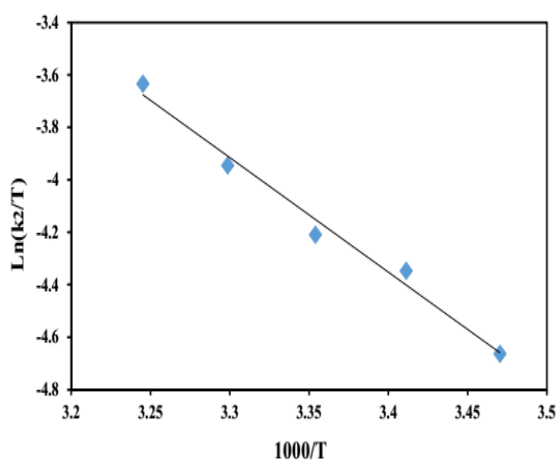


Fig. 6: Eyring plot for the reaction of [Pt(*p*-tolyl)₂(L)] with MeI in acetone.

Table 2: The data of activation parameters.

ΔS^\ddagger	ΔH^\ddagger	Ea
-110.3390	36.2919	38.7679

Large obtained negative value of ΔS^\ddagger indicated typical of oxidative addition reactions by the S_N2 mechanism which involves nucleophilic attack of the metallic

center to the methyl group of MeI and the formation of [Pt(Me)(*p*-tolyl)₂(L)]⁺ cationic intermediate. This mechanism is well-established for the platinum(II) complexes from the previous works [5].

Conclusions

Two new platinum complexes containing a chelating ligand, with nitrogen donor atoms were synthesized and kinetic studies of reaction of MeI with the platinum(II) complex was investigated in different temperatures and rate constants, k_{obs} and k_2 , Ea, ΔH^\ddagger and ΔS^\ddagger were calculated. These values showed that this kind of reaction occurred by the S_N2 mechanism.

Acknowledgment

We gratefully acknowledge the support of this work by Damghan University Research Council.

References

- [1] J. P. Collman, L. S. Hegedus, J. R. Norton, R. G. Finke, "Principles and Applications of Organotransition Metal Chemistry", 1987, Mill Valley University Science, 2nd Ed., 279-294, CA, USA.
- [2] W. Lu, B. X. Mi, M. C. W. Chan, Z. Hui, C. M. Che, N. Zhu, S. T. Lee, "Light-emitting tridentate cyclometalated platinum (II) complexes containing σ -alkynyl auxiliaries: tuning of photo-and electrophosphorescence", *J. Am. Chem. Soc.*, 126 (2004) 4958-4971.
- [3] L. M. Rendina, R. J. Puddephatt, "Oxidative addition reactions of organoplatinum (II) complexes with nitrogen-donor ligands", *Chem. Rev.*, 97 (1997) 1735-1754.
- [4] D. C. Harris, "Nonlinear least-squares curve fitting with Microsoft Excel Solver", *J. Chem. Edu.*, 75 (1998) 119-121.
- [5] (a) M. Crespo, R. J. Puddephatt, "Cationic intermediates in oxidative addition reactions of alkyl halides to d⁸ complexes: evidence for the S_N2 mechanism", *Organometallics*, 6 (1987) 2548-2550.
 (b) P. K. Monaghan, R. J. Puddephatt, "Reactivity and mechanism in the oxidative addition of iodoalkanes and di-iodoalkanes to a dimethylplatinum (II) complex.", *J. Chem. Soc. Dalton Trans.*, 3 (1988) 595-599.

Determination of the Second Order Rate Constants, Activation Energy, Entropy and Enthalpy of Activation Changes

Bita Shafaatian*, Vajihah Hasani

School of Chemistry, Damghan University, Damghan 3671641167, Iran

*shafaatian@du.ac.ir

Abstract: New complexes of organoplatinum(II) and organoplatinum(IV) containing dinitrogen chelated ligand were synthesized and characterized by FT-IR, ¹H NMR, UV/Vis, elemental analysis and conductometry. The platinum complexes have been found to possess 1:1 metal to ligand stoichiometry and the molar conductance data revealed that the metal complexes were non-electrolytes. The platinum(II) and platinum(IV) complexes exhibited square planar and octahedral coordination geometry, respectively. Moreover, oxidative addition reaction of iodomethane with platinum(II) complex in 15, 20, 25, 30 and 35 °C was studied and calculation of rate constants was done using curve fitting with Microsoft Excell solver. Moreover, activation energy, entropy and enthalpy of activation were calculated using Arrhenius and Eyring plot, respectively. From the obtained data, S_N2 mechanism was suggested for the oxidative addition reaction.

Keywords: Kinetic; Oxidative Addition; Organoplatinum; Chelate

Introduction

Platinum complexes are relatively easily oxidized or reduced in two-electron processes between the three main oxidation states, so that oxidative addition and reductive elimination reactions are facile. Furthermore, since the predominant geometry for the +2 oxidation state is square planar and for the +4 oxidation state is octahedral, oxidative addition accompanied by the addition of two fragments to the platinum(II) and reductive elimination accompanied by loss of two fragments from platinum(IV) are both particularly favourable. Although, platinum(0) exhibits a wider range of geometries than the other two oxidation states, the loss of ligands to form two coordination platinum(0) complexes is relatively facile. Equilibrium of transformation of platinum during oxidative addition and reductive elimination reaction can be accompanied by addition or loss of two fragments [1].

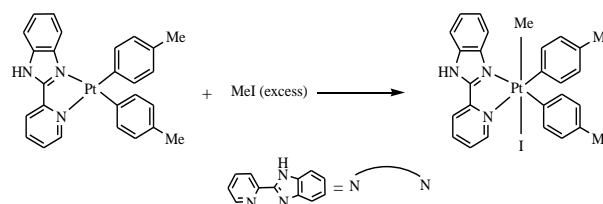
Materials and method

All chemicals were reagent grade quality purchased from commercial sources and used as received. All reactions were carried out in an argon atmosphere and dry solvents. After preparation of the complexes, which were usually air-stable, they were dried in high vacuum to remove traces of solvents. Electronic absorption spectra of the complexes were recorded in acetone solvent on an Analytik Jena Specord 205 spectrophotometer.

Results and Discussion

The oxidative addition of alkyl halides with square-planar complexes of platinum is often a key step in catalytic reactions in order to gain insights about the

intrinsic properties of the reaction constituents [2,3]. Thus, the oxidative additions of iodomethane to [Pt(MeC₆H₄)₂(NN)], were studied by using UV-Vis absorption spectroscopy to monitor the reaction (Scheme 1). The disappearance of the MLCT band for the platinum(II)



Scheme 1. Oxidative addition reaction.

complex at $\lambda_{\text{max}} = 448 \text{ nm}$ was used to monitor the reaction in acetone (Fig. 1).

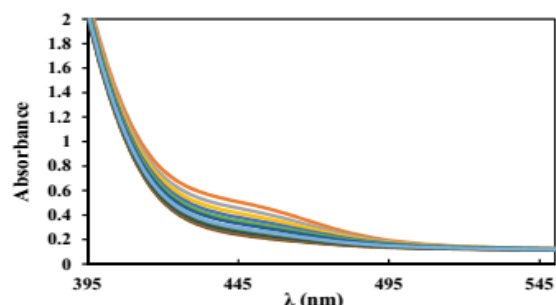


Fig.2: Changes in the UV-Vis spectrum during the reaction of [Pt(MeC₆H₄)₂(NN)], (3 mL of $5 \times 10^{-4} \text{ M}$), with iodomethane in acetone at T=25 °C, successive spectra recorded at intervals of 50 s.

The yellow color of the platinum(II) complex changed

to a very pale yellow upon oxidation to platinum(IV) complex. In this case, excess of methyl iodide was used and the reaction followed good first-order kinetics. The pseudo-first-order rate constants (k_{obs}) can be calculated with curve fitting by using Microsoft Excell solver [4]. Curve fittings plots in acetone were shown in Figs.2 and 3.

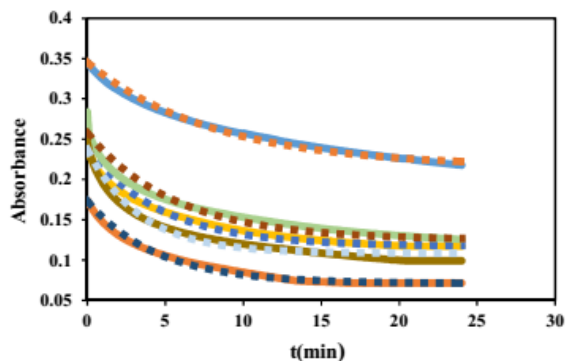


Fig.2: Curve fitting for the reaction of $[Pt(MeC_6H_4)_2(NN)]$, with methyl iodide in acetone at $T=30\text{ }^\circ\text{C}$.

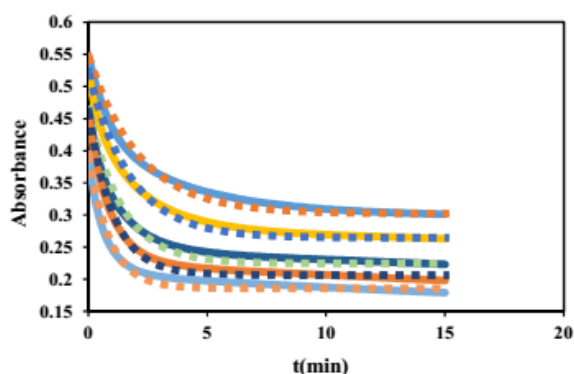


Fig.3: Curve fitting for the reaction of $[Pt(MeC_6H_4)_2(NN)]$, with methyl iodide in acetone at $T=35\text{ }^\circ\text{C}$.

Graphs of these first-order rate constants against the concentrations of methyl iodide gave good straight line plots passing through the origin, showing a first-order dependence of the rate on the concentration of the iodomethane (Fig.4). The overall second-order rate constants (k_2) can be obtained from the slopes of these similar figures.

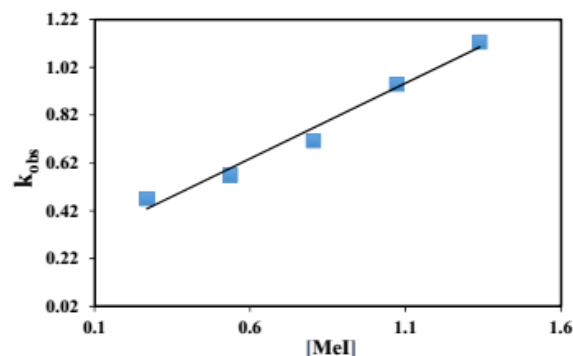


Fig. 4:Plot of first-order rate constants (k_{obs}) for the reaction of $[Pt(MeC_6H_4)_2(NN)]$, with MeI in acetone at different temperatures vs concentration of methyl iodide at $T=35\text{ }^\circ\text{C}$.

The second order rate constants were given in Table 1.

Table 1: Second order rate constants

Temp($^\circ\text{C}$)	15	20	25	30	35
k_2	0.0814	0.1547	0.2317	0.2522	0.6325

The activation energy, E_a , was obtained from the Arrhenius equation as following:

$$\ln k_2 = \ln A - E_a/RT$$

The Arrhenius plot was shown in Fig. 5.

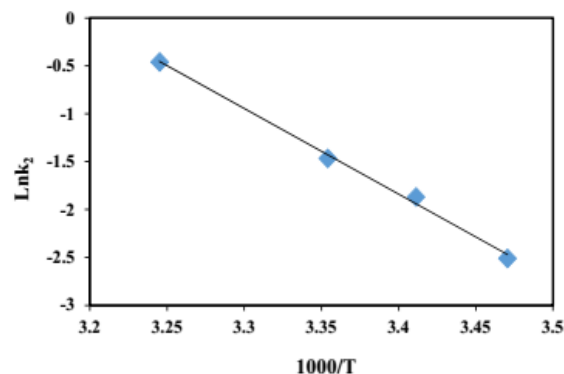


Fig. 5:Arrheniusplot for the reaction of $[Pt(MeC_6H_4)_2(NN)]$ with iodomethane in acetone.

Furthermore, entropy and enthalpy of activation were obtained from the Eyring equation:

$$\ln(k_2/T) = \ln(k'/h) + \Delta S^\ddagger/R - \Delta H^\ddagger/RT$$

The Eyring plot was shown in Fig. 6.

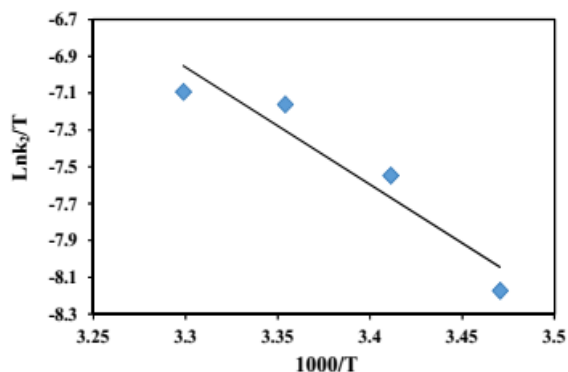


Fig. 6: Eyring plot for the reaction of [Pt(MeC₆H₄)₂(NN)] with methyl iodide in acetone.

The activation parameters were reported in Table 2.

Table 2: Activation parameters data

ΔS^\ddagger	ΔH^\ddagger	Ea
-80.6736	52.9538	74.3414

Kinetic studies of the oxidative addition reaction of methyl iodide with platinum(II) complex in different temperatures indicated that the reaction occurred by the S_N2 mechanism [5].

Conclusions

Kinetic studies of the oxidative addition reaction of iodomethane with platinum(II) complex in different

temperatures were performed and second order rate constants and activation parameters were calculated. The large negative of ΔS^\ddagger showed that the reaction was occurred by the S_N2 mechanism.

Acknowledgment

We gratefully acknowledge the support of this work by Damghan University Research Council.

References

- [1] F.R. Hartly "The chemistry of platinum and palladium", 1973, Applied Science, London.
- [2] J. K. Jawad, R. J. J. Puddephatt, "Electronic and steric effects on the rate of oxidative addition of methyl iodide to diaryl(2,2'-bipyridyl)platinum(II) complexes", *Dalton Trans. Chem. Soc.*, (1977) 1466-1469.
- [3] A. Capape, M. Crespo, J. Granell, M. Font-Bardía, & X. Solans, "A comparative study of the structures and reactivity of cyclometallated platinum compounds of N-benzylidenebenzylamines and cycloplatination of a primary amine", *Dalton Trans.*, 20(2007)2030-2039.
- [4] D. C. J. Harris, "Nonlinear least-squares curve fitting with microsoft excel solver", *Chem. Edu.*, 75(1998) 119.
- [5] B. Shafaatian, B. Heidari, "Synthesis, characterization, crystal structure, solvatochromism, fluorescence and electrochemical studies of new organometallic platinum complexes, kinetic investigation of oxidative addition reaction", *J. Organomet. Chem.*, 780(2015) 34-42.

Theoretical Study on the Kinetics of the Reactions Between 1,3,5-Trioxane with OH Radical

V.Saheb*, A.Bahadori

Master of Science in Physical Chemistry, University of Shahid Bahonar, Kerman, Iran

aidin.bahadory@gmail.com

Abstract: Theoretical investigations have been performed on the kinetics of bimolecular reaction of $C_3H_6O_3$ and OH radical. In this research, two probable pathways for hydrogen absorption processes are considered. Optimization of the structures, and calculation of energies, vibrational frequencies and moments of inertia for all the stationary points are carried out by using MP2(full) method along with the 6-31+G** basis set. Single-point energy calculations on the optimized points are performed at the CBS-QB3 level of theory. Transition state theory is employed to compute the thermal rate constants for two reaction channels over the temperature range 200-3000K.

Keywords: 1,3,5-Trioxane, Hydroxyl radical, Transition State Theory, Rate constant

Introduction

1,3,5-trioxane, also called trioxane or trioxin, is a chemical compound with molecular formula $C_3H_6O_3$. It is a white crystalline solid with a characteristic odor resembling that of chloroform. This molecule is a six-membered ring trimer of CH_2O using acid catalysts with alternating carbon and oxygen atoms. Thus, 1,3,5 trioxane is interesting as a model of how C-H bond strength and reactivity change upon cyclization. The production of plastics (polyoxymethylene plastics, POM) is the most important commercial application of trioxane and requires extremely pure material. Since trioxane depolymerizes to produce formaldehyde, it can be used in almost all formaldehyde reactions, especially when anhydrous formaldehyde is desired.

The reaction of 1,3,5-trioxane with OH radical is of importance because of atmospheric considerations. Only one experimental data is reported on the measurement of the rate constant of the reaction of hydroxyl radical with 1,3,5-trioxane. These determinations were performed over the temperature range 292-597 K. The technique employed is laser photolysis to generate the OH radicals, and laser-induced fluorescence (LIF) to directly monitor their decay under pseudo-first-order conditions. The results fit the following Arrhenius equations: $k = (1.36 \pm 0.20) \times 10^{-11} \exp[-(460 \pm 100)/RT] \text{ cm}^3 \text{ s}^{-1}$. To date, no experimental data is reported on the kinetics and mechanism of title reaction. In this research, the potential energy surface (PES) for bimolecular reaction of $C_3H_6O_3$ and OH radical is explored by M06-2X method. Next the rate constant for reaction paths are computed by using transition state theory (TST).

Method

The structures for all of the stationary points, i.e., minimum energy structures, van der Waals complexes, saddle points and products are optimized at the MP2(full) /6-31+G** level of theory. Single-point

calculations on the optimized geometries are performed at the CBS-QB3 level of theory. Quantum chemical calculations were performed with the Gaussian 09 package of programs.

Transition-state theory (TST) is used to compute the thermal rate coefficients. According to the TST, the canonical rate constant, $k(T)$, is given by the following equation:

$$k(T) = \Gamma \frac{k_B T}{h} \frac{Q_t^\ddagger Q_r^\ddagger}{Q_t Q_r Q_v} \exp(-E_0/k_B T)$$

where h is Planck's constant, k_B is Boltzmann's constant, T is the temperature, Q_t , Q_r and Q_v are the translational, rotational and vibrational partition functions for the reactants, respectively. Q_t^\ddagger and Q_r^\ddagger represent the corresponding values for transition state. Γ is the tunneling factor.

Results and Discussion

The hydrogen abstraction reaction of OH radicals from $C_3H_6O_3$ occurs via axial and equatorial positions. Based on the present theoretical calculations on the reaction, the reaction proceeds through a common van der Waals complex vdW1 with an energy of $-22.43 \text{ kJ mol}^{-1}$ lower than the reactants. Next, the reaction proceeds via two transition states (TS1 and TS2) corresponding to axial and equatorial hydrogen atoms on $C_3H_6O_3$. The potential energy profile of the reaction is shown in Figure 1. The energies of the transition states TS1 and TS2, relative to the reactants, are $-8.23 \text{ kJ mol}^{-1}$ and 7.63 kJ mol^{-1} , respectively. The later transition states lead to the van der Waals complexes vdW1B and vdW2B, respectively. The relative energies of the complexes are $-114.37 \text{ kJ mol}^{-1}$ and $-94.097 \text{ kJ mol}^{-1}$, respectively. Next, vdW1B and vdW2B give the products P1+H₂O and P2+H₂O, respectively. The product P1 and P2 are $106.61 \text{ kJ mol}^{-1}$ and $86.98 \text{ kJ mol}^{-1}$ more stable than the reactants, respectively.



Here, it is attempted to compute the rate constant for two general reaction paths by using transition state theory (TST). The latter calculations are underway and will be presented and discussed in the conference.

Table 1. vibrational frequencies and moments of inertia for the reaction, transition states for bimolecular reaction of

	Frequency (cm ⁻¹)	Moment of inertia	
Reactant	305.9, 305.9, 480.5, 523.5, 523.5,	96.1857	
	756.7, 966.8, 966.8, 994.4, 1005.2,	96.1858	
	1098.8, 1098.8, 1214, 1214, 1258.1,	172.8132	
	1274.6, 1354.4, 1354.4, 1424.5,		
	1466.9, 1466.9, 1550.9, 1550.9,		
	1569.7, 3045.7, 3045.7, 3057.6,		
	3264.6, 3264.6, 3266.8		
	1317.7i, 68.8, 92.3, 115, 295.9,	148.6111	
	310.6, 470.1, 517.7, 525.3, 687.2,	235.2553	
	767.9, 912.4, 956.9, 970.4, 998.1,	260.2523	
1019.5, 1106.1, 1119.7, 1218.5,			
1224.1, 1255, 1286, 1356.6, 1365.4,			
1416, 1450.9, 1473.3, 1482.5, 1552,			
1569.2, 3094.6, 3098.3, 3249.5,			
3272.1, 3275.1, 3806.2			
TS1	2133.5i, 54.7, 83.1, 170.2, 261.4,	101.4949	
	287.2, 418.3, 518.6, 522.5, 734.4,	280.6160	
	800.6, 834.5, 969.5, 983.1, 1016.4,	351.4160	
	1023.4, 1099.4, 1106.4, 1186.1,		
	1221.8, 1239.1, 1267.9, 1311.2,		
	1349.8, 1385.6, 1444.5, 1464.2,		
	1537.4, 1550.2, 1564.6, 3060.5,		
	3064.7, 3075.1, 3270.9, 3272.8,		
	3808.1		
	TS2	2133.5i, 54.7, 83.1, 170.2, 261.4,	101.4949
		287.2, 418.3, 518.6, 522.5, 734.4,	280.6160
		800.6, 834.5, 969.5, 983.1, 1016.4,	351.4160
		1023.4, 1099.4, 1106.4, 1186.1,	
		1221.8, 1239.1, 1267.9, 1311.2,	
		1349.8, 1385.6, 1444.5, 1464.2,	
1537.4, 1550.2, 1564.6, 3060.5,			
3064.7, 3075.1, 3270.9, 3272.8,			
3808.1			

C₃H₆O₃ and OH radical.

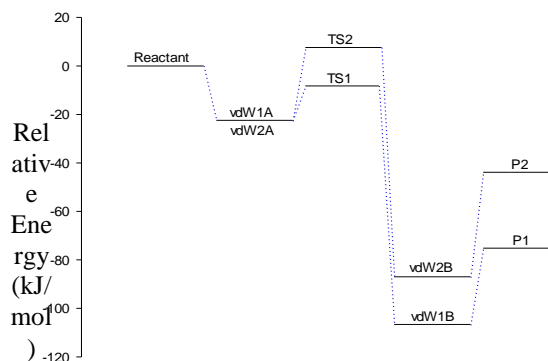
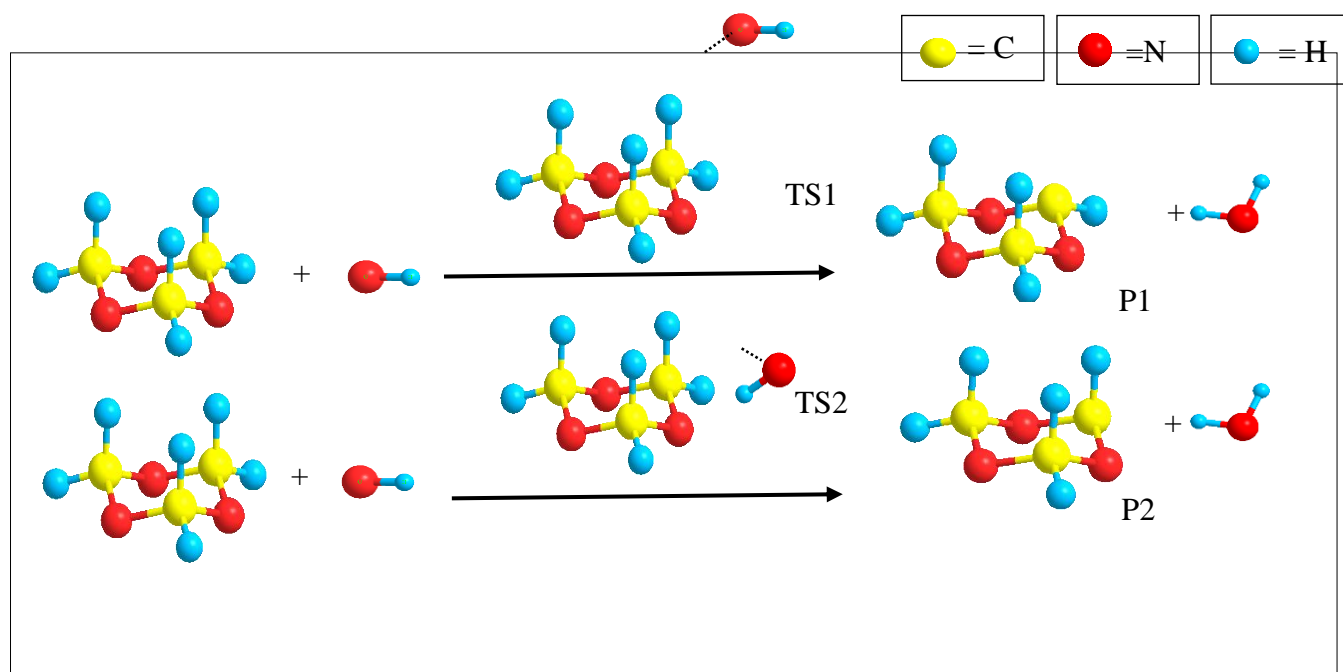


Figure 2. Relative energies for potential energy surface of the C₃H₆O₃ + OH reaction. The energy values are given in kJ mol⁻¹ and are calculated using CBSQB3 theory.

References

- [1] Lindström B, Pettersson LJ. A brief history of catalysis. *CatTech*. 2003 Aug 1;7(4):130-8.
- [2] Dhanya S, Pushpa KK, Naik PD. Measurement of kinetic parameters of gas-phase reactions relevant to atmospheric chemistry. *Current Science*. 2012 Feb 10;102(3):452.
- [3] Miller WH. Beyond transition-state theory: a rigorous quantum theory of chemical reaction rates. *Accounts of chemical research*. 1993 Apr;26(4):174-81.
- [4] Bunker DL. *Theory of elementary gas reaction rates*. Pergamon; 1966.



Estimation and optimization of Kinetic Parameters for thermal decomposition of MDF by genetic algorithm

M. H. Ahmadi Azghandi*

Applied Chemistry Department, Faculty of Petroleum and Gas (Gachsaran),
Yasouj University, Gachsaran, 75813-56001, Iran.
[*mhahmadia58@gmail.com](mailto:mhahmadia58@gmail.com), m.ahmadi@yu.ac.ir

Abstract: In this study, the Genetic algorithm method, as evolution strategy, through simultaneous thermogravimetric analysis experiments was used for modelling the burning behaviour of medium density fiberboard (MDF) and estimate pyrolysis kinetic parameters.

Thermal degradation kinetic parameters (e.g. E_a , A and n) were calculated by Kissinger–Akahira–Sunose method (KAS). According comparison made between kinetic properties predicated by the genetic algorithm, experimental and KAS method is found that GA could effectively contribute to the estimation of precise activation energy (E_a) and reaction order (n) values with least amount of experimental work and most accuracy.

Furthermore, the four components of MDF, hemicellulose, cellulose, lignin, and resin were considered during the modelling of MDF decomposition.

Keywords: Genetic algorithm; Kinetics; TGA; E_a .

Introduction

Differences in the activation energy (E_a) values from values from differential and integral isoconversional methods (model free) have been already reported. Since long ago it was understood that these differences may be due to the temperature integral approximations used in integral methods. However, the activation energy obtained from these (isoconversional) methods has no physical meaning and it is called the apparent activation energy.

Since the late 2000s, with the development of computational equipment and software, several effective estimation methods have been improved to calculate the triplet kinetic parameters (e.g. E_a , $\log A$ and n).

In these methods, numerical simulation of a single TG thermogram as a new strategy was used for calculation of kinetic parameters. This numerical simulation is also called an inverse problem.

The existences of more than one main convergence region and/or many minor local optima in each region are the major obstacles for explaining the inverse problem. However, there are many approaches to solve such optimization problem (e.g. stochastic methods, deterministic methods, heuristics etc).

In the last decade, several scientific researches tried to apply different optimization algorithms to the inverse problem of thermal degradation kinetics parameters estimation such as the genetic algorithms (GA) [1,2], least-squares method [3,4] and PEAKFIT [5].

In spite of the fact that genetic algorithm is a versatile and powerful tool, its use has a number of difficulties. Results obtained by GA are strongly dependent on the initial setup of algorithm parameters such as mutation probability, population size and crossover probability or selection mechanism.

The least-squares and PEAKFIT techniques can be applied for this reaction, but these approaches are only suitable for reactions that are well separated. It is noting that both least-squares and PEAKFIT methodologies are similar to GA while the kinetic parameters are adjusted to produce TG curves to fit the experimental data. However, GA may be useful when complex degradation with multiple steps is simulated; the large number of kinetic parameters must be adjusted by user to the modelling process impractical.

An extensive literature survey revealed the kinetic parameters calculated for the decomposition of wood vary over a range. Thus, GA is used to search for the kinetic parameters that produce the best fit TG curves. Also, the objective of this research is to investigate the mechanisms of MDF pyrolysis and obtain a set of kinetic properties that are applicable for pyrolysis modelling for the particular MDF used.

Materials and method

Case studies

Wood is a very complex material, where the main components are cellulose and lignin. Its thermal behaviour is not simple and overlapping processes seem to be involved.

The MDF panel is a lightweight, wood product that consists of resin, cellulose, lignin and hemicellulose and thermal behaviour its very complex. Hence, in the current study we investigated MDF panel made by a local (Iran) manufacturer with thicknesses of 18 mm and weight of 10-15mg.

TG

Thermogravimetry (TG) testing was conducted on a SDT Q600 by TA Instruments. A sample of powder with 6.0 mg was placed in an aluminium oxide crucible. Sample was heated from 25 to 1000 °C with four heating rates (5, 10, 15, and 20 °C/min). Pure nitrogen gas was used as a purge gas with a flow rate of 20 mL/min.



Kinetic methods

TG provides an ideal environment of controllable atmosphere and heating rate, with negligible transport effects and thermal gradient during degradation of small solid sample. Mass loss rate (MLR) could be expressed based on reaction temperature, T , and conversion percent, α . So Mass loss rate could be written as:

$$d\alpha/dt = \beta(d\alpha/dT) = k(T)f(\alpha)$$

where, α is the conversion percent, t is the time, β is the heating rate and T is the temperature. $k(T)$ is the reaction rate, which could be described by the Arrhenius law, so the above equation could be changed to

$$d\alpha/dt = A \exp(-E_a/RT) f(\alpha)$$

where E_a is the activation energy, and A is the pre-exponential factor. Isoconversional method is a commonly used way to calculate kinetic parameters by using temperature and derivative thermogravimetry (DTG) data at the same conversion with different heating rates. The most commonly used ones are KAS method.

Kissinger-Akahira-Sunose method (KAS)

KAS method is based on the expression:

$$\ln(\beta/T^2) = \ln(AE/R) - E/(RT) \quad (1)$$

Plotting $\ln(\beta/T^2)$ against $1/T$ obtained from data at different heating rates should be a straight line which could give us the value of activation energy.

Genetic algorithm

GA is a heuristic scientific method based on Darwin's biological evolutionism, which has been widely applied to solve high dimensional optimization problem for parameter optimization in engineering and science areas, such as biotechnology and building construction. Meanwhile, it has also been applied to the optimization of kinetic triplet calculation and chemical reaction mechanisms. A brief introduction about genetic algorithm is described in the following sections.

Generation, individual, and gene

The operation of genetic algorithm is initialized by creation of a new generation. Each set of parameters in generation is called one individual. One parameter in the individual is defined as one gene. In chemical dynamic solution process, one reaction corresponds to one set of triplet. For this reaction, four set of triplet is considered (Fig.1). The parameter in individual is called gene, e.g., E_a is one gene. All individuals could make up one population. The initial population is the first generation. Each gene value of one individual is determined by:

$$g_j^i = g_{j,min}^i + r(g_{j,max}^i - g_{j,min}^i)$$

where $g_{j,max}^i$ and $g_{j,min}^i$ are the upper and lower bounds of the i -th gene, the j -th individual. And r is a random number distributed in the interval $[0, 1]$.

Fitness

Fitness is defined as difference between numerical calculations and experimental results. For each individual, it has its own corresponding fitness, which could be used to judge being preserved or eliminated. The lower-fitness means that the individual values are far from theoretical ones, and these individuals should be eliminated. On the contrary, higher-fitness individuals then would be preserved. In thermal degradation kinetics, the fitness of individuals in one generation is calculated as:

$$\phi = a \left(\sum |MLR_{exp} - MLR_{cal}| \right)^{-1} + (1 - a) \left(\sum |m_{exp} - m_{cal}| \right)^{-1}$$

where a is considered as the weight coefficient, indicating a weight factor to fitness between MLR and mass. In this paper, the weight coefficient is 0.5, i.e. two parts, mass and MLR, are divided equally.

Results and Discussion

Estimation of A and E by KAS Method

The TG data of 5, 10, and 20 K/min are used to determine kinetic parameters, while the case of 60 K/min is used later for validation. The activation energy can be estimated from the slope of $-(E/R)$ by a linear fit of three experimental points, and substituting back into eq 1 gives the pre-exponential factor. Table 1 list the obtained T , A and E as well as fitting condition (R^2) for the proposed four-step kinetics under three heating rates.

Table 1. Kinetic parameters (KAS method)

reaction	β ($\frac{K}{min}$)	T (K)	R^2	E (kJ/mol)	log A (1/s)
resin	5	485	0.9856	132	11.5
	10	507			
	20	520			
hemicellulose	5	566	0.9999	155	12.6
	10	598			
	20	611			
cellulose	5	621	0.9958	190	13.7
	10	648			
	20	659			
lignin	5	660	0.9965	198	13.2
	10	690			
	20	705			

Optimized Search Methods and Ranges

In spite of the fact that genetic algorithm is able to create a large search space in a complex landscape, it takes longer computational time to converge when the number of optimized parameters becomes large. In addition to, if the search ranges are too large, attain to the best solutions become more difficult. Thus, if a good initial guess and an appropriate research range are provided, the better and fast convergence is very likely to be achieved.

As Wenlan [5] and Li [6] showed, when component is near the maximum decomposition rate without other major reaction peaks nearby, the value of |DDTG| (second derivatives of thermogravimetry) curve is very likely to drop rapidly to a local minimum.

$$|DDTG| = \left| \frac{d^2 \left(\frac{m}{m_0} \right)}{dT^2} \right|$$

Figures 1 show the |DDTG| curves of DMF, and four local minimums can be observed in the |DDTG| curves. Here, we select a range of the peak temperature as ± 10 K of the local minimum of the |DDTG| curve. Using the same Kissinger's method, the range of A and E can be found. The parameters to be determined in this research are mass fractions and kinetic parameters. The optimized GA search method was conducted with the n-order Arrhenius equation and TG data at different heating rate (i.e. 5, 10, 20 K/min) and the GA codes in MATLAB (R2015a) are used to perform the search. Table 2 lists the best solution of kinetic parameters. The results demonstrate that the four-step decomposition scheme is reasonable and GA is able to obtain good solutions. Also, it is found that the four-step decomposition mechanism and the calculated kinetic parameters work well for the prediction of the experimental DTG curves at different heating rates.

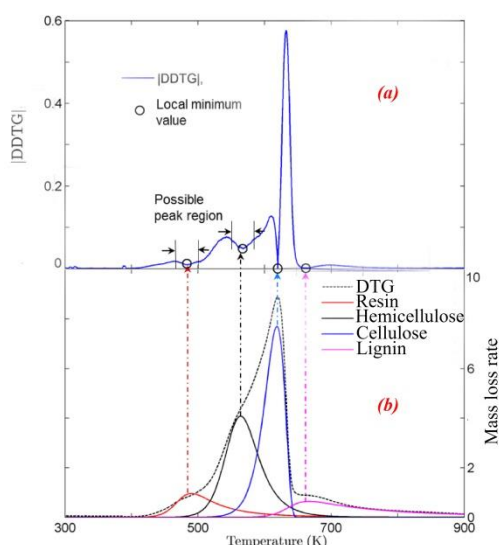


Figure 1. Experimental curves of (a) |DDTG| and (b) DTG.

Conclusions

In the current study, TGA experiments were conducted to investigate the pyrolysis kinetics of MDF. On the basis of the decomposition of MDF, the related kinetic properties are determined. These are useful inputs for modeling the burning behavior of MDF. The four components of MDF, hemicellulose, cellulose, lignin, and resin were considered during the modelling of MDF decomposition. In this work, genetic algorithm was used to optimize the kinetic properties. The kinetic

properties determined by the genetic algorithm and KAS are found to be consistent with the Kissinger-Akahira-Sunose method. However, according to the comparison made between experimental and predicted kinetic parameters of thermal degradation process calculated from GA methods, the proposed prediction effort could effectively contribute to the estimation of precise activation energy (E_a) and reaction order (n) values with least amount of experimental work and most accuracy.

Table 2. Kinetic triplet of each reaction in DMF degradation.

reaction		E(kJ/mol)	log A(1/s)
1	1.2	138	11.3
2	1.38	146	13.2
3	2.04	185	13.5
4	1.54	202	13.8

References

1. C. Lautenberger, G. Rein, C. Fernandez-Pello "The application of a genetic algorithm to estimate material properties for fire modeling from bench-scale fire test data", *Fire Safety Journal*, 41 (2006) 204–214.
2. B. Saha, A. K. Ghoshal "Hybrid genetic algorithm and model-free coupled direct search methods for pyrolysis kinetics of ZSM-5 catalyzed decomposition of waste low-density polyethylene", *Industrial & Engineering Chemistry Research*, 46 (2007) 5485–5492.
3. M. Grnli, M. J. Antal, G. Vrhgyi "A round-robin study of cellulose pyrolysis kinetics by thermogravimetry", *Industrial & Engineering Chemistry Research*, 38 (1999) 2238–2244.
4. M. Becidan, G. Vrhgyi, J. E. Hustad "Thermal decomposition of biomass wastes: A kinetic study", *Industrial & Engineering Chemistry Research*, 46 (2007) 2428–2437.
4. K.A. Trick, T.E. Saliba, S.S. Sandhu "A kinetic model of the pyrolysis of phenolic resin in a carbon/phenolic composite", *Carbon*, 35 (1997) 393–401.
5. W. Xu, J. Li, F. Liu, Y. Jiang, Z. Li, L. Li "Study on the thermal decomposition kinetics and flammability performance of a flame-retardant leather", *Therm. Anal. Calorim.*, DOI 10.1007/s10973-016-5974-9.
6. K. Y. Li, D. S. W. Pau, Y. N. Hou, J. Ji "Modeling Pyrolysis of Charring Materials: Determining Kinetic Properties and Heat of Pyrolysis of Medium Density Fiberboard", *Ind. Eng. Chem. Res.*, 53 (2014) 141–149.

Investigation of kinetic and surface adsorption of anionic dye on Layered double hydroxide/Nickel -Copper ferrite spinel magnetic nanocomposite

N.Sohrabi^{*a}, N.Rassoli^{*a}, M.oftadeh^a, M.Haghshenas^a

^aDepartment of Chemistry, Payame Noor University University, Tehran, P.O.19395-3697, Iran

* nsohrabi48@gmail.com

Abstract: Organic dyes are widely used in industries such as textile, cosmetics, printing, and paper. Organic dyes are an important class of pollutants in wastewater, and it is necessary to find a broad spectrum adsorbent that can effectively remove different kinds of organic dyes. To date, various technologies have been applied to remove organic dyes in industrial effluents, including filtration, oxidation, adsorption and ion exchanges. Among these technologies, adsorption technology is one of the most effective methods for dye removal due to its low cost, high efficiency, simplicity and insensitive to toxic substances. Layered double hydroxides (LDHs), because of their structure and high anionic exchange capacity, have received considerable attention in recent years. The adsorption performance were evaluated by the removal of Congored dye and Layered double hydroxids (Ni_{0.5}Cu_{0.5}Fe₂O₄-NiFe-LDH) (Ni_{0.5}Cu_{0.5}Fe₂O₄-MgFe-LDH) (Ni_{0.5}Cu_{0.5}Fe₂O₄-CaFe-LDH) (NiFe-LDH) (MgFe-LDH) (CaFe-LDH). Meanwhile, kinetic models, FTIR spectra, X-ray diffraction pattern and scanning electron microscope (SEM) were applied to the experimental data to examine uptake mechanism. Therefore, our work suggests the novel magnetic layered double hydroxides (Ni_{0.5}Cu_{0.5}Fe₂O₄-Ni Fe-LDH) (Ni_{0.5}Cu_{0.5}Fe₂O₄-Mg Fe-LDH) (Ni_{0.5}Cu_{0.5}Fe₂O₄-Ca Fe-LDH) to be applicable for organic dyes wastewater treatment.

Keywords: Organic Dyes, wastewater, Surface Adsorption, spinel magnetic nanocomposite, Layered double hydroxide/Nickel -Copper

Introduction

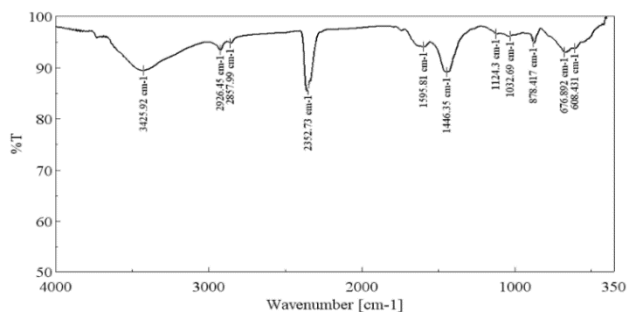
Organic dyes are widely used in industries such as textile, cosmetics, printing, and paper. However, the organic dyes are well known for causing pollution to water resulting in various undesirable consequences [1–3]. Hence, removal of dyes has gained much attention in the past years [4]. To date, various technologies have been applied to remove organic dyes in industrial effluents, including sedimentation, filtration, coagulation, oxidation, adsorption, ion exchange, and biology treatments [5–7]. Among these technologies, adsorption technology is one of the most effective methods for dye removal due to its low cost, high efficiency, simplicity, easy to perform, and insensitive to toxic substances [8,9]. Layered double hydroxides (LDHs), known as the anionic clays or hydrotalcite clays, can be expressed as the following general formula:

$[M_{1-x}^{II}M_x^{III}(OH)_2] \cdot [A_{x/n}^{n-} \cdot mH_2O]$, where M^{II} and M^{III} represent divalent and trivalent metal ions, respectively, within the brucite-like layers and Aⁿ⁻ is an interlayer anion [10–12]. Due to the attractive properties such as compositional flexibility, anion exchangeability, and biocompatibility, LDHs have received much attention in many fields, such as catalysts, polymer nanocomposites, electrochemistry, and biotechnology [13–17]. Since the interlayer anions are easily exchangeable, the anions in the interlayer can be

exchanged by other anions so that it makes LDHs useful for many applications, such as the sorption of many hazardous inorganic and organic ions from aqueous solution. The adsorption performance were evaluated by the removal of Congored dye and Layered double hydroxids (Mg Fe-LDH) (Ni_{0.5}Cu_{0.5}Fe₂O₄-Mg Fe-LDH).

Materials and method

Preparation of samples MgFe-LDH, Ni_{0.5}Cu_{0.5}Fe₂O₄-MgFe-LDH were prepared by co-precipitation method. This work aims at preparing an adsorbent to effectively remove dye Congored from aqueous solutions. Meanwhile, kinetic model, FTIR were applied to the experimental data to examine uptake mechanism. The utilization of the “memory effect” of LDH for the adsorption of dye was also confirmed by the FTIR analysis. The strong and broad bands centered around 3425.92 cm⁻¹ are associated with the OH stretching vibrations of the hydroxyl groups in the layers and interlayer water molecules [18]. The water deformation band is observed at 1595.81 cm⁻¹. D_{3h} of interlayer NO₃⁻ vibration appears at 1446.35 cm⁻¹ and 878.417 cm⁻¹ in the layered double hydroxide. The shoulder at 608.431 cm⁻¹ is assigned to M-O lattice vibrations. The effects of different parameters on Congored dye adsorption, such as effect of adsorbent dose, effect of contact time and effect of concentration Congored dye have been studied.



Effect of adsorbent dose

The effect of the adsorbent dose on the adsorption of congedred dye studied. It can be seen from Fig. 2 that the adsorption of congedred dye increases rapidly with the increase in adsorbent dose. The increase in adsorption with an increase in amount adsorbent can be attributed to increased surface area and the availability of more adsorption sites.

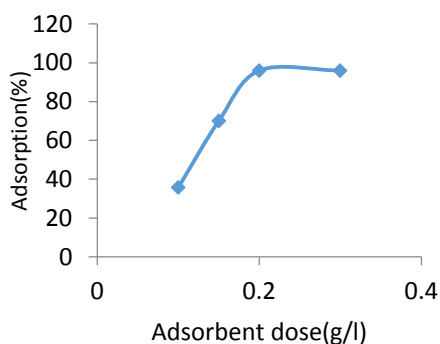


Fig. 2. Effect of the contact time on congedred dye adsorption onto magnetic $Ni_{0.5}Cu_{0.5}Fe_2O_4$ -MgFe-LDH

Adsorption kinetic

As presented in Fig. 3, kinetic studies were carried out to determine congedred dye removal from solution. The adsorption process of congedred dye on $Ni_{0.5}Cu_{0.5}Fe_2O_4$ -MgFe-LDH are analyzed using the Lagergren pseudo-first or pseudo-second order kinetic model which was given by Eqs. (1) and (2), respectively [19,20].

$$\log(q_e - q_t) = \log q_e - k_1 t / 2.303 \quad (1)$$

$$\frac{t}{q_t} = \frac{1}{k_2 q_e^2} + \frac{1}{q_e} t \quad (2)$$

where q_e and q_t are the amounts of MO adsorbed at equilibrium (mg/g), and at time (t in h), respectively, k_1 and k_2 are the pseudo-first order rate constant (h^{-1}) and pseudo-second order rate constant ($g \text{ mg}^{-1} h^{-1}$), respectively.

Results and Discussion

This result implies that $Ni_{0.5}Cu_{0.5}Fe_2O_4$ -MgFe-LDH would result in a better catalytic and adsorption activity than that for MgFe-LDH. By utilizing the unique “memory effect” of LDHs, $Ni_{0.5}Cu_{0.5}Fe_2O_4$ -MgFe-LDH could be used as a multifunctional adsorbent for anionic dye adsorption. The incorporation of $Ni_{0.5}Cu_{0.5}Fe_2O_4$ with MgFe-LDH is potentially a promising method to facilitate the separation and recovery of MgFe-LDH from solution with the magnetic separation technique, so MgFe-LDH cannot become another source of contaminant. The magnetic separation technique can also reduce the wastewater treatment cost and spread the application of MgFe-LDH as potential adsorbents in environmental pollution cleaning.

resolution. Figure and Table legends should be typed in single-spaced, Times New Roman. Captions for tables go above of each table. Captions for

Conclusions

This result implies that $Ni_{0.5}Cu_{0.5}Fe_2O_4$ -MgFe-LDH would result in a better catalytic and adsorption activity than that for MgFe-LDH. By utilizing the unique “memory effect” of LDHs, $Ni_{0.5}Cu_{0.5}Fe_2O_4$ -MgFe-LDH could be used as a multifunctional adsorbent for anionic dye adsorption. The incorporation of $Ni_{0.5}Cu_{0.5}Fe_2O_4$ with MgFe-LDH is potentially a promising method to facilitate the separation and recovery of MgFe-LDH from solution with the magnetic separation technique, so MgFe-LDH cannot become another source of contaminant. The magnetic separation technique can also reduce the wastewater treatment cost and spread the application of MgFe-LDH as potential adsorbents in environmental pollution cleaning.

References

- [1] Z. Aksu, Process Biochem. 40 (2005) 997.
- [2] B.H. Hameed, A.A. Ahmad, J. Hazard. Mater. 164 (2009) 870.
- [3] Z. Aksu, J. Yener, Waste Manage. 21 (2001) 695.



بیستمین کنفرانس شیمی فیزیک ایران
دانشکده علوم پایه - دانشگاه اراک
۱۳۹۶ مرداد ۲۹-۳۱



20th Iranian Physical Chemistry Conference

- [4] G. Mezohegyi, F.P. van der Zee, J. Font, A. Fortuny, A. Fabregat, J. Environ. Manage. 102 (2012) 148.
- [5] K. Swaminathan, S. Sandhya, A. Carmalin Sophia, K. Pachhade, Y.VSubrahmanyam, Chemosphere 50 (2003) 619.
- [6] C.A.K. Gouvêa, F. Wypych, S.G. Moraes, N. Durán, N. Nagata, P. Peralta-Zamora, Chemosphere 40 (2000) 433.
- [7] C. O'Neill, F.R. Hawkes, D.L. Hawkes, S. Esteves, S.J. Wilcox, Water Res. 34(2000) 2355.
- [8] J. Guo, R.Y. Wang, W.W. Tjiu, J.S. Pan, T.X. Liu, J. Hazard. Mater. 225–226 (2012) 63.
- [9] Y.-E. Miao, R.Y. Wang, D. Chen, Z.Y. Liu, T.X. Liu, ACS Appl. Mater. Interfaces 4 (2012) 5353.
- [10] R.Z. Ma, Z.P. Liu, L. Li, N. Iyi, T. Sasaki, J. Mater. Chem. 16 (2006) 3809.
- [11] G.R. Williams, D. O'Hare, J. Mater. Chem. 16 (2006) 3065.
- [12] A.I. Khan, D. O'Hare, J. Mater. Chem. 12 (2002) 3191.
- [13] B. Sels, D. De Vos, M. Buntinx, F. Pierard, A. Kirsch-De Mesmaeker, P. Jacobs, Nature 400 (1999) 855.
- [14] F. Leroux, J.-P. Besse, Chem. Mater. 13 (2001) 3507.
- [15] Z. Yang, W.W. Tjiu, W. Fan, T.X. Liu, Electrochim. Acta 90 (2013) 400.
- [16] Z. Gu, B.E. Rolfe, A.C. Thomas, J.H. Campbell, G.Q. Lu, Z.P. Xu, Biomaterials 32(2011) 7234.
- [17] H.F. Bao, J.P. Yang, Y. Huang, Z.P. Xu, N. Hao, Z.X. Wu, G.Q. Lu, D.Y. Zhao, Nanoscale 3 (2011) 4069.
- [18] M. Bouraada, M. Lafjah, M.S. Ouali, L.-C. deMénorval, Basic dye removal from aqueous solutions by dodecylsulfate- and dodecyl benzene sulfonate intercalated hydrotalcite, J. Hazard. Mater. 153 (2008) 911–918.
- [19] W. Plazinski, W. Rudzinski, Kinetics of solute adsorption at solid/solution interfaces: a theoretical development of the empirical pseudo-first and pseudo-second order kinetic rate equations, based on applying the statistical rate theory of interfacial transport, J. Phys. Chem. B 110 (2006) 16514–16525.
- [20] W. Plazinski, W. Rudzinski, Studies of the kinetics of solute adsorption at solid/solution interfaces: on the possibility of distinguishing between the diffusional and the surface reaction kinetic models by studying the pseudo-first-order kinetics, J. Phys. Chem. C 111 (2007) 15100–15110.

Novel TiO₂ NPs Loaded on Activated Carbon as a Green and High Efficient Absorbent : Synthesis, Characterization, Kinetic and Equilibrium Studies of the Adsorption of Bismarck Brown and Thymol Blue from Aqueous Solutions

Saideh Bagheri^{a*}, Hossein Aghaei^a and Mehrorang Ghaedi^b

^a Department of Chemistry, Science and Research Branch, Islamic Azad University, Tehran P.O.Box14515-755,
Tehran, Iran.

^b Chemistry Department, Yasouj University, Yasouj 75918-74831, Iran.

*S_bagheri2010@yahoo.com

Abstract: The present study focuses on the development of an effective methodology to obtain the optimum removal conditions assisted by ultrasonic to maximize the simultaneous removal of Bismarck Brown (BB) and Thymol Blue (TB) dyes on TiO₂ nanoparticles loaded on activated carbon (TiO₂-NPs-AC) in aqueous solution using response surface methodology (RSM). The experimental equilibrium data were fitted to the conventional isotherm models such as Langmuir, Freundlich, Temkin and Dubinin–Radushkevich. The Langmuir isotherm was found to be the best model for the explanation of experimental data. From the Langmuir isotherm, the maximum monolayer capacity (Q_{max}) was found to be 100 and 50 mg g⁻¹ for BB and TB, respectively at optimum conditions. Kinetic evaluation of experimental data showed that the BB and TB adsorption processes followed well pseudo-second-order.

Keywords: TiO₂-NPs-AC; dye; Central composite design; Response surface methodology; Ultrasonicated adsorption

1. Introduction

Dyes as most abundant and hazardous pollutants in high extent presence in wastewater of dye manufacturing, textile and paper industries [1,2]. Their emittance and appearance in water media as associated with some difficultly accurate and safe treatment of such pollutants containing media. Some of accomplished hazards and difficultly from water [3,4]. In the present work, TiO₂ nanoparticles-loaded on AC (TiO₂-NPs-AC) as a novel adsorbent was simply synthesized and subsequently characterized by field emission scanning electron microscopy (FE-SEM) (not shown), Fourier transform infrared spectroscopy (FTIR) (not shown). In dyes removal process, the effects of important variables such as (initial BB and TB concentration, pH, adsorbent mass and sonication time) were investigated and optimized by central composite design (CCD) under response surface methodology (RSM). It was shown that the adsorption of BB and TB follows the pseudo-second-order rate equation. The Langmuir model was found to be applied for the equilibrium data explanation.

2. Materials and method

2.1. Chemicals And Materials

All chemicals used in this work were of analytical grade and obtained from Merck, Bismarck Brown, Thymol Blue, activated carbon, sodium hydroxide, hydrochloric acid, activated carbon, sodium hydroxide, hydrochloric

acid, ethanol and titanium tetra chloride were also from Merck (Germany). To adjust the pH of reaction mixture, a solution of 0.1 mol L⁻¹ KOH was used. All aqueous solutions were prepared with ultrapure water and freshly prepared solutions were used for all chemical procedures.

2.2. Measurements of dye uptake

Small central composite design as most applicable type of RSM was applied for modeling and the optimization of effects of concentration of BB (X₁) and TB (X₂) dyes, PH (X₃), amount of adsorbent (X₄) and contact time (X₅) on the ultrasonic-assisted adsorption of BB and TB by TiO₂-NPs-AC. Five independent variables were set at five levels at which the R% of BB and TB as response was determined

and shown in Table 1.

Table 1 Matrix for the central composite design (CCD).

Factors	levels					Star points = 2.0	
	Low (-1)	Centra l (0)	High(+1)	-α	+α		
BB Concentration (mg L ⁻¹)	10	15	20	5	25		
TB Concentration (mg L ⁻¹)	10	15	20	5	25		
pH	5.0	6.0	7.0	4.0	8.0		
Adsorbent mass (g)	0.015 0	0.025	0.0350	0.005	0.045		
Sonication time (min)	2.0	4.0	6.0	2.0	6.0		
Ru n	X 1	X 2	X 3	X 4	X 5	R % _{DSB}	R % _{MO}
1	10	20	7	0.035	2	98	100

2	15	15	4	0.025	4	95	95
3	20	20	7	0.035	6	97.9	99.4
4	25	15	6	0.025	4	98	100
5	15	15	6	0.025	4	94.45	94.87
6	10	10	7	0.015	2	88	88
7	10	10	7	0.035	6	100	100
8	15	15	8	0.025	4	97.5	95.77
9	15	15	6	0.025	4	95	95
10	15	15	6	0.025	4	94.7	95
11	20	10	7	0.015	6	95	95
12	10	10	5	0.035	2	100	100
13	15	15	6	0.025	4	95	95
14	15	5	6	0.025	4	97	99
15	10	20	5	0.035	6	100	100
16	15	15	6	0.025	4	95	95
17	20	20	5	0.015	6	73	81.8
18	15	15	6	0.005	4	70	78.8
19	20	10	5	0.015	2	80	96.47
20	20	10	7	0.035	2	99.69	100
21	10	20	5	0.015	2	88.5	90
22	20	20	5	0.035	2	100	98.45
23	15	25	6	0.025	4	95	95
24	15	15	6	0.045	4	100	100
25	15	15	6	0.025	8	99.48	98.52
26	10	10	5	0.015	6	99.33	100
27	5	15	6	0.025	4	100	100
28	10	20	7	0.015	6	100	96
29	15	15	6	0.025	4	94.57	94.7
30	20	20	7	0.015	2	80	81.7
31	20	10	5	0.035	6	100	100
32	15	15	6	0.025	4	95	95

3. Results and Discussion

3.1. Response Surface Plots

The 3D RSM surfaces corresponding to R%BB and R%TB were depicted and considered to optimize the significant factors and to give useful information about the possible interaction of variables. For example Fig 3 that the dye removal percentage changes versus the adsorbent dosage. The positive increase in the dye removal percentage with increase in adsorbent mass is seen. Significant diminish in

removal percentage at lower amount of TiO₂-NPs-AC is attribute to higher ratio of dye molecules to the vacant sites of the adsorbent.

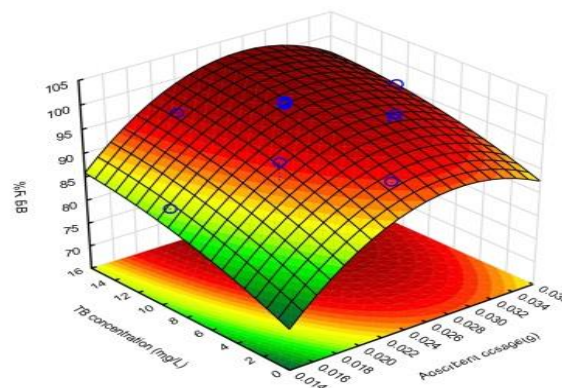


Fig.1. Response surfaces for the BB dye removal: initial TB concentration– adsorbent dosage.

3.1. Adsorption Equilibrium Study

The experimental adsorption equilibrium data was evaluated for studying the mechanism of BB and TB dyes adsorption onto TiO₂-NPs-AC using different models such as Langmuir, Freundlich, Temkin, Dubinin–Radushkevich isotherms [5, 6, 7] in their conventional linear form. Subsequently, their corresponding constants were evaluated from the slopes and intercepts of respective lines (Table 2). , It was concluded that the Langmuir isotherm is the best model to explain the BB and TB dyes adsorption onto TiO₂-NPs-AC.

Table 2 The resultant values for the studied isotherms in connection to BB and TB dyes adsorption onto TiO₂-NPs-AC.

Isotherm	parameters	Value of parameters ForBB	Value of parameters for TB
Langmuir	$q_m/(\text{mg g}^{-1})$	100	50
	$b/L \text{ mg}^{-1}$	0.487	1.53
	R^2	0.998	0.997
Freundlich	$1/n$	0.55	0.24
	$p/ (L \text{ mg}^{-1})$	4.09	3.66
	R^2	0.982	0.985

3.2. Kinetic Study

The kinetic of reactions in adsorption process is strongly influenced by several parameters related to the state of the solid and to the physico-chemical conditions under which sorption is occurred. To investigate the sorption processes of TB and BB dyes onto the adsorbent, different kinetics models such as pseudo-first order and pseudo-second-order models (Tables 2 and 3) [8]. As a result, the adsorption fits to the pseudo-second-order

better than the pseudo-first-order kinetic model for both dyes.

Table 3 The resultant values for the studied Kinetic in connection to BB and TB dyes adsorption onto TiO₂-NPs-AC.

Model	parameters	Value of parameters for BB	Value of parameters for TB
pseudo-First-order kinetic	k1/(min-1)	0.987	1.43
	qe/(calc) (mg g-1)	17.92	10.155
	R2	0.95	0.95
pseudo-Second-order kinetic	k2/(min-1)	0.154	0.507
	qe(calc) (mg g-1)	56.15	53.46
	R ²	0.999	0.999

4. Conclusions

1. Ultrasound assists the whole adsorption time leading to omit undesirable effects.
2. Combined ultrasound-assisted/nanoparticles adsorption as an efficient dye removal method. Experimental design based response surface methodology was used for optimization.
3. We demonstrate a methodology for simultaneous dyes removal from aqueous solution.
4. Nanoparticles shows considerable advantages on the removal yield of dyes.

Acknowledgment

The author expresses their appreciation to the Science and Research Branch Islamic Azad University, Tehran, Iran for financial support of this work.

References

- [1] F.N. Azad, M. Ghaedi, K. Dashtian, S. Hajati, A. Goudarzi, M. Jamshidi, Enhanced, simultaneous removal of malachite green and safranin O by ZnO nanorod loaded, activated carbon: modeling, optimization and adsorption isotherms, *New J. Chem.* 39 (2015) 7998–8005.
- [2] M. Jamshidi, M. Ghaedi, K. Dashtian, A. Ghaedi, S. Hajati, A. Goudarzi, E. Alipanahpour, Highly efficient simultaneous ultrasonic assisted adsorption of brilliant green and eosin B onto ZnS

nanoparticles loaded activated carbon: artificial neural network modeling and central composite design optimization, *Spectrochim. Acta Part A Mol. Biomol. Spectrosc.* 153 (2016) 257–267.

[3] A. Asfaram, M. Ghaedi, S. Agarwal, I. Tyagi, V.K. Gupta, Removal of basic dye auramine-O by ZnS: Cu nanoparticles loaded on activated carbon: optimization of parameters using response surface methodology with central, composite design, *RSC Adv.* 5 (2015) 18438–18450.

[4] A. Asfaram, M. Ghaedi, S. Hajati, A. Goudarzi, Ternary dye adsorption onto MnO₂ nanoparticle-loaded activated carbon: derivative spectrophotometry and modeling, *RSC Adv.* 5 (2015) 72300–72320.

[5] M. Ghaedi, A. Hassanzadeh and S. N. Kokhdan, *J. Chem. Eng. Data*, 56(2011), 2511–2520.

[6] M. Ghaedi, B. Sadeghian, A. A. Pebdani, R. Sahraei, A. Daneshfar and C. Duran, *Chem. Eng. J.*, 187(2012), 133–141.

[7] S. Hajati, M. Ghaedi, B. Barazesh, F. Karimi, R. Sahraei, A. Daneshfar and A. Asghari, *J. Ind. Eng. Chem.*, 20(2014), 2421–2427.

[8] Y. Wong, Y. Szeto, W. Cheung, G. McKay, Pseudo-first-order kinetic studies of the sorption of acid dyes onto chitosan, *Journal of applied polymer science*, 92(2004) 1633-1645.

Theoretical Study of tautomerism of methyl uracil in the gas phase

Shapourramazani*, [AkramNoshadizadeh](#)

Department of Chemistry, Yasouj University, 75914 Yasouj, Iran

Email: ramazani@yu.ac.ir

Abstract: The current work is a theoretical study of the tautomerism of 1-methyluracil (1-Mu) in the gas phase. Three structures were found in the isomerization reaction of 1-methyluracil. Two possible unimolecular pathways for 1-methyluracil have been studied. In these two reactions, the hydrogen abstractions N—H→O was considered. The potential energy surface for trajectories was determined for 3 tautomers and 2 transition states. All dynamics calculations were performed by VTST/MT using the MPWB1K level with the 6-311++G(d,p) basis set to build the potential energy surface, calculations are performed using the GAUSSRATE9.1 program.

Keywords: Kinetics, Potential- Energy Surface, Rate Constant, Tunneling.

Introduction:

Uracil is one of the four [nucleobases](#) in the [nucleic acid](#) of [RNA](#) that is derived from pyrimidines. In [DNA](#), the uracil nucleobase is replaced by [thymine](#). Uracil is a [demethylated](#) form of thymine. One of the derivatives of the uracil is 1- methyl-uracil. The importance of 1-methyl-uracil is the presence of methyl group on N1. The crystalline structures imply the presence of weak interactions between hydrogen bonds in this molecule. Of the two nitrogen atoms, the N1 that is connected to the methyl group loses its chance for direct involvement in hydrogen bond creating. [1]

In spite of its natural conditions, the N3 is susceptible to hydrogen bonding, but according to the crystalline structures and calculated parameters (by quantum computing by DFT density theory using the Gaussian 98 software), it was found that most of the protections and less affected by interactions. Because Uracil is one of the four [nucleobases](#) in the [nucleic acid](#) of [RNA](#), it plays a key role in the spread of HIV in the cell, so changing the function of 1-methyl-uracil to uracil is very important in this regard. [2,3]

Computational details:

Ab initio calculations were carried out using the Gaussian 03 program. The geometries of all the stationary points were optimized at the MPWB1K [4] and MP2 [5] levels, and Single-point calculations on the optimized MP2 geometries at the CCSD(T) level with the 6-311+g(d) basis set were carried out to obtain more accurate energies for the stationary points along the PES. Harmonic vibrational frequencies were obtained at the same level of theory

to characterize stationary points as local minima or first-order saddle points and to obtain zero-point vibration energy corrections. All dynamics calculations were performed by VTST / MT [6] using the MPWB1K level with the 6-311 ++ G (d, p) basis set to build the potential energy surface. Calculations are performed using the GAUSSRATE9.1 program.

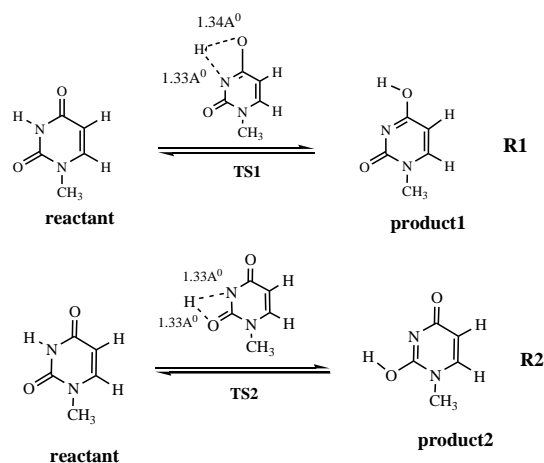


Fig.1. Reactions R1 and R2.

Results and discussion

The potential energy surface (PES) for reactions R1 and R2 (Figure 1) and relative energies are shown in Figure 2. Relative energies of all species in the reaction R1 and R2 at the mp2/6-311++g(d,p)//ccsd(t)/6-311+g(d) level. In the path R1, with hydrogen transfer from N₈ to O₁₁ and gives us a transition state (TS₁) and other time in path R2, with hydrogen transfer from N₈ to O₁₀ that gives

us(TS₂). As shown in figure 2, transition state for R1 is, 584.47 (kJ mol⁻¹) higher than reactant and for R2 is 604.63 (kJ mol⁻¹) higher than reactant. Relative free energy, enthalpy and entropy of various structures in the gas at 298.15 K are shown in Table 1.

Dynamics calculations were performed by VTST/MT using the MPWB1K level. The minimum energy paths were searched from 6.0 Å⁰ in the reagents valley up to 6.0 Å⁰ in the product valley using the step size of 0.02 bohr. The Hessian calculations were performed at 0.2 Å⁰ intervals. The Page-McIver algorithm was used to follow the minimum energy path (MEP), which is an algorithm for analyzing the normal process analysis at each point along the path. With this information, we can calculate both the vibrational partition function along the MEP and the ground state vibrationally adiabatic potential curve. It is using a method based on VTST method to calculate the rate constants for reactions R1 and R2. All of the result will be reported in the conference.

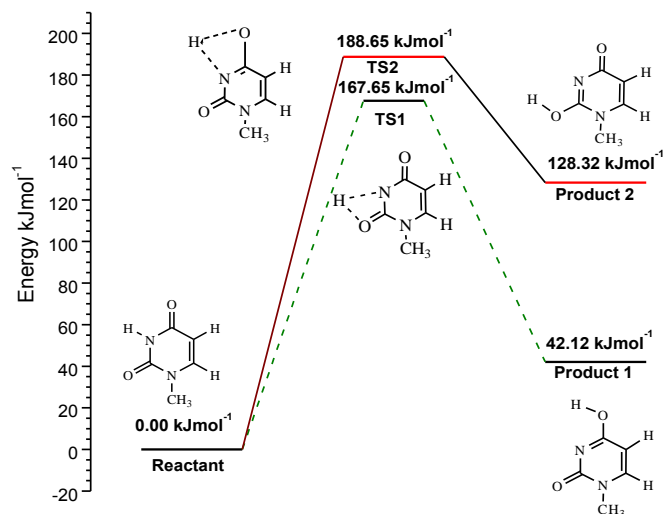


Fig.2. Relative energies of different species in kJ mol⁻¹ at the mp2/6-311++g(d,p)//ccsd(t)/6-311+g(d) level. All values are corrected for zero pointenergies.

Table 1. Relative free energy, enthalpy and entropy (kJ mol⁻¹) of various structures in the gas phase at 298.15 K.

Parameter \ path	R1	R2
$\Delta H(kJ/mol)$	39.69	392.87
$\Delta H^\ddagger(kJ/mol)$	165.03	188.51
$\Delta G(kJ/mol)$	42.28	398.79
$\Delta G^\ddagger(kJ/mol)$	165.45	188.45
$\Delta S(kJ/mol)$	42.14	391.54
$\Delta S^\ddagger(kJ/mol)$	168.48	187.87

Conclusions

The present study used 3 structures as tautomers of 1-methyluracil. Two hydrogen transfer reactions were carried out. The minimum energy path of R1 consists of one transition state and in the other one (R2) has also one transition state. Reactant is 42.12 (kJ mol⁻¹) more stable than product1. According to results, ΔG of product1 is 42.27, ΔH is 39.68 and ΔS is 168.47(kJ mol⁻¹) and barrier energy for reaction R1 is 167.65(kJ mol⁻¹). According to results, ΔG of product2 is 188.44, ΔH is 399.87 and ΔS is 391.53 (kJ mol⁻¹) and barrier energy for reaction R2 is 188.66(kJ mol⁻¹). Dynamics calculations were performed by VTST/MT using the MPWB1K level.

References

- [1] H. Azijn; I. Tirry, J. Vingerhoets; M.-P. De Béthune; G. Kraus; K. Boven; D. Jochmans; E. Van Craenenbroeck; G. Picchio; L. T. Rimsky, Antimicrob “TMC278, a Next-Generation Nonnucleoside Reverse Transcriptase Inhibitor (NNRTI), Active against Wild-Type and NNRTI-Resistant HIV-1” *Agents Chemother*, 54 (2010) 718–727.
- [2] N. Sluis-Cremer; N. A. Temiz; I. Bahar “Conformational Changes in HIV-1 Reverse Transcriptase Induced by Nonnucleoside Reverse Transcriptase Inhibitor Binding” *Curr. HIV Res*, 2 (2004) 323-332.
- [3] M.P. De Béthune “Non-nucleoside reverse transcriptase inhibitors (NNRTIs), their discovery, development, and use in the treatment of HIV-1 infection: A review of the last 20 years (1989–2009)” *Antivir. Res*, 85 (2010) 75–90.
- [4] Y. Zhao, D.G. Truhlar “Hybrid Meta Density Functional Theory Methods for Thermochemistry, Thermochemical Kinetics, and Noncovalent Interactions: The MPW1B95 and MPWB1K Models and Comparative Assessments for Hydrogen Bonding and van der Waals Interactions” *J. Phys. Chem, A*, 108 (2004) 6908-6918.
- [5] C.h. Møller, M.S. Plesset “The Pure Rotational Spectra of AuCl and AuBr” *Phys. Rev*, 46(1934) 618-622.



Isotherm and Kinetic Modeling of Adsorption of Acridine Orange Using Eucalyptus-Wood Based Activated Carbon Modified with Maghemite Nanoparticles

T. Momeni Isfahani*

Department of Chemistry, Arak Branch, Islamic Azad University, Arak, Iran
P.O. Box 38135-567, Arak 38135-567, Iran
*t-momeni@iau-arak.ac.ir

Abstract: In this study, activated carbon (AC) was prepared from low cost and locally available source such as eucalyptus wood, the activated carbon modified with $\gamma\text{-Fe}_2\text{O}_3$. The activated carbon was produced by the acid treatment of the carbon obtained from eucalyptus wood. The prepared nanomaterial was characterized by field emission scanning electron microscopy (FE-SEM), X-ray diffraction (XRD) and vibrating sample magnetometer (VSM) to examine their size and magnetic moment. The $\gamma\text{-Fe}_2\text{O}_3$ nanoparticle loaded activated carbon ($\gamma\text{-Fe}_2\text{O}_3\text{-NPs-AC}$) was used as novel adsorbent for the removal of acridine orange. The Freundlich and Langmuir isotherms were studied. The Langmuir was found to be most applicable isotherm which predicted maximum monolayer adsorption capacities of 154.74 mg g^{-1} for the adsorption of dye. The pseudo-second order model was found to be applicable for the adsorption kinetics.

Keywords: *Maghemite nanoparticles, Acridine Orange, activated carbon*

Introduction

Chromium is widely detected in surface water and groundwater at sites associated with industrial activities. Industrial sources such as chrome plating, electronic and et al. release hexavalent chromium, Cr(VI), in effluent streams with a high level of mobility and a notoriously toxicity of mutagenic and carcinogenic. The methods generally used to Cr(VI) removal from wastewaters. An alternative clean treating route that has received much attention is photocatalytic reduction in the presence of some semiconductor materials such as titania (TiO₂) [1, 2]. Ultraviolet (UV) light, visible light, sunlight, or ultrasonic sources are commonly used for this purpose [3].

The main step is charge carrier generation. The technique of ultrasound, on the other hand, has received much attention as an advanced oxidation process for treating contaminants in water. The most important chemical effect of ultrasound is by passing the waves through liquid medium in the generation of many cavities. This leads to develop high temperatures and high pressures within the cavities during their collapse [3]. The consequences of these extreme conditions are the cleavage of dissolved oxygen molecules and water molecules into $\cdot\text{H}$ and $\cdot\text{OH}$ radicals. The reactions of these entities with each other and with H₂O and O₂ yield the products of HO₂ \cdot radical and H₂O₂. In this media, organic compounds are decomposed and inorganic compounds are oxidized or reduced[3].

In this work, photo-reduction was performed with very low amounts of nanotitania particles, and modeled via RSM. Meanwhile, to the best of our knowledge, effect of sono-assisted photocatalytic reduction process of the hexavalent chromium, Cr(VI), has not been reported for this case so far. The ultrasound activity has been in cavitation regime i.e. based on chemical and physical influence of ultrasonic waves. Effects of operational parameters as well as redaction kinetics are also investigated on the reduction of Cr(VI). The investigated two reduction processes also has been compared in term of energy consumption required.

Materials and method

All the used chemicals were of analytical grade. Titanianano particles (P-25, purity >99.5%, 75% anatase, 25% rutile) was supplied by Plasma Chem. According to the manufacturer report, the specific surface area and particle size were about 50 m²/g and 21 nm, respectively. Potassium dichromate, 1,5-diphenylcarbohydrazide (DPC), acetone, sulfuric acid and sodium hydroxide, potassium iodine, sodium thiosulfate, acetic acid and starch indicator all obtained from Merck Company.

Deionized water (conductivity less than 0.08 $\mu\text{S}/\text{cm}$) was utilized for the solution.

Initial solutions of Cr(VI) were prepared with 5.0 mg/L of potassium dichromate and after adjustment of pH with either dilute sulfuric acid or sodium hydroxide, one liter solution was transferred into the reactor. After addition of desired amounts of the TiO₂, sonication and temperature adjustment were established and the UV lamp and ultrasonic generator were switched on to initiate the ultrasonic-assisted photocatalytic process. Samples of 2 mL were taken out at different times. The nano particles were separated with vigorous centrifuging and the residual concentration of Cr(VI) ions was analyzed by colorimetry method. H₂O₂ concentrations were determined spectrophotometrically by iodide method. The changes of concentrations was followed by using UV-Vis spectrophotometer (Jasco, V-630). Experimental data were analyzed using Design Expert software, V. 8.0.5 Trial.

Results and Discussion

The variable parameters initial pH, the catalyst dosage, temperature and reaction time, having influence on the desired response of *RE*. A quadratic mathematical reduced expression for modeling reduction efficiency in terms of given variables was obtained as:

$$\begin{aligned}
 RE = & 28.36 - 12.06x_{\text{pH}} + 4.34x_{\text{TiO}_2} + 10.96x_T + 7.63x_T - 4.45x_{\text{pH}}x_T \\
 & - 3.61x_{\text{pH}}x_T + 3.61x_Tx_T + 4.68x_{\text{pH}}^2 - 4.61x_{\text{TiO}_2}^2 + 3.07x_T^2 + 2.07x_T^2 \quad (1)
 \end{aligned}$$

The results show that *RE* ranges from 8.9 to 82.2% under different conditions. The major parameters that influence the rate and conversion of Cr(VI) to Cr(III) are pH, temperature, and the loading of the TiO₂ respectively. The photocatalytic Cr(VI) reduction rate is less sensitive to time change. The efficiency decreases with pH and increases with temperature. The process dependency to pH can be attributed to the surface charge properties of the photocatalyst. An increase in temperature would enhance mobilization of the reacting species and favoring the reaction rate with respect to the reaction activation energy. After screening the factors and their interactions, a maximum of 81.5% Cr(VI) reduction is predictable with titania dosage of about 33.1 mg/L, and other conditions at their limit used values of pH 2.5, temperature of 36 °C and reaction time of 120 min. The confirmatory experiment run showed a Cr(VI) reduction efficiency of 80.6% under these conditions. This closeness confirms the validity of the model (Fig. 1).

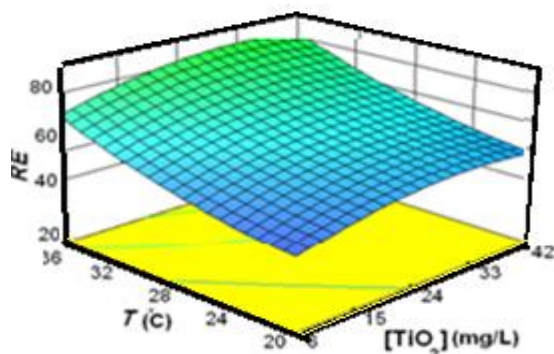


Fig.1: Response surface plot of thereduction efficiency as a function pH and T: [TiO₂]=33.1 mg/L and time=120 min.

Fig. 2 demonstrates the enhancement of photocatalytic (UV/TiO₂) reduction of Cr(VI) when the process is assisted with ultrasonic irradiation. About 96% of the Cr(VI) reduces under the above- mentioned operating conditions. This efficiency is only about 81% for the UV/TiO₂ and 60% only photolysis processes under the same conditions.

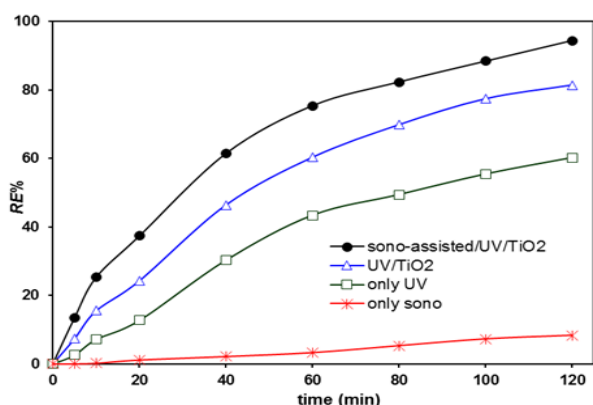


Fig.2: Effect of the different component of the sono-assisted photocatalytic process on the reduction efficiency:pH=2.5, [TiO₂]=33.1 mg/L and T=36 °C.

It is clearly obvious that the substrate trends to reduces several times higher when sonocation is employed. It should be mentioned that sensible reduction was appropriate when sono-assisted/UV/TiO₂ process was used.

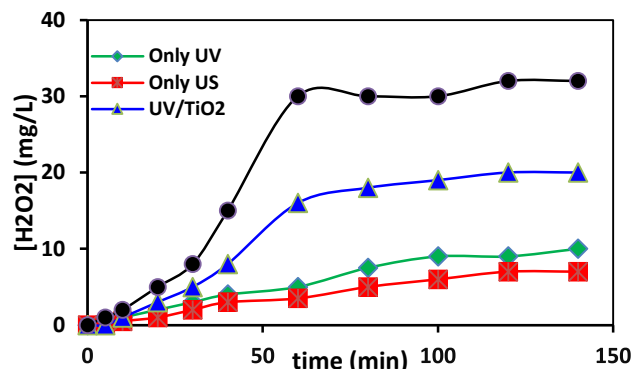


Fig.3: Comparing of H₂O₂ generation in the different Cr reduction processes; pH of 2.5 and T= 35 °C

Therefore, it can be said that cavitation process is occurred in the solution and during aqueous sonolysis, reactive radicals such as hydroxyl radicals are produced and recombined into H₂O₂[3] and the observed enhanced effect of ultrasonic on photocatalytic process relates to chemical on ultrasonic due to action to its increases through the solution. In the present investigations, this was confirmed analytically and the concentration of H₂O₂ formed during aqueous sonolysis was monitored. It can be seen from Fig.3 that H₂O₂ concentration firstly increase with time and then after approximately 40 min, the accumulate H₂O₂ reach steady-state concentrations and remained almost constant. The reason of observation is thought to be the fact that the decomposition of the H₂O₂ is occurred in the sono-assisted process reactor.

Owing to practical applications, the reduction kinetic of Cr(VI) in photocatalytic and sono-assisted photocatalytic processes were investigated under the optimum conditions. Here, a preliminary power law kinetic model was used for modeling the experimental data [4]:

$$r = -\frac{d[\text{Cr(VI)}]}{dt} = k[\text{Cr(VI)}]^n \quad (2)$$

for which the differential method of analysis, based on the provided data of concentration at different times was employed for finding the rate at each appropriate concentration. The goodness of fitting in agreement with Eq. (3). Kinetic parameters of the used reduction processes along with the coefficient of determination (R²) are given in Table 1.

Table1: Kinetic parameters of the Cr(VI) reduction; pH of 2.5 and [TiO₂]=33.1 mg/L, T= 35 °C and 120 min.

Reaction	Order	Rate constant	R ²
Only photolysis	1.50	5.87×10 ⁻³ (mg/L) ^{-0.5} /min	0.945
UV/TiO ₂	0.98	1.37×10 ⁻² (mg/L) ^{0.02} /min	0.960
Sono-assisted UV/TiO ₂	0.97	2.54×10 ⁻² (mg/L) ^{0.03} /min	0.980

There are several vital factors in selecting a waste treatment technology. Electrical energy consumption, E_E , is the main parameter in the photochemical processes economic. [5].

The investigated two reduction processes can also be compared in term of energy consumption required. Indeed, it is of high importance with industrial scale applications point of view. The energy required to reach a 60% (for instance) reduction of Cr(VI) with UV/TiO₂ process, appropriate to 60 min required time (Fig. 2), is 0.25kWh (UV lamp of 250 W). It is while assisting this process with the ultrasonic irradiation (sono-assisted/UV/TiO₂ process) leads to the reduction in energy consumption as low as 0.19kWh (250W UV lamp and 50W ultrasound) to achieve the same reduction efficiency of 60%, appropriate to required time of only 38 min. Also this energy (in kWh/m³) can be obtained according to the proposal of the photochemistry commission of the International Union of Pure and Applied Chemistry (IUPAC), for first order reactions as [5]:

$$E_E = \frac{38.4P}{Vk} \quad (3)$$

where P is the electric power (kW) of the photochemical system, V is the volume (L) of the solution in the reactor, and, k is the rate constant (in unit of 1/min).

So, the electrical energy related to both the photocatalytic and sono-assisted photocatalytic reduction of 5.0 mg/L of Cr(VI) solution, after 120 min treatment, and under conditions of pH 2.5, 33.1 mg/L of TiO₂ and 36 °C, are given in Table 2. Comparing E_E values related to sono-assisted/UV/TiO₂ with the corresponding UV/TiO₂ process in Table 2.

A valid criterion in this regard can be proposed as process efficiency (PE) when RE is assigned to unit electrical energy consumption and unit photocatalyst concentration, given in the empirical equation of:

$$PE = \frac{RE}{E_E \times [TiO_2]} \quad (4)$$

where E_E and $[TiO_2]$ are the electrical energy consumption in kWh/m³ and the catalyst loading in mg/L. Generally, PE reflects the efficiency achievement with respect to the level of energy consumption as well as the amount of catalyst.

Table2: Comparing the performance of different photocatalytic Cr(VI) reduction processes; pH of 2.5 and $[TiO_2]=33.1$ mg/L, $T=35$ °C and 120 min.

Reaction	RE	E_E	PE
----------	------	-------	------

UV/TiO ₂	81	608.7	4×10^{-3}
Sono-assisted UU/TiO ₂	96	453.6	6.4×10^{-3}

Conclusions

Reduction of Cr(VI) ion in water by Sono-assisted/UV/TiO₂ process can be performed effectively. The reaction rate can be described with a pseudo first order kinetic concentration. It is obvious that a mild electrical energy consumption is relevant in US/UV/TiO₂ process. Results shows that PE values for Cr(VI) ion in the US/UV/TiO₂ are significantly higher than UV/TiO₂ value.

References

- [1] G. Donmez, Z. Aksu, "Removal of chromium (VI) from saline wastewaters by *Dunaliella* species", *Process Biochem*, 38 (2002) 751–62.
- [2] W. Wu, J. Peng, "Linear control of electrochemical tubular reactor system—Removal of Cr(VI) from wastewaters", *J Taiwan Inst Chem Eng*, (2011) 498-505.
- [3] C. Joseph, L. Gianluca, "Sonophotocatalysis in advanced oxidation process: a short review", *Ultrason Sonochem*, 16 (2009) 583–589.
- [4] J. Saien, R. Ardjmand, "Photocatalytic decomposition of sodium dodecyl benzene sulfonate under aqueous media in the presence of TiO₂". *Phys Chem Liq*, (2003) 519–31.
- [5] J. Bolton, K. Bircher, "Figures-of-merit for the technical development and application of advanced oxidation technologies for both electric and solar-driven systems", *Pure Appl Chem*, (2001) 627–37.



بیستمین کنفرانس شیمی فیزیک ایران
دانشکده علوم پایه - دانشگاه اراک
۳۱-۲۴ مرداد ۱۳۹۶



20th Iranian Physical Chemistry Conference

الکتروشیمی

Electrochemistry

A First-Principles Theoretical Study on Electrochemical Properties of Ni(II) N₂O₂ Schiff Base Complexes

M. H. Fekri^{a*}, M. Darvishpour^a

^a Department of Chemistry, Ayatollah Aozma Boroujerdi University, Broujerd, Iran
Fekri_1354@yahoo.com

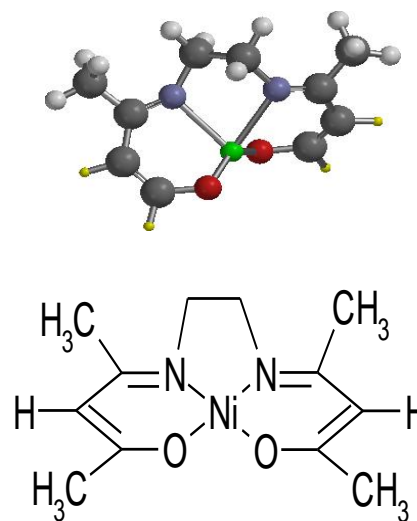
Abstract: Electrochemical methods of analysis used in the electro-chemical decomposition in solving various problems, including the use of mineral and organic substances. Now days, with the help of new methods and devices are able to determine the extent nano gram of substances. Computational methods can be replaced experimental methods oxidation potential revive to obtain complexes to which save time and cost. In regard to the first row transition metal Schiff base complexes as catalysts in catalytic processes are used in the calculation of oxidation potential revive their biochemistry that you can experience to accelerate the catalytic reactions this research, is considered. Structural and electrochemical properties of a theoretical study of the best way to present this series of complexes, and the results are compared with experimental data. The present research, calculations and computations of [Ni(Chel)] (where Chel =BAE (bis(acetylaceton) ethylenediimine), BFE (bis(1,1,1-trifluoroacetylaceton) ethylenediimine and BCE= bis(3-chloroacetylaceton)ethylenediimine. are described. electrode potentials in DMSO solvent. For this purpose, the HF calculations with the 6-311G basis set were utilized. The calculated values were compared with the experimental data that obtained by cyclovoltametry (CV).

Keywords: Ni(II); Solvent effect; HF; half-wave potential; CPCM.

Introduction

Schiff bases have been widely used as ligands because of the high stability of coordination compounds with different oxidation states. The π -system in a Schiff base often imposes a geometrical constriction and affects the electronic structure as well. Transition metal Schiff base complexes have been studied as catalysts in organic redox and electrochemical reduction reactions [1-4]. The electrochemical methods also provide highly valuable information regarding catalytic processes since catalytic conversions are frequently accompanied by change in the structure of the complex and the oxidation state of the metal, however, the electrochemical approaches for these purposes have not been fully explored [5,6,7]. The ability to calculate redox potentials accurately using the theoretical methods would be advantageous in a number of different areas, particularly where the experimental measurements are difficult, due to the complex chemical equilibria and the reactions of the involved chemical species. Recently, a number of reports, dealing with the electrode potential calculation of several biomolecules, have been published in the literature [8-9].

Our goal in the present study is to investigate metal-mediated deduction processes by theoretical methods. synthesis and characterization of [Ni(Chel)] reported in literature [10]. The electrochemical properties of Ni(II) complexes with tetradentate Schiff base ligands investigated, also (Fig. 1).



Chel	R'	X	M
BAE	CH ₃	H	Ni
BFE	CF ₃	H	Ni
BCE	CH ₃	Cl	Ni

Fig. 1. The structure of Schiff bases and Ni(Chel) complexes.

Results and Discussion

A Pentium IV personal computer system was used and the initial geometry optimization was performed with

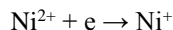


Comp.	Solvent	ΔG_{solv}^0 (a.u.)		$\Delta \Delta G_{\text{solv}}^0$ (kJ mol ⁻¹)	ΔG_{tot}^0 (kJ mol ⁻¹)
		Ni ²⁺	Ni ⁺		
BAE Ni	DMSO	-0.260334	-0.343559	218.50984	29.46861
BCE Ni		-0.329726	-0.235411	247.62401	-8.165305
BFE Ni		-0.218432	-0.078307	367.89815	132.18944

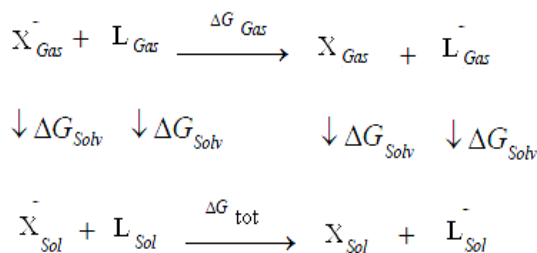
hyperchem (version 10) for all the abinitio calculations, also Gaussian 03 was employed.

In this study, the chemical structure of all of the complexes were optimized using Gaussian 03 program at HF/ 6-311G level of theory and the half-wave potentials were obtained from output results.

In this work, the nickel metal which is used Redox reaction is as follows:



Optimized geometry for all the complexes Schiff base in the gas phase and liquid phase is done with the method HF and Basis set 6-311G. Gibbs free energy in the gas phase are as follows:



$$\Delta G_{\text{gas}}^0 = G_{\text{gas}}^0(\text{Ni}^+) - G_{\text{gas}}^0(\text{Ni}^{2+})$$

Gibbs free energy in the solvent phase are as follows:

$$\Delta G_{\text{tot}}^0 = \Delta G_{\text{gas}}^0 + \Delta \Delta G_{\text{solv}}^0$$

And finally obtained E^0 from the following equation .

Comp.	ΔU_{gas}^0 (a.u.)		ΔG_{gas}^0 (a.u.)		ΔG_{gas}^0 (kJ mol ⁻¹)
	Ni ²⁺	Ni ⁺	Ni ²⁺	Ni ⁺	
BAE Ni	-2229.85	-	-2229.91	-2229.82	247.97
BCE Ni	-3147.67	-3147.57	-3147.72	-3147.63	239.45
BFE Ni	-2823.03	-2823.23	-2823.10	-2823.29	-500.08

$$\Delta G^0 = nF(E^0 - E_{\text{ref}}^0)$$

n: The number of displaced electrons

F: Faraday constant

E_{ref}^0 : The experimental value (0.197 V)

Cyclic voltammetry of Gibbs energy is as follows in the gas phase and solution.

Table 1. Gibbs free energy in the gas phase and internal energy of Ni (II) (chel).

Table 2. Gibbs free energy and The final free energy changes of the DMSO solvent

The Gibbs energy is in atomic units. Hartree (1Hartree=2625488.7Jmol⁻¹) and $E_{1/2}$ is in terms of volt.

The Gibbs energies at 298.15K, Solvation energies, and half-wave potentials were calculated using Polarisable Continuum Models (PCM).

It could be inferred that differences between computational and experimental values of $E_{1/2}$ in CPCM method is in the range of 0.003-0.049V and IEFPCM method is 0.19-0.044V, while that of COSMO method is 0.699-0.430V. Table 4 showed $E_{1/2}$ values from left to right across a period in the trend of COSMO < IEFPCM < CPCM.

The computational values of $E_{1/2}$ and their experimental data in DMSO along with three different methods are listed in table 3.

Table 3. Comparison of results of half-wave potentials calculated with experimental in three methods CPCM, IEF and COSMO in Dymethylsolfixide

Comp.	DMSO	
	$E_{1/2}^{\text{cal}}$ (V)	$E_{1/2}^{\text{exp}}$ (V)
BAE Ni	1.973	-1.901
BCE Ni	1.736	-1.705
BFE Ni	-3.399	-1.360

Conclusions

The electrochemical behavior of MnL_6^{n+} was studied in DMSO solvent, with 29,8 donor number. We expect good correlation between the redox potentials. In this study CV was carried out on Mn (III) reduction and determined the half-wave potentials ($E_{1/2}$).

Acknowledgment

The authors express their appreciation to postgraduate office of Ayatollah Alozma Boroujerdi University for financial support of this work.

References

- [1] Canali, L., and Sherrington, D.C., *Chem. Soc. Rev.*, 28 (1998) 85.
- [2] Isse, A.A., Gennaro, A., and Vianello, E., *J. Electroanal.Chem.*, 444 (1998) 241.
- [3] Pletcher, D., and Thompson, H., *J. Electroanal. Chem.*, 464 (1999) 168.
- [4] Okada, T., Katou, K., Hirose, T., Yuasa, M., and Sekine, I., *J. Electrochem. Soc.*, 146 (1999) 2562.
- [5] Isse, A.A., Gennaro, A., and Vianello, E., *J. Electroanal. Chem.*, 444 (1998) 241.



بیستمین کنفرانس شیمی فیزیک ایران
دانشکده علوم پایه - دانشگاه اراک
۲۱-۲۴ مرداد ۱۳۹۶



20th Iranian Physical Chemistry Conference

- [6] Okada, T., Katou, K., Hirose, T., Yuasa, M., and Sekine, I., *J. Electrochem. Soc.*, 146 (1999) 2562.
- [7] Jäger, E.G., Schuhmann, K., and Görls, H., *Inorg. Chim. Acta.*, 255 (1997)295.
- [8] Namazianm, M., and Norouzi, P., *J. Electroanal. Chem.*, 573 (2004) 49.
- [9] Reynolds, C. A., King, P. M., and Richards, W. G., *Nature*, 334 (1998) 80.
- [10]. Kianfara, A.H., Zargarib, S., and Khavasic, H.R., *J. Iran. Chem. Soc.*, 7 (2010) 908.

Application of a New Macrocyclic-PVC Electrode to Potentiometric Studies of Cr(III) Ion and Its Computational studies

M. H. Fekri^{a*}, M. Darvishpour^a

^a Department of Chemistry, Ayatollah Aozma Boroujerdi University, Broujerd, Iran.
Fekri_1354@yahoo.com

Abstract: A new macrocyclic ligand as a neutral carrier in the construction of a new PVC membrane electrode selective to Cr(III) ion was prepared. The electrode exhibits a good potentiometric response for Cr(III) over a wide concentration range 1.0×10^{-4} to 1.0×10^{-1} M with a slope 20.4 ± 0.5 mV/decade and low detection limit of 8.9×10^{-5} M. It has a fast response time ≤ 20 s. The best performance was observed with the membrane having the PVC- ligand- acetophenone- oleic acid composition 6:1:7:1. The electrode assembly was also used as indicator electrode in the potentiometric titration of Cr(III) with EDTA. The structure of the ligand was also studied by HF calculations using a standard 6-31G* basis set and LanL2DZ.

Keywords: PVC membrane; Cr(III); sensor; potentiometry; New Macrocyclic; HF, LanL2DZ.

Introduction

Ion-selective electrodes (ISEs), especially those with neutral carrier-based solvent polymeric membranes, have been studied for more than three decades, and are now routinely employed for direct potentiometric measurements of various ionic species in environmental, industrial and clinical samples [1,2,3]. The increasing use of ion sensors in the fields of environmental, agricultural and medicinal analysis is stimulating analytical chemists to develop new sensors for the fast, accurate, reproducible and selective determination of various species. In the past few decades, considerable efforts have led to the development of selective sensors for alkali and alkaline earth metals and for heavy metals. Among heavy metals, trivalent metals have received less attention in spite of their widespread occurrence in rocks, alloys, food products, sea- and fresh-water, plants and animals [4].

A significant number of macrocyclic compounds including crown ethers, cryptands, aza-crowns and thiacycrowns, which have been synthesized in various cavity sizes and shapes have already been exploited for the fabrication of poly (vinyl chloride) membrane electrodes for transition and heavy metal ions [5,6].

Fabrication of a new ion specific ISE with high selectivity and sensitivity, wide linear concentration range, long lifetime, good reproducibility and low cost is always in need. A literature survey revealed that a large number of ISE based on PVC membrane were reported for many inorganic ions [7], but to the best of our knowledge, very little reports were appeared on PVC-based trivalent ions.

The first report on Cr(III) was in 1980 [8]. In 1987 a Cr(III) selective electrode with PVC membrane based on 8-quinoline-dithiocoboxilate was described [9]. In 1989 another ion selective electrode based on

chromium dithizonate was built that was a precipitate based selective electrode [10]. A PVC-based Cr(III)-selective electrode, which was recently been prepared, is based on 4-methylaminoazobenzene [11]. Gholivand et al. used a Cr(III)-selective electrode based on glyoxal bis(2-hydroxyanil) [12].

In this paper, the ligand (Fig. 1) used as an ionophore in fabrication of ISEs for determination of Cr(III) and studied its structure by ab initio HF calculations using a standard 6-31G* basis set and LanL2DZ.

Experimental

A new macrocyclic ligand (Fig. 1) Tetrahydrofuran (THF), dibutyl phthalate (DBP), acetophenone (AP), oleic acid (OA), high relative molecular weight PVC, chloride and nitrate salts of all other cations and reagents used (all from Merck or Fluka) were of the highest purity available and used without any further purification.

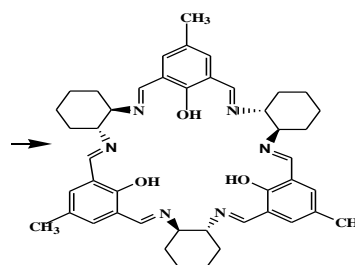


Fig. 1. Structure of used ionophore.

Potentiometric and pH measurements were carried out using a metrohm digital pH/mV meter ion analyzer in stirred solution. In all instances, an Ag-AgCl / KCl (sat.) electrode (Azar electrode company, Urmia, Iran)

was used in conjunction with the respective indicator electrode. A Haoke model FK2 circulation water bath was used control the temperature of the test solution.

A mixture of PVC, oleic acid, acetophenone and ionophore to give a total mass of 100 mg, was dissolved in about 2 mL of THF and the solution was mixed well. The resulting clear mixture was transferred into a glass dish of 2 cm diameter. The solvent was evaporated slowly until an oily concentrated mixture was obtained. A pyrex tube (5 mm o.d.) was dipped into the mixture for about 10 s so that a nontransparent membrane of about 0.2 mm thickness was formed. The tube was then pulled out from the mixture and kept at room temperature for about 2 h. The tube was then filled with internal solution 1.0×10^{-3} M Cr(III) chloride with pH = 3. The electrode was finally conditioned for 24 h by soaking in a 1.0×10^{-2} M Cr(III) chloride solution with pH = 3. The potential measurements were carried out with the following assembly:

Ag/AgCl / 3 M KCl / internal solution (1.0×10^{-3} M CrCl_3 , 1.0×10^{-3} M HCl) / PVC membrane / test solution / 3 M KCl / Ag-AgCl.

A mixture of PVC, oleic acid, acetophenone and ionophore to give a total mass of 100 mg, was dissolved in about 2 mL of THF and the solution was mixed well. Membrane composition are listed in Table 1. The resulting clear mixture was transferred into a glass dish of 2 cm diameter. The solvent was evaporated slowly until an oily concentrated mixture was obtained.

A pyrex tube (5 mm o.d.) was dipped into the mixture

Ionophor	Composition, %			Slope	Linear range, M
	PVC	Plastisizer	Additive		
-	32.0	63.0 (AP)	5.0 (OA)	3.1	-
1.5	29.0	63.5 (DBP)	6.0 (OA)	24.2	1.0×10^{-3} - 1.0×10^{-1}
1.5	27.0	65.0 (AP)	6.5 (OA)	17.1	1.0×10^{-3} - 1.0×10^{-1}
2.0	28.0	65.5 (AP)	4.5 (OA)	22.5	1.0×10^{-4} - 1.0×10^{-1}
2.0	28.0	64.0 (AP)	6.0 (OA)	23.5	1.0×10^{-4} - 1.0×10^{-1}
3.0	30.5	61.0 (AP)	5.5 (OA)	21.6	1.0×10^{-4} - 1.0×10^{-1}
4.7	28.0	62.0 (AP)	5.3 (OA)	18.5	1.0×10^{-4} - 1.0×10^{-1}
4.8	31.1	59.0 (AP)	5.1 (OA)	22.1	1.0×10^{-4} - 1.0×10^{-1}
6.8	40.0	47.4 (AP)	5.8 (OA)	20.4	1.0×10^{-4}- 1.0×10^{-1}
9.5	32.0	52.5 (AP)	6.0 (OA)	31.7	1.0×10^{-3} - 1.0×10^{-1}

for about 10 s so that a nontransparent membrane of about 0.2 mm thickness was formed. The tube was then pulled out from the mixture and kept at room temperature for about 2 h. The tube was then filled with internal solution 1.0×10^{-3} M Cr(III) chloride with pH=3. The electrode was finally conditioned for 24 h by soaking in a 1.0×10^{-2} M Cr(III) chloride solution with pH = 3.

Table 1. Optimization of the membrane ingredients.

Results and Discussion

The macrocyclic ligand as a carrier was found to be highly responsive to Cr(III) with respect to several other metal ions. Therefore, we studied in detail the performance of the plasticized PVC membrane containing this ionophore for Cr(III) in aqueous solution. In order to test the performance of the membrane characteristics, various operation parameters including selectivity, response time, sensitivity, lifetime, linear range, the influence of pH and the membrane composition on the response of the electrode were investigated.

It is well known that the sensitivity and selectivity of the ion-selective sensors not only depend on the nature of ionophore used, but also significantly on the membrane composition and the properties of plasticizers and additives used [13-16]. Thus, the influences of the membrane composition, the nature and amount of plasticizers and amount of oleic acid as an additive on the potential response of the Cr(III) sensor were investigated.

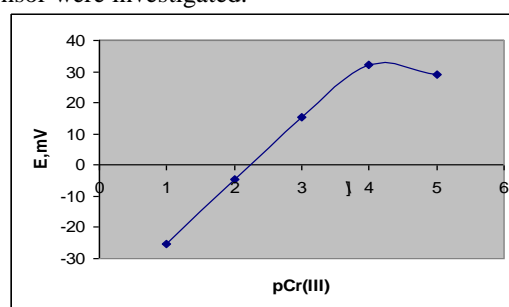


Fig. 2. Calibration plot of the Cr(III)-ISE based on ionophore.

Among the different composition studied, membrane 8 incorporating 40.0 % PVC, 47.4 % AP, 5.8 % OA and 6.8 % ionophor shows the best sensitivity. The calibration plot is shown in Fig. 2, which indicates a linear range from 1.0×10^{-4} to 1.0×10^{-1} M Cr(III) with a Nernstian slope of 20.4 ± 0.5 mV/decade of Cr(III) concentration and low detection limit of 8.9×10^{-5} M. It has a fast response time ≤ 20 s. The best performance was observed with the membrane having the PVC-ligand-acetophenone-oleic acid composition 6:1:7:1.

The response time of the electrode was measured after successive immersion of the electrode in a series of chromium solution, in each of which the Cr(III) concentration was increased tenfold, from 1.0×10^{-5} to 1.0 M. At lower concentrations, however, the response time was longer and reached 20 s for a Cr(III) concentration of 1.0×10^{-4} M. The actual potential versus time traces is shown in Fig. 4 for Cr(III) concentration of 1.0×10^{-4} M.

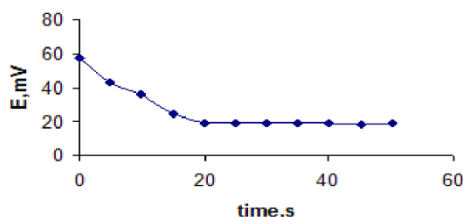


Fig. 3. The response time of Cr(III)-ISE based on ionophore for Cr(III) concentration of 1.0×10^{-4} M.

To evaluate the reversibility of the electrode, a similar procedure in the opposite direction was adopted. The measurements were performed in the sequence of high-to-low (from 1.0×10^{-2} to 1.0×10^{-3} M) sample concentration and the results are shown in Fig.5. This Figure shows that the potentiometric response of the electrode is reversible, although the times needed to reach equilibrium values were longer than that of low-to-high sample concentration [17].

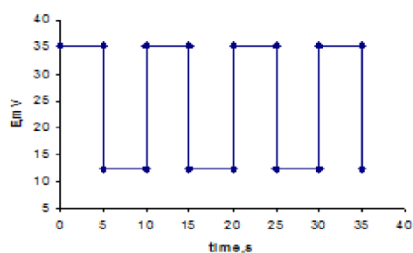


Fig. 4. Dynamic response characteristics of the Cr(III)-electrode for several high-to-low sample cycles.

The practical applicability of the electrode was tested by using it as an indicator electrode to determine the end point in the potentiometric titration of Cr(III) with EDTA solution. 20 ml of 1.0×10^{-4} M Cr(III) solution was titrated against 1.0×10^{-3} M EDTA solution.

The potential data are plotted against the volume of EDTA (Fig.5). Although the changes observed in potentials are not large, the end point is quite sharp and a perfect stoichiometry is observed.

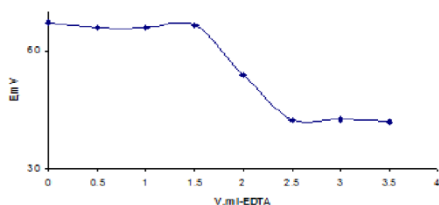


Fig. 5. Potentiometric titration curve for 20 ml 1.0×10^{-4} M Cr(III) with 1.0×10^{-3} M EDTA.

We performed a full geometry optimization at HF level of theory, using 6-31G* basis set for ionophore and for formed Cr(III) complex used effective core potential (ECP) standard basis set, LanL2DZ basis set for Cr(III) and 6-31G* for all other atoms.

The calculation methods showed stabilisation energy for ligand and its complex are 2258.70 Hartree mol⁻¹ and -3500.17 Hartree mol⁻¹ respectively. The calculations predicted nonplanar structure for ligand.

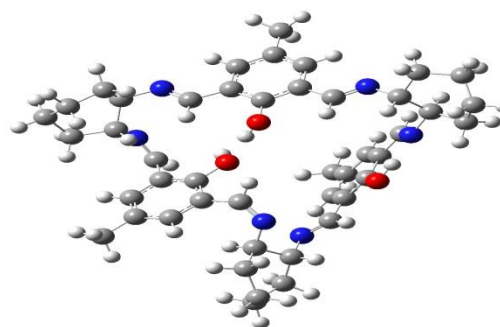


Fig. 6. structure of optimized ligand.

Conclusions

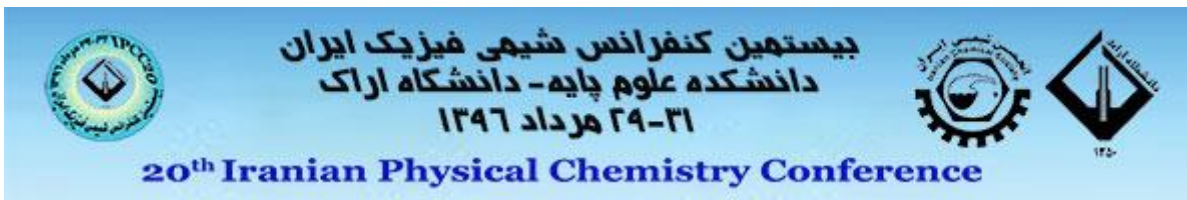
The membrane sensor incorporating ionophore as the electroactive phase can be used to determine Cr(III) in the wide concentration range. The sensor exhibited good reproducibility over a useful lifetime about 2 months. This electrode is superior to the existing electrodes with regard to the slope, pH range, response time and selectivity over a number of catio. The present electrode permits the direct measurement of Cr(III) in real samples without prior separation steps, thus considerably simplifying the determination procedure with respect to the other analytical methods used.

Acknowledgment

The authors express their appreciation to postgraduate office of Ayatollah Ahozma Boroujerdi University for financial support of this work.

References

- [1]. T. S. Light, Industrial use and application of ion selective electrodes, *J. Chem. Educ.* 74 (1997) 171.
- [2]. C. C. Young, Evolution of blood chemistry analyzers based on ion selective electrodes, *J. Chem. Educ.* 74 (1997) 177.
- [3]. M. H. Fekri, H. Khanmohammadi, M. Darvishpour, *Int. J. Electrochem. Sci.*, 6 (2011) 1679.
- [4]. S. P. Parker, *McGraw-Hill Concise Encyclopaedia of Science and Technology*, McGraw-Hill, New York, 1984, 390.
- [5]. G. J., Moody, B. B. Saad., J. D. R. Tomas, *Sel. Electrode Rev.*, 10 (1998) 71.
- [6]. M. H. Fekri, H. Khanmohammadi, M. Darvishpour, *Int. J. Electrochem. Sci.* 6 (2011) 1679.



- [7]. P. Buhlmann, E. Pretschm, E. Bakker, *Chem. Rev.*, 96 (1998) 1593.
- [8]. Y. Masuda, E. I. Shida, K. Hivaga, *Nippon Kagaku kaishi*, 10 (1980) 1453.
- [9]. O. A. Lebedeva, E. Yu Yanson, *Fromotkrtiya Izobret*, 39 (1987) 195.
- [10]. M. C. Chattopadhyaya, *J. Indian Chem. soc.*, 66 (1989) 54.
- [11]. A. Abbaspour, A. Izadyar, *Talanta*, 53 (2001) 1009.
- [12]. M. B. Gholivand, F. Sharifpour, *Talanta*, 60 (2003) 707.
- [13]. N. A. El-Ragheh, A. M. Kosasy, S. S. Abbas, S. Z. El-Khateeb, *Anal. Chem. Acta*, 418 (2000) 93.
- [14]. M. hmsipur, M. Yousefi, M. R. Ganjali, *Anal. Chem.*, 72 (2000) 2391.
- [15]. S. R. Sheen, J. S. Shih, *Analyst*, 117 (1992) 1691.
- [16]. S. S. Badavy, A. F. Shoukry, Y. M. Assa, *Analyst*, 111 (1986) 1363.
- [17]. T. Poursaberi, M. Hosseini, M. Taghizadeh, H. Pirelahi, M. Shamsipur, M. R. Ganjali, *Microchem. J.*, 72 (2002) 77.

Polythiophene supported MnO₂ nanoparticles as nano-stabilizer for simultaneously electrostatically immobilization of D-amino acid oxidase and hemoglobin as efficient bio-nanocomposite in fabrication of dopamine bi-enzyme biosensor

J. Ghodsi^a, Y. Shoja^a, A. A. Rafati^{a*}

^a Department of Physical Chemistry, Faculty of Chemistry, Bu-Ali Sina University, P.O.Box 65174, Hamedan, Iran
rafati_aa@yahoo.com

Abstract: A novel, highly selective and sensitive voltammetric bi-enzyme biosensor for sensing dopamine (DA), in presence of H₂O₂ which resulted as D-alanine enzymatic oxidation, was fabricated on the basis of simultaneously electrostatically immobilization of D-amino acid oxidase (DAAO) and hemoglobin (Hb) on MnO₂ nanoparticles (MnO₂ NPs) enriched poly thiophene (PTh). Cyclic voltammetry was applied for electropolymerization of thiophene on GCE surface and MnO₂ NPs dispersed on PTh network by soaking PTh/GCE in potassium permanganate (KMnO₄) solution. Excellent catalytic properties and large surface area of MnO₂ NPs/PTh composite caused it was used as an enzymes immobilization host in this developed bi-enzyme biosensor. The biosensor was characterized by SEM, EDX and CV techniques. The performance of the modified bi-enzyme biosensor was investigated in terms of its response time, detection limit, sensitivity, stability and selectivity in a lab environment. The composite of DAAO-Hb/MnO₂ NPs/PTh to construct a bi-enzyme biosensor in this study showed a linear response with DA in the concentration range of 0.04-9.0 μM with R-squared value of 0.994 (for S/N=3) and its sensitivity and detection limit were about 12.801 μA/μM and 41 nM respectively. Also this bi-enzyme biosensors exhibited high selectivity, rapid response (5 s) and long-term stability (42 days).

Keywords: *Bi-enzyme biosensor; Dopamine; MnO₂ nanoparticles; D-amino acid oxidase; Hemoglobin; Immobilization.*

Introduction

Dopamine, (DA), is belonged to catecholamine neurotransmitters which are an important group of biogenic compounds that are mediators in transmitting messages between neurons. It has proved that changes in DA levels to be important in efficient brain functions for example dopamine deficiency results in Parkinson's disease and people with low dopamine activity may be more prone to addiction [1]. Several mono enzymatic biosensors have been reported for dopamine (DA) and some other catechol amines determination by using tyrosinase, laccase and horseradish peroxidase as one of the simplest and most accurate methods. But often traditional DA biosensors have some disadvantages such as low conductivity, low reproducibility, low stability and high over potential. Hence, development of biosensor is still in need for DA measurement in real samples. In recent years, bi-enzyme biosensors have been attached great attentions to overcome these problems. Bi-enzyme biosensors show high selectivity, stability and sensitivity because their low applied potential decreases the noise levels and background currents and eliminates the undesirable oxidation of electroactive interferes species. In these biosensors, peroxidase enzyme, (POx), like horse radish peroxidase, in

combination with oxidase enzyme have been studied for the substrate detection in the way of direct or mediated electron transfer. In this regard hemoglobin (Hb), has intrinsic peroxidase like activity commercial availability, structure and relatively higher stability. Therefore it could be an appropriate alternative for horseradish peroxidase, specifically for reducing the fabrication cost and improving the biosensor performance. However, there are only few reports on the measurement of catecholamines or phenolics compounds using Hb-modified biosensors [1].

Many metal oxides are applied for immobilization of enzymes that among of them MnO₂ nanoparticles have been widely interested due to their unique properties such as good biocompatibility, high surface/volume ratio, low cost, strong electrocatalytic activity, high energy density and high conductivity. On the other hand, conductive polymers have ability to effectively transfer electric charge produced by the biochemical reactions to electronic circuit in biosensors. Polythiophene (PTh) is one type of the most interested conducting polymers which are useful in many applications such as solar cells, sensors, biosensors, organic field effect transistor, super capacitors, light emitting diodes and electrochromic devices [2].



Recently, the composite containing conductive polymers and MnO_2 are paid more consideration for construction various electrodes because of their excellent stability, high conductivity and good mechanical flexibility.

In this work, for the first time, DA was measured by using D-alanine enzymatic catalyzed oxidation. Indeed Hb was applied as electrocatalyst for DA oxidation in presence of H_2O_2 which was in situ generated by D-amino acid oxidase, (DAAO)-catalyzed oxidation of D-alanine, while in most oxidase/peroxidase bi-enzyme biosensor POx (herein Hb), catalyzes the H_2O_2 response. D-amino acids (DAAs) have an important role in life science since several DAAs are found to have physiological functions in mammals. For example D-alanine in the gland, anterior pituitary, plasma and pancreas might have a physiological function to the insulin regulation. Thus it can be said measurement of DA in presence of DAAs like D-alanine is possible and necessary. For this purpose, PTh electropolymerized on glassy carbon electrode (GCE) surface by applying cyclic voltammetry and MnO_2 nanoparticles dispersed on to PTh/GCE by directly soaking PTh/GCE into a potassium permanganate solution. Then Hb and DAAO were electrostatically immobilized on MnO_2 nanoparticles. The enzymes were positively charged and could assemble with negatively charged MnO_2 nanoparticles by electrostatic interaction. Hb could catalyze the oxidation of DA and avoid the interferences. As far as we know, MnO_2 nanoparticles/PTh nanocomposite was used in fabrication of biosensor for the first time in this study but it has various applications in other electrochemical fields.

Materials and method

Dopamine (DA), folic acid (FA), uric acid (UA) and ascorbic acid (AA) were obtained from darou pakhsh.co (Iran). DAAO (EC 1.4.3.6, DAAO) was from porcine kidney (1.5 units mg^{-1} of solid), D-alanine, Hb and tetrabutylammonium perchlorate (TBAPC), were purchased from Sigma-Aldrich. Thiophene was from Merck. All other reagents were of analytical grade and used without further purification. All electrochemical measurements were performed at 50 mM in a phosphate buffer (PB) of pH 6.0 and all experiments were carried out at room temperature (25 ± 0.1 °C).

To fabricate of DAAO-Hb/ MnO_2 NPs/PTh/GCE bi-enzyme biosensor as working electrode, CV was applied for electropolymerization of thiophene at GCE surface in deaerated acetonitrile solution containing 0.01 M TBAPC and 5×10^{-3} M thiophene monomer to prepare PTh/GCE. The electrode potential was cycled between 0.0 and 1.7 V at a scan rate of 50 mVs^{-1} for 20 cycles in a cyclic voltammetry regime. After electropolymerization, the PTh/GCE was kept at a

reducing potential (-0.2 V) for 10 min to undope from the original electrolyte anion. Solution was bubbled with N_2 for 5 min before electropolymerization.

The dispersion and formation of MnO_2 NPs on PTh/GCE were carried out according previous literature. In detail, PTh/GCE was soaked in 10 mM potassium permanganate solution for 10 min. MnO_2 nanoparticles grew in the PTh/GCE surface during this soaking process. The obtained electrode washed with PBS and dried at room temperature. The DAAO-Hb/ MnO_2 NPs/PTh/GCE was prepared by dipping of MnO_2 NPs/PTh/GCE in to solution, which was containing DAAO and Hb in PBS (100 mM, pH =6). As expected from isoelectric points of DAAO, Hb and MnO_2 the DAAO and Hb electrostatically were immobilized onto the surface of MnO_2 / PTh/GCE. Isoelectric points of DAAO, Hb and MnO_2 NPs are about 7.0, 7.0 and 4.5, respectively; so, in the pH = 6, positively charged DAAO and Hb can immobilize onto the negatively charged MnO_2 NPs. Optimized experimental parameters including dipping time, pH, DAAO and Hb concentration for maximum DAAO and Hb immobilization were obtained and applied for the next preparation of bi-enzyme biosensor. The amount of immobilized DAAO and Hb on MnO_2 NPs was investigated from the difference in UV-Vis absorbance of DAAO and Hb solution in about 280 nm before and after treating with MnO_2 NPs. UV-Vis absorbance of DAAO and Hb was related to DAAO and Hb concentration by applying a standard calibration curve for them (obtained as milligrams per milliliter of DAAO and Hb vs. UV-Vis absorbance at ~ 280 nm). Finally the obtained bi-enzyme biosensor washed with PBS buffer of pH =6 to remove the unimmobilized DAAO and Hb.

Results and Discussion

Electrocatalytic response of the bi-enzyme biosensor was characterized by CV measurements. Figure 1 shows the CV voltammograms of four differently modified GCE in 100mM PBS (pH = 6.0) containing fix amount of D-alanine (200 μM) and DA (5 μM). As can be concluded from this figure, no electrocatalytic reduction or oxidation peak was observed at bare GCE, PTh/GCE and MnO_2 NPs/PTh/GCE surface (curve a, b and c respectively). The redox peak current corresponding to DA by DAAO-Hb/ MnO_2 NPs/PTh/GCE were appeared at around 0.17 V for anodic peak and 0.11 V for cathodic peak respectively (curve d). It can be said this modified bi-enzyme biosensor exhibits high electrocatalytic activity for oxidation of DA which is related to the simultaneous presence of Hb as electrocatalyst and MnO_2 NPs/PTh composite in this modified GCE. MnO_2 NPs/PTh composite not only is used as nano-stabilizer for enzymes immobilization in developed bi-enzyme biosensor, but also increases the electrode surface area

due to a well-organized packaging of PTh film that electropolymerized on GCE surface and high surface/volume ratio of MnO₂ NPs dispersed on PTh film. Oxidation mechanism of DA by proposed bi-enzyme biosensor is shown in figure 2.

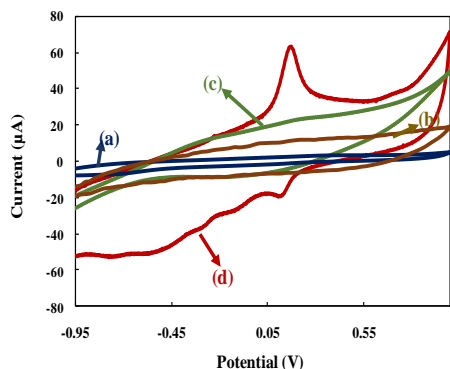


Fig.1: CVs of (a) bare GCE, (b) PT/GCE, (c) MnO₂ NPs/PTh/GCE and (d) DAAO-Hb/MnO₂ NPs/PTh/GCE in PBS solution (100mM, pH=6) containing 200 µM D-alanine and 5 µM DA at scan rate of 100 mV/s.

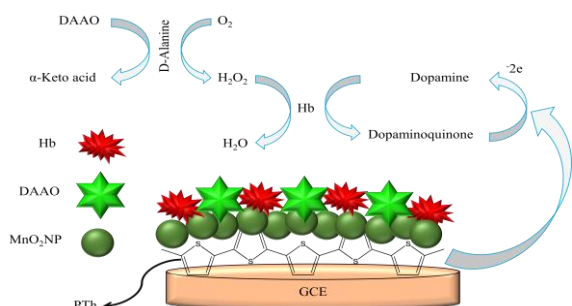


Fig.2: Oxidation mechanism of DA by DAAO-Hb/MnO₂ NPs/PTh/GCE bi-enzyme biosensor.

Determination of DA was carried out by using differential pulse voltammetry (DPV), method. Figure 3 shows the respective calibration curve of DAAO-Hb/MnO₂ NP/PTh/GCE with correlation coefficients of 0.994. According to this results the modified biosensor has the detection limit of 41 nM (at S/N of 3) in linear range concentration of 0.04-9.0 µM, a rapid current response time (within 5 s) to DA and possess the sensitivity of 12.801 µA µM⁻¹. The good linear response to the DA concentration ($R^2=0.994$), an excellent linear range, high sensitivity, low detection limit and high stability modification process suggest that the developed bi-enzyme biosensor in this study can be comparable or even better than other previously reported works.

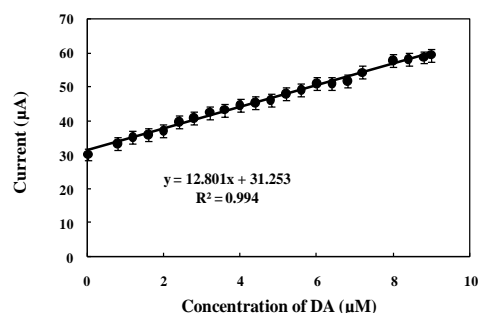


Fig.3: Calibration curve obtained from DPVs voltammograms data for DA in range 0.04-9.0 µM.

Conclusions

Summarily in this work, we described a bi-enzyme biosensor for DA sensing base on electrostatically immobilization of DAAO and Hb on MnO₂ NPs/PTh network modified GCE. PTh was electropolymerized on GCE surface and MnO₂ NPs loaded on PTh by soaking the PTh network in KMnO₄ solution. The fabricated bi-enzyme was characterized by SEM, EDX and CV. The experimental results showed excellent characteristics for detection and measurement of DA such as good linear range ($R^2 = 0.994$), low detection limit (41 nM), high sensitivity (12.801 µA/µM), rapid response time (5 s), good storage stability (42 days) and an average recovery of 97.5% in human serum samples. These results confirmed an efficient catalytic property of GCE modified with DAAO-Hb/MnO₂ NPs/PTh composite for detection and determination of DA that could offer a reliable bi-enzyme biosensor for other phenolic compounds.

Acknowledgment

The authors greatly acknowledge Bu-Ali Sina University for the financial support.

References

- [1] J. Ghodsi, A. A. Rafati, Y. Shoja, M. Najafi "Determination of dopamine in the presence of uric acid and folic acid by carbon paste electrode modified with CuO nanoparticles/hemoglobin and multi-walled carbon nanotube", *Journal of The Electrochemical Society*, 162 (2015) 69-74.
- [2] A. Hajian, A. A. Rafati, A. Afraz, M. Najafi "Electrosynthesis of Polythiophene Nanowires and Their Application for Sensing of Chlorpromazine", *Journal of The Electrochemical Society*, 161 (2014) B196-B200.

Electrochemical investigation of the corrosion behavior of mild steel in 0.5 M phosphoric acid solution by Metoprolol tablet as a green inhibitor

F. Mohammadinejad^a, S. M. A. Hosseini^{b*}, M. Shahidi^c, M. J. Bahrami^d

^{a,b}Department of chemistry, Shahr Bahonar University, Kerman, 76169-14111, Iran

^cDepartment of chemistry, Islamic Azad University, Kerman, 7635131167, Iran

^dDepartment of Science Farhangian University, Kerman, 76175173, Iran

*Corresponding author: s.m.a.hosseini@uk.ac.ir

Abstract: The effect of metoprolol tablet as green inhibitor on the corrosion behavior of mild steel (st37) in 0.5 M phosphoric acid solution was investigated using potentiodynamic polarization and electrochemical impedance spectroscopy (EIS). The inhibition efficiency was found to increase with increasing inhibitor concentration. Potentiodynamic polarization measurements indicated that corrosion current density decreased with increasing the inhibitor concentration. The EIS measurements showed that by addition of the inhibitor up to a certain concentration, the charge transfer resistance increases and the double layer capacitance decreases. It was found that the investigated compounds exhibit a good inhibition effect especially at 50-400 ppm range of concentration, which makes it commercially important. Polarization curves indicated that metoprolol tablet acts as a mixed type inhibitor. The adsorption of the inhibitor on the alloy surface in 0.5 M phosphoric acid solution followed the Langmuir isotherm. The results obtained from analysis of EIS data was in good agreement with those achieved by the polarization measurements.

Keywords: *Metoprolol tablet, Electrochemical impedance spectroscopy (EIS), Potentiodynamic polarization, phosphoric acid*

1. Introduction

The protection of metals against corrosion by H₃PO₄ has been the subject of much study since it has been used in many industrial processes especially in fertilizer production [1]. Mild steel has been extensively studied from both theoretical and practical viewpoints. Acid solutions are widely used in the chemical industry for several purposes such as acid pickling, industrial acid cleaning, oil well oxidizing, etc. Because of the general acid solution, inhibitors are commonly used to reduce the corrosion attack on metallic materials. The utilization of inhibitors is one of the most practical methods of protecting metals and alloys against corrosion, especially for material in acidic media [2-3]. The use of inhibitors is one of the best options of protecting metals and alloys against corrosion. Several inhibitors in use are either synthesized from cheap raw material or chosen from compounds having hetero atoms in their aromatic or long-chain carbon system. However, most of these inhibitors are toxic to the environment containing heavy metals. This has prompted the search for green corrosion inhibitors [4]. A number of heterocyclic compounds containing N, O and S either in the aromatic or long chain carbon system have been reported to be effective inhibitors [5-7]. Most of organic inhibitors are expensive, toxic and have negative effect on the environment this properties restrict its use to inhibit the metal corrosion. Thus it is important and necessary to develop low cost and environmentally safe corrosion inhibitors [8-9]. In the recent years drugs has been used as corrosion

inhibitors. According to Eddy and Odoemelam, the use of drugs for the inhibition of the corrosion of metals has some advantages over the use of some organic/inorganic inhibitors because of their eco-environmental nature [10]. Drugs are nontoxic, cheap, negligible negative effects on environment, so it suggested replacing the traditional toxic corrosion inhibitors [11]. In this work the inhibition effect of metoprolol tablet on corrosion of mild steel in 0.5 M phosphoric acid solution was investigated. The choice of this drug as corrosion inhibitor was made on the basis of their low toxicity and high solubility in acidic media. The aim of the present work is to investigate the metoprolol tablet inhibition action of for the corrosion of mild steel. Electrochemical impedance spectroscopy (EIS) and potentiodynamic polarization methods were employed to evaluate corrosion rate of mild steel and inhibition efficiency of the inhibitor.

2. Materials and method

Metoprolol tablet was used as corrosion inhibitor, in this study. Fresh solutions of 0.5 M phosphoric acid were prepared for each experiment using analytical reagent (85% H₃PO₄) and distilled water. The concentration range of inhibitor employed was 50-400 ppm in 0.5 M phosphoric acid solution. Mild steel samples of the (in wt%) : C 0.17; Si 0.5; Mn 1.4 ; S 0.045 ; Fe balance was used. The sample were mechanically cut into 1 cm². Prior to all measurements, the samples were polished using different grades of emery papers (600-2000), then washing with distilled water and acetone and finally dried in air.



Potentiodynamic polarization and EIS measurements were used to study the corrosion behavior of mild steel in 0.5 M H₃PO₄ solution without and with addition of different amounts of metoprolol tablet using a potentiostat/galvanostat Autolab 302 N (EcoChemie, Netherland) supported by a frequency response analyzer FRA-2 and Nova 1.9 software. A platinum plate electrode was used as the counter electrode (CE) and a saturated calomel electrode (SCE) as reference electrode and the working electrode (WE) is made of mild steel st37. The potentiodynamic polarization measurements were carried out after the EIS experiments. To determine the optimal concentration of the inhibitor, electrochemical experiments were performed in the concentration range of 50_400 ppm. For the polarization measurement, the potential of the electrode was scanned from -200 to +200 mV versus corrosion potential at a scan rate of 1 mV/s. The frequency range in EIS experiments was 100 mHz up to 100 kHz and the amplitude was 10mV.

3. Results and Discussion:

3.1. Electrochemical impedance spectroscopy:

Electrochemical impedance spectroscopy has been employed in order to investigate the surface layer created by inhibitor. The effect of metoprolol tablet concentrations on the impedance behavior of mild steel in 0.5 M H₃PO₄ solution at 25 °C is shown in Fig1. Inhibitor efficiency can also be evaluated by charge transfer resistance according to the below equation:

$$\frac{R'_{ct} - R_{ct}}{R_{ct}} \times 100$$

where R_{ct} and R'_{ct} are charge transfer resistances of mild steel in the absence and presence of inhibitor, respectively. Inhibition efficiencies increased with the concentration of inhibitor and further increase in the inhibitor concentration did not cause any appreciable change in the inhibition performance of the inhibitor. Calculated efficiency by charge transfer resistance is in close correlation with those obtained from polarization results. Fig.2 shows the electrical equivalent circuit employed to analyze the impedance plots. In this Fig., R_s is the solution resistance and R_{ct} is the charge transfer resistance.

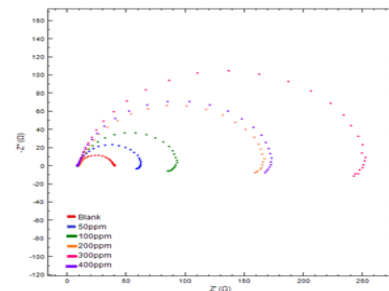


Fig1: Nyquist plots for mild steel in 0.5 M H₃PO₄ solution in the absence and presence of different concentrations of inhibitor 25°C.

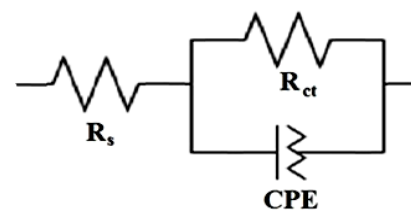


Fig2. The electrical equivalent circuit used to fit the experimental EIS data

3.2. Potentiodynamic polarization:

Fig.3 illustrates the potentiodynamic polarization curves of mild steel in 0.5 M H₃PO₄ solution in the absence and presence of various concentrations of the inhibitor. The relevant parameters are gathered in Table 1 as corrosion current density (i_{corr}), corrosion potential (E_{corr}) and inhibition efficiency (IE%). The corrosion current density decreased as the concentration of the inhibitor increased up to 400 ppm, and then decreased at higher inhibitor concentrations. Addition of inhibitor to acid media affected both cathodic and anodic branches of the polarization curves. But the corrosion potential did not change noticeably. Therefore, metoprolol tablet behaved as a mixed type inhibitor. In addition to the above parameters, Table 1 presents the values of corrosion inhibition efficiency (IE) that were calculated using the below equation:

$$(IE\%) = \frac{i_{corr} - i'_{corr}}{i_{corr}} \times 100$$

Where i_{corr} and i'_{corr} are the corrosion current densities in the uninhibited and inhibited cases, respectively. The IE values reveal that the inhibition is more pronounced at higher concentrations. The concentrations above 300 ppm did not affect the IE values. The results show that the inhibitor acts as an effective inhibitor.

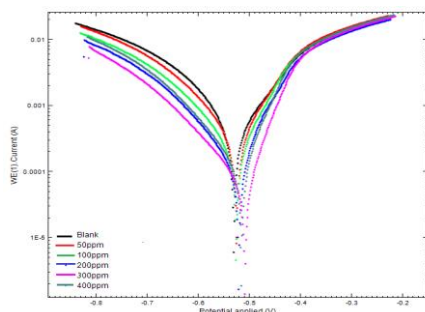


Fig3: Polarization curves for mild steel in 0.5 M H₃PO₄ solution in the absence and presence of different concentrations of inhibitor at 25°C.

Table1. Polarization parameters and the corresponding inhibition efficiencies for mild steel in 0.5 M H₃PO₄

C/ppm	$i_{corr}/\mu A\ cm^{-2}$	- E _{corr} /mV	IE(%)
Blank	626.97	530.85
50	413.01	525.91	34.13
100	229.26	526.49	63.43
200	151.94	521.48	75.77
300	71.57	509.48	88.6
400	128.34	516.31	79.53

Conclusions

The results indicated that metoprolol tablet acts as an effective inhibitor. The inhibition efficiency increased with inhibitor concentration up to a certain concentration, and decreased with increase in temperature. Polarization curves shows that this drug acts as a mixed type inhibitor. The EIS measurements indicated that by addition of the inhibitor up to a certain concentration, the charge transfer resistance increases and the double layer capacitance decreases.

References

1. M. Ozcan, R. Solmaz, G. Kardas, I. Dehri, Adsorption properties of barbiturates as green corrosion inhibitors on mild steel in phosphoric acid, *Colloid Surface A*, 325(2008), 57-63.
2. M. J. Bahrami, S. M. A. Hosseini, P. Pilvar, Experimental and theoretical investigation of

organic compounds as inhibitors for mild steel corrosion in sulfuric acid medium, *Corros. Sci.*, 52(2010), 2793-2803.

3. S. M. A. Hosseini, M. Salari, M. Ghasemi, 1-Methyl-3-pyridine-2-yl-thiourea as inhibitor for acid corrosion of stainless steel, *Mater. Corros.*, 60(2009), 963-968.
4. B.E.A. Rani & B.B.J. Basu, "Green inhibitors for corrosion protection of metals and alloys An overview", *International Journal of Corrosion*, 2012, 1-15, 2012
5. I.B.Obot, N.O.Obi-Egbedi, S.A.Umoren, "Adsorption characteristics and corrosion inhibitive properties of Electrochemical Science, 4,863-877, 2009.
6. E.E. Ebenso, H. Alemu, S.A. Umoren, & I.B.Obot, "Inhibition of mild steel corrosion in sulphuric acid using alizarin yellow GG dye and synergistic iodide additive", *International Journal of Electrochemical Science*, 8,1325-1339,2008.
7. S.A. Umoren, I.B. Obot, E.E. Ebenso, & N. O. Obi-Egbedi, "Synergistic inhibition between naturally occurring exudates gum and halide ions on the corrosion of mild steel in acidic medium", *International Journal of Electrochemical Science*, 3, 1029-1043, 2008.
8. R.T.Loto, C.A. Loto & A.P.I. Popoola, "Corrosion inhibition of thiourea and thiadiazole derivatives: a review", *Journal of Materials and Environmental Science*, 3,885-894,2012.
9. D.G. Ladha, U.J. Naik & N.K. Shah, "Investigation of cumin (*Cuminum Cyminum*) extract as an eco-friendly green corrosion inhibitor for pure Aluminium in acid medium", *Journal of Materials and Environmental Science*, 4,701-708,2013.
10. N.O. Eddy & S.A. Odoemelam, "Norfloxacin and Sparfloxacin as corrosion inhibitors for zinc. Effect of concentrations and temperature", *Journal of Materials Science*, 4, 87-96, 2008.
11. A.S. Mahdi, "Amoxicillin as green corrosion inhibitor for concrete reinforced steel in simulated concrete pore solution containing chloride", *International Journal of Advanced Research in Engineering and Technology*, 5, 99-107, 2014.

Electrochemical oxidation of 2,5-diethoxy-4-morpholinoaniline in the presence of *p*-toluenesulfinic acid: Experimental and theoretical study

Hadi Beiginejad ^a

^a Faculty of Science, Malayer University, P. O. Box 65719, Malayer, Iran.

E-mail: h.beiginejad@malayeru.ac.ir

Abstract: Electrochemical oxidation of 2,5-diethoxy-4-morpholinoaniline (**1**) in aqueous solution has been investigated both experimentally and theoretically to bring hints into the connection of thermodynamic and oxidation potential. The experimental results were obtained using cyclic voltammetry and controlled potential coulometry. Also the theoretical results were calculated at DFT (B3LYP) level of theory and 6-311G (p,d) basis sets. The result of this work shows that the electrochemical generated *p*-quinonedimine (**1a**) participates in the hydrolysis reaction and is converted to *p*-benzoquinone. It was found that species with larger ΔG_{tot} value have more positive oxidation potentials. Also electrochemical oxidation of **1** in the presence of *p*-toluenesulfinic acid (TSA) was studied in view point of thermodynamic.

Keywords: *Cyclic voltammetry; para-quinonedimine; Hydrolysis; para-benzoquinone; Density Functional Theory (DFT).*

Introduction

Electrochemistry provides very versatile means for the electrosynthesis and mechanistic studies. Using electrochemical methods with a wide time window (submicroseconds to hours) thermodynamic and kinetic information about the reactions of organic and inorganic species were obtained. It is known that cyclic voltammetry is a powerful technique for investigation of electrochemical reactions that are coupled with chemical reactions [1]. Electrochemical studies of amines at various conditions indicate that mechanism of aromatic amines is quite complex, and leads to a variety of products depending on their structure and electrolysis conditions [2].

Materials and method

Experimental: Cyclic voltammetry was performed using a micro Autolab model TYPE III. Required electrolysis were performed using a potentiostat/galvanostat system (Behpajooch model 2065), and also a divided cell was used for coulometry. The working electrode used in the voltammetry experiments was a glassy carbon disk (1.8 mm diameter) and a platinum wire was used as the counter electrode. The working electrode used in controlled-potential coulometry was an assembly of four carbon rods (31 cm²) and a large platinum gauze was used as counter electrode. The working electrode potentials were measured vs. Ag/AgCl.

Computational study: The geometries of all species in the gas phase were fully optimized at Density functional theory (DFT), B3LYP levels of theory using the Gaussian 03. The standard 6-311G (p,d) basis set were used for all species. To calculate solvation

energies the Conductor-like Polarizable Continuum Model (CPCM) with the setting ICOMP = 0, have been used at the above levels of theory. The optimized atomic radii were invoked via the solvent keyword RADII =UAHF. Then solvation free energies were obtained using the SCFVAC keyword. The values of -6.28 kcal/mol and -262.5 kcal/mol have been used for Gibbs free energy of H⁺ at gas phase (ΔG^0 (g,H⁺)) and its solvation energy in solution (ΔG^0 (s,H⁺)), respectively. Also the value energy -0.86 kcal/mol was used for a free electron at 298 K in our calculation [3].

Results and Discussion

Fig. 1 shows the first and the second cycles of cyclic voltammogram (CV) of 2,5-diethoxy-4-morpholinoaniline (**1**) in aqueous solution containing phosphate buffer (pH 3.0).

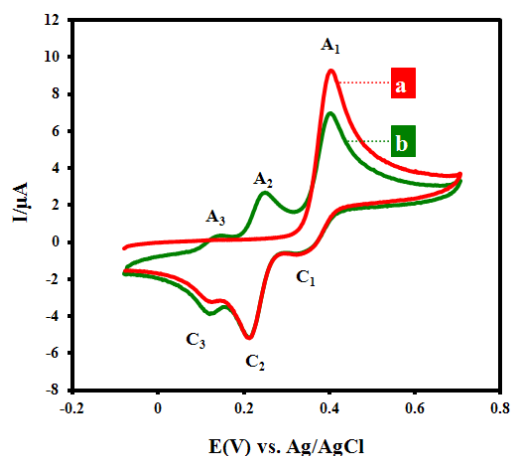
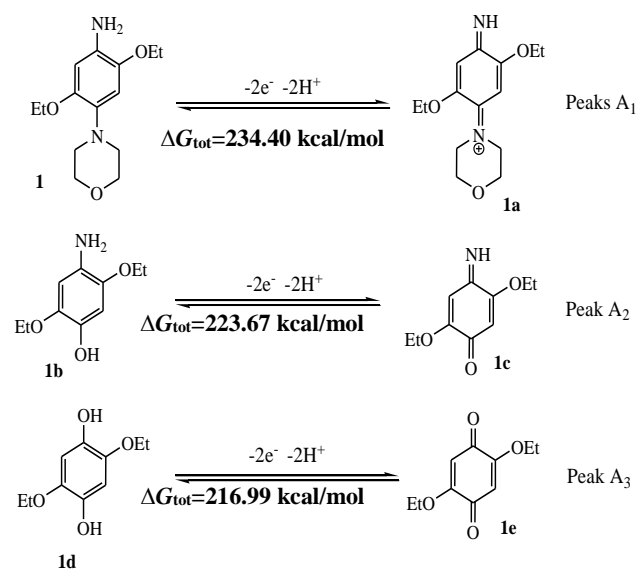


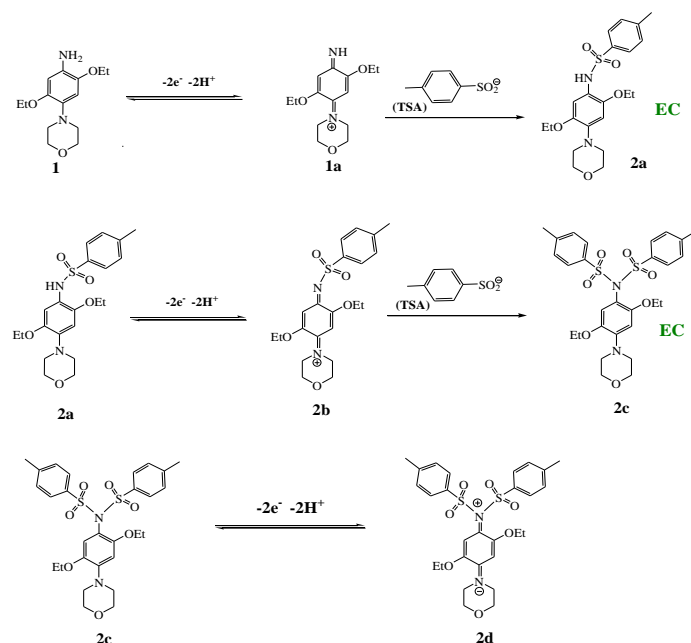
Fig.1: The first and the second cycle of CVs of 2,5-diethoxy-4-morpholinoaniline (**1**) (1.0 mM) at a glassy

carbon electrode, in phosphate buffer solution (pH=3.0); scan rate: 50 mV s⁻¹.

Fig.1, *curve-a* exhibits one anodic peak at 0.44 V and three cathodic peaks at 0.39, 0.25 and 0.18 V vs. Ag/AgCl, respectively. The second cycle of CV shows two new anodic peaks (A₂ and A₃) at less positive potentials. Electrochemical oxidation of **1** shows that, within a two-electron process, it oxidized to *p*-quinonediimine (**1a**). Our electrochemical study showed that produced *p*-quinonediimine (**1a**) after two step hydrolysis convert to **1e** (scheme 1). At first, oxidation potentials of **1** and products of hydrolysis were obtained by the use of CV, then ΔG of oxidation of studied species were calculated using B3LYP/6-311+G (p,d) method. As shown ΔG_{tot} varies in the order $\Delta G_{1d} > \Delta G_{1b} > \Delta G_{1a}$. In other word the results show that species with larger ΔG_{tot} value have more positive oxidation potentials. Electrochemical oxidation of **1** in the presence of *p*-toluenesulfinic acid (TSA) as a nucleophile was studied. In this work monosulfone and disulfone derivatives of **1** were synthesized just by controlling the applied potential. Calculated results indicate that the ΔG_{tot} of the electrochemical oxidation of monosulfone specie (**2a**) is more positive than **1**, and **2a** is formed via an EC mechanism. Also ΔG_{tot} of disulfone specie (**2c**) is more positive than **1** and **2a**. So, the oxidation of **2c** is more difficult than the oxidation of **1** and **2a**, and consequently the final product is formed via an ECEC mechanism.



Scheme 1: Calculated ΔG_{tot} of **1** and its related species.



Scheme 2. Proposed mechanism for the electrochemical oxidation of 2,5-diethoxy-4-morpholinoaniline (**1**) in the presence of *p*-toluenesulfinic acid (TSA).

Conclusions

The calculated results indicate that oxidation potential of **1** and its substituted species are directly dependent on the ΔG_{tot} , and continuance of reactions during electrolysis is dependent on ΔG_{tot} of produced species on the surface of electrode. The current study indicates that theoretical studies along with empirical research can be useful in displaying electrochemical reactions mechanisms.

References

- [1] A. J. Bard, L. R. Faulker, "Electrochemical Methods", 2001, 2nd Ed., Wiley, New York.
- [2] H. Beiginejad, D. Nematollahi, Electrochemical oxidation of 2,5-diethoxy-4-morpholinoaniline in aqueous solutions, *Electrochimica Acta*, 114 (2013) 242–250.
- [3] H. Beiginejad, D. Nematollahi, M. Bayat, F. Varmaghani, A. Nazarpour, Experimental and theoretical analysis of the electrochemical oxidation of catechol and hydroquinone derivatives in the presence of various nucleophiles, *J. Electrochem. Soc.* 160 (2013) H693-H698.

Efficient Factors on ring cleavage rate of some 4-phenylurazole species in electrochemical oxidation process

Hadi Beiginejad^a

^a Faculty of Science, Malayer University, P. O. Box 65719, Malayer, Iran.

Tel.: +988512355404 Fax: +988512355404.

E-mail: h.beiginejad@malayeru.ac.ir

Abstract: Electrochemical oxidation of some 4-phenylurazole species (**1-5**) has been investigated theoretically to provide insight into the influence of some factors on the ring cleavage reaction rate. It was reported that the electrochemically produced form (**1ox-5ox**) are unstable and participate in ring cleavage reaction, and also observed homogeneous rate constants of ring cleavage reaction of them were determined using digital simulation technique. The effect of charge of reaction site (C_1) and N_1-C_1 bond order (Wiberg Bond Indices, WBIs) on the hydrolysis rate constant were studied. All calculations were performed using Density Functional Theory (DFT) B3LYP level of theory and 6-311G (p,d) basis set. Results of the present research indicate that the rate of ring cleavage increases upon increasing positive charge of C_1 , and also the rate of ring cleavage decreases upon increasing WBIs of N_1-C_1 .

Keywords: 4-phenylurazole species, ring cleavage, WBIs, positive charge.

Introduction

Electrochemical methods are widely applied to study of the reactions of electroactive compounds. They can be used to obtain both thermodynamic and kinetic information. Among electrochemical techniques, cyclic voltammetry has been used as a powerful independent route for qualitative and quantitative characterization of complex electrode processes. Electrochemical oxidation of some 4-phenylurazole derivatives (**1-5**) was studied and rate constants of ring cleavage of produced **1ox-5ox** were estimated using digital simulated cyclic voltammograms [1]. Also theoretical study indicates that positive charge of reaction site (C_1) and N_1-C_1 bond orders (Wiberg Bond Indices, WBIs) are effective on the rate of hydrolysis of amines [2]. Using experimental data (rate of ring cleavage) in one hand and reported theoretical data in the other hand, in this work dependence rate of ring cleavage on positive charge of C_1 and WBIs was studied.

Materials and method

Experimental: Cyclic voltammetry was performed using an Ivium potentiostat/galvanostat (model vertex). The working electrode used in the voltammetry experiments was a glassy carbon disk (1.8 mm diameter) and a platinum wire was used as the counter electrode. The working electrode potentials were measured vs. SCE.

Computational study: The geometries of all species in the gas phase were fully optimized at Density functional theory (DFT), B3LYP level of theory using the Gaussian 03. The standard 6-311G (p,d) basis set was used for all species[3]. The Wiberg Bond Indices (WBIs) of C_1-N_1 bonds were calculated with the

Natural Bond Orbital (NBO) method at mentioned level of theory [4].

Results and Discussion

Figure 1 shows cyclic voltammogram (CV) of 4-phenylurazole (**1**) in water containing phosphate buffer (pH = 3.0) at a glassy carbon electrode. The voltammogram shows one anodic peak (A_1) at 0.58 V vs. SCE which correspond to the transformation of **1** to **1ox** with an irreversible feature. This electrochemical behavior shows that the produced **1ox** is unstable and participates in hydrolysis reaction (Scheme 1) [1]. Changing the scan rate indicated that the peak current ratio (I_{pC1}/I_{pA1}) is strongly related to the scan rate and increases upon increasing the scan rate [1]. Electrochemical oxidations of other substituted species (**2-5**) were studied in aqueous solution too. On the basis of the mechanism presented in Scheme 1, it is appeared that the following factors are effective on hydrolysis reaction rate.

- 1) Electrophilicity of C_1 .
- 2) N_1-C_1 bond order (Wiberg bond indexes, WBIs).

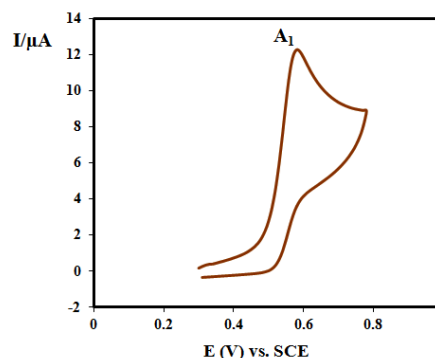
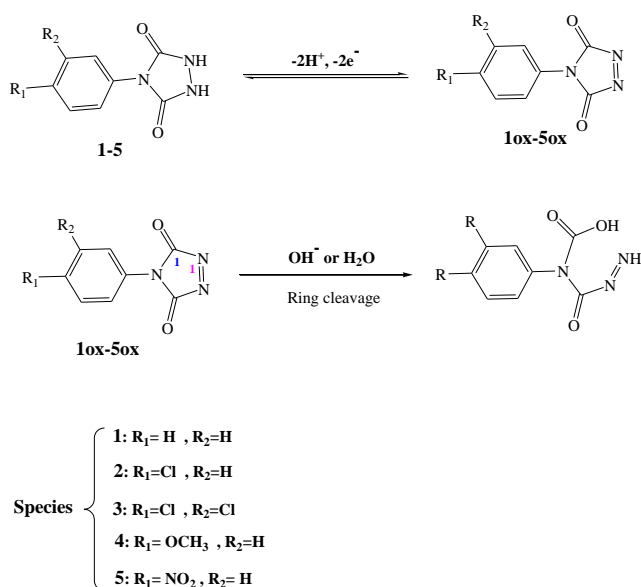


Figure 1. Cyclic voltammograms of 1.0 mM 4-phenylurazole (**1**) in phosphate buffer solution (pH = 3.0) at a glassy carbon electrode. Scan rate 50 mV/s.

The reported observed homogeneous rate constants of hydrolysis were found to vary in the order (5) > (3) > (2) (1) > (4). These changes are consistent with the changes in the positive charge on C₁ atom in **1ox**, **2ox**, **3ox**, **4ox** and **5ox**. As shown in table 1, the positive charge on C₁ atom was found to vary in the order **5ox** > **3ox** > **2ox** > **1ox** > **4ox**. The positive charge on C₁ atom increases and consequently the electrophilicity of the C₁ atom increases and makes it more susceptible to nucleophilic attack by hydroxide ion or water. As shown in table 1 the hydrolysis reaction rate increases upon increasing positive charge of C₁.

The strength of N₁-C₁ bond is an important factor in the hydrolysis reaction rate. The hydrolysis rate constant is inversely proportional to the strength of N₁-C₁ bond. Wiberg bond indexes of N₁-C₁ bond is an indicative of strength of this bond. Using NBO analysis Wiberg bond indexes of N₁-C₁ bonds in species **1ox-5ox** were calculated. The results indicate that WBIs of N₁-C₁ bond was found to vary in the order **4ox** > **1ox** > **2ox** > **3ox** > **5ox**. In other word the larger the WBIs of N₁-C₁ bond of studied species, the less the value of the ring cleavage rate constant (Table 1).



Scheme 2: The structure of studied 4-phenylurazole species and oxidative ring cleavage mechanism of them.

Table 1. Obtained homogeneous rate constants of ring cleavage reaction (*k*_{obs}), WBIs of N₁-C₁ and positive charge on C₁ for studied species (**1ox-5ox**).

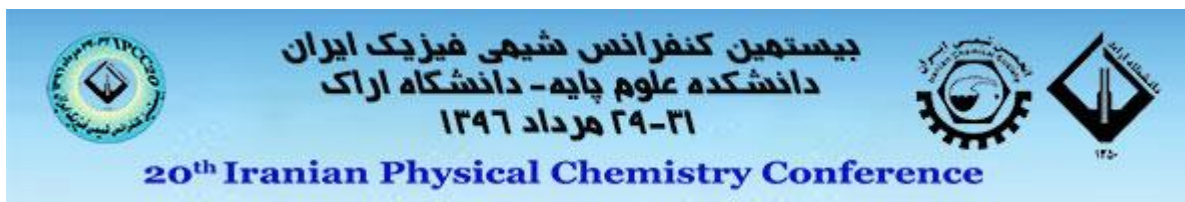
species	<i>k</i> _{obs}	WBIs (N ₁ -C ₁)	positive charge (C ₁)
1ox	0.22	1.0328	0.78318
2ox	0.43	1.0294	0.78344
3ox	1.03	1.0251	0.78374
4ox	0.16	1.0367	0.78233
5ox	2.56	1.0212	0.78458

Conclusions

In this work relation between rates of ring cleavage of 4-phenylurazole species (**1ox-5ox**) and positive charge of C₁ and WBIs of N₁-C₁ were studied. The results show that the N₁-C₁ bond order (WBIs) and charge on the reaction sites has significant roles on impermanence of oxidized form (**1ox-5ox**).

References

- [1] F. Varmaghani, D. Nematollahi, S. Mallakpour "Oxidative Ring Cleavage of 4-(4-R-phenyl)-1,2,4-triazolidine-3,5-diones: Electrochemical Behavior and Kinetic Study", *J. Electrochem. Soc.*, 159 (2012) F174-F180.
- [2] H. Beiginejad, D. Nematollahi, F. Varmaghani, M. Bayat "Efficient Factors on the Hydrolysis Reaction Rate of Some Para-Aminophenol Derivatives in Acidic pHs", *J. Electrochem. Soc.* 160 (2013) H469-H473.
- [3] M. J. Frisch et al., Gaussian 03, revision B. 04, Gaussian, Inc., Pittsburgh, PA, 2003.
- [4] P. M. W. Gill, B. Johnson, W. Chen, M. W. Wong, C. Gonzalez, and J. A. Pople, Gaussian 03, Version D. 01, Gaussian, Inc., Pittsburgh, PA, 2005.



Investigation of Walden Rule for Sodium Glutamate in Aqueous Solutions of Glucose at 298.15 K

Nader Molavi^{a*} Rahman Salamat Ahangari Ph.D^{b**}

^{**}Assistant Professor ^{*}MSc. student Department of Chemistry Azarbaijan Shahid Madani University, Tabriz-Iran

^aEmail: azer.shimi@yahoo.com ^bEmail: r.a.salamata@gmail.com

Abstract: Walden constants of Monosodium Glutamate (MSG) electrolyte solution in aqueous saccharide (glucose) measured, considering density and bulk viscosity and relative dielectric constant for the mixture of water - organic at 298.15 K. Thermodynamic data on NaGlu aqueous solutions are useful e.g. for the modeling of the influence of the ion channels on the signal transmission in a human body cell. By use of the theory of the conductivity of Onsager (DHO), theoretical conductivity were evaluated and compare well with experimental in very dilute solutions and then Walden products were calculated, consequently were analyzed based upon the interactions of ion- ion and ion - water and organic solvents in the three-component mixture[1].

Keywords: conductivity molar; dissolved tripartite; Walden product; Onsager;MSG

1. Introduction

MSG is used in the food industry as a flavor enhancer, carbohydrates hold a key position in living nature and have been the focus a huge interest over the past few decades because of their abilities to preserve biosystems such as cells, vaccines, or therapeutic proteins employed in the food, pharmaceuticals, and cosmetics industries. Indeed, saccharides such as glucose can be added to biologically active solutions to overcome the limited stability range of proteins. Carbohydrates and metal cations coexist in biological fluids, and the interactions between carbohydrates and metal cations are a subject of current interest because of the importance of carbohydrate-metal complexes in chemistry and biology. The Walden product constant as well as conducting molar has been studied dilution infinite mixed aqueous solution - to (glucose) extracted [2].

2. Experimental Section

2.1. Chemicals. Sodium Glutamate (>99.5%) at 100 °C for 24 hours in the oven is placed and then weighed, dried at room temperature to constant weight reached by EDTA salt solution, the salt is standard. As well as the deionized water six step distillation and specific conductivity of 2.2 micro siemens centimeter taken during testing of nitrogen gas with a purity of 99.995 percent is used Merck also (>99.5% glucose) with high purity water with a molar mass of 198.17 was used in this study. ρ is a density mix solvents, η viscosity solution, D gradient density, d_s density solution[3].

2.2. Thermostat: Thermostat Julabo-5 is used of the type. With approximately less than $\pm 0.05\%$ at temperature program has proved in the cell walls can be use to be tested in order to maintain the temperature.

2.3. Conductivity measurement: Experimental measurements is done with it 4510 Conductivity Meter devices calibrated and temperature coefficient correction was made. In this experiment[4, 5], certain values of the mixed aqueous solution - organic (glucose) on certain amounts of potassium chloride solution spilled at every step gas N₂ inert atmosphere is carried out in solution. At each time interval of about 10 minutes with constant conductivity in the 4510 Conductivity Meter numbers are read. Density and viscosity and dielectric constant references [2], the harvest reference[2] is polynomial on it by the numbers fit. In all treatments of proven thermostat temperature of 298 K was on schedule. From the weights and the corresponding solution densities d , the concentrations molar c were determined. A linear change of d with increasing salt content for diluted solutions was assumed, $d = d_s + D\tilde{m}$, where \tilde{m} is the molality of the electrolyte (moles of electrolyte per kilogram of solution). the density gradient D is considered to be independent of temperature[6]. The measuring procedure including the corrections and the extrapolation of the sample conductivity to infinite frequency are described in the literature. The measured conductivity data are given in Table 1 as a function of the temperature-independent molality. They can be converted to the temperature-dependent molarities by use of the relationship $C = \tilde{m}d$ Taking into account the sources of error (calibration, titration, measurements, impurities)[7]. The specific conductivities are certain within 0.08%. No hydrolysis correction was made in data analysis

3. Results and Discussion

Dielectric constants of Mix solvents (water + glucose) are reported in Table 1, and the conductivities molar



respectively of NaGlu in mixtures water + glucose are collected in Tables 1, [1]. The experimental data were analyzed using the conductivity molar in the form suggested by DHO two- parameter iterative method were used to obtain the limiting molar conductivity Λ^∞ and the distance parameter a Debye-Huckel by nonlinear leastsquares iterations[6, 8, 9].

$$\kappa^2 = (8\pi N_A e_0^2 / 1000 \epsilon K T) I$$

$$I = \alpha c$$

$$\Lambda / \alpha = \Lambda^\infty - (S_2 + S_1 \Lambda^\infty)$$

$$\omega = 0.5859$$

$$S_2 = \frac{FZe_0}{3\pi\eta} \kappa, \quad S_1 = \frac{e_0^2 \omega}{6\epsilon K T} \kappa$$

$$\text{Walden product Constant} = \eta \Lambda^\infty$$

The input data for the calculation of the coefficients were the solvent properties given in Table 2 . dilution, and the amount of organic solvent is reduced by increasing the percentage of Walden product. This behavior can be attached to the given facts[10].

- to reduce the dielectric constant of the mixture ratio, and the electrostatic attraction between ions increases, and hence, the number of ions decreases in free mode.
- possible association polysaccharide cation and reduces ion mobility.
- increasing the viscosity of aqueous electrolyte solutions microscopic organic, reduced ion mobility association constants ions increased, resulting in reduced value of its molar conductivity.

Fig.1 Variation the limiting Conductivities Molar of NaGul with w/w% water+glucose of at 298.15k

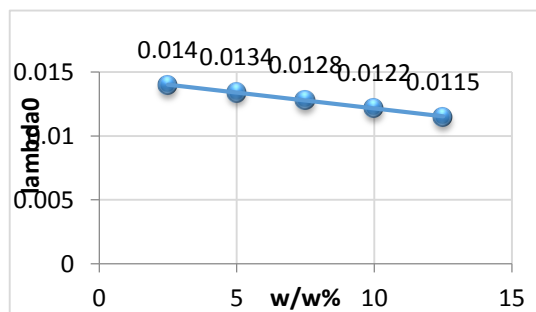


Fig 2. Variation the Walden Rule of NaGul

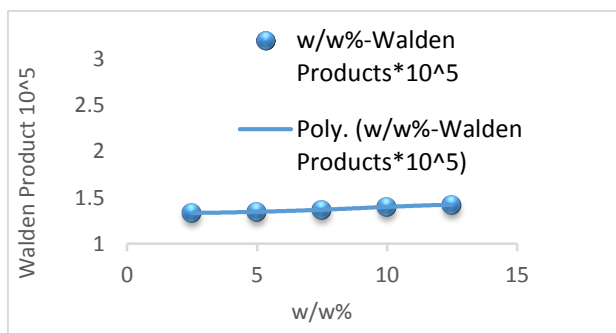


Table1. density,viscosity,dielectric mix solvents water+glucose[3]*

w/w%	ρ	$(\eta)10^3$	ϵ	D	ds
2.5	1.005	0.9517	78.11925	0.0501	1.10127
5	1.0145	1.0042	77.5135	0.0518	1.11195
7.5	1.024	1.0692	76.90775	0.0508	1.1209
10	1.0335	1.1467	76.302	0.0502	1.13183
12.5	1.043	1.2367	75.69625	0.0517	1.14187

*Units ρ and ds , $kgdm^{-3}$; η , $pa.s$; D, $kg^2mole^{-1}dm^{-3}$

For an electrolyte at infinite dilution conductivity molar of aqueous glucose solution (Figure 1). Based on the conclusions of Tsurko et al and Hoskins et al., The hydrogen bonds between water molecules is far more powerful than the water with other compounds.(Na⁺) ions are smaller and have a high density ion, and an increasing number of solvent molecules grades to keep hydrated. Therefore, the number of (Na⁺)more hydrated. With approval of Na+ hydration can be reached this conclusion[11]. By reducing the dielectric constant of the solvent mixture, electrostatic attractions between cations and anions increases, amount Walden product Constant ($\Lambda^\infty \eta$) increases with increasing slowly dissolving. Given the uncertainty in the experimental viscosity and conductivity molar(Figure 2)., it can be reasonably expected. Some of the experimental points will deviate from the linear relationship.This shows that the ionic radius is not affected by ion solvation of ions in the solution are considered a major factor in their dissolution.a similar result in the water mixed with the organic solvent is observed.This behavior seems to be preferred by solvation caused by ions with water molecules Which, in turn, changes in viscosity microscopic molecules of sugar in sugar replacement instead of solvation is hydrated with water[12].In addition, by increasing the interaction of ions with saccharides, which leads to a larger radius of ion solvation and thus reduce ion mobility causes.

Table 2. Value of Limiting Conductiitty molar,Walden Product Obtained for NaGlu in water + glucose at 298.15 k



w/w %	Λ^∞	η	$(\Lambda^\infty \eta) 10^5$	
2.5	0.014	0.00095 17	1.33238	
			1.34562	
5	0.0134	0.00100 42	8	
				1.3685
		0.012 8	0.00106 92	76
				1.3989
		0.012 2	0.00114 67	74
				1.4222
		0.011 5	0.00123 67	05

Unit: $\Lambda^\infty, \text{sm}^2 \text{mole}^{-1}$

4. Conclusion

NaGlu electrolyte solution conductivity in mixed aqueous - Organics were measured. conductivity at infinite dilution (Λ^∞), and Walden Product constant were calculated in aqueous saccharide. Values Λ with increasing molality sugar dropped and the water

molecules in the solvation partnerships were with molecules of glucose replacement and ions attributed in solvation by increasing sugar concentration decreases and deviations from the Walden constant in glucose + water solution were more pronounced in higher dielectric constants of the mixed solvents [13].

References

For journals:

- [1] Tsurko, E.N., R. Neueder, and W. Kunz, *Activity of water, osmotic and activity coefficients of sodium glutamate and sodium aspartate in aqueous solutions at 310.15 K*. Acta Chim. Slov, 2009. **56**: p. 58-64..
- [2] Bes, M., et al., Conductometric study of ion association of divalent symmetric electrolytes: I. CoSO 4, NiSO 4, CuSO 4 and ZnSO 4 in water. Journal of molecular liquids, 2005. **118**(1): p. 111-118.
- [3] Zhuo, K., et al., *Conductivity in NiSO 4-d-glucose-water solutions at 278.15-308.15 K*. Fluid Phase Equilibria, 2009. **284**(1): p. 50-55.



Ion Pair Studies of Potassium Chloride in Mixed (Glucose-Water) Solvents at 298.15 K

Nader Molavi^{a*} Rahman Salamat Ahangari Ph.D^{b**}

^{a*}Assistant Professor ^{**}MSc. student Department of Chemistry Azarbaijan Shahid Madani University, Tabriz-Iran

^aEmail: azer.shimi@yahoo.com ^bEmail:r.a.salamata@gmail.com

Abstract:The electrical conductivity of solution in mix solvents of saccharide+ water was measured as a function of temperature at 298.15 K. Electrostatic interactions have been observed to play important roles in the kinetics of protein-protein association. Ionic strength, by its ability to modulate the magnitude of electrostatic interactions, has often been conveniently used to test their presence. Association constant of electrolyte solutions of potassium chloride in the mix solvents of water and organic (glucose) were evaluated. A comparative study was accomplished using the equations of Debye-Huckel-Onsager, Fuoss 1958 and ion-pair theory of Bjerrum. The resulted association constants of the paired ion is interpreted and compared well and are in compliance [1].

Keywords: Ion Paired, Bjerrum, Association Constant, Debye-Huckel-Onsager, Fuoss 1958

Introduction

Recently, there has been an increasing amount of work concerning the measurement of thermodynamic properties of electrolytes in mixtures of solvents, because their composition is important in industrial, chemistry, biological and other fields. With a better understanding of fixed ions extracted Association as well as in the theoretical study of them would be a correct answer to the nearest reasoning was investigated. The interactions of ions - ions and ion - solvent has an ionic association is fixed in an organic solvent and water mixed reviews many of the questions on the biology and agricultural biotechnology and justified Food industry. Ion concentration can be fixed as a corrective quantity in the processes of ion-ion electrolyte solutions put forward in relation to see corrected [2].

Materials and method

(Potassium chloride >99.5%) at 110 ° C for 24 hours in the oven is placed and then weighed, dried at room temperature to constant weight reached by EDTA salt solution, the salt is standard. As well as the deionized water six step distillation and specific conductivity of 2.2 micro Siemens per centimeter taken during testing of nitrogen gas with a purity of 99.995 percent is used Merck also 99.5% glucose with high purity water with a molar mass of 198.17 was used in this study [3]. and Thermostat (of the type Julabo-5 Germany) is used with accuracy approximately less than $\pm 0.05\%$ a temperature program can be used proved to be tested in order to maintain the temperature in the cell walls Certain values of the mixed aqueous solution - organic (glucose) on given amounts of potassium chloride solution spilled at every step, In order to purge the system, inert atmosphere of gas N₂ is carried out in solution. At each time interval of about 10 minutes with constant conductivity in the Conductivity Meter

values are read. Density and viscosity and dielectric constant taken from references and also calculated by a polynomial method. In all treatments of proven thermostated temperature of 298.15 K was on schedule for the purpose of calibrations. From the weights and the corresponding solution densities d , the molar concentrations c were determined [6]. A linear change of d with increasing salt content for diluted solutions was assumed, $d = d_s + D\tilde{m}$, where \tilde{m} is the molality of the electrolyte (moles of electrolyte per kilogram of solution). The density gradient D is considered to be independent of temperature. The measuring procedure including the corrections and the extrapolation of the sample conductivity to infinite frequency are described in the literature [7]. The measured conductivity data are given in Table 1 as a function of the temperature-independent molality. They can be converted to the temperature-dependent molarities by use of the relationship $c = \tilde{m}d$

Taking into account the sources of error (calibration, titration, measurements, impurities) the specific conductivities are certain within 0.08%. No hydrolysis correction was made in data analysis [7].

Results and Discussion

Dielectric constants of water + glucose mixtures are reported in reference [8], and the molar conductivities of KCl in water + glucose mixtures are collected in reference [9], respectively. The experimental data were analyzed using the conductivity molar in the form suggested by Pethybridge and Taba. 3 two-parameter iterative method were used to obtain the limiting molar conductivity Λ^∞ and the distance parameter a (closest approach) was optimized by non-linear least-squares iterations [10, 11].



DHO

$$\kappa^2 = (2000N_A e_0^2 / \epsilon_0 \epsilon K T) I$$

$$K_A = \frac{(1-\alpha)f_A}{c\alpha^2 f_{\pm}^2}$$

$$\log f_{\pm} = -\frac{A' z I^{0.5}}{1+\kappa a}$$

$$A' = (z e_0^2 / \epsilon) \frac{e^{\kappa a}}{1+\kappa a}$$

$$K_A = 4\pi N_A b^3 \int_2^b e^y y^{-4} dy$$

$$K_A \equiv 4\pi N_A a^3 e^b / (1000b)$$

$$b = z_i e_0^2 / \epsilon a K T$$

Bjerrum

Fuoss 1958

$$K_A = 4\pi N_A a^3 e^b / 3000$$

$$K_A = \frac{(1-\alpha)}{c\alpha^2}$$

EXP

The lower limit, a , of the association integral is the distance of closest approach of cation and anion (contact distance) $a' = a^+ + a^-$ calculated from the ionic radii of the metal ion ($a^+ = 0.133$ nm for K^+) and ($a^- = 0.181$ nm for Cl^-). From extended investigations on electrolyte solutions in amphiprotic hydroxylic solvents (water, alcohols), it is known that the upper limit of association is given by an expression of the type $a = a' + ns$

where s is the length of an oriented solvent molecule and n is an integer, $n = 0, 1, 2, \dots$. Here, s is the length of an OH-group, d_{OH} , and $s = 0.28$ nm.

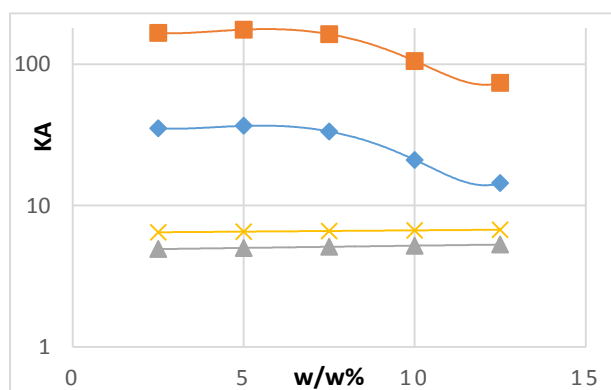


Fig1: Variations of Association constant calculated by model and experimental value; DHO EXP

Studying of Electron Transfer Rate Constant of Cytochrome c Immobilized on Nanoparticle Decorated Hybrid System by Cyclic Voltammetry Technique

Bjerrum Fuoss of KCl with w/w% water+glucose at 298.15 K

For an electrolyte at infinite dilution molar conductivities of KCl in aqueous glucose solution (Figure 1). Based on the conclusions of Galma et al and Baron et al., The hydrogen bonds between water molecules is far more powerful than the water with other compounds. Potassium ions are small and have a high charge density, and an increasing number of solvent molecules keep hydrated. Therefore, the number of (K^+) more hydrated. With approval of K^+ hydration can be reached proper conclusion[9]. In addition, by increasing the interaction of ions with saccharides, which leads to a larger radius of ion solvation and thus reduce ion mobility causes.

Conclusions

conductivity solution electrolyte KCl in mixed aqueous - Organics were measured. Conductivity Molar at infinite dilution (Λ^∞). The breakdown of the overall ionic conductivity molar conductivity diluted to low concentrations to obtain[13]. according to the Fig1 Match the ion concentration constant in the equation Fuoss and Bjerrum is well represented. Onsager theoretical and practical ion accumulation has near constant values (FIG.1)[8].

It can be deduced that the association constant ion electrolyte solutions to meet the practical need to provide modeling. In addition, by increasing the interaction of ions with saccharides, which leads to a larger radius of ion solvation and thus reduce ion mobility causes.

References

For journals:

- [1] Pinho, S.P. and E.A. Macedo, *Solubility of NaCl, NaBr, and KCl in water, methanol, ethanol, and their mixed solvents*. Journal of Chemical & Engineering Data, 2005. **50**(1): p. 29-32.
- [2] Bes, M., et al., *Conductometric study of ion association of divalent symmetric electrolytes: I. CoSO₄, NiSO₄, CuSO₄ and ZnSO₄ in water*. Journal of molecular liquids, 2005. **118**(1): p. 111-118.
- [3] Zhuo, K., et al., *Conductivity in NiSO₄-d-glucose-water solutions at 278.15-308.15 K*. Fluid Phase Equilibria, 2009. **284**(1): p. 50-55.

V. Alizadeh^{a*}, A. Jamali Moghaddam^b

^{a,b}Department of Petroleum Engineering, University of Garmsar, Garmsar, Postal code 3581755796, Iran

*valializadeh.chem@gmail.com

Abstract: A hybrid of cytochrome c (cyt c) and a 4-5 nm gold nanoparticle (AuNP) on Au electrode (AuE) was prepared. In the hybrid system, AuNPs was attached to the AuE via 1,6 hexandithiol (1,6 HDT) monolayer and capped with captopril (capt) molecule then electrostatically conjugated with cyt c. The AuE/AuNP/cyt hybrid system was characterized by cyclic voltammetry (CV). CV shows a very closely ideal protein voltammetric response with low peak separation in both low and very high scan rates. It is suggested that on curved AuNPs, the density of immobilized cyt c smaller than AuNP free monolayer and resultant low electrostatic repulsion between cyt c molecules during reduction or oxidation. Moreover, enhancement of the interfacial electron transfer (ET) rate of AuE/AuNP/cyt system compared with capt/cyt c was observed. This study gave fast rate constants, $1 \times 10^9 \text{ cm}^3 \text{ mol}^{-1} \text{ s}^{-1}$ for bimolecular and 69.6 s^{-1} for tunneling ET rate constants.

Keywords: Cytochrome c, Gold nanoparticle, Captopril, Cyclic Voltammetry, Electron transfer Rate Constant.

Introduction

Electron transfer (ET) in redox proteins plays a central role in a variety of fundamental biological processes, such as respiration and photosynthesis. Furthermore, the role of protein is also fundamental for bioelectrocatalysis, bioelectronics, biosensors and, more recently, in nanobiotechnology [1-3]. Improving the efficiency of charge transfer through target molecules and across interface, is a key challenge in molecular electronics, particularly in protein-based systems since electronic coupling between the protein and the electrode is relatively weak. However, self-assembled monolayers (SAMs) which provide a highly ordered interfacial environment, has offered solutions for coupling the protein redox centre physically and electronically to the electrode surface for efficient biological ET. However, the ET rate constant of such systems is slow and decays exponentially with increasing chain length of the SAMs that is consistent with an electron tunneling mechanism [4]. The use of nanoparticle-protein hybrid systems has recently been proposed to overcome this problem by employing nanoparticles (NPs) as nanoelectrodes, which facilitate electrical communication and electron relay between the electrode and redox region of the protein, thus achieving an enhanced rate of ET[5].

The present study addresses specifically the role of AuNPs in long-rang ET of cyt c. The hybrid system was prepared and its electrochemical properties were studied. These studies showed significant interfacial ET enhancement with very closely to ideal voltammetric response of cyt c compared to cyt c immobilized onto the AuNP free pure captopril SAM. The significant enhancement in ET rate of cyt c immobilized onto this NP decorated SAM, is related to the presence of the AuNPs. Furthermore, nearly ideal voltammetric response of cyt c may be related to curvature of underlying NPs [6]. Nanoscale curvature

causes pronounced changes in the redox properties of electroactive ligands so that on curved smaller NPs, redox ligands, here cyt c, are farther from each other relative to planar surfaces. Thus, electrostatic ligand-ligand repulsions on smaller NPs are very low and redox ligands are easily oxidized or reduced.

Materials and method

The bovine heart cytochrome c (cyt c), captopril (capt) (>98%), 1,6 hexandithiol (1,6 HDT) (>98%), HAuCl₄.3H₂O (>99%), NaBH₄ (>99.9%), chloroform (>99.8%), toluene (>99.9%) from Sigma-Aldrich and tetra-octylammonium bromide (TOAB), H₂SO₄ (supra pure), ethanol (99.8%), potassium phosphate, potassium hexacyanoferrate (III) and potassium hexacyanoferrate (II) (supra pure) from Fluka as a redox probes, were used as received. Milli-Q water was used to prepare all aqueous solutions and for rinsing. Electrochemical measurements were carried out using a CHI-900 (CH Instrument, Austin, TX). AuNPs were synthesized by Brust-Schiffrin method in the absence of thiol molecule (by two step procedure)[7]. The resulting solution of Au colloidal particles was characterized using a UV-VIS spectrum, which yielded a strong absorption at 524 nm and transmission electron microscopy (TEM) which indicated a particle sizes of 4-5 nm. Cleaned AuE was immediately immersed in an ethanolic solution of 1,6 HDT (0.01 M) for 24h. For AuNP immobilization, the 1,6 HDT-modified electrode after rinsing by ethanol, was transferred to a solution containing TOAB stabilized AuNPs for several hours. Modification of immobilized AuNP on 1,6 HDT SAM by capt, was achieved by rinsing the electrode by toluene and ethanol followed by immersion into a 0.01 M ethanolic solution of capt for several hours. Cyt c/AuNP hybrid system was prepared by immersion of

AuNP-modified electrode into a 20 μM cyt c solution for 1.5h.

Results and Discussion

The Au/1,6 HDT, Au/1,6 HDT/AuNP and Au/1,6 HDT/AuNP/Capt Electrodes, were characterized by CV and electrochemical impedance spectroscopy. Comparison of the redox probe voltammetric behavior at the bare AuE and 1,6 HDT SAM, confirming the formation of a more compact and almost defect free film of the 1,6 HDT molecules on the bare AuE surface. This blocking the electronic communication between the redox probe and the underlying AuE surface is proved by the disappearance of the probe faradaic current at the 1,6 HDT SAM compared to the bare AuE. After the immobilization of AuNPs on the 1,6 HDT SAM, the faradaic current of the redox probe reappeared. The attachment of the AuNPs on the blocking 1,6 HDT SAM, provides an efficient ET path and reveals the quasireversible cyclic voltammogram of the redox probe. After chemisorption of capt on Au/1,6 HDT/AuNP SAM, for electrostatic immobilization of cyt c, the electrochemical response of the redox probe was suppressed. The response of the probe depends on the degree of ionization of the capt carboxylate endgroup and resultant negative charges. Further electrochemical characterization of the AuE, AuE/1,6 HDT, AuE/1,6 HDT/AuNP and AuE/1,6 HDT/AuNP/Capt electrodes, was performed by EIS. The Nyquist plots recorded at bare AuE and modified electrodes are presented in Fig. 1.

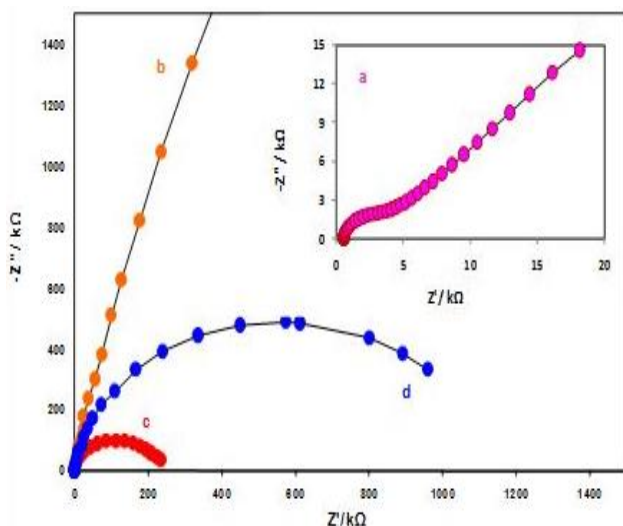
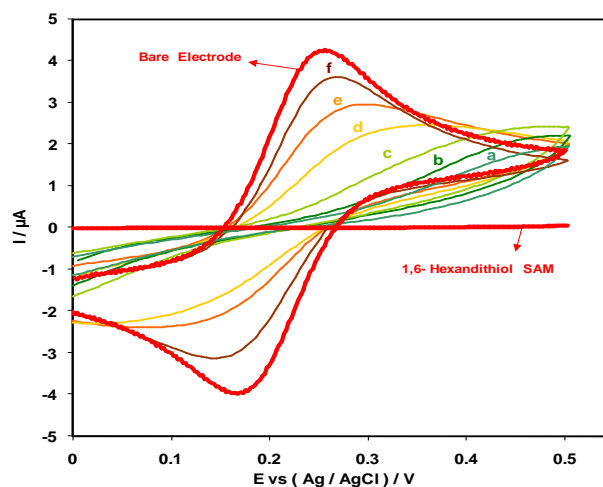


Fig.3: Nyquist plots for (a) bare AuE, (b) AuE/1,6 HDT SAM, AuE/1,6 HDT/AuNP and (d) AuE/1,6 HDT/AuNP/Capt modified electrodes in a 1 mM solution of

$\text{Fe}(\text{CN})_6^{3-/4-}$, and at potential 0.25 V. The frequency was swept from 100 kHz to 0.1 kHz.

These observations indicate the formation of AuNP decorated SAM for immobilization of cyt c and studying of its electrochemical properties onto this SAM. For investigation of time effect on the quantity of AuNP immobilization on the 1,6 HDT SAM, cyclic voltammetry was used in the presence of ferrocyanide after various times of AuNPs adsorption. Fig. 2 shows that the ferrocyanide voltammetric response on the 1,6 HDT SAM, is affected after immersion times of this electrode into the AuNPs containing solution. These results indicate significantly increase in the rate of ET,



purely due to the immobilization of AuNPs on 1,6 HDT SAM.

Fig.2: Cyclic voltammetry of bare AuE and AuE/1,6 HDT SAM after immersion into the AuNP containing solution at the deposition times of (a) 1.5 (b) 3 (c) 4.5 (d) 8 (e) 11 and (f) 20 h, in the presence of 1mM $\text{Fe}(\text{CN})_6^{4-}$ in 100mM phosphate buffer and pH 7.2 at scan rate of 50 mV/s.

The AuNP decorated SAM was prepared as a platform for assembly of cyt c and its electrochemical studies. Cyt c was attached to the AuNP through electrostatic binding by capt as a linker molecule. Fig. 3 shows the voltammetric response of cyt c after baseline-subtraction, in order to show better the electrochemical behavior of cyt c on AuNP decorated SAM.

Current-Distance curves carried out in 4 electrode system to kinetics investigations of cyt c immobilized on nanoparticulated surface. The below reaction shows the mediated ET, in which the redox mediator $\text{Fe}(\text{CN})_6^{4-}$, is oxidized at the working electrode 1 and regenerated at the substrate surface (working electrode 2) through bimolecular ET with the cyt c with a bimolecular rate constant, k_{BI} .

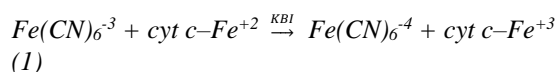
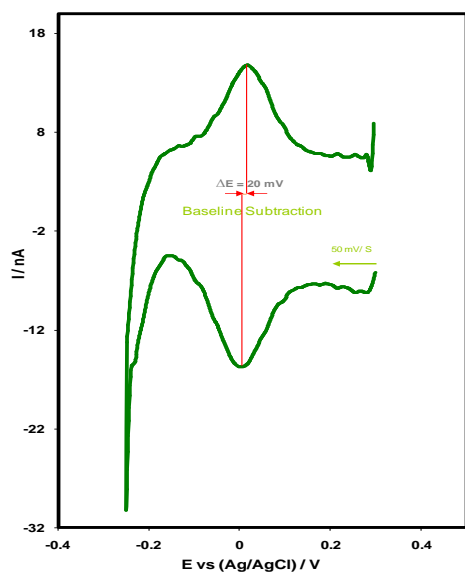
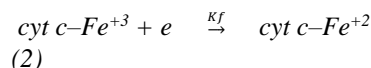


Fig. 6. Cyclic voltammetry of AuE/1,6,HDT/AuNP/capt /cyt c electrode after baseline subtraction in the 100mM phosphate buffer solution pH 7.2 at scan rate of 50 mV/s.

Simultaneously, by applying sufficiently negative potentials to the substrate, the cyt c-Fe⁺² regenerates through tunneling ET with a tunneling rate constant, k_f .



Regeneration of Fe(CN)₆⁴⁻ depends on tunneling ET through the SAM which has a Butler-Volmer dependency on substrate potential. The rate constants for mediated ET were measured by the new developed methodologies[8]. The heterogeneous rate constant, k_{eff} , from fitting the experimental rate constant to theory one is:

$$k_{eff} = k_{BI} \frac{k_f \Gamma}{k_{BI} c + k_f + k_b} \quad (3)$$

Γ and c are surface coverage and probe concentration, respectively. There are two limiting cases: a) At high substrate overpotentials, where substrate potential (E_{sub}) is more negative than the cyt c formal potential, and $k_{BI} c \ll k_f + k_b$, the heterogeneous rate constant, k_{eff} , in equation 3 becomes

$$k_{eff} = k_{BI} \Gamma \quad (4)$$

Here the overall rate of ET becomes limited by the bimolecular ET rate constant, k_{BI} .

b) At low substrate overpotentials, substrate potential is not much more negative than cyt c formal potential

and $k_{BI} c \gg k_f + k_b$, the rate constant, k_f , for the tunneling ET controlling the ET processes and then the heterogeneous rate constant, k_{eff} , in equation 3 becomes

$$k_{eff} = k_f \Gamma / c \quad (5)$$

The values of k_{eff} obtained by fitting the experimental current-distance curves to the theory versus Γ , ranging from 1.78 to 8.35 pmolcm⁻² in a low potential of substrate. This plot shows a linear relationship between k_{eff} and Γ with slope of 4×10^8 cm³mol⁻¹s⁻¹ and k_f of 200 s⁻¹. The standard tunneling rate constant, k^0 , for ET is equal to 69.6 s⁻¹, calculated using k_f value and Butler-Volmer equation. The values of k_{eff} vs Γ obtained in upper range of overpotential, $E_{sub} = -200$ mV. k_{eff} has a linear relationship with Γ , and using limiting equation in high overpotentials, k_{BI} was obtained as 1×10^9 cm³mol⁻¹s⁻¹.

A comparison of the obtained k^0 values for this nanoparticulated SAM (69.6 s⁻¹) and pure cap SAM (46.4 s⁻¹), shows that the enhanced ET rate constant is strongly due to the presence of AuNP through the SAM. The most important factor in AuNP-induced interfacial ET rate enhancement is probably due to the strong electronic coupling of cyt c to the AuNP than directly to the capt-modified surface or to any thiol-modified surface.

Conclusions

AuNP decorated SAM was prepared and cyt c linked electrostatically to the AuNPs through the capt molecules. A well-defined reversible voltammetry was observed for the redox mediator and the assembled cyt c on the nanoparticulated surface. It is concluded that the AuNP facilitate the electronic coupling between the protein redox center and the AuE. Obtained tunneling ET rate constant confirms the AuNP rol as an excellent ET relay. This hybrid system can applied to studying of other redox proteins and design protein based devices.

References

- [1] J. Zhang, A.M. Kuznetsov, I.G. Medvedev, Q. Chi, T. Albrecht, P.S. Jensen, J. Ulstrup, Chem. Rev, 108 (2008) 2737-2791.
- [2] H. Wang, R. Yang, L. Yang, W. Tan, ACS Nano, 3 (2009) 2451-2460.
- [3] N. Li, R. Yuan, Y. Chai, S. Chen, H. An, W. Li, J. Phys. Chem. C, 111 (2007) 8443-8450.
- [4] C. Léger, P. Bertrand, Chem. Rev, 108 (2008) 2379-2438.
- [5] A.F. Loftus, K.P. Reighard, S.A. Kapourales, M.C. Leopold, JACS, 130 (2008) 1649-1661.
- [6] H.D. Hill, J.E. Millstone, M.J. Banholzer, C.A. Mirkin, ACS Nano, 3 (2009) 418-424.



Thermodynamic study of the (KCl + N,N-dimethylformamide + water) system based on potentiometric measurements at T=298.2K

T. Nasiri-Louhesara, B. Ghalami-Choobar*

Department of Chemistry, Faculty of Science, University of Guilan, Rasht, Iran

*B-Ghalami@guilan.ac.ir

Abstract: In this work, the results relating to the mean activity coefficients measurements of KCl in the (N,N-dimethylformamide + water) mixed solvent system using the potentiometric method have been reported. The electromotive force (emf) measurements were performed on the galvanic cell of type: Ag | AgCl | KCl (m), N,N-dimethylformamide (wt.%), H₂O (1-wt) % | K-ISE, in various mixed solvent systems containing 10, 20 and 30% mass fraction of N,N-dimethylformamide over ionic strength ranging from 0.0496 to 2.3500 mol kg⁻¹ at T=298.2 K. The modeling of this ternary system was made based on the Pitzer ion-interaction model. The values of the mean activity coefficients, the excess Gibbs free energy for the series under investigated system were determined.

Keywords: Activity coefficient; Ion selective electrode; N,N-dimethylformamide; KCl; Pitzer model

Introduction

Knowledge of thermodynamic properties of electrolyte solutions is of great interest because of their applications in the fields of chemistry, chemical engineering, biology and industrial processes such as seawater desalination and solvent extraction [1,2]. Addition of inorganic salts into the mixed solvents (water + organic agent) or some organic solvents into electrolyte solutions affects on the physicochemical properties of reference solutions. Therefore, investigation of these mixed systems can be a very important matter in theoretical and application study of fluid chemistry, such as the separation and purification of mixed salts [3] and the concentration distillation [4]. For this purpose, an accurate description of the thermodynamic properties of electrolyte systems is required. N,N-dimethylformamide (DMF) is widely used as a solvent and reaction medium in different fields such as chemical synthesis and chemical engineering processes. Some investigations have been performed on the activity coefficients of electrolytes in DMF + water mixtures [5, 6]. As a continuation of our previous studies on KCl in mixed solvent system [7], we present herein the activity coefficients and the excess Gibbs free energy for KCl in various mixed solvent systems containing 10, 20 and 30% mass fraction of DMF at 298.2 K.

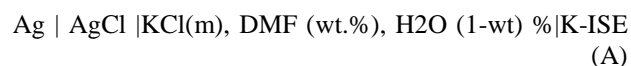
Materials and method

KCl and DMF were purchased from Merck and Sigma-Aldrich and were of > 0.99 mass fraction purity. Double distilled water was used throughout all experiments. Dibutyl phthalate (DBP), potassium tetrakis (p-chlorophenyl) borate (KTP CIPB), high weight poly(vinylchloride) (PVC), and tetrahydrofuran (THF) used were purchased from Merck and Fluka chemical

company and all of them were of analytical reagent grade. These chemical were used without further purification. The stock aqueous solutions of electrolyte were prepared from potassium chloride, DMF and double-distilled water by adding weighted amounts of KCl and DMF into the proportion volume of double-distilled water. All of the potentiometric measurements were made using a digital multimeter (Martini instruments Mi180) whose resolution was 0.1 mV. The output of the multimeter was connected to a personal computer by the RS232 connector for data acquisition. The Mi5200 software together with Microsoft Excel (Office2007) software were used for data acquisition and calculations. The solutions were continuously stirred using a magnetic stirrer (Delta Model HM-101) at a slow constant rate to avoid concentration gradients in the test solutions. A Model GFL circulation water bath was used to control the temperature of the test solution at T=298.2 K. Analytical balance (A&D) with accuracy 0.1 mg was used in preparation of the stock solutions.

Results and Discussion

The mean activity coefficients for KCl in the mixed solvent (DMF–water) were determined from the emf measurements using the following cell according to Eq. (1).



$$E = E^0 + s \log(\gamma_{\pm} I) \quad (1)$$

The emf of the cell (A) was measured at different series of electrolyte molalities in DMF–water mixed solvents



through changing of electrolyte concentration with standard addition method. Table 1 shows the values of measured emf and the obtained mean activity coefficients of the KCl electrolyte in 10% of DMF mass fraction in mixed solvent as a function of KCl molality. Fig. 1 presents the variation of the KCl mean activity coefficient versus molality of electrolyte in different mass fraction of DMF in mixed solvents.

Table1: Ionic strength of KCl electrolyte (I), mean activity coefficients (γ_{\pm}), and emf values of KCl in 10% mass fraction of DMF in mixed solvent.

I(mol.kg ⁻¹)	E(mV)	$\gamma_{\pm, KCl}$
0.0496	-30.3	0.7927
0.0976	0.5	0.7344
0.2521	45.6	0.6406
0.4980	76.6	0.5713
0.7506	95.4	0.5336
1.0001	108.8	0.5119
1.2505	119.5	0.4994
1.4995	128.2	0.4937
1.7497	136.1	0.4933
2.0001	145.9	0.4974
2.2501	151.7	0.5057

The Pitzer ion interaction model was used for the experimental data correlation and calculation of thermodynamic properties for under investigated system. According to the Pitzer model, the mean activity coefficient in molal based (γ_{\pm}) for KCl in the mixed solvent is described as:

$$\ln \gamma_{\pm, KCl} = f^{\gamma} + B_{KCl}^{\gamma} I + 1.5 C_{KCl}^{\phi} I^2 \quad (2)$$

Where

$$f^{\gamma} = -A_{\phi} \left[\frac{\sqrt{I}}{1+b\sqrt{I}} + \left(\frac{2}{b} \right) \ln(1+b\sqrt{I}) \right] \quad (3)$$

$$B_{KCl}^{\gamma} = 2\beta_{KCl}^{(0)} + \frac{2\beta_{KCl}^{(1)}}{\alpha^2 I} \left[1 - \left(1 + \alpha\sqrt{I} - \frac{\alpha^2 I}{2} \right) e^{-\alpha\sqrt{I}} \right] \quad (4)$$

In these equations α and b are assumed to be constant with values of 2.0 and 1.2 kg^{1/2}mol^{1/2}, respectively, both in water and in DMF–water mixtures; I indicates the total ionic strength on a molality scale. B^{γ} and C^{ϕ} represent the second and third virial coefficients, respectively. The variation of B^{γ} with ionic strength is given by Eq. (4). $\beta^{(0)}$, $\beta^{(1)}$ and C^{ϕ} show solute specific interaction Pitzer parameters for electrolyte solution. The symbol A_{ϕ} denotes the Debye–Hückel (DH) parameter for the osmotic coefficients, depends on the temperature and solvent properties, defined by Eq. (5).

$$A_{\phi} = \frac{1.4006 \times 10^6 d_s^{1/2}}{(\epsilon_r T)^{3/2}} (kg^{1/2} \cdot mol^{-1/2}) \quad (5)$$

where d_s is the solvent density (kg m⁻³); ϵ_r the solvent relative permittivity; and T the Kelvin temperature.

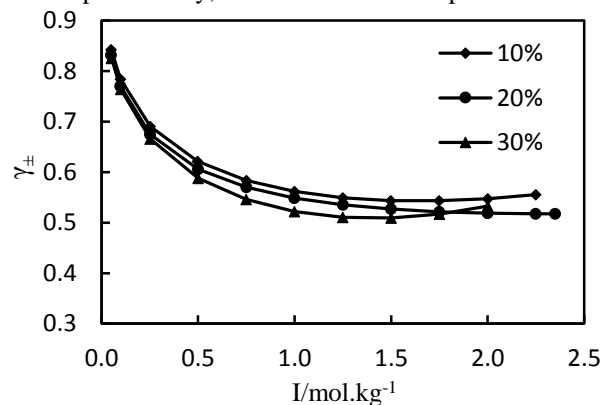


Fig.4: The mean activity coefficients for KCl versus molality of electrolyte in various DMF–water mixed solvent system containing 10, 20 and 30% mass fraction of DMF at 298.2K.

The Pitzer ion-interaction parameters ($\beta^{(0)}$, $\beta^{(1)}$ and C^{ϕ}) together with E^0 and s were determined by combining Eqs. (1) and (2) by an iteration minimization procedure employing the Microsoft Excel (solver) program. The obtained parameters were used to predict the thermodynamic properties of under investigation system by the Pitzer model. The excess Gibbs free energy for all of the under investigation series can be calculated using Eq. (6).

$$G^E = 2IRT(1 - \phi + \ln \gamma_{\pm}) \quad (6)$$

Fig.2 shows the plot of the excess Gibbs free energy versus the molality of electrolyte in different mass fraction of DMF in mixed solvents. It can be seen that



the excess Gibbs free energy is reduced by increasing the mass fraction of DMF in mixed solvent.

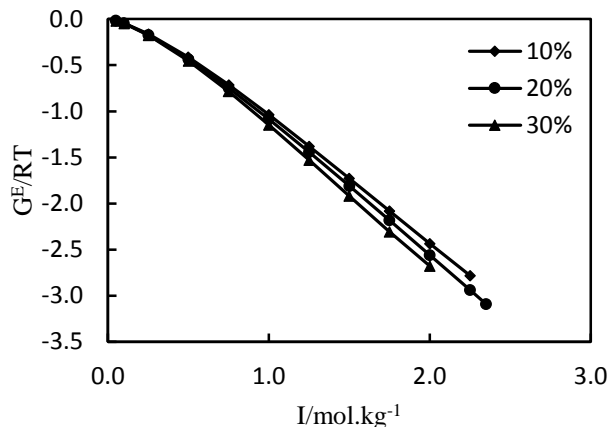


Fig.2: Variation of excess Gibbs free energy (G^E/RT) with molality of KCl in various DMF-water mixed solvent system containing 10, 20 and 30% mass fraction of DMF at 298.2K.

Conclusions

The mean activity coefficients of KCl in the KCl + DMF + water system were determined by a potentiometric method using a solvent polymeric ion-selective membrane electrode and Ag–AgCl electrodes at temperature of 298.2 K. We used the Pitzer ion-interaction model to obtain the Pitzer parameters ($\beta^{(0)}$, $\beta^{(1)}$ and C^ϕ) and the other thermodynamic properties such as the excess Gibbs free energy. It can be concluded that the Pitzer ion-interaction model satisfactorily describes the system under investigated.

References

- [1] M. T. Zafarani-Moattar, R. Majdan-Cegincara, Viscosity modelling and prediction of aqueous mixed electrolyte solutions, *Ind. Eng. Chem. Res.*, 48 (2009) 5833-5844.
- [2] N. M. Konstantinova, M. S. Motornova, M. N. Mamontov, D. I. Shishin, I. A. Uspenskaya, Partial and integral thermodynamic properties in the sodium chloride-water-1-butanol(isobutanol) ternary systems, *Fluid Phase Equilib.*, 309 (2011) 20-29.
- [3] M. Anzar, R. N. Araujo, J. F. Romanato, G. R. Santos, S. G. Avila, Salt effects on liquid-liquid equilibrium in water + ethanol + alcohol + salt systems, *J. Chem. Eng. Data*, 45 (2000) 1055-1059.

[4] W. F. William, Salt effect in distillation: a literature review II, *Can. J. Chem. Eng.*, 55 (1977) 229-239.

[5] F. Deyhimi, A. Ebrahimi, H. Roohi, K. Koochaki, Determination of activity coefficients, osmotic coefficients, and excess Gibbs free energies of HCl in N,N-dimethylformamide + water mixed solvent systems by potentiometric measurements, *J. Chem. Eng. Data*, 49 (2004) 1185-1188.

[6] L. Wang, S. Li, Q. Zhai, H. Zhang, Y. Jiang, W. Zhang, M. Hu, Thermodynamic study of RbCl or CsCl in the mixed solvent DMF + H₂O by potentiometric measurements at 298.15 K, *J. Chem. Eng. Data*, 55 (2010) 4699-4703.

[7] T. Nasiri-Lohesara, B. Ghalami-Chooabar, Thermodynamic study and modeling of the (KCl + diethanolamine + water) ternary system based on potentiometric measurements at T= (298.2 and 308.2) K, *J. Mol. Liq.* 232 (2017) 440-448.



Fabrication of a coated graphite electrode for selective determination of magnesium

*F. davudi^{1,2}, A. Ghaemi², M. Rezaeimanesh^{1,2}

¹ Department of Chemistry, Khouzestan Science and Research Branch, Islamic Azad University, Ahvaz, Iran

² Department of Chemistry, Ahvaz Branch, Islamic Azad University, Ahvaz, Iran

*f.davudi@yahoo.com

arezooghaemi@yahoo.com*

p.rezaeimanesh70@gmail.com

Abstract: In this project a magnesium selective coated graphite electrode based on dibenzo-18-crown-6 as a neutral ionophore incorporated in polyvinyl chloride (PVC) membrane in tetrahydrofuran (THF) has been fabricated. The best operation obtained in the membrane including: 4.0 mg dibenzo-18-crown-6, 1.0 mg sodium tetraphenylborate (NaTPB), 65.0 mg dioctylphthalate (DOP) and 30.0 mg PVC. This electrode had a good selectivity respect to Mg²⁺ cation, with a Nernstian slope of 29.1±0.7 mV.decade⁻¹ in a linear concentration range of 1.0×10⁻¹ M-1.0×10⁻⁵ M. The detection limit of the electrode was 8.9×10⁻⁶ M. The proposed sensor had a fast response time of 10 sec and good reproducibility. The effects of the pH and possible interfering ions were investigated, and it could be used in pH range of 3-12.

Keywords: Magnesium (II) cation, Ion selective electrode, Potentiometry.

1. Introduction:

Potentiometric ion selective electrodes (ISEs) are one of the most important types of chemical sensors. A significant number of ionophores, including crown ethers, cryptands, aza-crowns, thiocrowns and thio compounds, have been exploited for the fabrication of polyvinyl chloride (PVC) membrane electrodes for the determination of alkali, alkaline earth, transition and heavy metal ions [1,2]. Ionophores used in sensors should have rapid exchange kinetics and adequate complex formation constants in the membrane. Moreover, ionophores should be soluble in the membrane matrix and have sufficient lipophilicity to prevent leaching from the membrane into the sample solution. In addition, the selectivity of neutral carrier-based ISEs is governed by the stability constant of the neutral carrier-ion complex and the partition constant between the membrane and sample solution [3]. Changes in the structure of the ionophore, such as replacing oxygen with nitrogen or sulfur and/or introducing other constituents into the macrocyclic and noncyclic core, may alter the ligand binding strength and selectivity of the sensor [4].

2. Experiment

2.1. Materials and method:

The dibenzo-18-crown-6, sodium tetraphenylborate (NaTPB), dibutyl phthalate (DBP), dioctyl sebacate (DOS), dioctyl phthalate (DOP), nitrobenzene (NB), polyvinyl chloride (PVC), tetrahydrofuran (THF), acid nitric, magnesium nitrate and sodium hydroxide were purchased from Merck and Fluka. Potentiometer (Zag Chemi Co, Iran, Model PTR-79) and glass electrode Ag/AgCl (Azar Electrode, Iran) were used for potential difference and pH measurements, respectively. pH measurements were made with a digital pH meter (Horiba, Japan, Model pH F-11). Hot

plate magnetic stirrer (Pars Faraso, Iran, Model F-60) and digital scale (Sartorius, Swiss, Model PB210D) was used.

2.2. Electrode preparation

The electrodes were prepared from graphite bars (3 mm diameter and 50 mm long). The graphite bars were polished and put in a concentrated HNO₃ solution overnight to clean the surface of the electrodes. Then, the bars were rinsed with THF and once again polished and washed with distilled water and allowed to dry. A shielded copper wire was glued to one end of the graphite bar and the bar was inserted into the end of a polyethylene tube. A mixture of PVC, plasticizer, ionophore (dibenzo-18-crown-6) and the membrane additive (NaTPB) to give a total mass of 100 mg was dissolved in about 2 ml of THF and the solution was mixed well. The graphite bar was coated by dipping into the membrane solution for a few seconds and allowed to dry overnight. The electrode was conditioned for 24 h in 0.001 M magnesium nitrate solution and stored in mild concentration solutions of magnesium nitrate, when not in use. The coating solutions were stable for several days and could be used for construction of new membranes.

2.3. Potential measurements

The potential was measured for test solutions by varying the concentration in the range of 1.0×10⁻⁸ to 1.0×10⁻¹ M. The solution of Mg(NO₃)₂ was prepared by sequential dilution of the appropriate stock solution. The potential measurement was carried out at 25±0.1°C using an Ag/AgCl as a reference electrode with the following cell assembly:

Ag/AgCl; KCl(satd.) | Mg²⁺ sample solution | ion selective membrane | graphite bar



3. Results and discussion

3.1. Optimization of the membrane composition

The sensitivity and selectivity obtained for a given ionophore depend significantly on the membrane composition and the nature of the plasticizer and additive used [5,6]. Therefore, the effect of the membrane composition on the potential response of the Mg(II) electrode was investigated. The results are summarized in Table 1. As a result, membrane composition of 30% PVC, 4% dibenzo-18-crown-6, 1% NaTPB and 65% DOP (membrane no. 1) exhibits the best Nernstian slope (29.1 mV/decade) and linear concentration range (from 1.0×10^{-5} to 1.0×10^{-1} M). The calibration curve for this sensor is shown in Fig. 1. The detection limit of this sensor, as determined from the intersection of the two extrapolated segments of the calibration graph is 8.9×10^{-6} M. The standard deviation of 3 replicate measurements is ± 0.7 mV/decade. The proposed sensor was very stable and could be used for 35 day without observing any change in its response characteristics. It is well known that the presence of lipophilic anions in cation-selective membranes based on neutral carriers not only diminishes the ohmic resistance and enhances the response behavior and selectivity, but also, in cases where the extraction

capability is poor, increases the sensitivity of the membrane electrodes [7-9].

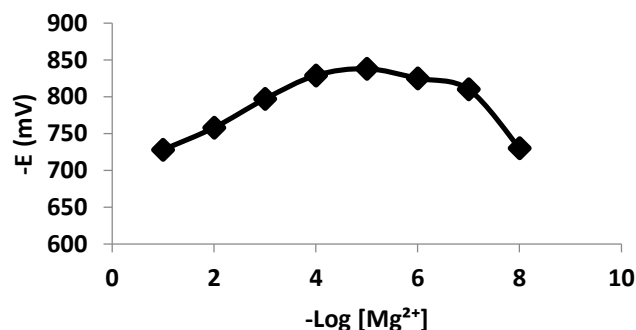


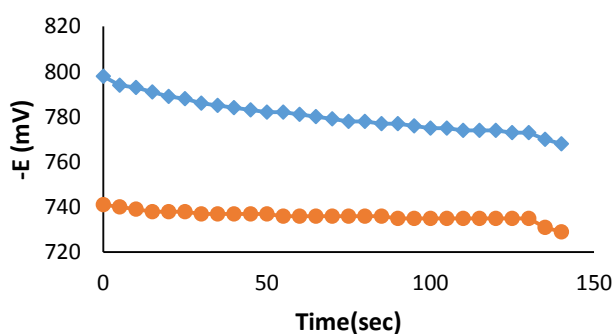
Fig. 1. Calibration curve of the Mg^{2+} selective sensor based on dibenzo-18-crown-6.

3.2. Static and dynamic response time

For analytical purposes, response time is one of the most important factors that are taken into account. Therefore, the static response time of the proposed sensor (membrane no. 1) was studied by plotting the potential response vs. time, at 1.0×10^{-3} M and 1.0×10^{-2} M of Mg^{2+} ion solutions (Fig. 2). As is evident in this figure, in the whole concentration range, the sensor reaches its equilibrium response in a short time (~ 10 s) and no change is observed in 130 second.

Table 1. Optimization of the membrane ingredients. No.	Composition (wt. %)				Linear range (M)	Slope (mV/decade)
	PVC	Plasticizer	NaTPB	Ionophore		
1	30	4	1	(DOP) 65	10^{-5} - 10^{-1}	29.1 \pm 0.7
2	30	5	3	(DOP) 62	10^{-5} - 10^{-1}	26.2 \pm 0.5
3	30	7	3	(DOP) 60	10^{-5} - 10^{-1}	35.0 \pm 1.0
4	30	3	2	(NB) 65	10^{-4} - 10^{-1}	23.2 \pm 0.7
5	30	5	1	(DOS) 64	10^{-5} - 10^{-1}	26.4 \pm 4.0
6	30	7	3	(DBP) 60	10^{-5} - 10^{-1}	22.8 \pm 3.0

Fig. 2. Static response time curves of the Mg^{2+} selective sensor (\bullet 1.0×10^{-2} M, \blacklozenge 1.0×10^{-3} M).



For any ion selective sensor, dynamic response time is an important factor. In this study, the practical response time of the proposed sensor was recorded by changing the Mg^{2+} concentration in solution in a concentration range of 1.0×10^{-5} to 1.0×10^{-1} M and the results are shown in (Fig. 3). From this figure, it can be derived that the electrode reaches its equilibrium response rapidly (10 s), in the whole concentration range. This is most probably due to the fast exchange kinetics of the complexation-decomplexation of Mg^{2+} ions with the ionophore at the test solution-membrane interface.

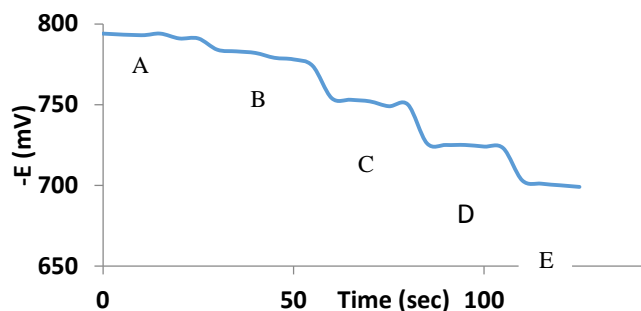


Fig. 3. Dynamic response time of the Mg^{2+} selective sensor for step changes in the concentration of Mg^{2+} : (A) 1.0×10^{-5} M, (B) 1.0×10^{-4} M, (C) 1.0×10^{-3} M, (D) 1.0×10^{-2} M, (E) 1.0×10^{-1} M.

3.3. Effect of pH

The relationship between the pH and the potentials of the proposed ion selective electrode was investigated by measuring the potential at a pH range of 1.0-14.0. Experimentally, the pH was adjusted with dilute solutions of HNO_3 and $NaOH$. The effect of the pH on the proposed ion selective electrode is shown in Fig. 4. As shown in the figure, the potential remained constant over a pH range of 3.0-12.0. Therefore, the working pH range of the proposed electrode is 3.0-12.0. A significant change in the potential response was observed at pHs greater than 12.0, which may be due to the formation of hydroxyl complexes of Mg (II) cations, which reduce the free cation concentration in solution. The observed drift in the electrode potentials at pHs less than 3.0 may be due to the protonation of the ion carrier in solution.

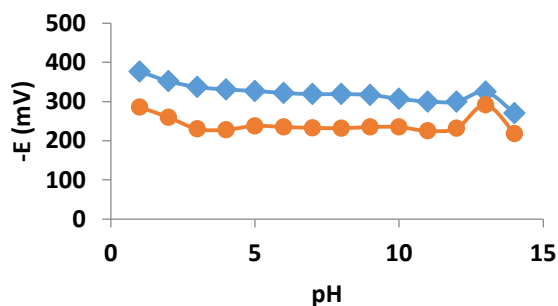


Fig. 4. Effect of the pH of test solutions on potential response of the Mg^{2+} selective sensor (\bullet 1.0×10^{-2} M, \blacklozenge 1.0×10^{-3} M).

4. Conclusion

A PVC membrane electrochemical sensor incorporating dibenzo-18crown-6 as a macromolecule ionophore was successfully used to determine magnesium (II) cation over a concentration range of 1.0×10^{-5} - 1.0×10^{-1} M. The sensor displayed a Nernstian slope of 29.1 ± 0.7 mV. decade⁻¹ and a response time of 10 s. The proposed sensor showed high sensitivity, stability and working concentration range to Mg (II) cation.

References

- [1] M. Mazloum, M. Salavati Niassary, M. K. Amini, *Sens. Actuators B* 82 (2002) 259.
- [2] H. A. Zamani, M. R. Ganjali, H. Behmadi, M. A. Behnajady, *Mater. Sci. . Eng. C* 29 (2009) 1535.
- [3] E. Bakker, P. Bühlmann, E. Pretsch, *Chem. Rev.* 97 (1997) 3083.
- [4] V. Alexander, *Chem. Rev.* 95 (1995) 273.
- [5] S. Amarchand, S. K. Menon, Y. K. Agrawal, *Electroanalysis* 12 (2000) 522.
- [6] A. Ghaemi, H. Tavakkoli, T. Mombeni, *Mater. Sci. Eng. C* 38 (2014) 186.
- [7] E. Bakker, P. Buhlmann, E. Pretsch, *Chem. Rev.* 97 (1997) 3083.
- [8] M. R. Ganjali, M. Emami, M. Salavati-Niasari, *Bull. Korean Chem. Soc.* 23 (2002) 1394.
- [9] R. Eugster, P. M. Gehrig, W. E. Morf, U. E. Spichiger, W. Simon, *Anal. Chem.* 63 (1991) 2285.

Thermodynamic investigation of Sodium Nitrate in N,N Dimethylformamide aqueous mixtures based on potentiometric measurements at T=298.2K

^aE. Hadizadeh, ^aB. Ghalami-Chooabar*, ^aP. Mossayyebzadeh

^aDepartment of Chemistry, Faculty of Science, University of Guilan, Rasht, Iran

*B-Ghalami@guilan.ac.ir

Abstract: In this work, the thermodynamic properties of the ternary (NaNO₃+DMF+water) system were reported using the potentiometric method. The potentiometric measurements were performed on the galvanic cell of the type: NO₃-ISE|NaNO₃ (m), DMF (W/W%), H₂O|Na -ISE, in various mixed solvent systems containing 0, 5, 10, 15 and 20.% mass fraction of DMF over total ionic strengths from 0.0100 mol·kg⁻¹ to 2.500 mol·kg⁻¹ at T= 298.2 K and P= 0.1 MPa. The obtained results were interpreted by using Pitzer ion interaction model. Then, Pitzer parameters ($\beta^{(0)}$, $\beta^{(1)}$ and C^φ) for each of them were determined and utilized to calculate the values of mean activity coefficients for the whole series of under investigated electrolyte solutions.

Keywords: Thermodynamic properties; Activity coefficients; Sodium Nitrate; N,N Dimethylformamide

Introduction

Knowledge of thermodynamic properties of electrolyte solutions is of great interest because of their applications in the fields of chemistry, chemical engineering, biology and industrial processes such as sea water desalination and solvent extraction. Addition of inorganic salts in to the mixed solvents (water + organic agent) or some organic solvents in to electrolyte solutions effect on the physicochemical properties of reference solution. Therefore, investigation of these mixed systems can be a very important matter in theoretical and application study of fluid chemistry, such as the separation and purification of mixed salts and the concentration distillation [1].

Materials and method

The potentiometric measurements were performed on the galvanic cell of the type: NO₃-ISE|NaNO₃ (m), DMF (W/W%), H₂O|Na -ISE, in various mixed solvent systems containing 0, 5, 10, 15 and 20% mass fraction of DMF, over total ionic strengths from 0.0100 mol·kg⁻¹ to 2.5000 mol·kg⁻¹ at T = 298.2 K and P= 0.1 MPa. All of the potentiometric measurements were made using a digital multimeter (Martini instruments Mi180) whose resolution was 0.1 mV [2]. Then, Experimental activity coefficients of sodium nitrate were calculated using Nernst equation;

$$E = E^0 + \text{slog} (\gamma_{\pm \text{NaNO}_3} I) \quad (1)$$

The “E⁰” and “I” are the experimental standard potential of cell and the total ionic strength on a molality scale respectively.

The Pitzer ion interaction model was used for the experimental data correlation and calculation of thermodynamic properties for under investigated system. According to the Pitzer formula, the mean activity coefficient in molal based (γ_{\pm}) for NaNO₃ in the mixed solvent is written as:

$$\ln \gamma_{\pm} = f^{\gamma} + I\beta^{\gamma} + 1.5C^{\varphi} I^2 \quad (2)$$

$$f^{\gamma} = -A\varphi \left[\sqrt{I} / (1 + b\sqrt{I}) + (2/b) \ln(1 + \sqrt{I}) \right] \quad (3)$$

$$\beta^{\gamma} = 2\beta^{(0)} + 2\beta^{(1)} \{ [1 - \exp(-\alpha\sqrt{I})(1 + \alpha\sqrt{I} - \alpha^2 I/2)] / (\alpha^2 I) \} \quad (4)$$

In these equations “ α ” and “ b ” are constant with values of 2.0 and 1.2 kg^{1/2} mol^{-1/2}, respectively. “ B^{γ} ”, and “ C^{γ} ” represent the second and third virial coefficients, respectively. The variation of B^{γ} with ionic strength is given by Eq. (4). $\beta^{(0)}$, $\beta^{(1)}$ and C^{γ} symbolize solute-specific interaction Pitzer parameters for electrolyte solution. The symbol A_{φ} denotes the Debye–Hückel parameter for the osmotic coefficients, depends on the temperature and solvent properties, defined by [1]

$$A_{\varphi} = \frac{1.4006 \times 10^6 d_s^{1/2}}{(\epsilon_r T)^{3/2}} (Kg^{1/2} \cdot mol^{-1/2}) \quad (5)$$

Results and Discussion

In this work, the mean activity coefficients for NaNO₃ in the mixed solvent (NaNO₃+ DMF+ Water) system were determined in various mixed solvent systems containing 0, 5, 10, 15 and 20% mass fraction of DMF at T= 298.2 K.

Tables 1 illustrates molality of NaNO₃, the values of measured emf and the obtained mean activity coefficients of NaNO₃ in aqueous DMF solutions containing 5% mass fractions of DMF.

Fig.1 shows the values of mean activity coefficients for NaNO₃. It can be seen that the mean activity coefficients is reduced by increasing the mass fraction of DMF in the mixed solvent system.

Table 1. Values of NaNO_3 moles per 1 kg of (DMF 5% + water) mixed solvent, m , emf data, E , and mean activity coefficient of NaNO_3 , $\gamma_{\pm \text{NaNO}_3}$, in DMF + water mixtures at 298.2 K and $P = 0.1$ MPa.

$m(\text{mol}\cdot\text{kg}^{-1})$	$E(\text{mV})$	$\bar{\alpha}_{\pm}$
0.0100	-143.4	0.8982
0.0999	-36	0.7540
0.2498	8.4	0.6733
0.4996	37.5	0.6043
0.7493	50.4	0.5599
0.9991	65	0.5257
1.2489	79.1	0.4970
1.4987	85.1	0.4716
1.7485	91.6	0.4484
1.9982	92.5	0.4268
2.2480	93	0.4064
2.4978	95.6	0.3868

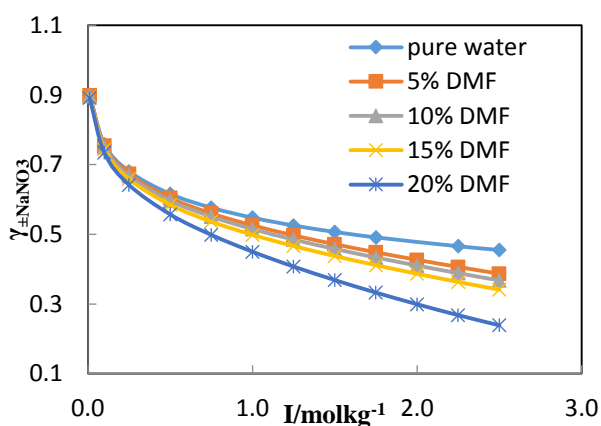


Fig. 1. Plot of the values of NaNO_3 mean activity coefficients

versus ionic strength in pure water and (DMF + water) mixtures at $T = 298.2$ K.

Conclusions

The thermodynamic research of ($\text{NaNO}_3 + \text{DMF} + \text{water}$) system was performed using a solvent polymeric ion-selective membrane electrode and Ag-AgCl electrodes at $T = 298.2$ K. The galvanic cell consisting of Na-ISE and NO_3 -ISE electrodes were used to study the thermodynamic properties of $\text{NaNO}_3 + \text{DMF} + \text{H}_2\text{O}$ system at $T = 298.2$ K. The emf measurements were made for NaNO_3 in various mass fraction (%) of DMF containing 0, 5, 10, 15, and 20% over the entire range of total ionic strengths. The parameters of Pitzer model were determined for the whole data set of ternary system. The obtained parameters were used to calculate the thermodynamic properties such as mean activity coefficient and excess Gibbs free energy.

References

- [1] T. Nasiri-Lohehsara, B. Ghalami-Choobar "Thermodynamic study and modeling of the ($\text{KCl} + \text{diethanolamine} + \text{water}$) ternary system based on potentiometric measurements at $T = (298.2 \text{ and } 308.2)$ K", *Molecular Liquids* 232 (2017) 440–448.
- [2] B. Ghalami Choobar, P. Mossayyebzadeh Shalkoohi "Activity Coefficient Measurements and Thermodynamic Modeling of ($\text{CaCl}_2 + \text{l-Alanine} + \text{Water}$) System Based on Potentiometric Determination at $T = (298.2, 303.2 \text{ and } 308.2)$ K", *J. Chem. Eng. Data*, 60 (2015) 2879–2894.



Synthesis of TiO₂ nanorods on the transparent conductive oxide substrates for photoelectrochemical Generation of H₂

Samaneh Taghipour ,Hussein Gharibi* ,M Azimzade

Department of Chemistry, Faculty of Science, Tarbiat Modares University, P.O. Box 14115-175, Tehran, Iran
gharibi.modares@gmail.com

Abstract: In this work we synthesized TiO₂ nanorods on the transparent conductive oxide substrate (FTO, fluorine doped tin oxide) and investigated photovoltaic properties of TiO₂ nanorods under illumination. TiO₂ photoanodes were synthesized using a hydrothermal method and annealed at 450 °C to obtain better crystallinity. FESEM image proves formation of the TiO₂ nanorods and X-ray diffraction show that TiO₂ nanorods are formed properly. Photoelectrochemical properties were measured using linear sweep voltammetry and chronoamperometry techniques at 0.5 M Na₂SO₄ as electrolyte. In this work we synthesized TiO₂ nanorods on the transparent conductive oxide substrate (FTO, fluorine doped tin oxide) and investigated photovoltaic properties of TiO₂ nanorods under illumination. TiO₂ photoanodes were synthesized using a hydrothermal method and annealed at 450 °C to obtain better crystallinity. FESEM image proves formation of the TiO₂ nanorods and X-ray diffraction show that TiO₂ nanorods are formed properly. Photoelectrochemical properties were measured using linear sweep voltammetry and chronoamperometry techniques at 0.5 M Na₂SO₄ as electrolyte. All photoelectrochemical measurements were performed in a three-electrode electrochemical system, using an Ag/AgCl as the reference electrode and a platinum foil as the counter electrode.

Keywords: TiO₂ nanorods, water splitting, photoanode, photocatalysis, hydrothermal

1. Introduction

Due to the increasing energy demands and growing environmental concerns, efficient utilization of the solar energy has become a crucial way to solve these issues. Hydrogen production by solar water splitting in PEC cells has attracted a great attention in artificial photosynthesis owing to its promise for direct conversion of sunlight into the chemical bonds of fuels. Metal oxide semiconductors (such as TiO₂, ZnO, Fe₂O₃, WO₃) as well as their composite materials have been widely used as photoanode in PEC cells [1-2]. TiO₂ has been intensively studied as the photocatalyst to date due to its favorable band-edge positions for water splitting, high resistance to photocorrosion, excellent physical and chemical stability, nontoxicity, low-cost and abundance. A common approach for improving photoelectrochemical properties of photoanodes is photo-management with introducing micro and nanometric roughness on the photoanodes surfaces specially 1-dimensional structure (nanorods). In photoelectrochemical water splitting on a semiconductor photoanode, under illumination, conduction band electrons are transferred to a counter electrode (typically Pt) to reduce water to H₂ and valence band holes are used to oxidize water [3].

There are three key factors influencing the photoelectrolysis reaction: (1) light absorption and carrier excitation (electron-hole formation), (2) charge separation and (3) charge transfer. A photocatalytic reaction, usually involves light absorption by the semiconductor followed by transition of electron from low energy level to high energy level. This transition is called as electron-hole separation [5].

In this research we have used TiO₂ nanorods as a semiconductor photoanode because of their large surface area originating from its special shape and favorable band-edge positions for water splitting and consequently generation of H₂.

2. Materials and method

Synthesis of TiO₂ nanorods

The TiO₂ nanorods were prepared by hydrothermal method. Firstly, 24 mL of 36% hydrochloric acid, 24 mL of deionized water and 0.8 mL of titanium butoxide (97% Aldrich) were mixed in a Teflon-lined stainless steel autoclave. A piece of FTO substrate, cleaned sequentially in deionized water, acetone and ethanol by ultrasonic agitation, was put into the autoclave 'upside down' and then kept at 150 °C for 20 h to obtain TiO₂ nanorods array. TiO₂ nanorods array were obtained after rinsed with deionized water



and ethanol for several times and the following annealing at 450 °C for 0.5 h in air [8].

All photoelectrochemical measurements were performed in a three-electrode electrochemical system, using an Ag/AgCl as the reference electrode and a platinum foil as the counter electrode. The working electrode was TiO₂ nanorods photoanode and 0.5 M Na₂SO₄ aqueous solution was used as electrolyte. The illumination source was 500 W Xe lamp with a light intensity of 100 mW/cm² and the photoanode was irradiated from backside.

3. Results and Discussion

Figure 1 shows the XRD patterns of TiO₂ nanorods grown on the FTO substrate. The relation between the FTO substrate and TiO₂ with a small lattice mismatch plays a key role in driving the nucleation and growth of the TiO₂ nanorods on the FTO as substrate. Strong and sharp diffraction peaks can be observed and the patterns can be identified as tetragonal rutile phase TiO₂. The (002) diffraction peak of TiO₂ nanorods array was the strongest peak, indicating TiO₂ nanorods grew along c-axis direction. Figure 1 illustrates the pattern of eleven peaks due to the Bragg reflection of crystalline oxide screens (backgrounds) and various crystalline phases of the titanium dioxide. The crystalline phases of the oxidation of nanorods synthesized in both forms are rutile and anatase. The crystalline network of rutile, tetragonal with lattice constants $a = 4.5924$, $b = 4.5924$ and $c = 2.9575$ angstrom and angles $\gamma = \alpha = \beta = 90$ degrees, having diffraction from plates (110), (211), (002) and (112). Anatase crystalline phase has a tetragonal crystal network with network constants $a = 3.7300$, $b = 3.7300$ and $c = 9.3700$, and $\gamma = \alpha = \beta = 90$ degrees and has a diffraction of plates (103) and (116).

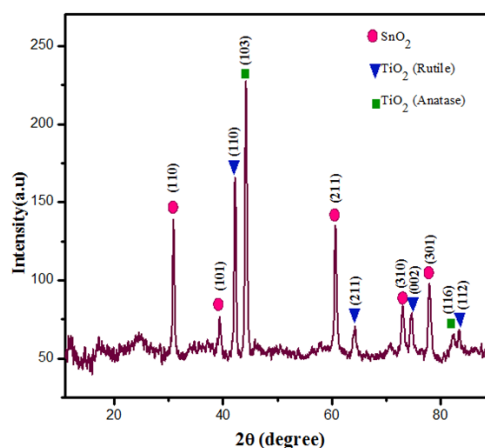


Figure 1. XRD pattern of TiO₂ NRs

Figure 2 shows typical cross section FESEM images of the TiO₂ nanorods film grown at 150 °C for 20 h. FESEM images reveal that the entire surface of the FTO substrate is covered with TiO₂ nanorods.

According to convenient band positions of TiO₂, holes at TiO₂ nanorods can be injected into the solution, while photogenerated electrons are injected into contact (charge collector) and then to the Pt as counter electrode and leads to generation of H₂ on the Pt surface.

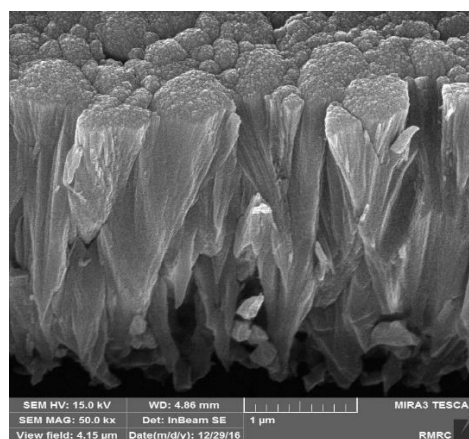


Figure 2. Cross section FESEM image of the TiO₂ nanorods grown on the FTO substrate.

Figure 3 and 4 show the measured photocurrent density for the TiO₂ nanorods under sudden on and off switching (at a constant bias voltage of 0.5 V vs. Ag/AgCl electrode) and as a function of applied bias voltages ranging from 0 to 1.2 V, respectively,

Under illumination, the resulting photoinduced charge accumulation at annealed



TiO₂ nanorods is believed to be the reason for the relatively high current density. The possible mechanism of the observed photoinduced charge accumulation at annealed TiO₂ nanorods can be explained because of better crystallinity and better tenacity of the TiO₂ nanorods on the FTO substrate. As can be seen in figure 3, photocurrent density is very stable after 6 cycles and this show that the TiO₂ nanorods photoanode is very stable and has a good resistance against photocorrosion.

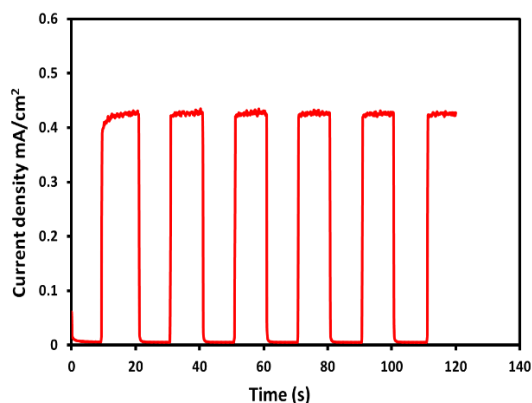


Figure 3. chronoamperometry data recorded at 0.5 V vs Ag/AgCl. Ag/AgCl.

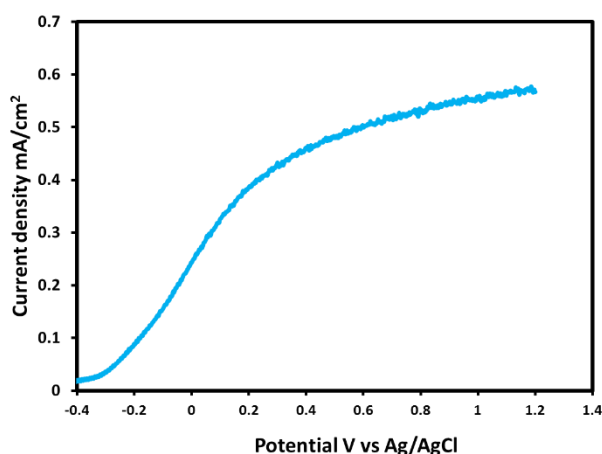


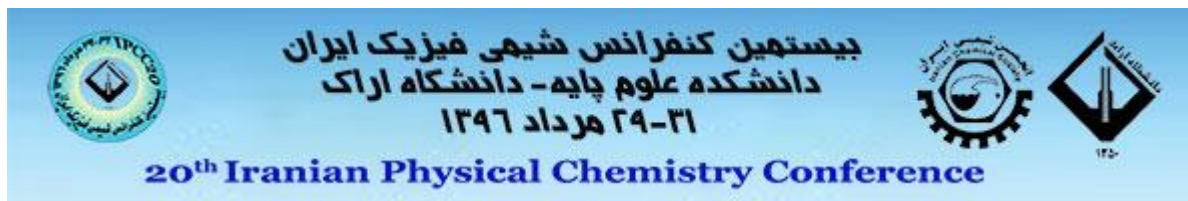
Figure 4. J-V curves under illumination (100 mW/cm²) versus Ag/AgCl at various bias voltages.

Conclusions

In conclusion, we have synthesized TiO₂ nanorods as an effective photoanode with high effective surface area originating from its shape for water splitting and generation of H₂ under illumination.

References

- [1] Zou, Zhigang, et al. "Direct splitting of water under visible light irradiation with an oxide semiconductor photocatalyst." *nature* 414.6864 (2001): 625-627
- [2] Warren, Scott C., et al. "Identifying champion nanostructures for solar water-splitting." *Nature materials* 12.9 (2013): 842-849
- [3] Momeni, Mohamad Mohsen, Yousef Ghayeb, and Mahsa Davarzadeh. "Single-step electrochemical anodization for synthesis of hierarchical WO₃-TiO₂ nanotube arrays on titanium foil as a good photoanode for water splitting with visible light." *Journal of Electroanalytical Chemistry* 739 (2015): 149-155.
- [4] Hoang, Son, et al. "Enhancing and NH₃: synergistic effects between Ti³⁺ and N." *Journal of visible light photo-oxidation of water with TiO₂ nanowire arrays via cotreatment with H₂* the American Chemical Society 134.8 (2012): 3659-3662.
- [5] Li, Di, et al. "Visible-light-driven photocatalysis on fluorine-doped TiO₂ powders by the creation of surface oxygen vacancies." *Chemical Physics Letters* 401.4 (2005): 579-584.
- [6] Xu, Fang, et al. "Au nanoparticles modified branched TiO₂ nanorod array arranged with ultrathin nanorods for enhanced photoelectrochemical water splitting." *Journal of Alloys and Compounds* 693 (2017): 1124-1132.
- [7] Li, Chunhe, et al. "Visible-light-driven water splitting from dyeing wastewater using Pt surface-dispersed TiO₂-based nanosheets." *Journal of Alloys and Compounds* 699 (2017): 183-192.
- [8] Chaudhary, Deepti, et al. "A ternary Ag/TiO₂/CNT photoanode for efficient photoelectrochemical water splitting under visible light irradiation." *International Journal of Hydrogen Energy* 42.12 (2017): 7826-7835.



Investigating the effect of graphite electrodes structures on the synthesized graphene using electrochemistry method

Z. Mehrvar^a, M. A. Kiani^a, H. Sayahi^{a*}

^a Chemical & Chemical Engineering Research Centre of Iran

* hanisayahi@yahoo.com, sayahi@ccerci.ac.ir

Abstract: In this study, a simple and efficient approach is reported to product graphene using electrochemical exfoliation of graphite electrodes, in acidic solutions. The electrolyte concentration, applied voltages, electrodes distance and preparation time were taken as control parameters to optimize the produced graphene structures. The optimized graphene sample was prepared in a H₂SO₄ (0.5 M) at a bias of +10 V. The interlayer spaces, crystallite size and the average number of layers were determined by XRD. Surface morphology, layer thickness and characteristics of obtained samples were investigated by Scanning Electron Microscopy (SEM), Atomic Force Microscopy (AFM), and FTIR. The obtained results confirmed the graphene structures.

Keywords: Graphene, Graphite Electrode, electrochemical synthesis, electrochemical saving energy

Introduction

Graphene, a two-dimensional material formed from sp² bonded carbon atoms packed in a honeycomb crystal lattice, has become one of the most exciting research topics in the last decade because of their extraordinary mechanical, optical, electronic, and electrochemical properties [1], [2]. Various methodologies such as scotch-tape isolation, epitaxial growth, bottom-up synthesis from aromatic precursors, and chemical vapor deposition of gaseous reagents do not seem readily scalable because of high cost, process complexity and/or low yield. Beyond that, wet chemical approaches, including reduction of graphene oxide (GO) and liquid-phase exfoliation of graphite, may present plausible alternatives for manufacturing graphene on a large scale. Electrochemical exfoliation of graphite has drawn increasing attention over the last few years as a potentially scalable method. Generally, it involves the use of an electrolyte (e.g., aqueous or non-aqueous solution) and an electrical current to drive structural expansion at a graphite electrode.[3] Electrochemical exfoliation of graphite has drawn increasing attention over the last few years as a potentially scalable method. Generally, it involves the use of an electrolyte (e.g., aqueous or non-aqueous solution) and an electrical current to drive structural expansion at a graphite electrode. According to the charge of the intercalated ions, the graphite electrode works as an anode or cathode and representing oxidation or reduction reactions, respectively. In contrast to other exfoliation processes, this method is not equipment-intensive and is typically performed under ambient conditions.[4]

In this study, we report a simple, cost-effective electrochemical approach to produce graphene by electrochemical exfoliation of graphite electrode, in acidic electrolytes. X-ray powder diffraction (XRD) was used to determinate the number of graphene layers, the distance interlayers, and the size of graphene crystallites. The obtained materials were also investigated by FT-IR Spectroscopy, Scanning Electron Microscopy (SEM), and Atomic Force Microscopy (AFM).

Materials and method

All reagents were of analytical grade and used without further purification. All solutions were prepared using double distilled water. Sulfuric acid was purchased from Merck chemicals. graphite electrode with high purity (99.99%) were used.

Results and Discussion

The electrochemical exfoliation process of graphite electrodes to product graphene (Fig. 1) was shown that it is significantly dependent on a couple of parameters which affects the quality of the final products: the electrolyte concentration and the applied bias voltages. The influence of the applied bias potential and electrolyte concentration, was studied in the 1–10 V of potentials and in the 0.2–1 M concentration, Respectively.

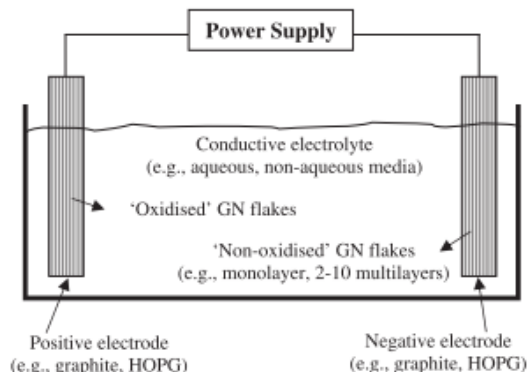


Fig. 1 Schematic of an electrochemical cell.

The XRD analysis was used to characterize the crystalline nature and phase purity of the synthesized materials (Fig. 2). The mean crystallites size (D) for each sample was calculated from full width at half maximum (FWHM) of the XRD pattern, using the Debye-Scherrer equation, as previously reported by other research groups.

The interlayer distance (d) was found using Bragg equation [5], [1]. The average number of graphene layers (n) was calculated by "Eq. 1":

$$n = \frac{D}{d} \quad (1)$$

FT-IR spectroscopy was applied to identify the functional groups which are expected to be attached to the graphene sheets. The intense broad band at 3430 cm^{-1} is attributed to the characteristic vibration of the OH group. The bands at 2922 and 2850 cm^{-1} are the stretching vibrations of CH_2 groups and 1362 cm^{-1} are C=C groups. (Fig 3)

The graphene morphology was further confirmed by SEM analysis (Fig 4). It can be observed the thin and crumpled nanosheets which are randomly arranged and over-lapped with each other.

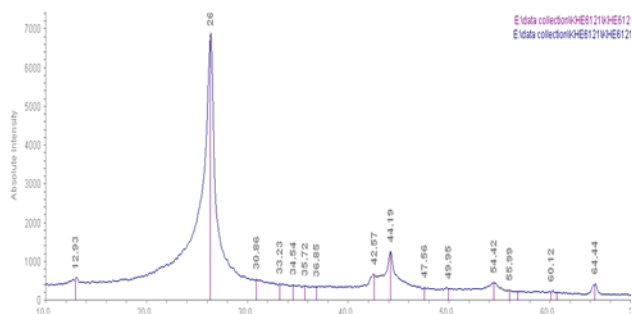


Fig. 2 The XRD patterns of the samples

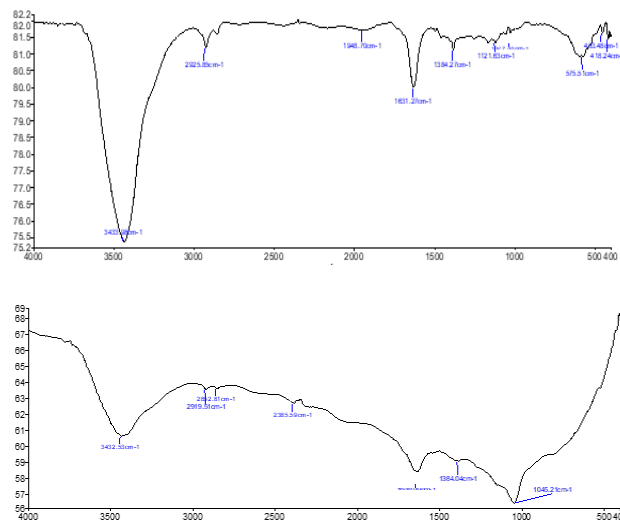


Fig. 3 FTIR spectra of samples

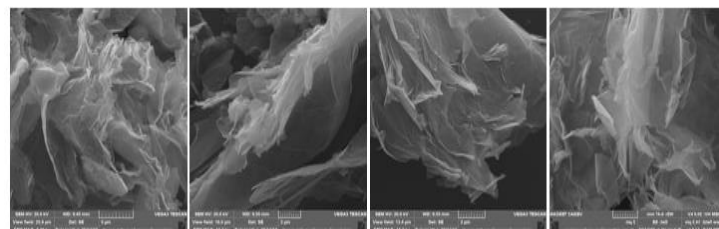


Fig. 4 SEM images of the samples

The typical AFM image of the sample (Fig. 5) reveals a graphene Flake with an average thickness, corresponding to multi-layer graphene.

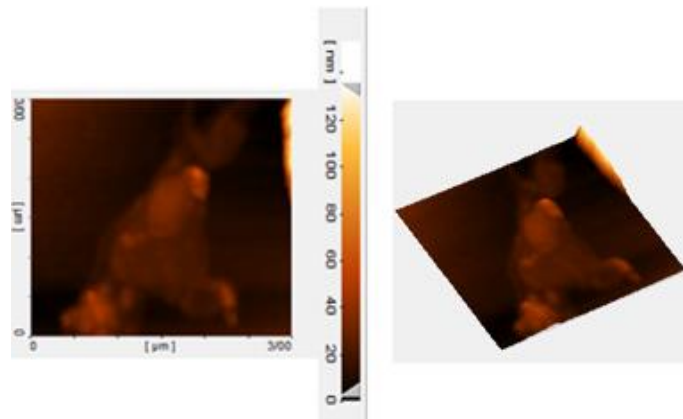


Fig. 5 The typical AFM image of the sample

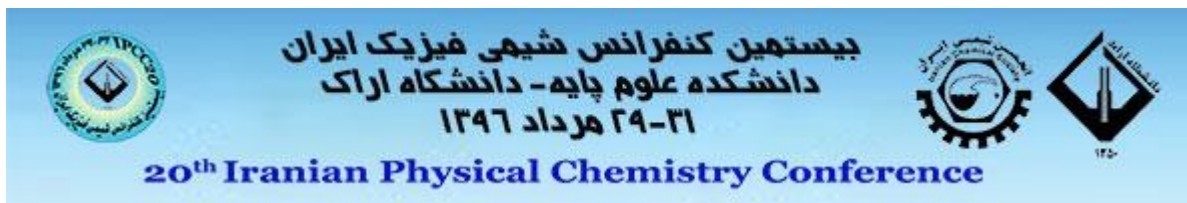


Conclusions

In conclusion, a one-step method of the synthesis of high quality graphene by electrochemical exfoliation of graphite electrode using acidic electrolyte. Different electrochemical parameters (e.g. applied bias, electrolyte concentration) were studied in details. In all of the as-prepared materials a mixture of few-layer and multi-layer graphene was present. The experimental conditions for the optimum sample were as follows: 0.5 M electrolyte concentration, 10 V applied bias and 30 min exfoliation time. This method, like other methods, has some disadvantages and advantages, but showed that it is a simple, cost-effective and efficient way to produce high quality graphene sheets. Obviously, the reported method can be optimized to produce less graphene layers.

References

- [1] M. Coroş *et al.*, "Simple and cost-effective synthesis of graphene by electrochemical exfoliation of graphite rods," *RSC Adv.*, vol. 6, no. 4, pp. 2651–2661, 2016.
- [2] A. Ambrosi and M. Pumera, "Electrochemically Exfoliated Graphene and Graphene Oxide for Energy Storage and Electrochemistry Applications," *Chem. - A Eur. J.*, vol. 22, no. 1, pp. 153–159, 2016.
- [3] C. T. J. Low, F. C. Walsh, M. H. Chakrabarti, M. A. Hashim, and M. A. Hussain, "Electrochemical approaches to the production of graphene flakes and their potential applications," *Carbon N. Y.*, vol. 54, no. April 2013, pp. 1–11, 2013.
- [4] S. Yang, M. R. Lohe, K. M?llen, and X. Feng, "New-Generation Graphene from Electrochemical Approaches: Production and Applications," *Adv. Mater.*, vol. 28, no. 29, pp. 6213–6221, 2016.
- [5] N. S. Faal, M. M. Saffari, and E. Bazyar, "X-ray Diffraction : A Multifunctional method for Graphene type structure characterization," *Icnl*, no. March, pp. 9–11, 2014.



Calcium measurement using ion selective electrode based on a macromolecule ionophore

Sh. Lovineh^{1,2}, A. Ghaemi^{2*}

¹ Department of Chemistry, Khouzestan Science and Research Branch, Islamic Azad University, Ahvaz, Iran

² Department of Chemistry, Ahvaz Branch, Islamic Azad University, Ahvaz, Iran

arezooghaemi@yahoo.com*

Shaghayegh.louvineh@gmail.com

Abstract: A new PVC based membrane using benzo-18-crown-6 as an ionophore has been developed as a calcium ion selective electrode. The electrode comprises of ionophore (4%), PVC (30%) and plasticizer (63%). The electrode shows a linear dynamic response in the concentration range of 1×10^{-5} M to 1×10^{-1} M with a Nernstian slope of 29.8 mV/decade and a detection limit as 4×10^{-6} M. The proposed sensor shows reasonably good selectivity with respect to alkali, alkaline earth and transition metal ions. It can be used in the pH range 5–12. The proposed electrode also was applied for the direct determination of Ca^{2+} cation in doubly distilled deionized water samples spiked with different concentrations calcium. This electrode was also used for determination of Ca^{2+} in real samples with a very good recovery.

Keywords: Calcium (II) cation, Ion selective electrode, Potentiometry.

1. Introduction:

Ion-selective electrodes (ISEs) possess many advantages over traditional methods of analysis and provide accurate, reproducible, fast, and regular selective determination of various ionic species. In addition, ion-selective electrodes allow non-destructive, on-line monitoring of particular ions in a small volume of sample without any pretreatment. Because of these merits, the use of ISEs is increasing day by day in medicinal, environmental, agricultural, and industrial fields [1,2]. Macrocyclic ligands have been widely used as suitable neutral carriers for the construction of membrane selective electrodes especially for alkali and alkaline earth metal cations [3,4].

In the present study, a novel PVC-membrane sensor based on benzo-18-crown-6 as a neutral carrier for the selective and sensitive determination of Ca (II) cations in aqueous media was developed.

2. Experimental

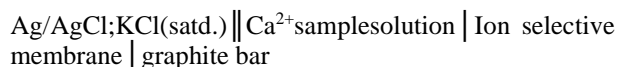
2.1. PVC membrane-coated electrode

The electrodes were prepared from a graphite bars (3mm diameter and 50mm long). The graphite bars were polished and put in a concentrated HNO_3 solution overnight to clean the surface of the graphite bars. Then, the bars were rinsed with THF and once again polished and washed with distilled water and allowed to dry. A mixture of ionophore (benzo-18-crown-6) and PVC, plasticizer (DOP) and carbon powder (for increasing the electrical conduction and mechanical stability of coated

membrane) to give a total mass 300 mg was dissolved in about 5 ml of THF and the solution was mixed well. The graphite bar was coated by dipping it into the membrane solution for a few seconds and allowed to dry overnight. The electrode was conditioned in 0.001 M Calcium nitrate for 24 h, and stored in mild concentration solutions of Calcium nitrate, when not in use. The coating solution was stable for several days and could be used for construction of new membranes.

2.2. Apparatus and potential measurements

All potential measurements were made with a potentiometer having ± 0.01 mv accuracy with an Ag/AgCl reference electrode. All measurements were carried out at 25 °C with a cell type:



The potential readings were made after the potential reached to a constant value. The performance of the electrode was investigated by measuring the potential of Ca^{2+} solutions over the range of 1.0×10^{-8} to 1.0×10^{-1} M. The data were plotted as observed potential vs the logarithm of Ca^{2+} cation concentration.

3. Results and discussion

3.1. Effect of membrane composition on the sensor response and calibration curve

It is well known that some important features of the PVC-based membranes, such as the nature and amount

of the ionophore, the properties of the plasticizer, the plasticizer/ PVC ratio and especially the nature of the additives used, significantly influence the sensitivity and selectivity of the ion selective sensors [5,6]. Thus, different aspects of preparation of membranes based on benzo-18-crown-6 were investigated and the results are given in Table 1.

The best response was observed with the membrane composed of the following ingredients: 30.0 mg PVC, 63.0 mg DOP, 4.0 mg benzo-18-crown-6 and 3.0 mg NaTPB (membrane No. 3). The characteristic properties of this optimized coated membrane were studied and the calibration curve for Ca^{2+} cation is shown in Figure 1. Over the concentration range from 1.0×10^{-5} to 1.0×10^{-1} M of the cation, the electrode potential response was linear with the logarithm of Calcium cation concentration. The slope of the calibration curve was found to be: 29.8 ± 1.2 mV/decade. The limit of detection, as determined from the intersection of the two extrapolated segments of the calibration graph, was 4.0×10^{-6} M.

3.2. Analytical performance

The proposed Ca^{2+} sensor was found to work well under laboratory conditions. This electrode was used to determine the end-point in the potentiometric titration of Ca^{2+} with EDTA solutions. Two typical titration curves are shown in Fig. 2. In this process, 25 ml of 1.0×10^{-2} M and 25 ml of 1.0×10^{-3} M calcium nitrate solutions were titrated with 1.0×10^{-1} M and 1.0×10^{-2} M EDTA solutions, respectively. As can be seen, the end points of titration are sharp and this titration method can determine the amount of calcium ion accurately.

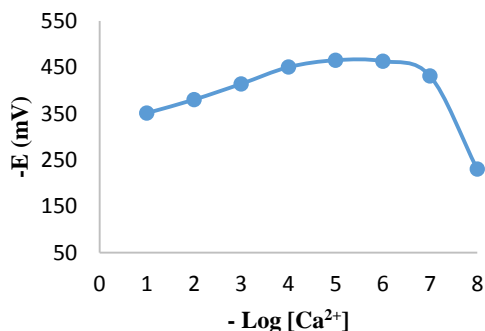


Fig. 1. Calibration curve of the Ca^{2+} selective sensor based on benzo-18-crown-6.

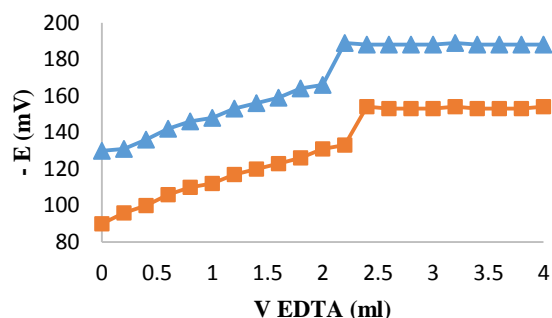


Figure 2. Potentiometric titration curves of 25 ml of Ca^{2+} (\blacksquare 1.0×10^{-2} M and \blacktriangle 1.0×10^{-3} M) with 1.0×10^{-1} M and 1.0×10^{-2} M of EDTA solutions, respectively.

3.3. Effect of pH

The pH dependence of the proposed electrode potential was investigated over the pH range of 1.0–14.0 for 1.0×10^{-3} and 1.0×10^{-2} M of Ca^{2+} ion solutions. The graphical results shown in Fig. 3 indicate that the potential was independent of pH in the range of 5.0–12.0 pH units.

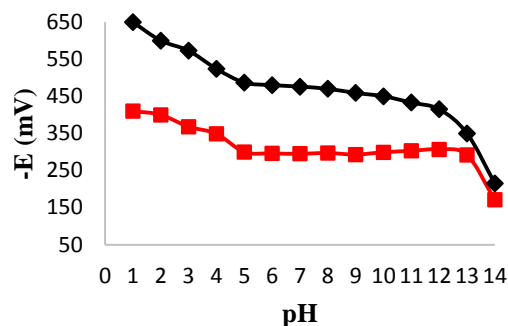


Fig. 3. Effect of pH on potential response of the Ca^{2+} selective sensor using (\blacksquare) 1.0×10^{-2} M and (\blacklozenge) 1.0×10^{-3} M of Ca^{2+} solutions.

Table 1. Optimization of the membrane ingredients.

No.	Composition (wt. %)				Linear range (M)	Slope (mV/decade)
	PVC	Ionophore	NaTPB	Plasticizer		
1	30	6	4	(NB) 60	10^{-8} - 10^{-5}	19.9±1.8
2	30	4	2	(DOP) 64	10^{-6} - 10^{-3}	23.3±0.4
3	30	4	3	(DOP) 63	10^{-5} - 10^{-1}	29.8±1.2
4	30	4	3	(DOS) 63	10^{-7} - 10^{-5}	31.0±1.0
5	30	5	4	(DBP) 61	10^{-8} - 10^{-4}	30.0±1.4

3.4. Determination of Ca²⁺ ion in real samples

The proposed sensor was also successfully applied to the direct determination of calcium (II) in real samples using standard addition method and the results are shown in Table 2. As can be seen, the recoveries of calcium from different water samples are in the range of 85.0-92.0%. Results indicate that the composition of the real samples do not interfere significantly on the detection of Ca²⁺ ions. In fact, the accuracy of calcium recovery in different solution samples is almost quantitative.

Table 2. Potentiometric determination of Ca²⁺ ion in different real samples using the Ca²⁺ selective sensor.

Real water samples	Added Ca ²⁺ concentration (M)	Found Ca ²⁺ concentration (M)	Recovery (%)
Delester	3.0×10^{-4}	2.6×10^{-4}	86.6
Ahvaz water	2.0×10^{-4}	1.7×10^{-4}	85.0
Mango water	5.0×10^{-3}	4.6×10^{-3}	92.0

4. Conclusion

A PVC membrane electrochemical sensor incorporating benzo-18-crown-6 as an ionophore was successfully used to determine calcium(II) cations over a concentration range of 1.0×10^{-5} – 1.0×10^{-1} M. The sensor displayed a Nernstian slope of 29.8±1.2 mV decade⁻¹. The Ca (II) selective membrane sensor can be used for the direct determination of Ca (II) cations in real samples.

References

- [1] M. Mazloum, M. Salavati Niassary, M. K. Amini, Sens. Actuators B 82 (2002) 259.
- [2] M. Shamsipur, M. R. Ganjali, A. Rouhollahi, A. Moghimi, Anal. Chim. Acta 434 (2001) 23.
- [3] E. Bakker, P. Bühlmann, E. Pretsch, Chem. Rev. 97 (1997) 3083.
- [4] V. Alexander, Chem. Rev. 95 (1995) 273.
- [8] M. Shamsipur, M. Yousefi, M. Hosseini, M. R. Ganjali, Anal. Chem. 74 (2002) 5538.
- [5] V. K. Gupta, A. K. Singh, S. Mehtab, B. Gupta, Anal. Chim. Acta, 566 (2006) 5.
- [6] M. R. Ganjali, T. Poursaberi, M. khoobi, A. Shafiee, M. Adibi, M. Pirali-Hamedani, P. Norouzi, Int. J. Electrochem. Sci., 6 (2011) 717.

New Coated Graphite Potentiometric Sensor based on benzo-18-crown-6

Sh. Lovineh^{1,2}, A. Ghaemi^{2*}

¹ Department of Chemistry, Khouzestan Science and Research Branch, Islamic Azad University, Ahvaz, Iran

² Department of Chemistry, Ahvaz Branch, Islamic Azad University, Ahvaz, Iran

arezooghaemi@yahoo.com*

Shaghayegh.louvime@gmail.com

abstract: In this project, a highly selective calcium coated graphite electrode was prepared by benzo-18-crown-6 as an ionophore into plasticized polyvinylchloride (PVC) membrane. The best response characteristic was observed using the membrane composition of dioctyl phthalate (DOP) = 63.0 mg, PVC = 30.0 mg, sodiumtetraphenylborate (NaTPB) = 3.0 mg and benzo-18-crown-6 = 4.0 mg. The electrode has a fast response time of 10 s, with a satisfactory reproducibility and relatively long life time of 28 days without significant drift in potential. This electrode reveals a very good selectivity toward Ca²⁺ ion over a wide range of alkali, transition and heavy metal cations.

Keywords: Calcium (II) cation, Ion selective electrode, Potentiometry.

1. Introduction:

Since the investigations relating to ionophore based ISE in 1970s, increasing number of papers are being published because of the simple operation and good selectivity characteristics. Ca²⁺ sensitive electrodes were among the first commercially available ISEs [1–4]. Electrically neutral lipophilic ligands containing an appropriate number of binding sites of high solvating ability can behave as ionophores for alkali and alkaline earth cations. The macrocyclic polyethers have cavities that can take up alkali and alkaline earth cations [5,6]. Complexation occurs between cation and the ethereal oxygen of the crown ether, and the resulting complexes are highly stable and selective. These lipophilic ethers when incorporated into membranes, behave as ionophore based ion selective electrodes for alkali and alkaline earth cations. Very few studies are available in literature on the old crown ethers that were used as ion selective electrodes. Gahan and co-workers have investigated the interaction of monoazapolyoxacrown ethers with Pb²⁺, Hg, Cd and Zn by potentiometry [7,8].

2. Experiment

2.1. Materials and method:

Potentiometer (Zag chemi co, Iran, Model PTR-79) and glass electrode Ag/AgCl (azar electrode, Iran) were used for potential different and respectively. pH measurements were made with a digital pH meter (Horbia, Japon, Model pH F-11). Hot plate magnetic stirrer (Pars faraso, Iran, Model F-60) and digital scale (Sartorius, Swiss, Model PB210D) was used.

2.2. Electrode preparation

The general procedure for preparation of the PVC membrane was to mix thoroughly 30 mg of powdered PVC, 63 mg of plasticizer DOP, and 3 mg of additive NaTPB in 3

ml of THF. To this mixture was added 4 mg of ionophore benzo-18-crown-6 and the solution was mixed well. The solvent was allowed to evaporate at room temperature. After 24 h, transparent membrane of 10 mm diameter was cut, attached to a pyrex glass tube. The tube was then filled with internal filling solution (1.0×10⁻³ M Ca²⁺). The electrode was finally conditioned for 8 h by soaking in a 1.0×10⁻² M solution of Ca²⁺.

2.4. Apparatus and potential measurements

All potential measurements were made at 25.0 ± 0.1 °C with a digital pH/mV meter model PTR-79 (Zag Chimi, Iran) having ±0.01 mV accuracy with an Ag/AgCl reference electrode. The potential build up across the electrode was measured using the galvanic cell of the following type:

Ag|AgCl; KCl (satd.) Ca²⁺ sample solution ion selective membrane graphite bar.

The performance of each electrode was investigated by measuring the potential of Ca²⁺ solutions with concentrations ranging from 1.0 × 10⁻⁸ to 1.0 × 10⁻¹ M by serial dilution of the 0.1 M stock solution at constant pH. The solutions were stirred and potential readings recorded when a steady state value was attained. The observed potential versus the logarithm of the Ca²⁺ ion concentration was plotted.

3. Results and discussion

3.1. Effect of membrane composition

It is well known that the sensitivity and selectivity obtained for a given ionophore depend significantly on the membrane composition and the nature of solvent mediator and additives used [9]. As is shown in Table 1, the best sensitivity is obtained for membrane number 3 with PVC: DOP: NaTPB: benzo-18-crown-6 weight percent ratio of 30.0: 63.0: 3.0: 4.0 that resulted in the Nernstian behavior

of the sensor over a wide concentration range. The calibration curve for this sensor is shown in (Fig. 1). The emf response of this sensor of varying Ca^{2+} concentration depicts a wide linear range from 1.0×10^{-5} to 1.0×10^{-1} M with a Nernstian slope of 29.8 ± 1.2 mV/decade. The limit of detection, as determined from the intersection of the two extrapolated segments of the calibration graph, is 4.0×10^{-6} M.

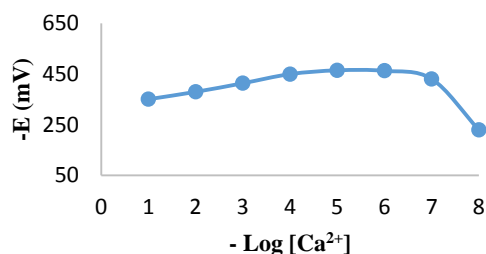


Fig. 1. Calibration curve of the Ca^{2+} selective sensor based on benzo-18-crown-6.

3.2. Response time characteristics of the proposed sensor

The response time is an important factor for ion selective sensors. The static response time of the sensor was studied by plotting the potential response vs. time, at 1.0×10^{-3} M and 1.0×10^{-2} M of Ca^{2+} ion solutions (Fig. 2). As is evident in this figure, in the whole concentration range, the sensor reaches its equilibrium response in a short time (~ 10 s) and potentials stay constant for about ~ 140 s. This is most probably due to the fast exchange kinetics of complexation–decomplexation of Ca^{2+} cation with the ion carrier at the test solution–membrane interface.

Dynamic response time of the sensor has been recorded by changing solutions with different Ca^{2+} concentrations. The measurement sequence was from the lower (1.0×10^{-5} M) to the higher (1.0×10^{-1} M) concentrations and the results are shown in (Fig. 3). As it is seen, the sensor reached the equilibrium response in a very short time of about 15 s. To evaluate the reversibility of the sensor response, similar measurements were carried out in the sequence of high-to-low (1.0×10^{-2} to 1.0×10^{-3} M) sample concentrations. The results indicate that the potentiometric response of the sensor is reversible (Fig. 4). The sensing behavior of the electrode remained unchanged when the potentials were recorded either from low-to-high concentrations or vice versa.

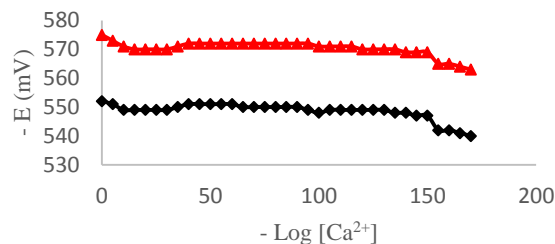


Fig. 2. The response time curves of the Ca^{2+} selective sensor (\blacklozenge 1.0×10^{-2} M, \blacktriangle 1.0×10^{-3} M).

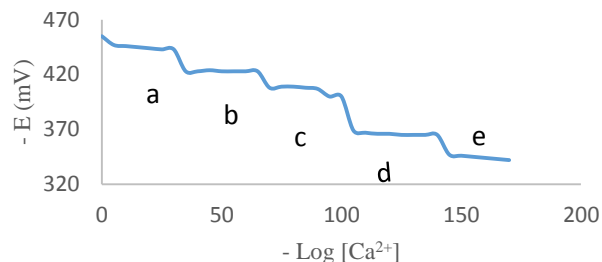


Fig. 3. Dynamic response of the Ca^{2+} selective sensor for step changes in concentration of Ca^{2+} cations: (a) 1.0×10^{-5} M, (b) 1.0×10^{-4} M, (c) 1.0×10^{-3} M, (d) 1.0×10^{-2} M, and (e) 1.0×10^{-1} M.

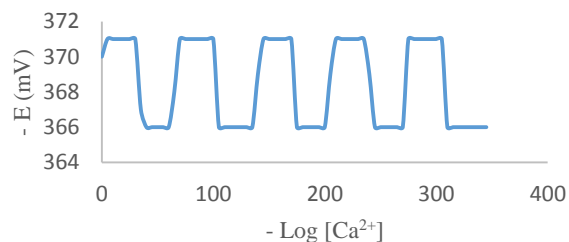


Fig. 4. . Response characteristics of the Ca^{2+} selective sensor for several high-to-low (1.0×10^{-2} to 1.0×10^{-3} M) sample cycles.

3.3. Potentiometric selectivity

The most important characteristic of a sensor is the selectivity, as it reflects its utility for target sample. The potentiometric selectivity coefficients of the proposed coated graphite sensor were determined by the separate solution method (SSM) [10,11], using the respective nitrate salts at 0.01 M concentration according to the following equation:

$$\text{Log} K_{ij}^{\text{pot}} = \frac{(E_j - E_i)Z_i F}{2.303RT} + \left(1 - \frac{Z_i}{Z_j}\right) \text{log} a_i$$

where E_i and E_j are the measured potentials of primary (Ca^{2+}) and interfering ions and z_i and z_j are their respective

Table 1. Optimization of the membrane ingredients.

No.	Composition (wt. %)				Linear range (M)	Slope (mV/decade)
	PVC	Ionophore	NaTPB	Plasticizer		
1	30	6	3	(NB) 62	10^{-5} - 10^{-1}	21.9±1.7
2	30	3	2	(DOP) 65	10^{-8} - 10^{-6}	18.5±1.8
3	30	6	4	(DOP) 60	10^{-8} - 10^{-6}	29.0±2.2
4	30	7	-	(DOP) 63	10^{-4} - 10^{-1}	13.9±0.6
5	30	4	3	(DOP) 63	10^{-5} - 10^{-1}	29.8±1.2

Table 3. General performance characteristics of some Calcium (II) ion selective sensors

Ref. no.	Response time (s)	Linear range (M)	pH range	Slope (mV/decade)	Detection limit (M)
[12]	4	10^{-7} - 10^{-1}	---	28.0	2.0×10^{-8}
[13]	15	10^{-6} - 10^{-1}	8-11	---	---
[14]	30	10^{-5} - 10^{-1}	3-11	28.0±0.2	4.0×10^{-6}
[15]	10	10^{-7} - 10^{-1}	3.5-9	29.5±0.5	---
[This work]	10	10^{-5} - 10^{-1}	5-12	29.8±1.2	4.0×10^{-6}

charges. The K_{Ca_j} pot of mono-, di- and trivalent cations was measured and the results are shown in Table 3. It is obvious from the selectivity coefficient data that alkali, transition and heavy metal cations could not significantly disturb the Ca^{2+} ion selective sensor function. As it is evident from the data in Table 3, most of the selectivity coefficients of interfering ions are low (less than 1.0×10^{-1}) indicating no significant interference in the performance of the sensor (except for Ag^+ and Zn^{2+}) and the sensor can, therefore, be used for Ca^{2+} determination in the presence of several other ions.

Table 2. Selectivity coefficient values observed for Ca^{2+} selective sensor no. 5 for various interfering ions using separate solution method

Interfering ions	Selectivity coefficients (K_{Cd_j} pot)
K^+	$2/4 \times 10^{-5}$
Cd^{2+}	$4/2 \times 10^{-6}$
Sr^{2+}	$1/7 \times 10^{-3}$
Cu^{2+}	$5/1 \times 10^{-5}$
Fe^{3+}	$4/0 \times 10^{-8}$
Zn^{2+}	$1/2 \times 10^{-1}$
La^{3+}	$2/6 \times 10^{-4}$
Ag^+	$8/9 \times 10^{-2}$
Cr^{3+}	$3/4 \times 10^{-3}$

4. Conclusion

The investigations demonstrate the utility of the coated graphite sensor incorporating benzo-18-crown-6 as

electroactive phase in determining Ca^{2+} cation in the concentration range of 1.0×10^{-5} to 1.0×10^{-1} M. This sensor exhibits either comparable or better performance to the existing electrodes, already reported by many researchers for the determination of Ca^{2+} ions, regarding linear concentration range, pH range, response time and detection limit (Table 3). Therefore, the proposed sensor is a good addition to the existing list of the Calcium (II) ion selective sensors reported till date.

References

- [1] M.S. Frant, Analyst 119 (1994) 2293.
- [2] M.S. Frant, J. Chem. Edu. 74 (1997) 159.
- [3] G.J. Moody, J.D.R. Thomas, Ion Selective Electrodes Rev. 1 (1979)3.
- [4] W. Simon, D. Ammann, D. Oebme, M. Morf, Acad. Sci. 52 (1978)307.
- [5] C.J. Pedersen, J. Am. Chem. Soc. 84 (1967) 7017.
- [6] J.J. Christensen, D.J. Eatough, R.M. Izatt, Chem. Rev. 74 (1974) 351.
- [7] K. Byriel, K.R. Dunster, L.R. Gahan, C.H.L. Kennard, J.L. Latten, I.L. Seann, P.A. Duckworth, Inorg. Chim. Acta 205 (1993) 191-198.
- [8] K. Byriel, K.R. Dunster, L.R. Gahan, C.H.L. Kennard, J.L. Latten, I.L. Seann, P.A. Duckworth, Polyhedron 11 (1992) 1205-1212.
- [9] N. Tavakkoli, M. Shamsipur. Anal. Lett. 29 (1996)2269.
- [10] Y. Umezawa, K. Umezawa, H. Sato, Pure Appl. Chem. 67 (1995)507.
- [11] R.P. Buck, E. Lindner, Pure Appl. Chem. 66 (1994) 2527.
- [12] El.Jammal A. Bouklouze A.A. Patriarche G.J..Talanta, 38: 929-935, 1991.
- [13] Yi-long M. Xiao-hong R. Shi-ming Z. Journal of Tongji Medical University, 12: 98-102, 1992
- [14] Kumar A. S.K. Mittal. Sensors and Actuators, B, 99: 340-343., 2004.
- [15] Kumar A. Sameena M. ScienceDirect, Sensors and Actuators B, 123: 429-436.,2007



بیستمین کنفرانس شیمی فیزیک ایران
دانشکده علوم پایه - دانشگاه اراک
۱۳۹۶ مرداد ۲۹-۳۱



20th Iranian Physical Chemistry Conference

Iron (III) selective measurement based on kryptofix 5 as a carrier

N. Boroujerdi^{1,2}, A. Ghaemi^{2*}

¹ Department of Chemistry, Khouzestan Science and Research Branch, Islamic Azad University, Ahvaz, Iran

² Department of Chemistry, Ahvaz Branch, Islamic Azad University, Ahvaz, Iran

arezooghaemi@yahoo.com*

Brj.nadi@gmail.com

Abstract: In this research project, a highly selective iron coated graphite electrode was prepared by kryptofix 5 as a macromolecule ionophore into plasticized polyvinylchloride (PVC) membrane. The best response characteristic was observed using the membrane composition of nitrobenzen (NB) = 65.0 mg, PVC = 30.0 mg, sodium tetraphenylborate (NaTPB) = 2.0 mg and kryptofix 5 = 3.0 mg. The sensor exhibits a Nernstian slope (19.5 ± 0.5 mV/decade) in a linear concentration range of 1.0×10^{-5} to 1.0×10^{-2} M. The detection limit of the electrode is 6.3×10^{-6} M. The electrode has a fast response time of 10 s, with a satisfactory reproducibility and relatively long life time of 5 weeks without significant drift in potential. The electrode operates in the wide pH range of 4-11.

Keywords: Iron (III) cation, Ion selective electrode, Potentiometry.

1. Introduction:

Over the past 40 years, the application of carrier-based ion-selective electrodes (ISEs) has evolved to well-established routine analytical technique [1]. During the last four decades, a number of IESs with polymeric membranes have been reported [2,3]. The development of selective membrane electrodes based on neutral carriers is one of the most promising trends in ionometry [4,5]. Crown ethers have been demonstrated as highly selective complexing agents for many metal ions. They can be applied in separation and determination of metal ions through molecular recognition. Generally, crown ether forms a complex with a metal ion that fits well in its cavity. A number of methods are available today to measure ion-ionophore formation constant. In some cases, a good correlation between selectivity coefficients and the ratio of experimental formation constants obtained in ordinary polar solvents has been observed [6]. However, most ion carriers form very weak complexes in such solvents [7], and most ionophores cannot be characterized with this approach. Therefore, a direct measurement of complex formation constants within the solvent polymeric membrane phase has been shown to yield more meaningful results [8].

2. Experimental

2.1. Electrode preparation

The general procedure for preparation of the PVC membrane was to mix thoroughly 30 mg of powdered PVC, 65 mg of plasticizer NB, and 2 mg of additive NaTPB in 3 ml of THF. To this mixture was added 3 mg of ionophore kryptofix 5 and the solution was mixed well. The graphite bar was coated by dipping it into the membrane solution for a few seconds and allowed to dry overnight. The electrode was conditioned in 0.001 M iron nitrate for 24 h, and stored in mild concentration solutions of iron nitrate, when not in use. The coating solution was stable for several days and could be used for construction of new membranes.

2.2. Emf measurements

All emf measurements were carried out with the following assembly:

$\text{Ag}/\text{AgCl}; \text{KCl}(\text{satd.}) \parallel \text{Fe}^{3+} \text{ samplesolution} \mid \text{Ion selective membrane} \mid \text{graphite bar}$

The potentiometric measurements were performed with a Metrohm pH meter E516 at $25.0 \pm 0.18^\circ\text{C}$. Activities were calculated according to the Debye-Huckel procedure.

Table 1. Optimization of the membrane ingredients.

No.	Composition (wt. %)				Linear range (M)	Slope (mV/decade)
	PVC	Ionophore	NaTPB	Plasticizer		
1	30	3	2	(NB) 65	10^{-5} - 10^{-2}	19.5 ± 0.5
2	30	4	3	(NB) 63	10^{-5} - 10^{-2}	18.2 ± 2.2
3	30	5	4	(DOP) 61	10^{-6} - 10^{-1}	23.7 ± 2.7
4	30	4	3	(DOP) 63	10^{-8} - 10^{-5}	25.8 ± 1.0
5	30	4	4	(DOS) 62	10^{-8} - 10^{-4}	15.0 ± 0.7
6	30	5	5	(DBP) 60	10^{-8} - 10^{-6}	21.0 ± 2.1

3. Results and discussion

3.1. Effect of membrane composition

It is well known that the sensitivity and selectivity obtained for a given ionophore depend significantly on the membrane composition and the nature of solvent mediator and additives used [9]. Thus, the influences of the membrane composition, nature, and amount of plasticizer and NaTPB as a lipophilic additive on the potential response of the Fe(III) sensor were investigated and the results are summarized in Table 1. It is seen that, the use of 65% (w/w) NB in the presence of 30% (w/w) PVC, 3% (w/w) ionophore, and 2% (w/w) NaTPB (No. 1, Table 1) resulted in the best sensitivity, with a Nernstian slope of 19.5 ± 0.5 mV per decade over a wide dynamic range.

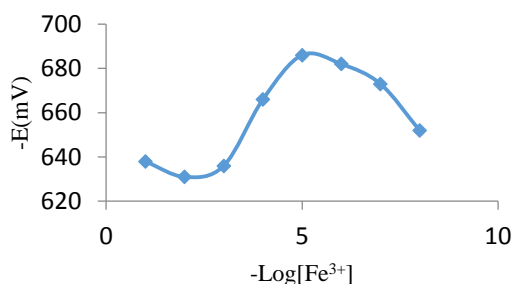


Fig. 1. Calibration curve of the Fe³⁺ selective sensor based on kryptofix 5.

3.2. pH effect on potential response

The influence of pH on the potential response of the optimized sensor was tested over a pH range of 1.0-14.0 (concentrated NaOH or HNO₃ solutions were employed for the pH adjustment) and the result is shown in Fig. 2. As it is seen, the pH effect of the test solutions (1.0×10^{-3} M and 1.0×10^{-4} M) on the potential response of the iron sensor was found to remain constant in the pH range of

4.0-11.0. The observed drift at higher pH values could be due to the formation of some hydroxyl complexes of Fe (III) in the solution. At the lower pH values, the potentials decreased. This is due to the existence of nitrogen donor atoms in the structure of the ionophore which can be easily protonated, indicating that the sensor responds to hydrogen ions.

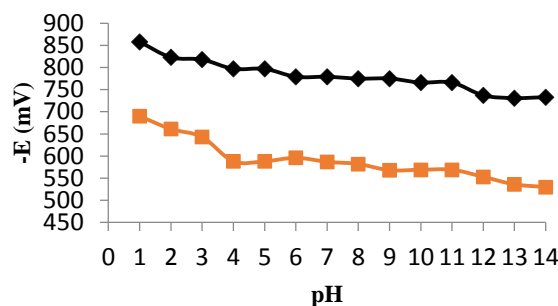


Fig. 2. Effect of pH on potential response of the Fe³⁺ selective sensor using (■) 1.0×10^{-3} M and (◆) 1.0×10^{-4} M of Fe³⁺ solutions.

3.3. Static and dynamic response time

For analytical purposes, response time is one of the most important factors that are taken into account. Therefore, the static response time of the proposed sensor (membrane no. 1) was studied by plotting the potential response vs. time, at 1.0×10^{-4} M and 1.0×10^{-3} M of Fe³⁺ ion solutions (Fig. 3). As is evident in this figure, in the whole concentration range, the sensor reaches its equilibrium response in a short time (~ 10 s) and no change is observed in 140 second.

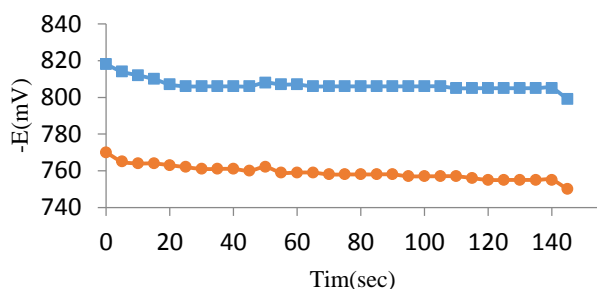


Fig. 3. Static response time curves of the Fe^{3+} selective sensor (\bullet 1.0×10^{-3} M, \blacksquare 1.0×10^{-4} M).

For any ion selective sensor, dynamic response time is an important factor. In this study, the practical response time of the proposed sensor was recorded by changing the Fe^{3+} concentration in solution in a concentration range of 1.0×10^{-5} to 1.0×10^{-2} M and the results are shown in Fig. 4. From this figure, it can be derived that the electrode reaches its equilibrium response rapidly (10 s), in the whole concentration range. This is most probably due to the fast exchange kinetics of the complexation-decomplexation of Fe^{3+} ions with the ionophore at the test solution-membrane interface.

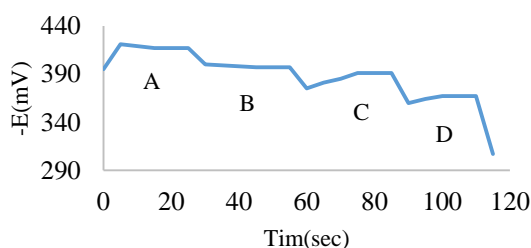


Fig. 4. Dynamic response time of the Fe^{3+} selective sensor for step changes in the concentration of Fe^{3+} : (A) 1.0×10^{-5} M, (B) 1.0×10^{-4} M, (C) 1.0×10^{-3} M, (D) 1.0×10^{-2} M.

4. Conclusion

Kryptofix 5 can be used as an excellent supramolecule ion carrier for construction of a PVC-based coated graphite ion selective sensor for determination of iron ions.

References

- [1] P. Buhlmann, E. Pretsch, E. Bakker. *Chem. Rev.* 98 (1998) 1593.
- [2] R. K. Mahajan, M. Kumar, V. Sharma, I. Kaur. *Analyst* 126 (2001) 505.
- [3] S. K. Srivastva, V. K. Gupta, S. Jain. *Anal. Chem.* 68 (1996) 1272.

[4] D. Diamond. *J. Incl. Phenom. Macrocycl. Chem.* 19 (1994) 149.

[5] D. M. Petrukhin, E. N. Avdeeva, A. F. Zhukov, I. B. Polosuchina, S. A. Krylova, S. L. Rogatinskaya, G. V. Bodvin, N. P. Nesterova, Y. M. Polikarpov, M. I. Kabachnik. *Analyst* 116 (1991) 715.

[6] H. R. Wuhrmann, W. E. Morf, W. Simon. *Helv. Chim. Acta* 56 (1973) 1011.

[7] R. Bliggendorfer, G. W. Suter, W. Simon. *Helv. Chim. Acta* 72 (1989) 1164.

[8] Y. Ma, R. Yuan, Y. Chai, X. Liu, *Mater. Sci. Eng. C* 30 (2010) 209.

[9] H. A. Zamani, M. Rohani, A. Zangeneh-Asadabadi, M. S. Zabihi, M. R. Ganjali, M. Salavati-Niasari, *Mater. Sci. Eng. C* 30 (2010) 917.



بیستمین کنفرانس شیمی فیزیک ایران
دانشکده علوم پایه - دانشگاه اراک
۳۱-۲۹ مرداد ۱۳۹۶



20th Iranian Physical Chemistry Conference

بیو شیمی فیزیک

Bio-Physical Chemistry

Preparation and characterization of drug-loaded poly(methyl methacrylate) nanoparticles by a microemulsion method

Azar Kajbafvala^a, Alireza Salabat^{a,b*}

^a Department of Chemistry, Faculty of Science, Arak University, 38156-8-8349, Arak, Iran

^b Institute of Nanosciences & Nanotechnology, Arak University, 38156-8-8349, Arak, Iran

*Corresponding Author: a-salabat@araku.ac.ir

Abstract: This work was aimed to synthesis and characterization of drug-loaded poly(methyl methacrylate) (PMMA) nanoparticles by use of a simple microemulsion method. The PMMA nanoparticles were characterized by Fourier Transform Infrared Spectroscopy (FTIR), Dynamic Light Scattering (DLS) and Transmission Electron Microscopy (TEM) analysis. The zeta potential of the QU-loaded PMMA latex also was measured by the Zetasizer. The particles had the size of below 10 nm and were spherical with narrow size distribution with PDI value of 0.36. The zeta potential was obtained about -20 mV that was confirmed good stability of the system. Consequently, this route was very useful for pharmaceutical carriers in drug delivery aims.

Keywords: *Poly(methyl methacrylate); Nanoparticle; Microemulsion*

Introduction

Polymeric nanoparticles are introduced as novel drug delivery vehicles for poor water soluble drugs. These types of nanoparticles have gained top attention because of their small particle size, enlarged surface/volume ratio and increased number of molecules or atoms on their surfaces [1]. These properties have made them very satisfactory in different fields such as semiconductors, catalysts, drug delivery aims and so on. PMMA is a biocompatible and non-toxic polymer which can be used as a suitable carrier for delivery of various classes of drugs such as anti-oxidants [2]. Various methods have been reported for synthesis of polymer nanoparticles. Microemulsion polymerization is of the simplest and common techniques for preparation of polymer nanoparticles [3].

Materials and method

Quercetin hydrate was purchased from Sigma-Aldrich Co., USA. Methyl methacrylate, Tween 80, ammonium persulfate (APS), ethanol (99%) and methanol were prepared from Merck Co.

Preparation of quercetin-loaded PMMA nanoparticles

In order to prepare QU encapsulated PMMA nanoparticles a microemulsion polymerization method has been used. In this procedure a required amount of tween 80 as surfactant was mixed with distilled water in a glass reactor equipped with a magnetic stirrer, a thermometer and a reflux condenser. After completely mixing, weighted quantity of initiator (APS) was added to the system. When the temperature was reached 80°C, quantified QU dissolved in monomer (MMA) was ceaselessly added in small droplets.

Characterization

Fourier transform infrared spectroscopy

The compositions of the synthesized pure polymer as well as investigation of the drug-excipient possible interactions were analyzed using FTIR (Galaxy series 5000, Unicam Co.).

Dynamic light scattering

The mean size of particles and polydispersity index (PDI) of the drug-loaded polymer latex has been carried out DLS technique (Malvern Zetasizer Nano-ZS, UK). The mean diameter of diluted latex was measured at room temperature with scattering angle of 90°.

Transmission electron microscopy

Morphology and size of the QU-loaded PMMA nanoparticles was determined using transmission electron microscopy instrument (TEM, EM10C, Zeiss, Germany).

Results and Discussion

Mechanism of QU encapsulation in PMMA nanoparticles

In O/W microemulsion polymerization, many of the surfactant molecules are aggregated toward each other to form micelles. After initiating drop addition of QU dissolved in monomer into the surfactant aqueous solution, these molecules will be entrapped by tail groups of surfactants molecules, because of the hydrophobic nature of QU and MMA. By continuing supplementation of monomer including drug to the

reaction mixture, they will be captured in core of micelles. This protocol could cause that most of the monomer and drug molecules snared in micelles [4]. By adding initiator, micellar nucleation was initiated. Continuous addition of drug in monomer units in this stage could cause growth of polymer chain. Schematic representation of the above steps is given in Fig. 1.

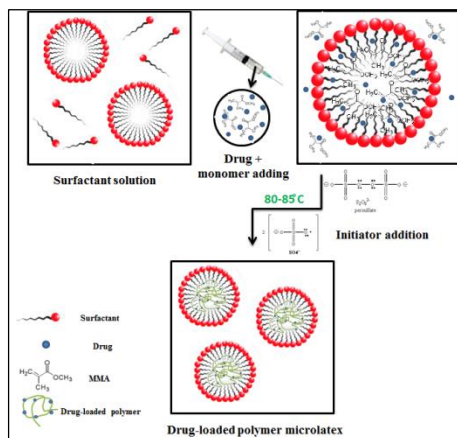


Fig. 1: Fig. 1. Schematic representation of the mechanism of microemulsion polymerization.

Characterization

FT-IR analysis

Fig. 2(a) shows the distinctive peaks of pure QU as aromatic bending and stretching at 1095-1614 cm^{-1} , -OH phenolic bending at 1213-1429 cm^{-1} , C=O stretching at 1655 cm^{-1} and broad phenolic -OH around 3300 cm^{-1} [6].

The FTIR spectrum of the prepared pure PMMA nanoparticles in Fig. 2(b) represents its major characteristic peaks as stretching of -CH₃ group at 2953 and 2876 cm^{-1} , bending of -CH₃ at 1388 cm^{-1} , a sharp peak for stretching of -C=O at 1732 cm^{-1} and stretching peak for -C-O at 1149 cm^{-1} . Based on the obtained spectrum data, it was verified that the synthesized product is pure PMMA nanoparticles. As can be seen from Fig. 2(c), FTIR spectrum of QU-loaded PMMA nanoparticles, the basic peaks of QU and PMMA were observed at their positions corresponds to their neat materials. This evidence indicated absence of chemical interactions between QU and PMMA nanoparticles.

DLS and TEM results

Fig. 3(a) represents size distribution by intensity diagram for the optimized formulation (F3) of QU-loaded PMMA nanoparticles obtained by dynamic light scattering. As can be seen, the mean hydrodynamic size of nanoparticles was obtained about 6.5 nm and PDI value measured as 0.36. The PDI value for polymer nanoparticles indicates good uniformity in the particle size.

In Fig. 3(b), the zeta potential curve for the optimized formulation (F3) of QU-loaded PMMA nanoparticles has been shown. This diagram exhibit mobility distribution of nanoparticles. The zeta potential value was obtained as -21.9 mV.

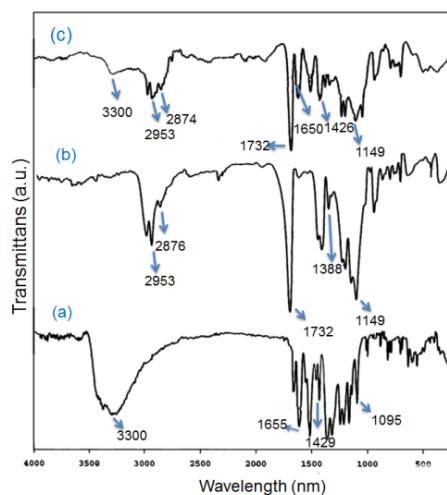


Fig. 2. FT-IR spectra of QU (a), pure PMMA (b) and QU-loaded PMMA (c) nanoparticles.

A microscopic image of electron transmission of QU-loaded PMMA nanoparticles are shown in Fig. 4. An average diameter of about 8 nm was obtained for the nanoparticles which were calculated by image analyzer, which was in agreement with DLS results. The obtained uniform spherical shape for polymeric latex. The TEM result also indicates that polymer nanoparticles do not aggregate and have good monodispersity with uniform particle size.

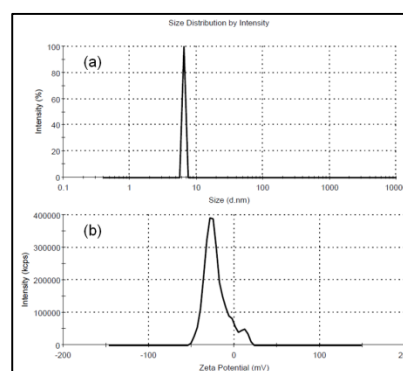


Fig. 3. (a) Dynamic light scattering and (b) zeta potential curve for the QU-loaded PMMA nanoparticles.

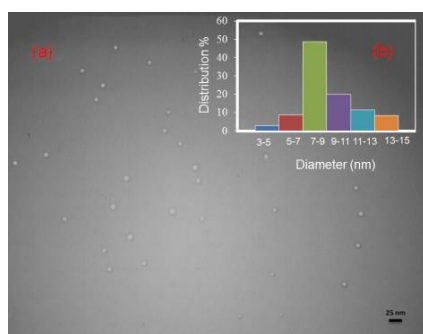


Fig. 4. (a) TEM image of QU-loaded PMMA nanoparticles, (b) histogram of the particle size distribution.

Conclusions

In this study, we have synthesized very small QU-loaded PMMA nanoparticles via microemulsion polymerization without the need of co-surfactant. FT-IR analysis was represented basic peaks of QU and PMMA and confirmed that QU and PMMA interactions had physical nature. The size, morphology, homogeneity and stability of the prepared nanoparticles were determined by DLS and TEM which confirmed that they were spherical nanoparticles with very low particle size and good stability.

Acknowledgment

The financial support from Arak University Research Council is gratefully acknowledged (grant no. 93-14365).

References

- [1] S. Kumar, D. Kumar, N. Dilbaghi N "Preparation, characterization, and bio-efficacy evaluation of controlled release carbendazim-loaded polymeric nanoparticles", *Environ Sci Pollut Res*, 24 (2017) 926-937.
- [2] A. Bettencourt, A.J. Almeida "Poly (methyl methacrylate) particulate carriers in drug delivery", *J Microencapsul*, 29 (2012) 353-367.
- [3] A. Kajbafvala, A. Salabat, A. Salimi A "Formulation, characterization and in-vitro/ex-vivo evaluation of quercetin-loaded microemulsion for topical application", *Pharm Dev Technol*, (2016) 1-30.
- [4] H. Wang, Q. Pan, G.L. Rempel "Micellar nucleation differential microemulsion polymerization", *Eur Polym J*, 47 (2011) 973-980.



Energetics of Ion Permeation Process through Mechanosensitive Channels of Large Conductance by Adaptive Biasing Force Method

Vahid Fadaei Naeini^{a*}, Majid Baniassadi^a, Masumeh Foroutan^b

^a School of Mechanical Engineering, College of Engineering, University of Tehran, Tehran, Iran

^b Department of Physical Chemistry, School of Chemistry, College of Science, University of Tehran, Tehran, Iran

*v.fadaei.n@ut.ac.ir

Abstract: In this study, the permeation process of oppositely charged ions through mechanosensitive channels of large conductance is investigated using the steered molecular dynamics (SMD) simulation along with adaptive biasing force technique. Since some of the mentioned amino acids exist in the interior pore of the other membrane proteins, studying the mechanism of interaction of these basic components with different substrates and their role in the gating process of the utmost importance. The barriers of energy and their location required for the ion to permeate through the different sidechains of the channel are studied by the potential of mean force. Furthermore, it was demonstrated that the selective function of Val21 sidechain on oppositely charged ions arises from the completely different electrostatic interaction of the sidechain with the ions.

Keywords: Ion Permeation; Membrane Protein; Adaptive Biasing Force; Molecular Dynamics Simulation

Introduction

Transport of ions, water molecules and the other substrates to the outside or inside of the cell through the membrane is considered as one of the processes that the proper functioning of the cells depends on it entirely. Permeation of the ions through the transmembrane proteins is a method for ion transport across the membrane. Mechanosensitive (MS) channels are pervasive membrane proteins in prokaryotic and eukaryotic cell membranes. The gating function in MS channels causes some conformational changes to reach the open and closed states in response to mechanical stimuli such as tension, shear, and pressure.

It is worth noting that the water and ion permeation into the cell adjust the cell volume and play an essential role in cell migration mechanism (1). Molecular dynamics (MD) simulation as a numerical method to analyze the gating process and obtain a more comprehensive view about the role of the structural components of these channels during the gating process. Beckstein *et al.* performed a numerical study about the energy barriers for permeation in nanopores using the potential of mean force ions and drew a comparison between MD simulation results and continuum-electrostatic calculations (2). Molecular dynamics simulation was used to determine the different molecular structures of the MscL during the gating process (3). MD simulations of Mycobacterium Tuberculosis of Bacterial MscL (Tb-MscL) embedded in a bilayer membrane and of its helical bundle alone in the solvent were performed (4). The gating function of MS channels is also investigated in the presence of membrane and it was found that the flattening of the transmembrane helices leads to a significant increase

in pore radius (5). Moreover, the crucial role of water molecules as a facilitating agent in ion permeation is investigated and the effective structural elements of the protein on gating process were identified. The threshold value of the force that makes the channel to open and causes a significant change in the channel diameter and conductance was evaluated by MD simulations (6, 7). Similar to this study, Gullingsrud *et al.* assessed the effects of membrane lateral tension on the channel opening state (8). Ollila *et al.* calculated three-dimensional pressure fields for nanoscale systems and found the distinction in pressure profiles for curved and planar membranes (9). They denoted that the membrane protein can tune the tension and elastic properties of the bilayer. Vanegas *et al.* have presented a comprehensive research about the effects of the membrane lateral tension on applied force to the channel and identified some interactions with a crucial role in force transduction between membrane and protein (10). Bavi *et al.* amphiphate N-terminus end of the transmembrane helices accomplish a fundamental task in the gating function of the protein (11).

According to the preceding studies, it seems that the energetics of the ion permeation through each region of the channel require a further study that will be addressed in the present work. In SMD simulation, a vertical bias force is applied to the potassium and chloride ions separately to pull them through the interior pore of the channel. Finally, the energetic parameters are calculated using adaptive biasing force method.

Methods

In this section, further details about the system specifications, equilibrium and non-equilibrium



simulations are provided. Modeling process was initiated using the crystal structure of Tb-MscL (PDB entry 1MSL) (12). A patch of Palmitoyl-oleoyl-phosphoethanolamine membrane with the size of $(126 \times 126) \text{ \AA}^2$ was built and used as the natural environment. The protein was embedded into the membrane patch and aligned with the membrane properly. A water box with the specified size of $(117 \times 117 \times 153) \text{ \AA}^3$ in x, y and z directions respectively, was built to solvate the system. A specific ion concentration of 0.2 M KCl was created. Finally, the simulation system contained ~ 156000 atoms, including 35029 water molecules. All simulations were carried out using the parallel molecular dynamics program NAMD (13) with a non-bonded cutoff of 12 \AA . The MD simulation procedure was performed in four steps sequentially. It is noteworthy that a CHARMM22 parameter file for proteins (14,15) with NBFIX modification was used as the main force field of the system. Periodic cell dimensions was set up to $(120 \times 120 \times 156) \text{ \AA}^3$ in x, y and z directions respectively. Particle mesh Ewald (PME) method was hired for the full long-range electrostatics interactions (16). Bonds to all hydrogen atoms were supposed to be rigid using the SHAKE algorithm (17). Langevin thermostat was used to set temperature of the system on the constant amount of 310 K. Moreover, pressure of the system was controlled in a constant level of 1 atm using the Langevin piston (18). The potassium and chloride ions was pulled with spring constant $k=1 \text{ kcal/mol.\AA}^2$. Potential of mean force (PMF) for ion permeation was obtained by adaptive bias force technique with the window size of the 5 (\AA). About 6 ns of force biased simulation was done on the system. There are three side chains that operate as filters and possibly have stronger molecular interaction with the ions, including the non-polar sidechain Val21, the acidic sidechain Glu104, and the Thr115 sidechain are detectable. The main tight gate of the channel in the undeformed structure of the protein corresponds to the Glu104.

Results and Discussion

In this section, the ion permeation process is investigated with an energetic standpoint. The root mean square of deviation (RMSD) for backbone of the protein without hydrogens is displayed in Fig. 1.

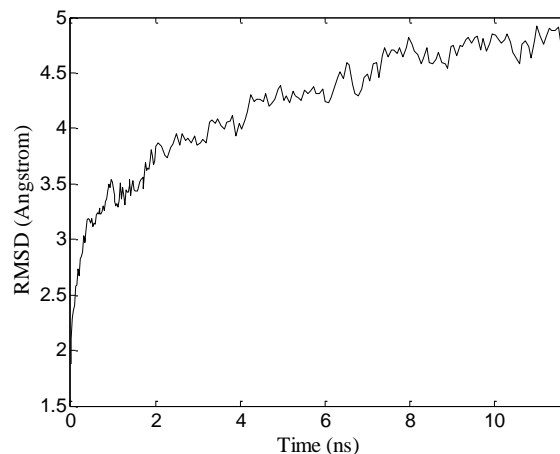
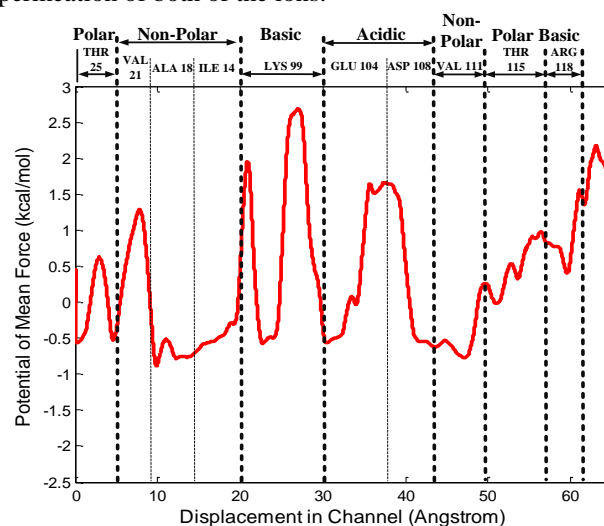
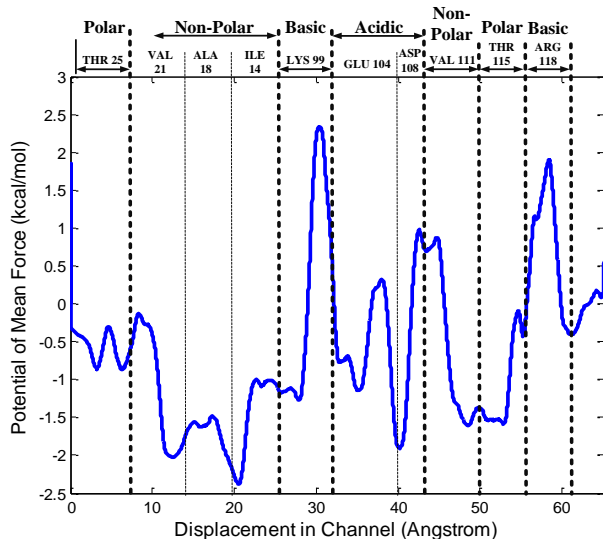


Fig. 1: RMSD for backbone of the protein

It can be deduced from Fig. 1 that the protein structure was equilibrated after 10 ns. Ion permeation can also be characterized by changes in the free energy of the substrate on a pathway which is known as the potential of mean force (PMF). Fig. 2 illustrates the PMF during permeation of both of the ions.



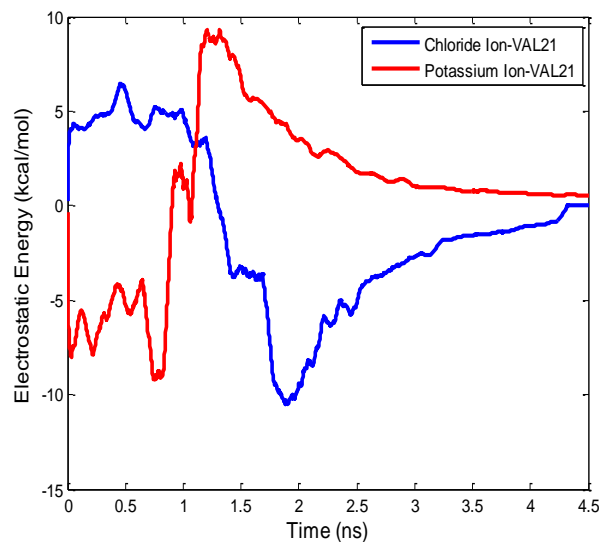
(a)



(b)

Fig. 2: Potential of mean force as a function of the ion displacement in channel for (a). Potassium, (b) Chloride Ion

As this study focuses on Val21 and Glu104 sidechains, for the sake of brevity the energy barrier in these regions are investigated. In Fig. 2, the energy barriers for permeation through each sidechain of the interior pore in the MscL are indicated and both types of the ions situate in local minima after permeating through Val21 sidechain. However, the potassium ion has a greater amount of the energy barrier for breaching Val21 sidechain. The energy barrier for chloride ion permeation through the acidic sidechain of Glu104 is also smaller than the barrier for potassium ion. The electrostatic interaction energies between the ions and Val21 were obtained in order to investigate the selective function of Val21 filter when interacting with different ions. Fig. 3 shows the different trend for electrostatic interaction energies during permeation of oppositely charged ions.



(b)

Fig. 3: Electrostatic interaction energies for ion-Val21 interaction

Conclusions

The acquired results of this study, represents the role of effective factors on permeation of ions through a mechanosensitive channel of large conductance. Despite the higher energy barrier for permeation of positive charged ion from non-polar sidechain Val21, the ion with negative electric charge permeate through the sidechain with a larger repulsive acceleration. The selective function of the non-polar sidechain Val21 is investigated and it was shown that VAL21 sidechain behaves differently with oppositely charged ions.

References

- [1]. Beckstein, O., K. Tai, and M.S.P. Sansom. 2004. Not ions alone: Barriers to ion permeation in nanopores and channels. *J. Am. Chem. Soc.* 126: 14694–14695.
- [2]. Sukharev, S., S.R. Durell, and H.R. Guy. 2001. Structural Models of the MscL Gating Mechanism. *Biophys. J.* 81: 917–936.
- [3]. Elmore, D.E., and D.A. Dougherty. 2001. MD Simulations of Wild-Type and Mutant Forms of the Mycobacterium tuberculosis MscL Channel. *Biophys. J.* 81: 1345–1359.
- [4]. Gullingsrud, J., D. Kosztin, and K. Schulten. 2001. Structural Determinants of MscL Gating Studied by MD Simulations. *Biophys. J.* 80: 2074–2081.
- [5]. Colombo, G., S.J. Marrink, and A.E. Mark. 2003. Simulation of MscL Gating in a Bilayer under Stress. *Biophys. J.* 84: 2331–2337.
- [6]. Bilston, L.E., and K. Mylvaganam. 2002. Molecular simulations of the large conductance mechanosensitive (MscL) channel under mechanical loading. *FEBS Lett.* 512: 185–190.
- [7]. Gullingsrud, J., and K. Schulten. 2003. Gating of MscL Studied by SMD. *Biophys. J.* 85: 2087–2099.



- [8]. Jeon, J., and G.A. Voth. 2008. Gating of the MS Channel Protein MscL: The Interplay of Membrane and Protein. *Biophys. J.* 94: 3497–3511.
- [9]. Ollila, O.H.S., H.J. Risselada, M. Louhivuori, E. Lindahl, I. Vattulainen, and S.J. Marrink. 2009. 3D Pressure field in lipid membranes and membrane-protein complexes. *Phys. Rev. Lett.* 102: 78101.
- [10]. Vanegas, J.M., and M. Arroyo. 2014. Force transduction and lipid binding in MscL: A continuum-molecular approach. *PLoS One.* 9: e113947.
- [11]. Bavi, N., D.M. Cortes, C.D. Cox, P.R. Rohde, W. Liu, J.W. Deitmer, O. Bavi, P. Strop, A.P. Hill, D. Rees, B. Corry, E. Perozo, and B. Martinac. 2016. The role of MscL amphipathic N terminus indicates a blueprint for bilayer-mediated gating of mechanosensitive channels. *Nat. Commun.* 7: 11984.
- [12]. Chang, Geoffrey, et al. "Structure of the MscL homolog from *Mycobacterium tuberculosis*: a gated MS ion channel." *Science* 282.5397 (1998): 2220-2226.
- [13]. Phillips, J.C., R. Braun, W. Wang, J. Gumbart, E. Tajkhorshid, E. Villa, C. Chipot, R.D. Skeel, L. Kalé, and K. Schulten. 2005. Scalable MD with NAMD. *J. Comput. Chem.* 26: 1781–1802.
- [14]. Mackerell, A.D., D. Bashford, M. Bellott, R.L. Dunbrack, J.D. Evanseck, M.J. Field, S. Fischer, J. Gao, H. Guo, S. Ha, L. Kuchnir, K. Kuczera, F.T.K. Lau, C. Mattos, S. Michnick, T. Ngo, D.T. Nguyen, B. Prodhom, W.E. Reiher, B. Roux, M. Schlenkrich, J.C. Smith, R. Stote, J. Straub, M. Watanabe, J. Wio, D. Yin, and M. Karplus. 1998. All-Atom Empirical Potential for Molecular Modeling and Dynamics Studies of Proteins. *J. Phys. Chem.* 5647: 3586–3616.
- [15]. Mackerell, AD and Bashford, D and Bellott, M and Dunbrack, RL and Field, MJ and Fischer, S and Gao, J and Guo, H and Ha, S and Joseph, D. and others, and D. others Mackerell, AD and Bashford, D and Bellott, M and Dunbrack, RL and Field, MJ and Fischer, S and Gao, J and Guo, H and Ha, S and Joseph. 1992. Self-consistent parameterization of biomolecules for molecular modeling and condensed phase simulations. In: *Faseb Journal. FEDERATION AMER. SOC. EXP. BIOL.* 9650 ROCKVILLE PIKE, BETHESDA, MD 20814-3998. pp. A143----A143.
- [16]. Darden, T., D. York, and L. Pedersen. 1993. Particle mesh Ewald: An $N \cdot \log(N)$ method for Ewald sums in large systems. *J. Chem. Phys.* 98: 10089–10092.
- [17]. Ryckaert, J.P., G. Ciccotti, and H.J.C. Berendsen. 1977. Numerical Integration of the Cartesian Equations of Motion of a System with Constraints: MD of Alkanes. *J. Comput. Phys.* 23: 327–341.
- [18]. Feller, S.E., Y. Zhang, R.W. Pastor, and B.R. Brooks. 1995. Constant pressure molecular dynamics simulation: The Langevin piston method. *J. Chem. Phys.* 103: 4613–4621.

Atomic determinants for inducing β conformation in protein structure

B. Shokri^{*a}, K. Khalifeh^b, M. Vahedpour^a & E. Heshmati^b.

^aDepartment of Chemistry, Faculty of Science, University of Zanjan, Zanjan, 4537138791, Iran

^bDepartment of Biology, Faculty of Science, University of Zanjan, Zanjan, 4537138791, Iran

* heshmati@znu.ac.ir

Abstract

Statistical analysis on existing structural files of proteins indicates that 400 possible dipeptides are differently distributed in defined structural classes of proteins. We took 12 favorable dipeptides for beta conformation along with 12 dipeptides that are not significantly found in this conformation. The structures were geometrically optimized at DFT level (B3LYP 6-311++g**) and their physico chemical properties including bond lengths, bond angles, torsion angles and charge distribution on specific atoms were calculated by Gaussian 09 program. For mimicking the beta sheet secondary structure, in our peptide model; the ϕ and ψ torsion angles were constraint to β conformation. The output of the computational study was statistically compared using T-test analysis and it was found that the bond lengths of N-H and $C_{\alpha 1}-C_1$ are significantly different in two datasets. It was also revealed that bond angles including $C1-N1-H2$ and $H2-N2-C\alpha 2$ are different in two groups. However, there was no significant difference in specifying torsion angles for the planarity of peptide plane.

Concerning the importance of N-H group in forming the hydrogen bonds as well as dipole-dipole interaction in protein folding; it may be concluded that the peptide plane dictates its structural roles *via* its N-H moiety.

Keywords: Protein; Dipeptide; Conformation; DFT; Gaussian.

Introduction

Different aspects of life is directly depends on the concert function of different proteins. On the other hand correct function of individual proteins is due to its unique tertiary structure [1]. It is generally accepted that all information for a protein to take its ultimate functional structure is hidden in its amino acid sequence [2]. Therefore, elucidating the sequence-structure relationship or folding problem is one of the classical challenges in biophysics and structural biology that is currently an open problem. In these regard, the majority of investigations have been performed by considering the single amino acids as building blocks of proteins. While, it is possible to consider a polypeptide chain as a string of peptide planes which act as linkers of two adjacent amino acids. This assumption is confirmed by observing different pattern of distribution of dipeptides in different protein structural classes. According to previous statistical analysis on defined protein structural classes [3] followed by determination of the conformational distribution of the first and second positions of representative dipeptides in the context of secondary structural elements [4] it was concluded that dipeptides are differently distributed along the

sequence proteins. In order to find appropriate explanation for observing unbiased distribution of some dipeptides, here we prepared two different datasets of dipeptides including preferred and avoidable dipeptides for β conformation, respectively and performed chemical quantum computations.

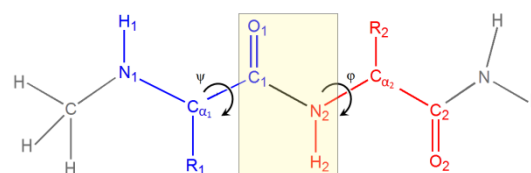


Figure 1. Schematic drawing of a dipeptide which demonstrates two constituent's residues (blue and red color fonts) and a peptide plane between them as well as main torsion angles, ψ and ϕ . For computational purposes, N- and C- termini are capped by CH_3 and NH_2 , respectively.

Materials and method

Dipeptides structure

According to our previous study, the neighbor effect is highly correlated to the local conformation of constructing residues. Based on the quantitative values obtained for the first and second positions of individual dipeptides for beta-beta conformation, we selected 12



high score structures as favorable bete-bete conformation including Pro-Lys, Pro-Gly, Pro-Cys, Asn-Thr, Asn-Cys, Lys-Asn, Gly-Thr, Gly-Asn, Asp-Val, Asp-Phe, Asp-Glu and Cys-Asp. These structures were compared with 12 low score structures (bete-bete conformation avoidant) including Phe-Glu, Phe-Phe, Phe-Thr, Ile-Glu, Ile-Phe, Ile-Met, Ile-Gln, Leu-Phe, Met-Ile, Val-Ser, Val-Trp and Tyr-Arg. In these structures, all geometrical parameters were allowed to change except torsion angles in which they were constrained to accept the values for bete-beta conformation.

Computational method

The dipeptide structures were firstly optimized using DFT level (B3LYP, Becke's three parameter hybrid functional using Lee-Yang-Parr correlation function) with the basis set 6-311++g(d,p). After optimization, frequency calculation was performed and NBO keyword was used to calculate charge distribution.

All calculations were performed by Gaussian 09 program and water solvent effects were included using CPCM model.

Statistical Analysis

Upon calculation of the sample means and respective standard deviations, the pairwise comparisons between means of two groups were performed using a two tailed T-test with degrees of freedom equal to 22. The difference between two subsets of data is considered statistically significant if the t-test gives a significance level P (P value) less than 0.1.

Results and Discussion

It have been reported that side chains (-R groups) as well as ϕ and ψ torsion angles in both sides of peptide plane have prominent effects on its properties. In order to investigate the effect of side chains on the peptide bond features, in peptide model (Fig. 1); we constrained the ϕ and ψ torsion angles to β conformation and more importantly dipeptides which tend to gain β conformation were used. As can be seen in peptide model of Fig. 1, we used four main parameters for the comparison of preferred and avoided groups: bond lengths that are directly or indirectly involved in the peptide bond (C_1-O_1 , C_1-N_2 and N_2-H_2 accompanied by $C_{\alpha 1}-C_1$ and $N_2-C_{\alpha 2}$), bond angles ($C_1C_{\alpha 1}O_1$, $C_{\alpha 1}-C_1-N_2$, $C_1-N_2-H_2$, $H_2-N_2-C_{\alpha 2}$, C_1-

$N_2-C_{\alpha 2}$), torsion angles ($C_{\alpha 1}-C_1-N_2-C_{\alpha 2}$ and $O_1-C_1-N_2-H_2$) and charge distribution around $C_{\alpha 1}$, C_1 , O_1 , N_2 , H_2 , $C_{\alpha 2}$.

Table 1 shows the bond length and angles as well as torsion angles demonstrating that the difference between two datasets in bond length is only significant in $C_{\alpha 1}-C_1$ and N_2-H_2 bonds. $C_{\alpha 1}-C_1$ is indirectly involved in peptide bond, but directly in ψ torsion angle. Therefore, it appears that in β conformation the R-groups can influence that bond length which is directly involved in ψ torsion angle. Since the N_2-H_2 bond of peptide plane has critical role in formation of specific types of hydrogen bond essential for secondary structural stability of proteins, then the resulting data of Table 1 indicate that the pattern of hydrogen bonds for β conformation is probably induced by the type of side chain in both sides of peptide plane.

The calculated values for bond and torsion angles of peptide plane in Table 2 show that two bond angles including $C_1-N_2-H_2$ and $H_2-N_2-C_{\alpha 2}$ are significantly different between two groups. Surprisingly, both angles are directly linked to N_2-H_2 bond which has different behavior in bond length as mentioned above. These finding together demonstrates that the pattern of hydrogen bonds is determined by effects of R groups on bond parameters (length and angle) of N_2-H_2 at the peptide plane. There are also two torsion angles in Table 1 including $C_{\alpha 1}-C_1-N_2-C_{\alpha 2}$ and $O_1-C_1-N_2-H_2$ which shows the planarity of peptide plane. The values of these torsion angles reveal that the peptide plane for both groups is not completely planar, but it has some degrees of deviation from the planarity.

Conclusions

It was found that the physico-chemical parameters originated mainly from the N_2-H_2 moiety is of great importance for directing the first and second positions of a given dipeptide toward β conformation. Since this group is directly going out from the peptide plane it may be concluded that peptide plane near ϕ torsion angle determines the pattern of hydrogen bond as well as dipole-dipole interaction. Therefore the flexibility of this torsion angle helps the plane to orient itself in accord with local conformation.

References

- [1] C. A. Orengo, A. E. Todd, and J. M. Thornton,



- [2] C. B. Anfinsen, "Principles that Govern the Folding of Protein Chains," *Science* (80-.), vol. 181, no. 4096, pp. 223–230, 1973.
- [3] M. Ghadimi, E. Heshmati, and K. Khalifeh, "Distribution of dipeptides in different protein structural classes: An effort to find new similarities," *Unpubl. Data*, 2017.
- [4] M. Ghadimi, K. Khalifeh, and Emran Heshmati, "Neighbor Effect and Local Conformation in Protein Structures," *Amino Acids*, vol. Accepted A, 2017.

Table 1. The values of bond lengths which directly or indirectly involved in peptide plane.

	Bond angle					Torsion angle					N2-C α 2		
	C α 1-C1-O1	C α 1-C1-N2	C1-N2-H2	H2-N2-C α 2	C1-N2-C α 2	C α 1-C1-N2-C α 2	O1-C1-N2-H2	C α 1-C1	C1-O1	C1-N2		N2-H2	
Preferred dipeptides for β conformation	CD	120.515	115.830	119.105	116.619	124.053	176.558	181.273	1.537	1.232	1.352	1.011	1.461
	DE	121.092	115.542	117.155	117.218	123.512	177.510	191.096	1.534	1.235	1.354	1.013	1.461
	GN	120.914	115.814	118.843	116.837	123.558	174.421	183.100	1.526	1.232	1.356	1.011	1.456
	GT	120.819	115.900	119.332	116.710	123.951	178.163	178.319	1.526	1.232	1.355	1.010	1.453
	KN	120.912	115.815	118.844	116.836	123.558	174.417	183.100	1.526	1.232	1.356	1.011	1.456
	NC	121.023	115.642	118.623	116.912	123.203	176.812	187.840	1.535	1.231	1.357	1.012	1.458
	PC	122.449	114.782	119.104	116.792	123.584	173.914	183.612	1.533	1.228	1.361	1.011	1.455
	PG	122.362	114.683	118.952	117.204	123.765	175.719	180.545	1.534	1.230	1.358	1.010	1.451
	PK	122.254	114.802	118.956	116.867	123.915	175.290	182.465	1.534	1.230	1.358	1.010	1.458
	DF	121.218	115.511	117.003	117.305	123.098	177.534	192.585	1.534	1.234	1.356	1.013	1.458
NT	120.881	115.680	119.206	116.819	123.918	178.857	180.926	1.535	1.232	1.353	1.010	1.454	
DV	121.138	115.436	116.526	117.649	123.016	177.979	193.441	1.534	1.235	1.356	1.013	1.460	
Avoided dipeptides for β conformation	FE	120.738	115.902	118.979	116.703	124.118	178.016	182.096	1.534	1.233	1.352	1.010	1.461
	FF	120.879	115.933	119.002	116.943	123.724	177.152	182.785	1.534	1.232	1.355	1.011	1.458
	FT	120.907	115.849	119.321	116.794	123.881	178.835	179.038	1.533	1.232	1.354	1.010	1.453
	IE	121.563	115.557	118.985	116.585	124.029	176.881	181.730	1.535	1.233	1.356	1.010	1.460
	IF	121.651	115.628	119.113	116.638	123.684	176.425	182.520	1.535	1.232	1.358	1.010	1.457
	IM	121.732	115.526	119.074	116.633	123.728	176.248	182.470	1.534	1.232	1.358	1.010	1.458
	IQ	121.674	115.575	119.079	116.715	123.710	176.700	182.308	1.534	1.232	1.358	1.010	1.459
	LF	121.948	115.229	119.138	116.815	123.904	175.035	181.540	1.542	1.230	1.359	1.010	1.456
	MI	120.768	115.844	118.529	116.466	123.478	171.819	186.882	1.534	1.231	1.355	1.010	1.458
	VS	121.769	115.543	119.006	116.542	123.532	175.152	183.690	1.534	1.231	1.360	1.011	1.455
VW	121.607	115.621	119.062	116.673	123.809	177.191	182.411	1.534	1.232	1.357	1.010	1.457	
YR	120.918	115.927	119.015	116.768	123.782	176.685	183.194	1.533	1.232	1.355	1.011	1.459	
t-test	0.838	0.129	0.066	0.005	0.112	0.903	0.153	0.080	0.841	0.733	0.065	0.430	



Dominant factors on the micellization of cationic urethane gemini surfactants in aqueous solution

S. Fayaz zadeh¹, P. S. Pourhosseini^{1,*}, and F. Najafi²

¹Faculty of Biological Sciences, Alzahra University, Tehran, 1993893973 I.R. Iran

²Department of Resin and Additives, Institute for Color Science and Technology, Tehran, 1668836471 I.R. Iran

*p.pourhosseini@alzahra.ac.ir

Abstract

A series of novel cationic urethane gemini surfactants with polymethylene spacer chain length of 2, 4 and 6 carbon atoms were studied. Electrical conductivity measurements were performed in aqueous solution at 25 °C to obtain important system parameters such as the critical micelle concentration (CMC) as well as the average degree of micellar ionization (α). The change of Gibbs free energy (ΔG°) of micellization was also calculated. Results show that at experimental conditions, the supramolecular nanomicelles self-assemble spontaneously and their CMC values vary with spacer chain length. Further, the average degree of micellar ionization (α) is mainly determined by the size of the gemini surfactant nanomicelles.

Keywords: gemini surfactant, nanomicelle, conductivity, CMC

Introduction

Gemini surfactants are newly developed amphiphilic molecules that have two hydrophilic head and hydrophobic tail groups linked by a spacer (Figure1) [1-3].

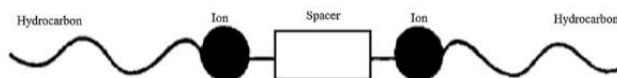


Fig.1. Schematic representation of a gemini surfactant [4]

The position of the spacer chain could be either at or near the head groups. It may be at the hydrophobic tail as well (Figure2) [1-3]. Depending on the characteristics of the head group, gemini surfactants are classified in four groups: anionic, cationic, non-ionic and zwitterionic. The latter contains a head group with two oppositely charged groups (Figure 3) [5,6]. The first report on dimeric surfactants concerned bisquaternary ammonium halide surfactants [7]. The hydrophobic tail can be short or long, and the spacer group can be polar (polyether), non-polar (aliphatic or aromatic), rigid (benzene) or flexible (methylene) [6].

Nowadays gemini surfactants have attracted a great attention of the scientific and industrial communities, due to their interesting properties with respect to conventional surfactants, such as lower toxicity, higher degrees of biodegradability, higher foaming capacity and optimal activity at extreme conditions of temperatures, pH levels and salinity. They are utilized in various industries like pharmaceuticals, food, painting, agriculture, paper, mineral processing, electronics, as well as personal care.

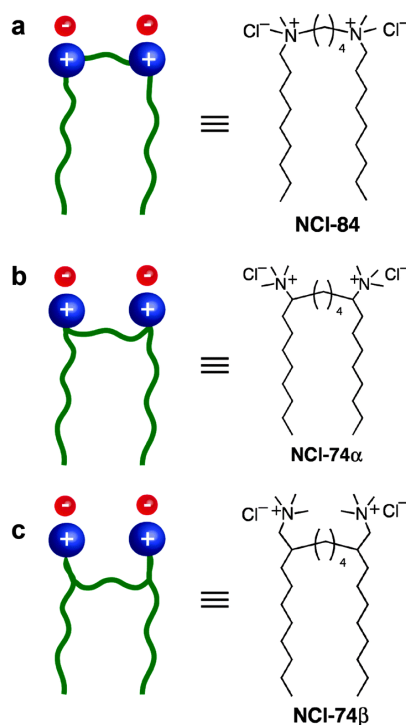


Fig.2. Schematic representation of the spacer position in bisquaternary ammonium cationic gemini surfactants [8]

A list of applications of dimeric surfactants in the above-mentioned industries is as follows:

- Pharmaceuticals: emulsions, dispersions, fouling.
- Household products: dirt removal, foam control.
- Paints & coatings: cleanliness, wetting, adhesion, dispersion stabilizing.
- Semi-conductors: cleanliness, adhesion of thin layers, characterization of surface treatments.
- Crude oil: oil recovery.
- Paper: printing, adhesion in packaging.
- Biomaterials: stabilizing, tissue adhesion [5].



Several studies have shown that gemini surfactants have a much lower CMC and a higher efficiency to decrease the surface tension of water than the corresponding monomeric surfactants. However, it should be considered that the length of the spacer chain, the tail and spacer hydrophobicity, and the tail dissymmetry greatly affect the properties of Gemini surfactants [9].

The aim of this study is to characterize the micellization behavior of a series of cationic Gemini surfactants varying in polymethylene spacer chain length (2, 4, 6). The CMC, the average degree of ionization of the micelles and the ΔG° of micellization of surfactants determined by conductivity measurements are reported.

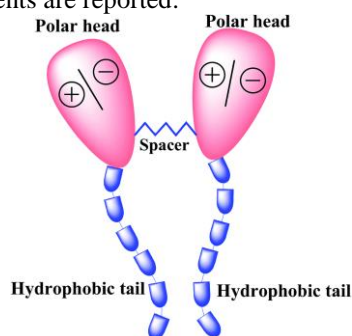


Fig.3. Schematic representation of a zwitterionic gemini surfactant [10]

Materials and methods

Materials

A series of bisquaternary ammonium cationic gemini surfactants were previously synthesized in our laboratory. Surfactants only differ in the number of methylene units in the spacer chain (2, 4, 6). All other chemicals were of analytical grades and used as received from Merck Chemicals. Phosphate-buffered saline (PBS; 137 mM NaCl, 2.7 mM KCl, 10 mM Na_2HPO_4 , 1.8 mM KH_2PO_4 , pH 7.4) was prepared and used.

Methods

Conductivity measurements were performed by a LCR meter instrument (GPS Inc., 3138B, England). A given volume of the PBS solution was titrated with small aliquots of a known concentration of gemini nanomicelles and the conductance changes were recorded. All measurements were carried out at 298 ± 1 K. Conductance was obtained at the frequency of 1KHz and the voltage of 0.1v, using platinum hexafluoride electrodes. The calibration procedure of cell was performed using a KCl solution (0.01 M) at room temperature. The cell constant was 0.55 cm^{-1} .

Results

The CMC of the surfactants in PBS solution pH 7.4, was determined from the plot of the specific conductivity changes vs. the surfactant concentration.

The CMC was taken as the concentration at the intersection of the two linear regions of the plot above and below the breakpoint.

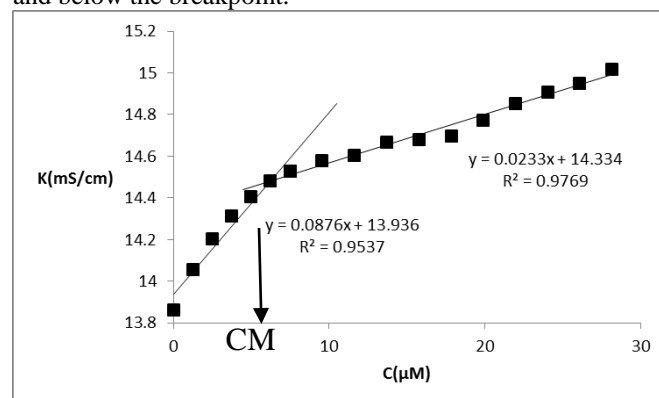


Fig.4. Specific conductivity vs. concentration for gemini surfactant with the spacer chain length of 6.

The average degree of micellar ionization (α) was obtained from the conductivity plots as the ratio of the slopes above and below the CMC for the surfactant solutions.

Also the change of standard Gibbs free energy of micellization, $\Delta G^\circ_{\text{mic}}$, per mole of hydrocarbon chain, for double chain surfactants, was calculated using the equation below [11],

$$\Delta G^\circ_{\text{mic}} = RT(1/2 + \beta) \ln \text{CMC} - (RT/2) \ln 2 \quad \text{Eq. (1)}$$

where R is the gas constant, T is the absolute temperature, and β is the degree of counter ion binding to micelles, defined as,

$$\beta = 1 - \alpha \quad \text{Eq. (2)}$$

Table 1. micellar parameters obtained for nanomicelles of three gemini surfactants with different spacer chain length

Gemini surfactant nanomicelles (spacer chain length)	Average size of the nanoparticles (nm)	CMC(μM)	A (%)	$\Delta G^\circ_{\text{mic}}$ (kJ/mol)
C6	156.7	4.72	18	-41.0
C4	138.6	5.8	11	-42.4
C2	162.9	6.25	27	-37.4

Discussion

Table 1 shows that the values of $\Delta G^\circ_{\text{mic}}$ have a considerably great negative amount, implying that the micellization process (micelle formation) is spontaneous. According to the calculated $\Delta G^\circ_{\text{mic}}$ values, it can be seen that gemini surfactant nanomicelles with the spacer length of 4 are the most stable nanomicelles in the aqueous solution among other gemini surfactants at room temperature (298 ± 1), owing to the greatest $\Delta G^\circ_{\text{mic}}$ value.



Table 1 also demonstrates that the value of the CMC is decreased by increasing the length of spacer chain. Since the spacer chain has a composition of repeated CH₂ units, increasing the spacer length results in the enhancement of hydrophobicity of the molecule. Therefore, micelle formation occurs in lower surfactant concentrations.

Table 1 also indicates the degree of ionization of the micelles (α), which is highly dependent on the size of the nanomicelles. As nanomicelles of the spacer length of 4 has the smallest size and the lowest degree of ionization.

Conclusions

In this work, CMC of the cationic gemini surfactants with different spacer chain lengths was investigated using conductivity measurements. The results indicate that the CMC decreases with the increase of spacer chain length. Gemini surfactant micelles form spontaneously in aqueous solutions. The degree of ionization of the micelles depends on the size of the micelles.

Acknowledgements

The authors thank the Research Council of Alzahra University for their financial support.

References

1. F.M. Menger, J.S. Keiper "Gemini surfactants", *Angew Chem Int Edit* 39(2000)1906–1920.
2. M.F. Gouzy, B. Guidetti, C. Andre´-Barres, I. Rico-Lattes, A. Lattes, C. Vidal "Aggregation behavior in aqueous solutions of a new class of asymmetric bipolar amphiphiles investigated by surface tension measurements", *J Colloid Interface Sci* 239(2001) 517–521.
3. R. Zana -"Dimeric and oligomeric surfactants. Behavior at interfaces and in aqueous solution: a review" , *Adv Colloid Interfac* 97(2002) 205–253
4. F. Menger, C. Littauc "Gemini surfactants: a new class of self-assembling molecules", *J Am Chem Soc* 115(1993) 10083-10090.
5. RK Sharma, "Surfactants: Basics and Versatility in Food Industries", *Pharma Tutor* 2 (2014)17-29.
6. D. Shukla, V. Tyagi, " Anionic gemini surfactants: a distinct class of surfactants", *J Oleo Sci* 55(2006) 215–226.
7. C.A. Bunton , L.Robinson, J. Schaak and M.F. Stam , "catalysis of nucleophilic substitutions of dicationic detergents, *J.Org. chem.* ; 36 (1971) 2346-2350.
8. M.H. Mondal, S.Malik, B. Saha "modernization of surfactant chemistry in the age of gemini and bio-surfactants: a review", *RSC Adv.* 5(2015) 92707-92718.
9. M. Nilsson, C. Cabalerio-Lago, A.J.M. Valente, O. Soderman, "Interactions between gemini surfactants, 12-s-12, and β -cyclodextrin as investigated by NMR diffusometry and electric conductometry" , *Langmuir* 22 (2006) 8663-8669.
10. G.P. Sorenson, M. Mahanthappa "Unexpected role of linker position on ammonium gemini surfactant lyotropic gyroid phase stability", *Soft Matter* 12(2016) 2408-2415.
11. R. Zana "critical micellization concentration of surfactants in aqueous solution and free energy of micellization", *Langmuir* 12(1996) 1208-1211.



Bovine Serum Albumin interactions with Schiff base study by spectroscopic techniques

H. Dezhampanah* and S. Jampur

Department of Chemistry, Faculty of Science, University of Guilan, P.O. Box: 1914, Rasht, Iran

*h.dpanah@guilan.ac.ir

Abstract: A new Schiff-base compound Ternary Cu (II) complexes of Schiff - base tyrosine amino acid derivatives and phnan troline heterocycle (A) was synthesized and the interaction between this Schiff base and bovine serum albumin (BSA) was investigated by fluorescence and Fourier transform infrared spectroscopies. A marked decrease in the fluorescence intensity of BSA was observed upon addition of Schiff base when excitation wavelength was set at 295nm. Based on the fluorescence quenching calculation, the quenching constant (K_q), apparent quenching constant (K_{sv}), binding constant (K_b) and binding site number (n) were obtained. The quenching mechanism was suggested as static quenching according to the Stern–Volmer equation. In addition, the infrared spectra of BSA in the absent and present of Schiff base was studied.

Keywords: Schiff base; BSA; Fluorescence; FTIR; quenching constant.

Introduction

Protein is an important chemical substance in our life and the major target of many types of medicine in the body. Studying the structure and function of protein is an important project in biochemistry, chemistry and medical. Serum albumins are the most abundant proteins in the circulatory system and play very important roles in transporting and disposing of many endogenous and exogenous compounds. Bovine serum albumin (BSA) is usually selected as the protein model, because of its abundance, low cost, ease of purification, stability, medical importance and ligand binding properties. Moreover all the studies are consistent with the fact that human and bovine serum albumins are homologous proteins [1].

Aromatic Schiff Bases are a large class of organic compounds being from condensation reaction of aromatic aldehyde and amine [2]. The applications of Schiff base-metal complexes in biology have gained importance as they show antimicrobial, antifungal, antibacterial, antiviral, antipyretic, antidiabetic and antitumor activities [3].

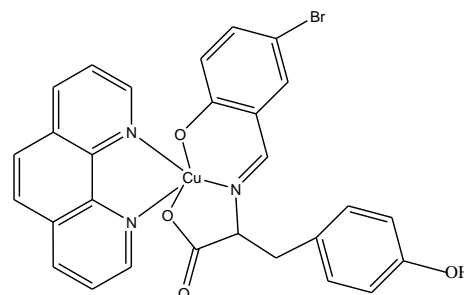
Materials and method

Schiff base complex (A) (scheme1) solution by dissolving in methanol. Bovine serum albumin was dissolved in distilled water. Phosphate buffer with PH =7.4 containing 0.44 gr Na_2HPO_4 , and 0.30 gr NaH_2PO_4 and 250 ml distilled water was prepared.

The exact concentration of BSA was determined spectrophotometrically using at 278 nm. Solutions of A were prepared in methanol.

All fluorescence emission spectra were recorded at λ_{ex} =295 nm, using slits of 2.5 nm. The fluorescence quenching studies were conducted at the same temperature. FT-IR measurements were performed at

the room temperature by an ALPHA FT-IR Spectrometer (Bruker) optics using KBr pellet in range of 4000-400 cm^{-1} . BSA concentrations were fixed at 60 μM and Schiff concentration varied from 0 to 45 μM (0:1, 0.5:1 and 1:1.5).



Scheme. 1. Chemical structure of A

Results and Discussion

Fluorescence quenching is a process which decreases the fluorescence intensity of a given substance. The mechanisms of quenching are usually classified as dynamic or static quenching. Dynamic quenching is collisional and encounters between quencher and the fluorophore, but static quenching, is due to complex formation [4]. The fluorescence spectra of BSA in the presence of different concentrations of Schiff base are shown in Fig1. It can be observed that increasing the concentration of A decreased the fluorescence intensity of BSA with 7 nm, red shift in the maximum wavelengths, respectively. The variation of F_0/F versus total concentration of A-BSA (Fig. 2). The plot of $F_0/(F_0 - F)$ vs $1/[Q]$ (Fig.3) in equation 2, yields f^{-1} as the intercept on the y axis and $(K_b)^{-1}$ as the slope. Thus, the ratio of the ordinate and the slope gives K_b . The number of A bound per protein (n) is calculated from of equation 3 (Fig. 4, Table 1).

$$\frac{F_0}{F} = 1 + K_{sv}[Q] \quad (1)$$



$$\frac{F_0}{(F_0 - F)} = \frac{1}{fK_b[Q]} + \frac{1}{f} \quad (2)$$

$$\log \frac{(F_0 - F)}{F} = n \log[Q] + \log K_s \quad (3)$$

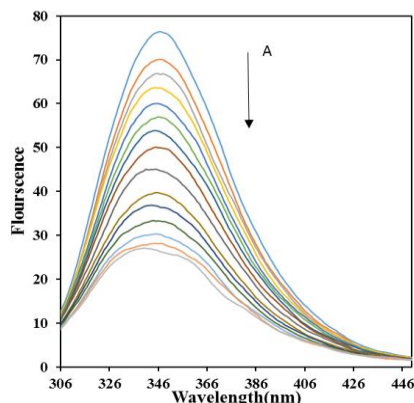


Fig. 1. Fluorescence quenching of BSA-Schiff base solution.

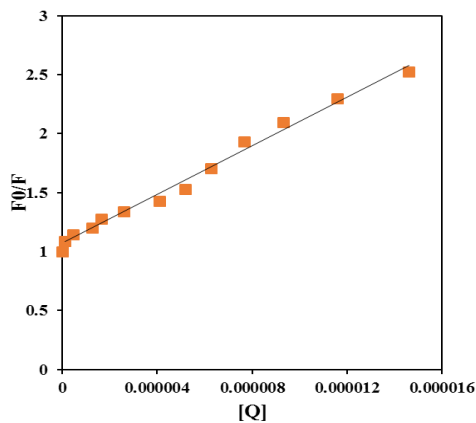


Fig. 2. . The variation of F_0/F versus total concentration of Schiff base complex.

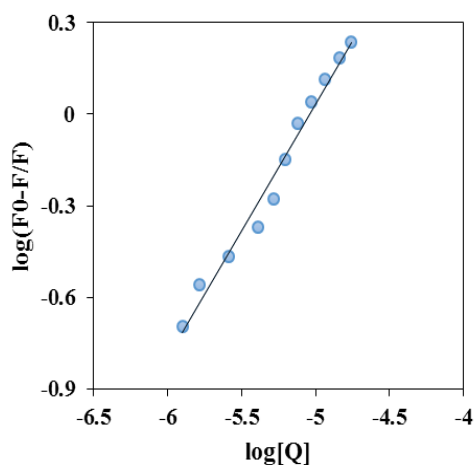


Fig. 3. The plots of $\log \frac{(F_0 - F)}{F}$ as a function of $\log [Q]$.

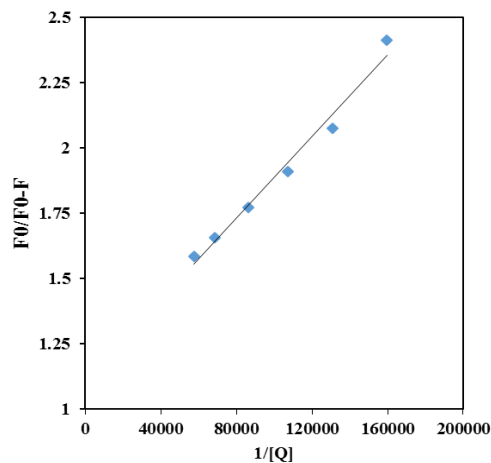


Fig. 4. The plot of $F_0/(F_0 - F)$ as function of $1/[Q]$.

Table1: Stern–Volmer constant, Binding constants, quenching constant and binding sites.

protein	K_{SV} ($L \text{ mol}^{-1}$)	K_b ($L \text{ mol}^{-1}$)	K_q	n
BSA	1.03×10^5	1.38×10^5	5.15×10^{13}	1

The BSA interaction with Schiff base A was analyzed by FTIR spectroscopy. The result of BSA interaction with A compound at low concentration of A showed an eminent increase in intensity and a decrease at high concentration of A.

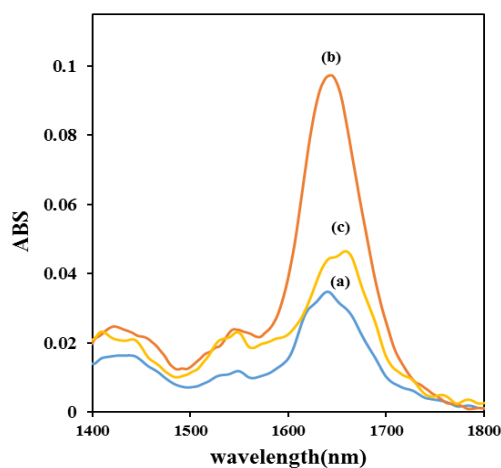


Fig. 5. FTIR spectra in the region of $1500\text{-}1800 \text{ cm}^{-1}$ of (a) BSA, (b) BSA-0.5 A and (c) BSA-1.5 A.

Conclusions

Based on the results of the present study, the interaction between a Schiff base complex and BSA has been investigated using molecular modeling and different optical techniques. It was shown that the



fluorescence of BSA has been quenched due to reacting with Schiff base complex. So, on the basis of spectroscopic studies this Schiff base complex bind strongly to BSA. At the end, increasing of concentration of A change the structure of BSA in secondary compound.

References

- [1] Y. Xiang, F. Wu “Study of the interaction between a new Schiff-base complex and bovine serum albumin by fluorescence spectroscopy”, *Spectrochimica Acta Part A*, 77 (2010) 430-436.
- [2] J. Gao, Y. Gue, J. Wang, Z. Wang, X. Jin, C. Cheng, Y. Li, K. Li “Spectroscopic analyses on interaction of o-Vanillin-d-Phenylalanine,

- o-Vanillin-l-Tyrosine and o-Vanillin-l-Levodopa Schiff Bases with bovine serum albumin (BSA)”, *Spectrochimica Acta Part A* 78, (2011) 1278–1286.
- [3] A. Ray, B. Koley Seth, U. Pal, S. Basu “Nickel (II)-Schiff base complex recognizing domain II of bovine and human serum albumin: Spectroscopic and docking studies”, *Spectrochimica Acta Part A* 92, (2012) 164–174.
- [4] F. Dezhampannah, R. Firouzi, L. Hasani “Spectroscopy and Molecular Modeling Study on Binding of Nickel Phthalocyanine to Human Serum Albumin”, *Protein & Peptide Letters*, 23 (2016) 800-807.

Aqueous Solubility of Poorly Water-Soluble Drug Ibuprofen in Micellar Media: Effect of Head Groups Charge

F. Teymouri, M. Jabbari*

School of Chemistry, Damghan University, Damghan, 36716-41167, Iran

*m_jabari@du.ac.ir

Abstract : In this study, equilibrium solubility of ibuprofen (IBP) as a poorly water-soluble drug was determined in pure water and in aqueous micellar solutions consisting of anionic SDS, cationic CTAB and non-ionic Brij-35 surfactants with different concentrations and charged head groups. The solubility data show that, irrespective of the surfactant type, the solubility of IBP in the micellar media increased compared to water by increasing solution concentration. Moreover, the non-ionic surfactant Brij-35 in lower concentrations than ionic surfactants CTAB and SDS can solve the drug ibuprofen better. This behaviour is a consequence of the interactions between the drug and the micelles under study.

Keywords: *Ibuprofen; Solubility; Micellar effect; Aqueous media.*

Introduction

Drugs with low water solubility are predisposed to low and variable oral bioavailability and therefore to variability in clinical response [1].

Ibuprofen (IBP; Figure 1) with chemical name 4-isobutyl-2-phenyl-propionic acid, is a well-known nonsteroidal anti-inflammatory drug widely used in inflammatory therapy [2,3].

Although ibuprofen is used widely nowadays in therapeutics, the physico-chemical information such as solubility for this drug is not abundant; the only knowledge of the solubility is in several solvents [4]. One of the classical approaches to improve the aqueous solubility of hydrophobic drugs, which is still being used in the pharmaceutical industry, is to use appropriate surfactants [5]. Surfactants are a large group of pharmaceutical excipients, which are used in a wide variety of drug delivery vehicles as solubilizers, emulsifiers, foamers, wetting agents, etc. Above the critical micelle concentration (CMC), surfactant molecules form micelles (colloidal structures of different shape) which are composed of hydrophobic core and hydrophilic surface [6].

In this work, we were investigated the influence of micelle on aqueous solubilization of the drug ibuprofen (IBP) by using a shake-flask method. The aqueous solution of three different surfactants containing a cationic CTAB (cetyl tri methyl ammonium bromide), non-ionic Brij-35 (Polyethylene glycol dodecyl ether) and an anionic SDS (sodium dodecyl sulphate), in above their CMC were used as micellar media. Finally, the physico-chemical effects of these micelles are discussed based on the interactions available between the drug and micelle species.

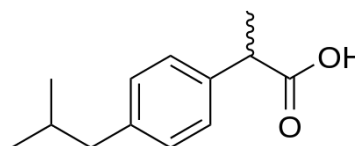


Figure 1. Chemical structure of ibuprofen.

Materials and method

The chemicals are pro analysis grade consist of the solvent ethanol ($\geq 99.9\%$) and the surfactants SDS ($\geq 99\%$), CTAB ($\geq 99\%$) and Brig-35 ($\geq 99\%$). All solutions used in this study were prepared with double distilled water.

In this study, the analytical isothermal shake-flask method was used for assaying the solubility of the drug ibuprofen. In this method, an excess of IBP was added to 10 mL of water into a glass flask. The mixture was stirred using a magnetic stirrer running at 450 rpm for 24 h, and then allowed to stand in water baths kept at constant temperature 25 °C. After this time, the supernatant solution was filtered (at isothermal condition), to ensure that it was free of particulate matter before sampling. All these steps were repeated for micellar solution containing excess of the drug ibuprofen. The micellar media of anionic SDS, cationic CTAB and non-ionic Brij-35 surfactants were used in different concentrations above CMC: 1.5 - 8.5 mM for CTAB, 0.09 - 0.8 mM for Brij35 and 8.5 - 20 mM for SDS.

The Concentration of ibuprofen in water and aqueous micellar media were determined by measuring UV absorbance of saturation solutions in the wavelength range of 200 to 450 nm, after appropriate dilution of them.

Before preparation of saturation solutions, an external calibration curve was plotted by using standard

solutions of ibuprofen in the appropriate concentration range in the organic solvent ethanol. From the linear fitting of data at the wavelength of the maximum absorbance ($\lambda_{\max}=263.5$ nm), the value obtained for the molar absorbance coefficient (ϵ) was 350.52 and 317.64 L mol⁻¹ cm⁻¹ for ethanolic and aqueous micellar solution of IBP, respectively. These values were utilized for calculating ibuprofen molarity as solubility in different media analyzed. For each the solubility data reported, at least three measurements were performed.

Results and Discussion

The solubility of ibuprofen in terms of the molar concentration (molar solubility, S_m) was calculated by using the absorbance data obtained for the saturated samples of IBP in pure water and different aqueous solution of the micelles under study. The experimental values of ibuprofen solubility expressed in molarity at atmospheric pressure are given in Table 1. It can be seen in Table 1 that the equilibrium solubility of ibuprofen in the different micellar media increases with the increasing the concentration of micelles in the solution.

Table 1. Experimental values of ibuprofen solubility (S_m) in water and micellar solutions at 25 °C.

[Brij] mM	S_m	[SDS] mM	S_m	[CTAB] mM	S_m
0.09	5.09×10^{-4}	8.5	1.71×10^{-3}	1.5	1.69×10^{-3}
0.15	7.43×10^{-4}	12	2.41×10^{-3}	2.5	2.42×10^{-3}
0.30	1.02×10^{-3}	15	3.03×10^{-3}	4.5	5.07×10^{-3}
0.50	1.48×10^{-3}	18	4.11×10^{-3}	6.5	6.79×10^{-3}
0.80	2.12×10^{-3}	20	4.70×10^{-3}	8.5	9.54×10^{-3}
H ₂ O	2.95×10^{-4}				

The solubility of a drug molecule in water is likely to depend on various diverse structural factors and physico-chemical properties such as the size, shape, hydrophobicity of substituent groups and their effect on the water structure, degree of ionization and other solute-solute and solute-solvent interactions.

Surfactant micelles can be pictured as having a nonpolar interior and a relatively polar interfacial region. The interior of the micelle is generally considered the locus of solubilization for nonpolar solubilize such as aromatic compounds [7]. The drug ibuprofen is a compound with low solubility in water [3]. It is also known to exist in the anionic state with one charge in neutral aqueous solution, because the carboxylic OH group dissociates resulting in a mixture of neutral and anionic species ($pK_a = 4.8$) [2]. The

site of solubilization within a micelle is closely related to the chemical nature of the solubilize [8]. Based on concentration range used in this work for each of surfactant micelles, non-ionic surfactant (Brij-35) was found to be a better solvent system as compared to ionic surfactants. Amongst ionic surfactants, ibuprofen had higher solubilization efficiency in cationic surfactant (CTAB) as compared to the anionic surfactant (SDS). The slope of plots in Figure 2 well shows the solubilization behavior of ibuprofen. This behavior can be correlated to the structure and electrostatic interactions between the negatively charged ibuprofen and the head groups of micelle surface.

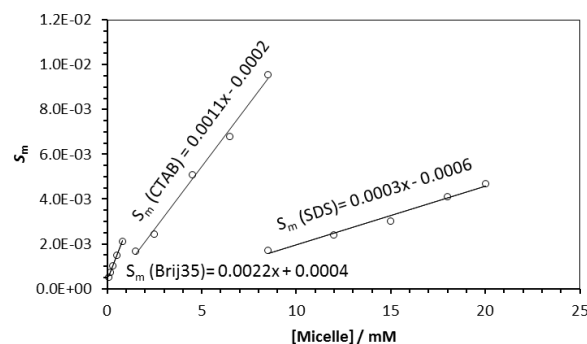


Fig 2. Plot of solubility in terms of the concentration of micelles used in aqueous media

Conclusions

The use of aqueous micellar systems as reaction medium is wide and varied. In this work, the influence of different concentration of the surfactants (anionic, cationic and non-ionic) on the extent of ibuprofen solubilization was investigated. It was found that the solubility of IBP in the micellar media increased compared to water by increasing solution concentration. Also, non-ionic surfactant Brij-35 is a better medium compared to ionic surfactants CTAB and SDS for more solubility of ibuprofen in water.

References

- [1] H. D. Williams, N. L. Trevaskis, S. A. Charman, W. N. Charman, "Strategies to address low drug solubility in discovery and development", *Pharmacological reviews*, 65 (2013) 315-499.
- [2] M. A. Filippa, E. I. Gasull, "Ibuprofen solubility in pure organic solvents and aqueous mixtures of cosolvents: Interactions and thermodynamic parameters relating to the solvation process" *Fluid Phase Equilibria*, 354 (2013) 185-190.
- [3] C. O. Rangel-Yagui, H. W. L. Hsu "Micellar solubilization of ibuprofen: influence of surfactant



head groups on the extent of solubilisation”, *Brazilian Journal of Pharmaceutical Sciences*, 41 (2005) 237-246.

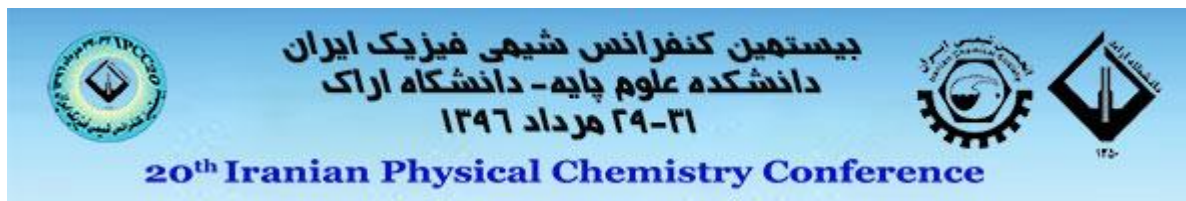
[4] S. Wang, Z. Song, J. Wang, “Solubilities of ibuprofen in different pure solvents”, *Journal of Chemical & Engineering Data*, 55 (2010) 5283-5285.

[5] V. P. Torchilin, “Micellar nanocarriers: pharmaceutical perspectives”, *Pharmaceutical research*, 24 (2007) 1-16.

[6] K. Stoyanova, Z. Vinarov, “Improving Ibuprofen solubility by surfactant-facilitated self-assembly into mixed micelles”, *Journal of Drug Delivery Science and Technology*, 36 (2016) 208-215.

[7] J. Xi, R. Guo, “Effects of pH and micelle on the radical scavenging ability of puerarin”, *Journal of Dispersion Science and Technology*, 30 (2009) 857-864.

[8] D. Attwood, A. T. Florence, “FASTtrack Physical Pharmacy”, 2012, Pharmaceutical Press, 2ndEd., London.



Inclusion Complex of β -CD-DZ as a nanocarrier: Preparation, Spectroscopic characterization, Thermodynamic parameters and molecular modelling Study

F. Fateminasab^a, A. K. Bordbar^{a*}

^aDepartment of Chemistry, University of Isfahan, Isfahan, 8174673441, Iran

*Email: ftmfatemi61@gmail.com and akbordbar@gmail.com

Abstract: The β -CD-DZ inclusion complex was prepared via freeze-drying method and characterized by using various spectroscopic techniques. The phase solubility diagram and Job plot showed the formation of a soluble complex of A_L type (1:1 stoichiometric IC) with improved solubility and stability. The thermodynamic parameters for the β -CD-DZ IC formation were determined and analyzed on basis of involved driving forces. The results showed the reaction process in mainly entropy driven and endothermic that assigned the predominant role of hydrophobic interaction in the formation of β -CD-DZ complex. In conclusion, a comprehensive computational study has been done on formation process of β -CD-DZ IC using molecular docking methods. In case of β -CD-DZ IC, the results of thermodynamic parameters, molecular docking confirmed stable complex formation between β -CD-DZ and also DZ included into a narrow site of inner cavity of β -CD.

Keywords: β -Cyclodextrin (β -CD), Daidzein (DZ), ¹H-NMR, inclusion complex (IC) and Molecular docking

Introduction

Daidzein (DZ) (Scheme 1-a), one of the most important isoflavones, is often found in soy foods. It has a varieties of biological activities including antioxidant, anti-inflammatory and antitumor and playing important role in female hormone. In spite of the most importance of DZ, low solubility in aqueous media, low bioavailability in oral absorption [1] and bitter taste have been limited its clinical applications. However, these limitations could be removed if DZ is encapsulated into suitable nanocarriers.

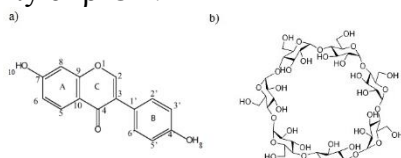
Cyclodextrins (CDs) are family of cyclic oligosaccharides that have Doughnut-shape structure. Native CDs, containing of linked 6,7 and 8 D-glucopyranose units by α -(1 \rightarrow 4) glycosidic bonds, are named α -, β - or γ -CD, respectively [2]. The β -CD molecule (Scheme 1-b) has a hydrophilic outer surface and a relatively hydrophobic nanocavity [3] and has been used properly to improve the solubility of poor soluble guests, visible or UV

light and heat, controlled release of drugs and flavours and etc.[4] The encapsulation could be done by formation of an IC between the host CD molecule and the guest, where CD, the “host”, includes, totally or partly, drug molecules “guest” by physical forces.[2] The applications of CDs in food industry, pharmaceuticals, protection and analytical chemistry[5] are based on their inclusion complexation ability with a number of molecules.

In this research, the ability of β -CD, as a nanocarrier and protective factor that improve the solubility and bioavailability of DZ, for targeting delivery of this compound was investigated. In this regard, the IC of DZ with β -CD is prepared by the freeze-drying method and characterized by ¹H-NMR spectroscopy and SEM technique. Phase solubility diagram for DZ in the IC determined. The thermodynamic parameters for the IC formation were determines and analyzed on basis of involved driving forces. An inclusive computational study has also been done on



formation process of this IC using molecular docking method. The result reveal detailed molecular features of the complex formation including the orientation of DZ in the nanocavity of β -CD.



Scheme 1. a) Structure of DZ, b) β -CD

Materials and method

Materials

β -CD (98 %, Sigma-Aldrich) and DZ (>99 %, Sigma Aldrich) were purchased. All solvents (acetone, DMSO and DMSO-d₆) were of high purity and obtained from Merck Company (Germany). The phosphate buffer saline prepared (PBS, 10mM, pH=7.4), as the solvent in all the studies performed.

Preparation and characterization of β -CD-DZ IC

8mL β -CD 5 mg/mL dissolved in deionized water and 9 mg DZ were dissolved in 8 mL acetone in glass capped vials. These solutions were mixed and put on the magnetic stirrer for 1 day. After that, the mixture was centrifuged and the supernatant was separated and freeze dried (VaCo5, Zirbus, Germany; -50°C, 130×10⁻³mBar) for preparing of the solid form of β -CD-DZ IC that was stored at 4 °C. Then IC characterized by using ¹H-NMR spectroscopy and SEM techniques.

Phase solubility diagram

The β -CD solution with various concentrations were prepared in PBS, Then, 1 mL portion of DZ solution (180 μ M) was added to 5 mL of each these β -CD solutions in the glass capped vials. The vials were stirred gently for 3 days at 25 °C. After that the samples were filtered and DZ concentration in the filtrates was

determined by measuring the absorbance at 245nm using UV-vis Spectrophotometer (Perkin Elmer, Lambda 265, USA).

UV-vis absorption spectroscopy and thermodynamic parameters

All absorption spectra of β -CD-DZ complexes were recorded by UV-vis Spectrophotometer equipped with a thermostat that control the temperature within ± 0.1 °C precision. For UV-vis titration experiments, DZ solution (2000 μ L, 30 μ M) was put on a quartz cuvette and titrated with fixed amounts of 20 μ L solution of the β -CD (300 μ M), sequentially. The UV-vis absorption spectra were recorded in the range of 235–450 nm. The corrected absorption data for dilution was analyzed by using the Benesi-Hildebrand method Eq. (1) as follow:

$$\frac{1}{\Delta A_i} = \frac{1}{\Delta A_{max}} + \frac{1}{K_a \Delta A_{max} [\beta - CD]_i} \quad (1)$$

Where ΔA_i is the difference of measured absorbance at 245 nm in i^{th} step with the absorbance of free DZ, $[\beta - CD]_i$ is the total concentration of β -CD in the i^{th} step of titration, ΔA_{max} is the absorption difference between bound and free DZ and K_a is the associative binding constant for formation of β -CD-DZ complex. The spectroscopic binding experiments were carried out at 20, 25, 30 and 35 °C. The estimated binding constants were used for calculation of ΔG° using the Gibbs famous equation, $\Delta G^\circ = -RT \ln K_a$. The other thermodynamic parameters (ΔH° and ΔS°) were determined using the following Eq. (2):

$$\ln(K_a) = -\frac{\Delta H^\circ}{RT} + \frac{\Delta S^\circ}{R} \quad (2)$$

Where R and T are universal gas constant (J. mol⁻¹.K⁻¹) and absolute temperature (K), respectively.

Molecular modelling

Molecular docking calculations were performed using the software AutoDock 4.2.6. The initial

structure of β -CD were extracted from the webserver:

(<http://upjv.q4md.forcefieldtools.org/REDDDB/projects/F-85/>). The .pdbqt file constructed. Macromolecules were considered rigid, while all torsional bonds of DZ were freely rotating. The grid box was set to $40 \times 40 \times 40$ grid point cubic box for β -CD and the grid point spacing was set to 0.375 \AA in each dimension. The LGA was adopted to model the interactions of the β -CD-DZ IC. For calculation, set of 250 docking run for ligand was performed and for run, a maximum 25,000,000 GA operations carried out. The inclusion energy was calculated based on the ranking functions, and their configurations were ranked into the clusters from the lowest to highest binding energy.

Results and Discussion

Characterization of β -CD-DZ IC

All $^1\text{H-NMR}$ experiments were carried out in DMSO-d_6 at 298K in the range of 0 to 10 ppm using NMR (Bruker, Ultra shield 400 MHz, Germany). All $^1\text{H-NMR}$ analysis were recorded for three samples β -CD, DZ and the β -CD-DZ IC (1:1). Chemical shift changes ($\Delta\delta$) were calculated according to Eq. (3):

$$\Delta\delta = \delta_{\text{complex}} - \delta_{\text{guest}} \quad (3)$$

Where δ_{complex} and δ_{guest} are the chemical shifts of IC and β -CD, respectively.

As shown in Table (1), for studying the inclusion behaviour of β -CD-DZ, the $^1\text{H-NMR}$ spectra of β -CD, DZ and IC β -CD-DZ were compared. According to Table 1, the most chemical shift change is observed for H-5 ($\Delta\delta=0.089$ ppm) and 6-OH ($\Delta\delta=0.0782$ ppm) groups which could be an indicative that DZ is more located on the narrow side of the cavity of β -CD. Accordingly, the NMR study confirms the formation of IC and the location of DZ in the narrow side of β -CD cavity.

The FE-SEM obtained for DZ, β -CD, and β -CD-DZ IC are illustrated in Fig 1. DZ arranged in columns (Fig 1-a), for β -CD (Fig 1-b) has a rhombus shape, and also for freeze dried DZ: β -CD IC the form of amorphous powder circular could be observed (Fig 1-c)

Table 1. ^1H -chemical shift (δ [ppm]) corresponding to pure β -CD and DZ and β -CD-DZ IC

DZ	δ [ppm]	β -CD-DZ	$\Delta\delta = \delta_{\text{complex}} - \delta_{\text{DZ}}$
7-OH	9.5783	9.6096	0.0313
4'-OH	10.8295		
H-5	8.0324	8.1646	0.1322
H-2'/6'	7.4479	7.4423	-0.0056
H-8	6.8741	6.8662	-0.0079
H-3'/5'	6.7986		
H-6	6.978	6.8883	-0.0897
H-3	8.3428	8.3595	0.0167
β -CD	δ [ppm]	β -CD-DZ	$\Delta\delta = \delta_{\text{complex}} - \delta_{\beta\text{-CD}}$
2-OH	5.7398	5.7593	0.0195
H-1	4.8362	4.9069	0.0707
6-OH	4.4606	4.5388	0.0782
H-3	3.6578	3.7281	0.0703
H-2	3.5542	3.5713	0.0171
H-5	3.3324	3.4214	0.089

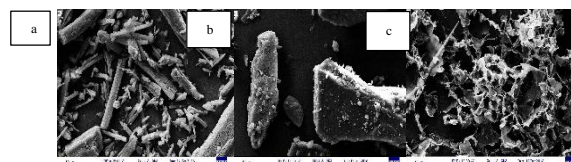


Fig.1. The FE-SEM images for A) DZ, B) β -CD and C) IC of DZ: β -CD

Phase solubility diagram

The apparent stability constant (K_s) of the complexes was calculated from the phase-solubility diagrams according to the following Eq. (4):

$$K_s = \frac{\text{slope}}{S_0(1 - \text{slope})} \quad (4)$$

Where S_0 is y-intercept, (the intrinsic solubility of DZ in water in the absence of CD).

Fig. 2 shows the phase-solubility diagram for DZ with β -CD. According to the phase solubility diagram results, the solubility of DZ increased as a linear function of the β -CD concentration. Based on Higuchi and Connors's theory [6], the diagram shown in this figure belongs to A_L -type group; and therefore represents the 1:1 stoichiometric between DZ and β -CD in the complex. The value of 1091.87 M^{-1} for the apparent stability constant (K_s) of β -

CD-DZ complex at 25°C was obtained with respect to Eq. (4). From these results, we found that solubility of DZ improved via complexation with β -CD.

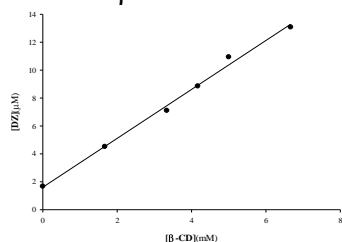


Fig. 2. Phase solubility diagram for β -CD and DZ at 25 °C

Thermodynamics of DZ- β -CD complex formation

As shown in Fig. 3-a, the absorbance increased in all spectral region due to the addition of β -CD at 25 °C. The same behaviour was observed at all other studied temperatures. The spectral titration data were analyzed on basis of Eq.1 and the corresponding plots were shown in Fig. 3-b. The high linearity of these plots represents the formation of 1:1 complex that is in agreement with the results of phase diagram task.

The values of associative binding constant for formation of β -CD-DZ IC, K_a , at various temperatures have been calculated and the results are shown in Table 2.

Table 2. Thermodynamic parameters for the formation of IC between DZ and β -CD

T(K)	$K_a(M^{-1})$	$\Delta G(kJ/mol)$	$\Delta H(kJ/mol)$	$\Delta S(J/mol)$
293.15	27091.20±964.62	-99.90±9.21	37.43±6.59	213.12±21.94
298.15	40500.00±1950.91	-100.97±9.29		
303.15	51366.70±14342.44	-102.04±9.36		
308.15	57250.00±2775.72	-03.10±9.44		

The results represents the reaction process in mainly entropy driven and endothermic that assigned the predominant role of hydrophobic interaction in the formation of DZ: β -CD complex.

Molecular Docking

Molecular docking was employed to investigate the interaction of β -CD with DZ in the IC. IC between β -CD:DZ showed two hydrogen bonds

between H of -OH (B ring) of DZ with O of -OH (C-6) and O of -OH (B ring) of DZ with H of -OH (C-6) of glucopyranose units (No. 4 and 2) of the narrower truncated cone. (Fig. 5) ΔG° obtained from molecular docking for interaction of β -CD with DZ is -5.97 kcal/mol. Comparison of the molecular docking results of β -CD to the titration absorption spectroscopy data showed that ΔG° and binding constant (K_a) results were in good agreement with each other. The results of molecular docking for β -CD were compared to the experimental data of 1H -NMR and showed that the most chemical shift in $\delta_{complex}$ belongs to the primary hydroxyl (C6) that located in the narrower truncated cone.

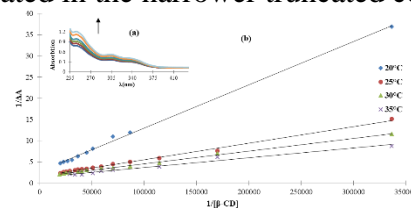


Fig. 3-a) Increase of the UV-vis absorption spectra for DZ (30 μ M) with different concentration of β -CD in the PBS (pH=7.4) at 25°C. b) Benesi-Hildebrand plot ($1/\Delta A$ vs. $1/[\beta\text{-CD}]$) for absorption titration data of DZ in the presence of different concentration of β -CD at 20, 25, 30 and 35°C

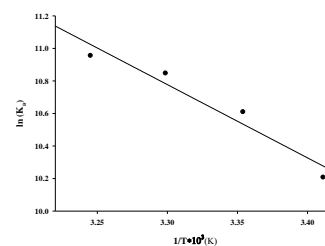


Fig.4. The van't hoff plot for IC between DZ and β -CD

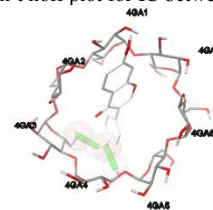


Fig. 5. Molecular docking for β -CD with DZ

Conclusions

The results of this work show that DZ was complexed with β -CD to form an inclusion complex by the freeze drying method in molar ratios of 1:1. The β -CD-DZ IC was studied using UV-vis spectroscopy, 1H -NMR, SEM.

Phase solubility diagram by using UV-vis spectroscopy analysis showed that DZ could form 1:1 stoichiometry inclusion complex with β -CD. The thermodynamic parameters for the β -CD-DZ IC formation showed the reaction process in predominantly entropy driven and endothermic and thus the main role of hydrophobic interaction in the formation of β -CD-DZ complex and this result in agreement with the computational study. ¹H-NMR spectroscopy showed that the formation of inclusion complex between β -CD-DZ and the location of DZ (Bring) in the narrow side of β -CD cavity and this result was confirmed by molecular docking.

Acknowledgment

The authors gratefully acknowledge Research Council of Department of chemistry, Isfahan University of Iran for fellowships and financial supports.

References

- [1] Bilia, A. R.; Isacchi, B.; Righeschi, C.; Guccione, C.; Bergonzi, M. C. Flavonoids Loaded in Nanocarriers: An Opportunity to Increase Oral Bioavailability and Bioefficacy. *Food Nutr. Sci.* **2014**, *5*, 1212–1227.
- [2] Sangpheak, W.; Kicuntod, J.; Schuster, R.; Rungrotmongkol, T.; Wolschann, P.; Kungwan, N.; Viernstein, H.; Mueller, M.; Pongsawasdi, P. Physical Properties and Biological Activities of Hesperetin and Naringenin in Complex with Methylated P-Cyclodextrin. *Beilstein J. Org. Chem.* **2015**, *11*, 2763–2773.
- [3] Khuntawee, W.; Wolschann, P.; Rungrotmongkol, T.; Wong-Ekkabut, J.; Hannongbua, S. Molecular Dynamics Simulations of the Interaction of Beta Cyclodextrin with a Lipid Bilayer. *J. Chem. Inf. Model.* **2015**, *55*, 1894–1902.
- [4] Yatsu, F. K. J.; Koester, L. S.; Lula, I.; Passos, J. J.; Sinisterr, R.; Bassani, V. L. Multiple Complexation of Cyclodextrin with Soy Isoflavones Present in an Enriched Fraction. *Carbohydr. Polym.* **2013**, *98*, 726–735.
- [5] Li, S.; Purdy, W. C. Cycodextrins and Their Applications in Analytical Chemistry. *Chem. Rev.* **1992**, *92*, 1457–1470.
- [6] T. Higuchi and K. A. Connors. Phase-Solubility Techniques. *Adv. Anal. Chem. Instrum.* **1965**, *4*, 212–217.

Biophysical Studies on the Interaction of Cationic Urethane Gemini Surfactant with Insulin

P. S. Pourhosseini ^{a,*}, R. Ghasemi Tabesh ^a, A. A. Saboury ^b, F. Najafi ^c

^a Faculty of Biological Sciences, Alzahra University, Tehran 1993893973, Iran

^b Institute of Biochemistry & Biophysics, University of Tehran, Tehran 1417614411, Iran

^c Department of Resin and Additives, Institute for Color Science and Technology, Tehran 1668814811, Iran

*p.pourhosseini@alzahra.ac.ir

Abstract: The interaction of cationic urethane gemini surfactant, having two methylene units in spacer (C2), with insulin was studied in phosphate-buffered saline PBS, pH 7.4, at 25 °C as a function of surfactant concentration. The investigation dealt with fluorescence spectroscopy, in which the Stern-Volmer plot of acrylamide quenching experiment was studied. The values of F_0/F versus acrylamide concentration were depicted, where F_0 and F were the fluorescence intensity in the absence and presence of acrylamide. Results show that the slope of the Stern-Volmer plot decreases continuously upon increasing the surfactant concentration. This observation indicates the progressive restricted accessibility of tyrosines to the environment, which is the consequence of either increasing the helical content of the protein or shielding effect of the hydrophobic interior of the nanomicelles.

Keywords: *Insulin; acrylamide; fluorescence spectroscopy; quenching*

Introduction

Proteins are the most important functional biomacromolecules in living organisms because they participate in all life processes. They can bind to a variety of ligands, such as fatty acids, metal ions, and surfactants. Since the late 18th century, the interaction of proteins with surfactants have been under thorough investigation because their mixtures have very important applications in biosciences [1-2]. The effect of surfactant on protein stability and structure depends on the specificities of the surfactant, such as the charge (anionic, cationic, neutral), nature of the polar group, hydrophobicity of tail, etc.) [3].

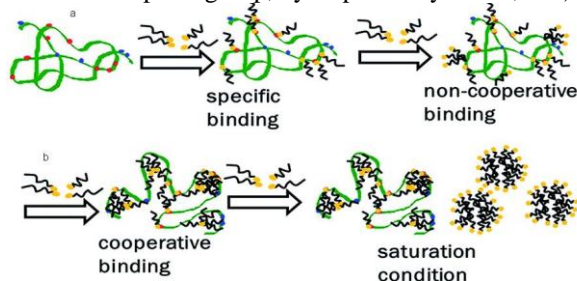


Fig.1. Schematic representation of conventional surfactant-protein interactions in a non-cooperative (a) and cooperative (b) manner.

It has already been reported that monomeric detergents bind to the native state of the protein as conventional ligands, that is, they bind to a small number of sites in a saturable manner (Fig.1). The interaction of ionic surfactant with

proteins leads to the denaturation of the protein and formation of poorly soluble complexes, while non-ionic surfactants do not denature globular proteins (Fig.2)

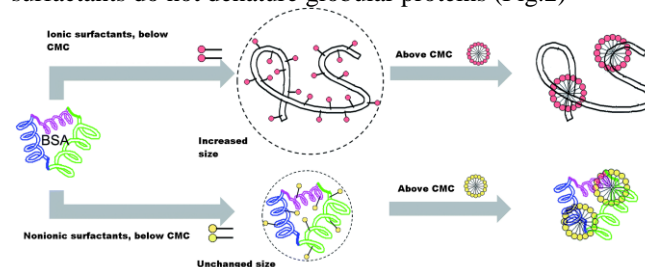


Fig.2. Interaction of ionic (top), and nonionic (bottom) surfactants with protein.

Some recent reports on new generation of surface active agents called as “Gemini surfactants” also suggest their potential role in protein stability and activity. Interaction of gemini surfactants with proteins shows that they have stronger binding with proteins as compared to conventional surfactants. This difference in binding is intensely governed by the two long hydrocarbon chains and two ionic head groups attached covalently to a spacer group (Fig.3) [4].

This work is an attempt to get deeper insight on the effect of cationic urethane gemini surfactant with a spacer length of $-(CH_2)_2-$, abbreviated as (C2), on insulin structure using fluorescence spectroscopy.

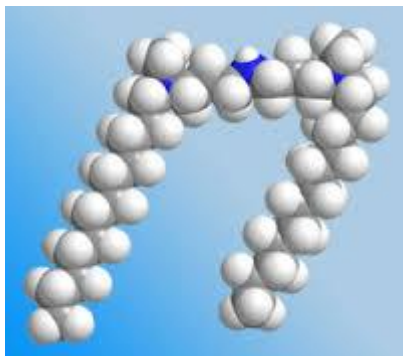


Fig.3. Schematic representation of a gemini surfactant.

Materials and methods

Cationic urethane gemini surfactants having 2 methylene units in spacer (C2) were previously synthesized in our laboratory. Human medicinal insulin was purified by dialysis against PBS, pH7.4, before use. All other chemicals were of analytical grades and used as received from Merck Chemicals. Phosphate-buffered saline (PBS; 137 mM NaCl, 2.7 mM KCl, 10 mM Na₂HPO₄, 1.8 mM KH₂PO₄, pH 7.4) was prepared according to reference [5].

Micellar dispersions: Stock solutions of nanomicelles were prepared by dissolving a given amount of surfactant in phosphate-buffered saline (PBS, pH 7.4). Samples were stirred for 30 min at room temperature and then sonicated in a bath sonicator for 15 min to obtain a homogenized dispersion.

Sample preparation: Aliquots of the stock solutions were mixed to a final concentration of 0.2 mg/mL protein, and gemini surfactant (C2) varying from 0, 90, 172, 238, 303, and 355 μ M, corresponding to [surfactant]/[protein] molar ratios of 0, 3, 5, 7, 9, and 10, respectively. Samples were incubated for 30 min at 25 °C prior to the experiment.

Acrylamide quenching: Acrylamide quenching studies of the intrinsic fluorescence were performed by adding 3 μ L aliquots of 4.0 M acrylamide stock solution to each sample. Excitation was done at 276 nm and the fluorescence emission was followed immediately at 303 nm. The final concentration of acrylamide in each sample varied from 0-700 mM. Fluorescence intensities were corrected for dilution effects.

Results and discussion

Conclusions

Acrylamide quenching experiments provide valuable proof of the structural changes in the protein upon addition of the gemini surfactant. Results show that the microenvironment around tyrosines is rearranged upon interaction with the surfactant. This rearrangement induces structural changes in

Significant evidence for the structural changes taking place in hexameric insulin upon its interaction with the surfactant (C2) was obtained by studying the fluorescence quenching of acrylamide as a neutral quencher. Fig. 4 shows the Stern-Volmer plots of human insulin upon increasing the molar ratio of [C2]/[protein]. It is observed that the slope of the plot decreases continuously upon increasing the [C2]/[protein] molar ratio from 3 to 10. The decrease in the slope indicates that tyrosines are less accessible to acrylamide. A comparison of these results with those of FUV CD provides interesting points about the microenvironmental changes around tyrosines. For instance, FUV CD data indicate that there is a +3% change in the helical content of the protein at the molar ratio of 3. As three of the four tyrosines of insulin are located in helices [6], the observation of decreased tyrosine accessibility is in accord with the far-UV CD data and reflects the shielding of these fluors by the helix structure. On the other hand, at molar ratios higher than 3 far-UV CD data show changes in the helical content of the protein in the opposite manner. These changes are -5%, -10%, -3%, and -4.5% for molar ratios of 5, 7, 9, and 10, respectively. Knowing the cmc of gemini surfactants, the restricted accessibility of tyrosines at these molar ratios indicate that at the molar ratios of 5 to 10 tyrosines are exposed to the environment but buried in the hydrophobic interior of the micelles.

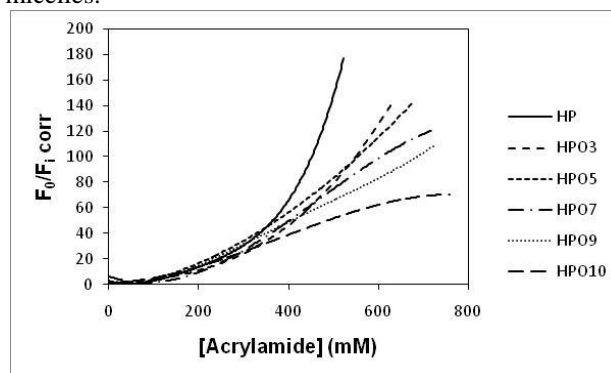


Fig.4. Stern-Volmer plots of human insulin as a function of [C2]/[protein] molar ratio at 25 °C. F₀ and F: fluorescence intensities in the absence and presence of acrylamide, respectively. Protein: 0.2 mg/mL. HP, HPO3, HPO5, HPO7, HPO9, and HPO10 refers to [C2]/[protein] molar ratio of 0, 3, 5, 7, 9, and 10, respectively.

the protein the extent of which depends on surfactant concentration.

Acknowledgments The authors thank the Iran National Science Foundation (INSF) and Research Council of University of Tehran for their financial support.

References

- [1] D. Wu, G. Xu, Y. Sun, H. Zhang, H. Mao, Y. Feng
"Interaction between proteins and cationic gemini surfactant" *Biomacromolecules*, 8 (2007) 708-712.
- [2] T. Sharma, N. Dohare, M. Kumari, U.K. Singh, A.B. Khan, M. S. Borseb, R. Patel "Comparative effect of cationic gemini surfactant and its monomeric counterpart

on the conformational stability and activity of lysozyme" *Royal Soc. Chem.*, 7 (2017) 16763-16776.

- [3] Y. Pi, Y. Shang, C. Peng, H. Liu, Y. Hu, J. Jiang
"Interactions between bovine Serum albumin and gemini surfactant alkanediyl- α,ω -bis(dimethyldodecyl-ammonium bromide)" *Biopolymers*, 83 (2006) 243-249.

[4] S. Mondal, M.L. Raposo, G. Prieto, S. Ghosh
"Interaction of myoglobin with cationic and nonionic surfactant in phosphate buffer media" *J. Chemical Eng. Data*, 61 (2016) 1221-1228.

[5] J. Sambrook, E.F. Fritsch, T. Maniatis "Molecular Cloning, A Laboratory Manual", 1989, (CSH Cold Spring Harbor Laboratory Press), 2nd edn., Book 3 Appendix B, New York, USA.

[6] P.S. Pourhosseini, A.A. Saboury, F. Najafi, M.N. Sarbolouki "Interaction of insulin with a triblock copolymer of PEG-(fumaric-sebacic acids)-PEG: Thermodynamic and spectroscopic studies" *Biochimica et Biophysica Acta. Proteins and Proteomics* 1774 (2007) 1274-1280.

Spectroscopic Studies on the Interaction Between Etofylline and Human Serum Albumin

D. Mohammad-Aghaie^{a*}, F. Hamed^a

^aDepartment of Chemistry, Shiraz University of Technology, Shiraz, (71555-313), Iran

*d-agmaie@sutech.ac.ir

Abstract: Human serum albumin (HSA) principally tasks as a transport carrier for a vast variety of natural compounds and pharmaceutical drugs. The present work is devoted to investigate the molecular interaction of 1,3-Dimethyl-7-(hydroxyethyl) xanthine (etofylline) with HSA under physiological conditions, using UV-visible and fluorescence spectroscopies. Fluorescence quenching titration carried out in 50 mM sodium phosphate buffer, pH 7.4 at different temperatures (298, 303 and 310K). Spectroscopic observations along with the Stern-Volmer equation were employed to determine the quenching mechanism. Fluorescence data revealed that etofylline quenches the intrinsic fluorescence of HSA through static quenching. The results obtained by spectroscopic studies will be of biological significance in pharmacology and clinical medicine.

Keywords: Human serum albumin; Etofylline; Fluorescence spectroscopy

Introduction

Among several transport proteins in blood, human serum albumin (HSA) is the most abundant protein; which is synthesized by the liver. HSA is unique due to its functions such as capability to bind and transport drugs and other endogenous and exogenous molecules, resulting in their selective delivery. HSA also regulates blood pH and colloidal osmotic pressure. X-ray crystallographic analysis has indicated that HSA is composed of a single polypeptide chain of 585 amino acids and has a heart-shape structure. It has a single tryptophan at amino acid position 214, showing distinctive fluorescence properties[1]. Etofylline (7-(2-hydroxyethyl)-1,3-dimethylpurine-2,6-dione or Hydroxy- ethyl theophylline) is one of derivatives of theophylline (methylxanthine). Theophylline and its compounds have been used in asthma[2].

Binding of drugs to the plasma protein is important because this phenomenon affects their pharmacodynamic and pharmacokinetic behaviors. These interactions influence distribution, bioavailability and elimination of ligands. Therefore, designing new more effective drugs, and better determination of their pharmacokinetic properties, requires a clear view of a drug-transport proteins, mainly drug-HSA interaction[3].

Fluorescence spectroscopy is a suitable technique to determine binding mechanism and calculate binding parameters, due to its high sensitivity and simple operational action. In this study, uv-vis absorption and fluorescence spectroscopies were used to investigate HSA-etofylline interactions. The stern-Volmer equation was used to analyse the mechanism (static or dynamic) of fluorescence quenching[1].

Materials and methods

HSA was purchased from “Sigma chemical Co” and used without further purification. Etofylline, was made by the known method[4]. Concentration of HSA was determined by spectrophotometric method at $\lambda=280$ nm and molar extinction coefficient of $\epsilon = 35700 \text{ M}^{-1} \text{ cm}^{-1}$ [1]. The solutions of HSA ($10 \mu\text{mol L}^{-1}$) and etofylline (1 mmol L^{-1}) were prepared by dissolving known amounts of the solid substances in 50 mM sodium phosphate buffer, pH 7.4. Solutions were used freshly after preparation and kept at 0–4 °C in the dark environment for maximum 3 days.

The uv-visible absorbance spectra of HSA in the presence and absence of etofylline were recorded on a T90⁺ UV-vis spectrophotometer instrument (PG Instrument Ltd., United Kingdom), where the quartz cuvette of 1.0 cm optical path was employed in the range of 240–300 nm. Fixed concentration of HSA ($10 \mu\text{mol.L}^{-1}$) was titrated with increasing amounts of drug stock solution (1 mmol.L^{-1}).

HSA fluorescence measurements were carried out on a Cary-Eclipse spectrophotometer (Varian model, Australia) using a 1.0 cm optical path quartz cell and a circulating water bath. The excitation wavelength was 280 nm, and band widths of both excitation and emission were set at 5 nm. HSA solution ($10 \mu\text{M}$) was titrated by addition of etofylline solution (1mM) using microinjection (to give a concentration ranging from 0-75 μM). Fluorescence intensities were measured at three different temperatures (298, 303 and 310 K). All samples were kept for 3 min at a fixed temperature, then the emission spectra were recorded in the range of 285-500nm. Control measurements were performed by adding identical amounts of etofylline in the absence of HSA, therefore the final spectra were acquired by subtracting the spectra of etofylline in the absence of HSA from the total spectra in presence of HSA.

Synchronous fluorescence spectroscopy, is a simple and effective method, able to measure fluorescence quenching and the possible shift of the maximum emission wavelength (λ_{max}). It also can reflect the change of microenvironment around the chromophore. In this study, synchronous fluorescence spectra of HSA in presence of different concentrations of ligand were recorded. The synchronous spectra are a characteristic of typical Trp residue fluorescence at $\Delta\lambda(\lambda_{em}-\lambda_{ex}) = 60$ nm, while they are characteristic of the typical Tyr residue fluorescence at $\Delta\lambda = 15$ nm[5].

Results and Discussion

UV-visible absorption studies

The probability and quality of complex formation between HSA and etofylline were studied at around 280 nm by UV-visible absorption spectroscopy and the obtained spectra are illustrated in Fig. 1. The UV absorption intensity of HSA increases through addition of etofylline. This result indicates the change in the protein microenvironment with concentrations of etofylline. Fig. 1 also reflects the dependence of HSA-etofylline complex absorption on the etofylline concentration at 298 K. The HSA concentration was fixed at $10 \mu\text{mol L}^{-1}$ and etofylline was used at different concentrations (a-e): 0, 20, 39, 57 and 74 mol L^{-1} .

Fluorescence quenching

The fluorescence intensity of protein may decrease upon a variety of molecular interactions. This can be attributed to the change in the molecular microenvironment of protein in the vicinity of the chromophores due to the drug-protein binding interactions[1,5]. Fig. 2 shows the fluorescence emission spectra of HSA with various amounts of etofylline following an excitation at 280 nm. It could be seen that the fluorescence intensity of HSA is dropped regularly with the increase in etofylline concentration, indicating that etofylline can bind to the HSA and quench the Trp intrinsic fluorescence intensity.

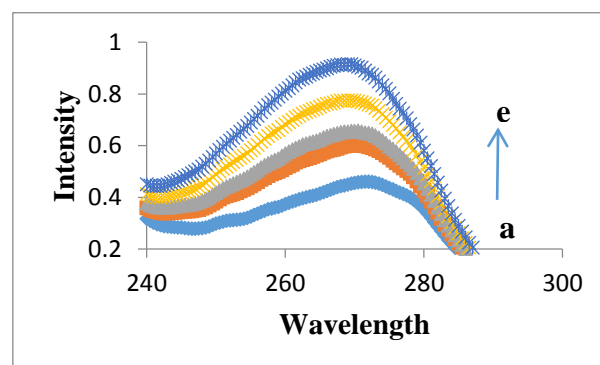


Fig.2: UV-visible absorbance spectra of the binding of etofylline to HSA at 298 K.

Quenching mechanism

Fluorescence quenching is any process which decreases the fluorescence intensity of the fluorophore. The fluorescence can be quenched both by collision and by complex formation between quencher and fluorophore. The former is referred to as the dynamic quenching and the latter is known as the static quenching mechanism. These two probable mechanisms are distinguished from each other by the differences in the temperature-dependent behavior of the system.

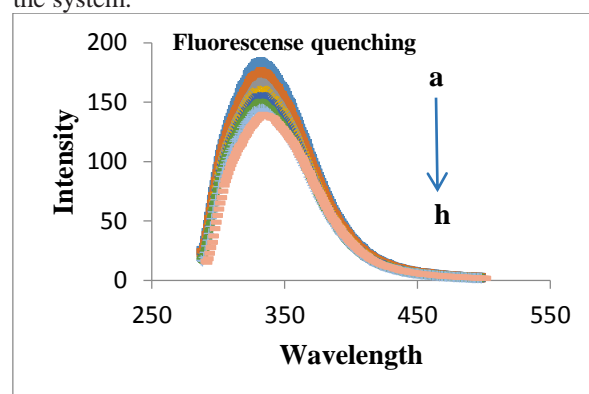


Fig.3: Fluorescence spectra of HSA at 298 K. HSA: $10 \mu\text{mol L}^{-1}$, etofylline (a-h): 0, 10, 20, 29, 38, 48, 57 and $65 \mu\text{mol L}^{-1}$.

Dynamic quenching depends mainly on diffusion. Since higher temperatures result in higher diffusion coefficients, the dynamic quenching constants are expected to increase when the temperature rises. In contrast, increasing the temperature can decrease both the complex stability and the value of the static quenching constants[6]. Stern-Volmer plots help to determine the quenching mechanism:

$$\frac{F_0}{F} = 1 + K_{sv} [Q] = 1 + K_q \cdot \tau_0 [Q] \quad (1)$$

In Eq.(1), F_0 and F respectively represent the fluorescence intensities in the absence and presence of the quencher with concentration $[Q]$. K_{sv} is the Stern-

Volmer quenching constant, k_q is the biomolecular quenching rate constant (dynamic quenching), and τ_0 is the average lifetime of the biomolecule in the absence of the quencher with a value of 10^{-8} s for HSA[1].

Fig. 3 shows the Stern–Volmer plots of F_0/F versus quencher concentrations at different temperatures (298, 303 and 310 K) at $\lambda_{ex}=280$ nm. The Stern–Volmer curves are linear, and the slopes decrease with the rising temperature (Table 1). It is already known that, K_{sv} values decrease with an increase in temperature for static quenching, though the reverse effect is observed for dynamic quenching. The K_{sv} values, in our study, decrease with an increase in temperature, which is an indication of static quenching mechanism.

Synchronous fluorescence of HSA with etofylline

Synchronous fluorescence gives information about the molecular environment in the vicinity of the chromophores, and has several advantages, such as sensitivity, spectral simplification and avoiding different perturbing effects. As already mentioned the $\Delta\lambda$ values of 15 or 60 nm, between the excitation and emission wavelengths in synchronous fluorescence gives rise to the characteristic information of Tyr and Trp residues respectively[7]. According to Fig.4 (a and b), the intensity of the fluorescence peak of $\Delta\lambda=60$ nm decreases more significantly with etofylline addition compared with the $\Delta\lambda=15$ nm peak. This means that etofylline addition has a greater effect on the fluorescence of Trp. Since no shifts are observed in their peak maximums, one can conclude that there is no polarity change around the Trp or Tyr residues.

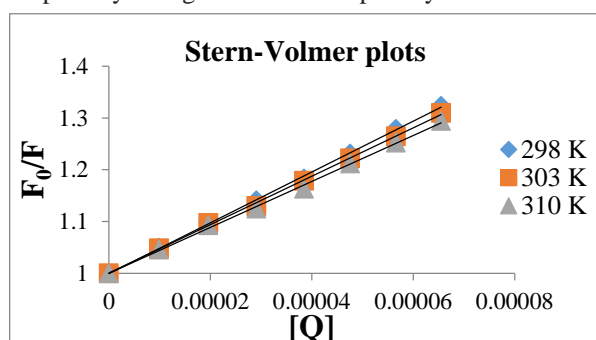


Fig. 3. SternVolmer plots for the fluorescence quenching of HSA by etofylline at different temperatures at $\lambda_{ex}=280$ nm.

Table1: Stern–Volmer dynamic quenching constants of HSA-drug system at different temperatures with $\lambda_{ex}=280$ nm..

T	K_{sv} (10^3)	R^2
298	4.90 ± 0.05	0.9995
303	4.67 ± 0.09	0.9990
310	4.43 ± 0.05	0.9983

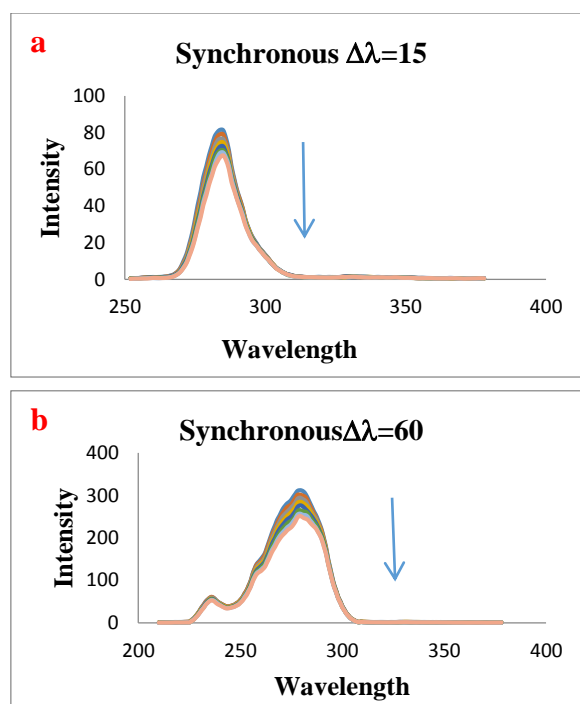


Fig. 4 Synchronous fluorescence measurements for HSA in the presence of etofylline with $\Delta\lambda=15$ nm (a) and $\Delta\lambda=60$ nm (b), respectively.

Conclusions

In this study, the interaction of etofylline with HSA was investigated by molecular spectroscopy methods including UV-visible, conventional and synchronous fluorescence spectroscopies. The results showed that etofylline quenches the intrinsic fluorescence of HSA through static quenching mode. On the other hand synchronous fluorescence spectra provided some information about the molecular environment around the Tyr and Trp residues. The biological significance of this work is evident since albumin serves as a carrier molecule for most drugs and the interactions of etofylline with HSA has not been characterized so far.

References

- [1] P. Daneshgar, A. Moosavi-Movahedi, P. Norouzi, M. R. Ganjali, A. Madadkar-Sobhani and A. A. Saboury, "Molecular interaction of human serum albumin with paracetamol: spectroscopic and molecular modeling studies" *Int. J. Biol. Macromol.*, 45 (2009) 129-134.



بیستمین کنفرانس شیمی فیزیک ایران
دانشکده علوم پایه - دانشگاه اراک
۲۱-۲۴ مرداد ۱۳۹۶



20th Iranian Physical Chemistry Conference

[2] K.D. Tripathi, "Essentials of Medical pharmacology", 2013, 7th Ed, 218-227, New Dehli, India.

[3] N. Shahabadi, M. Falsafi, S. Hadidi, "Molecular modeling and multispectroscopic studies of the interaction of hepatitis B drug, adefovir dipivoxil with human serum albumin", *J. Lumin*, 167(2015) 339-346.

[4] A. Kleeman, J. Engel, B. Kutscher, D. Reichert, "Pharmaceutical Substances" 2008, 5th Ed, Thieme, Stuttgart.

[5] N. V. Rakotoarivelo, P. Perio, E. Najahi and F. Nepveu, "Interaction between Antimalarial 2-Aryl-

3H-indol-3-one Derivatives and Human Serum Albumin" *J. Phys. Chem. B*, 118 (2014) 13477-13485.

[6] B. Valeur, "Molecular Fluorescence: Principles and Applications" 2001, Wiley-VCH Verlag GmbH.

[7] J.L. Yuan, Z. Lv, Z.G. Liu, Z. Hu, G.L. Zou, "Study on interaction between apigenin and human serum albumin by spectroscopy and molecular modeling", *J. Photochem. Photobiol. A* 191 (2007) 104-113.

Investigation of Interaction of New Platinum Complexes Containing Phosphine Ligand with DNA

BitaShafaatian*, AtiyehKazempour, Maryam Noori

School of Chemistry, Damghan University, Damghan 3671641167, Iran

*shafaatian@du.ac.ir

Abstract: New complexes of platinum(II) containing phosphine ligand were synthesized and characterized by FT-IR, ¹H NMR, ³¹P NMR UV/Vis, elemental analysis and conductometry. In synthesized complexes, the ligand was coordinated to the metal center via phosphorous donor atoms. The interaction of these complexes with DNA was investigated by UV-Vis spectroscopy in order to calculation of binding constants (K_b). The results revealed hypochromism effects which generally indicate the intercalative binding nature of the interaction. Viscosity measurements were used to further elucidate the nature of the interactions between the complexes and DNA. Moreover, thermodynamic of these interactions were studied and thermodynamic parameters containing ΔG , ΔH and ΔS were calculated.

Keywords: Platinum Complex; Phosphine ligands; DNA Interaction

Introduction

Platinum is a third row transition metal with a d^{10} electron configuration that is readily oxidized to Pt(II) and Pt(IV) respectively. The dicationic d^8 configuration almost always forms compounds with square planar geometry.

Platinum complexes were used as anticancer drugs. Cisplatin (CDDP) is a relatively small coordination compound of platinum (Pt) that was approved in 1978 for the clinical treatment of various cancers [1]. Thirty-nine years since its FDA approval cisplatin has remained one of the most commonly prescribed chemotherapeutic drugs. However, the clinical application of cisplatin is limited due to toxic side effects, such as kidney damage and cellular resistance (either intrinsic or acquired). Due to these issues, numerous cisplatin analogues have been synthesized and investigated with varying anti-neoplastic activity. Currently, only two cisplatin analogues have been approved [2].

Materials and method

All reagents were commercially available and were used as received. Calf thymus DNA (CT-DNA) was purchased from Sigma-Aldrich. Reagents used for the physical measurements were of spectroscopic grade. All the DNA binding experiments were done in 10 mM Tris-HCl buffer (pH=7.4) containing 50 mM NaCl. A solution of CT-DNA gave a ratio of UV absorbance at 260 and 280 nm >1.8 , indicating that the DNA was sufficiently free from protein. Electronic absorption spectroscopic experiments were carried out at 27 °C, keeping the complex concentration constant (10.0 μ M) while varying the DNA concentration from 0 to 15.0 μ M. Absorbance values were recorded in the range of 227-375 nm after each successive addition of DNA

solution, followed by an incubation time of 10 min. CT-DNA in Tris-HCl buffer solution (pH=7.4) was used as a reference.

Results and Discussion

In this work two new platinum complexes were synthesized and used in order to investigate of their interaction with DNA (Fig. 1) UV-Vis spectroscopy is one of the most important techniques for studying the interaction binding of complexes to DNA. Thus; this technique was used to the investigation of DNA interaction with the synthesized metal complexes. The absorption spectra of these complexes in the absence and presence of DNA were shown in Figs 2 and 3.

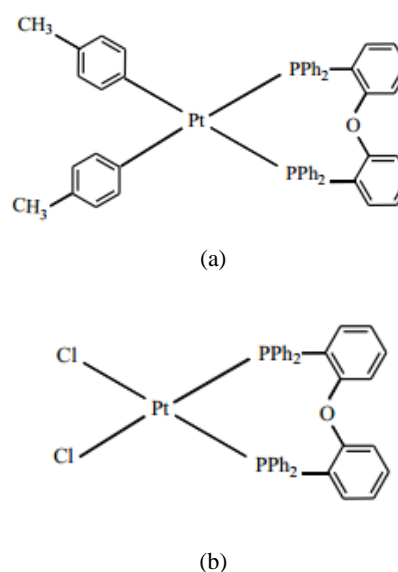


Fig. 1: The structure of [Pt (*p*-tolyl)₂(phosphine) (a) and the [Pt Cl₂(phosphine) (b).

The absorption bands at 230 and 231 nm are due to the intraligand π - π^* transitions. As seen, during the



titration of these complexes with CT-DNA (0–22 μM), both bands exhibit hypochromic and indicating the intercalative binding characteristics of the interactions for complexes

with DNA [3]. For verifying the binding strength of complexes with DNA, the intrinsic binding constants (K_b) were calculated by the following equation [4]:

$$[\text{DNA}]/(\epsilon_a - \epsilon_f) = [\text{DNA}]/(\epsilon_b - \epsilon_f) + 1/K_b(\epsilon_b - \epsilon_f)$$

where, $[\text{DNA}]$ is the concentration of DNA in base pairs, ϵ_a is the apparent extinction coefficient obtained by calculating $A/[\text{complex}]$, ϵ_f corresponds to the extinction coefficient of the complex in its free form and ϵ_b refers to the extinction coefficient of the complex in the fully bound form. In the plot of $[\text{DNA}]/(\epsilon_a - \epsilon_f)$ versus $[\text{DNA}]$, K_b is given by the ratio of slope to intercept. The binding constants (K_b) for these complexes (a) and (b) were obtained 2.80×10^5 and 2.75×10^5 , respectively.

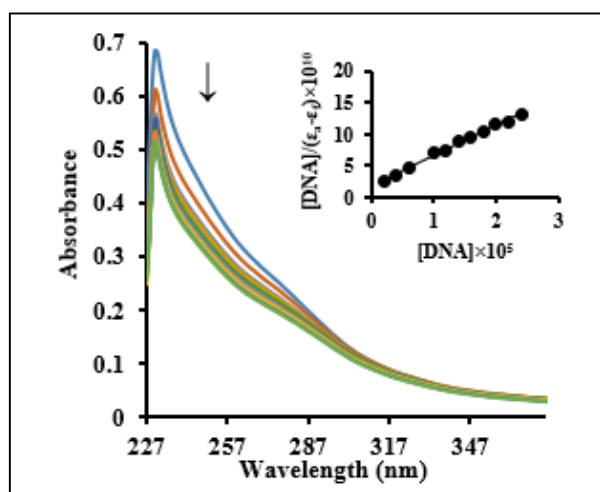


Fig. 2: UV spectra of the organoplatinum(II) complex (a) during the titration with CT-DNA; $[\text{Complex}] = 10 \mu\text{M}$, $[\text{CT-DNA}] = 0\text{--}22 \mu\text{M}$. Inset: Plot of $[\text{DNA}]/(\epsilon_a - \epsilon_f)$ versus $[\text{DNA}]$.

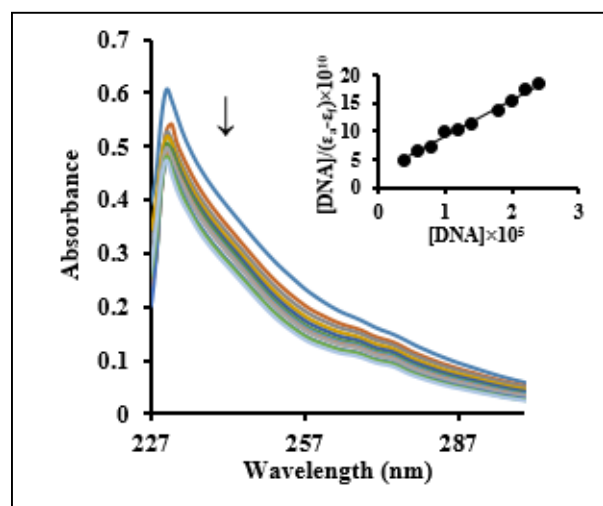


Fig.3: UV spectra of the platinum complex (b) during the titration with CT-DNA; $[\text{Complex}] = 10 \mu\text{M}$, $[\text{CT-DNA}] = 0\text{--}22 \mu\text{M}$. Inset: Plot of $[\text{DNA}]/(\epsilon_a - \epsilon_f)$ versus $[\text{DNA}]$.

Thermodynamic studies

The thermodynamic data can explain the model of interaction between the platinum complexes and calf thymus DNA. According to the thermodynamic data, interpreted as follows, the model of the interaction between a complex and DNA may be (1) $\Delta H > 0$ and $\Delta S > 0$, hydrophobic forces; (2) $\Delta H < 0$ and $\Delta S < 0$, van der Waals interactions and hydrogen bonds; and (3) $\Delta H < 0$ and $\Delta S > 0$, electrostatic interactions. The thermodynamic parameters, ΔS , ΔH and ΔG , were calculated from the binding constants (K_b) according to the following Van 't Hoff equations:

$$\ln K = -\Delta H/RT + \Delta S/R, \quad \Delta G = \Delta H - T\Delta S$$

The positive amounts of ΔH and ΔS show hydrophobic forces between DNA and these platinum complexes. The resulted Van 't Hoff plots were shown in Figs. 4 and 5.

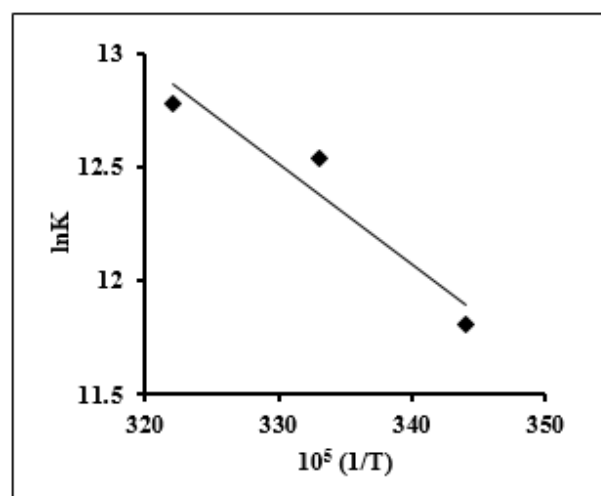


Fig. 4: Van't Hoff plot for the interaction of the platinum complex (a) and CT-DNA at pH 7.4.

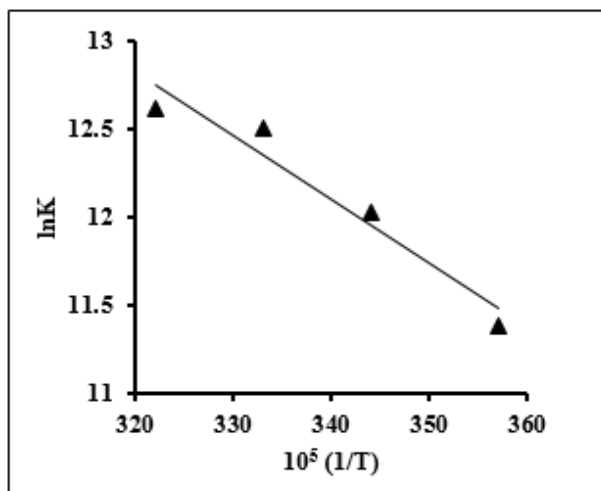


Fig. 5: Van't Hoff plot for the interaction of the platinum complex (b) and CT-DNA at pH 7.4.

The Thermodynamic parameters for binding of these complexes with DNA were given in Table 1 and 2.

Table 1: Thermodynamic parameters for binding of complex (a) to CT-DNA in 0.01 M tris buffer, pH 7.4

T (K)	Complex (a)		
	ΔH (kJ mol ⁻¹)	ΔS (J mol ⁻¹ K ⁻¹)	ΔG (kJ mol ⁻¹)
290			-28.57
300	36.66	224.96	-30.82
310			-33.07

Table 2: Thermodynamic parameters for binding of complex (b) to CT-DNA in 0.01 M tris buffer, pH 7.4

T (K)	Complex (b)		
	ΔH (kJ mol ⁻¹)	ΔS (J mol ⁻¹ K ⁻¹)	ΔG (kJ mol ⁻¹)
280			-26.78
290			-28.82
300	30.26	203.74	-30.86
310			-32.89

Viscosity measurements

UV-Vis spectra are not sufficient to investigate a binding mode and viscosity measurements, which is very sensitive to length increase, is used in order to support binding mode of complexes to DNA. A classical intercalative mode affords a considerable increase in viscosity for the DNA solution due to the entirely increase in DNA length due to the increasing in separation of base pairs and increasing the overall DNA length [5]. However, non classical intercalation of complex may cause a kink on the DNA helix and decrease its length with a concomitant decrease in its

viscosity [6]. The relative viscosity of DNA is increased in the presence of the complexes. These data indicate that these complexes can bind to DNA by intercalation binding modes which are consistent with the obtained absorption spectroscopic data.

Conclusions

New complexes of Platinum containing a bidentate phosphine ligand were synthesized and characterized by different methods.

The interactions of these complexes with DNA were investigated by UV-Vis spectroscopy and viscosity measurements. The results revealed hypochromic effects which generally indicate the intercalative binding nature of the interaction. Moreover, K_b and thermodynamic parameters were calculated for these interactions. The positive amounts of ΔH and ΔS show hydrophobic forces between DNA and these platinum complexes.

Acknowledgment

We gratefully acknowledge the support of this work by Damghan University Research Council.

References

- [1] F. Arnesano and G. Natile "Mechanistic insight into the cellular uptake and processing of cisplatin 30 years after its approval by FDA", *Coord. Chem. Rev.*, 253 (2009) 2070-2081.
- [2] C. A. Rabik and M. E. Dolan "Molecular mechanisms of resistance and toxicity associated with platinating agents", *Cancer Treat. Rev.*, 33 (2007) 9-23.
- [3] M. N. Patel, C. R. Patel, H. N. Joshi "Metal-based biologically active compounds: synthesis, characterization, DNA interaction, antibacterial, cytotoxic and SOD mimic activities", *Appl. Biochem. Biotechnol.*, 169 (2013) 1329-1345.
- [4] M. Mathew, A. J. Gary, G. J. Palenik, *J. Am. Chem. Soc.*, 92 (1972) 3197-3198.
- [5] F. Mohammadtabar, B. Shafaatian, A. Soleymanpour, S. A. Rezvani, B. Notash "Synthesis, spectral characterization, X-ray crystal structure, electrochemical studies, and DNA interactions of a schiff base pro-ligand and its homobimetallic complexes containing the cysteamine moiety", *Transition Met. Chem.*, 41 (2016) 475-484.
- [6] L. S. Lerman "Structural considerations in the interaction of DNA and acridines", *J. Mol. Biol.*, 3 (1961) 18-30.

Destabilization of glucose oxidase by increasing concentration of ionic liquid: Insight from molecular dynamics simulation

F. Janati-Fard^{a,*}, M.R.Housaindokht^{a,b}, H.Monhemi^b

^aBiophysical Chemistry Laboratory, Department of Chemistry, Faculty of Science, Ferdowsi University of Mashhad, Mashhad, 9177948974, Iran

^bDepartment Research and Technology Center of Biomolecules, Faculty of Science, Ferdowsi University of Mashhad, Mashhad, 9177948974, Iran

*fjanatifard@gmail.com

Abstract: Ionic liquid (IL) containing solvents can change the structure, dynamics and stability of proteins. In order to investigate the mechanism by which ILs induce structural changes in a large multimeric protein, we studied the interactions of glucose oxidase (GOx) with two different concentration of IL, 1-ethyl-3-methylimidazolium bromide. Molecular dynamics simulations showed that enzyme has an unstable conformation at higher IL concentration. It was found that IL, at higher concentration, reduces intermolecular hydrogen bond and unfold enzyme structure. To the best of our knowledge, this is the first study that bears detailed structural mechanism about the IL effects on glucose oxidase.

Keywords: *Glucose oxidase; Ionic liquid; Molecular dynamics simulation*

Introduction

Ionic liquids (ILs) have gained widespread attention from the academic and industrial research communities due to their unusual and useful properties [1]. ILs are non-volatile, non-flammable, and highly stable, thus possessing great potential as environment friendly green solvents [2]. Glucose oxidase (GOx) is a dimeric enzyme containing two subunits and two flavin adenine dinucleotide (FAD) cofactors [3]. GOx has found in the food industry for the glucose removal from dried eggs, for the removal of oxygen from fruit juices, for the production of gluconic acid, and as a source of hydrogen peroxide in food preservation [4]. Molecular dynamics (MD) simulations on biomolecules in hydrated ionic liquids could provide detailed information of molecular interactions. However, in contrast to the large amount of experiments, the theoretical studies on the effects of ILs on protein structures are quite few so far [5-8].

Considering these, the aim of this work is to investigate the effect of two different concentration of IL on the behaviour of glucose oxidase using MD simulation.

Materials and Method

Molecular dynamics (MD) simulations were performed using GROMACS 5.0.4 with a GROMOS 43a1 forcefield [9]. The crystal structure of GOx used for the simulation was obtained from the Protein Data Bank (PDB ID: 1GPE) [10].

Parameters for FAD which were not present in the GROMOS force field were taken from the work of van den Berg et al [11]. The IL parameters referring to the GROMOS forcefield were supplied by calculating the atomic charges of the IL via electrostatic surface potential fits based on CHelpG procedure [12], at the

same level of theory, in conjunction with PRODRG application. LINCS algorithm [13] was employed to fix the chemical bonds between the atoms of the protein and the systems constitutes. To maintain a constant temperature and pressure for various components during simulations, the Berendsen coupling algorithm was applied [14]. Then 50 ns, molecular dynamics simulation was performed.

Results and Discussion

MD process was performed on the GOx during the 50 ns time interval in the presence of two ionic liquids by GROMACS software. The structure information such as RMSD, RMSF, radius of gyration and hydrogen bonding between GOx and solvent molecules were obtained at room temperature.

Root mean square deviation (RMSD) value is a useful estimation for quantifying stability of the tertiary structure of the proteins [15]. RMSD of the GOx in the presence of 10 and 20% (v/v) ionic liquid was obtained. As seen in Fig. 1, the system reaches a stable state after about 50 ns. Fig. 1 shows that GOx has more structural changes (RMSD) in the presence of higher concentration of ionic liquid. These results indicate that a significant destabilization of the overall protein occurred upon treatment of GOx with 20% (v/v) ionic liquid.

The root mean-square fluctuation (RMSF) value is a measure of the macromolecular flexibility, which shows the deviation between the position of a particle and some reference positions [16]. Additionally, RMSF for GOx with 10 and 20% of IL were shown in Fig. 2. RMSF values tend to increase with increasing concentration, which indicate that 20%IL-treated GOx has unfold structure, compared to 10% IL-treated GOx.

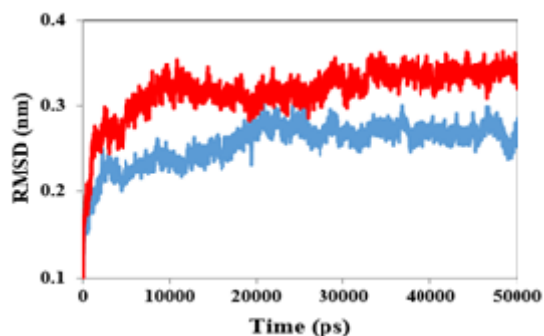


Fig.4: Root mean square deviation (RMSD) for GOx in the presence of 10% (blue) and 20% (red) IL.

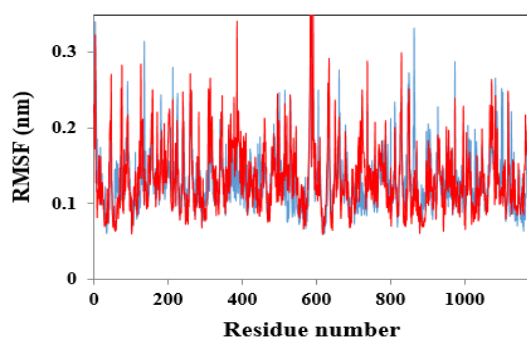


Fig.2: Average root mean square fluctuation (RMSF) for GOx in the presence of 10% (blue) and 20% (red) IL.

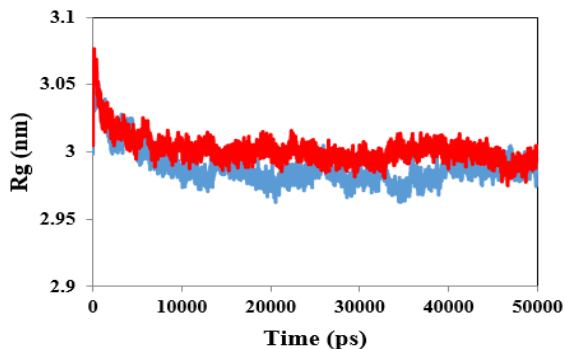


Fig.3: Radius of gyration (Rg) for GOx in the presence of 10% (blue) and 20% (red) IL.

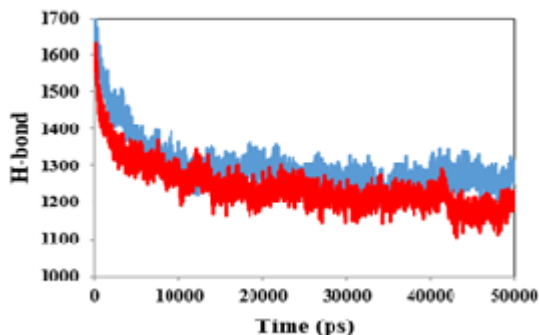


Fig.4: Hydrogen bond (H-Bond) for GOx in the presence of 10% (blue) and 20% (red) IL.

Radius of gyration (R_g) describes the equilibrium conformation of a total system, which could be as an indicator of protein structure compactness [17]. Fig. 3 displays the radius gyration of GOx in the presence of 10 and 20% (v/v) ionic liquid. The results prove that the GOx structure at higher concentration of IL has been unfolded.

Fig.4 shows intermolecular hydrogen bond of GOx in the presence of 10 and 20% (v/v) IL. It is obvious that hydrogen bond in system with 20% ionic liquids is decreased so the GOx structure has been unfolded. Totally, ionic liquid can affect poly peptide chain and change its hydrogen bond. As sites of hydrogen bond is fixed in poly peptide, by addition of IL the number of hydrogen bond in protein decrease.

Conclusions

In this work, to understand the effect of different concentration of IL on the behavior of a multimeric enzyme, the structure, conformation, stability in IL-treatment GOx were investigated using molecular dynamic simulation. According to the MD simulation, IL at higher concentration alters the conformational structure of the enzyme resulting in a decrease in the stability. Furthermore, at high concentration of IL, the enzyme interactions showed an increase in radius gyration and decrease in hydrogen bond offering unfolding process of enzyme.

References

- [1] G.A. Baker, S. Baker, S. Pandey, F.V. Bright "An analytical view of ionic liquids", *Analyst*, 130 (2005) 800–808.
- [2] S. Park, R.J. Kazlauskas "Biocatalysis in ionic liquids –advantages beyond green technology", *Current Opinion in Biotechnology*, 14 (2003) 432–437.
- [3] W. N.Ye, D. Combes "The Relationship between the Glucose Oxidase Subunit Structure its Thermostability", *Biochimica et Biophysica Acta*, 999 (1989) 86–93.
- [4] S.B. Bankar, M.V. Bule, R.S. Singhal, L. Ananthanarayan "Glucose oxidase-An overview", *Biotechnology Advances*, 27 (2009) 489–501.
- [5] M. Haberler, O. Steinhauser "On the influence of hydrated ionic liquids on the dynamical structure of model proteins: a computational study", *Physical Chemistry Chemical Physics*, 13 (2011) 17994–18004.
- [6] M. Haberler, C. Schroder, O. Steinhauser "Solvation studies of a zinc finger protein in hydrated ionic liquids", *Physical Chemistry Chemical Physics*, 13 (2011) 6955–6969.
- [7] N. M. Micaelo, C. M. Soares "Protein structure and dynamics in ionic liquids. Insights from molecular dynamics simulation studies", *The Journal of Physical Chemistry B*, 112 (2008) 2566–2572.



- [8] M. Klahn, G. S. Lim, P. Wu “How ion properties determine the stability of a lipase enzyme in ionic liquids: A molecular dynamics study”, *Physical Chemistry Chemical Physics*, 13 (2011) 18647–18660.
- [9] E. Lindahl, B. Hess, D. van der Spoel “GROMACS: A Message-Passing Parallel Molecular Dynamics Implementation”, *Computer Physics Communications*, 91 (1995) 43–56.
- [10] G. Todde, S. HovmÖller, A. Laaksonen, F. Mocchi “Glucose oxidase from penicillium amagasakiense: Characterization of the transition state of its denaturation from molecular dynamics simulations”, *Proteins*, 82 (2014) 2353–2363.
- [11] P.A.W. van den Berg, K. Anton Feenstra, A.E. Mark, H.J.C. Berendsen, A.J.W.G. Visser “Dynamic conformations of flavin adenine dinucleotide: Simulated molecular dynamics of the flavin cofactor related to the time-resolved fluorescence characteristics”, *The Journal of Physical Chemistry B*, 106 (2002) 8858–8869.
- [12] T.C.F. Gomes, J. Vicozo da Silva, L.N. Vidal, P.A.M. Vazquez, R.E. Bruns “Chelp G and QTAIM atomic charge and dipole models for the infrared fundamental intensities of the fluorochloromethanes”, *Theoretica Chimica Acta*, 121 (2008) 173–179.
- [13] B. Hess, H. Bekker, H.J.C. Berendsen, J.G.E.M. Fraaije “LINCS: A linear constraint solver for molecular simulations”, *Journal of Computational Chemistry*, 18 (1997) 1463–1472.
- [14] H.J.C. Berendsen, J.P.M. Postma, W.F. van Gunsteren, A. DiNola, J.R. Haak “Molecular Dynamics with Coupling to an External Bath”, *The Journal of Chemical Physics*, 81 (1984) 3684–3690.
- [15] F. Janati-Fard, M.R. Housaindokht, H. Monhemi “Investigation of structural stability and enzymatic activity of glucose oxidase and its subunits”, *Journal of Molecular Catalysis B: Enzymatic*, 134 (2016) 16–24.
- [16] T.W. Allen, O.S. Andersen, B. Roux “On the importance of atomic fluctuations, protein flexibility, and solvent in ion permeation”, *The Journal of General Physiology* 124(2004), 679–690.
- [17] M.Y. Lobanov, N.S. Bogatyreva, O.V. Galzitskaya “Radius of gyration as an indicator of protein structure compactness”, *Molecular Biology*, 42 (2008) 623–628.

Fluorescence study on the interaction between Nickel (II) Complex [Ni(bin)₂OAC] and bovine serum albumin

N.Sohrabi^{*a}, M.Eslami Moghadam^{*a}R. Amrolahi

^aDepartment of Chemistry, Payame Noor University University, Tehran, P.O.19395-3697, Iran

* nsohrabi48@gmail.com

Abstract: The interaction of Nickel (II) Complex [Ni(bin)₂OAC] and bovine serum albumin (BSA) was studied by fluorescence spectroscopy at room temperatures. The results revealed that Nickel (II) Complex [Ni(bin)₂OAC] caused the fluorescence quenching of BSA through a static quenching procedure. The binding constants (K_b), and the number of binding sites (n), were obtained to be 1.11×10^6 and 1.040 at 298K, respectively. The primary binding pattern between Nickel (II) Complex [Ni(bin)₂OAC] and BSA was interpreted as hydrophobic interaction. In this study, it was decided that new water soluble compound of binicotinic acid ligand with formula [Ni(bin)₂OAC], (bin= 2,2-bipyridine-3,3-dicarboxylic) will be designed and synthesized.

Keywords: Bovine serum albumin (BSA), Fluorescence spectra, Interaction, [Ni(bin)₂](OAC)₂

Introduction

Recently, chiral coordination polymers have become a topic of intense interest due to their intriguing potential application in enantioselective absorption and catalysis, porous materials, nonlinear optical materials and magnetic materials [1]. Bridging ligands with twisted conformation spacers which exhibit atropisomer chirality have been extensively employed to build chiral coordination polymers and are proven to be efficient for chiral generation and transmission. Taking this into consideration, 2,2-bipyridine-3,3-dicarboxylic acid (H₂bpy-3,30-dc), which is characteristic of multifunctional O coordination sites, structural flexibility and conformational freedom, is chosen as the building block to study the formation of chiral coordination polymers through spontaneous resolution [2]. The atropisomer chiral bridging mode of the ligand has the potential to translate the chirality of the first metal center to the second one. The presence of uncoordinated nitrogen atoms of the ligand is expected to form intermolecular hydrogen bonds [3], which might be homochiral and strong enough to control the chiral aggregation. Herein, d⁸ metal were chosen as the metal center. Serum albumins are the major soluble proteins in the circulatory system. They play an important role in the transport and deposition of many drugs molecules in the blood. Since the overall distribution, metabolism and efficacy of many drugs in the body are correlated with their affinities towards serum albumin, the investigation of albumin–drug binding is imperative. In this paper, bovine serum albumin (BSA) is selected as our protein model because of its long-standing interest in protein community and structural homology with human serum albumin. Recently, many studies have been carried out to investigate the interaction of proteins with drugs by

NMR, CD, ROD, Raman, attenuated total reflectance-Fourier transform infrared (ATR-FT-IR), UV–vis absorbance (UV) and fluorescence spectroscopy (FS). Measurement of quenching of albumin's natural fluorescence is an important method to study its interaction with several substances[4]. In this paper, the interaction between Nickel (II) Complex [Ni(bin)₂OAC] and BSA has been investigated using FS. The binding constants were calculated.

2. Materials and method

2.1. Apparatus

Fluorescence intensity changes were studied by using a Scinco spectrofluorimeter, FS-2 model, equipped with a 1.0 cm quartz cell.

2.2. Materials

Bovine serum albumin (BSA) were purchased from Sigma-Aldrich chemical company. All other chemical reagents were of analytical reagent grade and were used as purchased without further purification. All experiments were performed in 5 mM phosphate buffer at pH 7.0 at 25 °C. The buffer solution includes (1.53 mM KH₂PO₄ and 0.97 mM K₂HPO₄) dissolved in the double distilled water. The doubly distilled water was used to prepare the buffer solutions

2.3. Procedures

A 1.5 mL solution, containing appropriate concentration of ligand (1.3×10^{-4} mol/L), was titrated by successive additions of a 1.5045×10^{-5} mol/L stock solution of BSA. Titrations were done manually by using micro-pipette. The fluorescence spectra were then measured at 298 K.

Results and Discussion

3.1. Fluorescence quenching spectra

Fig. 1 shows the emission spectra of BSA in the presence of various concentrations of ligand. It is observed that the fluorescence intensity of BSA decreases regularly with the concentration increase of ligand, but there is no significant emission wavelength shift with the addition of ligand. These data indicate that Complex [Ni(bin)2OAC] could interact with BSA and quench its intrinsic fluorescence.

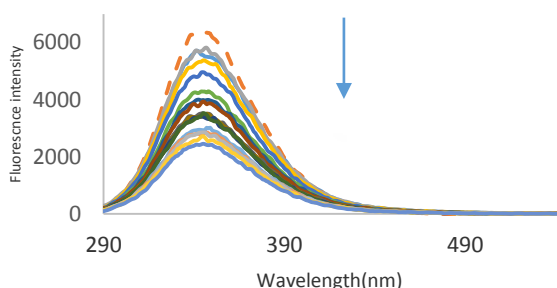


Fig. 1. Fluorescence spectra of BSA with Various of Complex [Ni(bin)2OAC] at 298K, (pH=7), c(BSA) =0.2mg/ml, c(ligand)= 1.3×10^{-4}

3.2. Principles of fluorescence quenching

Fluorescent quenching can occur in two different mechanisms, static quenching and dynamic quenching. For dynamic quenching, the mechanism can be described by the Stern–Volmer equation:

$$F_0/F = 1 + K_q \tau_0 [Q] = 1 + K_{sv} [Q] \quad (1)$$

where F_0 and F represent the fluorescence intensities in the absence and in the presence of quencher, respectively. K_q is the quenching rate constant of the biomolecule, K_{sv} the dynamic quenching constant, τ_0 the average lifetime of the biomolecule without quencher, and $[Q]$ the concentration of quencher. In order to confirm the quenching mechanism, the procedure of the fluorescence quenching was first assumed to be a dynamic quenching process.

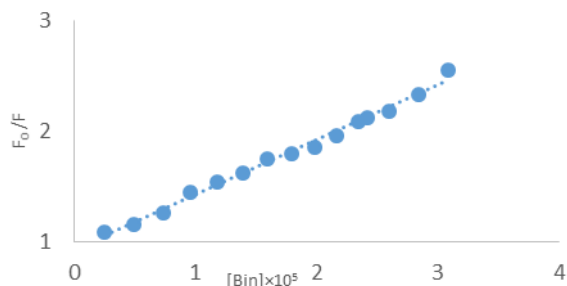


Fig. 2. Stern–Volmer plots of BSA for the quenching of BSA by Complex [Ni(bin)2OAC] at 298 K, (pH=7), c(BSA)=0.2mg/ml,

Fig. 2 displays the Stern–Volmer plots of the quenching of BSA fluorescence by Complex [Ni(bin)2OAC] at room temperature. The corresponding dynamic quenching constants for the interaction between Complex [Ni(bin)2OAC] and BSA are found to be $K_{sv} = 4.9 \times 10^3$ (298 K, $r = 0.9923$). When the fluorescence lifetime of the biopolymer is taken as 10^{-8} s [5-7], the quenching rate constant K_q at room temperatures was calculated to be 4.9×10^{11} (298 K). According to the literatures [8], for dynamic quenching, the maximum scatter collision quenching constant of various quenchers with biopolymers is 2.0×10^{10} L mol⁻¹ s⁻¹. Obviously, the rate constant of protein quenching procedure initiated by ligand is greater than the K_q of the scatter procedure. This means that the quenching is not initiated by dynamic collision but from the formation of a complex. Meanwhile, we find that the quenching rate constants are so high. The first reason is that the ion strength under the experimental condition is lower and the fluorescent quantum yield of BSA increases compared to the other studies [9-11]. Lower concentration of ligand can lead to fluorescence quenching of BSA. The second reason is that there may be a strong binding between BSA and ligand.

3.3. Binding constant and binding sites

For static quenching, the relationship between fluorescence quenching intensity and the concentration of quenchers can be described by Eq. (2) [12-13]:

$$\log(F_0 - F)/F = \log K_b + n \log [Q] \quad (2)$$

where K_b is the binding constant, and n is the number of binding sites per BSA. After the fluorescence quenching intensities on BSA at 350 nm were measured, the double-logarithm algorithm was assessed by Eq. (2). Fig.3 shows the double-logarithm curve ($\log(F_0 - F)/F$ vs. $\log[\text{ligand}]$), the interaction between ligand and BSA agrees well with the site-binding model underlined in Eq. (2). The results suggest that there is a strong binding force between ligand and BSA [15-16]. The values of n approximately equal to 1 indicate the existence of just a single binding site in BSA for ligand.

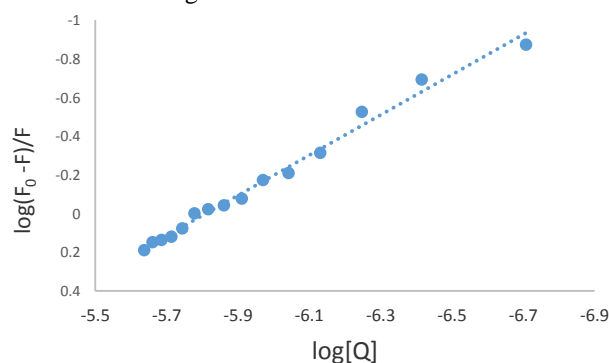


Fig. 3: The plot of $\log(F_0 - F)/F$ vs. $\log[\text{ligand}]$ at 298K, pH=7



4. Conclusions

A fluorescence method for the rapid and simple determination of the interaction between Complex [Ni(bin)2OAC] and BSA was provided. The results obtained give preliminary information on the binding of Complex [Ni(bin)2OAC] to BSA. The experimental results show that the fluorescence quenching of BSA by Complex [Ni(bin)2OAC] is a result of the formation of ligand-BSA complex. Static quenching is confirmed to result in the fluorescence quenching. Hydrophobic interaction force plays a major role in stabilizing the complex. The results of synchronous fluorescence spectroscopy indicate that the conformation of BSA is not changed in the presence of Complex [Ni(bin)2OAC].

4. References

- [1]. A. Assalit, T. Billard, S. Chambert, R. Bernard " 2,2-Bipyridine-3,3-dicarboxylic carbohydrate esters and amides. Synthesis and preliminary evaluation as ligands in Cu(II)-catalysed enantioselective electrophilic fluorination" *J. Photochem. Photobiol*, 20(2009) 593-601
- [9]. Hu, Y.J., Liu, Y., Zhang, L.X., Zhao, R.M., Qu, S.S." Studies of interaction between colchicine and bovine serum albumin by fluorescence quenching method", *J. Mol. Struct*, 750(2005) 174-178.
- [10]. Liu, L., Y.M., Sun, G.Z., X.F." Study on the interaction between colchicine and bovine serum albumins by fluorescence method. Chin", *J. Anal. Chem.* 32(2004) 615-618.
- [11]. Zhou, N., Liang, Y.Z., Wang, P." Characterization of the interaction between furosemide and bovine serum albumin", *J. Mol. Struct*, 872(2008) 190-196.
- [12]. Eftink, M.R., Ghiron, C.A." Fluorescence quenching of indole and model micelle systems", *J. Phys. Chem*, 80(1976) 486-493.
- [13]. Feng, X., Lin, Z., Yang, L., Wang, C., Bai, C. "Investigation of the interaction between acridine orange and bovine serum albumin", *Talanta*, 47(1998) 1223-1229.
- [14]. Wei, X.F., Liu, H.Z."The interaction between Triton X-100 and bovine serum albumin", *Chin. J. Anal. Chem.* 28(2000) 699-701
- [15]. Sulkowska, A., Rownicka, J." Effect of guanidine hydrochloride on bovine serum albumin complex with antithyroid drugs: fluorescence study" *J. Mol. Struct*, 704(2004) 291-295.
- [16]. Zhang, Y.Z., Zhou, B., Liu, Y.X., Zhou, C.X., Ding, X.L., Liu, Y."Fluorescence study on the interaction of bovine serum albumin with *p*-aminoazobenzene" *J. Fluoresc*, 18(2008)109-118
- [2]. X. Lixia, F. Wenhua, L. Xin, M. Lei " Syntheses of Zn or Cd complexes from dicarboxylate ligand exhibiting an axial chirality and auxiliary ligand" *Chin. J. Anal. Chem*, 423(2014)79-83
- [3]. K. Chryssou, V.J. Catalano, R. Kurtaran, P. Falaras " Synthesis and characterization of bdmppdc bpyRu (II) complex for dye-sensitized solar cells [where bdmpp is 2,6-bis(3,5-dimethyl-*N*-pyrazoyl)pyridine and dc bpy is 2,2-bipyridine-4,4-dicarboxylic acid]" , *Inorganica Chim*, 328 (2002) 204-209
- [4]. Bose, B., Dube, A." Interaction of Chlorin p6 with bovine serum albumin and photodynamic oxidation of protein" *J. Photochem. Photobiol*, 85(2006) 49-55. (2006).
- [5]. Athina, P., Rebecca, J.G., Richard, A.E." Interaction of flavonoids with bovine serum albumin: fluorescence quenching study" *J. Agric. Food Chem.* 53(2005) 158-163.
- [7]. Lakowicz, J.R.: Principles of Fluorescence Spectroscopy. Plenum, New York/London (1983)
- [8]. Lakowicz, J.R., Weber, G." Quenching of fluorescence by oxygen-probe for structural fluctuations in macromolecules" *Biochem*, 12(1973) 4161-4170 .

Lipase Immobilization on Metal-Organic Framework and Evaluation of Initial Enzyme Concentration Effect

Atefeh Zare, Abdol-Khalegh Bordbar *

Department of Chemistry, University of Isfahan, Isfahan, 81746-73441, Iran.

*akbordbar@gmail.com

Abstract: In the study, one of the metal-organic frameworks, MIL-101-NH₂ (Cr), was synthesized by solvothermal method and functionalized with 2,4,6-trichloro-1,3,5-triazine (TCT). Amino MIL-101(Cr) and its chemical functionalized form (TCT@NH₂-MIL-101(Cr)) were used as support for *Candida rugosa* lipase (CRL) immobilization. The effect of initial CRL concentration on the enzyme loading and the immobilized enzyme activity were investigated. The result indicated that with increasing the amount of enzyme loading, the corresponding specific activity decreases. The amount of enzyme loading was determined by Bradford method. The catalytic activity of the immobilized lipase was assayed by the hydrolysis of *p*-nitrophenyl palmitate (*p*-NPP). FT-IR spectra, XRD diffraction and FE-SEM analysis were used to confirm successive synthesis, functionalization and immobilization.

Keywords: Lipase, Immobilization, Metal-organic framework

Introduction

Enzymes as versatile bio-catalyst are capable of catalyzing reactions with up to 10¹⁷-fold rate accelerations. They often display high regio- and chemoselectivity while operating under mild conditions [1]. However, the reaction conditions in an industrial surrounding differ quite often from the natural environment. This may lead to enzyme denaturation [2]. Immobilizing enzymes on solid supports offer to enhance enzyme stability in storage and operational conditions.

Metal-Organic Frameworks (MOFs) are a new class of organic-inorganic hybrid porous crystalline materials in which metal ions, as coordination centres, are linked together with a variety of polyatomic organic bridging ligands [3][4]. A wide range of potential applications has been reported for MOFs such as gas storage, separation, catalysis, sensing, biomedicine [5]. Moreover, this materials are promise candidates for enzyme immobilization due to tunable pore size, high surface area and remarkable physical and chemical properties [6].

In this study, NH₂-MIL-101 (Cr) was synthesized and modified with 2,4,6-trichloro-1,3,5-triazine (TCT). NH₂-MIL-101 (Cr) and its chemically modified form were used for *Candida rugosa* lipase (CRL) immobilization. The effect of initial CRL concentration on the enzyme loading and the immobilized enzyme activity for two supports were investigated the results were compared.

Materials and Method

Materials

CRL (Type VII, nominal activity >> 700 U mg⁻¹), *p*-nitrophenyl palmitate (*p*-NPP), Arabic gum, 2-aminoterephthalic acid and Coomassie Brilliant Blue G-250 were purchased from Sigma-Aldrich. Ethanol (96%), isopropyl alcohol (99.7%), sodium hydroxide, TCT, component of MIL-101(Cr) and tetrahydrofuran (THF)

were supplied from Merck. NaH₂PO₄.2H₂O and Na₂HPO₄.12H₂O were used for preparing 50 mM phosphate buffer solution (PBS).

Synthesis and Activation of Supports

MIL-101(Cr)-NH₂ was prepared following the procedure reported by Lin et al. [7]. The obtained NH₂-MIL-101(Cr) was functionalized with TCT in terms of the following procedures: Briefly, 0.1 g NH₂-MIL-101(Cr) and 0.2 g TCT were dispersed in 10 mL THF. The mixture was reacted and stirred under certain conditions. Then, the chlorinated amino MIL was washed with THF several times to remove the unreacted TCT and dried at room temperature.

Enzyme Immobilization

To investigate the effect of initial lipase concentration on the enzyme loading and activity, the solid supports (3mg) were suspend in 5 mL of lipase solution (with different concentration) for 24h at room temperature. The immobilized lipase were separated by centrifugation and washed three times with 50 mM PBS (pH 7.5). The amount of enzyme loading was determined by measuring the initial and final concentration of CRL in the immobilization medium using the Bradford method [8].

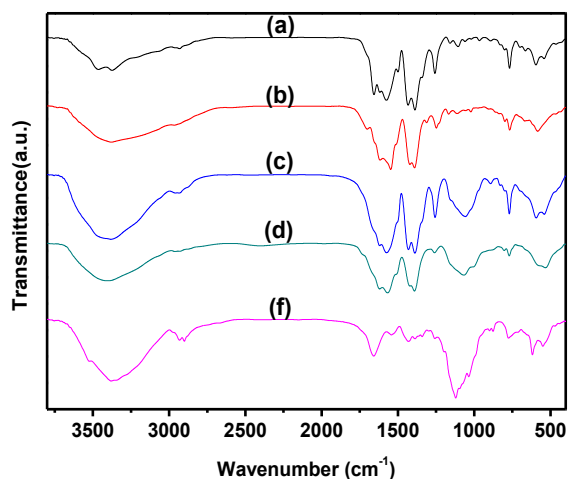
Assessment of Lipase Activity

The catalytic activity of immobilized lipase was assayed by the hydrolysis of *p*-nitrophenyl palmitate (*p*-NPP) to *p*-nitrophenol and palmitic acid. The substrate solution was prepared by mixing one volume of *p*-NPP solution and 9 volume of buffer solution containing PBS (50 mM, pH 7.5), Arabic gum, 2%, Triton X-100, 4% and NaCl 1%. The immobilized lipase was incubated in 3 mL of substrate solution at room temperature for 4 min. After 5 min centrifugation, the absorbance of released *p*-nitrophenol was measured at 410 nm in a UV/VIS spectrophotometer as a criterion of enzyme activity.

Results and Discussion

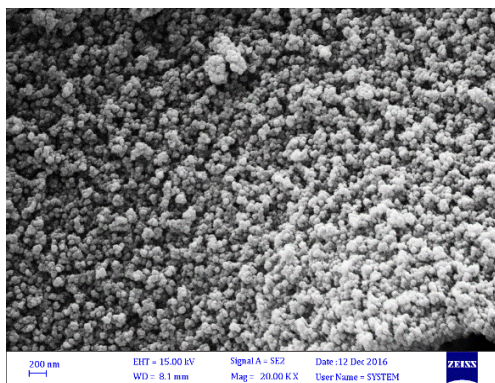
Characterization

The FTIR spectra of NH₂-MIL, TCT@NH₂-MIL, CRL@NH₂-MIL, CRL@TCT@NH₂-MIL and free CRL are shown in Fig. 1. In Fig. 1a, the double peaks at 3490 cm⁻¹ and 3380 cm⁻¹ were clearly observed, which were ascribed to the asymmetrical and symmetrical stretching vibration adsorption of the amine groups [7]. The observed peaks at 1624 cm⁻¹ and 1338 cm⁻¹ correspond to the N-H bending vibration and the characteristic C-N stretching of aromatic amines, respectively. In Fig. 1b, the absence of the double peaks at 3490 cm⁻¹ and 3380 cm⁻¹ indicates that the amino MIL is chlorinated. The appearance of peaks at

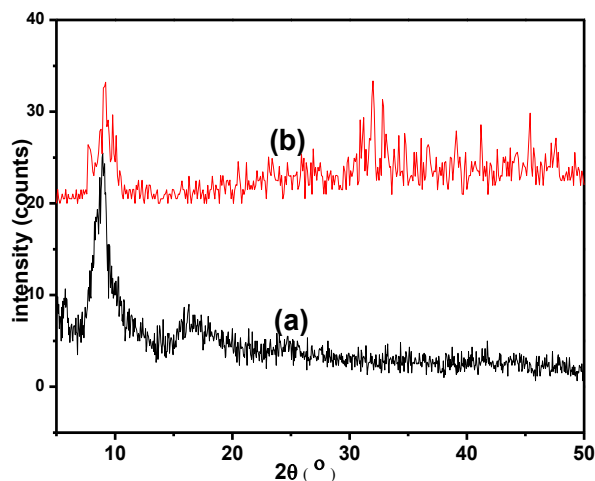


1000-1200 cm⁻¹ in Fig. 1c and d confirm the lipase immobilization.

Fig. 1. The FTIR spectra of (a) NH₂-MIL, (b) TCT@NH₂-MIL, (c) CRL@NH₂-MIL, (d) CRL@TCT@NH₂-MIL, (f) free CRL



The morphology of NH₂-MIL-101(Cr) were investigated by FE-SEM (field emission scanning



electron microscopy) Fig. 2 indicates the uniform size distribution of the amino MIL particles and their spherical shape.

Fig. 2. SEM image of NH₂-MIL-101(Cr)

Fig. 3 shows the PXRD pattern for NH₂-MIL-101(Cr) and CRL@TCT@NH₂-MIL. These patterns confirm that the structure of support remains nearly intact after the modification with the agent and immobilization steps. The observed additional peaks at 32° in Fig. 3b attributed to immobilized CRL.

Fig. 3. XRD patterns of (a) NH₂-MIL, (b) CRL@TCT@NH₂-MIL

Effect of initial concentration of lipase

The different initial CRL concentration in medium immobilization was applied and its effect on the enzyme loading for two supports was investigated (Fig. 4). For NH₂-MIL-101(Cr) the amount of CRL loading increased greatly with the initial lipase concentration in solution. However, in the case of TCT@NH₂-MIL, at first, the amount of enzyme loading increased then leveled off at 28 μg mg⁻¹. It has been reported that functionalization of MIL reduces its surface area [9] therefore, the observed differences in loading capacity of the supports can be attributed to less surface area of TCT@NH₂-MIL Compared with NH₂-MIL.

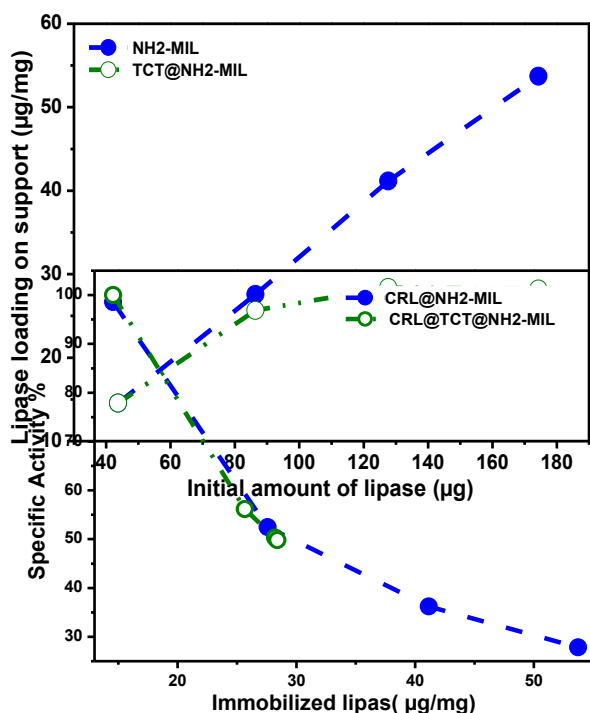


Fig. 4. The variation of enzyme loading vs. initial concentration of lipase for various MIL supports

The effect of different amounts of the CRL added on specific activity of the immobilized lipase for two supports is shown in fig. 5. With increasing the amount of enzyme loading, the corresponding specific activity decreases, in the both cases. It is considered that the higher CRL loading makes the enzyme form an intermolecular steric hindrance, which restrains the diffusion of the substrate and product. Therefore, the relative activity decreased.

Fig. 5. Effect of lipase initial concentration on the specific activity of immobilized enzyme

Conclusions

In the study, we have demonstrated the successful CRL immobilization on NH₂-MIL-101(Cr) and its chemical functionalized form (TCT@NH₂-MIL-101(Cr)). The influence amount of different initial CRL concentration in medium immobilization on enzyme loading and specific activity is investigated. The results show there is the highest specific activity for two supports at the lowest amount of enzyme loading. Because, at the higher CRL loading the enzyme molecules form an intermolecular steric hindrance.

References

[1] M. Marciello, M. Filice, and J. M. Palomo, "Different strategies to enhance the activity of lipase catalysts," *Catal. Sci. Technol.*, 2 (2012)

1531.

[2] A. Liese and L. Hilterhaus, "Evaluation of immobilized enzymes for industrial applications," *Chem. Soc. Rev.*, 42 (2013) 6236–49.

[3] A. U. Czaja, N. Trukhan, and U. Muller, "Industrial applications of metal-organic frameworks," *Chem. Soc. Rev.*, 38 (2009) 1284–1293.

[4] D. S. Raja, W.-L. Liu, H.-Y. Huang, and C. Lin, "Immobilization of Protein on Nanoporous Metal-Organic Framework Materials," *Comments Inorg. Chem.*, 35 (2015) 332–350.

[5] E. Gkaniatsou, C. Sicard, R. Ricoux, J.-P. Mahy, N. Steunou, and C. Serre, "Metal-organic frameworks: a novel host platform for enzymatic catalysis and detection," *Mater. Horiz.*, 4 (2017) 55–63.

[6] X. Wu, M. Hou, and J. Ge, "Metal-organic frameworks and inorganic nanoflowers: a type of emerging inorganic crystal nanocarrier for enzyme immobilization," *Catal. Sci. Technol.*, 5 (2015) 5077–5085.

[7] Y. Lin, C. Kong, and L. Chen, "Direct synthesis of amine-functionalized MIL-101(Cr) nanoparticles and application for CO₂ capture," *RSC Adv.*, 2 (2012) 6417.

[8] M. M. Bradford, "A rapid and sensitive method for the quantitation of microgram quantities of protein utilizing the principle of protein-dye binding," *Anal. Biochem.*, 72 (1976) 248–254.

[9] F. Zadehahmadi *et al.*, "Synthesis and characterization of manganese(III) porphyrin supported on imidazole modified chloromethylated MIL-101(Cr): A heterogeneous and reusable catalyst for oxidation of hydrocarbons with sodium periodate," *J. Solid State Chem.*, 218 (2014) 56–63.

Thymine and Its Derivatives: A Computational Study

M. Esnaashari^a, M. Namazian^{*a}, M. R. Noorbala^a

^aDepartment of Chemistry, Yazd University, Yazd, Iran

*e-mail: namazian@yazd.ac.ir

Abstract: Nucleic acid biopolymers include the DNA and RNA molecules. DNA is composed of a sugar deoxyribose, a phosphate group, and an inimitable sequence of the nitrogenous bases adenine (A), guanine (G), cytosine (C), and thymine (T). Thymine is usually only existing in DNA. The chemical properties of thymine and some of its derivatives in which, the oxygen atoms of thymine are replaced with sulfur atoms, have been studied theoretically. The roles of sulfur atoms on ionization energy, electron affinity, proton affinity and radical reactions of thymine have been investigated. Density functional theory (DFT) has been used to optimize molecular geometries.

Keywords: Thymine; DFT; Ionization energy; Electron affinity; Proton affinity

Introduction

Recently, there has been considerable interest in the change of DNA and RNA, which may cause many illnesses. DNA is made of adenine, guanine, cytosine and thymine bases, while RNA is made of adenine, guanine, cytosine and uracil. These bases due to the biological significance were studied theoretically. One of molecular methods for spontaneous alterations is related to tautomerism of DNA bases [1].

Bai and Barbatti in 2016 with replacement of oxygen atoms with sulfur in thymine showed that the electronic absorption and properties of intersystem crossings of these derivatives depended on situation of substituent and the number of replacement severely [2].

In the present work, we have studied thermodynamic properties of thymine and its derivatives including of ionization energy, electron affinity and proton affinity with a reliable DFT method.

Computational and method

The geometries of thymine molecule and some of its derivatives were optimized by density functional theory at the level of B3LYP/6-31G (2df, p) as recommended by Curtiss [3]. Then single-point energies have been calculated by means of M06-2X/aug-cc-pVTZ method [4].

Results and Discussion

Ionization is the process by which an atom or a molecule acquires a positive charge by losing one electron to form ions and is equal to the energy

changes of the following reaction:



The studied molecules are shown in Fig1. The ionization energies are calculated for the stable forms of these molecules. The energies which are calculated at M06-2X/aug-cc-pVTZ level of theory are reported in Table1.

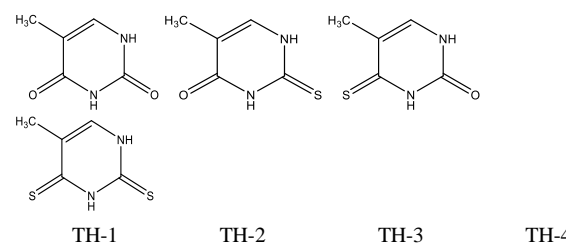
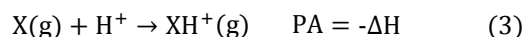


Fig.1: Thymine (TH-1) and its derivatives (TH-2 to Th-4).

The electron affinity (EA) is the change of energy of a process, in which a molecule gains an electron to form an anion, as shown in the following reaction:



Proton affinity is change of enthalpy of a process by which a molecule reacts with H⁺ as shown below:



For the protonation process, there are different sites to be protonated. These most active sites which are presented in Fig.2 are oxygen or sulfur atoms.

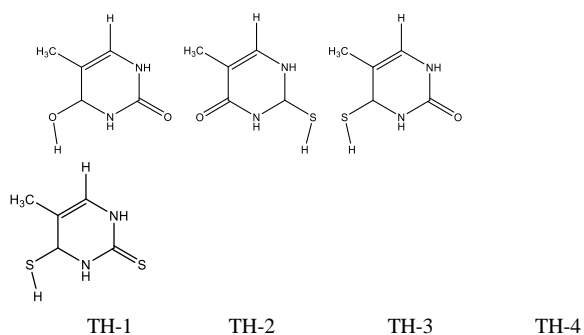


Fig.2: Protonated molecules of thymine and its derivatives.

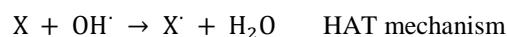
The final results of IE, EA and PA are presented in Table1. According to the values in this table, with the replacement of oxygen atoms with sulfur in thymine, the ionization energy decreases. The reason is that for larger molecules with sulfur atoms, the valence electrons are less affected by the effective load of the nucleus and therefore, less energy is required to remove the electron.

Fig. 2 shows the most stable protonated form when proton is attached the molecule. It is also worth noting that with the replacement of sulfur, EA and PA are increased. These are expected results so that with the increase of the size of molecules, the charged species are more stable compared to smaller species (TH-1).

Table1: The ionization energy (IE), electron affinity (EA) and proton affinity (PA) of thymine and some of its derivatives in eV, calculated at the level of M06-2X/aug-cc-pVTZ.

	IE	EA	PA
TH-1	8.91	0.05	8.83
TH-2	8.59	0.43	8.87
TH-3	8.29	0.84	9.07
TH-4	8.37	1.14	9.03

The reaction of a molecule with hydroxyl radical can be a model to investigate the radical stabilization energy (RSE) of studies species based on HAT and RAF mechanisms [5]:



(4)



The products of reaction (4) and (5) are shown in Fig.3

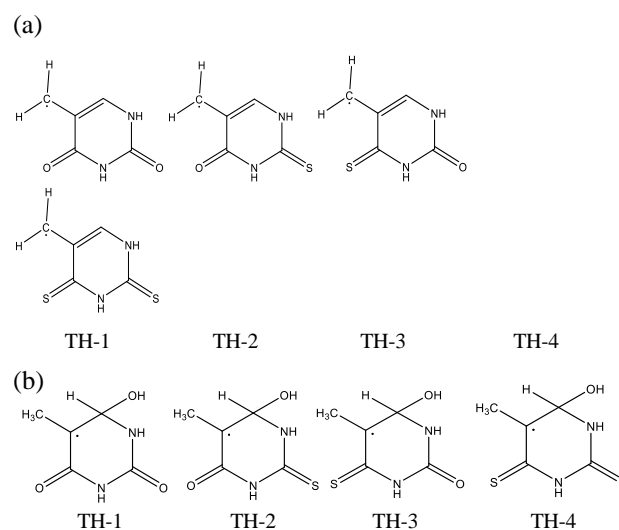


Fig.3: (a) The products of HAT reaction and (b) The products of RAF reaction

The change of enthalpies for the radical reactions of studied species with hydroxyl radical, reactions (4) and (5) are presented in Table 2. The values are in kJ/mol for both HAT and RAF mechanisms. As explained earlier, a hydrogen atom is transferred between molecule and hydroxyl radical for HAT and the hydroxyl radical is attached to molecule for RAF mechanism.

Table2: The change of enthalpies for the radical reactions of studied species with hydroxyl radical, reactions (4) and (5), in kJ/mol, based on HAT and RAF mechanisms s explained in text.

	HAT Reaction (4)	RAF Reaction (5)
TH-1	-117.9	-130.6
TH-2	-121.0	-128.2
TH-3	-110.8	-150.0
TH-4	-114.8	-150.0

For the radical reaction of HAT, with the replacement of oxygen atoms with sulfur, the change

of enthalpies are insignificant while for the reaction of RAF, the replacement of one oxygen by a sulfur atom increases RSE significantly.

Conclusions

In this study, the effects replacement of oxygen atoms with sulfur on the change of thermodynamic properties and radical reactions of thymine has been examined theoretically. As valence electrons of sulfur have more accessible than oxygen, sulfur substituent helps molecule to ionized more easily. In the case of electron affinity and proton affinity, the small charge densities on molecule with sulfur atom, result in the increase of EA and PA.

References

- [1] D. Jiao, H. Wang, Y. Zhang, Y. Tang, "A DFT study of thymine and its tautomers", *Can. J. Chem.*, 87 (2009) 406-415.
- [2] S. Bai, M. Barbatti, "Why replacing different oxygen of thymine with sulfur causes distinct absorption and intersystem crossing?", *J. Phys. Chem. A*, 120 (2016) 6342-6350.
- [3] L. A. Curtiss, P. C. Redfern, K. Raghavachari, "Gaussian-4 theory", *J. Chem. Phys.*, 126 (2007).
- [4] D. G. Truhlar, Y. Zhao, "Density functionals with broad applicability in chemistry", *Acc. Chem. Res.*, 41 (2008) 157-167.
- [5] F. Tureček, "Computational studies of radicals relevant to nucleic acid damage", *Advances in Quantum Chemistry*, 52 (2007) 89-120.



Investigation of *Candida Rugosa* Lipase Immobilization on the Modified Graphene Oxide

F. Jafarian^a, A. K. Bordbar^{a*}

^aDepartment of Chemistry, University of Isfahan, Isfahan, 81746-73441, Iran

*bordbar@chem.ui.ac.ir

Abstract : The attention to green methodologies have enlarged the usage of enzymatic technology in industrial processes. Enzyme immobilization can lead to increase stability and improve the reusability of enzyme. In this project, candida rugosa lipase (CRL) was immobilized on the surface of modified graphene oxide nanosheets. Initially, the graphene oxide (GO) was synthesized by Hummer method. Afterward, it was activated for covalent attachment of enzyme by designing appropriate reaction based on the use of cyanuric chloride (CC) as an appropriate chemical linker. Several techniques such as XRD, FESEM and FTIR was applied to characterize nanosheets in various stages of synthesis and after immobilization of CRL enzyme. The optimized conditions were determined for the immobilization process of CRL. The optimal time and initial concentration of CRL for immobilization at room temperature were respectively specified about three hours and 47.42 μg/mL. Under these conditions, the amount of immobilized CRL was 14.46 μg per mg of support (GO@CC) and relative activity% was 97.99%.

Keywords: immobilization, candida rugosa lipase, graphene oxide, cyanuric chloride

1. Introduction

Enzymes as a green catalysts, play an important role in biochemical reactions. Lipases are a class of enzymes which catalyze the hydrolysis of long chain triglycerides, esterification, interesterification, alcoholysis and acidolysis [1]. Accordingly, they are widely used biotechnological and industrial processes including food, paper, pulp, detergent, oleo-chemical, biodegradable polymer, cosmetics and perfumery, pharmaceutical and waste treatment [2]. However, the application of lipase is difficult and expensive because of its aqueous solubility and instability. Immobilization technique is often used to increase lipase performance. Generally, five significant strategies for enzyme immobilization are: adsorption, entrapment, ionic interaction, covalent binding, and cross-linking [3-4]. Although, immobilized enzyme has displayed advantages to the free enzyme, such as reusability, improved thermal, pH and storage stability, the reduction of catalytic activity after enzyme immobilization is a problem that could be attribute to low loading, large stereospecific blockade, damage of the active site. [5]. Therefore searching for new efficient supports and methods to immobilize enzymes is still an interesting topic for researchers. Hereunto, a variety of nanomaterials have been investigated as supports [6]. GO has been recently attended in various fields of scientific research due to its inexpensively, stability, high surface area, two-dimensional structures and biocompatibility. The easy dispersion of GO in water and other polar solvents refers to the unique characteristics of its surface that rich in hydroxyl, epoxide, carboxyl groups. So these advantages make GO a promising carrier in enzyme immobilization [7]. In fact, horseradish peroxidase (HRP) [8] glucose oxidase [9] lipase [10] have been successfully immobilized onto GO through various methods. In this

project, GO was prepared by hummers method [11] and, then, a composite of GO and cyanuric chloride (GO@CC) was synthesized via relatively proposed convenient method. GO@CC have been then examined as support for immobilization of *Candida Rogosa* Lipase (CRL). Thenceforward, the structure of GO was characterized by using X-ray powder diffraction (XRD) and a field emission scanning electron microscopy (FESEM) technique. The functionalization of GO surface and CRL immobilization on GO@CC was confirmed by Fourier transform infrared spectrum measurements (FTIR). The optimum conditions such as CRL initial concentration and the time for immobilization of CRL were investigated.

2. Experimental

2.1. Materials

Candida rugosa lipase (lyophilized powder, Type VII, nominal activity ≥ 700 U mg⁻¹), para-nitrophenyl palmitate (p-NPP, $\geq 98.0\%$), bovine serum albumin (BSA), N,N-diisopropylethylamine (DIPEA) and Coomassie Brilliant Blue G-250 were purchased from Sigma Chemical Co. (St. Louis, MO, USA), Isopropyl alcohol (99.7%), Triton X-100 and Arabic gum were purchased from Dae-Jung chemicals, The preparation of GO was according to the Hummers method, Cyanuric chloride (CC) and Tetrahydrofuran (THF) were obtained from Merck.

2.2. Instrumentations

X-ray powder diffraction spectrum of GO and natural graphite was obtained by a Bruker D8-advance X-ray diffractometer with Cu K α radiation ($\lambda = 0.1540$ nm). To determine the structure and size of GO, a field emission scanning electron microscopy (FESEM) instrument (SIGMA VP-500, ZEISS Germany) was used. The FTIR spectra were recorded by a Fourier



transform Infrared Spectroscopy (JASCO FTIR-6300, Japan) in the range of 4000–400 cm^{-1} . The activity of immobilized CRL on support and the concentration of CRL solution were detected by an UV-Vis spectroscopy system (PERKIN, USA).

2.3. Preparation GO and GO@CC

The GO powder was prepared by a modified Hummers method. After that, a suspension of 100 mg of GO powder and 20 mL anhydrous THF was magnetically stirred at 0°C for 5 hours with a solution containing of 0.1mmol of CC and 500 μL of DIPEA in THF. The product was purified by centrifuging with anhydrous THF several times and dried under vacuum.

2.4. CRL Immobilization on GO@CC

The mixture of 3 mg of GO@CC and 3 mL of phosphate buffer solution (PBS, 50 mM, pH 7.5) containing CRL was shaken for 2 hour at room temperature. After centrifuging, the solid and the supernatants were collected separately and the solid was washed with the PBS.

2.5. CRL Loading measurement

The supernatant was then used to measure the concentration of the residual CRL and determine the CRL loading on support by UV-Vis spectroscopy through the Bradford method. CRL loading on GO@CC is defined as the enzyme amount difference between the total enzyme used and the residual enzyme present in the supernatant after immobilization.

2.6. Activity assay

The enzyme activity was measured by the hydrolysis of p-NPP as a substrate. For preparing the substrate, 45 mg of (p-NPP) was dissolved in 15mL of propane-2-ol and Separately 0.2g of Triton X-100 and 0.05g of gum arabic was added to 45mL of phosphate buffer (50 mM, pH = 7.5). After that, 2mL of the first solution was mixed with 18 mL of the second solution. For enzyme activity assay, 3 mL of the assay solution was added to 0.1 mL of free enzyme or enzyme immobilized. After 7 min of reaction, the absorbance of released p-nitrophenol was detected at 410 nm in a UV-Vis spectrophotometer. One unit of lipase activity (1U) is defined as the amount of enzyme that produces 1 μmol of p-nitrophenol per minute. Relative activity were determined by the following equations:

$$\text{Relative activity} = A_2 * 100 / A_1 \quad (1)$$

Where A_2 is the activity of the immobilized enzyme and A_1 is the activity of the free enzyme .

3. Results and Discussion

3.1. Characterization of GO, GO@CC, and GO@CC@CRL

Fig. 1. Shows the XRD patterns for natural graphite (G) and GO. The pattern of GO has a peak around 2θ

= 10.86° and the most intense peak for graphite at $2 = 26.11$ is absent in GO sample.

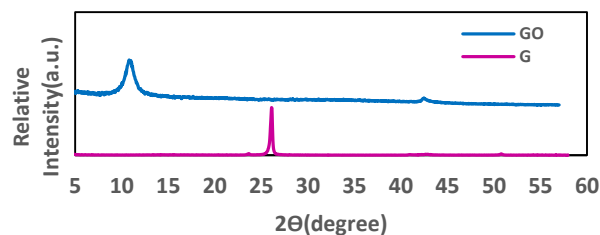


Fig.1: XRD pattern of graphite (G) and GO

The FESEM image of GO surface is shown in Fig. 2. It is detected that GO containing of thin sheets (about 22nanometers). This result proves two dimensional nanosheets of GO with high surface to volume ratio.

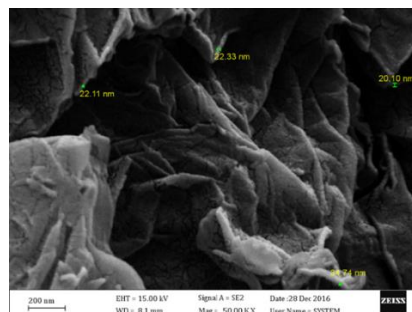


Fig.2: FESEM image of GO

According to Fig.3, the FTIR spectrum of GO displays the peaks characteristic of the vibrations of oxygen-containing functional groups, such as the O-H group stretching vibrations at 3409 cm^{-1} , the C=O stretching at 1729 cm^{-1} and C-O stretching of C-O-C of the epoxide group at 1048 cm^{-1} . After reaction with cyanuric chloride new peaks at 1430 and 1458 cm^{-1} , characteristic of the C-N and C=N stretching vibrations, indicate the presence of CC units on the GO surface. The FTIR spectrum of GO@CC@CRL shows the intense and broad absorption band of the amine ($-\text{NH}_2$) stretching vibration at 3427 cm^{-1} . The peak at 1396 cm^{-1} of the C-N stretching vibration, and at 1627 cm^{-1} and at 1710 cm^{-1} of the symmetric and asymmetric of C=O stretching vibrations, can be assigned to the amide (CO-NH_2) and carboxylic acid (CO_2H) groups, respectively.

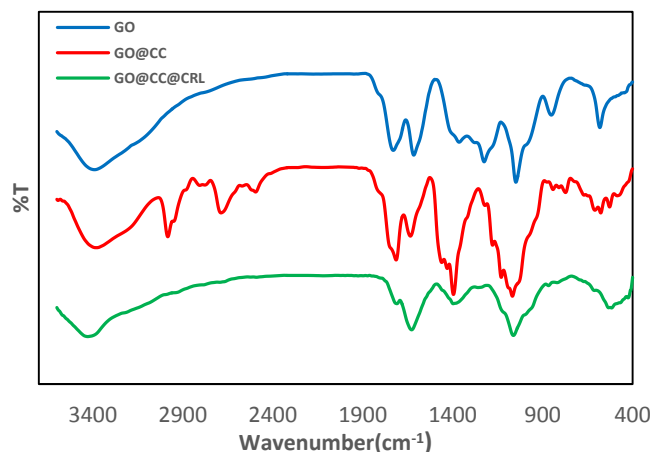




Fig.3: FTIR spectra of GO, GO@CC and GO@CC@CRL

3.2. CRL immobilization parameters

3.2.1. Initial Concentration of CRL

In this section, different concentrations of the CRL solution (12.85 – 69.28 $\mu\text{g}/\text{mL}$) were used for immobilization on 3 mg of GO@CC at room temperature.

As shown in Fig. 4, the amount of immobilized CRL increased with increasing the initial amount of CRL and the relative activity reached a maximum value at 47.42 $\mu\text{g}/\text{mL}$ of CRL and remained approximately constant with increasing initial amount of CRL. It seems that optimal initial concentration for immobilizing of CRL on GO@CC under these conditions is 47.42 $\mu\text{g}/\text{mL}$.

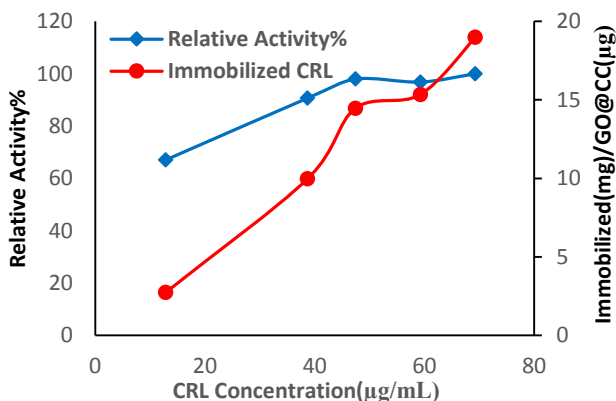


Fig.4: Effect of the initial concentration of CRL on the amount of immobilized CRL and relative activity

3.2.1. Time of immobilization

The amount of immobilized CRL (μg) on 1mg of GO@CC and the relative activity of CRL versus reaction time are shown in Fig. 4. It was found that, by increasing the reaction time from 1 to 3 hours, the amount of immobilized CRL increased and, then, it decreased after 3 hours. The relative activity of CRL increased with reaction time up to 3 hours and approximately remained constant after about three hours. Therefore, optimal time could be 3 h

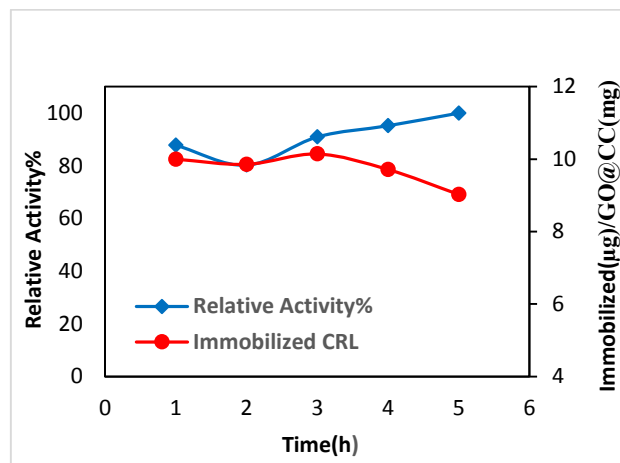


Fig.4: Effect of reaction time on the amount of immobilized CRL and relative activity

Conclusions

This work described a new method for the covalent immobilization of CRL on the surface of functionalized GO nanosheets. The XRD pattern and FESEM of GO proved that GO was successfully synthesized. The FTIR spectrum confirmed the modification of GO with cyanuric chloride and immobilization of CRL onto GO@CC. Subsequently, GO@CC served as a two-dimensional carrier for CRL. The Optimal immobilization time was measured three hours and optimum initial concentration of CRL solution at room temperature was specified about 47.42 μg per mg of GO@CC. These results demonstrate that the over loading of enzyme molecules on GO@CC could be lead to some unfavorable protein-protein interactions that successively, reduce the enzyme activity.

Acknowledgment

The authors are grateful to the Center of Excellence of Research Council of the University of Isfahan for financial supports of this work.

References

- [1] N. Gandhi "Applications of Lipase", *JASCO*, 74(6) (1997).
- [2] P. Choudhury, B. Bhunia "Industrial Application of Lipase: A Review", *Pharm. J.*, 1(2) (2015) 41-47.
- [3] N. Nisha, S. Arun Karthick, S. Gobi "A Review on Methods, Application and Properties of Immobilized Enzyme", *Chem. Sci. Rev. Lett.*, 1 (2012) 148-155.
- [4] N. R. Mohamad, N. H. C. Marzuki, N. A. Buang, F. Huyop, R. A. Wahab "An overview of technologies for immobilization of enzymes and surface analysis techniques for immobilized enzymes", *Biotechnol. Biotechnol. Equip.*, 29 (2015) 205-220.



- [5] K. Blank, J. Morfill, H. E. Gaub, "Site-specific immobilization of genetically engineered variants of *Candida antarctica* lipase B", *ChemBioChem.*, 7 (2006) 1349.
- [6] W. Shuai, R. K. Das, M. Naghdi, S. K. Brar, M. Verma, "A review on the important aspects of lipase immobilization on nanomaterials", *Biotechnol. Appl. Biochem.*, (2016) 1-20.
- [7] J. Zhang, F. Zhang, H. Yang, X. Huang, H. Liu "Graphene oxide as a matrix for enzyme immobilization", *Langmuir*, 26 (2010) 6083–6085.
- [8] F. Zhang, B. Zheng, J. Zhang, X. Huang "Horseradish peroxidase immobilized on graphene oxide Physical properties and applications in phenolic compound removal", *J. Phys. Chem. C*, (2010) 8469–8473.
- [9] Y. Liu, D. Yu, C. Zeng, Z. Miao, L. Dai "Biocompatible graphene oxide-based glucose biosensors", *Langmuir*, 26 (2010) 6158–6160.
- [10] Q. Li, F. Fan, Y. Wang, W. Feng, P. Ji "Enzyme Immobilization on Carboxyl-Functionalized Graphene Oxide for Catalysis in Organic Solvent", *Ind. Eng. Chem. Res.*, 52 (2013) 6343–6348.
- [11] W. S. Hummers, R. E. Offeman "Preparation of Graphitic Oxide", *J. Am. Chem. Soc.*, 80 (1958) 1339.



Mechanistic Characters of Ion Permeation through Mechanosensitive Channels of Large Conductance: A Steered Molecular Dynamics Study

Vahid Fadaei Naeini^{a*}, Majid Baniassadi^a, Masumeh Foroutan^b

^a School of Mechanical Engineering, College of Engineering, University of Tehran, Tehran, Iran

^b Department of Physical Chemistry, School of Chemistry, College of Science, University of Tehran, Tehran, Iran

*v.fadaei.n@ut.ac.ir

Abstract: In this study, the permeation process of oppositely charged ions through mechanosensitive channels of large conductance is investigated using the steered molecular dynamics (SMD) simulation. The results suggest that the mechanism of interaction between the ion and the key residues of the channel can vary according to the ion charge. Since some of the mentioned amino acids exist in the interior pore of the other membrane proteins, studying the mechanism of interaction of these basic components with different substrates and their role in the gating process of the utmost importance. It was mentioned that Val21 sidechains interact with the ion as a selective filter in transmembrane domain.

Keywords: Ion Permeation; Mechanosensitive Channels of Large Conductance; Molecular Dynamics Simulation

Introduction

Mechanosensitive (MS) channels are pervasive membrane proteins in prokaryotic and eukaryotic cell membranes. The gating function in MS channels causes some conformational changes to reach the open and closed states in response to mechanical stimuli such as tension, shear, and pressure. These types of proteins play a pivotal role in physiological processes such as senses of touch, hearing, and regulation of blood pressure as transducers of mechanical stimulations into an electrical signal.

One of the research areas of interest in studying MscL function is to identify the diverse mechanisms for gating function of these channels. MD simulation is used as a numerical method to analyze the gating process and obtain a more comprehensive view about these channels during the gating process. Beckstein et al. performed a numerical study about the energy barriers for permeation in nanopores using the potential of mean force ions and drew a comparison between MD simulation results and continuum-electrostatic calculations (1). They found that the continuum-electrostatic model doesn't consider the role of water molecules in the pore. MD simulation was used to determine the different molecular structures of the MscL during the gating process (2). Simulations of Mycobacterium Tuberculosis of Bacterial MscL (Tb-MscL) embedded in a membrane and of its helical bundle alone in the solvent were performed (3). It was found that the spatial structure of helix bundle is not stable at physiological pH, while this behavior is stabilized by decreasing the pH condition. The gating function of MS channels was investigated in the presence of membrane and it was found that the flattening of the transmembrane helices leads to a significant increase in pore radius (4). The threshold value of the force that makes the channel to open and causes a significant change in the channel diameter and conductance was evaluated by MD

simulations (5, 6). Similar to this study, Gullingsrud et al. assessed the effects of membrane lateral tension on the channel opening state (7). Jonggu et al. utilized the MD simulations to find the reciprocal effects of membrane and protein on each other during the gating function (8). Based on their observations, the opening of the channel was caused only by applying an explicit lateral bias force to each of the five subunits of MscL in the radially outward direction. Additionally, MD simulations were employed to describe the interplay of main structural segments of the channel during the opening (9, 10). Patch-clamp experiments were applied to investigate the conformational changes and conductance alterations in MscL during their function (11). Deplazes et al. studied the conformational changes related to gating with a higher level of conformational sampling than previous studies by combining coarse graining simulations with FRET and EPR experiments (12).

According to the preceding studies, it seems that the mechanical characteristics in ion permeation through the interior pore of a MS channel require a further study that will be addressed in the present work. In SMD simulation, a vertical force is applied to the potassium and chloride ions separately to pull them through the interior pore of a MS channel with an almost constant velocity.

Methods

Modeling process was initiated using the crystal structure of Tb-MscL (PDB entry 1MSL) (13). A patch of Palmitoyl-oleoyl-phosphoethanolamine membrane with the size of (126×126) Å² was built and used as the natural environment. The protein was embedded into the membrane patch and aligned with the membrane properly. A water box with the specified size of (117×117×153) Å³ in x, y and z directions respectively, was built to solvate the system. A specific ion



concentration of 0.2 M KCl was created. Finally, the simulation system contained ~156000 atoms, including 35029 water molecules and 332 lipid headgroups. All simulations were carried out using the parallel molecular dynamics program NAMD (14) with a non-bonded cutoff of 12 Å. The MD simulation procedure was performed in four steps sequentially. It is noteworthy that a CHARMM22 parameter file for proteins (15,16) with NBFIX modification was used as the main force field of the system. Periodic cell dimensions was set up to (120×120×156) Å³ in x, y and z directions respectively. Particle mesh Ewald (PME) method was hired for the full long-range electrostatics interactions (17) with PME grid spacing about 1 Å. Bonds to all hydrogen atoms were supposed to be rigid using the SHAKE algorithm (18). Langevin thermostat was used to set temperature of the system on the constant amount of 310 K. Moreover, pressure of the system was controlled in a constant level of 1 atm using the Langevin piston (19). The potassium and chloride ions was pulled with spring constant $k=1$ kcal/mol.Å². About 6 ns of force biased simulation was done on the system. There are three side chains that operate as filters and possibly have stronger molecular interaction with the ions, including the non-polar sidechain Val21, the acidic sidechain Glu104, and the polar sidechain Thr115 are detectable. The main tight gate of the channel in the undeformed structure of the protein corresponds to the Glu104. Thr115 sidechain in cytoplasmic domain is considered as a nucleophilic sidechain. Given this premise, Thr115 sidechain will have a strong interaction with the positively charged ion naturally.

Results and Discussion

In this section, the ion permeation is studied based on mechanical parameters of the process. The root mean square of deviation (RMSD) for backbone of the protein without hydrogens resulted from the equilibrium simulation is displayed in Fig. 1.

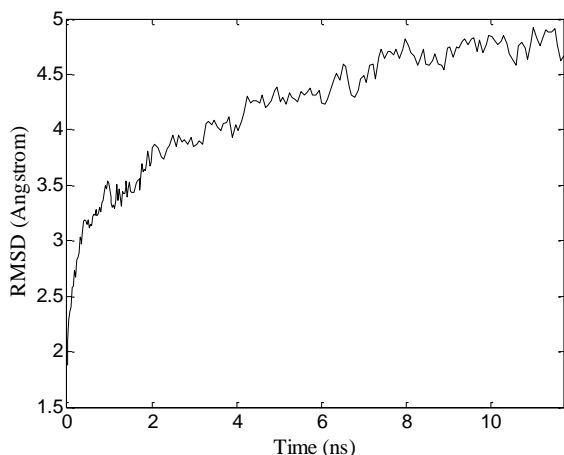


Fig. 4: RMSD for backbone of the protein

It can be deduced from Fig. 1 that the protein structure was equilibrated after 10 ns and would be ready for non-

equilibrium simulation. Fig. 2 displays the running average of the SMD force required to pull the ion inside the cavity vs. position of the ion taken over 0.3 (ns) windows.

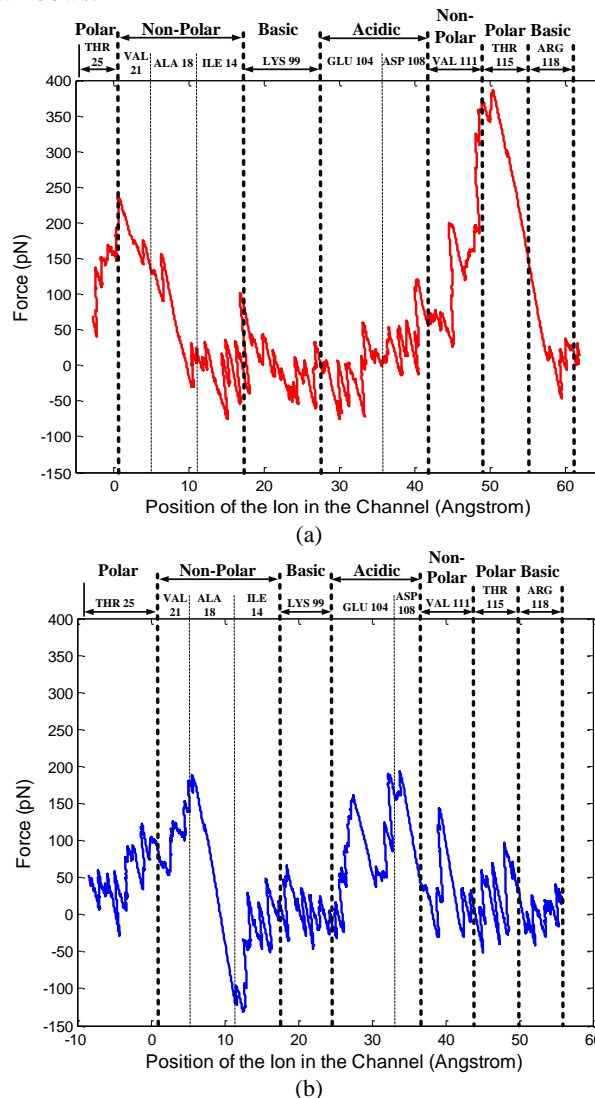


Fig. 5: The SMD force vs. position of the ion in case of: (a). Potassium, (b). Chloride ion permeation

In both graphs of Fig. 2, two peaks can be observed that take place in the interval between 0 Å to 10 Å. These peaks can be attributed to the opening of non-polar sidechains of Val21 to pass the ion through this region. According to Fig. 2.(a), a strong interaction is foresighted between the nucleophilic sidechain Thr115 and potassium ion as well. In Fig. 2.(b), during permeation through Val21, the SMD force for chloride ion has a local maximum about 200 pN, and then the force drops sharply. Almost the same amount of force is required for potassium ion to cross the barrier of Val21, but the repulsive force acting on potassium after entering the polar region is less than chloride –see Fig. 2.(a). According to Fig. 2.(b), the SMD force required to permeate the chloride ion through the acidic sidechains of



the interior pore as well as non-polar sidechain Val111 also reaches to local maximum values.

Conclusions

The acquired results of this study, represents the role of effective factors on permeation of ions through a mechanosensitive channel of large conductance. This study utilized biophysical parameters to investigate the different events in ion permeation. In this regard, the key residues of the pore were identified using the SMD simulation. The SMD force illustrated that Thr115 interacts with K^+ much stronger than Cl^- . However, negatively charged ion required a larger SMD force to permeate through the acidic sidechains of Glu104 than the positive one. Collectively, MD simulation of the process of ion permeation at the atomic scale can lead to an improved level of understanding for reconstruction of the ion transport cycle.

References

- [1]. Beckstein, O., K. Tai, and M.S.P. Sansom. 2004. Not ions alone: Barriers to ion permeation in nanopores and channels. *J. Am. Chem. Soc.* 126: 14694–14695.
- [2]. Sukharev, S., S.R. Durell, and H.R. Guy. 2001. Structural Models of the MscL Gating Mechanism. *Biophys. J.* 81: 917–936.
- [3]. Elmore, D.E., and D.A. Dougherty. 2001. MD Simulations of Wild-Type and Mutant Forms of the *Mycobacterium tuberculosis* MscL Channel. *Biophys. J.* 81: 1345–1359.
- [4]. Gullingsrud, J., D. Kosztin, and K. Schulten. 2001. Structural Determinants of MscL Gating Studied by MD Simulations. *Biophys. J.* 80: 2074–2081.
- [5]. Colombo, G., S.J. Marrink, and A.E. Mark. 2003. Simulation of MscL Gating in a Bilayer under Stress. *Biophys. J.* 84: 2331–2337.
- [6]. Bilston, L.E., and K. Mylvaganam. 2002. Molecular simulations of the large conductance mechanosensitive (MscL) channel under mechanical loading. *FEBS Lett.* 512: 185–190.
- [7]. Gullingsrud, J., and K. Schulten. 2003. Gating of MscL Studied by SMD. *Biophys. J.* 85: 2087–2099.
- [8]. Jeon, J., and G.A. Voth. 2008. Gating of the MS Channel Protein MscL: The Interplay of Membrane and Protein. *Biophys. J.* 94: 3497–3511.
- [9]. Anishkin, A., V. Gendel, N.A. Sharifi, C.-S. Chiang, L. Shirinian, H.R. Guy, and S. Sukharev. 2003. On the Conformation of the COOH-terminal Domain of the MscL. *J. Gen. Physiol.* 121: 227–244.
- [10]. Sawada, Y., M. Murase, and M. Sokabe. 2012. The gating mechanism of the bacterial MscL revealed by MD simulations: from tension sensing to channel opening. *Channels (Austin).* 6: 317–331.
- [11]. Sukharev, S., M. Betanzos, C.S. Chiang, and H.R. Guy. 2001. The gating mechanism of the MscL. *Nature.* 409: 720–724.
- [12]. Deplazes, E., M. Louhivuori, D. Jayatilaka, S.J. Marrink, and B. Corry. 2012. Structural Investigation of MscL Gating Using Experimental Data and Coarse Grained MD Simulations. *PLoS Comput. Biol.* 8: e1002683.
- [13]. Chang, Geoffrey, et al. "Structure of the MscL homolog from *Mycobacterium tuberculosis*: a gated MS ion channel." *Science* 282.5397 (1998): 2220–2226.
- [14]. Phillips, J.C., R. Braun, W. Wang, J. Gumbart, E. Tajkhorshid, E. Villa, C. Chipot, R.D. Skeel, L. Kalé, and K. Schulten. 2005. Scalable MD with NAMM. *J. Comput. Chem.* 26: 1781–1802.
- [15]. Mackerell, A.D., D. Bashford, M. Bellott, R.L. Dunbrack, J.D. Evanseck, M.J. Field, S. Fischer, J. Gao, H. Guo, S. Ha, L. Kuchnir, K. Kuczera, F.T.K. Lau, C. Mattos, S. Michnick, T. Ngo, D.T. Nguyen, B. Prodhom, W.E. Reiher, B. Roux, M. Schlenkrich, J.C. Smith, R. Stote, J. Straub, M. Watanabe, J. Wio, D. Yin, and M. Karplus. 1998. All-Atom Empirical Potential for Molecular Modeling and Dynamics Studies of Proteins. *J. Phys. Chem.* 5647: 3586–3616.
- [16]. Mackerell, AD and Bashford, D and Bellott, M and Dunbrack, RL and Field, MJ and Fischer, S and Gao, J and Guo, H and Ha, S and Joseph, D. and others, and D. others Mackerell, AD and Bashford, D and Bellott, M and Dunbrack, RL and Field, MJ and Fischer, S and Gao, J and Guo, H and Ha, S and Joseph. 1992. Self-consistent parameterization of biomolecules for molecular modeling and condensed phase simulations. In: *Faseb Journal. FEDERATION AMER. SOC. EXP. BIOL.* 9650 ROCKVILLE PIKE, BETHESDA, MD 20814-3998. pp. A143---A143.
- [17]. Darden, T., D. York, and L. Pedersen. 1993. Particle mesh Ewald: An $N \cdot \log(N)$ method for Ewald sums in large systems. *J. Chem. Phys.* 98: 10089–10092.
- [18]. Ryckaert, J.P., G. Ciccotti, and H.J.C. Berendsen. 1977. Numerical Integration of the Cartesian Equations of Motion of a System with Constraints: MD of Alkanes. *J. Comput. Phys.* 23: 327–341.
- [19]. Feller, S.E., Y. Zhang, R.W. Pastor, and B.R. Brooks. 1995. Constant pressure molecular dynamics simulation: The Langevin piston method. *J. Chem. Phys.* 103: 4613–4621.



بیستمین کنفرانس شیمی فیزیک ایران
دانشکده علوم پایه - دانشگاه اراک
۳۱-۲۹ مرداد ۱۳۹۶



20th Iranian Physical Chemistry Conference

شیمی سطح و حالت جامد

Surface Chemistry and Solid State

A theoretical study of gas adsorption on Boron nitride Nanocone induced with Zn-porphyrin

Sattar Arshadi*, Hojatollah Rahimi

*Department of chemistry, Payame Noor University, 19395-4697, I.R. of Iran

*chemistry_arshadi@pnu.ac.ir

Abstract: The electronic structure of a boron nitride Nano cone with 120 disclination, and some properties that derive from this structure, were studied by density-functional theory calculations. We design Porphyrin-doped on apex of boron nitride Nano cone. The stabilities and electronic properties of Zinc -porphyrin induced boron nitride nano cones (Zn-P-BNNC) and their interaction with CO₂ and O₂ gaseous molecules on the internal and external sites are investigated for exploring their potential usage as Nano sensors. Moreover the atomic charges calculated by using Natural Bond Orbital (NBO). The results indicated that dipole moments and energy gaps could reveal the effects of porphyrin on the properties of BNNC. Furthermore the results show that the Zn- P-BNNC is the good and selective sensor for the O₂ gas in the presence of CO₂ gas.

Keywords: Porphyrin, Nanocone, Sensor, Boron Nitride

Introduction

Recently, the study of gas adsorption on nanostructures and the importance of gas control have attracted considerable attention in theoretical and experimental studies [1-2].

Porphyrins are a group of heterocyclic macrocycle compounds, composed of four modified pyrrole subunits interconnected at their alpha carbon atoms through methine bridges [3]. The porphyrin ring structure is aromatic, with a total of 26 electrons in the conjugated system and may be deeply colored. The chemistry of porphyrins and similar macrocycles is an interesting field of research [4]. The current and still rising appeal of porphyrins arises from the remarkable versatility of these molecules and their host-guest metal complexes. These complexes are formed with the majority of the elements in the periodic table [5].

The O₂ sensor is mounted in the exhaust manifold to monitor how much unburned oxygen is in the exhaust as the exhaust exits the engine. Monitoring oxygen levels in the exhaust is a way of gauging the fuel mixture. It tells the computer if the fuel mixture is burning rich (less oxygen) or lean (more oxygen).

The aim of this study is the investigation of structure and electronic properties of BN nanocone molecule (BNNC), the effect of making defect with elimination of B and N atoms and insertion of porphyrin like structure in nanocone (PIC70F). In the next step, the effects of insertion of Zn²⁺ in porphyrin cavity (Zn-P-BNNC) were studied. Finally, Zn-P-BNNC ability for sensing of O₂ gas was examined. The obtained results may provide a new insight to the gas sensing and monitoring nanotechnology.

Materials and method

After the optimization of P-BNNC it was found that the diameter of cavity is equal to 4.12 Å. The size of created cavity is in a way that it can adsorb the Zn metal ions and produce Zn-P-BNNC.

the adsorption energies were corrected using BSSE correction through the counterpoise method with "ghost" atoms [37] according to the following equation:

$$E_{ads}^{BSSE} = E_{M-PIC70F/gas} - [E_{M-PIC70F/gas\ ghost} + E_{gas/M-PIC70F\ ghost}]$$

Where the E_{ads}^{BSSE} is the BSSE corrected adsorption energy. The "ghost" gas and M- P-BNNC corresponds to additional basis wave functions centered at the position of the CO₂ and O₂ or the Cr Zn-P-BNNC, without any atomic potential.

The full natural bonding orbital (NBO) calculations were done on all optimized structures in order to study the electronic structure and obtain the charge transfer energy.

Results and Discussion

At first, the accuracy of the applied method was scrutinized to describe the structural parameters of BNNC, O₂ and CO₂ molecules in gas phase

The calculated E_b energies of BNNC, P- BNNC, Zn-P-BNNC (Figs. 1) are -5.99, -5.92 and -5.43 eV, respectively. The negative values of E_b show that the studied compounds are stable.

The adsorption energies of Zn²⁺ inserted in P-BNNC was -612.31 kJ.mol⁻¹. Hence, chemisorption of Zn²⁺ into P-BNNC is very strong. The HOMO and LUMO

energies of P-BNNC have been faintly increased after chemisorption of Zn^{2+} into cavity of this molecule.

The adsorption of O_2 and CO_2 gas molecules on Zn-P-BNNC were studied.

The reported data showed that all the BSSE corrected adsorption energies (E_{ads}^{BSSE}) for interaction between gas molecules and exterior site of Zn-P-BNNC were negative which indicated that the adsorption process was favourable in standard temperature and pressure (STP). Also, the negative value of E_{ads}^{BSSE} showed that the adsorption process was exothermic.

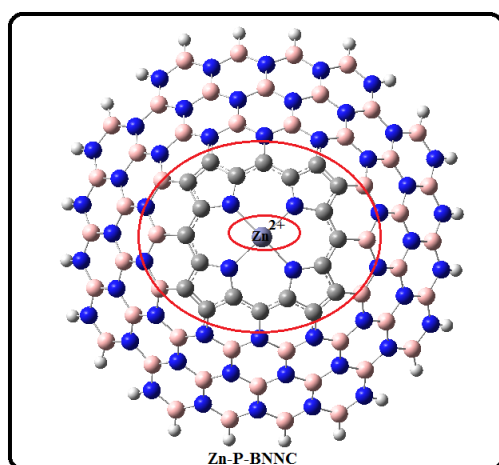


Fig.1 Zn-porphyrin induced BNNC

In electronic industry, the control of HOMO-LUMO energy difference (E_g) was considered as a most important function for improving the instrument. So, reducing or adjustment the E_g of BNNC is one of the important cases for controlling the sensing properties of nanocone.

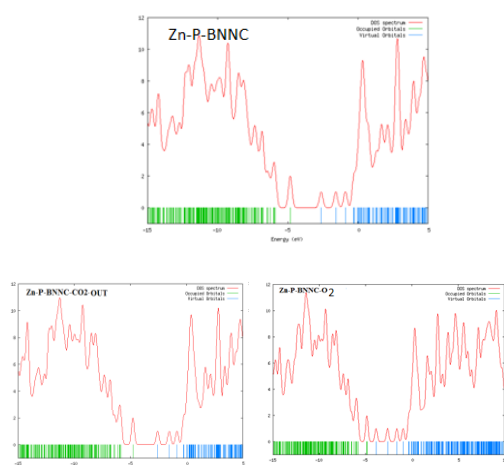


Fig.2 The density of state (DOS) plots of Zn-P-BNNC, Zn-P-BNNC- CO_2 and Zn-P-BNNC- O_2 .

The results revealed that during the adsorption of only O_2 gas molecule on Zn-P-BNNC, the amount of E_g have been considerably decreased. Based on calculated E_{ads}^{BSSE} and E_g , it is expected that the Zn-P-BNNC could be a promising candidate in gas sensor design for selective detection of O_2 even in the presence of CO_2 . However, the E_g amount of Zn-P-BNNC has not been changed significantly in the presence of CO_2 gas molecules (Fig. 2). So, it is not considered as a suitable sensor for this gas.

Conclusions

The CO_2 gas molecule adsorbed only on the Zn metal atom on the exterior site but, the O_2 molecule was adsorbed from both the exterior and interior site of Zn-P-BNNC. However, the O_2 gas molecule has high adsorption only from interior site of Zn-P-BNNC. With the adsorption of CO_2 gas on Zn-P-BNNC, the band gap is approximately constant and so, the conductivity of Zn-P-BNNC molecule has not significantly changed.

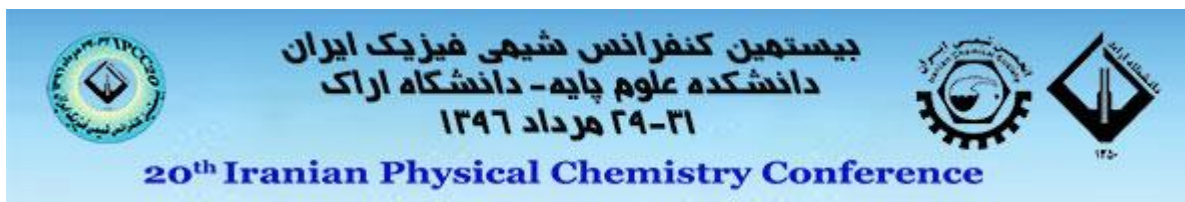
The noticeable point is that the amount of Zn-P-BNNC band gap, as well as conductivity, has significant change with the adsorption of O_2 gas on its interior site. So, the Zn-P-BNNC is the good and selective sensor for the O_2 gas in the presence of CO_2 gas. The density of state (DOS) and Natural bond orbital (NBO) calculations has confirmed the above results.

Acknowledgment

This work has done with financial support of Payame Noor University.

References

- [1] Ghosh A, Late DJ, Panchakarla LS, Govindaraj, A, Rao, C. N. R. NO_2 and humidity sensing characteristics of few-layer graphenes. *J Exp Nanosci.* 2009;4:313-322.
- [2] Chougule MA, Nalage SR, Shashwati S, Patil VB. Development of nanostructured ZnO thin film sensor for NO_2 detection. *J Exp Nanosci.* 2014;9:482-490.
- [3] Zhu L, Yi Y, Shuai Z, Schmidt K, Zojer E. Structure to Property Relationships for Multiphoton Absorption in Covalently Linked Porphyrin Dimers: A Correction Vector INDO/MRDCI Study. *J Phys Chem A.* 2007;111:8509-8518.
- [4] Purtaş S, Köse M, Tümer F, Tümer M, Gölcü A, Ceyhan G. A novel porphyrin derivative and its metal complexes: Electrochemical, photoluminescence, thermal, DNA-binding and superoxide dismutase activity studies. *J Mol Struct.* 2016;1105:293-307.



Error Analysis and Kinetic Aspect of Doxycycline Adsorption onto Graphene nanosheet

R. Rostamian*, H. Behnejad

Department of Physical Chemistry, School of Chemistry, University College of Science, University of Tehran, Tehran, Iran.
*r.rostamian@gmail.com, r.rostamian@ut.ac.ir

Abstract: In current research which belong to environmental engineering science, the adsorption behavior of doxycycline (DCN) as an antibiotic in veterinary onto graphene oxide nanosheets in aqueous solution was evaluated. The time factors influencing the adsorption of antibiotics and error analysis were studied. Non-linear regressions were carried out in order to define the best fit model. To do this, eight error functions were applied to predict the optimum model. Among various kinetic models, the experimental data were well fitted by pseudo second-order (PSO) kinetic model. The study showed that GOS can be removed more efficiently in a short time from water solution.

Keywords: Graphene nanosheet, Kinetic study, Adsorption, Error analysis.

Introduction

Wastewater evacuation is one of the main sources of antibiotics. To estimate concentrations of the most widely used pharmaceuticals in wastewater treatment plants and their release to the environment, plentiful studies have been carried out. There are many studies which have reported presence of some antibiotics including ciprofloxacin, trimethoprim, sulfamethoxazole, tetracycline and doxycycline in effluent waters [1, 2].

Nanomaterials can operate as a pivotal factor in antibiotics decontamination because they contain high specific surface areas, many active sites and abundant functional groups. Graphene oxide nanosheet is a nanomaterial consisting of carbon sheets with carboxylate groups in the periphery and has a thickness of a single atom. The basal surfaces of graphene oxide contain hydroxyl and epoxide functional groups which are uncharged but polar and are capable of $\pi - \pi$ interactions. High specific area, ample active sites and abundant functional groups of GOS aid in the elimination of antibiotics from large volumes of aqueous solutions. In antibiotic interactions, positively charged side chains and aromatic side chains promote GOS adsorption. Because of presence the plenty functional groups and the large surface are on the GOS, it contains potentially larger adsorption capacities than most nanomaterials. Actually a few studies are focusing on the studies of GOS adsorption in the environment [1-2]. Among these published researches, $\pi - \pi$ interactions (due to the wide accessibility of delocalized π electrons at the GOS surface) are commonly invoked to illustrate adsorption rate which can overlap in a stacking arrangement with π electrons within the benzene ring in the organic adsorbate structure. Hydrophobic, electrostatic, other diverse π interactions, dispersion (van der Waals) interactions and hydrogen bonding with oxygen-containing impurities (for example carboxyl functional groups) may also be considerable adsorption mechanisms depending on adsorbent and adsorbate properties. As we know, charged surface functional

groups may increase the wettability of surfaces, alter π electron donating character of C SP² also improve colloid stability, evaluate electrostatic repulsion or attraction [2].

This study systematically investigated the performance of GOS as potent adsorbent to removing DCN.

Materials and method

Graphene oxide nanosheet (GOS) (with purity: 99.5% - thickness: 2-18 nm, less than 32 layers, pH: 7 - 7.7 (30 °C), volume resistivity: 4×10^{-4} ohm.cm, diameter: 4-12um) was purchased from US-NANO company and DCN was purchased from Chinese company. All Solutions were prepared with double distilled water Batch experiments were done to measure DCN adsorption capacities. Solutions of desired concentration were prepared by diluting the stock solution using double distilled water. Shaker was used to mix the suspensions (DCN solution-adsorbent) at 150 rpm and 25.0 °C for all tested conditions [2].

Initial identical concentrations of DCN were used. Adsorbent and solution of DCN were mixed and allowed to contact at different contact times. Then the samples were centrifuged at 4000 rpm for 10 min and filtrated. The residual DCN concentrations in the solutions were measured. The sorption capacity q_t (mg g⁻¹) of GOS was calculated using [3]:

$$q_t = \frac{C_0 - C_t}{W} \times V \quad (1)$$

where C_0 is the initial ion concentration (mg L⁻¹) and C_t is the remaining metal concentration (mg L⁻¹) at time t, V is the volume of ion solutions (L), and W is the adsorbent amount (g).

Error Analysis

To the best of our knowledge, linear regression has been one of the best tools describing the best fitting which mathematically analyses the adsorption systems and checks the theoretical hypothesis of a model. So, because of attending the model for the adsorption system, it is essential to study the data using



the error analysis [3]. The eight mathematically precise error functions were employed and the obtained parameters were tabulated in Table 1.

Table 1. Lists of error functions [1].

Error function	Definition/expression
Sum squares error	$\sum_{i=1}^n (q_{calc} - q_{meas})^2$
Average relative error	$\frac{100}{n} + \sum_{i=1}^n \left \frac{q_{e.meas} - q_{e.calc}}{q_{e.meas}} \right $
Sum of absolute error	$\sum_{i=1}^n q_{e.meas} - q_{e.calc} $
Marquardt's percent standard deviation	$100 \sqrt{\frac{1}{n-p} \sum_{i=1}^n \left(\frac{q_{e.meas} - q_{e.calc}}{q_{e.meas}} \right)^2}$
The coefficient of determination	$R^2 = \frac{(Q_{meas} - \overline{Q_{calc}})^2}{\sum_{i=1}^n (Q_{meas} - \overline{Q_{calc}})^2 + (Q_{meas} - Q_{calc})^2}$
Standard deviation of relative errors	$\sqrt{\frac{\sum_{i=1}^n [(q_{e.meas} - q_{e.calc})_i - ARE]_i^2}{n-1}}$
Nonlinear chi-square test	$\sum_{i=1}^n \left(\frac{(q_{e.calc} - q_{e.meas})^2}{q_{e.meas}} \right)$
Residual root mean square error	$\sqrt{\frac{1}{n-2} \sum_{i=1}^n (q_{e.meas} - q_{e.calc})^2}$

In these equations, q_{meas} is the measured antibiotic concentration; q_{calc} is the calculated antibiotic concentration with model, n is the number of observations in the experimental data and $\overline{q_{calc}}$ is the average of q_{calc} .

Results and Discussion

Fig. 1 represents DCN adsorption on GOS with shaking time (0-900 min). This figure indicates that while the adsorption of DCN is quite rapid initially, the rate of adsorption becomes slower with the passage of time and reaches a constant value and equilibrium was reached 200 minutes.

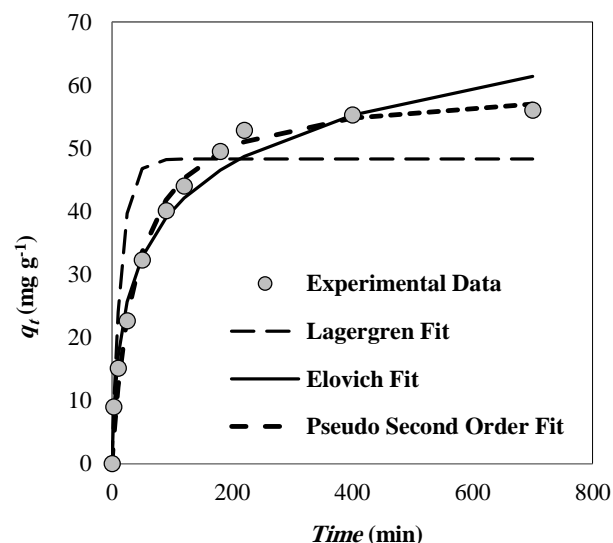


Fig.1. Kinetic adsorption of DCN onto GOS at 298.15 K.

The initial faster rate may be due to the availability of the uncovered surface area of the adsorbents, since the adsorption kinetics depends on the surface area of the adsorbent. The kinetic data were fitted with kinetic models (Fig 1) [1-3]. Error analysis values shows that, the pseudo-second order (PSO) model shows the sorption kinetics better which informs adsorption on GOS is controlled by multiple processes [2].

Conclusions

The kinetic studies at 298.15 K showed that GOS can be effectively utilized for the removal of DCN from water samples in a few times therefore GOS is a very good sorbent to removal DCN from water samples. The obtained error analysis data shows that the pseudo-second order kinetic model explains the adsorption in a better way.

References

- [1] R. Rostamian, H. Behnejad, "A unified platform for experimental and quantum mechanical study of antibiotic removal from water", *Journal of Water Process Engineering*, 17 (2017) 207-215.
- [2] R. Rostamian, H. Behnejad, "A comparative adsorption study of sulfamethoxazole onto graphene and graphene oxide nanosheets through equilibrium, kinetic and thermodynamic modeling", *Process Safety and Environmental Protection*, 102 (2016) 20-29.
- [3] Rostamian, Rahele, Mojgan Najafi, and Amir Abbas Rafati. "Synthesis and characterization of thiol-functionalized silica nano hollow sphere as a novel adsorbent for removal of poisonous heavy metal ions from water: Kinetics, isotherms and error analysis."

Selective Hydrogenation of Benzene to Cyclohexane on Various Ni- Supported Catalysts

N. Parsafard ^{a*}, M. H. Peyrovi ^b, Z. Mohammadian ^b

^aKosar University of Bojnord, Department of Applied Chemistry, North Khorasan, 9415615458, Iran

^bFaculty of Chemistry Science and Petroleum, Department of Physical Chemistry, University of Shahid Beheshti, Tehran, 1983963113, Iran

*n_dastmoozeh@sbu.ac.ir

Abstract: This report aims to reduce the benzene as a model reaction using catalytic hydrogenation. In this research, we developed a series of catalysts with different supports such as Ni/HMS, Ni/HZSM-5, Ni/HZSM5-HMS, Ni/Al₂O₃ and Ni/SiO₂. The various Ni-supported catalysts were evaluated for the hydrogenation reaction of benzene at 130–190 °C. The results showed that Ni/Al₂O₃ catalyst has better ability than other prepared catalysts for this reaction, such as a maximum benzene conversion (>99%), good cyclohexane selectivity (>55%), the best yield (>52%) and appropriate catalytic stability against coke deposition. It seems that the catalytic acidity is effective parameter compared to other factors such as surface properties and metal dispersion.

Keywords: Catalytic hydrogenation; Benzene conversion; Selectivity; Stability.

Introduction

Arenes are the most threatening materials to life especially due to their carcinogenic effects. On this basis, the hydrogenation reaction as one of the most important methods is used to saturate these contents in the petroleum industry [1-5]. Among the aromatic compounds, benzene is mostly used as a reaction model to study the performance of the hydrogenation catalysts [1, 3]. So far a lot of catalysts have been used for the hydrogenation of benzene [5, 6]. Various published researches reported many affecting parameters on the catalytic activity of metal-based catalysts in the hydrogenation reaction such as the nature of support, acidity, support's interaction with an active metal, metal particle size and etc. [7, 8]. Achieving the highest possible performance in catalytic reaction processing is an essential purpose of the chemical industry.

In aiming to develop the catalysts with the highest activity and process stability, we focus our effort on detecting the best support for this process according to characterization analysis and catalytic performances especially catalytic stability.

Materials and method

Herein, the catalytic behavior of 25 wt% Ni supported catalysts was taken into account for the benzene hydrogenation reaction. A solution of Ni(NO₃)₂·6H₂O (Merck) with appropriate concentration for 25 wt% loading of nickel was used for the impregnation of Al₂O₃, SiO₂, HMS, HZSM-5 and HZSM5/HMS (as ZH) supports [9-11]. The catalysts were mixed with this solution at room temperature and evaporated at 85 °C. The impregnated materials were dried at 110 °C and calcined in flowing air at 300 °C for 4 h.

In the present work, the catalytic features (activity and selectivity), the effects of reaction temperature and residence time on the catalytic activity and stability for the hydrogenation reaction of benzene (Bz) in a fixed-bed reactor have been compared.

Ni/Catal	S _{BE} T m ² / g	V _p cm ³ / g	d _p nm	C _N i n m	d _{Ni} %	Ni wt %	Ac μmolNH ₃ /g _{ca} ta
HMS	763	0.74	3.9	8.9	17. 3	24. 3	65
ZH	674	0.58	3.4	8.2	15. 7	23. 9	237
HZSM5	406	0.21	2.1	7.9	10. 4	24. 7	223
SiO ₂	310	0.67	8.6	6.3	22. 3	24. 9	69
Al ₂ O ₃	158	0.64	16. 2	7.1	14. 3	23. 7	296

Results and Discussion

Table 1. Physicochemical properties of prepared catalysts. After characterizing the catalysts and diagnosing their suitability as an acidic support by various analyzing methods as XRD, XRF, FTIR, UV-vis DRS, NH₃-TPD, Py-IR, H₂ chemisorption, nitrogen adsorption-desorption and TGA techniques that some results of these analysis were summarized in Table 1, the catalytic performance was investigated over Bz as a model for the hydrogenation reaction.

This reaction was done in presence of H₂ to saturate the Bz. Firstly, the catalytic activity was performed over the prepared catalysts in 130-190 °C. The effect of temperature on conversion in the vapor phase of the Bz hydrogenation over various supported catalysts is shown in Fig. 1. Under our experimental conditions, the only detectable product for the hydrogenation of benzene was cyclohexane (CH). As can be seen in this

figure, the catalysts presented high activity in this reaction as a function of reaction temperature. The maximum conversion in benzene hydrogenation (>99%) was achieved for Ni/Al₂O₃ at 130 °C, while Ni/HMS and Ni/ZH were shown 61% and 54%, respectively, and the maximum activity (>59%) for Ni/SiO₂ at 170 °C and for Ni/HZSM5 (>52%) at 190 °C.

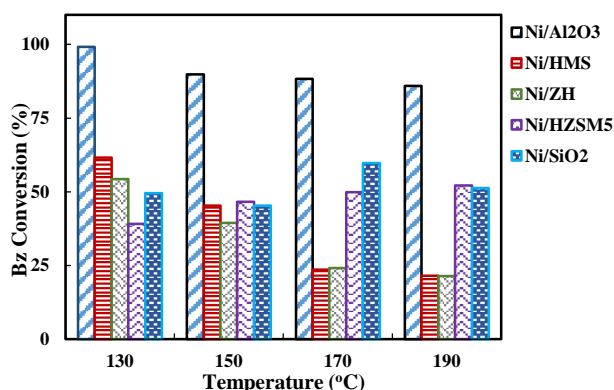


Fig. 1. Dependence of conversion on temperature in Bz hydrogenation for various catalysts.

Fig. 2 shows the dependences of the catalysts selectivity to cyclohexane in Bz hydrogenation. Selectivity toward cyclohexane produced ($S_{CH}(\%)$) was calculated by the following equation,

$$S_{CH}(\%) = \frac{\text{percentage of BZ transformed into CH}}{\text{total amount of Bz converted}} \quad (1)$$

The results show that Ni/SiO₂ catalyst has the best selectivity (75% at 130 °C) toward CH. This implies that Ni/SiO₂ catalyst has a tendency to preferably hydrogenate Bz.

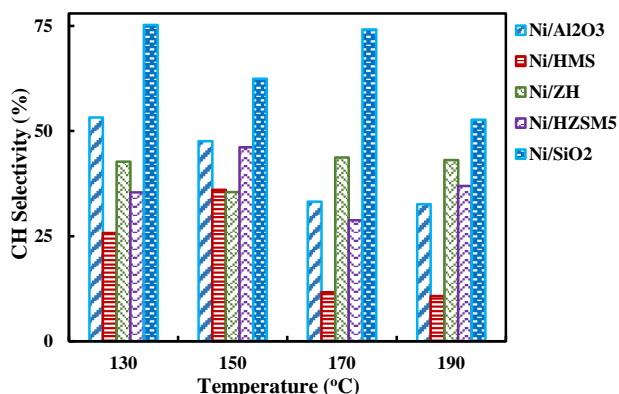


Fig. 2. Dependence of CH selectivity in benzene hydrogenation on temperature for various catalysts.

In order to understand the deactivation of prepared catalysts and the coke formation during the reaction, the activity with respect to stream time (72 h) at 150 °C was examined and shown in Fig. 3.

The activity of the prepared catalysts has the maximum decrease in the first 10 h. It seems that the greatest amount of coke deposition is formed in this period of

time. According to the occurred changes in the catalysts activities and the amount of coke deposition, Ni/HZSM5 catalyst showed better stability than other catalysts in this reaction without coke content. However, Ni/HMS catalyst even after 72 h on stream has more activity than other catalysts.

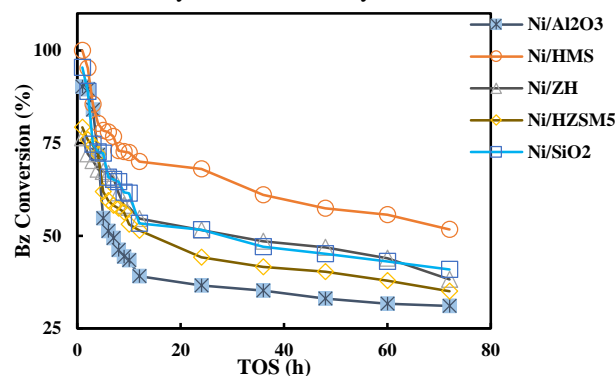


Fig. 3. The overall conversions as a function of time on stream (72 h)

The results of TG/DTA show that the amount of coke deposited on various catalysts is close together and very low (Fig. 4). Since all five catalysts reveal almost similar on stream stability with a loss in conversion after 72 h, the deactivation during the constant-temperature reaction test is not significant.

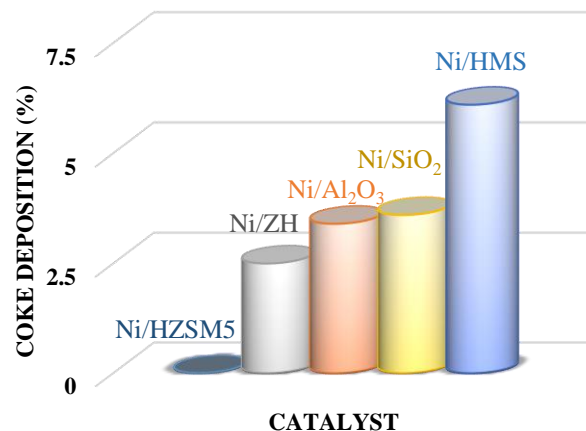


Fig. 4. Coke deposition at 150 °C over various catalysts.

Conclusions

In summary, the various porous supports were successfully synthesized and their physicochemical properties were characterized by various techniques. A detailed structural/catalytic study was carried out for the benzene hydrogenation reaction. Among the synthesized catalysts, the maximum benzene conversion (99.19%) in the benzene cut was achieved over Ni/Al₂O₃ at 130 °C. Also the best CH selectivity (above 75%) and the lowest coke amount (0 wt.%) were obtained for Ni/SiO₂ and Ni/HZSM5,



respectively. From the conversion, selectivity and stability results, it cannot be concluded that one catalyst is the best catalyst. For this reason, the yield of reaction was calculated as multiplication of conversion and selectivity.

These results are summarized in Table 2 given below.

Table 2. Benzene Yield (Conversion*Selectivity/100) of the prepared catalysts.

Ni/Catal.	Al ₂ O ₃	HMS	ZH	HZSM5	SiO ₂
130 °C	52.8	15.9	23.2	13.8	37.2
150 °C	42.7	16.3	14.0	21.5	28.3
170 °C	29.3	2.7	10.5	14.4	44.3
190 °C	28.0	2.3	9.2	19.2	27.0

According to these results, the best catalytic behaviour was reached by Ni/Al₂O₃ catalyst at 130 °C, with the best yield and the appropriate stability.

References

- [1] N. A. Bakar, M. M. Bettahar, M. A. Bakar, S. Monteverdi, J. Ismail "Low temperature activation of Pt/Ni supported MCM-41 catalysts for hydrogenation of benzene", *Journal of Molecular Catalysis A: Chemical*, 333 (2010) 11-19.
- [2] J. Mahmoudi, M. N. Lotfollahi, A. H. Asl "Comparison of synthesized H-Al-MCM-41 with different Si/Al ratios for benzene reduction in gasoline with propylene", *Journal of Industrial and Engineering Chemistry*, 24 (2015) 113-120.
- [3] R. Wojcieszak, S. Monteverdi, M. Mercy, I. Nowak, M. Ziolek, M. M. Bettahar "Nickel containing MCM-41 and AlMCM-41 mesoporous molecular sieves: characteristics and activity in the hydrogenation of benzene", *Applied Catalysis A: General*, 268 (2004) 241-253.
- [4] Y. Ma, Y. Huang, Y. Cheng, L. Wang, X. Li "Biosynthesized ruthenium nanoparticles supported on carbon nanotubes as efficient catalysts for hydrogenation of benzene to cyclohexane: An eco-friendly and economical bioreduction method", *Applied Catalysis A: General*, 484 (2014) 154-160.
- [5] S. Lu, W. W. Lonergan, J. P. Bosco, S. Wang, Y. Zhu, Y. Xie, J. G. Chen "Low temperature hydrogenation of benzene and cyclohexene: a comparative study between γ -Al₂O₃ supported PtCo and PtNi bimetallic catalysts", *Journal of Catalysis*, 259 (2008) 260-268.
- [6] L. Zhu, H. Sun, H. Fu, J. Zheng, N. Zhang, Y. Li, B. H. Chen "Effect of ruthenium nickel bimetallic composition on the catalytic performance for benzene hydrogenation to cyclohexane", *Applied Catalysis A: General*, 499 (2015) 124-132.
- [7] K. Y. Tsai, I. Wang, T. C. Tsai "Zeolite supported platinum catalysts for benzene hydrogenation and naphthene isomerization", *Catalysis Today*, 166 (2011) 73-78.
- [8] A. Lewandowska, S. Monteverdi, M. Bettahar, M. Ziolek "MCM-41 mesoporous molecular sieves supported nickel-physico-chemical properties and catalytic activity in hydrogenation of benzene", *Journal of Molecular Catalysis A: Chemical*, 188 (2002) 85-95.
- [9] M. Rostamizadeh, A. Taeb "Synthesis and characterization of HZSM-5 catalyst for methanol to propylene (MTP) reaction", *Synthesis and Reactivity in Inorganic, Metal-Organic, and Nano-Metal Chemistry*, 46 (2016) 665-671.
- [10] N. Parsafard, M. H. Peyrovi, M. Rashidzadeh "n-Heptane isomerization on a new kind of micro/mesoporous catalyst: Pt supported on HZSM-5/HMS", *Microporous and Mesoporous Materials*, 200 (2014) 190-198.
- [11] S. Therdthianwong, C. Siangchin, A. Therdthianwong "Improvement of coke resistance of Ni/Al₂O₃ catalyst in CH₄/CO₂ reforming by ZrO₂ addition", *Fuel Processing Technology*, 89 (2008) 160-168.

Kinetics Study of Selective Hydrogenation in Aromatics Mixture over Ni-W Composite Catalysts

N. Parsafard ^{a*}, M. H. Peyrovi ^b, Z. Mohammadian ^b

^aKosar University of Bojnord, Department of Applied Chemistry, North Khorasan, 9415615458, Iran

^bFaculty of Chemistry Science and Petroleum, Department of Physical Chemistry, University of Shahid Beheshti, Tehran, 1983963113, Iran

*n_dastmoozeh@sbu.ac.ir

Abstract: Ni-W/HZSM5-HMS catalysts were evaluated for benzene hydrogenation reaction at 130–190 °C. Kinetics of benzene hydrogenation was investigated under various hydrogen and benzene pressures and the effect of reaction conditions on catalytic performance was studied. The results showed that these catalysts have a good ability for this reaction. For more study, two kinetic models have been selected and tested to describe the kinetics for this reaction. Both used models, the power law and Langmuir-Hinshelwood, provided a good fit towards the experimental data and allowed to determine the kinetic parameters. The kinetics evaluations were shown that the catalyst with Ni/W=1.5 could perform this hydrogenation reaction with appropriate rate.

Keywords: Benzene hydrogenation; Kinetics; Power law model; Langmuir-Hinshelwood model.

Introduction

The selective hydrogenation of unsaturated compounds to reduce their concentration according to the environmental regulations and also their important role in the octane number of fuels, is the main process in the petrochemical industry. The selective hydrogenation of benzene because of high performance and octane number saving compared to other methods is taken into consideration [1, 2]. In this study, the hydrogenation of benzene was done in three-phase system (liquid feed, solid catalyst and hydrogen gas) using continuous fixed bed micro reactor. In order to activation of catalysts, before the reaction, they were placed under hydrogen gas stream. Thermodynamically, the standard formation enthalpy (ΔH_f°) of cyclohexane is lower than cyclohexene and also Gibbs free energy of cyclohexane is about 75 kJ/mol. Besides that, since the reactivity of cyclohexene is much more than of benzene, so cyclohexane will be the result as a main product [3, 4]. Design and preparation of green, thermally stable and low-cost catalysts is one of the challenges in the hydrogenation reaction. To enhance the dispersion of the active phase, variety of meso, micro-meso materials such as metal oxides (SiO_2 , Al_2O_3 , ZrO_2 , ...), zeolites, carbon compounds and recently composites have been applied [1, 3, 5, 6]. Among various metals, nickel resulted to similar electronic features with metals likes platinum and palladium and cost-effectiveness is preferred in the industry [5]. The hydrogenation process affects by different factors as acidity, preparation method, partial pressure of hydrogen, reaction temperature, metal loading percentage and etc. [6, 7]. In the present work, the kinetics of selective hydrogenation reaction was

evaluated in benzene and toluene mixture solution and investigated these effective parameters on this process.

Materials and method

The composite support (HZSM-5/HMS) with 40 wt% of HZSM-5 was prepared using the method described in ref. [8]. After the preparation of this support, nickel (II) nitrate hexa hydrate (as nickel source) and ammonium meta tungstate hydrate (as tungsten source) solutions with different amounts were co-impregnated. After evaporation of the solvent, these catalysts were dried in a static air at 110 °C overnight and calcined at 300 °C for 4 h.

A kinetic study was carried out to determine the reaction order and activation energy for hydrogenation of benzene over Ni-W/HZSM-5(x)-HMS, where x represents the nominal Ni/W ratios (that are equal to 0.25, 0.67, 1.5 & 4). Two kinetic models (power law (PL) and Langmuir-Hinshelwood (LH)) were used to investigate the kinetics of this reaction. The partial orders of this reaction and other kinetic parameters were calculated based on the simplest model (PL model). The reaction orders with respect to benzene concentration (2-8 vol%) and hydrogen pressure (2.6-5.9 Pa) were estimated at various temperatures (130-190 °C). In this method, the partial pressure of hydrogen and benzene were changed respectively for evaluating the order of benzene and hydrogen.

Results and Discussion

As mentioned, the PL model was chosen as a simplest kinetic equation. The reaction orders of benzene and hydrogen were determined in separate experiments. To obtain the reaction order of benzene, the catalysts were examined at temperature range of 130-190 °C for a series of reaction mixtures containing various



concentrations of benzene (2-8 vol.% with 2 mL min⁻¹ flow rate) while maintaining constant the H₂ flow rate at 40 mL min⁻¹. After each reaction, catalysts were cleaned in a flow of H₂ while heating at 350 °C before cooling to 130 °C and continuing the other step of reaction. In the same step, the reaction order of H₂ was obtained. In this step, the flow rate of H₂ was varied between 20 and 45 mL min⁻¹ while maintaining the benzene at 6 vol%. In this condition and at a constant temperature, the logarithmic representations of reaction rate against hydrogen or benzene pressures are mostly linear and their slopes express the order of reaction for the component with varying pressure. The reaction rate was defined as follows,

$$r \left(\frac{\text{mol}}{\text{g.s}} \right) = \frac{\text{Bz flow rate} \left(\frac{\text{ml}}{\text{s}} \right) \cdot \text{Bz density} \left(\frac{\text{g}}{\text{ml}} \right) \cdot \text{conv}(\%)}{\text{Bz molar weight} \left(\frac{\text{g}}{\text{mol}} \right) \cdot \text{weight of catalyst (g)} \cdot \text{impregnated metal (wt.\%)} \quad (1)$$

The partial reaction orders were calculated with respect to the empirical kinetic equation,

$$r \left(\frac{\text{mol}}{\text{g.s}} \right) = k P_{H_2}^n P_{Bz}^m \quad (2)$$

where n and m are the partial orders of hydrogen and benzene respectively and k is the rate constant.

The reaction orders for benzene on the Ni-W supported catalysts at a constant temperature were measured -0.88 to -0.11 orders while for hydrogen were found 0.78 to 1.34 (Table 1). The negative order for benzene indicates its self-inhibition on bi metallic catalysts. As can be seen in this table, the reaction orders of H₂ and benzene increase with reaction temperature, probably due to a substantial decrease in the coverage of each reactant.

Table 1. Kinetic parameters for benzene hydrogenation.

Tem p	orders	x=4.00	x=1.50	x=0.67	x=0.25
Power law model					
130	n_{H_2}	0.78	0.87	0.91	1.22
150	n_{H_2}	0.78	0.88	0.92	1.27
170	n_{H_2}	0.81	0.88	0.92	1.27
190	n_{H_2}	0.82	0.90	0.95	1.34
130	m_{Bz}	-0.14	-0.14	-0.88	-0.43
150	m_{Bz}	-0.14	-0.12	-0.40	-0.36
170	m_{Bz}	-0.11	-0.12	-0.25	-0.29
190	m_{Bz}	-0.11	-0.10	-0.21	-0.11
	E_{app}^{act} (kJ/mol)	20.80	16.69	55.25	69.80
Langmuir-Hinshelwood model					
K	E_{app}^{act} (kJ/mol)	28.4	25.5	33.5	52.1
	A (mol/g.s)	4.2×10^{-15}	2.8×10^{-18}	4.3×10^{-15}	7.3×10^{-13}
K_{Bz}	ΔH_{ads-Bz} (kJ/mol)	-3.6	-3.6	-3.6	-3.6
	A_{Bz} (atm ⁻¹)	0.09	0.09	0.09	0.09
K_{H_2}	ΔH_{ads-H_2} (kJ/mol)	-40.9	-32.2	-53.7	-55.0
	A_{H_2} (atm ⁻¹)	1.5×10^{19}	3.3×10^{15}	3.5×10^{12}	7.4×10^{12}

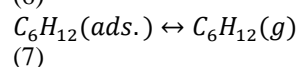
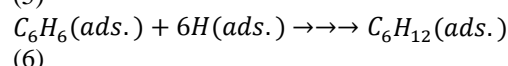
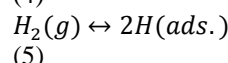
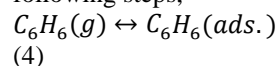
The temperature dependence of the reaction rate constant (k) was evaluated according to the logarithmic form of the Arrhenius equation,

$$\ln k = \ln A - \frac{E_{app}^{act}}{RT} \quad (3)$$

It should be noted that the activation energies for our prepared catalysts in this reaction was determined at similar condition for conversion levels less than 10% where the best linear correlation was observed between the logarithmic rate constant (ln k) and the inverse temperature ($\frac{1}{T}$).

The results of apparent activation energies (Table 1) calculated for the impregnated Ni-W catalysts are in good agreement with that reported in the literatures [9]. The range of activation energies for the reaction of benzene hydrogenation calculated from the Arrhenius plot is 16.69-69.80 kJ mol⁻¹. The kinetics study indicates that the activation energy in the benzene hydrogenation carried out on Ni-W/HZSM-5(1.5)-HMS (16.69 kJ mol⁻¹) is lower than that other prepared catalysts. This low amount of activation energy confirms that this micro/mesoporous molecular sieve are very attractive support for Ni-W active in the hydrogenation reaction with much easier and faster performance of reaction.

Arising from the above-described experimental data, a Langmuir-Hinshelwood mechanism is proposed for the hydrogenation of benzene over Ni-W supported catalysts. According to this model, the hydrogenation reaction of benzene is generally regarded to proceed following steps,



In this mechanism has been assumed that one molecule of benzene and three dissociated molecules of hydrogen are chemisorbed on the same type of separated active sites at the surface. Then these pre-adsorbed molecules simultaneously react as step 6 (rate determining step) in many consecutive mini-steps. According to this step, the theoretical rate equation would be as follows,

$$r = \frac{k K_H P_H K_{Bz} P_{Bz}}{(1 + K_H^{1/2} P_H^{1/2} + K_{Bz} P_{Bz})^3} \quad (8)$$

where k is the rate constant, K_H and K_{Bz} are the chemisorption equilibrium constants ($K_i = \frac{k_i}{k_{-i}}$) and P_H and P_{Bz} are the hydrogen and benzene partial pressures, respectively.

The same set of experiments was done as the experiments of the PL model and the kinetic



parameters of the expanded Eq. (8) have been estimated and listed in Table 1. These results show that the activation energies calculated via the LH model are almost lower than the activation energies measured in the PL model. This observation is probably due to the simplicity of PL model and the lack of consideration of the H₂ and benzene adsorptions in the PL model. The data in Table 1 show negative values for the adsorption heats of Bz and H₂ that are based on the exothermic nature of the Bz hydrogenation reaction. The pre-exponential factor of adsorption for Bz (A_{Bz}) is lower than that of the H₂ (A_{H_2}). This probably implies a faster and stronger adsorption of H₂ over the prepared catalysts. The parameters obtained were used to simulate the selectivity to Bz products for different prepared catalysts. The results of calculated Bz selectivity vs. experimental Bz selectivity were presented in Fig. 1. The calculated data of LH model present a same trend of experimental data, but the accuracy at low conversions is slightly bad.

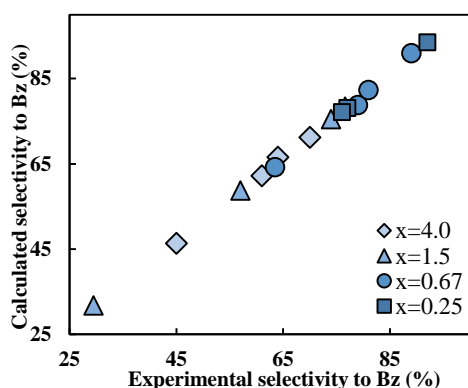


Fig. 1. Estimated data by power law model for various catalysts.

According to the results obtained of these two models, the LH model presents the less accuracy than the PL model (Fig. 2). This is probably because the power law has a simpler expression versus numerical adjustment.

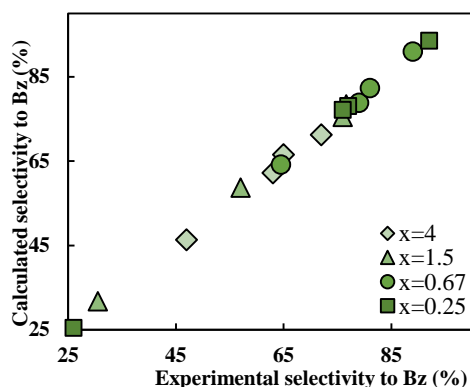


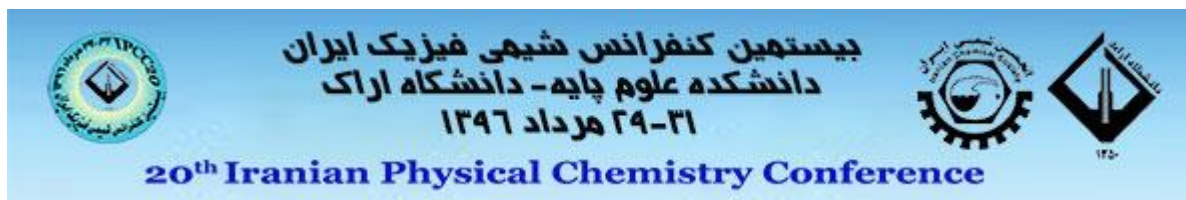
Fig. 2. Estimated data Langmuir-Hinshelwood model for various catalysts.

Conclusions

In summary, a series of micro/mesoporous catalysts with different amounts of Ni/W ratios were successfully synthesized. A series of kinetic tests performed with these catalysts under various operating conditions showed that the catalyst with Ni/W=1.5 could perform this hydrogenation reaction with appropriate rate. The activation energies calculated in this work confirm that micro/mesoporous molecular sieves are attractive supports for nickel/tungsten active for the hydrogenation of benzene. A question arises as to whether competitive or non-competitive adsorption of benzene or hydrogen occurs during this catalysis reaction. The observed increase in both hydrogen and benzene orders with increasing reaction temperature is described on the basis of a non-competitive adsorption of two components. However, in some literature [10], competitive adsorption was reported. As a result, both reactant molecules (benzene and hydrogen) are adsorbed on the surface sites during catalysis reaction that their strength of adsorption effects on reaction orders.

References

- [1] X. Liu, C. Meng, Y. Han "Substrate-mediated enhanced activity of Ru nanoparticles in catalytic hydrogenation of benzene", *Nanoscale*, 4 (2012) 2288-2295.
- [2] X. Yan, Q. Zhang, M. Zhu, Z. Wang "Selective hydrogenation of benzene to cyclohexene over Ru-Zn/ZrO₂ catalysts prepared by a two-step impregnation method", *Journal of Molecular Catalysis A: Chemical*, 413 (2016) 85-93.
- [3] P. Zhang, T. Wu, T. Jiang, W. Wang, H. Liu, H. Fan, Z. Zhang, B. Han "Ru-Zn supported on hydroxyapatite as an effective catalyst for partial hydrogenation of benzene", *Green Chemistry*, 15 (2013) 152-159.
- [4] H. Spod, M. Lucas, P. Claus "Continuously conducted selective hydrogenation of benzene to cyclohexene in a four-phase system", *Chemical Engineering & Technology*, 38 (2015) 1340-1342.
- [5] Y. Wan, C. Chen, W. Xiao, L. Jian, N. Zhang "Ni/MIL-120: An efficient metal-organic framework catalyst for hydrogenation of benzene to cyclohexane", *Microporous and Mesoporous Materials*, 171 (2013) 9-13.
- [6] M. H. Peyrovi, N. Parsafard, M. A. Hajiabadi "Ni-W catalysts supported on HZSM-5/HMS for the hydrogenation reaction of aromatic compounds: effect of Ni/W ratio on activity, stability, and kinetics", *International Journal of Chemical Kinetics*, 49 (2017) 283-292.
- [7] M. H. Peyrovi, M. R. Toosi "Study of benzene hydrogenation catalyzed by nickel supported on alumina in a fixed bed reactor", *Reaction Kinetics and Catalysis Letters*, 94 (2008) 115-119.



[8] N. Parsafard, M. H. Peyrovi, M. Rashidzadeh "n-Heptane isomerization on a new kind of micro/mesoporous catalyst: Pt supported on HZSM-5/HMS", *Microporous and Mesoporous Materials*, 200 (2014) 190-198.

[9] A. Lewandowska, S. Monteverdi, M. Bettahar, M. Ziolk "MCM-41 mesoporous molecular sieves supported nickel-physico-chemical properties and catalytic activity in hydrogenation of benzene",

Journal of Molecular Catalysis A: Chemical, 188 (2002) 85-95.

[10] R. Wojcieszak, S. Monteverdi, M. Mercy, I. Nowak, M. Ziolk, M. M. Bettahar "Nickel containing MCM-41 and AlMCM-41 mesoporous molecular sieves Characteristics and activity in the hydrogenation of benzene", *Applied Catalysis A: General*, 268 (2004) 241-253.

Synthesis of n-type and p-type CuInS₂ thin films via simple SILAR method

H. Alehdaghi^a, M. Zirak^{a*}

^aDepartment of physics, Hakim Sabzevari University, Sabzevar, 9617976487, Iran

*m.zirak@hsu.ac.ir

Abstract: Among various CuInS₂-related heterojunctions, it is expected that CIS-based p-n junctions are high-performance photo-active electrodes. Herein, both n-type and p-type CuInS₂ thin films were synthesized via facile successive ion layer adsorption and reaction (SILAR) method, using aqueous (A-CIS) and methanolic (M-CIS) SILAR solutions, respectively. Based on UV-visible transmission spectra, M-CIS thin films were more transparent with larger band gap energy (1.6 eV) than A-CIS thin films (1.5 eV). The A1-mode Raman peak of M-CIS thin film was located at 293 cm⁻¹ which has a red shift of 5 cm⁻¹ as compared to A-CIS one, indicating that M-CIS has smaller CuInS₂ nanoparticles. The Mott-Schottky plots revealed that A-CIS is an n-type semiconductor, while M-CIS thin films have p-type semiconducting behavior, which is due to different Cu/In ratio in these thin films. The obtained results can be very useful to prepared CIS-based p-n junctions toward high performance solar-based devices.

Keywords: *CuInS₂ thin film; p-n heterojunction, SILAR; solar-based devices*

Introduction

CuInS₂ (CIS) is a semiconductor with narrow band gap energy of 1.45 eV. It has a high extinction coefficient of $\alpha=10^5$ cm⁻¹ in the visible region [1, 2]. In addition, CIS is free of toxic elements with satisfactory and stable performance under sun-light irradiation [3]. Therefore, it is an interesting material for solar energy conversion applications.

Among various CuInS₂-related heterojunctions, it is expected that CIS-based p-n junctions are high-performance photo-active electrodes [4]. the space charge region (depletion layer), caused by p-n junction, depletes the electrons and an internal electrostatic field is established. Therefore, electrons (e⁻) and holes (h⁺) diffuse to opposite directions, leading to reduce e⁻-h⁺ recombination [2]. It is reported that semiconducting behavior of CIS can be tuned between n-type and p-type by changing the synthesis parameters. For example, CIS exhibits p-type semiconductivity when Cu to In atomic ratio exceeds 1 [2, 5]. It is very important to develop a simple and reliable protocols to synthesis CIS with desired semiconducting behavior.

Herein, we have employed facile successive ion layer adsorption and reaction (SILAR) method, with two different natures of SILAR solutions (aqueous and methanolic solutions) to obtain n-type and p-type CuInS₂ thin films. The obtained results can be very useful to prepared CIS-based p-n junctions toward high performance solar-based devices.

Materials and method

Copper (II) nitrate trihydrate (KESHI company, China), Sodium sulfide nonahydrate (Na₂S.9H₂O, Acros), Indium(III) nitrate hydrate (Sigma), Indium tin

oxide (ITO) sheets (30 Ω/□) and absolute methanol (Merck) were used as received without any further purification.

The CIS thin films prepared with aqueous-SILAR solutions (A-CIS) as following: the pre-cleaned ITO substrates were successively immersed in three separated aqueous solutions namely 0.10 M In(NO₃)₃ for 60 s, 1.25×10⁻³ M Cu(NO₃)₂ for 30 s, and 0.135 M Na₂S for 4 min., to remove unabsorbed ions, the electrode was rinsed with DI water for 1 min after each immersion step. These three immersion steps were considered as one SILAR cycle. 10 SILAR cycles were repeated to obtain the final thin films. After that, the thin films were annealed in Ar environment at 350 °C for 1.5h to prepare crystallized CIS thin films. The M-CIS thin films were synthesized as same as A-CIS layers, except that methanol was used instead of water as solvent and Na₂S was dissolved in methanol/water (7:3, v/v) solvent.

A PGENERAL T6 spectrophotometer was utilized to obtain the UV-Visible absorption spectra of the samples. To identify the samples composition structure, an Invia Renishaw Raman microscope (with exciting laser wavelength of 514.5 nm) was employed. A three-electrode setup (the synthesized thin films as working electrode, saturated calomel electrode (SCE) as reference electrode and Pt wire as counter electrode) was connected to a CHI 660D electrochemical workstation (Shanghai Chenhua Instrument Co., China) to measure all electrochemical analyses. the Mott-Schottky tests were done in 50 mM Na₂S aqueous solution by applying AC voltage varying from -0.2 to 0.2 V with frequency of 1 kHz and 5mV amplitude

Results and Discussion



UV-Visible transmission spectra of synthesized samples have been shown in Fig. 1. As it can be seen, the sample prepared via aqueous solutions (A-CIS) has less transmittance than M-CIS one, meaning that aqueous solutions have resulted in more ion absorption and consequently thicker layer has formed on ITO substrate. The band gap energy (E_g) of the layers were evaluated via Tauc plots [6] (Fig. 1 b). based on Fig. 1 b results, the E_g of M-CIS and A-CIS was determined to be 1.6 and 1.5 eV respectively. Larger E_g of M-CIS is related to formation of smaller particles and thinner CuInS_2 film on ITO substrate.

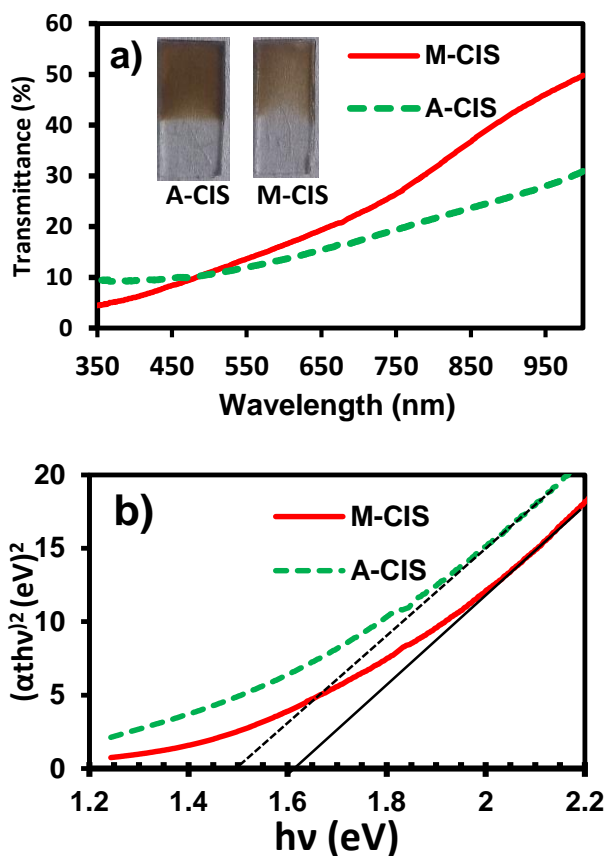


Fig. 1: a) UV-Visible transmission spectra and b) related Tauc plots of A-CIS and M-CIS thin films. The inset of a) is photograph of prepared samples.

The compositions of the synthesized thin films were more characterized via Raman spectroscopy. The obtained Raman spectra have been shown in Fig. 2. There is a dominant peak located at 293 and 298 cm^{-1} for M-CIS and A-CIS, respectively. The observed peak is related to A1-mode of CuInS_2 crystal structure [7]. The A1-mode of M-CIS has a shift toward lower frequencies as compared to the A-CIS thin film, which can be attributed to optical phonon confinement and formation of smaller CuInS_2 nanoparticles [7]. The Raman results are in good agreement with obtained UV-Visible transmission data.

To determine that the synthesized $\text{CuInS}_2/\text{ITO}$ thin films are n-type or p-type semiconductor, the Mott-Schottky tests were done and the results have been shown in Fig. 3.

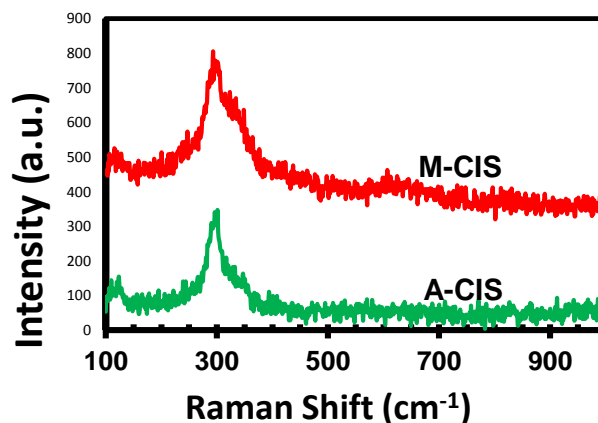


Fig. 2: Raman spectra of M-CIS and A-CIS thin films.

The Mott-Schottky relationship for semiconductors are expressed as following [8]:

$$\frac{1}{C^2} = \frac{2}{\epsilon\epsilon_0 e N_d A^2} \left[(E - E_{\text{FB}}) - \frac{kT}{e} \right], \text{ for n type (1)}$$

$$\frac{1}{C^2} = \frac{2}{\epsilon\epsilon_0 N_a A^2} \left[(-E + E_{\text{FB}}) - \frac{kT}{e} \right], \text{ for p type (2)}$$

Where " ϵ_0 " and " ϵ " are the permittivity of vacuum and semiconductor, respectively. " e " is the electron charge, " k " is Boltzmann's constant, " T " is operation temperature, " N_a " and " N_d " are the acceptor and donor densities, respectively. " E ", " E_{FB} " and " C " are the electrode potential, flat-band potential and depletion-layer capacitance, respectively [8]. Based on above equations, the Mott-Schottky plots have positive and negative slopes for n-type semiconductor and a negative slope for p-type one.

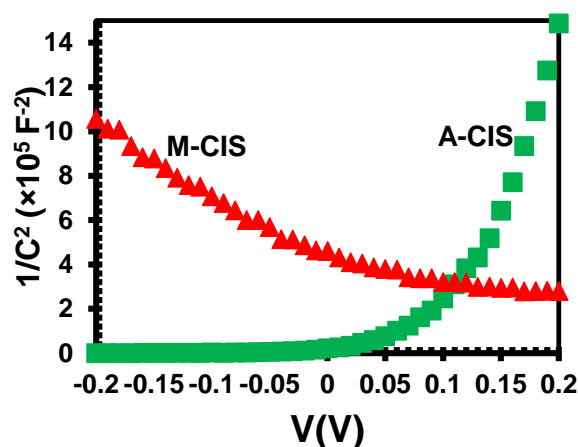


Fig. 3: Mott-Schottky plots of CuInS_2 thin films.



As it can be seen from Fig. 3, the A-CIS has a positive slope and M-CIS has a negative slope. Therefore, the CuInS₂ thin films prepared with aqueous SILAR solutions have n-type semiconducting behavior. On the other hand, the CIS thin films prepared with methanolic SILAR solutions are p-type semiconductors. The reason may be related to different Cu/In ratio in A-CIS and M-CIS thin films [2].

Conclusions

The CuInS₂ thin films were prepared by simple SILAR method using aqueous (A-CIS) and methanolic solutions (M-CIS). The Raman results indicated that the M-CIS thin film has smaller nanoparticles than A-CIS one. The A-CIS thin films were more opaque with smaller band gap energy. The Mott-Schottky plots revealed that A-CIS is an n-type semiconductor, while M-CIS thin films have p-type semiconducting behavior, which is due to different Cu/In ratio in these thin films.

Acknowledgment

The Authors would like to thank Research and Technology Council of the Hakim Sabzevari university for supporting the work.

References

- [1] J. Kolny-Olesiak, H. Weller, "Synthesis and Application of Colloidal CuInS₂ Semiconductor Nanocrystals", *ACS Applied Materials & Interfaces*, 5 (2013) 12221-12237.
- [2] Y.-X. Yu, W.-X. Ouyang, Z.-T. Liao, B.-B. Du, W.-D. Zhang, "Construction of ZnO/ZnS/CdS/CuInS₂ Core-Shell Nanowire Arrays via Ion Exchange: p-n

Junction Photoanode with Enhanced Photoelectrochemical Activity under Visible Light", *ACS applied materials & interfaces*, 6 (2014) 8467-8474.

[3] G.S. Wang, H.Y. Wei, J.J. Shi, Y.Z. Xu, H.J. Wu, Y.H. Luo, D.M. Li, Q.B. Meng, "Significantly enhanced energy conversion efficiency of CuInS₂ quantum dot sensitized solar cells by controlling surface defects", *Nano Energy*, 35 (2017) 17-25.

[4] L.C. Jia, Y.B. Wang, Q.Q. Nie, B. Liu, E.Z. Liu, X.Y. Hu, J. Fan, "Aqueous-synthesis of CuInS₂ core and CuInS₂/ZnS core/shell quantum dots and their optical properties", *Materials Letters*, 200 (2017) 27-30.

[5] K. Das, S.K. Panda, S. Gorai, P. Mishra, S. Chaudhuri, "Effect of Cu/In molar ratio on the microstructural and optical properties of microcrystalline CuInS₂ prepared by solvothermal route", *Materials Research Bulletin*, 43 (2008) 2742-2750.

[6] M. Zirak, M. Zhao, O. Moradlou, M. Samadi, N. Sarikhani, Q. Wang, H.-L. Zhang, A. Moshfegh, "Controlled engineering of WS₂ nanosheets-CdS nanoparticle heterojunction with enhanced photoelectrochemical activity", *Sol. Energy Mater. Sol. Cells*, 141 (2015) 260-269.

[7] E. Rudigier, I. Luck, R. Scheer, "Quality assessment of CuInS₂-based solar cells by Raman scattering", *Applied physics letters*, 82 (2003) 4370-4372.

[8] Y. Liu, Y.-X. Yu, W.-D. Zhang, "MoS₂/CdS Heterojunction with High Photoelectrochemical Activity for H₂ Evolution under Visible Light: The Role of MoS₂", *The Journal of Physical Chemistry C*, 117 (2013) 12949-12957.

Effect of lithium doping in electron injection layer on the LED performance in reverse structure

M. Zirak^a, H. Alehdaghi^{b,*}

^aDepartment of physics, Hakim Sabzevari University, Sabzevar, 9617976487, Iran

^{*}hasan.aldaghi@gmail.com

Abstract: light emitting diodes (OLEDs) are one the newest lighting in industrial lighting which can be a promising candidate in this area. A typical reverse OLED is made from cathode, injection/transport electron and hole layers, emissive layer (EM). Electrons and holes after injection to EM are recombined in emissive layer which is an organic material. In reverse structure, holes inject EM well while electrons cannot be easily injected to emissive layer. Here, effect of lithium doped zinc oxide (LZO) on the led performance was investigated. The results showed that lithium can be increased conductivity of injection electron layer and facile to inject electron to emissive layer.

Keywords: lighting; OLED; injection electron; lithium doping; thin film

Introduction

Deep research on organic light emitting diodes (OLEDs) starts with Tang's research [1]. After that time researchers focused on this area with higher acceleration [2–6]. OLEDs are made of several thin layer consist of injection/transport electron and hole layers and an emissive layer which is a place for electron and hole recombination. Regarding deposition method of layers which is very easy to scale up and doesn't need to vacuum systems, OLEDs are a good candidate to substitute of another lighting in industry lighting. According to configuration there are two structure for OLEDs; conventional and reverse. In conventional usually ITO is used to anode and metals with low workfunction are used to cathode (Ca, Al, LiF/Al) [7] and in reverse structure ITO is used to cathode and metals with high workfunction are used to anode (Au, Ag and Pt) [8]. In reverse structure one of challenging issue is injection of electron to emissive layer [9]. Therefore work on injection electron layer in reverse structure is very important [10].

Here, we used lithium doped zinc oxide (LZO) introduced an electron injection layer leading to increase efficiency and decrease turn on voltage. Varying of amount of lithium, the optimum condition was obtained. Current-voltage, luminance-voltage, and efficiency-luminance characteristic of devices was well indicated that how lithium can affect on LED performance.

Materials and method

Lithium doped Zinc Oxide (LZO) precursor was prepared with solving of zinc acetate.4H₂O and lithium acetate (sigma Aldrich) in ethanol at concentration of 100 mM for zinc precursor. The milky solution was

refluxed at 60 °C for 12 h. the solution would be suitable for deposition after filtration. Values of percent volume lithium was selected 2%, 10%, and 30%. About 30 nm LZO deposited top on clean ITO/glass substrate. To prepare clean ITO/glass, it was down by successive cleaning in acetone, methanol, and IPA in ultrasonic bath, each for 15 min. Finally, the substrates were treated by UV/ozone irradiation for 15 min to avoid any organic contaminant. The LZO thin film were baked at 200 °C for 15 min. To increase electron injection ability Cs₂CO₃ ultrathin deposited top of LZO layer. The precursor of Cs₂CO₃ was dissolve in 2-methoxyethanol with 5% volume concentration. After layer is emissive polymer, here is PDY or super yellow, deposited about 70 nm. After that samples moved to vacuum chamber at pressure of 10⁻⁹ torr. Two successive layers of MoO₃ and Ag were deposited at rate of 0.2 nm/s with 10 nm and 100 nm, respectively. Finally, the devices are encapsulated in the glove box.

The current-voltage and luminance–voltage characteristics are measured using Konica Minolta CS100A luminance meter (with 0.001 cd accuracy) coupled with a Keithley 2635A (with pico Ampere accuracy) voltage and current source meter, with a 1 sec time steps (in continuous mode).

Results and Discussion

The configuration of devices fabricated and related thickness has been showed in Fig. 1. Electrons are injected from ITO/LZO/Cs₂CO₃ and holes from Ag/MoO₃ injected to emissive layer. In emissive layer the reached electrons and holes are recombined and emit light. Due to transparency of ITO/LZO/Cs₂CO₃ layers light exits from bottom of device. In Fig. 2 current-voltage (J-V) characteristic of three device of



fabricated has been drawn. In the linear presentation J-V it is seen that with increasing of lithium dopant conductivity of devices improved. In this trend can be attributed to being of meal properties of lithium. In the fact, increasing of lithium amount in LZO thin film leads to have a more conductive layer. The maximum of current for three device is approximately is the same (300 mA/cm^2). In the rest, semi-logarithmic representation J-V characteristic is observed. The magnitude order of measured range of current variation is about 10, it means the current starts from 10^{-8} mA/cm^2 to about 300 mA/cm^2 . According to this figure, device fabricated with LZO (30%) has better diodic properties. It is noted that Cs_2CO_3 ultrathin layer is a factor to improve electron inject characteristic.

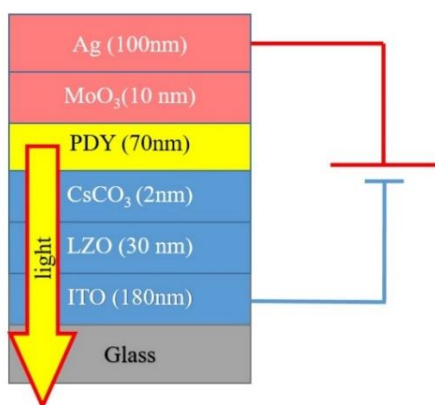


Fig. 1: configuration of LED and related thickness

Luminescence-voltage characteristic of the devices is depicted in Fig. 3. These behavior is very similar to J-V properties. The maximum luminance is 21 cd/m^2 for device fabricated to LZO (20%). Regarding to higher conductivity in LZO (30%) we too have lower turn on voltage for the related device. In every device, luminescence is dropped suddenly that according to J-V characteristic it can be due to degradation of devices in very high current.

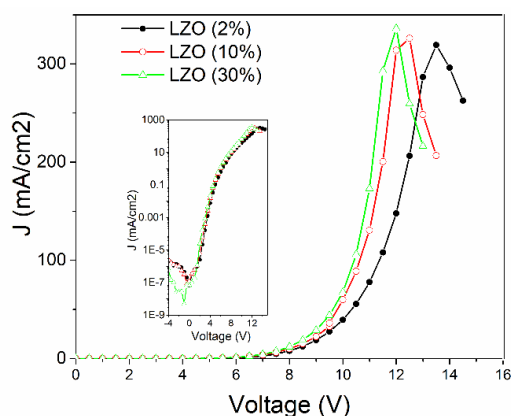


Fig. 2: current-voltage characteristic of LEDs fabricated by different amount of lithium doping in ZnO

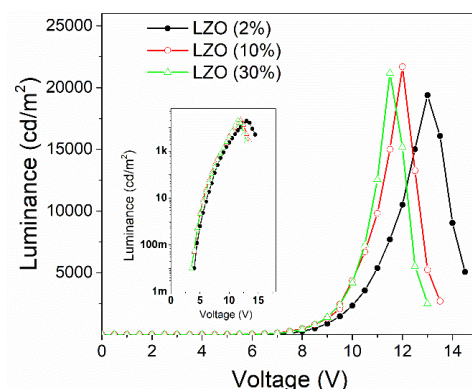


Fig. 3: effect of lithium doping in ZnO layer on the Luminescence-voltage characteristic.

Performance of a LED is indicated when its efficacy is measured. In order to compare devices performance current-luminescence-voltage (J-L-V) was recorded with measuring of J-V and L-V simultaneously. Fig. 3 shows current efficiency or efficacy (a) and power efficiency versus on luminance (b). In Fig. 3 (a) is seen that efficacy of device fabricated by LZO(10%) is the best although turn on voltage of LZO(30%) is the lowest. the efficacy of LEDs can reach to 7.5 cd/A that is very acceptable for inverted structure. Higher efficacy means LED emits light in lower current that causes to increase the device performance and lifetime. Conductivity of LZO (30%) is so high that it cannot have a good efficacy due amount of current is higher than luminance in comparing to other devices. If a device turns on in low voltage and low current, it has high power efficiency. The highest power efficiency owns to LZO (10%) (In Fig. 3 (a)) with amount of 2.3 lm/W . lithium doping leads to electron inject to emissive layer better.

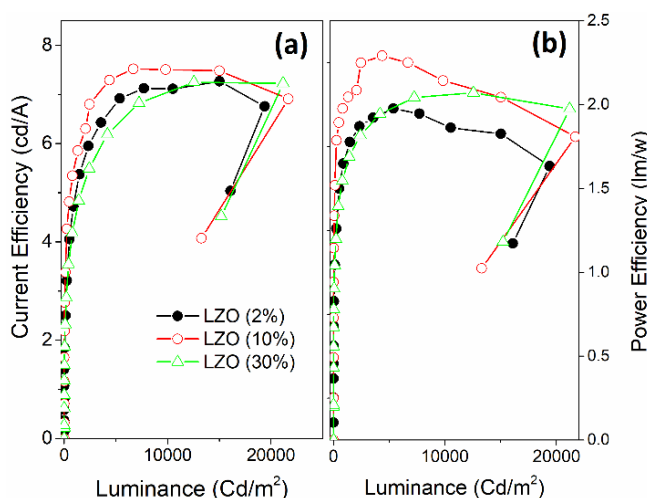


Fig.4: effect of lithium doping in ZnO layer on current efficiency (a) and power efficiency (b)

Conclusions

In aim to understand and compare of effect of lithium doping in ZnO thin film, different amount of lithium was mixed to Zn precursor. After baking, LZO thin film prepared to enter a LED device. From J-V characteristics it was concluded conductivity of LZO is improved as amount of lithium is increased. The lowest turn on voltage owned to device fabricated to LZO (30%). According to the efficiency results it was indicated efficiency of device fabricated by LZO (10 %) is the best and optimum due to facile injection of electrons to emissive layer.

References

- [1] C. W. Tang, S.A. Vanslyke, Organic electroluminescent diodes, *Appl. Phys. Lett.* 51 (1987) 1913.
- [2] J.H. Youn, S.J. Baek, H.P. Kim, D.H. Nam, Y. Lee, J.G. Lee, J. Jang, Improving the lifetime of a polymer light-emitting diode by introducing solution processed tungsten-oxide, *J. Mater. Chem. C* 1 (2013) 3250. doi:10.1039/c3tc00855j.
- [3] S. Reineke, F. Lindner, G. Schwartz, N. Seidler, K. Walzer, B. Lüssem, K. Leo, White organic light-emitting diodes with fluorescent tube efficiency., *Nature*. 459 (2009) 234–8.
- [4] W. Gu, X. Liu, X. Pi, X. Dai, S. Zhao, L. Yao, D. Li, Y. Jin, M. Xu, D. Yang, G. Qin, Silicon-quantum-dot light-emitting diodes with interlayer-enhanced hole transport, *IEEE Photonics J.* 9 (2017). doi:10.1109/JPHOT.2017.2671023.
- [5] J. Lee, C. Jeong, T. Batagoda, C. Coburn, M.E. Thompson, S.R. Forrest, Hot excited state management for long-lived blue phosphorescent organic light-emitting diodes, *Nat. Commun.* 8 (2017) 15566. doi:10.1038/ncomms15566.
- [6] C.W. Tang, S. A. Vanslyke, Organic electroluminescent diodes, *Appl. Phys. Lett.* 51 (1987) 913.
- [7] J.H. Lee, C.I. Wu, S.W. Liu, C.A. Huang, Y. Chang, Mixed host organic light-emitting devices with low driving voltage and long lifetime, *Appl. Phys. Lett.* 86 (2005) 1–3.
- [8] H.J. Bolink, E. Coronado, J. Orozco, M. Sessolo, Efficient polymer light-emitting diode using air-stable metal oxides as electrodes, *Adv. Mater.* 21 (2009) 79–82. doi:10.1002/adma.200802155.
- [9] M. Sessolo, H.J. Bolink, Hybrid organic–inorganic light-emitting diodes, *Adv. Mater.* 23 (2011) 1829–1845.
- [10] H.J. Bolink, E. Coronado, D. Repetto, M. Sessolo, E.M. Barea, J. Bisquert, Inverted Solution Processable OLEDs Using a Metal Oxide as an Electron Injection Contact, *Adv. Funct. Mater.* 18 (2008) 145–150.



Study of the effects of acidic after treatment on the gamma alumina powder properties

Zahra shahidian*¹, [Azadeh papan](#)¹, Fatemeh Tavakolzadeh¹, Sara Beshkoofeh¹

¹ Iranian Institute of Research and Design in Chemical Industries (Acecr), Karaj, Iran

Azadeh_papan@yahoo.com

Abstract

Increasing the pore volume and pore diameter of gamma alumina powder is the purpose of this research. In order to increase the pore volume and pore diameter of gamma alumina powder, the effects of acidic after treatment on physical chemistry of gamma alumina are studied. In this regard, the boehmite powder from the Azarshahr Nephelinsite ore is calcinated at 650 °C for 6 hours and gamma alumina powder is obtained. In order to obtain the gamma alumina powder with desired pore volume and pore diameter, after treatments in hydrochloric acid and nitric acid and after treatment with different steps (first, second and third steps) on the boehmite powder are performed. The pore volume, pore diameter and surface area of the final prepared gamma alumina were studied by the BET techniques and the results shows that after treatment in hydrochloric acid and nitric acid with third steps are effective to increase the pore volume and pore diameter of the gamma alumina powder.

Keywords: *gamma alumina; catalyst support; acidic after treatment; catalytic HDT.*

Introduction

Catalytic hydrotreating (HDT) is one of the most important processes in the petroleum refining industry. It is applied to treat almost all of the refinery streams, from straight-run distillates to vacuum residua. The reaction conditions of the HDT process vary with the type of feedstock; while light oils are easy to desulfurize, desulfurization of heavy oils is much more difficult. The HDT reactions take place in catalytic reactors at elevated temperatures and pressures typically in the presence of a catalyst consisting of an alumina base impregnated with transition metals [1].

Due to upgrade heavy crude oil, catalysts need to have wide pores to allow for diffusion of such large molecules to the catalytic sites. However, increasing catalyst porosity leads to reduction in surface area and consequently decrease in specific activity. For heavy feeds, adequate porosity is essential since it is necessary to achieve a large metal-retaining capacity to extend the catalyst life, which decreases rapidly due to coking and metal deposition. Therefore, the textural properties of the catalyst could be of greater importance than surface area and chemical composition of the surface [2, 3].

For hydrotreating catalysts, alumina is being the most commonly used support because it combines virtually all of the above-listed characteristics. Gamma alumina because of high surface area, is stable at the temperatures used in hydrotreating, easily formed in spheres or extrudes and inexpensive [4-7].

The alumina powder can be easily prepared in the laboratory or can be obtained in sufficiently large quantities from the commercial companies. In general, the following alumina in the laboratory steps are followed for preparation of: precipitation, hydrothermal transformation (aging), centrifugation and filtration, washing, drying, shaping of the support

(crushing, grinding, extrudes, etc.), drying and calcination. Each of the above steps has a particular effect on the properties of the final support [8,9].

The catalytic performance of a catalyst depends on its different components such as support and active metal. Usually, the behaviour of the active phase is influenced by the type of support material; therefore, it becomes necessary to select an optimum support material according to the criteria of interaction with active phases, acid-base properties, textural properties, stability, extrusion properties, and cost at commercial scale. These properties become critical when the catalyst is being used for heavy oil hydro processing. Therefore, taking all properties into consideration, the most used support for hydro processing of heavy crude oil has been alumina [10, 11].

In this research all of the doing after treatments on the boehmite powder that are caused to increase the pore volume and pore diameter of gamma alumina powder (which is used as the catalyst support in hydrotreating unit of Imam Khomeini refinery) are studied. Gamma alumina powder is prepared of the boehmite powder calcination and because of the prepared gamma alumina properties is different from the commercial sample (surface area, pore volume, pore diameter), so it is needed to after treatment until the properties of the prepared gamma alumina powder is closed to the commercial sample. In the experimental section of this paper, all of the after treatments such as acidic after treatment and the number of acidic after treatment steps that are affected on the considered surface properties of gamma alumina powder are studied.

Experimental

1-materials and equipment



Boehmite powder from the Azarshahr Nephelinsite ore, nitric acid, hydrochloric acid and deionized water are all materials that are used in this research. The equipment's are oven, furnaces, Buchner funnel and stirrer. The surface properties are studied by BELLSORP-II mini device.

2- Boehmite powder

In this test, the boehmite powder is calcinated at 650°C for 6 hours and gamma alumina powder is obtained.

3- The effects of hydrochloric acid after treatment

At first, 13 gr boehmite powder is added to 100 ml deionized water. Then 4.5 cc hydrochloric acid is added to the boehmite solution and is stirred at 50°C for 40 min. Then is filtered and is calcinated at 650°C for 6 hours. (Sample 1)

3-1- The effects of the number of hydrochloric acid after treatment steps

In this test, the effects of the number of hydrochloric acid after treatment steps on the physical chemistry properties of gamma alumina powder are investigated, the obtained gamma alumina is kept in hydrochloric acid 10% for two days in laboratory conditions. Then it is washed with water for several times and dried in oven and calcinated at 650°C for 6 hour (the first step). (Sample 2)

In the second step, the previous prepared gamma alumina powder is kept in hydrochloric acid 10% for two days in laboratory conditions. Then it is washed with water for several times and dried in oven and calcinated at 650°C for 6 hours (the second step). (Sample 3)

In the final step, the prepared gamma alumina from the second step is kept in hydrochloric acid 10% for two days in laboratory conditions for the third time. Then it is washed with water for several times and dried in oven and calcinated at 650°C for 6 hours (the third step). (Sample 4)

4- The effects of nitric acid after treatment

In this section, 13 gr boehmite powder is added to 100 ml deionized water. Then 4.5 cc nitric acid is added to the boehmite solution and is stirred at 50°C for 40 min. Then is filtered and is calcinated at 650°C. (Sample 5)

4-1- The effects of the number of nitric acid after treatment steps

The other parameter that is influenced on the physical chemistry properties of the gamma alumina powder is to increase the steps of acidic after treatment. At first, the powder is kept in nitric acid 65% for two days. Then it is washed with water for several times and dried in oven and calcinated at 650°C for 6 hours (the first step aging). (Sample 6)

In the next step, the obtained gamma alumina powder of the previous step is kept in nitric acid 65% for two days. Then it is washed with water for several times and dried in oven and calcinated at 650°C for 6 hours (the second step aging). (Sample7)

In the final step, the obtained gamma alumina of the second step aging is kept in nitric acid 65% for two days. Then it is washed with water for several times and dried in oven and calcinated at 650°C for 6 hours (the third step aging). (Sample 8)

Results and Discussion

The BET test is done for all samples and boehmite powder and gamma alumina powder and the results of surface area, pore volume and pore diameter are listed in table 1.

Table 1: the BET results of gamma alumina powder, boehmite powder and samples

	Surface area (m ² /g)	Pore volume (cc/g)	Pore diameter (nm)
Boehmite powder	211	0.67	12.69
Gamma alumina	244	0.54	8.9
Sample 1	216	0.58	10.88
Sample 2	243	0.72	11.88
Sample 3	244	0.82	13.56
Sample 4	262	1.38	21.04
Sample5	221	0.6	10.89
Sample 6	226	0.76	10.88
Sample 7	227	0.82	14.8
Sample 8	263	1.04	15.84

According to the experimental tests and BET results, the following results are founded:

- 1- The results show that the properties of obtained gamma alumina with after treatment in nitric acid and hydrochloric acid are improved and pore volume and pore diameter are increased.
- 2- The results show that after treatment in hydrochloric acid is lead to further increase in pore volume and pore diameter than nitric acid.
- 3- By increasing the steps of acidic after treatment, acidic ions are activated and it is caused to improve the physical chemistry properties of gamma alumina.
- 4- By increasing the steps of the acidic after treatment, the surface properties of gamma alumina are improved.

Conclusions

According to the results, although, the obtained gamma



alumina powder from hydrochloric acid after treatment has better pore diameter and pore volume, because of a little hydrochloric acid is remained in the obtained gamma alumina powder is not selected as the best method.

The best after treatment that cause to desired pore volume and pore diameter, is nitric acid after treatment with third steps and because of the all nitric acid is burned in furnaces and is removed of the gamma alumina powder that is selected as the best method.

References

- [1] J. Ancheytad, Deactivation of heavy oil hydroprocessing catalyst, 2016, published by John Wiley & Sons, Inc., 39-49, Hoboken, New Jersey.
- [2] M. Absi-Halabi, A. Stanislaus and H. Al-Zaid, Applied Catalysis A: General, 101 (1993)117-128.
- [3] R.J.Quan, R.A.Ware, .C.W.Hung and J. Wel. Advances in Chemical Engineering, 14 (1988)95.
- [4] H.Toulhoat and J.C.Plumall. In "Catalysts in Petroleum Refining 1989". D.L.Trim, S.Akashah, M. Absl-Halabi and A. Bishara (editors), 1990, Elsevier, 463, Amsterdam.
- [5] V.J.Lostaglio and J.D.Carruthers, Chem, Eng. Progr. (1986), 46.
- [6] D.L.Trimm and A. Staislaus. Appl. Catal. 21(1986) 215.
- [7] T. One, Y.A. Jacobs (editors), 1983, Elsevier, 631, Amsterdam.
- [8] B.C. Lippens and J.J.Steggerda, in "Physical and Chemical Aspects of Adsorbents and Catalysts", 1970, Linsen (editors), 171 Academic Press, london.
- [9] W.H. Gitzen, Alumina as a Ceramic materials, 1970, The American Ceramic Society, Columbs, Ohlo.
- [10] P. Burtin, J.P.Brunella, M.Pijolat and M.Soustell, Appl. Catal. 34(1987) 225.
- [11] M.Absi-Halabi, A. Stanlslaus and H.Al-zald, G. Poncelet, P.A. Jacobs, P. Grange and B. Delmon (Editors), "Preparation of Catalysts V", 1991,(studies in surface science and catalysis ,vol.63),Elsevier, 155,Amsterdam.



Investigation of hydrogen adsorption & storage on G-C₃N₄: fuel cell application

S.Rostami^{a*}, A.Nakhaei Pour^a, H. Oliaei Torshizi^a

Department of chemistry, faculty of science, Ferdowsi University of Mashhad, Iran
Siroosrostami90@gmail.com

Abstract: In this paper we experimentally worked on hydrogen storage on G-C₃N₄ in ambient temperature and 20 bar pressure. Also we determined thermodynamical properties of hydrogen adsorption. we synthesized pure G-C₃N₄ by Urea Precursor and it proved by XRD and FT-IR spectra. Results show that the pure G-C₃N₄ adsorption isotherm matched to Freundlich adsorption isotherm and ΔH_{ad} , ΔG_{ad} and ΔS_{ad} obtained about (-27 kJ/mol), (+21 kJ/mol) and (-161 J/K) respectively. Result showed pure G-C₃N₄ have low hydrogen storage and could not consider as candidate for hydrogen storage materials and must equip with other materials like metal oxide, transitional metal and ... to promote capacity of G-C₃N₄ compounds for fuel cell application.

Keywords: hydrogen, G-C₃N₄, Storage

Introduction

Carbon compounds have been considered as candidate for hydrogen storage because of lightweight, porosity and etc. nowadays researchers have been attempted to modify the structure of carbon compounds to enhance hydrogen storage. G-C₃N₄ considered as some of these materials which have higher hydrogen storage than similar activated carbon. Researchers attributed these properties to presence of C-N bonds instead of C-C bonds increase hydrogen storage [1-3].

Materials and method

G-C₃N₄ have been synthesized by urea precursor like each preparation methods have been observed elsewhere [4]. for experimental preparation G-C₃N₄ we used Urea precursor, were purchased from Merk as received without additional purification. we put crucible with Urea in furnace and raised temperature to 550 °C step by step (4 step in hour) and hold this circumstance for 2 hours at last we observed yellow G-C₃N₄ product. Previous processes yielded yellow product then milled and made pellet and put 1.5 gr in sample tube then checked out apparatus from gas leaking. G-C₃N₄ was proved by FT-IR, XRD spectra and specific surface area obtained ($S_{BET} = 27 \text{ m}^2/\text{gr}$). Hydrogen adsorption carried out by home-made volumetric adsorption apparatus and system checked for leaking presence. Also we carried out adsorption processes in different temperatures to find thermodynamical parameters.

Results and Discussion

For finding thermodynamical properties we used Equation 1 so hydrogen storage of substrate obtained in different temperature had been showed in Fig.1 and ΔH_{ad} calculated.

$$d \ln P / d(1/T) = \Delta H_{ad} / R \quad \text{Eq.1}$$

In this experiment we obtained ΔH_{ad} , about -28 kJ/mol.

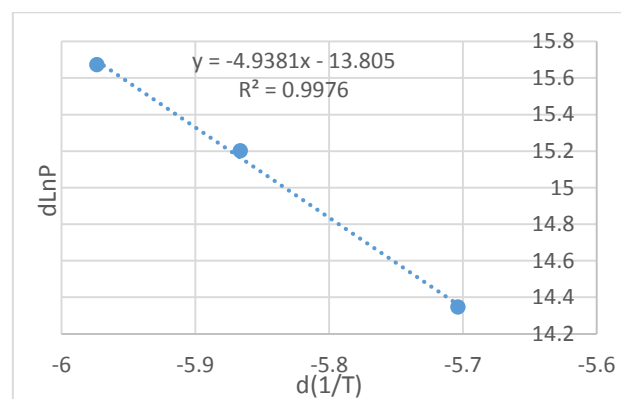


Fig.1: Hydrogen adsorption in different temperature.

Also we obtained adsorption capacity of G-C₃N₄ substance and evaluated the Langmuir, Temkin and Freundlich isotherms. Results show that the hydrogen adsorption on G-C₃N₄ have better adjustment by Freundlich adsorption isotherm., (Fig.2-4) presented as follow:

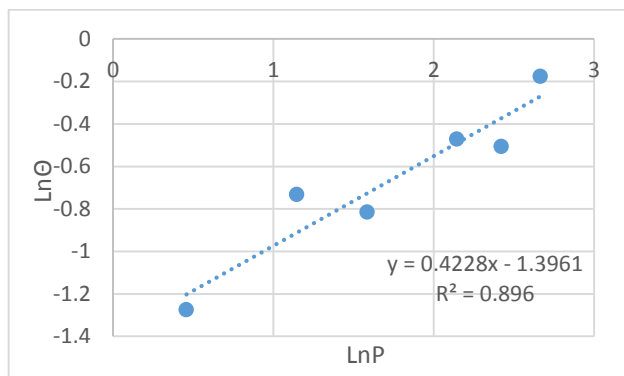


Fig.2: Freundlich isotherm.

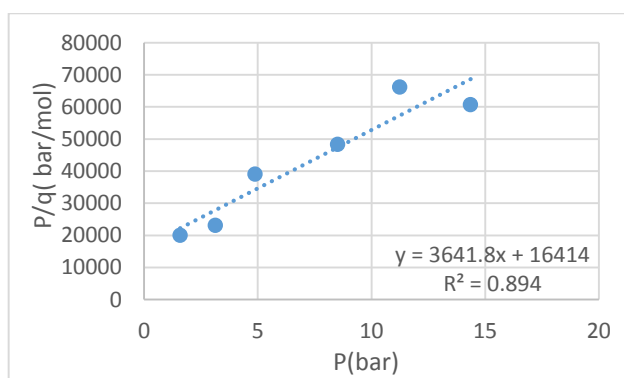


Fig.3: Langmuir isotherm.

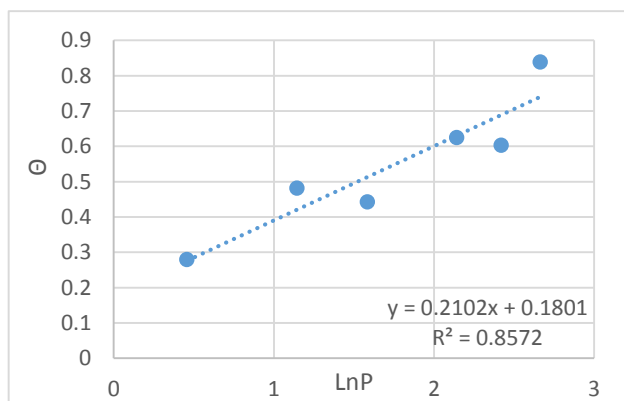


Fig.4: Temkin isotherm.

According to equation 2 and 3 we be able to find thermodynamical properties. Q_m is amount of monolayer of hydrogen molecules adsorbed on adsorbent surface and b_L is Langmuir constant.

$$\Delta G = \Delta H - T\Delta S \quad \text{Eq.2}$$

$$\Delta G = -RT \ln b_L \quad \text{Eq.3}$$

ΔG_{ad} (kJ)	ΔH_{ad} (kJ)	ΔS_{ad} (J/K)	Q_m (mmol/gr)	b_L (1/bar)
+21.014	-27.360	-161.24	0.2745	2.1619×10^{-4}

Conclusions

United states of department of energy (USDOE) aimed finding Adsorbent with 7.5 wt% H_2 storage capacity until 2020. Also $G-C_3N_4$ considered carbon material for hydrogen storage because of lightweight but our studies showed pure $G-C_3N_4$ cannot be reliable adsorbent and it is necessary to modified with other materials to enhance $G-C_3N_4$ hydrogen capacity to reach USDOE target.

References

- [1] L. Zubizarreta, A. Arenillas "Carbon materials for H_2 storage" international journal of hydrogen energy, (2008).
- [2] Asalatha A.S. Nair, R. Sundara "Hydrogen storage performance of palladium nanoparticles decorated graphitic carbon nitride, international journal of hydrogen energy, 40(2015) 3259-3267"
- [3] M J. Bojdys, J o Muller "Ionothermal Synthesis of Crystalline, Condensed, Graphitic Carbon Nitride" chemistry- a European journal, (2008).
- [4] B. Zhu, P. Xiaa "Isoelectric point and adsorption activity of porous $g-C_3N_4$ ", Applied Surface Science, (2015).

Determination of hydrogen storage capacity of MOF (Zn5): Fuel cell application

S. Rostami^{a*}, A. Abolghasem Pour^a, A. Nakhaie pour^a, A.R. Salimi^a

Department of chemistry, faculty of science, Ferdowsi University of Mashhad, Iran
Siroosrostami90@gmail.com

Abstract: In this article we studied preparation and hydrogen storage on metal - organic framework (MOF) Zn5 at ambient temperature and 20 bar pressure. A lot of articles indicated these compounds have high internal specific surface area and porosity. We synthesized MOF(Zn5) and proved by FT-IR spectra and melting point analysis. Resultant data showed MOF (Zn5) adsorption isotherm matched to Langmuir adsorption isotherm. Also we obtained total hydrogen storage in mentioned condition and showed about 0.25 wt% hydrogen storage. This result clarified pure MOF (Zn5) still far from United states department of energy target and must modify by other compound to promote its storage capacity.

Keywords: MOF(Zn5), hydrogen, storage

Introduction

Increasing urban population and growing industries, a side and drawback of fossil fuels in other side have desired new energy sources such as wind, sea, wave and solar energy and etc. nowadays hydrogen energy have been considered as substitutional clean energy instead of fossil fuels. But some disadvantages have inhibited to achieve this target such as hard compressibility of hydrogen, volatility, safety and These obstacles motivated researcher and countries to modify new adsorbent to prevail these problems. Recently researchers familiarized to new family of compounds which called Metal-Organic Framework (MOF). These materials have had essential properties such as high specific surface area and high internal free space[1-3]. In this paper we deal with some of these materials called MOF(Zn5).

Materials and method

The preparation of microsized crystals was performed by mixing Zn(NO₃)₂.6H₂O (0.29 g, 1 mmol), 1,4-benzenedicarboxylic acid (H₂-BDC) (0.08 g, 0.5 mmol), and N,N-dimethylformamide (DMF) (9.5 g, 130 mmol) at room temperature. The obtained mixture after stirring was heated to 120°C in a Teflon-lined stainless steel autoclave at a rate of 1 °C/min for 24h. Crystallization was carried out under static conditions and cold to room temperature at a rate of 0.5°C /min. The resulting solid was filtered and repeatedly washed with DMF, and dried at room temperature. The samples were stored in a vacuum desiccator to avoid water adsorption [4]. The adsorption processes have been done by home-made adsorption apparatus that made up in Ferdowsi university and gas leaking have been checked out in each process. We put 0.6 gr (Zn5) in tube sample and heated by furnace to 300 °C and

completely vacuumed for two hours. Then let adsorbent cooled down to ambient temperature (22±2). Amount of hydrogen uptake equalled to difference between amount of hydrogen in first pressure (primitive pressure and amount of remained hydrogen in previous experience) and amount of hydrogen in equilibrium pressure. It must note that the volume of sample obtained by Helium gas.

Results and Discussion

In this paper we studied hydrogen adsorption on MOF(Zn5) at ambient temperature(22±2°C) and 20 bar pressure. MOFs family have high porosity and extended in last decade. Result showed Zn5 adsorption isotherm is in agreement with Langmuir isotherm(Fig.1-3). Linear form of Langmuir equation introduced as below:

$$P/q = 1/(bq_m) + P/q_m \quad \text{Eq.1}$$

q_m is amount of monolayer of hydrogen adsorbed on surface (0.23392 mmol/gr) and b is Langmuir constant that explained ratio of k_{ad}/k_{dis} (1.75171×10^{-3} (1/bar)).

Also results depicted in (Fig.4) illustrated the capability of MOF(Zn5) to uptake about 0.25 H wt% in mentioned condition.

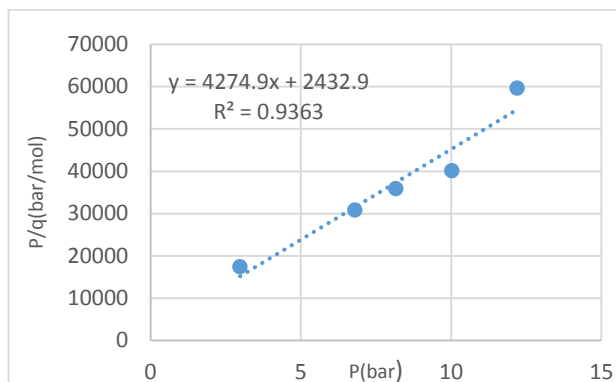


Fig.1: Langmuir adsorption isotherm.

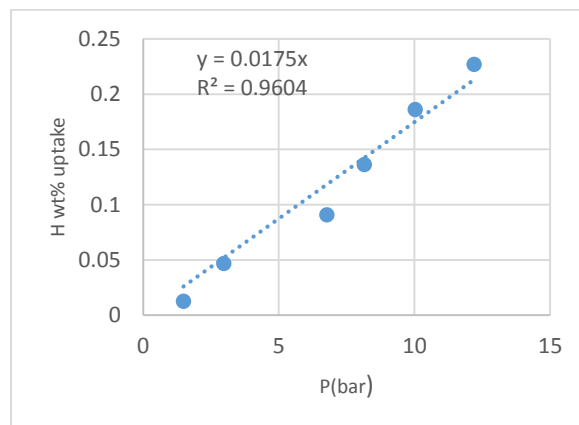


Fig.4: hydrogen uptake in 22±2°C.

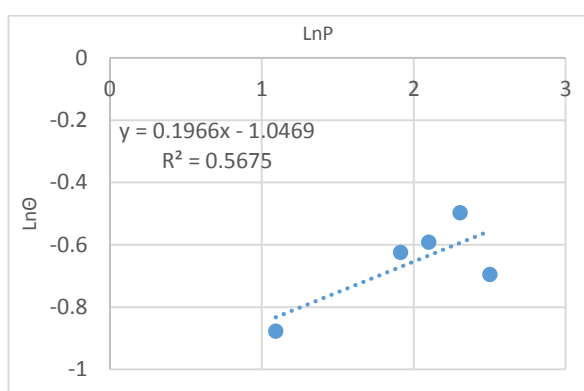


Fig.2 Freundlich adsorption isotherm.

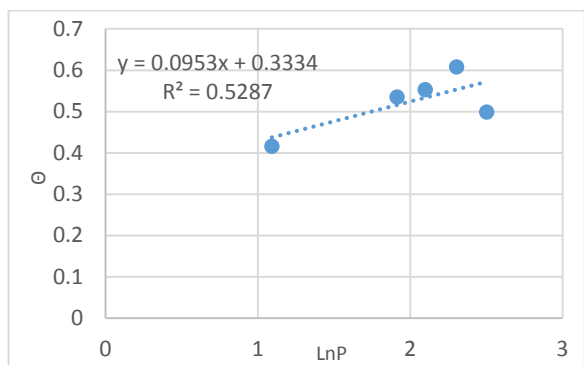


Fig.3: Temkin adsorption isotherm.

Conclusions

We studied hydrogen storage in MOF(Zn5) at ambient temperature and 20 bar pressure. Result showed Zn5 has 0.25 wt% hydrogen uptake and this result is far from United States department of energy (USDOE). It is reasonable for enhancing hydrogen storage must modified with additional substances such as transition metal, metal oxide, alloy and etc.

References

- [1] Henrietta W. Langmi, J.R, Brian North, Hydrogen Storage in Metal-Organic Frameworks: A Review. *Electrochimica Acta*, (2014)
- [2] M. Latroche, C. Serre, Hydrogen Storage in the Giant-Pore Metal-Organic Frameworks MIL-100 and MIL-101. *Angewandte Chemie International Edition*, (2006).
- [3] H. Rasool Abid, J.Shang, Synthesis, characterization, and CO2 adsorption of three metal-organic frameworks (MOFs): MIL-53, MIL-96, and amino-MIL-53. *Polyhedron*, (2016)
- [4] M. Sabo, A. Henschel "Solution infiltration of palladium into MOF-5: synthesis, physisorption and catalytic properties" *J. Mater. Chem.* 17(2007) 3827-3832

Selective Catalytic Oxidation of *o*-xylene to Phthalic Anhydride over VPO/HZSM-5: An Optimization Study

A. Monajemi^a, V. Mahdavi^{*a}

^aDepartment of Chemistry, Surface Chemistry and Catalysis Division
 Faculty of Sciences, Arak University, Arak 38156-8-8349, Iran

*Ali_Monajemi2011@yahoo.com

Abstract: Selective gas-phase oxidation of *o*-xylene to phthalic anhydride over VPO/HZSM-5 catalysts was investigated. The catalysts with various P/V ratio were facilely synthesized by impregnation method. The prepared catalysts were characterized by several techniques such as SEM, TPD-NH₃, H₂-TPR, FT-IR, BET and XRD. The effects of P/V ratio (1.6–2.4), reaction temperature (350–450 °C), O_x/O₂ ratio (0.15–0.60) and gas hourly space velocity (G.H.S.V) of O₂/N₂ (600–1200 h⁻¹) on yield of PA were studied by Box–Behnken design. The influence of independent factors and their quadratic interactions were examined by means of the Analysis of Variance (ANOVA). Present results indicate that P/V ratio has a different effect on the conversion and selectivity of PA. The catalyst with P/V ratio = 2.0, O_x/O₂ ratio = 0.37, G.H.S.V of 770 h⁻¹ and reaction temperature of 370 °C produced maximum yield of PA (80.7 %). The analysis revealed that the predicted results agree well with the experimental data (P/V ratio = 2.0, O_x/O₂ ratio = 0.38, G.H.S.V of the carrier gas = 900 h⁻¹ and reaction temperature of 400 °C with 74.3% yield).

Keywords: VPO/HZSM-5 catalyst; phthalic anhydride; selective oxidation; *o*-xylene

Introduction

Vanadium oxide-based catalysts is commonly used for several important industrial reactions, including in the oxidation of *n*-butane (VPO) and of benzene (supported V-MoO) to maleic anhydride, production of phthalic anhydride from *o*-xylene oxidation, in the reduction of NO_x with ammonia and production of sulphuric acid by oxidation of SO. Growing annual production of phthalic anhydride (5.5 million tons in 2015) is indicative of importance of its applications in the manufacture of polyester resins, phthalate plasticizers, phthalocyanine dyes and numerous fine chemicals.

The industrial reaction process was carried out in range of 380–400°C, near atmospheric pressure to give maximum conversion of *o*-xylene (100%) and good selectivity to phthalic anhydride (70–75%). Recently, the main object of several investigations demonstrated that V₂O₅ can be highly dispersed on the surface of anatase obtaining an active and selective V/Ti/O catalyst. The formation of polymerized and isolated vanadia species on the surface and its strong interaction with the support have important influences on reaction performance and improve long life in the *o*-xylene oxidation.

At present work, a novel VPO/HZSM-5 catalyst (P/V molar ratio from 1.6 to 2.4) at constant total weight percentage of V and P atoms = 20% was prepared by impregnation method. The effect of the preparation condition (or independent factors), such as P/V ratio supported on HZSM-5 (A) and operation conditions, such as reaction temperature (B), O_x/O₂ molar ratio

(C) and Gas hourly space velocity (G.H.S.V) (D) on the performance and activity of the catalyst were investigated. Response surface methodology (RSM) was used in order to optimize the selective oxidation reaction along with desirable PA selectivity. The interaction between reaction parameters (factors) and *o*-xylene conversion were evaluated to find the optimum conditions for achievement the highest yield of PA. Powder X-ray diffraction (XRD), Scanning electron microscopy (SEM) and temperature-programmed desorption of NH₃ (TPD-NH₃) were employed to characterize the texture and structure of the catalysts.

Materials and method

The VPO-2.0 catalyst (unsupported) was synthesized according to a literature procedure through an organic route using isobutyl alcohol and benzyl alcohol as reducing agents. A mixture of V₂O₅ (4.85 g), 2-butanol (99%, 30 mL) and benzyl alcohol (anhydrous, 99.8%, 20 mL) was refluxed at 150°C for 3 h. The color of the solution changed from yellow-orange to black-green. Then, 7.30 mL of phosphoric acid (85%) was added to obtain the P/V molar ratio of 2. The resulting solution was then heated again to 120°C and maintained under reflux with constant stirring for 5 h. After, the suspension was filtered and turquoise blue solid (VOHPO₄·0.5H₂O) was washed with isobutanol and acetone, respectively, then further dried in air at 130 °C for 24 h. VPO-*x* /HZSM-5 catalysts with *x* ranged from 1.6 to 2.4 were prepared by the impregnation method. In a typical experiment, 1.185 gram of V₂O₅ (0.0066 mol) was dissolved in a mixture of 2-butanol (99%) and benzyl alcohol (anhydrous, 99.8%) and then



refluxed at 150 °C for 3 h, required amount of phosphoric acid (1.78 ml, 85%) was drop-wise added to obtain P/V = 2. Then, a given amount of H-ZSM-5 (9.15 gr) was impregnated with the impregnation liquid for another 5 h of refluxing under vigorous stirring to make VPO-2.0/ HZSM-5 sample. VPO-x / HZSM-5 samples with P/V= 1.6, 1.8, 2.2 and 2.4 molar ratio were also prepared according to previous section. The total weight percentage of V and P atoms was 15%. Finally, the gel was removed by filtration, washed thoroughly with water and dried at 130 °C overnight. Both unsupported and supported precursors were calcined in a programmable muffle furnace at 800°C for 2 h in air flow with heating rate of 2 °C.min⁻¹ to produce pure vanadium phosphorus oxide (VPO or (VO)₂P₂O₇) and VPO/HZSM-5 powders. The surface area of prepared VPO-2.0 (with P/V=2.0 molar ratio) was 28.5 m²/gr.

Results and Discussion

The X-ray diffraction patterns of the HZSM-5 and synthesized samples, VPO-2.0 and VPO/ HZSM-5 with various P/V molar ratio from 1.6 to 2.4 molar ratio are presented in Fig. 1 (I, II). As before mentioned, all of samples were calcined in air flow at 800 °C for 2 h. According to PDF No. 44-0003, The HZSM-5 characteristic peaks appear at 2θ value of 7.87, 8.81, 23.09, 23.86, 24.34, 29.20 and 29.88. Besides, the diffractogram of synthesized VPO-2.0 is also presented in Fig.1 and the peaks observed at 2θ = 22.8, 28.3, 29.2, 33.6, 37.7, 46.2 and 49.5° indicates the presence (VO)₂P₂O₇ (JCPDS: 41-698), while the peaks appeared at 2θ = 12.1, 19.3, 25.2° confirm the presence of β-VOPO₄ (JCPDS: 27-948), respectively. Fig.2 depicted the selective oxidation reaction in the presence of VPO/ HZSM-5 catalysts. The specific surface area (S_{BET}), pore volume and pore diameter for HZSM-5, pure VPO-2.0 and VPO/HZSM-5 catalysts of this study are tabulated in Table 1. As compared with the pure VPO-2.0, Using of HZSM-5, not only enhanced specific surface area of the supported samples but also improved the dispersion of active phase significantly. It is apparent that, by increasing of P/V molar ratio, BET surface areas are gradually decreased from 352 m² g⁻¹ with micro-pore volume of 0.13 cm³/g to 292 m² g⁻¹ with micro-pore volume of 0.10 cm³/g.

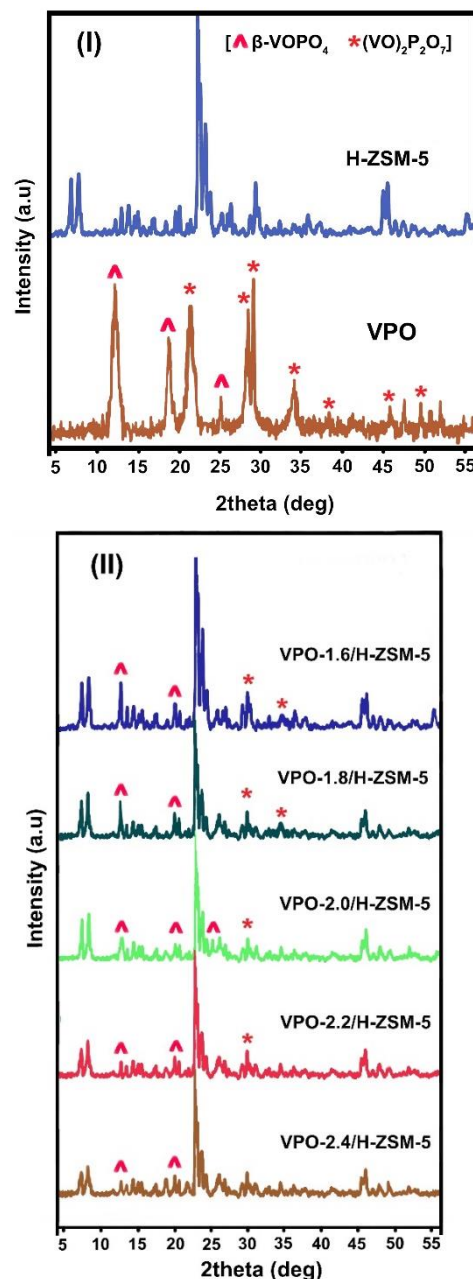


Fig.1: The chemical reaction for selective oxidation of o-xylene to PA

From results of Table 1, could be related to interaction between support and unreacted phosphoric acid, which are causing to decrease specific surface area and micro-pore volume probably by blocking the pores. In order to gain a better understanding of the interaction effects of variables on conversion and selectivity, 3D surface plot for the measured responses were formed based on the model equations (Eq. 1- 2).

Table1. Results of BET surface area, pore size distribution measurements, acidic properties various VPO/HZSM-5 catalysts.



VPO-X/HZSM-5 Catalysts	BET _{sa} (m ² /g) ^a	Mv (cm ³ /g) ^b	Apd (Å) ^c	Tad (μmol/g) ^d
HZSM-5	380	0.138	22.6	438.5
VPO-2.0	28.5	0.047	48.1	1860.4
1.6	352	0.130	22.9	825.2
1.8	338	0.125	23.7	972.6
2.0	323	0.121	26.3	1005.5
2.2	310	0.112	29.2	987.3
2.4	292	0.100	34.6	821.7

a surface area b Micropore volume c Average pore diameter d Total ammonia desorption

The results of surface response 3-D plots of OX conversion and PA selectivity as a function of two independent variables: (a, e) P/V molar ratio on the HZSM-5 and OX/O₂ ratio; (b, f) G.H.S.V and P/V molar ratio; (c, g) OX/O₂ ratio and temperature, (d, h) G.H.S.V and temperature are shown in Fig. 3(a)–(h), respectively.

Table 2. Experimental range and levels for Box-Behnken design

Independent variables	Range and level		
	-1	0	1
P/V molar ratio, A	1.6	2	2.4
Temperature (°C), B	350	400	450
o-xylene/O ₂ molar ratio, C	0.15	0.30	0.60
G.H.S.V(h ⁻¹), D	600	900	1200

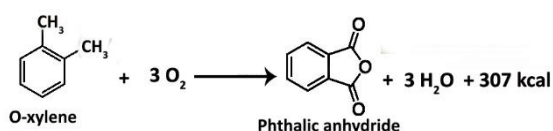


Fig.2: The chemical reaction for selective oxidation of o-xylene to PA

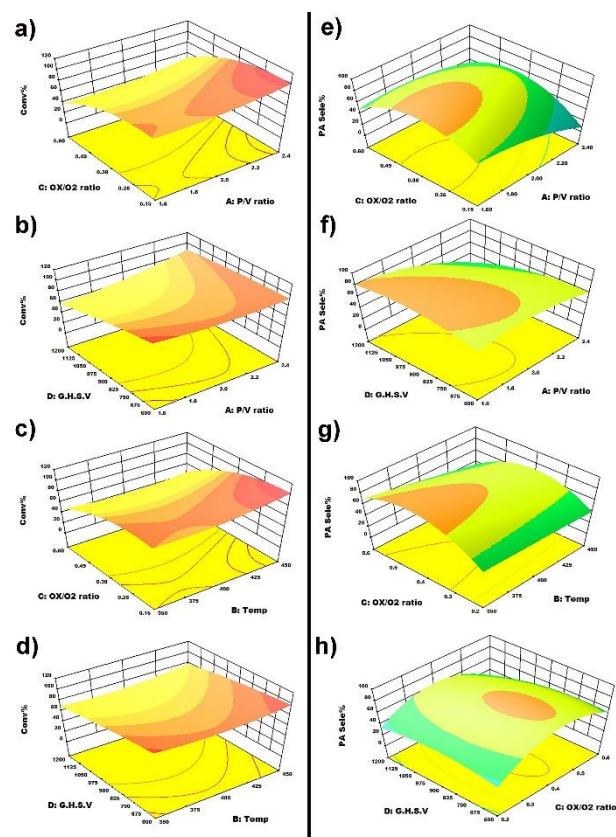


Fig.3: surface plots describing the response surface for: (Left: OX conversion, Right: PA selectivity)

$$(1) \text{ OX Conv}(\%) = 82.0 + 6.45A + 2.91B - 25.22C - 11.51D + 0.08AB + 0.57AC + 8.93AD - 3.70BC + 1.87BD - 6.92CD + 5.11A^2 + 6.30B^2 - 16.67C^2 - 2.15D^2$$

$$(2) \text{ PA Sele}(\%) = 81.24 - 15.97A - 10.04B + 4.48C - 6.14D - 14.35AB + 9.52AC - 11.68AD - 6.88BC - 6.75BD - 5.75CD - 10.86A^2 - 0.45B^2 - 31.93C^2 - 10.52D^2$$

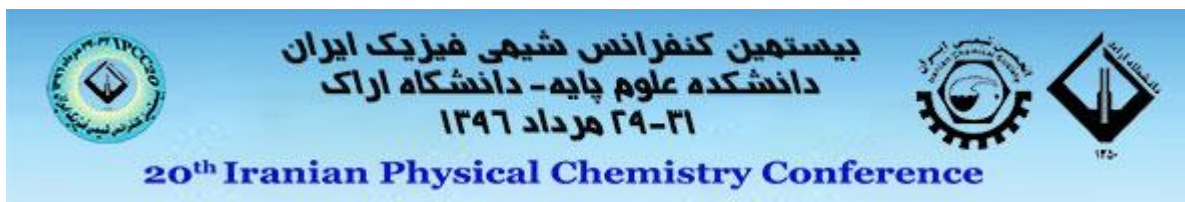
Conclusions

A response surface model, based on the Box-Benken technique, was developed to describe the conversion of o-xylene, PA selectivity and yield. Temperature programmed desorption of ammonia (NH₃-TPD) showed that the amount of strong acid sites decreased by increasing of P/V ratio while number of total acid sites significantly increased. X-ray diffraction patterns and temperature programmed reduction (H₂-TPR) showed that the catalysts with high P/V ratio (VPO-2.2/HZSM-5 and VPO-2.4/HZSM-5) have more amounts of reducible V⁵⁺ species, which is mainly because of highly dispersed β-VOPO₄ and γ-VOPO₄ species. Also, we found that the catalytic activity and product distributions depend on reaction temperature, B/B+L ratio and V⁵⁺/V⁴⁺ ratio. The obtained results

from ANOVA showed that the most significant factor affecting the conversion of OX and PA selectivity were P/V molar ratio and OX/O₂ molar ratio, respectively. Coefficient of determination (R²) value of 0.9955 and 0.9864 obtained from Eqs. (1) and (2) shown that quadratic polynomial regression model could properly interpret the experimental data. Thus, weak-medium strength acid sites efficiently promoted the oxidation reaction. With P/V ratio = 2.0, O_x/O₂ ratio = 0.37, G.H.S.V of 770 h⁻¹ and reaction temperature of 370 °C, we could achieve the highest yield of PA (80.7%). Also, to show the validity of this prediction, we run the experiment at this condition and gained 79.3% for the yield of PA. These studies confirm that the predicted values are fully compatible with the experimental values.

References

- [1] I.E. Wachs, Catalysis science of supported vanadium oxide catalysts, *Dalton Transactions*, 42 (2013) 11762-11769.
- [2] A.S. Kootenaei, J. Towfighi, A. Khodadadi, Y. Mortazavi, Stability and catalytic performance of vanadia supported on nanostructured titania catalyst in oxidative dehydrogenation of propane, *Applied Surface Science*, 298 (2014) 26-35.
- [3] S. Bagheri, N. Muhd Julkapli, S. Bee Abd Hamid, Titanium dioxide as a catalyst support in heterogeneous catalysis, *The Scientific World Journal*, 14 (2014) 21-51.
- [4] T. Mongkhonsi, L. Kershenbaum, The effect of deactivation of a V₂O₅/TiO₂ (anatase) industrial catalyst on reactor behavior during the partial oxidation of o-xylene to phthalic anhydride, *Applied Catalysis A: General*, 170 (1998) 33-48.
- [5] T. Zhang, J. Liu, D. Wang, Z. Zhao, Y. Wei, K. Cheng, G. Jiang, A. Duan, Selective catalytic reduction of NO with NH₃ over HZSM-5-supported Fe-Cu nanocomposite catalysts: The Fe-Cu bimetallic effect, *Appl. Catal. B* 148-149 (2014) 520-531.
- [6] J. Hu, Z. Lu, H. Yin, W. Xue, A. Wang, L. Shen, S. Liu, Aldol condensation of acetic acid with formaldehyde to acrylic acid over SiO₂-, SBA-15-, and HZSM-5-supported V-P-O catalysts, *J. Ind. Eng. Chem.* 40 (2016) 145-151.



Investigation of 4-chlorophenol degradation over a new designed Pt/ γ -Al₂O₃ nanocatalyst synthesized by microemulsion method

A. Keshavarz¹, A. Salabat^{1,2*}

¹ Department of Chemistry, Faculty of Science, Arak University, 38156-8-8349, Arak, Iran

² Institute of Nanosciences & Nanotechnology, Arak University, 38156-8-8349, Arak, Iran

*Corresponding E-mail address: a-salabat@araku.ac.ir

Abstract: The objective of the present study is degradation study of 4-chlorophenol (4-CP) as highly toxic pollutant by a new designed Pt/ γ -Al₂O₃ nanocatalyst. The proposed shaped controlled nanocatalyst was synthesized in microemulsion systems containing 25% or 0% HCl. The prepared nanocatalysts were characterized by several techniques such as scanning electron microscopy (SEM), cyclic voltammetry (CV) and X-ray diffraction (XRD). The effect of some important parameters such as initial concentration of 4-CP (10-50 mg/L), solution pH (3-11), and temperature (20-40 °C) on the degradation process was investigated by Box–Behnken design. The obtained results showed that HCl concentration of the microemulsion system can affect the catalytic activity of Pt/ γ -Al₂O₃. It is confirmed that the catalyst synthesized in microemulsion system containing 25% HCl is most effective and maximum degradation was obtained at pH=11, [4-CP]₀=50 mg/L and reaction temperature of 40°C.

Keywords: 4-chlorophenol (4-CP); Microemulsion; Pt/ γ -Al₂O₃; Nanocatalyst.

Introduction

Removal and degradation of phenolic compounds such as 4-chlorophenol (4-CP), as pollutant materials, from wastewater of different industries is an interesting subject [1]. 4-CP that is a useful material to synthesize numerous chemical products is commonly found in wastewater and exhibit high toxicity and poor biological degradability. Many articles published in recent years to show the effect of pH, temperature and initial concentration[2-4] on degradation process. it is important to find the best combination of these main parameters and design a suitable process in order to maximizing the degradation efficiency of 4-CP. The application of modelling tools such as response surface methodology (RSM) due to provide more information with fewer experiments and extremely reduce cost have interested by researchers. The most active catalysts degradation of chloroaromatic compounds are supported by noble metal nanoparticles such as Pd, Pt, and Rh[5-7]. Design of new catalyst with high activity for degradation of 4-CP by economically and green approach is significant importance. The catalytic activity depends on nanoparticles size, metal dispersion on support and shape or metal surface area. Particle morphology and support-induced electronic effects can govern catalytic activity[8]. Martinez-Rodriguez et al. synthesized cubic Pt NPs by microemulsion method at different HCl or H₂SO₄ concentrations[9,10].

The aim of this study is to introduce modified Pt/ γ -Al₂O₃ nanocatalyst synthesized by microemulsion system to enhance degradation of 4-CP from aqueous solution. Then an experimental design approach applied to study the effects of some key parameters on the degradation of 4-chlorophenol such as solution pH, initial 4-CP concentration, and temperature. The optimization of degradation reaction was performed by response surface methodology (RSM). UV-vis spectrophotometry has been applied for the monitoring of 4-CP concentrations for evaluating the degradation percent (R %).

Materials

Hexachloroplatinic acid (H₂PtCl₆) (99%), n-heptane, 2-butanol, 4-chlorophenol (4-CP), sulphuric acid, HCl and NaOH were obtained from Merck Company and used as received. The nonionic surfactant poly(ethylene glycol) *p*-(1,1,3,3-tetramethylbutyl)-phenyl ether (TX-100) with purity of 98% was purchased from Acros Company and used without further purification. Alumina (γ -Al₂O₃) was obtained from Japan Aerosil with surface area of 110 m²/g. All of the solutions were prepared by deionized water.

Catalyst preparation

Pt/ γ -Al₂O₃ was synthesized by a recently reported method at two different microemulsion systems: Briefly, 0.1M acidic solution of H₂PtCl₆ was added to



microemulsion system containing n-heptane, TX-100 and 2-butanol. The mixture was placed at room temperature for 3 hours with stirring. The Pt ions in this solution were reduced by addition of NaBH₄ induced in another microemulsion system. The γ -Al₂O₃, as a supporting material was added to the prepared Pt colloidal suspensions. Then by slow addition of THF to the colloid system the Pt nanoparticles precipitated on γ -Al₂O₃. The obtained product was dried at room temperature for 24 hours and calcined at 600°C.

Results and discussion

Catalysts characterization

The SEM image, XRD pattern and cyclic voltammetry of the Pt/ γ -Al₂O₃ nanocatalysts were obtained. It was found from SEM image the catalyst keep the layer structure of the γ -Al₂O₃ support and Pt nanoparticles well dispersed on the support. As an interesting result from XRD pattern the intensity of surface (111) has been reduced and surface (200) increased for Pt nanoparticles synthesized in HCl-microemulsion system. Finally the CV results showed the amount of (111) sites is nearly negligible for the nanoparticles prepared in HCl-microemulsion system, which is coincidence with other observations.

Analysis of data of the response surface model

Three important factors for degradation of 4-CP including pH (3-11), temperature (20-40°C) and initial concentration of 4-CP (10-50 mg/L) are considered as independent variables. Analysis of variances (ANOVA) was used to investigate the effects of main factors and their interactions.

Degradation of 4-CP by H₂ streaming has advantages as the ability of reaching high conversion levels at low temperature and pressure. It is found that increasing the temperature significantly increases 4-chlorophenol degradation over the two catalysts, that is in agreement with results obtained by Díaz and et al.[5].

It was understood that degradation reaction of 4-CP took place smoothly effected with concentration of 4-CP. However as shown in surface response plot, results for catalyst synthesized in Pt-HCl microemulsion representative more effect concentration to degradation. It may be due to existence high surface to volume ratio in this catalyst.

As indicated in surface response plot, catalyst activity increased by increasing solution pH for both catalysts, confirm other researches [11,12].

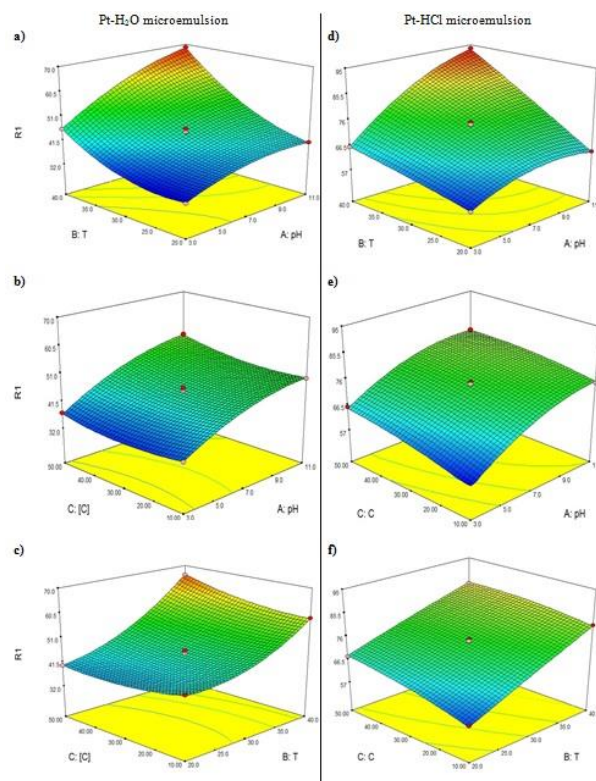


Fig1. Response surface plots showing effective factors and their mutual effects on degradation of 4-CP by Pt/ γ -Al₂O₃ catalyst synthesized at Pt-H₂O microemulsion (a-c) and synthesized at Pt-HCl microemulsion (d-f).

Conclusions

In this paper a modified form of Pt/ γ -Al₂O₃ synthesised in microemulsion system was introduced as a new and efficient catalyst for degradation of 4-CP. The response surface model with three important factors reaction by three levels, based on the Box-Benken design was applied to describe the degradation of 4-CP. Obtained results of degradation percentages (R %) for Pt/ γ -Al₂O₃ at HCl-microemulsion showed a good potential for 4-CP degradation. The observed data was analysed by analysis of variance (ANOVA). The optimal conditions for 4-CP degradation were solution pH, reaction temperature and initial 4-CP concentration respectively equal to 8.8, 40°C and 50 mg/L for the catalyst synthesised in Pt-H₂O and 11, 40°C and 35 mg/L for catalyst synthesis in Pt-HCl microemulsion.



Acknowledgment

The financial support from Arak University and Iran National Science Foundation is gratefully acknowledged (grant no. 95818034).

References

- [1] S. Wang, B. Yang, T. Zhang, G. Yu, S. Deng, J. Huang, Catalytic hydrodechlorination of 4-chlorophenol in an aqueous solution with Pd/Ni catalyst and formic acid, *Industrial & Engineering Chemistry Research*, 49 (2010) 4561-4565.
- [2] N. Graham, C.-c. Jiang, X.-Z. Li, J.-Q. Jiang, J. Ma, The influence of pH on the degradation of phenol and chlorophenols by potassium ferrate, *Chemosphere*, 56 (2004) 949-956.
- [3] R.I. Yousef, B. El-Eswed, The effect of pH on the adsorption of phenol and chlorophenols onto natural zeolite, *Colloids and Surfaces A: Physicochemical and Engineering Aspects*, 334 (2009) 92-99.
- [4] Y. Jiang, C. Petrier, T.D. Waite, Sonolysis of 4-chlorophenol in aqueous solution: effects of substrate concentration, aqueous temperature and ultrasonic frequency, *Ultrasonics Sonochemistry*, 13 (2006) 415-422.
- [5] E. Díaz, J.A. Casas, Á.F. Mohedano, L. Calvo, M.A. Gilarranz, J.J. Rodríguez, Kinetics of the hydrodechlorination of 4-chlorophenol in water using Pd, Pt, and Rh/Al₂O₃ catalysts, *Industrial & Engineering Chemistry Research*, 47 (2008) 3840-3846.
- [6] L. Calvo, A. Mohedano, J. Casas, M. Gilarranz, J. Rodríguez, Treatment of chlorophenols-bearing wastewaters through hydrodechlorination using Pd/activated carbon catalysts, *Carbon*, 42 (2004) 1377-1381.
- [7] G. Evdokimova, S. Zinovyev, A. Perosa, P. Tundo, Selectivity issues in the catalytic multiphase reduction of functionalized halogenated aromatics over Pd/C, Pt/C, and Raney-Ni, *Applied Catalysis A: General*, 271 (2004) 129-136.
- [8] G. Yuan, M.A. Keane, Liquid phase catalytic hydrodechlorination of chlorophenols at 273 K, *Catalysis communications*, 4 (2003) 195-201.
- [9] R.A. Martínez-Rodríguez, F.J. Vidal-Iglesias, J. Solla-Gullón, C.R. Cabrera, J.M. Feliu, Synthesis of Pt nanoparticles in water-in-oil microemulsion: effect of HCl on their surface structure, *Journal of the American Chemical Society*, 136 (2014) 1280-1283.
- [10] R.A. Martínez-Rodríguez, F.J. Vidal-Iglesias, J. Solla-Gullón, C.R. Cabrera, J.M. Feliu, Synthesis and Electrocatalytic Properties of H₂SO₄-Induced (100) Pt Nanoparticles Prepared in Water-in-Oil Microemulsion, *ChemPhysChem*, 15 (2014) 1997-2001.
- [11] N. Jadbabaei, T. Ye, D. Shuai, H. Zhang, Development of palladium-resin composites for catalytic hydrodechlorination of 4-chlorophenol, *Applied Catalysis B: Environmental*, 205 (2017) 576-586.
- [12] G. Yuan, M.A. Keane, Liquid phase hydrodechlorination of chlorophenols over Pd/C and Pd/Al₂O₃: a consideration of HCl/catalyst interactions and solution pH effects, *Applied Catalysis B: Environmental*, 52 (2004) 301-314.

How can Pt-free catalysts act as an efficient catalyst?

Elham Moharramzadeh Goliaei^{a*}, Seifollah Jalili^{a,b}

^aDepartment of Chemistry, K. N. Toosi University of Technology, P.O. Box 15875-4416, Tehran, Iran

^bComputational Physical Sciences Research Laboratory, School of Nano-Science, Institute for Research in Fundamental Sciences (IPM), P.O. Box 19395-5531, Tehran, Iran

*emoharramzadeh@mail.kntu.ac.ir

Abstract: By utilizing density functional theory calculations with empirical pair potentials (DFT-D), the catalytic activity of Ag-based catalysts supported on Nitrogen(N)-doped graphene was studied. It is found that supported pure Ag-based catalyst shows higher activity in oxygen reduction reaction because of significant decrease in O₂ adsorption energy and higher charge transfer to O₂, although alloying of Ag cluster with metal in the presence of N-doped graphene sheet show lower catalytic activity compared to pure silver cluster. All data including adsorption energies, Bader charge analyses, PDOS plots and O-O bond lengths suggest that both of these systems can act as an efficient catalyst like Pt/C.

Keywords: Ag cluster; Oxygen reduction reaction; Bader charge analysis

Introduction

Over the past few decades, the production of clean energy has received considerable attention from the scientists. The act of fuel cells is undeniable, given their useful performance in the production of clean energy [1-4]. In the search for electrocatalysts, many studies have been conducted using non-precious metal catalysts, such as iron [5-9] and silver [10,11] nanoparticles deposited on support. Among these efforts, adding heteroatoms [12] or defects [13] in graphene are appropriate ways to enhance the adhesion of metal catalysts and add to the electrochemical activity of graphene sheets. Jin and coworkers recently designed a new way to deposit Ag on N-doped graphene utilizing single-stranded DNA and AgNO₃ [14]. They claimed that silver cluster supported on N-doped graphene exhibit ORR catalytic activity in alkaline media with more electrochemical stability than other electrocatalysts using other materials like Pt/C.

Here, DFT-D calculations are applied to investigate the interaction between cluster and support and to predict their activity.

Materials and method

The DFT calculations are carried out using the Perdew-Burke-Ernzerhof (PBE) [15] functional and projector-augmented-wave (PAW) pseudopotentials [16]. The Quantum Espresso package [17] was used to perform all calculations. The DFT-D method [18] are utilized to include weak dispersive interactions. Geometry optimization are carried out until all forces are smaller than 0.05 eV/Å. 30 Å vacuum was applied in the z-direction. For O₂ adsorption, the Γ point is used.

Results and Discussion

According to our publishing results [19], the total densities of states for N-doped graphene is investigated, all results have shown that N-doped graphene shows metallic character. Among different N-doped positions, pyridinic position, formed by removing one carbon atom

and substituting three carbon atoms, shows higher activity due to the sharp peak below the Fermi level. So, the focus of this study is on the pyridinic position. Not only the adsorption of Ag cluster on the pyridinic position is exothermic, but also the O₂ adsorption energy is negative according to the following equation:

$$E_{\text{ads}} = E(\text{Ag-O}_2\text{@N/G}) - E(\text{Ag@N/G}) - E(\text{O}_2)$$

Where total energies of complex, Ag supported on N-graphene and O₂ molecule are shown by $E(\text{Ag-O}_2\text{@N/G})$, $E(\text{Ag@N/G})$ and $E(\text{O}_2)$, respectively. On the other hand alloying of Ag cluster with metal in the presence of N-doped graphene sheet, show positive adsorption energy. In pure Ag cluster after supporting the O-O bond length increase from 1.23 Å (in the gas phase) to 1.277 in the complex system [19]. In alloying system this value reaches to 1.281 Å. In pure Ag cluster and alloying cluster transfer of electrons from Ag to O₂ leads to elongation of the O-O bond. So, the positive charges of Ag atoms after adsorption of O₂ reach to more positive values. According to the electronic structure analyses, we can answer to two important questions. The PDOS data explain what leads to the elongation of O₂ bonds and why alloying leads to endothermic O₂ adsorption compared to the pure cluster.

As shown in Figures 1(a) and (b), the position of d orbitals of silver exactly is in the middle of 2π and $2\pi^*$ orbitals of O₂ molecules so charge transfer from d orbitals of silver to O₂ molecules leads to elongation of O-O bond lengths. On the other hand, when we compare O₂ molecules peaks which are located at -6.25 eV, it is obvious that in the pure cluster O₂ peaks are more broadened and delocalized compared to that on the supported cluster with sharp peaks. So, according to this fact, it is expected that the O₂ adsorption energy on the pure silver cluster is more exothermic compared to the

Ag alloying system.

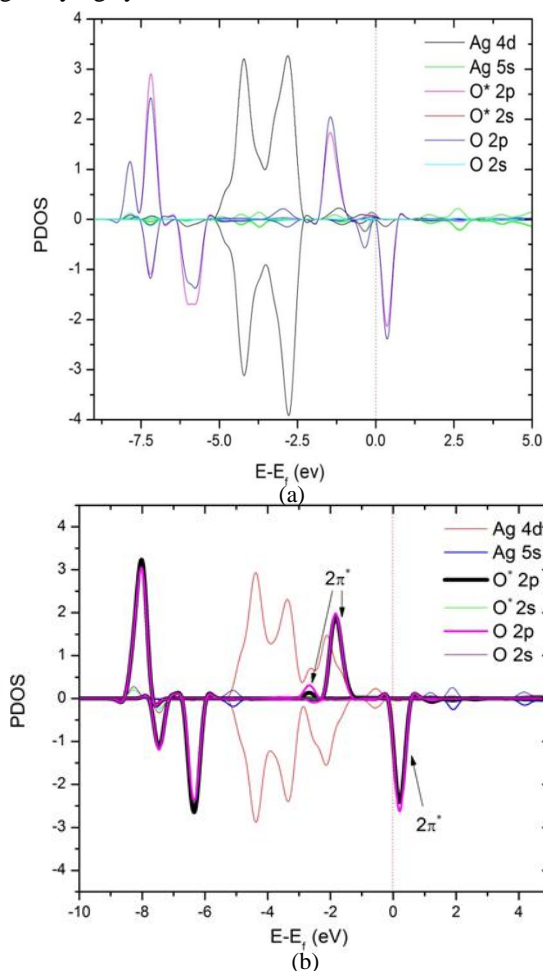


Fig.2: PDOS diagrams for (a) O_2 adsorbed on Ag cluster [19]
(b) O_2 adsorbed on the Ag alloying system.

It should be mentioned that the rate-determining step for ORR on silver is the adsorption of O_2 molecules on the surface. So, due to exothermic adsorption of O_2 on the pure silver cluster, it would be a better catalyst compared to alloying system. On the other hand, the low O_2 adsorption energy and elongation of the O_2 bond act as two key parameters to propose a catalyst able to act as an electrocatalyst for ORR. In this view both of these systems are active, although pure silver exhibit more catalytic activity.

Conclusions

To sum up, the catalytic activity of Ag cluster and alloying of Ag cluster in ORR in the presence of N-doped graphene sheet was investigated. The O_2 adsorption energies and Bader charge analyses have shown that pure silver cluster is a better catalyst compared to alloying of Ag cluster.

References

- [1] F. Jaouen "Recent advances in non-precious metal catalysis for oxygen-reduction reaction in polymer electrolyte fuel cells", *Energy Environ Sci*, 4 (2011) 114-130.
- [2] I. Katsounaros, S. Cherevko, A. R. Zeradjanin, K. J. Mayrhofer "Oxygen electrochemistry as a cornerstone for sustainable energy conversion", *Angew Chem Int Ed*, 53 (2014) 102-121.
- [3] K. B. Liew "Non-Pt catalyst as oxygen reduction reaction in microbial fuel cells: A review", *Int J Hydrogen Energy*, 39 (2014) 4870-4883.
- [4] R. Li "Nitrogen and phosphorus dual-doped graphene/carbon nanosheets as bifunctional electrocatalysts for oxygen reduction and evolution", *ACS Catal*, 5 (2015) 4133-4142.
- [5] E. Proietti, et. al. "Iron-based cathode catalyst with enhanced power density in polymer electrolyte membrane fuel cells", *Nat Commun*, 2 (2011) 416-1-416-9.
- [6] W. Yang, X. Liu, X. Yue, J. Jia, S. Guo "Bamboo-like carbon nanotube/Fe₃C nanoparticle hybrids and their highly efficient catalysis for oxygen reduction", *J Am Chem Soc*, 137 (2015) 1436-1439.
- [7] W. Ding, et. al. "Shape fixing via salt recrystallization: a morphology-controlled approach to convert nanostructured polymer to carbon nanomaterial as a highly active catalyst for oxygen reduction reaction", *J Am Chem Soc*, 137 (2015) 5414-5420.
- [8] Y. Hu, et. al. "Hollow spheres of iron carbide nanoparticles encased in graphitic layers as oxygen reduction catalysts", *Angew Chem Int Ed*, 53 (2014) 3675-3679.
- [9] W. J. Jiang et. al. "Understanding the high activity of Fe-NC electrocatalysts in oxygen reduction: Fe/Fe₃C nanoparticles boost the activity of Fe-Nx", *J Am Chem Soc*, 138 (2016) 3570-3578.
- [10] E. J. Lim, S. M. Choi, M. H. Seo, Y. Kim, S. Lee, W. B. Kim "Highly dispersed Ag nanoparticles on nanosheets of reduced graphene oxide for oxygen reduction reaction in alkaline media", *Electrochem Commun*, 28 (2013) 100-103.
- [11] Z. Wang, et. al. "Carbon supported Ag nanoparticles with different particle size as cathode catalysts for anion exchange membrane direct glycerol fuel cells", *Renew Energy*, 62 (2014) 556-562.
- [12] X. K. Kong, C. L. Chen, Q. W. Chen "Doped graphene for metal-free catalysis", *Chem Soc Rev*, 43(2014) 2841-2857.
- [13] D. E. Jiang, V. R. Cooper, S. Dai "Porous graphene as the ultimate membrane for gas separation", *Nano Lett*, 9 (2009) 4019-24.
- [14] S. Jin, et. al. "Stable silver nanoclusters electrochemically deposited on nitrogen-doped graphene as efficient electrocatalyst for oxygen reduction reaction", *J Power Sources*, 274 (2015) 1173-1179.
- [15] J. P. Perdew, K. Burke, M. Ernzerhof "Generalized gradient approximation made simple", *Phys Rev Lett*, 77 (1996) 3865-8.
- [16] P. E. Blöchl "Projector augmented-wave method", *Phys Rev B*, 50 (1994) 17953-17979.
- [17] P. Giannozzi, et. al. "QUANTUM ESPRESSO: a modular and open-source software project for quantum.



Vanadium phosphorus oxide composite as an efficient catalyst for hydrocarbon oxidations using tert-Butyl hydroperoxide

S.Golmohammadi^a, V.Mahdavi^a

^aDepartment of Arak University, Arak, 38156 879, Iran

*sobhan.50sat@yahoo.com

Abstract: Calcined vanadium phosphorus oxide (VPO) prepared by an organic method is found to be an active and effective catalyst for the oxidation of various alkanes such as cyclohexane, n-hexane and cycloheptane in acetonitrile solvent using the environmentally benign oxidant, tert-Butyl hydroperoxide, where the oxidation mechanism is believed to involve a reversible V⁴⁺/V⁵⁺ redox cycle. *This heterogeneous catalyst at the end of the reaction is easily separated by the least cost of the product. This reaction is investigated in a polar and nonpolar solvent with different dielectric constant. Cobalt metal is also used as a catalyst enhancer and TBHP as an oxidizing agent. After catalytic tests and determining the best catalyst and ideal amount of cobalt percent improvement, detection and analysis will be done by analyzing XRD, SEM, TGA, IR*

Keywords: Cyclohexane; VPO Catalyst; TBHP; Oxidation; Acetonitrile

Introduction

Oxidation of hydrocarbons is a key process in the chemical industry due to the wide ranging utility of the ensuing functionalized compounds as raw materials and intermediates in industrial and pharmaceutical chemistry.[1] Partially oxygenated hydrocarbons are used as building blocks in the manufacture of plastics and synthetic fibers. For example, oxidation products of cyclohexane, cyclohexanone and n-hexane important raw materials for the production of adipic acid and caprolactam used for the manufacture of nylon.[2]

Current processes for the production of these highly desired oxygenates in many cases involve stringent conditions, which may include high temperatures and pressures, strong acids, free radicals and corrosive oxidants.[3,4] Therefore, a major challenge in this field is to find reaction pathways that afford the primary product with high selectivity at high conversion of the hydrocarbon. Characterized rather extensively by various techniques such as, FT-IR,[29] , XPS, XRD, SEM,. The better performance of this catalyst has been ascribed to the availability. We have very recently accomplished an unprecedented and efficient oxidation of cyclohexane over VPO catalyst using tert- Butyl hydroperoxide in acetonitrile under a atmosphere

Materials and method

Vanadium phosphorus oxide (VPO) catalyst with a P/V of 1.1 was prepared by refluxing an appropriate quantity (10 g) of V₂O₅ in a mixture of isobutanol (30 mL) and benzyl alcohol (15 mL) for 12 h, followed by addition of the required quantity of 85% H₃PO₄ (P/V ¼ 1.1) and refluxing for a further 6 h to give a light green precipitate.[17,20] The precipitate was filtered off, dried at 110 °C overnight and then calcined in air at 400 °C for 4 h. Oxidations of various alkanes were conducted in a 100 mL round-bottomed flask fitted with a reflux condenser and a magnetic stirrer. In a typical reaction procedure, 12.5 mmol substrate was mixed with 10 mg of calcined VPO catalyst, 10 mL solvent and 50 mmol of 30% tert- Butyl hydroperoxide and the mixture was kept at 50–70 °C using a heating mantle with vigorous stirring under atmosphere. The reaction mixture was sampled at regular intervals and the aliquot extracted with ether.[6,7]

Results and Discussion

The VPO catalysts are prepared by a variety of methods, all of which, however, eventually result in the same active phase. The most important of the synthesis steps is the initial preparation of the active phase precursor, vanadyl hydrogen phosphate hemihydrate, (VO)HPO₄·0.5H₂O,



which is then thermally decomposed and activated inside a reactor.[7] The two main methods for the preparation of this precursor involve the reduction of V⁵⁺ (V₂O₅) to V⁴⁺ either in water by HCl or hydrazine or the reduction in an organic phase (2-butanol) in the presence of another reducing agent such as benzyl alcohol. The catalyst prepared by the organic route is rather more popular. Therefore, vanadium phosphorus oxide (VPO) with a P:V We have earlier found that calcined VPO catalyst prepared by the organic route is highly active for the oxidation of cyclohexane [9] using tert-Butyl hydroperoxide and acetonitrile at 65 C under nitrogen atmosphere where the maximum activity is obtained at a substrate-to- catalyst ratio of 385.19. Acetone is also found to be another successful solvent. However, the reaction is much slower in solvents such as 1,4- dioxane and methanol whereas other solvents such as dichloromethane, methyl t-butyl ether, tetrahydrofuran and dimethyl sulfoxide are not found to be useful. Acetonitrile activates tert-Butyl hydroperoxide by forming an perhydroxyl anion (OOH⁻), which nucleophilically attacks the nitrile to generate a peroxy-carboximidic acid intermediate, which is a good oxygen transfer agent. Acetone also activates tert-Butyl hydroperoxide[8] in a similar way but to a lesser extent than acetonitrile.[9]

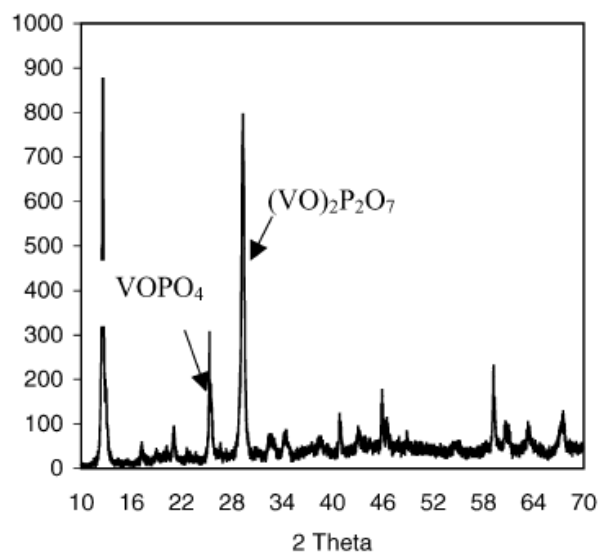
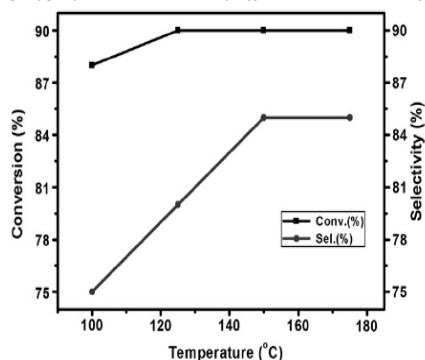
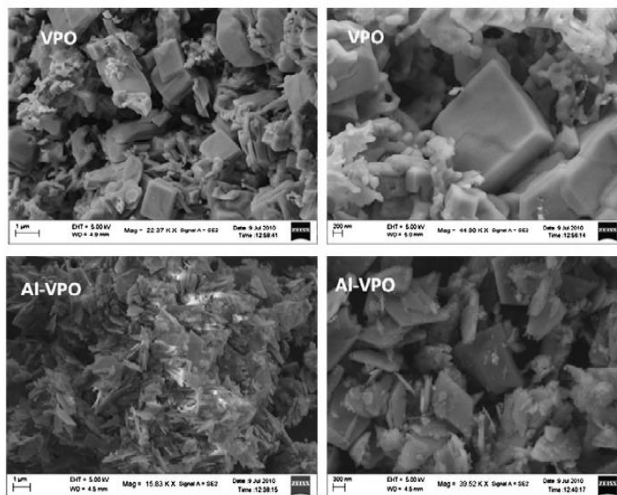


Fig. 1. XRD spectra of the VPO catalyst.

XRD spectra of the catalyst after calcination show high intensity peaks at 2θ values of 23.18, 28.48 and 29.98 characteristic of the presence of vanadyl pyrophosphate phase ((VO)₂P₂O₇) and also low intensity peaks at 2θ values of 22.08, 26.08 and 28.98 characteristic of VOPO₄ phase (Fig.1) [10]. This suggests that vanadium in the calcined catalyst sample is predominantly in V⁴⁺ state with the presence of a small amount of V⁵⁺ species. The mechanism of formation of this phase involves the solubilization of V⁵⁺ through the formation of vanadium cyclohexane followed by its reduction to V₂O₄ by the organic alcohol (benzyl alcohol). On the addition of H₃PO₄, V₂O₄ reacts with H₃PO₄ to form (VO)HPO₄·0.5H₂O at the solid-liquid interface which on calcination forms (VO)₂P₂O₇ [11]. The BET surface area of the calcined VPO catalyst is found to be 10 m² g⁻¹.

Scanning electron microscopy studies:

The FE-SEM micrograph of the catalysts revealed that the samples possess a slate-like morphology (Fig.2). Further, aggregates without regular shapes are observed in VPO. This is the reason for the low surface area of the VPO catalyst than of Al-VPO. However, the morphology of VPO was not affected significantly by Aldoping.



Effect of reaction temperature

To accomplish better toluene conversion and maximum p-cymene selectivity, liquid-phase isopropylation of toluene was carried out over 5 wt.% Al-VPO catalyst at various reaction temperature, and the results are depicted in Fig. 3.[9] It has been found that the toluene conversion increases up to 150 C and remains constant thereafter. This could be attributed to the coke deposition caused by dealkylation, which in turn leads to the oligomerization of olefins. On the other hand, the increase in toluene conversion at lower temperatures may be due to the clustering of alcohols around the Brønsted acid sites of the catalyst through H-bonding[10]. As a result, its dissociation to cyclohexan carbocations will be suppressed at higher temperatures. But at higher temperatures, the alcohols will have a decreased tendency to form molecular clusters, and so they can freely form carbonium ions via protonation.[11]

Conclusions

In summary, the calcined VPO catalyst with a P/V ratio 1.1 is found to be a very active catalyst for the oxidation of alkanes, especially cycloalkanes such as cyclopentane, cyclohexane, cycloheptane, cyclooctane, cyclodecane and adamantane, to their respective oxygenates using hydrogen peroxide under nitrogen atmosphere. The active center for the oxidation is believed to be (VO)₂P₂O₇ sites (V⁴⁺) in combination with dynamic V⁵⁺ sites involving a reversible redox cycle. The VPO catalyst can also be successfully reused for the reaction

Acknowledgment

URP is a postgraduate research participant at the National Risk Management Research Laboratory administered by the Oak Ridge Institute for Science and Education through an interagency agreement between the US Department of Energy and the US Environmental Protection Agency. We also thank

References

- (a) D. H. R. Barton, M. J. Gastinger and W. B. Motherwell, *J. Chem. Soc., Chem. Commun.*, 1983, 731; (b) J. M. Thomas, *Nature (London)*, 1985, 314, 669; (c) T. Ito and J. H. Lunsford, *Nature (London)*, 1985, 314, 721.
- U. Schuchardt, W. A. Carvalho and E. V. Spinace, *Synlett*, 1993, 10, 713.
- (a) K. U. Ingold, *Aldrichim. Acta*, 1989, 22, 69; (b) J. C. Russell, *US Pat. 3 665028*, 1972 (Halcon).
- R. A. Sheldon and J. K. Kochi, *Metal-Catalyzed Oxidation of Organic Compounds*, Academic Press, New York, 1981.
- V.I. Pa[^]rvulescu, D. Dumitriu and G. Poncelet, *J. Mol. Catal. A: Chem.*, 1999, 140, 91.
- (a) E. V. Spinace, H. O. Pastore, U. Schuchardt, *J. Catal.*, 1995, 157, 631; (b) M. H. Zahedi-Niaki, M. P. Kapoor and S. Kaliaguine, *J. Catal.*, 1998, 177, 231.
- W. A. Carvalho, P. B. Varaldo, M. Wallau and U. Schuchardt, *Zeolites*, 1997, 18, 408.
- R. Raja, G. Sankar and J. M. Thomas, *J. Am. Chem. Soc.*, 1999, 121, 11 926
- (a) S. Ueno, K. Yamaguchi, K. Yoshida, K. Ebitani and K. Kaneda, *Chem. Commun.*, 1998, 295; (b) K. Yamaguchi, K. Ebitani and K. Kaneda, *J. Org. Chem.*, 1999, 64, 2966; (c) K. Yamaguchi, K. Mori, T. Mizugaki, K. Ebitani and K. Kaneda, *J. Org. Chem.*, 2000, 65, 6897; (d) U. R. Pillai, E. Sahle-Demessie and R. S. Varma, *Tetrahedron Lett.*, 2002, 43, 2909.
- E. A. Lombardo and L. M. Cornaglia, *Appl. Catal. A: Gen.*, 1995, 127, 125.
- (a) G. Centi (Ed.), *Vanadyl Pyrophosphate Catalysts*, *Catal. Today* 16 (1993) 1.

A highly efficient oxidation of cyclohexane over VPO catalysts using tert-Butyl hydroperoxide

M.H.Farghadani^a, V.Mahdavi^a

^aDepartment of arak University, Arak, 38156 879, Iran

*mhfarghadany@yahoo.com

Abstract : A highly efficient oxidation of cyclohexane to cyclohexanol and cyclohexanone is accomplished over calcined vanadium phosphorus oxide (VPO) catalysts in a relatively mild condition using tert-Butyl hydroperoxide under a atmosphere condition. This heterogeneous catalyst at the end of the reaction is easily separated by the least cost of the product. This reaction is investigated in a polar and nonpolar solvent with different dielectric constant. After catalytic tests and determining the best catalyst ,detection and analysis will be done by analyzing XRD, SEM, TGA, IR, The activity and selectivity of vanadium phosphate (VPO) catalysts on the mesoporous KIT-6 support for green oxidation of cyclohexane to cyclohexanone and cyclohexanol were studied using H₂O₂.

Keywords : Cyclohexane ; VPO Catalyst ; TBHP ; Oxidation ; Acetonitrile

Introduction

The well-known pyrophosphate phase catalysts (vanadium pyrophosphate oxides) are fascinating and complex catalytic system which have been the subject of extensive research for the past decades due to their unique ability to catalyze various oxidation reactions [1]. These catalysts have shown extremely good activities in selective oxidation of butane to maleic anhydride and hence they are used as the major components of industrial catalysts. It is generally accepted that well crystallized vanadyl pyrophosphate (VP) is the major phase in industrial vanadium phosphate catalysts. The (VO)₂P₂O₇ phase has been mostly prepared from the thermal treatment of VOHPO₄·0.5H₂O via a topotactic transformation during the catalyst activation. The most common commercial formulations for the preparation of this hemihydrate precursor is reduction of V₂O₅ with organic reductive agents [2] such as a mixture of isobutanol and benzyl alcohol. Although, the use of VP phase as catalyst for liquid phase oxidation reactions is very restricted, Pillai and Sahle-Demessie showed that the vanadyl pyrophosphate phase is a good catalyst for the oxidation of cycloalkanes but not for linear alkanes. Apart from these, the VP phase has been used for liquid phase oxidation of different hydrocarbons such as cycloheptane and cyclooctane and styrene [2,3].

All reagents were used as received without further purification. Hydrogen peroxide (35%) and H₃PO₄ (85%) solution in water were purchased from Merck KGaA, Darmstadt, Germany. Cyclohexane (Extra pure), acetonitrile (HPLC grade), ethylacetate, acetic acid, methyl ethyl ketone (MEK), and acetone were purchased from Sigma-Aldrich Co. Tetraethyl orthosilicate (TEOS> 98%) was purchased from Dae-Jung, S Korea.

Results and Discussion

The actual contents of catalyst components (vanadium) were estimated using ICP-AES technique. The contents of vanadium are in good agreement with those of nominal values. The prepared catalysts were denoted as 34wt% VPK-6 and 27wt% VPK-6 based on vanadium content. The crystal structure of (VO)₂P₂O₇ consists of infinite double chains of VO₆ octahedral which are coupled by effective spin-spin exchange interactions[4]. To prove the valence of V in the(VO)₂P₂O₇ sample, the XPS spectra of the 27wt% VPK-6 catalyst is shown in Figure 1. It is observed that the V₂p binding energies of catalyst are 517.2 and 524.6 eV, corresponding to the energy levels V₂p_{3/2} and V₂p_{1/2}, respectively. Spin orbit coupling creates a V₂p split, hence the vanadium oxidation states of catalyst is approximately 4+, and the sample is in the form of (VO)₂P₂O₇. The O1s peak in VP appears at 532.2 eV. It can be well fitted with only one component attributed to O²⁻ ions of the lattice [4,5].

Materials and method

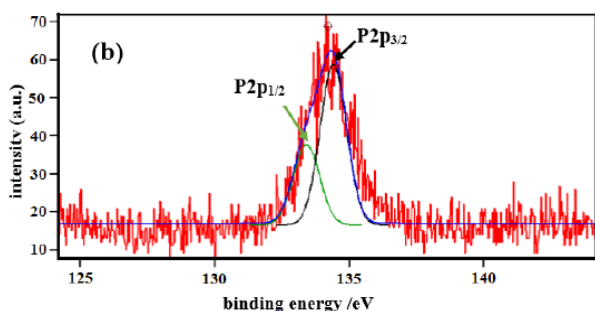
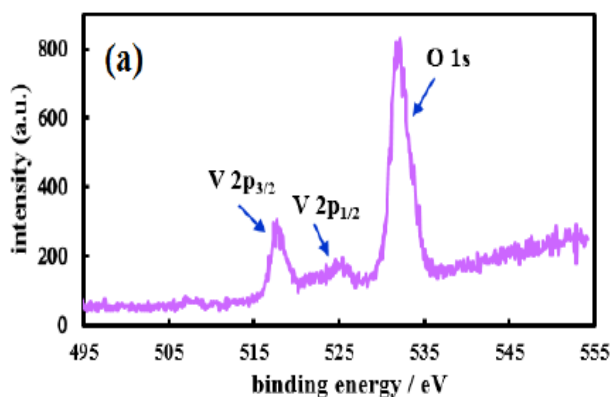


Fig. 1. XPS spectra of 27wt% VPK-6 a) V 2p and O 1s b)

The small-angle XRD patterns of KIT-6 and VPK-6 catalysts after calcination are shown in Figure 2. For the pure KIT-6 sample can be observed that the main peak appears at 2θ of 0.98 and two small peaks appear at 2θ of 1.70 and 1.96°, respectively. This confirms successful synthesis of KIT-6 silicate and exhibits well-resolved Bragg reflections, which is characteristic of highly ordered 3-D cubic *Ia3d* symmetry. With successive loading of VP onto KIT-6, there is a slight decline in the intensity of the d211 peak gradually, whereas the d420 and d431 peaks disappear. This was ascribed to the partial blocking of KIT-6 mesopores by VP species and the cubic *Ia3d* symmetry of the support is synchronously maintained [6].

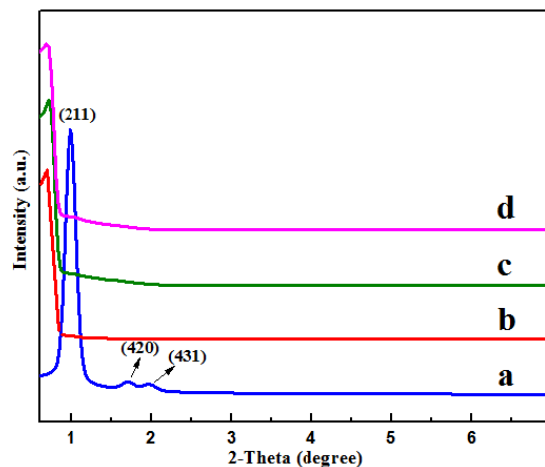
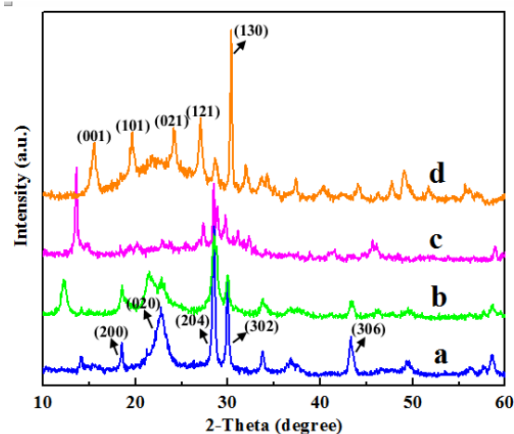


Fig. 2. Small-angle XRD patterns of mesoporous materials a) KIT-6 b) 34wt% VPK-6 c) 27wt% VPK-6 d) 27wt% VPK-6 after 5 times recycling.

According to the wide-angle XRD patterns, it is evident from Figure 3 that the VPK-6 catalyst before the calcination process (Fig. 3d), shows high intensity peak at $2\theta = 30.35^\circ$ is due to the plane (130) with principal d-spacing at 2.93 Å, corresponds to the diffraction patterns of vanadyl hydrogen phosphate hemihydrate phase (VOHPO₄ 0.5H₂O) as the precursor of supported vanadyl pyrophosphate [7]. This is in accordance with ICDD Card No 01-084-0761. As can be seen the XRD



spectra of VPK-6 catalyst with different VP loadings after the calcination process, VOHPO₄ 0.5H₂O precursor is converted to (VO)₂P₂O₇ structure as the major phase. It shows high intensity peaks at 2θ values of 18.48, 22.84, 28.46, 29.94 and 43.25 are due to the planes (200), (020), (204), (302) and (306) with principal d-spacing at 4.80, 3.89, 3.15, 2.98, and 2.09 Å which correspond well to the vanadyl pyrophosphate phase ((VO)₂P₂O₇ phase) [ICDD Card No 00-041-0698].

Fig. 3. The wide-angle XRD patterns of mesoporous a) 34wt% VPK-6, b) 27wt% VPK-6, c) 27wt% VPK-6 after 5 times recycling, d) catalyst before calcination.

The images of the catalysts (Fig. 4 b, c) showed that VP particles covered the KIT-6 template with uniform shape. These platelets particles are agglomerated into a beautiful rosebud shape clusters which are made up of (VO)₂P₂O₇ platelets. This result is due to adding PEG in the catalyst preparation. The presence of PEG in the synthesis medium would lower interfacial surface energy which leads to the generation of fine particles [8,9]. The morphological SEM images corroborate the X-ray diffractograms shown in Figure 3. The qualitative local EDX Conclusions In summary, in the present study two new catalysts, KIT-6 supported vanadium was successfully synthesized and characterized. The catalysts then were used to the liquid-phase selective and green oxidation of cyclohexane to cyclohexanol and cyclohexanone. Effects of reaction parameters such as mole ratio of reactants, reaction time and temperature were examined to find higher substrate conversions and product selectivity. analysis demonstrates that nanoparticles dispersed well over the support including vanadium and phosphorous. Moreover, it is evident from Figure 5 (b, c) that elemental mapping analysis shows phosphorous and vanadium finely dispersed on the KIT-6.

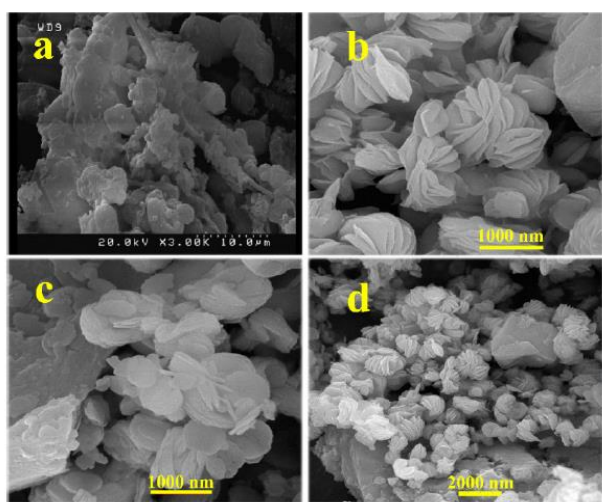


Fig 4. SEM images of (a) KIT-6, (b, c) 27wt% VPK-6, (d) 27wt% VPK-6 after 5 times recycling.

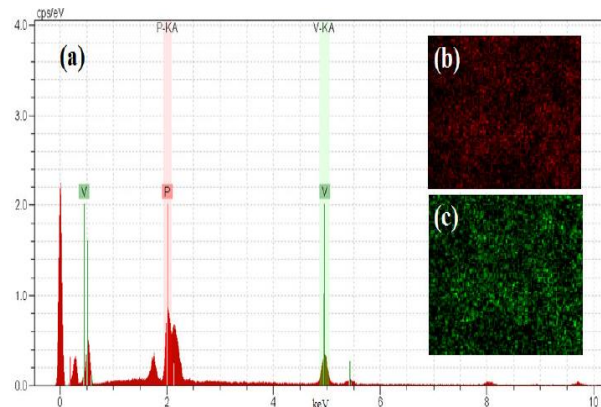


Fig 5. EDX spectrum for (a) 27wt% VPK-6 and elements distribution maps recorded (b) phosphorous (c) vanadium.

Acknowledgment

We thank arak University of Technology (Iran) for the financial support of this work.

References

- [1] F. Wang, J.-L. Dubois, W. Ueda, Catalytic performance of vanadium pyrophosphate oxides (VPO) in the oxidative dehydration of glycerol, *Appl. Catal. A: Gen.* 376 (2010) 25-32.
- [2] V. Mahdavi, H.R. Hasheminasab, Liquid-phase efficient oxidation of cyclohexane over cobalt promoted VPO catalyst using tert-butylhydroperoxide, *J. Taiwan Inst. Chem. Eng.* 51 (2015) 53-62.
- [3] E. Mikolajska, E.R. Garcia, R.L. Medina, A.E. Lewandowska, J.L.G. Fierro, M.A. Banares, Alumina support-stabilized nanoscaled vanadium-phosphorous mixed oxides as new catalysts for propane ammoxidation, *Appl. Catal. A: Gen.* 404 (2011) 93-102.
- [4] J.C. Ganley, F. Thomas, E. Seebauer, R.I. Masel, A priori catalytic activity correlations: the difficult case of hydrogen production from ammonia, *Catal. Lett.* 96 (2004) 117-122.
- [5] V. Kalevaru, N. Madaan, A. Martin, Synthesis, characterization and catalytic performance of titania supported VPO catalysts for the ammoxidation of 3-picoline, *Appl. Catal. A Gen.* 391 (2011) 52-62.
- [6] Y. Kamiya, S. Ueki, N. Hiyoshi, N. Yamamoto, T. Okuhara, Preparation of catalyst precursors for selective oxidation of n-butane by exfoliation-reduction of VOPO₄·2H₂O in primary alcohol, *Catal. Today* 78 (2003) 281-290.
- [7] M. O'Connor, B. Hodnett, Preparation of vanadium-phosphorus oxide catalysts: I. Dissolution and reduction of vanadium pentoxide and isolation of the precursor, *Appl. Catal.* 42 (1988) 91-104.



Kinetic Studies of DMSO Deuteration Process and Introduction of an Ideal Isotopic Exchange Reactor Type

A.A. Rezaei^a, Z. Rezaei Sarlak^a, P. Mobalegholeslam^a, A. Amiri Majed^{*a}

^a Research & GC management, MESBAH ENERGY Co., Arak, Iran, 15875/7339

*aamirimajed@gmail.com

Abstract: The kinetics of the deuterium exchange reaction of dimethyl sulfoxide (DMSO) and deuterium oxide (D₂O) has been studied at 80°C in the presence of sodium carbonate as a catalyst using ¹H-NMR detection of isotopic content of the DMSO. Reaction conditions were optimized via experimental design according to the Taguchi algorithm. The reaction order and rate constant at 80°C have been determined. In the basis of obtained data, ideal type of reactor for deuterium exchange between DMSO and D₂O has been proposed.

Keywords: dimethyl sulfoxide; deuterium oxide; kinetic; deuterium exchange

Introduction

Hydrogen-deuterium exchange (H/D exchange) is a chemical reaction in which a covalently bonded hydrogen atom is replaced by a deuterium atom. It can be applied to easily exchangeable protons, where H/D exchange occurs in the presence of a deuterium source, without any catalyst. Acid, base or metal catalyst, coupled with high temperature or pressure, can facilitate the H/D exchange reaction. Therefore, characterization of reaction's mechanism, kinetic and thermodynamic would be a key step in deuteration process.

A fundamental challenge in chemical kinetics is the determination of the reaction's rate law from experimental information. Our knowledge about reaction's mechanism and kinetics is a conducting tool to quantify the relationship between production rate, reactor size and selected operating conditions. Applying an ideal reactor allow us to quantify reactor performance as a function of its size and selected operating conditions. Therefore, the rate laws applying to different kinds of chemical reactions are common practice of chemical kinetics textbooks. However, the case of isotope exchange reaction is often ignored despite of the importance of this sort of phenomenon.

It has been motivated us to study the rate law of isotope exchange reaction between dimethyl sulfoxide and deuterium oxide as a deuterium source. Deuterated dimethyl sulfoxide is one of the most consuming deuterated solvent and it is produced via deuterium exchange reaction with deuterium oxide in the presence of sodium carbonate as a catalyst.

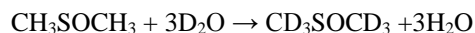
Materials and method

Dimethyl sulfoxide, acetonitrile and sodium carbonate were purchased from Merck Co., deuterium oxide was prepared from Arak Heavy Water complex. Isotope exchange reaction was done in sealed tubes. The reaction mixture was heated in HACH-LANGE GmbH. COD reactor model LT200. The samples were diluted by

deuterium oxide before analysis. Acetonitrile was added as an internal standard into samples and ¹H-NMR spectra were recorded using BRUKER-¹H 300MHz.

Results and Discussion

Deuterated DMSO is produced by isotope exchange reaction of DMSO with deuterium oxide as deuterium source in the presence of sodium carbonate as basic catalyst.



Optimum design of a reactor is a key step in an industrial process. Reactor design and the evaluation of the kinetic parameters have to be based on experimental results that preferably were done at conditions similar to those contemplated for the large scale process.

There have been two experimental methods for obtaining required data:

The first method is concentration Measurements vs. time in a batch reactor and the other is Concentration Measurement in a differentiation reactor.

The experimental data are analyzed mathematically via the following methods:

- Differentiation
- Integral
- Half life
- Initial speed
- Liner regression
- Non-liner regression

In this study, concentration values were measured versus time in the batch reactor.

Effective parameters on the isotope exchange such as sodium carbonate concentration, D₂O/DMSO mol ratio, temperature and time were optimized using experimental design. The optimum conditions were applied for kinetic



studies and data evaluation was performed in the constant volume reactor. The concentration variations were measured as a function of time by ¹H-NMR. Obtained data was used for determining reaction order and reaction rate constant according to **Eq.1**.

$$-\frac{dC_A}{dt} = k_A C_A^n \quad (1)$$

where, k is the reaction rate constant and n in the reaction order.

The logarithm form of above **Eq.1**:

$$\ln\left(-\frac{dC_A}{dt}\right) = \ln k_A + n \ln C_A \quad (2)$$

There are three common methods for calculating $\left(-\frac{dC_A}{dt}\right)$:

- Graphical divergence
- Numerical differentiation formulas
- Differentiation of polynomial fit to the data

In this study, numerical differentiation formula has been employed.

$$t_1 - t_0 = t_1 - t_2 = \Delta t \quad (3)$$

Time	t_0	t_1	t_2	t_3	t_4
Concentration (mol/dm ³)	C_{A0}	C_{A1}	C_{A2}	C_{A3}	C_{A4}

$$\left(-\frac{dC_A}{dt}\right)_{t_0} = \frac{-3C_{A0} + 4C_{A1} - C_{A2}}{2\Delta t} \quad (4)$$

$$\left(-\frac{dC_A}{dt}\right)_{t_i} = \frac{1}{2\Delta t} [(C_{A(i+1)} - C_{A(i-1)})] \quad (5)$$

$$\left(-\frac{dC_A}{dt}\right)_{t_5} = \frac{C_{A3} - 4C_{A4} + C_{A5}}{2\Delta t} \quad (6)$$

The graph of $\log(-r_A)$ versus $\log C_A$ (**Fig. 1**) was plotted using obtained experimental results. According to **Eq. 2**, the slope of this curve shows the reaction order and intercept presents the rate constant of isotope exchange reaction.

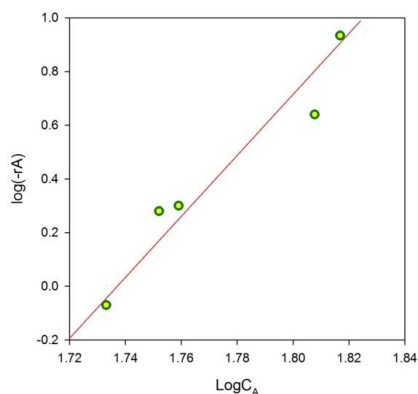


Fig.1. The plot of $\log(-r_A)$ vs. $\log C_A$

Fig.1. reveals that n and k values are 1.4 and $0.645 \frac{Lit^{0.4}}{mol^{0.4} \times t}$, respectively.

The $-\frac{1}{r_A}$ is plotted versus mole fraction of deuterated dimethylsulfoxide (X_A) in **Fig. 2**. As shown in Fig. 2, the A domain presents required volume for a plug reactor and A+B domain shows the mixed reactor volume. Consequently, the plug type of reactor is the best choice for the studied isotope exchange reaction.

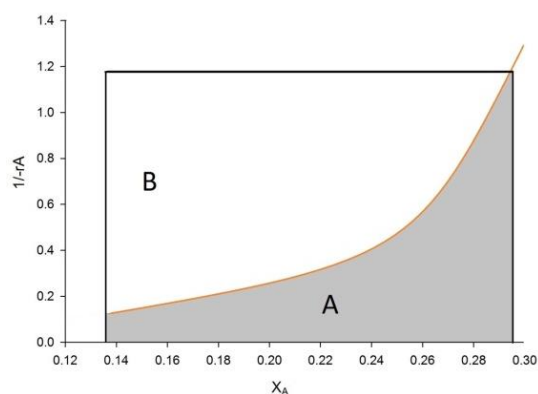


Fig. 2. The plot of $1/r_A$ vs. X_A

Conclusions

Isotopic exchange reaction of dimethyl sulfoxide has been studied in the presence of sodium carbonate base. Deuterium oxide was used as a deuterium source. At first, the reaction parameters were optimized using experimental design according to the Taguchi algorithm. Then, Dimethylsulfoxide-d6 concentration was measured during the isotope exchange reaction using ¹H-NMR technique. Obtained data were evaluated mathematically, both the reaction order and rate constant were determined from the plot of $\log(-r_A)$ vs. $\log C_A$, which they are 1.4 and $0.645 \frac{L^{0.4}}{mol^{0.4} \times t}$, respectively. Also, the graph of $1/r_A$ vs. X_A was plotted and the best reactor type was selected. Plug reactor is preferred to the other types of reactor because of its required volume is minimized.

Acknowledgment

We thank research and quality control management, MESBAH ENERGY complex for supporting this study and preparing required samples.

References

- [1] S. R. Logan, "the kinetics of isotopic exchange reactions", *journal of chemical education*, 67 (1990) 371-373.



[2] F. Mata-Perez, J. F. Perez-Benito, “the kinetic rate law for autocatalytic reactions” *journal of chemical education*, 64 (1987) 925-927.

[3] O. Levenspile, “*Chemical reaction engineering*”, 1999, Wiley, 3rd Ed, 106-112, New York, U.S.A

[4] S. Fogler, “*Elements of chemical reaction engineering*”, 2016, Prentice hall, 5th Ed, 106-112, New York, U.S.A



Using Electrolysis for Accurate Measurement of Oxygen Isotopes Abundance in ¹⁸O enriched Water

B. Dadpou^{*a}, F. Faridani^a, V. azami^a, Z. Sharifnejad^a

^a Research & GC management, MESBAH ENERGY Co., Arak, Iran, 15875/7339

^{*}bita.dadpou@gmail.com

Abstract: A new system is introduced to measure the relative isotopic abundance of oxygen isotopes in the water using gas chromatography-mass spectrometry. Electrolysis process was done with an undivided cell equipped with platinum anode, copper as cathode and CuSO₄ as electrolyte. Water is transformed into oxygen gas and then, produced gas is subsequently analyzed with a GC-MS instrument. Obtained results revealed that it is reliable, cheap, and fast and can be easily automated. The new method would be an acceptable alternative to the traditional H₂O-CO₂ equilibrium method.

Keywords: Electrolysis; Water; Oxygen 18; GC-MS instrument

Introduction

The chemical element oxygen has three stable isotopes, ¹⁶O, ¹⁷O and ¹⁸O, with abundances of 99.76, 0.035 and 0.2%, respectively. Oxygen is one of the most abundant elements in the earth and stable oxygen isotopes are used in studies of the ocean, atmosphere, cryosphere and the continents.

Observation of ¹⁸O variation provides worthy information on the hydrological cycle. ¹⁸O is often enriched in saline lakes because of a high degree of evaporation, while high-altitude and cold-climate precipitation is low in ¹⁸O. Therefore, development of accurate and facile method for measurement of ¹⁸O/¹⁶O is the essential step in hydrological interpretations.

Sample preparation is a vital stage in isotope ratio measurement. Various methods are introduced in the literatures; (a) reduction with heated metals such as uranium and zinc, (b) reduction on heated filament, (c) reduction by calcium hydride and lithium aluminum hydride, (d) equilibration of water with CO₂ or some organic compounds and (e) electrolysis.

In the electrolysis of water, the electrolytic fractionation factor with respect to the ¹⁶O/¹⁸O isotopes is only about 1.01-1.03.

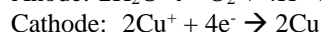
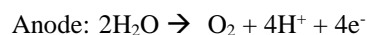
Isotopic ratio mass spectrometry (IRMS) is the most accurate method for determination of isotope ratio. Other methods have been selected according to cost, available time and figure of merit. Limitation in IRMS availability has motivated us to combine electrolysis method for sample preparation and gas chromatography-mass spectrometer for isotope ratio determination.

Materials and method

Copper sulfate, phosphorous pentoxide and Molecular sieve were obtained from Merck Co., the GC-MS system used in this paper was Perkin-Elmer (Clarus SQ8 model) equipped with one Elite-5MS column.

In the first step of the study, we developed an electrolysis cell, in which we could capture the oxygen gas produced from O¹⁸ enriched water. The electrolysis system is shown

in Fig. 1. The anode is made of platinum, the cathode of copper. Anhydrous CuSO₄ was used an electrolyte, thereby avoiding hydrogen gas production. The electrolytic reactions that occur are:



The measurement procedure with this setup is as follows: First, electrolyte has to be added to the sample. The electrolyte concentration was optimized (0.94 molality) and then 2 ml of electrolytic solution was put into the electrolysis cell. In order to remove the air dissolved in the solution, the electrolytic solution was evacuated until 20mbar, weighted, frozen and evacuated again. Subsequently, the electrolysis was started by adjusting voltage so that, the electrolysis current was stabilized at 30 mA. During the electrolysis, the sample was continuously stirred using a standard magnetic stirrer, to avoid the build-up of concentration gradient. After 40 minutes enough oxygen was produced for GC-MS analysis. Sample was passed from a drying agent (P₂O₅ or Molecular sieve) to absorb the inevitable water vapor from oxygen gas. Dried oxygen gas was injected to the GC-MS instrument.

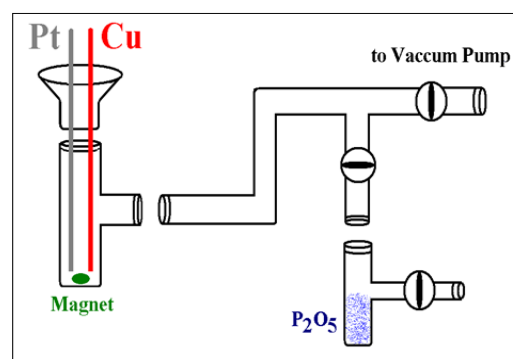


Fig.1. Schematic of electrolysis cell

Results and Discussion



Injected sample into gas chromatograph was characterized using mass spectrometry as detection device. In this way, the masses 32, 33, 34 and 36 amu were monitored with SIM method and base peak intensity (BPI) was determined for all samples. In fact, BPI shows the peaks intensity in every second and it is more accurate than the total ion current (TIC) because of the baseline peaks will be removed from sample data. The equations 1-3 were used for calculating mol% of ¹⁷O and ¹⁸O in water samples.

$$R = \left\{ \left[\frac{\text{Average of } \langle BPI \rangle_{34 \text{ or } 33}}{2} \right] / \left[\text{Sum of } \langle BPI \rangle_{32,33,34,36} \right] \right\} \quad (1)$$

$$\%_o = \left\{ \left[R * 10^6 / 2005 \text{ or } 375 \right] - 1 \right\} \quad (2)$$

$$w/w \% = \{ R * 100 \} \quad (3)$$

Where, R is isotope ratio, ‰ is part per thousand and w/w% is weight percent. The values 2005 and 375 equal to ¹⁸O and ¹⁷O concentrations in VSMOW standard, respectively. The obtained results for air and water samples are listed in Table 1 for 9 times of injection. Electrolysis-MS readout is compared with obtained results using laser spectroscopy instrument. Laser spectroscopy technique is designed for determination mol% ¹⁸O in the natural abundance range and the enriched sample must be diluted. From this point of view, the new developed method is user-friendly.

Table 1. The obtained results for oxygen isotope analysis of water samples

Sample	mol% ¹⁸ O	mol% ¹⁷ O	mol% ¹⁸ O LGR readout
DM water	0.33177	0.1705	0.1995
Sample 1	1.4216	0.2701	1.4
Sample 2	2.4179	0.3333	2.39
Sample 3	3.3530	0.3723	3.2
Air	0.2043	0.0692	-

During electrolysis process, less than 0.7% of the total amount of water is electrolyzed. This makes the sulfate concentration change negligible, and the Cu built-up not problematic.

Conclusions

The δ D/H values obtained for the different water sample by the electrolysis technique are listed in Table 1. The obtained results confirmed that reproducibility and accuracy is good for enriched sample, and analysis data of tap water is affected with fractionation and temperature variation during electrolysis. Therefore, this method isn't reliable for oxygen isotope ratio measurements in the natural abundance range.

Acknowledgment

We thank research and quality control management, MESBAH ENERGY complex for supporting this study and preparing required samples.

References

- [1] H. A. J. Meijer, W. J. Li “the use of electrolysis for accurate ¹⁷O and ¹⁸O isotope measurements in water”, *Isotope Environ. Health Stud.*, 34 (1998) 349-369.
- [2] A. Ijiri, U. Tsunogai and T. Gamo “a simple method for oxygen-18 determination of milligram quantities of water using NaHCO₃ reagent” *Rapid Communications in Mass Spectrometry*, 17 (2003) 1472-1478.
- [3] M. S. Iqbal, F. Rashid, N. A. Javed “an electrolytic device for preparation of hydrogen and oxygen from water for isotopic analysis” *Talanta*, 38(1991) 603-605.
- [4] C. A. M. Brenninkmeijer, P. Kraft and W. G. Mook “oxygen isotope fractionation between CO₂ and H₂O” *Isotope Geoscience*, 1(1983) 181-190.
- [5] W. A. Brand, “high precision isotope ratio monitoring techniques in mass spectrometry” *journal of mass spectrometry*, 31 (1996) 225-235.

The evaluation of electrochemical and physical properties of cationic membranes in the electro-dialysis reversal system of the Imam Khomeini Petrochemical Complex

A. R. Khodabakhshi*,

Department of Chemistry, Faculty of Science, Arak University, Arak 38156-8-8349, Iran

*A-khodabakhshi@Araku.ac.ir

Abstract: The electrical and physical properties of cation exchange membranes which have been used in the Imam Khomeini Petrochemical Complex for two years, have been studied. These membranes are used in the electro-dialysis reversal (EDR) system for purification of wastewater. Ion exchange capacity, water content, membrane potential, selectivity and energy consumption have been the properties, which evaluated in this study.

The reduction of membranes performance can be attributed to the absorption of iron ions and polyvalent metal ions on the membrane ion exchange sites.

Keyword: Ion exchange capacity; Electrochemical properties; Water content; Membrane potential; Selectivity

Introduction

Membrane processes are currently used in several branches of industry, such as food-processing industry and the treatment of effluents and water, to resolve the technological problems of purification and concentration, and to improve quality of the products while ensuring an environmental protection [1-2].

The ion exchange membranes with improved electrochemical and morphological properties are important in chemical and waste treatment applications. Their economic interest is obvious since they are based on simple, low energy-consuming and relatively inexpensive technologies [2].

A major problem associated with the use of the membranes is ageing. Particularly it is important in electro dialysis of solutions containing weak organic acids, where a great part of the costs is related to the replacement of the membranes [3].

In this study the cation exchange membranes which have been used in the Imam Khomeini Petrochemical Complex for two years, have been compared with the new membranes. The ion exchange membranes are used in the electro-dialysis reversal (EDR) system for purification of wastewater. The purpose of this study was to evaluate the electrochemical and physical properties of cationic membranes. Ion exchange capacity, water content, membrane potential, selectivity, ionic flux and energy consumption have been the properties, which evaluated in this study.

Materials and method

All chemicals used for this work were used from Merck Inc..

The membranes used in this study were provided in pairs by Imam Khomeini Petrochemical Complex. Each pair consisted of a sample of a new membrane and another retired from an EDR module after two years of use.

Measurement of water content was determined from the difference in weight between the drying and the swollen membranes [2]. For this aim membranes were immersed in distilled water for 24 hr, and then taken out and its surface wiped by filter paper and weighed. Then, these weighed wet membranes were dried at fixed temperature (50 °C) for 4 hr until constant weight as dry-membrane achieved. The water content can be calculated from the following equation:

$$\text{Water content} = [(W_{\text{wet}} - W_{\text{dry}})/W_{\text{dry}}] * 100\%$$

Ion exchange capacity (IEC) is defined as milli-equivalent of ion exchange group included in a 1 gr dry membrane. The IEC was determined through titration. In order to measure the ion exchange capacity of the membranes, a sample membrane is left at first in a 1 M HCl solution for 24 hr, for converting the exchange group to an H type, and then washed with water sufficiently and kept in it for 24 hr until the washed water does not exhibit acidity recognized by the reaction with methyl red. Next the membrane is immersed in a 1 M NaCl solution for 24 hr and washed sufficiently with water. The immersed solution and washed water are collected and finally H ions dissolved in to the collected solution are analyzed with a 0.1 M NaOH and a phenolphthalein indicator (A meq). At final, the membrane is wiped with filter paper and dried in oven at 50 oC for 4 hr and then weighed (W gr). The IEC can be calculated from the following equation:

$$\text{IEC} = (A/W)$$

The relationship between the IEC and water content as fixed ion concentration (FIC) can be calculated using this equation:

$$\text{FIC} = \frac{\text{IEC}}{\text{Water content}}$$

There is a relationship between FIC and membrane selectivity[5].



When both surfaces of an IEM are in contact with solutions of different concentrations, an electrical potential is developed across the membrane due to the tendency of oppositely charged ions to move with various velocities and mobilities. The magnitude of this potential depends on the electrical characteristics of the membrane along with the nature and concentration of the electrolyte solution. This parameter was measured using a two-cell glass apparatus (Fig. 1) in which an equilibrated membrane of 13.85 cm² effective area was integrated between the cells. At ambient temperature (25 °C), an electrolyte solution with concentration C₁ = 0.1 mol L⁻¹ and a solution with C₂ = 0.01 mol L⁻¹ were poured into the cell compartments on either side of the membrane. Both sections were stirred vigorously using magnetic stirrers to minimize the effect of boundary layers on the measurement. The potential difference developed across the membrane was measured after 10 min by connecting both compartments to a saturated calomel electrode and using a digital auto multimeter (DEC 330FC, China)[5].

The measurements were repeated for 15 min with the potential being measured every minute until a constant value (E_{measure}) was obtained. The membrane potential generated between the solutions in contact with both membrane surfaces is expressed by the Nernst equation which was used in the calculation of transport number of ions as follows:

$$E_{\text{measure}} = (2t_i^m - 1) \left(\frac{RT}{nF} \right) \ln \left(\frac{a_1}{a_2} \right)$$

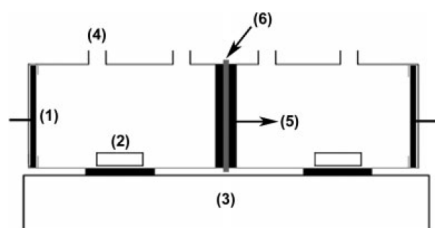


Fig.1. Schematic of test cell: 1- platinum electrode; 2- magnetic bar; 3- stirrer; 4- orifice; 5- rubber ring; 6- membrane[5].

The energy consumption (E) can be calculated using following equations [5]:

$$E = \frac{\int_{t=0}^{t=t} I \times V \times dt}{\Delta n \times M_w}$$

Results and Discussion

Water content

Suitable water content in the membranes can give better

ion paths and improve membrane permselectivity. In contrast, too high a water content provides more and wider transfer channels to transport co-ions and counter-ions, decreasing the ion selectivity, and leads to the formation of a loose membrane structure. Table 1 shows the water content for all membranes.

IEC

The results indicate that a dropping of IEC from 1.7 to 1.28 (meq g⁻¹) (Table 1). This may be attributed to adsorption properties of membranes sites for metal ions which cause decreasing of interaction between ions and membrane surface.

Selectivity

The worked membranes exhibited lower FIC compared to fresh one (Table 1). The higher FIC in the fresh membrane can control the channels for counter-ion transport in the membranes and therefore increase the ion selectivity.

Membrane potential

The membrane potential for worked membranes has been decreased again compared to fresh one (Table 2).

Energy consumption

The energy consumption has been increased for worked membranes because of low IEC and current efficiency. The fresh membrane showed better current efficiency and lower energy consumption because of the higher ionic flux and permeability for ions (Table 2).

Table1: The water content and IEC for fresh and worked membranes.

membrane	Water content(%)	IEC(meq/g)	FIC
Worked1	48	1.25	2.6
Worked2	49	1.28	2.61
Worked3	47	1.29	2.74
Worked4	46	1.27	2.76
Average	47.5	1.27	2.67
Fresh	61	1.7	2.78

Conclusions

The results showed that about 20% of the performance of the membranes has decreased compared with the new membranes. This can be attributed to the absorption of iron ions and polyvalent metal ions on the ion exchange sites of the membranes.

Table2: Membrane potential and Energy consumption for fresh and worked membranes.

membrane	Membrane potential (v)	Energy consumption (kJ/g)
Worked1	38	19
Worked2	35	21
Worked3	37	20
Worked4	36	16
Average	36.5	19
Fresh	45	14

Acknowledgment

In The authors are grateful to Arak Petrochemical Corporation for financial support during this research.

References

- [1] H. Strathmann, Membrane Science and Technology Series, 9, Ion-exchange Membrane Separation Processes, Elsevier, Amsterdam, 2004.
- [2] L. -C. Juang, D.-H. Tseng, H.-Y. Lin, Membrane processes for water reuse from the effluent of industrial park wastewater treatment plant: a study on flux and fouling of membrane, *Desalination* 202 (2007) 302–309.
- [3] R. Ghalloussi, W. Garcia-Vasquez, N. Bellakhal, C. Larchet, L. Dammak, P. Huguet , D. Grande, Ageing of ion-exchange membranes used in electrodialysis: Investigation of static parameters, electrolyte permeability and tensile strength, *Separation and Purification Technology* 80 (2011) 270–275.
- [4] Tongwen Xu, Ion exchange membranes: State of their development and perspective, *Journal of Membrane Science* 263 (2005) 1–29.
- [5] A.R. Khodabakhshi, S.S. Madaeni, S.M. Hosseini, Comparative studies on morphological, electrochemical, and mechanical properties of S-polyvinyl chloride based heterogeneous cation-exchange membranes with different resin ratio loading, *Ind. Eng. Chem. Res.* 49 (2010) 8477–8487.